THE

[redacted]OURNAL OF

PHYSICS

AND

CHEMISTRY

OF SOLIDS

AN
INTERNATIONAL
JOURNAL

VOLUME 30 NUMBER
MAY 1969

Editor-in-Chief
HARVEY BROOKS
Cambridge, Mass.

Associate Editors

H. B. G. CASIMIR
Eindhoven

B. CHALMERS FRAZER
Brookhaven

JACQUES FRIEDEL
Paris

I. M. LIFSHITZ
Khar'kov

PERGAMON PRESS NEW YORK · OXFORD · LONDON · PARIS

THE JOURNAL OF PHYSICS AND CHEMISTRY OF SOLIDS

Editors

Prof. Harvey Brooks (*Editor-in-Chief*), *217 Pierce Hall, Harvard University, Cambridge* 38, *Mass., U.S.A.*

Prof. Dr. H. B. G. Casimir, *N.V. Philips' Gloeilampenfabrieken, Eindhoven, The Netherlands*

Dr. B. Chalmers Frazer, *Brookhaven National Laboratory, Upton, Long Island, New York, U.S.A.*

Prof. Jacques Friedel, *Laboratoire de Physique des Solides, Bâtiment 210, Faculté des Sciences, 91-Orsay, France*

Prof. I. M. Lifshitz, *Physico-Technical Institute, Academy of Science, Yumorskii tupik, Khar'kov, U.S.S.R.*

Editorial Advisory Board

U.S.A.

E. N. Adams, White Plains, N.Y.
D. Alpert, Urbana, Ill.
L. Apker, Schenectady, N.Y.
J. Bardeen, Urbana, Ill.
D. S. Billington, Oak Ridge, Tenn.
R. G. Breckenridge, Canoga Park, Calif.
Leo Brewer, Berkeley, Calif.
E. Burstein, Philadelphia, Penn.
J. A. Burton, Murray Hill, N.J.
N. Cabrera, Charlottesville, Va.
G. C. Danielson, Ames, Iowa
G. J. Dienes, Long Island, N.Y.
J. C. Fisher, Schenectady, N.Y.
F. G. Fumi, Chicago, Ill.
H. K. Henisch, University Park, Penn.
F. Herman, Palo Alto, Calif.
C. Herring, Murray Hill, N.J.
A. R. von Hippel, Cambridge, Mass.
J. H. Hollomon, Washington, D.C.
W. V. Houston, Houston, Texas
H. B. Huntington, Troy, N.Y.
H. M. James, Lafayette, Ind.
C. Kittel, Berkeley, Calif.
W. Kohn, La Jolla, Calif.
J. A. Krumhansl, Ithaca, N.Y.
A. W. Lawson, Riverside, Calif.
H. W. Leverenz, Princeton, N.J.
O. T. Marzke, Pittsburgh, Penn.
B. T. Matthias, La Jolla, Calif.
L. R. Maxwell, Silver Spring, Md.
J. E. Mayer, La Jolla, Calif.
J. W. Mitchell, Charlottesville, Va.
E. W. Montroll, Rochester, N.Y.
D. Pines, Urbana, Ill.
M. H. L. Pryce, Los Angeles, Calif.
G. T. Rado, Washington, D.C.
H. Reiss, Thousand Oaks, Calif.
J. R. Reitz, Dearborn, Mich.
A. Rose, Princeton, N.J.
R. A. Smith, Cambridge, Mass.
R. Smoluchowski, Princeton, N.J.
F. H. Spedding, Ames, Iowa
D. Turnbull, Cambridge, Mass.
J. H. Van Vleck, Cambridge, Mass.
B. E. Warren, Cambridge, Mass.
E. P. Wigner, Princeton, N.J.
B. H. Zimm, La Jolla, Calif.

Canada

R. E. Burgess, Vancouver
W. B. Pearson, Ottawa

United Kingdom

M. Born, Bad Pyrmont
A. Charlesby, Shrivenham, Berks.
W. J. Dunning, Bristol
F. C. Frank, Bristol
H. Jones, London
A. B. Pippard, Cambridge
O. C. Simpson, Baldock, Herts.
K. W. H. Stevens, Nottingham
F. C. Tompkins, London

Czechoslovakia

J. Tauc, Praha

France

E. F. Bertaut, Grenoble
A. Guinier, Orsay
Louis Néel, Grenoble
Louis Weil, Grenoble

Germany

Ulrich Dehlinger, Stuttgart
R. Hilsch, Göttingen
G. Leibfried, Aachen
E. Mollwo, Erlangen
H. Pick, Stuttgart
W. Welker, Erlangen

Israel

I. Estermann, Haifa

Italy

F. G. Fumi, Palermo

Japan

Toshinosuke Muto, Tokyo

The Netherlands

A. Michels, Amsterdam
G. W. Rathenau, Eindhoven

Sweden

J. O. Linde, Stockholm
Per-Olov Löwdin, Uppsala

Switzerland

G. Busch, Zurich
P. Scherrer, Zurich

U.S.S.R.

G. S. Zhdanov, Moscow

Publishing Offices

American Continent: Pergamon Press Inc., Maxwell House, Fairview Park, Elmsford, N.Y. 10523.

Rest of the World: Pergamon Press Ltd, 84–86 *Malahide Road, Coolock, Dublin* 5.

***Published monthly.** Annual subscription for libraries, research establishments and all other multiple-reader institutions,* £60 ($150.00); *private individuals, whose Departmental Libraries subscribe, may obtain this Journal for their personal use at a reduced price of* £6 ($15.00) *per annum, including postage. All subscription enquiries are to be addressed to The Manager, Subscriptions Department, Pergamon Press, Headington Hill Hall, Oxford OX3 0BW, England. Back issues are available, write for Back Issues Price Lists.*

Copyright © 1969 Pergamon Press Ltd.

PERGAMON PRESS, INC.
MAXWELL HOUSE, FAIRVIEW PARK, ELMSFORD, N.Y. 10523
HEADINGTON HILL HALL, OXFORD OX3 0BW

carbon

SV02

Editor-in-Chief: S. Mrozowski

'Carbon' is a journal devoted to the physics, chemistry and to scientific aspects of the technology of a class of materials ranging from organic crystals and polymers, through chars and carbons, to graphite. It provides a source of information on important research on these materials, and occasional reviews of limited problems. A special reference section to research published elsewhere is also included.

Papers published recently
R N Katz: Effect of post deposition heat treatment on the flexural strength of pyrolytic graphite
Y Tamai, Y Nishiyama and M Takahashi: Carbon deposition on iron and nickel sheets from light hydrocarbons
R E Woodley: The oxidation of boronated graphite
E S Golovina and L L Kotova: The role of sublimation and self-diffusion of carbon in interaction with carbon dioxide
P D Zavitsanos: Mass spectrometric analysis of carbon species generated by laser evaporation

Published bi-monthly
Please write for further information and inspection copy
Details of other journals in this field can also be sent to you

Pergamon Press
Headington Hill Hall Oxford OX3 0BW England
Maxwell House Fairview Park Elmsford New York 10523 USA

11/68

NEW FROM PERGAMON

ANTENNAS IN INHOMOGENEOUS MEDIA

J. Galejs, *Sylvania Electronic Systems, Waltham, Mass*

Treats impedance calculations of antennas for a number of different environments.
The reader is assumed to be familiar with basic electromagnetic field theory.
The first part of the book contains material covering a general course on antenna theory, while the remainder is suitable for more specialised graduate courses. There are extensive numerical results and this material is useful as a reference for design engineers.
The material on antennas in magnetoionic media will be of special interest to space experiments and design of antenna probes.

312 pages £7 $18.00

STRUCTURE AND APPLICATION OF GALVANOMAGNETIC DEVICES

H. Weiss, *Siemens-Aktiengesellschaft, Erlangen*

In presenting a summary of work done so far in the field of galvanomagnetic compounds and their applications, the author has attempted to give a simplified explanation of the physics of galvanomagnetic effects. The book is not intended to be just a bibliography of the subject but reflects the author's own experience in this field, and the part of the book which deals with the design of devices, their applications and the related circuit problems reflects the author's practical experience in the field.

Contents:
Basic Physical Considerations—Design and Fabrication of Galvanomagnetic Devices—Properties of Galvanomagnetic Devices - Applications of the Hall Effect -Applications of the Magnetoresistance Effect Other Possibilities of Controlling the Electrical Properties of Semiconductors by Means of a Magnetic Field

376 pages £7 $18.00

STRUCTURE, PROPERTIES AND PREPARATION OF PEROVSKITE TYPE COMPOUNDS

Francis S. Galasso, *United Aircraft Research Laboratories, East Hartford, Conn.*

A detailed and up-to-date reference source which brings together in one volume information on approximately 500 perovskite-type compounds. Includes the various methods of preparing powders, their films and single crystals of perovskite-type compounds, the structure of these compounds and their properties
This book is unique in that it covers in detail compounds with one structure
Recently perovskite-type compounds have been investigated as superconductors, laser modulators and catalysts and the chapters containing these topics will be of special interest to researchers in these fields.

218 pages £3 10 0. $9 00

TYPE II SUPERCONDUCTIVITY

D. Saint-James, G. Sarma and E. J. Thomas

The first book to deal specifically with Type II superconductors describes in some detail both the reversible and irreversible properties of these superconductors. Intended primarily for experimentalists working in the field of superconductors it will also be of value to theoretical physicists and research metallurgists studying the properties of superconductors

300 pages £5.5 0 $14.00

SOLID-LIQUID EQUILIBRIUM

R. Haase and H. Schonert, *Institute of Physical Chemistry, Aachen*

This well-written book enumerates the basic principles of the subject and deals with the one-component systems, binary systems and ternary systems.
The various systems are treated rigorously and extensively and illustrated by numerous examples

288 pages £4.0 0.

Pergamon Press
Headington Hill Hall Oxford OX3 0BW England
Maxwell House Fairview Park Elmsford New York 10523 USA

CORROSION SCIENCE

Editor-in-Chief: L L SHREIR

'Corrosion Science' is the official journal of the Corrosion and Protection Society, and is associated with Centre Belge d'Etude de la Corrosion.
Its primary purpose is to publish original research in the fields of corrosion science and technology, which makes an important contribution to an understanding of the phenomena of corrosion and its control in practice.
The scope covers high temperature oxidation, passivity, anodic oxidation, aqueous and fused salt corrosion, bio-chemical corrosion, stress-corrosion cracking, and mechanisms and methods of corrosion control.
Papers range from the highly theoretical to the essentially practical, with the intention of producing a publication in which there is an appropriate balance between corrosion science and technology.

Papers published recently
J S Armijo and B E Wilde: Influence of Si content on the corrosion resistance of austenitic Fe-Cr-Ni alloys in oxidizing liquid
A B Ijzermans and A J van der Krogt: Pitting corrosion of an austenitic Cr-Ni stainless steel in H_2SO_4 containing H_2S
Z Zembura: Relationship between metallic corrosion and limiting current using the rotating disk method
J E Antill, K A Peakall and J B Warburton: Oxidation of mild and low-alloy steels in CO_2 based atmospheres

Monthly
Write for further details and an inspection copy of this journal, and information on other journals in the field.

Pergamon Press
Headington Hill Hall Oxford OX3 0BW England
Maxwell House Fairview Park Elmsford New York 10523 USA

11/68

ELECTROCHIMICA
Acta

Editor-in-Chief T P Hoar Cambridge

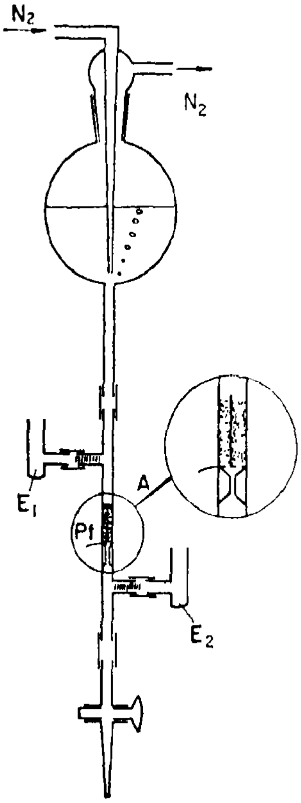

is an international journal of pure and applied electrochemistry, published under the auspices of the International Committee for Electrochemical Thermodynamics and Kinetics (CITCE).

Executive Editorial Board
T P Hoar, University of Cambridge
J O'M Bockris, University of Pennsylvania
N Ibl, Swiss Federal Institute of Technology
P Van Rysselberghe, Stanford University
G Valensi, Faculté des Sciences de Poitiers

It publishes papers on every branch of this field, and, since its inception in 1959, has included contributions from nearly every electrochemical laboratory of importance. Over 200 papers are presented each year, either as original reports or as serious critical reviews. In this way, it is possible to keep electrochemists up-to-date with modern work in the whole of the fast-growing field of electrochemistry.

Recently published papers include
N A Pangarov, L A Uvarov and A T Vagranyan:
Preferred orientation of electrodeposited nickel crystallites at high temperatures
E Gileadi, L Duic and J O'M Bockris:
A comparison of radiotracer and electrochemical methods for the measurement of the electrosorption of organic molecules
A Sanfeld, C Devillez and M Lubelski:
Influence of molar volumes, polarization and activity coefficients on the repulsion between two plane layers
W E Triaca, C Solomons and J O'M Bockris:
The mechanism of the electrolytic evolution and dissolution of chlorine on graphite

Published monthly
For further information and an inspection copy write to

11/68

Pergamon Press
Headington Hill Hall Oxford OX3 0BW England
Maxwell House Fairview Park Elmsford New York 10523 USA

J. Phys. Chem. Solids Pergamon Press 1969. Vol. 30, pp. 1025–1036. Printed in Great Britain.

INTERACTION BETWEEN POINT DEFECTS IN NONSTOICHIOMETRIC COMPOUNDS

J. B. LIGHTSTONE* and G. G. LIBOWITZ

Ledgemont Laboratory, Kennecott Copper Corporation Lexington, Mass. 02173, U S A.

(*Received* 5 *June* 1968; *in revised form* 29 *November* 1968)

Abstract – The variation in thermodynamic activity as a function of nonstoichiometry was derived for binary compounds exhibiting large deviations from stoichiometry. The assumptions were made that only one type of point defect is present in high concentrations, and that there are pair-wise interactions among the randomly distributed defects. It is shown that comparisons of experimentally determined activities with the theoretically derived relations may be used to deduce the type of point defect which is predominantly responsible for the nonstoichiometry, and to determine the free energy of interaction between the defects. Experimental hydrogen activities in yttrium and cerium hydrides, and thorium activities in thorium monocarbide are analyzed in this manner.

INTRODUCTION

THE PRESENCE of point defects in a compound will in general imply a deviation from stoichiometry, δ, so that a compound whose stoichiometric formula is MX_x may have a real composition which corresponds to the apparent formula $MX_{x\pm\delta}$. The positive sign is used when the compound has a higher X/M ratio than the stoichiometric composition, and the negative sign is used when the X/M ratio is less than the stoichiometric ratio. It has been shown in previous papers[1, 2] that, neglecting electronic defects, for noninteracting, randomly distributed atomic point defects, the functional dependence of the thermodynamic activity of one of the components (e.g. of X) on δ is characteristic of the types of point defects which are present. This characteristic dependence was used to identify the defects in $UH_{3-\delta}$, $LaH_{2+\delta}$ and $CeCd_{6+\delta}$, which have moderately large deviations from stoichiometry in the 0·01–0·26 range.

For systems exhibiting relatively large deviations from stoichiometry, interactions between defects become important. In the present paper, the previous treatment[1] is extended to include the possibility of interaction between like defects. A comparison of the theoretically derived variation of activity with nonstoichiometry with that determined experimentally is then used to characterize the defect structure of various compounds, and also to provide information on the free energy of interaction between like defects.

THEORETICAL TREATMENT

There are six possible types of simple point defects which may occur in a compound of stoichiometric formula MX_x. They are M vacancies, X vacancies, M interstitials, X interstitials, M substitutionals, by which is meant M atoms on normal X sites, and X substitutionals. The total free energy, G, of a crystal having an arbitrary defect structure may be written:

$$G = G(N, N_{M(M)}, N_{X(X)}, N_{IM}, N_{IX}, N_{M(X)}, N_{X(M)}) \qquad (1)$$

where N is the number of M sites, $N_{M(M)}$ is the number of M atoms on M sites, N_{IM} is the number of M atoms in interstitial sites, and $N_{M(X)}$ is the number of M atoms in substitutional positions. $N_{X(X)}$, N_{IX} and $N_{X(M)}$ are the corresponding X quantities.

An expression for the free energy, G, will be made up of four sets of terms: (1) the free energy of the ideal perfect crystal, which is considered to be the starting material; (2) the free energy change, other than that arising from changes in the configurational entropy, when isolated simple point defects are formed by adding or removing atoms between the perfect crystal and reservoirs of M and X in their standard states; (3) the free energy of interaction between point defects; and (4) the configurational entropy of distribution of the defects on the various sublattices. The distribution of electrons and holes will be neglected. Therefore, the relation will apply only to systems where the defects are unionized or to metallic compounds where the distribution of electronic charge is unimportant.

**Present address*: Union Carbide Corporation, Linde Division, P.O. Box 44, Tonawanda, N.Y. 14150, U S A

The present treatment, which is a modification and generalization of those used by Anderson[3] and Libowitz[4], is equivalent to a zeroth or Bragg-Williams approximation [5], where it is assumed that despite the interaction between the defects, the defects are nevertheless randomly distributed, so that the number of defect pairs is the random number of defect pairs that would obtain in the absence of any interaction, and the configurational entropy will be that for ideal mixing. We shall further only consider interaction between like defects.

With these approximations, we have that:

$$
\begin{aligned}
G = {} & N\mu'_{MX_s} \\
& + (N - N_{M(M)} - N_{X(M)})g_{\square M} \\
& + (sN - N_{X(X)} - N_{M(X)})g_{\square X} \\
& + N_{M(X)}g_{M(X)} + N_{X(M)}g_{X(M)} \\
& + N_{IM}g_{IM} + N_{IX}g_{IX} \\
& + \frac{z_M}{2}\frac{(N - N_{M(M)} - N_{X(M)})^2}{N}\xi_{\square M} \\
& + \frac{z_X}{2}\frac{(sN - N_{X(X)} - N_{M(X)})^2}{sN}\xi_{\square M} \\
& + \frac{z_X}{2}\frac{N^2_{M(X)}}{sN}\xi_{M(X)} + \frac{z_M}{2}\frac{N^2_{X(M)}}{N}\xi_{X(M)} \\
& + \frac{z_I}{2}\frac{N_{IM}}{\alpha N}\xi_{IM} + \frac{z_I}{2}\frac{N^2_{IX}}{\alpha N}\xi_{IX} \\
& + kT\Bigg[N_{M(M)}\ln\frac{N_{M(M)}}{N} + N_{X(M)}\ln\frac{N_{X(M)}}{N} \\
& + (N - N_{M(M)} - N_{X(M)})\ln\frac{(N - N_{M(M)} - N_{X(M)})}{N} \\
& + N_{X(X)}\ln\frac{N_{X(X)}}{sN} + N_{M(X)}\ln\frac{N_{M(X)}}{sN} \\
& + (sN - N_{X(X)} - N_{M(X)})\ln\frac{(sN - N_{X(X)} - N_{M(X)})}{sN} \\
& + N_{IM}\ln\frac{N_{IM}}{\alpha N} + N_{IX}\ln\frac{N_{IX}}{\alpha N} \\
& + (\alpha N - N_{IM} - N_{IX})\ln\frac{(\alpha N - N_{IM} - N_{IX})}{\alpha N}\Bigg].
\end{aligned}
\tag{2}
$$

$N\mu'_{MX_s}$ is the free energy of the ideal perfect crystal from which the real crystal is derived. There are sN X sites, and αN interstitial sites, so that α is characteristic of the crystal structure. $g_{\square M}$ is the change in free energy other than the contribution from configurational entropy when an M atom is removed from the crystal to some standard state, such as vapor at 1 atm pressure, to form a vacancy. There are $(N - N_{M(M)} - N_{X(M)})$ M vacancies and $(sN - N_{X(X)} - N_{M(X)})$ X vacancies. g_{IM} is the free energy of formation of an M interstitial by addition of an M atom to the crystal from the same standard state of M. $g_{M(X)}$ is the free energy of formation of an M substitutional by removal of an X atom from a normal X-site to X in its standard state, and the addition of an M atom to that site from M in its standard state. $g_{\square X}$, g_{IX} and $g_{X(M)}$ are the corresponding X quantities. The symbol ξ is used to denote a pairwise free energy of interaction between like defects, so that $\xi_{\square M}$, for example, describes the pairwise free energy of interaction between M vacancies. A positive value of ξ implies a repulsion between defects, and a negative ξ an attraction. z_M is the number of nearest neighbor normal M sites surrounding a given M site. z_X is the coordination number of X sites by X sites, and z_I is the coordination number of interstitial sites by interstitial sites. It is further assumed that only one kind of interstitial site is available.

From equation (2), we find that:

$$\begin{aligned}\mu_{M(M)} &\equiv \frac{\partial G}{\partial N_{M(M)}}\\ &= -g_{\square M} - z_M\xi_{\square M}\frac{(N - N_{M(M)} - N_{X(M)})}{N}\\ &\quad + kT\ln\frac{N_{M(M)}}{N - N_{M(M)} - N_{X(M)}} \qquad (3)\end{aligned}$$

where $\mu_{M(M)}$ is the chemical potential of M atoms on M sites. Similarly we have that:

$$\begin{aligned}\mu_{X(X)} &\equiv \frac{\partial G}{\partial N_{X(X)}}\\ &= -g_{\square X} - z_X\xi_{\square X}\frac{(sN - N_{X(X)} - N_{M(X)})}{sN}\\ &\quad + kT\ln\frac{N_{X(X)}}{sN - N_{X(X)} - N_{M(X)}}. \qquad (4)\end{aligned}$$

$$\begin{aligned}\mu_{IM} &\equiv \frac{\partial G}{\partial N_{IM}}\\ &= g_{IM} + z_I\xi_{IM}\left(\frac{N_{IM}}{\alpha N}\right)\\ &\quad + kT\ln\frac{N_{IM}}{\alpha N - N_{IM} - N_{IX}}. \qquad (5)\end{aligned}$$

$$\begin{aligned}\mu_{IX} &\equiv \frac{\partial G}{\partial N_{IX}}\\ &= g_{IX} + z_I\xi_{IX}\left(\frac{N_{IX}}{\alpha N}\right)\\ &\quad + kT\ln\frac{N_{IX}}{\alpha N - N_{IM} - N_{IX}}. \qquad (6)\end{aligned}$$

$$\begin{aligned}\mu_{M(X)} &\equiv \frac{\partial G}{\partial N_{M(X)}}\\ &= -g_{\square X} + g_{M(X)}\\ &\quad - z_X\xi_{\square X}\frac{(sN - N_{X(X)} - N_{M(X)})}{sN}\\ &\quad + z_X\xi_{M(X)}\left(\frac{N_{M(X)}}{sN}\right)\\ &\quad + kT\ln\frac{N_{M(X)}}{sN - N_{X(X)} - N_{M(X)}}. \qquad (7)\end{aligned}$$

$$\begin{aligned}\mu_{X(M)} &\equiv \frac{\partial G}{\partial N_{X(M)}}\\ &= -g_{\square M} + g_{X(M)}\\ &\quad - z_M\xi_{\square M}\frac{(N - N_{M(M)} - N_{X(M)})}{N}\\ &\quad + z_M\xi_{X(M)}\frac{N_{X(M)}}{N}\\ &\quad + kT\ln\frac{N_{X(M)}}{N - N_{M(M)} - N_{X(M)}}. \qquad (8)\end{aligned}$$

$\mu_{X(X)}$, μ_{IM}, μ_{IX}, $\mu_{M(X)}$, and $\mu_{X(M)}$ are the chemical potentials of X atoms on X sites, M atoms in interstices, X atoms in interstices, M atoms on X sites, and X atoms on M sites, respectively.

At equilibrium:

$$\left(\frac{\partial G}{\partial N}\right)_{N(X),N_{M(M)},N_{IM},N_{IX},N_{X(M)},N_{M(X)}} = 0.$$

If we impose this condition on equation (2), we have that:

$$\begin{aligned}0 &= \mu'_{MX_s} + g_{\square M} + sg_{\square X}\\ &\quad + \frac{z_M\xi_{\square M}}{2}\\ &\quad \times\frac{(N - N_{M(M)} - N_{X(M)})(N + N_{M(M)} + N_{X(M)})}{N^2}\\ &\quad + \frac{z_X\xi_{\square X}}{2}\\ &\quad \times\frac{(sN - N_{X(X)} - N_{M(X)})(sN + N_{X(X)} + N_{M(X)})}{sN^2}\\ &\quad - \frac{z_X\xi_{M(X)}}{2}\frac{N^2_{M(X)}}{sN^2} - \frac{z_M\xi_{X(M)}}{2}\frac{N^2_{X(M)}}{N^2}\\ &\quad - \frac{z_I\xi_{IX}}{2}\frac{N^2_{IX}}{\alpha N^2} - \frac{z_I\xi_{IM}}{2}\frac{N^2_{IM}}{\alpha N^2}\\ &\quad + kT\ln\left[\left(\frac{N - N_{M(M)} - N_{X(M)}}{N}\right)\right.\end{aligned}$$

$$\times\left(\frac{sN-N_{\square(X)}-N_{M(X)}}{sN}\right)^{s}$$

$$\times\left(\frac{\alpha N-N_{IM}-N_{IX}}{\alpha N}\right)^{\alpha}\Bigg]. \qquad (9)$$

We also have the following conditions of internal equilibrium:

$$\mu_{M(M)}=\mu_{IM}=\mu_{M(X)}=\mu_{M} \qquad (10)$$

$$\mu_{X(X)}=\mu_{IX}=\mu_{X(M)}=\mu_{X} \qquad (11)$$

where μ_M is the chemical potential of M atoms and μ_X the chemical potential of X atoms in the defect crystal. We may also write:

$$\mu_X = kT\ln a_X \qquad (12a)$$

$$\mu_M = kT\ln a_M \qquad (12b)$$

where a_X and a_M are the activities of X and M relative to the same standard states previously considered

The deviation from stoichiometry in the compound $MX_{s\pm\delta}$ is given in terms of the numbers of defects by the relation:

$$s\pm\delta=\frac{N_{\square(M)}+N_{X(M)}+N_{IX}}{N_{\square(X)}+N_{M(X)}+N_{IM}} \qquad (13)$$

where the negative sign is used for negative deviations from stoichiometry.

It is therefore possible to compute the relationships between activity and δ, using equations (3–13), and to compare the derived relationships with experimental data to obtain information about the defect structure. In order to characterize the system, it is sufficient to express the relations in terms of the activity of only one of the components. We will assume that the X component is the more volatile, or the one whose activity is more easily measured. Therefore, the following discussion will be presented in terms of a_X. However, a similar treatment may be used for the M component and a_M. We will consider only larger deviations from stoichiometry where only one type of defect is predominant and the concentrations of all other defects may be considered negligible. Therefore, by algebraic manipulation of equations (3–13), six relationships between a_X and δ were derived, on the assumption that one kind of point defect alone contributes to the observed nonstoichiometry. It is convenient to discuss these relationships in terms of the general equation:

$$y_i(a_X,\delta)=p_i(g_i)+q_i(\xi_i)x_i(\delta) \qquad (14)$$

where i represents the type of defect assumed to be present in predominant concentration. y_i is some function of a_X and δ, which is different for each type of assumed defect, i. p_i is a constant, containing the formation energy, g_i, of the defect i. q_i is another constant, containing the pairwise interaction energy, ξ_i, between i defects, and x_i is some function of δ, also characteristic of the nature of the defect i. A plot of y_i vs. x_i should therefore yield a straight line if, and only if, we do in fact have i type defects present. In this way the nature of the point defects present may be identified, and the free energy of interaction, ξ_i, may be determined from the slope of the line, q_i. For positive deviations from stoichiometry the relations are as follows:

M *vacancies*

If we eliminate $g_{\square M}$ from equations (4) and (9) and use equations (11–13), we obtain:

$$\ln\left[a_X\left(\frac{s+\delta}{\delta}\right)^{1/s}\right]=\frac{1}{skT}(\mu'_{MX_s}+g_{\square M})+$$

$$+\left(\frac{z_M\xi_{\square M}}{2skT}\right)\frac{\delta(2s+\delta)}{(s+\delta)^2}. \qquad (15)$$

X *interstitials*

From equations (6), (11), (12) and (13) we have that:

$$\ln\left[a_X\left(\frac{\alpha-\delta}{\delta}\right)\right]=\frac{g_{IX}}{kT}+\left(\frac{z_I\xi_{IX}}{\alpha kT}\right)\delta. \qquad (16)$$

X *substitutionals*

Multiplying equation (4) by s and adding equation (8) yields [in view of equation (11)]:

$$(s+1)\mu_X = -(g_{\square M} + s g_{\square X}) + kT \ln \left[\left(\frac{N_{X(X)}}{sN - N_{X(X)}}\right)^s \frac{N_{X(M)}}{N - N_{M(M)} - N_{X(M)}} + z_M \xi_{X(M)} \frac{N_{X(M)}}{N}\right].$$

Substituting the expression for $(g_{\square M} + s g_{\square X})$ obtained from equation (9) into the equation above, and using equations (12) and (13) leads to the following relationship:

$$\ln\left[a_X\left(\frac{s+1+\delta}{\delta}\right)^{1/(s+1)}\right] = \frac{1}{(s+1)kT}(g_{X(M)} + \mu'_{MX_g}) + \frac{z_M \xi_{X(M)}}{2(s+1)kT} \frac{\delta(2s+\delta+2)}{(s+1+\delta)^2}. \quad (17)$$

For negative deviations from stoichiometry, we have the following relations:

X *vacancies*

From equations (4, 11–13), we find that:

$$\ln\left(\frac{\delta a_X}{s-\delta}\right) = -\frac{g_{\square X}}{kT} - \frac{z_X \xi_{\square X}}{skT}\delta. \quad (18)$$

M *interstitials*

Equations (3) and (5) may be set equal to each other according to equation (10). If we then substitute the expression for $g_{\square M}$ obtained from equation (9) and the expression for $g_{\square X}$ obtained from equation (4) into the resulting equation, we get the following relation [using equations (12) and (13)].

$$\ln a_X + \frac{1}{s} \ln \left[\frac{\alpha^\alpha (s-\delta)^\alpha \delta}{(\alpha s - \alpha\delta - \delta)^{\alpha+1}}\right]$$

$$= \frac{\mu'_{MX_g} - g_{IM}}{skT} - \left(\frac{z_I \xi_{IM}}{2\alpha skT}\right) \frac{\delta(2s-\delta)}{(s-\delta)^2}. \quad (19)$$

M *substitutionals*

Equations (3) and (7) may be set equal to each other according to equation (10). If we then substitute the expression for $g_{\square M}$ obtained from equation (9) and the expression for $g_{\square X}$ obtained from equation (4) into the resulting equation, we get the following relation [using equations (12, 13)].

$$\ln a_X + \frac{s}{s+1} \ln[(s^2+s-s\delta)\delta^{1/s}] - \ln(s+1)(s-\delta) = \frac{\mu'_{MX_g} - g_{M(X)}}{(s+1)kT} \left(\frac{z_X \xi_{M(X)}}{2s(s+1)kT}\right) \frac{\delta(2s+2-\delta)}{(s+1-\delta)^2}. \quad (20)$$

COMPARISON WITH EXPERIMENTAL DATA

Yttrium dihydride

The rare earth dihydrides exhibit very large deviations from stoichiometry, and in cases such as yttrium hydride, where the nonstoichiometry may be as high as 50 per cent ($\delta = 1{\cdot}0$), the simple relations[2] derived under the assumption of no interaction are not applicable. In this paper, equations (18–20) are applied to the activity data of Yannopoulos *et al.*[6] for negative deviations from stoichiometry in yttrium dihydride. Figure 1 shows graphs of y_i as a function of x_i (according to equation (14)) at 651°C for various assumptions of the nature of the defect.

It can be seen that only for the case of hydrogen vacancies is a straight line relationship obtained. For yttrium interstitials, the plot of y_i vs. x_i shows a deviation from the straight line (indicated by the dashed curve) at lower values of x_i. In the case of Y substitutionals the curvature is more pronounced. The inference, therefore, is that the nonstoichiometry in $YH_{2-\delta}$ is, not unexpectedly, due to hydrogen vacancies.

In the plot of $y_{\square H}$ vs. $x_{\square H}$, the point at lowest δ does not fall on the straight line. Such deviations of the theoretical curve from the experimental points are to be expected at

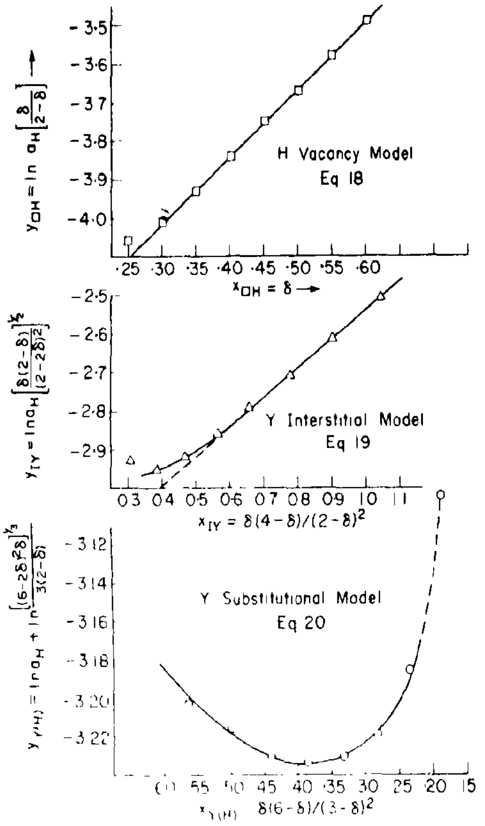

Fig. 1. Graph of y_i vs x_i according to equation (14) for $YH_{2-\delta}$ at 651°C calculated from the hydrogen activity data of Yannopoulos *et al* [6]

lower values of δ because the assumption was made in deriving the theoretical relations that only one type of defect is present in predominant concentrations; this is not true in the vicinity of the stoichiometric composition. The stoichiometric composition does not imply a perfect crystal, but rather that there are two opposite types of defects present in equivalent concentrations. (These are usually referred to as intrinsic defects.) Therefore, as the stoichiometric composition is approached, the concentration of the second type of defect becomes significant and the assumption that only one type of defect is present is no longer valid.

Similar comparisons between equations (18–20) and experimental data at 601°, 701°, 750°, 800°, 850°, 899 and 949°C were also made. Since the intrinsic defect concentration increases with temperature, the value of δ at which the experimental points start to deviate from the calculated curve also increases. In addition, at very high deviation from stoichiometry ($\delta > 0{\cdot}65$), the simple Bragg-Williams random distribution model no longer holds, and deviations from straight line behavior also occur at high values of δ. It was found that the region of applicability of these relations varied from $\delta = 0{\cdot}30$–$0{\cdot}60$ at 601°C to 0·40–0·65 at 949°C. Figure 2 shows a comparison of experimental data with calculated curves at 949°C.

The free energy of interaction between hydrogen vacancies, $\xi_{\square H}$, may be calculated at each temperature from the slopes, $q_{\square H}$, in equation (14). The interaction energy was found to be negative, which implies attraction between vacancies, and to decrease linearly with temperature as shown in Fig. 3. From this curve, values of −2·35 kcal/mole and −1·37 cal/deg mole were calculated for the enthalpy and entropy of vacancy pair formation, respectively. This latter value may be interpreted as the change in vibrational entropy in the crystal on formation of vacancy pairs from single vacancies.

Cerium dihydride

In order to illustrate the application of these relations to compounds exhibiting positive deviations from stoichiometry, equations (14–17) were used in an analysis of the activity data of Lundin [7] on cerium hydride. This is shown for the 300°C isotherm in Fig. 4. Although the differences are not as great as in the case of yttrium dihydride, curvature is observed for the cerium vacancy and hydrogen substitutional defect models while a straight line is obtained with the assumption of hydrogen interstitials. The deviation of the point at $\delta = 0{\cdot}40$ from the straight line is probably due to the breakdown of the random distribution of defects approximation at large defect concentrations. Isotherms at 400°, 500°, 550°,

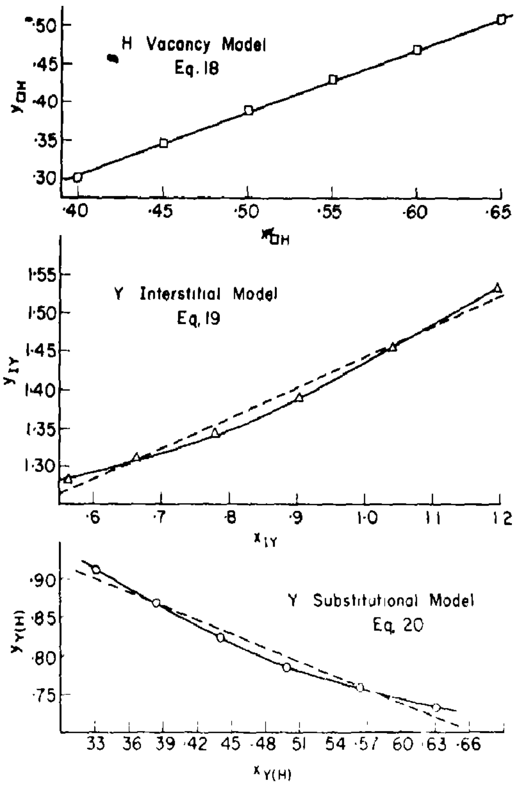

Fig. 2. Graphs of y_i vs. x_i according to equation (14) for $YH_{2-\delta}$ at 949°C, calculated from hydrogen activity data of Yannopoulos *et al.*[6].

600° and 650°C also gave best agreement with the interstitial hydrogen model. More pronounced differences in curvature among the three defect models are observed at higher temperatures as illustrated by the 550°C isotherms in Fig. 5. Thus, it may be assumed that interstitial hydrogen is the predominant defect at large positive deviations from stoichiometry in cerium hydride. This is in accordance with neutron diffraction[8] and NMR studies[9] of the rare earth dihydrides. The points at low values of δ fall on the straight line at temperatures up to 650°C, which implies lower intrinsic defect concentrations than in yttrium dihydride.

Table 1. Hydrogen interstitial interaction energies in cerium dihydride

Temp. (°C)	Interaction energy (kcal/mole) Lundin	Korst and Warf
300	0·42	
400	0·30	
500	0·22	
550	0·20	0·21
600	0·17	0·19
650	0·18	0·15
700		0·19
750		0·22

The computed values for the free energy of interaction between hydrogen interstitials are shown in the second column of Table 1. At lower temperatures, the interaction energy decreases with increasing temperature as it does for vacancies in yttrium dihydride. At temperatures above 500°C, however, the

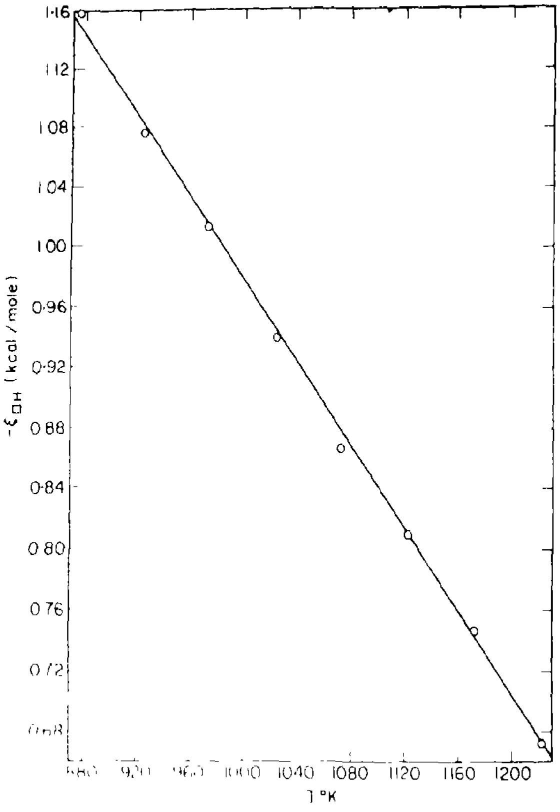

Fig. 3. Temperature variation of interaction energy between hydrogen vacancies in yttrium dihydride, YH_{2-x}.

interaction energy appears to remain constant at about 0·2 kcal/mole. Interaction energies calculated from the activity data of Korst and Warf[10] are also shown in Table 1. Since there was a greater degree of scatter in their data, it was not possible to differentiate among the three types of defects by observing the fit to a best straight line as in Figs. 4 and 5. Nevertheless, assuming that the defects were hydrogen interstitials as indicated by Lundin's data, it was possible to calculate the interaction energies shown in Table 1. It is seen that these values are in good agreement with those obtained from Lundin's data.

Whereas there was an attraction between vacancies in yttrium dihydride, in the case of cerium dihydride, the positive interaction energies correspond to repulsion between the hydrogen interstitials.

Thorium carbide

Thorium monocarbide has the NaCl-type structure and is normally carbon deficient with a homogeneity range of about $ThC_{0.60}$ to $ThC_{0.95}$ at temperatures below 1350°C[11]. More recently, Satow[12] observed a homogeneity range of $ThC_{0.70}$ to $ThC_{0.95}$ at 1000°–1200°C.

In this compound, thorium is the component whose thermodynamic activities are more easily measured. Therefore, in order to analyze the activity data of Satow[12] in terms of equations (15–20), it is more convenient to write the formula of the compound

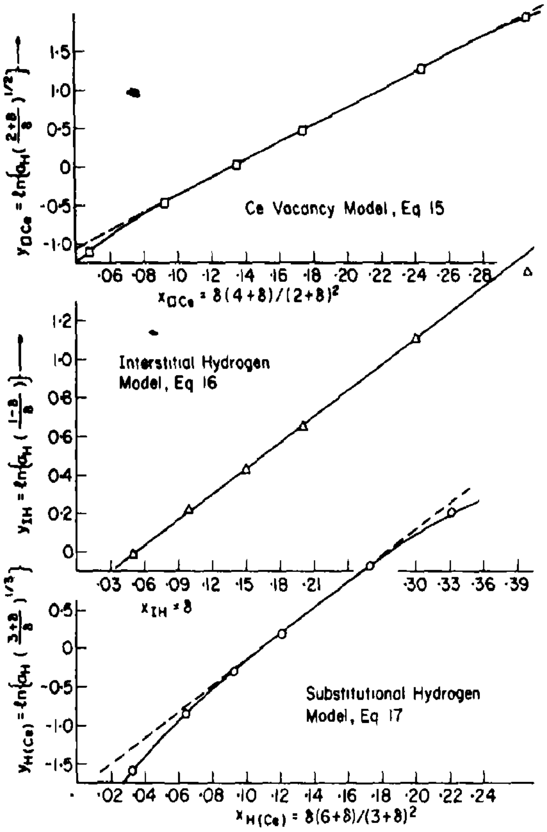

Fig. 4 Graphs of y_i vs x_i according to equation (14) for $CeH_{2+\delta}$ at 300°C, calculated from the hydrogen activity data of Lundin[7].

as $CTh_{1+\delta}$, such that carbon corresponds to the M, and thorium to X in these equations. Comparison of the data at 1000°K with equations (15–17) is shown in Fig. 6. Except at $\delta = 0{\cdot}086$ ($x_{\square C} = 0{\cdot}154$) where the concentration of intrinsic defects is probably significant, the experimental points are in best agreement with the carbon vacancy model. This is in accordance with the results of density measurements[12] which also indicate that carbon vacancies are the predominant defects in nonstoichiometric thorium monocarbide. Data at 1100° and 1200°K give curves similar to those shown in Fig. 6.

The interaction energy between carbon vacancies was found to be positive and independent of temperature over the range 1000°–1200°K as shown in Table 2. The positive value implies a repulsion between carbon vacancies.

Table 2. Carbon vacancy interaction energies in thorium monocarbide

Temp. (°K)	$\xi_{\square C/\square C}$ (kcal/mole)
1000	10·5
1100	9·6
1200	10 0

DISCUSSION

The theoretical development followed here and in [1] differs in one important respect from those commonly given. Previous treatments do not list the complete set of independent variables specifying the configuration

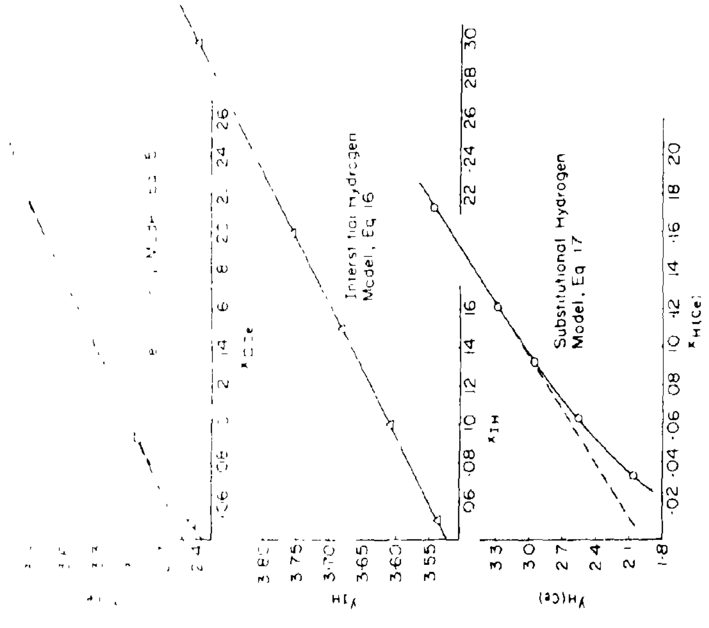

Fig. 5. Graphs of y_i vs. x_i according to equation (14) for $CeH_{2+\delta}$ at 550°C, calculated from the hydrogen activity data of Lundin[7].

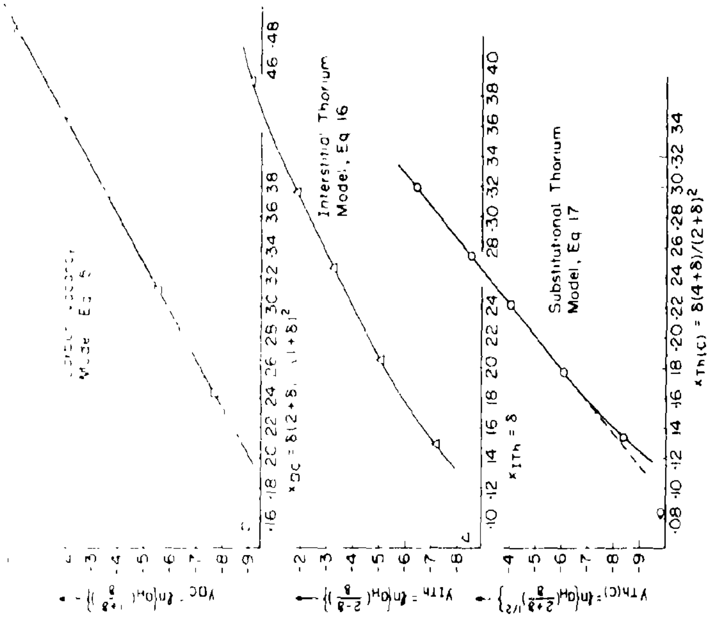

Fig. 6. Graphs of y_i vs. x_i according to equation (14) for thorium monocarbide, $CTh_{1+\delta}$, at 1000°K, calculated from the thorium activity data of Satow[12].

of the crystal; the number of sites is usually considered to be constant. As a result, one relationship defining the equilibrium situation is lost. Here we recognize N as a variable, obtaining equation (9) when G is minimized with respect to it. The essential role of equation (9) is that of providing a relationship between the activities of the two crystal components. The net result is that a different functional relationship between thermodynamic activity and deviation from stoichiometry is obtained for each type of defect.

At very low deviations from stoichiometry, the interaction between defects can usually be neglected and the expressions involving activity and δ given in [1] are applicable. However, if the interaction energy is large, the interactions must be taken into consideration, particularly at larger values of δ as indicated by the last term in equations (15–20). This is illustrated in Fig. 7.

As mentioned on page 1030, the Bragg Williams random distribution assumption does not hold at very high deviations from stoichiometry in the vicinity of a phase boundary. One would also expect the relationships derived in this study to be valid only for low values of ξ/kT. This condition is met by $YH_2(\xi/kT \simeq 0{\cdot}3)$ and $CeH_2(\xi/kT \simeq 0{\cdot}1)$. However, the fact that the equations are applicable to thorium monocarbide, where the calculated value of ξ/kT appears to be 5 at 1000°C, is surprising.

Finally, it is of interest to compare the values of the defect interaction energies for hydrides obtained here with those computed for similar type hydrides by other investigators. Takeuchi and Suzuki[13] calculated defect interactions in both hydrogen deficient and hydrogen excess plutonium dihydride from the hydrogen activity data of Mulford and Sturdy[14]. Assuming that the hydrogen deficiency was due to empty tetrahedral sites,

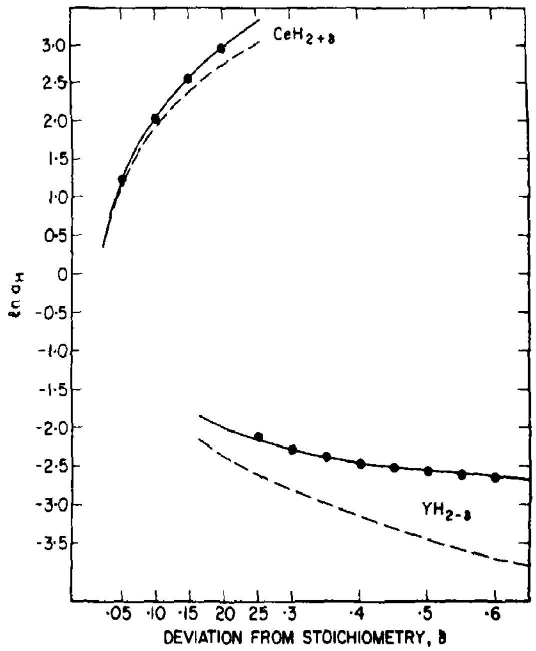

Fig. 7. Camparison of experimental hydrogen activities in yttrium and cerium hydrides at 650°C with activities calculated assuming both interaction between defects (solid lines) and no interaction between defects (dashed lines).

they obtained an expression similar to equation (18). If their interaction energies are put in terms of equation (18), the value calculated for the vacancy-vacancy interaction is −1·7 kcal/mole and is approximately temperature independent over the range 500°–700°C. This is comparable with values of −1·3 to −1·0 kcal/mole for vacancies in yttrium dihydride. Similarly, their value for interstitial hydrogen interaction energy corresponds to a temperature-independent 0·33 kcal/mole in the temperature range 300°–500°C. This value appears to be in agreement with the average value given in Table 1 for cerium dihydride in that temperature range. More recently in a study of lanthanum dihydride, Messer and Hung[15] obtained hydrogen interstitial interaction energies ranging from 0·30 kcal/mole at 250°C to 0·18 at 450°C. These values are slightly lower than the values for cerium hydride at the corresponding temperatures.

REFERENCES

1. LIBOWITZ G. G. and LIGHTSTONE J. B., *J. Phys. Chem. Solids* **28**, 1145 (1967).
2. LIBOWITZ G. G. and LIGHTSTONE J. B., In *Proc. Sixth Rare Earth Research Conf.*, AFOSR 67-1214, pp. 132–141. Gatlinburg, Tenn. (1967).
3. ANDERSON J. S., *Proc. R. Soc.* **A185**, 69 (1946).
4. LIBOWITZ G. G., *J. appl. Phys.* **33**, 399 (1962).
5. BRAGG W. L. and WILLIAMS E. J., *Proc. R. Soc.* **A145**, 699 (1934), *ibid* **A151**, 540 (1935)
6. YANNOPOULOS L. N., EDWARDS R. K. and WAHLBECK P. G., *J. phys. Chem* **69**, 2512 (1965).
7. LUNDIN C. E., *Trans. AIME* **236**, 978 (1966).
8. HOLLEY C. E., MULFORD R. N. R., ELLINGER F. H., KOEHLER W. C. and ZACHARIASEN W. H., *J. phys. Chem.* **59**, 1226 (1955)
9. SCHREIBER D. S. and COTTS R. M., *Phys. Rev.* **131**, 1118 (1963).
10. KORST W. L. and WARF J. C., *Inorg. Chem.* **5**, 1719 (1966)
11. STORMS E. K., In *The Refractory Carbides*, pp 157–158. Academic Press, New York (1967).
12. SALOW T., *J. nucl. Mater.* **21**, 255 (1967)
13. TAKEUCHI S. and SUZUKI K., *Trans. Jap. Inst. Metals* **3**, 41 (1962).
14. MULFORD R. N. R. and STURDY G. E., *J. Am. chem. Soc.* **77**, 3449 (1955); *ibid.* **78**, 3897 (1956).
15. MESSER C. E. and HUNG G. W., *J. phys. Chem* **72**, 3958 (1968).

J. Phys. Chem. Solids Pergamon Press 1969. Vol. 30, pp. 1037-1042. Printed in Great Britain

ETUDE PAR RAYONS X DE LA DILATATION DE NaCl A HAUTE TEMPERATURE

E. LAREDO
Instituto Venezolano de Investigaciones Científicas, Apartado 1827, Caracas, Venezuela

(*Received* 8 *November* 1968)

Résumé—Nous avons mesuré la dilation thermique linéaire par diffraction de rayons X sur des monocristaux de NaCl entre la température ambiante et 770°C (près du point de fusion) On montre que la dépendence en température de la dilatation thermique de NaCl à des températures supérieures à 550°C, peut se relier à la concentration de paires de lacunes libres génerées thermiquement (défauts de Schottky). Nous avons séparé dans la dilatation thermique le terme dû aux défauts, cette partie 'anomale' croît exponentiellement avec $1/T$°K, et on détermine une énergie d'activation de 2 eV qui est en bon accord avec celle déduite des études de conductivité ionique. Nous discutons les ordres de grandeur des différents termes qui interviennent dans l'expression de la partie 'anomale' du coefficient de dilatation thermique

Abstract—Linear thermal expansion has been measured by means of X-ray diffraction on single crystals of NaCl between room temperature and 770°C (near the melting point) It is shown that the temperature dependence of the thermal expansion of NaCl at temperature above 550°C can be related to the concentration of thermally generated free vacancy pairs (Schottky defects) We have separated in the thermal expansion the term due to defects; this 'anomalous' part increases exponentially with $1/T$°K and has an activation energy of 2 eV in good agreement with the activation energy deduced from studies of ionic conductivity. We also discuss the order of magnitude of the different terms that contribute to the 'anomalous' part of the thermal expansion.

INTRODUCTION

DANS DE nombreux solides cristallins la dilatation thermique présente à haute température une anomalie attribuée à la formation accélérée de défauts ponctuels à l'approche de la fusion.

Pour les halogénures alcalins les mesures du coefficient de dilatation effectuées ne sont pas toujours concluantes en ce qui concerne la création de paires de Schottky.

Fischmeister[1] a mesuré le paramètre de NaCl polycristallin par des techniques photographiques et diffractométriques. Le comportement qu'il observe à haute température semble incompatible avec l'interprétation liée aux défauts ponctuels. Il explique ses résultats dans un simple modèle de Gruneïsen. Fletcher [2] a montré que l'analyse utilisée par Fischmeister n'était pas assez sensible pour garantir cette conclusion.

Parmi les autres mesures du coefficient de dilatation qui ont été publiées nous noterons les déterminations du coefficient macroscopique α effectuées par Eucken et Dannöhl [3], grâce à des mesures de variations de capacité, et par Enck et Dommel[4] avec un dilatomètre automatique enregistreur.

Merriam *et al.*[5] ont interprété la variation de α rapportée par Eucken *et al.* à haute température comme résultant de la somme de deux termes, une contribution normale et une contribution anormale attribuée aux défauts de Schottky. Ils en ont conclut à la nécessité de nouvelles mesures de paramètre cristallin et de conductivité électrique aux environs du point de fusion.

Nous rapportons ici les résultats de la première partie de notre étude sur la détermination de paramètre du NaCl monocristallin.

METHODE EXPERIMENTALE ET RESULTATS

La chambre chauffante adaptée au diffractomètre Philips à axe horizontal a déjà été décrite[6]. L'échantillon utilisé est une lamelle monocristalline de 1 mm d'épaisseur et 1 cm^2

de section. Ces lamelles sont clivées à partir de monocristaux de 20 cm^3 préparés au laboratoire, par la méthode de fusion avec gradient de température[7]. Le produit de départ est du NaCl Johnson et Matthey spectroscopiquement pur.

La température est mesurée par un thermocouple situé à 1 mm au-dessous de l'échantillon. Celui-ci est maintenu par des ressorts en Tungstène qui conservent leur élasticité à haute température. L'étalonnage en température rendu necessaire par le gradient de température entre le thermocouple et la surface diffractante du cristal est donné par les points de transformation allotropique de AgI, NH_4Cl, $KClO_4$, CsCl et SO_4Li_2. A l'équilibre, la température est stable à mieux que ±2°C.

La géométrie du montage[8] ne nous permet d'étudier qu'une seule rangée du réseau réciproque à la fois. Nous avons choisi la rangée {h00} car elle comporte les raies les plus intenses du spectre. Le rayonnement utilisé est du MoKα, qui nous permet d'atteindre la réflexion (1400). L'optique du diffractomètre est différente de celle utilisée dans la montage classique pour poudres: nous n'utilisons qu'une fente de 50 μ à l'entrée ainsi que les deux systèmes de Soller, puisque l'échantillon monocristallin sert de canaliseur.

Les aberrations classiques en géometrie de poudre sont ici négligeables. Il ne reste que l'erreur de zéro dont nous tenons compte dans l'extrapolation finale pour $\theta = 90°$, de la droite $a = f$ (cotg θ), (Fig. 1). La précision relative va de 4×10^{-5} à 7×10^{-4} quand la température augmente. En effet le facteur de Debye diminue fortement l'intensité des raies aux grands angles à haute température (pour la raie (1400) exp-2 M passe de 0·1 à 20°C, à $0{\cdot}3 \times 10^{-3}$ à 763°C).

Nous avons effectué 28 mesures de paramètre entre 50°C et 763°C. Le gradient de température existant dans le cristal nous a empêchés d'effectuer des mesures plus proches du point de fusion (801°C), car la face du cristal en contact avec la platine commençait à fondre lorsque la surface diffractante atteignait 780°C. Nos résultats expérimentaux ainsi que ceux de Fischmeister, sont groupés sur la Fig. 2 où nous avons porté $a_T - a_{273} = f(T)$. Jusqu'à 550°C, Δa croît d'une façon quasilinéaire. Au-dessus de cette température s'amorce la dilatation anomale que nous suivons jusqu'à 770°C. Fischmeister n'indique pas la précision de ses mesures qui diffèrent des notres à haute température. Il dit cependant ne pas prétendre à une grande précision. L'étalonnage visuel en température de sa

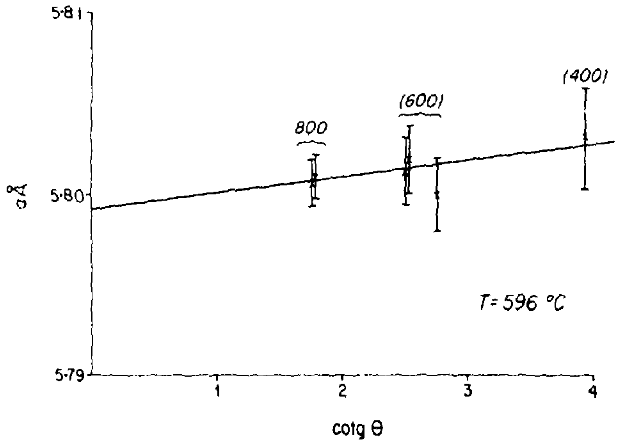

Fig. 1 Détermination du paramètre cristallin de NaCl pur à 596°C, $a = 5{\cdot}799_2$ Å.

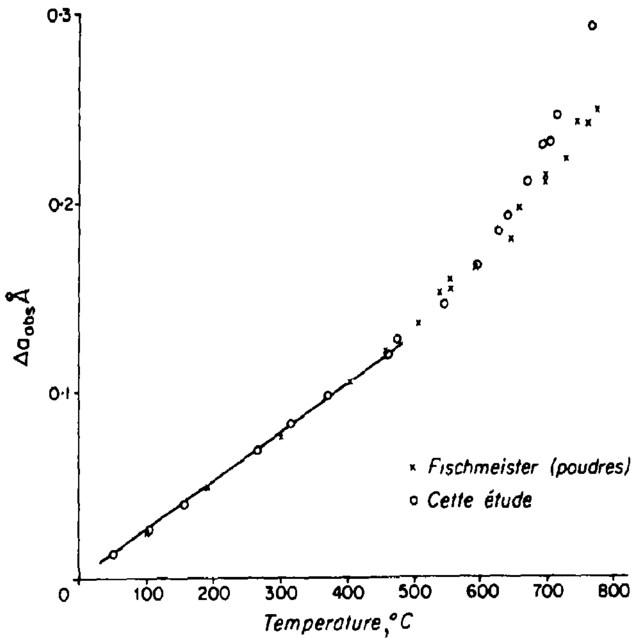

Fig. 2. Variation de $\Delta a = a_T - a_{273}$ avec la température.

chambre pourrait expliquer en partie ces différences.

ANALYSE DE RESULTATS

L'effet des défauts ponctuels sur le volume du cristal peut provenir soit des effets de taille soit de l'influence du défaut sur la cohésion et par conséquent sur la coefficient de dilatation. L'analyse de Merriam *et al.* est basée sur cette deuxième contribution.

La prise en considération simultanée des deux effets est possible dans un calcul simple qui permet cependant de contrôler les ordres de grandeur.

En toute rigueur, dans un modèle linéaire, on peut écrire quela variation totale de volume observée est à une température T:

$$dV_{obs} = \frac{\partial V}{\partial T} dT + \frac{\partial V}{\partial n} dn$$

ou encore

$$dV_{obs} = \left[\alpha'(T,n) + \frac{\partial \alpha'}{\partial n} dn\right] dT + \frac{\partial V}{\partial n} dn \quad (1)$$

où $\alpha'(T.n)$ est le coefficient absolu de dilatation thermique à la température T, n le nombre total de défauts dans le cristal et $\partial V/\partial n$ l'expansion absolue due à un défaut. En faisant l'approximation $(\partial\alpha'/\partial n) = (d\alpha'/dn) = K$ dans (1) nous séparons le terme dû uniquement à la température, sans création de défauts:

$$dV_{obs} = \left[\alpha'(T,0) + \int_0^n \frac{d\alpha'}{dn} dn\right] dT + \frac{\partial V}{\partial n} dn$$

et

$$dV_{obs} - dV_{ext} = dV_T = \left[\int_0^n \frac{d\alpha'}{dn} dn\right] dT + \frac{\partial V}{\partial n} dn$$

où dV_{ext} est la dilatation thermique sans contribution des défauts. Il est plus facile de raisonner sur les coefficients de dilatation thermique car l'évaluation de α' $(T.0)$, pour le réseau parfait, se fait par une extrapolation linéaire de la representation $\alpha' = f(T)$ de basse température, avec $d\alpha'(T.0)/dT > 0$.

Finalement:

$$\frac{dV_T}{dT} = Kn + \frac{\partial V}{\partial n}\frac{dn}{dT}. \quad (2)$$

Connaisant la loi de variation de la concentration des défauts avec la température $n = N \exp-(W_s/2kT)$, où W_s est l'énergie nécessaire pour créer une paire de lacunes libres dans le cristal, nous pouvons écrire (2) de la façon suivante:

$$\frac{\mathrm{d}V_T}{\mathrm{d}T} = \left(K + \frac{\partial V}{\partial n}\frac{W_s}{kT^2}\right) N \exp-\frac{W_s}{2kT}.$$

Nos mesures ne sont pas suffisament précises pour pouvoir en tirer un coefficient de dilatation instantané. Nous calculerons plutôt le coefficient moyen de dilatation linéaire relative défini par

$$\bar{\alpha} = \frac{1}{T-273}\int_{273}^{T} \alpha\, \mathrm{d}T,$$

et $\alpha = \frac{1}{3}(\alpha'/V)$; $\bar{\alpha}$ est ainsi directement comparable aux données expérimentales et

$$\bar{\alpha} = \frac{1}{T-273}\frac{\Delta a}{a_0},$$

est représenté sur la Fig. 3 ainsi que $\Delta\bar{\alpha}$ partie anomale du coefficient de dilatation. Le calcul de l'erreur commise sur $\bar{\alpha}$ montre que celle-ci atteint 2% dans le domaine de température qui nous intéresse. La coude dans le coefficient de dilatation se place à 550°C comme dans les mesures de conductivité électrique de Etzel et Maurer[9], la pureté de leurs échantillons étant comparable à celle de nos cristaux.

$\Delta\bar{\alpha}$ peut être relié au nombre de défauts par l'équation (2)

$$3\Delta\bar{\alpha}\Delta T = K\Delta T\left\langle\frac{n}{V}\right\rangle + \frac{\partial V}{\partial n}\frac{n}{V} \qquad (3)$$

où $\langle n/V\rangle$ est la valeur moyenne de la concentration des défauts créés dans l'intervalle $\Delta T = T - 273°\mathrm{K}$; et

$$\left\langle\frac{n}{V}\right\rangle\Delta T = \frac{1}{V}\int_{273} \exp-\frac{W_s}{2kT}\,\mathrm{d}T.$$

Des intégrations par parties successives nous permettent d'écrire:

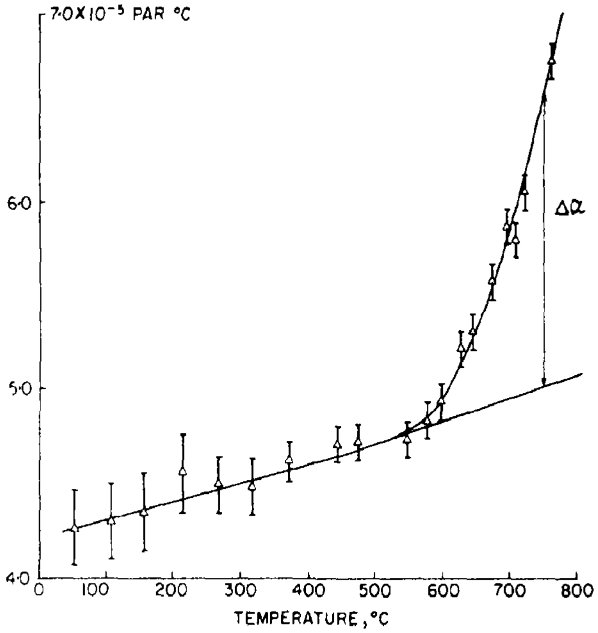

Fig. 3. Variation avec la température du coefficient de dilatation thermique moyen du NaCl La ligne continue représente l'extrapolation des résultats expérimentaux de basse température.

$$\left\langle\frac{n}{V}\right\rangle\Delta T=\left[\frac{n}{V}\frac{2kT^2}{W_s}\left(1-\frac{4kT}{W_s}+\frac{24k^2T^2}{W_s^2}-\ldots\right)\right]_{273}^{T}$$

et enfin:

$$3\Delta\bar{\alpha}\Delta T=\frac{n}{V}\left[K\frac{2kT^2}{W_s}\left(1-\frac{4kT}{W_s}+\frac{24k^2T^2}{W_s^2}-\ldots\right)+\frac{\partial V}{\partial n}\right]. \quad (4)$$

Le comportement $3\Delta\bar{\alpha}\Delta T$ en fonction de la température dépendra de l'importance relative des deux termes dans le deuxième membre de l'équation (4) que nous allons évaluer. Au point de fusion $T = 1{\cdot}07\times 10^3$ °K, $(W_s/2kT) = 11{\cdot}21$, $\Delta T = 1074$°K et $K \simeq \alpha(V/N) \simeq 4\times 10^{-3}$ Å^3 par degré.

On peut déterminer une valeur acceptable de $\partial V/\partial n$ à partir des déplacements des ions premiers voisins du défaut calculés par Brauer (10) soit $\xi_{\boxminus} = 0{\cdot}110$ et $\xi_{\boxplus} = 0{\cdot}096$.

En considérant comme Eshelby[11] la dilatation du cristal comme une déformation homogène élastique isotrope, on obtient:

$$\Delta V = 4\pi a^3\gamma\xi \text{ avec d'après[12] } \gamma = \frac{3(1-\sigma_0)}{1+\sigma_0}.$$

On aboutit finalement à $(dV/dn) \simeq 102$ Å^3. En portant ces ordres de grandeur dans (4) nous constatons que le premier terme peut être négligé devant le second.

En conséquence le comportement de ln $3\Delta\bar{\alpha}\Delta T$ en fonction de $1/T$ devrait être linéaire. La pente de la droite obtenue (Fig. 4), nous permet de calculer une valeur pour $(W_s/2) = 1{\cdot}00\pm 0{\cdot}05$ eV à comparer avec $(2{\cdot}02/2)$ eV valeur admise pour la création de paires de Schottky dans le NaCl.

Il semble donc que l'anomalie constatée peut se relier à la création de ces défauts à haute température.

DISCUSSION

La discussion des ordres de grandeur de n, pour une température donnée, celle de la fusion par exemple est instructive.

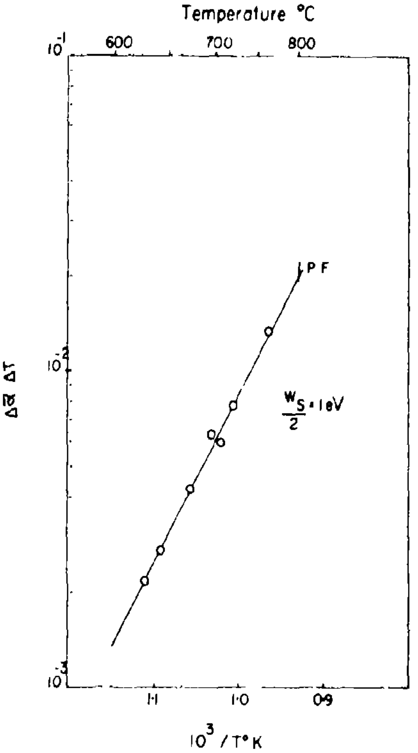

Fig. 4. Dépendence logarithmique de $\Delta\bar{\alpha}\Delta T$ en fonction de $10^3/T$. W_s est l'énergie de formation d'une paire de Schottky

En négligeant le premier terme dans (4), on obtient $(n/N) \simeq 3\times 10^{-2}$, soit le même ordre de grandeur que celui tiré par Merriam *et al.* des mesures de Eucken et Dannöhl en appliquant un modèle mis au point pour la production de défauts crées par irradiation X.

Etzel *et al.* déduisent des mesures de conductivité électrique une valeur de $(n/N) \simeq 10^{-4}$ à la fusion. Ils ne tiennent pas compte du facteur multiplicatif, supérieur à 1 qu'introduit l'entropie de vibration plus forte pour les ions au voisinage du défaut. Il semble donc que les mesures de conductivité électrique soient à réanalyser et à étendre plus près du point de fusion. C'est ce que nous entreprenons actuellement.

REFERENCES

1. FISCHMEISTER H. F., *Acta crystallogr* 9, 416 (1956).
2. FLETCHER G. C., *Phil. Mag.* 2, 639 (1957)

3. EUCKEN A. et DANNÖHL W., *Z. elektrochem.* **40**, 814 (1934).
4. ENCK F. D. et DOMMEL J. G., *J. appl. Phys.* **36**, 839 (1965).
5. MERRIAM M. F., SMOLUCHOWSKI R. et WIEGAND D A., *Phys. Rev.* **125**, 65 (1962).
6. BENVENISTE M., LAREDO E., BERGÉ P. et TOURNARIE M., *J. Phys.* **26**, 189 (1965)
7. BENVENISTE M., Thèse, 3ᵉ Cycle, Paris (1963).
8. LAREDO E., Thèse, 3ᵉ Cycle, Paris (1965).
9. ETZEL H. W. et MAURER R. J., *J. chem. Phys.* **18**, 1003 (1950).
10. BRAUER P., *Z. Naturf.* **7a**, 372 (1952).
11. ESHELBY J. D., In *Solid State Physics*, Vol. 3. Academic Press, New York.
12. LEIBFRIED G., *Z Phys.* **135**, 23 (1953).

J. Phys. Chem. Solids Pergamon Press 1969. Vol. 30, pp. 1043–1058. Printed in Great Britain.

VIBRATIONAL PROPERTIES OF AN ADSORBED SURFACE LAYER ON A SIMPLE MODEL CRYSTAL*

LEONARD DOBRZYNSKI† and D. L. MILLS
Department of Physics, University of California, Irvine, Calif. 92664, U.S.A.

(*Received* 20 *September* 1968; *in revised form* 6 *November* 1968)

Abstract—We consider the influence of an adsorbed layer of atoms on the vibrational properties of a simple model crystal. The change in specific heat and entropy are computed for arbitrary temperatures, assuming the defect layer differs only in mass from the atoms in the bulk crystal. The Montroll–Potts model of lattice dynamics is used for this purpose. We also explore the existence of surface modes above the vibrational band of the host matrix for this model, along with in-band resonances and low frequency surfaces modes. The results of the specific heat and entropy calculation are compared with an expansion valid in the high temperature regime.

I. INTRODUCTION

THE PURPOSE of this paper is to explore the influence of an adsorbed layer of atoms on the surface of a three dimensional crystal. We employ a simple model of the crystal, along with the assumption that the surface layer differs from atomic layers in the bulk only in mass. The formalism we employ is easily applied to more general situations, where force constants as well as mass changes occur in the surface layer. We feel that the simple mass defect layer offers a qualitative feeling for the influence of an adsorbed layer on the properties of the crystal, while the algebra remains quite simple for our model.

We describe the bulk crystal by the Montroll–Potts model that has been employed earlier in work on point defects in bulk crystals[1]. While it is known that for the semi-infinite solid, the predictions of this model disagree with the theory of elasticity[2] because the model is not rotationally invariant, nonetheless we feel the model gives reasonable rough estimates of the changes in the thermodynamic properties associated with the defect layer.

We present an analytic study of the change in low temperature specific heat associated with the defect layer. Numerical computations extend this result to arbitrary temperatures, for two values of the mass change. The change in entropy is also calculated. We present the numerical results for the case where the mass of the atoms in the surface layer is half that of the bulk, and then the case where it is twice the bulk value. The numerical results are compared to a high temperature expansion for the specific heat and entropy. The coefficients of the terms in the high temperature expansion are also given for the Montroll–Potts f.c.c. and b.c.c. lattices.

Also, we find that when the defect layer is lighter than the bulk atoms, surface modes above the bulk vibrational bands appear. These modes are expected to persist in more general models.

All of the computations described above are carried out using a Green's function technique.

The effects of layers of defect atoms on crystal surfaces have been investigated theoretically for one and two dimensional

---

*Supported in part by the Air Force Office of Scientific Research, Office of Aerospace Research, U.S. Air Force under AFOSR Grant Number 68–1448

†*Permanent address:* Institut Superieur d'Electronique du Nord, 59-Lille, France.

geometries[3–5]. In the three dimensional crystal, high temperature expansions of the entropy have been discussed[6–7]. The only experimental work we are aware of which deals with localized vibration modes associated with defects on crystal surfaces is the work of Pliskin and Eischens[8]. However, a number of measurements of the desorption entropy have been reported[6].

2. GENERAL CONSIDERATIONS

Let us consider a three dimensional lattice of atoms. We consider a large macrocrystal in the form of a cube, with sides of length L, with periodic boundary conditions applied to all physical quantities. If there are N atoms in the crystal, with one atom per unit cell, we introduce a $3N$ column vector **u**, which gives the displacements of the atoms from their equilibrium position. In the harmonic approximation, the time independent equations of motion for **u** assume the form

$$(\mathbf{D}-\omega^2\mathbf{I})\mathbf{u}=0 \tag{2.1}$$

where we introduce the dynamical matrix **D** that depends on the details of the microscopic forces between atoms, ω is the frequency of the motion, and **I** the identity matrix.

We begin by considering a perfect, simple cubic crystal with atoms of mass M. Let $\mathbf{D}^{\circ}$ denote the dynamical matrix of this lattice. Then, following Maradudin and Wallis[9], we create two (100) free surfaces by setting to zero all atomic force constants that describe interactions which cross a fictitious plane that lies between two (100) planes of atoms in the bulk crystal. We denote the dynamical matrix of the crystal in the presence of the two free surfaces by $\mathbf{D}^S$, and write $\mathbf{D}^S=\mathbf{D}^{\circ}+\mathbf{V}^S$, where $\mathbf{V}^S$ is the perturbation produced by the 'bond breaking' procedure. Finally, we simulate an adsorbed monolayer of atoms by changing the mass of the atoms in one of the surface layers, along with the intra-layer force constants, and interactions which couple the surface layer to the remainder of the semi-infinite crystal. We assume the atomic structure of the surface layer is the same as a (100) layer of atoms in the bulk. We let $\mathbf{V}^A$ denote the perturbation produced in $\mathbf{D}^S$ by the mass and force constant changes associated with the 'formation' of the adsorbed layer. Then if **D** is the dynamical matrix of the final crystal,

$$\mathbf{D}=\mathbf{D}^S+\mathbf{V}^A.$$

It will be convenient to introduce the following Green's functions

$$\mathbf{G}^{\circ}=(\omega^2\mathbf{I}-\mathbf{D}^{\circ}+i\epsilon)^{-1} \tag{2.2}$$

$$\mathbf{G}^S=(\omega^2\mathbf{I}-\mathbf{D}^S+i\epsilon)^{-1} \tag{2.3}$$

and

$$\mathbf{G}=(\omega^2\mathbf{I}-\mathbf{D}+i\epsilon)^{-1} \tag{2.4}$$

where ϵ is a positive, infinitesimal number.

The functions $\mathbf{G}^S$ and **G** may be constructed from the Green's function $\mathbf{G}^{\circ}$ of the unperturbed crystal by employing the relations

$$\mathbf{G}^S=\mathbf{G}^{\circ}(\mathbf{I}-\mathbf{G}^{\circ}\mathbf{V}^S)^{-1} \tag{2.5}$$

$$\mathbf{G}=\mathbf{G}^S(\mathbf{I}-\mathbf{G}^S\mathbf{V}^A)^{-1}. \tag{2.6}$$

The frequencies of the localized modes and resonance modes that arise from the perturbations $\mathbf{V}^S$ and $\mathbf{V}^A$ respectively may be found from the conditions

$$\mathrm{Re}\{\det|\mathbf{I}-\mathbf{G}^{\circ}\mathbf{V}^S|\}=0 \tag{2.7}$$

$$\mathrm{Re}\{\det|\mathbf{I}-\mathbf{G}^S\mathbf{V}^A|\}=0. \tag{2.8}$$

We shall find it desirable to compute the changes in thermodynamic properties of the system that occur in the presence of $\mathbf{V}^S$ and $\mathbf{V}^A$. Suppose we consider a quantity F which is a function of the normal mode frequencies $\omega^2(\mathbf{q})$ of the perfect crystal described by the dynamical matrix $\mathbf{D}^{\circ}$. Let F have the form

$$F=\sum_{\mathbf{q}} f(\omega^2(\mathbf{q})). \tag{2.9}$$

The change in the quantity F that results from the perturbation $V^S(V^A)$ is given by Lifshitz [10] formula

$$\Delta F_{S(A)} = -\frac{1}{\pi}\int \mathrm{d}E \frac{\mathrm{d}f(E)}{\mathrm{d}E}\eta_{S(A)}(E) \qquad (2.10)$$

where the phase angle $\eta(E)$ is given by

$$\eta_S(\omega) = -\operatorname{Arg}\det|\mathbf{I}-\mathbf{G}^\circ\mathbf{V}^S| \qquad (2.11)$$

and

$$\eta_A(\omega^2) = -\operatorname{Arg}\det|\mathbf{I}-\mathbf{G}^S\mathbf{V}^A|. \qquad (2.12)$$

The result in equation (2.10) takes due account of localized states, when equations (2.11) and (2.12) are understood to be the generalized phase shifts as employed by deWitt[11] and Toulouse[12].

3. PROPERTIES OF THE MONTROLL–POTTS MODEL IN THE PRESENCE OF A FREE SURFACE

The Montroll–Potts model[1] consists of a monatomic simple cubic lattice of atoms, with nearest neighbor interactions of an especially simple kind. If $\mathbf{u}(\mathbf{l}) = (u(\mathbf{l}), v(\mathbf{l}), w(\mathbf{l}))$ is the displacement from equilibrium of the atom in lattice site $\mathbf{l}$ of the perfect crystal, then the potential energy term in the Hamiltonian is assumed to have the form

$$V = \tfrac{1}{2}\beta\Big\{\sum_{\mathbf{l}}\sum_{\delta}[u(\mathbf{l})-u(\mathbf{l}+\delta)]^2 + [v(\mathbf{l})-v(\mathbf{l}+\boldsymbol{\delta})]^2+[w(\mathbf{l})-w(\mathbf{l}+\boldsymbol{\delta})]^2\Big\}. \qquad (3.1)$$

This simple form of V allows one to easily deduce the form of the phonon dispersion curves and eigenvectors of the infinitely extended, perfect crystal. A study of the influence of a free surface on the properties of this model crystal has recently been completed[13]. In this section, we recall some results of this study, as well as derive the form of the Green's function $\mathbf{G}_S$ defined above, before proceeding to the discussion of the influence of an adsorbed layer.

It is well known that the force constants associated with the Montroll–Potts model fail to satisfy the conditions imposed by considerations of rotational invariance of the Hamiltonian with respect to rigid body rotations. Ludwig and Lengeler[2] have pointed out that this lack of rotational invariance is the source of the disagreement between the theory of elasticity, and the long wavelength properties of the Montroll–Potts model applied to the semi-infinite crystal. Because of this, the predictions of the model for temperatures very small compared to the Debye temperature θ_D may be of doubtful validity.

In this paper, we will be concerned with the influence of the adsorbed layer on the thermodynamic properties of the crystal at temperatures comparable to θ_D. We feel within this model, we are able to obtain order of magnitude estimates for the quantities of interest to us, in this temperature range. The simplicity of the model enables much of the work to be performed in simple analytical form, so it provides a reasonable first approach to the problems at hand.

In the infinitely extended crystal, there is one threefold degenerate phonon branch for each wave vector $\mathbf{k}$. The frequency of a phonon of wave vector $\mathbf{k}$ is given by

$$\omega^2(\mathbf{k}) = \frac{2\beta}{M}(3-\cos\varphi_x-\cos\varphi_y-\cos\varphi_z)$$

where M is the atomic mass, $\varphi_x = k_x a$, $\varphi_y = k_y a$, and $\varphi_z = k_z a$. A convenient choice of unnormalized eigenvectors is the set

$$\mathbf{u}_i(\mathbf{l}) = \hat{n}_i \exp(i\mathbf{k}\cdot\mathbf{l})$$

where $\hat{n}_1 = \hat{x}$, $\hat{n}_2 = \hat{y}$ and $\hat{n}_3 = \hat{z}$. We will often omit degeneracy indices in the subsequent discussion.

Now consider the effect of two free surfaces formed between the layers with $l_z = 0$ and $l_z = 1$, by the method described in Section 2. If $V^{(S)}_{\alpha\beta}(\mathbf{l}\mathbf{l}')$ is an element of the perturbation matrix $\mathbf{V}_S$ defined in the last section, it is convenient to introduce the Fourier transformed quantity

$$V^{(S)}_{\alpha\beta}(\varphi_x\varphi_y;l_zl'_z)=\sum_{l'_xl'_y}V^{(S)}_{\alpha\beta}(\mathbf{ll'})\exp[i\varphi_x(l_x-l'_x)+i\varphi_y(l_y-l'_y)] \qquad (3.2)$$

since introduction of the free surfaces does not destroy the periodicity of the crystal in the x and y directions. For the Montroll–Potts model, one has the simple form

$$V^{(S)}_{\alpha\beta}(\varphi_x\varphi_y;l_zl'_z)=\delta_{\alpha\beta}\beta(\delta_{l_z0}\delta_{l'_z1}+\delta_{l_z1}\delta_{l'_z0}-\delta_{l_z0}\delta_{l'_z0}-\delta_{l_z1}\delta_{l'_z1}), \qquad (3.3)$$

where $\delta_{ll'}$ is the usual Kronecker symbol.

From the criteria in equations (2.7) and 2.8), for a given φ_x and φ_y one finds no surface modes (Rayleigh waves) in this model, however there does exist a band of resonant modes at the bottom of the bulk band, with $\varphi_z=0$[13]. For a more sophisticated model in which the force constants satisfied the conditions imposed by rotational invariance, one would necessarily find a Rayleigh wave mode[2]. However, it is interesting to note that in the Montroll–Potts model, one does obtain a T^2 term in the low temperature specific heat that is proportional to the surface area, with a coefficient comparable to that obtained by Maradudin and Wallis[9] in their study of a rotationally invariant model. In the Montroll–Potts model, the surface specific heat has been computed at all temperatures[13]. The results for the surface specific heat, and the entropy are given in Figs. 1 and 2.

We next compute the Green's function G^S, defined above in equation (2.5). When the appropriate matrix elements of equation (2.5) are taken between eigenvectors of the pure crystal $\mathbf{G}_S$ will depend on φ_x and φ_y; since translational symmetry in the x and y directions is unaffected, these quantities are good quantum numbers. Furthermore, for the Montroll–Potts model, $G^{(S)}_{\alpha\beta}$ $(\varphi_x\varphi_y;$ $l_zl'_z)$ will be diagonal in the cartesian indices α and β. Let us define

$$X=3-\cos\varphi_x-\cos\varphi_y;\quad E=\frac{M}{2\beta}\omega^2$$

and $\zeta=X-E$. The Green's function $\mathbf{G}_{0\beta}\mathbf{ll'}$ of the infinitely crystal may be written

$$\mathbf{G}^0_{\alpha\beta}(\mathbf{ll'})=\frac{\delta_{\alpha\beta}}{N_S}\sum_{l'_xl'_y}G^0(\varphi_x\varphi_y;l_z-l'_z)\exp[i(l_x-l'_x)\varphi_x+i(l_y-l'_y)\varphi_y]$$

where N_S is the number of atoms in a (100) layer. One has

$$G^0(\varphi_x\varphi_y;l_z)=\frac{M}{4\pi\beta}\int_{-\pi}^{+\pi}\mathrm{d}\varphi_z\frac{\cos(l_z\varphi_z)}{\cos(\varphi_z)-\zeta+i\epsilon}=\frac{M}{\beta}\frac{t^{1+|l_z|}}{t^2-1}$$

where

$$t=\begin{cases}\zeta-\sqrt{(\zeta^2-1)}, & \zeta<1\\ \zeta+i\sqrt{(1-\zeta^2)}, & -1<\zeta<+1\\ \zeta+\sqrt{(\zeta^2-1)}, & \zeta<-1.\end{cases} \qquad (3.4)$$

These three cases correspond to ω^2 below ($\zeta>1$), inside, and above ($\zeta<1$) the bulk band.

Then, by employing equation (2.5) and (3.3) one easily obtains the result $G^S_{\alpha\beta}=\delta_{\alpha\beta}G^S$, where

$$G^S(l_zl'_z)=G^0(l_z-l'_z)+\frac{\beta}{M}\times\frac{[G^0(l_z-1)-G^0(l_z)][G^0(l'_z)-G^0(l'_z-1)]}{1-\frac{2\beta}{M}[G_0(1)-G_0(0)]}. \qquad (3.5)$$

For convenience, we have surpressed explicit reference to the variables φ_x and φ_y. By using the expressions above for G^0, it is simple to show that

$$G^S(\varphi_x\varphi_y;l_zl'_z)\equiv 0$$

if l_z and l'_z lie on opposite sides of the bond-cutting plane $l_z=\frac{1}{2}a$. Thus, we can remove

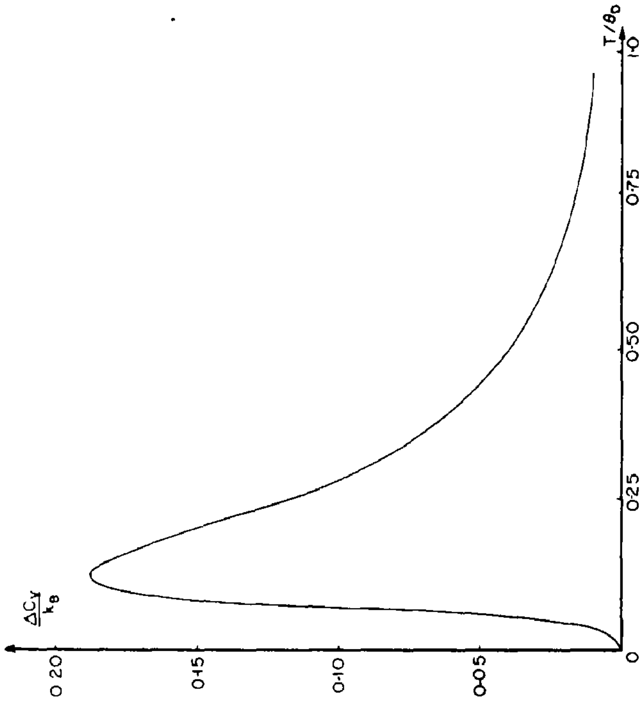

Fig. 1. The surface specific heat per surface atom for the Montroll–Potts model, plotted as a function of (T/θ_D), where θ_D is the bulk Debye temperature.

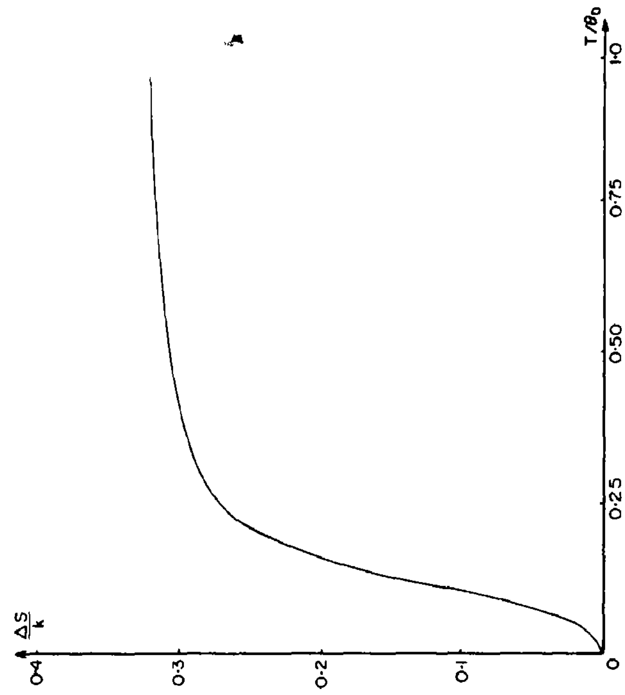

Fig. 2 The surface entropy/surface atom for the Montroll–Potts model, plotted as a function of (T/θ_D), where θ_D is the bulk Debye temperature.

one half of the crystal from the problem, since there are no matrix elements of G^S that couple the two halves. Thus, in the rest of the paper, we confine our attention to the case where both l_z and l_z' are greater than unity, i.e. both l_z and l_z' lie in the semi-infinite portion of the crystal in the upper half space. For both l_z and l_z' in this range, $\mathbf{G}^S$ reduces to the remarkably simple form

$$G^S(\varphi_x\varphi_y;l_zl_z') = G^0(\varphi_x\varphi_y;l_z-l_z') + G^0(\varphi_x\varphi_y;l_z+l_z'-1). \quad (3.6)$$

4. DYNAMICAL PROPERTIES OF THE ADSORBED LAYER IN THE MONTROLL-POTTS MODEL

In this section, we examine the influence of an adsorbed layer of atoms on the dynamical properties of the semi-infinite crystal described in the previous section. In a real crystal, one may expect the atomic force constants within the adsorbed layer to differ greatly from their values in the bulk, while the force constants that couple the adsorbed layer to the remainder of the crystal will also be greatly different. While it is in principle straightforward to include these effects in the formalism, we shall only examine in detail the case where the mass of the layer on the surface differs from the mass of the atoms in the bulk. Force constant changes will be ignored in the present work. Since it is well known that the stiffening of force constants will increase vibrational frequencies, while the converse is true if they are decreased, the effect of force constant softening near the surface may be expected to be qualitatively similar to an increase in mass in this region. The converse will hold if the force constants are stiffened.

There are two methods by which we may introduce an adsorbed layer in our model. First, we may begin with the semi-infinite crystal in the space $l_z > 0$ described at the end of the previous section. Suppose this crystal contains N atoms. Then we may add a layer of N_S atoms to the surface, in a layer which has the same atomic arrangement as a (100) plane in the bulk, but perhaps characterized by a different mass or different force constants. We may then compute the change in thermodynamic properties of the system of (N_S+N) atoms. Alternatively, we may begin with the semi-infinite crystal, then change the masses and force constants in the surface region, but retaining the same total number of atoms in the system. When one computes the thermodynamic properties of these two systems, one finds that the thermodynamic functions of the first system contain contributions from N_S additional bulk atoms. This is quite obvious physically, nonetheless we provide a check of this statement in the discussion in the Appendix.

We shall adopt the second of the two approaches described above, since the change in the Hamiltonian introduced by the creation of the adsorbed layer may be described by a perturbation $\mathbf{V}_A$ as described in Section 2 without the need for introducing new dynamical variables. As mentioned above, we suppose the adsorbed layer differs in mass from a bulk layer, but for simplicity we ignore changes in force constants and atomic arrangement. Note that from the discussion in the Appendix, one sees that the properties of our model are independent of the spacing between the adsorbed layer and the first plane of bulk atoms at $l_z = 1$.

If M is the mass of the bulk atoms, and M_S the mass of an adsorbed atom in the surface layer, let us define

$$\alpha = \frac{M_S - M}{M}.$$

From Section 2, it is seen that the information we require is contained in the quantity det $|\mathbf{I}-\mathbf{G}_S\mathbf{V}_A|$. From the results of the previous section, it is a straightforward matter to show

$$\det|\mathbf{I}-\mathbf{G}_S\mathbf{V}_A| = 1+2\alpha\frac{Et}{t-1} \quad (4.1)$$

where t is defined in equation (3.4). We can use this result to study the occurrence of surface modes and in band resonance modes in our model. Since as we mentioned earlier, the Montroll–Potts model is known to fail to give an adequate account of Rayleigh waves in the semi-infinite crystal, it is not clear that modes with the properties discussed below would occur in a more realistic model. Nonetheless, since the local modes and in-band resonances are averaged over in the computation of the thermodynamic properties, it will be useful to describe their properties.

(i) *Localized surface modes outside the bulk band*

For a given value of φ_x and φ_y, one obtains the frequency of the localized modes by examining the frequency at which the determinant in equation (4.1) vanishes. By rearranging this equation, and employing the definition of the variable t, one finds the condition for the occurrance of a localized mode is

$$(1+2\alpha E)[X-E\pm\sqrt{((X-E)^2-1)}]=1 \tag{4.2}$$

where the upper sign is employed for frequencies above the band, and the lower sign for frequencies below the band. Equation (4.2) may be rearranged to read

$$2\alpha(\alpha+1)E^2+(1+2\alpha-2\alpha X)E+1-X=0. \tag{4.3}$$

We have obtained equation (4.3) by moving the square root to the right hand side, then squaring the whole equation. This procedure can introduce spurious roots, so the solutions of equation (4.3) must be inserted back into equation (4.2) to determine which roots are spurious.

For a surface layer of light masses ($\alpha < 0$), we find a band of localized states with energy E_0 given by

$$E_0=\frac{2\alpha X-1-2\alpha-\sqrt{(4\alpha^2(X^2-1)+4\alpha(X-1)+1)}}{4\alpha(\alpha+1)}. \tag{4.4}$$

The localized surface modes exist only for the dimensionless frequency E_0 greater than $(-1/\alpha)$.

When $\alpha > 0$ (a heavy adsorbed layer), one obtains a localized mode below the bulk band, with the frequency given by

$$E_a=\frac{2\alpha X-2\alpha-1+\sqrt{(4\alpha^2(X^2-1)+4\alpha(X-1)+1)}}{4\alpha(\alpha+1)} \tag{4.5}$$

In Fig. 3, we show the position of the localized bands and their widths as a function of the mass change parameter α. Figures 5 and 6 illustrate the dispersion curves for special directions, for the two cases $M_S=2M$ and $M_S=(M/2)$.

Lengeler and Ludwig[14] have studied the localized modes occurring at a (001) plane of isotopic defects immersed in a bulk crystal. Their model differs from our model only by the fact that they employed different values for the force constant for motion perpendicular to the line joining two atoms, compared to motion parallel to the line between the atoms. We have examined this problem for our model, using the Green's function approach. We find the following expressions for the local mode frequencies associated with a (100) plane of isotopic defects immersed in the bulk of the crystal

$$E=\frac{X-\sqrt{1+\alpha^2(X^2-1)}}{1-\alpha^2};\quad \alpha>0$$

$$E=\frac{X+\sqrt{1+\alpha^2(X^2-1)}}{1-\alpha^2};\quad -1<\alpha<0.$$

Figure (1) shows these bands as a function of α. Upon comparing Figs. 3 and 4, it is apparent that the local mode frequencies associated with the impurity surface layer are lower than

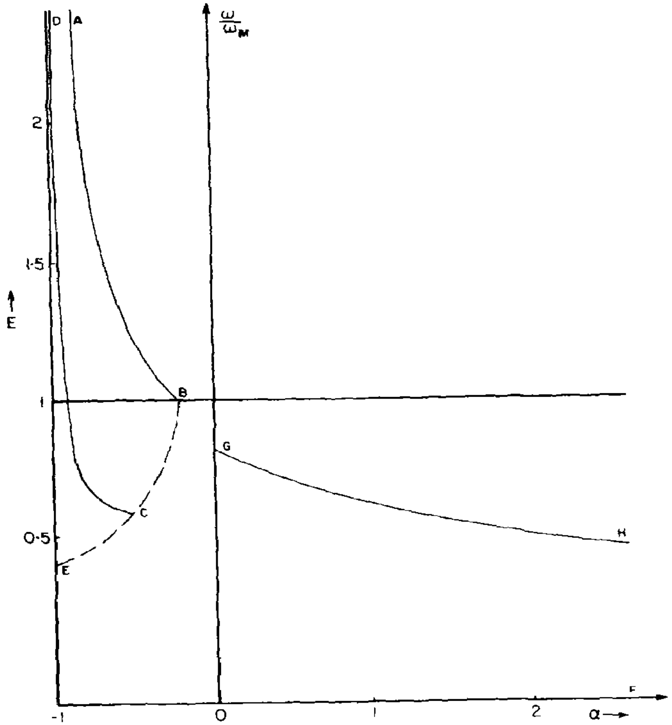

Fig 3 Frequencies of localized states associated with an adsorbed layer of mass defect atoms. The modes in the region *ABCD* lie above the bulk band, while those in the region *FOGH* lie below. The dashed line represents the resonant states at $E = -(1/\alpha)$

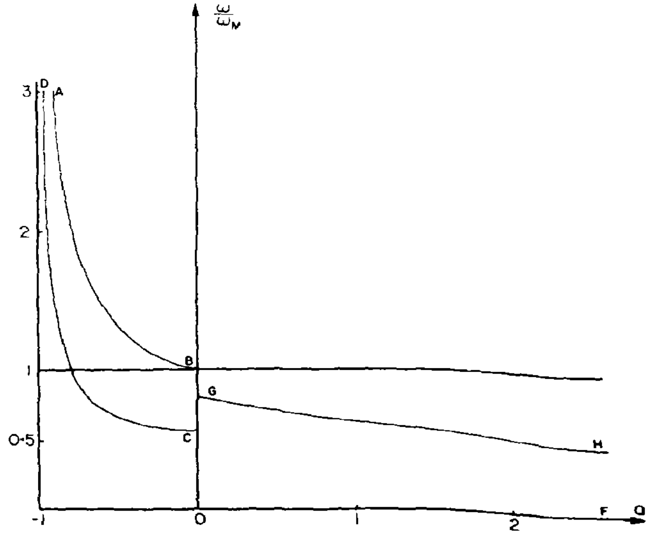

Fig. 4. Frequencies of localized modes associated with a (100) layer a isotopes immersed in a bulk crystal. The modes in region *ABCD* lie above the bulk band, while those in region *FOGH* lie below.

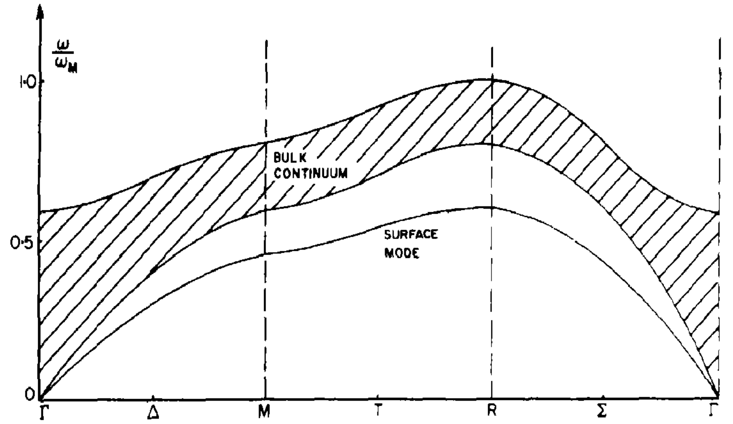

Fig. 5. Vibrational spectrum for a (100) adsorbed layer of heavy atoms of mass $M_S = 2M$. Figure 7 gives directions of propagation used on this figure.

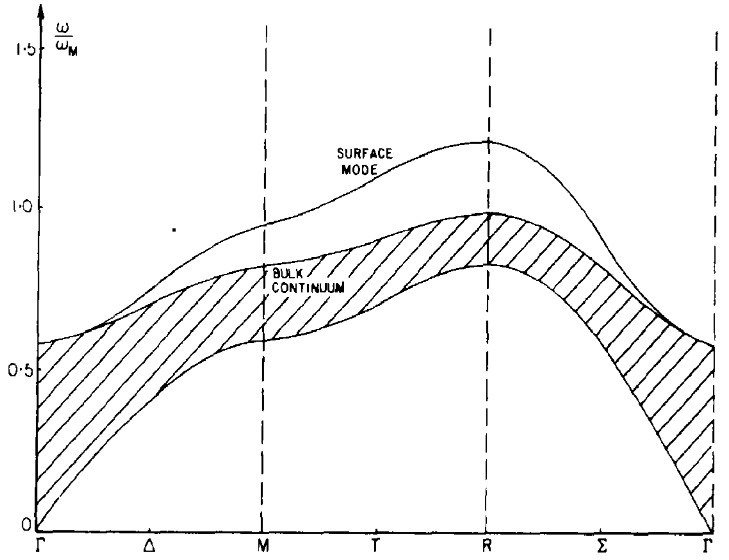

Fig. 6. Excitation spectrum for a (100) adsorbed layer of atoms of mass $M_S = (1/2)M$ on the crystal surface. Figure 7 gives the directions of propagation employed in this figure.

the local mode frequencies for the same layer immersed in the bulk. This is physically reasonable, since the atoms in the surface layer are coupled to fewer atoms than those in the bulk, so the frequency of the local modes must decrease when the layer is moved toward the surface. It is also interesting to note that for $\alpha < 0$ (light mass impurities), one has surface modes above the band only for certain ranges of propagation directions. This is true for the adsorbed surface layer, as well as the layer of isotopes immersed in the bulk.

We have also investigated the occurrence of surface modes above the band for light mass defect layers adsorbed on the f.c.c.

and b.c.c. 'Montroll–Potts crystal'. We find results that are very similar to the results described above.

(ii) *The occurrence of in-band resonance modes*

For values of E inside the bulk spectrum, for a given value of φ_x and φ_y, one finds

$$\det|\mathbf{I}-\mathbf{G}_S\mathbf{V}_1| = 1+\alpha E - i\alpha E\left(\frac{1+X-E}{1-X+E}\right)^{1/2}.$$

Recall that in terms of the variable E, the bulk spectrum lies in the range

$$X-1 \leq E \leq X+1.$$

X is a function of φ_x and φ_y, and ranges over the range 1–5. We can next form the expression for the phase shift $\eta_1(E)$, defined in equation (2.12). One has

$$\eta_1(E) = \tan^{-1}\left\{\frac{\alpha E}{1+\alpha E}\left(\frac{1+X-E}{1-X+E}\right)^{1/2}\right\}. \quad (4.6)$$

At the bottom of the band, where $E = X-1$,

$$\eta_1(E) = \frac{\pi}{2}\operatorname{sgn}(\alpha).$$

At the top of the band, where $E = X+1$,

$$\eta_1(E) = \begin{cases} 0 & \text{for } \alpha > (-1/E) \\ -\pi & \text{for } -1 < \alpha < (-1/E). \end{cases}$$

It is interesting that one may deduce the criterion for occurrence of localized modes by examining the difference between the phase shift at the top and bottom of the band. This point has been stressed by one of us in an earlier discussion[15].

From equation (2.6), one sees that an in-band resonance occurs (i.e. $\eta = \pi/2$) if

$$E = E_R = -(1/\alpha)$$

for $X-1 < E_R < X+1$. The conditions under which this resonance levels is a sharp, well-defined feature in the density of states may be explored by noting that the change in density of phonon modes associated with the presence of the adsorbed level is

$$\Delta n(E) = +\frac{3}{\pi}\frac{\mathrm{d}\eta_1}{\mathrm{d}E} = \frac{3}{\pi}\frac{\partial}{\partial E}\tan^{-1}\left(\frac{\mathscr{I}(E)}{R(E)}\right)$$

where $R(E) = \operatorname{Re}\det(\mathbf{I}-\mathbf{G}^S\mathbf{V}^S)$ and $\mathscr{I}(E) = \operatorname{Im}\det(\mathbf{I}-\mathbf{G}^S\mathbf{V}^S)$. For energies near the resonance energy E_R, $\Delta n(E)$ is given by the well known relation

$$\Delta n(E) \approx \frac{1}{\pi}\frac{\Gamma}{(E-E_R)^2+\Gamma^2}, \quad \text{with}$$

$$\Gamma = \mathscr{I}(E)/(\partial R/\partial E).$$

The resonance is well-defined when $|\Gamma/E_R| \ll 1$.

After some simple algebra, one finds

$$|\Gamma/E_R| = \left(\frac{\alpha(1+X)+1}{\alpha(1-X)-1}\right)^{1/2} = \left(\frac{[1+X]-E_R}{[1-X]+E_R}\right)^{1/2}.$$

The resonance level is sharp and well-defined if E_R is near the top of the band ($E_R \approx 1+X$). As E_R decreases, the resonance level becomes broad, and ceases to be a prominent feature in the change $\Delta n(E)$ in the density of states.

Notice that the phase shift $\eta_A(E)$ equals $(\pi/2)$ sgn (α) at the bottom of the band ($E = X-1$). If the energy is moved below $(X-1)$ the phase shift suffers a discontinuous jump to π if $\alpha > 0$ (and a local mode exists below the band), or to 0 if $\alpha < 0$. Thus, one finds the jump in $\eta_A(E)$ contributes a delta function singularity to the change in density of states.

5. THE VARIATION OF THE THERMODYNAMIC FUNCTIONS IN THE PRESENCE OF THE ADSORBED LAYER

In equation (4.6), we have found the variation of the phase shift for frequencies E inside the band of allowed frequencies. In addition, we have also found the frequencies of the various localized modes for the simple model described above. When this information is combined with the Lifschitz formula of equation (2.10), we have enough information to compute the various thermodynamic quantities.

Let us briefly recall the variation of $\eta_1(E)$ with the dimensionless frequency variable E. First suppose $\alpha > 0$ (heavy masses adsorbed on the surface). For $E <$ the frequency E_a of the bound state below the band, $\eta_A(E) = 0$. At $E = E_a$, $\eta_A(E)$ jumps discontinuously to the value $+\pi$, and remains at this value until $E = X-1$, the bottom of bulk band for the given φ_x and φ_y. Then η_A drops suddenly to the value $(\pi/2)$, since we saw from equation (2.6) that $\eta_1 \rightarrow +(\pi/2)$ for $E \rightarrow X-1$ from above. The phase shift drops from $\pi/2$ at $E = X-1$ to zero at $X+1$, the band maximum. $\eta_A(E) \equiv 0$ for all $E > X+1$.

For $\alpha < 0$, $\eta_A(E) \equiv 0$ for all $E < X-1$, since there are no surface modes below the bulk band in this case. At $E = X-1$, $\eta_1(E)$ jumps to the value $-\pi/2$. If there are no local modes above the band $\eta_{1(E)} \rightarrow 0$ for this φ_x and φ_y as $E \rightarrow X+1$. If there is a mode split off above the band, $\eta_A(E) \rightarrow -\pi$ at the top of the band, and jumps back to zero at the frequency E_0 of the bound state.

We begin by integrating the Lifschitz formula by parts, noting from the preceding discussion that $\eta_A(0) = \eta_A(\infty) = 0$. Then

$$\Delta F = \frac{1}{\pi}\int \mathrm{d}E f(E) \frac{\mathrm{d}\eta_A(E)}{\mathrm{d}E}.$$

Noting that the phase shift $\eta_1(E)$ is a function of φ_x and φ_y, and the three-fold degeneracy of the phonon branches in the Montroll-Potts model, the function to be inserted into this result is the form

$$\eta_A(E) = \frac{3N_S}{(2\pi)^2}\int \mathrm{d}\varphi_x \mathrm{d}\varphi_y \eta_A(\varphi_x \varphi_y, E)$$

where we have on the right side the function of equation (4.6), with the φ_x and φ_y dependence explicitly indicated. N_S is the number of atoms in the surface layer.

(i) *The low temperature region*, $T \ll \theta_D$

At low temperatures, the temperature dependent properties are dominated by the long wave length vibrations. One may expand the various quantities in a power series in φ_x and φ_y, for $\varphi_y \ll 1$. We define $\varphi^2 = \varphi_x^2 + \varphi_y^2$.

First consider the case $\alpha > 0$ (an adsorbed layer of heavy masses). From the discussions above, one finds a localized surface mode below the bulk band in this case. When φ_x, $\varphi_y \ll 1$, the frequency of this mode is

$$E_a \cong (X-1) - \tfrac{1}{2}\alpha\varphi^4 + \ldots$$

where the bottom of the band is given by

$$E_{\mathrm{min.}} = X - 1 \cong \tfrac{1}{2}\varphi^2 + \ldots .$$

Thus, for $\alpha > 0$, the frequency of the surface mode differs from that of a bulk mode propagating parallel to the surface only in the φ^4 terms. While this behavior is physically unrealistic, since as we pointed out before the theory of elasticity demands the existence of Rayleigh waves, we feel the present model will offer a crude feeling for the change in thermodynamic properties.

Then the surface mode contribution to $(\mathrm{d}\eta_A/\mathrm{d}E)$ is given by

$$\frac{\mathrm{d}\eta_A}{\mathrm{d}E} \cong 3\pi\delta(E_a) \cong 3\pi\delta(E - \tfrac{1}{2}\varphi^2)$$

where the φ^4 terms are neglected in the last statement. As we mentioned above, there is a delta function contribution to $(\mathrm{d}\eta_4/\mathrm{d}E)$ at the energy $E_{\mathrm{min.}}$, because of the jump in η_A at this point. For both $\alpha > 0$, and $\alpha < 0$ one has from this source

$$\frac{\mathrm{d}\eta_A}{\mathrm{d}E} = -\frac{3\pi}{2}\delta(E - \tfrac{1}{2}\varphi^2)$$

where again we ignore the φ^4 terms.

The contribution to the specific heat from these two terms is easily computed, using the results given above. It is easy to see that one gets a contribution

$$\Delta C_{v_0} = \frac{9}{2\pi} k_B \frac{M}{\beta} \operatorname{sgn}(\alpha) \zeta(3) \frac{(k_B T)^2}{\hbar^2} + \varphi(T^4).$$

Let us now compute the contribution to C_v from the change in density of states in the bulk region, $E > X-1$. For small values of E, and small values of φ, one has

$$\tan\eta \cong \frac{2^{1/2}\alpha E}{\sqrt{(E-\frac{1}{2}\varphi^2)}},$$

and the Lifschitz formula may be written in a form valid in the low temperature region:

$$\Delta F = \frac{3N_S}{(2\pi)^2} \int_0^\infty \mathrm{d}^2\varphi \int_{1/2\varphi^2}^\infty \mathrm{d}E f(E) \frac{\mathrm{d}\eta}{\mathrm{d}E}$$
$$= \frac{3N_S}{(2\pi)^2} \int_0^\infty \mathrm{d}E f(E) \int_0^{2E} \mathrm{d}^2\varphi \frac{\mathrm{d}\eta}{\mathrm{d}E}.$$

Upon introducing a new variable,

$$x^2 = E - \frac{\varphi^2}{2}$$

then integrating over x^2 rather than φ, and applying the result to the computation of the specific heat, we obtain a contribution

$$\Delta C_{v_1} = -\Delta C_{v_0} + \frac{6\pi^2}{5} \alpha \left(\frac{M}{\beta}\right)^{3/2} \frac{k_B^4 T^3}{\hbar^3} + \ldots.$$

The total change in specific heat that occurs because the surface layer has mass M_S rather than the bulk value M is then given by

$$\Delta C_v = N_S \frac{144}{5} \sqrt{3}\pi^2 \alpha k_B \left(\frac{T}{\theta_D}\right)^3 + \text{order of } T^4$$

where we have introduced a Debye temperature θ_D using the definition

$$k_B \theta_D = \hbar\omega_M = \hbar\left(\frac{12\beta}{m}\right)^{1/2}$$

where ω_M is the maximum bulk vibration frequency.

The result exhibited in equation (5.1) shows that altering the mass of the surface layer does not change the coefficient of the T^2 term found earlier[13]. We feel this is a reasonable result which would survive in a more sophisticated model, in which Rayleigh waves appear in the long wavelength limit. It seems reasonable that the presence of one single atomic layer of defects should not alter the propagation velocity of a Rayleigh wave, in the long wavelength limit. If this is so, one would be surprised if the coefficient of the T^2 term in the low temperature specific heat would change. Thus, while we have not computed the coefficient of the T^2 term in a more general and physically plausible model, we feel that the result exhibited in equation (5.1) is plausible, from an intuitive point of view.

Because the contribution to the surface specific heat from the adsorbed layer varies as T^3, and the contribution from the free surface itself is proportional to T^2, the effect of the adsorbed layer is the smaller by roughly a factor of (T/θ_D) at low temperatures. Thus, when $T \ll \theta_D$, it may be quite difficult to observe the contribution from the adsorbed layer. Also, it would be difficult to distinguish this term from a change in the Debye temperature.

(ii) *The change in thermodynamic properties for a general value of* T

We have computed the change in specific heat for general values of T by resorting to an electronic computer. One can perform the integrations over φ_x and φ_y by integrating over one eighth of the two dimensional Brillouin zone of Fig. 7. In this manner the integral $\int \mathrm{d}\varphi_x \mathrm{d}\varphi_y \eta_A(\varphi_x \varphi_y, E)$ may be evaluated for fixed E. One can then perform the remaining integration over the energy

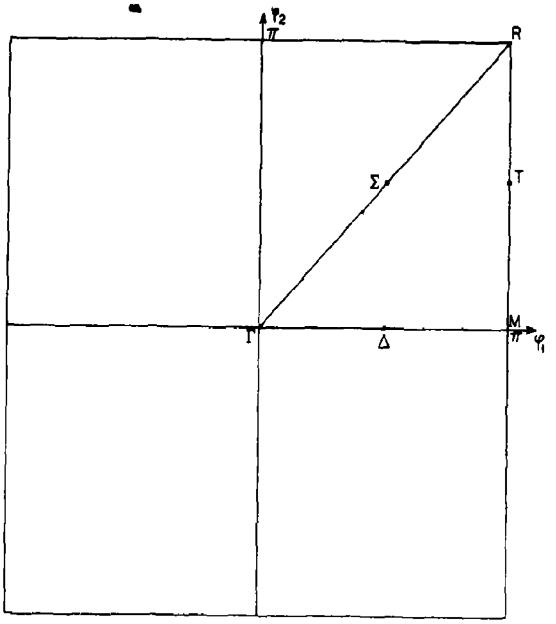

Fig. 7. Brillouin zone for surface problems associated with a (100) face of a simple cubic crystal.

variable numerically. The detailed computations follow closely the method employed in the work of Dobrzynski and Leman cited above[13]. As in the earlier work, β and M are chosen to represent the average elastic constants and masses of MgO. We have taken

$$\frac{\beta}{M} = 0{\cdot}125 \times 10^{28}\,(\text{c.p.s})^2.$$

The Debye temperature then assumes the value

$$\theta_D \cong 935°\text{K}.$$

The change in specific heat has been computed as a function of temperature for the two cases $M_S = M/2$ and $M_S = 2M$. The results are exhibited in Fig. 8. The result for the entropy variation ΔS is displayed in Fig. 9.

In Figs. 8 and 9, we show the change in thermodynamic quantities when the mass of the surface layer is *changed* from the bulk value M to $(\frac{1}{2})M$ or $2M$. If one wants the *total* change in S and C_v due to adsorption of a monolayer of atoms of mass M_S, one has to add to the values given in the figures the bulk value of S and C_v, per atom. The total effect of a free surface of atoms of mass M_S is then found by adding to this result the changes exhibited in Figs. 1 and 2.

The sign of the effects displayed in Figs. 8 and 9 may be understood by noting that decreasing the mass of the surface atoms raises all the vibrational frequencies. This has the effect of decreasing the specific heat, as seen in Fig. 8. So long as the total number of atoms remains fixed, when $T \gg \theta_D$, $\Delta C_v \to 0$, since the specific heat approaches the classical equipartition value. Thus, the general trend of the results in Figs. 8–9 may be understood intuitively.

It may be possible to observe the kind of changes in C_v and S reported here by experimental study of crystals on which light gases have been adsorbed.

sions employed in this section may be utilized to compute the high temperature forms of ΔS and ΔC_v in a straightforward manner for models which do not suffer from the difficulties of the Montroll–Potts model. As we stated earlier, we feel our results provide a rough estimate of these quantities. When more detailed experimental data is available, then computations with realistic models may provide useful information that will lead to a detailed understanding of the nature of the adsorbed layer.

REFERENCES

1. MONTROLL E. W. and POTTS R. B., *Phys. Rev.* **102**, 72 (1956).
2. LUDWIG W. and LENGELER B., *Solid State Commun.* 2, 83 (1964).
3. HORI J. and ASAKI T., *Prog. theor. Phys.* **31**, 49 (1964).
4. ASAKI T. and HORI J., In *Proc. Intl. Conf. Lattice Dynamics*, p. 571. Copenhagen (1963).
5. KAPLAN H., *Phys. Rev.* **125**, 1271 (1962).
6. DEGRAS D. A., *Nuovo Cim. N-2-Suppl.* **5**, 420 (1967).
7. DOBRZYNSKI LEONARD, In *Proc. Colloque de Physique des Surfaces dans les Gaz Raréfiés. Saclay, 1968*. To be published.
8. PLISKIN W. A. and EISCHENS R. P., *Z. phys. Chem.* **24**, 11 (1960).
9. MARADUDIN A. A. and WALLIS R. F., *Phys. Rev.* **148**, 945 (1966).
10. LIFSCHITZ E. M., *Nuovo Cim. Suppl.* **4**, 7716 (1956).
11. deWITT B. S., *Phys. Rev.* **103**, 1565 (1956).
12. TOULOUSE G., *Solid State Commun.* **4**, 593 (1966).
13. DOBRZYNSKI LEONARD and LEMAN G., *J. Phys.* To be published.
14. LENGELER B. and LUDWIG W., In *Proc. Intl. Conf. Lattice Dynamics*, p. 439. Copenhagen (1963).
15. MILLS D. L., *J. Phys.* Suppl. on No. 2, Vol. 28, p. C-1 (1967).
16. SALTER L., *Proc. R. Soc.* **233**, 418 (1956).
17. CYROT-LACKMANN F., *J. Phys. Chem. Solids* **29**, 1235 (1968).
18. DOBRZYNSKI LEONARD and FRIEDEL J., In *Surface Sci.* To be published.

APPENDIX

In the text of the paper, we considered a semi-infinite crystal of atoms of mass M. We then simulated a layer of adsorbed atoms by changing the mass of the atoms in the surface layer from M to $M_S \neq M$. The change in thermodynamic quantities was then computed.

In this Appendix, we consider a semi-infinite crystal of mass M. We then add a new layer of atoms of mass $M_S \neq M$. We shall see that the change in thermodynamic properties of this case is the same as that obtained in the text, except for the contribution of N_S bulk atoms, since there are N_S more atoms in the second case, compared to the first case. While this result is obvious from an intuitive point of view, it is interesting to see that the result follows in a straightforward way from the phase shift formulation.

We begin by considering the equations of motion for the atomic displacements. Since translational invariance with respect to the two directions parallel to the surface layer is not destroyed, we seek solutions proportional to $\exp(i\varphi_x l_x + i\varphi_y l_y)$, where the x and y axis lie in the surface. We denote the displacement of the atoms in the surface layer by w $\exp(il_x\varphi_x + il_y\varphi_y)$, and the displacement of a bulk atom by $u_{l_z} \exp(il_x\varphi_x + il_y\varphi_y)$, where $l_z = 1, 2, \ldots$ is an index of the atomic plane parallel to the surface in which the bulk atom lies.

For our model, in which atoms in the adsorbed layer differ only in mass from the bulk atoms, the equations of motion assume the form

$$[\omega^2 M_S - 2\beta(2-\cos\varphi_x - \cos\varphi_y)]w + \beta[u_1 - w] = 0 \tag{A.1}$$

$$\omega^2 M u_1 - \beta[(5 - 2\cos\varphi_x - 2\cos\varphi_y)u_1 - u_2] + \beta[w - u_1] = 0 \tag{A.2}$$

with the equations of motion of atoms in the plane $l_z \geq 2$ remain unperturbed by the adsorbed layer.

By employing equation (A.1), we can eliminate the variable w from equation (A.2), so equation (A.2) depends only on u_1 and u_2. By examining the resulting equation, one may construct the form of an effective perturbation V_A (recall the definition given in Section 2). Using the Green's of equation (3.6), one finds

$$\det|\mathbf{I} - \mathbf{V}_A\mathbf{G}^S| = \frac{-t - 2E(\alpha+1) + 2X - 1}{(t-1)[2(\alpha+1)E + 1 - 2X]} \tag{A.3}$$

where the variables t, E, α and X are defined in Section 4 of the text.

The phase shift $\eta_A^{(+)}$ associated with the perturbation from the added layer band may be found from equation (A.3) for frequencies inside the bulk band

$$\tan\eta_A^{(+)} = -\left(\frac{1+X-E}{1-X+E}\right)^{1/2} \frac{(\alpha+1)E - (X-1)}{(\alpha+1)E - X}. \tag{A.4}$$

For $\alpha = 0$ (the mass of the added layer is the same of that of the bulk atoms), we call the phase shift η_0. From equation (A.4), one may show that

$$\eta_A^{(+)} = \eta_0 + \eta_A \tag{A.5}$$

where η_A is the phase shift studied in the text, when the mass of the surface layer was changed.

Equation (A.5), when inserted into the computation of the thermodynamic quantities, provides a proof of the desired result.

J. Phys. Chem. Solids Pergamon Press 1969. Vol. 30, pp. 1059–1062. Printed in Great Britain.

CONDUCTION-ELECTRON SPIN RESONANCE IN ALKALINE-EARTH HEXABORIDES

L. W. RUPP Jr. and P. H. SCHMIDT
Bell Telephone Laboratories, Incorporated, Murray Hill, N.J. 07971, U.S.A.

(*Received* 30 *August* 1968; *in revised form* 4 *November* 1968)

Abstract – Conduction-electron spin resonance (CESR) has been observed in polycrystalline samples of *n*-type CaB_6, SrB_6 and in a single crystal plate of BaB_6. The CESR signals are observable over the temperature range from 1·4°K to room temperature and are characterized by temperature independent intensities, positive *g*-shifts and line widths on the order of a few gauss

RECENTLY there has been considerable interest in the alkaline-earth hexaboride system. Studies of these materials include several theoretical calculations of the band structure[1–3] as well as measurements of the Knight shift[4] and the Hall effect[5–7]. The Hall measurements indicate that the metal hexaborides (MB_6) are semiconducting in nature which is in agreement with the calculations of Longuet-Higgins and Roberts [2] and Yamazaki [3].

The crystal structure of the MB_6 compounds has been experimentally investigated by Kiessling[8] using X-ray analysis, and he finds the simple cubic structure shown in Fig. 1. The six boron atoms are arranged at the vertices of a regular octahedron. The octahedra, in turn, are bonded together forming a clathrate-like lattice of boron atoms with the metal atom M in the interstices. Thus the M sites have full cubic point symmetry while the boron sites have tetragonal symmetry.

We have observed magnetic resonance signals in the alkaline-earth hexaborides. The samples used in our experiments were prepared by heating the reactants (alkaline-earth granules and 100 mesh boron powder) to approximately 1850°C for 30 min in a partial pressure of argon gas (0·5 atm. at room temperature). The constituents were contained in spot welded tantalum tubes. The hexaborides samples contain less than 30 ppm metallic impurities in their final form. All samples were *n*-type as determined from thermal probe measurements. The structure and composition of all samples were confirmed by powder X-ray analysis to insure the presence of only the hexaboride phase. The small single BaB_6 crystals grew in the shape of rectangular prisms with typical dimensions of 0·50 × 0·25 × 0·10 mm. The CaB_6 and SrB_6 single crystals were nearly cubic in shape with typical dimensions of 0·01 and 0·07 mm respectively. A large crystal of BaB_6 (2·6 × 2·6 × 0·25 mm thick) was examined when samples of small crystallites failed to yield reliable resonance signals.

A small quantity (~ 50 mg) of these single crystals were placed between two layers of Parafilm to form a thin package ~6 × 12 mm in area. The samples were then placed inside a rectangular TE_{101} cavity resonant near either 12 or 18 GHz. The derivative of the surface resistance, dR/dH, was measured versus the applied magnetic field using a conventional homodyne spectrometer. The magnetic field was applied in the plane of the package and could be rotated to align the d.c. magnetic field either parallel or perpendicular to the linearly polarized microwave magnetic field in order to check the magnetic-dipole character of the observed absorptions.

Using the configuration described above,

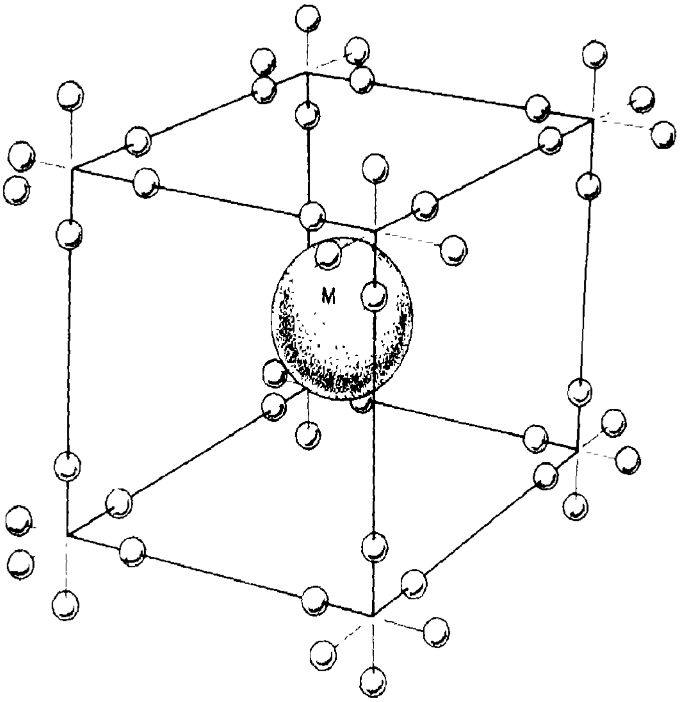

Fig. 1. Metal hexaboride crystal structure (M represents any of the alkaline-earth or rare-earth atoms)

single asymmetric magnetic dipole transitions were observed in both CaB_6 and SrB_6 multicrystalline samples and in a single crystal plate of BaB_6. The resonance linewidths were sufficiently narrow to permit precise g-value determinations: $g(CaB_6) = 2{\cdot}0034 \pm 0{\cdot}0002$, $g(SrB_6) = 2{\cdot}0076 \pm 0{\cdot}0005$ and $g(BaB_6) = 2{\cdot}0312 \pm 0{\cdot}0005$. The line centers H_0 which yielded the quoted g-values were defined after Feher and Kip[9], since the line shapes had Dysonian asymmetry due to spin diffusion[10].

The CaB_6 samples were investigated between room temperature and 4·2°K. The temperature dependence of the resonance is shown in Fig. 2. The principal basis for concluding that the observed resonance is due to the conduction electrons is that the line intensity proved independent of temperature. Such behavior is characteristic of temperature-independent Pauli paramagnetism of a degenerate conduction-electron gas.

The linewidth ΔH of the CESR signal in CaB_6 proved to be $\approx 1{\cdot}3$ G, which corresponds to a spin-lattice relaxation time $T_1 \lesssim 0{\cdot}8 \times 10^{-7}$ sec. The g-value $2{\cdot}0034 \pm 0{\cdot}0002$ was measured relative to that of a lithium metal reference[11]. The CaB_6 therefore displayed a positive temperature independent. g shift $(\delta g \equiv g - 2{\cdot}0023)$ of $+(11 \pm 1) \times 10^{-4}$. As the temperature was varied from 295 to 4·2°K the asymmetry ratio (ratio of maximum positive to maximum negative slope values) increased from $\sim 1{\cdot}3$ to $\sim 2{\cdot}5$. This is not surprising since the microwave skin depth is presumably decreasing with respect to the spin diffusion distance as the temperature is lowered.

Magnetic resonance was also investigated in several multicrystalline SrB_6 samples and the general behavior was similar to that of the CaB_6 resonance. In particular essentially temperature independent intensity was observed. A CESR linewidth of ~ 7 G $(T_1 \lesssim$

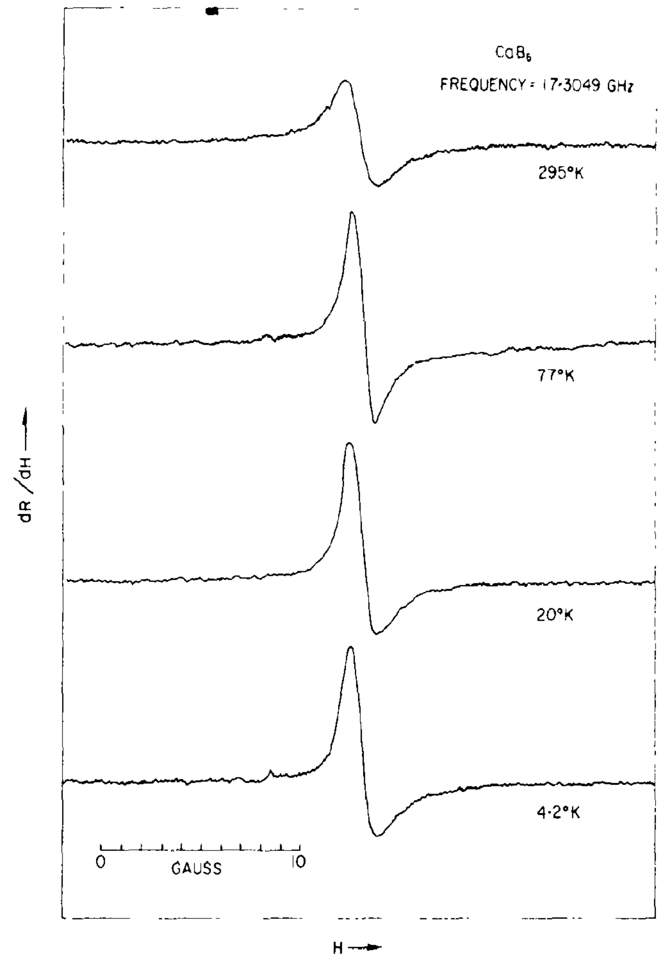

Fig. 2. Experimental traces of the conduction-electron spin resonance signal of CaB_6 crystals at various temperatures.

$0{\cdot}14 \times 10^{-7}$ sec) was observed and this material proved to have a positive g-shift of $+(53 \pm 2) \times 10^{-4}$.

Several multicrystalline BaB_6 samples were investigated, but failed to yield reproducible resonance signals. A large single crystal of BaB_6 was prepared and exhibited a positive g-shift of $+(289 \pm 2) \times 10^{-4}$. The CESR signal in BaB_6 was also temperature independent with a linewidth of $\sim 6{\cdot}2$ G($T_1 \lesssim 0{\cdot}16 \times 10^{-7}$ sec).

The progression of the g-shifts, as shown in Table 1, is qualitatively to be expected since the spin-orbit interaction λ should increase as some power of the atomic number of the alkaline-earth and $\delta_g \propto \lambda/\Delta E$ where ΔE is a characteristic energy band gap[12] which is, of course, unknown for these hexaborides.

On the same basis, however, one should

Table 1

Material	g	δg	ΔH
CaB_6	$2{\cdot}0034 \pm 0{\cdot}0002$	$+(11 \pm 1) \times 10^{-4}$	1·3 G
SrB_6	$2{\cdot}0076 \pm 0{\cdot}0005$	$+(53 \pm 2) \times 10^{-4}$	7 G
BaB_6	$2{\cdot}0312 \pm 0{\cdot}0005$	$+(289 \pm 2) \times 10^{-4}$	6·2 G

expect a similar monatonic increase in the resonance linewidths ΔH as the alkaline-earth changes from Ca through Ba, since there is a close relationship between the g-shift and the spin-lattice relaxation time T_1. Very crudely one expects

$$\Delta H \propto \frac{1}{T_1} \propto \frac{\delta_g^2}{\tau}$$

where τ is the momentum scattering lifetime due to lattice imperfections[12]. Since it is likely that $\tau \lesssim 10^{-14}$ sec at room temperature one could expect T_1 values $\lesssim 10^{-10}$ sec corresponding to line widths of ~ 1000 G. In practice we find $T_1 \gtrsim 10^{-8}$ sec. assuming the observed linewidths to be due to simple lifetime broadening. The lack of a simple progression of the observed linewidths suggests that they are in fact inhomogeneous due to strains and/or concentration gradients and that the true T_1 values are even longer than 10^{-8} secs. While clearly incompatible with the Elliott-Yafet theory this situation is not at all novel. Similar discrepancies exist for the case of CESR in In_2O_3[13] and in a number of other degenerate semiconductors investigated by Muller and Schneider[14]. Therefore, more theoretical effort is required in order to resolve an apparently quite general problem.

We are presently attempting to obtain large, single crystal specimens of CaB_6 and SrB_6 to determine if larger values of T may be obtained. Clearly a study of the isomorphic rare earths with the alkaline-earth hexaborides is indicated and is actively being pursued at this time.

Acknowledgements—The authors wish to thank Dr. W. M. Walsh, Jr and Dr. P S. Peercy for their constructive comments of this manuscript.

REFERENCES

1. FLODMARK S., *Ark. Fys.* **9**, 357 (1955).
2. LONGUET-HIGGINS H. C. and ROBERTS M. DE V., *Proc R. Soc* **A224**, 336 (1954)
3. YAMAZAKI M., *J. phys. Soc. Japan* **12**, 1 (1957).
4. MCNIFF E. J., Jr and SHAPIRO S., *J. Phys. Chem. Solids* **24**, 939 (1963).
5. EUBANK W. R., PRUITT L. E. and THURNAUER H., In *Boron: Synthesis, Structure, and Properties* (Edited by J. A. Kohn, W. F. Nye and G. K. Gaule), pp 116–127 Plenum Press, New York (1960).
6. JOHNSON R. W and DAANE A. H., *J. chem. Phys.* **38**, 425 (1963).
7. WALDEN R H., Private communication.
8. KIESSLING R., *Acta chem scand* **4**, 209 (1950)
9. FEHER G and KIP A F., *Phys. Rev.* **98**, 337 (1955).
10. DYSON F. J., *Phys. Rev* **98**, 349 (1955).
11. VANDERVAN N S., *Phys. Rev.* **168**, 787 (1968).
12. YAFET Y., In *Solid State Physics* (Edited by F Seitz and D. Turnbull), Vol 14, p. 1 Academic Press, New York (1963)
13. WALSH W. M., Jr., REMEIKA J P. and RUPP L. W., Jr., *Phys. Rev.* **152**, 223 (1966)
14. MULLER K. A and SCHNEIDER J., *Phys. Lett.* **4**, 288 (1963).

J. Phys. Chem. Solids Pergamon Press 1969. Vol. 30, pp. 1063–1070. Printed in Great Britain.

ELASTIC AND ANELASTIC BEHAVIOR OF SEVERAL DELTA-STABILIZED PLUTONIUM ALLOYS AT LOW TEMPERATURES

M. ROSEN and G. EREZ
Nuclear Research Center, Negev, Israel

and

S. SHTRIKMAN
Weizmann Institute of Science, Rehovot, Israel

(*Received* 4 *November* 1968)

Abstract– The temperature dependence of the elastic moduli, adiabatic compressibilities, Debye temperatures and ultrasonic wave attenuations of several delta-stabilized plutonium alloys (with aluminum and cerium) has been investigated in the range 4·2–300°K. The behavior of the elasticity and anelasticity of these alloys, similar to alpha plutonium, was found to be inconsistent with the antiferromagnetic model. The observed anomalies in the longitudinal wave attenuation in these alloys, support the possible existence of a cooperative electron transition in the vicinity of 65°K. It is shown that the cooperative effect, as manifested by the anomalies in the longitudinal wave attenuation, is due to the plutonium itself. Alloying additions serve as diluents and weaken the interaction which leads to the cooperative phenomenon. The behavior of both longitudinal and transverse wave attenuations at temperatures above 130°K indicates the possibility of operation of a thermally-activated interband electron transfer.

1. INTRODUCTION

THE BEHAVIOR of the elastic moduli and ultrasonic attenuations of the monoclinic α plutonium at low temperatures has been discussed in a recent paper[1]. It was shown that the temperature dependence of the elastic moduli in the region of the electrical resistivity anomaly[2] is at variance with that expected from an antiferromagnetic transition[3, 4], as required by the phenomenological theory of Landau-Lihshitz[5]. The elastic properties, being the second derivatives of the lattice potential with respect to strain are very sensitive to magnetic ordering phenomena and invariably exhibit anomalies in the adiabatic compressibility at the transition points[3, 4]. The antiferromagnetism hypothesis for plutonium, was deduced by analogy with the behavior of α manganese[6] and rare earth metals[7]. However, the elastic and anelastic behavior of plutonium at low temperatures[1] provides strong evidence against a magnetic transition. On the other hand, the existence of an anomaly in the ultrasonic attenuation was found to attributable to a cooperative electron transition at 66°K[1]. The occurrence of a sharp peak in the longitudinal wave attenuation accompanied by a normal temperature dependence of the transverse attenuation was found to be consistent with Pippard's theories[8, 9] for inter- and intraband transitions of electrons in a metal possessing a complex band structure. Relative changes in the bands due to a varying band population of electrons are expected to induce a cooperative phenomenon, manifested by a peak in the longitudinal attenuations.

Anomalies in the electrical resistivity, similar in character to that of α plutonium[2], were also observed in β plutonium[10] (body centered monoclinic), in several δ-stabilized (f.c.c.) plutonium alloys[11], and in monoclinic plutonium-neptunium alloys[12].

The objective of the present study was to experimentally verify the validity of the proposed cooperative electron transition for plutonium[1] by demonstrating its independence of the crystallographic structure (f.c.c. instead of monoclinic), and the chemical and magnetic character of the minority constituents. Aluminum and cerium alloying additions were selected, since both stabilize plutonium in the f.c.c. δ-phase[11], and cerium carries a magnetic moment, while aluminum does not. The experimental aim of this investigation was to determine the temperature dependence of the ultrasonic attenuations and elastic moduli with particular emphasis on the region from 4·2° to 100°K.

2. EXPERIMENTAL

The simultaneous determination of the longitudinal and transverse sound wave velocities and their respective attenuations were carried out by means of an ultrasonic pulse technique at a frequency of 10 MHz. Experimental details and the method of data processing has been described elsewhere[13]. Nevertheless mention will be made of several problems encountered in low temperature ultrasonic work with plutonium. The specimen holder assembly was on the inside of a cryogenic glovebox, containing a 'cold finger' which was immersed in a liquid helium cryostat. Since the ultrasonic transmitting and receiving components were on the outside of the glovebox, quite long coaxial cables had to be used, thus necessitating careful impedance matching. The ultrasonic couplant between the specimen disks and the piezoelectric transducers caused some difficulties, particularly for unalloyed α plutonium. A variety of adhesives and application procedures were tried out. The most satisfactory coupling was achieved with a low-viscosity (about 1000 cP) Dow Corning 200 Adhesive[14] applied as a very thin layer which solidified under pressure in a laboratory vice for the period of about 48 hr. In most cases such a bond withstood repeated low temperature runs. Measurements were generally performed during warming from 4·2 to 300°K at a rate of 0·5°K min^{-1}.

The δ-stabilized plutonium samples were prepared from plutonium metal loaned through the courtesy of the French A.E.C. The metal was electrorefined (to about 300 ppm impurities by weight) by the fused-salt method [15] and subsequently melted and cast *in vacuo* in an induction furnace together with an appropriate amount of high-purity aluminum (or cerium). Due to the small quantity of metal which was available the following procedure had to be adopted. First, two Pu–5*a*/o Al disks, 10 mm in dia. by about 6 mm thick, were prepared for the ultrasonic measurements. Then, these disks were remelted, together with additional aluminum, in order to obtain a richer aluminum alloy. The Pu–Ce alloys were prepared in a similar manner. Before machining, the cast cylinders were heat-treated at 720°K for about 50 hr [16]. Metallographic examination revealed a homogeneous structure.

The machined disks were hand-lapped to a parallelism of faces to within 2×10^{-3} mm. The thickness was measured to $\pm 5 \times 10^{-4}$ mm. Room temperature densities of these alloys were determined by means of a fluid displacement technique in a bath of monobromobenzene. The following average densities, to within ±0·01 g·cm^{-3}, were obtained for the alloys used in this study.

Alloys	Density (g·cm^{-3})
Pu–5*a*/oAl	15·50
Pu–11*a*/oAl	15·19
Pu–5*a*/oCe	15·26
Pu–10*a*/oCe	15·00

Temperature was measured by means of a calibrated helium-gas thermometer in the range 4·2–35°K. Copper-constantan thermocouples were used at higher temperatures. The estimated error in the temperature measurement is ±0·5°K.

The estimated experimental error in the

determination of the elastic moduli is 0·2 per cent. The relative point-to-point precision was better by a factor of 2. Temperature variation of the ultrasonic attenuation was measured to within 1 per cent.

3. RESULTS

Measurements of the longitudinal and transverse attenuations and sound wave velocities were carried out on two Pu–Al (5 and 11*a*/o) and two Pu–Ce (6 and 10*a*/o) alloys in the δ-stabilized f.c.c. phase. Noteworthy, as will be illustrated later is the qualitative similarity in the temperature dependence of the ultrasonic attenuations and Debye temperatures between these alloys with each other and with unalloyed α plutonium[1]. Plots of these properties are shown for Pu–5*a*/oAl (Figs. 1–3) and Pu–6*a*/oCe (Figs. 4–6).

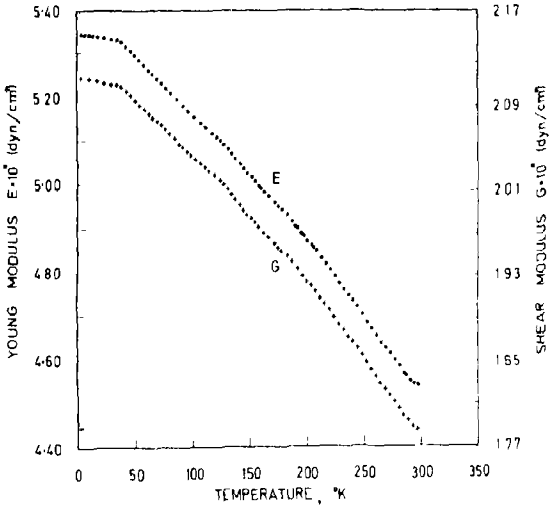

Fig. 1. Temperature dependence of the Young (E) and shear (G) moduli of Pu–5%Al alloy.

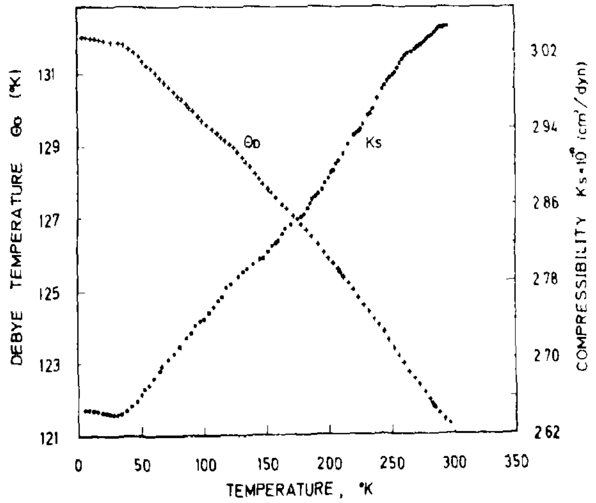

Fig. 2. Temperature dependence of the adiabatic compressibility (K_s) and Debye temperature (θ_D) of Pu–5%Al alloy

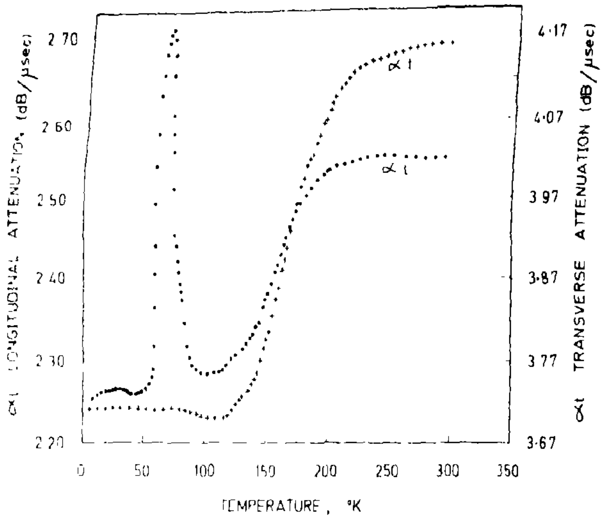

Fig. 3 Temperature dependence of the longitudinal (α_l) and transverse (α_t) attenuation of Pu-5%Al alloy

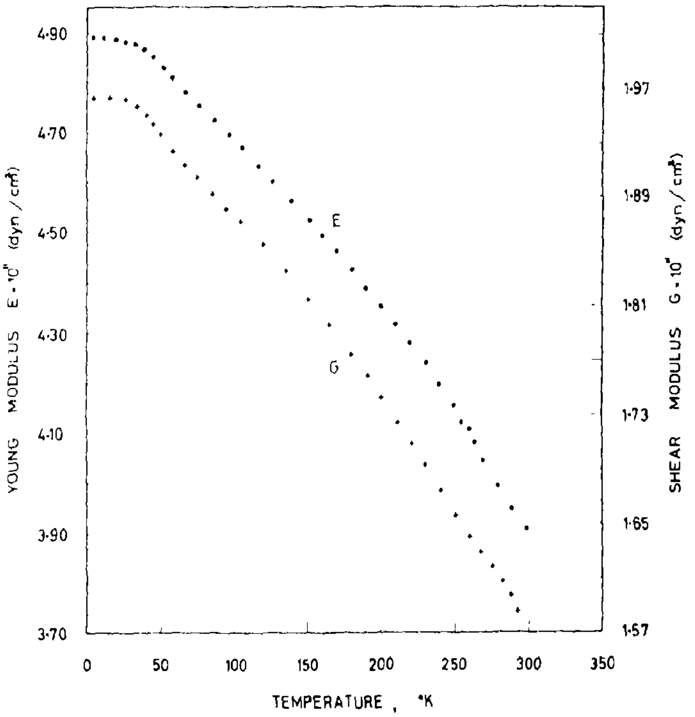

Fig. 4 Temperature dependence of the Young (E) and shear (G) moduli of Pu-6a/oCe alloy.

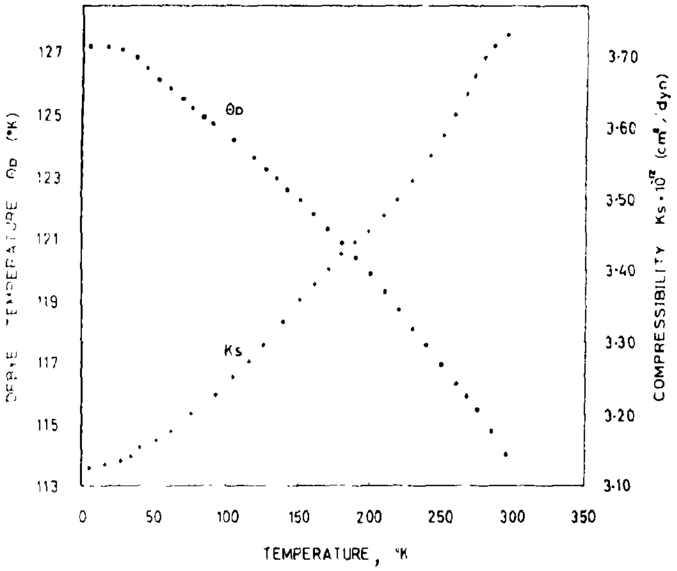

Fig 5. Temperature dependence of the adiabatic compressibility (K_s) and Debye temperature (θ_D) of Pu-6*a*/0Ce alloy

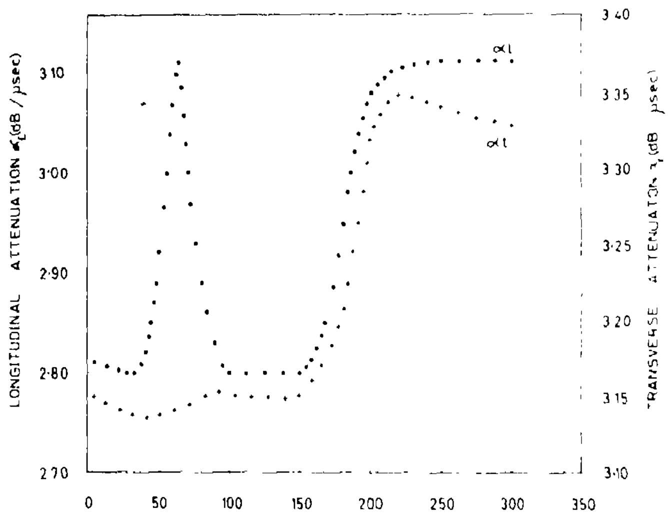

Fig. 6. Temperature dependence of the longitudinal (α_l) and transverse (α_t) attenuation of Pu-6*a*/0Ce alloy.

Similar to the behavior of α plutonium[1] the elastic moduli (E and G) of these alloys, the adiabatic compressibility (Ks) and Debye temperature (θ_D), as computed from the sound velocities do not reveal any anomalies in the temperature region of the electrical resistivity maximum[11]. In contrast, the temperature variation of the longitudinal wave attenuation (α_l) in Figs. 3 and 6, similar to the longitudinal attenuation in α plutonium[1], display sharp peaks in the neighborhood of 65°K. In this temperature range the attenuation of the transverse waves (α_t) is smooth, as was also observed in α plutonium. Both α_l and α_t in the Pu–Al and Pu–Ce alloys (Figs. 3 and 6) start increasing from about 130° up to 230°K, where they level off to their room temperature values.

The elastic moduli of the δ-stabilized alloys (Figs. 1 and 4) approach 0°K with zero slope, as required by the third law of thermodynamics[17]. Above 30°K the moduli assume a nearly linear temperature dependence up to the ambient. The effect of alloying additions on the elastic properties at 4·2 and 300°K, in the four alloys investigated is shown in Table 1.

Table 1. *Influence of alloying additions on the elastic properties of* Pu–Al *and* Pu–Ce *alloys*

Alloy	Temperature (°K)	$\Delta L/\Delta C$ (dyn·cm^{-2}/at.%)	$\Delta K_s/\Delta C$ (cm^2·dyn^{-1}/at.%)	$\Delta\theta_D/\Delta C$ (°K/at.%)
Pu–Al	4·2	$0{\cdot}09 \times 10^{11}$	$0{\cdot}03 \times 10^{-12}$	1·2
	300	$0{\cdot}08 \times 10^{11}$	$0{\cdot}04 \times 10^{-12}$	1·2
Pu–Ce	4·2	$0{\cdot}03 \times 10^{11}$	$0{\cdot}01 \times 10^{-12}$	0·75
	300	$0{\cdot}02 \times 10^{11}$	$0{\cdot}01 \times 10^{-12}$	0·75

4. DISCUSSION

The experimental results of this study show that the temperature dependence of the ultrasonic attenuations and the elastic moduli of the δ-stabilized alloys (Figs. 1–6) depict almost exactly the behavior of these properties in α plutonium[1]. The absence of any anomalies in the elastic moduli agrees with the results of magnetic susceptibility[18], neutron diffraction[19] and specific heat[20] measurements on δ-stabilized plutonium alloys. Furthermore, the Landau *et al.* criteria[5, 21] for a magnetic transition in the δ-stabilized alloys are not fulfilled, indicating that the antiferromagnetic model[2, 22, 23] for these alloys is not adequate.

The results of the present investigation show that the longitudinal wave attenuations (α_l) develop well-defined peaks in the vicinity of 65°K, Figs. 3 and 6. In this temperature region, the transverse attenuations (α_t) vary smoothly. The integrated areas under the longitudinal attenuation anomalies ($S = \oint d\alpha_l \cdot dT$), is shown in Fig. 7. Noteworthy is the fact that S of the four alloys investigated fall on a straight line which crosses the ordinate (100%Pu) at the value of S for unalloyed α plutonium[1]. Extrapolation of this line to $S = 0$, i.e. to the composition of a plutonium alloy in which the attenuation anomaly would vanish, hits the abscissa at 77·5%Pu. Figure 7 also indicates that the amount rather than the physico-chemical properties of the δ-stabilizing addition is of importance. The similarity in the behavior of the longitudinal wave attenuations (α_l) points towards the operation of one common mechanism which is responsible for the anomalies in both α and δ plutonium. The occurrance of these anomalies in the longitudinal attenuation only, whereas the transverse one remains unaffected, is in accord with Pippard's requirements[8,9] for inter- or intraband electron transitions. A quantitative description of this mechanism must await the knowledge of the Fermi surface and the band structure of plutonium. Recent attempts to determine the band structure of plutonium have not proven to be successful[24]. However, the occurrence of a maximum in the temperature dependence of the thermoelectric power[25] in the region of the anomalies in α_l, appears to qualitatively support the electron transition mechanism.

The anomalies in the longitudinal attenuations in α and δ plutonium can be attributed

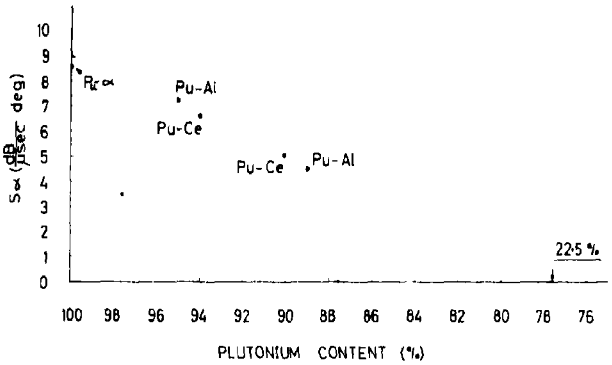

Fig 7. Variation of the integrated area S below the longitudinal attenuation anomaly as a function of the Pu content (in at. %) in α plutonium and several δ-stabilized Pu–Al and Pu–Ce alloys

to the existence of a *cooperative electron transition*, rather than to a temperature dependent thermally assisted transfer of electrons. Figure 7 suggests that the extent of the cooperative effect is dependent on the concentration of plutonium atoms in the lattice. The crystallographic environment (whether monoclinic or cubic) and the magnetic properties of the alloying addition (cerium with, and aluminum without a magnetic moment) do not exert any detectable influence. Apparently, the bands responsible for the cooperative transition are derived from energy levels of the plutonium atom itself. The cooperative effect, manifested by peaks in the longitudinal attenuation is due to changes in the band structure which in turn depend on changes in the electron population. At the temperature of the peak in α_l, at about 65°K, the band overlap should be maximal. Aluminum and cerium additions act as 'diluents' only, thus decreasing the strength of interaction between the plutonium atoms, and consequently diminishing the cooperative effect. Figure 7 shows that addition of more than 22 per cent of foreign atoms, in solid solution will completely destroy the interaction. The anomaly in the longitudinal attenuation (and therefore the cooperative phenomenon) will vanish.

Above 130°K, both longitudinal (α_l) and transverse (α_t) attenuations, increase. A similar behavior was observed in α plutonium [1]. The rise in the attenuations occurs in the temperature range where the electrical resistivities display negative slopes[2, 11]. A gradual, thermally-assisted transfer of electrons from the narrow $5f$ bands to the conduction bands[26, 27] may be responsible for the decrease in the electrical resistivity with increasing temperature. Well-established theories of ultrasonic attenuations[28, 29] show that both attenuations α_l and α_t are expected to be proportional to the electrical conductivity. This is in agreement with the observations in the plutonium alloys (Figs. 3 and 6). However, the leveling off of the attenuations at temperatures above 230°K should be elucidated.

Table 1 illustrates the effect of the alloying additions on the elastic properties at 4·2 and 300°K. The relative influence of aluminum appears to be stronger than that of cerium. A similar behavior was observed in the residual electrical resistivity, at absolute zero, in Pu–Al and Pu–Ce alloys[30]. One possible reason is the larger change in the electron-atom ratio in the Pu–Al alloys. The metallic valence of Pu(~ 4) is closer to Ce(3·6) than to Al(3)[31]. Furthermore, localized strains in the lattice should affect the elastic moduli. The difference between the metallic radii of δ plutonium and that of aluminum is −13% compared with +4% for the cerium atom[31].

Thus, the aluminum atom will increase the elastic energy of the lattice, thereby raising the absolute values of the elastic moduli.

Acknowledgements—The authors would like to extend their gratitude to the French A.E.C. for providing the plutonium metal. One of us (M.R.) wishes to acknowledge the benefit of stimulating discussions and correspondence with Professors J. Friedel (Orsay, Paris), A. B. Pippard (Cambridge) and R. B. Coles (Imperial College, London)

REFERENCES

1. ROSEN M., EREZ G. and SHTRIKMAN S., *Phys. Rev. Lett.* **21**, 430 (1968)
2. SANDENAW T. A. and GIBNEY R. B., *J. Phys. Chem. Solids* **6**, 81 (1958).
3. ROSEN M., *Phys. Rev.* **165**, 357 (1968)
4. ROSEN M., *Phys. Rev.* **166**, 561 (1968)
5. LANDAU L. D. and LIFSHITZ E. M., *Statistical Physics* Pergamon Press, Oxford (1958)
6. LEE J. A., MEADEN G. T. and MENDELSSON M., *Cryogenics* **1**, 52 (1960)
7. BRODSKY M. B., *Phys. Rev.* **163**, 484 (1967).
8. PIPPARD A. B., *Phil. Mag.* **46**, 104 (1955)
9. PIPPARD A. B., *Low Temperature Physics* (Edited by C. de Witt, B. Dreyfus and P. GP. de Gennes), p. 3. Gordon and Breach, New York (1962)
10. KING E. and LEE J. A., *Cryogenics* **3**, 177 (1963)
11. LEE J. A., HALL R. O. A., KING E. and MEADEN G. T., *Plutonium 1960* (Edited by E. Grison, W. B. H. Lord and R. D. Fowler), p. 39. Cleaver-Hume, London (1961)
12. OLSEN C. E. and ELLIOTT R. O., *Phys. Rev.* **139**, A437 (1965)
13. ROSEN M., *Phys. Rev.* **174**, 504 (1968)
14. Dow Corning Co., Inc., Midland, Michigan, USA.
15. BLUMENTHAL B. and BRODSKY M. B., *Plutonium 1960* (Edited by E. Grison, W. B. H. Lord and R. D. Fowler), p. 171. Cleaver-Hume, London (1961).
16. WILKINSON W. D., *Physical Metallurgy of Plutonium*, Interscience, New York (1960).
17. HUNTINGTON H. B., *Solid State Physics* (Edited by F. Seitz and D. Turnbull), Vol. 7, p. 213. Academic Press, New York (1958).
18. LUNSFORD J. L. and KMETKO E. A., *Plutonium 1965* (Edited by A. E. Kay and M. B. Waldron), p. 214. Chapman and Hall, London (1967).
19. ROOF R. B., Los Alamos Scientific Laboratory Rep., No. LA-2912. Unpublished (1963)
20. SANDENAW T. A., *J. Phys. Chem. Solids* **23**, 1241 (1962).
21. LANDAU L. D. and KHALATNIKOV J. M., *Dokl. Akad. Nauk SSSR* **96**, 469 (1954).
22. ROCHER Y. A. and FRIEDEL J., *J. Phys. Chem. Solids* **18**, 196 (1961).
23. ROCHER Y. A., *Adv. Phys.* **11**, 233 (1962)
24. KMETKO E. A. and WABER J. T., *Plutonium 1965* (Edited by A. E. Kay and M. B. Waldron), p. 244. Chapman and Hall, London (1967).
25. MEADON G. T., *Proc. R. Soc.* **A276**, 553 (1963).
26. ZACHARIASEN W. H., *The Metal Plutonium* (Edited by A. S. Coffinberry and W. N. Miner), p. 99 University of Chicago Press, Chicago (1961).
27. SMOLUCHOWSKI R., *Phys. Rev.* **125**, 1577 (1962)
28. MASON W. P., *Phys. Rev.* **97**, 557 (1955).
29. KITTEL C., *Quantum Theory of Solids*, p. 326. Wiley, New York (1963)
30. ELLIOTT R. O., OLSEN C. E. and LOUIE J., *J. Phys. Chem. Solids* **23**, 1029 (1962)
31. GSCHNEIDNER K., *Rare Earth Alloys* Van Nostrand, Princeton, N.J. (1961).

J. Phys. Chem. Solids Pergamon Press 1969. Vol. 30, pp. 1071-1076. Printed in Great Britain.

ANISOTROPIC ELECTRICAL BEHAVIOR OF THE BLUE POTASSIUM MOLYBDENUM BRONZE, $K_{0\cdot30}MoO_3$*

D. S. PERLOFF, M. VLASSE and A. WOLD

Departments of Physics and Chemistry and Division of Engineering, Brown University, Providence, R.I. 02912, U.S.A.

(*Received* 23 *September* 1968; *in revised form* 1 *November* 1968)

Abstract—Cleavable platelets of the blue potassium molybdenum bronze, $K_{0\cdot30}MoO_3$, were prepared by the electrolysis of mixtures of potassium molybdate and molybdenum (VI) oxide. X-ray diffraction studies were performed in order to relate the morphological habit of these crystals to the actual crystal structure. Results of the X-ray study and considerations of crystal structure motivated an investigation of the electrical resistivity along certain significant crystallographic directions. An anisotropy in the electrical resistivity of approximately 1-1/2-2 orders of magnitude was observed throughout the temperature range 80°-340°K. In addition, a change from semiconducting to metallic behavior, which occurs at approximately 180°K, was also sensitive to sample orientation.

INTRODUCTION

THE CRYSTAL structures of the red and blue potassium molybdenum bronzes, K_xMoO_3, have been determined by Stephenson and Wadsley[1] and Graham and Wadsley[2] on single crystals prepared by the electrolysis of mixtures of potassium molybdate and molybdenum (VI) oxide[3]. These bronzes were assigned to the monoclinic system, space group C2/m, and were shown to be layer structures in which potassium ions are responsible for bonding infinite two-dimensional layers of distorted molybdenum-oxygen (Mo–O) octahedra. Wold, Kunnmann, Arnott and Ferretti[3] and Bouchard, Perlstein and Sienko[4] have studied the electrical properties of unoriented samples of the red and blue bronzes. The red bronze was found to be semiconducting; the blue bronze exhibited a change from semiconducting to metallic behavior above approximately 175°K. Bouchard *et al.*[4] and Morris and Wold[5] have found that the magnetic susceptibilities of powders are weak and nearly temperature-independent over a wide range of temperature.

In this study, the electrolytic technique of Perloff and Wold[6] was used to prepare thin cleavage platelets of the blue potassium molybdenum bronze. Careful control of the conditions of growth prevented admixture of the red phase with the blue. X-ray diffraction studies showed that the orientation of the growth-cleavage face can be directly related to the manner in which the Mo–O layers are stacked to form the layer structure. A comparison of the ionic interactions within the Mo–O layer of the blue potassium molybdenum bronze with ionic interactions in certain transition metal oxides suggested the existence of a significant anisotropy in the electrical resistivity. An investigation of this possibility is the basis for the current study of electrical properties.

STRUCTURAL CONSIDERATIONS

The blue potassium molybdenum bronze has been shown to crystallize in the monoclinic system, space group C2/m[2]. This bronze has the ideal crystallographic formula $K_{0\cdot30}MoO_3$ when all available K sites are occupied. The structure, which consists of infinite two-dimensional layers of distorted

---

*This research has been supported by A.R.P.A. and Grant No. N.S.F. GP-6824

Mo–O octahedra, is represented in Fig. 1. Adjacent Mo–O layers are bonded through K ions which occupy interlayer interstices formed by O ions. A cell of sides *a* and 2*c* is shown in Fig. 2 which is a projection of the structure on the (010) plane. The [102] direction corresponds to the minor diagonal of this cell and the *b*-axis is perpendicular to the plane of the figure. The plane defined by the [010] direction (*b*-axis) and the [102] direction can be associated with the stacking of the Mo–O layers. The X-ray diffraction studies carried out in this investigation demonstrate that these crystals cleave by the separation of adjacent Mo–O layers. A detailed consideration of the structure of the Mo–O layer is thus a prerequisite to orienting crystals for electrical measurements.

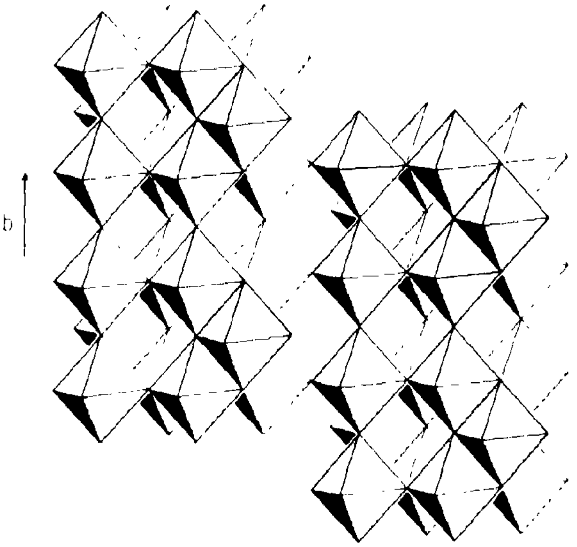

Fig. 1. A portion of the infinite two-dimensional molybdenum-oxygen layer of the blue potassium molybdenum bronze, $K_{0.30}MoO_3$, showing its orientation with respect to the monoclinic *b*-axis or [010] direction. Four clusters, consisting of ten idealized Mo–O octahedra, are represented.

Stephenson and Wadsley[1] and Graham and Wadsley[2] describe the Mo–O layer in terms of subunits or clusters of ten distorted Mo–O octahedra. These clusters share octahedral corners along the monoclinic *b*-axis and also perpendicular to this direction, thereby forming the infinite two-dimensional Mo–O layer. Moreover, these clusters are highly important in conferring electrical and magnetic[4] properties upon the potassium molybdenum bronzes. In particular, the electrical properties must be described in terms of ionic interactions which extend throughout the crystal and are responsible for the formation of energy bands. These interactions, however, differ significantly from one direction to another because of the manner in which the clusters are bonded to each other.

Goodenough[7, 8] has rationalized the electrical behavior of certain transition metal oxides having large cation–cation separations by employing one-electron energy-band diagrams in which cation–anion–cation interactions are responsible for the formation of π-bands. Transition metal oxides such as ReO_3 and the tungsten bronzes Na_xWO_3 (cubic) and In_xWO_3[9] (hexagonal) exhibit isotropic metallic conductivity which is accounted for by this concept. The potassium molybdenum bronzes, K_xMoO_3, are also

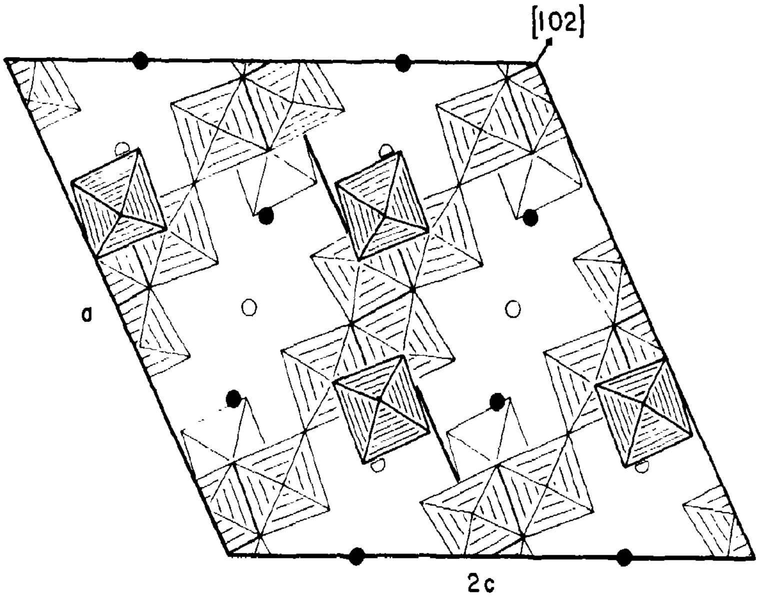

Fig. 2. A projection of the blue potassium molybdenum bronze structure on the (010) plane showing a cell of dimensions a and $2c$. The [102] direction is parallel to the minor diagonal of this cell. Solid and open circles represent inter-layer potassium ions at different levels of the unit cell

amenable to this type of description, since continuous short cation–cation separations are not available for the formation of energy bands. It is clear that the role of the anion in these structures must be carefully considered.

Parallel to the monoclinic b-axis of the blue potassium molybdenum bronze, infinite chains of corner-sharing distorted Mo–O octahedra extend throughout the Mo–O layer, as shown in Fig. 1. Thus continuous chains of cation–anion–cation interactions are available for forming π-bands. Perpendicular to the b-axis, in the [102] direction shown in Fig. 2, a geometrically complex set of ionic interactions is responsible for band-formation. Cation–cation interactions are present within clusters but cation–anion–cation interactions connect adjoining clusters. Geometrical considerations alone, therefore, would lead one to anticipate a significant difference in the electrical resistivity for the two directions under consideration.

EXPERIMENTAL

Preparation

Large blue potassium molybdenum bronze crystals (~ 8 × 4 × 1 mm) were grown by the electrolysis of potassium molybdate–molybdenum (VI) oxide mixtures under carefully controlled conditions. The growth cell consisted of recrystallized aluminum oxide crucibles nested to form a double-cell in which cathode and anode compartments are separated by a permeable wall. The cell geometry and electrode-thermocouple configuration are described elsewhere[6].

Shattuck Chemical Co. reagent grade potassium molybdate was fused for 2 hr at 850°C in a Coors porcelain crucible and then ground. Fisher Scientific Co. reagent grade molybdic anhydride was mixed in the desired molar proportions with potassium molybdate, fused for two hours at 650°C in a platinum crucible, and then ground to a fine powder.

Electrolysis was conducted for a period of three days at a regulated current of 20 mA. The blue bronze crystals were prepared under the conditions used by Wold *et al.*[3] 3·35 MoO_3 : 1·00 K_2MoO_4 at a melt temperature of 550°C.

X-ray study

X-ray diffraction studies were carried out by means of a Burger precession camera using molybdenum radiation ($\lambda(MoK\alpha) = 0{\cdot}7106$ Å). A large representative single crystal with a well-developed cleavage face and a secondary cleavage edge was chosen for the study. The crystal was mounted about the cleavage edge which was subsequently identified as the [010] direction. All other pertinent crystallographic directions were determined by rotation about this direction. The results indicate that the cleavage face corresponds to the $(20\bar{1})$ plane which includes the *b*-axis and the [102] direction. In addition, cell parameters were determined which compare favorably to those of Graham and Wadsley[2]: $a = 18{\cdot}249 \pm 0{\cdot}009$ Å, $b = 7{\cdot}559 \pm 0{\cdot}005$ Å, $c = 9{\cdot}862 \pm 0{\cdot}006$ Å and $\beta = 117°30' \pm 5'$.

An X-ray diffraction investigation was carried out on finely divided powder in order to study the possibility of a crystallographic transition. A Norelco powder diffractometer with monochromatic radiation (AMR-202 focussing monochromator) and a copper source ($\lambda(CuK\alpha_1) = 1{\cdot}5405$ Å) was employed. Liquid nitrogen and room temperature X-ray diffraction patterns exhibited no significant differences in the positions or intensities of the diffraction peaks.

Electrical measurements

Crystals of the blue potassium molybdenum bronze were cut in the shape of rectangular slabs by using a 0·011 in. thick circular diamond blade in conjunction with a Micromech Mfg. Corp. Precision Wafering Machine. The morphology of the crystals permitted orientation with respect to the [010] direction or *b*-axis. Specimens were cut parallel to the monoclinic *b*-axis which were of the approximate dimensions 1·0 mm along the [102] direction, 5·0 mm along the [010] direction, and 0·2 mm along the stacking direction of the Mo–O layers. Specimens were also cut perpendicular to the *b*-axis which were approximately 1·0 mm along the [010] direction, 3·0 mm along the [102] direction, and 0·1 mm along the stacking direction of the layers.

D.C. resistivity measurements were carried out using a conventional four-probe technique. Current was supplied by a Princeton Applied Research Model TC-100.2AR Voltage/Current Source; voltage was monitored with a Keithley 149 Milli-Microvoltmeter. Ohmic contact was verified by checking that the IR/I ratio was constant over a wide range of currents and that this ratio was independent of the polarity of the current source. Contacts to the crystals were of pure indium applied ultrasonically by means of a specially adapted Sonobond Corp. Model S-O-HN-56-4 ultrasonic soldering unit. In all cases, data points were taken with the sample at thermal equilibrium during both a cooling and heating cycle.

RESULTS AND DISCUSSION

The results of resistivity measurements carried out over the temperature range 80°–340°K are provided in Fig. 3 which is a plot of $\log \rho$ vs. $1000/T$ for samples oriented along the [010] and [102] directions. Samples 20*A* and 20*B* were cut from the same crystal and give results so similar that no distinction has been made between data points in Fig. 3. Samples 1*A* and 2*A* were cut from different crystals; data for these specimens suggest that the absolute value of resistivity varies from specimen to specimen. It is clear from Fig. 3 that the difference in resistivity for the two crystallographic directions studied is approximately 1–1/2–2 orders of magnitude over the entire temperature range. These results confirm the ideas proposed above concerning the dependence of the electrical properties of the blue potassium molybdenum

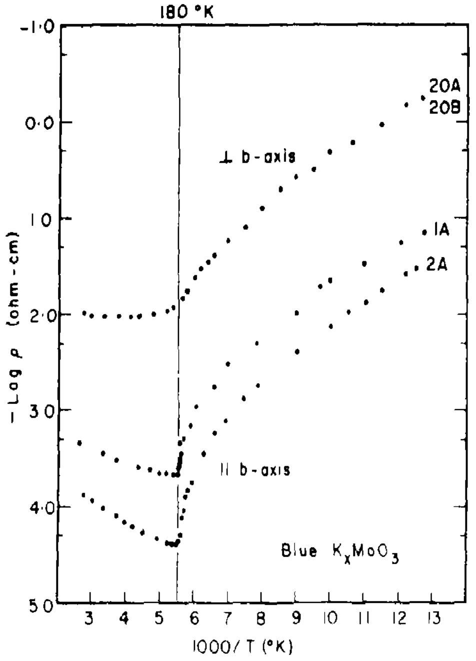

Fig. 3 Plot of log ρ vs. $100/T$ for representative samples of the blue potassium molybdenum bronze oriented parallel to the monoclinic *b*-axis, along the [010] direction, and perpendicular to the *b*-axis, along the [102] direction At 180°K a transition from semiconducting to metallic behavior occurs which is not related to an apparent structural change.

bronze on the geometrical structure of the infinite two-dimensional Mo–O layers.

The data supplied in Fig. 3 are in general agreement with those of Bouchard *et al.*[4] for unoriented samples of the blue bronze to the extent that a marked change in electrical behavior is observed at approximately 180°K. The data presented here suggest that this change corresponds to a transition from semiconducting to metallic behavior in samples oriented parallel to the *b*-axis. For these samples, the resistivity increases linearly as a function of temperature above approximately 180°K. Samples oriented perpendicular to the *b*-axis, however, exhibit a resistivity which is virtually constant at temperatures in excess of 180°K.

The change from semiconducting to metallic behavior in the blue potassium molybdenum bronze cannot be related to a structural change that is large enough to detect by X-ray diffraction studies of powder samples. Morris and Wold[5], however, observe a change from weak diamagnetic to weak Pauli paramagnetic susceptibility in the neighborhood of 180°K. These data correspond to a condition in which the electrons donated to the Mo–O layers by ionized K atoms are spin-paired in the semiconducting state but free in the metallic state.

Bouchard *et al.*[4] have suggested that spin-pairing of electrons may occur within molecular orbitals associated with the Mo–O clusters. The possibility also exists that spin-pairing may occur through the formation of Mo^{IV}, d^2, ions. These relatively large ions could be accommodated by the two highly distorted Mo–O octahedra of each Mo–O cluster which are isolated from one another but share edges with four adjoining Mo–O octahedra (Figs. 1 and 2). The additional distortion induced in these Mo–O octahedra at low temperatures by the presence of a Mo^{IV} cation would then appear as small displacements of the Mo ion and the two O ions involved in K–O bonding. This small distortion could not be detected by conventional X-ray diffraction studies.

In this study, electrical properties of the blue potassium molybdenum bronze, $K_{0.30}MoO_3$, were investigated along crystallographic directions which were selected after a careful consideration of crystal structure. The results of this investigation suggest that any study of directionally dependent physical properties is meaningful only when the orientation of the crystals is known. Without this knowledge, the relationship between structure and properties cannot validly be deduced.

Acknowledgements – The authors wish to acknowledge the contribution of Mr. P. Brandler who participated in crystal preparation and in carrying out electrical measurements

REFERENCES

1. STEPHENSON N. C and WADSLEY A. D., *Acta crystallogr.* **18**, 241 (1965).
2. GRAHAM J. and WADSLEY A. D., *Acta crystallogr.* **20**, 93 (1966).

3. WOLD A., KUNNMANN W., ARNOTT R. J. and FERRETTI A., *Inorg. Chem.* **3**, 545 (1964).
4. BOUCHARD, Jr. G. H., PERLSTEIN J. and SIENKO M. J., *Inorg. Chem.* **6**, 1682 (1967).
5. MORRIS B. L. and WOLD A., *Rev. scient. Instrum.* In press.
6. PERLOFF D. S. and WOLD A., *J. Phys. Chem. Solids, Suppl.* **28**, 361 (1967).
7. GOODENOUGH J. B., *Bull. Soc. Chim. Fr.* **4**, 1200 (1965).
8. GOODENOUGH J. B., *J. appl. Phys.* **37**, 1415 (1966).
9. BOUCHARD R. J. and GILLSON J. L., *Inorg. Chem.* **7**, 969 (1968).

J. Phys. Chem. Solids Pergamon Press 1969. Vol. 30, pp 1077–1082. Printed in Great Britain

PRESSURE-INDUCED TRANSFORMATION BEHAVIOR OF SOME QUASI-BINARY ALLOYS OF InSb

PHILIP N. ADLER*
General Telephone & Electronics Laboratories Inc. Bayside, N.Y. 11360, U.S.A.

(*Received 8 May 1968, in revised form 25 October 1968*)

Abstract – Two systems, InSb–InAs and InSb–GaSb, with compositions to 20 mol. % alloying compound were studied to 70 kbar at room temperature. Both InAs and GaSb additions were found to raise the transformation pressure of InSb, but each behaves differently. Possible elevated pressure phase equilibria is considered. A relationship between transformation and electronic structure is indicated based on the internal energy change at transformation being a relatively uniform percentage of the electronic energy gap of the low pressure, semiconductor phase. Instability of the zinc-blende form at a critical percentage of the bonding energy is suggested.

1. INTRODUCTION

Most of the III–V compounds, as well as Si and Ge, transform from their zinc-blende type structure to a denser elevated pressure form [1, 2]. The results of Minomura and Drickamer[1] indicate that the transformation pressure at room temperature for these materials decreases, almost linearly, with increasing average atomic number. Jamieson [3] and Musgrave[4] have pointed out relationships between the transformation pressure and the electronic energy gap of the semiconductor atmospheric pressure form. These factors suggest that transformation is dependent on electronic structure.

The pressure-induced transformation behavior of InSb has been extensively reported upon[5–9] with transformation taking place sluggishly at about 22 kbar at room temperature. The present work reports on a study of the transformation behavior of two quasi-binary alloys of InSb. These systems were investigated to explore their elevated pressure phase equilibria and to possibly clarify the significance of electronic structure to transformation.

Alloys of InSb containing 1–20 mol.% InAs or GaSb were prepared and studied at pressures to 70 kbar at room temperature. Study of alloys containing InBi was also attempted, but solid solution in InSb could not be attained as was previously indicated[10]. The presence of particles of InBi was found to have no significant effect on the transformation behavior of the InSb matrix phase.

2. EXPERIMENTAL PROCEDURE

2.1 *Alloy preparation*

Complete solid solution in the quasi-binary systems InSb–GaSb[11–14] and InSb–InAs[13] has been reported, but equilibrium is difficult to attain. Preparation techniques such as long-time annealing of powders[12, 13] slow directional freezing[13, 15, 16], and zone equilization[13, 14, 16] have been utilized with some reported success. Long-time annealing of powders was selected for these studies. Samples of InSb, GaSb, and InAs of semiconductor purity were obtained within the Laboratory or, as was the case for most of the InSb used, cast using 99·999 + per cent purity elements. The compounds were ground to less than 270 mesh, appropriately mixed blended and compacted. Spectrographic analysis performed before and after powder preparation indicated no significant change in the starting purity of about 99·99 per cent. Alloys of InSb containing 1, 2, 5, 10 and 20 mol % alloying compound were prepared. Samples were capsuled in vacuum and heat treated at 525°C for extended times. Periodic X-ray examination made to evaluate the extent of homogenization eventually indicated that a state was reached where continued heat treatment seemed ineffective. This was the case after 105 days for the InSb–InAs alloys. The InSb–GaSb alloys were annealed for 116 days.

2.2 *Pressure testing*

Tests were conducted using a 200 ton NBS-type Barogenics Tetrahedral Apparatus. The sample, 1·5 × 1·5 × 7 mm, was contained in a 3·4 mm dia. AgCl cylinder

---

**Present address*: Research Dept., Grumman Aircraft Engng Corp., Bethpage, N.Y. 11714, U.S.A.

placed within a 23·5 mm edge-length pyrophyllite tetrahedron. Calibration of this configuration[17] with Ce, Bi, Tl and Ba indicated pressure values to have an average deviation of ±0·4 kbar. (Use of the solid AgCl transmitting medium, as is the case for the presently reported work, imparts a shearing component to the applied stress so that the term 'pressure' is a simplification for the stress system being imposed.) Pressure was increased with fixed holding times at successive pressure increments. Transformation behavior was indicated by a resistance decrease during a holding period and continued resistance change at subsequent increments. Resistance values, measured with a Keithley 503 Milliohmeter, were plotted as a function of pressure and time on an X–Y recorder. Loading rates varied from about 0·4 kbar/5 min hold to 0·8 kbar/2 min hold through the pressure range of interest. Two to five tests were run for each alloy.

3. RESULTS AND DISCUSSION

3.1 *Sample description*

To characterize the powder-compacted alloys, procedures such as microstructure examination, electron microprobe analysis, X-ray precision lattice parameter determination, and X-ray diffraction line broadening were utilized. A uniform single phase was indicated for alloys containing GaSb, whereas InAs rich particles were still observed. For these cases, matrix compositions were found to be within 10 per cent of the intended compositions, except for the 20 per cent InAs alloy where a 15·3 mol.% composition was indicated. Over the investigated composition range, the InSb–InAs system exhibited ideal volume behavior, whereas negative volume deviations, suggesting greater than ideal solution bonding, was observed for the InSb–GaSb system. This is illustrated by the lattice parameter measurements shown in Fig. 1 and differs from those previously reported[13]. Nonhomogeneity, as interpreted by diffraction line broadening, was less than ± 0·7 mol.%, but higher for the 5 per cent GaSb alloy (±1·7 per cent) and the 15·3 per cent InAs alloy (±1·2 per cent).

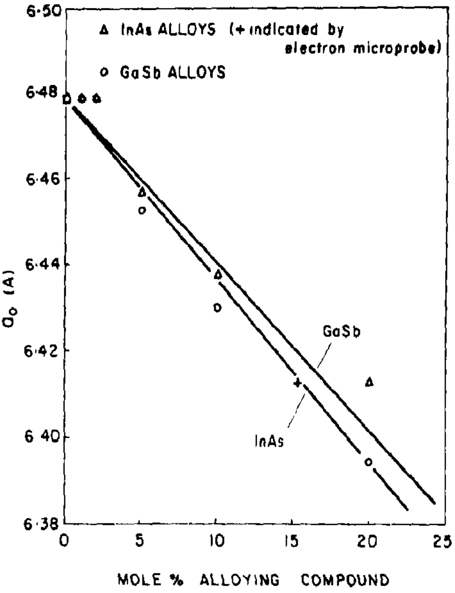

Fig. 1. Lattice parameter as a function of alloying for InSb rich alloys containing InAs or GaSb (Lines indicate ideal volume behavior).

3.2 *Resistance behavior*

The resistance behavior of InSb in the vicinity of transformation is significant to delineating onset. This behavior has been reported to be dependent on sample crystallinity[8] and is shown in Fig. 2 for single crystal, polycrystalline and powder-compacted samples. Indicated increments are a result of the experimental loading procedure during the 3–4 order of magnitude resistance decrease accompanying this sluggish room temperature transformation[6, 7]. For the powder-compacted sample, a resistance maximum occurs at a pressure which is too low to be attributable to transformation; also, no indication of transformation was observed during long time holding periods at slightly higher pressures. Therefore, the presence of a resistance decrease prior to transformation may not necessarily be indicative of heterogeneous nucleation as suggested by Smith, King and Gebbie[8] but may rather reflect on pressure-dependent electronic transport in a polycrystalline semiconductor. The resistance behavior for the alloy compounds, while differing for each system, was similar to that illustrated for the powder-compacted sample.

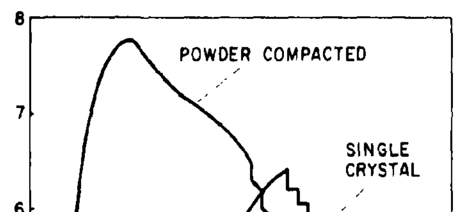

Fig 2. Resistance behavior of different forms of InSb

3.3 *Transformation behavior*

Transformation pressures for compound and alloy compounds are indicated in Tables 1 and 2, respectively. The behavior of InAs and GaSb alloys are quite different with the rate at which the transformation pressure increases with alloying, dP/dX, steadily increasing for As substitution of Sb and steadily decreasing for Ga substitution of In. Extrapolation of the alloy results reveals that both systems do not intersect the transformation pressure of the pure components, InAs or GaSb. (These latter points were determined with samples of the polycrystalline compounds used for alloy preparation.)

Since Jamieson has indicated that the elevated pressure forms of InSb and InAs differ[3], at least one three-phase reaction must exist in what is assumed to be a quasi-binary system between these components. The present results confirm this but do not unequivocally indicate the type of behavior which exists.

Both InSb and GaSb are reported to have the same elevated pressure structure[3], so that existence of a three-phase reaction within this assumed quasi-binary system is not essential. However, the transformation data indicate almost zero slope, dP/dX, at higher GaSb concentrations; in addition, an inflection must exist if the curve is to be extrapolated to the pure component. These conditions suggest either imminent immiscibility[18] or the existence of a monotectoid type miscibility gap.

The binary equilibria of both systems do not appear to be simply represented by complete

Table 1. *Values of* n *and* N *for some* III–V *compounds*

Compound	P_t* (kbar)	$E\dagger_{g}$ (eV)	$-(V_t-V_c)$‡ (cm³/mole)	$-\Delta V_t$ (cm³/mole)	n $\left(\frac{\text{strain energy}}{\text{band gap energy}}\right)$	N $\left(\frac{\text{internal energy change at transformation}}{\text{band gap energy}}\right)$
InSb	21	0·50	1·9	7·7	0·021	0·21
GaSb	66	0·92	3·3	5·2	0·062	0·22
InAs	69	0·64	2·5	5·8	0·070	0·36
AlSb	115	1·4	4·6	5·0	0·098	0·23

*Value for AlSb that of Minomura and Drickamer[1], remainder presently obtained.

†E_g and dE_g/dP based on values summarized by Madelung[24].

‡V_t based on Jamieson's values[3].

§Value for InSb that of Hanneman *et al* [9] remainder reported by Jamieson[3].

Table 2. *Values of* n *and* N *for* III–V *alloy compounds*

InSb alloy	P_t (kbar)	E_{gt}^* (eV)	$-(V_t-V_i)$† (cm³/mole)	$-\Delta V_t$† (cm³/mole)	n (strain energy / band gap energy)	N (internal energy change at transformation / band gap energy)
1% GaSb	21·7	0·51	1·9	7·7	0·021	0·22
2% GaSb	23·3	0·51	2·0	7·7	0·024	0·23
5% GaSb	24·3	0·55	2·1	7·6	0·024	0·22
10% GaSb	27·0	0·58	2·3	7·5	0·028	0·22
20% GaSb	27·9	0·60	2·2	7·2	0·027	0·21
1% InAs	21·3	0·50	1·9	7·7	0·021	0·22
2% InAs	22·5	0·51	2·0	7·7	0·023	0·22
5% InAs	22·1	0·48	1·9	7·6	0·023	0·23
10% InAs	23·5	0·48	2·0	7·5	0·026	0·24
15·3% InAs	28·2	0·53	2·3	7·4	0·032	0·25

*Based on atmospheric pressure E_g data of Woolley and Evans[25], Ivanov-Omskii and Kolomiets[26], and Woolley and Warner[27] and calculated mean values of dE_g/dP.

†Based on mean obtained from Jamieson's results[3], ΔV_t for InSb that of Hanneman *et al.*[9].

solid solubility in both ambient and elevated pressure forms, but since even the elevated pressure form of InSb is still under discussion [19, 20], additional information would be required to clarify existing equilibria.

3.4 *Transformation and electronic structure*

Different relationships have been suggested to obtain some insight into the cause of transformation for the Group IV and III–V materials. Jamieson[3] points out that an empirical basis between $P_t\Delta V_t$ and $\frac{1}{2}E_g$, where P_t and ΔV_t are the pressure and volume change at transformation, respectively, and E_g the electronic band gap at atmospheric pressure. Since $-P_t\Delta V_t$ is the approximate free-energy difference between the atmospheric and elevated-pressure forms at atmospheric pressure, a relationship between the band gap and the free-energy difference was suggested. However, the band gap in these materials generally increases with increasing pressure[21]. Since the free-energy difference would continually decrease with pressure, becoming zero at transformation, this relationship does not appear generally applicable.

If we consider the system at transformation, $-P_t\Delta V_t$ is also indication of the approximate internal energy increase accompanying transformation, i.e.

$$\Delta G = \Delta E + P\Delta V - T\Delta S \qquad (1)$$

where G is the Gibbs free energy, E the internal energy, and S the entropy. At transformation, $\Delta G = 0$, and

$$\Delta E_t = -P_t\Delta V_t + T_t\Delta S_t. \qquad (2)$$

The empirical basis reported by Jamieson may therefore be an indication of a relationship between the electronic structure of the semiconductor form and the internal energy change at transformation since the entropy term, $T\Delta S$, probably makes a comparatively small contribution for most of the compounds being considered. For the transformation in InSb, a value of 0·022 eV for $T\Delta S$ can be obtained from the results of Hanneman, Banus, and Gatos[9]. This value compares favorably with the value of 0·023 eV for an analogous temperature-induced transformation in tin from a diamond cubic to a denser tetragonal form[22].

Musgrave[4] has suggested that transformation is brought about by a destabilizing electronic configuration which occurs when the conduction-band becomes critically populated and thereupon develops two correlations between transformation pressure and the electronic band gap. For the first, thought responsible for initiation of the phase change, the hydrostatic strain-energy of compression is considered equal to the energy required by a critical number of electrons/atom to jump the band gap and initiate instability. A modified form is given in equation (3).

$$W = \int_{V_i}^{V_t} P\mathrm{d}V = nE_{gt} \qquad (3)$$

where W is the isothermal work of compression, n the critical number of electrons/atom to initiate transformation, and E_{gt} the band gap at transformation. If the volume is assumed to be linearly dependent upon pressure over the range being considered, as is almost the case for GaAs[23] which has the same zinc-blende structure, then

$$W \cong \tfrac{1}{2} P_t(V_t - V_i) = nE_{gt} \qquad (4)$$

or

$$n = \frac{1}{2}\frac{P_t(V_t - V_i}{E_{gt}}. \qquad (5)$$

The other correlation relates the work done during the volume contraction associated with transformation to the approximate energy necessary to make a critical number of electrons/atom cross the band gap and complete the transformation. This can be represented by a form of equation (2) in which the entropy term is considered negligible. Thus,

$$NE_{gt} \cong -P_t\Delta V_t \qquad (6)$$

where N is the critical number of electrons/atom to complete transformation. A more exact statement would be,

$$NE_{gt} = \Delta E_t = -P_t\Delta V_t + T_t\Delta S_t \qquad (7)$$

or

$$N = -\frac{P_t\Delta V_t + T_t\Delta S_t}{E_{gt}}. \qquad (8)$$

A critical occupancy in the conduction band is difficult to rationalize in light of the fact that the presence of extrinsic carriers do not appear significant to the transformation pressure[1]. Instead, we will consider n in equation (5) as the ratio of the strain energy introduced during compression to the band gap energy and N in equation (8) as the ratio of the internal energy change at transformation to the band gap energy. Since the band gap is some measure of the bonding in the covalent zincblende structure, these ratios are a means of comparison to the bonding energy in the semiconductor phase at transformation.

Determination of these ratios is attempted in Table 1 for some III–V compounds and in Table 2 for the alloy compounds presently investigated. A value of 0·023 eV was assumed for the entropy term. Values of P_t were presently determined except as indicated, and energy converted to electron volts considering a one electron to atom equivalence. For Table 2, interpolation was necessary to assign values for E_{gt}, $V_t - V_i$, and ΔV_t. This was done for E_{gt} using the expression

$$E_{gt} = E_g + P_t\frac{\mathrm{d}E_g}{\mathrm{d}P} \qquad (9)$$

where $\mathrm{d}E_g/\mathrm{d}P$ is a mean coefficient obtained considering the contribution of the components proportional to their concentration. Similar means were used for determining $V_t - V_i$ and ΔV_t.

The values of n for the compounds listed in Table 1 vary by a factor of almost 5 whereas N is relatively constant except for the InAs value. For the alloy compounds listed in Table 2, a systematic trend in the variation of n is indicated whereas N deviates slightly only for the higher concentration alloys of InAs. Considering the probable inaccuracies in the elevated pressure values, the consistency of N may be fortuitous, but does suggest that a relationship exists. It appears that at some critical value of the band gap energy, approximately 22 ± 1 per cent, sufficient energy can be supplied by transformation to a denser state to cause instability of the zinc-blende type of structure. The denser phase of higher internal energy is stable since the overall free energy is reduced by the volume and entropy contributions.

Deviation in N for InAs and higher concentration InAs alloys is not explainable in terms of inaccuracies in the elevated-pressure band gap[28] or volume information[3] although corroborating information is not available, and the optically determined band gap coefficient, dE_g/dP, appears somewhat anomolous in relation to other III–V compounds[21]. The internal energy change, however, is dependent upon an assumed entropy term in equation (8). Since the elevated-pressure form of InAs, rocksalt type, differs from that of the antimonides, the assumed 0·023 eV is not applicable. In fact, the entropy change must be negative for agreement with the N value of the antimonides if the other factors in equation (8) are correct. For a similar change in CdTe, from zinc-blende to a rocksalt structure, ΔS appears to be positive[29]. Knowledge of the slope of dP/dT for the solid–solid transition in InAs might possibly clarify this anomoly.

Acknowledgements – The author is grateful to Dr. C. D. Dickinson for relevant discussions and critical reading of the manuscript, P. Lublin for electron microprobe and X-ray evaluation, G. P. Werber for alloy preparation and conducting the pressure testing program, A. Calvano for X-ray measurements, and J. Black for supplying samples of III–V compounds.

REFERENCES

1 MINOMURA S. and DRICKAMER H. G., *J. Phys. Chem. Solids* **23**, 451 (1962)
2 JAYARAMAN A., KLEMENT W., Jr. and KENNEDY G. C., *Phys. Rev.* **130**, 540 (1963)
3 JAMIESON J. C., *Science* **139**, 845 (1963)
4 MUSGRAVE M. J. P., *Proc. phys. Soc.* **84**, 585 (1964).
5. GEBBIE H. A., SMITH P. L., AUSTIN I. G., and KING J. H., *Nature* **188**, 1095 (1960).
6. JAYARAMAN A., NEWTON R. C. and KENNEDY G. C., *Nature* **191**, 1288 (1961).
7 PONYATOVSKII E. G. and PERESADA G. I., *Dokl. Akad. Nauk SSSR* **144**, 129 (1962).
8. SMITH P. L., KING J. H. and GEBBIE H. A., In *Physics and Chemistry of High Pressures*, p. 140. Soc. Chem. Ind., London (1963).
9. HANNEMAN R. E., BANUS M. D. and GATOS H. C., *J. Phys. Chem. Solids* **25**, 293 (1964).
10 PERETTI E. A., *Trans. AIME* **212**, 79 (1958)
11 GORYUNOVA N. A. and FEDOROVA N. N., *J. Tech. Phys. Moscow* **24**, 1339 (1955).
12. WOOLLEY J. C., SMITH B. A. and LEES D. G., *Proc. phys. Soc.* **69B**, 1339 (1956)
13 WOOLLEY J. C. and SMITH B. A., *Proc. phys. Soc.* **72**, 214 (1958).
14. IVANOV-OMSKII V. I. and KOLOMIETS B. T., *Soviet Phys. solid St.* **1**, 834 (1959).
15 WOOLLEY J. C. and WARNER J., *J. electrochem. Soc.* **111**, 1142 (1964).
16. WOOLLEY J. C., EVANS S. A. and GILLETT C. M., *Proc. phys. Soc.* **74**, 244 (1959).
17. ADLER P. N. and WERBER G. P., *Rev. scient. Instrum.* **36**, 1886 (1965).
18. ADLER P. N. and MARGOLIN, H. *Acta Metall* **14**, 1645 (1966).
19. KASPER J. S. and BRANDHORST H., *J. chem. Phys.* **41**, 3768, (1964).
20. McWHAN D. B. and MAREZIO M., *J. chem. Phys* **45**, 2508 (1966).
21 PAUL W., *J. appl. Phys.* **32**, 2082 (1961)
22 LUMSDEN J., In *Thermodynamics of Alloys*, p. 93 Inst. of Metals, London (1952)
23 McSKIMIN H. J., JAYARAMAN A. and ANDREATCH P., Jr., *J. appl. Phys.* **38**, 2362 (1967)
24. MADELUNG O., In *Physics of III–V Compounds*, p. 49 Wiley, New York (1964)
25 WOOLLEY J. C. and EVANS J. A., *Proc. phys. Soc.* **78**, 354 (1961).
26 IVANOV-OMSKII V. I. and KOLOMIETS B. T., *Dock. Acad. Nauk SSSR* **127**, 135 (1959).
27. WOOLLEY J. C. and WARNER J., *Can. J. Phys* **42**, 1879 (1964)
28 EDWARDS A. L. and DRICKAMER H. G., *Phys. Rev.* **122**, 1149 (1961).
29 JAYARAMAN A., KLEMENT W., Jr. and KENNEDY G. C., *Phys. Rev.* **130**, 2277 (1963)

J. Phys. Chem. Solids Pergamon Press 1969. Vol. 30, pp. 1083–1090. Printed in Great Britain.

THE Ga–GaAs–GaP SYSTEM: PHASE CHEMISTRY AND SOLUTION GROWTH OF $GaAs_xP_{1-x}$

MORTON B. PANISH
Bell Telephone Laboratories, Incorporated, Murray Hill, N.J. 07974, U.S.A

(*Received* 24 *October* 1968)

Abstract – Liquidus isotherms at 900°, 1000°, 1100°, 1200° and 1300°C have been determined for the $GaAs_xP_{1-x}$ primary phase field of the Ga–GaAs–GaP ternary system. The corresponding solidus isotherms were determined at 900°, 1100°, 1200° and 1300°C and crystallization paths for the solid and liquid estimated. The ternary phase diagram was used to establish the conditions for liquid epitaxial growth of $GaAs_xP_{1-x}$ layers on GaP and for the growth of crystallites of predictable composition. No solid–solid miscibility gap was observed in the temperature range studied

INTRODUCTION

THE GaAs–GaP system is one of several mixed III–V crystal systems in which there is an energy gap range which is partially in the visible region of the spectrum, and which is dependent primarily upon the gross composition of the crystal. This paper is the third in a series of studies of such systems[1,2], which are of considerable interest because of their potential value for optoelectronic devices. An understanding of the phase chemistry of these systems is particularly useful for the development of solution growth techniques. Such techniques have, for GaAs and GaP, generally provided materials with more efficient radiative recombination than is obtained with materials prepared by vapor growth or from the melt[3–9]. GaAs–GaP alloys are generally prepared by vapor growth techniques[10–12], and the most extensive descriptions of band gap changes with composition and of the electrical, optical and electro-optic properties are for such materials [12–14].

In this paper the 900°–1300°C liquidus-solidus isotherms in the $GaAs_xP_{1-x}$ primary phase field of the Ga–GaAs–GaP system are presented along with the corresponding solid solubility isotherms at 900°, 1100° and 1200° and 1300°C. The preparation of solution grown epitaxial layers by simple techniques based upon information inherent in the phase information is described.

EXPERIMENTAL

Determination of the liquidus–solidus isotherms

Two techniques were used for the determination of the liquidus–solidus isotherms, differential thermal analysis, and an optical technique. In both cases the materials used were Ga, GaAs and GaP of semiconductor grade. The DTA method used here is the same as that which was described earlier [15,16] for the study of several other ternary systems. Once the general features of the isotherms had been established, it was more convenient and more precise to use an optical technique, in which the sample mixture to be studied was sealed into an evacuated quartz capsule and then heated in a furnace provided with a window. The mixtures were heated until they were visually observed to be completely liquid, then cooled slowly until the first crystallization on the melt surface was observed, and then very slowly heated while shaking the furnace. The temperature at which the last solid dissolved was taken as the liquidus temperature for that mixture. The disappearance of the last solid was particularly simple to observe in this system because the crystals float on top of the liquid surface where they are easily observed because of the effective emissivity difference between their relatively rough surface and the smooth liquid surface. The observed liquidus temperatures were confirmed by holding the furnace at just below the just above the observed transition temperature while observing the liquid surface, to eliminate the possibility of errors due to too rapid heating.*

Liquid epitaxy and solution growth of $GaAs_xP_{1-x}$

Solution growth. Once the liquidus isotherms were established, crystal platelets of $GaAs_xP_{1-x}$ were grown in quartz ampoules by slow cooling (~ 5°/hr) liquid mixtures with compositions on or near to a given isotherm, from the temperature of first formation of solid to 20°C below that temperature and then quenching the ampoule in water. Actually the same samples which were used in the optical studies described above were generally used for growth of platelets.

During the quench only very small crystals were grown and an additional thin layer of mixed crystal was deposited upon the larger crystals grown during the slow cooling. After removal of the Ga (mechanically and by dissolution in HCl solution), the larger crystals were separated for later analysis.

Solution epitaxy. The tipping technique used in this work was similar to that described by Nelson[3], except that a modification which facilitated removal of the solution from the growing crystal at any temperature was devised. This was done by allowing a weighted graphite ram to push the solution off the seed at the desired time and temperature. Once this was done, the apparatus containing the crystal was removed from the tipping furnace and cooled. Most of the layers were grown in a graphite boat under flowing H_2 on $\bar{1}\bar{1}\bar{1}$ (P) oriented undoped vapor grown GaP prepared by an open tube halogen transport process[17]. Several layers were grown on solution grown GaP platelets.

The best control of the composition of the regrown layer was obtained when the tipping was done at a temperature which corresponded to the temperature of first formation of solid for the solution used. Generally, therefore, the solution was prepared by adding together the required amounts of Ga, GaAs and GaP to yield a solution which would be completely liquid above the tipping temperature, with the solid precipitating below that temperature. Cooling rates for growth of the epitaxial layers were 2°–5°C/minute.

Analysis for As *and* P. The solid solubility isotherms corresponding to several of the liquidus isotherms were determined by analysis of the crystals or epitaxial layers grown on or near to several of the isotherms. In all cases polished cross sections of the crystals were prepared and analyzed for Ga and As with an electron beam microprobe by observation of the x-radiation due to electron beam exitation of those atoms.

RESULTS AND DISCUSSION

Liquidus isotherms in the Ga–As–P *ternary phase diagram*

The only thermal effect studied in this work was that for the first formation of solid upon slowly cooling or heating the liquid. The data for the various compositions studied, both by the DTA and optical techniques are tabulated in Table 1 and Table 2 and are plotted as isoarsenic curves in Fig. 1. For Fig. 1 the Ga–As binary diagram of Thurmond[18] was used as the zero phosphorus limit. Temperatures for the various liquidus isotherms were obtained by extrapolation and interpolation of the data plotted in Fig. 1. These isotherms are plotted in Fig. 2 with

---

*The observed temperatures for first precipitation of $Ga_xAs_{1-x}P$ were about 15° lower than the observed last temperature at which solid was present upon heating. This supercooling effect leads to some discrepancy in DTA (cooling) and optical (heating) data. The latter are a more reliable indication of the correct transition temperature.

Table 1. *Differential thermal analysis determinations of the liquids temperature*

Ga	at. % As	P	T°C liquidus
96·35	2·00	1·65	989
92·15	7·00	0·85	981
93·70	2·00	4·30	1093
89·80	7·00	3·20	1083
84·40	14·00	1·60	1100

Thurmond's Ga–As and Ga–P binaries[14] as limits. For convenience in reading the data, Fig. 2 is plotted in rectilinear coordinates rather than the triangular coordinates generally used for ternary systems.

Table 2. *Optical determinations of the liquidus temperature and the corresponding measured solidus composition*

at. % – liquid Ga	As	P	T°C	at % As in solid
98·55	0·80	0·65	913	17·50
97·50	0·20	0·50	902	14·00
95·70	4·00	0·30	903	32 00
94·40	5·50	0·10	900	46·00
84·30	13·70	2·00	1100	
84·70	7 00	8·30	1220	6 50
79 50	14·00	6·50	1220	17·00
73·40	22·50	4·10	1210	27·50
68·30	30 00	1·70	1220	45·50
72·50	14·00	13·50	1312	10·60
61 25	30 00	8·75	1300	26·00
52·50	40·00	7·50	1305	

Solid solubility isotherms – crystallization paths

Solid solubility isotherms corresponding to the liquidus isotherms of Fig. 2 were obtained by analysis of epitaxial layers and crystal platelets of $GaAs_xP_{1-x}$ grown as described in the experimental part above. Most of the data were obtained for the 1100°C isotherm (Table 3), but data were also

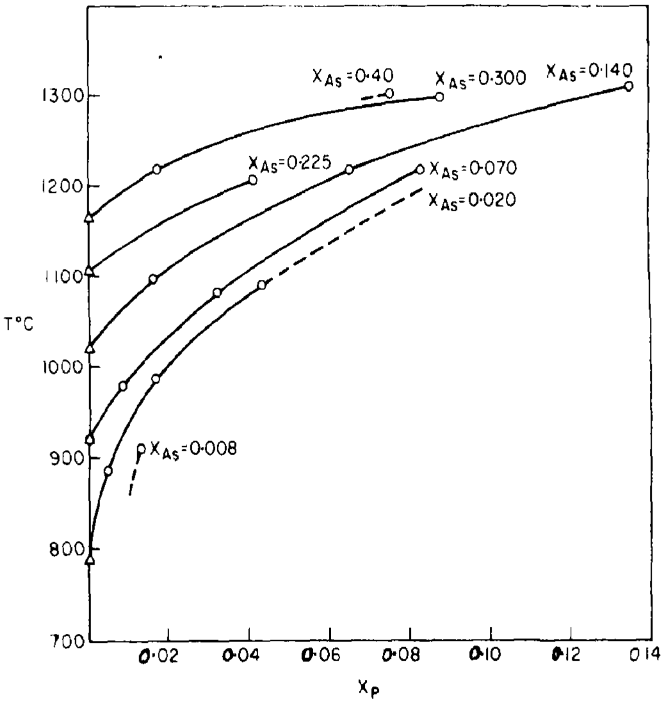

Fig. 1 Isoarsenic plots of the liquidus temperature as a function of the atom fraction phosphorus, χ_P, in the liquid.

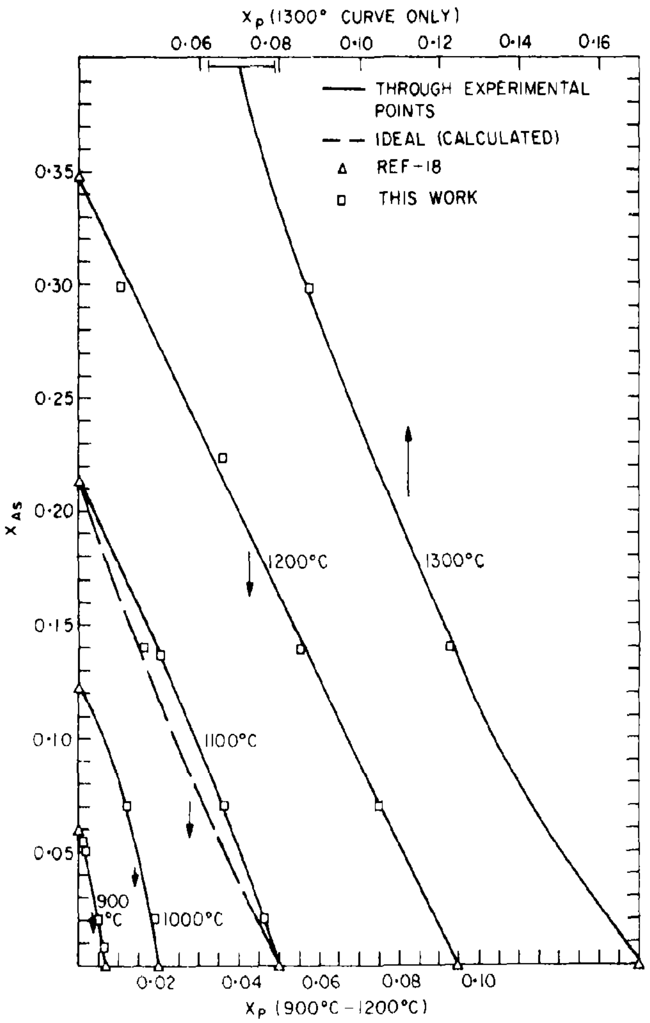

Fig. 2. Liquidus isotherms for the $GaAs_xP_{1-x}$ primary phase field. Note: For all points the sum of the atom fractions of the components in the liquid, $\chi_{Ga}+\chi_{As}+\chi_P=1$. At 1100°C one calculated curve is shown.

obtained for the 900°, 1200° and 1300°C isotherms. All of the data are tabulated in Tables 2 and 3 and plotted in Fig. 3.

The epitaxial layers were grown only at 1100°C. The solid solubility data obtained for several such layers was more scattered than the data obtained with the slow grown crystallites. This may be the result of the faster growth conditions which occur with the epitaxial growth procedure. In general, the quality of the epitaxial growth layers was poorer on vapor grown than on solution grown GaP substrates, and in general, layers with high GaAs concentration were worse than layers with low GaAs concentration.

The crystallization paths for this system are of interest because they show, for crystals grown with the growing surface at equilibrium with the liquid, the composition range to be expected for a crystal grown over a known temperature range. We do not expect that in any growth procedure the entire crystal will

Table 3. *Composition data for* $GaAs_xP_{1-x}$ *crystals grown from* 1100 *to* 1080°C

at. % – liquid Ga	 As	 P	Solid As	Growth type
94·32	1·00	4·65	2·30	platelet
91·90	4·00	4·10	8·30	epitaxial
91·90	4·00	4·10	6·30	platelet
88·75	8·00	3·25	13·50	epitaxial
88·75	8·00	3·25	15·10	platelet
85·70	12·00	2·30	25·60	platelet
82·60	16·00	1·40	32·00	epitaxial
82·60	16·00	1·40	38·50	platelet
80·40	9·00	0·60	49·00	epitaxial
80·40	9·00	0·60	46·50	platelet

come into equilibrium with the liquid, but rather, that each part of the crystal has, for slow growth, a composition characteristic of the temperature at and solution from which it was grown. This assumption is supported by the fact that the slow platelet growth data and the much more rapid epitaxial growth data of Fig. 3 are essentially in agreement, and by self diffusion data for As^{20} in GaAs which indicate that self diffusion of the group V element is very slow. The liquidus and solidus data reported here in Figs. 2 and 3 have been interpolated so that the crystallization paths for several overall compositions could be estimated. For this purpose the 'isogallium arsenide' plots of liquidus temperature vs the atom fraction of arsenic in the liquid, χ_{As}, shown in Fig. 4 were constructed. The interpolated solidus isotherms are shown along with experimental curves on Fig. 3, and the interpolated liquidus isotherms are shown in the triangular diagram of Fig. 5.

In a triangular diagram such as that of Fig. 5, tie lines connecting the solid and

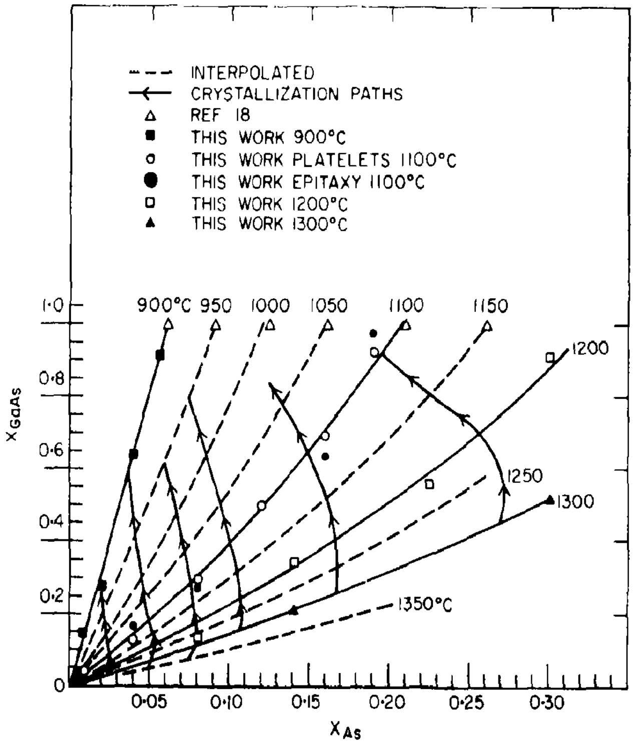

Fig. 3. Solidus isotherms and solidus crystallization paths for the solid. Note The liquid composition on any solidus isotherm is completely defined by one component (in the case χ_{As}) and in the solid the atom fractions of GaAs and GaP, $\chi_{GaAs}+\chi_{GaP} = 1$

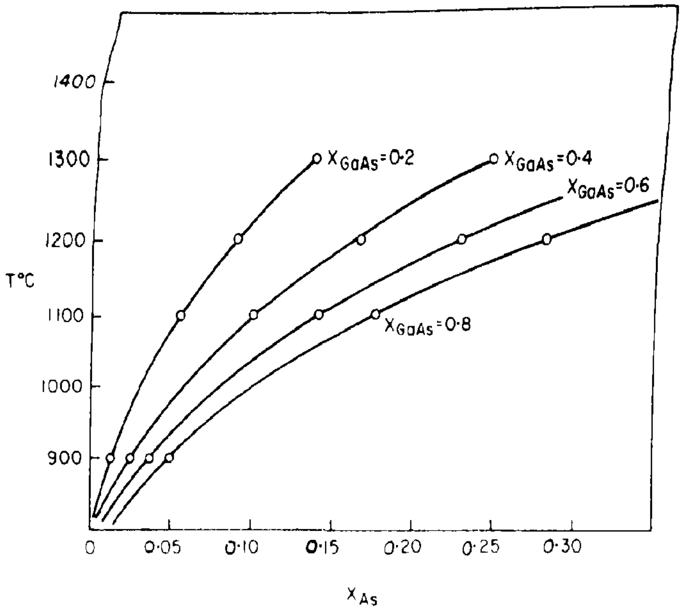

Fig. 4 Plots of the transition temperature as a function of the concentration of arsenic in the liquid for several solidus compositions

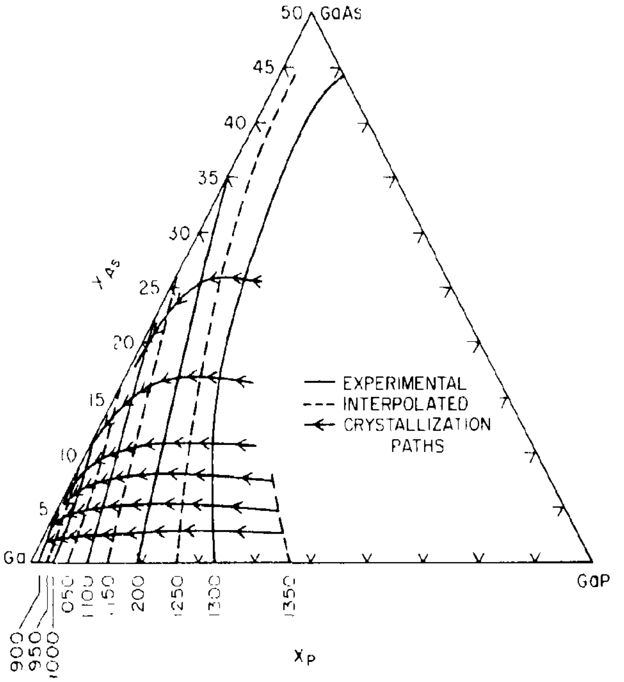

Fig. 5 Liquidus isotherms and liquidus crystallization paths

liquid compositions are tangent to the liquidus crystallization path. In this work the solid and liquid crystallization paths were obtained graphically with an extrapolation and interpolation procedure for isotherms at 50°C intervals. These curves are shown in Figs. 3 and 5. They illustrate, for several starting liquidus compositions, the instantaneous liquidus and solidus compositions at the liquid-solidus interface during precipitation of the solid upon cooling.

Thermodynamic properties of the system

The isotherms of Fig. 2 are quite simple. The addition of P to a solution of Ga and As depresses the arsenic solubility in such a manner that most of the curves of Fig. 2 are almost linear. Since the liquidus isotherm shapes depend upon interactions among the components in the liquid and in the solid as well as upon the stability of pure solid components, it is of interest to try to understand how these factors contribute to the isotherm shape in the Ga–As–P system.

For the equilibrium of the mixed $GaAs_xP_{1-x}$ solid with the ternary liquid we may write

$$GaAs_{(s)} \rightleftarrows Ga_{(l)} + As_{(l)} \tag{1}$$

$$K_{GaAs} = \frac{\gamma_{Ga}\chi_{Ga}\gamma_{As}\chi_{As}}{\gamma_{GaAs}\chi_{GaAs}} \tag{2}$$

$$GaP_{(s)} \rightleftarrows Ga_{(l)} + P_{(l)} \tag{3}$$

$$K_{GaP} = \frac{\gamma_{Ga}\chi_{Ga}\gamma_{P}\chi_{P}}{\gamma_{GaP}\chi_{GaP}} \tag{4}$$

with the restrictions

$$\chi_{Ga} + \chi_{As} + \chi_{P} = 1 \tag{5}$$

and

$$\chi_{GaAs} + \chi_{GaP} = 1. \tag{6}$$

The subscripts Ga, As and P refer to those elements in the liquid, and the subscripts GaAs and GaP refer to those compounds in the solid. Reactions (1) and (3) show formally, the equilibrium between the components of the mixed crystal solid and the liquid, K_{GaAs} and K_{GaP} are the equilibrium constants for equations (1) and (3), and the γ's and χ's are activity coefficients and atom or mole fractions for the components in the liquid or the solid.

From equations (1–6)

$$\frac{K_{GaAs}\gamma_{GaAs}}{\gamma_{As}}(\chi_P - \chi_P^2 - \chi_{As}\chi_P) + \frac{K_{GaP}\gamma_{GaP}}{\gamma_P}(\chi_{As} - \chi_{As}^2 - \chi_{As}\chi_P) = \frac{\gamma_{GaAs}\gamma_{GaP}}{\gamma_{Ga}\gamma_{As}\gamma_P}K_{GaAs}K_{GaP}. \tag{7}$$

The activity coefficients for the various components in the liquid and the solid are not known except at the binary limits. It is not expected, however, that those for the liquid will vary over very wide limits since As and P are chemically quite similar. Thus, although neither of the binary systems Ga–As or Ga–P are ideal, or even regular[18, 19], we may as a first approximation treat the liquid as ideal from the point of view that we are taking γ_{Ga}, γ_{As} and γ_P to be constants incorporated into the equilibrium constants. The solid solutions of $GaAs_xP_{1-x}$ are not expected to be ideal since the lattice match for GaAs and GaP is poor ($A_{GaAs} = 5{\cdot}6532$ Å [21], $A_{GaP} = 5{\cdot}4505$ Å[21]). However, again as a first approximation, we may take γ_{GaAs} and γ_{GaP} to be unity. The binary equilibrium constants as obtained from the binary liquidus curves[18, 19] may then be used with equation (7) to calculate liquidus isotherms for the completely ideal system. This has been done for the 1100°C isotherm in Fig. 2. The calculated curve is in fair agreement with the experimental curve and reflects primarily the lack of sensitivity of equation (7) to nonideality in the solid.

CONCLUSIONS

Liquidus isotherms in the $GaAs_xP_{1-x}$ primary phase field of the Ga-GaAs-GaP ternary system have been determined from 900° to 1300°C. The data thus obtained were used to establish the growth conditions for the preparation of solution grown epitaxial layers and crystal platelets on several of the isotherms. The composition data for the grown crystals was used to construct the solid solubility isotherms corresponding to the liquidus isotherms and to estimate the crystallization paths for the solid and the liquid at several compositions. No evidence for a solid–solid miscibility gap was found.

Acknowledgements – The author would like to acknowledge the work of S. Sumski who helped with the experimental measurements and C. Kim who did the electron beam microprobe measurements.

REFERENCES

1. PANISH M. B. and SUMSKI S., *J. Phys. Chem. Solids*, **30**, 129 (1969).
2. PANISH M. B., LYNCH R. T. and SUMSKI S., *Conf. Preparation of Electronic Materials* Metallurgical Society of A.I.M.E., Chicago, August (1968); Trans. A.I.M.E., In press (1969).
3. NELSON H., *RCA Rev.* **24**, 603 (1963).
4. DOUSMANIS G. C., NELSON H. and STAEBLER D. L., *Appl. Phys. Lett.* **5**, 174 (1964).
5. PILKUHN M. H., RUPRECHT and WOODALL J., *IEEE J. quant. Electron.* **1**, 184 (1965).
6. PANISH M. B., QUEISSER H. J., DERICK L. and SUMSKI S., *Solid-St. Electron.* **9**, 311 (1966).
7. QUEISSER H. J. and PANISH M. B., *J. Phys. Chem. Solids* **28**, 1177 (1967).
8. PANISH M. B., *J. Phys. Chem. Solids* **29**, 409 (1968).
9. LOGAN R. A., WHITE H. G. and TRUMBORE F. A., *Appl. Phys. Lett.* **10**, 206 (1967).
10. WOLFE C. M., NEUSSE C. J. and HOLONYAK N., Jr., *J. appl. Phys.* **36**, 3790 (1965).
11. TEITJEN J. J. and AMICK J. A., *J. electrochem. Soc.* **113**, 275 (1966).
12. THOMPSON A. G., WOOLLEY J. C. and RUBENSTEIN M. *Can. J. Phys.* **44**, 2927 (1966).
13. HOLONYAK N., Jr., *Trans. metall. Soc. A.I.M.E.* **230**, 276 (1964)
14. MARUSKA H. P. and PANKOVE J. I., *Solid-St. Electron.* **10**, 917 (1967).
15. PANISH M. B., *J. Phys. Chem. Solids* **27**, 291 (1966).
16. PANISH M. B., *J. electrochem. Soc.* **114**, 516 (1967)
17. LUTHER L. C. and ROCCASECCA D. D., *J. electrochem. Soc.* **115**, 850 (1968).
18. THURMOND C. D., *J. Phys. Chem. Solids* **26**, 785 (1965).
19. ARTHUR J., *J. Phys. Chem. Solids* **28**, 2257 (1967).
20. GOLDSTEIN B., *Phys. Rev.* **121**, 1305 (1961).
21. GIESECKE G., *Semiconductors and Semimetals, Physics of III–V Compounds* (Edited by R. K. Willardson and A. C. Beer). Vol. 2. Academic Press, New York (1966)

J. Phys. Chem. Solids Pergamon Press 1969. Vol. 30, pp. 1091–1096. Printed in Great Britain.

AN INTERPRETATION OF THE *P–T* DIAGRAM FOR TIN

M. J. P. MUSGRAVE
Department of Mathematics, Imperial College, London, S.W.7

(*Received* 31 *May* 1968; *in revised form* 23 *October* 1968)

Abstract – Kinematic paths, defined in terms of lattice modes, are suggested for the transitions between white tin (Sn I) and (i) the liquid and (ii) the simple b.c.t. form (Sn II).

Calculations, based on a lattice dynamical model of white tin, which examine the variation of effective elastic constants necessary to fit the observed *P–T* diagram are reported and compared with the phase lines implied if similar calculations are based wholly on observed values of $\Delta c_{ij}/\Delta T$. Results indicate that, if the path suggested for (ii) is to yield the observed phase line, the shear stiffness $\frac{1}{2}(c_{11}-c_{12})_{\text{eff}}$ near the triple point (34 kbars, 583°K) must be very small.

1. INTRODUCTION

In 1966 Barnett, Bean and Hall[1] presented a *P–T* diagram for tin which is reproduced in Fig. 1 with additional captions relevant to the present note. The essential points are *S*, the m.p. at 1 bar, 503°K; the triple point *T*, 34 kbars, 583°K; the SnI–SnII transition point at room temperature U, 92 kbars, 298°K.

The phase SnII, first indicated by the experiments of Stager *et al.*[2] (1962), was structurally investigated by Jamieson[3] (1962) and found to have a simple body-centred unit cell, initially considered cubic; an interpretation of the kinematics of the transitions, in terms of two lattice modes calculated from a dynamical model for tin originally used to discuss the grey-white tin transition, was subsequently given by Musgrave (1963 (a, b); hereafter I and II). The two modes believed to provide the kinematic path between SnI and SnII are optical modes of *z*-polarization (∥ to *c*-axis) which have remarkably low frequencies at 300°K and atmospheric pressure.

Experimental determination of the phonon dispersion curves for SnI by inelastic neutron scattering[6] (Long Price, 1964) has since given satisfactory corroboration to the general shape of the dispersion curves derived from (I) and, in particular, has provided strong confirmation for the existence of the relevant low frequency optical modes.

The present note seeks to interpret the phase diagram further in terms of the model which, though simple, appears to contain significant elements of the real force field within the crystal.

2. THE PHASE DIAGRAM

Briefly, we enquire whether (i) along the segment *ST*, melting is a consequence of the vanishing of the effective shear stiffness, $\frac{1}{2}(c_{11}-c_{12})_{\text{eff}}$, which governs macroscopic displacements of the form $(u, -u, 0)$; (ii) along the segment *TU*, the change of crystal structure occurs owing to the vanishing of the stiffness of a compound displacement in the z-direction involving modes $\omega_{\text{TO}}(q)$ where $q = (2\pi/a')[1, 0, 0]$ and $q = [0, 0, 0]$. The former mode (*A*) causes atoms in planes $x = na'$ and $x = (n+1/2)a'$ to vibrate in antiphase, the latter mode (*B*) causes atoms of one simple b.c.t. lattice to move in antiphase with respect to the other simple b.c.t. lattice of the structure. The kinematic path from SnI → SnII may be represented by the combination $2(A)+(B)$ and transforms an oblique parallelopiped of typical vertices $(a'/2, 0, 3c/4)$, $(a'/2, 0, -c/4)$, $(0, a'/2, c/4)$,

$(0, a'/2, -3c/4)$ into a rectangular cell which, with the atom at $(0, 0, 0)$, forms the simple b.c.t. cell of SnII. (See reference II for further details and a figure.)

Neither of these hypotheses is essentially novel. The inability to offer elastic stiffness to shear deformation has long been acknowledged a criterion of the liquid state. The first calculations of solid-liquid phase lines based on setting a shear stiffness to zero are usually attributed to Born[13], although he mentions that Brillouin[14] had made more primitive calculations on the same basis. Born presented detailed calculations for a b.c.c. lattice. Subsequent experimental data (e.g. Alers and Neighbours[15]), have shown that linear extrapolations of the temperature dependence of shear stiffnesses over tens or hundreds of °K imply melting points appreciably higher than observed. Nevertheless, such extrapolation does afford an indication of the reduction of stability with respect to the various shear modes.

In the case of tin, the shear stiffness $\frac{1}{2}(c_{11}-c_{12})$ is roughly one quarter the value of the remaining shear stiffness $\frac{1}{2}(c_{33}-c_{13})$, c_{44}, c_{66}, $(c_{11}+c_{12}-4c_{13}+c_{33})/6$ at 300°K, 1 bar, yet it has the temperature coefficient of greatest magnitude. Consequently extrapolation of the stiffness $\frac{1}{2}(c_{11}-c_{12})$ as a function of temperature implies a m.p. within 70°K of observation while corresponding extrapolations of the other shear stiffnesses imply m.p. of 1000°K or more above the observed value. Since sequential breakdown or melting certainly occurs in some highly anisotropic structures (e.g. liquid crystal forms), the possibility of analogous behaviour in simpler materials, though over much smaller (perhaps experimentally unachievable) temperature ranges, seems worth consideration.

The second hypothesis is conceptually the same as the instability invoked by Cochran [16] to interpret ferroelectric transitions though here a superposition of two modes is required and larger atomic displacements are involved.

The evidence which suggests that propositions (i) and (ii) might be valid approximations to the kinematics of the transitions is offered below.

3. THE MELTING LINE (*ST*)

The elastic constants of SnI were measured over a range of temperature by Rayne and Chandrasekhar[7] (1960) and the temperature coefficients for the elastic constants $(\Delta c_{ij}/\Delta T)$ derived from their measurements at 77° and 300°K are shown in Table 1 denoted by (R.&.C). It will be remarked that the observed coefficient for the shear stiffness $(c_{11}-c_{12})(-4{\cdot}81\times10^{8}\,\text{dyn. cm}^{-2}/°\text{K})$ is exceptionally high when considered as a percentage of the total constant $(1{\cdot}29\times10^{11}\,\text{dyn. cm}^{-2})$. Rectilinear extrapolation indicates that the stiffness would vanish in the region of 570°K. However, the magnitude of the negative coefficient may be expected to increase and it is not unreasonable to suppose $c_{11}-c_{12}$ might vanish at 503°K, the m.p. at 1 bar, (*S* in Fig. 1). Assuming that the associated displacements determine the initial mode of melting and that they continue to do so along *ST*, the force field represented by the force constants k_j of (1), may be recalculated from a set of $(c_{ij})_{\text{eff}}$ in which $(c_{11}-c_{12})_{\text{eff}}=0$. In this way, a structure unstable to a given shear but otherwise stable to homogeneous displacement may be contrived and the melting process may be attributed to the collapse of this shear stiffness.

It is important to note that the expression for the shear constant in terms of the atomic force constants of the rigid ion model described in reference I has the form

$$c_{11}-c_{12}=F-G^2/H_B \qquad (1)$$

where

$$F=\frac{1}{c}\left[\frac{k_1}{1+\rho^2}+\frac{k_3}{1+9\rho^2}+4\rho^2(k\phi'-k\phi'\phi')\right] \qquad (2a)$$

$$G=\frac{2\rho}{c^{1/2}}\left[\frac{k_1}{1+\rho^2}+\frac{3k_3}{1+9\rho^2}-4(k\phi'-k\phi'\phi')\right] \qquad (2b)$$

$$H_B=\frac{4[\rho^2k_1+4(k\phi'-k\phi'\phi')]}{1+\rho^2}+\frac{36\rho^2k_3}{1+9\rho^2} \qquad (2c)$$

with the notation of (I) in which, $\rho = c/2a'$, 1/2 (axial ratio of the tetragonal cell); k_1, k_2, k_3 are extensional stiffness between first, second and third neighbours; $k\phi'$, $k\phi'\phi'$ are an angular and an interaction stiffness respectively for angles $\phi' = \cot^{-1}(\rho^2-1)/2\rho \approx 150°$ in the tetrahedral coordination of first neighbours.

In particular, H_B is the stiffness of the lattice mode (B).

The form of (1) shows clearly that $H_B > 0$ even when $c_{11}-c_{12} \to 0$; consequently, the stiffness of the compound displacement $2(A)+(B)$ must possess a positive (B) component and its vanishing must depend on a negative (A) component which, until it attains a sufficient magnitude, affords no path to a state of lower free energy than the liquid.

An alternative possibility is that instability of the (A) mode might initiate melting. We reconsider this possibility later (Section 6(viii)).

4. THE SOLID-SOLID LINE (TU)

The experimental evidence for the non-reconstructive character of this transition is very strong[8] (Barnett, Bennion and Hall, 1963) and encourages an interpretation of it as an 'atomic buckling' process related to the instability of normal modes.

The lattice modes (A) and (B) can provide a compound displacement which offers a kinematic path between the two solid phases SnI-SnII. The necessary ratio of displacements (A): (B) is 2:1 and it is necessary that the deformation energy of the compound displacement should vanish for the compound mode to account for the transition

$$\text{i.e.}\quad 4H_A + H_B \to 0 \tag{3}$$

where

$$H_A = \frac{4[\rho^2 k_1 + 4k\phi']}{1+\rho^2} + \frac{36\rho^2 k_3}{1+9\rho^2} + \frac{16\rho^2 k\phi}{(1+\rho^2)(1+2\rho^2)} \tag{4}$$

and H_B, as defined by (2c), are the stiffnesses of the (A) and (B) modes in the notation of (I). $k\phi$ is an angular stiffness for angles $\phi = \cot^{-1}[-\rho^2/(1+2\rho^2)^{1/2}] \approx 95°$ in the tetrahedral coordination of first neighbours.

The segment TU can now be defined by $H_A = -H_B/4$ which condition expresses the zero stiffness of the displacement which forms a path between the structures.

5. THE TRIPLE POINT (T)

The triple point is defined by the intersection of the transition lines ST and TU discussed above. In order that the suggested interpretation may be acceptable overall, we require that

(i) $(c_{11}-c_{12})_{\text{eff}} = 0,\quad 4H_A + H_B > 0$ along ST,

(ii) $(c_{11}-c_{12})_{\text{eff}} = 0 = 4H_A + H_B$ at T,

(iii) $(c_{11}-c_{12})_{\text{eff}} > 0,\quad 4H_A + H_B = 0$ along TU.

The values of physical parameters necessary for the fulfilment of these conditions have been estimated and their plausibility considered.

6. VALUES OF THE PHYSICAL PARAMETERS FOR THE PROPOSED INSTABILITIES

The observed data on SnI show that the axial ratio (c/a') remains substantially constant over a large range of pressure and temperature. In addition, the temperature coefficients of the elastic constants at atmospheric pressure over the range 100°-300°K are, except in the case of c_{13}, measured quantities. Pressure coefficients are not so readily available, however, using arguments analogous to those of Musgrave and Pople [9] (1962), the $(c_{ij})_{\text{eff}}$ can be expressed in terms of c^*_{ij}, the constants implied by the actual atomic dimensions, and the pressure P. Taking advantage of the approximate constancy of axial ratio, it has been assumed that

$$c_{ij}^* = c_{ij}(c) = c_{ij}(c_R) + \left(\frac{\Delta c_{ij}}{\Delta c}\right)_{c_R} \cdot \Delta c, (i, j = 1, 2 \ldots . 6) \quad (5)$$

where $\Delta c = c - c_R = AP + BP^2 + C(T - T_R) + D(T^2 - T_R^2)$ and the values $A = 6{\cdot}63 \times 10^{-4}$ Å/kbar; $B = 1{\cdot}20 \times 10^{-6}$ Å/kbar²; $C = 9{\cdot}54 \times 10^{-5}$ Å/kbar; $D = 1{\cdot}04 \times 10^{-7}$ Å/kbar² were determined from the data of Barnett, Bean and Hall[1] and Lee and Raynor[12] (1954). In conjunction with the values of Rayne and Chandrasekhar[7] (1960) for $\Delta c_{ij}/\Delta T$, $\Delta c_{ij}/\Delta c = (\Delta c_{ij}/\Delta T)/(\Delta c/\Delta T)$ may be obtained for all c_{ij} except c_{13}.

Calculations using the above approximations and the data in Table 1 afford the following results: (see Fig. 1)

Curve (1)

(i) the melting line ST can be attributed to the shear constant $\frac{1}{2}(c_{11} - c_{12})_{\text{eff}} \to 0$, if the slope $\Delta(c_{11} - c_{12})/\Delta T = -0{\cdot}75$, (Units 10^8 dyn. cm^{-2}/°K)

(ii) the line TU can be attributed to the instability of the compound mode $2(A) + (B)$ if $\frac{1}{2}(c_{11} - c_{12})_{\text{eff}}$ is calculated as in (i) and $c_{13}(T) = 2{\cdot}740$, $c_{13}(U) = 5{\cdot}084$. Values of $\frac{1}{2}(c_{11} - c_{12})$ are all positive.

(iii) the value of $\Delta c_{12}/\Delta T$ required for (i) and (ii) implies $c_{12}(R) = 7{\cdot}08$, c.f. 5·92 (obs) (Units 10^{11} dyn. cm^{-2}); however this implies a very low value of the shear constant $\frac{1}{2}(c_{11} - c_{12})(R) = 0{\cdot}075$ (calc.), c.f. 0·65 (obs).

(iv) the value of $c_{13}(R)$ calculated from $c_{13}(T)$ and $c_{13}(U)$ is 2·114, c.f. 2·25 (original model), 2·8–4·4 (obs).

Curve (2)

(v) the line ST' is obtained if $\Delta(c_{11} - c_{12})/\Delta T = -4{\cdot}81$ (obs) is used with the criterion $\frac{1}{2}(c_{11} - c_{12})_{\text{eff}} \to 0$,

(vi) if, consistent with (v), c_{13} is calculated to make $H_1 + H_B/4 \to 0$ at U and $c_{13}(R) = 2{\cdot}114$, then $\Delta c_{13}/\Delta T = -1{\cdot}22$ and $T'U$ is obtained, similar calculation with $c_{13}(R) = 2{\cdot}00$, $\Delta c_{13}/\Delta T = -1{\cdot}32$ yields a curve similar to (2) shifted towards TU, the triple point T' is then located in the region 800°K, 20 kbars.

Curve (3)

(vii) using similar criteria as in (v) and (vi), the intermediate value of $\Delta(c_{11} - c_{12})/\Delta T = -1{\cdot}50$ yields the line ST'' and in conjunction with $c_{13}(R) = 2{\cdot}114$, $c_{13}(U) = 5{\cdot}050$, $\Delta c_{13}/\Delta T = -1{\cdot}19$ yields the line $T''U$.

Finally we may note: (viii) if the line ST is reproduced by requiring $H_1 \to 0$ and thus determining c_{13} while all other parameters are allotted their observed values as for curve (2), then only a very small change in slope at T is obtained when the criterion is altered to $H_1 + H_B/4 \to 0$, owing to the small magnitude of $|H_1 - H_B| \propto p^2 k\phi'/(1 + 2p^2) + k\phi'\phi'$.

These findings indicate that if the SnI–SnII change is occasioned by the instability of the compound mode and an appreciable

Table 1. Elastic stiffnesses (c_{ij}; units, 10^{11} dyn.cm^{-2}) and temperature coefficients ($\Delta c_{ij}/\Delta T$; units, 10^8 dyn.cm^{-2}/°K) of white tin (SnI) *(after Rayne and Chandrasekhar)*

ij	11	33	44	66	11–12	13	
c_{ij}	7 23	8 84	2·20	2 40	1·29	2·8–4·4	(obs) (R & C)
						2·25	(1963 model)
					0 15 (1)		
					0·97 (2)	2·114	(curves (1–3))
					0·31 (3)		
$-\Delta c_{ij}/\Delta T$	4·0 (R & C)	5·0 (R & C)	1 9 (R & C)	1 7 (R & C)	0 75	1·22	(curve (1), fit to STU)
					4 81 (R & C)	1·26	(curve (2), $ST'U$)
					1·50	1·19	(curve (3), $ST''U$)

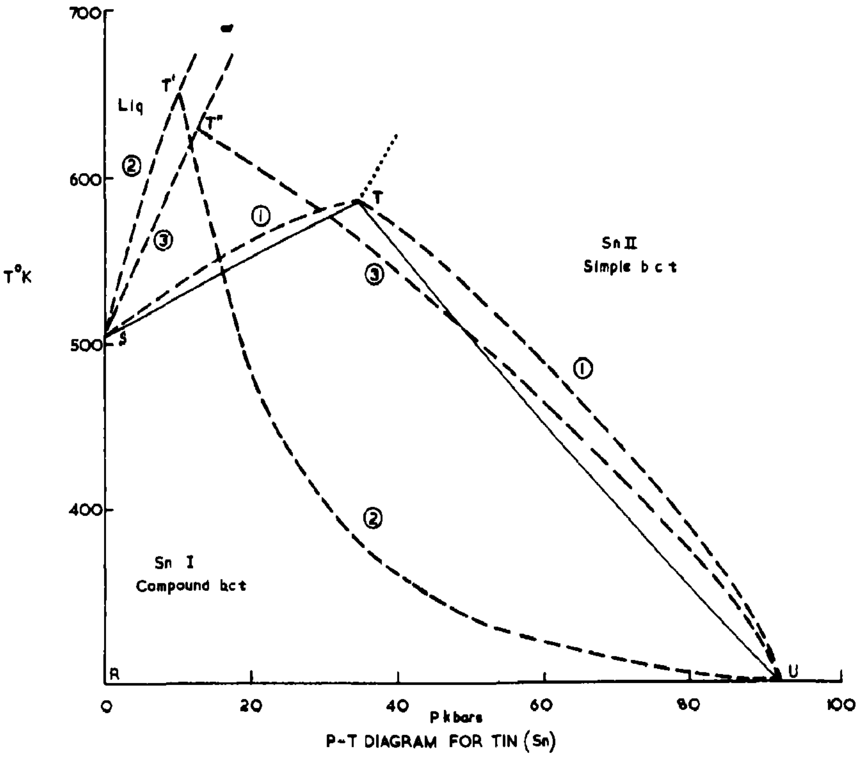

Fig. 1. Observed and calculated phase lines for tin. ——— line segments between observed points; ----- calculated lines: (1) fit to *STU*, (2) based on observed values of all parameters, (3) based on observed values except $\Delta(c_{11}-c_{12})/\Delta T = -1 \cdot 50 \times 10^{8}$ dyn.cm^{-2}/°K.

change of slope from *ST* to *TU* is to occur, the melting is not attributable to the variation of the constant c_{13} to whose value $H_\perp$ and $H_\parallel$ are most sensitive. If melting is to be associated with a simple instability, the criterion $\frac{1}{2}(c_{11}-c_{12})_{\text{eff}} \rightarrow 0$ is suggested by the observed temperature coefficients. The calculations here reported indicate that a very low value of this parameter in the neighbourhood of the triple point is necessary if the proposed interpretation of the phase diagram is to afford a valid approximation.

7. DISCUSSION

It is evident that the calculations here offered are based on far from rigorous assumptions and it may well be that the kinematics of the phase changes has been over-simplified. However, while the thermodynamic free energies of two phases undoubtedly decide their relative stabilities, they provide no information about the kinematic path between the structures. The class of non-reconstructive or displacive transitions includes a number of cases in which such paths may be very simple and these offer an important opportunity to discuss the precise atomic movements involved in phase changes. From this point of view, it is contended that the present discussion, though imperfect, is meaningful since it is susceptible to test and may stimulate complementary investigations.

Long Price[10] (1967) has pointed out that results from Mössbauer experiments and specific heat measurements do not offer support for the suggested modes of transition along *TU*. However, measurements at atmospheric pressure cannot be regarded as ideally relevant and the dependence on (P,T) of the constants involved remains of crucial interest.

The macroscopic shear $(u,-u,\mathrm{o})$ which is suggested as the mode of melting might initially be expected to give rise to large vibrational amplitudes in the x and y directions as compared to the z-direction. However, there is internal strain along the z-direction associated with this shear so that marked anisotropy cannot be expected. Radial distributions in the liquid state have been compared with crystallographic data for white tin (SnI) but opinions appear to differ about the conclusions to be drawn from this evidence[11] (See Furukawa, 1962). A careful investigation of lattice amplitudes along the line ST would nevertheless be worthwhile. Measurements of $\frac{1}{2}(c_{11}-c_{12})$ in the neighbourhood of ST would also be most interesting. Similarly, it would be valuable to have further measurements of c_{13} as a function of (P,T).

The possibility of watching the pressure-dependence of the (A) mode in an inelastic scattering experiment should not be overlooked although it must be recognized that high-pressure techniques are generally suited to smaller samples than are required for work with neutrons. A further possibility is that analogous work on the P–T diagram for InSb would show a similar pattern and be interpretable in similar terms.

Acknowledgement—I wish to acknowledge the able assistance of Miss A. Kemp with the computations which are here reported.

REFERENCES

1. BARNETT J. D., BEAN V. E. and TRACY HALL H., *J. appl. Phys* **37**, 875 (1966).
2. STAGER R. A., BALCHAN A. S. and DRICKAMER H. G., *J. chem. Phys.* **37**, 1154 (1962).
3. JAMIESON J. C., Houston Meeting of the Geological Society of America (1962).
4. MUSGRAVE M. J. P., *Proc. R. Soc.* **A272**, 503 (1963), (I).
5. MUSGRAVE M. J. P., *J Phys. Chem. Solids* **24**, 557 (1963), (II).
6. LONG PRICE D. *Conf. Inelastic Scattering*, Vol. 1, p. 109. International Atomic Energy Agency, Vienna (1965).
7. RAYNE J. A. and CHANDRASEKHAR B. S., *Phys. Rev.* **120**, 1658 (1960).
8. BARNETT J. D., BENNION R. B. and HALL H. T., *Science* **141**, 1041 (1963).
9. MUSGRAVE M. J. P. and POPLE J A., *J. Phys. Chem Solids* **23**, 321 (1962).
10. LONG PRICE D, *Proc. R. Soc.* **A300**, 25 (1967).
11. FURUKAWA K., *Rep Prog Phys.* **25**, 395 (1962).
12. LEE J. A. and RAYNOR G. V, *Proc phys. Soc.* **B67**, 737 (1954)
13. BORN M., *J chem. Phys* **7**, 591 (1939).
14. BRILLOUIN L., *Phys Rev.* **54**, 916 (1938)
15. ALERS G A and NEIGHBOURS J.R., *J. Phys. Chem. Solids* 7, 58 (1958).
16. COCHRAN W., *Adv. Phys* **9**, 387 (1960).

J. Phys. Chem. Solids Pergamon Press 1969. Vol. 30, pp. 1097–1112. Printed in Great Britain.

THE INFLUENCE OF STATIC ATOMIC DISPLACEMENTS ON THE DIFFUSE INTENSITY SCATTERED BY SOLID SOLUTIONS

H. E. COOK
Metallurgy Department, Scientific Laboratory, Ford Motor Company,
Dearborn, Mich. 48121, U.S.A.

(*Received* 19 *September* 1968; *in revised form* 22 *October* 1968)

Abstract—The diffraction theory for solid solutions given by Matsubara and subsequently extended by Kanzaki and by Krivoglaz is used to examine the asymmetry in the diffuse intensity scattered by β brass and Cu_3Au and also the asymmetry in the satellite intensity diffracted by artificially produced silver–gold layered structures. Good agreement is found between the observed and predicted asymmetries.

1. INTRODUCTION

WHEN X-rays are diffracted by a crystal, their distribution in reciprocal space consists of sharp, intense Bragg peaks regularly spaced in a weak diffuse intensity. The Bragg peaks result from X-rays reflected in phase by the lattice planes; whereas, the diffuse intensity results from X-rays scattered by lattice imperfections such as phonons, dislocations, and impurity atoms. Phonon-scattered X-rays are by far the major portion of the diffuse intensity scattered by a pure, well-annealed crystal. In solid solutions X-rays are also scattered by the solute (impurity) atoms and by the static displacements resulting from the size difference between the solute and solvent atoms. These intensities which add to that from phonons, often constitute the major portion of the diffuse intensity scattered by a solid solution.

Matsubara[1] has shown that the Born and von Kármán[2, 3] microscopic theory of elasticity, developed for the dynamic properties of crystal lattices, can also be used to estimate the *static* distortions in solid solutions and, thus, the diffuse intensity of X-rays scattered by them. In this approach, which has been significantly extended by Kanzaki[4] and by Krivoglaz[5], the net force acting on an atom is separated into an internal force and a lattice force. The internal force is related to the solute distrubition and is assumed to be proportional to the size difference between solute and solvent atoms. The lattice force is assumed, as in the dynamic theory, to be proportional to the displacements of the atoms from their sites on the average lattice. The principal result used in the diffraction equations is the Fourier representation of the equilibrium balance between the internal and lattice forces. This is a linear relationship between the Fourier coefficients of the solute distribution and those of the displacement field, which on substitution into the diffraction equations allows the diffuse intensity (neglecting thermal diffuse scattering) to be written solely as a function of the solute distribution for a particular alloy system and composition.

In this paper the Matsubara, Kanzaki and Krivoglaz (M.K.K.) theory is used to analyze the diffuse intensity scattered by solid solutions of cubic symmetry. This provides a test of the theory while elucidating its important applications. The first portion is a review of the M.K.K. theory in which the equations are written in a form suitable for an analysis, which follows, of the asymmetry in the diffuse short-range order 'peaks' of β brass[6] and Cu_3Au[7]. Application of the equations to satellite theory[8–12] is then considered in an examination of the asymmetry in intensity of satellites diffracted by artificially produced silver–gold layered structures[13]. Finally, the results are summarized and the advantages and limitations of the theory are discussed.

2. THEORY

The diffraction equations for solid solutions

The scattered amplitude in electron units for a binary, substitutional alloy is

$$a(h) = \sum_p [f + (f_2 - f_1) q(p)] \times \exp\{-2\pi i s(h) \cdot [x(p) + u(p)]\}, \quad (1)$$

where f_1 and f_2 are the atomic scattering factors of components one and two respectively, f is the mean atomic scattering factor of the alloy, and $q(p)$ is the 'composition variation' at site (p):

$$q(p) = \begin{cases} 1 - c \text{ if an atom of component two is at site } (p), \\ -c \text{ if not,} \end{cases}$$

in which c is the atom fraction of component two. The single index (p) is shorthand for the triplet (p_1, p_2, p_3) determined from the vector

$$\mathbf{x}(p) = p_1\mathbf{a}_1 + p_2\mathbf{a}_2 + p_3\mathbf{a}_3$$

from the origin to site (p) on the undistorted lattice where $\mathbf{a}_1$, $\mathbf{a}_2$, and $\mathbf{a}_3$ are the usual, nonprimitive, lattice translation vectors of the b.c.c. or f.c.c. lattice. Thus, each p_i will be either an integer or half integer. The vector $\mathbf{u}(p)$ is the equilibrium displacement of the atom at site (p), and $\mathbf{s}(h)$ is the usual vector in 'diffraction space' or h-space:

$$\mathbf{s}(h) = (\mathbf{S} - \mathbf{S}_0)/\lambda_R$$

where $\mathbf{S}_0$ and $\mathbf{S}$ are unit vectors in the direction of the incident and diffracted beams, respectively, and λ_R is the wavelength of the radiation. The single index (h) is shorthand for (h_1, h_2, h_3) determined from the vector $\mathbf{s}(h)$ written in the form:

$$\mathbf{s}(h) = h_1\mathbf{b}_1 + h_2\mathbf{b}_2 + h_3\mathbf{b}_3, \quad (2)$$

where $\mathbf{b}_1$, $\mathbf{b}_2$ and $\mathbf{b}_3$ are the reciprocal lattice vectors:

$$\mathbf{b}_i \cdot \mathbf{a}_j = \delta_{ij},$$

in which δ_{ij} is the Kronecker delta.

The function $q(p)$, defined only at the lattice sites, can be represented by the Fourier polynomial:

$$q(p) = \sum_g Q(g) \exp[i\mathbf{k}(g) \cdot \mathbf{x}(p)], \quad (3)$$

where (g) is shorthand for (g_1, g_2, g_3) determined from the wave vector:

$$\mathbf{k}(g) = 2\pi(g_1\mathbf{b}_1 + g_2\mathbf{b}_2 + g_3\mathbf{b}_3). \quad (4)$$

If for simplicity, we assume that the crystal is a large cube containing L^3 unit cells then each

$$g_i = \frac{m_i}{L}, \qquad (i = 1, 2, 3)$$

where m_i is one of the integers $-n, -n+1, \ldots, n-1, n$ which determine the coordinate g_i of an 'allowed' site (g) in the first Brillouin zone; the summation in equation (3) is over all the sites (g) in the zone. Similarly, we can write the Cartesian components of the displacements as

$$u_i(p) = \sum_g U_i(g) \exp[i\mathbf{k}(g) \cdot \mathbf{x}(p)].$$

When the product $\mathbf{s}(h) \cdot \mathbf{u}(p)$, which appears in the argument of the exponential in equation (1), is small, it follows that

$$\exp\{-2\pi i \mathbf{s}(h) \cdot [\mathbf{x}(p) + \mathbf{u}(p)]\}$$
$$\simeq [1 - 2\pi i \mathbf{s}(h) \cdot \mathbf{u}(p)] \exp[-2\pi i \mathbf{s}(h) \cdot \mathbf{x}(p)]. \quad (5)$$

This approximation will usually be valid in a (roughly) spherical region about the origin of diffraction space extending to the nearest Bragg peaks. As the distance, $|\mathbf{s}(h)|$, from the origin increases so does the error in the approximation. Upon replacing the exponential in equation (1) by the right-hand side of equation (5) and $q(p)$ and $\mathbf{u}(p)$ by their respective Fourier polynomials, we find that the *diffuse* intensity (neglecting thermal diffuse scattering and the higher order term involving the product of $\mathbf{u}(p)$ and $q(p)$ in the amplitude expression) is†

$$\begin{aligned} i(h=h'+g) &\equiv |a(h)|^2 \\ &\simeq N^2|(f_2-f_1)Q(g) \\ &\quad -(2\pi if/a)h_jU_j(g)|^2 \qquad (6) \end{aligned}$$

where N is the number of atoms in the crystal.

The force-balance equations

For cyclic boundary conditions, Krivoglaz [5] has shown using the microscopic theory that the equilibrium balance between the solute and lattice forces yields the relation:

$$U_j(g) = -\Theta_j(g)Q(g). \qquad (7)$$

A derivation of this equation is given in Appendix A. The function $\Theta_j(g)$ which connects the solute and displacement Fourier coefficients can be written in a relatively simple form when the wave vector is in either the [100], [110] or [111] directions (summation convention is not implied here)[14]:

$$\Theta_j(g) = \frac{\Phi_j(g)}{h\Phi_{j1}(g)+k\Phi_{j2}(g)+l\Phi_{j3}(g)}$$

$$\text{(high symmetry direction)}, \qquad (8)$$

where h, k and l, either zero or one denote the high-symmetry direction $[hkl]$. The functions $\Phi_j(g)$ and $\Phi_{jk}(g)$ are the Fourier transforms of the solute-lattice and lattice coupling parameters[14], respectively. (The lattice coupling parameters are often called 'atomic force constants'.) The general expressions for these transforms and for the function $\Theta_j(g)$ are given in Appendix A.

Equation (7) allows the displacement Fourier coefficients in the intensity expression, equation (6), to be replaced by the product $-\Theta_j(g)Q(g)$. After this replacement, the intensity, in Laue units, is given by

$$\begin{aligned} I(h=h'+g) &\equiv \frac{i(h)}{N|f_2-f_1|^2c(1-c)} \\ &\simeq \frac{C(g)}{|f_2-f_1|^2}\Big|(f_2-f_1) \\ &\quad +(2\pi if/a)h_j\Theta_j(g)\Big|^2 \qquad (9) \end{aligned}$$

where

$$C(g) = C(-g) \equiv \frac{NQ(g)Q^*(g)}{c(1-c)}. \qquad (10)$$

Since the solute variation $q(p)$ and the components $u_i(p)$ of the displacement vector are assumed to obey cyclic boundary conditions, it follows that their Fourier coefficients are periodic in h-space:

$$Q(g) = Q(h'+g)$$

$$U_j(g) = U_j(h'+g),$$

and likewise the function connecting them in equation (7):

$$\Theta_j(g) = \Theta_j(h'+g).$$

We may, therefore, write equation (9) in the simpler form[5]:

$$\begin{aligned} I(h) &\simeq \frac{C(h)}{|f_2-f_1|^2}\Big|(f_2-f_1) \\ &\quad +(2\pi if/a)h_j\Theta_j(h)\Big|^2. \qquad (11) \end{aligned}$$

---

† Summation over repeated subscripts is implied and $(h'+g)$ is shorthand for $(h_1'+g_1, h_2'+g_2, h_3'+g_3)$ where (h') is the site of the Bragg peak nearest (h).

This equation relates the diffuse intensity in Laue units to the function $C(h)$, defined by equation (10). This function equals the diffuse intensity when there is no size difference and is usually termed the short-range order intensity.

The size-effect intensity and the Huang peak

Borie[15], in his formulation of this problem, found it advantageous to break the diffuse intensity into three terms: the short-range order intensity, the 'size-effect' intensity[16], and the Huang peak[17]. These separate intensities are also included in equation (11). The short-range order intensity at site (h) is, of course, $C(h)$. The presence of the size-effect intensity and the Huang peak is somewhat obscure and it is advantageous to discuss them for a simpler form of equation (9), the intensity along the [100] direction in h-space scattered by a random distribution of solute on an f.c.c. lattice. For this case it is well known that the short-range order intensity, given by equation (10), is uniform and equal to unity. If, for simplicity, only nearest neighbor interactions are assumed, then the long wave relations in Table A.5 for f.c.c. crystals can be used to express the coupling parameters uniquely in terms of the macroscopic elastic constants:

$$a_1 = ac_{11}/4,$$

$$\hat{\alpha}_1 = a^2\eta(c_{11}+2c_{12})/16$$

where $\eta(=da/adc)$ is the linear expansion coefficient per unit composition change. With this assumption, it follows from equation (8) and the expressions for $\Phi_I(h)$ and $\Phi_{II}(h)$ in Table A.2 that

$$\Theta_I(h_1,0,0) = \left(\frac{a\eta}{4}\right)\left(\frac{c_{11}+2c_{12}}{c_{11}}\right)\left(\frac{i\sin\pi h_1}{1-\cos\pi h_1}\right).$$

Thus, if the scattering factors are real, the intensity given by equation (11) is

$$I(h_1,0,0) = 1-2B\frac{h_1\sin\pi h_1}{1-\cos\pi h_1} + B^2\left(\frac{h_1\sin\pi h_1}{1-\cos\pi h_1}\right)^2 \qquad (12)$$

for this example where

$$B = \pi f\eta(c_{11}+2c_{12})/[(f_2-f_1)2c_{11}].$$

The first term, unity, on the right-hand side of equation (12) is the short-range order intensity. The second and third terms are the size-effect intensity and the Huang peak, respectively. The functions

$$\frac{\sin\pi h_1}{1-\cos\pi h_1}, \frac{h_1\sin\pi h_1}{1-\cos\pi h_1}, \left(\frac{h_1\sin\pi h_1}{1-\cos\pi h_1}\right)^2$$

are shown in Fig. 1. The first is asymmetric about every Bragg peak: $h_1 = 0, 2, 4, \ldots$ Multiplication by h_1 yields a term proportional to the size-effect intensity which is symmetric about the origin but asymmetric about the other Bragg peaks and the superlattice positions: $h_1 = 1, 3, 5, \ldots$ The square of this function is proportional to the Huang peak for this direction in h-space. It is zero at the superlattice reflections but very large in the vicinity of the Bragg peaks. (The approximation in equation (6) will, therefore, break down very close to a Bragg peak.)

Evaluating the Warren short-range order parameters

Now that we are confident that the three intensities described by Borie are included in equation (9), we shall not continue with a separate consideration of each because no advantage is realized here by doing so. Often only the short-range order intensity is of interest:

$$C(h) = I(h)G(h), \qquad (13)$$

where from equation (11),

$$G(h) = \frac{|f_2 - f_1|^2}{|(f_2 - f_1) + (2\pi i f/a) h_j \Theta_j(h)|^2} \tag{14}$$

is a function which converts $I(h)$ upon multiplication into the short-range order intensity at (h). Because this operation 'corrects' the diffuse intensity for the 'size-effect' and Huang modulations, we will term $G(h)$ the intensity correction function.

Since equation (13) relates the short-range order intensity at (h) to the diffuse intensity there, it allows us to obtain the Warren short-range order parameters defined by the equation:

$$\alpha(p) = \frac{1}{z} \iiint_{B-Z} \times C(h) \exp\left[2\pi i s(h) \cdot x(p)\right] \mathrm{d}h_1 \, \mathrm{d}h_2 \, \mathrm{d}h_3 \tag{15}$$

where z is the number of atoms in a unit cell and the integral is over the first Brillouin zone. From equation (13), we see that:

$$\alpha(p) = \frac{1}{z} \iiint_{B-Z} I(h) G(h) \times \exp\left[2\pi i s(h) \cdot x(p)\right] \mathrm{d}h_1 \, \mathrm{d}h_2 \, \mathrm{d}h_3. \tag{16}$$

This equation, first obtained by Krivoglaz[5], should be very useful for extracting the short-range order parameters from the diffuse intensity. The equation has a simple form and includes, properly, the 'size-effect' and Huang corrections in the function $G(h)$. This correction function is valid, in principle, over the entire Brillouin zone, the volume of integration; whereas, the 'size-effect' correction of Warren, Averbach, and Roberts is only valid near the superlattice positions (unless a large number of Fourier coefficients are used) and equations for the Huang peak based on continuum elasticity theory are valid only in the vicinity of the Bragg peaks.

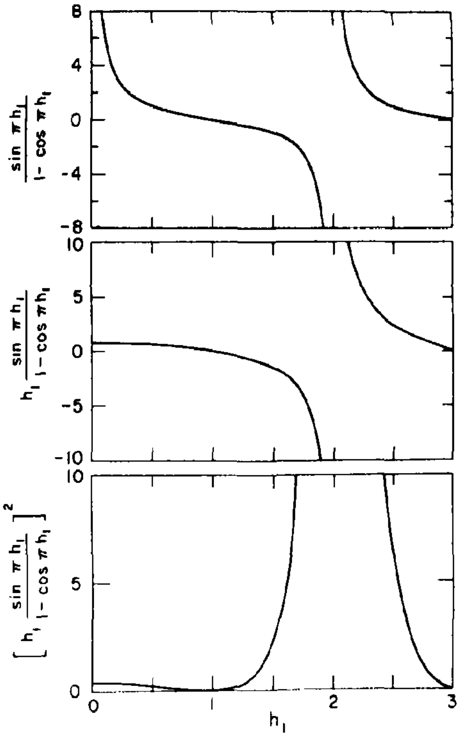

Fig. 1. Functions related to the diffuse scattering by static displacements when the solute is randomly distributed: $(\sin \pi h)/(1 - \cos \pi h)$ is asymmetric about every Bragg peak; multiplied by h it yields a function proportional to the size-effect intensity[16]. The square of the latter is proportional to the Huang peak[17].

3. THE DETERMINATION OF THE SOLUTE-LATTICE COUPLING PARAMETERS

The function $G(h)$ can be evaluated from the atomic scattering factors, the elastic constants and the lattice and solute-lattice coupling parameters. The lattice coupling parameters have been measured for a substantial number of pure crystals and ordered alloys. Thus rough estimates for a variety of disordered alloys can be obtained by interpolating the pure-crystal values or by averaging the values coupling the displacements of the different types of atoms in the ordered crystal. Moreover, the lattice coupling parameters can be measured directly for disordered alloys in which the mass difference between solute and solvent atoms is small

[18–20]. The most extensive measurements are for the niobium-molybdenum system[19].

As we shall now show, the solute-lattice coupling parameters can be determined from an analysis of the asymmetry in intensity of the diffuse short-range order peaks provided that the lattice coupling parameters are known. To do this it is necessary to obtain the intensity ratio

$$R(\epsilon) = I(h''+\epsilon)/I(h''-\epsilon) \qquad (17)$$

where (h'') is a superlattice position and $(h''-\epsilon)$ and $(h''+\epsilon)$ are sites equally distant from (h'') on a line from the origin passing through the superlattice position. Since the short-range order intensity, C in equation (10), is the same at $(h''\pm\epsilon)$, the theoretical value for this ratio is from equation (13):

$$R(\epsilon) = G(h''-\epsilon)/G(h''+\epsilon). \qquad (18)$$

We see from the definitions of $G(h)$, equation (14), and the function $\Theta_i(h)$, equation (8), that the solute-lattice coupling parameters can be evaluated by fitting the theoretical ratio, equation (18), to experimental intensity ratios. After the solute-lattice coupling parameters have been determined in this manner, they can be used with the lattice coupling parameters and atomic scattering factors to determine the correction function, $G(h)$, itself.

To demonstrate this method, we have fitted the function $R(\epsilon)$ to the intensity ratios measured by Walker and Keating[6] and by Moss[7] along the [100] direction in h-space for β brass and Cu_3Au, respectively. The lattice coupling parameters for these systems have not been measured directly and it is necessary, therefore, to estimate them. Thus the values for the solute-lattice coupling parameters will also be estimates. This is of little consequence for our purposes since the analyses provide a test of the theory and do yield a set of self-consistent coupling parameters adequate for the determination, along the [100] direction, of the intensity correction function, $G(h)$, and the short-range order intensity, $C(h)$.

Using the values tabulated in Tables A.1 and A.2 for the Fourier transforms of the coupling parameters, we find from equation (8) that

$$\Theta_1(h_1,0,0) = \frac{i[\hat{\Psi}_1 \sin \pi h_1 + \hat{\Psi}_2 \sin 2\pi h_1]}{\Psi_1(1-\cos \pi h_1)+\Psi_2(1-\cos 2\pi h_1)} \qquad (19)$$

and

$$\Theta_2(h_1,0,0) = \Theta_3(h_1,0,0) = 0,$$

when the wave vector is in the [100] direction. The coefficients Ψ_1, Ψ_2, $\hat{\Psi}_1$ and $\hat{\Psi}_2$, which can be interpreted as interplanar coupling parameters, are given by the relations:

$$\hat{\Psi}_1 = 8\hat{\alpha}_1$$

$$\hat{\Psi}_2 = 2\hat{\alpha}_2 + 8\hat{\alpha}_3 \qquad \text{(b.c.c.)}$$

$$\Psi_1 = 8\alpha_1$$

and

$$\Psi_2 = 2\alpha_2 + 8\alpha_3$$

for b.c.c. crystals, and by

$$\hat{\Psi}_1 = 8\hat{\alpha}_1 + 16\hat{\beta}_3$$

$$\hat{\Psi}_2 = 2\hat{\alpha}_2 + 8\hat{\alpha}_3 \qquad \text{(f.c.c.)}$$

$$\Psi_1 = 8\alpha_1 + 16\beta_3$$

and

$$\Psi_2 = 2\alpha_2 + 8\alpha_3$$

for f.c.c. crystals. The shorthand notation used for the coupling parameters is described in Tables A.3 and A.4.

β Brass

We have estimated the lattice coupling parameters for disordered β brass by averaging those for the ordered alloy[21] coupling the displacements between copper–copper and zinc–zinc atoms. These values were then corrected to the temperature, 543°C, where the diffuse intensity was measured[6] by requiring them to obey the first long wave relation for b.c.c. crystals in Table A.5, c_{11} being evaluated from the results of McManus [22]. The values estimated are†

$$\alpha_1 = 8315, \alpha_2 = 3817, \alpha_3 = 1116.$$

The function

$$R(\epsilon_1, 0, 0) = G(1-\epsilon_1, 0, 0)/G(1+\epsilon_1, 0, 0)$$

is shown in Fig. 2 for three ratios of $\hat{\Psi}_2/\hat{\Psi}_1$–the individual values being determined from the long wave relation:

$$\hat{\Psi}_1 + 2\hat{\Psi}_2 = a^2\eta(c_{11}+2c_{12}) \qquad \text{(b.c.c.)}$$

which follows from the b.c.c. long wave relations in Table A.5. The value for

$$\eta = \frac{da}{a\,dc_{Zn}} = 0{\cdot}068$$

was obtained from the composition variation of the lattice parameter reported by Beck and Smith[23]; the lattice parameter a is 3·0 Å at 543°C. The scattering lengths for the isotopes of zinc (natural) and copper (98·3% Cu^{65})[6, 24] were substituted for f_2 and f_1, respectively, following the convention of zinc being component two used in the determination of the sign of η. The points are the intensity ratios $I(1+\epsilon_1, 0, 0)/I(1-\epsilon_1, 0, 0)$ at 543°C measured by Walker and Keating[7].

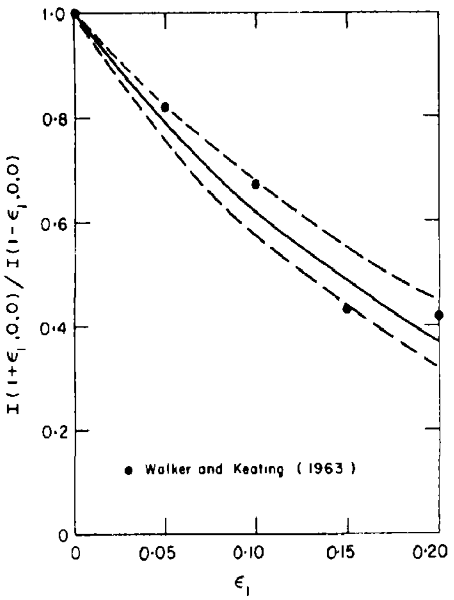

Fig. 2. Ratio of the diffuse intensities at equal distances ϵ_1 about the 100 (superlattice) position along the [100] direction in β brass h-space at 543°C[6] The curves are theoretical ratios obtained using the following interplanar coupling parameters:

Curve	Ψ_1	Ψ_2	$\hat{\Psi}_1$	$\hat{\Psi}_2$
Lower dashed	$6{\cdot}65 \times 10^4$	$1{\cdot}65 \times 10^4$	$1{\cdot}78 \times 10^{-4}$	0
Solid (best fit)	$6{\cdot}65 \times 10^4$	$1{\cdot}65 \times 10^4$	$1{\cdot}6 \times 10^{-4}$	$5{\cdot}6 \times 10^{-6}$
Upper dashed	$6{\cdot}65 \times 10^4$	$1{\cdot}65 \times 10^4$	$1{\cdot}42 \times 10^{-4}$	$1{\cdot}48 \times 10^{-5}$

The best fit is obtained for the ratio $\hat{\Psi}_2/\hat{\Psi}_1 = 0{\cdot}035$ and is shown by the solid curve. The lower dashed curve is for $\hat{\Psi}_2 = 0$ and the upper for a ratio of 0·104. A repeat of this procedure using the 111 short-range order peak would allow $\hat{\alpha}_2$ and $\hat{\alpha}_3$ to be determined independently since they appear as coefficients of different functions in this case (See Table A.1).

The values $\hat{\Psi}_1 = 1{\cdot}58 \times 10^{-4}$, $\hat{\Psi}_2 = 5{\cdot}6 \times 10^{-6}$, for the best fit in Fig. 2 were used to obtain the short-range order intensity using equation (9). The results are listed in Table 1. The intensity $I(1 \pm \epsilon_1, 0, 0)$, uncorrected for the size-effect, is seen to be very asymmetric about the superlattice position. The short-range order intensity given by equation (13), however, is symmetric within experimental error. Walker and Keating[6] used the method of Warren, Averbach and Roberts[16] to

---

†All lattice coupling parameters are given in units of dyn/cm, and all solute-lattice coupling parameters are given in units of dynes.

Table 1. *Diffuse intensity of β brass at* 543°C [6]

	Measured intensity [6]†		Short-range order intensity, equation (13)	
ϵ_1	$I(1-\epsilon_1, 0, 0)$	$I(1+\epsilon_1, 0, 0)$	$C(1-\epsilon_1, 0, 0)$	$C(1+\epsilon_1, 0, 0)$
0	9·00	9·00	9·0	9·0
0·05	8·40	6·95	7·5	7·9
0·10	6·45	4·30	5·3	5·7
0·15	4 55	1·95	3·4	3·1
0·20	3·05	1·28	2·2	2·4

†The thermal diffuse intensity has been subtracted.

correct for the size effect and the resulting short-range order peak was still significantly asymmetric. This was interpreted as a peak displacement to lower angles in contrast to short-range order studies on copper–gold alloys where a shift to higher angles is observed. The peak shifts in both systems seem to be a result of inadequate size-effect corrections and are not related to fine structure such as ordered nuclei, often suggested as a possible cause of this effect in copper–gold alloys.

Cu_3Au

The function $R(\epsilon_1, 0, 0)^{-1}$ and the intensity ratios $I(1-\epsilon_1, 0, 0)/I(1+\epsilon_1, 0, 0)$ measured by Moss[7] for Cu_3Au at 405° and 450°C are shown in Fig. 3. Since the elastic constants do not change markedly between these temperatures[25], the microscopic theory predicts that the intensity ratio $I(1-\epsilon_1, 0, 0)/I(1+\epsilon_1, 0, 0)$ should be the same at both temperatures. This is in fact observed, even though the individual intensities changed significantly between the two temperatures [7].

The lattice coupling parameters for pure copper[26] (neither those for pure gold nor those for the ordered alloy have been measured) and the high temperature elastic constants for Cu_3Au[25] were used to estimate Ψ_1 and Ψ_2 for the alloy:

$$\Psi_1 = 10{\cdot}6 \times 10^4, \Psi_2 = 0{\cdot}32 \times 10^4.$$

The dashed curve in Fig. 3 was calculated using these values with the assumption of solute-lattice coupling between nearest-neighbors only:

$$\hat{\Psi}_2 = 0$$

and

$$\hat{\Psi}_1 = \frac{a^2\eta}{2}(c_{11} + 2c_{12})$$
$$= -4{\cdot}3 \times 10^{4} \qquad (20)$$

at 405°C. The value for

$$\eta = \frac{da}{adc_{Cu}}$$
$$= -0{\cdot}148$$

was obtained from the lattice parameter measurements compiled by Pearson[27], and the value of 3·77 Å was used for the lattice parameter, a. The Thomas-Fermi-Dirac values were added to the real and imaginary parts of the Hönl correction[28] in the evaluation of the atomic scattering factors f_1 and f_2 for gold and copper, respectively.

The fit cannot be improved by assuming that solute-lattice coupling parameters for second or third neighbors are non-zero. It can, however, be improved by assuming that the ratio of interplanar coupling parameters, Ψ_2/Ψ_1, in the alloy is greater than for pure copper. The solid curve is for $\hat{\Psi}_1$ equal to the value given by equation (20) and for a ratio

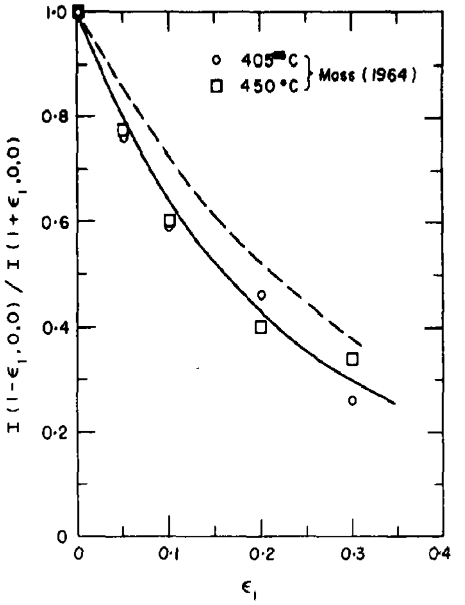

Fig. 3. Ratio of diffuse intensities at equal distances ϵ_1 about the 100 (superlattice) position along the [100] direction in Cu_3Au h-space at 405° and 450°C[7]. The curves are theoretical ratios obtained using the following interplanar coupling parameters:

Curve	Ψ_1	Ψ_2	$\hat{\Psi}_1$	$\hat{\Psi}_2$
Dahsed (Ψ_1 and Ψ_2 estimated from pure Cu force constants[26])	$10\cdot6\times10^4$	$0\cdot32\times10^4$	$4\cdot3\times10^{-4}$	0
Solid (best fit)	$7\cdot75\times10^4$	$1\cdot07\times10^4$	$4\cdot3\times10^{-4}$	0

of $\Psi_2/\Psi_1 = 0\cdot138$, which from the relation $\Psi_1 + 4\Psi_2 = 2ac_{11}$ yields:

$$\Psi_1 = 7\cdot75\times10^4, \Psi_2 = 1\cdot07\times10^4.$$

These values were used to obtain the short-range order intensity from the measured values of $I(h_1, 0, 0)$[7], and the results are listed in Table 2. The short-range order intensity $C(h_1, 0, 0)$ is, within experimental error, symmetric about the superlattice position as required by theory.

4. SATELLITES IN SILVER-GOLD LAYERED STRUCTURES

The Fourier representation of the force balance, equation (7), expresses a correlation between the composition and displacement modulations. If, for example, the composition modulation is a sine wave:

$$q(p) = A \sin \mathbf{k}(g)\cdot\mathbf{x}(p)$$

the displacement modulation will be a cosine wave of the same wave vector:

$$u_j(p) = i\Theta_j(g)A \cos \mathbf{k}(g)\cdot\mathbf{x}(p).$$

The displacement equation follows because the proportionality coefficient, $\Theta_j(g)$, in the force balance equation is purely imaginary with $\Theta_j(g) = -\Theta_j(-g)$. (This can be shown to follow from equation A-6 and the properties of the Fourier transforms of the coupling parameters[14].) A correlation of this type between the composition and displacement modulations is intuitive and is always assumed in discussions on satellite theory[8-12] in which the intensity scattered by a planar lattice having a sinusoidal composition modulation of long wavelength is usually calculated. That theory, however, incorporates a strain parameter which is known only to be proportional to the size difference. The important influence of elastic anisotropy on the strain parameter, for example, is not included.

The satellite problem can also be treated by the M.K.K. theory, which is not limited to a planar lattices and long wavelength composition modulations and uses elasticity theory to determine the strain parameter or, more generally, the function $\Theta_j(h)$. Since the M.K.K. theory uses Fourier methods, the resulting equations can be applied directly to the satellite intensity problem.

Satellites about a 222 peak diffracted by a silver-gold, layered structure are shown in Fig. 4. The structure was produced by evaporating alternate layers of silver and gold onto a mica substrate and was used to study interdiffusion over short distances at low temperatures[13]. The particular, as-evaporated, specimen shown in Fig. 4 had a mean composition of 32·0 at. pct gold, a total thickness

Table 2. Diffuse intensity of Cu_3Au *at* 405° *and* 450°C [7]

Temperature (°C)	ϵ_1	Measured intensity [7]† $I(1-\epsilon_1, 0, 0)$	$I(1+\epsilon_1, 0, 0)$	Short-range order intensity, equation (13) $C(1-\epsilon_1, 0, 0)$	$C(1+\epsilon_1, 0, 0)$
405	0	13·13	13·13	13·13	13·13
	0·05	9·02	11·85	10·05	10·59
	0·10	4·23	7·12	5·12	5·58
	0·20	1·23	2·66	1·81	1·68
	0·30	0·47	1·80	0·79	0·91
450	0	6·56	6·56	6·56	6·56
	0·05	4·85	6·28	5·40	5·61
	0·10	2·92	4·83	3·60	3·85
	0·20	1·09	2·67	1·60	1·68
	0·30	0·54	1·55	0·92	0·78

†The thermal diffuse and Compton modified intensities have been subtracted

of 4710 Å and the average spacing for each silver plus gold layer was ≈ 33 Å. The satellites resulted from X-rays scattered by the Fourier coefficient of the composition modulation having a wavelength equal to the 33 Å layer spacing. (Although not shown in Fig. 4, satellites associated with the higher harmonics of the composition modulation were sometimes observed in the as-evaporated films, particularly at low angles where the intensity is greatest.) According to satellite theory, the atom with the largest scattering factor, gold, is smaller in solution than the other atom, silver because the satellite at higher angles is more intense[11].

Only the 111 and 222 Bragg peaks were observed for the θ–2θ scan of this specimen in which a normal to the substrate bisected the angle formed by the incident and diffracted beams. This indicates that most of the grains in the film had their [111] direction perpendicular to the substrate. Furthermore, it follows that the wave vector $\mathbf{k}(g)$ for the Fourier coefficient associated with the satellites is in the [111] direction:

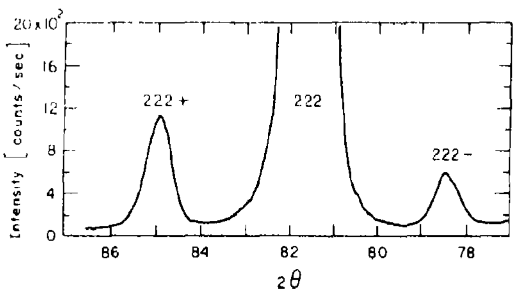

Fig. 4. Chart scan of intensity about 222 peak diffracted by Ag-32 at pct Au layered structure showing asymmetry in satellite intensity caused by the correlation between scattering factor and displacement modulations.

$$\mathbf{k}(g) = 2\pi g(\mathbf{b}_1 + \mathbf{b}_2 + \mathbf{b}_3) \tag{21}$$

of magnitude

$$\begin{aligned} k(g) &= 2\pi/\lambda, \\ &= 2\pi\sqrt{3}g/a \end{aligned} \tag{22}$$

where the wavelength λ is equal to the mean thickness of a gold plus silver layer.

Since equation (9) is written for the intensity scattered by a sinusoidal composition wave, it can be used for a quantitative evaluation of the asymmetry in satellite intensity. When the wavelength is large compared to the lattice parameter a, we can estimate the satellite intensities from equation (9) by replacing the trigonometric functions which appear in the explicit expressions for $\Phi_i(g)$ and $\Phi_{ij}(g)$ (see Table A.2) by the leading terms in their expansions about $g_i = 0$; $i = 1, 2, 3$. The sums of coupling parameters which then occur can be expressed in terms of the macroscopic elastic constants using the long wave relations in Table A.5 On doing this we find

$$S(n \pm d/\lambda) \approx KN(A^2/4)\left|(f_2 - f_1) - \frac{(n \pm d/\lambda)f\eta 3(c_{11} + 2c_{12})}{(\pm d/\lambda)(c_{11} + 4c_{44} + 2c_{12})}\right|^2 \quad (23)$$

for the satellite intensity at site (h, h, h) in which each $h = h' \pm g = n \pm d/\lambda$ where d is the spacing between 111 planes and n is the order of the reflection—$n = 0$ for satellites about the origin, $= 1$ about 111 peak, $= 2$ about 222, etc. The parameter K includes the various corrections such as the Lorentz, polarization, etc., which convert the theoretical intensity in electron units to the measured intensity. The various corrections used are described in Appendix B.

To test equation (23) against the measured satellite intensities, we have calculated the ratio $S(n + d/\lambda)/S(n - d/\lambda)$ as a function of η. (The elastic constants were interpolated from those tabulated by Huntington[29].) The result is shown in Fig. 5 for a 32 at.pct Au specimen where the measured intensity ratio is shown as a horizontal line. The calculated ratio fits the measured ratio at $-\eta = 0{\cdot}0033$. This value is in good agreement with the value 0·0037 estimated from the precision lattice parameter data for Sachs and Weerts[30]. Results of this calculation for other layered structures used in the diffusion measurements are shown in Table 3. (Several specimens having very short wavelengths ($\approx 7{\cdot}5$ Å) were used in the diffusion experiments[13], but the intensity of these satellites was appreciable only about the 000 reflection where the procedure described here for estimating η cannot be used.) The results are summarized in Fig. 6 where the lattice parameters and slopes $da/dc = a\eta$ are compared with the measurements of Sachs and Weerts[30]. The lattice parameters of the layered structures were determined from the position of the 222 peak and thus are not highly accurate. The change in lattice parameter as a result of diffusion is more reliable and is, roughly, equal to the difference between the lattice parameter of the homogeneous alloy measured by Sachs and Weerts and the Vegard's Law value. Moreover, the value of η changed as diffusion progressed. The values determined from the as-deposited structures, listed as η_0 in Table 3, are less in absolute value than those obtained after appreciable diffusion had occurred. The

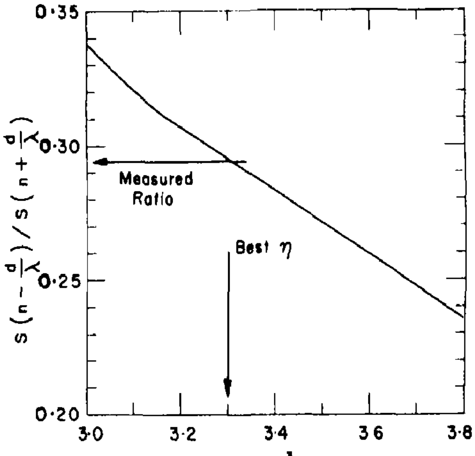

Fig. 5. The theoretical variation of the satellite intensity ratio as a function of η. The calculations are for satellites about the 222 Bragg peak of a 32 at.pct Au specimen having a 33 Å layer spacing. Plots of this type were used to determine η from the measured satellite intensity ratios.

Table 3. η values obtained from ratios of satellite intensity diffracted by silver–gold layered structures

Composition (at.pct) Au	Wavelength (Å)	$\eta_0 \times 10^3$	$\eta \times 10^3$	Estimated $\eta \times 10^3$†
18·1	22·1	−3·1	−5·1	−5·9
32·0	33·5	−2·3	−3·3	−3·7
37·9	19·5	−2·2	−3·0	−2·9
37·9	21·6	−2·3	−2·8	−2·9
50·0	24·2	−1·1	−2·4	−1·7
50·0	24·4	−0·9	−1·3	−1·7

†Estimated from the precision lattice parameter measurements of Sachs and Weerts[30]

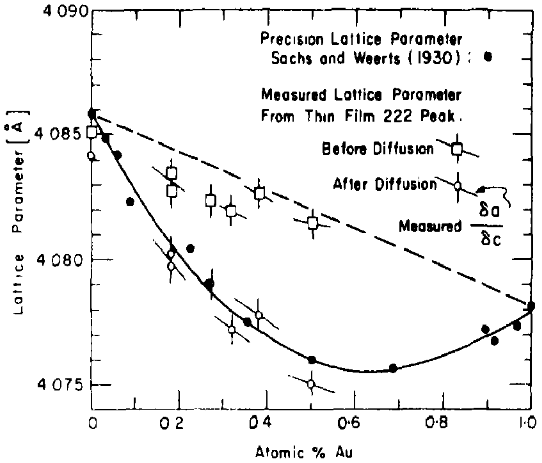

Fig. 6 Changes in lattice parameter and da/dc ($=a\eta$) during annealing of the layered structured compared with the difference between the Vegard's law and homogeneous solid solution values for these quantities[30]

latter are listed as η and were measured when the mean value of the satellite intensities was between 0·3 and 0·4 of their mean value in the as-deposited structures. They agree quite well with values estimated from the slope of a smooth curve through the precision lattice parameters. Thus, as diffusion progressed, the lattice parameter and η ($= da/adc$) changed from their Vegard's Law values to the homogeneous solution values. It was important to recognize this in the diffusion experiments because the change in η was a major source of the initial non-linear behavior in the log intensity versus time curves used to determine the diffusivities. (See, for example, Fig. 2 in reference [13].)

5. SUMMARY AND DISCUSSION

The results presented here support the M.K.K. theory. Agreement between the η values obtained from the satellite intensity ratios and the values obtained from the precision lattice parameter measurements of Sachs and Weerts is particularly significant because the constants in the expression for the satellite intensity, equation (23), were not at our disposal. In the analyses of the asymmetry in the diffuse short-range order peaks, the coupling parameters were chosen so that the theoretical expression for the intensity ratio, $R(\epsilon)$ in equation (18), agreed with the experimental ratios obtained from the results of Walker and Keating[6] for β brass and of Moss[7] for Cu_3Au. It is important to note, however, that a major prediction of the theory and one which could be tested without knowing the coupling parameters was the invariance of the intensity ratio to changes in the amount of short-range order, Fig. 3.

Selecting the solute-lattice coupling parameters such that the theoretical intensity ratio fits the experimental ratio is, of course, a method for evaluating these coupling parameters. A proper evaluation, however, awaits a direct determination by neutron diffraction techniques of the lattice coupling parameters for the disordered alloys. The β brass system appears promising for this because the phonon groups are not excessively wide for the disordered alloy[21] and the asymmetry of the short-range order peak is pronounced.

The methods used are sufficient, nevertheless, to determine the function $\Theta_j(h)$ with reasonable accuracy. The latter can be used in conjunction with the scattering factors to obtain the intensity correction function, $G(h)$, given by equation (14). Multiplication of the measured diffuse intensity in Laue units (corrected for background, Compton modified, and thermal diffuse scattering) by $G(h)$ yields the short-range order intensity, equation (13). As shown by Tables 1 and 2, the short-range order intensity obtained by this method was, as required, symmetric about the superlattice reflection sites. A useful property of the intensity correction function should be its insensitivity to variations in short-range order since once it has been determined for a particular system it will not need to be re-evaluated for subsequent experiments in which the short-range order intensity is varied.

Acknowledgements—The author is grateful to Drs. C. B. Walker and D. T. Keating and to Professor S. C. Moss who so kindly supplied their diffuse intensity measurements; the silver–gold layered structures were prepared and examined at Northwestern University as part of a research program directed by Professor J. E. Hilliard and supported by the National Science Foundation. The author would like to thank Professor P. Perio and Dr. D. de Fontaine for several stimulating discussions concerning satellite theory and is indebted to Dr. T. L. Johnston and Professor Hilliard for critical reviews of an earlier manuscript.

REFERENCES

1. MATSUBARA T. J., *J. phys. Soc. Japan* **7**, 270 (1952).
2. BORN M. and VON KÁRMÁN T., *Phys. Z* **13**, 297 (1912); *ibid.* **14**, 15 (1913).
3. BORN M. and HUANG K., In *Dynamical Theory of Crystal Lattices*. Oxford University Press, Oxford (1954).
4. KANZAKI H., *J. Phys. Chem. Solids* **2**, 24, 107 (1957).
5. KRIVOGLAZ M. A., *Soviet Phys. JETP* **34**, 139 (1958).
6. WALKER C. B. and KEATING D. T., *Phys. Rev.* **130**, 1726 (1963).
7. MOSS S. C., *J. appl. Phys.* **35**, 3547 (1964).
8. DANIEL V. and LIPSON H., *Proc. R. Soc.* **A181**, 368 (1943); *ibid.* **A182**, 378 (1944).
9. HARGREAVES M. E., *Acta crystallogr.* **4**, 301 (1951).
10. JEHANNO G. and PERIO P., *J. Phys. Radium* **23**, 854 (1962); *ibid.* **25**, 966 (1964).
11. GUINIER A., In *X-ray Diffraction in Crystals, Imperfect Crystals, and Amorphous Bodies*, pp 279–282. Freeman, San Francisco (1963).
12. DE FONTAINE D., In *Local Atomic Arrangements Studied by X-ray Diffraction* (Edited by J. B. Cohen and J. E. Hilliard), pp. 51–94. Gordon and Breach, New York (1966).
13. COOK H. E. and HILLIARD J. E., *J. appl Phys.* In press (1969).
14. COOK H. E. and DE FONTAINE D., *Acta Metall.* In press.
15. BORIE B., *Acta crystallogr.* **10**, 89 (1957); *ibid.* **12**, 280 (1959).
16. WARREN B. E., AVERBACH B. L. and ROBERTS B. W., *J. appl. Phys.* **22**, 1493 (1951).
17. HUANG K., *Proc. R. Soc.* **A190**, 102 (1947).
18. WOODS A. D. B. and POWELL B. M., *Phys. Rev. Lett.* **15**, 778 (1965).
19. POWELL B. M., MARTEL P. and WOODS A. D. B., To be published.
20. NG S C and BROCKHOUSE B. N., *Solid State Commun.* **5**, 79 (1967).
21. GILAT G. and DOLLING G., *Phys. Rev.* **138**, A1053 (1965).
22. MCMANUS G. M., *Phys. Rev* **129**, 2004 (1963).
23. BECK L. H. and SMITH C. S., *J. Metals* **4**, 1079 (1952).
24. KEATING D. T, NEIDHARDT W. J. and GOLAND A. N, *Phys. Rev.* **111**, 261 (1958).
25. SIEGEL S, *Phys. Rev.* **57**, 537 (1940).
26. SINHA S. K., *Phys. Rev.* **143**, 422 (1966).
27. PEARSON W. B, In *A Handbook of Lattice Spacings and Structures of Metals and Alloys*, Fig. 83. Pergamon Press, Oxford (1958).
28. DAUBEN C. H. and TEMPLETON D. H., *Acta crystallogr* **8**, 841 (1955).
29. HUNTINGTON H. B., *Solid St Phys.* **7**, 214 (1958).
30. SACHS G. and WEERTS J, *Z. Phys.* **60**, 481 (1930).

APPENDIX A

A derivation of the Fourier representation of the force balance

The coupling parameters which appear in the expression for $\Theta_j(g)$ can be defined and clarified most suitably through a derivation of equation (7). A derivation of the equation is given here because of this and because the equation is central to the diffraction theory in that it allows the diffuse intensity, equation (9), to be written solely as a function of the solute distribution for a particular alloy.

Let us assume that the atoms are arranged initially on a perfect reference lattice and that an internal force field is introduced—acting outwardly about the larger atoms and inwardly about the smaller—which displaces the atoms from the sites of the reference lattice to their equilibrium positions. Such a description of the atomic arrangement can be based in an analytic manner upon an expansion of the net force acting upon an atom in powers of the displacements of the atoms from their sites on the reference lattice:

$$-F_i(p) = \mu_i(p) + \sum_{p'} \varphi_{ij}(p, p')u_j(p') + \ldots \quad i = 1, 2, 3. \tag{A-1}$$

The coefficient $-\varphi_{ij}(p,p')$ represents the force on the atom at site (p) in direction i resulting from a unit displacement of the atom at site (p') in direction j. The negative value of the leading term in the expansion, $-\mu_i(p,p')$, represents the internal force field or initial force. When the atoms are arranged on a Bravais lattice, the initial force can be related to the solute distribution by the equation[14]:

$$-\mu_i(p) = \sum_{p'} \varphi_i(p,p')q(p') \qquad \text{(A-2)}$$

where $q(p')$ is the solute variation at site (p') as defined in Section 2. If a single solute atom is present in an infinite host crystal and located at site (p'), we have that $(C = 0)$

$$q(p) = \begin{cases} 1 & p = p' \\ 0 & p \neq p' \end{cases} \qquad \text{(A-3)}$$

Thus in this limit, $-\varphi_i(p,p')$ (for $i = 1, 2, 3$) represent the components of the initial force field which is centered about the solute atom. In conformity with this limiting behavior, the coefficients $\varphi_i(p,p')$ have been termed the solute-lattice coupling parameters[14]. Following this nomenclature, it is convenient to term the coefficients $\varphi_{ij}(p,p')$ the lattice coupling parameters.

At equilibrium the net force is zero and it follows from equations (A-1) and (A-2) that

$$\sum_{p'} \varphi_{ij}(p'-p)u_j(p') = -\sum_{p'} \varphi_i(p'-p)q(p'), \quad i = 1,2,3 \qquad \text{(A-4)}$$

where terms higher than first order in equation (A-1) were assumed to be negligible and the coupling parameters were assumed to depend only upon the difference $(p'-p)$. These assumptions denote the harmonic approximation which is invoked so that the displacements can be related to the solute distribution in a simple, analytic manner. The Fourier representation of the force balance given by equation (A-4) is obtained by multiplying both sides of the equation by $\exp - i\mathbf{k}(g)\cdot\mathbf{x}(p)$ and summing over p and $p' - p = r$

$$\Phi_{ij}(g)U_j(g) = -\Phi_i(g)Q(g), \; i = 1,2,3 \qquad \text{(A-5)}$$

The functions

$$\Phi_i(g) = \sum_r \varphi_i(r)\exp i\mathbf{k}(g)\cdot\mathbf{x}(r)$$

and

$$\Phi_{ij}(g) = \sum_r \varphi_{ij}(r)\exp i\mathbf{k}(g)\cdot\mathbf{x}(r)$$

are the Fourier transforms of the solute-lattice and lattice coupling parameters, respectively. The solution to the linear system given by equation (A-5) is[5, 14]

$$U_i(g) = -\Theta_i(g)Q(g), \; i = 1,2,3$$

where

$$\Theta_i(g) = \bar{\Phi}_{ij}(g)\Phi_j(g) \qquad \text{(A-6)}$$

and the function $\bar{\Phi}_{ij}(g)$ is an element of the inverse matrix associated with the matrix having elements $\Phi_{ij}(g)$. This key result, which was first given in a slightly different form by Matsubara[1], relates the Fourier coefficients of the displacements, $U_i(g)$, to those of the solute distribution, $Q(g)$, by a linear equation and allows the intensity to be written as a function of the Fourier coefficients $Q(g)$ of the solute distribution on replacing $U_i(g)$ in equation (9) by $-\Theta_i(g)Q(g)$.

For convenience, the Fourier transforms of the coupling parameters are given in Table A.1 for the b.c.c. lattice and in Table A.2 for the f.c.c. lattice – the (g) notation being replaced by the (h) notation for the diffraction equations. The shorthand notation used for the various coupling parameters is described in Tables A.3 and A.4. The 'long wave relations' which relate the coupling parameters to the elastic constants are given in Table A.5. These relations were obtained from a comparison of the microscopic and continuum theory expressions for the elastic energy in the limit $\mathbf{k}(g) \to 0$, i.e. at long wavelengths[14]. These Tables have been taken directly from [14] where coupling parameters beyond third-neighbors were assumed to be zero.

Table A.1. Fourier transforms of b.c.c. coupling parameters

Lattice

$$\begin{aligned}\Phi_{11}(h) = {} & 8\alpha_1(1-\cos\pi h_1\cos\pi h_2\cos\pi h_3) \\ & + 2\alpha_2(1-\cos 2\pi h_1) + 2\beta_2(2-\cos 2\pi h_2 \\ & - \cos 2\pi h_3) + 4\alpha_3[2-(\cos 2\pi h_2+\cos 2\pi h_3) \\ & \times \cos 2\pi h_1] + 4\beta_3(1-\cos 2\pi h_2\cos 2\pi h_3)\end{aligned}$$

$$\begin{aligned}\Phi_{12}(h) = {} & 8\gamma_1\sin\pi h_1\sin\pi h_2\cos\pi h_3 + 4\gamma_3\sin 2\pi h_1 \\ & \sin 2\pi h_2\end{aligned}$$

Solute-lattice

$$\begin{aligned}\Phi_1(h) = {} & i[8\hat{\alpha}_1\sin\pi h_1\cos\pi h_2\cos\pi h_3 + 2\hat{\alpha}_2\sin 2\pi h_1 \\ & + 4\hat{\alpha}_3(\cos 2\pi h_2+\cos 2\pi h_3)\sin 2\pi h_1]\end{aligned}$$

Table A.2. Fourier transforms of f.c.c. coupling parameters

Lattice

$$\begin{aligned}\Phi_{11}(h) = {} & 4\alpha_1(2-\cos\pi h_1\cos\pi h_2-\cos\pi h_1\cos\pi h_3) \\ & + 4\beta_1(1-\cos\pi h_2\cos\pi h_3) + 2\alpha_2(1-\cos 2\pi h_1) \\ & + 2\beta_2(2-\cos 2\pi h_2-\cos 2\pi h_3) \\ & + 8\alpha_3(1-\cos 2\pi h_1\cos\pi h_2\cos\pi h_3) \\ & + 8\beta_3[2-(\cos 2\pi h_2\cos\pi h_3+\cos\pi h_2\cos 2\pi h_3) \\ & \times \cos\pi h_1]\end{aligned}$$

$$\begin{aligned}\Phi_{12}(h) = {} & 4\gamma_1\sin\pi h_1\sin\pi h_2 + 8\gamma_3\sin\pi h_1\sin\pi h_2\cos 2\pi h_3 \\ & + 8\delta_3(\sin 2\pi h_1\sin\pi h_2+\sin\pi h_1\sin 2\pi h_2) \\ & \times \cos\pi h_3\end{aligned}$$

Solute-lattice

$$\begin{aligned}\Phi_1(h) = {} & i[4\alpha_1(\cos\pi h_2+\cos\pi h_3)\sin\pi h_1 \\ & + 2\hat{\alpha}_2\sin 2\pi h_1 + 8\hat{\alpha}_3\sin 2\pi h_1\cos\pi h_2\cos\pi h_3 \\ & + 8\beta_3(\cos\pi h_2\cos 2\pi h_3+\cos\pi h_3\cos 2\pi h_2) \\ & \times \sin\pi h_1]\end{aligned}$$

Table A.3. *Lattice coupling parameter shorthand notation*

B.C.C.	F.C.C.
$\varphi_U(\frac{1}{2},\frac{1}{2},\frac{1}{2}) = \begin{pmatrix} -\alpha_1 & -\gamma_1 & -\gamma_1 \\ -\gamma_1 & -\alpha_1 & -\gamma_1 \\ -\gamma_1 & -\gamma_1 & -\alpha_1 \end{pmatrix}$	$\varphi_U(\frac{1}{2},0,\frac{1}{2}) = \begin{pmatrix} -\alpha_1 & 0 & -\gamma_1 \\ 0 & -\beta_1 & 0 \\ -\gamma_1 & 0 & -\alpha_1 \end{pmatrix}$
$\varphi_U(1,0,0) = \begin{pmatrix} -\alpha_2 & 0 & 0 \\ 0 & -\beta_2 & 0 \\ 0 & 0 & -\beta_2 \end{pmatrix}$	$\varphi_U(1,0,0) = \begin{pmatrix} -\alpha_2 & 0 & 0 \\ 0 & -\beta_2 & 0 \\ 0 & 0 & -\beta_2 \end{pmatrix}$
$\varphi_U(1,0,1) = \begin{pmatrix} -\alpha_3 & 0 & -\gamma_3 \\ 0 & -\beta_3 & 0 \\ -\gamma_3 & 0 & -\alpha_3 \end{pmatrix}$	$\varphi_U(1,\frac{1}{2},\frac{1}{2}) = \begin{pmatrix} -\alpha_3 & -\delta_3 & -\delta_3 \\ -\delta_3 & -\beta_3 & -\gamma_3 \\ -\delta_3 & -\gamma_3 & -\beta_3 \end{pmatrix}$

Table A.4. *Solute-lattice coupling parameter shorthand notation*

B.C.C.	F.C.C.
$\varphi_I(\frac{1}{2},\frac{1}{2},\frac{1}{2}) = \begin{pmatrix} \hat{\alpha}_1 \\ \hat{\alpha}_1 \\ \hat{\alpha}_1 \end{pmatrix}$	$\varphi_I(\frac{1}{2},0,\frac{1}{2}) = \begin{pmatrix} \hat{\alpha}_1 \\ 0 \\ \hat{\alpha}_1 \end{pmatrix}$
$\varphi_I(1,0,0) = \begin{pmatrix} \hat{\alpha}_2 \\ 0 \\ 0 \end{pmatrix}$	$\varphi_I(1,0,0) = \begin{pmatrix} \hat{\alpha}_2 \\ 0 \\ 0 \end{pmatrix}$
$\varphi_I(1,0,1) = \begin{pmatrix} \hat{\alpha}_3 \\ 0 \\ \hat{\alpha}_3 \end{pmatrix}$	$\varphi_I(1,\frac{1}{2},\frac{1}{2}) = \begin{pmatrix} \hat{\alpha}_3 \\ \hat{\beta}_3 \\ \hat{\beta}_3 \end{pmatrix}$

Table A.5. *Long wave relations*

B C C

$$2\alpha_1 + 2\alpha_2 + 8\alpha_1 = ac_{11}$$
$$2\alpha_1 + 2\beta_2 + 4\alpha_3 + 4\beta_3 = ac_{41}$$
$$4\gamma_1 + 8\gamma_3 = a(c_{12} + c_{14})$$
$$4\hat{\alpha}_1 + 2\hat{\alpha}_2 + 8\hat{\alpha}_3 = \frac{a^2\eta}{2}(c_{11} + 2c_{12})$$

F.C.C.

$$4\alpha_1 + 4\alpha_2 + 16\alpha_1 + 8\beta_3 = ac_{11}$$
$$2\alpha_1 + 2\beta_1 + 4\beta_2 + 4\alpha_1 + 20\beta_3 = ac_{41}$$
$$4\gamma_1 + 8\gamma_3 + 32\delta_3 = a(c_{12} + c_{44})$$
$$8\hat{\alpha}_1 + 4\hat{\alpha}_2 + 16(\hat{\alpha}_3 + \hat{\beta}_3) = \frac{a^2\eta}{2}(c_{11} + 2c_{12})$$

APPENDIX B

Correction factors for satellite intensities

The coefficient K which appears in the expression for the satellite intensity, equation (23), is the product of several terms:

$$K = (K')(L)(P)(T)(D) \qquad \text{(B-1)}$$

where K' is a constant independent of the diffraction angle and thus cancels out when the intensity ratios are taken. The coefficient,

$$L = \frac{1}{\sin\theta} \qquad \text{(B-2)}$$

is the Lorentz factor where θ is the diffraction angle, and

$$P = (1 + \cos^2 2\alpha \cos^2 2\theta)/(1 + \cos^2 2\alpha) \qquad \text{(B-3)}$$

is the polarization factor where α is the diffraction angle for the monochromator which was doubly-bent lithium fluoride for these experiments, copper K_α radiation was used. The coefficient,

$$T = 1 - \exp(-2\mu t/\sin\theta)$$

in which μ is the linear absorption coefficient and t is the specimen thickness (measured by an interferometric technique) corrects for the finite thickness of the specimen, and D is the usual Debye–Waller factor.

The largest error in the determination of η by this method probably arises from the improper Lorentz factor. The single crystal factor was chosen, equation (B-2), because of the strong preferred orientation of the evaporated specimens. A rough check of the validity of this choice was made by comparing the corrected intensity ratio of the Bragg peaks. For the several specimens studied, this ratio (222/111) – which should be unity – was 0·8 using the single crystal factor but was 1·5 using the powder Lorentz factor. This indicates that the proper factor, as expected, is somewhere between the two but nearer the single crystal value. In this respect it is important to note that a twenty per cent error in the satellite intensity ratio will yield only about a ten per cent error in η. The error resulting from the incorrect Lorentz factor was smallest for the 32·0 at. pct gold specimen because the factor is rather insensitive to diffraction angle in the vicinity of the 222 peak; η would only change from $-3{\cdot}3 \times 10^{-3}$ to $-3{\cdot}5 \times 10^{-3}$ for this specimen if the powder factor were used.

The Thomas-Fermi-Dirac values were used for the scattering factors; the real and imaginary parts of the Hönl correction given by Dauben and Templeton[28] were added to these values.

The measured intensity ratios and the product $L\times P\times T\times D$ are listed in the Table below for the specimens studied:

Table B.1

Composition (at. pct)Au	Wavelength (Å)	Thickness (Å)	$S\left(n-\frac{d}{\lambda}\right)\Big/S\left(n+\frac{d}{\lambda}\right)$			$L\times P\times T\times D$	
			(As evaporated)	(Annealed)	n	$\left(n-\frac{d}{\lambda}\right)$	$\left(n+\frac{d}{\lambda}\right)$
18·1	22·1	3690	1·14	0·885	1	0·766	0·515
32·0	33·5	4710	0·48	0·294	2	0·229	0·207
37·9	19·5	5640	1·31	1·18	1	1·12	0·732
37·9	21·6	5640	1·21	1·13	1	1·09	0·747
50·0	24·2	2700	1·32	1·12	1	0·703	0·483
50·0	24·4	2700	1·40	1·28	1	0·703	0·483

J. Phys. Chem. Solids Pergamon Press 1969. Vol. 30, pp. 1113–1118. Printed in Great Britain.

A LOCAL APPROXIMATION FOR EXCHANGE AND CORRELATION IN BAND STRUCTURE CALCULATIONS*

LUIZ G. FERREIRA†

Departamento de Física, Faculdade de Filosofia, Ciências e Letras, Universidade de São Paulo, Brazil and Material Theory Group, Department of Electrical Engineering, Massachusetts Institute of Technology, U.S.A.

(*Received* 20 *June* 1968; *in revised form* 16 *October* 1968)

Abstract—This paper deals with an approximation for exchange and correlation, in the form of an effective potential, to be used in band structure calculations. The present approximation differs from the earlier expressions by being dependent on the kinetic energy of the electron. The derivation follows the formalism of Green functions in the many-body systems, in the random phase approximation. We also present a relaxation time operator, which can be calculated simultaneously with the energy bands, and which may have some implications in the band theory itself.

1. INTRODUCTION

IN BAND structure calculations it is very convenient to have a local approximation for exchange and correlation. By local we mean an approximation in the form of an effective potential which depends only on the coordinates of the electron, instead of an integral operator such as the classic exchange term of the Hartree–Fock equation. A very simple and attractive solution to this problem has been given by Slater in 1951[1]. In Slater's solution, one uses locally an average exchange of a free electron gas with the same density as the local density of the actual problem. One drawback in Slater's method is that the Coulomb screening of the electron is not taken into account. As it has been emphasized elsewhere, the screening should be a specially important effect in the region of low electron density[2, 3]. To remedy this situation, Robinson, Bassani, Knox and Schrieffer have proposed a correction to Slater's formula which takes screening into account in the Fermi–Thomas approach[4]. Besides these two methods, there occurs in the literature, some other proposals which are either a correction to Slater's scheme[5–7], or which are applicable just to special situations[8, 9]. For instance, the paper by Kohn and Sham[5] may be considered in the first category, since they give a better method to average the exchange and correlation of a free electron gas over the occupied states. Again based on Slater's ideas, one has Liberman's paper[6] and the present work. Their novelty lies in the introduction of a kinetic-energy dependent exchange. As a matter of fact the present work differs from Liberman's mainly in that we include the effect of Coulomb screening (correlations). In the same category, we have the work by Lindgren[7] which takes into account the breakdown of Koopman's theorem in the case of atoms, by a small correction on Slater's exchange. In the second category we have some attractive schemes to meet special situations, such as the method used by Golin[8]. Finally, the work by Kleinman[9] might also be put in this second category, since it deals exclusively with those situations where the pseudo-potential is weak, namely the case of conduction electrons in

---

*Work partially supported by the Conselho Nacional de Pesquisas, the Fundação de Amparo à Pesquisa do Estado de São Paulo, Brazil, and by the Material Theory Group, Massachusetts Institute of Technology, U.S.A.

†*Present address:* Departamento de Física, Faculdade de Filosofia, Ciências e Letras, Caixa Postal 8105, São Paulo (SP), Brazil.

metals. The present article differs from the approaches above in that we consider a local exchange and correlation dependent not only on the local charge density, but also on the local kinetic energy of the electron (unlike Kleinman which considers the dependence on the average kinetic energy of the electron, and unlike Liberman which neglects correlation altogether).

A kinetic energy dependent exchange and correlation must be introduced to account for the physical fact that the positive cloud around an electron is velocity dependent. Indeed, the ability of the medium to react to the presence of an electron depends upon the speed of the latter. Fast electrons cannot be screened while slow electrons are easily surrounded by a cloud of holes. The dependence of the exchange and correlation upon the kinetic energy of the electron shows up very clearly, for instance, in the classical Hartree–Fock exchange term in the problem of a free electron gas[10]. Our approximation for the exchange will be, as Slater's, local and dependent on the electronic density, but unlike the latter we shall deal with a kinetic energy dependent exchange and we shall include the effects of screening as well. This energy dependence is not problematic if one uses a method, such as the APW, in which the energy eigenvalue is determined by trial error, and interpolation. For the methods of band determination in which the eigenvalue is not a necessary parameter in the calculation of the matrix elements of the secular equation, one could use the formula below, without much imprecision, assuming an average eigenvalue for the band to be determined. The local approximation for exchange and correlation is explained in part 2, while in part 3 we discuss the possibilities and implications of a relaxation time operator to band theory.

2. A LOCAL APPROXIMATION FOR THE MASS OPERATOR

In order to include the Coulomb screening into the wave equation, one should proceed from the techniques of electrodynamics. A good general reference to these techniques as applies to solid state problems is the book by Bonch–Bruevich and Tyablikov[11]. Instead of the Hartree–Fock exchange term we now deal with the mass operator, which, within the framework of band theory (assumption of negligible damping of the quasi-electron states) and random phase approximation, becomes

$$M(x,y) = -iG(x,y)D(y,x) \tag{1}$$

where D is the screened Coulomb interaction

$$D^{-1}(x,y) = D^{(0)-1}(x,y) + i2G(x,y)G(y,x). \tag{2}$$

$D^{(0)}$ is the unscreened interaction

$$D^{(0)}(x,y) = \frac{2}{|\mathbf{x}-\mathbf{y}|}\,\delta(x_0-y_0) \tag{3}$$

x and y specify the space and time location of a point, and G is the Green function for the electron under the hypothesis of negligible damping of the quasi-electron states:

$$\begin{aligned} G(x,y) = i\int \mathrm{d}\nu\, \phi(\mathbf{x},\nu)\phi^*(\mathbf{y},\nu) \\ \times \exp[-iE_\nu(x_0-y_0)] \\ \times [\theta(x_0-y_0)\theta(E_\nu-\mu) - \theta(y_0-x_0)\theta(\mu-E_\nu)]. \end{aligned} \tag{4}$$

Here $\phi(\mathbf{x},\nu)$ is the complete set of self-consistent eigenstates of a wave equation where only the Hermitean part of equation (1) intervenes. In equation (4), one must sum over these states and the function θ is just the step function. By a local approximation to exchange and correlation we understand the substitution of the real part of equation (1) by

$$\mathrm{Re}[M(x,y)] \rightarrow e(\mathbf{x})\delta(\mathbf{x}-\mathbf{y})\delta(x_0-y_0) \tag{5}$$

which makes the wave equation dependent only on the spatial coordinates of one point. $e(\mathbf{x})$ can thus be treated in the same way as an added potential. To attain such a localization of the mass operator, we recur to the basic idea behind the WKB method in quantum mechanics, and which possibly oriented Slater in the formulation of his approximation. That is, we substitute each small crystalline region where the electron moves by a free electron gas with the same electronic density as that of the small region being considered. Further, the mass operator is substituted by the eigenvalue of that operator in the problem of the free electron gas for a plane wave state with the *same kinetic energy* as that of the Bloch state at the small crystalline region. *Both, the kinetic energy of the electron and the charge density are function of position, but complete localization of the mass operator is attained by these means.* The real part $e(K)$ of the eigenvalue of the mass operator in the free electron gas for a plane wave with kinetic energy K^2 is

$$\begin{aligned} e(K) = {} & -\frac{1}{\Pi^2}\int \frac{\mathrm{d}^3k}{k^2}\theta(k_f-|\mathbf{k}+\mathbf{K}|)\,\mathrm{Re} \\ & \times\left[\frac{1}{\epsilon(\mathbf{k}, E_{\mathbf{k}+\mathbf{K}}-K^2)}\right] \\ & +\frac{1}{\Pi^3}\int\frac{\mathrm{d}^4k}{k^2}\,\mathrm{Im}\left[\frac{1}{\epsilon(\mathbf{k},k_0)}\right]P \\ & \times\frac{E_{\mathbf{k}+\mathbf{K}}-K^2}{(E_{\mathbf{k}+\mathbf{K}}-K^2)^2-k_0^2} \end{aligned} \tag{6}$$

where in the second term P means the principal value. If one uses in equation (6) $\epsilon = 1$ one readily obtains the conventional Hartree–Fock exchange of the electron gas. In our approximation, one must use the RPA dielectric constant quoted in reference[12]. The exact value of $e(K)$ has been obtained elsewhere, in the neighbourhood of the Fermi surface $K \simeq k_f$[13]. Outside this region, it is almost impossible to perform the integrations. Fortunately, one is helped by the fact that the second term in equation (6) is small for the densities one finds in band problems, and in the first, due to the special relation between the wave vector and the frequency occurring in the dielectric constant ϵ, one has

$$\mathrm{Re}\left[\frac{1}{k^2\epsilon(\mathbf{k}, E_{\mathbf{k}+\mathbf{K}}-K^2)}\right]=\frac{1}{k^2+k_e^2} \tag{7}$$

where k_e is the effective screening wave number and is approximately equal to the Fermi–Thomas wave number defined below. It is to be expected that only for very low densities k_e should cease to follow k_{ft} to become proportional to k_f. In this way one obtains the expression for $e(K)$ when

$$E = K^2 > 0$$

$$\begin{aligned} e(K) = {} & \\ & -\frac{2}{\Pi}\left\{\frac{k_f^2+k_e^2-K^2}{4K}\ln\frac{(K+k_f)^2+k_e^2}{(K-k_f)^2+k_e^2}+k_f\right. \\ & \left.+k_e\left[\mathrm{tg}^{-1}\frac{K-k_f}{k_e}-\mathrm{tg}^{-1}\frac{K+k_f}{k_e}\right]\right\} \end{aligned} \tag{8.a}$$

which can be continued for negative values of the kinetic energy E:

$$\begin{aligned} e(K) = {} & \\ & -\frac{2}{\Pi}\left\{\frac{k_f^2+k_e^2+K^2+2Kk_e}{2K}\mathrm{tg}^{-1}\frac{2k_fK}{k_e^2+k_f^2-K^2}\right. \\ & \left.+k_f-2k_e\mathrm{tg}^{-1}\frac{k_f}{k_e-K}\right\} \end{aligned} \tag{8.b}$$

where E = kinetic energy (8.c)
n = electronic density (8.d)
$k_f = |3\Pi^2 n)^{1/3}$ (8.e)
$k_{ft} = (4k_f/\Pi)^{1/2}$ (8.f)
$K = |E|^{1/2}$ (8.g)
$k_e = k_{ft}$ (8.h)

(the atomic unit system is used throughout these expressions). Figure 1 illustrates the energy dependence of $e(K)$, and compares the present approximation with those of Slater and Robinson *et al.* In order to be rigorous one should use in equation (6) the self-consistent RPA dielectric constant, that is, the dielectric constant where instead of just k^2 one uses $k^2+e(k)$ as the energy of a plane wave $\mathbf{k}$. From the expression for the RPA dielectric constant[12], one sees that

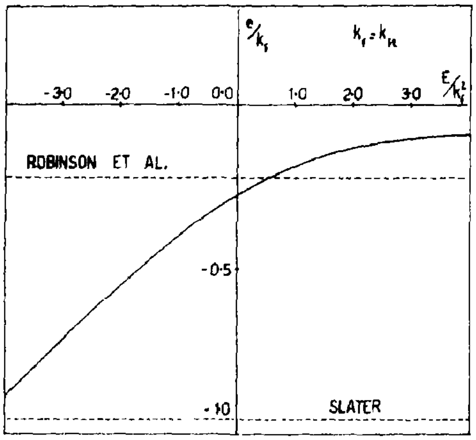

Fig. 1. Behaviour of exchange-correlation as a function of the kinetic energy, for the case of $k_f = k_{ft}$. Dashed lines represent Slater's and Robinson *et al* approximations.

the main effect of this correction is to modify the Fermi–Thomas wave number to

$$k'_{ft} = \frac{2k_f}{v_f} k_{ft} \tag{9}$$

where k_{ft} is given by equation (8.f), k'_{ft} is the modified screening wave number, and v_f is the self-consistent velocity at the Fermi surface, that is v_f is $2k_f$ plus the derivative of equation (8.a). Proceeding in this way one soon finds out that the solution to equation (9) is, for all practical purposes, given by equation (8.f), the self-consistent correction being negligible.

Figure 1 shows that while Slater's exchange is too strong because it is not screened, that of Robinson *et al.* is quite accurate, as long as the classically inaccessible regions of negative kinetic energy do not play a much important role in determining the energy eigenvalue of the electron. In fact, Robinson *et al.* exchange is equal to an average of our expression within the kinetic energy region of $0 \leq E/k_f^2 \leq 1$. Since the exchange $e(k)$ does not vary much within this region, Robinson *et al.* exchange may lead to sound results in many cases. For instance, by using a different averaging technique, Kohn and Sham found an exchange value just 30 per cent smaller. For high precision work, however, it would be better to use the kinetic energy dependence of equation (8). One must remember that the kinetic energy is the difference between the eigenvalue and the potential energy and is a function of position.

3. A RELAXATION TIME OPERATOR

The mass operator of equation (1) is non-Hermitean. One may deal with its imaginary part in the same way we dealt with its real part, by localizing it in space and time. Again, this localization can be accomplished by the same means. Again, the algebra is much simplified if one uses:

$$\mathrm{Im}\left[\frac{1}{k^4\epsilon(\mathbf{k},E_{\mathbf{k}+\mathbf{K}}-K^2)}\right] = -\frac{\mathrm{Im}[\epsilon(k,E_{\mathbf{k}+\mathbf{K}}-K^2)]}{(k^2+k_d{}^2)^2} \tag{10}$$

where k_d is similar to k_{ft}. We start from the imaginary part in the form

$$\begin{aligned} f(K) = &-\frac{1}{\Pi^2}\theta(K-k_f)\int\frac{d^3k}{k^2}\theta(K^2-E_{\mathbf{k}+\mathbf{K}}) \\ &\times\theta(E_{\mathbf{k}+\mathbf{K}}-k_f^2)\mathrm{Im}\left[\frac{1}{\epsilon(\mathbf{k},K^2-E_{\mathbf{k}+\mathbf{K}})}\right] \\ &+\frac{1}{\Pi^2}\theta(k_f-K)\int\frac{d^3k}{k^2}\theta(k_f{}^2-E_{\mathbf{k}+\mathbf{K}}) \\ &\times\theta(E_{\mathbf{k}+\mathbf{K}}-K^2)\mathrm{Im}\left[\frac{1}{\epsilon(\mathbf{k},E_{\mathbf{k}+\mathbf{K}}-K^2)}\right]. \end{aligned} \tag{11}$$

The final formula one obtains has different analytic expressions for different regions in the positive kinetic energy axis. We list below some values which may be used to obtain an interpolated formula valid for the positive energies: (a) near $K = 0$, the imaginary part is quadratic in K, and at $K = 0$ it assumes the value

$$f(0)=\frac{k_{ft}^2}{2k_f}\left[-\ln\left(1+k_f^2/k_d^2\right)+\frac{k_f^2/k_d^2}{1+k_f^2/k_d^2}\right]\leqslant 0. \quad (12.a)$$

(b) For $K \lesssim k_f$

$$\left[-\frac{k_f}{2k_d^3}\operatorname{tg}^{-1}\frac{2k_f}{k_d}-\frac{k_f^2/k_d^2}{4k_f^2+k_d^2}\right]\times(K-k_f)^2\leqslant 0. \quad (12.b)$$

(c) For $K \gtrsim k_f$ take the negative of equation (12.b). (d) For $K = 3k_f$, a good interpolated value is

$$f(3k_f)=\frac{k_{ft}^2}{2k_f}\frac{0{\cdot}261k_f^4/k_d^4}{k_f^3/k_d^3+0{\cdot}75k_f^2/k_d^2+0{\cdot}166k_f/k_d+0{\cdot}154}\geqslant 0. \quad (12.c)$$

This interpolated expression is exact for $k_f/k_d = 0, 1, \infty$. (e) For $K \to \infty$

$$f(K)=\frac{k_{ft}^2}{2k_fK}\left[\frac{4k_f^2+k_d^2}{8k_d}\operatorname{tg}^{-1}\frac{2k_f}{k_d}-\frac{k_f}{4}\right]\geqslant 0. \quad (12.d)$$

For $E < 0$, again we continue the function. However, if in equation (11) we integrate from $k = 0$, $f(K)$ turns out to be non-analytic at $K = 0$. This non-analycity is associated with the long range part of the Coulomb interaction and can be eliminated if in equation (11) we integrate from $k = k_0$. After the continuation to negative kinetic energies we can make $k_0 = 0$. The resulting expression is: (f) For $E \leqslant 0$

$$f(K)=\frac{k_{ft}^2}{2k_f}$$

$$\times\left\{1{\cdot}5-0{\cdot}5\ln\frac{(k_f^2+k_d^2-K^2)^2+4k_f^2K^2}{k_d^4}\right.$$

$$-k_d^2\frac{k_f^2+k_d^2-K^2}{(k_f^2+k_d^2-K^2)^2+4k_f^2K^2}$$

$$-\frac{k_d^2(3k_d^2+4K^2)+(K^2+k_f^2)^2}{16Kk_d^3}$$

$$\times\ln\frac{(K+k_d)^2+k_f^2}{(K-k_d)^2+k_f^2}+$$

$$+\frac{k_d^2(k_d^2+4K^2)-(k_f^2+K^2)^2}{4k_d^2}$$

$$\left.\times\frac{k_d^2-K^2-k_f^2}{(k_d^2+k_f^2-K^2)^2+4k_f^2K^2}\right] \quad (12.e)$$

with

$$k_d = k_{ft} \quad (12.f)$$

and the definitions (8.c–8.g). In Fig. 2 we plot the behaviour of $f(K)$ as a function of the kinetic energy for a medium density case.

Equation (12) defines an operator which can be used to calculate the electron-electron relaxation time of a Bloch state. In most situations, this relaxation will be largely dominated by the electron-phonon and electron-impurity interactions. The importance of equation (12) lies in that it yields a check on the band structure calculation through the following means: It is well known that the relaxation time changes sign at the Fermi energy. Therefore, the relaxation time oper-

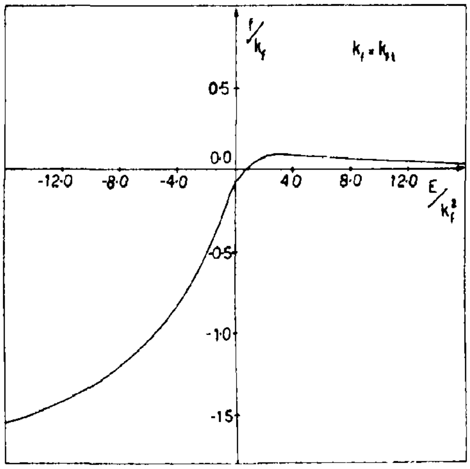

Fig. 2. Behaviour of the relaxation time operator as a function of the kinetic energy, for the case of $k_f = k_{ft}$.

ator may also be used to determine the Fermi energy which can be compared with that obtained from the band calculation.

REFERENCES

1. SLATER J. C., *Phys. Rev.* **81**, 385 (1951).
2. HERMAN F. and SKILLMAN S., *Bull. Am. phys. Soc.* **7**, 214 (1962).
3. PAYNE H., *Phys. Rev.* **157**, 515 (1967).
4. ROBINSON J. E., BASSANI F., KNOX R. S. and SCHRIEFFER J. R., *Phys. Rev. Lett.* **9**, 215 (1962).
5. KOHN W. and SHAM L. J., *Phys. Rev.* **140**, A1133 (1965).
6. LIBERMAN D. A., *Phys. Rev.* **171**, 1 (1968).
7. LINDGREN I., *Ark. Fys.* **31**, 59 (1965).
8. GOLIN S., *Phys. Rev.* **140**, A993 (1965).
9. KLEINMAM L., *Phys. Rev.* **160**, 585 (1967).
10. KITTEL C., *Quantum Theory of Solids*, Chap. 5, p. 90 Wiley, New York (1963).
11. BONCH-BRUEVICH V. L. and TYABLIKOV S. V., *The Green Function Method in Statistical Mechanics* North-Holland, Amsterdam (1962).
12. PINES D., *Elementary Excitations in Solids*, Chap. 3, p. 144 Benjamin, New York (1964).
13. QUINN J. and FERRELL R., *Phys. Rev.* **112**, 812 (1958).

J. Phys. Chem. Solids Pergamon Press 1969. Vol. 30, pp. 1119–1124. Printed in Great Britain.

ELECTRICAL PROPERTIES OF NbO and NbO_2*

JAMES A. ROBERSON

Metallurgy and Ceramics Research Laboratory Aerospace Research Laboratories, Wright-Patterson Air Force Base, Ohio 45433, U S A.

and

ROBERT A. RAPP

Department of Metallurgical Engineering, Ohio State University, Columbus, Ohio 43210, U.S A.

(*Received* 8 *August* 1968; *in revised form* 7 *October* 1968)

Abstract – The thermoelectric power and electrical conductivity were measured for NbO and NbO_2 as functions of temperature at the limiting oxygen activities for the thermodynamic stability of each of the compounds. The electrical properties of NbO_2 were essentially independent of oxygen pressure in the temperature range 50–1000°C, and the properties of NbO showed only a small dependence on oxygen activity The thermoelectric power and electrical conductivity of NbO indicate that metallic bonding exists in this compound. This bonding is discussed on the basis of Kreb's model for the influence of homopolar bonds on the structure of inorganic compounds. The thermoelectric power and electrical conductivity of NbO_2 indicate that this compound is an *n*-type intrinsic semiconductor. The nature of the predominant ionic defect in NbO_2 and its dependence on oxygen activity are discussed.

1. INTRODUCTION

THE ELECTRICAL properties of NbO and NbO_2 have not been sufficiently established because the low oxygen pressures required for the stability of these compounds are difficult to achieve and maintain experimentally. The low-temperature conductivity measurements of Meissner *et al.*[1] indicated metallic behavior for NbO. Without presenting any data, Kolchin and Sumarokova[2] reported that NbO is characterized by metallic conduction, and that NbO_2 appears to be a semiconductor. Kusenko and Geld[3] measured the heat content, coefficient of thermal expansion, and electrical conductivity of NbO_2 as a function of temperature. A discontinuous change in C_p and a heat of transformation of about 700 cal/mol. were found at about 1040°K; these changes would indicate a phase transition of the second kind which is not surprising in view of the low-temperature antiferromagnetism of NbO_2. In a recent paper, Janninck and Whitmore[4] reported on the electrical conductivity and thermoelectric power of NbO_2 in the temperature range 196°–1273°K. The purified argon atmosphere which was used did not allow maintenance of a stable composition (stoichiometry); however, the electrical properties of the *n*-type semiconductor NbO_2 were found to be independent of composition.

In the present investigation, the electrical conductivities and the thermoelectric powers of NbO and NbO_2 were measured over a range of temperature and oxygen pressure.

2. EXPERIMENTAL PROCEDURES

In the preparation of the oxides, Nb powder† was preliminarily oxidized in air to Nb_2O_5. Nb_2O_5 was mixed with Nb and sintered in vacuum to produce NbO. NbO was mixed with Nb_2O_5 and sintered in vacuum to produce NbO_2. An alternative technique involved equilibration of a phase with a two-phase mixture in adjacent combustion boats at a high temperature. Thus, a large amount of NbO/NbO_2 could be used to convert a small amount of Nb to NbO or to convert Nb_2O_5 to NbO_2. All of these preliminary sintering and equilibration treatments were done at about 1000°C. Phases were identified with an X-ray diffractometer. Dense, hard, NbO pellets of 8 mm dia. and 2 mm thickness were subsequently prepared by sintering at 1730°C in vacuum for 100 hr. NbO_2 pellets of similar size were prepared by sintering at 1500°C in vacuum for 24 hr.

---

*This paper is based on a portion of a thesis by J. A. ROBERSON submitted in partial fulfillment of the requirements for the degree of Master of Science in Metallurgical Engineering, The Ohio State University, in 1966.

†Spectrographic analysis indicated metallic impurities of 200 ppm Fe, 100 ppm Si, 30 ppm each of Ca, Mg, Cr, Ni and Hf, and trace amounts of Al, Mo, Zr, Na.

The thermoelectric powers and electrical conductivities of NbO and NbO_2 were determined as a function of temperature at oxygen pressures which corresponded to the limits of stability (and stoichiometry) for each phase. These oxygen activities were established and maintained by the equilibration of the specimen with a coexisting condensed phase (for example, at 1000°C: P_{O_2} (Nb/NbO) = $10^{-21·8}$ atm, P_{O_2} (NbO/NbO_2) = $10^{-21·0}$ atm and P_{O_2} (NbO_2/Nb_2O_5) = $10^{-17·8}$ atm).

The specimen was held between 2 Pt foils which served as the electrical contacts (two-probe measurements). Two Pt/Pt + 13 per cent Rh thermocouples, which had been calibrated against a Bureau of Standards couple, were welded to the Pt foils. The Pt wires of the thermocouples also served as electrical leads. A large pill of the phase desired for coexistence equilibrium was placed behind one of the Pt foils. Thus, the electrical properties of NbO were measured in equilibrium with Nb and then in equilibrium with NbO_2; likewise the properties of NbO_2 were measured in equilibrium with NbO and then in equilibrium with oxygen-deficient Nb_2O_5. The absence of any detectable reaction by either phase served as evidence that equilibrium coexistence was maintained. For the thermoelectric power measurements, a temperature difference of about 10–20°C was maintained across the specimen; a uniform temperature zone was established for electrical conductivity measurements. The quartz combustion tube was evacuated and outgassed, and then sealed while measurements were made. The electrical conductivities were calculated from potentiometric measurement of the voltage across a specimen for the passage of a small (0·02 to 0·5 mA) d.c. current. The ohmic behavior of the specimens for these d.c. measurements was established.

3. RESULTS AND DISCUSSION

NbO: The variation of the thermoelectric power of NbO with temperature is shown in Fig. 1. The cooler end of the specimen was negative, which indicates that the majority carrier is excess electrons. All values of the thermoelectric power have been corrected for the thermal emf of the Pt lead wires: this emf was always in opposition to that generated by the specimen. The correction factors (−0·05 to −0·3 mV) depended upon the temperature gradient and average temperature of the specimen and were large relative to the measured voltages (0·03 to 0·1 mV) for NbO. The data in Fig. 1 represent values of dE/dT at various temperatures, so that the slopes of the lines are d^2E/dT^2. The

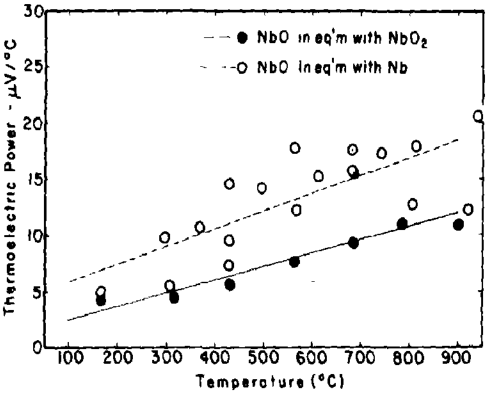

Fig. 1. The effects of temperature and oxygen activity on the thermoelectric power of NbO.

lines shown were calculated according to a least-squares fit of the data. The Peltier heat ($\pi = FT(dE/dT)$) and the Thomson heat ($\mu = -FT(d^2E/dT^2)$) can be computed from these results. The thermoelectric power of NbO had a small positive dependence upon temperature; the low value of the thermoelectric power for NbO indicates that the concentration of the predominant charge carrier (excess electrons) is very high. These observations indicate behavior characteristic of a metal rather than a semiconductor.

The electrical resistivity of NbO, shown in Fig. 2, is low and has a small positive temperature coefficient which also indicates behavior characteristic of a metal[1]. Both Figs. 1 and 2 show small though significant differences between the properties at the two phase boundaries. Even though NbO is metallic, the electron concentration should vary with the oxygen content which in turn varies with the oxygen activity.

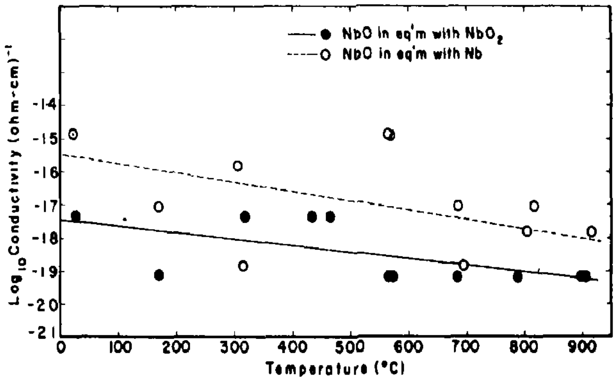

Fig. 2. The effects of temperature and oxygen activity on the electrical conductivity of NbO.

In contrast to Pauling's rules[5] by which an ionic crystal lattice is described in terms of cations surrounded by polyhedra of anions, Krebs[6] has pointed out the predominant role of the electronic configuration of the anion in determining the structure of inorganic compounds which possess significant covalent bonding contributions. In the NaCl-type NbO lattice, the six non-hydrid $2p$ electrons of the oxygen anion establish covalent, resonance bonds with octahedral symmetry to four nearest-neighbor Nb ions. (This bonding may be contrasted to that in which the oxygen ions possess four pairs of hydrid sp^3 electrons, so that homopolar bonds of tetrahedral symmetry are required). Brauer[7] has shown that a fourfold coordination in NbO is fulfilled on the NaCl-type lattice which usually requires a sixfold coordination because one quarter of both the niobium and oxygen sites of the NbO lattice are vacant. Two of the five outer electrons of the niobium atom may form resonance bonds with the $2p$ electrons of the four neighboring oxygen atoms. The three remaining electrons per niobium ion may adopt significant overlap with the electronic wave functions of neighboring cations, but this can only be determined by experiment. From the observed electrical properties of NbO, metallic behavior is evident. Therefore, the conclusion that the Nb ions possess nonbonding electrons with considerable overlap is justified.

NbO_2: The dependence of the thermoelectric power of NbO_2 on temperature is shown in Fig. 3. This plot shows the results of four specimens which were tested in equilibrium

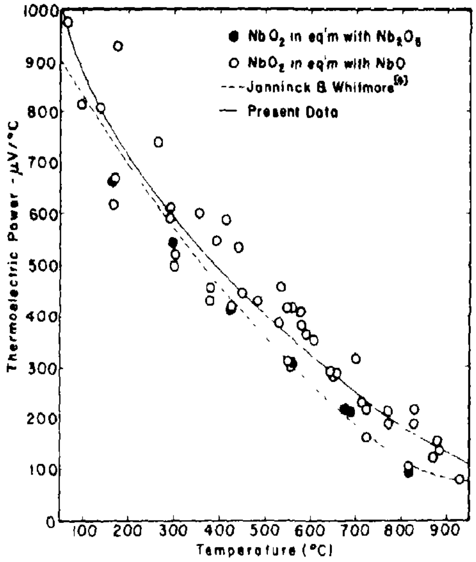

Fig 3 The effects of temperature and oxygen activity on the thermoelectric power of NbO$_2$.

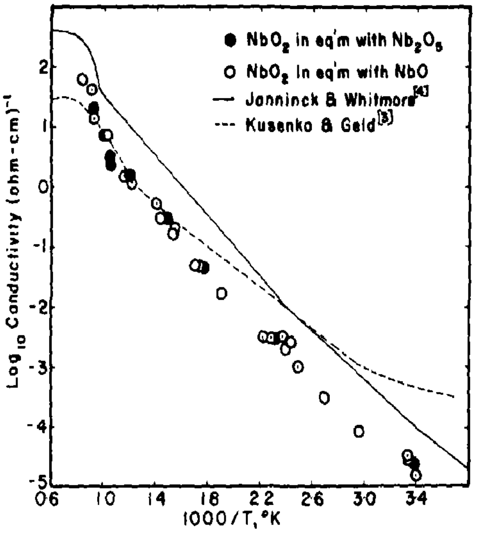

Fig 4 The effects of temperature and oxygen activity on the electrical conductivity of NbO$_2$.

with NbO and one in equilibrium with oxygen-deficient Nb$_2$O$_5$. The polarity of the specimen indicated predominant *n*-type semiconduction. Within the experimental scatter, the thermoelectric power of NbO$_2$ was found to be independent of the oxygen activity. The values are in agreement with the measurements of Janninck and Whitmore[1] who also reported that the thermoelectric power was independent of specimen stoichiometry.

In Fig. 4, the temperature dependence of the electrical conductivity of NbO$_2$ is presented. The difference in magnitude between these values and those of Janninck and Whitmore is probably due to differences in specimen preparation procedure; however, the temperature dependencies from the two studies are essentially identical. Agreement with Kusenko and Geld[3] is not satisfactory. The observed independence of the conductivity of oxygen activity indicates that NbO$_2$ is an intrinsic semiconductor. The ohmic behavior (lack of specimen polarization) with the application of d.c. potentials rules out the possibility that the P_{O_2}-independent conduction was predominantly ionic conduction.

The *n*-type behavior found in the thermoelectric power study for this intrinsic electronic conductor indicates that the mobility of conduction electrons exceeds that of the positive holes in NbO$_2$. The slope of the line through the conductivity data in Fig. 4 yields an activation energy of 0·43 eV.

In a rough approximation which is often applied, the energy gap between the valence and conduction bands in an intrinsic semiconductor is equal to twice the activation energy for conduction. If this value, 0·86 eV, is accepted as the energy for electron and hole pair formation without any contribution representing an energy for motion of charge carriers, then one may solve the equation for the density of electrons and holes [8]:

$$n_i = n = p = 2\left(\frac{2\pi kT}{h^2}\right)^{3/2} (m_e^* m_h^*)^{3/4} \times \exp\left(-\frac{E_g}{2kT}\right) \qquad (1)$$

if one makes the further assumption that $m_e^* \approx m_h^* \approx m_0$, the rest mass for free electrons. The solution at 1000°K is that $n_i = 1·0$

$\times 10^{18}$ cm^3. This value can now be used in the equation for conductivity:

$$\sigma = n_i e(\mu_e + \mu_h) \tag{2}$$

to give $(\mu_e + \mu_h) = 62$ (cm^2/Vsec).

Alcock, Zador and Steele[9, 10] have reported the oxygen deficiency* in NbO_{2-x} over the relatively high oxygen activity portion of its range of existence. At temperatures between 950 and 1050°C these authors reported the composition $NbO_{1.988}$ at oxygen activities still much higher than NbO_2-NbO equilibrium. In particular, the oxygen activity dependence of the oxygen deficiency in NbO_{2-x} was reported as

$$\frac{d\log x}{d\log P_{O_2}} = -1. \tag{3}$$

Alcock *et al.* suggested that this large P_{O_2}-dependence may result from intrinsic electronic disorder; the P_{O_2} dependence of the electrical conductivity of this study does establish intrinsic electronic disorder in NbO_2. As will be shown in the following discussion, equation (3) is consistent with the predominance of interstitial Nb ions in NbO_2; however, the magnitude of the deviations from stoichiometry reported by Alcock *et al.* are far too large for a self-consistent defect model for NbO_2.

In principle, a predominance of either interstitial Nb ions of charge z plus, $Nb_i^{z\cdot}$, or oxygen vacancies of charge y plus, $V_O^{y\cdot}$, may account for the oxygen deficiency in NbO_{2-x}†. Knowing that intrinsic electronic defects predominate, the nature of the predominant ionic defect should establish the P_{O_2}-dependence of the non-stoichiometry (x in NbO_{2-x}). The equilibrium for $Nb_i^{z\cdot}$ may be expressed

$$O_2(g) + Nb_i^{z\cdot} + ze' \rightleftharpoons 2O_O + Nb_{Nb}. \tag{4}$$

With the usual assumption of a dilute solution of defects, the equilibrium constant for equation (4) is

$$K_4 = \frac{1}{P_{O_2}[Nb_i^{z\cdot}]n^z} \tag{5}$$

where $[Nb_i^{z\cdot}]$ represents the interstitial ion concentration expressed in cation fraction. If oxygen vacancies were the predominant ionic defect, then the equilibrium would be expressed.

$$O_2(g) + 2V_O^{y\cdot} + 2ye' \rightleftharpoons 2O_O \tag{6}$$

with the equilibrium constant

$$K_6 = \frac{1}{P_{O_2}[V_O^{y\cdot}]^2 n^{2y}} \tag{7}$$

where $[V_O^{y\cdot}]$ is the concentration of oxygen vacancies expressed as anion fraction.

For an intrinsic semiconductor, the simplified charge neutrality expression[11, 12] is $n = p$ independent of P_{O_2}. If niobium interstitials are predominant in NbO_{2-x} with $[Nb_i^{z\cdot}]$ equal to $x/2$, equation (5) with n independent of P_{O_2} yields

$$\frac{d\log[Nb_i^{z\cdot}]}{d\log P_{O_2}} = \frac{d\log x}{d\log P_{O_2}} = -1. \tag{8}$$

On the other hand, if oxygen vacancies are presumed to be predominant, with n independent of P_{O_2} and $[V_O^{y\cdot}]$ equal to $x/2$, equation (7) yields

$$\frac{d\log[V_O^{y\cdot}]}{d\log P_{O_2}} = \frac{d\log x}{d\log P_{O_2}} = -\frac{1}{2}. \tag{9}$$

Because the predictions of equations (8) and (9) do not depend upon the valences, z plus, of the niobium interstitial, or y plus, of the oxygen vacancy, these valences could not be decided from an experimentally established value of d $\log x$/d $\log P_{O_2}$. With the determination of the predominant ionic defects, a standard Kröger and Vink[11, 12] graphical representation of the defect equilibria in NbO_2 at 1000°C could be constructed; the entire existence range of NbO_2 would lie within a central zone in which $n = p$ would represent the simplified neutrality condition.

---

*The term 'oxygen deficiency' does not imply that the predominant ionic defects are oxygen vacancies.

†The atomic defect notation of Kroger and Vink[11,12] has been used

The predominance of interstitial niobium in NbO_2 is required to explain the predominant cation diffusion in NbO_2 found in previous marker movement observations by the present authors[13]. Hurlen[14] has suggested that the rutile lattice should favor the formation of interstitial cations. While the equation (3) from experiment seems to support the prediction of equation (8) and thereby establish the predominance of interstitial cations, the absolute magnitudes of the reported nonstoichiometry in NbO_{2-x} are unrealistically large. Extrapolation of the 1000°C data of Alcock *et al*[9, 10] according to equation (3) to the low oxygen activity corresponding to NbO–NbO_2 equilibrium coexistence yields a value of x equal to 0·96. The composition $NbO_{1\cdot 04}$ would correspond to almost one interstitial niobium ion per cation lattice site. This calculated interstitial concentration is 40 times greater than that for the composition proposed by Brauer [7].

Janninck and Whitmore[4] reported from isopiestic equilibrations that the composition of NbO_2 for NbO–NbO_2 coexistence at 1100°C is $NbO_{1\cdot 9975}$. The composition of NbO_2 for NbO_2–NbO_2O_5 coexistence at 1100°C was reported as $NbO_{2\cdot 0030}$. While the permeability of vitreous silica to molecular oxygen[15, 16] may cause some difficulty in the isopiestic technique at 1100°C, the difference in compositions reported by Janninck[4] and Alcock[9, 10] are so large that the validity of equation (3) cannot be accepted from the available measurements. Further investigation of the P_{O_2}-dependence of the composition of NbO_{2-x} in the low oxygen activity range should identify the predominant ionic defect in oxygen-deficient NbO_2.

Presuming tentatively that interstitial cations are predominant in NbO_{2-x}, the more conservative estimate of the maximum interstitial cation concentration of Janninck and Whitmore[4] is $7{\cdot}3 \times 10^{19}$ per cm^3 at 1100°C. However, intrinsic electronic behavior requires $n = p \gg [Nb_i^{z\cdot}]$. The conductivity behavior for NbO_2 is anomalous at temperatures above 1000°K (see Fig. 4). Therefore, equation (1) cannot be used to calculate n_i at 1100°C for comparison with the values for $[Nb_i^{z\cdot}]$ of Janninck and Whitmore. Only if the niobium interstitials $Nb_i^{z\cdot}$ were unionized (z = zero) could the interstitial concentration exceed the electronic concentration for an intrinsic semiconductor, but this defect does not seem realistic.

REFERENCES

1. MEISSNER W., FRANZ H., and WESTERHOFF H., *Ann. Phys.* **17**, 593 (1933)
2. KOLCHIN P. O., and SUMAROKOVA N. V., *Atom. Energy* **17**, 168 (1961).
3. KUSENKO F. G. and GELD P. V., *Izv. Vysshikh Uchebn Zavendenii. Tavetn. Met.* **3**, 102 (1960)
4. JANNINCK R. F. and WHITMORE D. H., *J. Phys. Chem. Solids* **27**, 1183 (1966).
5. PUALING L., *The Nature of the Chemical Bond.* Cornell University Press, New York (1960)
6. KREBS H., *Acta crystallogr.* **9**, 95 (1956).
7. BRAUER G., *Z. anorg. Chem.* **248**, 1 (1941).
8. KITTEL C., *Introduction to Solid State Physics*, 2nd Edn., p. 350. Wiley, New York (1956).
9. ALCOCK C. B., ZADOR S. and STEELE B. C. H., *Proc. Br. ceram. Soc.* **8**, 231 (1967).
10. ZADOR S., In *Electromotive Force Measurements in High Temperature Systems*, Inst. Min. Metall., London (1967).
11. KROGER F. A. and VINK H. H., In *Solid State Physics*, Vol. 3. Academic Press, New York (1956).
12. KROGER F. A., In *The Chemistry of Imperfect Crystals*. North-Holland, Amsterdam (1964)
13. ROBERSON J. A. and RAPP R. A., *Trans. Met. Soc. AIME* **239**, 1327 (1967).
14. HURLEN T., *Acta chem. scand.* **13**, 365 (1959)
15. NORTON F. J., *Nature* **191**, 701 (1961)
16. NORTON F. J. and SEYBOLT A. V., *Trans. Met. Soc. AIME* **230**, 595 (1964).

J. Phys. Chem. Solids Pergamon Press 1969. Vol. 30, pp. 1125–1134. Printed in Great Britain.

THE OPTICAL PROPERTIES OF ORTHORHOMBIC SULPHUR CRYSTALS IN THE VACUUM ULTRAVIOLET

B. E. COOK* and W. E. SPEAR*
Physics Department, University of Leicester, Leicester, England

(*Received* 1 *August* 1968; *in revised form* 7 *October* 1968)

Abstract—The normal incidence reflectivity of natural (111) faces of orthorhombic sulphur has been measured for photon energies between 2·5 and 14 eV. The results were found to be largely independent of the surface treatment. A reflectometer designed for the present work is briefly described. The optical constants of orthorhombic sulphur over the above energy range have been derived by a Kramers–Kronig analysis of the experimental data. The extrapolation procedure is discussed and the internal consistency of the results is tested by the application of sum rules. The computed absorption coefficient is in satisfactory agreement with the measured data near the absorption edge. The spectral features of the $\epsilon_2(\omega)$ curve have been interpreted with some success in terms of the tentative band model suggested by Gibbons. The general agreement supports the model and also the previously published interpretation of the electronic transport mechanism in this material

1. INTRODUCTION

THE WORK described in this paper is concerned with reflectivity measurements on orthorhombic sulphur crystals, their analysis and interpretation. Our particular interest in this typical molecular crystal arose from electrical transport measurements[1, 2] which indicated that orthorhombic sulphur provides a good example of the two basic small polaron transport mechanisms predicted by Holstein [3]. An excess electron propagates by an intermolecular hopping process; a generated hole, on the other hand, is far less localized on the S_8 molecule than the electron and moves through the lattice in a comparatively narrow polaron band. The molecular orbital analysis of the S_8 molecule carried out by Gibbons[4] and his suggested band model for the crystalline solid lent considerable support to the above interpretation and also clarified the physical reasons for the observed transport behaviour.

The aim of the present investigation has been to provide independent new information on the electronic structure of orthorhombic sulphur by which the suggested model can be tested and put on a more quantitative basis. In addition the experimental results extend our knowledge of the optical constants of the material to photon energies of about 14 eV (880 Å), well beyond the range of previous measurements[5].

2. EXPERIMENTAL ARRANGEMENT

The vacuum monochromator used in this work contains a 1 m normal incidence concave grating as the dispersive element, and the radiation is provided by a high voltage d.c. discharge in hydrogen. The monochromator is operated without windows; the required vacuum conditions are obtained by a combination of pumping at the source, grating, and specimen chamber, and by the provision of high pumping impedance junctions between these components. Under typical operating conditions, the source is run at a pressure of ~ 1 Torr, whereas the monochromator and the specimen chamber are at pressures of 10^{-4} and $3{\cdot}10^{-5}$ Torr., respectively. The exit slit of the instrument is preceded by a system of filters that may be inserted into the exit beam, and also by a liquid nitrogen trap that prevents the streaming of diffusion pump oil into the specimen chamber

Detection is achieved by the normal photomultiplier-sodium salicylate combination. The results of an absolute calibration show that the intensity of the exit beam of the monochromator, at slit widths of 1 mm (resolving power ~ 30 Å) exceeds 10^{10} photons sec^{-1} for wavelengths down to 1000 Å. Below this figure the emission falls off sharply and reflectivity measurements could not be made below 850 Å.

**Present address*: Department of Physics, The University, Dundee, Scotland.

The principle of the reflectometer designed for the present work is illustrated in Fig. 1. The beam reflected from the specimen *A* travels the path SABC. When the rotating arm *OB*, carrying the mirror, is turned into position *OB′*, the shorter springloaded arm *OA* engages and moves the specimen out of the path of the light. In this position the salicylate screen *C* receives the reference beam *SAB′C*. The particular feature of the arrangement is that, except for the near normal incidence reflection at the specimen, both beams travel identical optical paths, and are reflected from the same mirror at the same angle. Accordingly, both beams are detected with equal efficiency, and absolute values of the reflectivity are measured. Also, the arrangement enables very small angles of incidence (~ 2°) to be employed without a corresponding increase in path length. Evaporated aluminium mirrors, with a thin overcoating of MgF_2[6], were used in most of the experiments.

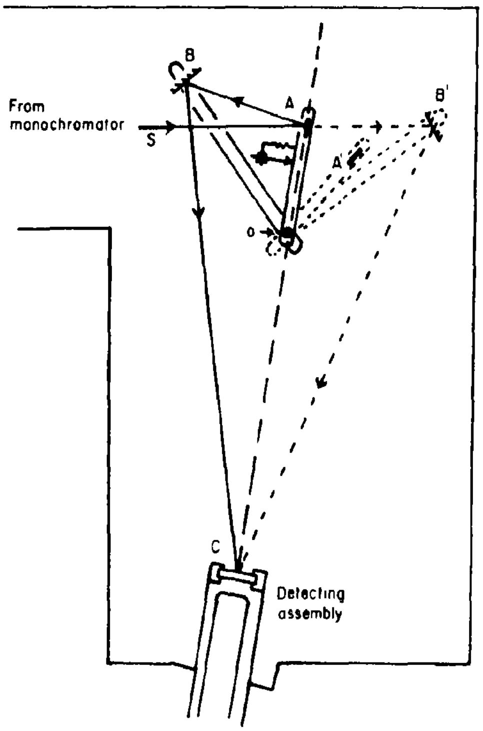

Fig. 1. Reflectometer used in the experiments. The specimen is mounted at *A* and a small mirror at *B*. Rotation about *O* turns the arms into positions *OA′* and *OB′* for the measurement of the incident beam.

Large orthorhombic sulphur specimens were grown by controlled evaporation of carbon disulphide from a saturated sulphur solution. The resulting crystals were of the well known bi-pyramid habit with natural (111) faces that were ideal for reflectivity work.

3. EXPERIMENTAL PROCEDURE AND RESULTS

The resolving power used in the majority of measured spectra was low (~ 30 Å) because of the limited intensity available in some parts of the spectral range. The corresponding energy resolution varied from 0·01 eV at 5000 Å to 0·40 eV at 850 Å, although this was improved upon for some measurements in spectral regions of particular interest. In most experiments data were taken in a 'point by point' manner and included up to 300 readings in any one run. Although obviously tedious, such a procedure allowed reliable corrections for stray light to be made when necessary. In spite of the limitation placed upon the resolution of fine structure, the use of comparatively low resolving power had certain advantages in this work. Averaged values of the reflectivity, suitable for the evalutaion of the phase angle, were determined for successive, adjoining frequency intervals which extended over the whole of the spectral range.

Although at the slit widths used, measurements could be performed easily for most wavelengths above 1000 Å, the low light intensities encountered below this figure, and in certain narrow regions below 1500 Å, made the use of filters necessary in order to correct for the effect of polychromatic stray light. The intensities of both the reflected and reference beams were measured with and without thin fused silica filters inserted before the exit slit. Stray light of wavelength shorter than the cut-off of Spectrosil (~ 1600 Å) could not therefore be discriminated against. However, experiments with different grades of fused silica filters indicated that most of the stray light came from a wavelength range above 2100 Å and was probably due to scattered zero order radiation. Data below 1000 Å should, however, be regarded with some caution.

As a check on the performance of the monochromator and reflectivity apparatus, measurements were taken on cleaved and etched germanium samples. The results agreed with published data[7, 8] for photon energies of up to 14 eV, with the exception of a local broad deviation at approximately 8 eV. The size of the discrepancy depended strongly upon specimen preparation and was reduced for crystals subjected to repeated etching.

It is well established that surface conditions may significantly affect the results of reflectivity measurements. It was therefore considered essential to undertake a thorough experimental investigation into the dependence of the S_8 data upon surface treatment. Results were obtained for crystals washed in distilled water or in volatile solvents, such as Benzene, Acetone and Toluene. One freshly grown specimen was studied, whilst other specimens had been exposed to the laboratory atmosphere for periods from a few days to a year. The surprising feature of all these results was the complete lack of dependence of the reflectivity spectra upon the above surface treatment over the whole experimental range. However, the monochromator environment itself was found to be a source of gradual contamination, and it was essential to prevent the build up of diffusion pump oil films on the specimen surfaces by the use of the liquid nitrogen trap mentioned earlier.

A total of nine specimens was studied, and the reflectivity curve shown in Fig. 2 is typical of the results obtained for the reflection of unpolarised light from a (111) plane at an angle of incidence of about 2°. The variation in the reflectivity spectra from different specimens is confined to comparatively small changes in the absolute and relative magnitudes of spectral features such as the position of peaks, minima, and shoulders. The only significant differences occurred in the region beyond the 9·5 eV peak. The position of the subsequent minimum varied from 10·1 to 10·5 eV, and although always present, it sometimes occurred at higher reflectivity values.

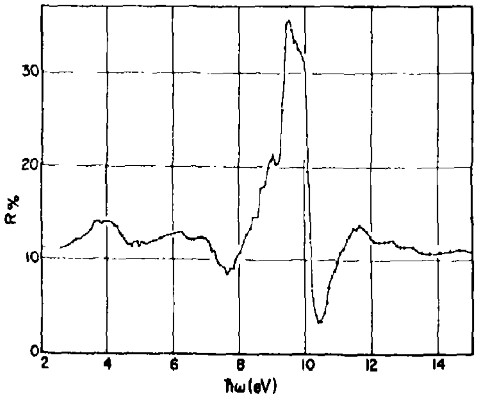

Fig. 2. The spectral dependence of the measured reflectivity from a (111) plane of orthorhombic sulphur. Angle of incidence about 2°, unpolarised light.

4. ANALYSIS OF RESULTS

The Kramers–Krönig relation used in the analysis of the results gives the phase change on reflection, $\theta(\omega_0)$, for radiation of angular frequency ω_0,

$$\theta(\omega_0) = \frac{\omega_0}{\pi}\int_0^\infty \frac{\ln R(\omega)}{\omega^2-\omega_0^2}\,\mathrm{d}\omega. \tag{1}$$

The principal difficulty in applying equation (1) lies in the fact that the integral is taken from 0 to ∞, whereas the range of the experimentally determined reflectivity function $R(\omega)$ is limited. The common argument, first introduced by Jahoda[9], that only the reflectivity data in the immediate vicinity of the singularity at $\omega = \omega_0$ contribute substantially to the phase angle θ, is in fact mistaken. The reason is that the integrand changes sign across the singularity, and if R is varying slowly, θ is evaluated from the difference of two very nearly equal contributions. Under these conditions the 'tails' of the integral cannot be ignored and it is essential that data must be obtained over as wide an energy range as possible, even if this means going beyond the region of particular interest.

In most treatments, the integral in equation (1) is split into 3 components. We define an interval (a, b) over which the experimental data extend, and write

$$I_1(\omega_0) = \frac{\omega_0}{\pi}\int_0^a \frac{\ln R(\omega)}{\omega^2-\omega_0^2}\,\mathrm{d}\omega \tag{2}$$

$$I_2(\omega_0) = \frac{\omega_0}{\pi}\int_a^b \frac{\ln R(\omega)}{\omega^2-\omega_0^2}\,\mathrm{d}\omega \tag{3}$$

$$I_3(\omega_0) = \frac{\omega_0}{\pi}\int_b^\infty \frac{\ln R(\omega)}{\omega^2-\omega_0^2}\,\mathrm{d}\omega. \tag{4}$$

In the present analysis, I_2 was evaluated directly from the experimental data by means of a computer programme based on the three point Simpson procedure. The step length was fixed at 0·05 eV and thus approximately 300 data points were included, ensuring that fine structure was not lost. It is often possible to evaluate the low frequency component I_1 by extrapolating the reflectivity data in accordance with tabulated refractive indices. In the case of sulphur, there is no appreciable absorption in the range $0 < \omega_0 < a$, so that the reflectivity remains constant. Equation (2) can then be integrated analytically to give

$$I_1(\omega_0) = -\frac{1}{2\pi}\ln R(a)\ln\left(\frac{\omega_0+a}{\omega_0-a}\right). \qquad (5)$$

Thus the high frequency contribution I_3 presents the real difficulty. There are several procedures that may be adopted, but all of these rely on one of two possible criteria: the total phase angle must be zero in regions of negligible absorption and the computed values of the extinction coefficient k should agree with absorption data in spectral regions where direct absorption measurements can be made. A number of extrapolation methods have been developed for the calculation of I_3, amongst them those of Philipp and Taft[7] and Rimmer and Dexter[10]; a somewhat different approach has been used by Roessler[11]. As remarked by Stern[12], there exists at present no entirely satisfactory method of data analysis, in that most procedures appear to be of an essentially arbitrary character.

In the analysis of the present data it appeared slightly more direct to appeal to the calculated $I_1 + I_2$ values and use these to choose a suitable form for $I_3(\omega_0)$, than to search for an extrapolation that would give the required fit. The choice is guided by knowledge of the various expressions for I_3 that have been derived from extrapolated reflectivities, and by the need for the corresponding behaviour of R to be physically acceptable. The analytical form of $I_3(\omega_0)$ chosen was

$$I_3(\omega_0) = -\left(A + B\ln\left|\frac{b+\omega_0}{b-\omega_0}\right|\right). \qquad (6)$$

The success of this expression in giving the desired low frequency fit is made evident by reference to Fig. 3, in which the total phase

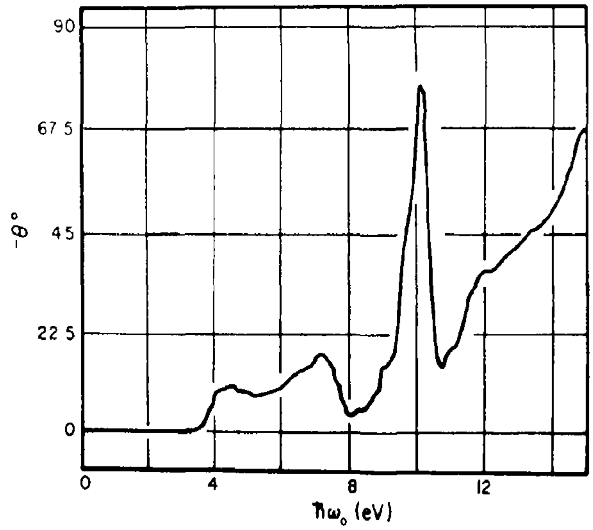

Fig 3 Plot of the phase angle $\theta(\omega_0)$ obtained from a Kramers–Kronig analysis of the reflectivity data

angle $\theta(\omega_0)$ is plotted. The second term in equation 6 is similar to the expression for I_1, and corresponds to a constant R over the range (b, ∞). The constant A may be regarded as a correction factor that compensates for any structure in R beyond the upper limit b. The discussion in the next section indicates that such structure is likely to exist. The values of A and B have been determined in the present work by means of a computer programme that obtains a least-mean-square fit between I_3 and $I_1 + I_2$ over the range $a < \omega_0 < \omega_{k>0}$. However, A and B may also be determined from the solution of simultaneous equations, at two frequencies ω_p and ω_q, $(a < \omega_p, \omega_q < \omega_{k>0})$ and the results thus obtained are included in Table 1 The consistency of the A and B values in Table 1 is very satisfactory, particularly when it is compared with a similar check based on the Roessler method, (c.f. reference[11] Table 1).

Having obtained the phase angle θ as a function of photon energy, it now becomes possible to calculate the spectral dependence of the optical constants. Fig. 4 shows the absorption coefficient $\alpha(\omega)$ and Fig. 5 the real and imaginary parts of the dielectric constant, $\epsilon_1 = n^2 - k^2$ and $\epsilon_2 = 2nk$, where $k = \alpha\lambda/4\pi$. Before proceeding to the discussion of these results, the following general comments are relevant. The shape and the spectral characteristics of the ϵ_2 curve (Fig. 5) are almost completely determined by the experimental data through the integral I_2. The interpretation of the results in Section 6, based on the features of the ϵ_2 curve, is therefore largely unaffected by the extrapolation procedure used in the Kramers–Krönig analysis. On the other hand, absolute magnitudes of the derived optical constants are sensitive to the magnitude of $\theta(\omega_0)$ and thus depend fairly critically on the general consistency of the analysis.

Table 1. *Check of consistency of the procedure used in the Kramers–Krönig analysis. The constants* A *and* B *in equation* (6) *have been determined from different pairs of frequencies,* ω_p *and* ω_q, *in the fitting range and are compared with the values from a least mean square fit*

ω_p (eV)	ω_q (eV)	A	B
1·00	1·50	8·00	34·00
1·50	2·00	8·12	33·40
2·00	2·50	7·93	34·40
1·00	2·00	8·04	34·05
1·20	2·80	8·12	33·54
Least mean square values $(1·0 < \hbar\omega_0 < 3·0)$eV		8·072	33·86

5. DISCUSSION

5.1 *The absorption coefficient*

In Fig. 4 the derived spectral dependence of the absorption coefficient is compared with experimental data. The graph includes the measurements of Spear and Adams[5] and of Hellyer[13] employing both single crystal and thin film specimens. The relative absorption data on thin films obtained by Rathenau [14], using photographic detection, have also been fitted to the absorption edge. The computed values of α lie exactly on the experimental edge, and at higher photon energies are intermediate between Hellyer's results and the data of Rathenau. Bearing in mind the difficulties associated with experimental determinations of α in regions of high absorption, the agreement is satisfactory. The lack of structure in the thin film results is not surprising.

At higher photon energies, the absorption coefficient shows a distinct minimum at 8·05 eV. The value of k at this energy is only about 4 per cent of the value of n and it is possible that the absorption at the minimum may be smaller than the computed values. Even with the determined values, the transmission of a 1000 Å film of sulphur at 8·05 eV would be as high as 50 per cent. Such a film deposited on a substrate of lithium or magnesium fluoride, could be useful as a band pass filter.

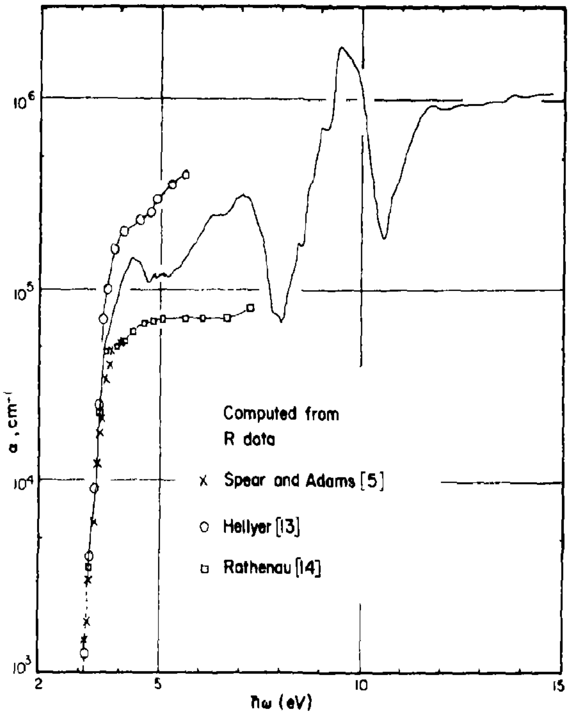

Fig. 4 The spectral dependence of the computed absorption coefficient α, compared with experimental data

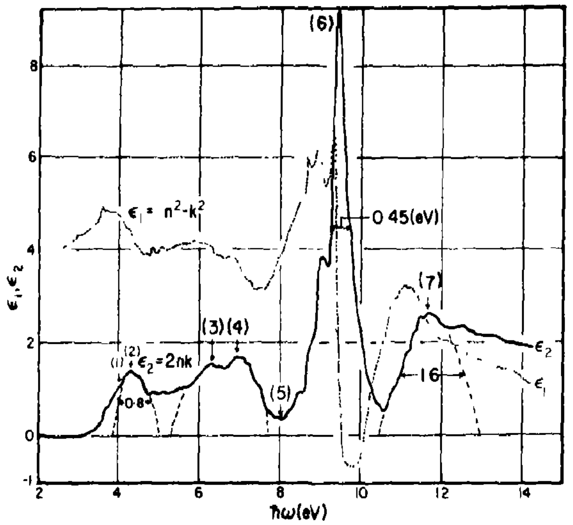

Fig. 5 The real and imaginary parts ϵ_1, ϵ_2, of the complex dielectric constant. The numbers above certain features of the ϵ_2 curve are used in the discussion (Section 6)

5.2 *Classical analysis of the peak in $\epsilon_2(\omega)$ at 9·4 eV*

In view of the sharpness of the 9·4 eV peak, it is reasonable to consider it in isolation, and fit it to the classical dispersion theory which gives

$$\epsilon_2(\omega) = 2nk = \frac{Ne^2}{m\,\epsilon_0}\frac{\omega g}{(\omega_0^2-\omega^2)^2+\omega^2 g^2}. \qquad (7)$$

In equation (7), N is the number of electrons per unit volume that can oscillate in response to an incident electromagnetic wave of frequency ω, and g is the damping coefficient. The analysis leads to $N = 3{\cdot}1\,.\,10^{22}\,\mathrm{cm}^{-3}$ which indicates that the effective number of electrons per atom participating in the interaction is $n_{\mathrm{eff}} = 0{\cdot}80$.

5.3 *Application of sum rules*

The application of the Kramers-Kronig dispersion relations to the various optical constants results in expressions known as 'sum rules' (e.g. reference[8]). Such expressions are useful because they constitute a check on the self consistency of the data obtained. The following relations have been applied:

$$\int_0^\infty n\alpha\,\mathrm{d}\lambda = (n_0^2-1)\,\pi^2 \qquad \text{(a)}$$

where n_0 is the zero frequency value of the refractive index.

Graphical integration of the function $n\alpha$ between $\lambda = 800\,\text{Å}$ and $\lambda = \infty$ led to a value of 13·4, as compared with the value of approximately 30 for $(n_0^2-1)\pi^2$.

$$\int_0^\infty \alpha\,\mathrm{d}\lambda = (n_0-1)2\pi^2 \qquad \text{(b)}$$

Integration of the computed values for α between the same wavelength limits as above gives 8·5, which compares with $(n_0-1)\,2\pi^2 = 20$.

These results indicate that the spectral region studied experimentally by no means includes all of the significant optical transitions. Each of the above integrations yields very nearly the same proportion of the predicted value (43 per cent and 45 per cent respectively), which confirms the internal consistency of the analysis.

A third sum rule is

$$\int_0^{\omega_0} \omega\epsilon_2(\omega)\,\mathrm{d}\omega = \frac{2\pi^2 Ne^2}{m}\,n_{\mathrm{eff}}. \qquad \text{(c)}$$

The integral has been evaluated for a series of ω_0 and the effective number of electrons per atom, n_{eff}, is plotted as a function of energy in Fig. 6. Each sulphur atom contributes 6 outer electrons to molecular states, two of which are instrumental in bonding. At around 15·5 eV (800Å), n_{eff} has reached a value of 2·6. Thus 44 per cent of the available 'molecular' oscillator strength contributes up to this energy. The similarity between this figure and the two previous results implies that the optical properties of S_8 are dominated by transitions involving the six electrons per atom that move in molecular orbitals.

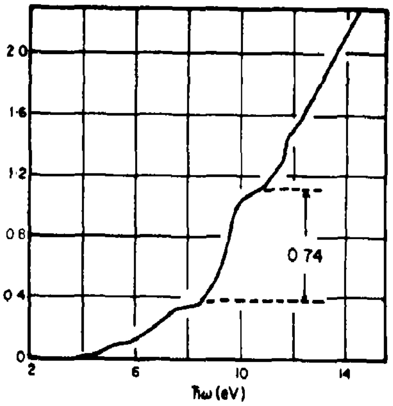

Fig. 6. Plot of the effective number of electrons per atom n_{eff}, which contribute at photon energy $\hbar\omega$. The curve has been calculated for sum rule (c).

The detailed shape of Fig. 6 is of some interest. In general, a 'plateau' signifies that one set of transitions are exhausted, and the subsequent sharp rise indicates that another system comes into play. Pronounced structure of this type occurs at 8 and 10·5 eV, and the difference between the 'saturation levels' is 0·74. This increase in the number of electrons per atom effectively participating in interactions with the electromagnetic radiation is associated with the strong 9·4 eV peak in the $\epsilon_2(\omega)$ curve and should be compared with the figure of 0·8 for n_{eff} obtained in the previous section.

6. INTERPRETATION OF THE RESULTS

The imaginary part of the dielectric constant $\epsilon_2(\omega)$ shown in Fig. 5 is mainly dependent upon the joint density of states function $g(E_{jj'})$ for the relevant bands in which the initial and final states j and j' of the transition are situated. It is likely that the matrix elements governing a particular transition $j \rightarrow j'$ do not change greatly over the Brillouin zone. It will be assumed that the only significance of the matrix elements is to make certain transitions strong and others weak.

In the following, an attempt is made to interpret some of the main features of the $\epsilon_2(\omega)$ curve in terms of the molecular orbital analysis of the S_8 molecule recently carried out by Gibbons[4]. As this work is unpublished a brief summary of the results is included here.

Gibbons analysed the S_8 ring in terms of $3sp^3$ hybrid orbitals and used Slater $3s$ and $3p$ atomic wavefunctions in his calculations. Of the hybrid orbitals, two are occupied by 'lone pair' electrons, and the remaining two are engaged in forming the covalent bonds with neighbouring sulphur atoms. As the atoms are brought together to the S_8 configuration, the resulting interaction leads to the molecular states illustrated in Fig. 7. The significant effect is the splitting of the σ and σ^* states caused by the strong overlap of the bonding orbitals. The lone pair orbitals forming the molecular π system overlap far less strongly, so that the π and π^* energies are likely to lie fairly close. In the molecular crystal lattice, the overlap between molecular wavefunctions is relatively small, so that a close correspondance would be expected between the electronic structure of the isolated molecule and the band structure of the crystal, as indicated in Fig. 7.

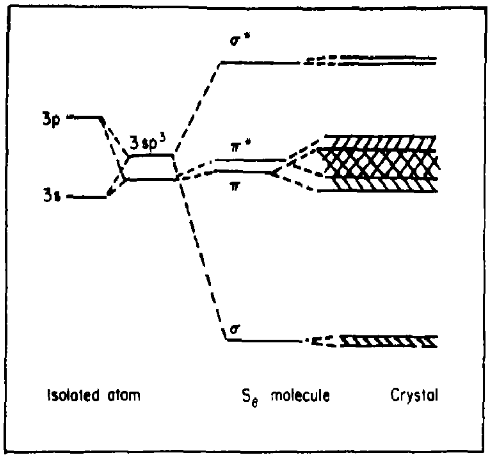

Fig. 7. Molecular orbital analysis of the S_8 molecule and suggested band scheme for the crystal (after Gibbons) The highest full band is formed from π^* and π orbitals, the σ^* orbitals form the narrow hopping level.

It should be emphasised that the suggested band scheme is essentially qualitative, although Gibbons has estimated the widths of the highest filled band, (π^*), and of the lowest empty band (σ^*), by means of the Bloch tight binding approach. The values of 0·8 eV and $2 \cdot 10^{-2}$ eV respectively support the published interpretation[2] of the transport mechanisms in sulphur.

The above model now forms the basis for the tentative assignment of the transitions shown in Fig. 8. The numbers in brackets represent transitions which are associated with the similarly labelled features of $\epsilon_2(\omega)$ in Fig. 5. The first band, peaking at about 4·3 eV is assigned to transitions from the π^* filled band to the σ^* hopping level. This is supported by transient photoconductivity measurements[5], which showed that above about 4 eV electrons and holes are generated in pairs, with rapidly rising quantum efficiency. The activation energy associated with the

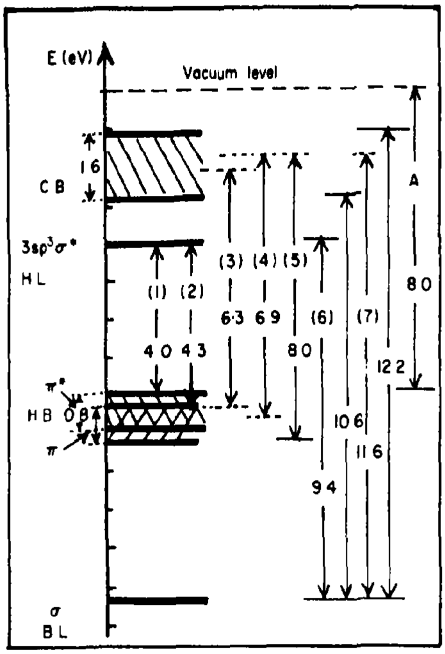

Fig 8. Suggested interpretation of the main features of the $\epsilon_2(\omega)$ curve The transitions are numbered to correspond to particular features in Fig. 5 All energies in eV C B . conduction band, H L.: hopping level: H.B · hole band. B L.: bonding level. The broken lines indicate regions of high density of states in the relevant bands.

intrinsic generation has been placed near 4·2 eV. The absorption below about 4 eV was found to result from predominantly non-photoconductive processes. As the final state of the transitions, the σ^* level, is extremely narrow, the part of the band above about 4·0 eV in Fig. 5 should reflect the density of states in the π^* band. According to the selection rules, $\pi^* \rightarrow \sigma^*$ transitions are allowed ($g \rightarrow u$), whereas those from $\pi \rightarrow \sigma^*$ are not. The width of the band is about 0·8 eV and transitions (1) and (2) are shown in Fig. 8 in accordance with the above discussion.

The next prominent spectral feature in the $\epsilon_2(\omega)$ curve is a second band containing the peaks centred on 6·3 eV[3] and 6·9 eV[4]. It is thought to be connected with transitions from the (π^*, π) full band into a comparatively wide conduction band lying above the σ^* hopping level. Nothing is known about the character of this band, except that in principle it could be formed from $4s\sigma$ orbitals, δ levels derived from $3d$ states, or from a mixture of the two. In the following we have assumed that the band possesses $3d$ character, firstly because this leads to a more acceptable interpretation, and secondly because $3d$ orbitals appear to play an important role in sulphur compounds, such as SF_6. Bonding orbitals derived from the $3d$ states have both u and g symmetry and thus transitions from the π^* and π states into the conduction band are allowed. It is possible that peaks (3) and (4) are due to these transitions although other interpretations are feasible. The minimum at 8 eV (5) probably reflects the convoluted widths of the π, π^* and conduction bands. Photoemission studies at present in progress [13] lead to a threshold energy of about 8 eV. Transition A in Fig. 8 therefore fixes the top of the π^* band with respect to the vacuum level.

The most prominent feature in $\epsilon_2(\omega)$ is the large peak at 9·4 eV (6) which requires for its explanation a transition between two narrow, well defined energy levels. This immediately suggests the allowed transitions between $3sp^3\sigma$ and $3sp^3\sigma^*$. According to Gibbons the widths of these levels should be considerably smaller than the measured half-width of 0·45 eV. This could possibly be accounted for by the strong coupling of the electrons to the molecular vibrational modes. The structure on the low energy side of this peak is of interest, and work at higher resolution and at low temperatures, at present in progress, should provide more detailed information.

The last feature is the band associated with peak (7) at 11·6 eV. Since emission occurs for photon energies above 8 eV, this band must be connected with levels below the valence band. An obvious possibility is the allowed transition from the narrow σ band into the conduction band. The minimum at 10·6 eV (Fig. 5) locates the bottom of this band which has an estimated halfwidth of 1·6 eV. This assignment is consistent with the information deduced from peaks (3) and (4).

7. CONCLUSIONS

(1) The optical constants of orthorhombic sulphur between 2·5 and 14 eV are summarised in Fig. 5. The results were obtained from reflectivity measurements on (111) planes. The spectral features are largely unaffected by surface treatment.

(2) The spectral dependence of the absorption coefficient derived from the Kramers-Kronig analysis is in satisfactory agreement with direct measurements near the absorption edge. This supports the validity of the analysis as do the sum rule applications.

(3) The principal features of the $\epsilon_2(\omega)$ curve have been tentatively assigned to the transitions shown in Fig. 8, which is based upon the orbital calculations of Gibbons.

Acknowledgements – The authors would like to thank Miss Mary Simpson for valuable help with the computations and Dr. D. Greenaway for useful comments and advice. A Research Studentship given to one of us (B.F.C.) by the Science Research Council is gratefully acknowledged.

REFERENCES

1. ADAMS A. R. and SPEAR W. E., *J. Phys. Chem. Solids* **25**, 1113 (1964)
2. GIBBONS D. J. and SPEAR W. E., *J. Phys. Chem. Solids* **27**, 1917 (1966)
3. HOLSTEIN T., *Ann. Phys.* **8**, 343 (1959).
4. GIBBONS D. J., Private communication. To be published.
5. SPEAR W. E. and ADAMS A. R., *J. Phys. Chem. Solids* **27**, 281 (1966).
6. CANFIELD L. R. *et al.*, *Appl. Optics* **5**, 54 (1966)
7. PHILIPP H. R. and TAFT E. A., *Phys. Rev.* **A113**, 1002 (1959)
8. PHILIPP H. R. and EHRENREICH H. *Phys. Rev.* **A129**, 1550 (1963).
9. JAHODA F. C., *Phys. Rev.* **A107**, 1261 (1957)
10. RIMMER M. P. and DEXTER D. L., *J. appl. Phys.* **31**, 775 (1960)
11. ROESSLER D. M., *Br. J. appl. Phys.* **17**, 1313 (1966)
12. STERN F., In *Solid State Physics* (Edited by F. Seitz and D. Turnbull), Vol. 15, p. 299. Academic Press, New York (1963)
13. HELLYER F. G., Private communication. University of Leicester.
14. RATHENAU G., *Physica* **3**, 42 (1936)

J. Phys. Chem. Solids Pergamon Press 1969. Vol. 30, pp. 1135-1146. Printed in Great Britain

TRANSIENT PROCESSES IN SPIN-WAVE SYSTEMS WITH MAGNETIC DIPOLE RADIATION-II. EXPERIMENTAL INVESTIGATIONS*

B. DESORMIÈRE and E. MILOT
C.F.T H., B.P. 11, 92-Bagneux, France
and
H. Le Gall
Laboratoire du Magnétisme, C.N.R.S., 92-Bellevue, France

(*Received* 24 *September* 1968)

Abstract—The harmonic and anharmonic transient evolutions of the power absorbed by a ferromagnetic system which is suddenly submitted to an electromagnetic excitation of constant amplitude, is experimentally studied under perpendicular pumping. We show the influence of the magnetic dipole radiation of the uniform magnons in narrow line-width crystals, like YIG and lithium ferrite, on the transient and steady-state absorption processes. When the ferromagnetic system is overcoupled, the absorbed r.f. power reaches, in the harmonic case the linear steady-state level after an overshoot due to the retardation of the radiation processes with respect to the direct photon-magnon processes of absorption. In the same way, in the anharmonic case, the overcoupled ferromagnetic system leads to a non-linear steady-state absorption level, higher than the steady-state linear level. The experimental results are in good agreement with the theory that we developed earlier, we can deduce from the theory the characteristics of the parametrically excited spin-waves. Finally, we have shown that the magnetic dipole radiation of the uniform magnons is the basic mechanism of tunable band pass filters and limiters using the ferromagnetic resonance. Expressions are derived for the selectivity of these devices and for the residual energy contained in the spike of the limiters. These expressions are in agreement with the experimental results.

1. INTRODUCTION

In part I[1] a general theory was given for linear and nonlinear transient processes of a ferromagnetic system submitted to a microwave excitation, in the case where the r.f. magnetic field is perpendicular to the applied d.c. field (perpendicular pumping). Since the theoretical work of Suhl[2] who interpreted the non-linear behavior of the ferromagnetic crystals at high power level, many experiments have been perfomed on this subject. However, most of the experimental results are devoted to the determination of the excitation threshold of parametric spin-waves and of the imaginary part of the r.f. steady-state susceptibility. The study of the transient processes is of great interest both from a fundamental point of view as a research tool for the basic dynamic processes occuring in ferromagnetic crystals and from a practical point of view, because it gives information on the linear and nonlinear behavior of some micro-wave devices such as circulators, phaseshifters, limiters and filters. Indeed, these devices are submitted mainly to r.f. pulses with duration of about a few microseconds and for fundamental studies the use of r.f. pulses allows a more detailed observation of the phenomena and also avoids heating effects.

Recently, Schlomann *et al.*[3] have studied the transient evolution of a spin-wave system under parallel pumping conditions. This technique presents the advantage of studying the evolution of a spin-wave mode[4] only. However the parallel pumping is a non-linear process (three-boson transitions with des-

---

*This work was supported in part by the Direction des Recherches et Moyens d'Essais (Paris).

truction of one photon and creation of two magnons) and is not of the same practical interest as perpendicular pumping, used in most microwave ferrite devices. Perpendicular pumping is a linear process (one photon is absorbed and one uniform magnon created) where the harmonic and anharmonic transient evolution can be independently studied.

In addition, in part I we explained the importance of the dipolar radiation of the uniform magnons, which produces reverse magnon–photon transitions. Thus, we have shown that a narrow line-width ferrimagnetic sample having a high filling factor in the microwave cell, becomes a mirror for the r.f. excitation: all the incident power is re-radiated. This radiation, which has been neglected by most authors, is fundamental both from a scientific point of view, because it modifies widely the dynamical properties of the materials, and from a practical point of view because it is the basis of microwave filters and limiters. In experiments we can use samples having a narrow line-width and a large diameter, which leads to high radiation, because the radiated field can then be taken into account.

The present paper is divided into 6 sections. In Section 2 the influence of the magnetic dipole radiation on the transient and steady-state evolution of the uniform mode is discussed in the harmonic case. The contribution of the radiated field to the relaxation rate of the uniform magnons η_0 is given. Section 3 describes the transient evolution of the uniform mode when the three-magnon non-linear processes occur. The changes in the threshold and transient growth of the spinwaves, produced by the dipolar radiation, are determined. In Section 4 we analyze the possibility of a direct observation of the magnetic dipole radiation. For this purpose, the expression of the r.f. power radiated by a spherical ferrimagnetic sample, placed between two crossed waveguides, is derived. We discuss this device upon which the filters are based. In addition, an analytical expression of the energy contained in the spike of the r.f. pulses transmitted through a limiter is derived and compared with the experimental results. The analytical expressions describing the time evolution of the uniform mode, the absorbed power and the radiated field, given in the part I are correct as long as the spin-wave populations do not become too high. In order to check qualitatively the experimental results which give the full evolution of the phenomena towards the steady-state, we have performed, in Section 5, numerical calculation of the transient absorbed power by making some simplifying assumptions. Finally, Section 6 describes the experimental arrangement used in this study.

2. TRANSIENT HARMONIC PROCESSES

In the conventional ferrimagnetic resonance experiments the main source of linear damping is produced by two-magnon transitions due to the magnetic surface and volume inhomogeneities, as proposed by Clogston *et al.*[5]. One uniform magnon is destroyed and one $k\neq 0$ magnon is created. Then the magnetoelastic coupling transfers the energy from the magnon system to the phonon bath with two and three-boson transitions[6]. This model is correct if the linear relaxation rate η_0 of the uniform mode is large, as it is in polycristalline samples or in some single-crystals having surface pits, dislocations, vacancies or slowly or rapidly relaxing impurities. In that case, the uniform mode population, as deduced from the magnon operator is weak[7]:

$$c_0 \sim \frac{q}{\eta_0} \tag{1}$$

where q is the electromagnetic field operator which determines the amplitude of the r.f. excitation. In the last few years because of progress in crystal-growth techniques, it has been possible to obtain ultra-pure single-crystals having quasi perfect crystallographic structure. The relaxation rate of these samples is very low as in yttrium–iron granet and lithium ferrite. Thus, according to equation (1) the number of uniform magnons increases as η_0 decreases. In that case a new process of damping is observed for the uniform mode. The dipolar energy of the uniform magnons results in a magnetic dipole radiation which increases when η_0 decreases. With this new process, the general expression of the microwave power actually absorbed by a ferromagnetic crystal, in the harmonic and anharmonic cases, is [1].

$$P_a = \hbar\omega[\alpha(c_0 q^+ + c_0^+ q) \\ -(\beta' c_0^+ c_0 + \beta'^* c_0^+ c_0)] \quad (2)$$

where $2\pi\hbar$ is the Planck constant and α' and β' are two parameters which represent respectively the direct processes of absorption and the reverse processes of radiation. c_0^+ and q^+ are hermitian conjugates of c_0 and q.

All the constants in the present paper have the same definitions as in [1]. The first two terms of equation (2) represent the number of the incident photons which are coupled per time unit to the uniform magnons, and the last two terms give the number of photons re-emitted by dipolar radiation. Figure 1 shows the linear relaxation of the uniform mode with the correction of the radiation.

The experimental study of the transient evolution of the uniform mode is performed by using r.f. pulses having fast time rising ($\leq 10^{-8}$ sec). In order to avoid transient effects in the microwave cavities, the sample is placed at the center of a wave-guide at the distance l from a tunable short (Fig. 2). From the equation of motion of the magnetic system, we have shown[1] that the dipolar radiation produces two effects; first, the resonance frequency ω_0 is shifted and becomes:

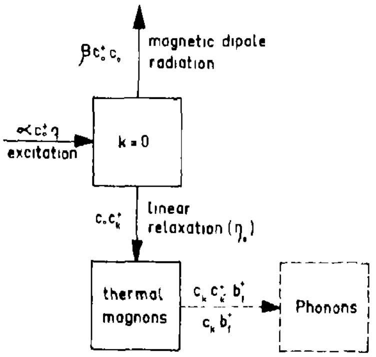

Fig 1 Schematic diagram of the linear relaxation with magnetic dipole radiation

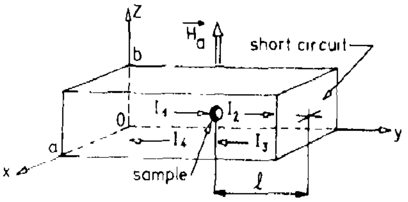

Fig 2 Microwave set-up.

$$\omega_L = \omega_0 + \tfrac{1}{2}\beta_0\eta_0 \sin 2k_g l \quad (3)$$

and then, the relaxation rate η_0 of the uniform mode increases:

$$\eta_L = \eta_0(1 + \beta_0 \cos^2 k_g l). \quad (4)$$

β_0 is the filling factor defined by:

$$\beta_0 = \frac{4\pi V}{ab\lambda_g} \cdot \frac{4\pi M_0}{\Delta H_0}$$

where ΔH_0, M_0 and V are respectively the uniform mode line-width, the magnetization and the volume of the sample; λ_g is the wavelength of the r.f. field in the wave-guide of dimensions a and b (Fig. 2). Even if the incident r.f. excitation is kept at a constant value, the transient growth of the uniform mode amplitude c_0 leads to a time variation of the radiated field. Thus, the effective r.f. field on the crystal is no longer constant but varies according to:

$$h_x(-l, t) = 2i\left(\frac{2\pi\hbar\omega}{V_1}\right)^{1/2}(q - q^+) \\ \times \left(1 - \frac{\beta_l}{1+\beta_l}\right)(1 - e^{-\eta_l t})$$

with

$$\beta_l = \beta_0 \cos^2 k_g l .$$

From these considerations, if P_{inc} is the constant incident power, the evolution of the power P_a absorbed effectively by the sample is:

$$\frac{P_a}{P_{inc}} = \frac{4\beta_l}{(1+\beta_l)^2}(1 - e^{-\eta_l t} + \beta_l e^{-\eta_l t} - \beta_l e^{-2\eta_l t}) . \quad (5)$$

If p_{inc} is suddenly suppressed at the time $t=t_c$ at which time the steady-state is reached, the evolution of P_a is given by:

$$\frac{P_a}{P_{inc}}_{t>t_c} = -\frac{4\beta_l^2}{(1+\beta_l)^2} e^{-2\eta_l(t-t_c)} \quad (6)$$

The minus sign before equation (6), shows that Pa is reradiated by the crystal.

The experimental verification of equations (5) and (6) have been obtained with a spherical YIG single crystal (1·56 mm in dia.) placed at the center of a rectangular wave-guide at C-band ($\omega/2\pi$ = 5·3 GHz) at a distance l from the tunable short. By moving the short-circuit, we vary the term β_l, through the term $\cos^2$, of interaction between the r.f. excitation and the magnetic system. Hence, the radiation rate, defined by:

$$y = \frac{\beta_l}{1+\beta_l}$$

depends on l.

Figure 3 shows the absorbed power evolution when the r.f. field is applied at t=0, for different values of β_l. In these experiments P_{inc} is not too large, in order to avoid non-linear processes ($P_{inc} \leq$ 1 mW). The steady-state absorption is the same when β_l=0·5 and 2 in these cases, the incident power is not entirely absorbed (P_a/P_{inc} = 0·88). Indeed, when β_l< 1, the magnetic system is under-coupled and 12 per cent of P_i is de-coupled from the uniform mode, whereas if β_l< 1 all the incident power is coupled to the uniform mode. In this last case the magnetic system is over-coupled and 12 per cent of the absorbed power is re-radiated after an overshoot. In Fig. 3, the case β_l=5 is obtained by decreasing the wave-guide height to 5 mm.

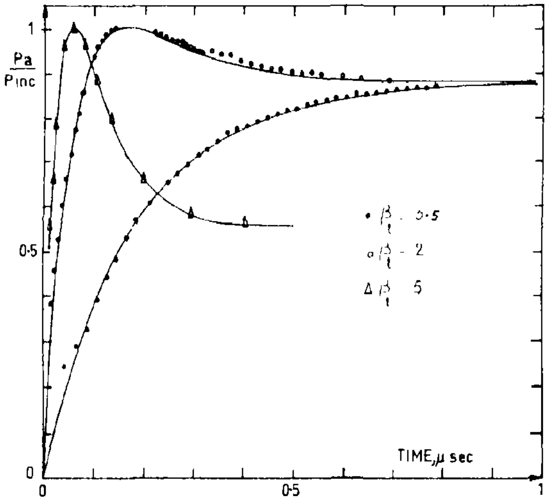

Fig. 3 Transient harmonic evolution of the r.f. power absorbed at resonance by a YIG single-crystal, for different values of the coupling factor.

This increases the filling factor. At critical coupling ($\beta_l=1$), all the incident power is absorbed in the steady-state ($P_a/P_{inc}=1$). The origin of the overshoot can be simply explained. Indeed, as shown in reference [1], the amplitude c_0 has an exponential evolution:

$$c_0 \sim (1-e^{-\eta_l t}) .$$

From equation (2), we deduce immediately that the number of photons effectively absorbed per time unit is given by the difference between a quantity which increases as c_0 (term $\alpha' c_0 q^+$) and a quantity which increases slowly as c_0^2 (term $\beta' c_0^+ c_0$). When $\beta_l > 1$, the radiation terms are large but their reaction arises only after a relatively extended time.

In Fig. 4, the radiated power after the suppression of the r.f. excitation is plotted on a logarithmic scale for two values of β_l. The slope of the curves gives the relaxation rate η_l since equation (6) leads to:

$$l_N \frac{P_{inc}}{P_a} = 2\eta_L t - l_N \frac{4\beta_l^2}{(1+\beta_l)^2} .$$

Then, from equation (4), we deduce the linewidth ΔH_0 of the uniform mode:

$$\Delta H_0 = 2\eta_L/\gamma(1+\beta_l) .$$

The good agreement between the theoretical and experimental results justifies our assumptions particularly when we consider the magnetic dipole radiation of the uniform magnons. We must introduce this process in the study of transient and steady state phenomena for narrow line-width samples, because the dipolar energy of the uniform mode produces a radiated field. Finally, the radiated power measured, when the r.f. excitation is suppressed, gives an accurate method to determine the low relaxation rates, since it is not necessary to know the value of the d.c. magnetic field; so, at room temperature, we obtain, for the YIG sample that we use, a line-width equal to 0·274 Oe.

3. TRANSIENT ANHARMONIC PROCESSES

The experimental results described in this section concern mainly the first-order anharmonic processes induced by the coupling coefficient f_k, defined in [1], which leads to the transfer of energy from a $k = 0$ magnon to a pair of parametric magnons $\pm k$, as shown in Fig. 5. In the anharmonic case, the dipolar

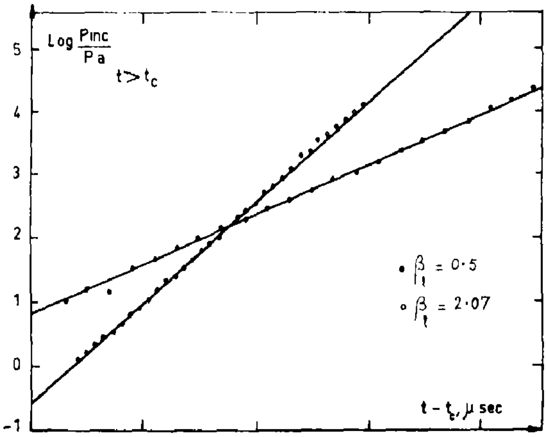

Fig. 4 Time evolution of the power radiated by a YIG single-crystal at resonance when the r.f. excitation is suppressed at the time t_c.

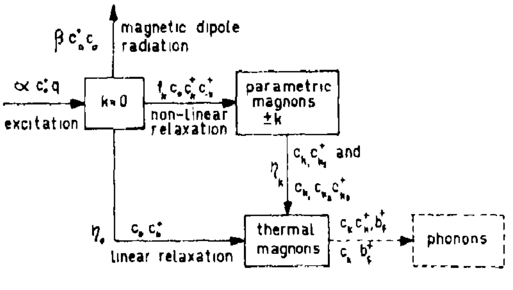

Fig. 5. Schematic diagram of the linear relaxation with magnetic dipole radiation.

radiation also modifies strongly the critical threshold of the spin-waves and the transient and steady-state evolutions of the magnetic system.

For a given material, the spin-wave threshold is an intrinsic parameter which depends mainly on η_0, η_k and f_k. We have seen in section 2 that the relaxation rate η_0 is modified by the dipolar radiation. Thus, the measurements of the threshold must be corrected by a radiation factor. From equation (56) and (59) of [1], we obtain the relation between the measured threshold h^c_{inc} and the intrinsic threshold h^c_{int} which is independent of the radiation:

$$h^c_{inc} = \frac{(1+\beta_l)}{\cos k_a l} h^c_{int} \tag{7}$$

with

$$h^c_{int} = \frac{\eta_0 \eta_k}{g_k} \tag{8}$$

and

$$g_k = \pi (g\gamma)^2 \left(\frac{\omega_i + Dk^2 + \omega_k}{4\omega_k}\right) \sin 2\theta_k .$$

These properties are described in Fig. 6. The variation of the r.f. susceptibility is given at the resonance conditions, as a function of $(h^c_{inc})^{-1}$ for two values of the coupling factor ($\beta_l = 0{\cdot}26$ and $0{\cdot}71$). We used a lithium ferrite sample for which the three-magnon cut-off frequency is higher than the r.f. excitation frequency ($\omega_0 = 5{\cdot}3$ GHz). For the two values of β_l mentioned above, the curves are the same; thus there is a single value of the intrinsic threshold which is independent of the strength of radiation.

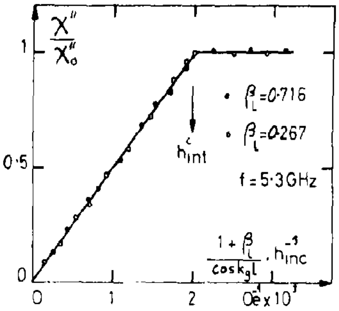

Fig. 6. R.F. susceptibility at resonance of a lithium ferrite sample as a function of the inverse of the intrinsic excitation, for two values of the coupling factor.

The transient study has been performed quantitatively for the first-order processes only. Indeed, the response observed for the second-order processes if very complex. In this latter case, both the saturation phenomena, produced by the parametric spin-wave excitation, and a resonance frequency shift, due to the fold-over effect, arise during the transient processes. We observed a modulation of the reflected power and a large difference in the steady-state absorption between the cases where the sample is tuned to resonance at low or high steady-state level. For the first-order processes, the resonance frequency is the same at low and high power levels. In Fig. 7, the traces a and b describe the typical time responses of the magnetic system. Trace 7 (a) shows the transient evolution of the absorbed power P_a when $\beta_l < 1$, for different values of r.f excitation. Trace 7 (b) shows the non-linear evolution of P_a when $\beta_l > 1$. In the two cases, the evolution of the absorbed power and the radiated field, as long as the parametric spin-wave reaction does not become too large, are given by [1]:

$$\frac{P_a}{P_{inc}} = \frac{4\beta_l}{(1+\beta_l)^2}\left[1 - (1-\beta_l)\sum_{k\neq 0} U_k(t) - \beta_l\left(\sum_{k\neq 0} U_k(t)\right)^2\right] \tag{9}$$

$$h_r = -i\left(\frac{2\pi\hbar\omega}{V_1}\right)^{1/2}\frac{2\beta_l}{1+\beta_l}(q-q^+)$$
$$\times\left[1-\sum_{k\neq 0}U_k(t)\right]. \quad (10)$$

The factors of equations (9) and (10) are the same as in [1]. $U_k(t)$ describes the time exponential growth of the mode k. Figure 8 shows a typical result of the power absorbed, at 5·3 GHz, by a lithium ferrite sample when $\beta_l = 0{\cdot}355$. In this case, the level of the incident power applied is 12 *dB* above the threshold. The linear evolution is very fast, and the linear steady-state is reached before the spin-wave amplitude becomes too large. Figure 9 represents, on a logarithmic scale, the non-linear evolution of P_a. This curve shows clearly that an exponential evolution of the spin-wave population, can be obtained over a relatively long period ($t \simeq 200$ nsec). Hence, in equation (9) the quadratic term can be neglected at the beginning of the spin-wave reaction and the discrete summation over k can be restricted to a very narrow packet.

By assuming that only one parametric mode is excited, we deduce the spin-wave relaxation rate η_k from the time variation of P_a given by equation (9):

$$\frac{\Delta P_a(t)}{P_{inc}} = \frac{4\beta_l}{(1+\beta_l)} - \frac{P_a(t)}{P_{inc}}$$
$$\simeq \frac{4\beta_l(1-\beta_l)}{(1+\beta_l)^2}F_k \exp 2\eta_k\left(\frac{h_{inc}}{h^c_{inc}}-1\right)t \quad (11)$$

with F_k as defined in [1]. η_k is then determined from the measurements of P_a and h_{inc}/h^c_{inc}. The results agree with those obtained by the parallel pumping technique[8-10] (see Table 1).

4. DIRECT OBSERVATION OF THE MAGNETIC DIPOLE RADIATION

The foregoing theory can be applied to explain the behavior of microwave filters and limiters using ferromagnetic resonance.

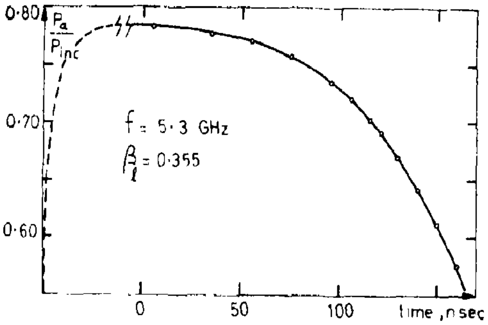

Fig. 8. Transient anharmonic evolution of the power absorbed at resonance by a lithium ferrite single-crystal, when the ferromagnetic system is undercoupled. The time decrease of P_a is produced by the built-up of the three-magnon processes

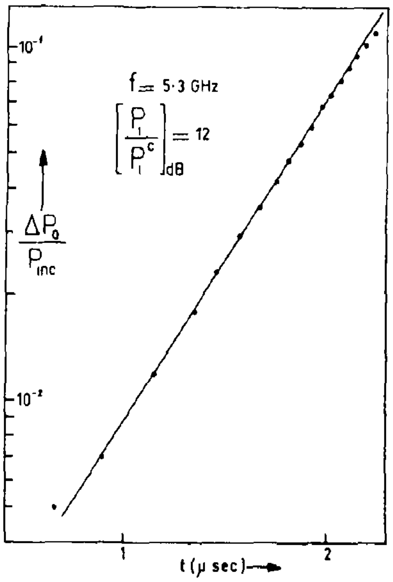

Fig. 9 Determination of the spin-wave relaxation rate in a lithium ferrite sample, from the time variations of the power absorbed by the sample.

Table 1. *Experimental results for lithium ferrite* ($\omega_k/2\pi = 2{\cdot}65$ GHz)

Magnetization direction (Oe)	[100]	[110]	[111]
ΔH	5·2	5·33	5·63
ΔH_k	0·33	0·45	0·72
h^c_{inc}	$0{\cdot}52\times10^{-3}$	$0{\cdot}77\times10^{-3}$	$1{\cdot}12\times10^{-3}$

Degrasse first described such a filter which can be tuned over a wide frequency range and can limit the transmitted power when the incident signal exceeds a threshold[11]. Carter[12] and Patel[13] have given the first interpretation of this device, by showing the analogy between the properties of the magnetic resonator and those of equivalent current loops. The validity of their model is restricted and cannot describe fully the junction defined by the filter. A theory of the filter is given below from the more fundamental assumptions of the magnetic dipole radiation we have developed in [1].

To do that we take the microwave set-up, shown in Fig. 10. Two short-circuited waveguides have a common circular hole at the center of their larger side. A ferrimagnetic sphere (for example YIG) is placed at the center of this hole. From the properties of the dipolar radiation, we shall determine the power transmitted by the sample from the wave-guide 1 to the wave-guide 2 in the linear case (filter) and in the non-linear case (limiter). The transient evolution will give the residual energy of the limiter spike. Finally we compare these theoretical properties with the experimental data.

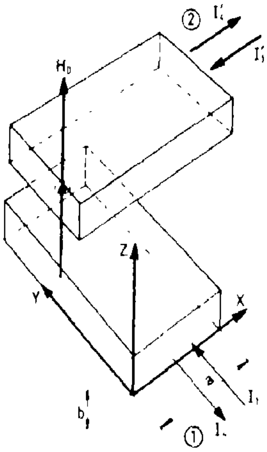

Fig. 10. Microwave set-up for a direct observation of the magnetic dipole radiation of the uniform magnons.

Linear case

In order to simplify the derivations, the following assumptions are made: (a) The two wave-guides are uncoupled when the ferrimagnetic crystal is off-resonance. (b) The sample is in the short-circuit plane of the two waveguides. (c) Only the TE_{10} mode is excited.

We have seen that a dipolar radiation is equivalent to a current source i_d and a voltage source v_d[1]. With the assumptions mentioned above, the complex amplitudes of the r.f. field, near the sample, are in the wave-guide 1:

$$\left.\begin{aligned} H_x &= 2\left(h_{inc_x} - i\frac{K'}{ab}m_x\right) \\ H_y &= 0 \end{aligned}\right\} \quad (11)$$

and in the wave-guide 2:

$$\left.\begin{aligned} H_x &= 0 \\ H_y &= -i\frac{2K'}{ab}m_y. \end{aligned}\right\} \quad (12)$$

a and b are the wave-guide dimensions, $K' = 2\pi V''/\mu_0\lambda_g$ and V' is the volume fraction of the sample which radiates in each wave-guide. In addition, from equation (16) of [1], only a wave I_4' is propagating in the wave-guide 2 with the amplitude:

$$I_4' = -v_d/Z_g$$

where Z_g is the characteristic impedance of the wave-guide. Then, the power radiated in the wave-guide 2 is given by:

$$P_r = \tfrac{1}{2}Z_g|I_4'^{*}I_4'| = \frac{1}{2}\left|\frac{v_d^{*}v_d}{Z_g}\right|. \quad (13)$$

From equations (15, 28 and 29) of [1], we obtain:

$$P_r = Z_g\frac{K'^2}{ab}\frac{2g\mu_B M_0}{V}b_0{}^{+}b_0. \quad (14)$$

The amplitude b_0 of the uniform mode is (equation 40 of [1]):

$$b_0 \approx \frac{i\alpha q}{\hbar \delta\Omega'}(1-e^{i\delta\Omega' t}) \qquad (15)$$

with

$$\delta\Omega' = \omega_0 - \omega + i\eta_L'$$

$$\eta_L' = \eta_0(1+2\beta_0')$$

$$\beta_0' = \frac{4\pi V'}{ab\lambda_g}\frac{4\pi M_0}{\Delta H_0}.$$

Equation (15) is different from the solution (43) obtained in [1] because the coupling of the sample to the wave-guides introduces a factor $2\beta_l$ in η_l. Finally, since the incident power in the wave-guide 1 is

$$P_{inc} = \frac{ab}{4} Z_g h_{inc_x}^2 \qquad (16)$$

the power radiated in the wave-guide 2 becomes:

$$P_r(t) = \frac{4\beta_0'^2 P_{inc}}{(1+2\beta_0')^2 + ((\omega_0-\omega)/\eta_0)^2} \times (1-e^{i\delta\Omega' t})^2. \qquad (17)$$

The expression (17) describes the time evolution of the power transmitted through a resonator having for Q-factor $\omega_0/2\eta_0$ and the input and output coupling coefficients β_0'.

We designed such a filter based on the magnetic dipole radiation. In order to improve the characteristics we chose a strip-line set-up with two lithium ferrite spheres situated on each side of a coupling hole between the two strip-lines. This filter is magnetically tuned between 4·9 and 8 GHz. Figure 11 shows the selectivity of such a device.

Non-linear case = the limiter

If the incident power P_{inc} exceeds the threshold P_{inc}^c in the device described above, three-magnon transitions arise and limit the amplitude b_0 of the uniform mode to a maximum value b_0^{crit}. Since the spin-wave radiation can be neglected in our case, the only re-emitted power in the wave-guide 2 is due to the uniform mode radiation. Thus equation (14), given above for the linear case, is still correct, if the linear amplitude b_0 is replaced by the non-linear solution obtained from by Equations (45–7) of [1]. These latter equations of motion are modified in the present device only by the introduction of the radiation of the sample in the wave-guide 2 (equation (12)). Following the method described in [1], it is straight-forward to derive the power radiated in the wave-guide 2, at the beginning of the spin-wave reaction:

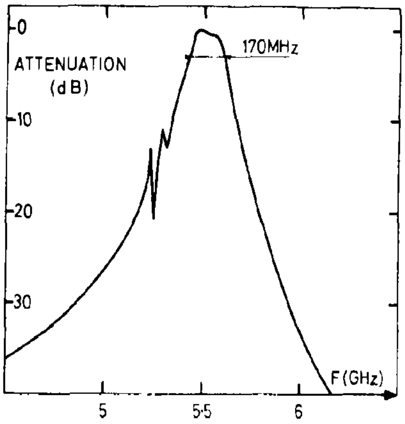

Fig. 11. Selectivity of a transmission filter or limiter using lithium ferrite resonators.

$$P_r(t) = \frac{4\beta_0'^2 P_{inc}^c}{(1+2\beta_0')^2 + ((\omega_0-\omega)/\eta_0)^2} \times \left[\frac{h_{inc}}{h_{inc}^c} - \frac{|f_k|^2 n_k{}^0}{\eta_k(2\rho_k - 2\eta_k + \eta_L')}\exp Nt\right]^2 \qquad (18)$$

with

$$N = \frac{2i\eta_L'\eta_k}{\delta\Omega'}\left(\frac{h_{inc}}{h_{inc}^c} - 1\right).$$

For simplification, it is assumed that only a parametric spin-wave state is excited above the threshold. We can evaluate the energy contained in the spike of the limiter. We define this energy by the hatching area in Figure 12, i.e.:

$$E(P_{inc}) = \int_{t_1}^{t_2} P_r(t)\,\mathrm{d}t$$

$$= \frac{4\beta_0'^2 P_{inc}}{(1+2\beta_0')^2 + ((\omega_0-\omega)/\eta_0)^2} \times (t_2-t_1) \tag{19}$$

where t_1 and t_2 are determined by the intersection of the steady-state level with respectively the linear increase and the approximated non-linear decrease of the radiated power.

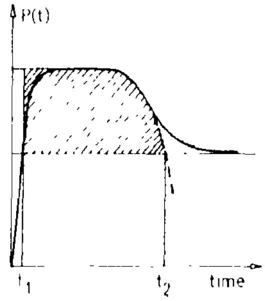

Fig. 12 Definition of the residual energy contained in the spike of a transmission limiter

The expression (19) has been compared with the experimental results obtained at 5·3 GHz on a limiter in which the magnetic dipole is a spherical lithium ferrite single crystal all of whose parameters have been determined experimentally [10]. Figure 13 shows that the calculation (19) is correctly verified over the 20 *dB* dynamic range of limitation. Equations (17) and (18) give the same selectivity of the device in the linear and non-linear behavior. The 3 *dB* band-pass is 170 MHz. In Fig. 13, the difference between theoretical and experimental results, when $P_{inc} > 1$ W, has two origins; first, when P_{inc} is very high, spin-waves arise before the uniform mode reaches its linear steady-state level; second, the assumption, that only a single spin-wave mode is excited, is no longer correct and we must consider in our calculations a spin-wave packet Δk.

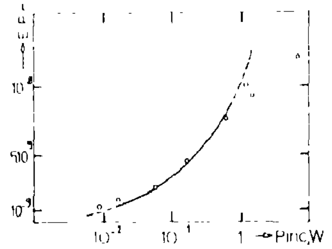

Fig. 13 Variation of the residual energy of the spike of a transmission limter as a function of the incident power. The solid curve is given by the theory

5. NUMERICAL INVESTIGATIONS

The transient evolution of the power absorbed in the anharmonic case is correctly described, at the beginning of the spin-wave growth, by the analytical expression (9). But it is not possible to obtain an anlytical solution which defines the full evolution of the magnetic system towards the non-linear steady-state. So, we have made numerical calculations to solve the equation of motion by using the simplifying assumption that only one spin-wave mode is excited. This assumption is not fully correct, but readily gives a numerical solution which, in the overcoupling case ($\beta_l > 1$), verifies qualitatively the evolution of P_a. Indeed, the time variation of the magnetic system is complex in this latter case, as shown from the experimental observation (Fig. 7(b)) and the numerical results (Fig. 14).

When $\beta_l > 1$, the spin-wave build-up gives an increase of P_a, which reaches the maximum value P_{inc}, and then decreases to a non-linear steady-state level higher than the linear steady-state level. When $\beta_l < 1$ we obtain the classic evolution described in Fig. 15.

6. EXPERIMENTAL TECHNIQUES

The r.f. power absorbed under perpendicular pumping gives directly the evolution of the uniform mode. The reaction of the parametric spin-waves on the uniform mode indirectly modifies this power. So we must use the theoretical result, obtained in [1] to deduce,

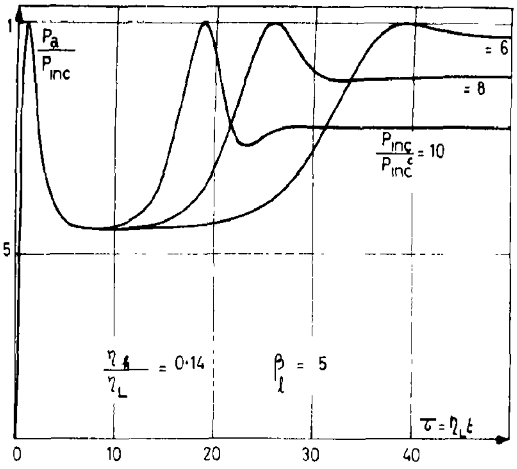

Fig. 14. Theoretical transient evolution of the absorbed r.f. power, obtained from numerical integration of the dynamic equations, when the magnetic system is overcoupled ($\beta_l > 1$).

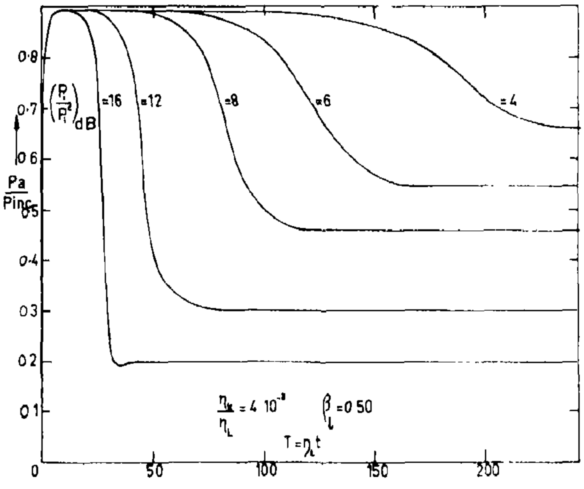

Fig. 15. Theoretical evolution of the absorbed r f power, obtained from numerical integration of the dynamic equations, when the dynamic system is undercoupled. ($\beta_l < 1$).

from the measurements, the characteristics of the parametric modes. We have replaced the conventional perturbation technique of a cavity by using a sample placed in a waveguide, in order to avoid the cavity transient effects.

The coupling factor β_l can be adjusted by moving the tunable short which limits the wave-guide (Figs. 2 and 16). The incident and reflected power are separated by a three-port circulator. The absorbed power is deduced from the reflected power. A thermostatically controlled c.w. klystron gives 50 mW at 5·3 GHz. A diode switch produces the r.f. pulses with a rise time less than 10 n sec. The pulses are amplified by a c.w. travelling wave tube

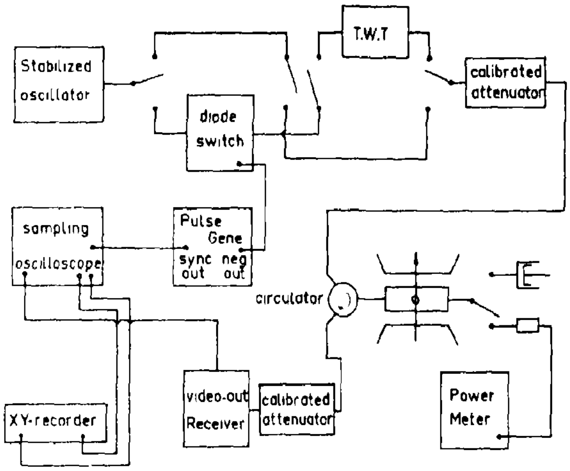

Fig 16 Schematic diagram of the experimental circuit

which can give a maximum power of 20 W. The reflected wave is analysed through a sampling oscilloscope and a X–Y recorder, which magnifies any part of the transient phenomena. The sample is placed at the center of a rectangular wave-guide at C-band whose height can be reduced to increase the filling factor. Finally by means of three manual switches, a low or high level signal, c.w. or pulsed shaped, can be applied to the sample.

CONCLUSIONS

We have studied in detail the time dependence of the microwave absorption in the YIG and lithium ferrite samples under perpendicular pumping. The experimental results are in good agreement with theory. We have shown that the dipolar radiation of the uniform magnons widely modifies the transient and steady-state phenomena, mainly in the narrow line-width materials. We have interpreted the behavior of the microwave filters and limiters, using the ferromagnetic resonance, from the dipolar radiation properties of the magnetic system. The experimental results confirm the validity of such a model.

Acknowledgements—The authors are indebted to E. Banerjea for carrying out the computer calculations. They also wish to thank C. Chauvin for his technical assistance

REFERENCES

1. LE GALL H., DESORMIERE B. and MILOT E., *J Phys. Chem. Solids* **30**, 979 (1969)
2. SUHL H., *J Phys. Chem Solids* **1**, 209 (1957).
3. SCHLOMANN E., *J. appl Phys.* **34**, 1998 (1963); SCHLÖMANN, E., *Izv Acad. Nauk SSSR* **28**, 454 (1964). Translation by Columbia Technical Translations, *Bull Acad. Sci. USSR* **28**, 366, JOSEPH R I and SCHLOMANN E., *J. appl. Phys.* **38**, 1915 (1967).
4. LE GALL H., *C r. hebd. Séanc Acad. Sci., Paris* **258**, 502 (1964); *C r. hebd. Séanc Acad. Sci., Paris* **258**, 3986 (1964); *J. appl. Phys* **36**, 1203 (1965)
5. CLOGSTON A. M., SUHL H., WALKER L. R., ANDERSON P W., *J. Phys. Chem. Solids* **1**, 129 (1956)
6. AKHIEZER A. I., *J Phys.* **10**, 217 (1946).
7. LE GALL H., MILOT E and DESORMIÈRE B., *Solid State Commun.* **5**, 637 (1967)
8. LE CRAW R. C. and SPENCER E. G., *J phys. Soc Japan, Suppl. B1.* **17**, 401 (1962).
9. DENTON R. T. and SPENCER E. G., *J. appl Phys* **33**, 1300 S (1962).
10. DESORMIÈRE B. and MILOT E., *I.E.E.E. Trans. Magnet.* **3**, 402 (1967)
11. DEGRASSE R. W., *J. appl. Phys.* **30**, 155 S (1959).
12. CARTER P S., *I.R E. 1960 Intl Convention Rec* **3**, 130 (1960)
13. PATEL C N., Tech. Rep No. 411–1. Stanford University (1961)

J. Phys. Chem. Solids Pergamon Press 1969. Vol. 30, pp. 1147–1150. Printed in Great Britain

PROPRIETES OPTIQUES DE COUCHES MINCES D'INDIUM DANS L'ULTRA VIOLET EXTREME

J. C. LEMONNIER, G. STEPHAN, Y. Le CALVEZ et Mme S. ROBIN
Laboratoire de Spectroscopie, Faculté des Sciences de Rennes (35), France

(*Received* 16 *September* 1968)

Resumé – On détermine à partir de mesures de pouvoirs réflecteurs les constantes optiques de couches minces d'indium évaporées *in situ*. Les résultats sont donnés pour le domaine spectral 4,1 à 63 eV et montrent la présence de transitions interbandes et d'une oscillation de plasma. Nous comparons nos résultats avec ceux d'autres auteurs concernant le pouvoir réflecteur, l'absorption, la courbe de densité d'états dans la bande de conduction et les pertes d'énergie caractéristiques des électrons.

Abstract – Optical constants of thin films of In evaporated *in situ* are obtained from reflectance measurements. Results are given for the spectral range 4·1–63 eV and show transitions and a collective oscillation. They are compared with other measurements concerning reflectance, absorption, optical density of states, and characteristic energy losses.

L'INDIUM A déjà fait l'objet d'études expérimentales et théoriques en ce qui concerne la détermination de ses propriétés optiques et électroniques dans le domaine de l'ultraviolet. Des mesures de pouvoir réflecteur ont été effectuées par Walker *et al.*[1] sous une incidence quasi normale entre 7,5 et 22 eV, par Huebner[2] entre 4,2 et 11,2 eV pour des incidences de 20° et 70°. Walker[1] a également mesuré la transmission d'une couche de 800 Å d'épaisseur, Hunter a déterminé les constantes optiques entre 11,4 et 16,7 eV (1085 à 744 Å)[3] et mesuré la transmission de films d'indium d'épaisseurs variables[4]. Afin de compléter vers les grandes énergies les mesures existantes, nous avons entrepris l'étude des propriétés optiques et électroniques de l'indium de 4,1 eV à 63 eV (3000 à 195 Å).

L'indium pur à 99,999% est disposé dans des creusets de tungstène; la couche métallique se forme directement dans l'enceinte de mesure sur des supports de pyrex soigneusement nettoyés ou des lames de mica fraîchement clivé. C'est ce dernier support qui nous a donné les meilleurs résultats quant à l'aspect des miroirs obtenus et à la reproductibilité de leurs propriétés optiques. La vitesse d'évaporation était de l'ordre de 800 à 1000 A/s et le vide dans le réflectomètre de 10^{-6} Torr. environ. Les mesures ont été effectuées à l'aide des appareillages déjà décrits[5, 6]. Au-dessous de 1000 Å, nous utilisons la source Morlais-Robin[7] avec une circulation d'argon fournissant un spectre de raies.

Nous avons mesuré les pouvoirs réflecteurs pour quatre angles d'incidence, soit 20°, 45°, 60°, 70°, ce qui nous a permis de déterminer les constantes optiques à l'aide de tables numériques ou d'abaques (méthode des deux angles d'incidence). La Fig. 1 donne le pouvoir réflecteur ramené à la lumière naturelle d'une couche d'épaisseur voisine de 2000 Å pour les incidences de 20° et 70° jusque 16 eV et pour 60° et 70° au-delà de cette énergie. En incidence normale le pouvoir réflecteur décroît rapidement vers 10 eV pour devenir très faible (inférieur à 2%) vers 16 eV. Nous constatons l'existence d'un maximum vers 7,7 eV analogue à celui trouvé par Huebner[2] mais aucun pic de réflexion n'apparaît au voisinage de 16 eV alors que la courbe de Walker[1] y montre un maximum important. Le même phénomène avait déjà été signalé pour l'étain et le bismuth. On

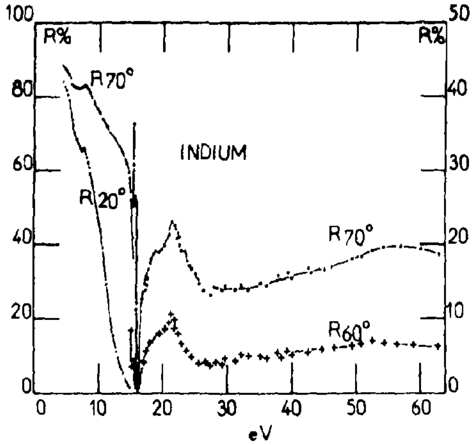

Fig. 1. Pouvoir réflecteur en lumière naturelle d'une couche d'indium d'épaisseur 2000 Å pour les incidences de 20°, 60° et 70° (R_{20}, R_{60} et R_{70})

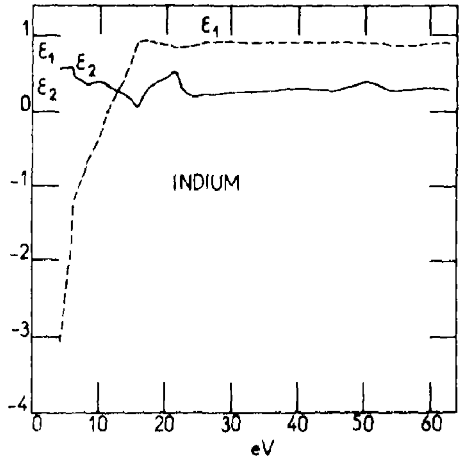

Fig. 2 Partie réelle (ϵ_1) et partie imaginaire (ϵ_2) de la constante diélectrique

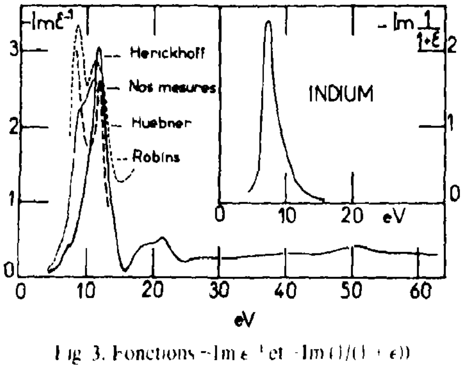

Fig. 3. Fonctions $-\mathrm{Im}\,\epsilon^{-1}$ et $-\mathrm{Im}(1/(1+\epsilon))$

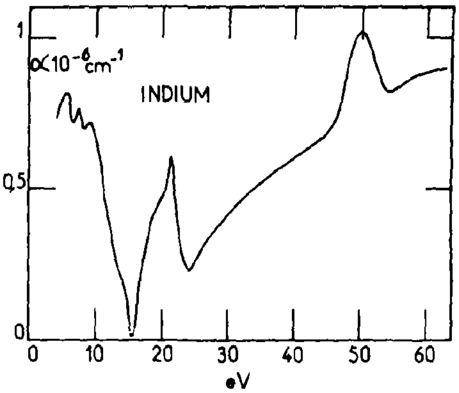

Fig. 4 Coefficient d'absorption $\alpha = (4\pi k/\lambda)$.

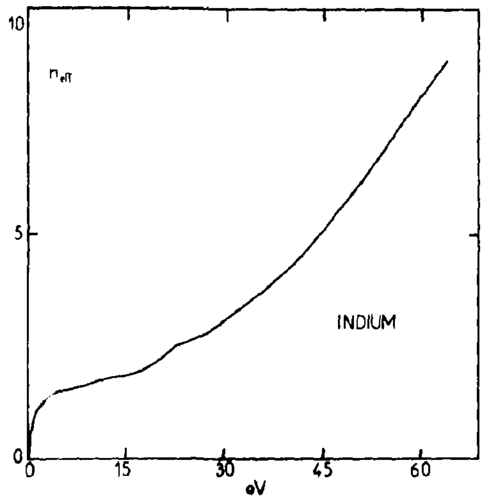

Fig. 5 n_{eff} en fonction des énergies.

peut penser que ce maximum de réflexion situé dans une bande de transmission est plutôt dû à un phénomène d'interférences. On note deux maxima a vers 18,4 et 21,4 eV et un plus large au voisinage de 54 eV.

Nous avons représenté sur la Fig. 2 les parties réelle ϵ_1 et imaginaire ϵ_2 de la constante diélectrique, sur la Fig. 3 les fonctions $-\mathrm{Im}(\epsilon^{-1})$ et $-\mathrm{Im}(1/(1+\epsilon))$ et sur la Fig. 4 le coefficient d'absorption $\alpha = (4\pi k/\lambda)$. L'indium solide possède trois électrons de conduction par atome: 2 électrons 5*s* et un électron 5*p*. En outre dans l'atome d'indium les niveaux 5*s* et 5*p* sont séparés des niveaux

$4d$ par une énergie de l'ordre de 16 eV[8]. On peut donc prévoir l'existence de transitions interbandes au voisinage de cette énergie. L'allure des courbes ϵ_2 et α vers 16 eV montre effectivement l'existence de transitions interbandes correspondant aux niveaux $N_{\mathrm{IV,V}}$ situés respectivement à 16,3 et 15,6 eV[8]. D'autre part entre 16 et 23 eV, la contribution des électrons libres doit être nulle (leur longueur d'onde de coupure est 1065 Å); on peut donc penser que, pour cet intervalle d'énergie, ϵ_2 décrit l'excitation des électrons $4d$ vers la bande de conduction et représente alors la courbe de la densité d'états $N(E)$ pour celle-ci, la bande $4d$ étant considérée comme plate. En effet, la contribution à ϵ_2 pour ce groupe de transitions interbandes peut s'écrire[9]

$$\epsilon_2(\omega) = \frac{2\pi e^2 h}{m\omega} N(E) f_{i,c}(k)$$

où

$$N(E) = \frac{1}{V} \int_{ZB} \frac{\mathrm{d}S_K}{\mathrm{grad}_k(E_c(k) - E_j(k))}$$

(V: volume de la zone de Brillouin)

est la densité des états combinés des bandes c et j, si on considère que les éléments de matrice $f_{j,c}(k)$ sont constants dans la zone de Brillouin. Nous pouvons donc comparer les mesures de $N(E)$ de Koyama[10] à la courbe $\epsilon_2(\omega)$ L'allure des deux courbes est la même, ce qui vient confirmer les approximations ci-dessus. La bande de conduction de l'indium comporte deux maxima de densité d'états séparés de 3,4 eV environ. La distance entre le bas de la bande et le niveau de Fermi serait alors d'environ 7,7 eV pour l'indium. Gaspari et Das[11] ont trouvé le niveau de Fermi à 8,3 eV au-dessus du bas de la bande située à Γ_1. L'allure des courbes ϵ_1, ϵ_2 et $-\mathrm{Im}(\epsilon^{-1})$ indique l'existence d'une oscillation de plasma à 11,6 eV; la fréquence théorique calculée en considérant que l'indium possède trois électrons libres est 12,6 eV. Nous pouvons également comparer nos résultats aux autres mesures optiques ainsi qu'aux pertes caractéristiques d'énergie (Tableau 1).

La position du pic principal situé vers 11,5 eV et correspondant au plasma de volume varie quelque peu suivant les auteurs et les méthodes mais il faut remarquer que la valeur trouvée est toujours inférieure à la valeur théorique 12,6 eV. Les écarts enregistrés doivent être attribués sans doute aux conditions expérimentales et aux états de surface des différents échantillons. La fonction $-\mathrm{Im}(1/(1+\epsilon))$ présente un maximum vers 7,7 eV correspondant au plasma de surface, la valeur théorique étant de 8,9 eV. Cet écart est dû au fait que la couche étudiée ne doit pas être totalement libre d'oxyde, et qu'il existe une transition interbande à proximité vers 6 eV[12, 13].

La Fig. 5 montre le nombre d'électrons n_{eff} participant aux transitions électroniques

Tableau 1. Résultats obtenus par différents auteurs entre 4 et 63 eV: maxima des fonctions $-\mathrm{Im}(\epsilon^{-1})$ *obtenues à partir des mesures optiques et maxima des pertes d'énergie caractéristiques*

Mesures optiques $-\mathrm{Im}(\epsilon^{-1})$ (eV)				Pertes d'energie caracteristiques (eV)			
Nos mesures	Hunter [3]	Huebner [2]	Robins [16]	Henckoff [15]	Kleinn [13]	Balabanova [14]	Gauthe [12]
6,2					5,9		5,7
7,4		8,7	8,7				
11,7	11,5	10,8	11,3	11,8	12,2	12,1	
18							
21,4					22,3	24	20,5
50							

entre 0,1 et 63 eV et déterminé à partir de la règle de sommation

$$\int_0^{\omega_0} \omega\epsilon_2\, d\omega = \frac{\pi N e^2}{2m\epsilon_0} n_{eff}.$$

Entre 0,1 et 2,3 eV nous avons utilisé les valeurs de ϵ_2 calculées à l'aide des constantes optiques déterminées par Golovashkin[17]. Nous observons d'abord une brusque augmentation de n_{eff} due à l'excitation des électrons libres puis après une variation plus lente n_{eff} arrive à la valeur 2,5 vers 21 eV. La transition interbande située au voisinage de cette énergie provoque un brusque changement de pente. Ensuite, n_{eff} continue à croître pour atteindre la valeur 8 vers 60 eV.

BIBLIOGRAPHIE

1. WALKER W. C., RUSTGI O. P. et WEISSLER G. L., *J. opt. Soc. Am.* **49**, 471 (1959).
2. HUEBNER R. H., ARAKAWA E. T., HAMM R. N. et MAC RAE R. A., Optical Constants of Evaporated Metal Films of Silver and Indium. O.R.N.L. TM. 1104 (1965).
3. HUNTER W. R., *J. Phys.* **25**, 154 (1964).
4. HUNTER W. R., *J. Phys.* **25**, 148 (1964).
5. LE CALVEZ Y., STEPHAN G. et ROBIN Mme S., *Optica Acta* **15**, 583 (1968).
6. STEPHAN G., LEMONNIER J. C. et ROBIN Mme S., *J. opt. Soc. Am.* **57**, 486 (1967).
7. MORLAIS M. et ROBIN S., *C. r. hebd. Séanc. Acad. Sci. Paris* **259**, 1489 (1964).
8. SANDSTROEM A. E., *Handb. Phys.* **30**, 226 (1957).
9. PHILLIPS J. C., *Solid State Physics* (Édité par F. Seitz et D. Turnbull), Vol. 18, p. 55, Wiley, New York (1966).
10. KOYAMA R., SPICER W. E., ASHCROFT N. W. et LAURENCE W. E., *Phys. Rev. Lett.* **19**, 1284 (1967).
11. GASPARI G. D. et DAS T. P., *Phys. Rev.* **167**, 660 (1968).
12. GAUTHE B., *Phys. Rev.* **114**, 1265 (1959).
13. KLEINN W., *Optik* **11**, 226 (1954).
14. BALABANOVA L. A., BREDOV M. M. et KOTOV B. A., *Soviet Phys. solid St.* **4**, 60 (1962).
15. HERICKOFF R. J., ARAKAWA E. T. et BIRKHOFF R. D., Characteristic energy loss studies of electron-bombarded Al, Cd, In, Mg and Zn foils with vacuum ultraviolet spectroscopy. O.R.N.L. TM-1107 (1965).
16. ROBINS J. L., Unpublished Ph.D. Dissertation. University of Western Australia, Nedlands, Western Australia (1961).
17. GOLOVASHKIN A. I., LEVCHENKO I. S., MOTULEVICH G. P. et SHUBIN A. A., *Soviet Phys. JETP* **24**, 1093 (1967).

J. Phys. Chem. Solids Pergamon Press 1969. Vol. 30, pp. 1151–1160. Printed in Great Britain

ELECTRICAL CONDUCTION IN Li-DOPED CoO

A. J. BOSMAN and C. CREVECOEUR
Philips Research Laboratories, N. V. Philips' Gloeilampenfabrieken, Eindhoven-Netherlands

(*Received* 23 *August* 1968)

Abstract—The electrical conductivity and the Seebeck coefficient of p-type CoO doped with Li have been measured on ceramic samples in the temperature region 150°–1300°K. It is concluded that the large temperature-dependence of the conductivity is almost completely determined by the change in the charge-carrier concentration. In order to calculate from the measurements the drift mobility μ_D as a function of temperature two extreme cases for the temperature dependence of the density of states N_t are assumed, viz. N_t is constant and N_t proportional to $T^{3/2}$. In the discussion the results of Hall-effect measurements are also considered.

INTRODUCTION

POLYCRYSTALLINE p-type CoO doped with Li was first investigated by Verwey *et al*[1]. The resistivity (ρ) was found to vary exponentially with temperature: $\rho = \rho_0 \exp Q/kT$. Depending on the Li concentration the value of the activation energy (Q) varied from 0·4 to 0·6 eV. The activation energy was thought to be due to ionization of the Li^+–Co^{3+} acceptors. It was assumed that free holes could move through the lattice by an unhampered interchange of electrons between Co^{3+} ions and Co^{2+} ions. The same model had also been used for the electrical conduction in non stoichiometric or Li-doped NiO[2, 3].

From similar measurements for Li-doped CoO Heikes *et al.*[4] suggested that the temperature dependence of ρ is entirely due to the mobility (μ_D), which should then increase exponentially with temperature. They considered the conduction mechanism to be a thermally activated diffusion process (hopping model). The activation energy for this diffusion process was assumed to arise from the trapping of holes by lattice polarization induced by the holes themselves.

The conception of a mobility exponentially increasing with temperature was first introduced by Morin[5] in his interpretation of ρ and Seebeck-effect measurements for the case of Ti-doped α-Fe_2O_3 and Li-doped NiO. He assumed the density of states (N_t) for the transport level to be temperature-independent and to be equal to the number of ionic sites/cm^3. The transport term (A) occurring in the expression for the Seebeck coefficient (α) was assumed to be zero. In later years different authors[6–8] arrived at the same conclusion from data for ρ and α viz. that electrical conduction in NiO indeed has to be regarded as a thermally activated hopping process. However, recent investigations by Ksendzow *et al.*[9], Zhuse *et al.*[10], Bosman *et al.*[11] and Austin *et al.*[12] have led to the conclusion that there is no coercive reason to introduce the hopping model in the case of NiO.

From recent data for ρ and the Hall coefficient (R_H) for non stoichiometric or Li-doped CoO it was found by Zhuse *et al.*[13], Austin *et al.*[12] and Van Daal *et al.*[14] that the Hall mobility (μ_H) is almost temperature-independent. The temperature region considered extended from 200° to 1500°K[14]. This result was considered to be in conflict with the hopping model. Fisher *et al.*[15], however, concluded from resistivity and gravimetric measurements that μ_D does increase exponentially with temperature between 1200°–1600°K, with an activation energy of 0·3 eV. Their results for α[15, 16] were also interpreted in terms of the hopping model. Furthermore these authors arrived at the conclusion that in the temperature region under consideration electrons may already contribute to electrical conduction. Shelyck *et al.*[17], from data for ρ and α obtained on single crystals between 900°–1500°K, arrive at a different conclusion. In their opinion the behaviour of ρ is governed mainly by the charge carrier concentration (p) and not by the drift mobility.

The electrical properties of CoO below room temperature have scarcely been investigated. Bruck *et al.*[18] and Austin *et al.* [12] have measured α down to low temperatures for the case of non stoichiometric polycrystalline material and Li-doped single crystals, respectively. Their results are not well understood and definite conclusions cannot be drawn.

In this paper data will be given for ρ and α between 145°–1300°K obtained on Li-doped ceramic CoO. From these data μ_p has been calculated as a function of temperature. In the discussion the results of Hall-effect measurements[14] are also considered.

EXPERIMENTAL

Li-doped CoO was prepared by heating an intimate mixture of Li_2CO_3 and very pure CoO at 800°C for some hours in nitrogen containing about 100 ppm of oxygen. CoO was made by decomposition of $CoCO_3$. The latter material was manufactured starting from very pure Co(grade: Johnson–Matthey). After milling the sintered Li-doped CoO powder it was pressed into disks and bars. Finally the samples were, packed in platinum, fired at 1300°C for 24 hr in nitrogen containing 10 ppm of oxygen. This oxygen pressure was maintained during cooling in the furnace to prevent the formation of Co_3O_4 at the grain boundaries. The density of the samples was about 93 per cent of the ideal value.

The d.c. resistivity was measured on bars as well as on disks. In both cases four electrodes were used for the measurements. Below room temperature, in a limited temperature range, a.c. resistivity measurements were also performed. This limitation in temperature is a consequence of the restricted frequency interval available (100Hz–2MHz). Moreover, at low temperatures the occurrence of dipole losses[19] gives an extra limitation. The a.c. measurements are meant to verify whether the measured values of the resistivity indeed represent the resistivity of the bulk. The d.c. measurements of ρ at high temperatures were performed in nitrogen containing 10 ppm of oxygen.

The Seebeck effect below room temperature was determined by measuring the voltage and temperature of two copper blocks between which the sample (bar) was mounted, using In–Hg as contact material. For the high temperature measurements of α two methods were used. In one method cylindrical samples were clamped between hollow platinum blocs of which the voltage and temperature were measured. Only the plane ends of the bars made electrical contact with the platinum blocs. In the other method the voltage and temperature were measured with thin thermocouples which were mounted in narrow and deep holes in the bar. For electrical contacts painted Pt contacts (Degussa) were used. The high temperature measurements of α were also performed in nitrogen containing 10 ppm of oxygen.

RESULTS

In Fig. 1 values of ρ obtained from d.c. measurements on CoO with Li dopes varying between 0·006 at.% and 9·0 at.% are presented as a function of $1/T$. Results of a.c. measurements are also given. At room temperature d.c. and a.c. values of ρ are practically the same. At lower temperatures, however, a.c. values are somewhat lower. The activation energies derived from a.c. data are some hundredths of an eV lower than those obtained from d.c. measurements.

For the weakly doped samples the decrease of ρ with increasing T above 800°K is due to the presence of Co vacancies (V_{Co}). In the

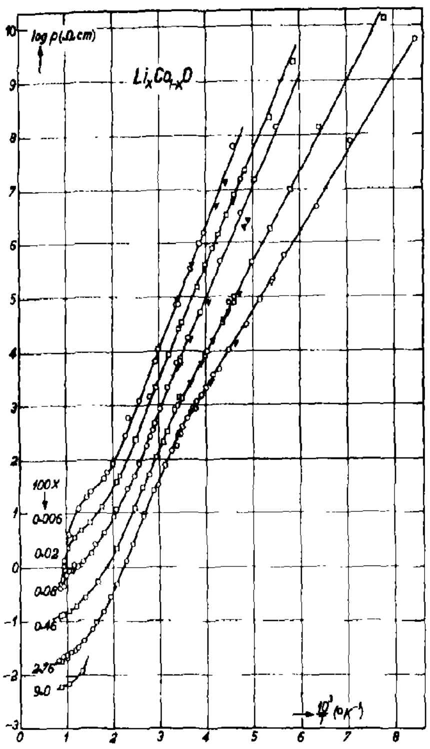

Fig. 1. Resistivity ρ as a function of reciprocal temperature for p-type Li-doped ceramic CoO. ○,□: from d.c. measurements, ▼: from a.c. measurements.

preparation of the samples these V_{Co}'s had been frozen in during cooling. According to Fisher *et al.*[15] the concentration of V_{Co}'s: $[V_{Co}]$ at 1300°C and a partial oxygen pressure of 10^{-5} atm., as derived from gravimetric measurements, amounts to 0·07 at.%. This is in agreement with our ρ data (Fig. 1). The conductivity at 1200°K of the weakly doped samples corresponds with the conductivity of a sample doped with about 0·1 at.% Li. (see also Fig. 4).

In Fig. 2 experimental values for α have been plotted as a function of T for CoO containing 0·08 at.% Li. The temperature range considered extends from 145° to 1300°K. The inset of Fig. 2 shows the high-temperature data on a larger scale. Here also results for CoO containing 0·006 at.% Li are shown.

In the case of NiO a maximum was found for α at low temperatures[9, 11]. This has been attributed to the occurrence of impurity conduction. For the case of CoO no such behaviour of α is found in the temperature range considered. Even at the lowest temperature α increases with decreasing temperature. The decrease of α above 800°K is due to the increase in free charge carrier concentration

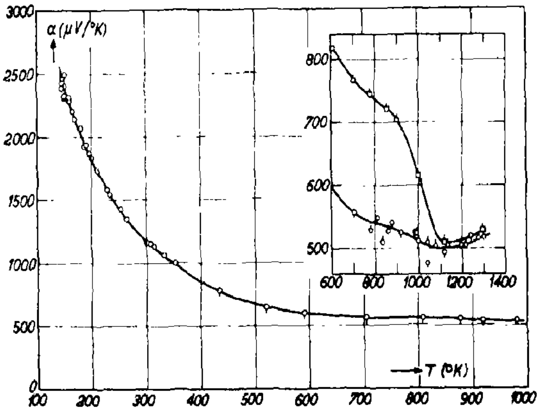

Fig. 2. Seebeck coefficient α as a function of temperature for CoO containing 0·08 at.% Li. (○,ȯ,ọ). The inset shows the high temperature measurements on a larger scale. Here also the measurements on CoO containing 0·006 at.% Li (□̇) are presented.

originating from the V_{Co} acceptors. For the low-doped samples this drop in α is quite pronounced. Above 1100°K α increases again with T. Recently this behaviour of α was also found by other investigators[16]. Li-doped NiO had already been found to show an increase of α at high temperatures[11].

Figure 3 illustrates the marked influence of oxidation of the material on the behaviour of α at low temperatures. Curve 1 was obtained on a sample prepared as described above. After the sample has been heated in oxygen at 800°C for 1 hr the behaviour of α changes completely (curve 2). This change may be ascribed to the presence of small amounts of Co_3O_4 formed during the heat treatment. Finally curve 3 was obtained by heating the sample again, but now at 1000°C in nitrogen containing 10^{-4} atm. oxygen. After this heat treatment the sample was quenched in the same gas atmosphere. Curve 3 and curve 1 practically coincide. It was furthermore found that below room temperature ρ was not influenced by the heat treatment in oxygen at 800°C.

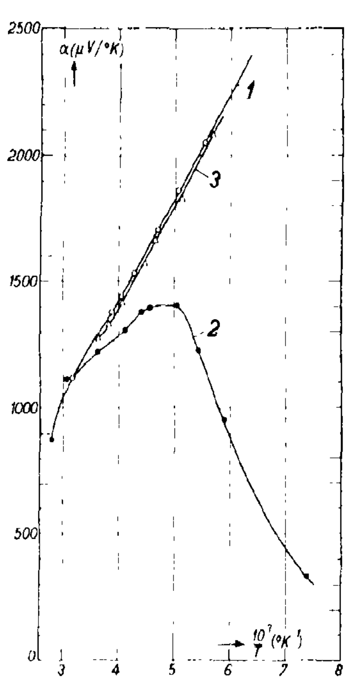

Fig. 3. Seebeck coefficient α as a function of reciprocal temperature for CoO containing about 0·1 at.% Li. In this Figure the influence of oxidation is demonstrated. Curve 1: original sample, curve 2: after heating at 800°C in O_2, curve 3: after a second heat treatment, but now at 1000°C in N_2 containing 10^{-4} atm O_2.

The results for α completely disagree with those given by Bruck *et al.*[18] and Austin *et al.*[12]. Oxidation might have influenced their results which show large resemblance to curve 2 in Fig. 3. In the case of Bruck *et al.* for example the samples were quenched from high temperatures in air.

DISCUSSION

(A) Resistivity

As can be seen in Fig. 1, in the case of CoO doped with Li, ρ depends markedly on T and [Li]. Below room temperature $\log\rho$ is a linear function of $1/T$. The values for the activation energy (Q) vary between 0·43–0·29 eV. As already mentioned, Q values obtained from a.c. data of ρ are some hundredths of an eV less. For most of the samples especially those with a high [Li], the temperature dependence of ρ suddenly changes at room temperature. This change may be connected with the antiferromagnetic order of CoO below 290°K. Above about 500°K the temperature dependence gradually decreases, pointing to exhaustion of the Li^+–Co^{3+} acceptors.

At high temperatures ρ decreases linearly with [Li] (see Fig. 4) except for the low-doped samples where conduction due to V_{Co}'s dominates. It may be assumed that at 1200°K practically all Li^+–Co^{3+} acceptors are ionized, the more so as the value of the density of states (N_v) is relatively large (see Section (*B*)). As will be shown, the concentration of compensating donors is small compared to [Li] so that in the exhaustion region the number of free holes p approximately equals the Li concentration. It follows then that $\mu_p = 0·25$ cm^2/V sec at 1200°K. Since $p \leqslant$ [Li] the value calculated for μ_p is a lower limit. This value of

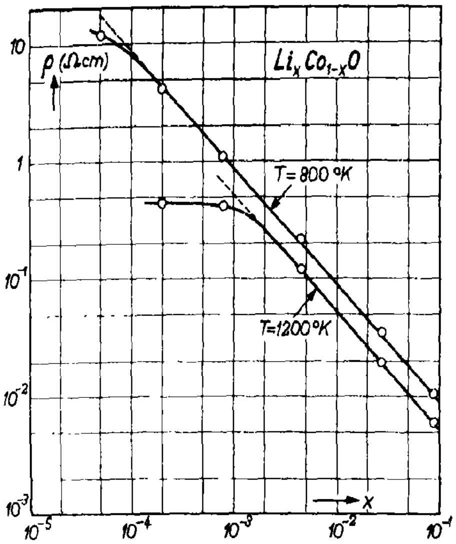

Fig. 4. Resistivity ρ of CoO doped with Li at 800° and 1200°K as a function of the Li concentration. At low [Li] conduction due to Co vacancies dominates.

μ_h agrees well with those obtained from measurements of ρ and gravimetric measurements on non-stoichiometric polycrystalline material ($\mu_h = 0{\cdot}4$ cm^2/Vsec at 1620°K)[15] and on non-stoichiometric single crystals ($\mu_h = 0{\cdot}30$ cm^2/Vsec at 1500°K)[17].

The value for Q below T_N reaches a lower limit of about 0·29 eV for large values of [Li]. This value is considerably larger than that for the case of Li-doped NiO, where this limiting value is about 0·15 eV[4, 6]. The fact that Q does not go to zero for highly doped samples has been used as an argument in favour of the hopping model[4], because in the absence of a thermally activated mobility one would expect Q to go to zero for large values of Li if the ionization energy of the acceptors is determined by Coulomb forces. Dielectric loss measurements performed on low-doped samples[19] however, suggest that a hole bound to a Li^+ ion corresponds to a Co^{3+} ion in the low-spin state. Movement of the hole around the Li^+ ion proved to be a thermally activated hopping process with an activation energy (Q') of 0·20 eV. It was supposed that this energy was necessary to bring the Co^{3+} ion from the low-spin state in the high-spin state, which is necessary for electron transfer between the high-spin Co^{3+} ion and a neighbouring high-spin Co^{2+} ion. When freed from the Li^+ ion, however, the hole corresponds to a Co^{3+} ion in the high-spin state (see Section (*C*)). The energy Q' may therefore be expected to enter into the total ionization energy Q. This may be one of the reasons why the energy Q for highly doped samples remains so large. Still another reason might be found in the formation of new centers consisting of neighbouring Li^+ ions to which a hole is stronger bound than to a single Li^+ ion.

In order to calculate from the ρ data the behaviour of the mobility μ_h as a function of temperature (see Section (*C*)) the results of the Seebeck effect measurements were used. In the next section (*B*) these Seebeck effect measurements will be discussed.

(*B*) *Seebeck effect*

If electrical conduction can be ascribed to one kind of charge carriers, viz. free holes, the Seebeck coefficient can be written as [20]

$$\alpha = \frac{k}{e}\left(\frac{E_F}{kT}+A\right) = \frac{k}{e}\left(\ln\frac{N_r}{p}+A\right) = \frac{k}{e}\,2{\cdot}3\,\log\frac{N_r e^A}{p} \tag{1}$$

Here E_F is the energy distance of the Fermi level above the transport level, A is the energy transport term, N_t is the effective density of states at the transport level and p is the number of free holes. E_F can be written as (see equation (1)):

$$E_F = e\alpha T - AkT \tag{2}$$

In Fig. 5 we have plotted E_F as a function of T for two values of A for the sample containing 0·08 at.% Li (see Fig. 2). At low temperatures E_F decreases with temperature. This is to be expected for a partially compen-

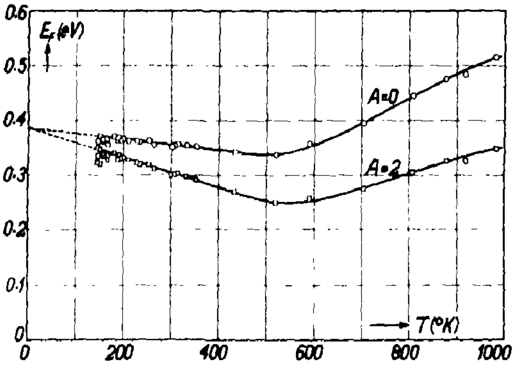

Fig. 5. The fermi level E_F as a function of temperature of CoO containing 0·08 at % Li, calculated from the Seebeck coefficient α (see Fig. 2) using the equation $E_F = e\alpha T - AkT$

sated semiconductor, because in that case[21] if $p \ll N_D$

$$E_F = E_A - kT \ln \frac{N_A - N_D}{N_D} \qquad (3)$$

where E_A is the energy level of the acceptors with respect to the transport level, and N_A and N_D are the respective concentrations of acceptors and donors. It is assumed that the impurity degeneracy is equal to unity. It can be calculated from Fig. 5 that N_D/N_A is 0·27 and 0·05 for A is 0 and 2 respectively.

For the sample under consideration it was not possible to determine the degree of compensation N_D/N_A by chemical analysis, because due to oxidation of the material the [Co^{3+}] was larger than the [Li^+]. If only Li acceptors and a certain amount of donors are present the [Co^{3+}] should be smaller than the [Li^+]. From dielectric loss measurements [19], however, it has been found that for small [Li^+], viz. smaller than 0·01 at.%, the amount of donors was about 0·004 at.%. If this amount of donors is also present in the sample under consideration the degree of compensation is 0·05, leading to a value for A of about 2.

Extrapolation of E_F to $T = 0$ gives $E_A = 0{\cdot}38^5$ eV (see equation (3)). This value found for E_A practically equals the value of 0·40 eV for Q following from ρ data below T_N. This implies that below T_N μ_D is hardly temperature-dependent. The temperature dependence of ρ is practically completely determined by the variation in the number of free holes p, which, for a partially compensated semiconductor, depends on temperature as

$$p = N_v \frac{N_A - N_D}{N_D} \exp\left(-\frac{E_A}{kT}\right) \qquad (4)$$

as long as $p \ll N_D$, viz. in the low temperature region.

As can be seen in Fig. 5, equation (3) holds up to about 500°K. Above this temperature p is certainly no longer negligible compared to N_D. There, the behaviour of E_F and p as a function of T is approximately the same as that of an uncompensated semiconductor. From Fig. 1 it can be seen that above 500°K the temperature dependence of ρ indeed significantly decreases.

At T_N, ρ shows a change of slope whereas α exhibits no change of temperature dependence. In the low temperature region (below 500°K) E_F is independent of N_v (see equation (3)). It follows then (see equation (1)) that a sudden change of N_v at T_N will not be reflected in α. In the same temperature region p on the contrary is proportional to N_v (see equation (4)) and an increase of N_v will be reflected as an extra decrease of ρ. The fact that around T_N the Hall coefficient R_H has the same temperature dependence as ρ[14], also may be an indication that the behaviour of ρ around T_N is connected with the charge carrier concentration p.

The quantity $N_v e^A$ (see equation (1)) can be calculated from the data for α if p is known. For this low-doped sample (0·08 at.% Li) the concentration p can be obtained at 1200°K from the corresponding value of ρ and the value of 0·25 cm²/Vsec for μ_D. It is then found that $N_v e^A = 0{\cdot}4\,N$, where N is the number of Co ions/cm³. Because A should be equal or greater than zero this means that at 1200°K $N_v \leq 0{\cdot}4\,N$, i.e. N_v is significantly smaller than the maximum value N. This phenomenon had also been found for NiO[11]. It is thus very likely that N_v will increase with temperature which will lead to an increase of α with temperature at high temperatures. This has indeed been found (see Fig. 2).

(C) *Temperature dependence of* μ_D

From the data for ρ and α, μ_D as a function of T can be calculated, if the temperature dependences of N_v and A are known. Unfortunately this is not the case. There are indications that N_v increases with temperature, but the exact dependence cannot be obtained from the data for α at high temperatures. In what follows two extreme cases will be considered, viz. N_v = constant and $N_v \sim T^{3/2}$ as for a broad-band semiconductor. For both cases the term A will be assumed to be constant with respect to temperature.

In Fig. 6 we have plotted $\alpha/2{\cdot}3k/e = \log N_v e^A/p$ vs. $\log \rho = \log 1/p e\mu_D$ for the sample containing 0·08 at.% Li (see Figs. 1, 2). If the quantity $N_v e^A \mu_D$ is temperature independent a straight line with slope 1 has to be expected. It can be seen that in the whole temperature region (145°–1200°K) practically a straight line with slope 1 is found. The variation of $N_v e^A/p$ is only a factor of 5 smaller than the variation of $\rho = 1/pe\mu_D$, which changes by a factor of 10^9. This implies that the quantity $N_v e^A \mu_D$ increases with temperature in the temperature region under consideration only by a factor of 5.

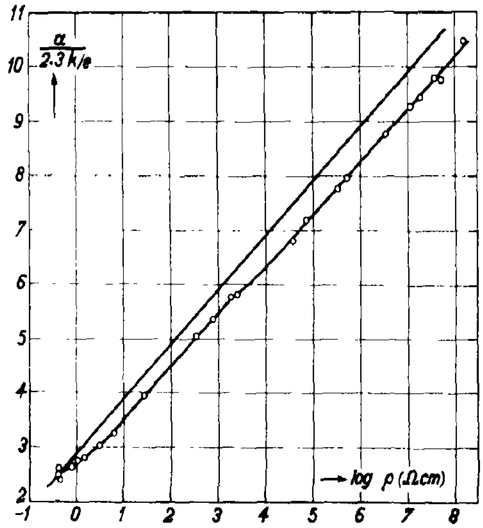

Fig. 6. $\alpha/2{\cdot}3\ k/e$ vs. $\log \rho$ for the sample containing 0·08% Li (see Figs. 1 and 2). The straight line has slope 1 and was drawn through the point obtained at 1200°K.

The straight line in Fig. 6 is a line with slope 1 drawn through the point corresponding to $T = 1200$°K. At this temperature $\mu_D = 0{\cdot}25$ cm^2/Vsec. Assuming $N_v e^A$ to be constant with respect to temperature the relative increase of $\log \rho$ compared with $\alpha/2{\cdot}3k/e$ gives directly the decrease of μ_D compared with the value of μ_D at 1200°K. In Fig. 7 μ_D obtained in this way is given as a function of $1/T$(curve 1). Assuming $N_v \sim T^{3/2}$ curve 2 is obtained. This curve has been calculated by multiplying the μ_D values of curve 1 by the factor $(1200°\text{K}/T)^{3/2}$. We have also plotted the Hall mobility μ_H measured on a sample also containing about 0·08 at.% Li.

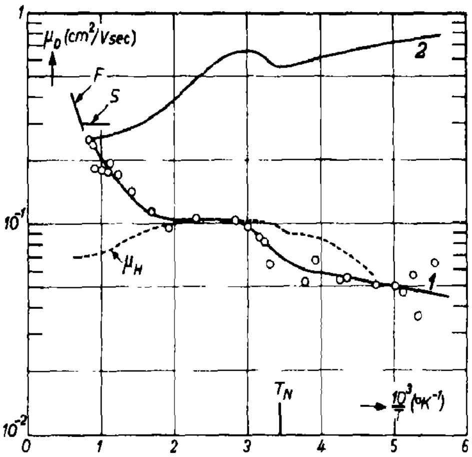

Fig. 7. Drift mobility μ_D and Hall mobility μ_H of CoO containing 0·08 at.% Li as a function of reciprocal temperature. Curves 1 and 2 are calculated from conductivity and Seebeck-effect measurements using N_v = constant and $N_v \sim T^{3/2}$, respectively.

At 1200°K μ_H is almost a factor of 4 lower than μ_D. This difference had already been mentioned earlier[14, 17]. It cannot be due to a contribution of electrons having a higher mobility than the holes, since the value for

μ_H at 1200°K and even at 1500°K remains constant if the number of free holes p is enlarged by a factor of ten[14]. Depending on the assumptions, as far as the behaviour of N_v is concerned, the difference between μ_H and μ_D increases (curve 2) or decreases (curve 1) with decreasing T. Below 500°K μ_D of curve 1 and μ_H practically coincide. The decrease of μ_H as well as μ_D (curve 1) below room temperature is most probably only apparent because the $\rho_{d.c.}$ values are somewhat too large, as shown by the a.c. measurements. Above 500°K μ_H decreases slightly with temperature, while on the contrary μ_D increases. For curve 2 μ_D decreases with temperature in the whole region. The slight increase of μ_D just above T_N, which can be seen in curve 1 as well as in curve 2, may also be only apparent. Neglect of possible details in the behaviour of N_v and A around T_N can easily lead to erroneous values of μ_D.

The absence of an activation energy in the mobility is an indication that a hole when freed from a Li^+ ion corresponds to a Co^{3+} ion in the high-spin state. In that case electron transfer between neighbouring Co^{3+} and Co^{2+} ions can easily take place (one electron process). For the case that Co^{3+} is in the low-spin state, electron transfer between neighbouring Co^{3+} and Co^{2+} ions will be severely hampered because it is then a many electron process (see Section (*A*)).

At this moment we have no further indications as to which assumption for the behaviour of N_v is most appropriate. Values for μ_D as calculated for constant N_v (curve 1) are fairly well in agreement with those for μ_H, but as long as the difference between μ_H and μ_D at high temperatures cannot be explained the agreement at lower temperatures could be accidental. Only from direct measurements of μ_D can it be decided which of the two curves agrees most with reality.

In Fig. 7 we have also presented the results for μ_D obtained by Fisher *et al.*[15] (F) and Shelyck *et al.*[17] (S). The results of Shelyck *et al.* were also obtained from ρ and α data assuming $N_v \sim T^{3/2}$. The temperature dependence of μ_D as found by Shelyck *et al.* closely resembles that of curve 2. The results of Fisher *et al.* were obtained from resistivity and gravimetric measurements. It was assumed that at all temperatures the bulk was in equilibrium with the gas atmosphere and that the V_{Co}'s are completely (singly) ionized. Their results agree most with curve 1, although the temperature dependence they found is significantly greater. However, if we combine their ρ and α data different results are obtained. Assuming N_v and A to be constant, μ_D then even decreases with increasing T*, in contradistinction to curve 1, indicating that their experimental results do not agree with ours.

The analysis given in this section was restricted to low-doped samples, because we are primarily interested in the electrical conduction mechanism in pure CoO. Results for μ_D and μ_H obtained from ρ,α and R_H measurements performed on highly doped samples (2·7 at.% Li) show some differences compared with those given in Fig. 7. Except at high temperatures μ_D and μ_H are somewhat lower than for the lightly doped samples. Around T_N (250°–370°K) μ_H increases with temperature from 0·025 cm²/Vsec to 0·06 cm²/Vsec. The sudden increase of conductivity above T_N for this dope concentration is thus partly attributable to the mobility. Below room temperature α increases with decreasing temperature. Down to 140°K no maximum has been found. The temperature dependence of α is somewhat smaller than that of log ρ. If indeed only one type of charge carrier contributes to electrical conduction, a difference in activation energy in α and ρ of 0·05 eV is found.

(*D*) *Small polaron model*

According to Holstein[22] electrical con-

---

[*] At $P(O_2) = 1$ atm. α decreases exponentially with temperature ($Q\alpha = 0{\cdot}54$ eV). Under the same circumstances σT increases exponentially with temperature with an activation energy of 0·58 eV, indicating that σ only increases with an activation energy of 0·46 eV.

duction for a small polaron semiconductor, having a strong coupling between charge carriers and lattice, is a thermally activated hopping process above $T_c \approx \hbar\omega_0/2k$ ($\omega_0 =$ longitudinal optical mode frequency).

Below T_c electrical conduction is characterized by a narrow polaron band. In the hopping regime, μ_D increases exponentially with temperature. In the polaron band regime μ_D decreases almost exponentially with temperature. The Hall mobility μ_H for a three site configuration above T_c as calculated by Friedman and Holstein[23], also increases exponentially with temperature, albeit with a smaller activation energy, and is much larger than the drift mobility μ_D. For a four site configuration, the Hall constant R_H should be normal, implying that μ_H equals μ_D at all temperatures.

According to Firsov[24] and Lang *et al.* [25] the transition temperature T_c is much lower than the value calculated by Holstein and is given by $T_c = \hbar\omega_0/2k\ln S_T$, where S_T is a parameter characterizing the electron phonon interaction. The behaviour of μ_D in the hopping regime as found by Holstein was confirmed by these authors.

The behaviour of μ_H is still a controversial question. Schnakenberg[26] has calculated that μ_H is almost temperature independent in the hopping regime, whereas Firsov[24] asserts that μ_H decreases experimentially with temperature in the hopping regime. Very recently Holstein and Friedman [27], also starting with Kubo's conductivity formula and restricting the calculations to the three site configuration, confirmed their earlier obtained results. As far as the magnitude of μ_H is concerned, it was found by all authors that for a three site configuration the Hall mobility is considerably larger than the drift mobility.

If CoO would be a small polaron semiconductor with a strong coupling constant the transition temperature T_c can be expected to be 450°K[28] or lower. The drift mobility μ_D, calculated for the case that N_v is constant (curve 1, Fig. 7), indeed increases with temperature above 500°K, pointing to small polaron conduction with a coupling constant $\gamma \approx 5$. This result, however, strongly depends on the assumption N_v is constant. The α data at high temperatures suggest that this assumption is not correct. Moreover, the most probable value for the transport term A was found to be 2, indicating that the charge carriers transport kinetic energy. These two facts militates against the small polaron model for the case of CoO. Also the behaviour of the Hall mobility seems not to be in favour of the small polaron model.

Recently it was concluded by Austin *et al.* [29] from near and far infrared absorption measurements that the charge carriers in CoO are small radius polarons, some of the carriers being bound to impurities. These measurements on CoO were performed at 290°K. In our opinion there is no doubt that at this temperature the number of free charge carriers is negligible compared with the number of bound charge carriers. The absorption found experimentally therefore cannot be due to free carriers. These results thus cannot be used to support the assumption that free charge carriers in CoO are small polarons.

CONCLUSION

It is concluded that the large temperature dependence of the conductivity is due to variation of the charge carrier concentration. The ionization energy of the Li^+-Co^{3+} acceptor is about 0·43 eV for lightly doped material. With increasing Li concentration it decreases and reaches a lower limit of about 0·29 eV. This relatively high value is explained by assuming that a Co^{3+} ion neighbouring a Li^+ ion is in the low-spin state, whereas Co^{3+} in the pure lattice is in the high-spin state. This assumption is based on the differences in behaviour of a moving hole when bound to a Li^+ ion (dielectric loss measurements) or freed from the Li^+ ion (conductivity measurements).

The temperature variation of the drift mobility between 145°–1200°K is almost negligible compared with the variation of the number of free holes. The value of μ_D at 1200°K is 0·25 cm²/Vsec. Below 1200°K for $N_v \sim T^{3/2}$ and A is constant, μ_D calculated from ρ and α data decreases with increasing temperature, whereas for N_v is constant and A is constant, μ_D increases significantly with temperatures only above 500°K.

It is concluded that the experimental results throw serious doubts on the applicability of the small polaron theory for the case of CoO.

REFERENCES

1. VERWEY E. J. W., HAAYMAN P. W., ROMEYN F. C. and VAN OOSTERHOUT G. W., *Phil. Res. Rept* **5**, 173 (1950).
2. DE BOER J. H. and VERWEY E. J. W., *Proc. phys. Soc.* **49**, 59 (1937).
3. VERWEY E. J. W., *Semiconducting Materials*, p. 151. Butterworths, London (1951).
4. HEIKES R. R. and JOHNSTON W. D., *J. chem. Phys.* **26**, 582 (1957).
5. MORIN F. J., *Phys. Rev.* **83**, 1005 (1951); **93**, 1195 (1954); **93**, 1199 (1954); *Bell Syst. tech. J.* **37**, 1047 (1958).
6. VAN HOUTEN S., *J. Phys. Chem. Solids*, **17**, 7 (1960).
7. PARRAVANO G., *J. chem. Phys.* **23**, 5 (1954).
8. KOIDE S., *J. phys. Soc. Japan* **20**, 123 (1965).
9. KSENDZOW M., AMSEL'M N. L., VASILEVA I. I. and LATYSHEVA V. M., *Fiz. Tverd. Tela* **5**, 1537 (1963), English transl.: *Soviet Phys. solid St.* **5**, 1278 (1963).
10. ZHUSE V. P. and SHELYKH A. I., *Fiz. Tverd. Tela* **8**, 629 (1966), English transl. *Soviet Phys. solid St.* **8**, 509 (1966).
11. BOSMAN A. J. and CREVECOEUR C., *Phys. Rev.* **144**, 763 (1966).
12. AUSTIN I. G., SPRINGTHORPE A. J., SMITH B. A. and TURNER C. E., *Proc. phys. Soc.* **90**, 157 (1967).
13. ZHUSE V. P. and SHELYKH A. I., *Fiz. Tverd. Tela* **8**, 629 (1966); English Transl.: *Soviet Phys. solid St.* **8**, 509 (1966).
14. VAN DAAL H. J. and BOSMAN A. J., *Phys. Rev.* **158**, 736 (1967).
15. FISHER B. and TANNHAUSER D. S., *J. chem. Phys.* **44**, 1663 (1966).
16. FISHER B. and WAGNER J. B., *J. appl. Phys.* **38**, 3838 (1967).
17. SHELYKH A. I., ARTEMOV K. S. and SHVAIKO-SHVAIKOVSKII V. E., *Fiz. Tverd. Tela* **8**, 883 (1966); English transl.: *Soviet Phys. solid St.* **8**, 706 (1966).
18. BRUCK A. and TANNHAUSER D. S., *J. appl. Phys.* **38**, 2520 (1967).
19. BOSMAN A. J. and CREVECOEUR C., *J. Phys. Chem. Solids* **29**, 109 (1968).
20. JOFFE A. F., *Physics of Semiconductors*. Infosearch, London (1960).
21. BLAKEMORE J., *Semiconductor Statistics*. Pergamon Press, Oxford (1962).
22. HOLSTEIN T., *Ann. Phys.* **8**, 325 and 343 (1959).
23. FRIEDMAN L. and HOLSTEIN T., *Ann. Phys.* **21**, 494 (1963).
24. FIRSOV Yu. A., *Fiz. Tverd. Tela* **5**, 2749 (1963); English transl. *Soviet Phys. solid St.* **5**, 1566 (1964).
25. LANG I. G. and FIRSOV Yu. A., *ZhETF* **43**, 1843 (1962); English transl.: *Soviet Phys. JETP* **16**, 1301 (1962).
26. SCHNAKENBERG J., *Z. Phys.* **185**, 123 (1965).
27. HOLSTEIN T. and FRIEDMAN L., *Phys. Rev.* **165**, 1019 (1968).
28. MARSHALL R., MITRA S. S., GIELISSE P. J. and PLENDL J. N., *Proc. 7th Int. Conf. on the Physics of Semiconductors*, p. 1101. Dunod, Paris (1964).
29. AUSTIN I. G., CLAY B. D., TURNER C. E. and SPRINGTHORPE A. J., *Solid State Commun.* **6**, 53 (1968).

J. Phys. Chem. Solids Pergamon Press 1969. Vol. 30, pp. 1161–1172. Printed in Great Britain.

THERMODYNAMICS OF ELECTROCALORIC PHENOMENA IN KCl:OH. PARAELECTRIC COOLING

W. N. LAWLESS
Research and Development Laboratories, Corning Glass, Works, Corning, N.Y. 14830, U.S A.

(*Received* 15 *August* 1968)

Abstract—The thermodynamics of low-temperature electrocaloric phenomena in alkali halides doped with polar impurities is developed, making use of the models for the tunneling splitting, dielectric saturation, and dipole correlations that pertain to KCl:OH. The thermodynamic theory is in good quantitative agreement with published data on the specific heat, adiabatic-depolarization temperature changes, and electrocaloric coefficient for KCl:OH, using a dipole moment of about 3·7 debye (*D*). The calculated hydroxyl concentrations, however, are consistently somewhat larger than the experimental concentrations.

The observed concentration dependences of the final depolarization temperature and of the electrocaloric coefficient are explained quantitatively as arising from the dipole–dipole interactions contribution to the specific heat. The lowest temperature achievable in KCl:OH by the process of adiabatic depolarization is estimated to be 0·205°K (consistent with a tunneling splitting of 0·30°K), starting from an initial temperature of 1·27°K.

1. INTRODUCTION

THE SUGGESTION that low-temperature paraelectric materials might be useful for refrigeration by the process of adiabatic depolarization appears to have been first made by Gränicher[1], in relation to the low-temperature ferroelectric $SrTiO_3$. This process is the dielectric analog of the well-known process of magnetic cooling[2]. Subsequently, Hegenbarth[3] investigated the low-temperature electrocaloric properties of $SrTiO_3$ and (Ba, Sr)TiO_3 crystals, and found that the magnitude of the electrocaloric coefficient dropped off rapidly for these materials below about 17°K.

Recently, the discovery of low-temperature parelectric behavior in certain hydroxyl-doped alkali halides, such as KCl:OH, has revitalized interest in paraelectric cooling, particularly because the temperature range where paraelectric properties are manifested can be controlled by the hydroxyl concentration[4]. In fact, parelectric heating and cooling in the He temperature range have been observed in KCl:OH[4–7].

The purpose of this paper is to develop the model thermodynamics of electrocaloric effects in doped salts, such as KCl:OH, in such a way as to include the limitations due to dielectric saturation, dipole–dipole interactions, and the zero-field splitting, and to make comparisons with experimental data. As will be seen below, the simple thermodynamic theory is in good quantitative agreement with the published electrocaloric data, so that certain predictions can be made from the theory for optimizing the paraelectric cooling in these materials.

We will first develop the general equilibrium thermodynamics for *T* and *E* independent (where *E* will always be the external applied field), and then the various models of the properties of OH^- dipoles in KCl will be reviewed (e.g. the dipole–dipole interactions, the ground-state splitting) and the corresponding thermodynamic quantities derived. The resulting model thermodynamics will then be compared to experimental data on the specific heat, adiabatic-depolarization temperature changes, and the electrocaloric coefficient for KCl:OH. The c.g.s.–e.s.u. system of units will be employed.

2. MODEL THERMODYNAMICS

The combined first and second laws of the thermodynamics of dielectrics (excluding ferroelectrics) is

$$TdS = dU - EdP$$

or

$$dS = \frac{1}{T}\left[\left(\frac{\partial U}{\partial T}\right)_E - E\left(\frac{\partial P}{\partial T}\right)_E\right]dT + \frac{1}{T}\left[\left(\frac{\partial U}{\partial E}\right)_T - E\left(\frac{\partial P}{\partial E}\right)_T\right]dE. \quad (1)$$

Now, equating the mixed partial derivatives of the entropy from equation (1) in the usual fashion yields the relation

$$\left(\frac{\partial U}{\partial E}\right)_T = T\left(\frac{\partial P}{\partial T}\right)_E + E\left(\frac{\partial P}{\partial E}\right)_T, \quad (2)$$

which shows the interesting property that if P is any function of the ratio (E/T), then

$$\left(\frac{\partial U}{\partial E}\right)_T = 0.$$

This fact, that the internal energy does not depend on E at constant T, is analogous to the fact that the internal energy of a perfect gas at constant temperature is independent of pressure. Thus, when work is done to polarize a material for which $P = P(E/T)$ in an isothermal process, an equal quantity of heat flows out of the material, analogous to the isothermal compression of an ideal gas. This property could be very useful for detecting the onset of dipole ordering (see below).

Substituting equation (2) in (1) leads to the useful Maxwell relation,

$$\left(\frac{\partial S}{\partial E}\right)_T = \left(\frac{\partial P}{\partial T}\right)_E, \quad (3)$$

Equation (2) is now integrated w.r.t. E and then differentiated w.r.t. T to give

$$\left(\frac{\partial U}{\partial T}\right)_E = C_0 + T\int_0^E \left(\frac{\partial^2 P}{\partial T^2}\right)_E dE + E\left(\frac{\partial P}{\partial T}\right)_E \quad (4)$$

where an integration by parts has been used, and

$$C_0 = \left(\frac{\partial U}{\partial T}\right)_{E=0}$$

the zero-field specific heat. Substituting equations (2) and (4) into equation (1) leads us to the desired form of the TdS equation for these materials

$$TdS = \left(C_0 + T\int_0^E \left(\frac{\partial^2 P}{\partial T^2}\right)_E dE\right)dT + T\left(\frac{\partial P}{\partial T}\right)_E dE, \quad (5)$$

on which our discussion below of electrocaloric properties will be based.

Consider now the quantities $C_0(T)$ and $P(E, T)$ which enter equation (5) and which encompass the properties of the OH$^-$ impurity substituted at a Cl$^-$ site in the KCl lattice. There are three contributions to C_0: a lattice phonon contribution, a dipole–dipole interactions contribution, and a Schottky contribution from the tunneling states. The lattice contribution is the familiar Debye expression expression (note that we are concerned with temperatures in the He range)

$$C'_0 = 234nk(T/\Theta_D)^3 \equiv \alpha T^3. \quad (6)$$

where n is the number of atoms per unit volume.

The dipole-interactions contribution occurs because the impurity dipoles order locally with decreasing temperature in an antiparallel correlation[8]; consequently, an expenditure of energy is required to break up these correlations in raising the temperature. The internal energy of the dipole system due to dipole–dipole interactions, U_d, has been calculated previously[8] and these results are shown in Fig. 1 (solid line) for U_d vs. $\gamma \propto T$; ϵ_m is the dielectric constant of the host lattice, d is the anion–cation separation, N is the impurity dipole concentration in cm^{-3}, and μ_e is a dipole moment which characterizes the strength of the dipole interaction[8]. These data were calculated on the basis of a two-dipole approximation where the interacting dipoles have equilibrium positions along [100] in the NaCl-type lattice (as is the case for OH^- in KCl[9]). The tensorial interaction energy and the lattice symmetry were taken into account in these calculations (see [8] for further details).

We will approximate $U_d(\gamma)$ by the dotted curve in Fig. 1 for the sake of convenience, and this approximation is quite accurate except at high temperatures; however, since we are interested in the derivative of U_d, this approximation should be reliable. Therefore, from Fig. 1, we find that the dipole–dipole interactions contribution to the specific heat is

$$C_0'' = \frac{\partial U_d}{\partial T} \simeq 2{\cdot}33 N^2 \mu_e^2/\epsilon_m T. \qquad (7)$$

This approximation is valid only in the dipole-ordering temperature range.

The third contribution to C_0 arises from the tunneling states. That is, the sixfold degeneracy of the ground state is tunneling split into a ground-state singlet A_{1g} of energy -2Δ, a triplet state T_{1u} of zero energy, and a doublet state E_g of energy Δ, where Δ is the zero-field splitting; this level system has been apply discussed[7, 10]. The Schottky contribution from these tunneling states is given by[7, 12]

$$C_0''' = 6Nk\frac{y^2(2e^{-2y}+3e^{-3y}+e^{-5y})}{(1+3e^{-2y}+2e^{-3y})^2}, y = \Delta/kT. \qquad (8)$$

Consider next the polarization function, $P(E, T)$; if we assign the external field to be

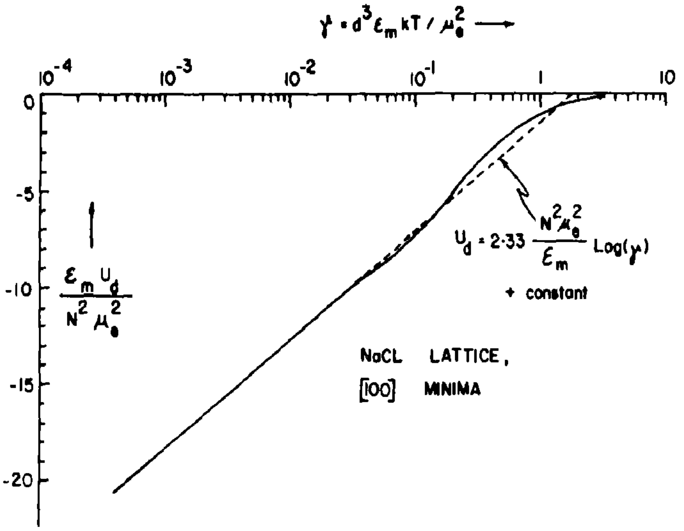

Fig. 1. The temperature dependence of the internal energy U_d due to dipole interactions for a random array of dipoles situated at Cl sites in the NaCl-type lattice with [100] equilibrium positions [8]. The quantities plotted are both dimensionless, and the symbols are explained in the text. The linear approximation (dashed line) is used in the thermodynamic treatment.

along [100] (i.e. along an equilibrium direction of the OH$^-$ dipole in the crystal lattice), then

$$P(E,T) = P^{(0)}(E,T) + N\mu\left(\frac{\sinh z}{2+\cosh z}\right), \qquad z = \bar{\mu}E/kT \qquad (9)$$

where $P^{(0)}(E,T)$ is the polarization of the host lattice. (Our discussion beyond this point will be constrained by the assignments that the dipole equilibria and the applied field are along [100]; for different orientations, equation (9) and the relations below derived from equation (9) are considerably altered.) We have introduced two more dipole moments in equation (9): The dipole moment, μ, characterizes the macroscopic polarization of the dipole system including the local moments induced in the host lattice by the impurity, and $\bar{\mu}$ contains a Lorentz correction which enables us to write the external field strength E explicitly (we will postpone until later a discussion of these various dipole moments).

It will be noticed from equation (5) that the T-derivatives of $P(E,T)$ are required, and we will assume that

$$\frac{\partial P^{(0)}}{\partial T} \cong 0$$

because the dielectric constant of pure alkali halides such as KCl is a very weak function of temperature in the He temperature range [4] (This, however, may not be the case with other materials, e.g. the thallous halides[11]).

3. COMPARISON WITH EXPERIMENTAL DATA ON KCl:OH

We have now established all the ingredients of a thermodynamic treatment of these salts, and in this section we will compare the above thermodynamic quantities with experimental data.

Zero-field specific heat

The zero-field specific heat, C_0, given by the sum of equations (6–8), contains two concentration-dependent contributions. For the dipole-interactions contribution, C_0'' the concentration N determines the dipole-ordering temperature range, whereas for the Schottky contribution, C_0''', the concentration is an amplitude factor, the function of y in equation (8) having a maximum at $y = 1{\cdot}37$ independent of concentration. This is not surprising, since C_0'' reflects a cooperative effect, C_0''' a single-particle effect. Therefore, for very dilute concentrations $C_0 \cong C_0' + C_0'''$, and the specific heat data of Harrison[12] on KCl:OH ($\sim 0{\cdot}6$ ppm) have revealed this Schottky contribution to be in good quantitative agreement with Equation (8) for $\Delta/k \simeq 0{\cdot}34$°K. This specific-heat value of the zero-field splitting is in very good agreement with the value from paraelectric-resonance measurements [13], $\Delta/k = 0{\cdot}30 \pm 0{\cdot}03$°K. Consequently, we will adopt the value $\Delta/k = 0{\cdot}30$°K below.

On the other hand, for temperatures *above* the peak of the Schottky term at $\simeq 0{\cdot}2$°K and for larger concentrations, $C_0 \cong C_0' + C_0''$, where the deviation from the T^3 behavior is proportional to T^{-1} in the dipole-ordering temperature range. The zero-field specific heat data of Shepherd[7] for KCl:OH above 0·4°K show such a deviation, and in Fig. 2 are shown these specific heat data, where C_0T is plotted vs. T^4 for three different concentrations. (For curve C in Fig. 2, the C_0''' contribution was subtracted from the experimental C_0 data, using the 'optical' concentration in equation (8) and the above-mentioned value of Δ/k.) That is, according to equations (6) and (7), C_0T vs. T^4 should be linear with a slope α and intercept $2{\cdot}33N^2\mu_e^2/\epsilon_m$. Although the experimental data that can be so plotted conveniently are meager, there is clear indication in Fig. 2 that these curves do, in fact, have finite intercepts indicative of the dipole ordering contribution. These intercept values are given in Fig. 2, and using the OH$^-$ concentrations determined optically by Shepherd[7] and the value [4] $\epsilon_m = 4{\cdot}3$, we find values of μ_e ranging

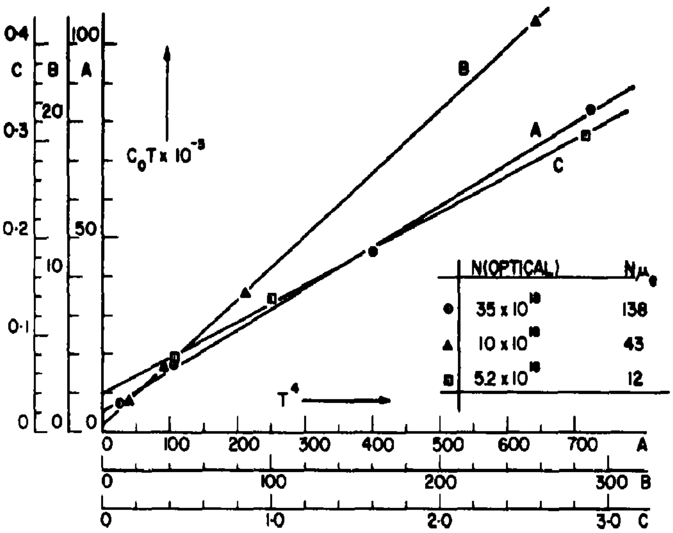

Fig 2. Zero-field specific heat data of KCl:OH in the dipole ordering temperature range [7]. The non-zero intercepts of C_0T vs. T^4 allow the determination of $N\mu_0$, according to equation (7), and these data are shown in the figure.

from 2·3 to 4·3 D from these intercepts. These dipole moment values are in good agreement with values determined from other sources, but it has to be pointed out that these 'optical' concentrations are subject to some question. We shall return to this question below.

The values of the slopes in Fig. 2 range from 94 to 107, indicating debye temperatures from 178° to 187°K. This is a surprising result, since pure KCl has a debye temperature of 230°K; however, as pointed out by Sheperd[7] the specific heat data for all concentrations in the temperature range above the data shown in Fig. 2 do exhibit a lowered debye temperature from the pure crystal value. Nor is this case of KCl:OH an isolated case of this phenomenon; Harrison *et al.*[14] found a debye temperature of 466°K for NaF doped with about 0·3 ppm OH⁻, a value which is about 6 per cent smaller than debye temperatures reported for NaF from other sources. The reason for this unusually large effect on the phonon spectrum resulting from small hydroxyl concentrations is not clear.

Field dependence of the specific heat

From equation (5), the field-dependent specific heat is given by

$$C_E = C_0 + T\int_0^E \frac{\partial^2 P}{\partial T^2}\,\mathrm{d}E \tag{10}$$

and it is shown in Appendix A that

$$C_E = C_0 + \frac{Nk\mu}{\bar{\mu}}\frac{Z^2(1+2\cosh Z)}{(2+\cosh Z)^2},\quad Z = \bar{\mu}E/kT, \tag{10'}$$

using equation (9) for $P(E, T)$. Equation (10′) predicts a peak in $C_E - C_0$ of 1·31 $Nk\mu/\bar{\mu}$ at $z = 2{\cdot}90$, and is identical to the expression used by Shepherd[7] in interpreting his $C_E - C_0$ data if $\mu = \bar{\mu}$, although the method of derivation was different than that presented here. Since Shepherd has considered this electrocaloric property, it will not be pursued here.

Adiabatic-depolarization temperature changes: paraelectric cooling in KCl:OH

In order to solve for the temperature change upon adiabatic depolarization (dS =

0)), we must solve the differential equation obtained from equation (5),

$$C_0\mathrm{d}T + T\mathrm{d}T\int_0^E \frac{\partial^2 P}{\partial T^2}\mathrm{d}E = -T\left(\frac{\partial P}{\partial T}\right)_E \mathrm{d}E.$$

the transformation $x = \int_0^E (\partial P/\partial T)\mathrm{d}E$ allows this integration, and we find that

$$\int_0^{E_i}\left(\frac{\partial P}{\partial T}\right)_i \mathrm{d}E - \int_0^{E_f}\left(\frac{\partial P}{\partial T}\right)_f \mathrm{d}E = \int_{T_i}^{T_f} C_0\mathrm{d}T/T \qquad (11)$$

where the subscripts i and f refer to the initial and final temperatures and fields, respectively. Alternately, we could have written down equation (11) directly using the Maxwell relation equation (3) in equating the entropy changes. The next step is to substitute equations (6–9) into equation (11) and perform the indicated integrations: when this is done we find that (setting $E_f = 0$)

$$\begin{aligned} T_f^3 = {} & T_i^3 - 3Nk(\mu/\alpha\bar{\mu})F(Z_i) \\ & + \frac{6{\cdot}99N^2\mu_e^2}{\alpha\epsilon_m}\left(\frac{1}{T_f} - \frac{1}{T_i}\right) \\ & + \frac{3Nk}{\alpha}[\ln 6 - g(y_f)],\ Z_i = \bar{\mu}E_i/kT_i, \\ & y_f = \Delta/kT_f. \end{aligned} \qquad (12)$$

The term in equation (12) involving $F(Z)$ derives from the polarization entropy change of the dipole system, and it is shown in Appendix B that

$$F(Z) = \frac{Z\sinh Z}{2+\cosh Z} - \ln\left(\frac{2+\cosh Z}{3}\right). \qquad (13)$$

The term involving ln6–$g(y)$ comes from the tunneling states and was calculated using the relation

$$S = Nk\ln Z + U/T$$

for the entropy of the dipole system, where Z is the partition function (see also [7]). The function $g(y)$ is given by

$$g(y) = \ln(1+3e^{-2y}+2e^{-3y}) + \frac{6y(e^{-2y}+e^{-3y})}{(1+3e^{-2y}+2e^{-3y})}. \qquad (14)$$

We have set $g(y_i) = \ln 6$, because we assume that the initial temperature is considerably greater than Δ/k; as we shall see, this is valid for KCl:OH data.

The functions $F(Z)$ and ln6–$g(y)$ are shown plotted in Fig. 3; $F(Z)$ saturates for $Z \simeq 8$, and this fact is useful for estimating the practical quantity E_i/T_i.

The adiabatic-depolarization relation equation (12) clearly indicates the limitations due to the dipole interactions and the tunneling splitting, as both of these terms are *additive*. Also, the effect of the dipole interactions introduces a term *quadratic* in the concentration N, and this fact has some interesting consequences, as will be seen below.

In order to compare equation (12) to experimental data, we are faced with the dilemma of the three dipole moments we have introduced, namely μ, $\bar{\mu}$, and μ_e, because our knowledge of these moments is imperfect. According to Fröhlich[15],

$$\mu = \left(\frac{2\epsilon_m+1}{2\epsilon_m+n_0^2}\right)\left(\frac{2+n_0^2}{3}\right)\mu_v$$

$$\bar{\mu} = \frac{3\epsilon_m}{2\epsilon_m+1}\mu$$

$$\mu_e = \left(\frac{2+n_0^2}{3}\right)\left(\frac{3\epsilon_m}{2\epsilon_m+n_0^2}\right)\mu_v = \bar{\mu}$$

where μ_v is the vacuum moment and n_0 is the refractive index of a 'liquid' composed of the impurity dipoles. On the other hand, Mahan[16] and Ham[17] have studied this dipole-moment problem and concluded that the Onsager–Fröhlich cavity approximation is probably not applicable to a substitutional dipole. Furthermore, the spectroscopic studies on KCl:OH have been interpreted[18] in terms of a displacement of the center-of-mass of the hydroxyl group, and this in turn

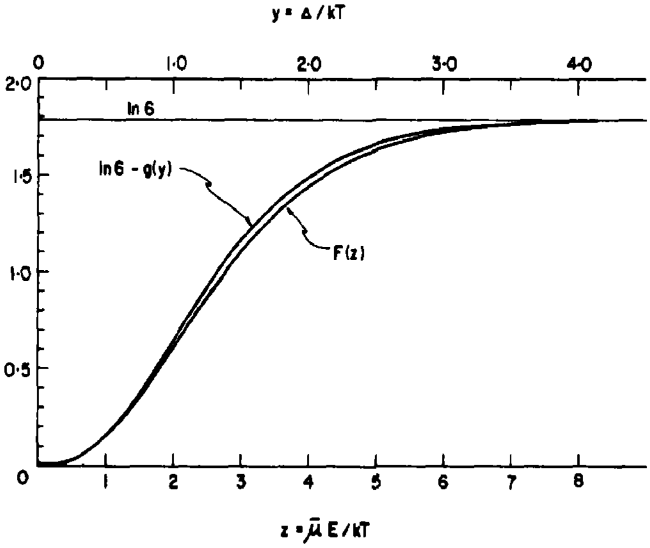

Fig. 3. Numerical data for the functions ln6$-g(y)$ and $F(z)$ which enter the adiabatic-depolarization relation, equation (12).

raises serious problems about the dipole moments. Consequently, for our purposes here, it seems reasonable to set

$$\bar{\mu} = \mu_p = \mu$$

in discussing equation (12); we shall discuss the possible implications of this approximation below.

Now Shepherd[7] has published data on the adiabatic depolarization of KCl:OH, and the data for the crystals showing the largest temperature drops are shown in Fig. 4. The curves in Fig. 4 were calculated according to equation (12) as follows: equation (12) can be solved for the concentration N, and since the data points for each crystal in Fig. 4 involve the same N, a set of μ-values can be determined relative to a reference data point using the data in Fig. 3. The coefficient $\alpha \simeq 100$ was used from Fig. 2. These fitting calculations yielded $\mu = 3{\cdot}66 \pm 0{\cdot}43$ debye and $\mu = 3{\cdot}80 \pm 0{\cdot}50$ debye for the two sets of data, as shown. These μ-values were then used in equation (12) to determine the corresponding concentrations, $N = 36{\cdot}2 \pm 2{\cdot}0 \times 10^{18}\,\text{cm}^{-3}$ and $N = 10{\cdot}6 \pm 2{\cdot}0 \times 10^{18}\,\text{cm}^{-3}$, respectively. Subsequently, the curves shown in Fig. 4 were drawn using these data.

It is seen that equation (12) describes the experimental data very well, and the dipole-moment fitting parameters shown in Fig. 4 agree closely with other estimates[7, 13, 18] and are consistent with the intercept values given in Fig. 2. The concentrations are in semi-quantitative agreement with the 'optical' concentrations reported by Shepherd[7] N (12) $= 36{\cdot}2 \times 10^{18}\,\text{cm}^{-3}$ and N(optical) $= 10^{19}\,\text{cm}^{-3}$; and N (12) $= 10{\cdot}6 \times 10^{18}\,\text{cm}^{-3}$ and N(optical) $= 5{\cdot}2 \times 10^{18}\,\text{cm}^{-3}$.

These concentrations are about twice as large as the 'optical' concentrations, and one reason for this may be our inexact knowledge of the various dipole moments and the coefficient α from Fig. 2. On the other hand, there is some disagreement in the literature [19] on the optical method of determining the OH^- concentration from the 204 mμ absorption band[20].

As mentioned above, the effect of dipole-dipole interactions introduces a term quadratic in N into equation (12), with the

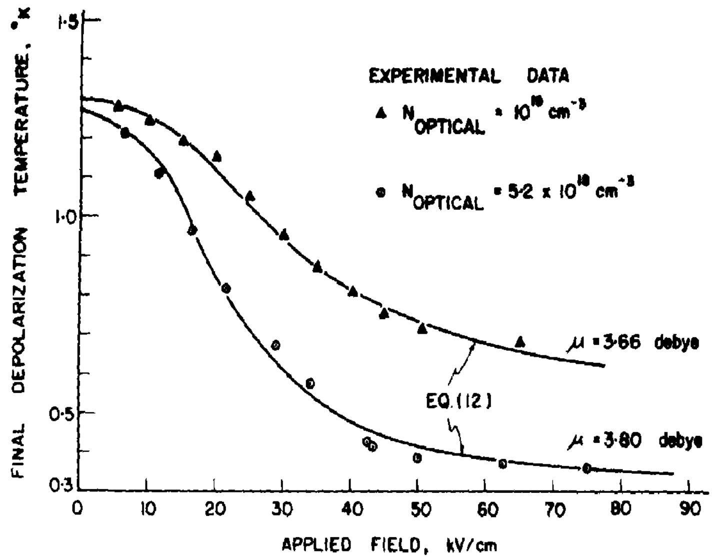

Fig. 4. Comparison of equation (12) with the observed adiabatic-depolarization data for KCl OH of [7]. A single-dipole moment fitting parameter was used in equation (12) for each curve, and these moments are shown on the respective curves. The calculated hydroxyl concentrations were $36{\cdot}2 \times 10^{18}$ and $10{\cdot}6 \times 10^{18}$ for the upper and lower curves, respectively. The debye temperature obtained from Fig. 2 was used in equation (12)

consequence that an *optimum* N exists which *maximizes* the temperature decrease during adiabatic depolarization. This is a very practical result, and may be understood physically as follows: At low concentrations, the available controllable entropy of the dipole system (namely, $Nk \ln 6$) is small and the temperature changes are correspondingly small; as N is increased, the controllable entropy is increased, but on removal of the field the dipoles do not entirely revert to the disordered state but rather begin to order locally, thus lowering the zero-field entropy of the dipole system. Therefore, the temperature change involved in going from the $E \neq 0$ to $E = 0$ state is not as large as would otherwise be the case. Upon further increasing N, the dipole ordering becomes more complete in the adiabatic depolarization step, and the temperature change becomes smaller. An optimum concentration thus exists which represents a compromise between the competing effects of the controllable entropy of the dipole system and entropy decrease due to dipole ordering.

This optimum concentration and the lowest achievable temperature can be obtained from equation (12), knowing T_i, E_i, μ, α, ϵ_m, and Δ; for a given set of initial conditions, the lowest final temperature is given by the transcendental equation

$$[F(Z_i) - \ln 6 + g(y_f)]^2$$
$$= 3{\cdot}11\left(\frac{\alpha}{\epsilon_m}\right)\left(\frac{\mu}{k}\right)^2\left(\frac{1}{T_f}-\frac{1}{T_i}\right)(T_i^3 - T_f^3) \quad (15)$$

and the optimum concentration for achieving this T_f is given by

$$\mathrm{N}_{\text{optimum}} = \frac{0{\cdot}378}{\mu}\left[\frac{\alpha\epsilon_m(T_i^3 - T_f^3)T_iT_f}{T_i - T_f}\right]^{1/2}. \quad (16)$$

As an example, Fig. 5 shows T_f vs. N plotted according to equation (12) for $T_i = 1{\cdot}27$°K, $\Delta/k = 0{\cdot}30$°K, $\alpha = 100$, $\epsilon_m = 4{\cdot}3$, and $\mu = 3{\cdot}73$ D (the average value from Fig. 4), for $E_i = 36$ kV/cm and $E_i = 110$ kV/cm (this

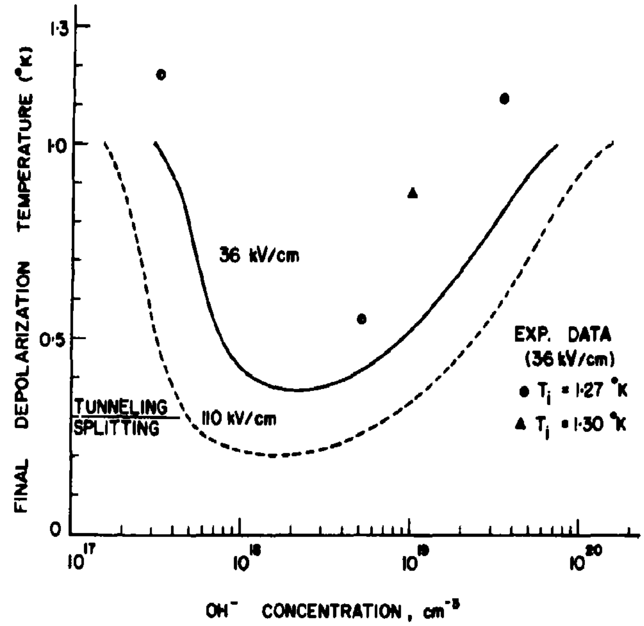

Fig. 5. Predicted final depolarization temperature as a function of hydroxyl concentration for KCl:OH according to equation (12), for the initial conditions $T_i = 1{\cdot}27°\text{K}$, and $E_i = 36$ kV/cm and $E_i = 110$ kV/cm. An average dipole moment, $\mu = 3{\cdot}73$ D from Fig. 4, and the debye temperature from Fig. 2 were used. The tunneling splitting is shown in the figure, and the experimental data are from [7].

latter value is the estimated saturation value for KCl:OH according to Fig. 3). The experimental points due to Shepherd[7] are also shown in Fig. 5 (the value $E_i = 36$ kV/cm was chosen to include all the data reported by Shepherd). The experimental data display an optimum-concentration effect, and agree reasonably well with the predictions of equation (12), given the reservations expressed above regarding the dipole-moment strength, etc.

The data in Fig. 5 indicate that the lowest achievable temperature with KCl:OH by the process of adiabatic depolarization is 0·205°K, corresponding to a concentration of $1{\cdot}50 \times 10^{18}\,\text{cm}^{-3}$. These calculations also illustrate that the tunneling splitting ultimately limits T_f for this optimum concentration, and that the minimum T_f approximately coincides with the peak of the Schottky specific-heat contribution, equation (8); i.e. $T_f \simeq \Delta/1{\cdot}37k$.

Electrocaloric coefficient in KCl:OH

The electrocaloric coefficient is defined by

$$\beta_E = \left(\frac{\partial T}{\partial E}\right)_s$$

and equation (12) is just the integrated form of this quantity. From equation (5)

$$\beta_E = -\frac{N\mu}{C_E}\frac{Z(1+2\cosh Z)}{(2+\cosh Z)^2}, Z = \bar{\mu}E/kT, \quad (17)$$

where C_E is given by equation (10′).

Lüty[6] has reported $(\Delta T/\Delta E)$-data on KCl:OH, and for the fields and temperatures used, equation (17) may be approximated by ($Z \ll 1, y \ll 1$).

$$\beta_E \cong \frac{-N\mu Z}{3\alpha T^3 + 6{\cdot}99N^2\mu^2/\epsilon_m T + NkZ^2}. \quad (18)$$

Here also, equation (18) predicts that a concentration exists which maximizes the electrocaloric coefficient, according to

$$N_{\max} = \frac{T^2}{\mu}\sqrt{(\alpha\epsilon_m/2\cdot 33)} \qquad (19)$$

and correspondingly from equation (18)

$$\beta_{\max} \cong \frac{-\mu E T\sqrt{(\alpha\epsilon_m/2\cdot 33)}}{6k\alpha T^3 + \mu E^2\sqrt{(\alpha\epsilon_m/2\cdot 33)}}. \qquad (20)$$

Equations (19) and (20) are in good qualitative agreement, and reasonably good quantitative agreement, with Lüty's experimental data[6], as may be seen from Table 1; the above-mentioned data for μ, α, etc. were used in equations (19) and (20) in calculating the results shown in Table 1.

The experimental data in Table 1 show that $N_{\max}$ is apparently independent of E and increases with T, in agreement with equation (19), although there are insufficient data to check the predicted T^2 behavior Also, the $\beta_{\max}$ data increase (negatively) with both T and E, in agreement with equation (20).

4. SUMMARY AND DISCUSSION

The simple thermodynamic model developed in this paper succeeds in explaining several of the observed thermodynamic properties of KCl:OH, both qualitatively and quantitatively, in a straightforward and consistent fashion: From the zero-field specific heat data of Fig. 2, the coefficient α of equation (6) was determined and subsequently used in equation (12) in the fitting of the adiabatic-depolarization data shown in Fig. 4. This fitting yielded a dipole moment of about 3·7 debye, which is consistent with the intercept values shown in Fig. 2 according to equation (7) and with other estimates in the literature. These data were next used for comparison of the theory with the observed positions and heights of the electrocaloric-coefficient peaks. In all these calculations, the literature values for the zero-field splitting and host-lattice dielectric constant were adopted.

The calculated hydroxyl concentrations are in reasonable quantitative agreement with the experimental values, although there is a tendency for these calculated concentrations to be consistently larger than the experimental values. It is suggested that this may be due to our inexact knowledge of the three dipole moments that were introduced, but which were later equated for the sake of expediency. For example, the dielectric data[4] on KCl:OH have been explained[8] using μ (from equation (9)) $\simeq$ 1·9 D, and μ_e (from equation (7)) $\sim$ 4·4 D consequently, equating $\mu_e = \mu$ in equation (12) has the effect of increasing the N in the dipole-interactions term.

The agreement with experiment, in particular with the observed concentration-dependence of the final depolarization temperature and of the electrocaloric coefficient, is strong evidence for the importance of the dipole–dipole interactions which

Table 1. *Electrocaloric-coefficient data for* KCl:OH

T (°K)	E (kV/cm)	$(N_{\max})$ calc	$(N_{\max})$ obs *	$(\beta_{\max})$ calc.	$(\beta_{\max})$ obs.†
4·0	20	$58\cdot3 \times 10^{18}$	29×10^{18}	$-2\cdot45 \times 10^{-3}$	$-0\cdot438 \times 10^{-3}$
2·8	20	$28\cdot6 \times 10^{18}$	20×10^{18}	$-4\cdot62 \times 10^{-3}$	$-1\cdot15 \times 10^{-3}$
2·0	20	$14\cdot6 \times 10^{18}$	14×10^{18}	$-7\cdot58 \times 10^{-3}$	$-2\cdot97 \times 10^{-3}$
2·0	40	$14\cdot6 \times 10^{18}$	13×10^{18}	$-8\cdot58 \times 10^{-3}$	$-3\cdot52 \times 10^{-3}$

*Determined optically [6]

†Reference [6]

introduce the term quadratic in N in equation (12). It is worth noting that the specific heat C_0'' calculated on the basis of an Ising model [21] is *independent* of N, and hence, does not lead to these concentration dependencies.

The electrocaloric coefficient, equation (17), contains much useful information, in addition to that indicated by equations (19) and (20). The specific heat C_E appearing in the denominator of β_E has a maximum at $Z = 2{\cdot}90$, whereas the explicit function of Z in equation (17) has a maximum at $Z = 2{\cdot}16$; both of these extrema are concentration independent. Therefore, $|\beta_E|$ has a maximum at $Z = 2{\cdot}16$ and a minimum at $Z = 2{\cdot}90$, if the collective term and Schottky term are ignored (i.e. small N, large T), and

$$|\beta_E|_{\max} = \frac{0{\cdot}518N\mu}{\alpha T^3 + 1{\cdot}12Nk(\mu/\bar{\mu})}$$

$$|\beta_E|_{\min} = \frac{0{\cdot}451N\mu}{\alpha T^3 + 1{\cdot}31Nk(\mu/\bar{\mu})}.$$

In particular, if β_E is measured isothermally by varying E, then the dipole moment $\bar{\mu}$ can be determined from the β_E peaks,

$$k/\bar{\mu} = \frac{2{\cdot}37}{|\beta_E|_{\min}} - \frac{2{\cdot}72}{|\beta_E|_{\max}}.$$

In conclusion, there are two refinements to the thermodynamic theory which deserve mention, in addition to the dipole-moments problem. First, the elastic-dipole nature [6, 22] of the OH^- impurity has been ignored above, and the *elastic* dipole–dipole interactions will contribute to C_0'', although the evidence presented here would seem to argue that this contribution is small compared to the electrostatic contribution.

Second, in writing down equation (9) we have implicitly assumed that the field E is always large enough to break up the dipole correlations. The effect of these correlations is to alter the $P(E/T)$-curve given by (9) in the low-field region (depending on N), thus altering the integrals which enter equations (10) and (11), because the correlated dipoles do not contribute to P statistically. The seriousness of this consideration obviously depends on the concentration, and Shepherd [7] in fact has found that at high concentrations the specific heat concentrations given by equation (10′) fall considerably below the corresponding 'optical' concentrations.

The onset of this dipole ordering could be detected experimentally in view of equation (2), since *prior* to dipole ordering, $P = P(E/T)$ (provided that $P^{(0)}$ in equation (9) is a weak function of E and T), so that in the isothermal polarization of the material, an equal quantity of heat flows out of the material. This would not be the case, however, when dipole ordering ensues.

Acknowledgement – The author is grateful to Dr Brent Wedding of this laboratory for helpful discussions and for reading the typescript

REFERENCES

1 GRÄNICHER H., *Helv. Phys. Acta* **29**, 211 (1956).
2 See GARRETT C. G. B., In *Magnetic cooling* Wiley, New York (1954); BARRON R., In *Cryogenic systems*. McGraw-Hill, New York (1966).
3 HEGENBARTH E., *Cryogenics* **1**, 242 (1961); *Phys. Status Solidi* **2**, 1544 (1962); *ibid.* **8**, 59 (1965).
4. KANZIG W., HART H. R., JR and ROBERTS S., *Phys. Rev. Lett.* **13**, 543 (1964)
5. KUHN U. and LUTY F., *Solid State Commun.* **3**, 31 (1965)
6 LUTY F., *J. Phys* Suppl 8–9. **28**. C4-120 (1967).
7. SHEPHERD I. W., *J. Phys. Chem Solids* **28**, 2027 (1967).
8 LAWLESS W. N., *Phys Kondens Materie* **5**, 100 (1966): the specific-heat expressions in this paper, immediately preceeding Fig 5, are linear in the concentration *N*, this is a misprint as may be seen from Fig. 5 and equation (30), *ibid.* **5**, 403 (1966)
9. KUHN U. and LÜTY F., *Solid State Commun.* **3**, 31 (1965).
10. SHORE H. B., *Phys Rev.* **151**, 570 (1966).
11. SAMARA G. A., *Phys. Rev.* **165**, 959 (1968)
12. HARRISON J. P., *Rev scient. Instrum.* **39**, 145 (1968).
13. FEHR G., SHEPHERD I. W. and SHORE H. B., *Phys. Rev. Lett.* **16**, 500 (1966).
14. HARRISON J. P., LOMBARDO G. and PERESSINI P. P., *J Phys. Chem. Solids* **29**, 557 (1968)
15. FRÖHLICH H., In *Theory of Dielectrics*. Oxford University Press, London (1958).
16. MAHAN G. D., *Phys. Rev.* **153**, 983 (1967).
17. HAM F. S., Unpublished

18. LAWLESS W. N., *J. Phys. Chem. Solids* **28**, 1755 (1967); BRON W. E. and DREYFUS R. W., *Phys. Rev.* **163**, 304 (1967).
19. CHAU C. K., KLEIN M. V. and WEDDING B., *Phys. Rev. Lett.* **17**, 521 (1966); KLEIN M. V., KENNEDY S. O., GIE TAN IK and WEDDING B., *Mat. Res. Bull.* (1968).
20. FRITZ B., LUTY F. and ANGER J., *Z. Phys.* **174**, 240 (1963).
21. KLEIN M. W., *Phys. Rev.* **141**, 489 (1966).
22. NOWICK A. S. and HELLER W. R., *Adv. Phys.* **12**, 251 (1963).

APPENDIX A

The polarization is a function of $Z = \bar{\mu}E/kT$, so that

$$\frac{\partial^2 P}{\partial T^2} = \frac{1}{T^2}\left[\left(Z^2\frac{\partial^2 P}{\partial Z^2}\right) + 2Z\frac{\partial P}{\partial Z}\right]$$

Therefore,

$$T\int_0^E \frac{\partial^2 P}{\partial T^2}\mathrm{d}E = \frac{k}{\bar{\mu}}\left(Z^2\frac{\partial P}{\partial Z}\right)_{Z=0}^{Z=\bar{\mu}E/kT}$$

and equation (10′) results when equation (9) is used in the above.

APPENDIX B

The integrals on the left-hand side of equation (11) can be solved by noting that

$$\left(\frac{\partial P}{\partial T}\right)\mathrm{d}E = -\frac{k}{\bar{\mu}}Z\left(\frac{\partial P}{\partial Z}\right)\mathrm{d}Z,$$

which can be integrated by parts,

$$-\frac{k}{\bar{\mu}}(ZP)_0^{\bar{\mu}E/kT} + \frac{k}{\bar{\mu}}\int_0^{\bar{\mu}E/kT} P\mathrm{d}Z,$$

and the remaining integral is tabulated for P from equation (9) (note that P–$P^{(0)}$ is to be used), resulting in equation (13).

J. Phys. Chem. Solids Pergamon Press 1969. Vol. 30, pp. 1173–1180. Printed in Great Britain.

DETERMINATION OF THE SURFACE HETERODIFFUSION COEFFICIENT BY THE METHOD OF MASS TRANSFER

Ya. E. GEGUZIN, Yu. S. KAGANOVSKY and V. V. SLYOZOV
A. M. Gorky State University, Institute of Single Crystals, Physico-Technical Institute, Kharkov, U.S.S.R.

(*Received* 22 *July* 1968)

Abstract—In the paper a method of determination of the surface heterodiffusion coefficient D_s is suggested which is based on the observation of the transfer of macroscopic quantities of substance A along the substrate B. Both the diffusion mass transport between solid and liquid phases of substance A and the two-dimensional coalescence of A on substrate B are considered.

The obtained formulae are then used for numerical calculations of the values of D_s basing upon the data on qualitative observations of the surface heterodiffusion from other publications.

1. INTRODUCTION

At present the mass transfer technique is widely used for the determination of self-diffusion coefficients[1–4].

Information on the surface diffusion coefficient may be obtained from the data on the volume of the transported material, which enables the experimentally observable changes in the object geometry.

As far as we know the mass transfer experiments were not used for the determination of the surface heterodiffusion coefficients although the first qualitative tests[5], in which the surface diffusion was discovered consisted in observing the changes of the silver condensate on glass due to the silver mass transport via the surface heterodiffusion mechanism.

In the present paper we discuss the possibilities of exploiting the experiments on the transport of substance A along substrate B for the determination of the heterodiffusion coefficient D_s of A along B.

2. FORMULATION OF THE PROBLEM

Presentation of the calculations proper should be prefaced with the discussion of the origin of gradients which provide directed surface fluxes. Possibilities of determination of D_s in principle from the data on the mass transfer are also to be analysed.

Two substantially different factors may cause the gradient of the chemical potential which determines directed mass transport.

Consider now the first of them. Let a supercooled liquid drop of substance A be situated near a crystallized particle of the same substance. The adsorbed gas densities near the solid and the liquid phases will be different due to the different values of energy necessary for the transition of an atom from the condensed into the two-dimensional adsorbed phase. An elementary evaluation of the arising gradient of the chemical potential is

$$\nabla\mu_1 \simeq \frac{\mu_l - \mu_c}{x} \approx \frac{Q_m \Delta T}{x T_m} \tag{1}$$

where μ_c and μ_l are the chemical potentials of the two-dimensional gas adsorbed near the crystalline and the liquid phases respectively, $\Delta T = T_m - T$ is the system supercooling, Q_m, the latent melting heat; T_m, the melting temperature and x is the distance between the particles.

The second factor is the difference of the adsorbed gas densities near two particles of different curvature. In this case

$$\nabla\mu_2 = \frac{\gamma\Omega}{x}\Delta K \tag{2}$$

where $\Delta K = 1/R_1 - 1/R_2$ is the difference of the particle curvatures, γ, the surface tension and Ω is the atom volume.

Comparing the gradients $\nabla\mu_1$ and $\nabla\mu_2$ one can easily see that for reasonable values of their determining constants, $\nabla\mu_1 \simeq 10^4\nabla\mu_2$. Thus, under other equal conditions the mass transport between the regions of different phase states should have a substantially greater rate than in case of coalescence of particles of the same phase states.

For the mass transfer experiment to serve as a source of information on the surface diffusion coefficient it is necessary that the surface diffusion flux should greatly overcome that through the gaseous phase, i.e. that the condition should be met:

$$\frac{D_a n_a}{D_g n_g R} \gg 1. \tag{3}$$

Here D_a stands for the adatom diffusion coefficient, D_g is the gaseous phase diffusion coefficient, n_g is the atom density in the gas, n_a is the number of adatoms on a unit surface and R is radius of a particle of a hemispheric shape.

From condition (3) it follows that the equilibrium vapour pressure of substance A adsorbed on the surface B ($p_0 \simeq n_g/kT$) must satisfy the inequality

$$p_0 \ll \frac{D_s kT}{D_g a^2 R}. \tag{4}$$

Here $D_s \simeq D_a n_a a^2$, a is the lattice parameter.

For the reasonable values of constants in (4) (kT) $\simeq 10^{-14}$ erg, $D_g \simeq 10^{-1}$ cm^2/sec, $D_s \simeq 10^{-5}$ cm^2/sec, $R \simeq 10^{-4}$ cm, $a \simeq 10^{-8}$ cm) we obtain $p_0 \ll 10^2$ dyn/cm^2. Note that the values involved in this evaluation refer to the elevated temperatures. As the temperature drops the inequality (4) is still better satisfied.*

In actual conditions the required difference of densities of the particles in the two-dimensional adsorbed gas and the 'spatial' one may occur because the potential barrier preventing the penetration of atoms into the two-dimensional adsorbed gas is lower than that for the 'spatial' gas by the value of the adsorption energy.

Thus in many cases the process of mass transfer between the granules of A on substrate B is determined by the two-dimensional diffusion flux, the surface heterodiffusion coefficient thus determining the kinetics of the process.

Regardless of the type of gradient the equation governing the steady-state diffusion along the surface may be written as [6]

$$\frac{\partial\xi}{\partial t} = D_a\nabla^2\xi + q - \frac{\xi}{\tau} = 0 \tag{5}$$

where $\xi = a^2 n_a$ is the adatom concentration.

In this equation the possible interchange between the diffusing adatoms of substance A and its saturated (equilibrium) vapour is taken into account: q stands for the relative number of particles incident upon a unit surface per unit time from the gaseous phase, τ is the mean time of 'life' of atom A in the adsorbed state on substrate B. However equation (5) does not take into account the leakage of diffusing adatoms into the bulk of the substrate. For the most part of real systems and the experimental conditions this disregard is quite admissible.

Hereafter equation (5) is being solved under the assumptions on the geometry of the system chosen to provide the most clear observations of the mass transport for each of the two types of gradients.

3. DIFFUSION MASS TRANSPORT BETWEEN THE REGIONS OF SOLID AND LIQUID PHASES

Consider the substance transfer between a supercooled liquid film and a crystal. For simplicity's sake we assume that the film edge and the crystal front are parallel (Fig. 1)

---

*Holding of the inequality (4) may be achieved by an artificial method consisting in carrying out the test in the inert gas atmosphere under pressure, so that $D_g \sim 1/p$ [10]. This method, however, may negatively affect the results of determination of D_s because of the interaction of the inert gas and the substrate

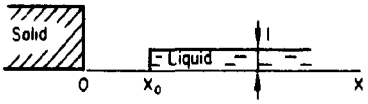

Fig. 1. An illustration to the calculation of the rate of growth of the yard free of liquid.

and the film thickness l is much less than that of the crystal L. The last assumption permits to consider the mass transport to be accompanied by the film edge displacement (x_0) only, the crystal front remaining unmoved. It is worth noting that the problem discussed is by its physical sense the problem of kinetics of the crystal growth from the supercooled liquid, when the substance supply to the crystal is due to the surface diffusion mechanism.

For the discussed geometry, equation (5) must be solved under the conditions

$$\xi|_{x=0} = \xi_c; \quad \xi|_{x=x_0} = \xi_l \qquad (6)$$

$$x_0|_{t=0} = b$$

and

$$q = \xi_l/\tau. \qquad (7)$$

Condition (7) arises from the fact that the flux of substance from the gaseous phase onto the surface is independent of the coordinate and equals the number of particles evaporated from a unit surface per unit time near the liquid phase front; this, in turn, occurs because of a much greater rate of achieving the homogeneous concentration in the gas compared to that on the surface.

Denoting $\eta = \xi_l - \xi$; $\omega^2 = D_a\tau$; $\xi = x/\omega$ one may re-write equation (5) as

$$\frac{d^2\eta}{d\xi^2} = \eta \qquad (8)$$

the boundary conditions becoming

$$\begin{aligned} \eta(0) &= \xi_l - \xi_c = \Delta \\ \eta(\xi_0) &= 0; \quad \xi_0 = x_0/\omega. \end{aligned} \qquad (9)$$

The solution of (5) is

$$\eta(\xi) = \Delta\left(\cosh\xi - \frac{\sinh\xi}{\tanh\xi_0}\right). \qquad (10)$$

The flux at the point x_0 satisfies the equation

$$j(x_0) = D_a\frac{d\eta}{dx}\bigg|_{x=x_0} = a^2\frac{\rho_l l}{m}\frac{dx_0}{dt} \qquad (11)$$

(ρ_l is the liquid phase density, m is the mass of one molecule of substance A), which with regard of (10) yields

$$\frac{dx_0}{dt} = \frac{\alpha}{\omega}\frac{D_a\Delta}{\sinh(x_0/\omega)}. \qquad (12)$$

Here $\alpha = m/\rho_l l a^2 \simeq a/l$ (a is the lattice parameter of substance A).

Integrating (12) we come to

$$\cosh\frac{x_0}{\omega} - \cosh\frac{b}{\omega} = \alpha\Delta D_a t/\omega^2. \qquad (13)$$

Under a reasonable assumption $x_0 \ll (D_a\tau)^{1/2}$, meaning that during the time τ an adatom covers the diffusion distance which surpasses the separation x_0 of the liquid and crystalline phases*) we may write the equation in the form

$$x_0^2 = b^2 + 2\alpha\Delta D_a t \qquad (14)$$

(neglecting the terms of order $\sim(x/\omega)^4$)

The quantity $\Delta = \xi_l - \xi_c$ involved in the equations may be expressed in terms of the chemical potentials of adatoms near the solid and liquid phases. Indeed, with $\Delta/\xi_0 \ll 1$:

$$\Delta\mu = \mu_l - \mu_c = kT\ln(\xi_l/\xi_c) \simeq kT\Delta/\xi_c. \qquad (15)$$

As

$$\Delta\mu = Q_m\frac{\Delta T}{T_m} \qquad (16)$$

---

*The necessary inequality is met when the adsorption heat of A-atoms on substrate B is of considerable magnitude, of about $20\,kT$.

it follows from (15) and (16)

$$\Delta = \frac{\xi_c}{kT} Q_m \frac{\Delta T}{T_m}. \qquad (17)$$

Q_m and T_m in (16) and (17) being the melting heat and the melting temperature of substance A respectively, $\Delta T = T_m - T$.

It proves useful to tie the wanted value D_s and the adatoms diffusion coefficient D_a with the relation

$$D_s = D_a \xi_c = D_{0s} \exp(-Q_s/kT). \qquad (18)$$

Equation (18) actually is the definition of the surface heterodiffusion coefficient similar to that of the surface self-diffusion which is known to be related to the adatom self-diffusion coefficient D_a and the adatoms concentration ($\xi_a = n_a/N_0 = a^2 n_a$) as

$$D_s = D_a \xi_a.$$

Having in mind the definition (18) of D_s one may re-write (14) as

$$x_0^2 = h^2 + 2\alpha D_s t \Psi \qquad (19)$$

where $\Psi = \Delta\mu/kT = Q_m \Delta T/kT T_m$.

A peculiarity of the considered diffusion process is that with the temperature decreasing the value of the chemical potential grows (see equation (19)) while the heterodiffusion coefficient also decreases. The temperature dependence of the mass transport rate is thus a curve with a maximum. This circumstance may be used for the determination of the activation energy Q_s not from the temperature dependence of D_s, as it is usually done, but from the position of the maximum on the curve $dx_0^2/dt = f(T)$. From the condition $d/dT(dx_0^2/dt) = 0$ it follows

$$Q_s \simeq \frac{kT^*}{1-(T^*/T_m)} \qquad (20)$$

where T^* is the temperature of the curve maximum. Note that $Q_s \simeq 10\,kT$ so $T_m - T \simeq 10^{-1} T_m$ and the maximum of $dx_0^2/dt = f(T)$ may be reliably found in the experiment.

4. TWO-DIMENSIONAL DIFFUSION COALESCENCE

Consider a particle of substance A (no matter solid or liquid) of a hemispheric shape placed on substrate B. The radius (R) of such a particle may change with time because of the material transfer via the mechanism of surface diffusion or diffusion within the gas:

$$\frac{dR}{dt} = \left(\frac{dR}{dt}\right)^s + \left(\frac{dR}{dt}\right)^g$$

or

$$\frac{dR}{dt} = D_g \frac{\partial C^g}{\partial r}\bigg|_{r=R} + D_a \frac{a}{R} \frac{\partial \xi}{\partial r}\bigg|_{r=R}. \qquad (21)$$

Here D_g is the diffusion coefficient within the gas, $C^g = a^3 n^g$ where n^g is the number of gas particles in a unit volume; a is the lattice parameter, $\xi = a^2 n_a$ and n_a denotes the number of adatoms on a unit surface. The values of $\partial\xi\partial r|_{r=R}$ and $\partial C^g/\partial r|_{r=R}$ are to be found from the solution of equation (5) and

$$D_g \nabla^2 C^g = \frac{\partial C^g}{\partial t} = 0. \qquad (22)$$

Hereafter we intend to consider this given particle to belong to an ensemble of similar particles of various radii; so we define the meanings of C^g and ξ at the infinity as

$$C^g\Big|_{r\to\infty} = \bar{C}^g; \quad \xi\Big|_{r\to\infty} = \bar{\xi} \qquad (23)$$

where $\bar{C}^g$ and $\bar{\xi}$ are determined by the ensemble in a self-congruent way.

Near the surface of a particle the conditions are met

$$C^g\Big|_{r=R} = C_\infty^g + \frac{\alpha^g}{R}; \quad \xi\Big|_{r=R} = \xi_\infty + \frac{\alpha^s}{R} \qquad (24)$$

where $C_\infty^g = a^3 p_0/kT$ is the concentration near the plane, p_0 is the equilibrium vapour pressure; $\alpha_g = (2\gamma a^3/kT)C_\infty^g$; ξ_∞ has the meaning of the equilibrium concentration of the two-dimensional gas adjacent the surface of infinite curvature radius, $\alpha^s = (2\gamma a^3/kT)\,\xi_\infty$ and γ is the surface tension of A.

Equations (5) and (22) are to be solved under boundary conditions (23) and (24).

The solution of (22) readily follows

$$\left(\frac{\mathrm{d}R}{\mathrm{d}t}\right)^g = \frac{D_g C_\infty{}^g}{R}\left(\Delta'^g - \frac{2\gamma a^3}{kTR}\right) \qquad (25)$$

$\Delta'^g = (\bar{C}^g/C_\infty{}^g) - 1$.

When solving (5) we must take into account that the relative number of particles incident upon the surface from the gas satisfies

$$q = \bar{\xi}/\tau. \qquad (26)$$

So we obtain

$$\left(\frac{\mathrm{d}R}{\mathrm{d}t}\right)^s = D_a \frac{a}{R}\frac{\partial \xi}{\partial r}\bigg|_{r=R}$$

$$= D_a \frac{a}{R}\left(\Delta^s - \frac{\alpha^s}{R}\right)\frac{K_0'(x)}{\omega K_0(x)}\bigg|_{x=R/\omega} \qquad (27)$$

$K_0(x)$ being the modified Bessel function, $\Delta^s = \bar{\xi} - \xi_\infty$, $\omega = (D_a\tau)^{1/2}$.

Two limiting cases deserve consideration: (i) $R \ll \omega$. Expression (27) takes the form

$$\left(\frac{\mathrm{d}R}{\mathrm{d}t}\right)^s = D_a \frac{a}{R^2 \ln(2\omega/R)}\left(\Delta^s - \frac{\alpha^s}{R}\right)$$

$$= D_a \frac{a\xi_\infty}{R^2 \ln(2\omega/R)}\left(\Delta'^s - \frac{2\gamma a^3}{kTR}\right) \qquad (28)$$

$$\Delta'^s = (\bar{\xi}/\xi_\infty) - 1.$$

(ii) $R \gg \omega$, instead of (27) we get

$$\left(\frac{\mathrm{d}R}{\mathrm{d}t}\right)^s = \frac{D_a}{R}\frac{a}{\omega}\left(\Delta^s - \frac{\alpha^s}{R}\right)$$

$$= \frac{D_a}{R}\frac{a}{\omega}\xi_\infty\left(\Delta'^s - \frac{2\gamma a^3}{kTR}\right). \qquad (29)$$

Comparison of (28, 29) and (25) brings us to a condition under which $(\mathrm{d}R/\mathrm{d}t)^s \gg (\mathrm{d}R/\mathrm{d}t)^g$. Indeed, Δ'^s and Δ'^g being of the same order, it follows from the written inequality

$$\frac{D_a a \xi_\infty}{D_g R C_\infty{}^g \ln\left(\frac{2\omega}{R}\right)} \gg 1 \quad \text{when} \quad R^2 \ll D_a\tau \qquad (30)$$

$$\frac{D_a a \xi_\infty}{D_g \omega C_\infty{}^g} \gg 1 \quad \text{when} \quad R^2 \gg D_a\tau.$$

Condition (30) is practically equivalent to (3) which was derived from general considerations. If we consider the given particle as an element of the ensemble of similar particles of various radii, scattered chaotically on the substrate we may derive the asymptotic size distribution of the particles and also the time dependence of their average size.

At $t \to \infty$, with $\Delta^g \to 0$ and $\Delta^s \to 0$ the law of mass conservation in the ensemble of particles involved in the self-consistent mass transport, may be written as

$$\frac{2\pi}{3}\int_0^\infty f(R)R^3\,\mathrm{d}R = Q_0 = \text{const.} \qquad (31)$$

Here $f(R)$ is the size distribution normalized by the unit surface, Q_0 is the total volume of matter of the particles per 1 cm^2. The calculations of $\bar{R}(t)$, $f(R,t)$, $\Delta^s(t)$ and the number of particles per 1 cm^2 of the substrate surface, $N^s(t)$, is absolutely the same as in the paper by Lifshitz and Slyozov[7]. So we present only the results.

There exist two cases when the mass transport is determined mainly by the surface heterodiffusion mechanism.

$$\text{(i)} \qquad \bar{R}^2 \ll D_a\tau; \quad \frac{(D_a\alpha^s a t)^{1/2}}{D_a\tau} \ll 1\,. \qquad (32)$$

At $t \to \infty$ the desired asymptotic formulae are

$$\bar{R}^4 = \left(\frac{4}{3}\right)^3 \frac{D_a\alpha^s a t}{\frac{1}{4}\ln(2\omega/R)} \qquad (33)$$

$$N^s(t) = Q_0\Big/\frac{2\pi}{3}\bar{R}^3;\quad \Delta^s(t) = \alpha^s/\bar{R}(t) \quad (34)$$

$$f(R,t) = \begin{cases} \frac{4}{3}N^s(t)\frac{\exp(-3\psi/4)}{\bar{R}\cdot g} & \text{when} \quad R < \frac{4}{3}\bar{R} \\ 0 & \text{when} \quad R \geq \frac{4}{3}\bar{R} \end{cases} \quad (35)$$

$$\psi = \psi(u) = \frac{7}{4}\ln\left(1-\frac{3u}{4}\right) + \frac{1}{6\left(1-\frac{3u}{4}\right)} + \frac{11}{18}\ln\left[\left(\frac{3u}{4}+1\right)^2+2\right] + \frac{1}{18\sqrt{2}}\arctan\left(\frac{1+\frac{3u}{4}}{\sqrt{2}}\right) - \frac{7}{9};$$

$$u = R/\bar{R};\quad g = \frac{1}{4u^3}\left(u-\frac{4}{3}\right)^2\left[\left(u+\frac{3}{4}\right)^2+\frac{g}{8}\right].$$

Note that the factor $(\frac{4}{3})^{1/3}\ln(2\omega/R)$ in (33) may be within the experimental accuracy replaced by a unit and be considered time-independent in the conditions of isothermal experiment. It also shows a very slow rate of variation with temperature changes, compared to $\exp(-Q_s/kT)$, say, where Q_s is the heterodiffusion activation energy.

(ii) $$\bar{R}^2 \gg D_a\tau.$$

In this case we obtain at $t \to \infty$

$$\bar{R}^3 = \frac{4}{9}D_a\frac{a}{\omega}\alpha^s t \quad (36)$$

$$f(R,t) = \begin{cases} 40\frac{N^s(t)\,u^2\exp[-1/1-(2u/3)]}{(u+3)^{7/3}(\frac{3}{2}-u)^{11/3}} & \text{when} \quad u < \frac{3}{2} \\ 0 & \text{when}\ u \geq \frac{3}{2} \end{cases}$$

$N^s(t)$ and $\Delta^s(t)$ are again given by (34).

5. SOME EXPERIMENTAL RESULTS

The theory that was developed above gives formulae which may be useful for the determination of heterodiffusion coefficients from the experimental data on the mass transport.

I. The mass transfer between the regions of solid and liquid phases.

$$D_s = \frac{1}{2\alpha\Psi}\frac{dx_0^2}{dt} = \frac{l}{2\Psi a}\frac{dx_0^2}{dt}. \quad (37)$$

II. The mass transfer via the coalescence between the grains of the same phase:

$$\begin{aligned} &\text{(a)}\quad \bar{R}^2 \ll D_a\tau;\quad D_s = \frac{kT}{2\gamma a^4}\frac{\Delta\bar{R}^4}{\Delta t} \\ &\text{(b)}\quad \bar{R}^2 \gg D_a\tau;\quad \frac{D_s}{\omega} = \frac{kT}{\gamma a^4}\frac{\Delta\bar{R}^3}{\Delta t}. \end{aligned} \quad (38)$$

The experiments carried out with $\bar{R}^2 \gg D_a\tau$ cannot be used to obtain the value D_s, giving D_s/ω only.

The formulae derived may be fitted to the results of some experiments in which the kinetics of surface heterodiffusion was quantitatively studied. We shall make use of the results of two experimental works. One of them dealt with the diffusion of potassium on the surface of quartz[6], another with the diffusion of gold along the (100) surface of the single crystal NaCl[8].

Wegener[6] studied the condensation of dispersed ($\sim 1\,\mu$) drops of potassium from the gaseous phase on the surface of the silica glass. The melted potassium is known to be easily supercooled; the drops remained liquid even at 23°C – that is being supercooled by 41°C. On the photos of [6] which illustrate the time variations of the drops' condensate structure one can easily see two pronounced effects.

In the vicinity of a casually crystallized drop there appears later a constantly growing site (a 'yard') free of other drops. At the same time the crystallized bulk grows which is an evidence for the mass transport from the liquid into the crystalline phase.

Also clearly seen on the photos is the coalescence process, i.e. the growing of drops with the diminution of their number.

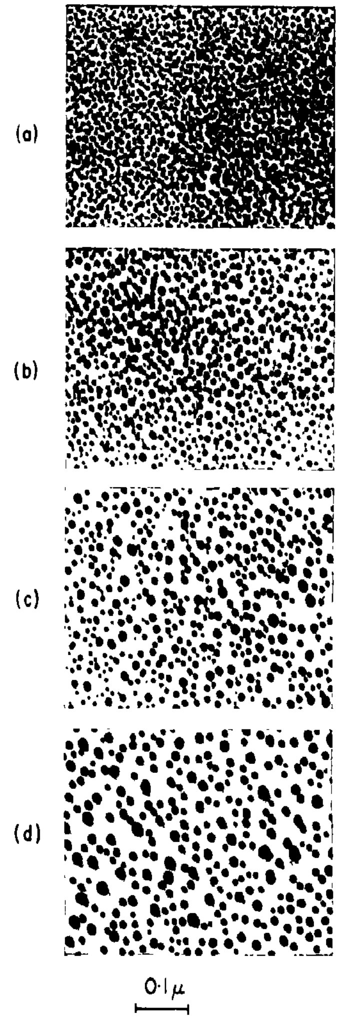

Fig. 2. Two-dimensional diffusion coalescence of gold particles on (100) surface of the single crystal NaCl. $T = 280$°C; (a) $t = 0$; (b) $t = 1h$; (c) $t = 4$h; (d) $t = 7h$.

Geguzin *et al.*[8] investigated the coalescence of dispersed drops of gold forming on the (100) surface of single crystal NaCl, which gold was condensed from a molecular beam. The replica technique was used and the ectron microscoping. It is worth reminding t Bassett in his well known works[9] used formation of gold grains to decorate thin ls of the ion crystals surface relief.

gure 2 represents a succession of photos ch clearly illustrates the process of gold ains coalescence.

Having plotted the time dependence of the ard's' linear dimensions from the photos of 6] (Fig. 3) one can evaluate (from equations (37)) the surface diffusion coefficient of potassium on quartz at the temperature 23°C. The calculations give the value of $D_s \simeq 2\times 10^{-7}$ cm^2 sec^{-1}. Note that this calculation involves a certain inaccuracy, because the results of an experiment of an axially symmetrical geometry are being interpreted on the basis of equation (37) which was derived for the one-dimensional case. The error is not, however, essential provided the 'yard's' radius x_0 is of the order of the dimensions of the crystal. The diffusion coefficient must also determine the kinetics of the supercooled potassium drops coalescence*.

From the photos of [6] we have plotted the curves of the size distribution of drops. D_s has been evaluated from equation (38) from the time dependence of the average size of drops. The value obtained is $D_s = 5\times 10^{-7}$ cm^2 sec^{-1} which is in good agreement with the evaluation from the 'yard's' growth kinetics.

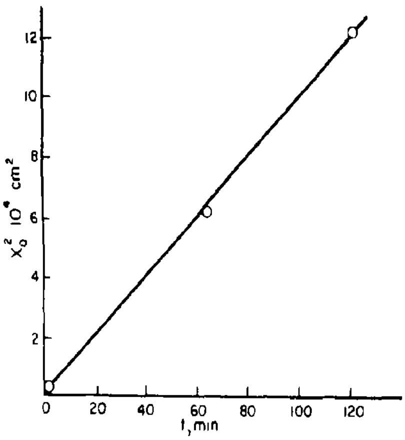

Fig. 3. Time-dependence of the linear dimension of the 'yard' on potassium-quartz (From the photos of Wegener [6]).

From the photos presented in Fig. 2 we have plotted the size distribution of the grains of gold and established the dependence $\bar{R}^4 = f(t)$ (Fig. 4). In agreement with (38) it appears to be $\bar{R}^4 \sim t$. The surface heterodiffusion coefficient of gold on the NaCl surface was calculated from the inclination of $f(t)$. At $T = 280°C$ it equals D_s 10^{-16} cm^2 sec^{-1}. The reasons of such a small value must be investigated.

The experimental results and their processing, in particular, the coincidence of the values of D_s as calculated from the kinetics of the formation of the 'yard' and from the coalescence of the potassium drops on quartz

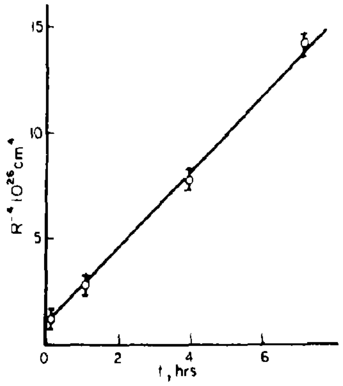

Fig. 4 Time-dependence of the average radius of gold particles coalescenting on the surface of NaCl, $T = 280°C$

---

*Rigorously, the diffusion coefficient D_s as found from (37) must differ from the value found from the kinetics of liquid drops coalescence (D_s') inasmuch as the equilibrium concentrations of adatoms near the crystalline and liquid phases are different. It is obvious that

$$\frac{D_s'}{D_s} = \frac{\xi_l}{\xi_c} = 1 + \frac{Q_m}{kT_m}\frac{\Delta T}{T} = 2.$$

In case the coalescence investigated was that of crystalline grains and not of liquid drops, the meanings of D_s from (37) and (38) would be the same.

serve as an evidence for the plausibility of the initial assumptions and derivations.

Acknowledgement – In conclusion the authors express their gratitude to I. M. Lifshitz for his interest and fruitful discussions

REFERENCES

1. MULLINS W. W., *J. appl. Phys.* **28**, 333 (1957), *J. appl. Phys.* **30**, 77 (1959).
2. BLAKELY J. M., *Prog. Materials Sci.* **10**, 393 (1963)
3. GJOSTEIN N. A., Review of Surface Self-Diffusion. Paper for ASM-AIME Symposium on *Surfaces: Structure, Energetics and Kinetics* (1962).
4. GEGUZIN YA. E., Poverkhnostnaya diffuziya i rastekaniye. *USSR Acad. Sci.* Moscow (1969).
5. ESTERMANN J., *Z. phys. Chem.* **106**, 403 (1923).
6. WEGENER H., *Z. Phys.* **139**, 464 (1954).
7. LIFSHITZ I. M. and SLYOZOV V. V., *J. Phys. Chem. Solids* **19**, 35 (1961).
8. GEGUZIN YA. E., KAGANOVSKY YU. S. and KALININ V. V., *Soviet FTT*. **11**, No. 1 (1969).
9. BASSETT G. A., *Phil. Mag.* **3**, 1042 (1958).
10. GEGUZIN YA. E. and OVCHARENKO N. N., *Soviet Phys.* Crystallogr. **6**, 1 (1961).

J. Phys. Chem. Solids Pergamon Press 1969. Vol. 30, pp. 1181–1187. Printed in Great Britain.

DENSITY OF STATES AND THE ELECTRONIC SPECIFIC HEAT: PALLADIUM*

E. D. THOMPSON†
Solid State Division, Oak Ridge National Laboratory, Operated by Union Carbide Corporation,
for the U.S. Atomic Energy Commission, Oak Ridge, Tenn. 37830, U.S.A.

(*Received* 28 *August* 1968, *in revised form* 14 *November* 1968)

Abstract—By a non-random trial and error procedure, density-of-states functions are calculated for palladium which yield the experimentally determined electronic specific heat. We find that considerable structure is required in this function in the chemical potential energy region. We conclude, however, that palladium's electronic specific heat and paramagnetic susceptibility cannot be fitted with the same density of states function.

1. INTRODUCTION

FROM RECENT inelastic neutron scattering results on pure palladium[1], it has been concluded that the electronic specific heat $C_v(T) = \gamma(T)T$ shows considerable structure at low temperature. It is the purpose of this paper to study the implications that such structure in $\gamma(T)$ has as regards the density-of-states function under the assumption of temperature-independent energy bands. From this density-of-states function, the paramagnetic susceptibility $\chi(T)$ is calculated and compared with the "experimental" results on palladium[1, 2].

There have been three approaches to the temperature dependence of $\gamma(T)$ and $\chi(T)$ arising from structure in the density of states function. The first approach is motivated by the methodology of Taylor series expansions[3]. However, such expansions are so slowly convergent as to be practically useless for 'peaky' density of states functions such as have been found for the transition metals[4]. The second approach is a numerical calculation based on analytically described density of states functions. Calculations have been carried out by Stoner[5, 6], Wohlfarth [7, 8], and Elcock, Rhodes and Teviotdale[9] and these calculations, plus the extensions which we have done on the latter's work but not reported on here, provide very important guidelines for this study.

The third approach is a numerical calculation based upon numerically described density of states functions[2, 10, 11]. These density of states functions have been generated under the assumption of the rigid band theory of alloying and the measured low temperature specific heat coefficients $\gamma(0)$ for a series of alloys. Using the density of states generated in this manner, these authors have calculated $\gamma(T)$ and $\chi(T)$ for a particular alloy over a broad temperature range and have obtained reasonable agreement with earlier experiments.

As the calculational procedure used here differs from that of previous authors[2, 10, 11], the necessary formulae are derived and the calculational procedure is given in Section 2.

In Section 3, the 'experimental' electronic specific heat for palladium is by a fitted non-random trial and error selection of density of states functions. Given a density of states function, it is now a straightforward matter of numerical integration to find γ and χ but such is not the case for the inverse. The situation is quite analogous to that found between the lattice mode spectral density and the lattice specific heat[12] and between the magnon mode density and the magnetization [13]. The non-unique density of states functions which we find all contain definitive structure close to the chemical potential on an energy scale such that this structure would be obscured by present density of states function calculations[14].

---

*Research sponsored by the U.S. Atomic Energy Commission under contract with Union Carbide Corporation.

†*Permanent address:* Case Western Reserve University, Cleveland, Ohio.

2. BASIC FORMULAE AND CALCULATIONAL PROCEDURE

Given $n(\epsilon)$, the density of electronic states function, then Δn, the change in the number of electrons in the system at temperature T compared with that absolute zero, is given by the relationship

$$\Delta n = \int_{-\infty}^{\mu} f(x)n(\epsilon)\,\mathrm{d}\epsilon - \int_{-\infty}^{0} n(\epsilon)\,\mathrm{d}\epsilon. \qquad (1)$$

In (1), $f = [1+\exp(x)]^{-1}$, $x = (\epsilon-\mu)/T$, and the origin of energy has been selected such that the chemical potential equals zero at $T = 0$°K. Using $f(x) = 1-f(-x)$, (1) can be rewritten in the form,

$$\Delta n = T\left\{\int_{0}^{\infty} f(x)[n(\mu+Tx)-n(\mu-Tx)]\,\mathrm{d}x + \int_{-\mu/T}^{0} n(\mu+Tx)\,\mathrm{d}x\right\}. \qquad (2)$$

This form is more convenient than (1) for calculational purposes, as the first integral can be truncated as $f(x) \approx e^{-x}$ for large x.

For a system with a fixed number of electrons, equation (2) with $\Delta n = 0$ is an integral equation defining the chemical potential at temperature T. Rather than solve this equation directly as previous authors have done[2, 10] using an iterative/interpolation scheme, we may instead find the chemical potential by the following procedure. If we take the temperature derivative of (1) and then set this derivative equal to zero, we obtain the differential equation for the chemical potential,

$$\frac{\mathrm{d}\mu}{\mathrm{d}T} = -\frac{\int_{-\infty}^{\infty} xf'(x)n(\mu+Tx)\,\mathrm{d}x}{\int_{-\infty}^{\infty} f'(x)n(\mu+Tx)\,\mathrm{d}x}. \qquad (3)$$

In this equation, $f'(x) = -df/dx$ and is a symmetric, positive function in x. Moreover, f' is a rapidly decreasing function of $|x|$ and the integrals in (3) may be truncated. Integrating (3) subject to the boundary condition $\mu(0) = 0$, we then obtain

$$\mu(T) = -\int_{0}^{T} \mathrm{d}T' \frac{\int_{-\infty}^{\infty} xf'(x)n(\mu(T')+T'x)\,\mathrm{d}x}{\int_{-\infty}^{\infty} f'(x)n(\mu(T')+T'x)\,\mathrm{d}x} \qquad (4)$$

In Section 3, we find the chemical potential by carrying out the integration specified in equation (4) by numerical means, and have used equation (2) as a correction term to prevent errors in the numerical integration from propagating and accumulating. We have found generally that the correction term is of the order of 1 per cent or less of the change in μ calculated from the first order difference approximation to (4) with $\Delta T = 20$°K. At first glance, this procedure seems just as complex the direct solution of equation (2). However, the integrals appearing in equation (3) are already available for the forward integration of (4), as the same integrals enter into the expressions for the magnetic susceptibility and the electronic specific heat.

The unenhanced susceptibility at zero field, χ, is given by the relationship

$$\chi(T) = 2\beta^2 \frac{\partial}{\partial_{\mu_T}} \int_{-\infty}^{\infty} f(x)n(\epsilon)\,\mathrm{d}\epsilon \qquad (5)$$

where β is the Bohr magneton and the derivative is taken at constant temperature. Carrying out the derivative and changing the variable of integration, (5) becomes

$$\chi(T) = 2\beta^2 \int_{-\infty}^{\infty} f'n(\mu + Tx)\mathrm{d}x \qquad (6)$$

which is just the integral appearing in the denominator in (3) multiplied by $2\beta^2$.

The energy U of the electronic system in the approximation being considered here is given by the equation

$$U = \int_{-\infty}^{\infty} \epsilon n(\epsilon) f(x)\mathrm{d}\epsilon, \qquad (7)$$

and the specific heat at constant volume, $C_v = \gamma(T)T$, is defined as the temperature derivative of (7). Taking this temperature derivative, using equation (3), and changing the variable of integration, the coefficient $\gamma(T)$ can then be expressed as

$$\gamma(T) = \int_{-\infty}^{\infty} x^2 f'n(\mu + Tx)\,\mathrm{d}x - \frac{\{\int_{-\infty}^{\infty} xf'n(\mu + Tx)\,\mathrm{d}x\}^2}{\int_{-\infty}^{\infty} f'n(\mu + Tx)\,\mathrm{d}x}. \qquad (8)$$

Expressions analogous to (8) appear to have first been given by Shimizu[10], but (8) differs in two respects. First we have used an energy normalized to T as the variable of integration. Second, we have chosen the zero-point of energy at T equal to the chemical potential $\mu(T)$. Because of these choices, we see immediately that the temperature dependence of γ depends on the density of states function through the shifting of the origin by $\mu(T)$ and the relative stretching of the energy scale about this origin by $1/T$. While both the shifting and stretching give rise to temperature dependence in γ, the latter appears to give rise to the more pronounced and sharper changes.

While $\gamma(T)$ must be (and is) independent of the choice of origin, the relative magnitudes of the two subtractive terms in (8) are dependent on this choice. In fact, by an appropriate choice of origin, the second term in (8) can be made to vanish, as can be seen from the equivalent, compact positive expression

$$\gamma(T) = \int_{-\infty}^{\infty} \left(x + \frac{\mathrm{d}\mu}{\mathrm{d}T}\right)^2 f'(x) n(\mu + Tx)\,\mathrm{d}x. \qquad (9)$$

Equations (3), (6) and (8) for the quantities $\mathrm{d}\mu/\mathrm{d}T$, $\chi(T)$, and $\gamma(T)$ respectively form the basis for numerical study. Before proceeding, it is worthwhile to point out that the integrals involve the weighting functions f', xf', and x^2f', functions which are plotted in Fig. 1. All these functions decrease exponentially for large x and hence the only part of the density of states function involved in defining the quantities is that part in the neighborhood of $\mu(T)$. Moreover, the functions f', xf', and x^2f' have maximums at $x = 0{\cdot}0$, $1{\cdot}544$, and $2{\cdot}40$ respectively. This means that the three basic integrals appearing in the equations depend on the density of states in different energy regions.

For instance, the integral for the susceptibility depends on f' and hence the susceptibility depends most strongly on the density of states at $\mu(T)$. A look at Fig. 1 gives us a rough guideline that $\chi(T)$ depends on the density of states in the energy range $\mu(T) - 2T < \epsilon < \mu(T) + 2T$.

On the other hand, the specific heat depends on all three integrals. We have found numerically that quite often $|\mathrm{d}\mu/\mathrm{d}T| < 1$, in which case Equation (9) shows that the specific heat depends primarily upon the integral involving x^2f'. Under these circumstances, a look at Fig. 1 gives us the guideline that $\gamma(T)$ depends upon the density of states in the energy ranges $\mu(T) + T < \epsilon < \mu(T) + 4{\cdot}5T$ and $\mu(T) - 4{\cdot}5T < \epsilon < \mu(T) - T$ and not at all on the density of states in the energy region with $\epsilon \approx \mu(T)$. If $\mathrm{d}\mu/\mathrm{d}T = 0$ (a symmetric density of states function), then, strictly speaking, $\gamma(T)$ does not depend upon

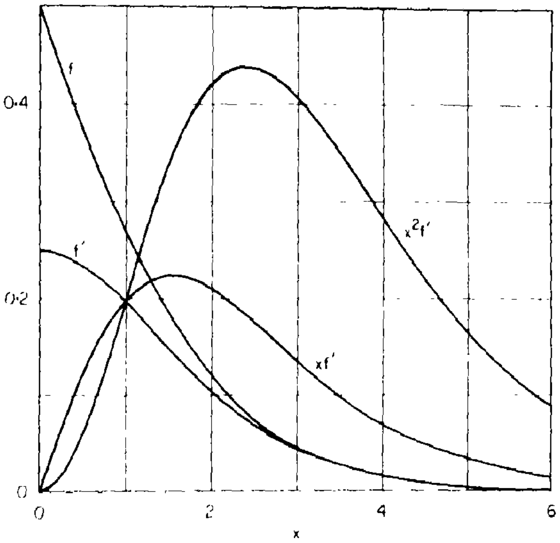

Fig. 1 The weighting functions multiplying the density of states function in the thermodynamic integrals The functions f, f', xf', and x^2f', as defined in the text, are plotted as functions of the normalized energy These plotted functions show the energy range(s) of the density of states function which contributes primarily to the integrals defining the susceptibility, the chemical potential temperature derivative, and the specific heat coefficient.

the density of states at the chemical potential except for the limiting temperature $T = 0$.

Similar considerations apply to $d\mu/dT$, and the obvious symmetry of the weighting functions can naturally be taken into account.

3. PALLADIUM

The normalized specific heat coefficient of palladium is shown as the circles in Fig. 2 as calculated from the recent results of Miiller and Brockhouse[1]. Two main features are observed in the temperature dependence of $\gamma(T)$. First, we observe the sharp decline to 0·3 at 1000°K, almost reaching this value, in fact, by 600°K. Second, we observe a local minimum at 75°–100°K and a local maximum at 150°K superimposed upon this sharp decline.

We interpret this structure in $\gamma(T)$ as follows. The sharp decline occurs due to a sharp (compared to 600°K) decrease in the density of states at an energy 700°–800°K from the chemical potential at absolute zero. Moreover, the mean of the density of states at ±1500°K and farther from $\epsilon = 0$°K is 0·3 to 0·4, the exact value depending on the magnitude of the chemical potential temperature derivative at $T = 1000$°K. The minimum results from a sharp dip in the density of states, the width and energy of the dip being determined by the requirement that the hump in x^2f' shown in Fig. 1 fits inside this dip at 75°K. Hence, the dip begins at $\epsilon = 150$°K and ends at $\epsilon = 375$°K. In order for the local maximum to occur, the density of states function must obtain approximately its value at $\epsilon = 0$°K for $|\epsilon| > 375$°K before the sharp decrease at $|\epsilon| \approx 750$°K. The chemical potential is, of course, temperature-dependent (unless the density of states function is symmetric about 0°K), but this temperature dependence changes only the detailed numbers (magnitudes and energies of changes in the density of states function) and not the general required features.

With these general features in mind, we

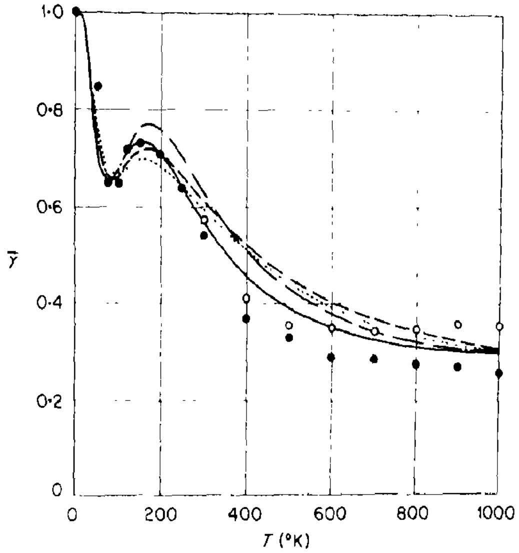

Fig. 2. The normalized specific heat coefficient of palladium as a function of temperature. The circles are the specific heat coefficients as calculated from the corresponding circles in Fig. 3 of [1] The open and closed circles are obtained by two different approximations for the anharmonic corrections as described in this reference. The curves are the theoretically calculated specific heat coefficients, the lining in this figure corresponding to that in Fig. 3.

have calculated the specific heat coefficient for various piecewise linear density of states functions, and the results of these calculations are shown in Fig. 2. The corresponding density of states functions are shown in Fig. 3. The corners and the infinite slopes can all be smoothed without affecting appreciably the calculated results.

We observe that the local minimum and maximum are obtained with a dip in the density of states function either above, below, or on both sides of the chemical potential at absolute zero. There appears no way here to determine among these alternatives, and the band structure calculations give no indication of such a dip (or dips)[15]. Neither do the density of states functions constructed from the low temperature alloy γ-values and the rigid band theory of alloying[2, 11]. It appears that fine structure, such as the dip envisioned here for explaining the anomaly in the specific heat γ, is washed out of the density of states function in proceeding from the element to the alloys[16].

The calculated sharp decrease in $\gamma(T)$ with T is in rough agreement with the experimental results although the curvature is not as large in the 300°–600°K temperature range. To obtain this curvature, it appears necessary to modify the density of states function in the following manner. The density of states should equal $\cong 0{\cdot}1$ at $\epsilon \cong -750$°K (just after the large drop in the density of states) and then increasing to its asymptotic value (0·28, 0·50 and 0·6, depending on which curve in Fig. 3 we are modifying) at -2500° to -3000°K. By this modification, γ in the 200°–400°K temperature range will be decreasing towards its asymptotic value of 0·1. At 400°K, however, $\bar{\gamma}$ begins to sample the increasing density of states at $\epsilon \cong -2000$, and, at $T = 1000$°K, $\bar{\gamma}$ is relatively insensitive to the density of

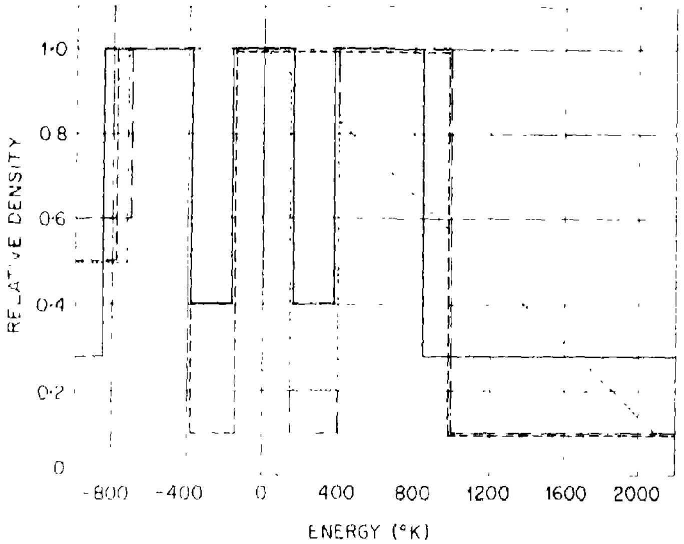

Fig. 3. The piecewise-linear density of states functions used in the calculation of the specific heat coefficients shown in Fig. 9. The lining in the density of states function shown here and in the specific heat coefficients shown in Fig. 2 correspond. Some of the lines in this figure have been shifted slightly for clarity. The number of states per spin atom between 0°K and the obvious top of the band are as follows: —— 0·12, ----- 0·17, — — — 0·13, and —·— 0·17. These values are obtained by scaling the relative density of states to 1·97 states/eV-atom at 0°K, which yields the experimental $\gamma(0°K) = 9{\cdot}3$ mJ/°K²-mole[18].

states in the energy range $|\epsilon| < 1500$°K. Hence, we would obtain the correct value for $\bar{\gamma}$ at $T = 1000$°K and steepen the slope at $T = 300$°K, which effectively increases the curvature in the appropriate region. There can be structure in the density of states curve for $|\epsilon| > 1000$°K which would not be reflected in $\gamma(T)$. For instance, at $T = 500$°K, $\gamma(T)$ depends effectively on a thermal smear of the density of states function over the range $750° < |\epsilon| < 2500$°K, and any fine structure with widths of the order of 200°K would not appear in $\gamma(T)$ at this temperature.

The rigid band theory of alloying and the low temperature γ values of alloys predict $\gamma(T)$ for palladium[2, 11] which decreases with increasing temperature and which agrees asymptotically with the experimental value at $T = 2000$°K. However, the calculated value is almost a factor of 2 too large at $T = 500$°K. The alloy data give a long-range energy tail to the peak in the density of states function and this tail appears responsible for the difference between the calculated and experimental γ at intermediate temperatures. We conclude that this tail is not present in the density of states for the element palladium.

While we have been able to adequately represent the specific heat results, such is not the case for the paramagnetic, unenhanced susceptibility. The normalized susceptibility, calculated from the density of states functions in Fig. 3, decreases to 0·8 at 100°K, remains relatively constant in the temperature range 200°–300°K, and then decreases smoothly to $\cong 0{\cdot}52$ at 1000°K. Using an orbital contribution $\chi_{\text{orb}} = 70 \times 10^{-6}$ e.m.u./mole [17], a temperature-dependent enhancement $E(T) = [1 - I\chi(T)]^{-1}$ with $E(0) = 5{\cdot}5$, and the scaling in the density of states necessary to obtain $\gamma(0)$, we obtain a calculated susceptibility agreeing with the experimental values [11] at $T = 0$ and 1000°K but differing by a factor of 1/2 in the range 200°–500°K. Shimizu *et al.* [11] have had the opposite experience of being able to fit the susceptibility (except for the small maximum at 80°K) but not the specific heat coefficient. It thus appears impossible to fit both the susceptibility and the specific heat coefficient of palladium with one density of states function within the assumptions made here.

REFERENCES

1. MILLER A. P. and BROCKHOUSE B. N., *Phys. Rev Lett* **20**, 798 (1968).
2. HINDLEY N. K. and RHODES P., *Proc. phys. Soc* **81**, 717 (1963).
3. WILSON A. H., In *The Theory of Metals*, 2nd Edn Chap. 6. University Press, Cambridge (1958).
4. WOHLFARTH E. P. and CORNWELL J. F., *Phys. Rev Lett.* **7**, 342 (1961).
5. STONER E. C., *Phil Mag.* **25**, 899 (1938)
6. STONER E. C., *Proc. Leeds Phil. Lit. Soc.* **3**, 403 (1938).
7. WOHLFARTH E. P., *Phil. Mag.* **42**, 374 (1951).
8. WOHLFARTH E. P., *Proc. phys. Soc* **60**, 360 (1948).
9. ELCOCK E. W., RHODES P. and TEVIOTDALE A., *Proc. R. Soc.* **A221**, 53 (1954).
10. SHIMIZU M., TAKAHASHI T and KATSUKI A., *J phys. Soc Japan* **17**, 1740 (1962).
11. SHIMIZU M., TAKAHASHI T. and KATSUKI A., *J. phys. Soc. Japan* **18**, 240 (1963).
12. deLAUNAY J. In *Solid State Physics* (Edited by Seitz and Turnbull), Vol 2, p. 219. Academic Press, New York (1956).
13. GEORGE P. K. and THOMPSON E. D., *J. Phys. Chem. Solids* **28**, 2539 (1967).
14. HODGES L., EHRENREICH H. and LANG N. D., *Phys. Rev.* **152**, 505 (1966).
15. FREEMAN A. J., FURDYNA A. M. and DIMMOCK J. O., *J. appl. Phys.* **37**, 1256 (1966)
16. EDWARDS S. F., *Proc. phys. Soc.* **85**, 1 (1965).
17. PLACE C. M. and RHODES P., *J. appl. Phys.* **39**, 1282 (1968).
18. HOARE F. E. and YATES B., *Proc. R Soc.* **A240**, 42 (1957)

J. Phys. Chem. Solids Pergamon Press 1969. Vol. 30, pp. 1189–1195. Printed in Great Britain.

Te^{125} MÖSSBAUER EFFECT STUDY OF NEUTRON CAPTURE EFFECTS IN PbTe, Te AND TeO_2*

J. F. ULLRICH† **and D. H. VINCENT**

Department of Nuclear Engineering, University of Michigan, Ann Arbor, Mich. 48104, U.S.A.

(*Received* 28 *August* 1968; *in revised form* 4 *November* 1968)

Abstract – The Mössbauer emission spectra of Te^{125} in PbTe, Te metal, and TeO_2 have been measured following neutron capture in Te^{124}. Mössbauer data for each sample were taken after the source irradiation and following thermal annealing. The irradiation conditions were chosen so that only the thermal neutron capture induced defects should have a significant effect on the environment of the Mössbauer emitting nuclei Comparison of the data taken before and after the source annealing showed no differences in linewidth, isomer shift, quadrupole splitting, or resonance intensity within the standard deviations of the parameters. The results show that the thermal neutron capture process in Te^{124} does not affect the Te^{125} Mössbauer spectra. The possible reasons for this are discussed. The results also indicate that the anomalous isomer shift reported by Stepanov and Aleksandrov in a similar experiment on PbTe is probably caused by a high background of fast neutron induced displacements.

1. INTRODUCTION

CHANGES in the structure of Mössbauer emission spectra due to the presence of neutron capture induced displacements have been studied in processes involving both neutron activation of the first excited state of the Mössbauer nuclide[1–3] and neutron activation of an isomeric state parent[4, 5]. Because of the short lifetime of the first excited state of Mössbauer nuclides (10^{-10}–10^{-5} sec), the neutron activation of this state and the Mössbauer measurement must be done simultaneously. Thus, the first type of experiment must be done in a neutron beam. However, if the Mössbauer nuclide has a long-lived isomeric state, then the neutron activation and the Mössbauer measurement can be done at different times. In the second type of experiment the neutron irradiation can be done in-pile and the Mössbauer measurement can be made at leisure after the irradiation.

The principle advantage of the second type of experiment is that it avoids the usual problems of low neutron intensity and high background radiation associated with neutron beam experiments. There is one limitation, however, in the use of in-pile irradiations for investigating radiation effects; the measurements are restricted to materials with defect annealing temperatures greater than the reactor irradiation temperature (generally 50°C or higher). This severely limits the number of potential experiments. This, of course, is not true if low temperature irradiations are possible; however, low temperature irradiation facilities are not available at most reactors.

Sn^{119} and Te^{125} are two Mössbauer nuclides that offer favorable thermal neutron capture cross sections, isomeric state half-lives, and resonant gamma ray energies for use in the second type of experiment. Previous Mössbauer investigations of the effect of neutron irradiation on the resonant emission spectra of these nuclides have given some evidence of recoil induced changes in the electronic configuration about the emitting nuclei.

Hannaford *et al.*[4] found a small satellite peak in the emission spectrum of Sn^{119} in Mg_2SnO_4 following neutron activation. The

---

*Research supported by the National Science Foundation, Grant No. Gk-871.

†*Present address*: Scientific Laboratory, Ford Motor Company, Dearborn, Michigan

intensity and isomer shift of the satellite peak indicated that approximately 25 per cent of the Sn atoms had suffered a recoil induced valency change. The valency change was clearly shown to be attributable to neutron capture induced displacements.

Stepanov and Aleksandrov[5] recently reported a Mössbauer measurement on Te^{125} in PbTe following neutron activation. The measurement showed an anomalous isomer shift. The PbTe source measured against a PbTe absorber had an isomer shift of 1·7 mm/sec (measured 20 days after the end of the irradiation) when, in fact, there should be no isomer shift if the source and absorber are chemically identical. The anomalous isomer shift indicated that the *s*-electron configuration of the PbTe source had been altered by the irradiation. The anomalous isomer shift was observed to decrease exponentially with time with a mean life of 10 ± 3 days. This indicated that the defect structure was annealed at room temperature.

The measurements reported in this paper were also done on Te^{125} following neutron activation. In addition to a measurement on PbTe, measurements were also made on Te metal and TeO_2. Mossbauer measurements were made on each of the three materials following the source irradiation and then following thermal annealing of the same source. The two spectra were then compared to see if there were any changes in the hyperfine spectra caused by neutron capture induced displacements.

Contrary to the results of Stepanov and Aleksandrov the Mössbauer spectrum for PbTe reported in this paper showed no anomalous isomer shift after the neutron irradiation. In fact, no changes were observed in the hyperfine spectra of any of the three materials.

The difference between these results for PbTe and those of Stepanov and Aleksandrov yields considerable insight into the defect mechanisms involved. The measurements reported in this paper were made with irradiation conditions chosen so that the Mössbauer spectra should only be affected by displacements caused by the thermal neutron capture process. The results indicate that the thermal neutron capture process in Te^{124} does not have an effect on the Mössbauer spectra of the Te^{125}. In conclusion, the anomaly observed by Stepanov and Aleksandrov in PbTe is probably the result of a high concentration of displacements induced by mechanisms other than thermal neutron capture. The most likely mechanism is fast neutron elastic scattering.

2. RADIATION EFFECTS

The Mössbauer isomeric state parent $Te^{125m}(58d)$ is produced by thermal neutron capture in Te^{124} (i.e. $Te^{124} + n_{th} \rightarrow Te^{125m} + \gamma$). The Te^{125m} nucleus can be introduced into the lattice as a defect if the recoil energy from the (n, γ)-reaction is greater than the minimum energy for displacement, E_d, which is typically of the order of 25 eV. The recoil energy arises from the emission of the 6·4 MeV of excitation energy of Te^{125} by 'prompt' gamma rays. By conservation of momentum the emitted gamma rays impart kinetic energy to the emitting nucleus.

A calculation of the mean recoil energy requires knowledge of the gamma rays emitted in the de-excitation process, including their energies, emission probabilities, and time and angular correlation. Unfortunatley the capture gamma ray energy spectrum has not been measured for neutron capture in Te^{124}; therefore the mean recoil energy cannot be accurately estimated.

In general the mean recoil energy for capture gamma ray emission is low (of the order of E_d). This means that the number of displaced atoms produced per thermal neutron captured is small; subsequently, the number of possible defect configuration is small. This is a particularly nice feature for Mössbauer measurements since the resultant Mössbauer spectrum is a weighted sum of the spectra characteristic of each defect configuration.

The isolation of displacements which are induced specifically by thermal neutrons is often very difficult when doing in-pile irradiations. This is due to the 'background' effects caused by displacements due to other recoil processes. All of the types of radiation present in a reactor (i.e. fast neutrons, gamma rays, etc.) can produce displacements through either scattering processes or nuclear reactions. For most elements the ratio of defects produced by thermal neutron capture to those produced by fast neutron scattering is less than one[6]. Thus, fast neutrons are usually responsible for most of the radiation effects observed with in-pile irradiations.

Under some conditions the Mössbauer effect measurement provides a means of separating displacements due to thermal neutron capture from those arising from fast neutrons and other sources. This is possible because the characteristic hyperfine interactions are, for the most part, only influenced by the 'local' electronic environment (atomic electrons and first few near neighbour atoms).

The fraction of the resonant emissions which have hyperfine structure characteristic of a defect environment is related to the probability that a defect is within the 'local' environment of an emitting nucleus. For defects produced by thermal neutron capture this probability should be nearly equal to 1 since the emitting nucleus itself is in a defect position. On the other hand, defects produced by other types of radiation are randomly located with respect to the emitting nuclei. Hence the probability that these defects are within the 'local' environment of an emitting nucleus is of the order of the ratio of the defect density to the appropriate atomic density.*

In order to minimize the effect of displacements caused by other types of radiation, the density of defects must be kept much less than the number density of atoms. Since the defect density is a linear function of the total radiation dose (in the absence of self annealing), it is possible to minimize the effect of undesirable displacements by proper choice of irradiation fluxes and times.

The measurements reported in this paper were carried out under conditions where the thermal neutron capture effects played a dominant role. Fast neutron scattering was the principal source of additional displacements; however, the estimated density of these displacements was $\sim 10^{-4}$–10^{-3} of the tellurium atom density. Thus, the fraction of Mössbauer emitting nuclei which are in close proximity to a fast neutron displaced atom is very small. The fast neutron induced displacements then should have little effect on the Mössbauer spectra.

3. EXPERIMENTAL PROCEDURE

(*A*) *Sources and absorbers*

The PbTe, Te metal and TeO_2 used in the measurements as sources were prepared from Te enriched to 94 per cent in Te^{124}. The PbTe† and Te metal powders were pressed into thin discs and then sintered in a hydrogen atmosphere at 550°C for 3 hr and 350°C for 6 hr, respectively. The TeO_2 was prepared from nitric acid solution following the procedure of Marshall[7]. This procedure results in TeO_2 with the tetragonal crystal structure. The structures of the materials were all verified by X-ray diffraction measurement.

The materials to be used as sources were irradiated in the Ford Nuclear Reactor. Samples were generally irradiated in fluxes of 10^{12}–10^{13} neutrons/cm^2-sec for periods of 10–15 days. The total thermal neutron doses for the PbTe, Te and TeO_2 samples reported on in this paper were 8×10^{17}, 9×10^{17} and 8×10^{18} neutron/cm^2, respectively. The fast neutron doses were a factor of 12 lower.

---

*The atomic density used here must take into account the range of the hyperfine interactions (referred to as the 'local' environment). This density will be smaller than the number density of atoms for long range interactions and will approach the number density for short range interactions (hyperfine interactions affected only by the atomic electrons).

†Prepared by New England Nuclear Corp., Boston, Mass.

The sample temperatures during the irradiation were measured to be ~45°C.

After the Mössbauer measurement was made following the source irradiation, the sources were all annealed to restore any displaced atoms to normal lattice sites. The PbTe and Te sources were annealed in a hydrogen atmosphere at 400°C for 11 hr and 350°C for 12 hr, respectively. The TeO_2 was dissolved in HNO_3 and recrystallized following the procedure in the initial preparation.

The Mössbauer measurements for PbTe and Te were made using a single line absorber of PbTe (17·5 mg/cm^2) enriched to 95 per cent in Te^{125}. The measurements for TeO_2 were made using a single line absorber of $Te(OH)_6$ (39 mg/cm^2) with a natural abundance of Te^{125} (7 per cent).

(*B*) *Apparatus*

The Mössbauer measurements were made using the 35·6 keV gamma ray resonance in Te^{125}. Details of the decay scheme and the relevant Mössbauer parameters have previously been reported[8].

The 35·6 keV gamma rays were detected using a xenon–nitrogen filled proportional counter. With this detector the 35·6 keV gamma ray is only partially resolved from the intense background due to the Te K_α and K_β X-rays at 27·4 and 31·2 keV. The gamma ray can best be discriminated by using the escape peak at 7·0 keV. All measurements were made with the single channel analyzer set at the escape peak energy.

The signal-to-noise ratio of the escape peak was further improved by using a 5 mil copper (113 mg/cm^2) absorber to reduce the X-ray intensity. This increased the signal-to-noise ratio by a factor of 3·5 with only a factor of 0·33 reduction in the count rate. The 8·0 keV copper X-rays which are generated in this absorber are almost completely absorbed in the 20 mil aluminum window on the proportional counter.

The resonant absorption spectra were taken using a time mode Mössbauer spectrometer. The multichannel analyzer was calibrated using the magnetic hyperfine spectrum of Fe^{57} in iron metal. Calibration runs were made before and after each Te run to check the constancy of the equipment.

The source and absorber were both cooled to liquid nitrogen temperature in a styrofoam insulated dewar similar to the one described by DeWaard *et al.*[9]. The source and absorber temperatures were not externally controlled and were generally ~ 82°K.

4. RESULTS

The results of the measurements on PbTe, Te and TeO_2 are shown in Fig. 1. The data points shown are those taken in the Mössbauer measurements immediately following the

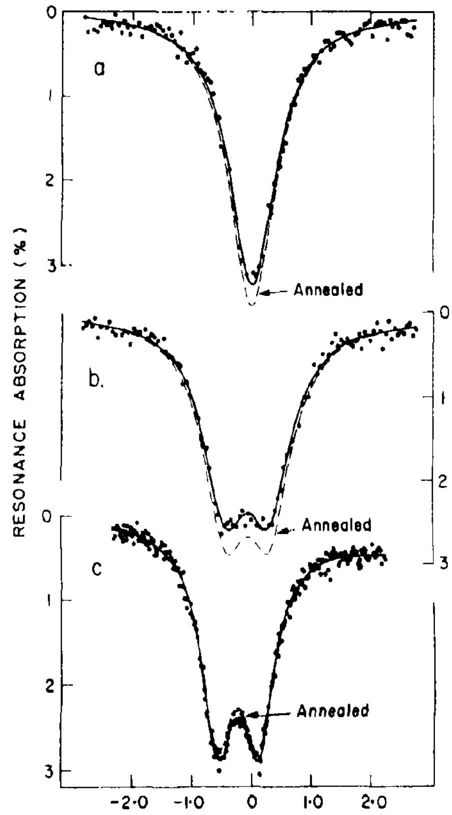

Fig. 1. Resonance absorption spectra taken before and after source annealing for: (a) PbTe; (b) Te metal; (c) TeO_2.

irradiations. The solid line is the least squares fit to the data with an assumed spectral shape. A single line of Lorentzian shape was fit to the PbTe spectrum and two lines of Lorentzian shape (quadrupole split) were fit to the Te and TeO_2 spectra.

The spectra characteristic of the normal lattices were obtained after treating the sources to restore any displaced atoms to normal lattice sites. The results of the curve fitting to the Mössbauer spectra taken after annealing are shown in Fig. 1. by the dashed lines.

The parameters obtained from the least squares fit to the spectra taken before and after annealing are listed in Table 1. The standard deviations of the parameters listed in the table are calculated from the error matrix generated in the final iteration of the least squares fitting routine. It is apparent from this tabulation that the linewidth, the isomer shift and the quadrupole splitting for the three materials are identical in the two runs within the standard deviations of the parameters.

Table 1. Parameters obtained from the least squares fit to the data of Fig. 1

Source		Linewidth (mm/sec)	Isomer shift* (mm/sec)	Quadrupole splitting (mm/sec)	Resonance intensity†
PbTe	– Pre-anneal	9·60 ± 0·23	0·07 ± 0·05	0	0·0324 ± 0·0003
	Post-anneal	9·58 ± 0·22	0·03 ± 0·04	0	0·0351 ± 0·0003
Te	– Pre-anneal	9·07 ± 0·24	– 0·44 ± 0·08	7·51 ± 0·14	0·0197 ± 0·0004
	Post-anneal	8·83 ± 0·26	– 0·41 ± 0·09	7·35 ± 0·15	0·0221 ± 0·0005
TeO_2	– Pre-anneal	6·42 ± 0·12	– 1·98 ± 0·04	6·72 ± 0·11	0·0226 ± 0·0002
	Post-anneal	6·49 ± 0·12	– 1·99 ± 0·04	6·89 ± 0·11	0·0219 ± 0·0002

*Shift relative to PbTe for the PbTe and Te source and $Te(OH)_6$ for the TeO_2 source.

†Maximum resonance intensity uncorrected for background.

The only parameter which shows a significant variation between runs is the resonance intensity. In all cases the variation in resonance intensity (3–11 per cent) is greater than the standard deviation in the intensity parameter (1–2 per cent). However, this standard deviation reflects only the statistical uncertainty in the fitting and does not include a contribution due to variations in experimental conditions. Several experimental factors can have a significant effect on the measured resonance intensity. These include the detector signal-to-noise ratio, the source and absorber temperature, and the experimental geometry. An accurate comparison of resonance intensities for two different runs requires that these factors not only remain stable during the course of each run but be exactly reproducible for each run. In both respects the conditions for our experiments were not the most desirable. Runs were generally of the order of 4–5 days in duration; this, of course, put a limitation on the temperature and electronic stability. In addition, the samples had to be removed between runs for annealing; this made exact reproducibility of all conditions difficult. A careful analysis of the stability and reproducibility of all the previously mentioned factors for our measurements indicates that the experimental uncertainty in the resonance intensity amounts to about 10 per cent.

As a result, the observed variations in the resonance intensity are only of the order of the uncertainty in the measured intensity. To see if the variations in resonance intensity for each material were reproducible, the sets of measurements were repeated using new sources. This second set of measurements for each material (only the measurements with the best statistics are reported in this paper) did not show the same variation in resonance intensity as the first set. In all cases the magnitude of the change was different and in one case even the direction of the change was different. Again, as in the first set of measurements, the resonance intensity changes ranged up to about 10 per cent.

From this evidence we conclude that if there are any f value changes in any of the materials due to the source irradiation, the change is certainly less than 10 per cent of the normal f value. To determine whether or not there indeed is a real f value change would require that the experimental conditions be much better controlled than in our measurements.

The quadrupole splittings for Te and TeO_2 obtained in our measurements are in agreement with previously reported values. All previous results, except for a recent measurement by Pasternak and Bukshpan[10], are summarized in a paper by Violet and Booth [11]. For comparison with previous results, the values obtained for the quadrupole splitting in our measurements are $0{\cdot}75 \pm 0{\cdot}01$ cm/sec and $0{\cdot}69 \pm 0{\cdot}01$ cm/sec* for Te metal and TeO_2, respectively.

To compare isomer shifts with the values tabulated by Violet and Booth, our values have all been referred to a Te source. With respect to a Te source, the isomer shifts are $-0{\cdot}04 \pm 0{\cdot}01$ cm/sec and $+0{\cdot}02 \pm 0{\cdot}01$ cm/sec for PbTe and TeO_2†, respectively. The isomer shift for TeO_2 agrees with the value obtained by Violet and Booth; however the isomer shift for PbTe is less than the value reported by Stepanov *et al.*[12].

5. DISCUSSION

Our measurements show no clearly resolved changes in the Mössbauer hyperfine spectra of Te^{125} which could be attributed to neutron capture induced recoils. There are several possible explanations for the lack of any observable effects; however, it is difficult to establish any conclusive explanation due to the lack of supplemental information.

First, the changes in the hyperfine structure may be too small to be resolved. The broad lines of the Te^{125} resonance, of course, make observation of small changes in the hyperfine spectra very difficult. It is also very difficult to theoretically predict the isomer shift and electric quadrupole splitting that might occur for various possible defect configurations.

Second, there may be insufficient recoil energy on the average to displace the atoms from their normal lattice sites.

Third, defect annealing may occur at the reactor irradiation temperature of 45°C. Previous measurements indicate that such annealing probably does occur in Te metal, but definitely not in PbTe. A study of electron bombardment effects on Te metal showed that the defects anneal fairly rapidly even at room temperature[13]. Rather extensive measurements of the Hall coefficient, the Seebeck coefficient, the electrical resistivity and the thermal conductivity of PbTe both during and following thermal and fast neutron irradiation show little annealing below temperatures ~ 150°C[14, 15]. There are no previous measurements of radiation effects in TeO_2.

It is quite clear from our results that the thermal neutron capture process in Te^{124} does not lead to any significant changes in the Mössbauer hyperfine spectra. The PbTe data, in particular, give evidence that the isomer shift anomaly observed by Stepanov and Aleksandrov is probably caused by displacements induced by other types of reactor radiation. All the measurements reported in this paper were made within approximately three weeks after the end of the irradiation. Using Stepanov and Aleksandrov's annealing curve, an isomer shift of at least 1·5 mm/sec should have been observed if the anomaly was caused by neutron capture induced recoils.

---

*The values quoted here are the average values obtained from several runs

†The TeO_2 isomer shift was obtained by combining the results reported in this paper with an additional measurement with a PbTe source and Te(OH)6 absorber which showed an isomer shift of $-0{\cdot}13 \pm 0{\cdot}01$ cm/sec

The most likely cause of the isomer shift anomaly observed by Stepanov and Aleksandrov is fast neutron induced displacements. No information is given on the fast neutron flux used in their irradiation; however, if it is assumed that the fast flux is $\frac{1}{10}$ the magnitude of the thermal flux quoted in their paper and that there is no saturation of defects, the Te defect density could be as large as $\frac{1}{5}$ the Te atomic density. Thus the Stepanov and Aleksandrov measurement seems to have been carried out under irradiation conditions where 'background' displacements have a high enough density to significantly affect the Mössbauer spectrum.

REFERENCES

1. HAFEMEISTER D. W. and SHERA E. B., *Phys. Rev Lett* **14**, 593 (1965).
2. FINK J. and KIENLE P., *Phys. Lett.* **17**, 326 (1965).
3. BERGER W. G., FINK J. and OBENSHAIN F. E., *Phys. Lett.* **25A**, 466 (1967).
4. HANNAFORD F., HOWARD C. J. and WIGNALL J. W. G., *Phys. Lett.* **19**, 257 (1965).
5. STEPANOV E. P. and ALEKSANDROV A. YU., *JETP Lett.* **5**, 83 (1967).
6. WALKER R. M., *J. nucl. Mater.* **2**, 147 (1960).
7. MARSHALL H., In *Inorganic Syntheses* (Edited by L. F. Audrieth), Vol. 3. McGraw-Hill, New York (1950).
8. See *Mössbauer Effect Data Index* (Compiled by A. H. Muir Jr., K. J. Ando and H. M. Coogan). Interscience, New York (1966)
9. DeWAARD H., DEPASQUALI G. and HAFEMEISTER D., *Phys. Lett* **5**, 217 (1963).
10. PASTERNAK M. and BUKSHPAN S., *Phys. Rev.* **163**, 297 (1967).
11. VIOLET C. E. and BOOTH R., *Phys. Rev.* **144**, 225 (1966).
12. STEPANOV E. P., ALESHIN K. P., MANAPOV R. A., SAMOILOV B. N., SKLYAREVSKY V. V. and STANKEVICH V. G., *Phys. Lett.* **6**, 155 (1963).
13. VAN LINT V. A. J., WIKNER E. G. and MILLER P. H., Jr., Rep. No. GA-1513 (1960).
14. DANKO J. C., KILP G. R. and MITCHELL P. V., *Adv. Energy Conversion* **2**, 79 (1962).
15. FROST R. T., CORELLI J. C. and BALICKI M., *Adv. Energy Conversion* **2**, 77 (1962).

J. Phys. Chem. Solids Pergamon Press 1969. Vol. 30, pp. 1197–1205. Printed in Great Britain.

THE HIGH TEMPERATURE ELASTIC MODULI OF ALUMINUM*

D. GERLICH† and E. S. FISHER
Argonne National Laboratory, Argonne, Ill. 60439, U.S.A.

(*Received* 4 *November* 1968)

Abstract—Measurements of the elastic moduli of aluminum over the temperature range 300°–930°K are reported. These data together with those reported for $T < 300$°K, show that all elastic moduli, including the shear moduli, vary smoothly with the temperature, up to the melting point, in contrast to other measurements at lower ultrasonic frequencies. From the data, a high temperature Grüneisen constant of 2·17 is calculated. The temperature dependence of the shear moduli at room temperature is calculated from Leigh's model, and the results of this calculation are compared with the experimentally determined data, and with the pressure dependence of the elastic moduli.

INTRODUCTION

MANY of the thermoelastic properties of aluminum have been measured over the past several years, and a number of measurements of the elastic moduli have been reported[1–3]. Of the latter measurements, Sutton's data[1] cover the temperature range up to 500°C. These measurements were done by the composite oscillator method, at a relatively low frequency (50 kc/sec), and are partially inconsistent with the measurements of Kamm and Alers[2]. As such measurements are sensitive to sample geometry and, also, might be affected by dislocation motion, there is an interest in measuring the high temperature elastic moduli of aluminum by an ultrasonic technique at much higher frequencies, carrying the measurements up to near the melting point of the material.

In Leigh's theoretical calculation of the shear moduli of aluminum[4], it was shown that the elastically isotropic character is due to the electron overlap over the hexagonal faces in the Brillouin zone. This model has served as a basis for interpreting the pressure dependence of the shear moduli of aluminum [5]. In the present work that part of the temperature dependence of the shear moduli which is not caused by thermal expansion is quantitatively compared with calculations based on Leigh's model and with parameters derived from the pressure dependence of the elastic moduli.

EXPERIMENTAL TECHNIQUES

The aluminum single crystals used in the present work were grown by the Bridgeman method, from stock of at least 99·999 per cent purity. The single crystal boules were oriented by back reflection Laue X-ray diffraction, mounted in lapping rings, and ground down to size. Since pure aluminum has a tendency towards recrystallization at relatively low temperatures, great care was exercised in order to minimize the degree and depth of cold worked metal. The specimens were first machine lapped then hand lapped with 15 μ diamond powder. Following this the surfaces were etched to remove all manifestations of cold work indicated by the Laue technique and finally hand lapped flat and parallel with 3 μ diamond powder. After each experimental run the specimen was etched, examined for presence of new grains and then the surfaces were refinished for the next measurement. The specimens used for the present work were in

---

*Work sponsored by the U.S. Atomic Energy Commission.

†*Permanent address:* Physics Department, Tel Aviv University, Ramat Aviv, Israel.

the shape of a button 2–3 mm thick and 5–6 mm lateral dimensions. Thicknesses were measured to within 0·01 per cent accuracy. Two sets of samples were prepared; one set with faces corresponding to a (110) crystalline plane and the other set with faces corresponding to a (100) crystalline plane.

The elastic moduli were determined by measuring the ultrasonic wave velocities of longitudinal and shear waves in different crystalline directions. The waves were generated by crystalline quartz transducers, X cut for the longitudinal waves, Y cut for shear waves. The wave frequencies varied from 48 to 54 Mc/sec for the longitudinal waves and between 18 and 22 Mc/sec for the shear waves.

The wave velocity was determined by the phase comparison technique[6], using a fused silica buffer rod. The sample was bonded to the top of the buffer rod with a phenolic resin[7] and a furnace placed around the sample and the upper part of the buffer rod. The transducer was attached to the lower end of the buffer rod, thus remaining at room temperature during the whole course of the measurement. Temperatures were monitored with a chromel-alumel thermocouple. The whole assembly was placed in an evacuated bell jar prior to the start of the measurements.

With the available crystalline directions, the sound velocity in five different propagation modes could be determined. The displacement and propagation directions together with the relations of the sound velocity to the three elastic moduli c_{11}, c_{12}, and c_{44}, are described in Table 1. Also defined in the same table are the longitudinal modulus C_L, and two shear moduli C, and C'. From the five experimentally determined velocities, v_1 to v_5, the three elastic moduli c_{11}, c_{12}, and c_{44}, were computed by a least square fit.

In the phase comparison method, the sound velocity v, at temperature T, is given by:

$$v = 2lf_n/(n+\phi/2\pi) \qquad (1)$$

where f_n is the resonant frequency, n the number of wavelengths of the sound in the sample, l the length of the sound path, and ϕ the phase angle between the incident and reflected sound waves. The phase angle was assumed to be insignificant in the present compution. In view of close agreement between our measurements at 300°K and those of Kamm and Alers[2] and Schmunk and Smith[5], the error in neglecting $\phi/2\pi$ is probably less than 0·2 per cent.

A stiffness modulus at a given temperature is obtained from the relation:

$$\rho v^2 = c = c_0(l_0/l)(f_n/f_n^0)^2 \qquad (2)$$

where ρ is the mass density and c_0, l_0, and f_n^0 are values measured at 293°K. Thus by measuring f_n as a function of temperature for a constant n, the elastic moduli as a function of temperature may be evaluated.

Table 1. Different available propagation modes, and the relation of their sound velocity to elastic moduli

Velocity	Propagation direction	Particle motion direction	Relation of velocity to elastic moduli
v_1	[110]	[110]	$\rho v_1^2 = (c_{11}+c_{12}+2c_{44})/2$
v_2	[110]	[001]	$\rho v_2^2 = c_{44}$
v_3	[110]	$[1\bar{1}0]$	$\rho v_3^2 = (c_{11}-c_{12})/2$
v_4	[100]	[100]	$\rho v_4^2 = c_{11}$
v_5	[100]	in (100) plane	$\rho v_5^2 = c_{44}$
$C_L = (c_{11}+c_{12}+2c_{44})/2$		$C = c_{44}$	$C' = (c_{11}-c_{12})/2$

RESULTS

The f_n/f_n^0 ratios as a function of temperature for the five different propagation modes, are shown in Figs. 1–3. The values of the elastic moduli, and the bulk modulus B, were calculated from the smoothed curves drawn through the experimental points in Figs. 1–3, the absolute values of the elastic moduli at 293°K, and the thermal expansion data given by Toulokian[8]. The values of the moduli listed in Table 2 were obtained from a least square fit. A value of 2·697 g/cm^3 was used for the 293°K density. It is interesting to note that all elastic moduli vary smoothly over the whole temperature range up to 3°K below the melting point. No abrupt change in the shear moduli close to the melting point could be detected.

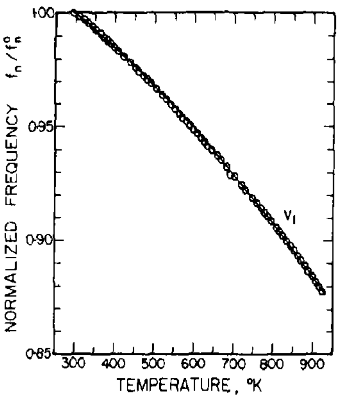

Fig. 1. Resonance frequency as a function of temperature for longitudinal waves in the [110] direction

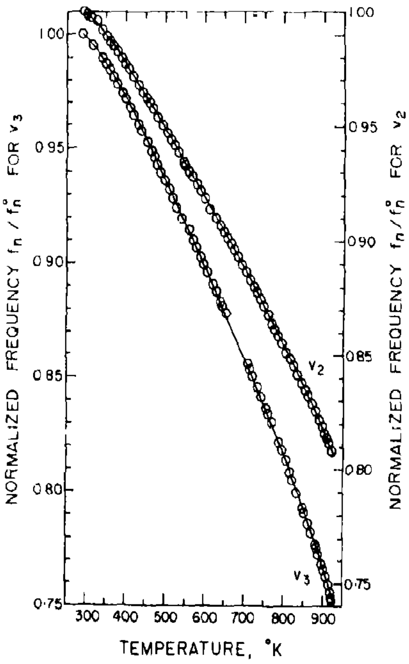

Fig. 2. Resonance frequency as a function of temperatures for the two shear waves in the [110] direction

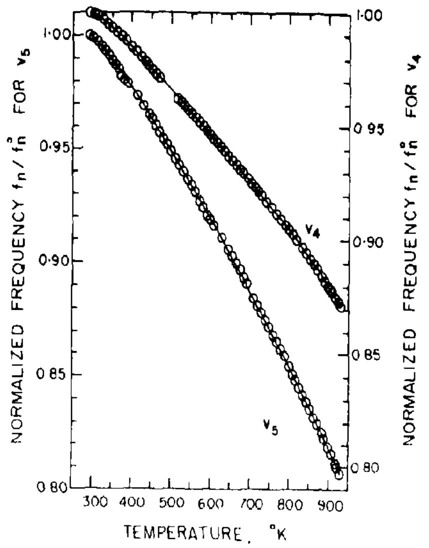

Fig. 3. Resonance frequency as a function of temperature for longitudinal and shear waves in the [100] direction.

In order to check the internal consistency of the data, two separate sets of elastic moduli were computed from the experimental data. One set was determined from the velocities v_1, v_2, and v_3, while the second set was calculated from the velocities v_3, v_4, and v_5. Denoting these two sets of moduli by c'_{ij} and c''_{ij} and denoting the moduli obtained from the least square fit by c_{ij}, the quantities $\Delta c'_{ij}/c_{ij}$ and $\Delta c''_{ij}/c_{ij}$ were calculated as a function of the temperature. Here,

$$\Delta c'_{ij} = c_{ij} - c'_{ij} \tag{3a}$$

$$\Delta c''_{ij} = c_{ij} - c''_{ij}. \tag{3b}$$

Table 2. Numerical values of c_{11}, c_{12}, c_{44}, *and* B, *as a function of temperature (Units are* 10^{11} dyn/cm^2*)*

Temp. (°K)	c_{11}	c_{12}	c_{44}	B
293	10·649	6·039	2·828	7·576
300	10·643	6·035	2·821	7·571
325	10·567	6·012	2·795	7·530
350	10·489	5·992	2·762	7·491
375	10·394	5·971	2·726	7·445
400	10·297	5·950	2·687	7·399
425	10·195	5·930	2·649	7·352
450	10·086	5·905	2·612	7·299
475	9·983	5·883	2·574	7·250
500	9·880	5·862	2·532	7·201
525	9·772	5·839	2·493	7·150
550	9·663	5·808	2·453	7·093
575	9·560	5·782	2·413	7·041
600	9·457	5·758	2·372	6·991
625	9·348	5·724	2·332	6·932
650	9·239	5·700	2·291	6·880
675	9·134	5·676	2·248	6·829
700	9·023	5·642	2·205	6·769
725	8·916	5·615	2·162	6·715
750	8·806	5·586	2·120	6·659
775	8·694	5·560	2·076	6·605
800	8·580	5·527	2·032	6·545
825	8·458	5·494	1·989	6·482
850	8·334	5·460	1·945	6·418
875	8·211	5·427	1·900	6·355
900	8·081	5·392	1·855	6·288
925	7·950	5·359	1·810	6·223

The magnitude of the quantities $\Delta c'_{ij}/c_{ij}$, and $\Delta c''_{ij}/c_{ij}$ indicates the consistency of the data. They are shown as a function of the temperature in Fig. 4. As can be seen, the deviations are of the order of $\frac{1}{2}$ per cent or less.

The results for C_l, C, and C', together with the low temperature data[2, 3] and Sutton's data[1], are plotted in Figs. 5–7. As can be seen, the present results agree very well with the low temperature data and with Sutton's data for C, and C'. They disagree completely, however, with Sutton's C_l results.

Several investigators have reported large variations in the value of Young's modulus for aluminum that are caused by dislocation motion in polygonized polycrystalline material [9, 10]. The high degree of consistency between the velocities measured for the five different modes indicates that dislocation motion effects in the present measurements were not significant.

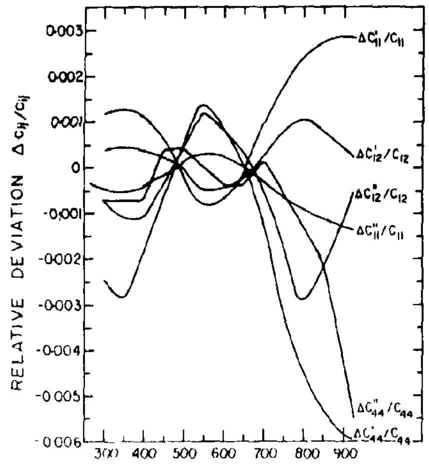

Fig. 4. Consistency of experimental data over the measured temperature range

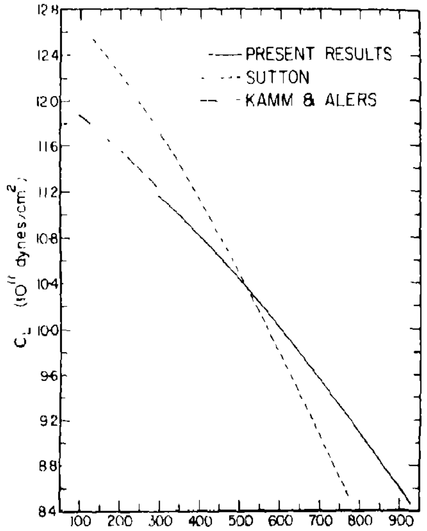

Fig. 5. Comparison of present data with others for C_l.

DISCUSSION

From the values of the high temperature elastic moduli, the Grüneisen constant,

$$\gamma = (3\alpha B^T C_V/V) \qquad (6)$$

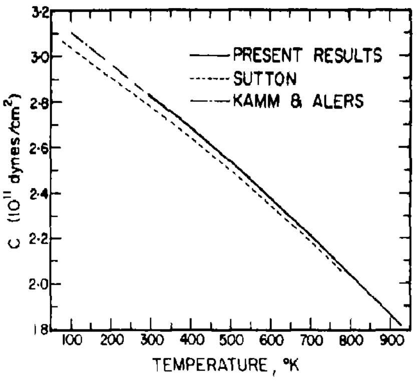

Fig. 6 Comparison of present data with others for C.

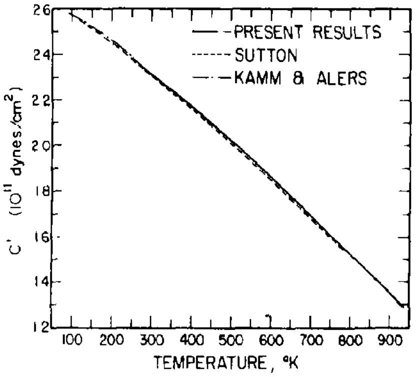

Fig. 7 Comparison of present data with others for C'.

may be calculated. Here α is the linear thermal expansion coefficient, B^T the isothermal bulk modulus, C_V the specific heat at constant volume and V the volume. The high temperature C_V data were taken from [8] and α was computed by fitting a second degree polynomial to the high temperature expansivity data[8]. The value of γ of 2·17 agrees very well with the high temperature limiting value γ_H of 2·27 determined from the third order elastic moduli[11].

The shear moduli C and C' for aluminum have been calculated theoretically by Leigh [4]. He represents C and C' as a sum of the form

$$C = C_E + C_F = C_E + C_{FI} + C_{FII} \quad (7a)$$

$$C' = C'_E + C'_F = C'_E + C'_{FI} + C'_{FII} \quad (7b)$$

where E is the Coulombic contribution, F the Fermi energy contribution, FI the Fermi energy contribution from the filled first Brillouin zone and FII the Fermi energy contribution from the overlap electrons. The form of the individual terms appearing in equations (7a), and (7b) is shown in Table 3. Here a is the lattice parameter, e the electronic charge, Z the numerical density of the valence electrons in the cell, m^* the effective mass of the valence electrons, (1·03 electronic masses [12]), Ω the atomic volume, n_h and n_s the number of electrons per atom in the second Brillouin zone overlapping a pair of hexagonal and square faces respectively, N_h and N_s the corresponding densities of states at the Fermi level and E_h and E_s the average energies over the hexagonal and square faces.

From the values of C, C', the Fermi energy ζ_0 and the density of states $N(\zeta_0)$ at the Fermi energy, the parameters appearing in his model may now be determined, following the same procedure as Leigh's[4]. The value of ζ_0 is obtained either from soft X-ray absorption measurements[13], or from the free electron gas model, both methods yielding 11·8 eV.

Table 3. The form of the individual contribution to the shear moduli C *and* C'

	E	FI	FII
C	$0{\cdot}9479Z^2e^2/(2\Omega a)$	$h^2/(m^*a^5)$	$\frac{1}{\Omega}\left(\frac{8}{3}n_hE_h - \frac{16}{3}N_hE_h^2 + 2n_sE_s\right)$
C'	$0{\cdot}1058Z^2e^2/(2\Omega a)$	$h^2/(3m^*a^5)$	$\frac{1}{\Omega}\left(\frac{8}{3}n_hE_h + 2n_sE_s - 2N_sE_s^2\right)$

$N(\zeta_0)$ is evaluated from the electronic specific heat[14], its value being 0·592 per eV per atom. As Leigh's calculation applies only to 0°K the athermal values of C and C' should be used[15]. These quantities, obtained by extrapolating to 0°K from the high temperature portion of the curves in Figs. 6 and 7 are shown in Table 4. The values of the parameters appearing in Leigh's model, as calculated from the above quantities, are shown in Table 5 together with values of the same parameters as determined from an energy band calculation for aluminum[12]. As can be seen, the agreement between the two sets of data is quite good. From the values of the parameters shown in Table 5 the individual contributions to C and C' are evaluated and are shown in Table 6.

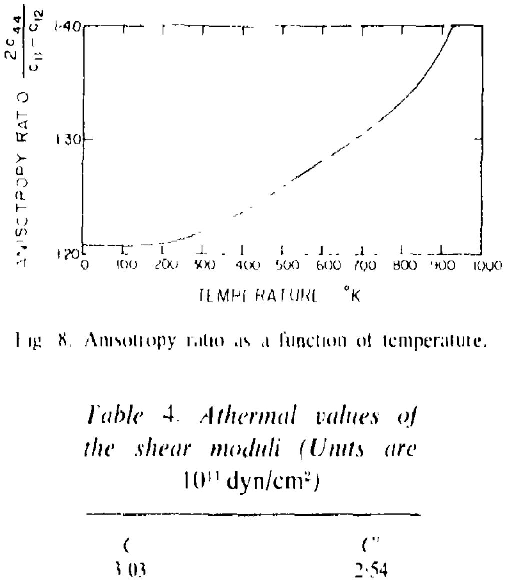

Fig. 8. Anisotropy ratio as a function of temperature.

Table 4. Athermal values of the shear moduli (Units are 10^{11} dyn/cm^2)

C	C'
3·03	2·54

Table 6. Values of the individual contributions to C and C' (Units are 10^{11} dyn/cm^2)

	C	C'
Coulomb (E)	11·473	1·281
Fermi full zone	4·633	1·544
hexagonal overlap	−13·021	5·881
square overlap	0·216	−5·829
Net Fermi (F)	−8·172	1·596
$E+F$	3·301	2·877

As can be seen from Table 6, the Coulombic contribution to C and C' is strongly anisotropic, the near isotropy of aluminum being caused by the Fermi energy contributions[4]. The anisotropy ratio $A = 2c_{44}/(c_{11}-c_{12})$ as a function of temperature is shown in Fig. 8. There is a remarkable change in the temperature dependence of A near 200°K. In terms of Leigh's model this suggests that the Fermi energy contribution decreases relative to the Coulombic contribution with increasing temperature. More specifically, it suggests that the contribution from the overlap on the square faces increases relative to that from the hexagonal faces, thus causing C' to decrease faster than C as the temperature increases above 200°K.

The experimentally measured temperature coefficients of the elastic moduli are a sum of an explicit and implicit temperature dependence[16], where the implicit dependence is caused by the change in volume with temperature:

$$\left(\frac{d \ln c_{ij}}{dT}\right)_P = \left(\frac{\partial \ln c_{ij}}{\partial T}\right)_V - 3\alpha B^T\left(\frac{\partial \ln c_{ij}}{\partial P}\right)_T \tag{8}$$

Table 5. Values of the parameters appearing in Leigh's model as obtained from experimental measurements and band calculations

	Z	E_h (eV)	N_h (eV* atom)$^{-1}$	n_h (atom)$^{-1}$	E_s (eV)	N_s (eV* atom)$^{-1}$	n_s (atom)$^{-1}$
Experimental	7	9·0	0·130	0·243	11·2	0·024	0·010
Band calculation		9·8	0·122	0·228	11·0	0·029	0·024

where P is the pressure, B^T the isothermal bulk modulus. The second term on the right hand is the part due to the volume change. The values of the experimentally observed temperature coefficients and the calculated explicit and implicit contributions at 300° and 900°K for aluminum, as well as the same parameters for copper, silver, and gold[17, 18], at 300°K, are given in Table 7. Here, total denotes

$$\left(\frac{\mathrm{d}\ln c_{ij}}{\mathrm{d}T}\right)_P$$

explicit

$$\left(\frac{\partial\ln c_{ij}}{\partial T}\right)_V,$$

and implicit

$$-3\alpha B^T\left(\frac{\partial\ln c_{ij}}{\partial P}\right)_T.$$

The explicit and implicit temperature coefficients for B, C and C' are plotted in Fig. 9. These values were obtained from the slopes of the B, C and C' vs. temperature curves and the values[5] of $\mathrm{d}B/\mathrm{d}P$, $\mathrm{d}C/\mathrm{d}P$ and $\mathrm{d}C'/\mathrm{d}P$, assuming the latter to be temperature independent. It is interesting to note that while $(\partial\ln C/\partial T)_V$ and $(\partial\ln C'/\partial T)_V$ are negative over the whole range 0°–900°K $(\partial\ln B/\partial T)_V$ remains positive throughout as in copper silver and gold[17, 18], but is of relatively small magnitude and decreases with increasing temperature.

It is also to be noted that the temperature dependence of C of Al due to the volume change is about 3 times as large as the intrinsic change in C at 300°K. For C', however, the volume change contribution is only about 1·2 times the intrinsic change at 300° and 900°K. The relatively large intrinsic contribution to C', as compared to C and B, is consistent with that observed in copper, silver and gold.

Since the volume change contributions to C and C' are about the same (Fig. 9), it seems that the increase in the anisotropy ratio, A, with temperature is caused then by the large intrinsic change in C', rather than the effects of the volume increase. As mentioned above, these intrinsic changes may be associated with a temperature dependence in n_h and n_s. If we assume that of all the parameters appearing in Leigh's model, only E_h, E_s, N_h and N_s depend explicitly on temperature, and that the temperature dependence is the same as for the free electron gas[19], i.e.

$$E = E^\circ - \frac{(\pi kT)^2}{6E^\circ} \tag{9a}$$

$$N \propto E^{1/2} \tag{9b}$$

then from equations (7a) and (7b) the following expressions for the explicit temperature dependence of C and C' are obtained:

$$\frac{\partial C}{\partial T} = -\left(\frac{8n_h}{3E_h} - \frac{40N_h}{9} + \frac{2n_s}{E_s}\right)\frac{\pi^2k^2T}{6\Omega} \tag{10a}$$

$$\frac{\partial C'}{\partial T} = -\left(\frac{8n_h}{3E_h} + \frac{2n_s}{E_s} - 5N_s\right)\frac{\pi^2k^2T}{6\Omega}. \tag{10b}$$

Introducing the values of the parameters from Table 5 into the above equations the numerical values for $(\partial\ln C/\partial T)$ and $(\partial\ln C'/\partial T)$ at 300°K are obtained, as shown in Table 8. Also shown in the same table are the results of a more elaborate calculation, based on similar assumptions, reported by Bernstein [20]. As can be seen, there is a large discrepancy between the theoretically calculated and the experimentally measured explicit temperature dependence of the shear moduli (Table 7). The calculations show a positive temperature dependence for both shear moduli. Furthermore, the relative magnitudes for C and C' are reversed.

The many simplifying assumptions that appear in the above calculations are possibly responsible for the failure of Leigh's model to explain the explicit contributions to the temperature dependence of C and C'. On the

Table 7. The values of $\left(\frac{d \ln c_{ij}}{dT}\right)_P$, $\left(\frac{\partial \ln c_{ij}}{\partial T}\right)_V$, *and* $3\alpha B^T\left(\frac{\partial \ln c_{ij}}{\partial T}\right)_T$ *for* Al, Cu, Ag *and* Au, *at* 300°K

(*Units are* 10^{-4} deg^{-1})

	Al	Cu	Ag	Au
Total, *C*	−5·24 −9·78 (900°K)	−3·68	−4·02	−2·98
Explicit, *C*	−1·28 −2·90 (900°K)	−1·64	−1·15	−0·01
Implicit, *C*	−3·96 −6·88 (900°K)	−2·04	−2·87	−2·97
$\frac{\text{Explicit}}{\text{Implicit}}$, *C*	0·32 0·42 (900°K)	0·80	0·40	0·003
Total, *C′*	−6·24 −12·10 (900°K)	−4·26	−4·02	−2·98
Explicit, *C′*	−2·83 −5·40 (900°K)	−2·64	−2·26	−1·31
Implicit, *C′*	−3·41 −6·70 (900°K)	−1·62	−2·39	−2·08
$\frac{\text{Explicit}}{\text{Implicit}}$, *C′*	0·83 0·81 (900°K)	1·63	0·95	0·63
Total, *B*	−2·51 −4·08 (900°K)	−1·60	−1·85	−1·66
Explicit, *B*	0·79 0·49 (900°K)	1·06	1·54	0·94
Implicit, *B*	−3·30 −4·57 (900°K)	−2·66	3·42	−2·60
$\frac{\text{Explicit}}{\text{Implicit}}$, *B*	−0·24 −0·11 (900°K)	−0·40	−0·45	−0·36

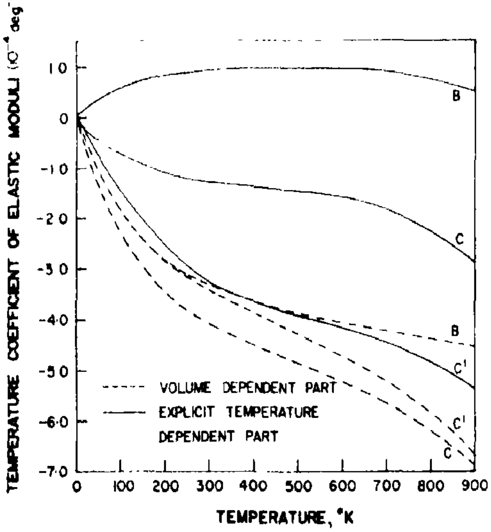

Fig. 9. The explicit and implicit temperature coefficient for *B*, *C* and *C′*, as a function of temperature

other hand, it is more probable that in the temperature range with which we are concerned, the explicit temperature dependence is primarily a function of the thermal vibrational energy changes. An examination of Table 7 reveals that *C′* having a much greater explicit temperature dependence than *C* is

Table 8. The theoretically calculated explicit temperature dependence of the shear moduli of aluminum at 300°K (*Units are* 10^{-4} deg^{-1})

	$\frac{\partial \ln C}{\partial T}$	$\frac{\partial \ln C'}{\partial T}$
Present results	0·006	0·001
Bernstein's results	0·037	0·017

clearly common to aluminum, copper, silver and gold, and may then be characteristic of f.c.c. metals in general. This suggests that the explicit contributions in aluminum are indeed more dependent on the vibrational characteristics of the f.c.c. structure than on the electronic contributions to the elastic moduli.

Schmunk and Smith[5] have shown that the implicit temperature dependence which arises from the volume thermal expansion can be accounted for by Leigh's model if electron transfer between hexagonal and square face overlaps are introduced. Thomas [11], however, has found the model inadequate in accounting for his measurements of the third order elastic moduli of aluminum.

CONCLUSIONS

Although the major part of the temperature dependence of the elastic moduli of aluminum can be attributed to the change volume with temperature, there is a large volume independent contribution to C' that causes notable increase in elastic anisotropy for temperatures above 200°K. This contribution cannot be attributed to the temperature dependence of the Fermi energy contribution to the shear moduli via Leigh's model, by assuming a T^2 dependence for the Fermi energy. A correlation with existing data for copper, silver and gold, indicates that a relatively high explicit temperature dependence for C' is common to f.c.c. metals and is a result of the increase of the vibrational energy with temperature.

Acknowledgements—The authors wish to express their indebtedness to S. Rothman and L. Nowicki for providing the aluminum single crystals, and to D. Dever for technical help. One of us (D. G.) wishes to thank the Metallurgy Division, Argonne National Laboratory, for the award of a summer appointment, during the tenure of which the present work was carried out.

REFERENCES

1. SUTTON P M., *Phys. Rev.* **91**, 816 (1953).
2. KAMM G. N. and ALERS G. A., *J. appl. Phys.* **35**, 327 (1964).
3. VALLIN J., MONGY M., SALAMA K and BECKMAN O., *J. appl. Phys.* **35**, 1825 (1964).
4. LEIGH R. S., *Phil. Mag.* **42**, 139 (1951).
5. SCHMUNK R. E., and SMITH C. S., *J. Phys. Chem. Solids* **9**, 100 (1959).
6. McSKIMIN H. J., *IRE Trans. Ultras. Engrg* UE–5, 25 (1957).
7. FISHER E. S. and RENKEN C. J, *J. acoust. Soc Am.* **35**, 1005 (1963).
8. *Thermophysical Properties of High Temperature Solid Materials* (Edited by Y. S. Touloukian). Vol. 1. McMillan, New York (1967).
9. FRIEDEL J., BOULANGER C. and CRUSSARD C., *Acta Metall.* **3**, 380 (1955).
10. BENIEVA T YA, LARIKOV L. N. and POLOTSKIN I. G., In *Internal Friction in Metals and Alloys*, p. 42. Consultants Bureau, New York (1967).
11. THOMAS J., *Phys. Rev.* **175**, 955 (1968).
12. SEGALL B., *Phys. Rev.* **124**, 1797 (1961).
13. SKINNER H. W. B, *Phil. Trans. R Soc.* **A239**, 95 (1940).
14. PHILLIPS N. E., *Phys. Rev.* **114**, 676 (1959).
15. HUNTINGTON H. B., *Solid State Physics* (Edited by F. Seitz and D. Turnbull), p. 213. Academic Press, New York (1958).
16. LAZARUS D., *Phys. Rev.* **76**, 545 (1949)
17. OVERTON W. C. and GAFFNEY J, *Phys. Rev.* **98**, 969 (1955).
18 NEIGHBOURS J. R. and ALERS G. A., *Phys. Rev* **111**, 707 (1958).
19. MOTT N. F. and JONES H., *The Theory of the Properties of Metals and Alloys*. Claredon Press, Oxford (1936).
20. BERNSTEIN B. T., *Phys. Rev.* **132**, 50 (1963).

J. Phys. Chem. Solids Pergamon Press 1969. Vol. 30, pp. 1207-1213. Printed in Great Britain.

MÖSSBAUER SPECTRA OF RARE EARTH SILICIDES AND GERMANIDES

I. SHIDLOVSKY and I. MAYER
Department of Inorganic and Analytical Chemistry, The Hebrew University, Jerusalem, Israel

(*Received* 29 *October* 1968)

Abstract—The Mössbauer effect was used to study the oxidation states of europium and ytterbium silicides and germanides and to determine characteristics of the chemical bond in rare earth silicides and germanides. Results show that Eu is in the divalent state in the $EuSi_2$ and $EuGe_2$ compounds, while Yb is divalent in $YbSi_2$, mostly divalent in $YbGe_{1.75}$ and trivalent in Yb_5Si_3. Isomer shifts obtained in the case of Dy_5Si_3 and Dy_5Ge_3 were larger than those obtained for $DySi_2$ and $DyGe_2$ indicating shorter Dy-Dy bond in the Dy_5X_3 compounds, in good agreement with crystallographic data.

1. INTRODUCTION

THE MÖSSBAUER effect has been used to study the oxidation states of Eu and Yb silicides and germanides, and to determine the nature of the chemical bond in rare earth silicides and germanides. Results given here include the Mössbauer spectra of EuX_2, Dy_5X_3, DyX_2, (X = Si, Ge), Yb_5Si_3, $YbSi_2$ and $YbGe_{1.75}$. The crystal structures are Mn_5Si_3 type hexagonal for the M_5X_3 type compounds[1], $ThSi_2$ type tetragonal for $EuSi_2$[2], and orthorhombic (distorted $ThSi_2$ type) for $DySi_2$[2] and $DyGe_2$[3]. $YbSi_2$[4] has the AlB_2 type hexagonal structure, while $YbGe_{1.75}$ is hexagonal with a Th_3Pt_5 type lattice[5].

2. EXPERIMENTAL

Dy and Yb compounds were prepared by melting the metals with Si or Ge in an induction furnace under an argon protective atmosphere. Europium compounds were prepared in sealed quartz tubes filled with argon.

The Mössbauer spectra were taken with the following sources. Gd^{161} in the form of GdF_3 was used for the dysprosium compounds: the energy of the γ-rays was 25·6 keV. Yb^{170} in the form of $TmAl_2$ was used for the ytterbium compounds: the γ-rays emitted an energy of 84 keV (this source was used as it emits an unsplit line with almost natural width at 4·20°K). Europium compounds were studied by 22 keV γ-rays of Eu^{151} isotope. The γ-rays were obtained from a Sm^{151} source in the form of Sm_2O_3.

The absorption was recorded automatically on a multichannel pulse height analyser as described previously[6, 7]. In all measurements of the Dy compounds, the source was at room temperature, and in the case of the Eu and Yb compounds the sources were kept at the measurement temperature. The γ-rays were detected by a NaI(Tl) scintillation counter.

3. RESULTS AND DISCUSSION

Compounds of dysprosium

The absorption spectra of the compounds at 293° and at 4·2°K are given in Figs. 1 and 2. Table 1 lists isomer shifts, those relative to the source (DyF_3) being caused by changes in the density of 6*s* conduction electrons at the nucleus of the dysprosium atom in the different compounds.

The results show that the compounds can be arranged in pairs, each pair giving the same isomer shift. For the Dy_5Si_3 and Dy_5Ge_3 pair, the isomer shift is twice as large as that for $DySi_2$ and $DyGe_2$. The increasing isomer shift in the Dy_5X_3 compounds and the

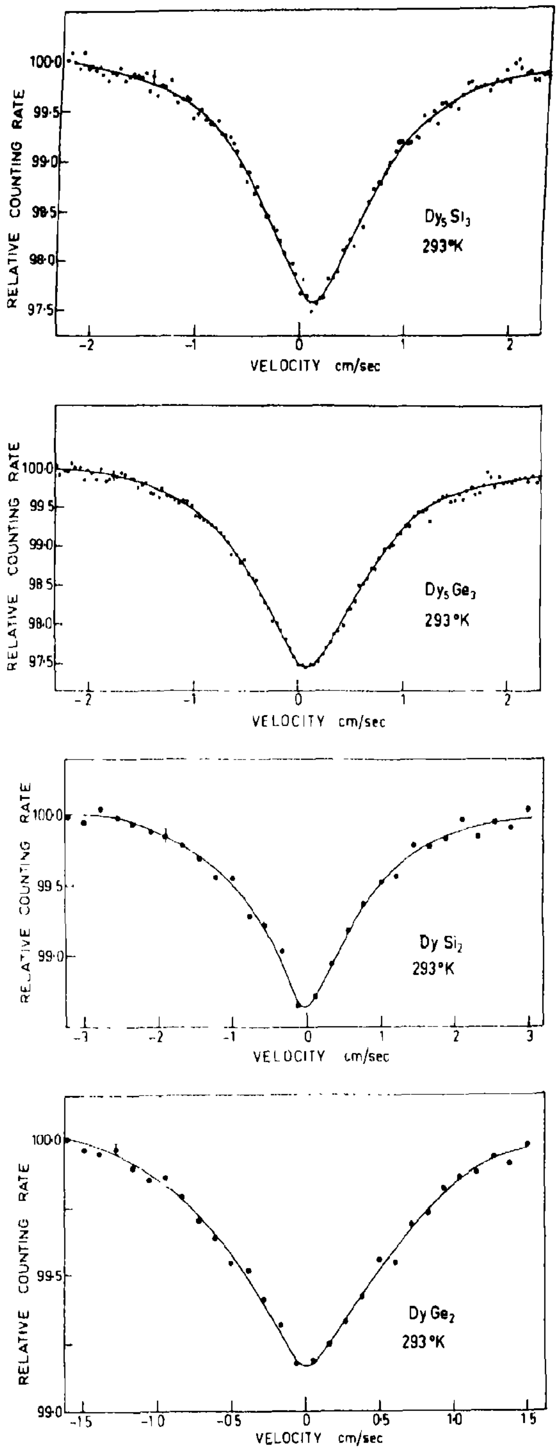

Fig. 1. Mossbauer spectra of silicides and germanides of dysprosium at 293°K

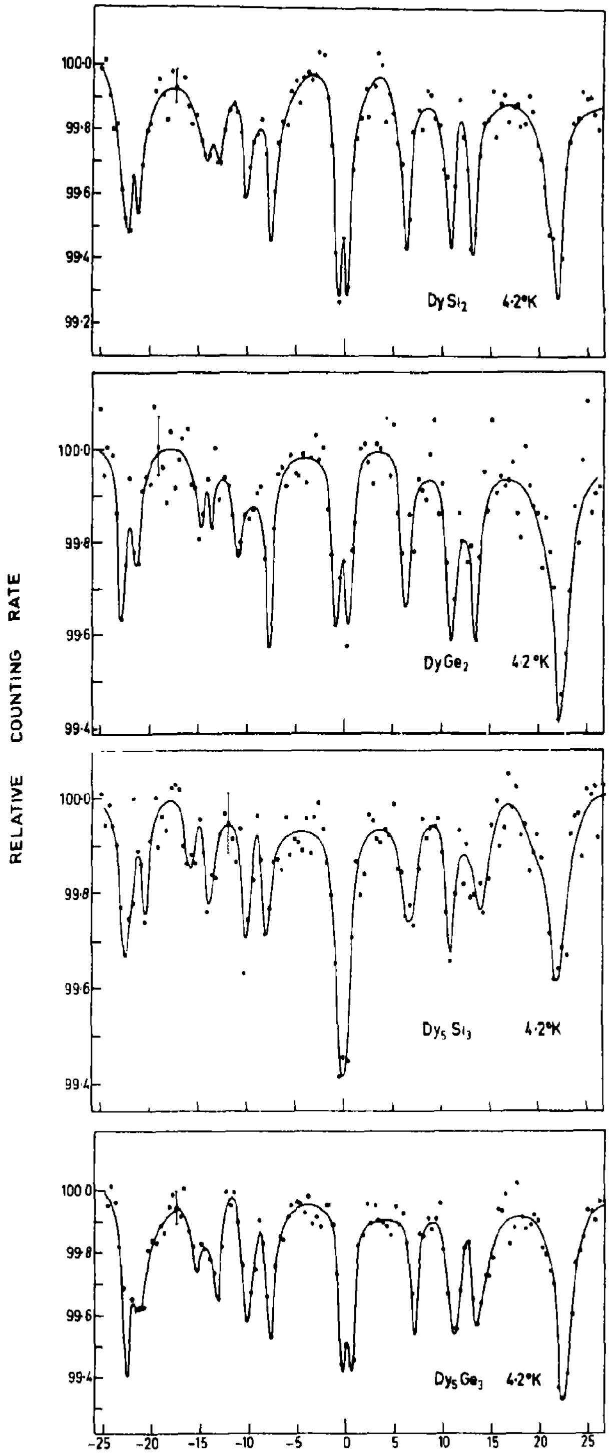

Fig 2. Mössbauer spectra of silicides and germanides of dysprosium at 4·2°K.

Table 1. *Isomer shift, the overall splitting and the ratio* H$_{eff}$*/free ion value in the dysprosium compounds*

	Isomer shift (mm/sec)	Overall splitting (cm/sec)	H_{eff}/free (ion value)
Dy_5Ge_4	+1·14 ± 0·20	44·9	1·03 ± 0·02
Dy_5Si_4	+1·42 ± 0·20	44·8	1·025 ± 0·02
$DyGe_2$	+0·42 + 0·20	45·2	1·035 + 0·02
$DySi_2$	−0·17 ± 0·40	44·3	1·015 ± 0·02

consequent increase in the number of the 6*s* conduction electrons must be related to decreasing distance of Dy–Dy bonds in these compounds, the number of 6*s* electrons being maximal in the dysprosium metal[8]. This finding is in good agreement with crystallographic data, which have shown the shortest distance in the Dy_5X_4 compounds to be 3·14–3·16 Å, and ~ 3·86 Å[1] in the case of the DyX_2 type compounds.

At 4·2°K, all the compounds were found to be magnetically ordered. The overall splitting and the values of H_{eff} relative to those of the 'free ion'—the ions in the gaseous state—are given in Table 1. These results are in good agreement with those obtained for the bulk magnetization of $DySi_2$[9], $DyGe_2$[3] and Dy_5Ge_4[10]. The effective magnetic moment found is in good agreement with the values found for the free ion.

Compounds of ytterbium

The spectrum of $YbSi_2$ at 4·2°K given in Fig. 3 is symmetric and unsplit. The isomer shift measured by calculating the positions of the centroids of the absorption spectrum at half the maximum height is Γ = 3·6 mm/sec. These results are similar to those obtained in the case of $YbAl_2$,[11] where Yb is divalent as determined by E.S.R. measurements. Divalent ytterbium being diamagnetic, no splitting should occur through the influence of magnetic field. The experimental width is less than twice the minimum possible width, which is $2\Gamma n$ = 2 mm/sec. From the above evidence it may be concluded that Yb in $YbSi_2$ is divalent.

The absorption spectrum of $YbGe_{1.75}$ is given in Fig. 4. While the line width in this case is almost the same as that found for $YbSi_2$, indicating that Yb is divalent in

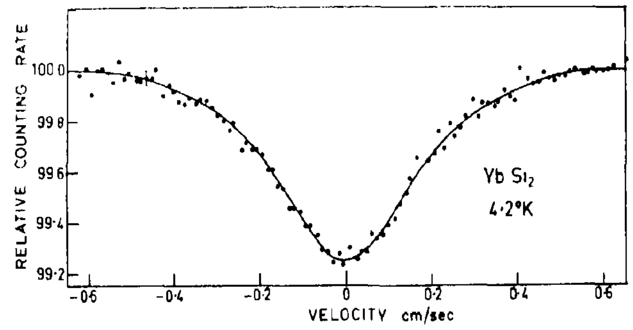

Fig. 3. Mossbauer spectrum of $YbSi_2$ at 4·2°K

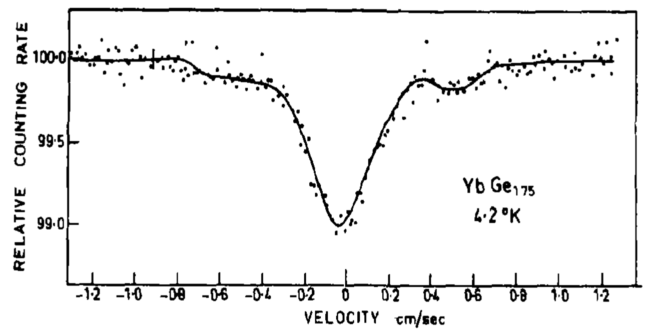

Fig. 4. Mössbauer spectrum of $YbGe_{1·75}$ at 4 2°K.

$YbGe_{1·75}$, the two symmetric shoulders appearing in the spectrum might originate from the hyperfine spectrum of Yb^{+3}, which is composed of five lines, as found in $YbNi_2$ [12] where Yb is trivalent. Comparison of shoulder and line areas in the hyperfine spectrum leads to the hypothesis that the shoulders can be related to the two end lines of the hyperfine spectrum and that a maximum of 25 per cent of the Yb in the $YbGe_{1·75}$ is in the trivalent state.

The absorption spectrum of Yb_5Si_3 at 4·2°K given in Fig. 5 is asymmetric. Its width, measured at half the height of the maximum absorption, is 14·8 mm/sec., i.e. seven times as large as the natural width ($2\Gamma n$). Three peaks of unequal intensity and line width can be detected on the spectrum, possibly as a consequence of quadrupole interaction, as found by Nowik *et al.*[12] for $YbNi_5$, where ytterbium is trivalent. The ytterbium in Yb_5Si_3 may therefore be concluded to be trivalent.

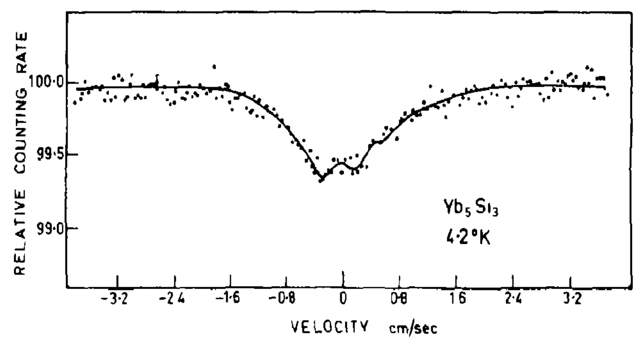

Fig. 5. Mössbauer spectrum of Yb_5Si_3 at 4·2°K.

Compounds of europium

The absorption spectra of $EuSi_2$ at 83°K and of $EuGe_2$ at 293°K are given in Figs. 6 and 7.

The spectra of the two compounds at the above temperatures were unsplit. The isomer shifts in the spectra of $EuSi_2$ and $EuGe_2$ relative to Eu_2O_3 are listed in Table 2. A comparison of these shifts to those obtained

Table 2. Isomer shift and the effective magnetic field for the europium compounds

	Isomer shift (mm/sec)	H_{eff} (KOe)
$EuSi_2$	−10·6 ± 0·3 (83°K)	286 ± 10 (4·2°K)
$EuGe_2$	−11·5 ± 0·2 (295°K)	229 ± 10 (4 2°K)

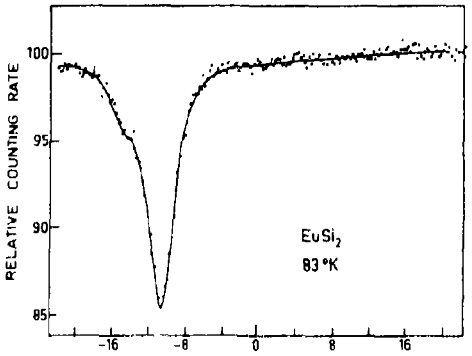

Fig. 6. Mossbauer spectrum of EuSi$_2$ at 83°K.

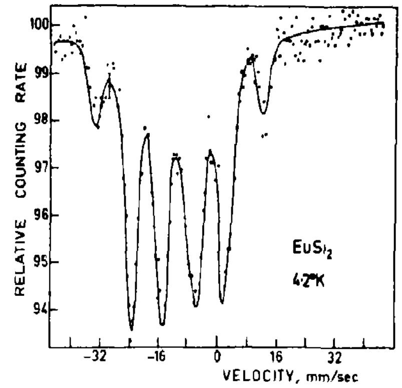

Fig. 8. Mossbauer spectrum of EuSi$_2$ at 4·2°K.

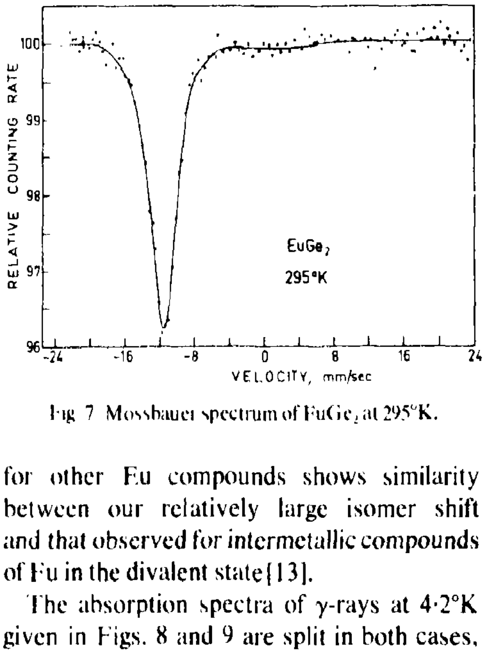

Fig. 7. Mossbauer spectrum of EuGe$_2$ at 295°K.

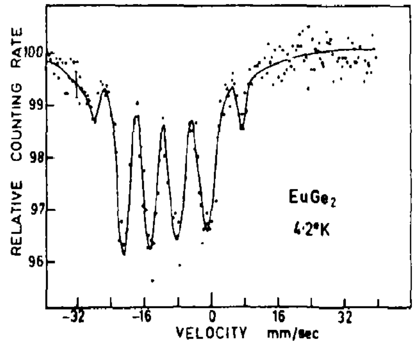

Fig. 9. Mossbauer spectrum of EuGe$_2$ at 4·2°K.

for other Eu compounds shows similarity between our relatively large isomer shift and that observed for intermetallic compounds of Eu in the divalent state[13].

The absorption spectra of γ-rays at 4·2°K given in Figs. 8 and 9 are split in both cases, proving that Eu is divalent in the compounds. In the case of Eu^{+3}, the spectra of compounds not containing iron are known to be unsplit, since the overall angular momentum J of Eu^{+3} is equal to zero. Only compounds of Eu^{+2} give hyperfine magnetic interactions at low temperatures.

A maximum isomer shift in divalent Eu compounds was obtained for salts with strongly electronegative anions, e.g. EuF$_2$[13] and EuSO$_4$[14], where the shift was −1·50 mm/sec. The electronic configuration of Eu^{+2} in these salts is $4f^7 5s^2 5p^6$. In the intermetallic compounds of europium, the isomer shift has a smaller absolute value owing to the contribution of the conduction electrons to the density of the electronic charge in the nucleus. The formal electronic configuration of Eu in this case is $4f^7 5s^2 5p^6 6s^x$, where x is equal to the number of the $6s$ conduction electrons.

The isomer shift in EuSi$_2$ is similar to the shift obtained in the case of EuAl$_4$, EuS, EuSe and EuO[13], and is much smaller than in salts with more electronegative anions. One possible explanation of these great differences might be that more covalent bonding takes place by $4p$ and $5p$ electrons than does in the salts. This conclusion appears correct, particularly with EuSi$_2$ and EuGe$_2$, where the Si and Ge tend to form covalent bonds.

$H_{\text{eff.}}$—the effective magnetic field—was calculated from the hyperfine interaction at 4·2°K, and is given in Table 2. When the values of $H_{\text{eff.}}$ obtained from $EuSi_2$ were inserted in the diagram of $H_{\text{eff.}}$ vs I.S., as was proposed by Wickman *et al.*[13], good agreement with the experimental line was obtained for different europium compounds.

Acknowledgement—The authors extend their thanks to Professor S. Ofer of the Department of Physics of the Hebrew University for helpful suggestions and advice.

REFERENCES

1. MAYER I. and SHIDLOVSKY I., *Inorg. Chem.* In press.
2. PERRI J. A., BINDER I. and POST B., *J. phys. Chem.* **63**, 616 (1959).
3. SEKIZAWA K., *J. phys Soc. Japan* **21**, 1137 (1966).
4. MAYER I. P., BANKS E. and POST B., *J. phys. Chem.* **66**, 693 (1962).
5. SMITH G. S., JOHNSON Q. and THARP A. G., *Acta crystallogr* **18**, 1085 (1965).
6. NOWIK I. and OFER S., *Phys. Rev.* **132**, 241 (1963).
7. ATZMONY M., MUALEM A. and OFER S., *Phys. Rev* **136**, B 1237.
8. NOWIK I., OFER S. and WERNICK J. H., *Phys. Lett.* **20**, 232 (1966).
9. SEKIZAWA K. and Yagukochi K., *J phys. Soc Japan* **21**, 274 (1966).
10. BUSCHOW K. A. J. and FAST J. F., *Phys status Solidi* **21**, 593 (1967).
11. WILLIAMS H. J., WERNICK J. H., NESBITT E. A. and SHERWOOD R. C., *J. phys. Soc. Japan* **17**, 91 (1962).
12. NOWIK I., OFER S. and WERNICK J. H., *Phys. Lett.* **24A**, 89 (1967).
13. WICKMAN H. H., NOWIK I., WERNICK J H., SHIRLEY D. A. and FRANKEL R. B., *J. appl. Phys.* **37**, 1246 (1966).
14. NOWIK I. and OFER S., *Rev. Mod. Phys.* **36**, 392 (1964).

J. Phys. Chem. Solids Pergamon Press 1969. Vol. 30, pp. 1215–1223. Printed in Great Britain.

MECHANISM OF THERMAL DECOMPOSITION OF POTASSIUM PERMANGANATE IN THE SOLID PHASE

V. V. BOLDYREV
Institute of Chemical Kinetics and Combustion, Siberian Branch of the USSR Academy of Sciences, Novosibirsk, U.S.S.R.

(*Received* 24 *April* 1968; *in revised form* 23 *October* 1968)

Abstract—This study of the mechanism of thermal decomposition of potassium permanganate illustrates the possibility of applying the methods and conceptions of solid-state physics in solving problems related to the investigation of chemical reactions in solids.

It was found that the elementary stages of the thermal decomposition of permanganate, which is a semiconductor of the *n*-type, are associated with electron transition from one anion site to another. This viewpoint provides an explanation for the mechanism of the action of catalysic additives and the influence of the solid products formed in the course of the reaction of thermal decomposition, as well as for the mechanism whereby the rate of thermal decomposition of permanganate is affected by preliminary irradiation. The latter is interpreted as the result of the concurrent catalytic action of manganese dioxide and inhibiting action of manganate formed on thermolysis and radiolysis of permanganate. The physical processes occurring during the chemical reactions under investigation are discussed.

DESPITE THE fact that thermal decomposition of potassium permanganate has been the subject of much investigation into topochemical reactions[1–4] and that a considerable number of works devoted to investigating this process have been published, many details of the mechanism call for further study and are not yet well understood. This is especially true of those which deal with the elementary stages of the process, the correlation between the physical properties of permanganate and its reactivity, the mechanism of catalysic action of additives and the action of the products formed as a result of thermolysis and radiolysis of permanganate.

This induced us to carry out an investigation of the thermal decomposition of potassium permanganate, aimed at ascertaining the nature of the mechanism of thermal decomposition and whether it is associated with electron transition in the lattice; if electron transition actually does take place, how does it occur and how, from this viewpoint, is the mechanism of the action of catalytic additives and of the solid reaction products on the rate of the process to be explained. The results obtained in the course of the investigations are outlined in this article.

1. PHYSICO-CHEMICAL PROPERTIES OF POTASSIUM PERMANGANATE AND THE PECULIARITIES OF THE MECHANISM OF ITS THERMAL DECOMPOSITION

As is well known, thermal decomposition of potassium permanganate begins to occur at a noticeable rate at temperatures ranging from 205° to 280°C. To describe the chemical reaction, most authors use the following schematic equation:

$$2KMnO_4 \rightarrow K_2MnO_4 + MnO_2 + O_2$$

according to which the thermal decomposition of permanganate results in the formation of two solid products, namely manganese dioxide and potassium manganate, and one gaseous product, oxygen. The deviations from this scheme, recorded in some cases[5] seem to be related to secondary reactions.

It follows from the above scheme that thermolysis of permanganate is a typical redox reaction. At the same time Roginsky and

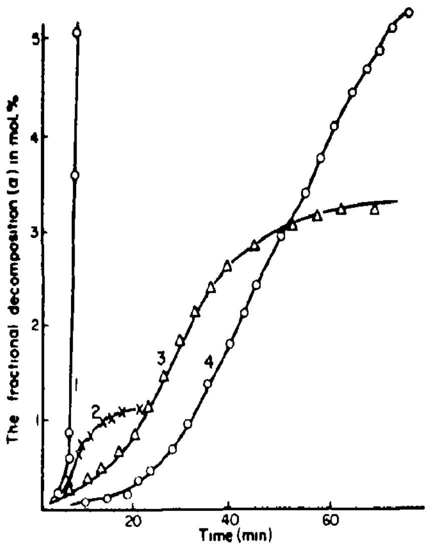

Fig. 1. Thermal decomposition of potassium permanganate in solid solution at 235°C. (1) decomposition of permanganate crystals; (2) decomposition of permanganate with its content in solid solution in perchlorate equal to 2·1 mol %; (3) the same, but with $KMnO_4$ content equal to 5·6 mol %; (4) the same, but with the $KMnO_4$ content equal to 14·6 mol %

Schultz[3] proved that the rate of thermal decomposition of permanganate changes in the presence of additions of such oxides which are generally active in redox catalysis. It may therefore be assumed that considerable importance in thermolysis may be attributed to the excitation and transition of the electron. It was of interest to ascertain the nature of this transition: whether we are dealing with local electron transition or whether, when potassium permanganate is heated, electron transition may occur that augments conductivity; to find out where precisely this electron transition takes place and whether it is essential for the process of thermal decomposition.

To give an answer to the first of these questions, an investigation was made into the nature of the basic current carriers in potassium permanganate, proceeding from a study of the electrical conductivity of permanganate, the transfer numbers and the thermoelectromotive force. It appeared that at temperature ranging from 170° to 210°C the electrical conductivity of potassium permanganate (both the single crystals and the pressed by pressure 10^4/cm^2 were investigated) varies from 10^{-8} to $10^{-6}\,\Omega$ and accordingly permanganate is close to semiconductors. Measurement of the transfer numbers by Tubandt's method has shown[6] that the anion component of electrical conductivity is not revealed, while the cation component does not exceed 5–9 per cent. Therefore the electrical conductivity of permanganate is, in the main, not of an ionic nature.

Additional information on the nature of the current carriers was obtained by measuring the thermoelectromotive force of potassium permanganate in form of the presed pellets, which was carried out by the differential method relative to metallic tin. It was found that the thermoelectromotive force of potassium permanganate has a negative sign, which points to the electronic nature of permanganate conductivity. From the experimental data obtained by employing the generally accepted methods of studying semiconductors[7], it was determined that the activation energy $E_0 = 1{\cdot}62 \pm 0{\cdot}03$ and $E_t = 0{\cdot}62 \pm 0{\cdot}03$, the ratio of the mobilities of the electrons and vacancies $\mu_n/\mu_p = 4{\cdot}93$ and the ratio of the effective masses of the positive holes and electrons $m_p^*/m_n^* = 1{\cdot}89$. We were unable to determine individually the values of the mobility and the effective masses for the electrons and the holes, since we did not succeed in determining the magnitude of Hall's constant for permanganate.

In the case of potassium permanganate it is difficult to presume anion-to-cation electron transition similar to that generally considered, for instance, in thermolysis of azides[8], if one takes into consideration the very high values of the activation barrier which have to be overcome as well as the fact that the composition of the products formed in thermolysis of permanganate do not conform to the supposed mechanism of decomposition.

More probable is the assumption that the electron transition accounting for conductivity occurs not between anion and cation, but inside the anion-lattice. As a result of such a transition, chemically stable anion sublattice sites are formed in the lattice, on which an extra electron is captured, as well as anion sub-lattice sites which have electrons and should be chemically unstable[9]. To check the correctness of this assumption, a study was made of the thermal decomposition of potassium permanganate comprising a solid solution in potassium perchlorate. Since the temperature of thermal decomposition of potassium perchlorate is considerably higher than that at which appreciable decomposition of permanganate sets in, and, judging from the position of the potassium perchlorate absorption edge in the u.v. spectrum[10] it should be characterized by a considerable magnitude of the forbidden band, when analyzing the thermal decomposition of potassium permanganate in solid solution and the related electron transitions, potassium perchlorate may be considered as an inert matrix in which permanganate ions are uniformly distributed.

On sufficient dilution, a part of these ions will be surrounded on all sides by perchlorate ions and they may be regarded as single ions; another part of the ions which have as their closest neighbour at least one permanganate ion, will form in the perchlorate lattice dimers, trimers, etc., consisting of permanganate ions.

If the above-suggested scheme of the mechanism of thermal decomposition of permanganate is actually realized, then it should be expected that at the temperature at which thermal decomposition of permanganate begins to proceed at an appreciable rate, the single permanganate ions in the solid solution will be stable, unlike those which enter into the composition of dimers, trimers, etc., which will decompose under these conditions. Proceedings from test results obtained[11], it is possible to estimate approximately for each given concentration of permanganate ions the relative proportion of each definite group of permanganate ions occurring in the solid solution. For this reason the correctness of the assumption regarding the mechanism of the elementary stages of permanganate thermolysis could be checked by determining the degree of decomposition of permangatate on heating its solid solutions in perchlorate up to a temperature of 235°C, at which temperature pure permanganate decomposes rapidly.

The results of our experiments have shown that at a temperature of 235°C there occurs not complete, but only partial decomposition of permanganate in the solid solution. When the concentration of the solid solution changes, the degree of transformation changes in the same direction as the ratio of the permanganate ions forming groups to the single ions, according to evaluation made in [11].

Hence, the presence of pairs of permanganate ions in the lattice, indispensable for electron transition from one anion site to another, is a substantial factor in the elementary stages of the process of thermal decomposition of permanganate. Accordingly, the scheme of the process may be expressed as

$$\begin{tikzcd} 2\mathrm{MnO}_4^{-1} \arrow[r, shift left, "k_1"] & \mathrm{MnO}_4 \arrow[l, shift left, "k_2"] \arrow[d, "k_3"] + e(\mathrm{MnO}_4^{-2}) \\ & \mathrm{MnO}_2 + \mathrm{O}_2 \end{tikzcd}$$

which is in agreement with the experimentally determined composition of the permanganate thermolysis products. Assuming that a stationary condition is achieved rapidly in the system in the course of the process, the rate of chemical transformation may be put down as

$$V = \frac{k_1 \cdot k_3}{k_2[e] + k_3} \cdot C$$

where C is the concentration of MnO_4^{-1} ions per unit of interphase surface. It follows from this equation that the factors which lead to a rise in the concentration of free electrons in the permanganate lattice will result in a reduced of the reaction. A reduction of the concentration of the electrons should, on the contrary, accelerate thermolysis.

2. MECHANISM OF THE EFFECT OF CATALYTIC ADDITIONS ON THE RATE OF THERMAL DECOMPOSITION OF PERMANGANATE AND THE INFLUENCE OF THE PRODUCTS FORMED AS A RESULT OF ITS THERMAL DECOMPOSITION AND RADIOLYSIS

Let us consider now from the viewpoint of the suggested mechanism of permanganate thermolysis the possible mechanism of the effect of additives consisting of various semiconductor oxides on the rate of the process, as well as the mechanism of the influence exerted on the decomposition rate by the solid products formed as a result of permanganate thermolysis and radiolysis. As has already been mentioned, Roginsky and Schlutz[3], as far back as 1928, proved that additions of some oxides, as, for example, NiO and CuO, accelerate the process of chemical decomposition of potassium permanganate. This may be assumed from the viewpoint of the conceptions advanced in our work, provided there is a drop in the concentration of free electrons in permanganate, resulting from contact between the additive and permanganate. Applying to this case the conceptions regarding the role of contact phenomens in chemical transformations in the solid phase, advanced by various authors[12–14], it may be supposed that this may result from the appearance of a contact potential difference at the point of contact of the additive and permanganate crystals if the work function of the additive electron will be greater than that of the permanganate electron. Measurement (made with the aid of a vibrating condenser) of the electron work function of the permanganate and that of substances used as additives (NiO, CuO, MnO_2), under conditions close to those under which the process of thermal decomposition takes place, has shown that, actually, the additives accelerating the thermal decomposition of permanganate are generally characterized by a greater work function of the electron as compared with permanganate*.

Closely associated with the mechanism of the action of catalytic additives is the question regarding the mechanism of the influence on the rate of the process of the solid products formed as a result of thermolysis or, in other words, the question regarding the nature of autocatalysis during thermal decomposition of permanganate. It follows from the general scheme that thermal decomposition results in the formation of two solid reaction products: manganese dioxide and potassium manganate. Both in thermal and in radiative decomposition manganese dioxide becomes at once separated as an independent phase[15]. As to the catalytic effect of manganese dioxide on the rate of thermal decomposition of permanganate, various publications contain contradictory data. Roginsky's data[3] to the effect that additives excercise a catalytic influence are in disagreement with the results obtained by Simchen[16] who did not detect any catalytic effect of manganese dioxide. For this reason, employing methods similar to those previously applied in studying permanganate thermolysis[3, 4, 17], we conducted special experiments to find out whether manganese dioxide has any catalytic effect on the decomposition of permanganate. The results of the experiments given in the diagram (Fig. 2) indicate that manganese dioxide influences thermal decomposition of permanganate, but that the effectiveness of the influence of a given additive, as well as the magnitude of the preparation is obtained and on its prehistory. Four preparations of manganese dioxide were tested: a commercial preparation; a preparation isolated from the products of thermal decomposition of permanganate by treating them with an aqueous KOH solution; one obtained by the dry method by heating manganese nitrate[11] at 170°C; one synthesized by the wet method

---

*The work function of $KMnO_4$ by 180°C is 4·7–4·9 eV.

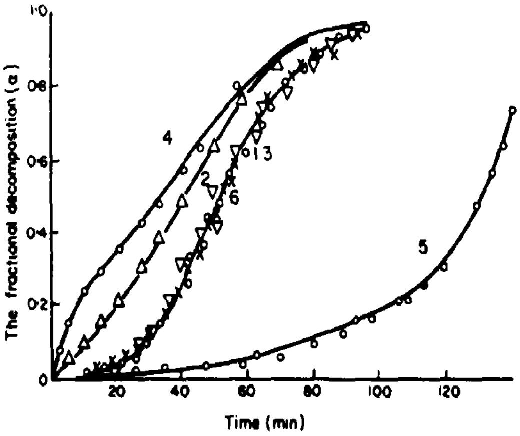

Fig. 2. Influence of MnO and $K_3(MnO_4)_2$ additives on the rate of thermal decomposition of potassium permanganate at 220°C. (1) decomposition of permanganate at 220°C with an additive MnO_2 (commercial reagent); (2) the same with an addition of MnO_2 obtained by thermal decomposition of $KMnO_4$; (3) with an addition of MnO_2 obtained by heating $Mn(NO_3)_2$ at 170°C; (4) with an addition of MnO_2 synthesized by oxidation of a 5 per cent $MnSO_4$ solution heated to 60°C; (5) with an addition of $K_3(MnO_4)_2$ (cocrystallization); 6-decomposition of permanganate without any additive

by oxidizing a 5 per cent manganese sulphite solution heated to 60°C. The second and the last preparations proved to be the most active ones. The first and the third preparations of manganese dioxide practically had no effect on the rate of thermal decomposition of permanganate. It was found, at the same, that the work function of an electron of the active manganese dioxide preparations is, as a rule, considerably greater than that of potassium permanganate preparation under similar conditions.

We failed to find in any publications data concerning the nature of the effect on the decomposition rate, of the other solid product formed in thermal decomposition of potassium permanganate: potassium manganate. Our experiments have shown that whereas a mechanical mixture of permanganate with manganate decomposes at the same rate as pure permanganate, coprecipitation of permanganate and manganate from and alkaline solution leads to a decrease in the rate of thermal decomposition of permanganate. Concurrently, the conductivity of the crystals increases. A detailed roentgenostructural examination of this preparation[18] made it possible to establish that, in addition to K_2MnO_4, a new phase, isostructural $Ba_3(AsO_4)_2$ and $KMnO_4 \cdot K_2CrO_4$, is formed under such conditions. The phase was identified as a double salt with a composition of $K_3(MnO_4)_2$. Hence, when there is adequate contact with permanganate, potassium manganate, the second solid product of thermal decomposition of potassium permanganate, may affect the rate of thermal decomposition as a heterophase addition, either by itself as a K_2MnO_4 phase, or by comprising the phase corresponding in composition to the double salt $K_3(MnO_4)_2$. Measurement of the work function of the electron of these two compounds under conditions close to those of thermal decomposition of permanganate has shown that both of them have a smaller electron work function as compared with permanganate. Therefore the inhibiting action which they exert on the thermal decomposition of potassium permanganate may be related to enrichment of the permanganate lattice with electrons in the region adjacent to the point of contact with the additive. Another reason for the inhibiting action may be the formation of donor levels when small amounts of manganate ions enter the permanganate lattice.

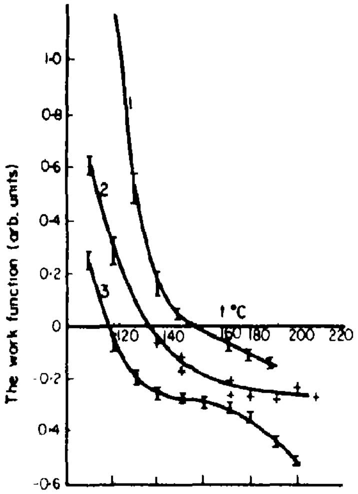

Fig. 3. Change in the work function of the electron with the temperature for $K_3(MnO_4)_2$ (1), $KMnO_4$ (2), MnO_2 (3).

The recorded experimental catalytic action of solid products formed upon thermal decomposition of potassium permanganate appears to result from concurrent catalyzation of the process by manganese dioxide and inhibition of the process by potassium manganate.

3. MECHANISM OF THE INFLUENCE OF PRELIMINARY IRRADIATION ON THE RATE OF THERMAL DECOMPOSITION

The influence of preliminary irradiation on the rate of subsequent thermal decomposition of potassium permanganate was analysed by us in previous papers[17, 19]. We showed that the cause of acceleration of thermal decomposition resulting from preliminary irradiation of permanganate lies not in the formation of displaced atoms in the permanganate lattice, but in the accumulation of radiolysis products which catalyze thermal decomposition of permanganate upon subsequent heating. Since, according to Glemser and Butenuth[15], manganese dioxide and potassium manganate are the main products formed in permanganate radiolysis, it may be assumed that the mechanism of their influence on the rate of thermal decomposition is similar to the one we have considered above of the catalytic action of the products formed upon thermal decomposition of permanganate. The basic difference between these two processes can be attributed, apparently, to the different spatial distribution of the product formed upon thermal decomposition and radiolysis. Whereas in thermal decomposition the initial centres of the reaction are chiefly formed on the surface on the permanganate crystal[20], permanganate radiolysis occurs in the interior of the crystal.

4. CHANGE IN THE PROPERTIES OF PERMANGANATE IN THE COURSE OF ITS THERMAL AND RADIATIVE DECOMPOSITION

To trace changes occurring in the permanganate-reaction products system during thermal and radiative decomposition of potassium permanganate, measurements were made of the electrical conductivity* and thermoelectromotive force of permanganate in form of pressed pellets in the course of the process.

The change in the electrical conductivity of potassium permanganate at the various stages of its thermal decomposition is shown in Fig. 4 where the degree of decomposition is plotted on the x-axis, and the relative change in electrical conductivity σ/σ_0 on the y-axis. It is evident from the figure that, as permanganate decomposes, its electrical conductivity first increases and then dimini-

---

*The experimental procedure is described in our previous papers[6, 21].

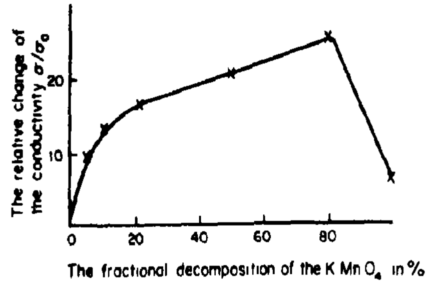

Fig. 4 Change in the electrical conductivity of potassium permanganate in the course of its thermal decomposition at 140°C. σ/σ_0 change in the electrical conductivity relative to the conductivity of nondecomposed permanganate under similar conditions.

shes. An assumption was made that such a character of the change in electrical conductivity is due to the fact that at the deeper stages of decomposition of permanganate there is a change in the ratio of the donor and acceptor levels in the system, or that it results from an increase in the relative amount of the product which has acceptor properties, or from depletion or chemical changes in the components in the system, branched off beyond the donor levels.

A study of the curves representing the temperature dependence of the conductivity of permanganate partly decomposed as a result of preliminary heating to the decomposition temperature, shows the presence of a typical loop which is not to be found in the case of pure permanganate. Such a loop is also observed on the curve of preliminary irradiation of permanganate and on the curve of permanganate cocrystallized with manganate ion (Figs. 5, 6).

Similar results were obtained in studying the temperature dependence of the thermo-electromotive force of permanganate crystals (Fig. 7). On the curves corresponding to irradiated permanganate crystals containing an admixture of manganate ions, there is a maximum which can be attributed to the presence in the system of an additional number of donor levels disappearing at temperatures of the order of 140°C. This

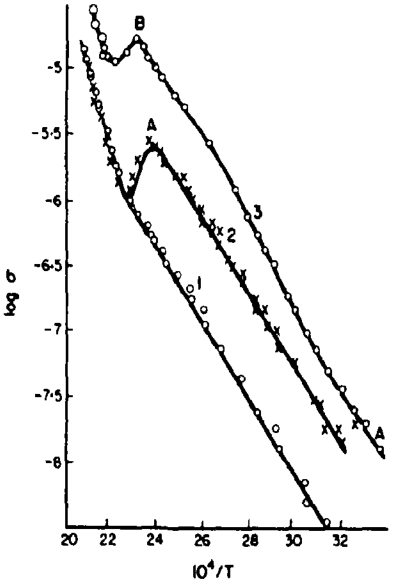

Fig. 5. Dependence of conductivity of potassium permanganate partly decomposed as a result of preliminary heating on the temperature for; (1) potassium permanganate; (2) potassium permanganate partly decomposed (10 per cent); (3) $KMnO_4$ cocrystallized with K_2MnO_4.

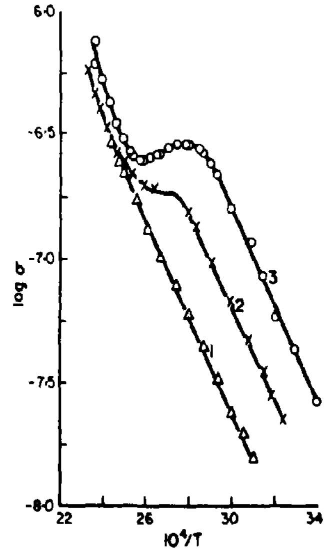

Fig. 6. Dependence of conductivity of irradiated potassium permanganate exposed to various X-ray irradiation doses on the temperature for: (1) nonirradiated $KMnO_4$; (2) irradiation dose $10^8\,r$; (3) the same, but irradiation dose $5 \times 10^8\,r$.

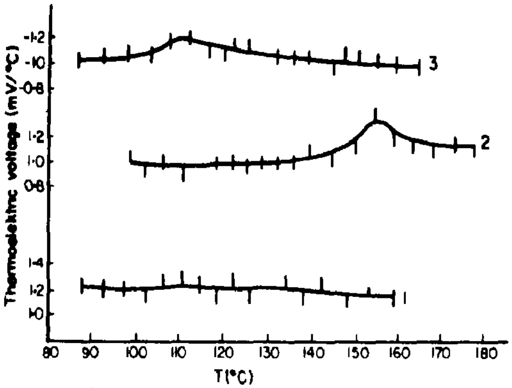

Fig. 7 Dependence of differential thermoelectromotive force on the temperature for: (1) $KMnO_4$; (2) $KMnO_4$ with an additive of K_2MnO_4; (3) $KMnO_4$ X-ray irradiation dose 5×10^6 r

correlates with the moment of transition from the maximum to the minimum on the electrical conductivity curve.

The disappearance of the donor levels cannot, apparently, be attributed to the trivial phenomenon of depletion of the donor levels, which sometimes occurs in semiconductors[22], since in the case of permanganate $\Delta E \gg KT$. This is also attested by the closeness of the magnitudes characterizing the dependence of conductivity on the temperature before and after the anomalous region. Therefore it would apparently be more correct to consider chemical changes, such, for instance, as the disproportionation of manganate, possible under these conditions.

$$2K_2MnO_4 \rightleftarrows KMnO_4 + K_3MnO_4$$

as the cause for the drop in electrical conductivity in the course of decomposition of permanganate and the appearance of anomalous sections on the curves representing the dependence of electrical conductivity and thermoelectromotive force on the temperature. The above considerations make it possible to understand the sharp acceleration of the process of thermal decomposition of potassium permanganate on heating it above 140–150°C[20]. This can evidently be explained by the decrease in the relative amount of manganate which is an inhibitor of thermal decomposition of permanganate as shown above.

CONCLUSIONS

The above results indicate how successfully the conceptions, procedures and methods of solid-state physics can be applied in solving the problems related to chemical reactions in solids. It can be seen in the case of the reaction of thermal decomposition of potassium permanganate that the elementary stages of decomposition are associated with electron transition from one anion site to another. This point of view provides an explanation for the mechanism of the action of catalytic additions, the influence of the solid products formed in the course of the reaction of thermal decomposition, and the mechanism of the effect of preliminary irradiation on the rate of subsequent thermal decomposition.

Acknowledgements—The author wishes to avail himself of the opportunity to express his sincere gratitude to A. N. Oblivantsev, A. A. Kabanov, E. M. Uskov, G. London, O. P. Korobeinichev, V. K. Zhuravlyov and B. G. Erenburg who participated in the experimental part of the work and in the discussion of the results, as well as to Dr. E. Tappe (Institute of Physical Chemistry, German Academy of Sciences) for the helpful discussion of the results of the work.

REFERENCES

1. PINKUS A., *Helv. Chim. Acta* 1, 145 (1918).
2. MOLES E. and CRESPI M., *Z. phys. Chem.* **100**, 337 (1922).
3. ROGINSKY S. and SCHULTZ E., *Z. phys. Chem.* **A138**, 21 (1928).
4. PROUT E. and TOMPKINS E., *Trans. Faraday Soc.* **40**, 488 (1944).
5. PETERS H., RADEKE K. H. and TILL L., *Z. anorg. allg. Chem.* **346**, 1, 1 (1966).
6. TRUBITSYN A. M., KABANOV A. A., BOLDYREV V. V and MAKOVIK A. K., *Soviet Phys. solid St.* **6**, 249 (1964)
7. BUSCH G. and WINKLER U., *Ergebn. exakt. Naturw* **29**, 145 (1956).
8. GREY P., *Q. Rev.* **17**, 440 (1963).
9. JONOV G. V. and DYATKINA M. E., *J. Struct. Chem. USSR* **6**, 1 (1965)
10. MAYCOCK I. H., PAI VERNECKER V. R. and GORZYNSKI C. S., *Spectrochim. Acta.* **A23**, 2849 (1967)
11. BERLINGER J., *J. chem. Phys.* **29**, 537 (1958).
12. MOTT N., *Disc. Faraday Soc.* 837 (1938).
13. YEROFEYEV B. V., *Izv. Inst. fis. org. khim. AN BSSR*, 7, 15 (1959).
14. ZAKHAROV Y. A. and SAVELIYEV G. G., *Kinetics and Catalysis* 7, 55 (1966).
15. GLEMSER O. and BUTENUTH G., *Optika* **10**, 42 (1953).
16. SIMCHEN E. A., *Bull. Soc. chim. Fr* **5**, 638 (1954).
17. BOLDYREV V. V. and OBLIVANTSEV A. N., *Kinetics and Catalysis* 3, 887 (1962).
18. ERENBURG B. G., BOLDYREV V V, ANIKINA L. D. and MIKHAILOV J. I., *J. Struct Chem.* 9, 536, 7 (1968).
19. BOLDYREV V. V., OBLIVANTSEV A. N., RAITZIMRING A. M, and USKOV E. M, *Dokl. AN SSSR* **166**, 891 (1966).
20. HILL R. A. W., RICHARDSON R. T. and ROGER B. W., *Proc. R. Soc.* **A291**, 208 (1966).
21. BOLDYREV V. V., KABANOV A. A., TRUBITSYN A. M., OBLIVANTZEV A. N., USKOV E. M. and TSHELYSHOV V. V., *J. phys. Chem.* **41**, 1783 (1967).
22. SMITH R. A., *Semiconductors*. Cambridge University Press, Cambridge (1959).

J. Phys. Chem. Solids Pergamon Press 1969. Vol. 30, pp. 1225–1235. Printed in Great Britain.

THE NEODYMIUM MOLYBDATE-TUNGSTATE SYSTEM

K. NASSAU, P. B. JAMIESON* and J. W. SHIEVER
Bell Telephone Laboratories, Incorporated Murray Hill, N J. 07971, U S.A.

(*Received* 15 *October* 1968)

Abstract – The $Nd_2(MoO_4)_3$–$Nd_2(WO_4)_3$ system has been investigated by means of differential thermal analysis and X-ray diffraction. Four distinct solid phases exist in the system, for all of which single crystals have been prepared. The high temperature (β–) form of $Nd_2(MoO_4)_3$ crystallizes in the previously established β-$Gd_2(MoO_4)_3$ structure, with Mo in tetrahedral and Nd in octahedral co-ordination. The three remaining phases have structures closely related to that of tetragonal scheelite ($CaWO_4$): the low temperature (α–) form of $Nd_2(MoO_4)_3$ has a basically undistorted tetragonal structure, but contains a complicated ordering arrangement of Nd atoms over the Ca sites, the low temperature (α–) $Nd_2(WO_4)_3$ phase, extending over much of the system, has the α–$Eu_2(WO_4)_3$ structure in which distortions from the scheelite structure are marked but the ordering arrangement is simple, and the higher temperature (β–) form of $Nd_2(WO_4)_3$ is closely related to the α-form. Relations between the structures are discussed. The effect of deviation from stoichiometry in the system was also studied In the off-stoichiometric system $Nd_2O_3\,.\,3{\cdot}4MoO_3$–$Nd_2O_3\,.\,3{\cdot}4WO_3$, similar phase relationships exist, the main difference being that the α–$Nd_2(MoO_4)_3$ phase extends above the α–$Nd_2(WO_4)_3$ phase for compositions between about 2·5 and 35 mol. % $Nd_2O_3\ 3{\cdot}4WO_3$.

INTRODUCTION

THE RESULTS of a comprehensive study of trivalent molybdates and tungstates of the type $L_2(MO_4)_3$ were presented in a previous paper[1]. Among the rare-earth compounds alone at least six different phases were recognized and have been confirmed in other investigations[2-4]. The structures of three of these phases are closely related to that of tetragonal scheelite ($CaWO_4$)[5-7] by the substitution of two trivalent ions for every three Ca^{2+} ions. Ordering of the cations and subsequent lattice distortions give rise to the different structure types. Detailed studies of the atomic arrangement in monoclinic α-$Eu_2(WO_4)_3$[8] and in monoclinic (pseudo-tetragonal) β-$Nd_2(MoO_4)_3$[9, 10] have now been made. Since the low temperature (α-) form of $Nd_2(WO_4)_3$ has the α-$Eu_2(WO_4)_3$ structure, the $Nd_2(MoO_4)_3$-$Nd_2(WO_4)_3$ pseudo-binary system was investigated in order to understand the relationships between the different scheelite-type structures. The results herewith reported are based on powder and single crystal X-ray diffraction measurements in association with differential thermal analysis, annealing, quenching, and crystal growth experiments.

EXPERIMENTAL

Reagent grade oxides (WO_3 – Amend Drug and Chemical Co.; MoO_3 – Matheson, Coleman and Bell; 99·9 per cent Nd_2O_3 dried at 900°C – Michigan Chemical Corp.) were ground together in stoichiometric amounts, sintered, and reground at least three times to yield $Nd_2(MoO_4)_3$ and $Nd_2(WO_4)_3$. Intermediate samples were prepared by mixing these two end-members in appropriate amounts and firing and regrinding at least twice. Some intermediate samples prepared directly from the oxides gave identical results. All sintering was performed below 950°C to avoid premature formation of the high-temperature $Nd_2(MoO_4)_3$ phase which is quite stable once formed. Off-stoichiometric compositions were prepared in a similar manner from the oxides. The growth of single crystal end-members is described below.

**Present address*: Department of Chemistry, University of Aberdeen, Old Aberdeen, Scotland.

Powder X-ray diffraction photographs were taken with a Phillips 114·6 mm Debye–Scherrer camera using *V*-filtered CrK radiation, or with a Nonius Guinier camera using Ni-filtered CuK radiation. Guinier photographs were calibrated using KCl as a standard. Single crystal X-ray photographs were taken on precession and Weissenberg cameras using Zr-filtered MoK radiation. High temperature powder X-ray diffraction measurements were made using a GE XRD3 diffractometer with an MRC high temperature attachment as previously described[1].

Differential thermal analysis (DTA) curves were obtained from a DuPont 900 machine using platinum cups in a stream of air at a heating rate of 20°/min. All delays observed were endothermic on heating. On cooling they were exothermic, but cooling values were not used because of the considerable supercooling usually observed. For quenching, samples contained in folded platinum foil were held for at least one hour at the desired temperature in a vertical tube furnace and then dropped into liquid nitrogen. The quenching rate was estimated as greater than 500°C per sec.

PHASE DIAGRAM RESULTS

The DTA thermal delays indicating phase transitions or melting points are shown in Fig. 1. Boundary lines were drawn and areas identified from a scrutiny of X-ray powder diffraction photographs of both sintered (low temperature) and quenched (high temperature) phases. Fields were labeled α for low-temperature and β for high-temperature phases. The previous designations[1, 4] of these phases are given in Table 1, as are the temperature and compositional ranges of the phases observed. Based on Fig. 1, a plausible phase diagram such as that of Fig. 2 can be suggested; for simplicity, two-phase regions are not labeled. This is merely a possible phase diagram that is non incon-

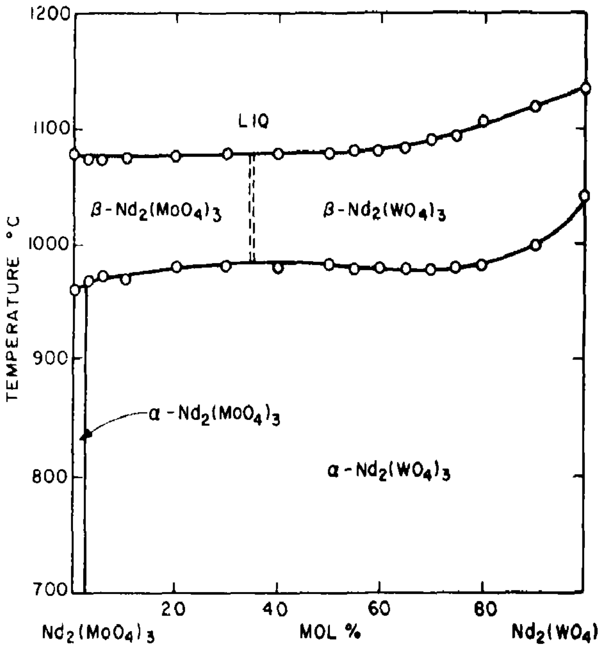

Fig. 1. Differential thermal analysis results for the Nd$_2$(MoO$_4$)$_3$–Nd$_2$(WO$_4$)$_3$ system.

Table 1

Phase	α-$Nd_2(WO_4)_3$	β-$Nd_2(WO_4)_3$	α-$Nd_2(MoO_4)_3$	β-$Nd_2(MoO_4)_3$
Previous designation[a]	A	D	N	L
Structure type[b]	α-$Eu_2(WO_4)_3$[c]	β-$Nd_2(WO_4)_3$	α-$Nd_2(MoO_4)_3$[d]	β-$Gd_2(MoO_4)_3$[e]
True unit cell	Monoclinic-$C2/c$ $a = 7{\cdot}73$ Å $b = 11{\cdot}58$ Å $c = 11{\cdot}48$ Å $\beta = 109{\cdot}6°$		Monoclinic-$C2$ $a = 27{\cdot}02$ Å $b = 11{\cdot}70$ Å $c = 11{\cdot}85$ Å $\beta = 105{\cdot}3°$	Monoclinic-$C2$[f] $a = 10{\cdot}46$ Å $b = 10{\cdot}46$ Å $c = 10{\cdot}82$ Å $\beta = 90{\cdot}0°$
Sub-cell	Pseudo-tetragonal (highly distorted) $a = 5{\cdot}28$ Å $c = 11{\cdot}58$ Å	Pseudo-tetragonal $a \sim 5{\cdot}3$ Å $c \sim 11{\cdot}6$ Å	Tetragonal-$I4_1/a$ $a = 5{\cdot}30$ Å $c = 11{\cdot}70$ Å	Tetragonal-$P\bar{4}2_1m$[f] $a = 7{\cdot}40$ Å $c = 10{\cdot}82$ Å
Temperature field for pure end-member	below 1045°C	1045–1135°C[h]	below 960°C	960–1080°C[f,g]
Composition range in stoichiometric system (mol. % $Nd_2(WO_4)_3$)	~ 2·5–100	~ 35–100	0–~ 2·5	0–~ 35
Composition range in WO_3-rich system (mol % Nd_2O_3 . 3·4WO_3)	~ 0·5–100	~ 35–100	0–~ 0·5 below ~ 800°C 0–~ 35 above ~ 800°C	0–~ 50

[a] See [1] and [4]

[b] For isostructural compounds see [1].

[c] See [8].

[d] See [9, 10]

[e] See [13].

[f] If this compound is ferroelectric at room temperature, as is the isostructural $Gd_2(MoO_4)_3$, then these results apply only to the ferroelectric modification of the β-$Nd_2(MoO_4)_3$ phase, existing metastably below its Curie temperature, above the Curie temperature one would then have γ-$Nd_2(MoO_4)_3$.

[g] The same values were obtained by Rode *et al.*[4].

[h] Melting point given as 1130°C by Borchard[3], and as 1250°C by Plyuschev and Amosov[11]

sistent with the data and obeys the phase rule.

In order to investigate the possibility of congruent growth of single crystals of the α-$Nd_2(MoO_4)_3$ phase from the melt, the depression of the melting point of $Nd_2(MoO_4)_3$ by excess MoO_3 was examined (Fig. 3). The small change observed indicates that crystal growth, if at all feasible, would require a very large excess. Investigation of the corresponding $Nd_2(WO_4)$-WO_3 system (Fig. 4) revealed a much steeper slope, with the α-$Nd_2(WO_4)_3$ phase appearing to melt congruently at approximately 13 mol. % WO_3 excess, corresponding to the composition $Nd_2O_3 . 3{\cdot}4WO_3$. It should be stated that, with the exception of Fig. 2, the various composition-temperature plots are not intended to represent valid phase diagrams; these could, however, be inferred in the same way as Fig. 2 was obtained from Fig. 1.

Investigation of the system $Nd_2O_3 . 3{\cdot}4MoO_3$-$Nd_2O_3 . 3{\cdot}4WO_3$ gave the results summarized in Fig. 5 and in Table 1. In this system the α-$Nd_2(MoO_4)_3$ phase overrides the α-$Nd_2(WO_4)_3$ phase so that an identical phase change is produced by variation of either composition or temperature.

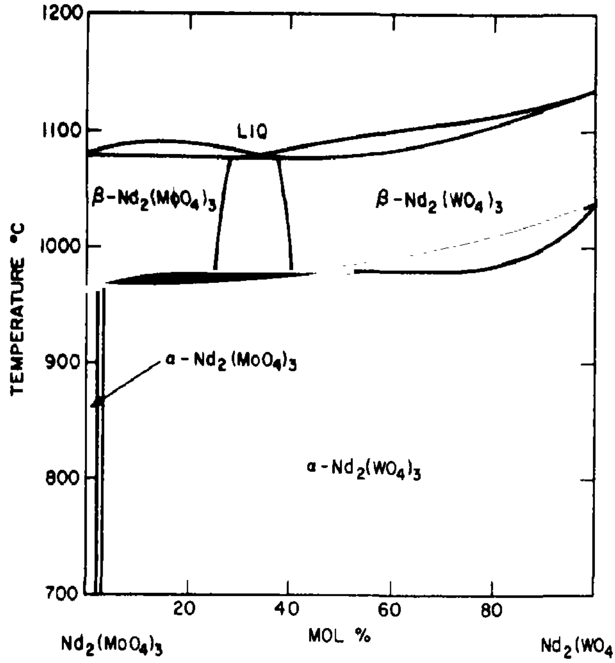

Fig. 2. Proposed phase diagram for the Nd$_2$(MoO$_4$)$_3$–Nd$_2$(WO$_4$)$_3$ system based on Fig. 1.

CRYSTAL GROWTH

Crystals of β-Nd$_2$(WO$_4$)$_3$ are readily grown in inch-size boules by Czochralski pulling from the melt as previously described[1]. When the crystals are cooled through the transition temperature of 1045°C, they transform nondestructively to α-Nd$_2$(WO$_4$)$_3$. A large heat emission with cooling is observed for this transition during DTA.

Crystals of β-Nd$_2$(MoO$_4$)$_3$ may also be pulled from the melt[1], but do not transform readily to the α-form; crystals cooled fairly rapidly to room temperature have remained untransformed after several years.

Since it was not possible to lower the melting point of Nd$_2$(MoO$_4$)$_3$ below the transition temperature of 960°C by addition of a small excess of MoO$_3$, crystals of the α-form were prepared by a sintering process. The temperature of a sample of Nd$_2$(MoO$_4$)$_3$ was cycled through a range of 30°C just below the transition temperature for four days in a covered platinum crucible. Crystals of poor quality were obtained from stoichiometric samples, but crystals of high quality, up to 2 mm in longest dimension, were prepared in this way from starting material having the composition Nd$_2$O$_3$. 3·4MoO$_3$. By the end of the growth period essentially all the excess MoO$_3$ has been lost by sublimation. The crystals grew in the form of tetragonal bipyramids with the {102} faces dominant (Fig. 6). Spectrochemical analysis showed the crystals to be essentially stoichiometric:

	wt.% Nd	wt.% Mo
Sample 5257	37·6, 37·4	37·2, 37·0
Calculated for Nd$_2$(MoO$_4$)$_3$	37·55	37·46

Crystals of all these phases have the typical lilac neodymium color, being blueish-purple in daylight and reddish-purple under a tungsten lamp. Diffuse reflectance spectra in the 0·45–0·90 μ range have been reported for α-Nd$_2$(MoO$_4$)$_3$ and for α-Nd$_2$(WO$_4$)$_3$[1].

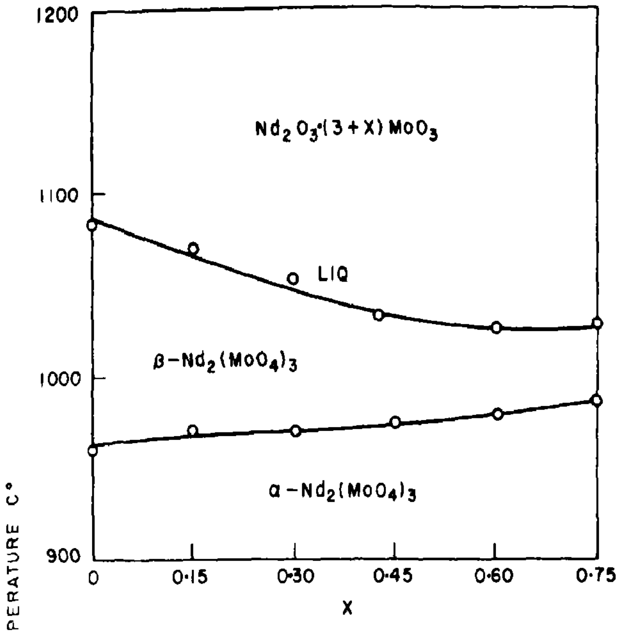

Fig. 3. Differential thermal analysis results for the $Nd_2O_3 . (3+x)MoO_3$ system.

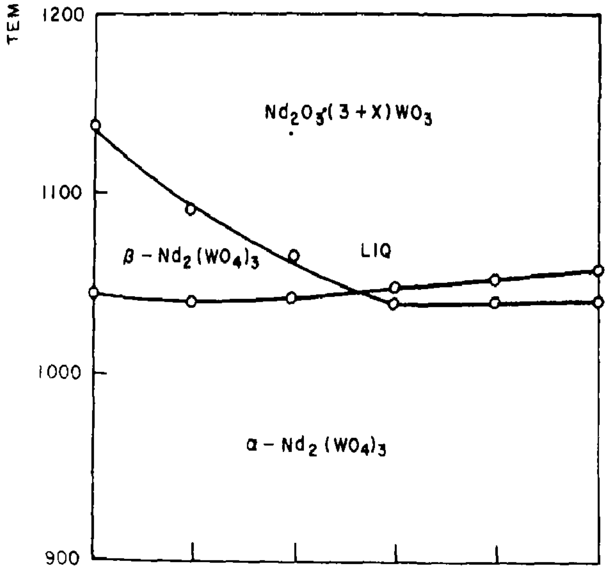

Fig. 4. Differential thermal analysis results for the $Nd_2O_3 . (3+x)WO_3$ system.

VARIATION IN UNIT CELL DIMENSIONS

Since three of the four phases in the system have structures related to that of scheelite ($CaWO_4$),[5–7], the most appropriate way to follow structural variations with composition and temperature is by a study of dimensional changes in the basic scheelite-like unit cell. For the end-members of the low-temperature series, cell constants were measured directly from single crystal X-ray photographs (Table 1); for intermediate compositions, the cell constants were calculated from indexed powder patterns. Table 2 contains the X-ray powder pattern for $\alpha-Nd_2(MoO_4)_3$, indexed

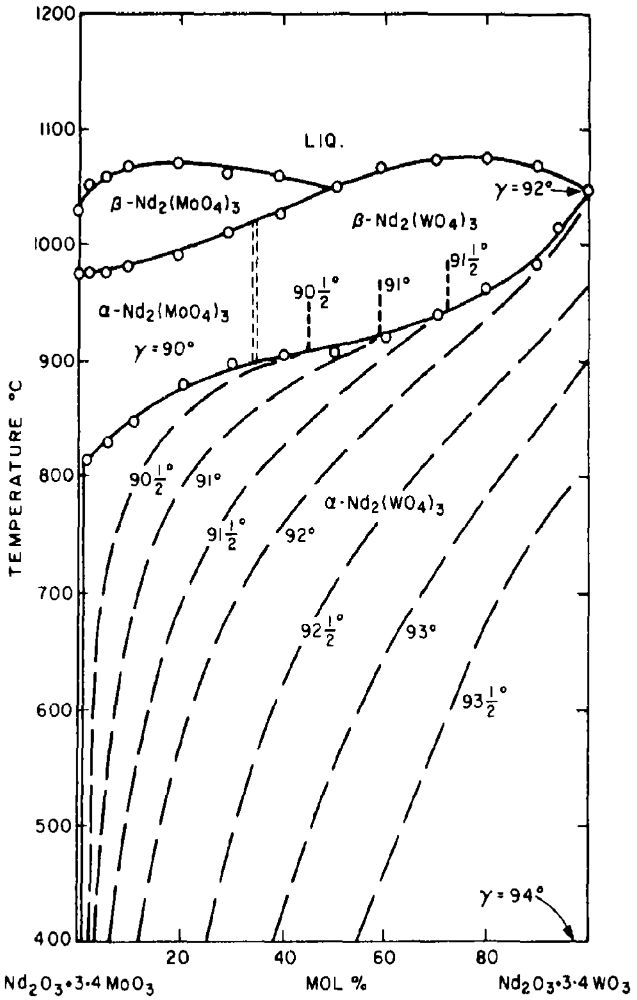

Fig. 5. Differential thermal analysis and γ values from X-ray diffraction for the $Nd_2O_3 \cdot 3{\cdot}4MoO_3$–$Nd_2O_3 \cdot 3{\cdot}4WO_3$ system

on the basis of the tetragonal scheelite-like cell; indexed powder data for α-$Nd_2(WO_4)_3$ have been presented elsewhere[1].

The change in cell constants with compositional variation in both the stoichiometric and off-stoichiometric systems is presented in Fig. 7. For the α-$Nd_2(MoO_4)_3$ phase the scheelite cell is geometrically tetragonal, with $a = b$ and with γ, the angle between the a- and b-axes, equal to 90°. Immediately following the transition to the α-$Nd_2(WO_4)_3$ phase there begins a rapid change in all constants, followed by a more gradual change, with the angle γ increasing with increasing tungstate content to a value of about 94° for $Nd_2(WO_4)_3$.

For high-temperature specimens only the change in γ was plotted, as determined from the degree of splitting of the 'tetragonal' 112 line on high-temperature powder diffraction traces. The splitting could be influenced also by differences between a and b, but large differences would be required where γ is near 90° to cause a noticeable effect; the greatest

Fig. 6. Crystals of α-$Nd_2(MoO_4)_3$ grown during sintering: the longest is 2 mm in length.

Table 2. Indexed powder X-ray diffraction pattern of α-$Nd_2(MoO_4)_3$, *using tetragonal (scheelite) parameters* a = 5·298 Å, c = 11·705 Å[9]. *All lines with calculated intensities > 1 are included*

h k l	d_{calc} (Å)	d_{obs} (Å)	I_{calc}	I_{obs}
*		5·88		10
*		5·07		5
011	4·83		4	
112	3·16	3·15	100	100
004	2·926	2·919	14	20
020	2·649	2·643	19	20
114	2·306	2·308	2	5
*		2·170		5
024	1·964	1·961	29	30
220	1·873	1·870	12	15
116	1·730	1·727	15	20
312	1·611	1·608	14	25
132	1·611		10	
224	1·578	1·575	10	15
008	1·463	1·461	2	5
*		1·404		5
040	1·325	1·324	3	5
028	1·281	1·280	6	10
316	1·271	1·269	4	15
136	1·271		6	
332	1·222	1·217	4	5
044	1·207	1·207	4	5
420	1·185	1·183	2	5
240	1·185		2	
228	1·153	1·158	3	5

Superlattice reflections which cannot be indexed in the tetragonal (scheelite) subcell.

difference between *a* and *b* for low-temperature samples is less than 0·01 Å which has negligible influence on the calculated value of γ. The variation in γ, calculated with the assumption that *a* and *b* remain essentially equal, was determined over parts of the whole α-$Nd_2(WO_4)_3$ region for the off-stoichiometric system (Fig. 8). In this diagram, the temperagure T is expressed as a reduced temperature T/T_{tr}, where T_{tr} is the transition temperature for the composition under investigation. The results are presented as contours in Fig. 5. It should be noted that the absolute values of γ, particularly at the higher temperatures, may be in error by up to +0·3°; it is the trends which are significant.

Variation in γ with increasing temperature, determined as described in the preceding paragraph, was investigated also for a sample of pure $Nd_2(WO_4)_3$ (Fig. 9). No significant change in γ is observed at the $\alpha \rightarrow \beta$ transition, although DTA results indicate a large heat absorption for this transformation.

DISCUSSION

Prior to a discussion of the interesting structural transformations involved in this study, it is useful to consider briefly the crystal structures of the four phases encountered in the system.

β-$Nd_2(MoO_4)_3$: Crystals of metastable β-$Nd_2(MoO_4)_3$ are isostructural with the previously examined β-$Gd_2(MoO_4)_3$, which has an orthorhombic true cell and a tetragonal sub-cell[13, 14] (Table 1). The atomic arrangement within the subcell of $Gd_2(MoO_4)_3$ has been determined[13] and contains two crystallographically independent MoO_4 tetrahedra, with Gd in six-fold octahedral coordination. This is in contrast to the scheelite-based structures in which Nd exhibits eightfold coordination. There is thus little resemblance between the β-$Nd_2(MoO_4)_3$ structure and the three remaining structures in the system, which probably explains the sluggish conversion of β-$Nd_2(MoO_4)_3$ to α-$Nd_2(MoO_4)_3$ on cooling, and makes β-$Nd_2(MoO_4)_3$ (just as the isostructural β-$Gd_2(MoO_4)_3$) a metastable material at room temperature. In addition, β-$Nd_2(MoO_4)_3$ is presumably ferroelectric by analogy with the ferroelectricity reported(15) for the isostructural molybdates of Sm, Eu, Tb, Dy and Gd (in this case the high temperature form above the Curie temperature would then be designated γ-$Nd_2(MoO_4)_3$, metastable below 960°C and stable above 960°C).

α-$Nd_2(MoO_4)_3$: One characteristic of the α-$Nd_2(MoO_4)_3$ phase, as shown above, is that the γ angle for the scheelite-like sub-cell is exactly 90°. X-ray examination of single

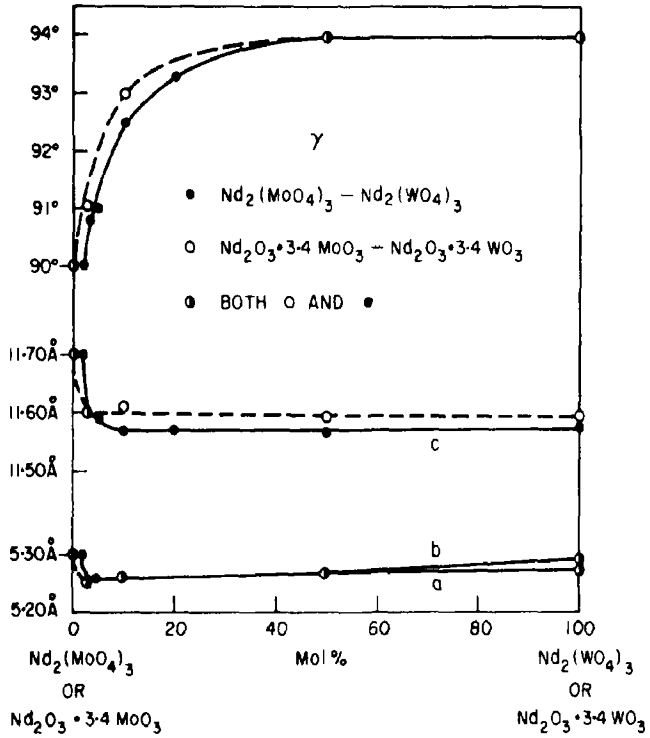

Fig. 7. Scheelite sub-cell dimensions in the $Nd_2(MoO_4)_3$–$Nd_2(WO_4)_3$ and $Nd_2O_3 \cdot 3{\cdot}4MoO_3$–$Nd_2O_3 \cdot 3{\cdot}4WO_3$ systems.

crystals of $Nd_2(MoO_4)_3$ indicated that the sub-cell is truly tetragonal, with $a = b$ and with tetragonal diffraction symmetry. The tetragonal unit cell is given in Table 1. The structure has now been completely determined[9, 10] with respect to this unit cell with $\frac{2}{3}$ Nd in each Ca position of the scheelite structure. This occupancy, however, is not random. Ordering of the Nd atoms results in additional weak scattering corresponding to the monoclinic cell given in Table 1. The transformation matrix from the tetragonal to the monoclinic unit cell is $(510/0\bar{1}0/\bar{1}20)$. Figure 10(a) illustrates the complicated arrangement of Nd atoms over the sites available. In this structure, each Mo atom has 4 nearest-neighbor oxygen atoms which form an undistorted tetrahedron; each Nd atom is dodecahedrally coordinated to 8 oxygen atoms.

α-$Nd_2(WO_4)_3$: The structure of α-$Nd_2(WO_4)_3$ is the same as that of α-$Eu_2(WO_4)_3$, for which atomic positions have been determined[8]. This structure is again based on a scheelite subcell, but a highly distorted one in which the angle γ is 94·0°; the true cell is monoclinic (Table 1). The ordering arrangement of 2Nd atoms for every 3 Ca positions of scheelite is much simpler than in α-$Nd_2(MoO_4)_3$; along each 'tetragonal' axis every third site is regularly vacant (Fig. 10(b)). Coordination of the metal atoms is similar to that in α-$Nd_2(MoO_4)_3$, but with considerable distortions of the MoO_4 tetrahedron and NdO_8 dodecahedron.

β-$Nd_2(WO_4)_3$: Because of the ready conversion of β-$Nd_2(WO_4)_3$ to α-$Nd_2(WO_4)_3$, no single crystals of the β phase are available at room temperature; determination of the structure would require a single-crystal X-ray

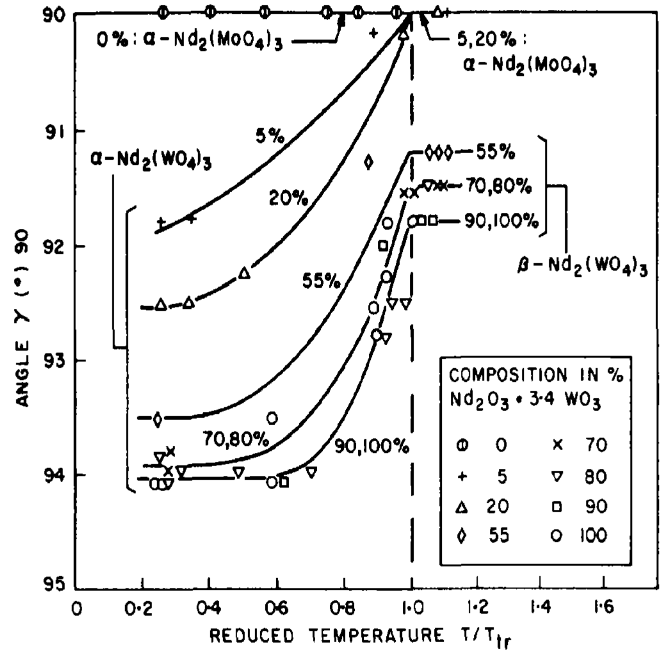

Fig. 8. Scheelite sub-cell γ values in terms of the transition temperature T_{tr} in the $Nd_2O_3 . 3{\cdot}4MoO_3$-$Nd_2O_3 . 3{\cdot}4WO_3$ system

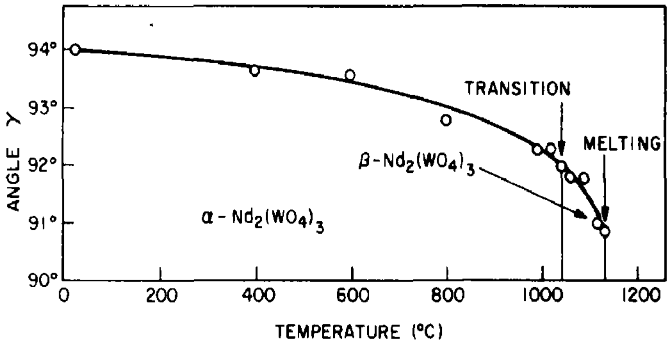

Fig. 9. Scheelite sub-cell γ values for $Nd_2(WO_4)_3$.

diffraction study above 1045°C. High temperature powder X-ray diffraction, however, indicates that the structure is probably also scheelite-based, and the easy transition to α-$Nd_2(WO_4)_3$ accompanied by a continuous variation of γ (Fig. 9) suggests a close relationship between the two structures.

The differences between the three scheelite-based structures in the $Nd_2(MoO_4)_3$-$Nd_2(WO_4)_3$ system are related to the large number of possible arrangements for which 2 Nd atoms replace 3Ca atoms in the $CaWO_4$ structure. The crystal structures of α-$Nd_2(WO_4)_3$ and of α-$Nd_2(MoO_4)_3$ may be thought of as two extreme cases: in α-$Nd_2(WO_4)_3$ (Fig. 10(b)) the ordering arrangement is one of the simplest possible and the distortions of the scheelite cell are the largest

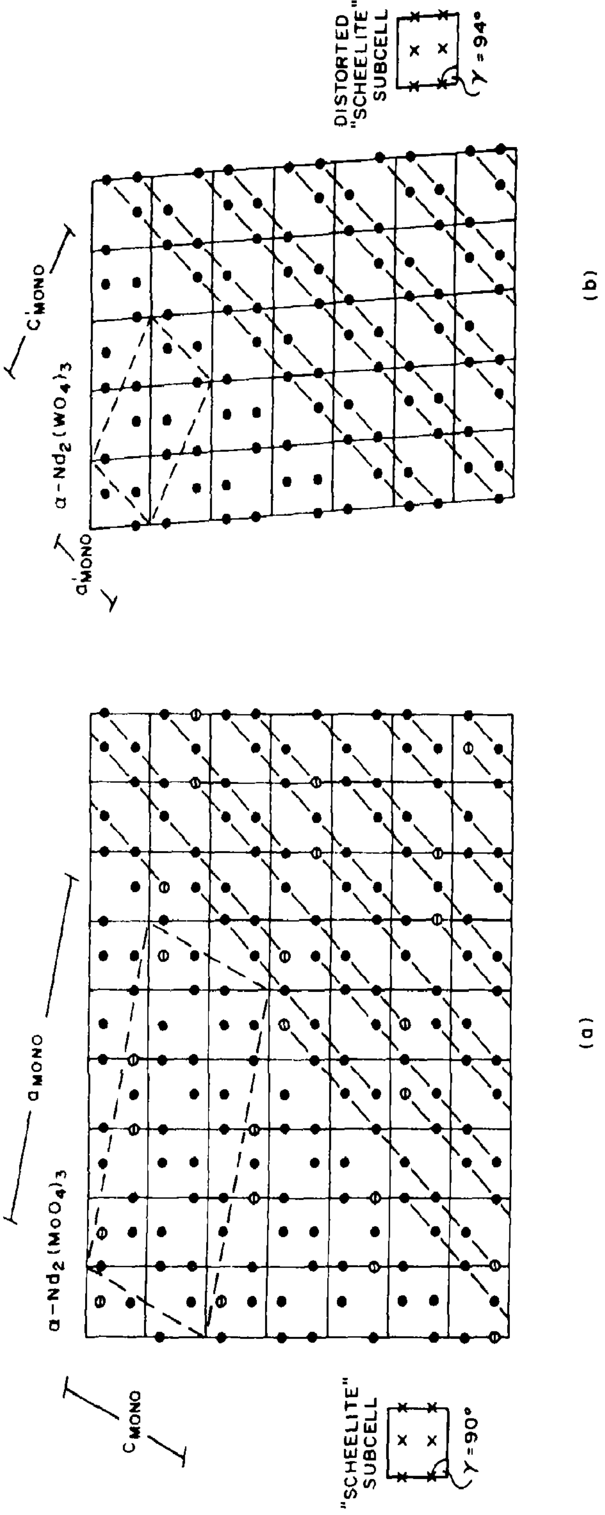

Fig. 10. The arrangement of Nd atoms in the α-Nd$_2$(MoO$_4$)$_3$ and α-Nd$_2$(WO$_4$)$_3$ structures. Solid circles represent Nd sites, hatched circles represent incompletely occupied Nd sites.

observed; in α-$Nd_2(MoO_4)_3$ (Fig. 10(a)) the scheelite cell is completely undistorted but the ordering arrangement is particularly complicated. The β-$Nd_2(WO_4)_3$ structure, for which γ lies between 90° and 92°, would appear to correspond to another variant of Nd arrangements, probably intermediate between the α-$Nd_2(MoO_4)_3$ and α-$Nd_2(WO_4)_3$ structures.

The transformation from the α-$Nd_2(WO_4)_3$ to the α-$Nd_2(MoO_4)_3$ structure may be accomplished by either increase of the Mo:W ratio or by increase of temperature (Fig. 5). In either case the scheelite subcell angle γ shows a gradual decrease to almost 90° before the α-$Nd_2(MoO_4)_3$ phase is reached (Fig. 8), followed by an abrupt change at the transition as γ becomes exactly 90°. That this is indeed a discontinuous change is demonstrated by the large latent heat associated with this presumably first order transformation.

The relationship between the α-$Nd_2(MoO_4)_3$ and α-$Nd_2(WO_4)_3$ structures can be discussed in terms of sheets of Nd atoms. The α-$Nd_2(WO_4)_3$ structure (Fig. 10(b)) contains continuous sheets of Nd atoms parallel to 'tetragonal' (110), with every third sheet systematically absent. The α-$Nd_2(MoO_4)_3$ structure contains similar sheets of Nd atoms, but continuous only in the 'tetragonal' c direction. One structure could thus be derived from the other by a system of localized faulting plus the scheelite cell distortion. There is, therefore, the possibility of the formation of intermediate structures. Without detailed evidence from single-crystal X-ray studies, it is impossible to be certain that the Mo-rich end of the α-$Nd_2(WO_4)_3$ field truly has the α-$Nd_2(WO_4)_3$ structure. The heat associated with the transition does suggest that the major part of the faulting occurs suddenly at $\gamma = 90°$ or at least very close to it.

One of the interesting points to emerge from this study is the equivalence of an increase in the Mo:W ratio with an increase in the temperature for structural transformations in this pseudo-binary molybdate-tungstate system. Mo and W atoms are almost identical in their crystallochemical characteristics (ionic radii, polarizabilities, coordination preferences, etc.) and in many such systems (e.g. $CaWO_4$:$CaMoO_4$, $Er_2(WO_4)_3$: $Er_2(MoO_4)_3$ and $In_2(WO_4)_3$: $In(MoO_4)_3$)[17] no change in structure is observed between molybdate and tungstate. In the present instance the addition of less than 3 mol.% $Nd_2(WO_4)_3$ causes the transition from the complex order of the tetragonal subcell of α-$Nd_2(MoO_4)_3$ to the simple order by distorted subcell of α-$Nd_2(WO_4)_3$.

Acknowledgements—We wish to thank D. J. Nitti, C. D. Capio and Mrs. A. Cooper for obtaining the X-ray powder diffraction photographs and traces, and G. M. Loiacono, R. N. Storey and J. S Barshatky for assistance with some preliminary work Helpful discussions with S. C. Abrahams are gratefully acknowledged.

REFERENCES

1. NASSAU K., LEVINSTEIN H J and LOIACONO, G. M., *J. Phys. Chem. Solids* **26**, 1805 (1965)
2. AMOSOV V M, TRUNOV V. K and KOVBA L. M., *Vest. Mosk Univ* **1965**, 23 (1965).
3. BORCHARD H J, *J. chem. Phys.* **39**, 504 (1963).
4. RODE E. Ya., LUSANOVA G. V, KUZNETZOV V. G. and GOCHMAN L. Z, *Z Neorg Khim.* **13**, 1295 (1968).
5. ZALKIN A. and TEMPLETON D H, *J chem. Phys* **40**, 501 (1964).
6. KAY M. I, FRAZER B C and ALMODOVAR, I, *J chem. Phys.* **40**, 504 (1964).
7. BURBANK R. D., *Acta crystallogr.* **18**, 88 (1965).
8. TEMPLETON D. H. and ZALKIN A., *Acta crystallogr* **16**, 762 (1963).
9. JAMIESON P. B., ABRAHAMS S C. and BERNSTEIN J L., *J. chem Phys.* To be published.
10. JAMIESON P B, DE FONTAINE D and ABRAHAMS S. C., *J appl Cryst.* To be published.
11. PLYUSCHEV V. E. and AMOSOV V M, *Dokl Akad. Nauk. SSSR* **157**, 131 (1964).
12. YA. RODE E., BALAGINA G. M, IVANOVA M. M. and KARPOV V N., *Z. Neorg Khim.* **13**, 1451 (1968).
13. ABRAHAMS S. C. and BERNSTEIN J. L., *Amer Cryst. Assn. Winter Meeting. 1966*. Abstract N1 To be published.
14. BERNSTEIN J. L., *Z Kristallogr* **122**, 315 (1965)
15. BORCHARDT H. J and BIERSTEDT P. E., *J appl Phys.* **38**, 2057 (1967).
16. SMITH D. K., Rep. No UCRL-50264 Lawrence Radiation Laboratory, University of California, Livermore, Calif. (1967)
17. NASSAU K., Unpublished observations.

J. Phys. Chem. Solids Pergamon Press 1969. Vol. 30, pp. 1237–1239. Printed in Great Britain.

NEW MELTING LAW AT HIGH PRESSURES*

L. MARSHALL LIBBY
University of Colorado and The Rand Corporation, Calif. 90406, U.S.A.

and

F. J. THOMAS
The Rand Corporation, Santa Monica, Calif. 90406, U.S.A.

(*Received* 20 *September* 1968)

Abstract—A new melting law at high pressures relating the change in molar volume to the change in molar entropy upon melting, of the form

$$C+\ln(V_L^m-V_S^m)=\alpha(S_l^m-S_s^m),$$

is shown to fit the data presently available.

THE EMPIRICAL melting law for high pressures recently described by Kennedy[1] and Kraut and Kennedy[2, 3] which relates the melting temperature T^m and the specific volume of solid V_s^m linearly as,

$$T^m=A+BV_s^m \tag{1}$$

along the melting curve[4], is apparently not a consequence of the Clapeyron equation. However, it is known (as discussed by Kraut and Kennedy) that deviations from the linearity of (1) occur, for example at very high compressions in the alkali metals, and at very low compressions[2, 5] for argon and helium, providing, of course, that available melting data and compressibility data are taken at face value. In addition, no melting law adequately predicts initial negative slopes of melting curves or maxima in melting curves where changes in coordination of the liquid take place.

Stishov has pointed out[6] that if one rewrites the Kennedy relation in the differential form

$$\frac{\mathrm{d}V_s^m}{\mathrm{d}T_m}=\text{const.} \tag{2}$$

and combines it with an empirical relation observed by Zhokhovskii[7],

$$\frac{\mathrm{d}\ln\Delta V_{SL}^m}{\mathrm{d}T_m}=\text{const.}' \tag{3}$$

where $\Delta V_{SL}^m=(V_L^m-V_S^m)$ is the change in volume on melting, one obtains,

$$\frac{\mathrm{d}\ln\Delta V_{SL}^m}{\mathrm{d}V_S^m}=\text{const.}'' \tag{4}$$

Equation (4) has been shown by Stishov to hold for such different substances as gases, alkali salts, and metals, over large volume changes, and this behavior leads him to conclude that "a universal connection exists between the volumes of the liquid and solid phases along the melting curve."

The significance may be that entropy is dominant, for ΔS^m would be expected to depend on density change, and this dependence is basic to the validity of equations (1–4).

Accordingly we propose a new melting law at high pressure, of the form

$$C+\ln(V_L^m-V_S^m)=\alpha(S_L^m-S_S^m) \tag{5}$$

which relates the change in volume ΔV_{LS}^m to the change in entropy ΔS_{LS}^m upon melting.

---

*Research supported in part by U.S. Atomic Energy Commission Contract AT(11-1)-1537.

The data presently available, plotted in the form of equation (5) in Figs. 1(a) and 1(b), show good agreement with linearity.

Keeping in mind that the entropy change ΔS^m along the melting curve can be written, from the Clapeyron equation, as

$$\Delta S^m_{sl} = \Delta V^m_{sl}(\mathrm{d}P/\mathrm{d}T^m) \qquad (6)$$

we observe that substitution of (6) into (5) leads to an integral equation of state along the melting curve:

$$\int_{T_1}^{T_2} \frac{[C+\ln \Delta V^m_{sl}]}{\Delta V^m_{sl}} \mathrm{d}T^m = \alpha(P_2-P_1). \qquad (7)$$

It should be clearly understood that these relations are proposed to hold only for normally melting substances, i.e. substances where the melting temperature changes monotonically with pressure. The relations herein proposed may not hold for the very light gases at extremely low pressures and temperatures where quantum mechanical effects may take place, nor for substances with negative melting slopes nor rare substances where change in coordination number of the liquid causes maxima in the melting curve; see discussion[1] by Kraut and Kennedy.

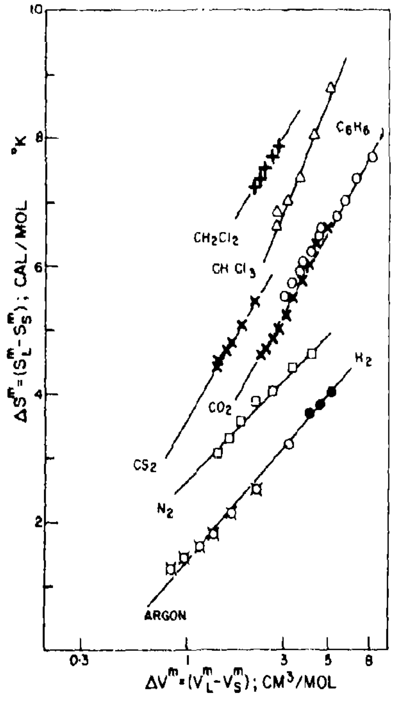

Fig. 1(a).

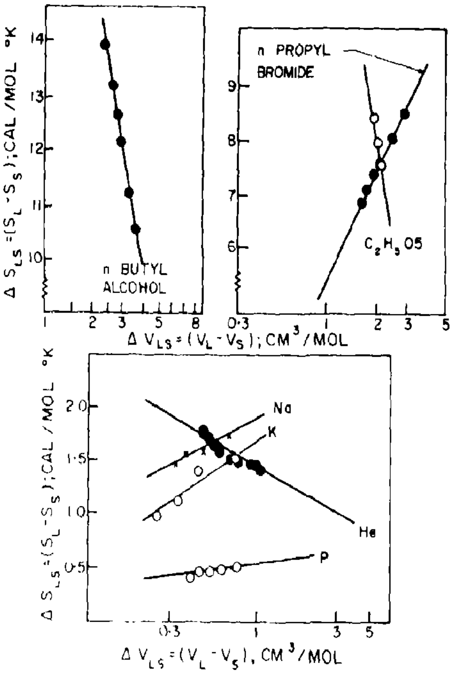

Fig 1(b).

Figs 1(a–b) Plot of $[C+\ln(V_l - V_s) = \alpha(S_l - S_s)]$ for various substances, taken along the melting curves, S in units of cal/mol °K and V in units of cm³/mol.

Acknowledgements – We thank W. F. Libby for calling our attention to the Kennedy relation. We thank G. C. Kennedy for helpful discussions about the data.

REFERENCES

1. KENNEDY G. C., *J. geophys Res.* 70, 1979 (1965).
2. KRAUT E. A. and KENNEDY G. C., *Phys. Rev. Lett.* 16, 608 (1966).
3. KRAUT E. A. and KENNEDY G. C., *Phys. Rev.* 151, 668 (1966).
4. LIBBY W. F., *Phys. Rev. Lett.* 17, 423 (1966). According to footnote (1) in his paper the Kennedy relation holds both for isothermal compressions and along the melting curve.

5. LUEDEMANN H. D. and KENNEDY G. C., *J. geophys. Res.* **73**, 2795 (1968); KRAUT E. A. and KENNEDY G. C., *Phys. Rev.* **151**, 668 (1966).
6. STISHOV S. M., *JETP Lett.* **6**, 97 (1967).
7. ZHOKOVSKII M. K., *State Committee on Standards and Measures*, p. 69, (1964) as quoted in reference [6].
8. Data at the melting point from KENNEDY G. C., *American Institute of Physics Handbook* (Edited by E. D. Gray), 2nd Edn, pp. 4–34. McGraw-Hill, New York (1963); *Thermodynamic Functions of Gases* (Edited by F. Din). Butterworths, New York (1962); DUGDALE J. S. and SIMON F. E., *Proc. R. Soc.* **218**, 291 (1953); DWYER R. F., COOK G. A., BERWALDT O. E. and NEVINS H. E., *J. phys. Chem.* **43**, 801 (1965); BRIDGEMAN P. W., *Proc. Am. Acad. Arts Sci.* **74**, 399 (1942).

J. Phys. Chem. Solids Pergamon Press 1969. Vol. 30, 1241-1249. Printed in Great Britain.

EXISTENCE OF AIR-GAPS IN SPECIMEN-ELECTRODE CONTACTS AND THEIR EFFECT ON DIELECTRIC RELAXATION PHENOMENA IN KCl AND NaCl*

DEMITRIOS MILIOTIS† **and DUK N. YOON**
Department of Physics and Materials Research Laboratory, University of Illinois, Urbana, Ill. 61801, U.S.A

(*Received* 14 *August* 1968)

Abstract – Dielectric relaxation effects previously reported in KCl and NaCl with and without divalent impurities are reexamined in the 35 Hz–10 mHz range at temperatures between 200° and 700°C. It is demonstrated that, except for those effects which can be unambiguously attributed to the well-known divalent impurity-vacancy interaction, the relaxation at high frequencies and the polarization at low frequencies observed previously can be explained by the presence of air-gaps between the specimen and electrodes. A correct method for measuring the true ionic conductivity of ionic crystals is suggested.

INTRODUCTION

Dielectric relaxation and polarization phenomena in alkali- and silver-halides have been widely studied. Breckenridge[1,2] first observed dispersions in the dielectric constants of many alkali- and silver-halides with and without added divalent impurities. These dielectric losses, which occurred at several different temperatures at a fixed frequency for some specimens, were attributed to the relaxation processes involving various complexes of the divalent impurities and vacancies. It was later discovered, however, that many of the relaxation peaks reported by Breckenridge could not be reproduced[3–6] and that some irregularities in the loss curves were caused by improper electrodes[3].

Recently, Sastry and Srinivasan[7], Economou and Sastry[8] and Economou[9] observed dispersion in the dielectric constants of KCl, NaCl, and KBr crystals at the temperatures between 600° and 700°C in the frequency range between 1 and 10 mHz. These losses were attributed to the relaxation of anion and cation vacancy pairs.

Dielectric losses in the 1–10 kHz range at temperatures between 100° and 500°C were also reported in NaCl[10,11], KCl[12], LiF[13] and NaCl doped with Ca[11]. These loss peaks, in most cases, were shown to be clearly distinguished from those[23] due to the divalent impurity-vacancy relaxation.

In the low frequency range between 50 and 1000 Hz, Friauf[14] observed dielectric dispersion in AgBr at 200°–300°C. Later, Jacobs and co-workers[15–17] reported very large capacitance variation in the same frequency range in KCl with and without divalent impurities. Similar effects were also observed in NaCl by Bean[24].

The interfacial polarization caused by a uniform layer of high resistance between the specimen and the electrodes was suggested as a possible explanation of these losses[10,24]. However, the nature of this high resistance layer or a method of eliminating it was never suggested. The low-frequency relaxation effects have been discussed most extensively in terms of theories of interfacial polarization developed by Friauf[14], MacDonald[18] and Beaumont and Jacobs[17]. In these

---

*Supported in part by the U.S. Advanced Research Projects Agency under Contract SD-131 and by the U.S. Atomic Energy Commission under Contract AT(11-1)-1198

†*Present address:* Department of Physics, University of Athens, Athens, Greece.

theories the interfacial polarization is described in terms of a Debye layer of charge at the electrodes. The most important parameter for interpreting the experimental results is the degree of charge blocking at the electrodes. The observed magnitude of the capacitance and its dependence on frequency could not be consistently explained by assuming various degrees of blocking within the framework of these theories. Also, the results of d.c. measurements[19] could not be satisfactorily understood by this model.

Upon a careful examination of most of the experimental results described so far, two characteristic problems become evident: first, the irreproducibility of the data, and second, the large dependence on the material and condition of the electrodes. It is therefore suspected that these phenomena may not represent any physical processes inherent in the specimens or their contacts with the electrodes.

In this paper it is shown that the relaxation phenomena in KCl and NaCl observed earlier, except those which can be unambiguously attributed to the divalent impurity-vacancy relaxation, are probably caused by the existence of actual gaps between the specimen and the electrodes. For convenience these gaps will be called 'air-gaps'. The theory of Maxwell-Wagner[20] interfacial polarization, in which the air-gap is one of the dielectric layers, is briefly reviewed. The validity of this model is demonstrated by experimental observations on specimens with deliberately introduced air-gaps. It is then shown that the high-frequency relaxation effects, which would be caused by large air-gaps, can be eliminated by improving the contact between the specimen and the electrodes.

In the low-frequency region, the observed strong dependence of the a.c. and d.c. relaxation effects on the nature of the contacts is also explained most consistently by the air-gaps. While Friauf's and MacDonald's theories assume that the degree of charge blocking is uniform at all areas of the specimen-electrode contacts, the present model suggests that only part of the areas are completely blocked by the air-gaps. The d.c. observations suggest that for a given applied voltage the areas of good contact show no blocking effect.

Finally, based on these considerations, a method of measuring the true ionic conductivity in ionic crystals is suggested.

MAXWELL-WAGNER POLARIZATION WITH AIR-GAP

A specimen of conductance G_S and capacitance C_S with an air-gap of capacitance C_A can be represented by the parallel G_S and C_S in series with C_A. The effective total parallel conductance G and capacitance C, which are the quantities usually measured experimentally, are written as [20]

$$C = C_\infty + \frac{C_0 - C_\infty}{1+\omega^2\tau^2} \qquad (1)$$

$$G = G_\infty - G_0 - \frac{G_\infty - G_0}{1+\omega^2\tau^2} \qquad (2)$$

where ω is the angular frequency, and C_0 $(=C_A)$, $C_\infty(=(C_AC_S)/(C_A+C_S))$, G_0, and $G_\infty(=G_S(C_A/(C_A+C_S))^2)$ are the effective capacitance and conductance at the low and high frequency limits, respectively. τ is the relaxation time given by

$$\frac{1}{\tau} = 2\pi f_0 = \frac{G_S}{C_A + C_S}. \qquad (3)$$

f_0 is the frequency at which the maximum dispersion occurs.

If the air-gap thickness d_A is small compared to the sample thickness d_S, f_0 is given by

$$f_0 = \frac{\sigma_S d_A}{2\pi\epsilon_0 d_S} = \frac{G_\infty - G_0}{2\pi(C_0 - C_\infty)} \qquad (4)$$

where ϵ_0 is the dielectric constant of the air and σ_S is the conductivity of the sample.

These relations show that the Maxwell-Wagner relaxation is indistinguishable from the simple orientation polarization of the Debye theory. Also, these equations are of the same form as the solutions of the MacDonald [18] and Friauf[14] theories with completely blocking electrodes. In this case, however, τ is determined by the thicknesses of the specimen and the air-gap.

When the air-gaps between the specimen and the electrodes can be divided into groups with different average values of d_A, the frequency dependence of the total effective capacitance and conductance will resemble the curves shown in Fig. 1. The average relaxation frequency f_0 and the corresponding d_i can be calculated from equation (4) by taking for C_0, C_∞, G_0, G_∞, the values of the measured capacitance and conductance at the low and high frequency limits of the particular dispersion region. As the sample temperature is increased, the f_0's will increase linearly with conductivity if the air-gap sizes remain constant.

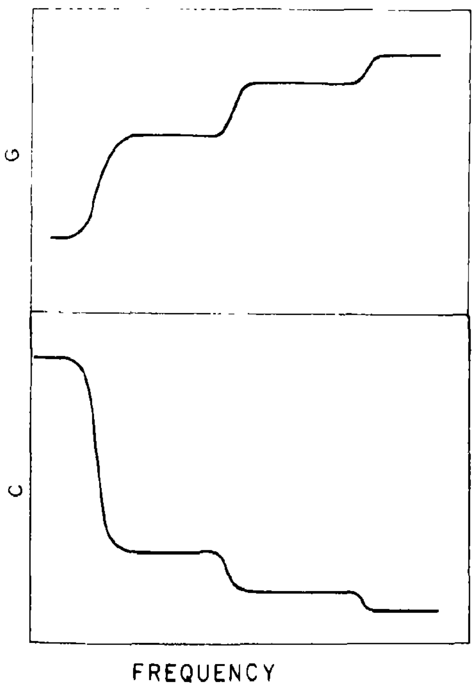

Fig. 1 The expected frequency dependence of the total effective conductance G and capacitance C caused by air-gaps of different thicknesses

EXPERIMENTAL RESULTS AND DISCUSSIONS

The a.c. measurements were made by standard capacitance bridge techniques. The bridges used were: for the 35–5000 Hz range, a General Radio Type 1603-A and 716-C with a Hewlett-Packard 302 A wave analyzer; for the 5–500 kHz range, a Boonton Model 75 C; and for the 500 kHz–10 mHz range, a General Radio Type 821-A. For d.c. measurements, a potential of about 4·3 V was supplied by two Willard DH-5-1 batteries, and the current was measured with a Hewlett-Packard recorder connected across a standard resistor in series with the specimen. Because the recorder response time was about 0·5 sec, the current immediately after the battery switch was turned on could not be measured.

The KCl and NaCl samples were supplied by the Harshaw Company. The samples with divalent impurities were grown in this laboratory. NaCl–Ca samples contained about 0·55 per cent Ca and KCl–Sr samples, about 0·03 per cent Sr by weight. Typical sample dimensions were 0·5 × 0·5 × 0·15 cm.

Two different sample holders were used. The first sample holder, which will be called Sample Holder I, is the commonly used coaxial line type[25] with platinum sheets hard soldered to nickel pieces. A spring was attached at the end of the electrode with a coaxial rod. The spring tension was varied from about 200 g/cm^2 to 1000 g/cm^2. The two electrodes appeared to be almost parallel to each other, and no particular care was taken to make them optically flat or parallel. The second sample holder, Sample Holder II, was a simple C-clamp with 12 mil thick platinum sheets as electrodes and two pieces of flat alumina and Refrasil cloth as insulators. Because of the swivel seat at one end of the clamp and slight deformation of the platinum sheets under tightening of the clamp, the contact between the specimen and electrodes appeared excellent.

To improve the contacts, silver paint was applied on some specimens. It was found, however, that improper use of the silver paint could have adverse effects, and great care was necessary for its proper use. After the application of the silver paint the samples were left at room temperature for more than four days to dry the organic material slowly. Then samples were placed in an oven and the temperature was slowly increased to about 200°C. If the drying time was less than four days, small bubbles were formed between the specimen surface and the paint when exposed to high temperatures. Large diffusion of silver into the specimens can also cause errors. It was found that at 700°C, when Sample Holder II was used, silver diffused rapidly into the specimens and the measured conductivity increased rapidly with time. Up to about 600°C, however, the silver diffusion appeared to be small within the usual duration of experiments. In Sample Holder I, no significant diffusion of Ag was observed even at 700°C.

(*A*) *Deliberately introduced air-gaps*

Experiments were performed on a crystal with deliberately introduced air-gaps to demonstrate the validity of the equivalent circuit model described earlier. On both sides of a KCl crystal 0·05 mm-deep grooves were cut with a milling machine, so that only the four corners were in contact with the electrodes. The contact areas were about 10% of the total specimen surface area.

The results of measurements on this sample at 380°C are shown in Fig. 2. The dispersion is due to the 0·05 mm air-gaps, because the frequency, f_0, and the dependence of the effective conductance and capacitance on frequency can be accurately predicted from the size of the air-gap and estimated conductivity of the specimen from equation (4).

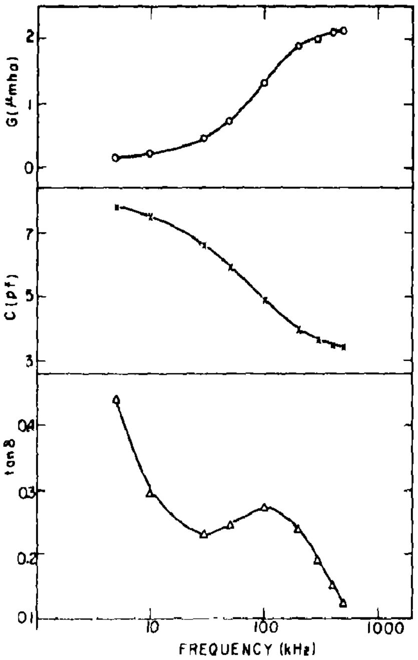

Fig. 2. The dispersion observed in a KCl sample with deliberately introduced air-gap at 380°C. The dissipation factor, tan δ, was calculated from G and C.

As the temperature is increased to about 600°C, this dispersion region moved to the mHz range, and another dispersion appeared in the low (35–1000 Hz) frequency range. This low frequency dispersion, which is caused by the contacts at the four corners, will be discussed later. The initial (about 0·5 sec after the application of the step voltage) d.c. conductance was about one-tenth of the expected value and the steady state value was even less.

(*B*) *High frequency dispersion*

The high frequency dispersions usually observed in ordinary experimental situations will now be discussed. Table 1 shows some of the typical dispersions we observed in NaCl and KCl crystals; the temperature and frequency ranges are consistent with those reported earlier[10–13]. Sample Holder I was used with flat and apparently parallel electrodes. The samples had cleaved surfaces. Initially, only small spring pressure was applied, and these dispersions were observed

Table 1. The relaxation frequencies, f_0, *observed in the kHz range at temperatures,* T_m, *the estimated thicknesses,* d_A, *and the fractional areas,* A'/A_S *of the air-gaps causing these relaxations. The conductivity,* σ, *was calculated from the observed conductance at the high frequency limit*

Sample	T_m (°C)	d_S (cm)	σ (μmho/cm)	f_0 (kHz)	d_A (mm)	A'/A_S
KCl	566	0·13	1·1	35	0·022	0·76
NaCl	546	0·15	2·5	60	0·020	0·40
NaCl-Ca	220	~0·1	~0·3	3	~0·006	0·88

at fixed temperatures before heating the samples close to their melting points. In case of NaCl-Ca, the dispersion listed here is clearly distinguished from another dispersion caused by the divalent impurity and vacancy interaction. The air-gap thickness, d_A, was estimated from the observed f_0 using equation (4). The ratio between the air-gap area, A', and the total specimen area, A_S, was estimated from G_0 and G_∞. These values do not necessarily represent the actual size of the gaps, because the dispersions show the net effect of the gaps on both sides of the specimen surfaces.

The following observations suggest that these relaxations are caused by air-gaps. First, the reproducibility of the dispersion frequency, f_0, was extremely poor under, presumably, identical experimental conditions. Secondly, as the contacts were improved, the dispersion consistently decreased, and after the specimens were kept at temperatures close to the melting points under high spring tension for about one hour, the dispersion disappeared almost completely. Figure 3 shows the dispersion curves observed in an NaCl sample before and after raising the temperature of the specimen to 750°C. With careful application of silver paint or with the use of Sample Holder II, the dispersions also disappeared.

These dispersions will be shifted to mHz range as temperature is increased close to the melting points. The losses which occur in the mHz range were given special attention, because these were earlier attributed to the vacancy-pair relaxation by Sastry, Economou, and Srinivasan[7–9]. Losses similar to those reported by Sastry, Economou, and Srinivasan were sometimes found in KCl when Sample Holder I was used with a low spring pressure. However, when the specimen was left at about 700°C for a few hours, the loss

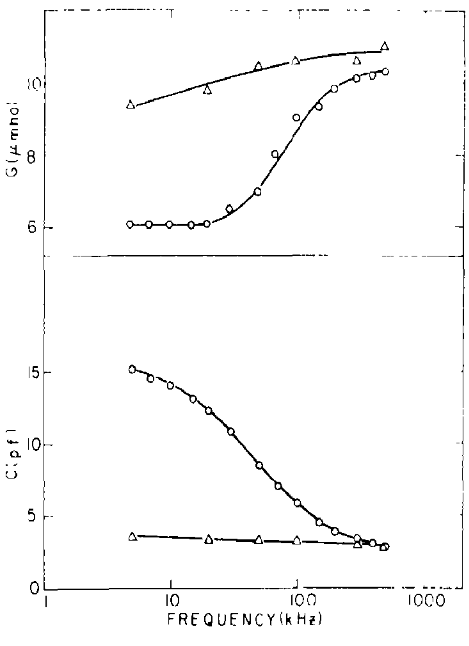

Fig. 3. The dispersion observed in an NaCl sample at 546°C before (the circles) and after (the triangles) raising the temperature close to the melting point.

peak became smaller. When higher pressure was applied, the peak immediately disappeared almost completely. Again, with silver paint application or with Sample Holder II, no loss was observed in this frequency range. Figure 4 shows the result in Sample Holder I with a silver painted specimen.

Analysis of Sastry and Srinivasan's[7] data at 703°C shows that their air-gap thickness was probably about 7×10^{-3} cm. Using equation (4) and values of G_0, G_∞, C_0, and C_∞ given in their paper, the observed f_0 can be predicted fairly accurately. Economou's observation that the loss peak frequency, f_0, was independent of the sample thickness could not be substantiated; the apparent loss frequencies varied almost randomly from sample to sample regardless of their thickness.

The dispersions which are usually attributed to the divalent impurity-vacancy pair in NaCl–Sr could not be eliminated by improving contacts. If this relaxation were caused by air-gaps, the expected thickness of the gaps are so large that they could have been easily eliminated. Also, many careful previous measurements[23] show that this is a volume phenomenon.

(C) *Low frequency dispersion*

It is obvious from the discussions thus far, that if extremely thin air-gaps exist between the specimen and electrodes, high-capacitance dispersions will be found in the low-frequency region. The question to be dealt with here is whether any such air-gaps were the direct cause of the high-capacitance dispersions in the 300–1000 Hz range observed by Friauf [14] and Jacobs and co-workers[15–17].

With common electrode techniques of heating the sample between the electrodes to temperatures close to the melting points, applying silver paint, or evaporating platinum, it is not difficult to imagine, that at some portions of the specimen-electrode contact area, actual gaps of extremely small size will exist. In fact, it was pointed out by Panchenko[21] that extreme caution is necessary to reduce air-gaps with these techniques even at low temperatures. In addition, the contacts can become worse at the temperatures at which measurements are performed, because the thermal expansion coefficients of the alkali-halide crystals are about ten times larger than those of the usual noble metal electrode materials.

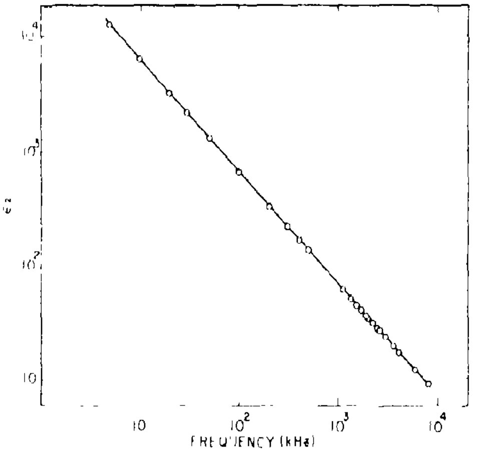

Fig. 4 The observed frequency dependence of the imaginary part of the dielectric constant, ϵ_2, of KCl at 693°C

Although attempts to eliminate the dispersions presumably caused by extremely small air-gaps were not successful, the following observations strongly suggest that the air-gaps were the direct cause of the low frequency dispersions reported previously [14–17].

First, there was a strong dependence of the relaxation effects on the surface condition of the specimens, which can be most readily and consistently explained by air-gaps. The a.c. measurements shown in Fig. 5 were performed with Sample Holder II. With this sample holder, the observed low frequency dispersion effects did not significantly change after heating the samples close to the melting point. The d.c. measurements shown in Fig. 6 were performed immediately after the a.c. measurements.

Although these curves represent the superposition of many dispersion frequencies

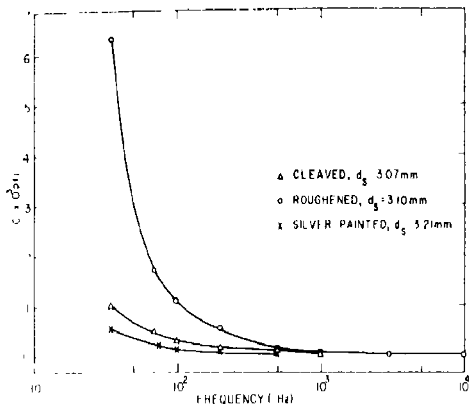

Fig. 5. The observed frequency dependence of the capacitance in KCl–Sr samples of different surface conditions at 603°C.

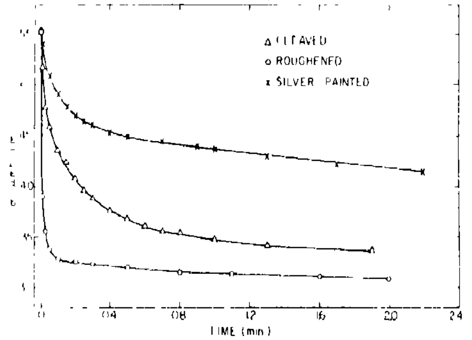

Fig. 6. The observed effective conductivity, σ, as a function of time after applying a step voltage, for KCl–Sr samples of different surface conditions at 603°C.

caused by air-gaps of varying thicknesses, both a.c. and d.c. measurements show the expected variation of the air-gap sizes with the surface condition; the d.c. results show that the specimen whose surface was roughened with sandpaper has large air-gaps covering large areas, whereas the silver painted specimen has predominantly smaller gaps, causing the slower decay of the d.c. current. Since the dispersion region in the silver-painted specimen is mostly at very low frequencies, the capacitance observed at the measured frequency range is smaller in the silver painted specimen than in the roughened specimen. The cleaved sample shows intermediate behavior between these two cases. Actually, a similar systematic dependence of the dispersion effect for different electrodes is quite evident from the data of Allnatt and Jacobs [15].

Secondly, the large steady state d.c. conductivity shows that, at least with the particular voltage (4·3 V) applied, transfer of charges between the specimen and electrodes is not impeded at most of the contact area. In addition, the steady state conductivity appears to increase with improving contact. It is difficult to attribute such large d.c. conductivity to electron conduction, as suggested by Jacobs and Maycock [16].

Finally, direct observation of the contacts indicates the presence of air-gaps. For direct observation of the contact area, a cleaved KCl sample was placed in Sample Holder I with 6 mil thick platinum sheets on both faces. It was kept at 700°C for 1 hr under high spring tension and slowly cooled to room temperature after reducing the spring tension. The crystal was intact and the platinum sheets appeared to be firmly attached to it. The sample was then cleaved through the middle, and the contact area was observed under the microscope from the cleaved end of the crystal.

The contact area, which covered about half of the crystal surface, could be clearly distinguished from the non-contact area. Some evidence for the occurrence of thermal etching in the non-contact suggests that the gap was present also at high temperatures. The thickness of the gaps observed under the microscope was extremely small.

The presence of air-gaps explains the confusion in the previous attempts to interpret these polarization effects in terms of a Debye layer of charges within the crystals. Since the polarization is determined by the thickness and area of the gaps, the existence of the Debye layer caused by blocking of the charge can be viewed as a consequence of the existence of the gap.

Although no experimental observations on AgBr were made, it seems possible that the polarization effects in AgBr observed by Friauf[14] were also caused by air-gaps. The effects in AgBr were observed at lower temperatures because the conductivity of AgBr is higher than KCl or NaCl at the same temperature. In fact, in any ionic crystals, the existence of air-gap in the specimen-electrode interface will cause polarization effects.

CONCLUSIONS

It was shown in this paper that the relaxation effects in KCl and NaCl observed in the kHz and mHz range, except those which can be unambiguously attributed to the divalent impurity and vacancy interaction, can be eliminated by improving the contact between specimen and electrodes. The existence of actual gaps is the most likely cause of the apparent relaxation effects.

Also, in the low frequency range, air-gaps appear to provide the best explanation for the high-capacitance polarization effects, although the effects could not be completely eliminated by usual electrode techniques.

One important aspect of the present work is that a correct way of measuring the ionic conductivity can be suggested. With a d.c. technique, Sutter and Nowick[22] suggested that the *final* steady-state conductivity, and not the initial conductivity, represented the true ionic conductivity. Although they were probably correct, at least in part, in interpreting the time dependent polarization observed at low temperatures as real dielectric phenomena, they also assumed that the contact was perfect. Since the contacts are shown to be imperfect in this paper, *neither* the initial nor the final d.c. conductivity gives the true ionic conductivity under ordinary experimental situations. Instead, a.c. techniques should be used. The existence of large air-gaps may be easily checked by extending the measurements to fairly high frequencies, and large gaps can be easily eliminated by usual methods of improving contacts. Since the low-frequency dispersions, probably caused by very small gaps, are difficult to eliminate, the frequencies must be above this range to measure the correct ionic conductivity. At very high frequencies, however, the dipole orientations of the divalent impurity-vacancy pair can cause error in the measured conductivity.

Although only KCl and NaCl were measured experimentally in this work, these conclusions should apply to other alkali-halides, silver-halides, and ionic crystals in general.

Acknowledgements—The authors would like to express their appreciation to Professor R. J. Maurer and Professor D. Lazarus for helpful suggestions and discussions.

REFERENCES

1. BRECKENRIDGE R. G., *J. chem. Phys.* **16**, 959 (1948)
2. BRECKENRIDGE R. G., *J. chem. Phys.* **18**, 913 (1950)
3. HENVIS B. W., DAVISSON J. W. and BURSTEIN E., *Phys. Rev.* **82**, 774 (1951)
4. HAVEN Y., *J. chem. Phys.* **21**, 171 (1953)
5. HAVEN Y., *Rep. Conf. Defects in Crystalline Solids*, p. 261. Bristol (1955)
6. JACOBS G., *Naturwissenschaften* **42**, 575 (1955).
7. SASTRY P. V. and SRINIVASAN T. M., *Phys. Rev.* **132**, 2445 (1963).
8. ECONOMOU N. A. and SASTRY P. V., *Phys. Status Solidi* **6**, 135 (1964)
9. ECONOMOU N. A., *Phys. Rev.* **135**, 1020 (1964)
10. WIMMER J. M. and TALLAN N. M., *J. appl. Phys.* **37**, 3728 (1966)
11. KESSLER A. and MARIANI E., *Czech. J. Phys.* **B14**, 757 (1964)
12. SANO R. and TOMIKI T., *J. phys. Soc. Japan* **21**, 1697 (1966)
13. MAITROT M. *et al.*, *C. r. hebd. Seanc. Acad. Sci.*, *Paris* **B264**, 1549 (1967)
14. FRIAUF R. J., *J. chem. Phys.* **22**, 1329 (1954)
15. ALLNATT A. R. and JACOBS P. W. M., *J. Phys. Chem. Solids* **19**, 281 (1961).
16. JACOBS P. W. M. and MAYCOCK J. N., *J. chem. Phys.* **39**, 757 (1963).
17. BEAUMONT J. H. and JACOBS P. W. M., *J. Phys. Chem. Solids* **28**, 657 (1967)
18. MACDONALD J. R., *Phys. Rev.* **92**, 4 (1953).
19. ALLNATT A. R., JACOBS P. W. M. and MAYCOCK J. N., *J. chem. Phys.* **43**, 2526 (1965).
20. See for example VON HIPPEL A. R., *Dielectrics and Waves*, p. 228. Wiley, New York (1954).

21. PANSCHENKO V. V., *Fiz. Tverd. Tela* **6**, 584 (1964); Eng. transl.-*Soviet Phys. solid St.* **6**, 457 (1964).
22. SUTTER P. H. and NOWICK A. S., *J. appl. Phys.* **34**, 734 (1963).
23. See for example LIDIARD A. B., *Handbuch der Physik*, Vol. XX, p. 312. Springer, Berlin (1957).
24. BEAN C. P., Thesis, University of Illinois (1952).
25. WATKINS G. D., *Phys. Rev.* **113**, 91 (1959).

J. Phys. Chem. Solids Pergamon Press 1969. Vol. 30, pp. 1251–1259. Printed in Great Britain.

SECOND-RANK TENSOR ANION POLARIZABILITIES IN SOME RUTILE GROUP CRYSTALS

CHARLES O. POLLARD, Jr.*

Department of Geology, Florida State University, Tallahassee, Fla 32306, U.S.A.

(*Received* 21 *February* 1968; *in revised form* 1 *August* 1968)

Abstract—Straightforward computation of anion polarizability elements for light electric vector vibration parallel with, then normal to, the plane of three cations bonded to each anion [either (110) or (110)] in six rutile-group minerals yields the following values.

	α cation (Å^3)	$\alpha^{\parallel}$ anion (Å^3)	$\alpha^{\perp}$ anion (Å^3)
TiO_2(Rutile)	2·5	35·1	22·6
SnO_2(Cassiterite)	30·5	10·5	23·6
GeO_2	11·9	18·0–18·7	7·0–5·4(Depending on n_ϵ)
MgF_2(Sellaite)	7·9	7·2	8·0
ZnF_2	9·9	10·0	13·0
NiF_2	15·0	7·6	10·4

(The values are in rationalized units, and for lowest available visible refractive indices The isotropic cation polarizalities are 'input' data.) Actually, the tetragonal character of these minerals precludes rigorous separation of the two elements for vibration normal to the cation plane and parallel to the cation plane, but normal to the *c*-axis. These two elements are linearly related. The linear relation is solved by the approximation that the parallel element of this relation and the element for vibration parallel both with the cation plane and with the *c*-axis are equal This approximation improves as the three bond lengths approach equality. Of the minerals reported, only cassiterite has all nearest-neighbor bond lengths essentially equal; anion polarizability values are hence more nearly rigorous in this respect for cassiterite than for the other minerals. Reiteration with all the values is necessary for refinement

INTRODUCTION

A RIGOROUS model relating ion properties to crystal optical behavior demands anisotropic polarizabilities. On the other hand, attributing anisotropy to each ion gives rise, for most crystals, to equations that are intractable. Hence, in the present paper, the anion polarizability alone is represented as a second-rank tensor. The method developed is applicable for crystals referable to orthogonal axes with only one anion type and environment. The method is demonstrated by the computation of anion polarizability tensors in six rutile-group compounds.

The assumptions used are similar to those in works by Bolton, Fawcett and Gurney (BFG)[1] and by Field[2]. These assumptions include the following: (a) ions polarized by electric fields with the frequency of visible light can be well approximated as point dipoles at the ionic sites, (b) cation polarizabilities can be represented as isotropic, and (c) the dispersion exhibited in some rutile compounds is a relatively insignificant deviation from the conditions of the Maxwell ($n^2 = K$) relation. Assumption *c* is of particular interest, of course, because the real part of the dielectric constant is strictly

---

*[*] *Present address*: Crystal Physics Branch and Geophysical Sciences, Georgia Institute of Technology, Atlanta, Georgia 30332, U.S.A.

equal to the difference between the squares of the real and imaginary parts of the refractive index at frequencies where dispersion is observed. Whereas no absorption data are available giving imaginary parts of refractive indices for polarized light in the rutile minerals, assumption *c* is unavoidable. The method developed by BFG[1] had been the basis for the calculation of anisotropic anion polarizabilities in the following rutile group compounds: rutile-TiO_2 (by BFG); and rutile, GeO_2, and stishovite-SiO_2 (all by Field). The present method is similar to that of BFG in that the original equations are essentially equivalent. The differences are in the modes of solution and simplifying assumptions. The rutile group is chosen for study because there is considerable variation in cation field strength, and because there is some 'biaxial' asymmetry at the anion sites.

The system of units used is Lorentz–Heaviside, or, equivalently, cm g sec, rationalized.

THE METHOD

Equation (1) describes the anistropic response of ion l' with polarizability tensor elements $(\alpha_{l'})_{ij}$ to a local electric field with components $(E_{l'})_j$ by the development of a dipole with components $(\mu_{l'})_i$:

$$(\mu_{l'})_i = (\alpha_{l'})_{ij}(E_{l'})_j. \qquad (1)$$

(The prime is necessary because of future notation difficulties.) The second-rank tensor subscript notation and summation convention is as presented in Nye[3].

The local fields are determined by the combination of the macroscopic field and the dipole fields of the other ions, which creates a cyclic dependence of local fields on other local fields. In general, the present method of accounting for these electrostatic interactions is similar to that introduced by Bragg[4], who used the logic inherent in the Lorentz–Lorenz equation. A fictional cavity is constructed around the central unit cell, in the form of an expanded unit cell. See BFG[1] for a discussion of the merits of this cavity shape. The local electric field $\vec{E}_{l'}$ can then be equated to the sum $(\vec{E}+\vec{A}^{l'}+\vec{B}^{l'})$. The last two terms are corrections to the macroscopic electric field $\vec{E}$. $\vec{A}^{l'}$ represents the field from the distant dipoles, outside the cavity, acting collectively as a continuum. $\vec{B}^{l'}$ represents the sum of dipole fields from ions inside the cavity. The size of the cavity is the important factor in bringing about a convergence of the sum $(\vec{A}^{l'}+\vec{B}^{l'})$ to a value near that of the real interaction field.

The components of the macroscopic polarization (dipole moment per unit volume) of a crystal can be represented by summing the components of the individual dipoles in a given volume, as shown in equation (2).

$$(U_1U_2U_3)P_i = \sum_{l'=1}^{W} (\alpha_{l'})_{ij}(E_j + A_j^{l'} + B_j^{l'}) \qquad (2)$$

where U_1, U_2, U_3 are unit cell dimensions; P_i is the *i*-component of macroscopic polarization; l' identifies the original ion, at which the various quantities are evaluated (n.b.—the l' ion occupies the origin of axes and the origin changes for each term in the series); and W is the number of ions in the unit cell.

The components of $\vec{E}$, $\vec{A}^{l'}$, and $\vec{B}^{l'}$ can also be evaluated in terms of other tensor relations with P. The tensor matrices χ_j (dielectric susceptibility) and β_j (Lorentz cavity factor) are already diagonal for orthogonal crystal systems.

$$E_j = \frac{1}{\chi_j}P_j \qquad (3a)$$

and

$$A_j^{l'} = \beta_j P_j \qquad (3b)$$

where $\chi_j = (n_j^2 - 1)$, by the Maxwell relation; and

$$\beta_1 = \frac{2}{\pi}\tan^{-1}\left\{\frac{U_2U_3}{U_1\sqrt{(U_1^2+U_2^2+U_3^2)}}\right\}, \text{etc. [1, 2].}$$

$B^{l'}$ depends on the evaluation of the dipolar fields of all other dipoles within the cavity. Ions need only be located in the central unit cell, as incremental lattice translation locates counterpart ions. Because changing the l' ion can locate new sets of ions on faces, edges, and corners of unit cells and of the Lorentz cavity, it is necessary to introduce a second index (l, which only in combination with l' denotes a given ion in any unit cell). Reference to a particular ion in a particular unit cell requires the integer values of l', l, m_1, m_2 and m_3, where m_i indicates one from the set of lattice planes normal to the i-axis. Then

$$\vec{B}^{l'} = \sum_{l=1}^{V'} \sum_{m_1=-t}^{t} \sum_{m_2=-t}^{t} \sum_{m_3=-t}^{t} \vec{\nabla}[(\vec{\mu}_l^{l'} \cdot \vec{\Gamma})/4\pi r^2]$$

in which[5] V' is the number of ions shared by, or belonging to, the central unit cell (The prime indicates that V' is dependent on the value of l' and the prime on the first capital sigma indicates the convention that the term when $l' = l$ is excluded if $m_1 = m_2 = m_3 = 0$.); t is the number of unit cells to each side of the central unit cell within the Lorentz cavity (If $t = 2$, there are 125 unit cells in the Lorentz cavity.); $\vec{\nabla}$ is the gradient operator; $\vec{\mu}_l^{l'}$ is the dipole moment of the ion l when l' is at the origin; r is the distance from the origin to the ion l, or one of its $[(2t+1)^3 - 1]$ counterparts, as determined from the relation

$$r = \sqrt{(U_1^2(m_1 + X_l^{l'})^2 + U_2^2(m_2 + Y_l^{l'})^2 + U_3^2(m_3 + Z_l^{l'})^2)}$$

if $(U_1 X_l^{l'})$, $(U_2 Y_l^{l'})$, and $(U_3 Z_l^{l'})$ are the coordinates of the l ion relative to the l' ion at the origin; and

$\vec{\Gamma}$ is the unit vector from the origin to ion l or one of its counterparts, the components being determined by the relations

$$\Gamma_1 = (m_1 + X_l^{l'})U_1/r, \text{etc.}$$

Hence, if δ_{jq} is the Kronecker delta and

$$(G_l^{l'})_{jq} = (G_l^{l'})_{qj} = \sum_{m_1=-t}^{t} \sum_{m_2=-t}^{t} \sum_{m_3=-t}^{t} \frac{(3\Gamma_j\Gamma_q - \delta_{jq})}{4\pi r^3}$$

then

$$B_j^{l'} = \sum_{l=1}^{V'}{}' (G_l^{l'})_{jq}(\mu_l^{l'})_q$$

where each $(G_l^{l'})_{jq}$ is the sum of geometrical factors relating the contributions from the q-components of the l dipole and its counterparts to the j-component of the local field at the origin (l' ion).

Determining the local fields that affect the values of the $(\mu_l^{l'})_q$ presents the same difficulties as evaluating the local fields $\vec{E}_{l'}$, in equation (1). To solve this problem, the local field is separated into macroscopic, Lorentz, and dipolar portions, as was done for the $\vec{\mu}_{l'}$ dipoles, but a value of zero is assigned to the dipolar portion. It is thought that the method presented here is an improvement because the (arbitrarily) nil dipole interaction correction affects not the central ion l', as it does in methods based on Lorentz-Lorenz reasoning, but the other ions l.

$B_j^{l'}$ is then approximately given by

$$B_j^{l'} = \sum_{l=1}^{V'}{}' (G_l^{l'})_{jq} \left[\frac{(\alpha_l^{l'})_{qs}}{h_l^{l'}}\right]\left[\beta_s + \frac{1}{(n_s^2 - 1)}\right] P_s \quad (4)$$

where all symbols have been explained except $(\alpha_l^{l'})_{qs}$, which is the same as the qs-element of polarizability for the ion l in the central unit cell when the l' ion is at the origin; and $h_l^{l'}$, which is 8 if the l ion is on a corner of the unit cell, 4 if the l ion is on an edge, 2 if the l ion is on a face, and unity otherwise, all when the l' ion is at the origin.

Combining equations (2), (3), and (4), and letting

$$\left[\beta_j + \frac{1}{(n_j^2 - 1)}\right] = \gamma_j$$

$$(U_1 U_2 U_3)P_i = \sum_{l'=1}^{W} (\alpha_{l'})_{ij}\left[\gamma_j P_j + \sum_{l=1}^{V'}{}'(G_l^{l'})_{jq} \times \frac{(\alpha_l^{l'})_{qs}}{h_l^{l'}} \gamma_s P_s\right].$$

Application of three linearly independent polarization vectors to this equation could yield the nine independent equations necessary to attain values for the nine polarizability tensor elements $(\alpha_{l'})_{ij}$ of one ion l'. Rather than to attempt solution of these nine simultaneous quadratic equations, a further simplification is introduced. The anisotropic polarizability elements $(\alpha_l^{l'})_{qs}$ at the l dipoles are replaced by isotropic polarizabilities $\alpha_l^{l'}$. Three sets of three linear simultaneous equations in $(\alpha_{l'})_{1j}$, $(\alpha_{l'})_{2j}$, and $(\alpha_{l'})_{3j}$ are thereby obtained when any three linearly independent polarization vectors are applied:

$$(U_1U_2U_3)P_i = \sum_{l'=1}^{W} (\alpha_{l'})_{ij}\left[\gamma_j P_j + \sum_{l=1}^{V'}{}'(G_l^{l'})_{jq} \cdot \frac{\alpha_l^{l'}}{h_l^{l'}}\gamma_q P_q\right]. \qquad (5)$$

Equation (5) is the general equation, which is valid in the absence of detailed symmetry information or additional simplifying assumptions only for minerals with one ion per unit cell. One such assumption that has been made is that ions with demonstrably small polarizabilities (such as many cations) can be assigned isotropic polarizabilities without introducing substantial error.

THE RESULTS

Even though the cations are here represented to be isotropic, it is still only possible to obtain polarizability elements for one anion, unless all anions happen to be symmetrically equivalent. The anions in rutile crystals are equivalent, and conveniently are related by reflections and rotations of 180°.

With the incorporation of equation (6), the axis-transformation law specialized for reflection or rotation only through 180°, the equivalent elements $(\alpha_{l'})_{ij}$ of any one set of symmetrically equivalent ions in the unit cell are appropriately equated.

$$(\alpha_{l'})_{ij} = a_{ii}^{l'}a_{jj}^{l'}\,(\alpha_{l''})_{ij} \qquad (6)$$

where the l'' in $(\alpha_{l''})_{ij}$ is indicative of a selected individual l' dipole with which reverse symmetry operations can bring the other l' dipoles into equivalence, and where the $a_{ii}^{l'}$ and $a_{jj}^{l'}$ are direction cosines appropriate for relating each other anion to l'' (the cosines assume values of ±1·0). For convenience, the three unit polarization vectors ($[P_1, P_2, P_3]$ = [1, 0, 0], [0, 1, 0], and [0, 0, 1]) are chosen and equation (5) is specialized:

$$C_{ijm}(\alpha_{l''})_{ij} = K_{im} \qquad (7)$$

where

$$C_{ijm} = \sum_{l'=l''}^{W} a_{ii}^{l'}a_{jj}^{l'}\left[\gamma_j P_j + \sum_{l=1}^{V'}{}'(G_l^{l'})_{jq}\left(\frac{\alpha_l^{l'}}{h_l^{l'}}\right)\gamma_q P_q\right]$$

and

$$K_{im} = (U_1U_2U_3)P_i - \sum_{l'=1}^{(l''-1)} \alpha_l^{l'}\left[\gamma_i P_i + \sum_{l=1}^{V'}{}'(G_l^{l'})_{ij}\left(\frac{\alpha_l^{l'}}{h_l^{l'}}\right)\gamma_j P_j\right]$$

with $P_m = 1$ and the other $\bar{P}$ components zero. Obviously, the ions must be numbered so those are first that are to be approximated to be isotropic (in this case, cations); hence, l'' in equation (6) is one more than the number of cations.

A Fortran IV program was constructed for calculation of the C_{ijm} and K_{im} of equation (7). The program was shown to represent correctly the computation of these values by a hand check for a hypothetical mineral with only one cation and one anion per unit cell. Computations were then carried out for rutile-TiO_2, cassiterite-SnO_2, GeO_2, sellaite-MgF_2, ZnF_2 and NiF_2, all with the rutile structure. The ions in a rutile mineral occupy the general sites[6] given in Table 1, in which the numbering is for this paper only. D assumes a different value for each mineral, as shown in Table 2. (D_1 in Table 2 is the value D would have if all nearest-neighbor bond lengths were

Table 1. *General ion locations in rutile-group minerals (See Table* 2 *for values of* D *in specific minerals)*

Ion (I′)	X_I^2	Y_I^2	Z_I^2	Type	V′
1	0	0	0	Cation	15
2	$\frac{1}{2}$	$\frac{1}{2}$	$\frac{1}{2}$	Cation	15
3(I'')	$(\frac{1}{2}+D)$	$(\frac{1}{2}+D)$	$\frac{1}{2}$	Anion	13
4	$(\frac{1}{2}-D)$	$(\frac{1}{2}-D)$	$\frac{1}{2}$	Anion	13
5	D	$(1-D)$	0	Anion	13
6	$(1-D)$	D	0	Anion	13

equal and the U_1 and U_3 values remained the same; D_1 is given to demonstrate the extent that the anion site symmetry differs from uniaxial.) Anion 3 is chosen as I'', to which all the other equivalent anions are transformable by symmetry operations. V' is also given, representing the number of ions belonging to or shared by the unit cell centered on ion I'.

Along with D and D_1, the other data used in the computations are given in Table 2. The lowest visible refractive indices available in the literature were sought, to avoid as much as possible dispersion effects from absorption peaks in the ultraviolet[7]. (Besides the comments concerning dispersion in the introductory section of this paper, a comment is necessary about the desirability of computing complex polarizabilities to represent dispersion of polarizabilities. For the same reasons that the real polarizability elements of one ion only can be calculated, it would be possible to determine complex elements for only one ion—in this example, an anion. This neglects those dispersive mechanisms that have little to do with anions; e.g. cationic electronic transitions, and charge-transfer transitions. Another suggestion—that the extrapolation of visible indices to infinite wavelength be used—implies that this value would allow computation of electronic polarizability elements from the static dielectric constants. One of the approximations in the equations derived here is that the macroscopic electric field is constant throughout the Lorentz cavity, which is only about 0·01 of the wave-length of visible light. The approximation obviously does not introduce much error. Additionally, data for such an extrapolation are available only for rutile, cassiterite, and sellaite. It is also doubtful whether the extrapolated indices could be trusted because of the sensitivity of the slope of the dispersion curve to the difference between the resonance frequency and the frequencies of visible light.) The high dispersion in the rutile oxides and the high cation polarizabilities are undesirable because the conditions of assumptions in the derivation are then not strictly fulfilled, but these are considered to be merely disadvantages of the rutile group.

For each rutile-group mineral computed and obviously because of the symmetry of anion site 3, the following coefficients were not zero: C_{111}, C_{121}, C_{212}, C_{222} and C_{333}. The following constants were not zero: K_{11}, K_{22} and K_{33}. The five coefficients were within an order of magnitude of unity and the three constants were within an order of magnitude of one hundred; the other constants and coefficients were within 10^{-15} of zero, and were considered nil. Moreover, it was observed for each mineral that $C_{111}=C_{222}$, $C_{121}=C_{212}$ and $K_{11}=K_{22}$. (Computed C_{111}, C_{121}, C_{333}, K_{11} and K_{33} values are reported in Table 3.) With these observations in mind, equations (7) can be rewritten as follows:

$$C_{111}(\alpha_3)_{11}+C_{121}(\alpha_3)_{12}=K_{11} \tag{8a}$$

$$C_{121}(\alpha_3)_{21}+C_{111}(\alpha_3)_{22}=K_{11} \tag{8b}$$

$$C_{333}(\alpha_3)_{33}=K_{33}. \tag{8c}$$

The site symmetry of anion 3 allows near-complete solution of these equations. At the same time, it is desirable to transform the polarizability tensor by rotation 45° about X_3, which refers polarizability to its principal axes. (Anion 3, along with all other anions, then lies on the intersection of a 'new' m_1 and an m_3 mirror plane.) The polarizability elements for the new orientation are primed

Table 2. Data for computation of anion polarizability tensor elements in six rutile group minerals

Compound (mineral name)	$U_1 = U_2$ (Å)	U_3 (Å)	n_ω	n_ϵ	D	D_1	Cation $\alpha_i{}^P$ (Å^3)	Anion $\alpha_i{}^P$ (Å^3)	Comments
TiO_2 (Rutile)	4·594[8]	2·959[8]	2·5555[9]	2·8294[9]	0·306[8]	0·302[8]	2·51[1]	28·90[1]	6907·5 Å Indices
TiO_2 (Rutile)			2·6124[1]	2·8993[1]					5893 Å Indices Check against sources [1] and [2]
SnO_2 (Cassiterite)	4·737[8]	3·185[8]	1·9836[10]	2·0818[10]	0·307[8]	0·307[8]	30·50[11]	28·90[1]	7152 Å Indices
GeO_2	5·395[8]	2·860[8]	1·99[12]	2·05[12] 2·10	0·307[8]	0·303[8]	11·9[11]	28·90[1]	5893 Å Indices.
MgF_2 (Sellaite)	4·625[8]	3·052[8]	1·37599[13]	1·38771[13]	0·303[8]	0·304[8]	7·92[11]	8·04[11]	7065·8 Å Indices. Anion $\alpha_i{}^P$ differs from other fluorides because of slight discrepancy within source [11]
MgF_2 (Sellaite)			1·3775[14]	1·3889[14]					5893 Å Indices. Computed before discovery of source [13]
ZnF_2	4·7034[15]	3·1335[15]	1·510[16]	1·526[16]	0·303[15]	0·306[15]	9·93[11]	8·09[11]	5893 Å indices or white indices (source neglects to say)
NiF_2	4·6506[15]	3·0836[15]	1·526[17]	1·560[17]	0·302[15]	0·305[15]	15·04	8·09[11]	5893 Å indices (?). Cation $\alpha_i{}^P$ calculated for NiF_2 by methods of source [11]

Table 3. Computed values for C_{111}, C_{121}, C_{333}, K_{11} and K_{33}; t is the integer such that there are $(2t+1)^3$ unit cells in the Lorenz cavity; thus the larger t the more accurate the values

	t	C_{111} $\left(\frac{\text{statcoul}}{\text{Å}^2}\right)$	C_{121} $\left(\frac{\text{statcoul}}{\text{Å}^2}\right)$	C_{133} $\left(\frac{\text{statcoul}}{\text{Å}^2}\right)$	K_{11} (statcoul.Å)	K_{33} (statcoul.Å)
TiO_2 (6407 5 A indices)	1	4·6825	0·7053	2·6349	139·529	92·275
	2	4·6875	0·6891	2·6250	139·554	92·225
	3	4·6876	0·6847	2·6249	139·558	92·217
	4	4·6876	0·6829	2·6248	139·560	92·213
TiO_2 (5893 Å)	1	4·6825	0·7053	2·6349	142·657	93·457
SnO_2 (7152 Å)	1	4·5614	3·0091	2·8772	58·131	30·596
	2	4·5558	2·9841	2·8884	58·237	30·383
	3	4·5542	2·9772	2·8916	58·270	30·318
GeO_2 (5893 Å, $n_\epsilon = 2{\cdot}05$)	1	4·7685	1·8706	2·4631	69·656	44·710
	2	4·7698	1·8481	2·4606	69·762	44·4
	3	4·7691	1·8418	2·4618	69·783	44·4
GeO_2 (5893 Å, $n_\epsilon = 2{\cdot}10$)	1	4·7685	1·8706	2·4631	69·656	46·356
	2	4·7698	1·8481	2·4606	69·762	46·145
	3	4·7691	1·8418	2·4618	69·783	46·104
MgF_2 (7065·8 Å)	2	4·1933	0·8659	3·6135	31·495	26·073
MgF_2 (5893 Å)	1	4·1946	0·8733	3·6109	31·666	26·192
	2	4·1933	0·8659	3·6135	31·675	26·175
ZnF_2 (5893 Å)	1	4·1836	1·0000	3·6327	46·721	36·501
	2	4·1817	0·9923	3·6366	46·728	36·488
NiF_2 (5893 Å)	1	4·2142	1·5275	3·5716	35·606	27·061
	2	4·2106	1·5175	3·5787	35·602	27·070

in equation (9), and the anion subscript 3 is dropped, as this is the only ion of interest.

$$\alpha'_{11} = \alpha'_{22}\left(\frac{C_{121}+C_{111}}{C_{121}-C_{111}}\right) - \frac{2K_{11}}{(C_{121}-C_{111})} \qquad (9)$$

$\alpha'_{33} = K_{33}/C_{333}$, and

$$\alpha'_{12} = \alpha'_{21} = \alpha'_{13} = \alpha'_{31} = \alpha'_{23} = \alpha'_{32} = 0.$$

Without other assumptions, it is not possible to solve for α'_{11} and α'_{22} explicitly. The relationship between them is obviously linear. Because $C_{111} > C_{121}$ and C_{111}, C_{121}, C_{333}, K_{11}, and K_{33} are positive in each case, the slope of the line is negative and the α'_{11} and α'_{22} intercepts are positive.

Listed in Table 4 are values for $a^{\parallel}$ and $\alpha^{\perp}$ (polarizability elements for application of a local field to anion 3 first parallel, then perpendicular, to the plane of three cations to which anion 3 is bonded). $\alpha^{\parallel}$ and $\alpha^{\perp}$ are obtained by assuming that the slight differences in bond lengths are of so little consequence that $\alpha'_{22} = \alpha'_{33}$. This is the assumption made by BFG[1] and Field[2] for all their computations. A comparison of $\alpha^{\parallel}$ and $\alpha^{\perp}$ for TiO_2 by BFG and Field with those of this work is provided in Table 4. The alternative results are obviously comparable, considering the much greater accuracy (greater t) sought by BFG and Field. The results obtained are considered to be adequate for future iterative refinement. $\alpha^{\parallel}$ and $\alpha^{\perp}$ values for GeO_2 are

Table 4. $\alpha^{\parallel}$ and $\alpha^{\perp}$ for six rutile group minerals. The values given are for the most accurate (largest t) C_{111}, C_{121}, C_{333}, K_{11} and K_{33} values. Where pertinent, the values are compared to BFG[1] and Field[2]. Because the $\alpha^{\parallel}$ and $\alpha^{\perp}$ are obviously dependent on the cation polarizability, this value is also indicated

	t	Cation polarizability (Å^3)	$\alpha^{\parallel}$ (Å^3)	$\alpha^{\perp}$ (Å^3)
TiO_2 (6407·5 Å indices)	4	2·5	35·1	22·6
TiO_2 (5893 Å)	1	2·5	33·5	23·7
	7[1]	2·5	32·4	21·7
	13[2]	2·6	32·1	22·0
SnO_2 (7152 Å)	3	30·5	10·5	23·6
GeO_2 (5893 Å, n_ϵ = 2·05)	3	11·9	18·0	7·0
GeO_2 (5893 Å, n_ϵ 2·10)	3	11·9	18·7	5·4
	13[2]	1·3	21·4	16·6
MgF_2 (7065·8 Å)	2	7·9	7·2	8·0
MgF_2 (5983 Å)	2	7·9	7·2	8·0
ZnF_2 (5893 Å)	2	9·9	10·0	13·0
NiF_2 (5893 Å)	2	15·0	7·6	10·4

also compared with those by Field, with less success. Field approximated the scalar polarizability of Ge to be 1·26 Å^3 by the assumption that the polarizability varies directly with the cube of the ionic radius. The value for the Ge polarizability from Tessman, Kahn and Shockley[11] (11·9 Å^3) is used herein. This difference in cation polarizabilities explains the observed differences in computed anion polarizabilities.

Yamaka and Narita[18] have reported some effects of the development of permanent anionic dipoles in response to finite electric fields at anion sites in unilluminated rutile crystals. These dipoles are of no concern to the present computations, because equations (9) are satisfied by the additional dipole moments that are induced in the anions by the illumination fields.

SUMMARY

A method to compute optical anion polarizability tensors in selected minerals is developed, by restriction and approximation in the general equations until they can be solved. By this approach, it is possible to describe anion polarizabilities in the rutile group more completely than before. The linear relationship between α'_{11} and α'_{22} in equation (9) is, in a sense, a generalization of the 'point' relationship between $\alpha^{\parallel}$ and $\alpha^{\perp}$. Considerable knowledge of the anion environment in the form of symmetry information not incorporated in the general equations is still required for solution for $\alpha^{\parallel}$ and $\alpha^{\perp}$.

The available anisotropic anion polarizabilities for rutile-group compounds included rutile TiO_2, GeO_2 and stishovite-SiO_2 (with assumed structure). This list is extended, in Table 4, to include values also for cassiterite-SnO_2, sellaite-MgF_2, NiF_2 and ZnF_2, all obtained by the present method.

Acknowledgements—The National Science Foundation supported this work in two categories, initially under a

Cooperative Graduate Fellowship, and later under grant GP-5114. The advice of Dr. G. W. DeVore was invaluable. The kindness of Dr. W. G. Field in providing an otherwise inaccessible copy of his thesis is gratefully acknowledged. Thanks are due to Mr. Alan Niedoroda for help in computer programming, and to the Georgia Institute of Technology for stenographic assistance. I am also sincerely grateful to Dr. A. L. Stanford and Dr. A. J. C. Wilson for reading the manuscript.

REFERENCES

1. BOLTON H. C., FAWCETT W. and GURNEY I. D. C., *Proc. phys. Soc.* **80**, 199 (1962).
2. FIELD W. G., *The Structural Dependence of Refractive Indices*, 198 pp., Unpublished Ph.D. thesis, Harvard University, Cambridge (1965).
3. NYE J. F., *Physical Properties of Crystals* Oxford University Press, Oxford (1957).
4. BRAGG W. L., *Proc. R. Soc.* **A105**, 370 (1924)
5. Von HIPPEL A., *Dielectrics and Waves*, Wiley, New York (1954).
6. BAUR W. H., *Acta crystallogr.* **14**, 209 (1961).
7. RADHAKRISHNAN T., *Proc. Ind. Acad. Sci.* **35**, 117 (1952)
8. BAUR W. H., *Acta crystallogr.* **9**, 515 (1956).
9. *Gmelins Handbuch der Anorganischen Chemie*, Titan 41, 481 pp. Verlag Chemie, Weinheim (1951).
10. DEER W. A., HOWIE R. A. and ZUSSMAN M. A., *Rock Forming Minerals*, Vol 5, Nonsilicates, 371 pp Wiley, New York (1962).
11. TESSMAN J. R., KAHN A. H. and SHOCKLEY W., *Phys. Rev.* **92**, 890 (1953).
12. WINCHELL A. N. and WINCHELL H., *The Microscopical Characters of Artificial Inorganic Solid Substances*, 3rd Edn, 439 pp. Academic Press, New York (1964).
13. DUNCANSON A. and STEVENSON R. W. H., *Proc. phys. Soc.* **72**, 1001 (1958).
14. MALLARD E., *Bull. Soc. fr. Minér. Cristallogr.* **11**, 302 (1888).
15. BAUR W. H., *Acta crystallogr.* **11**, 488 (1958).
16. INGERSON E., and MOREY G. W., *Am. Miner.* **36**, 778 (1951).
17. *Gmelins Handbuch der Anorganischen Chemie*, Nickel 57, Teil B, Lief. 2, 451 pp. Verlag Chemie, Weinheim (1966).
18. YAMAKA E. and NARITA K., *Phys. Lett.* **33**, 645 (1966)

J. Phys. Chem. Solids Pergamon Press 1969. Vol. 30, pp. 1261–1271. Printed in Great Britain.

ELECTRICAL PROPERTIES OF β-PHASE NiAl

H. JACOBI, B. VASSOS and H. -J. ENGELL
Max-Planck-Institut für Metallforschung, Institut für Metallkunde, Stuttgart, Germany

(*Received* 29 *July* 1968)

Abstract – The variation of the electrical resistivity of the intermetallic compound β-NiAl at 77° and 298°K is characterized by a sharp minimum at the stoichiometric composition and can be explained by electron scattering from constitutional point defects. The Hall coefficient shows proportionality to the electrical conductivity and changes the sign twice within the homogeneity range. Positive and negative contributions to the Hall coefficient are interpreted by the shape of the Fermi surface relative to the Brillouin zones. Room temperature values of the absolute thermoelectric power and of the high frequency conductivity measured by optical methods indicate that the Fermi surface overlaps into higher Brillouin zones in ⟨110⟩ direction, when the Al-concentration approaches 50 at.%. From the low energy part of the conductivity spectra effective electron masses were computed. Absorption maxima found at 1·5, 2·5, 4 and 5 eV are attributed to interband transitions of electrons. The compositional dependence of the hydrogen solubility suggests that hydrogen dissociates into proton and electron, the solubility being primarily controlled by the electron potential. Thus the rapid rise in Fermi energy between 46 and 50 at % Al simultaneously causes the solubility to decrease.

INTRODUCTION

THE INTERMEDIATE phase β-NiAl belongs to the electron phases which are formed at definite electron concentrations, as was first pointed out by Hume-Rothery. Assuming that aluminum contributes three valence electrons to the conduction band and nickel none, a valence electron to atom ratio of 1·5 is obtained which gives rise to the stability of the large family of β-phases that crystallize in the primitive cubic CsCl-type structure every atom being surrounded by eight un-like next neighbor atoms.

β-NiAl exhibits a wide range of homogeneity of approximately 40–55 at.% Al at room temperature and congruent melting at the stoichiometric composition[1]. It maintains its ordered atomic arrangement probably over the entire temperature range of stability up to 1638°C, as can be concluded from high temperature X-ray measurement[2] and thermodynamic investigation of the compound[3].

The different defect structures at deviation from the equiatomic composition, vacancies of nickel at an excess of aluminum and anti-structure atoms of nickel on the other side of the concentration of maximum order, together with a remarkable change in colour as a function of composition, both phenomena of which were first reported in the early work of Bradley and Taylor[4] in 1937, may be considered as the most interesting features of this phase besides its relatively high stability.

All these factors including the simple structure make the β-phase NiAl a very suitable substance for the study of the basic nature of intermetallic compounds as well on the metallurgical as on the physical and chemical side. The purpose of the work described in this paper is to provide more information on the electronic structure of the NiAl compound by measuring several electrical properties as the d.c. conductivity, the high-frequency conductivity, the Hall coefficient and Seebeck coefficient on the very same sample in dependence of the composition within the homogeneity range, correlating the properties among each other and explaining them by a rigid band model. The energetical change in the accommodation of electrons on varying the concentration of the component elements reflects in the hydrogen solubility as will be shown in a subsequent part of this paper.

PREPARATION OF THE SAMPLES

Using an induction furnace weighed amounts of 99·99% aluminum and 99·9% nickel were melted in Al_2O_3 crucibles under an atmosphere of purified argon to avoid vaporization and cast into a heated copper mould yielding 15 mm dia. cylindrical ingots of relatively coarse grained polycristalline material. After a homogenization annealing for 1 week at 1100°C the samples were allowed a 24 hr cool down to room temperature and rectangular parallelepiped shaped specimens (55 × 12 × 0·7 mm) cut out with a water cooled carborundum disk preceeding slowly under a constant load. Other conventional methods as for example rolling, machining or grinding were unsuccessful in view of the extreme brittleness of the material. Finally the specimens were given a metallographic polish. Little difficulty was experienced in this preparation procedure providing samples uniformly free from visible porosity except for those ranging from 53 at.% Al to the Al-side phase boundary, which often cracked during the cutting process.

ELECTRICAL RESISTIVITY

Measurements of the electrical resistivity have been carried out at room temperature and the temperature of liquid nitrogen by the usual potentiometric method. The pronounced minimum, Fig. 1, which occurs in the resistivity vs. composition curve provides strong evidence that the electrical conductivity is controlled primarily by the changes in the mobility or relaxation time rather than by the density of the charge carriers. Such a behaviour reveals a strong metallic character of the compound. The lattice potential in an ideal crystal is a periodic function of the coordinates in space, on the other hand the introduction of impurity atoms or constitutional defects with deviation from stoichiometry causes a disruption of periodicity resulting in a scattering of electron waves and increase in resistivity which in an ideal solution of interstitials in a pure metal, for instance nitrogen dissolved in nickel, is a linear function of the number of defects. Let us discuss this point in more detail for β-NiAl.

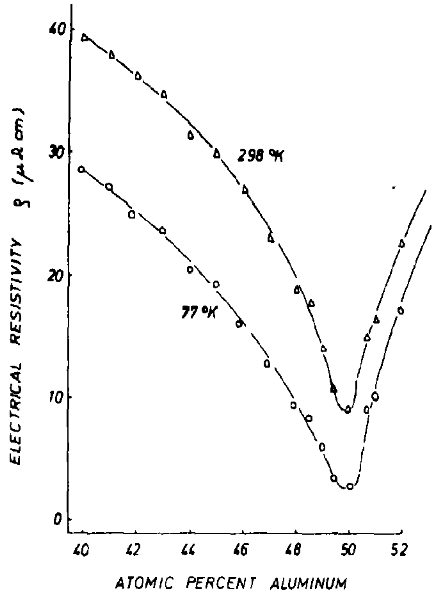

Fig. 1. Electrical resistivity of β-NiAl as a function of composition.

Assuming as a first attempt point defects distributed statistically over the lattice sites one can easily show that except for very small deviations from the equiatomic composition the number of substitutional wrong nickel atoms Ni_{Al} is equal to half the nickel excess $\Delta N : Ni_{Al} = \frac{1}{2}|\Delta N|$. The number of vacancies of nickel V_{Ni} is equal to the deficiency in Nickel $-\Delta N : V_{Ni} = |\Delta N|$. Further, $\Delta N = N_{Ni} - N_{Al}$. If proportionality between the restistivity and the concentration of both types of defects is assumed, slopes differing by a factor of 2 are expected for both branches of the curve, the resistivity increasing at a faster rate in the Al-rich portion of the homogeneity range which is confirmed quite well by the experimental values given here and by Guzeva[5]. However this explanation in a strict sense could hold only if the defects were of the same kind, so that in fact the steeper slope on the vacancy defect side can be ascribed partially to a greater scattering cross section of the vacancies relative to that of the antistructure atoms.

Concerning the arrangement of defects in NiAl, West[6] has explained his room temperature NMR results by assuming that instead of randomly distributed vacancies, as was originally proposed by Bradley and Taylor[4], highly ordered microdomains of Ni_2Al_3 configuration could possibly exist in a NiAl matrix. Similarly nickel atoms on aluminum sites were thought to assemble in such a way as to leave a maximum amount of order in the alloy. Diffraction studies by Hughes[7] supported this hypothesis and quite recently electrical resistivity measurements on NiAl conducted by Yamaguchi *et al.*[8] disclosed the two branches to flatten out after initially steep slopes leaving two sharp knees at 49·5 and 52 at.% Ni in the resistivity curve which were interpreted by suggesting clustering of the defects. Although our values lying in fact considerably lower by almost 5 $\mu\Omega$cm around 52 at.% Ni do not confirm these knees the possibility of defect interaction at low temperature and accordingly a contribution to the characteristics of the resistivity curve cannot be ruled out with certainty.

In the vicinity of the stoichiometry the treatment must be modified to account for a finite degree of intrinsic disorder with both types of defect coexisting in thermodynamic equilibrium, resulting in a residual electrical resistance at the equiatomic composition. Comparing Guzeva's and our results some discrepancy arises in locating the minimum of the resistivity curve. He had found out that both the electrical conductivity and the lattice constant passed through a maximum at 51 at.% Al which was assumed to correspond to the onset of vacancy formation allowing for some aluminum atoms in excess to be accommodated on nickel sites[4,5,9]. But since the resistivity minimum is clearly determined by the defect structure and there is no reason for it to be shifted away from the concentration of maximum order, it is believed that the whole problem might be governed by the equilibration of the alloys, by the oxidation of powder specimens and differences in chemical analysis.

The residual electrical resistance ratio $\rho^{298°K}/\rho^{77°}$ which reaches a sharp peak at the equiatomic composition amounting to 2·8 indicates by its low value the existence of a significant number of intrinsic defects at the stoichiometric composition. The difference in the electrical resistivities at both temperatures plotted versus the composition of the alloys gives constant values of approximately $\rho^{298°K}-\rho^{77°K} = 11\ \mu\Omega$cm for the nickel excess part and 6 $\mu\Omega$cm for the Al-rich side of the homogeneity range with a gradual transition between 47 and 50 at.% Al.

It is also interesting to note that the compound β-CoAl which has the same structure and the same types of defect shows a resistivity vs. composition curve quite similar to that of NiAl the values being higher by about one order of magnitude[8]. This additional feature might be explained by the different filling of the *d*-band of the transition metal in both compounds. While the *d*-band in NiAl may be regarded as completely filled even at the nickel rich boundary of the phase, states in the *d*-band of CoAl are left vacant, involving an increased scattering probability of *s*-electrons by inhomogeneities of the crystal lattice, because of the possibility of transitions not only into *s*-levels but also into *d*-levels.

ABSOLUTE THERMOELECTRIC POWER

The thermal e.m.f. of β-NiAl against copper and constantan serving simultaneously as thermocouples for the registration of the temperatures of the hot and cold junction, 35° and 15°C respectively, were converted to the absolute thermoelectric power S and plotted in Fig. 2. An addition of aluminum to the nickel rich compound causes a positive change in S, which is rather sharp in the

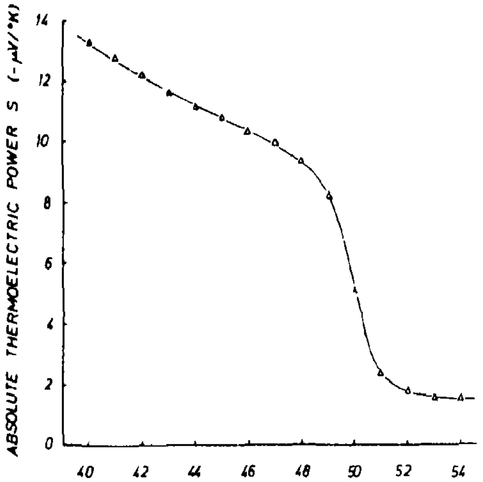

Fig. 2. Absolute thermoelectric power of β-NiAl at room temperature as a function of composition

neighborhood of the stoichiometric composition but nearly vanishes at an excess of aluminum. Although the thermoelectric power represents an electrical transport property and thus is expected to be sensitive to the mean free path of the electrons, it is seen immediately from the shape of the curve that electron scattering by lattice defects is not at all or only to a negligible extent determining the value of S. A satisfactory mathematical treatment explaining the negative values encountered with metals like Na and K with spherical Fermi surfaces was derived by Mott and Jones[10]:

$$S = \frac{\pi^2 k^2 T}{3e}\left\{\frac{d\ln\sigma_{(E)}}{dE}\right\}_{E=E_f}$$

e = charge of an electron; $\sigma_{(E)}$ = electrical conductivity; E_f = Fermi energy; k = Boltzmann constant. Modifications and proposals to fit the equation for metals and alloys with anisotropic Fermi surfaces are still in a speculative stage today, particularly the interpretation of the positive sign of the thermoelectric power which was observed for instance with noble metals and several primary solid solutions of nickel.

However some qualitative conclusion according to Ziman's[11] zone boundary contact theory may be obtained from our experimental results. The Fermi surface in NiAl is probably a rather complicated one and makes contact with the second zone boundary much earlier than a spherical surface could do. It even seems quite possible that the Fermi surface expands into higher Brillouin zones when the Al-concentration approaches the stoichiometric composition.

HALL COEFFICIENT

Recognition that the use of electrical resistance measurements alone is merely concerned with information on whether or not metallic type of conduction is present but does not allow to distinguish between a conduction mechanism in one band or several bands and between a spherical or an anisotropic Fermi surface overlapping zone boundaries stimulated the investigation of a galvanomagnetic property.

The Hall coefficient vs. composition curve illustrated in Fig. 3 is clearly controlled by the

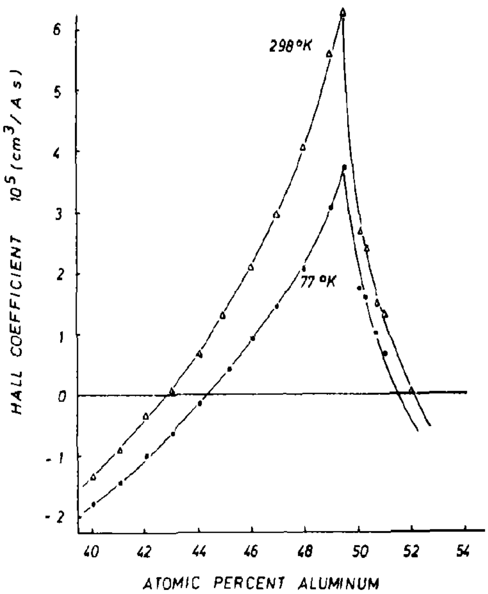

Fig. 3. Hall coefficient of β-NiAl as a function of composition

conductivity and thus by the scattering of electrons from point defects showing again the feature of dropping off extremely rapidly when an Al-excess is contained in the alloys. The whole curve is moved along the ordinate axis but no shift in the direction of the concentration axis is observed if the experiment is conducted at a higher temperature. While conductivity and Hall coefficient vary in the same way regarding scattering from lattice defects, it is evident that they are influenced just in an opposite sense by the scattering from phonons which further indicates an essentially different temperature dependence of the partial conductivities in the operative bands.

From these considerations it follows that the concentration dependence of the Hall coefficient alone is not sufficient to detect the topology of the Fermi surface or to observe interaction between the Fermi surface and the zone boundaries when the Fermi surface expands due to an increase in electron concentration by the addition of aluminum. Of major importance is the change in sign twice within the homogeneity range which enables us to learn more about the distortion and shape of the Fermi surface, since the positive contribution to the Hall coefficient is not connected with holes in the d-band of the transition metal[12], as was already pointed out above.

Under the driving force of a constant magnetic and electric field the electrons move on the Fermi surface and in a plane perpendicular to the direction of the magnetic field where the intersection of both in k-space leads to the orbit of the electron, which may have electron-character if it includes occupied states, or hole-character as for example in empty corners of otherwise filled zones, yielding a negative and positive sign of the Hall coefficient respectively. An identical definition might be given by considering the curvature of the Fermi surface.

Electron theory of solids shows how discontinuities in electron energy arise at certain planes in various directions in k-space leading to the conception of Brillouin zones, the construction of which is based on the reciprocal lattice of the solid. In addition the valence electrons that occupy the highest energy levels form the Fermi surface in k-space and it is the ability of the Fermi surface to interact with the zone boundaries, e.g. by distortion, contact, overlapping and intersecting several zone boundaries, by which some of the electronic properties can be interpreted. Imagining a sphere in the interior of the Brillouin zones of the primitive cubic CsCl structure of NiAl, illustrated in Fig. 4, expanding due to an increase in the number of valence electrons, this sphere first would overlap the (100) cube planes of the first zone, then expand in ⟨110⟩ direction over the cube edge into the second, third and fourth zone and at last reach the corners in ⟨111⟩ direction. Calculations by Jones[13] predicted that an inscribed sphere makes contact with the cube edge at an electron to atom ratio of 1·48 in agreement with Hume-Rothery's rule. On the other hand modern topological

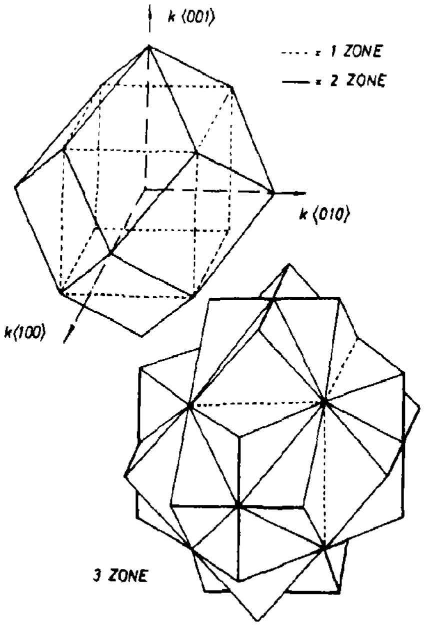

Fig. 4. Brillouin zones for the CsCl type structure.

investigation of the Fermi surfaces in electron phases revealed that contact is often made at a lower electron to atom ratio. Vice-versa it was proved by Lipson and Taylor[14] studying ternary β-phases like Ni–Cu–Al that a number of 3 electrons per unit cell does not necessarily give rise to phase instability, considerably higher values up to 3·39 electrons per unit cell having been observed.

Applying these generally accepted ideas, our results substantiate the conclusion that the Fermi surface in β-NiAl is highly anisotropic. Contact is established already at the nickel rich phase boundary associated with neck formation in ⟨110⟩ direction, which enables hole-like orbits around the cube corners to contribute with a positive sign to the Hall coefficient. The rather sharp decrease towards negative values and the change in sign of the Hall coefficient when the aluminum concentration exceeds 50 at. % might be favored partially by electrons accommodated in the higher zones after the Fermi energy has passed the gap in energy existing at the cube edge in ⟨110⟩ direction.

HIGH-FREQUENCY CONDUCTIVITY

The logical extension of the work described above was an investigation of the optical properties not only in view of their close relation to the band structure, but also because the alloys undergo an appreciable change in colour with composition:

40 at. % aluminum	yellow
45 at. % aluminum	pink–grey
48 at. % aluminum	blue–grey
50 at. % aluminum	blue
52 at. % aluminum	silvergrey–blue
55 at. % aluminum	silvergrey.

As the results of optical measurements are known to be rather sensitive to contamination, oxidation and distortion, the surface-preparation was performed with great care by finally polishing with alumina and cleaning to a mirrorlike surface with alcohol, immediately before the specimen was placed in the optical apparatus. Very thin oxide layers which possibly were left on the alloy surfaces were found to be of minor influence on the characteristic features of the energy spectra of the optical properties, giving rise to small changes in the absolute values whereas the energy position of the minima and maxima was not affected.

Our discussion will be restricted to the high-frequency conductivity σ which was computed from experimental results obtained by means of a modification of the old Drude method, in the spectral energy range extending between

$$0{\cdot}7 < E < 5\,\text{eV}$$
$$1{\cdot}6\times10^{14} < \nu < 1{\cdot}2\times10^{15}\,\text{1/sec}$$
$$18000 > \lambda > 2500\,\text{Å}.$$

Physical significance is given to the high-frequency conductivity via its correlation with the absorption behavior of the electrons being proportional to the absorbed energy regardless of the detailed process by which this absorption takes place. In order to distinguish between absorption mechanisms like intraband transitions, interband transitions and plasma oscillations of electrons one has to compare the spectral functions of various optical constants. The low energy part of the absorption spectrum, shown in Fig. 5 for a NiAl alloy with stoichiometric composition, predominantly originates from intraband transitions, that is the movement of electrons at the Fermi surface, and may be described with the simple Drude formula

$$\sigma_{(\omega)} = \frac{N_c e^2}{m_{\text{eff}}^{\text{opt}}}\,\frac{1/\tau}{(\omega^2 + 1/\tau^2)}$$

(N_c = number of conduction electrons; ω = frequency), containing an optical effective electron mass $m_{\text{eff}}^{\text{opt}}$ and a relaxation time τ, which both were found independent of the energy below 1·3 eV. Some typical values of the optical effective mass, listed in the table below, are in good agreement with optical masses reported by Rechtien *et al.*[15], but

40 at. % aluminum	2·68 m
42 at. % aluminum	2·44 m
46 at. % aluminum	2·85 m
50 at. % aluminum	3·54 m
54 at. % aluminum	2·9 m

(m = mass of the electron).

somewhat higher than the thermal effective mass ratio $m_{\mathrm{eff}}^{\mathrm{th}}/m = 2{\cdot}2$ computed by Seitchik and Walmsley[16] for a 50 at. % alloy on the basis of specific electronic heat data. The part of the intraband absorption may be approximately separated from the other absorption processes when an extrapolation is made towards higher photon energies. In turn an extrapolation to zero frequency yields optical d.c. resistivities of much higher value than those reported above, no explanation being present at the moment.

Besides the investigation of free electron behavior concerned with intraband transitions and effective masses the Drude theory may be explored to compute plasma frequencies at which collective oscillations of the free electrons take place yielding a slightly concentration dependent plasma energy around $E_p = 7{\cdot}5$ eV throughout the homogeneity range. This value of course could not be verified experimentally as it lies outside the sensitivity range of the available optical instruments. Further evidence for the absence of collective oscillation absorption maxima in the investigated energy region is given by the comparison between the spectral functions of the real and imaginary part of the dielectric constant and the energy loss function. Coincidence of zero or extreme values, required for free electron collective phenomena to be present, could not be observed. The maxima which were found in the absorption spectra are thus ascribed to interband transitions. These transitions can occur if the energy of the incident photons is equal to the energy separation between two levels of different bands and unoccupied states are available in the upper band. The high-frequency conductivity is therefore a very valuable help in determining the energy gaps between distinct bands, however, the main problem to be solved usually is to decide which energy levels are involved in the transition.

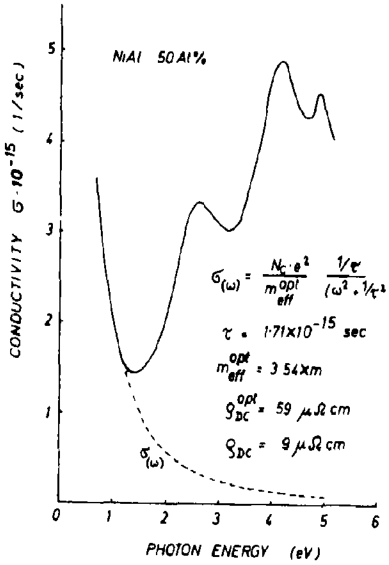

Fig. 5. High frequency conductivity of a stoichiometric NiAl alloy as a function of photon energy and extrapolation of the low energy part by means of the Drude formula.

Conductivity spectra for four characteristic compositions of the β-phase NiAl have been plotted in Fig. 6. It can be seen the existence of four absorption maxima at 1·5, 2·5, 4 and 5 eV. The small peak at 1·5 eV is shifted towards higher energies diminishing in absorption strength and vanishes before the Al-concentration reaches the equiatomic composition. Coincidently with the disappearing of the 1·5 eV absorption peak the much stronger 2·5 eV peak emerges. It is displaced to lower photon energies with increasing electron concentration and reaches its highest absorption strength at the concentration of maximum order. The other two maxima at 4 and 5 eV seem to be uneffected by the composition of the alloys regarding their energy position, while the strength of the 5 eV peak is gradually increasing with addition of aluminum.

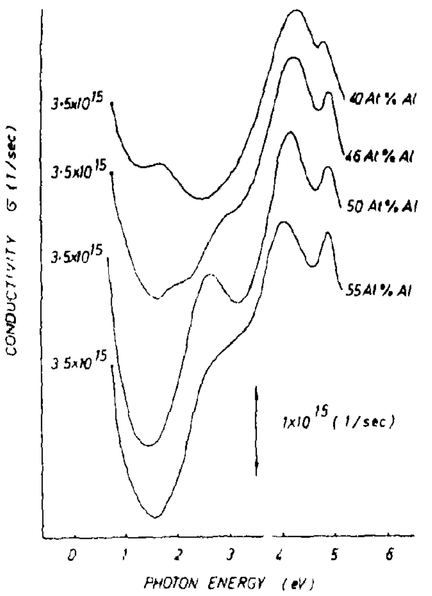

Fig. 6. Conductivity spectra of alloys with different composition in the homogeneity range of β-NiAl.

Information on the particular energy levels that take part in the band to band transition is gained from the concentration dependence of the conductivity maxima. If rigid bands are admitted, any change in the characteristics of extrema with composition can be interpreted by assuming that the Fermi surface is involved. This means that either electrons from a bound state can be lifted to the Fermi energy or that electrons are raised from the Fermi level to an upper empty energy band.

Using these general ideas the absorption peak at 4 eV may be specified as a transition of electrons from the bound state, for instance from the *d*-band to higher s- or p-like conduction bands above the Fermi surface. In contrast to this the concentration dependent absorption peaks at 1·5 and 2·5 eV are most probably associated with the Fermi surface, the 1·5 eV peak for instance with a transition from the *d*-band to the Fermi surface and the 2·5 eV peak with an absorption process originating from the intersection and overlap of the Fermi surface near the (110) zone face. Similarly the 5 eV peak seems to correspond to a Fermi surface transition. A detailed explanation for the origin of this peak cannot be given at the moment, but further investigation on the temperature dependence of the optical properties is planned to elucidate this point.

The situation as it may apply to a 50 at. % alloy is illustrated in principle in Fig. 7. It represents energy bands in ⟨110⟩, the preferred direction of the transition, and a projection on the (001) reciprocal lattice plane, which was chosen for the reason that this plane is the only one allowing the Fermi surface to completely surround the first Brillouin zone. The shaded area indicating the region of occupied states is far from being a sphere with electrons accomodated in the upper bands and necks being formed at the (110) zone face, the Fermi surface itself bulging out in ⟨100⟩ direction towards the corners of the second zone.

A mechanism which could account for the 2·5 eV absorption edge is a transition within the (110) plane between nearly parallel energy

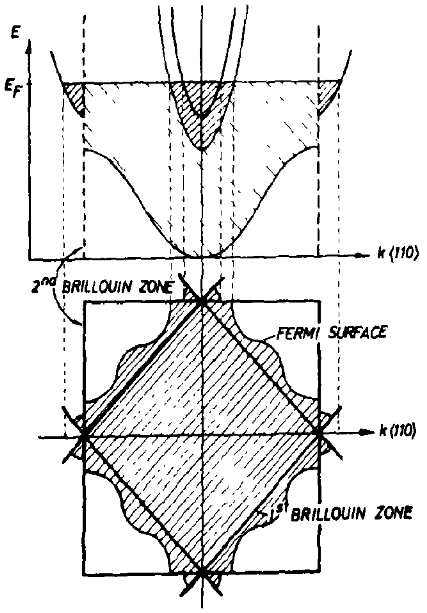

Fig. 7. Projection of Brillouin zones and Fermi surface on the (100) plane in *k*-space and corresponding energy bands.

bands which are most likely to occur in all polyvalent metals as was discussed in general by Harrison[17]. He predicted the energy gap and absorption strength on the basis of geometrical considerations of the Fermi surface and Brillouin zone. Moving in the (110) zone face from the 'cap' in the upper zone to the outer part of the 'neck' in the lower zone the energy gap for the transition across the plane remains nearly constant, but it will grow if we move out of the plane. The absorption strength is proportional to the area which is left between the projections of neck and cap on the (110) plane and thus by the growth in neck diameter and rate at which electrons are accommodated in the higher zone when the valence electron concentration of the alloy is increased by the addition of aluminum. From this picture we conclude that the origin of the rather rapid rise of the conductivity maximum at 2·5 eV is a sharp increase in the energy of the electrons in the composition range between 46 and 50 at. % aluminum, which is responsible not only for appreciable changes in the physical properties as shown above but also favors the formation of the vacancy type defect and by this quite a lot of other properties.

HYDROGEN SOLUBILITY

A further object of this investigation was to provide thermodynamical evidence for the rapid rise in electron energy in the vicinity of the equiatomic composition in β-NiAl. As thermodynamics is mainly concerned with energetical changes in systems due to variations in composition and temperature, the usual treatment in this case consequently would consist of a determination of the energy associated with an isothermal transfer of electrons from any standard state to the alloy, yielding a chemical potential or a chemical activity of the electrons. In contrast it is well known that electrons do not represent true component elements of a system and that their concentration cannot be varied independently, so that we have to apply some indirect method, for instance, an increase in electron concentration by dissolving hydrogen in the compound following the equation

$$\tfrac{1}{2}H_2 \rightarrow H^+ + e^-.$$

The relative amount of hydrogen absorbed as a function of composition gives us the chemical potential of hydrogen in the alloy which now must be separated into the contributions from protons and electrons, a treatment which is not rigorously possible, but which has been fruitfully applied to many metallic systems, demonstrating that the hydrogen solubility can be explained predominantly either on the basis of the electronic structure or the disposition of the hydrogen ion in the lattice.

For the measurement of the hydrogen absorption the electrochemical charging method of Devanathan[18] was chosen which yields a higher sensitivity than gas volumetric methods, if the hydrogen solubility is very small. Hydrogen is electrochemically evolved on the cathodic side of a NiAl membrane (30 mm dia., 0·8 mm thick), migrates along a sharp concentration profile to the other side of the membrane where it is anodically extracted from the alloy. Both compartments of the teflon cell, shown in Fig. 8, contained as electrolyte pre-electrolized 0·1 N NaOH, the potentials at the cathodic and anodic side being maintained at −850 mV s.c.e. and 0 mV s.c.e. respectively and the temperature at 80°C. The counterelectrodes and reference electrodes were kept in separate polyethylene vessels connected to the cell by polyethylene tubing with capillary ends.

The permeation of hydrogen is measured by the anodic current density of oxidation of the diffusing hydrogen. A certain time after the beginning of the experiment the current starts from a very low dead value gradually increasing as long as the concentration profile of hydrogen is being built up, and reaches

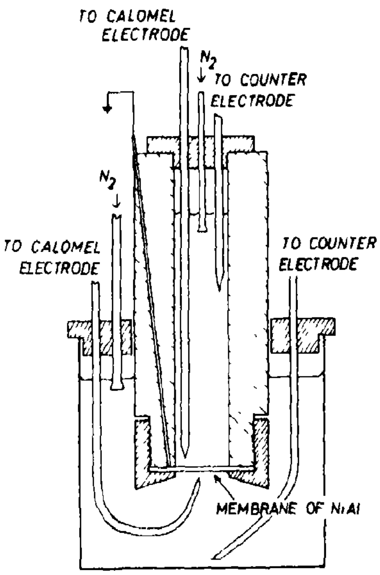

Fig. 8. Electrochemical cell for the measurement of the hydrogen solubility.

a steady-state value, when the profile becomes stable. From the slope of the transition part of the curve one obtaines the diffusion coefficient of hydrogen whereas the steady-state current is evaluated in view of the solubility of hydrogen at the cathodic side surface of the membrane.

As can be seen from the experimental results in Fig. 9 there is no doubt that the dissolved hydrogen must be dissociated into protons and electrons far apart from each other, every hydrogen atom contributing one valence electron, which is incorporated in the conduction band and raises the Fermi energy. Oppositely, imagining that the hydrogen were dissolved as neutral atom without under-going any type of bond in the alloy, this would lead us to discuss the solubility from the geometrical point of view and we would expect a sharp increase in the solubility as soon as we have aluminum in excess, since then a relatively high amount of vacant sites in the Ni-sublattice would be available for the accommodation of hydrogen. These arguments however are in contradiction to the experimental results.

Following a derivation of Wagner[19] the equilibrium condition for the above chemical reaction may be formulated as

$$\tfrac{1}{2}\mu_{H_2} = \mu_{H^+} + \mu_{e^-}$$

where μ is the chemical potential of the hydrogen gas, the protons and the electrons. For very diluted solutions of the protons in the solid phase one is permitted to write

$$\tfrac{1}{2}{}_{H_2} + RT \ln p_{H_2}^{1/2} = \mu_{H^+} + RT \ln c_{H^+} + \mu_{e^-}$$

μ_{H^+} being the potential of the protons extrapolated to unity concentration and p_{H_2} the virtual hydrogen fugacity at the cathodic metal surface, held constant for all compositions. Rearrangement of the terms yields the concentration of the dissolved hydrogen:

$$c_H = p_{H_2}^{1/2} \cdot \exp(\mu_{H_2} - \mu_{H^+} - \mu_{e^-}/RT).$$

The significant composition effect on c_{H^+} may be interpreted as an increase of the

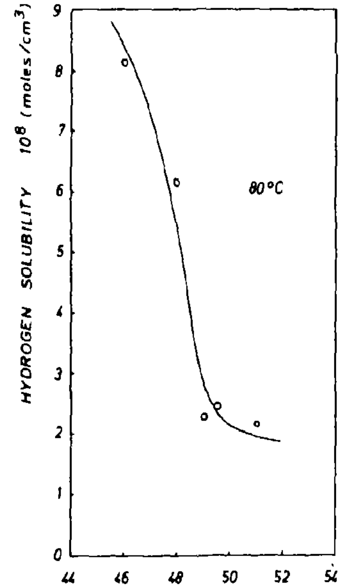

Fig. 9. Hydrogen solubility in β-NiAl as a function of composition under −850 mV s.c.e. cathodic potential in 0·1 N NaOH.

electron potential with Al concentration μ_e- which is only partially compensated for by a decrease of the proton potential μ_{H^+}. It may be possible that despite the generally accepted idea that the protons are completely shielded by the conduction electrons there is still some electrostatic interaction with the Al^{3+} -ions on the Ni-excess side of the stoichiometry where the H^+ -ion may be placed on interstitial sites, which would correspond to a relative rise in the chemical potential of the protons. This assumption is supported by the fact that the high stability of the β-phase NiAl cannot be explained by the valence electron structure alone, but must be ascribed to a considerable amount of electrostatic interaction between the bound electrons of the metal ions.

Lieser and Witte[20] who have measured the hydrogen solubility in the Ni–Al system in a compositon range extending between pure nickel and the β-phase between 400° and 600°C have interpreted the concentration dependence of the solubility by the change in enthalpy of the proton only, which was correlated to the polarization of the valence electrons and outer bound electrons of nickel. This treatment including the neglection of the influence of the electrons, that are stripped off from the hydrogen atoms seems to be useful as long as the Fermi energy lies in the d-band and as long as the standard dissolution entropy does not vary with composition. These conditions have been accomplished on the nickel side of the Ni–Al system, but are not fullfilled in the homogeneity range of the β-phase. While the standard entropy term was found constant throughout the whole composition range up to the β-phase, $\Delta S^0 = -18$ cal/grad ½-mole H_2, there has been observed a considerable decrease in the vicinity of 50 at. %, for example $\Delta S^0 = -12$ cal/grad ½ mole H_2 for a 54 at. % Al alloy. Although the authors estimated some uncertainty in this value, it could perhaps be understood by a different position of the hydrogen in the lattice, on interstitial sites and in vacancies of nickel.

REFERENCES

1. HANSEN M. and ANDERKO K., In *Constitution of Binary Alloys*, p. 119. McGraw-Hill. New York (1958).
2. VANDERVOORT R. R. *et al.*, *Trans. ASM* **59**, 930 (1966).
3. STEINER A. and KOMAREK K. L., *Trans. Met. Soc. A.I.M.E.* **230**, 786 (1964).
4. BRADLEY A. J. and TAYLOR A., *Proc. R. Soc.* **A159**, 62 (1937).
5. GUSEVA L. N., *Dokl. Akad. Nauk. SSSR* **77**, 415 (1951).
6. WEST G. W., *Phil. Mag.* **9**, 979 (1964).
7. HUGHES T., Ph.D. dissertation, Northwestern University.
8. YAMAGUCHI Y. *et al.*, *J. appl. Phys.* **39**, 231 (1968).
9. COOPER M. J., *Phil. Mag.* **8**, 805 (1963).
10. MOTT N. F. and JONES H., In *The theory of Properties of Metals and Alloys*, p. 310 Clarendon Press, Oxford (1936)
11. ZIMAN J. M., In *Electrons and Phonons*, p. 262 Clarendon Press, Oxford (1960).
12. HÖHL M., *Z. metallk.* **51**, 85 (1960).
13. MOTT N. F. and JONES H., In *The Theory of Properties of Metals and Alloys*, p 172 Clarendon Press, Oxford (1936).
14. LIPSON H and TAYLOR A., *Proc. R. Soc.* **A173**, 232 (1939).
15. RECHTIEN J. J. *et al.*, *J. appl. Phys.* **38**, 3045 (1967).
16. SEITCHIK J A. and WALMSLEY R H. *Phys. Rev.* **131**, 1473 (1963).
17. HARRISON W A., *Phys. Rev.* **147**, 467 (1966).
18. DEVANATHAN M. A. V. and STACHURSKI Z., *Proc. R. Soc.* **A270**, 90 (1962).
19. WAGNER C., In *Thermodynamics of Alloys*, p 43. Addison-Wesley, London (1952).
20. LIESER K. H. and WITTE H., *Z. elektrochem. Ber. Bunsenges. phys. Chem.* **61**, 367 (1957).

J. Phys. Chem. Solids Pergamon Press 1969. Vol. 30, pp. 1273–1276. Printed in Great Britain.

TECHNICAL NOTES

Magnetic properties of U_3P_4 and U_3As_4 single crystals

(*Received* 7 *October* 1968; *in revised form* 27 *November* 1968)

STUDIES of the magnetic properties of U_3P_4[1] and U_3As_4[2] powders have led to the conclusion that these uranium compounds are ferromagnetic at low temperatures, and this has been supported in the case of U_3P_4 by a neutron diffraction study[3]. However, the discrepancy between the paramagnetic and ferromagnetic moments in U_3P_4 ($2{\cdot}77\,\mu_B$ and $1{\cdot}16\,\mu_B$ per U ion respectively) and the low value found for the entropy change associated with its magnetic ordering[4] suggest that these compounds may not be simple ferromagnets. In the present work, magnetic measurements were made on single crystals of these compounds. The results show the existence of an extremely large magnetocrystalline anisotropy with the easy axis of magnetization along a [111] direction in the cubic unit cell. In addition toroids of U_3P_4 ceramic were used for hysteresis studies which established the presence of a zero-field magnetization.

To prepare U_3P_4, uranium metal was powdered by forming UH_3 at 300°C and decomposing the latter at 500°C in a purified hydrogen stream. The metal was then heated to 900°C in a stream of yellow phosphorous vapor mixed with hydrogen to form U_3P_4. X-ray diffraction showed the material to be U_3P_4 with a trace amount of UO_2.

To prepare U_3As_4, stoichiometric amounts of the elements were weighed and placed as lumps at opposite ends of a quartz ampoule. The uranium only was heated, converted to the hydride and decomposed as above. The ampoule was evacuated, sealed and heated to 600°C to allow the arsenic to vaporize and react with the uranium powder. The end containing the uranium was then further heated to 900°C to complete the reaction.

Single crystals of these compounds were prepared by an iodide transport process. About two grams of powder were placed at one end of a 100 cm^3 quartz ampoule 2·5 cm in dia. with care being taken to prevent powder from coating the walls of the opposite end of the ampoule. The ampoule was evacuated to 10^{-6} mm pressure, outgassed at 400°C, cooled, and filled with iodine corresponding to a concentration of 1–2 mg per cm^3. The sealed ampoule was placed in a tube furnace having a temperature difference of about 50° between its ends. Transport took place from the cooler end containing the powder to the hotter end which was kept at 1040°C for U_3P_4 and 940°C for U_3As_4. Crystals with dimensions of up to a few millimeters were obtained. The arsenide crystals were washed in dilute hydrochloric acid with no noticeable effect, but the phosphide reacted readily with acid and was best cleaned with water or alcohol.

For the magnetic measurements, crystals were oriented after the predominant faces ([211], [110] and [310]) were identified. A vibrating sample magnetometer was used to obtain the component of magnetization along the applied field as the crystal was rotated to allow the field to take on all direction in a (110) plane. Polycrystalline samples were also measured.

In Fig. 1 are shown the angular variations of the observed specific magnetization (σ_θ) of U_3P_4 and U_3As_4 single crystals in a field of 15,000 Oe at 73°K. The curves drawn through the experimental points consist of segments of four circles passing through the origin with centers on [111] directions and diameters equal to the observed σ_θ for these

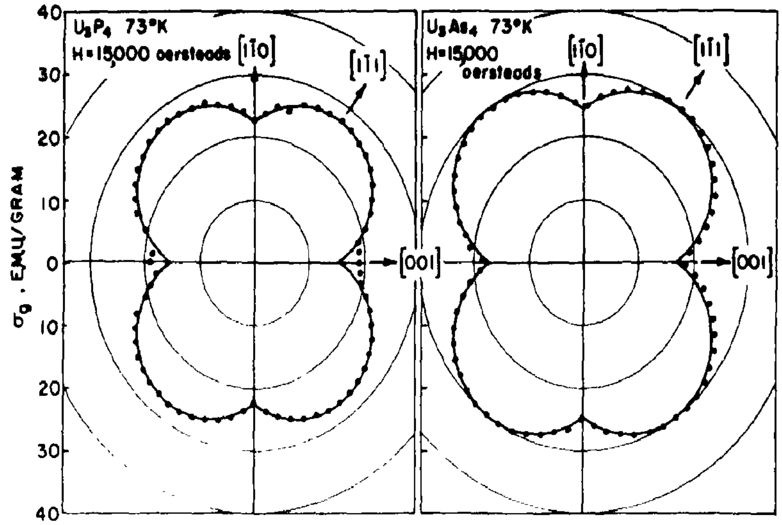

Fig. 1. Measured specific magnetizations of U_3P_4 and U_3As_4 in (110) plane.

directions. The close fit except near [100] is assumed to indicate that the magnetization is strongly constrained to lie in a [111] direction and switches to whichever one of the eight such directions is closest to the applied field. The observed component of magnetization should therefore be expected to vary as the cosine of the angle between the field and the nearest [111] direction, such variation in polar coordinates being the observed circles.

This evidence that the magnetizations in U_3P_4 and U_3As_4 do not align with the field but rather with the [111] direction closest to it requires a reinterpretation of observed magnetization data on polycrystalline or powder samples. Assuming a random orientation of crystallites, it can be shown that the observable magnetization of such materials should be $\sqrt{3}/2$ times that along [111]. As a check of this relationship, magnetic measurements were made on samples consisting of many small crystals randomly oriented in the magnetometer sample holder. These results for U_3P_4 and U_3As_4 are listed in Table 1. The specific magnetizations σ_0 at 15,000 Oe and 73°K for the single crystal samples agree well with those calculated from the data obtained with polycrystalline samples. The specific magnetizations for these polycrystalline samples were extrapolated to $1/H = 0$ and divided by $\sqrt{3}/2$ to obtain the magnetizations $\sigma_{\infty 73^\circ}$ for the [111] directions. From these, the crystal moments per uranium atom were calculated. Also in Table 1 are the effective paramagnetic moments and paramagnetic Curie temperatures observed using the larger polycrystalline samples.

For the hysteresis studies, ceramic toroids were prepared. The phosphide powder was ground together with 10 volume per cent of paraffin dissolved in toluene and dried. The mixture was pressed in a steel die at 5000 kg/cm^2, and the resulting toroids were then placed on a flat quartz plate in a heavy-walled quartz tube. The toroids were heated slowly to 400°C under vacuum and sealed off after the paraffin was evaporated. They were then heated at 1180°C for about 110 hr. The ceramic density was determined from measurements of the weight and dimensions of the toroid. The toroids were about 1 cm in dia. with a cross section of about 0·025 cm^2.

Each of the two toroids prepared was first wound with a 50-turn secondary coil and then

Table 1.

	$\sigma_{g\,15{,}000,73°\mathrm{K}}$ (e.m.u/g)	$\sigma_{g\,\infty,73°\mathrm{K}}$ (e.m.u./g)	μ_{ferro} (Bohr magnetons)	μ_{para} (Bohr magnetons)	θ (°K)
U_3P_4					
Powder		23·0(85°) [1]	1·16 [1]	2·77 [1]	138 [1]
Polycrystalline	23·8	24·3	1·22	2·8	144 ± 5
[111] calculated	27·5	28·1	1·41		
[111] obs. single crystal	27·7				
U_3As_4					
Powder			1·42 [4]	2·81 [4]	198 [4]
Polycrystalline	25·6	26·0	1·57	2·8	205 ± 5
[111] calculated	29·6	30·0	1·82		
[111] obs. single crystal	30·0				

with a 250-turn primary coil for producing the magnetic field, H. The primary coil was driven with a two-cycle burst of 60 Hz current with a peak value of 10 As. The magnetic field was indicated by the horizontal deflection of an oscilloscope which monitored the voltage across a current shunt. This current shunt, along with the toroid winding, an RCA 40429 triac gate, a 15 Ω resistor, and the 120 V a.c. power line, constituted the current drive circuitry. The voltage induced in the toroid secondary was integrated to gave a signal proportional to B which was applied to the vertical input of the oscilloscope. In addition, a voltage proportional to H was substracted from the vertical input to compensate for the H contribution to B and any extraneous mutual inductance between windings. It was adjusted to give no vertical deflection with the sample well above the Curie temperature. The hysteresis loops so obtained therefore represent a plot of $4\pi M$ vs. H.

The two toroids prepared had bulk densities of 8·0 and 8·6 g/cm^3 as compared with a theoretical density of 10·0 g/cm^3. The values of the coercive field, H_c, remanent and saturation magnetization, $4\pi M_r$ and $4\pi M_s$, are plotted vs. temperature in Fig. 2. The latter is somewhat less than the expected value of 2500 G at 75°K, but most significant is the high value of 200 Oe obtained for the coercive

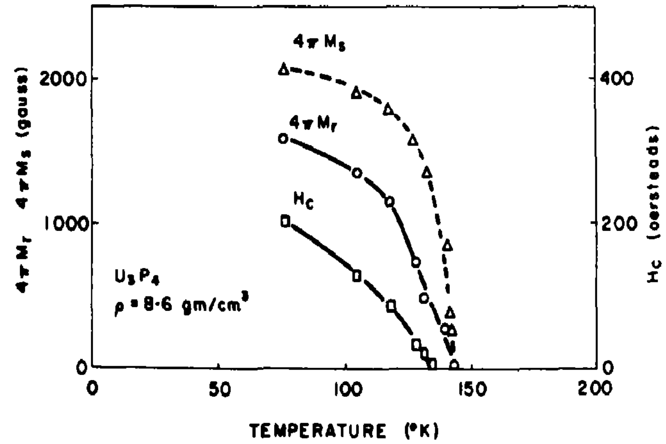

Fig. 2. Saturation and remanent magnetization and coercive field of U_3P_4 (ρ = 8·6 g/cm^3) vs. temperature.

field. This is at least partly due to the high porosity (14–20 per cent) of the ceramic, but could also reflect the high anisotropy noticed during the single crystal study.

In this Th_3P_4 type structure the uranium ions have a $\bar{4}$ local symmetry, and it could be expected that their crystal field might constrain the individual moments to lie along [100] directions as observed for DySb and some related antimonides. If all the magnetic ions were then to remain magnetically equivalent there would exist three magnetic sublattices with mutually perpendicular moments adding to a resultant magnetization along [111]. This is what was observed, and it is consistent at least qualitatively with the low value found for the saturation magnetization relative to the paramagnetic value. Several such three or six sublattice noncollinear ferrimagnetic structures were considered, and most were found to agree with the published neutron diffraction data almost as well as the ferromagnetic model. They have many equivalent forms and might therefore contribute to the entropy of the ordered state. If so, this could explain the observed low entropy difference between the ordered and the paramagnetic state.

It appears that the exact nature of the magnetic ordering in U_3P_4 and U_3As_4 will remain uncertain until a more definitive neutron diffraction study is undertaken.

General Telephone and
Electronics Laboratories,
Bayside, N.Y. 11360, U.S.A.

C. F BUHRER

REFERENCES

1. TRZEBIATOWSKI W and TROC R , *Bull. Acad. pol Sci , Ser. Sci. Chim* 11, 661 (1963)
2. TRZEBIATOWSKI W., SEPICHOWSKA A. and ZYGMUNT A., *Bull. Acad. pol Sci., Ser. Sci. Chim* **12**, 687 (1964)
3. CISZEWSKI R., MURASIK A and TROC R , *Phys. Status Solidi* **10**, K85 (1965)
4. STALINSKI B., BIEGANSKI Z. and TROC, R. *Phys. Status Solidi* **17**, 837 (1966).
5. BUSCH G. and VOGT, O. *J appl. Phys* **39**, 1334 (1968).

J. Phys. Chem. Solids Vol. 30, pp. 1276–1279.

Temperature dependence of the elastic constants of single crystal lithium*

(*Received* 3 *October* 1968;
in revised form 28 *October* 1968)

THE SINGLE crystal elastic constants of lithium were first measured by Nash and Smith[1]. Each of the three elastic constants were measured at 195°, 155° and then at 78°K. The temperature dependence of the elastic constants was determined from these independent measurements. In a later study, the elastic constants of Li and dilute Li–Mg alloys were determined at room temperature Trivisonno and Smith[2].

Since a more precise technique for measuring the elastic constants and their temperature dependence is now available, it was decided to directly measure the temperature dependence of the elastic constants of Li in the region 78°–190°K, since they are of theoretical interest and are not accurately known. It was also felt that the more accurate low temperature measurements would clear up a slight discrepancy between the ultrasonic and isothermal compressional measurements of the bulk modulus at 78°K. This discrepancy, (which is just outside of the accuracies of the two experiments), is unexpected because of the good agreement over the entire temperature range between the ultrasonic and isothermal data for all the other alkali metals and was initially felt to be related to the Martensitic phase transformation[3], which occurs slightly below 78°K in lithium.

The furnace used to grow the single crystals was similar to those employed in the previous studies, except that heat was supplied by means of nichrome wire wrapped around the furnace instead of by means of a hot plate.

---

*Work supported in part by Air Force Grant No. 68-1479.

The lithium used to grow the crystals was nominal purity lithium obtained from the Lithium Corporation of America. The crystals were oriented by a Laue transmission technique and acoustic specimens were prepared with orientations along the [110] and [100] directions.

The relative and absolute velocity measurements were made using an ultrasonic pulse echo technique with a Mg buffer rod between the acoustic specimen and the transducer. This technique is described in a recent publication[4]. Measurements were made between 90° and 195°K by immersing the sample holder in a liquid freon temperature bath. The temperature was varied by a small resistance heater and measured with a thermocouple. Once these measurements were completed, the crystals were immersed in liquid nitrogen and the values of the elastic constants were determined at 78°K. Attempts were also made to measure the elastic constants below 78°K by pumping on the liquid nitrogen. However, the crystals underwent a phase transformation just below 78°K and the elastic constants could not be measured in this region. The phase transformation was easily detected because it was accompanied by a loud ping and a substantial change in the transit time. The phase transformation could also be induced at 78°K by straining the crystals and then plunging them into the liquid nitrogen bath. X-ray diffraction verified that these specimens were polycrystalline. For those crystals which did not undergo a phase transformation, the velocities at 78°K were in excellent agreement with the values extrapolated from 90°K.

The method used to determine the elastic constants from the measured sound velocities in various crystallographic directions is given by Neighbours and Smith[5]. The values of the elastic constants shown in table 1 have been corrected to take into account the deviation of the actual direction of propagation from the [110] direction. The notation $C = C_{44}$, $C' = (C_{11} - C_{12})/2$ and $C_n = (C_{11} + C_{12} + 2C_{44})/2$ has been used. A comparison with Nash's elastic constants and anisotropy at 78°K shows a difference of about 1–5 per cent with the present data. The comparison between Trivisonno and Smith's measured room temperature elastic constants and the extrapolated elastic constants of this study shows agreement within 1 per cent. The elastic constants C_{11} and C_{44} were also measured on a [100] crystal and the values of C_{11} are given in Table 1. The agreement between the values of C_{11} and C_{44} as measured on the [100] and those measured or calculated from data taken on [110] crystals is within 1 per cent. Identical results are expected because in the [100] direction, $C'_{55} = C'_{66} = C_{44}$.

The temperature dependence of the elastic constants was determined by making an absolute measurement at 90°K and measuring the change in transit time as a function of temperature between 90° and 200°K. The system used was capable of measuring a 1 nsec change in 10 μsec, so that temperature dependence measurements could be made with high precision. Plots of the elastic constants vs. temperature are remarkably linear. The quantity dC/dT was obtained from these plots and values of dC/dT for the elastic constants C_{11}, C_n, C_{44}, and C are listed in Table 2 along with those obtained by Nash. It is seen that the $(dC/dT)p$ are quite different for all the elastic constants. This is to be expected not only because of the increased accuracy in transit time measurements, but also because the previous determination of the temperature dependence was inferred from independent measurements at three different temperatures.

The adiabatic bulk modulus, B_s, was computed from the three directly measured elastic constants and the results are shown in Table 3. Nash's data and the value of B_t given by Swenson[6] are also included in this table. The isothermal bulk modulus, B_t, was computed from B_s and the values in Table 3 clearly show that the present ultrasonic data and the isothermal compressional data

Table 1. Values of the adiabatic elastic constants, the elastic anisotropy and the density of lithium. The elastic constants are in units of 10^{10} *dyn. cm*$^{-2}$*, and the density is in units of g.cm*$^{-3}$

Temp. (deg)	C_s	C_{44}	C'	C_{11}	C_{12}	A	C_{11}^*	ρ
78	24·22	10·94	1·108	14·44	12·11	9·87	14·23	0·5454
110	23·78	10·63	1·098	14·29	12·03	9·68	14·09	0·5443
150	23·24	10·26	1·086	14·10	11·87	9·44	13·91	0·5423
190	22·68	9·89	1·074	13·92	11·72	9·21	13·72	0·5401
298†	21·23	8·89	1·042	13·42	11·30	8·53	13·23	0·5326

*Directly measured on [100] crystals.
†Extrapolated

Table 2. Values of $(\mathrm{d}C/\mathrm{d}T)_p$ *in units of dyn. cm*$^{-2}$. deg^{-1}*. These values were determined for the temperature interval 90° to 195°K*

$\mathrm{d}C_{44}/\mathrm{d}T$	$\mathrm{d}C'/\mathrm{d}T$	$\mathrm{d}C_{11}/\mathrm{d}T$	$\mathrm{d}C_s/\mathrm{d}T$	$\mathrm{d}B_s/\mathrm{d}T$	Reference
$10·26 \times 10^7$	$-0·6 \times 10^7$	$11·8 \times 10^7$	$-21·45 \times 10^7$	$-11·1 \times 10^7$	Nash
$9·31 \times 10^7$	$-0·3 \times 10^7$	$-4·70 \times 10^7$	$-13·6 \times 10^7$	$-3·07 \times 10^7$	Present work

are in good agreement over the entire temperature interval. Since the elastic constants are known to 1 per cent in the present experiment, compared to the 3–5 per cent listed by Nash, the bulk modulus, which is essentially determined by the difference between C_s and C_{11}, is now known more accurately. The discrepancy between Nash's data and the compressional data at 78°K is therefore not associated with a Martensitic phase transformation but with the difficulty in accurately determining the bulk modulus.

Table 3. Values of the adiabatic and isothermal bulk moduli of lithium in units of 10^{10} *dyn. cm*$^{-2}$

Temp (deg)	B_s	$B_{t(\mathrm{calc})}$	B_t (Swenson)	B_s (Nash)
78	12·9	12·8	12·3	13·3
100	12·8	12·7	12·2	
150	12·6	12·4	12·1	12·5
200	12·4	12·2	11·9	12·0
298	12·0	11·6	11·2	

Acknowledgements – The authors wish to thank Professor H. C. Nash of the John Carroll University Physics Department for the many helpful suggestions and stimulating discussions that he contributed during the undertaking of this problem.

John Carroll University,
Cleveland, Ohio 44106,
U.S.A.

T SLOTWINSKI
J. TRIVISONNO

REFERENCES

1. NASH H. C. H. and SMITH C. S., *J. Phys. Chem Solids* **9**, 133 (1959).
2. TRIVISONNO J. and SMITH C. S., *Acta Metall.* **9**, 1064 (1961).
3. BARRETT C. S., *Phys. Rev.* **72**, 245 (1947).
4. KOLLARITS F. J. and TRIVISONNO J., *J. Phys. Chem Solids*, **29**, 2133 (1968).
5. NEIGHBOURS J. R. and SMITH C. S., *J. appl. Phys.* **21**, 1338 (1950).
6. SWENSON C. A., *J. Phys. Chem Solids* **27**, 33 (1960).

J. Phys. Chem. Solids Vol. 30, pp. 1279–1281.

Some ESR studies of *F* centers in highly pure and doped KCl crystals

(*Received* 28 *October* 1968)

THE INCREASED *F* center growth in alkali halide crystals containing Ca impurity [1–4] and the absence of this increase in crystals doped with Cd[5] or Pb[6] impurity has not been explained satisfactorily. A suggestion has been made that on *X*-irradiation the apparent increase in the growth rate may be due to centers formed by Ca which may give rise to optical absorption under the *F* band[3]. We have measured the ratio of the electron spin resonance absorption (ESR) and the optical absorption in the pure and Ca doped irradiated crystals in order to find out whether of not the 'Ca induced' centers are *F* centers.

The narrowing of the *F* center ESR absorption line on optically bleaching the colored crystal is well-known[7]. We have investigated the shape of *F* center ESR line on thermally bleaching the additively colored crystals of KCl in dark.

Highly pure *H* crystals of KCl with background divalent cation impurity concentration $C_i \sim 1$ ppm, 'pure' *B* crystals $C_i \sim 10$ ppm and doped *D* crystals containing 1 per cent by weight $CaCl_2$ in the melt were prepared as described earlier[3, 4, 8]. The methods of quenching or slowly cooling the crystals, *X*-irradiation, additive coloration, and optical and ESR absorption measurements have also been described earlier[4, 8, 9]. Care was taken to keep the colored crystals in dark and the crystals were handled in weak red torch light for cleaving, mounting, etc. The exposure of the crystals to light in the *F* band during optical absorption measurements was kept as low as possible.

The optical absorption at the *F* peak in a *D* crystal, whether additively colored or irradiatively colored, was found to be much larger than in *H* or *B* crystal colored under identical conditions, as found by other authors[1–3]. ESR absorption spectra of the colored *H*, *B* and *D* crystals in dark were measured and carefully analysed. In all cases a gaussian ESR line of half-width 46 G with $g = 1{\cdot}9957 \pm 0{\cdot}0005$, characteristic of the *F* centers in KCl, was observed. The height of the ESR line is plotted as a function of the absorption coefficient α (cm^{-1}) at the *F* peak in Fig. 1 for both the *B* and the *D* crystals for a typical experiment with *X*-irradiated *B* and *D* crystals. It is seen from the figure that the height of the observed ESR line is proportional to the value of α at the *F* peak in both *B* and *D* crystals. These results suggest that the increase in the optical absorption at the *F* peak in the Ca doped crystal is due to the increase in the *F* center concentration and not due to the presence of Z_1 or other 'Ca induced' centers giving optical absorption near the *F* peak as suggested by Jain and Parashar[3]. The *D* crystals bleached with visible light lying in the *F* band showed a complex ESR line of half-width (peak to peak) 55 G presumably due to the formation of Z_1 centers[10].

To study the influence of thermal bleaching on *F* center ESR absorption, an additively colored *H* crystal quenched from the coloring temperature 560°C was annealed in dark at 300°C for different times and its optical and ESR absorption were studied. The optical absorption measurements showed that the colored and quenched crystals had mainly *F* band and a small *M* band[9]. The ESR absorption results, on annealing the crystal for different times at 300°C, in dark, shown in Fig. 2, reveal some new features. Curve 1 shows the characteristic *F* center ESR line [7, 9] of half-width 46 G with $g = 1{\cdot}9957$ observed in a quenched crystal Curves 2–6 are the observed ESR spectra of the crystal after annealing for 5, 15, 30, 60 and 90 min, respectively at 300°C in dark. The curves show that for initial annealing period up to 15 min, the half-width of the ESR line

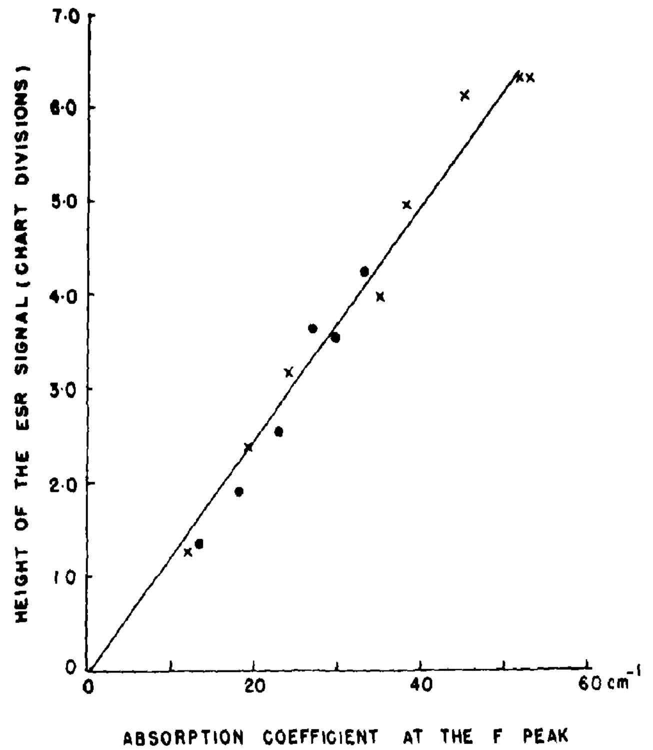

Fig. 1 Plot of the height of the ESR signal as a function of the absorption coefficient at the F band peak in X-irradiatively colored pure (● ● ●) and calcium doped (× × ×) KCl crystals at room temperature in dark.

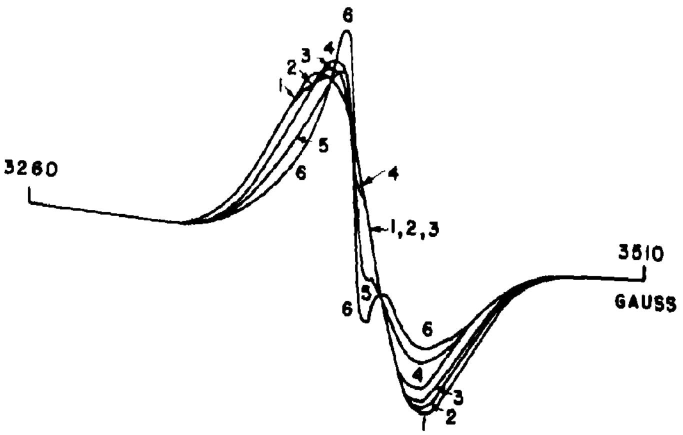

Fig. 2 First derivative trace of the ESR spectrum, taken from the recorder chart at room temperature, for additively colored KCl crystal in dark. Curve 1 for the quenched crystal from the coloring temperature. Curves 2–6 were obtained after heating the same crystal at 300°C for 5, 15, 30, 60 and 90 min respectively, and then quenching to room temperature.

decreases from 46 to 40 G, but the g value remains unchanged. On annealing for times $>$ 15 min the ESR spectra is found to be a superimposition of two lines, a sharp line superimposed over the F center ESR line. The sharp ESR absorption line is Lorentzian in shape, has a g value of 1·9997 and half-width 2·5 G and is associated with the colloidal particles of potassium metal giving an optical absorption band at 730 nm as discussed earlier[9].

The narrowing of the F center ESR line on annealing the colored crystal at 300°C in dark for short times ($\leqslant$ 15 min observed by us is similar to the narrowing of the F center ESR line on optically bleaching the crystal at room temperature[7, 9]. It has been suggested that the observed narrowing of the F center ESR line in optically bleached crystals is due to the formation of loose clusters of F centers[7] (with 4–5 interionic distances between the F centers). The narrowing in case of thermal bleaching observed by us is small (from 46–40 G) as compared to the narrowing observed in the case of optical bleaching (from 46 to 33 G). It is likely that, in dark, only a small number of clusters of the F centers is formed at 300°C, and these clusters rapidly change into potassium colloidal particles.

National Physical Laboratory,
New Delhi-12,
India

S. C. JAIN*
V. K. JAIN†
G. D. SOOTHA

REFERENCES

1. CRAWFORD J. H. and NELSON C. M., *Phys. Rev Lett.* **5**, 314 (1960).
2. SCHULMAN J. H. and COMPTON W. D., *In Color Centers in Solids*. Pergamon Press, Oxford (1962).
3. JAIN S. C. and PARASHAR D. C, *Phys. Lett.* **4**, 36 (1963).
4. JAIN S. C. and MEHENDRU P. C., *Phys. Rev.* **140**, A957 (1965).
5. JAIN S. C., SOOTHA G. D. and JAIN R. K., *J. Phys. C. (Solid State Physics, Proc. Phys. Soc., London)*. **1**, 1220 (1968).
6. SIBLEY W. A., SONDER E. and BUTLER C. T., *Phys. Rev.* **136**, A537 (1964).
7. SEIDAL H. and WOLF H. C., *Phys. Status Solidi* **11**, 3 (1965).
8. JAIN S. C. and SOOTHA G. D., *J. Phys. Chem. Solids* **26**, 267 (1965).
9. JAIN S. C. and SOOTHA G. D., *Phys. Rev.* **171**, 1075 (1968).
10. JAIN S. C. and RADHAKRISHNA S., *J. Scient. Ind. Res.* **26**, 324 (1967).

---

*Also at the Indian Institute of Technology, New Delhi-29.

†*Present address* Department of Physics, University of Utah, U.S.A.

J. Phys. Chem. Solids Vol. 30, pp. 1281–1282

Zeeman effect of bound excitons in CuCl

(*Received* 7 *October* 1968)

ZEEMAN effect of the ν_2(25,654 cm^{-1}) line[1] and the satellites lines ν_2^1 (25,665 cm^{-1}) ν_2^3 (25,670 cm^{-1}) have been studied at temperatures between 20°K and 1·9°K. These lines are observed on the low energy side of the $n = 1$ exciton line, both in absorption and in emission. The experiments were carried out in absorption[2] with thick crystals (100 μ) purified by zone melting and in emission with thin film (1 μ thick). The samples are immersed in the refrigerating liquid. High pulsed magnetic fields up to 180 kG are used (condensators battery: 2000 μF, 3000 V) synchronized with a flash (10^{-5} sec), triggered at maximum field. Luminescence is excited with the same flash associated with UG 11 Schott filter. The spectra are recorded photographically with a Bauch and Lomb grating spectrograph of high dispersion (4 Å/mm). The main line ν_2 splits into four well definite components (Fig. 1). In a magnetic field of 120 kG splitting and polarisation are as follows: (1) (25,646 cm^{-1}) π; (2) (25,652 cm^{-1}) σ; (3) (25,657 cm^{-1})σ; (4) (25,663 cm^{-1})π. This splitting is the same in absorption and in emission and varies linearly with the magnetic field. In absorption, thermalization effects occur in the ground state so that only two components are seen at 1·9°K and four at 20°K. This effect permits to identify the g

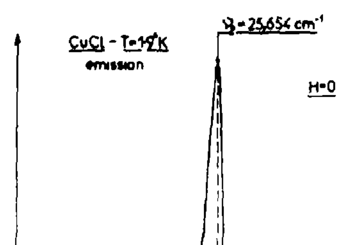

Fig. 1. Zeeman effect of the emission line ν_2 of a thin recrystallised layer, 1 μ thick.

factor of the excited state ($g = 2·05$) and the g factor of the ground state ($g = 1·1$). These results compared with theoretical calculation of the g value from the known band structure of CuCl, enable us to attribute the ν_2 line to an exciton bound to neutral acceptor. The other line $\nu_2{}^1$ behaves similarly in magnetic field while $\nu_2{}^3$ shows no splitting.

Laboratoire de Spectroscopie
et d'Optique du Corps Solide,
Associe au C N R S.,
Institut de Physique,
Universite de Strasbourg,
France

M. CERTIER
C. WECKER
S. NIKITINE

REFERENCES

1. NIKITINE S., RINGEISSEN J. and CERTIER M., *Acta phys. Polon.* **26**, 745 (1964).
2. CERTIER M., WECKER C. and NIKITINE S., *C.r. hebd. Séanc. Acad. Sci., Paris* **266**, 1215 (1968).

J. Phys. Chem. Solids Vol. 30, pp. 1282–1285.

High pressure transformations of transition metal difluorides*

(*Received* 25 *July* 1968;
in revised form 4 *October* 1968)

INTRODUCTION

THE DIFLUORIDES of the first-row transition metals have the tetragonal rutile structure with 6, 3 coordination, or monoclinic distortions of it in the case of CuF_2 and CrF_2. The radius ratios of the cation to anion, 0·50–0·60, are below the critical ratio of 0·73 for the 8, 4 coordination of the fluorite structure, according to empirical rules for hard sphere models[1]. However, the recent theoretical calculations of Lombardi and Jansen[2] involving three ion interactions, give a radius ratio of 0·636 for separation of the stability region for the fluorite versus rutile structures. The transformation from rutile to fluorite structures may be produced under high pressure. Other experiments[3, 4] on ZnF_2 and MnF_2 revealed the phase transformations under high pressure, from 20 to 140 kbars, to orthorhombic structures with basically the 6, 3 coordination and no transformation to the fluorite structure.

We have investigated the stability under high pressure of the transition-metal difluorides, CrF_2, MnF_2, FeF_2, CoF_2, NiF_2 and CuF_2. This was part of a study on reactions of the transition-metal fluorides.

EXPERIMENTAL

The experimental work was done in a girdle high-pressure apparatus described by Young *et al.*[5]. The transition-metal difluorides were all commercially available. The

---

*Supported by the U. S. Army Research Office, Durham.

Table 1. *X-ray powder diffraction data for* NiF_2 (*II*)

hKl	d_{obs} in Å	d_{calc} in Å	$I_{obs.}$	$I_{calc.}$
1 1 0	3·30	3·298	210	250
0 1 1	2·57	2·579	50	61
1 0 1	2·53	2·545	100	82
0 2 0	2·41	2·388	20	15
2 0 0	2·24	2·281		8
1 1 1		2·245	50	42
1 2 0	2·12	2·115	30	11
2 1 0	2·06	2·058	< 5	3
1 2 1	1·75	1·741	100	70
2 1 1	1·70	1·709	125	81
2 2 0	1·65	1·649	50	46
0 0 2	1·53	1·532	30	23
1 3 0	1·51	1·503	20	15
3 1 0	1·45	1·449	20	13
2 2 1	1·43	1·452	10	6
0 3 1	1·42	1·413	30	33
1 1 2	1·39	1·390	30	33
3 0 1	1·36	1·362	20	23
1 3 1		1·349		< 1
3 1 1	1·307	1·310	10	2
2 3 0		1·305		< 1
0 2 2	1·291	1·290	10	6
3 2 0		1·282		1
2 0 2	1·270	1·272	5	4
122	1·242	1·241		3
212		1·229	10	< 1
2 3 1	1·204	1·201	15	9
0 4 0		1·194		5
3 2 1	1·183	1·183	20	16
1 4 0	1·166	1·155	< 5	2
4 0 0	1·138	1·138	15	9
2 2 2	1·123	1·123	50	38
4 1 0	1·103	1·109	15	1
3 3 0		1·100		18
1 4 1	1·086	1·081	15	26
1 3 2	1·075	1·073	15	21
2 4 0	1·063	1·058	15	14
3 1 2	1·052	1·053	30	20
4 1 1	1·042	1·043	30	21
3 3 1	1·029	1·034	15	< 1
4 2 0		1 029		9
2 4 1	1·008	1·000	< 5	1
0 1 3	0·996	0·999	30	13
1 0 3		0·997		17
2 3 2		0·994		1
1 1 3	0·975	0·976	10	6

materials were contained in short carbon, nickel, or platium tubes, about 2 mm in dia. by 2·5 mm height, with chromel–alumel thermocouples on both ends. The samples were heated indirectly by four carbon-rod electrical heaters, 1 cm long surrounding them in the lavite media. Runs were made at pressures from 20 to 90 kilobars at temperatures up to 900°C. Samples were quenched after two hours at the maximum temperature. After quenching and release of pressure the samples were examined by X-ray diffraction 57·3 mm dia. cameras with FeKα, CuKα or CrKα radiation.

RESULTS

The experiments on stability of the transition-metal difluorides revealed phase transformations of NiF_2, CoF_2 and MnF_2, under pressure, from the tetragonal rutile structure to orthorhombic phases, but not in the case of FeF_2. CuF_2 and CrF_2, with monoclinic structure, did not exhibit a phase transformation up to 900°C at 90 kbars, although the CuF_2 melts at a lower temperature. The pressure-temperature dependence of the phase transformation of NiF_2 was investigated. The transformation temperature decreased from about 600°C at 20 kbars to 375°C at 90 kbars. Transformation for other difluorides was determined for samples quenched from 900°C at 90 kbars.

The high-pressure phases of NiF_2 and CoF_2 had orthorhombic structures with axial ratio b/a of 1·02. Table 1 lists the powder diffraction data for NiF_2. The observed intensities were estimated with reference to the powder pattern of the normal rutile form of NiF_2. The calculation of intensities and parameters was one using the Argonne MET-153 modified least-squares program of Busing, *et al.*[6]. Table 2 list unit-cell dimensions for NiF_2 and CoF_2. The volume change from the phases is less than the error of 0·5 per cent in calculation of the unit-cell dimensions. The extinctions indicated space group Pnnm or Pnn2. The cell distortions from the rutile tetragonal structure were mainly in the a axis to the orthorhombic a and b axis and negligible along the c axis. Thus the orthorhombic distortion depended on the change in the fluorine position x,y parameters from the x,x parameter of the rutile structure. The powder X-ray diffraction intensities were not sufficient to resolve choice of space groups. Calculations for the more symmetrical Pnnm with Ni or Co in $(2a)$ 000; and F in $(4g)$ x,y,o; indicate that the parameters for the F ions are $x = 0{\cdot}282 \pm 0{\cdot}007$, $y = 0{\cdot}315 \pm 0{\cdot}007$ with an R factor of 0·33 for $|F|^2$. These give interatomic M – F distances, 4 at 2·03 ± 0·04 Å and 2 at 1·98 ± 0·04 Å as compared to 2·01 ± 0·01 Å and 1·98 ± 0·01 Å for the rutile phase[7]. The space group Pnn2 would introduce additional z parameters for both Ni and F ions which could shift the x,y parameters of the F ion. The resolution of this structure would require at least data from a single crystal which were not obtainable.

Reactions of the fluorides with oxide materials led to the discovery of nickel oxyfluoride and cobalt oxyfluoride. The nickel oxyfluoride was made by reaction of $NiO + NiF_2$ in nickel capsules at 800°C and 50 kbars. It is a solid solution, $NiO_XF_{2\text{-}2X}$ for $0 < x < 0{\cdot}37$, an increase in unit-cell distortion according to the b/a-axial ratio from 1·02 to 1·09. There is also an increase in refractive

Table 2. Unit cell dimensions of high pressure phase of NiF_2 *and* CoF_2

(Å)	*ao*	*bo*	*co*	*v*
NiF_2	4·56 ± 0·01	4·77 ± 0·01	3·065 ± 0·005	$66{\cdot}6 \pm 0{\cdot}3^3$
CoF_2	4 64 ± 0·02	4·80 ± 0·02	3·16 ± 0·01	$70{\cdot}3 \pm 0{\cdot}4^3$

index with mean value from 1·600 for $x = 0$ to 1·654 for $x = 0{\cdot}33$. The structure of the solid solution may be either anion defect or nickel excess. Since densities could not be obtained, this question is not resolved. The $CoO_xF_{2\text{-}2x}$ solid solution has similar composition range with the same orthorhombic structure. In contrast no solid solution in the fluorides was found for FeO–FeF_2 and MnO–MnF_2 system.

Batelle Memorial Institute,
Columbus Laboratories,
505 King Avenue,
Columbus,
Ohio 43201,
U.S.A

A. E. AUSTIN

REFERENCES

1. PAULING L., *The Nature of the Chemical Bond.* Cornell University Press, New York (1960).
2. LOMBARDI E. and JANSEN L., *Phys. Rev.* **151**, 694 (1966).
3. KABALKINA S. S. and POPOVA S. V., *Dokl. Akad. Nauk SSSR* **153**. 1310 (1963); *Crystallography* **8**, 1141 (1964).
4. AZZARIA L. and DACHILLE F., *J. phys. Chem.* **65**, 889 (1961).
5. YOUNG A. P., ROBBINS P. B. and SCHWARTZ C. M., *High Pressure Measurement* (Edited by AA Giardini and E. C. Lloyd), pp. 262–273 Butterworths, New York (1963).
6. BUSING W. R., MARTIN K. O and LEVY, H. A., A Fortran Crystallographic Least-Square Program. Publication No. ORNL-TM-305, Oak Ridge National Laboratory, Tennessee
7. BAUER W. H., *Acta crystallogr.* **11**, 488 (1958)

J. Phys. Chem. Solids Vol. 30, pp. 1285–1286.

A variational method for anisotropic effective mass theory

(*Received* 25 *September* 1968)

It is well known that for the case of anisotropic effective masses it is difficult to solve the Schrödinger quations for a Coulomb potential, even for the case where two of the masses are the same. Use is made usually of a variational principle (e.g. Roberts[1]; see also references there to earlier work). We wish to draw attention to a different variational principle which applies to arbitrary potentials and can be formulated for the case of three different anisotropic masses.

As is well known, (Morse and Feschbach [3]) for a bound state the Schrödinger equation for wave vector $|4\rangle$

$$(H_0+H_I)|\Psi\rangle = E|\Psi\rangle \tag{1}$$

is exactly equivalent to the integral equation

$$|\Psi\rangle = G_0H_I|\Psi\rangle. \tag{2}$$

In equations (1) and (2) H_0 is the kinetic energy operator, H_I the potential operator, and G_0 the Green's operator defined by

$$G_0 = (E-H_0)^{-1}. \tag{3}$$

For a Coulomb potential and scalar mass (2) can be solved directly[1].

The functional

$$\Lambda = H_I - H_IG_0H_I \tag{4}$$

is stationary for solutions $|4\rangle$ satisfying (2) and therefore (1). By expanding $|4\rangle$ in a complete set $|\mathbf{n}\rangle$

$$|\Psi\rangle = |\mathbf{n}\rangle\,\langle n|\Psi\rangle = \sum_n \alpha_n|n\rangle \tag{5}$$

and defining matrix elements

$$\Lambda_{nn'} = \langle n|\Lambda|n'\rangle. \tag{6}$$

The stationary condition gives

$$\frac{\partial\Lambda_{nn'}}{\partial\alpha_n} = \sum_{n'}\alpha_{n'}\Lambda_{nn'} = 0, \quad n = 0,1,2.\ldots \tag{7}$$

The set of homogeneous equations (2) have a solution provided their determinant vanishes; the energies for which this occurs are the eigenvalues of (1). For the anisotropic mass problem we take units such that

$$H_0=\frac{k_x^2}{2m_1}+\frac{k_y^2}{2m_2}+\frac{k_z^2}{2m_3}. \tag{8}$$

$G_0(\mathbf{r},\mathbf{r}',E)$ is now given by

$$G_0(\mathbf{r},\mathbf{r}',E)=\int\frac{e^{i\mathbf{k}(\mathbf{r}-\mathbf{r}_1)}}{E-\frac{k_x^2}{2m_1}-\frac{k_y^2}{2m_2}-\frac{k_z^2}{2m_3}}\times\frac{d\mathbf{k}}{(2\pi)^3} \tag{9}$$

By making the transformations $k_x=\beta_1\alpha_x$, $k_y=\beta_2\alpha_y$, $k_z=\beta_3\alpha_z$, where $(2m_1)^{1/2}=\beta_1$ etc., the integrations in (9) can be carried out to give for negative energies

$$G(\mathbf{q},\mathbf{q}',E)=-\frac{1}{4\pi}(\beta_1\beta_2\beta_3)\exp-[E^{1/2}|\mathbf{q}-\mathbf{q}_1|] \tag{10}$$

where $\mathbf{q}$ is a vector with components $(x\beta_1, y\beta_2, z\beta_3)$. For isotropic effective masses equation (10) of course reduces to the usual result for the free particle Green's function. Equation (10) can now be substituted into (6) and, provided that $\Lambda_{nn'}$ can be evaluated numerically or analytically, the equation $\det|\Lambda_{nn'}|=0$ gives a condition from which the eigenvalues can be determined.

Department of Applied Mathematics,
and Mathematical Physics,
University College,
Cardiff,
Wales

T. LUKES

REFERENCES

1. KURSUNOGLU B., In *Modern Quantum Theory* Freeman, San Francisco (1962).
2. ROBERTS P. J., *J. Phys. Chem. Solids* **28**, 1353 (1967).
3. MORSE P. M. and FESCHBACH M., In *Methods of Theoretical Physics*, McGraw Hill, New York (1953)

J. Phys. Chem. Solids Vol. 30, pp. 1286–1289

Photocapacitive effects in ZnS

(*Received* 20 *August* 1968,
in revised form 19 *September* 1968)

INTRODUCTION

PHOTOCAPACITIVE effects observed in ZnS phosphors[1–4] have long been a subject of controversy. It was originally thought that the dielectric constant can increase on illumination because of the additional polarizability of electrons in traps[1]. Later[2,3] the idea was discarded, in the belief that the densities and polarizabilities could never be high enough to account for the observed capacitance increase and that electrons in traps could not produce the Debye type relaxation actually observed[5].

More recently, Fröhlich and co-workers [6,7] have developed a theory of interacting polarons which predicts a much higher polarizability for electrons localized in traps than had been expected hitherto, and Dominik and MacCrone[8] have since obtained experimental results on reduced rutile which are in agreement with Fröhlich's predictions. Moreover, recent measurements by Broser and Reuber[9] on single crystal ZnS have likewise suggested that a genuine photodielectric effect can be observed at liquid nitrogen temperature. These authors made repeated measurements on specimens irradiated at 78°K and temporarily raised to higher temperature to induce electron leakage from traps. After each high-temperature excursion, the capacitance diminished, and this was interpreted as arising from the successive diminution in the number of trapped electrons. On the other hand, the use of a Schering Bridge on small specimens did not permit any high degree of accuracy. Time relationships and direct comparisons of trap population and photocapacitance were not explored. In view of this, it was decided to subject the conclusion to further tests.

MEASUREMENTS

A vapor grown ZnS:Cu hexagonal single crystal (blue light emission) was provided by Professor F. E. Williams, University of Delaware. It had a thickness of 0·36 mm and

Table 1. *Typical capacitance dispersion of* ZnS : Cu *single crystal*

(*a*) Under darkness, no previous irradiation, at 80°K

Freq. (KHz)	Capacitance (pF)	Dissipation factor
1	1·12	0·0002
2	1·12	0·0001
4	1·12	0·0001
8	1·12	0·0001
10	1·11	0·0001
20	1·11	0·0001
50	1·11	0·0001
100	1·11	0·0001

(*b*) Under darkness, with previous u.v. irradiation, at 80°K

	1 KHz		10 KHz	
Time (hr min)	Cap. (pF)	Diss. factor	Cap. (pF)	Diss. factor
0 [under irradiation]			8·7	
5	1·60	0·523	1·13	0·0084
17	1·25	0·248	1·12^{5}	0·0037
43	1·20	0·189	1·11^{7}	0·0025
1.00	1·16	0·140	1·11^{7}	0·0021
1 15	1·15	0·109	1·11^{4}	0·0023
1·30	1·15^{5}	0·102	1·11^{0}	0·0072
1 45	1·14^{8}	0·101^{2}	1·11^{0}	0·001^{2}
2·00	1·14^{4}	0·093^{2}	1·11^{0}	0·0015
2.23	1·14^{0}	0·078^{4}	1·11^{0}	0·0010

was transparent. Evaporated gold contacts were applied to two sides. The dark capacitance was 1·5 pF at room temperature (25°C) and about 1·1 pF at 80°K. Its almost non-dispersive behavior is shown in Table 1(a). The measurements were made with a GR 1615-A transformer ratio bridge which reads capacitance to 10^{-5} pF and dissipation factors to 0·000001 at 1 KHz. The available precision was thus much higher than in the experiments referred to above. The specimen was illuminated at 80°K, leading to a capacitance increase to 8·7 pF. On cessation of the light, this value decayed as shown in Table 1(b). After 2 hr, the capacitance at 10 KHz regained its pre-illumination value. Such measurements were made between 100 Hz and 100 KHz, with very little dispersion over the whole range, except initially as shown by the data for 1 and 10 KHz. The presence of faint fluorescence can account for this, in view of the fact that ZnS:Cu is photoconductive.

DISCUSSION AND CONCLUSIONS

In order to estimate the fraction of traps which releases electrons during the photocapacitive delay, measurements of thermoluminescence were initiated after varying periods of storage at 80°K. They showed (Fig. 1) that after 2 hr (within which the capacitance returned to its pre-illumination value) the overwhelming proportion of electrons were still in traps and could be released by heating in the usual way. The results were almost independent of heating rate.

Two other possibilities follow: (a) The observed photocapacitive effects are after

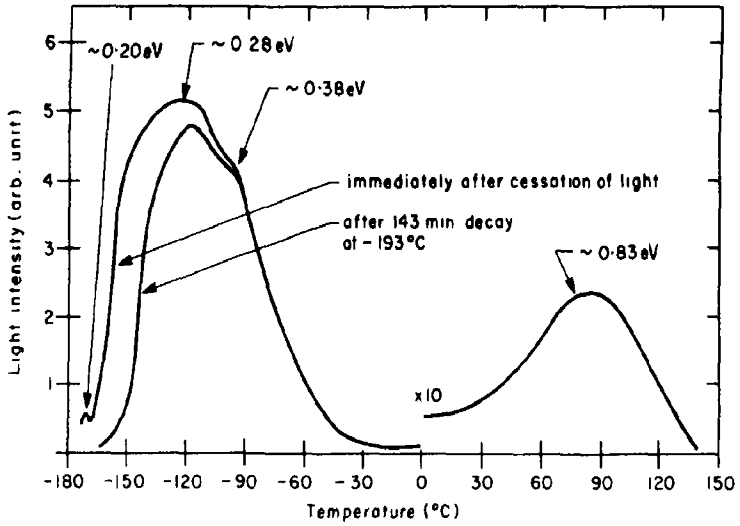

Fig. 1. Glow curves of ZnS:Cu before and after decay of photocapacitance

all due to photoconduction. The results obtained by Broser and Reuber would then have to be ascribed to their lower sensitivity, their failure to take account of decay relationships, and to possible contact problems. (b) The excited electrons become disturbed over two types of traps: a majority over deep traps of low polarizability and a few of shallower traps (~ 2 hr decay time) of much higher polarizability. This would be phenomenologically in harmony with the observations, and thermoluminescent glow curves do, indeed, yield evidence of a second, shallower trap level at about 0·20 eV. On the other hand, the shallow traps contain only a minute fraction of the total number of excited electrons, and there is at present no independent evidence that this dielectric behavior is radically different from that of normal traps. For the time being, at any rate, interpretation (a) is therefore more appropriate.

It has been suggested by Kallmann and Mark[10] that applied d.c. fields may diminish the trapped electron population, because of the reduced probability of retrapping, once electrons are thermally released from traps. A corresponding decrease of photocapacitance with field was observed. The present measurements on ZnS:Cu confirmed that the photocapacitance with field was observed. The present measurements on ZnS:Cu confirmed that the photocapacitance was indeed decreases when field less than 10^3 V/cm were applied. However, when the field was further increased, the photocapacitance increased likewise. The interpretation is thus in doubt. With field ionization of traps in ZnS ruled out[11], the field effects on photocapacitance are more likely to be due to space charge processes near the electrodes, as suggested by Bube[12].

Acknowledgements—This work was supported by contract number DA-44-009-AMC-581 (T) of the U S Army Mobility Equipment Research and Development Center, Night Vision Laboratory

Materials Research Laboratory,
The Pennsylvania State University,
University Park,
Penn. 16802,
U.S.A.

S. LEE
H. K. HENISCH

REFERENCES

1. GARLICK G. F. J. and GIBSON A. F., *Proc. R. Soc.* **A188**, 485 (1947).
2. KALLMANN H., KRAMER B. and PERLMUTTER A., *Phys. Rev.* **89**, 700 (1953)
3. DROPKIN J. J. and EWALD P., Polytechnic Inst. of Brooklyn, N. Y., Rep. No. NBONR-26313 (1953).
4. KRISPIN P. and LUDWIG W., *Phys. Status Solidi* **5**, 573 (1964).
5. FRÖHLICH H., *Theory of Dielectrics*, Chaps. 3–11. Oxford Press, Oxford (1958).
6. FRÖHLICH H., MACHLUP S. and MITRA T. K., *Phys Kondens. Materie* **1**, 359 (1963).
7. SUSSMAN J. A., *Proc. phys. Soc.* **79**, 758 (1962).
8. DOMINIK A. K. and MAC CRONE R. K., *Phys. Rev.* **163**, 756 (1967).
9. BROSER I and REUBER C., *J. Phys. Chem. Solids* **27**, 527 (1966).
10. KALLMANN H. and MARK P., *Phys. Rev.* **105**, 1445 (1957).
11. MIYASHITA K. and HENISCH H. K., *Solid-St. Electron.* **9**, 29 (1966).
12. BUBE R. H., *Photoconductivity of Solids*, p. 292. Wiley, New York (1960).

J. Phys. Chem. Solids Vol. 30, pp. 1289–1293.

Photoluminescence in lightly doped epitaxial GaAs: Cd and GaAs: Si

(*Received* 17 *September* 1968)

IN THIS NOTE it is shown that the dominant radiative recombination observed in high quality epitaxial *p*-type cadmium doped GaAs is in quantitative agreement with the predictions of the simple theory[1, 2] for conduction band-acceptor recombination. Both the spectral shape and position of the peak of the strong emission near 1·49 eV are investigated as a function of temperature between 2° and 80°K and found to be in excellent agreement with elementary theory. In addition, it is shown that the behavior of one component from a group of three lines near 1·49 eV observed in silicon doped *n*-type GaAs is also quantitatively consistent with the band-acceptor mechanism. This is in sharp contrast to the situation in bulk grown GaAs where it has recently been demonstrated that the dominant radiative emission near 1·49 eV is ascribed to donor–acceptor recombination [3]. The occurrence of different recombination mechanisms in bulk and epitaxial GaAs is not surprising in view of the greatly improved quality and purity of the epitaxial material.

Improved epitaxial growing techniques are now providing undoped samples of *n*-type GaAs with high mobilities, 50,000–100,000 cm^2 V^{-1} sec^{-1}, and decreased residual impurity content, 10^{14}–10^{15} donors (and acceptors) per cc. In these high purity samples it is possible to unambiguously identify spectral lines associated with 'added' impurities. Recombination radiation arising from the residual foreign impurities is present only weakly if at all. Epitaxial GaAs samples lightly doped with shallow acceptors Cd and Si are investigated. The GaAs: Cd samples are *p*-type, doped to a cadmium concentration of about 4×10^{16}/cc, well below the concentration where significant interaction between acceptors occurs. Some concentration broadening was observed for Cd concentrations in excess of 10^{17}/cc. Both *n*- and *p*-type GaAs: Si samples have been studied. The data presented here is from a *p*-type sample containing 10^{15}/cc silicon.

The line shape for conduction band to acceptor recombination has been predicted from both detailed balance arguments [4] and by direct calculation [1, 2]. Taking the latter view, it is possible to calculate directly the absorption coefficient $\alpha(\hbar\omega)$ in cm^{-1} and the radiative recombination rate $R(\hbar\omega)\, d(\hbar\omega)$. Making the appropriate and well-known assumptions [5] about the equality of momentum matrix elements involved in absorption and emission, it is straightforward to relate $\alpha(\hbar\omega)$ and $R(\hbar\omega)$,

$$R(\hbar\omega) = G(\hbar\omega)\, V_{\mathrm{EN}}\alpha(\hbar\omega)\left(\frac{n_u n_l'}{n_l n_u' - n_u n_l'}\right) \qquad (1)$$

where V_{EN} = energy velocity of optical radiation field. In a dielectric, the energy velocity is equal to the group velocity,

$$V_G = \left(\frac{\mathrm{d}[\omega n(\omega)]}{c\,\mathrm{d}\omega}\right)^{-1}$$

and

$$G(\hbar\omega) = \frac{n^2(\hbar\omega)(\hbar\omega)^2}{\pi^2\hbar^3c^2V_G} = \begin{array}{l}\text{density of modes}\\ \text{of radiation field.}\end{array}$$

Here $n_u(n'_u)$ is the number of filled (empty) states at the higher energy ϵ_u and $n_l(n'_l)$ is the number of filled (empty) states at the lower energy ϵ_l.

The form of equation (1) can be simplified by introducing the Fermi distribution functions. Lasher and Stern[6] have shown that the ratio $n_un'_l/(n_ln'_u - n_un'_l)$ can always be reduced to $\langle\exp[(\hbar\omega - \Delta F)/KT] - 1\rangle^{-1}$ for transitions involving band states or effective mass impurity states. Here $\Delta F = F_n - F_p$ is the difference in the quasi-Fermi levels for electrons and holes. Hence within the approximation that the carrier distributions are adequately described by quasi-Fermi levels (i.e. the rate of thermalization of the carriers is much more rapid than the recombination rate), the spontaneous radiative recombination rate is given by a slightly generalized van Roosbroeck–Shockley relation,

$$R_{\mathrm{SP}}(\hbar\omega) = G(\hbar\omega)\,V_{\mathrm{EN}}\,\alpha(\hbar\omega)/\langle\exp[(\hbar\omega - \Delta F)/KT] - 1\rangle. \tag{2}$$

In examining experimental results, attention is usually focused on the spectral dependence of the emission with the absolute magnitude given only secondary interest. Accordingly we drop the constants of proportionality and further consider the region of the $\hbar\omega/KT \gg 1$; then,

$$R_{\mathrm{SP}}(\hbar\omega) \propto \alpha(\hbar\omega)(\hbar\omega)^2 \exp(-\hbar\omega/KT). \tag{3}$$

The spectral dependence is thus contained primarily in the absorption coefficient $\alpha(\hbar\omega)$ and the exponential $\exp(-\hbar\omega/KT)$. The energy dependence of $\alpha(\hbar\omega)$ is rather different for donor-band and acceptor-band transitions in GaAs and assumes a particularly simple form in the second instance. Because of the large difference in the conduction and valence band masses ($m_v/m_c \sim 10$), the donors are much more diffuse than the acceptors. The Fourier expansion of the relatively more compact acceptors requires an appreciable portion of k-space, leading to a density of states which is nearly independent of k for $k < 1/a^*$. Since the absorption coefficient depends on energy essentially through the product of the band density of states with the impurity induced density of states (i.e. the Fourier coefficients), the energy dependence for absorption involving acceptors reduces principally to that of the density of states in the conduction band [for parabolic bands, $\epsilon_c(k)^{1/2}$] for photon energies near $\hbar\omega = \epsilon_G - \epsilon_A$ irrespective of the exact nature of the acceptor state involved[7]. Detailed calculations utilizing the quantum defect functions discussed in[8] have been performed for both donor and acceptor states in GaAs. It is found that the form of the absorption coefficient (or recombination radiation) due to donor valence band transitions depends strongly on the donor binding energy; on the other hand, for acceptor-conduction band transitions the absorption coefficient varies as $\epsilon_c(k)^{1/2} = (\hbar\omega - \epsilon_G - \epsilon_A)^{1/2}$ for small values of $\epsilon_c(k)$ irrespective of the acceptor binding energy ϵ_A, just as anticipated from the density of states arguments above. Thus, the recombination spectrum due to band to acceptor transitions should in most instances approximate the energy dependence predicted by Eagles[1].

$$R(\hbar\omega)\alpha(\hbar\omega - \epsilon_G + \epsilon_A)^{1/2} \times \exp[-(\hbar\omega - \epsilon_G + \epsilon_A)/KT]. \tag{4}$$

In Fig. 1, the photoluminescence spectra of GaAs:Cd for two temperatures, 20° and 80°K, is compared with the line shape for conduction band to acceptor transitions predicted from equation (4). The measurements were

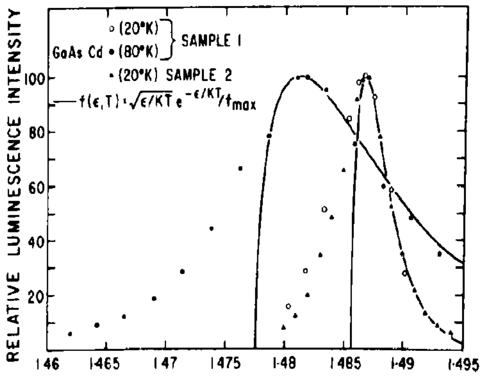

Fig 1 Comparison of the photoluminescence line shape observed from GaAs : Cd with that calculated from equation (4) for two temperatures.

obtained from front surface luminescence. The experimental apparatus and techniques have been discussed elsewhere[9]. Corrections for self-absorption were considered and found to be small.

Matching the peaks of the calculated line shapes to the experimental values yields the binding energy of the acceptors. Assuming a band gap of $\epsilon_G = 1{\cdot}521$ eV at $T = 20$°K, the binding energy of the Cd acceptor is found to be $\epsilon_A = 34{\cdot}5$ meV. Utilizing the binding energy calculated at one temperature, say 20°K, both the position and shape of emission bands can be predicted for other temperatures if the temperature variation of the band gap is known. The predicted curve for 80°K follows taking $\epsilon_A = 34{\cdot}5$ meV and Sturge's value for the band gap of $\epsilon_G = 1{\cdot}512$[10]. Excellent agreement between experiment and simple theory is obtained for the peak and high energy portion of the spectral line at all temperatures in excess of 15°K. At lower temperatures other broadening mechanisms dominate the free carrier distribution broadening described by equation (4) and prevent further line narrowing.

The deviation of the experimental line shape from theory on the low energy side appears to arise from the presence of a weaker emission line ~ 3·0 meV below the band-acceptor emission. However, other broadening mechanisms such as phonon emission may be operative precluding an unambiguous explanation. The analogous low energy shoulder seen in Fig. 2 for silicon doped gallium arsenide at 20°K emerges as a dominant line at lower temperatures, say 2°K. In fact an additional lower energy line (~ 1·486 eV) is also distinguished in GaAs : Si. The temperature dependence of the three lines (~ 1·486, 1·489 and 1·492 eV) has recently been investigated in some detail[10] in a number of different samples of varying silicon concentrations. In that work, the 1·489 eV line is ascribed to excitons bound to ionized acceptors and the 1·486 eV emission is identified as donor–acceptor pair recombination. The arguments for these assignments will not be repeated here. In the present note we restrict our attention to the band-acceptor recombination at 1·492 eV. As with GaAs : Cd excellent agreement between the predicted line shape of band-acceptor emission and the observed emission at 1·492 eV obtains. The comparison for $T = 20$°K is shown in Fig. 2

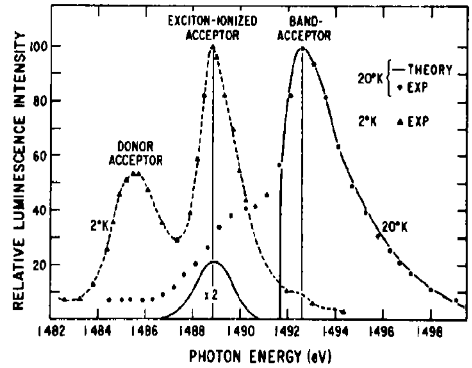

Fig. 2. Comparison of observed and calculated band-acceptor recombination in GaAs : Si The lower energy lines at 1·486 and 1·489 eV are ascribed to donor-acceptor and bound exciton recombination, respectively (see [10]).

assuming an acceptor binding energy of $\epsilon_1 = 30$ eV and a band gap of 1·521 eV.

Sturge's[11] determination of the temperature dependence of the band gap is shown in Fig. 3. At finite temperature the emission energy at the peak of the band-acceptor recombination differs from the band gap because of the thermal energy of the free carriers. In the approximation of parabolic bands the energy distribution of the carriers is Maxwellian, $\epsilon^{1/2} \exp[-\epsilon/KT]$. According to the simple theory of equation (4), the spectral dependence of the recombination radiation is also determined by the free carrier distribution with $\epsilon = h\omega - \epsilon_G + \epsilon_1$. The peak of the Maxwellian distribution moves to higher energy with increasing temperature causing the peak in the emission energy to occur increasingly further above the band gap with increasing temperature. In Fig. 3 the resulting temperature dependence of the peak of the emission predicted from equation (4) is compared with the measured temperature dependence for GaAs:Cd and GaAs:Si. Hence, it appears that in these materials, photoluminescence provides a direct measure of the carrier distribution in the conduction band. It might also be possible to determine changes in the carrier distribution resulting from external perturbations such as electric fields or infrared radiation.

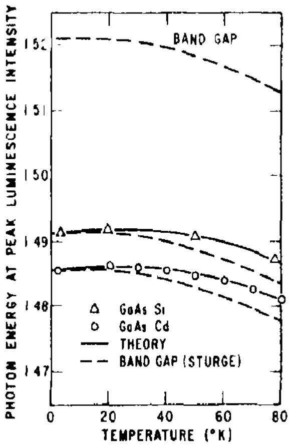

Fig. 3. Temperature dependence of the predicted and measured values for the position of the peak intensity of the band to acceptor emission bands in GaAs:Cd and GaAs:Si.

The ability of theory for band to acceptor transitions to predict both the shape and position of the emission bands in GaAs:Cd and GaAs:Si observed near 1·49 eV constitutes a strong indication that these bands are due to recombination of conduction electrons with holes trapped on acceptor levels. Similar but less complete comparisons have been obtained for Mg-doped GaAs yielding an ionization energy near 30 meV for that impurity center.

Acknowledgements – The authors wish to thank Hal Bogardus for numerous discussions and for making available recent experimental results prior to their publication which aided materially in reducing the ambiguity in interpreting the present data, and Professor J. S. Blakemore for several discussions.

Royal Radar Establishment, E. W. WILLIAMS
Malvern,
Worc., England
and
Texas Institute Incorporated, H. BARRY BEBB
Dallas, Texas 75222,
U.S.A.

REFERENCES

1. EAGLES D. M., *J. Phys. Chem. Solids* **16**, 76 (1960).
2. DUMKE W. P., *Phys. Rev.* **132**, 1998 (1968).
3. LEITE R. C. C. and DiGiovanni A. E., *Phys. Rev.* **153**, 841 (1967); LEITE R. C. C., *Phys. Rev.* **157**, 672 (1967).
4. VAN ROOSBROECK W. and SHOCKLEY W., *Phys. Rev.* **94**, 1558 (1954).
5. FOWLER W. B. and DEXTER D. L., *Phys. Rev.* **128**, 2154 (1962).
6. LASHER G. and STERN F., *Phys. Rev.* **133**, A553 (1964), BLAKEMORE J. S., *Phys. Rev.* **163**, 809 (1967).
7. JOHNSON E. J., In *Semiconductors and Semimetals* (Edited by R. K. WILLARDSON and A. C. BEER), Vol 3, p. 204. Academic Press, New York (1967).
8. BEBB H. B. and CHAPMAN R. A., *J. Phys. Chem. Solids* **28**, 2087 (1967); BEBB H. B. and WILLIAMS E. W., *Bull. Am. Phys. Soc.* **13**, 26 (1968).

9. WILLIAMS E W and CHAPMAN R A, *J appl. Phys.* **38**, 2547 (1967).
10. BOGARDUS E. H., BEBB H. B. and REYNOLDS R. A., *Bull. Am. Phys. Soc.* **13**, 497 (1968); BOGARDUS E. H. and BEBB H. B., *Phys. Rev.*, To be published; GILLEO M., HILL D. E. and WILLIAMS F. V., *Bull. Am. Phys. Soc.* **12**, 656 (1967).
11. STURGE M. D., *Phys. Rev.* **127**, 768 (1962); the smaller value of the band gap estimated by Nathan and Burns [*Phys. Rev.* **129**, 125 (1968)] resulted from assuming that the high energy line near 1·513 eV (at $T < 20°K$) occurring in emission is the same (free exciton) line observed in absorption by Sturge at 1·517 eV. However, in sufficiently pure epitaxial GaAs the free exciton occurs in emission near 1 516 eV, the 1·513 eV line often observed in emission is probably due to excitons bound to shallow donor impurities

---

J. Phys. Chem. Solids Vol 30, p. 1293.

Comment on the application of configuration coordinates to the red emission of gallium phosphide

(*Received* 27 *November* 1967;
in revised form 5 *July* 1968)

In a recent publication[1] an attempt was made to account for the width and peak position of the red emission band (at 7000 Å) of p-type GaP, doped with Zn and O, using the concept of configuration coordinates which is widely employed in the study of II–VI and I–VII compounds[2].

The red luminescence is emitted by pairs of deep donors (oxygen) and shallow acceptors (zinc)[3, 4]. The large width of the red emission band may be caused by the vibrations of the impurity atoms on the donor and acceptor sites as well as of the host lattice.

A simplified description of such vibrations may be obtained by the assumption of a single configuration coordinate. As it may well be the first time that the concept of configuration coordinates is applied in the domain of III–V compounds it may be useful to point out some limits of its applicability.

In[1], two quantities of the theory involved were derived from the dependence of the half-width ΔE of the emission band on temperature, i.e. the Franck–Condon energy shift E_{FC} (the difference between available transition energy and peak position) and the characteristic energy $\hbar\omega$ of the vibrations at the excited state. The following equation was used:

$$(\Delta E)^2 = (2{\cdot}36)^2 \cdot E_{FC} \cdot \hbar\omega \cdot (1+2n) \quad (1)$$

where $\bar{n}$ is the mean quantum number of the oscillator involved whose temperature-dependence is given by:

$$\bar{n} = [\exp(\hbar\omega/kT)-1]^{-1}. \quad (2)$$

Equations (1) and (2) contain a single phonon energy. As it is now known[3] different phonon energies play a role in the peak broadening so that the value found of 20 meV represents at best some average of the actual phonon energies. The high temperature approximation of equation (1) yields the value of E_{FC}. The oscillators in the ground and excited states may, however, have different force constants ($K' \neq K$) necessitating the extension of equation (1) by an additional multiplier (K/K') so that at the most the product $E_{FC} \cdot (K/K')$ can be obtained.

J. A. W van der DOES de BYE

Philips Research Laboratories,
N. V. Philips' Gloeilampenfabrieken.
Eindhoven – Netherlande

REFERENCES

1. MORGAN T. N., PILKUHN M. H. and LORENZ M R., *Int. Conf. Luminescence, Budapest, August 23–30, 1966*. Preprints **D10**, 104 (1966).
2. See for instance: LAX M., *Photoconductivity Conf., Atlantic City, November 4–6, 1954*. Wiley, New York (1956); CURIE D., *Luminescence Crystalline*. Dunod, Paris (1960).
3. MORGAN T. N., WELBER B. and BHARGAVA R. N., *Phys. Rev.* **166**, 751 (1968), HENRY C H., DEAN P. J. and CUTHBERT J. D., *Phys Rev.* **166**, 754 (1968).
4. VAN DER DOES DE BYE J. A. W., *Phys. Rev* **147; 2**, 589 (1966).

J. Phys. Chem. Solids Vol. 30, pp. 1294–1295.

Some observations on dislocation etching in copper

(Received 3 June 1968)

IN THE COURSE of an investigation[1] of easy glide in copper single crystals utilizing the chemical etch pit technique several features of pitting were observed which have not been reported previously. The etchant used was that of Livingston[2], (90 parts water, 25 hydrochloric acid, 15 acetic acid, 1 bromine).

The appearance of an etched {111} surface is shown in Fig. 1. Light and dark pits were determined by Livingston[3] to be due to dislocations of the same type but of opposite sign which, because they intersect the etching surface obliquely, give rise to pits of different depth—the light pits being shallower. It can be seen that a pit does not have a constant slope from centre to edge; this is especially noticeable in the light pits, which have a pronounced dark border. This effect also appears in interferometric micrographs of both light and dark pits shown by Hulett and Young[4, Fig. 1].

Figure 2 is an electron micrograph of dark (*A*) and light (*B*) pits. A border region of high slope is visible on the light pit. Optically such a pit might be mistaken for a flat-bottomed dark pit, indicating that the dislocation responsible for it had moved away from the pit position, but it is clear from the electron micrograph that the pit is pyramidal. Regions of high slope (i.e. the dark pit and the edges of the light pit) are covered with small features which, through the use of latex shadowing balls on the replica, were determined to be protuberances on the pit walls. Similar features appear in Young's[5] electron micrographs.

Pits in a crystal which was etched, stressed, and re-etched are shown in Fig. 3. Five varieties of pit appear in the field shown. Pit *A* is a dark pit at a position from which the dislocation did not move; *B* a dark pit from which the dislocation moved; *C* a light pit, dislocation unmoved; *D* a light pit, dislocation moved; *E* a new pit. A dark annulus appears near the centre of pit *C*, a dark region is apparent around the centre of pit *A*, and the new pit *E* appears to be a light pit with a dark border. These observations suggest that when etching (or re-etching) begins a transient effect occurs, consisting of the generation of a slope higher than the steady state slope, As etching continues this region moves towards the edges of the pit as illustrated in Fig. 4. This accounts for the dark border on light pits discussed above. Hulett and Young[4] have reported similar transient effects when current density is changed in electrolytic etching.

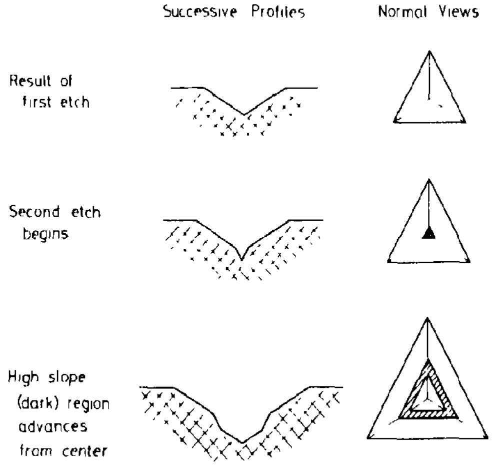

Fig. 4. Possible mechanism of re-etching unmoved dislocation (profiles are drawn symmetrically and with exaggerated slopes for clarity).

It may be noticed in Fig. 3, that the flat bottom in pit *D* is larger than that in *B*. Hullet and Young[4] have shown from the kinematic theory of etching that the rate of advance of a slope discontinuity depends on the etching characteristic followed. Higher spreading velocity for a flat bottom in a shal-

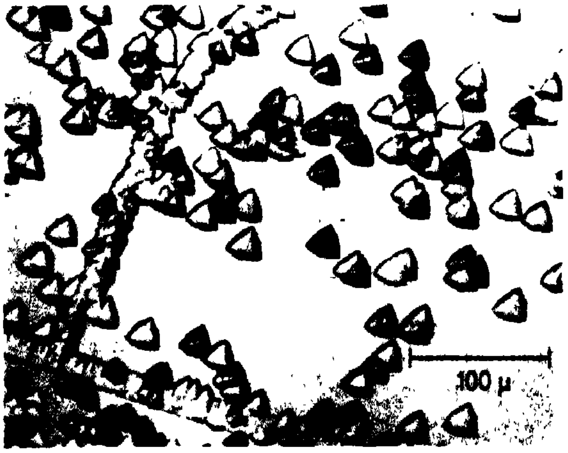

Fig. 1. Dislocations revealed by Livingston's etchant on a {111} copper surface.

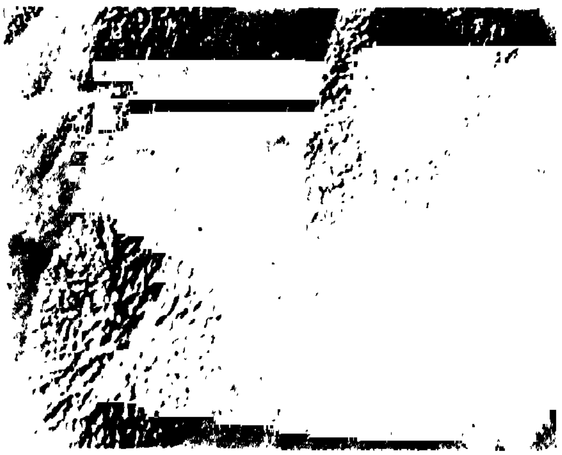

Fig. 2. Electron micrograph of a surface replica showing internal structure of dark (*A*) and light (*B*) pits.

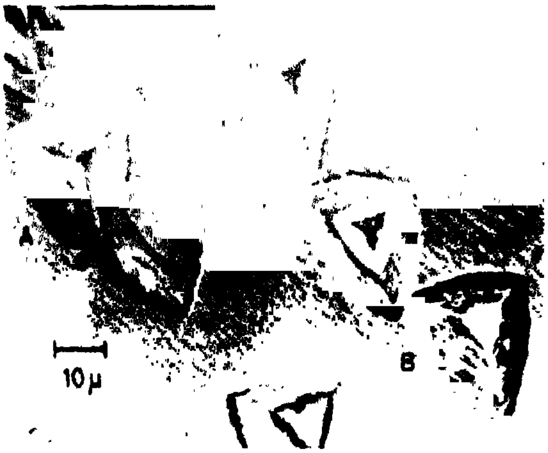

Fig. 3. Re-etching behaviour of light and dark pits.

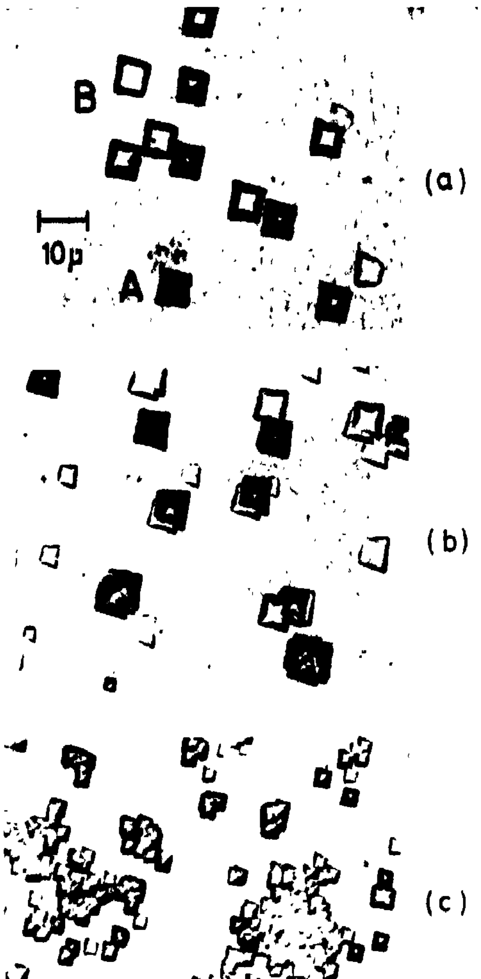

Fig. 5. Pits formed with Livingston's etchant on a {100} copper surface (a) unstrained (b) 0·2 per cent strain (c) 0·8 per cent strain.

low pit as compared to a deeper one implies that the etching characteristic is Type I, i.e.

$$\left(\frac{\partial^2 J}{\partial \rho^2} < 0\right)$$

where J is the step flux and ρ the step density. However if such a characteristic is being followed, the leading edges of a pit should be diffuse rather than sharp, and in Fig. 3 this does not seem to be the case.

The light-dark etching effect is not confined to {111} surfaces. Figure 5 shows a {100} surface etched with Livingston's etchant. No determination of the types of dislocation giving rise to the various pits has been made, but some of the features mentioned above for {111} pitting can be seen, for example dark pits (A) and light pits with dark borders(B). A light-dark effect on the {100} surface is expected according to Livingston's explanation, since the {111} slip planes intersect {100} obliquely. The etch-pit clusters shown in Figs. 5(b) and (c) after strains of 0·2 and 0·8 per cent are more equi-axed than is commonly observed in copper. This is thought to be due to the orientation of the crystal, whose tensile axis was on the [001]-[011] tie line so that two slip systems were equally stressed.

It may be wondered why Fig. 5(c) does not show such a pronounced light-dark effect, as does Fig. 5(b) since presumably dislocations of opposite sign are still present. The author's view is that when a light-dark effect occurs, it can be taken as evidence that dislocations of opposite sign are present; but when the effect is absent, no conclusions about the dislocation population can be drawn. Even in crystals where dislocations of opposite sign are known to be present (e.g. copper single crystals strained in tension) the effect does not always occur; presumably it is quite sensitive to such factors as crystallographic orientation of the surface, quality of surface polish, orientation of the specimen surface in the etching bath, and amount of agitation. Contrast is also strongly affected by the microscope aperture settings. In the author's experience the most pronounced light-dark effect occurs when no agitation is used during etching and the surfaces to be etched are horizontal in the etching bath.

Acknowledgements – Drs. J. D. Livingston and F. W Young, Jr. and Prof. A. S. Argon gave helpful advice. The research programme was supported by the National Science Foundation under grants G-24840 and NSF-GK-596.

Massachusetts Institute of Technology,
Cambridge,
Massachusetts, U.S.A.

W T. BRYDGES*

REFERENCES

1. ARGON A. S and BRYDGES W T *Phil. Mag.* **18**, 817 (1968).
2. LIVINGSTON J. D., *Acta Metall.* **10**, 229 (1962).
3. LIVINGSTON J D., In *Direct Observations of Imperfections in Crystals* (Edited by Newkirk and Wernick), p. 115. Interscience, New York
4. HULETT L. D., Jr and YOUNG F W. Jr., *J. Phys Chem. Solids* **26**, 1287 (1965).
5. YOUNG F. W. Jr., *J. appl. Phys.* **33**, 749 (1962)

**Present address:* Corning Glass Works, Sullivan Park, Corning, N.Y. 14830, U.S.A.

J. Phys. Chem. Solids Pergamon Press 1969. Vol. 30, pp. 1297–1308. Printed in Great Britain

ANTIPHASE BOUNDARIES IN SEMICONDUCTING COMPOUNDS

D. B. HOLT
Metallurgy Department, Imperial College, London S.W. 7, England

(*Received* 23 *September* 1968; *in revised form* 16 *December* 1968)

Abstract – Within crystals of semiconducting compounds regions can exist between which reversals of crystallographic polarity occur These regions are antiphase domains. Antiphase boundaries (*APBs*) are crystallographic defect surfaces and type 2 *APBs* incorporate non-stoichiometric excess atoms of one of the constituents of the compound. The geometry of *APBs* and their interactions with grain boundaries and with dislocations in semiconducting compounds with the sphalerite structure are treated and the properties of *APBs* are discussed. The evidence for their existence is reviewed and the techniques available for their study are outlined

INTRODUCTION

MANY PARTIALLY ordered alloys contain anti-phase boundaries. These are surfaces across which the occupation of the sub-lattices of the ordered superlattice changes. That is, on one side (in one domain) one type of site is occupied by *A* atoms, the second type of site being occupied by *B* atoms; on the other side of the boundary, however, (in the other anti-phase domain) the first type of site is occupied by *B* atoms and the second type by *A* atoms. The anti-phase domain size is a function of the degree of disorder. Much work both theoretical[1-4] and experimental[5, 6] has been done on this phenomenon.

The sphalerite structure characteristic of most of the important III–V and II–VI compounds is an ordered superlattice. Each of the elements of the compound with this structure occupies the sites of an f.c.c. sublattice. Each f.c.c. sublattice is offset by a quarter of a body-diagonal of the f.c.c. structure cell from the sites of the other sublattice as shown in Fig. 1. The wurtzite structure characteristic of a number of the remaining III–V and II–VI compounds and the chalcopyrite structure in which a number of ternary semiconducting compounds crystallize are closely related ordered superlattices. For crystallographic simplicity however attention will, in the main, be confined in this paper to the sphalerite structure of the more important materials. The general treatment developed applies *pari passu* to the other structures as well, however. The possibility that antiphase domains might occur in these structures has not previously been considered in the literature. There is evidence, however, as outlined below, arising from research on the dissimilarities between (1 1 1) *A* faces and $(\bar{1}\,\bar{1}\,\bar{1})$ *B* faces which shows that antiphase domains do occur. (Here *A* denotes atoms of the lower valence element in the compound and *B*, atoms of the element with the higher valency). This conclusion has not been explicitly deduced previously however.

The sphalerite and wurtzite structures are non-centrosymmetric. Hence there is in the [1 1 1] direction in the sphalerite structure, a definite order of occurrence of the (1 1 1) planes of atoms of the two chemical species constituting the compound as illustrated in Fig. 2. That is, the structure exhibits polarity in the ⟨1 1 1⟩ directions. The opposite sides of {1 1 1} slices of materials with the sphalerite structure are physically and chemically distinguishable in a number of simple and important ways[7]. This implies that sphalerite structure materials part predominantly along either Type I or Type II {1 1 1} planes, since

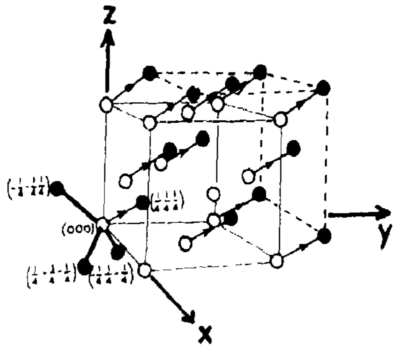

Fig. 1. A f.c.c. unit cell of the sphalerite structure is drawn with fine solid lines. Part of another face centred cubic unit cell is shown by dotted lines. The latter cell is occupied by black atoms displaced by $\frac{1}{4}, \frac{1}{4}, \frac{1}{4}$ in terms of the lattice parameter along the three crystallographic axes from the white atoms of the first unit cell. The coordinates are given for the four black atoms to which the white atom at the origin is bonded. The pairs of atoms connected by arrows are the basis of the structure.

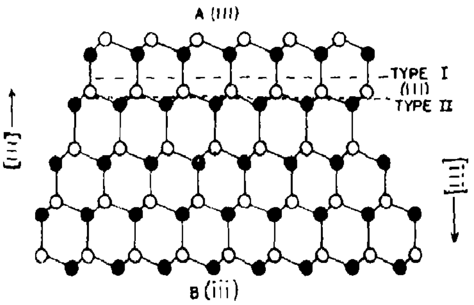

Fig. 2. Sphalerite structure projected onto the $(1\bar{1}0)$ plane. The sequence of atoms in the {111} and {111} directions are reversed, that is, these directions have polarity. If the material always or predominantly parts on type I planes rather than type II planes, then (111) planes and (111) planes are surfaced by atoms of different type. That this does occur is shown by the existence of many experimentally observed dissimilarities between (111) and (111) planes[7].

only in this case are opposite faces predominantly of atoms of the different chemical species. It is therefore very probable that they part essentially along Type I planes as indicated in Fig. 2. In two cases it was observed that the character of the surface varied from one area to another[8–10] and evidence of polarity reversal across twin boundaries has been reported[11]. These observations are evidence of the existence of polarity-reversal domains, that is, of antiphase domains and boundaries as will be discussed below.

GEOMETRY OF ANTIPHASE BOUNDARIES IN THE SPHALERITE STRUCTURE

It is possible either for the *A* atoms (those of the lower valence element in the compound) to occur on the (000) (white atom) sites of Fig. 1 and the *B* atoms therefore on the ($\frac{1}{4}\frac{1}{4}\frac{1}{4}$) (black atom) sites or for the *A* atoms to occupy the ($\frac{1}{4}\frac{1}{4}\frac{1}{4}$) sites. Changing from the one occupation scheme to the other creates antiphase domains between which polarity is reversed as shown for example in Fig. 3. The interface between antiphase domains is an antiphase boundary (*APB*). It can also be seen in Fig. 3 that the nature of, for example, the top surface of the material changes across antiphase boundaries. That is, the presence of *APB*'s changes a surface from (111) *A* type to $(11\bar{1})$ *B* type. Conversely observations of changes in surface type from one area to another[8–10] constitute evidence of the existence of antiphase boundaries in the material. Assuming that all atoms have four tetrahedral bonds, all bonds crossing *APB*'s must connect like atoms, that is, they are wrong bonds and have higher energy than right bonds connecting unlike atoms. This follows since bonds connect neighbouring sites which are normally occupied by unlike atoms. Across an *APB* however the occupancy of the sublattices has been interchanged so that across an *APB* neighbouring sites are occupied by like atoms.

In the sphalerite (and wurtzite) structures there are just two sublattices and only two ways in which they can be occupied. It therefore follows that *APB*s in these structures are incapable of forming a metastable foam structure[1]. That is, three domains cannot be in contact for there are only two ways in which the sub-lattices can be occupied. Two of the hypothetical three domains must have the same occupation scheme and no *APB* separates them. This means that *APB*s must either be closed surfaces (possibly coinciding with grain boundaries, as discussed below)

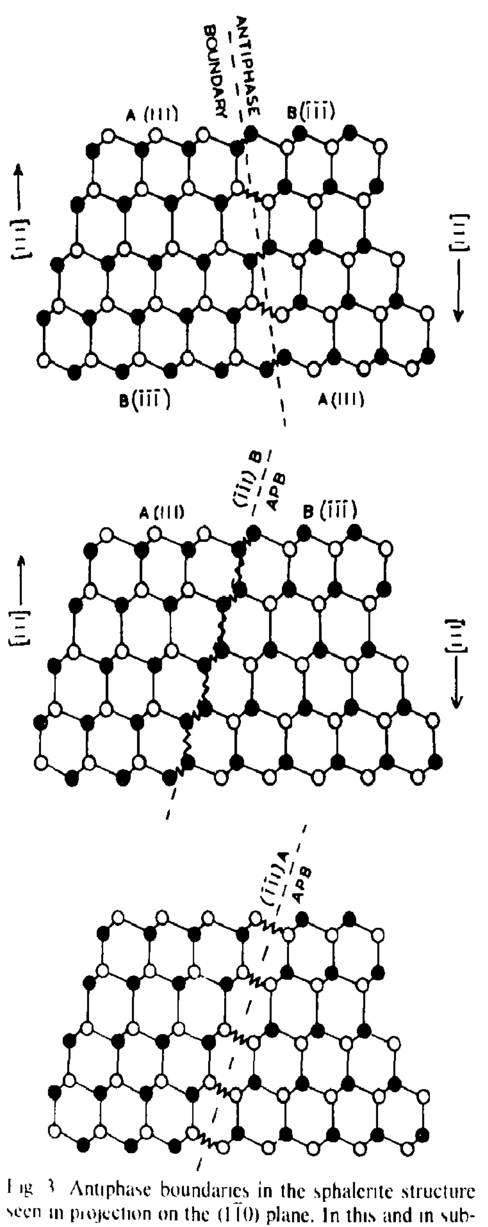

Fig. 3. Antiphase boundaries in the sphalerite structure seen in projection on the (1 1̄ 0) plane. In this and in subsequent figures zig-zag lines denote wrong bonds. (a) (1 1 3̄) antiphase boundary. This is a type 1 *APB*. Equal numbers of wrong *A–A* bonds (white–white) and of wrong *B–B* bonds (black–black) cross the boundary. The total numbers of the two types of atom in the material are unaffected by the presence of this *APB*. (b) (1̄ 1̄ 1̄) *B* antiphase boundary which is of type 2 and involves wrong *B–B* bonds only. More *B* atoms than *A* atoms are incorporated in material containing type 2 *B APB*s. (c) (1̄ 1̄ 1) *A* antiphase boundaries are also of type 2 but incorporate a non-stoichiometric excess of *A* atoms into the material.

or emerge at free surfaces. Thus the domain structure in monocrystalline materials with either the sphalerite or wurtzite structures can only take the form of a matrix of one domain type containing domains of the other type in the form of included volumes. The structures observed by etching both GaAs (which has the sphalerite structure[8] and CdS (which has the wurtzite structure)[9] were of this form. Such a substructure is unstable and at elevated temperatures will tend to anneal out, eliminating the high energy *APB*'s[9]. Unstable foam structures are conceivable in which pairs of *APB*s intersect to divide the crystal into four domains which are alternately phase and antiphase around the line of intersection of the *APB*s.

The vectors translating the points of one sub-lattice to those of the other sublattices are of the form $a/4\langle 111\rangle + L$, where L is any f.c.c. lattice vector. Any plane that contains an $a/4\langle 111\rangle$ vector will therefore include sites of both sublattices. These will be called type 1 planes. (These are not to be confused with the Type I {111} planes shown for example in Fig. 2. The two similar terms are in standard use.) Planes containing no $a/4\langle 111\rangle + L$ vectors will contain sites of one sublattice only and will be called type 2 planes. All bonds crossing an *APB* are wrong bonds. If the atomic planes on either side of the boundary are of type 1, therefore, wrong bonds connecting both species of atom must be involved. Antiphase boundary planes of type 2, however, involve atoms and wrong bonds of one kind only. Only in the latter case are there more of this kind of atom than of the other in the material in consequence of the existence of the *APB*. That is, only type 2 *APB*'s can affect and be affected by deviations from stoichiometry. Examples of *APB*'s illustrating these facts are given in Figs. 3(a–c).

The condition that a plane $(u\ v\ w)$ contains a direction $h\ k\ l$ is that the normal to the plane and the direction be at right angles. That is, the scalar product of the two directions must be zero:

$$hu + kv + lw = 0. \tag{1}$$

Thus type 1 planes are those for which

$$[u\,v\,w] \cdot \langle 111 \rangle = 0$$

while for type 2 planes

$$[u\,v\,w] \cdot \langle 111 \rangle \neq 0.$$

All type 1 planes contain equal numbers of A and B sites. This can be shown by treating two cases: Type 1 (i) planes contain just one $a/4\langle 111 \rangle$ vector. Hence each A site in the plane is coupled to a B site displaced by $a/4\langle 111 \rangle$ from it. Type 1(ii) planes contain two $a/4\langle 111 \rangle$ vectors at 109°28′ (the tetrahedral angle) to one another. Thus to each A site correspond two B sites displaced from it by the two $a/4\langle 111 \rangle$ vectors i.e. at the ends of the two tetrahedral bonds lying in the plane (Fig. 1). However since the interbond angle at both A and B atoms is the same the sites lie in parallel rows forming a zig-zag chain containing equal numbers of A and B atoms. The plane of a type 1 (ii) *APB* is of course fully determined by the two $\langle 111 \rangle$ vectors that it contains. For example, the plane $(u\,v\,w)$ containing the $[111]$ and $[\bar{1}11]$ directions, is $(01\bar{1})$.

The only type 1 (ii) planes are those of the form $\{110\}$*.

Since type 2 planes contain sites of one sublattice (One atomic species) only, there must be neighbouring parallel planes in the other sublattice containing only atoms of the other kind. Hence, depending upon where the type 2 *APB* is formed all the bonds will be either wrong A–A type or wrong B–B type. Thus type 2 *APB*'s can occur in either $\{u\,v\,w\}$ A or in $\{u\,v\,w\}$ B forms. An example illustrating this fact is given in Figs. 3(b, c).

ANTIPHASE BOUNDARIES AND GRAIN BOUNDARIES

To each grain boundary across which the misorientation corresponds to a tilt about a $\langle 110 \rangle$ or a $\langle 100 \rangle$ axis in the diamond structure, there correspond two physically distinguishable grain boundaries in the sphalerite structure. In the case of $\langle 110 \rangle$ tilt axis boundaries it was shown in a previous paper that the two boundaries correspond to tilts of θ and of $\Theta = 180° + \theta$[12]. Rotation through 180° about a $\langle 110 \rangle$ axis is an operation which interchanges the occupation of the two sphalerite sublattices. Thus a $\Theta\langle 110 \rangle$ grain boundary is also describable as a θ boundary plus an *APB*. This is illustrated in Figs. 4(a, b) for the case of the upright and inverted (111) twins in the sphalerite structure[12]. Figure 4(c) is an example of the way in which twin boundaries and an *APB* may be connected.

In the case of $\langle 100 \rangle$ tilt axis grain boundaries the two boundaries in the sphalerite structure corresponding to a single boundary in the diamond structure have misorientations of θ and $\theta + 90°$ (plus inversion). Again a rotation of 90° about a $\langle 100 \rangle$ axis plus inversion through a centre of symmetry is a polarity inverting operation, since the $\langle 100 \rangle$ axes in the sphalerite structure are $\bar{4}$ inversion tetrad axes. Therefore a $(\theta + 90° + \text{inversion})\langle 100 \rangle$ boundary is equivalent to $a\theta\langle 100 \rangle$ grain boundary plus an *APB*. An illustrative example is given in Fig. 5.

Thus *APB*'s may be associated with changes of orientation (grain boundaries) in whole or in part. Which situation will obtain depends upon the conditions under which the specimens were prepared. If the material formed by coalescence during growth of grains that nucleated with unconstrained or only partially constrained orientation and occupation of the sublattices, *APB*'s must be expected sometimes to be associated with the grain boundaries. In the case of CdS studied by Rozgonyi and Foster[10] it appears that *APB*'s occurred

---

*Equation (1) is the same expression as that employed to distinguish between type 1 and type 2 *APB*'s in centrosymmetric superlattices However there is no shear vector that will transform one antiphase domain into the other in the sphalerite or wurtzite structures i.e there is no antiphase vector. Therefore the arguments[6] in terms of the necessity or otherwise for removing material in order to form the *APB* which are used to justify equation (1) in centrosymmetric materials don't apply here.

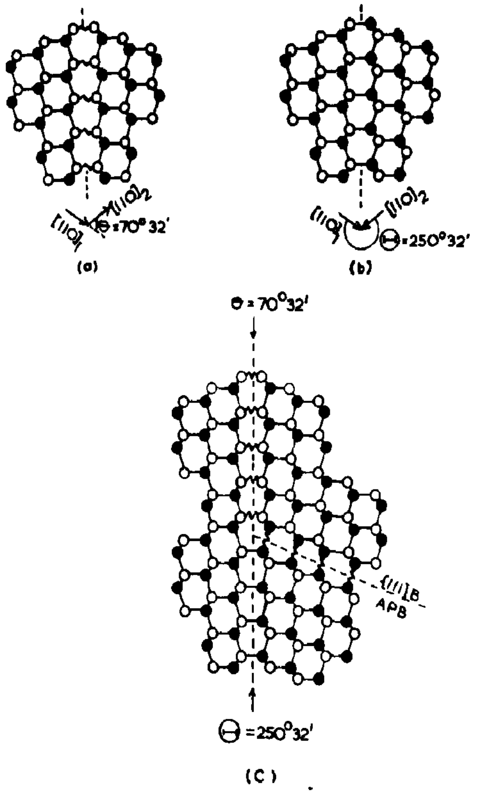

Fig. 4. {111} twin boundaries in the sphalerite structure (a) Inverted twin boundary (b) Upright twin boundary. (c) Join of a {111} *B* antiphase boundary and {111} twin boundaries.

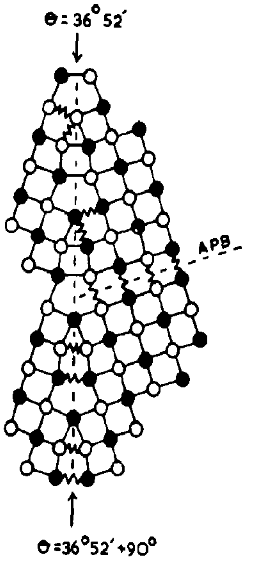

Fig. 5. Join between grain boundaries in the sphalerite structure having tilt axis [001] and a (110) median plane with an antiphase boundary.

only in coincidence with grain boundaries in both vapour phase grown bulk polycrystalline samples and in films, evaporated or sputtered onto Au-coated quartz and sapphire. When films are grown epitaxially all the grains that coalesce to form the film have the same or nearly the same orientation due to the influence of the substrate. It need not be the case in general that the occupation of the sublattices be the same throughout all these separately nucleated volumes however. In such cases then the *APB*s would not be associated with grain boundaries. The antiphase domains so formed would occur on an electron microscopic scale. In the case of bulk single crystals there are no grain boundaries and the antiphase domains constitute isolated volumes with the common crystallographic orientation. Where they intersect the free surface they will produce isolated polarity inversion areas as in the case of the (0001) surface of CdS investigated by Wilson[9].

An important special case of the association of an *APB* with a grain boundary is that of the inverted twin shown in Fig. 4(a). Inverted twins were found to occur frequently in BeO [11] although they are not known to exist in other materials.

ANTIPHASE BOUNDARIES AND DISLOCATIONS

What were previously described as inverted stacking faults in dissociated dislocations in the sphalerite structure[13] are antiphase domains two (111) planes thick and bounded by partial dislocations. Figure 6 indicates the way in which a 60° dislocation can dissociate to form such an inverted stacking fault. Movement of either or both of the partials can widen the stacking fault, that is, increase the volume of the antiphase domain. In this way dislocations can play a role in order-disorder transformations and can interact with

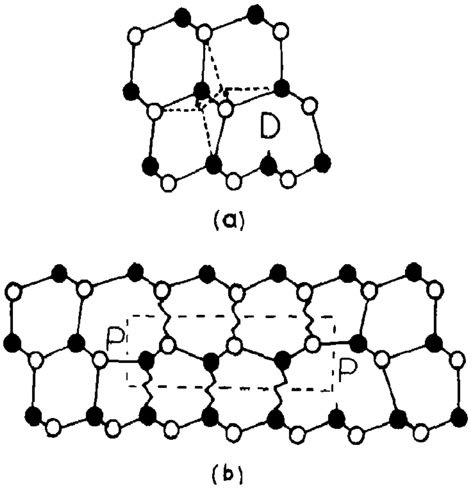

Fig 6 One mode of dissociation of a 60° dislocation in the sphalerite structure to form an inverted stacking fault. (a) 60° dislocation The arrows indicate the sense in which the double atom ribbon running normal to the figure must be rotated and rebonded as indicated by the dotted lines. (b) Resultant form of extended dislocation when three double atom ribbons have been so rotated. Partial dislocations run normal to the figure at the positions marked *P* The dotted lines bound an antiphase domain which can be extended by movement of the partial dislocations.

*APB*s. However in diamond and sphalerite-structure materials dislocations have not been observed to be dissociated[14] except in the case of AlN[15, 16] and the II–VI Compounds ZnS[15, 17, 19] CdS[20] and ZnSe[19, 21]. In the case of ZnS it has been established that the wurtzite-sphalerite phase transition occurs through the movement of partial dislocations drawing stacking faults behind them[22, 23]. Thus dislocation dissociation is unlikely to be important in many of the III–V compounds but may well be significant in most II–VI materials.

The defect structures considered above are idealized. Real defects must often be more complex due to segregation of impurities and to interactions with gross defects such as precipitates, voids, cracks etc.

ENERGIES OF ANTIPHASE BOUNDARIES

The energy of antiphase boundaries in the sphalerite structure will be the sum of terms due to nearest-neighbour interactions, to long-range ionic interactions and non-stoichiometric contributions. The nearest neighbour interaction term can be obtained by multiplying the number of each kind of wrong bond per unit area by the extra energy of that kind of wrong bond. The long-range ionic term could be obtained from a calculation of the change in the Modelung constant resulting from the introduction of the *APB*. The effect of conditions favouring non-stoichiometry would have to be treated in terms of the chemical potentials of the elements in a system consisting of the crystal in contact with material reservoirs of the two constituents of the compound.

None of these terms can be treated in a general way. Existing treatments of *APB*s consider nearest neighbour interactions alone. Even in the case of the wrong bond term which involves nearest neighbour interactions alone the generalized expression employed by Cahn and Kikuchi cannot be used here as it applies only to structures in which each atom is at a centre of symmetry[2]. Moreover no experimental observations of the preferred orientations of *APB*s in sphalerite structure materials are available, against which to test any expressions for *APB* energies as functions of orientation. In this paper therefore the wrong bond term alone will be discussed and that only for a few simple cases.

Any bond that crosses an antiphase boundary plane, **p**, must be a wrong bond. The condition that a plane **p** must be crossed by a vector **t** is that the projection of **t** on **p** equal or exceed the interplanar spacing $1/p$[1]. The bonds in the sphalerite structure all have vectors $\mathbf{t} = \langle 111 \rangle$ and it would be possible to proceed in this way to determine the types of bond cut by any given plane, the numbers of each type cut per unit area and to multiply these numbers by the increase in energy per bond $E_{AA} - E_{AB}$ or $E_{BB} - E_{AB}$ as the case might be[1].

It will suffice for present illustrative purposes, however to consider the (100), (110) and (111) planes. Drawings of the atomic structures of these planes were given in a previous paper[24] and it was shown that the number of bonds crossing unit area was given by

$$N_s = \frac{n}{\mathbf{q}_1 \times \mathbf{q}_2}$$

where $\mathbf{q}_1 \times \mathbf{q}_2$ is the unit mesh of the crystallographic plane in question and n is the number of cross-boundary bonds associated with that mesh. For the (100) plane it was shown that $N_s = 4/\lambda^2$ where λ is the lattice parameter of the compound. These bonds are all of the same kind i.e. (100) is a type 2 *APB* plane. Thus there are two cases: (100)*A APB*'s have a wrong bond energy per unit area of $4/\lambda^2$ $(E_{AA} - E_{AB})$ and (100)*B APB*s have a wrong bond energy per unit area of $4/\lambda^2\,(E_{BB} - E_{AB})$. Similarly for (110) planes $N_s = 2\sqrt{2}/\lambda^2$ with equal numbers of both kinds of wrong bonds present i.e. (110) is a type 1 *APB* plane. Thus the wrong bond energy per unit area for (110) *APB*s is given by $\sqrt{2}/\lambda^2\{E_{AA} + E_{BB} - 2E_{AB}\}$. For (111) planes $N_s = 4/\sqrt{3}\lambda^2$ and the bonds are all the same kind (type 2 *APB*s). Thus the two cases are: (111) *A* with an energy per unit area due to wrong bonds of $4/\sqrt{3}\lambda^2\{E_{AA} - E_{AB}\}$ and (111) *B* with a wrong bond of energy of $4/\sqrt{3}\lambda^2\{E_{BB} - E_{AB}\}$.

Thus for example (111)*B APB*s are of lower energy than are (100)*B APB*s in sphalerite structure compounds in which the bonding is predominantly covalent so that the wrong bond energy term is more important than is the ionic energy term. It is also clear that specimens grown under conditions favouring non-stoichiometry are likely to contain a greater area per unit volume of type 2 *APB*s than are specimens of stoichiometric composition. Type 2 *APB*s will therefore also be referred to as non-stoichiometric *APB*s.

While type 2 *APB*'s, if atomically planar, contain all *A* or all *B* atoms it is geometrically possible to produce *APB*s with any ratio of *A*–*A* to *B*–*B* bonds. This is done by means of a stepped structure with successive steps in positions e.g. as in Figs 3(b) and 3(c) or in Type I and Type II (111) positions as shown in Fig. 2. Each kind of step in such cases will contain atoms and wrong bonds of one kind only. The ratio of the areas of the steps of the two kinds then gives the ratio of *A* to *B* atoms. This amounts, microscopically, to considering high-index planes which are very near to a type 2 *APB* orientation. The types of *APB*s occurring on a number of low-index crystallographic planes are listed in Table 2.

PHYSICAL AND CHEMICAL EFFECTS OF *APB*s IN SEMI CONDUCTING COMPOUNDS

The occurrence of antiphase domains in crystals of semiconducting compounds with the wurtzite or the sphalerite structure will affect the overall value for the sample of polarity-dependent properties. Certain physical parameters measured in polar directions, reverse sign when the polarity is reversed. If the sample contains equal volumes of matrix and antiphase material the averaged value of such a parameter will be zero. The effect of the presence of any volume percentage of antiphase material will be to reduce the measured value of the parameter proportionally. Examples of polarity dependent parameters are the piezoelectric and pyroelectric constants. The sign of the surface charge for a given stress or temperature depends upon the polarity[25, 26]. Wilson[9] measured the piezoelectric constant, d_{31}, of CdS crystals containing apparent antiphase domains and found the measured value to vary linearly with the 'average density' of these antiphase domains intersecting the {0001} surface of the sample. Other well-known polarity dependent properties of sphalerite, and wurtzite, structure compounds are the etching and crystal growth behaviour of the {111} and {0001} surfaces[7].

The electrical and optical properties of *APB*s should resemble those of grain boundaries. As the periodicity of the lattice potential is disturbed by *APB*s, scattering of charge carriers can occur. Since like-neighbour bonds occur across *APB*'s the possibility of trapping and recombination of charge carriers arises. Type 2 *APB*s contain like-neighbour pairs of one chemical element only. They must therefore be expected to have large electrostatic charges. The data necessary for a quantitative discussion are not available. However it is possible to indicate the qualitative causes and consequences of this surface charge. In compounds that are predominantly covalently bonded the wrong bonds that occur have either more or less than two electrons per sp^3 hybrid orbital and should be readily excited so that electrons may tend to be either lost (donor action) or gained (acceptor action). The resultant charges are likely to be less than in the case of grain boundaries containing dangling bonds which have been observed to have charges as great as $2{\cdot}5 \times 10^{12}$ electrons per cm^{-2} or one per 10^3 atoms in the surface. Such surface charges in semiconductors would result in band bending and in extreme cases might result locally in majority charge carrier sign reversal[12]. In predominantly ionically bonded compounds type 2 *APB*'s would automatically have a charge of the sign of the ions involved and of the order of 10^{15} electrons cm^{-2} i.e. one per ion in the surface. Such surface charges are not energetically possible and may be avoided either by a change in the valence state of the atoms concerned, or by the incorporation of impurity atoms, or by adopting an atomically non-planar configuration for example stepped from *A* to *B* atom positions as discussed above, or by the non-occurrence of boundaries in such orientations. If charged surfaces do occur in ionically bonded compounds they will produce screening space charge regions containing an excess of the vacancies of the appropriate charge sign (reference [12] and the references listed therein).

Type 2 *APB*'s accommodate a non-stoichiometric excess of one element. Thus APB's are one of the forms of structural defect to which non-stoichiometry can give rise[4]. The influence of non-stoichiometric conditions in the formation of APB's may be direct or indirect. The direct mechanism is that in which a high chemical potential of one element during crystal growth or annealing promotes the incorporation of a non-stoichiometric excess of that element and lowers the energy of type 2 *APB*s.

A possible indirect mechanism is that which has been found responsible for the occurrence of long period stacking order structures[27] and periodic antiphase structures[28–33] in alloys. On this approach, periodic antiphase structures (which are not known to occur in semiconducting compounds) or long period stacking order structures (polytypes[34]) would be explained as occurring in order to alter the positions of certain Brillouin zone boundaries so that the Fermi surface just fills the zone. In other words the structural defects, *APB*s or stacking faults, occur despite their surface energy of formation because of a net energy minimization resulting from a lowering of the energy of the valence electrons in the sample. Particular structures, i.e. particular polytypes or periodic antiphase structures, would then be expected to occur for particular electron/atom ratios. These ratios would vary with either impurity content or with the deviation from stoichiometry. These forms of defect structure would then be a consequence of the thermodynamic conditions during growth or annealing of the crystals. Regularly faulted or antiphase structures apparently also occur as phases of fairly definite composition in certain non-stoichiometric oxides[35].

The fact that non-stoichiometric excess atoms can occur in forms other than as statistically distributed isolated point defects involves an alteration in the traditional viewpoint. Cahn and Kikuchi[4] pointed out that in addition to the various forms of isolated point defect, deviations from stoichiometry in alloys could lead to the formation of a precipitate phase containing the excess of the major species or to the adsorption of the major species on to a network of domain walls.

In addition in semiconductors with tetrahedral co-ordination structures regular superlattice-like vacancy arrays called sponges appear to be geometrically and energetically possible (Hornstra J. H., Private communication) and polytypes do, and periodic antiphase structures might occur. Deviations from stoichiometry can be very large by the usual semiconductor standards. In the one case that has been intensively studied, that of GaAs, nonstoichiometric point defect concentrations of $10^{19}\,\mathrm{cm}^{-3}$ seem to occur. (The literature on this point was reviewed previously[36]) If this were entirely accomodated on antiphase boundaries with 10^{15} atom sites cm^{-2}, $10^{4}\,\mathrm{cm}^{2}$ of Type 2 *APB* per cc would result. Much larger deviations from stoichiometry are common in oxides and may well occur in the II–VI compounds. Effects of heat treatments that are usually attributed to alterations in point defect concentration may be partially due to the formation of other types of nonstoichiometric structural defects [37].

METHODS FOR OBSERVING *APB*s

Transmission electron microscopy has proved to be the most powerful technique for the study of *APB*'s in alloys and it is likely to be the most useful method in the case of semiconducting compounds too. Certain features of the structure factor for the sphalerite structure, however, lead to changed diffraction contrast conditions for *APB*s in sphalerite-structure materials as compared with the materials hitherto studied. It seems desirable therefore to discuss these points here.

The positions of the atoms in sphalerite-structure materials may be given in terms of their co-ordinates in an f.c.c. unit cell (Fig. 1) as A atoms at $u_Av_Aw_A = 000$, $\frac{1}{2}\frac{1}{2}0$, $\frac{1}{2}0\frac{1}{2}$ and $0\frac{1}{2}\frac{1}{2}$ and B atoms at $u_Bv_Bw_B = \frac{1}{4}\frac{1}{4}\frac{1}{4}$, $\frac{3}{4}\frac{3}{4}\frac{1}{4}$, $\frac{3}{4}\frac{1}{4}\frac{3}{4}$ and $\frac{1}{4}\frac{3}{4}\frac{3}{4}$. Substituting these values into the expression for the structure factor for the *h k l* reflection

$$F_{hkl} = \sum_{uvw's} f e^{2\pi i(hu+kv+lw)}$$

leads to the expression

$$F_{hkl} = [f_A + f_B e^{\pi/2i(h+k+l)}][1 + e^{\pi i(h+k)} + e^{\pi i(h+l)} + e^{\pi i(k+l)}]$$

where f_A and f_B are the atomic scattering factors for the two constituent elements of the compound. The second factor in the structure factor is that for the f.c.c. space lattice and is equal to 4 when h, k and l are all even or all odd and is equal to zero when h, k and l are mixed even and odd integers. The first term is the basis structure factor. For permitted reflections (h k and l all even all odd) therefore

$$F_{hkl} = 4(f_A + f_B \exp i\pi/2\,(h+k+l))$$

which represents both the phase and the amplitude of the reflected wave. There are four cases of permitted reflection, details of which are given in Table 1.

The effect of interchanging the occupation of the sublattices across an *APB* is to interchange f_A and f_B in the Structure Factor. In case 0 of Table 1, $f_A + f_B$ becomes $f_B + f_A$ which involves neither phase nor amplitude change and no *APB* contrast arises in dark field electron micrographs using such reflections. In case 1, $f_A + if_B$ becomes $f_B + if_A$ which does not alter the amplitude but involves a phase change as indicated in Fig. 7 and Table 1 which depends upon the relative magnitudes of f_A and f_B and therefore varies from one compound to another. Case 3 is similar to case 1 except as can be seen in Fig. 7 the sign of the phase change is reversed. Case 2, superlattice, reflections undergo a phase change π across APBs and strong *APB* contrast occurs in dark field micrographs. In the alloy systems studied hitherto only superlattice reflections (analogous to case 2) gave contrast at APBs and no analogues of cases 1 and 3 existed. The reflections permitted by the sphalerite structure factor are listed in Table 2 together with the reflection case and the *APB* type of the corresponding atomic reflecting planes in each instance.

Table 1. Cases of permitted reflections in the sphalerite structure (All permitted reflections must have h, k, l *all even or all odd)*

Case	$h+k+l=$	Type of reflection	Structure factor F_{hkl}	Reflected intensity $\lvert F_{hkl}\rvert^2$	Magnitude of *APB* phase change	Relative *APB* contrast
0	$4n$	Fundamental	$4(f_A+f_B)$	$16(f_A+f_B)^2$	0	0
1	$4n+1$	Fundamental	$4(f_A+if_B)$	$16(f_A^2+f_B^2)$	$\tan^{-1}\frac{fA}{fB}-\tan^{-1}\frac{fB}{fA}$	Depends on compound
2	$4n+2$	Superlattice	$4(f_A-f_B)$	$16(f_A-f_B)^2$	π	strong
3	$4n+3$	Fundamental	$4(f_A-if_B)$	$16(f_A^2+f_B^2)$	$\tan^{-1}\frac{fA}{fB}\ \tan^{-1}\frac{fB}{fA}$	Depends on compound

The *APB* phase changes for type 1 and 3 reflections for any given compound are of opposite sign as indicated in Fig. 7

Table 2. Permitted reflections in sphalerite structure materials

hkl	$h^2+k^2+l^2$	Reflection case	*APB* contrast	*APB* type for $\{hkl\}$ planes	Actual atomic plane indices
1 1 1	3	3	D.O.C.	2(non-stoichiometric)	{111}
2 0 0	4	2	strong	2(non-stoichiometric)	{100}
2 2 0	8	0	0	1(stoichiometric)	{110}
3 1 1	11	1	D.O.C.	2(non-stoichiometric)	{311}
2 2 2	12	2	strong		{111}q.v.
4 0 0	16	0	0		{100}q.v.
3 3 1	19	3	D.O.C.	2(non-stoichiometric)	{331}
4 2 0	20	2	strong	2(non-stoichiometric)	{210}
4 2 2	24	0	0	1(stoichiometric)	{211}
5 1 1	27	3	D.O.C.	2(non-stoichiometric)	{511}
3 3 3		1	D.O.C.		{111}q.v

The distance from the undeflected beam to an *hkl* reflection on an electron diffraction pattern is proportional to the square root of $h^2+k^2+l^2$, given in the second column. The reflection case number refers to the listing in Table 1 and is the remainder when $h+k+l$ is divided by four. The terms used in the *APB* contrast column are defined in columns 6 and 7 of Table 1

Table 3 lists for a number of the most practically important III–V and II–VI compounds the actual *APB* phase changes for the first two cases 1 and 3 reflections, namely ⟨311⟩ and ⟨111⟩. These are fairly large for compounds of elements of widely differing atomic number and in these compounds *APB* contrast should be readily detectable for ⟨311⟩ and ⟨111⟩ reflections.

The presence of *APB*'s can also be detected in semiconducting compounds by observing any polarity dependent property of the material. The only experimental observations thus far have been made in this way and especially by etching[8–10], and this is the simplest method for detecting the presence of macroscopic antiphase domains. The electrical effects of *APB*s would appear to be worth investigating. The sign of the piezoelectric or pyroelectric surface charge on polar surfaces must reverse from matrix to antiphase domain. Large surface potential changes should therefore occur at *APB*s and be detectable by decoration with fine particles of high dielectric constant[38]. Of course in more highly conducting specimens, such surface changes quickly flow away, so that this type of technique is applicable only to large band gap materials. Electron mirror microscopy which is sensitive to extremely small

Table 3. APB phase changes for case 1 and case 3 reflections

Compound atomic nos.	Reflections	f_A	f_B	$\tan^{-1}\frac{fA}{fB}-\tan^{-1}\frac{fB}{fA}$
InSb	311	4·62	4·81	1°17′
49–51	111	7·44	7·64	1° 9′
GaAs	311	2·93	3·07	8°53′
31–33	111	5·13	5·35	4°25′
GaP	311	2·81	1·67	28°42′
31–15	111	4·35	3·41	13°39′
CdS	311	4·16	2·00	38°40′
48–16	111	6·95	3·46	37° 7′
ZnS	311	2·74	1·82	22°51′
30–16	111	4·90	3·34	21°34′
ZnSe	311	2·88	3·16	5°21′
30–34	111	5·02	5·47	4°34′
ZnTe	311	3·12	4·62	21°57′
50–52	111	5·23	7·52	21°26′

Values of Sin $\theta/\lambda = 1/2\ d_{hkl}$ were calculated from values of lattice parameters taken from Aven and Prener[39] and from Wyckoff[40]. Values of f_A and f_B were then obtained from the tables in Appendix A3.1 in Hirsch *et al.*[5].

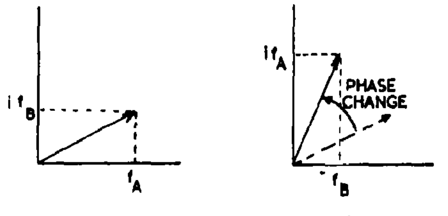

CASE 1 (311)

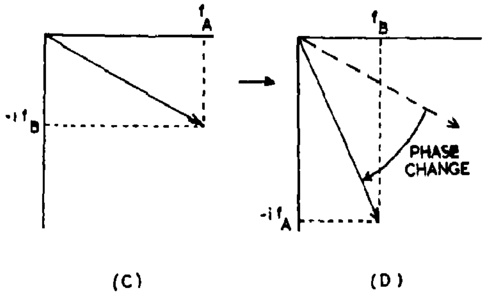

CASE 3 (111)

Fig. 7. Phase changes in case 1 $(h+k+l=4n+1)$ ((a) to (b)) and in case 3 $(h+k+l=4n+3)$ ((c) to (d)) reflections on crossing *APB*'s. The values of f_A and f_B are those for the (311) and (111) reflections of CdS.

variations in surface potential and scanning electron microscopy in which voltage contrast can be obtained for potential changes of the order of a volt may also prove useful for observing *APB*'s through their electrical effects.

Acknowledgements—It is a pleasure to thank Professor F. C. Frank and Dr. P. R. Swann for helpful discussions and Professor J. G Ball for the provision of research facilities. This work was done under a C.V D. contract and is published by permission of the Ministry of Defence (Navy Department).

REFERENCES

1. FLINN P. A., *Trans. metall. Soc. A.I.M.E.* **218**, 145 (1960).
2. CAHN J. W. and KIKUCHI R., *J. Phys. Chem. Solids* **20**, 94 (1961).
3. KIKUCHI R and CAHN J. W., *J. Phys. Chem. Solids* **23**, 137 (1962).
4. CAHN J W. and KIKUCHI R., *J. Phys. Chem Solids* **27**, 1305 (1966).
5. HIRSCH P. B., HOWIE A., NICHOLSON R. B., PASHLEY D. W. and WHELAN M. J., In *Electron Microscopy of Thin Crystals*, pp. 378–387. Butterworths, New York (1965).
6. MARCINKOWSKI M. J., In *Electron Microscopy and the Strength of Crystals* (Edited by G. Thomas and J Washburn), pp. 333–439. Interscience, New York (1963).
7. BARBER H. D. and HEASELL E. L., *J. Phys. Chem. Solids* **26**, 1561 (1965).
8. BOBB L. C., HOLLOWAY H., MAXWELL K. H and ZIMMERMAN E., *J. appl Phys.* **37**, 4687 (1966).
9. WILSON R. B., *J. appl. Phys.* **37**, 1932 (1966)
10. ROZGONYI G. A. and FOSTER N. F., *J. appl Phys.* **38**, 5172 (1967).

11. AUSTERMAN S. B. and GEHMAN W. G., *J. Mater. Sci.* **1**, 249 (1966)
12. HOLT D. B., *J. Phys. Chem. Solids* **25**, 1385 (1964).
13. HOLT D. B., *J. Phys. Chem. Solids* **23**, 1353 (1962)
14. ALEXANDER H. and HAASEN P., *Solid St. Phys.* To be published.
15. BLANK H., DELAVIGNETTE P. and AMELINCKX S., *Phys. Status Solidi* **2**, 1660 (1962).
16. DRUM C. M., *Phil. Mag.* **11**, 313 (1965).
17. CHADDERTON L. T., FITZGERALD A. G. and YOFFE A. D., *Phil. Mag.* **8**, 167 (1963)
18. BLANK H., DELAVIGNETTE P., GEVERS R. and AMELINCKX S., *Phys. Status Solidi* **7**, 747 (1964)
19. FITZGERALD A. G., MANNAMI M., POGSON E. H. and YOFFE A. D., *J. appl. Phys.* **38**, 3303 (1967)
20. CHIKAWA J. I., *Jap. J. appl. Phys.* **3**, 229 (1964)
21. FITZGERALD A. G., MANNAMI M., POGSON E. H. and YOFFE A. D., *Phil. Mag.* **14**, 197 (1966)
22. SECCO D'ARAGONA F., DELAVIGNETTE P. and AMELINCKX S., *Phys. Status Solidi* **14**, K 115 (1966)
23. SECCO D'ARAGONA F. and DELAVIGNETTE P., *J. de Physique* **27**, Colloque C 3, 121 (1966)
24. HOLT D. B., *J. Phys. Chem. Solids* **27**, 1053 (1966).
25. AUSTERMAN S. B., BERLINCOURT D. A. and KRUEGER H. H. A., *J. appl. Phys.* **34**, 339 (1963).
26. ARLT G. and QUADFLIEG P., *Phys. Status Solidi* **25**, 323 (1968)
27. SATO H., TOTH R. S. and HONJO G., *J. Phys. Chem. Solids* **28**, 137 (1967).
28. SATO H. and TOTH R. S., *Phys. Rev.* **124**, 1833 (1961)
29. SATO H. and TOTH R. S., *Phys. Rev.* **127**, 469 (1962).
30. SATO H. and TOTH R. S., In *Alloying behaviour and Effects in Concentrated Solid Solutions* (Edited by T. B. Massalski), p. 295. Gordon and Breach, New York (1965).
31. SATO H. and TOTH R. S., *Phys. Rev.* **139A**, 1581 (1965).
32. SATO H. and TOTH R. S., *Phys. Rev. Lett.* **8**, 239 (1962)
33. TOTH R. S. and SATO H., *J. appl. Phys.* **33**, 3250 (1962).
34. VERMA A. R. and KRISHNA P., *Polymorphism and Polytypism in Crystals*. Wiley, New York (1966).
35. ANDERSON J. S. and HYDE B. G., *J. Phys. Chem. Solids* **28**, 1393 (1967)
36. HOLT D. B., *J. Mater. Sci.* **1**, 280 (1966).
37. BLANC J., BUBE R. H. and WEISBERG L. R., *J. Phys. Chem. Solids* **25**, 225 (1964).
38. BRAFMAN O., SCHACHER G. and STEINBERGER I. T., *J. appl. Phys.* **36**, 668 (1965).
39. AVEN M. and PRENER J. S., In *Physics and Chemistry of II–VI Compounds*. North-Holland, Amsterdam (1967).
40. WYCKOFF R. W. G., In *Crystal Structures*, Vol. 1, Chap. 3, Table, p. 29. Interscience, New York (1960)

J. Phys. Chem. Solids Pergamon Press 1969. Vol. 30. pp. 1309–1314. Printed in Great Britain.

OXYGEN SELF-DIFFUSION IN UNDOPED AND DOPED COBALTOUS OXIDE*

W. K. CHEN and **R. A. JACKSON**†
Metallurgy Division, Argonne National Laboratory, Argonne, Ill. 60439, U S A.

(*Received* 7 *October* 1968; *in revised form* 12 *December* 1968)

Abstract – The diffusion coefficient of O–18 in CoO has been measured in the temperature range from 1175° to 1560°C. Diffusion was measured in undoped CoO crystals and in crystals containing from 0·1 to 0·5 molar percent of aluminum or lithium. The diffusion coefficient in the undoped crystals is represented by the expression, $D = 50 \exp[-(95{,}000 \pm 5000)]/RT$ cm²/sec. at $P_{O_2} = 0{\cdot}21$ atm At a constant temperature and a constant oxygen partial pressure, the diffusion coefficient in doped crystals was found to increase or decrease with increasing concentration of lithium or aluminum in the oxide crystals. The results are discussed in terms of oxygen diffusion by a vacancy mechanism.

1. INTRODUCTION

COBALTOUS oxide is an oxygen-excess oxide exhibiting a p-type semi-conduction. The predominant defect in this non-stoichiometric oxide has been considered to be a cobalt ion vacancy. At high temperatures and at oxygen partial pressures near one atomsphere, the cobalt vacancy is believed to be predominantly singly ionized. This is supported by a number of experimental findings, such as electrical conductivity[1–4] and self-diffusion of cobalt ions[5] are approximately proportional to the one-fourth power of equilibrium oxygen partial pressure at a constant temperature. While a careful study has been done on cation self-diffusion in polycrystalline CoO[5], little information concerning oxygen self-diffusion in CoO at high temperatures is available. The purpose of this study was to obtain meaningful results for oxygen diffusion in CoO and to look for the possible diffusion mechanism of oxygen in this oxide.

2. EXPERIMENTAL

(*A*) *Material*

All diffusion measurements were made on single crystals. The single crystals were grown by the Vernuil process in an arc-image furnace. The starting material for the undoped crystals was a 'baker analyzed' reagent grade cobalt oxide power (crystal series I). The doped cobalt oxide powders were obtained from decomposition of a cobalt oxalate mixed with a dopant oxalate. Mixtures of a cobalt oxalate and a dopant oxalate were obtained by co-precipitation from the well stirred mixed solution of nitrates with an ammonium oxalate. The oxalate precipitates were first dried and then decomposed at 1200°C in air to oxide powder for growing single crystals (crystal series II). Typical analysis of impurities in the crystals grown from two different lots of starting materials are shown in Table 1. The as-grown crystals were annealed at 1200°C in air for 24 hr before use.

(*B*) *Methods*

Oxygen diffusion was determined by the gas/solid O–18 isotopic exchange technique. The details of the apparatus and the procedures have been described previously[6]. The difference from the previous report will be described briefly here. The geometry of oxide sample in this experiment was a thin parallel-faced crystal wafer. The thin crystal wafers were cleaved from a crystal boule along a (100) cleavage plane. The cleaved crystal wafers were ground to uniform thickness of

---

*This work was performed under the auspices of the United States Atomic Energy Commission.

†Now a Graduate Student, Michigan State University, East Lansing, Michigan.

Table 1. Spectrographic analysis of impurities in the CoO crystals

	Conc. in wt.%			Conc in wt.%	
Elements	Series I	Series II	Elements	Series I	Series II
Ag	<0·001	<0·001	Na	<0·01	<0·01
Al	Trace?	(Dopant)	Ni	<0·08	<0·06
B	<0·01	<0·01	Si	F.T.	<0·01
Bi	<0·001	<0·001	Sn	<0·005	<0·01
Fe	Trace	<0·01	Ti	<0·01	<0·01
K	<0·05	<0·05	Zr	<0·01	<0·02
Li	<0·001	(Dopant)			
Mn	Trace	Trace			

about 400–700 μm and both surfaces were finished with a 0·5 μm diamond paste. For each diffusion run the total surface area of the solid sample was about 5 cm^2.

The solution of Fick's equation for diffusion of a tracer into a thin wafer of thickness $2l$, with the assumption of an instantaneous phase-boundary reaction is given by Crank [7].

$$\frac{C_t - C_0}{C_i - C_0} = \exp\left(\frac{Dt}{l^2\alpha^2}\right) \operatorname{erfc}\left(\frac{Dt}{l^2\alpha^2}\right)^{1/2} \qquad (1)$$

where C_i and C_0 are the initial concentrations of O–18 in the gas phase and in the solid phase respectively, C_t is the concentration of O–18 in the gas phase at time t, α is the ratio of the number of gram-atoms of oxygen in the gas phase to that in the solid, and D is the diffusion coefficient in the solid. Equation (1) is not an exact solution but is a good approximation when $(Dt/l^2\alpha^2)^{1/2}$ is less than 0·3. (The largest value used in this study was about 0·15). Because of the nature of equation (1), the diffusion coefficient was obtained numerically. The quantity $(C_t - C_0)/C_i - C_0)$ was obtained by mass-spectrometric analysis of the concentrations of O–18 in the gas phase at the diffusion annealing time $t = 0$ and after a certain time interval, t. With the experimentally obtained value of $(C_t - C_0)/(C_i - C_0)$ and the value of α calculated from the initial condition, $(Dt/l^2)^{1/2}$ was obtained graphically. The diffusion doefficient was evaluated from the slope of a linear plot of $(Dt/l^2)^{1/2}$ vs. $(t)^{1/2}$.

The O–18 enrichment in the oxygen gas was between 12 and 17 per cent. The volume of the water-cooled Vycor exchange vessel was 335 cc. In all cases, the crystal samples were initially equilibrated with natural oxygen gas at the same temperature and pressure as were used for the exchange annealing. At the start of isotopic exchange, the crystals were first heated in O–18 enriched gas to about 950°C for a period of 10 min to ensure that the crystal surface was initially saturated with O–18. The O–18 concentration in the gas phase at this point was taken as the initial concentration C_i at $t = 0$. The mole fraction of O–18 was calculated from the peak height of masses 32, 33, 34, 35, and 36 determined with a Consolidated Electrodynamics Model 21–620 mass spectrometer.

3. RESULTS AND DISCUSSIONS

The decrease in O–18 concentration in the gas phase as a function of annealing time is shown in Fig. 1. Included in Fig. 1, is a plot of the change in the background when the susceptor assembly was heated to 1215°C without presence of the oxide crystal sample in the system. The change in the background was within the experimental error. Figure 2 shows typical plots of the experimental points plotted as $(Dt/l^2)^{1/2}$ vs. $(t)^{1/2}$. All plots indicate a linear relation between $(Dt/l^2)^{1/2}$ and $(t)^{1/2}$ and the straight line is extrapolated to the origin. Edwards *et al.*[8], have shown that such a plot should show a curvature or, if a

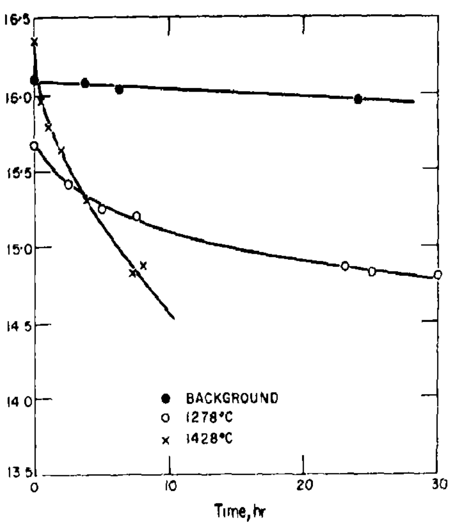

Fig. 1. Change in O-18 concentration in the gas phase as a function of exchange annealing time

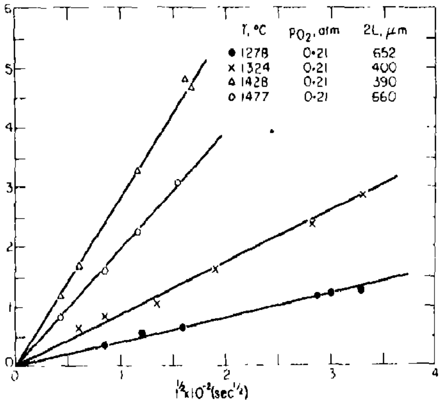

Fig 2 Typical plots of a non-dimensional parameter, $(Dt/l^2)^{1/2}$ vs. $(t)^{1/2}$.

curvature is too small to be distinguishable from a straight line, the extrapolation of a straight line should be offset from the origin if the rate of the exchange process is limited by the gas/solid phase boundary reaction. Therefore, it is reasonable to assume that oxygen diffusion in the oxide crystal is the rate determining process in the isotopic exchange in this experiment and the diffusion coefficient can be calculated with equation (1).

(A) Undoped oxide

The diffusion coefficients have been determined for undoped CoO crystals (from series I) at a constant oxygen pressure in the temperature range 1175°–1560°C. The results are plotted as $\log D$ vs. $1/T$ in Fig. 3. A least squares fit of the data to the Arrhenius Equation gives

$$D = 50 \exp[-(95{,}000 \pm 5000)/RT] \text{ cm}^2/\text{sec}. \tag{2}$$

The data previously measured by Thompson [9] at the lower temperatures is also included in Fig. 3. The reason for the obvious discrepancy between Thompson's result and the present result is not certain. Since a mullite tube was used as an isotopic exchange vessel in Thompson's work, the isotopic exchange between the tube wall and the gas might have been substantial which contributed to the apparent higher diffusion coefficient.

Recently, Holt[10] reported a study of oxygen diffusion in CoO by the proton activa-

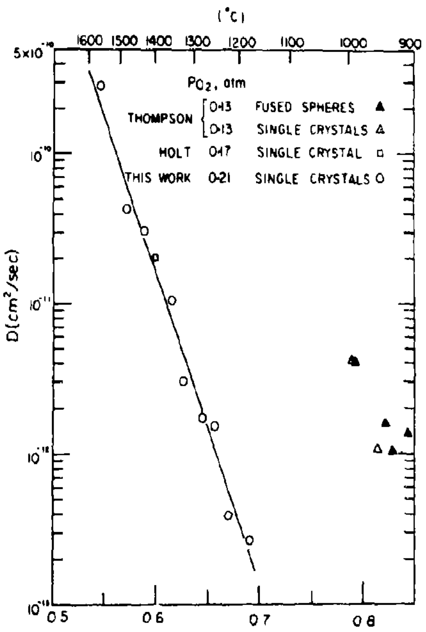

Fig. 3. Temperature dependence of the oxygen diffusion coefficient in CoO at $P_{O_2} = 0{\cdot}21$ atm, plotted as $\log D$ vs $1/T$.

tion technique. In this method the penetration of the O–18 tracer in the oxide crystal is determined by the nuclear reaction, $^{18}O(p,n)^{18}F$, in conjunction with autoradiography. Since the relative rate of the gas/solid phase boundary reaction with respect to bulk diffusion is immaterial in this type of analysis, more direct information on the oxygen diffusivity can be obtained if sufficiently accurate measurement can be made. From the only available penetration plot in the paper (Fig. 7 in [10]), one obtains $D \simeq 2\times 10^{-11}$ cm²/sec at 1400°C and at $P_{O_2} = 0{\cdot}17$ atm. This result is in good agreement with the present results, as shown in Fig. 3. This agreement further substantiates the assumption made in the present analysis that the bulk diffusion is the rate determining process in the oxygen isotopic exchange in CoO crystals at the high temperatures.

Equation (2) may be compared with the diffusion coefficient expressed in the form of the transition-state theory of Eyring[11], i.e.

$$D = \left(\frac{RT}{Nh}\right) d^2 \exp\left(\frac{\Delta S^*}{R}\right) \exp\left(-\frac{\Delta H^*}{RT}\right) \quad (3)$$

Where ΔH^* and ΔS^* are activation enthalpy and activation entropy respectively, R is the gas constant, T is the temperature in °K, N is Avogadro's number, h is Plank's constant and d is the elementary jump distance. Taking $T = 1600$°K and $d = 3{\cdot}02$ Å (i.e. the nearest neighbor distance between two oxygen ions in the CoO lattice), one obtains $\Delta S^* \simeq 14{\cdot}4$ e.u./mole and $\Delta H^* = 95{,}000$ cal/mole. Both ΔS^* and ΔH^* consist of terms associated with formation and migration of defects that are responsible for the migration of O–18 tracer. From the argument of Mott and Gurney[12], the large value of ΔS^* is more consistent with vacancies rather interstitials as being the predominant defects for the oxygen diffusion. Empirically, O'Keeffe[13] has also pointed out that ΔS^* will be large and positive for oxygen diffusion in the metal oxides by vacancies and, on the other hand, ΔS^* will be expected to be small or a negative value by interstitials.

Attempts have been made to study the influence of oxygen pressure on the diffusion with O–18 enriched oxygen gas as well as O–18 enriched CO–CO$_2$ gas mixtures. In the case of CO–CO$_2$ gas mixtures, it was difficult to maintain a constant CO/CO$_2$ ratio in the closed gas-phase throughout the course of the exchange anneal. Therefore, the results have been inconclusive.

(B) Doped oxides

The defect equilibrium in the oxide can be influenced by the incorporation of oxides of uni- and trivalent cations. Thus, substitution of Li$^+$ for Co^{2+} diminishes cation vacancies while Al^{3+} increases their concentration. By virtue of the Shottky product relation, the defects in the anion sublattice may also be influenced in the following manner. For undoped CoO, the simple reactions, among other possibilities, may be

$$\tfrac{1}{2}O_{2(gas)} \rightarrow O_0^{2-} + V'_{Co} + e^+ \quad (4)$$

$$(1-\delta)CoO \rightarrow Co_{(1-\delta)}O_{(1-\delta)} + \delta V'_{Co} + \delta V^{\cdot}_0 \quad (5)$$

where O_0^{2-} is an oxygen ion in the anion lattice site, V'_{Co} and $V^{\cdot}_0$ are a singly-ionized cobalt ion vacancy and a singly-ionized oxygen ion vacancy respectively, and e^+ is a positive hole which may be associated to Co^{2+}. Applying the law of mass action to reactions (4) and (5) and with the neutrality condition, $[e^+] \simeq [V'_{Co}]$, one obtains the concentration of oxygen ion vacancy, $[V^{\cdot}_0]$, in the undoped oxide,

$$[V^{\cdot}_0] = (K_s \cdot K_4^{-1/2}) P_{O_2}^{-1/4} \quad (6)$$

where K_4 and K_s are equilibrium constant for reactions (4) and (5) respectively, and P_{O_2} is the equilibrium partial pressure of oxygen.

Incorporation of univalent Li$^+$ or trivalent Al^{3+} in CoO can be considered to take place by the substitution of the cobalt ions in the lattice by the dopant ions thereby creating negatively charged ($\mathrm{Li}_{\mathrm{Co}}'$) or positive charged ($\mathrm{Al}_{\mathrm{Co}}^{\cdot}$) centers relative to the lattice. Assuming all the dopants are ionized at the high temperatures, the following approximation for the neutrality condition has to be considered in the doped oxides;

$$[e^{+}] = [V_{\mathrm{Co}}'] + [\mathrm{Li}_{\mathrm{Co}}'] \tag{7}$$

for the Li-doped oxide, and

$$[e^{+}] + [\mathrm{Al}_{\mathrm{Co}}^{\cdot}] = [V_{\mathrm{Co}}'] \tag{8}$$

for the Al-doped oxide. From reactions (4) and (5), and equation (7) or (8) one obtains the concentrations of oxygen vacancies,

$$[V_{0}^{\cdot\cdot}] = \frac{2K_{s}}{-[\mathrm{Li}_{\mathrm{Co}}'] + \{([\mathrm{Li}_{\mathrm{Co}}'])^{2} + 4K_{4}P_{0_2}^{1/2}\}^{1/2}} \tag{9}$$

and

$$[V_{0}^{\cdot\cdot}] = \frac{2K_{s}}{[\mathrm{Al}_{\mathrm{Co}}^{\cdot}] + \{([\mathrm{Al}_{\mathrm{Co}}^{\cdot}])^{2} + 4K_{4}P_{0_2}^{1/2}\}^{1/2}} \tag{10}$$

in the Li-doped oxide and Al-doped oxide, respectively. The experimentally observed dependence of the oxygen diffusion coefficient on dopant concentration, at a constant temperature and at a constant oxygen partial pressure, is shown in Fig. 4. The oxide crystals from series II were used to determine the diffusion coefficients shown in Fig. 4. The apparent small discrepancy between the diffusion coefficients of the undoped crystals obtained from series I (see Fig. 3) and from series II (see Fig. 4) was probably due to the difference in impurity level in the two series of crystals. Since more chemical processes were involved in the preparation of the starting material for growing the series II crystals, one may expect higher multivalent impurities in these crystals. The broken-line in Fig. 4 shows the concentration of oxygen vacancies, in the unit of mole fraction, calculated from expressions [9] and [10]. The fitting parameter ($K_4^{1/2} \cdot P_{0_2}^{1/4}$) was found to be 6×10^{-3} mole fraction. The reasonable agreement between the observed dependence of the oxygen diffusion coefficient and the estimated dependence of oxygen vacancy concentration on the concentration of dopants in Fig. 4 confirms the assumption that all the dopants are ionized at the high temperatures and tends to favor the migration of oxygen ions via oxygen vacancies.

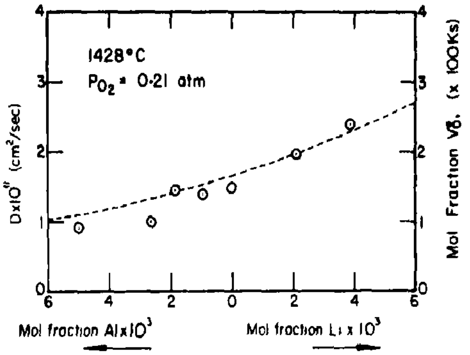

Fig. 4. Dependence of the oxygen diffusion coefficient in CoO(O) on the dopant concentration at $P_{O_2} = 0{\cdot}21$ atm and at 1428°C. The broken line indicates the concentration of oxygen vacancies calculated from expressions (9) and (10). Ks is the equilibrium constant for reaction (5) at 1428°C.

Acknowledgements—The authors wish to acknowledge the guidance and many suggestions afforded to them by D. W. Readey and N. L. Peterson Throughout the course of this work, frequent discussions with M. L. Volpe have been very valuable. This work was performed under the auspices of the United States Atomic Energy Commission.

REFERENCES

1. WAGNER C and KOCH E., *Z. phys. Chem.* **B32**, 439 (1936).
2. EROR N. G., Jr and WAGNER J. B., Jr., paper presented at *Fall Meeting of Met. Soc., AIME*. Cleveland, Ohio (1963), EROR N. G., Jr, Ph.D Thesis, Northwestern University (1965)
3. DUGUESNOY A and MARION F., *C. r. hebd. Séanc. Acad. Sci., Paris* **256**, 2862 (1963).
4. FISHER B. and TANHAUSER D S., *J chem. Phys.* **44**, 1663 (1966).
5. CARTER R. E. and RICHARDSON F. D., *J. Metals* **6**, 1244 (1954).
6. CHEN W. K. and JACKSON R. A., *J chem. Phys.* **47**, 1144 (1967).
7. CRANK J., In *Mathematics of Diffusion*, p 52 Clarendon Press, Oxford (1956).
8. EDWARDS H. S., ROSENBERG A. F. and

BITTEL J. T., Aeronautical System Division, Wright-Patterson Air Force Base, Ohio, Rep. No ASD-TDR-63-635 (1963).
9. THOMPSON B. A., Ph.D. Thesis, Rensselaer Polytechnic Institute (1962).
10. HOLT J. B., *Proc. Br. ceram. Soc.* 9, 157 (1967).
11. STEAN A. E. and EYRING H., *J. phys. Chem.* **44**, 955 (1940).
12. MOTT N. F. and GURNEY R. W., In *Electronic Processes in Ionic Crystals*, p. 29. Clarendon Press, Oxford (1940).
13. O'KEEFFE M., Diffusion in Oxides and Sulfides, In *Sintering and Related Phenomena, Proc. Intl Conf. Notre Dame, 1965* (Edited by G. C. Kuczynski, N. A. Hooton and C. F. Gibbon), p. 57. Gordon and Breach, New York (1967).

J. Phys. Chem. Solids Pergamon Press 1969. Vol. 30, pp. 1315–1320. Printed in Great Britain.

IMPURITY HALIDE DIFFUSION IN SILVER CHLORIDE AND SILVER BROMIDE*

A. P. BATRA and L. SLIFKIN
Department of Physics, University of North Carolina at Chapel Hill, Chapel Hill, N.C. 27514, U.S.A

(*Received* 9 *December* 1968)

Abstract—Using the standard microtome-sectioning technique, the diffusion of bromide and iodide tracers in silver chloride and of chloride and iodide tracers in silver bromide has been studied. In silver chloride both bromide and iodide ions diffuse with the same activation energy as that of the chloride ion. In silver bromide the Arrhenius plots are curved: whereas the iodide ion has the same temperature-dependent activation energy as does bromide, the chloride ion appears to have a rather higher value at high temperatures, with all three energies approaching the same value at low tempeatures. These results are discussed in terms of vacancy mechanisms.

INTRODUCTION

THE DIFFUSION of a variety of cationic impurities in silver halides has recently been reviewed[1, 2]. Very little attention, however, has so far been given to the diffusion of anionic impurities. In silver halides, the dominant equilibrium disorder is of the cation Frenkel type; that is, interstitial silver ions and silver ion vacancies. There is no evidence for the presence of anion Frenkel disorder, presumably because of the large energy required to form an interstitial halide ion; however, the existence of a relatively small degree of Schottky disorder, silver ion and halide vacancies, has been inferred from experiments on ionic conductivity[3, 1], self-diffusion of halide[4–7], and dislocation climb[8]. Fouchaux and Simmons[9], by comparing the thermal expansion of the lattice parameter with that of the bulk crystal, have estimated an upper limit of 9×10^{-5} for the fractional Schottky defect concentration at the melting point of silver chloride, and a lower limit of 1·45 eV for the formation energy. Layer, Miller and Slifkin[3, 1] observed an enhancement in the ionic conductivity after quenching very pure silver chloride crystals from near the melting point, from which may be deduced a quenched-in concentration of about 10^{-4}.

The self-diffusion of chloride ion in silver chloride was measured by Compton and Maurer[4], and by Reade and Martin[5]. In addition, Lakatos and Lieser[6] have extended the data down to 150°C and have observed a rather sharp break at about 300°C in the Arrhenius plot. For bromide ion diffusion in pure silver bromide, Tannhauser[7] also obtained a non-linear Arrhenius plot, which appears to show a continuous curvature. In addition, he found that doping with cadmium, which should decrease the concentration of halide vacancies, did indeed cause a depression of the bromide diffusion coefficient. Tannhauser suggested that the diffusion proceeds by both single vacancies and by cation–anion vacancy pairs. Furthermore, the large activation volume observed by him lends support to this view.

In the alkali halides, which have predominantly Schottky defects, the halide impurity tracers[10] have been found to diffuse with approximately the same activation energy as for halide self-diffusion, but with a different frequency factor. With monovalent cations, however, Arai and Mullen[11] have observed a systematic effect of the ion size on diffusion by measuring the diffusivity of rubidium in

---

*Supported by the U.S. Atomic Energy Commission (Contract AT-(40–1)-2036).

sodium chloride, potassium chloride and rubidium chloride; the activation energy progressively decreases as the ionic radius of the host increases.

It is recognized that both the effective charge of the diffusing ion and its relative size should in general influence the diffusion parameters. The charge effect does not exist for diffusion of halide (or monovalent cation) in alkali or silver halides. In an attempt to understand the effect of the ionic size on anion diffusion in silver halides, the diffusivities of the bromide and iodide ions in silver chloride and those of the chloride and iodide ions in silver bromide are reported in this paper.

EXPERIMENTAL

Single crystals of zone-refined silver bromide, kindly supplied by Dr. James E. LuValle of Fairchild Space and Defense Systems, and of Harshaw silver chloride were used in this experiment. The silver bromide had been prepared from 99·999 per cent pure ASARCO silver and fractionally distilled Dow bromine. Conductivity measurements on typical samples yielded an estimate of the divalent impurity content of about 4 ppm for the silver bromide and 5 ppm for the silver chloride. Diffusion specimens with 1 cm^2 rectangular cross sections were prepared by polishing on successively finer grades of silicon carbide paper, and finally on a polishing cloth soaked in 5 per cent KCN. A microtome-cut surface was used for diffusion, the terminal cuts being only one micron thick in order to minimize strain and surface curvature. All specimens were annealed at approximately 30°C below the melting point for a day or two; they were then cooled to room temperature at a rate of 10° per hour.

The Cl^{36} (specific activity 14 mCi/g) and Br^{82} (27 Ci/g) radioisotopes were obtained from Nuclear Science and Engineering Corporation, and I^{131} (6 Ci/g) from New England Nuclear Corporation. All three tracers were in the form of silver halide dissolved in NH_4OH. A solution of the appropriate tracer, in a quantity small enough to insure thin-film geometry, was placed on the face of the specimen and allowed to dry. The specimen was placed in a vycor insert which was then encapsulated in a pyrex tube, either under a vacuum of about 10^{-6} Torr, or in a helium atmosphere. The diffusion anneals lasted from several hours to over a month, during which the temperature was usually controlled to about ±0·5°C. Warm-up corrections to the duration of the anneal were applied wherever necessary. The encapsulated hot specimens were air-cooled, and then quenched in water.

The sides of each specimen were polished through a depth of about $6(Dt)^{1/2}$ to eliminate surface diffusion effects. The specimen was then aligned on the microtome to within $\pm 2\mu$, by means of an optically flat mirror with a long optical arm. Usually fifteen to twenty sections through the diffusion zone were taken. All the above-mentioned procedures were carried out in yellow safe-light for silver chloride and in red safe-light for silver bromide.

The thickness of each section was determined from its weight. For measurement of the Cl^{36} activity, the sections were dissolved in NH_4OH and then dried in a planchet to obtain a uniform geometry for thin window beta counting. The Br^{82} and I^{131} activities were counted with a scintillation detector and a single channel analyzer. The counting data were corrected for the counter dead-time, background, and decay, when necessary.

RESULTS

The thin-film solution[12] to the diffusion equation is given by

$$c(x,t) = [c_0/(\pi Dt)^{1/2}] \exp(-x^2/4Dt) \quad (1)$$

where $c(x,t)$ is the concentration of the tracer atoms at a distance x from the surface at time t, c_0 is the initial surface concentration and D

is the diffusion coefficient. The diffusion coefficients were calculated from the penetration plots of ln c vs. x^2. With few exceptions these plots were good Gaussians (at low temperatures, the diffusion plots of chloride ion in silver bromide and of bromide ion in silver chloride exhibited a slight downward curvature in a small region near the surface, due to tracer evaporation and to surface diffusion).

The total error, random and systematic, for each measurement of D is believed to be no more than 5 per cent. One source of error of concern is the measurement of the diffusion temperature. The monitoring thermocouple, although within the furnace cavity, was outside the capsule and presumably did not record the actual temperature of the sample during the initial stages of heating. To check the accuracy of the warm-up correction, additional runs were made by diffusing zinc, a fast diffusing impurity[13], into silver chloride for different lengths of time at a particular temperature. These tests indicated that for the diffusion anneal times used in the present work the error in determining the warm-up correction is not serious.

Table 1 gives a summary of the data. Figure 1 shows the temperature dependence of the

Table 1. *Diffusion of halide impurities in silver chloride and silver bromide*

Host crystal	Diffusing ion	Temperature (°C)	D (cm²/sec)
Silver Chloride	Bromide	449·9*	$8\cdot84 \times 10^{-10}$
		427·6	$3\cdot46 \times 10^{-10}$
		405·7	$1\cdot41 \times 10^{-10}$
		384·3	$5\cdot86 \times 10^{-11}$
		369·9	$3\cdot32 \times 10^{-11}$
		350·6	$1\cdot39 \times 10^{-11}$
		332·9	$5\cdot34 \times 10^{-12}$
		304·8	$1\cdot28 \times 10^{-12}$
	Iodide	448·3	$1\cdot75 \times 10^{-9}$
		421·2	$6\cdot64 \times 10^{-10}$
		397·9	$2\cdot52 \times 10^{-10}$
		359·7	$5\cdot16 \times 10^{-11}$
		334·7	$1\cdot62 \times 10^{-11}$
		307·5	$3\cdot70 \times 10^{-12}$
Silver Bromide	Chloride	413·1	$7\cdot05 \times 10^{-10}$
		412·2	$6\cdot08 \times 10^{-10}$
		402·5	$3\cdot47 \times 10^{-10}$
		387·7	$1\cdot10 \times 10^{-10}$
		369·1	$3\cdot40 \times 10^{-11}$
		355·7	$1\cdot46 \times 10^{-11}$
		331·8	$3\cdot97 \times 10^{-12}$
		320·6	$1\cdot81 \times 10^{-12}$
		305·5	$6\cdot80 \times 10^{-13}$
	Iodide	415·0	$7\cdot82 \times 10^{-10}$
		397·7	$2\cdot81 \times 10^{-10}$
		383·4	$1\cdot14 \times 10^{-10}$
		363·3	$3\cdot63 \times 10^{-11}$
		344·8	$1\cdot24 \times 10^{-11}$
		322·0	$3\cdot09 \times 10^{-12}$
		302·2	$9\cdot20 \times 10^{-11}$
		292·4	$5\cdot08 \times 10^{-13}$

*This run, at a temperature within a few degrees of the melting point, gave a slightly high diffusion coefficient (see Fig. 1), and is not included in the least-squares analysis.

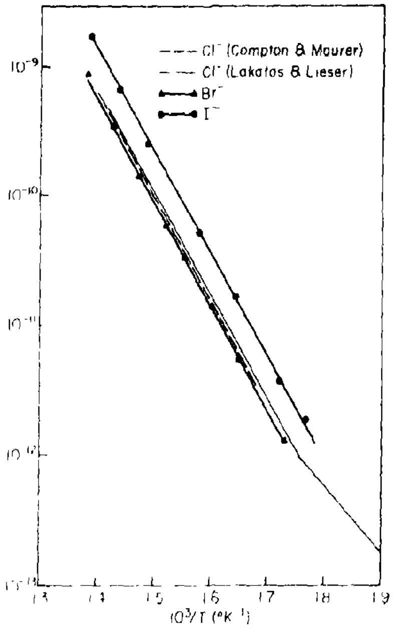

Fig. 1 Temperature dependence of D for halide ions in silver chloride

diffusion coefficients for bromide and iodide tracers in silver chloride, along with the results on the self-diffusion of chloride ion, by Compton and Maurer[4] and by Lakatos and Lieser[6]. Least-squares fits of these data were made to an Arrhenius relation, $D = D_0 \exp(-Q/RT)$. The values of Q, the diffusion activation energy, and D_0, the frequency factor, are listed in Table 2. It is seen that the activation energies for all three halide tracers are the same, within experimental error. The frequency factors vary by no more than a factor of two, and show no systematic progression as a function of size or mass of the tracer.

The Arrhenius plots for diffusion of chloride and iodide tracers in silver bromide are shown in Fig. 2; Tannhauser's results[7] for self-diffusion of the bromide ion are included for comparison. These plots are all definitely curved over the entire temperature range investigated, and thus no unique Q and D_0 can be assigned.

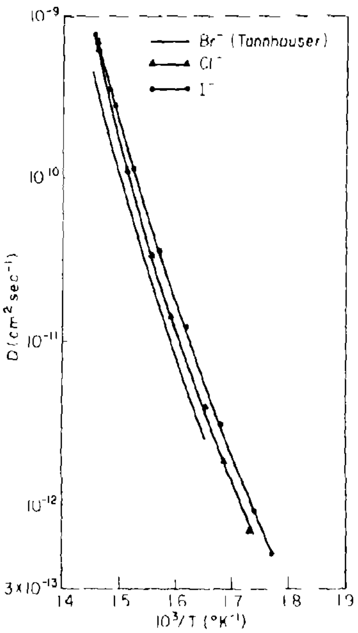

Fig. 2. Temperature dependence of D for halide ions in silver bromide.

Table 2. Arrhenius parameters for diffusion of halide ions in silver chloride

Diffusing ion	Q (kcal/mole)	D_0 (cm²/sec)	Reference
Chloride	37·0	133	Compton and Maurer[4]
Chloride			
(above 300°C)	36·3	85	
(below 300°C)	22·6	$4{\cdot}4 \times 10^{-1}$	Lakatos and Lieser[6]
Bromide	36·6 ± 0·2	90 ± 14	Present work
Iodide	36·2 ± 0·2	167 ± 21	Present work

DISCUSSION

As is well known, the difference between the activation energy for impurity diffusion and that for self-diffusion arises from (i) the change in the formation energy of a vacancy, (ii) the change in the migration energy, and (iii) the temperature dependence of the correlation factor. The temperature dependence of the correlation factor can be neglected when the *D*'s and *Q*'s of host and impurity ions are very nearly the same, as in the present case. Mullen's calculations[14] for the alkali halides indicate that the contribution from the migration term would be dominant for a homovalent ion larger than the host ion. Qualitatively, this occurs because the barrier ions must be displaced to a greater extent in order to effect interchange with a vacancy. In the case of a small impurity ion, however, the situation might be entirely different. The host ions around such an impurity would normally be relaxed inwards and this strain would further increase if a vacancy happened to be at an adjacent site. Thus it does not seem unreasonable to assume that the energy of formation of a vacancy next to a small impurity would be rather large and might therefore be the dominant factor in the activation energy difference. The results of the present investigation, however, do not entirely agree with this picture.

Although the diffusion coefficients of both bromide and iodide ion in silver chloride differ from that of the host chloride ion, the three tracers are seen to have approximately the same activation energy (Fig. 1), in spite of widely differing ionic radii[15] (Cl^-: 1·81 Å; Br^-: 1·95 Å; I^-: 2·16 Å). The various contributions to the change in the activation energy for impurity diffusion could conceivably just cancel each other; this would seem to be improbable. An interesting model which could explain this constancy of activation energy has been suggested by Condit[16]. One notes that for halide diffusion, the jumping ion must push through a 'gate' formed by four neighboring silver ions. Also, the relative ease of producing interstitial silver ions suggests that the plot of energy vs. silver ion displacement must have a metastable minimum at the interstitial site, with an energy maximum at an intermediate displacement. Suppose, now, that the jumping chloride ion displaces some of the gate ions beyond the value corresponding to this energy maximum; if this were so, then these gate ions would spontaneously relax further into the interstitial minima, thereby producing a more open gate at no additional cost in energy. It would then follow that even somewhat larger ions, such as bromide or iodide, could jump through such a gate with no greater migration energy than that required for the chloride ion.

In silver bromide the Arrhenius plots are curved (Fig. 2). At temperatures near the melting point, the activation energy for the chloride diffusion appears to be much larger than for the bromide and iodide ions, but all three activation energies become nearly the same at the lower temperatures. It has been argued[7] that the self-diffusion of the bromide ion might be due to two different mechanisms, predominantly single bromide vacancies at higher temperatures and mainly neutral associated vacancy pairs at lower temperatures. The bromide and iodide tracers behave similarly, but the chloride ion, being smaller, possibly repels a vacancy at a nearest neighbor site; this would give rise to a higher activation energy at the higher temperatures where the diffusion is assumed to take place via single bromide vacancies. On the basis of this model, one proposes that the formation of the neutral vacancy pairs, on the other hand, is insensitive to the size of the diffusing ion. Admittedly, this is at best only a speculation.

Although the effect of altering the size of the jumping ion on the frequency factor D_0 is theoretically very complicated, one can crudely discuss it on the basis of a simple Einstein model. Here D_0 is proportional to the frequency of vibration of the diffusing ion, which varies inversely as the square root of its mass. On the other hand, a larger atom would be coupled more strongly to its neighbors, and as a consequence would have a higher frequency of vibration. Thus these two factors influence D_0 in opposite directions. On this basis, our data seem to show that for the large iodide ion the stronger coupling is the dominant consideration. This may be understood from the fact that on a hard sphere model of both silver chloride and silver bromide, the halide ions do not touch one another; for the iodide impurity ion, however, in either silver chloride or silver bromide there is now an appreciable overlap, thereby increasing the local vibration frequency.

In any event, the present experimental results on halide diffusion in silver halides certainly do show much less variation than might have been intuitively expected on the basis of simple theoretical models.

Acknowledgement – The helpful assistance of Marvin H Greene is gratefully acknowledged.

REFERENCES

1. SLIFKIN L. M., *Proc. Symp. Mass Transport in Oxides*, p. 1. Natl Bur. Standards, Washington, D.C. (1968).
2. SÜPTITZ P. and TELTOW J., *Phys. Status Solidi* **23**, 9 (1967).
3. LAYER H., MILLER M. and SLIFKIN L., *J. appl. Phys.* **33**, 478 (1962).
4. COMPTON W. D. and MAURER R., *J. Phys. Chem. Solids* **1**, 191 (1956).
5. READE R and MARTIN D., *J. appl. Phys.* **31**, 1965 (1960).
6. LAKATOS E. and LIESER K., *Z. phys. Chem., Neue Folge* **48**, 213 (1966).
7. TANNHAUSER D, *J. Phys. Chem. Solids* **5**, 224 (1958).
8. CHILDS C., FUKAI A., McGOWAN W. and SLIFKIN L., To be published.
9. FOUCHAUX R. and SIMMONS R., *Phys. Rev.* **136A**, 1664 (1964).
10. BEAUMONT J C. and CABANÉ J., *C.r. hebd Séanc. Acad. Sci., Paris* **252**, 113 (1961).
11. ARAI G. and MULLEN J. G., *Phys. Rev.* **143**, 663 (1966)
12. CRANK J., In *Mathematics of Diffusion*. Clarendon Press, Oxford (1956).
13. BATRA A P and SLIFKIN L., To be published.
14. MULLEN J. G., *Phys. Rev.* **143**, 658 (1966).
15. KITTEL C., In *Introduction to Solid State Physics*. Wiley, New York (1966).
16. CONDIT R., Private communication.

J. Phys. Chem. Solids Pergamon Press 1969. Vol. 30, pp. 1321–1326. Printed in Great Britain.

ON THE PHASE TRANSITION IN MIXED VALENCE TYPE OXIDES

JUN TATENO
Japan Atomic Energy Research Institute, Tokai-mura, Naka-gun, Ibaraki-ken, Japan

(*Received* 30 *April* 1968; *in revised form* 2 *December* 1968)

Abstract—The origin of phase transitions occuring in some mixed valence-type oxides is attributed to electronic ordering. In these transitions the ordering energy is found to be proportional to the activation energy of hopping conduction in low temperature phase The ordering energy is estimated based on the electronic ordering mechanism and by considering the energy of crystalline distortion The ordering energy numerically calculated for U_4O_9 agrees fairly well with the observed

INTRODUCTION

SOME OXIDES of transition elements, lanthanides and actinides are called mixed valence type oxides, in the crystal lattice of which cations are in different valence states such as di- and tri-valent in Fe_3O_4. Electrical properties of these compounds are characterized by relatively high conductivity (about 200 Ω^{-1} cm^{-1} for Fe_3O_4 at room temperature) and low carrier mobility (less than one cm^{2}V^{-1}sec^{-1} for Fe_3O_4 even at high temperature), and the conduction mechanism is explained by "hopping" of electron between cations in different valence states. It has been found that order–disorder type phase transitions occur in many of these compounds. For example in the case of Fe_3O_4, a transition occurs at about 120°K and is attributed to ordering of Fe^{2+} and Fe^{3+} in the octahedral sites of spinel structure[1–3]. This phenomena is also expressed as ordering of electrons on Fe ions in octahedral sites. In the other compounds the origin of the phase transition is not known. Recently experimental data on the physical properties of these compounds have been reported actively, especially as to lanthanides and actindies. In this paper a relationship between the electrical conduction and the phase transition is discussed based on existing data. A model of the transition mechanism which occurs in some mixed valence type oxides is also discussed.

EXISTING DATA ON ELECTRICAL CONDUCTION AND PHASE TRANSITION

In the case of oxides with hopping conduction mechanism, electrical conductivity σ is described as[4]

$$\sigma = ne\mu,\quad \mu = \frac{eD}{kT},\quad D = a^2p,$$
$$p = \nu\exp(-W/kT) \qquad (1)$$

where n is carrier concentration. D is diffusion coefficient, a is distance of hopping, p is transition probability, ν is frequency of lattice vibration and W is activation energy of hopping. Consequently, a straight line should be obtained if $\log_e(\sigma T)$ is plotted vs. $1/T$. According to the small polaron theory[5], the activation energy W is considered to be due to displacement nearest neighbor O^{2-} ions (lattice distortion). Some examples of the hopping conduction mechanism are cited and the values of activation energy calculated from existing data using equation (1) are given below.

Measurement of the electrical conductivity of Fe_3O_4 was done by Verwey *et al.*[2] and Calhoun[6]. The conductivity changes discontinuously at the phase transition point (about 120°K). Verwey presumed that the phase transition is due to ordering of electrons, and this is supported by neutron diffraction[7] and Mössbauer effect[8] experi-

ments. This ordering changes the crystal structure slightly, from orthorhombic (in the low temperature phase) to cubic[9]. The transition temperature varies depending on the deviation from stoichiometry. Values of the activation energy recalculated from the above experimental data are listed in Table 1. Results on the other compounds described below are also listed.

Honig *et al.*[10] showed that the conduction mechanism in PrO_x ($1·50 < x < 1·80$) is hopping of electrons. This is considered to be true of Pr_6O_{11}. The electrical conductivity was measured by Noddak *et al.*[11]. Hyde *et al.*[12] reported an order-disorder phase transition at about 670°K.

Aronson *et al.*[13] showed that the conduction is by electronic hopping in UO_{2+x} and U_4O_{9-y}. U_4O_9 is considered to have the same mechanism. A λ-type anomaly of specific heat was found in U_4O_9 at about 340°K[14]. The transition temperature changes with deviation from stoichiometry[15]. The conductivity changes discontinuously at the transition point as in Fe_3O_4[15]. In our laboratory this transition was ascertained to be of neither magnetic[16] nor ordinary dielectric origin[17]. Belbeoch *et al.*[18] reported that a very slight change occurs in the crystal structure from trigonal to cubic at this point.

The activation energy of the electrical conductivity in U_3O_8 changes at about 720°K[19]. Many authors[20–25] reported a higher order phase transition in α-U_3O_8 and the reported values of transition temperature range from 480° to 720°K. This fact is considered to show that the transition temperature varies widely according to the deviation from stoichiometry of U_3O_8. It was reported that a slight change in the crystal structure occurs and that the symmetry changes from hexagonal to orthorhombic at this point[20].

The activation energies (W_1 in the high temperature phase, W_2 in the low temperature phase) of hopping conduction calculated from the data in the above reports are listed in Table 1. This table contains also the ordering energies E_{ord} represented by $E_{ord} = kT_{tr}$, where T_{tr} is the phase transition temperature. *A plot of E_{ord} vs. W_2 is shown in Fig. 1. From this we find a linear relation as*

$$W_2 = 10E_{ord}. \qquad (2)$$

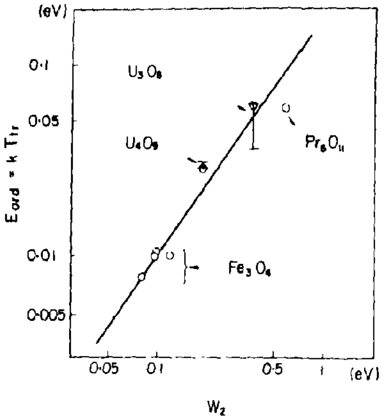

Fig. 1. Relationship between the ordering energy $E_{ord} = kT_{tr}$, and the activation energy of hopping conduction in low temp. phase in some mixed valence type oxides.

DISCUSSION

In addition to the linear relationship of equation (2), these phase transitions have other common features: the transition temperature varies considerably with deviation from stoichiometry, and the transition is accompanied by a slight change in the crystal structure or symmetry. From these features of the phase transitions which occur in some mixed valence type oxides, we may conclude that these phase transitions have the same origin, and that the origins related to some electronic ordering, as shown in Fe_3O_4. Anderson[26] calculated the ordering energy of Fe^{2+} and Fe^{3+} ion in Fe_3O_4 based on difference in Madelung energy between in ordered and disordered phase. The calculated ordering energy is 2–3 eV, and this value is much higher than observed value, 0·01 eV (from $T_{tr} = 120°K$). He assumed that this phase transition is related to only long range order, and that short range order kept even in

Table 1. *Phase transitions and activation energies for electrical conduction in some mixed-valence type oxides*

Compound	Transition temperature T_{tr} (°K)	$E_{ord} = kT_{tr}$ (eV)	Activation energy of hopping conduction (eV)		Crystal structure*		Reference
			W_1 (high temp. phase)	W_2 (low temp. phase)	High temp. phase	Low temp. phase	
Fe_3O_4	119·4	0·0103	0·048	0·10	cubic	orthorhombic	[6]
$Fe_3O_{4\cdot011}$	117·6	0·0101	0·039	0·12			[2]
$Fe_3O_{3\cdot984}$	111·1	0·0096	0·069	0·10			
$Fe_3O_{3\cdot977}$	100·0	0·0082	0·079	0·079			
Pr_6O_{11}	673	0·0580		0·59	cubic		[11],[12]
$U_4O_9(UO_{2\cdot25})$	338	0·0291	0·18	0·18	cubic	trigonal	[14],[15]
$UO_{2\cdot248}$	337	0·0290					[15]
$UO_{2\cdot211}$	352	0·0303					
$UO_{2\cdot127}$	370	0·0318					
α-U_3O_8	723	0·0623	0·51	0·37			[19]
α-U_3O_8	718~ 423	0·0618~ 0·0364			hexagonal	orthorhombic	[20–25]

*A slight change occurs in each case.

the high temperature phase. The calculated value based on this assumption is still much higher than the observed value.

Semiconductor-to-metal transitions and transitions due to the Jahn–Teller effect are other types of phase transitions observed in transition-metal oxides. Many authors[27–30] have shown that the energy of a crystalline structure distortion contribute to the ordering energy in the phase transitions. There are also many examples of the crystallin distortion due to ordered cations in spinel structure[31]. In this paper we take into account the crystalline distortion energy in calculating the energy of phase transitions due to electronic ordering.

A crystalline distortion due to electronic ordering may be treated as follows. First we consider a set of ions microscopically. As the cations are in different valence states (Fe^{2+} and Fe^{3+}, for example), the shape of configulation of these ions is different from that of the ions where the cations are in same valence state (as $Fe^{2.5+}$) This 2·5 valent cation represents either the result from statistical randomness or the model indicated by Verwey, in which a electron transfers from cation to cation. Here we represent this microscopic distortion by the displacement of an anion. The anion located between cations in different valence states (Fe^{2+} and Fe^{3+}) is attracted by unbalanced Coulomb force, and it displaces to one direction (from central position to Fe^{3+}). The degree of this displacement is possible to estimate by considering the electrostatic energy and the elastic energy. An electric field E is produced by the cations in different valence states. We consider only nearest neighbor interaction hereafter. The field induces polarization, which is composed of two parts, a pure electronic part and a part due to displacement of ion. The latter part of the polarization is considered to correspond to the crystalline distortion. The displacement of the anion is limited by the increasing elastic energy, which is proportional to the square of polarization. When we write the polarization due to ionic displacement by p, the internal energy increment per anion is expressed by

$$u = -pE + \tfrac{1}{2}\gamma p^2 \tag{3}$$

where γ is a constant. By using Np instead of p, we get the energy increment per unit volume

$$U = -NpE + \tfrac{1}{2}\gamma(NP)^2 \tag{4}$$

where N is the number of dipoles per unit volume. Minimizing equation (4) with respect to Np $(\partial U/\partial(Np) = 0)$ gives the equibrium displacement at absolute zero temperature, that is,

$$U_0 = -\frac{E^2}{2\gamma}, \quad (Np)_0 = \frac{E}{\gamma} \tag{5}$$

where suffix 0 expresses the equibrium state at absolute temperature $T = 0$. As the temperature increases, some electrons in ordered state are excited to random state. The Coulomb interaction term in equation (4) must be changed, thus we get new equibrium Np, which is related to the net distortion of crystal at finite temperature. That is,

$$U = -NpsE + \tfrac{1}{2}\gamma(Np)^2 \tag{6}$$

where s is order parameter. Using $\partial U/\partial(Np) = 0$, we can get the energy for the equibrium distortion,

$$U = -\frac{(Es)^2}{2\gamma}. \tag{7}$$

To estimate the elastic energy, one may use the information from the compressibility data and the infrared spectra. In this paper we adopt the latter. The Szigeti relations are available for a small sphere sample[32, 33]:

$$\tfrac{1}{2}\gamma P^2 = \tfrac{1}{2}NM_{\text{red}}\omega_s{}^2Q^2 \tag{8}$$

$$P = e^*NQ \tag{9}$$

and

$$M_{\text{red}}\omega_s{}^2 = 2\beta \tag{10}$$

where P is infrared polarization, N is the number of dipoles per unit volume, M_{red} is the reduced mass of ion pair, Q is the displacement of an ion, e^* is the effective ionic charge defined by Szigeti, and β is the force constant. ω_s is the small sphere eigenfrequency defined as

$$\omega_s = \frac{\epsilon_0 + 2}{n^2 + 2}\,\omega_{t0} \qquad (11)$$

where ω_{t0} is the transverse eigenfrequency of lattice vibration, ϵ_0 is the static dielectric constant, and n is the refractive index. Here we note that, in equations (3–7), we treat the interaction between one dipole p and the microscopic field E, we consider the resultant distortion instead of the resultant polarization. On the other hand, in equations (8–10), the resultant polarization, P, interacts with the external field in a small sphere sample, where the electric field is corrected due to the self field[32]. In spite of the difference in these treatment, we consider that the data of infrared spectra is useful to estimate the force constant between cation and anion and to estimate the elastic term in equation (6). From equations (8–10) we get

$$\gamma = \frac{2\beta}{e^{*2}N}. \qquad (12)$$

Substituting this in equation (7), we get

$$U = -(e^*Es)^2N/4\beta. \qquad (13)$$

In equation (13), e^*E expresses the Coulomb interaction between an anion and ordered cations. Then e^* is the effective charge of an anion. If we define e^+ as the effective charge difference between cations in different valence state, and if we take into account only nearest neighbor interactions, we can write

$$E = e^+/r^2 \qquad (14)$$

where r is the distance between cation and anion. Substituting equation (14) in (13), we obtain

$$U = -(e^*e^+s)^2N/4\beta r^2. \qquad (15)$$

From this expression for internal energy, we can estimate the transition temperature according to the Bragg–Williams approximation. Neglecting the volume change, we may use the following relations:

$$F = U - TS \qquad (16)$$

$$U = -vN's^2 \qquad (17)$$

$$S = k \log W \qquad (18)$$

and

$$W = \frac{N(\alpha)!N(\beta)!}{N(A\alpha)!N(B\beta)!N(A\beta)!N(B\beta)!} \qquad (19)$$

where F is the free energy associated with electronic ordering, S is the entropy, $N(\alpha)$ and $N(\beta)$ are the number of cations in the valence states of $\alpha+$ and $\beta+$ respectively (if we put $N(\alpha) = N(\beta) = N'$, then the total number of cations is $2N'$), and $N(A\alpha)$ etc. express the number of α-valent cations on sublattice A etc. Minimizing F with respect to the order parameter, s, gives

$$s = \tanh\frac{vs}{kT} \qquad (20)$$

and thus

$$v = kT_{\text{tr}}. \qquad (21)$$

From definition of the ordering energy E_{ord}, $E_{\text{ord}} = v$. Since the number of ion pairs in equation (8) is equal to $2N'$ in equation (17), we obtain from equations (15), (17) and (21)

$$E_{\text{ord}} = \frac{(e^*e^+)^2}{2\beta r^4}. \qquad (22)$$

In the case of U_4O_9, the observed value for the ordering energy is 0·029 eV. If we assume that the characteristic properties of the lattice vibrations in U_4O_9 are not so different from those of UO_2, we can use the values of the effective charge and the force constant of UO_2 reported by Axe *et al.*[34] in order to calculate the equation (22) for U_4O_9. They found from i.r. reflectivity experiments that the effective charge of an oxygen ion, e^*, was $1{\cdot}15e$, where e is the charge of electron, and that the force constant, β, was 23×10^4 dyn/cm. The effective charge difference between U^{4+} and U^{5+} should be $0{\cdot}58e$. For the distance between cation and anion in U_4O_9 we adopt $r = 2{\cdot}35 \times 10^{-8}$ cm[35]. Numerical calculation of equation (19) for U_4O_9 using these values gives the ordering energy $E_{\text{ord}} = 0{\cdot}026$ eV, a value which agrees fairly well with observed. It is difficult to discuss the relation expressed by equation (2) quantitatively in the present state.

SUMMARY AND CONCLUSION

1. In some mixed valence type oxides, phase transitions occur, which have common features, such as changes in electrical properties and crystal symmetry at the transition point, and variation of transition temperature with deviation from stoichiometry.

2. These phase transitions appear to have the same origin, electronic ordering.

3. There is an apparent linear relationship between the activation energy for hopping conduction in the low temperature phase and the ordering energy of the phase transition.

4. The ordering energy can be expressed in the terms of the effective charges of the ions and the force constants of the lattice.

Acknowledgements – We would like to thank Professor Keiji Naito and Mr Tamotsu Ishii for many useful discussions

REFERENCES

1 VERWEY E. J. W., *Nature* **144**, 327 (1939).
2. VERWEY E. J. W and HAAYMAN P W, *Physica* **8**, 979 (1941).
3. VERWEY E. J. W., HAAYMAN P W. and ROMEIJN F. C., *J. chem. Phys* **15**, 181 (1947)
4. HEIKES R. R. and JOHNSON W. D., *J. chem. Phys.* **26**, 582 (1957).
5. YAMASHITA J. and KUROSAWA T., *J. phys. Soc Japan* **15**, 802 (1960).
6. CALHOUN B. A., *Phys. Rev.* **94**, 1577 (1954).
7 HAMILTON W. C., *Phys. Rev.* **110**, 1050 (1958).
8. BAUMINGER R. *et al.*, *Phys. Rev.* **122**, 1447 (1961).
9. BICKFORD L. R., *Rev. mod. Phys.* **25**, 75 (1953).
10 HONIG B. G., CELLA A. A. and CORNWELL J. C., In *Rare Earth Research II*, p. 555. Gordon and Breach, New York (1964).
11. NODDACK Von W. and WALCK H., *Z. Elektrochem.* **63**, 269 (1959).
12. HYDE B. G., BEVAN D. J. M. and EYRING L., In *Rare Earth Research II*, p. 277. Gordon and Breach, New York (1964).
13 ARONSON S., RULLI J. E. and SCHANER B E., *J. chem. Phys.* **35**, 1382 (1961).
14. GOTOO K. and NAITO K., *J. Phys. Chem. Solids* **26**, 1673 (1965).
15 NAITO K et al., *Solid State Commun.* **5**, 349 (1967)
16 GOTOO K, NOMURA S. and NAITO K., *J. Phys. Chem. Solids* **26**, 1679 (1965).
17. TATENO J and NAITO K., To be published.
18. BELBEOCH B., BOIVINEAU J. C. and PERIO P, *J Phys. Chem. Solids* **28**, 1267 (1967).
19. GEORGE A. M. and KARKHANAVALA M. D., *J. Phys. Chem. Solids* **24**, 1207 (1963).
20. HOEKSTRA H R. *et al.*, *J. phys. Chem* **59**, 136 (1955)
21 NOTZ K J, HUNTINGTON C. W. and BURKHARDT W., *I and EC Process Design and Develop.* **1**, 213 (1962)
22. ERMISCHER W, HAUSER O. and SCHENK M, *J nucl. Mater.* **16**, 341 (1965).
23. BESSONOV A. F., STREKALOVSKII V. N. and UST'YANOV V. M., *Kristallografiya* **10**, 570 (1965).
24 WESTRUM E F, Jr, Private communication.
25. RACHEV V V, KOVBA L M. and IPPOLITOVA E. A., *Dokl. Akad. Nauk SSSR* **159**, 1371 (1964).
26 ANDERSON P. W., *Phys. Rev* **102**, 1008 (1959).
27 KAWAKUBO T., *J phys. Soc. Japan* **20**, 516 (1965).
28 ROBBRECHT G. G. and DE KLERCK E F., *Physica* **31**, 1033, 1575 (1965).
29. ADLER D. *et al.*, *Phys. Rev.* **155**, 851 (1967).
30. ADLER D and BROOKS H., *Phys. Rev.* **155**, 826 (1967).
31. HAAS C., *J. Phys. Chem. Solids* **26**, 1225 (1965).
32. FRÖHLICH H., *In Theory of Dielectrics*, p. 149. Oxford University Press, Oxford (1949).
33. SZIGETI B., *Trans Faraday Soc.* **45**, 155 (1949).
34. AXE J. D. and PETIT G. D., *Phys. Rev.* **151**, 676 (1966).
35. ISHII T., Private communication

J. Phys. Chem. Solids Pergamon Press 1969. Vol. 30, pp. 1327–1334. Printed in Great Britain.

ELECTRICAL CONDUCTION AND ELECTRON MICROSCOPY OF VITREOUS SOLIDS IN THE K_2O-SiO_2 SYSTEM

Y. P. GUPTA
Northrop Corporate Laboratories, Northrop Corporation, Hawthorne, Calif. 90250, U S A.
and
U. D. MISHRA*
Philco Ford Corporation, Blue Bell, Pennsylvania U.S.A

(*Received* 12 *September* 1968, *in revised form* 2 *December* 1968)

Abstract – Both the electrical conductivity and phase separation by replication electron microscopy of the vitreous K_2O–SiO_2 solids from 10–43·3 mole % K_2O are investigated. Inflexions in the activation energy of conduction vs. composition are observed around 33, 20 and 11 mole % K_2O. The activation energy of conduction is derived from the experimental electrical conductivities obtained in the temperature range, 70°–300°C for all compositions excepting 10–15 mole % K_2O, for which the temperature range was 100°–300°C. The observed inflexions in the resistivity and its temperature dependence around 33 and 20 mole % K_2O compositions seem to be related to the occurrence of phase separation in the potash-silica glasses of 15–43·3 mole % K_2O. The inflexion around 11 mole % K_2O is probably related to a large change in the structure of the silica network upto about this composition.

1. INTRODUCTION

EXPERIMENTAL investigations of ionic conduction in alkali silicate, Li_2O-B_2O_3-SiO_2 and Na_2O-B_2O_3-SiO_2 glasses[1–5] generally show kinks in the activation energy of electrical conduction and conductance vs. the composition of the glass. According to the current models of ionic conduction[4, 6, 7], these inflexions are either attributed to changes with composition in the glass structure or are accounted for on the basis of compound formation or phase separation. There is evidence of phase separation in the Na_2O-SiO_2 [4, 8], Li_2O-SiO_2[4], PbO-B_2O_3[9] and some binary and ternary alkali silicate glasses[10]. On the other hand, changes in the ESR spectra of alkali borate glasses[11] at about 30 mole % alkali oxide have been ascribed to changes, principally, in the environment of the boron nucleus. In the Cs_2O-SiO_2 glasses, the activation energy for electrical conduction and the NMR chemical shift of Ca^{133} show inflexions at about the same composition (i.e. 25 mole % Cs_2O). The break in activation energy has been assigned to changes in the environment of the caesium ion[5]. Leventhal and Bray[12] examined the NMR chemical shift of Pb^{207} in compounds and glasses of PbO-SiO_2 and PbO-B_2O_3. Although the model of a random network of structural groupings, characterizing the crystalline compounds, is consistent with their observations on the PbO-SiO_2 glasses, it is not yet established. For the PbO-B_2O_3 glasses, their model is much less satisfactory when tested against the NMR chemical shift of the B^{11} nucleus.

For the alkali silicate glasses, in particular, the break is found at 33 mole % Li_2O in the Li_2O-SiO_2 glasses[3], although in one study of Li_2O-SiO_2 glasses a break is reported at about 15 mole % Li_2O[4]. In the Na_2O-SiO_2[1, 3] and K_2O-SiO_2[3, 13] glasses, the activation energy shows kinks around 22 mole % metal oxide, yet only the potash glasses exhibit a corresponding change in the electrical conductivity. At 33 mole %

---

*Now, at the Control Data Corporation, Minneapolis, Minnesota

Na_2O in the Na_2O–SiO_2 glasses there is, apparently, no change in the activation energy but a kink is observed in the electrical conductance. However, Mazurin and Borisovskii[2] observed an inflexion in electrical conductance vs. composition at 33 mole % K_2O in the K_2O–SiO_2 glasses but not at 22 mole % K_2O. In the Cs_2O–SiO_2 glasses[5] a break is reported in the activation energy of conduction vs. composition at 25 mole % Cs_2O. Moreover, for glasses containing $Cs_2O > 25$ mole %, the electrical conductivity tends to decrease and the activation energy increases with increasing Cs_2O, whereas for the other alkali silicate glasses, the electrical conductivity generally increases and the activation energy decreases with increasing alkali oxide.

The alleged breaks in the Li_2O–SiO_2 and Na_2O–SiO_2 glasses can be attributed to phase separation, experimentally observed by electron microscopy[4, 8]. However, the replication electron microscopy of etched sample surfaces of a 7·5 mole % K_2O–SiO_2 glass was inconclusive about liquid–liquid immiscibility in the K_2O–SiO_2 glasses[4].

Cahn and Charles[14] have analyzed thermodynamically the question of metastable immiscibility in the alkali silicate glasses and conclude that metastable immiscibility in the K_2O–SiO_2 glasses, although theoretically feasible, is unlikely to occur because of the possible lowering of the critical temperature. Recently, Moriya *et al.*[10], based on a correlation between the heats of formation of metasilicates and the ionic potentials, suggested a consolute temperature of about 750°C for the K_2O–SiO_2 system. If the suggested consolute temperature is correct, it is indeed surprising that no immiscibility has been observed in the K_2O–SiO_2 glasses. To examine the controversial data on electrical conduction in the potash-silica glasses and to understand the reasons for the alleged breaks in the activation energy for conduction vs. composition, a study of electrical conduction and electron microscopic examination of glasses in the K_2O–SiO_2 system was undertaken. The results of this study are reported here.

2. EXPERIMENTAL PROCEDURE

2.1 *Sample preparation*

Potassium silicate glasses in batches of 50–100 g were prepared from anhydrous potassium carbonate and 'pure' silica powder prebaked at 1000°C for 8–10 hr. Table 1 shows the analyses of SiO_2 and K_2CO_3. Stoichiometric amounts of silica and anhydrous K_2CO_3, further dried at about 100°C, were mixed for several hours in a mixer. The mixture, contained in a platinum crucible, was slowly heated to and held at about 900°C for about 2 hr in an atmosphere of dry 4:1 argon and

Table 1. *Analyses of* SiO_2 *and* K_2CO_3

Spectrographic analysis of SiO_2 (As oxides of the elements)		Analysis of anhydrous K_2CO_3 (%)	
Si	Principal constituent	As	0·0000
Mg	< 0·0005%	Fe	0·0001
Fe	0·004%	Pb	0·0002
Al	0·004%	Na	0·020
Cu	< 0·0005%	Insolubles	0·002
Ca	0·0005%	N	0·0005
		PO_4	0·0005
		SO_4	0·003
		NH_4OH ppt	0·001
		Ca and Mg ppt	0·0003
		SiO_2	0·003
		Loss on Heating (285°C)	0·400

oxygen. The temperature was then slowly raised to at least 200°C above the liquidus temperature of the glass. The melt was held at this temperature for 18–20 hr and then cooled in air. Each glass was further homogenized by remelting the crushed glass. In all cases, the glass was clear and bubble free. The composition of the various glasses, shown in Table 2, was determined from: (i) loss in weight of glass, assuming that in all cases the entire weight loss could be attributed to loss of K_2O; and (ii) wet chemical analysis of typical glasses.

Specimens for conductivity measurements were obtained by remelting the glass in a mixture of dry 4:1 argon and oxygen for 3–4 hr in 1·5 cm dia. × 1·5 mm deep platinum cups at about 200°C above the liquidus temperature. All samples were cooled at a rate of about 15°C/min. On visual examination under reflected or transmitted light all specimens were apparently homogeneous. To obtain samples with uniform thickness and flat surfaces, specimens were polished on both sides first on silicon carbide paper and then lapped on a lap machine. The polished specimen was washed with acetone and dried at about 120°C in a continuously evacuated quartz tube. Both surfaces of the specimen were then coated by Dupont liquid bright platinum paint and fired for a couple of minutes at suitable temperatures to obtain a conductive coating. Compositions in excess of 43·3 mole % K_2O could not be investigated because of (i) generally increased hygroscopicity of these compositions and (ii) the difficulties with the maintenance of the conductive coating.

2.2 *Electrical conductivity measurement*

The experimental arrangement, used to measure electrical conductivity, is shown in Fig. 1. The platinum coated specimen was set upon a platinum foil electrode supported on a sintered, polished alumina disc, affixed to a ¼ in dia. alumina tube. An inverted alumina crucible, with the inner bottom lined with the second platinum foil electrode, was kept at the specimen top. Lead wire connections were spot-welded to the platinum foil electrodes. To keep the specimen in position and ensure good electrical contact, a slight pressure was exerted on the crucible. Two chromel-alumel thermocouples, one on each side of the specimen, were used to measure the temperature of the sample. A resistance furnace controlled within ±0·5°C at temperatures near 500°C and having a constant temperature zone of more than 1 in. was used. D.C. conductance was measured in an atmosphere of dry oxygen and argon, 1:4 at 10^2–10^4 V/cm in the temperature range 70°–300°C, save 100°–300°C for glasses with $K_2O \leq 15$ mole % since these glasses had too low a conductivity to be measured precisely below 100°C. A General Radio, Model 1608-A, impedance bridge was used with an accuracy of 0·1% ± 0·005% of full scale in the lowest range and 0·2% ± 0·005% of full scale in the highest range. The desired voltage was set by use of a high impedance d.c. voltmeter. Conductivity, σ, or resistivity, ρ, was calculated by Ohm's law.

Before making conductivity measurements, specimens were annealed at 425°C for about 36 hr. Some specimens were annealed at 425°C for 200 hr. As shown by a typical case in Fig. 2, no appreciable difference in electrical conductance due to the prolonged annealing (e.g. 200 hr) was noticed. The above annealing schedule was adequate for each composition since practically a steady state value of conductivity was thus achieved. Moreover, the annealing temperature of 425°C is well below the suggested critical temperature[10] for metastable immiscibility. The conductivity of the samples was measured on cooling as well as heating in steps of about 20°C. The specimen was held at each temperature for a sufficiently long time (≃ 30 min.) to achieve steady state values of conductivity. In no case did the experimental data obtained on cooling and heating differ significantly; compare Fig. 2.

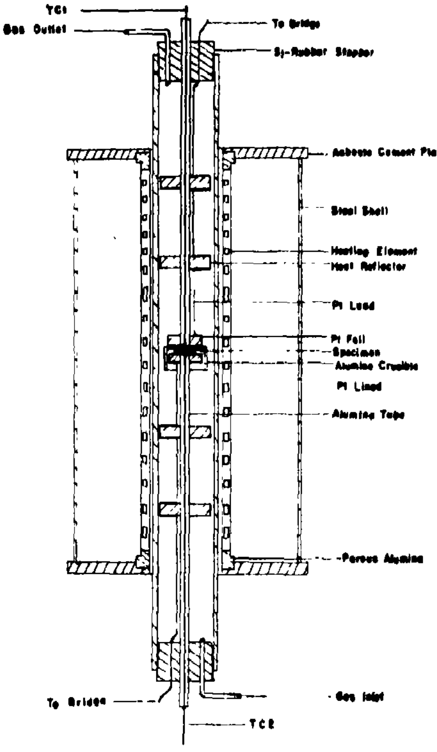

Fig. 1 Experimental arrangement for conductivity measurements.

Measurements were made on a typical glass using specimens of varied volume/surface ratio. In the temperature range of this study, conductivity was not influenced by varying the volume/surface ratio by about 5. For specimens of repeat melts the variations in electrical conductance at any temperature and the activation energy were, respectively, less than 5% and ±100 cal/g. mole.

2.3 *Electron microscopy of the* K_2O–SiO_2 *glasses*

Glass specimens, used for conductivity measurements, were fractured, examined under natural light and then replicated to observe the fractured surfaces. Under normal daylight, glass samples with K_2O in excess of

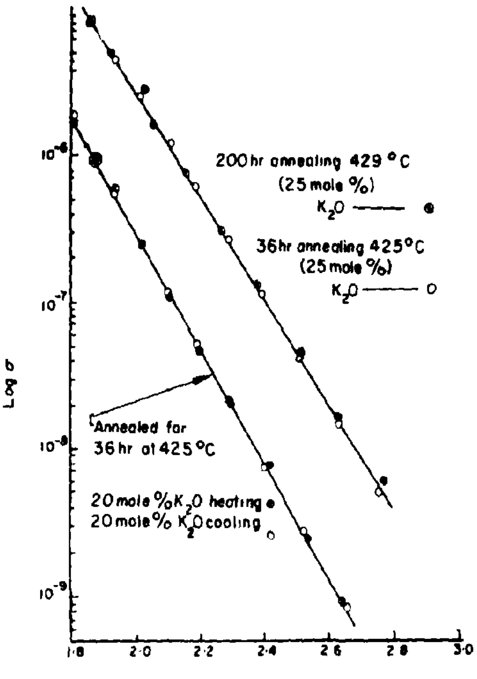

Fig 2 Conductivity vs reciprocal temperature at different annealing times and on heating and cooling

32·5 mole % appeared very slightly light bluish (hardly perceptible), presumably due to the presence of the second phase All other specimens appeared completely clear and transparent.

Next, the fractured surfaces were etched in 1 : 1 HF for a few seconds and replicated again. The replicating procedure consisted of (i) softening the cellulose tape with acetone and applying it to the sample, (ii) allowing the tape to dry and gently removing it from the specimen. (iii) shadowing the tape at an angle of 45° with *Pt–Pd* alloy followed by carbon, and (iv) dissolving the primary cellulose replica in warm acetone leaving only the carbon replica attached to the alloy film. The electron micrographs of the fractured surfaces are not presented since either no or only very fine scale structures, having no correlation with the gross structures of the etched specimens, were observed. The significance of this observation is considered later. Typical electron micrographs of etched surfaces of the various glasses are shown in Figs. 3(a–r)

3. RESULTS AND DISCUSSION

The theory of electrical conduction in single phase alkali silicate glasses has been discussed by Stevels[15] in terms of the mobility of alkali ions between adjacent interstices in the glass network. For moderate field strengths ($\leqslant 10^5$ V/cm) the resistivity, ρ, is given by equation (1).

$$\log\rho = \log\rho_0 + \Delta H^*/2{\cdot}3RT = A + B/T \quad (1)$$

where $A = \log\rho_0 = \log[2h\exp(-\Delta S^*/R)/e^2\lambda^2 n]$; $B = \Delta H^*/2{\cdot}3\,R$; and h, T, e, λ, n, R, ΔH^* and ΔS^* are, respectively, the Planck's constant, absolute temperature, charge of the mobile ion, jump distance, number of ions/cc, gas constant and the activation energy and entropy for electrical conduction.

The parameters, ρ_0 and ΔH^*, obtained by a least squares fit of the experimental data to equation (1), are shown in Table 2.

In a single phase system, a change in ΔH^* is generally attributed to either a change in the mechanism of conduction or in structure, or both. If however, a dispersed phase is present in a glassy matrix, both the conductivity and its temperature dependence would depend on the volume fraction, electrical properties, and distribution of the dispersed phase; e.g. whether the second phase is continuous or discontinuous.

Figure 4 shows a plot of $A = \log\rho_0$ vs. log M, where M is the concentration of K^+ ions

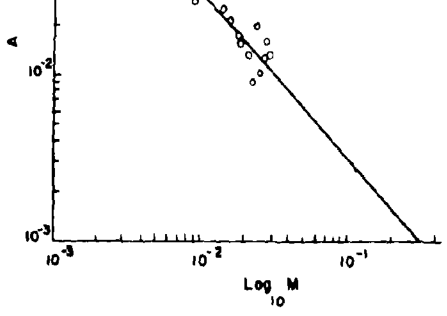

Fig. 4. Plot of A vs. $\log_{10} M$.

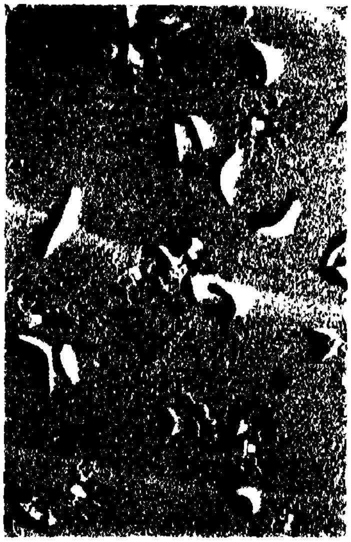

Fig. 3(a). Electron micrograph of a replicated etched surface of a K_2O-SiO_2 glass (10 mole % K_2O). Magnification 21,000.

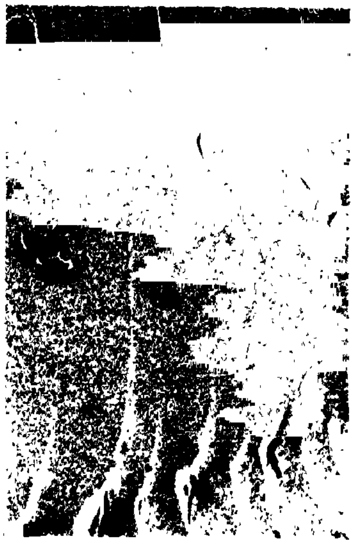

Fig. 3(b). Electron micrograph of a replicated etched surface of a K_2O-SiO_2 glass (11·25 mole % K_2O). Magnification 21,000.

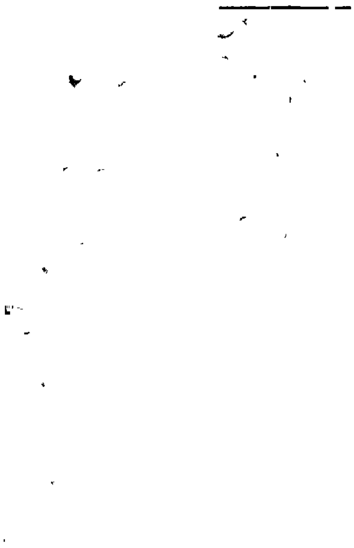

Fig. 3(c). Electron micrograph of a replicated etched surface of a K_2O-SiO_2 glass (12·5 mole % K_2O). Magnification 21,000.

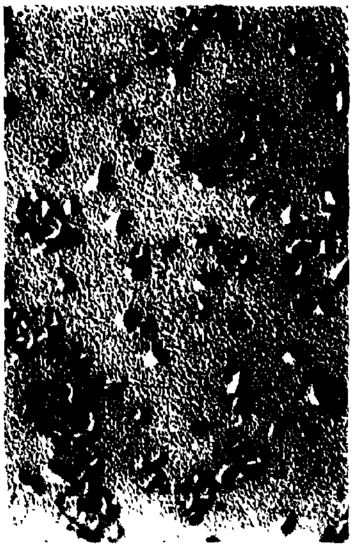

Fig. 3(d). Electron micrograph of a replicated etched surface of a K_2O-SiO_2 glass (13·75 mole % K_2O). Magnification 21,000.

Fig. 3(e). Electron micrograph of a replicated etched surface of a K_2O-SiO_2 glass (15·0 mole % K_2O). Magnification 21,000.

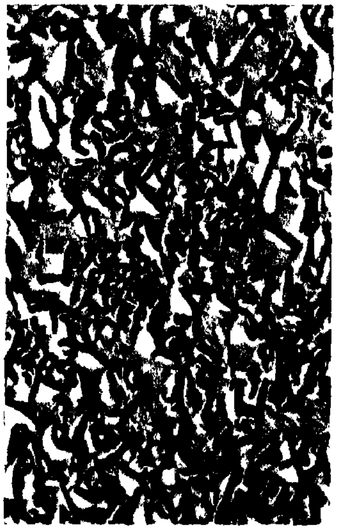

Fig. 3(f). Electron micrograph of a replicated etched surface of a K_2O-SiO_2 glass (17·5 mole % K_2O). Magnification 21,000.

Fig. 3(g). Electron micrograph of a replicated etched surface of a K_2O-SiO_2 glass (20 mole % K_2O). Magnification 21,000.

Fig. 3(h). Electron micrograph of a replicated etched surface of a K_2O-SiO_2 glass (22·5 mole % K_2O). Magnification 21,000.

Fig. 3(i). Electron micrograph of a replicated etched surface of a K_2O-SiO_2 glass (25 mole % K_2O). Magnification 21,000.

Fig. 3(j). Electron micrograph of a replicated etched surface of a K_2O-SiO_2 glass (27·5 mole % K_2O). Magnification 21,000.

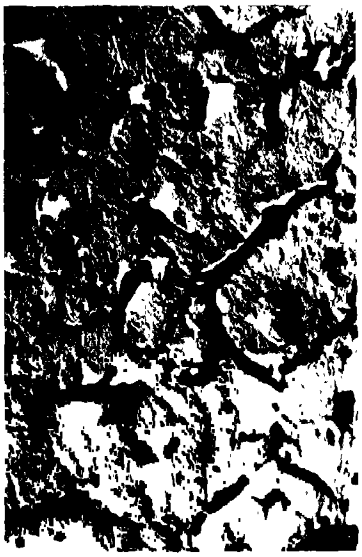

Fig. 3(k). Electron micrograph of a replicated etched surface of a K_2O-SiO_2 glass (30 mole % K_2O). Magnification 21,000.

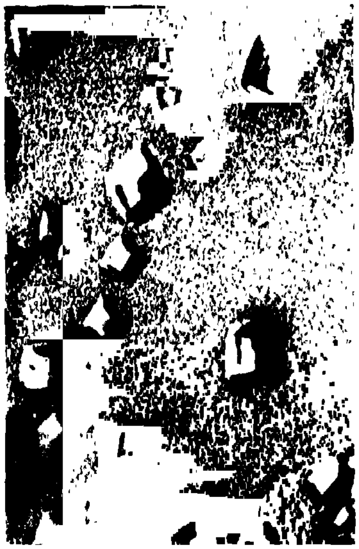

Fig. 3(l). Electron micrograph of a replicated etched surface of a K_2O-SiO_2 glass (32·5 mole % K_2O). Magnification 24,500.

Table 2. Composition and electrical resistivity of K_2O-SiO_2 *glasses*

Batch composition mole % K_2O	Mole % K_2O from weight loss	Mole % K_2O from chem. analy.	$\rho_0 \times 10^2$ (Ω cm)	Activation energy (kcal/g mole)
10·00	9·88	9·94	1·66 ± 0·24	22·68 ± ·087
11·25	11·07		3·42 ± 0·38	21·67 ± ·056
12·50	12·03	12·25	2·77 ± 0·3	21·25 ± ·063
13·75	13·47		3·77 ± 0·38	20·85 ± ·054
15·00	14·80	14·50	1·76 ± 0·18	20·81 ± ·063
17·53	17·53		1·31 ± 0·16	19·75 ± ·059
20·00	19·73		2·43 ± 0·26	18·59 ± ·060
22·50	22·38	22·90	2·09 ± 0·31	17·58 ± ·094
25·00	24·95		1·72 ± 0·2	17·13 ± ·057
27·50	27·36		1·59 ± 0·16	16·66 ± ·053
30·00	29·84	29·74	1·13 ± 0·12	16·14 ± ·053
32·50	32·39		0·89 ± 0·13	15·71 ± ·093
35·00	34·77	34·80	1·96 ± 0·27	15·06 ± ·081
37·50	37·33	37·33	1·03 ± 0·12	15·33 ± ·056
40·00	39·96	39·76	1·28 ± 0·17	15·49 ± ·067
41·34	41·26	41·29	1·59 ± 0·16	15·68 ± ·044
43·30	43·29	42·72	1·32 ± 0·16	15·62 ± ·060

in g atom/cc. A straight line: $A = -\log_{10}M - 3{\cdot}5$ fits the experimental data and is in good agreement with Myuller's[16] equation: $A = -\log_{10}M - P_e$ where $P_e = 3{\cdot}7 \pm 1$ was deduced from a semi-theoretical expression for ion mobility. Myuller's expression is compatible with the conductivity data for a wide variety of simple alkali silicates, borates and borosilicates. Since a constant value of P_e implies a constant ΔS^*, the change in the activation energy for electrical conduction dominates the variation in resistivity and the conduction mechanism in these glasses is essentially the same. These observations are consistent with the results of Owen and Douglas[17] who reported a linear relation between $\log \rho$ and the activation energy for d.c. conduction in a very wide range of composition of other alkali glasses.

Since most of the current in the potash-silica glasses is carried by the K^+ ions, the activation energy of conduction in these glasses may, therefore, determine at a specific temperature the number of mobile K^+ ions and the extent to which the local structure impedes their migration. A change in the activation energy with glass composition must then indicate a change in the concentration as well as the environment of the mobile K^+ ions, including, of course, an effect of any phase separation that may possibly occur in glass.

The experimental activation energy, ΔH^*, is plotted vs. mole % K_2O in Fig. 5. The activation energy for transport of the K^+ ions in pure silica is taken from the work of Verhoogen[18] on trace diffusion of K^+ into fused silica in an electrical potential gradient. Figure 5 shows inflexions in the activation energy around compositions 33, 20 and 11 mole % K_2O. Moreover, for glasses with K_2O above 33 mole %, the activation energy tends to increase slightly, with an accompanying increase in resistivity. The kinks around 33 and 20 mole % also appear to be present in the plot of $\log \rho$ vs. composition, Fig. 6. By comparison, the electrical conductivity data of Kuznetsov and Meljnikova[13] for potash-silica glasses from 18–38 mole % K_2O suggest a break around 22 mole % K_2O in

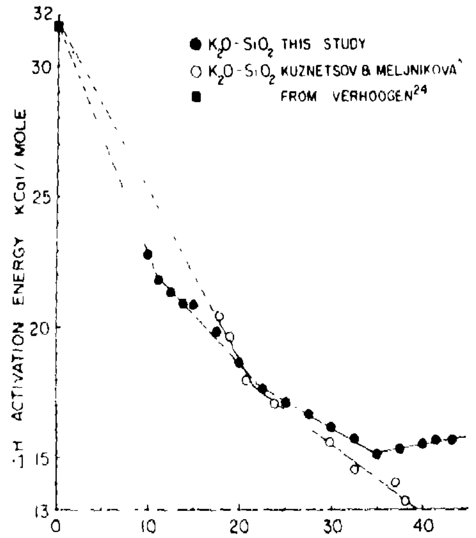

Fig. 5. Activation energy vs mole % of K_2O.

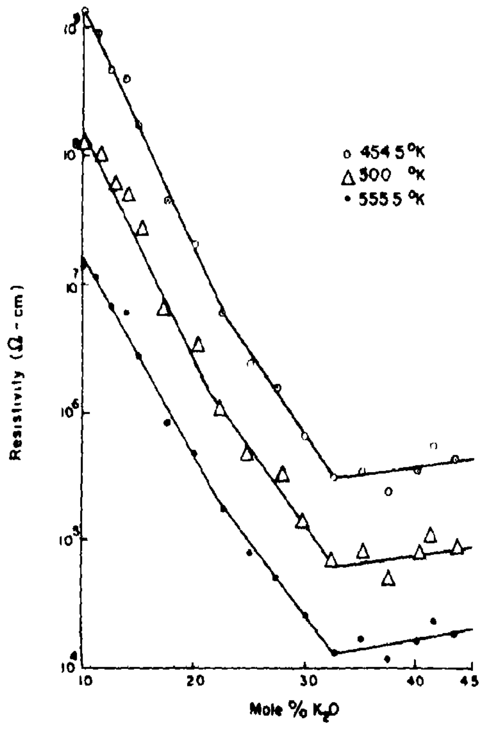

Fig. 6. Logarithm of resistivity vs. mole % K_2O.

both the activation energy and log ρ vs. composition. Since beyond 32 mole % K_2O data were obtained only on 37 and 38 mole % K_2O glasses, the inflexion around 33 mole % K_2O may not have been observed. However, the resistivity data of Mazurin and Borisovskii[2] on potash glasses from 15 to 40 mole % K_2O at two different temperatures show a break in resistivity around 33 mole %.

However, with some effort it is possible to draw continuous curves through the experimental data of Figs. 5 and 6, at least in the 11–33 mole % K_2O range. In this sense, the inflexion around 20 mole % K_2O is somewhat ambiguous although such a discontinuity in slope occurs in all curves obtained by drawing the best lines through a maximum number of points. In fact, if one relies on the accuracy of the present resistivity data it seems that drawing a continuous curve through the experimental points is more a result of an implicit presumption that the resistivity in the potash silica system varies only continuously with K_2O. Since in cases where the resistivity change is gradual a relatively large change in slope of a continuous curve (as is certainly the case around 20 mole % K_2O in the present measurements) is indicative of the discontinuity, it is more realistic to draw the best lines through a maximum number of points. Also, in view of the electron microscopic evidence of phase separation and the discussion presented later, inflexions around 33, 20 and 11 mole % K_2O appear reasonable.

Two-liquid immiscibility may occur stably (above the liquidus) or metastably (below the liquidus). When phase separation occurs either by spinodal decomposition or by nucleation and growth, one of the phases inevitably moves in composition closer to compound limits if compounds occur in a binary system. In addition to compounds similar to those in the systems Li_2O-SiO_2 and Na_2O-SiO_2, a compound $K_2O.4SiO_2$ is formed in the K_2O-SiO_2 system. The formation of this compound may reduce the range of possible liquid–liquid metastable immiscibility. According to Rey[19] the range of positive deviation from ideality, wherein immiscibility may result, extends to about 10 mole % K_2O, but on the basis of liquid immiscibility observed for lithia and soda silica glasses [4], potash silica glasses containing 7·5 or 15 mole % K_2O are expected to be more prone to phase separation. Contrary to this, Charles [4] observed that the dielectric loss in the K_2O-SiO_2 glasses is quite appreciable and increases to a maximum value towards the 30 mole % K_2O glass, which may suggest the presence of a submicroscopic segregation or phase separation in this glass. Moreover, the recent estimate of the critical temperature (750°C) for liquid–liquid immiscibility in the K_2O–SiO_2 glasses[10] makes phase separation quite probable in these glasses.

Typical electron micrographs, Figs. 3(a–r), of the etched surfaces of the various K_2O-SiO_2 glasses show dark regions of the fast etching phase as etched valleys along with areas of the slower etching phase. The observed structure in most cases is well below 0·2–0·25 μ. Transmission electron microscopy and diffraction from different parts of several thin film glass specimens showed the films to be initially amorphous, as indicated by the diffuse diffraction patterns typical of liquids. However, on constant exposure to intense electron beam some films tended to devitrify. Under the conditions of sample preparation and annealing of these glasses, it appears that phase separation first increases towards the 20 mole % K_2O glass. The fast etching phase is apparently richer in K_2O and probably has a variable composition although relatively closer to potassium tetrasilicate. Exceeding 20 mole % K_2O, phase separation still occurs until in the 32·5 mole % K_2O glass there are observed a few well defined etch shapes, associated with the occurrence of a few particles of a crystalline phase, possibly $K_2O.4SiO_2$ in a disilicate matrix. When the K_2O content exceeds 33 mole %, an increasing amount of a highly continuous fast etching separate phase appears with varying composition but probably nearer the potassium disilicate glass.

The absence of gross structure on fracture replication, as indicated earlier, suggests that both phases excepting that in the 32·5 mole % K_2O glass are vitreous, apparently resulting from liquid–liquid immiscibility. This seems to be supported by the fact that the gross structure on fracture replication is generally seen when the material is either polycrystalline or the fracture characteristics of the two phases are dissimilar; such as may be the case for a crystalline phase in a glassy matrix. Moreover, the structures observed from the etched fractured surfaces resemble those reported by Charles[4], and Douglas *et al.*[10] for glasses with liquid–liquid immiscibility.

Moreover, the electron micrographs, presented here, clearly show no evidence of any artifact effects because: (a) the observed structures change in a regular manner with increasing K_2O, (b) the replication techniques are similar to those of other authors[4, 8, 10], and (c) the same replication technique shows crystallization in the 32·5 mole % glass and not in others which further substantiates the conclusions of the preceding paragraph.

Briefly, the separation of the disilicate-like phase concurs with the appearance of the inflexion around 33 mole % K_2O. The nearly constant activation energy for conduction in the potash-silica glasses with K_2O exceeding 33 mole % is indicative of conduction principally in the disilicate-like phase.

The inflexion around 20 mole % K_2O is apparently due to a gradual increase of the tetrasilicate-like phase in glasses of compositions from 15 to 20 mole % followed by an increasing appearance of the disilicate-like phase in glasses with more than 20% K_2O. The gradual decrease in the activation energy of conduction is probably due to conduction through phases of slightly varying compositions. In fact, depending on the extent of phase separation in glasses on either side of the 20 mole % K_2O glass, the inflexion in this region could occur in the range, 20–25 mole % K_2O.

The inflexion around 11 mole % K_2O in the activation energy vs. composition is *uncertain* because (a) it is predicted simply from a combination of the present data with the only diffusion[18] and some well-characterized conductivity data on glasses with low alkali content[17], and (b) the lack of data on conductivity of the K_2O–SiO_2 glasses with less than 10 mole % K_2O make it difficult to observe a break in log ρ vs. composition.

However, if the resistivity of silica[17] having a few ppm Na^+ ions is included in Fig. 6 (e.g. resistivity is 8×10^{13}, $1{\cdot}5\times10^{15}$ and 9×10^{16} Ω-cm at 555°, 500° and 454°K, respectively) and it is assumed that the resistivity of fused silica with low concentrations of Na^+ or K^+ ions is nearly the same, a break around 11 mole % K_2O appears quite likely. Moreover, Bockris *et al.*[20, 21] reported at 10–12 mole % metal oxide a rather sharp change in the thermal expansion coefficient and the activation energies for viscous flow and electrical conduction in binary molten alkali silicates. This was inferred to be due to a marked change in the structure of liquid silicates in this composition range. It is likely that the structural features of the molten alkali silicates are retained in the solid potash-silica glasses upto about 12 mole % K_2O, particularly when the electron micrographs show practically no evidence of phase separation in the 10–12 and 7·5[4] mole % K_2O glasses, except that due to minor local composition fluctuations, characteristic of single phases.

4. SUMMARY

The activation energy of electrical conduction in the K_2O–SiO_2 glasses of 10–43·3 mole % K_2O show inflexions around 11, 20 and 33 mole % K_2O. The inflexions around 20 and 33 mole % K_2O, also observed in the electrical resistivity vs. composition plots, are apparently related to the occurrence of phase separation, observed by replication electron microscopy, in the K_2O–SiO_2 glasses. The inflexion around 11 mole % K_2O is probably associated with a relatively large structure change upto this composition in the silica network.

Acknowledgements – The financial support for this research from the Graduate School of the University of Minnesota and the United States Atomic Energy Commission is gratefully acknowledged.

REFERENCES

1. SEDDON E., TIPPETT E. J. and TURNER W. E. S., *J. Soc. Glass Technol.* **16**, 450 (1932).
2. MAZURIN O. V. and BORISOVSKII E. S., *Soviet Phys. Tech. Phys.* **2**, 243 (1957).
3. KUZNETSOV A. Ya., *Russ. J. Phys. Chem.* **33**, 20 (1959).
4. CHARLES R. J., *J. Am. Ceram. Soc.* **46**, 235 (1963).
5. MILBERG M. E., OTTO K. and KUSHIDA T., *Phys. Chem. Glasses* **7**, 14 (1966).
6. ANDERSON O. L. and STUART D. A., *J. Am. Ceram. Soc* **37**, 573 (1954)
7. ISARD J. O., *J. Soc. Glass Technol.* **43**, 113T (1959).
8. TRAN T. L. and SELLA C., *C.r. hebd. Séanc. Acad Sci., Paris* **258** (17), 4243 (1954)
9. ZARZYCKI J. and NANDIN F., *Phys. Chem. Glasses* **8**, 11 (1967).
10. MORIYA Y., WARRINGTON D. H. and DOUGLAS R. W., *Phys. Chem. Glasses* **8**, 19 (1967).
11. LEE S. and BRAY P. J., *J. chem. Phys.* **40**, 2982 (1964).
12. LEVENTHAL M. and BRAY P. S., *Phys. Chem. Glasses* **6**, 113 (1965).
13. KUZNETSOV A. YA. and MELJNIKOVA I. G., *Z. Fiz. Khim.* **24**, 1209 (1950)
14. CAHN J. W and CHARLES R. J., *Phys. Chem. Glasses* **6**, 181 (1965).
15. STEVELS J. M., *Progress in Theory of the Physical Properties of Glass.* Elsevier, Amsterdam (1948), *Handbuch der Physik*, Vol. 20, p. 350. Springer, Berlin (1957).
16. MYULLER R. L., *Soviet Phys. solid St.* **2**, 1213 (1968).
17. OWEN A. E. and DOUGLAS R. W., *J. Soc. Glass Technol.* **43**, 159T (1959).
18. VERHOOGEN, J., *Am. Miner.* **37**, 637 (1952).
19. REY M., *Discuss. Faraday Soc.* 257 (1948).
20. BOCKRIS J. O'M., MACKENZIE J. D. and KITCHENER J. A., *Trans. Faraday Soc.* **51**, 1734 (1955)
21. BOCKRIS J. O'M., TOMLINSON J. W. and WHITE J. L. *Trans. Faraday Soc.* **52**, 299 (1956).

J. Phys. Chem. Solids Pergamon Press 1969. Vol. 30, pp. 1335–1340. Printed in Great Britain.

ANTIFERROMAGNETIC RESONANCE IN $LiMnPO_4$

P. R. ELLISTON*, J. G. CREER and G. J. TROUP
Physics Department, Monash University, Clayton, Victoria, Australia

(Received 27 November 1968)

Abstract – Antiferromagnetic resonance at millimetre wavelengths has been observed in single crystals of $LiMnPO_4$($T_N \approx 35°K$). The data have been compared with the Nagamiya-Yosida theory for a collinear orthorhombic antiferromagnet. A best fit to the theory is given by taking $(2\lambda K_1)^{1/2} = 37{\cdot}9 \pm 0{\cdot}5$ kG and $(2\lambda K_2)^{1/2} = 62 \pm 2$ kG at 4·2°K, in good agreement with independent pulsed-field spin-flop data.

INTRODUCTION

ORTHORHOMBIC $LiMnPO_4$, lithiophilite, is antiferromagnetic below about 35°K[1]. A variety of studies has been made on this system[1–4] including spin-flop experiments and preliminary antiferromagnetic resonance experiments reported by us[5, 6]. In the present paper we give detailed antiferromagnetic resonance data at millimetre wavelengths in pure single crystals of $LiMnPO_4$, and compare our results with the Nagamiya–Yosida theory[7–9]. Unlike many systems investigated since the early work on $CuCl_2 . 2H_2O$[10], $LiMnPO_4$ possesses a collinear spin system, and is perfectly orthorhombic. The Nagamiya–Yosida theory should therefore provide a good description of antiferromagnetic resonance in this system, as it does in $CuCl_2 . 2H_2O$.

CRYSTAL AND MAGNETIC STRUCTURE

Lithiophilite is isomorphous with olivine, with Li in inversion sites[11] as in other $LiXPO_4$ compounds[4], and Mn in mirror-plane sites. The space group is Pnma with $a = 10{\cdot}46$ Å, $b = 6{\cdot}10$ Å and $c = 4{\cdot}744$ Å[11].

An antiferromagnetic spin configuration collinear with the a axis was postulated by Mays[1] from nuclear magnetic resonance experiments. Mays' model has been subsequently confirmed by neutron diffraction[2].

EXPERIMENTAL TECHNIQUES

Single crystals of $LiMnPO_4$ were synthesized by the flux-melt method[12]. Orange crystals up to 3 mm in size were obtained. Smaller crystals, about 1 mm, were generally used for the resonance measurements. The larger crystals tended to show structure in the recorded lines (making line-position difficult to determine), while smaller crystals did not; we tentatively ascribe this to propagation effects, although we have not made a detailed study of the effect.

Specimens were identified and oriented by back-reflection X-ray photographs, and mounted on a rotatable holder in a broad-band millimetre spectrometer[6].

EXPERIMENTAL RESULTS AND DISCUSSION

As previously mentioned, the a axis is the most favoured axis of magnetization in $LiMnPO_4$. The spin-flop data of Ranicar and Elliston[5] further indicate that the least favoured axis is the b axis. In the notation of Nagamiya and Yosida the a and b axes then correspond to the x and z axes respectively.

In the paramagnetic state above the Néel point an isotropic resonance line with $g = 2{\cdot}00 \pm 0{\cdot}01$ is observed. This paramagnetic resonance broadens and weakens near 35°K. The Néel point thus obtained is $T_N = 34{\cdot}6 \pm 0{\cdot}4$°K, in agreement with Mays'[1] value ($T_N = 34{\cdot}85 \pm 0{\cdot}1$°K).

Since Mn^{2+} is an S-state ion, a g-value close to 2 in the paramagnetic state is not unexpected. We take the same g-factor for the antiferromagnetic state, an assumption which has been shown to be quite reasonable for other materials[8, 9, 13].

---

*Present address: Eaton Electronics Laboratory, McGill University, Montreal, Canada.

Below T_N antiferromagnetic resonance is observed. No hysteresis in the data was recorded, although runs were usually made with increasing magnetic field.

If a magnetic field H_0 is applied along the x axis, the Nagamiya-Yosida theory predicts resonances above and below the critical (spin-flop) field H_c [$= (c_1/\alpha)^{1/2}$]. These modes are given by

$$(\omega/\gamma)^2 = (1/2)[(1+\alpha^2)H_0^2+c_1+c_2 \pm \{(1-\alpha^2)^2H_0^4+2(1+\alpha)^2H_0^2(c_1+c_2) + (c_2-c_1)^2\}^{1/2}]; \quad H_0 < H_c \qquad (1)$$

where the low- and high-frequency modes are given by $-$ and $+$ respectively;

$$(\omega/\gamma)^2 = H_0^2 - c_1; \quad H_0 > H_c \qquad (2)$$

and

$$(\omega/\gamma)^2 = c_2 - c_1; \quad H_0 > H_c$$

where ω is the angular frequency, $\gamma(= ge/2mc)$ the gyromagnetic ratio, and

$$c_1 = 2\lambda K_1,\ c_2 = 2\lambda K_2,\ \alpha = 1 - \chi_{\parallel}/\chi_{\perp}$$

where $\lambda(= 1/\chi_{\perp})$ is the molecular field coefficient, K_1 and K_2 are the anisotropy energy constants ($K_2 > K_1 > 0$), and $\chi_{\parallel}$, $\chi_{\perp}$ are the parallel and perpendicular susceptibilities.

Under certain conditions resonance may also be observed at $H_0 = H_c$[8, 9].

For H_0 along the y axis the resonance condition is

$$(\omega/\gamma)^2 = H_0^2 + c_1. \qquad (3)$$

With a microwave frequency of 67·6 Gc/s ($\omega/\gamma = 24·1$ kG) and H_0 along the a axis in LiMnPO$_4$, we observe two resonances at low temperatures. The linewidths between inflexion points at 4·2°K are about 250 G for the low-field line and about 400G for the high-field line. We identify these resonances with two of the modes given above: the low-frequency mode of (1), and (2). The high-field mode, equation (2), allows a direct determination of c_1 at the temperature of measurement, providing the g-factor, or γ, is known. From equation (2) we obtain, at 4·2°K, $c_1^{1/2} = 37·9 \pm 0·5$ kG, in good agreement with spin-flop measurements[5]. Knowing $c_1^{1/2}$ we can determine $c_2^{1/2}$ from the low-field mode, provided α is known. Rather than determine α from molecular field theory, it is usually obtained experimentally, since this generally gives better agreement between theory and the resonance data[14].

Mays[1] gives α at 4·2°K obtained from NMR and direct susceptibility measurements. We arbitrarily take $\alpha = 0·95$ at 4·2°K, a value between those given by Mays. Actually, at this temperature (where α is of the order of unity) the resonance expressions are somewhat insensitive to the choice of α. From equation (1) we then obtain $c_2^{1/2} = 62 \pm 2$ kG at 4·2°K, taking $c_1^{1/2} = 37·9 \pm 0·5$ kG. This value of $c_2^{1/2}$ is in good agreement with the value of 65 ± 3 kG obtained from spin-flop measurements in the ab plane[5].

Knowing c_1, c_2, α, and γ, all the parameters in the Nagamiya-Yosida theory are specified. The frequency dependence of the various resonances for $\omega/\gamma < 60$ kG is shown in Fig. 1. The 67·6 Gc/s points are, of course, those from which c_1 and c_2 (and hence the theoretical curves) have been determined. No resonance at the critical field is predicted for this temperature at the frequencies used, in agreement with observation. The 135·5 *Gc/s* ($\omega/\gamma = 48·4$ kG) data for H_0 along the c axis are in good accord with equation (3).

The angular dependence of the resonances in the ac plane is shown in Fig. 2. The theoretical expressions for this plane are complicated; they were solved, using an iterative technique, with the aid of a computer. The

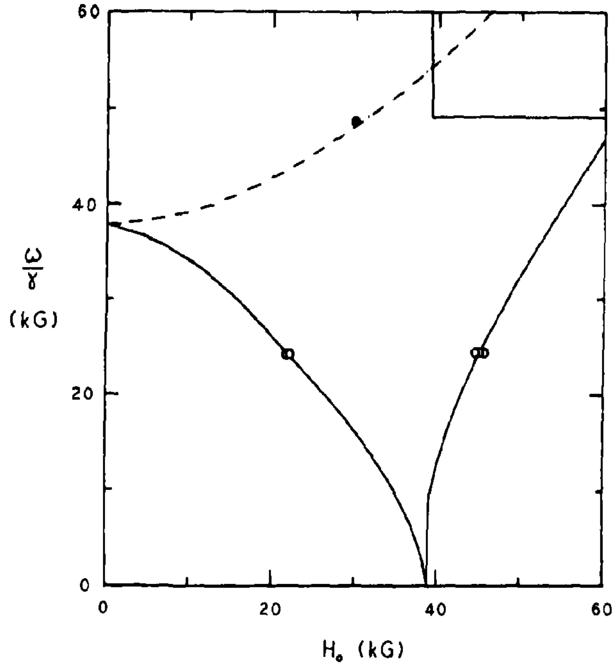

Fig. 1. Frequency dependence of antiferromagnetic resonance at 4·2°K. Open circles are for H_0 along a axis, and full circles for H_0 along c axis. Curves are from Nagamiya–Yosida theory with $(c_1)^{1/2} = 37{\cdot}9$ kG and $(c_2)^{1/2} \doteq 62$ kG.

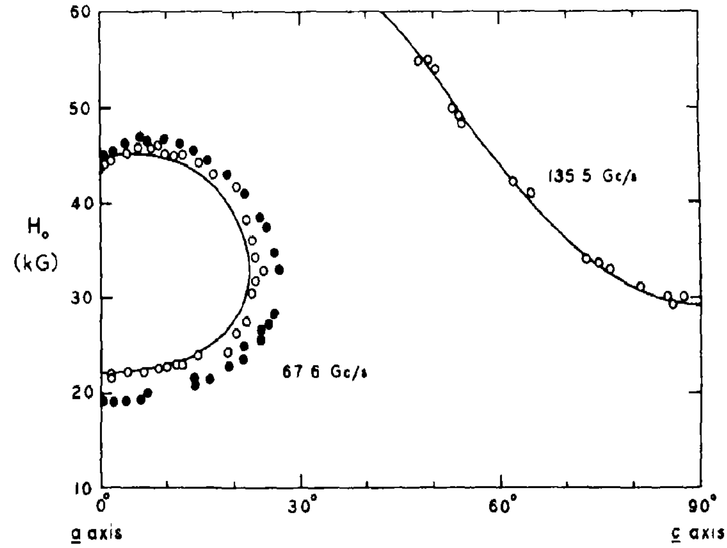

Fig. 2. Angular dependence of antiferromagnetic resonance with H_0 in ac plane. Open circles are for 4·2°K, and full circles for 18·5°K. Curves are from Nagamiya–Yosida theory.

theoretical curves for the above values of c_1, c_2 and α are shown as solid lines in Fig. 2; the agreement with the data is good.

It appears likely that close to the a axis the high-field line at 67·6 Gc/s shows a small 'dip' in the resonance field value similar to that which has been observed in $CuCl_2 . 2H_2O$ [15, 16] and $NiCl_2 . 6H_2O$[17]. In $CuCl_2 . 2H_2O$ Yamazaki and Date[16] have observed an anomalously broad line in the region of the dip; this also occurs in $LiMnPO_4$, although experimentally we were not able to study the behaviour in detail. The origin of the dip in these materials is not clear.

The angular dependence in the ab plane at 67·6 Gc/s is shown in Fig. 3 for $T = 4{\cdot}2$°K. Again we obtain good agreement between theory and experiment, using c_1, c_2 and α as before.

Finally, the temperature dependence of the resonances at 67·6 Gc/s is shown in Fig. 4. Resonance for H_0 along the c axis is observed at this frequency for T greater than about 28°K. Above $T \simeq 32$°K broad resonances are also observed for H_0 along the a axis; these correspond to the high frequency (+) mode of equation (1).

In order to compare the temperature-dependence data with theory we need to know $\alpha(T)$. In the absence of published data we proceed as follows: the critical field H_c is given by

$$H_c^2 = 2\lambda K_1/\alpha = 2K_1/\alpha\chi_\perp$$

so that generally

$$\alpha(T) = 2K_1(T)/H_c^2(T)\chi_\perp(T).$$

Assuming that $\alpha(0) = 1$ and $\chi_\perp(T)$ is constant below T_N (expected for a simple antiferromagnet) we have

$$\alpha(T) = K_1(T)H_c^2(0)/K_1(0)H_c^2(T).$$

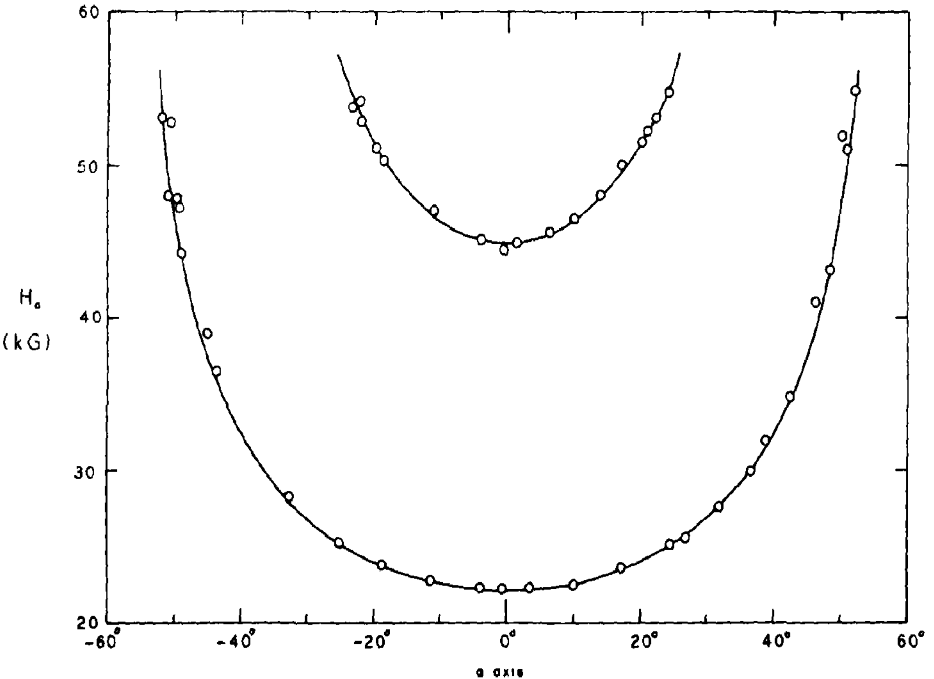

Fig. 3. Angular dependence of antiferromagnetic resonance with H_0 in ab plane at 67·6 Gc/s and $T = 4{\cdot}2$°K. Curves are from Nagamiya–Yosida theory.

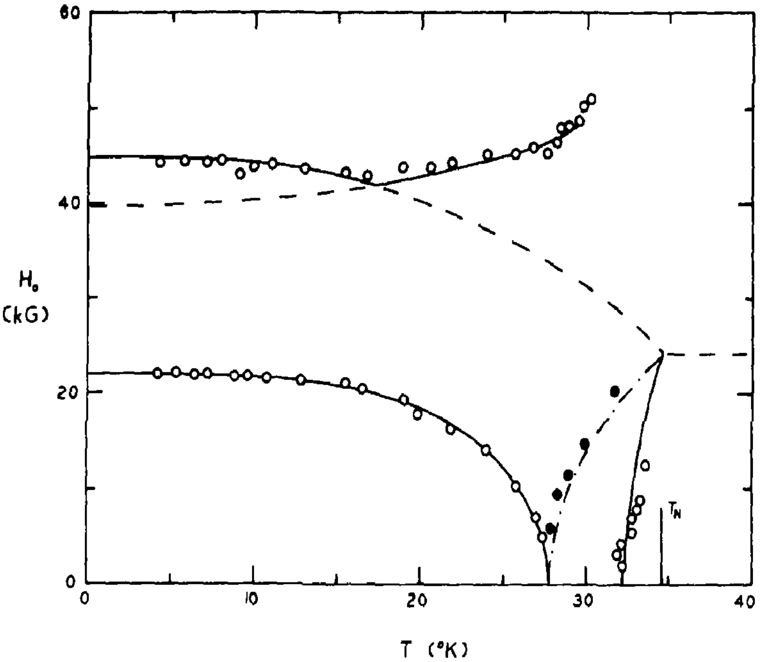

Fig. 4. Temperature dependence of antiferromagnetic resonance at 67·6 Gc/s. Open circles are for H_0 along a axis, and full circles for H_0 along c axis The curves are explained in the text.

Following Abkowitz and Honig[14] we assume

$$K_1(T)/K_1(0) = K_2(T)/K_2(0) = B^2_{5/2}(T/T_N)$$

where $B_{5/2}(T/T_N)$ is the reduced Brillouin function for the spin 5/2 appropriate to Mn^{2+} in LiMnPO$_4$.

Hence

$$\alpha(T) = B^2_{5/2}(T/T_N)\,.\,H_c{}^2(0)/H_c{}^2(T).$$

$H_c(T)$ has been experimentally determined by Ranicar and Elliston[5]; using their data we can predict $\alpha(T)$. Implicit in the above assumptions are the variations of $c_1(T)$ and $c_2(T)$:

$$c_1(T)/c_1(0) = K_1(T)/K_1(0) = B^2_{5/2}(T/T_N)$$
$$= c_2(T)/c_2(0).$$

Knowing $c_1(T)$, $c_2(T)$ and $\alpha(T)$, we can now compare the experimental data with the Nagamiya–Yosida theory. The theoretical curves, taking $T_N = 34{\cdot}6$°K, are shown in Fig. 4, with $[c_1(4{\cdot}2)]^{1/2} = 37{\cdot}9$ kG, and $[c_2(4{\cdot}2)]^{1/2} = 62$ kG. The curve starting at about 40 kG for $T = 0$°K, and shown as a solid line above 17·4°K, is a best fit to the spin-flop phase boundary determined by Ranicar and Elliston. Above 17·4°K, the spin-flop mode given by equation (2) is not observed; instead, the resonance occurs at the critical field.

The exchange field H_E in an antiferromagnet can be determined from the perpendicular susceptibility, since $H_E = M_0/\chi_\perp$ (where M_0 is the sublattice magnetization). At 4·2°K, using $\chi_\perp(4{\cdot}2) = 0{\cdot}043$ cm^3/mole[1], we obtain $H_E = 320$ kG for LiMnPO$_4$. The anisotropy field $H_A = K_1M_0$ can be determined from H_E and c_1, since $c_1 = 2H_EH_A$. With $c_1{}^{1/2} = 37{\cdot}9$ kG we obtain $H_A = 2{\cdot}2$ kG. A necessary requirement of the Nagamiya–Yosida theory is that the exchange field be much greater than the applied and anisotropy fields; this requirement is therefore well satisfied in $LiMnPO_4$.

CONCLUSIONS

Antiferromagnetic resonance in $LiMnPO_4$ is well described by the Nagamiya–Yosida theory. At 4·2°K, the parameters chosen to give the best agreement between theory and experiment are $c_1^{1/2} = 37{\cdot}9 \pm 0{\cdot}5$ kG and $c_2^{1/2} = 62 \pm 2$ kG, in good agreement with independent pulsed-field magnetization measurements.

Acknowledgements—We are grateful to Mr A. Vas for growing single crystals of $LiMnPO_4$. One of us (P. R. Elliston) acknowledges a Radio Research Board grant.

REFERENCES

1. MAYS J. M., *Phys. Rev.* **131**, 38 (1963)
2. NEWNHAM R. E., SANTORO R. P. and REDMAN M. J., *J. Phys. Chem. Solids* **26**, 445 (1965).
3. MERCIER M. and GAREYTE J., *Solid State Commun.* **5**, 139 (1967).
4. SANTORO R. P. and NEWNHAM R. E., *Acta crystallogr.* **22**, 344 (1967).
5. RANICAR J. H. and ELLISTON P. R., *Phys. Lett.* **25A**, 720 (1967).
6. ELLISTON P. R. and TROUP G. J., *Proc. phys. Soc.* **92**, 1040 (1967).
7. YOSIDA K., *Prog. theor. Phys.* **7**, 425 (1952).
8. NAGAMIYA T., *Prog. theor. Phys.* **11**, 309 (1954).
9. NAGAMIYA T., *Prog. theor. Phys.* **15**, 306 (1956).
10. for references see Foner S., In *Magnetism* (Edited by G. T. Rado and H. Suhl), Vol. 1, p. 408. Academic Press, New York (1963).
11. GELLER S. and DURAND J. L., *Acta crystallogr.* **13**, 325 (1960).
12. ZAMBONINI F. and MALOSSI L., *Z. Kristallogr.* **80**, 442 (1931).
13. FONER S., *Phys. Rev.* **130**, 183 (1963)
14. ABKOWITZ M. and HONIG A., *Phys. Rev.* **136**, A1003 (1964).
15. GARBER M. and GERRITSEN H. J., *Physica* **22**, 189 (1956).
16. YAMAZAKI H. and DATE M., *J. phys. Soc. Japan* **21**, 1615 (1966).
17. DATE M. and MOTOKAWA M., *J. phys. Soc. Japan* **22**, 165 (1967)

J. Phys. Chem. Solids Pergamon Press 1969. Vol. 30, pp. 1341–1352. Printed in Great Britain

SUR L'EVOLUTION EN FONCTION DE LA COMPOSITION DE PROPRIETES SEMI-CONDUCTRICES A DES PROPRIETES METALLIQUES AU SEIN D'UNE PHASE DE TYPE 'BRONZES OXYGENES DE VANADIUM'

A. CASALOT et P. HAGENMULLER
Service de Chimie Minérale Structurale de la Faculté des Sciences de Bordeaux, associé au C.N.R.S.,
351, cours de la Libération, 33 Talence, France

(*Received* 20 *November* 1968)

Resumé—Dans les phases $M_xV_2O_5\beta$, la nature du métal inséré influe beaucoup moins que le taux d'insertion x. Nos mesures montrent que lorsque celui-ci n'est pas trop important, les phases $Cu_xV_2O_5\beta$ sont des semi-conducteurs. Les propriétés physiques évoluent, au fur et à mesure de l'accroissement de x, marquant le passage d'un état localisé, caractérisé par un paramagnétisme de Langevin et une conduction par sauts vers un état délocalisé (paramagnétisme indépendant de la température et conduction de type métallique). Une telle évolution qui s'effectue sans discontinuité apparente n'a à notre connaissance jamais été observée antérieurement

1. INTRODUCTION

LA THÉORIE des bandes prédit pour l'anhydride vanadique V_2O_5 un caractère fortement isolant par suite de l'absence à l'état fondamental de tout électron d. Des mesures de conductivité électrique en fonction de la température infirment cependant cette théorie; elles impliquent un caractère semi-conducteur avec une énergie d'activation de l'ordre de 0,2 eV[1–2].

Ioffe étudiant des échantillons de V_2O_5 par résonance paramagnétique électronique conclut à la présence de quelques atomes de vanadium tétravalent ($3d^1$), entrainant une conduction par sauts[3–4]. Ce résultat a été confirmé ultérieurement par l'étude de propriétés physiques des phases $M_xV_2O_5\alpha$ qui peuvent être considérées comme des solutions solides d'ions M^{n+} dans V_2O_5 et qui comportent ainsi nx atomes V^{4+}[5].

Les phases $M_xV_2O_5\beta$ ont fait l'objet d'études diverses et contradictoires[6–7]. Sohn a déterminé sur des monocristaux de phases β de composition proche de $Na_{0,33}V_2O_5$ des énergies d'activation de 0,06 eV et des moments magnétiques effectifs de $2\,\mu_B$ environ par atome de vanadium tétravalent[8]. Il confirmait que l'élément inséré était totalement ionisé, opinion déjà énoncée par Gendell, Cotts et Sienko, qui constataient l'absence de tout déplacement de Knight lors de mesures de R.M.N. effectuées sur $Li_{0,33}V_2O_5\beta$[9]. Perlstein, poursuivant sur le plan électrique les travaux de Sohn, a montré par effet Hall que le nombre de porteurs devenait constant à une température proche de celle de Debye [10]. Ces auteurs proposaient pour la phase $Na_{0,33}V_2O_5$ un mécanisme de conduction par sauts.

Nous avons abouti à une conclusion analogue en expliquant les propriétés électriques et magnétiques de divers bronzes oxygénés de formules $Na_xV_2O_5$ ($0,22 \leq x \leq 0,40$), $K_xV_2O_5$ ($0,19 \leq x \leq 0,27$) et $Ag_xV_2O_5$ ($0,29 \leq x \leq 0,41$) étudiés pour la première fois dans tout leur intervalle de composition[5–11]

La phase $Cu_xV_2O_5\beta$, isotype des précédentes[12] présentait un intérêt tout particulier en raison de l'étendue de son domaine d'existence ($0,26 \leq x \leq 0,64$ à 600°C) qui permettait d'étudier des échantillons beaucoup plus riches en porteurs.

2. PROPRIETES MAGNETIQUES

La susceptibilité molaire χ_m a été déterminée entre 77° et 625°K environ grâce à l'emploi d'une balance magnétique de type Faraday. La susceptibilité paramagnétique χ_p s'en déduit:

$$\chi_p = \chi_m - \chi_D - N\alpha. \qquad (1)$$

Dans cette relation χ_D représente la contribution dramagnétique de tous les atomes et $N\alpha$ un terme correctif lié au paramagnétisme de Van Vleck du réseau. Cette valeur, assez difficile à déterminer expérimentalement se calcule néanmoins par méthode graphique. Elle s'est avérée dans tous les cas étudiés très voisine de celle de V_2O_5. $N\alpha$ possède une valeur proche de 120 μuem c.g.s. et reste indépendant de la température[5–13–14].

Alors que leurs homologues du potassium suivent rigoureusement un loi de Curie-Weiss dans tout le domaine de température envisagé[11], il n'en est pas de même pour les phases $Cu_xV_2O_5\beta$. Elles ne suivent en effet une loi de Curie-Weiss qu'à température suffisamment élevée. En deçà elles présentent une légère incurvation.

Si cette température de transition est toujours voisine de 220°K pour les phases $Ag_xV_2O_5\beta$, pour les phases Cu_x-$V_2O_5\beta$ elle varie: les courbes $\chi_p^{-1} = f(T)$ deviennent linéaires pour des températures d'autant plus élevées que le taux d'insertion est plus grand (Fig. 1).

Nous avons déduit des courbes obtenues à température élevée les valeurs des constantes de Curie molaires C_m et atomiques $C_{V^{4+}}$, les températures de Curie θ, les moments effectifs P_m et les températures T_M limites inférieures d'application de la loi de Weiss. Toutes ces données sont regroupées au Tableau I.

La croissance de la température de Curie en fonction du taux d'insertion répond pour cette série à une loi d'allure parabolique (Fig. 2). Il semble en être de même pour le moment magnétique P_m des phases $Cu_xV_2O_5\beta$. Les valeurs de P_m obtenues pour des taux d'insertion élevée en cuivre sont très supérieures à la valeur théorique ($P_m = 1{,}73\ \mu_B$) correspondant au seul paramagnétisme de

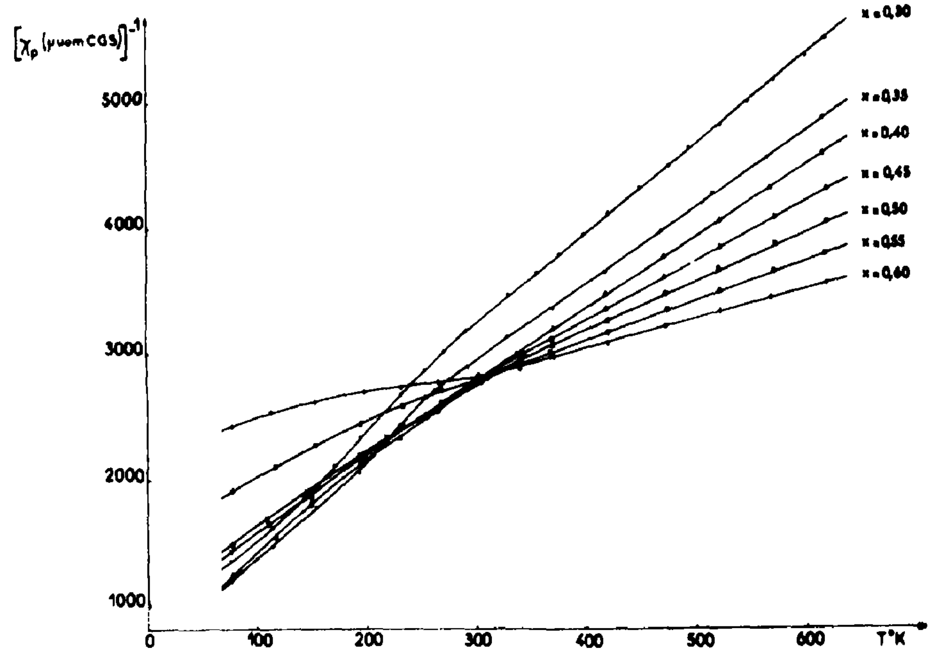

Fig. 1. Variation avec la température de l'inverse de la susceptibilité paramagnétique.

Tableau 1

Compositions	T_M (°K)	C_m	$C_{V^{4+}}$	P_m (μ_B)	θ (°K)
$Cu_{0,30}V_2O_5\beta$	310	0,146	0,488	1,97	−175
$Cu_{0,35}V_2O_5\beta$	300	0,165	0,473	1,94	−195
$Cu_{0,40}V_2O_5\beta$	295	0,183	0,456	1,91	−220
$Cu_{0,45}V_2O_5\beta$	300	0,210	0,468	1,93	−290
$Cu_{0,50}V_2O_5\beta$	310	0,246	0,492	1,98	−380
$Cu_{0,55}V_2O_5\beta$	335	0,316	0,575	2,14	−580
$Cu_{0,60}V_2O_5\beta$	350	0,400	0,666	2,31	−800

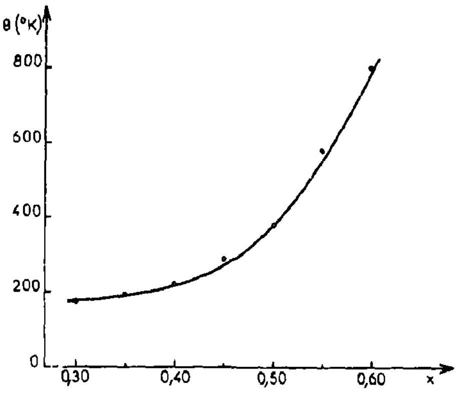

Fig. 2. Variation de la température de Curie en fonction du taux d'insertion.

spin. On pouvait être tenté à première vue d'expliquer cet accroissement brutal de P_m avec x par la formation d'ions cuivriques $Cu^{2+}(d^9)$ dont le nombre augmenterait en fonction du taux d'insertion. L'étude chimique semble exclure une telle possibilité.

Le modèle proposé pour d'autres séries $M_xV_2O_5\beta(M = Na, K)$ (forte localisation des électrons d du vanadium et existence dans le diagramme des corrélations électroniques de multiplets serrés) s'avère satisfaisant pour nos deux séries tant que les valeurs de P_m restent inférieures à $2\mu_B$. Il n'est plus valable lorsque x devient supérieur à 0,50 ($P_m > 2\mu_B$). Cette croissance de P_m correspond à des valeurs anormalement basses du point de Curie qui tend rapidement vers -∞, propriété qui annonce l'apparition d'un paramagnétisme de Pauli.

Il semblerait donc que les phases étudiées évoluent d'un état localisé vers un état métallique lorsque le taux d'insertion augmente. Cette interprétation est confirmée para l'évolution de la susceptibilité molaire χ_p avec x à température donnée (Fig. 4). Les isothermes de susceptibilité χ_p ont toutes tendance à se recouper pour une valeur de x légèrement supérieure à 0,60. Les isothermes qui caractérisent la variation avec x de la susceptibilité molaire par atome de vanadium tétravalent χ_p/x (susceptibilité atomique) devraient de leur côté pratiquement être indépendantes du taux d'insertion dans l'hypothèse d'une localisation. Ce résultat n'est pas confirmé par l'expérience puisqu'en fait les diverses isothermes χ_p/x décroissent linéairement avec x (Fig. 5). Les diverses droites obtenues, à l'exception peut être de l'isotherme obtenue à 77°K, convergent vers la valeur $x = 0,667$ qui correspond à la limite cristallographique supérieure théorique des phases β.

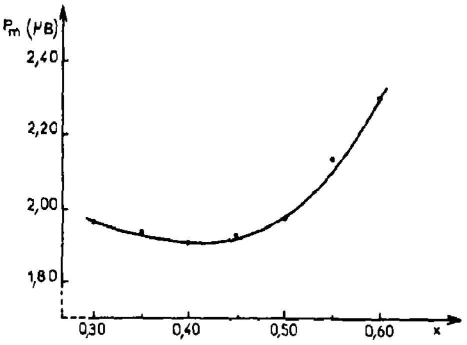

Fig. 3. Variation du moment magnétique effectif en fonction du taux d'insertion.

Cette évolution semble impliquer que la composition $Cu_{0,667}V_2O_5$, si elle existait, possèderait un paramagnétisme indépendant de la température. La valeur de χ_p, qui est de 300 μuem c.g.s. environ, reste cependant supérieure aux valeurs habituellement mises en évidence pour un paramagnétisme de Pauli. Elle suppose une bande de conduction encore étroite.

Lorsque le taux d'insertion x augmente les phases β paraissent donc évoluer effective-

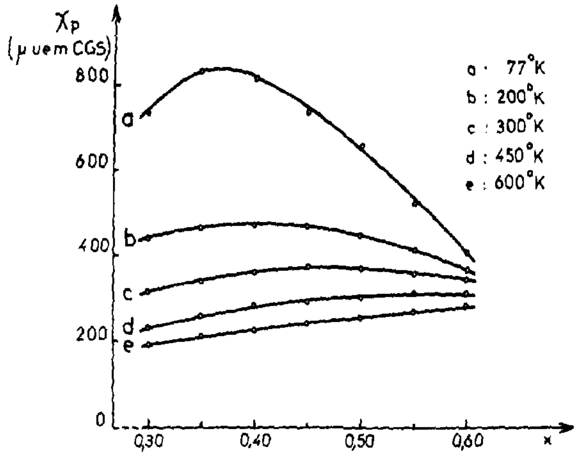

Fig. 4 Variation isotherme des susceptibilités molaires en fonction du taux d'insertion.

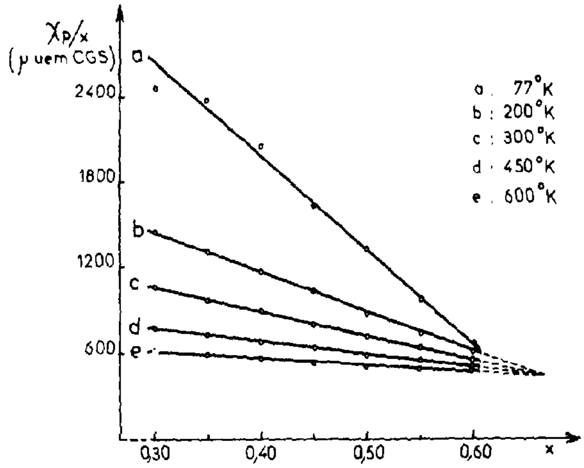

Fig. 5 Variation isotherme des susceptibilités atomiques en fonction du taux d'insertion.

ment d'un état localisé vers un état délocalisé. Ce résultat, qui sera confirmé par les mesures électriques et de chaleur spécifique à basse température est important. Nous ne connaissons pas d'autre exemple de phases comportant un domaine d'existence dans lequel au caractère semi-conducteur se substituent progressivement des propriétés métalliques.

3. CONDUCTIVITE ELECTRIQUE

Les mesures de conductivité ont été effectuées sur une cellule utilisant la méthode des quatre pointes. La conductivité est déterminée pour une très large gamme de températures (de 77° à 800°K) sur des échantillons frittés. L'absence de monocristaux suffisamment gros nous a conduits à préparer des barreaux parallélépipédiques obtenus par compression d'une poudre de granulométrie connue sous $1,5 \times 10^9$. Pascals et frittage prolongé 20°C environ au-dessous du point de fusion. Ce frittage est effectué en ampoule scellée et sous atmosphère d'argon afin d'éviter tout départ d'oxygène. Avant chaque manipulation les échantillons sont dégazés à 300°C sous vide pendant une heure.

La Fig. 6 rassemble les résultats relatifs à l'évolution de la conductivité σ des phases $Cu_xV_2O_5\beta$ avec la température. Pour chaque composition le logarithme de la conductivité varie linéairement avec l'inverse de la température selon une loi de type:

$$\sigma = \sigma_0 \exp\left(-\frac{\Delta E}{kT}\right). \qquad (2)$$

Une telle loi implique un caractère semi-conducteur. Dans la mesure où, comme l'a déterminé Perlstein par mesures d'effet Hall sur $Na_{0,33}V_2O_5$, le nombre de porteurs est constant, ce résultat implique également une variation exponentielle de la mobilité; celle-ci est alors caractéristique d'une conductivité par sauts[15].

Nous déduisons l'énergie d'activation ΔE de la pente des courbes obtenues. ΔE subit une discontinuité à une température T_E qui augmente avec x, mais qui est très éloignée de la température T_M précédemment définie. L'existence d'une cassure vers 95°K pour la composition $Cu_{0,35}V_2O_5\beta$ laisse supposer que le changement de pente se manifeste encore pour la composition $x = 0,30$, mais se situe à une température inférieure à celle de l'azote liquide.

Les énergies d'activation observées sont toujours plus faibles à haute température (ΔE_{HT}) qu'à basse température (ΔE_{BT}). Elle sont rassemblées au Tableau 2. Les valeurs de ΔE_{HT} sont voisines de celles obtenues pour les phases $Na_xV_2O_5\beta$[10–11]. Cette similitude

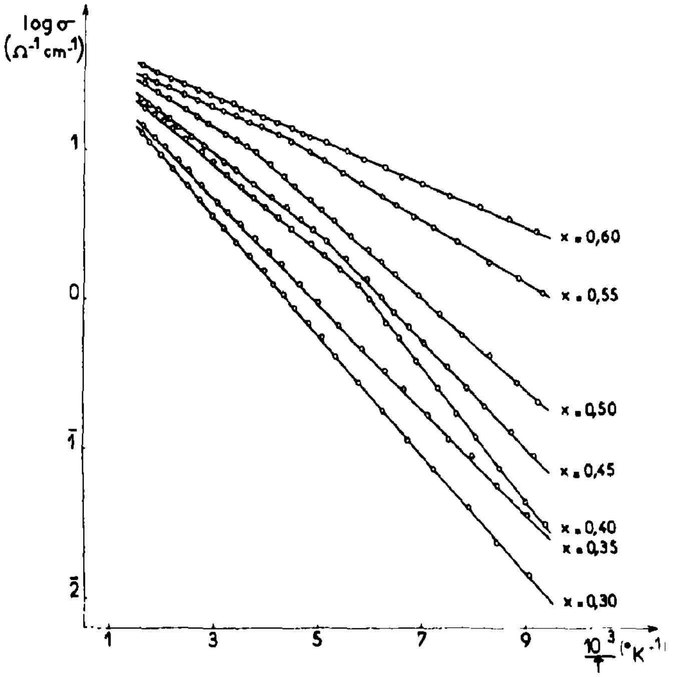

Fig. 6. Variation du logarithme de la conductivité avec l'inverse de la température.

Tableau 2

Compositions	T_L (°K)	E_{BT} (eV)	$\log\sigma(\Omega^{-1}\text{cm}^{-1})$ pour $T = 125$°K	E_{HT} (eV)	$\log\sigma(\Omega^{-1}\text{cm}^{-1})$ pour $T = 400$°K
$Cu_{0,30}V_2O_5\beta$			$\bar{2},56$	$0,076 \pm 0,003$	0,75
$Cu_{0,35}V_2O_5\beta$	95		$\bar{2},95$	$0,068 \pm 0,003$	0,86
$Cu_{0,40}V_2O_5\beta$	175	$0,090 \pm 0,006$	$\bar{1},10$	$0,058 \pm 0,004$	1,04
$Cu_{0,45}V_2O_5\beta$	200	$0,070 \pm 0,005$	$\bar{1},40$	$0,050 \pm 0,003$	1,11
$Cu_{0,50}V_2O_5\beta$	275	$0,057 \pm 0,005$	$\bar{1},73$	$0,039 \pm 0,002$	1,26
$Cu_{0,55}V_2O_5\beta$	235	$0,039 \pm 0,003$	0,36	$0,030 \pm 0,002$	1,36
$Cu_{0,60}V_2O_5\beta$		$0,023 \pm 0,002$	0,65	$0,023 \pm 0,002$	1,42

des énergies d'activation implique que le mécanisme de conduction ne dépend pas de la nature de l'élément inséré mais du squelette de composition $(V_2O_5)_n$ qui capte l'électron *s* introduit avec chaque atome *M*.

Les énergies d'activation à basse et haute température diminuent de manière sensiblement linéaire (Fig. 7). Elles s'écrivent:

$$\Delta E = -ax + b. \qquad (3)$$

A l'aide de cette relation, nous avons calculé les valeurs de *x* pour lesquelles s'annuleraient ΔE_{HT} et ΔE_{BT}. Ces valeurs (respectivement $x = 0,67$ et $x = 0,72$) correspondraient pour des monocristaux à une conduction de type métallique; elles ne diffèrent pas sensiblement de la valeur limite $x = 0,667$ qui répond au maximum d'insertion au sein de la phase β. Si on tient compte du fait qu'une phase de caractère métallique peut comporter à l'état pulvérulent une conductivité croissant avec la température par suite de la présence d'une faible énergie d'activation due en fait à l'existence de joints de grains, ce résultat implique que la conductivité devient métallique dès lors que *x* est suffisamment élevé. Une telle remarque confirme l'étude magnétique précédente.

Le report de la relation (3) dans l'équation (2) se traduit pour une température donnée par une variation linéaire de $\log\sigma$ avec le taux d'insertion *x*:

$$\log\sigma = a'x + b'. \qquad (4)$$

Les isothermes de variation du logarithme de la conductivité obéissent pratiquement à une loi de ce type: l'écart maximal n'est que de 0,2 unités logarithmiques par exemple pour l'isotherme à 125°K (Fig. 8). L'existence d'une relation linéaire du type (4) constitue une justification certaine de l'utilisation de barreaux frittés pour les mesures de conductivité à condition de considérer leurs variations relatives et non pas leurs valeurs

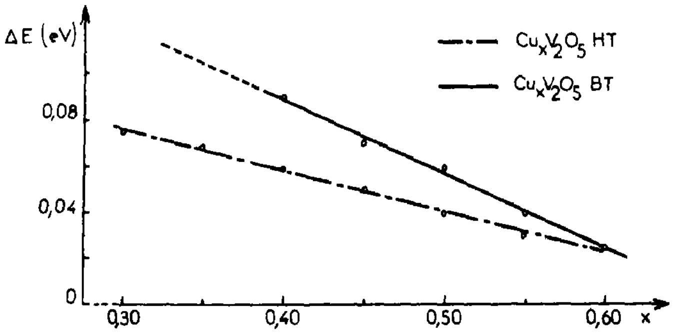

Fig. 7. Variation des énergies d'activation en fonction du taux d'insertion.

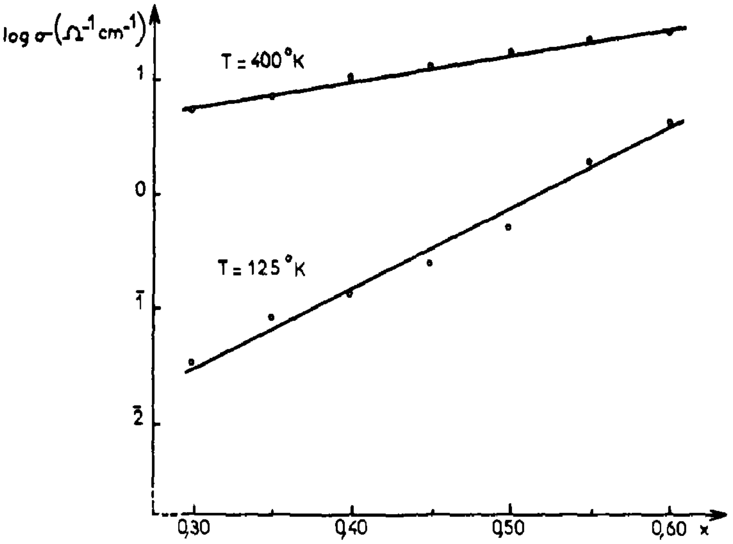

Fig. 8. Variation isotherme du logarithme de la conductivité en fonction du taux d'insertion.

absolues. Ce résultat ne saurait nous faire oublier en effet le rôle important que jouent les résistances de joints de grains. Comme nous l'avons déjà fait remarquer, elles inhibent fortement la conductivité (Perlstein a mesuré par exemple des conductivités sur monocristal cent fois supérieures aux nôtres pour des compositions voisines), elles sont susceptibles également d'entrainer une légère augmentation de l'énergie d'activation.

L'accroissement du taux d'insertion x du métal, dont le corollaire est l'augmentation du nombre d'atomes de vanadium porteurs d'électrons d, entraine une attraction plus faible des ligandes oxygénés et par conséquent un abaissement de la barrière de potentiel qui piège ces électrons d. Dans la mesure où l'énergie d'activation ΔE correspondrait sensiblement à l'énergie nécessaire pour effectuer un saut entre atomes de vanadium à travers cette barrière selon le mécanisme proposé par Galy, Casalot et Pouchard pour les phases $Na_xV_2O_5\beta$[16], cette décroissance de ΔE avec x s'expliquerait ainsi très logiquement.

Dans l'état de nos connaissances, nous considèrerons que ce mécanisme de conduction par sauts évolue sans discontinuité apparente vers une conduction de type métallique.

4. POUVOIR THERMOELECTRIQUE

A température ambiante le pouvoir thermoélectrique α des phases $M_xV_2O_5\beta$ (M = Na, Cu, Ag) ne dépend pratiquement que du taux d'insertion x (Fig. 9).

La valeur que nous obtenons pour la composition $Na_{0,33}V_2O_5$ ($\alpha = -116\,\mu V/°K$) est intermédiaire entre celles mesurées par Ornatskaya ($\alpha = -100\,\mu V/°K$)[7] et Perlstein ($\alpha = -136\,\mu V/°K$)[10]. La valeur négative de α implique que pour les phases β les porteurs de charge sont des électrons et que la conductivité est donc de type n. La valeur absolue élevée est typique d'autre part pour un semi-conducteur.

Goodenough a proposé une relation pour relier α à la concentration c en porteurs de charge par l'intermédiaire de l'entropie thermique S^*[17]:

$$\alpha = -\frac{k}{e}\left[\frac{S^*}{k} + \mathrm{Log}\left(\frac{1-c}{c}\right)\right]. \qquad (5)$$

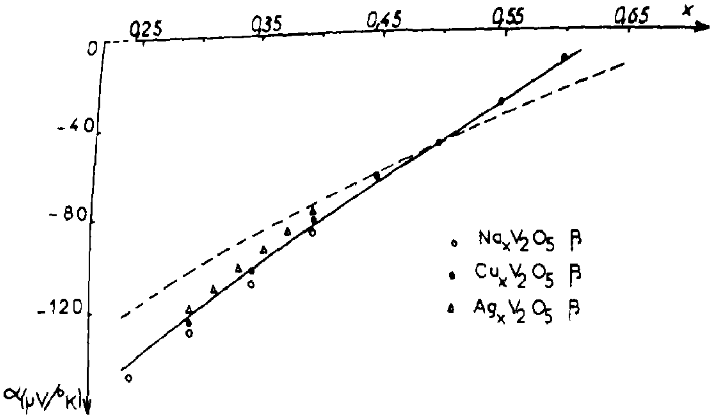

Fig. 9 Variation du pouvoir thermoélectrique des phases $M_xV_2O_5\beta$ à 300°K en fonction du taux d'insertion

La concentration en électrons par atome de vanadium est égale à $x/2$ puisque Perlstein a montré par mesures d'effet Hall pour les phases $Na_xV_2O_5\beta$ que le nombre de porteurs est égal au nombre d'électrons d[10]. Le pouvoir thermoélectrique varierait donc selon une relation du type:

$$\alpha = A + B \operatorname{Log}\left(\frac{2-x}{x}\right). \qquad (6)$$

Nous avons déterminé empiriquement les valeurs des constantes A et B à partir de la valeur du pouvoir thermoélectrique de $Cu_{0,50}V_2O_5$. La courbe théorique ainsi obtenue, que nous avons mentionnée en pointillé sur la Fig. 9, ne coincide pas en fait avec les valeurs expérimentales. La courbe en trait plein qui correspond à la formule (5), mais où c représente le nombre x de porteurs de charge est par contre en plein accord avec les données de l'expérience.

Cette contradiction entre la relation de Goodenough établie pour des semi-conducteurs extrinsèques et nos valeurs expérimentales exclut donc ce type de conduction. Il semble que cette relation aurait besoin d'être adaptée pour que sa validité s'étende aux semi-conducteurs par sauts; la relation que nous proposons a toutefois l'avantage de faire intervenir le nombre d'électrons qui est proportionnel à x, et le nombre de sites disponibles lui-même proportionnel à $1-x$.

La diminution de la valeur absolue de α avec le taux d'insertion, qui tombe à 12 μV/°K pour $Cu_{0,60}V_2O_5$ confirme en tout cas le passage progressif de propriétés semi-conductrices à un caractère métallique.

La variation avec la température du coefficient de Seebeck des phases $M_xV_2O_5\beta$ est conforme à la théorie établie par Heikes pour les semi-conducteurs par sauts[15]. Dans de tels matériaux α dépend des constantes thermodynamiques:

$$\alpha = \frac{k}{e}\left[\frac{\Delta H - T\Delta S}{kT} + Cte\right]. \qquad (7)$$

Les mesures ont été effectuées à diverses compositions (Fig. 10).

Tant que la température T est relativement faible le terme $T\Delta S$ est négligeable devant le terme enthalpique; α varie alors proportionnellement à l'inverse de la température. Lorsque ce terme devient prépondérant par suite de l'accroissement de la température le pouvoir thermoélectrique est indépendant de T. Ce changement de mécanisme s'effectue assez brutalement et à une température d'autant plus basse que le nombre de porteurs est plus élevé.

Nous ne connaissons pas en fait l'influence

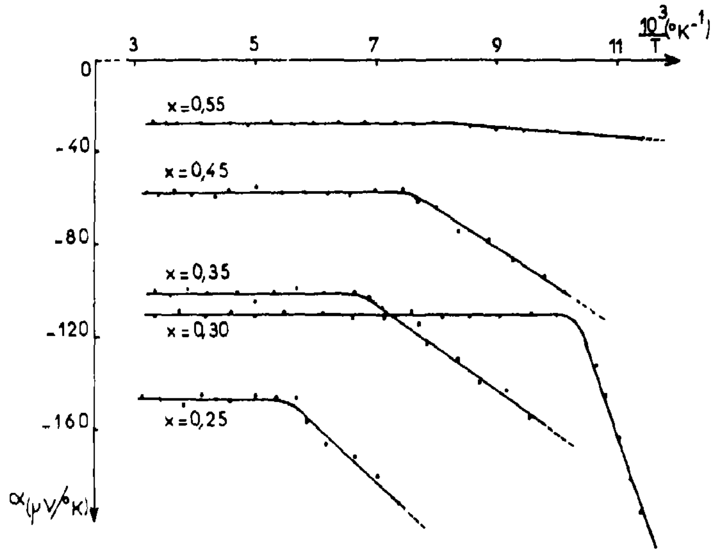

Fig. 10 Variation du pouvoir thermoélectrique avec l'inverse de la température

du taux d'insertion donc du nombre de porteurs de charge sur les diverses grandeurs thermodynamiques. Leur détermination quantitative que ne permet pas pour le moment la théorie de Heikes apporterait une confirmation à notre hypothèse et validerait sans ambiguité aucune la théorie de la semi-conduction par sauts.

5. DENSITE D'ETATS AU NIVEAU DE FERMI

Des mesures de chaleur spécifique effectuées à des températures comprises entre 1, 5° et 10°K environ[†] semblent suivre avec la température une loi de type:

$$C = \gamma T + \beta T^3. \qquad (8)$$

L'existence d'une ordonnée à l'origine γ non nulle correspond à une valeur très élevée de la densité d'états au niveau de Fermi $n(E_F)$. Ce résultat implique pour les bronzes $\mathrm{Cu}_x\mathrm{V}_2\mathrm{O}_5\beta$ l'existence d'une bande de conduction particulièrement étroite.

La diminution progressive de la densité d'états pour des taux d'insertion élevés nous incite cependant à admettre un élargissement progressif de la partie occupée de la bande de conduction (Fig. 11).

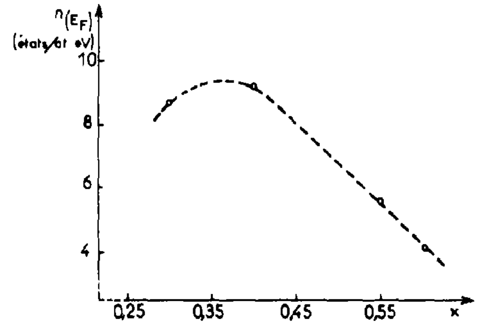

Fig. 11. Variation de la densité d'états au niveau de Fermi en fonction du taux d'insertion.

Cette première étude est trop fragmentaire pour permettre la détermination du profil exact de la bande de conduction en fonction du taux d'insertion, mais elle confirme la complexité des mécanismes de conduction dans les bronzes oxygénés de vanadium.

[†] Cette étude a été réalisée au Laboratoire de Physique des Solides de la Faculté des Sciences d'Orsay grâce à l'aimable collaboration de M. Jacques Bonnerot et de M. Jean-Pierre Mercurio.

6. DISCUSSION

Les diverses propriétés physiques étudiées permettent de conclure qu'au fur et à mesure qu'augmente au sein des phases β le taux d'insertion se produit une évolution progressive d'un mécanisme de semi-conduction par sauts vers des propriétés métalliques, l'apparition d'une délocalisation électronique pouvant être attribuée à l'élargissement progressif dans la structure de bandes d'une bande de conduction partiellement remplie.

L'étude structurale des phases $M_xV_2O_5\beta$ révèle que les atomes de vanadium occupent deux types de sites: ils sont soit en positions octaédriques déformées (sites A) soit en positions bipyramidales (sites B). Les plus courtes distances entre atomes de vanadium proches voisins varient selon la nature de ces sites: les distances A–A sont de 3,12 Å, les distances B–B de 3,01 Å, les distances A–B de 3,14 Å. Les volumes respectifs de la bipyramide et des octaèdres laissent présager une prédominance du vanadium tétravalent dans les sites A[18].

La distance critique R_c de Goodenough, valeur limite en-dessous de laquelle un recouvrement direct des orbitales t_{2g} d'un élément de la première série de transition conduit à une délocalisation électronique, est de 2,87 Å pour le vanadium tétravalent dans un site octaédrique[19]. Toutes les distances vanadium–vanadium s'avérant supérieures à cette valeur critique, nous ne pouvions nous attendre a priori à une conductivité métallique de ce type.

Une théorie de Goodenough justifie cependant les propriétés métalliques de quelques composés oxygénés des éléments de transition T pour lesquels les distances interatomiques cation–cation sont supérieures à R_c. Cette théorie envisage la possibilité d'un recouvrement indirect des orbitales d de cations voisins par l'intermédiaire d'orbitales p_π de l'oxygène. Un tel mécanisme qui s'applique aux bronzes de vanadium exige la réalisation simultanée de deux conditions[20]: (a) L'atome d'oxygène considéré ne doit engager au maximum que trois liaisons σ avec les atomes métalliques les plus proches; il faut, en effet, qu'une au moins des orbitales de l'oxygène soit disponible pour l'établissement d'une liaison π dans les chaînons T–O–T. A l'orbitale moléculaire π liante qui en résulte correspond une orbitale moléculaire π^* anti-liante susceptible de s'étendre sur tout le réseau. (b) Le nombre d'électrons anti-liants n_e par cation doit être inférieur à trois, de manière à ce que cette bande π^* son soit pas totalement remplie.

Plusieurs atomes d'oxygène (Fig. 12) sont susceptibles de former des liaisons π avec les orbitales d_{t2g} du vanadium dans la mesure où le polyèdre oxygéné peut être assimilé à un octaèdre non déformé (symétrie O_h). Si les chaînons V–O–V restent très isolés dans les directions de l'axe a, ils s'allongent par contre d'une manière continue dans la direction de l'axe de croissance b et pourraient donner ainsi naissance à une bande π^* antiliante. Compte-tenu des distorsions importantes qui existent dans la structure des phases β, cette bande semble être la seule qui puisse éventuellement constituer une bande de conduction. Les distances V–O n'étant pratiquement pas modifiées lorsque le taux d'insertion évolue, la largeur de cette bande est indépendante de la composition.

Or les diverses mesures physiques ont révélé le passage progressif d'un mécanisme de conduction par sauts à une conduction de type métallique, autrement dit de niveaux d'énergie discrets à une bande partiellement remplie dont la partie occupée est d'autant plus large que le nombre de porteurs est plus élevé.

Lorsque x est faible les niveaux occupés de la bande de conduction constituent une zone extrêmement étroite par suite du petit nombre d'atomes de vanadium porteurs de charge. Ces porteurs d'électrons d sont isolés les uns des autres et n'ont que peu de chances d'entrer statistiquement en interaction.

Le passage des électrons d sur des vanadiums résulte de l'agitation thermique et de son action sur le réseau. Chaque électron n'est

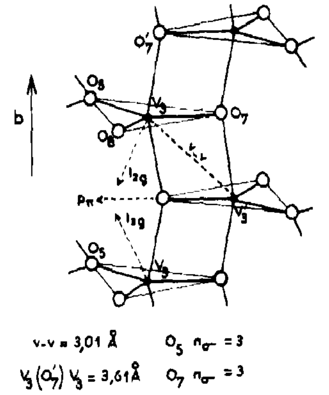

Chaînes bipyramidales (sites B)

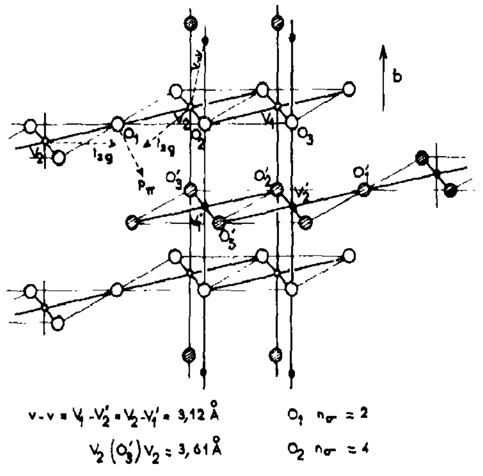

Chaînes octaèdriques (sites A)

Fig. 12. Possibilités schématiques de recouvrement des orbitales dans les chaines bipyramidales et octaédriques de la phase $Cu_xV_2O_5\beta$.

donc délocalisé qu'à courte distance, sur quelques atomes de vanadium proches voisins. Les domaines qui se forment ainsi au sein des chaînes V–O–V parallèles à l'axe *b* sont pratiquement isolés les uns des autres. La conduction résulterait de sauts électroniques entre ces divers chaînons par-delà une barrière de potentiel. Les sauts exigent alors une énergie d'autant plus faible que ces chaînons sont plus nombreux, donc plus rapprochés.

La croissance du taux d'insertion implique un accroissement simultané du nombre de vanadiums tétravalents, donc de celui des électrons 3*d*. Le nombre de chaînons de délocalisation croissant parallèlement, la probabilité de rencontre de ces chaînons, et par conséquent leur extension, augmente également. Il en résulte que les possibilités d'interactions au sein de ces chaînons s'accroissent. Ce phénomène explique l'élargissement progressif de la partie occupée de la bande de conduction au fur et à mesure que la délocalisation devient importante (Fig. 13). Les mesures de chaleur spécifique montrent que cette extension graduelle coincide avec une diminution de la densité d'états au niveau de Fermi.

ΔE est théoriquement nul lorsque la délocalisation de l'électron *d* est totale le long de l'axe *b*. Dans un monocristal nous devrions observer alors une conductivité métallique, si cette bande n'est pas complètement remplie. Des mesures d'anisotropie électrique ef-

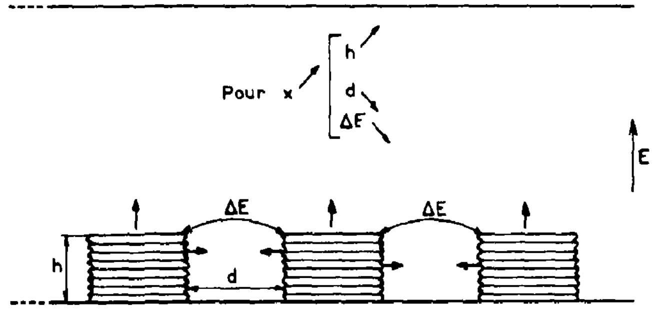

Fig. 13. Evolution du remplissage de la bande de conduction par accroissement du taux d'insertion.

fectuées sur des monocristaux des phases $M_xV_2O_5\beta$ seraient seules susceptibles de montrer que la conduction s'effectue préférentiellement le long de l'axe *b*. Le passage progressif du caractère semiconducteur à une conduction de type métallique laisse supposer que dans le réseau l'un au moins des trois sites relatifs au vanadium est occupé préférentiallement: pour $x = \frac{2}{3}$ un tiers seulement des vanadiums disponibles est susceptible en effet de fournir un électron *d*.†

REFERENCES

1. BRIDGMANN P. W., *Proc. Am. Acad. Arts Sci* **79**, 127 (1951).
2. HAEMERS J., *C.r. hebd. Séanc. Acad. Sci., Paris* **259**, 3740 (1964)
3. PATRINA I. B. et IOFFE V. A., *Fiz. Tverd. Tela* **6**, 3227 (1964).
4. DIMITRIEVA L. V., IOFFE V. A. et PATRINA I. B., *Fiz. Tverd. Tela* 7, 2754 (1965).
5. CASALOT A., CAZEMAJOR H., HAGENMULLER P., POUCHARD M. et ROCH J., *Bull. Soc. chim. Fr* 1, 85 (1968).
6. FLOOD H., KROG T. et SØRUM H., *Tidss. Kr. Kjemi Bergv. Met.* **3**, 36 (1946).
7. ORNATSKAYA E. I., *Fiz. Tverd. Tela* **6**, 1254 (1962).
8. SOHN J. B., thèse de Doctorat, Université de Cornell (1965).
9. GENDELL G., COTTS R. et SIENKO M. J., *J. chem. Phys.* **37**, 220 (1962).
10. PERLSTEIN J. H., thèse de Doctorat, Université de Cornell (1967).
11. POUCHARD M., CASALOT A., VILLENEUVE G. et HAGENMULLER P., *Mat. Res. Bull.* **2**, 877 (1967).
12. CASALOT A., DESCHANVRES A., HAGENMULLER P. et RAVEAU B., *Bull. Soc. chim. Fr* **6**, 1730 (1965).
13. GROSSMAN G., PROKURENKO O. W. et ARIJA S. M., *Z. anorg. allg. Chem.* **305**, 121 (1960).
14. CASALOT A., *Bull. Soc. chim. Fr.*, **3**, 725 (1969).
15. HEIKES R. R. et JOHNSTON W. D. *J. chem. Phys.* **26**, 582 (1957)
16. GALY J. CASALOT A. et POUCHARD M., *Liaisons Inter Atomiques et Proprietés Physiques des Composés Mineraux*. Sedes, Paris (1969).
17. GOODENOUGH J. B., *Czech. J. Phys.* **17B**, 304 (1967).
18. WADSLEY A. D., *Acta crystallogr.* **8**, 695 (1955).
19. GOODENOUGH J. B., *J. appl. Phys.* **37**, 1415 (1966).
20. GOODENOUGH J. B., *Bull. Soc. chim. Fr.* **4**, 1200 (1965).

---

†La Direction des Recherches et Moyens d'Essais nous a aidé matériellement pour ce travail

J. Phys. Chem. Solids Pergamon Press 1969. Vol. 30, pp. 1353-1374. Printed in Great Britain.

THE CREATION OF *F* CENTERS IN LITHIUM FLUORIDE BETWEEN 77° AND 600°K AND THEIR INTERPRETATION BY A RECOMBINATION MODEL OF INTERSTITIAL-VACANCIES

P. DURAND*, Y. FARGE† and M. LAMBERT
Laboratoire de Physique des Solides‡, Faculté des Sciences d'Orsay, Bat 210, Orsay, 91 France

(*Received* 18 *November* 1968)

Abstract – In pure LiF crystals, the number of *F* centers generated by X-ray irradiation between 200° and 600°K is proportional to the square root of the irradiation time. At room temperature, for the same irradiation time, the number of *F* centers increases proportionately to the square root of the radiation intensity. At irradiation temperatures higher than 400°K a fraction of *F* centers clusters to form large agglomerates observable by small angle X-ray scattering. One assumes that the radiation creates KI Frenkel pairs per unit time (I being the radiation intensity) and that interstitials thus created diffuse towards *F* centers or towards traps which are assumed to be agglomerates of interstitials: the calculation leads to a generation law of *F* centers proportional to $(It)^{1/2}$ in good agreement with experimental results. One thus verifies this model by studying the disappearance of *M* centers by X-ray irradiation below 250°K: such a bleaching occurs through trapping of free interstitials by these centers.

INTRODUCTION

THE IONIZING radiations in alkali halides displace halogen ions by a mechanism not yet clearly explained, which we shall call the primary process. To this process, are added other processes depending strongly on the temperature of irradiation and bound to the mobility of the defects created (H, H', V_K, α, F centers, etc...)[1, 2].

At low temperature (4°K), the generated defects are stable[2]: it is thus possible to indirectly study the primary process by observing the kinetics of formation of the various generated centers. Numerous hypothesis have been made on this process. The first one, due to Seitz[3] and presently abandoned, suggested that vacancies are generated from dislocations. The second one, proposed by Varley[4], invokes a multiple ionization of a halogen ion and its ejection into an interstitial position. The third one, developed by Klick [5] and by Williams[6] uses the simple ionisation of two neighbouring halogens. Finally, the last one, actually the most probable one, has been simultaneously proposed by Pooley [7] and Hersch[8]: the primary process would be due to an electron-hole recombination. This recombination can be radiative without creation of *F* centers; it can also be non radiative and the energy thus released to the lattice gives rise to a Frenkel pair. The yield of this primary process varies with temperature as the probability of the non radiative recombination increases strongly with temperature.

At higher temperature and in particular at room temperature, the effects are much more complex due to the mobility of the H, H', V_K, and α centers. In general, near 300°K, one considers two distinct stages of generation of *F* centers as a function of the time of irradiation: a stage of rapid generation followed by a slow one[9]. According to all publications[2], it appears that the first stage is due to the presence of impurities in the crystals, the second one being more intrinsic. The influence of impurities is such that it is necessary to study very pure crystals with concentrations of F centers greater than the residual concentration of impurities if one wants to reach the intrinsic creation of F centers at room temperature. Very few studies have been made in this range of concentrations. Srinavisan and Compton[10] in KCl purified by zone melting have not observed the first stage. Etzel and Allard[11] in the purest NaCl crystals have not observed it either. Sonder and Templeton[12] have studied the saturation which appears for strong concentrations in KCl $\approx 4 \times 10^{18}$ F centers per cc.

**Present address:* Laboratoire de Recherches de l'EDF, 92 Fontenay aux Roses, France.

†*Present address:* Laboratory of Atomic and Solid State Physics Cornell University, Ithaca, N.Y. 14850, U.S.A.

‡Associé au CNRS.

Such studies performed essentially on KCl crystals have never been done on LiF samples. Like other alkali halides, lithium fluoride can be colored with X-rays, γ-rays or far ultraviolet[13]. By X-rays irradiation one observes essentially defects of the Frenkel type[14]. Other studies have been published on this question[15, 16], but they are in general old and have been performed on fairly impure crystals with small doses of irradiation.

To reach the intrinsic creation of F centers between 77° and 600°K, we have studied the formation of F centers in pure samples with large concentration of F centers (5×10^{17} to 10^{19} F centers per cc). We have thus been able to interpret our experimental results in terms of an interstitial-F centers recombination model.

ORIGIN OF SAMPLES AND EXPERIMENTAL TECHNICS

All samples used have been cleaved from the same Harshaw block. Ionic conductivity and flow-stress measurements* have been done at the laboratory: the crystals have a very low impurity concentration. These results are close to the analysis of Klick and his coworkers[17] on LiF samples of the same origin, the only impurity present with an appreciable concentration being oxygen†. Taking no account of oxygen, we can consider that our samples were extremely pure (impurity concentration lower than 5 ppm). The Harshaw block has been slightly irradiated with γ-rays to be cleaved; samples were plates of 15/100 to 25/100 mm thickness. They have been thermally bleached during one hour near 500°C.

Irradiations[18, 19]

Crystals have been irradiated with non-filtered X-rays with a copper tube (or molybdenum) at 45 KV and 8 mA. Samples were at 4 cms from the anticathode. In irradiations at temperatures lower than room temperature, the sample was in vacuum and brought into contact with the cool part of a cryostat filled with a cooling liquid. In this case, optical absorption has been measured at the same temperature as the irradiation temperature. Irradiations at temperatures between 300° and 500°K have been made in an apparatus with oil circulation, the temperature of oil being regulated with a water bath. Finally, above 500°K we have used a small furnace. In these last cases, optical absorption of samples has been measured at room temperature.

Optical measurements

Optical measurements have been done with a Cary 14 spectrometer and the number of F centers calculated with the Smakula's formulae. In the case of high concentrations, it is not possible to measure the absorption at the top of the F band: for each temperature we have measured the wavelength where the optical absorption is one half the absorption at the top of the F band. We have thus extrapolated the F band absorption. The error introduced is not larger than the error due to the measurements of the crystal thickness: to obtain high F center concentrations, we have studied very thin crystals and we have introduced an important relative error on the thickness measurements (this last error is systematic and does not vary with the X-ray dose for a given sample).

---

*Cagnon has observed a flow-stress of 80 g per mm^2 in non-irradiated samples[20].

†We have effectively measured in the near infrared an absorption band at 2·7 μ which could be correlated to the O_2 impurity[21].

In all cases, the number of complex centers of small size (M, R, N_2) was much less than the number of F centers. The number of M centers, the most numerous, was less than 8 per cent of the number of F centers: for example, in a sample irradiated 181 hr at 50°C*, $1{\cdot}02\times10^{19}$ F centers per cc have been formed with only $7{\cdot}5\times10^{17}$ M centers per cc. The M center absorption gives an absorption band in the F band equal to 70 per cent of the absorption of two F centers[22]: the correction to obtain the exact number of F centers (isolated + coagulated into M centers) would be no larger than 5 per cent. Such a correction, which is of the order of magnitude of the experimental error, has not been made.

Study of clusters by small angle X-ray scattering

Large clusters of F centers are in fact aggregates of lithium atoms whose electronic density is very low compared with the density of the whole crystal. When the size of clusters is between five and a few hundred angstroms, they can be studied by small angle X-ray scattering. A beam of monochromatic X-rays of wavelength λ with normal incidence to the surface of the LiF crystal is scattered by F center clusters (Fig. 1). If these defects have a relatively uniform size, the scattering curve can be approximated by a gaussian in the domain of small angles[24]. The scattering power† is written:

$$I(\epsilon) = N(\rho-\rho_0)^2V^2\exp\left(-\frac{4\pi^2R^2\epsilon^2}{3\lambda^2}\right) \quad (1)$$

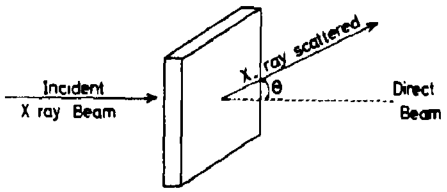

Fig. 1. Small angle scattering of X-rays.

N being the number of aggregates of volume V, $\rho-\rho_0$ being the difference between electronic densities of aggregate and crystal, R being the radius of gyration of an aggregate.

From the analysis of experimental curves, one can determine: (1) their radius a which for spherical aggregates is

$$a = (5/3)^{1/2}R \quad (2)$$

(2) the total number of aggregates per unit volume of the crystal.

One can deduce from these two results the number of F centers included in these clusters that is to say the equivalent concentration of F centers per unit volume.

In the case of small clusters, the scattering power is very low. It is necessary to use an extremely sensitive apparatus: measurements have been performed with the apparatus built by Levelut[25] using the CuK$_\alpha$ radiation ($\lambda = 1{\cdot}54$ Å).

1. FIRST PART—EXPERIMENTAL RESULTS

(1) *F center creation at room temperature*

At room temperature, the number of F centers increases proportionately to the square root of the irradiation time in a concentration domain included between 5×10^{17} and 1×10^{19} F centers per cc (Figs. 2 and 3). For a given irradiation time, the number of F center created is proportional to the square root of the radiation intensity (Fig. 4).

(2) *F center creation at temperatures larger than 300°*K

The creation law $N_F = Kt^{1/2}$ is always observed in samples irradiated above room temperature (Fig. 5). The constant K varies

---

*The efficiency of the M centers formation is the largest[23] at that temperature.

†The scattering power is the ratio of the intensity scattered by the sample to the intensity scattered by one electron in the same experimental conditions.

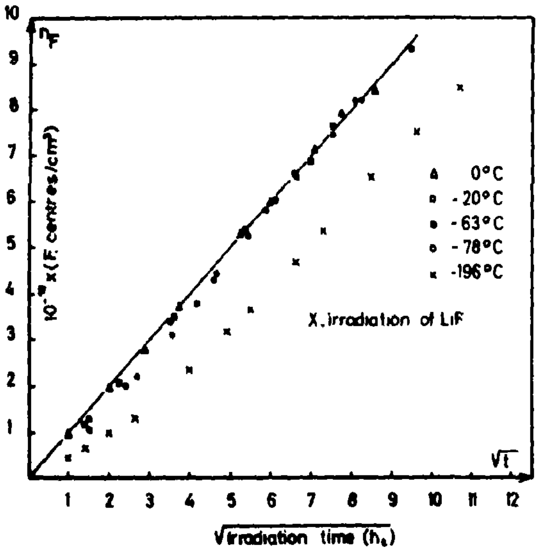

Fig. 7. Variations of the number of F centers vs the square root of the irradiation time in LiF crystals X-irradiated below room temperature

is 420°K. The optical absorption observed at 5000 Å by thermal bleaching at 530°K of LiF irradiated at room temperature[26] becomes visible at 480°K and is important at 520°K (Fig. 8): we have suggested that this band could be due to an electron excess color center larger than the N center; such a suggestion seems confirmed by the formation of this defect by irradiation at high temperature. On Fig. 9, we have represented the optical density of the top of the absorption bands for each complex color center versus the irradiation temperature after an irradiation time of 60 hr.

Measurements by small angle X-ray scattering: optical methods do not permit the observation of large aggregates of F centers. But we have shown that small angle X-ray scattering can give this information on these aggregates. This method is much less sensitive than optical method: for each irradiation temperature, we have just studied the more strongly irradiated samples. Experimental results are represented on Fig. 10*; in ordinate the scattering power taken back to one per molecule of LiF, i.e. with the gaussian approximation

$$f(\epsilon) = x(\rho-\rho_0)^2V^2\exp\left(-\frac{4\pi^2R^2\epsilon^2}{3\lambda^2}\right) \quad (3)$$

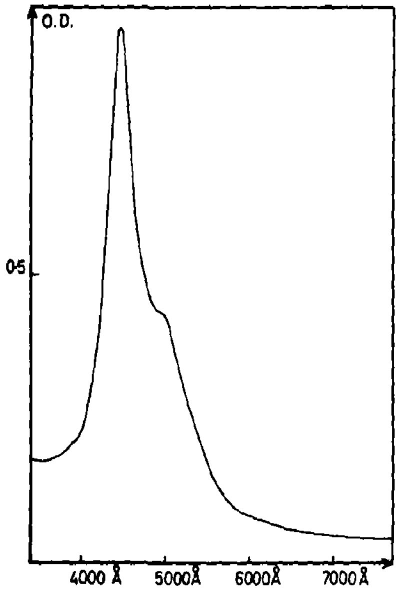

Fig. 8. Optical absorption spectrum of LiF crystal irradiated at 520°K

---

*We thank Mrs Dartyge who has performed these experiments.

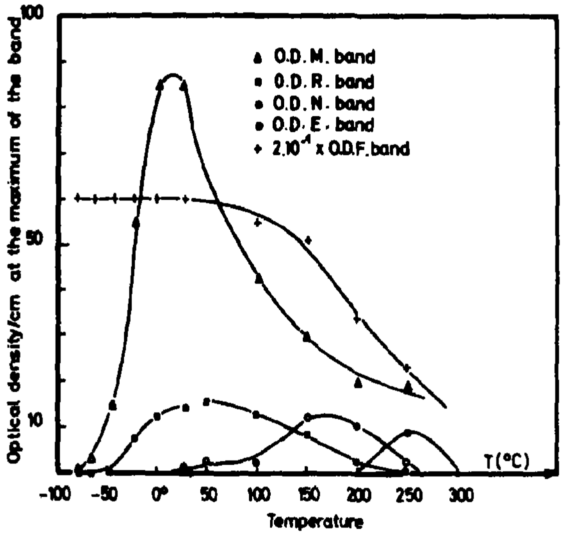

Fig 9. Optical density of the top of the absorption band for each complex color centers vs. the irradiation temperature after an irradiation time of 60 hr

x being the ratio of the number of clusters versus the number of LiF molecules in the same volume of crystal.

When irradiation temperature is higher than 420°K, large aggregates of *F* centers appear and their size is relatively uniform: the scattered intensity obeys Guinier's law (Fig. 11), so that we can determine in the same time the size and the number of aggregates. In Table 1 we have brought together all the results obtained as a function of temperature and irradiation time.

One can see that the total number of *F* centers created at high temperature (isolated +

Table 1. *Aggregates of* F *centers formed by irradiation*

Irradiation temperature	473°K	523°K	593°K
Irradiation time (hr)	116	238	123
Number of isolated *F* centers per cc (optical measurements)	$5{\cdot}9 \times 10^{18}$	$5{\cdot}9 \times 10^{18}$	$2{\cdot}3 \times 10^{18}$
Size of aggregates (Å)	10	11·7	14·6
Number of *F* centers in one aggregate	262	427	820
Number of agglomerated *F* centers per cc	2×10^{18}	$3{\cdot}3 \times 10^{18}$	$6{\cdot}1 \times 10^{18}$
Total number of *F* centers (isolated + clustered)	$7{\cdot}9 \times 10^{18}$	$9{\cdot}2 \times 10^{18}$	$8{\cdot}4 \times 10^{18}$
Number of *F* centers formed in the same conditions at 300°K	$1{\cdot}05 \times 10^{19}$	$1{\cdot}47 \times 10^{19}$	$1{\cdot}06 \times 10^{19}$
Number of agglomerates per cc	$0{\cdot}76 \times 10^{16}$	$0{\cdot}77 \times 10^{16}$	$0{\cdot}74 \times 10^{16}$

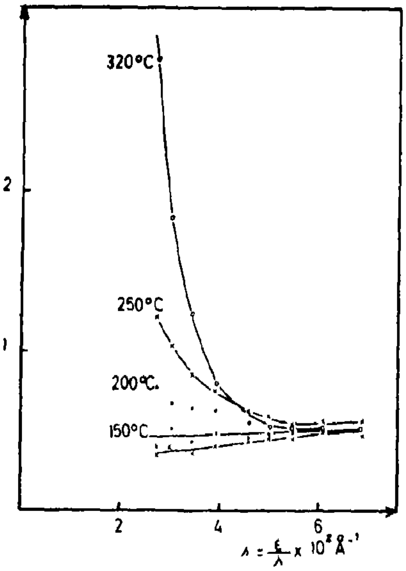

Fig. 10 The scattering X-ray power vs. scattering angle in samples X-irradiated at several temperatures

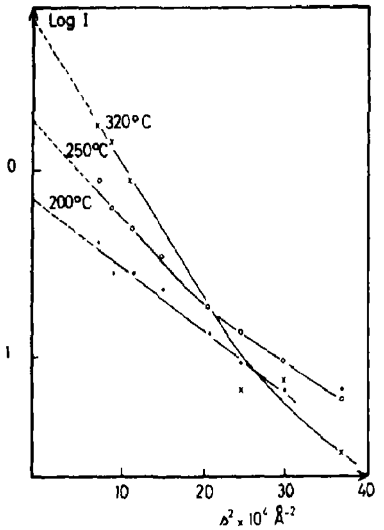

Fig. 11 Observation of a Guinier's law for the scattered intensity in the three samples of Fig. 10.

clustered) is approximately the same as the number of F centers which are formed at room temperature when no clustering effect is present. One can also observe that the number of clusters is the same in the three cases ($\simeq 0{\cdot}76 \times 10^{16}$ per cc) though their sizes are different. This experimental result seems to indicate that they are not randomly formed, but grow on determined sites of the crystal (impurities or other defects).

2. SECOND PART–INTERPRETATION OF THE RESULTS IN A RECOMBINATION MODEL OF INTERSTITIALS WITH *F* CENTERS AND TRAPS

We have experimentally obtained a simple law of F center generation in the vicinity of room temperature: $N_F = K\sqrt{(It)}$. This generation proportional to the square root of the irradiation time has already been observed in other alkali halides, as reported by Goldstein[27] for potassium iodide irradiated with ultraviolet. Similarly, if one reconsiders certain experimental results, one notices that some growth curves are parabolic: Etzel and Allard[11] in natural NaCl crystals (Baden); Srinavisan and Compton[10] in KBr purified by zone melting; Rabin and Klick[28] in pure NaCl; Sonder and Templeton[12] in pure KCl before saturation. It then appears that the law which we observed in LiF in the range of strong concentrations would be a general and intrinsic law as it has only been observed in the purest samples.

In order to interpret these results, it is necessary to conceive a formation process leading to a generation rate of F centers inversely proportional to the number of F centers present in the crystals ($dN_F/dt \propto 1/N_F$). Goldstein[27] with Pooley's hypothesis has proposed a mechanism based on the alteration of the primary process due to F centers already created. This suggestion has the disadvantage of not taking into account interstitials mobile at this temperature (cf. the Ueta's results[29]). Varley[30] tried for the first time to take into account the recombination of interstitials and F centers: the F centers created after irradiation correspond to a certain number of interstitials trapped on the dislocations or grain boundaries. His model leads to a generation of F centers proportional to the square root of t, but it appears that the number of dislocations is insufficient to explain the high F center concentrations which one can obtain. By analyzing experimental data from a similar point of view we shall show that interstitials recombine with *F* centers. In order to establish our model, we shall also discuss the nature of the traps which, by trapping interstitials, permit the creation of *F* centers.

(1) *Introduction of the model*

The interstitial *F* center recombination was essentially revealed by a method of irradiation pulses. During the irradiation pulses, one could observe transient color centers which then rapidly disappear. Schulman and Boag [31] have studied LiF, NaCl, KCl and KBr at room temperature: they found many transient bands in the ultraviolet, and they have attributed these bands to hole centers (H, V_K...). Compton[32] found that in KCl and KBr the number of *F* centers continues to increase several microseconds after the end of the irradiation pulse and that a large number of *F* centers disappears spontaneously after a few seconds. It is quite probable that these *F* centers are destroyed by the trapping of *H* centers mobile at this temperature. Finally, much more recently, Ueta[29] performed a systematic study in KCl and KBr and measured the activation energy for the disappearance of *H* centers. He has shown that a portion of *H* centers and of V_1 centers (probably an *H* center associated with an impurity[33]) recombined among themselves or with *F* centers. Other experimental methods indicate that interstitial-vacancy recombinations occur under irradiation[34, 35].

In LiF, it is only very recently that Chu and Mieher[36] have shown evidence for the *H* center: a halogen atom associated with an ion to form a molecular ion X_2^- in a $\langle 111 \rangle$ direction. This defect becomes instable above 60°K so that *H* center is very mobile under 77°K as in other alkali halides.

Knowing that interstitials formed by irradiation in LiF remain in the crystal[29], we shall discuss in our interpretation a model in which the interstitial-vacancy recombinations play an important part. The interstitials not captured by the *F* centers are then trapped by traps. At first, we shall assume that these traps are in a fixed number, that they have an infinite capacity. We shall discuss later this approximation.

(2) *Approximate theoretical solution*

We shall assume that the number of interstitial-vacancy pairs directly created per unit time is proportional to the radiation intensity: KI pairs per cc per sec, I being the radiation intensity. We shall also assume that these pairs are created continuously during irradiation and that, during irradiation, there exists X free interstitials per unit volume uniformly distributed in the crystal.

We shall assume that at time t_0 the crystal contains a number Y of *F* centers and N traps and that the interstitial lifetime under these conditions at a temperature T of the experiment is small compared with the time t_0, that is to say, small compared with the duration of irradiations. We shall therefore assume that the number of *F* centers is practically constant during the lifetime of an interstitial (steady state approximation). Our calculation will therefore not be valid during the first stages of irradiation.

Let us consider the evolution of an interstitial created at time t_0 ($\tau = 0$). Let x be the probability of existence of this free interstitial; x obeys the equation (4):

$$\mathrm{d}x/\mathrm{d}\tau = -K_1xY - K_2xN. \tag{4}$$

The first term of the expression on the right represents the recombination interstitial-vacancies, the second term, the recombination interstitial-traps, K_1 and K_2 are coefficients which take into account at the same time the mobility of interstitials and the effective capture cross section of interstitials by a vacancy or by a trap. Only the mobility varies with temperature, that is to say that the ratio K_1/K_2 is temperature independent.

Y being constant during the lifetime of the interstitial, one can solve equation (4):

$$x(\tau) = \exp - (K_1Y + K_2N)\tau. \quad (5)$$

During interval of time dt_0 about t_0, $KI dt_0$ interstitials have been created. At time $t = t_0 + \tau$, there remains dX given by expression (6):

$$\begin{aligned} dX &= KIx(t-t_0)\,dt_0 \\ &= KI\{\exp - (K_1Y + K_2N)(t-t_0)\}\,dt_0 \quad (6) \end{aligned}$$

the total number of free interstitials per unit volume after time t of irradiation is given by (7):

$$X(t) = \int_{t_0=0}^{t_0=t} KI\{\exp - (K_1Y + K_2N)(t-t_0)\}\,dt_0. \quad (7)$$

Since the exponential is only different from zero in the vicinity of $t = t_0$, we can assume that Y is constant in the integral (7):

$$X(t) = KI\{1 - \exp - (K_1Y + K_2N)t\}/(K_1Y + K_2N). \quad (8)$$

In expression (8), for a sufficiently great duration of irradiation, the number of free interstitials X is approximately inversely proportional to the number Y of F centers. This expression is only valid under irradiation. If one stops the irradiation, free interstitials disappear in very short time.

We can calculate the probability $y(\tau)$ of having an F center left after time τ. Let $x_1(\tau)$ be the probability for the interstitial considered above to recombine with an F center, $y(\tau) = 1 - x_1(\tau)$ and

$$dx_1/d\tau = K_1xY = K_1Y\exp - (K_1Y + K_2N)\tau \quad (9)$$

$$\begin{aligned} x_1 &= \int_0^\tau dx_1 \\ &= K_1Y\{1 - \exp - (K_1Y + K_2N)\tau\}/(K_1Y + K_2N). \quad (10) \end{aligned}$$

Then:

$$\begin{aligned} y(\tau) = {} & K_2N/(K_1Y + K_2N) \\ & + K_1Y\{\exp - (K_1Y + K_2N)(t-t_0)\}/(K_1Y + K_2N). \quad (11) \end{aligned}$$

This expression contains two terms: a term of the steady state stage inversely proportional to the F center concentration in the crystal and a term of the transient stage which leads to an excess of F centers under irradiation. When the irradiation is interrupted, only the contribution of the steady state regime remains. Of the $KI\, dt_0$ F centers created under irradiation, there will therefore remain $dY = KI\, y(t-t_0)\, dt_0$ F centers after final recombination. Thus neglecting the second term of equation (11) and writing that $t = t_0$,

$$dY/dt = KIK_2N/(K_1Y + K_2N). \quad (12)$$

(a) *Behaviour in the vicinity of room temperature.* Around 300°K, the interstitial lifetime is so short (from Ueta's results[29]) that one can neglect the transient term of equation (11). Equation (11) gives then:

$$K_1Y^2/2 + K_2NY = KIK_2Nt. \quad (13)$$

As the number of F centers is large, one can assume that almost all interstitials recombine with F centers, that is to say that $K_1Y \gg K_2N$. It therefore follows:

$$Y = (2KIK_2Nt/K_1)^{1/2}. \quad (14)$$

Law of generation: therefore Y varies proportionately to $\sqrt{It}$ in agreement with our experimental results.

Behaviour as a function of temperature: as K_1/K_2 is temperature independent $Y(t)$ will only vary with T if $K \times N$ varies with T. According to our experimental results, one sees that this rate is temperature independent between 200° and 400°K in LiF: this would indicate that KN is almost independent of T in all this range of temperature. We shall discuss this in more detail later on.

(b) *Behaviour at high temperature.* According to our calculation, the total number of F centers generated must increase proportionately to the square root of t. But at high temperature ($T > 400$°K), a portion of the F

centers cluster to form agglomerates, whose sizes increase with the irradiation temperature. Results of small angle X-ray scattering show that large size clusters are formed rapidly and that the total number of *F* centers formed (isolated + agglomerated) for a given time of irradiation is almost the same as at room temperature. Such a result seems to indicate that there is a thermodynamical equilibrium under irradiation between *F* centers and clusters of *F* centers of which the number is almost constant and of which the size increases slowly during irradiation. For a given temperature, the ratio of the clustered *F* centers to the isolated ones should be the same, so that the total number of *F* centers (isolated + clustered) should increase proportionately to $\sqrt{t}$; if such a thermodynamical equilibrium exists, the number of isolated *F* centers will obey the same law. In other words the number of *F* centers should always be proportional to the $\sqrt{t}(Y = A\sqrt{t})$ but the coefficient A should diminish when the irradiation temperature increases, which is in good agreement with our experimental results.

Finally, the observation of large clusters of *F* centers by small angle X-ray scattering confirms the existence of large interstitial clusters. Indeed, in the case where only small interstitial clusters would exist, they would be in large number and the *F* centers would annihilate with these small clusters before being able to agglomerate among themselves in large numbers.

(c) *Behaviour at low temperature*. At low temperature, the interstitial lifetime increases. One can therefore predict two effects which shall overlap. On the one hand, the transient term of equation (11) can become important, the number and size of traps of interstitials varying little with respect to irradiation at room temperature. On the other hand, the interstitials now have the time to meet other interstitials and thus form small clusters.

The second effect has already been experimentally observed: the Oak Ridge group[37] in KCl and Commins[38] in KBr have shown that the size of interstitial clusters is smaller, the lower the temperature of irradiation. Cagnon[39], in LiF, comes to the same conclusion from measurements of the elastic limit. It is difficult to treat such a problem theoretically and therefore in this article, we shall not try to interpret our experiments in samples irradiated at low temperature.

3. EXPERIMENTAL VERIFICATION OF THE MODEL: DISAPPEARANCE OF *M* CENTERS BY *M* CENTER-INTERSTITIAL RECOMBINATION

We have repeated and completed in LiF experiments originally done by Schnatterly and Compton in KCl[34]. For this purpose, we have irradiated under different conditions (at temperatures below the temperature of formation of *M* centers) crystals containing excess electron centers created by irradiation.

In Fig. 12 (curve a) one sees that the disappearance of *M* centers proceeds in two steps, first a rapid one, and then a second and slower one which can be described by first order kinetics, in agreement with results already published on KCl. The first step is due to an electronic rearrangement: the electrons freed by irradiation transform the F_3^+ centers into *R* centers (Fig. 12, curve b), which leads to a rapid decrease of the *M* band as the absorption band of the F_3^+ center overlaps with that of the *M* center[40]. We have

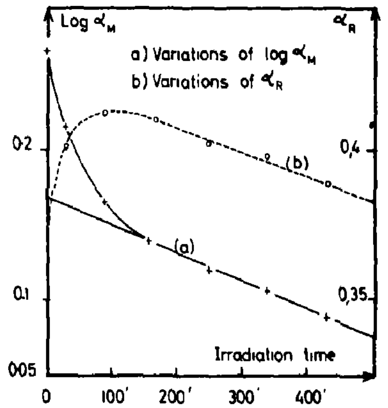

Fig. 12. Variation of the *M* and R_2 bands vs the irradiation time in LiF crystal irradiated at 196°K (sample was previously γ-irradiated, dose ≈ $2\times10^7 R$) (a) Variation of the *M* band, (b) Variation of the R_2 band.

only studied the second step which we can, as Schnatterly and Compton, attribute to a recombination of interstitial on M centers.

(a) *Theoretical results: disappearance of M centers via interstitials M centers recombination*

When the interstitial lifetime is sufficiently small, equation (8) which gives $X(t)$, the number of free interstitials under irradiation, becomes:

$$X(t) = KI/(K_1Y + K_2N). \qquad (15)$$

If one irradiates a crystal containing a number Z of M centers (formed by irradiation at room temperature), at a temperature where the α centers are not mobile, these centers will disappear obeying the following kinetics:

$$\mathrm{d}Z = -K_3XZ\,\mathrm{d}t \qquad (16)$$

K_3 being a coefficient which depends on temperature as K_1 and K_2. It therefore follows:

$$\mathrm{d}Z/Z = -K_3KI\,\mathrm{d}t/(K_1Y + K_2N). \quad (17)$$

Assuming that during the disappearance of M centers, the number Y of centers varies little, and that this number is sufficiently big so that $K_1Y \gg K_2N$ one obtains:

$$Z = Z_0 \exp\{-K_3KI(t-t_0)/K_1Y\} \quad (18)$$

Z_0 being the number of M centers at the beginning of irradiation.

(b) *Experimental results, verification of equation* (18)

First order kinetics: according to our model, the M centers should disappear according to a first order kinetics; this is in good agreement with the observations of Schnatterly and Compton in KCl and with ours in LiF (Fig. 11, curve a).

Variation of the speed of the kinetics with the number of F *centers:* according to our model, the straight line $\log Z/Z_0$ as a function of t has a slope of $-K_3KI/K_1Y$, that is to say a slope which is inversely proportional to the number of F center. We have experimentally verified this theoretical result in samples containing various concentrations of F centers (Fig. 13). This result is important in so far as it confirms that M centers disappear by trapping of interstitials and not by dissociation under irradiation (there would then be no reason for the speed of the kinetics to depend on the number of F centers present in the crystal).

This result is also important as it permits us to obtain the quantity K_3KI/K_1, that is to say a value close to KI the primary rate of generation, as K_3 and K_1 do not differ by more than a constant geometrical factor, ratio of the effective capture cross sections of an interstitial by an F center and by a M center $K_3/K_1 \simeq 2$.

Variation of the speed of the kinetics with radiation intensity: in accordance with theoretical predictions of equation (18), we have found the rate of disappearance of M centers to be proportional to the radiation intensity. We have displayed, in Fig. 14 our results on a sample previously irradiated with

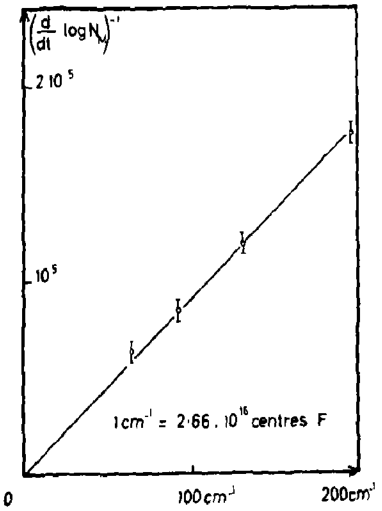

Fig. 13 Variation of the disappearance speed of the M band under X-irradiation at 196°K vs. the inverse number of F centers (equation (18)).

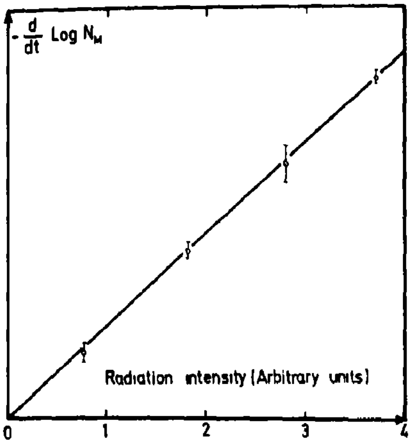

Fig. 14. Variation of the disappearance speed of the *M* band under X-irradiation vs. the radiation intensity.

γ-rays ($3{\cdot}3\times10^7$ Roentgens at 320°K) and re-irradiated with unfiltered X-rays from a tube with a copper anticathode (the abscissa is the radiation intensity and the ordinate, $-\mathrm{d}\log Z/\mathrm{d}t$, Z being the M center number at time t).

Variation of the speed of kinetics with temperature: as Schnatterly and Compton in KCl, we found that the speed of the kinetics represented by equation (17) depends on temperature. We have obtained in two different samples an activation energy of 0·11 eV (Fig. 15). According to our model this result would mean that the quantity K obeys the equation:

$$\begin{cases} K = K_0 \exp -W/kT \\ \text{with } W = 0{\cdot}11\ \text{eV} \end{cases} \tag{19}$$

that is to say the rate of primary generation of Frenkel pairs varies very simply with temperature.

These experiments form a verification of our initial hypothesis: the F center creation is strongly conditioned by the recombination of interstitials with F centers.

4. DISCUSSION OF VARIOUS RESULTS

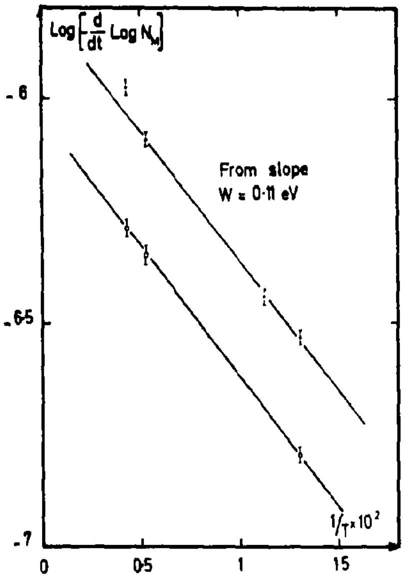

Fig. 15. Variation of the logarithm of the disappearance speed of the *M* band under X-irradiation vs. $1/T$ measured in two crystals containing different concentrations of *F* centers.

The calculation which we have made leads to an F center generation proportional to $\sqrt{t}$, which is in perfect agreement with our experimental results. These experiments which we have performed on the M center disappearance by re-irradiation at low temperature have shown that the choosen model is the good one as it permits the prediction of the various observed effects. In this paragraph we shall discuss the previous hypothesis.

(1) *Primary creation rate KI*

In our calculations, we have made the hypothesis that irradiation creates KI Frenkel pairs per unit time, the free interstitials recombining later on with traps or with F centers: this hypothesis is experimentally verified by the measurements on the kinetics of M centers disappearance during re-irradiation under 260°K. The primary effect is therefore proportional to radiation intensity. This important result excludes a certain number of proposed mechanisms for the primary process: in particular, the mechanism involving the simultaneous ionization of two neighbouring halogens which would lead to a primary creation proportional to the square of the radiation intensity[6].

It is more difficult to interpret the temperature variation of K (equation (18)). In particular, in KCl, by similar methods, Schnatterly and Compton[34] have observed an activation energy of 0·07 eV which they have interpreted as the interstitial activation energy; Itoh, Royce and Smoluchowski[35] have obtained the same activation energy for an interstitial halogen ion. Finally, Ueta[29] in recent experiments by pulse irradiation has obtained a similar activation energy for the H center disappearance. It therefore seems that the primary process depends on the mobility of interstitials. Further experiments should therefore permit one to understand the primary process of defect formation.

Finally, one can compare the creation rate KI measured from equation (18) with the energy received by the crystal. With a copper anticathode X-ray tube and a sample situated approximately 5 cm from this anticathode, one can estimate the energy flux on the sample to be 5×10^{16} eV/sec cm². After about an hour of irradiation approximately 10^{18} F centers per cc are formed in a 0·2 mm thick sample which only retains ten per cent of the incident energy. One could then easily verify that one needs approximately 10^{3} eV in order to create an F center. KI can be estimated from equation (18). With the same radiation at 196°K, we have measured:

$$-\mathrm{d}\log Z/dt = K_3KI/K_1Y = 3{\cdot}04\times10^{-5}\ \mathrm{sec}^{-1} \tag{20}$$

in a crystal containing approximately 5×10^{18} F centers per cc. Assuming that the effective capture cross section of an interstitial by an M center is approximately double that by an F center ($K_3/K_1 \simeq 2$) one then obtains:

$$KI(196°\mathrm{K}) = 7{\cdot}6\times10^{13}$$

and

$$\begin{cases} KI = 4{\cdot}9\times10^{16}\exp - W/kT \\ W = 0{\cdot}11\ \mathrm{eV}. \end{cases} \tag{21}$$

In a crystal 0·2 mm thick, we shall then expect $9{\cdot}4\times10^{14}\exp - W/kT$ Frenkel pairs created per unit time. Only 5×10^{15} eV/sec of in incident radiation is absorbed in the crystal; so that at high temperature, only few electron-volts will be necessary (approximately 7 eV according to our estimate) to create a Frenkel pair. Such a coarse estimate brings us back to Pooley's mechanism of deexcitation of an exciton.

(2) *Interstitial lifetime*

It would be interesting to see from our measurements if the interstitial lifetime in LiF is small as we had assumed in the beginning of our calculations. This lifetime τ can be deduced very simply from equation (5):

$$\tau^{-1} = K_1Y + K_2N. \tag{22}$$

K_1 and K_2 depend only on the interstitial activation energy. As mentioned above the interstitial activation energy is unknown. However Chu and Mieher[36] in LiF have observed that the ⟨111⟩ orientated H center becomes unstable at 60°K. The jump frequency $\nu\exp - W/kT$ equals one at this temperature with $W = 0{\cdot}15$ eV. We shall take this estimated value as the activation energy of H centers in LiF.

It is now easy to calculate the K_1 coefficient by assuming a random diffusion. If Z is the number of halogen interstitial sites neighbouring an F center and N_0 the number of interstitial sites per unit volume, the probability of destroying an F center by an interstitial can be written as:

$$ZX\nu_i/N_0 \tag{23}$$

where $\nu_i = \nu_0\exp - W'/kT$ is the interstitial frequency jump. It then follows that:

$$K_1 = Z\nu_i/N_0. \tag{24}$$

In LiF with results of Chu and Mieher (8 interstitial positions for each halogen ion) $N_0 = 4{\cdot}6\times10^{23}$. $Z = 8$ and $\nu = 10^{13}\ \mathrm{sec}^{-1}$:

$$K_1 = 8\times10^{-11}\exp - W'/kT \qquad (25)$$

W' being the activation energy of the H center.

In order to calculate the interstitial lifetime, we must also know the quantity K_2N. Assuming that the number of traps is constant, K_2N can be estimated from experimental results by using equation (14) as we know all other parameters. In a crystal containing 10^{19} F centers per cc after a room irradiation of 100 hr, we obtain*:

$$K_2N = 3{\cdot}1\times10^{7}\exp - W'\times kT \qquad (26)$$

It is then possible to calculate numerically the order of magnitude of τ at the beginning of irradiation ($Y=0$) and when the number F centers is much greater than the number of traps ($K_1Y \gg N_2N$). We have obtained the following results for different temperatures.

Table 2. Estimation of the halogen interstitial lifetime calculated from formulas (22), (25) *and* (26)

Temperature (°K)	Beginning of irradiation (sec)	with 5×10^{18} F centers (sec)
77	67	5·2
200	$0{\cdot}13\times10^{-3}$	10^{-5}
300	$12{\cdot}9\times10^{-6}$	10^{-6}

The interstitial lifetime is always extremely short under the condition of course that the activation energy that we have used corresponds to that of the halogen interstitial. The steady state approximation which we have developed above is therefore quite justified as well as the approximation in which K_1Y very rapidly becomes much larger than K_2N.

(3) *Discussion about traps*

In our calculation, we have assumed that interstitials are trapped by traps whose number being constant becomes quickly much smaller than the number of F centers when the irradiation time increases. This assumption is verified by experimental results on the disappearance of M centers under X-irradiation by interstitial trapping†. The rate of these kinetics is inversely proportional to the number of F centers; if the number of traps were much larger than the number of F centers, one should observe a kinetics independent of Y (in equation (15), in the first case, $X(t) \simeq KI/K_1Y$ and in the second case $X(t) \simeq KI/K_2N$).

One can say now that interstitials cluster and form aggregates whose number is smaller than the number of F centers. Such a result is in good agreement with several experimental data: recently, Sonder and Walton[41] have deduced from thermal conductivity measurements at very low temperature that the irradiation of KCl produces interstitial clusters, the size of which is larger when irradiation takes place at room temperature rather than at low temperature. By the same method, Neumaier[42] has also observed large interstitial clusters in LiF irradiated at room temperature. These interstitials cannot form three-dimensional clusters because there is not sufficient room in the lattice: as in metals [43] they could form small dislocation loops the size and the number of which vary according to irradiation conditions. Under this assumption, we shall now discuss our experimental results that is to say that KIK_2N/K_1 does not depend on the irradiation time and on the irradiation temperature.

---

*If $K_2 \sim K_1$ which is reasonable, one obtains $N = 3{\cdot}9\times10^{17}$ per cc. Such a number of traps is reasonable if they arise from impurities.

†One could also assume that free interstitials form stable di-interstitials: when the number of F centers is sufficiently large, interstitials are essentially trapped by F centers and the rate of disappearance of M centers would be also inversely proportional to the number of F centers. In appendix A, we show that such a model gives a creation law for F centers in complete disagreement with our experimental results: $Y \alpha I^{2/3} t^{1/3}$.

(a) Variation of K_2N with the irradiation dose. The ratio K_2N/K_1 is equal to σ_2N/σ_1 in which σ_1 and σ_2 are capture cross sections of an interstitial by an F center and by a trap. σ_1 is obviously constant and does not vary during irradiation. One must therefore discuss variations of σ_2. We shall analyse two cases: the first one where the size of the traps is constant and their number varies, the second one where the size of the traps varies during irradiation and their number remains constant. In both cases we shall assume that traps are small circular dislocation loops all having the same radius r. These loops can only trap interstitials on their circumference, that is to say that σ_2 is proportional to the radius of the loop (if there is no long or medium range interaction between the loop and free interstitials).

σ_2 constant and N variable: The total number of interstitials trapped after an irradiation time t is equal to Y. Then N is proportional to Y with $N = A \times Y$. Equation (4) becomes

$$\mathrm{d}x/\mathrm{d}\tau = -K_1xY - K_2AxY \qquad (29)$$

so that

$$\mathrm{d}Y/\mathrm{d}t = KIK_2Y/(K_1Y + K_2AY) = \text{constant}. \qquad (30)$$

In this case, the number of F centers created would be proportional to the irradiation time which is contrary to experimental results.

σ_2 variable and N constant: The radius of the loops is proportional to $Y^{1/2}$, i.e. $K_2 = AY^{1/2}$ (A being a constant). Equation (4) becomes:

$$\mathrm{d}x/\mathrm{d}\tau = -K_1xY - AxY^{1/2}. \qquad (31)$$

The problem is solved as previously (the steady state approximation) and one obtains in the vicinity of room temperature:

$$\mathrm{d}Y/\mathrm{d}t = KIAY^{1/2}/(K_1Y + ANY^{1/2}) \qquad (32)$$

or, for high F center concentrations:

$$Y\alpha(It)^{2/3}. \qquad (33)$$

Here again, we find a theoretical law in disagreement with experimental results. But we have assumed that for a dislocation loop, σ_2 is proportional to its radius: this is only true if there are no interactions between the loop and the isolated interstitials. If our hypothesis of small dislocation loops is correct, our results indicate that σ_2 varies slowly with radius of loops: dislocation loops distort the lattice at a fairly large distance and the size of the interaction domain between a dislocation loop and an interstial should vary much less rapidly than the loop size (It is only true if the size of the interaction domain is much larger than the radius of the loop: it is the case of very little loops).

Experimental verification of the weak variation of the number of traps N *with irradiation doses*. There is a method capable of telling us if the number of interstitial traps varies with irradiation dose at a given temperature. This method which we have already mentioned previously was first used by Sonder *et al.*[37] and repeated more recently by Commins[38]: one studies the kinetics of disappearance of F centers at room temperature under irradiation with F light. The F centers transformed into α centers recombine on traps. We shall now describe theoretically the phenomenon by assuming that we have a number Y of F centers, N traps and that, under F light irradiation, a portion pI of F centers is ionized (I being the F light intensity). The F center number disappearance kinetics is then given by:

$$\mathrm{d}Y = -pIYK_4N\,\mathrm{d}t \qquad (34)$$

K_4 being a factor in which appears the α mobility and the effective capture cross section of this center by one of the N traps. One then has:

$$Y = Y_0\exp\{-pIK_4N(t-t_0)\} \qquad (35)$$

Y_0 being the number of *F* centers at the beginning of *F* light irradiation.

If our model is correct, one must expect the number of *F* centers to decrease according to a first order kinetics and at a given temperature the coefficient of this exponential only to depend on *I* and *N*.

We have irradiated a series of samples previously coloured by γ-rays with the help of an unfiltered mercury vapour lamp. We have observed that the *F* centers disappear according to a first order kinetics in the samples least irradiated*. In the most irradiated samples one observes a much more complex kinetics (Fig. 17): this result is interpretable in first approximation by assuming that the traps are not all of the same size and that their number varies under the u.v. irradiation. We have then measured the average slopes which are shown in the next table:

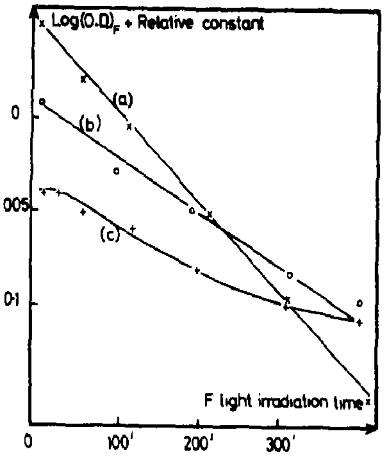

Fig. 17. Variations of the logarithm of the number of *F* centers vs. the irradiation time in LiF crystals irradiated with *F* light at room temperature and containing different concentrations of *F* centers (γ doses: (a) $6{\cdot}6\times10^6\,R$, (b) $1{\cdot}3\times10^7\,R$, (c) $3{\cdot}3\times10^7\,R$).

Table 3. *Average value of* pIK_4N, *speed of reaction (34)*

Dose (roentgens)	$6{\cdot}6\times10^6$	$1{\cdot}32\times10^7$	$1{\cdot}65\times10^7$	$2{\cdot}31\times10^7$	$3{\cdot}3\times10^7$
pIK_4N (equation (34))	$8{\cdot}7\times10^{-6}$	$5{\cdot}8\times10^{-6}$	$4{\cdot}45\times10^{-6}$	$5{\cdot}30\times10^{-6}$	$3{\cdot}55\times10^{-6}$

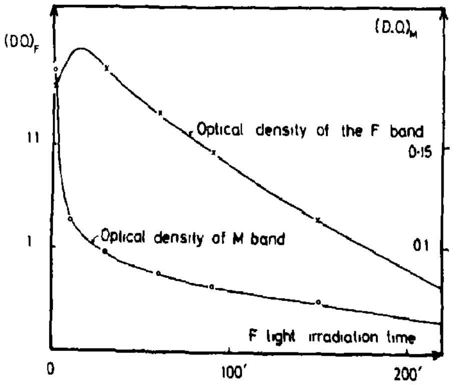

Fig. 16. Variations of the *F* and *M* bands in LiF crystal under *F* light irradiation at room temperature (sample was previously γ-irradiated, dose = $6{\cdot}6\times10^6\,R$).

One therefore sees from the results obtained at room temperature under the present approximation that the number of traps is practically independent of irradiation time†.

---

*One can easily see that the effect of *F* light is a disappearance of *F* centers by trapping and not a clustering to form agglomerates: in all the first stages of *F* irradiation, the number of *M* centers decreases abruptly while there is a corresponding increase in the number of *F* centers (Fig. 16).

†According to equation (34), the rate of the reaction varies with temperature through *p* and K_4: *p* is the rate of ionisation of *F* centers which varies very slightly with temperature and K_4 a diffusion coefficient which brings in the activation energy of the α center. In LiF, indirect considerations[44] lead one to think that this energy is of the order of 1 eV. Therefore the kinetics[34] would vary very quickly with *F* light irradiation temperature But Dubois *et al.*[45] found that the precedent reaction depends on temperature with an activation energy of 0·16 eV. Identical experiments have led us to similar results. Such a disagreement can be interpreted by recalling that neither Dubois nor we have utilized purely monochromatic *F* light. It is therefore probable that the light used detraps interstitials (a loop of interstitials can give rise to an absorption band and an optical excitation could detrap an interstitial) and that the energy of 0·16 eV is the energy for such a detrapping after an optical excitation. In any case, whether the bleaching process is due to detrapping of interstitials or by vacancy diffusion towards traps, our results indicate that the number of traps varies very little with the irradiation dose.

(*b*) *Variations of K_2N with temperature.* Let us recall equation (14) giving the kinetics of generation of F centers and equation (19) giving the variation of K with temperature.

$$\begin{cases} Y = (2K/K_2Nt/K_1)^{1/2} \\ K = K_0 \exp - W/kT \text{ with } W = 0.11\ eV. \end{cases} \quad (36)$$

If K_2/K_1 does not vary with temperature as we have assumed until now, Y will vary with T according to $\exp - W/2kT$, which is quite contrary to our experimental results as we have observed that the number of F centers is almost temperature independent between 200° and 600°K. If our model is a good one, we must therefore bring in a corrective term in equation (14) which compensates for the variation of K with T. This term can be due to the variation of N with T: we have mentioned that the size of interstitial clusters is lower in samples irradiated at low temperature than at high temperature[41]. This term can also be due to a variation of K_2/K_1: if traps are dislocation loops, the lattice is strained around loops and the activation energy of an interstitial will change when it arrives near the loop. However we are not able at present to explain correctly creation curves of F centers at different temperatures with our model but the discrepancy between experimental results and theoretical predictions is not contrary to the model.

5. THE INTERPRETATION OF HARDENING BY IRRADIATION UNDER THE HYPOTHESIS OF SMALL DISLOCATION LOOPS

In various alkali halides, the hardening by irradiation is observed to be proportional to the square root of the number of generated F centers[46]. In LiF irradiated at room temperature, Cagnon[47] has observed the same law. Until now, this result was interpreted starting from a theory of Fleischer[48] according to which the hardening of crystals by point defects is proportional to the square root of the number of defects (in the dislocation slip plane the average distance between two defects is proportional to the square root of the number of defects in this plane).

Under the assumption of a constant number of dislocation loops with a size increasing under irradiation, the problem becomes completely different. Saada and Wasburn[49] on the one hand and Kroupa[50] on the other have studied the effect of small dislocation loops on metal hardening. Their theoretical results are contradictory as the first ones have predicted that the hardening should be proportional to $N \times r$ (N being the number of loops and r the loop radius, while the second one predicts a hardening proportional to $(N \times r)^{1/2}$.

To the extent where dislocation loops made up with interstitials are neutral, the problem is formally similar to that of metals. In the absence of definite theoretical calculations, one can however say that, if the hardening is proportional to the square root of the number of F centers, i.e. to the square root of the total number of interstitials, it will also be proportional to the dislocation loop radius (their number remaining constant), in agreement with Saada and Washburn's calculations. The assumption of dislocation loops therefore is not in disagreement with the hardening observed by various authors.

CONCLUSION

The model developed here gives a good interpretation of the creation of F centers in pure LiF between 200° and 600°K. Essential points of this model are the following: free interstitials formed by incident radiation diffuse towards F centers or towards traps: to obtain a good agreement between theory and experiment, the number of these traps as well as the capture cross section of an interstitial by such a trap have to vary slowly with irradiation. Disappearance of M centers by irradiation below 250°K indicates also that traps are much less numerous than F centers in crystals containing more than 10^{18} F

centers per cc. Little dislocation loops of interstitials could be such traps if the size of the interaction domain between a dislocation loop and an interstitial varies much less rapidly than the loop size. According to our model, we would observe a variation of the creation rate of F centers with temperature which is not observed experimentally: however, we have admitted that the activation energy of the H center diffusing towards a F center is the same as when H centers diffuse towards a trap: if traps are dislocation loops, the crystal could be strained around a loop and the activation energy of an interstitial changes when it arrives near the loop.

Other models give the same creation law for F centers, particularly, if one can consider that each incident particle of the radiation acts as an irradiation pulse at a microscopic scale whether interstitials form di-interstitials or big agglomerates. In Appendix B, we analyze this case in detail; studying conditions of application in lithium fluoride, we show that the probability of such a process is low.

SUMMARY

We display a certain number of experimental results on the generation of F centers in LiF and we explain these results with the help of a recombination model of free interstitials with F centers or traps.

(1) *Experimental results in* LiF

Between 200° and 600°K, the number of F centers generated by X-ray irradiation is proportional to the square root of the irradiation time.

At room temperature we have also observed that, for the same irradiation time, the number of F centers increases proportionately to the square root of the radiation intensity.

At higher temperature ($T > 400°$K) a fraction of the F centers cluster to form big agglomerates which can reach a radius of 10 Å.

(2) *Theoretical interpretation in* LiF

Starting hypothesis: we assume that the radiation creates KI Frenkel pairs per unit time (I being the radiation intensity), that the interstitials thus created diffuse towards the F centers or towards traps. These traps quickly become less numerous than the number of F centers when irradiation time increases. The number of traps varies slightly with the irradiation time.

With these assumptions, the calculation leads to a generation of F centers proportional to $(It)^{1/2}$.

This model is verified by studying the disappearance of M centers by X-ray irradiation under 250°K. It is shown that the M centers disappear after trapping of interstitials. The study of the disappearance kinetics permits directly to obtain the number of free interstitials under irradiation. One then verifies that this number is proportional to the radiation intensity and inversely proportional to the number of F centers in accordance with theoretical predictions. These measurements also make it possible to obtain the variation of K (rate of primary generation) with temperature: one then shows that K obeys the equation:

$$\begin{cases} K = K_0 \exp - W/kT \\ \text{with } W = 0{\cdot}11 \text{ eV}. \end{cases} \qquad (19)$$

Acknowledgements—We would like to thank Professors J. Friedel and A. Guinier for their constant interest in this work. Drs Y. Quéré and J. Bonnelle have helped us with enlightening discussions. Mrs E. Dartyge performed the small angle X-ray scattering experiments, for which we are deeply grateful. We also thank Dr J. J. Hauser who translated and re-read this manuscript.

REFERENCES

1. SCHULMAN J. H. and COMPTON W. D., In *Colors centers in Solids*. Pergamon Press, Oxford (1964).
2. CRAWFORD J. H., *Adv. Phys.* **17**, 93 (1968).
3. SEITZ F., *Rev. Mod. Phys.* **26**, 7 (1954).
4. VARLEY J. H. O., *Nature* **174**, 886 (1954); *J. nucl. Energy* **1**, 130 (1954).
5. KLICK C. C., *Phys. Rev.* **124**, 703 (1961).

6. WILLIAMS F. E., *Phys. Rev.* **126**, 70 (1962).
7. POOLEY D., *Solid State Commun.* **3**, 241 (1965); *Proc. phys. Soc.* **87**, 245 (1966); *Proc. phys. Soc.* **87**, 257 (1966).
8. HERSCH H. N., *Phys. Rev.* **148**, 928 (1966).
9. GORDON R. B. and NOWICK A. S., *Phys. Rev.* **101**, 977 (1956).
10. SRINAVISAN T. M. and COMPTON W. D., *Phys. Rev.* **137**, A264 (1965).
11. ETZEL H. W. and ALLARD J. G., *Phys. Rev. Lett.* **2**, 452 (1959).
12. SONDER E. and TEMPLETON L. C., *Phys. Rev.* **164**, 1106 (1967).
13. WARNEK P., *J. opt. Soc. Am.* **55**, 921 (1965).
14. BALZER R., PEISL H. and WAIDELICH W., *Phys. Status Solidi* **15**, 495 (1966).
15. PRIMAK W. and WOLFE G., *Phys Rev.* **132**, 1612 (1963).
16. WIEGAND D. A., TURNER R. C. and SMOLUCHOWSKI R., *J. Phys. Chem. Solids* **27**, 1251 (1966).
17. KLICK C. C., CLAFFY E. W., GORBICS S. G., ATTIX F. H., SCHULMAN J. H. and ALLARD G. J., *J. appl. Phys.* **38**, 3867 (1967).
18. DURAND P., FARGE Y., LAMBERT M. and SMOLUCHOWSKI R., *J. Phys.* **28**, C4, 154 (1967).
19. DURAND P., Thèse de 3^e Cycle, Orsay (1967)
20. CAGNON M., Private communication.
21. STOEBE T. G., *J. Phys. Chem. Solids* **28**, 1375 (1967)
22. DUBOIS M., BERGE P., BLANC G. and ADAM-BENVENISTE M., *C. r. hebd. Séanc. Acad. Sci. Paris* **263**, 771 (1966); DUBOIS M. and BERGE P., *J. Phys.* **28**, 815 (1967)
23. FARGE Y., LAMBERT M. and SMOLUCHOWSKI R., *Solid State Commun.* **4**, 333 (1966).
24 FOURNET G. and GUINIER A., *Small Angle Scattering of X-rays*. Wiley, New York (1955)
25. LEVELUT A. M. and GUINIER A., *Proc. Conf. Small Angle X-ray Scattering*. Gordon and Breach, New York (1967).
26. FARGE Y., LAMBERT M., LETTELLIER B. and GUINIER A., *C. r. hebd. Séanc. Acad. Sci., Paris* **260**, 485 (1965).
27. GOLDSTEIN F. T., *Solid State Commun.* **4**, 621 (1966); *Phys. Status Solidi* **20**, 379 (1967).
28. RABIN H. and KLICK C. C., *Phys. Rev.* **117**, 1005 (1960).
29. UETA M., *J. phys. Soc. Japan* **23**, 1265 (1967).
30. VARLEY J. H. O., *J. Phys. Chem. Solids* **23**, 985 (1962).
31. SCHULMAN J. H. and BOAG J. W., *Phys. Status Solidi* **3**, 516 (1963).
32. COMPTON D. M. J., *'Color center Symposium* at University of Illinois (1965).
33. DELBECQ C. J., Private communication.
34. SCHNATTERLY S. and COMPTON W. D., *Phys. Rev.* **135**, A227 (1964).
35. ITOH N., ROYCE B. S. H. and SMOLUCHOWSKI R., *Phys. Rev.* **137**, A1010 (1965).
36. CHU Y. H. and MIEHER R. L., *Bull. Am. Phys. Soc.* **13**, 661 (1968); *Phys. Rev. Lett.* **20**, 1289 (1968).
37. SONDER E., SIBLEY W. A., ROWE J. E. and NELSON C. M., *Phys. Rev.* **153**, 1000 (1967).
38. COMMINS J. D. C. and WEDEPHOL P. T., *Solid State Commun.* **4**, 537 (1966).
39. CAGNON M., Private communication.
40. FARGE Y., TOULOUSE G. and LAMBERT M., *J. Phys.* **27**, 287 (1966).
41. SONDER E. and WALTON D., *Phys. Lett.* **25A**, 222 (1967).
42. NEUMAIER R., Private communication.
43. MAKIN M. J., WHAPHAM A. D. and MINTER F. J., *Phil. Mag.* **6**, 465 (1961), *Phil. Mag.* **7**, 285 (1962).
44. EISENSTADT M., *Phys. Rev.* **132**, 630 (1963).
45. DUBOIS M., BERGE P., BLANC G. and ADAM-BENVENISTE M., *C. r. hebd. Séanc. Acad. Sci., Paris* **261**, 1243 (1965).
46. SIBLEY W. A. and RUSSEL J. R., *J. appl. Phys.* **36**, 810 (1965); SIBLEY W. A. and SONDER E., *Phys. Rev.* **128**, 540 (1962).
47. CAGNON M., X^e Colloque de Métallurgie, Saclay (1966).
48. FLEISCHER R. L., *Acta Metall.* **10**, 835 (1962); *J. appl. Phys.* **33**, 3504 (1962).
49. SAADA G. and WASHBURN J., *J. phys. Soc. Japan* **18**, suppl. 1, 43 (1963).
50. KROUPA F., *J. Phys.* **27**, C3, 154 (1966).
51. ITOH N., *J. Phys. Chem. Solids* **27**, 197 (1966).
52. DAMASK A. C. and DIENES G. J., *Phys. Rev.* **125**, 444 (1962); DIENES G. J. and DAMASK A. C., *Phys. Rev.* **125**, 447 (1962); DIENES G. J. and DAMASK A. C., *Phys. Rev.* **128**, 2542 (1962).
53. YOUNG C. R., *J. appl. Phys.* **27**, 1 (1956).

APPENDIX A

Creation of F *centers with the hypothesis of formation of di-interstitials*

It is reasonable to think that at room temperature, interstitials form big agglomerates (cf. our previous discussion). It is however interesting to ask what type of generation is expected in a case where interstitials would form di-interstitials. Such a calculation has more than an academic interest as this defect probably exists in crystals irradiated in the vicinity of 80°K* We shall perform a calculation similar to the one performed above. Let us take an interstitial created at time t and x its probability of not being trapped. In the case of formation of di-interstitials, x obeys the following equation.

$$\mathrm{d}x/\mathrm{d}t = -K_1xY - K_2xX. \tag{A.1}$$

As previously, one assumes that during the interstitial lifetime, the number Y of F centers and the number X of free interstitials vary very little. At time τ after time t, one would have:

$$x = \exp -(K_1Y + K_2X)\tau \tag{A.2}$$

If KI is the number of free interstitials created by irradiation per unit time, one would have:

---

*As suggested by Itoh[51] the V_4 center observed in KCl and KBr could be this di-interstitial oriented along ⟨100⟩ directions which disappears thermally near 200°K.

$$X(t) = \int_{\tau=t}^{\tau=0} KI \exp -(K_1Y + K_2X)\tau \, d\tau \quad (A.3)$$

$$X(t) = \frac{KI}{K_1Y + K_2X}\{1 - \exp -(K_1Y + K_2X)t\}. \quad (A.4)$$

In the vicinity of room temperature, the lifetime is assumed to be very small:

$$X(t) \simeq KI/(K_1Y + K_2X) \quad (A.5)$$

$$X = \{-K_1Y + (K_1^2Y^2 + 4K_2KI)^{1/2}\}/2K_2. \quad (A.6)$$

If we also assume that the number of F centers is big, i.e. that $4K_2KI/K_1^2Y^2 \ll 1$* we obtain by expansion:

$$X = KI/K_1Y - K_2(KI)^2/K_1^3Y^3 + \dots \quad (A.7)$$

we can now calculate the number of F centers generated during a period of time dt:

$$dY/dt = KI - K_1XY \quad (A.8)$$

using (A.7), it follows that,

$$dY/dt = K_2(KI)^2/K_1^2Y^2 \quad (A.9)$$

$$Y = \left(\frac{3K_2K^2I^2t}{K_1^2}\right)^{1/3}. \quad (A.10)$$

Thus, according to equation (A.10), we see that at room temperature, if one would form stable di-interstitials, the number of F centers would increase proportionately to $t^{1/3}$ and to $I^{2/3}$. The experimental results are in total disagreement with such a theoretical prediction (experimental results show that $Y \alpha (It)^{1/2}$ Finally Y depends on temperature through $(K_2/K_1^2)^{1/3}$ while we found it to be temperature independent between 220° and 400°K.

The hypothesis of di-interstitials stable at room temperature is therefore in disagreement with experimental results. At lower temperatures the various approximations which we have made are no longer valid and one should make a computer calculation similar to the one made for metals by Damask and Dienes[52].

APPENDIX B

The formation of F *centers during pulse irradiation*

The theoretical treatment of pulse irradiations is valid in the two following cases: in the case when the time which separates two irradiation pulses is much larger than the recombination time of interstitials, and also in the case when one can consider an X photon as a pulse on a microscopic scale. In this second case, it would be necessary for the energy of the X-ray photon at the time when it disintegrates on an electron on site $\mathbf{r}_0$ to be contained in a sphere of radius R centered at $\mathbf{r}_0$ and such that, during the lifetime of interstitials, the various spheres don't overlap. In LiF, we shall show that this hypothesis is not valid. We shall consider two cases successively. On the one hand, as previously, we shall assume that interstitials are clustered in traps the number of which varies little during irradiation. On the other hand, we shall assume that interstitials form stable di-interstitials.

(1) *Finite number of traps with infinite capacity*

Study of a pulse. At time $t(\tau = 0)$, we already have a number Y of F centers and we suddenly inject X_0 interstitials. If X is the number of interstitials:

$$dX/d\tau = -K_1XY - K_2NX \quad (B.1)$$

$$dY/d\tau = -K_1XY \quad (B.2)$$

if we assume that Y is almost constant between two pulses, we obtain:

$$X = X_0 \exp -(K_1Y + K_2N)\tau \quad (B.3)$$

We can then simply show that the number of F centers created during this pulse ΔY is given by the following expression:

$$\Delta Y = K_2NX_0/(K_1Y + K_2N). \quad (B.4)$$

Generalization to P pulses per sec. The ΔY F centers are created during a time Δt such that $P \times \Delta t = 1$, P being the number of pulses per unit time We can write expression (B.4) under the form:

$$\Delta Y = PK_2NK_0\Delta t/(K_1Y + K_2N). \quad (B.5)$$

If we assume that $K_2N \ll K_1Y$, we can then integrate (B.5), which gives:

$$Y = (2PK_2NX_0t/K_1)^{1/2}. \quad (B.6)$$

If I_p is the intensity of the pulse (proportional to the number of incident particles per pulse):

$$X_0 = KI_p. \quad (B.7)$$

K being a constant which describes the primary process. We then have:

$$Y \propto (PI_pt)^{1/2} \quad (B.8)$$

The number of F centers generated is then proportional to the square root of the number of pulses per unit time, of the intensity of each pulse and of time.

(2) *Formation of di-interstitials*

Study of a pulse. In this case, equations (B.1) and (B.2) can be written

$$dX/d\tau = -K_1XY - K_2X^2 \quad (B.9)$$

$$dY/d\tau = -K_1XY. \quad (B.10)$$

Assuming Y to be constant we obtain.

$$X = K_1X_0Y \exp -K_1Y\tau/\{(K_1Y + K_2X_0) - X_0K_2 \exp -K_1Y\tau\} \quad (B.11)$$

---

*$4K_2KI - (K_1Y)^2$ is of the same magnitude order as $4KI - K_1Y^2$. With our previous estimations: $4KI \simeq 10^{17} \exp -W/kT$ (equation 22) and $K_1Y^2 \simeq 10^{28} \exp -W/kT$ (equation 25) with 10^{18} F centers per cc. The preceeding inequality is verified.

The number Y_0 of F centers destroyed by trapping of an interstitial during a pulse is:

$$Y_0 = \int_0^\infty K_1 X Y \mathrm{d}t \qquad \text{(B 12)}$$

$$Y_0 = \left\{K_1 Y \log\left(1 + \frac{K_2 X_0}{K_1 Y}\right)\right\}/K_2 \qquad \text{(B.13)}$$

The number of F centers created during this pulse will be.

$$\Delta Y = X_0 - Y_0 = X_0 - \left\{K_1 Y \log\left(1 + \frac{K_2 X_0}{K_1 Y}\right)\right\}/K_2 \qquad \text{(B 14)}$$

If we assume that there already is a certain number of F centers, $K_2 X_0/K_1 Y \ll 1$ and that we can expand the logarithm in expression (B.13), we obtain.

$$\Delta Y = K_2 X_0^2/2K_1 Y + \ldots \qquad \text{(B.15)}$$

Generalization with P pulses per sec The ΔY F centers are created during a time Δt such that $P \times \Delta t = 1$

$$\Delta Y = P K_2 X_0^2 \Delta t/2K_1 Y \qquad \text{(B 16)}$$

$$Y = (K_2 X_0^2 P t/4K_1)^{1/2} \qquad \text{(B 17)}$$

or writing that $X_0 = K I_p$ (equation (B 7))

$$Y \propto I_p (Pt)^{1/2} \qquad \text{(B 18)}$$

In this case, the number of F centers created must be proportional to the square root of the number of pulses per second and irradiation time

We then see that the theory has led us to a generation law proportional to the square root of irradiation time, whether interstitials are captured by a constant number of traps or the same interstitials form stable di-interstitials.

If an X-ray irradiation can be considered as a pulse irradiation, it would be normal to observe a law in square root of t However, we shall show that such a hypothesis is not realistic For this purpose we shall use the values calculated by Mrs. Bonnelle for the mean free paths of characteristic K line radiations emitted by the F^- and Li^+ ions in LiF and the mean free path of photoelectrons.

(a) *Absorption of the characteristic* K *radiation emitted by* F^- *and* Li^+ *in* LiF. The absorption coefficient of $K_\alpha F$ (18·27 Å) is equal to 2430 cm^{-1}: if one assumes that the intensity of radiation is negligible when it is reduced to 1 percent of its original value, the thickness of LiF in which the absorption takes place is $z = 19\,\mu$. Taking into account the experimental data or existing approximations, it is difficult to calculate the absorption coefficient of K_α of Li (240 Å) One can only say that its absorption coefficient will vary much more than that of $K_\alpha F$.

(b) *Trajectory of 45 keV electrons in* LiF. The photoelectrons created by irradiation have at the most an energy of 45 keV, which is the maximum energy of incident photons. If one assumes the relation proposed by Young[53] (in principle valid under 20 keV), one would get for the mean free path·

$$R_\mu \simeq 0{\cdot}042\, E_{\mathrm{keV}}^{1.3} \times \rho_{\mathrm{Al}}/\rho_{\mathrm{LiF}} \simeq 6\mu. \qquad \text{(B 19)}$$

The practical trajectory, often called the penetration depth, is the thickness of a foil beyond which one can no longer detect any incident particle. It is obvious that electrons do not propagate in the medium along a straight line and the real average trajectory of electrons defined as the average length travelled by the particle before losing all its kinetic energy is longer than the practical trajectory. It can be one to three times longer.

So it is seen that the energy of a photon, from the time when it is transferred to an electron, will be entirely contained in a sphere with a radius far greater than 19 μ. An order of magnitude calculation shows that under experimental conditions, about 10^{14} X photons disintegrate per unit volume and per unit time, that is to say, a volume of 10^{10} Å^3 for each photon If interstitials recombine in about 10^{-3} seconds at room temperature, one can consider that during this time, the photon disintegrates in a volume 10^{13} Å^3. We see that this volume is much larger than the volume in which the energy of the disintegrated photon is localized in the same point of the crystal, there will therefore be interstitials created by many photons at the same time and one cannot say that the photons are behaving as pulses

J. Phys. Chem. Solids Pergamon Press 1969. Vol. 30, pp. 1375–1384. Printed in Great Britain.

INTERPRETATION OF THE CREATION OF *F* CENTERS BY IONIZING RADIATION ABOVE 77°K BY A RECOMBINATION MODEL OF INTERSTITIALS AND VACANCIES

Y. FARGE*

Laboratoire de Physique des Solides†, Faculte des Sciences, Bat. 210, Orsay, 91 France

(*Received* 18 *November* 1968)

Abstract—In pure samples, the first stage of *F* centers creation by ionizing radiations is not observed: one explains theoretically the creation of *F* centers assuming that interstitials formed by the primary process diffuse towards *F* centers or toward traps which are big aggregates of interstitials. With this model, one can also explain the saturation which has been studied by Sonder and Templeton. Addition of other traps (surfaces, dislocation lines, impurities) changes the theoretical creation curve and permits one to partially explain the first stage of *F* center creation in alkali halides.

1. INTRODUCTION

IN THE PRECEDING paper[1], we reported a study on the creation of *F* centers in pure LiF irradiated by X-rays between 77° and 650°K. We have observed that the number of *F* centers above 220°K increases proportionately to the square root of the flux $I \times t$, I being the radiation intensity and t the irradiation time. We have thus developed a model of recombination of interstitials with *F* centers or with traps under irradiation. We have made the following hypothesis: the number of traps is constant and the capture cross section of an interstitial by such traps does not vary considerably with the irradiation time (This is probably the case if traps are small dislocation loops of interstitials). Under this hypothesis, we have found a theoretical law in agreement with experimental results. It was possible to verify the model experimentally: if crystals containing *M* centers are irradiated with X-rays at temperatures where formation of *M* centers cannot occur by diffusion, *M* centers are destroyed by interstitial trapping. From the speed of this reaction one can measure the number of free interstitials under irradiation. Assuming that the radiation creates KI Frenkel pairs per unit time (primary creation rate), we obtained the number X of free interstitials under irradiation:

$$X = KI/(K_1Y + K_2N) \tag{1}$$

Y being the number of *F* centers in the crystal at this time t of the irradiation; K_1Y is the probability per unit time that an interstitial is trapped by *F* centers; and K_2N is the probability per unit time that an interstitial is trapped by traps.

If the number of *F* centers is larger than that of traps ($K_1Y \gg K_2N$) equation (1) becomes:

$$X = KI/K_1Y. \tag{2}$$

We have thus experimentally verified this equation in LiF, and we have found that the primary creation rate varies very simply with irradiation temperature:

$$K = K_0 \exp -W/kT \tag{3}$$

with $W = 0{\cdot}11$ eV.

---

*[*] *Present address:* Laboratory of Atomic and Solid State Physics, Cornell University, Ithaca, N.Y. 14850, U.S.A.

[†] Laboratoire associe' au C.N.R.S.

In this paper, we shall determine whether the model developed in the case of lithium fluoride crystals can be extended to other alkali halides. We shall show that it can explain a certain number of experimental results obtained by several authors these past years.

As in LiF, interstitials are mobile at liquid nitrogen temperature[2] in a large number of alkali halides: the creation of F centers above 77°K is modified by the recombination of interstitials with F centers or with traps. In pure samples, traps can only be surfaces or residual impurities; and in impure samples, traps can be impurities, dislocation lines and so on. We shall successively analyze both cases.

2. F CENTER CREATION IN PURE ALKALI HALIDES

(A) *Creation in pure samples*

It is well known that the F center creation by ionizing radiations occurs in two distinct stages in alkali halides[2]. A first stage of fast coloration which is very sensitive to impurities, dislocations and a second slower one which seems more intrinsic. Particularly, in the purest samples[3], the first stage has not been observed and if one analyzes published creation curves, one observes that in general the number of F centers increases proportionately to the square root of irradiation time for irradiation at room temperature. It therefore seems that this law is an intrinsic law of creation because it is observed in the purest samples. This law has also been observed in crystals colored with u.v. light in the exciton spectral range: Goldstein[4] in pure KI, Goldberg[5] in pure KI and RbI as well as in KCl and KBr doped with I^- and irradiated with u.v. light in the I^- absorption band. The model developed for LiF can thus be applied to other alkali halides giving the following creation law, Y being the number of F centers:

$$Y = (KIK_2Nt/K_1)^{1/2}. \qquad (4)$$

As we have done in LiF, this model can be verified by studying the disappearance of M centers under X-rays by interstitial trapping. These experiments have been partially performed by Schnatterly and Compton (S.C.) in KCl[6] before our own experiments in LiF. Theoretically the disappearance of M centers under X-irradiation obeys kinetics:

$$\frac{dN_M}{dt} = -K_3N_MX = -K_3\frac{N_MKI}{K_1Y+K_2N}. \qquad (5)$$

The relaxation time τ of the M center concentration is thus the following:

$$\tau = \frac{K_1Y+K_2N}{K_3KI} = \frac{K_1}{K_3KI}Y+\frac{K_2N}{K_3KI}. \qquad (6)$$

Equation (6) has been verified by S.C. in KCl; they have measured at 90°K:

$$\tau(90°\text{K}) = 33\text{ min} + 16{\cdot}7\,N_F \times 10^{-17}\text{ min}. \qquad (7)$$

We can thus calculate KI assuming that the ratio $K_3/K_1 = 2$ (capture cross sections of an interstitial by F center and M center). From equations (6) and (7), one finds:

$$KI(90°\text{K}) \simeq 5\times10^{13}\text{ Frenkel pairs}\times\text{sec}^{-1}. \qquad (8)$$

Assuming that $K_2 \simeq K_3$, an estimation of the number N of traps can be obtained

$$N \simeq 10^{17}\text{ cm}^{-3}. \qquad (9)$$

This last value is of the same magnitude order as the value calculated in LiF (we had found $N = 3{\cdot}9\times10^{17}$).

S.C. have observed that the M center decay time varies with temperature above 100°K with a simple exponential law giving an activation energy equal to 0·072 eV. In equation (6), τ varies with temperature only if K varies with T because K_1, K_2 and K_3 have the same temperature dependence due to the activation energy of H center. That is to say:

$$K = K_0 \exp - W/kT \qquad (10)$$

with $W = 0{\cdot}072$ eV.

From these experiments, it is possible to obtain the variation of the primary creation rate with T in KCl which obeys the same law as that observed in LiF. One can relate this result to those obtained by Royce and Treacy in KBr[7]: they have found that the primary creation rate K (vacancy formation efficiency) increases from 135 to 300°K and obeys equation (10) with $W = 0{\cdot}07$ eV. It therefore seems that in all alkali halides, K obeys equation (10) in a given range of temperature (with a given activation energy for each alkali halide).

The activation energy which appears in equation (10) is always close to the activation energy for the displacement of H centers: in LiF, from results obtained by Chu and Mieher[8], we have estimated the activation energy of H centers to 0·15 eV and we have measured $W = 0{\cdot}11$ eV. In KCl, Ueta[9] has observed by pulse irradiation techniques that after a pulse, H centers disappear with a temperature time constant which gives an activation energy equal to 0·075 eV, a value very close to that measured by S.C. (equation (10)). In KBr, agreement is not so good (Ueta's measurements for H disappearance give 0·09 eV and Royce's measurements for the primary creation rate give 0·07). Therefore, it appears that the efficiency of the primary creation by ionizing radiation in alkali halides strongly depends on irradiation temperature; it also seems that the activation energy which describes this dependence is always close to the activation energy of H centers. This condition can be fortuitous and in this case the non-radiative decay creating a F center is thermally activated.

This variation of the primary process with temperature has also been observed by Goldberg[5] in u.v. irradiated KI, RbI, KCl:I^- and KBr:I^-. He has found the following activation energies: KCl:I^- (0·05 eV), KI (0·05 eV) and RbI (0·03). The energies of KCl: I^- (0·05 eV) and pure KCl (0·07 eV) are different; this difference seems to indicate that the thermal activation of the primary process occurs through a thermal-activated non-radiative decay and that the migration energy of H centers does not occur.

S.C. have suggested that the variation of M center decay time with temperature can be directly related to the H center activation energy. However, in our model, such is not the case because the ratio of the number of interstitials trapped by M centers to the number trapped by F centers or traps is always the same whatever the speed of interstitials.

Goldstein[4] and Goldberg[5] have interpreted the $(It)^{1/2}$ creation law assuming that the primary creation rate decreases when the number of F centers increases: electron-hole recombination occurring on F centers without displacement. Such a model does not take into account that free interstitials (H centers) can recombine with F centers or other traps.

(B) *Study of saturation*

We can study the saturation which must arise when α centers created by irradiation are sufficiently mobile to recombine with interstitial traps. In LiF, we have not reached the saturation, but in KCl, Sonder and Templeton[10] (S.T.) have reached it for a number of F centers of the order of 3 to 7×10^{18} centers per cc. The essential results are: (1) If one irradiates pure KCl crystals at room temperature, the number of F centers increases parabolically; it then deviates from this law to arrive at saturation. (2) The value at saturation decreases when temperature increases. If one calls Y_∞ the number of F centers at saturation, S.T. have observed that Y_∞ obeyed the law:

$$Y_\infty \propto \exp - W'/kT \qquad (11)$$

with $W' = 0{\cdot}4$ eV.

(3)The saturation depends weakly and in a reversible manner on the radiation intensity. (4) Finally, one cannot describe the approach to saturation by simple kinetics.

We have studied this saturation using S.T.'s suggestion: under irradiation a certain number of α centers exist which can diffuse and recombine on trapped interstitials.* In our preceding paper[1], we found that the number dY of F centers created during the time dt obeys equation (12) if the lifetime of interstitials is very short compared to variations of the number of F centers (steady state approximation).

$$dY = KIK_2 N dt/(K_1 Y + K_2 N). \qquad (12)$$

Under the S.T. hypothesis, equation (12) becomes in the vicinity of room temperature:

$$dY = KIK_2 N dt/(K_1 Y + K_2 N) - dY_1. \qquad (13)$$

The first term on the right represents the number of F centers generated taking into account the interstitial-F center recombination. The second term represents the number of F centers which have disappeared by recombining with interstitial clusters. If one assumes that at a given temperature α centers exist only under irradiation, then:

$$dY_1 = aK_1 INY dt. \qquad (14)$$

In this equation, we assume that the number of α centers is proportional to the radiation intensity ($N_\alpha = aIY$) and to the number of F centers. The coefficient K_1 is, among other things, proportional to $\exp - W_\alpha/kT$, W_α being the halogen vacancy activation energy. The equation becomes:

$$dY/dt = NI(KK_2 - aK_1K_4Y^2 - aK_2K_4NY)/(K_1Y + K_2N). \qquad (15)$$

Saturation comes in when $dY/dt = 0$. Assuming that in the vicinity of saturation $Y_\infty \gg N$, $(K_1K_4Y_\infty^2 \gg K_2K_4NY_\infty)$, one obtains:

$$Y_\infty = (KK_2/aK_1K_4)^{1/2}. \qquad (16)$$

1. *Variations of Y with T*. We have mentioned above that K_2/K_1 is almost independent of temperature so that only K and K_4 depend on T. By analogy with our results in LiF, we can assume that $K \ \alpha \exp - 0{\cdot}7/kT$, the value measured by Schnatterly and Compton for the disappearance of M centers by X-ray irradiation in the vicinity of 100°K (equation (10)). One therefore sees that Y_∞ is proportional to the following expression:

$$Y_\infty \ \alpha \exp - (0{\cdot}07 - W_\alpha)/2kT \qquad (17)$$

assuming that K_1 varies with temperature according to $\exp - W_\alpha/kT$.

This result is in good agreement with the experimental results of S.T.: for the same intensity, Y_∞ decreases when temperature increases. The curve log Y_∞ as a function of 1/T is a straight line giving an activation energy $(W_\alpha - 0{\cdot}07)/2$. This would indicate, taking the activation energy measured by S.T., that the α center activation energy in KCl would be equal to 0·87 eV, which is in agreement with direct measurements[12] and with theoretical estimates[13]. The agreement could be improved by taking into account the fact that the number of α centers with respect to the number of F centers is probably not constant with temperature.

2. *Kinetics describing saturation*. Equation (15) shows that it is impossible to describe the approach to saturation with the help of a simple kinetic law, which is again in good agreement with the results of S.T.

3. *Variations of Y_∞ with intensity*. According to equation (16), Y_∞ is independent of the radiation intensity, which is in contradiction with experimental results of S.T.: they have observed a weak variation of Y_∞ with

---

*Matthews *et al.*[11] have observed that the creation of F centers by γ-radiations is strongly inhibited when the sample is irradiated at the same time with F light, i.e. when some F centers are ionized.

I. In fact, it is probable that one of the hypothesis of equation (14) is wrong: it is not evident that under irradiation, the ratio of the number of α centers to the number of F centers is rigorously proportional to the irradiation intensity, especially when this intensity is multiplied by a factor larger than 100 when one passes from γ irradiation to a β irradiation of the order of 1 MeV.

Theoretical estimate of Y_∞

One can estimate Y_∞ starting from equation (6) and from parameters which we can determine in KCl. It is easy to calculate K_1, the probability of capture of an interstitial by an F center:

$$K_1 = \frac{p\,.\,\nu}{N_i}\exp - W'/kT \tag{13}$$

p being the number of interstitial halogen sites around a vacancy ($p = 6$ if H center migrates along $\langle 110\rangle$ directions by an interstitialcy mechanism). $\nu \exp - W/kT$ being the frequency jump of interstitial from a site to a neighboring site. N_i being the number of interstitial sites per cc ($12 \times N_{Cl^-}$, and N_{Cl^-} the number of halogen sites per cc). It leads to:

$$K_1 \simeq 6 \times 10^{-10} \exp - W'/kT \tag{14}$$

assuming that $\nu \simeq 5 \times 10^{12}\ \mathrm{sec}^{-1}$.

We can estimate K_2/K_4, ratio of the capture probability of an interstitial by a trap to the capture probability of an α center by the same trap. Neglecting terms of entropy in frequency jumps, we come to:

$$K_2/K_4 \simeq \exp - \frac{W' - W_\alpha}{kT}. \tag{15}$$

KI can be calculated from S.C.'s experiments combined with equations (7) and (10):*

$$KI = K_0 I \exp - W/kT$$
$$= 5{\cdot}5 \times 10^{17} \exp - W/kT \tag{16}$$

with $W = 0{\cdot}072$ eV.

Using the value measured by S.T. for $(W - W_\alpha)$ we obtain:

$$Y_\infty = 5 \times 10^{19}/(aI)^{1/2}. \tag{17}$$

Not knowing aI, it is difficult to use this last equation. One can simply notice that our calculation for KCl gives a resonable value for Y_∞ with respect to the value observed by S.T.

It would be interesting to perform the same experiments as S.T in alkali halides for which W_α is small. One should observe a value of Y_∞ which is the smaller W_α.

Remark: A similar calculation based on the hypothesis of detrapping interstitials from N traps by irradiation helped by an activation energy close to W_α would lead to the same theoretical result. Experiments by Matthew *et al.*[11] seem however to show that the good assumption is the one (proposed by S.T.) which we used.

3. EXTRINSIC GENERATION

Defects in ionic solids can have various influences on the generation of F centers by ionizing radiations[2]. On one hand, as suggested by Pooley[14], they can modify the primary generation mechanism, the electron-hole recombination occuring on an impurity without Frenkel pair generation. On the other hand, as suggested by Ikeya *et al.*[15] defects can create new traps for interstitials. Surfaces, dislocations, chemical impurities, etc..., can act as defects. We shall study the second assumption and we shall show that it can explain a large number of results, particularly in the case of crystals doped with positive divalent impurities.

(1) *Theoretical study*

As previously, we assume that the radiation creates KI Frenkel pairs per unit time. Under irradiation $X(t)$ free interstitials exist which can be trapped by the $Y(t)$ F centers, by the N traps whose number is constant (same traps as in the intrinsic case) and by new traps which can be impurities or similar traps. At the beginning of irradiation the number of these traps is M_0 and it decreases with irradiation time because a part of them have been filled by interstitials. At the time t of irradiation, only $M(t)$ impurity traps remain. Quantities $X(t)$, $Y(t)$ and $M(t)$ obey equations:

---

*S.C. have used a high flux X-ray tube and very probably in S.T. γ-ray irradiations, KI was smaller.

$$\mathrm{d}X/\mathrm{d}t = KI - K_1XY - K_2XN - K_3XM \tag{18}$$

$$\mathrm{d}Y/\mathrm{d}t = KI - K_1XY \tag{19}$$

$$\mathrm{d}M/\mathrm{d}t = -K_3XM. \tag{20}$$

In the right-hand side of equation (18), the last three terms represent the capture of free interstitials by F centers, by the N traps and by the M traps. We have done numerical calculations on Univac 1108 computer using numerical values given for KCl by equations (14) and (16) and assuming that $K_2 \simeq K_3 \simeq K_1$.

In Fig. 1, we have reported F center creation curves at room temperature for several concentrations of saturable traps: the two stages of creation can be observed and extrapolation of the second stage gives at $t = 0$ the number of saturable traps.* For low concentrations of saturable traps, the creation law is parabolic which is the case of pure crystals. One can easily see that the second stage is not a saturation because it occurs when the number of saturable traps becomes negligible and then one has the intrinsic generation.

On one of Fig. 1 curves, we have analyzed the approach of the pseudo-saturation (2nd stage) and we have verified that this approach is exponential as experimentally observed by Alvarez-Rivas and Levy[16] (Fig. 2). Such a result is normal as the extrinsic creation rate

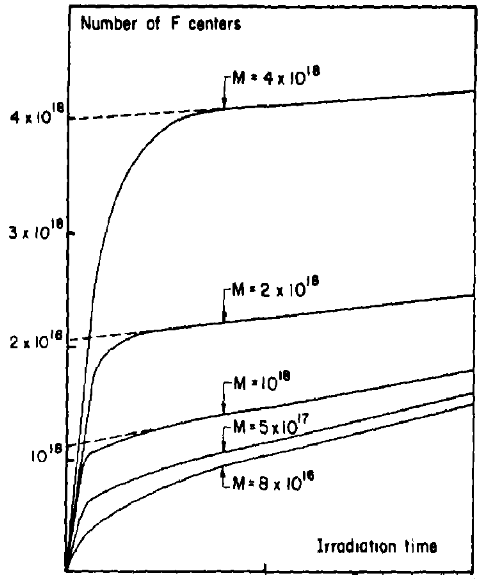

Fig. 1 Theoretical creation curves of F centers at 280°K with several concentrations of the M saturable traps. ($KI = 5{\cdot}5 \times 10^{17}$ exp $- W/kT$ and $N = 2 \times 10^{16}$, N being the number of non saturable traps).

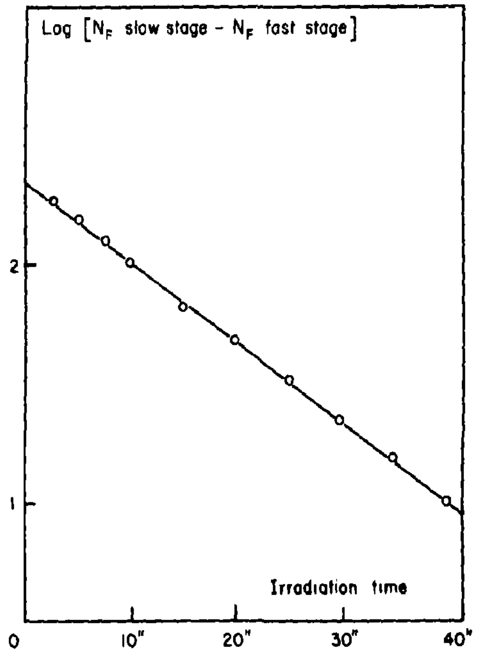

Fig. 2. Analysis of the approach of the saturation in one of the cases of Fig. 1 ($M = 4 \times 10^{18}$).

---

*The second stage occurs more quickly with irradiation time in these theoretical curves than in usual experimental creation curves. Probably because KI determined from experiments of S.C using a powerful X-ray tube is much higher than in usual experiments.

is fast and the intrinsic one much slower: the extrinsic creation rate decreases exponentially as the number of unfilled saturable traps.

On Fig. 3, we have reported theoretical creation curves for several irradiation temperatures. Such curves are similar to those experimentally observed by several authors in KCl[2]: the number of *F* centers created is lower at low temperatures than at high temperatures and the first stage seems to disappear.

It is also interesting to study the influence of the radiation intensity. Theoretical creation curves are represented on Fig. 4 with several irradiation intensities. However, calculations show that the number of *F* centers created is the same for a same integrated flux, whatever the radiation intensity. It is well known that the first stage of creation is critically dependent on the radiation intensity [17] but experimental results are conflicting. In fact, we have neglected electronic processes, impurity processes ($OH^- \rightarrow U+F$ conversion[18]) and variations of the primary process with some impurities as suggested by Pooley[14]: such effects can be intensity dependent.

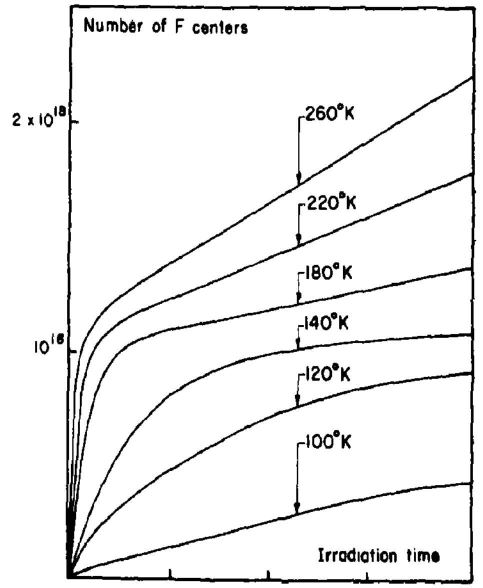

Fig. 3. Theoretical creation curves of *F* centers at several temperatures ($M = 10^{18}$, $N = 2\times 10^{16}$ and $KI = 5{\cdot}5\times 10^{17}$ exp$-W/kT$).

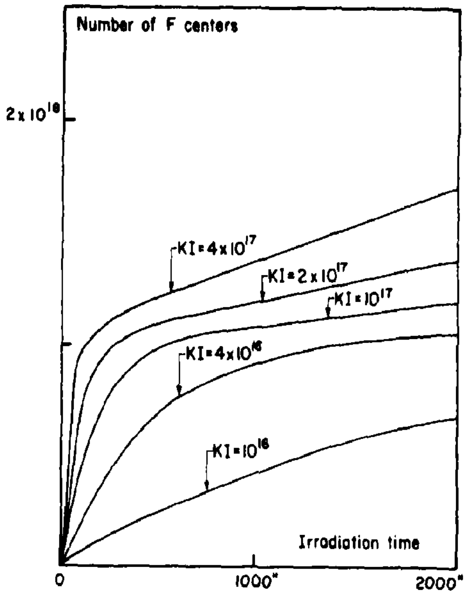

Fig. 4. Theoretical creation curves of *F* center at 280°K with several radiation intensities ($M = 10^{18}$ and $N = 2\times 10^{16}$).

From this last result, we can conclude that the first stage can be interpreted by a recombination of interstitials on saturable traps but other effects are added to the first one: normally the first stage would be complex. This conclusion is in good agreement with experimental results of Alvarez-Rivas and Levy[16].

Finally on Fig. 5 we have represented the influence of the number N of non-saturable traps with 10^{18} saturable traps per cc. As it was easy to anticipate, the first stage disappears when N increases: the intrinsic generation becomes important and screens the extrinsic one.

(2) *Interpretation of some experimental results*

If the model of interstitial-vacancy recombination is not able to explain all

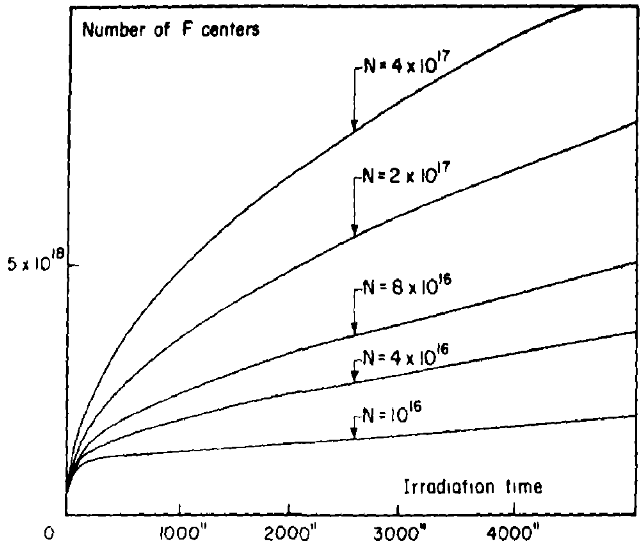

Fig. 5. Theoretical creation curves of F centers at 280°K with several concentrations of non-saturable traps ($KI = 5{\cdot}5 \times 10^{17}$ and $M = 10^{18}$).

experimental results on the first stage, we can however interpret correctly some experimental results with different types of saturable traps.

(a) *Influence of the surface.* In our model the surface can only be of importance in small crystals and in the very first stages of irradiation, as long as the F centers do not trap more efficiently than the surface. The only experimental results have been obtained in whiskers of NaCl and KCl by Gol'denberg *et al.*[19] and by Ballaro *et al*[20]. They have observed a first stage of generation which is more important in whiskers than in bulk crystals. Thus it seems that the surface plays an important part in this case.

(b) *Influence of dislocations.* It is well known that dislocations considerably increase the importance of the first stage of generation[2]. We can assume that dislocations introduce new saturable traps for interstitials. Alvarez-Rivas and Levy[16] have shown that the value at saturation of the first stage increases proportionately with the strain applied to the crystal during previous deformation. If one assumes that the number of dislocations introduced is approximately proportional to this strain this would indicate that the saturation sets in when all the traps created by dislocations have been filled. The assumption that dislocation lines can act as traps for interstitials is therefore reasonable. ESR studies should lead to the observation of new defects which would be halogen atoms trapped on dislocation lines.

(3) *Influence of positive divalent impurities*

In alkali halide crystals doped with divalent impurities, several authors[2] have found that the rate of the saturation of the first stage is proportional to the number of isolated positive ion vacancies (dissociated thermally and stabilized by quenching). With the assumption of interstitial-defects recombination, Ikeya *et al.*[15] have suggested that interstitials are trapped by isolated vacancies, saturation setting in when all traps have been filled. The new defect formed (neutral interstitial and cation vacancy) would form an X_2^- molecular ion with one of the six neighboring X^- ions in the ⟨100⟩ direction: this defect would be nothing else but the center observed with ESR by Hayes and Nichols[21].

Ikeya *et al.*[15] have also observed that the rate of generation in the very first stages (linear portion before saturation) varies with temperature according to an exponential law giving an activation energy of 0·07 eV. This linear part in our model corresponds to the moment when, at the beginning of irradiation, the F centers are in small number compared to the cation vacancies and when most of these cation vacancies have not yet trapped interstitials; i.e. each Frenkel pair created by the primary process gives rise to an F center as the corresponding interstitial will be trapped by a cation vacancy. The rate of generation studied by Ikeya is the rate of the primary process K.

One can thus conclude from these experiments that K varies according to equation (10), the activation energy measured by Ikeya *et al.* being very close to the energy measured by Schnatterly and Compton. Such an agreement between two different methods indicates that the first stage of generation in crystals doped with divalent impurities is indeed due to the trapping of interstitials by isolated cation vacancies.[*]

This mechanism is in contradiction with the one proposed by Crawford and Nelson[23]: they had suggested that, after capturing a hole, a neighboring halogen atom jumped inside the cation vacancy and the anion vacancy thus formed went away by diffusion. The activation energy of such a mechanism should be close to 1 eV, the jump energy of α centers in KCl, which is in complete contradiction with Ikeya's results.

The mechanism proposed by Ikeya is in agreement with the results of Sibley and Russel[24]: they have observed in KCl doped with Ca^{2+} that the elastic limit of crystals increases that much lower with the concentration of F centers the higher the concentration of Ca^{2+}. This indicates that, the hardening being caused by interstitials, these interstitials are fewer the higher the doping level of the crystals (the halogen atom corresponding to the F center created is not in an interstitial position but in the cation vacancy and does not contribute to the hardening).

4. CONCLUSION

The model of interstitial-F-centers recombination permits to explain a great number of experimental results on the creation of F centers in alkali halides: the creation law proportional to the square root of the irradiation time in the purest samples, the saturation observed by Sonder and Templeton[10] in pure KCl for high F center concentration, the first stage of creation in samples doped by divalent impurities or in crystals previously strained. However, we have not taken into account other effects which could be of importance: electronic effects in the first and second stages, variations of the primary creation rate with impurities as suggested by Pooley or chemical transformations ($OH^- \rightarrow U \rightarrow F$) as suggested by Crawford [18].

REFERENCES

1. DURAND P., FARGE Y. and LAMBERT M., *J. Phys. Chem. Solids* **30**, 1353 (1969)
2. CRAWFORD J. H. Jr, *Adv. Phys.* **17**, 93 (1968).
3. ETZEL H. W. and ALLARD J. G., *Phys. Rev. Lett.* **2**, 452 (1959); RABIN H and KLICK C. C, *Phys. Rev* **117**, 1005 (1960); SRINAVISAN T. M. and COMPTON W. D., *Phys. Rev.* **137**, A264 (1965)
4. GOLDSTEIN F. T., *Solid State Commun.* **4**, 621 (1966), *Phys Status Solidi* **20**, 379 (1967).
5. GOLDBERG L. S., Ph.D. Thesis, Cornell University, Unpublished.
6 SCHNATTERLY S and COMPTON W. D., *Phys. Rev.* **135**, A227 (1964).
7. ROYCE B. S. H. and TREACY D. J., Color Centers in alkali halides. *Intl. Symp. Rome* (1968).
8. CHU Y. H. and MIEHER R. L., *Phys. Rev. Lett* **20**, 1289 (1968).
9. UETA M., *J. phys. Soc. Japan* **23**, 1265 (1967).
10. SONDER E. and TEMPLETON L. C., *Phys. Rev.* **164**, 1106 (1967).
11. MATTHEWS J. W. and MALLARD W. C., *Phys. Rev.* **146**, 611 (1966).
12. LAURENT J. F. and BERNARD J., *J. Phys. Chem. Solids* **3**, 7 (1957).
13. CADET M. and GAUTIER P., *J. Phys.* **28**, 445 (1967).

---

[*] In LiF, Laj and Bergé[22] measuring the number of electric dipoles by the ionic thermocurrent method have concluded that the effect of irradiation is also the disappearance of isolated cation vacancies.

14. POOLEY, D., *Proc. phys. Soc.* **89**, 723 (1966).

15. IKEYA M., KUSAS K., OKADA T., ITOH N., and SUITA T., *J. phys. Soc. Japan* **20**, 289 (1965); IKEYA M., ITOH N., OKADA T. and SUITA T., *J. phys. Soc. Japan* **21**, 1304 (1966); ITOH N. and IKEYA M., *J. phys. Soc. Japan* **22**, 1170 (1967).

16. ALVAREZ-RIVAS J. L. and LEVY P. W., *Phys. Rev.* **162**, 816 (1967).

17. HARRISSON P. G., *J. chem. Phys.* **37**, 388 (1962); *Phys. Rev.* **131**, 2505 (1963); ABRAMSON E. and CASPARI M. E., *Phys. Rev.* **129**, 536 (1963); AGULLO-LOPEZ F., *Phys. Status Solidi* **22**, 483 (1967).

18. CRAWFORD J. H. Jr., *Proc. Conf. Color Centers and Crystal Luminescence*. Turin, Italy (1960). AGULLO-LOPEZ F., ALVAREZ-RIVAS J. L. and SANCHEZ C., Private communication.

19. GOL'DENBERG S. U. and MEKILA-GAILSAZYAN I. Ya., *Soviet Phys. solid St.* **6**, 2790 (1965).

20. BALLARO S., CHIAROTTI G., CUBIOTTI G. and GRASSO V., *J. Phys. Chem. Solids* **26**, 729 (1965).

21. HAYES W. and NICHOLS G. M., *Phys. Rev.* **117**, 993 (1960).

22. LAJ C. and BERGE P., *J. Phys. Chem. Solids* **30**, 845 (1969).

23. CRAWFORD J. H. Jr. and NELSON C. M., *Phys. Rev. Lett.* **5**, 314 (1960).

24. SIBLEY W. A. and RUSSEL J. R., *J. appl. Phys.* **36**, 810 (1965).

J. Phys. Chem. Solids Pergamon Press 1969. Vol. 30, pp. 1385–1402. Printed in Great Britain.

EFFET SHUBNIKOV DE HAAS DANS Cd_3As_2: FORME DE LA SURFACE DE FERMI ET MODELE NON PARABOLIQUE DE LA BANDE DE CONDUCTION†

I. ROSENMAN‡§

Laboratoire Central des Industries Electriques, 92 Fontenay-aux-Roses, France

(*Received* 18 *November* 1968)

Résumé – On a mesuré la magnétorésistance oscillatoire dans des monocristaux d'Arséniure de Cadmium (Cd_3As_2), dont les concentrations électroniques sont comprises entre 1.10^{18} et 8.10^{18} cm^{-3}. La période et l'amplitude des oscillations ont été étudiées tant en fonction de la concentration que de l'orientation cristallographique. La température est comprise entre 4,2° et 40°K, et l'induction magnétique a une valeur maximum de 5 Wb/m^2. On décrit les méthodes de préparation et de traitement des monocristaux et les techniques expérimentales utilisées (filtrage TBF, variation $1/B \propto t$ . . .). Le dépouillement des résultats, effectué sur ordinateur, conduit aux conclusions suivantes: (1) La surface de Fermi proposée pour Cd_3As_2 se compose d'un seul ellipsoïde allongé suivant l'axe cristallographique d'ordre 4, et de révolution autour de celui-ci; le rapport des axes de l'ellipsoïde est 1,18. (2) La masse cyclotron transverse, relative à la surface de Fermi, varie avec la concentration passant de 0.042 à 0,065 m lorsque celle-ci passe de 2,60 à 8,30 × 10^{18} cm^{-3}. Cette variation est en accord avec un modèle non parabolique de la bande de conduction. Le carré l'élément de matrice d'interaction obtenu est $P^2_{cv} = 15$ eV.

Abstract – The oscillatory magnetoresistance has been measured in Cadmium Arsenide monocrystals (Cd_3As_2) with electron concentrations in the range 1–8.10^{18} cm^{-3}. The oscillations period and amplitude variation have been studied versus concentration and cristallographic orientation. Temperatures were in the range 4·2°–40°K and magnetic fields with a maximum value of 5 Wb/m^2. Methods of preparation and doping the sample crystals are described as well as experimental techniques used in this study (V.L.F. Filtering, $1/B \propto t$ programming, .) Experimental results were processed by a computer. Main results are. (1) The proposed Fermi Surface of Cadmium Arsenide consists of only one ellipsoid prolate in the 4-fold axis direction. the anisotropy axis ratio is 1·18. (2) The transverse cyclotron mass, on the Fermi Surface, varies with the concentration from 0·042 to 0·065 m when the latter varies from 2·60 to 8·30 × 10^{18} cm^{-3}. This variation is consistent with a non parabolic model for the conduction band. The square of the interaction matrix element is found to be $P^2_{cv} = 15$ eV

1. INTRODUCTION

L'OBJET de ce travail est l'étude des propriétés électroniques de Cd_3As_2 monocristallin en utilisant les effets de transport isothermes aussi bien classiques que quantiques. Ce sont surtout ces derniers et plus particulièrement la magnétorésistance oscillatoire, ou effet Shubnikov–de Haas (SdH), qui nous intéresseront.

On sait que l'effet SdH se manifeste par un comportement oscillatoire de la magnétorésistance lorsqu'on fait varier l'induction magnétique B à laquelle est soumis le cristal. Le phénomène est périodique en $1/B$, la période des oscillations est inversement proportionnelle à la section extrêmale de la surface de Fermi, par un plan perpendiculaire à l'induction magnétique. L'effet SdH, dont il n'y a pas de théorie applicable pour une surface de Fermi non sphérique, obéit cependant à des lois analogues à celles qui régissent l'effet de Haas Van Alphen (susceptibilité oscillatoire), mieux connu[1]; tous deux ont leur origine dans la quantification des niveaux d'énergie d'un électron dans un cristal en présence d'une induction magnétique (niveaux de Landau). Un travail très complet sur l'effet SdH a été publié récemment par

---

†Travail effectué grâce à l'aide de la Direction des Recherches et Moyens d'Essais (D.R.M.E.).

‡Ce travail fait partie d'une Thèse de Doctorat d'Etat ès-Sciences Physiques soutenue à la Faculté des Sciences de Paris (1967 non publiée).

§Actuellement au Groupe de Physique des Solides de l'E.N.S. Tour 23 Faculté des Sciences de Paris.

Kubo *et al.*[2]; il a été fait dans l'hypothèse où la masse effective est isotrope et constante, et en tenant compte de l'élargissement des niveaux de Landau sous l'effet des collisions. L'expression de la magnétoconductivité oscillatoire est très complexe; nous ne donnerons que le résultat obtenu pour la magnétorésistivité oscillatoire, lorsqu'on généralise 'hardiment' l'expression de Kubo au cas d'une surface de Fermi de forme quelconque, mais assez simple, en tenant compte des résultats obtenus par Lifshitz et Kosevich[3] dans le calcul de l'effet SdH pour une surface de Fermi de forme complexe, sans tenir compte de l'élargissement des niveaux dû aux collisions.

Dans le cas d'une S.F. composée d'un seul ellipsoide, et B étant orienté suivant la direction d'un axe principal de l'ellipsoide, on a:

$$\sigma_{zi} = \sigma_{iz} = 0, \quad i = x, y$$

et l'on peut inverser séparément les composantes 'transversales' et 'longitudinale' du tenseur de conductivité. De plus l'induction magnétique étant élevée ($\omega_c t \gg 1$), on a lorsque les parties oscillatoires sont faibles:

$$\frac{\Delta\tilde{\rho}_{zz}}{\rho_0} = -\frac{\Delta\tilde{\sigma}_{zz}}{\sigma_0} \qquad (1.01)$$

$$\frac{\Delta\rho_{xx}}{\rho_0} = (\mu B)^2 \frac{\Delta\sigma_{xx}}{\sigma_0}. \qquad (1.02)$$

On obtient dans ces conditions:

$$\frac{\Delta\rho_0}{\rho_0} = A_0 B^{1/2} \sum_{r=1}^{\infty} \frac{(-1)^r}{r^{1/2}} T \times \left[\exp\left(\frac{-2\pi^2 krm^*}{\hbar eB} T_D\right)\right] \Big/ \left[Sh\left(\frac{2\pi^2 krm}{\hbar eB} T\right)\right] \cos\left(\frac{2\pi r S_m}{heB} - \gamma\right). \qquad (1.03)$$

C'est l'expression de la partie oscillatoire $\Delta\tilde{\rho}$ de la magnétorésistance relative à une section extrêmale de la S.F.

ρ_0 est la résistivité en l'absence d'induction magnétique

k est la constante de Boltzmann

S_m est l'aire extrêmale des sections de la S.F. par des plans perpendiculaires à l'induction magnétique B, mesurée dans l'espace des quantités de mouvement.

$m^* = (1/2\pi)(\partial S_m/\partial E_F)$ est la masse cyclotron relative à la direction considérée.

r est l'indice, entier, de l'harmonique.

γ est la constante de phase

$\gamma = +(\pi/4)$ dans le cas d'une bande parabolique.

A est un tenseur dont les termes sont indépendants de l'induction magnétique B et de la température T. Dans le modèle isotrope et parabolique, B étant orienté suivant Oz, on a:

$$A_{zz} = \pi^2 k\left(\frac{2m}{heE_F}\right)^{1/2} \quad (E_F \text{ est l'énergie de Fermi}) \qquad (1.04)$$

$$A_{xx} = \tfrac{1}{2}A_{zz} \qquad (1.05)$$

Enfin, dans le facteur d'amortissement, T_D est appelé température de Dingle et s'écrit[2]:

$$T_D = \frac{\hbar}{2\pi k\tau_l} \qquad (1.06)$$

où τ_l est le temps de relaxation de la quantité de mouvement, mesuré pour $B = 0$.

On voit d'après (1.03) que la période fondamentale des oscillations est:

$$P = \frac{he}{S_m}. \qquad (1.07)$$

Après ce rappel des formules qui nous serviront à l'interprétation des expériences, nous allons exposer ces dernières.

Bien que de nombreux travaux aient été publiés ces dernières années sur Cd_3As_2 (cf. par. 2), les résultats obtenus restent très fragmentaires, car presque tous ont porté sur des polycristaux. Notre étude porte uniquement sur des monocristaux pour différentes concentrations électroniques. Plusieurs questions se posaient à propos de l'Arséniure de Cadmium (Cd_3As_2): Quelle est la forme des surfaces isoénergie et quels sont les paramètres qui les définissent? Comment se répartissent-elles dans l'espace réciproque? La (ou les) bande(s) de conduction est (sont) elle(s) parabolique(s) ou non?

C'est à ces questions que nous avons tenté de répondre en utilisant l'effet Shubnikov de Haas comme moyen d'investigation, Cd_3As_2 étant un semi-conducteur à haute mobilité et dégénéré aux températures où nous l'étudions.

La 2ème partie rappelle quelques propriétés de Cd_3As_2. La 3ème partie de ce travail décrit la préparation des monocristaux et les traitements thermiques nécessaires à l'obtention de monocristaux dopés. La 4ème partie décrit les méthodes expérimentales utilisées. Les résultats expérimentaux sont rappelés dans la 5ème partie.

Enfin, l'interprétation de ceux-ci fait l'objet de la dernière partie de ce travail, dans laquelle nous proposons un modèle pour la structure de bande de Cd_3As_2.

2. QUELQUES PROPRIETES DE Cd_3As_2

L'Arséniure de Cadmium (Cd_3As_2) est un composé intermétallique II–V; c'est un semi-conducteur de type *n*. Sa température de fusion est 721°C. Il présente un point de transformation en phase solide à 578°C, ce qui est une source de multiples difficultés dans la préparation et le traitement des monocristaux. Ses propriétés sont encore mal connues à ce jour. Différentes structures cristallographiques one été proposées au cours du temps, la première ayant été un maille cubique. Actuellement, la structure retenue est celle d'une maille 'quadratique multiple' similaire à celle de Zn_3As_2 et contenant 32 molécules de Cd_3As_2[4].

L'étude de la structure électronique de Cd_3As_2 a fait objet de nombreux travaux, au cours des dernières années, qui ont porté soit sur les effets de transport soit sur les effets optiques. Ces études ont pratiquement toutes porté sur des polycristaux[5–13], les échantillons monocristallins de dimensions suffisantes étant trés difficiles à obtenir. Rappelons les principaux résultats:

> Cd_3As_2 est un semiconducteur de type *n*, dégénéré jusqu'à environ 200°C, la concentration électronique est toujours voisine de $2 \cdot 10^{18}\ cm^{-3}$ pour le matériau pur.
>
> Des énergies d'activation, comprises entre 0,04 eV et 0,6 eV, ont été mesurées et interprétées comme représentant la largeur de la bande interdite.
>
> Les effets de transport classiques ont permis de déterminer une 'masse effective moyenne' de l'ordre $m^* = 0{,}045$ m (polycristaux)[6]. Une étude de celle-ci en fonction de la concentration électronique (polycristaux) laisse supposer l'existence de deux bandes de conduction[5].

Signalons qu'il est difficile de comparer les résultats des différents travaux, les masses effectives ne correspondant pas aux mêmes définitions, ni aux mêmes concentrations de porteurs.

Nous nous sommes attachés à obtenir des monocristaux de différentes concentrations électroniques, comprises dans une gamme assez étendue, afin de pouvoir étudier l'influence de celle-ci sur les propriétés électroniques.

Nous allons donc décrire rapidement la méthode de préparation et de traitement des monocristaux de Cd_3As_2, avant de passer aux expériences à proprement parler.

3. PREPARATION ET TRAITEMENT DES MONOCRISTAUX

Elle s'effectue en plusieurs étapes[14]. Dans un premier stade, on obtient des polycristaux de Cd_3As_2 par co-fusion de Cadmium et d'Arsenic, en proportion stoechiométrique, à 800°C dans un tube en quartz scellé sous vide. Le matériau ainsi obtenu est purifié au moyen d'une distillation à 550°C dans un courant d'hydrogène trés lent; de petits cristaux de diverses formes se déposent sur certaines régions des parois du tube. Ils sont refondus sous forme d'un lingot qui est placé à l'extrémité d'un tube de quartz scellé sous vide; l'autre extrémité du tube est terminée en pointe. L'ampoule est enfermée dans un four en argent à deux zones de températures, voisines de 460°C. On tire très lentement l'ampoule de la zone chaude vers la zone froide. L'Arséniure de Cadmium vient se déposer et former un monocristal dans la partie froide de l'ampoule. La vitesse de tirage est de 1 mm/jour.

On coupe les monocristaux au moyen d'une scie à électro-érosion, après les avoir orientés aux Rayons X.

Il est très difficile d'obtenir des monocristaux de Cd_3As_2 avec des concentrations électroniques très différentes de $2\cdot10^{18}\,cm^{-3}$, car l'existence du point de transformation en phase solide à 578°C rend impossibles les les traitements thermiques à des températures supérieures à celle-ci. Nous avons essayé diverses méthodes pour obtenir des monocristaux dopés:

(1) *Tirage* des monocristaux à partir de Cd_3As_2 polycristallin préalablement dopé: résultat négatif, la concentration électronique finale étant toujours $2.10^{18}\,cm^{-3}$;

(2) *Tirage* en présence de dopant: pas de résultat car la présence d'un élément étranger empêche la croîssance de monocristaux, sauf en ce qui concerne le Sélénium avec lequel on n'obtient toutefois que $2.10^{18}\,cm^{-3}$;

(3) *Dopage par diffusion*: les traitements devant s'effectuer à une température assez basse (< 578°C), nous avons fait des expériences en utilisant divers éléments:

éléments à faible température de fusion (Li, Ga, Cd, In, S, Hg, I)
éléments à pression de vapeur élevée (Se, Te)
cuivre (préalablement évaporé sur l'échantillon)
lithium colloïdal déposé sur l'échantillon.

Les éléments diffusent plus facilement dans les polycristaux que dans les monocristaux. Dans ceux-ci, seuls paraissent efficaces, le lithium colloïdal qui joue le rôle de donneur ($n \simeq 8.10^{18}\,cm^{-3}$) et le selenium qui serait plutôt accepteur ($n \simeq 1{,}1.10^{18}\,cm^{-3}$). La température optimale semble être de 450°C, et la durée de traitement optimale de 4 à 5 jours. Tous les cristaux obtenus sont de type *n*.

Le dopage s'effectue donc sur des monocristaux préalablement orientés et découpés. On effectue un polissage à l'alumine après le traitement. Les dimensions finales des échantillons sont $1\times1\times6\,mm^3$. On y applique des fils de cuivre (dia. 6/100 mm) avec de la soudure à l'étain après avoir nettoyé la surface par du chlorure de zinc.

Nous allons à présent décrire les méthodes expérimentales utilisées au cours de ce travail:

4. METHODES EXPERIMENTALES

4.1 *Partie magnétique*

Les expériences nécessitant des températures basses et des inductions magnétiques élevées, nous avons utilisé une bobine supraconductrice Westinghouse équipée de son alimentation stabilisée et de son cryostat, et produisant une induction magnétique maximum de 50 kG, dans un cylindre de 25,4 mm de diamètre.

A l'intérieur de la bobine supra-conductrice se trouve l'extrémité de l''anti-dewar', double paroi en tube très fin (3/10 mm), d'acier inoxydable, qui reçoit le porte-échantillon. Les expériences se font soit en transférant de l'hélium liquide dans l'enceinte expérimentale de l''anti-dewar', soit en y maintenant de l'hélium gazeux. Le contact thermique avec le bain d'hélium principal, est réalisé en maintenant une pression d'environ 5 Torr. d'hélium entre les parois de l''anti-dewar'.

On mesure le niveau d'hélium liquide grâce à une sonde à capacité.

4.2 *Porte-échantillon*

Il est constitué par un plateau orientable commandé de l'extérieur du cryostat par un système 'roue tangente-vis sans fin'. Ceci permet de faire tourner l'échantillon de 360° autour d'un axe horizontal (le champ magnétique est vertical), dans le centre de la bobine supra-conductrice. Une rotation lente et continue peut être réalisée par un petit moteur synchrone. La résolution angulaire est de 20′, l'enregistrement électrique de l'angle est obtenu grâce à un potentiomètre hélicoïdal monté coaxialement avec la commande de rotation. Une résistance Allen-Bradley de 33Ω-1/10 W, alimentée par un courant constant de 100μA, fixée sur le porte-échantillon, sert aux mesures de températures de l'échantillon. Celles-ci sont régulées pour les mesures comprises entre 4,2°K et 50°K. Le principe de régulation est le suivant: la ddp mesurée sur la résistance potentiométrique est envoyée sur un amplificateur opérationnel muni d'un circuit de compensation, qui sert de référence pour fixer la température désirée. La ddp d'erreur ainsi produite commande un transistor réglant le courant dans une résistance de chauffage de 50 Ω en constantan, scellée à la base du porte-échantillon.

La stabilité des températures réalisées de cette facon est d'environ 0,05°K au voisinage de 4,2°K, et reste raisonnable jusqu'à 50°K.

4.3 *Mesure et programmation des inductions magnétiques*

La variation de l'induction magnétique B peut être telle que: (1) B soit proportionnel au temps (2) ou bien $1/B$ soit proportionnel au temps. Le 1er type de variation est utilisé dans la mesure de l'effet Hall ou de la magnétorésistance non oscillatoire.

Nous utilisons le 2éme type de variation ($1/B \propto t$) pour la mesure de l'effet Shubnikov de Haas: nous avons vu en effet que la variation oscillatoire de la magnétorésistance était périodique en $1/B$. La programmation $1/B \propto t$ a donc pour effet de transformer la partie oscillatoire de la magnétorésistence en un effet de variation périodique (amorti) en fonction du temps. Ceci est très avantageux, car on peut alors utiliser la technique de filtrage ou de différenciation en basse fréquence, pour ne garder de la magnétorésistence que la partie oscillatoire. Il est ainsi possible d'étudier les différentes parties de la surface de Fermi, chacune de celles-ci étant caractérisée par une période bien déterminée.

La variation $1/B \propto t$ est réalisée grâce à un circuit constitué d'éléments linéaires et produisant une *ddp* v, servant à commander l'intensité I délivrée par l'alimentation régulée de la bobine supra-conductrice; v est telle que $1/v \propto t$.

Le circuit très simple, représenté sur la Fig. 1, fonctionne d'après les équations suivantes:

on a, quel que soit la valeur de la résistance fixe r:

$$v = ri = \frac{rV}{R+r} \qquad (4.1)$$

k'' etant la constante de la bobine supraconductrice (en G/A) et k'/k'' étant la constante de proportionnalité entre la ddp de commande v de l'alimentation et le courant I qu'elle délivre, on a:

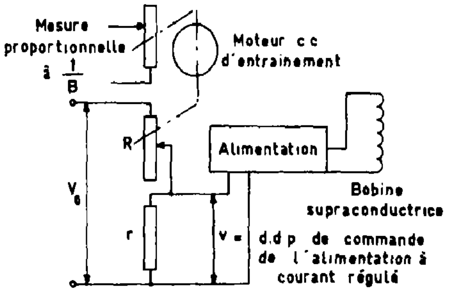
Mesure proportionnelle à $\frac{1}{B}$
Moteur c c d'entrainement
R
Alimentation
Bobine supraconductrice
V_0
r
v = d.d p de commande de l'alimentation à courant régulé

Fig. 1. Schèma de réalisation de la variation de l'induction magnétique B, telle que $1/B \propto t$.

$$\frac{1}{B} = \frac{1}{k''I} = \frac{1}{k'v} = \frac{1}{k'rV}(R+r). \qquad (4.2)$$

Il suffit donc de faire varier R linéairement en fonction du temps t

$$R = R_0 \pm kt \qquad (4.3)$$

R_0 étant la valeur initiale du potentiomètre helicoïdal R, pour obtenir la variation désirée de l'induction magnétique soit:

$$\frac{1}{B}-\frac{1}{B_0}=\pm Kt. \qquad (4.4)$$

La vitesse et le domaine de variation peuvent être réglés en fonction des nécessites (cf. plus loin).

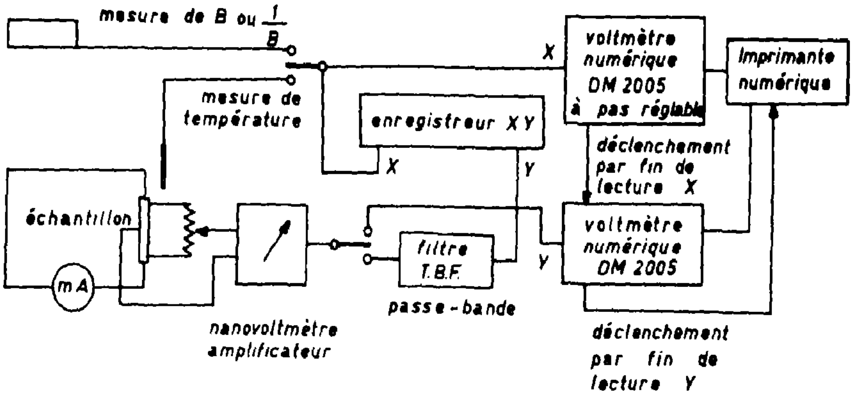
mesure de B ou $\frac{1}{B}$
mesure de température
enregistreur XY
X
Y
X
voltmètre numérique DM 2005 à pas réglable
Imprimante numérique
déclenchement par fin de lecture X
échantillon
mA
filtre T.B.F.
passe-bande
Y
voltmètre numérique DM 2005
nanovoltmètre amplificateur
déclenchement par fin de lecture Y

Fig. 2 Schéma de l'enregistrement des mesures.

4.4 *Mesure galvanomagnétiques*

Les mesures galvanomagnétiques sont faites en courant continu constant; ce dernier est délivré par une alimentation stabilisée Hewlett Packard ou P.A.R.; on mesure les ddp au moyen d'un nanovoltmètre-amplificateur Astrodata.

La magnétorésistance oscillatoire correspond à des ddp oscillatoires faibles (10 nV à 10 μV), noyés dans celles que proviennent des effets monotones (100 μV à 1 mV). La programmation $1/B\alpha t$, décrite précédemment, est telle que la période des oscillations est constante et toujours comprise entre 3 et 20 sec. La sortie du nanovoltmètre est branchée sur l'entrée d'un filtre électronique TBF Kronhite 330 A, qui élimine les *ddp* qui n'ont pas la période de l'effet Shubnikov de Haas. On peut mesurer ainsi des variations oscillatoires relatives de la magnétorésistance de 10^{-4}.

Les effets sont enregistrés sur un enregistreur XY et/ou dans un système numérique d'acquisition de données, composé de deux voltmètres numériques Dynamco DM 2005 et d'une imprimante Venner (Max. 5 couples de points par sec); ce procédé facilite l'exploitation des résultats par un ordinateur Univac 1107. La Fig. 2 donne un schéma de l'appareillage. La précision des mesures sur les coefficients galvanomagnétiques est d'environ 10%.

5. RESULTATS EXPERIMENTAUX

Après avoir indiqué quelles sont les caractéristiques des différents monocristaux étudiés nous exposerons les résultats obtenus, tant pour les effets galvanomagnétiques 'classiques', que pour les effets oscillatoires. Pour ces derniers, nous ne donnerons qu'une très petite partie des résultats expérimentaux acquis. En effet, plusieurs centaines de courbes de variation de la magnétorésistance oscillatoires ont été tracées au cours de ce travail, en étudiant ses variations, soit avec l'orientation relative des axes cristallins et de l'induction magnétique, soit avec la température, soit encore avec la concentration électronique.

5.1 *Caractéristiques des échantillons étudiés*

Nous avons fait des expériences sur 2 types de monocristaux de Cd_3As_2: (a) *Type 1*: l'axe cristallographique d'ordre 4-axe *c*-parallèle à la direction du courant; (b) *Type 2*: l'axe cristallographique d'ordre 4-axe *c*-

perpendiculaire à la direction du courant;

Les axes cristallins sont orientés suivant les arêtes de l'échantillon.

Le Tableau 1 donne les caractéristiques des échantillons étudiés.

La résistivité varie linéairement avec la température, mais présente deux régions à pentes différentes (300°K à env. 80°K, et 80°K à env. 15°K); elle ne varie plus (résistivité résiduelle) en-dessous d'environ 15°K.

5.2 *Effets galvanométriques classiques*

Effet Hall: La résistivité de Hall est proportionnelle à l'induction magnétique; on peut donc définir un coefficient de Hall, R. Celui-ci diminue légèrement lorsque la température diminue $R(300°\text{K})/R(78°\text{K}) = 1{,}05$. Cette variation s'explique très bien en tenant compte du 2ème terme du développement de Sommerfeld des intégrales de Fermi, étant donné que le gaz électronique n'est pas complètement dégénéré à 300°K.

Magnétorésistance: Ni la magnétorésistance transversale, ni la longitudinale ne sont nulles. Cette dernière est même négative dans plusieurs échantillons, quelle que soit la température. Aucune ne se sature quand on augmente l'induction magnétique B jusqu'à 50 kG. Pour une valeur de B donnée, la magnétorésistance reste constante lorsque la température varie dans le domaine où la mobilité se sature ($T < 15°\text{K}$).

5.3 *Effets oscillatoires quantiques*

Les oscillations de la magnétorésistance ont été mesurées dans un domaine de températures comprises entre 1,5° et 40°K, et à partir d'inductions magnétiques qui, dans les meilleurs cas, étaient telles que $\mu B \sim 5$. Nous avons également enregistré de très faibles oscillations de la résistivité de Hall, de même période que celles de la magnétorésistance pour la même orientation.

La détermination de la période des oscillations se fait de la facon habituelle en numérotant les extrema de la magnétorésistance: en effet, la magnétorésistance oscillatoire peut s'écrire:

$$\frac{\widetilde{\Delta\rho}}{\rho_0} = M(X, T) \cos 2\pi \left(\frac{X}{P} + \delta\right); \quad (5.1)$$

$$X = 1/B; \quad \delta = \frac{1}{8} \text{ théoriquement.}$$

$M(X, T)$ est une fonction lentement variable devant la fonction cosinus (grands nombres quantiques). Les maxima correspondent aux valeurs entières de l'argument $(X/P) + \delta = N$. Les minima correspondent aux valeurs demi-entières de l'argument: $(X/P) + \delta = N + 1/2$.

On détermine donc la période en portant en abscisses les valeurs de X correspondant aux extrema et en ordonnées la suite des nombres entiers et demi-entiers: la période est l'inverse de la pente. Un exemple est donné sur la Fig. 3. Les courbes sont la copie de celles obtenues sur l'enregistreur XY (on trace directement en abscisse $X = 1/B$).

On constate immédiatement que la S.F. du Cd_3As_2 est anisotrope: les périodes étant différentes suivant que la direction de B est parallèle ou perpendiculaire à l'axe c; la Fig. 4 représente pour l'ensemble des échantillons la variation de la période en fonction de l'angle $(\mathbf{B}, c)$.

La Fig. 5 représente l'amplitude de l'effet SdH en fonction de $X = 1/B$ pour plusieurs températures. Comme on pouvait s'y attendre, l'amplitude pour X fixé diminue rapidement lorsque la température augmente.

Remarquons également que la période des oscillations ne varie pas en fonction de la température, ce qui est en accord avec le fait que le gaz d'électrons est très dégénéré dans les monocristaux étudiés et que toutes les impuretés qui jouent le rôle de donneurs sont ionisées.

6. INTERPRETATION DES RESULTATS

Nous nous attacherons essentiellement aux résultats des effets oscillatoires quantiques qui permettent de déterminer la structure de bande avec plus de précision que les effets classiques. Ces derniers nous aideront à vérifier la validité du modèle proposé à partir

Tableau 1. *Caractéristiques des échantillons étudiés*

	Résistivité ($\mu\Omega$cm)			Coeff. de Hall (cm^{3}Cb^{-1})			Mobilité, (cm^{2}V^{-1}s^{-1})			n_H (10^{18}cm^{-3})	n_{SdH} (10^{18}cm^{-3})	Orientation† cristall type n°
Température échantillon	300 (°K)	78 (°K)	4,2 (°K)	300 (°K)	78 (°K)	4,2 (°K)	300 (°K)	78 (°K)	4,2 (°K)	4,2 (°K)	4,2 (°K)	
m.p. 1	321	85.6	51	2.30	2,30	2,50	7 300	27 400	46 000	2,50	2,61	1
m.p. 3	217	54.7	36.3	3.13	2,82	3,04	12 000	47 500	71 800	2,08	2,40	2
m.p 4	190	52.3	34.2	2.40	2,33	2,92	15 600	56 500	86 500	2,14	2,11	2
m.p. 131	221	59	40.4	3,85	3,72	3.63	14 600	54 700	79 800	1,73	1.94	2
m.p 142	380	114	80.8	5.49			14 700	53 600	69 000	1.14	1.12	1
m.p. 151	278	76.3	39.7	3.31		3.47	12 000	43 700	84 300	1,88	1.87	1
m.p. 144	241	56.2	25.5	2.26			10 700	45 800	101 000	2,77	2,42	1

†Orientation cristallographique: type 1: axe d'ordre 4—axe c—parallèle à la direction du courant électrique I, type 2: axe d'ordre 4—axe c—perpendiculaire direction au courant électrique I. Les axes cristallins sont orientés suivant les arêtes du cube.

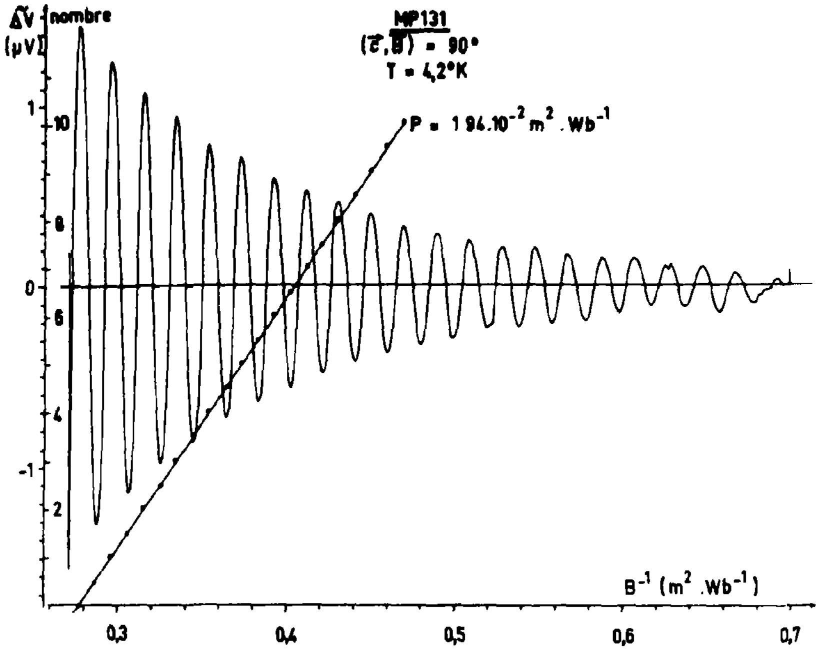

Fig. 3. Oscillations de la magnétorésistance transversale: échantillon; m.p. 131, température. 4·2°K. Orientation cristalline: (c,B) = 90° c étant l'axe d'ordre 4. Les extrêma sont alignés: la période est $P = 1{,}94.10^{-2}\ m^2\ Wb^{-1}$. $1\mu V$ correspond à $\Delta\rho/\rho_0 = 1{,}4.10^{-2}$ ρ_0 étant la résistivité à champ magnétique nul. Cette courbe a été obtenue *après* filtrage TBF. Les cercles et les points représentent respectivement les maxima et les minima.

de l'étude de l'effet SdH. Nous étudierons d'abord la variation angulaire des périodes, puis la variation des amplitudes.

6.1 *Variation angulaire des périodes et forme de la surface de Fermi de* Cd_3As_2

La période du fondamental des oscillations, associée à une seule aire extrêmale de la surface de Fermi, est donnée comme on l'a vu au par. 1 par:

$$P = \frac{eh}{S_m} \qquad (6.1)$$

S_m est la section extrêmale de la S.F. (dans l'espace de la quantité de mouvement) par un plan perpendiculaire à l'induction magnétique. Pour l'ensemble des monocristaux étudiés dans ce travail, nous n'avons observé qu'une seule période fondamentale dans chaque monocristal pour une orientation donnée; par conséquent:

La surface de Fermi ne présente qu'une *seule section* extrêmale pour une orientation donnée. Elle ne peut donc comporter qu'une seule vallée ou plusieurs vallées identiques se déduisant les unes des autres par translation.

De plus, il n'y a qu'un seul type de porteurs qui soit dégénéré (électrons).

La période ne varie pas lorsque, lors d'une rotation du cristal autour de son axe d'ordre 4, celui-ci étant perpendiculaire à l'induction magnétique: la S.F. est donc, comme on pouvait s'y attendre, de révolution autour de l'axe *c*.

On peut essayer d'approximer la surface de Fermi de Cd_3As_2 par un (ou plusiers) ellipsoïde(s).

Nous allons supposer que l'équation de dispersion n'est pas parabolique, mais correspond à une 'bande de Kane'.

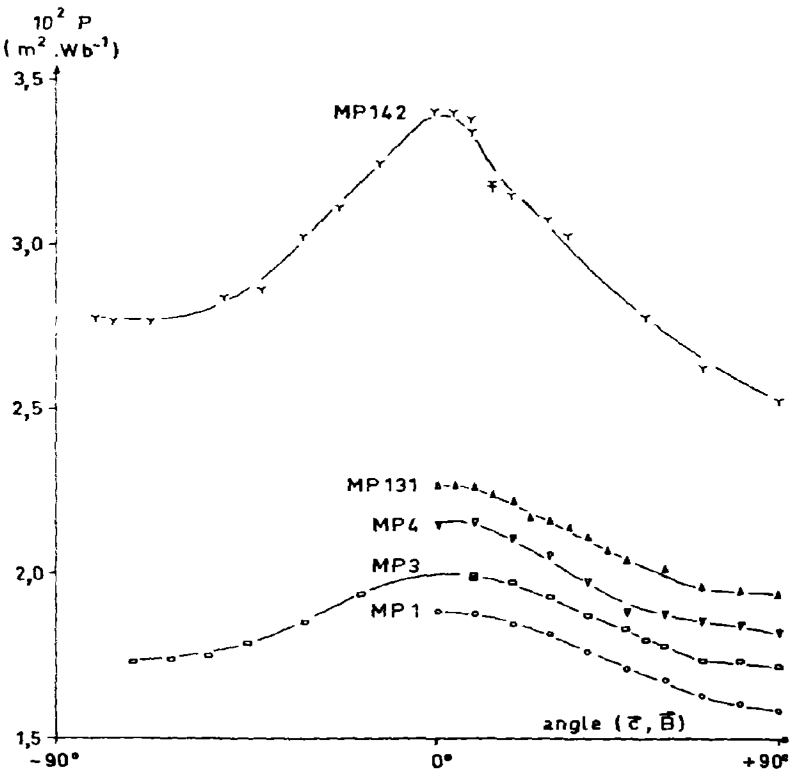

Fig. 4. Variation de la période des oscillations en fonction de l'orientation relative de l'axe cristallographique c et de l'induction magnétique **B**, pour différents échantillons.

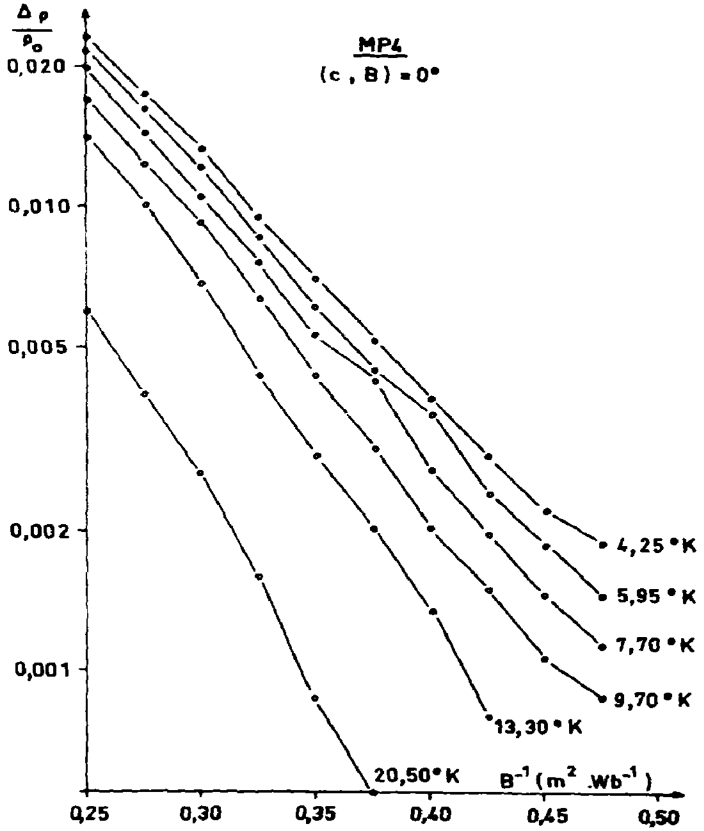

Fig. 5. Variation de l'amplitude des oscillations de la magnétorésistance en fonction de l'*inverse* de l'induction magnétique pour plusieurs températures. Echantillon m.p. 4. Orientation cristallographique telle que (c. **B**) = 0. L'échelle des ordonnées est logarithmique. On constate *que la variation est linéaire*.

La généralisation du calcul de Kane, au cas d'une surface isoénergie anisotrope a été effectuée par Cohen[15].

En suivant Cohen, on peut écrire, dans le *système des axes principaux*, l'équation de dispersion pour les états de la bande de conduction, sous la forme suivante:

$$E(\mathbf{p})\left(1+\frac{E(\mathbf{p})}{E_G}\right)=\frac{p_1^2}{2m_{01}^*}+\frac{p_2^2}{2m_{02}^*}+\frac{p_3^2}{2m_{03}^*} \qquad (6.2)$$

E_G est la largeur de la bande interdite d'interaction (qui peut inclure l'effet de plusieurs bandes).

$E(p)$ est l'énergie; nous ne considérerons que l'énergie de Fermi E_F, car seuls les porteurs situés sur la surface de Fermi participent à l'effet Shubnikov de Haas. m_{0i}^* sont les masses effectives principales au bas de la bande de conduction.

La section extrêmale d'un ellipsoïde de Fermi (6.2), par un plan de cosinus directeurs $(\alpha_1, \alpha_2, \alpha_3)$ perpendiculaire à l'induction B, $B = B(\alpha_1, \alpha_2, \alpha_3)$, est:

$$S_m = 2\pi E_F\left(1+\frac{E_F}{E_G}\right) \times\frac{(m_{01}^* m_{02}^* m_{03}^*)^{1/2}}{(m_{01}^*\alpha_1{}^2+m_{02}^*\alpha_2{}^2+m_{03}^*\alpha_3{}^2)^{1/2}}. \qquad (6.3)$$

Si, de plus, le plan contient un des axes principaux, par exemple l'axe p_2, alors $\alpha_2 = 0$, la période P des oscillations donnée par (6.1) et (6.3) vérifie la relation

$$P^2=\left[\frac{e\hbar}{E_F(1+E_F/E_G)}\right]^2\frac{m_{01}^*\sin^2\theta+m_{03}^*\cos^2\theta}{m_{01}^*m_{02}^*m_{03}^*} \qquad (6.4)$$

où $\theta = (\mathbf{B}, \mathbf{p}_3)$, l'induction B étant située dans le plan $(\mathbf{p}_1, \mathbf{p}_3)$, on voit donc que la variation de P^2 en fonction de $\sin^2\theta$ doit être linéaire, lorsque la S.F. est un ellipsoïde.

Nous avons lissé les résultats expérimentaux obtenus pour la variation angulaire des périodes par la formule ci-dessous, en utilisant le critère des moindres carrés.

$$P^2(\theta) = A\sin^2(\theta-\phi)+B\cos^2(\theta-\phi) \qquad (6.5)$$

θ est l'angle $(\mathbf{B}, \mathbf{p}_3)$, ϕ représente un décalage d'angle introduit pour corriger les erreurs systématiques provenant d'une désorientation de l'échantillon, A et B se déduisent de la formule (6.4).

Le programme est effectué sur une Univac 1107. La correction est généralement de quelques degrés au maximum.

La Fig. 6 représente les résultats des calculs de lissage. On constate que la variation de la période correspond bien à une Surface de Fermi ellipsoïdale ($m_{01}^* = m_{02}^*$ car l'ellipsoïde est de révolution autour de l'axe **c**, ici l'axe 3). La déviation quadratique moyenne, par rapport à une section ellipsoïdale, est comprise entre 0,7 et 5,5% suivant les échantillons.

L'ellipsoïde de Fermi est allongé suivant la direction de l'axe **c** du cristal. le rapport des masses effectives est:

$$\frac{m_{03}^*}{m_{01}^*}=\frac{B}{A}=1{,}415\ \text{(moyenne)}$$

Le rapport des axes de l'ellipsoïde est:

$$\frac{P_\parallel}{P_\perp}=\left(\frac{B}{A}\right)^{1/2}=1.185;\quad \begin{array}{l} P_\parallel: \bar{B}\parallel\bar{c} \\ P_\perp: \bar{B}\perp\bar{c}. \end{array}$$

Le nombre N de vallées ellipsoïdales de la S.F. s'obtient en comparant le nombre n_{SdH} d'électrons par ellipsoïde de Fermi obtenu à partir de l'effet SdH et le nombre total de porteurs n_H obtenu à partir de l'effet Hall:

$$n_H = n_{SdH}N_V \qquad (6.6)$$

$$n_{SdH}=\frac{V}{4\pi^3}=\frac{1}{3\pi^2}\left(\frac{2e}{\hbar}\right)^{3/2}\left(\frac{1}{P_1P_2P_3}\right)^{1/2} \qquad (6.7)$$

V volume limité par une ellipsoïde de Fermi, P_i sont les périodes principales ($P_1 = P_2$).

Nous avons porté l'ensemble des résultats sur le Tableau 2. On en déduit: $N_V = 1$

Il n'y a done qu'un seul ellipsoïde de Fermi.

Nous allons à présent étudier les masses effectives

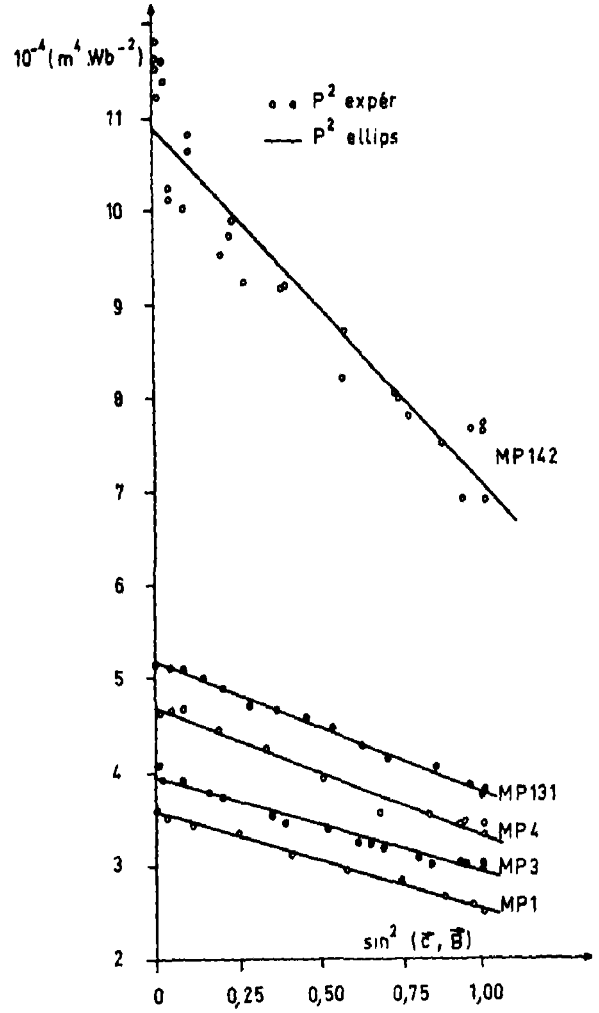

Fig. 6. Variation du carré de la période en fonction de $\sin^2 \varphi$ où φ est l'angle de l'induction avec l'axe c: lissage par la méthode des moindres carrés, pour une variation correspondant à un ellipsoïde ○●P^2 expér, ——P^2 ellips.

6.2 *Variation de l'amplitude des oscillations avec la température et détermination des masses effectives*

La formule donnant la partie oscillatoire de la magnétorésistance est très complexe dans le cas où la S. F. se compose de plusieurs ellipsoïdes (cf. par. 1). Dans notre cas, celui de Cd_3As_2, d'une part la S.F. se compose d'un seul ellipsoïde, et d'autre part les harmoniques de la fréquence fondamentale sont très attenués, grâce en particulier à la technique de filtrage TBF. On peut donc se limiter à un seul terme dans la partie oscillatoire; l'amplitude du fondamental est alors:

$$\left|\frac{\tilde{\Delta\rho}}{\rho_0}\right| = MX^{1/2}\left[T\exp\left(-\frac{2\pi^2 kT_D X m^*}{\hbar e}\right)\right] \Big/ \left[Sh\left(\frac{2\pi^2 kTXm^*}{\hbar e}\right)\right]; \quad X = 1/B \qquad (6.8)$$

Tableau 2. Résultats des mesures des périodes: lissage des résultats par un modèle ellipsoïdal de la surface de Fermi

Echantillon	10^4 (Périodes)^2 (M^4/Wb^2) calculées		Rapport d'anisotropie	Déviation quadratique moyenne par rapp. ellips.	Concentration électronique par ellipsoïde	Concentration électronique totale (Effet Hall)	Nombre de vallées n_H/n_{SdH}
	A	B	B/A	(%)	n_{SdH} (10^{18}cm^{-3})	n_H (10^{18}cm^{-3})	N_r
m.p. 1	2,53	3,55	1,405	0,7	2,61	2,50	1
m.p. 3	2,895	3,94	1,36	1,0	2,40	2,08	1
m.p. 4	3,31	4,66	1,41	1,0	2,11	2,14	1
m.p. 131	3,77	5,18	1,37	1,5	1,95	1,73	1
m p. 142	7,14	10,97	1,54	5,5	1,12	1,14	1
m.p. 151		5,52†			1,87‡		
m.p. 144		3,92†			2,42‡		
m.p. 20§	0,61	0,61	1,00		8,30‡		

†Périodes mesurées.

‡En supposant une anisotropie de 1,40.

§Mesures effectuées sur un échantillon de faible mobilité, dopé au lithium.

m^* est las masse effective cyclotron définie par:

$$m^* = \frac{1}{2\pi}\left(\frac{\partial S_m}{\partial E}\right)_{E_F} \quad \text{(cf. par. 1)} \qquad (6.9)$$

T est la température, T_D est la température de Dingle (cf. par. 1), reliée à un temps de relaxation et M est une constante.

Pour B fixé ($X = 1/B$), on obtient m^* à partir de la variation de l'amplitude en fonction de la température

$$\left|\frac{\Delta\rho}{\rho_0}\right| = M'(X)\frac{T}{Sh(2\pi^2 kTXm^*/\hbar e)}. \qquad (6.10)$$

Nous avons mis au point un programme de lissage, par le critère des moindres carrés pour analyser la variation de l'amplitude des oscillations.

La difficulté provient du fait que le paramètre à déterminer (m^* out T_D) ne figure pas linéairement dans les formules. Nous nous sommes fortement inspirés d'un programme mis au point par Soule *et al.*[16]. Les calculs ont été faits sur un ordinateur Univac 1107. Du fait de la non linéarité, il est nécessaire de partir de valeurs d'approche des paramètres. Les calculs ont été faits pour différentes valeurs de l'induction magnétique. La dispersion est assez faible, environ 3%. La Fig. 7 donne un exemple de lissage. On constate que l'on ne peut pas approximer la fonction hyperbolique par une exponentielle: les variations ne sont pas linéaires lorsque l'échelle des ordonnées est logarithmique. D'où la nécessité d'utiliser un programme de lissage non linéaire.

Nous donnons sur le Tableau 3, en fonction des concentrations électroniques des différents échantillons étudiés, les valeurs des masses effectives obtenues lorsque B est parallèle à l'axe c du cristal.

Tableau 3. Variation de la masse effective, en fonction de la concentration électronique lorsque l'induction magnétique est parallèle à l'axe c

Echantillon	P^* (m^2/Wb)	m^*/m	n_{SdH} (10^{18}cm^{-3})
m.p. 1	0,0188	0,042	2,61
m.p. 3	0,0198	0,0437	2.40
m.p. 4	0,0216	0,0395	2.15
m.p. 131	0,0227	0,0395	1.95
m.p. 142	0,0331	0,031	1.12
m.p. 20	0.0078	0,065	8,30

*P est la période des oscillations.

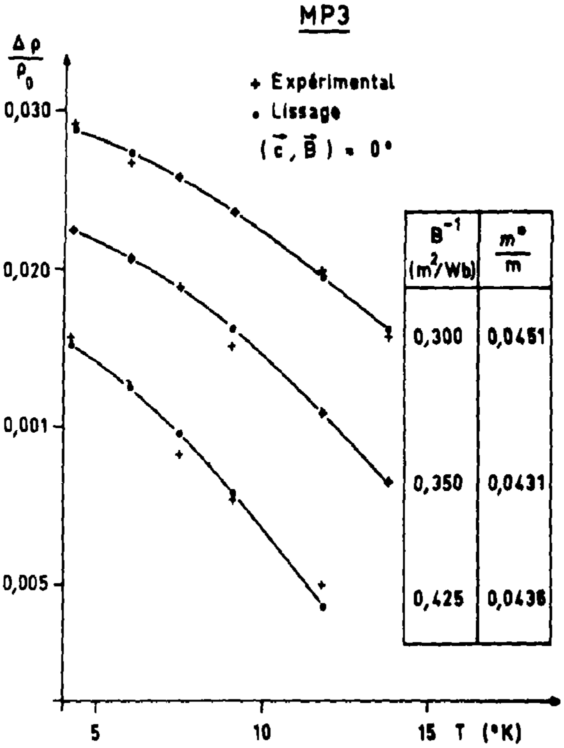

Fig. 7. Détermination de la masse effective cyclotron à partir de la variation des amplitudes oscillatoires en fonction de la température. Comparaison des valeurs expérimentales et des valeurs calculées par lissage non linéaire, par les moindres carrés. Echantillon m.p. 3 (c, B) = 0°. + expérimental, ( ) lissage. On prend pour valeur de m^*, la moyenne obtenue pour plusieurs inductions magnétiques.

On voit que la masse effective cyclotron varie sensiblement en fonction de la concentration électronique, ce qui nous oblige à envisager un modèle non parabolique de la bande de conduction, comme on a commencé à le faire au par. 6.1.

6.3. *Modèle non parabolique de la bande de conduction*

Nous nous limiterons à la direction où **B** est parallèle à l'axe c, en tenant compte du fait que $m^*_{02} = m^*_{01}$, car l'ellipsoïde de Fermi est de révolution autour de **c**.

Dans ces conditions, la période P est obtenue à partir de l'équation (6.4) en faisant $\theta = 0$.

$$P = \frac{e\hbar}{E_F(1+E_F/E_G)}\frac{1}{m^*_{01}} \qquad (6.11)$$

et la masse cyclotron correspondante est:

$$m^* = \frac{1}{2\pi}\left(\frac{\partial S_m}{\partial E_F}\right)_{\theta=0} = \left(1+\frac{2E_F}{E_G}\right)m^*_{01}. \qquad (6.12)$$

D'où il résulte, en éliminant l'énergie de Fermi une relation entre la masse cyclotron et la période[17]:

$$\left(\frac{m^*}{m}\right)^2_{\theta=0} = \left(\frac{m^*_{01}}{m}\right)^2 + \frac{4}{m}\frac{e\hbar}{E_G}\frac{m^*_{01}}{m}\frac{1}{P}. \qquad (6.13)$$

m est la masse de l'électron libre.

Il suffit donc de tracer la variation du carré de la masse cyclotron mesurée, en fonction de l'inverse de la période: si le modèle est vérifié, on doit trouver une droite. Nous avons représenté cette variation sur la Fig. 8. On

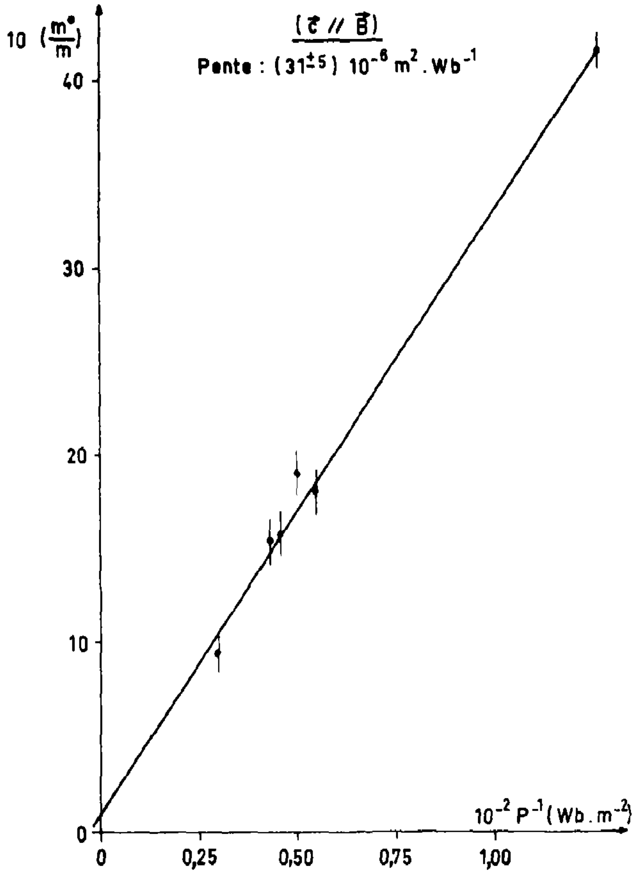

Fig. 8. Variation du carré de la masse cyclotron en fonction de l'inverse de la période. La variation linéaire obtenue est en accord avec un modèle non parabolique de la bande de conduction. La pente est de $(31 \pm 5)\ 10^{-6}\ m^2\ Wb^{-1}$. orientation: (c, B) = 0°.

constate que la variation est raisonnablement représentée par une droite. La pente de cette droite est:

$$s = (31 \pm 5) 10^{-6} \frac{m^2}{W_b}.$$

Cette pente est reliée au carré P_{cv}^2 de l'élément de matrice de l'opérateur impulsion pris entre les états de la bande de valence et la bande de conduction[17], on a dans notre cas:

$$P_{cv}^2 = \frac{E_G}{m_{01}^*/m} = \frac{4e\hbar}{ms}. \qquad (6.14)$$

On trouve:

$$P_{cv}^2 = (15 \pm 2)\ \text{eV}$$

Cette valeur est voisine de celle trouvée pour les composés II–VI et III–V:

InSb $P_{cv}^2 = 20\,\text{eV}$
CdTe $P_{cv}^2 = 17\,\text{eV}$.

La droite représentée sur la Fig. 8 n'est pas définie assez précisément pour que l'on puisse déterminer la masse effective en bas de bande m_{01}^* et obtenir ainsi grâce à (6.14), la largeur de la bande interdite d'interaction E_G. On ne peut donc pas calculer exactement l'énergie de Fermi. On peut avoir une limite inférieure E_F^0 de E_F, en utilisant les équations

(6.11) et (6.12) et en supposant la bande parabolique, m^* étant la masse cyclotron mesurée. On trouve alors que E_F^0 varie de 0, 11 eV pour l'échantillon le moins dopé à 0, 23 eV pour le plus dopé, les températures de Fermi correspondantes étant de 1300° et 2650°K, bien supérieures aux températures d'expériences qui sont inférieures à 40°K.

Connaissant les masses effectives, on peut déterminer les températures de Dingle en étudiant la variation de l'amplitude des oscillations en fonction de l'induction magnétique: il suffit de se rapporter à la formule (6.8).

6.4 *Températures de Dingle*

Elles ont été déterminées par le lissage de la variation des amplitudes en fonction de $X = 1/B$, toujours en utilisant le critère des moindres carrés. Ici, le programme à réaliser est plus simple que pour la détermination de m^*: en effet, on voit d'après la formule (6.8) que l'on peut linéariser l'expression nécessaire au calcul de T_D, et l'on obtient:

$$\begin{aligned} V &= \log\left[X^{-1/2}\left|\frac{\Delta\rho}{\rho_0}\right|\frac{sh(CXT)}{T}\right] \\ &= \log A - CXT_D \qquad (6.15) \end{aligned}$$

avec $C = (2\pi^2 k m^*/eh)$. A est un paramètre indépendant de la température et de l'induction magnétique.

Nous donnons dans le Tableau 4 les températures de Dingle, à 4,2°K, obtenues par le procédé décrit. A titre de comparaison, nous y avons fait figurer les valeurs $T_D(H)$ calculées à partir de la mobilité de Hall: en utilisant le résultat de Kubo

Tableau 4. Valeurs des températures de Dingle et des temps de relaxation

Echantillon	$T_D(SdH)$ (°K)	$T_D(H)$ (°K)	$\tau(SdH)_{sec}$	τf_{sec}
m.p. 1	14,3	1,1	$0,85.10^{-13}$	$1,12.10^{-12}$
m.p. 3	7,8	0,6	$1,55.10^{-13}$	$2,16.10^{-12}$
m.p. 4	17	0,7	$0,71.10^{-13}$	$1,62.10^{-12}$
m.p. 131	7,2	0,7	$1,68.10^{-13}$	$1,80.10^{-12}$
m.p. 142	11,4	1,0	$1,06.10^{-13}$	$1,22.10^{-12}$

$$T_D(H) = \frac{\hbar}{2\pi k\tau_f} = \frac{\hbar}{2\pi k}\frac{e}{\mu m_1^*} \qquad (6.16)$$

où τ_f est le temps de relaxation. On a également indiqué les valeurs de ce dernier, calculé à partir de μ et de T_D

$$\tau_f = \frac{m_1^*\mu}{e} \qquad (6.17)$$

$$\tau(\mathrm{SdH}) = \frac{\hbar}{2\pi k T_D}. \qquad (6.18)$$

On voit qu'il y a un ordre de grandeur de différence entre les paramètres d'amortissement obtenus à partir de l'effet Shubnikov de Haas et ceux obtenus à partir de la mobilité de Hall. Ce résultat peut avoir plusieurs causes:

(1) Il y a probablement des causes d'amortissement supplémentaires provenant par exemple des inhomogénéités dans la répartition des impuretés dans les échantillons.

(2) La théorie utilisée est approximative.

Nous allons à présent résumer les résultats des effets galvanomagnétiques classiques et voir s'ils corroborent ou non la structure de bande proposée pour Cd_3As_2: un seul ellipsoïde allongé suivant l'axe c du cristal.

6.5. *Effets galvanomagnétiques classiques*

Nous avons mesuré la résistivité, le coefficient de Hall et la magnétorésistance:

6.5.1. *Résistivité.* Nous avons mesuré, pour plusieurs échantillons, l'anisotropie de la résistivité à 300°, 78° et 4,2°K. La théorie étendue à un modèle non parabolique prévoit dans le cas d'un ellipsoïde de Fermi allongé suivant l'axe c, que l'on a, lorsqu'on fait l'hypothèse de l'isotropie des temps de relaxation ($\tau_3 = \tau_1$), par manque d'autres données concernant Cd_3As_2:

$$\frac{\rho_{33}}{\rho_{11}} = \frac{m_{03}^*}{m_{01}^*}. \qquad (6.19)$$

On trouve une valeur moyenne de 1,56, pour ce rapport, qui est en accord raisonnalbe, compte tenu des erreurs expérimentales avec le rapport d'anisotropie de masse effective de 1,41, trouvé au par. 6.1 d'après la variation angulaire des périodes.

6.5.2. *Effet Hall*. La théorie prévoit qu'il n'y a qu'un seul coefficient de Hall et qu'il est indépendant du tenseur de masses effectives

$$R_{312} = R_{213} \qquad (6.20)$$

$$R_{ijk} = \left|\frac{\rho_{ijk}}{B}\right|, \qquad (6.21)$$

ρ_{ijk} sont les composantes du tenseur de résistivité de Hall.

l'induction magnétique **B** est orientée suivant l'axe **k**

le vecteur de densité de courant suivant l'axe **j**

la ddp de Hall est mesurée suivant l'axe **i**.

Nous avons vérifié sur l'échantillon m.p. 131 que le rapport (R_{312}/R_{213}) reste constant et voisin de 1, aux erreurs d'expériences près: il vaut 1,04. Pour cela, nous avons fait varier l'induction magnétique de 0,140 à 1,06 Wb/m^2, à deux températures différentes: $T = 300°K$ et $T = 78°K$.

Les résultats des mesures d'effet Hall sont donc également en accord avec le modèle de surface de Fermi proposé.

Voyons à présent la magnétorésistance:

6.5.3. *Magnétorésistance*. La théorie prédit que la magnétorésistance est nulle, dans le cas où il n'y a qu'un ellipsoïde et si l'on se limite au premier terme du développment de Sommerfeld. Même si l'on tient compte des termes d'ordre supérieur du développement de Sommerfeld, on peut montrer que dans notre hypothèse la magnétorésistance doit être proportionnelle à B^2 aux faibles inductions.

Or, des expériences dont nous n'indiquons ici que les résultats nous ont montré que: (1) Le gaz d'électrons est dégénéré et l'on observe cependant de la magnétorésistance; (2) Celle-ci ne varie pas comme B^2; (3) De plus, elle ne correspond pas au 2ème terme du développement de Sommerfeld de l'intégrale de transport. En effet, la variation avec la température que nous avons mesurée n'est pas celle qui est prédite par ce développement et qui doit être en T^2 pour les phonons acoustiques[18]. (4) Signalons également que nous avons observé de la magnétorésistance (aussi bien longitudinale que transversale) négative, dans certains échantillons.

Ces quatre observations ne peuvent pas s'expliquer par l'existence d'un seul type de porteur dégénéré et d'une surface de Fermi composée d'un seul ellipsoïde. Ce point reste obscur. L'explication de ces phénomènes pourrait être recherchée dans les deux voies suivantes:

L'existence d'un second type de porteurs, non dégénéré, de faible concentration et d'assez forte masse effective. Cette hypothèse qui semble expliquer les résultats obtenus dans des mesures de la piézorésistance sur Cd_3As_2[19], notamment la très grande anisotropie de celle-ci, permettrait de rendre compte de l'existence d'une magnétorésistance positive.

L'influence des inhomogénéités qui peuvent produire de la magnétorésistance, aussi bien négative que positive[18].

CONCLUSION

Nous avons utilisé l'effet Shubnikov de Haas pour déterminer la structure de bande de Cd_3As_2, semiconducteur dégénéré de type *n*.

En associant la variation de l'induction magnétique en $1/B \propto t$ et les techniques de filtrage électronique *TBF* avec une exploitation des résultats sur ordinateur, on améliore considérablement les résultats obtenus.

La surface de Fermi proposée se compose d'un seul ellipsoïde allongé suivant laxe *c*, et de révolution autour de celui-ci. Le rapport des axes est de 1,18 et se conserve dans le domaine de concentration étudié.

De plus, la masse cyclotron à la surface de

Fermi varie avec la concentration passant de 0,042 m à 0,065 m lorsque celle-ci varie de 2,60 à 8,30.10^{18} cm^{-3}, dans une direction où l'induction B est parallèle à l'axe c. Cette variation est en accord avec un modèle non parabolique de la bande de conduction.

La valeur du carré de l'élément de matrice, qui caractérise l'interaction de la bande de conduction et de la bande de valence, a été déterminée. On trouve $P_{cv}^2 = 15\,\mathrm{eV}$, valeur voisine de celles intervenant dans les composés III–V (20 eV).

Des mesures plus précises, en particulier sur les effets oscillatoires seraient nécessaires pour déterminer la largeur de la bande interdite d'interaction et la masse effective en bas de bande, ainsi que pour expliquer la magnétorésistance.

REFERENCES

1. LIFSHITZ I. M. et KOSEVICH A. M., *Soviet Phys JETP* **2**, 636 (1956).
2. KUBO R., MYAKE S. J. et HASHITSUME N., *Solid State Physics* (Edité par Seitz et Turnbull), Vol 17, p. 269, Wiley, New York (1965)
3. LIFSHITZ I. M. et KOSEVICH A. M., *J. Phys. Chem. Solids* **4**, 1 (1958).
4. ZDANOWICZ W., LUKASZEWICZ K. et TRZEBIATOWSKI W., *Bull. Acad. polon. Sci., Ser. Sci. Chim.* **12**, 169 (1964).
5. SEXER N., *J. Phys. Rad.* **22**, 807 (1961); *Phys. Status Solidi* **14**, K43 (1966); Thèse, Paris (1965).
6. ZDANOWICZ W., *Proc. Int. Conf. Semicond. Phys Prague 1960*, p. 1095; *Acta Phys. Polon.* **20**, 647 (1961); *ibid.* **21**, 541 (1962), *ibid.* **25**, 663 (1964).
7. UGAI Y. et ZYUBINA T. A., *Izv. Akad. Nauk. SSSR Neory. Mat.* **1**, 860 (1965).
8. LOVETT D. R. et BALLENTYNE D. W. G., *Brit. J. Appl. Phys.* **18**, 1399 (1967).
9. TURNER W. J., FISCHLER A. S. et REESE W. E., *Phys. Rev.* **121**, 759 (1961)
10. MOSS T. S., *Proc. phys. Soc.* **B63**, 167 (1950).
11. HAIDEMENAKIS E. D., *Solid State Commun.* **4**, 65 (1966); *Bull. Am. Phys.* **11**, 401 (1966); *Supp. J. phys. Japan* **21** (1966).
12. SAINT MARTIN J. P. et ROSENMAN I., *Phys. Status Solidi* **11**, 789 (1965).
13. ROSENMAN I., These, Paris (1967) (Bibliographie plus complète sur Cd_3As_2).
14. KOLTIRINE B. et CHAUMEREUIL M., *Phys. Status Solidi* **13**, K1 (1966).
15. COHEN M. H., *Phys. Rev.* **121**, 387 (1961).
16. SOULE D. E., McCLURE J. W. et SMITH L. B., *Phys. Rev.* **134**, 1453 (1964).
17. ELLET M. R., HORST R. B., WILLIAMS L. R. et CUFF H. F., *Proc. Int. Conf. Phys. Semicond. Kyoto 1966*, *Supp. J. phys. Soc. Japan* **21**, 666 (1966).
18. BEERS A. C., *Galvanomagnetic effects in semiconductors Supp. 4* to *Solid St. Physics* (1963).
19. CLAVAGUERA M. T., Thèse 3e cycle, Paris (1969) A paraître

J. Phys. Chem. Solids Pergamon Press 1969. Vol. 30, pp. 1403–1406. Printed in Great Britain.

INFRARED DIELECTRIC DISPERSION IN DIVALENT EUROPIUM CHALCOGENIDES

J. D. AXE
IBM Watson Research Center, Yorktown Heights, N.Y. 10598, U.S.A.

(*Received* 18 *November* 1968)

Abstract—The infrared reflectivity of EuO, EuS and EuSe have been measured at room temperature. The results were analyzed by classical dispersion theory to obtain dielectric response and the long wavelength optical phonon frequencies of these materials. Distortion of the valence electrons by short range forces appears to be an important factor in determining the effective charges of the ions.

THERE HAS been considerable recent interest in the magnetic, magneto-optical, and electrical transport properties of divalent rare earth compounds with the Group VI elements [1–3]. We wish to report the results of an i.r. optical study of the dielectric dispersion and optical phonon modes in three europium chalcogenides, EuO, EuS and EuSe.

EuO crystals were grown by Dr. M. Shafer using a previously reported procedure[4]. The EuS and EuSe crystals were grown from a melt in an evacuated tungsten crucible by Holtzberg. Surfaces suitable for specular reflectance were prepared by standard metallographic polishing procedures on single crystal or polycrystalline specimens of all three materials. With both EuO and EuSe it was possible to also make measurements on cleavage faces. The reflectivity was measured at near-normal incidence by point-by-point comparison with an aluminized surface at many frequencies between 50 cm^{-1} and 4000 cm^{-1}. A grating monochromator provided radiation with a spectral bandwidth ranging between 1 cm^{-1} and 10 cm^{-1}. All measurements were made at room temperature.

Reflectivity data, representative of the three materials, is shown in Fig. 1–3. Two different methods were used to derive the optical constants from the measured reflectivity. The first consisted of a least-square adjustment of the parameters of a classical oscillator response function of the form,

$$\hat{\epsilon}(\omega) - \epsilon_\infty = \sum_{i=1}^{N} \Delta\epsilon_i \Omega_{ti}^2 / (\Omega_{ti}^2 - \omega^2 + i\gamma_i\omega). \quad (1)$$

The best fitting reflectivities derivable from this functional form are shown as solid lines in Figs. 1–3. For EuS and EuSe a single resonant term in equation (1) provided a satisfactory representation of the observed reflectivity data. This is entirely in accord with our expectations based upon the existence of a single transverse optic phonon frequency for materials with the cubic rock salt structure. In EuO, however, besides a strong primary resonance at about 200 cm^{-1}, it was necessary to assume another much weaker resonance at higher frequencies in order to account for the pronounced dip in the reflectivity seen at about 350 cm^{-1}.

In the second method of analyzing the reflectivity data use was made of the phase shift dispersion relation[5] in order to calculate all the pertinent optical constants. For any one sample the dielectric response resulting from this procedure was very similar to that predicted by the best fitting classical oscillator response function. Since this latter procedure furnishes a much more economical summary of the derived optical constants, we have chosen to report only these results, given in Table 1. With regard to these results, it must be pointed out that relatively minor, but definite, differences were observed in the measured reflectivities of different samples

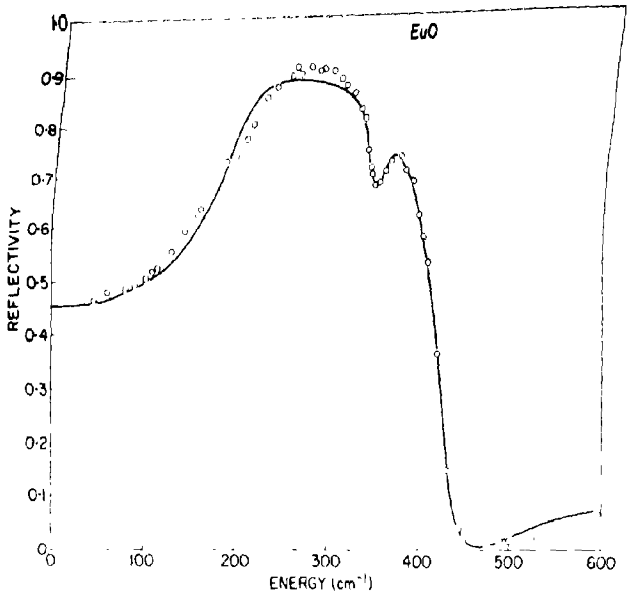

Fig. 1. The i.r. reflectivity of EuO. The circles represent measured data points. The solid curve is a least-square fit to a classical damped oscillator form.

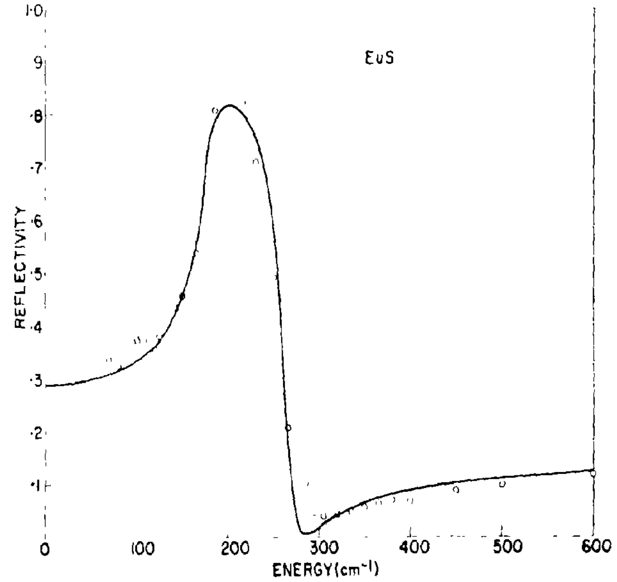

Fig. 2. The i.r. reflectivity of EuS.

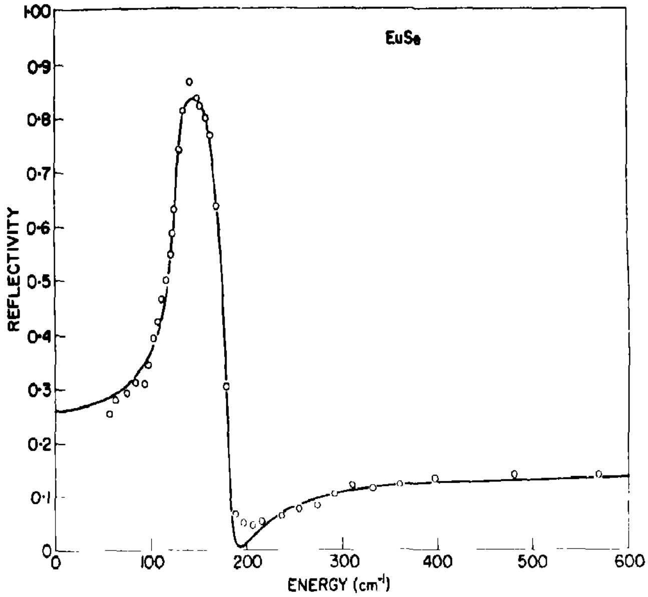

Fig. 3. The i.r. reflectivity of EuSe.

Table 1. Summary of classical dispersion analysis of the i.r. dielectric response of three europium chalcogenides

	Ω_t (cm⁻¹)	γ (cm⁻¹)	$\Delta\epsilon$	Ω_l (cm⁻¹)	e_t^*/e
EuO			ϵ_∞ = 5·3 ± 0·4		1·12
Mode 1	199·3 ± 1·5	23·0 ± 1·3	18·5 ± 3·6	346·3 ± 1	
Mode 2	350·1 ± 1·4	25·7 ± 2·1	0·08 ± 0·01	426·8 ± 5	
			ϵ_0 = 23·9 ± 4·0†		
EuS			ϵ_∞ = 5·0 ± 0·6		1·01
	178·4 ± 2·0	12·1 ± 3·2	6·1 ± 0·9	266·5 ± 1·8	
			ϵ_0 = 11·1 ± 1·5		
EuSe			ϵ_∞ = 4·7 ± 0·2		0·97
	127·8 ± 0·5	9·5 ± 2·0	4·7 ± 0·6	182 ± 3	
			ϵ_0 = 9·4 ± 0·8		

†The error limits shown on ϵ_∞, $\Delta\epsilon$ and ϵ_0 represent (indirectly) estimates of the absolute accuracy of the reflectivity measurements at various wavelengths. The error limits on the other quantities represent deviations between least square fitting at two or more samples of the same material

of the same material. It is possible that some of the discrepancies arose in surface preparation, but since it was not clear that this was the only factor, we chose to separately fit the results from all samples and to treat the results on an equal footing. The values given in Table 1 are thus an average set of parameters which fit no single set of data. The error limits, however, were chosen large enough to include the variations found among individual samples.

Berreman[6] has shown that the presence of microscopic pits or foreign inclusions in an otherwise specular surface can give rise to spurious structure in the reflectivity spectrum of a substance similar to that observed in our EuO samples. The effect we observed was not introduced during surface preparation since it was clearly present in cleaved and polished surfaces alike. The possibility remains that inclusions of some sort distributed throughout the bulk of the material are responsible, but it appears more likely that the observed minor mode is intrinsic to EuO and associated with multiple phonon absorption. In this regard it is of interest to note that the reflectance spectra of the isomorphic alkaline earth oxides MgO, CaO and SrO all appear to show very similar (and incompletely understood) structure near the short wavelength edge of the principle restrahl band[7].

The parameters ω_t are to be identified with the frequency of the long-wavelength transverse optic modes. Estimates of the frequencies of the longitudinal optic modes, Ω_l, which are important in any discussion of electron–phonon coupling, were obtained from the poles of $[\hat{\epsilon}(\omega)]^{-1}$[8], and are also listed in Table 1.

Another quantity of interest which can be derived from these measurements is the Szigeti effective charge of the ions, arrived at by correcting the fundamental mode resonance strength, $\Delta\epsilon$, for electronic polarization effects due to local electric fields[9, 10].

$$(e_s^*)^2 = \left(\frac{9v}{4\pi e^2}\right)\frac{\Delta\epsilon}{(\epsilon_\infty + 2)^2}\mu\Omega_l^2 \qquad (2)$$

where v = unit cell volume and $\mu = m_+m_-/(m_+ + m_-)$ is the 'reduced mass' of the unit cell. In fully ionic compounds the deviation of e_s^* from the formal ionic charge is taken to be a measure of the distortion of the outer electron shells by interatomic repulsive forces. A relationship between the effective charge and the electronic polarizability of ions, α, has been noted for several types of materials, and simple shell model considerations suggest the effective charge for series of chalcogenide compounds MX, should be related to a dimensionless polarizability parameter $x = (K\alpha_x/e^2)$ in an approximately linear way[10, 11]. $(K = \mu\Omega_t^2)(\epsilon_0+2)/(\epsilon_\infty+2)$ is the effective short range force constant coupling the positive and negative sublattices[9]. The fact that such a correlation is indeed possible (Fig. 4) suggests that ion shell distortion is important in determining the effective charges of simple chalcogenide compounds, although undoubtedly covalency also plays some role in reducing the effective charges.

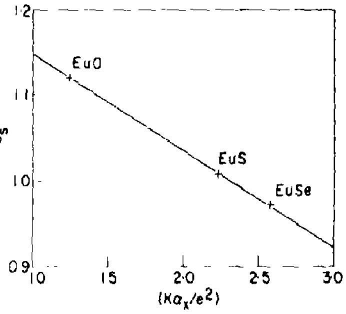

Fig. 4. A correlation of the Szigeti effective charges, e_s^*, of the europium chalcogenides with the reduced electronic polarizabilities of the anions (The polarizabilities, α_x, are taken from Tessman, Kahn and Shockley, *Phys. Rev.* **92**, 890 (1953)).

Acknowledgements—We thank Dr. F. Holtzberg and Dr. M. Shafer for kindly supplying the samples upon which these measurements were performed, and Dr. S. Methfessel and Dr. S. von Molnar for several useful discussions. We also acknowledge the capable technical assistance of J. H. Kaplan and R. Hammer throughout this work.

REFERENCES

1. HOLTZBERG F., MCGUIRE T. R. and METHFESSEL S., *J. appl. Phys.* **37**, 976 (1966).
2. SUITS J. C., ARGYLE B. E. and FREISER M. J., *J. appl. Phys.* **37**, 1391 (1966).
3. MOLNAR VON S. and METHFESSEL S., *J. appl. Phys.* **38**, 959 (1967).
4. MCGUIRE T. R. and SHAFER M. W., *J. appl. Phys.* **35**, 984 (1964).
5. See, for example, STERN F., In *Solid State Physics*, Vol. 15, p. 333. Academic Press, New York (1963).
6. BERREMAN D. W., *Phys. Rev.* **163**, 855 (1967).
7. JACOBSEN J. L. and NIXON E. R., *J. Phys. Chem. Solids* **29**, 967 (1968).
8. BARKER A. S., Jr., *Phys. Rev.* **136**, A1290 (1964).
9. SZIGETI B., *Proc. R. Soc.* **A204**, 51 (1950).
10. COCHRAN W., *Phil. Mag.* **4**, 1082 (1959).
11. AXE J. D. and PETTIT G. D., *J. Phys. Chem. Solids* **27**, 621 (1966).

J. Phys. Chem. Solids Pergamon Press 1969. Vol. 30, pp. 1407–1410. Printed in Great Britain.

A STUDY OF THE SUPERCONDUCTIVITY OF ANTIMONY UNDER PRESSURE AND A SEARCH FOR SUPERCONDUCTIVITY IN ARSENIC*

J. WITTIG
Institute for Pure and Applied Physical Sciences, University of California, San Diego, La Jolla, Calif. 92037, U.S.A.

(*Received* 18 *November* 1968)

Abstract—The high pressure phase of antimony stable above 85 kbar is superconducting. The transition temperature is 3·55°K at 85 kbar, decreasing very slightly with pressure. Neither an analogous phase transformation nor superconductivity was found in arsenic up to 200 kbar.

SUPERCONDUCTIVITY of pure Sb was first observed below about 2·7°K in a metastable phase of unresolved structure which was prepared by releasing pressure in excess of 100 kbar at 77°K[1]. Preliminary results on the behavior of thin films of Sb condensed onto a cold substrate at helium temperatures reveal superconductivity[2], if the vapor consists at least in part of Sb-atoms[3] besides a variety of Sb-molecules normally found in the vapor. These widely different quenching techniques apparently are capable of producing metastable structures which are metallic and superconducting in contrast to normal rhombohedral Sb. For a better understanding of these data, it is desirable to report the superconducting properties of Sb under true equilibrium conditions at high pressure. The recent discovery of superconductivity of metallic phosphorus under pressure[4, 5], prompted this search for superconductivity in antimony and arsenic which are in the same column of the periodic table.

The high pressure apparatus and the experimental procedure have been described in detail[6]. The electrical resistance of high purity powder samples is studied in its dependence on pressure or temperature. Fig. 1 is a typical plot of the room temperature resistance of Sb against press force which shows a large resistance increase[7] caused by a first order lattice transformation at about 85 kbar (pressure according to Bridgman's old 'V-scale'). As might be expected, as well as from the position of antimony in the periodic table and the various quenching experiments cited above, this high pressure phase, in fact, turned out to be superconducting.

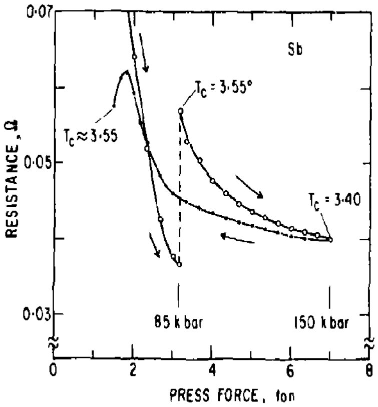

Fig. 1. Room temperature resistance of Sb vs. press force. For this specimen T_c was measured at 85 kbar, 150 kbar and, for a two phase sample, again at 85 kbar.

At room temperature the phase transformation went to completion at constant pressure generally within a few minutes (cf. Fig. 1. Resistance drift indicated by the vertical dashed line at 85 kbar). After cooling the

---

*Research sponsored by the Air Force Office of Scientific Research, Office of Aerospace Research, United States Air Force, under AFOSR grant number AF-AFOSR-631-67.

sample in this state of compression at 85 kbar, we found repeatedly a critical temperature of 3·55°±0·02°K (Fig. 2, curve 1). As discussed elsewhere[6] the midpoint of the transition ($R/R_n = 0·5$) is considered as a representative value of T_c belonging to the mean sample pressure. On further increase of pressure, T_c is shifted only *very slightly* (in contrast to the majority of non-transition metal superconductors) to lower temperatures, T_c being 3·40°K at about 150 kbar (Fig. 2, curve 2). Several independent measurements at intermediate pressures revealed superconducting transitions between these temperatures. Thus the very small negative pressure dependence of T_c ($dT_c/dp \approx 2·5 \times 10^{-6}$°K/bar) has been clearly confirmed for this high pressure phase between 85 and 150 kbar.

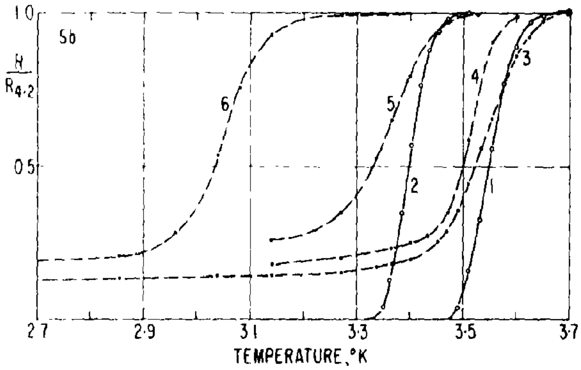

Fig. 2. Superconducting transition curves of SbII 1: p = 85 kbar. 2: 150 kbar, 3: 85 kbar, 4, 5, 6: pressure successively removed to ambient at 4°K.

From X-ray work there is still remarkable uncertainty concerning the sequence and even the structure of pressure induced polymorphs of Sb[1, 8]. An additional simple-cubic phase is claimed to exist in a narrow pressure interval between about 70 and 85 kbar[8] in close analogy to the cubic phase of phosphorus at high pressures[9] which is superconducting [5]. Therefore, it was decided to examine this pressure interval more carefully in order to see whether this phase is also superconducting.

By means of the inhomogeneous pressure distribution along the sample length on the pressure releasing cycle it is easy to study a two-phase sample; the two phases being spatially separated but electrically connected in series. Thus the pressure was removed at room temperature until just a small portion of the sample had reconverted to the low pressure phase as evidenced from a slight resistance drop (cf. Fig. 1). The center part of the specimen, always experiencing a higher pressure, remained in the high pressure phase. At low temperatures, a superconducting transition was found around 3·55°K (Fig. 2, curve 3) which undoubtedly belongs to that part of the sample which is still in the high pressure phase. A normal conducting 'tail' indicated that the reconverted portion of the sample in the low pressure phase is not superconducting down to 1·3°K, if at all. Hysteresis of the reverse phase transformation on the pressure releasing cycle may inhibit the formation of an intermediate cubic phase between 70 and 85 kbar in this experiment. Therefore, an analogous experiment was done on the pressure *increasing* branch. Starting from zero pressure, the pressure distribution is known to be very inhomogeneous along the sample upon a second application of load in this opposed anvil device. Utilizing this feature one easily gets a two phase sample similar to that during the release of pressure. The low temperature measurement again gave a resistance drop at 3·55°K and a normal tail down to the lowest temperature due to the untransformed portion of the sample.

Thus the present low temperature data clearly show that if an intermediate simple-cubic phase really exists, it must be non-superconducting or superconducting with the same T_c as the high pressure phase (i.e. approx. 3·55°K).

On further release of pressure at 4·2°K in several steps the superconducting transition successively shifts to lower temperatures (Fig. 2, curves 3–5). Finally, at ambient pressure a broad transition between 2·9° and 3·2°K was observed (Fig. 2 curve 6). The location of this broad zero pressure transition was not reproducible. Two independent experiments gave transitions between 2·7° and 3·1°K. However, these temperatures are very close to that observed previously ($T_c = 2{\cdot}7$°K) for samples which were similarly quenched at liquid nitrogen temperature[1].

From the X-ray pictures of Sb at high pressure (90 kbar) and of the quenched phase at zero pressure, there was already some doubt concerning the identity of these phases [1]. This view is strongly corroborated by the present T_c-measurements. Under the plausible assumption that the sign of dT_c/dp will not change below 85 kbar for the high pressure phase, one would expect a T_c higher than 3·55°K at zero pressure for the pure retained high pressure phase, contrary to our observation. The broad zero pressure transitions (which cannot be attributed to pressure inhomogeneity) are another indication that the high pressure phase cannot be quenched to zero pressure without partial or full transformation into another modification.

Arsenic, now in the periodic table nearly completely surrounded by elements which possess superconducting metallic modifications under high pressure, very likely will become superconducting if the covalent bonds of the normal semimetallic rhombohedral structure are destroyed. Yet no similar high pressure phase transformation as in Sb has been observed. Three runs were made on As to pressures as high as 200 kbar (the ultimate limit of the present unsupported opposed anvil press, using heavily workhardened pistons). No resistance anomaly with pressure was found at room temperature, and no sign of superconductivity was detected at this pressure down to 1·3°K.

Apparently, as a general feature, both As and Sb have much higher transformation pressures to the first truly metallic modification than their neighboring elements in the fourth and sixth column of the periodic table: Ge (~ 115 kbar) and Se (~ 130 kbar), Sn (~0 kbar) and Te (~43 kbar) respectively. If there exists a lattice transformation in As at higher pressures to a structure which is isomorphous to the high pressure phase of Sb we predict a higher T_c (about 5°K) for this hypothetical superconducting As than for Sb at 85 kbar. Despite the lack of full verification by X-ray structure determination under pressure, there seems to be a strong tendency among nontransition elements of the same group, especially following the 3*d* and 4*d* transition series, to adopt isomorphous crystal structures under pressure. A compari-

Table 1. *Superconducting transition temperatures of non-transition metals following the* 3d *and* 4d *transition series*

	Zn	GaII	GeII	As	SeII
T_c, °K	0·85	6·4[10]	5·4[11]	?	~ 6·7[12]
P, kbar	0	~35	~115	(>200)	~130
Lattice structure	hcp	fct	bct	?	?

	Cd	In	Sn	SbII	TeII
T_c, °K	0·52	3·4	3·7	3·6[This work]	~4·5[11]
P, kbar	0	0	0	~85	~43
Lattice structure	hcp	fct	bct	hcp(?)[1, 8]	?

son of the critical tempeatures T_c of such pairs (Zn–Cd, hcp, isomorphous and metallic already at ambient pressure; GaII–In, fct; GeII–Sn, white tin structure; SeII–TeII, structure still unknown) shows that so far without exception the lighter element has the higher T_c.

This can readily be seen from Table 1 which contains the relevant data. The pressures listed are the transformation pressures to the metallic phase or zero if the element is metallic already at ambient pressure.

In order to see whether this empirical rule for the magnitude of T_c for the special class of non-transition metals considered here is not completely fortuitous, it would be most helpful to have a structure determination of the superconducting modification SeII and TeII. In addition, a search for superconductivity in As at the highest pressures which can be achieved today in static high pressure apparatus, very likely will provide some check for the outlined general rule. It should be noted, however, that the apparent trend of the T_c-values does not hold for the sixth period: the high pressure modification BiIII which presumably is isomorphous to SbII[1] has a much higher T_c (7·2°K) than SbII.

Acknowledgements – Thanks are due to Professor B. T. Matthias and Professor H. L. Luo for their critical comments in connection with this note.

REFERENCES

1. McDONALD T. R. R., GREGORY E., BARBERICH G. S., McWHAN D. B., GEBALLE T. H. and HULL G. W., Jr., *Phys. Lett.* **14**, 16 (1965).
2. BAUMANN F., *Verh. Deut. Phys. Ges.* **3**, 214 (1966) and Private communication.
3. BAUMANN F., KESSLER J. and ROESSLER W., *J. appl. Phys.* **38**, 3398 (1967).
4. BERMAN I. V. and BRANDT N. B., *Soviet Phys. JETP Lett.* **7**, 323 (1968).
5. WITTIG J. and MATTHIAS B. T., *Science* **160**, 994 (1968)
6. EICHLER A. and WITTIG J., *Z. angew. Phys.* **25**, 319 (1968).
7. VERESHCHAGIN L. F., SEMERCHAN A. A., KUZIN N. N. and POPOVA S. V., *Soviet Phys. Doklady* **6**, 41 (1961).
8. VERESHCHAGIN F. and KABALKINA S. S., *Soviet Phys. JETP* **20**, 274 (1965)
9. JAMIESON J. C., *Science* **139**, 1291 (1963)
10. BUCKEL W. and GEY W., *Z. Phys.* **176**, 336 (1963)
11. WITTIG J., *Z. Phys.* **195**, 215 (1966).
12. WITTIG J., *Phys. Rev. Lett.* **15**, 159 (1965).

J. Phys. Chem. Solids Pergamon Press 1969. Vol. 30, pp. 1411-1416. Printed in Great Britain.

MELTING OF GERMANIUM TO 65 KBAR*

S. N. VAIDYA, J. AKELLA and G. C. KENNEDY
Institute of Geophysics and Planetary Physics, University of California, Los Angeles, Calif. 90024, U.S.A.

(*Received* 13 *November* 1968)

Abstract—Melting curve of germanium has been determined to 65 kbar in a single stage piston-cylinder apparatus. The melting curve is slightly concave towards the pressure axis. This trend is apparently in agreement with Bundy's data replotted on the revised pressure scale.

INTRODUCTION

THE MELTING curve of germanium was first reported by Hall[1] up to a nominal pressure of 180,000 atm. The results of Hall's measurements in belt apparatus were revised by Bundy and Strong[2] who showed that the pressure of 180,000 atm in Hall's experiment corresponded roughly to 100 to 110 kbars. Hall's melting data did not extrapolate to the 1 atm melting point. The initial slope of the revised melting curve was −5·5°C/kbar. Jayaraman *et al.*[3] reported the melting curve of germanium along with those of some other semiconductor compounds. These determinations were made in piston-cylinder apparatus. The melting curve reported by these authors extrapolates to the 1 atm melting temperature of 936°C and has a constant slope of −3·8°C/kbar up to 50 kbar. Bundy[4] has reinvestigated the phase diagrams of germanium and silicon to 200 kbar and 1000°C in belt apparatus by observation of electrical resistance changes. Bundy reported that the melting curve of germanium had a slope of −3·3°C/kbar up to the triple point of the semiconducting, the metallic and the liquid phases at 103 ± 5 kbar and 600 ± 15°C. The triple point co-ordinates estimated by Jayaraman *et al.* from the extrapolation of their melting data and by analogy with the phase diagram of InSb are 115 kbar and 500°C.

The nature of the semiconductor to metal transition in germanium at about 120 kbar at room temperature has been studied by Minomura and Drickamer[5] using a high pressure electrical resistance cell and by Jamieson[6] in the X-ray anvil apparatus. Bates *et al.*[7] have reported on the metastable phases of germanium.

The present study reports the melting curve of germanium to 65 kbar as determined in single stage piston-cylinder apparatus and compares it with those of Jayaraman *et al.* and Bundy.

EXPERIMENTAL METHODS

The experiments were performed in an end-loaded single stage piston-cylinder apparatus previously described (Cohen *et al.*[8]). High pressures were achieved by monitoring the unsupported length of the piston and by making this length very small at the highest pressure. It has been shown by Haygarth and Kennedy[9] that the crushing strength of tungsten carbide piston can be increased by reducing the length of unsupported piston. The pistons were fitted with a stationary and sliding binding rings of Vascomax 300 steel with 2 per cent interference in order to control the length of unsupported piston. The details of this method have been described elsewhere [10, 11]. Pressure vessels, with bushing of Carboloy 55A grade (tungsten carbide with 13 per cent cobalt binder) and pistons of Carboloy 883 grade (with 6 per cent binder) were used in the present work.

---

*Publication no 718 Institute of Geophysics and Planetary Physics, University of California, Los Angeles, Calif 90024, U.S.A.

Intrinsic germanium of 99·99+purity was used in the present experiments. The one atmosphere melting temperature obtained from the extrapolation of our melting curve is 938°C, the value quoted in the literature is 936°C.

Conventional furnace assembly[12] was employed in the present experiments except that boron nitride filled the graphite furnace instead of talc. Thermocouple and sample contamination took place when talc filled the graphite furnace, possibly because of decomposition of talc into enstatite and water at high temperature. The boron nitride parts were fired at 480°C for 48 hr to free them from ammonia and water.

It is difficult to find a suitable encapsulating material for germanium since it alloys readily with almost all metals[13]. The experiments employing molybdenum and tantalum capsules gave lower melting temperatures and X-ray examination of the material showed evidence of alloying. Alloying was also observed in niobium capsules when the experiments extended over long period Graphite apparently does not alloy with germanium and was used as the encapsulating material in these reported experiments. Quartz crucibles lined with graphite have been used under vacuum for casting rods of germanium of high purity[14]. A platinum foil 0·004 in. thick followed by a tantalum disc (0·01 in.) was placed between the graphite capsule and the thermocouple. The platinum foil prevented reaction between tantalum and graphite.

Temperatures were measured with Pt-$Pt_{10}Rh$ thermocouples in all the experiments. Chromel-alumel thermocouples were tried in some experiments, but they did not give reproducible results. The melting and freezing at different pressures was detected by differential thermal analysis. The rate of heating and cooling in the present experiments ranged from 6 to 8°C/sec. At a given pressure the melting and freezing temperatures were taken at least four times before datum points were considered fixed. Approximately 70 such datum points were taken—these deviated only 1–2°C from a smooth curve.

The assembly was initially compressed to the maximum pressure planned for the experiment. The temperature was then taken to the melting temperature. The melting and freezing temperatures were taken on decompression and compression cycles. The correction for friction was applied by assuming the friction to be symmetrical and the true pressure was obtained by interpolation. The double value of friction was roughly 4 kbars at the maximum pressure of 65 kbar. The final pressures are believed to be accurate to ±0·5 kbar.

The difference between the sample and the thermocouple seal temperature was determined in a separate experiment in order to apply the correction for the pressure effect on the e.m.f. of Pt–$Pt_{10}Rh$ thermocouples. The difference between the sample and thermocouple seal temperatures was found to be a function of the sample temperature and was independent of pressure.

RESULTS

The results from the present work along with those of Jayaraman *et al.*[3] and Bundy [4] are presented in Fig. 1. The corrections for effect of pressure on Pt–$Pt_{10}Rh$ thermocouple e.m.f. were taken from the recent results of Getting and Kennedy[15] (Table 1). These experiments up to 30 kbar show a monotonic rise in thermocouple e.m.f. correction with pressure and temperatures and therefore the values of correction at higher pressure were obtained by extrapolation. The temperature corrections to the Pt–$Pt_{10}Rh$ thermocouple ranged from 4°C at 10 kbar and 900° to 18·8°C at 50 kbar and 600°C. These values are roughly half of those reported by Hanneman and Strong[16, 17] from their experiments in 'belt' apparatus and calculations.

The melting curve from the present study shows a curvature towards the pressure axis. The initial slope of our corrected melting curve is −3·24°C/kbar. Jayaraman *et al.*[3]

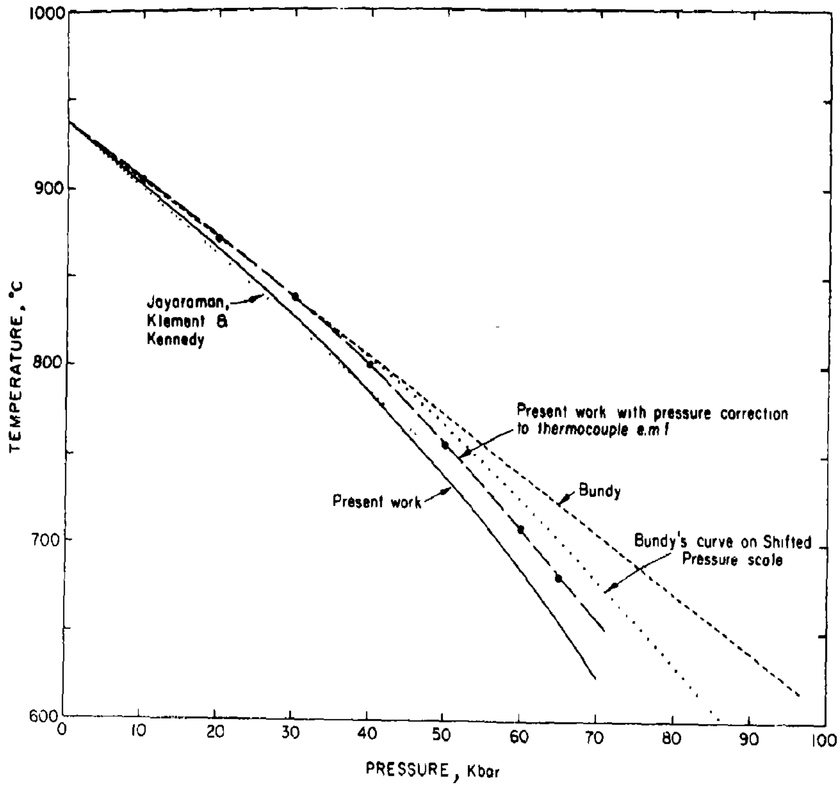

Fig. 1. Melting temperature of germanium vs. pressure.

Table 1.

Pressure (kbar)	T_m(uncorrected) (°C)	T_m(corrected) (°C)
0	936	936
10	900	904
20	860	867
30	827	838·5
40	785	800·5*
50	738	757*
60	685	707*
65	657	681*

*The correction for pressure effect on Pt-$Pt_{10}Rh$ thermocouple e.m.f. taken from extrapolation of the experimental data of Getting and Kennedy[15] to 30 kbar

and Bundy[4] reported the slope of melting line as −3·8°C/kbar and −3·3°C/kbar respectively. The initial slope obtained from the Clapeyron equation is −3·4 to −3·5°C/kbar[4].

The melting temperatures observed in the present work are 6–10° lower than Bundy's values, and are 3–4° higher than those of Jayaraman *et al.* at 20–25 kbar. At higher pressure as the melting curve becomes concave towards the pressure axis, melting temperatures a few degrees lower than those of Jayaraman *et al.* were obtained.

Bundy's calibration of belt apparatus in the lower pressure range is based on Bi I–II, Ba I–II, and Bi III–V, transitions taken as 25, 58 and 88 kbar respectively. The value of the Bi I–II transition pressure measured in a rotating piston apparatus is 25·38 kbar (Kennedy and La Mori[18]) and 25·499 kbar in a piston-cylinder apparatus with a dead weight piston gauge (Hydemann[19]). The pressures of the Ba I–II and Bi III–V transitions have been recently established from detailed studies in the piston-cylinder apparatus. Resistance observations of the sample embedded in a

9. HAYGARTH J. C. and KENNEDY G. C., *Rev. scient. Instrum* **38**, 1590 (1961).
10. HAYGARTH J. C., LEUDEMANN H. D., GETTING I. C. and KENNEDY G. C., *J. Phys. Chem. Solids* **30**, 1417 (1969).
11. AKELLA J., VAIDYA S. N. and KENNEDY G. C., To be published.
12. KLEMENT W., COHEN L. H. and KENNEDY G. C., *J. Phys. Chem. Solids* **27**, 171 (1966)
13. HANSEN M. and ANDERKO K., In *Constitution of Binary Alloys*, McGraw-Hill, New York (1968)
14. SEILER K. O., U.S. Patent No. 2,780,539 quoted in *Chem. Abs* **51**, 6492 i.
15. GETTING I. C. and KENNEDY G. C., To be published.
16. HANNEMAN R. E. and STRONG H. M., General Electric Technical Information Series, Rep. No. 65-RL-4033 X (1965)
18. KENNEDY G. C. and LA MORI P. N., *J. geophys. Res*. **67**, 851 (1962)
19. HEYDEMANN P. L. M., *J. appl. Phys*. **38**, 2640 (1967)
20. HAYGARTH J. C., GETTING I. C. and KENNEDY G. C., *J. appl. Phys*. **38**, 4557 (1967).
21. LINDEMANN F. A., *Phys. Z.* **11**, 609 (1910).
22. PINES D., In *Elementary Excitations in Solids*, pp. 34–37. Benjamin, New York (1964).
23. GILVARRY J. J., *Phys. Rev.* **102**, 308 (1956).
24. GSCHNEIDNER K. A. Jr., In *Solid State Physics* (Edited by F. Seitz and D. Turnbull), Vol. 16, pp. 378–381. Academic Press, New York (1964).
25. SIROTA N. N., In *Semiconductors and Semi Metals* (Edited by R. K. Willardson and A. C. Beer), Vol. 4, p. 139. Academic Press, New York (1968).
26. KRAUT E. A. and KENNEDY G. C., *Phys. Rev.* **151**, 668 (1966).
27. GILVARRY J. J., *Phys. Rev. Lett.* **16**, 1089 (1966).
28. VAIDYA S. N. and GOPAL E. S. R., *Phys. Rev. Lett* **17**, 635 (1966)
29. BRIDGMAN P. W., *Proc. Am. Acad. Arts Sci.* **76**, 71 (1948)
30. BRIDGMAN P. W., *Proc. Am. Acad. Arts Sci.* **76**, 55 (1948).

J. Phys. Chem. Solids Pergamon Press 1969. Vol. 30, pp. 1417–1424. Printed in Great Britain.

DETERMINATION OF PORTIONS OF THE BISMUTH III-V AND IV-V EQUILIBRIUM BOUNDARIES IN SINGLE-STAGE PISTON-CYLINDER APPARATUS*

J. C. HAYGARTH†, H. D. LUEDMANN‡, I. C. GETTING and G. C. KENNEDY
Institute of Geophysics and Planetary Physics, University of California, Los Angeles, Calif. 90024, U.S.A.

(*Received* 19 *September* 1968; *in revised form* 16 *October* 1968)

Abstract—The Bi III–V and IV–V equilibrium boundaries were studied by monitoring electrical resistance changes. Extrapolation of the III–V data to 25°C yields an equilibrium transition pressure of 77·5 ± 1·0 kbar. The extrapolation also agrees within experimental error with the pressure of 78·2 kbar determined in a separate experiment at 22°C. The use of the transition as a calibration point is discussed, and a procedure for estimating the compression-stroke transition pressure from the equilibrium transition pressure is proposed. This involves adding 2 kbar to the equilibrium pressure at room temperature.

INTRODUCTION

RECENT work[1] has shown that the pressure of the barium I–II transition at room temperature is 55·0 ± 0·5 kbar, about 4 kbar lower than the previously accepted value. This suggests that the pressures assigned to other calibration points at higher pressures may also be in error. In this paper, we describe a redetermination of portions of the bismuth III–V and IV–V equilibrium boundaries, with particular emphasis on a more accurate estimation of the pressure of the bismuth III-V transition at room temperature, and a precautionary note on its use as a high pressure calibration point.

EXPERIMENTAL

End-loaded piston-cylinder apparatus as described by Boyd and England[2] was used, with modifications to enable it to reach higher pressures. The discovery[3] that the crushing-strength of cemented tungsten carbide pistons increases as the unsupported length decreases has already been used to achieve pressures necessary to observe the barium I–II transition[1]. A limitation of the apparatus is the rather short travel allowed to the piston, as a result of the need to keep the unsupported length of the piston less than that at which breakage occurs[3]. In this study, the piston was fitted with a sliding binding ring, shown in Fig. 1, positioned so as to split up the unsupported length of the piston into two unequal segments. This increases the available piston travel without increasing the unsupported length of the piston. Dividing the piston into two shorter exposed segments allows it to withstand higher stresses. The available travel is not reduced because the sliding binding ring allows the piston to move through it after it collides with the face of the pressure vessel. The exposed length does not increase as quickly on decompression as it decreased on compression because some permanent compaction of the sample occurs on the first compression. In addition, the strength of pistons at very small exposed lengths appears to be higher than was previously realized[3]. The sliding binding ring was of the same material as the stationary binding

---

*Publication no. 690, Institute of Geophysics and Planetary Physics, University of California, Los Angeles, Calif. 90024, U.S.A.

†*Present address:* E. I. Du Pont de Nemours & Co., Inc. Central Research Department, Experimental Station, Wilmington, Del. 19898, U.S.A.

‡*Present address:* Institut fur Physikalische Chemie und Elektrochemie Universitat Karlsruhe, 75 Karlsruhe, Kaiserstrasse 12, Germany.

Three experiments were done, as follows. The piston was first advanced until all the travel was used; no measurements were made during this process because of the unknown force necessary to move the sliding binding-ring. The transition temperature was measured at 0·8 kbar intervals, and 0·4 kbar intervals in the region of the III–IV–V triple point, on decompression to about 45 kbar and on recompression to about 70 kbar. It was then checked at a few pressures on decompression, and on a second recompression, to make sure that the measurements were reproducible.

The transition temperature at a given compression was found by raising the temperature until the transition was partially completed, then reducing the temperature until the back reaction began to run. A dead span temperature interval in which the reaction does not run detectably in either direction with both phases present was found. This temperature interval was independent of the relative amounts of the two phases present. It ranged in size from about 4° at the lowest temperature to about 0·5° near the triple point for the III–V boundary, and was 0·5° for the IV–V boundary near the triple point and less at higher temperatures. The transition temperature was taken as the mid-point of this interval. This method of locating the boundary is referred to later as the isobaric method. It is essential, however, that both phases be present during location of the transition temperature, since continuous heating of pure Bi IV or Bi III leads to a small degree of super heating of these phases into the stability field of Bi V, while continuous cooling of pure Bi V yields a marked degree of supercooling into the stability field of Bi IV or Bi III. Both the extent of superheating and supercooling increase with decreasing temperature along the phase boundaries. These findings are contrary to the report of Klement *et al.* [4]. The magnitude of the superheating and supercooling varied erratically from one temperature cycle to the next, and was little affected by changing the heating and cooling rate. The rate of the V–III and V–IV reactions appeared to increase with the degree of supercooling at any given pressure.

The III–IV boundary was detected, and found to be associated with large hysteresis, confirming the findings of Klement *et al.*[4]. The hysteresis was so large that occasionally the metastable III–V boundary was observed in the neighborhood of the III–IV–V triple point. The III–IV reaction was so sluggish that no attempt was made to delineate accurately the equilibrium boundary.

The III–V boundary was also studied at a number of constant temperatures by cycling the pressure. These experiments are referred to later as the isothermal experiments. The pressure was changed in 0·2 kbar intervals every 0·5 min or every 2·5 min, and the pressures at which the transition began to run on compression and decompression noted. The I–II boundary was also studied at room temperature in this way, to test the validity of the procedure used to calculate the sample pressure.

The III–V boundary was also observed at room temperature using a set-up similar to that described for the barium transition[1]. In this case the pressure was varied continuously at about 0·2 kbar per second.

In all experiments, the pressure of the oil activating the hydraulic ram that drove the piston was measured with a Heise Bourdon-type gage. Since the gage was new it was assumed to be accurate within the limits guaranteed by the manufacturer, and was not calibrated. At the start of each experiment the gage was set to zero when sensing the oil-pressure generated by the weight of the hydraulic ram piston; this eliminated the need to correct for this quantity later. The friction resisting motion of the ram when it was applying no load to the high-pressure piston was unobservable.

RESULTS AND DISCUSSION

The data from the isobaric experiments were in the form of thermocouple e.m.f.'s and oil-pressure values for measurements taken on compression and decompression. They were plotted and resulted in two similar curves whose separation was the double-valued friction. This was made up of the friction between the piston and the pressure chamber bore, and the hysteresis due to the shear strength of the pressure medium. It ranged from about 1·2 kbar at the highest temperature to 1·6 kbar near the triple point for the IV-V boundary, and from about 1·6 kbar near the triple point to 3·0 kbar at the lowest temperature for the III-V boundary. On the assumption that the friction was symmetrical, the mean of compression and decompression values was taken at fixed values of thermocouple e.m.f. The validity of this procedure has been questioned by Pistorius *et al.*[5] but their results and arguments do not appear applicable to this study because the pressure found in these experiments for the I-II boundary at room temperature by assuming symmetrical friction was in good agreement with that reported by Heydemann[6] and Kennedy and La Mori[14].

The corrected oil-pressure values were converted to real pressures by multiplying by the ratio of the area of the hydraulic ram piston to the area of the high-pressure piston. The latter was calculated as described earlier[1]. The diameter of the high-pressure piston was obtained in the present case by adding 0·0068 ± 0·0068 cm to the final diameter of the upper end of the piston. After taking into account the errors introduced in reading the oil-pressure and in calculating the area of the piston, the uncertainty in calculated pressure was estimated to be ±1·2 per cent.

Thermocouple e.m.f's were converted to temperature by reference to the standard tables[7]. A long extrapolation of some preliminary data obtained by one of us (I.C.G.) on the calibration of chromel-alumel thermocouples under pressure suggests that temperature corrections of 2–3° downward might be expected over the investigated region of the III–V boundary. This corresponds to a shift of about 0·3 kbar downward in equilibrium pressures. However, even the sign of the temperature correction is uncertain. Excluding consideration of the pressure effect, temperatures are believed to be accurate to ±2°.

The results of the isothermal experiments, including the single experiment at room temperature, were treated by taking the mean of the oil-pressures at which the transition started on compression and decompression, and converting to real pressures as above.

The results are plotted in Fig. 3. Circles represent points from the isobaric measurements, except that points on the metastable projection of the III–V boundary are shown as squares. Triangles denote points derived from the isothermal experiments, and the point represented by a diamond is the result of the room temperature experiment.

The data for the isobaric experiments, in which the equilibrium transition temperature was measured, were fitted to polynomials of degree two through ten using a least-squares technique with the U.C.L.A. IBM 360 computor. For both the III–V and IV-V boundaries the standard deviation was essentially constant for all polynomials, and the coefficients of the terms of degree higher than 2 vanishingly small. With P in kbar and T in °K the second degree equations were

$$P_{\text{III-V}} = 96{\cdot}343 - 1{\cdot}4431 \times 10^{-3}T - 2{\cdot}0774 \times 10^{-4}T^2$$

and

$$P_{\text{IV-V}} = 54{\cdot}192 + 1{\cdot}0425 \times 10^{-1}T - 2{\cdot}3354 \times 10^{-4}T^2.$$

The standard deviations were 0·08 kbar and 0·09 kbar respectively. Combination of these expressions gives the III–IV–V triple point coordinates as 174·6°, 54·3 kbar, which compares well, especially as to temperature, with

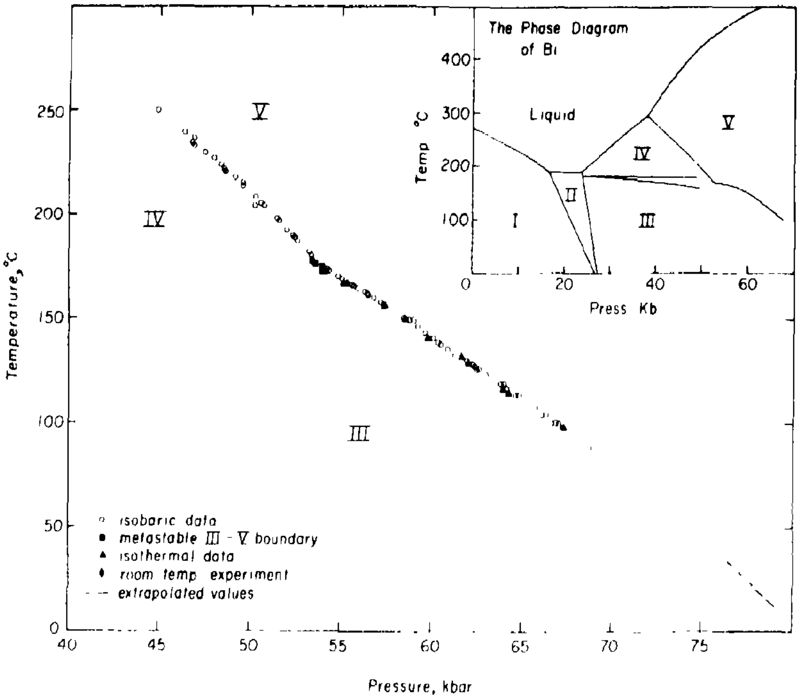

Fig. 3 Bismuth III–V and IV–V equilibrium boundaries.

the result of Klement *et al.*[4], namely 174°, 52·6 kbar.

To facilitate extrapolation of the III–V boundary to room temperature, it is desirable to apply a constraint outside the range of measurement. One is supplied by the third law of thermodynamics; since at $T = 0. \Delta S_{\text{III-V}} = 0$, we have

$$(\partial P/\partial T)_{T=0} = 0.$$

This condition is met when the coefficient of the linear term of the polynomial fitting the data is equal to zero; it is interesting to note that this is very nearly the case for the polynomial chosen already to describe the III–V data, since

$$(\partial P/\partial T)_{T=0} = -1{\cdot}4 \times 10^{-3}\,{}^{\circ}\text{K kbar}^{-1}.$$

When the computer program was adjusted to set the coefficient of the linear term equal to zero automatically, the standard deviations were again essentially constant for all the polynomials, and the second degree equations were

$$P_{\text{III-V}} = 96{\cdot}048 - 2{\cdot}0949 \times 10^{-4} T^2$$

and

$$P_{\text{IV-V}} = 79{\cdot}490 - 1{\cdot}2628 \times 10^{-4} T^2.$$

The standard deviations were 0·08 kbar and 0·10 kbar respectively. The equation for the IV–V boundary is included because it gives a more realistic value for the metastable IV–V equilibrium pressure at zero °K.

Both equations for the III–V boundary yield the same value for the transition pressure at 25°, namely 77·5 kbar; the predicted absolute zero transition-pressures, 96·343 and 96·048 kbar, differ only by 0·3 kbar. The extrapolated transition pressure at 22° is 77·9 kbar, in good agreement with the measured value of 78·2 kbar.

The pressure proposed for the III–V equilibrium boundary at 25° is 77·5 ± 1·0 kbar allowing for absolute uncertainties in both pressure and temperature determinations. The standard deviation of the data from the expression with which they were extrapolated is less than one-tenth of the accuracy estimation. Previous estimates of the III–V transition pressure at room temperature have ranged from 88–90 kbar by Bridgman[8] and Vereshchagin *et al.*[9] to 73·8 ± 1·3 kbar by Jeffery *et al.*[10]. The consensus of recent opinion has favored a value near 80 kbar as reported by Klement *et al.*[4], Stark and Jura[11], and Giardini and Samara[12]. In considering these values it is necessary to make a distinction between experiments measuring the equilibirum pressure and those measuring the pressure at which the transition starts on compression, because it is often the case that the latter is higher than the former. This is discussed at length by Bridgman[13].

Of the four[4, 8, 10, 11] papers in which the estimated pressure is assumed to be the equilibrium pressure, only two[4, 8] describe the use of apparatus appropriate to measuring pressure directly. The others[10, 11] describe techniques in which an indirect method of calibration was used. The value of 78–82 kbar suggested by Klement *et al.*[4] was tentative and based on a long extrapolation of sparse data obtained in double-stage piston–cylinder apparatus, where pressure determinations are less certain than with single stage apparatus. Considering this, the agreement with the present result is good. The fact that Bridgman[8] reports a value about 10 kbar above the present value is consistent with the finding that Bridgman pressures of a number of transitions frequently used as calibration points[1, 14]. It is difficult to discuss the values reported by the other workers because of the indirect pressure calibration procedures[10–12] and the fact that the equilibrium pressure was not determined in all cases[9, 12].

The transition-pressures determined in the isothermal experiments by taking the mean of the pressures at which the transition ran on compression and decompression agree well with the data determined by the isobaric method, as shown by Fig. 3. The double-valued friction and the mean pressure were both independent of the length of time between pressure changes, suggesting that the relaxation-time for friction and for transient pressure-gradients in the pressure-medium was short compared to the pause between pressure changes. However, at any particular temperature the difference between compression values was larger for the isothermal technique than for the isobaric technique. The difference increased with decreasing temperature. The isobaric curve separations is a measure of the friction between the piston and the pressure-chamber bore plus the effects due to the shear strength of the pressure-medium. The isothermal curve separation includes these quantities and also any hysteresis associated with the transition itself. The difference between the isobaric and isothermal curve separation is then evidently a measure of the hysteresis of the transition. The fact that both the isothermal and the isobaric methods yielded the same transition-pressures, as shown in Fig. 3, suggests that the hysteresis is symmetrical, that is, that the tendency of III to 'superpress' into the stability field of V is the same as the tendency of V to 'underpress' into the stability field of III. The amount of superpressing required to nucleate and grow Bi V from Bi III at room temperature is estimated to be 2–2·5 kbar by extrapolating the difference between the isothermal and isobaric observations. This figure is in good agreement with the value of 3·8 kbar for superpressing plus underpressing reported Jeffery *et al.*,**10**..

Since the transition starts to run on compression at a pressure higher than the equilibrium pressure, a knowledge of the equilibrium pressure alone is insufficient to allow use of the transition as a calibration point. A reasonable procedure for using the III–IV transition in calibration work may be to take the pressure at which the transition runs on compression as being approximately 2 kbar above the equilibrium pressure. Thus at 25°C the equilibrium value of the transition is 77·5 ± 1 kbar and in a typical calibration experiment, the transition should be observed on compression at pressures of circa 79·5 kbar. Caution is necessary, however, because of the unknown effect of shear on the equilibrium 'pressure' and on the magnitude of the hysteresis, and because there is no guarantee that the above procedure would be valid under all conditions, especially in view of the demonstrated existence of large pressure gradients in some types of high-pressure apparatus[15].

Acknowledgements—We wish to thank Dr. W. Klement for many helpful discussions, and Mr. L. Faus and Mr. J. Yamane for their skill and patience in machining the many intricate parts required. We are also indebted to the Army Research Office, Durham, North Carolina for partial financial support under contract DA-31-124-ARO-D

REFERENCES

1. HAYGARTH J. C., GETTING I. C. and KENNEDY G. C., *J. appl. Phys.* **38**, 4557 (1967).
2. BOYD F. R. and ENGLAND J. L., *J. geophys. Res.* **65**, 741 (1960).
3. HAYGARTH J. C. and KENNEDY G. C., *Rev. scient. Instr.* **38**, 1590 (1967).
4. KLEMENT W. Jr., JAYARAMAN A. and KENNEDY G. C., *Phys. Rev.* **131**, 632 (1963).
5. PISTORIUS C. W. F. T., RAPOPORT E. and CLARK J. B., *Rev. scient Instrum.* **38**, 1741 (1967).
6. HEYDEMANN P. L. M., *J. appl. Phys.* **38**, 2640 (1967).
7. N. B. S. Circular no. 561 (1955).
8. BRIDGMAN P. W., *Proc. Am. Acad. Arts Sci* **74**, 425 (1942).
9. VERESHCHAGIN L. F., ZUBOVA E. V., BUIMOVA I. P. and BURDINA K. P., *Soviet Phys. Docklady* **11**, 585 (1967).
10. JEFFERY R. N., BARNETT J. D., VANFLEET M. R. and HALL H. T., *J. appl. Phys.* **38**, 3172 (1966).
11. STARK W. and JURA G., ASME paper no. 64-WA/PT-28 (1965).
12. GIARDINI A. A. and SAMARA G. A., *J. Phys. Chem. Solids* **26**, 1523 (1965).
13. BRIDGMAN P. W., In *The Physics of High Pressure*, Bell, London (1958).
14. KENNEDY G. C. and LA MORI P. N., *J. geophys. Res.* **67**, 851 (1962).
15. See, for example, MONTGOMERY P. W., JURA G. H. and JURA G., In *High Pressure Measurement* (Edited by A. A. Giardini and E. C. Lloyd), p. 1. Butterworths, New York (1963).

J. Phys. Chem. Solids Pergamon Press 1969. Vol. 30, pp. 1425–1428. Printed in Great Britain.

PHOTOLUMINESCENCE OF TRIGONAL SELENIUM SINGLE CRYSTALS

H. ZETSCHE and R. FISCHER
Physikalisches Institut der Universität Frankfurt/M., Germany

(*Received* 18 *October* 1968)

Abstract – Photoluminescence of trigonal Se single crystals has been investigated in the temperature range from 2° to 50°K. Between 1·80 and 1·86 eV seven lines are found, most of them with a phonon satellite. The associated phonon energy is 28·5 meV. The relative intensities of the lines depend strongly and non-monotonically on temperature. An interpretation of the luminescence is attempted, using a model with five levels within the band gap.

INTRODUCTION

PHOTOLUMINESCENCE of trigonal Se single crystals near the band gap was investigated earlier by Queisser and Stuke[1]. Their measurements were restricted to 20°K, where they found three lines, each with a phonon satellite. We now measured the photoluminescence between 2° and 50°K and found a marked temperature dependence. The luminescence between 1·80 and 1·86 eV contains seven lines. It is, however, only near 4°K, that they are all visible. Most of the lines have a one-phonon satellite. A first interpretation of the luminescence is attempted, using a model with five levels within the band gap.

EXPERIMENTAL ARRANGEMENT

The trigonal Se single crystals used were grown from the vapour phase. They had the form of needles or platelets, depending on the content of Cl and Tl in the Se raw material (*). No dependence of the luminescence on these differences in the starting material was found.

The crystals were directly immersed into the cooling medium. We used liquid He for $T \leq 4$°K, liquid H_2 for $T = 20$°K, and He gas for other temperatures up to 50°K. We measured the temperature of the cooling medium near the crystals. The temperature of the samples itself could be somewhat higher due to heating in connection with their excitation. This temperature difference, however, was estimated to be less than 0·3°K in the case of liquid He and H_2. The crystals were excited by a He-Ne-laser with photon energy of 1·96 eV(†). The irradiated power was about 1 mW. The polarization of the exciting light could be adjusted parallel or perpendicular to the *c*-axis of the crystals. The luminescence being emitted from the illuminated face of the crystals was analysed with a double grating spectrometer and detected with a cooled photomultiplier.

RESULTS

Typical spectra for each of the temperatures 2°, 4°, 20° and 50°K are shown in Fig. 1. The polarization of the exciting light is $E \perp C$ for the 2°K-spectrum and $E \parallel C$ for the others.

At 50°K the structure within the spectrum becomes comparable in its order of magnitude with the noise level, inhibiting measurements at yet higher temperatures.

At 20°K the luminescence contains four lines: (2:1), 3, 4 and 6, and some structure on the lower energy side of line 6. Sometimes this structure is resolved into three peaks with energy separation equal to that of the

---

*Most of the crystals were grown by G. Weiser, Phys. Inst. der Universität Marburg, Germany.

†At 20°K the effect of excitation with higher photon energy was studied (HBO 200 Hg-lamp from Osram with a filter absorbing between 1·7 and 2·5 eV). No significant change in the luminescence spectrum was found.

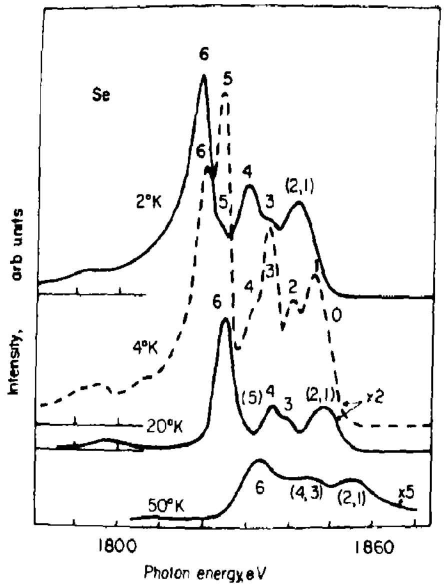

Fig. 1. Luminescence spectra at different temperatures. Peaks carrying the same index are attributed to the same recombination process

Table 1. Energies and wave-lengths of the luminescence peaks at 4°K

Peak Nr.	Wave-length (Å)	Energy (eV)
0	6704	1·849
1	6718	1·846
2	6734	1·841
3	6755	1·835
4	6772	1·831
5	6798	1·824
6	6811	1·820
2′	6842	1·812
3′	6862	1·807
5′	6906	1·795
6′	6919	1·792

Error. $\Delta\lambda = \pm 2.5$ Å for lines 0–6; $\Delta\lambda = \pm 4$ Å for lines 2′–6′.

lines (2:1), 4 and 6. There is no dependence of the luminescence on the polarization of the exciting light at this temperature. Our results are thus in full agreement with those of Queisser and Stuke concerning crystals grown from the vapour phase[1]. In addition we resolve their peak *B* into two lines 3 and 4.

At 4°K we find seven lines, 0–6, and a structure on the low energy side of line 6. The energies of all peaks, as taken from a selected spectrum with especially good line resolution, are given in Table 1. The symbols 2′–6′ in the table refer to the maxima within the structure below peak 6. In addition there sometimes appears a broad background band at 4°K with maximum at the energy of peak 6 and a halfwidth of about 50 meV. This background causes a marked reduction in line resolution.

At 4°K the luminescence depends on the polarization of the exciting light. If this polarization is changed from $E \parallel C$ to $E \perp C$, the intensities of the lines 1, 3 and 5, normalized respectively to those of the lines 2, 4 and 6 decrease. The intensity of the background band relative to that of the lines increases by a factor between 2 and 10.

At 2°K we have experimental data only for $E \perp C$. The spectra at this temperature are similar to those at 20°K (Fig. 1). The only difference consists in the appearance of a peak 5 at 2°K and in the fact, that the 2°K-spectrum seems to be superposed upon a background band as reported for 4°K. Neither peak 5 nor a background band is ever found in a 20°K-spectrum.

A striking feature of our results is a great variation in the data obtained for the same sample, at fixed temperature, and with fixed polarization of the exciting light. We believe that this variation is due to a strong dependence of the luminescence on the location of the illumination spot on the crystal. In particular the intensities of the peaks 1, 3 and 5, normalized respectively to those of the peaks 2, 4 and 6 depend strongly on the illumination spot, being in some cases much smaller than shown in Fig. 1. Such a reduction of the lines 1, 3 and 5 hardly affects the shape of the spectra at 2° and 20°K, but completely alters that of the 4°K-spectrum. Thus, at 4°K there sometimes appear spectra quite similar to those at 2°K. The absolute energies of the lines also show a variation with illumination spot up to 4 meV; the energy distances between the lines, however, remain fixed. Finally we find a variation of the intensity of the background band seen at 4° and 2°K.

The temperature dependence of the luminescence may be seen from Fig. 1. The lines carrying the same index are assumed to be identical in the sense, that they stem from the same process. This assumption is supported by measurements at intermediate temperatures.

We find: (1) As far as the lines remain visible, their relative spacings do not change with temperature. (2) The absolute energies of the lines shift to higher values with increasing temperature (see e.g. peak 6 in Fig. 1). Between 4° and 50°K the increase in energy is 15 ± 4 meV. The temperature coefficient at 50°K is $dE/dT = (2{\cdot}5 \pm 1) \times 10^{-4}$ eV/°K. The relatively large error is caused by the variation with illumination spot described above. (3) The intensities of peaks 1, 3 and 5, normalized respectively to those of the peaks 2, 4 and 6 depend non-monotonically on temperature: At 4°K these intensities occasionally are larger than unity, whereas at 2° and 20°K they always are smaller than unity (Fig. 1).

INTERPRETATION

From Table 1 one sees, that the lines 6 and 6′, 5 and 5′ etc. are all equally spaced. The difference in energy is $28{\cdot}5 \pm 1$ meV. According to Lucovsky *et al.*[2] three of the optical phonons in Se each have an energy between 28 and 29·4 meV at $q = 0$. We therefore interpret the lines 2′–6′ seen at 4°K as one-phonon satellites of the lines 2–6. At 20° and 2°K only the satellites of the strong lines 4 and 6 are clearly seen.

No definite interpretation of the lines 1–6 can as yet be given. We suggest a term scheme as shown in Fig. 2. The transitions from the upper level group to the lower one produce the lines 1–6 as indicated. Line 0 probably has a different origin. The energy distances between the levels α to ϵ are completely determined by the energies of the luminescence lines. The distances within the two level groups are independent of the temperature and the crystal point considered, whereas the separation of the two groups increases with increasing temperature and changes from point to point in the crystal. The latter may be due to local strains or potential fluctuations within the crystal.

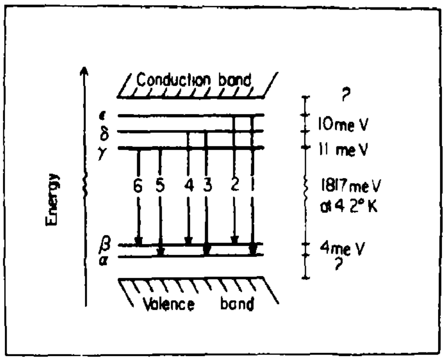

Fig. 2 Model to explain the luminescence in trigonal Se α to ϵ denote 5 energy levels within the band gap. The arrows indicate the recombination process leading to the different luminescence lines.

The intensities of the lines 2, 4 and 6 are of the same order of magnitude even at 2°K (Fig. 1). This implies, that electrons excited to the levels γ, δ, and ϵ do not thermalize. If they did, the Boltzmann factor ($\approx e^{-60}$ between level γ and δ at 2°K) would completely suppress the energetically higher lines 2 and 4 (Fig. 2). Thus transitions between the levels γ, δ, and ϵ must be forbidden.

The relative intensities of the lines 1, 3 and 5 depend non-monotonically on temperature. This could be explained within our model by the following mechanism: If we take the level α to lie about 10 meV above the valence band, the concentrations of the impurities or lattice defects producing the states α and β can be adjusted in such a way, that the calculated Fermi energy E_F varies non-monotonically with temperature: E_F lies below the level α at 4°K but above this level at 2° and 20°K. Thus the concentration of holes in the level α normalized to that in the level β has its maximum value at 4°K decreasing to higher and lower temperatures. The temperature dependence of the relative line intensities thereby is explained at least qualitatively.

The dependence of the relative line intensities on the location of the illumination spot on the crystal may be caused by a spatial variation in the concentrations of the lattice defects or impurities producing the levels α and β.

An explanation of the background band has to start from the experimental result, that its intensity increases, if the polarization of the exciting light is changed from $E\|C$ to $E\perp C$. Thus, the states which participate in the recombination process producing the band must be excited mainly with $E\perp C$. In order to find such states we have to investigate the mechanism by which our exciting light ($\hbar\omega = 1{\cdot}96$ eV) is absorbed for $E\|C$ and $E\perp C$ respectively:

(1) The absorption coefficient of trigonal Se at 1·96 eV is larger for $E\perp C$ than for $E\|C$*. Thus more photons are absorbed near the surface of the crystal for $E\perp C$ than for $E\|C$. Nevertheless we do not believe the band to be due to surface recombination, since even for $E\perp C$ only 0·5 per cent of the irradiated power is absorbed within the first 100 Å from the surface, whereas for this polarization direction the intensity of the band is equal to that of the lines in order of magnitude.

(2) According to Roberts *et al.*[4] trigonal Se has an indirect band gap at 1·82 eV ($E\|C$ and $E\perp C$). The gap for direct transitions is located at the symmetry point H in the Brillouin zone and has an exciton associated with it[3, 5, 6]. The energies given in the literature are not unique (compare e.g. [3] and [6]). Therefore we do not know, whether photons with an energy of 1·96 eV excite electrons into the direct conduction band minimum, or, instead of this, create the excitons associated with this minimum. It is well established, however, that both excitations are allowed only for $E\perp C$. Thus either of these states may be in some way connected with our background band.

(3) Recent absorption measurements on trigonal Se[6] show absorption edges at 1·857, 1·870 and 1·880 eV for both polarization directions. They may be interpreted as caused by direct excitation of electrons from the valence band into the levels γ, δ, and ϵ of our model. Thus the line-luminescence probably is excited by this mechanism.

Acknowledgements—We thank Professor H. J. Queisser for stimulating this work and supporting it by valuable advice. We are indebted to Professor J. Stuke for helpful discussions and to G. Weiser for preparing most of the crystals.

---

*The absorption coefficients of trigonal Se at 1·96 eV are $5{\cdot}4\times10^{3}\,\mathrm{cm}^{-1}$ for $E\perp C$ and $2\times10^{4}\,\mathrm{cm}^{-1}$ for $E\|C$ according to absorption measurements made by Fischer. See also Fig. 9 in [3].

REFERENCES

1. QUEISSER H. J. and STUKE J., *Solid State Commun.* **5**, 75 (1967).
2. LUCOVSKY G., MOORADIAN A., TAYLOR W., WRIGHT G. B. and KEEZER R. C., *Solid State Commun.* **5**, 113 (1967).
3. TUTIHASI S. and CHEN I., *Phys. Rev.* **158**, 623 (1967).
4. ROBERTS G. G., TUTIHASI S. and KEEZER R. C., *Phys. Rev.* **166**, 637 (1968).
5. HENRION W., *Phys. Status Solidi* **20**, K145 (1967).
6. FISCHER R., QUEISSER H. J. and ZETSCHE H., Contribution to the *9th Int. Conf. on the Physics of Semiconductors*. Moscow (1968).

J. Phys. Chem. Solids Pergamon Press 1969. Vol. 30, pp. 1429–1434. Printed in Great Britain.

MAGNETIC AND ELECTRICAL PROPERTIES OF $Co_{1-x}Cu_xRh_2S_4$

F. K. LOTGERING
Philips Research Laboratories, N.V. Philips' Gloeilampenfabrieken, Eindhoven, Netherlands

(*Received* 2 *October* 1968)

Abstract—Samples of $Co_{1-x}Cu_xRh_2S_4$ with $0·1 \leqq x \leqq 1$ show a practically temperature-independent resistivity of 10^{-2}–$10^{-3}\,\Omega$ cm and a positive Seebeck coefficient decreasing from 125 μV/deg for $x = 0·1$ to $\approx 25\,\mu$V/deg for $0·5 \leqq x \leqq 1$. The material is antiferromagnetic for $0 \leqq x < 0·4$, shows spontaneous magnetization for $\approx 0·4 \leqq x \leqq \approx 0·7$ and is paramagnetic for $\approx 0·7 \leqq x \leqq 1$. The strongest spontaneous magnetization occurs at $x = 0·5$ and a moment of $\approx 0·8\,\mu_B$/molecule is found.

The conduction is attributed to holes in the valence band. The occurrence of a small saturation moment in the composition range $0·4 \leqq x \leqq 0·7$ is explained tentatively and attributed to double exchange between Co^{2+} and Co^{3+} on tetrahedral sites.

1. INTRODUCTION

THE COMPOUNDS $CoRh_2S_4$ and $CuRh_2S_4$, which crystallize in the normal[1, 2] spinel structure, exhibit a completely different electrical and magnetic behaviour. $CoRh_2S_4$ is an antiferromagnetic semiconductor[1], while $CuRh_2S_4$ shows metallic conduction[3] and a small, nearly temperature-independent susceptibility[2, 3].

According to Blasse[1], the antiferromagnetism of $CoRh_2S_4$ arises from ordering of the Co^{2+} spins at tetrahedral sites (*A* sites), the Rh^{3+} ions at octahedral sites (*B* sites) being in the non-magnetic, low-spin t_{2g}^6 state. From the high Néel temperature $T_N = 400$°K it is seen that the exchange interaction between the Co^{2+} spins is anomalously strong for *AA* interaction in a spinel. Blasse's interpretation has been confirmed by the magnetic properties of $CoRH_{2-x}Cr_xS_4$[4]. For example, the magnetic behaviour of $Co[Rh_{1·5}Cr_{0·5}]S_4$ points to a triangular ferrimagnetic spin configuration with canted Co^{2+} spins for $T < T_C = 60$°K and an antiferromagnetic ordering of Co^{2+} spins for $T_C < T < T_N = 360$°K. This has recently been confirmed by neutron-diffraction work on this substance by Plumier[5], who observed a Yafet and Kittel type of ordering at 4·2°K and an antiferromagnetic ordering of the Co_3O_4 type[6] at 80° and 290°K. It seems therefore quite certain that the ordering in $CoRh_2S_4$ is also of the same type, i.e. a simple antiferromagnetic ordering in two *A* sublattices with an antiparallel alignment of nearest neighbours.

The electrical and magnetic properties of $CuRh_2S_4$ have been discussed by Lotgering and Van Stapele[3] (see also Section 4 of this paper).

The present paper gives experimental work on the series of mixed crystals between $CoRh_2S_4$ and $CuRh_2S_4$. The interesting point is that the 1:1 mixed crystal between an antiferromagnetic compound and a substance containing no magnetic ions is found to be spontaneously magnetized.

2. PREPARATION

Samples of $Co_{1-x}Cu_xRh_2S_4$ with $x = 0·01$, 0·10, 0·25, 0·35, 0·40, 0·45, 0·50, 0·55, 0·60, 0·65 and 0·75, and a sample of $Co_{0·5}Cu_{0·5}Rh_{1·5}Ti_{0·5}S_4$ were prepared by firing intimate mixtures of $CoRh_2S_4$, $CuRh_2S_4$ and $CuTi_2S_4$ for 24—110 hr at 800°C in evacuated silica ampoules, and then quenching them. All samples were ground and fired for a second time and, in some cases, for a third time in the same way. Resistivities and Seebeck coefficients were measured on sintered pellets prepared from powders pressed hydrostatically under a pressure of 13 kbar/cm^2.

The X-ray diagrams of most preparations showed a pure spinel phase and very weak extra reflections were observed in some cases. The X-ray diagram of a starting mixture of $CoRh_2S_4$ and $CuRh_2S_4$ obtained using a low rotation speed of the spectrometer showed only one spinel phase with a cell edge of 9·776 Å. The formation of mixed crystals cannot therefore be detected using the X-ray diagrams, but appears from the physical properties.

3. EXPERIMENTAL RESULTS

A practically temperature-independent resistivity was measured on the samples $Cu_{1-x}Co_xRh_2S_4$ with $0{\cdot}1 \leq x \leq 1$ at temperatures between 80°K and room temperature. Figure 1 gives the resistivity ρ and the Seebeck coefficient as a function of composition. The resistivity of $Co_{0{\cdot}5}Cu_{0{\cdot}5}Rh_{1{\cdot}5}Ti_{0{\cdot}5}S_4$ was found to change gradually from $\log \rho = -0{\cdot}5$ at 80°K to $\log \rho = -1{\cdot}1$ at room temperature and the Seebeck coefficient was $+240\ \mu$V/deg.

The value $\rho = 10^4\ \Omega$ cm at 80°K given in Fig. 1 has been reported by Blasse[1]. We prepared $CoRh_2S_4$ several times, but all these samples were far from pure and showed much lower resistivities. We succeeded, however, in preparing[4] a pure sample of $CoRh_{1{\cdot}5}Cr_{0{\cdot}5}S_4$ on which we measured $\log \rho = 2{\cdot}1$ and 1·3 at 80° and 273°K, respectively, and a Seebeck coefficient of +260 μv/deg at room temperature. Since a replacement of a part of the trivalent rhodium in $CoRh_2S_4$ by trivalent chromium will have no significant influence on the conduction, the value reported by Blasse seems to be reliable for pure $CoRh_2S_4$.

The magnetic behaviour changes with the Cu content in such a way that three composition ranges may be distinguished. (a) Antiferromagnetic range for $0 \leq x < \approx 0{\cdot}4$. Figure 2 gives the reciprocal susceptibility χ_m^{-1} as a function of temperature for $x = 0$, 0·10, 0·25 and 0·35. The susceptibility measured at 4·5°K on the samples with $x = 0{\cdot}25$ and 0·35 was found to be field-independent. At high temperatures a Curie-

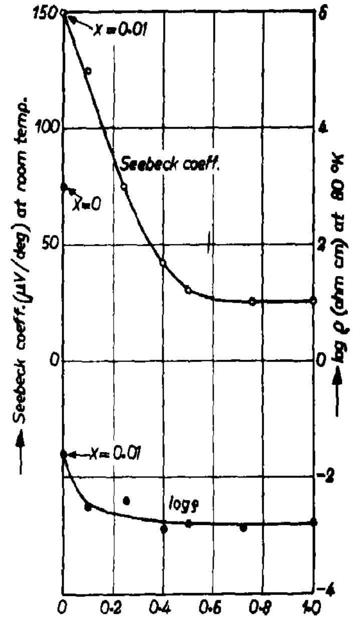

Fig. 1. $Co_{1-x}Cu_xRh_2S_4$. Seebeck coefficient at room temperature and logarithm of the resistivity at 80°K as a function of composition. Resistivity for $x = 0$ after Blasse[1].

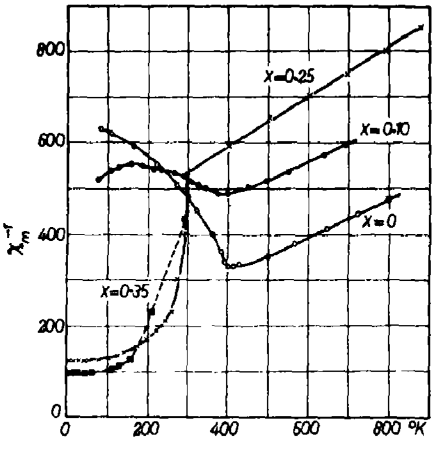

Fig. 2. $Co_{1-x}Cu_xRh_2S_4$ with $0 \leq x \leq 0{\cdot}35$. Reciprocal molar susceptibility as a function of temperature. Curve for $x = 0$ after measurements by Blasse (Private communication).

Weiss law holds. For $x = 0$ and $x = 0{\cdot}10$ the temperature at which the $\chi_m^{-1} - T$ curve has a minimum is interpreted as the Néel temperature. For $x = 0{\cdot}25$ the $\chi_m^{-1} - T$ curve shows a kink at 295°K and we found that

$\chi_m^{-1}-T$ curves measured at lower temperatures are poorly reproducible. Certain antiferromagnetics like $CaMnO_3$ and $LaCrO_3$ have been observed to show similar behaviour [7]. We therefore think that $Co_{0.75}Cu_{0.25}Rh_2S_4$ is predominantly antiferromagnetic with $T_N = 295°K$. (b) Ferromagnetic range for $\approx 0{\cdot}4 < x < \approx 0{\cdot}7$. The samples with $0{\cdot}40 \leq x \leq 0{\cdot}65$ show spontaneous magnetization and the maximum moment occurs for $x = 0{\cdot}5$ (Figs. 3 and 6). One sample with $x = 0{\cdot}5$ was saturated at 4·5°K in a field of 20 kOe, whereas other samples with $x = 0{\cdot}5$ and all samples of other composition were found to be not completely saturated at 20 kOe. (For $x = 0{\cdot}4$ the magnetization even increases strongly with H). Specimens with $x = 0{\cdot}50$ and 0·60 were quenched from 800°C or slowly cooled with annealing treatments of 50 hr at 700°, 600° and 500°C. The magnetization measured on these samples can be seen in Fig. 6. The $\chi_m^{-1}-T$ curves for $x = 0{\cdot}4$, 0·5 and 0·6 obey a Curie-Weiss law at temperatures above ~ 500°K and show complicated shapes at lower temperatures (Figs. 4 and 5). We observed that the $\chi_m^{-1}-T$ curves measured on two samples I and II with $x = 0{\cdot}6$, which were both quenched from 800°C, show temperature hysteresis at

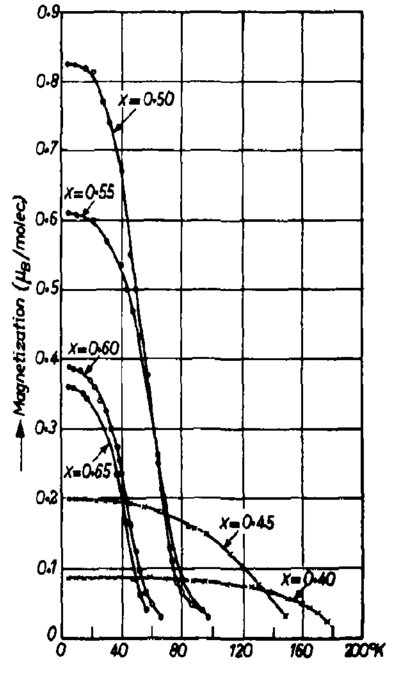

Fig. 3. $Co_{1-x}Cu_xRh_2S_4$ with $0{\cdot}40 \leq x \leq 0{\cdot}65$. Magnetization at $H = 9$ kOe as a function of temperature.

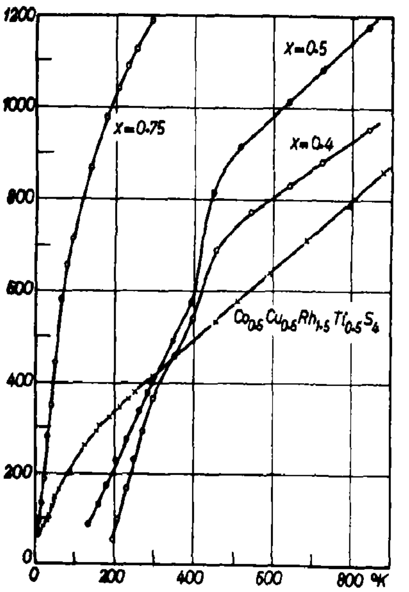

Fig 4. $Co_{1-x}Cu_xRh_2S_4$ with $x = 0{\cdot}4$, 0·5, 0·75 and $Co_{0.5}Cu_{0.5}Rh_{1.5}Ti_{0.5}S_4$ Reciprocal molar susceptibility as a function of temperature.

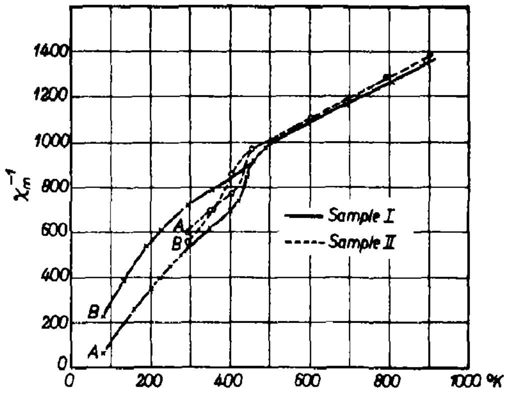

Fig. 5 $Co_{0.4}Cu_{0.6}Rh_2S_4$. $\chi_m^{-1}-T$ curves measured for increasing T (starting from A) on two quenched samples that were prepared separately. After the measurement at ≈ 900°K, the sample was measured again at 510°K and χ_m was found to be unchanged. Then the sample was cooled and the $\chi_m^{-1}-T$ curve starting from B was measured for increasing T.

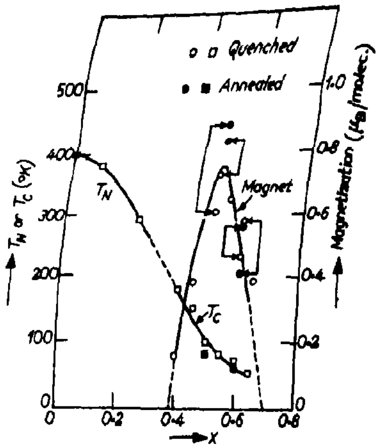

Fig. 6. $Co_{1-x}Cu_xRh_2S_4$ Néel temperature T_N, Curie temperature T_c and magnetization measured on quenched and annealed samples at 4·5°K for $H = 20$ kOe as a function of composition.

$T < \sim 500$°K whereas the Curie-Weiss part of the curve at $T > 500$°K is well reproducible (Fig. 5). A quenched sample with $x = 0{\cdot}5$ showed hysteresis of the type of sample II given in Fig. 5. (c) Paramagnetic range for $\approx 0{\cdot}7 < x \lesssim 1$. The $\chi_m^{-1} - T$ curve measured on the sample with $x = 0{\cdot}75$ (Fig. 4) does not show any indication of magnetic ordering at temperatures down to 4·5°K.

4. DISCUSSION

The conducting properties of $Co_{1-x}Cu_xRh_2S_4$ can easily be explained using a model for the electronic structure of sulphospinels given by Lotgering and Van Stapele[3]. A detailed interpretation of the magnetic properties is much more difficult, however, and we will only discuss the origin of the spontaneous magnetization observed.

In reference[3] the properties of $CuRh_2S_4$ are explained with the aid of an energy level scheme (Fig. 7(a)) which consists of a broad valence band containing 1 hole/molecule and narrow bands far below the top of the valence band for the d electrons of Rh^{3+} and Cu^+. The p-type metallic conduction is attributed to hole conduction in the valence band and the observation of a small and temperature-independent susceptibility is explained by the absence of magnetic ions. The valencies can be represented by the formula $Cu^+|Rh_2^{3+}|S_3^{2-}S_1^-$ where S^- denotes a hole in the valence band.

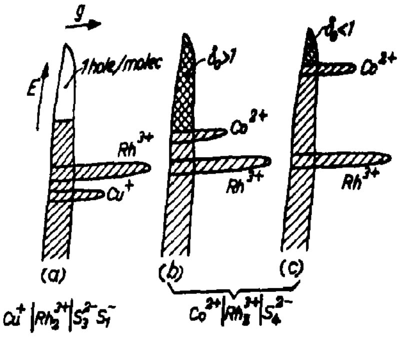

Fig. 7. Energy level schemes for (a) $CuRh_2S_4$ and (b) or (c) for $CoRh_2S_4$. The energy E is plotted schematically versus the density of states g, and $\int g\mathrm{d}E$ gives the number of states per molecule.

The properties of $CoRh_2S_4$ (see introduction) point to valencies represented by $Co^{2+}|Rh_2^{3+}|S_4^{2-}$. This corresponds to an energy-level scheme with a filled valence band and a filled Co^{2+} band, which may lie above or below the top of the valence band. A model with a d band above the top of the valence band can be excluded because this would lead to an electrical behaviour as discussed in[8] and observed on $Fe_{1-x}Cu_xCr_2S_4$ [8, 9], which is completely different from that of $Co_{1-x}Cu_xRh_2S_4$. For example, $Fe_{0.5}Cu_{0.5}Rh_2S_4$ is a semiconductor, in contrast with $Co_{0.5}Cu_{0.5}Cr_2S_4$, which shows p-type metallic conduction (Fig. 1).

We assume therefore that the Co^{2+} band is situated below the top of the valence band. There are two possibilities $\delta_0 > 1$ or $\delta_0 < 1$ (Figs. 7(b) and (c)), where δ_0 is the number of valence-band states per molecule with energies above the top of the Co^{2+} band. From the schemes for $CuRh_2S_4$ and $CoRh_2S_4$ given in Fig. 7, the schemes for the mixed crystals $Co_{1-x}Cu_xRh_2S_4$ can be drawn. One finds two cases represented by the formulae

$$Co^{2+}_{1-x}Cu_x{}^+|Rh_2{}^{3+}|S^{2-}_{4-x}S_x{}^- \quad \text{for } 0 \leqq x \leqq 1 \tag{1}$$

if $\delta_0 > 1$, and

$$\left.\begin{array}{l} Co^{2+}_{1-x}\,Cu_x{}^+|Rh^{3+}|S^{2-}_{4-x}S_x{}^- \\ \qquad\qquad \text{for} \quad 0 \leqq x \leqq \delta_0 \\ Co^{2+}_{1+\delta_0-2x}Co^{3+}_{x-\delta_0}Cu_x{}^+|Rh_2{}^{3+}|S^{2-}_{4-\delta_0}S_{\delta_0}{}^- \\ \qquad\qquad \text{for} \quad \delta_0 \leqq x \leqq \dfrac{1+\delta_0}{2} \\ Co^{3+}_{1-x}Cu_x{}^+|Rh_2{}^{3+}|S^{2-}_{5-2x}S^-_{2x-1} \\ \qquad\qquad \text{for} \quad \dfrac{1+\delta_0}{2} \leqq x \leqq 1 \end{array}\right\} \tag{2}$$

if $\delta_0 < 1$ and the width of the Co^{2+} band is neglected.

For $\delta_0 < 1$ as well as for $\delta_0 > 1$ the number of holes S^- in the valence band increases with x. Both models thus explain the decrease of ρ from $10^3\,\Omega$ cm for $x = 0$ to $\sim 10^{-2}\,\Omega$ cm for $x = 0{\cdot}01$ or $0{\cdot}05$ and the low resistivity ($\rho = 10^{-2} - 10^{-3}\,\Omega$ cm) as well as the occurrence of p-type conduction observed for $0{\cdot}1 \leqq x \leqq 1$ (Fig. 1).

We will now discuss the magnetic properties. According to our model, the magnetic ions are exclusively Co^{2+} and Co^{3+} occupying A sites. There are two complications: (i) the presence of Cu^+ on A sites will cause fluctuations of the mutual surroundings of the magnetic ions, and (ii) the observed saturation moment of $1{\cdot}6\,\mu_B$/Co at $x = 0{\cdot}5$ is much smaller than the moment expected for a parallel alignment of the spins of Co^{2+} or Co^{3+} ions (~ 3 to $4\,\mu_B$/Co) and points therefore to a complicated spin ordering. It will be difficult to give a detailed interpretation of the magnetic behaviour of such a complicated system and our discussion will be restricted to the origin of the spontaneous magnetization.

According to our model with $\delta_0 < 1$, cobalt is present as a mixture of Co^{2+} and Co^{3+} for a composition range $\delta_0 \leqq x \leqq (1+\delta_0)/2$ (Formula (2)) that is determined by only one parameter δ_0. It is remarkable that, putting $\delta_0 = 0{\cdot}4$, this condition yields the range $0{\cdot}4 \leqq x \leqq 0{\cdot}7$, in which the materials show spontaneous magnetization (Fig. 6). For $\delta_0 = 0{\cdot}4$ our model gives therefore a natural explanation of the composition range in which spontaneous magnetization occurs if we assume that the spontaneous magnetization is caused by the presence of cobalt in two valency states. This suggests a ferromagnetic coupling of Co spins by double exchange between Co^{2+} and Co^{3+} occupying equivalent A sites. Further, a combination of antiferromagnetic superexchange (as observed in $CoRh_2S_4$) and ferromagnetic double exchange interactions between the Co ions may result in a spin-canted ground state as pointed out by de Gennes[10] for $La_{1-y}Me_yMnO_3$ (Me = Ca, Sr, Ba) with small values of y. In this way our model can also explain the observation of saturation moments much smaller than expected for a parallel alignment of the cobalt spins.

The relatively small difference between the magnetization measured on quenched and annealed samples (Section 3, Fig. 6) may be caused by differences in the mutual surroundings of copper and cobalt ions at A sites.

The sample of $Co_{0{\cdot}5}Cu_{0{\cdot}5}Rh_{1{\cdot}5}Ti_{0{\cdot}5}S_4$ was prepared with the purpose of filling the valence band and the Co^{2+} band so that cobalt occurs in the one valence state according to $Co^{2+}_{0{\cdot}5}Cu^+_{0{\cdot}5}Rh^{3+}_{1{\cdot}5}Ti^{4+}_{0{\cdot}5}S^{2-}_4$. It is then expected that the material will no longer be ferromagnetic and metallic. This is indeed found experimentally (Section 3 and Fig. 4).

We will now comment briefly on the paramagnetic properties, which are difficult to understand.

From the straight part of the $\chi_m{}^{-1} - T$ curves given in Figs. 2 and 4 we find Curie constants of 2·4–2·7 per gram atom Co. This corresponds to g factors of 2·3–2·4 in agreement with values[11, 12] reported for Co^{2+} at tetrahedral sites. If, however, the observed susceptibilities (Figs. 2 and 4) are corrected for diamagnetism ($-2{\cdot}0 \times 10^{-4}$ per mole) and the Van Vleck susceptibilities[13, 3] of

Co^{2+} and Rh^{3+} ($4 \cdot 0 \times 10^{-4}$ and $1 \cdot 6 \times 10^{-4}$ per gram atom, respectively), we find straight $\chi_m^{-1} - T$ curves corresponding to Curie constants much lower than expected for Co^{2+} at A sites (e.g. $C_m = 1 \cdot 5$ for $CoRh_2S_4$). Such a disagreement, which may be connected with the strong exchange interactions, has also been found for $CoRh_{2-x}Cr_xS_4$[4]. In these cases it is clear that no reliable information about the ionic valencies or the strength of the interactions can be obtained from the paramagnetic data.

From Fig. 6 it is seen that T_N and T_C plotted vs. x lie on a smooth curve. This suggests the existence of a close relation between the antiferromagnetic ordering for $x < 0 \cdot 4$ and the ferromagnetic ordering for $x > 0 \cdot 4$, and may be seen as a support of our model, which attributes the spontaneous magnetization for $x > 0 \cdot 4$ to decompensation of the antiferromagnetic ordering at $x < 0 \cdot 4$. On the other hand, the observed magnetic behaviour does not agree* with de Gennes' theory[10]. For example, this theory predicts a transition from the canted spin configuration to the paramagnetic state via an antiferromagnetic state, and this is not observed for $x = 0 \cdot 4$, $0 \cdot 5$ and $0 \cdot 6$. The shape of the $\chi_m^{-1} - T$ curves measured are complicated and show temperature hysteresis (Figs. 2 and 4). It will be interesting to investigate whether spin ordering occurs in the region between T_C and the temperatures (~500°K) at which a Curie–Weiss law starts to hold.

The author wishes to stress that the interpretation given is meant to be tentative and is far from settled. Several other models that were envisaged failed to give an unforced explanation of the low saturation moment of $Co_{0 \cdot 5}Cu_{0 \cdot 5}Rh_2S_4$. For example, we could not think of any simple ordering of the copper and cobalt ions on the A sites capable of explaining the observed spontaneous magnetization as arising from ferrimagnetism. In the case of a partial ionic ordering, the author would expect the heat treatment to have a larger influence on the magnetization and the Curie temperature than observed for $x = 0 \cdot 5$ and $0 \cdot 6$.

The behaviour of $Co_{1-x}Cu_xRh_2S_4$ has much resemblance with that of $Mn_{1-x}Li_xSe$ [14]. In both cases the material is antiferromagnetic for $x = 0$ and becomes, with increasing x, spontaneously magnetized with small saturation moments. Although a detailed interpretation[14] of the properties of $Mn_{1-x}Li_xSe$ is difficult, it is clear that the replacement of Mn^{2+} by $Mn^{3+} + Li^+$ for increasing x plays an essential part. The analogy of both systems can therefore be seen as an indication of a replacement of Co^{2+} in $CoRh_2S_4$ by $Co^{3+} + Cu^+$ in the case of $Co_{1-x}Cu_xRh_2S_4$.

Acknowledgements—The author is indebted to Drs C. Haas and R. P. van Stapele for stimulating discussions and to G. H. A. M. van der Steen, J. F. Fast and P. R. van Ijzendoorn for preparing the samples and performing the measurements.

REFERENCES

1. BLASSE G., *Phys. Lett.* **19**, 110 (1965).
2. BLASSE G. and SCHIPPER D. J., *J. inorg. nucl. Chem* **26**, 1467 (1964)
3. LOTGERING F. K. and VAN STAPELE R. P., *J. appl. Phys.* **39**, 417 (1968).
4. LOTGERING F. K., *J. Phys. Chem. Solids* **29**, 699 (1968)
5. PLUMIER R., Private communication.
6. ROTH W. L., *Bull. Am. phys. Soc., Series II*, **8**, 213 (1963).
7. JONKER G. H., *Physica* **12**, 707 (1965)
8. LOTGERING F. K., BAN STAPELE R. P., VAN DER STEEN G. H.A.M. and VAN WIERINGEN J. S., *J. Phys. Chem. Solids* **30**, 799 (1969)
9. HAACKE G. and BEEGLE L. C., *J. appl. Phys.* **39**, 656 (1968).
10. DE GENNES, P. G., *Phys. Rev.* **118**, 141 (1960).
11. VAN STAPELE R. P., BEIJERS H. G., BONGERS P. F. and ZIJLSTRA H., *J. chem. Phys.* **44**, 3719 (1966).
12. HAM F. S., LUDWIG G. W., WATKINS G. D. and WOODBURY H. H., *Phys. Rev. Lett.* **5**, 468 (1960).
13. COSSEE P., Thesis, Leiden (1956).
14. HEIKES R. R., McGUIRE T. R. and HAPPEL R. J., *Phys. Rev.* **121**, 703 (1961).

---

*The author found recently that the magnetic behaviour of $La_{1-y}Ba_yMnO_3$ with $0 \leqq y < 0 \cdot 1$ is neither in agreement with De Gennes'[10] predictions (to be published).

J. Phys. Chem. Solids Pergamon Press 1969. Vol. 30, pp. 1435–1452. Printed in Great Britain.

LONG WAVELENGTH OPTICAL ABSORPTION OF BROMINATED SILVER BROMIDE*

P. B. P. PHIPPS† and F. A. KRÖGER

Department of Materials Science, University of Southern California, Los Angeles, Calif. 90007, U.S.A.

(*Received* 23 *September* 1968)

Abstract—This paper describes an attempt to measure the acceptor ionization energy, E_a, of neutral silver vacancies in silver bromide through optical absorption. The optical absorption spectrum of silver bromide was investigated from the band edge to $< 0{\cdot}08$ eV while the crystal was at temperatures up to 400°C in equilibrium with bromine at pressures up to one atmosphere. Trapped hole absorption was not observed. A weak absorption that was observed can be interpreted as a free hole transition from the top of the valence band ($L_{4,5}$) to L_8 originated from spin orbit splitting. Combination of absorption and conductivity data leads to a temperature dependence of the hole mobility $v_h = 8 \times 10^6 \times T^{-2{\cdot}69}$ cm$^2V^{-1}$sec^{-1}. The absence of a noticeable absorption due to neutral silver vacancies suggests that these centers are shallow acceptors with $E_a \leq 0{\cdot}1$ eV. Values of the forbidden gap calculated from conductivity data are close to the optical values, but show a somewhat larger temperature dependence

INTRODUCTION

SILVER bromide is a material in which both ionic and electronic conductivity have been observed. Studies relating to the ionic conduction are by now almost classic[1, 2]. Studies of the conduction of pure and doped crystals with appropriate blocking electrodes have yielded values for the electronic conductivity [3, 4]. These data together with the results of other investigations make it possible to determine the thermodynamic parameters regulating the formation of the charged defects V'_{Ag}, $Ag_i^{\cdot}$, e', $h^{\cdot}$ [5]. Here and throughout the paper, the defect notation of Kröger and Vink [6] is used. Neutral species such as V_{Br}^{x}, V_{Ag}^{x}, $(V_{Ag}^{x})_2$, which dominate the imperfection chemistry of non-stoichiometric alkali halides, cannot be detected by conductivity measurements. Information concerning these species should be obtained from other experiments. So far such information is scarce. Spin resonance attributed to V_{Ag}^{x} was shown to be due to iron[7]; an optical absorption observed with chlorinated silver chloride[8], tentatively assigned to V_{Ag}^{x}[5], was shown to correspond to a positive species, probably free holes[9]. The only information concerning V_{Ag}^{x} available at present was deduced from the drift mobility of holes in brominated AgBr at $T > 200$°C. If the drift mobility is supposed to be limited by trapping of holes at V_{Ag}^{x}, analysis leads to a value of the ionization energy of V_{Ag}^{x} of $E_a \approx 0{\cdot}12$ eV[10], somewhat below a previously estimated value of $0{\cdot}2$ eV[5, 11]. The present paper describes an attempt to detect the presence of V_{Ag}^{x} and determine its properties through measurement of the optical absorption corresponding to electronic (hole) transitions between the valence band and the V_{Ag}^{x} acceptor level. If it is assumed that the Smakula equation holds in this case, previous estimates of the concentration of the neutral silver vacancies allow us to estimate the intensity of the expected optical absorption. The Smakula equation relates the extinction coefficient k to the concentration of absorbing centers, N:

$$N = \frac{8{\cdot}2 \times 10^{16}}{M} \frac{n_0}{(n_0^2+2)^2 f} \int k(E)\,\mathrm{d}E. \quad (1)$$

---

*This work was supported by the Directorate of Chemical Sciences, Air Force Office of Scientific Research, under grant AF-AFOSR-986-66

†Now at IBM Research Laboratory, Monterey and Cottle Roads, San Jose, Calif. 95114, U.S.A.

Here M is the number of molecules AgBr per cm^3: $2{\cdot}07\times 10^{22}$; n_0 is the refractive index, 2·2; f is the oscillator strength of the absorption, ≤ 1; E is the photon energy in eV, and N is the concentration of centers expressed as a mole fraction. The absorption coefficient k is defined by $k = -1/d \ln I/I_0$, I_0 being the intensity of the incident beam corrected for reflection, I is the intensity of the transmitted beam, and d is the thickness of the crystal. Instead of k we shall use α, the absorption coefficient defined by

$$\alpha = -\frac{1}{d}\log_{10} I/I_0 \mathrm{cm}^{-1} = k/2{\cdot}303.$$

From [5], $N = [h^{\cdot}] = 159 p_{\mathrm{Br}_2}^{1/2} \exp(-1{\cdot}05 + E_a/kT)$. Taking $p_{\mathrm{Br}_2} = 0{\cdot}25$ atm., $T = 315$°C and $E_a = 0{\cdot}12$ eV leads to $\int \alpha \, \mathrm{d}E \leq 0{\cdot}8$ eV cm^{-1}. Dexter[12] has criticized the use of the classical expression for the ratio of the effective electric field to that in free space on which the Smakula formula is based, and advocates the use of the free space field for calculating the strength of absorption in crystals. This modifies the Smakula equation to

$$N = \frac{0{\cdot}9\times 10^{16} n_0}{Mf}\int k(E)\,\mathrm{d}E \qquad (1\mathrm{a})$$

and leads to a reduction of the estimated absorption strength by a factor 5·2 to $\int \alpha \, \mathrm{d}E \leq 0{\cdot}15$ eV cm^{-1}. In any case the absorption should be observable for a crystal thickness of ≈ 1 cm. Its peak may be expected anywhere from 15 to 1·5 mμ, i.e. at photon energies between 0·08 and 0·8 eV.

In addition, free hole absorption as observed with AgCl[8, 9] must be expected. As we shall see, our investigation showed the latter, but absorption due to V_{Ag}^{x} was not observed. The implication is that either $f \ll 1$ or that this center is present in concentrations smaller than expected.

MATERIALS

Preliminary measurements were made on a crystal of silver bromide kindly donated by Dr. F. Moser of the Eastman Kodak Company. Crystals were also prepared by the following procedure[13]. Silver nitrate and ammonium bromide (analytical reagents) were recrystallized and then made into M/50 solution at 60°C. Aluminium and iron were suspected as probable impurities because their hydrous oxides might not be removed from solution by filtering. An attempt was made to coprecipitate these ions from each solution by the following procedure. The hot solutions of ammonium bromide and silver nitrate were adjusted to a pH ≈ 2 with nitric acid in order to dissolve the oxides. Then the pH was adjusted to 6 with ammonium hydroxide, and enough of each solution was added to the other to form an appreciable precipitate. This was discarded and then the pH was readjusted to ~2 and the main precipitation effected in the ammonium bromide. The filtrate was washed with water, then alcohol, and dried at 110°C in the dark. The powder was melted in a quartz crucible in 0·2 atm. of bromine and 0·8 atm. of nitrogen, and the crystal pulled at 0·3 cms/hr. No part of the apparatus in contact with the bromine gas was made of metal. Crystals doped with cadmium were grown from a melt to which cadmium metal was added. The cadmium reacted rapidly with the bromine and dissolved in the melt forming a clear solution. The concentration of cadmium in the crystal was calculated using the known distribution coefficient[14]. Spectrographic analysis showed concentrations given in Table 1. The crystals were cut with a razor blade, etched thoroughly in concentrated HCl, ground flat using carborundum, and polished using filter paper wet with diethylamine. They did not

Table 1. *Spectrographic analysis*
(mol. fr. $\times 10^6$)

Element	Cd	Mg+Ca	Fe	Al
Undoped	< 30	7	8	< 5
Cd Doped	540	6	21	< 5

darken rapidly in room light but were stored in the dark.

APPARATUS

The rapid response to bromine[8] and the quickness of precipitation processes in silver bromide precluded the use of quenched samples. The apparatus shown in Fig. 1 was designed to allow the spectrum to be observed from ~ 0·4 to 16 μ while a 1 cm thick crystal was at temperatures up to 420°C in bromine pressures up to one atmosphere with rigorous exclusion of oxygen. A single crystal of NaCl, which does not show absorption in this spectral region, was used as a blank. The difference in reflectivity between AgBr and NaCl was calculated from the refractive index at the wavelength of the sodium *D* line.

The light sources used were a constant-power 'globar' and a tungsten lamp with a sodium chloride window. A single beam Leiss double monochromator with sodium chloride

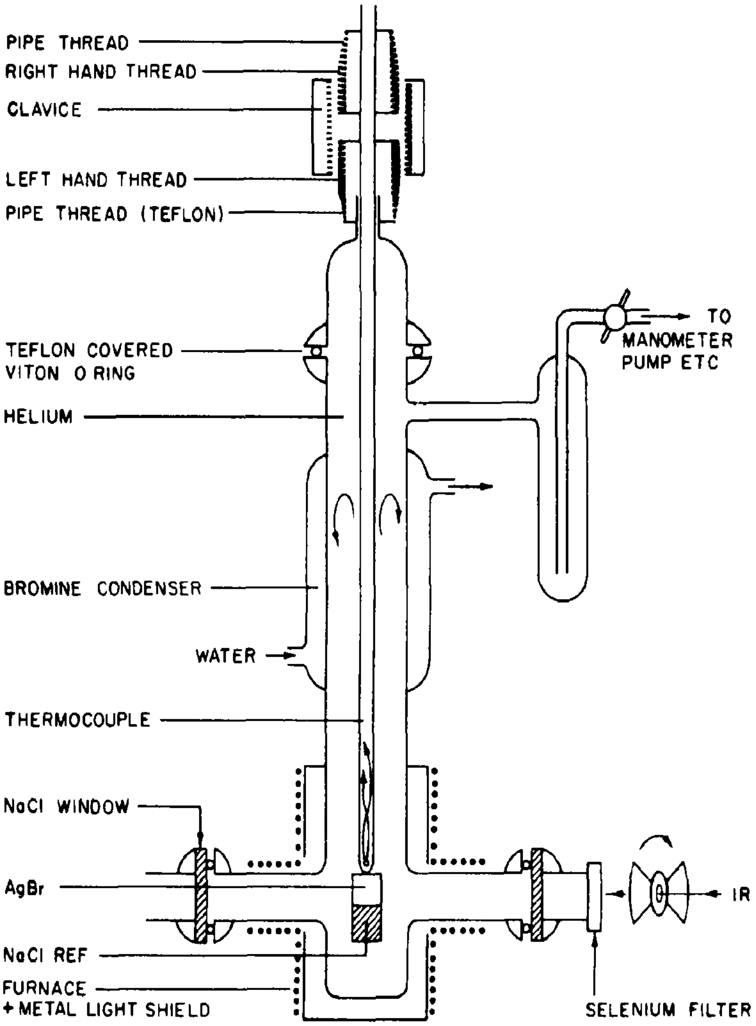

Fig. 1. The infrared absorption cell used for temperatures up to 400°C and controlled bromine pressures up to one atmosphere.

prisms was used in combination with a high sensitivity Reeder thermocouple and Brower synchronous detector. An image of the light source was formed at unit magnification on the crystal with a Perkin Elmer spherical mirror. For measurements at photon energies $1{\cdot}6\,\text{eV} > h\nu > 1{\cdot}2\,\text{eV}$ radiation of shorter wavelengths was cut off by interposing a filter consisting of cast and quenched selenium. For measurements at wavelengths less than one micron, the incident light was passed through a second monochromator with a broader band pass than the prism instrument which was detecting the transmitted light. Both measures were taken to avoid photochemical changes caused by short-wave radiation which were slow to reverse.

EXPERIMENTAL PROCEDURE AND RESULTS

In a preliminary experiment the absorption spectrum of bromine was measured for temperatures up to 400°C and was found to be in excellent agreement with previous measurements[15]. It was also shown that neither bromine nor any impurity present gave rise to absorption with an absorption coefficient (for Br_2 per atm. of bromine) greater than $0{\cdot}01\,\text{cm}^{-1}$ from 1 to $17\,\mu$. The absorption at 4750 Å which does not vary with temperature could not be used to measure the bromine pressure because silver bromide is photographically active at this wavelength. The pressure was set using the van Doorn method [16], or was estimated from the temperature of the side arm[17].

No valve which could withstand attack by hot bromine proved reliably leak tight (as monitored by a mass spectrometer leak detector) unless lubricated with a small amount of Kel F 90 halogen resistant grease. The light which passed through the sodium chloride reference crystal suffered progressive attenuation when the crystal was held at temperatures greater than 300°C while using the van Doorn method. This was believed to be due to the decomposition of a volatile compound produced by reaction with the grease. Furthermore the surface of the silver bromide appeared to be roughened by heating in bromine. A random error of $\pm 0{\cdot}15\,\text{cm}^{-1}$ in the absorption coefficient relative to sodium chloride was attributed to these factors. Although the sodium chloride was always checked as a reference, an alternative technique proved more precise. The crystals were equilibrated with bromine at a known temperature and pressure, and the spectrum measured by comparison with the sodium chloride. This was repeated for several temperatures at a given pressure. Then the silver bromide was placed in the beam and the transmission at four convenient wavelengths was measured as the crystal was heated, and subsequently cooled, at a given pressure of bromine. The logarithm of the observed transmitted light was plotted against the reciprocal temperature as shown in Fig. 2. The difference between this line and an unknown constant level, $\log_{10} I_0$, gives the absorption coefficient: $\alpha = 1/d \log_{10}(I_0/I)$. Since α is proportional to the number of centers causing the absorption N, and N is expected to vary exponentially in reciprocal temperature (at least in the low-temperature range), we expect α to vary exponentially in reciprocal temperature at low temperatures. The I_0 which made the low-temperature extinction coefficient vary exponentially in reciprocal temperature was chosen by trial and error. Measurements at other wavelengths and/or pressures give the same slope within experimental error. Figure 3 demonstrates this for two wavelengths. Figure 4 shows similar data for cadmium doped crystals. All the curves tend to flatten at high temperatures, some even bend slightly down at the highest temperature. The temperature dependence of the tail absorption is essentially the same at all wavelengths. The bromine pressure dependence of the α's thus determined is shown in Fig. 5 and the spectral distribution of the absorption is shown in Figs. 6–8.

It is found that for pure as well as cadmium doped crystals, bromination causes an extra

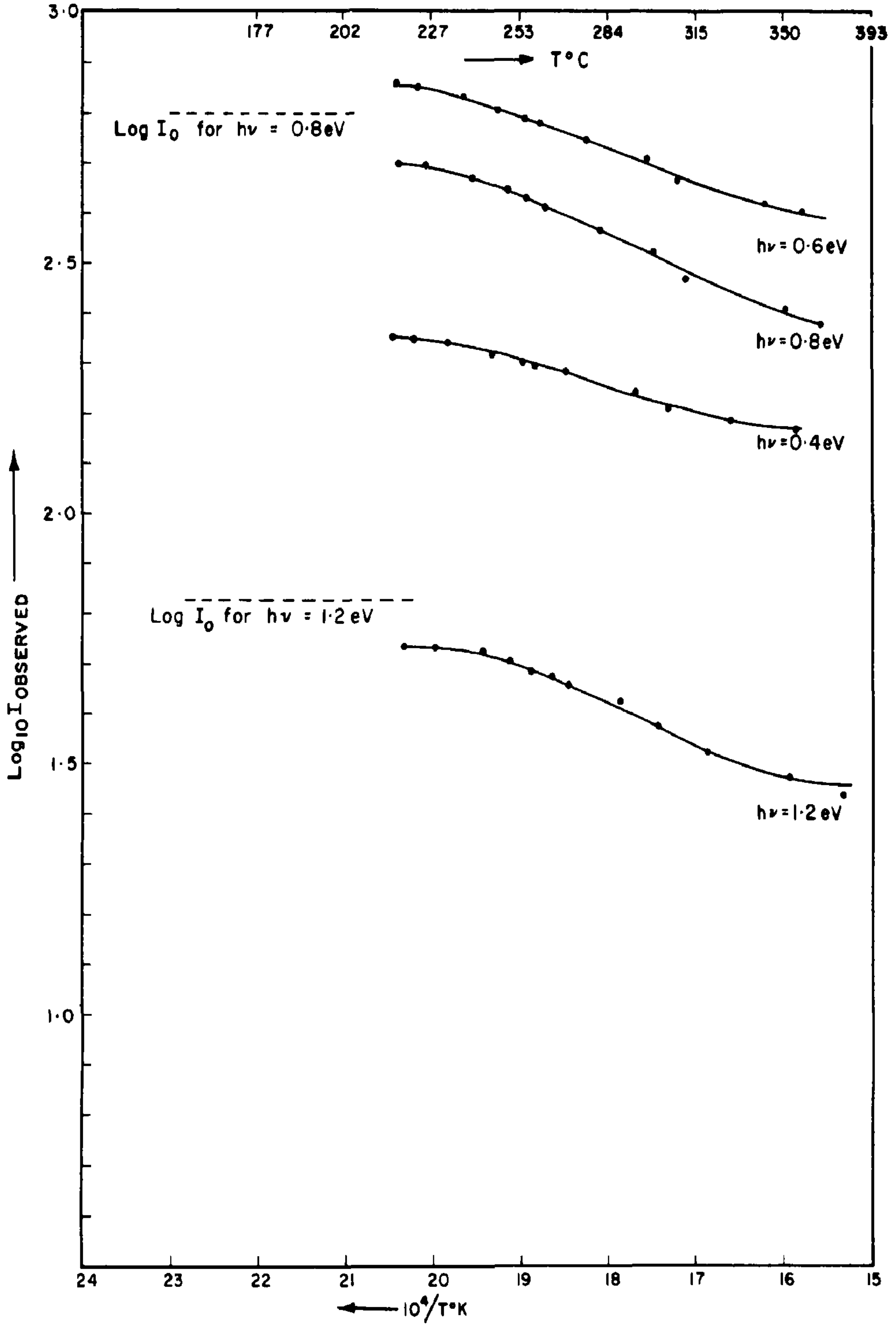

Fig. 2. The intensity of transmitted light as a function of temperature for a 1 cm thick crystal of undoped AgBr at $p_{Br_2} = 1$ atm.

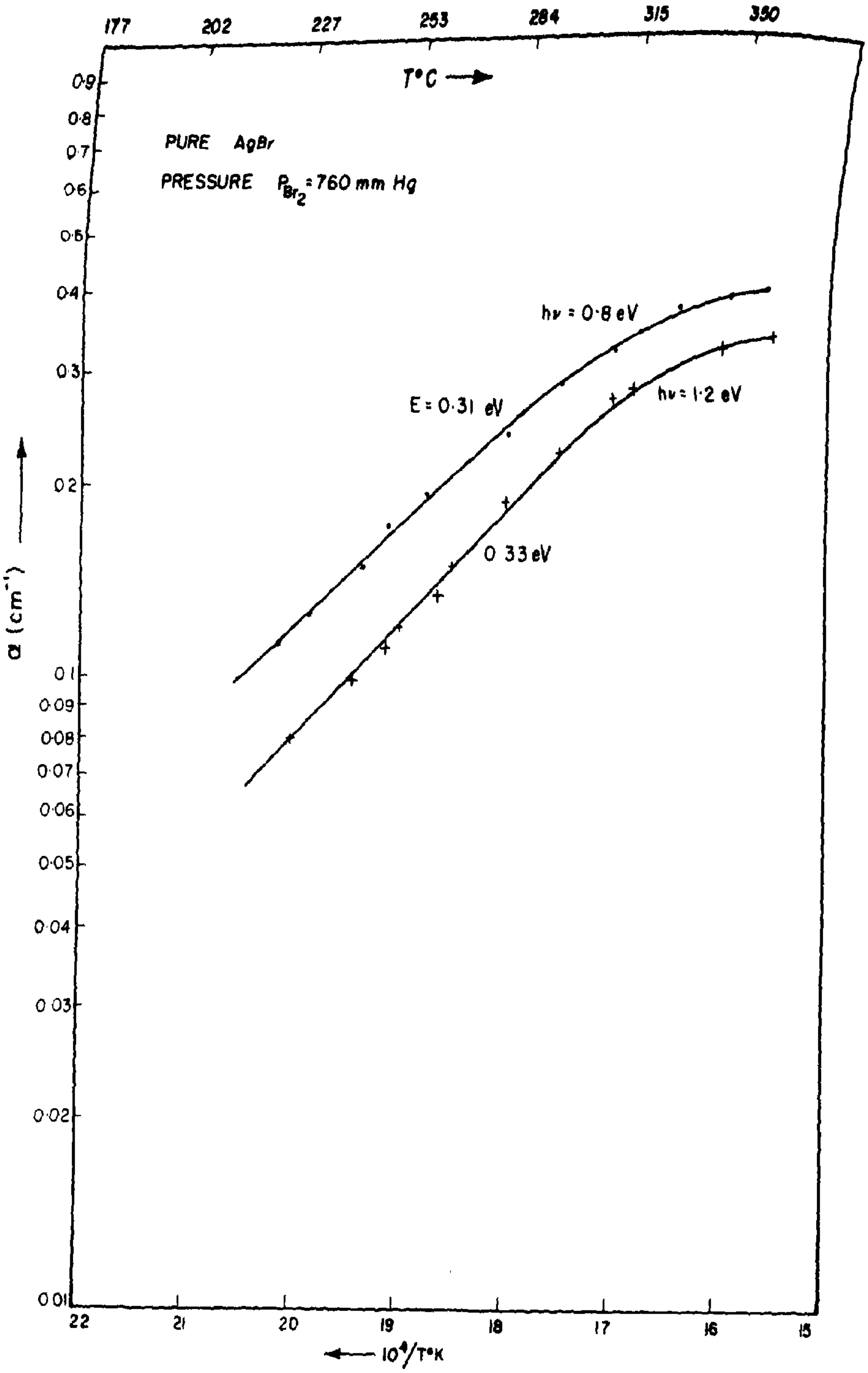

Fig. 3 The temperature dependence of the absorption coefficients for undoped AgBr derived from Fig 2, and the activation energy E obtained.

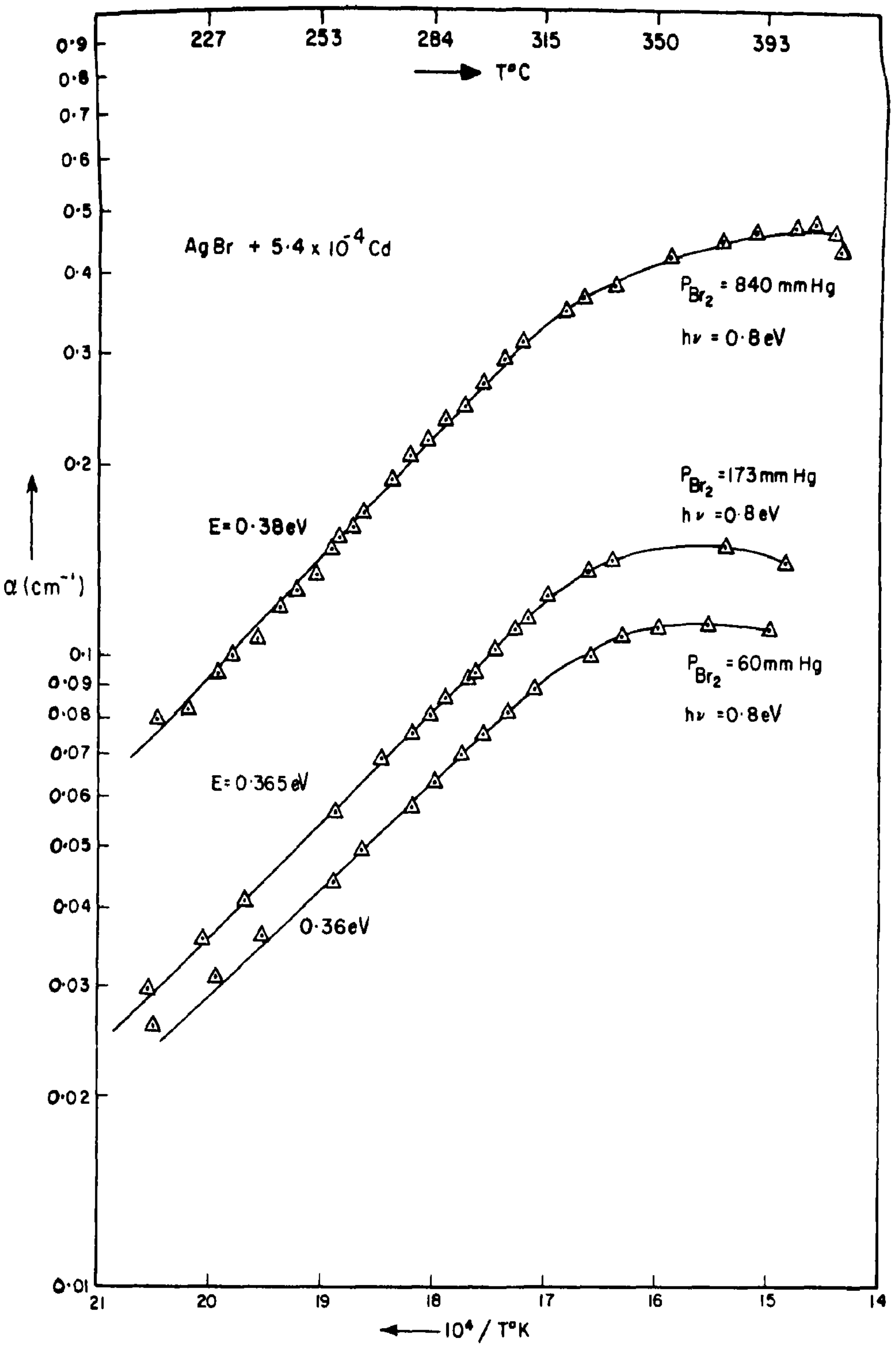

Fig. 4. The temperature dependence of the absorption coefficients for AgBr + 5·4 × 10^{-4} Cd at three different pressures, and the activation energies, *E*, obtained

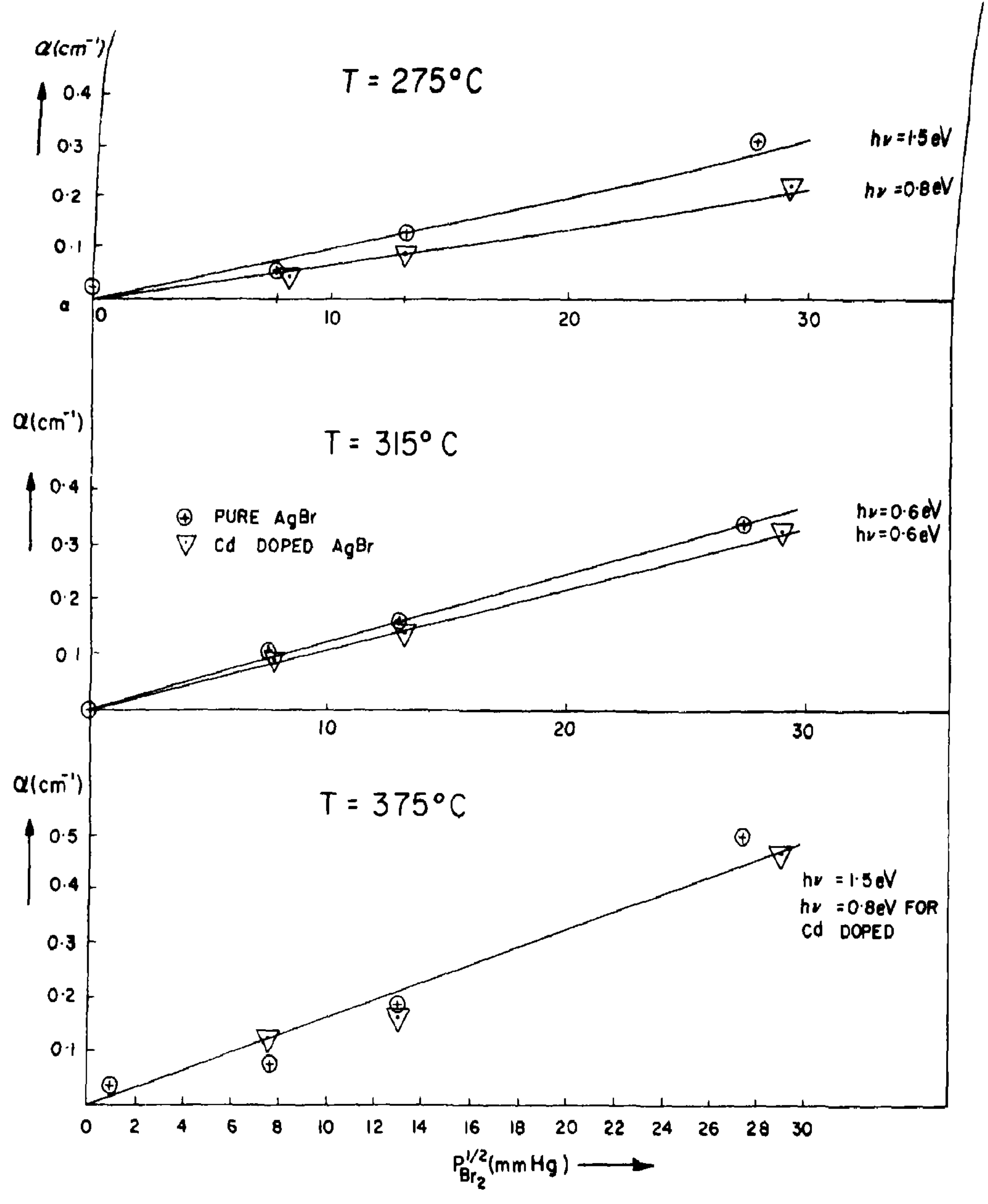

Fig. 5 The absorption induced by bromination plotted against the bromine pressure for undoped AgBr and AgBr + 5·4 × 10^{-5} mole fraction of cadmium

absorption extending from the fundamental absorption edge (which varies from 2·4 eV at 140°C to 2·05 eV at 400°C, all at $\alpha = 0{\cdot}44$ cm^{-1}) to a cut-off independent of temperature at ≈0·08 eV. A similar absorption was previously indicated by the reflection spectrum of electrolytically brominated AgBr[18]. Some of our spectra show a structure in the long-wave part of the absorption. We are not quite certain that this is significant; it may be due to the presence of water which absorbs in this region. The absorption strength is

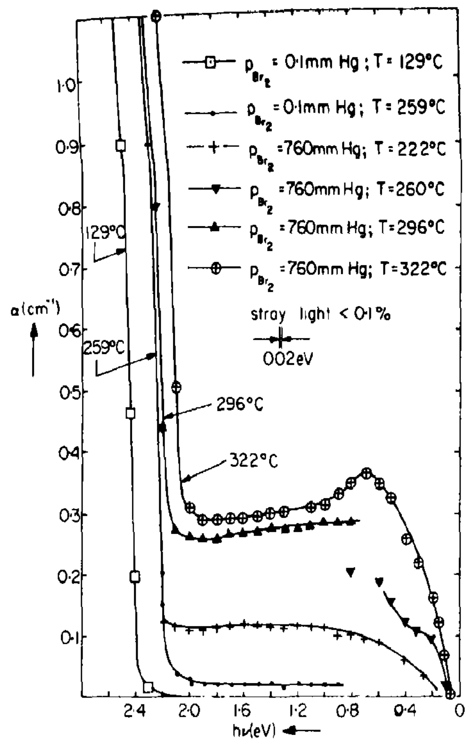

Fig. 6 The spectral distribution of the absorption of undoped AgBr at 0·1 and 760 mm Hg at various temperatures.

proportional to $p_{Br_2}^{1/2}$. Cadmium doping decreases the strength of the absorption at the lower temperatures, but does not affect it at higher temperatures.

DISCUSSION

Assignment of the spectrum; defect equilibria

If it is assumed that the absorption cross section of a given defect is independent of temperature or at most weakly dependent on temperature, the dependence of the observed absorption on p_{Br_2} and on the cadmium concentration as observed must be determined exclusively by the concentration of the defect involved.

Bromination may be expected to give rise to three simple defects, viz. V_{Ag}^{x}, V'_{Ag} and $h^{\cdot}$. The concentrations of these defects formed under equilibrium conditions are found by applying the methods of defect chemistry to the various defect disorder and formation reactions. The concentrations of all charged defects present must satisfy the neutrality condition:

$$[e'] + [V'_{Ag}] = [h^{\cdot}] + [Ag_i^{\cdot}] + [Cd_{Ag}^{\cdot}]. \quad (2)$$

Native ionic defects are formed as a result of Frenkel disorder:

$$Ag_{Ag}^{x} + V_i^{x} \rightarrow Ag_i^{\cdot} + V'_{Ag}$$

and in equilibrium,

$$[Ag_i^{\cdot}][V'_{Ag}] = K_{F'}. \quad (3)$$

In the bromine-rich part of the phase field in which we are interested, electrons may be neglected. Holes are formed mainly as a result of bromination

$$\tfrac{1}{2}Br_2(g) \rightleftarrows Br_{Br}^{x} + V'_{Ag} + h^{\cdot},$$

$$\text{giving } [h^{\cdot}][V'_{Ag}] = K_{Br_2V'h}\, p_{Br_2}^{1/2} \quad (4)$$

Neutral vacancies V_{Ag}^{x} are in equilibrium with V'_{Ag} and $h^{\cdot}$ through

$$V_{Ag}^{x} = V'_{Ag} + h^{\cdot}, \; [h^{\cdot}][V'_{Ag}]/[V_{Ag}^{x}] = K_a.$$

We can also formulate the formation of V_{Ag}^{x} as as a result of bromination

$$\tfrac{1}{2}Br_2(g) \rightleftarrows Br_{Br}^{x} + V_{Ag}^{x}, \; [V_{Ag}^{x}] = K_1 p_{Br_2}^{1/2}. \quad (6)$$

Evidently (4–6) are not independent: $K_{Br_2V'h} = K_1 K_a$. A general solution for the concentration of holes in Cd-doped AgBr as $f(p_{Br_2})$ is found by solving the equations (2–5)

$$[h^{\cdot}] = \tfrac{1}{2}(1 + K_{F'}K_{Br_2V'h}^{-1}p_{Br_2}^{-1/2})^{-1}\{-[Cd] + ([Cd]^2 + 4K_{F'} + 4K_{Br_2V'h}\,p_{Br_2}^{1/2})^{1/2}\}$$

$$\approx \tfrac{1}{2}[Cd]K_{F'}^{-1}K_{Br_2V'h}\,p_{Br_2}^{1/2} \times \{-1 + (1 + 4K_{F'}/[Cd]^2)^{1/2}\}.$$

At high temperatures where V'_{Ag} and $Ag_i^{\cdot}$ are

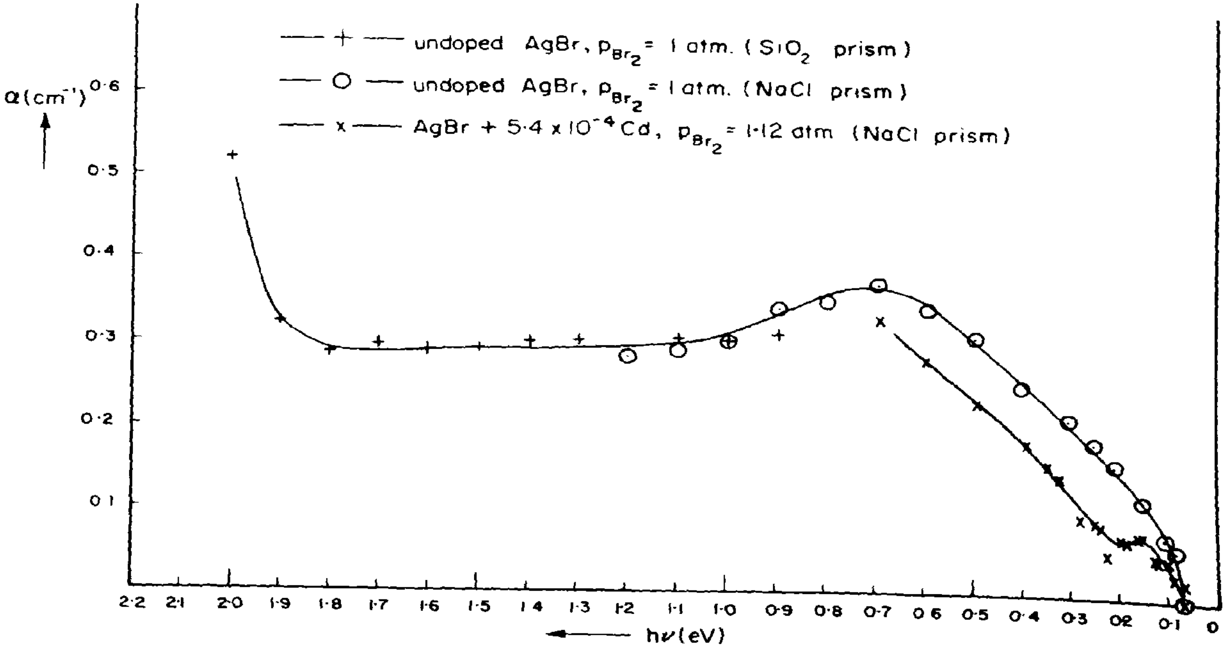

FIG. 7. The spectral distribution of the absorption caused by bromination at 315°C and a bromine pressure p_{Br_2} of 1 and 1·12 atm respectively, for undoped AgBr and AgBr + 5·4 × 10^{-4} Cd.

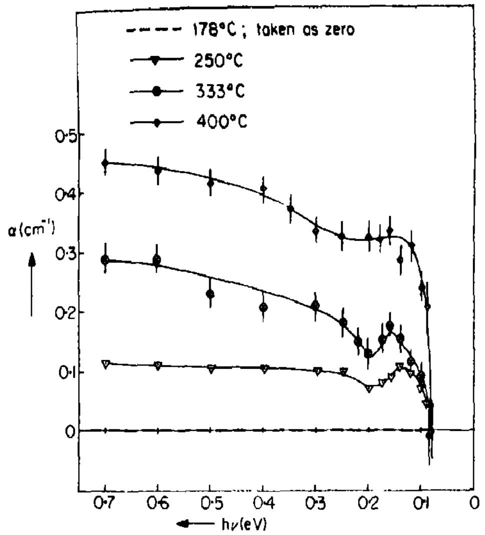

Fig. 8. Long-wave part of the bromine induced absorption for undoped AgBr at $p_{\mathrm{Br_2}} = 1{\cdot}25$ atm at various temperatures.

the dominant charged species, $4K_{F'} \gg [\mathrm{Cd}]^2$, and (7) reduces to

$$[h^{\cdot}] \approx K_{F'}^{-1/2}K_{\mathrm{Br_2}\nu h}p_{\mathrm{Br_2}}^{1/2}. \tag{8}$$

At low temperatures when $[\mathrm{Cd}_{\mathrm{Ag}}^{\cdot}] \gg [\mathrm{Ag}_i^{\cdot}]$ and $[\mathrm{Cd}_{\mathrm{Ag}}^{\cdot}] \approx [V'_{\mathrm{Ag}}] \gg K_{F'}^{1/2}$, (7) reduces to

$$[h^{\cdot}] = [\mathrm{Cd}_{\mathrm{Ag}}^{\cdot}]^{-1}K_{\mathrm{Br_2}\nu h}p_{\mathrm{Br_2}}^{1/2}. \tag{9}$$

The temperature dependence of the hole density and the mobility

Figure 10 shows the temperature dependence of the concentrations of the various defects in Cd-doped AgBr at $p_{\mathrm{Br_2}} = 1$ atm.

As shown by equations (6–9), both $[h^{\cdot}]$ and $[V_{\mathrm{Ag}}^{x}]$ are proportional to $p_{\mathrm{Br_2}}^{1/2}$ but whereas (6) shows $[V_{\mathrm{Ag}}^{x}]$ to be independent of the cadmium concentration under all circumstances, the hole concentration is independent of the cadmium concentration at high temperatures, but inversely proportional to it at low temperatures. Our absorption data fit the theory if the absorption is assigned to free holes, the temperature range covered corresponding to high and medium temperatures.

That we are dealing with free holes is also indicated by the similarity between $\log[h^{\cdot}]$ as $f(1/T)$ as obtained by Raleigh[4] and the absorption coefficients found by us, both showing a linear section at lower temperatures, and a flattening and a weak maximum at higher temperatures. The possibility that absorption due to V_{Ag}^{x} is contributing markedly to the absorption in the discussed range is unlikely, since the absorption was found to be suppressed by $\mathrm{Cd}_{\mathrm{Ag}}^{\cdot}$; as we have seen, neutral V_{Ag}^{x} would not be affected. Furthermore, the activation energy would be ≈0·93 eV[5], while we observe 0·32 eV (see below) – a discrepancy well outside the range of possible errors.

Although the curves for the absorption and the hole concentration have a similar appearance, the slopes are not quite the same. Raleigh's data for pure AgBr in the linear region can be represented by [4, 5]:

$$[h^{\cdot}] = 1{\cdot}74 \times 10^{-2}p_{\mathrm{Br_2}}^{1/2} \times \exp(-0{\cdot}44\, eV/kT) \text{ mol. fr.} \tag{10}$$

The observed temperature dependence of the integrated absorption is represented by

$$\int \alpha\, \mathrm{d}E = 2{\cdot}84 \times 10^{2}p_{\mathrm{Br_2}}^{1/2} \times \exp(-0{\cdot}32\, eV/kT) \text{ eV cm}^{-1}. \tag{11}$$

A similar discrepancy exists for the cadmium-doped crystal. Inspection of Fig. 10 shows that in the temperature range $17 < 10^4/T < 19$

$$[h^{\cdot}] = 6 \times 10^{-2}p_{\mathrm{Br_2}}^{1/2} \exp(-0{\cdot}5\, eV/kT) \text{ mol. fr.} \tag{12}$$

The integrated absorption, on the other hand, is given by

$$\int \alpha\, \mathrm{d}E = 6{\cdot}7 \times 10^{2}p_{\mathrm{Br_2}}^{1/2} \times \exp(-0{\cdot}37\, eV/kT) \text{ eV cm}^{-1}. \tag{13}$$

Both sets of data indicate a similar decrease

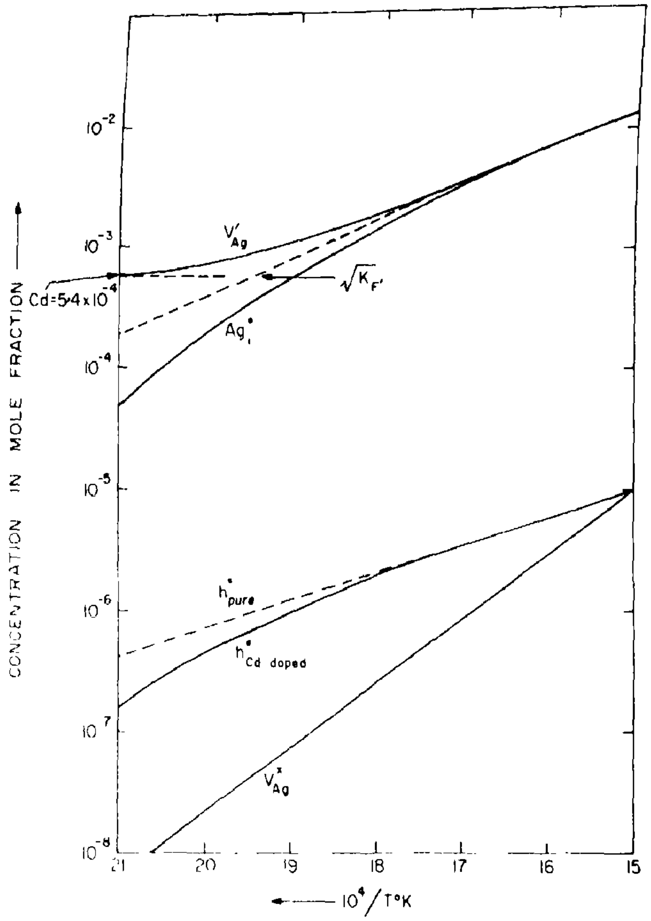

Fig. 9. The temperature dependence of the defect concentrations for a crystal of AgBr + $5\cdot4 \times 10^{-4}$ Cd in a bromine pressure of 1 atmosphere, assuming an acceptor ionization energy $E_a = 0\cdot12$ eV for V'_{Ag}.

of the absorption per hole with increasing temperature, (10) and (11) giving

$$\bar{\alpha} = \int \alpha \, dE/2\cdot07 \times 10^{22}[h^\cdot]$$
$$= 7\cdot9 \times 10^{-19} \exp(0\cdot12\, eV/kT)\ \text{eV cm}^2 \quad (14)$$

and (12) and (13) give a similar result.

Although absorption coefficients may decrease with increasing temperature as a result of a variation of occupation of levels when transitions starting at these levels have different transition probabilities, such a decrease is of the form $\propto \{1 - \exp(-E/kT)\}$ rather than $\propto \exp E/kT$. Therefore we are inclined to believe that the difference between the slopes of (10) and (11) and (12) and (13) is due to an error in either the hole concentration or the absorption. An error in the former may have arisen by the use at higher temperatures of a temperature dependence of the hole mobility $v_h = 1\cdot5 \times 10^{14} T^{-5\cdot5}$ cm^{2}V^{-1}sec^{-1} determined at $T < 100$°C [19, 4, 5].

The temperature dependence of v_h required to bring (10) and (11) into line can be found by dividing the hole conductivity σ_h as given by Raleigh[4] in his Fig. 4, by $\int \alpha\, dE$ as given by equation (11) or by Fig. 3 using $\int \alpha\, dE = 1\cdot59 \times \alpha_{0\cdot8eV}$ eV cm^{-1}:

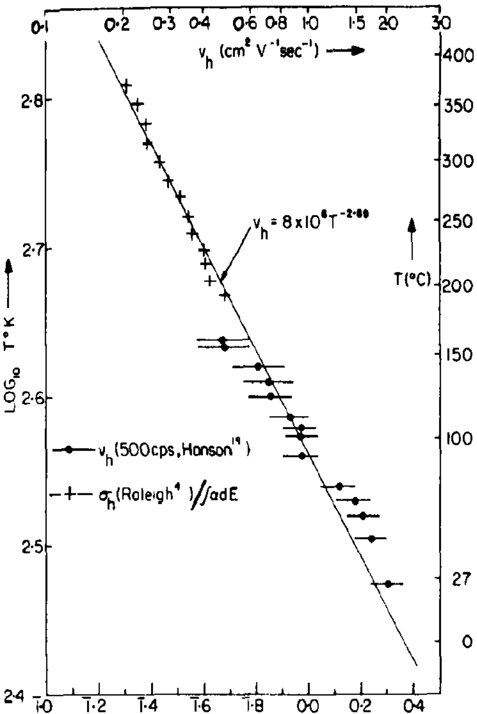

Fig. 10 Experimental data for the Hall mobility of holes, v_h, measured at 500 c/s by Hanson[19] compared to v_h as $f(\log T)$ derived from conductivity data by Raleigh[4] and our optical absorption data, using equation (15)

$$\frac{\sigma_h}{\int \alpha\, dE} = 2{\cdot}07\times 10^{22}\frac{[h^{\cdot}]qv_h}{\bar{\alpha}[h^{\cdot}]}$$

$$= 2{\cdot}07\times 10^{22}\, qv_h/\bar{\alpha}\ \mathrm{V^{-2}\,sec^{-1}}. \quad (15)$$

Here q is the electronic charge, $1{\cdot}6\times10^{-19}$ C, and $\bar{\alpha}$ is the integrated absorption per hole, supposedly independent of temperature. Taking into account that according to Hanson [19] (v_h)100°C ≈ 1 cm²V⁻¹ sec⁻¹, we find $\bar{\alpha} = 2{\cdot}53\times10^{-17}$ eV cm². This is in excellent (though probably fortuitous) agreement with $(\bar{\alpha})_S = 2{\cdot}3\times10^{-17}$ eV cm² as calculated from the Smakula formula (1) with $f = 1$, but is ≈ 4× smaller than $(\bar{\alpha})_D = 1{\cdot}2\times10^{-16}$ eV cm² as calculated from Dexter's modified more correct formula (1^a). As indicated by Dexter [12] the numerical factor in both formulas must be expected to increase if exchange and covalency are taken into account, which reduces $(\bar{\alpha})_D$. This quantity is further reduced if we take $f < 1$; $f \approx 0{\cdot}25$ would lead to quantitative agreement. Since this is a reasonable value, we feel that the agreement is satisfactory. Figure 11 shows $\log v_h$ as $f(\log T)$ arrived at in this manner. A relation

$$v_h = 8\times10^6 T^{-2\cdot69}\,\mathrm{cm^2V^{-1}\,sec^{-1}} \quad (16)$$

describes both Hanson's and our data from 27 to 380°C. Note the absence of an inflexion at high temperature where σ_h and $\int \alpha\, dE$ have a maximum.

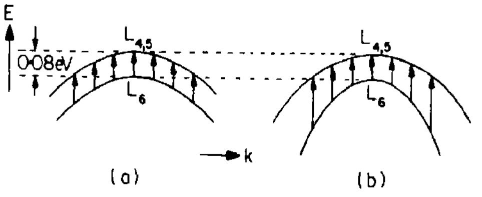

Fig 11. Qualitative form of energy versus the wave vector for branches of the valence band near L_1: (a) in the [111] direction, (b) in directions other than [111]

The exponent of −2·69 found now is more acceptible than the value −5·5 arrived at previously on the basis of Hanson's data only. Similar values have been observed with several semiconductors (Table 2). Negative exponents of this magnitude are believed to result from acoustical scattering combined with inter valley and/or optical mode scattering [25–28]. The band structure of AgBr shows several valleys with energy extrema in close proximity[29, 30]. In addition this compound is also partly polar. Thus both types of scattering may well play a role.

Interpretation of the hole spectrum in terms of the band structure

The hole spectrum observed is a broad band, possibly with some structure in the long-wave region, with a sharp cut-off at 0·08 eV. It should result either from intraband transitions or from transitions between different valleys or branches of the structure. The shape of

Table 2. Strongest high-temperature temperature dependences of carrier mobilities in semiconductors ($v \propto T^{-n}$)

Substance	Carriers	Method of measurement	n	Reference
Si	e'	drift	2·5	[20]
		conductivity	2·6	[22]
	h	drift	2·7	[20]
		conductivity	2·3	[22]
Ge	h	drift	2·3	[21]
GaAs	h	Hall effect	2·1	[23]
PbS, PbSe, PbTe	e', h	Hall effect	2·2 –2·5	[24]

the absorption near the cut-off indicates a dependence

$$\alpha = \frac{A}{h\nu}(h\nu - E_0)^{1/2} \tag{17}$$

with $E_0 = 0{\cdot}08$ eV rather than

$$\alpha = \frac{A}{h\nu}(h\nu - E_0)^{3/2}. \tag{18}$$

This seems to indicate that we are dealing with a direct, allowed transition[31].

The calculated band structure[29] shows that the top of the valence band is L_3, split by spin-orbit coupling into a pair of Kramers doublets $L_{4,5}$ and L_6, with a splitting of $\approx 0{\cdot}08$ eV. On the other hand there is a state $\Sigma_4 \approx 0{\cdot}1$ eV below $L_{4,5}$. A transition, $\Sigma_4 \rightarrow L_{4,5}$, though of approximately the right energy would be indirect and can be excluded. On the other hand the direct transition $L_{4,5} \rightarrow L_6$, though of exactly the observed energy, is parity forbidden: at L_3, viewed from a silver site, all wave functions have even parity. Away from L_3, parity is no longer exact, and there are non-vanishing matrix elements of the electric dipole moment, leading to allowed absorption. Normally the spin-orbit splitting increases with the distance from L_3, and therefore the increased absorption occurs at a gradually increasing frequency: the absorption then has a tail as described by equation (18) – which does not fit our data.

Thus we seem to be in an impasse, the two types of possible transitions having the wrong frequency dependence. A possible solution of this dilemma was suggested by Pryce[32]. The spin-orbit splitting is different along [111] and in other directions. Along [111] it is essentially equal to the difference between the expectation value of the spin orbit parameters, λ_{4p} on Br^- and λ_{4d} on Ag^+. The weight associated with the amount of $Br^-(4p)$ and $Ag^+(4d)$ changes only slowly near L_3, and therefore the splitting along [111] is insensitive to small displacements from L_3 (Fig. 11(*a*)). As a result transitions polarized $\perp$[111] but at points other than L_3 where parity is no longer exact, are allowed but still have a frequency close to that at L_3. In directions different from [111] additional splitting occurs due to the fact that the orbital degeneracy of L_3 is resolved; this dominates quickly over the spin-orbit coupling and gives rise to transitions at larger frequencies (Fig. 11(*b*)). As a result we get a total absorption with a sharp long-wave edge at E_0 corresponding to the splitting near L_3, extending to shorter wave lengths due to contributions from non-[111] directions. This type of transition therefore may be held responsible for the absorption near the cut-off at 0·08 eV. It possibly accounts for the absorption at shorter wavelengths. It may well be, however, that the latter is at least partly due to the indirect transition $\Sigma_4 \rightarrow L_{4,5}$. In both cases our analysis would be affected in that the total absorption cross section is not completely independent of temperature, but has the tendency to increase with temperature. This will lead to $v_h \propto T^{-n}$ with n even smaller than the value found by us.

The ionization energy of the native acceptor

The absence of a noticeable absorption due to $V^{\mathrm{x}}_{\mathrm{Ag}}$ indicates that either the oscillator strength $f \ll 1$, or that $[V^{\mathrm{x}}_{\mathrm{Ag}}] < 10^{-6}$ for $T \leq 320°\mathrm{C}$, $p_{\mathrm{Br}_2} \leq 1$ atmosphere. The latter in turn would indicate that $V^{\mathrm{x}}_{\mathrm{Ag}}$ acceptor level is close to the valence band, with $E_a \leq 0{\cdot}1$ eV. E_a can also be estimated from the temperature dependence of the drift mobility of holes as deduced from the rate of bromination[10]. Combination of

$$(v_h)_{\mathrm{drift}} = 3{\cdot}1 \times 10^{-9} \exp(0{\cdot}77\, eV/kT) \quad \mathrm{cm}^2\mathrm{V}^{-1}\mathrm{sec}^{-1} \qquad (19)$$

found for $T > 200°\mathrm{C}$[33] with the temperature dependence of v_h as given by (16) leads to

$$R = (v_h)_{\mathrm{drift}}/v_h = 8{\cdot}7 \times 10^{-8} \exp(0{\cdot}632\, eV/kT). \qquad (20)$$

Assuming the drift mobility to be limited by trapping at V'_{Ag} with the formation of $V^{\mathrm{x}}_{\mathrm{Ag}}$,

$$R = \frac{[h^{\cdot}]}{[h^{\cdot}] + [V^{\mathrm{x}}_{\mathrm{Ag}}]} = \frac{1}{1 + [V^{\mathrm{x}}_{\mathrm{Ag}}]/[h^{\cdot}]} = \frac{1}{1 + [V'_{\mathrm{Ag}}]/K_a} = \frac{1}{1 + K_F'^{1/2}/K_a}. \qquad (21)$$

Here K_a is the equilibrium constant of the ionization reaction $V^{\mathrm{x}}_{\mathrm{Ag}} \rightarrow V'_{\mathrm{Ag}} + h^{\cdot}$;

$$K_a = \frac{[h^{\cdot}][V'_{\mathrm{Ag}}]}{[V^{\mathrm{x}}_{\mathrm{Ag}}]} = \tfrac{1}{2} A_h g_v \exp(-E_a/kT)$$

with $g_v = 12$ and $A_h = 2{\cdot}34 \times 10^{-7}\ (m_h^*/m)^{3/2}\ T^{3/2}$ (mol. fr.), and K'_F is the equilibrium constant of the Frenkel disorder, which determines $[V'_{\mathrm{Ag}}]$ in the temperature range concerned. Taking $K'_F = 3{\cdot}1 \times 10^5 \exp(-1{\cdot}22\, eV/kT)$ (mol. fr.) we find $E_a = -0{\cdot}10$ eV, which is unacceptable: E_a must be positive. Since the previously used stronger temperature dependence of v_h led to a plausible value for E_a, this may be seen as evidence against the temperature dependence of v_h as found in this work. It is also possible, however, that (19) is somewhat in error. Considering the narrow temperature range from which it was deduced this is not unlikely. Correction of (19) to an expression with a weaker temperature dependence will make E_a positive. However, at most a small absolute value may be attained—in agreement with the limitation $E_a < 0{\cdot}1$ eV found above.

The thermal and optical band gaps

The change in the temperature dependence of v_h represented by (16) also affects the result for the intrinsic electronic excitation constant K_i as $f(T)$ arrived at by combining our data for the hole concentration in AgBr in contact with bromine, with Ilschner's data for the electron conduction in AgBr in equilibrium with silver[34] and the free enthalpy of formation of AgBr. For a constant absorption cross section $\bar{\alpha} = 2{\cdot}53 \times 10^{-17}$ eV cm², as found above, (11) gives

$$[h^{\cdot}] = 5{\cdot}53 \times 10^{-4} p_{\mathrm{Br}_2}^{1/2} \exp(-0{\cdot}32\, eV/kT)\ \mathrm{mol.\ fr.} \qquad (22)$$

From this we find for the equilibrium constant of bromination with the formation of silver ion vacancies and holes

$$K_{\mathrm{Br}_2Vh} = 3{\cdot}1 \times 10^{-1} \exp(-0{\cdot}93\, eV/kT) \quad (\mathrm{mol.\ fr.})^2\ \mathrm{atm.}^{-1/2} \qquad (23)$$

Following the path outlined in reference [10] we obtain instead of equation (16) of that paper:

$$K_i = [e'][h^{\cdot}]$$

$$= 4{\cdot}07 \times 10^{48} \exp(-3{\cdot}26\, eV/kT)\ \text{cm}^{-6}. \quad (24)$$

Equating this with the theoretical expression

$$K_i = g_c g_v A_e A_h \exp(\beta/k) \exp(-E_i^{\circ} eV/kT)$$

with E_i the band gap and g_c and g_v weight factors of the conduction and valence bands,

$$E_i = E_i^{\circ} - \beta T\ eV$$

$$g_c = 1,\ g_v = 12,\ A_{e,h}$$

$$= 4{\cdot}84 \times 10^{15} \left(\frac{m^*_{e,h}}{m}\right)^{3/2} T^{3/2}\ \text{cm}^{-3}$$

$m_e^* \approx m_h^* = 0{\cdot}27$ m, writing $T^3 \approx 1{\cdot}88 \times 10^9 \exp(-0{\cdot}11\, eV/kT)$ leads to

$$E_i^{\circ} = 3{\cdot}15\ \text{eV} \quad \text{and} \quad \beta = 1{\cdot}7 \times 10^{-3}\ \text{eV/deg.}$$

Figure 12 shows how this compares to the optical values for E_i as a function of temperature. There is agreement of the absolute value of E_i near 500°K, but the temperature dependence and the value of E_i° are somewhat too large, the linear part of the optical absorption edge varying with temperature according to $(E_i)_{\text{opt}} = (2{\cdot}9 - 1{\cdot}2 \times 10^{-3}T)$ eV if we consider the whole temperature range or by $(E_i)_{\text{opt}} = (2{\cdot}97 - 1{\cdot}36 \times 10^{-3}T)$ eV if we concentrate on the range 100–300°C. Considering the many steps involved in the analysis, the discrepancy is not so large that it disqualifies the model. This is true in particular because both the

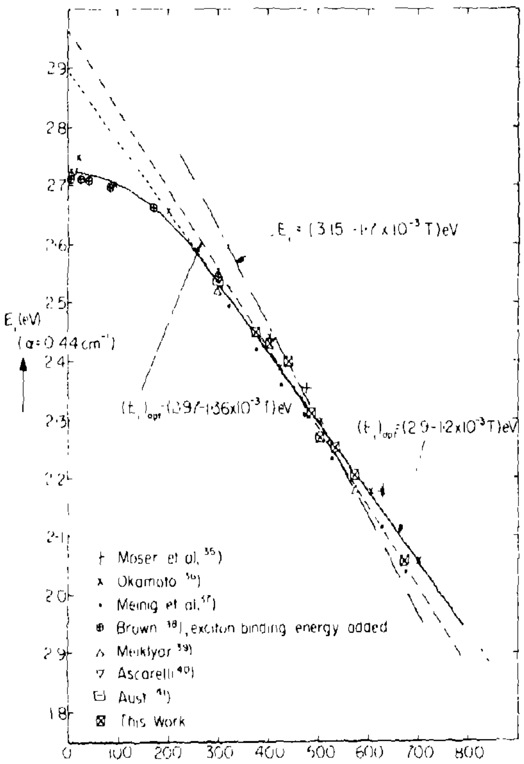

Fig. 12. The optical bandgap $(E_i)_{\text{opt}}$ as $f(T)$ according to various authors, and the bandgap E_i as deduced from polarization experiments with v_h as $f(T)$ as given by equation (17) and Fig. 10.

optical gap and its temperature dependence are themselves somewhat arbitrary. The data of Figs. 6 and 12 are represented by a modified Urbach relation[42]: $k = 6{\cdot}8 \times 10^4 \exp\{0{\cdot}8(h\nu - 2{\cdot}9)eV/kT\}$. Thus the value of k chosen to define the band edge affects the temperature dependence of the edge observed.

It has so far been tacitly assumed that the absorption edge of AgBr is due to band to band and exciton transitions, without allowing for transitions involving the defects of the native Frenkel disorder or non-stoichiometry. These should give rise to absorption bands in the tail of the fundamental absorption similar to the 'greek' bands in the alkali halides, and as a result the observed edge should be found at a somewhat longer wavelength than corresponds to the band to band transition. Since the concentration of Frenkel defects increases with temperature, the displacement should be largest at higher temperatures. Evidently this effect, if present, would weaken the temperature dependence of the forbidden gap as deduced from the optical data and thus tends to increase rather than decrease the discrepancy discussed above.

CONCLUSIONS

Silver bromide shows an absorption from the band edge to 0·08 eV whose intensity increases with the square root of the bromine pressure and with increasing temperature. The band is depressed by positively charged species and is identified as a free hole transition from $L_{4,5} \rightarrow L_6$. No absorption due to neutral silver vacancies was observed. If the oscillator strength f of the absorption by these centers is ≈ 1, the absence of absorption implies that the concentration of these centers is low, which in turn indicates that V_{Ag}^{x} is a shallow acceptor, with a separation between its acceptor level and the valence band $\leq 0{\cdot}1$ eV.

Combination of the absorption and conductivity data leads to a hole mobility described by $v_h = 8 \times 10^6 T^{-2{\cdot}69}$ cm^{2}V^{-1} sec^{-1}. Values of the forbidden gap calculated from conductivity data with the changed hole mobility are close to the values indicated by optical absorption but show a somewhat larger temperature dependence.

Acknowledgements – The authors gratefully acknowledge profitable discussions with, and comments on the manuscript by, Dr. W. G. Spitzer.

REFERENCES

1 KOCH E. and WAGNER C., *Z. phys. Chem.* **B38**, 295 (1937); TELTOW J., *Ann. Phys.* **5**, 63, 71 (1940); EBERT I and TELTOW J, *Ann. Phys.* **15**, 268 (1955).
2. MÜLLER P., *Phys. Status Solidi* **12**, 545 (1965)
3. ILSCHNER B., *J. chem. Phys.* **28**, 1109 (1958).
4. RALEIGH D. O., *J Phys. Chem. Solids* **25**, 329 (1965).
5. KRÖGER F A., *J. Phys. Chem Solids* **26**, 901 (1965).
6 KRÖGER F A, In *The Chemistry of Imperfect Crystals*. North-Holland, Amsterdam (1963).
7 HAYES W., PILBROW J. R. and SLIFKIN L., *J. Phys. Chem. Solids* **25**, 1417 (1964).
8. MOSER F., *J. appl. Phys* **33S**, 343 (1962).
9. ULRICI W., KOSWIG H. D and STASIW O., *Phys. Status Solidi* **12**, 545 (1965).
10. KRÖGER F. A, *J. Phys. Chem. Solids* **27**, 1697 (1966); *ibid.* **28**, 528 (1967)
11. KRÖGER F. A, In *The Chemistry of Imperfect Crystals*, p 952. North-Holland, Amsterdam (1963)
12 DEXTER D. L., *Phys. Rev.* **101**, 48 (1956).
13. NAIL N R., MOSER F, GODDARD P F and URBACH F., *Rev. scient Instrum* **28**, 275 (1957)
14. SUPTITZ P, *Ann. Phys.* **9**, 133 (1962).
15 SEERY D J. and DOYLE B., *J. phys. Chem.* **68**, 2263 (1964); RAO J. and VENKATESWARLU P. R., *J. molec. Spectrosc.* **13**, 288 (1964).
16 VAN DOORN C Z., *Rev. scient Instrum* **32**, 755 (1961).
17. SCHEFFER F. E. C. and VOOGD M., *Rev Trav chim. Pays-Bas Belg.* **45**, 21 (1926); RAMSAY W and YOUNG S, *J. chem. Soc* **49**, 453 (1886)
18. AMSLER H, *Z Elektrochem.* **57**, 801 (1953)
19. HANSON R. C., *J. phys. Chem.* **66**, 2376 (1962).
20. LUDWIG G. W. and WATTERS R. L., *Phys. Rev* **101**, 1699 (1956).
21. PRINCE M. B, *Phys. Rev* **92**, 681 (1953).
22. MORIN F J. and MAITA J P., *Phys. Rev.* **96**, 28 (1954)
23. HILSUM C and ROSE-INNES A. C., In *Semiconducting III–V Compounds* Pergamon Press, Oxford (1961).
24. ALLGAIER R S. and SCANLON W W, *Phys. Rev.* **111**, 1029 (1958); SMITH R. A., *Physica* **20**, 1910 (1954).
25. BLATT F. J., In *Physics of Electronic Conduction in Solids*, p. 265 a f McGraw-Hill, New York (1968).

26. HERRING C., *Bell Syst. tech. J.*, **34**, 237 (1955).
27. EHRENREICH H. and OVERHAUSER A. W., *Phys. Rev.* **104**, 331, 649 (1956).
28. BROWN D. M. and BRAY R., *Phys. Rev.* **127**, 1598 (1962)
29. SCOP P. M., *Phys. Rev.* **139A**, 934 (1965).
30. BASSANI F., KNOX R. S and BEALL FOWLER W., *Phys. Rev.* **137A**, 1217 (1965).
31. SMITH R. A., In *Wave Mechanics of Crystalline Solids*, p. 403 a.f Chapman and Hall, London (1961).
32. PRYCE M. H. L., Private communication
33. JAENICKE W. and EISENMANN E., *Naturwissenschaften* **52**, 491 (1965)
34. ILSCHNER B., *J. chem. Phys.* **28**, 1109 (1958).
35. MOSER F. and URBACH F., *Phys. Rev.* **102**, 1519 (1956).
36. OKAMOTO Y., *Nachr. Akad. Wiss. Gott. Math. Phys.* Kl., IIa Nr 14 (1956).
37. MEINIG K., METZ S. and TELTOW J., *Phys. Status Solidi* **2**, 1556 (1962).
38. BROWN F. C., *J. phys. Chem.* **66**, 2368 (1962).
39. MEIKLYAR P. V., *Soviet Phys. solid St.* **4**, 105 (1962).
40. ASCARELLI G., *Phys. Rev. Lett.* **20**, 44 (1968).
41. AUST R. B., *Phys. Rev.* **170**, 784 (1968).
42. URBACH F., *Phys. Rev.* **92**, 1324 (1953).

J. Phys. Chem. Solids Pergamon Press 1969. Vol. 30, pp. 1453–1464. Printed in Great Britain.

ZEEMAN PERTURBATIONS ON SHALLOW ACCEPTOR STATES IN GERMANIUM

P. J. LIN-CHUNG and R. F. WALLIS
Naval Research Laboratory, Washington, D.C. 20390, U.S.A.

(*Received* 12 *September* 1968)

Abstract – Based on the effective mass theoretical approach, the magnetic field splittings of the shallow acceptor states in Ge have been studied. In this calculation, we have used the acceptor wave functions previously obtained by Mendelson and James. It is found that the g-factor for the ground state Γ_8 quartet, so obtained, is in close agreement with the one calculated by Suzuki, Okazaki and Hasegawa using full six component envelope functions. The Zeeman splitting for the excited Γ_6 doublet appears to be quite large. The g-factors for the Γ_7 doublet and other excited states have been calculated. The Zeeman splittings of Raman transitions involving the ground state multiplet and a low-lying excited state multiplet of even parity have also been determined

1. INTRODUCTION

EXPERIMENTAL investigations of the Zeeman splittings of the i.r. absorption lines associated with acceptor impurities in germanium have been reported by several authors. Fisher and Fan have studied the Group II impurities copper and zinc[1] as well as the Group III impurity boron[2]. Shenker, Swiggard, and Moore[3] have recently reported results for the Group II impurity beryllium.

Theoretical investigations so far appear to be restricted to the Zeeman splitting of the impurity ground state which, in the absence of a magnetic field, is four-fold degenerate. Bir, Butikov and Pikus[4] calculated the ground state Zeeman splittings using four-component wave functions of the Kohn–Schechter type[5]. Suzuki, Okazaki and Hasegawa[6] have used six-component wave functions to treat the ground state splittings and have obtained results somewhat different from those of Bir, Butikov and Pikus.

In the present paper we calculate the Zeeman splittings of the ground state and several excited states for shallow acceptors in germanium using effective mass theory and four-component wave functions of Mendelson and James[7]. The intensities of the various Zeeman components of i.r. absorption lines are estimated in lowest order approximation. The Zeeman splittings of Raman transitions involving the ground state multiplet and a low-lying excited state multiplet of even parity are calculated for germanium.

2. THEORETICAL DEVELOPMENT

In the effective mass approximation, it is known that the wave functions of shallow acceptor states may be expressed in the form

$$\psi(\mathbf{r}) = \sum_j F_j(\mathbf{r})\varphi_j(\mathbf{r}) \qquad (1)$$

where the φ_j are the degenerate Bloch functions at the valence band edge in the pure crystal, and the $F_j(\mathbf{r})$ are the so-called envelop functions which satisfy the following coupled effective mass equations

$$\sum_{j'} \left(D_{jj'}^{\alpha\beta} p_\alpha p_\beta + \frac{e}{\epsilon r}\delta_{jj'}\right) F_{j'}(\mathbf{r}) = EF_j(\mathbf{r}). \quad (2)$$

$D_{jj'}^{\alpha\beta}$ in equation (2) represents the inverse effective mass tensor; p_α, p_β are the components of the momentum operator along α and β directions respectively; ϵ is the static dielectric constant of the crystal.

The valence band edge of Ge has Γ_8 symmetry and is four-fold degenerate. Thus, in the very strong spin-orbit coupling limit, the sum over j in equation (1) and the sum over j' in equation (2), run over the four degenerate states, namely, the $m_j = \frac{3}{2}, \frac{1}{2}, -\frac{1}{2}, -\frac{3}{2}$ states of the Γ_8 valence band edge.

Kohn and Schechter[5] first used trial functions of the form

$$F_j(\mathbf{r}) = \sum_l \sum_k C_{lk} A_j^{lk}(\theta, \varphi) r^l e^{-\alpha_l r}.$$

The angular functions $A_j^{lk}(\theta, \varphi)$ are linear combinations of spherical harmonics of order l and are determined by the symmetry properties of the impurity states[5].

Mendelson and James[7] then adopted a more general radial function such that

$$F_j(\mathbf{r}) = \sum_l \sum_k C_{lk} A_j^{lk}(\theta, \varphi) r^l f_l(r). \quad (3)$$

The coefficients C_{lk} and the radial functions $f_l(r)$ were obtained by means of a variational calculation and were presented by Mendelson and James in numerical form.

In contrast to the radial functions of Kohn and Schechter, the radial functions of Mendelson and James contain nodes for some of the excited states. They therefore seem more suitable for use in our calculation which involves excited impurity states.

For a number of states of interest, however, the Mendelson and James functions do not have nodes. The improved numerical nodeless functions could be fitted very closely by an analytical form

$$f_l(r) = a_l r^{n_l} e^{-\alpha_l r}.$$

Here, in general, n_l is not an integer.

As we shall see in the computation of the absorption coefficients in the Zeeman spectrum, it proves necessary to replace the numerical form of each individual wave function by an analytical form. The reason is that a numerical integration for the matrix elements appearing in Appendix 2 always shows slow convergency.

In the presence of a magnetic field, a new set of coupled effective mass equations is introduced as follows

$$\sum_{j'} \left[D_{jj'}^{\alpha\beta} \left(p_\alpha + \frac{eA_\alpha}{c} \right) \left(p_\beta + \frac{eA_\beta}{c} \right) + \left(\boldsymbol{\mu}_s \cdot \mathbf{H} + \frac{e^2}{\epsilon r} \right) \delta_{jj'} \right] F_{j'}(\mathbf{r}) = EF_j(\mathbf{r}) \quad (4)$$

where A_α is the α-th component of the vector potential for the external magnetic field and $\boldsymbol{\mu}_s$ is the free electron magnetic moment.

For convenience, equation (4) may be expressed in matrix form. Furthermore, the Hamiltonian on the left-hand side of the equation may be divided into two parts:

$$\mathcal{H} F = (\mathcal{H}^{(0)} + \mathcal{H}_{\text{Zeeman}}) F = EF. \quad (5)$$

One part is the unperturbed part, $\mathcal{H}^{(0)}$, which is identical to the left hand side of equation (2) and is of the following form:

$$\mathcal{H}^{(0)} = \begin{bmatrix} \frac{3B}{2}\left(\frac{\partial^2}{\partial x^2}+\frac{\partial^2}{\partial y^2}\right) - (A-B)\left(\frac{\partial^2}{\partial x^2}+\frac{\partial^2}{\partial y^2}+\frac{\partial^2}{\partial z^2}\right) - \frac{2}{r} & i\sqrt{3}N\left(\frac{\partial^2}{\partial x\partial z} - i\frac{\partial^2}{\partial y\partial z}\right) & -\frac{1}{2\sqrt{3}}B\left(\frac{\partial^2}{\partial x^2}-\frac{\partial^2}{\partial y^2}\right)+\frac{iN}{\sqrt{3}}\frac{\partial^2}{\partial x\partial y} & 0 \\ i\sqrt{3}N\left(\frac{\partial^2}{\partial x\partial z} + i\frac{\partial^2}{\partial y\partial z}\right) & +\frac{3B}{2}\left(\frac{\partial^2}{\partial x^2}+\frac{\partial^2}{\partial y^2}\right) - (A+B)\left(\frac{\partial^2}{\partial x^2}+\frac{\partial^2}{\partial y^2}+\frac{\partial^2}{\partial z^2}\right) - \frac{2}{r} & 0 & -\frac{1}{2\sqrt{3}}B\left(\frac{\partial^2}{\partial x^2}-\frac{\partial^2}{\partial y^2}\right)+\frac{iN}{\sqrt{3}}\frac{\partial^2}{\partial x\partial y} \\ \frac{1}{2\sqrt{3}}B\left(\frac{\partial^2}{\partial x^2}-\frac{\partial^2}{\partial y^2}\right) - \frac{iN}{\sqrt{3}}\left(\frac{\partial^2}{\partial x\partial y}\right) & 0 & \frac{3B}{2}\left(\frac{\partial^2}{\partial x^2}+\frac{\partial^2}{\partial y^2}\right) - (A+B)\left(\frac{\partial^2}{\partial x^2}+\frac{\partial^2}{\partial y^2}+\frac{\partial^2}{\partial z^2}\right) - \frac{2}{r} & -i\sqrt{3}N\left(\frac{\partial^2}{\partial x\partial z} + i\frac{\partial^2}{\partial y\partial z}\right) \\ 0 & \frac{1}{2\sqrt{3}}B\left(\frac{\partial^2}{\partial x^2}-\frac{\partial^2}{\partial y^2}\right) - \frac{iN}{\sqrt{3}}\frac{\partial^2}{\partial x\partial y} & i\sqrt{3}N\left(\frac{\partial^2}{\partial x\partial z} + i\frac{\partial^2}{\partial y\partial z}\right) & -\frac{3B}{2}\left(\frac{\partial^2}{\partial x^2}+\frac{\partial^2}{\partial y^2}\right) - (A-B)\left(\frac{\partial^2}{\partial x^2}+\frac{\partial^2}{\partial y^2}+\frac{\partial^2}{\partial z^2}\right) - \frac{2}{r} \end{bmatrix}.$$

The other, the Zeeman part, $\mathscr{H}_{\text{Zeeman}}$, may, in turn, be considered as composed of two terms, the symmetric term, coming from $e/c\,(D_{jj'}^{\alpha\beta}+D_{jj'}^{\alpha\beta})(p_\alpha A_\beta+A_\alpha p_\beta)$, and the antisymmetric term coming from $\boldsymbol{\mu}_s\cdot\mathbf{H}$ and $e/c\,(D_{jj'}^{\alpha\beta}-D_{jj'}^{\beta\alpha})(p_\alpha A_\beta+A_\alpha p_\beta-p_\beta A_\alpha-A_\beta p_\alpha)$; $\alpha\neq\beta$. The antisymmetric term gives a simple expression in terms of a constant K introduced by Luttinger[8]. When the gauge $\mathbf{A}=(-\frac{1}{2}yH,\frac{1}{2}xH,0)$ is used for a magnetic field in the (001) direction, we obtain

$$\mathscr{H}_{\text{Zeeman}}^{\text{Antisym.}}=\frac{2}{3}(mK+1)\frac{e\hbar}{2mc}\mathbf{J}_z\cdot\mathbf{H}=-\frac{\kappa e\hbar}{mc}J_zH.$$

We ignored the quadratic terms in the magnetic field and assumed that the constant q defined in [8] is equal to zero. The total $\mathscr{H}_{\text{Zeeman}}$ will then take the form

$$\mathscr{H}_{\text{Zeeman}}=\begin{bmatrix}\left(A+\frac{B}{2}\right)iH\left(y\frac{\partial}{\partial x}-x\frac{\partial}{\partial y}\right)\;3\kappa\beta H & \frac{NH}{2\sqrt{3}}\left(y\frac{\partial}{\partial z}+ix\frac{\partial}{\partial z}\right) & \frac{\sqrt{3}BiH}{2}\left(y\frac{\partial}{\partial x}+x\frac{\partial}{\partial y}\right)+\frac{NH}{2\sqrt{3}}\left(x\frac{\partial}{\partial x}-y\frac{\partial}{\partial y}\right) & 0\\ -\frac{NH}{2\sqrt{3}}\left(y\frac{\partial}{\partial z}\;\;ix\frac{\partial}{\partial z}\right) & +\left(A-\frac{B}{2}\right)iH\left(y\frac{\partial}{\partial x}-x\frac{\partial}{\partial y}\right)-\kappa\beta H & 0 & \frac{\sqrt{3}BiH}{2}\left(y\frac{\partial}{\partial x}+x\frac{\partial}{\partial y}\right)-\frac{NH}{2\sqrt{3}}\left(x\frac{\partial}{\partial x}-y\frac{\partial}{\partial y}\right)\\ +\frac{\sqrt{3}BiH}{2}\left(y\frac{\partial}{\partial x}+x\frac{\partial}{\partial y}\right)+\frac{NH}{2\sqrt{3}}\left(x\frac{\partial}{\partial x}-y\frac{\partial}{\partial y}\right) & 0 & \left(A-\frac{B}{2}\right)iH\left(y\frac{\partial}{\partial x}-x\frac{\partial}{\partial y}\right)+\kappa\beta H & -\frac{NH}{2\sqrt{3}}\left(y\frac{\partial}{\partial z}+ix\frac{\partial}{\partial z}\right)\\ 0 & \frac{\sqrt{3}BiH}{2}\left(y\frac{\partial}{\partial x}+x\frac{\partial}{\partial y}\right)+\frac{NH}{2\sqrt{3}}\left(x\frac{\partial}{\partial x}-y\frac{\partial}{\partial y}\right) & \frac{NH}{2\sqrt{3}}\left(y\frac{\partial}{\partial z}-ix\frac{\partial}{\partial z}\right) & \left(A+\frac{B}{2}\right)iH\left(y\frac{\partial}{\partial x}-x\frac{\partial}{\partial y}\right)+3\kappa\beta H\end{bmatrix}\tag{6}$$

The parameters A, B, N and κ characterizing the effective mass and the g-factor of the valence band edge of germanium are taken as $-13{\cdot}08(\hbar^2/2m)$, $-8{\cdot}94(\hbar^2/2m)$, $-34{\cdot}62(\hbar^2/2m)$ and $3{\cdot}9$ respectively[6]. When the strength of the magnetic field is not very large, $\mathscr{H}_{\text{Zeeman}}$ may be considered as a perturbation potential which acts on the ground state quartet or excited state multiplets and gives rise, as a first order effect, to a splitting of all multiplets. If the J-M_J representation is taken for the multiplets, the g-factor corresponding to the component M_J of a multiplet is simply given by

$$g_J^{(M_J)}=\frac{1}{M_J\beta H_z}\langle F^{(M_J)}|\mathscr{H}_{\text{Zeeman}}|F^{(M_J)}\rangle.\tag{7}$$

The shift in energy of the component of a multiplet from its unperturbed state is then

$$\Delta E=g_J^{(M_J)}M_J\beta H_z.\tag{8}$$

The ground acceptor state, being predominantly s-like, belongs to the Γ_8 irreducible representation, while the p-like excited acceptor states belong to doubly degenerate Γ_6, Γ_7 and four-fold degenerate Γ_8-p irreducible representations. Finally, one of the low-lying excited states belongs to the irreducible representation Γ_8-s. In Appendix 1, we list the trial functions for these states used in [7] and in the present calculation.

In order to obtain a detailed understanding of the Zeeman absorption spectra of Ge doped with group III impurities, we compute the g-factors for the various levels, examine the selection rules of optical transition between these levels and determine the relative absorption coefficient of each component line in the spectrum.

The g-factors calculated from equation (7) are given by:

$\Gamma_8 - s$:

$$g_{3/2} = \frac{2}{3}\cdot 4\pi\bigg\{\kappa\bigg[-3c_{01}{}^2\langle f_0{}^2\rangle - \frac{2}{5}c_{21}{}^2\langle f_2{}^2\rangle$$

$$-\frac{1}{15}c_{22}{}^2\langle f_2{}^2\rangle\bigg] + A\bigg[\frac{2}{15}c_{22}{}^2\langle f_2{}^2\rangle$$

$$-\frac{4\sqrt{3}}{15}c_{21}c_{22}\langle f_2{}^2\rangle\bigg]$$

$$+B\bigg[-\frac{1}{15}c_{22}{}^2\langle f_2{}^2\rangle + \frac{2\sqrt{3}}{15}c_{21}c_{22}\langle f_2{}^2\rangle$$

$$-\frac{\sqrt{3}}{5}c_{01}c_{22}t_1\bigg]$$

$$+N\bigg[\frac{1}{5}c_{01}c_{21}t_1 - \frac{1}{5\sqrt{3}}c_{01}c_{22}t_1$$

$$+\frac{\sqrt{3}}{15}c_{21}c_{22}\langle f_2{}^2\rangle\bigg]\bigg\}.$$

$$g_{1/2} = 8\pi\bigg\{\kappa\bigg[-c_{01}{}^2\langle f_0{}^2\rangle + \frac{2}{5}c_{21}{}^2\langle f_2{}^2\rangle$$

$$-\frac{1}{5}c_{22}{}^2\langle f_2{}^2\rangle\bigg]$$

$$+A\bigg[-\frac{2}{15}c_{22}{}^2\langle f_2{}^2\rangle - \frac{4\sqrt{3}}{15}c_{21}c_{22}\langle f_2{}^2\rangle\bigg]$$

$$+B\bigg[-\frac{1}{15}c_{22}{}^2\langle f_2{}^2\rangle - \frac{2\sqrt{3}}{15}c_{21}c_{22}\langle f_2{}^2\rangle$$

$$-\frac{\sqrt{3}}{5}c_{01}c_{22}t_1\bigg]$$

$$+N\bigg[\frac{1}{5}c_{01}c_{21}t_1 + \frac{1}{5\sqrt{3}}c_{01}c_{22}t_1$$

$$+\frac{\sqrt{3}}{15}c_{21}c_{22}\langle f_2{}^2\rangle\bigg]\bigg\}$$

where

$$t_1 = \langle f_0 f_2\rangle + \frac{1}{3}\left\langle rf_0\frac{\mathrm{d}f_2}{\mathrm{d}r}\right\rangle - \frac{1}{3}\left\langle rf_2\frac{\mathrm{d}f_0}{\mathrm{d}r}\right\rangle$$

$$\langle f^2\rangle = \int_0^\infty f^2 r^2\,\mathrm{d}r.$$

$\Gamma_8 - p$:

$$g_{3/2} = \frac{2}{3}\cdot 4\pi\bigg\{\kappa\bigg[-\frac{1}{3}c_{11}{}^2\langle f_1{}^2\rangle + \frac{20}{9}c_{12}{}^2\langle f_1{}^2\rangle$$

$$-\frac{3}{7}c_{31}{}^2\langle f_3{}^2\rangle + \frac{24}{35}c_{32}{}^2\langle f_3{}^2\rangle - \frac{8}{35}c_{33}{}^2\langle f_3{}^2\rangle$$

$$-\frac{3384}{8575}c_{34}{}^2\langle f_3{}^2\rangle - \frac{8}{3\sqrt{3}}c_{11}c_{12}\langle f_1{}^2\rangle$$

$$-\frac{48}{35}c_{31}c_{32}\langle f_3{}^2\rangle - \frac{144}{35}c_{31}c_{33}\langle f_3{}^2\rangle$$

$$-\frac{288}{245}c_{31}c_{34}\langle f_3{}^2\rangle - \frac{192}{35}c_{32}c_{33}\langle f_3{}^2\rangle$$

$$+\frac{1728}{1225}\langle f_3{}^2\rangle + \frac{96}{245}c_{33}c_{34}\langle f_3{}^2\rangle\bigg]$$

$$+A\bigg[\bigg(-\frac{2}{3}c_{11}{}^2 + \frac{4}{9}c_{12}{}^2 - \frac{4}{3\sqrt{3}}c_{11}c_{12}\bigg)\langle f_1{}^2\rangle$$

$$+\bigg(-\frac{4}{5}c_{31}{}^2 + \frac{136}{175}c_{32}{}^2 - \frac{48}{35}c_{33}{}^2$$

$$+\frac{936}{1225}c_{34}{}^2 - \frac{8}{5}c_{31}c_{32} + \frac{96}{35}c_{32}c_{33}$$

$$-\frac{288}{175}c_{32}c_{34} - \frac{144}{35}c_{33}c_{34}\bigg)\langle f_3{}^2\rangle\bigg]$$

$$+B\bigg[\bigg(-\frac{1}{5}c_{11}c_{31} - \frac{8}{25}c_{11}c_{32} + \frac{12}{5}c_{11}c_{33}$$

$$+\frac{24}{35}c_{11}c_{34} - \frac{2\sqrt{3}}{3}c_{12}c_{31} + \frac{8\sqrt{3}}{15}c_{12}c_{32}$$

$$+\frac{8\sqrt{3}}{5}c_{12}c_{33} - \frac{104\sqrt{3}}{175}c_{12}c_{34}\bigg)t$$

$$+\bigg(\frac{1}{3}c_{11}{}^2 + \frac{4}{9}c_{12}{}^2 + \frac{2}{3\sqrt{3}}c_{11}c_{12}\bigg)\langle f_1{}^2\rangle$$

$$+\bigg(-\frac{2}{5}c_{31}{}^2 - \frac{64}{175}c_{32}{}^2 - \frac{48}{35}c_{33}{}^2$$

$$-\frac{288}{1225}c_{34}{}^2 - \frac{28}{35}c_{31}c_{32} + \frac{24}{35}c_{32}c_{33}$$

$$+\frac{144}{175}c_{32}c_{34}\bigg)\langle f_3{}^2\rangle\bigg]$$

$$+N\bigg[\bigg(\frac{7}{15}c_{11}c_{31} + \frac{56}{75}c_{11}c_{32} + \frac{7\sqrt{3}}{45}c_{12}c_{31}$$

$$-\frac{8\sqrt{3}}{45}c_{12}c_{32} - \frac{8\sqrt{3}}{15}c_{12}c_{33} + \frac{8\sqrt{3}}{25}c_{12}c_{34}\bigg)t$$

$$+\bigg(-\frac{2}{9}c_{12}{}^2 + \frac{1}{3\sqrt{3}}c_{11}c_{12}\bigg)\langle f_1{}^2\rangle + \bigg(\frac{52}{175}c_{32}{}^2$$

$$-\frac{24}{35}c_{33}{}^2 + \frac{180}{1225}c_{34}{}^2 - \frac{10}{35}c_{31}c_{32} - \frac{16}{35}c_{31}c_{33}$$

$$-\frac{51}{175}c_{31}c_{34}-\frac{92}{175}c_{32}c_{33}+\frac{48}{245}c_{32}c_{34}$$

$$-\frac{204}{245}c_{33}c_{34}\biggr)\langle f_3{}^2\rangle\biggr]\biggr\}.$$

$$g_{1/2}=8\pi\biggl\{\kappa\biggl[\biggl(-c_{11}{}^2+\frac{4}{3}c_{12}{}^2+\frac{8}{\sqrt{3}}c_{11}c_{12}\biggr)\langle f_1{}^2\rangle$$

$$+\biggl(-\frac{1}{7}c_{31}{}^2-\frac{24}{7}c_{33}{}^2-\frac{5832}{8575}c_{34}{}^2+\frac{8}{175}c_{32}{}^2$$

$$+\frac{16}{35}c_{31}c_{32}+\frac{48}{35}c_{31}c_{33}-\frac{96}{245}c_{31}c_{34}$$

$$-\frac{192}{35}c_{32}c_{33}-\frac{3264}{1225}c_{32}c_{34}$$

$$+\frac{864}{245}c_{33}c_{34}\biggr)\langle f_3{}^2\rangle\biggr]$$

$$-A\biggl[\biggl(-\frac{2}{3}c_{11}{}^2+\frac{4}{9}c_{12}{}^2+\frac{4}{3\sqrt{3}}c_{11}c_{12}\biggr)\langle f_1{}^2\rangle$$

$$+\biggl(-\frac{4}{5}c_{31}{}^2+\frac{136}{175}c_{32}{}^2-\frac{48}{35}c_{33}{}^2+\frac{936}{1225}c_{34}{}^2$$

$$+\frac{8}{5}c_{31}c_{32}+\frac{96}{35}c_{32}c_{33}+\frac{288}{175}c_{32}c_{34}$$

$$+\frac{144}{35}c_{33}c_{34}\biggr)\langle f_3{}^2\rangle\biggr]$$

$$+B\biggl[\biggl(-\frac{1}{5}c_{11}c_{31}+\frac{8}{25}c_{11}c_{32}-\frac{12}{5}c_{11}c_{33}$$

$$+\frac{24}{35}c_{11}c_{34}+\frac{2\sqrt{3}}{3}c_{12}c_{31}+\frac{8\sqrt{3}}{15}c_{12}c_{32}$$

$$+\frac{8\sqrt{3}}{5}c_{12}c_{33}+\frac{104\sqrt{3}}{175}c_{12}c_{34}\biggr)t$$

$$+\biggl(\frac{1}{3}c_{11}{}^2+\frac{4}{9}c_{12}{}^2-\frac{2}{3\sqrt{3}}c_{11}c_{12}\biggr)\langle f_1{}^2\rangle$$

$$+\biggl(-\frac{2}{5}c_{31}{}^2-\frac{64}{175}c_{32}{}^2-\frac{48}{35}c_{33}{}^2-\frac{288}{1225}c_{34}{}^2$$

$$+\frac{28}{35}c_{31}c_{32}+\frac{24}{35}c_{32}c_{33}-\frac{144}{175}c_{32}c_{34}\biggr)\langle f_3{}^2\rangle\biggr]$$

$$-N\biggl[\biggl(\frac{7}{15}c_{11}c_{31}-\frac{56}{75}c_{11}c_{32}-\frac{7\sqrt{3}}{45}c_{12}c_{31}$$

$$-\frac{8\sqrt{3}}{45}c_{12}c_{32}-\frac{8\sqrt{3}}{15}c_{12}c_{33}-\frac{8\sqrt{3}}{25}c_{12}c_{34}\biggr)t$$

$$+\biggl(-\frac{2}{9}c_{12}{}^2-\frac{1}{3\sqrt{3}}c_{11}c_{12}\biggr)\langle f_1{}^2\rangle$$

$$+\biggl(\frac{52}{175}c_{32}{}^2-\frac{24}{35}c_{33}{}^2+\frac{180}{1225}c_{34}{}^2+\frac{10}{35}c_{31}c_{32}$$

$$+\frac{16}{35}c_{31}c_{33}-\frac{51}{175}c_{31}c_{34}-\frac{92}{175}c_{32}c_{33}$$

$$-\frac{48}{245}c_{32}c_{34}+\frac{204}{245}c_{33}c_{34}\biggr)\langle f_3{}^2\rangle\biggr]\biggr\}$$

where

$$t=\frac{5}{7}\langle f_1f_3\rangle+\frac{1}{7}\biggl\langle rf_1\frac{\mathrm{d}f_3}{\mathrm{d}r}\biggr\rangle-\frac{1}{7}\biggl\langle rf_3\frac{\mathrm{d}f_1}{\mathrm{d}r}\biggr\rangle.$$

Γ_7:

$$g_{1/2}=8\pi\biggl\{\kappa\biggl[4c_1{}^2\langle g_1{}^2\rangle+\frac{8}{175}c_3{}^2\langle g_3{}^2\rangle\biggr]$$

$$+A\biggl[-\frac{4}{3}c_1{}^2\langle g_1{}^2\rangle-\frac{136}{175}c_3{}^2\langle g_3{}^2\rangle\biggr]$$

$$+B\biggl[\frac{4}{3}c_1{}^2\langle g_1{}^2\rangle-\frac{64}{175}c_3{}^2\langle g_3{}^2\rangle$$

$$+\frac{4\sqrt{2}}{5}c_1c_3t'\biggr]$$

$$+N\biggl[-\frac{2}{3}c_1{}^2\langle g_1{}^2\rangle+\frac{52}{175}c_3{}^2\langle g_3{}^2\rangle$$

$$+\frac{4\sqrt{2}}{15}c_1c_3t'\biggr]\biggr\}.$$

Γ_8:

$$g_{1/2}=8\pi\biggl\{\kappa\biggl[-\frac{20}{3}c_1'^2\langle h_1{}^2\rangle-\frac{24}{35}c_3'^2\langle h_3{}^2\rangle\biggr]$$

$$+A\biggl[-\frac{4}{3}c_1'^2\langle h_1{}^2\rangle-\frac{136}{175}c_3'^2\langle h_3{}^2\rangle\biggr]$$

$$+B\biggl[-\frac{4}{3}c_1'^2\langle h_1{}^2\rangle+\frac{64}{175}c_3'^2\langle h_3{}^2\rangle$$

$$+\frac{4\sqrt{2}}{5}c_1'c_3't''\biggr]$$

$$+N\biggl[-\frac{2}{3}c_1'^2\langle h_1{}^2\rangle+\frac{52}{175}c_3'^2\langle h_3{}^2\rangle$$

$$-\frac{4\sqrt{2}}{15}c_1'c_3't''\biggr]\biggr\}$$

where

$$t' = \frac{5}{7}\langle g_1 g_3\rangle + \frac{1}{7}\left\langle r g_1 \frac{\mathrm{d}g_3}{\mathrm{d}r}\right\rangle - \frac{1}{7}\left\langle r g_3 \frac{\mathrm{d}g_1}{\mathrm{d}r}\right\rangle$$

$$t'' = \frac{5}{7}\langle h_1 h_3\rangle + \frac{1}{7}\left\langle r h_1 \frac{\mathrm{d}h_3}{\mathrm{d}r}\right\rangle - \frac{1}{7}\left\langle r h_3 \frac{\mathrm{d}h_1}{\mathrm{d}r}\right\rangle.$$

The relation, $g_{(M_J)} = g_{(-M_J)}$, holds for all the above irreducible representations.

Using the values of the e's and f's obtained from [7], we have calculated the numerical values of the g-factors. The results are summarized in Table 1. In addition, to show the positions of the levels with and without a magnetic field, we display a schematic diagram in Fig. 1. The figure is exaggerated for clarity. On the left hand side of the diagram, we label the levels both by group representation notations and by the conventional designations.

It is seen in Table 1 that the values of $g_{3/2}$ and $g_{1/2}$ for the ground state $\Gamma_8 - s$ agree reasonably well with the values obtained by Suzuki *et al.*[6]. This indicates that, in the case of Ge, four-component wave functions are accurate enough to represent the true effective mass wave functions. The discrepancy in the results of [4] is attributed to the neglect of the most important contribution to $\mathscr{H}_{\text{Zeeman}}$ i.e. the symmetric term

$$(e/c)(D^{\alpha\beta}_{jj'} + D^{\beta\alpha}_{jj'})(p_\alpha A_\beta + A_\alpha p_\beta).$$

The g-factor for Γ_6 appears to be exceedingly large. It leads us to believe that, for large magnetic fields, the first-order perturbation treatment of $\mathscr{H}_{\text{Zeeman}}$ can no longer be valid for levels close to Γ_6. However, the Zeeman spectrum in the energy range close to the Γ_6 level has so far not been observed experimentally.

In the estimation of the optical absorption coefficient we have employed the dipole approximation and zero-th order wave functions. The absorption coefficient α_{ij} associated with transitions from the initial state i to the final state j under this approximation is proportional to $(E_j - E_i)|\int \psi_i^*(\mathbf{r})\mathbf{r}\psi_j \times (\mathbf{r})\mathrm{d}^3\mathbf{r}|^2$ where $\mathbf{r}$ is in the direction of the electric vector of the radiation. Neglecting the slow variation of the modulating functions $F_j(\mathbf{r})$ over a unit cell and replacing $|\phi_j(\mathbf{r})|^2$ by its average value in a unit cell, we can write the absorption coefficient

$$\alpha_{ij} \sim (E_j - E_i)\left|\int F_i^*(\mathbf{r})\mathbf{r}\mathbf{F}_j(\mathbf{r})\right|^2. \quad (9)$$

Equation (9) then specifies selection rules and relative absorption coefficients for strong electric dipole transitions. The expressions for the integrals $\int F_i^*(\mathbf{r})\mathbf{r}F_j(\mathbf{r})\mathrm{d}\mathbf{r}$ are shown in Appendix 2. The selection rules for strong electric dipole transitions are as follows:

(*a*) *For transitions between* $\Gamma_8 - \mathrm{s}$ *and* $\Gamma_8 - \mathrm{s}$ *multiplets:*

$\Delta m_j = 1, -3$ allowed for right-circularly radiation.
$\Delta m_j = -1, 3$ allowed for left-circularly polarized radiation.
$\Delta m_j = \pm 2$ allowed for radiation with $\mathbf{E}\|\mathbf{H}$.
$\Delta m_j = 0$ forbidden transition.

(*b*) *For transitions between* Γ_7 *and* Γ_8-s *multiplets:*

$\Delta m_j = 1$ allowed for right-circularly polarized radiation.
$\Delta m_j = -1$ allowed for left-circularly polarized radiation.
$\Delta m_j = \pm 2$ allowed for radiation with $\mathbf{E}\|\mathbf{H}$.
$\Delta m_j = 0$ forbidden transition.

Table 1. *The* g-*factors* $g_{1/2}$ *and* $g_{3/2}$ *for the acceptor levels of* Ge, *when* H ∥ [001]

	(8 + 00)	(8 + 01)	(8 − 01)	(8 − 02)	(8 − 11)	(7 − 0)	(7 − 1)	(6 − 0)
$g_{1/2}$	−0·9720	−1·5260	−2·9732	−3·6585	−3·1768	1·9974	2·8706	11·822
$g_{3/2}$	0·2879	−0·0827	0·2470	−0·0831	0·2551			

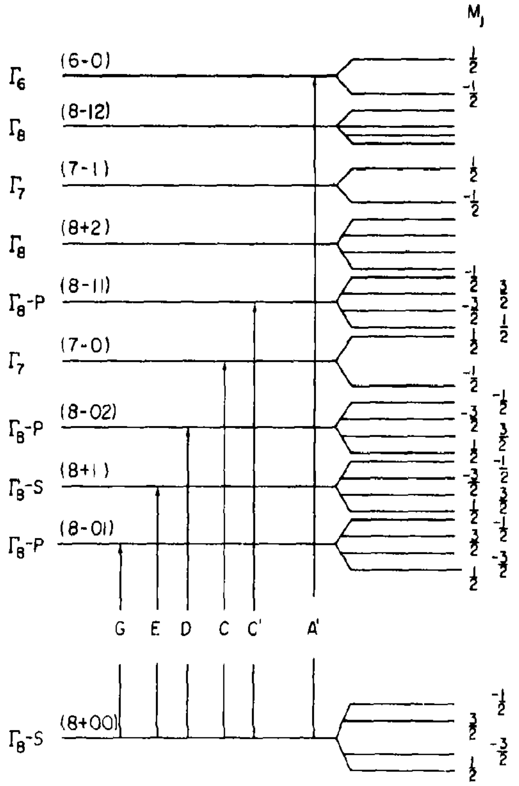

Fig. 1. Schematic diagram of the acceptor ground state and p-like excited states in germanium without (left side of drawing) and with magnetic field (right side of drawing). Conventional designations for the levels and the optical transitions are shown

(*c*) *For transitions between* Γ_6 *and* $\Gamma_8 - s$:

$\Delta m_j = -1$ allowed for right-circularly polarized radiation.

$\Delta m_j = 1$ allowed for left-circularly polarized radiation.

$\Delta m_j = \pm 2$ forbidden transition.

$\Delta m_j = 0$ allowed for radiation with $\mathbf{E} \| \mathbf{H}$.

A complete list of the Zeeman spectrum lines can be found in Table 2. Some of the lines in the Zeeman spectrum are very close to each other energy and may not be resolvable by experiment. Thus, roughly speaking, there are only four distinct G lines, four D lines, two C lines, four C' lines and two A' lines for $\mathbf{E} \perp \mathbf{H}$ transitions, and three G lines, four D lines, two C lines, four C' lines, and two A' lines for $\mathbf{E} \| \mathbf{H}$ transitions. The relative absorption coefficients for some of the lines are shown in Fig. 2. We should bear in mind that this calculation of the absorption coefficients is based on the assumption that there exists no collision broadening. More accurate estimates rely upon the use of more accurate wave functions as well as the inclusion of collision broadening mechanisms.

We notice that in Fig. 2, the absorption coefficients of the D and C lines are an order of magnitude greater than the G lines. Owing to the fact that the integral in equation (9) converges slowly when r is large, the estimates of the absorption coefficients of the C' and A' lines suffer from the lack of analytic expressions for the $(6-0)$ and $(8-11)$ wave

Table 2. Positions of Zeeman spectrum lines for Ge(E_G, E_D, *etc. are the positions of corresponding lines without magnetic field*)

	Right-circularly polarized	Left-circularly polarized	$E\parallel H$
	$E_G-1{\cdot}918\beta H$	$E_G-1{\cdot}973\beta H$	$E_G+1{\cdot}055\beta H$
$(8-01)\rightarrow(8+00)$	$E_G-0{\cdot}857\beta H$	$E_G-0{\cdot}802\beta H$	$E_G-0{\cdot}115\beta H$
G lines	$E_G+1{\cdot}973\beta H$	$E_G+0{\cdot}857\beta H$	$E_G+0{\cdot}115\beta H$
	$E_G+0{\cdot}802\beta H$	$E_G+1{\cdot}918\beta H$	$E_G-1{\cdot}055\beta H$
	$E_D-2{\cdot}261\beta H$	$E_D-2{\cdot}315\beta H$	$E_D+1{\cdot}397\beta H$
$(8-02)\rightarrow(8+00)$	$E_D-0{\cdot}361\beta H$	$E_D-0{\cdot}307\beta H$	$E_D-0{\cdot}611\beta H$
D lines	$E_D+0{\cdot}307\beta H$	$E_D+0{\cdot}361\beta H$	$E_D+0{\cdot}611\beta H$
	$E_D+2{\cdot}315\beta H$	$E_D+2{\cdot}261\beta H$	$E_D-1{\cdot}397\beta H$
$(7-00)\rightarrow(8+00)$	$E_C+0{\cdot}567\beta H$	$E_C+0{\cdot}513\beta H$	$E_C-1{\cdot}431\beta H$
C lines	$E_C-0{\cdot}513\beta H$	$E_C-0{\cdot}567\beta H$	$E_C+1{\cdot}431\beta H$
	$E'_C-2{\cdot}020\beta H$	$E'_C-0{\cdot}559\beta H$	$E'_C+1{\cdot}157\beta H$
$(8-11)\rightarrow(8+00)$	$E'_C-0{\cdot}614\beta H$	$E'_C-2{\cdot}074\beta H$	$E'_C+0{\cdot}358\beta H$
C' lines	$E'_C+2{\cdot}074\beta H$	$E'_C+0{\cdot}614\beta H$	$E'_C-0{\cdot}358\beta H$
	$E'_C+0{\cdot}559\beta H$	$E'_C+2{\cdot}020\beta H$	$E'_C-1{\cdot}157\beta H$
$(6-0)\rightarrow(8+00)$	$E'_A+5{\cdot}425\beta H$	$E'_A+5{\cdot}479\beta H$	$E'_A+6{\cdot}397\beta H$
A' lines	$E'_A-5{\cdot}479\beta H$	$E'_A-5{\cdot}425\beta H$	$E'_A-6{\cdot}397\beta H$

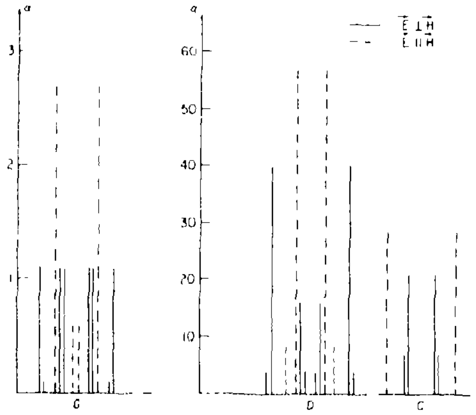

Fig. 2. Relative absorption coefficients of the component lines of G, D and C lines. The solid lines represent the optical transitions with $\mathbf{E}\perp\mathbf{H}$; the broken lines represent those with $\mathbf{E}\parallel\mathbf{H}$.

functions and incomplete numerical information of these wave functions at large r.

The transition between $(8+00)$ and $(8+01)$ i.e. the E line, is forbidden for strong electric dipole transitions but is Raman-active. It should therefore be of interest to examine the Raman spectrum in low magnetic fields. We have evaluated the g-factors for the $(8+01)$ state and listed them in Table 1. The cross section for Raman scattering in the dipole approximation is proportional to the following quantity

$$W=\frac{\omega_F}{\omega_I}|A_{fi}|^2$$

$$=\frac{\omega_F}{\omega_I}\left|\frac{1}{m}\sum_r\left[\frac{(\boldsymbol{\epsilon}_F^*\cdot\boldsymbol{\pi})_{fr}(\boldsymbol{\epsilon}_I\cdot\boldsymbol{\pi})_{ri}}{E_i+\hbar\omega_I-E_r}+\frac{(\boldsymbol{\epsilon}_I\cdot\boldsymbol{\pi})_{fr}(\boldsymbol{\epsilon}_F^*\cdot\boldsymbol{\pi})_{ri}}{E_i-\hbar\omega_F-E_r}\right]\right|^2. \quad (10)$$

Here, $\boldsymbol{\pi}=\mathbf{p}+(e/c)\mathbf{A}$; i, r, f refer to the components of the $(8+00)$ state, the intermediate states and the components of the $(8+01)$ state, respectively; m is the free electron mass; $\boldsymbol{\epsilon}_I$, $\boldsymbol{\epsilon}_F$, ω_I, ω_F are the polarizations and frequencies of the incident and emitted photons, respectively.

According to equation (10), there exist selection rules for the strong Raman transitions between the $(8+00)$ and $(8+01)$ multiplets. For $\boldsymbol{\epsilon}_I\perp\mathbf{H}$, $\boldsymbol{\epsilon}_F\perp\mathbf{H}$, the transitions with $\Delta m_j=0$, ± 2 are allowed. For $\boldsymbol{\epsilon}_I\parallel\mathbf{H}$ and $\boldsymbol{\epsilon}_F\parallel\mathbf{H}$, only $\Delta m_j=0$ are allowed transitions. Finally, for $\boldsymbol{\epsilon}_I\parallel\mathbf{H}$, $\boldsymbol{\epsilon}_F\perp\mathbf{H}$, $\boldsymbol{\epsilon}_F\parallel\mathbf{H}$, $\Delta m_j=\pm 1$, ± 3 are allowed transitions. These polarization rules also hold for transitions among the ground state components.

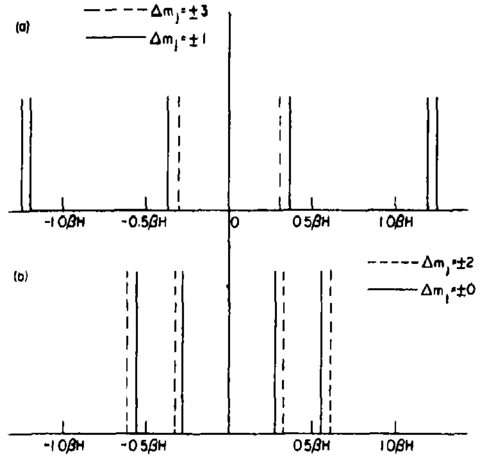

Fig. 3. (a) The splitting of the Raman E line in magnetic fields, when $\epsilon_l \| \mathbf{H}$, $\epsilon_F \perp \mathbf{H}$ or $\epsilon_l \perp \mathbf{H}$, $\epsilon_F \| \mathbf{H}$. Both $\Delta m_j = \pm 1$ (solid lines) and $\Delta m_j = \pm 3$ (broken lines) are allowed transitions. (b) The splittings of the Raman E line in magnetic fields when $\epsilon_l \perp \mathbf{H}$, $\epsilon_F \perp \mathbf{H}$ (both solid and broken lines); and when $\epsilon_l \| \mathbf{H}$, $\epsilon_F \| \mathbf{H}$ (solid lines only). The zero position is the position of the unperturbed E line.

Based on the selection rules and the g-factors obtained in this calculation, the splittings of the Raman E line in low magnetic fields are found and displayed in Fig. 3. It is seen that, for the polarizations $\epsilon_l \| \mathbf{H}$, $\epsilon_F \perp \mathbf{H}$ or $\epsilon_l \perp \mathbf{H}$, $\epsilon_F \| \mathbf{H}$, four distinct lines may be observed, whereas for the polarization $\epsilon_l \| \mathbf{H}$, $\epsilon_F \| \mathbf{H}$ or $\epsilon_l \perp \mathbf{H}$, $\epsilon_F \perp \mathbf{H}$, only two lines may be resolved.

In the case of Raman induced transitions among the ground state components, no line will be observed when $\epsilon_l \| \epsilon_F \| \mathbf{H}$. That is due to the fact that, for this polarization, no transitions other than $\Delta m_j = 0$ are allowed. For $\epsilon_l \perp \mathbf{H}$, $\epsilon_F \perp \mathbf{H}$ one line with energy $0{\cdot}05\beta H$ is produced by Raman scattering. For $\epsilon_l \| \mathbf{H}$, $\epsilon_F \perp \mathbf{H}$ or $\epsilon_l \perp \mathbf{H}$, $\epsilon_F \| \mathbf{H}$ three lines with energies $0{\cdot}918\beta H$, $0{\cdot}972\beta H$, $0{\cdot}864\beta H$, respectively, appear.

3. COMPARISON WITH EXPERIMENT

Experimentally, the C and D lines of both B- and Cu-doped germanium and the D line of Zn-doped germanium have been observed to split into two components[1, 2] in a magnetic field. Recently, more interesting results were obtained for Be-doped Ge[3]. It is found that at 30 kG, the G line splits into four components consistent with our present calculation. Four components of the D line and two components of the C line were also observed. Apparently, at such a relatively high magnetic field, 30 kG, the spacing between the split-off components is comparable to the spacing between the C and D lines. The interaction between the components of the C and D lines has a tendency to push the D component lines to lower energies. Indeed, in[3], the components of the D line are all shifted toward the low energy region as expected. For the purpose of checking our computed results on C, D, and other lines, experiments with higher spectral resolution and performed under lower magnetic fields on group III impurities therefore seem most desirable. Such experiments are now underway at the Naval Research Laboratory.

Apparently, no experimental data are available for the splittings of the Raman E line under magnetic field. Wright and Mooradian[9] observed the Raman E line of acceptors in Si without magnetic field. However, no observation of the electronic Raman scattering from acceptor impurities in Ge has been reported.

REFERENCES

1. FISHER P. and FAN H. Y., *Phys. Rev. Lett.* **5**, 195 (1960).
2. FISHER P. and FAN H. Y., *Phys. Rev. Lett.* **2**, 456 (1959).
3. SHENKER H., SWIGGARD E. M. and MOORE W. J., *Trans. metall. Soc A.I.M.E.* **239**, 347 (1967).
4. BIR G. L., BUTIKOV E. I. and PIKUS G. E., *J. Phys. Chem. Solids* **24**, 1467 (1963).
5. KOHN W. and SCHECHTER D., *Phys. Rev.* **99**, 1903 (1955).
6. SUZUKI K., OKAZAKI M. and HASEGAWA H., *J. phys. Soc. Japan* **19**, 930 (1964).
7. MENDELSON K. S. and JAMES H. M., *J. Phys. Chem. Solids* **25**, 729 (1964).
8. LUTTINGER J. M., *Phys. Rev.* **102**, 1030 (1956).
9. WRIGHT G. B. and MOORADIAN A., *Phys. Rev. Lett.* **18**, 608 (1967).

APPENDIX 1

Envelope functions for the acceptor states of Ge

(i) $\Gamma_8 - s$:

$$F^{(3/2)} = c_{01}\begin{bmatrix}1\\0\\0\\0\end{bmatrix} f_0 + c_{21}\begin{bmatrix}P_{2,0}\\0\\-\frac{\sqrt{3}}{4}(P_{2,2}+P_{2,-2})\\0\end{bmatrix} f_2 + ic_{22}\begin{bmatrix}0\\P_{2,1}\\-\frac{i}{4}(P_{2,2}-P_{2,-2})\\0\end{bmatrix} f_2$$

$$F^{(1/2)} = c_{01}\begin{bmatrix}0\\1\\0\\0\end{bmatrix} f_0 + c_{21}\begin{bmatrix}0\\-P_{2,0}\\0\\-\frac{\sqrt{3}}{4}(P_{2,2}+P_{2,-2})\end{bmatrix} f_2 + ic_{22}\begin{bmatrix}-P_{2,-1}\\0\\0\\-\frac{i}{4}(P_{2,2}-P_{2,-2})\end{bmatrix} f_2$$

$$F^{(-1/2)} = c_{01}\begin{bmatrix}0\\0\\1\\0\end{bmatrix} f_0 + c_{21}\begin{bmatrix}-\frac{\sqrt{3}}{4}(P_{2,2}+P_{2,-2})\\0\\-P_{2,0}\\0\end{bmatrix} f_2 + ic_{22}\begin{bmatrix}\frac{i}{4}(P_{2,2}-P_{2,-2})\\0\\0\\-P_{2,1}\end{bmatrix} f_2$$

$$F^{(-3/2)} = c_{01}\begin{bmatrix}0\\0\\0\\1\end{bmatrix} f_0 + c_{21}\begin{bmatrix}0\\-\frac{\sqrt{3}}{4}(P_{2,2}+P_{2,-2})\\0\\P_{2,0}\end{bmatrix} f_2 + ic_{22}\begin{bmatrix}0\\\frac{i}{4}(P_{2,2}-P_{2,-2})\\P_{2,-1}\\0\end{bmatrix} f_2$$

(ii) Γ_7

$$F^{(1/2)} = c_1\begin{bmatrix}P_{1,1}\\0\\-\sqrt{3}P_{1,-1}\\2iP_{1,0}\end{bmatrix} g_1(r) + c_3\begin{bmatrix}\frac{3}{4}(P_{3,1}+P_{3,-3})\\-\frac{i\sqrt{3}}{2}(P_{3,2}+P_{3,-2})\\-\frac{\sqrt{3}}{4}(7P_{3,-1}-P_{3,3})\\-3iP_{1,0}\end{bmatrix} g_3(r)$$

$$F^{(-1/2)} = c_1\begin{bmatrix}-2iP_{1,0}\\\sqrt{3}P_{1,1}\\0\\-P_{1,-1}\end{bmatrix} g_1(r) + c_3\begin{bmatrix}3iP_{3,0}\\\frac{\sqrt{3}}{4}(7P_{3,1}-P_{3,-3})\\-\frac{i\sqrt{3}}{2}(P_{3,2}+P_{3,-2})\\\frac{3}{4}(P_{3,-1}+P_{3,3})\end{bmatrix} g_3(r)$$

(iii) Γ_6

$$F^{(1/2)} = c'_1\begin{bmatrix}\sqrt{3}P_{1,-1}\\2iP_{1,0}\\P_{1,1}\\0\end{bmatrix} h_1(r) + c'_3\begin{bmatrix}-\frac{\sqrt{3}}{4}(7P_{3,-1}-P_{3,3})\\3iP_{3,0}\\\frac{3}{4}(P_{3,1}+P_{3,-3})\\\frac{i\sqrt{3}}{2}(P_{3,2}+P_{3,-2})\end{bmatrix} h_3(r)$$

$$F^{(-1/2)} = c'\begin{bmatrix}0\\-P_{1,-1}\\-2iP_{1,0}\\-\sqrt{3}P_{1,1}\end{bmatrix} h_1(r) + c'_3\begin{bmatrix}-\frac{i\sqrt{3}}{2}(P_{3,2}+P_{3,-2})\\-\frac{3}{4}(P_{3,-1}+P_{3,3})\\-3iP_{3,0}\\\frac{\sqrt{3}}{4}(7P_{3,1}-P_{3,-3})\end{bmatrix} h_3(r)$$

(iv) Γ_8-p:

$$F^{(3/2)}=c_{11}\begin{bmatrix}0\\ iP_{1,-1}\\ P_{1,0}\\ 0\end{bmatrix}f_1+c_{12}\begin{bmatrix}0\\ \frac{i}{\sqrt{3}}P_{1,-1}\\ -\frac{2}{\sqrt{3}}P_{1,0}\\ -iP_{1,1}\end{bmatrix}f_1+c_{31}\begin{bmatrix}\frac{\sqrt{3}}{4}(5P_{3,-2}-P_{3,2})\\ 0\\ 0\\ -\frac{i\sqrt{3}}{4}(5P_{3,1}+P_{3,-3})\end{bmatrix}f_3$$

$$+c_{32}\begin{bmatrix}\frac{\sqrt{3}}{2}(P_{3,2}+P_{3,-2})\\ \frac{3i}{4}(P_{3,-1}+P_{3,3})\\ -3P_{3,0}\\ -\frac{i\sqrt{3}}{4}(7P_{3,1}-P_{3,-3})\end{bmatrix}f_3+c_{33}\begin{bmatrix}\frac{3\sqrt{3}}{2}(P_{3,2}+P_{3,-2})\\ \frac{i}{2}(15P_{3,-1}+P_{3,3})\\ 5P_{3,0}\\ i\sqrt{3}P_{3,-3}\end{bmatrix}f_3+c_{34}\begin{bmatrix}-\frac{\sqrt{3}}{14}(9P_{3,2}-3P_{3,-2})\\ \frac{3i}{4}(3P_{3,-1}-P_{3,3})\\ -3P_{3,0}\\ \frac{3\sqrt{3}i}{28}(5P_{3,1}+P_{3,-3})\end{bmatrix}f_3$$

$$F^{(1/2)}=c_{11}\begin{bmatrix}iP_{1,1}\\ 0\\ 0\\ P_{1,0}\end{bmatrix}f_1+c_{12}\begin{bmatrix}-\frac{i}{\sqrt{3}}P_{1,1}\\ 0\\ -iP_{1,-1}\\ -\frac{2}{\sqrt{3}}P_{1,0}\end{bmatrix}f_1+c_{31}\begin{bmatrix}0\\ -\frac{\sqrt{3}}{4}(5P_{3,2}-P_{3,-2})\\ \frac{i\sqrt{3}}{4}(5P_{3,-1}+P_{3,3})\\ 0\end{bmatrix}f_3$$

$$+c_{32}\begin{bmatrix}-\frac{3i}{4}(P_{3,1}+P_{3,-3})\\ \frac{\sqrt{3}}{2}(P_{3,2}+P_{3,-2})\\ \frac{i\sqrt{3}}{4}(7P_{3,-1}-P_{3,3})\\ 3P_{3,0}\end{bmatrix}f_3+c_{33}\begin{bmatrix}-\frac{i}{2}(15P_{3,1}+P_{3,-3})\\ \frac{3\sqrt{3}}{2}(P_{3,2}+P_{3,-2})\\ i\sqrt{3}P_{3,3}\\ -5P_{3,0}\end{bmatrix}f_3+c_{34}\begin{bmatrix}\frac{3i}{4}(3P_{3,1}-P_{3,-3})\\ \frac{\sqrt{3}}{14}(9P_{3,-2}-3P_{3,2})\\ -\frac{3\sqrt{3}i}{28}(5P_{3,-1}+P_{3,3})\\ -3P_{3,0}\end{bmatrix}f_3$$

$$F^{(-1/2)}=c_{11}\begin{bmatrix}-P_{1,0}\\ 0\\ 0\\ -iP_{1,-1}\end{bmatrix}f_1+c_{12}\begin{bmatrix}-\frac{2}{\sqrt{3}}P_{1,0}\\ iP_{1,1}\\ 0\\ \frac{i}{\sqrt{3}}P_{1,-1}\end{bmatrix}f_1+c_{31}\begin{bmatrix}0\\ -\frac{i\sqrt{3}}{4}(5P_{3,1}+P_{3,-3})\\ \frac{\sqrt{3}}{4}(5P_{3,-2}-P_{3,2})\\ 0\end{bmatrix}f_3$$

$$+c_{32}\begin{bmatrix}-3P_{3,0}\\ -\frac{i\sqrt{3}}{4}(7P_{3,1}-P_{3,-3})\\ -\frac{\sqrt{3}}{2}(P_{3,2}+P_{3,-2})\\ \frac{3i}{4}(P_{3,-1}+P_{3,3})\end{bmatrix}f_3+c_{33}\begin{bmatrix}5P_{3,0}\\ -i\sqrt{3}P_{3,-3}\\ -\frac{3\sqrt{3}}{2}(P_{3,2}+P_{3,-2})\\ \frac{i}{2}(15P_{3,-1}+P_{3,3})\end{bmatrix}f_3+c_{34}\begin{bmatrix}3P_{3,0}\\ \frac{3\sqrt{3}i}{28}(5P_{3,1}+P_{3,-3})\\ -\frac{\sqrt{3}}{14}(9P_{3,2}-3P_{3,-2})\\ -\frac{3i}{4}(3P_{3,-1}-P_{3,3})\end{bmatrix}f_3$$

$$F^{(-3/2)}=c_{11}\begin{bmatrix}0\\ -P_{1,0}\\ -iP_{1,1}\\ 0\end{bmatrix}f_1+c_{12}\begin{bmatrix}iP_{1,-1}\\ \frac{2}{\sqrt{3}}P_{1,0}\\ -\frac{i}{\sqrt{3}}P_{1,1}\\ 0\end{bmatrix}f_1+c_{31}\begin{bmatrix}i\frac{\sqrt{3}}{4}(5P_{3,-1}+P_{3,3})\\ 0\\ 0\\ -\frac{\sqrt{3}}{4}(5P_{3,2}-P_{3,-2})\end{bmatrix}f_3$$

$$+c_{32}\begin{bmatrix}-\frac{i\sqrt{3}}{4}(7P_{3,-1}-P_{3,3})\\ 3P_{3,0}\\ -\frac{3i}{4}(P_{3,1}+P_{3,-3})\\ -\frac{\sqrt{3}}{2}(P_{3,2}+P_{3,-2})\end{bmatrix}f_3+c_{33}\begin{bmatrix}-i\sqrt{3}P_{3,3}\\ -5P_{3,0}\\ -\frac{i}{2}(15P_{3,1}+P_{3,-3})\\ -\frac{3\sqrt{3}}{2}(P_{3,2}+P_{3,-2})\end{bmatrix}f_3+c_{34}\begin{bmatrix}-\frac{3\sqrt{3}i}{28}(5P_{3,-1}+P_{3,3})\\ 3P_{3,0}\\ -\frac{3i}{4}(3P_{3,1}-P_{3,-3})\\ \frac{\sqrt{3}}{14}(9P_{3,-2}-3P_{3,2})\end{bmatrix}f_3$$

where

$$P_{0,0}=1$$
$$P_{1,0}=z/r,\ P_{1,\pm1}=(x\pm iy)/r$$
$$P_{2,0}=z^2-\tfrac{1}{2}(x^2+y^2)/r^2,\ P_{2,\pm1}=z(x\pm iy)/r^2,\ P_{2,\pm2}=(x\pm iy)^2/r^2$$
$$P_{3,0}=z(z^2-\tfrac{3}{5}r^2)/r^3,\ P_{1,\pm1}=(z^2-\tfrac{1}{5}r^2)(x\pm iy)/r^3$$
$$P_{3,+2}=z(x\pm iy)^2/r^3,\ P_{3,\pm3}=(x\pm iy)^3/r^3.$$

APPENDIX 2

Nonvanishing matrix elements of $\langle F_i|\mathbf{r}|F_j\rangle$

$$\langle F^{1/2}(\Gamma_8-p)|\mathbf{r}|F^{3/2}(\Gamma_8-s)\rangle=\langle F^{-1/2}(\Gamma_8-p)|\mathbf{r}|F^{-3/2}(\Gamma_8-s)\rangle^*=-i(\lambda_1-\lambda_2)(\mathbf{i}-i\mathbf{j}).$$

$$\langle F^{-1/2}(\Gamma_8-p)|\mathbf{r}|F^{3/2}(\Gamma_8-s)\rangle=-\langle F^{1/2}(\Gamma_8-p)|\mathbf{r}|F^{-3/2}(\Gamma_8-s)\rangle=-(\lambda_1+2\lambda_2)\mathbf{k}.$$

$$\langle F^{-3/2}(\Gamma_8-p)|\mathbf{r}|F^{3/2}(\Gamma_8-s)\rangle=-\langle F^{1/2}(\Gamma_8-p)|\mathbf{r}|F^{-1/2}(\Gamma_8-s)\rangle$$
$$=-\langle F^{-1/2}(\Gamma_8-p)|\mathbf{r}|F^{1/2}(\Gamma_8-s)\rangle^*=\langle F^{3/2}(\Gamma_8-p)|\mathbf{r}|F^{-3/2}(\Gamma_8-s)\rangle^*=-i\sqrt{3}\lambda_2(\mathbf{i}+i\mathbf{j}).$$

$$\langle F^{-3/2}(\Gamma_8-p)|\mathbf{r}|F^{-1/2}(\Gamma_8-s)\rangle=\langle F^{3/2}(\Gamma_8-p)|\mathbf{r}|F^{1/2}(\Gamma_8-s)\rangle^*=i(\lambda_1+\lambda_2)(\mathbf{i}-i\mathbf{j}).$$

$$\langle F^{1/2}(\Gamma_8-p)|\mathbf{r}|F^{-1/2}(\Gamma_8-s)\rangle=-\langle F^{-3/2}(\Gamma_8-p)|\mathbf{r}|F^{1/2}(\Gamma_8-s)\rangle=(\lambda_1-2\lambda_2)\mathbf{k}.$$

$$\langle F^{1/2}(\Gamma_7)|\mathbf{r}|F^{3/2}(\Gamma_8-s)\rangle=\frac{1}{\sqrt{3}}\langle F^{-1/2}(\Gamma_7)|\mathbf{r}|F^{1/2}(\Gamma_8-s)\rangle$$
$$=\frac{-1}{\sqrt{3}}\langle F^{1/2}(\Gamma_7)|\mathbf{r}|F^{-1/2}(\Gamma_8-s)\rangle^*=-\langle F^{-1/2}(\Gamma_7)|\mathbf{r}|F^{-3/2}(\Gamma_8-s)\rangle^*=\cdot\lambda_3(\mathbf{i}-i\mathbf{j})$$

$$\langle F^{-1/2}(\Gamma_7)|\mathbf{r}|F^{3/2}(\Gamma_8-s)\rangle=\langle F^{1/2}(\Gamma_7)|\mathbf{r}|F^{-3/2}(\Gamma_8-s)\rangle^*=2i\lambda_3\mathbf{k}.$$

$$\langle F^{1/2}(\Gamma_6)|\mathbf{r}|F^{3/2}(\Gamma_8-s)\rangle=-\langle F^{-1/2}(\Gamma_6)|\mathbf{r}|F^{-3/2}(\Gamma_8-s)\rangle^*$$
$$=-\sqrt{3}\langle F^{-1/2}(\Gamma_6)|\mathbf{r}|F^{1/2}(\Gamma_8-s)\rangle=\sqrt{3}\langle F^{1/2}(\Gamma_6)|\mathbf{r}|F^{-1/2}(\Gamma_8-s)\rangle^*=\sqrt{3}\lambda_1(\mathbf{i}+i\mathbf{j}).$$

$$\langle F^{1/2}(\Gamma_6)|\mathbf{r}|F^{1/2}(\Gamma_8-s)\rangle=\langle F^{-1/2}(\Gamma_6)|\mathbf{r}|F^{-1/2}(\Gamma_8-s)\rangle^*=-2i\lambda_4\mathbf{k}.$$

where

$$\lambda_1=\frac{4\pi}{3}c_{01}c_{11}\langle r^4f_0f_1\rangle+\frac{16\sqrt{3}\pi}{45}c_{21}c_{12}\langle r^6f_2f_1\rangle+\frac{4\pi}{210}\left[\frac{48}{5}c_{21}c_{32}-72c_{21}c_{33}+14\sqrt{3}c_{22}c_{31}\right]\langle r^8f_2f_3\rangle.$$

$$\lambda_2=\frac{4\pi}{3\sqrt{3}}c_{01}c_{12}\langle r^4f_0f_1\rangle+\frac{4\pi}{15}(c_{21}c_{11}-c_{22}c_{12})\langle r^6f_2f_1\rangle+\frac{4\pi}{210}\left[6c_{21}c_{31}-\frac{468}{35}c_{21}c_{34}+\frac{28\sqrt{3}}{5}c_{22}c_{32}\right]\langle r^8f_2f_3\rangle$$

$$\lambda_3=\frac{4\pi}{3}c_{01}c_1\langle r^4f_0g_1\rangle+\frac{4\pi}{15}(2c_{21}c_1+\sqrt{3}c_{22}c_1)\langle r^6f_2g_1\rangle-\frac{8\pi}{75}(3c_{21}c_3-\sqrt{3}c_{22}c_3)\langle r^8f_2g_3\rangle.$$

$$\lambda_4=\frac{4\pi}{3}c_{01}c_1'\langle r^4f_0h_1\rangle-\frac{4\pi}{15}(2c_{21}c_1'-\sqrt{3}c_{22}c_1')\langle r^6f_2h_1\rangle-\frac{8\pi}{75}(3c_{21}c_{3'}+\sqrt{3}c_{22}c')\langle r^8f_2h_3\rangle.$$

i, **j**, **k** are unit vectors along (100), (010), (001) directions respectively.

J. Phys. Chem. Solids Pergamon Press 1969. Vol. 30, pp. 1465-1481. Printed in Great Britain.

HYDROXIDE AND OXIDE IMPURITIES IN CALCIUM HALOPHOSPHATES

J. S. PRENER, W. W. PIPER and R. M. CHRENKO
General Electric Research and Development Center, Schenectady, New York, U.S.A.

(*Received* 25 *October* 1968; *in revised form* 16 *December* 1968)

Abstract – A number of defects giving rise to specific optical absorption and fluorescence, and to the formation of color and paramagnetic centers upon X-ray irradiation, can be produced in polycrystalline $Ca_{10}(PO_4)_6F_2$ (calcium fluorapatite). Heating in vacuum results in the formation of F ion vacancies. Heating in water vapor introduces OH ions which substitute for F ions and heating in water vapor followed by heating in vacuum results in the formation of oxide ion impurities at F ion sites and F ion vacancies which can associate. Models for several color and paramagnetic centers proposed on the basis of the results of earlier EPR studies on single crystals are supported. A new paramagnetic defect consisting of a hole trapped at an O–OH ion pair is reported for the first time. Some ideas on the defects responsible for extrinsic u.v. absorption bands seen previously in fluorapatite are presented. Finally, chlorapatite is shown to behave in an analogous manner.

INTRODUCTION

THE APATITES form a large group of naturally occurring and synthetic compounds having the generic formula $M_{10}(YO_4)_6X_2$[1]. Most commonly the M are positive divalent ions, the YO_4 are groups such as PO_4^{3-} and VO_4^{3-}, and the X are halide or hydroxide ions, although much more complex compositions are possible[2]. The apatites discussed in this paper are $Ca_{10}(PO_4)_6F_2$ and $Ca_{10}(PO_4)_6Cl_2$, henceforth referred to as F-apatite and Cl-apatite. The apatite crystal structure is based on a primitive hexagonal lattice with $P6_3/m$ space group symmetry[3–6]. The important structural feature for the purposes of this paper concerns the packing and immediate surroundings of the halide ions in the structure. The F-ions with point symmetry C_{3h} form linear chains along the 6_3 screw axis (*c*-axis) and diffusion may be expected to occur with relative ease along these chains[7]. In Cl-apatite and in calcium hydroxy-apatite the Cl^- and OH^- ions also lie on the screw axis but their *z* parameters and the orientation of the O–H dipoles along this axis are more complex[3, 8, 9].

Good methods for the synthesis of polycrystalline F- and Cl-apatite powders have been developed as a result of their use as fluorescent lamp phosphors. Large single crystals have been grown by the Kyropoulos method[10] and by the flux method[9]. These crystals both pure and doped have been used for the study of color and paramagnetic centers[11–13] and for a variety of optical studies[9, 10, 14, 15]. The *epr* studies of defects formed in X-irradiated F-apatite were sufficiently detailed to suggest a simple set of defect models consistent with all the experimental facts. The presence of hyperfine interactions with nearby *F* and *P* nuclei permitted the identification of the position of these defects in the host lattice with almost complete certainty. Table 1 summarizes the final models proposed for the defects observed after X-raying F-apatite crystals[12]. The symbols O and V represent, respectively, an O impurity at an F site and an F ion vacancy. Multiple symbols represent defects associated as nearest neighbors. The superscripts 0, +, and – give the charges of the defects relative to the singly negative F ions which they replace. Although it was necessary to subject the F-apatite crystals to a dose of X-rays before the color and paramagnetic centers could be observed, the fact was well

Table 1. *Summary of defects seen in F-apatite single crystals*[12]

Defects observed after X-ray irradiation	Absorption band maximum (‖c) at 300°K	EPR spectrum lable[(a)]
O^0	none	H II
V^0	450 nm	II
$(O–V–V)^0$	760 nm	III
$(V–O–V)^0$	448 nm	I[(b)]
$(O–V–V)$	610 nm	none[(c)]
$(O–V)^+$	none	H I[(b)]

[(a)] H II and H I are hole excess center, the remaining ones are electron excess centers.

[(b)] Not stable at room temperature Observed by X-ray irradiation at 77°K

[(c)] Not a paramagnetic defect

documented that the atomic defects were not created by the X-rays[11]. Free electrons and holes, created by the X-rays found their way to a trap with a suitable charge state to create the observed centers. Thus, only the charge state of the defect was changed by irradiation, and a thermal anneal at 500°C was sufficient to permit the centers to relax to their initial charge states. Therefore, corresponding defects originally present in the F-apatite crystals quite probably were O^-, V^+, $(V–O–V)^+$ and $(O–V)^0$. These defects whose concentrations varied among the many crystals grown all involve oxide and F^- ion vacancies either isolated or in various associations. It was not possible, however, to control the chemistry during crystal growth and thus provide a further test for the proposed models. In particular, the presence of O as part of the defects could not be positively identified by *epr* studies.

In addition to the formation of color and paramagnetic centers under X-ray irradiation, extrinsic u.v. absorption bands were observed in as-grown Cl- and F-apatite crystals[9, 10]. The intensity of these bands varied among different crystals but their origin was unknown since, again, it was not possible to control the chemistry adequately during crystal growth. Upon examination of pure F-apatite powder which had been prepared to have a stoichiometric composition, it was observed that none of the defects listed in Table 1 could be created in any appreciable quantity by X-rays. Further, diffuse reflectance measurements of the material indicated reflectance in the ultraviolet larger than 0·9 (compared with MgO taken as 1·0) out to 185 nm.

The purpose of this paper is to describe chemical procedures by which the composition of polycrystalline stoichiometric F-apatite could be modified so as to observe the color and paramagnetic centers and the extrinsic u.v. absorption bands previously seen in single crystals. By correlating the observed changes in optical and *epr* spectra with the chemistry of the F-apatite system, it has been possible to further substantiate the correctness of the models as given in Table 1. The extrinsic u.v. absorption bands have been produced and some clues have been provided as to the nature of the defects associated with the bands. In addition, several new *epr* spectra are observed. For one of these (spectrum HV), a model for the defect is proposed. Although this paper is primarily concerned with F-apatite, we also show that Cl-apatite behaves in an analogous manner.

MATERIALS AND METHODS OF MEASUREMENT

The F- and Cl-apatites were prepared by solid phase reactions from $CaHPO_4$, $CaCO_3$, and CaF_2 or $CaCl_2$.* The single crystals of F-apatite were grown from a CaF_2 flux[9] or from the melt[10].

For the diffuse reflectance measurements, monochromatic light from a Cary Model 14R spectrophotometer was allowed to fall on the samples pressed into shallow cups (0·8 mm deep) at an incident angle of 40°. A cone of the diffusely reflected radiation was detected by a suitable photomultiplier and recorded. Corrections for fluorescence were made where necessary and all reflectances are given relative to that of freshly smoked MgO taken as unity. Fluorescence emission spectra, corrected for the spectral sensitivity of the detector and spectrometer, were obtained using a Jarrell–Ash 0·5 m monochromator and filtered GEH85–C3 high pressure Hg arc as the exciting source. Infrared transmission measurements were made using a Beckman IR-7 spectrophotometer and standard KBr pressed disk techniques.

---

*The apatite samples were kindly supplied to us by the Chemical Products Plant, Lamp Division, General Electric Co., Cleveland, Ohio.

For the production of color and paramagnetic centers, the powdered samples were pressed into the shallow cup used for reflectance measurements and mounted on a water-cooled brass block. These samples were usually exposed for 30 min to the X-ray beam from a *W* target filtered by 10 ml Al and operated at 50 kV and 20 mA. These conditions insured approximately homogeneous exposure and concentrations close to saturation.

For *epr* measurements the irradiated powder was remounted dry in a teflon sleeve centered in a cylindrical TE 011 cavity. The magnetic resonance measurements were made at 77°K in a balanced bolometer spectrometer operating at 14 Ghz. Details of this spectrometer have been described elsewhere[16].

Measurements of the absolute concentration of the paramagnetic defects in powder samples have been made with the aid of a calibrated sample of phosphorous-doped silicon.* By taking proper account of the differences of line shape, line width, and saturation characteristics between this standard and the *epr* signals in F-apatite, the signals obtained with apatite could be converted to defect concentrations. A sample of MgO:Cr^{3+} was used to correct for variations in the spectrometer sensitivity as described in an earlier paper[12]. Comparison of signal amplitudes before and after crushing a single crystal yielded the additional factor needed to calibrate signal strengths in powder samples. The estimated accumulated error for the absolute calibration of the hole center concentrations is probably about ±25 per cent whereas relative concentrations are about ±5 per cent. The absolute concentrations of the trapped electron centers are about a factor of two less certain.

EPR SPECTRA

Three of the major centers which have been studied in single crystals of fluoroapatite have been labelled II, III and H II. The most probable defects which could give rise to these spectra were concluded to be those described in Table 1. The associated *epr* spectra may be adequately described by the spin Hamiltonian

$$\mathscr{H} = \beta S\cdot g\cdot H + S\cdot A\cdot I_F - \gamma_F\beta_N H\cdot I_F$$

where g and A are axially symmetric tensors and I_F is the spin of one or two nearest neighbor fluorine nuclei[12]. The parameters for these centers are included in Table 2.

Table 2. EPR *parameters of defects in F-apatite*

EPR spectrum	$g_\perp$	$g_\parallel$	$A_\perp$ (G)	$A_\parallel$ (G)
I(b)	1·9994	1 9983	21	32
II	1·9995	1·9984	17	26
III	2 0000	1·9995	3	4
V(a)	2·0024	2·0024	4	4
VI(a)	2·0012	2·0024	0	0
HI(b)	2·0582	2·0019	5·8	0
H II	2·0522	2·0018	7·0	0
H V	2·0548	2·0018	6·1	0

(a) Powder samples only

(b) Observed only upon irradiation at 77°K

These three centers have been observed in the powder samples and will be discussed in the next section. The powder spectrum may be predicted by averaging the single crystal parameters over all directions in space. Alternatively a single crystal whose color

---

*Samples of this material were distributed by E. A. Gere (Bell Telephone Laboratories) to colleagues active in *epr* work *circa* 1961. G. W. Watkins kindly furnished us with part of the sample given to him.

center properties are known can be ground up. Both of these approaches have been employed to correlate powder and single crystal spectra. Representative single crystal and powder spectra are shown in Fig. 1.

To further confirm the identity of III and H II, a powder sample in the oxide state was X-irradiated near 77°K and transferred to the resonance cavity without experiencing appreciable warming. As was earlier reported for single crystals[12], H I and I were observed which converted to H II and III as soon as the sample had been exposed to room temperature.

In addition to the defects described above, at least three additional centers in appreciable concentrations have been observed in powders. These are labelled V, VI and H V and their resonance parameters are included in Table 2. By a suitable water vapor treatment the H V center has been reproduced in single crystals. The parameters for this center are extremely close to those for H II, except that the hyperfine interaction is with only one

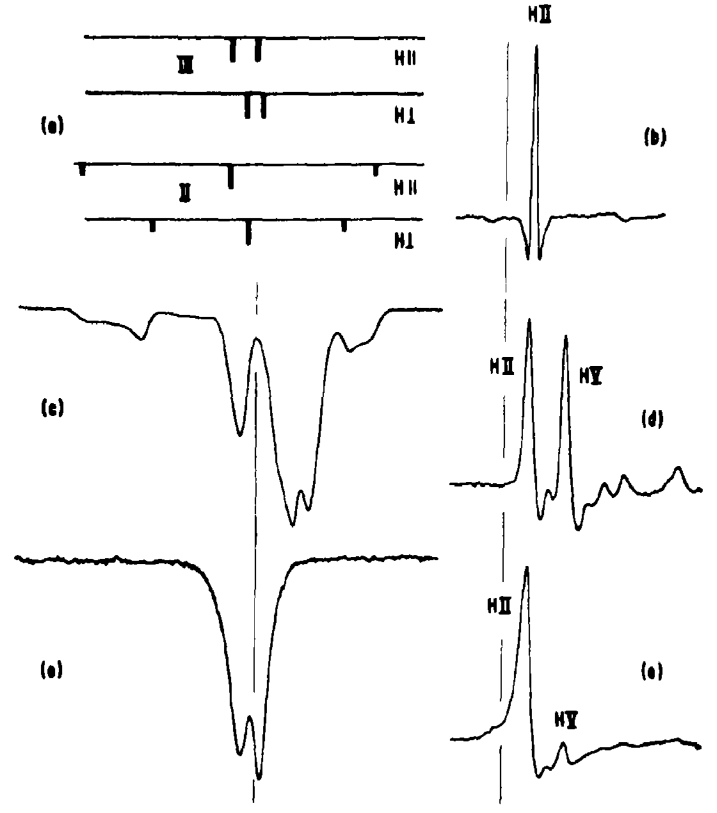

Fig. 1. EPR spectra of X-ray induced defects in single crystals and powders of F-apatite. (a) Single crystal line positions of II and III with H ⊥ *c*-axis and H ∥ *c*-axis. (b) Single-crystal spectrum of H II with H ⊥ *c*-axis. (c) Powder spectrum of II and V in the vacuum state (d) Powder spectra of H II and H V. (e) Powder spectra of H II and III in the oxide state. These spectra are all recordings of the dispersion derivative. Due to long relaxation times, the centers near g = 2 are recorded out-of-phase.

fluorine nucleus and is somewhat smaller. The defect which we believe responsible for the H V spectrum will be discussed later in this paper.

The g-values of the V and VI centers are very close to the free electron g-value. Although g-shifts and hyperfine splittings are extimated they are quite tentative since these parameters are quite small and there is a real possibility that one or both centers are in fact composite. These spectra have not been seen in single crystals. The absence of observable V and VI spectra in F-apatite powders into which we have introduced oxide impurities, as described below (see sample FA-43, Table 3) suggests that the failure to see these spectra in single crystals may be due to the high concentration of these impurities. The defects responsible for these spectra are, at present, unknown, and shall not be considered further in this paper.

Table 3. Molar concentrations (ppm) of paramagnetic defects in various states of F-apatite after X-ray irradiation

Sample	State	II	III	V	VI	HII	HV
FA-0	Virgin	2				0·2	
FA-45	Vacuum[(a)]	25		80			
FA-40	Hydroxide[(b)]	3			90	1	0·5
FA-43	Oxide[(c)]	10	90			50	6
FA-48	Hydroxide[(d)]	1·5			60	2	3

[(a)] Sample FA-0 fired 16 hr at 1000°C in vacuum.

[(b)] Sample FA-0 fired 16 hr at 1000°C in argon saturated with water vapor at room temperature.

[(c)] Sample FA-40 refired 16 hr at 1000°C in vacuum.

[(d)] Sample FA-43 refired 16 hr at 1000°C in wet argon.

CHEMICAL MODIFICATION OF F-APATITE

The sample of F-apatite powder was placed in a platinum boat within a quartz container and heated to 1000°C in the presence of one of two ambients. The first ambient was a vacuum, although it was observed that equivalent results could be obtained by substituting a flowing stream of high purity argon. The second ambient consisted of a slow stream of argon which was saturated with water vapor at room temperature.

Initial heating of a F-apatite sample under either of these conditions produced irreversible changes in the sample. Combinations of treatments produced further changes. In all, three states of the F-apatite could be produced, in addition to the virgin (initial) state of the powder. These three modified states of F-apatite will be referred to as the vacuum state, the hydroxide state, and the oxide state for reasons which will become evident shortly. These states are characterized by their ultraviolet and i.r. optical absorption, by their fluorescence, and by the nature and concentration of color and paramagnetic centers produced upon X-ray irradiation. The treatments necessary to arrive at any of these states are summarized in Fig. 2.

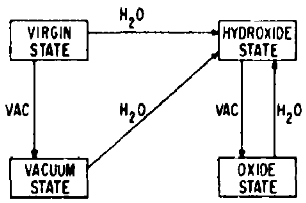

Fig. 2. Chemical treatments of virgin F-apatite powder at 1000°C required to produce each of the three states referred to in the text.

1. *The virgin state*

Before F-apatite powder is subjected to any of the heat treatments, its diffuse reflectance is greater than 0·90 (Fig. 3(a)), although there is evidence of some absorption near 250 nm and 190 nm. Infrared absorption measurements from 4000 to 650 cm^{-1} show strong bands below 2500 cm^{-1} due to the PO_4^{3-} vibrations and weak sharp bands at 3540 and 745 cm^{-1} arising from the substitution of hydroxide for fluoride ions as we shall discuss shortly. Six other very weak bands not intrinsic to F-apatite are seen. Three of these appear to be due to CO_3^{2-} ion vibrations, but the origins of the others are not known. When such a virgin state sample is irradiated by X-rays, none of the defects listed in Table I are produced in any appreciable concentration, although weak *epr* signals for II and H II can be identified, as indicated in Table 3. A resonance signal near a *g*-value of 2 and about 15 gauss wide at a concentration of 200 ppm is seen only in F-apatite powder in the virgin state. Such a strong signal could mask weak III, V, or VI *epr* signals. The color center which correlates with the *epr* II spectrum can be seen as small reflectance minima at 450 and 370 nm (Fig. 4(a)). Both bands are due to the same color center, since the absorption is dichroic[11, 12].

In summary, both optical and *epr* spectra indicate the presence, in low concentrations, of hydroxide and carbonate impurities, some unknown impurities or defects, and two of the defects listed in Table I. In the next three subsections we show that the various chemical treatments outlined in Fig. 2 cause very marked changes in the optical and *epr* spectra, and that these changes can be understood in terms of modifications in the composition of the F-apatite.

2. *The vacuum state*

After the powder has been heated in a vacuum there are changes observed in the optical and *epr* spectra which can be understood in terms of the chemical reaction:

$$\mathrm{Ca_{10}(PO_4)_6F_2} \xrightarrow[\text{vac.}]{1000^\circ\mathrm{C}} \mathrm{Ca_{10-\epsilon}(V_{Ca}^{2-})_\epsilon(PO_4)_6F_{2(1-\epsilon)}}(V^+)_{2\epsilon}+\epsilon\mathrm{CaF_2} \quad (1)$$

where V_{Ca}^{2-} refers to a vacant Ca ion site. Although no effects are observed which can be ascribed to a loss of Ca, recent work, to be published, indicates that in Cl-apatite, both Ca and Cl ion vacancies are created by a vacuum anneal.

In this state there are no changes in the diffuse reflectance spectrum until the sample has been X-irradiated. After X-irradiation, strong minima in the diffuse reflectance are

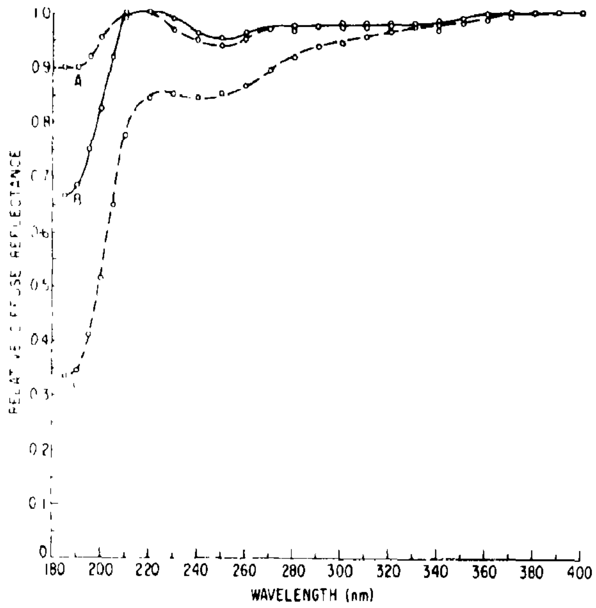

Fig. 3. (a) Diffuse reflectance spectra of F-apatite powder as made by solid phase reactions, (b) after heating for 16 hr at 1000°C in argon saturated with water vapor; and (c) after heating 16 hr at 1100°C in argon saturated with water vapor.

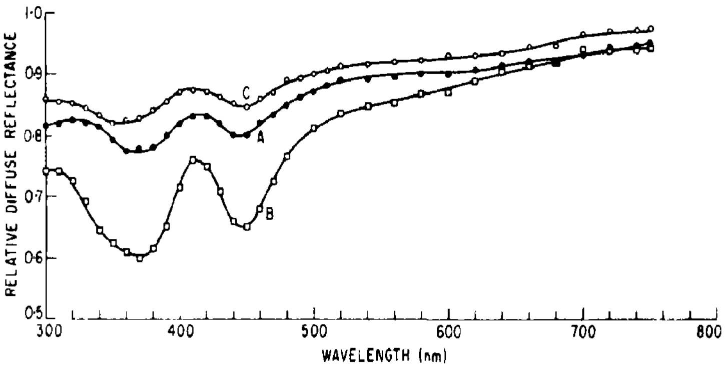

Fig. 4. Diffuse reflectance spectra of F-apatite X-ray irradiated at room temperature for 30 min. (a) virgin F-apatite; (b) F-apatite heated 16 hr at 1000°C in vacuum; and (c) F-apatite heated 16 hr at 1000°C in argon saturated with H_2 at room temperature.

seen at 450 nm and at 370 nm (Fig. 4(b)). Examination of the sample in the *epr* spectrometer reveals that the concentration of the H center has increased about a factor of ten as shown in Table 3. Thus, the defect labelled V^0 in Table 1 is supported by the chemistry of this experiment. Since no foreign impurities are introduced in the vacuum anneal, the observed *epr* and optical spectra are ascribable to a native defect. CaF_2 is probably the most volatile component of F-apatite, and the defect was already known to be on a F site [12]. The *epr* signal V is also observed, but as already discussed, the defect responsible for this spectrum is unknown.

3. *The hydroxide state*

After heating a virgin or vacuum state sample of F-apatite in a flowing stream of argon which had been saturated with water vapor at room temperature, changes are observed in the u.v. and i.r. optical absorption. These changes can be explained by the chemical reaction

$$Ca_{10}(PO_4)_6F_2 + 2\epsilon H_2O \rightarrow Ca_{10}(PO_4)_6(OH)^0_{2\epsilon}F_{2(1-\epsilon)} + 2\epsilon HF \quad (2)$$

where $(OH)^0$ represents a hydroxyl ion impurity replacing a F ion. The liberation of HF was detected analytically by passing the exit gas through a dilute alkali solution. Reactions of this type have been studied previously [8, 17, 18], but no optical or magnetic properties have been reported.

The diffuse reflectance in the vicinity of 190 nm is decreased as shown in Figs. 3(b) and 3(c). In Fig. 5 is shown the infrared optical absorption of F-apatite after heating in water vapor. The sharp band at 3540 cm^{-1} (2·83 μ) with a half width of 10 cm^{-1} is due to the O–H stretching vibration. It is seen at 3560 cm^{-1} in $Ca_5(PO_4)_3OH$ [19], and at 3700 cm^{-1} in the free OH radical [20]. The small differences in the vibrational frequency of OH observed in various solids has been taken as an indication of H bonding to neighboring ions [21]. This same band is also seen in F-apatite crystals grown from a CaF_2 flux and the absorption has been found to occur only for incident radiation polarized parallel to the *c*-axis. This is as expected for a molecule with $C_{\infty v}$ symmetry, with its rotational axis parallel to the *c*-axis of the apatite crystal and is in accord with the disposition of the OH groups in $Ca_5(PO_4)_3OH$ as determined by neutron diffraction [3]. The sharp absorption band at 745 cm^{-1} (13·4 μ), seen in Fig. 5, is most probably due to a librational mode of the hydroxyl ion. It was found that for any one sample the peak absorbance values of the 3540 cm^{-1} and

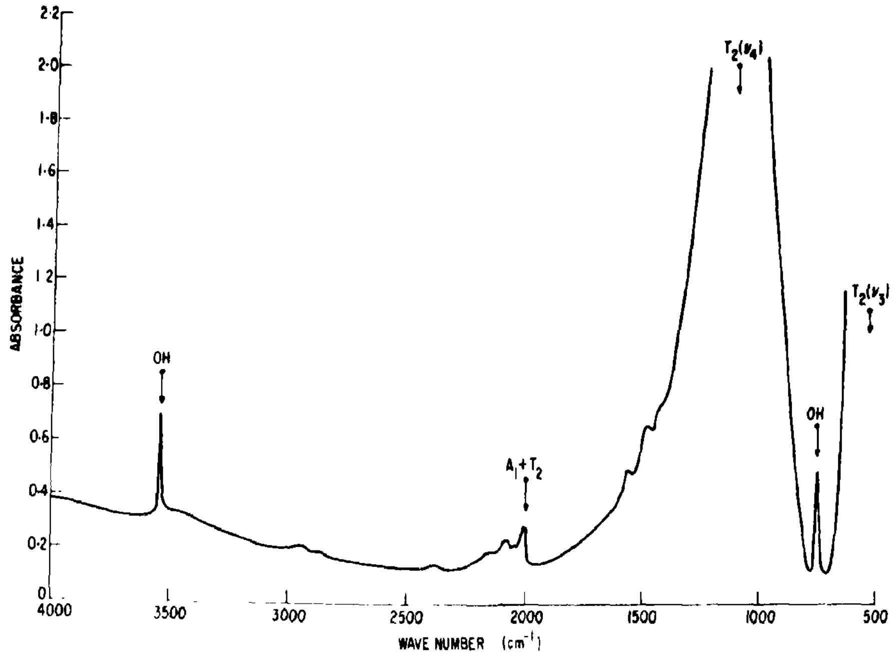

Fig. 5. Infrared absorption of F-apatite heated for 16 hr at 1000°C in argon saturated with water vapor. The OH vibrational and librational bands are marked. The other labeled absorption bands are due to PO_4 vibrations.

745 cm^{-1} bands were the same within experimental error. By using D_2O instead of H_2O the 3540 cm^{-1} band shifted to 2598 cm^{-1}. The ratio of observed frequencies, 1·363, is in good agreement with the expected value of 1·372 calculated from the reduced masses. The 745 cm^{-1} band could no longer be seen after heating in D_2O, since the decrease in frequency would place the band in the region of strong intrinsic absorption.

By comparing the maximum absorbance in the i.r OH bands with the absorbance of the intrinsic band at 1990 cm^{-1} (the structured absorption between 1990 and 2060 cm^{-1} is due to the A_1+T_2 (ν_4) combination vibration of the $PO_4{}^{3-}$ ion) errors due to differences in sample preparation could be minimized. The ratio of the average of the peak absorbances at 3540 cm^{-1} and 745 cm^{-1} to that at 1990 cm^{-1} can be taken as a measure of the $(OH)^0$ content in F-apatite. In Table 4 this ratio is given in the third column. To be compared is sample FA-40 with FA-0 and FA-45. The increase in i.r absorbance and decrease in far u.v. reflectance in going from the virgin or vacuum state to the hydroxide state is obvious.

In order to get more quantitative data on the relation between the ultraviolet reflectance, i.r. absorption, and the hydroxyl ion content, four samples were fired at 1000°C in flowing argon saturated with water vapor at room temperature for varying periods of time. The results are given in Table 5. The relative i.r. absorbance increases with increasing firing time in water vapor. From the measured diffuse reflectance at 190 nm, the product of the absorption coefficient and particle diameter were calculated using Johnson's analysis[22]. Aside from the approximations inherent in the theory, there are several experimental sources of error contributing to the uncertainty of the values listed in the third column. The atom fraction of missing

Table 4. Optical properties of F*-apatite in various states*

Sample	State	Relative i.r. absorbance[a]	Relative diffuse reflectance 190 nm	Relative diffuse reflectance 250 nm	Fluorescence
FA-0[b]	Virgin	0·6	0·90	0·96	No
FA-45	Vacuum	0·0	0·88	0·96	No
FA-40	Hydroxide	2·6	0·68	·95	No
FA-43	Oxide	0·5	0·15	·19	Yes
FA-48	Hydroxide	3·1	0·56	·94	No

[a] Average value of absorbance at 3540 and 745 cm^{-1} divided by absorbance at 1900 cm^{-1}.

[b] See Table 3 for sample treatments.

Table 5. Correlation of the i.r. absorption, u.v. reflectance and fluorine content in F*-apatite*

Firing time (hr)	Relative i.r. absorbance[a] A	Particle diameter times absorption coefficient at 190 nm[b] B	Atom fraction of missing fluorine[c] C	Value of A/C	Value of B/C
8	2·0	0·020	0·12	17	0·17
16	2·6	0·030	0·14	19	0·21
32	2·9	0·037	0·18	16	0·21
64	4·0	0·069	0·24	17	0·29

[a] Average value of absorbance at 3540 and 745 cm^{-1} divided by absorbance at 1990 cm^{-1}.

[b] Calculated from measured diffuse reflectance by taking 0·9 for the reflectance of MgO (see Cl-apatite section) and using the equation given by Johnson[22] for a powder with a refractive index of 1·63.

[c] Calculated from fluorine analysis. The analysis was kindly performed for us by the Analytical Group of the Lamp Metals and Components Department, Lamp Division, General Electric Co., Cleveland, Ohio.

F ions was determined by chemical analysis of the fired samples, for fluorine. The relative constancy of the values in the fifth column indicates that F ions are replaced by OH ions and allows a determination of the OH content in other samples from infrared absorption data. From the integrated absorbance (expressed in cm^{-2}) under the 3540 cm^{-1} band and the OH ion concentration (in cm^{-3}), the computed value of the integrated absorption coefficient per OH ion is $6{\cdot}0\pm0{\cdot}7\times10^{-18}$ cm. This is 3·3 times larger than for the OH ion in KCl[23]. The values in the last column are not constant, possibly due to the errors involved in calculating the values of B. There is, however, qualitative agreement between the OH content and the u.v. absorption near 190 nm.

For the hydroxide state the diffuse reflectance spectrum after X-ray irradiation is similar to that of F-apatite in the virgin state (Fig. 4c). The *epr* spectra (Table 3) of hydroxide state F-apatite show no large concentration of any of the paramagnetic defects given in Table 1. The II center is present in about the same concentration as in the virgin state. The H II spectrum which is attributed to an O^0 defect appears at a low concentration of 1 ppm, a concentration slightly greater than that in the virgin state. The H V spectrum increases from 0·5 to 3 ppm with increasing firing time. The III spectrum is not observed, although a low concentration would be hidden by the intense VI spectrum.

In summary, we conclude that heating florapatite in an ambient containing water vapor results in the replacement of some of the fluoride ions by OH ions in accord with equation (2). This conclusion is based on the observations that fluorine is detected in the exhaust gas, that OH vibrational and librational absorption bands appear at 3540 and 745 cm^{-1}, that in single crystals these i.r. absorption bands occur only for incident radiation polarized parallel to the c-axis, and that there is a linear relationship between the i.r. absorbance of the OH ions and the missing atom fraction of fluoride ions. The decrease in reflectance observed near 190 nm after heating in water vapor indicates the presence of an absorption band which may be due to the $(OH)^0$ defects. An absorption band at 204 nm in KCl has been attributed to OH impurities whose vibrational absorption is observed at 3570 cm^{-1} (2·8 μ)[23].

4. *The oxide state*

The oxide state of F-apatite is produced by subjecting a sample in the hydroxide state to a vacuum heat treatment or by heating such a sample in a stream of dry inert gas such as argon. In going from the hydroxide to the oxide state very marked changes are observed in the u.v. reflectance, the i.r. absorption, and in the reflectance and *epr* spectra after X-ray irradiation. These observed changes are reversible and are consistent with a predominant chemical reaction

$$Ca_{10}(PO_4)_6(OH)^0_{2\epsilon}F_{2(1-\epsilon)} \underset{H_2O}{\overset{\text{vac or inert gas}}{\rightleftarrows}} Ca_{10}(PO_4)_6O_\epsilon^-V_\epsilon^+F_{2(1-\epsilon)}+\epsilon H_2O. \quad (3)$$

As discussed below, the experimental evidence suggests that the oxide ion impurities and vacancies are present both as isolated defects at F-sites and as associated defects. In addition, as discussed in the next section, oxide ions might reside next to residual OH ions which could explain the new paramagnetic center, HV, which appears after X-ray irradiation. The oxide state of F-apatite could not be produced by firing virgin F-apatite directly in oxygen gas for 16 hours at 1000°C. Under these conditions, oxygen behaves as an inert gas. The existence of mixed fluor-oxyapatites has been suggested by Bredig *et al.* [24] but no properties of these materials were given.

In the u.v. an extremely strong broad absorption band appears at 250 nm and the absorption near 190 nm is greatly increased as shown in Fig. 6. Concurrently, the optical absorption due to the OH vibration and libration is reduced several fold from its value in the hydroxide state of F-apatite. These effects are illustrated by the data given for sample FA-43 in Table 4.

It was also found that excitation within the strong 250 nm absorption produced red fluorescence. The fluorescence spectra taken at 77°K and at room temperature are shown in Fig. 7. The excitation spectrum at room temperature of this fluorescence was found to consist of a broad band peaking near 250 nm.

Upon X-ray irradiation of F-apatite in the oxide state several defects already studied in single crystals are seen for the first time in appreciable concentrations; namely, the defects listed in Table 1 whose labels are O^0, $(O–V–V)^0$ and $(O–V–V)^-$. The diffuse reflectance spectrum (Fig. 8) clearly shows the bands at 610 and 760 nm attributed to (O–V–V) and $(O–V–V)^0$, respectively, as well as the band at 450 nm due to V^0. The band at 350 nm is a composite one and is due to the fact that the absorption of the color centers is dichroic[11, 12]. In going from the hydroxide to the oxide state, the *epr* data in Table 3 (compare samples FA-40 and FA-43) show a very large increase in the intensity of the III spectrum attributed to $(O–V–V)^0$ as well as the H II spectrum attributed to O^0. The H V spectrum and the II spectrum which we have attributed to $(O–OH)^0$ and to V^0 centers also increase in intensity. The V and VI spectra are not observed.

Upon refiring oxide state F-apatite in water vapor, the u.v. and color center reflectance, the i.r. absorption spectra, and the *epr*

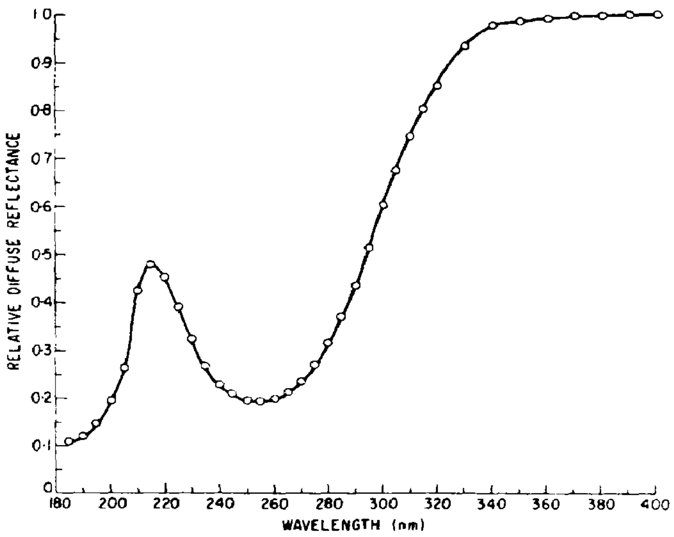

Fig. 6. Diffuse reflectance of F-apatite after heating first for 16 hr at 1000°C in wet argon (see Fig. 3(b)) and then in a vacuum at 1000°C for 16 hr

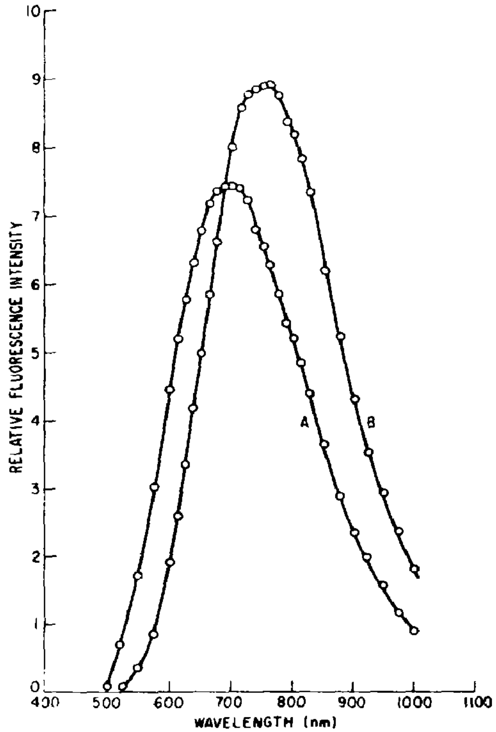

Fig. 7. Fluorescence spectra of F-apatite after heating first for 16 hr at 1000°C in wet argon and then in a vacuum at 1000°C for 16 hr: (a) room temperature, (b) 77°K.

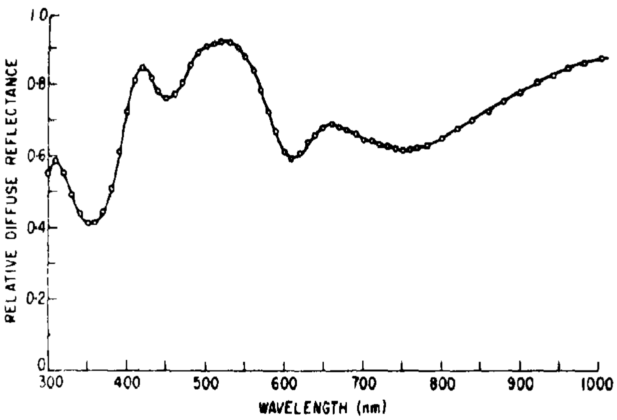

Fig 8. Diffuse reflectance, after X-ray irradiation, of F-apatite fired for 16 hr at 1000°C in argon saturated with H_2O vapor at room temperature and then refired for 16 hr at 1000°C in vacuum.

spectra (with the exception of the H V spectrum) all revert to those characteristic of the hydroxide state. The red fluorescence also disappears. These effects are tabulated in Tables 3 and 4 where samples FA-48 and FA-40 are to be compared with sample FA-43. The reversibility of the reaction as given by equation (3) is therefore reflected in the reversibility of the optical and *epr* spectra.

The decrease in intensity of the OH vibrational absorption in going from the hydroxide state to the oxide state and its reversibility upon refiring in water vapor strongly suggests the formation of oxide ion impurities at fluoride sites. This is supported by the observation that mixed calcium fluor-oxy-apatites of composition $Ca_{10}(PO_4)_6O_xF_{2(1-x)}$ could be synthesized directly by a solid phase reaction from $CaHPO_4$, $CaCO_3$, and CaF_2. The strong optical absorption at 250 and 190 nm was observed in these synthetic samples and the absorption was found to increase with increasing values of x. These samples were also fluorescent and became strongly colored under X-ray irradiation. We might also note that oxide ion impurities in KCl have been shown to absorb in a band at 210 nm[25].

Most significant as we have seen, is the marked appearance of several color and paramagnetic centers in F-apatite when it is in the oxide state. The models for these centers given previously[12] involve either electrons or holes trapped at isolated oxide impurities or at oxide ion-fluoride ion vacancy associates and are therefore supported by the chemical and optical data. The strong ultraviolet absorption and associated fluorescence found in oxide state F-apatite is also most likely due to defects containing oxygen. However, as discussed in the next section, we cannot, at this time, identify their structure with any certainty.

CHEMICAL MODIFICATION OF F-APATITE SINGLE CRYSTALS

The H V paramagnetic center observed in polycrystalline F-apatite had not been previously seen in F-apatite single crystals grown either from the melt or a CaF_2 flux. It was of some interest, therefore, to obtain, by suitable chemical treatment, F-apatite single crystals containing a high enough concentration of H V centers that their point-symmetry and hyperfine interactions might be studied by *epr* and Endor techniques.

F-apatite single crystals which had been grown from the melt[10] were heated for several days at 1000°C in water vapor. Upon X-ray irradiation of these treated crystals, it was quite evident that the crystals were no longer homogeneous. Diffusion fronts, evidenced by regions of different color (after X-ray irradiation) were easily seen. The fast direction for diffusion was parallel to the c-axis of the crystal. As indicated in the introduction, the crystal structure of F-apatite is such that diffusion would be expected to occur relatively easily along the fluoride ion chains parallel to the c-axis. These crystals did contain, however, an easily measurable concentration of H V centers. The resonance parameters were measured and are summarized in Table 2. Measurements at intermediate angles of the magnetic field agreed with a model of a hyperfine interaction with one fluorine nucleus. An Endor experiment which would have verified that the nuclear interaction was with a fluorine nucleus was unsuccessful. As already noted, this resonance with $H \perp c$ and with $H \parallel c$ has been seen in polycrystalline F-apatite in the oxide state and at a somewhat lower concentration in the hydroxide state formed from the oxide state by heat treatment in water vapor. That the H V center contains an oxide ion seems most reasonable from the chemical methods needed to produce it. From the fact that it is not observed in as-grown crystals but only after treatment in water vapor, from the similarity of the *epr* parameters to those of the H II center (Table 2) and from the observation of hyperfine interaction with only one neighboring fluoride ion, we suggest that the most likely crystalline defect, which upon X-ray irradiation yields the H V center, is an $(O\text{–}OH)^-$ associated pair lying in the F ion chain. This defect has the proper charge state to trap a hole thus producing the paramagnetic center $(O\text{–}OH)^0$. The trapped hole would have the same electronic configuration as in the H II center but would be in a slightly different crystalline field and exhibit hyperfine interaction with only one fluorine.

Another question of interest is the identification of the defect responsible for the strong absorption at 250 nm. We therefore looked, in single crystals, for a correlation between changes in the intensity of the optical absorption band near 250 nm and changes in the concentration of various oxygen-containing defects upon X-ray irradiation and subsequent annealing. If the defect responsible for the absorption is simply converted into one of the paramagnetic or color centers by capture of a charge carrier produced by the X-rays, then a decrease in absorbance should be observed which is proportional to the increase in concentration of that particular center. The reverse should be true during the annealing out of the paramagnetic and color centers either thermally or by exposure to 365 nm radiation.

The melt-grown crystal examined for any such correlation exhibited a very strong dichroic absorption band peaking near 260 nm and contained the defects 0^-, $(O\text{–}V\text{–}V)^+$, V^+, and quite probably $(O\text{–}V)^0$. By grinding and polishing a thin enough sample the absorbance near 260 nm could be measured. The techniques for measuring the absorption coefficient using polarized incident radiation have been described in an earlier paper[12]. The shape of the absorption band is shown in Fig. 9 for both polarized and unpolarized radiation. The unpolarized curve is in good agreement with the diffuse reflectance curves for oxide-state F-apatite powders, and we shall assume that they arise from the same defects. The shape of the band for radiation polarized parallel to the *c*-axis is Gaussian with a width at half-maximum intensity of 0·77 eV at room temperature. Upon X-ray irradiation, the shape of the band did not change detectably but its intensity decreased. Upon annealing, after X-ray irradiation, the intensity increased again and after a complete anneal of the X-ray induced centers the optical absorbance could be brought back to its initial value.

The concentration of O^0 centers after X-ray irradiation or annealing was determined by measuring the strength of the H II signal as described earlier. The measurements of the intensity of the color center absorption bands at 610 nm and 760 nm using incident radia-

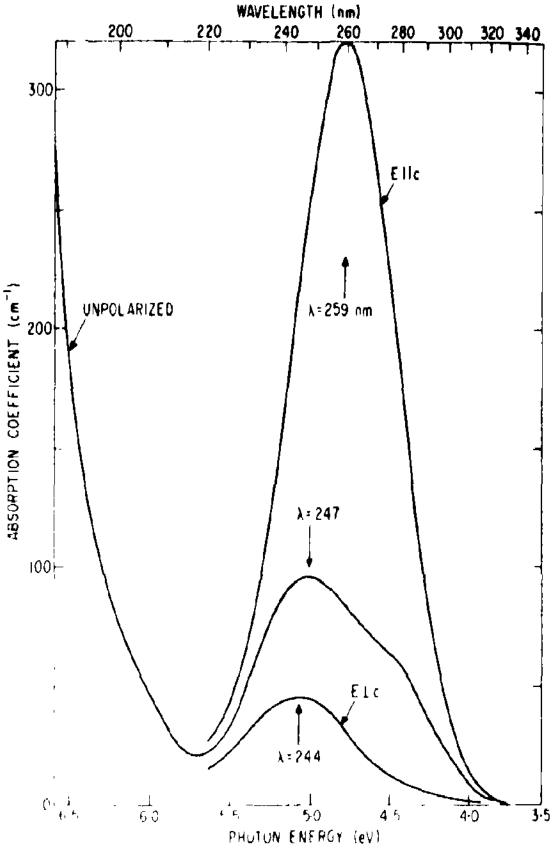

Fig. 9. Optical absorption spectrum of a melt grown F-apatite single crystal at room temperature

tion polarized parallel to the *c*-axis gave a measure of the concentration of the (O–V–V)$^-$ and (O–V–V)^0 defects, respectively.

Although the absolute concentration of the optical and *epr* centers were of the same order of magnitude, the data taken after many X-ray irradiation and annealing cycles failed to indicate any simple correlation between changes in the intensity of the 250 nm absorption band and changes in the concentration of the O^0, (O–V–V)^0 or (O–V–V)$^-$ defects. We conclude, therefore, that the defect responsible for the 250 nm absorption band in oxygen doped F-apatite powders is neither O$^-$ nor (O–V–V)$^+$ (assuming that the only other charge states give rise to the two color centers). Since there is evidence that the defect (O–V)^0 (assumed to be responsible for H 1) does not change its charge state upon X-ray irradiation at room temperature[12], one may also conclude that this is not the defect responsible for the u.v. absorption. One cannot rule out the possibility that the absorption band is a composite one, although the half width of the band did not change by more than ±5 per cent throughout the series of treatments. At present, therefore, we do not have a model for the defect responsible for the ultraviolet absorption and concurrent red fluorescence in oxide state F-apatite. In Table 6, which summarizes the various defects observed in polycrystalline F-apatite we have labelled the defect responsible for the strong absorption at 250 and 190 nm and for the red fluorescence by the symbol

Table 6. Summary of defects seen in polycrystalline F-*apatite*(a)

Defect	Optical absorption bands	EPR label	State
$(OH)^0$	< 190 nm 3540, 745 cm^{-1}	none	Hydroxide
O_x(c)	250 nm < 190 nm	none	Oxide
O^0		H II	Oxide
V^0	450(b) nm	II	Vacuum, Oxide
$(O\text{–}V\text{–}V)^0$	760(b) nm	III	Oxide
$(O\text{–}V\text{–}V)^-$	610(b) nm	none	Oxide
$(O\text{–}OH)^0$		H V	Oxide, Hydroxide

(a)The first two defects are seen in F-apatite after suitable chemical treatments. The remaining five defects are color and paramagnetic centers and can be observed only after X-ray irradiation of the treated samples.

(b)There are additional bands in the vicinity of 350–370 nm due to excitation to higher excited levels of the defect.

(c)See section of text entitled Chemical Modification of F-apatite single crystals.

O_x (suggesting some presently undetermined relation to the presence of oxygen at the fluorine site).

CHEMICAL MODIFICATION OF POLYCRYSTALLINE Cl-APATITE

The diffuse reflectance spectra of virgin state Cl-apatite powders exhibit strong reflectance minima at 190 nm as previously described by Johnson[10]. We found that firing in a stream of anhydrous HCl at 1000°C for as little as one hour gave a material which below 240 nm is a better diffuse reflector than MgO smoked on a $MgCO_3$ backing. The diffuse reflectance of such a treated sample of Cl-apatite is shown in Fig. 10(a). No changes were observed upon heating such a sample either in vacuum or in dry argon. It was not possible to treat F-apatite similarly by heating in an HF atmosphere, since decomposition of the F-apatite was found to occur probably through the formation of gaseous POF_3.

When Cl-apatite, which had been previously treated with HCl was refired at 1000°C in wet argon for several hours, it exhibited a significant decrease in diffuse reflectance below 240 nm as shown in Fig. 10(b). Refiring this material again in HCl resulted in a diffuse reflectance curve identical to that in Fig. 10(a). Refiring a water vapor fired Cl-apatite in vacuum or in an inert gas at 1000°C for 16 hours resulted in strong absorption below about 320 nm as shown in Fig. 10(c). Orange fluorescence (Fig. 11) was also observed when this sample was excited within this absorption band. Finally, the reflectance shown in Fig. 10(c) could be reversed to that in Fig. 10(b) by water vapor firing or to Fig. 10(a) by HCl firing. Concurrently the orange fluorescence disappeared. The changes in optical properties of Cl-apatite following a high temperature firing in water vapor, or in water vapor followed by vacuum are thus very similar to those found in F-apatite. Although differences were observed in the coloration of the different samples of Cl-apatite upon X-ray irradiation, no studies of color or paramagnetic center formation were made since very little is known about these defects in this material. Strong OH vibrational bands at 3590 cm^{-1} (2·78 μ) and a weaker one at 3500 cm^{-1} (2·86 μ) were found, however, in water vapor fired Cl-apatite. These OH bands were removed by HCl firing.

In analogy with F-apatite, we can designate Cl-apatite having the u.v. reflectance shown in Fig. 10(a) as virgin state; that shown in Fig. 10(b) as hydroxide state; and that shown in

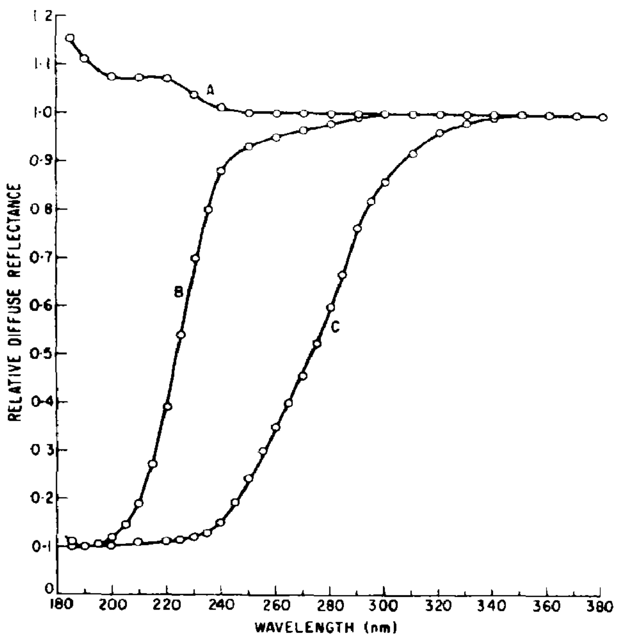

Fig. 10. Diffuse reflectance spectra of Cl-apatite powder: (a) after heating at 1000°C for 1 hr in a stream of anhydrous HCl; (b) sample (a) after reheating for 8 hr at 1000°C in argon saturated with water vapor; and (c) sample. (b) after reheating at 1000°C for 16 hr in vacuum.

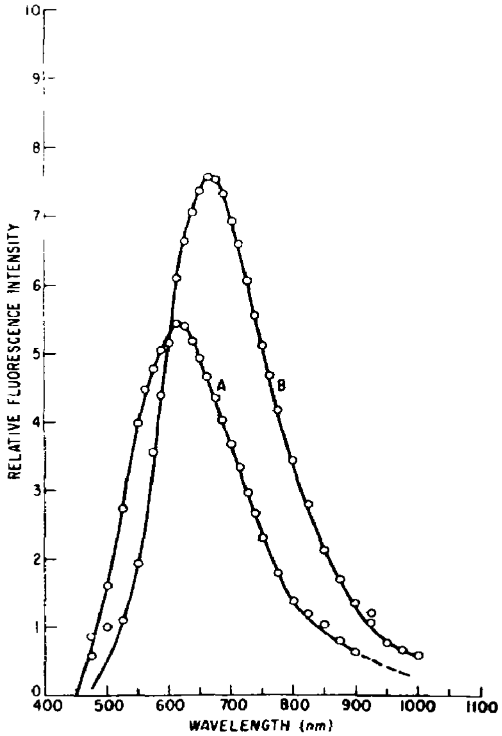

Fig. 11. Fluorescence spectra of Cl-apatite after heating for 8 hr at 1000°C in wet argon and then in a vacuum at 1000°C for 16 hr: (a) room temperature; (b) 77°K.

10(c) as oxide state. The various chemical reactions occurring in Cl-apatite may, therefore, be summarized

Virgin state ⇄ hydroxide state

$$\mathrm{Ca_{10}(PO_4)_6Cl_2 + 2\epsilon H_2O \rightleftarrows}$$

$$\mathrm{Ca_{10}(PO_4)_6(OH)^0_{2\epsilon}Cl_{2(1-\epsilon)} + 2\epsilon HCl}$$

Hydroxide state ⇄ oxide state

$$\mathrm{Ca_{10}(PO_4)_6(OH)^0_{2\epsilon}Cl_{2(1-\epsilon)}} \overset{\text{vac.}}{\rightleftarrows}$$

$$\mathrm{Ca_{10}(PO_4)_6O_\epsilon^-V_\epsilon^+Cl_{2(1-\epsilon)} + \epsilon H_2O}$$

Oxide state → virgin state

$$\mathrm{Ca_{10}(PO_4)_6O_\epsilon^-V_\epsilon^+Cl_{2(1-\epsilon)} + 2\epsilon HCl \rightarrow}$$

$$\mathrm{Ca_{10}(PO_4)_6Cl_2 + \epsilon H_2O.}$$

Acknowledgements—The aid of C. R. Trzaskos in the *epr* work and of A. M. LaTorre in the sample preparation and in the optical studies on powder samples are acknowledged with thanks

REFERENCES

1. VAN WAZER J. R., In *Phosphorous and Its Compounds*, pp. 530–538. Interscience, New York (1958).
2. KREIDLER E., PhD Thesis, Pennsylvania State University (1967).
3. KAY M. I., YOUNG R. A. and POSNER A. S., *Nature* **204**, 1050 (1964).
4. HENDRICKS S B., JEFFERSON M. E. and MOSELEY V. M., *Z. Kristallogr.* **81**, 352 (1932).
5. MEHMEL M., *Z. Phys. Chem.* **15**, 223 (1932).
6. NARAY-SZABO St., *Z. Kristallogr.* **75**, 387 (1930).
7. BEEVERS C. A. and MACINTYRE D. B., *Mineral Mag.* **27**, 254 (1944–46).
8. YOUNG R. A. and ELLIOT J. C., *Arch. Oral Biol.* **11**, 699 (1966).
9. PRENER J. S., *J. electrochem. Soc.* **114**, 77 (1967).
10. JOHNSON P. D., *J. electrochem. Soc.* **108**, 160 (1961).
11. SWANK, R. K. *Phys. Rev.* **135**, A 266 (1964).
12. PIPER W. W., KRAVITZ L. C. and SWANK R. K., *Phys. Rev.* **138** A 1802 (1965).
13. PIPER W. W., KRAVITZ L. C., SWANK R. K. and PRENER J. S., *Int. Symp. on Color Centers in Alkali Halides*, Abstract No. 149, p. 115. University of Illinois, Urbana, Ill. (1965)
14. JOHNSON P. D., In *Luminescence of Organic and Inorganic Materials* (Edited by H. P. Kallman and G. M. Spruch), pp. 563–575. Wiley, New York (1962).
15. KINGSLEY J. D., PRENER J. S. and SEGALL B., *Phys. Rev.* **137**, A 189 (1965).
16. LUDWIG G. W. and WOODBURY H. H., *Solid State Phys.* **13**, 237 (1963).
17. SCHLEEDE A., MEPPEN B. and JØRGENSEN O. B., *Agnew. Chem.* **52**, 316 (1939).
18. WALLAEYS R., *Ann. Chim.* 7, 108 (1952).
19. BOURRET G., Thesis, La Faculte des Sciences de l'Universite de Toulouse, Toulouse, France (1965).
20. BASS A. M. and CARVIN P., *J. molec. Spectrosc.* **9**, 114 (1962).
21. NAKAMOTO K., MARGOSHES M. and RUNDLE R. E., *J. Am. chem. Soc.* **77**, 6480 (1955).
22. JOHNSON P. D., *J. opt. Soc. Am.* **42**, 978 (1952).
23. FRITZ B., LUTY F. and ANGER J., *Z. Phys.* **174**, 240 (1963).
24. BREDIG M. A., FRANK H. H. and FULDNER H., *Z. Elektrochem.* **39**, 959 (1933).
25. ROLFE J., *Phys. Rev. Lett.* **1**, 56 (1958).

J. Phys. Chem. Solids Pergamon Press 1969. Vol. 30, pp. 1483–1491. Printed in Great Britain.

FLUORESCENCE OF Nd^{3+} IN LITHIUM YTTRIUM FLUORIDE*

A. L. HARMER†, A. LINZ and D. R. GABBE
Center for Materials Science and Engineering and Department of Electrical Engineering, Massachusetts Institute of Technology, Cambridge, 02139, U.S.A.

(*Received* 25 *November* 1968)

Abstract—Crystals of the scheelite structure fluoride $LiYF_4$ have been grown doped with 0·24, 1·4 and 2·2 at. per cent Nd^{3+}. The polarized fluorescence and absorption, excitation spectra, lifetime decay and linewidths have been measured at 77° and 300°K. The optical data of $LiYF_4:Nd^{3+}$ have been compared with data on the isomorphous oxide $CaWO_4:Nd^{3+}$. The spectroscopic features of $LiYF_4:Nd^{3+}$ are: a long lifetime of 500 μsec which decreases rapidly with increasing Nd-concentration; a narrow linewidth of 2 cm^{-1} at 77°K; and a high absorption in the near infrared. These factors have been related to its potential as a laser material.

1. INTRODUCTION

IT IS WELL known that $CaWO_4$ (scheelite) is a good laser host for the trivalent rare earth ions. Lasers based upon the fluorescence of trivalent neodymium are of special interest because the Nd^{3+} ion has a large terminal to ground state splitting of approximately 2000 cm^{-1}. Therefore Nd^{3+} ions can be operated in 'four-level laser mode' having relatively low thresholds, which implies that continuous operation of such a laser is feasible. Laser action based upon the fluorescence of Nd^{3+} was first observed in a calcium tungstate host[1], and Nd^{3+}-doped $CaWO_4$ also served as the first continuously operated solid state laser[2]. Thus, it appeared interesting to examine the fluorescence of Nd^{3+} in other compounds having the scheelite structure, since such studies might suggest new laser materials.

For this study lithium yttrium fluoride ($LiYF_4$) doped with Nd^{3+} has been selected. This compound is isomorphous with $CaWO_4$ [3], with yttrium corresponding to calcium, lithium to tungsten, and fluorine to oxygen. The two lattices have similar cell dimensions: for $LiYF_4$ $a = 5{\cdot}26$ Å, $c = 10{\cdot}94$ Å and for $CaWO_4$, $a = 5{\cdot}21$ Å, $c = 11{\cdot}43$ Å. The substitution of yttrium by neodymium in $LiYF_4$ should be accomplished easily, since the radii, chemical and physical properties of the two ions are very similar. In the case of $CaWO_4$, the substitution of Ca^{2+} by Nd^{3+} requires some form of charge compensation [4]. This produces a distortion of the crystal field around the Nd^{3+} ions, which results in shorter radiative lifetimes, broader linewidths and extra lines which appear in the fluorescent spectrum[5]. These effects, which usually have an adverse influence on laser performance, should be absent in Nd^{3+}-doped $LiYF_4$. In this paper, the fluorescence, absorption and excitation spectra and lifetime decay of $LiYF_4:Nd^{3+}$ are presented and compared with data of $CaWO_4:Nd^{3+}$. These measurements have also been related to the potential of $LiYF_4:Nd^{3+}$ as a laser material.

2. CRYSTAL GROWTH

Crystals of $LiYF_4$ doped with Nd^{3+} were grown from the melt in a helium atmosphere by a modified Czochralski method. The phase diagram[3] for the system LiF-YF_3 shows the compound $LiYF_4$ has a peritectic point at 49 mole % YF_3 and 819°C, and a eutectic point at 19 mole % YF_3 and 695°C. Starting materials were anhydrous YF_3 and NdF_3 (from American Potash and Chemical Corporation) dried in a hydrofluorination tube furnace, and LiF in the form of single crystal chips (from Harshaw Chemical Company). Melt compositions ranged from 45 to 48 mole % total rare earth fluoride. A modified National Research Corporation Model 2804 pulling furnace was used. Details of the technique are described elsewhere [6]. Samples were grown with different Nd^{3+} melt concentrations of 5, 2 and 0·5 at. %. The actual concentration of Nd^{3+} present in the crystals was found by spectrographic analysis to be 2·2, 1·4 and 0·24 at. % respectively. Samples for spectroscopic measurements, measuring about 1·5 cm cube, were cut from the boules and oriented by Laue back reflection photographs.

---

*This work was supported by the Advanced Research Projects Agency under contract SD-90, and MITHRAS, a division of Sanders Associates, Inc. under prime contract with the Night Vision Laboratory, USAERDL, Fort Belvoir, Virginia.

†Submitted in partial fulfillment of the requirements for the degree of Master of Science in Electrical Engineering at the Massachusetts Institute of Technology. *Present address:* Clarendon Laboratory, Oxford, England.

3. EXPERIMENTAL RESULTS

(A) *Fluorescence spectra*

Continuous fluorescence was excited with light from a BH6 General Electric 1000 W mercury lamp filtered by a 10 cm thick saturated solution of $CuSO_4$. Fluorescent spectra were recorded with a Jarrell-Ash $\frac{1}{2}$ m spectrometer with a resolution of 3 Å, and a Glan prism was used to separate the different polarizations of the emitted light. The data were corrected for photomultiplier response, grating efficiency and polarization effects.

The near infrared emission spectra were examined in the two regions from 10,400 to 10,800 Å and from 8600 to 9100 Å. These correspond respectively, to transitions from the $^4F_{3/2}$ state to the $^4I_{11/2}$ and $^4I_{9/2}$ ground multiplets. The fluorescent spectra at 77°K and 300°K are shown in Figs. 1–4 for both polarizations: σ-spectrum ($E \perp c$) and π-spectrum ($E \parallel c$). The axial spectrum was found to be identical to the σ-spectrum showing that all the transitions are electric dipole type.

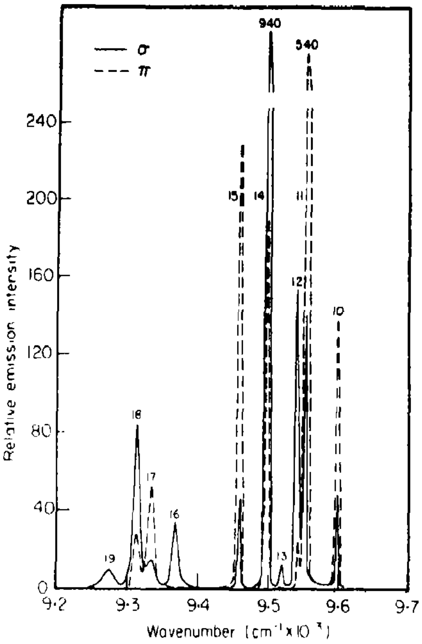

Fig. 1. Fluorescent spectrum of $^4F_{3/2} \rightarrow {}^4I_{11/2}$ transition of $LiYF_4$: 1·4 at. % Nd at 77°K.

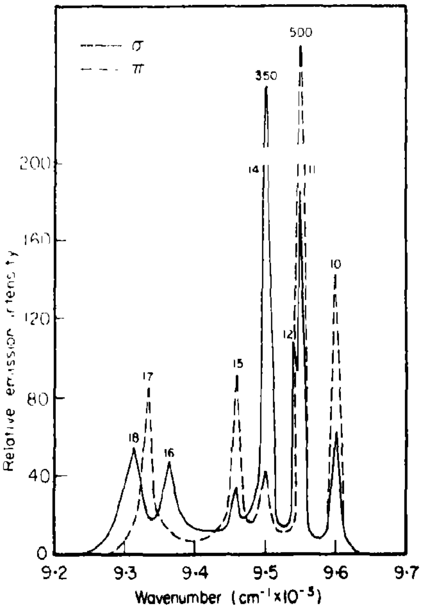

Fig. 2. Fluorescent spectrum of $^4F_{3/2} \rightarrow {}^4I_{11/2}$ transition of $LiYF_4$: 1·4 at. % Nd at 300°K.

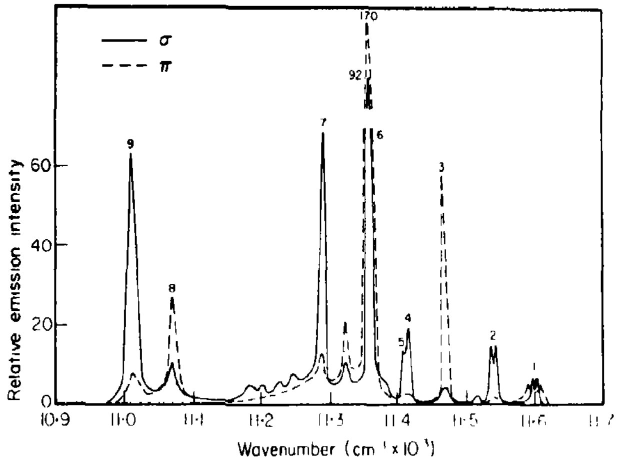

Fig. 3. Fluorescent spectrum of $^4F_{3/2} \rightarrow {}^4I_{9/2}$ transition of $LiYF_4$: 1·4 at. % Nd at 77°K.

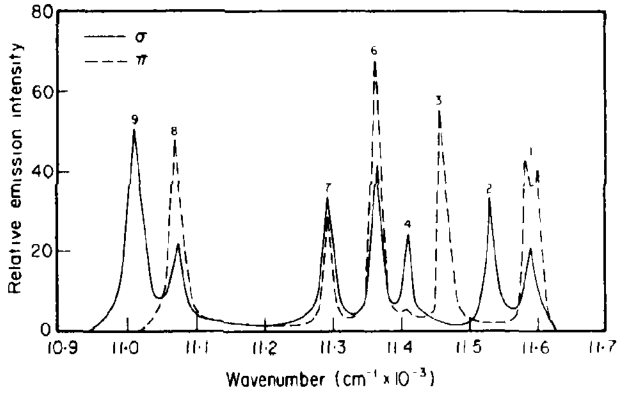

Fig. 4. Fluorescent spectrum of $^4F_{3/2} \rightarrow {}^4I_{9/2}$ transition of $LiYF_4$: 1·4 at. % Nd at 300°K.

Lines appearing in the $^4F_{3/2} \rightarrow {}^4I_{11/2}$ spectra generally have a much greater intensity than lines in the $^4F_{3/2} \rightarrow {}^4I_{9/2}$ spectra. The strongest line at 300°K occurs at 9548 cm^{-1}. The strongest line at 77°K occurs at 9497 cm^{-1}. At low temperatures a 'satellite' line appears on either side of this line. With 2·2 % Nd^{3+} doping the intensities of these satellites relative to the main line (9499 cm^{-1}) at 20°K were 0·33 for the line at 9496 cm^{-1} and 0·13 for the line at 9501 cm^{-1}. The linewidth of the main line at 9497 cm^{-1} (σ-polarization) decreases from 12 cm^{-1} at 300°K to 2 cm^{-1} at 77°K. The line shifts to higher energies by 3 cm^{-1} between 300° and 77°K. The linewidth does not seem to increase appreciably with increasing Nd doping concentration; it has the value 2·0 cm^{-1} for 0·24% Nd^{3+} doping and 2·3 cm^{-1} for 2·2 % Nd^{3+} doping, at 77°K.

In the $^4F_{3/2} \rightarrow {}^4I_{9/2}$ fluorescent spectra the lines at 11,599 and 11,538 cm^{-1} are split into doublets. The splitting is larger in the π-polarization, is independent of temperature and increases linearly with Nd doping concentration. The splitting is much larger than the splitting of the satellite lines, being 20 cm^{-1} for 2·2 % Nd doping. Some degree of quenching of fluorescent emission was found to occur in the more heavily doped samples. The mean ratio of fluorescent intensity was found to be 1:4·9:5·3 for 0·24:1·4:2·2 % Nd doping concentrations.

(B) *Absorption and excitation spectra*

Polarized absorption spectra were recorded with a Cary 14R spectrophotometer. The absorption spectra for σ and π polarizations at 300°K are given in Figs. 5 and 6. The level assignments have been made by comparison with the calculated $4f^3$ energy levels in the free ion[7, 8] and the observed energy levels of Nd^{3+} in $CaWO_4$[9]. The strongest absorption occurs in the near infrared in the groups $^4I_{9/2}$–$^4F_{5/2}$, $^4H_{9/2}$ and $^4I_{9/2}$–$^4F_{7/2}$, $^4S_{3/2}$, which are responsible for over 50 per cent of the total absorption.

Excitation spectra were recorded with a modified form of the continuous fluorescence apparatus. The exciting light was obtained from an Orion 1000 W xenon lamp passed through a ¼ m Bausch and Lomb monochromator (resolution 55 Å). Repetitive scanning of the exciting source, and sampling with a Technical Measurements Corporation CAT 1000 computer was used. The excitation spectra for the fluorescent line at 9497 cm^{-1} are given in Fig. 7. Considerable inaccuracy is present at the red end of the spectrum due to difficulty in normalization because of the structure of the xenon lamp output. However, the curves show that the most efficient energy transfer occurs in the three bands in the infrared which are responsible for 70 per cent of the total fluorescent emission.

(C) *Fluorescent lifetime*

Fluorescent lifetime decay under pulsed excitation was measured using a short light pulse from an E. G. and G. FX-33 xenon flashtube. Repetitive sampling employing a CAT 1000 computer was used to increase the signal-to-noise ratio. The variation of observed fluorescent lifetime of the $^4F_{3/2}$ level with Nd concentration, for $LiYF_4:Nd^{3+}$ at 77°K is shown in Fig. 8. The total error in each reading is ±1 per cent. The lifetime decreases approximately linearly with increasing Nd-doping concentration; from 570 μsec for 0·24% Nd^{3+} doping to 420 μsec for 2·2% Nd^{3+} doping. The lifetime at 300°K was found to be the same at 77°K, except that the lifetime of the sample containing

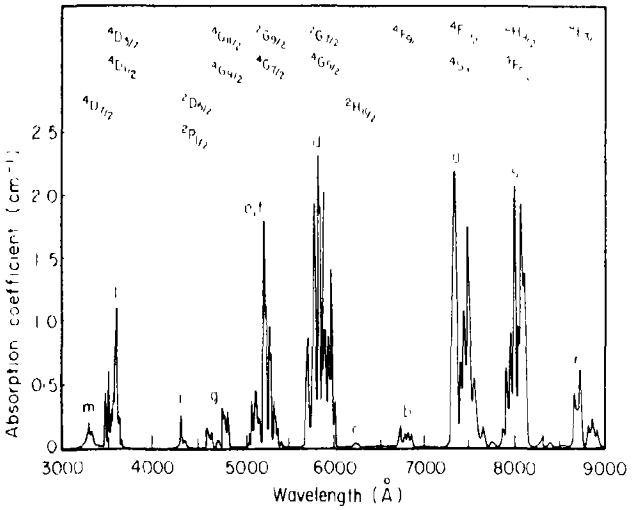

Fig. 5. Absorption spectrum for σ-polarization of $LiYF_4$:2·2 at. % Nd at 300°K.

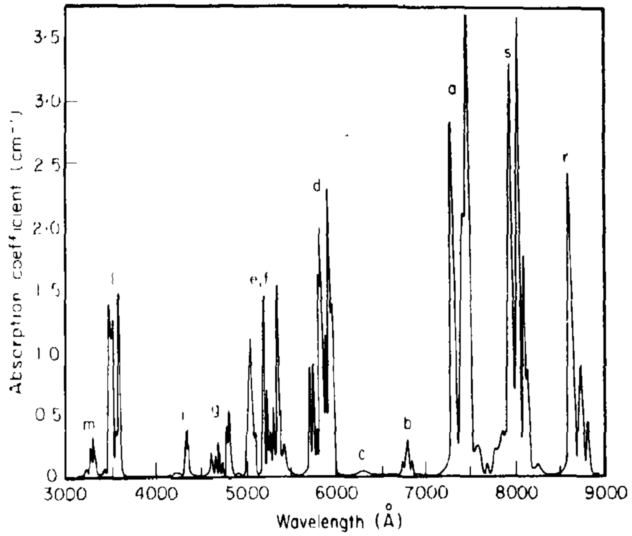

Fig. 6. Absorption spectrum for π-polarization of LiYF$_4$:2·2 at. % Nd at 300°K.

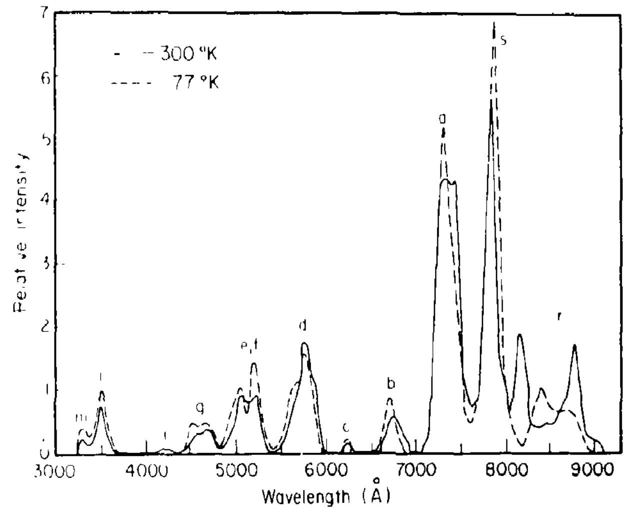

Fig. 7. Excitation spectra of 9497 cm^{-1} line in LiYF$_4$: 1·4 at % Nd

2·2% Nd^{3+} was longer at 300°K (440 μsec) than at 77°K (420 μsec). Figure 8 also shows the variation of lifetime for CaWO$_4$:Nd^{3+}: Na$^+$ [10] and LaF$_3$:Nd^{3+} [11], at 77°K.

4. DISCUSSION

Energy level diagram

The similarity of the fluorescent spectra for CaWO$_4$:Nd^{3+} [9, 12] and LiYF$_4$:Nd^{3+} shows that the Nd^{3+} ion is present in the same environment in both lattices. Thus the crystal field splitting of Nd^{3+} in LiYF$_4$ shown in Fig. 9. was derived by comparison with CaWO$_4$:Nd^{3+} [9, 12]. The splitting of the $^4F_{3/2}$ level is temperature dependent, having the value 59·5 ± 0·6 cm^{-1} at 77°K and 54·8 ± 0·6 cm^{-1} at 300°K. The center of gravity of the $^4F_{3/2}$ term is situated 130 cm^{-1}

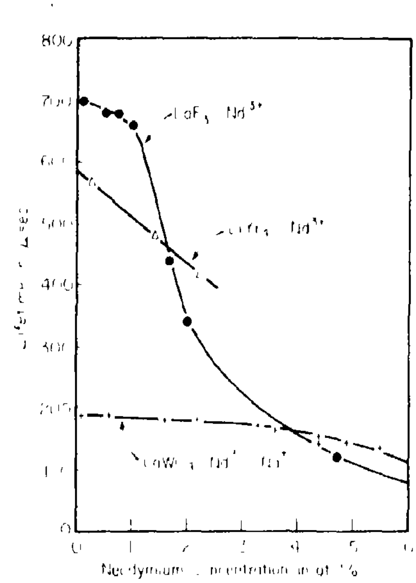

Fig. 8. Variation of fluorescent lifetime of $^4F_{3/2}$ level with Nd^{3+} concentration for LiYF$_4$:Nd^{3+}, CaWO$_4$:Nd^{3+} [10] and LaF$_3$:Nd^{3+} [11] at 77°K

higher in LiYF$_4$:Nd^{3+} than in CaWO$_4$:Nd^{3+}. The total splitting of the $^4I_{9/2}$ and $^4I_{11/2}$ is also greater in LiYF$_4$:Nd^{3+} but the splitting of the $^4F_{3/2}$ level is smaller. These results seem to indicate that the Nd^{3+} ion in LiYF$_4$ is situated in a stronger crystal field associated with the first coordination sphere of fluorine atoms around the Nd^{3+} ion.

Comparison with CaWO$_4$:Nd^{3+}

The fluorescent spectra of Nd^{3+} in CaWO$_4$ and LiYF$_4$ are very similar[9, 12]. Additional lines have been observed in the spectra of CaWO$_4$:Nd^{3+} which vary in intensity in crystals with different charge compensation [13] and can therefore be attributed to a disturbance of the crystal field around the Nd^{3+} ion by the form of charge compensation used. In CaWO$_4$:Nd^{3+} the linewidths are considerably broader (5·3 cm^{-1} at 77°K) than in LiYF$_4$:Nd^{3+}, and increase with increasing Nd^{3+} concentration[4]. This may be partly due to inhomogeneities of the crystal field produced by charge compensation, but may also be due to exchange effects. Further evidence for exchange effects is provided by the satellite lines which are observed at low temperatures around the main fluorescent line in LiYF$_4$:Nd^{3+}. These also occur in CaWO$_4$:Nd^{3+} with roughly the same intensity, and have been shown to be a direct result of Nd–Nd interaction[4]. Concentration quenching of fluorescent emission may also be attributed to exchange interaction between the Nd^{3+} ions. The splitting of the lines at 11,599 and 11,538 cm^{-1} in the $^4F_{3/2}-{}^4I_{9/2}$ fluorescent spectrum for LiYF$_4$:Nd^{3+} were also observed in CaWO$_4$:Nd^{3+}. These may possibly be due to Nd–Nd interaction but the energy splitting

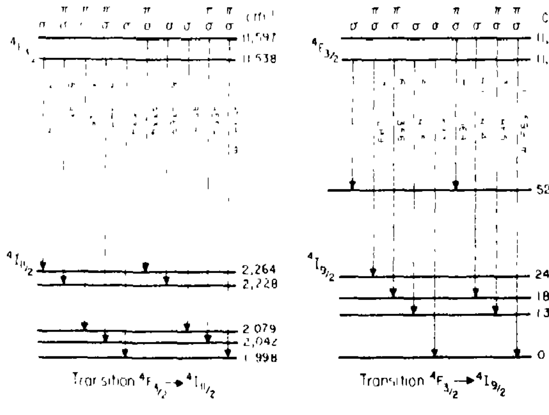

Fig. 9. Observed fluorescence transitions of Nd^{3+} in LiYF$_4$ at 77°K.

of 20 cm^{-1} is much greater than would be expected from exchange effects as indicated by the satellite lines.

The absorption and excitation spectra show important differences between $LiYF_4:Nd^{3+}$ and $CaWO_4:Nd^{3+}$. In $CaWO_4:Nd^{3+}$ absorption in the near infrared is much weaker and the two bands $^4I_{9/2} \rightarrow {}^4F_{5/2}$, $^2H_{9/2}$ and $^4I_{9/2} \rightarrow {}^4F_{7/2}$, $^4S_{3/2}$ contribute only 30 per cent of the total absorption between 3000 and 9000 A. In $LiYF_4:Nd^{3+}$ these bands are much more pronounced and are responsible for over 50 per cent of the total absorption. In $CaWO_4:Nd^{3+}$ the single group $^4I_{9/2} \rightarrow {}^2G_{7/2}$ contributes over 40 per cent. These differences are also exhibited in the excitation spectra. A comparison of the excitation spectra of $LiYF_4:Nd^{3+}$ with $CaWO_4:Nd^{3+}$ and $YAG:Nd^{3+}$[14] shows that YAG and $LiYF_4$ are alike since the absorption bands in the near infrared produce the greatest fluorescent output. In $CaWO_4:Nd^{3+}$ these bands are less pronounced and the broad absorption at 5800 A is responsible for the largest single contribution to the emitted fluorescence.

The variation of lifetime of the excited $^4F_{3/2}$ state with neodymium doping concentration also shows important differences between $LiYF_4:Nd^{3+}$ and $CaWO_4:Nd^{3+}$. The lifetime in $LiYF_4:Nd^{3+}$ is considerably longer than in $CaWO_4:Nd^{3+}$[10] or in other scheelite structure oxides[15]. The rate of decrease with increasing Nd concentration is considerably greater in $LiYF_4$ than in $CaWO_4$ but less than in LaF_3. The decrease of lifetime in LaF_3 was explained by cross relaxation[11]. This mechanism may also account for the behavior in $LiYF_4$, but a detailed analysis of all the levels of the ground multiplets is necessary to establish this argument. The different lifetimes exhibited by these materials have an important effect on laser performance. A long lifetime is useful for Q-switched laser operation but a rapidly decreasing lifetime for increasing Nd concentration implies that the performance declines rapidly at high impurity doping levels.

Potential use as a laser material

Consideration of the basic physical and optical properties of $LiYF_4:Nd^{3+}$ indicates its suitability as a prospective laser material. The host material is chemically stable and can be grown as rods of a reasonable length with good optical quality. The Nd^{3+} ion in $LiYF_4$ exists in a more homogeneous environment than in $CaWO_4$. This gives rise to a narrower linewidth which should produce a lower value of threshold. The lifetime of the $^4F_{3/2}$ level is three times longer in $LiYF_4:Nd^{3+}$ than in $CaWO_4:Nd^{3+}$ which is a desirable feature in Q-switched laser operation. The heavy absorption bands in the near infrared should result in lower thresholds for $LiYF_4:Nd^{3+}$ with cw xenon or tungsten lamp pumping, whereas with a xenon flashlamp pulsed at high current densities a better spectral match would be obtained in $CaWO_4:Nd^{3+}$ due to heavy absorption at 5800 A.

An estimate of the laser transition cross section was obtained by using a method employed by Neeland and Evtuhov[16]. In this method the radiative fluorescent lifetime for the laser transition is calculated from the total radiative lifetime of the fluorescent level and the branching ratio, i.e., the ratio of the photon rate for the laser transition only to the photon rate of all transitions originating from either of the $^4F_{3/2}$ levels. For $LiYF_4$:2·2% Nd^{3+} at 300°K, the branching ratio determined from the fluorescent spectra for the line at 10,530 A was 0·173. This gives a radiative lifetime for the laser transition of 1110 μsec. The laser transition cross section is given by

$$\sigma = \lambda^2/4\pi^2 n^2 \tau_l \Delta\nu$$

where λ is the laser wavelength, n is the refractive index, τ_l is the radiative lifetime for the laser transition, and $\Delta\nu$ is the linewidth. Taking $\lambda = 10{,}530$ A, $n = 1{\cdot}46$ and $\Delta\nu = 12{\cdot}5$ cm^{-1}, the equation gives $\sigma = 3{\cdot}2 \times 10^{-19} cm^2$.

This is only an estimate, since the branching ration was determined neglecting transitions from ${}^4F_{3/2}$ to ${}^4I_{13/2}$ and ${}^4I_{15/2}$. However, this should only affect the result by 15 per cent and the calculated cross section is probably accurate to within 30 per cent[17]. This estimated value for the laser transition cross section compares favorably with that of YAG[17] ($8{\cdot}8 \times 10^{-19}$ cm^2) or Nd-doped glass[18]. All these considerations suggest that $LiYF_4$:Nd^{3+} should be a reasonably efficient laser material.

Stimulated emission with pulsed optical pumping has been observed in $LiYF_4$:Nd^{3+} [19]. Laser oscillations occur at 10,530 A (σ-polarization) and 10,471 A (π-polarization). These originate from the lower and upper levels respectively of the ${}^4F_{3/2}$ state and terminate on the level at 2042 cm^{-1} of the ${}^4I_{11/2}$ state. These are also the strongest laser transitions in $CaWO_4$:Nd^{3+} and terminate on the equivalent level situated at 2016 cm^{-1}. Laser action in $CaWO_4$:Nd^{3+} has been examined extensively, and both pulsed and continuous operation have been achieved [1, 2, 9, 12]. The preliminary laser measurements of $LiYF_4$:Nd^{3+}[19] although made on lightly-doped rods or specimens of poor optical quality, nevertheless indicate that it is a high-gain material with a low threshold. However, it is difficult to compare the laser performance of $LiYF_4$:Nd^{3+} with $CaWO_4$:Nd^{3+}, since for a valid comparison the measurements must be made under the same conditions.

Various possibilities can be suggested for the development of other laser materials. The presence of a trivalent site in the lattice allows the possibility of double doping with other rare earths. Energy transfer has been observed from Ce^{3+} – Nd^{3+} in CeF_3[20], and thus it is possible that addition of Ce^{3+} to $LiYF_4$:Nd^{3+} would produce enhanced emission. Other materials of the form $LiMF_4$, where M is a trivalent rare earth, exist[3], and investigation of these compounds doped with Nd^{3+} might yield new laser materials.

5. SUMMARY

The absorption and emission spectra of $LiYF_4$:Nd^{3+} have been studied at 77° and 300°K and compared with corresponding data of $CaWO_4$:Nd^{3+}, which has a similar crystal structure. The near i.r. fluorescent spectrum corresponding to transitions from the ${}^4F_{3/2}$ level to the ${}^4I_{9/2}$ and ${}^4I_{11/2}$ terms of the ground multiplet was used to determine the crystal field splittings of these terms. These results seem to indicate that the Nd^{3+} ion is situated in a stronger field in $LiYF_4$. Evidence of exchange effects is provided by concentration quenching of the fluorescent emission above 1·4% Nd doping, and the presence of satellite lines.

Several features of $LiYF_4$:Nd^{3+} indicate its suitability as a prospective laser material. A long lifetime (three times as long as that observed in other scheelites) was found for the fluorescent decay. The linewidth of fluorescent emission is narrower in $LiYF_4$:Nd^{3+} than in $CaWO_4$:Nd^{3+} probably due to a more homogeneous crystal field. The excitation spectra showed that a higher percentage of the output radiation in $LiYF_4$:Nd^{3+} is derived from absorbed energy in the strong absorption bands in the near infrared. An estimate of the laser transition cross section gave $3{\cdot}2 \times 10^{-19}$ cm^2.

Acknowledgements – The authors wish to thank J. Kalnajs and K. Bangerskis for technical assistance, and C. S. Naiman and B. DiBartolo for helpful discussions. We are also grateful to A. Hook, L. Gillespie, G. M. Janney and F. Sharp of the Night Vision Laboratory for helpful discussion and assistance as well as the use of their laser facilities.

REFERENCES

1. JOHNSON L. F. and NASSAU K., *Proc. Instn Radio Engrs* **49**, 1704 (1961).
2. JOHNSON L. F., BOYD G. D., NASSAU K. and SODEN R. R., *Phys. Rev.* **126**, 1406 (1962).
3. THOMA R. E., WEAVER C. F., FRIEDMAN H. A., INSLEY H., HARRIS L. A. and YAKEL H. A., *J. phys. Chem.* **65**, 1096 (1961).
4. JOHNSON L. F., In *Quantum Electronics III* (Edited by N. Bloembergen and P. Grivet), Vol. 2, p. 1021. Columbia University Press, New York (1964).
5. VAN UITERT L. G., In *Luminescence of Inorganic Solids* (Edited by P. Goldberg), p. 465. Academic Press, New York (1966).

6. GABBE D. and HARMER A. L., In *Proc. Int. Conf. Crystal Growth*. Birmingham, England (1968) and to be published in *Intl. J. Crystal Growth*.
7. WYBOURNE B. G., *J. chem. Phys.* **32**, 639 (1960).
8. CARLSON E. and DIEKE G. H., *J. chem. Phys.* **34**, 1602 (1961)
9. JOHNSON L. F., *J. appl. Phys.* **34**, 897 (1963).
10. Data of M. Peterson quoted by NASSAU K., In *Optical Masers* (Edited by J. Fox), p. 451. Polytechnic Press, New York (1963).
11. ASAWA C. K. and ROBINSON M., *Phys. Rev.* **141**, 251 (1966)
12. JOHNSON L. F. and THOMAS R. A., *Phys. Rev.* **131**, 2038 (1963)
13. FEOFILOV P. P., KARISS Ya. E. and MOROZOV A. M., *Optika Spectrosk.* **17**, 481 (1964).
14. BRANDWIE R. A. and TELK C. L., *J. opt. Soc. Am.* **57**, 1221 (1967)
15. MOROZOV A. M., TOLSTOI M. N. and FEOFILOV P. P., *Optika Spectrosk.* **22**, 139 (1967)
16. NEELAND J. K. and EVTUHOV V., *Phys. Rev.* **156**, 244 (1967).
17. KUSHIDA T., MARCOS H. M. and GEUSIC J. E., *Phys. Rev.* **167**, 289 (1968).
18. MAUER P., *Appl. Optics* **3**, 433 (1964)
19. HARMER A. L., LINZ A., GABBE D., GILLESPIE L., JANNEY G. M. and SHARP E., *Bull. Am. Phys. Soc.* **12**, 1068 (1967) and to be published.
20. O'CONNOR J. R. and HARGREAVES W. A., *Appl. Phys. Lett.* **4**, 208 (1964)

J. Phys. Chem. Solids Pergamon Press 1969. Vol. 30, pp. 1493–1505. Printed in Great Britain.

VIBRATIONAL ABSORPTION OF CARBON AND CARBON–OXYGEN COMPLEXES IN SILICON

R. C. NEWMAN and R. S. SMITH*
J. J. Thomson Physical Laboratory, University of Reading, Berks., England

(*Received* 25 *November* 1968)

Abstract – Vibrational absorption of isolated carbon and carbon–oxygen complexes has been studied in silicon containing various carbon isotopes. The energies of the isolated carbon fundamentals and second harmonics have been determined at 290° and 77°K and compared with the corresponding results for boron. The strength of the local mode absorption has been remeasured and the high value of $\eta_0 \simeq 2{\cdot}5e$ has been confirmed. A search has been made for band mode absorption due to carbon with essentially negative results; this fits in with current theoretical ideas on long range impurity induced polarization effects in silicon.

Satellite lines near the carbon fundamental at 588, 640 and 690 cm^{-1} for ^{12}C and corresponding lines for ^{13}C and ^{14}C have been correlated in strength with satellite lines at 1104 and 1052 cm^{-1}. The latter lines show no splitting or broadening at 4·2°K when different carbon isotopes are present and it is concluded that they are due to vibrations of oxygen in a centre where the rotational motion is quenched. Detailed models of possible C–O pair structures are discussed and compared with isolated oxygen and Li–O centres. It is concluded that the carbon atom in the pair probably occupies a second or third neighbour site to the interstitial oxygen.

1. INTRODUCTION

In a previous paper [1], results were presented for the infra-red absorption due to the localized modes of vibration of isolated carbon impurity atoms in silicon single crystals. The energies of the fundamental modes were obtained for the three isotopes ^{12}C, ^{13}C and ^{14}C at room temperature and 77°K and weak second harmonics were observed for ^{12}C and ^{13}C at 63°K. A surprising result was the very strong local mode absorption due to the neutral carbon impurities, determined in samples containing radioactive ^{14}C. This absorption was about five times greater than that measured for B$^-$ ions in an equivalent concentration in compensated silicon crystals [2]. In this latter material, appreciable absorption also occurs in the band mode region [2, 3] in qualitative agreement with the theoretical predictions of Dawber and Elliott[4, 5]; in particular, there is a fairly sharp absorption peak at an energy slightly less than that of the Raman frequency as well as other features at still lower energies[2, 3]. No similar absorption was obviously present in the crystals containing carbon[1] although this region of the spectrum was not investigated in any detail.

In the theory of Dawber and Elliott[4,5], the coupling of the one phonon spectrum to the incident radiation is assumed to result from a static charge on the impurity atom. For example, boron would be present as B$^-$ ions in material compensated with an equal concentration of a donor impurity such as phosphorus. Clearly this theory is inadequate to explain the absorption arising from neutral impurities. Other recent theoretical models have taken into account charge sharing between the impurity and its neighbour and polarization effects of the host lattice [6–9]. These models give better agreement with experimental measurements of the magnitude of the infra-red absorption[8, 9] in samples containing boron and phosphorus, than the simpler theory of Dawber and Elliott. In addition, some consideration has been given to the problem of absorption from carbon atoms[9]. In view of this current interest, the strength of the local mode absorption bands due to carbon in silicon have been remeasured and a search has been made for band mode absorption, with particular emphasis on the region near the Raman frequency.

---

*Now at Allen Clark Research Centre, The Plessey Company Limited, Caswell, Towcester, Northants.

Another previous result[1] was the observation of a new absorption band at 1104 cm^{-1} (77°K) in samples which contained both carbon and oxygen. This band, which was tentatively ascribed to a vibrational mode of a complex involving the two impurities, has also been observed more recently by Pajot and Deltour[10] in a detailed investigation of the structure of the 9μ oxygen band[11–14]. Although carbon was not detected spectroscopically, chemical analysis of their samples showed it to be present in a high concentration. Modifications of the vibrational modes of an isolated oxygen atom are to be expected if a carbon impurity occupies a neighbouring site, thus providing a possible explanation of the observations. Similarly, modifications of the vibrations of the paired carbon atom would be expected and should lead to the formation of weak satellite lines in the region of the carbon local mode fundamentals. Observation of such structure would then essentially confirm the existence of carbon–oxygen pairs. Absorption lines in this region have now been detected and correlated in strength with the line at 1104 cm^{-1}. Consequently, a detailed discussion will be given for possible models of carbon–oxygen complexes.

2. EXPERIMENTAL

2.1 *Description of crystals*

The samples used in this investigation were kindly made available to us by the A.E.I. Central Research Laboratory and in some cases were the same as those used previously [1]. Pulled monocrystals doped with barium carbonate contained about 10^{18} cm^{-3} oxygen atoms and a variable concentration of carbon up to about 2×10^{18} cm^{-3}. These crystals contained less than 3×10^{14} cm^{-3} (limit of detection) of barium as determined by neutron activation analysis and had room temperature p-type resistivities in the range 5–50 Ω cm. Some of these samples with the lower resistivities showed a small amount of free carrier absorption at room temperature and also bands in the region of 34μ (77°K) which were identified with electronic transitions of boron impurities[15, 16]. It will be shown that new electronic transitions also occur near 15μ and 14·5μ from an unknown centre; however the total acceptor impurity content estimated from the integrated absorption in all these electronic lines was always consistent with the measured room temperature resistivity. These pulled crystals contained either naturally occurring carbon (1·1% ^{13}C), ^{12}C and ^{14}C in approximately equal concentrations, or ^{12}C and ^{14}C in a ratio of 2:1. Samples containing natural carbon but no measurable amount of oxygen grown by a meltback technique in vacuum were also examined.

2.2 *Determination of ^{14}C concentrations*

A thin window Geiger tube was used to count the emitted β-particles from both sides of each sample examined (a typical thickness was about 0·2 cm) and the average count rate R_{Si} was thus determined. Using the same geometry, a corresponding count rate R_{st} was obtained from a standard polymer source 0·77 mm in thickness. The rate R from either type of sample containing a concentration of ^{14}C of [C] is then given by

$$R = A\int_0^\infty [\mathrm{C}]f(x)\,\mathrm{d}x \qquad (1)$$

where A is a constant depending upon the geometry of the arrangement and $f(x)$ is the attenuation function for self absorption for β-particles originating from a layer of thickness dx at a depth x below the surface; the upper limit of infinity in the integral is justified because the samples were much thicker than the range of the β-particles. It has been shown that $f(x\rho)$ is independent of the particular material being investigated[17], where ρ is its density. Since [C] is essentially constant in a given silicon sample the following simple relation is obtained

$$[^{14}\mathrm{C}]_{Si} = \left(\frac{R_{Si}}{R_{St}}\right)\left(\frac{\rho_{Si}}{\rho_{St}}\right)[^{14}\mathrm{C}]_{St} \qquad (2)$$

providing small back-scattering corrections are ignored. From the quoted activity of the standard of 10·2 μC/gm and its measured density of 1·146 gm/cm^3, a value of 1·17 × 10^{17} atom cm^{-3} is deduced for $[^{14}\mathrm{C}]_{St}$, thus allowing $[^{14}\mathrm{C}]_{Si}$ to be determined for each sample.

2.3 *Infra-red absorption measurements*

Standard transmission measurements were made on samples at 290°C, 77°K and 4·2°K with a double beam grating Grubb Parsons Spectromaster instrument in the range 1–25 μ with a limiting resolution of about 1 cm^{-1} in the region of 9 μ and 2 cm^{-1} in the region of 17 μ. The instrument was flushed with dry air or nitrogen gas to minimise effects due to atmospheric absorption and was calibrated with various standard gases. Preliminary measurements at 290°K and 77°K have also been carried out by Devine with a high resolution grating instrument operating in vacuum over the wavelength range 16–100 μ.

Most measurements in the 1–25 μ region were however made by a differential technique with a high purity floating-zone silicon sample, or other samples as discussed below, in the reference beam of the spectrometer; the samples were cooled in separate cryostats for measurements at 77°K. The sample apertures were set up (without the samples) and an attenuator in the sample beam was adjusted to give a 100 per cent transmission reading on the recorder. The two samples of the same thickness d were then inserted and the relative transmission is given by

$$\frac{T}{T_{Si}} = \exp(-\alpha' d)\frac{1-R^2\exp[-2\alpha d]}{1-R^2\exp[-2(\alpha+\alpha')d]} \qquad (3)$$

where $R = 0{\cdot}3$ is the reflection coefficient for silicon and α and α' are the absorption coefficients due to intrinsic and impurity effects respectively. α' may be written as $\alpha' = \alpha_B + \alpha_L$ where α_B is a slowly varying function of wavelength, due for example, to free carrier absorption and α_L is due to absorption in a line. If α_B is negligible, as was the case in most of our samples, the intrinsic lattice absorption is completely eliminated from the recorded spectrum. Since α is known as a function of wavelength [18], it is a simple matter to compute α_L. The relative transmission could be usefully magnified instrumentally by a factor of up to ten and this allowed weak bands with an absorption coefficient of 0·025 cm^{-1} to be detected for the sample thickness of 0·2 cm used in this work.

3. DETAILS OF SPECTRA

3.1 *Absorption from isolated carbon impurities*

The energies of the fundamental modes for the three carbon isotopes were determined at 290°K and 77°K in a large number of samples and are given in Table 1. Previously, discrepencies were found in the position of the ^{12}C line depending upon which other isotopes were present [1]; no such effects were observed in the present work, presumably because of the higher instrumental resolution used. Corresponding results for the second harmonic absorption lines which had a strength relative to the fundamentals of 1·5 per cent are also given in Table 1. These lines were easily detectable, even at room temper-

Table 1. I.R. absorption energies for isolated carbon in silicon

Temp.	Line	ω(cm^{-1}) C^{12}	 C^{13}	 C^{14}	Δω cm^{-1}
290°K	Fundamental	604·9	586·3	570·3	5·9
	2nd harmonic	1205·8	1169·0		10
77°K	Fundamental	607·5	589·1	572·8	1·8*
	2nd harmonic	1211·1	1174·5		5·3
4·2°K	2nd harmonic	1211·4	1174·4		3·7

*Possibly instrumentally limited

ature, when the expanded differential technique was used as shown in Fig. 1. No data are available for the ^{14}C second harmonic line as its position at 1141·8 cm^{-1}, estimated from the results for ^{12}C and ^{13}C, lies on the side of the very intense structure due to oxygen in the 9μ region.

The strengths of the band for ^{14}C, taken as the product of peak absorption coefficient multiplied by the half width of the line, were determined at room temperature and 77°K for four samples and are shown in Fig. 2 as a function of the ^{14}C concentration (equation (2)). When the linewidth is taken into account the results at room temperature are very similar to those reported previously[1].

Attempts to detect measurable absorption at energies just below the Raman frequency [19] of 523 cm^{-1} due to the presence of carbon all produced negative results. These measurements were made at room temperature on (1) a sample containing ^{12}C in a concentration of 9×10^{17} atoms cm^{-3} (^{14}C calibration) but no measurable quantity of oxygen (9μ band at 77°K); and (2) on a sample containing ^{12}C and ^{13}C in a total concentration of $1{\cdot}6\times10^{18}$ cm^{-3} together with 10^{18} atom cm^{-3} of oxygen, measured differentially with respect to a reference sample having an identical oxygen content but a very low carbon concentration. In the latter experiment, the bands at 19·5 and 9μ associated with the normal interstitial oxygen centre [10–14], were completely eliminated (see Fig. 3 for 9μ region). These results indicate that any band mode absorption, due to carbon, in the region of the spectrum from 450 to 523 cm^{-1} must have an absorption coefficient of less than 0·03 cm^{-1} when the integrated absorption in the local mode region is 90 cm^{-2}.

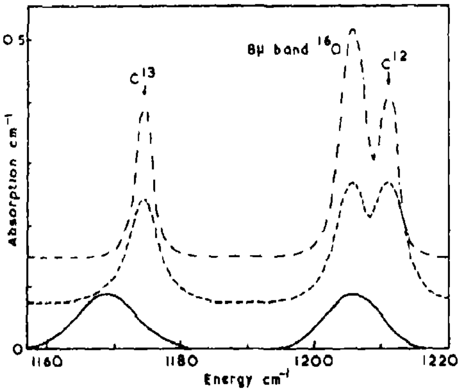

Fig. 1 Second harmonic absorption due to isolated ^{12}C and ^{13}C impurities and the 8μ oxygen band; ——293°K, --- 77°K, ---- 4·2°K; the zero of absorption for the low temperature results is displaced upwards for the purposes of clarity

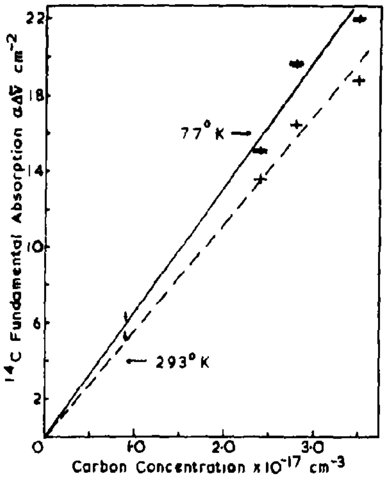

Fig. 2 Strength of the ^{14}C fundamental absorption band vs. ^{14}C concentration; —77°K, ---293°K.

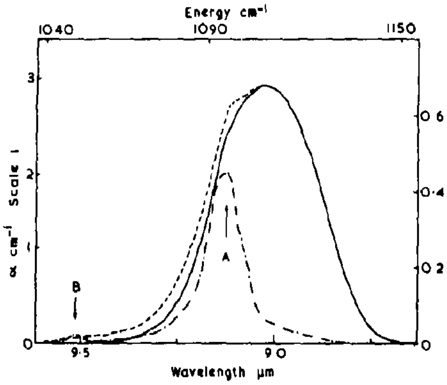

Fig. 3. Differential absorption spectrum in the 9μ oxygen region at room temperature;——sample (a) containing 10^{18} oxygen/cm^3 and no carbon versus undoped floating zone crystal;---sample (b) containing 10^{18} oxygen/cm^3 and $1{\cdot}6\times10^{18}$ carbon (^{12}C+^{13}C)/cm^3 vs. undoped floating zone crystal,---- differential spectrum between (b) and (a) showing lines A and B, right hand Scale applies to this spectrum.

Results of a preliminary investigation carried out by Devine have shown that any absorption lines due to carbon in the band region are in fact very small ($\alpha < 0{\cdot}1\ \mathrm{cm}^{-1}$) in the whole spectral range from 100–500 cm^{-1}.

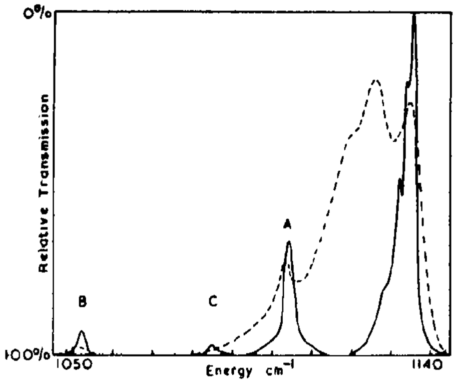

Fig. 4. Relative transmission of a sample containing 10^{18} oxygen/cm^3 and $1{\cdot}6 \times 10^{18}$ carbon ($^{12}C + {}^{13}C$) vs. undoped floating zone crystal showing lines A, B, and C,--- 77°K,——4·2°K

3.2 *Satellite lines in the region of 9 μ*

The structure in the region of 9μ from samples at room temperature is shown in Fig. 3. When carbon is present two new bands occur, line *A* being about six times as strong as line *B*. Line *A*, with a half width of 12 cm^{-1}, is very much sharper than the normal oxygen band which has a halfwidth of 36 cm^{-1}. The corresponding structure at 77°K and 4·2°K is shown in Fig. 4 where it is seen that the normal oxygen band sharpens and shows the fine structure[13–14] reported previously (See Table 2). Line *A* also sharpens and shifts to a higher energy at 4·2°K and two shoulders become apparent as shown in Fig. 5; a more detailed discussion of this figure is given in Section 4.2. Line *B* also shifts to a higher energy (Fig. 4) and another weak line *C* at 1085·1 cm^{-1} is detected at 4·2°K. High resolution measurements at 4·2°K on samples containing natural carbon, $^{12}C + {}^{14}C$ and $^{12}C + {}^{13}C$ failed to detect any isotope shift on any of these lines, confirming our previous lower resolution results obtained at 77°K for line *A*. However, the variations of the strength of these lines with the total carbon content of the samples (Fig. 6) suggests that they do arise from the vibration of a complex involving a carbon impurity. The presence of oxygen in the centre was indicated by the fact that these lines were absent in

Table 2. I.R. absorption energies of oxygen centres in the 9 μ region

Assignment	290°K		77°K		4·2°K	
	ω(cm^{-1})	Δω(cm^{-1})	ω(cm^{-1})	Δω(cm^{-1})	ω(cm^{-1})	Δω(cm^{-1})
Oxygen 8μ			1205·1		1205·7	4·4
Oxygen 9μ	1107·2	36	1134·9 1126·1		1136·2 1134·4 1132·6 1130·5 1128·3	1·0
Shoulder E of line A					1108·8	
line A	1093·6	12	1103·0	3·6	1103·9	2·1
Shoulder D of line A			1098·4		1099·0	
line C					1085·1	1·4
line B	1047·5	5	1051·9	2·8	1052·0	1·8

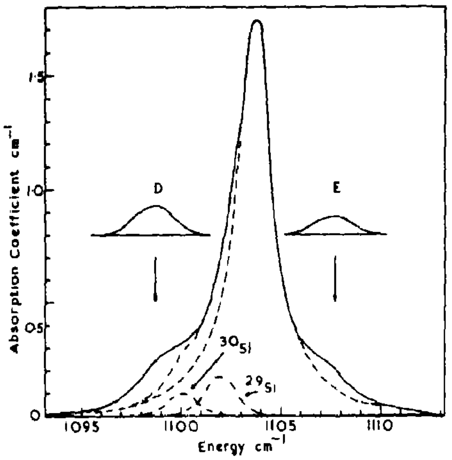

Fig. 5. Detailed structure of line A at 4·2°K; — observed absorption. --- expected contributions from the centres containing ^{28}Si, ^{29}Si and ^{30}Si (see discussion section of text). - - composite curve for the three Si isotopes; D and E remaining absorption

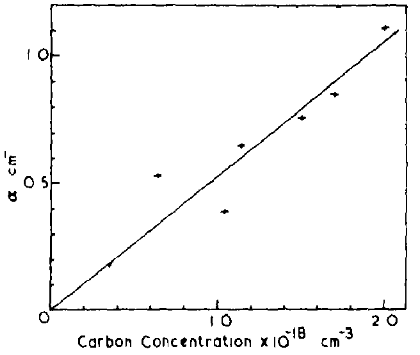

Fig. 6. Variation of line A for samples containing 10^{18} oxygen/cm^{3} and a range of carbon concentrations

samples which contained a high concentration of carbon but no oxygen.

3.3 *Satellite lines in the region of the carbon fundamental modes*

The satellite structure observed in the region of 16μ from a sample containing ^{12}C together with 10^{18} cm^{-3} atoms of oxygen, is shown in Fig. 7. The halfwidths of these bands were similar to those of the isolated carbon fundamentals, at corresponding temperatures and their integrated absorption remained essentially constant showing that they were due to single phonon absorption. Other measurements on samples containing ^{12}C + ^{13}C and ^{12}C + ^{14}C confirmed that there were three vibrational satellite lines associated with each carbon isotope, details of which are given in Table 3. Line *Y* for the ^{14}C isotope has not been observed as its position estimated from the data for the other isotopes, is almost coincident with the ^{12}C fundamental. At room temperature many of these lines were only present as shoulders on the strong fundamental bands, due to the increase in their linewidth with increasing temperature. The relative strength of the absorption in the three satellites was approximately 2:2:1 for X:Y:Z and was the same for all samples. The absorption in these lines increased with increasing carbon content of

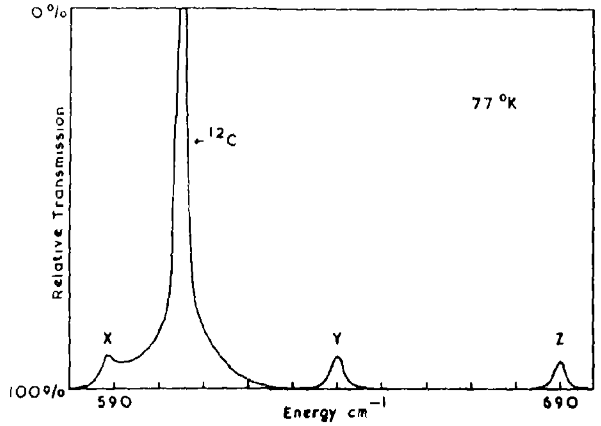

Fig. 7. Satellite structure in the region of the carbon fundamental absorption band when oxygen is present showing lines X, Y and Z.

Table 3. I.R. absorption energies of C–O *complexes in the region of the carbon fundamentals*

	line (°K)	X (cm^{-1})	Y (cm^{-1})	Z (cm^{-1})
C^{12}	290°	586·2*	636·7	683·8
	77°	588·5	640·1	689·9
C^{13}	290°	568·0*	617·8*	665·8
	77°	571·1	621·9	670·7
C^{14}	290°	552·9*	601†	650·2*
	77°	555·4	605†	656·8*

*Shoulders on stronger lines.

†Estimated positions; masked by C^{12} fundamental at 605 and 607·5 cm^{-1} at 290° and 77°K respectively.

the sample in a similar manner to lines *A* and *B*. In fact the strength of the absorption in the satellite line *Y*, summed over all the isotopes of carbon present, gave a very good correlation with the strength of line *A* as shown in Fig. 8. It was also established that there was no detectable satellite structure in this region in the oxygen free samples except for a small line at 589·1 cm^{-1} which corresponded in position and strength to the expected absorption from the 1·1 per cent abundance of the naturally occurring ^{13}C isotope. Likewise no satellite structure was observed from a sample which contained 10^{18} cm^{-3} oxygen atoms but a negligible carbon concentration. These results, taken in conjunction with those in Section 3·2 are taken to establish the existence of complexes involving carbon and oxygen.

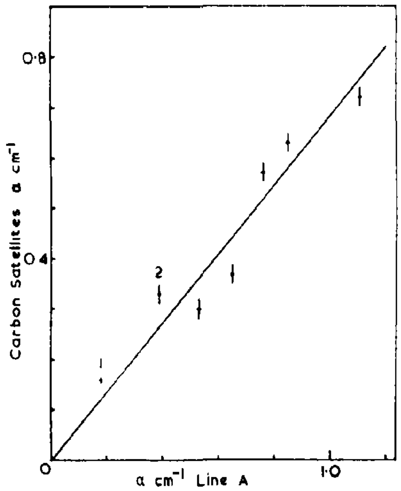

Fig 8 Peak absorption coefficient for satellite line A versus absorption coefficient in satellite line Y (summed over all carbon isotopes present) Point 1, sample contains ^{12}C; point 2, sample contains ^{12}C + ^{14}C, other points, samples with ^{12}C + ^{13}C.

3.4 *Absorption due to electronic transitions*

Observations of the sattelite structure described above were complicated to some extent in certain samples by the presence of two other lines at 669·3 cm^{-1} and 693·3 cm^{-1} (4·2°K) which increased strongly in absolute intensity as the temperature was reduced. This behaviour precludes the possibility that they were due to a one phonon absorption process. The strength of these lines showed a correlation with the boron content of the samples, as determined from the strength of the absorption at 34μ, and they were absent in samples which had been subjected to a 2 MeV electron irradiation with a dose of 5 × 10^{18} cm^{-2}. This treatment is known to introduce deep electronic levels which should lead to the ionization of any shallow acceptor levels present. All these observations indicate that these lines arise from electronic transitions of an acceptor centre, the nature of which is not known at present. It could be speculated that this centre involves a boron impurity paired with oxygen and/or carbon but no direct correlation with either of these latter two impurities was found. In view of the limited number of observations of this centre, which are anyway outside the scope of this investigation, no further discussion will be given. Other effects of the electron irradiation treatment will be presented elsewhere.

3.5 *Other absorption*

Apart from the lines due to the normal oxygen centre at 1206 cm^{-1} (8μ band) and 517 cm^{-1} (19μ band) and those described above the only other feature that was detected in some samples was a broad band near 21μ.

This band did not correlate with the carbon or oxygen concentrations, nor with the strength of the satellite structure described in Section 3.3, and its origin is not understood. No bands due to local mode absorption of boron were observed, as was to be expected for the low concentrations of this impurity which were present. A concentration of boron of 5×10^{19} cm^{-3} has been found to give a local mode peak absorption coefficient of about 100 cm^{-1}[2] and so a concentration of 5×10^{15} cm^{-3}, which was the highest value in the samples examined, would lead to $\alpha \simeq 10^{-2}$ cm^{-1} which was below the limit of detection.

4. DISCUSSION

4.1 *Isolated carbon impurities*

Since carbon and boron atoms have similar masses and both impurities are thought to occupy substitutional sites in silicon, it will be useful to compare and contrast the present results with the detailed observations for isolated boron ions[2].

A comparison of the energies of the carbon fundamental modes given in Table 1 with those for ^{11}B at 622·8 cm^{-1} and ^{10}B at 645·8 cm^{-1} (77°K), indicates that the required reduction in force constants relative to a simple isotopic impurity[4, 5] is almost the same for both impurities, being very marginly greater for boron. From the data in Table 1 it is seen that the energies of the second harmonic transitions for carbon are less than double those of the fundamentals by $3{\cdot}8 \pm 0{\cdot}2$ cm^{-1}. This is the same shift, within experimental error, as that obtained for boron impurities (3·7 cm^{-1}) and indicates that the degree of anharmonicity in the vibrational potential is also similar for the two centres. Unfortunately, details of the anharmonic constants, even in a static well approximation[20], cannot be determined without a knowledge of the energies of the third harmonic transitions. The relative strength of the second harmonic to the fundamental absorption, which depends on both the mechanical anharmonicity and the existence of a second order electric dipole moment, is also similar having values of 0·015 and about 0·02 for carbon and boron respectively. The linewidth of the carbon fundamentals of 1·8 cm^{-1} measured at 77°K (our previously reported value[1] of 5 cm^{-1} was obviously instrumentally limited) is somewhat lower than that of 3·5 cm^{-1} for boron. The reason for this difference is not clear, but it has been shown that there is extra satellite structure close to the boron fundamentals [21, 22] and second harmonics[2], possibly resulting from the electron irradiation treatment given to these samples, and this may have led to an apparent increase in the fundamental linewidth.

The results shown in Fig. 2 appear to indicate that the absorption in the carbon local mode lines increases by about 10 per cent when the sample temperature is lowered from 290 to 77°K, although it is well known that the absorption should be independent of temperature for a one phonon process. Similar effects have been observed for boron-lithium complexes in silicon[23] and hydrogen in calcium fluoride[20]. In the latter system, the discrepancy was attributed to a reduction in i.r. active two phonon processes, involving a local mode plus or minus a lattice mode, as the temperature was lowered. Such combination bands were relatively strong and easily observable and showed the expected variation in strength with temperature[20]. Similar bands have also been observed for boron-lithium complexes in a concentration of 2×10^{20} cm^{-3} in silicon[24] although these were relatively weak and were only revealed in experiments using the differential technique described in Section 2.3. Corresponding measurements on the present samples gave no clear indication of the existence of combination bands. The explanation of the change in absorption in the local modes is thus probably to be attributed to changes in the line shape as the temperature is lowered. These were also the conclusions relating to the work on boron lithium pairs in silicon[23].

The present results have shown that the local mode absorption from neutral carbon impurities is about six times greater than that observed from an equal concentration of B^- ions thus confirming our earlier result. It has been shown that the total integrated absorption in the band and local mode regions from substitutional impurities present in a concentration D, of mass M' and carrying a static charge e is given by

$$\int \alpha(\omega)\mathrm{d}\omega = \frac{2\pi^2 e^2 D}{\mathrm{n c M'}} \qquad (4)$$

where c is the velocity of light and n is the refractive index of silicon[4–5]. Application of this formula to the observations on boron doped silicon yielded a value of e close to unity[2]. Although this theory is not really meaningful for a neutral impurity, equation 4 has been used to define an apparent charge of $\eta_0 = 2{\cdot}5e$ for carbon, on the assumption that all the absorption occurs in the local mode region. The theory[4–5] predicts that about 32 per cent of the absorption should occur in the band for an impurity with an atomic mass of fourteen (^{14}C). However it has now been shown experimentally that band mode absorption for carbon in silicon is very small. It was found that the absorption coefficient due to this process, at frequencies just below the band limit, was less than $0{\cdot}03\ \mathrm{cm}^{-1}$ when the integrated local mode absorption from the carbon was $90\ \mathrm{cm}^{-1}$ ($\alpha_{\max} = 13\ \mathrm{cm}^{-1}$). For comparison the same local mode absorption from B^- ions would lead to a value of $\alpha \simeq 0{\cdot}25\ \mathrm{cm}^{-1}$ in the same region[2]. Hence any band mode absorption due to carbon is at least an order of magnitude smaller than that produced by B^- ions. This is the justification for ignoring band mode absorption (equation (4)) in evaluating the quantity η_0 for carbon impurities. The larger value of η_0 for carbon is perhaps not too surprising in view of the stronger lattice absorption in silicon carbide[25] compared with various III–V semiconducting compounds[26–28]. These observations are in accord with the current ideas of Leigh and Szigeti who will give a more detailed discussion elsewhere. It is interesting to note that similar large charge displacements must occur for neutral interstitial oxygen impurities which also produce very strong infra red absorption in silicon[12].

4.2 *Carbon-oxygen complexes*

The observations described in Sections 3.2 and 3.3 are considered to establish conclusively that carbon-oxygen complexes exist in as grown silicon when both impurities are present.

Before proceeding with a discussion of possible models for such complexes, it is necessary to recall briefly the interpretations that have been put forward to explain the fine structure of the 9μ band of the isolated interstitial oxygen centre. It now seems firmly established that an oxygen atom is bonded to two silicon host atoms in a triangular arrangement and that the oxygen may occupy any of the six equivalent interstitial positions around the normal [111] bond axis (D_{3d} symmetry) as shown in Fig. 9[13]. Because of this symmetry, the vibrational wavefunctions will be linear combinations of wavefunctions appropriate to each separate minimum (in azimuthal angle about the [111] axis) and each vibrational energy level will be split into

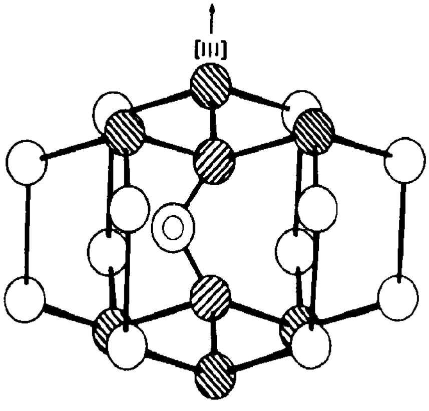

Fig. 9 Configuration of an interstitial oxygen impurity in the silicon lattice, ◎ oxygen atom: ▩ first neighbour site P; ▨ second neighbour site Q. ○ third neighbour site R.

groups of closely spaced sub-levels. Optical transitions can then only occur between certain pairs of sub-levels because of symmetry based selection rules. This is the essence of the interpretation given first by Hrostowski and Alder[13] to explain the apparently anomalous behaviour of the observed temperature dependence of the complicated fine structure in the 9 μ band. At low temperatures all the oxygen atoms are in their *lowest* vibrational sub-states and only certain transitions are permitted: on raising the temperature somewhat, a higher sub-level becomes populated and further transitions at lower energies occur: at still higher temperatures the various fine structure lines broaden and merge to give a very broad band 36 cm^{-1} in width at 290°K, and it is thought that free (hindered) rotation of the oxygen atom about the [111] axis takes place. More details of this fine structure, observed at a higher instrumental resolution, have subsequently been given by Pajot[14]. In a later publication however, Pajot and Deltour[10] put forward convincing evidence based upon the relative strengths of the various transitions, that much of the structure is due to isotope effects resulting from the silicon host lattice which contains 4·5% ^{29}Si and 3% ^{30}Si. Thus various fine structure lines are attributed to ^{28}Si$_2$O, ^{28}Si^{29}SiO, ^{28}Si^{30}SiO etc. complexes with adjacent separations of 1·9 cm^{-1}. This interpretation does not invalidate the earlier theoretical ideas of Hrostowski and Alder [13], but means that the structure to be interpreted is very much simpler, involving only three or four transitions with separations of about 7 cm^{-1} for each isotopic centre. Other lines at 1206 and 517 cm^{-1} were originally interpreted in terms of the two other i.r. active modes of vibration to be expected for the non-linear triangular arrangement of the Si–O–Si group of atoms[13]. More recently, the line at 1206 cm^{-1} has been re-interpreted [29] as a two phonon combination band involving excitations along and about (rotational) the Si–Si bond axis, and an explanation was given for the decrease in its strength as the temperature is raised. This possibility could be checked by the observation of the fundamental librational mode estimated to be at 67 cm^{-1} but this has not been reported so far. Other small lines at 9·5 μ and 9·7 μ have been observed[30] but these were tentatively attributed to the vibrations of clusters of oxygen atoms which are known to form during a heat treatment of silicon. It is concluded that the theory can account qualitatively for the observations on the 'simple' oxygen centre, but a more quantitative explanation is still awaited.

The effect of diffusing interstitial lithium impurities into silicon containing oxygen is also highly relevant to the present results. It is found[29] that the strength of the 9 μ band is decreased and a new band ascribed to oxygen–lithium pairs is formed at 1006·5 cm^{-1}. This band shows no fine structure, no anomalous broadening on raising the temperature and no isotope shift when ^{7}Li is replaced by ^{6}Li. The oxygen 8 μ band is also reduced but no new corresponding band due to the Li–O complexes is formed. These results led to the conclusion that the rotational motion of the oxygen atom around the Si–Si bond axis is quenched by the presence of the interstitial lithium atom; that is, the oxygen becomes trapped in one particular potential minimum. These observations are very similar to those for the present carbon–oxygen complexes which are now discussed in more detail.

The three lines *A*, *B* and *C* observed in the region of 9 μ showed no anomalous behaviour as the temperature was raised from 4·2 to 77°K, e.g. line *C* did not increase in strength at the expense of line *A*. It is therefore concluded that they are not fine structure transitions arising from a single centre analogous to those of the simple oxygen centre. In any case, the separations of 19 cm^{-1} between *A* and *C* and 33 cm^{-1} between *C* and *B* are considered to be too large to be interpreted in this way. The ratio of the strengths of lines *A* and *B* appeared to be the same in all of the samples examined but it was not possible to come to a similar conclusion for the weaker line *C* which was only detected at 4·2°K. On the basis of these observations alone, it is not clear whether lines *A* and *B* arise from two different defect centres, always present in the same relative concentrations, or if they are due to two distinct normal modes of vibration of a single defect centre. The former possibility is thought to be the more likely because only one normal mode of the isolated oxygen centre occurs in the 9μ region and only one line is observed from the Li–O complexes. It will therefore be assumed that the three lines arise from three different centres each involving oxygen. The presence of carbon in the centres giving lines *A* and *B* has been clearly demonstrated (Fig. 8), and the almost linear variation in the strengths with the total carbon content of the sample (Fig. 7) strongly suggests that only one carbon atom is involved in each centre. A similar conclusion cannot be reached for the oxygen impurities, as samples with a variable oxygen content but a constant carbon concentration were not available for examination. However, since it has been demonstrated that lines *A* and *B* are not due to defects consisting of oxygen clusters alone[30], we shall assume that they arise from carbon–oxygen pairs. The origin of line *C* is very uncertain and consequently it will not be considered further in this work.

The correlation between the strength of line *A* and the carbon satellite structure (Fig. 8) may be examined on a more quantitative basis. The maximum observed absorption in line *A* of $\alpha\Delta\tilde{\nu} = 4{\cdot}0\ \text{cm}^{-2}$ would correspond to $3{\cdot}1\times10^{16}$ oxygen atoms cm^{-3}, if the dipole moment were the same as that for the normal oxygen centre[12]. The total absorption in the satellite lines near the carbon fundamentals in the same sample corresponded to a carbon concentration of $9{\cdot}0\times10^{16}\ \text{cm}^{-3}$ with a similar assumption about the relevant dipole moment (η_0). This does not imply that the centre contains three carbon atoms and only one oxygen atom, as the value of η_0 is known to change when impurity pairing occurs; for example a value of $\eta_0 \simeq 0{\cdot}5e$ has been measured for boron-lithium pairs[23] compared with $\eta_0 \simeq e$ for isolated boron ions[2]. In this analysis it has been tacitly assumed that three carbon satellites *X*, *Y* and *Z* all arise from a single centre, mainly because all three lines have similar strengths. If lines *A* and *B* arise from separate centres, further satellite structure would be expected near the carbon fundamentals. However, line *B* was weaker than line *A* by a factor of six and the corresponding carbon satellite structure should then be weaker by about the same factor. This would imply a maximum absorption coefficient of about $0{\cdot}06\ \text{cm}^{-1}$ in each satellite line which is the limit of detection in this region of the spectrum. In fact no extra structure was observed. It is concluded that the satellite lines *X*, *Y* and *Z* and line *A* arise from the same centre, but that the measurements in the carbon local mode region give no further definite evidence about the origin of line *B*.

An important result of the present work is that neither line *A* nor *B* shows any detectable splitting or broadening when different carbon isotopes are present. This suggests that the oxygen atom in these centres is not bonded directly to the carbon atom; that is the carbon does not occupy site *P* in Fig. 9. In this case, structure is expected from the various silicon isotopes present by analogy with the observation of the normal 9μ band[10]. The detailed profile of line *A* shown in Fig. 5 clearly reveals two shoulders, but in addition, the main peak is found to be asymmetric. This asymmetry can be explained if the peak is really the profile of three unresolved lines (dashed curves in Fig. 5) with separations of $1{\cdot}9\ \text{cm}^{-1}$ and relative strengths of $1:0{\cdot}1:0{\cdot}065$ which are the expected ratios for occurence of the centres $^{28}\text{Si–O–}^{28}\text{Si}$, $^{29}\text{Si–O–}^{28}\text{Si}$ and $^{30}\text{Si–O–}^{28}\text{Si}$; the separation of $1{\cdot}9\ \text{cm}^{-1}$ is the same as that observed for the well resolved lines in the 9μ band structure[10]. This would then leave small unexplained bands *D* and *E* at

1098·9 cm^{-1} and 1107·3 cm^{-1}, on the low and high energy sides of the main peak. Similar effects were not observed for line *B*, possibly because of its much smaller strength. The sidebands of line *A* could in principle be fine structure features of the same type as those found for the isolated oxygen centre but against this interpretation, is the lack of anomalous effects as the temperature was raised from 4·2 to 290°K. In fact lines *A* and *B* remain relatively sharp at 290°K with half-widths of only 12 cm^{-1} and 5 cm^{-1} respectively compared with 36 cm^{-1} for the normal oxygen 9 μ band. This implies that the rotation of the oxygen about the Si–Si[111] axis is quenched in these centres as in the Li–O pair centre described above[29].

These results are explicable if the carbon atom occupies second or third neighbour sites *Q* or *R* in Fig. 9. Carbon is a much smaller atom than silicon and its presence in either of these sites would make the adjacent interstitial site very favourable for the oxygen atom from the point of view of lattice strain, apart from any chemical affinity between the two impurities. The strength of the interaction may be gauged from the relative strength of line *A* compared with the normal oxygen centre which shows that a fraction of about 3×10^{-2} of the oxygen atoms are paired in a sample containing 10^{18} cm^{-3} and 2×10^{18} cm^{-3} of oxygen and carbon atoms respectively. Assuming carbon is present in sites *Q*, the expected statistical fraction of pairs is only 2×10^{-4}.

A carbon atom occupying either site *Q* or *R* will have rhombic symmetry and this is expected to lead to a complete removal of the three-fold degeneracy of the localized modes of vibration of an isolated carbon atom with tetrahedral symmetry. This result is consistant with the observation of three satellite lines for each carbon isotope in the region of 16 μ, but does not allow the two types of site to be distinguished. The centre of gravity of the satellite structure for ^{12}C is at 639 cm^{-1}, which is a slightly higher energy than that of the isolated carbon fundamental at 605 cm^{-1}; however, the relatively close agreement does suggest that the carbon atom occupies substitutional sites in both centres[1]. The shift of 34 cm^{-1} to a higher energy could be explained by the local compression produced by the oxygen interstitial impurity. Similar shifts to successively higher energies have been observed for example when boron is paired with phosphorus, arsenic and antimony [21, 22, 31] which are progressively larger ions. This argument would then lead to a prediction of a lower oxygen vibrational frequency than for an isolated impurity, which is in agreement with the observations. Line *B* would then have the largest shift and might be due to an oxygen atom paired with a carbon atom in a second neighbour site *Q* (Fig. 9). Occupation of the third neighbour site *R* by the carbon atom could then account for the centre giving rise to line *A*. This would automatically make line *A* twice as strong as line *B* if sites *Q* and *R* were occupied by carbon on a purely statistical basis, with the assumption that the dipole moment was the same for the two centres. In fact line *A* was about six times as strong as line *B*.

In summary, it is concluded that the presence of a carbon atom close to an oxygen impurity leads to modified localized modes of vibration of both impurities in the 16 μ and 9 μ regions respectively. The results indicate that the carbon atom is in a site of rhombic symmetry and that the rotation of the oxyger about the Si–Si bond axis is quenched. Possible models for these centres have been proposed in which the carbon atom occupies substitutional second or third neighbour sit from the oxygen. These models are consisten with the observations, but cannot be taken a being firmly established; in particular furthe experiments would be required to determin whether the two new lines *A* and *B* in the 9 region are due to different centres or wheth they arise from two distinct normal modes vibration of a single centre.

Acknowledgements—The authors wish to thank R.

Rouse of A.E.I./G.E.C. for supplying the silicon crystals used in this investigation, R. S. Leigh and B. Szigeti for helpful discussions and permission to comment on some of their unpublished work, S. D. Devine for allowing us to quote some of his unpublished measurements and Professor E. W. J. Mitchell for providing the laboratory electron irradiation facilities. One of us, R.S.S. also wishes to thank the S.R.C. for a research studentship.

REFERENCES

1 NEWMAN R. C and WILLIS J B., *J. Phys. Chem. Solids* **26**, 373 (1965).
2 ANGRESS J F., GOODWIN A. R. and SMITH S. D., *Proc. R. Soc.* In press
3 ANGRESS J. F., GOODWIN A. R. and SMITH S. D , *Proc. R. Soc.* In the press.
4. DAWBER P. G and ELLIOTT R. J , *Proc R. Soc.* **273**, 222 (1963).
5. DAWBER P. G. and ELLIOTT R. J , *Proc Phys. Soc.* **81**, 453 (1963).
6 SZIGETI B., *J. Phys. Chem. Solids* **24**, 225 (1963).
7 LEIGH R. S. and SZIGETI B., *Proc. R. Soc.* **301A**, 211 (1967)
8. LEIGH R. S and SZIGETI B , *Phys. Rev. Lett.* **19**, 566 (1967)
9 LEIGH R S and SZIGETI B , In *Localized Excitation in Solids* (Edited by R F. Wallis), p 159. Plenum Press, New York (1968)
10. PAJOT B and DELTOUR J P , *Infrared Phys.* **7**, 195 (1967)
11 KAISER W., KECK P. H. and LANGE C. F., *Phys. Rev.* **101**, 1264 (1956)
12 KAISER W and KECK P H., *J. appl Phys.* **28**, 882 (1957)
13 HROSTOWSKI H. J and ALDER B. J , *J. chem Phys.* **33**, 980 (1960).
14 PAJOT B , *J. Phys. Chem. Solids* **28**, 73 (1967).
15 HROSTOWSKI H. J. and KAISER R. H , *J. Phys. Chem Solids* **4**, 148 (1958).
16 BURSTEIN E., PICUS G., HENVIS B. and WALLIS R , *J. Phys. Chem Solids* **1**, 65 (1956)
17. CALVIN M., HEIDELBERGER C., REID J. C., TOLBER B. M. and YANKWICH P. F., In *Isotopic Carbon*, p. 23. Wiley , New York (1949).
18. JOHNSON F. A., *Proc. phys. Soc.* **73**, 263 (1959).
19. RUSSELL J. P., *Appl. Phys. Lett.* **6**, 223 (1965).
20. ELLIOTT R. J., HAYES W., JONES G. D , MacDONALD H. F. and SENNETT C. T., *Proc. R. Soc.* **289A**, 1 (1965).
21. NEWMAN R. C. and SMITH R. S , *Solid State Commun.* **5**, 723 (1967).
22. NEWMAN R. C. and SMITH R. S In *Localized Excitations in Solids* (Edited by R. F. Wallis), p. 177. Plenum Press, New York (1968)
23. BALKANSKI M. and NAZAREWICZ W , *J. Phys. Chem. Solids* **27**, 671 (1966).
24. WALDNER M., HILLER M. A. and SPITZER W G , *Phys. Rev.* **140A**, 172 (1965).
25. SPITZER W G , KLEINMAN D A and FROSCH C J , *Phys. Rev.* **113**, 133 (1959)
26 KLEINMAN D A. and SPITZER W. G , *Phys. Rev.* **118**, 110, (1960).
27. HASS M. and HENVIS B W., *J Phys. Chem. Solids* **23**, 1099 (1962).
28. GIELISSE P. J., MITRA S. S , PLENDL J. N., GRIFFIS R. D , MANSUR L. C , MARSHALL R. and PASCOE E A , *Phys Rev* **155**, 1039, (1967).
29. CHRENKO R. M , McDONALD R. S. and PELL E. M , *Phys. Rev* **138A**, 1775 (1965)
30. KAISER W., HROSTOWSKI H. J. and THURMOND C. D , *Bull. Am. Phys. Soc.* **5**, 61 (1960).
31. TSVETOV V., ALLRED W and SPITZER W G , In *Localized Excitations in Solids* (Edited by R. F. Wallis), p. 185 Plenum Press, New York (1968).

Note added in proof Line *C* and shoulder *E* of line *A* correspond in both position and strength to the absorption expected from naturally occurring isolated ^{18}O and ^{17}O impurities respectively.

J. Phys. Chem. Solids Pergamon Press 1969. Vol. 30, pp. 1507–1511. Printed in Great Britain.

ON THE COEXISTENCE OF THE MAGNETIC PHASES IN CHROMIUM ALLOYS

B. LEBECH and K. MIKKE*
Danish Atomic Energy Commission, Research Establishment Risö, Roskilde, Denmark

(*Received* 25 *November* 1968)

Abstract – Detailed neutron diffraction investigations have been performed on Cr–Re alloys in order to explain the several observations in Cr alloys of the coexistence of a commensurable and an oscillatory magnetic phase. It is concluded that the individual magnetic phases probably occur in separate domains.

THE MAGNETIC properties of chromium and its alloys have recently attracted a considerable amount of interest both experimentally and theoretically. It is now generally assumed that these properties are closely related to the character of the Fermi surface of chromium metal. The essential feature is the instability of the Fermi surface against formation of exchange coupled electron-hole pairs. The condensation of such pairs gives rise to antiferromagnetism. This phenomenon resembles the formal description of excitonic insulators [1] where a condensation of coupled electron-hole pairs transforms a semiconductor or a semimetal into an insulator. The analogy applies in particular to the two-band model of antiferromagnetism in the form developed by Fedders and Martin[2]. As the theoretical models are still very crude and oversimplified there is a need for new and extensive experimental data.

In order to correlate the Fermi surface properties with the magnetic phenomena a number of neutron investigations on various chromium alloys have been made[3–11]. In the first detailed studies on Cr–Mn alloys by Hamaguchi *et al.*[4] the existence of a mixed commensurable (AF_0) and an oscillatory (AF_1) phase was discovered. This result was further supported by Møller *et al.*[5] for Cr–Mn and Cr–Re alloys, by Bastow[9] for Cr–Mn alloys and by Hoshino *et al.*[7] for Cr–Fe alloys. The careful studies by Koehler *et al.*[10] of Cr–Mn alloys, however, did not confirm the existence of a mixed phase. The interpretation of some of the experimental evidence can be given in terms of the single-band model of Tachiki and Nagamiya[12] and the recently developed two-band models[2, 13]. None of these models, however, explains the observed coexistence of the two magnetic phases over a rather wide range of temperatures or concentrations. It was thus one aim of the present studies of Cr–Re alloys[14] to clarify this problem. The hypothesis was that concentration gradients produced in the crystal during the growth process would give rise to an apparent mixed phase for the bulk crystal. However, due to the concentration gradients a variation of the relative intensities of the AF_0 and the AF_1 components would be observed across the crystal.

A specimen of Cr–0·78% Re which had earlier been found to have a very pronounced mixed phase region[5] was chosen for the more detailed studies. The single crystal bar obtained by the arc-zone melting technique[15] had a maximum length of 5 cm and irregular cross sections of approximately 0·7 cm^2. Investigations of the inhomogeneity of the solute concentration were made both by chemical and X-ray fluorescent analysis. An average concentration variation from 0·94 at.% to 0·65 at.% was found across the crystal, consistent with the neutron diffraction patterns to be discussed below. For a number of 50 $\mu \times 50\,\mu$ crystal regions X-ray fluorescent microprobe photographs were taken in search of microscopic inhomogeneities similar to those reported for Cr–Fe crystals[16]. Inhomogeneities of this kind were not found.

---

*Present address. Institute of Nuclear Research, Swierk, Poland.

The neutron diffraction measurements were performed at the fixed-scattering-angle neutron spectrometer[17] at the DR3 reactor at Riso. This type of instrument eliminates the second order reflection contamination and has a fixed scattering geometry. The crystal was mounted with its long axis almost vertical and a cadmium aperture was used to select narrow slices from the bulk crystal. In the first series of measurements three 2 mm wide horizontal crystal slices were in turn exposed to neutrons. The observed neutron diffraction patterns (for the top, central and bottom part of the crystal) showed a small but significant difference between the relative intensities of the AF_0 and the AF_1 peaks.

In the second series a 0·7 mm wide aperture selected a number of vertical layers from the crystal parallel to the open crystal surface[†]. From several detailed scans three patterns obtained at 95°K are shown in Fig. 1. The drastic variation of the relative intensities is easily seen. The central peak belongs to the AF_0 phase and the side peaks to the AF_1 phase. In comparison with the observations for horizontal crystal slices, the intensity variation is much more pronounced over a considerably smaller distance. Note that a pure AF_0 phase is found in the scan corresponding to the open crystal surface. The AF_1 phase could not be separated in such a clean form.

One of the regions with a small contribution from the AF_0 phase at 95°K was chosen for the next series of measurements. Patterns for 24 different temperatures were obtained, thus covering the temperature region of the previously found pronounced coexistence. Three examples of the diffraction patterns obtained are shown in Fig. 2. They are very involved and cannot be interpreted completely unambiguously. The temperature variation of the central peak intensity is displayed in Fig. 3. Compared to the analogous curve for the whole crystal, the transition to the AF_1 phase is much sharper and below the transition temperature the intensity drops considerably. Both the vertical layer scan and the temperature scan supports the view that the apparently coexisting phase is rather a mixture of single phase domains.

No fully convincing explanation could be found for the shape of the peaks shown in Fig. 2 (the insert Fig. 2(a) shows the nuclear peak (2, 0, 0) for comparison). It is known from measurements on several chromium alloys that the wave vector **Q** of the sinusoidal spin modulation changes abruptly from $0{\cdot}97\,\frac{2\pi}{a}$ to $\frac{2\pi}{a}$ at about 0·9 per cent excess electrons per atom. The observed broadening of the central peak (1, 0, 0) and the appearance of satellites very close to it, is in contradiction to this well established experimental fact[4, 5, 9, 10]. However, it is consistent with the recent model of Motizuki *et al.*[18] which predicts an abrupt change of **Q** from approximately $0{\cdot}97\,\frac{2\pi}{a}$ to a value less than $\frac{2\pi}{a}$ at roughly 1·5 per cent excess electrons per atom, followed by a continuous increase in **Q** with electron concentration to a final value $\frac{2\pi}{a}$. The broadening of the (1, 0, 0) peak can be explained by an instrumental effect such as insufficient collimation by assuming a **Q** variation similar to that of Motizuki *et al.* For **Q**

[†] The crystals were grown in moats of shape like a boat, thus leaving one surface of the melt free during the crystal growth process. This surface is referred to as the open crystal surface.

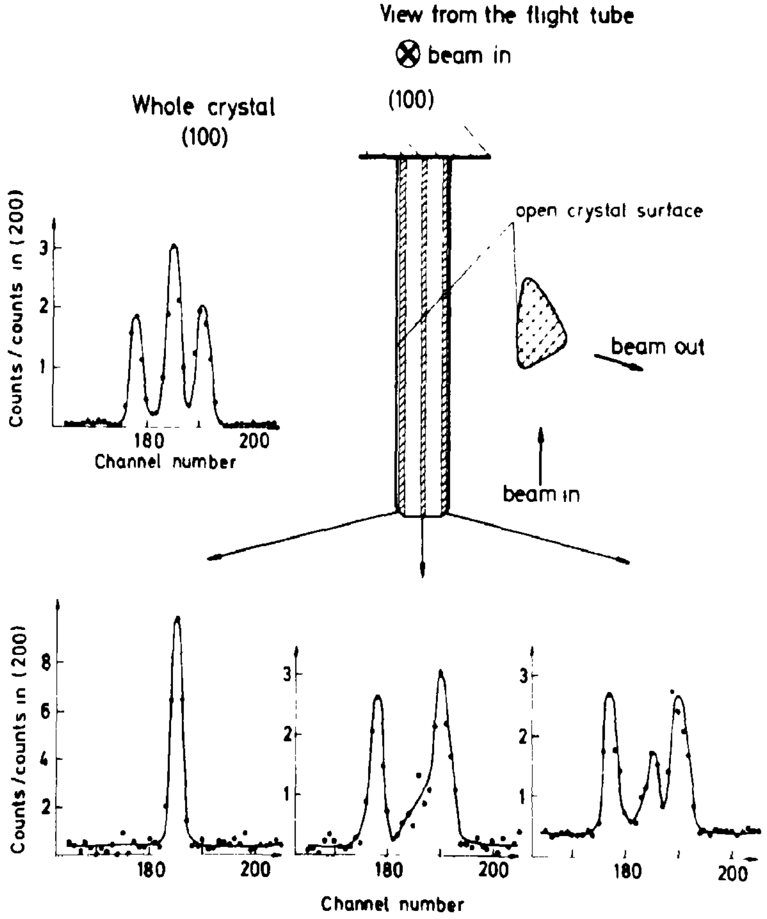

Fig. 1. Comparison of the diffraction patterns around (1, 0, 0) at 95°K for the whole sample and for three runs with different vertical slit positions indicated by the hatched regions on the sample. The cross-hatched area represents the horizontal cross section of the sample

values larger than $0{\cdot}98\frac{2\pi}{a}$ the collimation was such that the four satellites $(1, \pm\delta, 0)$ and $(1, 0, \pm\delta)$ would be added asymmetrically to $(1, 0, 0)$, while the satellites $(1\pm\delta, 0, 0)$ would be observed on each side of the $(1, 0, 0)$ peak. For **Q** values smaller than $0{\cdot}98\frac{2\pi}{a}$ the collimation was sufficiently strong to exclude observation of $(1, \pm\delta, 0)$ and $(1, 0, \pm\delta)$.

In addition to the observed magnetic inhomogeneities due to solute concentration variations, magnetic inhomogeneities induced by strains in the crystal are likely to occur [19–21]. Evidence of strains has been observed as marked differences in the relative intensities AF_0/AF_1 for scattering from the three cubic directions. It is thus possible that the strange shape of the above discussed diffraction patterns is a result of a specific combination of atomic and magnetic inhomogeneities.

On the basis of these experiments it can be concluded that the commensurable and oscillatory magnetic phases probably do not coexist within a single domain. In order to prove the non-coexistence of the magnetic

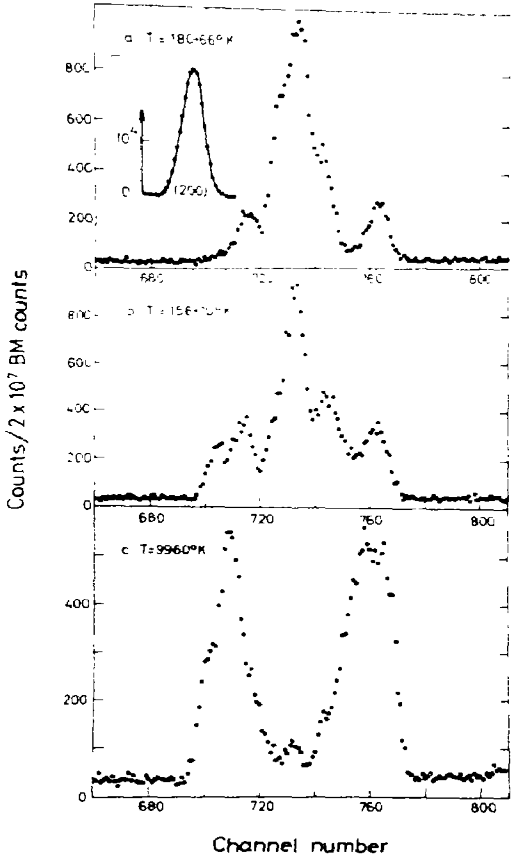

Fig. 2. Diffraction patterns observed around (1, 0, 0) for a selected part of the sample at 180·66°K (a), 156·70°K (b) and 99·60°K (c). The insert shows the nuclear peak (2, 0, 0) for comparison.

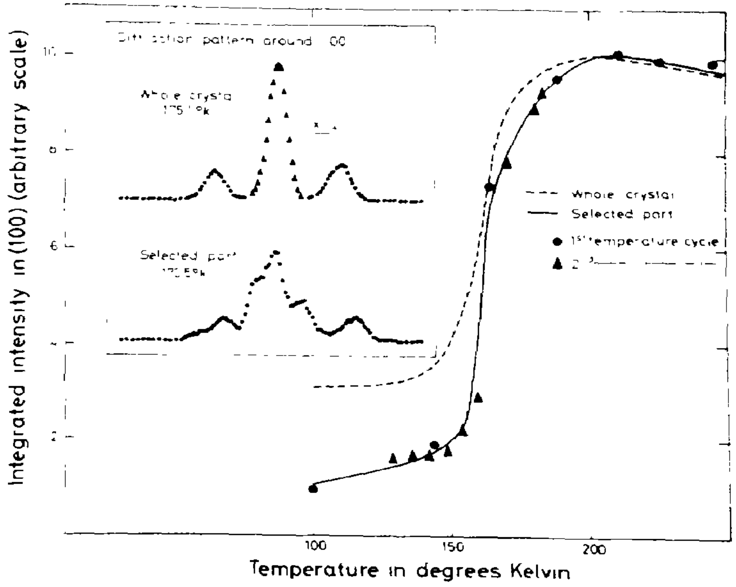

Fig. 3. Comparison of the temperature dependence of the integrated intensity in the magnetic peak at the (1, 0, 0) reciprocal lattice point for the whole sample and a selected part. The insert shows the diffraction patterns observed around (1, 0, 0) at temperatures close to the AF_1 to AF_0 transition.

phases, experiments should be carried out over very small ranges of temperature on highly homogeneous unstrained crystals. However, this requires substantial improvements in the crystal growing technique for chromium.

Acknowledgements—The authors are indebted to Professor A. R. Mackintosh and their collegues at Riso for many valuable discussions. The chemical analysis was performed by A. Thorboe and the X-ray fluorescent analysis by F. Lærke- Nielsen. We express our sincere thanks for their work. One of the authors (KM) expresses his thanks to the Danish Atomic Energy Commission for providing the research grant that made this work possible.

REFERENCES

1. ZITTARTZ J., *Phys. Rev.* **164**, 575 (1967).
2. FEDDERS P. A. and MARTIN P. C., *Phys. Rev.* **143**, 245 (1966).
3. KOMURA S. and KUNITOMI N., *J. phys. Soc. Japan* **20**, 103 (1964).
4. HAMAGUCHI Y., WOLLAN E. O. and KOEHLER W. C., *Phys. Rev.* **138**, A 737 (1965).
5. MØLLER H. B., TREGO A. L. and MACKINTOSH A. R., *Solid State Commun.* **3**, 137 (1965).
6. ARROTT A., WERNER S. A. and KENDRICK H., *Phys. Rev. Lett.* **14**, 1022 (1965).
7. HOSHINO S., ISHIKAWA Y., YAMADA Y. and YAMADA T., *J. phys. Soc. Japan* **20**, 1729 (1965).
8. SUZUKI T., *J. phys. Soc. Japan* **21**, 442 (1966).
9. BASTOW T. J., *Proc. phys. Soc.* **88**, 935 (1966).
10. KOEHLER W. C., MOON R. M., TREGO A. L. and MACKINTOSH A. R., *Phys. Rev.* **151**, 405 (1966).
11. KOMURA S., HAMAGUCHI Y. and KUNITOMI N., *Phys. Lett.* **24A**, 299 (1967).
12. TACHIKI M. and NAGAMIYA T., *Phys. Lett.* **3**, 214 (1963).
13. FALICOV L. M. and PENN D. R., *Phys. Rev.* **158**, 476 (1967).
14. LEBECH B. and MIKKE K. To be published.
15. CARLSON O. N., SCHMIDT F. A. and PAULSON W. M., *Trans. Am. Soc. Metals* **57**, 356 (1964).
16. ARROTT A., WERNER S. A. and KENDRICK H., *Phys. Rev.* **153**, 624 (1967).
17. BURAS B., MIKKE K., LEBECH B. and LECIEJEWICZ J., *Phys. Status Solidi* **11**, 567 (1965).
18. MOTIZUKI K., SHIBATANI A. and NAGAMIYA T., *J. appl. Phys.* **39**, 1098 (1968).
19. BASTOW T. J. and STREET R., *Proc. phys. Soc.* **86**, 1143 (1965).
20. WERNER S. A., ARROTT A. and KENDRICK H., *J. appl. Phys.* **37**, 1260 (1966).
21. WERNER S. A., ARROTT A. and KENDRICK H., *Phys. Rev.* **155**, 528 (1967).

J. Phys. Chem. Solids Pergamon Press 1969. Vol. 30, pp. 1513–1525. Printed in Great Britain.

MATTHIESSEN'S RULE AND THE ELECTRICAL RESISTIVITY OF IRON-SILICON SOLID SOLUTIONS

F. C. SCHWERER, J. W. CONROY and SIGURDS ARAJS*
Edgar C. Bain Laboratory for Fundamental Research, United States Steel Corporation Research Center, Monroeville, Penn. 15146, U.S.A.

(*Received* 30 *October* 1968; *in revised form* 25 *November* 1968)

Abstract—The electrical resistivities of iron–silicon solid solutions (0·97–7·7 a/o silicon) were measured between 4·2° and 310°K. Above 30°K the data were analyzed for deviations from Matthiessen's rule. Initially, abnormal negative deviations were observed, however, these anomalies could be ascribed to systematic changes with silicon content in the ideal resistivity. The ideal resistivity of the alloys was identical to that of pure iron when scaled in magnitude by a concentration-dependent parameter and when the temperature was scaled by a characteristic resistivity temperature. This characteristic temperature varied with silicon concentration in the same manner as the ferromagnetic Curie temperature and in marked contrast to the lattice Debye temperature. This similarity in dependence on silicon content suggests the resistivity is more critically dependent on the magnetic properties of the host metal than on its lattice dynamics. After the appropriate corrections to the ideal resistivity were made, the deviations from Matthiessen's rule were concentration independent as expected from some theories for high solute resistivity alloys. The corrected deviations were compatible with explanations involving anisotropies with respect to electron wave vector in the scattering processes and to a lesser extent with spin mixing theories involving anisotropies with respect to spin.

1. INTRODUCTION

In discussing the electrical resistivity of a metal for which there exist several distinct sources for the scattering of conduction electrons, it is customary to equate the total resistivity to a sum of resistivity increments, each increment arising from a different scattering source[1]. Thus, the resistivity as a function of temperature is written

$$\rho_{\mathrm{Total}} = \rho_0 + \rho_{\mathrm{Ideal}}(T) \qquad (1)$$

where ρ_{Total} is the total measured resistivity, $\rho_{\mathrm{Ideal}}(T)$ is a temperature-dependent contribution characteristic of a perfect host material, and ρ_0, nominally temperature independent, is due to scattering from lattice defects and impurities. This addition rule (Matthiessen's rule) depends on the various scattering processes being independent. In addition it is necessary to satisfy several criteria among which are that changes in the concentration and type of scattering center and changes in temperature must not change the band structure or alter the filled regions of k space of the host metal. However, even when these criteria are fulfilled (as one would expect them to be in dilute alloys) deviations from Matthiessen's rule $\Delta(=\rho_{\mathrm{Total}}-\rho_0-\rho_{\mathrm{Ideal}})$ will still occur if the scattering probability associated with each source is a different function of electron wave vector k_F (e.g. if the relaxation times have different anisotropies with respect to k_F). Dugdale and Basinski[2] have reported deviations from Matthiessen's rule in dilute noble metal alloys which could be explained in terms of differences in the anisotropy of the relaxation times associated with the various solute atoms and the anisotropy associated with phonon scattering (ρ_{Ideal}). Such differences in anisotropy are expected from considerations of the electronic states associated with the various solutes. The resultant deviations are temperature dependent both because the size of ρ_{ideal} relative to ρ_0 changes with temperature and because the anisotropy of the scattering from phonons is expected to be temperature dependent [3].

---

*Now with the Department of Physics, Clarkson College of Technology, Potsdam, New York.

Predictions of deviations from Matthiessen's rule based on relaxation time anisotropy arguments follow generally from electronic transport theory and are expected to be applicable to all metals. Using a different, more specialized model, Campbell, Fert and Pomeroy [4] have recently argued that deviations from Matthiessen's rule in iron alloys are evidence for two-current conduction. In their model for ferromagnetic metals, the conduction electrons are considered to be spin-polarized and consequently divided into subbands. Because the two bands will have different electronic properties, the scattering from impurities may be characterized with a different relaxation time in each subband. Momentum-conserving, spin-flip scattering which normally would not affect the resistivity, can now give a resistive contribution by transferring electrons into the low conductivity band. This spin mixing gives rise to deviations from Matthiessen's rule which are dependent upon the anisotropy with respect to spin for impurity scattering and upon the spin-flip scattering process. The latter is naturally expected to be temperature dependent.

From still a third point of view, temperature-dependent deviations from Matthiessen's rule have been interpreted as evidence for temperature-dependent impurity (or defect) scattering. Such temperature dependences may be associated with the scattering process itself [5]. However, in the case of ferrometals some theories predict a temperature dependence of the impurity resistivity due to changes in the electronic states available for scattering. Such changes would accompany changes in the spontaneous magnetization of the ferromagnetic matrix. For either form the thermal part of the impurity resistivity would be proportional to the impurity concentration.

Therefore, depending upon their origin, deviations from Matthiessen's rule in ferromagnetic alloys can furnish important clues to the electronic states associated with impurities or to the nature of the fundamental scattering processes in ferro-metals. All the above theories predict that the deviations Δ will be positive.

In this paper we are primarily concerned with deviations from Matthiessen's rule in iron-silicon alloys in the solid solution range (1–8 at. % silicon) for temperatures from 20° to 300°K at zero applied magnetic field. These choices of solute, solute concentrations, and temperature range were influenced by the following considerations: (1) A number of corrections for chemical and thermal volume changes become important in resistivity studies concerned with deviations from Matthiessen's rule. The parameters needed for these corrections are available in the literature for the iron-silicon system. (2) The solute concentrations must be sufficiently high to dominate the effects of residual impurities. Furthermore, there is an advantage to the analysis (the deviations become concentration independent) in having the solute resistivity also dominate the thermal resistivity (provided, of course, other high-concentration solute effects can be controlled). (3) In ferrometals there are effects associated with the spontaneous magnetization ($4\pi M_s$) which tend to obscure meaningful measurements of the scattering process resistivity [7]. Methods exist to accurately correct for these effects, however, they involve measurements over large ranges of applied magnetic fields (2 or 3 times $4\pi M_s$) in addition to measurements as a function of temperature and concentration. These spontaneous moment effects are most critical for high purity samples at low temperatures. This is an additional reason for large solute concentrations as well as for the lower temperature limit.

2. BACKGROUND

(a) *Experimental*

Deviations from Matthiessen's rule can be experimentally determined by measuring the resistivity ρ_{Total} as a function of temperature for a dilute alloy. The resistivity due to the solute element ρ_0 is the resistivity of this alloy measured at low temperatures where the ideal resistivity is negligible by comparison. If the solute atoms act independently the residual resistivity ρ_0 will be proportional to the solute concentration c. The ideal resistivity ρ_{Ideal} is measured for a pure sample of the host material (a sample with small ρ_0). Deviations from Matthiessen's rule are then determined as $\Delta = \rho_{\text{Total}} - \rho_{\text{Ideal}} - \rho_0$. Obviously it is necessary that the ideal resistivity not change with alloying. Such changes in ρ_{Ideal} for normal metals might, for example, be associated with changes in the phonon spectra due to the mass defects[8]. This source of deviation from Matthiessen's rule will be discussed in greater detail below but for the present we assume such effects to be negligible, either being initially absent or suitable corrections to the data having been made.

There are several simple corrections to the data which should be made to obtain information comparable with theoretical predictions. Since these corrections are often of the order of the observed deviations we detail in the following paragraphs the procedure we followed in correcting our data.

In practice the resistance R is measured for a particular sample at a temperature T and converted to resistivity by dividing by a geometrical factor G(=gauge length/cross sectional area). This geometrical factor was measured at 296°K and converted to that at temperature T by

$$G(T) = G(0)(1+\delta a(T)/a_0)$$

where

$$G(0) = G(296)(1+\delta a(296)/a_0)$$

and $(\delta a(T)/a_0)$ is the thermal change in lattice parameter from its value a_0 at 0°K. Failure to correct for this change in geometrical factor results in measured deviations which are the sum of the true deviations and the apparent deviation

$$\Delta^G_{\text{ThEx}} = -\rho_0(\delta a(T)/a_0)/(1+\delta a(T)/a_0). \qquad (2)$$

To relate the deviations from Matthiessen's rule to the scattering processes the various resistivities (ρ_{Total}, ρ_0, ρ_{Ideal}) should be compared at the same atomic volume[2]. *Thermal or chemical changes in volume can give rise to* apparent or erroneous deviations The resistivity of a dilute alloy (at vol. V) at temperature T is

$$\rho(T,V) = \rho_{\text{Ideal}}(T,V)+\rho_0(V)+\Delta_{\text{True}}(T,V).$$

The ideal resistivity $\rho_{\text{Ideal}}(V,T)$ differs from that of the pure material $\rho_{\text{Ideal}}(T,\Omega)$ by changes due to chemical expansion. To first order this change is

$$\rho_{\text{Ideal}}(T,V) = \rho_{\text{Ideal}}(T,\Omega)\left[1+\left(\frac{\mathrm{d}\ln\rho_{\text{I}}}{\mathrm{d}\ln V}\right)\left(\frac{\mathrm{d}\ln V}{\mathrm{d}c}\right).c\right].$$

Similarly because of thermal volume expansion the impurity resistivity at temperature T differs from that at 0°K by

$$\rho_0(V(T)) = \rho_0(V(0))\left[1+\left(\frac{\mathrm{d}\ln\rho_0}{\mathrm{d}\ln V}\right)\left(\frac{V(T)-V(0)}{V(0)}\right)\right]$$

The measured quantities are $\rho_{\text{Ideal}}(T,\Omega)$ and $\rho_0(V(0))$. Consequently the apparent deviations from Matthiessen's rule may be separated as follows

$$\begin{aligned}\Delta_{\text{Appar}} &= \rho_{\text{Total}}(T\ V)-\rho_{\text{Ideal}}(T,\Omega)-\rho_0(V(0))\\ &= \Delta_{\text{True}}+\Delta^R_{\text{ChEx}}+\Delta^R_{\text{ThEx}} \qquad (3)\end{aligned}$$

where

$$\Delta^R_{\text{ChEx}} = \rho_{\text{Ideal}}(T,\Omega)\left(\frac{\mathrm{d}\ln\rho_{\text{Ideal}}}{\mathrm{d}\ln V}\right)\left(\frac{\mathrm{d}\ln V}{\mathrm{d}c}\right).c \qquad (4)$$

and

$$\Delta^R_{\text{ThEx}} = \rho_0(V(0))\left(\frac{\mathrm{d}\ln\rho_0}{\mathrm{d}\ln V}\right)\left(\frac{\delta V(T)}{V(0)}\right) \qquad (5)$$

where c is the solute concentration Bridgeman[9] has determined the volume dependence of the ideal resistivity at room temperature as $(\mathrm{d}\ln\rho/\mathrm{d}\ln V) = +4{\cdot}0$ and from his data the volume dependence of the resistivity due to silicon impurities was inferred to be $(\mathrm{d}\ln\rho/\mathrm{d}\ln V) = -0{\cdot}5$. These quantities generally have weak temperature dependences over the range of principal interest in this study and consequently for these corrections were assumed to be constant. The thermal volume expansion $(\delta V(T)/V(0))$ was obtained from the thermal change in lattice parameter $(\delta a(T)/a_0)$ and a polynomial fit of data for pure iron as quoted by Pearson[10] was used to determine $(\delta a(T)/a_0)$. There is evidence[11] to suggest that the changes in thermal expansion with silicon content will not be significant to our application here and the thermal expansion of pure iron was assumed to describe that of the alloys. The experimental value [12] dln $a/dc = -0{\cdot}000237$ per a/o was used for the chemical expansion and consistent with the above assumption taken to be temperature independent.

The resultant corrections for an iron -1 *a*/0 silicon alloy are plotted in Fig. 1. Note that all three of these corrections are proportional to solute concentration *c* (equations (2, 4, and 5)).

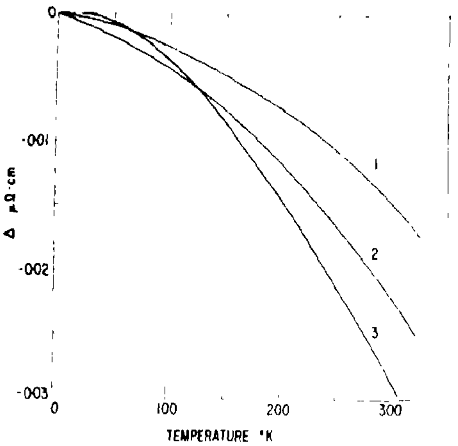

Fig. 1. Apparent deviations from Matthiessen's rule for iron with 1 a/o silicon due to (1) thermal expansion of geometrical factor, (2) thermal expansion of atomic volume, and (3) chemical expansion of at. vol.

(b) *Theoretical*

Theoretical expressions for the electrical conductivity may be derived from the Boltzmann transport equation[1]. Solution of this equation depends upon the scattering probabilities for the conduction electrons. Intuitively, it is reasonable to describe the effect of scattering on the electron distribution $f(\mathbf{K})$ by a relaxation time $\tau(\mathbf{k})$. Consequently, if several independent sources for scattering exist, the total scattering probability for an electron in a state described by k will be proportional to

$$\frac{1}{\tau(\mathbf{k})} = \sum_i \frac{1}{\tau_i(\mathbf{k})}$$

Under this assumption, the Boltzmann transport equation gives the electrical conductivity as

$$\sigma_{ij} = e^2 \int \tau(\mathbf{k}) v_i(\mathbf{k}) v_j(\mathbf{k})\, \mathrm{d}S_F / v_F|(\mathbf{k})|$$

where $\mathrm{d}S_F$ is a surface element on the Fermi surface and $v(k)$ are electron velocities. The electrical resistivity is the reciprocal of the electrical conductivity. If the $v(k)$ and the appropriate constant energy surfaces do not change, then Matthiessen's rule follows provided all scattering processes are described by relaxation times which have the same functional form of k. If, however, the different scattering processes are characterized by relaxation times with different anisotropies, then deviations from Matthiessen's rule occur and are given by

$$\Delta = \left\{ \int \frac{\tau_1(\mathbf{k})\tau_2(\mathbf{k})}{\tau_1(\mathbf{k}) + \tau_2(\mathbf{k})} \right\} - \left\{ \frac{\int \tau_1(\mathbf{k}) \int \tau_2(\mathbf{k})}{\int (\tau_1(\mathbf{k}) + \tau_2(\mathbf{k}))} \right\}^{-1} \tag{6}$$

where the integral sign denotes $\int v_i(\mathbf{k}) v_i(\mathbf{k})\, \mathrm{d}S_F / |v_F|$. If one of the scattering processes is dominant in strength (i.e. $\tau_1 \gg \tau_2$, $\rho_1 \ll \rho_2$) then

$$\Delta \doteqdot \frac{1}{\int \tau_1} \left[\frac{\int \tau_1 \int (\tau_2^2/\tau_1) - (\int \tau_2)^2}{(\int \tau_2)^2} \right]. \tag{7}$$

Since the bracket is independent of the relative strengths of τ_1 and τ_2 (τ_1 and τ_2 appear to equal powers in numerator and denominator), in this limit Δ is proportional to the weaker resistivity ρ_1 and the proportionality constant depends only on the relative anisotropies associated with the two scattering processes. In particular, if the solute resistivity dominates the ideal resistivity over the experimental temperature range, the deviations Δ will be proportional to $\rho_{\text{Ideal}}(T)$ and independent of solute concentration.

One method of simplifying these equations divides the Fermi electrons into two groups which characterize areas a_a and a_b of the Fermi surface with velocities v_a and v_b[2, 13]. The scattering from sources '1' and '2' is described by relaxation times τ_1 and τ_2 for electrons on region '*a*' and by $\alpha\tau_1$, $\beta\tau_2$ on region 'b'. Equation (6) then reduces simply to

$$\Delta = \frac{g(\alpha-\beta)^2(\rho_1\rho_2)}{\rho_1[\beta(1+\alpha g)^2]+\rho_2[\alpha(1+\beta g)^2]}$$

and if $\rho_1 \ll \rho_2$ this becomes

$$\Delta = \rho_1\left[\frac{(\alpha-\beta)^2}{\alpha(1+\beta)^2}\right] \tag{8}$$

where $g = (a_a v_a)/(a_b v_b)$ and in equation (8) has been absorbed into α and β.

Studies of electron transport properties in noble metals have shown that it is necessary to consider anisotropies in the relaxation times to explain the observed results[14]. Moreover, Deaton and Gavenda[15] have directly measured relaxation time anisotropies in copper; while Dugdale and Basinski[2] find that such considerations explain the deviations from Matthiessen's rule which they observe in noble metal alloys. In noble metals regions a and b are assigned to 'belly' and 'neck' electrons[2, 3]. The spatial extent of the impurity disturbance may cause 'neck' electrons (which have p-like components and hence greater probabilities of being found between nuclei) to be scattered more or less strongly than 'belly' electrons (principally s-like wave functions with large probabilities on the atomic site) giving rise to a non-unity value for β. Similarly at low temperatures where Umklapp processes are frozen out and small angle scattering dominates phonon scattering is expected to become relatively more effective for 'neck' electrons resulting in a temperature dependent anisotropy α.

In the electronically more complex transition metals we expect that scattering probabilities will also vary over the Fermi surface in ways characteristic of the scattering source. Theoretical considerations[16] suggest that the disturbance in electronic states varies greatly with the type of impurity present and there is experimental evidence to confirm these predictions (for example neutron diffraction[17] and Mössbauer spectroscopy)[18, 19]. Studies of the magnetoresistivity of nickel alloys in the context of Kohler's rule[20] (another rule whose validity depends on assumptions concerning the anisotropy in the relaxation times) indicates that at least for this transition metal host, these differences in impurity electronic states may also be manifest as differences in the relaxation time anisotropy. Consequently, deviations from Matthiessen's rule due to differences in the anisotropy of the relaxation times characteristic of the various scattering sources may well be important in iron alloys.

Another model which predicts deviations from Matthiessen's rule is one proposed by Campbell, Fert and Pomeroy[4]. In this two-current conduction model, parallel currents are carried by electrons in two subbands. The subbands are formed as a result of the spin polarization of the conduction electrons due to the ferromagnetic state of the host metal. Scattering of electrons in each band is characterized by a relaxation time ($\tau\uparrow$ or $\tau\downarrow$) which describes both impurity and thermal process scattering. Spin-flip scattering in which momentum is conserved would normally not affect the conductivity; however, if electrons in the two subbands have different relaxation times ($\tau\uparrow \neq \tau\downarrow$) this spin-mixing process can produce a resistive contribution in the form of deviations from Matthiessen's rule. The spin-mixing is characterized by a relaxation time $\tau\downarrow\uparrow$ and a 'resistivity' defined $\rho\uparrow\downarrow(T)$. For the impurity dominated limit one finds

$$\Delta = \left[\frac{\rho\uparrow(0)-\rho\downarrow(0)}{\rho\downarrow(0)+\rho\downarrow(0)}\right]^2 \left(\rho_{\text{Ideal}}(T)+\frac{1}{2}\rho\downarrow\uparrow(T)\right) \tag{9}$$

where it has been assumed that the contribution to the ideal resistivity is the same from each subband and that the impurity resistivity $\rho\downarrow(0)$, $\rho\uparrow(0)$ is spin dependent. Note that in this limit ($\rho_0 \gg \rho_{\mathrm{Ideal}}$) the deviation Δ is again independent of concentration and separates into a constant factor characteristic of a particular impurity and a temperature dependent component characteristic of the host metal. This latter component is the sum of the ideal resistivity and the spin mixing 'resistivity.' Both of these components are expected to be non-decreasing with increasing temperature.

Campbell, Fert and Pomeroy[4] have reported large deviations from Matthiessen's rule in iron alloys which they attribute to this spin-mixing process. At low temperatures, they find these deviations to be proportional to T^2 suggesting $\rho\downarrow\uparrow(T)$ is due to electron–electron interactions. Greig[21] has reported large deviations from Matthiessen's rule in nickel alloys which he also finds to be well described by spin-mixing considerations.

3. EXPERIMENTAL PROCEDURES AND RESULTS

Alloys of iron–silicon (0·97–7·66 a/o silicon) were prepared by levitation melting. These alloys along with high purity iron standards were sealed under vacua (10^{-6} Torr) in quartz tubes and homogenized for 1 week at 1000°C. The samples were machined to cylinders, 0·200 in. dia. and 2 in. long, a 20 mil thick surface layer being removed during machining. The samples were re-sealed in quartz tubes and recovered for 2 hr at 850°C. Iron wires were spot welded to the samples for potential probes. The large cross-sectional area was chosen to increase the accuracy with which the geometrical factor could be determined as well as to minimize adventitious size effects such as have recently been reported in connection with studies of grain boundary resistivities in iron[22, 23]. The cross-sectional area and gauge length were measured at 296°K and the geometrical factor determined to within 0·1 per cent. Representative chips from these alloys and from the iron standards were chemically analyzed for carbon, nitrogen, and silicon content. The silicon concentration was determined with relative accuracies of a few percent (several hundredths of an atomic percent) and the results are listed in Table 1. The residual carbon level was 0·002 w/o and the nitrogen ~ 0·001 w/o.

Three samples were mounted together in a heat leak in good thermal contact with one another and with calibrated germanium and platinum resistance thermometers. On several of the runs one of the samples was an iron standard. A constant current of 0·1 A was passed through the samples and the resistivity measured by a standard, four probe, nulling technique to ±0·005 μΩ-cm. The temperature was determined to within ±0·05°K. Measurements were typically made at 40–50 temperatures between 4·2° and 300°K. The iron standards and some of the alloys were run several times throughout the study and the data was reproducible within the limits given above.

Table 1. Alloy number, silicon concentration (at. %), residual resistivity (μΩ cm), *reduced characteristic temperature, and resistivity parameter for iron–silicon alloys studied*

Number	Concentration	ρ_0	θ_i/θ_0	β_i
0	0	0·08	1·000	1·000
1	0·97	6·27	1·006	0·999
2	1·81	11·48	0·973	0·949
3	2·74	18·51	1·005	0·999
4	3·85	23·53	0·977	0·934
5	4·74	30·37	0·955	0·897
			0·963	0·900
6	5·74	35·88	0·961	0·867
7	6·51	40·59	0·930	0·794
8	7·66	47·22	0·907	0·737

The data were corrected for thermal and chemical expansion as described above with the aid of a simple computer program. The magnitude of these corrections has already been illustrated in Fig. 1. In Fig. 2 we show data obtained from 4·2, to 50°K. The data taken at temperatures below 20° or 25°K showed considerable scatter as well as

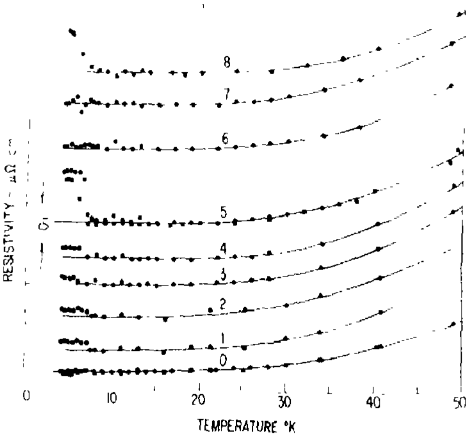

Fig. 2. Low temperature resistivity of iron–silicon solutions and iron standards. Each resistivity curve has been offset by a constant amount. See Table 1 for identification of alloys.

sudden, but reproducible, drops. The scatter may be associated with either the magnetic effects indicated in the introduction or with ferromagnetic resistivity anisotropies (cf. Smit[7]). However, the source of the sudden changes near 7°K is not now known. They are larger than those one would expect to arise from normal magnetoresistance effects in alloys with such large solute concentrations. Studies of the temperature and magnetic field dependence of the resistivity of dilute iron alloys with several different solutes are in progress and hopefull will help clarify the nature of these resistivity steps. Subsequent discussions will concern only the resistivity above 20°K.

The resistivity increments at 4·2°, 78° and 300°K were found to be well correlated with the silicon concentration. This is illustrated in Fig. 3 in which the solid lines are least square fits of the data to $\rho = \rho_{\text{Ideal}} + (\mathrm{d}\rho/\mathrm{d}c)c$.

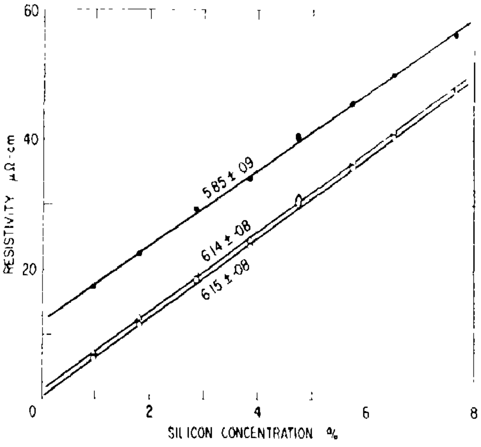

Fig. 3. Resistivity vs. at. % silicon at 4·2°K (○), 78°K (△), and 300°K (●). The straight lines are the least squares fit and the numbers are the respective slopes.

This correlation is somewhat improved if the data is fit to $\delta\rho \propto c(1-c)$ as expected from Nordheim's rule[1]. This correlation of $\delta\rho$ and silicon concentration supports the contention that we are studying the effects of independent silicon atoms. The resistivity increment per atomic percent silicon observed here is consistent with values previously reported[4, 24].

As expected $(\mathrm{d}\rho/\mathrm{d}c)$ is temperature dependent indicating, however, unexpected negative deviations from Matthiessen's rule. The thermal part of the resistivities for these alloys are shown in Fig. 4. The ideal resistivity of iron is shown as a dashed line. This change in the thermal component is even more striking for $\Delta(=\rho_{\text{Total}} + \rho_{\text{Ideal}} - \rho_0)$ as plotted in Fig. 5. These data have been corrected as described in Part 2 above, however, these negative deviations are also observed for the uncorrected data $\Delta = (R_{\text{Total}} - R_0)/G(296) - \rho_{\text{Ideal}}$.

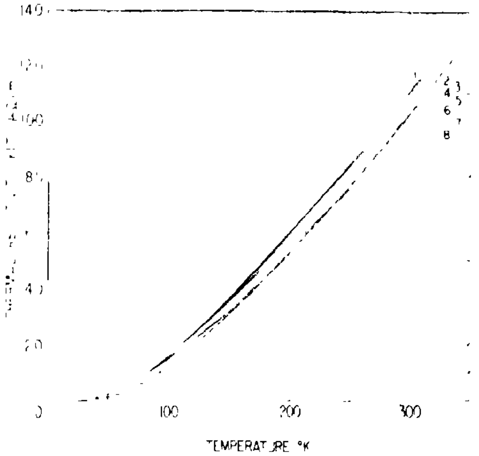

Fig. 4. Thermal component of the resistivity $r(T) = \rho_{\text{Total}} - \rho_0$ (solid lines), the ideal resistivity of pure iron (dashed line), and the normalized resistivity of solute-dominated, iron–silicon solid solutions (dotted line). See Table 1 for identification of alloys

The residual resistivities ρ_0 used in reducing the data were those values obtained by extrapolating the data as suggested by the solid curves in Fig. 2. In view of the uncertain origins of the increases in the resistivity on going below 7°K, this value was felt to be more indicative of the temperature independent solute resistivity. If these sudden changes are due to resistivity mechanisms which become important only below 7°K then they should be excluded from considera-

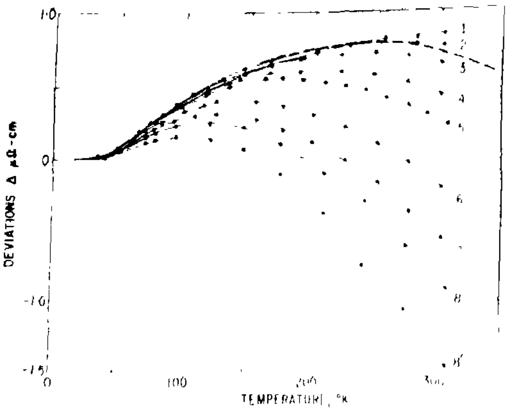

Fig. 5. Deviations from Matthiessen's rule corrected for thermal and chemical expansion (solid lines, see Table 1) and normalized deviations for solute-dominated, non-silicon solid solutions (top dashed line). Dashed line labeled 8' is uncorrected deviation for alloy number 8.

tion in discussions of the high temperature deviations. In effect this extrapolation means that we have defined the deviations such that they are zero (to within the resolution of our experiment) at 10°K. In the most extreme case (Sample 5) use of the actual resistivity value at 4·2°K would result in a uniform downward shift of the corresponding curve in Fig. 4 by ~ 0·15 μΩ cm. This would clearly remove the systematic variation with solute concentration which is observed. Although subsequent investigation may find the resistivity measured at 4·2°K to be the more meaningful, we feel that for the present the above considerations along with the systematic results obtained support the use of the extrapolated values.

4. ANALYSIS OF THE DATA

Several observations can immediately be made regarding these negative deviations. First, errors in the geometrical factor of the expected magnitude (0·1 per cent) could not produce this large an effect nor could these errors be expected to give such systematic behavior with concentration. Moreover, correction to the geometrical factors sufficient to eliminate these negative deviations would also cause large changes in the residual resistivity, ρ_0 and destroy the correlation between resistivity and concentration illustrated in Fig. 3. These alloys are still dilute enough that it is reasonable to expect little change in the electronic band structure; moreover band structure changes would also affect the residual resistivity ρ_0 concentration. Consequently, these changes are to be associated only with the temperature-dependent parts of the resistivity and most probably with changes in the ideal resistivity. From Fig. 4, it is apparent that there are similarities in the shapes of the thermal resistivity curves for the various alloys (and differences from that for the pure host, dashed line, Fig. 4).

As discussed (cf. equation (7)) the deviations from Matthiessen's rule become independent of concentration when the solute resistivity ρ_0 dominates the ideal resistivity. This is the case for the majority of the alloys over the temperature range studied here. Expecting these deviations to be temperature dependent, we write the thermal component of the resistivity $r(T)(=\rho_{\text{Total}}-\rho_0)$ as

$$r(T)=\rho_{\text{ideal}}(T)[1+f(T)] \tag{10}$$

where $r(T)(=\rho_{\text{Total}}-\rho_0)$ is the thermal component of the resistivity. For a normal metal, changes in ρ_{ideal} with alloying due to perturbations of the phonon spectra by the mass defects may be described as changes in the phonon characteristic (Debye) temperature. In analogy, we write the ideal resistivity of an iron–silicon solid solution as

$$\rho_{\text{ideal}}^{\text{Fe-Si}}(T)=\beta\rho_{\text{ideal}}^{\text{Fe}}(T\alpha) \tag{11}$$

where $\alpha^{-1}=\theta^r/\theta^0$ is the characteristic temperature θ^r for thermally excited scattering processes in the alloy reduced by that of the host θ^0 and β is a parameter introduced to provide for changes in the scattering strength. For scattering from phonons in a normal metal β would be proportional to θ_D^{-1} the inverse Debye temperature[25]. Both β and θ^r are expected to depend on solute concentration.

If deviations from Matthiessen's rule are due to differences in the anisotropies of the various scattering processes and if only a single scattering process dominates the ideal resistivity then the temperature dependence of $f(T)$ will also scale with the characteristic temperature θ^c. Consequently equation (10) may be written

$$r^c(T) = \beta^{\mathrm{Fe}}_{\mathrm{ideal}}(\alpha_c T)[1+f(\alpha_c T)] = \beta_c G(\alpha_c T) \tag{12}$$

where c denotes dependence on solute concentration. This means that the measured thermal component of the resistivity of a solid solution with solute concentration c when reduced by β_c will be a function only of the reduced temperature $\alpha_c T$. One method of testing for such a property is to expand $r^c(T)$ in a power series in T

$$r^c(T) = \sum_{i=1}^{N} B_i^c T^i = \sum_{i=1}^{N} (\beta_c \alpha_c^i) B_i^* T^i$$

where the B_i^* are independent of concentration. By forming ratios of the B_i^c for successive values of i, β_c may be eliminated and by again forming such ratios the following concentration-independent parameters are obtained

$$E_j = \frac{B_j^c B_{j-2}^c}{(B_{j-1}^c)^2} = \frac{B_j^* B_{j-2}^*}{(B_{j-1}^*)^2}, \quad j = 3, N.$$

The coefficients $(\beta_c \alpha_c^i B_i^*)$ were determined by fitting the measured data $r^c(T)$ with a ten term polynomial ($N = 10$). For each concentration c studied, the E_j, $j = 3, 10$ were calculated. The average standard deviation of the values for the nine samples about the average value of each E_j was less than 1·5 per cent, indicating this apparent shape similarly is real. The coefficient ratios

$$D_j^c = \frac{B_j^c}{B_{j-1}^c} = \alpha_c \frac{B_j^*}{B_{j-1}^*}, \quad j = 2, 10 \tag{13}$$

are proportional to α_c which in turn depends on solute concentration. For each value of j the coefficients D_j^c were fit to a polynomial in powers of solute concentration c. The results of this fit facilitated extrapolation to zero concentration, and by requiring $\alpha_c = 1$ at $c = 0$, the B^* ratios were eliminated from equation (13). An average of the values obtained for each value of j was used to define a value of α_c for each concentration.

With these values of α_c equation (12) was then used to determine β_c. The ideal resistivity of $\rho^{\mathrm{Fe}}_{\mathrm{ideal}}(T)$ was measured for a high purity iron standard. A low-silicon alloy was chosen as a relative standard with $\beta_c = 1$ and the deviation term $f(\alpha_c T)$ calculated from the data for this sample. This data was fit to a polynomial. With this analytical expression for $f(\alpha_c T)$ and with the values for α_c obtained above, equation (12) could be applied to define a value of β_c for each data point. An average of these values was constructed to define β_c for each concentration. The standard deviation of the β_c values for each sample about the average was about 1·5 per cent with no systematic deviations, again confirming the similarity in shapes of the resistivity curves. Extrapolation of α_c and β_c to zero concentration would permit a normalization of the curves to pure iron and an absolute determination of $f(T)$ $(=\Delta/\rho_{\mathrm{ideal}})$ for silicon in iron in the solute-dominated limit and with no perturbation on $\rho^{\mathrm{Fe}}_{\mathrm{ideal}}$. Such extrapolation yielded zero concentration values of α and β which were very close to unity and this re-normalization was not considered a serious modification.

With the aid of simple computer programs, the above analysis was performed for data corrected as described above, for uncorrected data, and for data corrected using other expressions for the thermal expansion. All analyses gave qualitatively the same results for data measured above 70°K. This scaling of the thermal resistivity is not a consequence of the corrections for thermal and chemical expansion. However, as pointed out above these corrections are all proportional to concentration and thus to a large measure have been implicitly incorporated by the scaling procedure. The corrected data is felt to have the most quantitative significance and is shown in Fig. 6 reduced as a plot of $f(\alpha^c T)[=\beta_c^{-1}r^c(T)-\rho_{\text{Ideal}}^{\text{Fe}}(\alpha_c T)]$ vs. $\alpha_c T$.

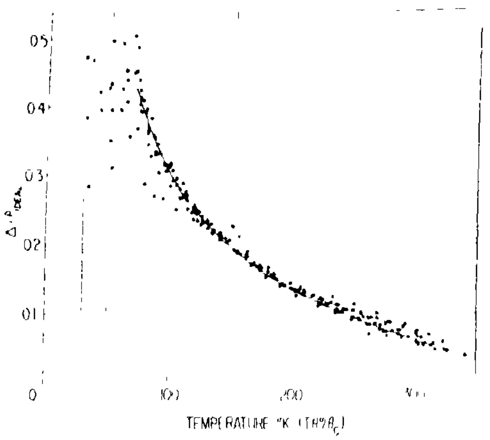

Fig. 6. Normalized plots of reduced deviations $\Delta/\rho_{\text{Ideal}}$. Solid curve represents solute-dominated limit, dashed line shows deviations for alloy No. 1 (see text). Error bars represent estimated resolution of $\Delta/\rho_{\text{Ideal}}$

Below 70°K errors in $f(\alpha_c T)=\Delta/\rho_{\text{Ideal}}$ become very large as both Δ and ρ_{Ideal} approach the limits of resolution of these measurements. For the high concentration alloys errors also exist due to the large residual restivities ($\sim 40\mu\Omega$ cm) relative to the small changes measured. The deviation of the reduced curve of the 0·97 a/o silicon alloy from the common curve at high temperatures in Fig. 6 is a result of the resistivity of the sample no longer being solute dominated (i.e. now $\rho_{\text{Ideal}} > \rho_0 \sim 6\mu\Omega$ cm). The decrease of $f(T)$ with increasing temperature is similar to that observed in noble metals and in those cases associated with a decrease in the relative importance of small angle scattering from phonons and the resultant decrease in the anisotropy of the thermal process scattering. The data normalized to zero concentration are also shown as the thermal resistivity $\beta_c^{-1}r(\alpha_c^{-1}T)$ in Fig. 4 (dotted lines) and as the concentration independent limit of the deviations from Matthiessen's rule in Fig. 5 (dashed lines).

As defined above the inverse of α_c is equal to the reduced characteristic temperature of the resistivity θ^c/θ_0, where θ_0 is characteristic of the host. In Fig. 7, θ_c/θ_0 and β_c are plotted against the square of the solute concentration.

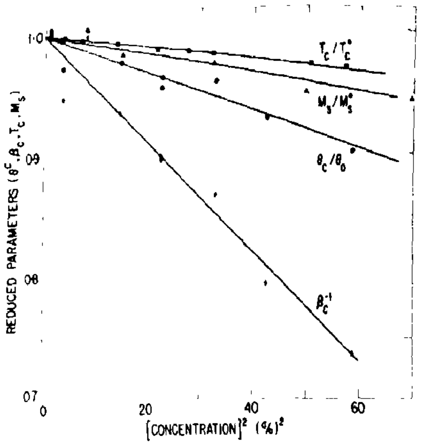

Fig. 7. Curie temperature[28] (○), saturation magnetization[29] (▲), characteristic resistivity temperature (●), and resistivity parameter ⊕ normalized to the corresponding values for pure iron as functions of solute concentration (in at. %) squared. Solid lines are least squares fits to the data

For the present, we note only the systematic decrease of these parameters with concentration. This systematic variation supports the physical significance of these parameters and the validity of this scaling procedure.

It is tempting to identify this characteristic resistivity temperature θ_c with other characteristic temperatures of iron solid solutions based on similarities in their dependences on solute concentration. For iron two such temperatures are the lattice Debye temperature and the ferromagnetic Curie temperature. Chessin[26] has measured the Debye temperature of iron–silicon alloys at 130° and 295°K by X-ray techniques and finds the lattice Debye temperature increases with silicon concentration up to about 7 a/o Si. From general arguments the Debye temperature is expected to vary as the square root of the ratio of an elastic constant to the effective mass per unit cell. Lytton[27] has found the elastic constants of iron to increase with silicon content and light silicon may be expected to decrease the mass per unit cell. Both of these variations predict increases in the Debye temperature with silicon concentration as observed by Chessin. On the other hand, the Curie temperature of iron–silicon solid solutions has been observed[28, 29] to decrease with increasing silicon content. This variation is in general complex[28] and analytical expressions for the dependence of the Curie temperature on silicon content have not been predicted. To obtain an analytical description of these variations, simple least square fits of the Curie temperature T_c, spontaneous magnetization M_s, the characteristic resistivity temperature θ_c, and the resistivity parameter β_c were made to half integral powers of silicon concentration from $\frac{1}{2}$ to 5. The data was generally fit best by a c^2 law and this is illustrated by the plots in Fig. 7.

The coefficient of c^2 for the resistivity temperature is about 2·5 times that of the Curie temperature T_c, however, the sign and magnitude of these coefficients are the same, as well as the power dependence of the variations. This factor of 2·5 would represent deviations of about 50 per cent if ascribed to errors in silicon concentration. In view of the correlation between intended alloy composition and chemical analyses and between the resistivity increment per solute atom observed here and those previously reported, errors of such magnitude are not likely. Taking such factors into account, the resistivity parameter (β_c) is roughly proportional to the square of the magnetization. Moreover, β_c increases with θ_c in contrast to the inverse proportionality predicted for scattering from phonons.

It must be pointed out that spin-mixing theory in the impurity-dominated limit (equation (9)) would predict a similar reduction of the data if the spin mixing term $\rho\uparrow\downarrow(T)$ was either negligible or arose from the same scattering process as the ideal resistivity. If however the spin mixing arises chiefly from electron–electron interactions, this contribution would not be expected to scale with the same characteristic temperature as the ideal resistivity. Bourquard, Daniel and Fert[30] have recently questioned if electron–electron collisions can be significant in producing deviations from Matthiessen's rule. Nevertheless, the appropriate modifications were made in the computer program to reduce the data as

$$r^c(T) = \beta^c \rho_{\text{Ideal}}(\alpha_c T) + f^c(T) \qquad (14)$$

where in this form β_c contains contributions from the term due to spin anisotropy in the impurity scattering (first brackets in equation (9)). The resultant reduction was not as good as that obtained with equations (7) and (12) and showed systematic deviations with temperature. However, deviations due to electron–electron scattering would be expected to be most important below 70°K where our data is not precise enough for such an analysis. It is important to mention that the best reduction of the data under equation (14) still shows a decrease of the deviations at high temperatures as is shown in Fig. 5 by the dashed line.

The analysis does indicate quite clearly that the total thermal resistivity cannot be obtained by scaling the ideal resistivity of pure iron with temperature-independent parameters. Some form of deviations from Matthiessen's rule are present even after appropriate corrections to $\rho_{\text{ideal}}(T)$ have been made. These deviations are temperature dependent but are not simply a constant multiple of the ideal resistivity. Moreover, these deviations are nearly concentration independent precluding any attempt to ascribe them to temperature-dependent scattering processes or to temperature dependences of the electronic states available for scattering.

5. SUMMARY

The electrical resistivity of iron–silicon solid solutions between 50° and 350°K show unexpected negative deviations from Matthiessen's rule. Such deviations were ascribed to changes in the ideal resistivity. In either relaxation time anisotropy or spin-mixing theories, deviations from Matthiessen's rule in solute dominated alloys ($\rho_0 > \rho_{\mathrm{Ideal}}$) are expected to be proportional to the ideal resistivity with proportionality factors which are independent of the solute scattering strength (ρ_0). In accordance with these two statements the thermal resistivity of these solid solutions was described well by

$$\rho_{\mathrm{Total}} = \rho_0 + \beta_c \rho^{\mathrm{Fe}}_{\mathrm{Ideal}}(T/\theta_c)[1 + f(T/\theta_c)]$$

where the residual solute resistivity ρ_0 is proportional to solute concentration and is temperature-independent. To a lesser extent the data could be reduced using a similar expression but with $f(T)$ independent of θ_c. This form is expected for spin-mixing processes if electron–electron collisions are important.

Data reduced in either fashion showed the qualitative feature of a decrease in Δ with increasing temperature above 250°K.

This does not seem compatible with spin-mixing theory as represented by equation (9) in which the first bracket is temperature independent and the temperature-dependent resistivities $\rho_{\mathrm{Ideal}}(T)$ and $\rho\ \downarrow\uparrow\ (T)$ are temperature non-decreasing. On the other hand such decreases are qualitatively understandable as a monotonic decrease in the anisotropy associated with thermal scattering processes when analyzed by equation (7) (or (8)), Fig. 6. Compatible with this interpretation is the observation that the temperature dependence of the deviations (i.e. of the anisotropy) scales with the same characteristic temperature as the ideal resistivity. In noble metals[2, 3] this behavior is associated with a decrease in the importance of small-angle scattering as longer wavelength phonons are excited. Consequently, we are inclined to attribute the deviations $\Delta(T)$ to the classic explanation-differences in the anisotropies of the various scattering processes.

One of the chief arguments for the necessity of spin-mixing considerations appears to be the large size of the deviations observed and consequently the large anisotropies needed to explain these deviations[4, 21]. A further test for the source of these deviations could involve the application of Kohler's rule to magnetoresistivity data. In at least one theory, the magnitude of the longitudinal magnetoresistivity at saturation depends on the anisotropy in the relaxation time of a conduction electron traveling in an orbit over the Fermi surface. At low temperatures where spin-mixing would be small, anisotropies with respect to spin would not contribute to the magnetoresistivity, whereas anisotropies within one band, which also give deviations from Matthiessen's rule, would affect the magnitude of the saturation value. Kohler's rule studies in nickel alloys interpreted in this way suggest that for some solutes considerable anisotropy is present in the scattering processes.

Continuing the discussion of the magnitude of the effect it must be noted that silicon has been observed to give rise to much smaller deviation than other solutes[4]. Although solutes giving larger deviations might improve the accuracy with which these deviations can be measured, these solutes usually have smaller resistivity increments per atomic percent solute. Consequently, it is more difficult to obtain solid solutions in the solute-dominated condition[31]. However, both theories suggest that only the magnitude and not the existence of these deviations depends on the solute present. Therefore having observed deviations in the iron-silicon system we think it reasonable to expect the results for silicon to be indicative of those for other solutes in iron.

Finally, the characteristic resistivity temperature θ_c varied with solute concentration in a manner similar to the ferromagnetic Curie temperature; both decrease, approximately quadratically, with silicon content. This is in marked contrast to the Debye temperature which increases with silicon concentration. The Debye temperature is expected to characterize the thermal component of the resistivity of normal metals for which phonon scattering is of chief importance. Consequently, this behavior suggests that the thermal component of the resistivity of iron is more critically dependent on the magnetic state than on the lattice dynamics in this temperature range. Theories [6, 32] predict that the ferromagnetic state may affect the resistivity either by presenting new sources for scattering or by altering the electronic states available for scattering. In the latter case deviations proportional to silicon concentration would be expected, whereas the observed deviations clearly had no such dependence. On the other hand, if the major ferromagnetic contributions are to the scattering processes (either as spin-disorder scattering at the host atoms or as spin-wave induced s–d transitions[33]) then the scaling laws observed here would be expected.

Acknowledgements—We gratefully acknowledge discussions with Drs. R. M. Fisher, L. J. Cuddy, G. P. Huffman, and Mr. L. Zwell and correspondence with Professors J. S. Dugdale, D Greig, and J. Silcox during the course of this work. We also wish to acknowledge the technical assistance of G. R. Dunmyre and the chemical analyses by G. W Momeyer.

REFERENCES

1 ZIMAN J. M., In *Electrons and Phonons*, pp. 285, 337 Clarendon Press, London (1960).
2. DUGDALE J. S. and BASINSKI Z. S., *Phys. Rev.* **157**, 552 (1967).
3. ZIMAN J. M , *Phys. Rev.* **121**, 1320 (1961).
4. CAMPBELL I. A , FERT A. and POMEROY A. R., *Phil, Mag.* **15**, 977 (1967).
5 BASINSKI Z. S., DUGDALE J. S., and HOWIE A., *Phil. Mag* **8**, 1989 (1963).
6. For a recent review of these ideas see BLATT F. J , In *Physics of Electronic Conduction in Solids*, p. 231 McGraw Hill, New York (1968).
7. cf. SMIT J., *Physica* **16**, 612 (1951); SCHWERER F. C. and SILCOX J., *Phys. Rev. Lett.* **20**, 101 (1968).
8. DAS S. B. and GERRITSEN A. N., *Phys. Rev.* **135**, A1081 (1960).
9. BRIDGMAN P. W., *Proc. Am. Acad. Sci., U.S.A.* **84**, 131 (1955).
10. PEARSON W. B., In *Handbook of Lattice Spacings and Structures of Metals*, Vol. 1, p. 626. Pergamon Press, Oxford (1958).
11. CAMERON D. I. and RUSSELL J. D , Lysaght's Central Res. Lab , Rep. No. 379, New Castle, N. S. W., Australia; Presented at the *AIME Conf., New York* (1968).
12. PEARSON W. B. In *Handbook of Lattice Spacings and Structures of Metals*, Vol 1, p. 656. Pergamon Press, Oxford(1958).
13. Similar results are obtained for a two-band model, cf. FARRELL T. and GREIG D., *Phys. Lett.* **24A**, 401 (1967).
14. cf. ZIMAN J. M., *Adv. Phys.* **10**, 1 (1961).
15. DEATON B. C. and GAVENDA J. D . *Phys. Rev.* **129**, 1930 (1963).
16. cf. FRIEDEL J., *Nuovo Cim.* **7**, 287 (1958); GOMES A. A., *J. Phys. Chem. Solids* **27**, 451 (1966); CAMPBELL I. A., *Proc. phys. Soc.* **89**, 71 (1966); CAMPBELL I. A. and GOMES A. A , *Proc. phys. Soc.* **91**, 319 (1967).
17. COLLINS M. F. and LOW G. G., *Proc. phys Soc.* **86**, 535 (1965)
18. JOHNSON C. E., RIDOUT M. S. and CRANSHAW T. E., *Proc. phys. Soc.* **81**, 1079 (1963).
19. STEARNS M. B., *Phys. Rev.* **147**, 439 (1966).
20 SCHWERER F. C., PhD Thesis, Cornell University, Ithaca, New York (1968).
21. GREIG D , *5th Annual Solid State Physics Conference*. University of Manchester (1968).
22. ARAJS S., OLIVER B. F. and MICHALAK J. T., *J. appl. Phys.* **38**, 1676 (1967).
23. HAWORTH C., Private communication
24. BOZORTH R. M., In *Ferromagnetism*, p. 76. Van Nostrand, Princeton, N. J. (1951).
25. ZIMAN J. M., In *Electrons and Phonons*, p. 364 Clarendon Press, London (1960).
26. CHESSIN H , *6th Intl Cong. Intl Union Crystallogr.* Rome, (1963).
27. LYTTON J. L., *J. appl. Phys.* **35**, 2397 (1964).
28. ARAJS S., *Phys. status Solidi* **11**, 121 (1965)
29. FALLOT M., *Ann. Phys.* **6**, 305 (1936)
30 BOURQUARD A , DANIEL E. and FERT A., *Phys. Lett.* **26A**, 260 (1968)
31. For the solubility limits of these iron base alloys see, for example, CAMERON D I. and RUSSELL J. D , Lysaght's Central Res. Lab., Rep. No. 379, New Castle, N. S. W., Australia; Presented at the *AIME Conf., New York* (1968).
32. COLES B. R., *Adv. Phys.* **7**, 63 (1958).
33. GOODINGS D. A., *Phys. Rev.* **132**, 542 (1963)

J. Phys. Chem. Solids Pergamon Press 1969. Vol. 30, pp. 1527-1533. Printed in Great Britain.

PRESSURE-INDUCED PHASE TRANSFORMATIONS IN THE B1 Ag-HALIDES

R. N. SCHOCK* and J. C. JAMIESON

Department of the Geophysical Sciences, University of Chicago, Chicago, Ill 60637, U.S.A.

(*Received* 20 *November* 1968)

Abstract—The structures which form with pressure from the Ag-halides in the B1-type have been investigated using X-ray powder diffraction techniques. It is proposed that AgCl transforms to a cinnabar (B9) type structure with $c = 7\cdot02$ Å, $a = 4\cdot06$ Å and $c/a = 1\cdot73$ and a $\Delta V/V_0$ at the transition of 8 per cent. This structure is stabilized due to overlap of electron orbitals resulting in the formation of two highly covalent collinear-bonds. AgBr transforms to the same structure with a volume change of the same magnitude, but at a slightly lower pressure. The structure to which B1–AgI transforms at 97 kbar is suggested to be tetragonal with $a = 5\cdot611$ Å, $c = 5\cdot020$ Å with $\Delta V/V_0$ at the transition approximately 13 per cent. Electrical conductivity measurements indicate that this transformation also involves a significant change to more covalent bonding.

INTRODUCTION

THE STRUCTURAL changes involved in the polymorphic transitions of NaCl-type (B1) structures with pressure have been the subject of considerable experimental effort and speculation. The most commonly postulated high-pressure structure has been the CsCl-type (B2) structure, mainly because of its higher cation–anion coordination. X-ray diffraction studies have indeed shown this to be the case in the alklai halides, except where the B2 structure is stable at atmospheric pressure due to cation–anion ionic-radius ratio. Such is not the case with the more covalently bonded Ag-halides. Jamieson and Lawson[1], using *in-situ* X-ray diffraction methods, showed that AgCl did not transform to this structure from the B1-type with pressure. Although actual identification was withheld, they suggested a tetragonal structure analogous to Hg_2Cl_2. Bassett and Takahashi [2] showed that the B1-type AgI did not transform to a B2-type. They were unable to index their high-pressure patterns.

This paper presents the results of high-pressure X-ray diffraction work on the Ag-halides, designed to determine the nature of these transitions. Bridgman[3] reported volume discontinuities at reported pressures of 88 kbar in AgCl and 84 kbar in AgBr at room temperature. These were the only transitions reported on compression of the B1-type atmospheric pressure phases. Based on comparison with a Bi transition at 88 kbar, Montgomery[4] placed the transition in AgCl at 76 ± 2 kbar at 25°C. Bridgman's[3] compression of the wurtzite (B4) modification of AgI showed a transition at about 3 kbar to a phase previously identified from a mixed-phase pattern[5] as the B1-type. Later, Van Valkenburg[6] showed the existence of two transitions in this region, the first to a PbO-type (B10) structure[7]. Slykhouse and Drickamer[8] reported an optical transition in AgI at 110 kbar but later revision[9] decreased this value to 97 kbar. These results partially reflect the present uncertainty in absolute pressure determinations in the 50–100 kbar range.

EXPERIMENTAL PROCEDURE

The apparatus and techniques for *in-situ* high-pressure X-ray diffraction studies have been described in detail[10]. Briefly, Zr filtered-MoKα radiation is collimated on a

---

*[*] *Present address:* University of California, Lawrence Radiation Laboratory, Livermore, Calif. 94550, U.S.A.

0·014 in dia. cylindrical sample, which has been diluted with amorphous boron to minimize absorption. The sample is pressurized between two tungsten-carbide anvils inserted through the top and bottom of a 114·6 mm Debye-Scherrer camera. Pressure is maintained and extrusion prevented through the use of a boron annulus, which permits the passage of X-rays. The technique was occasionally modified by utilizing a precompressed boron annulus, thereby reducing sample deformation and decreasing the width of diffraction lines. AgCl was reagent grade obtained from Allied Chemical, AgBr was as obtained from D. F. Goldsmith Corp. and AgI was from Mallickrodt and of unstated purity.

The electrical conductivity measurements were made in the same apparatus as that used for X-ray determinations except that the samples were not diluted with boron; and polystyrene, as well as the usual boron, was used at times to confine the sample. The current source and resistance network has already been described[11].

RESULTS AND DISCUSSION

AgCl

As pressure is increased the cubic B1-pattern of the low pressure phase is replaced by a non-cubic set of lines and this new pattern is stable to the highest achieved loads (estimated to be somewhat less than 150 kbar). Upon release of force this high-pressure phase reverts completely to the atmospheric form. A weak 2·363 Å line is observed in the after pattern, its absolute intensity increasing with the total time that the sample has been irradiated. Since this line is observed only in the after pattern and not in the starting material, it is concluded that interaction of the AgCl with X-rays serves to produce phonons which reduce silver-ions to produce the 111 Ag-metal reflection. The AgCl high-pressure pattern (Table 1) can be indexed as a hexagonal structure with $c = 7{\cdot}02$ Å, $a = 4{\cdot}06$ Å and $c/a = 1{\cdot}73$. Of the several hexagonal AX-type compound analogues, only the HgS-type (B9) structure ($Z = 3$, D_3^4-$P3_121$ space group) meets the density requirements for conversion from the B1-structure after 70–90 kbar of compression[3]. The calculated intensities in Table 1 were computed using the atom positions in normal cinnabar (HgS): $u = 0{\cdot}720$ (Ag) and $v = 0{\cdot}485$ (Cl).

Table 1. Analysis of experimental data on AgCl, high pressure form

d_{obs} (Å)	d_{calc} (Å)	hkl	$(I/I_0)_{obs}$	$(I/I_0)_{calc}$
3·145	3·141	101	*M*	19
2·832		boron	*W*	
2·482	2·482	102	*S*	100
2·288	2·339	003 (+Ag)	*M*−	5
2·030	2·030	110	*M*+	40
	1·950	111		10
	1·947	103		4
	1·757	112		2
1·702	1·705	201	*M*−	25
1·568	1·571	202	*W*	2
	1·569	104		1
	1·532	113		4
1·410	1·405	203 (+Ag?)	*M*	1
1·300	1·326	114	*M*	1
	1·305	211		5
	1·304	105		6
	1·243	212	*W*−	14
1·240	1·241	204		11
1·169	1·171	300	*W*	3
	1·169	006		4

The c/a ratio of 1·73 is lower than that of ideal HgS ($c/a = 2{\cdot}28$). Other compounds with this structure show c/a ratios of from 2·05 in the high-pressure form of HgTe[12] to 2·42 for HgO at 1 bar and 25°C. The calculated intensities in Table 1 show several departures from observed intensity values. The 003 and 203 lines should be too weak to be observed at all and the 111 and 212 reflection should perhaps be observed, which they are not. The two former anomalies may be explained by the presence of free Ag as mentioned before since Ag at a compression of 0·93 will have its 111 and 220 diffraction lines at 2·287 and 1·406 Å, respectively. Hence these lines may be assigned to free Ag rather than AgCl. This compression of Ag corresponds[13] to a pressure of 92 kbar, consistent with our pictures being taken well above the transition pressure.

The B9 structure can be derived from the B1-structure[14] by distorting the cubic anion lattice and repositioning the cations so as to attain more efficient packing along two of the original axes at the expense of the third. The cation–anion coordination is still 6 but with two very near, two intermediate and two furthest anion neighbors around each cation. This results in helical metal-anion chains running parallel to the c axis. Ionic Ag is significantly larger than Hg while ionic Cl is only slightly smaller than S and since the four longest cation-anion bonds in the B9 structure are very close to being in the [011] plane, this may account for the low c/a. The atom position-parameters were varied to try and obtain a better fit to the observed intensity data. In particular the 212 intensity is strongly dependent on the Ag parameter and diminishes rapidly as Ag is moved toward the cell edge. With $u = 0{\cdot}75$ and $v = 0{\cdot}450$ the intensity of 212 reflection is decreased to one-half that of the 204. Hence it is likely that the atom position-parameters deviate from ideal in the above manner.

The transitions of a B9-type structure with pressure in the group VIA compounds of Hg are from ZnS-type (B3) 4-fold coordinated structures. That AgCl apparently transforms to this structure from one that already has 6-fold coordination deserves some comment. Compounds either crystallizing with the B9-form or attaining it under pressure are notable in that they are only moderately ionic in character as opposed to the typically ionic alkali halides. This fact has been pointed out by Jayaraman *et al.*[15] who characterized these AX-compounds as intermediate between the metals and ionic crystals, based on the difference in electronegativity (ΔEN) of the constituent atoms and showed that they prefer the distorted B9 arrangement to the ideally ionic BI structure. The Ag-halides fall very close to the boundary between ionic and intermediate types. That they exist in ionic-type structures (B1) as well as intermediate types (B3, B4 and B10 for AgI) is in agreement with this concept. As pressure is increased on an ionic type (B1) structure, ΔEN will decrease as bond orbitals overlap to a greater degree until, barring a transformation dictated by space requirements, a structure more covalent in nature becomes energetically stable. The B9-type, considered as a simple distortion of a B1-type, is such a structure. Of the three Ag–Cl distances in the B9 structure (approx 2·0, 2·9 and 3·1 Å, compared with 2·61 Å in a Bl-lattice at their equilibrium) one is so short as to necessitate a strong covalent bond, while the other two in all probability are essentially ionic with their length dictated by the structure. To possess the two nearly collinear covalent bonds required by the B9-structure the Ag atom must utilize at least two of its electrons or have one donated from Cl. In the B9 structure of HgS, Hg has two 6s electrons with which to form bonds. However with only one 5s electron, Ag, would have to make use of an additional electron from its 4d sub-shell. Orgel[16] has shown that the tendency of Ag to occur in a linear environment is correlated with the small d–s separation in the Ag atom and that the loss in electrostatic energy due to a smaller number of neighbors is more than compensated by the stabilization due to d–s mixing in a low-symmetry environment. The bonds from the anion in the helical chain in the B9-structure are slightly greater than 90° and presumably represent utilization of p Cl orbitals. Thus the transformation from the B1- to B9-structure in AgCl may be considered to be due to increased overlap of electron orbitals as pressure is increased, until two covalent bonds are formed. Although the overall cation–anion coordination is unchanged, the increased strength of two of the bonds from each cation is compensated for by a slight relaxation in the remaining four bonds.

The cell parameters in Table 1 give a molar volume $V_p = 20{\cdot}12\ \mathrm{cm^3\ mole^{-1}}$. With the volume at the transition $V_t = 22{\cdot}13\ \mathrm{cm^3\,mole^{-1}}$ from Bridgman's compressibility data[3], $\Delta V = V_t - V_p = 2{\cdot}01\ \mathrm{cm^3\,mole^{-1}}$. This ΔV is the combined volume change at the transition and any volume decrement due to compression of the B9 structure. With $V_0 = 25{\cdot}73\ \mathrm{cm^3\,mole^{-1}}$, $\Delta V/V_0$ is 0·078 compared with Bridgman's $\Delta V/V_0$ at the transition of 0·016. The smallness of Bridgman's value is very likely due to his having achieved only partial transformation due to the sluggishness of the transition near the upper limit of his pressure range. We prefer our value.

The tetragonal Hg_2Cl_2 structure suggested in earlier work by Jamieson and Lawson[1] is not borne out by the present results where pattern quality is much improved. There is good correlation between d-spacings from both sets of data, however in the earlier work only five lines from a new phase could be separated from the B1-lines. This led to the fallacious suggestion.

AgBr

Although the patterns obtained from AgBr are quite inferior to those of AgCl due to sample absorption, three lines can be indexed as the hexagonal 101 at 3·16 Å (m-), 102 at 2·49 Å (m+) and 110 at 2·02 Å (w+). These may be satisfactorily fit by $a = 4{\cdot}0$ Å and $c = 7{\cdot}15$ Å. It is felt that this, combined with an absorption edge shift in AgBr at the transition similar to that in AgCl[8], is sufficient to indicate a B9-structure for the high-pressure form of AgBr. The mechanism of transition would be identical to that hypothesized for AgCl. The indicated c/a, 1·77, is slightly larger than that for AgCl. It is difficult, due to the poor patterns, to attain accuracy better than ±1 per cent in cell volume calculations. It is fairly certain, however, that the volume change at the transition is significantly greater than Bridgman's[13] $\Delta V/V_0$ of 0·011 for the same reason as in AgCl.

AgI

Several investigations have previously assigned the B1-structure to AgI above about 4 kbar[2, 5, 17]. In Table 2 we present a complete indexing of a pattern taken in the appropriate pressure range. The reason for presenting this data for a structure which seems already well established is to call attention to the small differences to be expected between d_{obs} and d_{calc} for a known structure and also to have available numerical d values for use in discussing patterns taken of AgI above its 97 kbar transition. The lattice parameter $a = 5{\cdot}815$ Å obtainable from this BI indexing corresponds to a pressure of 62 kbar using the cell edge data of Bassett and Takahashi[3]. The only available line from free Ag at 2·335 Å is in qualitative agreement with this pressure[13].

Table 2. Experimental data on B1 *phase of* AgI

d_{obs} (Å)	$(I/I_0)_{obs}$	hkl	d_{calc} (Å)
2·926	$S+$	200	2·908
2·483	W	boron	
2·335	W	(111 Ag)	
2·057	S	220	2·056
1·675	M	222	1·679
1·456	W	400	1·454
1·403	W =	boron	
1·330	$W-$	331	1·334
1·305	$M-$	420	1·303
1·185	$W+$	422	1·185
1·114	$W-$	511	1·119
1·029	W	440	1·028
0·971	W	600	0·969
0·921	W	620	0·919
0·877	W	622	0·877

The pattern obtained when AgI is compressed through its easily reversible transition at 97 kbar cannot be indexed as a B9-type structure. In Table 3 we present our data on this phase (or phases) together with that of Bassett and Takahashi[2]. At first glance there seems to be significant differences between the two sets of data and the possibility that the two patterns represent two distinct phases or assemblages of phases cannot be discounted. Indeed on the right hand side of Table 3 we present an indexing

Table 3. ***Diffraction patterns of*** **AgI** ***above 100 kbar***

(SJ) This study				(BT) Bassett and Takahashi [2]			
d_{obs} (Å)	Intens.	N	d_{calc} (Å)	d_{obs} (Å)	Intens.	N	d_{calc} (Å)
2·827	*S*	4	2·809	2·879	100	4	2·887
				2·656	30		
2·492	*W*	5	2·510	2·471	20		
				2·337	10		
2·291	*W*	6	2·291				
2·120	*W*	7	2·122	2·112	40		
1·982	*M+*	8	1·985				
1·764	*VW*	10	1·775				
1·716	*VW*						
				1·668	20	12	1·667
1·503	*VW*	14	1·500				
				1·442	20	16	1·443
1·405	*M*	16	1·403	1·417	10		
1·325	*M*	18	1·323	1·324	10	19	1·324

of a portion of their data as a B1 phase which is highly precise, $a = 5·773$ Å corresponding to a pressure slightly above 70 kbar. The strong 220 is missing, an effect which may be hypothesized as due to orientation in their stress system. No such interpretation may be made of our patterns but a much stranger set of systematic relations does appear in that for $a = 5·611$ Å calculated values for d from $d = a/\sqrt{N}$ may be obtained that are well within our experimental error except for one exceedingly weak reflection at 1·716 Å which may be entirely due to boron diffraction. The presence of the N value 7 precludes this indexing being truly cubic, while the presence of 7 and 14 together makes it impossible to choose a larger cubic cell. Using the cell data of Bassett and Takahashi [2], the B1 phase would have $a = 5·660$ Å at 100 kbar. This might lead one to suspect that at least some B1 phase is present and influencing the intensities and positions of lines such as 2·827, 1·982 or 1·405 Å. The absence of the expected 222 reflection (cf Table 2) suggests that the quantity present is small. Returning to Table 3, a glance at the values for N reveals that a great majority can be represented as h^2+k^2 while very few can be represented as h^2+hk+k^2 where h and k are integers. This immediately suggests tetragonal symmetry for a phase oriented so that reflections $hk0$ are accentuated. On this hypothesis we choose $a = 5·611$ Å and demand that a reasonable volume change be obtained from the volume 27·2 cm^3 mole^{-1} characteristic of the B1 phase at 100 kbar. For a 4 molecule cell this is found at $c = 5·020$ Å or $c/a = 0·894$ which gives a volume of 23·7 cm^3 mole^{-1}, a change of 12·8 per cent at the transition in excellent agreement with Van Valkenburg's [6] estimate of 10–20 per cent. This tetragonal fit is displayed in Table 4. All of our lines (SJ) could be fit by halving c and claiming two molecules per cell.

Table 4. *Quasi-tetragonal fit of high* AgI

hkl	d_{calc} (Å)	d_{obs}(SJ) (Å)	d_{obs}(BT) (Å)
200	2·805	2·827	2·879
022	2·510		
210	2·508	2·492	2 471
102	2·291	2 291 Ag(?)	2·337 Ag(?)
112	2·120	2·120	2·112
220	1·982	1·982	1·983
212	1·774	1·764	
310	1·774		
301	1 751		
311	1·672		1·668
003	1·669		
302	1·500	1·503	
312	1·448		1·442
400	1·402	1·405	1·417
330	1 322	1 325	1·324
331	1·278		1·293 (?)
223	1·276		
004	1·255	1·256	
420	1·254		
114	1·196	1·184	1·179
412	1·196		
332	1·170		

However this would rule out what we believe is one of the strongest arguments for accepting this simple picture. The cell parameters were obtained only from SJ data, yet on completing a full tetragonal calculation it was found that they also fit the data of Bassett and Takahashi completely with the exception of their reflection at 2·656 Å if reflections with *l odd were accepted. To sum up, what we are suggesting is that a composite pattern may be* obtained from the SJ and BT data. Both sets of data have been taken on highly oriented samples. In their case the X-ray beam passes parallel to the direction of applied force while in our case the converse is true. Since we are dealing with probable oriented samples in two different sets of apparatus it does not seem wise to try to suggest a more detailed structure using intensities and systematic absences, but the small numerical deviation of the tetragonal cell edges from cubic is similar to that in the known orthorhombic distortions of B1 in TlI or SnS[14, 18].

The electrical conductivity σ of AgI in its high-pressure phase was measured to check the data of Riggleman and Drickamer[9] and to carry the data of Schock and Katz[11] past the 97 kbar transition, in the hope that the pressure dependence of σ would shed further light on the type of structure that exists in this region. Due to the small sample size, no attempt was made to quantitize the data and instead σ/σ_0 was continuously plotted as a function of pressure. As pressure was increased, good qualitative agreement was obtained with the results of Schock and Katz. As the 97 kbar transition was approached σ decreased with increasing pressure, $d\sigma/dP$ likewise decreasing. At the transition a sharp decrease in σ, estimated to be 2–3 orders of magnitude, was observed. This result is in agreement with the observed blue shift[8] and sharp resistance increase[9] at these pressures. Above the transition σ increases rapidly at first, with $d\sigma/dP$ decreasing, with increasing pressure. The behavior below the transition is characteristic of ionic crystals where the charge is carried by diffusing ions, the activation energy for diffusion increasing with pressure. Above the transition, the behavior resembles that of a semi-conductor, the band-gap energy now being less than the activation energy for diffusion and decreasing with pressure. These results suggest that the transition in B1-AgI is, like that in AgCl, from a predominantly ionic crystal to one that is predominantly covalent in character. That the transition is not to the B9 structure must result from either atomic size or the inherent properties of the silver-iodine bond. Since HgTe, with a tellurium atom slightly larger than iodine, can exist in the structure[12], it is doubtful that size alone is the determining factor. Hg and Ag atoms are very nearly the same size.

The outer electrons in iodine are in the same shell as those of Ag and the compound AgI is expected to have a much lower contribution from ionic bonding than AgCl. With one more electron than Te in the well shielded $5p$ shell, the iodine atom is highly polarizable. These characteristics of the iodine atom may cause the B1 configuration not to transform to the B9 structure and to be stabilized to higher pressures at room temperature than either the chloride or the bromide. Periodic properties generally predict that as mean atomic number is increased in a group or isoelectronic combination of groups, identical structures become unstable at successively lower pressures, with high-pressure forms represented by the heavier materials. For example, compare AgCl and AgBr, and the B1–B2 transition in NaCl (300 kbar)[19], KCl (18 kbar) [1, 20], and RbCl (5·3 kbar)[20].

The specific structure stabilized in AgI at 100 kbar cannot be uniquely determined from the data available. It is likely that more refined work, perhaps including high temperature-high pressure determinations, may be necessary to delineate this structure.

In summary, B1 structures having small differences in the electro-negativities of their constituent atoms, appear to transform to structures in which at least some of the bonds are highly covalent. The inherent stability of the B1-type lattice is therefore a function of ΔEN and a lattice constant-atomic radius parameter, as well as the familiar cation-anion radius ratio.

Acknowledgements—We would like to acknowledge the donors of the Petroleum Research Fund administered by the American Chemical Society and NSF Grant GA-1270 for support of this work. We are grateful to J. Michael Bennett for providing the necessary computer programs.

REFERENCES

1. JAMIESON J. C. and LAWSON A. W., *J. appl. Phys.* **33**, 776 (1962).
2. BASSETT W. A. and TAKAHASHI T., *Am. Miner.* **50**, 1576 (1965).
3. BRIDGMAN P. W., *Proc. Am. Acad. Arts Sci.* **76**, (1945).
4. MONTGOMERY P. W., *Am. Soc. Mech. Engrs* Paper 64, WA/PT-18 (1964).
5. JACOBS R. B., *Phys. Rev.* **54**, 325 (1938).
6. VAN VALKENBURG A., *J. Res. natn. Bur. Stand.* **68A**, 97 (1964)
7. MOORE M. J. and KASPER J. S., *J. chem. Phys.* **48**, 2446 (1968)
8. SLYKHOUSE T. E. and DRICKAMER H. G., *J Phys Chem. Solids* **7**, 207 (1958).
9. RIGGLEMAN B M and DRICKAMER H G, *J. chem. Phys.* **38**, 2721 (1963).
10. JAMIESON J. C., In *Metallurgy at High Pressures and High Temperatures* (Edited by K. A. Gschneidner *et al.*), pp. 201–228. Gordon and Breach, New York (1964).
11. SCHOCK R N. and KATZ S., *J. chem. Phys.* **48**, 2094 (1968).
12. MARIANO A. N. and WAREKOIS E. P., *Science* **142**, 672 (1963).
13. CLARK S. P, *Geol. Soc. Amer. Mem.* 97 (1966).
14. WYCKOFF R W. G., In *Crystal Structures.* 2nd Edn, Vol. 1. Interscience, New York (1963)
15. JAYARAMAN A., KLEMENT W Jr, and KENNEDY G. C., *Phys. Rev.* **130**, 2277 (1963).
16. ORGEL L. E, *J. chem. Soc.* **4**, 4186 (1958).
17. PIERMARINI G J. and WEIR C. G, *J. Res. natn. Bur. Stand.* **66A**, 325 (1962)
18. KAFALAS, J A. and MARIANO, A N, *Science* **143**, 952 (1967).
19. BASSETT W. A, TAKAHASHI T, MAO M. and WEAVER J. S, *J. appl. Phys.* **39**, 219 (1968).
20. PISTORIUS C W. F. T., *J. Phys. Chem. Solids* **25**, 1477 (1964).

J. Phys. Chem. Solids Pergamon Press 1969. Vol. 30, pp. 1535–1547. Printed in Great Britain.

SUPERHYPERFINE INTERACTIONS IN THE EPR AND UPR SPECTRA OF $CaF_2:U^{4+}$

C. M. BOWDEN, H. C. MEYER, P. F. McDONALD and J. D. STETTLER
Solid State Physics Branch, Physical Sciences Laboratory, Redstone Arsenal, Alabama, U.S.A.

(*Received* 15 *August* 1968; *in revised form* 20 *November* 1968)

Abstract—Satellite components have been observed (at 9·0 GHz) in the EPR and UPR spectra of $CaF_2:U^{4+}$ in sites of C_{3v} symmetry, and interpreted on the basis of a theoretical model as superhyperfine structure. This structure is due to the interaction between the substitutional U^{4+} ion and its eight nearest neighbor F^- nuclei. Interpretation of the experimental results on the basis of the model indicates that the *shf* interaction is anisotropic and arises predominantly from the direct dipole–dipole interaction. The $2p_\sigma$-overlap contribution δA is within the range $0 \leq (\delta A/g_\parallel\beta) \leq 0{\cdot}4$ G

1. INTRODUCTION

THE ORIGINAL interest in uranium doped CaF_2 was based on its laser properties. Recently many forms of CaF_2:U other than the laser material $CaF_2:U^{3+}$ have been discovered. In particular, a very strong interaction has been observed between microwave phonons and the non-Kramers U^{4+} ion[1].

The free U^{4+} ion has a $5f^2$, $^3H_4$ ground state which is split by the cubic crystalline field of CaF_2 so that a T_2 triplet lies lowest. Although the U^{4+} presumably enters CaF_2 substitutionally for Ca^{2+}, nearby charge compensation or a static Jahn–Teller effect introduces a distortion along a [111] direction which splits the triplet into a singlet and a doublet. Spin relaxation studies indicate that the singlet is at least 6 cm^{-1} above the doublet[2]. Irrespective of the fact that no influence of the singlet upon either the EPR or UPR spectra has been observed, an effective spin of one formalism is necessary because of the non-Kramers character of the U^{4+} ion, i.e. the ground doublet can be split by crystalline fields of lower than trigonal symmetry. Thus the spin Hamiltonian which describes the interaction, within the ground triplet, of the magnetic electrons with the applied magnetic field and the crystalline electrostatic field is

$$\mathscr{H} = g_\parallel\beta H_zS_z + g_\perp\beta(H_xS_x + H_yS_y) + D[S_z^2 - \tfrac{1}{3}S(S+1)] + \sum_{i,j}\tau_{ij}S_iS_j, \quad (1)$$

where the axis of quantization is the trigonal axis of the U^{4+} site.* The effects of local random strains are represented by the fourth term in (1), where the τ_{ij} are linear in the strain components. This term is a perturbation to the Zeeman terms and the third or axial crystal field term, where $|D| \geq 6$ cm^{-1}. Under the conditions of the experiment described here only transitions within the ground doublet are observed. Hence, to first order in the τ_{ij}, equation (1) gives for the $\Delta M_s = \pm 2$ transitions

$$h\nu = 2g_\parallel\beta H_z \quad (2)$$

as the condition for resonant absorption. It is to be noted that the $\Delta M_s = 2$ transition is allowed in UPR but forbidden in EPR. The effects of the random strains in equation (1) are first, to give some $\Delta M_s = 0$ character to the transition, thus giving a non-zero EPR intensity for the microwave magnetic field parallel to the trigonal axis; and second, to broaden the UPR and EPR absorption lines to lower values of H_z, thus giving an asymmetrical line shape with the steeper slope on the high field side, as is experimentally observed[1]. A theoretical and experimental comparative study of the UPR and EPR

---

*The spin-1 formalism for non-Kramers doublets was first suggested by R. Orbach and applied to the interpretation of magnetic resonance of $CaF_2:U^{4+}$ by WETSEL G. C. and DONOHO P. L., *Phys. Rev.* **139**, A334 (1965).

strain broadened line shapes is the subject of a future publication[3].

Splittings of both the EPR and UPR lines have been reported[4]. The model for the U^{4+} ion represented by equation (1) does not explain this behavior. We report in this paper studies involving both EPR and UPR of these splittings, and propose an explanation for them in terms of superhyperfine interactions between the U^{4+} ion and its nearest neighbor fluorine ions.

2. THEORY

2.1 *SHF interactions*

We consider only the eight fluorines that are nearest neighbors of the U^{4+} impurity ion, assumed substitutional for the Ca^{2+} ion. Although a local trigonal distortion is indicated by the electronic spin Hamiltonian (1), the U^{4+} site is assumed to be an inversion center. Thus, the neighboring F^- ligands are magnetically equivalent in pairs about the impurity site for arbitrary direction of the field $\mathbf{H}_0$. For the α^{th} fluorine ($\alpha = 1, \ldots, 8$) we must add to equation (1) the Hamiltonian

$$\mathcal{H}^\alpha = \mathbf{S}\cdot\mathbf{A}^\alpha\cdot\mathbf{I}^\alpha - \gamma_N\mathbf{H}_0\cdot\mathbf{I}^\alpha, \tag{3}$$

where the tensor $\mathbf{A}^\alpha$ represents the electron-nuclear spin coupling and the second term is the nuclear Zeeman term. In the coordinate system defined for equation (1), there are no terms in equation (3) that couple the states of the ground doublet of the U^{4+} ion, provided we neglect the effects of random strains. Thus, the contributions of the nuclear spins may be found by diagonalizing only within a given M_s manifold.

In order to specify the $\mathbf{A}^\alpha$ tensor in terms of its principal components, we choose a coordinate system fixed at the α^{th} fluorine nucleus with coordinates π, μ, σ, where σ is the axis coincident with the bond axis between the fluorine and substitutional U^{4+} ion and π and μ are orthogonal axes perpendicular to the bond axis. These are chosen such that the bond axis, σ, the trigonal axis of the site z and π lie in the same plane. This is shown in Fig. 1(a), where ϕ is the angle between the bond axis σ and the trigonal axis z.

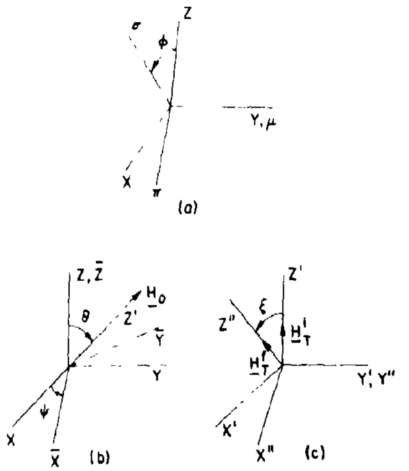

Fig. 1. (a) Relationship between the principal axis system for the interaction tensor $\mathbf{A}^\alpha$, (π, μ, σ), and the coordinate system (x, y, z), where z is the symmetry axis of the impurity site. The bond axis σ, the symmetry axis z, and π lie in the same plane. (b) Relationship between the applied field direction z' and the coordinate system (x, y, z), where z is the symmetry axis. The axes z', $\bar{y}$ and z all lie in the same plane. (c) Angular relation between the direction of the initial total field $\mathbf{H}_T{}^i$ at a given fluorine nucleus and the direction of the final total field $\mathbf{H}_T{}^f$ corresponding to the electronic spin transitions $M_s = -1 \rightarrow M_s = +1$ respectively.

If we neglect any distortion of the F^-2p electronic wave functions due to the lower symmetry of the impurity site relative to the Ca ion sites for the pure crystal, the (π, μ, σ) system is a principal axis system for the interaction tensor $\mathbf{A}^\alpha$. Thus, dropping the superscripts α, equation (3) can be written in the form

$$\mathcal{H}' = A^{\pi\pi}S_\pi I_\pi + A^{\mu\mu}S_\mu I_\mu + A^{\sigma\sigma}S_\sigma I_\sigma - \gamma_n\mathbf{H}_0\cdot\mathbf{I}. \tag{4}$$

Taking the symmetry axis z of the impurity site as the axis of quantization we look for the transformation $\mathbf{T}$ which transforms the electronic and nuclear spin components from the system (x, y, z) to the system (π, μ, σ). From Fig. 1(a)

$$\mathrm{T}(\phi)=\begin{pmatrix}\cos\phi & 0 & -\sin\phi\\ 0 & 1 & 0\\ \sin\phi & 0 & \cos\phi\end{pmatrix} \tag{5}$$

which gives, for contributions from the z component of the electronic spin,

$$S_\pi=-S_z\sin\phi,\quad S_\mu=0,\quad S_\sigma=S_z\cos\phi, \tag{6}$$

and for the nuclear spin variables

$$\begin{aligned} I_\pi &= I_x\cos\phi-I_z\sin\phi\\ I_\mu &= I_y\\ I_\sigma &= I_x\sin\phi+I_z\cos\phi. \end{aligned} \tag{7}$$

In order to simplify the transformation equations for the nuclear spin components, we define a new coordinate system $(\bar{x},\bar{y},\bar{z})$ in terms of the system (x,y,z) as shown in Fig. 1(b). The barred system is chosen such that z and $\bar{z}$ are coincident and $\bar{y}$ lies in the same plane with the applied magnetic field $\mathbf{H}^0$ and the axis $\bar{z}$. This defines an angle ψ between the x and $\bar{x}$ axes which is invariant for any pair of magnetically equivalent fluorines provided the field $\mathbf{H}_0$ is always in the $(1\bar{1}0)$ plane and the site axis z is in the $[1\bar{1}1]$ direction, which are the experimental conditions being described. The angle θ is the angle the applied magnetic field makes with the trigonal axis z. For the fluorine pair along the $[11\bar{1}]$ direction $\phi=0°$. For the fluorine pair along the $[111]$ direction in the plane of $\mathbf{H}_0$ and z, $\psi=\pi/2$. For $\mathbf{H}_0$ in the $(1\bar{1}0)$ plane the four F$^-$ nuclei out of the plane are magnetically equivalent with $\psi=75{\cdot}5°$.

If z' denotes the axis along which the applied field $\mathbf{H}_0$ is directed, the component of the total nuclear spin $\mathbf{I}$ along this axis is obtained from Fig. 1(b),

$$I_{z'}=-I_x\sin\psi\sin\theta+I_y\cos\psi\sin\theta+I_z\cos\theta. \tag{8}$$

Noting that in the principal axis system, (π,μ,σ), the symmetry of the p and s orbitals of the F$^-$ ion demands that there be only two independent elements of the tensor $\mathbf{A}$, i.e., the perpendicular component to the σ-bond axis $A_\perp$ and the element parallel to that axis $A_\parallel$, we have for the Hamiltonian (4)

$$\begin{aligned}\mathscr{H} &= [(A_\parallel-A_\perp)\sin\phi\cos\phi\, S_z\\ &\quad+\gamma_n H_0\sin\theta\sin\psi]I_x\\ &\quad-[\gamma_n H_0\sin\theta\cos\psi]I_y\\ &\quad+[(A_\perp+(A_\parallel-A_\perp)\\ &\quad\times\cos^2\phi)S_z-\gamma_n H_0\cos\theta]I_z.\end{aligned} \tag{9}$$

The neglect of the S_+ and S_- terms in equation (9) is based upon a perturbation approximation, valid for the UPR[1] and EPR [4] spectra, that the electronic singlet exerts no influence upon the transitions within the ground doublet. Equation (9) can be written in terms of the raising and lowering operators as

$$\begin{aligned}\mathscr{H} &= (A_1S_z+B_1)(I_++I_-)-iB_2(I_--I_+)\\ &\quad+(A_2S_z-C)I_z\end{aligned} \tag{10}$$

where

$$\begin{aligned} A_1 &= \tfrac{1}{2}(A_\parallel-A_\perp)\sin\phi\cos\phi\\ B_1 &= \tfrac{1}{2}\gamma_n H_0\sin\theta\sin\psi\\ A_2 &= A_\perp+(A_\parallel-A_\perp)\cos^2\phi\\ B_2 &= \tfrac{1}{2}\gamma_n H_0\sin\theta\cos\psi\\ C &= \gamma_n H_0\cos\theta.\end{aligned} \tag{11}$$

We thus have the resulting matrix elements

$$\begin{aligned} \langle\tfrac{1}{2}M_s|\mathscr{H}|\tfrac{1}{2}M_s\rangle &= \tfrac{1}{2}(A_2M_s-C)\\ \langle-\tfrac{1}{2}M_s|\mathscr{H}|-\tfrac{1}{2}M_s\rangle &= -\tfrac{1}{2}(A_2M_s-C)\\ \langle-\tfrac{1}{2}M_s|\mathscr{H}|\tfrac{1}{2}M_s\rangle &= (A_1M_s+B_1)-iB_2\\ \langle\tfrac{1}{2}M_s|\mathscr{H}|-\tfrac{1}{2}M_s\rangle &= (A_1M_s+B_1)+iB_2.\end{aligned} \tag{12}$$

Diagonalizing within the manifold M_s, we have the characteristic determinant

$$\begin{vmatrix} \frac{1}{2}(A_2M_s-C)-E & (A_1M_s+B_1)+iB_2 \\ (A_1M_s+B_1)-iB_2 & -\frac{1}{2}(A_2M_s-C)-E \end{vmatrix} = 0 \tag{13}$$

and the corresponding characteristic equation

$$E^2 = \tfrac{1}{4}(A_2M_s+C)^2+(A_1M_s+B_1)^2+B_2^2. \tag{14}$$

The contribution to the energy due to the superhyperfine interaction is therefore

$$\begin{aligned} E(M_s, m_I) = m_I\{&A_\perp^2+(A_\parallel^2-A_\perp^2)\cos^2\phi \\ &+2M_s(A_\parallel-A_\perp)\gamma_n H_z \\ &\times \sin\phi\cos\phi\sin\psi\tan\theta \\ &-2M_s[A_\perp+(A_\parallel-A_\perp)\cos^2\phi] \\ &\times\gamma_n H_z+\gamma_n^2 H_z^2\sec^2\theta\}^{1/2} \end{aligned} \tag{15}$$

where H_z is the component of the applied field $\mathbf{H}_0$ along the symmetry axis, z, of the site.

Consider now the Hamiltonian form for $\mathscr{H}$ specifically in terms of the Fermi S-contact, $2p_\sigma$-overlap, and direct dipole–dipole interactions. We will neglect overlap contributions from the $2p$ functions other than the component directed along the F^-–U^{4+} bond axis. The *shf* interaction Hamiltonian for the α^{th} fluorine is[5]

$$\begin{aligned} \overline{\mathscr{H}} = A_s\mathbf{S}\cdot\mathbf{I}+&(A_\sigma+A_D) \\ &\times\sum_{i}\sum_{\pi,\mu,\sigma} S_i I_r(3\cos^2\theta_{r\sigma}-1) \end{aligned} \tag{16}$$

where A_s is the interaction parameter for the isotropic interaction of the U^{4+} $5f$ electronic wavefunctions with the $1s$ and $2s$ functions of the fluorine ligand, A_σ and A_D are the $2p_\sigma$-overlap and direct dipole–dipole contributions respectively, and $\theta_{r\sigma}$ is the angle between the r axis and the σ-bond axis.

If the transformation equations (6) and (7) are used and the indicated summation is performed, equation (16) becomes

$$\begin{aligned} \overline{\mathscr{H}} = A_sS_zI_z+A_P[&(3\cos^2\phi-1)S_zI_z \\ &+3A_P\sin\phi\cos\phi\, S_zI_x] \end{aligned} \tag{17}$$

where $A_P = A_\sigma + A_D$. But, from equation (3)

$$\begin{aligned} \overline{\mathscr{H}} &= \mathbf{S}\cdot\mathbf{A}\cdot\mathbf{I} \\ &= A^{\pi\pi}S_\pi I_\pi+A^{\mu\mu}S_\mu I_\mu+A^{\sigma\sigma}S_\sigma I_\sigma. \end{aligned} \tag{18}$$

By using the transformations (6) and (7) this becomes

$$\begin{aligned} \mathbf{S}\cdot\mathbf{A}\cdot\mathbf{I} = {}&[A^{\pi\pi}\sin^2\phi+A^{\sigma\sigma}\cos^2\phi]S_zI_z \\ &+[A^{\sigma\sigma}-A^{\pi\pi}]\sin\phi\cos\phi\, S_zI_x. \end{aligned} \tag{19}$$

Comparing equations (17) and (19) we have the relations

$$\begin{aligned} &A^{\pi\pi}\sin^2\phi+A^{\sigma\sigma}\cos^2\phi = A_s+A_P(3\cos^2\phi-1) \\ &(A^{\sigma\sigma}-A^{\pi\pi})\sin\phi\cos\phi = 3A_P\sin\phi\cos\phi. \end{aligned} \tag{20}$$

Solving the two simultaneous equations (20) for $A^{\pi\pi}$ and $A^{\sigma\sigma}$, and writing $A^{\sigma\sigma}=A_\parallel$ and $A^{\pi\pi}=A_\perp$ yields

$$A^{\sigma\sigma}=A_\parallel=A_s+2A_P$$

and

$$A^{\pi\pi}=A^{\mu\mu}=A_\perp=A_s-A_P. \tag{21}$$

The excess charge of the U^{4+} ion would tend to distort the $2p_\sigma$ wavefunctions toward the impurity ion producing a higher spin density for these electronic wavefunctions in the vicinity of the paramagnetic electrons. Thus, the anisotropic overlap is expected to be much more dominant than the isotropic. Neglecting, then, overlap with the $1s$ and $2s$ F^- electronic wavefunctions, $A_s=0$ and equations (21) become

$$\begin{aligned} A_\parallel &= 2A_P \\ A_\perp &= -A_P. \end{aligned} \tag{22}$$

The Hamiltonian (9) can now be written as

$$\begin{aligned} \mathscr{H}' = {}&[3A_P\sin\phi\cos\phi\, S_z+\gamma_n H_0\sin\theta\sin\psi]I_x \\ &-[\gamma_n H_0\sin\theta\cos\psi]I_y \\ &+[A_P(3\cos^2\phi-1)S_z-\gamma_n H_0\cos\theta]I_z \end{aligned} \tag{23}$$

and the contribution to the energy (15) becomes

$$E(M_s, m_I) = m_I\{A_P{}^2[1+3\cos^2\phi] + 2M_s A_P \gamma_n H_z \times \sin\phi\cos\phi\sin\psi\tan\theta + 2M_s A_P[1-3\cos^2\phi]\gamma_n H_z + \gamma_n{}^2 H_z{}^2 \sec^2\theta\}^{1/2}. \quad (24)$$

With the applied magnetic field $\mathbf{H}_0$ in the $(1\bar{1}0)$ plane and the trigonal axis in the $[11\bar{1}]$ direction, there are three magnetically inequivalent sets of F$^-$ nuclei which interact with the U^{4+} ion. These are the pair along the site axis, $[11\bar{1}]$, the pair along the $[111]$ direction which lies in the plane of $\mathbf{H}_0$ and the site axis $[11\bar{1}]$, and the four nearest neighbors out of this plane. The angular dependence of the contribution of each of these sets of equivalent nuclei to the splitting of the electronic non-Kramers doublet was calculated from equation (24) and is presented in Fig. 2. The contribution to the interaction parameter A_P for each of the magnetically equivalent fluorine nuclei is that discussed in Section 5. Here, the energy level splitting is represented in frequency as a function of angle and gives the frequencies expected from an Endor experiment on CaF$_2$:U^{4+} corresponding to the selection rules $\Delta M_s = 0$, $\Delta m_I = \pm 1$.

2.2 *Calculation of the transition probabilities*

The interaction Hamiltonian for each fluorine can be written in terms of the total magnetic field $\mathbf{H}_T$ at the fluorine ligand site,

$$\begin{aligned}\mathcal{H}_i &= -\gamma_n \mathbf{H}_T{}^i \cdot I\\ \mathcal{H}_f &= -\gamma_n \mathbf{H}_T{}^f \cdot I\end{aligned} \quad (25)$$

where i and f denote the initial and final state respectively, corresponding to the electronic spin transitions $\Delta M_s = \pm 2$. If we denote the the initial spin states for the j^{th} nucleus of total spin $I = \frac{1}{2}$ by

$$\alpha_j = \begin{pmatrix}1\\0\end{pmatrix}^j \quad \text{and} \quad \beta_j = \begin{pmatrix}0\\1\end{pmatrix}^j \quad (26)$$

the initial spin states for an equivalent pair of nuclei, say $j = m$ and $j = n$, form a direct product space spanned by the product functions

$$\alpha_m\alpha_n, \beta_m\beta_n, \alpha_m\beta_n, \beta_m\alpha_n. \quad (27)$$

Let the angle between the initial and final total field directions at an F$^-$ nucleus be ζ. Then the unitary transformation that transforms the spinor functions α_j and β_j from the coordinate system where z' is along the direction of $\mathbf{H}_T{}^i$ to the system where z'' is along the direction of $\mathbf{H}_T{}^f$ is, from Fig. 1(c),

$$\begin{aligned}\mathbf{U}(\zeta) &= \exp[-i\zeta/2\, n \,.\, \sigma]\\ &= \cos\zeta/2 - i\sigma_y \sin\zeta/2\end{aligned} \quad (28)$$

or

$$\mathbf{U}(\zeta) = \begin{pmatrix}\cos\zeta/2 & -\sin\zeta/2\\ \sin\zeta/2 & \cos\zeta/2\end{pmatrix}. \quad (29)$$

Thus, the nuclear spinor functions of an equivalent pair transform from the initial to the final state as

$$\begin{aligned}\alpha_m\alpha_n &\to \alpha_m\alpha_n\cos^2\zeta/2 + \beta_m\beta_n\sin^2\zeta/2 + \tfrac{1}{2}(\alpha_m\beta_n + \beta_m\alpha_n)\sin\zeta\\ \beta_m\beta_n &\to \alpha_m\alpha_n\sin^2\zeta/2 + \beta_m\beta_n\cos^2\zeta/2 - \tfrac{1}{2}(\alpha_m\beta_n + \beta_m\alpha_n)\sin\zeta\\ \alpha_m\beta_n &\to \alpha_m\beta_n\cos^2\zeta/2 - \beta_m\alpha_n\sin^2\zeta/2 + \tfrac{1}{2}(\beta_m\beta_n - \alpha_m\alpha_n)\sin\zeta\\ \beta_m\alpha_n &\to \beta_m\alpha_n\cos^2\zeta/2 - \alpha_m\beta_n\sin^2\zeta/2 + \tfrac{1}{2}(\beta_n\beta_m - \alpha_n\alpha_m)\sin\zeta.\end{aligned}$$

The *shf* splitting of the electronic states by an equivalent pair of fluorine nuclei is presented schematically in Fig. 3. The relative transition probabilities for the electron-nuclear transitions are given in Table 1 in terms of the angle ζ. Thus, the ratio of the satellite intensity, p, to that of the central line, p_c, is

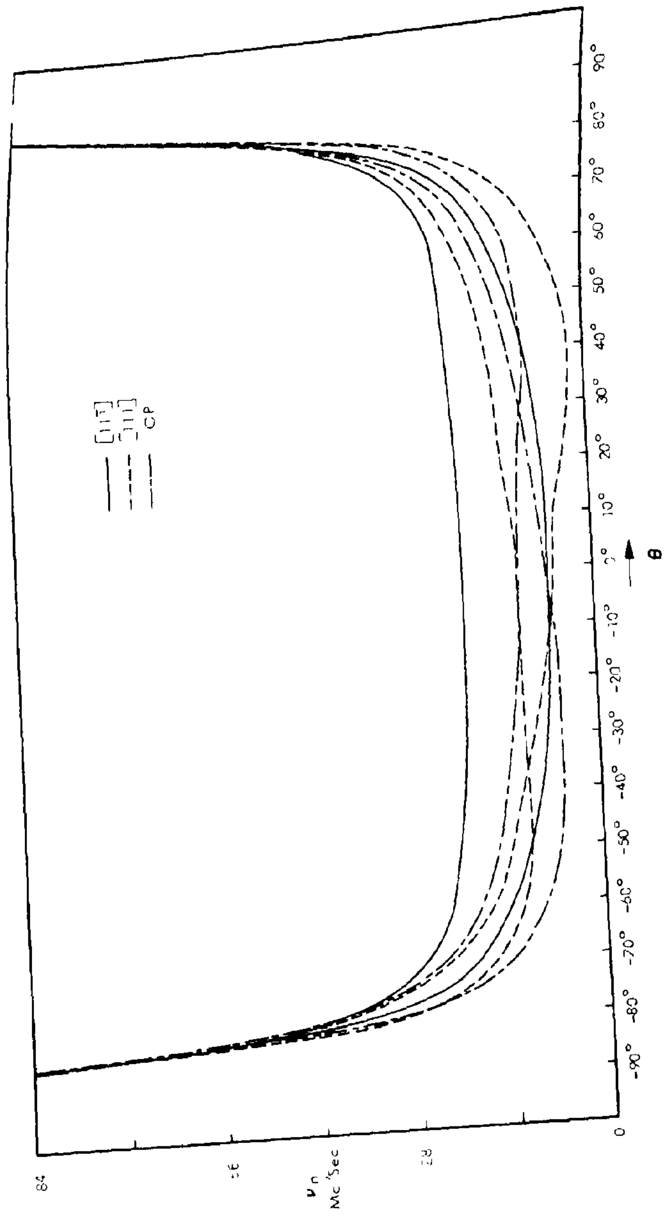

Fig. 2. Predicted contributions from each pair of magnetically equivalent nearest neighbor fluorine nuclei to the *shf* splitting of the electronic energy levels as a function of the angle θ between the symmetry axis z and the applied magnetic field $\mathbf{H}_0$. The frequencies are those expected from an Endor or Undor experiment.

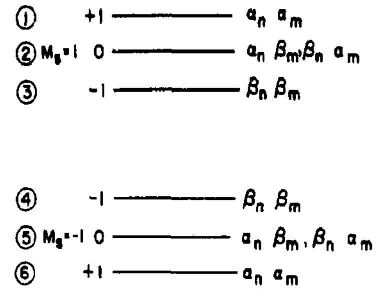
① +1 $\alpha_n\,\alpha_m$
② M_s=1 0 $\alpha_n\,\beta_m, \beta_n\,\alpha_m$
③ −1 $\beta_n\,\beta_m$
④ −1 $\beta_n\,\beta_m$
⑤ M_s=−1 0 $\alpha_n\,\beta_m, \beta_n\,\alpha_m$
⑥ +1 $\alpha_n\,\alpha_m$

Fig. 3. Schematic representation of the *shf* splitting of the electronic states by an equivalent pair of fluorine nuclei. The numbers on the left conveniently label the various energy levels corresponding to the indicated nuclear spin states.

Table 1

Transition from Fig. 3	$\lvert\Delta M_I\rvert$	Relative transition probability
4 → 3	0	$\cos^4\zeta/2$
6 → 1	0	$\cos^4\zeta/2$
6 → 3	2	$\sin^4\zeta/2$
4 → 1	2	$\sin^4\zeta/2$
5 → 2	0	$2(\cos^4\zeta/2+\sin^4\zeta/2)$
4 → 2	1	$\frac{1}{2}\sin^2\zeta$
5 → 3	1	$\frac{1}{2}\sin^2\zeta$
5 → 1	1	$\frac{1}{2}\sin^2\zeta$
6 → 2	1	$\frac{1}{2}\sin^2\zeta$

for the transitions, $\Delta M_s = \pm 2$, $\Delta M_I = 0, \pm 1, \pm 2$ respectively,

$$R_0 = \frac{1}{2}\,\frac{\cos^4\zeta/2}{(1-\frac{1}{2}\sin^2\zeta)} \tag{31a}$$

$$R_1 = \frac{1}{4}\,\frac{\sin^2\zeta}{(1-\frac{1}{2}\sin^2\zeta)} \tag{31b}$$

and

$$R_2 = \frac{1}{2}\,\frac{\sin^4\zeta/2}{(1-\frac{1}{2}\sin^2\zeta)}. \tag{31c}$$

We define now an angle ψ_{M_s} such that

$$\psi_{M_s} = \tan^{-1}\left(\frac{H_\perp}{H_\parallel}\right)_{M_s} \tag{32}$$

where $H_\parallel$ is the component of the total field $\mathbf{H}_T$ at a given fluorine site parallel to the trigonal axis and $H_\perp$ is the perpendicular component. Thus, in terms of the initial and final electronic states

$$\zeta = \psi_f - \psi_i = \left[\tan^{-1}\left(\frac{H_\perp{}^f}{H_\parallel{}^f}\right) - \tan^{-1}\left(\frac{H_\perp{}^i}{H_\parallel{}^i}\right)\right] \tag{33}$$

where i and f correspond to $M_s = -1, +1$ respectively. The total field $\mathbf{H}_T$ is defined in terms of the *shf* and nuclear Zeeman interactions,

$$-\gamma_n \mathbf{H}_T \cdot \mathbf{I} = [\mathbf{S}\cdot\mathbf{A} - \gamma_n \mathbf{H}_0]\cdot\mathbf{I}. \tag{34}$$

First, consider the equivalent fluorine pair along the $[11\bar{1}]$ direction. In this case $\phi = 0$ and from equation (23)

$$\begin{aligned} -\gamma_n \mathbf{H}_T \cdot \mathbf{I} &= 2A_p S_z I_z \\ &\quad - \gamma_n H_0 (I_z \cos\theta + I_x \sin\theta) \end{aligned} \tag{35}$$

giving

$$\begin{aligned} -\gamma_n H_{T_\parallel} &= 2A_p M_s - \gamma_n H_0 \cos\theta \\ -\gamma_n H_{T_\perp} &= -\gamma_n H_0 \sin\theta. \end{aligned} \tag{36}$$

So, for only anisotropic contribution to the *shf* interaction,

$$\tan\psi_{M_s} = \left(\frac{H_\perp}{H_\parallel}\right)_{M_s} = -\frac{\gamma_n H_z \tan\theta}{2A_p M_s - \gamma_n H_z}. \tag{37}$$

For the equivalent pair of nuclei located along the [111] direction, $\phi = 70{\cdot}5°$ and $\psi = \pi/2$. Thus

$$\tan\psi_{M_s} = \frac{3A_p' M_s \sin\phi\cos\phi + \gamma_n H_z \tan\theta}{A_p' M_s (3\cos^2\phi - 1) - \gamma_n H_z}. \tag{38}$$

If we consider the four fluorines located out of the plane of the applied field $\mathbf{H}_0$ and the trigonal axis, it is to be noted that these are strictly equivalent only in pairs due to inevitable slight misorientation of the crystal. However, for an equivalent pair $\phi = 70{\cdot}5°$, and, to a very close approximation, $\psi = 75{\cdot}5°$ for both pairs. It is simpler, in this case, to

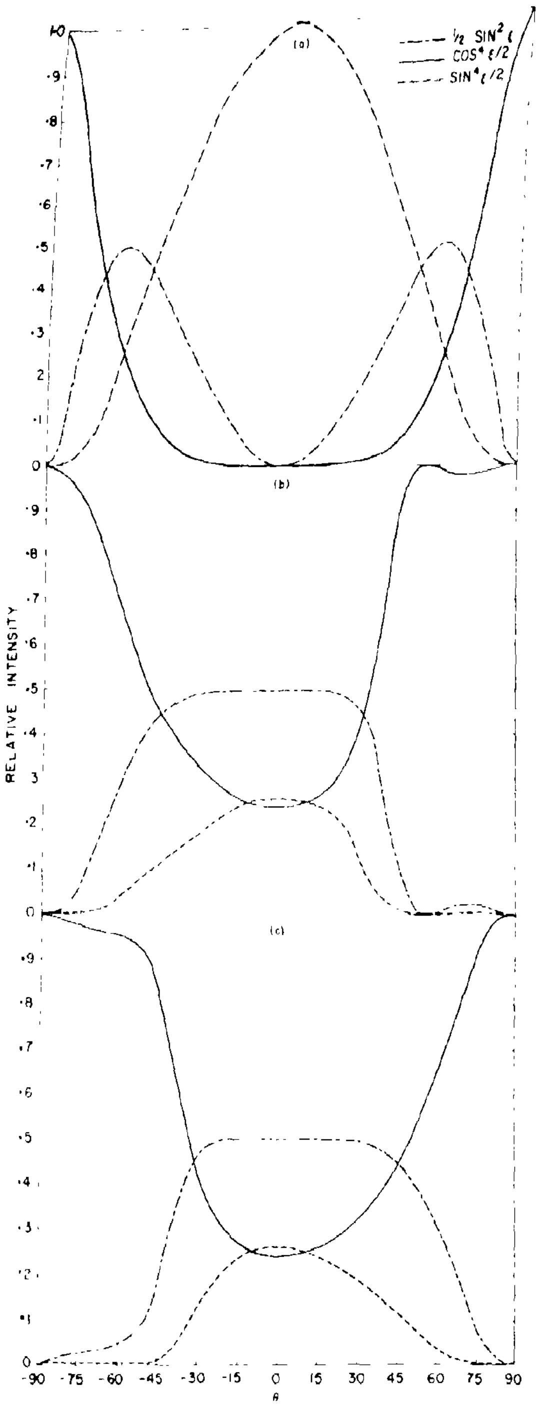

Fig 4 Angular dependency of the relative transition probabilities for the satellites arising from *shf* interaction between each of the various magnetically equivalent pairs of nearest neighbor *F* nuclei and the U^{4+} ion: (a) pair along the [111] direction; (b) pair along the [111] direction, (c) each of the pair located out of the plane (signified by OP) defined by the [11$\bar{1}$] and [111] directions. The angle θ is the angle between the symmetry axis z and the direction of the applied field $\mathbf{H}_0$

calculate $\cos\zeta$, where

$$\cos\zeta = \frac{\mathbf{H}_T{}^i \cdot \mathbf{H}_T{}^f}{|\mathbf{H}_T{}^i|\,|\mathbf{H}_T{}^f|}. \tag{39}$$

From equation (23), we have

$$-\gamma_n \mathbf{H}_{T\parallel} = [M_s A_p''(3\cos^2\phi - 1) - \gamma_n H_z]\mathbf{k} \tag{40a}$$

and

$$\begin{aligned} -\gamma_n \mathbf{H}_{T\perp} = {} & [3M_s A_p'' \sin\phi\cos\phi \\ & +\gamma_n H_z \sin\psi \tan\theta]\mathbf{i} \\ & -[\gamma_n H_z \cos\psi \tan\theta]\mathbf{j} \end{aligned} \tag{40b}$$

where **i**, **j** and **k** are unit vectors along the x, y and z axes respectively. Applying equations (40a and 40b) to (39), we get the following form for the angular dependence of ζ:

$$\zeta = \cos^{-1}\frac{-a + b\tan^2\theta}{\{[c + d\tan\theta + b\tan^2\theta][e - d\tan\theta + b\tan^2\theta]\}^{1/2}} \tag{41}$$

where a, b, c, d and e are given by

$$a = A_p''^2(3\cos^2\phi + 1) - \gamma_n{}^2 H_z{}^2 \tag{42a}$$

$$b = \gamma_n{}^2 H_z{}^2 \tag{42b}$$

$$\begin{aligned} \begin{pmatrix} c \\ e \end{pmatrix} = {} & A_p''^2(3\cos^2\phi + 1) \\ & \pm 2A_p''\gamma_n H_z(3\cos^2\phi - 1) + \gamma_n{}^2 H_z{}^2 \end{aligned} \tag{42c}$$

$$d = 6A_p''\gamma_n H_z \sin\phi\cos\phi\sin\psi. \tag{42d}$$

By using equations (33), (37), (38) and (41), the relative transition probabilities corresponding to each magnetically equivalent pair of fluorine nuclei were computed using a computer program, and their angular dependence is shown in Figs. 4(a–c). The values used for the parameters appearing in the equations were determined according to the discussion in Section 5.

3. THE UPR SPECTRUM

The *shf* splitting of an electronic state M_s is given by all possible values of the sum

$$E(M_s, M_I) = \sum_{\alpha=1}^{8} E^\alpha(M_s, m_I{}^\alpha) \tag{43}$$

where the $E^\alpha(M_s, m_I{}^\alpha)$ are obtained from (24) and $M_I = 0, \ldots, \pm 4$. For a given set of selection rules, the transitions between the electronic states produce components symmetrically distributed about the undisplaced electronic spin transition. In the region of magnetic fields of interest, and if we neglect terms of the order of $\Delta H_0/H_0$, the separations in gauss from the central line of the components corresponding to the transition $\Delta M_I = 0$, $\Delta M_s = \pm 2$ are obtained from all possible values of the sum

$$\begin{aligned} \Delta H(M_I) = \frac{\sec\theta}{2g_\parallel\beta} \sum_{\alpha-1}^{8} & [E^\alpha(M_s = 1, m_I{}^\alpha) \\ & -E^\alpha(M_s = -1, m_I{}^\alpha)] \end{aligned} \tag{44}$$

allowed by each value for M_I. A similar expression holds for the only other selection rule of interest, $\Delta M_s = \pm 2$, $\Delta M_I = \pm 1$.

In general, each equivalent pair of fluorines will contribute three components to an electronic level splitting. Since there are four equivalent pairs of nearest neighbor nuclei, an electronic level will be split into a total of $3^4 = 81$ components. The maximum number of transitions expected among these levels corresponding to the selection rule $\Delta M_s = \pm 2$ is 9^4. However, the intrinsic line width in the UPR spectrum of $CaF_2:U^{4+}$ is about 11 G at $\theta = 0°$, and thus, by far the majority of these components are completely unresolved. In fact due to this strain broadening, no resolution of the *shf* structure is expected on the basis of the model for the angle $|\theta| < 60°$, and none is observed.

At the higher angles, and consequently, large applied magnetic fields, the transitions corresponding to $\Delta M_I = \pm 2$, $\Delta M_s = \pm 2$ are not observed due to their relatively insignificant intensities, Figs. 4(a–c). The transitions corresponding to $\Delta M_I = 0$, $\Delta M_s = \pm 2$ have significantly high intensities for $|\theta| > 45°$ as indicated in Figs. 4(a–c), but calculations in terms of (44) show that these components are well within the line width of the central line for $|\theta| < 85°$. Since the experimental limitation of the applied magnetic field H_0 was 17 kG which corresponds approximately to $|\theta| = 84{\cdot}5°$, these components are not expected to be resolved in the experiment. This leaves only the components corresponding to transitions governed by $\Delta M_I = \pm 1$, $\Delta M_s = \pm 2$. The theory predicts that these components will not be resolved from each other due to line broadening. However, they are expected to be well resolved from the central component for angles $|\theta|$ in excess of 70°. The transition probabilities, though diminishing, are significant for angles $|\theta|$ through 85°, the main contribution in intensity arising from the equivalent nuclei along the $[11\bar{1}]$ direction, Figs. 4(a–c). In the region of high magnetic fields where the satellites are resolved, and for predominantly direct dipole–dipole contribution to the anisotropic interaction, the *shf* interaction is much smaller than the nuclear Zeeman term. Thus the observed spectrum should be composed of a central line arising from $\Delta M_I = 0$, $\Delta M_s = \pm 2$ components and two satellites arising from simultaneous nuclear spin electron spin flips, $\Delta M_I = \pm 1$, $\Delta M_s = \pm 2$, symmetrically spaced in magnetic field on either side of the central line and each separated from it by approximately one nuclear Zeeman energy.

4. EXPERIMENTAL

Single crystals of CaF_2 nominally doped with 0·03 and 0·007 molar percent U^{4+}, grown by Hargreaves of Optovac, were obtained with the long axis parallel to the [111] direction and a side plane perpendicular to the $[1\bar{1}0]$ direction. A conventional X-band UPR spectrometer[7] employing longitudinal elastic waves at 9·0 GHz was used at 4·2°K. The change in the absorption of ultrasonic waves was measured, as the applied magnetic field H_0 was varied through resonance, by observing the change in the height of an echo that resulted from one or more passes of an ultrasonic pulse through the sample. The EPR lines were obtained with a conventional EPR spectrometer using backward diode detection to improve the signal to noise ratio[8].

5. RESULTS

The observed splitting is into three components, a central higher intensity line and two lower intensity satellites for angles $|\theta| > 60°$. At the lower angles, the satellites are completely unresolved. The separation in gauss of the peak of the satellite components from the peak of the central component is plotted vs. $\sec^2\theta$ in Fig. 5. The measured intensity variation of the components is represented in Fig. 6 as the ratio of the satellite to central component intensity plotted against $\cos\theta$. In order to predict the contribution to the energy level splitting and relative intensities of the components for the various magnetically equivalent nuclei, the parameters A_P and $\gamma_n H_z$ in equation (24) were evaluated. In terms of the separation R between the U^{4+} and F^- nuclei the direct dipole–dipole contribution to A_P is $A_D = (g_\| \beta\beta_n g_F/R^3)$. Neglecting distortion of the lattice due to the impurity ion the nuclei–nuclei separation is $R = 2{\cdot}36$ Å; then for $g_F = 5{\cdot}257$[6], we have $(A_D/g_\|\beta) = 2$ G and from the UPR measurements $H_z = 1{\cdot}6$ kG giving $(\gamma_n H_z/g_\|\beta) = 2{\cdot}2790$ for $g_\| = 2{\cdot}01$.

With the dominant contribution to the *shf* interaction arising from the direct dipole–dipole interaction, the theory predicts a linear variation of ΔH with $\sec^2\theta$ in the angular region where the satellites are resolved, and the theoretical curves are shown as solid lines in Fig. 5 for both the high and low field satellites. The theoretical curves represent the intensity weighted average of the separation among the unresolved components from the undisplaced electronic component.

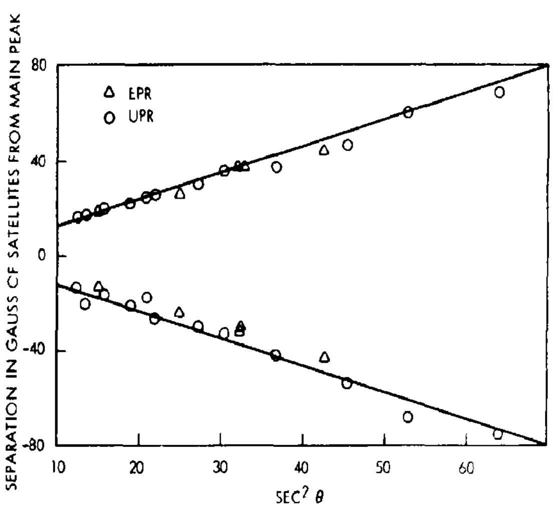

Fig. 5. Observed magnetic field separation, ΔH, of the high and low field satellites from the central component vs. $\sec^2\theta$, where θ is the angle between the symmetry axis z and the direction of the applied field H_0. The solid lines represent the angular dependency of the satellite separation calculated from the model.

It was found that in order to explain the intensity observations, it was necessary to ascribe to the F^- ions along the site axis an additional anisotropic contribution $(\delta A/g_{\parallel}\beta) = 0{\cdot}4$ G. This can be ascribed to $2p_\sigma$ overlap, and/or additional direct dipole–dipole contribution relative to that contributed by the remaining six nuclei. This may be due to a small difference, Δ, in the separation R of the nuclei of the ligands from the nucleus of the impurity. This additional anisotropic contribution is compatible with a model for local charge compensation for the U^{4+} impurity which ascribes F^- ions in the cubic interstitial positions as next nearest neighbors along the body diagonal$[11\bar{1}]$. The nearest neighbor fluorines along the site axis would tend to be moved closer to the impurity site, thus giving rise to the trigonal C_{3v} symmetry. The $2p_\sigma$ orbitals of these fluorines would therefore produce a slightly higher spin density in the neighborhood of the impurity ion than would the other nearest neighbor nuclei.

The method of determining the relative intensities and the separation of the various components in this instance is a particular application of the general method outlined by Clogston *et al.*[9]. The theoretical intensity ratios in Fig. 6 were calculated for each angle θ by weighting the intensity contributions from the various transitions according to magnetic field separation and intrinsic strain broadened line width. The theoretical curves for the intensity ratio for only equal direct dipole–dipole contribution from the eight nearest neighbor F^- nuclei are shown for comparison in Fig. 6. It is seen that this gives values which are slightly too small when compared with the distribution of the data points. As noted from Fig. 6 the theory predicts an asymmetry in intensities for the magnetic field orientation $\pm\theta$, about the trigonal axis z; however, the experimental error in the data is much too large to observe this effect for the line widths associated with the crystal used. Here, $+\theta$ is the angular direction such that increasing θ from $\theta = 0$ decreases the angle between the magnetic field H_0 and the σ-bond axis of the F^- nuclei located along the $[111]$ direction with the trigonal axis along the$[11\bar{1}]$direction.

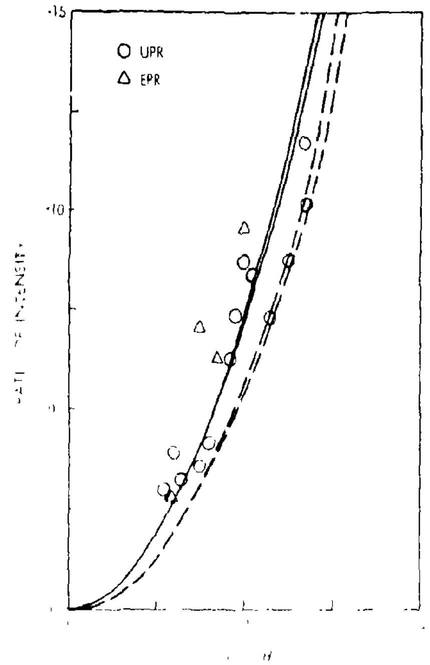

Fig. 6. Ratio of the observed satellite intensity to that of the central component vs cos θ, where θ is the angle between the symmetry axis and the direction of the applied field $\mathbf{H}_0$. The dashed curves were calculated from the model using only the undistorted lattice direct dipole-dipole interaction, whereas the solid curves were calculated with an additional anisotropic contribution $(\delta A/g_{\parallel}\beta) = 0{\cdot}4$ G for the equivalent fluorine pair located along the $[11\bar{1}]$ direction. In each set of curves, the upper one corresponds to $+\theta$ and the lower one to $-\theta$.

6. CONCLUSION

Comparison of the theoretical model with the experimentally determined separation of the *shf* structure and the comparison of the intensities in Figs. 5 and 6 shows good agreement between the predictions based on the theory and the experimental observations. In order to obtain good quantitative agreement with the experimental observations a slightly larger anisotropic *shf* interaction was ascribed to the nearest neighbor F^- ions along the trigonal axis than for the remaining six.

The relative intensity variation of the components with angle θ is much more sensitive in the *shf* coupling than the magnetic field separation at large angles of the field $\mathbf{H}^0$ relative to the trigonal axis. Thus, on the basis of the observed intensities, an additional anisotropic contribution δA is attributed to each nearest neighbor ligand along the trigonal axis and is given by $(\delta A/g_{\parallel}\beta) = 0{\cdot}4 \pm 0{\cdot}2$ G whereas the direct dipole-dipole contribution A_D from each of the remaining nearest neighbors is $(A_D/g_{\parallel}\beta) = 2$ G.

The observations of the satellite components in terms of their separation from the central component and their relative intensities are explained entirely in terms of direct dipole-dipole interaction of the U^{4+} ion with its eight nearest neighbor ligands with possibly a small amount of anisotropic $2p_{\sigma}$-overlap with the fluorine nearest neighbor ligands located along the trigonal axis. In terms of only direct dipole-dipole contribution, the term δA corresponds to a decrease in the U^{4+} nucleus-F^- nucleus separation of approximately 7 per cent or 0·2 Å. It is reasonable to suppose that this term, in itself, comprises significant contributions from both $2p_{\sigma}$-overlap and also direct dipole-dipole interaction.

The results of this experiment suggest a double resonance experiment similar to the Endor in EPR. The ultrasonic electron nuclear double resonance, or Undor, experiment would be quite significant in determination of the frequencies of the *shf* splitting, especially at lower angles where the structure is unresolved. The usual problems concerning the coil-cavity combination in Endor are not present in the Undor, since an r.f. coil may be wound directly upon the crystal[7] external to the UPR cavity without affecting the cavity Q in any manner.

Acknowledgements—The authors wish to express thanks to R. A. Shatas of this laboratory for some helpful suggestions during the course of this work and the preparation of the manuscript, and also to W. L. Kimber for his assistance in reducing the data.

REFERENCES

1. MEYER H. C., McDONALD P. F., STETTLER J. D. and DONOHO P. L., *Phys. Lett.* **24A**, 569 (1967)
2. WILKINSON E. L. and HARTMAN R. L., Private communication. Physical Sciences Laboratory, Redstone Arsenal, Alabama.

3. BOWDEN C. M., MEYER H. C., McDONALD P. F. and DONOHO P. L., Southeastern Section APS (1968), *Bull. Am. Phys. Soc.* To be published; BOWDEN C. M., MEYER H. C and DONOHO P. L. *Int. Symp. Quantum Theory*, University of Florida and Upsala (1969).
4. McLAUGHLAN S. D., *Phys. Rev.* **150**, 118 (1966).
5. MARSHALL W. and STUART R., *Phys. Rev.* **123**, 2048 (1961).
6. SULLIVAN W. H., *Trilinear Chart of the Nuclides*. Oak Ridge National Laboratory (1957).
7. MEYER H. C., DANIEL A. C. and DONOHO P. L., *Rev. scient. Instrum.* **37**, 1262 (1966).
8. HARTMAN R. L., BENNETT J. S and JENSEN R. A., *Bull. Am. Phys. Soc.* **13**, 244 (1968).
9. CLOGSTON A. M., GORDON J. P., JACCARINO V., PETER M. and WALKER L. R, *Phys. Rev.* **117**, 1222 (1960).

J. Phys. Chem. Solids Pergamon Press 1969. Vol. 30, pp. 1549–1559. Printed in Great Britain.

A MÖSSBAUER EFFECT STUDY OF THE METALLIC COMPOUNDS U_6 Fe AND Pu_6 Fe, AND THE RELEVANCE OF THE RESULTS TO THEORIES OF THE BEHAVIOUR OF ACTINIDE METALS

S. BLOW
Atomic Energy Research Establishment, Harwell, Didcot, Berks., England

(*Received* 12 *November* 1968)

Abstract – The intermetallic compounds U_6Fe and Pu_6 Fe were investigated using Mossbauer spectroscopy. From the Mössbauer point of view the results are straightforward: quadrupole pairs are seen in both materials at room temperature and low temperatures. Low temperature values for the splittings were 0·074 cm/sec for U_6Fe and 0·083 cm/sec for Pu_6Fe, the corresponding room temperature values were 0·069 and 0·073 cm/sec. Both quadrupole splittings and isomeric shift values are characteristic of Fe in the metallic state.

Recent electrical resistivity work has established that the temperature curves for Pu_6Fe and Pu metal are qualitatively very similar. In view of this investigation and our Mossbauer results we would be inclined to reject the hypothesis that Pu undergoes an antiferromagnetic transition at low temperatures. However, the situation is complex, and some space is devoted to a review and appraisal of the theories proposed to explain the properties of this most unusual metal

1. INTRODUCTION

THE TWO intermetallic compounds Pu_6Fe and U_6Fe were investigated during a study of the series of compounds formed by Fe with the actinides[1]. From the Mössbauer point of view the spectra, using Fe^{57} as the probe isotope, appear fairly straightforward – a quadrupole split pair of lines is seen. But this has some interesting consequences in relation to known facts about the actinide elements, especially Pu. This theme will be expanded upon through this paper.

2. EXPERIMENTAL TECHNIQUES

The preparation of absorber material is described later. The radioactive source was purchased from the Radiochemical Centre, Amersham, Bucks., U.K., and consisted of 10 mCi of Co^{57} electroplated onto Pd, and diffused into the metal matrix during annealing in a hydrogen atmosphere.

The source, which was kept at room temperature, was attached to a Goodmans V47 electromechanical transducer, and driven with a constant acceleration motion (linear voltage ramp).

The 14·4 keV radiation was detected by a $Xe-CH_4$ filled proportional counter, and the individual counts were stored in one of 256 channels of a Laben multichannel analyser. The analyser was operated in the multiscaler mode, with the channel switching synchronised to the ramp motion of the transducer.

Low temperatures were achieved by means of a standard 'X-ray' type cryostat, equipped with Melinex windows to allow the passage of low-energy γ-rays. Because of failure to surround the experimental space with liquid helium the lowest temperature we could obtain with the cryostat was 13°K. However, this is not too inhibiting from the general stand-point of this investigation.

The whole experimental procedure and instrumentation are described in detail elsewhere[1].

3. CRYSTALLOGRAPHY

The compounds belong to the tetragonal body-centred U_6Mn type, a fairly rare species found, it seems, only among actinide compounds. The space group is No: 140 in the International Table, D_{4h}^{18} in the Schoenflies notation.

There are 4 molecular groups (i.e. 28 atoms) in the basic unit cell, and the atomic positions are given by:-

$$(0, 0, 0; \tfrac{1}{2}, \tfrac{1}{2}, \tfrac{1}{2}) +$$

A_1 at $16(k)$: $\pm(x, y, 0); \pm(y, \bar{x}, 0);$

$$\pm(x, \bar{y}, \tfrac{1}{2}); \pm(y, x, \tfrac{1}{2});$$

with $x = 0{\cdot}214$, $y = 0{\cdot}102$.

A_2 at $8(h)$: $\pm(x, \tfrac{1}{2}+x, 0); \pm(\tfrac{1}{2}-x, x, 0)$

with $x = 0{\cdot}407$.

Fe at $4(a)$: $\pm(0, 0, \tfrac{1}{4})$.

The positions (k) and (h) have low point symmetries of m and mm respectively. The point symmetry at the (a) site is 42.

The Fe atoms are in linear chains along the edges and through the centre of the unit cell, all the chains being parallel to the c-axis.

Pu_6Fe: The lattice parameters are $a = 10{\cdot}404$ Å, $c = 5{\cdot}355$ Å. The Fe–2Fe distance $= c/2 = 2{\cdot}68$ Å. Fe – $8Pu_1$ = 2·81 Å. The Pu–Pu nearest neighbour distances vary from 2·71 Å up to 3·49 Å, the average being 3·23 Å. U_6Fe. The lattice parameters are $a = 10{\cdot}31$ Å, $c = 5{\cdot}24$ Å. The Fe–2Fe distance $= c/2 = 2{\cdot}62$ Å. The Fe–U, and U–U distances are proportionately less in this material than they are in Pu_6Fe. The data presented in this section have been extracted from references [2] and [3].

4. PREPARATION AND METALLOGRAPHY

The absorbers were made from high purity U and Pu wire, and from Fe metal enriched to about 94 per cent in the Mössbauer isotope Fe^{57} by means of electromagnetic separation.

Appropriate amounts of Fe and actinide material were arc-melted together in an argon atmosphere. Normally a slight excess of actinide was taken to preclude the possibility of formation of the AFe_2 compound (A = actinide).

U_6Fe material was annealed for 48 hr at 700°C in a vacuum furnace. The arc-melted Pu_6Fe button was similarly treated at the lower temperature of 420°C.

Metallographic sections taken on the annealed material indicated a generally single-phase substance, with occasional small platelets of free metal (actinide) and small dendritic growths of oxide (presumably UO_2 or PuO_2).

Containment is an extremely important problem when handling Pu, or Pu-bearing substances. The toxicity of the material demands that work be carried out in glove-boxes, or that careful methods of coating or containment be used.

Because we normally worked with brittle (easily powdered) materials we held such material in a solid suspension of polymethyl methacrylate, and worked with the absorber in the open lab. This was done by intimately mixing the absorber with perspex powder, heating to about 200°C, and pressing to about $\tfrac{1}{2}$-ton [= 4·982 kN] force on 1 cm^2 of area.

Unfortunately the A_6Fe compounds are relatively soft, and would not crush in a pestle and mortar. We thus experienced some difficulty in making a satisfactory U_6Fe absorber because of large particle size. This caused the low peak-to-background ratio seen in the spectra we analysed.

In making the Pu_6Fe absorber, the arc-melted button was cast into cylindrical shape down the 2 mm. dia. orifice at the centre of a copper hearth. After annealing, it was held in a pin vice and filed down against diamond. A much more homogeneous, small-particle size absorber resulted in this case.

5. RESULTS ON U_6FE

Spectra taken at 26°, 82° and 295°K were analysed on the basis of a forced fit to a quadrupole pair, and a picture of the 26°K fit is shown in Fig. 1. The data obtained are set out in Table 1.

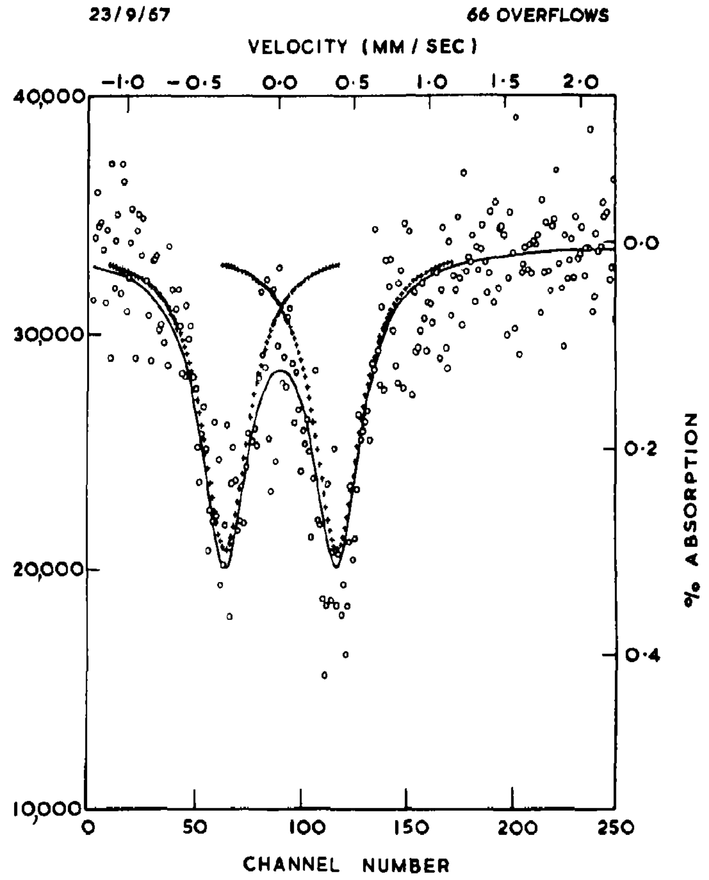

Fig. 1. Mössbauer absorption spectrum of 10 mg of U_6Fe at 26°K. the data points fitted to a quadrupole pair (One overflow = 65.535 counts in channel)

In Table 1 we see the usual slight increase in quadrupole splitting at the low temperatures together with the normal isomer shift in the positive direction, associated with the temperature difference betwcn source and absorber.

The peak height is small and the line-width varies somewhat, as a result, no doubt, of the small peak to background ratio. We ascribe an uncertainty of ±0·003 cm/sec in the velocity values quoted in Table 1.

Figure 2 shows the result of fitting two

Table 1. *Mössbauer parameters listed at different temperatures for* U_6Fe. *(All isomeric shift values are relative to sodium nitroprusside at zero)*

	26°K	82°K	295°K
Quadrupole splitting	0·074 cm/sec	0·074 cm/sec	0·069 cm/sec
Isomer shift	0·001 cm/sec	0·002 cm/sec	−0·011 cm/sec
Peak height	0·30%	0·30%	0·31%
Peak width	0·038 cm/sec	0·043 cm/sec	0·036 cm/sec

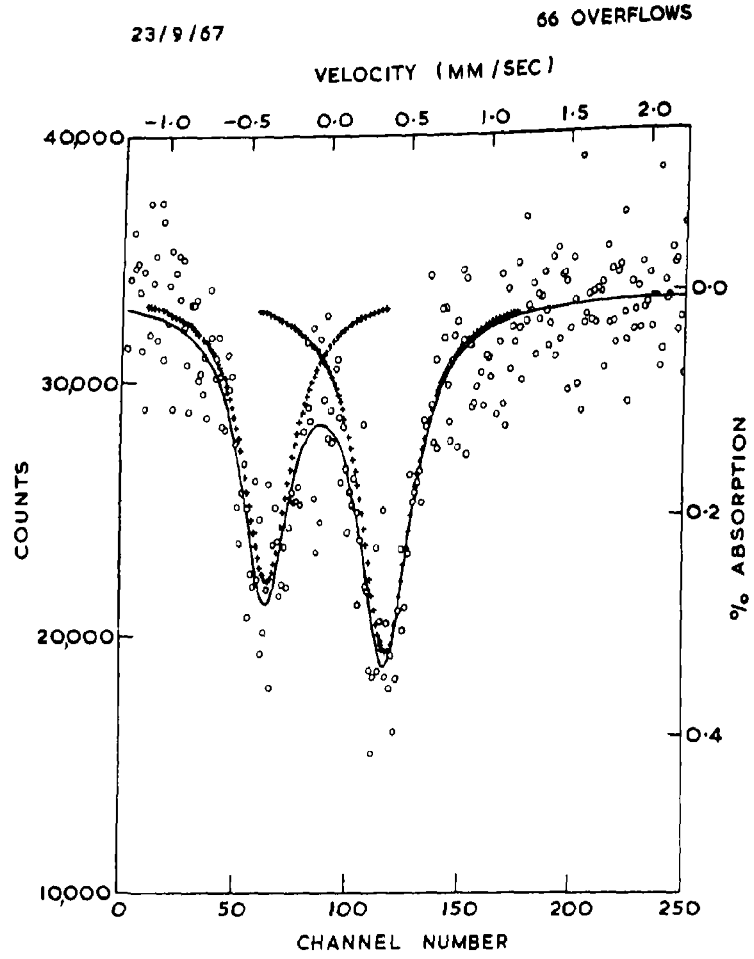

Fig. 2. Mössbauer absorption spectrum of 10 mg of U_6Fe at 26°K, the data points here being fitted to two independent peaks (One overflow = 65,535 counts in channel)

independent single peaks to the data points. It reveals what is apparent from a visual inspection that the right-hand peak (R.H.P) is both broader and more intense than the left-hand peak (L.H.P). Typical values are 0·34 per cent intensity and 0·052 cm/sec width for the R.H.P. as compared with 0·26 per cent intensity and 0·033 cm/sec width for the L.H.P.

We can suggest a reason for this occurrence by invoking the Goldanskii effect–anisotropy of the recoil-free fraction[4]. Otherwise it is very difficult to account for this phenomenon without suggesting either an instrumental failure, or the presence of a single background peak which implies the presence of a chemical form of Fe not revealed in the metallography or X-ray analysis. The possibility of a double quadrupole pair, very nearly superimposed, is also ruled out because the more intense line should then also be the narrower.

Independent confirmation of these experimental results has been provided by C. E. Johnson, A.E.R.E., Harwell, who also found a deeper and broader R.H.P. (Private communication). In other materials with which we worked, viz. UFe_2 at room temperature, Th_7Fe_3, and Pu_6Fe, we observed this same occurrence of a broad, deep R.H.P. compared with a narrower, less-intense L.H.P. in a quadrupole pair.

The compound U_6Fe has been reported as being a superconductor with a transition temperature at 3·86°K[5].

There is certainly no sign of magnetic splitting in the material down to 4·2°K, at which Johnson's lowest measurements were taken.

6. RESULTS ON PU_6FE

An absorber of 1 cm^2 cross-section containing 9·5 mg of finely powdered Pu_6Fe was used in the experiment. A diagram of a fit to a quadrupole pair is given in Fig. 3 for the data points accumulated at 16°K.

The results of the complete analysis are set out in Table 2. The general pattern is the same as for U_6Fe but there are certain features which make the results for Pu_6Fe more satisfactory.

Firstly, the peak width is the same at all three temperatures. Also the peak height increases in a consistent fashion the lower the temperature, as we would expect by virtue of the fact that the probability of recoilless absorption increases. The quadrupole splitting is a few per cent greater in Pu_6Fe, and the isomer shift is consistently more positive. This latter means that the s-electron density at the nuclear site is less in Pu_6Fe than in U_6Fe, due no doubt to the slightly larger lattice parameters in Pu_6Fe which allow a general expansion of the electron charge clouds and a consequent slight reduction in spatial charge density. The difference between room temperature and low temperature values for the isomer shift is almost exactly the same, indicating a very similar Debye θ value for the two crystalline lattices as one would expect.

Analyses were also made for Pu_6Fe on the basis of a fit of two independent peaks to the data points. The results are laid out in Table 3 in terms of peak heights and widths. Although the differences are not nearly so great as in U_6Fe the same general pattern is observed: the R.H.P. is more intense and broader than the L.H.P. The discrepancy is far less apparent at 16°K than at room temperature; this feature was not observed in U_6Fe.

These results on Pu_6Fe are interesting in relation to the work which other members of a Harwell–Oxford team have done on the physical properties of Pu, and in particular in view of the similarity between the resistance

Table 2. Mössbauer parameters listed at different temperatures for Pu_6Fe

	16°K	79°K	293°K
Quadrupole splitting	0·083 cm/sec	0·081 cm/sec	0·073 cm/sec
Isomer shift	0·010 cm/sec	0·009 cm/sec	−0·002 cm/sec
Peak height	1·47%	1·43%	1·18%
Peak width	0·037 cm/sec	0·037 cm/sec	0·037 cm/sec

Table 3. Peak heights and widths at different temperatures for Pu_6Fe

	16°K	79°K	293°K
Peak height R.H.P.	1·48%	1·46%	1·23%
Peak height L.H.P.	1·47%	1·41%	1·11%
Peak width R.H.P.	0·039 cm/sec	0·039 cm/sec	0·040 cm/sec
Peak width L.H.P.	0·036 cm/sec	0·035 cm/sec	0·035 cm/sec

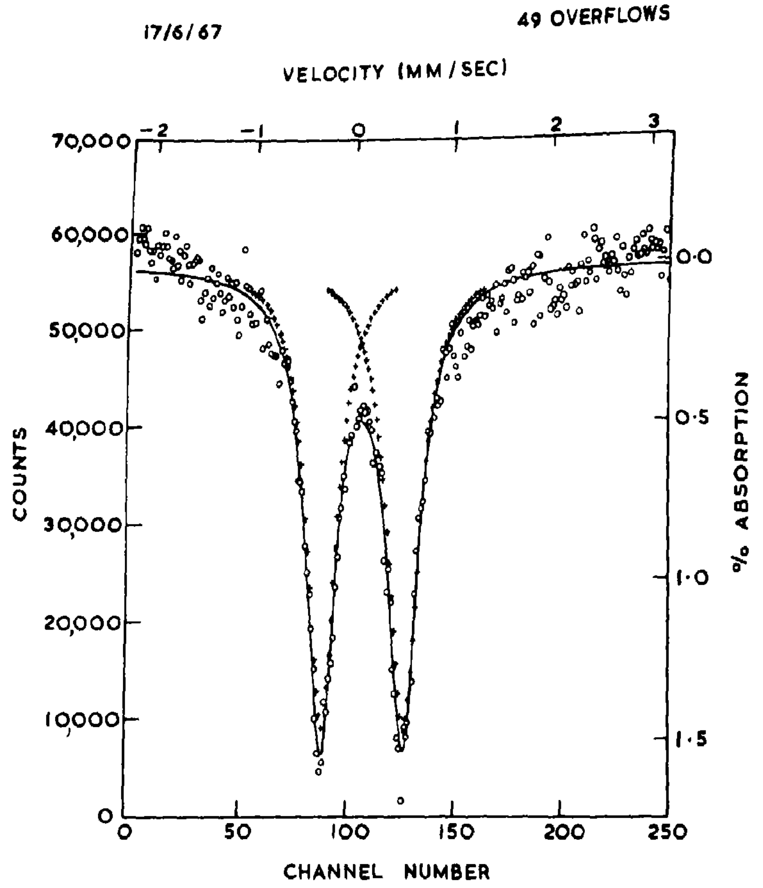

Fig. 3 Mossbauer absorption spectrum of 9.5 mg of Pu_6Fe at 16°K. the data points fitted to a quadrupole pair (One overflow = 65,535 counts in channel).

vs. temperature curves of Pu metal and Pu_6Fe.

7. THE METAL PLUTONIUM

We prepare the ground for further analysis by making a brief survey of experimental and theoretical work on the behaviour of the metal plutonium.

Plutonium is unique among metals in having six different crystallographic phases between room temperature and its low melting-point of 639·5°C. It was first produced in milligram quantities in 1943 as part of the wartime Manhattan project. Today, twenty-five years later, its many unusual physical properties have been widely explored, but a great deal of controversy still exists over the explanation of the metal's behaviour at low temperatures.

Much of the early low-temperature physical property discussion centred around the unusual electrical resistance vs. temperature curve for the metal which is reproduced in Fig. 4. From a small value at the lowest temperatures the resistance increases quite sharply to a maximum at about 90°K. From there on it has a small negative coefficient with respect to temperature, decreasing all the while up to the α-β phase transformation which takes place at about 130°C.

One of the early theories proposed to explain the unusual form of the resistance curve by invoking an antiferromagnetic

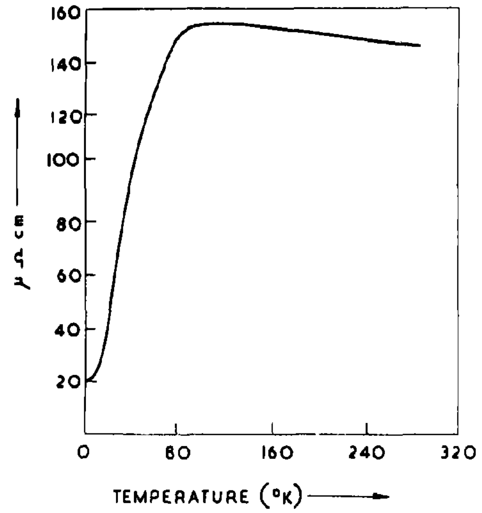

Fig. 4. The electrical resistivity of Pu metal.

transition at about, or somewhat below, 90°K. This was done by Sandenaw and Olsen[6], and by Lee, Meaden and Mendelssohn[7]. The proposition is eminently feasible for a number of reasons. Plutonium, besides having $7s$ and $6d$ electrons, will also have a number of f-electrons in an unfilled $5f$ shell and the atom should therefore possess a resultant magnetic moment. We compare with the unfilled $4f$ shell in the rare-earth series and find there that complicated types of helical antiferromagnetism are not an uncommon feature. Because of its $5f$ electrons and complicated crystallographic α-phase (monoclinic) we might well expect some similar type of magnetic condensation to occur in plutonium.

The basic explanation of the resistance drop is then the following. Each Pu atom possesses a magnetic moment. As the Pu lattice cools below the Néel point, the moments take up ordered directions relative to each other. The probability of electron scattering is considerably reduced for the ordered structure as opposed to the random paramagnetic state. Consequently the electrical resistance decreases.

Another cogent supporting feature for the antiferromagnetic theory was the form of the resistance curve for α-Mn, a known antiferromagnetic. This is very similar to that of Pu, except that after a few degrees above the resistance maximum, the temperature coefficient is positive and not negative as in Pu. This observation leads us naturally on to 'band' theories which have been proposed as an alternative to the antiferromagnetic theory.

By assuming that the density of states vs. energy of states graph for the metal consisted of a broad, low-density-of-states band containing $7s$ electrons, overlapped by a narrow, high-density-of-states band, containing $6d$ and $5f$ electrons, Lee and Hall[8] and Smoluchowski[9] were able to explain the negative temperature coefficient of α-plutonium by considering the Fermi level to be temperature dependent. In order to explain the resistivity maximum at low temperatures Smolchowski assumes, following Wilson[10], that the number of phonons available for interband scattering at low temperatures is drastically reduced by quantum selection rules. However, no independent evidence is available to support this theory.

The numerous physical measurements which have been made on Pu have not greatly clarified the situation. Magnetic susceptibility work indicates no anomaly in α-Pu near to the resistance maximum, but neither is there any anomaly to be found in α-Mn.

Specific heat measurements do show a λ-type anomaly in α-Mn, and very recent (1968) results on Pu indicate a similar, though much smaller, anomaly, together with a peaked minimum in the θ_D value at 60°K (P. W. Sutcliffe, Private communication).

Rocher[11] has also proposed an antiferromagnetic model with a Néel temperature at 60°K. He assumes that exchange coupling splits the $5f$ states into two levels and the difference in population of these levels contributes a magnetic moment of 0·3 Bohr magnetons. In support of his choice Rocher cites Meaden's thermoelectric power results (Fig. 5), the change in slope at 65°K indicating

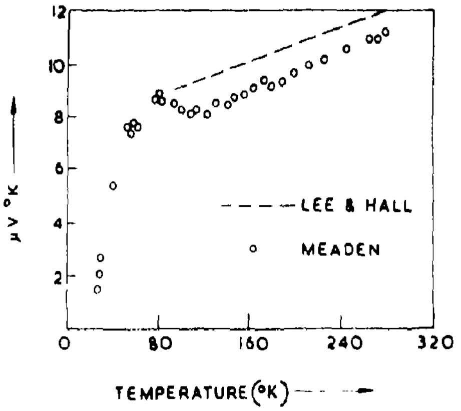

Fig. 5 The thermoelectric power of Pu metal

the Néel point. Results obtained by Lallement[12] indicate a minimum in Young's modulus between 50° and 60°K. This is interpreted in terms of a magnetic order-disorder transition.

Detailed results by Brodsky[13] showed that the Hall coefficient varies continuously from a positive value at room temperature to a negative value at 77°K, going through zero at 200°K. Brodsky proposes a band theory, and a change from hole to electron conduction to account for these phenomena. Brodsky observed no field dependence of the Hall coefficient over the temperature range of his investigation, and deduces that this precludes the existence of a Néel point at ~90°K. As measurements were not made below 77°K, this does not rule out the possibility of a 60°K Néel point.

The results and conclusions outlined above have been extracted primarily from the thesis of D. A. Wigley[14], written at the end of 1963.

Two years later, at the Third International Conference on plutonium held in London, November 1965, though more information was available, the uncertainty had, if anything, increased. Lallement, in a general review, felt that his measurements on expansion coefficient had not verified Rocher's theoretical predictions. On the other hand further measurements by Brodsky on the Hall coefficient had led him to reject his simple band structure theory and to propose that magnetic ordering takes place at 23°K. Lallement was led to conclude that all theories proposed to that date should be rejected.

8. RESISTANCE CURVE OF PU_6FE

In the autumn of 1967 some electrical resistance vs. temperature measurements were done on a number of intermetallic compounds containing Pu (J. Adamson and M. J. Mortimer, Private communication). In particular they found the curve for Pu_6Fe to be qualitatively very similar to that of pure Pu, though the residual resistivity was higher, and the position of the maximum was at about 120°K.

Referring back to the results detailed previously in Section 6 we can state that there is no indication of any magnetic splitting or even line broadening at 16°K compared with 293°K in Pu_6Fe. We may then infer, because of the close similarity in the resistance curves, that no magnetic condensation takes place in Pu, at least down to ~16°K which is lower than Brodsky's suggested value of 23°K.

There are, however, a number of points to discuss in respect of this inference which will now be considered in turn: (*A*) A different mechanism may operate in Pu_6Fe from that in Pu metal. Electrical resistance work is not a particularly selective measure, and it does not distinguish between a large variety of physical effects which may contribute. However, despite the differing crystallographic forms, the interatomic distances in Pu_6Fe are close to those in pure Pu. We conclude that it is most likely that the same basic mechanism is operating in both Pu_6Fe and Pu metal. (*B*) Iron does not take part in the ordering phenomenon in Pu_6Fe. This is a more serious objection though unlikely, we feel, in view of the fact that the average Fe-Pu distance is less than the average Pu-Pu distance (2·81 Å compared with 3·23 Å). It is interesting to consider here the behaviour of Fe as a dilute impurity in Cr metal.

Cr metal exhibits complicated magnetic behaviour and both Fe and Sn have been used as Mössbauer probes in the material. The Sn spectra (Sn is diamagnetic, of course) are reasonably straightforward: the single line observed at high temperature splits on cooling below the Néel point at 315°K, and a saturated hyperfine field of around 95 kG is observed. But for Fe in Cr, though splitting is observed below the Néel point, it indicates a small field of ~20 to 30 kG. Indeed, magnetic susceptibility measurements obey a Curie–Weiss law down to 2°K, which would indicate that the spins were quite free. On the assumption that the Fe spins were only loosely coupled to the Cr ordered spin state, a strong external magnetic field was applied to the material at 2°K in an attempt to order these Fe spins. However, no increase in broadening was achieved, which is indeed surprising. There has, though, been some doubt as to the purity of the material used (C. E. Johnson, Private communication).

At any rate we would expect to see at least some measurable broadening of the quadrupole lines of the Pu_6Fe spectrum at 16°K, if there exists at this temperature an ordered system of spins. (*C*) Filing has so strained the Mössbauer specimen that no magnetisation is observable. This is unlikely since we are concerned with preserving the presence of microscopic ordering rather than crystallite directional magnetisation (all the domains pointing in the same direction). We would not reckon that filing would disturb the microscopic order to any great extent. However, in order to check this a further experiment was done in which fresh filings were placed in a silica tube, which was evacuated and sealed. The filings were strain annealed for 24 hr at 250°C. The results we obtained from this second sample were substantially the same as before. (*D*) The line-widths we derived for Pu_6Fe are subject to experimental error and curve-fitting error, but we would reckon to be able to observe with ease an increase in line-width of 0·01 cm/sec., which corresponds to the presence of a magnetic field at the Fe nuclear site of some 3 kG in magnitude. The question of what this would mean in terms of Bohr magnetons on the Pu atoms has not been pursued.

9. FINAL COMMENTS

In the resistance-temperature curves of the actinide elements from thorium through to plutonium, there appears a consistent form of temperature rise from one element to the next, the resistance maximum first appearing (just) in Np, and being quite apparent in Pu (see Fig. 6).

A general outline of the possibility of this type of behaviour in the actinides was first made by Lee *et al.*[15]. They based their argument on a theoretical treatment by Varley[16] of the factors affecting the electronic contribution to the 'free energy' of a system, where the density of states at the Fermi surface changes sufficiently sharply with energy. A corollary of this treatment is that one could realise a negative value for the temperature coefficient of resistivity in the actinides over certain temperature ranges.

The suggestion is that in U, for example, one would also eventually see a resistance maximum if it were not for the fact that the α-β phase transformation intervenes first. This is, of course, mere conjecture, and can never be verified experimentally. Indeed it may well be that there is a significant step in going from U to Np if the 5*f* electrons make their first appearance in Np metal[17]. Th and U are well-known superconductors, and American workers[18] have reported that Pa goes superconducting as well. No transition temperature has been observed in either Np or Pu down to 0·4°K.

Neptunium would appear to be the critical element in the series, with its broad but definite resistance maximum situated at some 90 deg before the α-β phase change. In respect of Np some crucial work has been done by

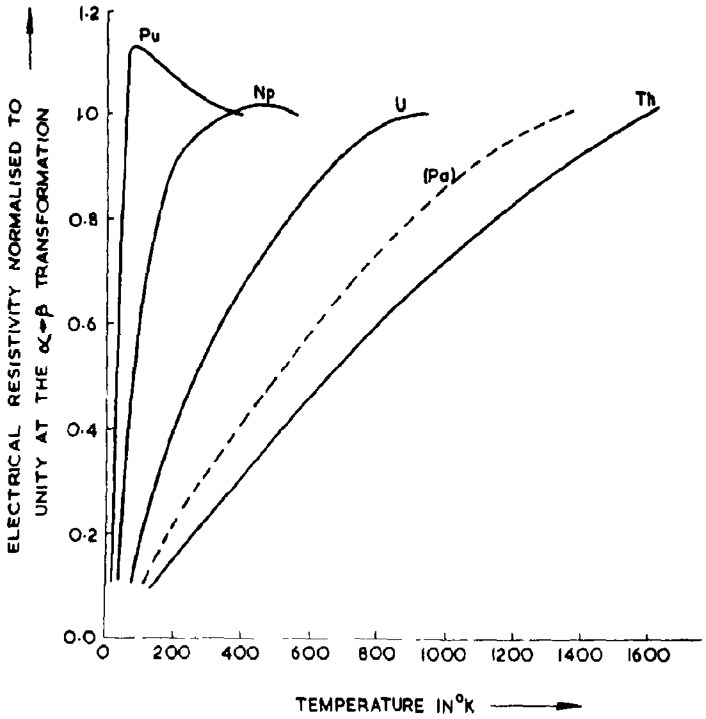

Fig. 6 The electrical resistivity vs. temperature curves for some actinide metals (Provided by E. King A. E. R. E., Harwell).

Stone (Private communication). Using a single line Am^{241} α-emitting source he investigated the Mössbauer spectrum of Np metal at 4·2°K. He found that there were two quadrupole split contributions in the spectrum arising from the two different crystallographic sites (the contributions were different in intensity by a factor of nearly 2 to 1 – a most surprising result in view of the equal population of the sites, but one which is irrelevant to the present discussion). There was thus no sign of magnetic splitting in Np metal though the temperature of 4·2°K is far and away below the resistance maximum.

The final solution to the actinide problem must be the result of direct measurement on the metals themselves, and in this respect the immediate future looks quite promising. By autumn 1968 the new Harwell refrigerator should be available to the group for resistance measurements down to 30 m/deg absolute, 0·030°K (this figure will probably be higher for Pu because of its high rate of self-heating). If Pu and Np prove to go superconducting we may not necessarily discount the antiferromagnetic theory. We would, however, view it with some reserve.

Hill and Matthias[19] have discussed superconductivity investigations made on U_6X compounds (where X is a ferromagnetic transition metal), and the role played by magnetic interactions in superconductivity involving transition metal elements.

In particular they outline theoretical work by Russian authors in which the co-existence of superconductivity with ferromagnetism[20], and with antiferromagnetism[21], is postulated. However, no experimental verification of these ideas has been produced and, indeed, conclusive evidence of the

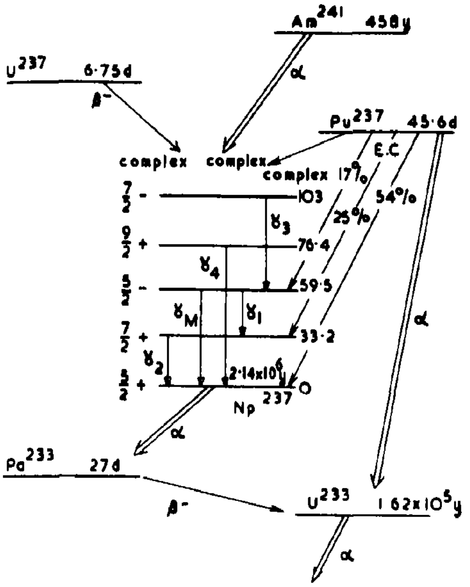

Fig 7. Radioactive parents' decay scheme to ground state of Np^{237}.

non-separation of superconducting and magnetic regions in the same sample will be difficult to achieve.

Lastly we mention the possibility of using Pu^{237} in Pu metal as a Mössbauer source, with a single peak NpO$_2$ absorber. With both source and absorber at 4·2°K we should easily be able to pick out a magnetically split contribution from the metallic source. Figure 7 indicates the different radioactive parent isotopes which can be used to populate the 59·6 keV excited state of Np^{237}.

Acknowledgements—The author would like to thank E. King and Dr. C. F Johnson for making available unpublished data, and for informative discussions with Dr. Johnson, and Dr. W. E Gardner. The computer programme used in the least-squares analysis of the data was prepared by Dr. N. R. Large. This work was carried out under the general supervision of Dr. K. Mendelssohn F R.S, and Dr. J. A. Lee, whose interest and encouragement were most welcome. During the course of this work the author was in receipt of a Harwell extramural research grant.

REFERENCES

1. BLOW S., D. Phil. Thesis, Oxford University (1968).
2. ELLINGER F H., In *The Metal Plutonium* (Edited by A. S. Coffinberry and W. N. Miner), p. 281. University of Chicago Press, Chicago, Ill. (1961).
3. WILKINSON W. D., In *Uranium Metallurgy*, Vol. II, p 1102 Interscience, New York, (1962).
4. GOLDANSKII V. I., MAKAROV E. F., and KHRAPOV V. V., *Zh. eksp. teoro Fiz.* **44**, 752 (1963); English transl *Soviet Phys. JETP* **17**, 508 (1963); see also *Phys. Lett* **3**, 344 (1963)
5. CHANDRASEKHAR B. S. and HULM J. K., *J. Phys. Chem. Solids* **7**, 259 (1958).
6. SANDENAW T. A, and OLSEN C. E, In *Plutonium 1960*, p. 59. Cleaver-Hume, London (1960).
7. LEE J. A., MEADEN G. T. and MENDELSSOHN K., *Cryogenics* **1**, 52 (1960).
8. LEE J. A. and HALL R O. A., *J. less-common Metals* **1**, 356. (1959)
9. SMOLUCHOWSKI R., *Phys Rev* **125**, 1577 (1962).
10. WILSON A. H., *Proc. R. Soc* **167**, 580. (1938)
11. ROCHER Y. A., *Phil. Mag. Suppl.* **11**, (43). 233. (1962).
12. LALLEMENT R., *Phys. Lett.* **6**, 182 (1963).
13. BRODSKY M. B, *Phys. Rev.* **131**, 137 (1963).
14. WIGLEY D. A., D Phil. Thesis, Oxford University. (1964).
15. LEE J. A, HALL R. O A., KING E. and MEADEN G. T, In *Plutonium 1960*, p. 39. Clever-Hume, London (1960).
16. VARLEY J H O., *Proc. R Soc.* **237A**, 413. (1956).
17. ZACHARIASEN W. H, In *The Metal Plutonium* (Edited by A. S. Coffinberry and W. N Miner), p. 99. University of Chicago Press, Chicago, Ill. (1961).
18. FOWLER R. D, MATTHIAS B. T., ASPREY L. B, HILL H H, LINDSAY J. D. G., OLSEN C. E. and WHITE R H, *Phys. Rev. Lett.* **15** (22), 860. (1965)
19. HILL H. H. and MATTHIAS B. T., *Phys. Rev.* **168**, 464 (1968).
20. AKHIEZER A. I. and AKHIEZER I. A., *Zh. eksp. teor. Fiz.* **43**, 2208 (1962); English transl., *Soviet Phys. JETP* **16**, 1560 (1963).
21. PRIVOROTSKII I. A, *Zh. eksp. teor. Fiz.* **43**. 2255 (1962); English transl., *Soviet Phys. JEPT* **16**, 1593 (1963).

J. Phys. Chem. Solids Pergamon Press 1969. Vol. 30, pp. 1561–1571. Printed in Great Britain.

MÖSSBAUER SPECTROSCOPY OF STOICHIOMETRIC AND NON-STOICHIOMETRIC MAGNETITE

J. M. DANIELS and A. ROSENCWAIG
Department of Physics, University of Toronto, Toronto 5, Ontario, Canada

(*Received* 23 *September* 1968; *in revised form* 12 *November* 1968)

Abstract–X-ray analysis, chemical analysis, magnetic measurements, and room temperature Mossbauer spectra, with and without the presence of a transverse magnetic field of 8 4 kG have been obtained for two samples of magnetite, one nearly stoichiometric and the other highly non-stoichiometric. The crystallographic structure of the non-stoichiometric sample has been found to be identical with that of the stoichiometric sample, and the vacancies located predominantly at the octahedral sites. The magnetic fields at the Fe nuclei in magnetite have been found to be negative and the Lamb–Mössbauer factor for octahedral and tetrahedral iron ions have been found to be equal within experimental error It has been established that the fast electron hopping process, present in magnetite, is essentially a pair-localized phenomenon, that is, limited to available (Fe^{2+}–Fe^{3+}) octahedral pairs, with the non-paired octahedral Fe^{3+} ions not participating in the hopping process. Significant delocalization of the process appears to occur only in highly stoichiometric samples.

1. INTRODUCTION

WE USED a sample of a commercial magnetite[*], which we shall refer to as Fe_3O_4-F, to test the resolution of a Mössbauer spectrometer, and noticed that the spectrum, Fig. 1(c), was different from that which we expected. Another sample, which we shall denote by Fe_3O_4–M, was prepared by heating α-Fe_2O_3 at 800°C in a stainless steel crucible in a CO–CO_2 atmosphere for 24 hr, followed by cooling in the same atmosphere. This sample gave the expected Mössbauer spectrum, as is shown in Fig. 1(a). Before describing our experiments we shall first review the principal facts about magnetite relevant to this investigation.

Magnetite has the inverse spinel structure [1]. The unit cell consists of a cage of 32 O^{2-} ions in a face centred cubic arrangement. The cations are distributed among the interstital positions of this lattice. There are 64 such sites with tetrahedral symmetry, of which a maximum of 8 are occupied, and 32 with octahedral symmetry, of which a maximum of 16 are occupied. Stoichiometric magnetite has all available interstital sites occupied by ferrous and ferric ions, the Fe^{2+} ions being all at octahedral sites. However, non-stoichiometric magnetites also exist, with various numbers of the available sites either vacant or occupied by impurity cations. It has been postulated that these vacancies and impurity cations are preferentially located at the octahedral sites[2]. Magnetite compositions range from that of stoichiometric Fe_3O_4 with 8 Fe^{3+} ions in tetrahedral and 8 Fe^{2+} + 8 Fe^{3+} ions in octahedral sites, to that of γ-Fe_2O_3 with 8 Fe^{3+} ions in tetrahedral and $13\frac{1}{3}$ Fe^{3+} ions in octahedral sites of the unit cell[3].

The magnetic properties of magnetite have been satisfactorily explained, on the assumption that the spins on the octahedral and tetrahedral cation sites form two antiferromagnetically coupled sublattices[4]. In addition, stoichiometric magnetite undergoes an order–disorder phase transition at ~ 120°K which is attributed to fast electron hopping among the Fe^{2+} and Fe^{3+} octahedral cations above 120°K[5]. Associated with this transi-

---

[*] This sample was obtained from the Fisher Scientific Company and although we were unable to obtain its exact method of preparation, we believe that the sample was prepared as a product in a reaction between an iron salt and an alkali.

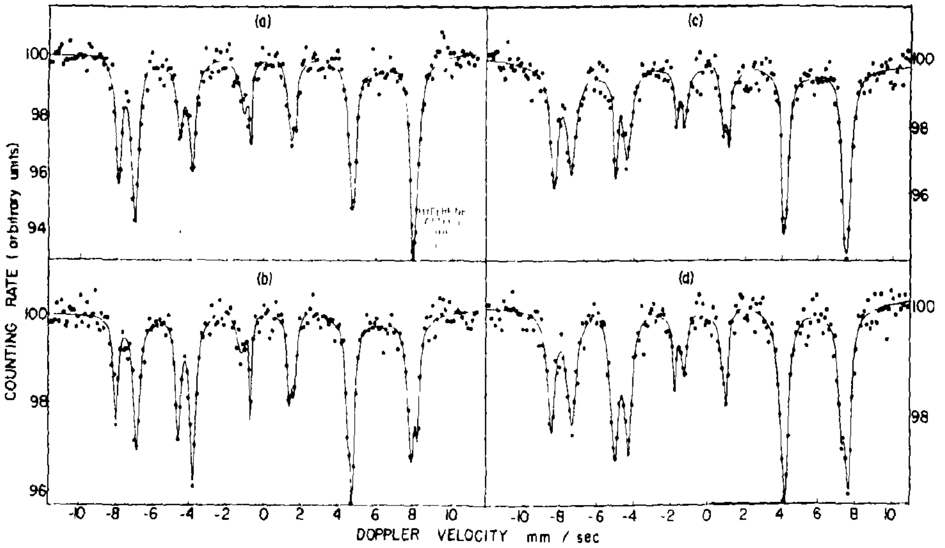

Fig. 1. Mössbauer spectra of magnetite samples Fe_3O_4–M and Fe_3O_4–F at 300°K. (a) Fe_3O_4–M in a transverse magnetic field $H_t = 0$ kG; (b) Fe_3O_4–M with $H_t = 8{\cdot}4$ kG; (c) Fe_3O_4–F with $H_t = 0$ kG; (d) Fe_3O_4–F with $H_t = 8{\cdot}4$ kG. Hyperfine patterns designated as (A) and (B) in Fig. 1(a) are discussed in the text.

tion is an anomaly in both the specific heat and electrical conductivity of magnetite at this temperature.

On the foregoing picture, one might expect three different Mössbauer spectra from magnetite, one from the Fe^{3+} ions in the tetrahedral sites, one from the Fe^{3+} ions in the octahedral sites, and another from the Fe^{2+} ions in the octahedral sites. In fact, in stoichiometric magnetite there are only two resolved spectra[6, 7]. Below 120°K these are identified as one due to the Fe^{3+} ions in both sites, and the other due to Fe^{2+} ions; above 120°K, the spectra change, and the two resolved spectra are generally identified as one due to the Fe^{3+} ions in the tetrahedral sites, and the other due to the entire set of Fe^{3+} and Fe^{2+} ions in the octahedral sites, i.e. one spectrum is due to all the tetrahedral cations, while the other is due to all the octahedral cations. The explanation for the spectral change is attributed to the electron exchange between ions at the octahedral sites, which is rapid above 120°K and slow below that temperature. This accounts for the indistinguishability of the Fe^{2+} and Fe^{3+} Mössbauer spectra (a process similar to motional narrowing) and for the increased electrical conductivity above 120°K.

Our investigation comprises a study of the Mössbauer spectra, in zero field and in a transverse field of 8400 G, measurements of the magnetic moment, and a chemical and X-ray analysis of the two samples of 'magnetite'. We propose that the fast electron exchange in magnetite above 120°K can be regarded in two distinct ways. On the one hand, it can be considered as an electron hopping back and forth within (Fe^{2+}–Fe^{3+}) octahedral pairs, and the transfer of the electron from the Fe^{2+} to the Fe^{3+} ion can be adequately described by a process involving only these two ions and the intervening oxygen anion, and not involving the rest of the lattice. We shall call such a process 'pair-localized' or simply 'localized hopping'. On the other hand, the electron exchange can be considered, as is usually done, as a more or less indiscriminate hopping of electrons among all the octahedral cations, and in this case the entire octahedral sublattice must be considered as being involved. This process we shall call 'delocalized hopping'. A consequence of localized hopping is that the Mössbauer spectra above 120°K should correspond to one spectrum arising from all the (Fe^{3+}–Fe^{2+}) pairs on the octahedral sites, and another arising from the remaining Fe^{3+} ions on both sites. A cursory examination of the Mössbauer spectra of Fe_3O_4-F seemed to indicate that this might be the correct interpretation of our spectra, and it is this hypothesis which we set out to test.

2. EXPERIMENTAL DETAILS AND RESULTS

(a) *X-ray analysis*

X-ray analysis, carried out by the Ontario Research Foundation, identified both Fe_3O_4–M and Fe_3O_4–F as single phase magnetites with the spinel structure. Since the Mössbauer spectrum obtained for Fe_3O_4–F can be easily explained on the basis that this sample is not really single phase but a mixture of 80 per cent magnetite and 20 per cent γ-Fe_2O_3, an extensive X-ray analysis was performed on Fe_3O_4–F to ascertain how much γ-Fe_2O_3 might be present.

An X-ray trace of the high-angle (553) doublet, present in both magnetite and γ-Fe_2O_3, is shown in Fig. 2. Here we see that there is a noticeable change in the lattice parameter as the composition is varied from stoichiometric Fe_3O_4 to γ-Fe_2O_3. Fe_3O_4–F has a lattice parameter which lies between that of stoichiometric Fe_3O_4 and γ-Fe_2O_3. If Fe_3O_4–F were in fact anything like a (80–20 per cent) mixture of Fe_3O_4 and γ-Fe_2O_3, we should expect to see more than one set of lines. If it were a mixture of phases of varying composition, we should expect the X-ray lines to be considerably broadened. These lines in Fe_3O_4–F are in fact somewhat broader than the corresponding lines for stoichiometric Fe_3O_4, but so are the lines in γ-Fe_2O_3. The observed broadening can therefore be attributed to the small size of the crystallites ($< 0{\cdot}1\,\mu$), which are known to be present in both the Fe_3O_4–F and the γ-Fe_2O_3 samples.

A further check can be made for the presence of γ-Fe_2O_3 in the Fe_3O_4–F since γ-Fe_2O_3 has certain weak characteristic X-ray lines which are not present in magnetite. Figure 3 shows X-ray traces in the region of two of these lines. (3·73 and 3·40 Å), for γ-Fe_2O_3, for two mechanical mixtures of stoichiometric magnetite and γ-Fe_2O_3, and for Fe_3O_4–F. It is seen from the traces that there is very little evidence of the presence of γ-Fe_2O_3 in Fe_3O_4–F. Finally, by performing a long count on the X-rays scattered in the direction of these two peaks, we were able, as shown in Fig. 4, to place an upper limit of 4 per cent on the amount of γ-Fe_2O_3 that may be present as a separate phase in Fe_3O_4–F. The X-ray evidence thus appears to strongly indicate that Fe_3O_4–F is essentially a single phase magnetite of definite composition.

(b) *Chemical analyses*

Chemical analyses for total iron and ferrous iron were carried out in the Department of Chemistry, University of Toronto. The results are shown in Table 1. Given also are the standard deviations of the average of about half a dozen measurements of each quantity.

(c) *Magnetometer measurements*

The magnetometer consisted of two coils, in series opposition and in series with a ballistic galvanometer, in a field of 3000 G. The sample was moved from the centre of one coil to the centre of the other. When samples of identical size and shape are used, the deflection of the ballistic galvanometer is proportional to the magnetic moment of the sample. We used a lucite tube packed with powered magnetite to ensure the latter. What we measured was the ratio of the magnetic moments of two samples of 'magnetite'. Because these samples had different grain size and packed differently, the masses required to fill the sample holder were different. The results are as follows:

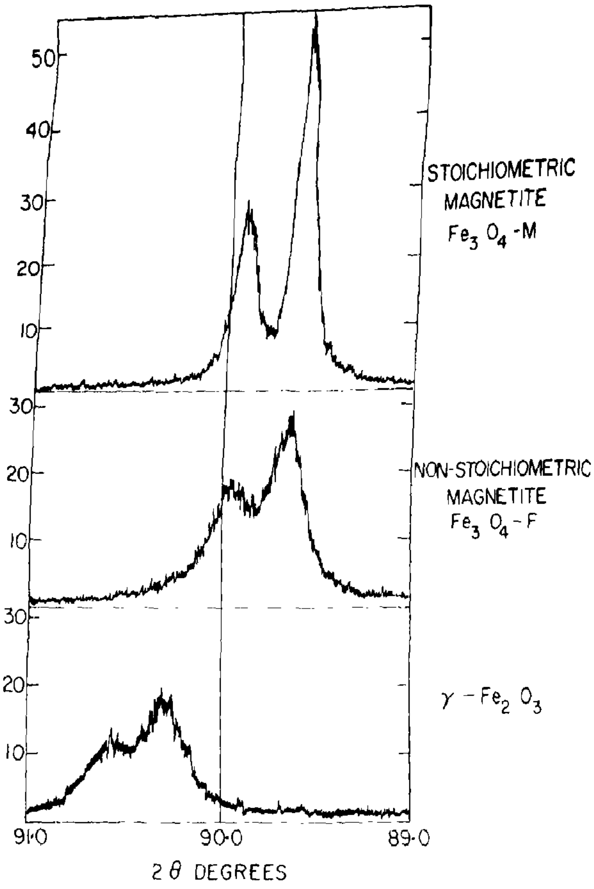

Fig. 2. X-ray traces of the high-angle (553) doublet in stoichiometric magnetite (Fe_3O_4-M), non-stoichiometric magnetite (Fe_3O_4-F), and in γ-Fe_2O_3.

Table 1. Chemical analyses of magnetite samples

Sample	Fraction by weight of total iron	S.D.	Fraction by weight of ferrous iron	S.D.	Composition
Stoichiometric Fe_3O_4	0·724		0·2412		$(Fe_2O_3)_{1\cdot0}\ (FeO)_{1\cdot0}$
Fe_3O_4-M	0·717	0·003	0·238	0·0002	$(Fe_2O_3)_{1\cdot00}\ (FeO)_{0\cdot97}$
Fe_3O_4-F	0·706	0·003	0·1784	0·0003	$(Fe_2O_3)_{1\cdot00}\ (FeO)_{0\cdot68}$

Mass of Fe_3O_4-M $= 0·995 \pm 0·001$ g

Mass of Fe_3O_4-F $= 0·589 \pm 0·001$ g.

(Magnetic moment of 1 g of Fe_3O_4-F)/(Magnetic moment of 1 gm of Fe_3O_4-M) $= 0·908 \pm 0·006$.

The value of the room temperature magnetic moment ratio is the average of 10 determinations, and the error given is the standard deviation of this average, computed from the observed scatter of the individual readings.

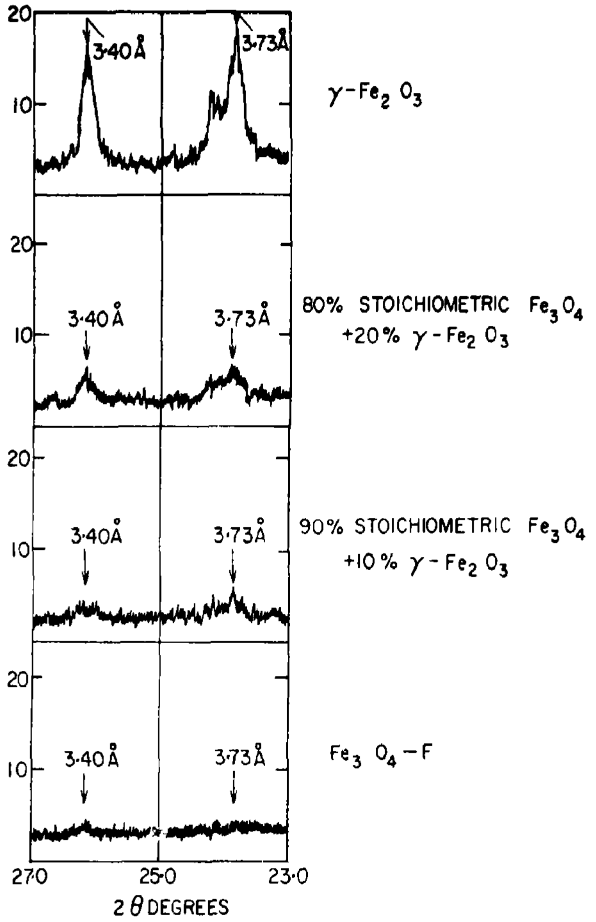

Fig. 3 X-ray traces of the characteristic γ-Fe_2O_3 lines, 3·40 and 3·73 Å, in γ-Fe_2O_3, in (80–20 per cent) and (90–10 per cent) mechanical mixtures of stoichiometric magnetite and γ-Fe_2O_3, and in the non-stoichiometric magnetite (Fe_3O_4–F).

(d) Mossbauer spectra

The spectrometer was a constant acceleration type similar to the one described by Wertheim[8]. The γ-rays were counted using a lithium drifted silicon detector and were displayed on a 400-channel pulse-height analyser. The absorbers were powdered magnetite of 46 mg/cm^2 held firmly between 2 mylar sheets of 0·0075 in. thickness. To obtain spectra in a transverse field, the absorber holders were placed between the poles of a permanent magnet whose field was 8400 G.

Assuming that the absorption line shape is Lorentzian, the parameters (position, height, area) of each line, and the standard deviations of these parameters, were obtained by the method of least squares, using an IBM 7094 computer. The Mössbauer spectrum of α-Fe_2O_3 was used to calibrate the spectrometer. The results of the measurements on the magnetite samples are displayed in Figure 1, and are summarized in Table 2. The ratio of the intensity of spectrum (A) to that of spectrum (B), β, (see caption of Fig. 1 for a definition of these spectra) is:

Table 2. *Parameters of Mössbauer spectra at* 300°K *of magnetite samples without and with transverse magnetic field*

Sample	Applied transverse magnetic field (kG)	Field at nucleus H_n (kG)	Isomer shift* ΔE (mm/sec)	Quadrupole shift $\|\epsilon\|$ (mm/sec)
Fe_3O_4–M				
Line group (a)	0·0	−498 ± 2	+0·41 ± 0·04	0·02 ± 0·04
Line group (b)	0·0	−463 ± 2	+0·77 ± 0·04	0·02 ± 0·04
Fe_3O_4–F				
Line group (a)	0·0	−497 ± 2	+0·38 ± 0·04	0·01 ± 0·04
Line group (b)	0·0	−462 ± 2	+0·76 ± 0·04	0·01 ± 0·04
Fe_3O_4–M				
Line group (a)	8·4	−504 ± 2	+0·39 ± 0·04	0·00 ± 0·04
Line group (b)	8·4	−457 ± 2	+0·74 ± 0·04	0·01 ± 0·04
Fe_3O_4–F				
Line group (a)	8·4	−504 ± 2	+0·39 ± 0·04	0·03 ± 0·04
Line group (b)	8·4	−456 ± 2	+0·73 ± 0·04	0·02 ± 0·04

* The isomer shift is measured relative to 310 stainless steel.

For Fe_3O_4–M, $\beta = 0{\cdot}575 \pm 0{\cdot}019$

For Fe_3O_4–F, $\beta = 0{\cdot}976 \pm 0{\cdot}043$.

The intensity ratios were obtained by fitting two Lorentzian curves simultaneously to the two resolved doublets at the left hand of the spectra in Fig. 1. In both the results just mentioned, the value of β quoted is the average of 14 determinations, and the error is the standard deviation of this average.

The changes in the magnetic fields at the nuclei, produced when the magnetite sample is placed in a transverse field of 8400 G, clearly identifies spectrum (A) with the ions in the tetrahedral sites, and spectrum (B) with ions in the octahedral sites, in both magnetite samples. The fact that the magnitude of the change in the nuclear magnetic fields is somewhat less than 8·4 kG can be attributed to incomplete magnetization and the presence of a small demagnetizing field. A closer examination of Fig. 1(c) and 1(d) indicates that the resolved lines on the left of the spectrum, belonging to spectrum (A) of Fe_3O_4–F, are not only shifted, but somewhat broadened in an external magnetic field. An attempt was made to resolve this line into two using the least squares curve fitting method. Indications were that it might well be a doublet with an unresolved separation of about 11 kG. If this is so, the following is a plausible identification of the origins of the two spectra in Fe_3O_4–F.

Spectrum (B), which originates with all the ions in the octahedral sites in stoichiometric Fe_3O_4, originates only with (Fe^{3+}–Fe^{2+}) pairs in the octahedral sites in non-stoichiometric magnetite. Spectrum (A), which originates with the ions in the tetrahedral sites in stoichiometric Fe_3O_4, originates with both the Fe^{3+} ions at the tetrahedral and the non-paired Fe^{3+} ions at the octahedral sites in non-stoichiometric magnetite. It is not an unreasonable assumption that the field at the nucleus would be relatively insensitive to the surroundings for an ion with this closed shell structure. Since spectrum (A) thus originates with ions of opposite spin directions, it is split in a magnetic field.

We shall now test our assumptions in a quantitative manner.

3. ANALYSIS OF THE RESULTS

Each of the observations just described leads to a linear equation connecting certain unknown quantities. For example, if x is the

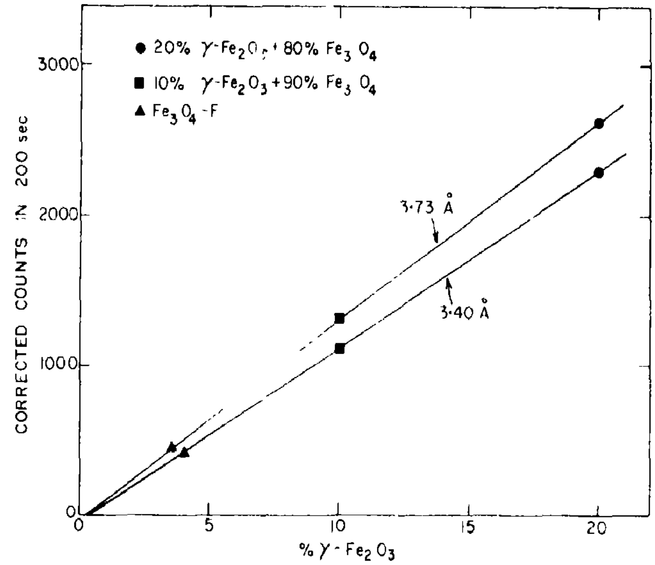

Fig. 4 The count rate, corrected for background for the 3·40 and 3·73 Å lines as a function of the amount of γ-Fe$_2$O$_3$ present as a separate phase in magnetite.

number of iron ions and y is the number of Fe^{2+} ions in the unit cell, then on the assumptions that (i) the Lamb-Mössbauer factors for the iron ions in octahedral and tetrahedral sites are the same, and (ii) Mössbauer spectrum (B) is identified with (Fe^{2+}-Fe^{3+}) pairs at the octahedral sites, and spectrum (A) with the rest of the ions, then:

$$(x-2y)=\beta\,.\,2y$$

where β is the ratio of the intensity of spectrum (A) to that of spectrum (B). Different hypotheses about the fast electron hopping process lead to different equations. In general, the number of equations related to the observations is greater than the number of unknowns, and the coefficients, which are measured quantities, are uncertain. The best solution to such a set of equations may be obtained by the method of least squares[9].

In particular, if we find an equation of the form

$$ax+by+cz+d=0 \qquad (1)$$

where x, y, z are unknowns, and a, b, c and d measured quantities with standard deviations $\sigma(a), \sigma(b), \sigma(c), \sigma(d)$, then let us write

$$\frac{ax+by+cz+d}{\sqrt{(x^2\sigma(a)^2+y^2\sigma(b)^2+z^2\sigma(c)^2+\sigma(d)^2)}}=\mathrm{E} \qquad (2)$$

Then, the best solution for an overdetermined set of such equations is that set of values of (x, y, z) which makes $\Sigma\mathrm{E}^2$ a minimum. This value of $\Sigma\mathrm{E}^2$ is the chi-squared for this solution, and standard tables of chi-squared may be used to estimate the goodness of the hypothesis which led to the set of equations which were solved.

The equations to be solved are the following. Let x be the number of iron ions in the unit cell, y the number of Fe^{2+} ions in the unit cell, and z the number of Fe^{3+} ions in tetrahedral sites of the unit cell. Then the chemical analyses give:

$$\frac{55{\cdot}85x}{55{\cdot}85x+(24-x)M+16{\cdot}0\times 32}=w_x \qquad (3)$$

$$\frac{55{\cdot}85y}{55{\cdot}85x+(24-x)M+16{\cdot}0\times 32}=w'_u \quad (4)$$

where w'_t and w'_u are the fractions by weight of total and ferrous iron. M is the average atomic weight of impurity cations. Since M is unknown, and is expected to be small, we have considered two extreme cases

(i) $M = 0$, i.e. the 'impurities' are all vacancies, and

(ii) $M = 55{\cdot}85$, i.e. the 'impurities' are elements like iron

For the magnetometer experiment, we make the assumption that the magnetic moment ratio measured at 300°K is not noticeably different from what we would obtain at 0°K. This is a reasonable assumption since the field used is of relatively high strength, and 300°K is a fairly small fraction of the Curie temperature of 900°K[10]. Assuming 5 Bohr magnetons for an Fe^{3+} ion, and 4 Bohr magnetons for an Fe^{2+} ion, the magnetic moment per unit cell is

$$\mu = 5x - y - 10z \quad (5)$$

Then, for Fe$_3$O$_4$-M, let us put

$$5x_M - y_M - 10z_M = \mu_M \quad (6A)$$

and for Fe$_3$O$_4$-F

$$5x_F - y_F - 10z_F = \mu_M R \quad (6B)$$

where R is the ratio of the moments of the unite cells of the two samples, and is given, in terms of R', the ratio of the moments of unit mass, by

$$R = R'\frac{55{\cdot}85x_F+(24-x_F)M+32\times 16}{55{\cdot}85x_M+(24-x_M)M+32\times 16}. \quad (7)$$

As mentioned in the previous section, there are two hypotheses which we wish to test for the interpretation of the Mössbauer spectra:

Hypothesis (A) The electron hopping occurs solely within (Fe^{2+}-Fe^{3+}) pairs. Then

$$x-2y=\beta\cdot 2y. \quad (8A)$$

Hypothesis (B) The electron hopping occurs among all the ions on the octahedral sites. Then

$$z=\beta(x-z) \quad (8B)$$

where β is the ratio of the intensity of spectrum (A) to that of spectrum (B).

In equations (8A) and (8B), it is assumed that the Lamb–Mössbauer factor for tetrahedral iron cations is essentially the same as that for octahedral iron cations.

To analyze the data for the Fe$_3$O$_4$–M sample sets of 3 equations in the 2 unknowns x and y were used. The first two equations were equations (3) and (4) for the chemical analysis, while the third was either equation (8A) or (8B). In equation (8B), the value of z was set to 8·0. In all, 4 sets of equations were used, in which hypotheses (A) and (B) were tested under the conditions $M = 0{\cdot}0$ and $M = 55{\cdot}85$.

From the last column of Table 3, we note that the values of χ^2 obtained are generally well within the reliability limits, especially for the hypothesis (A) cases. We can therefore conclude that the assumption that the octahedral and tetrahedral ions have nearly equal Lamb–Mössbauer factors, implicit in the way equations (8A) and (8B) have been written, is reasonable. Similarly the assumption that, for a nearly stoichiometric magnetite all the tetrahedral sites are occupied by Fe^{3+} ions, implicit by setting $z = 8{\cdot}0$, is also reasonable.

Most important, however, is the fact that, for both assumed values of M, hypothesis (A) gives a slightly lower value of χ^2 than does hypothesis (B). It would therefore appear that even in a slightly non-stoichiometric magnetite sample, such as Fe$_3$O$_4$–M, the localized electron hopping hypothesis seems to be preferred over the completely delocalized hypothesis.

Table 3. Results of least-squares analysis for Fe_3O_4-M

Sample	*M*	Electron hopping hypothesis	*x*	*y*	χ^2
Fe_3O_4-M	0·0	(A)	23·32 ± 0·57	7·53 ± 0·13	1·08
	0·0	(B)	23·10 ± 0·77	7·48 ± 0·18	1·22
	55·85	(A)	23·83 ± 0·35	7·69 ± 0·02	1·02
	55·85	(B)	23·75 ± 0·26	7·69 ± 0·02	2·58

In analyzing the Fe_3O_4-F sample, the results of the magnetometer experiment were included. Thus sets of 4 equations in the three unknowns, *x*, *y* and *z* were used. As in the previous analysis, 4 sets of equations testing hypotheses (8A) and (8B) under the two conditions for *M*, were used.

Table 4 lists the results of this analysis.

highly non-stoichiometric magnetite is limited to the available (Fe^{2+}-Fe^{3+}) octahedral pairs.

In stoichiometric magnetite, we do not expect any difference between hypothesis (8A) and (8B), because when the Fe^{2+} and Fe^{3+} ions on the octahedral sites are grouped into pairs, all the ions on the octahedral sites are used up. In addition, since there are no defects in the octahedral sites, there is no 'natural' way of grouping the ions into pairs. Under these circumstances, we would expect the electron hopping to be just as easy between pairs as within pairs, and this could be envisaged as a complete delocalization of the exchange. We should also expect a gradual change in the physical properties of magnetites, as the composition becomes less stoichiometric, until we arrive at the pair localized hopping which appears to be manifested, for example, by Fe_3O_4-F. A comparison of the values of χ^2 from Tables 3 and 4 appears to confirm such an assumption.

Table 4. Results of least-squares analysis for Fe_3O_4-F

Sample	*M*	Electron exchange hypothesis	*x*	*y*	*z*	χ^2
Fe_3O_4-F	0·0	(A)	22·014 ± 0·008	5·563 ± 0·001	7·927 ± 0·003	$4·5 \times 10^{-4}$
	0·0	(B)	21·9 ± 2·0	5·55 ± 0·37	7·91 ± 0·86	17·2
	55·85	(A)	23·417 ± 0·005	5·917 ± 0·0005	8·275 ± 0·003	$4·4 \times 10^{-1}$
	55·85	(B)	23·42 ± 0·92	5·92 ± 0·09	8·30 ± 0·63	18·9

The fit of the data for Fe_3O_4-F appears to be somewhat better for *M* = 0·0 than for *M* = 55·85. This is reflected, not in the values of χ^2 obtained, but rather in the fact that for *M* = 55·85 values of *z* greater than the permissible maximum of 8·0 have been calculated.

From the values of *z* obtained for *M* = 0·0, it is also apparent that the tetrahedral sites, even in this highly non-stoichiometric magnetite, are nearly completely occupied by Fe^{3+} ions, and, therefore, that the impurities and vacancies are predominantly located at the octahedral sites.

Of greater interest is the fact that the values of χ^2 obtained with hypothesis (8A) are remarkably small, while those obtained with hypothesis (8B) are considerably beyond the reliability limits. It would appear, therefore, that the fast electron exchange process in a

CONCLUSIONS

From the results of X-ray analysis and the magnetometer test, it would appear that non-stoichiometric magnetite has the same crystallographic structure as stoichiometric magnetite. In both cases, therefore, the unit cell consists of a cubic cage of 32 oxygen anions with up to 24 iron cations located at interstital positions, eight of which are tetrahedral and 16 are octahedral sites. This result agrees with the known fact that γ-Fe_2O_3, which may be considered as an extreme example of a non-stoichiometric magnetite, also has this same crystal structure[3].

As expected, the magnetic field at the Fe nuclei in magnetite proved to be negative, i.e. antiparallel to the direction of the local magnetization. In addition, Mössbauer spectroscopy in the presence of an external magnetic field, demonstrates in an easy and direct manner, the existence of two antiferromagnetically coupled sublattices in magnetite.

It has been found that the Lamb–Mössbauer factor for iron ions in octahedral and tetrahedral sites in Fe_3O_4 are equal within experimental error. This agrees with the previously obtained result[6], that below the transition point in magnetite, the hyperfine pattern due to the Fe^{3+} ions at the octahedral sites appears to have the same intensity as that due to the Fe^{3+} ions at the tetrahedral sites.

Both in highly as well as in slightly non-stoichiometric magnetite, nearly all of the available tetrahedral sites appear to be occupied by Fe^{3+} ions, with the vacancies and impurities predominantly located at octahedral sites. This result supports the evidence that in γ-Fe_2O_3, the vacancies are predominantly located at octahedral sites[11].

In highly non-stoichiometric magnetite, the available cation sites not occupied by iron ions appear to be vacant or occupied by impurities of low mass.

We have shown, in this experiment, that the fast electron exchange process, first proposed by Verwey[2, 5], and confirmed microscopically in 1961 by Bauminger *et al.* [6] by Mössbauer spectroscopy, is essentially a localized phenomenon, occurring principally within the available (Fe^{2+}–Fe^{3+}) octahedral pairs. In a highly non-stoichiometric magnetite, the process appears to be completely pair-localized while in a magnetite only slightly non-stoichiometric, the process appears to become somewhat delocalized. In general, any non-paired Fe^{3+} octahedral cation does not participate in this exchange process.

We are now able to explain, qualitatively, the results on conductivity measurements made by Verwey and Haayman[2] on magnetite samples of varying stoichiometry. Briefly, they found that magnetite exhibits a conductivity at room temperature many orders of magnitude higher than that of any other simple ferrite, and that there is a rapid decrease in electrical conductivity with increasing non-stoichiometry.

The fact that the room temperature conductivity of magnetites of all compositions is much higher than for other ferrites, can be attributed to the presence of the fast electron exchange process which occurs in all magnetites at this temperature. The existence of such a process obviously increases the mobility of the electrons under the presence of an applied electric field.

In a highly non-stoichiometric magnetite, the electronic wavefunctions, representing those electrons participating in the electron hopping process, are localized to regions in the octahedral sublattice containing an Fe^{2+} and an Fe^{3+} and the intervening O^{2-} ions. In a highly stoichiometric magnetite, these wavefunctions can become somewhat delocalized and extend over larger regions. In the singular case of a perfect lattice these wavefunctions can become Bloch or quasi-Bloch wavefunctions extending over the entire octahedral sublattice. Such an interpretation easily accounts for the observed critical dependence of the conductivity of magnetite on its stoichiometry. The rapid decrease in conductivity with only slight increases in non-stoichiometry is due, therefore, not to any disappearance of fast electron exchange, but rather to the localization of the electrons to regions encompassing available octahedral (Fe^{2+}–Fe^{3+}) pairs. Thus, if we consider two separate probablities or frequencies, one related to intra-pair election hopping ν_p and the other to inter-pair hopping ν_l, then ν_p is not critically dependent on lattice stoichiometry while ν_L is highly sensitive to lattice stoichiometry. In a perfect lattice $\nu_l \approx \nu_p$ while, in a highly non-stoichiometric lattice, $\nu_L \ll \nu_p$. Since macroscopic conductivity is more a function of ν_L than ν_p, the conductivity can be expected to decrease rapidly with increasing non-stoichiometry.

Acknowledgements—We should like to express our gratitude to Mr. K. R. Collins for carrying out the computation of the results of our measurements. This work was supported by the National Research Council of Canada.

REFERENCES

1. VERWEY E. J. W. and DE BOER J H., *Rec. Trav. Chim.* **55**, 531 (1936).
2. VERWEY E. J. W. and HAAYMAN P. W., *Physica* **8**, 979 (1941).
3. VERWEY E. J. W, *Z. Kristallogr.* **91**, 65 (1935).
4. NEEL L., *Annls. Phys.* **3**, 137 (1948).
5. VERWEY E. J. W., HAAYMAN P. W and ROMEIJN F. C., *J. chem. Phys.* **15**, 181 (1947).
6. BAUMINGER R., COHEN S. G., MARINOV A., OFER S and SEGAL E., *Phys. Rev* **122**, 1447 (1961).
7. ITO A., ONO K. and ISHIKAWA Y, *J phys. Soc Japan* **18**, 1465 (1963).
8. WERTHEIM G. K. In *Mossbauer Effect*, Chap. 2 Academic Press, New York (1964).
9. e.g. WHITTAKER E. T. and ROBINSON G. In *The Calculus of Observations*, 4th Edn p. 223 Blackie, Glasgow (1944).
10. SMIT J. and WIJN H P. J. In *Ferrites*, p. 161. Philips Technical Library (1959)
11. FERGUSON G. A., Jr. and HAAS M., *Phys. Rev* **112**, 1130 (1958).

J. Phys. Chem. Solids Pergamon Press 1969. Vol. 30, pp. 1573–1577. Printed in Great Britain.

OPTICAL ABSORPTION OF SELENIUM IN THE α-MONOCLINIC CRYSTAL AND SOME SOLVENTS

J. M. CAYWOOD and J. D. TAYNAI
California Institute of Technology, Pasadena, Calif. 91109, U.S.A.

(*Received* 25 *October* 1968)

Abstract—The optical absorption of α-monoclinic selenium has been measured over the range in wavelength 1·15–0·2775 μ. The data shows a well defined absorption edge at 2·25 eV with further structure appearing as changes in $d\alpha/dE$ at 2·85 eV and 3·75 eV. For comparison the absorption of selenium in solutions in which it is believed to exist in the same eight-membered puckered ring as in the crystal was measured. This absorption is qualitatively different from that of the crystal.

1. INTRODUCTION

In the course of investigations of α-monoclinic selenium in progress at this laboratory, it was discovered that although the optical properties of amorphous and trigonal selenium have been extensively studied[1–3], Prosser, alone, has reported measuring the optical constants of α-monoclinic selenium[4]. These measurements extend over the range in wavelength from 0·876 to 0·592 μ. However, in order to investigate the structure of the excited states one would like to extend these measurements to considerably shorter wavelengths. A technique has been developed to grow extremely thin platelets of α-monoclinic selenium which has allowed us to extend these measurements. To compare the optical absorption processes of a molecule in the crystalline environment (in which it might be considerably perturbed by the surrounding selenium molecules) with that of a molecule in a less perturbed condition, the optical absorption of selenium dissolved in various solvents in which it is believed to exist primarily as Se_8 molecules was also measured.

2. α-MONOCLINIC CRYSTALS

(A) *Sample preparation*

Small platelets of α-monoclinic Se were grown on quartz optical windows by controlled evaporation of a saturated solution of CS_2. The selenium solute was 99·99 per cent pure while the CS_2 was reagent quality. From the numerous platelets grown on the window several were chosen. These crystals were chosen because they were large (typical dimension of 200 μ), of uniform shape and of uniform thickness as determined by interference-contrast microscopy. Measurement of the angles formed by the edges of these platelets showed that the platelets correspond to those of the (101) face of the α-monoclinic crystal, as determined by Burbank, to within better than 10 min of arc[5, 6]. Figure 1 shows a crystal which is typical of those used in these investigations. Finally, an aluminum foil mask through which a hole of 100 μ diameter had been drilled was cemented over the platelet to define the light path through the crystal.

(B) *Experimental apparatus and procedure*

The monochromatic beam was provided by passing the light from the source through a Spex model 1400–11 double spectrometer using 600 line per mm gratings blazed at 5000 Å. Because this is a grating-type instrument care must be taken to avoid second (and higher) order radiation. This difficulty was avoided by employing as detectors vacuum photodiodes which had appreciable response only over an octave in wavelength

In this apparatus the light from the source was chopped, passed through the monochromator, focussed onto the sample assembly by a 90° off-axis paraboloid, front surfaced, reducing mirror, and detected by the aforementioned photodiode. The output of the photodiode was amplified, demodulated by a PAR model HR-8 phase lock amplifier and read from a digital voltmeter For calibration purposes similar measurements were made using a similar mask cemented to a clean quartz window

After the transmission measurements were completed, the masks were removed, the crystals were overcoated, and the thickness of the crystals was measured using the Nomarski interferometer attachment of a Reichert microscope To resolve the ambiguity inherent to interferometric measurement of sharp steps, measurements were made at the Th 5351 Å line and the Na D lines Consistency arguments were then used to unambiguously determine the thickness

(C) *Results*

With this system it was relatively easy to cover more than 3 orders of magnitude in relative transmission with good reproducibility and little scatter Figure 2 shows a plot of every second point from a data run on sample SeO4.

Figure 3 is a plot of $-(\ln T)/d$ for two samples of different thickness, where T is relative transmission and d the corresponding thickness. Sample SeO4 was 4102 ± 61 Å thick while SeO9 was 1060 ± 48 Å thick. The errors represent the 95 per cent confidence limits of the Student's test calculated from repeated measurements. Since the relative transmission, and not the absolute transmission, was measured, the highest transmission point of SeO9 was set at unity and the level of SeO4 was chosen to fit the two curves in the region of high absorption where reflections are unimportant. It can be seen that the fit is quite good throughout the region of high absorption. There is a well-defined change in the slope at 2·85 eV and a less well-defined change in slope around 3·75 eV. The fluctuations in the high energy region (above ~3·7 eV) are scatter, not structure. The measurements were extended to 1·15 μ in the case of SeO4, but no variations beyond those which could be attributed to interference were observed.

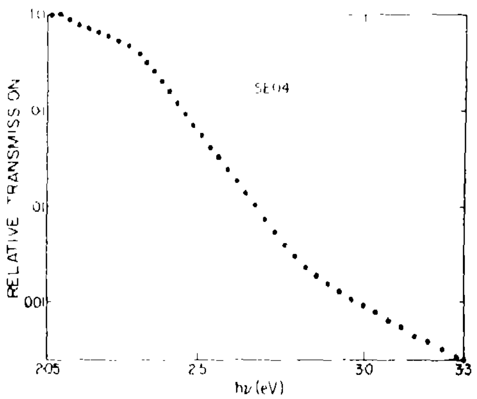

Fig. 2 Relative transmission of a typical platelet of α-monoclinic Se.

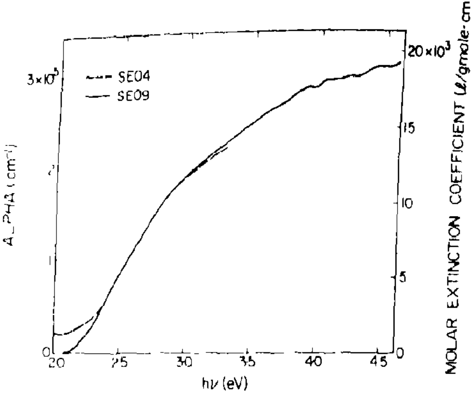

Fig. 3 Normalized absorption of two α-monoclinic Se crystals. SeO4 was 4102 ± 61 Å thick while SeO9 was 1060 ± 48 Å thick.

The planes of the Se_8 molecules are arranged approximately perpendicular to the (101) face. Since the angles formed by the edges of the (101) face differ by 4°, the orientation of molecular plane within the crystal could be determined. Measurements were made in which the electric vector was polarized approximately parallel and perpendicular to these planes. No large difference was noted between the transmission of the crystal for polarized and unpolarized light.

3. SOLUTIONS

(A) *Sample preparation and experimental procedure*

Transmission measurements were made of 99·99 per cent pure selenium dissolved in CS_2, in toluene, and in trichlorethylene (TCF). The CS_2 used was reagent grade The TCF was reagent grade which was subsequently distilled prior to use. The toluene was spectroscopic grade.

Transmission measurements employed a Cary model 14 spectrophotometer which uses a time sharing system

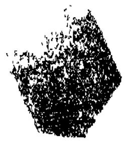

Fig. 1. A typical crystal used in the transmission measurements. This crystal was about 1800 Å in thickness.

to eliminate the effect of the solvent and container. To check this, the transmission cells were always filled with an unadulterated sample of the solvent to be employed and a transmission spectrum was taken before the solution was placed in the cell.

Concentration was determined by weighing the residue from repeated evaporations of known quantities of the solution and subtracting the weight of the residue from repeated evaporations of unadulterated solvent. The weight of the latter was always small (<3 per cent) with respect to the weight of the former.

(B) *Results*

In Fig. 4 is plotted the atomic extinction coefficient of an approximately saturated, room temperature solution of selenium in CS_2. Earlier workers have reported different results [7]. CS_2 begins to absorb strongly in the vicinity of 3·25 eV. It was found that because of this, special care had to be taken to obtain meaningful results in this region. The same coefficient for a solution of ½ of that concentration is the same to within the limits of the error bar. This demonstrates that there is no appreciable concentration effect. In addition to the random error indicated by the error bar on the graph there is a possible systematic error of ±7 with 90 per cent confidence from uncertainty in determination of the concentration.

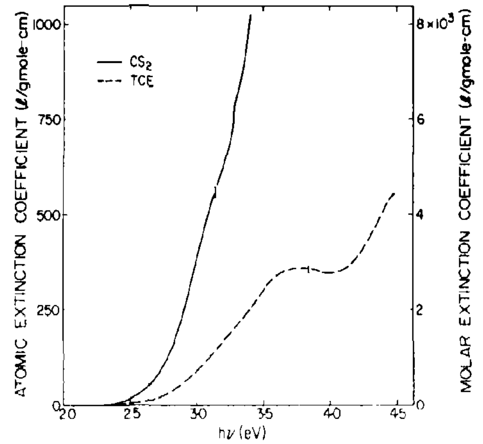

Fig. 4. Extinction coefficient of selenium dissolved in CS_2 and trichlorethylene (TCE)

Also shown in Fig. 4 is a plot of atomic extinction coefficient of selenium dissolved in TCE. The low solubility of selenium in TCE results in a possible systematic error from the concentration determination of ±23 with 90 per cent confidence for this curve. The data for toluene was qualitatively similar to that for TCE.

4. DISCUSSION

Using Prosser's values[4] for n and k and equation (5) of Appendix 1 to evaluate the transmission for wavelengths in the vicinity of 0·6 μ and selenium thicknesses of 0·1 μ one finds that the transmission of the selenium-quartz combination relative to clean quartz is about 0·98. This implies that the zero of the absorption constant, alpha, in Fig. 3, is correctly placed. Similarly evaluating equation (5) for a sample of 0·4 μ thickness one finds fair agreement with the baseline chosen for SeO4. One can then interpret all of the change in transmission of SeO9 as being due to absorption so that the curve in Fig. 3 does represent α as indicated. Absorption in SeO4 begins at the same energy as it does in SeO9, but, because of the reflection correction, has initially less effect until absorption dominates the loss whereupon the curve merges with that of SeO9. Extrapolation of the linear portion of the SeO9 curve to zero intercept yields an optical absorption edge of 2·25 eV at room temperature. This is in good agreement with Prosser[4]. A plot of the square root of α vs. photon energy is linear over the range 2·1–2·4 eV[8]. The optical absorption may quite generally be taken to be the density of occupied lower states times the density of unoccupied upper states times the square of the matrix element for the transition between these states, integrated over the energetically allowed transitions. Thus the breaks in $d\alpha/dE$ probably represent changes in the group symmetry of either the initial and/or the final states involved in the transition.

Turning to the measurements of Se in solution one might ask what evidence exists for believing the predominant molecular species in the solvent to be Se_8. If one takes a saturated solution of Se in CS_2 and places several drops on a microscope slide, the CS_2 will evaporate in about one minute leaving behind platelets of α-monoclinic selenium with dimensions of the order of $50\,\mu$. However, the thermodynamically stable crystalline form at room temperature and atmospheric pressure is the trigonal, which is composed of helical chains. The fact that one observes α-monoclinic crystals precipitated from the CS_2 solution tends to indicate that this is a kinetic process which deposits the molecules in the form in which they exist in the solution (i.e. Se_8). The same experiment with Se dissolved in TCE yields small α crystals. But a much larger proportion of the selenium is deposited in what appear to be amorphous globs than is the case with CS_2 solutions. This may indicate that in the case of TCE the selenium exists in the solution in other molecular forms besides Se_8. On the assumption that Se_8 is the predominant molecular species, the molar extinction coefficient is indicated on the right of Fig. 4.

Examining Fig. 4 one observes the extinction coefficient, ϵ, to increase approximately linearly with increasing photon energy from the onset of significant absorption in the vicinity of 2·7 eV to the vicinity of 3·3 eV for both the CS_2 and the TCE solutions. In the vicinity of 3·3 eV the slope of ϵ steepens for both solutions. Beyond this point the absorption of the CS_2 limits the range of measurement. The TCE data show a peak at 3·8 eV, a valley at 4·0 eV followed by an increase of undetermined extent.

The similarity of the shapes of the CS_2 and TCE curves at lower energies argues in favor of the same molecules in each while the difference in amplitude argues for a concentration difference for this molecule species in the two solutions. One possibility would be for there to be a preponderance of Se_8 molecules in the CS_2 while in the TCE about one half of the selenium is in the form of other molecular species. If a membrane which is permeable to the solvents, but not to Se_8 could be found, measurements of osmotic pressure could determine the molecular fractions.

Comparison of 'ϵ' for the case of the solid to the case of the solution (see Fig. 3 and 4) shows that in the solid the absorption edge has been shifted in energy by about 0·5 eV. However, $d\epsilon/dE$ in the linear regions of the two curves is approximately the same. This would lead one to believe that the intermolecular interactions in the solid, while not small (certainly stronger than Van der Waal's interactions), do not grossly perturb the density of states or the transition matrix elements.

5. SUMMARY

The optical absorption of selenium in the α-monoclinic crystal and in solutions of organic solvents has been observed. The absorption edge is 2·25 eV for the former and 2·7 eV for the latter. The intermolecular bonding is stronger than Van der Waal's in this crystal.

Acknowledgements—The authors wish to express their indebtedness to the Canadian Copper Refiners Ltd for supplying the selenium, to Mr S. Iizima for his valuable assistance in growing the crystals, and to Mr S. I. Kurtin for many valuable discussions concerning optical measurements. The authors, especially, wish to acknowledge many helpful discussions with Professors C. A. Mead and M-A. Nicolet, and Dr S. Geller.

REFERENCES

1. COLDWELL R. S. and FAN H. Y., *Phys. Rev* **114**, 664 (1959)
2. DOWD J. J., *Proc. phys. Soc.* **B64**, 783 (1951)
3. GILLEO M. A., *J. chem. Phys* **19**, 1291 (1951).
4. PROSSER V., *Cs. Cas. Fys* **10**, 35 (1960).
5. BURBANK R. D., *Acta crystallogr* **4**, 140 (1951)
6. IIZIMA S. *et al.*, To be published in *Proc. 1st Intl Symp* Physics of Se and Te.
7. FERGUSSON J. E. *et al.*, *J. inorg. nucl. Chem* **24**, 157 (1962)
8. MacFARLANE G. G. *et al.*, *Phys. Rev.* **108**, 1377 (1957).
9. KOLLER K., *Z. Phys* **110**, 45 (1938).

APPENDIX 1

In attempting to unravel the transmission data, one is faced with solving the problem of light passing from one medium through two dissimilar media, reemerging into a medium of the same index as the original medium. This problem may be solved in a straightforward, if tedious, manner by requiring the solution of the wave equation and its derivative to match at all three boundaries. Under the simplifying assumption of no absorption in the second layer (e.g. the quartz substrate in our case) the solution reduces to

$$T = 16/[G_1 + G_2\cos(4\pi\eta_2 d/\lambda) + G_3\sin(4\pi\eta_2 d/\lambda)] \quad (1)$$

where T is the ratio of transmitted to incident power, d is the thickness of the second layer, η_2 is the index of refraction of the second layer, and λ is the free space wavelength of the incident light.

$$\begin{aligned}
G_1 = {} & (A_1^2 - A_2^2 - A_3^2 - A_4^2 - A_5^2 + A_6^2)\cos(4\pi na/\lambda)\\
& + 2(A_1A_5 + A_3A_6)\sin(4\pi na/\lambda)\\
& + 2(A_1A_4 + A_2A_6)\sinh(4\pi ka/\lambda)\\
& + (A_1^2 + A_2^2 + A_3^2 + A_4^2 + A_5^2 + A_6^2)\\
& \times\cosh(4\pi ka/\lambda)\\
G_2 = {} & (A_1^2 + A_2^2 + A_3^2 - A_4^2 - A_5^2 - A_6^2)\cos(4\pi na/\lambda)\\
& + 2(A_1A_5 - A_3A_6)\sin(4\pi na/\lambda) \qquad (2)\\
& + 2(A_1A_4 - A_2A_6)\sinh(4\pi ka/\lambda)\\
& + (A_1^2 - A_2^2 - A_3^2 + A_4^2 + A_5^2 - A_6^2)\\
& \times\cosh(4\pi ka/\lambda)\\
G_3 = {} & 2(A_2A_5 - A_3A_4)\cos(4\pi na/\lambda) + 2(A_1A_6 - A_1A_2)\\
& \times\sin(4\pi na/\lambda) + 2(A_3A_4 - A_2A_5)\cosh(4\pi ka/\lambda)\\
& + 2(A_1A_3 - A_5A_6)\sinh(4\pi ka/\lambda)
\end{aligned}$$

where n and k are respectively the real and imaginary parts of the index of refraction of the first (e.g. selenium) layer, 'a' is the thickness of this layer and

$$\begin{aligned}
A_1 &= 2\\
A_2 &= n(\eta_2^2 + n^2 + k^2)/\eta_2(n^2 + k^2)\\
A_3 &= k(n^2 + k^2 - \eta_2^2)/\eta_2(n^2 + k^2)\\
A_4 &= n(n^2 + k^2 + \eta_0^2)/\eta_0(n^2 + k^2)\\
A_5 &= k(n^2 + k^2 - \eta_0^2)/\eta_0(n^2 + k^2)\\
A_6 &= (\eta_2^2 + \eta_0^2)/\eta_0\eta_2
\end{aligned} \qquad (3)$$

and η_0 is the index of the initial surrounding media. After considerable work one can show this to be a special case of a general relation derived by Koller[9].

The question arises of how to handle the sinusoidal terms of argument $4\pi nd/\lambda$. Since the monochrometer has a bandpass of about 10 Å in the configuration in which it was used it seems clear that one should average over the bandpass. Defining $\Delta\lambda$ to be the bandpass and λ_0 to be the nominal wavelength one obtains

$$T \cong 16/G_1\left[1 + \left(\frac{G_2^2 + G_3^2}{G_1^2}\right)^{1/2}\cos(4\pi\eta_0 d\Delta\lambda/\lambda_0^2 + \theta)\right]$$

where θ is a quantity which doesn't vary during the averaging. Then $\langle T\rangle = \int T\mathrm{d}(\Delta\lambda)/\int\mathrm{d}(\Delta\lambda)$, but since the argument of the cos goes through many cycles (~ 10) as $\Delta\lambda$ ranges over 10 Å

$$\langle T\rangle \cong \frac{N\int_0^{2\pi}\{16\mathrm{d}\varphi/[G_1(1 + ((G_2^2 + G_3^2)/G_1^2)^{1/2})\cos\varphi]\}}{N\int_0^{2\pi}\mathrm{d}\varphi} \qquad (4)$$

because the integral over a partial cycle is small with respect to the integral over many cycles. Therefore,

$$\langle T\rangle \cong \frac{16}{G_1[1 - ((G_2^2 + G_3^2)/G_1^2)]^{1/2}}. \qquad (5)$$

It might be asked why the $\cos\varphi$ term of equation (4) doesn't average to zero. One way of seeing this is to write

$$\frac{\mathrm{d}\varphi}{1 + a\cos\varphi} = \mathrm{d}\varphi\,(1 - a\cos\varphi + a^2\cos^2\varphi + \ldots)$$

and then note that while the first order term does average to zero over a cycle as expected, the second order term is always positive. The effect of the correction term, $(G_2^2 + G_3^2)/G_1^2$ is of the order of 0·2 to 4 per cent for cases that might be encountered in practice, values that are small enough to justify the approximation made, but large enough to affect the values calculated for n and k.

J. Phys. Chem. Solids Pergamon Press 1969. Vol. 30, pp. 1579–1585. Printed in Great Britain.

SPACE-CHARGE-LIMITED CURRENTS IN TETRACENE SINGLE-CRYSTALS

H. BAESSLER*, G. HERRMANN, N. RIEHL and G. VAUBEL
Physics Department, Technische Hochschule München, Germany

(*Received* 7 *August* 1968; *in revised form* 11 *October* 1968)

Abstract – It is established that gold and palladium form ohmic contacts for hole injection into sublimation grown tetracene crystals. Ohmic electron injecting contacts are formed by sodium and barium. The resulting SCL-currents can be described conventionally assuming an exponential trap distribution. Since the total trap density $H_0 = 3 \cdot 10^{15}\,\mathrm{cm}^{-3}$ and the distribution parameter $l = (T_c/T) = 4 \cdot 0 \pm 0 \cdot 3$ turn out to be equal for electron and hole traps, we conclude that the same defects are able to trap both electron and holes. Temperature variation of the SCL-currents yields the energetic distance of the Quasi-Fermi-level of electrons respectively holes from the lowest conduction respectively valence band. Its dependence on the applied voltage is in accordance with theory. The dependence of the SCL-currents on voltage and spacing of the electrodes can be described by $j \sim (F^{l+1}/d^{l})$.

INTRODUCTION

SPACE-charge-limited (SCL) currents are often used in the investigation of bulk properties of organic crystals[1(a–e)]. Therefore there is considerable interest in finding appropriate ohmic contacts. The energy condition for an hole-injecting contact to be ohmic is $\phi \approx I_c$ where ϕ denotes the work-function of the contact and I_c the work function of the crystal, i.e. the energy required to remove an electron from the valence band of the crystal into the vacuum. For an ohmic electron injecting contact $\phi \approx I_c - E_g = A_c$ (E_g = band gap, A_c is the energy which is set free when an electron from the vacuum is brought to the lowest conduction band of the crystal). For anthracene crystals ($I_c = 5 \cdot 65$ eV[2], $E_g = 3 \cdot 72$ eV[3], i.e. $A_c = 1 \cdot 93$ eV) these conditions are generally fulfilled only with electrolytic contacts[4, 5]. One exception is a Na–K-alloy which forms an (liquid) ohmic contact for electron injection at room temperature[6].

As energetics are more favorable for tetracene crystals ($I_c = 5 \cdot 25$ eV[7], E_g is proposed to be $3 \cdot 0$ eV[8], i.e. $A_c \approx 2 \cdot 25$ eV) it is expected that pure metals can be utilized which would be of considerable practical advantage. The present experiments show that indeed gold and palladium form ohmic contacts for hole injection and Na an Ba for electron injection without illumination. Investigation of the resulting SCL-currents yields information about trapping levels in tetracene and about the position of the Fermi-level in the bulk.

EXPERIMENTAL RESULTS

Tetracene crystals were grown by sublimation in a nitrogen atmosphere (20 Torr.). The starting material was obtained by Schuchardt and further purified by vacuum sublimation (1 . . . 3 times). At a growth time of two days crystals up to a thickness of 600 μ could be harvested. All metal contacts were evaporated at 10^{-5} Torr. to be ab-plane of the crystals. Oxidizable metals like Ba and Mg were covered with a protective Pd layer, thus the crystals with the contacts could be handled in air. Only the measurements with Na-contacts were performed at about 10^{-5} Torr. Currents were measured with a Cary vibrating reed electrometer, a Keithley $\mu\mu$-ammeter and a μ-ammeter, respectively.

RESULTS

It is well established that a KI/I_2 solution gives rise to a SCL-hole current in anthracene crystals[1(b)]. As the barrier heights for charge injection are lower with tetracene crystals, there is no reason why KI/I_2 should not form an ohmic contact to tetracene as well. Therefore we have used an aqueous solution of KI/I_2 as a reference electrode. The observed $j(V)$ curve indeed follows a power law $j \sim V^5$ which is typical for SCL-currents assuming the existence of an exponential trap distribution (Fig. 1).

**Present address:* Drexel Institute of Technology, Philadelphia, Pa. 19104, U.S.A.

As the values for the dark currents obtained with Na, Ba, Au, and Pd contacts fit the same power law $j \sim V^n$ with $n = 5{\cdot}0 \pm 0{\cdot}3$ over many orders of magnitude (see Fig. 1), we conclude that these metals also form ohmic contacts. The dependence of the current on crystal thickness can be used as a criterion whether the currents injected from these metals are really limited by a space charge located in trapping states exponentially distributed in energy. According to Mark and Helfrich[1(b)] the SCL-current should follow the law:

$$j = N_0\mu \,.\, e^{1-l}\left(\frac{\epsilon \,.\, \epsilon_0 \,.\, l}{H_0(l+1)}\right)^l\left(\frac{2l+1}{l+1}\right)^{l+1} \frac{V^{l+1}}{d^{2l+1}} \sim \frac{F^{l+1}}{d^l}. \quad (1)$$

N_0 is the effective density of states in the valence, respectively the conduction band, μ is the mobility, ϵ the dielectric constant, ϵ_0 the vacuum permittivity, e the elementary charge, H_0 the total trap density, d the crystal thickness, V the applied voltage and $l = T_c/T$ where T_c characterizes the trap distribution. The average value for l obtained from 15 $j(V)$ curves taken with different crystals and contacts (i.e. KI/I_2, Au, Pd, Na, Ba) is $l = 4{\cdot}0 \pm 0{\cdot}3$. A plot of the current density vs. crystal thickness at a constant field of $F = 9 \times 10^3$ V/cm yields the same l-value (The experimental points in Fig. 2 fit the relation $j \sim d^{-4}$). This presents evidence that the current is not only volume controlled but space-charge-limited. The former case is the more general one and includes the situation where the space charge is contracted within a narrow region near the injecting contact. For example, this can be the result of spatially inhomogeneous trap-emptying caused by barrier-lowering due to Frenkel–Poole effect. In this case the $j(V)$ curve should only depend on the electric field, but not on the thickness of the sample[9].

The polarity of the injected carriers was determined by combining an injecting contact with a non-injecting counterelectrode, e.g. water to which small amounts of MgOH were added in order to reduce the contact resistance. (Injection from the water electrode is negligible compared with injection by an ohmic contact). The results are summarized in Table 1.

Despite the fact that there is probably a residual energy barrier which has to be overcome thermally, Au and Pd form ohmic contacts for hole injection and Na and Ba form ohmic contacts for electron injection. With respect to the uncertainty of the values for the work-function, the error in the calculated barrier heights χ is quite large. Crude estimations, however, show that a thermal injection current of $j \geq 10^{-4}$ cm^{-2} is compatible with a barrier height $\chi \leq 0{\cdot}5$ eV. (10^{-5} cm^{-2} sets an upper limit for the current

Table 1. Comparison of calculated values for injection barrier heights and the 'polarity' of the injecting contact

Metal	ϕ (eV)[10]	$\chi_{+} = I_c - \phi$ (eV)	$\chi = \phi - A_c$ (eV)	Injected carriers
Au	4·78 .5·3[11]	0 . 0·47		holes
Pd	4·96 ..5·4[12]	0 ..0·3		holes
Na	2·3		0·05	electrons
Ba	2 55		0·3	electrons

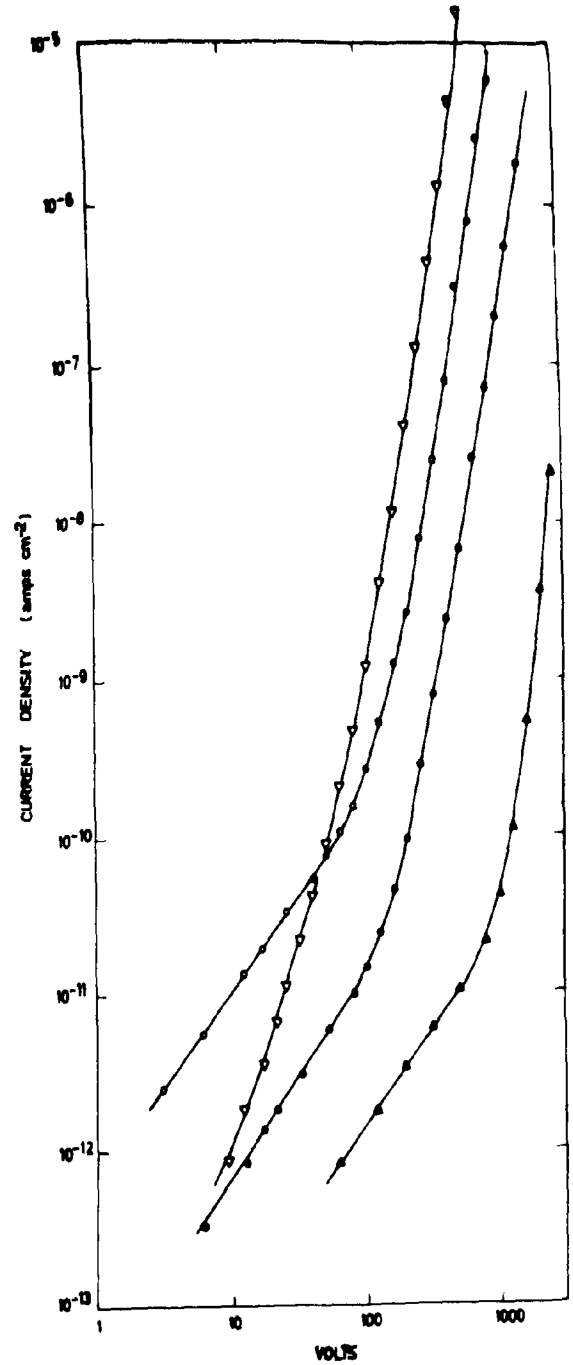

Fig. 1. Current voltage plots for various contact materials and various crystal thicknesses. —∇—∇—: Au-contacts at both sides ($d = 80\,\mu$); —○--○— KI/I_2 (positive), Mg (OH) (negative), ($d = 110\,\mu$), —●--●— Ba-contacts at both sides ($d = 220\,\mu$) (—▲--▲: Pb-contacts at both sides ($d = 240\,\mu$).

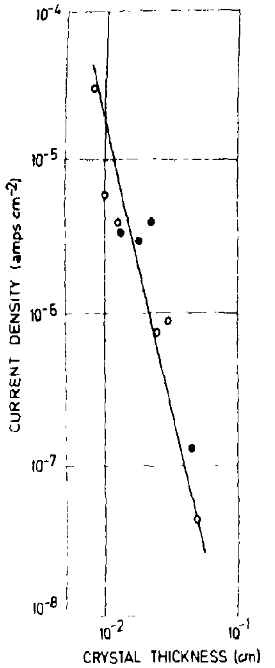

Fig. 2. Thickness dependence of the SCL-current at constant applied field (9×10^4 V/cm), open circles: hole currents, full circles: electron currents.

because of beginning thermal breakdown. Up to this value no deviation of the SCL current from $j \sim V^2$ is observed. Hence, the saturation value of the injection current must be at least 10^{-1} cm^{-2}).

The thermionic emission is given by $j = A'T^2 \exp(-\chi/kT)$. Inserting $T = 300°$K, $j \geq 10^{-1}$ and assuming $A' = 10^{-1}$ A cm^{-2} grad^{-2} yields $\chi \leq 0{\cdot}5$ eV. A similar value for χ is obtained if the assumption is made that the injection current is due to thermal excitation of charge carriers trapped at surface states rather than to the transfer of thermally excited hot metal electrons. In this case the saturation current should be given by $j = eN\nu \exp(-\chi/kT)$ [2]. $\nu \approx 10^{11}$ sec^{-1} is the attempt-to-escape frequency, N denotes the density of surface states. Experiments with anthracene have shown that N is in the order of 10^{13} cm^{-2} [14]. Inserting these values to equation (2) yields an upper limit for the distance of the surface Fermi-level fixed by surface charges from the conduction respectively the valence band: $\chi \leq 0{\cdot}55$ eV. The estimated values for the barrier heights ($\chi_- = \phi - A_c$, $\chi_+ = I_c - \phi$) listed in Table 1 are lower than 0·5 eV. Since they are calculated assuming that surface trapping can be neglected we must conclude that surface potentials ϕ due to trapped surface charges, which contribute to the barrier height, are lower than 0·5 eV.

Non-ohmic contacts

According to the work-functions it is expected that Pb ($\phi = 4{\cdot}0$ eV) and Mg ($\phi = 3{\cdot}7$ eV) will not form ohmic contacts to tetracene. This is confirmed by the measurements (see Fig. 1).

With lead contacts the current flowing at an external field of 4×10^4 V/cm is about four orders of magnitude lower than the SCL current at the same field and does not obey a power law. The same is true for the current observed with Mg-contacts. The temperature dependence of the current provides further evidence that Mg does not form an ohmic contact to tetracene. In the next section it will be shown that with an external voltage of 200 V applied to a 250 μ thick crystal, the activation energy of the SCL current is expected to be 0·83 eV. In contrast to this the current obtained with Mg-contacts follows an Arrhenius plot with an activation energy of $E = 1{\cdot}20 \pm 0{\cdot}02$ eV.

A straightforward explanation would be the following one: The current is a non-SCL injection current with E being the barrier height for injection of either holes or electrons [15]. Assuming the work-function $\phi_{Mg} = 3{\cdot}63$ eV [10], the estimated barrier heights are $\chi_- = 1{\cdot}38$ eV and $\chi_+ = 1{\cdot}62$ eV. The experimental value of 1·2 eV could be

---

[†] For thermionic emission from metals into unbound vacuum states it holds $A = 60$ Acm^{-2} grad^{-2}. A reduction of about 3 orders of magnitude for thermal emission into a narrow conduction band might be expected by comparing of the quantum yield for photoemission into vacuum states and into the lowest conduction band of anthracene [13].

identified with χ_-. However, the maximum thermionic injection current at room temperature which is compatible with a barrier height of 1·2 eV should be about 10^{-14} Acm^{-2}, whereas the observed current is about 10^{-11} Acm^{-2} at 10^4 V/cm. Furthermore, the field dependence of the current is not in accordance with the Schottky theory for thermionic emission. So far the origin of the current observed with weakly injecting contacts is not quite clear.

Application of SCL-currents

It has been shown that Au and Pd contacts give rise to SCL-hole currents and Na and Ba to SCL-electron currents. They can be used to determine the trap distributions for holes and electrons. As hole and electron currents show the same dependence on the spacing of the electrodes all $j(V)$-curves can be reduced to the same crystal thickness. After performing this procedure all SCL-$j(V)$-curves coincide. There is no systematic deviation between hole and electron currents. Hence both the hole and the electron trap distribution must be given by $h(E)\,dE = (H_0/kT_c)\exp(-E/kT_c)\,dE$ with the characteristic temperature $T_c = 1200 \pm 100$°K. In the case of holes, E is taken relative to the top of the valence band; in the case of electrons, it is taken relative to the lower edge of the lowest conduction band. If we assume a mobility $\mu = 0{\cdot}5\ \mathrm{cm^{-2}\,V^{-1}\,sec^{-1}}$ both for electrons and holes[16], an effective density of states $N_{\mathrm{eff}} = 4\times10^{21}\ \mathrm{cm^{-3}}$[1(a)] and a dielectric constant $\epsilon = 3{\cdot}8$ equation (1) yields a total concentration $H_0 = 2{\cdot}5\times10^{15}\ \mathrm{cm^{-3}}$ (error: a factor of 2) both for electron and hole traps. The numerical coincidence leads to the conclusion that the trapping sites for holes and electrons are identical.* This seems to be reasonable as they are preferentially associated with structural defects rather than with chemical impurities[18, 19]. These defects can be point defects or dislocations[20] at which the lattice parameters are changed. Using the Born formula $p^+ = p^- = (e^2/2r)(\epsilon - 1/\epsilon)$ as a rough estimate for the polarization energy of a localized charge in a medium with the dielectric constant ϵ it is evident that a change in the average molecular distance from r to r' causes a change in the polarization energy for a charge regardless of the sign of the charge:

$$\Delta p^+ = \Delta p^- = \frac{e^2}{2r}\frac{\epsilon-1}{\epsilon}\left(\frac{r}{r'}-1\right). \quad (2)$$

A trap is formed if $\Delta p > 0$, i.e. for $r > r'$. Our experiments showed that crystals grown from 1 to 3 times sublimed tetracene gave identical values for the parameters of the trap distribution. Only crystals grown from unpurified material had a slightly higher trap concentration and a distribution parameter $l = T_c/T = 5$ instead of 4 found with purer samples. This apparent independence of the trap distribution on the chemical purity of the crystals indicates that the binding energy of the trapped carriers mainly results from the structure dependent additional polarization energy and not from an enhanced electronic binding energy at impurity molecules having higher electron affinities or lower ionization energies.

If a certain trap distribution rather than a single trapping level is present in a crystal, the position of the quasi-Fermi-level depends on the magnitude of the stored charge and hence on the applied voltage V. In the case of an exponential distribution the energy distance of the Fermi level from the conductive state near the noninjecting contact can be expressed by

$$E_F(V) = kT_c \ln\left[\frac{(l+1)^2}{l(2l+1)}\cdot\frac{eH_0d^2}{\epsilon\epsilon_0V}\right]. \quad (3)$$

The density of free carriers, which is proportional to the current, is given by $n_f = N_{\mathrm{eff}}$

---

*Recently it has been found that this is true for surface traps in anthracene crystals, too[14]. For bulk trapping states in Harshaw-anthracene crystals a similar result was obtained[17]. With very pure anthracene crystals, however, it is often found that the concentration of electron traps is lower than that of hole traps[1(a)].

exp $(-E_F/kT)$. Therefore, the temperature dependence of the SCL-current yields E_F. With solid contacts the temperature dependence can be determined quite easily. The values for E_F at various voltages are plotted in Fig. 3. For comparison the theoretical curve is plotted as well. It is adjusted to fit the experimental point for $V = 400$ V. This corresponds to choosing $H_0 = 3{\cdot}3 \times 10^{15}\,\text{cm}^{-3}$ which is in good agreement with the trap concentration derived from the current-voltage plot.

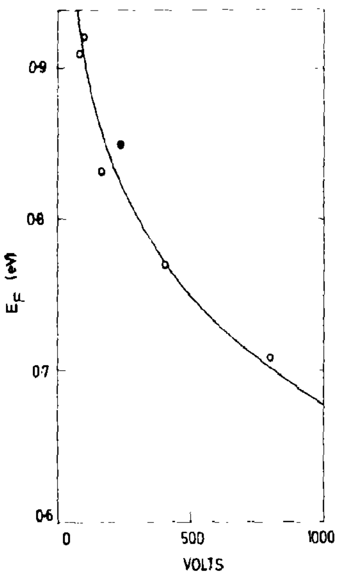

Fig. 3. Activation energy of the SCL-current versus applied voltage. (Crystal thickness 250μ) Open circles, hole currents injected from Au and Pd, full circles: electron current injected from Ba. The solid line is the theoretical dependence of the distance of the Quasi-Fermi-level from the valence respectively the conduction band on the applied voltage, normalized to the experimental point at 400 V.

The good agreement between experiment and theory provides evidence which is independent from the current-voltage-behavior that at least in the energy range $0{\cdot}92 \geqslant E_t \geqslant 0{\cdot}7$ eV the trap distribution is indeed very close to an exponential one. From the current-voltage plots which do not show any deviation from the power law $j \sim V^5$ up to $V = 3 \times 10^3$ V at a crystal thickness of 250μ one can infer an energy range $0{\cdot}9 > E_t > 0{\cdot}6$ eV in which the traps are distributed exponentially.

So far it seems that the trapping properties are quite analogous to that found with anthracene crystals grown under similar conditions. Therefore, one can suppose that the positions of the Fermi levels are approximately the same, too. Hence the threshold photon energy for optical release of trapped electrons (or holes) by direct transition to the conduction (resp. valence) band should be near 0·9 eV. This is just the value obtained by Many *et al.*[21] for the photoelectric response using a Na–K-alloy as one contact material which Mehl and Funk[6] have shown to give rise to an SCl-electron current.

REFERENCES

1. (a) HELFRICH W., In *Physics and Chemistry of the Organic Solid State* (Edited by Fox, Labes and Weissberger). Vol. III. Interscience, New York (1967).
   (b) ROSE A., *Phys. Rev* **97**, 1538 (1955).
   (c) MARK P. and HELFRICH W., *J. appl. Phys.* **33**, 205 (1962).
   (d) SUSSMANN A., *J. appl. Phys.* **38**, 2738 (1967).
   (e) HELFRICH W. and SCHNEIDER W. G., *J. chem. Phys.* **44**, 2902 (1966).
2. LYONS L. E. and MORRIS G. C., *J. chem. Soc.* 5192 (1960).
3. VAUBEL G. and BAESSLER H., *Phys. Lett* **27A**, 322 (1968).
4. HELFRICH W. and SCHNEIDER W. G., *J. chem. Phys* **44**, 2902 (1966)
5. MEHL W. and HALE J. M., *Adv. Electrochem. Engng* **6**, 399 (1967).
6. MEHL W and FUNK B., *Phys Lett.* **25A**, 364 (1967).
7. VILESOV F. I., ZAGRUTSKY A. A. and GARBUZOV D. Z., *Fiz. Tverd. Tela* **5**, 200 (1963).
8. GEACINTOV N., POPE M. and KALLMANN H., *J. chem. Phys.* **45**, 2639 (1966).
9. MEAD C. A., *Phys. Rev.* **128**, 2088 (1962)
10. *Handbook of Physics and Chemistry*, 46th Edn. Chemical Rubber Co
11. SACHTLER W. M. H., DORGELO G. J. H. and HOLSCHER A. A., *Surface Sci.* **5**, 221 (1966).
12. SUHRMANN R., OBER H. and WEDLER G., *Z. phys. Chem.* **29**, 1 (1961).
13. VAUBEL G. and BAESSLER H., *Phys. Status Solidi* **26**, 599 (1968).
14. BAESSLER H. and VAUBEL G., *Phys. Rev. Lett.* **21**, 615 (1968).
15. BECKER G., RIEHL N. and BAESSLER H., *Phys. Lett.* **20**, 221 (1966).

16. FRANKEVICH E. L. and BALAHANOV E. I., *Phys. Status Solidi* **14**, 523 (1966).
17. ZELSMANN H. R., Unpublished results.
18. McGHIE A. R., VOSCHENKOV A. M., REUCROFT P. J. and LABES M. M., *J. chem. Phys.* **48**, 186 (1968).
19. HELFRICH W. and LIPSETT F. R., *J. chem. Phys.* **43**, 4368 (1965).
20. WILLIAMS J. O. and THOMAS J. M., *Trans Faraday Soc.* **63**, 1720 (1967).
21. MANY A., LEVINSON I. and TEUCHER I., *Phys. Rev. Lett.* **20**, 1161 (1968); *ibid.* **21**, 57 (1968).

J. Phys. Chem. Solids Pergamon Press 1969. Vol. 30, pp. 1587–1601. Printed in Great Britain.

EQUATION OF STATE FOR CESIUM METAL TO 23 KBAR*

M. S. ANDERSON, E. J. GUTMAN, J. R. PACKARD† and C. A. SWENSON
Institute for Atomic Research and Department of Physics, Iowa State University,
Ames, Iowa 50010, U.S.A.

(*Received* 30 *September* 1968)

Abstract—An experimental equation of state has been determined for cesium metal at temperatures from 20° to 280°K and at pressures up to 23 kbar The results can be expressed analytically over the range 67–41 cm³/mole to an accuracy of 0·2 cm³ by the relationship

$$P(V, T) = (21{\cdot}5/2{\cdot}84)\,[(66{\cdot}5/V)^{2{\cdot}84} - 1] + 3{\cdot}65\times 10^{-3}(T - 10^\circ\mathrm{K})\ \mathrm{kbar},$$

where V is measured in cm³/mole. This relationship assumes that the isothermal bulk modulus is a function of volume only, that $(\partial B_T/\partial P)_T = 2{\cdot}84$, independent of temperature and volume, and that the molar volume and bulk modulus at $T = 0$ and $P = 0$ are respectively $V_0 = 66{\cdot}5$ cm³ and $B_0 = 21{\cdot}5$ kbar. A summary is given of similar parameters for the other alkali metals. This summary emphasizes the differences (on a reduced scale) between the equations of state for Li, Na, K and Rb (for which $(\partial B_T/\partial P)_T \sim 3{\cdot}8$), and for cesium The relatively greater softness of the P-V relation for cesium possibly is due to the extreme sensitivity to compression of the electronic band structure of this metal. Transition parameters are given also (from 77° to 300°K) for the CsI–II transition which occurs at approximately 22 4 kbars at room temperature.

INTRODUCTION

THE SIMILARITY of the alkali metals to ideal metals is closest for sodium, potassium and rubidium where the Fermi surfaces approach most closely to spherical shapes[1–4]. Lithium and cesium, on the other hand, are believed to have relatively more anisotropic Fermi surfaces[1–3, 5], and in the case of cesium, this anisotropy is predicted to be a strong function of pressure[1].

The simplest, first approximation, to the theory of the cohesive energy of the alkali metals makes use of this ideal behavior in a Wigner–Seitz type of calculation[6, 7]. A lattice of singly charged positive ion cores of radius r_c is assumed to be imbedded in an ideal free electron Fermi gas of equal charge density. The cohesive energy per atom for the metal is calculated in terms of the energy of an electrically neutral spherical volume (equal to the atomic volume) which contains the finite volume ion core at its center and a uniformly distributed electron gas outside this core. The major contributions to the volume-dependent cohesive energy of such a system involve the pure electrostatic energy of the ion core-free electron gas system and the quantum mechanical kinetic energy of the electron gas. Contributions due to correlations and exchange are small in this simplest picture[7]. Hence, one would expect the volume-dependent contributions to the cohesive energies of the alkali metals to differ primarily through a parameter which has the dimensions of a length (i.e. r_c)[8], and indeed this conclusion can be reached from our earlier equation of state data for sodium[9], potassium[10] and lithium[11] and recent data for rubidium[12].

These conclusions suggest a spherical Fermi surface for lithium although the precision of the pressure–volume data and the total compressions for this metal are quite small. The extreme compressibility of cesium and the calculated sensitivity of its Fermi surface to volume changes suggest that indeed cesium could differ appreciably from the other alkali metals in its equation of state at absolute zero[1, 2]. The pressure–volume relationships for the other four alkali metals are identical on a reduced plot of V/V_0 vs. P/B_0 (where V_0 and B_0 are the zero temperature and pressure values of the molar volume and the bulk modulus, respectively); Fermi surface effects could cause cesium to deviate from this common relationship.

---

*Work was performed in the Ames Laboratory of the U.S. Atomic Energy Commission. Contribution No. 2409.

†*Present address*. Minnesota Mining and Manufacturing Co., St. Paul, Minnesota.

Ham[1], Brooks[2], Okumura and Templeton[5], and Dugdale and his co-workers[3, 13, 14] have summarized evidence for the anisotropy of the cesium Fermi surface and its sensitivity to compression. Of particular importance are the experimental room temperature observations for cesium of a change in sign of the thermoelectric power at 400 bar [13] and a minimum in the electrical resistance at approximately 4 kbar[14]. A proper calculation of the cohesive energy must take these band structure effects into account [2, 8].

Bridgman reported a phase transition in cesium at room temperature at 23,500 kg/cm^2 [15, 16]. The volume change is quite small (0·006 V_0). Bardeen suggested that this transition is from the low pressure b.c.c. phase to a cubic-close-packed structure and is caused by an electrostatic interaction between the ion cores[17]. The nature of this transition (CsI–II) has been confirmed by the X-ray measurements of Hall *et al.*[18] Bridgman also discovered a room temperature phase transition at approximately 45,000 kg/cm^2 [16] which more recent work has shown actually consists of two phase transitions (CsII–III, III–IV) separated by approximately 1 kbar[18]. The volume change in these transitions is approximately 0·1 V_0 and is indicative of a change in the size of the ion core, or of a transition from one electronic state into another. These transitions have been studied in some detail by other workers[19–21].

The objective of the work presented in this paper is to produce equation of state data for cesium metal which are comparable with those we have reported for the other alkali metals [9–11]. Our interest is two-fold. First, we want to extend with greater precision earlier low temperature data for the absolute zero isotherm for cesium metal[22] to investigate by comparison with the other alkali metal data the possibilities for electronic effects. Second, we want to determine the thermal contributions to the equation of state. Heat capacity [23], X-ray lattice constant[24] and elastic constant[25] data exist to complement these latter measurements. For many substances (including the other alkali metals) the assumption can be made that to a few per cent the isothermal bulk modulus is independent of temperature at constant volume[26]. This, indeed, appears to be true for cesium also. In addition, we have obtained information as to the temperature dependence of the CsI–II transition which occurs at 22·4 kbar at room temperature.

EXPERIMENTAL DETAILS

The experimental apparatus and procedures which are used to obtain these piston-displacement data are the same as those described in an earlier paper on potassium[10]. The sample is placed in a thick-walled sintered tungsten carbide cylinder and the ends of the cylinder are closed by sintered tungsten carbide pistons. This assembly is placed in a hydraulic press and piston motion (proportional to volume change) is recorded as a function of applied force (pressure) for various sample holder temperatures from 20°K to the melting temperature of the sample at zero pressure.

The 99 per cent pure initial cesium metal as obtained from Mackay was triply distilled under vacuum for further purification and then was sealed in vacuum ampules for storage until it was melted into the sample holder under an argon atmosphere. Cesium metal is very plastic near room temperature, and extrusion occasionally occurred even when copper gaskets and metal back-up rings were used. We experienced no unusual instances of sample holder breakage at pressures to 24 kbar and conclude that there is no problem with cesium attacking our sample holders and weakening them.

Reliable pressure–volume data were obtained over a range of temperatures for two samples of cesium metal of different lengths and diameters. Cylinders of different bore (differing by a factor of two in area) are used to check for systematic errors, and the consistency of the results from these two different sample holders offers a means for evaluating the consistency of the final equation of state. Data were obtained from 1 to 14 kbar on a 0·328 in. long sample in the large diameter (0·354 in.) sample holder at 14 different temperatures in the following order; 270°, 219°, 169°, 82°, 128°, 178°, 43°, 20°, 64°, 99°, 146°, 248°, 287° and 200°K. Similar data, but from 1 (or 2) to 20 kbar, were obtained for a 0·275 in. long sample in the small diameter (0·250 in.) sample holder in 13 runs at the following temperatures (in the listed order); 107°, 158°, 202°, 83°, 242°, 214°, 265°, 125°, 219°, 77°, 41°, 20° and 63°K. Zero shifts in the displacement measuring system (a commercial dial indicator supported on fused quartz rods) are readily observable on raw data isobar plots (δL vs. T at constant pressure) as identical displacements in the data at all pressures and can be corrected for systematically by a simple additive correction. The relatively random order in which isotherm data were taken assists in identifying these shifts. Two such shifts (of maximum value approximately 2×10^{-3} in.) which were observed for each series of runs could be attributed to specific instances of jarring of the press system. A shift due to extrusion can be distinguished from a simple zero shift because it occurs at the highest pressures and results in a nonreproducible reading at the minimum pressure. Again, this can be compensated for and was found in one of the small sample holder runs.

The compressions are so large for cesium (see below) that our major uncertainty lies in the determination of the pressure associated with a given displacement. In each case at high temperatures (greater than 100°K) the double value of friction is of the order of 1 kbar, and it would be presumptuous to quote even relative pressures to a precision greater than 0·05 kbar. The friction effects essentially double at the lowest temperatures. Nevertheless, least squares computer fits through the graphically smoothed data as corrected for sample holder distortion and friction typically showed an r.m.s. deviation in pressure of 0·03 kbar and a maximum deviation of 0·05 kbar. As will be pointed out below, systematic differences between data taken with the two sample holders indicate an accuracy of 1 per cent of the total compression for the highest pressure runs. This is approximately 10^{-3} in. or ten times the smallest division on the dial indicator which measures piston displacement. The total correction for sample holder distortion is less than 10 per cent at maximum, and uncertainties in this quantity introduce a maximum error of 0·2 per cent in the final maximum compressions.

Three other sets of data were taken with the small diameter sample holder with results which agreed with those reported in this paper by roughly 5 per cent. Two of these gave reliable transition data for the CsI–II transition (which are reported below) but gave inconsistent P–V–T data. P–V–T data also were obtained for five runs on a 0·114 in. long sample in this sample holder which agree (except at room temperature) to 1 per cent with the longer sample data reported below. We do not feel that these P–V data are sufficiently reliable, however, to be included in this paper.

Our corrected data give the *change in length* of the sample as a function of temperature and pressure with a minimum pressure which is determined by friction (both in the press and in the sample holder) which is of the order of 1 to 2 kbar. The length of the sample at atmospheric pressure and 273°K (in the case of cesium) is determined by measuring the separation of the ends of the pistons with a micrometer and subtracting piston lengths, etc. The length change between atmospheric pressure and 1 or 2 kbar cannot be determined directly with our apparatus so we cannot ascertain directly the absolute length (or volume, which is assumed to be directly proportional to length) of the sample as a function of temperature and pressure. Once the absolute value of the length is fixed at one temperature and pressure, however, then the absolute sample lengths at all other experimental temperatures and pressures are determined. The zero pressure length (or volume) of the sample at temperatures other than the initial temperature at which it has been determined directly can be obtained by extrapolation of the experimental isotherms to zero pressure.

The procedure which is used to obtain these lengths has been described in the previous paper[10]. Most P–V isotherms can be represented very well by means of a function introduced by Birch[27, 28]:

$$P = P_0 + 3B_0/2[(y^7 - y^5)(1 - \xi(y^2 - 1))] \quad (1)$$

where $y^3 = V_0/V = L_0/L$. V_0(or L_0) and B_0 are the volume (length) and bulk modulus at the pressure P_0 and ξ is an arbitrary parameter which is of the order of 0 to ± 1. This relationship can be rewritten as

$$P = A + Bf(y) + Cg(y) \quad (2)$$

where $f(y)$ and $g(y)$ are functions of the experimental relative compressions. $A(P_0)$, B $(3B_0/2)$ and C $(3B_0\xi/2)$ can be determined by linear least squares fitting techniques for an assumed value of L_0 and the experimental values of $L(P)$. If equation (2) is an exact representation of the isotherm and, initially, the correct value for the compression between atmospheric pressure and 1 kbar has been assumed, A (or P_0) will be zero. If, however, the magnitude of A is greater than some predetermined value ($10^{-4}B_0$ in our case), a new choice of the initial compression is made by the computer, adjusted sample lengths are computed at each pressure for the same value of L_0, and a new least squares fit made. This is the procedure which we have used to determine our absolute sample lengths from the atmospheric pressure measurement of L_0 at 273°K and length change vs. pressure measurement from 1 to 14 (or 20) kbar near this temperature. The procedure is carried out for the full pressure data and also for only the data up to 0·5 full pressure to make sure that the extrapolation is not function-dependent.

Once an absolute value of the length vs. pressure relation has been determined for one isotherm, the experimental data give absolute values of the length for all other experimental values of the temperature and pressure for other isotherms. In particular, values of the sample length and bulk modulus at zero pressure are obtained by least squares fits of the data to equation (2) for which L_0 is chosen to make A (or P_0) less than $10^{-4}B_0$. Again, full pressure and half pressure fits are made to ensure that the extrapolations are not function-dependent. As was mentioned earlier in this section, r.m.s. deviations of the smoothed data from the fits are typically 0·03 kbar. The resulting values of B and C are used to represent the experimental isotherms and to calculate both the pressure and, after differentiation of equation (1), the isothermal bulk modulus for specific sample lengths or volumes. In general, values of the bulk modulus calculated from the full pressure and the half pressure representations of the isotherms agree to within 1 per cent in the region where the fits overlap.

Other functions are probably as useful or more useful than equation (1) for representing experimental P–V isotherms. These include the Murnaghan equation in its various forms [28, 29]:

$$(\partial B_T/\partial P)_T = n \quad (3a)$$

giving

$$B_T = B_0 + nP = B_0(V_0/V)^n \quad (3b)$$

and

$$P = B_0/n[(V_0/V)^n - 1] \quad (3c)$$

and the Tait equation[29, 30];

$$-(\partial P/\partial V)_T = J^{-1}(L+P). \quad (4)$$

MacDonald has discussed the application of curve-fitting techniques to these equations for representing experimental data and their relative suitability for this purpose[29]. He stresses that neither of these equations has any firm theoretical basis and each must be treated as a heuristic relationship which must be used with caution for extrapolation. Our experience has been that no experimental data are sufficiently precise so that a judgement can be made as to which of equations (1), (3) or (4) is 'correct.' Certainly, the power series representation of $\Delta V/V_0$ in terms of pressure as used by Bridgman for small compressions [31] and in the representation of earlier sodium data[9] is quite unsatisfactory.

The most convenient representation of our final equation of state is in terms of equations (3) since both B_T and $(\partial B_T/\partial P)_T$ are in principle readily obtainable from ultrasonic data [26]. Equation (3c) is difficult to use when the absolute length of the sample can be obtained only by extrapolation, as in our experiments. The aesthetically unpleasing procedure which was used to analyze our equation of state data involves using the Birch function fits to the individual isotherms (equation (1)) to obtain both pressures and bulk moduli as a function of temperature for fixed values of the volume and then to obtain the coefficients for equation (3) from a plot of these quantities (see below). This experiment involves systematic errors which cannot be evaluated (uncertainties in the friction correction, variation of the sample holder diameter with pressure and temperature, etc.) and which internal inconsistencies suggest introduce errors of the order of 0·5–1 per cent of the total compression. These are large when compared with the errors involved in the method of analysis. The final objective only can be to reproduce the data (to within an estimated experimental accuracy) using an equation of state which contains 'reasonable' parameters. Because of the uncertainties in the systematic errors, precise extrapolations of this equation of state are risky.

EXPERIMENTAL RESULTS

Figure 1 summarizes the experimental P–V–T results obtained for our two samples. The actual data $[L(T,P)/L_0(273°\text{K}, P=0)]$ have been converted to molar volumes by assuming the molar volume at 273°K and atmospheric pressure to be 70·00 cm^3[32, 33]. The use of data points on this plot is misleading. The actual data consist of a series of P–V isotherms, each of which has been graphically smoothed twice (before and after making the friction correction) before subtracting a smooth 'background' or sample holder distortion correction. The 'experimental points' have been read from the smooth isotherms at the specified pressures and are useful to show differences between the isotherms. The solid lines are calculated from an analytical equation of state which will be described in the next section.

The results for both samples and the calculated equation of state are in excellent agreement from 2 to 14 kbar (with maximum deviations of the order of 0·2 cm^3/mole). However, differences of up to twice this amount appear at the lowest temperatures and the highest pressures when the calculated and experimental values are compared. This effect is shown in Fig. 2 where the room temperature and absolute zero isotherms are plotted as calculated from our analytical relationship (full line) and as observed for the small sample holder (dashed line). In particular, the results suggest that the thermal expansion is approximately zero at 20 kbar. The deviation between the calculated curve and the experimental results indicates that the low temperature small sample holder data deviate

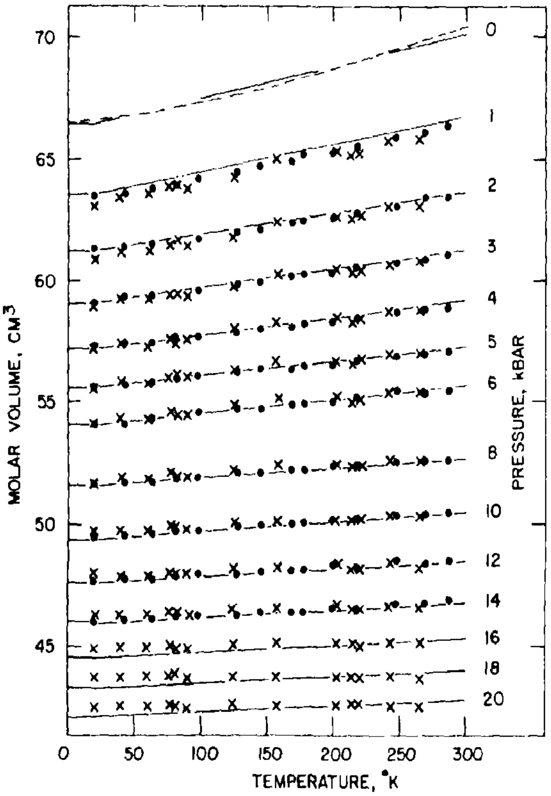

Fig. 1. The experimental equation of state for cesium metal. The 'experimental points' which are indicated have been read off the smoothed experimental isotherms at equal pressure increments, and indicate only the relative consistency of the various isotherms.

appreciably from both equations (1) and (3), and this is evident in our data analysis in the form of systematic deviations. The small sample holder (high pressure) data are not as smooth and are perhaps less reliable (for unknown reasons) than the large sample holder data on which our equation of state is based. Compressions as calculated from this equation of state may be in error at 20°K and 20 kbar by as much as 2 per cent; this results in an error in the molar volume at this temperature and pressure of less than 1 per cent. Because of this ambiguity, the following discussion will be applicable almost completely to pressures less than 14 kbar or molar volumes greater than 46 cm³.

The present data can be compared directly with earlier 10,000 atm, 4°K data[22], with Bridgman's room temperature data to 40,000 kg/cm²[15, 16] and with the X-ray data of Hall *et al.*[18]. The 10,000 atm, 4°K data give compressions which are too low by approximately 4 per cent at all pressures. The reason for this discrepancy is not known, but the present data are to be preferred because of the refinements in techniques which have been used in the current experiments. Bridgman's two sets of room temperature compression data[15, 16] disagree by 10 per cent at 20,000 kg/cm² ($\Delta V/V_0 = 0{\cdot}372$ and $0{\cdot}344$, respectively). The corresponding compression for the present results is 0·387. Bridgman's data were

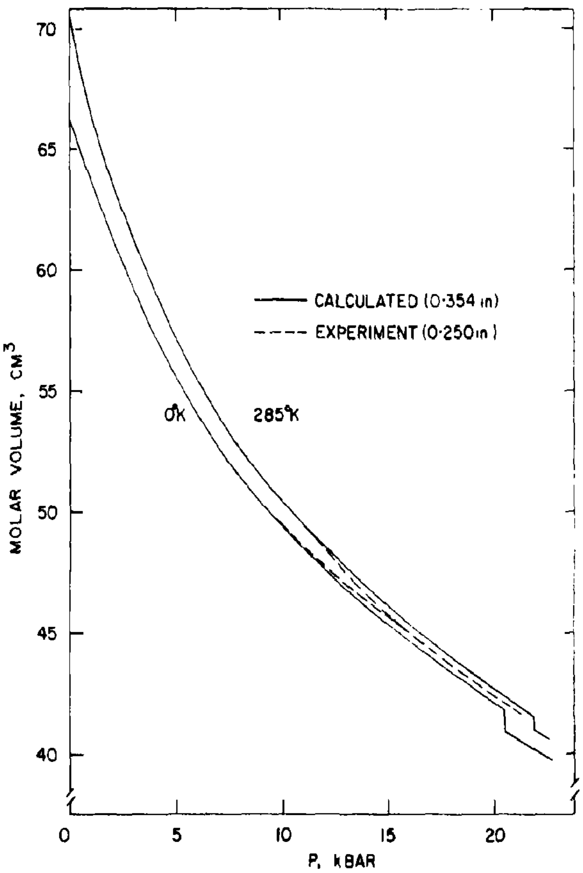

Fig. 2 Absolute zero and room temperature P-V isotherms for cesium metal The solid lines represent the large sample holder data and are extrapolations above 14 kbar The dashed lines represent the results obtained with the small sample holder.

obtained using a jacket of copper or aluminum around the alkali metals to prevent them from attacking the cylinder. This could have resulted in an unsuspected systematic error since we differ from Bridgman's piston displacement results for each of the alkali metals. The third possible comparison is with the X-ray measurements of Hall *et al.*[18], who were primarily concerned with structure determinations. A compression of 0·38 at 20,000 kg/cm^2 can be read from a figure in their paper. In all these instances, the agreement is perhaps within experimental accuracy if the most recent Bridgman determination is not considered.

The extrapolation of the large sample holder isotherms to zero pressure gives both the molar volume and the isothermal bulk modulus as a function of temperature. The results of these extrapolations are given in Figs. 3 and 4 where a comparison is made with other data. The molar volume curve is forced to coincide with 70·00 cm^3 at 273°K, with the molar volumes at other temperatures being determined by the relative zero pressure length changes. The data points shown in Fig. 3 were obtained from the extrapolation of the large sample holder data to zero pressure, and the error bars indicate the difference between the extrapolated molar volumes obtained using

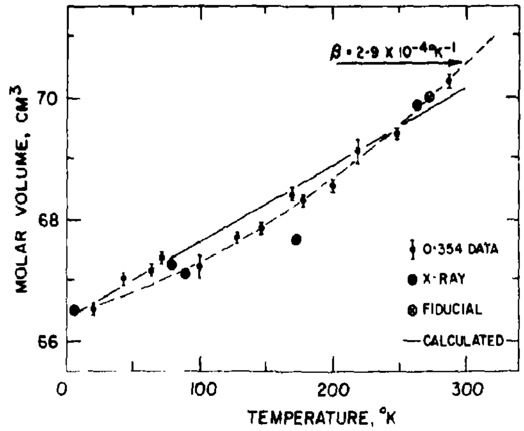

Fig. 3. The volume thermal expansion of cesium metal as obtained by extrapolation of the large sample holder data to zero pressure, and normalized to 70·00 cm³/mole at 273°K. Molar volumes as calculated from various X-ray measurements[24, 32] are shown also. See the text for details.

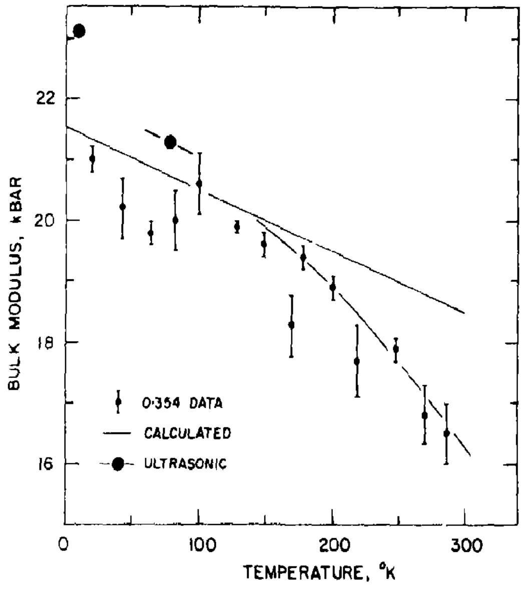

Fig. 4. The isothermal bulk modulus of cesium metal as obtained from the extrapolation of the individual large sample holder isotherms to zero pressure (see the text for details). Ultrasonic values for B_T[25] and its isobaric temperature dependence near 77°K are indicated.

the 2–7 kbar portion of the isotherms, and those obtained using the full 2–14 kbar range of the isotherms. The agreement is excellent and verifies our choice of equation (1) as a representation of the data. The extrapolations of the small sample holder data above 100°K confirm these results. The dashed curve in Fig. 3 is a smoothed representation of these data which also is plotted in Fig. 1 and is given numerically in Table 1. The slope of this curve at 300°K is consistent with the room temperature volume thermal expansion coefficient of cesium metal ($2{\cdot}9 \times 10^{-4}$ K^{-1})[34]. The solid line is the zero pressure molar volume as calculated from our equation of state (see below).

Table 1. A summary of the zero pressure thermodynamic data for cesium metal, as obtained in these measurements

T (°K)	$V_0^{(a)}$ (cm^3/mole)	$B_T^{(b)}$ (kbar)	$p^{*(c)}$ (kbar)	$U^{*(d)}$ (10^3 J/mole)	$\gamma_u^{(e)}$
0	66.5	21·5	0	0	
50	66·9	21·0	0·14	0·88	1·07
100	67·3	20·5	0·32	2·11	1·02
150	67·9	20·0	0·50	3·39	1·00
200	68·7	18·9	0·69	4·68	1 01
250	69·5	17·6	0·88	6·60	1·01
300	70·5	16·3	1·06	7·69	0·96

(a) All ±0·2 cm^3. From the dashed curve, Fig. 1.
(b) All ±1·0 kbar. From the dashed curve, Fig. 4.
(c) All ±0·1 kbar. From the dashed curve, Fig. 7
(d) Calculated from the data in [23].
(e) Calculated from equation (6).

Molar volumes corresponding to various X-ray lattice constant determinations are plotted in Fig. 3 also[32]. In particular, we agree well with molar volumes as calculated from Barrett's 5° and 77°K data[24] and disagree with an extrapolation by Martin[34] which predicts a smaller value of the molar volume. Our conclusion is that the molar volume of cesium metal at zero pressure and 0°K is 66·5 (±0·1) cm^3. Okumura and Templeton[5] have stated that their observed d*HvA* frequencies correspond to within 0·1 to 0·2 per cent with those calculated for a spherical Fermi surface from Barrett's lattice constant data and, hence, for a metal with the above molar volume.

Figure 4 shows our extrapolated values of $B_T(T, P = 0)$ as obtained from the large sample holder data; the length of the error bars indicates again the differences in the values of B_T as obtained from the full pressure and half pressure extrapolations. The extrapolations of the small sample holder isotherms give the same results above 100°K, but systematically larger (by 10 per cent) bulk moduli for the lower temperatures. We believe that this is due to the failure of the shapes of these low temperature high pressure isotherms to correspond to either equations (1) or (3). The solid line represents the temperature dependence of B_T at zero pressure as calculated from our analytic equation of state. The deviations from this equation of state at high temperatures probably are real and correspond to the deviations between the dashed and solid lines in Fig. 3. Table 1 contains smoothed values of B_T which correspond to the dashed line in Fig. 4.

Kollarits and Trivisonno give elastic constant data for cesium metal at 77° and 4°K and also give the temperature dependence of the elastic constants for a 15°K interval below 77°K[25]. The agreement between the present data and these elastic constant determinations of B_T and its isobaric temperature derivative (Fig. 4) is excellent for 77°K although the 4°K ultrasonic value perhaps is a bit high. The data shown in Fig. 4 agree reasonably well with those suggested by Martin[34].

Figures 5(a) and 5(b) show the parameters

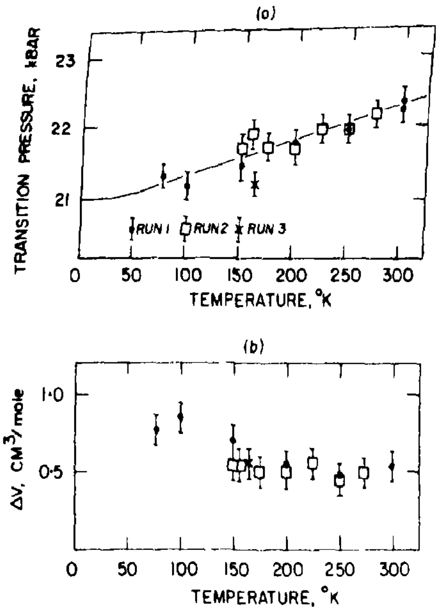

Fig. 5. Transition parameters for the CsI–II transition

(pressure, volume change) which we obtain for the CsI–II transition. The agreement between our room temperature transition pressure (22·4 ± 0·2 kbar) and those given by Kennedy and LaMori (22·6 ± 0·6 kbar)[19] and by Bridgman (23,300 kg/cm² or 22·5 kbar)[15, 16] is excellent and gives credence to our pressure determinations. Figure 5(a) complements the phase diagram of Kennedy *et al.* [20] which shows a strong increase in dP/dT for this transition as the melting line is approached.

The volume change shown in Fig. 5(b) (approximately $0{\cdot}006V_0$ or 0·5 cm³/mole) also is in agreement with Bridgman's results [15, 16]. This volume change appears to increase at low temperatures (below 150°K) while at the same time, experimentally, the transitions begin to show hysteresis which is much greater than (up to twice) the sample holder friction as it appears in the raw plots of length vs. pressure. This may or may not be significant, and no further checks were made. Early data on the phase diagram of cesium [20] suggest that the CsII–III transition would extrapolate to a triple point in this region, but more recent data[21] show the CsII–III and CsIII–IV phase lines to be parallel and the transition pressure to be practically temperature independent at approximately 45 kbar. The hysteresis associated with the CsI–II transition becomes so great at low temperatures (below 77°K) that we cannot observe the volume change.

This transition is sketched in Fig. 2 as occurring at constant volume on the basis of our postulated equation of state. If the experimental high pressure data were to be used, the molar volume at which the transition occurs would become greater at low temperatures. The entropy change along the transition line appears to be constant from 77° to 300°K and equal to approximately $0{\cdot}3R$, where R is the gas constant.

ANALYTICAL EQUATION OF STATE

The equation of state of a solid can be expressed as the sum of two terms,

$$P(V, T) = P_0(V) + P^*(V, T) \qquad (5)$$

where P_0 is the equation of state at absolute zero and P^* is the so-called thermal pressure which approaches zero at absolute zero. When lattice vibration contributions are dominant, as is true for cesium over our experimental range, the thermal pressure can be approximated by the Mie–Grüneisen equation of state[26].

$$P^*(V, T) = \gamma_G U^*/V. \qquad (6)$$

γ_G is a Grüneisen parameter which should be dependent only on volume at high temperatures ($T > \theta_D$), and U^* is the temperature-dependent internal energy of the solid. Since $\theta_D \sim 38$°K for cesium metal[23], most of our data refer to this 'high temperature' region. A considerable amount of information has been accumulated which suggests that to a first approximation P^* is a function only of temperature or, equivalently, that the bulk modulus is solely a function of volume[26]. This approximation will form the basis for the following analysis.

The equation of state must somehow involve an average of all of the isotherms which are indicated in Fig. 1. This could be done by means of a multi-parameter least squares analysis, but the relatively arbitrary variations in the detailed shapes of our experimental isotherms (shown by exploratory plots of B_T vs. P) appeared to make such an analysis of dubious value so an analytical equation of state was constructed from equations (3) in the following manner. The computer fits to the large sample holder isotherms were used to obtain values of $B_T(T, V)$ for integral values of V. Typical $B_T(T, V = \text{const.})$ plots are given in Fig. 6, where the scatter appears to be moderate. These data can be extrapolated easily to obtain the bulk modulus-volume relationship at absolute zero, $B_0(V)$ (Table 2). As is noted in Table 2, and is obvious in Fig. 6, $(\partial B_T/\partial V)_T \neq 0$ for both the smallest and the largest molar volumes. This effect is small and to within our experimental precision (±0·2 cm^3/mole) has no effect on our analytical equation of state. The P^* contribution to the equation of state also is quite small (see below) so $P_0(V)$ can be established most easily by extrapolating to $T = 0$ plots of $P(T, V = \text{const.})$. This was done using the computer fits to the large sample holder data for the same molar volumes for which the bulk moduli were calculated. A plot of $B_0(V)$ vs. $P_0(V)$ resulted in a straight line which could be represented to within a few per cent by $B_0 = 21{\cdot}5$ kbar and $n = 2{\cdot}84$ in equation (3(b)). This relationship, plus the assumption that $V_0 = 66{\cdot}50\,\text{cm}^3$, allows the construction of the $T = 0$ isotherm as

$$P_0(V) = (21{\cdot}5/2{\cdot}84)[(66{\cdot}5/V)^{2{\cdot}84} - 1]\ \text{kbar}. \tag{7}$$

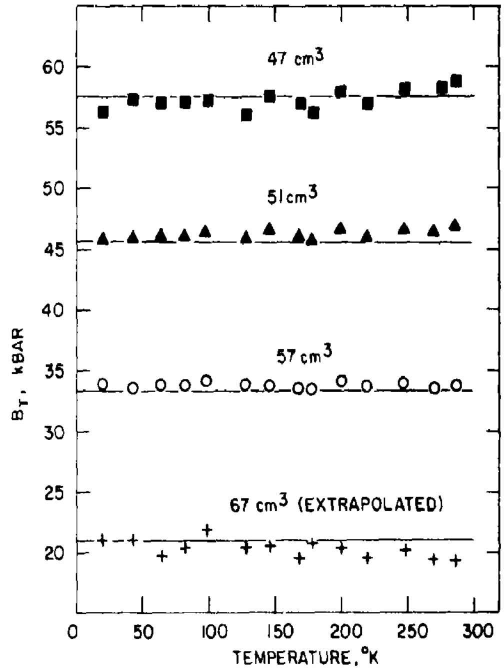

Fig. 6 The temperature dependence of the isothermal bulk modulus for cesium metal for several molar volumes The solid lines represent the values of $B_0(V)$ listed in Table 2

Table 2. The T = 0 *equation of state for cesium metal as obtained by extrapolation of the present large sample holder data only, and as calculated from equation* (7)

V_0 (cm³)	$P_0(V)$ (kbar) extrap[a]	$P_0(V)$ (kbar) calc.	$B_0(V)$ (kbar) extrap.[b]	$B_0(V)$ (kbar) calc.
41		22·32		84·9
43		18·55		74·2
45		15·38		65·2
47	12·7	12·71	57 ± 1[c]	57·6
49	10·5	10·45	51·0[c]	51·2
51	8·55	8·50	46·0[c]	45·6
53	6·9	6·87	41·5	41·0
55	5·45	5·41	37·3	36·85
57	4·15	4·16	33·7	33·30
59	3·1	3·07	30·5	30·21
61	2·1	2·11	27·6	27·48
63	1·25	1·26	25·3[d]	25·07
65	0·5	0·50	23·2[d]	22·93
66·5	0·0	0·0		21·50
67	(−0·15)	−0·16	21·0[d]	21·05
69	(−0·7)	−0·76	(19)	19·35

[a] All ± 0·05 kbar

[b] All ± 0·5 kbar unless otherwise noted

[c] $(\partial B_T/\partial T)_V = +1{\cdot}6\times10^{-3}$ kbar/°K

[d] $(\partial B_T/\partial T)_V = -6\times10^{-3}$ kbar/°K.

The extrapolated and calculated values of $P_0(V)$ and $B_0(V)$ are given in Table 2. The absolute zero intercepts of the solid lines in Fig. 1 and the $T = 0$ solid curve in Fig. 2 are given by equation (7).

Once $P_0(V)$ has been established, the thermal pressure can be calculated from equation (5). The results of this calculation (in terms of the computer fits to our individual isotherms) are shown in Fig. 7. This plot, which gives the temperature dependence of the deviation of the actual experimental pressure for a given molar volume from a smooth function (equation (7)), indicates that to within better than ±0·1 kbar the thermal pressure is independent of molar volume and is a linear function of temperature with $(\partial P/\partial T)_V = 3{\cdot}65\times10^{-3}$ kbar/°K. P^* is given as a function of temperature in Table 1. Equation (5) then can be written explicitly as

$$P(V,T) = (21{\cdot}5/2{\cdot}84)\left[(66{\cdot}5/V)^{2{\cdot}84} - 1\right] + 3{\cdot}65\times10^{-3}\,(T - 10°\mathrm{K})\ \mathrm{kbar}. \quad (8)$$

This relationship has been used to obtain the solid (calculated equation of state) lines in Figs. 1, 3, 4 and 6. The agreement with experiment for molar volumes is in general good to within ±0·2 cm³. The temperature dependence

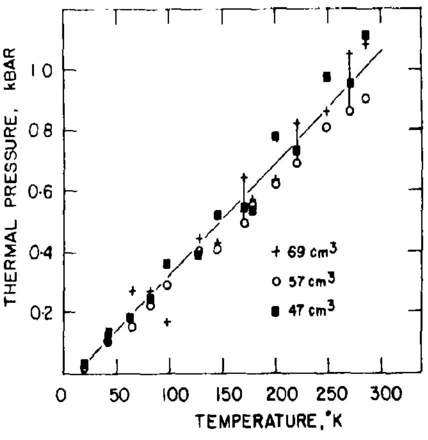

Fig. 7. The thermal pressure P^* as a function of molar volume. The scatter of the 'data points' shows clearly the consistency of the various isotherms.

of B_T at 67 cm³/mole shown in Fig. 6 as obtained from extrapolations of the isotherms to negative pressures indicates the same falling off of B_T at high temperatures as was mentioned in the discussion of Fig. 4. This is undoubtedly a real effect and reflects the influence of anharmonicity, vacancies, or other phenomena which we have not considered in our simple model.

Equation (6) expresses P^* in terms of the internal energy. Filby and Martin's heat capacity data[23] can be used together with our thermal expansions (Fig. 3, Table 1) and thermal pressures to obtain $\gamma_u(T, P = 0)$. The internal energy U^* for cesium metal (obtained by graphical integration) and γ_u as calculated from equation (6) are given in Table 1. The independence of γ_u on temperature at atmospheric pressure corresponds to similar behavior for potassium[10] and lithium[11] although perhaps not for sodium[9] where the present method of analysis had not been so well-defined. In any event, it is interesting that within our experimental precision, the equation of state of cesium metal can be defined completely with the parameters $B_0 = 21{\cdot}5$ kbars, $n = 2{\cdot}84$, $V_0 = 66{\cdot}5$ cm³, and $\gamma_u = 1{\cdot}00$ ($\pm 0{\cdot}04$), if the zero pressure C_p data are used.

The usual Grüneisen parameter is defined

$$\gamma_c = (\beta B_T V)/C_v.$$

Martin calculates $\gamma_c = 1{\cdot}16$ at 300°K[34] while we calculate 1·14 ($\pm 0{\cdot}06$), using essentially the same experimental data but our own value of B_T.

CONCLUSIONS

The equation of state for cesium metal (Fig. 1, equation (8)) follows very well the empirical relationships which have been found to hold for many other solids[26]. Indeed, it extends them over much greater relative temperature (in terms of T/θ_D) and volume (in terms of V/V_0 or P/B_0) ranges than before. The thermal equation of state of cesium, like that for lithium[11], sodium[9] and potassium [10], is expressable in terms of a volume-independent thermal pressure P^* which can be evaluated from a temperature-independent γ_u (equation (6)) and zero (atmospheric) pressure heat capacity data.

The absolute zero equation of state for cesium metal does differ from the other alkali metals, however. The similarities of the reduced equations of state for lithium, sodium and potassium have been pointed out previously[11]. Since that time elastic constant data have become available for rubidium both as a function of temperature at atmospheric pressure[35] and as a function of pressure at 200°K[12]. These then can be used to complement the present data for cesium to give a

Table 3. *A summary of the experimental* T = 0, P = 0 *thermodynamic parameters for the alkali metals*

	$(\partial B/\partial P)_T$ [a]		$B_0(V_0)$		V_0 [d]	B_0V_0	γ_u [e]	References [f]
	P–V–T	U.S.	P–V–T (kbar)	U.S.	(cm³)	(10⁵ J/mole)		
Li	$3{\cdot}6\ (\pm 0{\cdot}25)$		123	$128^{(b)}$	12·69	1·6	0·88	[11·36]
Na	$3{\cdot}9^5(\pm 0{\cdot}2)$	3·6–3·8	74	$73^{(b)}$	23·1	1·68	1·2	[9, 37–39]
K	$3{\cdot}8^5(\pm 0{\cdot}2)$	4·05	37·0	36·6	43·3	1·60	1·2	[10, 40, 41]
Rb		3·9	29	$30{\cdot}6^{(c)}$	53·0	1·62		[22, 12, 35]
Cs	$2{\cdot}8^4(\pm 0{\cdot}05)$		21·5	23·1	66·5	1·43	1·0	[42, 25]

(a) Assumed to be temperature-independent.

(b) 78°K.

(c) Extrapolated

(d) V_0 is as given in the various references and is reliable to 0·5 per cent.

(e) As defined by equation (6).

(f) P–V–T; high pressure ultrasonic; zero pressure ultrasonic.

complete picture of the equation of state for the alkali metals. Table 3 summarizes the relevant absolute zero data for the alkali metals and gives a comparison of piston-displacement and ultrasonic results for various parameters. The agreement in general is quite good, and this summary should be useful for future comparisons with theory. Values of γ_0 also are given which can be used with the heat capacity data summarized by Martin[34] to obtain the thermal contributions to the equations of state.

The striking feature of this compilation is that cesium is quite different from the other alkali metals, both in the value of the dimensionless parameter $n = (\partial B_T/\partial P)_T$ (which should be roughly temperature-independent) [26] and in the value of the characteristic energy B_0V_0. Previously[11], we pointed out that a common value of $(\partial B_T/\partial P)_T$ suggests that only two parameters (an energy and a length) are necessary to differentiate between the gross features of the volume-dependent contribution to the cohesive energy for lithium, sodium, potassium and (now) rubidium, while a common value of B_0V_0 implies that the energy parameter is the same for these four. This leaves only a characteristic length to differentiate between the four and, as we suggested in the introduction, this is qualitatively the 'core radius.' Cesium metal would appear to have a cohesive energy which presumably is dominated by band structure effects[1, 2]. It is surprising that these effects appear so markedly in the equation of state, and a direct verification of our conclusion would be most interesting.

REFERENCES

1. HAM F. S., *Phys. Rev.* **128**, 82 (1962). *Phys. Rev.* **128**, 2524 (1962).
2. BROOKS H., *Trans. metall. Soc. A.I.M.E.* **227**, 546 (1963).
3. DUGDALE J. S., *Science* **134**, 77 (1961).
4. SHOENBERG D. and STILES P. J., *Proc. R. Soc.* **A281**, 62 (1964).
5. OKUMURA K. and TEMPLETON I. M., *Proc. R. Soc.* **A287**, 89 (1965).
6. STOKES R. H., *Proc. Am. Chem. Soc.* **86**, 233 (1964); *J. Phys. Chem. Solids* **27**, 487 (1966).
7. RAICH J. C. and GOOD R. H., Jr., *J. Phys. Chem. Solids* **26**, 1061 (1965). This paper gives a summary of previous theoretical work.
8. ASHCROFT N. W. and LANGRETH D. C., *Phys. Rev.* **155**, 682 (1967); ASHCROFT N. W., *J. Phys. C (Proc. phys. Soc.)* **1**, 232 (1968). These papers discuss the 'hard core' picture from the standpoint of pseudo-potentials.
9. BEECROFT R. I. and SWENSON C. A., *J. Phys. Chem. Solids* **18**, 329 (1961). All pressures quoted in this paper are uniformly 3 per cent too small due to a calibration error. See [11] below.
10. MONFORT C. R. and SWENSON C. A., *J. Phys. Chem. Solids* **26**, 291 (1965).
11. SWENSON C. A., *J. Phys. Chem. Solids* **27**, 33 (1966).
12. SMITH C. S., Private communication.
13. MUNDY J. N. and DUGDALE J. S., *Phil. Mag.* **6**, 1463 (1961).
14. PHILLIPS D. and DUGDALE J. S., *Proc. R. Soc.* **A287**, 381 (1965).
15. BRIDGMAN P. W., *Proc. Am. Acad. Arts Sci.* **72**, 207 (1938).
16. BRIDGMAN P. W., *Proc. Am. Acad. Arts Sci.* **76**, 71 (1948).
17. BARDEEN J., *J. chem. Phys.* **6**, 372 (1938).
18. HALL H. T., MERRILL LEO, and BARNETT J. D., *Science* **146**, 1297 (1964).
19. KENNEDY G. C. and LaMORI P. N., *J. geophys. Res.* **67**, 851 (1962).
20. KENNEDY G. C., JAYARAMAN A. and NEWTON R. C., *Phys. Rev.* **126**, 1363 (1962).
21. JAYARAMAN A., NEWTON R. C. and Mc DONOUGH J. M., *Phys. Rev.* **159**, 527 (1967).
22. SWENSON C. A., *Phys. Rev.* **99**, 423 (1955). Due to an error in transposition, the data tabulated for cesium in this paper are for $\Delta V/V_{1500}$. $\Delta V/V_0$ can be obtained by multiplying the tabulated numbers by $V_{1500}/V_0 = 0.94$. The quoted values of the compressibility and ξ are correct. Dr. J. J. Gilvarry first brought this to our attention.
23. FILBY J. D. and MARTIN D. L., *Proc. R. Soc.* **A284**, 83 (1965).
24. BARRETT C. S., *Acta crystallogr.* **9**, 671 (1956).
25. KOLLARITS F. J. and TRIVISONNO J., *J. Phys. Chem. Solids*. To be published.
26. SWENSON C. A., *J. Phys. Chem. Solids* **29**, 1337 (1968).
27. BIRCH F., *J. geophys. Res.* **56**, 227 (1952).
28. ANDERSON O. L., *J. Phys. Chem. Solids* **27**, 547 (1966).
29. MACDONALD J. R. *Rev. mod. Phys.* **38**, 669 (1966).
30. GINELL R. and QUIGLEY T. J., *J. Phys. Chem. Solids* **27**, 1173 (1966).
31. BRIDGMAN P. W., In *The Physics of High Pressure*, 2nd Edn, Chap VI. Bell, London (1958).
32. PEARSON W. B., In *Handbook of Lattice Spacing and Structures of Metals*. Pergamon Press, Oxford (1958).

33. A smoothed tabulation of the pressure-volume relationships for the individual isotherms is available from SWENSON C. A., Physics Division, Ames Laboratory, Iowa State University, Ames, Iowa 50010. These are the data which make up Fig. 1.
34. MARTIN D. L., *Phys. Rev.* **139**, A150 (1965).
35. GUTMAN E. J. and TRIVISONNO J., *J. Phys. Chem. Solids* **28**, 805 (1967).
36. SLOTWINSKI T. and TRIVISONNO J., *J. Phys. Chem. Solids* **30**, 1276 (1969).
37. DANIELS W. B., *Phys. Rev.* **119**, 1246 (1960).
38. MARTINSON R. H., Cornell University, Ithaca, N. Y., Unpublished data.
39. DIEDERICH MARY E. and TRIVISONNO J., *J. Phys. Chem. Solids* **27**, 637 (1966).
40. SMITH P. A. and SMITH C. S., *J. Phys. Chem. Solids* **26**, 279 (1965).
41. MARQUANDT U. R. and TRIVISONNO J., *J. Phys. Chem. Solids* **26**, 273 (1965).
42. Present data.

J. Phys. Chem. Solids Pergamon Press 1969. Vol. 30, pp. 1603–1607. Printed in Great Britain.

THERMOELECTRIC POWER OF IONIC CRYSTALS–IV. THERMOELECTRIC POWER AND IONIC CONDUCTIVITY OF POTASSIUM IODIDE CONTAINING CADMIUM IODIDE

TOSHIO ITAMI, HIDEOKI HOSHINO and MITSUO SHIMOJI
Department of Chemistry, Faculty of Science, Hokkaido University, Sapporo, Japan

(*Received* 30 *September* 1968)

Abstract—The thermoelectric power of single crystals of pure potassium iodide and potassium iodide containing $2{\cdot}8 \times 10^{-2}$ and $1{\cdot}3 \times 10^{-3}$ mol % cadmium iodide was measured as a function of temperature between 450° and 630°C with graphite electrodes. The heat of transport for a cation vacancy was found to be −0·56 eV. Conductivity measurements were also made on pure crystals and on specimens doped with cadmium iodide as a function of temperature using graphite electrodes. The following values were found: heat of formation of a Schottky defect, 2·00 eV, heat of motion of a cation vacancy, 0·87 eV; entropy of activation for migration of a cation vacancy, $\Delta S_m/k = 4{\cdot}1$; entropy of formation of a Schottky defect, $\Delta S_s/k = 7{\cdot}1$, where k is the Boltzmann constant. It was found that platinum electrodes were not inert to potassium iodide crystals

INTRODUCTION

IT IS WELL known that in potassium iodide as well as other alkali halides the Schottky disorder[1] and cation vacancies play important roles in transport phenomena[1–3]. There have been many previous studies on potassium iodide, such as ionic conductivity measurements[4–8], dielectric loss measurements[9], self-diffusion[10] and theoretical calculations [11] on defect formation and migration. However, there has been no work on the thermoelectric power measurement of this salt. The purposes of this paper are, (i) to obtain ionic conductivity parameters, particularly, heat of motion of a cation vacancy, and (ii) to measure the thermoelectric power related to the heat of transport of defects. As before[12] graphite and platinum were employed as electrode materials because of their inertness. However, it was found that platinum electrodes were contaminated by potassium iodide crystals at high temperatures and the steady measurements of thermoelectric power and of ionic conductivity could not be made. On the other hand graphite electrodes were so stable that satisfactory results were obtained.

EXPERIMENTAL PROCEDURES

Single crystals of pure potassium iodide and potassium iodide containing cadmium iodide were prepared by the Kyropoulos technique. Cleaved specimens were used. The concentration of cadmium impurities was determined by the colorimetric method[13]. The experimental arrangements and techniques for thermoelectric power and ionic conductivity measurements were the same as before[12, 14]. Most ionic conductivity measurements were made in the temperature range from 440° to 640°C, but for pure crystals the measurements were performed up to near the melting point (684°C).

RESULTS

In Fig. 1 the thermoelectric power of pure potassium iodide crystals and potassium iodide crystals containing $2{\cdot}8 \times 10^{-2}$ and $1{\cdot}3 \times 10^{-3}$ mol. % cadmium iodide with graphite elec-

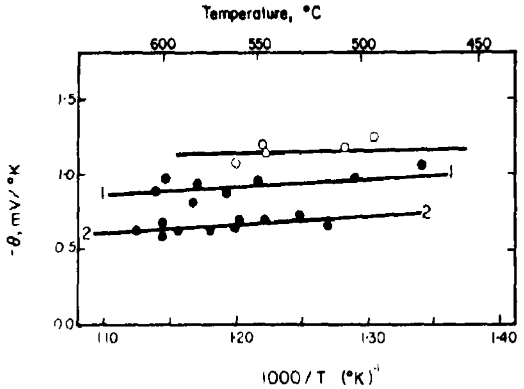

Fig. 1 Thermoelectric power of pure potassium iodide (open circles) and potassium iodide containing cadmium iodide in two different concentrations, (1) $1{\cdot}3\times10^{-1}$ mol % and (2) $2{\cdot}8\times10^{-2}$ mol %, as a function of temperature. All lines are obtained by the least squares method

trodes is plotted as a function of temperature. The experimental errors were about 10 per cent

The ionic conductivity as a function of temperature is shown in Fig. 2 for four potassium iodide crystals containing cadmium impurities and pure potassium iodide crystals. The experimental errors were about 5 per cent.

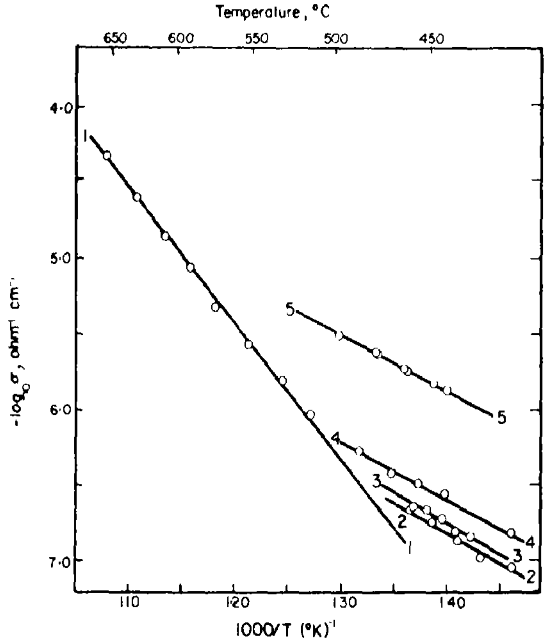

Fig. 2 Log$_{10}$ (specific conductivity) plotted against $1/T$ for pure potassium iodide and for solid solutions containing cadmium iodide. (1) pure KI; (2) KI + $1{\cdot}1\times10^{-3}$ mol % CdI$_2$. (3) KI + $1{\cdot}3\times10^{-1}$ mol % CdI$_2$; (4) KI + $2{\cdot}3\times10^{-1}$ mol. % CdI$_2$; (5) KI + $2{\cdot}8\times10^{-2}$ mol % CdI$_2$.

ANALYSES OF THE RESULTS

(1) *The mobility of a cation vacancy in potassium iodide and related parameters*

The methods of analyses of the data are the same as in Paper III[12]. From equation (4.2) in III, the observed temperature dependence of the mobility, μ, of a cation vacancy was represented by

$$\mu = (9580/T)\exp(-0{\cdot}87/kT)\ \text{cm}^2/\text{V sec}. \tag{4.1}$$

Compared with the theoretical expression for the mobility, (4.4) in III, we found that the heat of motion of a cation vacancy, h_m, was 0·87 eV and the frequency factor, ν_0, was $2{\cdot}55\times10^{14}\ \text{sec}^{-1}$, being expressed by

$$\nu_0 = \nu_D \exp(\Delta S_m/k). \tag{4.2}$$

Using the value of the Debye frequency, $\nu_D = 2{\cdot}9\times10^{12}\ \text{sec}^{-1}$[15], we obtained the entropy of migration of a cation vacancy, $\Delta S_m/k = 4{\cdot}0_5$.

As shown in Fig. 2 the conductivity of the pure crystal, σ_0, was expressed by

$$\sigma_0 T = 6{\cdot}92\times10^8 \exp(-1{\cdot}87/kT)\ \Omega^{-1}\text{cm}^{-1}\,^\circ\text{K}. \tag{4.3}$$

Using equation (4.8) in III, the expression for the mole fraction of a cation vacancy, $N^0_{(+)}/N$, in pure crystals was obtained as a function of temperature,

$$N^0_{(+)}/N = 34{\cdot}7\exp(-1{\cdot}00/kT). \tag{4.4}$$

From equation (4.9) in III, we found that the heat of formation of a Schottky defect, h_s, was 2·00 eV and the entropy of formation of a Schottky defect, $\Delta S_s/k$, was $7{\cdot}0_9$. In order to take into account the vibrational contribution to the entropy of defect formation, we found $\nu/\nu' = 1{\cdot}81$ for the change in vibrational frequency by making use of equation (4.11) in III.

(2) *Heat of transport*

Following the procedures discussed in Papers I–III[12, 14, 16] of this series, the expression of the thermoelectric power for impure crystals, $\theta(\xi)$, can be simplified in the form

$$e\theta(\xi) = Q^*_{(+)}/T - \partial(kT\ln\xi)/\partial T, \tag{4.5}$$

where $Q^*_{(+)}$ is the heat of transport of a cation vacancy and ξ is the ratio of the concentration of unassociated cation vacancies in a doped crystal to the concentration of cation vacancies in a pure crystal at the same temperature.

As shown in Fig. 1 the experimental points for the impure potassium iodide crystals satisfy the following expressions:

$$e\theta(\xi) = -0{\cdot}57/T - 0{\cdot}02\times10^{-3}\ \text{eV}/^\circ\text{K} \quad (2{\cdot}8\times10^{-2}\ \text{mol.}\ \%\ \text{Cd}^{2+}) \tag{4.6}$$

$$e\theta(\xi) = -0{\cdot}54/T - 0{\cdot}28\times10^{-3}\ \text{eV}/^\circ\text{K} \quad (1{\cdot}3\times10^{-3}\ \text{mol.}\ \%\ \text{Cd}^{2+}). \tag{4.7}$$

From equations (4.5)–(4.7) the mean value for the heat of transport of a cation vacancy, $Q^*_{(+)} = -0{\cdot}56$ eV, was obtained, because the heat of transport is independent of impurity concentration. The values of heat of transport of anion vacancies, $Q^*_{(-)}$, were obtained with the same method as before[12]. It was found that $Q^*_{(-)}$ was $-2{\cdot}7$ eV at 620°C.

DISCUSSION

As in the previous ionic conductivity measurements of the KI crystals in which the Pt[4, 5] and Ag foils[7] had been chiefly employed as electrodes, Pt foils were used in earlier stages of our measurements. However, no reproducible results were obtained and it was found that the KI crystals were slightly colored and the faces of Pt electrodes with which crystals were in contact were highly corroded under both the a.c. and d.c. methods. This kind of phenomenon was not encountered in our measurements for NaBr[14] and KBr [12]. It has been known[17] that KI crystals are colored by applying a d.c. voltage (e.g. 250 V at 520°C), while our conductivity measurements with Pt electrodes were made under a.c. methods in the temperature range between 440° ~ 680°C. Therefore the slight coloration of the KI crystals with Pt electrodes may be caused from other origins, such as the chemical reactivity of the KI crystals. Recently, it was found[18, 19] that the graphite electrodes might be better in view of their inertness. This was also recognized in our ionic conductivity measurements.

On the ionic conductivity of KI crystals Biermann[7] had measured the systems of pure crystals and KI crystals containing Pb^{2+} and Ba^{2+} in the temperature range 380° ~ 650°C, while no detailed analyses about individual ionic conductivity parameters had been made. Moreover, Lehfeldt[4] and Phipps and Partridge[5] had made measurements on pure KI crystals and pellets, respectively, and obtained the values of the 'effective activation energy' in the intrinsic region. Forbes and Lynch[6] have measured the ionic conductivity of KI crystals colored with I_2 in the temperature range from 90° ~ 200°C. On the other hand Ecklin *et al.*[8] have made the measurements on KI crystals containing Mg^{2+}, Ca^{2+} and Sr^{2+}. In Table 1 the values of ionic conductivity parameters on KI crystals are shown. The present value of the heat of activation for cation vacancies, 0·87 eV, is in good agreement with that of the theoretical result [11], 0·86 eV, which is based on the Einstein model of ionic solids. However, the values obtained from the dielectric loss measurement [9], 0·58 eV, and from other conductivity measurements, 0·65 eV[6] and 1·21 eV[8], were widely dispersed. On the heat of formation of a Schottky defect the fair agreement between the experimental value, 2·00 eV, and the theoretical one[11], 2·29 eV, is obtained, while the value obtained by Ecklin *et al.*[8] 1·59 eV, is too small. Of the values of 'effective activation energy', $h_m + (h_s/2)$, the experimental values[4, 5, 7] (1·87–1·48 eV) are scattered, while the present result, 1·87 eV, may be reasonable judging from the theoretical value, 2·00 eV[11]. The values of entropies of formation of a Schottky defect 7·1 k, and of migration for cation vacancies, 4·1 k, may be reliable in the light of the values obtained in the case of KBr crystals[12] (8·7 k and 4·0 k, respectively). As seen above, the values of the ionic conductivity parameters obtained by the present work are different from those obtained by the previous workers. This may partly be due to the difference of the electrode materials, that is, the graphite electrodes in the present case and the Pt or Ag electrodes in the previous ones[4, 5, 7].

Table 1. Numerical values of ionic conductivity parameters for potassium iodide crystals

h_m (eV)	h_s (eV)	$h_m + (h_s/2)$ (eV)	$\Delta S_s/k$	$\Delta S_m/k$	Method	Source
0·87	2·00	1·87	7·1	4·1	Conductivity	Present work
0·65					Conductivity	Forbes and Lynch[6]
0·58					Dielectric loss (+ SrI_2)	Dryden and Meakins[9]
1·21	1·59				Conductivity	Ecklin *et al.*[8]
0·86	2·29	2·00			Theoretical calculation	Mullen[11]
		1·77			Conductivity	Lehfeldt[4]
		1·61			Conductivity (pressed powder)	Phipps and Partridge[5]
		1·48			Conductivity	Biermann[7]
			8·7 (KBr)	4·0 (KBr)	Conductivity	Hoshino and Shimoji[12]

The results of thermoelectric power for pure KI crystals are shown in Fig. 1, along with those for KI crystals doped with CdI_2 in two different concentrations; $2{\cdot}8 \times 10^{-2}$ and $1{\cdot}3 \times 10^{-3}$ mol. %. The effect of the impurity is to make the thermoelectric power more positive. This may be due to the extra cation vacancies produced by impurities.

As a consequence of the interpretation of the homogeneous thermoelectric power using the Fokker–Planck equation it has been shown [12, 16] that the heat of transport is equal to the heat of activation for migration. For the KI crystals the absolute value of the heat of transport of cation vacancies is 0·56 eV and the heat of activation for migration of cation vacancies 0·87 eV. Since the value of the heat of transport may include some error[12, 16], these two values are fairly comparable to each other, being in fair agreement with the above theoretical conclusion.

REFERENCES

1. LIDIARD A. B., *Handb. Phys.* **20**, 246 (1957).
2. SEITZ F., *Rev. mod. Phys.* **18**, 384 (1946); *ibid.* **26**, 7 (1954).
3. SÜPTITZ P. and TELTOW J., *Phys. Status solidi* **23**, 9 (1967).
4. LEHFELDT W., *Z. Phys.* **85**, 717 (1933).
5. PHIPPS E. P. and PARTRIDGE F. G., *J. Am. chem. Soc.* **51**, 1331 (1929)
6. FORBES H. L. and LYNCH D. W., *J. Phys. Chem. Solids* **25**, 621 (1964)
7. BIERMANN W., *Z. phys. Chem.* **25**, 253 (1960).
8. ECKLIN D., NDLER C. and ROSSEL J., *Helv. phys. Acta* **37**, 692 (1964).
9. DRYDEN J. S. and MEAKINS R. J., *Discuss. Faraday Soc.* **23**, 39 (1957).
10. LAURENT J. F. and BÉNARD J., *J. Phys. Chem. Solids* **3**, 7 (1957).
11. MULLEN J. G., *Phys. Rev.* **143**, 658 (1966).
12. HOSHINO H. and SHIMOJI M., *J. Phys. Chem. Solids* **29**, 1431 (1968).
13. SANDELL E. B., In *Colorimetric Determination of Traces of Metals*. Interscience, New York (1959).
14. HOSHINO H. and SHIMOJI M., *J. Phys. Chem. Solids* **28**, 1169 (1967).
15. BANES R. B., *Z. Phys.* **75**, 723 (1932)
16. SHIMOJI M. and HOSHINO H., *J. Phys. Chem. Solids* **28**, 1155 (1967).
17. UCHIDA Y. and NAKAI Y., *J. phys. Soc. Japan* **8**, 795 (1953).
18. RALEIGH D. O., *J. phys. Chem.* **71**, 1785 (1967).
19. SANO R. and TOMIKI T., *J. phys. Soc. Japan* **21**, 1697 (1966)

J. Phys. Chem. Solids Pergamon Press 1969. Vol. 30, pp. 1609–1611. Printed in Great Britain.

A HIGH-PRESSURE SUPERCONDUCTING POLYMORPH OF CADMIUM TIN DIARSENIDE*

H. KATZMAN, T. DONOHUE† and W. F. LIBBY
Department of Chemistry, University of California, Los Angeles, Calif. 90024, U.S.A.
and
H. L. LUO and J. G. HUBER
Institute of Pure and Applied Physical Sciences, University of California, San Diego, Calif. 92110, U.S.A.

(*Received* 6 *September* 1968)

Abstract—A superconducting polymorph of $CdSnAs_2$ prepared at about 60 kbar and 25–450°C has been retained at atmospheric pressure and temperature. Its crystal structure is B1(NaCl) with a lattice constant of 5·679–5·695 Å depending on the temperature at which it was prepared. The superconducting transition temperature is also a function of the preparation temperature and varies from 1·79° to 2·29°K.

INTRODUCTION

THE EFFECT of high pressure on semiconducting compounds of the general formula $A^{III}B^{V}$ has been extensively and intensively studied[1] in recent years. We have extended these studies to one of the isoelectronic analogs with the general formula $A^{II}B^{IV}C_2^{V}$[2].

EXPERIMENTAL

The $CdSnAs_2$ was prepared from stoichiometric quantities of the elements (99·9+% purities) sealed in a quartz tube under an argon atmosphere, heated to 700°C for 48 hr, and then very slowly cooled to room temperature. All of the reflections observed on a Debye–Scherrer X-ray diffraction pattern of the cast samples were accounted for by the reported chalcopyrite structure with $a = 6{\cdot}093$ Å and $c/a = 1{\cdot}959$[3]. No extra lines were observed and the prepared material is believed to be homogeneous and single-phase.

Pressure was generated in a piston-cylinder apparatus with an internal graphite heater[4]. Appropriate modifications were made to allow the apparatus to reach 70 kbars[5]. The samples were contained in either boron-nitride or niobium capsules and the temperature was measured with a Cromel–Alumel thermocouple. No allowance was made for the effect of pressure on the thermocouple e.m.f.

Superconducting transitions were determined by monitoring the self-inductance of a coil containing the sample. The temperature was measured by determining the vapor-pressure of helium over the bath in which the samples were emerged.

RESULTS

During our first attempts to prepare a high-pressure phase we melted the samples after pressurizing to about 45 kbars. X-ray diffraction patterns taken after cooling to room temperature and releasing the pressure showed that the samples had converted to the B1 structure, but weak Cd_3As_2 lines and about 10 other unidentifiable lines were also present. In a recent paper[6] Storm, Jayaraman and Wernick report seeing SnAs, Cd_3As_2 and As after quenching from the melt.

---

*Work supported in part by the Chemical Directorate of the U.S. Air Force Office of Scientific Research, Grant No. AFOSR-67-1255A, and the Air Force Office of Scientific Research, Office of Aerospace Research, U.S. Air Force, under AFOSR Grant No. AF-AFOSR-631-67.

†National Science Foundation Summer Fellow.

However, we did not observe any As or SnAs lines.

In order to prevent the formation of these extra compounds we decided to try higher pressures and more moderate temperatures for longer periods of time. This method proved successful for producing *only* the high-pressure polymorph and the data obtained is reported in Table 1.

As can be seen from the table, both the lattice constant and superconducting transition temperature seem to be functions of the preparation temperature. This is probably due to a disordering effect becoming more important at higher temperatures. The crystal structure of the new phase is B1(NaCl) with the cadmium and tin atoms sharing one f.c.c. sublattice and the arsenic atoms on the other. Since the X-ray scattering factors for cadmium and tin are so similar it is impossible to tell by means of X-ray diffraction methods to what degree their sublattice is ordered. However, the apparent trend in both the lattice constant and transition temperature values suggest that the samples prepared at higher temperatures are more disordered. Attempts to anneal the samples at 100°C in an argon atmosphere resulted in almost complete conversion back to the chalcopyrite structure.

$CdSnAs_2$ is isoelectronic with InAs and Jamieson reports that the high-pressure modification of InAs also has the B1 structure[7]. In addition, the compound SnAs has the B1 structure with a lattice constant of 5·722 Å [8]. The high-pressure form of $CdSnAs_2$ can therefore be regarded as being based on this structure with half of the tin atoms replaced by cadmium atoms. SnAs is also a superconductor with a reported transition temperature of 3·41–3·65°K[8]. We pressurized a sample of SnAs at 60 kbars and 150°C for 20 hr and found no change in the crystal structure or the lattice constant. However, the superconducting transition temperature dropped slightly to 3·26–3·42°K. Since replacing Sn atoms with Cd atoms decreases the number of electrons in the system, it is not surprising that $CdSnAs_2$ has a lower transition temperature than SnAs.

Table 1

Sample #	Capsule	Pressure (kbar)	Temperature (°C)	Time (hr)	Lat constant (Å)	T_c (°K)
1	BN	64–68	25	22	*	1·84–2·20
2	BN	60–65	100	21	5·679 ± 0·003	2·17–2·29
3	BN	65–67	170	44	5·684	2·13–2·24
4	Nb	61–65	205–215	19	5·686	1·81–2·07
5	BN	58–64	200–210	22	5·688	2·00–2·20
6	Nb	45	900 (sample melted)	2	5·689†	1·92–2·03
7	BN	60–63	250–280	15	5·694	1·81–1·85
8	Nb	62–64	435–445	1-1/2	5·695	1·79–1·93

*Sample was only about 25 per cent converted to high-pressure structure and X-ray diffraction lines were too weak to determine accurate lattice constant.

†X-ray diffraction pattern also shows other phases (see text)

Acknowledgement—The press used was financed by National Aeronautics and Space Administration Grant No. 237-63

REFERENCES

1. KLEMENT W., Jr. and JAYARAMAN A., In *Progress in Solid State Chemistry* (Edited by H. Reiss), pp 289–376. Pergamon Press, Oxford (1966).
2. RAY B., *J. Mater. Sci.* **2**, 284 (1967).
3. PFISTER H., *Acta crystallogr.* 11, 221 (1958).

4. KLEMENT W. Jr., COHEN L. H. and KENNEDY G. C., *J. Phys. Chem. Solids* **27**, 171 (1966).
5. HAYGARTH J., *J. appl. Phys.* To be published.
6. STORM A. R., JAYARAMAN A. and WERNICK J. H., *J. Phys. Chem. Solids* **29**, 623 (1968).
7. JAMIESON J. C., *Science* **139**, 845 (1963).
8. GELLER S. and HULL G. W., Jr., *Phys. Rev. Lett.* **13**, 127 (1964).

J. Phys. Chem. Solids Pergamon Press 1969, Vol. 30, pp 1613–1627. Printed in Great Britain

NONSTOICHIOMETRY IN RARE-EARTH FLUORIDES*

E. CATALANO, R. G. BEDFORD and V. G. SILVEIRA
Lawrence Radiation Laboratory, University of California, Livermore, Calif 94550, U S A

and

H. H. WICKMAN
Bell Telephone Laboratories, Murray Hill, N.J. 07971, U S A.

(*Received* 3 *September* 1968)

Abstract—We report the results of a systematic survey of the rare-earth fluoride systems at 1500°C Stable fluorite phases with ideal composition LnF_2 were observed in the Sm, Eu, and Yb systems A compound with this structure was also observed in the Tm system, but equilibrium was not established The stable composition range of this phase in the Sm and Eu systems extends from $LnF_{2\cdot00}$ to $LnF_{2\cdot25}$. A second phase of unresolved structure extends from $LnF_{2\cdot25}$ to $LnF_{2\cdot45}$ in the Sm and Eu systems. Additional unresolved phases are also present in the Yb system SmF_3 (orthorhombic) is stoichiometric within experimental error.

The lattice parameters of the fluorite phases decrease as fluorine is added Bulk density measurements and X-ray densities indicate that the defect structure is due to F^- interstitials. With the possible exception of the Pr and Nd systems, where slight color changes were observed in the LnF_3, no reactions occur between Ln and LnF_3 at temperatures to 1600°C

Mössbauer spectra of the Eu system indicate that the europium is in either a Eu^{2+} or Eu^{3+} state for all phases in the system The relaxation time for any charge transfer process is greater than 10^{-8} sec (the lifetime of the ^{151}Eu nuclear excited state). Mossbauer spectra are consistent with the existence of the intermediate phases mentioned above

A few observations were made on mixed systems containing Sm + Pr and Sm + Nd fluorides

1. INTRODUCTION

THE CHEMISTRY and properties of Ln anhydrous halides have been reviewed in detail by Thoma[1]. The typical rare-earth (Ln) ion valence state is +3. Divalent states for some Ln halides have been reported in molten salt solutions and for Eu^{2+} and Sm^{2+} in aqueous solutions. The iodides LaI_2, NdI_2, $CeI_{2\cdot4}$, $PrI_{2\cdot5}$, $NdCl_2$, TmI_2, and YbI_2, and all of the divalent halides of Eu^{2+} and Sm^{2+} have been reported[2, 3]. Nonstoichiometry in EuF_2 and SmF_2 was discovered by Asprey, Ellinger and Staritzky[4] and independently in EuF_2 by Lee, Muir, and Catalano[5].

One expects the fluorides to be more stable than the other halides, and to be less susceptible to hydrolysis. Thus, they form a convenient system for study.

We survey the Ln–LnF_3 systems in order to examine the possibility of the reduction of LnF_3 by the corresponding Ln metal. In particular, we report the solid solution ranges of Eu and Sm near the low fluorine concentration side of the composition range. With respect to the latter, the work is a preliminary or 'coarse' study, as these systems are quite complex. We will present more detailed studies of the systems SmF_2–SmF_3 and EuF_2–EuF_3 in a future publication. Studies of the range of stoichiometry were made by metathetical synthesis followed by petrographic and X-ray analysis.

For those solid solutions of Eu and Sm fluorides at the low-fluorine-concentration side of the composition scale, there is apparently a single face centered cubic (f.c.c.) phase region. In this region, we have determined that the defect structure is due to interstitial fluoride ions. In the region $2\cdot25 \leq F/Ln \leq 2\cdot45$ for Sm and Eu, another phase of undetermined structure exists. This structure is one which is a very small distortion from the fluorite f.c.c. structure. The Mössbauer spectra for the Eu fluorides presented are consistent with this picture: they indicate the distinct existence of Eu^{2+} and Eu^{3+} ions in the solid solutions.

---

*This work was performed in part under the auspices of the U.S. Atomic Energy Commission.

Fluorite structure YbF_2 has also been prepared. The situation regarding solid solutions near $F/Yb \approx 2$ is still unclear. TmF_2 has been prepared, but to date, we have not obtained equilibrium conditions.

Solid solutions of the type CaF_2–YF_3[6, 7] and CaF_2, SrF_2, and BaF_2 with LnF_3[7–9] have been characterized. In the cases CaF_2–YF_3 and SrF_2–LaF_3[6–8] solid solutions with $M^{+3}/(M')^{+2}$ ranging from 0 to ≈ 1 have been shown to have interstitial fluoride ion defect structures. In cases where ionic radii of the divalent and trivalent cations are approximately the same, the f.c.c. lattice parameter increases with fluorine concentration.

The solid solutions of BaF_2–UF_3 investigated by D'Eye and Martin[10] are more analogous to the Eu and Sm fluoride systems reported here. In this system, the ratio of ionic radii of Ba^{2+} to U^{3+} is 1·35 Å/1·04 Å = 1·30. In the solutions of low fluorine concentrations, the fluoride lattice parameter decreases about 5 per cent per mole UF_3 dissolved. D'Eye and Martin have shown that the defect structure for these solutions is again due to interstitial fluoride ions. The lattice contraction in the EuF_2–EuF_3 and SmF_2–SmF_3 systems is about 2 per cent per mole of trivalent ion. For these systems, the ratio of divalent to trivalent ionic radii is approximately 1·12 Å/1·03 Å = 1·09.

We have prepared a small number of solid solutions of SmF_3 with PrF_3 and NdF_3 in the lower fluorine concentration region. Once more, f.c.c. solid solutions and solutions with the same but undetermined distorted cubic structures are obtained.

2. EXPERIMENTAL METHODS

(A) Preparation of divalent Ln *fluorides and solid solutions*

The trivalent Ln fluorides starting materials were prepared in either of two ways: (1) Commerically obtained LnF_3 of nominal 99·9 per cent purity (in the Ln) in a Pt boat were first dehydrated under HF and then fused under HF. (2) Commercially obtained Ln_2O_3 of nominal 99·9 per cent purity in a Pt boat were converted to LnF_3 with HF and then fused under HF. The only exception to the fusing of the LnF_3 under HF was for the preparation of EuF_3 which we will discuss below. For the cases PrF_3, NdF_3, and LaF_3, single crystals grown from the melt under an HF atmosphere were used as starting materials. Such treatment results in LnF_3 which are not susceptible to room temperature hydrolysis and which have small surface areas so that water adsorption is minimized.

Commercially obtained Ln metals in ingot form with < 1 per cent metallic impurities were used as starting materials. With the exception of Eu metal, the Ln metals were milled under dry hexane to remove the surface coating. They were then chipped under dry hexane with a tungsten carbide milling tool. The metals were transferred into a gloved dry box after pumping off the hexane in the air lock. The box could be evacuated to $\sim 2 \times 10^{-6}$ Torr. In use, Ar from a liquid Ar supply was used as the working gas in the box. Eu metal is much more susceptible to corrosion by air than any of the other Ln metals. The Eu ingot was directly transferred into the dry box. Pieces of Eu metal were cut as required after first removing the surface coating.

LnF_3 and Ln in the mole ratio of 2 to 1 and total amounts of 2–5 g were sealed in Ta or Mo crucibles. The crucibles had been previously heated in vacuum at 1800°C. LnF_3 was weighed out to 0·1 mg into weighed crucibles and transferred into the dry box. The Ln metal was then weighed and added, and the crucible lid pressed on. The filled crucible (now filled with Ar) was transferred out of the box, quickly weighed to 0·1 mg, then placed in a heat sink and transferred to an electron beam welding (EBW) box. The box and samples were pumped down to $\sim 5 \times 10^{-5}$ Torr, and kept evacuated for about 18 hr. The crucible lids were then closed by EBW. The sealed crucibles were again weighed to 0·1 mg in air. The reactions *per se*, were carried out at 1500°–1600°C, which insured melting the LnF_3 and any LnF_2 that formed. Normal procedure was to program the power to decrease slowly (to ~1000°C) in order to obtain reasonably large crystals from the melt and good separation if two phases remained. The crucibles were again weighed to 0·1 mg before being opened and the products examined. This enabled a check for leaky crucible seals. The LnF_2 produced in the above manner are stable in air for very long periods. EuF_2 was also prepared by reduction of EuF_3 (in Mo boats) by pure H_2 at temperatures of ~1500°C.

For the systems in which LnF_2 were formed as described above, additional compositions were prepared by metathetical synthesis from LnF_2 and LnF_3. The reactants in 0·5–5 g amounts were weighed into Ta, Mo, or Pt-10% Rh crucibles. These were then sealed after evacuation at $\sim 5\times10^{-5}$ Torr. by EBW. The sealed crucibles were kept at 1500–1600°C for approximately an hour and cooled slowly. Some solid solutions were prepared by metathetical synthesis from Ln metal and LnF_3 under the same conditions used for the preparation of LnF_2.

(B) *Chemical analyses*

Three types of chemical analyses were made: an F/Ln ratio, trace oxygen, and emission spectrographic. The oxygen analyses were made by γ-activation analysis[11].

Flouride is determined[12] by fusing the sample with NaOH, converting the NaF to HF on a cation exchange resin, eluting with water, and titrating the HF with standard NaOH. A separate portion of sample, for the rare-earth analysis, is fused with Na_2CO_3, then dissolved in water, and the rare-earth oxide is filtered off. The oxide is dissolved in a minimum of 6N HCl, diluted, adjusted to pH 6·0, and titrated with standard EDTA (ethylene-diamine-tetraacetic acid) solution. Relative standard deviations for fluorine and rare earths were 0·6 and 0·4 per cent, respectively.

(C) *Crystallographic, petrographic analyses and density determination*

Powder pattern photographs were obtained using CuK_α radiation with a Ni filter, FeK_α radiation with an Mn filter, CrK_α radiation with a V filter, and CoK_α radiation with an Fe filter. Si was used as an internal standard for lattice parameter measurements. Powdered samples were examined with transmitted light using a polarizing microscope.

Bulk densities at 35±0·1°C of Sm and Eu fluorides in the range $LnF_{2.00}$ to $LnF_{2.45}$ were measured to ±0·2 per cent using Ar and He gas displacement[13] on samples of ~4 g.

(D) *Mössbauer spectra*

The Mössbauer spectra were obtained with a conventional linear velocity drive spectrometer. A room-temperature source of $Sm_2{}^{151}O_3$ was used. The EuF_x samples were in the form of fine powders. Spectra were obtained at 77 and 4·2°K.

3. RESULTS AND DISCUSSION

(A) *Stability of the divalent* Ln *fluorides*

Divalent ions of all the lanthanides can be formed by reduction by γ-irradiation of LnF_3 in CaF_2[14]. The extent of divalent Ln ion formation is limited to a few per cent for most of the lanthanides. Sm^{2+}, Eu^{2+}, Tm^{2+}, and Yb^{2+} have also been formed by these same techniques in SrF_2 and BaF_2 hosts. An electrolytic method has also been used to reduce both Sm^{3+} and Tm^{3+} in solid CaF_2 [15]. Sm, Eu, Tm and Yb trifluorides have been reduced with alkaline earth metals[3].

Performing the reduction with the corresponding Ln metal itself provides a technique for investigating these systems without the problems and ambiguity introduced by the presence of another metal. Using this technique, fluorite structure SmF_2, EuF_2, TmF_2, and YbF_2 were obtained. The f.c.c. lattice parameters for TmF_2 and YbF_2 are $5{\cdot}59_7$ Å and $5{\cdot}59_9$ Å, respectively. The reaction goes to completion for the Sm, Eu, and Yb reductions, but not for Tm. The situation with respect to solid solutions and phases of the Yb fluorides is as yet unclear. Very slight reduction was evidenced by the color change for PrF_3 and NdF_3, but not enough reduction occurred to identify either a divalent fluoride or a solid solution either by X-ray or by petrographic techniques. Several nonmetallic crystalline phases were found with LuF_3. None of these were identified, but from the masses of Lu metal and nonmetallic phases which remained after reaction, it was evident that very little reduction had occurred. No reaction occurred in any of the other LnF_3–Ln systems.

(B) Samarium and europium fluorides

Since the Sm and Eu fluorides are quite similar, we shall discuss them together.

Nominal EuF_2 prepared by H_2 reduction of EuF_3 has been reported by a number of investigators[4, 5, 16]. The composition, lattice parameter, and color obtained seemed to by quite variable. Asprey *et al.*[4] noted the nonstoichiometric nature of nominal SmF_2, EuF_2 and YbF_2; and, Lee *et al.*[5] also noted it in EuF_2. Both sets of workers indicated that the Eu-rich composition was substoichiometric ($EuF_{1.93}$ and $EuF_{1.82}$). We shall discuss the lower limit of the solid solutions in some detail, and show that for both the Eu and Sm fluorides of lowest fluorine concentration, the compositions are $EuF_{2.00}$ and $SmF_{2.00}$ respectively.

1. *Composition scale*. The composition scale was essentially established by metathetical synthesis. Consistency tests and corrections to the initial scale were applied using the results of the physical and chemical analyses discussed below.

Some difficulties were initially encountered due to a reaction between Pt and the lower fluorides, which produced an intermetallic $EuPt_2$ or $SmPt_2$ of f.c.c. $MgCu_2$ structure and a higher fluoride. The lattice parameter of the $EuPt_2$ is 7·72 Å in agreement with Elliot[17]. In the Eu system, samples with F/Eu < 2·09 cannot be prepared in Pt containers. The minimum F/Sm that can be obtained at equilibrium in Pt containers is not less than 2·8.

For the Sm system, the composition scale problem is not too severe, since Sm metal is not susceptible to rapid corrosion and anhydrous SmF_3 is well-defined. 'Apparent' compositions were made up by synthesis from Sm and SmF_3 in Mo crucibles. Petrographic examination of the apparent composition $SmF_{1.99}$ showed the boules to be two-phase, there being an excess of Sm metal which physically separated from the nonmetallic phase. Samples very close to SmF_3 in composition were made up in Pt-10% Rh crucibles. The specific measured properties for the SmF_2–SmF_3 system are listed in Table 1.

For the Eu system, there are two difficulties in the use of direct synthesis to establish the composition scale. (1) In the preparation of the apparent compositions from Eu metal, the corrosion of the metal is a severe problem. This may be somewhat obviated by use of dry box techniques and by analyses for oxygen so as to apply preventive measures and to obtain some measure of the actual corrosion. This we have done, and the results of the trace oxygen analyses in the final compositions have indicated levels in and below tenths of per cents by weight. (2) EuF_3 is not a stable, well-defined material at temperatures of about 1400°C.

As indicated above, it is generally advantageous to fuse the trifluoride under HF. One then obtains a material which is not susceptible to hydrolysis at low temperatures. EuF_3 in Pt crucibles held at 1400°C under an HF atmosphere decomposes. It will be noted in the comments in Table 2 that a number of compositions develop high pressures at the melting point.

For the Eu system, three different sets of

Table 1. Physical properties of the SmF_2–SmF_3 *system (table includes only representative samples of a total of* 40 *preparations examined)*

F/Sm	X-ray analysis results		Density ($g\,cm^{-3}$)	Color, microscopic observations, miscellaneous comments
	(Structure)	(Å)		
1·98	f.c.c.	$5{\cdot}87_2$	$6{\cdot}10_3$	Two phases: Opaque metallic phase and almost-opaque crystalline phase. Crystals blue and transparent with very high optical density. Nonbirefringent.
2·00	f.c.c.	$5{\cdot}86_6$	$6{\cdot}11_8$	Appears to be single phase. Finely ground powder looks blue by reflected light. Almost opaque crystal; in very thin section, very dark blue transparent crystals. Nonbirefringent.
2·03	f.c.c.	$5{\cdot}86_8$	6·15	Appears to be single phase. Almost opaque crystals which are blue, transparent, with very high optical density. Nonbirefringent.
2·09	f.c.c.	$5{\cdot}85_8$	6·19	Appears to be single phase. Crystallites are almost opaque. In thin sections, small pieces transparent blue; larger pieces look transparent red. Nonbirefringent.
2·15	f.c.c.	$5{\cdot}84_9$	$6{\cdot}30_8$	Ground powder looks red under reflected light. Almost-opaque crystals. Dark red; transparent in thin section. Nonbirefringent.
2·20	f.c.c.	$5{\cdot}84_4$	6·38	Appears to be single phase. In thin section, crystals are transparent, very dark red, with high optical density. Nonbirefringent.
2·25	f.c.c.	$5{\cdot}84_3$	6·39	Crystals are dark red, transparent, with very high optical density. Nonbirefringent.
2·30	U.S.*	(5·82)†	6·45	Crystals give the appearance of being two-phase. Both are dark red, transparent, with high optical density. One is birefringent (red) and the other is nonbirefringent.
2·35	U.S.	(5·82)	6·58	Appears to be two-phase. Both dark red, transparent, with high optical density. One is birefringent (red), the other is nonbirefringent.
2·40	U.S.	(5·82)	$6{\cdot}63_4$	Appears to be two-phase. Both red and becoming lighter. One is birefringent (red), and the other is nonbirefringent.
2·45	U.S.	(5·82)	6·67	Appears to be two-phase. Bright red, transparent and birefringent (red) phase, with a red nonbirefringent phase.
2·50	U.S. +SmF_3‡	(5·79)		Two phases. Red, transparent, birefringent phase with brightly birefringent colorless phase.
2·60	U.S. +SmF_3	(5·79)		Two phases. Red, transparent, birefringent phase with brightly birefringent colorless phase.
2·70	U.S. +SmF_3	(5·79)		Two phases. Red, transparent, birefringent phase with brightly birefringent colorless phase.
2·80	U.S. +SmF_3	(5·79)		Two phases. Red, transparent, birefringent phase with brightly birefringent colorless phase.
2·90	U.S. +SmF_3	(5·79)		Two phases. Red, transparent, birefringent phase with brightly birefringent colorless phase.
3·00	SmF_3			Single phase. Colorless, transparent, brightly birefringent.

*U.S. = Undetermined structure.

†Lattice parameters, a; numbers in brackets are parameters calculated *as if* structure were f.c.c.

‡SmF_3-Orthorhombic, $a = 6{\cdot}66_9$Å, $b = 7{\cdot}05_9$Å, $c = 4{\cdot}40_5$Å.

preparations were examined: (a) Eu + 'A', (b) 'B' + 'A', and (c) EuF_2 and EuF_3.

The material 'A' was obtained in the following way. EuF_3 was first dehydrated and then kept under HF at 1200°C for several hours. It was then cooled under HF and quickly transferred into a Pt crucible. A lid was sealed on by EBW under 10^{-5} Torr. The crucible was then inductively heated to 1400°C in a vacuum furnace. It was kept at this temperature for only a few minutes, because the crucible leaked due to the very high internal pressures. The material within the crucible was found to have melted. Chemical analyses of the type listed above gave a composition for 'A' = $EuF_{2.99}$. This is the value we have used in the first two sets of preparations.

The material 'B' was obtained by hydrogen reduction of EuF_3 in a Pt crucible under a partial pressure of HF. This material was pulled as a large single crystal and is one of the specimens that was used for the ESR measurements in [5]. It was there quoted as having an F/Eu = 2·05 on the basis of the chemical analysis quoted in the reference. Chemical analyses on the type material listed above gave F/Eu = 2·07. We have not used this value for 'B'; instead, we have taken the composition $EuF_{2.09}$ for 'B.' This value gives the best consistency of lattice parameters and densities for set (b) as compared with sets (a) and (c).

For preparations (c), EuF_3 was dehydrated under HF at 800°C for several hours and then cooled under HF. It was quickly transferred to and stored in the dry box until used in the preparations. This material was analysed as having F/Eu = 2·97. The same crucible loading techniques as for Eu metal were then used. The EuF_2 was obtained by reducing this material in a Mo boat with H_2 at ~ 1300°C. The temperature was then raised to 1500°C so that the EuF_2 was molten while in contact with H_2.

We believe that the starting materials for preparation (c) most closely come to stoichiometric EuF_2 and EuF_3. The argument for the EuF_3 is that at the low temperature (800°C) for the dehydration under HF, we do not expect significant decomposition. For the EuF_2 prepared by H_2 reduction (in a Mo container), the argument rests on the consistency of the physical measurements. That is, for this material the X-ray lattice parameter is at the maximum value (and the same as that for those parameters obtained when excess Eu metal was present). The stoichiometry calculated from the measured density and the f.c.c. lattice parameter is $EuF_{2.00}$ to within the experimental accuracy (±0·2 per cent). The Mossbauer spectrum of this material shows no Eu^{3+} absorption. However, this material resembles one described by both Asprey *et al.*[4] and Lee *et al.*[5] as being substoichiometric. Also, chemical analysis (as mentioned above) for this material gives an F/Eu = 1·98. We will discuss this point in detail below.

Corrections to the F/Ln resulting from oxygen and cation impurities were negligible as compared to other experimental uncertainties for all sets of preparations. For preparations (a) and (b), density and X-ray lattice parameters allow relation to (c). As shown in Figures 1 and 2, the consistency is quite good. From the relation of sets (a) and (b) to set (c) we establish 'A' having F/Eu = 2·99 and 'B' having F/Eu = 2·09. It is to be noted that, although there were no difficulties in relating the chemical analyses for F/Sm in the SmF_2–SmF_3 system, we do not trust this kind of analysis for the EuF_2–EuF_3 system.

Attempts to prepare a homogeneous Eu-rich material by means of Eu-metal reaction in EBW-sealed Mo crucibles were unsuccessful. Apparently EuF_2 dissolves Eu metal to some extent at high temperatures. Excess Eu metal remains trapped in the resultant crystals of EuF_2 (which have X-ray f.c.c. lattice parameters that are identical with those of the material prepared by H_2 reduction of EuF_3 in Mo containers). This was evidenced by the optical properties (see Table 2 and below) of samples prepared in such a manner.

2. *Optical examination.* SmF_2 is a blue transparent nonbirefringent solid of very high optical density. As F/Sm increases from 2·00 to 2·10, the color changes very rapidly to a dark red. There is very little change in appearance from 2·10 to 2·25; then from 2·25 to 2·40, the optical density starts to decrease and a birefringence sets in with some of the crystallites being red birefringent and some being nonbirefringent. At F/Sm of 2·45 the material is predominately red birefringent. Above 2·45, it consists of the red birefringent phase together with a bright colorless highly birefringent material. Samples of apparent

Table 2. Physical properties of the EuF_2–EuF_3 *system (Table includes only representative samples of a total of* 40 *preparations examined)*

F/Eu	X-ray analysis results		Density ($g\ cm^{-3}$)	Color, microscopic examination, miscellaneous comments
	(Structure)	(Å)		
1·99	f.c.c.	$5{\cdot}83_8$	6·28	Black crystalline chunks. Under transmitted light, grey and transparent with many scattering centers. Nonbirefringent.
2·00	f.c.c.	$5{\cdot}84_0$	6·32	Prepared by H_2 reduction. Green with trace of yellow, crystalline chunks. Under transmitted light, transparent, colorless, nonbirefringent.
2·04	f.c.c.	$5{\cdot}83_9$	6·33	Greenish-brown under reflected light. Appears to be two-phase under transmitted light. Bulk is nonbirefringent. Some crystallites brown and birefringent (brown).
2·09	f.c.c.	$5{\cdot}83_4$	6·37	Apparently single phase. Brown under reflected light. Under transmitted light, yellow, transparent nonbirefringent
2·14	f.c.c.	$5{\cdot}82_2$	6·44	Brown under reflected light. Under transmitted light, light brown transparent crystals. Small amount of birefringence in thick sections.
2·20	f.c.c.	$5{\cdot}81_1$	6·56	Dark brown under reflected light. Under transmitted light, a yellow transparent and nonbirefringent phase.
2·25	f.c.c.	$5{\cdot}81_2$	6·63	Very dark brown. Under transmitted light, light-brown transparent crystals. A strange mosaic-like birefringence.
2·29	U.S.*	(5·78)†	6·67	Dark brown. Under transmitted light, light brown transparent crystals. A mosaic-like, bright-brown birefringence. Evidence for a pressure build-up in crucible.
2·33	U.S.	(5·78)	6·70	Brown. Under transmitted light-light brown, transparent, and brightly birefringent. Possibly two phases—both birefringent. Evidence for a pressure build-up in crucible
2·39	U.S.	(5·78)	6·76	Brown. Under transmitted light, brown, transparent and brightly birefringent. Evidence for pressure build-up in crucible.
2·44	U.S.	(5·78)	6·75	Brown Under transmitted light, light brown, transparent, very brightly birefringent. Evidence for pressure build-up in crucible.
2·50	U.S. + EuF_3‡	(5·78)		Deep gold color. Very birefringent under transmitted light. Evidence for pressure build-up in crucible.
2·57	U.S. + EuF_3	(5·78)		Gold colored. Very birefringent under transmitted light. Evidence for pressure build-up in crucible.
2·70	U.S. + EuF_3	(5·78)		Gold colored. Very birefringent under transmitted light. Evidence for pressure build-up in crucible.
2·80	U.S. + EuF_3	(5·78)		Gold colored. Very birefringent under transmitted light. Evidence for pressure build-up in crucible.
2·90	U.S. + EuF_3	(5·78)		Gold colored. Very birefringent under transmitted light. Evidence for pressure build-up in crucible.
2·99	EuF_3			Light beige. Brightly birefringent under transmitted light.

*U.S. = undetermined structure

†Lattice parameters, a; numbers in brackets are parameters calculated *as if* structure were f.c.c. for the strongest set of lines.

‡EuF_3-orthorhombic, $a = 6{\cdot}22_4$ Å, $b = 7{\cdot}01_0$ Å, $c = 4{\cdot}39_6$ Å.

compositions SmF_{3-x} (where x is small) are two-phase with what appears to be the phase identical to that with F/sm = 2·45 in equilibrium with SmF_3. This appears to be the case with $x \leqslant 0{\cdot}01$ within experimental accuracy. Apparently these optical observations would be consistent with the following: A solid solution extends from $SmF_{2{\cdot}00}$ to $SmF_{2{\cdot}25}$. The system may be two-phase from $SmF_{2{\cdot}25}$ to $SmF_{2{\cdot}47\pm0{\cdot}03}$, or may have a narrow two-phase region at $SmF_{2{\cdot}25}$, with a solid solution extending to $SmF_{2{\cdot}47}$. At higher fluorine concentrations, the system is two-phase SmF_3 in equilibrium with $SmF_{2{\cdot}47}$.

EuF_2 is a transparent, light yellow-green solid. With the addition of small amounts of fluorine, the color goes to dark brown when observed under reflected light. When examined under transmitted light in going from F/Eu of 2·00–2·25, the materials are nonbirefringent and change in color from very light yellow (nearly colorless) to light brown. For F/Eu > 2·25, the materials are light brown and birefringent. As the F/Eu ratio increases to 2·33, the brightness due to birefringence increases. The birefringene of these materials is not uniform, appears mosaic-like and brown in color. For materials 2·33 ≤ F/Eu ≤ 2·45, the birefringence becomes more uniform within each particle, lighter in color, and brighter. For samples with 2·5 ≤ F/Eu ≤ 3·00 the birefringence is very bright, but differences in optical appearances are quite small even though the samples do not appear to be homogeneous. At F/Eu ≈ 3·00, we cannot decide on the basis of the optical observations alone whether or not the phase corresponding to F/Eu ~ 2·45 is in equilibrium with EuF_3.

3. *X-ray examination.* Figure 1 and Tables

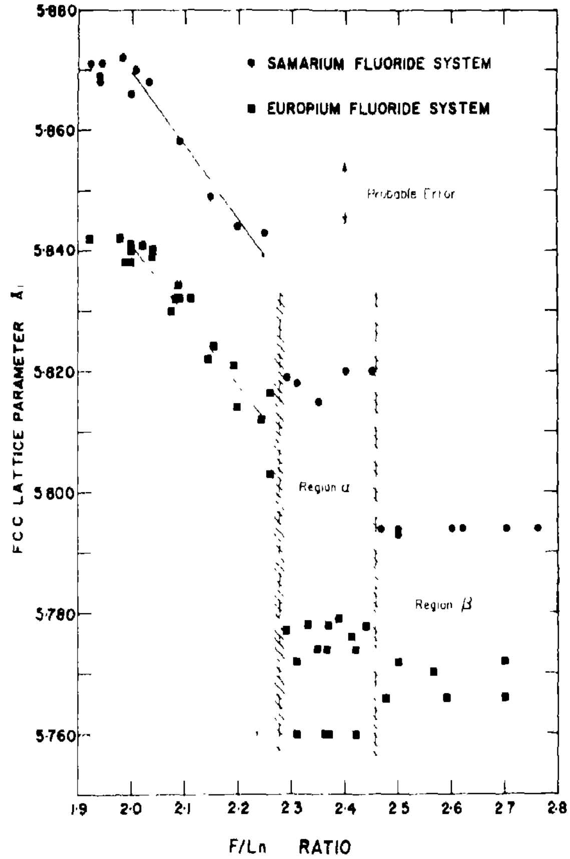

Fig. 1. The f.c.c. lattice parameters obtained from powder patterns using CuK_α radiation. For regions α and β, the structures are complex and undetermined, but are only a small distortion from cubic symmetry. The data in α and β are plotted as if the patterns were from f.c.c. lattices. For Eu in α, the patterns could be indexed as two f.c.c. lattices; these parameters are shown.

1 and 2 contain the data obtained for the Sm and Eu fluoride systems. For the range $2\cdot00 \leq \mathrm{F/Ln} \leq 2\cdot25$ the structure deduced from powder patterns is unequivocally f.c.c. From 2·25 to ~2·45 the structure is undetermined but is one which has a small distortion from cubic symmetry. Table 3 is a listing of lines for examples of materials within this region. The data in Fig. 1, regions α and β, are plotted *as if* the structures were actually the fluorite f.c.c. structures from the data obtained using CuK_α radiation. In region α for the Eu system, the powder patterns can *cursorily* be indexed as two f.c.c. structures with the lattice parameters as shown in Fig. 1 (when the data are obtained using CuK_α radiation).

Table 3. *d-Spacings for* $\mathrm{SmF}_{2\cdot40}$ *and* $\mathrm{EuF}_{2\cdot44}$

$\mathrm{SmF}_{2\cdot40}$*		$\mathrm{EuF}_{2\cdot44}$†	
d	Relative intensity‡	d	Relative intensity‡
3·51	w	4·01	w
3·34	s	3·31	vs
3·31	vs	2·87	s
2·89	s	2·49	vvw
2·47	vw	2·33	vvw
2·34	vw	2·22	vvw
2·23	vw	2·09	vvw
2·18	vvw	2·04	vs
2·14	vw	1·95	vvw
2·08	vvw	1·91	vvw
2·05	vs	1·74	vs
2·04	vs	1·67	s
1·98	vvw	1·63	vvw
1·93	vvw		
1·91	vvw		
1·86	vw		
1·74	vs		
1·73	s		
1·71	vw		
1·68	w		
1·67	w		

*CrK_α radiation, V Filter; $\lambda = 2\cdot2909$ Å.
†CoK_α radiation, Fe Filter; $\lambda = 1\cdot7902$ Å.
‡s, strong; w, weak; v, very.

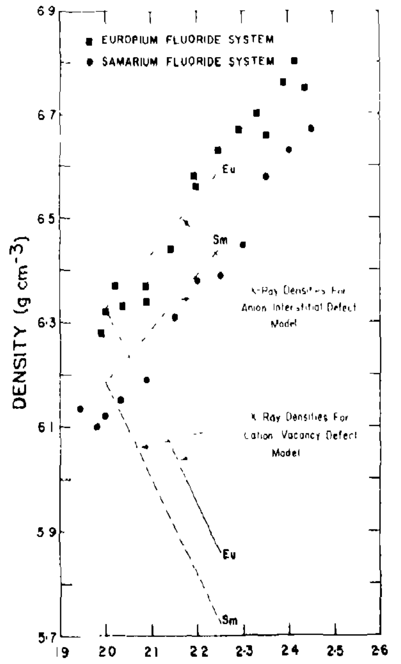

Fig. 2. Density vs. composition for the Sm and Eu fluoride systems.

For some six compositions for each of the Sm and Eu fluoride systems with $2\cdot25 \leq \mathrm{F/Ln} \leq 2\cdot45$, patterns were taken with CrK_α and CoK_α radiation in an attempt to elucidate the distorted f.c.c. structures. In the case of the Sm system, as the composition changes toward increased fluorine concentration, the structure appears to change from f.c.c. to rhombohedral and finally to tetragonal. Unfortunately, the patterns were such poor quality that measurement of the lattice parameter was not possible. In the Eu system, the patterns did not even allow this kind of structural interpretation to be made. For some samples in this composition range, it was possible to index the lines for this undetermined structure as postulated mixtures of rhombohedral and tetragonal structures, such as the oxyfluorides of the type reported by Zachariasen [18] for LaOF and YOF. That the phases actually prepared are not oxyfluorides we have demonstrated by: (a) Oxygen analyses. Oxygen occurs essentially as an impurity ranging up to several tenths of a per cent. (b) Preparation of EuOF and SmOF as pure phases and examination of the X-ray powder patterns of these phases and mixtures of them with EuF_3 and SmF_3, respectively. These patterns do not correspond to those found for materials with $2{\cdot}25 \leq F/Ln \leq 2{\cdot}45$.

As the F/Sm or Eu increases above 2·40, what appear to be orthorhombic trifluoride patterns begin to grow, and there is an apparent two-phase region for at least part of the composition range.

4. *Mössbauer spectra.* Several comprehensive reviews of the Mössbauer effect (ME), or recoil-free gamma-ray emission are available[19, 20]. The measurements reported here pertain only to the ^{151}Eu isotope with a nuclear excited state of ~21 keV above the nuclear ground state level. In the ME, the isomer shift for the recoil-free γ-absorption between source and absorber as a function of Doppler velocity occurs because the source and absorber nuclei are not in identical environments. Usually, source and absorber environments are not identical because of: (a) differing coulombic energies of source and absorber. (b) Interaction of a nuclear quadrupole moment (if present) and an electric field gradient (if present) at the nucleus. (c) Internal magnetic fields of electronic origin cause a Zeeman splitting of the nuclear levels. The isomer shift then depends on both nuclear and electronic properties. Semi-empirical, quantitative treatments of the isomer shift in the ME have been given[21–24]; the works of Brix *et al.*[24] and Shirley[23, 25] are particularly noteworthy for their treatment of the isomer shift in Eu^{151}. Another point is that the intensity of the absorption (or that measure of the fraction of nuclei absorbing γ-radiation in a recoil-free fashion) is partly a measure of how tightly bound the nucleus is to the crystalline lattice. The ME can yield much information on the chemical nature of the system.

ME effect data were obtained for some nineteen samples in the EuF_2–EuF_3 system. Data were taken at both 77 and 4·2°K. No Zeeman splittings due to internal magnetic fields of electronic origin were observed down to 4·2°K for any composition. This is consistent with the EPR data on a sample of low fluorine concentration[5].

Figure 3 shows ME spectra for six representative samples of the EuF_2–EuF_3 system taken at 77°K. One notes immediately that there are only two absorptions, well separated and resolved, which may be ascribed to Eu^{+2} and Eu^{3+} ions. If electrons can 'jump' between divalent and trivalent Eu sites, then the relaxation time for such a process must be considerably longer than the lifetime of the excited nuclear state in ^{151}Eu, which is $8{\cdot}8 \times 10^{-9}$ sec[26]. Figure 4 shows the isomer shifts for the Eu^{2+} and Eu^{3+} for all the ME data as a function of composition. Several features are evident in this plot. The most obvious is that the divalent peak is resolved into two peaks for $F/Eu > 2{\cdot}4$. (The splitting in the divalent peak may be seen in Fig. 3.) Note that the isomer shift plot for the divalent Eu corresponds to a *low resolution* phase plot and correlates quite well with the X-ray data in Fig. 1. The correlation can be seen by comparing Fig. 1 with Fig. 4. Note in Fig. 4, as F/Eu increases across what corresponds to region α in Fig. 1, the isomer shift for the Eu^{2+} ions becomes increasingly negative and finally splits for $2{\cdot}4 < F/Eu < 2{\cdot}5$.

The magnitude of the isomer shift is a measure of the net *s*-electron density at the nucleus. Values given by Brix *et al.*[24] for the isomer shift of divalent ^{151}Eu $(4f^7\,5s^2\,5p^6)$ relative to trivalent ^{151}Eu are $-1{\cdot}2$ to $-1{\cdot}5$ cm/sec where the electronic configuration is $4f^6\,5s^2\,5p^6$. The more ionic the divalent Eu, the larger is the negative value of the isomer shift, qualitatively indicating loss of the outermost 'valence' 6*s* electrons. A similar effect would also result from shielding, arising from an increase of core *f* or *d* electrons; however, for present purposes, this is probably of less importance than valence electron behavior. EuF_2 with an isomer shift δE of $-1{\cdot}42$ cm/sec, is one of the more ionic of the divalent Eu compounds. Eu metal has an isomer shift of $-0{\cdot}81$ cm/sec, consistent with an electronic configuration of $4f^7\ 6s^2$ (see

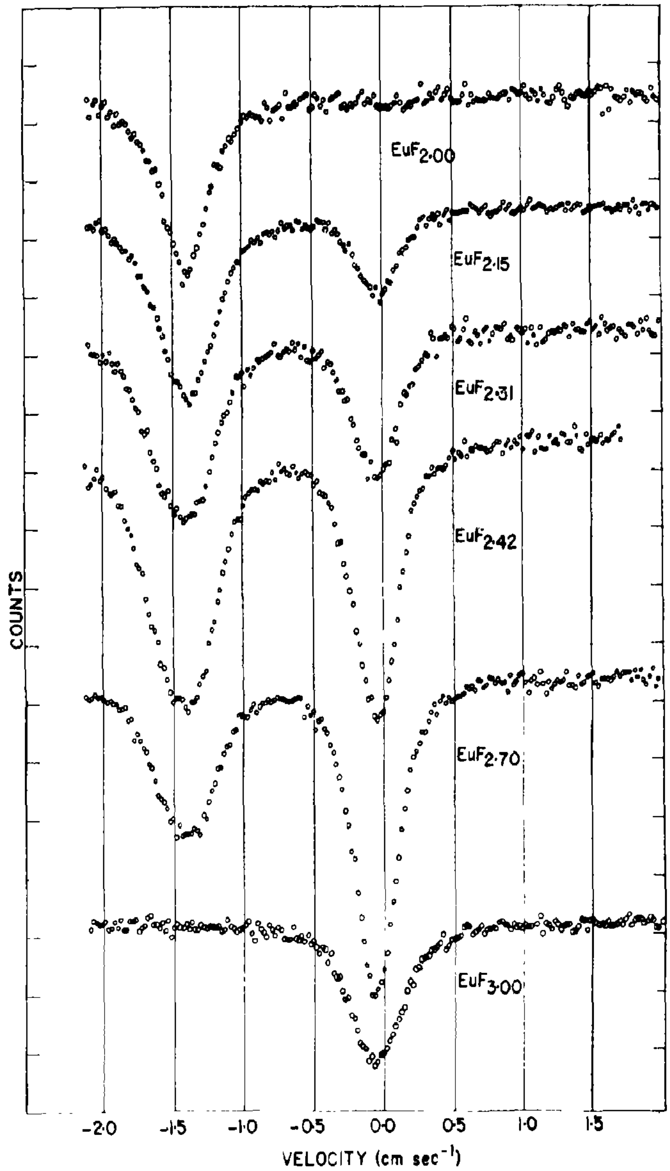

Fig 3. Mössbauer spectra. Six representative samples of the EuF_2–EuF_3 system taken at 77°K.

Barrett and Shirley[25]). The methods of Brix *et al.*[24] suggest an isomer shift of $-0{\cdot}9$ cm/sec for the two most physically reasonable configurations of Eu^{1+}. We note for the 77°K data in Fig. 4, that in one type of Eu^{2+} sites for $F/Eu > 2{\cdot}4$, the Eu^{2+} nuclei have δE values $\sim -1{\cdot}50$ cm/sec, and that in the other type of site, the δE is $\sim -1{\cdot}39$ cm/sec. The origin of these small changes in isomer shift accompanying phase transformation at $EuF_{2\cdot25}$, may be related to the observation of a concentration-dependent isomer shift in dilute Eu^{2+}: CaF_2 absorbers, as reported by Maletta, Heidrich, and Mössbauer

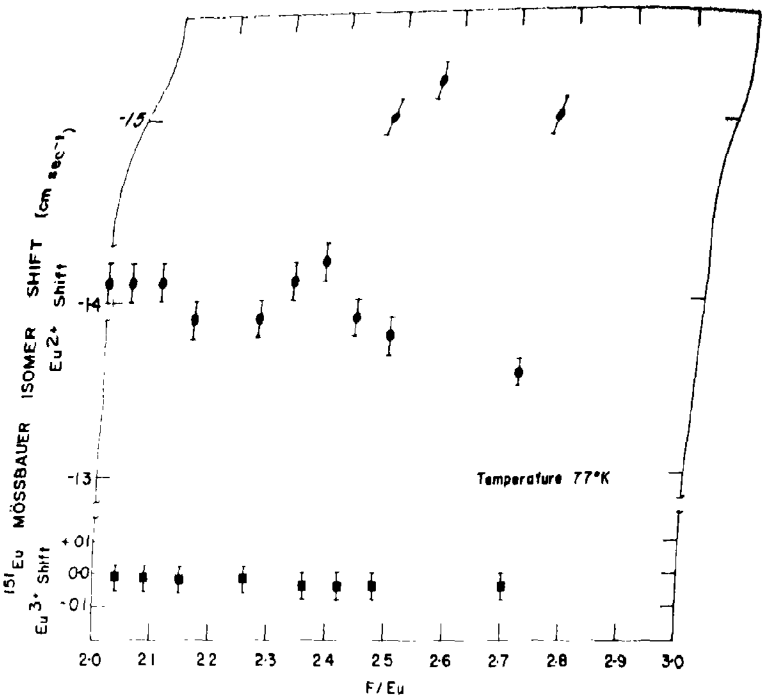

Fig. 4. ^{151}Eu Mössbauer isomer shift as function of F/Eu for the europium fluoride system

[27]. However, we do not at present have sufficient information to be able to meaningfully relate these observations to the bonding or other properties of europium in the present compounds. The isomer shift for the Eu^{3+} sites, although small, also exhibits a change in magnitude near F/Eu ~ 2·3. This near the f.c.c.-region α break in Fig. 1.

It is interesting to compare the observed intensity ratios of the ME lines for Eu^{2+} and Eu^{3+} in the specimens examined at 77°K with what one calculates from a hypothetical 'thin' absorber, which is a *physical* mixture of EuF_2 and EuF_3 (see Fig. 5). In Fig. 5, D is plotted as the ordinate and is the absorption coefficient, defined as

$$D = \frac{\text{Area}\,(Eu^{2+})/X(Eu^{2+})}{\text{Area}\,(Eu^{2+}) + \text{Area}\,(Eu^{3+})}$$

where $X(Eu^{+2})$ is the mole fraction of EuF_2 in the mixture and D represents the fractional deviation from 'ideal' behavior for each composition. For the hypothetical solid described above (where differences in recoil-free fractions are negligible), D will be unity and independent of concentration. On the other hand, the actual data of Fig. 5 give a representative situation with routine sample thickness (20 mg Eu/cm^2) and temperature (77°K); and, a noticeable deviation is observed. The point here is that the ME effect in real cases may not be directly amenable for determining concentrations of ions in solids without ancillary data, such as a deviation function or calibration procedure.

5. *Densities and defect structures.* The data for both Sm and Eu fluorides are shown in Fig. 2. These data are compared to theoretical curves based on an anionic interstitial defect model and a cationic vacancy model for the fluorite f.c.c. structure solid solutions.

The general trend of the data clearly indicates an anionic interstitial defect model as being the most reasonable model for both systems. The results clearly indicate this model despite an overall decrease in f.c.c. lattice parameter as fluoride ions are added.

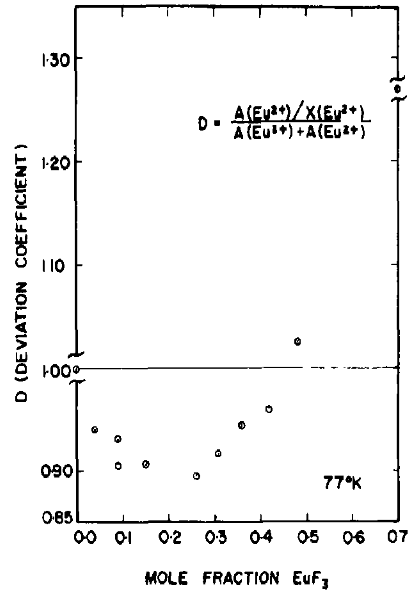

Fig. 5. Mössbauer intensity deviation coefficient vs mole fraction of EuF_3.

Thus, these systems are similar to the BaF_2-UF_3 system mentioned above[10]. The f.c.c. solid solution range in the BaF_2-UF_3 system extends to ~ 40 mole % UF_3.

Ippolitov *et al.*[9] and D'Eye and Martin [10] have adequately demonstrated that stable fluorite f.c.c. solid solutions do not require a close similarity in cationic sizes. Stability depends on both chemical and geometrical factors. That the geometrical sizes of the ions are important in the determination of the f.c.c. lattice parameter dependence on composition in solid solutions, has been demonstrated by Ippolitov *et al.*[9] for the systems CaF_2-LnF_3, SrF_2-LnF_3 and BaF_2-LnF_3. The range of f.c.c. solid solution in these systems cover from 33 to 55 mole % LnF_3 in MF_2. Unfortunately, the defect model for these systems has not been determined.

The curves for the theoretical vacancy and interstitial models were calculated for the fluorite f.c.c. structure using the density of the $F/Ln = 2{\cdot}00$ computed from the X-ray lattice parameters. The experimentally determined density for $EuF_{2{\cdot}00}$ agrees very well with that calculated from the X-ray lattice parameter. The experimentally determined density for $SmF_{2{\cdot}00}$ lies below that calculated from the X-ray lattice parameter.

That a density comparison between a continuous solution and a mixture of two phases is not distinguishable is illustrated by the continued linear behavior in the region α (Fig. 1). Although there are probably two or more discrete phases in the composition range $2{\cdot}00 \leq F/Ln \leq 2{\cdot}45$, they are all based on substitution of +3 ions for +2 ions in the cation lattice with interstitial fluoride ions. Fluoride ions probably first occupy central interstitial sites up to the point of the composition $F/Ln = 2{\cdot}25$. This corresponds to the beginning of region α. Continued occupation of F^- in edge positions to the point of adding one more F^- per unit cell may correspond to region β. This latter occupancy probably occurs in a layer-like manner and results in a distortion from cubic symmetry.

6. *Possibility of substoichiometric solutions* (LnF_{2-x}). The question as to whether some of the obtained low fluorine concentration compounds are really substoichiometric solutions is important particularly in view of published reports[4, 5] of the existence of stable substoichiometric EuF_2.

Let us first consider SmF_2 (and YbF_2). Here, metathetical synthesis of substoichiometric solutions have proved to yield samples in which metal inclusions could clearly be discerned by microscopic examination. In addition, compositions calculated by metathetical synthesis of nearly stoichiometric solutions and compositions obtained from chemical analyses always agreed. X-ray lattice parameters of *apparently* substoichiometric samples were always identical to the lattice parameters for SmF_2 (YbF_2) (see Fig. 1). Moreover, all samples prepared which were *apparently* substoichiometric were quite dark, occasionally with a metallic coating around the outside of crystalline chunks and in the boundaries between crystal grains. (These effects are much more discernable for YbF_2 than for SmF_2, which is optically very dense.) We conclude that such substoichiometric solutions are not stable at room temperature and that all of our observations and analyses are consistent with this conclusion.

This question is more difficult to answer for the europium case. Here, as we have mentioned above, the establishment of the composition scale was particularily difficult. More evidence was required, especially since analyses[4, 5] on some low fluorine concentration compounds gave F/Eu < 2·00. *All* the evidence we have accumulated, *except* for chemical analyses, interlocks and points to a lower limit of F/Eu = 2·00.

The conclusion that the low fluorine end of the solid solution is $EuF_{2\cdot00}$ is based on the following. The material obtained by H_2 reduction of EuF_3 in Mo boats corresponds to the low fluorine end of the composition range as evidenced by X-ray lattice parameter comparisons described in Section 3 (B). Agreement is obtained between the measured bulk density and the density calculated from the X-ray lattice parameter, if the composition is $EuF_{2\cdot00}$. Mössbauer effect data show only an Eu^{+2} isomer shifted absorption for this sample; none was observed for Eu^{0} or in the suspected vicinity for Eu^{+}. For samples of higher fluorine concentration, but for which chemical analysis indicated EuF < 2·00, isomer-shifted absorptions corresponding to Eu^{3+} *were observed*. Finally, one expects behavior similar to that for the Sm and Yb systems, for which the lower limit is $LnF_{2\cdot00}$. The accepted composition scale is therefore based on the values $EuF_{2\cdot00}$ for the H_2-reduced material, and $EuF_{3\cdot00}$ for material dehydrated under HF at 800°C (as explained in Section 3 (B)). The analytical result of $EuF_{2\cdot99}$ was taken for material 'A' as it was considered that decomposition was likely during melting, due to container failure.

These assumptions result in good agreement between the composition scales for series (a) and (c). Because the analytical results were apparently unreliable, the composition of material 'B' ($EuF_{2\cdot05}$) was established by its lattice parameter, using the accepted scale for series (c). The resulting scale for series (b), agrees with the other scales. Agreement between composition scales involves (1) agreement between lattice parameters and densities for samples of corresponding compositions calculated on the basis of the different scales over the region where these vary continuously, as well as (2) agreement between compositions for observed phase changes.

(C) Mixed fluorides of the type NdF_3–SmF_2 and PrF_3–SmF_2

A set of survey-type samples were prepared to examine fluorite f.c.c.-type solid solutions in mixed valance rare-earth fluoride systems. The NdF_3 and PrF_3 with SmF_2 were chosen for this preliminary survey since (1) pure starting materials for NdF_3 and PrF_3 were available as anhydrous single crystals, and (2) the Nd^{3+} Pr^{3+} and Sm^{2+} ions are highly colored (Sm ion species in the range of 2·00 ≤ F/Sm ≤ 2·45 are highly colored, and

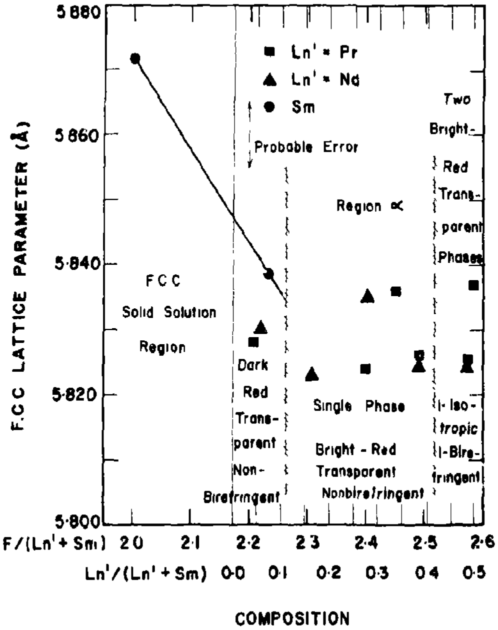

Fig. 6. Properties of mixed solutions of SmF_2 with PrF_3 and NdF_3.

characteristically colored according to the species present, as discussed in Section 3 (B). Sm^{2+} in dilute colorless and transparent solids such as $Sm^{2+}:CaF_2$ is a bright emerald green. (Incidently, the techniques described in this paper provide an extremely convenient method of preparing solid solutions of $Sm^{2+}:CaF_2$ and $Eu^{2+}:CaF_2$.) Pr^{3+} is green, and Nd^{3+} is lavender.

For solid solutions of this kind it is possible to vary one more degree of freedom besides the fluorine concentration; that is, it is also possible to vary the ratios of the two rare earths. Figure 6 is a composite of the X-ray data and the optical properties of the examined solid solutions. It is clear from the data presented that stable solid solutions are formed. Solid solutions of $Sm^{2+}:CaF_2$ prepared by the techniques described above using starting materials ranging in composition $2{\cdot}3 < F/Sm < 2{\cdot}6$ yielded solutions having the characteristic bright emerald green color of Sm^{2+}. This observation is consistent with what one would expect from a material whose ionic species are Sm^{2+} and Sm^{3+}. Definitive experiments involving perhaps optical spectra; ESR: and for solutions of EuF_2–LnF_3, the Mössbauer effect certainly would yield more detailed information regarding the +2 to +3 cationic ratios of both rare earths. It is hoped that some one will further investigate such systems.

Acknowledgements—We wish to thank E. Smathers and J. Hill for aid in the density measurements. Special thanks go to L. Rigdon for developing the quantitative analytical techniques. We thank K. Marsh for the oxygen γ-activation analyses. Special thanks go to E. Wrenn and R. Reiss for developing electron-beam welding equipment and techniques which made this study possible. We are grateful for the discussions with G. Smith on the X-ray structure data.

REFERENCES

1. THOMA R. E., In *Progress in the Science and Technology of the Rare Earths*, Vol. 2, p. 90. Pergamon Press, Oxford (1966).
2. TOPP N. E., In *The Chemistry of Rare Earth Elements*, pp. 63–70. Elsevier, Amsterdam (1965).
3. ASPREY L. B. and CUNNINGHAM B. B., In *Progress in Inorganic Chemistry* (Edited by F. A. Cotton), Vol. 2, pp. 269–272. Interscience, New York (1960).
4. ASPREY L. B., ELLINGER I. H. and STARITZKY E., *Proc. The Third Rare Earth Conf., Clearwater, Florida, April 1963* (Edited by K. S. Vorres), p. 11. Gordon and Breach, New York (1964).
5. LEE K., MUIR H. and CATALANO E., *J. Phys. Chem. Solids* **26**, 523 (1965).
6. SHORT J. and ROY R., *J. phys. Chem.* **67**, 1860 (1963).
7. ZINTL E. and UDGÅRD A., *Z. anorg. Chem.* **240**, 150 (1939).
8. KETELAAR J. A. A. and WILLEMS P. J H., *Rec. Trav. Chim.* **56**, 29 (1937).
9. IPPOLITOV E. G., GARASHINA L. S., MAKLACHKOV A. G., *Izv. Akad. Nauk. Neorg. Mat.* **3**, 73 (1967).
10. D'EYE R. W. M. and MARTIN F. S., *J. chem. Soc.* 1847 (1957).
11. ENGELMAN C., GOSSET J. and LOEUILLET M., *Bull. Soc. Chim. Fr.* 544 (1965).
12. RIGDON L. P. and SUNDERLAND W. E., Determinations of rare earths and fluoride in rare earth fluorides, UCRL-50383 (1968).
13. HILL J. H., FRAZER J. W. and SMATHERS E. R., Analytical chemistry Sect. Prog. Rep. Jan. 1–Dec. 31, 1966 (Compiled by J. Harrar). UCRL-50006-67-1.
14. McCLURE D. S. and KISS Z., *J. chem. Phys.* **39**, 3251 (1963).
15. GUGGENHEIM H. and KANE J. V., *Appl. Phys. Lett.* **4**, 172 (1964).
16. McGUIRE T. R. and SHAFER W. M., *J. appl. Phys.* **35**, 984 (1964).
17. ELLIOT R. P., *Proc. Fourth Rare Earth Res. Conf. Phoenix, Arizona, April 1964* (Edited by LeRoy Erying), p. 215 Gordon and Breach, New York (1965).
18. ZACHARIASEN W. H., *Acta crystallogr.* **4**, 231 (1951).
19. FRAUENFELDER M., In *The Mössbauer Effect*. Benjamin, New York (1962).
20. BOYLE A. J. F. and HALL H. E., *Rep. Prog. Phys.* **25**, 441 (1962).
21. KISTNER O. C. and SUNYAR A. W., *Phys Rev. Lett.* **4**, 412 (1960).
22. WALKER L. R., WERTHEIM G. K. and JACCARINO V., *Phys. Rev. Lett.* **6**, 98 (1961).
23. SHIRLEY D. A., *Rev mod. Phys.* **36**, 339 (1964).
24. BRIX P., HÜFNER S., KIENLE P. and QUITMANN D., *Phys. Lett.* **13**, 140 (1964).
25. BARRETT P. H. and SHIRLEY D. A., *Phys. Rev.* **131**, 123 (1963).
26. MUIR A. H., Jr., ANDO K. J., and COOGAN H. M., In *Mössbauer Effect Data Index 1958–1965*. Interscience, New York (1966).
27. MALETTA H., HEIDRICH W and MÖSSBAUER R. L., *Phys. Lett* **25A**, 295 (1967).

J. Phys. Chem. Solids Pergamon Press 1969. Vol. 30, pp. 1629–1631. Printed in Great Britain.

TECHNICAL NOTES

Activation energy from thermoluminescence and phosphorescence of α-Al_2O_3

(*Received* 26 *February* 1968; *in revised form* 13 *December* 1968)

THERMOLUMINESCENCE in α-Al_2O_3 crystals activated by short wavelength electromagnetic radiation has been studied by various authors [1–5]. As a result the main peaks in the glow curve are well-known.

However, the activation energies derived from these glow peaks, using expressions from [7–9] show large discrepancies, which in part may be due to the assumption of one discrete trap depth instead of a contribution of different depths. We like to suggest that the phosphorescence decay is less sensitive to such a distribution and therefore we investigated both phosphorescence and thermoluminescence in α-Al_2O_3 activated by ^{60}Co-gamma radiation. The analysis is given in terms of the monomolecular theory of Randall and Wilkins [6].

Phosphorescence decay was measured at a sequence of at least eight different temperatures on each of the ascending slopes of the four peaks in the glow curve of α-Al_2O_3 shown in Fig. 1.

The glow curve was obtained after one hour irradiation in a ^{60}Co-source, the dose was 16000 rad./hr. This dose saturated peaks II, III and IV while peak I reached $\frac{3}{4}$ of its saturation. The growth of luminescent intensity could be described as $I = I_\infty . \{1-\exp(-at)\}$.

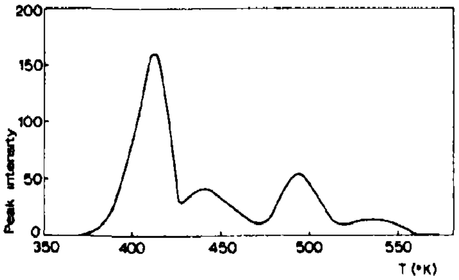

Fig. 1. Glow curve of α-Al_2O_3 after ^{60}Co-gamma radiation (dose 16,000 rad.).

For relative intensities and absorption constants see Table 1.

Table 1. *Saturation of four luminescent peaks following* $I = I_\infty . \{1-\exp(-at)\}$ *in a flux of* 16,000 *rad./hr*

	T_m (°K)	I_∞ rel. units	a (min^{-1})
Peak I	412	36	0·00153
Peak II	441	7	1·29
Peak III	494	8·5	0·0555
Peak IV	538	2·6	0·1245

In order to determine the phosphorescence decay of each of the following peaks we annealed the foregoing one at a temperature such that the rest of the glow curve remained essentially the same. The decay of phosphorescence for all four peaks turns out to be exponential over long periods of time; the measuring time is limited by the decay constant and the dark current of the photomultiplier.

In Fig. 2. the phosphorescence intensity I vs. time is given for peak IV, the phosphorescence decay of the other peaks is of the same nature. For each sequence the decay constants vs. T^{-1} were by least square method fitted to a straight line on a semi logarithmic scale using a digital computer (Fig. 3).

The slopes of the lines give the activation energy E, whereas extrapolation towards $T^{-1} = 0$ yields the frequency factor s; E and $\log s$ are tabulated in Table 2.

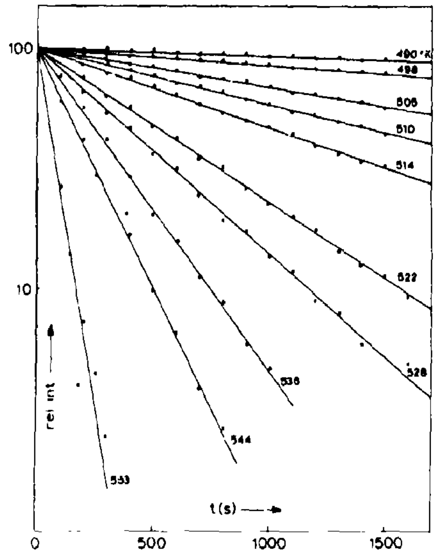

Fig. 2. Phosphorescence decay of peak IV, following $I = I_0 \exp(-at)$.

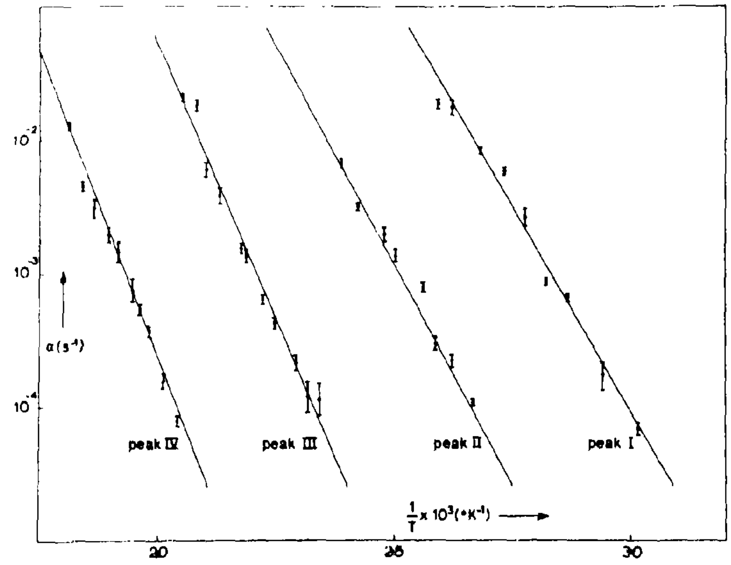

Fig. 3. Phosphorescence decay constants vs T^{-1} of four luminescent peaks in α-Al_2O_3 least squares fitted to a straight line

Table 2. Activation energies and frequency factors of four luminescent peaks

	Peak I	Peak II	Peak III	Peak IV
T_m (°K)	412	441	494	538
log s	14·3	13·6	15·4	14·7
E (eV)				
phosphorescence	1·22	1·31	1·65	1·82

The errors in the determination of E and log s are estimated to be about 1 and 10 per cent respectively.

DISCUSSION

The growth of the four luminescent peaks between 400 and 540°K in γ-activated α-Al_2O_3 is exponential, the growth-rates of which are listed in Table 1. The phosphorescence decay of these peaks is exponential too over long periods of time in spite of seemingly conflicting evidence in the literature[1, 5, 10]. Decay constants can be found in Fig. 3. In contrast to our work these authors observed the *transient phosphorescence at room temperature* immediately after excitation with visible light or u.v. The transient phosphorescence can be considered as the response of traps which are unstable at room temperature upon the sudden removal of the stimulating field. This phenomenon has also been observed by us after gamma excitation but it is not reported here. In our experiments we waited until this phenomenon had died out before we began our measurements.

The activation energies, derived directly from a plot of the phosphorescence decay constants vs. T^{-1} and the frequency factors given in Table 2 do not seem to be unreasonable.

Acknowledgements—One of the authors, J. B. van Tricht, wishes to express his thanks to Professor Dr. J. J. van Loef for his vivid interest in this work.

Reactor Instituut,
Delft,
The Netherlands

J. B. VAN TRICHT
B. A. M. VAN DER KRAAY

REFERENCES

1. GABRYSH A. F., EYRING H., LE FEBRE V. and EVANS M. D., *J. appl. Phys.* **33**, 3389 (1962)
2. VISHNEVSKY V. N., GNYP R. G., PIDZYRAILO N. S. and TOLCHINSKAYA R. M., *Ukr fiz. Zh.* **11**, 991 (1967)
3. GABRYSH A. F., KENNEDY J., EYRING H. JOHNSON V., *Phys. Rev.* **131**, 1543 (1963)
4. RIEKE J. K. and DANIELS F., *J. phys. Chem.* **61**, 629 (1957).
5. LEHMANN H. W. and GUNTHARD H. H., *J. Phys. Chem. Solids* **25**, 941 (1964).
6. RANDALL J. T. and WILKINS M. H. F., *Proc. phys. Soc.* **A184**, 366 (1945).
7. GROSSWEINER L. I., *J. appl. Phys.* **24**, 1306 (1953)
8. LUSHCHIK Ch. B., *Soviet Phys. JETP* **3**, 390 (1956)
9. BOOTH A. H., *Can. J. Chem.* **32**, 214 (1954)
10. COOP W. H. and HAMMOND J. A., *J. opt. Soc. Am.* **52**, 835 (1952).

J. Phys. Chem. Solids Vol 30, pp 1631–1635

Anion reduced ionic conductivity in LiF

(*Received* 25 *July* 1968, *in revised form* 22 *November* 1968)

THE EFFECT of aliovalent cations on the ionic conductivity of alkali halide crystals has been well documented. Both theoretical[1] and experimental studies[2, 3] have shown how these cations in solution lead to an increase in the ionic conductivity at low temperatures. To date, there has been little work on the effect of aliovalent anionic impurities on ionic conduction. It has been demonstrated that anions can bring about significant reductions in ionic conductivity, and can extend the range of intrinsic conduction to lower temperatures[4–6]. Since the only previous work on anion doping in LiF used OH^- as the dopant[7], experiments were undertaken to determine the effect of oxygen on the low temperature conductivity in LiF.

The starting materials were Fisher grade, reagent LiF powder and high purity Li_2O powder. Mixtures containing one, three, and five mole per cent Li_2O were prepared by thoroughly mixing the powders prior to melting. Single crystals were pulled from the melt at a rate of 1 in./hr with a rotation speed of 5 rev/min. The melt was contained in a high purity graphite crucible, which had been previously vacuum degassed. The furnace chamber was evacuated prior to melting, than filled with purified argon to a pressure of 5 psig. Single crystals with more than ~3 mole per cent Li_2O were almost completely cloudy, indicating the presence of gross precipitation; these crystals were not used for conductivity measurements. Slabs approximately 1 cm × 1 cm × 0·1 cm were cleaved from the transparent regions of the 'as-grown' crystals and Dag[8] was painted on the large surfaces to serve as electrodes.

The specimens were mounted between graphite electrodes in an evacuated stainless steel container. D.C. conductivity measurements were made by applying a constant 240 V to the specimens at room temperature; after the steady state current had been reached (monitored by a Keithly 610 A electrometer), heating was commenced. A furnace was placed around the container and slowly heated from room temperature to ~350°C at a rate of ~2·5°C/min. The temperature was measured by a thermocouple placed just above the specimen. Following the technique described by Sutter and Nowick[9], the steady state current was used to calculate the conductivity. However, at temperatures in excess of 300°C the discharge of ions, due to the constant voltage, was so rapid that the specimen was often destroyed. This necessitated the use of one-second pulsed voltages at these temperatures to measure the current. An oscilloscope was used to check that the currents measured by the electrometer were not due to initial transients. Following the conductivity measurements, the specimens were cleaved in half; one half used for infrared measurements, the other for chemical analysis. The results of the chemical analysis are shown in Table 1.

Figure 1 shows the results, upon heating, for specimens with 0·9 and 2·6 mole per cent Li_2O. These were grown from nominally doped mixtures of 1·0 and 3·0 mole per cent Li_2O. For comparison purposes, a conductivity curve for an undoped, nominally pure specimen is also shown. By assuming the data to fit a curve of the form $\sigma T = (\sigma T)_0 \exp - Q/KT$, a least squares analysis of the data was used to obtain the slope and intercept; these values are shown in Table 2.

As Fig. 1 shows, introduction of Li_2O in LiF brings about marked changes in the conductivity. A reduction in conductivity by as much as a factor of ~100 was observed for the specimen doped with 0·9 mole per

Table 1. *Chemical analysis (all in mole per cent)*

LiF powder (manufacturers analysis)	Li_2O powder	Undoped specimen	Oxygen doped specimens
0·001% Pb	< 0·001 Si	0·005% Mg	0·006% Mg
0·005% Cl		< 0·001% Fe	< 0·001% Fe
		< 0·001% Si	0·001% Si
		< 0·001% Cu	< 0·001% Cu

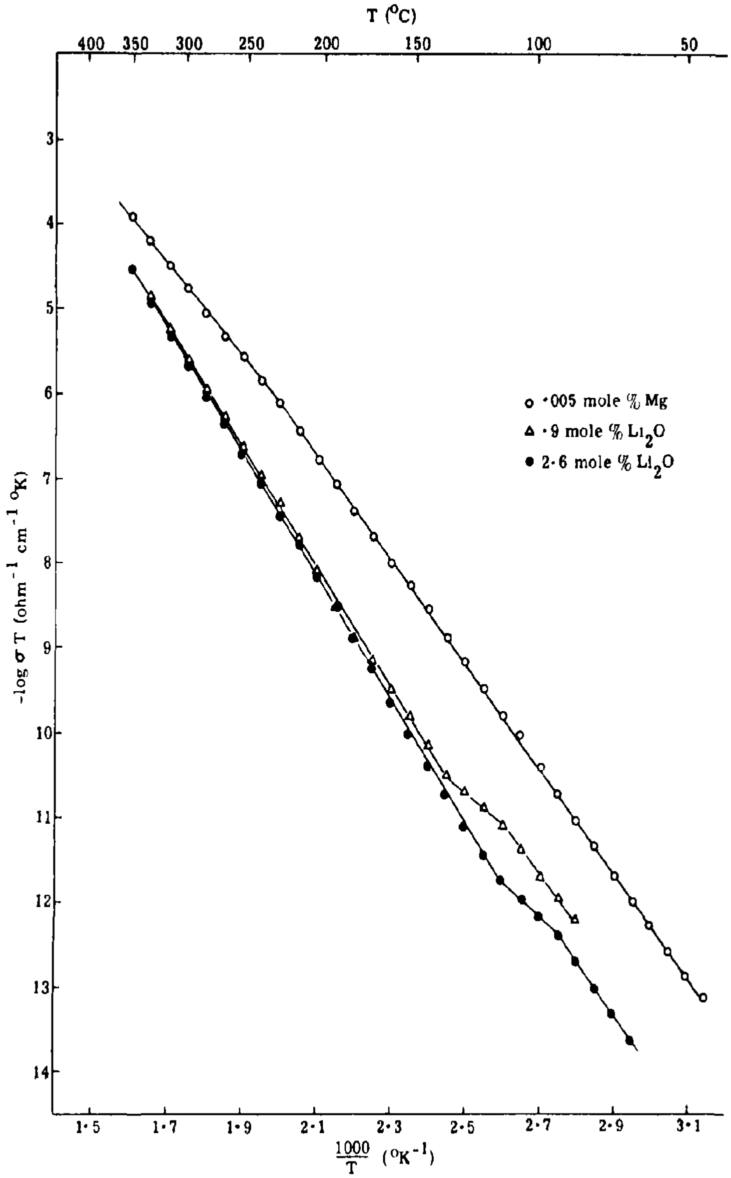

Fig. 1 Conductivity of LiF single crystals showing the effect of Li_2O

cent Li_2O, but a threefold increase in the Li_2O concentration produced no further decrease in conductivity. The decrease is accompanied by a region in which the activation energy associated with the conductivity shows a significant increase (Table 2). The temperature, at which this high activation energy region begins, increases with decreasing Li_2O concentration. Finally, the low temperature behavior of the oxygen doped crystals appears to be similar to the normal conductivity processes in anion-free LiF[10].

Large reductions in conductivity have been observed when alkali halide crystals were

Table 2. Constants for the equation $\sigma T = (\sigma T)_0 \exp - Q/KT$

Specimen	Temperature	$(\sigma T)_0$	Q
	(°C)	(Ω^{-1} cm^{-1} °K)	(eV)
LiF (undoped)	44–227	$8{\cdot}8 \times 10^5$	1·202
	227–394	$1{\cdot}7 \times 10^5$	1·131
LiF (0·9 mole per cent Li_2O)	84–111	$1{\cdot}0 \times 10^3$	1·079
	111–135	$1{\cdot}2 \times 10^{-1}$	0·774
	135–333	$6{\cdot}3 \times 10^6$	1·405
LiF (2·6 mole per cent Li_2O)	66–90	$1{\cdot}5 \times 10^4$	1·197
	90–111	$6{\cdot}0 \times 10^{-1}$	0·879
	111–352	$1{\cdot}6 \times 10^7$	1·454

doped with anions[4–6, 11–13]. This reduction in conductivity has usually been associated with the extension of intrinsic behavior to lower temperatures than could be obtained by a reduction in cation concentration. However, as will be shown, the results reported here cannot be considered an extension of intrinsic conductivity.

By extrapolating the results of recent conductivity measurements[14] in very pure LiF (with a divalent cation impurity concentration of ~ 0·1 ppm), the intrinsic conductivity (σT) at 127°C would be expected to be $4 \times 10^{-17} \Omega^{-1}$ cm^{-1} °K. In the specimen doped with 2·6 mole per cent Li_2O, the observed value of σT at the break in the curve, at 127°C, is $5 \times 10^{-11} \Omega^{-1}$ cm^{-1} °K. Because of the great difference between conductivity of the oxygen doped specimens and the high-purity LiF, it does not seem likely that the results presented here can be explained on the basis of intrinsic conduction.

All of the observations can be explained if it is assumed that the conductivity is controlled by the dissolution of either Li_2O or a multivalent metal oxide (MO) that had precipitated during previous cooling. At low temperatures, below the temperature range 110°–135°C (the exact temperature depending on the Li_2O concentration), the kinetics of solution of the oxide are so sluggish that normal conductivity processes[2] take place prior to what appears to be a transition range in the vicinity of 100°C.

If the upper part of the curve is assumed to be due to the solution of aliovalent cation oxides (MO), it does not seem likely, in view of the large oxygen concentration, that there would be sufficient aliovalent cations present at low temperatures to produce a conductivity region where the activation energy can be associated with that previously reported for Mg^{2+} vacancy association[14]. If we further assume that there are sufficient multivalent cations left after cooling to produce the low temperature region, then it is difficult to account for the upper part of the curve on the basis of the solution of MO.

As the temperature increases above the transition region, dissolution of the oxide begins. The temperature at which this dissolution begins appears to depend on the bulk Li_2O concentration. Once dissolution starts, because of the high activation energy associated with the process, the conductivity is only governed by dissolution of the oxide; hence, both specimens show the same conductivity. Similar behavior has been observed in KBr doped with K_2CO_3, and was attributed to precipitation of K_2CO_3[15].

Large reductions in the ionic conductivity of LiF doped with OH^- have been reported [7]. To eliminate the possibility that the behavior reported here is due to OH^- (formed by hydrolysis of Li_2O prior to, or during crystal growth), infrared examination of the specimens was performed. The i.r. spectra showed neither the sharp line spectra between

2·71 and 2·83 μ observed in crystals doped with >50 ppm Mg (the line spectra presumably associated with Mg:OH complexes); nor the broadband at 2·68 μ, which is thought[7] to be a measure of free OH^- ions in the crystal. While the specimen thickness is used in this study is three to six times less than Stoebe's[7] specimens, the dopant concentration is at least 20 times larger; thus the sensitivity for OH^- detection should be at least as good as in the earlier work. Analysis for oxygen showed the concentrations given in Fig. 1; no other anionic impurities were detected.

The conclusion is that the reduced conductivity observed in oxygen doped LiF specimens in the temperature range ~ 120°C to 350°C is due to the solution of Li_2O upon heating and its subsequent precipitation upon cooling.

Research Department, GARY GESCHWIND
Grumman Aircraft Engineering Corporation,
Bethpage, L.I., N.Y. 11714,
U.S.A

REFERENCES

1. LIDIARD A. B., In *Handbuch der Physik*, Vol XX. Springer, Berlin (1957).
2. DREYFUS R. W. and NOWICK A. S., *Phys. Rev.* **126**, 1367 (1962).
3. SUPTITZ P. and TELTOW J., *Phys. Status Solidi* **23**, 9 (1967)
4. GRUZENSKY P. M. and SCOTT A. B., *J. Phys. Chem. Solids* **21**, 128 (1961)
5. REDFERN B. A. W and PRATT P. L., *Proc. Brit. ceram. Soc.* **1**, 173 (1964).
6. PASHKOVSKII M. V., TSAL N. A. and TKACHUK A.D., *Soviet Phys. solid St.* **5**, 853 (1963).
7. STOEBE T. G., *J. Phys. Chem. Solids* **28**, 1375 (1967)
8. Dag Dispersion No. 154, Acheson Colloid Co., Port Huron, Michigan.
9. SUTTER P. H. and NOWICK A. S., *J. appl. Phys.* **34**, 734 (1963).
10. GESCHWIND G., *J. Am Ceram Soc* **51**, 539 (1968)
11. HAVEN Y., *Rec. Trav Chim.* **69**, 1471 (1950).
12. FRITZ B., LUTY F. and ANGER J., *Z. Phys.* **174**, 240 (1963).
13. KESSLER A. and MARIANI E., *Czech. J. Phys.* **178** (1967).
14. PERIO P., DUBOIS M., BERGE P. and BLANC G., *J. phys. Soc. Japan Suppl. III*, **18**, 363 (1963).
15. ROLFE J., *Can. J. Phys.* **42**, 2195 (1964).

J. Phys. Chem. Solids Vol. 30, pp. 1635–1636.

ESR study of simultaneous optical bleaching and X-irradiation of KCl

(*Received* 18 *November* 1968)

OPTICAL absorption studies of the production of F centers in KCl subjected to simultaneous optical bleaching and γ irradiation have been reported[1]. The ESR studies reported here yield results in close agreement with those of the optical absorption studies.

A helical slow wave assembly[2] was constructed of silver wire and magnetically coupled to the waveguide fields in the sample arm of a commercial *x*-band spectrometer system. Coaxial X-ray irradiation and white light illumination facilities were directed at a single crystal of KCl within the helical assembly. Irradiation was done at room temperature with 40 KVP X-rays at dose rates to samples up to 45,000 R/min. This arrangement was particularly convenient since no movement of the sample was necessary throughout the experiment.

Figure 1 illustrates the differences in the rates of production of F centers between crystals irradiated in darkness, bleached, and re-irradiated (crystal A) and crystals simul-

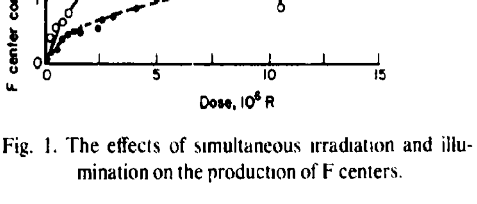

Fig. 1. The effects of simultaneous irradiation and illumination on the production of F centers.

taneously irradiated and bleached then irradiated in darkness (crystal B). The differences between the curves, as discussed in reference[1], vary as a function of dose rate precisely as determined by the optical absorption techniques.

This experiment serves to corroborate results obtained by other techniques and point out the usefulness of the helical assembly as a tool in radiation damage research.

Physics Department,
Emory University,
Atlanta, Ga. 30322,
U.S.A.

R. E PIAZZA*

REFERENCES

1. MATHEWS J. W., MALLARD W. C. and SIBLEY W. A., *Phys. Rev.* **146**, 611 (1966)
2. WEBB R. H., *Rev. scient Instr.* **33**, 732 (1962)

---

*Present address: Department of Physics and Astronomy, University of Massachusetts, Amherst, Mass 01002, U S A

J. Phys. Chem Solids Vol 30, pp 1636–1638

Distribution coefficient and acceptor valency of tin in bismuth

(*Received* 4 *November* 1968)

ONCE THE relation between the density of a dope material in bismuth and the excess charge carrier density it brings about is established, the saturation value of the Hall coefficient at very low temperatures enables one to determine the dope density in a region where spectrochemical analyses attain qualitative results only. In much the same way as has been followed with tellurium in bismuth[1], the valency of tin in bismuth is determined by radioactive tracer methods, and distribution coefficients are then inferred from Hall coefficient measurements.

Metallic tin was dissolved in a bismuth (99·9999 per cent spectrochemically pure) melt at 600°C. The tin had previously been irradiated with thermal neutrons and thus contained radioactive nuclei, viz. mainly Sn^{113}, Sn^{125}, and the latter's daughter Sb^{125}. A monocrystal was pulled from this melt. After Hall measurements were carried out, the sample was divided into parts of about 0·07 g. The activity of the isotope Sn^{113} ($t/2 = 118\,d$) in each part was measured through the photo peak of its 0·39 MeV gamma ray with a Ge(Li) detector. The results are given in Fig. 1. Comparison with the activity of a tin standard of known weight pertained to a tin density in the sample represented by the right-hand scale in Fig. 1. No explanation can be given for the fact that, contrary to expectations, the tin concentration found in the crystal parts grown first are relatively higher.

Hall coefficient measurements were carried out at 4·2°K. The Hall coefficients saturated in a magnetic field of 10 kG. Their saturation values were positive and from them the excess hole densities were derived[2]. A comparison of the hole densities with the tin densities is given in Fig. 1. The one-to-one correspondence found leads to the conclusion, already suggested by the periodic table and earlier drawn on less firmly based evidence[2], that tin is a monovalent acceptor in bismuth. Much uncertainty about this figure had existed[3].

From melts which contained about 70 wt ppm tin some crystals were pulled at different growth rates, the rotation rate being 15 rev/min. Values of the effective distribution coefficient of the dope material were deduced from the Hall coefficient saturation values following the procedure described above. The results are given in Fig. 2 as a function of growth rate. Burton, Prim, and Slichter[4] have given a theory that relates the effective distribution coefficients at different growth rates to the equilibrium distribution coefficient.

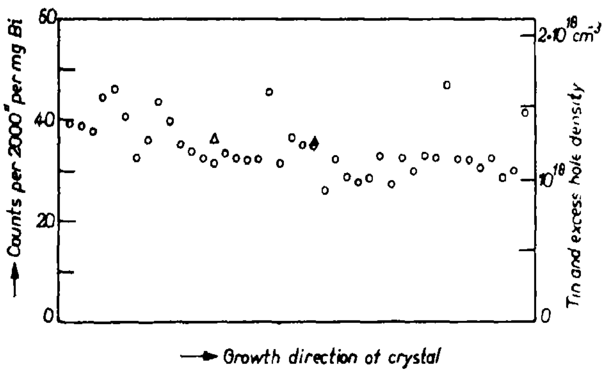

Fig. 1. Tin densities from radioactive tracer analysis (circles), and acceptor-added hole densities from Hall coefficient measurements (triangles) along the growth direction of a bismuth crystal.

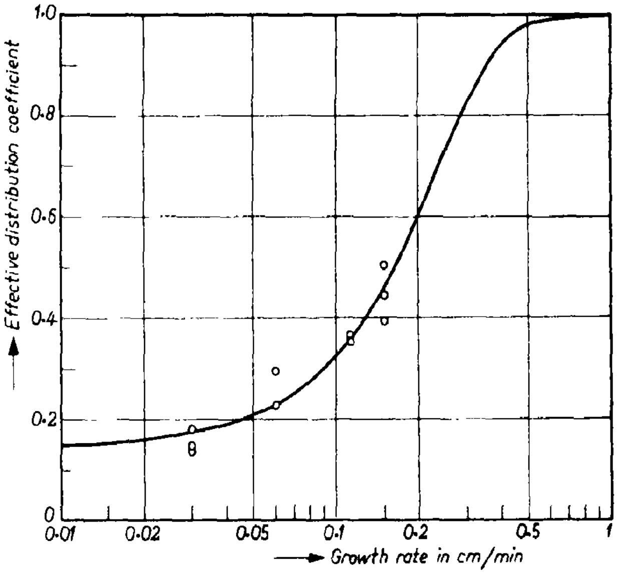

Fig. 2. Effective distribution coefficient of tin in bismuth as a function of crystal-growth rate, while the rotation rate was 15 rev/min The line gives the best fit of the experiments to theory.

Here the best fit with theory yields an equilibrium distribution coefficient of 0·13 for small amounts of tin in bismuth.

With the viscosity value of liquid bismuth cited in[1], the diffusion coefficient of tin in liquid bismuth at about 275°C is calculated to be $1{\cdot}6 \times 10^{-5}$ cm^2/sec. Niwa *et al.*[5] measured this diffusion coefficient in the temperature range 450°–600°C. The extrapolation of their data to 275°C results in a value of $2{\cdot}8 \times 10^{-5}$ cm^2/sec.

Acknowledgements—Thanks are due to Dr. E. Bruninx and Mr J. E. Crombeen for performing the radioactive tracer analysis.

J. M. NOOTHOVEN VAN GOOR
H. M. G. J. TRUM

Philips Research Laboratories,
N. V. Philips Gloeilampenfabrieken,
Eindhoven,
The Netherlands

REFERENCES

1. NOOTHOVEN van GOOR J. M. and TRUM H. M. G. J., *J. Phys. Chem. Solids* **29**, 341 (1968).
2. SCHULTZ B. H. and NOOTHOVEN VAN GOOR J. M., *Philips Res. Rep.* **19**, 103 (1964).
3. JAIN A. L. and KOENIG S. H., *Phys. Rev.* **127**, 442 (1961).
4. BURTON J. A., PRIM R. C. and SLICHTER W. P., *J. chem. Phys.* **21**, 1987 (1953).
5. NIWA K., SHIMOJI M., KADO S., WATANABE Y. and YOKOKAWA T., *Trans. Am. Inst. Min. Metall. Engrs* **209**, 96 (1957).

J. Phys. Chem. Solids Vol. 30, pp. 1638–1642.

Elastic Grüneisen parameters in crystals of low symmetry*

(*Received* 1 *November* 1968)

The Grüneisen parameters play an important role in the theory of anharmonic effects in solids, and their properties and behavior in cubic crystals have been extensively investigated[1–5]. Recently, Brugger[6] has formulated a generalized scheme of Gruneisen mode parameters in crystals of any symmetry. In the present note, the relations between the mode Gruneisen parameters and the pressure derivatives of the elastic moduli in several crystal classes of lower symmetry than cubic will be derived. The results will be applied to some materials where experimental data are available.

An anisotropic continuum model, neglecting dispersion, will be assumed. In addition, the discussion will be limited to crystal structures where the linear thermal expansion tensor α_{ij} referred to crystalline axes is diagonal, and the elastic compliance moduli s_{ij} obey the relation:

$$s_{ij} = 0; \quad i = 1, 2, 3; \quad j = 4, 5, 6. \qquad (1)$$

These assumptions limit the treatment to cubic, tetragonal, hexagonal and orthorhombic crystals.

The general mode Grüneisen parameter for a mode of wave vector **q** and polarization index p is defined as[7]:

$$\gamma^p_{jk} = -[\partial \ln \omega_p(\mathbf{q})/\partial \eta_{jk}]_T; \quad j, k = 1, 2, 3 \qquad (2)$$

where η_{ij} are the Lagrangian strains, $\omega_p(\mathbf{q})$ the frequency of the mode **q**, p. Confining the strain to hysrostatic pressure P, we have the relation[6]:

$$[\partial \ln \omega_p(\mathbf{q})/\partial P]_T = -s^T_{iijk}[\partial \ln \omega_p(\mathbf{q})/\partial \eta_{jk}]_T \qquad (3)$$

where summation over repeated indices is implied. In our case, $\eta_{ij} = 0$ for $i \neq j$, and as a result of equation (1) we have:

$$[\partial \ln \omega_p(q)/\partial P]_T = \sum_{i,j=1}^{3} s^T_{ij}\gamma^p_j(q) \qquad (4)$$

the mode gamma tensor being diagonal. Now, as we neglect dispersion, $\omega_p(q)$ is given by:

$$\omega_p(q) = qs_p(\theta, \phi). \qquad (5)$$

---

*This work was performed under the auspices of the United States Atomic Energy Commission.

But,

$$q \propto (L_1^2 + L_2^2 + L_3^2)^{-1/2} \tag{6}$$

where L_1, L_2 and L_3 are the lengths of the crystal parallel to the x, y and z axes, and $s_p(\theta, \phi)$ is the sound velocity for the mode $\mathbf{q}, p$. Hence, one obtains the relation:

$$[\partial \ln \omega_p(\mathbf{q})/\partial P]_T = (l^2 K_1^T + m^2 K_2^T + n^2 K_3^T) + [\partial \ln s_p(\theta, \phi)/\partial P]_T \tag{7}$$

where K_1^T, K_2^T and K_3^T are the isothermal linear compressibilities in the directions of the crystalline axes, and l, m, n, are the *direction cosines of* $\mathbf{q}$. Denoting the elastic stiffness modulus associated with the mode q, p by c_p, one obtains:

$$(\partial \ln \omega_p(\mathbf{q})/\partial P) = l^2 K_1^T + m^2 K_2^T + n^2 K_3^T - 0{\cdot}5\, K_1^T + 0{\cdot}5(\partial \ln c_p/\partial P)_T \tag{8}$$

where K_1^T is the isothermal volume compressibility. Thus, we have

$$\sum_{i,j=1}^{3} s_{ij}\gamma_j^p(\mathbf{q}) = l^2 K_1^T + m^2 K_2^T + n^2 K_3^T - 0{\cdot}5 K_1^T + 0{\cdot}5(\partial \ln c_p/\partial P)_T. \tag{9}$$

Defining now an averaged mode gamma

$$\gamma^p(\mathbf{q}) = \left(\sum_{i,j=1}^{3} s_{ij}\right)^{-1} \times \left[\sum_{i,j=1}^{3} s_{ij}\gamma_j^p(\mathbf{q})\right] \tag{10}$$

one obtains

$$\gamma^p(\mathbf{q}) = [l^2 K_1^T + m^2 K_2^T + n^2 K_3^T - 0{\cdot}5 K_1^T + 0{\cdot}5(\partial \ln c_p/\partial P)_T] \Big/ \left(\sum_{i,j=1}^{3} s_{ij}\right) \tag{11}$$

As can be seen the individual mode gammas $\gamma_i^p(\mathbf{q})$ cannot be deduced from the pressure derivatives of the elastic moduli alone, but only their weighted average. In order to determine the individual $\gamma_i^p(\mathbf{q})$, uniaxial as well as hysrostatic pressure derivatives of the elastic moduli are required.

The Grüneisen parameter, defined by

$$\gamma = \beta V \Big/ \left(C_V \sum_{i,j=1}^{3} s_{ij}\right) \tag{12}$$

where β is the volume expansion thermal expansion coefficient ($\beta = \alpha_1 + \alpha_2 + \alpha_3$), C_V the specific heat at constant volume V, is given by[7]

$$\gamma = \left[\sum_{q,p} C_p(\mathbf{q})\gamma^p(\mathbf{q})\right] \Big/ \left[\sum_{q,p} C_p(\mathbf{q})\right] \tag{13}$$

where $C_p(\mathbf{q})$ is the specific heat associated with the mode $\mathbf{q}, p$. The low and high temperature limits of the Grüneisen parameter, γ_L and γ_H may be easily calculated, as at the low temperature limit $C_p(\mathbf{q}) \propto c_p^{-3/2}$, while in the high temperature limit $C_p(\mathbf{q}) = kT$. Hence, in these two limiting cases the sum in equation (13) may be evaluated in a straight forward manner.

A computer program for the CDC 3600 computer which evaluates the averaged mode gammas $\gamma^p(\mathbf{q})$, as well as γ_L and γ_H in crystals of cubic, hexagonal, tetragonal and orthorhombic symmetry has been written. The input data to the program are the room temperature elastic moduli, their pressure derivatives, and the low temperature elastic moduli. The program computes the sound velocity in any direction by calculating the eigenvalues of the Christoffel determinant[8], as well as the pressure derivatives in any direction. From the latter quantities the $\gamma^p(\mathbf{q})$ as function of direction are determined. γ_L and γ_H are evaluated by numerical quadrature.*

The above program has been applied to three materials of hexagonal symmetry, where the values of the elastic moduli and their pressure derivatives are available, i.e. magnesium[9, 10], cadmium[11, 12] and cadmium sulfide[13, 14]. Since the hexagonal structure has transverse symmetry, the $\gamma^p(q)$ need only be evaluated as a function of the latitude angle θ. The results of the computation are shown in Figs. 1–3, where $p = 1$ is the longitudinal mode, $p = 2$ the fast shear mode, and

---

*A write-up of the program may be obtained from the author upon request.

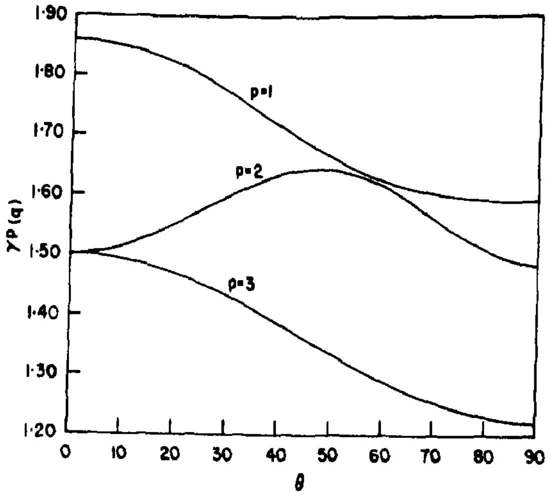

Fig. 1 $\gamma^p(\mathbf{q})$ as a function of θ for Mg.

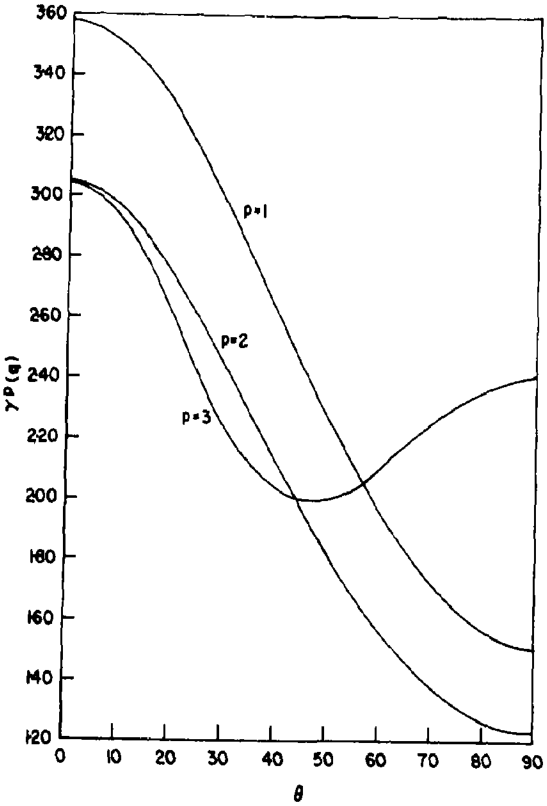

Fig. 2. $\gamma^p(\mathbf{q})$ as a function of θ for Cd.

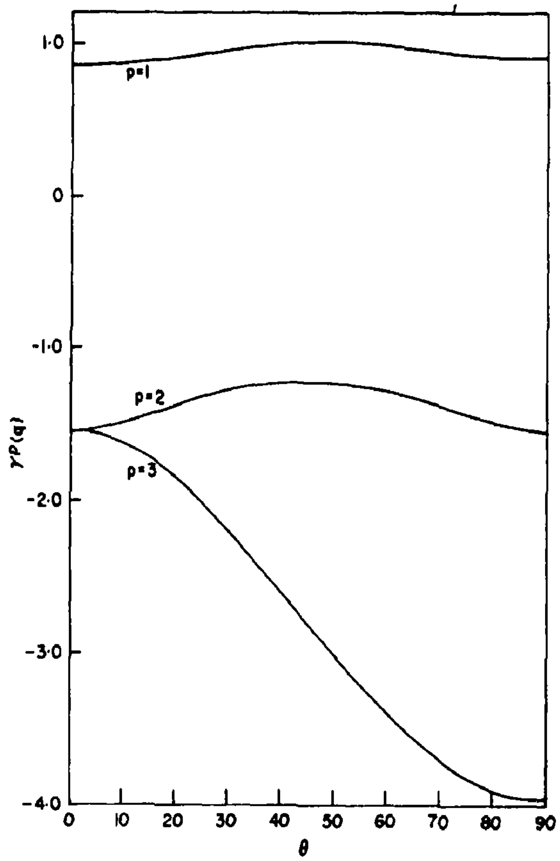

Fig. 3. $\gamma^p(q)$ as a function of θ for CdS.

Table 1. *The values of* γ_L *and* γ_H *for* Mg, Cd *and* CdS, *as obtained from elastic and thermal expansion data*

	Elastic data		Thermal expansion data	
	γ_l	γ_H	γ_L	γ_H
Mg	1·45	1·52	1·40(10°K) [7]	1·50(300°K) [7]
Cd	2·16	2·06	2·10(20°K) [16, 18]	1·86(300°K) [16, 18]
CdS	−2·19	−1·19	−2·34(20°K) [15, 18]	0·45(300°K) [15, 18]

$p = 3$ the slow shear mode. In Table 1 the values of γ_L and γ_H as obtained from elastic data, are compared with the similar quantities derived from thermal expansion data. As can be seen, the agreement between the two sets of data is very good for magnesium and cadmium, while in the case of cadmium sulfide, there are large discrepancies between the thermal expansion and elastic γ_H. This is not surprising, as such discrepancies are expected when optical phonons contribute appreciably to the lattice vibration spectrum [4], which is the case for cadmium sulfide. The thermal expansion value of γ_L contains probably some error, as the values of the low temperature thermal expansion coefficient were determined from data of the lattice parameter as a function of temperature [15].

It is interesting to note that the negative thermal expansion coefficient of cadmium at low temperatures [16, 17] is not reflected in $\gamma^p(\mathbf{q})$ becoming negative. This is probably due to the dominance of the modes with positive values of $\gamma^p(\mathbf{q})$ in the averaging process. On the other hand, in the case of cadmium sulfide, the $\gamma^p(\mathbf{q})$ for the shear modes are both negative throughout, as well as γ_L. This is in agreement with the fact that both thermal expansion coefficients of cadmium sulfide become negative at low temperatures.

Acknowledgements—The author wishes to express his gratitude to F. S. Fisher for many helpful discussions and comments. He is also indebted to the Metallurgy Division, Argonne National Laboratory, for the award of a summer appointment during the tenure of which this work was done.

Argonne National Laboratory,
Argonne, Ill 60439,
U.S.A.
D. GERLICH†

REFERENCES

1. SLATER J. C., In *Introduction to Chemical Physics* McGraw Hill, New York (1939).
2. SHEARD F. W., *Phil. Mag.* **3**, 1381 (1958).
3. COLLINS J. G., *Phil. Mag.* **8**, 323 (1963).
4. SCHUELE D. E. and SMITH C. S., *J. Phys. Chem. Solids* **25**, 801 (1964).
5. HIKI Y., THOMAS J. F., and GRANATO A. V., *Phys. Rev.* **153**, 764 (1957).
6. BRUGGER K., *Phys. Rev.* **137**, A1826 (1965).
7. COLLINS J. G. and WHITE G. K., In *Progress in Low Temperature Physics* (Edited by C. J. Gorter), Vol. IV, p. 450. North-Holland, Amsterdam (1964).
8. MASON W. B., In *Physical Acoustics and Properties of Solids*. Van Nostrand, Princeton, N.J. (1958).
9. EROS S. and SMITH C. S., *Acta metall.* **9**, 14 (1961).
10. SCHMUNK R. E. and SMITH C. S., *J. Phys. Chem. Solids* **9**, 100 (1959).
11. GARLAND C. W. and SILVERMAN J., *Phys. Rev.* **119**, 1218 (1960); *ibid.* **127**, 2287 (1962).
12. CORLL J. A., Case Inst. Technol. O.N.R. Tech. Rep. No. 6 (1962).
13. GERLICH D., *J. Phys. Chem. Solids* **28**, 2575 (1967).
14. CORLL J. A., *Phys. Rev.* **157**, 623 (2967).
15. REEBER R. R., *Proc. Symp. Therm. Exp. Solids* To be published
16. MADAIAH N. and GRAHAM G. M., *Can. J. Phys.* **42**, 221 (1964).
17. WHITE G. K., In *Proc. 7th Int. Conf. Low Temp. Phys.*, p. 685 University of Toronto Press (1961).
18. *American Instiute of Physics Handbook* McGraw Hill, New York (1957).

---

†*Permanent address*: Physics Department, Tel Aviv University, Ramat Aviv, Israel.

J. Phys. Chem. Solids Vol. 30, pp. 1642–1644.

Antiferromagnetic structures of USb and UBi*

(*Received* 28 *August* 1968, *in revised form* 1 *October* 1968)

THE URANIUM compounds with group VA elements (N, P, As, Sb, and Bi, denoted by v) that have the NaCl-type structure are antiferromagnetic. The values of the Néel temperature (T_N), the paramagnetic Curie temperature (θ), and the paramagnetic moment (n_p) increase along the series from UN to UBi. These properties and the high electrical conductivity were considered in a

---

*This work was performed under the auspices of the United States Atomic Energy Commission.

Table 1. *Properties of the* Uv *compounds in the ordered state*

Uv Compounds	Antiferromagnetic properties n_o at 5°K (μ_B)	Transition (°K)	n_o at 77°K (μ_B)	T_N (°K)	References
UN	0·75 ± 0·10	None		53 ± 2	[2]
UP	1·95 ± 0·05	22–24	1·72 ± 0·05	125 ± 2	[3–5]
UAs			1·89 ± 0·05	128 ± 3	[7]
			2·13 ± 0·05		[6]
USb	2·85 ± 0·08	None	2·78 ± 0·08	217 ± 4	This Note
UBi	3·0 ± 0·2	None	3·0 ± 0·2	285 ± 5	

proposed model[1] that accounts for the properties of the Uv compounds.

Neutron diffraction studies of UN[2], UP[3–5], and UAs[6, 7] have shown that the compounds have the Type-I antiferromagnetic structure with ferromagnetic sheets coupled antiferromagnetically. The uranium moments are perpendicular to the sheet and lie along one of the [001] directions.

This note reports the results of neutron diffraction studies for USb and UBi that are, by susceptibility measurements [8, 9], antiferromagnetic.

Polycrystalline samples of USb and UBi were prepared from arc-melted buttons. The lattice parameters as determined by X-ray diffraction are 6·200 ± 0·003 Å and 6·364 ± 0·003 Å for USb and UBi, respectively. Small amounts (< 1 per cent) of U_3Sb_4 were present in the USb sample, and larger amounts (~ 15 per cent) of other phases, such as UO_2 and U_3Bi_4, were present in the UBi sample.

The antiferromagnetic structure of both materials is Type-I, as determined by neutron diffraction. When both materials were cooled to 5°K, no abrupt change in the ordered moment occurred, such as was observed in UP[5]. The ordered moments (n_o) and Néel temperatures, together with the estimated limits of error, are given in Table 1. The moments were determined by using a theoretical form factor for the $5f^3$ configuration[3] to obtain f for the low-angle (110) and (201) reflections. The temperature factor for the uranium atom derived from the nuclear intensities was assumed for the magnetic intensities. Four other reflections at $\sin\theta/\lambda$ values between 0·2 and 0·3 could be measured with reasonable certainty in USb. The observed form factor values are all lower than those calculated from a $5f^3$ configuration. For the (310) ($\sin\theta/\lambda = 0{\cdot}256$ Å^{-1}) and (312) ($\sin\theta/\lambda = 0{\cdot}302$ Å^{-1}) reflections, the observed form factors are 0·66 ± 0·03 and 0·58 ± 0·03, respectively, whereas the corresponding calculated values are 0·73 and 0·64. Unresolved reflections of the additional phases in the UBi sample make measurements of the form factor in this material uncertain.

A summary of the ordered magnetic moments of the Uv compounds is given in Table 1. The moments increase from UN to UBi, which is similar to the behavior of other magnetic properties (see corresponding table in [1]).

Metallurgy Division,
Argonne National Laboratory,
Argonne, Ill. 60439,
U.S.A.

M. KUZNIETZ
G. H. LANDER
F. P. CAMPOS

REFERENCES

1. GRUNZWEIG J. and KUZNIETZ M., *J. appl. Phys.* **39**, 905 (1968); GRUNZWEIG J., KUZNIETZ M and FRIEDMAN F., *Phys. Rev.* **173**, 562 (1968).
2. CURRY N. A., *Proc. phys. Soc.* **86**, 1193 (1965).
3. SIDHU S. S., VOGELSANG W. and ANDERSON K. D., *J. Phys. Chem. Solids* **27**, 1197 (1966).
4. CURRY N. A., *Proc. phys. Soc.* **89**, 427 (1966).

5. HEATON L., MUELLER M. H., ANDERSON K. D. and ZAUBERIS D. D., *J. Phys. Chem. Solids* **30**, 453 (1969).
6. TROC R., MURASIK A., ZYGMUNT A. and LECIEJEWICZ J., *Phys. Status Solidi* **23**, K123 (1967).
7. WILLIAMS J. M., HEATON L. and CAMPOS F. P., *J. Phys. Chem. Solids* **29**, 1702 (1968).
8. TRZEBIATOWSKI W., SEPICHOWSKA A. and ZYGMUNT A., *Bull. Acad. Polon. Sci., Ser. Chim.* **12**, 687 (1964).
9. TRZEBIATOWSKI W. and ZYGMUNT A., *Bull. Acad. Polon. Sci., Ser. Chim.* **14**, 495 (1966).

J. Phys. Chem. Solids Vol. 30, pp. 1644–1646.

Rotational barrier height for OH⁻ ion trapped in KCl, KBr, NaCl and RbCl matrices

(*Received* 17 *July* 1968)

THERE HAS been a great deal of experimental [1–3] and theoretical interest [4–6] in the rotational motion of diatomic impurities in alkali halide matrices. The salient features of the various experimental investigations are explained on the basis of Devonshire model [7] for the hindered rotation of linear molecules in fields of octahedral symmetry. The Devonshire model enables one to calculate the barrier height from the experimental data of librational level of the impurity. Recently, Lawless [8] has calculated the barrier height for rotational motion of OH⁻ taking the point charge model. The point charge model is in fact not very correct and hence it is desired in the present work to calculate the barrier height on a more realistic approach. The multipole expansion method has been used to obtain an expression for the rotational barrier (K) for a diatomic impurity at a lattice site in ionic matrices. The method is very general and can be employed to any diatomic impurity, provided its quadrupole moment and hexodecapole moment are known.

The main interactions between the trapped impurity and one of its surrounding nearest neighbours are (i) between the charge of the matrix atoms and the multipole moments of the trapped impurity and (ii) between the multipole moments of the trapped molecule and the induced dipole moment in the ions of the host lattice. The explicit expression for these are well known [9]. These can be rearranged and written in terms of spherical harmonics as follows

$$V = \sum_{l=1}^{l=4} A_l(R_i) Y_0^{\,l}(\omega_i) \tag{1}$$

where the constant A_l's are given by

$$\begin{aligned}
A_0 &= 3\sqrt{\pi}\left[-\frac{\alpha_H \Theta_s^{\,2}}{R^8} + \frac{2}{3}\frac{C_H C_s}{R}\right]\\
A_1 &= \sqrt{\frac{4\pi}{3}}\left[-18\frac{\alpha_H \mu_s \Theta_s}{R^7} - \frac{C_H \mu_s}{R^2}\right]\\
A_2 &= \frac{4}{3}\sqrt{\frac{\pi}{5}}\left[-\frac{3}{2}\frac{\alpha_H \mu_s^{\,2}}{R^6} - \frac{18}{7}\frac{\alpha_H \Theta_s^{\,2}}{R^8} + \frac{3}{4}\frac{C_H \Theta_s}{R^3}\right]\\
A_3 &= \frac{4}{5}\sqrt{\frac{\pi}{7}}\left[-\frac{6\alpha_H \mu_s \Theta_s}{R^7} - \frac{5}{2}\frac{C_H \Omega_s}{R^4}\right]\\
A_4 &= \frac{16\sqrt{\pi}}{105}\left[-\frac{45}{8}\frac{\alpha_H \Theta_s^{\,2}}{R^8} + \frac{35}{8}\frac{C_H \phi_s}{R^5}\right.\\
&\qquad \left. - \frac{35}{48}\frac{C_s \phi_s \alpha_H}{R^8}\right].
\end{aligned} \tag{2}$$

The symbols having their usual meanings. Here $\omega(\theta,\phi)$ denotes the orientation of the ion relative to the 'R-frame'—a rectangular coordinate system, with the z axis along the internuclear axis vector **R**. In a rigid lattice, however, the total interaction energy of the rotating molecule due to the interaction (1) is given by

$$V_c = \sum_{i=1}^{\infty} \sum_{l} A_l(R_i) Y_0^{\,l}(\omega_i). \tag{3}$$

The summation over all the neighbours can easily be done by transforming the spherical harmonics from the R_i frame to another frame (say c-frame), which has its z-axis along the

Table 1. Calculated and experimental values of the barrier height

System	Librational frequency* (cm^{-1})	α_a† ($\times 10^{-24}\,\mathrm{cm}^3$)	α_c† ($\times 10^{-24}\,\mathrm{cm}^3$)	R‡ ($\times 10^{-8}\,\mathrm{cm}$)	K (exptal) (cm^{-1})	K (calculated) (cm^{-1})
KCl-OH^-	293	4·98	3·29	3·12	541·9	533·3
KBr-OH^-	304	6·44	3·29	3·25	565·3	400·0
NaCl-OH^-	385	4·98	1·57	2·80	743·3	747·1
RbCl-OH^-	265	4·98	4·56	3·26	483·5	496·6

*Reference [3].

†ROBERTS S., *Phys. Rev.* **81**, 865 (1951).

‡Reference [8].

symmetry axis of the lattice cage. This gives [10]

$$V_c = \sum_{l=1}^{\infty} \sum_{t} \sum_{m} Y_m{}^t(\Omega) A_t(R_i) D^t_{m0}(\alpha_i\beta_i\gamma_i). \quad (4)$$

Here $(\alpha_i\beta_i\gamma_i)$ are the Eulerian angles of rotations carrying the c-frame into the R_i-frame, D's are the rotation matrices and Ω stands for the orientation of the impurity ion in the 'c-frame'. In the f.c.c. lattice, the contribution of the first two shells of neighbours to the sum in (4) vanishes except when $t = 4$. This makes only quadrupole induced quadrupole, charge induced hexadecapole and hexadecapole charge interaction terms contribute to the crystalline field and hence to the barrier height. Thus the barrier height can be written in terms of molecular constants as follows

$$K = (9/2)\frac{\alpha_H\theta_S{}^2}{R^8} - (7/2)\frac{C_H\phi_S}{R^5} + (7/12)\frac{C_S\phi_S\alpha_H}{R^8}. \quad (5)$$

The symbols having their usual meanings. The subscripts H and S denote respectively the host lattice and solute (or trapped) ion.

In Table 1 the result of the calculations of the barrier heights are summarized. It is seen that with a value of $5{\cdot}8 \times 10^{-26}$ esu for the quadrupole moment and $-0{\cdot}83 \times 10^{-42}$ esu for the hexadecapole moment, the calculated barriers agree well with the experimental values. The values of quadrupole and hexadecapole moments are quite reasonable and are of the same order of magnitude as for other diatomic molecules (for HCl, $\phi = 0{\cdot}5 \times 10^{-42}$ e.s.u. [12, 13], and $\theta = 3{\cdot}7 \times 10^{-26}$ e.s.u. [11]).

Calculations of Lawless for OH^- trapped in these crystals involve a point charge model and a fitting of three parameters to one barrier height. Even this best fit leads to an unreasonably large dipole moment of OH^- (about 3½ times larger), which cannot be explained either by quantum mechanical considerations [14] or nonequilibrium mechanisms [15]. Even with the inclusion of induced moments, the large dipole moment of OH^- obtained by point charge model cannot be explained [16].

The result for KBr matrix needs special mention. The experimental barrier height for the KBr matrix comes out to be larger than that for KCl matrix. This seems to be erroneous and cannot be explained by us. The reason is as follows. If one considers the effect of only nearest neighbours, the OH^- ion faces the same type of cavity in KBr, consisting of six K^+ neighbours, as in KCl. The dimension of the cavity is larger in KBr than in KCl resulting in a smaller crystalline field. This is due to the fact that all multipole expansions depend upon some inverse power of the interionic separation. The larger separation in KBr will give rise to smaller barrier height. However, at the present moment we cannot say anything with confidence. It is also likely that barrier height depends upon the displaced anion radius for which no information is available. The ion size effect is known to play an effective part in diffusion processes in these crystals at high temperatures[17]. Experiments on NaBr and RbBr crystals will be useful from this aspect.

The experimental barrier height is obtained by using the Devonshire model to explain the librational frequencies. This at the first sight creates difficulty as two quite different barriers are needed to explain the librational and tunneling levels in hydroxyl doped alkali halides. Recently, it has been concluded [12, 18] that if the interaction of the lattice vibrations to the motion of the trapped molecule is also considered, the two phenomenon viz. the libration and tunneling can be explained from the same barrier. In the aforesaid paper, it is concluded that this barrier does not differ very much from that obtained by the librational level alone without considering the lattice vibrational effects.

Acknowledgement – The authors are thankful to Professor Krishnaji for his guidance

S. CHANDRA

Radio and Electrical Engineering Division,
N R C , Ottawa, Canada

and

Physics Department,
University of Allahabad
Allahabad, India

G K PANDEY
V K. AGRAWAL

REFERENCES

1. BOSOMWORTH D. R., *Solid State Commun.* **5**, 681 (1967).
2. NARAYANMURTI V., *Phys. Rev. Lett.* **13**, 693 (1964); SEWARD W. D. and NARAYANMURTI V., *Phys. Rev* **148**, 489 (1966).
3. WEDDING B. and KLEIN M. V., *Bull. Am. phys. Soc.* **11**, 228 (1966)
4. SHORE H B., *Phys. Rev. Lett.* **17**, 1142 (1966).
5. BAUR M. E. and SALZMAN W. R., *Phys. Rev. Lett.* **18**, 590 (1967).
6. BAUR M. E. and SALZMAN W. R., *Phys. Rev. Lett* **16**, 701 (1966); *Phys. Rev.* **151**, 710 (1966).
7. DEVONSHIRE A. F., *Proc. R. Soc.* **153**, 601 (1936).
8. LAWLESS W. N., *J. Phys. Chem. Solids* **28**, 1755 (1967).
9. KIELICH S., *Acta Phys. Polon* **22**, 65 (1962)
10. ROSE M E., In *Elementary Theory of Angular Momentum.* Wiley, New York (1957).
11. KRISHNAJI and PRAKASH V., *Rev. mod. Phys.* **38**, 690 (1966)
12. PANDEY G. K., *J chem. Phys.* **49**, 1555 (1968).
13. FRIEDMANN H and KIMEL S., *J. chem. Phys.* **47**, (1967).
14. LAWLESS W N., *Phys Rev Lett* **17**, 1048 (1966).
15. HART H. R., To be published.
16. CHANDRA S and AGRAWAL V. K, *Can J. Phys.* **45**, 2489 (1967).
17. ARAI G and MULLEN J. G, *Phys. Rev.* **143**, 663 (1966).
18. PANDEY G K and AGRAWAL V. K, *J. chem. Phys* To be published (1969).

J. Phys. Chem. Solids Pergamon Press 1969. Vol. 30, p. 1647. Printed in Great Britain.

ERRATUM

F. K. LOTGERING: Mixed crystals between binary sulphides or selenides with spinel structure. *J. Phys. Chem. Solids* **29**, 699 (1968).

THE PRINTER regrets that on page 706, the second and fourth lines respectively of the second column should read:

composition. If α depends on x, the $M_{0K}-x$
curvature and it can easily be shown that α

The fifteenth line of the first column on page 707 should read:

for $x = 1{\cdot}65$ ($\Theta \approx -500°\text{K}$, $T_c \approx 200°\text{K}$) it

On page 708, W should read W_1 in the second term of the first equation for $\cos\varphi$.

J. Phys. Chem. Solids Pergamon Press 1969. Vol. 30, pp. 1649–1660. Printed in Great Britain.

APPLICATION OF THE POLARON MODEL TO THE F' CENTER†

H. L. ARORA and **S. WANG**
Department of Physics, University of Waterloo, Waterloo, Ontario, Canada

(*Received* 28 *October* 1968; *in revised form* 3 *February* 1969)

Abstract—An approach for calculating the effects of electronic and ionic polarizations on a simple two-electron center such as the F' center is developed from the polaron model of electron-excess color centers. This approach and that described in a more recent work are applied to the study of effects of electronic and ionic polarizations on F' centers in KCl, KBr, and NaCl. From the comparison of the obtained theoretical results with experimental results of F' bands, we discuss which approach is more appropriate in treating the effects of crystalline polarization on the system of two trapped electrons. In addition, the possibility that the F' center in a typical alkali halide has a weakly bound excited state to which the optical transition can be made is shown. The wave functions and optical absorptions of F' centers in KCl, KBr and NaCl are also discussed.

1. INTRODUCTION

THE F' CENTER which is responsible for the F' band in colored alkali halide crystals is believed to consist of two electrons trapped at the lattice site of a missing negative ion. The F' band was identified with the direct ionization of an F'-center electron from the work of Pick[1], Domanic[2] and Seitz[3]. This identification implies that the F' center is the analog of an H^- ion and does not have a bound excited state. However, recent photoconductivity measurements by Crandall[4] suggest that the F' center in KBr could have a bound excited state with binding energy between 0·04 and 0·08 eV. This suggestion has not been justified and discussed theoretically.

In contrast to the F center, there are relatively few theoretical studies of the F' center. In the previous theoretical studies, both Pekar[5] and Cheban[6] treated the F' center by the dielectric-continuum-effective-mass model in calculating the thermal ionization energy of the F' center; Pincherle [7] used the semicontinuum model to calculate the ground-state energy of the F' center and discussed its binding energy using his calculated results of ground-state energies of the F' and F centers. Recently, La and Bartram[8] calculated the absorption energies of F' centers in NaCl, KCl and KBr by assuming that F' band is due to the direct ionization of the F' center rather than excitation to a bound excited state as in the case of the F center. In their calculation, the point-ion-lattice model of Gourary and Adrian is used to evaluate the potential of the trapped electron due to the lattice and the semicontinuum model of Krumhansl and Schwartz is adopted to obtain a correction for polarization. The theoretical F'-band energy calculated by the last authors for NaCl is in excellent agreement with the experimental value; however, their theoretical results for F' centers in KCl and KBr are considerably off the experimental values.

The aim of the present paper is twofold: (a) to extend the polaron model[9–11] to the F' center, a simple two-electron center for which one considers not only the effect of the electronic polarization but also the effect of ionic polarization (the last effect was omitted in reference [10], because it is not important in the problem considered there), and (b) to see which approach is more ade-

---

†Work supported in part by the National Research Council of Canada.

quate in treating the effects of electronic and ionic polarizations on a two-electron center.

Therefore, we propose first a method in Section 2(a), which is based on the basic idea of the polaron model but different from that in reference [10] for computing quantum states of a defect like the F' center. The basic difference between this method and that in reference [10] lies in the treatment of the electronic polarization on the system of two trapped electrons. The optical absorption energies of F' centers in KCl, KBr and NaCl are calculated on the basis of Crandall's suggestion[4] by using the proposed method, and given in Sections 2(b) and 2(c).

We then calculate in Section 3 the optical absorption energies of F' centers in the same crystals using the method developed in reference[10]. In the last section, we compare theoretical results obtained in Sections 2 and 3 with experimental results and discuss (i) the method for treating the effects of electronic and ionic polarizations on a two-electron center, (ii) the form of the wavefunction which adequately describes a defect such as the F' center, and (iii) the Crandall suggestion on the F' center.

2. CALCULATION A

(a) *Effective Hamiltonian*

Considering that the F' center is the F center plus an electron and adopting the approach used to treat the electronic and ionic polarizations in Section 3 of a recent paper[11], we write the Hamiltonian including the effect of electronic and ionic polarizations for the F' center in the form

$$H = \sum_{i=1}^{2} H_i + (e^2/r_{12}) + H_v + V_{q-v} + H_p + V_{q-p} \tag{1}$$

where H_i is given by

$$H_i = (p_i^2/2m_e) + \sum_{\alpha} V(\mathbf{r}_i - R_{\alpha 0}) - V(\mathbf{r}_i) + V_{ei-v} \tag{2}$$

for $|\mathbf{r}_i| < R$ and

$$H_i = (p_i^2/2m_e) + \sum_{\alpha} V(\mathbf{r}_i - \mathbf{R}_{\alpha 0}) - V(\mathbf{r}_i) + V_{ei-v} + V_{ei-p} \tag{3}$$

for $|\mathbf{r}_i| > R$, where R is the radius of a spherical region drawn about the trapping center and is so chosen that the ith trapped electron does not polarize the lattice for $|\mathbf{r}_i| < R$. As in the polaron model calculation of F center [9], this R is set numerically equal to the Mott-Littleton radius of negative ion vacancy. Here we have taken the origin of position vectors of the trapped electrons and ions at the center of the vacancy having an effective charge $+q$ (the trapping center, say). The first term in equation (2) is the kinetic energy of the ith trapped electron. $\sum_{\alpha} V(\mathbf{r}_i - \mathbf{R}_{\alpha 0})$ is the interaction of the ith trapped electron with all ions of the perfect lattice, i.e. when all the nuclei are at their equilibrium positions and the core and valence electrons of all ions are in their ground state. The third term represents the interaction of the ith trapped electron with the trapping center q. The second term in equation (1) is the Coulomb interaction between the two trapped electrons.

In the polaron model, H_v denotes the Hamiltonian of the virtual excitons which are introduced to describe the system of the crystalline valence electrons. The interactions of virtual excitons with the trapping center q and the ith trapped electron are, respectively, denoted by V_{q-v} and V_{ei-v} in the above equations. The expressions for these terms can be written in terms of creation and annihilation operators, $b_{\mathbf{w}}^*$ and $b_{\mathbf{w}}$, for excitons of wave vector $\mathbf{w}$, as those in reference [11]. H_p represents the Hamiltonian of the virtual phonons which are introduced to describe the system of ions. V_{q-p} and V_{ei-p} respectively stand for the interactions of virtual phonons with the trapping center q and the ith trapped electron, Corresponding expressions for H_p, V_{q-p}, and V_{ei-p} can be written in terms of creation and annihilation operators, $a_{\mathbf{k}}^*$ and $a_{\mathbf{k}}$, for phonons of wave vector $\mathbf{k}$[11].

Making a canonical transformation for the exciton part with the aid of an operator defined by $B_{\mathbf{w}} = b_{\mathbf{w}} - (V_w^*/E_w)$ and that for the phonon part with the use of the operator $A_{\mathbf{k}} = a_{\mathbf{k}} - (V_k^*/\hbar w_k)$ (see [11] for detail), we have

$$H = \sum_{i=1}^{2} \mathscr{H}_i + \frac{e^2}{r_{12}} + H_{ex} \tag{4}$$

where H_{ex} has the form

$$\begin{aligned} H_{ex} &= \sum_{\mathbf{w}} B_{\mathbf{w}}^* B_{\mathbf{w}} E_w \\ &\quad + \sum_{i=1}^{2} \sum_{\mathbf{w}} (V_w B_{\mathbf{w}}\, \mathrm{e}^{i\mathbf{w}\cdot\mathbf{r}_i} + c.c.) \end{aligned} \tag{5}$$

$\mathscr{H}_i$ is given by

$$\begin{aligned} \mathscr{H}_i &= (p_i^2/2m_e) - (Me^2/d) \\ &\quad + (1 - (1/\epsilon_\infty))(e^2/r_i) \end{aligned} \tag{6}$$

for $|\mathbf{r}_i| < R$ and

$$\mathscr{H}_i = (p_i^2/2m) - (e^2/\epsilon_s r_i) + H_{ph,i} \tag{7}$$

for $|r_i| > R$, with $H_{ph,i}$ given by

$$H_{ph,i} = \sum_{\mathbf{k}}{}_{i} A_{\mathbf{k}}^* A_{\mathbf{k}} \hbar\omega_k + \sum_{\mathbf{k}} (V_k A_{\mathbf{k}}\, \mathrm{e}^{i\mathbf{k}\cdot\mathbf{r}_i} + c.c.). \tag{8}$$

The notation used here is the same as in reference [11]. The first term in (5) is the Hamiltonian of exciton part and the second term is the interaction between excitons and the two trapped electrons. The first term in (8) is the Hamiltonian of phonons surrounding the ith trapped electron; the second term is the interaction between them. In writing (4), we have replaced $\sum_\alpha V(r_i - \mathbf{R}_{\alpha 0}) - V(\mathbf{r}_i)$ by the Madelung energy $(-Me^2/d)$ for $|\mathbf{r}_i| < R$ and $(p_i^2/2m_e) + \sum_\alpha V(\mathbf{r}_i - \mathbf{R}_{\alpha 0})$ by $(p_i^2/2m)$ for $|\mathbf{r}_i| > R$ using the effective mass approximation for the electron. We also set $V(\mathbf{r}_i)$ equal to (e^2/r_i) for $|\mathbf{r}_i| > R$. Since the phonons described by (8) occur only for $|\mathbf{r}_i| > R$, we shall adopt the method used for treating the exciton part in reference [10], where excitons occur only for $|\mathbf{r}_i| > R$, to treat the phonon part involved in the present problem. Following this method, we find that the contribution of the phonon part to the effective Hamiltonian is the self-energy of the trapped electrons due to their own phonon clouds plus the exchange effect of phonons between the two trapped electrons. This exchange effect reduces the repulsive Coulomb interaction between them. Therefore, the effective Hamiltonian for the F' center takes the form

$$H_{\mathrm{eff}} = \sum_{i=1}^{2} \mathscr{H}_{\mathrm{eff},i} + \frac{e^2}{\epsilon_1 r_{12}} + \langle F | H_{ex} | F \rangle \tag{9}$$

where $\mathscr{H}_{\mathrm{eff},i}$ has the same form as that of (6) for $|\mathbf{r}_i| < R$, and the form

$$\mathscr{H}_{\mathrm{eff},i} = (p_i^2/2m) - (e^2/\epsilon_s r_i) + \langle \Phi_i | H_{ph,i} | \Phi_i \rangle \tag{10}$$

for $|\mathbf{r}_i| > R$. ϵ_1 in the second term of (9) is introduced to account for the exchange effect of phonons between the two trapped electrons; (i) it is unity for the case in which the two trapped electrons are both inside the spherical region of radius R, because no phonons occur in this case, and (ii) $(1/\epsilon_1)$ is $(1 - (1/\epsilon^*))$ for the case in which the two trapped electrons are both outside the spherical region, because the exchange effect of phonons between two trapped electrons in this case gives the exchange energy $-(e^2/\epsilon^* r_{12})$ where $(1/\epsilon^*) = (1/\epsilon_\infty) - (1/\epsilon_s)$, ϵ_∞ being the high-frequency dielectric constant and ϵ_s the static dielectric constant for the crystal. Thus, ϵ_1 depends upon the electronic state in question (refer to the choice of ϵ_1 involved in the following sections). F denotes the wave function of all excitons. In the present section, we shall develop a method different from that introduced in reference [10] to evaluate the last term of (9), and so we write F in the Hartree form

$$F = \prod_{\mathbf{w}} f(\mathbf{w}) \tag{11}$$

where $f(\mathbf{w})$ is the wave function of the exciton of wave vector **w**. Φ_i denotes the wave function of phonons surrounding the ith trapped electron and, in the present approximation, has the form

$$\Phi_i = \prod_{\mathbf{k}} \varphi(\mathbf{k}). \tag{12}$$

where $\varphi(\mathbf{k})$ is the wave function of the phonon of wave vector **k**.

We shall take (9) as the basic form of the effective Hamiltonian in calculating quantum states involved in the optical absorption of the F' center in a typical alkali halide. The detailed form of (9) depends on the electronic state considered, because, in general, the contribution of the last term of (9) is a function of the electronic state under consideration.

(*b*) *Ground state*

To determine the one-exciton wave function $f(\mathbf{w})$, we assume that the electron-exciton interaction, i.e. the second term of (5) is a small perturbation on the system of crystalline valence electrons. Furthermore, we average the interaction over the electronic motion to give an interaction energy which depends on the exciton coordinate alone. In determining $f(\mathbf{w})$, we thus write

$$H_{ex} = \sum_{\mathbf{w}} B_{\mathbf{w}}^* B_{\mathbf{w}} E_w + 2 \sum_{\mathbf{w}} (V_w B_{\mathbf{w}} \rho_w + c.c.) \tag{13}$$

where ρ_w is given by

$$\rho_w = \int |\psi(\mathbf{r}_1, \mathbf{r}_2)|^2 \, e^{i\mathbf{w}\cdot\mathbf{r}_i} \, d^3r_1 \, d^3r_2, \; i = 1 \text{ or } 2. \tag{14}$$

$\psi(\mathbf{r}_1, \mathbf{r}_2)$ is the wave function of the two trapped electrons. Taking the second term in (13) as a perturbation and using first-order perturbation theory, we find

$$f(\mathbf{w}) = \left[1 - \frac{2V_w^* \rho_w^*}{E_w} B_{\mathbf{w}}^*\right] |0\rangle \tag{15}$$

here $|0\rangle$ represents the exciton's vacuum state. The normalization factor of $f(\mathbf{w})$ is set equal to one, because the crystal volume is assumed to be large in this calculation. Using these exciton functions and (5) for H_{ex}, we find

$$\langle F|H_{ex}|F\rangle = 4 \sum_{\mathbf{w}} \frac{|V_w|^2}{E_w} (\rho_w^* \rho_w - 2\, e^{i\mathbf{w}\cdot\mathbf{r}_i} \rho_w^*). \tag{16}$$

We note that in this approach a term like the second term of (20) in reference [10], i.e. the exciton exchange effect between the two trapped electrons, does not appear explicitly.

Following a method used for finding the contribution of excitons surrounding the ith trapped electron to the effective Hamiltonian in reference [10] to treat the last term of (10), we obtain

$$\langle \Phi_i|H_{ph,i}|\Phi_i\rangle = \sum_{\mathbf{k}} \frac{|V_k|^2}{\hbar\omega_k} (\rho_k^* \rho_k - 2\, e^{i\mathbf{K}\cdot\mathbf{r}_i} \rho_k^*). \tag{17}$$

For a given electronic wave function $\psi_g(\mathbf{r}_1, \mathbf{r}_2)$, equations (16) and (17) can be evaluated and hence the ground state may be determined from $E_g = \langle \psi_g(\mathbf{r}_1, \mathbf{r}_2)|H_{\text{eff}}|\psi_g(\mathbf{r}_1, \mathbf{r}_2)\rangle$ by using the variational method.

Pincherle[7] assumed that the problem of F' centers is analogous to that of the helium atom, with a nuclear charge equal to $+e$ for alkali halides. Thus he chose the product of two 1*s* hydrogenic wave functions as the trial wave function for the two electrons of the F' center in the ground state. This trial wave function implies that the two trapped electrons of up and down spins are in the same 1*s* orbital. In fact, the assumption of Pincherle is equivalent to saying that the F' center is analogous to a hydrogen negative ion H^-. In view of this and the fact that a hydrogen negative ion with two electrons of up and down spins in two different 1*s* orbitals is stable[12], we write the trial wave function for the ground state in the form

$$\psi_g(\mathbf{r}_1, \mathbf{r}_2) = N[\phi_\alpha(\mathbf{r}_1)\phi_\lambda(\mathbf{r}_2) + \phi_\alpha(\mathbf{r}_2)\phi_\lambda(\mathbf{r}_1)] \tag{18}$$

where N is the normalization factor of ψ_g; the form of ϕ_α and that of ϕ_λ are

$$\phi_\alpha(\mathbf{r}) = (\alpha^3/\pi)^{1/2}\,\mathrm{e}^{-\alpha r},$$
$$\phi_\lambda(\mathbf{r}) = (\lambda^3/\pi)^{1/2}\,\mathrm{e}^{-\lambda r} \qquad (19)$$

α and λ being variational parameters.

The detailed calculations of (16) and (17) for the $\psi_g(\mathbf{r}_1, \mathbf{r}_2)$ given by (18) are similar to those in reference [10] and we find

$$\langle F|H_{er}|F\rangle = 4\xi \qquad (20)$$

$$\langle \Phi_i|H_{ph,i}|\Phi_i\rangle = \xi'/\epsilon^* \qquad (21)$$

where ξ is given by equation (42) of reference [10] and $\xi' = \xi/(1-(1/\epsilon_\infty))$.

We have taken (20) and (21) as terms in the effective Hamiltonian to determine the ground state of F' centers in KCl, KBr, and NaCl using the variational method. The calculated minimum energy E_g and the corresponding variational parameters α and λ are summarized in Table 1. In calculating these results, we set $(1/\epsilon_1)$ appearing in the second term of (9) equal to $(1-(1/\epsilon^*))$. The reason for this is the following. The variational parameter α appearing in the hydrogenic 1*s* wave function has been calculated for the ground state of the *F* electron for the crystals considered here. From the calculated α, we have computed the average value of *r* of the *F* electron to be greater than the radius of the present spherical region, *R*. We then expect that the average value of $|\mathbf{r}_i|$ for the ground state of the F' center is considerably greater than *R*, because of the presence of the repulsive Coulomb force between the two trapped electrons. This means that the trapped electron described by the hydrogenic 1*s* wave function spends most of its time in the region where $|\mathbf{r}_i|$ is much larger than *R* and the exchange effect of phonons between the two trapped electrons is very strong. Thus $(1/\epsilon_1)$ approaches $(1-(1/\epsilon^*))$ in the present calculation (see the discussion following (10) for ϵ_1). As in reference [9], values for the constants are taken from Mott and Gurney [13]. We further note that the variational parameters α and λ in hydrogenic 1*s* wave functions are found to be the same in the present problem. This is not the case in the problem of the interstitial H^- ion in reference [10], because the 1*s* orbit involved there is very small and the Coulomb repulsive force between two trapped electrons of up and down spins is very strong. In contrast to this, however, for the case of the F' center, the Coulomb repulsive force between the two trapped electrons is weaker than that corresponding to the H^- center, because the interaction between the trapped electron and the trapping center, is box-like for $|\mathbf{r}_i| < R$ and Coulomb-like for $|\mathbf{r}_i| > R$ and hence the 1*s* orbital is larger. Thus $\psi_g(\mathbf{r}_1, \mathbf{r}_2)$ given by (18) can be reduced to $\Phi_\alpha(\mathbf{r}_1)\ \phi_\alpha(\mathbf{r}_2)$, which was first taken by Pincherle as the electronic trial wave function for the ground state of the F' center. It turns out that the ground-state wave function

Table 1. *Calculated variational parameters in* $\psi_g(\mathbf{r}_1, \mathbf{r}_2)$ *and* $\psi_e(\mathbf{r}_1, \mathbf{r}_2)$ *in which the* 1s *wave function is the hydrogenic* 1s *wave function, energy levels and absorption energies* ΔE *for* F′ *centers in* KCl, KBr *and* NaCl. *Variational parameters are given in* $Å^{-1}$ *and energies in eV (Calculation A)*

	α†	E_g	λ	β	E_e	ΔE
KCl	0·40	−3·05	0·40	0·20	−1·37	1·68
KBr	0·40	−2·91	0·35	0·20	−1·31	1·60
NaCl	0·45	−3·73	0·40	0·25	−1·69	2·04

†The two variational parameters in $\psi_g(\mathbf{r}_1, \mathbf{r}_2)$ are found to be the same.

determined here is nearly the same as that determined by Pincherle. Pincherle's function for KCl is shown to be rather more diffuse than that calculated by the square-well model in reference [8].

We have also taken the wave function

$$\psi_g(\mathbf{r}_1,\mathbf{r}_2) = (\gamma^3/7\pi)(1+\gamma r_1)\,e^{-\gamma r_1} \times (1+\gamma r_2)\,e^{-\gamma r_2} \qquad (22)$$

as the electronic trial wave function for the ground state of the F' center, which was first used by Pekar[5] for calculating the ground state of the F' center. The one-electron wave function involved in (22) (the modified $1s$ function, say) has been found to be better than the hydrogenic $1s$ wave function in determining the ground state of the F center in KCl or NaCl[9]. For this trial wave function, $\langle F|H_{ex}|F\rangle$ and $\langle\Phi_i|H_{ph,i}|\Phi_i\rangle$ given, respectively, by (16) and (17) are found to be

$$\langle F|H_{ex}|F\rangle = 4\eta(1-(1/\epsilon_x)) \qquad (23)$$

$$\langle\Phi_i|H_{ph,i}|\Phi_i\rangle = \eta/\epsilon^* \qquad (24)$$

where

$$\eta = e^2\left[\frac{5373}{25088}\gamma - \frac{1}{r_i} + \frac{e^{-2\gamma r_i}}{r_i} \times \left(1+\frac{17}{28}\gamma r_i + \frac{23}{42}\gamma^2 r_i^2 + \frac{\gamma^3 r_i^3}{7}\right)\right]. \qquad (25)$$

The corresponding minimum value of E_g and variational parameter γ are found to be those given in Table 2. The variational parameter γ determined here is 0·70 Å^{-1} for KCl, which is smaller than that determined by Pekar ($\gamma =$ 1·17 Å^{-1} for KCl). This means that ψ_g of (22) determined by the present method is more diffuse than Pekar's function and may not be much different quantitatively from the wave function calculated by La and Bartram [8]. Note that we set ϵ_i in H_{eff} equal to unity in calculating the expectation value of the H_{eff} for $\psi_g(\mathbf{r}_1,\mathbf{r}_2)$ given by (22), because the average value of $|\mathbf{r}_i|$ expected from the γ value of the F' electron is nearly the same as the value of R and hence the phonon exchange effect between the two electrons in the state described by (22) is small (cf. the discussion following equation (21)), and therefore it is omitted.

(c) *Excited state*

We now consider the lowest excited state of the F' center to which the optical transition can be made from its ground state with a large probability. From the atomic calculations we expect that the excited state of interest here should be the one in which one of the two trapped electrons is in the hydrogenic $1s$ (or modified $1s$) state and the other electron is in the $2p$ state. Thus we write the trial wave function for this electronic state as follows:

$$\psi_e(\mathbf{r}_1,\mathbf{r}_2) = (1/\sqrt{2})\,[\phi_{1s}(\mathbf{r}_1)\phi_{2p}(\mathbf{r}_2) + \phi_{1s}(\mathbf{r}_2)\phi_{2p}(\mathbf{r}_1)] \qquad (26)$$

with $\phi_{1s}(\mathbf{r}_i)$ having the same form as $\phi_a(\mathbf{r})$ in (19) and with $\phi_{2p}(\mathbf{r}_i)$ given by

$$\phi_{2p}(\mathbf{r}_i) = (\beta^5/\pi)^{1/2}\mathbf{r}_i\,e^{-\beta r_i}\cos\theta,\ i=1,2. \qquad (27)$$

Table 2. Calculated variational parameters in $\psi_g(\mathbf{r}_1,\mathbf{r}_2)$ and $\psi_e(\mathbf{r}_1,\mathbf{r}_2)$ in which the 1s *wave function is the modified* 1s *wave function, energy levels and absorption energies* ΔE *for* F' *centers in* KCl, KBr *and* NaCl. *Variational parameters are given in Å^{-1} and energies in eV (Calculation A)*

	γ	E_g	γ	β	E_e	ΔE
KCl	0·70	−3·58	0·65	0·08	−1·32	2·26
KBr	0·70	−3·66	0·60	0·08	−1·31	2·35
NaCl	0·80	−4·45	0·75	0·08	−1·50	2·95

This excited state is a singlet state as is the ground state. Here we expect that the optical transition from the ground state to a triplet state is highly forbidden and thus we do not consider any possible triplet state.

For the state described by (26), if we follow again the treatment used in Section 2(b) for evaluating $\langle F|H_{ex}|F\rangle$ in (9), equation (13) can be written as:

$$H_{ex} = \sum_{\mathbf{w}} B_{\mathbf{w}}^{*} B_{\mathbf{w}} E_{w} + \sum_{\mathbf{w}} [V_{w} B_{\mathbf{w}} (\rho_{wg} + \rho_{we}) + c.c.] \quad (28)$$

where

$$\rho_{wg} = \int \phi_{1s}^{2}(\mathbf{r}_{i})\, e^{i\mathbf{w}\cdot\mathbf{r}_{i}} d^{3}r_{i},$$

$$\rho_{we} = \int \phi_{2p}^{2}(\mathbf{r}_{i})\, e^{i\mathbf{w}\cdot\mathbf{r}_{i}} d^{3}r_{i}. \quad (29)$$

It was shown in references [9] and [10] that the interaction of excitons with the trapped electron in a large orbit cannot be averaged over the electronic motion in evaluating $\langle F|H_{ex}|F\rangle$. We expect from the work on the F center that the $2p$ orbital involved in $\psi_{e}(\mathbf{r}_{1}, \mathbf{r}_{2})$ is large and set $\rho_{we} = e^{i\mathbf{w}\cdot\mathbf{r}_{i}}$. Hence, we obtain from (28)

$$H_{ex} = \sum_{\mathbf{w}} B_{\mathbf{w}}^{*} B_{\mathbf{w}} E_{w} + \sum_{i=1}^{2} \sum_{\mathbf{w}} \left[V_{w} B_{\mathbf{w}} \frac{\rho_{wg} + e^{i\mathbf{w}\cdot\mathbf{r}_{i}}}{2} + c.c. \right]. \quad (30)$$

The physical meaning of the method used in deducing (30) from (28) is the same as that in Section V(B) of reference [10]. Taking the second term as a perturbation on the system of the crystalline valence electrons, we find that the corresponding one-exciton wave function in the first order perturbation theory is

$$f(\mathbf{w}) = [(1 - (V_{w}^{*}/2E_{w})) \times (2\rho_{wg}^{*} + e^{-i\mathbf{w}\cdot\mathbf{r}_{1}} + e^{i\mathbf{w}\cdot\mathbf{r}_{2}}) B_{w}^{*}]|0\rangle. \quad (31)$$

Using this $f(\mathbf{w})$ and equation (11), we obtain the expectation value of H_{ex} given by (5)

$$\langle F|H_{ex}|F\rangle = \sum_{\mathbf{w}} \frac{|V_{w}|^{2}}{E_{w}} [|\rho_{wg}|^{2} - 2\rho_{wg} e^{i\mathbf{w}\cdot\mathbf{r}_{i}} - \tfrac{3}{4}(e^{i\mathbf{w}\cdot(\mathbf{r}_{1}-\mathbf{r}_{2})} + c.c.) - \tfrac{3}{2}]. \quad (32)$$

On replacing the summation over **w** by an integration (see Section V(B) in reference [10] for detail), we find

$$\langle F|H_{ex}|F\rangle = e^{2}(1 - (1/\epsilon_{\infty}))[\tfrac{5}{16}\alpha - (1/r_{i}) + (e^{-2\alpha r_{i}}/r_{i})(1 + \alpha r_{i}) - (3/4r_{12}) - (3/2a)] \quad (33)$$

for ψ_{e} in which ϕ_{1s} is the hydrogenic 1*s* wave function and

$$\langle F|H_{ex}|F\rangle = e^{2}\left(1 - \frac{1}{\epsilon_{\infty}}\right)\left[\frac{5373}{25088}\alpha - \frac{1}{r_{i}} + \frac{e^{-2\alpha r_{i}}}{r_{i}}\left(1 + \frac{17}{28}\alpha r_{i} + \frac{23}{42}\alpha^{2} r_{i}^{2} + \frac{1}{7}\alpha^{3} r_{i}^{3}\right) - \frac{3}{4r_{12}} - \frac{3}{2a}\right] \quad (34)$$

for ψ_{e} in which ϕ_{1s} is the modified 1*s* wave function. The phonon part, i.e. $\langle\Phi_{i}|H_{ph,i}|\Phi_{i}\rangle$, for the optical excited state can be assumed to be the same as that for the ground state, because the optical transition occurs according to the Franck–Condon principle and thus Φ_{i} remains unchanged during the optical transition.

We have taken $\langle F|H_{ex}|F\rangle$ just found above and $\langle\Phi_{i}|H_{ph,i}|\Phi_{i}\rangle$ found in Section 2(b) for those in the effective Hamiltonian of (9) and calculated the energy of the optically excited state, i.e.

$$E_{e} = \langle\psi_{e}(\mathbf{r}_{1}, \mathbf{r}_{2})|H_{eff}|\psi_{e}(\mathbf{r}_{1}, \mathbf{r}_{2})\rangle + (e^{2}/a)(1 - (1/\epsilon_{\infty})) \quad (35)$$

for the crystals under consideration. We note that the last term is added such that E_{g} and E_{e} (or the one-electron energies), in the preceding and the present sections, are measured from the same reference point. This can be seen in the following discussion. In evaluating $\langle F|H_{ex}|F\rangle$ involved in the present work and in reference [10], we used Hartree-type self-consistent field (SCF) method for the $1s$ orbitals and an approach equivalent to the second-order perturbation (SOP) method (see [10]) for the $2p$ orbital. We thus expect from the work of reference [9] that $E_g = \langle\psi_g(\mathbf{r}_1, \mathbf{r}_2)|H_{\text{eff}}|\psi_g(\mathbf{r}_1, \mathbf{r}_2)\rangle$ and $\langle\psi_e(\mathbf{r}_1, \mathbf{r}_2)|H_{\text{eff}}|\psi_e(\mathbf{r}_1, \mathbf{r}_2)\rangle$ in this work and in reference [10] are not measured from the same reference point. In reference [9], $\langle F|H_{ex}|F\rangle$ was treated by both the SCF and the SOP methods for the F electron. The application of the SCF method to $\langle F|H_{ex}|F\rangle$ yields an r-dependent self-energy whereas the SOP method yields a constant self-energy $-\sum_{w}(|V_w|^2/E_w) \simeq -(e^2/a)(1-(1/\epsilon_\infty))$, which is measured from the bottom of the bare conduction band (which does not include the effects of the electronic polarization of the crystal). This constant self-energy can be interpreted as the energy shift of the bottom of the bare conduction band as a consequence of the interaction of the electron with its own exciton field. From the comparison of the form of (49) in reference [9] with that of (29) in that reference (where ϵ_{go} is not much different from ϵ_∞), we see that if one neglects the constant self-energy, i.e. $-(e^2/a)(1-(1/\epsilon_\infty))$, then the one-electron energies in the SOP method and in the SCF method are measured from the same reference point, namely from the bottom of the conduction band which includes the effect of the electronic polarization. We then see that in order that the zero energies involved in calculations of the ground state (with SCF) and the excited state (with SCF plus SOP) for a work of the present type and reference [10] are the same, we have to subtract a constant energy C from the total energy of the excited state (or add the constant energy C to the energy of the excited state in which one of the two trapped electrons is in the $1s$ orbital, and $2C$ to the energy of the ground state in which the two trapped electrons are both in the $1s$ orbital). From the form of $\psi_e(\mathbf{r}_1, \mathbf{r}_2)$ given in the present work and reference [10], we see that the two trapped electrons in the excited state of the F' center or in the U_1 center spend one half of their time in the $1s$ orbital and the other half in the $2p$ orbital. On the average, one of the two trapped electrons is in the $1s$ orbital and the other electron is in the $2p$ orbital. This $2p$ orbital has been treated by a method equivalent to SOP method in evaluating $\langle F|H_{ex}|F\rangle$ for $\psi_e(\mathbf{r}_1, \mathbf{r}_2)$. Therefore, the constant energy C, which should be subtracted from $\langle\psi_e(\mathbf{r}_1, \mathbf{r}_2)|H_{\text{eff}}|\psi_e(\mathbf{r}_1, \mathbf{r}_2)\rangle$ in bringing zero energies involved in E_g and E_e in a calculation of the present type at the same point, is $-(e^2/a)(1-(1/\epsilon_\infty))$. (It turns out that the last term of (54) in reference [10] should be replaced by $(e^2/a)(1-(1/\epsilon_\infty))$. This replacement brings theoretical absorption energy of the U_1 band in KCl closer to the experimental result.)

The E_e given by equation (35) has been calculated for KCl, KBr and NaCl. The computed values of E_e and the corresponding variational parameters for $\psi_e(\mathbf{r}_1, \mathbf{r}_2)$ including the hydrogenic $1s$ wave function and for another $\psi_e(\mathbf{r}_1, \mathbf{r}_2)$ including the modified $1s$ wave function are, respectively, summarized in Tables 1 and 2. The theoretical absorption energies obtained by taking the difference between E_g and E_e for F' centers in these crystals are also summarized in these tables. The values used for constants appearing in E_e are the same as those used in the ground state. The comparison of the present theoretical results with experimental results is given in the last section.

3. CALCULATION B

We shall now adopt a method developed in reference [10] to calculate the ground and excited states of the F' center. The only difference between the method of the preceding section and that in reference [10] is the treatment of $\langle F|H_{ex}|F\rangle$. The treatment for $\langle F|H_{ex}|F\rangle$ in reference [10] is the following. The wave equation corresponding to H_{ex} given by equation (5) is

$$\Big[\sum_{\mathbf{w}} B_{\mathbf{w}}^{*} B_{\mathbf{w}} E_{w} + \sum_{i=1}^{2} \sum_{\mathbf{w}} (V_{w} B_{\mathbf{w}} e^{i\mathbf{w}\cdot\mathbf{r}_i} + \text{c.c.})\Big] \times F = E_{ex} F. \quad (36)$$

This equation determines the state of an exciton cloud in which there are two electrons. The application of the second-order perturbation theory to equation (36) yields (see [10] for detail)

$$E_{ex} \equiv \langle F|H|F\rangle = \sum_{i=1}^{2} \langle F_i|H_{ex,i}|F_i\rangle - (1-(1/\epsilon_\infty)(e^2/r_{12}) \quad (37)$$

with $H_{ex,i}$ given by

$$H_{ex,i} = \sum_{\mathbf{w}}{}_{i} B_{\mathbf{w}}^{*} B_{\mathbf{w}} E_{w} + \sum_{\mathbf{w}} (V_{w} B_{\mathbf{w}}\, e^{i\mathbf{w}\cdot\mathbf{r}_i} + c.c.). \quad (38)$$

The first term in (38) is interpreted as the Hamiltonian of the virtual excitons surrounding the ith electron; the second term is the interaction between them. The wave function corresponding to $H_{ex,i}$ is denoted by F_i. Thus $\langle F_i|H_{ex,i}|F_i\rangle$ is the self-energy of the ith trapped electron due to its own exciton cloud. The last term of (37) is interpreted as an attractive Coulomb interaction due to the exchange of excitons between the exciton cloud surrounding the first electron and that surrounding the second electron. We now see that in the actual calculation of $\langle F|H_{ex}|F\rangle$ in reference [10], we treat the whole exciton cloud as two independent exciton clouds each surrounding one of the two trapped electrons. This picture is quite analogous to that appearing in the exciton theory of Haken[14]. In contrast to this, we treat the whole exciton cloud as one cloud throughout the calculation in Section 2 of the present paper.

Adopting the method developed in reference [10] and considering (37), we have from (9) the effective Hamiltonian of the F' center in an alkali halide

$$H_{\text{eff}} = \sum_{i=1}^{2} \mathscr{H}_{\text{eff},i} + (e^2/\epsilon_2 r_{12}) \quad (39)$$

where $\mathscr{H}_{\text{eff},i}$ is now given by

$$\mathscr{H}_{\text{eff},i} = (p_i^2/2m_e) - (Me^2/d) + (1-(1/\epsilon_\infty))(e^2/r_i) + \langle F_i|H_{ex,i}|F_i\rangle \quad (40)$$

for $|\mathbf{r}_i| < R$ and

$$\mathscr{H}_{\text{eff},i} = (p_i^2/2m) - (e^2/\epsilon_s r_i) + \langle F_i|H_{ex,i}|F_i\rangle + \langle \Phi_i|H_{ph,i}|\Phi_i\rangle \quad (41)$$

for $|\mathbf{r}_i| > R$. ϵ_2 in the last term of (39) is introduced to account for exchange effects of excitons and phonons between the two trapped electrons; it is (i) the usual high-frequency dielectric constant ϵ_∞ for the case in which the two trapped electrons are both inside the spherical region of radius R, because in this case only the exciton exchange occurs, and (ii) the usual static dielectric constant for the case in which the two trapped electrons are both outside the spherical region, because both the exciton and the phonon exchanges occur. In view of the discussion following equation (21) and that following equation (25) for the choice of a value for ϵ_1 in (9), we shall choose $\epsilon_2 = \epsilon_s$ in the following calculation involving $\psi_g(\mathbf{r}_1, \mathbf{r}_2)$ given by (18) and $\epsilon_2 = \epsilon_\infty$ in the calculation involving $\psi_g(\mathbf{r}_1, \mathbf{r}_2)$ given by (22).

We have also adopted H_{eff} given by (39) and followed the approaches used in Sections IV and V(B) of reference [10] to calculate the ground and excited states of the F' center in the crystals considered. The calculated results are summarized in Tables 3 and 4.

4. DISCUSSION AND CONCLUSIONS

Obviously, the accuracy of the present calculation depends mainly on the choice of R, the method used and the wave function employed. The value of R used in this work is chosen to be the same as that in the F-, center calculation[9]. This seems reasonable since the present R is defined (as in reference [9]) such that the ith trapped electron (equi-

Table 3. Calculated variational parameters in $\psi_g(\mathbf{r}_1, \mathbf{r}_2)$ and $\psi_e(\mathbf{r}_1, \mathbf{r}_2)$ in which the 1s *wave function is the hydrogenic* 1s *wave function, energy levels and absorption energies* ΔE *for* F′ *centers in* KCl, KBr *and* NaCl. *Variational parameters are given in* Å^{-1} *and energies in eV (Calculation B)*

	α†	E_g	λ	β	E_e	ΔE
KCl	0·40	−3·05	0·40	0·20	−1·41	1·66
KBr	0·40	−2·91	0·35	0·20	−1·33	1·58
NaCl	0·45	−3·73	0·40	0·25	−1·74	1·99

†The two variational parameters in $\psi_g(r_1, r_2)$ are found to be the same here also.

Table 4. Calculated variational parameters in $\psi_g(\mathbf{r}_1, \mathbf{r}_2)$ and $\psi_e(\mathbf{r}_1, \mathbf{r}_2)$ in which the 1s *wave function is the modified* 1s *wave function, energy levels and absorption energies* ΔE *for* F′ *centers in* KCl, KBr *and* NaCl. *Variational parameters are given in* Å^{-1} *and energies in eV (Calculation B)*

	γ	E_g	γ	β	E_e	ΔE
KCl	0·65	−3·02	0·65	0·08	−1·32	1·70
KBr	0·65	−3·10	0·60	0·08	−1·29	1·81
NaCl	0·75	−3·81	0·75	0·08	−2·11	1·70

valently, the *F*-center electron) is capable of polarizing the lattice and the effective mass approximation is valid for $|\mathbf{r}_i| > R$.

It turns out that the method described in Section 2 and that used in Section 3 give nearly the same results for quantities determining quantum states and the absorption energy of the *F*′ center, if we take the hydrogenic 1*s* wave function as the trial wave function for the 1*s* electronic orbital involved in the ground and excited states of the *F*′ center. The corresponding theoretical absorption energies (Tables 1 and 3) are in fairly good agreement with experimental frequencies of band maxima of *F*′ bands in KCl, KBr and NaCl (See Table 5 where theoretical absorption energies of La and Bartram[8] are also given, for comparison). On the other hand, if we take the modified 1*s* wave function as the trial wave function for the 1*s* electronic orbital involved in the wave functions considered, the method given in Section 2 and that in Section 3 lead to the result that the *F*′ band may be identified with the direct ionization of the *F*′ center (since $\beta = 0{\cdot}08\,\text{Å}^{-1}$). However, the corresponding theoretical absorption energies (Tables 2 and 4) of *F*′ centers are in poor agreement with experimental values. The largest discrepancy of absorption energies occurs in the method of Section 2. In view of this and the fact that the only difference between the two methods used is the treatment of the effect of the electronic polarization on the system of the two trapped electrons, and that the modified 1*s* wave function is more compact than the hydrogenic 1*s* wave function, we would conclude that the approach described in Section 2, for dealing with the electronic polarization, may not be applicable for a deep electronic state. Thus, we feel that, generally speaking, a method including explicitly the exchange effects of excitons and phonons between the two trapped electrons seems more appropriate in treating the effects of electronic and ionic polarizations on a two-electron center. However, these exchange effects have not been treated in more detail in this work and hence a rigorous study of these effects is called for. Such a study may improve the present theoretical results.

Furthermore, we see from the above discussion that the use of the hydrogenic $1s$ wave function for the $1s$ orbit involved in $\psi_g(\mathbf{r}_1, \mathbf{r}_2)$ and $\psi_e(\mathbf{r}_1, \mathbf{r}_2)$ may be more appropriate than that of the modified $1s$ wave function. It is worthwhile noting that the latter wave function is found to be a good wave function for describing the ground state of the F electron. The reason why the modified $1s$ wave function is not appropriate for the F' electron may be the following. In the case of the F' center, because of Coulomb repulsive force between the two trapped electrons, the size of the electronic orbit is larger than that in the F center. Hence the F' electron sees the negative ion vacancy as a unit positive point charge and, therefore, the hydrogenic $1s$ wave function is more reasonable than the modified $1s$ wave function.

The optically ionized excited state (i.e. the optically excited state for $\beta \to 0$) of the F' center is also calculated by setting β in E_e given by (35) equal to zero and minimizing the resulting E_e with respect to the variational parameter in the hydrogenic $1s$ wave function. We find that the energy of the optically ionized excited state of the F' center is $-1{\cdot}09$ eV for KCl, $-1{\cdot}14$ eV for KBr, and $-1{\cdot}40$ eV for NaCl. Comparing these values with the corresponding E_e listed in Table 1, we see that the optically ionized excited state is always above the optically excited state $\psi_e(\mathbf{r}_1, \mathbf{r}_2)$ of interest. We then conclude that the optically excited state to which the transition corresponding to the band maximum of the F' band can be made from the ground state of the F' center is a weakly bound state. The binding energy, obtained by taking the difference between the energy of the optically ionized state found above and E_e listed in Table 1, is found to be 0·28 eV for KCl, 0·17 eV for KBr, and 0·29 eV for NaCl. These binding energies are expected to be reasonable from the observed thermal binding energy, 0·04 ~ 0·08 eV, of the F' center in KBr[4], since, generally, the optical binding energy is larger than the thermal binding energy. We note that these optical binding energies are much less than those of the optical $2p$ excited states of F centers in typical alkali halides (approximately 0·5 eV, see [9]).

Thus, the above results lead to the conclusion that the F' band in a typical alkali halide is due to the optical transition from the ground state of the F' center to its $1s2p$-like singlet excited state modified by the crystal field.

We have not calculated the oscillator strength for the F' center, since a detailed form of the oscillator strength for an electron-excess center based on the polaron model is not yet established. Nevertheless, we would make a remark that in the polaron model the total oscillator strength of a color center having N trapped electrons may be greater than N, because of a small admixture of exciton oscillator strength. This remark is consistent with that proposed by Smith and Dexter from another point of view[15].

REFERENCES

1. (a) PICK H., *Ann. Phys.* **31**, 365 (1938); (b) *Nuovo Cim. suppl.* 7, 498 (1958)
2. DOMANIC F., *Ann. Phys.* **43**, 187 (1943)
3. SEITZ F., *Rev. mod. Phys.* **18**, 384 (1946)
4. CRANDALL R. S., *Phys. Rev.* **138**, A1242 (1965). The possibility that the F' center in KBr has a bound excited state is drawn from a discussion given in the last section of this reference.
5. PEKAR S. I., In *Untersuchungen uber die Elektronentheorie der Kristalle*. Akademie Berlin (1954).
6. CHEBAN A. G., *Optika Spectrosk.* **10**, 253 (1961), *ibid.* **14**, 269 (1963)
7. PINCHERLE L., *Proc. phys. Soc.* **A64**, 648 (1951)
8. LA S. Y. and BARTRAM R. H., *Phys. Rev.* **144**, 670 (1966).
9. WANG S., *Phys. Rev.* **153**, 939 (1967).
10. WANG S., *Phys. Rev.* **170**, 799 (1968).
11. CHEUNG T. H. and WANG S., *Phys. Status Solidi* **24**, 509 (1967)

12. CHANDRASEKHAR S., *Astrophys. J.* **100**, 176 (1944).
13. MOTT N. F. and GURNEY R. W., In *Electronic Processes in Ionic Crystals*. Clarendon Press, Oxford (1948).
14. HAKEN H., *In Polarons and Excitons* (Edited by C. G. Kuper and G. D. Whitfield), p. 312. Oliver and Boyd, London (1963).
15. SMITH D. Y. and DEXTER D. L., *Bull. Am. phys. Soc.* **13**, 439 (1968); *Intl. Symp. Color Centers in Alkali Halides, Rome, Italy*, Abstract No. 172 (1968).

J. Phys. Chem. Solids Pergamon Press 1969. Vol. 30, pp. 1661–1664. Printed in Great Britain.

SPIN-LATTICE COEFFICIENTS FOR SUBSTITUTIONAL Gd^{3+} IN CaF_2

C. M. BOWDEN†‡
Physics Department, Clemson University Clemson, S. C. 29631, U.S.A.

and

J. E. MILLER
Florida Institute of Technology Melbourne, Florida, U.S.A.

(*Received* 5 *July* 1968; *in revised form* 31 *January* 1969)

Abstract—For the purpose of evaluating the spin-lattice coefficients C_{11} and C_{44}, for $CaF_2:Gd^{3+}$ in cubic sites, uniaxial stress studies were conducted at room temperature on a single crystal of CaF_2 doped with 0·02 at. % Gd^{3+}. From the measured shifts of the magnetic field positions of certain of the fine structure components, corresponding to known increments in applied stress, the spin-lattice coefficients were evaluated in magnitude and sign Taking compressive stress as negative, the experimentally determined values are $C_{11} = -2{\cdot}4 \pm 0{\cdot}8 \times 10^{-13}$ cm/dyn and $C_{44} = -5{\cdot}5 \pm 1{\cdot}1 \times 10^{-13}$ cm/dyn.

INTRODUCTION

For the purpose of determining the effect of applied stress on the crystal field interaction of Gd^{3+} in CaF_2, unixial stress studies were conducted using an Optovac CaF_2 single crystal with approximately 0·02 at. % Gd^{3+} impurity substituted in cubic sites. The measurements were performed at room temperature with a Varian 4500 EPR spectrometer at 9·8 GHz. The stress was applied in increments to the crystal in the microwave cavity.

The results of these studies[1] were reported previously and, though they are revised here, they constitute the first report on the effect of uniaxial stress on the EPR spectrum of an S-state rare earth ion in a cubic field environment. The signs of the previously reported values for C_{11} and C_{44} correspond to the arbitrary choice of taking compressive stress as positive. Feher[2] reported results of uniaxial stress studies for the S-state ions of the iron group Mn^{2+} and Fe^{3+} in the cubic electrostatic field environment of MgO; these measurements were performed at x-band at 77°K. Recently, Calvo and Sroubek[3, 4] reported results of similar studies on two rare earth S-state ions, Gd^{3+} and Eu^{2+} in CaF_2; the measurements for these two ions were done at 9 GHz and 77°K, and 35 GHz and 300°K respectively. Our results are compared with the results given by these authors.

THEORY

The effect, on the EPR fine structure components, of the application of uniaxial stress, is described by the term added to the spin Hamiltonian,

$$\mathbf{S} \cdot \delta\mathbf{D} \cdot \mathbf{S} \tag{1}$$

which describes the perturbation to lower than cubic symmetry induced by the applied stress. The elements of the tensor $\delta\mathbf{D}$ can be written as a linear combination of the applied stress components, χ_{kl}, where

$$D_{ij} = \sum_{kl} C_{ijkl}\chi_{kl}. \tag{2}$$

---

†*Present address:* Solid State Physics Branch, Physical Sciences Laboratory, Redstone Arsenal, Alabama, U.S.A.

‡Work performed as part of a Ph.D dissertation under NASA Fellowship.

For an initially cubic symmetry, there are two independent coupling, or spin-lattice coefficients[5] which must be experimentally determined. In terms of the contracted Voight notation, these are C_{11} and C_{44}.

The development given by Feher[2] gives for the shift in resonance magnetic field position of a fine structure component corresponding to a first order shift in the energy levels due to applied uniaxial stress,

$$\delta H = -\frac{(2M_s-1)}{g\beta}\mathcal{D}(\theta,\phi,\chi_{ij}) \qquad (3)$$

where the component corresponds to the transition $M_s \rightarrow M_s - 1$; θ and ϕ are the polar angles of the applied magnetic field $\mathbf{H}_0$ relative to the crystal axes, and the χ_{ij} are the components of applied stress. The function $\mathcal{D}$ in terms of the spin-lattice coefficients is

$$\begin{aligned}\mathcal{D}(\theta,\phi,\chi_{ij}) = \tfrac{3}{2}\{C_{11}[\chi_{11}(\tfrac{3}{2}\sin^2\theta\cos^2\phi-\tfrac{1}{2})\\ +\chi_{22}(\tfrac{3}{2}\sin^2\theta\sin^2\phi-\tfrac{1}{2})+\chi_{33}(\tfrac{3}{2}\cos^2\theta-\tfrac{1}{2})]\\ +2C_{11}[\chi_{12}\sin^2\theta\sin\phi\cos\phi\\ +\chi_{23}\sin\theta\cos\theta\sin\phi\\ +X_{31}\sin\theta\cos\theta\cos\phi]\}. \qquad (4)\end{aligned}$$

EXPERIMENTAL

The uniaxial stress apparatus used in this experiment is shown in Fig. 1. A General Electric Quartz tube of about $\frac{1}{16}$ in. thick and $\frac{3}{8}$ in. in dia. and flared at the upper end, fits through the cavity and contains the crystal to be stressed, and the means for transmitting a force. The flared end rests on O-rings which are held in place in slots in the brass head. The micrometer barrel is mounted on a bearing which is rigidly imbedded in the brass cap, and the screw is slotted vertically, with the set screw, which screws in from the side of brass cap, riding in the slot. Hence, by turning the brass micrometer barrel, the micrometer screw is advanced without rotating. This is important due to the anisotropy of the ESR spectrum[6].

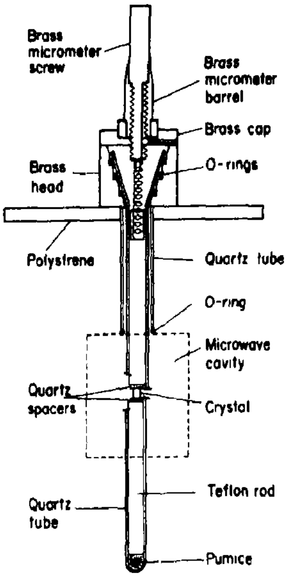

Fig. 1. Uniaxial stress apparatus. The quartz tube containing the crystal fits through the stacks of the Varian room temperature microwave cavity which operates in the TE 102 mode

The brass screw compresses a calibrated phosphore-bronze spring, and a force is transmitted to the sample by a teflon piston which is machined at the top so as to accommodate the spring. The sample rests between two quartz spacers each approximately $\frac{1}{8}\times\frac{3}{16}\times\frac{3}{16}$ in., which distribute the load on the end of the teflon rod. The base pedestal is also teflon and the lower end of the quartz tube is packed with pumice so that the load is uniformly distributed over the hemispherical surface.

The teflon gives only a very weak EPR signal and corresponds to a single very broad resonance with a g-value slightly less than the free electron value. Teflon does not bind with the quartz walls; however, as an added precaution, the piston was well greased with Dow Corning High Vacuum silicone grease, which shows no EPR signal.

Referring to the cubic crystalline axes and taking the applied stress, $\mathbf{P}$, in the [110] and the applied magnetic field, $\mathbf{H}_0$, parallel to the [001] direction, the magnetic field shift of the component corresponding to the transition $M_s \rightarrow M_s - 1$ under applied stress **P** is

$$\delta H = \frac{3}{4}\frac{(2M_s-1)}{g\beta}C_{11}P \qquad (5)$$

where $g = 1{\cdot}992$[7]. If now, $\mathbf{H}_0$ is taken parallel to the $[1\bar{1}1]$ direction, the magnetic field shift for each fine structure component becomes

$$\delta H = \frac{1}{2}\frac{(2M_s-1)}{g\beta}C_{44}P. \qquad (6)$$

It is to be noted that in (5) and (6) a positive increment δH corresponds to a shift to higher magnetic field.

For $\mathbf{H}_0$ parallel to the $[1\bar{1}1]$ direction, the observed shift in magnetic field position under the applied stress is shown in Fig. 2 for the magnetic dipole transitions $M_s = \frac{7}{2} \rightarrow M_s = \frac{5}{2}$ and $M_s = -\frac{3}{2} \rightarrow M_s = -\frac{5}{2}$. Zero initial stresses indicated on the graph actually corresponds to $20\,kg/cm^2$ to $30\,kg/cm^2$, so the stress values given are referred to the initial stress. With the magnetic field $\mathbf{H}_0$ in the [001] direction, the observed shifts under applied stress for the components corresponding to the transitions $M_s = -\frac{5}{2} \rightarrow M_s = -\frac{7}{2}$ and $M_s = \frac{5}{2} \rightarrow M_s = \frac{3}{2}$ are represented in Fig. 3. At the beginning of the final measurement for the $M_s = \frac{5}{2} \rightarrow M_s = \frac{3}{2}$ transition, the sample powdered. For the four transitions observed under applied stress, the magnetic field shift δH was to higher field for positive values of M_s and to lower field for negative values.

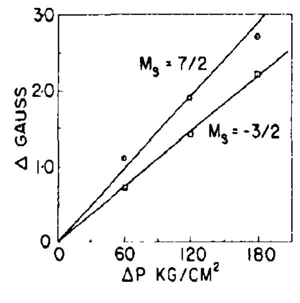

Fig. 2. Magnitude of the magnetic field shift, |δH|, of the indicated fine structure components vs. increase in uniaxial stress ΔP for H_0 parallel to [111] direction and P parallel to [110] direction, with H_0 perpendicular to P.

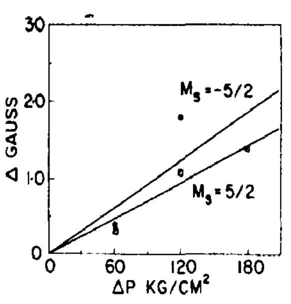

Fig. 3. Magnitude of the magnetic field shift, |δH|, of the indicated fine structure components vs. increase in uniaxial stress ΔP for H_0 parallel to [100] direction and P parallel to [110] direction, with H_0 perpendicular to P.

RESULTS AND DISCUSSION

From the magnitudes of the slopes of the lines drawn through the data points in Figs. 2 and 3 together with the sign of the slopes, the spin-lattice coupling coefficients were evaluated. These values are given in the Table along with the corresponding values quoted by Feher for Mn^{2+} and Fe^{3+} in MgO and the values given by Calvo *et al.* for Gd^{3+} and Eu^{2+} in CaF_2. No detectable change in the g tensor under applied stress was observed in our measurements.

The major source of the uncertainty in our measurements stems from an observed dependency of the stress characteristics of the crystal on its previous stress history. This is manifest as an observed departure of the magnetic field positions of the components from the initial values when the stress is reduced to the initial value. Another source of uncertainty is due to observed broadening of the resonance absorption as stress is applied. This broadening was about 3 per cent at maximum applied stress for the data shown in Fig. 2; however, it was as large as 15 per cent for that shown in Fig. 3. The larger scatter of the data shown in Fig. 3 is evidently

Table 1. Experimentally determined spin-lattice coefficients in units of 10^{-13} cm/dyn

	C_{11}	C_{44}	
MgO : Mn^{2+}	$+7{\cdot}1 \pm 0{\cdot}2$	$-2{\cdot}1 \pm 0{\cdot}1$	Feher[2]
MgO : Fe^{3+}	$+26 \pm 0{\cdot}8$	$-5{\cdot}5 \pm 0{\cdot}3$	Feher[2]
$CaF_2 \cdot Gd^{3+}$	$-2{\cdot}4 \pm 0{\cdot}8$	$-5{\cdot}5 \pm 1{\cdot}1$	**Bowden and Miller**
$CaF_2 : Gd^{3+}$	$-1{\cdot}8 \pm 0{\cdot}2$	$-3{\cdot}0 \pm 0{\cdot}3$	Calvo and Sroubek[3]
$CaF_2 : Eu^{2+}$	$-1{\cdot}7 \pm 0{\cdot}2$	$-10{\cdot}9 \pm 0{\cdot}1$	Calvo and Sroubek[3]

associated with this broadening which may be due largely to non-uniform distribution of the applied force caused by difficulty in polishing the ends of the crystal flat and parallel.

Comparing the values for the spin-lattice coefficients presented in Table 1, it is seen that they are well within the same order of magnitude for the four different cases. This is surprising, since it would be expected that the interaction would be less strong for the rare earth ions where the magnetic 4*f* electrons are inside filled 5*s* and 5*p* shells, than for the iron group ions, where the electrons of the half-filled 3*d* shell are exposed directly to the neighboring ligands. It seems that considerable admixture of higher energy states into the ground state is necessary in order to account qualitatively for the large values for the spin-lattice coefficients of the rare earth ions.

A theory using the point charge model and treating the relaxation process of an *S*-state ion in terms of spin-orbit interaction due to admixture of higher energy states into the ground state has been presented by Blume and Orbach[8] for the *S*-state ion of the iron group Mn^{2+} in a cubic environment. This theory predicts the correct order of magnitude for the coefficients, C_{11} and C_{44}, but fails to predict the correct signs as obtained from experiment[2]. Another theory presented by Leushin[9], which uses the spin-spin interaction between electrons as the relaxation mechanism, predicts the correct sign but does not give the correct ratio of the coefficients. A similar calculation for a rare earth ion in the *S*-state does not seem to exist in the literature.

Acknowledgements – Gratitude is expressed to R. A. Shatas of the Physical Sciences Laboratory for some helpful suggestions in the preparation of the manuscript

REFERENCES

1. BOWDEN C. M. and MILLER J. E., *Bull. Am. phys. Soc.* **13**, 245 (1968)
2. FEHER E. R., *Phys. Rev.* **136**, 145 (1964)
3. CALVO R. and SROUBEK Z., *Bull. Am. phys. Soc.* **13**, 901 (1968).
4. CALVO R., ISAACSON R. A. and SROUBEK Z., *Phys. Rev. Lett.* **21**, A2 (1968)
5. FUMI F. G. *Acta crystallogr.* **5**, 44 (1952)
6. KITTEL C. and LUTTINGER J. M., *Phys. Rev.* **73**, 162 (1948)
7. RYTER C., *Helv. Phys. Acta* **30**, 353 (1957).
8. BLUME M. and ORBACH R., *Phys. Rev.* **127**, 1587 (1962)
9. LEUSHIN A. M., *Soviet Phys. solid St.* **5**, 440 (1963).

J. Phys. Chem. Solids Pergamon Press 1969. Vol. 30, pp. 1665–1672. Printed in Great Britain.

A NEW HIGH PRESSURE PHASE OF $MnTiO_3$ AND ITS MAGNETIC PROPERTY

YASUHIKO SYONO, SYUN-ITI AKIMOTO, YOSHIKAZU ISHIKAWA and YASUO ENDOH
The Institute for Solid State Physics, The University of Tokyo Roppongi, Minato-ku, Tokyo, Japan

(*Received* 12 *November* 1968; *in revised form* 24 *January* 1969)

Abstract – A high pressure phase of $MnTiO_3$ II is newly synthesized at high pressures and temperatures. An equilibrium phase boundary between an atmospheric pressure phase of $MnTiO_3$ I and $MnTiO_3$ II is $P(\text{kb}) = 110 - 0{\cdot}044\,T(°\text{C})$. X-ray analysis of powder specimens has revealed that the high pressure phase $MnTiO_3$ II has the disordered ilmenite structure with the hexagonal lattice parameters of $a = 5{\cdot}2051$ Å, $c = 13{\cdot}699$ Å, $c/a = 2{\cdot}632$ and $V = 321{\cdot}4$ Å[3]. The transformation from $MnTiO_3$ I to $MnTiO_3$ II causes an expansion of the a axis by 1·3 per cent and a contraction of the c axis by 4·1 per cent, resulting a volume decrease of 1·6 per cent. Both Mössbauer effect and paramagnetic ESR measurements suggest that $MnTiO_3$ II is antiferromagnetic below $24° \pm 1°$K. The magnetic susceptibility obeys the Curie–Weiss law almost down to the Néel temperature and slightly deviates from it below T_N, in marked contrast with that of $MnTiO_3$ I. A possibility that the covalency of Mn^{2+} ions plays an important role both in the magnetic interactions and the crystal stability of manganese ilmenites is suggested.

1. INTRODUCTION

$MnTiO_3$, which has the ilmenite structure with rhombohedral $R\bar{3}$ symmetry, is a member of several titanate ilmenites $M^{2+}Ti^{4+}O_3$ (where M = Mg, Ni, Co, Fe, Mn and Cd). The ilmenite structure is an ordered corundum structure in which the Ti^{4+} and M^{2+} ions occupy alternate basal-plane layers of cationic sites. These ilmenites (except $MgTiO_3$ and $CdTiO_3$) are reported to be antiferromagnetic at low temperatures[1–3]. The magnetic structure is determined by the 90° exchange interaction in the layer and the intralayer exchange interaction through two oxygen layers. The magnetic properties of $MnTiO_3$ are quite different from those of other ilmenites [4, 5] and are reported not to be understood within the scope of the conventional crystalline field theory based on the molecular field approximation which was found to be successful for other ilmenites[6].

$MnTiO_3$ seems to be also rather different from other ilmenites from the crystallographic point of view. We have found that $MnTiO_3$ transforms into the disordered ilmenite structure with $R\bar{3}c$ symmetry at high pressures and temperatures. No phase transformation in ilmenites $MTiO_3$ has hitherto been found except $CdTiO_3$, which was reported to transform to a perovskite structure at high temperatures[7].

These characteristic features in the magnetic and crystallographic properties of $MnTiO_3$, which are clearly distinguished from those of other ilmenites, are expected to be closely related to each other. This paper is concerned with the magnetic and crystallographic studies of the disordered ilmenite $MnTiO_3$ II, which are mainly motivated by the anomalous properties of the atmospheric pressure phase $MnTiO_3$ I.

2. EXPERIMENTAL RESULTS

2.1 *Sample preparation and phase equilibrium study*

Starting materials for high pressure runs were powder specimen of $MnTiO_3$ I that had been prepared by intimately mixing $MnCO_3$ and TiO_2 in equimolar proportion, forming pellet and sintering at 1300°C for several hours in a CO_2 atmosphere. X-ray analysis indicated a single phase $MnTiO_3$ I for the quenched products.

Pressure was generated by a tetrahedral

anvil type high-pressure apparatus using pyrophyllite as pressure transmitting material. Pressure calibration was made on the basis of the pressure standard proposed by Jeffery et al.[8]. The heating element consisted of a pure graphite tube, and powder specimens were directly embedded in it. Temperature was measured with a Pt/13%Rh–Pt thermocouple without any correction for the pressure effect on the thermocouple e.m.f.

The specimen was abruptly cooled to room temperature before pressure was released, after being maintained at desired pressure-temperature condition for a sufficient time duration for an equilibrium (e.g. 15 min at 1300°C and 40 min at 900°C). The quenched specimen was examined by X-ray powder diffraction technique. Results of the phase relation study are indicated in Fig. 1, where open circles correspond to unchanged MnTiO$_3$ I and black circles to the newly found phase MnTiO$_3$ II. An equilibrium phase boundary between these two phases is determined as $P(\text{kb}) = 110 - 0{\cdot}044\,T(°\text{C})$. The reverse reaction starting from MnTiO$_3$ II, indicated by a square, revealed a monotropic reaction.

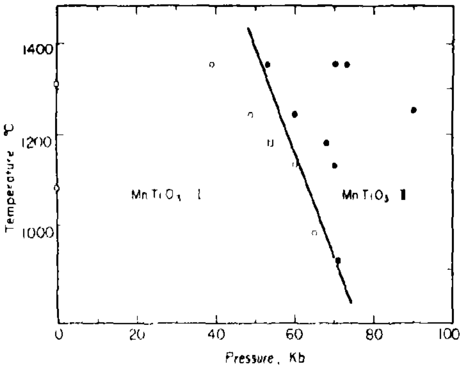

Fig. 1. Phase diagram of MnTiO$_3$ at high pressures and high temperatures. Hollow circle: MnTiO$_3$ I and full circle: MnTiO$_3$ II. Rectangular mark indicates a reverse reaction from MnTiO$_3$ II to MnTiO$_3$ I.

2.2 *Crystallographic properties*

X-ray diffraction lines of the newly synthesized, high pressure phase MnTiO$_3$ II were all indexed by rhombohedral indices with the corundum structure. The lattice parameters of both MnTiO$_3$ I and MnTiO$_3$ II are summarized in Table 1 together with observed *d*-spacings. The agreement between observed and calculated spacings is excellent.

Particular attention was paid to a search for the existence of the 111 diffraction line in the rhombohedral index, because this line is a superlattice line that characterizes the ordered ilmenite structure. However, no trace of this line could be detected, within experimental error, in the case of MnTiO$_3$ II. On the other hand, this 111 line, though weak, was distinctly observed in the case of MnTiO$_3$ I, which has the ordered ilmenite structure. The observed intensity ratio of the 111 diffraction line to the 110 line of MnTiO$_3$ I is about 5 per cent, which is reasonable in comparison with the intensity calculation using the atomic parameters determined by neutron diffraction[1].

Because of the complete absence of the 111 diffraction peak in MnTiO$_3$ II, it can be suggested that the cation distribution in MnTiO$_3$ II is random.

The unit cell length of the hexagonal *a* axis increases by about 1·3 per cent, while that of the *c* axis decreases by about 4·1 per cent, during the transformation from MnTiO$_3$ I to MnTiO$_3$ II. This results in a very large decrease of the *c*/*a* ratio, approaching to the ideal value for hexagonal close-packing, 2·45, and an increase by 2°22′ in the rhombohedral angle α. The volume decrease accompanied by the transformation is 1·6 per cent. With the aid of the Clapeyron–Clausius equation, this gives an entropy change of 0·5 cal/mol.°K during the transition.

It is also interesting to note here that such an order–disorder transformation in the ilmenite structure was found only in MnTiO$_3$. Other ilmenites MTiO$_3$(M = Fe^{2+}, Co^{2+}, Ni^{2+} and Mg^{2+}) do not show any transformation at pressures up to 90 kb at about 1300°C in the present study.

Table 1. *Cell parameters and* d-*spacings of* $MnTiO_3$ I *and* $MnTiO_3$ II

Rhombohedral index	$MnTiO_3$–I			$MnTiO_3$–II		
$h\,k\,l$	d_{obs}	d_{calc}	I	d_{obs}	d_{calc}	I
1 1 1	4·767	4·761	*vw*	—	4·566	—
1 1 0	3·779	3·776	*m*	3·769	3·765	*m*
2 1 1	2·785	2·785	*vs*	2 728	2·727	*vs*
$1\,0\,\bar{1}$	2·568	2·569	*s*	2·604	2·603	*s*
2 1 0	2·2609	2·2607	*m*	2·262	2·261	*w*
2 2 0	1·8882	1·8882	*m*	1·8827	1·8827	*s*
3 2 1	1·7460	1·7461	*m*	1·7162	1·7163	*w*
3 1 0	1·5213	1·5214	*m*	1·5254	1·5254	*m*
$2\,\bar{1}\,\bar{1}$	1·4831	1·4830	*w*	1·5025	1·5026	*m*
hexagonal	$a = 5{\cdot}1374 \pm 0{\cdot}0002$ Å $c = 14{\cdot}284 \pm 0{\cdot}001$ Å $c/a = 2{\cdot}7803 \pm 0{\cdot}004$ $V = 326{\cdot}5 \pm 0{\cdot}1$ Å^3			$a = 5{\cdot}2051 \pm 0{\cdot}0005$ Å $c = 13{\cdot}699 \pm 0{\cdot}003$ Å $c/a = 2{\cdot}6319 \pm 0{\cdot}0009$ $V = 321{\cdot}4 \pm 0{\cdot}1$ Å^3		
rhombohedral	$a_r = 5{\cdot}6096 \pm 0{\cdot}0005$ Å $\alpha_r = 54°30' \pm 1'$ $V_r = 108{\cdot}8 \pm 0{\cdot}1$ Å^3			$a_r = 5{\cdot}4666 \pm 0{\cdot}0011$ Å $\alpha_r = 56°52' \pm 2'$ $V_r = 107{\cdot}1 \pm 0{\cdot}1$ Å^3		

2.3 *Magnetic susceptibility measurements*

The magnetic susceptibility measurements were carried out by means of the conventional magnetic balance in a field up to about 10 kOe for the temperature range from room temperature to liquid He temperature. The absolute value of the susceptibility was calibrated by measuring the magnetic susceptibility of Mohr's salt. Temperature was measured by using the 2%Co-Au/Cu thermocouple, which was calibrated at liquid He, H_2 and N_2 temperatures.

Temperature dependences of magnetic susceptibility of both $MnTiO_3$ I and $MnTiO_3$ II are shown in Fig. 2. No field dependence of magnetic susceptibility for both substances was observed up to the maximum field examined. The magnetic susceptibility of $MnTiO_3$ I shows a broad maximum around 100°K, which is consistent with the previous

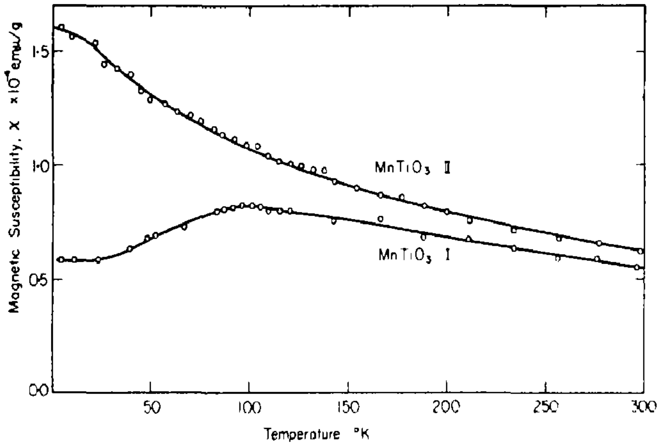

Fig. 2 Magnetic susceptibility vs. temperature of $MnTiO_3$ I and $MnTiO_3$ II

reports[4, 5]. On the contrary, the temperature dependence of magnetic susceptibility of $MnTiO_3$ II is strikingly different from that of $MnTiO_3$ I. It obeys a Curie-Weiss law down to the liquid hydrogen temperature and slightly deviates from it at 4·2°K, as shown in the inverse of magnetic susceptibility, χ^{-1} vs. T relation in Fig. 3. The effective Bohr magneton number determined from the Curie constant is $5{\cdot}95\,\mu_B$, which is reasonable for Mn^{2+} ions. The paramagnetic Curie temperature was determined as −175°K, rather smaller in absolute value than that of $MnTiO_3$ I, −210°K, which was determined from the measurements of high temperature susceptibility[9].

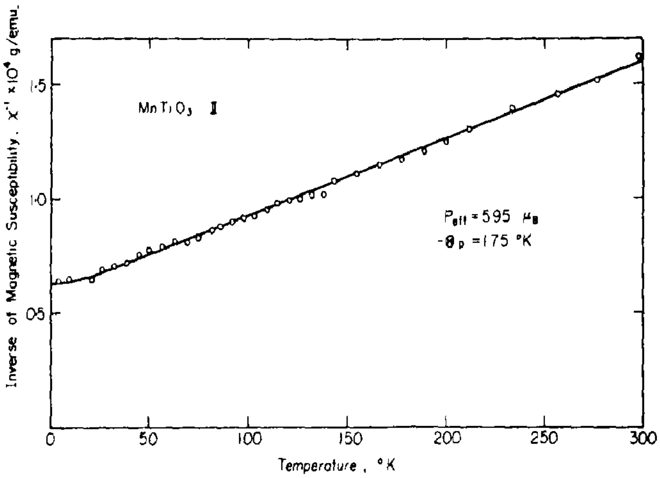

Fig. 3. Inverse of magnetic susceptibility vs. temperature of $MnTiO_3$ II.

2.4 *ESR study*

Paramagnetic resonance absorption was measured on powder samples of $MnTiO_3$ II at 95·3 MHz from 4·2 to 300°K. The ESR signal was observed by means of a waveguide reflection type spectrometer. Temperature was measured by using Au–Co/Pt thermocouple, which was attached to the bottom of the sample wave guide close to the specimen position. For the purpose of calibration, a small amount of DPPH crystal was also placed at the sample wave guide.

The g-factor of $MnTiO_3$ II was determined to be 2·0 at room temperature and showed no temperature dependence down to the Néel temperature. In the region of the Néel temperature, the line width increases exponentially and the resonance peak decreases rapidly as the temperature approaches T_N. In Fig. 4, the temperature dependence of the paramagnetic resonance absorption and the line width observed in $MnTiO_3$ II are presented. The Néel temperature, T_N, is estimated to be 24° ± 1°K by extrapolating the absorption and the inverse of line width to zero independently.

2.5 *Mössbauer study*

Mössbauer measurements were carried out on a 1 per cent $^{57}Fe^{2+}$ doped specimen of $MnTiO_3$. ^{57}Fe as Fe_2O_3 and TiO_2 were mixed with powder specimen of $MnTiO_3$ so as to give 1 mol. % $FeTiO_3$ in $MnTiO_3$. In order to make the iron divalent, the mixture was sintered in a controlled atmosphere of oxygen, which was produced by mixing CO_2 and H_2 gas in the ratio of 1. A high pressure polymorph of this iron doped $MnTiO_3$ was easily obtained, following the same procedure as mentioned in the preparation of pure $MnTiO_3$ II.

The Mössbauer spectrum measured at room

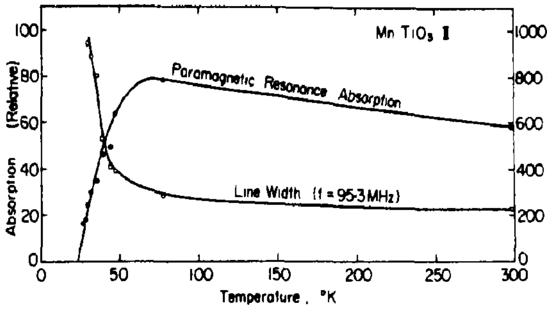

Fig. 4. Temperature dependence of paramagnetic resonance absorption (in arbitrary scale) and width of resonance line of $MnTiO_3$ II measured at the frequency of 95·3 MHz.

temperature was very similar to that of $FeTiO_3$, assuring Fe doped in $MnTiO_3$ is ferrous ion. The isomer shift and quadrupole splitting are 1·29 and 0·83 mm/sec for $MnTiO_3$ I and 1·22 and 1·32 mm/sec for $MnTiO_3$ II, respectively. The isomer shifts of both substances are almost comparable to that of $FeTiO_3$, 1·20 mm/sec[10]. However, the quadrupole splitting of $MnTiO_3$ II is considerably larger than that of $FeTiO_3$, 0·31 mm/sec.

The Mössbauer spectrum of $MnTiO_3$ II measured at 4·2°K showed an ordered magnetic structure. Although the resolution among each line was poor, the ordered Mössbauer spectrum resembles that of $FeTiO_3$. The internal field was roughly estimated to be about 150 kOe.

All of these experimental results suggest that $MnTiO_3$ II of the disordered ilmenite is antiferromagnetic at 4·2°K and the Néel temperature is 24°K.

3. DISCUSSION

We have concluded that the new high pressure phase of $MnTiO_3$ II has the disordered ilmenite structure. The most direct evidence for this is the absence of the 111 superlattice line. Considerable increase found both in entropy and the quadrupole splitting in the high pressure phase $MnTiO_3$ II, compared with those in $MnTiO_3$ I, also supports this conclusion.

We have very recently succeeded in synthesizing a similar disordered ilmenite $MnSnO_3$ at high pressures and temperatures[11]. In the case of $MnSnO_3$, the possibility of the ordered ilmenite structure can be eliminated more definitely than in the case of $MnTiO_3$ II, because of the marked difference in the atomic scattering factors of Mn and Sn. The crystallographic parameters, as shown in Table 2, are more similar to those of $MnTiO_3$ II, rather than those of $MnTiO_3$ I. This will be another evidence for the above conclusion.

The observed magnetic properties of $MnTiO_3$ II can also be explained rather satisfactorily from the viewpoint of the random distribution of Mn^{2+} and Ti^{4+} ions among four sublattice sites in the ilmenite structure. The temperature dependence of the magnetic susceptibility in $MnTiO_3$ II obeys the Curie-Weiss law almost down to the Néel temperature, in marked contrast with that of $MnTiO_3$ I, which has a very broad maximum above the Néel temperature. The similarity in the susceptibility vs. temperature curve of $MnTiO_3$ I to those of K_2NiF_4 and K_2MnF_4, which were reported to be the ideal two dimensional antiferromagnets[12, 13], suggests that the anomalous magnetic properties of $MnTiO_3$ I can also be understood as the characteristics of the two dimensional antiferromagnet. This is quite consistent with the antiferromagnetic

Table 2. Crystallographic parameters of some ilmenites $A^{2+}B^{4+}O_3$

	Hexagonal			Rhombohedral		$\|r_A - r_B\|$	
Substance	a(Å)	c(Å)	c/a	a_r(Å)	α_r	(Å)	Reference
$MnSnO_3$†	5·376	14·025	2·609	5·611	57°14′	0·09	[11]
$MnTiO_3$ II†	5·205	13·700	2·632	5·467	56°52′	0·12	*
$NiTiO_3$	5·031	13·788	2·741	5·437	55°07′	0·01	[1, 21]
$MgTiO_3$	5·052	13·893	2·748	5·471	54°58′	0·02	[21, 24]
$CoTiO_3$	5·066	13·920	2·748	5·485	55°00′	0·04	[3, 21, 24]
$FeTiO_3$	5·088	14·073	2·766	5·535	54°44′	0·06	[2, 21, 24]
$MnTiO_3$ I	5·138	14·283	2·780	5·609	54°30′	0·12	[1]
$MgGeO_3$‡	4·936	13·76	2·788	5·400	54°24′	0·13	[20]
$CdTiO_3$§	5·248	14·906	2·840	5·82	53°36′	0·29	[7, 16]
$MnGeO_3$‡	5·015	14·331	2·858	5·586	53°20′	0·27	[5, 19]
$CdSnO_3$§	5·454	14·968	2·744	5·900	55°02′	0·26	[17]

*Present study.

†Disordered ilmenite stabilized at high pressure.

‡Stabilized at high pressure.

§Transforms to a perovskite structure at high temperature and high pressure

structure of $MnTiO_3$ I determined by neutron diffraction, in which the 90° Mn–Mn interaction within the c layer plays a main role. Such two dimensional characteristics are possibly lost in $MnTiO_3$ II. The interlayer interaction in the disordered ilmenite $MnTiO_3$ II is drastically increased as the adjacent layer is no longer non-magnetic as in $MnTiO_3$ I.

In the disordered ilmenite structure, the nearest neighbor exchange interaction between four sublattice sites can be classified into four types: $J_a(\Gamma_a)$, $J_b(\Gamma_b)$, $J_c(\Gamma_c)$ and $J_d(\Gamma_d)$. (Symbols indicated in brackets are after the notation by Ishikawa and Akimoto [14].) J_a, J_b and J_d are the interlayer interactions, while J_c is the 90° intralayer interaction which is the most important in $MnTiO_3$ I. J_d is also a 90° interaction. If we assume that a magnetic structure of Cr_2O_3 type is realized in $MnTiO_3$ II, the Néel temperature T_N and the assymptotic Curie temperature, θ_p are given in the molecular field approximation to be

$$T_N = \tfrac{1}{2} C_m (3J_c + 3J_a - 6J_b + J_d) \times 0{\cdot}5$$
$$\theta_p = -\tfrac{1}{2} C_m (3J_c + 3J_a + 6J_b + J_d) \times 0{\cdot}5.$$

The factor 0·5 was multiplied because a half of every sublattice site is occupied by non-magnetic Ti ions in the case of $MnTiO_3$ II. When the concentration of non-magnetic atoms is 50 per cent, the probability of existence of magnetically isolated spins or clusters is quite small. Therefore, the molecular field approximation can be used to describe the magnetic properties of the inhomogeneous system[15].

The magnitude of the interaction $\frac{1}{2} C_m J_b$ is directly determined to be 25°K from the measured value of $T_N = 24$°K and $\theta_p = -175$°K. Assuming that the two 90° interactions, J_c and J_d, and the two 135° interactions, J_a and J_b, have almost the same magnitude, respectively, we can estimate the magnitude of $\frac{1}{2} C_m J_c$ to be 31°K. In this case, every interaction has almost the same magnitude, in quite contrast with the dominant 90° Mn–Mn interaction within the c layer in $MnTiO_3$ I. This will be a reason why typical features of two dimensional antiferromagnets are lost and an ordinary three dimensional antiferromagnetism seems to be established in $MnTiO_3$ II with the disordered ilmenite structure. However, it is to be noted here that the 90° Mn–Mn interaction has still almost a comparable magnitude with that of the 135° cation–anion–cation exchange interaction between adjacent layers in the disordered ilmenite $MnTiO_3$ II.

Secondly, we will discuss the stability of the crystal structure of $MnTiO_3$ from the viewpoint of crystal chemistry. In Table 2, crystallographic parameters of several substances $A^{2+}B^{4+}O_3$ with the ilmenite structure were tabulated together with the difference between the ionic radii of paired A^{2+} and B^{4+} ions, $|r_A - r_B|$. The table shows a tendency that the c/a ratio increases as the difference between ionic radii of divalent cations and the Ti^{4+} ion increases in the order of Ni^{2+}, Mg^{2+}, Co^{2+}, Fe^{2+}, Mn^{2+} and Cd^{2+} in the ilmenites $MTiO_3$. This fact suggests that the ilmenite structure becomes unstable if the difference in ionic radii exceeds a certain limiting value. Actually, the ilmenite structure seems to be realized only for the very restricted range of the value $|r_A - r_B| \leqslant 0{\cdot}13$, except for $CdTiO_3$, $CdSnO_3$ and $MnGeO_3$ (cf. Table 2).

This situation seems reasonable from the consideration that the ilmenite structure is basically identical with the corundum structure and a large mismatch in the size of paired ions may introduce a local strain energy. Ilmenite compounds with a large mismatch in the size of paired ions are relatively unstable compared with other ilmenites. Both ilmenites $CdTiO_3$[16] and $CdSnO_3$[16, 17] are unstable at high temperatures and high pressures, subjected to a phase transformation to the perovskite structure. Two germanates $MnGeO_3$[18, 19] and $MgGeO_3$[19, 20] are only stabilized in the ilmenite structure at moderately high pressures. $MnTiO_3$ is also a critical ilmenite because the difference between the ionic radii of ion pairs takes a boundary value. This is possibly a reason why the order–disorder transformation was only found in $MnTiO_3$ but not in other titanate ilmenites $MTiO_3$.

The order–disorder transformation occurs when the Gibbs free energies of the two phases become equal;

$$\Delta G = \Delta U - T\Delta S + P\Delta V$$

where ΔG and ΔU are differences of the Gibbs free energies and the internal energies of two phases. When the specimen is subjected to high pressure and temperature, the disordered ilmenite phase is stabilized because of the decrease in the energy due to $-T\Delta S$ and $P\Delta V$ terms at the cost of the increase in the internal energy change which consists of electrostatic ordering energy. At very high pressures such as some 10 kb, the $T\Delta S$ term is practically negligible compared with the $P\Delta V$ term. Therefore, since the change in the electrostatic ordering energy between the ordered and disordered ilmenite phases is nearly equal for all the ilmenites, the larger the volume difference between the ordered and disordered phases, the smaller the pressure at which a phase transformation takes place.

A volume difference between the ordered and disordered phases would be larger when the difference in the ionic radii of the paired ions of the ordered ilmenite is larger. The solid solutions between ilmenite $MTiO_3$ and hematite αFe_2O_3 where both ordered and disordered phases are realized by the change of composition give an evidence for that[21]. These considerations make us understand the present experimental results that only $MnTiO_3$ showed an order–disorder phase transformation among titanate ilmenites $MTiO_3$.

It is worth noticing that the relatively less stable ilmenites are realized only when they contain Cd^{2+} or Mn^{2+} ions, which have the electronic configuration d^{10} and d^5 respectively. Both the Cd–O and Cd–Cd distance in $CdTiO_3$ with the ilmenite structure have much smaller values than those in other cadmium oxygen compounds like $CdTiO_3$ with the perovskite structure[22]. This suggests that the Cd ion has a covalent character in the ilmenite structure. If we assume a similar covalency exists in the Mn^{2+} ion, both the anomalous magnetic properties and the crystal instability of the manganese ilmenites $MnTiO_3$ I or $MnGeO_3$ can be explained rather consistently.

Previous studies have revealed that the 90° exchange interaction is anomalously strong in $MnTiO_3$ I as in other manganese oxygen compounds. The 90° cation–anion–cation exchange interaction will be weak for Mn^{2+} ions since $MnBr_2$ and $MnCl_2$ with solely the 90° cation–anion–cation exchange interaction show very low Néel temperatures such as 2·16°K and 1·96°K, respectively[23]. The strong 90° interaction between Mn^{2+} ions in the oxides is considered to be due to the cation–cation interaction. It has been reported that the magnetic moment of the Mn^{2+} ion in the antiferromagnetic state of $MnTiO_3$ I determined by neutron diffraction is $4{\cdot}55\,\mu_B$[1] which is remarkably smaller than the value estimated from the high temperature susceptibility[9]. A possible interpretation of this fact is that the magnetic *d* electron expands more than the *d* electron wave function in the isolated atoms. It is interesting to suggest that such covalency effect may play an important role in stabilizing the ilmenite structure with the large mismatch of the paired ions. This may be a reason why only $MnGeO_3$, except for $MgGeO_3$, among $MGeO_3$ compounds, is stabilized in the ilmenite structure.

Acknowledgements—The authors are indebted to Dr. A. Ito for the Mossbauer measurements and Mr. M. Tanaka of the Department of Physics, the University of Tokyo for the ESR study.

REFERENCES

1. SHIRANE G., PICKART S. J. and ISHIKAWA Y., *J. phys. Soc. Japan* **14**, 1352 (1959).
2. SHIRANE G., PICKART S. J., NATHANS R. and ISHIKAWA Y., *J. Phys. Chem. Solids* **10**, 35 (1959).
3. NEWNHAM R. E., FONG J. H. and SANTORO R. P., *Acta crystallogr.* **17**, 240 (1964).
4. STICKLER J. J., KERN S., WOLD A. and HELLER G. S., *Phys. Rev.* **164**, 765 (1967).
5. SAWAOKA A., MIYAHARA S., AKIMOTO S. and FUJISAWA H., *J. phys. Soc. Japan* **21**, 185 (1966).
6. GOODENOUGH J. B. and STICKLER J. J., *Phys. Rev.* **164**, 768 (1967).
7. POSNJAK E. and BARTH T. F. W., *Z. Kristallogr.* **88**, 271 (1934).
8. JEFFERY R. N., BARNETT J. D., VANFLEET H. B. and HALL H. T., *J. appl. Phys.* **37**, 3172 (1966).
9. ISHIKAWA Y. and AKIMOTO S., *J. phys. Soc. Japan* **13**, 1298 (1958).
10. RUBY S. L. and SHIRANE G., *Phys. Rev.* **123**, 1239 (1961).
11. SYONO Y., SAWAMOTO H. and AKIMOTO S., *Solid State Comm.* In press (1969).
12. BREED D. J., *Physica* **37**, 35 (1967).
13. DE VRIES G., BREED D. J., MARSHALL F. P. and MIEDEMA A. R., *J. appl. Phys.* **39**, 1207 (1968).
14. ISHIKAWA Y. and AKIMOTO S., *J. phys. Soc. Japan* **12**, 1083 (1957).
15. ISHIKAWA Y., *J. appl. Phys.* **35**, 1054 (1964).
16. LIEBERTZ J. and ROOYMANS C. J. M., *Z. phys. Chem. Neue Folge* **44**, 242 (1965).
17. MORGENSTEIN-BARADAN I., POIX P. and MICHEL A., *C. r. hebd. Seanc. Acad. Sci., Paris* **256**, 692 (1963).
18. RINGWOOD A. E. and SEABROOK M., *Nature* **196**, 883 (1962).
19. RINGWOOD A. E. and SEABROOK M., *J. geophys. Res.* **68**, 4601 (1963).
20. RINGWOOD A. E. and SEABROOK M., *J. geophys. Res.* **67**, 1690 (1962).
21. ISHIKAWA Y. and AKIMOTO S., *J. phys. Soc. Japan* **13**, 1110 (1958).
22. BARTH T. F. W. and POSNJAK E., *Z. Krist.* **88**, 265 (1934).
23. GOODENOUGH J. B., In *Magnetism and the Chemical Bond*. Interscience, New York (1963).
24. AKIMOTO S. and SYONO Y., *J. chem. Phys.* **47**, 1813 (1967).

J. Phys. Chem. Solids **Pergamon Press 1969. Vol. 30, pp. 1673–1680. Printed in Great Britain.**

I.R. ABSORPTION CORRESPONDING TO TRANSITIONS OF HOLES FROM IMPURITY LEVELS TO THE VALENCE BAND IN SILICON AND GERMANIUM

TORSTEN STAFLIN
Physics Department and Institute of Optical Research, Royal Institute of Technology,
Stockholm 70, Sweden

(*Received* 24 *December* 1968)

Abstract – Absorption due to indirect transitions of holes from the boron levels to the valence band in silicon was recorded with the aid of penetrating exciting light. Two peaks for the absorption change produced by illumination were obtained which could be related to transitions from the two upper valence bands and from the lower valence band to the impurity level respectively. The participating phonon energies were determined and a value for the spin-orbit splitting in silicon was obtained. The measurements also made it possible to explain certain results from earlier measurements on boron-doped and indium-doped silicon. The absorption increase recorded as a function of the exciting light intensity was in good agreement with a curve calculated theoretically for the assumed conditions. From the results obtained, the conclusion may be drawn that the time interval during which the bound holes preserve their k values is considerably larger than the lifetime of the holes. Finally, some measurements were made on intrinsic and gold-doped germanium and the spectral distribution of the absorption due to a gold level was determined.

INTRODUCTION

IN PREVIOUS works, the impurity levels in silicon and germanium have been studied mainly with the aid of measurements of conductivity and transmission. Later on, investigations on silicon were made by the author according to a method in which the carriers were excited by light. The exciting light was chopped and the resulting modulation of the i.r. beam was recorded. This technique made it possible to detect both fast and slow effects[1–4]. By fast effects, we mean processes with the time constant $\tau \ll 1/f$ where f is the chopper frequency. A Perkin-Elmer spectrophotometer was used in the measurements. In the present work, the same technique was used to investigate the impurity absorption in boron-doped and gold-doped germanium. The crystals used were etched and polished rectangular plates 10 × 15 mm in area and 1–2 mm thick.

RESULTS AND DISCUSSION

Absorption due to boron levels in silicon

With the chopper 90° out of phase with the detector system (measurement of the slow effects), the dominant absorption change produced by illumination corresponds to transitions (1) and (7) from the valence band to the boron level, cf. Fig. 1 and was brought about by the exciting light which, by exciting electrons across the bandgap, caused an increase in the number of electron transitions from the conduction band to the impurity level (transition 2).

With the chopper in phase with the detector system, the dominant absorption change produced by illumination corresponds to transitions (6) and (8) in boron-doped silicon and was caused by the penetrating exciting light which, by exciting electrons from the impurity level to the conduction band (transition (5)) caused an increase of the hole

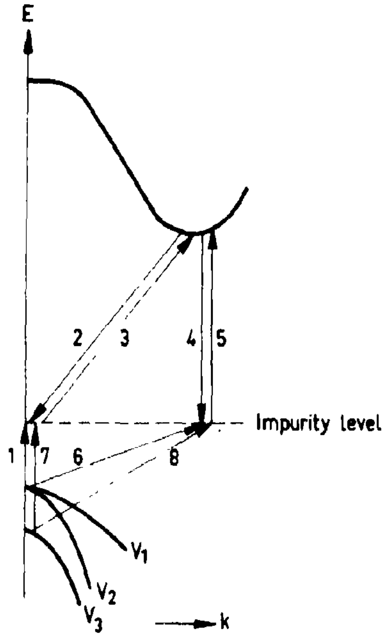

Fig. 1 The band structure of silicon v_1, v_2 and v_3 are the three valence sub-bands. The arrows indicate electron transitions. (2), (3), (6) and (8) are indirect transitions which can occur with the participation of phonons.

occupancy of the level. Emission and absorption corresponding to transitions (2–4) have been detected directly earlier[2, 5, 6].

From earlier measurements[4] on boron-doped silicon, it is evident that, with the chopper in phase with the detector system, no absorption change, due to free carriers, could be detected in considerable parts of the wavelength region. This is due to the fact that the lifetime of the free carriers is too small in strongly doped material, and the increase in the density of free carriers $S = Q\cdot\tau$ is consequently small. Q is the number of excited carriers per unit volume and unit time and τ is the lifetime. At about 0·10 eV, an absorption increase due to illumination was detected when no extra filters were used in the exciting light beam and penetrating light was present. By illuminating with the penetrating exciting light, electrons were excited from the boron level to the conduction band and, as a result, an absorption increase for the radiation whose photon energy corresponds to the transition between the acceptors and the valence band was obtained. One might therefore expect, if the transitions causing the absorption are mainly direct, an absorption curve with a sharp rise at about the photon energy corresponding to the ionization energy of the boron level. If, however, most of the transitions are indirect, viz. the transitions occur in interaction with phonons, a displacement of the rise in some direction should occur. The absorption curve recorded earlier[4] seems to be the result of indirect transitions. A rough estimate of the energy of the participating phonon was made. The recorded absorption is interpreted as being caused by the transitions between the valence band maximum of the v_1 and v_2 bands and impurity levels at the same k value, k_c, as the conduction band minimum.

In the present work, more accurate measurements, in which the region towards shorter waves was especially examined, were made on the band. As a result of this one more peak was detected, cf. Fig. 2, which thus made a more accurate interpretation possible. The curve recorded seems to be built up from a superposition of two different absorption curves, one due to indirect transitions from the maximum of the valence bands v_1 and v_2 to the impurity level and the other due to indirect transitions from the maximum of the v_3 band to the impurity level. The active impurity states seem to have k values around k_c. In the author's earlier works, where electrons were excited with white light across the bandgap up into the conduction band after which they recombined with the impurity level, the absorption corresponding to transitions from the valence band to the impurity level was recorded and an absorption decrease was obtained, corresponding to the direct transitions (1) and (7). This was to be expected from the works of Pokrovskii *et al.*[5] who have recorded recombination radiation due to electron transitions between

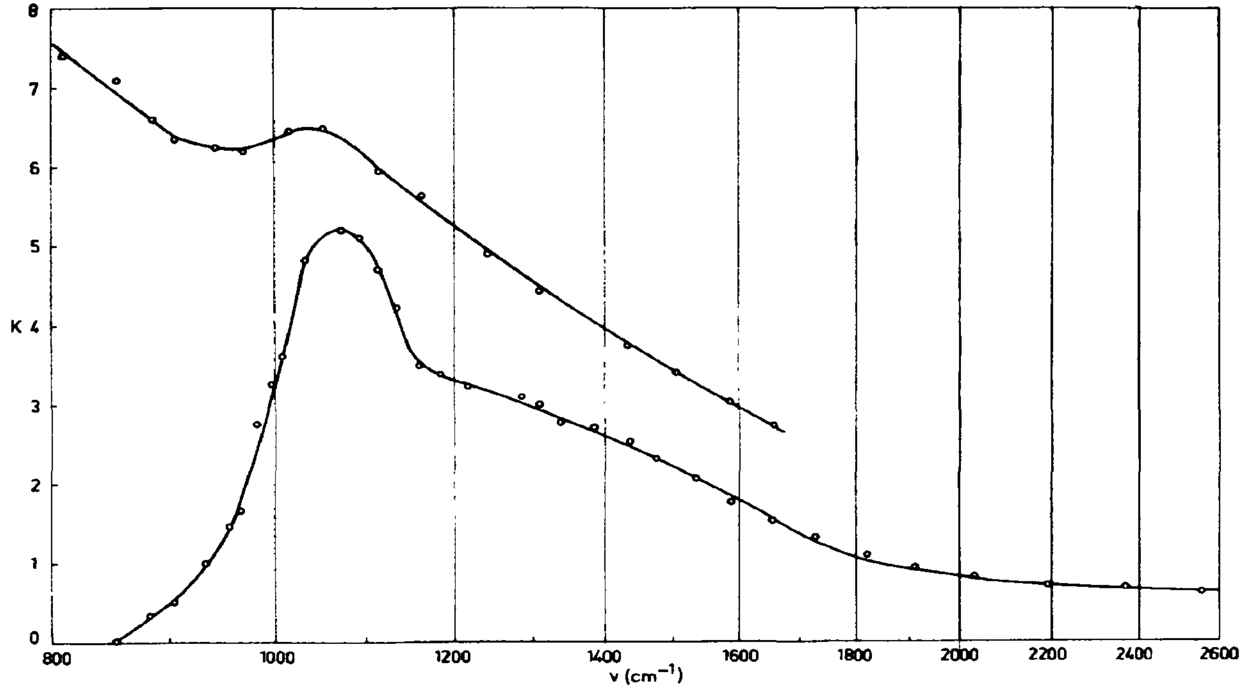

Fig 2. The change K in the absorption coefficient produced by illumination as a function of wave number ν for a boron-doped crystal with the resistivity 1·2 Ω cm at 95°K. The upper curve was registered with the chopper about 90° out of phase and the lower one with chopper in phase with the detector system. They illustrate the absorption distribution due to direct and indirect transitions between the valence band and the boron level respectively.

the conduction band minimum and the impurity level and have found that most transitions occur to states with $k \approx 0$ in boron-doped samples when white light was used. They have also found transitions to states with other k values, especially in silicon doped with impurities with a larger ionization energy where direct transitions have been recorded. It follows from their measurements that such impurity states exist. The present measurements support this last conclusion. In the present measurements, the main transitions seem to occur to states with $k = k_c$. This is a result of the method of excitation. In Fig. 3, the penetrating radiation is plotted and it is seen that the active exciting light comes from the region just outside the band edge and that the intensity increases toward lower energies and is large for a photon energy corresponding to the direct transition between the impurity level and the conduction band. The intensity is relatively small for energies corresponding to the indirect transitions occurring between the impurity level and the conduction band with the emission of a phonon which is a more probable process than the absorption of a phonon at the temperature 95°K. Direct transitions are more probable than indirect transitions. Most active states should therefore be situated at $k = k_c$ if the lifetime of the bound holes is small compared with the time interval during which these holes preserve their k values.

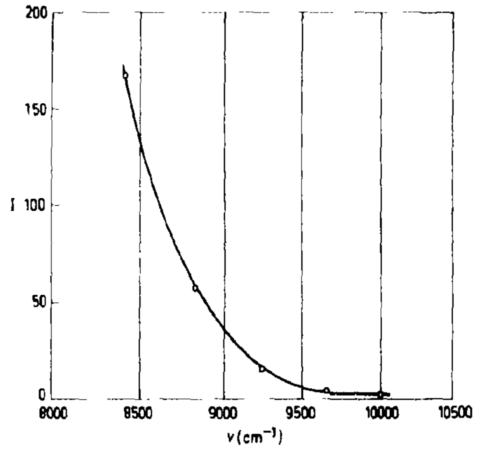

Fig. 3 The intensity of the penetrating i.r. light as a function of the wave number ν.

The curve in Fig. 2 shows that sharp increases are situated at about 0·105 and 0·143 eV. The first rise may be due to indirect transitions from the v_1 valence band to the most active states while the second may be due to indirect transitions from the v_3 band to the same impurity states. From these measurements, it is possible to obtain the energy values of the participating phonons and the spin-orbit splitting ΔE. From the first rise, the expression $0{\cdot}105 = 0{\cdot}046 + \hbar\omega$ is obtained and, from the second, $0{\cdot}143 = 0{\cdot}046 + h\nu_0 + \hbar\omega$. The value 0·046 is taken from earlier measurements of the ionization energy of the boron level. From the first expression we get, $\hbar\omega = 0{\cdot}059$ eV and, if this value is used in the second one, we find the value 0·038 eV for the spin-orbit splitting which agrees with our earlier determinations. A phonon with the energy 0·055 eV was also active in the recombination measurements of Pokrovskii *et al.* Macfarlane *et al.* studied the structure of the absorption edge in the temperature range 4·2°–415°K. In the whole range, a structure due to the emission of a phonon with the energy 0·058 eV was found. As in the present measurements, they could not find any structure due to absorption of this phonon at 90°K. Earlier measurements [2] at 330°K of the absorption corresponding to transitions of electrons from the boron level to the conduction band, i.e. direct measurements upon the type of transition which, in the present measurements, corresponds to the photon energy of the exciting light, show that the same phonon participates in this indirect transition. At 330°K one may expect transitions with the absorption of a phonon to take place to a large extent. From Figs. 10 and 11 in [2], it is seen that the absorption increase begins at 0·99 eV which gives the expression $0{\cdot}99 = E_k - \hbar\omega$, where E_k is the energy difference between the conduction band minimum and the impurity level. At 330°K, $E_k = 1{\cdot}05$ eV. This gives $\hbar\omega = 0{\cdot}06$ eV, a value in agreement with earlier determinations.

The present measurements provide an additional determination of the spin-orbit splitting in silicon[3] and also indicate that the boron hole states are spread to k values differing from zero.

The measurements of Pokrovskii *et al.*[5] also support this result. Their recombination curves show that the distribution of the density of states in k space is dependent upon the ionization energy which has also been indicated by theoretical treatment. The boron level, with its relatively small ionization energy, has the greatest density of states at $k = 0$ while the indium level, which has a larger ionization energy, seems to have a relatively greater density of states at $k = k_c$. These facts agree with both the present measurements and our earlier ones on boron-doped silicon.

The absorption change corresponding to transitions (1) and (7) was dominant when using a phase shift of 90° and with white light excitation since the density of states is greatest at $k = 0$ and transition (2) is dominant. With the chopper in phase with the detector system, an absorption change corresponding to transitions (6) and (8) was obtained by exciting electrons from the impurity level to the conduction band with light which had a high intensity in the energy region, corresponding to the energy gap for transition (5). The exciting light empties the level of electrons or fills it with holes. It is then possible for more electrons to be excited into the level (transitions (6) and (8)). There must be an increase in the hole density at $k = k_c$ if absorption due to transitions (6) and (8) is to be dominant. Another condition for this type of absorption is that the time interval during which the bound holes preserve their k values is large compared with the lifetime of the holes. The present results indicate that this is so.

Later measurements by Pokrovskii *et al.* [6] also point to the same conclusion. They gave curves for the recombination radiation due to electron transitions from the conduction band to the boron level. The increase in the conduction electron density was brought about in two ways, viz. by exciting electrons across the band gap with white light and also by exciting electrons from the impurity level to the conduction band by penetrating i.r. light. The same ways of excitation were used in the present work. With white light they recorded mainly the emission corresponding to the indirect transitions (2) with the emission of phonons with the energy 0·056 eV, viz. the very transitions which, in our measurements, were expected to cause the absorption change produced by illumination with white light (corresponding to transitions (1) and (7)) which is recorded with the chopper 90° out of phase with the detector system. With weak penetrating infra-red radiation, they obtained an emission band at about a photon energy of 1·11 eV which seems to correspond to direct electron transitions (4) between the conduction band minimum and the impurity level. The presence of such recombination radiation indicates that most holes are obtained with $k = k_c$ and that the time interval during which these holes preserve their k values is large compared with the lifetime of the holes. This is in agreement with the results of the present measurements where the absorption change produced by illumination with i.r. light was recorded with the chopper in phase with the detector system. This absorption change, corresponding to the indirect transitions (6) and (8), is considered to be due to the direct transitions (4) recorded by Pokrovskii.

Absorption due to indium levels in silicon

In indium-doped silicon, with the chopper 90° out of phase with the detector system, the dominant absorption change produced by illumination corresponded to transitions (6) and (8) from the valence band to the impurity level. It was produced by means of the exciting light which, by exciting electrons across the band gap, caused an increase of the electron occupancy of the impurity level. This change was due to an increase in the number of transitions from the conduction band to the impurity level (transitions (4))[3].

The measurements on indium-doped silicon at 90°K gave a curve with two peaks, cf. Fig. 11 in[3]. This curve is actually a superposition of two absorption curves, one due to transitions of electrons from valence bands v_1 and v_3 to the impurity level and the other due to transitions of electrons from the v_3 band to the impurity level. This curve is analogous to the one obtained for boron-doped silicon in the present work but the curves are obtained with different chopper phases and with different excitation techniques. While the curve for the indium-doped crystal was obtained with an excitation of electrons across the band gap and with the chopper 90° out of phase with the detector system, the curve for the boron-doped crystal was obtained with penetrating i.r. light and the chopper in phase with the detector system. That the curves are analogous is due, however, to the fact that the indium hole states are more widely spread in momentum space than the boron states. It was therefore possible to detect absorption corresponding to analogous transitions in boron-doped and indium-doped samples and, in this manner, obtain two sets of values for the participating phonons and for the spin-orbit splitting in silicon. In addition a value for the ionization energy of the indium levels could also be determined.

In Fig. 11 of reference[3], two sharp rises can be seen. The first seems to be due to indirect transitions of electrons, under interaction with phonons, from the valence bands v_1 and v_2 to the impurity level. With the phonon energy determined in the present work (see above), one would expect this rise to occur at a photon energy of 0·16 (ionization energy) + 0·06 (phonon energy) = 0·22 eV which is approximately in agreement with measurements on the indium level. The second rise, corresponding to indirect transitions between the v_3 band and the impurity level, should be situated at 0·16 (ionization energy) + 0·06 (phonon energy) + 0·04 (spin-orbit splitting) = 0·26 eV, approximately in agreement with the measurements.

Comparison between experimental measurements and a deduced theoretical curve for the absorption due to the boron level as a function of the exciting light intensity

The absorption corresponding to the indirect transitions (6) and (8) was used to study further the transitions to and from the boron level. The level was emptied of electrons using light, the photon energy of which was equal to the energy difference between the conduction band minimum and the boron level. The resulting absorption increase is a measure of the density change of the bound carriers. This change was consequently measured directly and corresponds to an equal increase in the electron density in the conduction band if the influence of the valence band can be neglected. This is the case when electrons with a larger probability make transitions to the impurity level rather than recombine with holes in the valence band or when the intensity of the exciting light is large so that the transitions between the impurity level and the conduction band are dominant. This method makes it possible to study transitions between acceptors and the conduction band more closely.

If we neglect the influence of the valence band and assume the above-mentioned conditions, the following equation is valid.

$$\frac{\mathrm{d}\Delta n}{\mathrm{d}t} = -\frac{\Delta n}{\tau} + \left(1 - \frac{\Delta n}{N}\right) \cdot s \qquad (1)$$

$$\tau = [r(2n_0 + \Delta n)]^{-1}$$

where Δn is the increase in the electron density in the conduction band due to the illumination, τ the lifetime of the carriers, N the density of the impurity centres, s the volume excitation rate, r a recombination constant and n_0 the density of the electrons in the conduction band without illumination. The steady state solution of this equation is

$$\Delta n = -\left(\frac{s}{2rN}+n_0\right)+\left[\left(\frac{s}{2rN}+n_0\right)^2+\frac{s}{r}\right]^{1/2} \quad (2)$$

and $\Delta n = k_1 \cdot K$.

K is the change, produced by the illumination, of the absorption coefficient corresponding to transitions between the valence band and the impurity level and k_1, is a constant. If q is the number of incoming quanta per unit surface and unit time and I is the intensity of the exciting light, the relations $q = k_2 \cdot I$ and $s = k_3 \cdot q$ are valid. k_2 and k_3 are constants. We then get $s = k_4 \cdot I$, where k_4 is a constant. If the expressions for Δn and s are used in equation (2), a relation of the following form is obtained.

$$K = -(\alpha+\beta I)+[(a+\beta I)^2+\gamma I]^{1/2} \quad (3)$$

where α, β and γ are constants. By measuring K as a function of I, the points in Fig. 4 are obtained from which it can be seen that the absorption change approaches saturation, when the light intensity increases, which means that the level has been entirely emptied of electrons. The constants α, β and γ were determined from three experimental points and the relation (3) was plotted (cf. Fig. 4). The agreement between the theoretical curve and the experimental points supports the interpretation made.

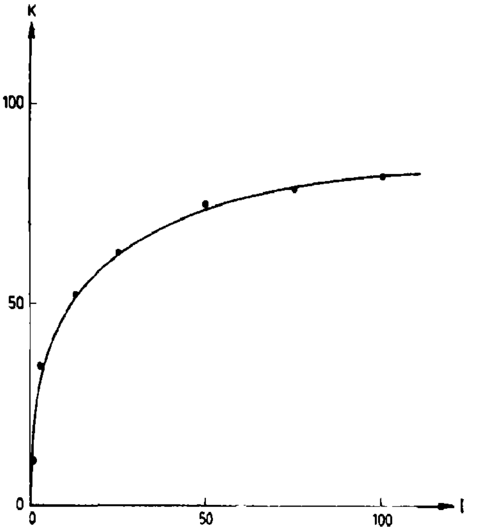

Fig. 4. The change K in the absorption coefficient as a function of the exciting light intensity for a boron-doped crystal with the resistivity 1·2Ωcm at 95°K. The chopper was in phase with the detector system and the measurements were made at the wave number 1070 cm^{-1} corresponding to the absorption peak. The points represent the experimental measurements and the solid line the theoretical curve. The absorption is due to indirect transitions between the valence band and the boron level. The Xenon light excites electrons from the level to the conduction band.

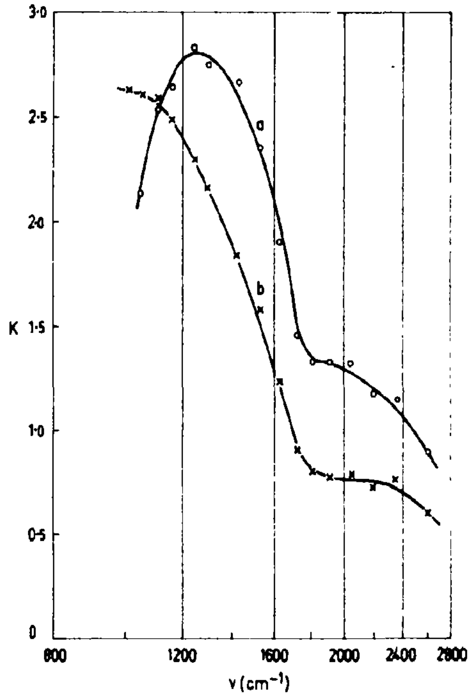

Fig. 5. The change K in the absorption coefficient produced by illumination as a function of wave number for two germanium crystals at 330°K: (a) a gold-doped crystal with the resistivity 8Ωcm The recorded absorption is a superposition of the absorption due to transitions between the valence sub-bands and the absorption due to the gold level. (b) An intrinsic crystal

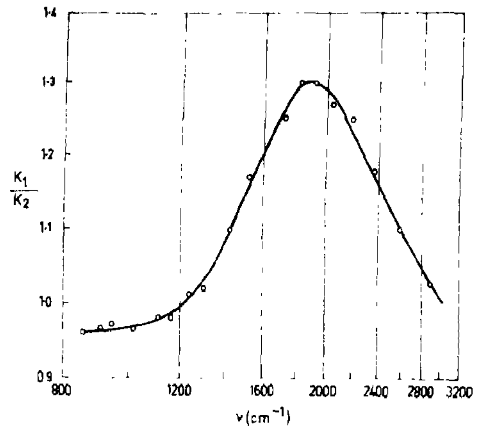

Fig. 6 K_1/K_2 as a function of the wave number ν at 330°K. K_1 and K_2 are the changes in the absorption coefficient produced by illumination of a gold-doped and an intrinsic crystal respectively.

Some measurements on germanium

Measurements on intrinsic and doped germanium were made in the present work to test the usefulness of the method on germanium. Since the absorption corresponding to the interband transitions in the valence band is dominant in the wavelength region in-investigated, the conditions are different from those in silicon. Measurements were made with the chopper approximately in phase with the detector system on both intrinsic and gold-doped germanium. As can be seen from Fig. 5, the interband transitions are dominant but, in the gold-doped material, an absorption due to the gold levels is distinguishable. In Fig. 6, the absorption of the gold-doped sample is plotted with the absorption of the intrinsic crystal as a reference. The curve represents the spectral distribution of the absorption due to a gold level. A sharp rise is seen at about 0·15 eV. This value corresponds to the ionization energy of a gold level.

The crystals upon which the measurements were made had the same dimensions and the same surface treatment. The resistivity of the gold-doped crystals was 8 Ωcm.

REFERENCES

1. STAFLIN T. and HULDT L., *Ark. Fys.* **20**, 527 (1961).
2. STAFLIN T., *J. Phys. Chem. Solids* **26**, 563 (1965).
3. STAFLIN T., *J. Phys. Chem. Solids* **27**, 65 (1966)
4. STAFLIN T., *Ark. Fys.* **31**, 413 (1966).
5. POKROVSKII Ya. E. and SVISTUNOVA K. I., *Soviet Phys. solid St.* **6**, 13 (1964).
6. POKROVSKII Ya. E. and SVISTUNOVA K. I., *Soviet Phys. solid St.* **7**, 1478 (1965).

J. Phys. Chem. Solids Pergamon Press 1969. Vol. 30, pp. 1681–1692. Printed in Great Britain.

NEW METHODS FOR DETERMINING ELECTRON TRAP PARAMETERS FROM THERMOLUMINESCENT OR CONDUCTIVITY 'GLOW CURVES'

PETER L. LAND

Metallurgy and Ceramics Research Laboratory, Aerospace Research Laboratories,
Wright-Patterson AFB, Ohio 45433, U.S.A

(*Received* 24 *August* 1968; *in revised form* 13 *December* 1968)

Abstract – A method of calculating electron or hole trap parameters from the inflection points and maxima of thermoluminescent or conductivity glow curves is described. Equations appropriate to simple theoretical models are discussed. Computer calculations are described in which initial rise data is used to calculate trap parameters from equations which are exact for a specific model. As a consequence, restrictions usually applied to initial rise data are reduced. The effect of temperature gradients on glow curve analysis is discussed

1. INTRODUCTION

SINCE THE early work of Randall and Wilkins [1], and their associates a number of approximate methods for calculating electron or hole trap energies, E, and frequency factors, ϕ, or velocity cross-section products, whichever is appropriate, from glow curves have been worked out. Usually these calculations utilize the temperature, T_*, corresponding to the maximum of the glow curve, the temperatures at half maximum, and the heating rate, β, to derive E and ϕ for some specific statistical model. Surprisingly, no one has considered using the inflection points of glow curves for such calculations. The temperatures for which the second derivative of a glow curve model is zero, together with T_* and β can be used to obtain E from a transcendental equation. The value of ϕ can then be gotten from the equation provided by setting the first derivative equal to zero at T_*. Equations appropriate to some simple models are discussed in this paper. In addition, the analysis of initial rise data is generalized to include a monomolecular rise, and a bimolecular rise as well as the usual exponential rise. This does not require additional labor if a computer is used in the analysis, and it may extend the range of usable data and generally improve confidence in calculated results. In the paper which follows this one, some simple energy band models having localized levels are discussed, and it is shown that several special cases lead to the forms for glow intensity, $I(T)$, used here.

For convenience, the symbols to be used in what follows are defined at this point:

$*, i$ ≡ The subscripts * and i indicate a temperature dependent function is to be evaluated at the temperature of maximum glow or at one of the two inflection temperatures respectively.

μ ∝ the initial density of trapped charge (set equal to one in calculated glow curves)

ϕ, Φ ≡ frequency factor which is determined by trap escape frequencies, recombination probabilities or density of states according to the requirements of a particular model

β heat rate = constant (set equal to one in calculated glow curves)

E ≡ the thermal activation energy for a trap

k ≡ Boltzman's constant

T ≡ temperature in degrees Kelvin

α ≡ E/k

X ≡ E/kT

$I(T)$ ≡ the glow intensity as a function of temperature

W ≡ $\exp(-\alpha/T)$

T_* ≡ the temperature at the glow peak maximum
T_i ≡ the temperature at a glow curve inflection point
T_1 ≡ the lower temperature inflection point
T_2 ≡ the higher temperature inflection point
Q ≡ $(T_i/T_*)^2$
τ ≡ $\exp(X_* - X_i)$
h ≡ $\int_{T_0}^{T} \mathrm{d}T \exp(-\alpha/T)/\beta$
H ≡ $\int_{T_0}^{T} \mathrm{d}T\, T^2 \exp(-\alpha/T)/\beta$.

The integrals represented by h and H occur in the glow intensity expressions given below. The lower limit of the integrals is set equal to zero. Integration by parts results in the asymptotic expansions:

$$h \cong TuW/X\beta$$

and

$$H \cong T^4 WU/\alpha\beta$$

with $u = 1 - 2/X + 6/X^2 - 24/X^3$, and $U = 1 - 4/X + 20/X^2 - 120/X^3$. The remaining terms of the series, which are truncated to give u or U, make negligible contributions for $X > 10$, a condition which holds for all cases of interest here. We also define for use below:

$$u' = 2 - u = 1 + 2/X - 6/X^2 + 24/X^3.$$

2. INFLECTION POINT METHOD FORMULI FOR SIMPLE MODEL GLOW CURVES

The formuli expressing the glow intensity $I(T)$ in this section are special cases of statistical models which have been discussed in the literature and of those treated in the following paper. The parameters ϕ and Φ which occur in the formuli are functions of the density of states, initial occupation numbers, transition probabilities or velocity cross-section products for a prescribed model. The glow intensity for the *simple monomolecular form*† is

$$I(T) = \mu\phi \exp(-\alpha/T - \phi h(T)). \quad (1)$$

The parameters ϕ and E satisfy the equations obtained by setting $\mathrm{d}I/\mathrm{d}T = 0$ and $\mathrm{d}^2I/\mathrm{d}T^2 = 0$ at T_* and T_i respectively. Thus

$$\phi/\beta = (X/WT)_* \quad (2)$$

and

$$[-2X + X^2 + \phi WT\beta^{-1}(\phi WT\beta^{-1} - 3X)]_i = 0. \quad (3)$$

If ϕ/β in equation (3) is replaced according to equation (2) one obtains

$$1 - 2/X_i - 3Q\tau + (Q\tau)^2 = 0. \quad (3')$$

The emitted light intensity for the *simple bimolecular form* is

$$I(T) = \mu\phi \exp(-\alpha/T)/[1 + \phi h(T)]^2. \quad (4)$$

The derivative conditions provide that

$$\phi/\beta = (X/Wu'T)_*, \quad (5)$$

and

$$[-2X + X^2 + 6P(P - X)]_i = 0 \quad (6)$$

with

$$P = [\phi WT/(1 + \phi h)\beta]_i;$$

or

$$1 - 2/X_i + 6R(R - 1) = 0 \quad (6')$$

with

$$R = \tau Q[u'_*(1 + \tau u_i Q/u'_*)]^{-1}.$$

When the electronic transitions giving rise to glow curves pass through a native energy band of a crystal, the glow intensity may take the *monomolecular form*

$$I(T) = \mu\Phi T^2 \exp[-\alpha/T - \Phi H(T)], \quad (7)$$

where the additional temperature dependence arises from the r.m.s. velocity, $v \propto \sqrt{T}$, and from the effective density of band states available for occupation, $N_c \propto T^{3/2}$[3]. The derivative conditions provide that

---

†Equations (1) and (4) are given by Curie[2] (pp. 161, 164) where $\phi = s$, the frequency factor for a trap. $I(T)$ is the number of photons/sec produced at T.

$$\Phi/\beta = [(2+X)/WT^3]_*. \quad (8)$$

and

$$[2+2X+X^2+L(L-6-3X)]_i = 0 \quad (9)$$

with

$$L \equiv (\Phi T^3 W/\beta)_i.$$

The *bimolecular form* for $N_c v \propto T^2$ is

$$I(T) = \mu\Phi T^2 \exp(-\alpha/T)/[1+\Phi H(T)]^2 \quad (10)$$

and the derivatives provide that

$$\Phi/\beta = M/(1-MH_*) \quad (11)$$

with

$$M \equiv [(1+X/2)/WT^3]_*;$$

and

$$[2+2X+X^2+6D(D-2-X)]_i = 0 \quad (12)$$

with

$$D = [\Phi T^3 W/(1+\Phi H)\beta]_i.$$

As was the case with ϕ/β, Φ/β can be replaced in equations (8) and (11) to provide a single equation for the energy.

Equations (3′) and (6′) can be written as

$$E = \frac{kT_* T_i}{|T_i - T_*|}\log_e(A/Q).$$

For equation (3′),

$$A = [3 \pm (5+8/X_i)^{1/2}]/2$$

and with $X_i = 25$, which is a reasonable trial value for all E and φ, $A = 0{\cdot}77$ and $2{\cdot}66$ for T_1 and T_2, respectively. For equation (6′),

$$A = Ru'_*/(1-Ru_i)$$

with

$$R = [3+(3 \pm 12/X_i)^{1/2}]/6$$

and with $X_i = 25$, $A = 0{\cdot}24$ and $3{\cdot}43$ for T_1 and T_2, respectively. One or two iterative changes in X_i provides an accurate value for E.

3. PROPERTIES OF MODEL GLOW CURVES

The first attempt to test equation (3′) was made on the theoretical curves given by Randall and Wilkins[1]. The results were unsatisfactory. We then calculated $I(T)$ according to equation (1) using their values for E, ϕ and β. It was found that the temperature values given on the abscissa of their Fig. 5, page 373, are shifted by 10 deg. The values of T_* and T_i judged from our curves when used in equations (2) and (3) gave values of E and ϕ in satisfactory agreement with those used in calculating the curves.

Figures 1 and 2 show $I(T)$ for the simple monomolecular and bimolecular forms, and the initial rise approximation to $I(T)$ (defined in the next section) for three values of E, with $\phi = 5{\cdot}8 \times 10^9$/sec, and with $\mu = 1/\text{cm}^3$ and $\beta = 1$°K/sec. Included in Fig. 2 is $I(T)$ for the monomolecular form when $N_c v \propto T^2$; the extra temperature dependence sharpens the peak somewhat, but the difference is rather insignificant. The curves broaden and decrease in amplitude with increasing energy while maintaining constant area. The initial rise approximation begins to fail significantly at approximately 10 per cent of I_*. The

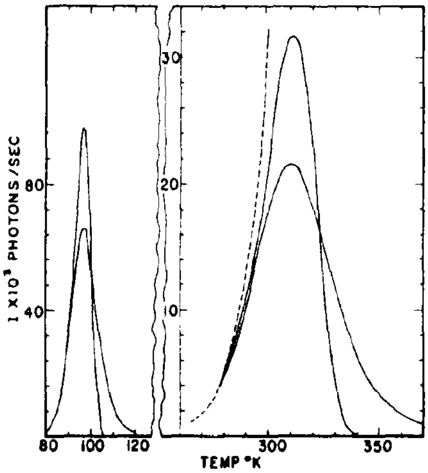

Fig. 1. Theoretical glow curves, $I(T)$, for monomolecular and bimolecular forms where $E = 0{\cdot}2$ eV at the left and $E = 0{\cdot}67$ eV at the right, with $\phi = 5{\cdot}8 \times 10^9$/sec, $\beta = 1$°K/sec and $\mu = 1$ are shown by the solid curves. The upper curves correspond to the monomolecular form and the lower curves to the bimolecular form. The dashed curve is the initial rise approximation for the same conditions

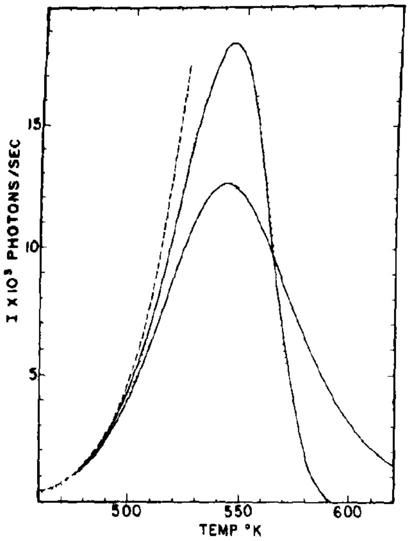

Fig. 2. Theoretical glow $I(T)$ for the simple monomolecular and simple bimolecular forms with $E = 1{\cdot}2$ eV, $\phi = 5{\cdot}8 \times 10^9$/sec, $\beta = 1$°K/sec and $\mu = 1/\text{cm}^3$ are shown respectively by the upper and lower solid curves. The dashed curve is the initial rise approximation for the same conditions. The dotted curve is the $I(T)$ for the monomolecular form with $N_c v \propto T^2$ when $E = 1{\cdot}2$ and with T_* chosen to be equal to that of the simple monomolecular form

maxima, T_*; inflection points, T_i; and intensity ratios, I_i/I_* for these curves are shown in Table 1. It is noteworthy that the I_i/I_* values are essentially independent of E for both the monomolecular and bimolecular forms. The extra temperature dependence when $N_c v \propto T^2$ has essentially no effect on the I_i/I_* values, but as will be seen the T_i values are different enough to shift the calculated energy by a few per cent if the simple rather than the $N_c v \propto T^2$ equations are used.

Figure 3 shows how the characteristics of the simple glow curve forms depend on ϕ with fixed E. It is seen that the I_i/I_* values are nearly independent of ϕ over a large range. It is also clear that the dependence of T_* on β (equation (2) or (5)), if used to calculate E by changing β [4, (see Section 3.1.3 of reference)], would require large changes for accurate results. Figure 4 shows how the values of E and ϕ calculated from equations (2, 3, 5) and (6) depend on the T_i values when T_* is fixed. The uncertainty in T_*-T_i is, of course, the major cause for uncertainty in calculated values, and this can be reduced by scale expansion during the experiment.

In picking the temperature of inflection points, one is guided not only by the points at which curvature changes, but also by the conditions that the I_i/I_* values of the forms for $I(T)$ being considered are almost independent of E and ϕ, and that T_1 and T_2 are symmetrically located about T_* as is evident from Table 1 and Fig. 3. The appropriateness of an $I(T)$ form is tested by whether or not the E and ϕ values calculated using T_1 and T_2 are consistent.

Table 1. The maxima and points of inflection of $I(T)$, and the intensity ratios for those $I(T)$ values, when $\phi = 5{\cdot}8 \times 10^9$/sec, for the simple glow curve models shown in Figs. 1 and 2. Similar results are included for $I(T)$ curves having the same T_* when $N_c v \propto T^2$

E	T_*	T_1	T_2	I_1/I_*	I_2/I	T_1	T_2	I_1/I_*	I_2/I_*
		Simple monomolecular				Monomolecular with $N_c v \propto T^2$			
0·20	97·2	93·3	101·0	0·687	0·536	93·6	100·7	0·688	0·536
0·67	311·0	299·3	322·6	0·688	0·535	300·1	321·8	0·689	0·535
1·20	545·2	525·1	565·3	0·688	0·534	526·5	563·9	0·690	0·534
		Simple bimolecular				Bimolecular with $N_c v \propto T^2$			
0·20	96·9	91·9	101·8	0·645	0·687	92·3	101·4	0·646	0·689
0·67	310·2	294·8	325·2	0·645	0·687	296·0	324·2	0·647	0·688
1·20	543·9	517·7	569·7	0·646	0·686	519·5	568·0	0·648	0·687

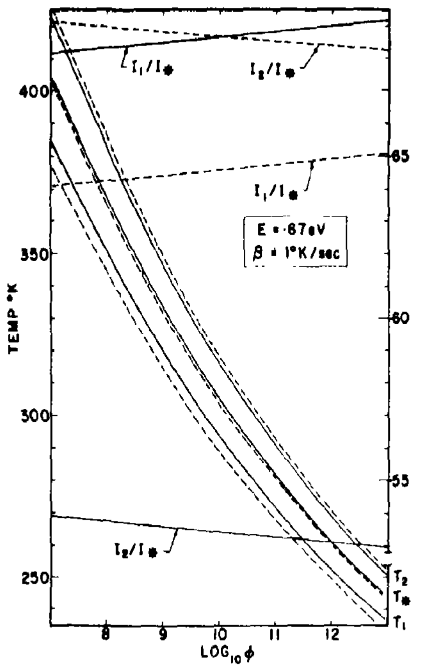

Fig. 3. This figure shows the dependence of T_*, T_1, T_2, I_1/I_* and I_2/I_* on ϕ with fixed E. The solid curves are for the simple monomolecular form, equation (1), and the dashed curves are for the simple bimolecular form, equation (4).

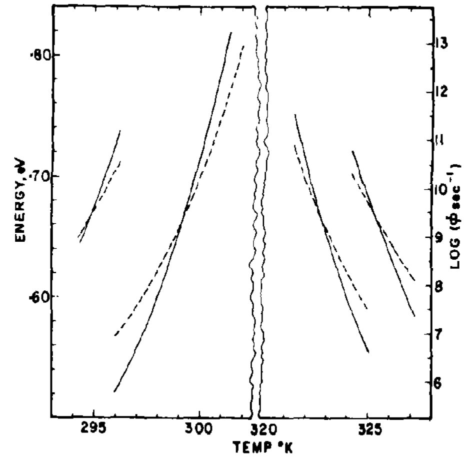

Fig. 4. The inner (outer) pair of solid curves show the dependence of E values on T_i and the inner (outer) pair of dashed curves show the dependence of ϕ values on T_i when calculated from equations (2) and (3), monomolecular form (equations (5) and (6), bimolecular form). T_* values are chosen to suit the case $E = 0{\cdot}67$ eV in Table 1.

The inflection point method and the initial rise method have been applied to a number of glow curves obtained from several crystals of Y_2O_3 and ThO_2. In many cases the peaks are compound and the inflection point method fails. In some cases the inflection point method is self consistant and agrees with the initial rise method: Table 2 shows values of E and ϕ for two of three major glow peaks from a crystal of Y_2O_3:Tb. The emission was characteristic of the Tb^{3+} ion in this sample whereas in undoped Y_2O_3 the emission spectrum is a broad curve usually peaked near 4400 Å and known to contain emission from more than one recombination center. The values of E and ϕ for the peak at 105·9°K are consistant for the two methods when a monomolecular form for $I(T)$ is assumed. The data is inconsistent for the glow peak at 157°K, but this peak is known to be complex from dosage studies. The temperature T_1 and T_2 were obtained by picking points of the glow curves where I_i/I_* had values as indicated at $\log\phi = 10$. (See Fig. 3).

4. A GENERALIZED INITIAL RISE ANALYSIS

The initial rise method of calculating energies utilizes the fact that $I(T)$ is always approximately equal to $\mu\phi\exp(-\alpha/T)$ at the leading edge of a glow curve. This method is limited because use of only the initial part of the glow curve rise is permitted[4. (see Section 3.2.1 of reference)] which may force one into the region where the uncertainty in background glow, I_0, is important. That is, in the initial rise method one works with the equation

$$E/kT \cong \log(I(T)-I_0) + \text{constant} \quad (13)$$

and one is restricted to $I(T)$ values much greater than the uncertainty in I_0. The first restriction is removed if one includes a correction factor for an appropriate form for $I(T)$ in equation (13) and utilizes all of the rise of a glow curve with increasing temperature. Thus one obtains

Table 2. Data and calculated values of E and ϕ for two glow peaks in $Y_2O_3{:}Tb$. T_* is the temperature at the glow peak maximum and β is the heating rate. TM1 and TM2 are the temperatures where $I_1/I_* = 0{\cdot}685$ and where $I_2/I_* = 0{\cdot}532$, respectively. TB1 and TB2 are the temperatures where $I_1/I_* = 0{\cdot}648$ and where $I_2/I_* = 0{\cdot}685$, respectively. The initial rise values for E and ϕ were calculated for a number of rises by the method described in Section 4, and the limits given represent the scatter in the calculated values

$T_* = 105{\cdot}9$°K	$\beta = 0{\cdot}627$°K/sec		$T_* = 157{\cdot}0$°K	$\beta = 0{\cdot}644$°K/sec	
	E	$\text{Log}_{10}\phi$		E	$\text{Log}_{10}\phi$
TM1 = 102·7°K	0·285 eV	12·5	TM1 = 151·7°K	0·380 eV	11·2
TM2 = 109·1	0·288	12·9	TM2 = 163·3	0·313	9·0
TB1 = 102·2	0·325	14 4	TB1 = 151·2	0·455	13·3
TB2 = 108·6	0·459	21·1	TB2 = 162·0	0·525	15·0
Initial rise	0·275 ± 0·02	12 6 ± 1	Initial rise	0·44 ± 0·03	13·4 ± 1

$$E = G\,[\log(I_n/I_m) + \Delta_{nm}] \qquad (14)$$

where

$$G = k/(1/T_m - 1/T_n)$$

and where T_n is the higher temperature and T_m is the lower temperature corresponding to the respective measured light intensity values I_n and I_m. The correction factor, Δ_{nm}, is

$$\Delta_{nm} = \phi(h_n - h_m) \qquad (15)$$

for the simple monomolecular form, and is

$$\Delta_{nm} = 2\log[(1+\phi h_n)/(1+\phi h_m)] \qquad (16)$$

for the simple bimolecular form. The correction factor is

$$\Delta = \Phi(H_n - H_m) - 2\log(T_n/T_m) \qquad (17)$$

for the monomolecular model with $N_c v \propto T^2$ and

$$\Delta = 2\log[T_m(1+\Phi H_n)/T_n(1+\Phi H_m)] \qquad (18)$$

for the bimolecular model with $N_c v \propto T^2$. Note that ϕ is different for the monomolecular and bimolecular forms, as is Φ.

A computer is useful to initial rise calculations, and if one is used, no additional labor is required by including the correction factor. Solving equation (14), together with an appropriate equation for Δ, by an iterative process, $\Delta_0 = 0 \rightarrow E_1$, $E_1 \rightarrow \Delta_1$, $\Delta_1 \rightarrow E_2$ etc., provides a condition where $|E_j - E_{j-1}| <$ any practical value. The value of T_* for the glow peak of interest is required for this calculation. One can, of course, retain the value of ϕ or Φ from the final iteration.

A program has been written which calculates E and ϕ according to equation (14) where $\Delta = 0$ and with Δ as given by equations (15) and (16). The calculations are done with both $m = n - 1$ and $m = 1$. For each rise average values of the parameters for a given curve are calculated.† The input data consists of thermocouple voltages and a voltage-temperature conversion table, the corresponding photomultiplier response values, time intervals, and the peak temperatures. The resulting calculated values of E and $\log\phi$ are inspected for consistency and the average values are plotted versus the maximum temperature attained during the rise. It is necessary to be cognizant of the order in which the initial rise data are taken and of the maximum temperature attained during each rise so that values affected by a peak lower, or higher, in temperature than the one being studied are properly understood. The peak temperature associated with a trap may shift upward with each successive rise if retrapping is significant; currently only one value for T per glow peak is used in the calculations so that the energies calculated from the final rises of a series may become erroneous because of the dependence of Δ on T_* (see note at end).

---

†Reference is made here to a method used by Halperin *et al.* where a series of initial rise curves are generated by a series of heating and cooling cycles, such that the maximum temperature attained is increased by some appropriate amount in each successive cycle[5].

Before the current work was undertaken, a program to calculate energies from equation (14) with $\Delta = 0$ only was used. The results obtained from the two programs are, for the most part, quite consistent; however, the output of the more recent program is more easily evaluated, scatter in the plotted results is reduced, and the confidence level is considerably improved.

Figure 5 illustrates the effect of including the appropriate correction factor in initial rise calculations. Calculated values of $I(T)$ for different models, with $E = 0{\cdot}67$ eV, are used as input data for equation (14). The correction, Δ, is set equal to zero or calculated according to equation (15) or (16). Study of the figure confirms that setting $\Delta = 0$, or use of an inappropriate Δ causes the calculated energy to begin diverging significantly from the correct value when $I(T)/I_* \approx 0{\cdot}1$. The calculated values of ϕ which diverge in a similar manner are not shown. Illustrated also is the fact that the Δ calculated for a simple monomolecular model, equation (15), when applied to $I(T)$ values calculated according to the monomolecular model with $N_c v \propto T^2$ gives an energy which is too large by about 6 per cent.

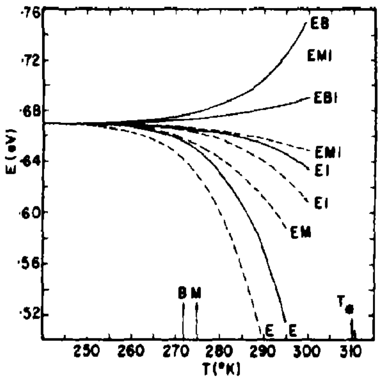

Fig. 5 The solid (dashed) curves are the energy values calculated from equation (14) using $I(T)$ values calculated for the simple monomolecular form, equation 1 (simple bimolecular form, equation (4)) with $E = 0{\cdot}67$ eV. The label E or $E1$ means that Δ is set equal to zero, M or B contained in a label means Δ is calculated according to equation (15) or (16), respectively. Omission or inclusion of 1 in a label means that $m = n - 1$ or $m = 1$, respectively. The dotted curve represents energy values calculated from equation (14) with Δ calculated according to equation (15) when $I(T)$ values used are from the monomolecular form with $N_c v \propto T^2$, equation (7), and with $m = n - 1$. The arrows labeled B and M mark the temperatures where $I(T)/I_* = 0{\cdot}1$ and the arrows labeled by T_* indicate the temperature of the maxima of the $I(T)$ values.

Limitations on the initial rise method have been discussed by Haake[6]. He concludes in his summary that values of E obtained in this way are often dubious and that ϕ values calculated from E and T_* by using a simple monomolecular form are often too inaccurate to be of any use. The following paper discusses conditions where the initial rise method can be quite limited for simple models. If traps are initially filled and if the retrapping rate is high, then a simple analytical form does not apply, and one does not expect a unique parameter ϕ nor a unique relation between T_* and E; however, with successive rises some traps empty and the glow curve tends toward a simple analytical form. Meanwhile the portion of the curve fitted with reasonable accuracy by an exponential increases toward a limit of $0{\cdot}1I_*$.

As shown in the following paper, the initial part (this can, of course, be a very small part) of a glow curve for all models considered there can be fitted by a monomolecular or bimolecular curve; however, the T_* for such curves can be either greater or less than the T_* observed. In most cases to be expected experimentally, including overlapping peaks, the observed T_* will be equal to or greater than the theoretical value, so that use of the experimental T_* in the monomolecular rise analysis will lead to values of E within the range of values obtained by the exponential rise analysis, if shifts in T_* which may occur with successive rises are taken into account.

The Author elected to refer to the method described here as a generalized initial rise analysis because the data from the initial part of a glow curve is analyzed in terms of an exponential, monomolecular or bimolecular curve. The analysis for the lowest data points yields essentially identical results for all cases, but when higher intensity data points are used there is a possibility of distinguishing the most appropriate fit of the three forms to the observed glow curve.

5. APPLICABILITY OF THE ABOVE RESULTS TO THERMALLY STIMULATED CURRENT MEASUREMENTS

Thermally Stimulated Current (TSC) and thermoluminescence glow curves take the monomolecular form if $n_c \propto \mathrm{d}n_a/\mathrm{d}t$, where n_c is the density of conduction electrons and n_a is the density of filled recombination centers. This will be true if a constant fraction of the charges released from traps of one kind make luminescent transitions to empty recombination centers and if the number of empty recombination centers remains approximately constant. Thus our equations apply directly to several published forms for TSC when ϕ is defined appropriately. Nicholas and Woods have reviewed methods of calculating the parameters significant to a model from current glow curves, and have shown some of the theoretical TSC equations[4]. Their equations (5, 6) and (8) correspond to the forms given here for $I(T)$ when ϕ is defined appropriately, except that their equations (5) and (8) contain misprints. (The correct equations are given by Haering and Adams, equations (2.4) and (2.10) [7]. Equation (6) given by Nicholas and Woods is said to be a TSC form for bimolecular recombination, and it has the same form as equation (4). In the following paper (equation (25a)) it is shown that

$$\sigma(T) \propto \exp(-\alpha/T)/[1+\phi h(T)] \quad (19)$$

is a TSC form which corresponds to a bimolecular form for thermoluminescence. The derivative conditions for equation (19) are given by equation (5) with u' replaced by $1-u$ and by equation (6) with 6 replaced by 2.

6. THE EFFECT OF TEMPERATURE GRADIENTS ON GLOW CURVE ANALYSIS

It can be argued that, in the analysis of glow curves, the use of the inflection point formuli provides no advantage over those based on the temperatures at which the glow is one half the maximum. The percent uncertainty in the temperature difference between the maximum and the inflection points is greater than that for the half maximum points since the differences are smaller in the former case. And, each of these methods, as well as the initial rise method, is a two point fit to a theoretical curve which is usually assumed to have two fixed parameters. (The initial rise method, of course, uses several points in pairs.)

On the other hand, it does seem desirable to have available several independent formuli providing two point fits for different parts of the same theoretical curve. The formuli presented here provide an essentially exact analysis for the assumed theoretical curves. This is not true for the formuli based on the half maximum points. It is also thought that a small temperature gradient in a transparent specimen should introduce smaller errors in the energy and frequency factor if calculated according to the inflection point analysis in lieu of other methods. This is true for the following example in any case.

The glow curves in Fig. 6 are based in the monomolecular form, and they were generated to correspond to situations where there is a linear temperature gradient between two surfaces, with a temperature difference ΔT, in a thermoluminescing transparent specimen, or in a specimen in which a current is being measured. It is assumed that there is no internal absorption. The temperatures on the

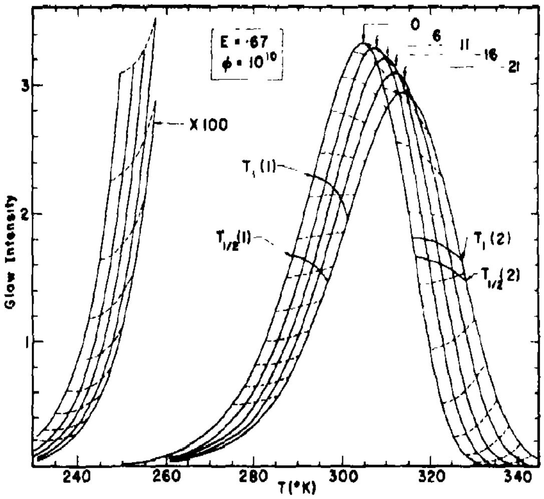

Fig. 6. These curves show the change from a simple monomolecular form which occurs when a linear temperature gradient exists in a thermoluminescing specimen. The numbers at the upper right are the assumed values for the temperature difference, ΔT, between opposing surfaces, and the arrows leading from the ΔT values indicate the temperature of the glow peak maximum. The temperature values on the absissa are those of the high temperature surface. Each dashed curve connects intensity values for a constant average specimen temperature. The inflection points and half maximum points are indicated by T_1 and $T_{1/2}$, respectively.

abscissa of Fig. 6 are those corresponding to the high temperature surface of a specimen. The glow curves shift upward in temperature and broaden as ΔT increases. Each dashed curve connects intensity values for a constant average specimen temperature; they have a positive curvature below the inflection points, and as will be seen, this causes the energy values calculated by the initial rise method to be too high. The positions of the maxima, inflection points, and half maximum points are also indicated, and it can be seen that the change in temperature for these points becomes progressively larger as one moves from point to point along the curve in the direction of increasing temperature. The second inflection point changes by an amount approximately equal to the change for a constant average temperature.

Figure 7 shows curves of the energy values calculated from the curves of Fig. 6 according to the usual initial rise analysis, and the monomolecular rise analysis. The calculations were done, as described in Chapter 4, (a) with the initial data point and all others, and (b) with neighboring data points. It can be seen that a temperature gradient increases the energy values calculated from the initial part of a glow curve. The energies calculated by the usual initial rise analysis fall off in the usual manner. The curves calculated according to the monomolecular rise analysis in Fig. 7(b) for the largest gradients would cross over the correct energy value if the curves were extended to T_*, but the one for a ΔT of 6°K probably would not.

Figure 8 shows the energy and frequency factor as calculated by various methods from the curves of Fig. 6. These values are plotted vs. ΔT. The energies calculated by the initial rise analysis are from the constant region and increase with increasing ΔT. The energies

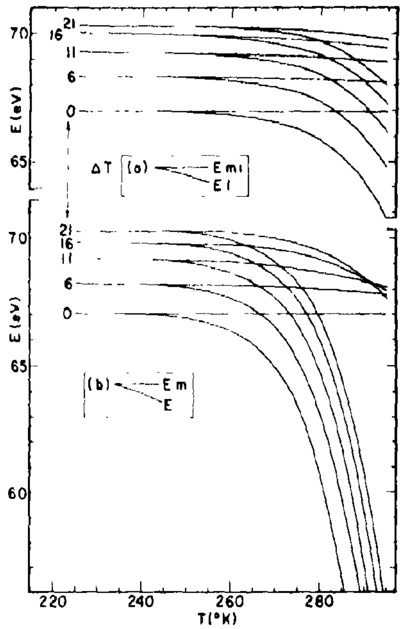

Fig. 7. Energy values calculated from the curves of Fig. 6. The lower branches of the curves are calculated by the exponential rise analysis, and the upper branches are calculated by the monomolecular rise analysis. The curves in 7(a) are calculated by using the initial data point with all others, for each case, and those in 7(b) are calculated by using neighboring data points (See the caption of Fig. 5).

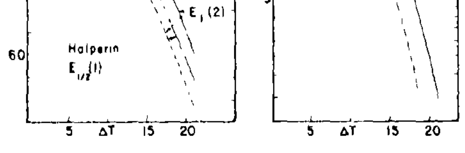

Fig. 8. Energy and frequency factors calculated from the curves of Fig. 6 by various methods.

calculated from half maximum temperatures are according to the formuli given by Luschik and Halperin, which use the upper, $T_{1/2}(2)$, and lower, $T_{1/2}(1)$, half maximum temperature, respectively[8, 9]:

$$\text{Luschik: } E = kT_*^2/[T_{1/2}(2) - T_*]$$

$$\text{Halperin: } E = 1{\cdot}72\,kT_*^2[1 - 5{\cdot}16\,kT_*/E]/[T_* - T_{1/2}(1)].$$

The values of E and ϕ calculated by using the inflection point formuli are denoted by $E_i(1)$, $E_i(2)$, $\phi_i(1)$ and $\phi_i(2)$ where 1 and 2 refer to the first and second inflection point, respectively. The solid curves are values calculated by using the temperatures at the actual inflection points. The dashed curves are values calculated by assuming that the intensity at the first and second inflection points is given by $0{\cdot}685I_*$ and $0{\cdot}534I_*$, respectively, and then using the corresponding temperatures in the inflection point formula. (The factors multiplying I_* are obtained from Fig. 3, and the reason for using this approach should be clear from the remarks pertaining to Fig. 3 and Table 1. The actual values of I_i/I_* are 0·67 and 0·57 for the first and second inflection points, respectively, when $\Delta T = 21$°K).

It seems clear that for small ΔT, the inflection point analysis yields the best values for E and ϕ, and that using the rule $I_i/I_* = 0{\cdot}685$ for the first inflection point, rather than relying solely on finding the point by the change in curvature, tends to yield improved values. It is also clear that, for this example, the Luschik formula is a rather poor approximation, since for $\Delta T = 0$ the calculated energy is in error by 7 per cent.

It is interesting that the values of ϕ in Fig. 8 calculated by the monomolecular rise analysis are rather insensitive to a temperature gradient. This is true because the shift in peak temperature compensates for the change in calculated energy. Likewise, the fact that energy values for small ΔT tend to be high when calculated by methods using the half maximum of inflection point temperatures is a result of increasing T_* in a range of ΔT where peak broadening has a less effective tendency to decrease the calculated energy.

The reason the inflection point analysis gives the best values for parameters when small temperature gradients are assumed for the example is that broadening is compensated by the shift in peak temperature. The broadening is never compensated by the shift in T_* for calculations from points below the half width points. Broadening would be compensated best by calculations using T_* and either of two points which move relatively (not necessarily absolutely) toward T_* as the gradient increases. These optimum points move above the inflection points as the gradient increases. This behavior would occur for all monomolecular and bimolecular curves, of course.

It seems reasonable to state that the ratio of $\Delta T/w$, where w is the width of a glow peak at half maximum provides a good qualitative measure of the error introduced by a gradient. For the example discussed here $w = 28°K$, which suggests that the condition $\Delta T/w = 0{\cdot}2$ would permit one to assume that errors due to gradients are less than 2 per cent for all analytical methods discussed.

The methods of evaluating trap activation energy in terms of shifts in peak temperature which result from changes in heating rate may be compromised by the effects of temperature gradients[4, 10]. Certainly, if the specimen being studied is transparent and sufficiently thick, the increase in temperature gradient accompanying an increase in heating rate tends to cause a larger increase in peak temperature than a simple analysis assumes. Substantial changes in heating rate are required in this method as can be seen from equation (2) and Fig. 3.

The effect of interference from a glow peak higher in temperature than one being analyzed is similar to that of a gradient, in that energies calculated by an initial rise analysis, in the constant region, tend to be too high. When a series of initial rise curves are generated as described in the footnote of Chapter 4, the charge in the trap responsible for the lowest existing glow peak is decayed most effectively. If the peak temperature of the glow for that trap changes, it will most likely shift upward. (See the following paper). Thus the reduction in magnitude, and possible shift both tend to increase the relative effect of a neighboring high temperature peak. Therefore, it can be expected that plots of energy vs. the maximum temperature attained during the successive rises will contain values which are higher than that appropriate to either trap, whenever the trap associated with the lower peak is in some intermediate state of decay. When properly understood, such points can be discounted.

7. DISCUSSION

Halperin and Braner have pointed out that neutrality conditions should be expressed as $\Delta n_d = \Delta n_a$ where n_d is the density of filled traps and n_a is the density of empty recombination centers, instead of as $n_d = n_a$ as has frequently been done[8]. They obtain formuli for trap energies for models where the ratios of parameters are changed in various ways, but they did not discuss the forms of $I(T)$ in detail nor the meanings of ϕ. The following paper does this, and discusses the conditions for which the simple monomolecular and bimolecular forms may be expected to occur.

Obviously the inflection points and maxima are universally applicable in the analysis of glow curves. For the forms discussed here, there are only two independent parameters so that the pairs of values T_*, T_1 and T_*, T_2 should yield consistent values for E and ϕ if the form used correctly describes a glow curve. Naturally it is desirable to clean the low temperature side of glow curves analyzed in this way.

The inflection point method, like half-width methods, will most likely yield energies which are too low when glow peaks are superimposed. We conclude that self consistency of values obtained by the inflection point method together with agreement with results of an initial rise analysis is good evidence of an elemental glow curve, i.e. a single trap and a single or effective single recombination center. There are, of course, other means of determining whether or not a glow curve is elemental. For example: Is the emission spectrum constant throughout the glow? Do decayed curves and undecayed curves with approximately equal areas have the same value for T_*? Does T_* change when curves of equal area are produced by excitation with different wavelengths?

One could easily calculate tables of E and ϕ vs. T_* and T_i for given I(T); this is not deemed necessary because with the general availability of computers the solutions are easily obtained. We will, of course, gladly share our IBM Fortran programs.

The analytical methods described have been applied to glow curves obtained from Y_2O_3 and ThO_2. As was pointed out earlier the generalized initial rise method does provide some improvement over the usual method. For one thing it removes the much discussed limitation of the upper limit of $I(T)$ values which one may include in a calculation.

In conclusion we add the somewhat unrelated remark that hyperbolic heat rates are undesirabe. This kind of heating has been used and is still being used because it simplifies the integrals contained in expressions for $I(T)$[11]. A linear heat rate can be maintained over a wider range and is more easily reproduced; and the integrals actually present little difficulty.

Acknowledgements – The author wishes to acknowledge that this and the following paper were substantially improved as a result of the referee's criticisms

REFERENCES

1. RANDALL J. T. and WILKINS M. H. F., *Proc. R. Soc.* **A184**, 366 (1945).
2. CURIE D., In *Luminescence in Crystals*. Methuen, London (1963).
3. DEKKER A. J., In *Solid State Physics*, pp. 314–315. Prentice-Hall, Englewood Cliffs, N. J. (1957).
4. NICHOLAS K. H. and WOODS J., *Br. J. appl. Phys.* **15**, 783 (1964).
5. NAHUM J. and HALPERIN A., *J. Phys. Chem. Solids* **24**, 823 (1963).
6. HAAKE C. H., *J. opt. Soc. Am.* **47**, 649 (1957).
7. HAERING R. R. and ADAMS E. N., *Phys. Rev.* **117**, 451 (1960).
8. HALPERIN A. and BRANER A. A., *Phys. Rev.* 117, 408 (1960).
9. LUSCHIK Ch. B., *Dokl. Akad. Nauk. SSSR* **101**, 641 (1955).
10. HOOGENSTRAATEN W., *Phillips Res. Rep.* **13**, 515 (1958).
11. HALPERIN A., LEIBOVITZ M. and SCHLESINGER M., *Rev. scient. Instrum.* **33**, 1168 (1962).

Note added in proof. The following paper discusses possible changes in peak temperature and shape as a glow peak is decayed If a specimen is quenched immediately after a TL glow curve reaches the second half width point, the density of trapped charge decays by about a factor of 10. In some cases several decades are available, and the data provides for a study of T_* vs. μ and for a comparison of E and ϕ values calculated by the different methods. If the glow is due to a single trap species, then the E and ϕ calculated according to different methods for an appropriate model should tend to converge. The values calculated from half width formuli should not agree exactly with those calculated by other methods since they are approximations. A test of the formuli of Halperin *et. al.*[8, p. 417] using the first half width points from curves generated with $E = 0·2$, 0·67 and 1·2 eV, each with $\phi = 0·58 \times 10^{10}$/sec yielded E equal to 0·204, 0·689 and 1·23 eV for the monomolecular formula and 0·189, 0·640 and 1·16 eV, respectively for the bimolecular formula. For curves generated with $\phi = 10^7$ and 10^{13}/sec, each with $E = 0·67$ eV, the E values calculated were 0·628 and 0·712 eV for the monomolecular and 0·545 and 0·679 eV for the bimolecular formula, respectively. Thus the half width formuli can yield values having significant error in E and, of course, in ϕ.

J. Phys. Chem. Solids Pergamon Press 1969. Vol. 30, pp. 1693–1708. Printed in Great Britain.

EQUATIONS FOR THERMOLUMINESCENCE AND THERMALLY STIMULATED CURRENT AS DERIVED FROM SIMPLE MODELS

PETER L. LAND
Metallurgy and Ceramics Research Laboratory, Aerospace Research Laboratories,
Wright-Patterson AFB, Ohio 45433, U.S.A.

(*Received* 24 *August* 1967; *in revised form* 11 *September* 1968)

Abstract—Equations for thermoluminescence and thermally stimulated currents are derived for simple models where transitions are strictly localized, where transitions are via a band; and where transitions are by overlap transfer. Analytical expressions for $I(T)$ and $\sigma(T)$ follow from assumptions about the relative densities of trapping states, filled trapping states, and empty recombination states; and from assumptions about the relative values of the different transition probabilities. The characteristics of glow curves are discussed in terms of relative values of the density and transition probability parameters. The models treated can be distinguished by variation of defect densities. It is shown that it is frequently possible to use experimental conditions for which the glow will have an analytical form, when the models discussed here are appropriate.

1. INTRODUCTION

THE PRECEDING paper describes a new method of calculating energy and frequency factors or velocity cross-section products from thermoluminescent and conductivity glow curves. In the course of showing that the forms used for thermoluminescence (TL) and thermally stimulated current (TSC) in that study are appropriate to most of the special cases appearing in the literature, the author concluded that it would be worthwhile to further generalize the previously recorded results, and to demonstrate that the simple analytical forms should frequently apply to glow curves describable in terms of simple models. The models and neutrality conditions used are essentially those used by Halperin and Braner who provide formuli for calculating the thermal energy, E, according to the maximum temperature and half width of the low temperature side of a glow curve[1]. However, here the overlap transfer model is generalized, and the emphasis is shifted more toward the form of the glow curves and the interpretation of the frequency factor, ϕ, instead of toward a method of deriving the trap activation energy. The band model discussed here is the same as that used by Dussel and Bube in discussing TSC[2]. The formulation used here, like that of Halperin and Braner, is less restrictive, however, in that it permits consideration of the possibility that the number of trapped charges may exceed the number of 'active' recombination centers, a situation which could occur as a result of the existence of some other 'inactive' recombination centers having a relatively very small cross-section.

The models treated describe strictly localized transitions, transitions via a band, and direct transfer transitions, and it is understood that transitions may involve undefined intermediate states. In obtaining solutions to the sets of equations involving time derivatives of occupation numbers, it is assumed that heating is linear, from an initial value of approximately 0°K, and that secular equilibrium exists between a trap being thermally activated and its excited state. In addition, it is assumed that electrons rather than holes are involved in the thermally stimulated transitions, but the results are, of course, applicable to hole models. The notation for occupation numbers; n_d, n_a and n_c is used because electron traps may be donor states, recombination centers may be acceptor states, and the excited states may be in a conduction band. For convenience the symbols to be used in what follows are defined here:

n_d = density of filled traps
n_c = density of electrons in a band
n_a = density of filled recombination centers
N_d = density of trapping states
N_c = density of band states
N_a = initial density of unoccupied recombination centers
m = initial density of filled traps
μ = smaller of N_a and m
μ' = larger of N_a and m
E = the thermal activation energy for a trapped electron
k = Boltzman's constant
T = temperature in degrees Kelvin
β = $\dot{T}$ = rate of heating = constant
t = time in sec
W = $\exp(-E/kT)$
h = $\int_0^T W \mathrm{d}T/\beta$

γ and s are transition probabilities per unit time, and describe transitions between a trap and its excited state

p and q are transition probabilities per unit time, and they describe transition rates from an excited state of a trap to a recombination state, by radiative and non-radiative transitions respectively

γ', s', p' and q' are quantities having units of $(\text{time} \times \text{density})^{-1}$ and can be regarded as a velocity times a cross section for recombination. They describe transitions analogous to those for the unprimed variables except that the excited state involved is not associated with the defect giving rise to the trapping state

ϕ is a function of some of the parameters: N_d, N_c, N_a, m, s, p, q, s', p' and q'

V = $\exp(-\phi h)$
U = ϕWV, a monomolecular glow curve
B = $\phi W(1+\phi h)^{-2}$, a bimolecular TL glow curve
T_* = a temperature at which a maximum in a glow curve occurs.

2. MODEL FOR LOCALIZED TRANSITIONS

It is assumed here that all charge transfer takes place within centers of one kind, each having one trapping state, one excited state and one recombination state; i.e. no transfer of charge among separate centers can occur. The time derivatives of the occupation numbers are

$$\dot{n}_d = -\gamma n_d + s n_c \tag{1}$$

$$\dot{n}_c = \gamma n_d - (s+p) n_c \tag{2}$$

$$\dot{n}_a = p n_c. \tag{3}$$

Equations (1–3) satisfy

$$n_d + n_c + n_a = m. \tag{4}$$

In equation (2) $\dot{n}_c$ is assumed to be small compared to the individual terms on the right hand side, so that for all times

$$n_c \cong n_d \gamma/(s+p). \tag{5}$$

According to the principle of detailed balance and the assumption that γ contains a Boltzman factor

$$\gamma = sW. \tag{6}$$

It is consistant with the preceding assumption that

$$n_d \cong m - n_a. \tag{7}$$

Equations (3–6) result in

$$\dot{n}_a = p(m-n_a)\gamma/(s+p). \tag{8}$$

When $\beta = \dot{T}$ = constant,

$$I(T) = mU \tag{9}$$

where

$$\phi \equiv ps/(s+p).$$

It is seen that ϕ is less than the smaller of s or p.

If there are several trapping states associated with a center and both radiative and non-radiative transitions are allowed for a recombination state then

$$I(T) = \frac{psm}{s+p+q+R} \exp(-E/kT - \phi h) \quad (10)$$

with

$$\phi = s(p+q+R)/(s+p+q+R)$$

where R represents the sum of the transition probabilities per unit time from the excited state of the trap being thermally activated to all other traps which would cause glow curves at higher temperatures. If one excited state is common to all traps, then R would be a sum over s values for these other traps if the s values are independent of temperature.

One could consider the case of localized transitions within a doubly charged center. There are ten charge configurations for two trapping states, one excited state and two recombination states. The occupation number time derivatives for this case would be linear and appropriate simplification would reduce this case to the singly charged defect case.

3. A MODEL WHERE ELECTRONS PASS THROUGH A CONDUCTION OR AN IMPURITY BAND

The glow curve equations derived in Sections 1–7 of this Chapter are based on the assumption that only one trapping state, one band and one recombination state of a kind are active, i.e. have changing occupation numbers, and that there are no non-radiative recombinations. Of course, this does not imply that $N_a = m$ since the active trap may have received charge from centers other than an active one or an active center may have provided charge during excitation from traps other than an active one. The density of band states available and the parameters governing transition rates from the band are treated as constants, which is appropriate for narrow bands. If it is desirable to include the temperature dependencies for the effective density of band states available for occupation[3], $N_c \propto T^{3/2}$, and for the r.m.s. electron velocity, $v \propto \sqrt{T}$, only minor modifications of the final forms are required, and they are discussed at the end of this section.

It is assumed that $n_a = 0$ initially, since filled recombination centers are inactive, and that $n_c = 0$ initially. The time derivatives of the occupation numbers are

$$\dot{n}_d = -\gamma' n_d (N_c - n_c) + s'(N_d - n_d) n_c \quad (11)$$

$$\dot{n}_c = \gamma' n_d (N_c - n_c) - [s'(N_d - n_d) + p'(N_a - n_a)] n_c \quad (12)$$

$$\dot{n}_a = p'(N_a - n_a) n_c. \quad (13)$$

Since $N_c \gg n_c$, $N_c - n_c$ is replaced by N_c in equations (11) and (12). The time derivatives, together with the assumed initial conditions, provide that

$$n_d + n_c + n_a = m. \quad (14)$$

As before, $\dot{n}_c$ is assumed to be much smaller than the individual terms on the right side of equation (12); hence

$$n_c = \gamma' N_c n_d / [s'(N_d - n_d) + p'(N_a - n_a)] \quad (15)$$

According to the principle of detailed balance and the assumption that γ' contains a Boltzman factor

$$\gamma' = s' W. \quad (16)$$

The further assumption that

$$n_d \simeq m - n_a \quad (17)$$

provides that

$$\dot{n}_a = \frac{p'\gamma' N_c}{s' - p'} \frac{(N_a - n_a)(m - n_a)}{n_a + G} \quad (18)$$

where

$$G \equiv [s'(N_d - m) + p'N_a]/(s' - p').$$

Integration of equation (18) gives

$$(1 - n_a/N_a)^F (1 - n_a/m)^f$$
$$= \exp\left(\int_0^T \frac{N_c p' \gamma'}{s' - p'} \frac{\mathrm{d}T}{\beta}\right) \quad (19)$$

where

$$F = (N_a + G)/(N_a - m)$$

and

$$f = -(m + G)/(N_a - m).$$

1. If $N_a \gg m$, the first factor in equation (19) may be set equal to unity. Then one obtains

$$I(T) = \dot{n}_a = mU\left[1 - \frac{m(s' - p')V}{s'N_d + p'N_a}\right]^{-1} \quad (20)$$

with

$$\phi = N_a N_c p' s'/(s'N_d + p'N_a). \quad (21)$$

This result will fail only if $s' \approx p'$ when $m \to N_d$.

2. If $m \gg N_a$, the second factor of equation (19) may be set equal to unity. Then one obtains

$$I(T) = N_a U\left[1 - \frac{N_a(s' - p')V}{s'(N_d - m + N_a)}\right]^{-1} \quad (22)$$

with

$$\phi = mN_c p'/(N_d - m + N_a). \quad (23)$$

This result will fail if $s' \gg p'$ when $m \to N_d$. It will also fail when p' is sufficiently large.

3. If $m = N_a$, a solution of equation (18) is

$$\log_e (1 - n_a/m) + C/(m - n_a) - C/m$$
$$= N_c p' s' h/(s' - p') \quad (24)$$

where

$$C \equiv m + G = s'N_d/(s' - p').$$

The log term can be neglected when $|m/C| \ll 1$; then

$$I(T) = mB\left[1 - \frac{m/C}{1 + \phi h}\right]^{-1} \quad (25)$$

with

$$\phi = mN_c p'/N_d.$$

4. When $s' \gg p'$ and $m \to N_d$, or when $p' \gg s'$, or more specifically when $\mu/|\mu + G| \gtrsim 0{\cdot}1$, then the initial part of a glow curve, perhaps only a very small fraction, can be represented by

$$\mu U \quad (26)$$

with

$$\phi_i = \frac{\mu' N_c p' s'}{s'(N_d - m) + p'N_a} \quad (27)$$

while the final part of the glow curve is given by the appropriate foregoing equation. The initial and final values of ϕ satisfy

$$\phi_f/\phi_i = G/(\mu + G). \quad (28)$$

When p' is sufficiently large the glow, $I(T)$, is given by mU with $\phi = N_c s'$; If $m > N_a$, this curve is cut off when

$$\int_0^T I(T)\,\mathrm{d}T/\beta = N_a. \quad (29)$$

When $s' \gg p'$ and $m \to N_d$, then $G \to 0$ and equation (26) holds approximately only when $n_a < 0{\cdot}1\,G$. In this case it can be seen that for $10\,G < n_a < 0{\cdot}1\,\mu$ an approximate solution of equation (18) is

$$n_a^2 = \mu\phi h$$

with

$$\phi = 2p'\mu' N_c.$$

Utilizing the expansion of h given in the introduction of the preceding paper it is seen that

$$I(T) \propto \exp(E/2kT)/T.$$

However for $I(T)$ to have this form requires that $G/\mu < 0{\cdot}01$ or that $m/N_a > 0{\cdot}99$ which is an unlikely situation. Thus $\log I$ vs. $1/T$ will have a slope between E/k and $E/2k$ when $n_a < 0{\cdot}1\,\mu$ as discussed by Bräunlich[4].

5. Up to this point only luminescence glow curves have been discussed. The TSC curves $\sigma(T)$ can be derived from equation (13) by using the solutions for $\dot{n}_a$. Thus when $N_a \gg m$, one obtains

$$\sigma(T) \propto n_c = \dot{n}_a/p'N_a \tag{20a}$$

corresponding to equation (20); and when $m \gg N_a$ one obtains

$$\sigma(T) \propto n_c = \frac{N_c m W}{(N_d - m + N_a)} \times \left[1 - \frac{N_a(s'-p')V}{s'(N_d - m + N_a)}\right]^{-1} \tag{22a}$$

corresponding to equation (22); and when $m = N_a$

$$\sigma(T) \propto n_c = \frac{N_c m W}{N_d(1+\phi h)}\left[1 - \frac{m/C}{(1+\phi h)}\right] \tag{25a}$$

where ϕ and C are defined as in equation (25). It is easily seen that the peak value of $\sigma(T)$ shifts from coincidence with $I(T)$ when $N_a \gg m$; to a difference predicted by

$$E/kT_*^2 = \epsilon\phi W/\beta(1+\phi h)$$

where W and h are functions of T_* and E, and where $\epsilon = 1$ for TSC and $\epsilon = 2$ for TL, when $m = N_a$, and $m/C \ll 1$; and finally to a case where $I(T)$ is monomolecular while $\sigma(T)$ is an exponential function (no peak) for the case $m \gg N_a$. As before, the restrictions $\mu/|\mu + G| \lesssim 0{\cdot}1$ apply to the results in this section.

6. In this section, numerical solutions of equation (18) with equations (19) or (24) will be discussed. The solutions for TSC are obtained at the same time by using equation (13). The purpose here is to illustrate the shape and characteristic of glow curves under conditions where the simple analytical forms don't apply. The dependence of peak temperatures for decayed traps, or for a reduction in dose are studied. A decayed trap results if the irradiated specimen has been previously preheated to a temperature which permitted some of the initially trapped charge to escape. For the model under consideration, the charge which escapes must go to the recombination centers: One can, however, use the results in thinking about a more general model. In considering the effect of a reduced radiation dose (all traps being initially empty for each irradiation) it is assumed that $N_a \propto m$. This is a reasonable assumption and appears to occur rather frequently if N_a is considered to be proportional to the total integrated TL intensity and if m is considered to be proportional to the integrated TL intensity from the glow peak being studied. There are, of course, many examples where the total glow and the glow from a single peak show different dependences on radiation dose. These possibilities will be discussed.

Decayed TL curves are obtained here by reducing m by a factor $10^{-\chi}$ when $N_a \geq m$. Thus

$$m(\chi) = 10^{-\chi}m(0)$$
$$N_a(\chi) = N_a(0) - m(0)[1 - 10^{-\chi}]$$
$$N_d(\chi) = N_d(0).$$

When $N_a \leq m$, N_a is reduced by a factor of $10^{-\chi}$ so that $m \rightarrow N_a$ and $N_a \rightarrow m$ in the above equations. A reduction in dose by a factor of $10^{-\chi}$, with the assumption $m \propto N_a$ is given by

$$m(\chi) = 10^{-\chi}m(0)$$
$$N_a(\chi) = 10^{-\chi}N_a(0)$$
$$N_d(\chi) = N_d(0).$$

In the actual calculations it was convenient to keep $m(\chi) = m(0) = 1/\text{cm}^3$, which only required multiplying through the above equations by $1/m(\chi)$. The condition $N_d(0) =$

$m(0)$ is used throughout this section, but the effect of having $N_a(0) > m(0)$ will be discussed.

In all calculations $E = 0{\cdot}67$ eV and $\beta = 1$°K/sec. The calculations used in generating Fig. 1 used $s'N_c = 10^{10}$/sec, so that when the ratio p'/s' was changed it was changed by changing p'. For all other figures of this section, $p'N_c = 10^{10}$/sec, and the ratio p'/s' is changed by changing s'.

Figure 1 shows how the characteristics of glow curves depend on the various parameters. Since m is defined to be 1/cm^3, all TL curves have unit area, excepting number 1 which is cut off to simulate a case where $N_a \ll m$ and $p' \gg s'$ (equation (29)). The areas under TSC curves are, of course, proportional to m only when the curves are monomolecular. The monomolecular and bimolecular forms are calculated with $\phi = 10^{10}$/sec, and the other curves are calculated with $s'N_c = 10^{10}$/sec; thus the initial part is the same for all curves. Some general features which can be seen from the figure and the foregoing equations are: (a) the initial rise of all glow curves is less than or equal to that of an exponential. (b) If $p' > s'$, TL and TSC curve shapes vary between those indicated by 1 and 4 or by 1_a and 4_a, respectively for all values of N_a/m. The approach to 4 or 4_a occurs when $p' \to s'$ and $N \to m$. The extreme cases 1 and 1_a occur when $p'/s' \to \infty$ and $N_a \ll m$. (c) If $s' = p'$ glow curves vary, as the ratio N_a/m decreases, from the monomolecular form, through the bimolecular forms (curves 4 and 4(a)) and back to a monomolecular form. The values of ϕ, of course, decreases for each successive form. (d) If $s' > p'$, TL and TSC curves will maintain an initial rise less than that of curves 3 and 3_a, respectively for all values of N_a/m. (e) If $N_a \ll m$ the TSC curves are monotonically increasing with increasing temperature. (f) Increasing p' sharpens all glow curves, and shifts maxima downward. Decreasing p' has the opposite effect. If the figure were more detailed it would be more apparent that curve 2 crosses over curve 3 once below the maximum and twice above the maximum. With sufficient further increase in p', curve 2 would peak before crossing over curve 3 and would cross over only one time.

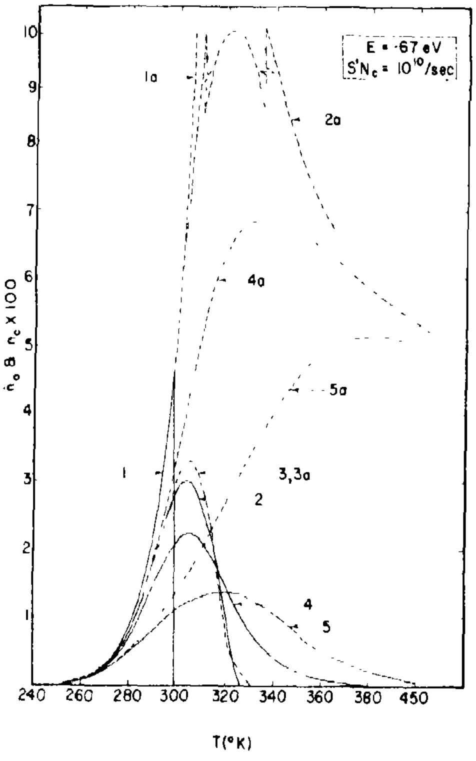

Fig. 1 TL (solid) and TSC (dashed) curves for $m = 1$/cm^3, $E = 0{\cdot}67$ eV, $\beta = 1$°K/sec and $s'N_c$ or ϕ equal 10^{10}/sec. Curves 1 and 1_a are for $N_a \ll m$, and $p' \gg s'$. Curves 2 and 2_a are for $N_a = m = N_d$ and $p'/s' = 10$. Curves 3 and 3_a are the monomolecular form with $N_a \gg m$ and $\phi = 10^{10}$/sec. Curves 4 and 4_a are the bimolecular forms (equations (25) and (25a)) for $N_a = m = N_d$ and $p' = s'$. Curves 5 and 5_a are for $N_a = m = N_d$ and $p'/s' = 0{\cdot}1$ The initial response of all curves is equal since the values of n_a and n_c are plotted

Figures 2–5 and Table 1 show the results of a numerical calculation using equations (18) and (24). The condition $m = N_a = 1$/cm^3, yields normalized TL curves. The value of $p'N_c = 10^{10}$/sec is used in all cases because the curves for decayed peaks or for reduced dose become independent of s'. The equiva-

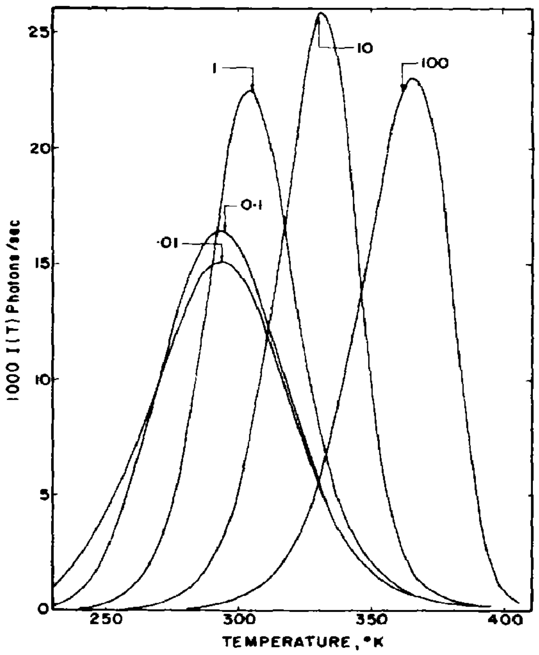

Fig. 2. TL intensity vs. temperature with the conditions $m = N_a = N_d = 1/\text{cm}^3$, $E = 0{\cdot}67$ eV, $p'N_c = 10^{10}$/sec, $\beta = 1$°K/sec, and for $p'/s' = 0{\cdot}01, 0{\cdot}1, 1, 10$, and 100 as indicated. The arrows indicate the first moment of each curve.

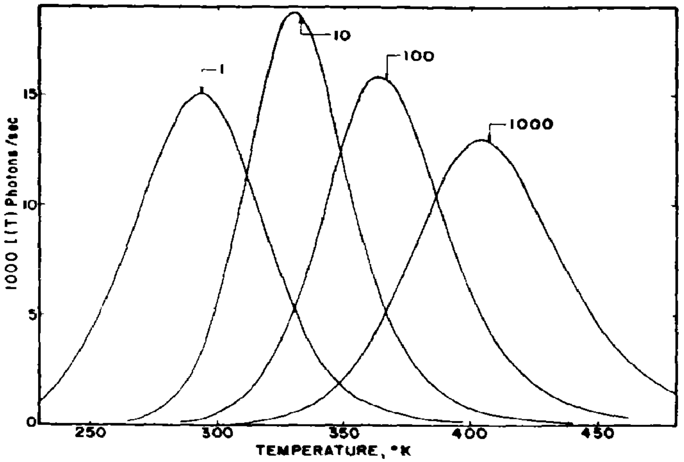

Fig. 3. The intensity vs. temperature for the conditions $p'/s' = 0{\cdot}01$, with $N_a = m = 1/\text{cm}^3$, $E = 0{\cdot}67$ eV, $p'N_c = 10^{10}$/sec, $\beta = 1$°K/sec, and for $N_d/m = 1, 10, 100$ and 1000 as indicated. The arrows indicate the first moment of each curve.

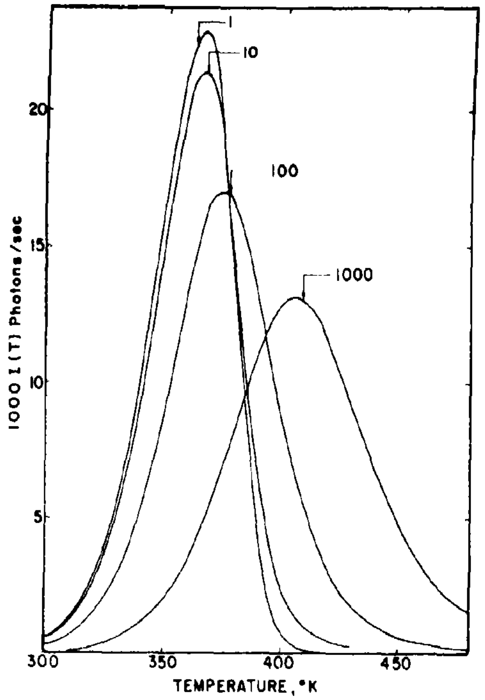

Fig. 4. TL intensity vs temperature for the conditions $p'/s' = 100$, with $N_a = m = 1/\text{cm}^3$, $L = 0.67$ eV, $p'N_c = 10^{10}$/sec, $\beta = 1$°K/sec, and $N_d/m = 1, 10, 100$ and 1000 as indicated. The arrows indicate the first moment of each curve.

lent of a reduction in the value of m and N_a is obtained by increasing N_d.

Figure 2 illustrates how the condition $m = N_a = N_d$ yields TL curves which tend toward a monomolecular, a bimolecular, or a broad curve which cannot be expressed in a simple analytical form, respectively for conditions $p' \gg s'$, $p' = s'$, or $p' \ll s'$. Thus the curve for $p'/s' = 100$ has the general appearance of a monomolecular curve, and Table 1 shows that the low temperature side of the curve is tending toward that of a monomolecular curve with $\log \phi = 8$. The curve for $p'/s' = 1$ is, of course, bimolecular with $\log \phi = 10$. Figures 3 and 4 illustrate that when $m = N_a$ the luminescence curves approach a bimolecular form (with $\log \phi = 7$ in the examples) as N_d/m increases, for all values of p'/s'. It is interesting that the difference between the first moments and the temperature of maximum glow increases for each example as the bimolecular form is approached. The change in curve amplitudes is not uniform for Figs. 2 and 3 because in some cases there is a competition between the trend toward a characteristic shape and the broadening which is associated with peaks occurring at the higher temperatures.

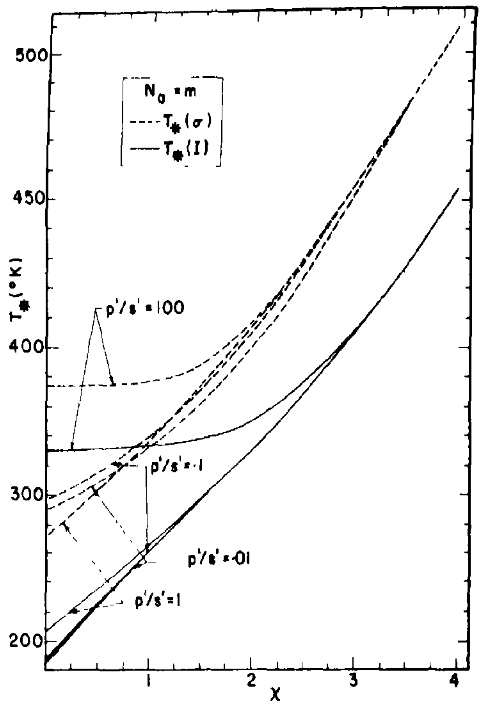

Fig. 5. The dependence of TL and TSC peak temperatures for a decayed trap or reduced dose when $m(0) = N_a(0) = N_d(0)$.

Figure 5 shows how TL and TSC peak temperatures shift as the amount of trapped charge is reduced by decay or by a reduction in dose (equivalent conditions for $m = N_a$) from the condition $m(0) = N_a(0) = N_d(0)$. When $p' > s'$ the initial shift is zero for both TL and TSC. When $s' \geqslant p'$ the initial TL peak temperature shift is approximately linear with χ, while the initial TSC shift occurs more slowly. When χ has increased sufficiently the shifts in peak temperature are described by the bimolecular forms (equation (25) and (25a)) and are thus independent of s'. It is

Table 1. This table shows how the characteristics of the curves in Figs. 2–4 vary with p'/s' and N_d/m. T_* and I_* are the temperature of maximum glow and the maximum glow respectively. $\bar{T}$ is the temperature at which $n_a = 0{\cdot}5$ m. ΔI is the percent deviation from $I(T)$ of an exponential rise calculated using equation (18) with $n_a = 0$ when $I(T) = I_*/10$. T_1 and T_2 are respectively the first and second inflection points of a curve, and I_1 and I_2 are the corresponding intensities. The characteristics of the monomolecular and bimolecular curves calculated with $E = 0{\cdot}67$ and $\beta = 1$ are given to illustrate the approach of curve characteristics to those of a bimolecular curve as N_d/m increases, or to those of a monomolecular curve as $p'/s' \rightarrow 100$

N_d/m	p'/s'	T_*	$1000I_*$	$\bar{T}$	ΔI	T_1	I_1/I_*	T_2	I_2/I_*
1	0·010	293·8	15·10	293·2	150·00	269·2	0·63	318·7	0·60
1	0·100	293·7	16·42	295·1	14·56	267·7	0·56	316·2	0·62
1	1·000	303·7	22·50	305·7	4·08	289·7	0·65	319·7	0·68
1	10·000	331·7	25·80	329·4	2·85	318·0	0·67	345·0	0·59
1	100·000	365·5	23·07	361·3	2·92	349·5	0·68	380·7	0·58
10	0·010	330·0	18·80	332·7	4·14	312·5	0·63	348·7	0·66
100	0·010	365·0	15·82	366·9	3·94	343·2	0·63	385·2	0·67
1000	0·010	404·0	12·98	407·4	3·78	378·0	0·64	430·0	0·69
10	100·000	366·5	21·45	363·2	2·95	348·7	0·66	381·2	0·62
100	100·000	375·0	17·00	375·5	3·32	355·0	0·65	393·5	0·65
1000	100·000	405·0	13·11	408·4	3·67	380·0	0·64	428·7	0·68
Monomolecular $\log\phi = 8, T_* = 366{\cdot}2$					2·98		0·683		0·536
Bimolecular $\log\phi = 7, T_* = 404{\cdot}0$					3·75		0·640		0·692

interesting that the T_*(TSC) for $p'/s' = 1$ crosses over the curves for p'/s' equal 0·1 or 0·01. This is related to the fact that T_*(TL) approaches a minimum value as s' increases with p' fixed and with $m = N_a = N_d$.

Figures 6 and 7 show that when $N_a(0) \geqslant m(0)$ all peak temperatures shift upward with increasing χ, with exception of the decayed TSC with $p' > s'$ which permits a decrease for small χ. The decayed curves approach a monomolecular form with $\phi_f =$ constant, (equation (20) or (20a)). The reduced dose curves approach a bimolecular form (equation (25) or (25a)) if $m \cong N_a$, or a monomolecular form if $N_a \gg m$. A comparison of Figs. 6 and 7 illustrates the convergence of TL and TSC peaks as $N_a(0)/m(0)$ increases; for a ratio greater than 10 the TL and TSC curves are essentially identical, and monomolecular with ϕ given by equation (21).

Figure 8 shows in more detail the behavior of TSC curves which show a negative shift in peak temperature. Part (a) shows that when $N_a(0$, $\gtrsim m(0)$ and $p' \gg s'$, decayed TSC peaks shift downward and become constant and equal to the TL peak temperatures. For the reduced dose case, the TL and TSC peaks are constant until $\chi \geqslant p'/s'$ where they start to shift upward. Part (b) and (c) are for $p'/s' = 10^7$. Part (b) shows that even when p'/s' is very large, $N_a(0)/m(0)$ must be close to unity before negative shifts in $T_*(\sigma)$ occur. The dependence of $n_c(\chi)_*$ is plotted to show that decaying a saturated trap which permits downward shifts in temperature for TSC does not decay the TSC peak magnitude much initially. When χ is sufficiently large the slope of $\log(n_c)_*$ vs. χ is minus one. The corresponding slope for TL magnitude is minus one at all times. This behavior can be understood by studying $m(\chi)/N_a(\chi)$ with increasing χ. The limiting behavior of the TSC with increasing χ is seen in equation (20a), where $\sigma(T) \propto m(\chi)/N_a(\chi)$. Part (c) simply shows the fraction of initially trapped charge which has recombined when a TSC peak occurs.

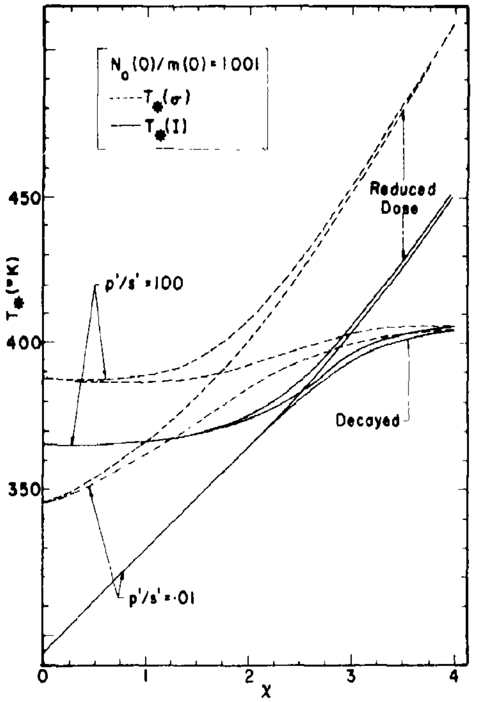

Fig. 6. The dependence of TL and TSC peak temperatures for a decayed trap and a reduced dose when $m(0) = N_d(0) = N_a(0)/1{\cdot}001$.

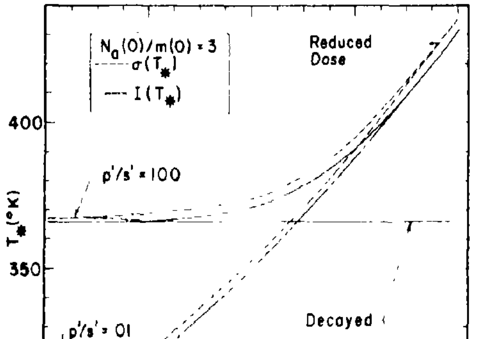

Fig 7. The dependence of TL and TSC peak temperatures for a decayed trap and a reduced dose when $m(0) = N_d(0) = N_a(0)/3$

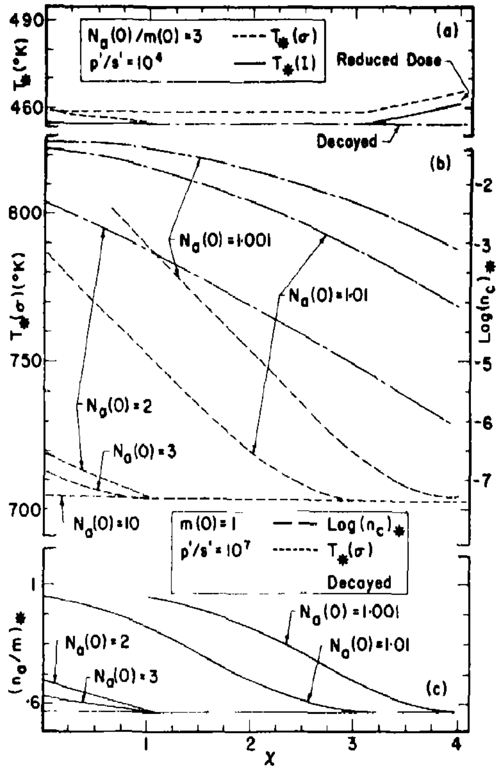

Fig. 8. Some characteristics of TL and TSC peak temperatures when $m(0) = N_d(0) < N_a(0)$ and when $p' \gg s'$. The TL peak temperature, not shown in part 'b', is 703·5°K for all cases.

When $p'/s' = 10^7$ and $N_a/m = 1{\cdot}001$, more than 99 per cent of the charge has recombined when the TSC peaks. The results shown in this and the preceding figures do not agree with the conclusions of Dussel and Bube concerning the conditions for which negative shifts in TSC peaks are most likely to be observed (top page 771, [2]).

The behavior of TL peak temperatures for the case $N_a < m$ are shown in Fig. 9. The TSC curves don't have maxima in most cases, but instead tend to become monotonically increasing with increasing temperature. When $N_a(0) < m(0)$ it is seen that curves for the TL peak temperature increase with decreasing dose, if $m \propto N_a$. The TL curve with $N_a(0)/m(0) = 0{\cdot}999$ approaches a bimolecular form while that for $N_a(0)/m(0) =$

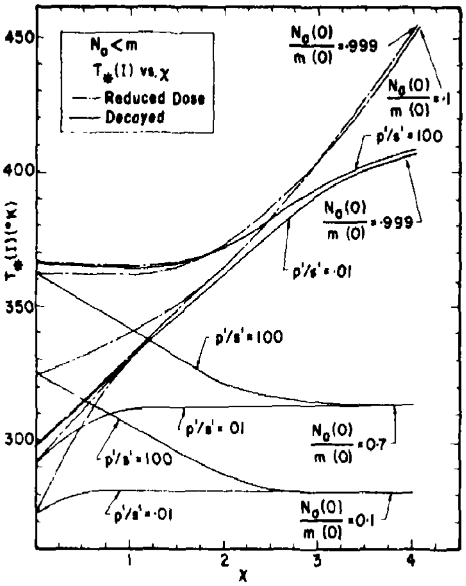

Fig. 9. The dependence of TL peak temperatures for a decayed trap and for a reduced dose when $m(0) = N_d(0) \geq N_a(0)$

0·1 approaches a monomolecular form. The TL peak temperature for the decayed case with $N_a(0)/m(0) = 0{\cdot}999$ decreases slightly when $p'/s' = 100$, and then increases to a constant value as χ increases. The corresponding curve with $p'/s' = 0{\cdot}01$ increases to a slightly smaller constant value given by equation (22) when the value for $N_a(\chi)/m(\chi)$ as $\chi \to \infty$ is inserted. When $N_a(0)/m(0) < 0{\cdot}7$, the decayed peak temperatures for $p' > s'$ shift downward and converge to a constant value which is common to the corresponding temperature maxima curves for $p' < s$.

Some further remarks concerning the band model under consideration are: (a) it is probable that most glow peaks if there are several in a glow curve will have a monomolecular form, or can be made to have by decay. (b) Glow peaks for which $N_a \approx m$ most probably would be the largest or last of a series. (c) The conditions for which glow curves have a simple analytical form are $\mu/|\mu + G| \leq 0{\cdot}1$. (d) The study of ϕ as a function of decay or dosage can yield useful information about the parameters on which ϕ depends. High dose levels tend to increase the dependence of ϕ on $s'N_d$ while low dose levels or decay tends to increase the dependence on p'. (e) It is unlikely that the condition $m = N_d$ can be fulfilled, since trapped charges may be released by the radiation which is causing them to be trapped. It is also possible that charge sources may be depleated before traps are filled. (f) The curves for peak temperature in Figs. 6–9 can be modified to correspond to conditions where $N_d(0) > m(0)$, by translating all curves toward the ordinate. The reduced dose curves are then correctly shown. The decayed curves must be shifted upward, with some change in shape, so that they are joined with the reduced dose curves at the ordinate. The shifts in peak temperature for reduced dose thus become negligible as $N_d(0)/m(0)$ increases. These statements and the one following can be confirmed by studying equations (21) and (23) in terms of χ. (g) If $N_a \gg m$ the peak temperature curves for decay are constant except when $m(0) \to N_d(0)$; the curves for reduced dose are constant initially if $p'N_a(0) \gg s'N_d(0)$, and begin to rise when $s'N_d(\chi)/p'N_a(\chi)$ excedes unity. If $p'N_a \ll s'N_d$ for all conditions, as could be the case if the number of available traps exceded the number of charge sources, then the reduced dose curves would have no constant region and the peak temperature curves for reduced dose and decay would form an acute angle. (h) The initial rise approximation, in which data from the leading edge of a glow curve is interpreted as an exponential rise, applies to a smaller fraction of the curve as the ratio ϕ_i/ϕ_f increases, or as p'/s' decreases. The approximation is better for TSC than for TL. Table 1, Column 6 illustrates how the condition $m = N_d$ when $s' \gg p'$ limits the use of initial rise data. For $p'/s' = 0{\cdot}01$, the value of an exponential rise obtained by setting $n_a = 0$ in equation (18), with T chosen so that $I(T)$ is 1/10, 1/100, or 1/1000 of the maximum, differs by 150, 8 or 0·8 per cent, respectively from $I(T)$. If a series of initial rise curves are made by warming part of the way through a peak several times (thus decaying the peak in steps) each rise can furnish data for a plot of log (I) vs. $1/T$. The intercepts of the initial and final plots would be different by a factor $(m\phi)_i/(m\phi)_f$ when m is sufficiently reduced. In the above example this factor would be $100\, m_i/m_f$. (i) The peak temperatures for TL and TSC for *decayed traps* will always shift upward or remain constant with the following exceptions: TSC peaks will shift downward if $p' \gg s'$ when $N_a \approx m \approx N_d$ initially. TL peak temperatures may shift downward if $p' > s'$ and $N_a < m$ initially. TSC peak temperatures may occur and shift downward initially if $p' > s'$ and if $N_a < m$ initially, but a peak fails to occur as the curve changes toward the limiting exponential form. (j) The peak temperatures for TL and TSC always increase with a *reduction in dose* if $N_a \propto m$. (There may, of course, be a range where they are approximately constant as in Fig. 8(a)). It is somewhat more general and sometimes appropriate to assume that $m = bt^q/(1 + bt^q/N_d)$ where t is the time of irradiation and b, q and N_d are constant, and to assume a similar form for N_a with a different set of constants. In this case or for any other dependence, the decreased dose peak temperature curves would fall above those for decayed traps so that only the same exceptions as noted in (i) above could apply to a rule specifying increasing peak temperature. It is clear from equation (23), if $m(0) > 10N_a(0)$ in some range, that peak temperatures can shift either downward or upward with decreasing dose according to the behavior of N_d/m and N_a/m. (k) It should be possible in cases to increase the separation of superimposed glow peaks by using selected glow levels. (l) The condition $N_a < m$ might apply to a case where trapping is due to a set of donor states N_d which are partially filled prior to irradiation when $N_a = 0$. (m) A series of initial rise curves (see (h) above) will give a value for energy which is too high if a glow peak is decayed to the point that a higher temperature glow peak contributes effectively to the initial rise.

7. When non-radiative transitions, retrapping by traps other than the thermally activated one, $(i = 1)$, or recombinations to more than one center occur, one can write the more general equations,

$$\dot{n}_c = \gamma_1' N_c n_d^1 - \Big[\sum\ (i, j) s_i' (N_d^i - n_d^i) + (p_j' + q_j')(N_a^j - n_a^j)\Big] n_c \quad (30)$$

$$\dot{n}_a^j = (p_j' + q_j')(N_a^j - n_a^j) n_c \quad (31)$$

where

$$m^1 = n_d^1 + n_c + \sum\ (i > 1, j) n_d^i - m^i + n_a^j \quad (32)$$

with the conditions $n_c = n_a^j = 0$ initially. If it is assumed that $s_1' N_d^1$ is not especially large, and that

$$N_d^i \gg n_d^i - m^i, i > 1 \quad \text{and} \quad N_a^j \gg n_a^j$$

then

$$I(T) = m^1 UJ/\rho \quad (33)$$

with

$$J = \sum\ (j) p_j' N_a^j$$

$$\rho = \sum\ (i > 1, j) s_i' (N_d^i - m^i) + (p_i' + q_i') N_a^j$$

and

$$\phi = s' N_c.$$

Here the curve is simple monomolecular, but the total glow is a complex function of excitation dose, the characteristics of which will be discussed later on. When equation (33) holds the glow peak temperature is an effective signature of the trapping defect.

8. When $N_c v \propto T^2$, all expressions for $I(T)$ are made to conform by changing s' to $S'\sqrt{T}$, p' to $P'\sqrt{T}$, and N_c to $N_c''\sqrt{T^3}$. The product ϕh can be changed to ΦH where

$$H \cong \int_0^T T^2 W \,\mathrm{d}T/\beta$$

and where Φ is obtained from the formuli for ϕ with s', p', and N_c replaced by S', P', and N_c'' respectively. The resulting expressions for $I(T)$ contain a factor T^2. Thus, for example, a monomolecular equation becomes

$$I(T) = \mu\Phi T^2 \exp(-a/T - \Phi H).$$

This extra temperature dependence is not very significant as is illustrated in Figs. 2 and 5 of the preceding paper.

4. A MODEL WHERE A TRAP AND EXCITED STATE ARE LOCALIZED AT THE SAME DEFECT, WHICH IS SPACIALLY SEPARATED FROM ALL RECOMBINATION CENTERS

If traps, excited states and recombination centers are each spacially separate from the other the results of Section 3 apply with N_c equal to the density of defects with which the excited state is associated. When one trapping state and one excited state are localized at the same defect, but spacially separated from all recombination centers, both linear and quadratic terms may occur in the occupation number time derivatives:

$$\dot{n}_d = -[\gamma + \gamma'(N_d - n_d - n_c)]n_d + [s + s'(N_d - n_d - n_c)]n_c \quad (34)$$

$$\dot{n}_c = [\gamma + \gamma'(N_d - n_d - n_c)]n_d - [s + s'(N_d - n_d - n_c) + p'(N_a - n_a)]n_c \quad (35)$$

$$\dot{n}_a = p'(N_a - n_a)n_c. \quad (36)$$

The unprimed factors, describe the rate of transitions between states associated with the same defect, while the primed factors describe the rate of overlap transitions between states associated with separate defects. The overlap transfer between states indicated may involve unspecified intermediate states. It has been assumed that the charge of a defect can change by one electron; that only one kind of trap, excited state, and recombination state are active; and that there are no non-radiative recombination transitions. Equations 34–36 satisfy

$$n_a + n_d + n_c = m \quad (37)$$

if n_a and n_c are equal to zero initially. It is again assumed that $\dot{n}_c$ is small compared to the separate terms on the right side of equation (35), so that

$$\frac{n_c}{n_d} = \frac{\gamma + \gamma'(N_d + n_a - m)}{s + s'(N_d + n_a - m) + p'(N_a - n_a)}$$

as before,

$$\gamma = sW, \quad \gamma' = s'W.$$

The additional assumption that $n_d \cong m - n_a$ permits one to write

$$\dot{n}_a = p'(N_a - n_a)(m - n_a) \left[\frac{s + s'(N_d + n_a - m)}{s + s'(N_d + n_a - m) + p'(N_a - n_a)}\right] W. \quad (38)$$

Integration of equation (38) gives

$$\left(\frac{N_a - n_a}{N_a}\right)^{A} \left(\frac{m - n_a}{m}\right)^{-(1+B)} \left(\frac{Z + n_a s'}{Z}\right)^{B} = \exp[h(T)] \quad (39)$$

where

$$A^{-1} = p'(N_a - m), B^{-1} = s + s'N_d, \text{ and } Z = s + s'(N_d - m).$$

1. If $N_d \gg m$, we define $s'' \equiv s + s'N_d$, then equation (38) reduces to

$$\dot{n}_a = \frac{p's''(N_a - n_a)(m - n_a)W}{s'' + p'(N_a - n_a)} \quad (40)$$

which is a form discussed by Halperin and Braner, if $s' = 0$[1]. The factor containing s' in equation (39) becomes unity thereby reducing the equation to the proper solution for equation (40).

If $N_a \gg m$, then the solution for equation (40) is

$$I(T) = mU \tag{41}$$

$$\phi = s''p'N_a/(s''+p'N_a).$$

This behavior is like that in equation (20) with s'' replacing $s'N_c$ and $s'N_d$.

If $m \gg N_a$, then the solution for equation (40) is

$$I(T) = N_a\mathrm{U}\,[1+pN_a s^{-1}\exp(-\phi h)]^{-1} \tag{42}$$

where $\phi = p'm$. Equation (42) is similar in behavior to equation (22). If p'/s' is very large, a situation analogous to equation (29) may occur; then the initial part of the glow is given by equation (41) with $\phi = s''$.

If $m = N_a$, then A in equation (39) is not well defined. Solving equation (40) for this condition yields

$$s''/p'm - s''/p'y + \log_e(y/m) = -h(T)$$

where $y - m - n_a$. If $p'm/s'' \leqslant 1$, then

$$I(T) = mB \tag{43}$$

with $\phi = p'm$.

The TSC for this model are given by

$$\sigma(T) \propto n_c = \dot{n}_a/p'N_a$$

when $N_a \gg m$, and by

$$\sigma(T) \propto n_c = mW$$

when $m \gg N_a$ and by

$$\sigma(T) \propto n_c = mW/[1+mp'h(T)]$$

when $m = N_a$.

2. When $m \to N_d$, the initial and final parts of a glow curve are described by equations (41–43), as appropriate, with $s'' = s$ and $s'' = s + s'N_d$, respectively. Thus shifts in peak temperature will occur if $s'N_d > s$. The behavior of glow peaks is like that for a strictly localized model or a band model according to whether the ratio $s'N_d/s$ is small or large. The model is distinguished from the band model discussed earlier because of the different dependence of ϕ on the trapping defect concentration. This is illustrated in Figs. 10 and 11 for a case where the glow peaks are monomolecular with $m \leqslant N_a$, and $m \propto N_a$.

A generalization of this model with assumptions similar to those in Chapter 3, Section 7, would result in monomolecular glow curves with $\phi = s$.

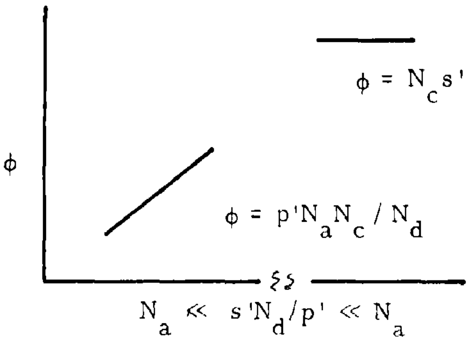

Fig. 10. The dependence of ϕ on N_a, if $m \propto N_a$ and $m \ll N_a$ for a band model with a monomolecular form.

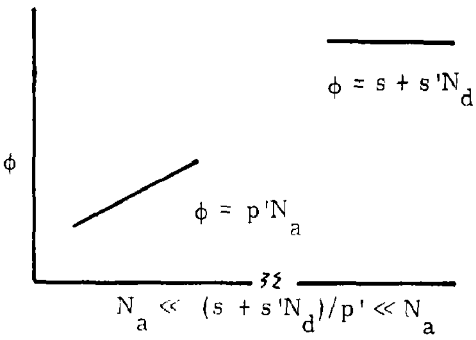

Fig. 11. The dependence of ϕ on N_a, if $m \propto N_a$ and $m \ll N_a$ for an exchange model with a monomolecular form.

5. DISCUSSION

If the traps occurring in a material become thermally activated at temperatures sufficiently different to prevent overlap of glow peaks, then it seems highly probable that low dose levels or peak cleaning, $m \ll N_a$, may result in glow curves having a simple analytical form. The simple monomolecular form is very likely to describe the glow from all peaks below the largest of a glow curve when the emission spectra is the same for all peaks, because this suggests a value of m/N_a small enough to make retrapping by the thermally activated trap negligible; in this case, even if glow peaks are superimposed, the leading edge of a cleaned glow curve should be simple monomolecular. A good check on whether or not monomolecular forms do apply should be afforded by simultaneous observations of TSC and TL curves having the same shape.

The simple non-localized systems having only three active states considered in most detail here obviously apply if all traps are filled by exciting to saturation (they may not be if one exhausts the sources or if the trap populations equilibrate without being filled), and if the recombination centers can be considered to be of one type. This procedure of preparing a material for measurements leading to evaluation of energy and frequency factors may or may not be desirable in that it can swamp out or eliminate some glow peaks, and in that it will not necessarily increase the probability of having glow curves with a simple analytical form. Making a series of initial rise curves (thus decaying each trap in turn) seems to be the best method, in general, of obtaining energies for a series of glow peaks in a complex glow curve. Frequently there are systematic shifts in the peak temperature, for some peaks, and systematic changes in peak areas, A_i, with changes in dose level. The temperature shifts; and the intercepts, slopes, and saturation levels of log A_t versus dose provide some information about the relative values of the parameters which influence the frequency factors, ϕ_i.

It does seem rather useless to obtain values for trap energies and frequency factors for a material exhibiting thermoluminescence without making an effort to identify the atomic configurations giving rise to traps, recombination centers or relevant intermediate states. If detailed thermodynamic histories and chemical analyses of several samples of a material are available, one can attempt to relate possible defect configurations to the characteristics of the thermoluminescence observed. For example, it would be most useful to be able to correlate the intensity of a glow peak with a defect density. Qualitative correlations can be made by studying glow peak intensity versus radiation dose, and quantitative correlations are possible for relative densities of defects giving rise to trapping states if the effect of enough of the parameters describing a general situation can be simplified. The complexity of a general situation is illustrated by equation (23), which is a simple case in that the band is a common excited state. To calculate a glow intensity from that equation, one must first calculate the charge distribution as a function of radiation dose, $I_0(\lambda)t$ and then calculate the redistribution over traps and centers upon heating to the temperature where the glow peak being analyzed occurs. The author intends to prepare a sequel to this paper which will treat some special cases of thermoluminescence intensity vs. radiation dose, and discuss the scope of the general problem in a way that should lead to a better understanding, at least for newcomers, to the field, of the meaning of glow curve characteristics and of their interpretations.

Thermoluminescence data, including emission spectra, glow intensity vs. dose or decay for specific conditions, plus other optical properties of a material can provide valuable information for use in establishing significant fixed (or changing) electronic charge distributions for study by magnetic resonance where direct measurement of ionic charge and of changes in charge densities are possible[5, 6]. In this respect it would seem generally desirable to use excitation radiation most likely to preserve the defect densities in a material.

The author is not aware of any terms which distinguish between retrapping by traps being thermally activated and by any others present, and therefore proposes use of the terms self and progressive retrapping, respectively. These terms, or some others, would be particularly useful in discussing thermoluminescence intensity versus radiation dose.

Acknowledgements – Figures drawn by John B. Ankeney. The author thanks Professor A. Halperin, Dr. David A. Lee, Mr Elward T Rodine, and Dr P. A. Hemenger for useful discussions pertaining to this work.

REFERENCES

1. HALPERIN A. and BRANER A. A., *Phys. Rev* **117**, 408 (1960).
2. DUSSEL A. G. and BUBE R. H., *Phys. Rev.* **155**, 764 (1967).
3. DEKKER A. J. In *Solid State Physics*. Prentice-Hall, Englewood Cliffs, N.J. (1957).
4. BRÄUNLICH P., *J. appl. Phys.* **38**, 2516 (1967).
5. MASON D. R., KOEHLER H. A. and KIKUCHI C., *Phys. Rev Lett.* **20**, 451 (1968).
6. HANSLER R. L. and SEGELKEN W. G., *J. Phys. Chem. Solids* **13**, 124 (1960).

Note added in proof: The decay of glow or conductivity at constant temperature is described by replacing $h(T)$ or $H(T)$ in formulae for $I(T)$ and $\sigma(T)$ by $t\exp(-E/kT)$ or $tT^2\exp(-E/kT)$, respectively

J. Phys. Chem. Solids Pergamon Press 1969. Vol. 30, pp. 1709–1718. Printed in Great Britain.

SECOND QUANTIZED FORMALISM FOR NON-ORTHOGONAL STATES

D. J. NEWMAN
Department of Physics, Queen Mary College, Mile End Road, London, E 1, England

(*Received 2 December 1968*)

Abstract—A simple method of manipulating annihilation and creation operators for non-orthogonal states is developed. This is applied in the context of crystal field theory to derive exact many electron matrix elements which are explicitly independent of the choice of basis set and linked cluster in form These are related to effective operators acting on free-ion open-shell states.

1. INTRODUCTION

IN THE present paper a formalism is developed which enables the second quantized form of many-body theory to be applied to systems where the single particle basis states are non-orthogonal. The most characteristic field of application is to assemblies of atoms in which the free electronic wave functions are only slightly perturbed. The basis functions normally used for such calculations are atomic Hartree–Fock functions.

Much work has already been done on the convergence problems that arise when non-orthogonal atomic wave functions are used in the determination of quantities such as binding energies and exchange energies of effectively infinite systems. Most recent are the papers of Arai[1,2] and the review article by Herring[3]. Our present aim is not to discuss convergence, but to consider the formal problems which arise in the case of a paramagnetic ion substituted into a crystalline environment. The very general algebraic results obtained in Sections 2 and 3 will, however, have a much wider range of possible application.

It may be supposed that an explicit formalism for non-orthogonal states is superfluous as, given a set of such states, we may always transform to orthogonal states, carry out the required algebraic analysis and then transform back to the original states for numerical evaluations. Quite apart from the fact that a transformation of this type is far from trivial, it must be emphasized that orthogonalization arises from the Pauli exclusion principle and is not just a question of mathematical convenience. That is to say, a many electron determinantal state with non-orthogonal component states is unchanged if all its components are mutually orthogonalized. If, however, the *whole set* of single electron basis states (unoccupied as well as occupied) are orthogonalized, a single determinant of non-orthogonal states will, in general, become a sum of determinants. Then the natural many-particle basis states, which are defined in terms of non-orthogonal atomic orbitals, take a complicated form. Our approach is designed to avoid this difficulty while retaining the natural many-particle basis states.

Bishton and Newman[4] have previously developed a diagrammatic method of expanding many-electron matrix elements in powers of the overlap integrals and shown that the first few terms in this expansion are in 'linked cluster' form. The present work takes advantage of a further result proved by the author[5] to ensure that all results obtained in this paper are expressed in a way which explicitly indicates that they are capable of expansion in terms of a linked cluster series in the overlap integrals to *arbitrary order*. This ensures the direct physical significance of our formulae and, at the same time, minimises the amount of numerical work required to evaluate them. The results derived in Section 5 generalize and extend the formulae obtained in[4].

Besides generating formulae useful in the numerical calculation of crystal field parameters, the new algebraic formalism may also be used to derive effective operators in crystal field theory which act between the states of an isolated paramagnetic ion and yet take into account the effects of the coordinated ligands. In particular, we wish to determine to what extent the formulation of effective operators given by Wybourne[6] can be generalized to cope with the real physical situation in which the crystal field has not only electrostatic contributions but also contributions due to the effects of overlap and covalency. It is shown in Section 5 that such effective operators exist in the 'exclusion model'[7] of both ordinary and correlation [8] crystal fields to all orders of overlap.

2. THE OVERLAP MATRIX

Consider a finite basis of non-orthogonal one electron states $|i\rangle$, $i = 1, \ldots, N$. The elements of the overlap matrix are written, for convenience, as $S_{ij} = \langle i|j\rangle$. We also define the inverse matrix S^{ij} so that

$$S^{ij}S_{jk} = \delta_k{}^i \tag{2.1}$$

with the usual summation convention. Following Chirgwin and Coulson[9] we shall treat S_{ij} as a *metric*, using it and its inverse to raise and lower indices. Throughout we take the non-orthogonal states $|i\rangle$ themselves as covariant (indicated by suffices). This tensor notation has the usual advantage that any tensor equation which is true for orthogonal states will also be true for an arbitrary non-orthogonal basis. Hence we avoid the need to make an explicit transformation to an orthogonal basis just in order to derive formulae which are valid for general non-orthogonal bases.

The $N \times N$ overlap determinant $\Delta_N = |S_{ij}|$ can be expanded in pivotal form[5] as

$$\Delta_N = S_{11}{}^{(1)}S_{22}, \ldots, {}^{(N-1)}S_{NN} \tag{2.2}$$

where the factors are defined by the recurrence relation

$$\begin{aligned} {}^{(r)}S_{mn} &= {}^{(r-1)}S_{mn} - {}^{(r-1)}S_{mr}\;{}^{(r-1)}S_{rn}/{}^{(r-1)}S_{rr}, \\ {}^{(0)}S_{mn} &= S_{mn}. \end{aligned} \tag{2.3}$$

It follows from (2.3) that the *pivotal overlaps* ${}^{(r)}S_{mn}$ are identically zero for $m, n \leq r$, and thus form an $(N-r)\times(N-r)$ dimensional matrix. We shall also find it convenient to raise an index on these quantities so as to define the *pivotal delta*

$${}^{(r)}\delta_k{}^i = S^{ij}\,{}^{(r)}S_{jk} \tag{2.4}$$

and the *contravariant pivotal overlap matrix*

$${}^{(r)}S^{il} = {}^{(r)}\delta_k{}^i\, S^{kl} = S^{ij}\,{}^{(r)}S_{jk}S^{kl}. \tag{2.5}$$

The pivotal delta has the following structure

$$\left.\begin{aligned} {}^{(r)}\delta_j{}^i &= \delta_j{}^i \text{ for } i > r, \\ &\neq 0 \text{ for } i \leq r, \quad j > r \\ &= 0 \text{ for } i \leq r, \quad j \leq r \end{aligned}\right\} \tag{2.6}$$

and the contravariant pivotal overlap matrix satisfies:

$${}^{(r)}S^{ij} = S^{ij} \text{ for } i \text{ or } j > r. \tag{2.7}$$

These new pivotal quantities also satisfy recurrence relations which may be obtained directly from equation (2.3):

$$\left.\begin{aligned} {}^{(r)}\delta_j{}^i &= {}^{(r-1)}\delta_j{}^i - {}^{(r-1)}\delta_r{}^i\;{}^{(r-1)}S_{rj}/{}^{(r-1)}S_{rr} \\ {}^{(r)}S^{ij} &= {}^{(r-1)}S^{ij} - {}^{(r-1)}\delta_r{}^i\;{}^{(r-1)}\delta_r{}^j/{}^{(r-1)}S_{rr} \end{aligned}\right\}. \tag{2.8}$$

The reader will find it easier to visualize the significance of the results in this and the following section if they are written out explicitly in the case of a basis with three non-orthogonal states. Most results were originally surmised in this way, general derivations being obtained afterwards.

It follows at once from equation (2.4) that

$$ {}^{(r)}S_{jt} = S_{jl}\,{}^{(r)}\delta_t^{\,l}. \qquad (2.9) $$

We may also prove the following more general result by induction, using the recurrence relation (2.3):

$$ {}^{(\overline{l,r})}S_{jt} = {}^{(l)}S_{ji}\,{}^{(r)}\delta_t^{\,i} \qquad (2.10) $$

where $\overline{l,r}$ indicates a pivotal sequence which runs to l or r, whichever is the greater. Rearrangement of the indices in this equation also gives

$$ {}^{(\overline{l,r})}S^{kl} = {}^{(l)}S^{kj}\,{}^{(r)}\delta_j^{\,l} \qquad (2.11) $$

$$ {}^{(\overline{l,r})}\delta_s^{\,k} = {}^{(l)}\delta_j^{\,k}\,{}^{(r)}\delta_s^{\,j} = {}^{(l)}S^{kl}\,{}^{(r)}S_{ls}. \qquad (2.12) $$

Successive application of the recurrence relations (2.3), starting from ${}^{(n)}S_{ij}$, leads to the equation

$$ {}^{(n)}S_{ij} = S_{ij} - \sum_{r=1}^{n} \frac{{}^{(r-1)}S_{ir}\,{}^{(r-1)}S_{rj}}{{}^{(r-1)}S_{rr}}. \qquad (2.13) $$

If the value of n is chosen to be N, ${}^{(N)}S_{ij}$ is identically zero and so are all terms in the sum with $r > ij$ where ij denotes the *smaller* of i and j.

Equation (2.13) then gives

$$ S_{ij} = \sum_{r=1}^{N} \frac{{}^{(r-1)}S_{ir}\,{}^{(r-1)}S_{rj}}{{}^{(r-1)}S_{rr}} = \sum_{r=1}^{ij} \frac{{}^{(r-1)}S_{ir}\,{}^{(r-1)}S_{rj}}{{}^{(r-1)}S_{rr}}; \qquad (2.14) $$

and raising indices

$$ \delta_j^{\,i} = \sum_{r} \frac{{}^{(r-1)}S_{jr}\,{}^{(r-1)}\delta_r^{\,i}}{{}^{(r-1)}S_{rr}}. $$

$$ S^{ij} = \sum_{r} \frac{{}^{(r-1)}\delta_r^{\,i}\,{}^{(r-1)}\delta_r^{\,j}}{{}^{(r-1)}S_{rr}}. \qquad (2.15) $$

Raising indices in equation (2.13) and using (2.15) we also obtain

$$ {}^{(n)}S^{ij} = \sum_{r=n}^{N} \frac{{}^{(r-1)}\delta_r^{\,i}\,{}^{(r-1)}\delta_r^{\,j}}{{}^{(r-1)}S_{rr}}. \qquad (2.16) $$

It has previously been remarked[5] that the recurrence relations show ${}^{(n)}S_{ij}$ to have a 'linked cluster' form in terms of the overlaps S_{ij}. That is to say the expansion of ${}^{(n)}S_{ij}$ is in the form of a sum of products of the overlaps S_{ij} such that no product can be factorized into separate parts having no state suffices in common. The recurrence relations similarly ensure that the expansion of ${}^{(r)}\delta_j^{\,i}$ is also of linked cluster form and the constructions given above demonstrate that all defined quantities have this form, including the inverse overlap matrix S^{ij}. The latter result has also been given by Arai[2].

The sums in the expressions for S_{ij}, S^{ij}, $\delta_j^{\,i}$ (equations (2.14) and (2.15)) are not explicitly in tensor form. This can be rectified if we introduce new bracketed indices defined by

$$ \delta^{i}(r) = {}^{(r-1)}\delta_r^{\,i}/\sqrt{{}^{(r-1)}S_{rr}}, $$
$$ S_i(r) = {}^{(r-1)}S_{ir}/\sqrt{{}^{(r-1)}S_{rr}}. \qquad (2.17) $$

Then

$$ \begin{aligned} \delta_r^{\,i} &= S_r(q)\,\delta^{i}(q) \\ S^{ij} &= \delta^{i}(q)\delta^{j}(q) \qquad (2.18) \\ S_{ij} &= S_i(q)S_j(q) \end{aligned} $$

if we also adopt the summation convention for pairs of bracketed indices. Pivots have been dropped in these expressions as they are implied by the bracketed indices. It is also convenient to define quantities with two bracketed indices:

$$ S(r, r+1) = S_{r+1}(r)/\sqrt{{}^{(r)}S_{r+1,r+1}}. \qquad (2.19) $$

3. OPERATOR FORMALISM

We now introduce covariant operators a_i^{+}, a_i which create and annihilate the (covariant) one electron states $|j\rangle$. These satisfy the well known anticommutation relations, viz:

$$ [a_i, a_j]_+ = 0, \qquad [a_i^{+}, a_j^{+}]_+ = 0, $$
$$ [a_i^{+}, a_j]_+ = S_{ij} \qquad (3.1) $$

(e.g. see Longuet-Higgins[10]). To verify (3.1) we only have to note that they are tensor equations which reduce to the correct form for orthogonal states.

Raising suffices we define the corresponding contravariant operators

$$a^{i+} = S^{ij}a_j^+, \qquad a^i = S^{ij}a_j \tag{3.2}$$

which create and annihilate electrons in mixed states with respect to the original basis. The following commutation relations are then easy to prove

$$[a^{i+}, a_j]_+ = [a^i, a_j^+]_+ = \delta_j^i, \qquad [a^{i+}, a^j]_+ = S^{ij}. \tag{3.3}$$

Using these operators we may construct the usual number operator which gives the number of electrons in a many electron state:

$$\hat{N} = a^{i+}a_i = S_{ij}a^{i+}a^j = S^{kl}a_k^+a_l. \tag{3.4}$$

This expression is clearly invariant with respect to arbitrary transformations of the basis states and has the correct form for an orthogonal basis

Pivotal operators are defined by

$${}^{(r)}a_n = {}^{(r)}\delta_n^i\, a_i, \qquad {}^{(r)}a_n^+ = {}^{(r)}\delta_n^i\, a_i^+. \tag{3.5}$$

They can be shown to satisfy the recurrence relation

$${}^{(r)}a_n = {}^{(r-1)}a_n - ({}^{(r-1)}S_{nr}/{}^{(r-1)}S_{rr})\,{}^{(r-1)}a_r, \qquad {}^{(0)}a_r = a_r \tag{3.6}$$

(and similarly for creation operators).

The operators ${}^{(1)}a_r^+$ create a set of $n-1$ states which are the states $|r\rangle$ orthogonalized with respect to state 1. Similarly the ${}^{(2)}a_r^+$ create $n-2$ states orthogonalized to states 1 and 2, and so on. Hence the recurrence relation specifies a step-by-step Schmidt orthogonalization procedure which finally produces creation operators ${}^{(r-1)}a_r^+$ for an orthogonal (but unnormalized) basis set. We might equally well have begun the theory at this point and used (3.6) to derive all the results obtained in the previous section.

Use of the recurrence relation (3.6) in conjunction with the basic commutation rules enables us to derive the following general commutation relation for pivotal operators:

$$[{}^{(t)}a_n^+, {}^{(r)}a_m]_+ = {}^{(\overline{r,t})}S_{nm} \tag{3.7}$$

where $\overline{r,t}$ indicates the greater of r and t. This is the basic result required for the algebraic manipulation of creation and annihilation operators. Important special cases are

$$[{}^{(r)}a_n^+, {}^{(r)}a_m^+]_+ = {}^{(r)}S_{nm} \tag{3.8}$$

and, for operators which generate Schmidt orthogonalized states,

$$[{}^{(r-1)}a_r^+, {}^{(s-1)}a_s]_+ = \delta(r,s)\,{}^{(r-1)}S_{rr}. \tag{3.9}$$

Here $\delta(r,s)$ is the Kronecker δ. The latter equation is not obviously in tensor form until we express it in terms of bracketed suffices (which we now see refer to *normalized* Schmidt orthogonalized states). Then

$$[a^+(r), a(s)]_+ = \delta(r,s) \tag{3.10}$$

where $a(r) = {}^{(r-1)}a_r/\sqrt{{}^{(r-1)}S_{rr}}$.

It is also convenient to define *pivotal contravariant operators*

$${}^{(r)}a^n = S^{nj}\,{}^{(r)}a_j = {}^{(r)}S^{nj}\,{}^{(r)}a_j = {}^{(r)}S^{nj}\,a_j. \tag{3.11}$$

These satisfy the commutation relations

$$\left.\begin{aligned} [{}^{(r)}a_m, {}^{(s)}a^{n+}]_+ &= [{}^{(r)}a^n, {}^{(s)}a_m^+]_+ = {}^{(\overline{r,s})}\delta_m^n \\ [{}^{(r)}a^m, {}^{(s)}a^{n+}]_+ &= [{}^{(r)}a^n, {}^{(s)}a^{m+}]_+ = {}^{(\overline{r,s})}S^{nm} \end{aligned}\right\} \tag{3.12}$$

It is worth noting that, as a result of equation (2.7), we have ${}^{(r)}a^n = a^n$ and ${}^{(r)}a^{n+} = a^{n+}$ if $r < n$.

Further results, which may be obtained by direct evaluation, are

$$a^{r\,(r)}a_t^{+} = -{}^{(r-1)}a_t^{+}a^{r} \qquad (t > r) \quad (3.13)$$

and

$${}^{(n)}a_r^{+} = a_r^{+} - [{}^{(n)}\hat{Q}, a_r^{+}]_{-} \quad (3.14)$$

where

$${}^{(n)}\hat{Q} = \sum_{s=1}^{n} \frac{{}^{(s-1)}a_s^{+}\,{}^{(s-1)}a_s}{{}^{(s-1)}S_{ss}}. \quad (3.15)$$

4. CONSTRUCTION OF MANY-ELECTRON STATES

An unnormalized n-electron determinantal state has the form

$$|n] = a_n^{+}a_{n-1}^{+}a_{n-2}^{+}, \ldots, a_2^{+}a_1^{+}|0] \quad (4.1)$$

where square brackets are used to distinguish many-electron from one-electron states and $|0]$ denotes the vacuum. Using the fact that ${}^{(s)}a_r^{+}\,{}^{(s)}a_r^{+} \equiv 0$ we can rewrite this expression in terms of the pivotal operators which create orthogonal states:

$$\begin{aligned} |n] &= {}^{(1)}a_n^{+}\,{}^{(1)}a_{n-1}^{+}, \ldots, {}^{(1)}a_2^{+}a_1^{+}\,|0] \\ &= {}^{(2)}a_n^{+}\,{}^{(2)}a_{n-1}^{+}, \ldots, {}^{(2)}a_3^{+}\,{}^{(1)}a_2^{+}a_1^{+}\,|0] \\ &= {}^{(n-1)}a_n^{+}\,{}^{(n-2)}a_{n-1}^{+}, \ldots. {}^{(1)}a_2^{+}a_1^{+}\,|0]. \end{aligned}$$

This procedure corresponds to rewriting a determinant in terms of orthogonal states. Hence

$$\begin{aligned} [n|n] = [0|a_1\,{}^{(1)}a_2, \ldots, {}^{(n-1)}a_n\,{}^{(n-1)}a_n^{+} \\ \times {}^{(n-2)}a_{n-1}^{+}, \ldots, a_1^{+}\,|0] \end{aligned}$$

and because of the commutation properties given by equation (3.9), a_1 can be moved to the left of a_1^{+} without changing the value of $[n|n]$, then ${}^{(1)}a_2$ can be moved to the left of ${}^{(1)}a_2^{+}$, and so on. Commuting each pair ${}^{(r-1)}a_r\,{}^{(r-1)}a_r^{+}$, starting from the right, we obtain the determinantal expression

$$[n|n] = {}^{(n-1)}S_{nn}\,{}^{(n-2)}S_{n-1,n-1}, \ldots, {}^{(1)}S_{22}\,S_{11} = \Delta_n \quad \text{(say)}.$$

In order to construct normalized states we divide by $\sqrt{\Delta_n}$, i.e. $|0) = |0]$ and

$$\begin{aligned} |n) = (\Delta_n)^{-1/2}\,|n] &= \frac{{}^{(n-1)}a_n^{+}}{\sqrt{{}^{(n-1)}S_{nn}}}, \ldots, \frac{a_1^{+}}{\sqrt{S_{11}}}\,|0) \\ &= a^{+}(n)\,a^{+}(n-1), \ldots, a^{+}(1)\,|0). \quad (4.2) \end{aligned}$$

In crystal field problems there is usually a degenerate set of free ion open-shell states that are split by the crystalline environment. Let the one electron open-shell states be distinguished by the label A, which is at least partly determined by the appropriate irreducible representation of the symmetry group at the site of the ion. In the case of only a single electron outside closed shells we may write

$$|n, A) = a^{+}(A)\,|n) \quad (4.3)$$

where n now denotes the complete collection of filled atomic shells which are taken into account explicitly in the theory. Similarly, for two electrons outside closed shells, we have

$$|n, B, A) = \frac{{}^{(n,B)}a_A^{+}}{\sqrt{{}^{(n,B)}S_{AA}}}\,\frac{{}^{(n)}a_B^{+}}{\sqrt{{}^{(n)}S_{BB}}}\,|n). \quad (4.4)$$

Even though state A is always chosen to be orthogonal to B, the state created by ${}^{(n)}a_A^{+}$ is not *necessarily* orthogonal to that created by ${}^{(n)}a_B^{+}$ unless A, B are associated with different irreducible representations of the site group. Because of the consequent simplifications, and the importance of this case in practice, it will be assumed in the following that A, B do indeed satisfy this criterion. We may then write, without ambiguity,

$$\begin{aligned} {}^{(n,B)}a_A^{+}/\sqrt{{}^{(n,B)}S_{AA}} = {}^{(n)}a_A^{+}\sqrt{{}^{(n)}S_{AA}} = a^{+}(A); \\ {}^{(n)}a_B^{+}/\sqrt{{}^{(n)}S_{BB}} = a^{+}(B). \quad (4.5) \end{aligned}$$

We shall also wish to consider excited states, arising from covalency and configuration interaction, in which an electron is transferred from one of the closed shells into the open shell. These have the form

$$|n-1,B,A) = \frac{{}^{(n-1)}a_A{}^{+}}{\sqrt{{}^{(n-1)}S_{AA}}}\frac{{}^{(n-1)}a_B{}^{+}}{\sqrt{{}^{(n-1)}S_{BB}}}|n-1)$$

$$\text{where}\quad |n-1) = \sqrt{{}^{(n-1)}S_{nn}}\,a^{n}|n) \quad (4.6)$$

if we assume for convenience that only one open shell state is already occupied and it is the electron in the n-th state which is transferred. According to equation (3.13) these excited states may also be expressed as

$$|n-1,B,A) = a^{n}\left(\frac{{}^{(n-1)}S_{nn}\,{}^{(n)}S_{AA}\,{}^{(n)}S_{BB}}{{}^{(n-1)}S_{AA}\,{}^{(n-1)}S_{BB}}\right)^{1/2}$$

$$\times\,|n,B,A).$$

5. EVALUATION OF MATRIX ELEMENTS

One and two particle operators in a many particle system may be written

$$\hat{F} = a^{i+}\,a^{j}\,\langle i|f|j\rangle = a^{i+}\,a^{j}\,F_{ij}$$

$$\hat{G} = \tfrac{1}{2}a^{i+}\,a^{j+}\,a^{k}\,a^{l}\,\langle ij|g|lk\rangle$$

$$= \tfrac{1}{2}a^{i+}\,a^{j+}\,a^{k}\,a^{l}\,\overline{G_{il}G_{jk}} \quad (5.1)$$

where the summations extend over *all* the states in the basis (not only those which are occupied). F_{ij} and $\overline{G_{il}G_{jk}}$ are introduced to display explicitly to covariant nature of these quantities. These expressions are manifestly invariant under arbitrary transformations of the basis states and have the correct form in the case of an orthonormal set, which is sufficient to establish their validity.

We shall be interested in evaluating $\hat{F}$, $\hat{G}$ and the unit operator between various n-particle states. This depends only on being able to evaluate products of contravariant operators between such states. The usual algebraic method of doing this is to commute the creation operators to the right. The simplest example is

$$\begin{aligned}(n|a^{i+}\,a^{j}|n) &= (n|S^{ij}|n) - (n|a^{j}\,a^{i+}|n)\\ &= S^{ij} - (n|{}^{(n)}a^{j}\,{}^{(n)}a^{i+}|n)\\ &= S^{ij} - (0|\,{}^{(n)}a^{j}\,{}^{(n)}a^{i+}|0)\\ &= S^{ij} - {}^{(n)}S^{ij}.\end{aligned}$$

It is therefore convenient to define ${}^{(n)}\bar{S}^{ij} = S^{ij} - {}^{(n)}S^{ij}$ which is zero for $i > n$ or $j > n$; i.e. for all the unoccupied states in $|n)$. Using the same method it is easy to show that

$$(n|a^{i+}\,a^{j+}\,a^{k}\,a^{l}|n) = {}^{(n)}\bar{S}^{il}\,{}^{(n)}\bar{S}^{jk} - {}^{(n)}\bar{S}^{ik}\,{}^{(n)}\bar{S}^{jl} \quad (5.2)$$

and the introduction of extra operators will simply increase the size of the determinantal expression on the right hand side. For this reason it is convenient to use an abbreviation for these determinants, writing

$${}^{(n)}\begin{bmatrix} i & j\\ l & k\end{bmatrix} = {}^{(n)}\bar{S}^{il}\,{}^{(n)}\bar{S}^{jk} - {}^{(n)}\bar{S}^{ik}\,{}^{(n)}\bar{S}^{jl}$$

and

$${}^{(n)}\begin{bmatrix} i & j & k\\ p & m & l\end{bmatrix} = {}^{(n)}\bar{S}^{ip}\;{}^{(n)}\begin{bmatrix} j & k\\ m & l\end{bmatrix}$$

$$-\,{}^{(n)}\bar{S}^{im}\;{}^{(n)}\begin{bmatrix} j & k\\ p & l\end{bmatrix} + {}^{(n)}\bar{S}^{il}\;{}^{(n)}\begin{bmatrix} j & k\\ p & m\end{bmatrix}$$

and so on. Hence the results for two, four, six and eight operators may be written

$$(n|a^{i+}\,a^{j}|n) = {}^{(n)}\bar{S}^{ij}$$

$$(n|a^{i+}\,a^{j+}\,a^{k}\,a^{l}|n) = {}^{(n)}\begin{bmatrix} i & j\\ l & k\end{bmatrix}$$

$$(n|a^{i+}\,a^{j+}\,a^{k+}\,a^{l}\,a^{m}\,a^{p}|n) = {}^{(n)}\begin{bmatrix} i & j & k\\ p & m & l\end{bmatrix}$$

$$(n|a^{i+}\,a^{j+}\,a^{k+}\,a^{l+}\,a^{m}\,a^{p}\,a^{q}\,a^{r}|n) =$$

$${}^{(n)}\begin{bmatrix} i & j & k & l\\ r & q & p & m\end{bmatrix}. \quad (5.3)$$

The interchange of a creation and annihilation operator in any of these expressions gives an appropriate overall change in sign combined with the substitution of $-{}^{(n)}S^{ij}$ for ${}^{(n)}\bar{S}^{ij}$ whenever the creation operator is to the right of the annihilation operator. Some examples of using this rule are given below:

$$(n|a^{i+}\,a^{k}\,a^{j+}\,a^{l}|n) = {}^{(n)}S^{ki}\,{}^{(n)}\bar{S}^{il} + {}^{(n)}\bar{S}^{ik}\,{}^{(n)}\bar{S}^{jl} \quad (5.4)$$

$$(n|a^l a^k a^{j+} a^{i+}|n) = {}^{(n)}S^{kj}\,{}^{(n)}S^{il} - {}^{(n)}S^{ki}\,{}^{(n)}S^{lj} \quad (5.5)$$

$$(n|a^{j+} a^k a^l a^{i+}|n) = {}^{(n)}S^{jk}\,{}^{(n)}\bar{S}^{il} - {}^{(n)}S^{ki}\,{}^{(n)}\bar{S}^{jl} \quad (5.6)$$

$$(n|a^{i+} a^{j+} a^k a^l a^{r+} a^t|n)$$

$$= {}^{(n)}\begin{bmatrix} i & j & r \\ t & l & k \end{bmatrix} + S^{rl}\,{}^{(n)}\begin{bmatrix} i & j \\ t & k \end{bmatrix} - S^{rk}\,{}^{(n)}\begin{bmatrix} i & j \\ t & l \end{bmatrix} \quad (5.7)$$

$$(n|a^r a^{i+} a^{j+} a^k a^l a^{t+}|n) = {}^{(n)}S^{tr}\,{}^{(n)}\bar{S}^{jk}\,{}^{(n)}\bar{S}^{il}$$

$$+ {}^{(n)}S^{jr}\,{}^{(n)}S^{tk}\,{}^{(n)}\bar{S}^{il} - {}^{(n)}S^{jr}\,{}^{(n)}S^{tl}\,{}^{(n)}\bar{S}^{ik}$$

$$- {}^{(n)}\bar{S}^{il}\,{}^{(n)}S^{tr}\,{}^{(n)}\bar{S}^{ik} - {}^{(n)}\bar{S}^{jl}\,{}^{(n)}S^{tk}\,{}^{(n)}S^{ir}$$

$$+ {}^{(n)}\bar{S}^{jk}\,{}^{(n)}S^{tl}\,{}^{(n)}S^{ir}. \quad (5.8)$$

The above results enable us to evaluate matrix elements which are of interest in crystal field theory to give expressions which are (a) independent of the choice of basis states, as is shown by their construction in terms of tensors; and (b) 'linked cluster' in form as is shown by their construction in terms of components which are known to be internally of this form. A trivial case occurs when all the electrons are in closed shells giving the extremely simple matrix elements

$$(n|\hat{F}|n) = {}^{(n)}\bar{S}^{ij}F_{ij}$$

$$(n|\hat{G}|n) = \tfrac{1}{2}\,{}^{(n)}\begin{bmatrix} j & i \\ k & l \end{bmatrix} \overline{G_{il}G}_{jk}$$

$$= \tfrac{1}{2}\,{}^{(n)}\bar{S}^{il}\,\overline{G_{il}G}_{jk}\,{}^{(n)}\bar{S}^{jk} - \tfrac{1}{2}\,{}^{(n)}\bar{S}^{ki}\,\overline{G_{il}\,{}^{(n)}\bar{S}^{lj}G}_{jk}. \quad (5.9)$$

The latter expression takes the usual form of direct coulomb minus exchange.

In crystal field theory, however, the matrix elements of interest are between states in which one or more electrons are outside closed shells. In ordinary crystal field theory only a single active electron has to be considered, so we require the matrix elements

$$(n,A|n,B) = S(A,B), \quad (5.10)$$

$$(n,A|\hat{F}|n,B) = F_{ij}[{}^{(n)}\bar{S}^{ij}S(A,B) + \delta^i(A)\,\delta^j(B)] \quad (5.11)$$

and

$$(n,A|\hat{G}|n,B) = \tfrac{1}{2}\overline{G_{jk}G}_{il}[\bar{S}(A,B)({}^{(n)}\bar{S}^{jk}\,{}^{(n)}\bar{S}^{il}$$
$$-{}^{(n)}\bar{S}^{jl}\,{}^{(n)}\bar{S}^{ik}) + 2\delta^i(A)(\delta^l(B)\,{}^{(n)}\bar{S}^{jk} - \delta^k(B)\,{}^{(n)}\bar{S}^{jl})] \quad (5.12)$$

where the terms containing the factor $S(A,B)$ vanish if the states A,B are associated with different irreducible representations of the site symmetry group.

In the 'exclusion model'[8] the crystal field energies are derived directly from the Hamiltonian $\hat{H} = \hat{F} + \hat{G}$ by solving the secular equation

$$|(n,A|\hat{H}|n,B) - E(n,A|n,B)| = 0.$$

All terms with a factor $S(A,B)$ in $(n,A|\hat{H}|n,B)$ may be written as $E_0S(A,B)$ so the secular equation reduces to

$$|(n,A|\hat{H}|n,B)_{\text{active}} - E'S(A,B)| = 0$$

where $E' = E - E_0$. Here the suffix 'active' indicates that all the (passive) contributions which merely shift the mean energy of all levels have been subtracted out. The active matrix elements are in linked cluster form and may be written in terms of effective operators acting between open shell states:

$$(n,A|\hat{F}|n,B)_{\text{active}} = F_{ij}\delta^i(A)\delta^j(B)$$
$$= \frac{(0|a_A\,{}^{(n)}\hat{F}\,a_B^{+}|0)}{\sqrt{({}^{(n)}S_{AA}\,{}^{(n)}S_{BB})}} \quad (5.13)$$

$$(n,A|\hat{G}|n,B)_{\text{active}} = \overline{G_{jk}G}_{il}\delta^i(A)(\delta^l(B)\,{}^{(n)}\bar{S}^{jk}$$
$$-\delta^k(B)\,{}^{(n)}\bar{S}^{jl})$$
$$= \frac{(0|a_A\,{}^{(n)}\hat{G}\,a_B^{+}|0)}{\sqrt{({}^{(n)}S_{AA}\,{}^{(n)}S_{BB})}} \quad (5.14)$$

where

$${}^{(n)}\hat{F} = F_{ij}\,{}^{(n)}a^{i+}\,{}^{(n)}a^j \quad (5.15)$$

and

$${}^{(n)}\hat{G} = \overline{G_{jk}G}_{il}({}^{(n)}\bar{S}^{jk}\,{}^{(n)}a^{i+}\,{}^{(n)}a^l - {}^{(n)}\bar{S}^{jl}\,{}^{(n)}a^{i+}\,{}^{(n)}a^k). \quad (5.16)$$

The free ion open shell states which appear in equations (5.13) and (5.14) are renormalized by a factor which depends explicitly on the state concerned, and which has not yet been absorbed into the effective energy operators. This is, however, possible in cases where the labels A, B etc. all refer to different symmetry orbitals. The operator

$$\hat{X} = \sum_{B} a_B{}^{+} a_B{}^{(n)}\bar{S}^{ij} a_i{}^{+} a_j \qquad (5.17)$$

satisfies

$$\hat{X} a_A{}^{+}|0) = (1 - {}^{(n)}S_{AA}) a_A{}^{+}|0).$$

Hence

$$(1 - \hat{X})^{1/2} a_A{}^{+}|0) = ({}^{(n)}S_{AA})^{-1/2} a_A{}^{+}|0)$$

so that the required normalization can be produced by an operator which is independent of A.

Some other matrix elements of interest in the 'exclusion model' are those for G between two particle states which contain contributions to the *correlation* crystal field[8]. For simplicity we now assume that $S(A, B) = \delta(A, B)$ so that the remaining passive contributions are explicitly independent of the open shell states. Then

$$\begin{aligned}(n, A, B|\hat{G}|n, A, B) = \overbracket{G_{il}G}_{jk}[\tfrac{1}{2}({}^{(n)}\bar{S}^{jk}\,{}^{(n)}\bar{S}^{il} \\ - {}^{(n)}\bar{S}^{jl}\,{}^{(n)}\bar{S}^{ik}) \\ + \delta^{l}(A)({}^{(n)}\bar{S}^{jk}\delta^{i}(A) \\ - {}^{(n)}S^{ij}\delta^{k}(A)) \\ + \delta^{l}(B)({}^{(n)}\bar{S}^{ik}\delta^{i}(B) \\ - {}^{(n)}\bar{S}^{ik}\delta^{l}(B)) \\ + \delta^{i}(A)\delta^{j}(B)(\delta^{k}(B)\delta^{l}(A) \\ - \delta^{l}(B)\delta^{k}(A))] \qquad (5.18)\end{aligned}$$

$$\begin{aligned}(n, A, B|\hat{G}|n, A, D) = \overbracket{G_{il}G}_{jk}[\delta^{l}(D)({}^{(n)}\bar{S}^{jk}\delta^{i}(B) \\ - {}^{(n)}\bar{S}^{ik}\delta^{j}(B)) \\ + \delta^{i}(A)\delta^{j}(B)(\delta^{l}(A)\delta^{k}(D) \\ - \delta^{k}(A)\delta^{l}(D))] \\ (B \neq D) \qquad (5.19)\end{aligned}$$

$$\begin{aligned}(n, A, B|\hat{G}|n, C, D) \\ = \overbracket{G_{il}G}_{jk}[\delta^{i}(A)\delta^{j}(B)(\delta^{k}(D)\delta^{l}(C) - \delta^{k}(C)\delta^{l}(D))] \\ (A, B \neq C, D). \qquad (5.20)\end{aligned}$$

The form of these results shows that the effective operator ${}^{(n)}\hat{G}$ given above is incomplete as it lacks the term which gives the (correlation) interactions between open shell electrons but which does not contribute to the one-particle field. The complete effective two-particle operator is given by

$$\begin{aligned}{}^{(n)}\hat{G} = \overbracket{G_{jk}G}_{il}({}^{(n)}\bar{S}^{jk}\,{}^{(n)}a^{i+}\,{}^{(n)}a^{l} - {}^{(n)}\bar{S}^{jl}\,{}^{(n)}a^{i+}\,{}^{(n)}a^{k} \\ + \tfrac{1}{2}{}^{(n)}a^{i+}\,{}^{(n)}a^{j+}\,{}^{(n)}a^{k}\,{}^{(n)}a^{l})\end{aligned}$$

as the reader may easily check by comparison with equations (5.18)–(5.20).

The required renormalization factor for the two-particle state $a_A{}^{+}a_B{}^{+}|0)$ in the presence of n particles in closed shells is

$$\begin{aligned}({}^{(n)}S_{AA}{}^{(n)}S_{BB})^{-1/2} = (1 - {}^{(n)}X_{AA} - {}^{(n)}X_{BB} \\ + {}^{(n)}X_{AA}{}^{(n)}X_{BB})^{-1/2} \qquad (5.21)\end{aligned}$$

when ${}^{(n)}S_{AA} = 1 - {}^{(n)}X_{BB}$. This factor is produced by the operator

$$(1 - \hat{Y}_1 - \hat{Y}_2)^{-1/2} \qquad (5.22)$$

where $\hat{Y}_1$ and $\hat{Y}_2$ are operators independent of the specific open-shell states A, B given by

$$\left.\begin{aligned}\hat{Y}_1 = \tfrac{1}{2}\sum_{C,D} a_C{}^{+}a_D{}^{+}a_D a_C{}^{(n)}\bar{S}^{ij}S^{kl}a_i{}^{+}a_k{}^{+}a_l a_j \\ \hat{Y}_2 = \tfrac{1}{2}\sum_{C,D} a_C{}^{+}a_D{}^{+}a_D a_C{}^{(n)}\bar{S}^{ij}\,{}^{(n)}\bar{S}^{kl}a_i{}^{+}a_k{}^{+}a_l a_j.\end{aligned}\right\} \qquad (5.23)$$

It can easily be verified that these operators satisfy the following equations if the labels A, B etc. all refer to different symmetry orbitals:

$$\hat{Y}_1 a_A{}^{+}a_B{}^{+}|0) = {}^{(n)}X_{AA}{}^{(n)}X_{BB}a_A{}^{+}a_B{}^{+}|0)$$

$$\hat{Y}_2 a_A{}^{+}a_B{}^{+}|0) = ({}^{(n)}X_{AA} + {}^{(n)}X_{BB})a_A{}^{+}a_B{}^{+}|0).$$

The formal expansion of the operator (5.22) then gives the factor (5.21).

The numerators in excited state (i.e. covalency and configuration interaction) calculations involve the matrix elements

$$\begin{aligned}(n,A|\hat{F}|n-1,A,B) = F_{ij}[&{}^{(n)}\bar{S}^{ij}S(Bn)\\ &+\delta^{i}(n)\delta^{j}(B)\\ &+\delta^{i}(A)\delta^{j}(A)S(Bn)\\ &-\delta^{i}(A)\delta^{j}(B)S(An)]\end{aligned} \qquad (5.24)$$

$$\begin{aligned}(n,A|F|n-1,C,B) &= F_{ij}(A)\delta^{i}(A)\\ &\times[\delta^{j}(C)S(Bn)-\delta^{j}(B)S(Cn)],\end{aligned} \qquad (A\neq B,C) \quad (5.25)$$

$$\begin{aligned}(n,A|\hat{G}|n-1,A,B) = \overbracket{G_{jr}G}_{is}[&({}^{(n)}\bar{S}^{is}\delta^{j}(A)\\ &-{}^{(n)}\bar{S}^{js}\delta^{i}(A))(\delta^{r}(A)S(nB)\\ &-\delta^{r}(B)S(nA))\\ &+\tfrac{1}{2}S(nB)({}^{(n)}\bar{S}^{is}\,{}^{(n)}\bar{S}^{jr}\\ &-{}^{(n)}\bar{S}^{ir}\,{}^{(n)}\bar{S}^{js})\\ &+\delta^{r}(B)(\delta^{j}(n){}^{(n)}\bar{S}^{is}\\ &-\delta^{i}(n){}^{(n)}\bar{S}^{js})\\ &+\delta^{j}(n)(\delta^{i}(A)\delta^{s}(A)\delta^{r}(B)\\ &-\delta^{i}(A)\delta^{r}(A)^{s}(B))]\end{aligned} \qquad (5.26)$$

$$\begin{aligned}&(n,A|\hat{G}|n-1,C,B)\\ &= \overbracket{G_{jr}G}_{is}[{}^{(n)}\bar{S}^{jr}\delta^{i}(A)(\delta^{s}(C)S(nB)-\delta^{s}(B)S(nC))\\ &\quad+\delta^{j}(n)\delta^{i}(A)(\delta^{s}(C)\delta^{r}(B)-\delta^{s}(B)\delta^{r}(C))]\end{aligned} \qquad (A\neq B,C) \quad (5.27)$$

where again we have taken ${}^{(n)}S(AB)=\delta(AB)$. The general overlap integral is

$$\begin{aligned}(n,A|n-1,C,B) &= S(AC)S(nB)\\ &-S(AB)S(nC);\end{aligned} \quad (\text{all } B,C). \quad (5.28)$$

An account of how such terms arise in crystal field theory is given in[7]. The isolation of effective operators is very much more complicated for excited state contributions and further discussion of this problem is deferred to a later publication.

6. DISCUSSION

The formalism developed in this paper provides the mathematical foundation of a many-body theory for non-orthogonal states. The basic algebraic result (equation (3.7)) is very simple, and allows us to derive matrix elements between many electron states with little manipulation.

As mentioned in the Introduction, the main application at present envisaged is to solve the basic problem which arises in formulating crystal field theory: To what extent can the crystalline environment be represented by the construction of effective operators which act on free ion open-shell states? The results obtained in this paper show that such operators exist at least in the case of the simple 'exclusion model' [7, 8] which does not include covalency and configuration interaction contributions.

An alternative application of the formulae given in the previous section is their use in straight numerical evaluations of contributions to the crystal field (such as those as in [7] and [11]. For this it is necessary to obtain the numerical values of the restricted set of pivotal deltas ${}^{(r-1)}\delta_r^{i}$ and the quantities

$${}^{(n)}\bar{S}^{ij} = \sum_{r=1}^{n} ({}^{(r-1)}\delta_r^{i}\,{}^{(r-1)}\delta_r^{j}/{}^{(r-1)}S_{rr})$$

which may easily be constructed from them. The ${}^{(r-1)}\delta_r^{i}$ may be evaluated from computed overlap integrals S_{ij} by means of the formula

$${}^{(r-1)}\delta_r^{i} = \delta_r^{i} - \sum_{s=1}^{r-1} ({}^{(s-1)}\delta_s^{i}\,{}^{(s-1)}\delta_s^{k}S_{kr})/({}^{(s-1)}\delta_s^{l}S_{ls})$$

which follows at once from (2.8). If it is only required to obtain results to a given order in the overlap integrals explicit expansions may be obtained using the diagrammatic method developed by Bishton and Newman [4].

Finally it should be remarked that one of the main advantages of the creation-annihilation operator formalism is that a simple linked-cluster diagrammatic representation of all terms in the perturbation series can be established using the Brueckner–Goldstone formalism[12]. This both simplifies the derivation of explicit formulae and allows classes of important terms to be identified and summed over. Although, in the present paper, we have only used algebraic methods, the tensor form of all equations makes it implicit that the expressions corresponding to the Brueckner–Goldstone diagrams may easily be generalised to the case of non-orthogonal states, without any changes being necessary in the diagrammatic representation itself. We shall use this method, in a later publication, to extend the results obtained herein.

Acknowledgements – The author is particularly indebted to Miss S. S. Bishton and Dr J. S. Marsh for helpful discussions.

REFERENCES

1. ARAI T., *Phys. Rev.* **134**, A824 (1964); *Prog. theor. Phys.* **36**, 473 (1966).
2. ARAI T., *J. Math. Phys.* **8**, 1018 (1967).
3. HERRING C., In *Magnetism* (Edited by G. T. Rado and H. Suhl), Vol. IIB. Academic Press, New York (1964).
4. BISHTON S. S. and NEWMAN D. J., *J. Phys. Chem Solids* **29**, 1245 (1968).
5. NEWMAN D. J., *Chem. Phys. Lett.* **1**, 684 (1968).
6. WYBOURNE B. G., *J. chem. Phys.* **48**, 2596 (1968).
7. ELLIS M. M. and NEWMAN D. J., *J. chem. Phys.* **47**, 1986 (1967).
8. NEWMAN D. J. and BISHTON S. S., *Chem Phys. Lett.* **1**, 616 (1968).
9. CHIRGWIN B. H. and COULSON C. A., *Proc. R. Soc.* **201A**, 196 (1950).
10. LONGUET-HIGGINS H. C., In *Quantum Theory of Atoms, Molecules and the Solid State* (Edited by P.- O. Lowdin), p. 105. Academic Press, New York (1966).
11. ELLIS M. M. and NEWMAN D. J., *J. chem. Phys.* **49**, 4037 (1968).
12. GOLDSTONE J., *Proc. R. Soc.* **A239**, 267 (1957).

J. Phys. Chem. Solids Pergamon Press 1969. Vol. 30, pp. 1719–1720. Printed in Great Britain.

THE STRUCTURE OF $Mn_{1\cdot88}Fe_{1\cdot12}O_4$

H. M. O'BRYAN, Jr. and H. J. LEVINSTEIN
Bell Telephone Laboratories, Incorporated, Murray Hill, N.J. 07971, U.S.A.

(*Received* 2 *December* 1968)

Abstract—The structure of slowly cooled $Mn_{1\cdot88}Fe_{1\cdot12}O_4$ is tetragonal at 300°K. Recent work which showed that the structure of similar material is cubic at 300°K is discussed in terms of the importance of thermal history and oxygen stoichiometry to the transition temperature.

IN MANGANESE ferrites with high Mn content a transition from the cubic to the tetragonal structure is sometimes observed as the temperature is decreased. Wojtowicz[1] has related this transformation to a cooperative Jahn–Teller distortion associated with Mn^{+3} ions on octahedral sites. As the amount of Mn^{+3} so situated increases, the degree of tetragonality and the temperature of the transition increase. Chemical composition and thermal history determine the amount of octahedral Mn^{+3}. McClure[2] has shown that at low temperatures there is an energetic preference of Mn^{+3} for octahedral sites. Consequently higher temperatures tend to randomize the distribution of Mn^{+3} and material quenched from high temperature will contain less octahedral Mn^{+3} and will have lower transition temperatures than slowly cooled material.

In a recent paper, Cervinka and Vetterkind [3] examined slowly cooled samples of $Mn_{1\cdot88}Fe_{1\cdot12}O_4$ with X-rays to determine the presence of any structural transition in the temperature range 4·2°–300°K. No transition was observed and the structure at 300°K was determined to be cubic. It was noted that the X-ray lines remained broad over the entire temperature range. To explain the absence of the expected transition from a cubic to a tetragonal structure, the existence of domains which were chemically inhomogeneous with respect to manganese was postulated. It is the purpose of this note to show that $Mn_{1\cdot88}Fe_{1\cdot12}O_4$, prepared in the manner of Cervinka and Vetterkind, has a transition from the cubic structure near 533°K, and is tetragonal at 300°K. Data showing the effect of thermal history on the structure of this ferrite are also presented.

A disk, 1·2 cm *Dx* 0·3 cm, was prepared by the usual ceramic techniques, fired at 1230°C in an atmosphere containing 0·6 Torr. oxygen for 6 hr and slowly cooled in nitrogen. The cooling conditions closely matched those of Cervinka and Vetterkind. As determined by X-ray fluorescent analysis the sample composition corresponded to $Mn_{1\cdot88\pm0\cdot02}Fe_{1\cdot12\pm0\cdot02}O_4$ where the oxygen content has been arbitrarily set at the stoichiometric amount. The sample was examined metallographically and by X- ray diffraction.

Under polarized light a polished section of the sample showed birefringence. To determine whether the birefringence was caused by polishing strains, the ferrite was etched chemically. The birefringence remained after etching, which indicates that the structure was non-cubic. In addition, the microstructure as revealed by the etching and shown in Fig. 1, exhibits a subgrain structure consisting of parallel bands whose orientation varies from grain to grain. The appearance of such bands in the microstructure has been shown to indicate tetragonality in the case of copper ferrite[4]. In that spinel the transformation from cubic to tetragonal structure is accomplished by a diffusionless martensitic double shear process and results in a lamellar microstructure in which the orientation differences between adjacent lamellae are functions of the degree of tetragonality. The shear band width as shown in Fig. 1 is too small to allow a study of the lamellae, but the band appearance indicates that at 300°K the manganese ferrite has indeed transformed to the tetragonal structure.

At room temperature the X-ray pattern showed the same line broadening and lack of distinct splitting, noted by Cervinka and Vetterkind. As the temperature was raised to 373°K, a splitting was observed, corresponding to $c/a = 1{\cdot}005$. This splitting became smaller at higher temperature but the broadness remained. Near 533°K a reversible transition to the cubic structure was observed.

To determine the importance of thermal history to the structure of $Mn_{1\cdot 88}Fe_{1\cdot 12}O_4$ a second sample, fired with the first but quenched in nitrogen rather than slowly cooled, was examined. At 300°K the structure of this sample was cubic as revealed by both metallography and X-ray analysis. No transition to the tetragonal structure was observed by X-rays over the temperature range 20° to 723°K. Throughout the lines remained sharp. This behavior is in agreement with the prediction that quenched material has a lower transition temperature. After a powdered sample of quenched material had been reheated near 773°K for 5 min, a transformation to the tetragonal structure was observed upon cooling. The appearance of the transition in this case indicates that rearrangement of Mn^{+3} has occurred during reheating.

The question which remains concerns the origin of the line broadness which caused Cervinka and Vetterkind to interpret the X-ray diffraction pattern of slowly cooled material as cubic rather than tetragonal. The fact that similar X-ray data were obtained at this laboratory when the material was also slowly cooled suggests that the line broadening originates from processes occurring during the slow cooling. The two causes which seem most probable, are lattice strains and variations in cation distribution.

Strain results from lattice mismatch between the lamellae which are formed when the ferrite transforms from the cubic structure. Since these lamellae are extremely small (well below the 1μ size of the shear bands which are shown in Fig. 1), an appreciable strain will have a significant effect on the width of the X-ray lines. Variations in cation distribution, on the other hand, cause line broadening by producing different degrees of tetragonality for the various parts of the sample. When during the cooling the oxygen content of the atmosphere surrounding the sample is not adjusted, a non-equilibrium situation develops and the oxygen stoichiometry of the sample changes. The rate at which such changes occur decreases with temperature and the final situation is a sample with a gradation of oxygen stoichiometry from the interior to the surface. Previous work has established that copper ferrite samples with identical thermal histories but different oxygen stoichiometries have different cation distributions[5]. A similar effect would be expected for manganese ferrite. Present data do not permit an assessment of the relative importance of the two sources in developing X-ray line broadness in $Mn_{1\cdot 88}Fe_{1\cdot 12}O_4$.

Acknowledgements – It is a pleasure to acknowledge the experimental assistance of H. G. Boyle and C. D. Capio.

REFERENCES

1. WOJTOWICZ P. J., *Phys. Rev.* **116**, 32 (1959).
2. McCLURE D. S., *J. Phys. Chem. Solids* **3**, 311 (1957).
3. CERVINKA L. and VETTERKIND D., *J. Phys. Chem. Solids* **29**, 171 (1968).
4. LEVINSTEIN H. J., SCHNETTLER F. J. and GYORGY E. M., *J. appl. Phys.* **36**, 1163 (1965).
5. O'BRYAN H. M., Jr., LEVINSTEIN H. J. and SHERWOOD R. C., *J. appl. Phys.* **37**, 1438 (1966).

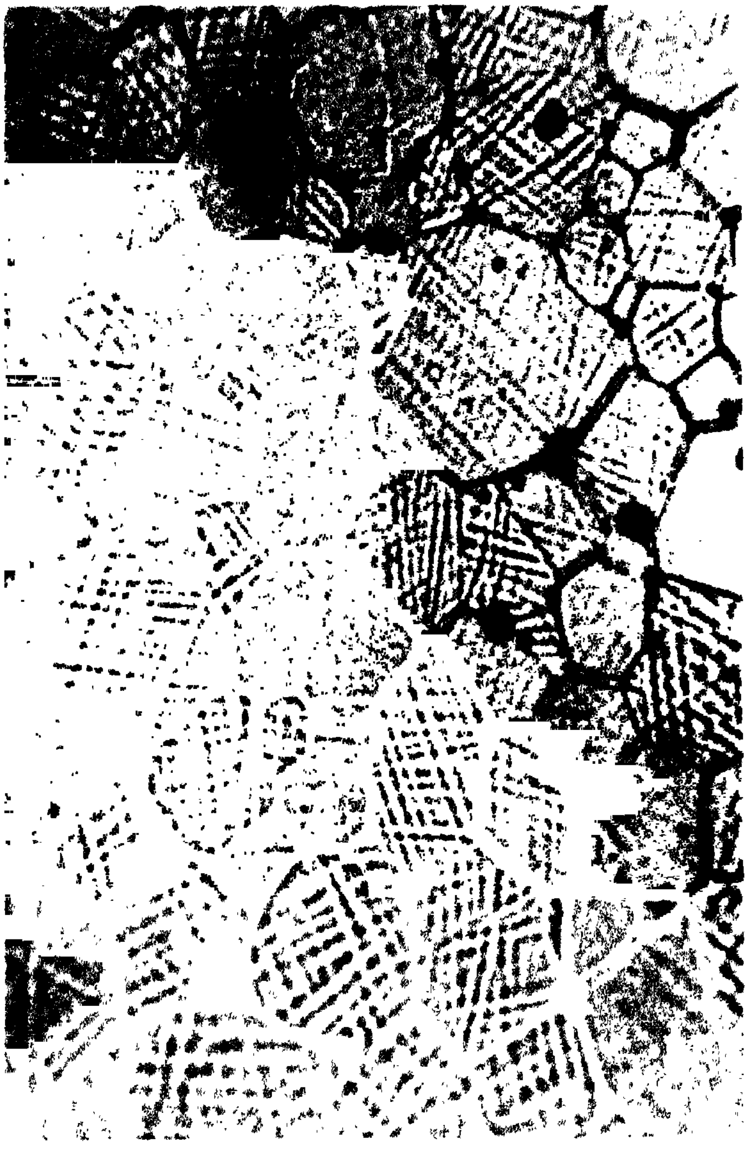

Fig. 1. Microstructure of slowly cooled $Mn_{1.88}Fe_{1.12}O_4$, 1600 ×.

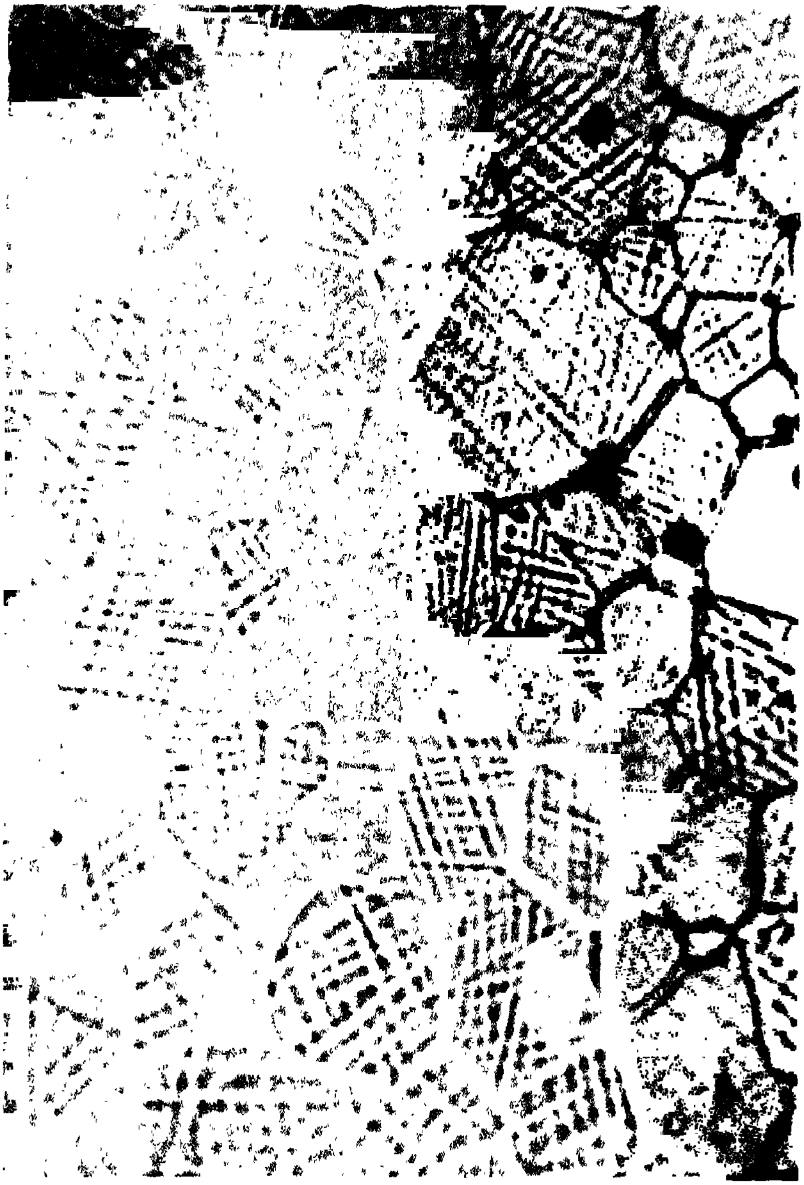

Fig. 1. Microstructure of slowly cooled $Mn_{1\,88}Fe_{1\,12}O_4$, 1600

J. Phys. Chem. Solids Pergamon Press 1969. Vol. 30, pp. 1721-1732. Printed in Great Britain.

AN X-RAY SINGLE CRYSTAL INVESTIGATION OF IRON-RICH ALLOYS OF IRON AND ALUMINUM-I. PHASE RELATIONS IN ALLOYS CONTAINING BETWEEN 14 AND 23 AT.% ALUMINUM

J. E. EPPERSON* and **J. E. SPRUIELL**
Department of Chemical and Metallurgical Engineering, University of Tennessee, Knoxville,
Tenn. 37916, U.S.A.

(*Received* 6 *November* 1968)

Abstract—An X-ray diffraction examination of alloy single crystals of Fe containing between about 14 and 23 at.% Al has revealed the existence of an intermediate temperature region in which long-range ordered phases based on the stoichiometric compounds Fe_3Al and FeAl coexist in equilibrium. This result is in excellent agreement with theoretical predictions which assume the Fe_3Al type phase disorders by a first order transformation in alloys containing less than about 25 at.% Al. The *K*-state phenomenon in the Fe–Al alloys is discussed in terms of a revised segment of the Fe–Al phase diagram based on the present results.

1. INTRODUCTION

DATING from nearly 40 years ago when Sykes and Evans[1] showed that the thermal expansion and electrical resistivity of certain Fe-rich alloys of Fe and Al were dependent on the thermal history, considerable research effort has been devoted to investigating alloys of the Fe–Al system. That the peculiarities in the physical properties as a function of temperature were associated with structural changes in the alloy was shown by the classical Debye-Scherrer X-ray investigation by Bradley and Jay[2]. Their X-ray study established the existence of two long-range ordered phases based on stoichiometric Fe_3Al and FeAl, in addition to the disordered phase, in alloys containing up to about 50 at.% Al. However because of the sluggishness of the kinetics and because the changes in physical and mechanical properties are often small and appear to be continuous, attempts to interpret these and subsequent experimental observations in terms of a phase equilibrium diagram have not met with complete success. In particular, the difficulty of obtaining convincing evidence for the coexistence of two phases in equilibrium has led to a controversy as to the thermodynamic order of the transformations, and, as a consequence, the form and details of construction of the phase diagram are not presently agreed upon.

Because of the voluminous literature concerning this alloy system, a complete survey of the literature is impractical here. A brief summary follows, and a more extensive review can be found in reference [3] and in the original publications cited therein. Examples of proposed diagrams of state inferred from experimental observations are shown in Fig. 1. Figure 1(a) was proposed by Taylor and Jones[4] on the basis of precision lattice parameters measured at temperature using powder specimens. The indicated phase boundaries were inferred from the systematic changes of slope in plots of the lattice parameters as a function of alloy composition for fixed temperatures. Resolved diffraction lines from two phases in equilibrium were not observed; it was estimated that the lattice parameters of the proposed two phases differed by about one part in

---

*[*] *Present address:* Oak Ridge National Laboratory, Oak Ridge, Tenn. 37830, U.S.A.

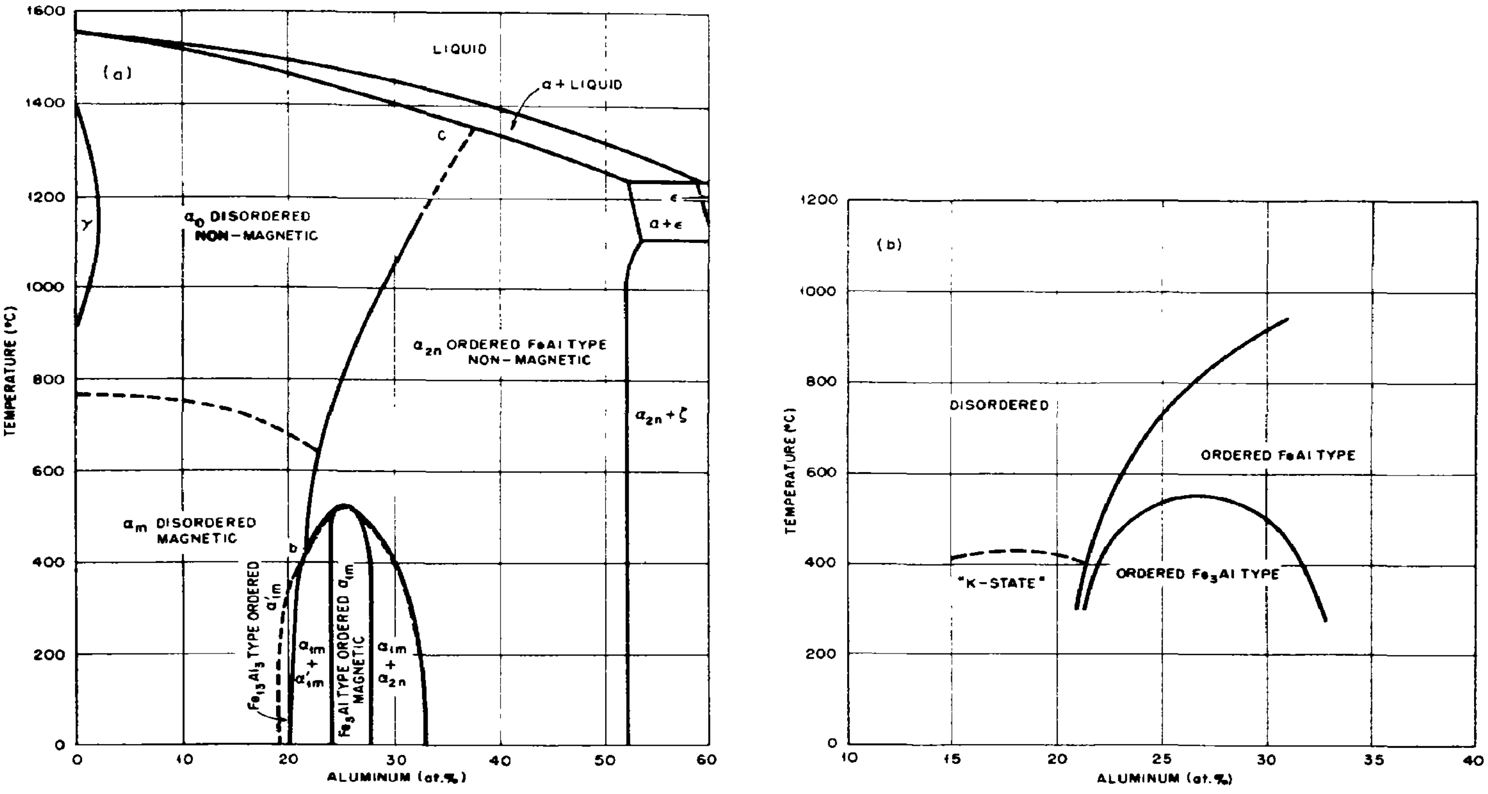

Figs. 1(a–b). Examples of phase equilibrium diagrams for the Fe-rich Fe–Al alloys which have been proposed based on experimental measurements. (a) After Taylor and Jones [4]; (b) after Davies [6].

1000. In support of the existence of two-phase regions as shown in Fig. 1(a), Lihl and Ebel[5] have reported pronounced broadening of the fundamental reflections over two corresponding ranges of composition. The latter authors, however, interpreted their results as indicating that the ordered Fe_3Al phase forms by a peritectoid transformation.

Still other experimental results have been interpreted quite differently as regards to the phase relations, an example of which is shown in Fig. 1(b). This diagram, reported by Davies[6], is consistent with the resistivity data of Seybolt[7], and the dilatometric measurements by Davies[6] and McQueen and Kuczynski[8].

In addition to the experimental work, statistical theoretical analyses have been performed, the results of which serve as useful guides in interpreting experimental results. Using quasi-chemical theory, Rudman[9] has shown that if the Fe_3Al type structure disorders by a first order transformation in alloys containing less than about 25 at.% Al while in higher Al alloys disorder proceeds from Fe_3Al to FeAl to the disordered phase by means of second order transformations, a phase diagram of the form shown in Fig. 2 should result. If, on the other hand, the Fe_3Al type structure disorders by a second order transformation at all compositions, Rudman predicted that the FeAl phase field should enclose the Fe_3Al field as shown in Fig. 1(b). Houska[10] extended the theoretical treatment to include magnetic interactions. These interactions were shown to have a significant effect on the position of the phase boundaries.

That the atomic arrangements in the conventionally denoted disordered phase are not random has been firmly established since the work by Thomas[11]. A more complete discussion of the short-range order occurring in these alloys is given by the authors in the succeeding paper[12], hereafter referred to as part II.

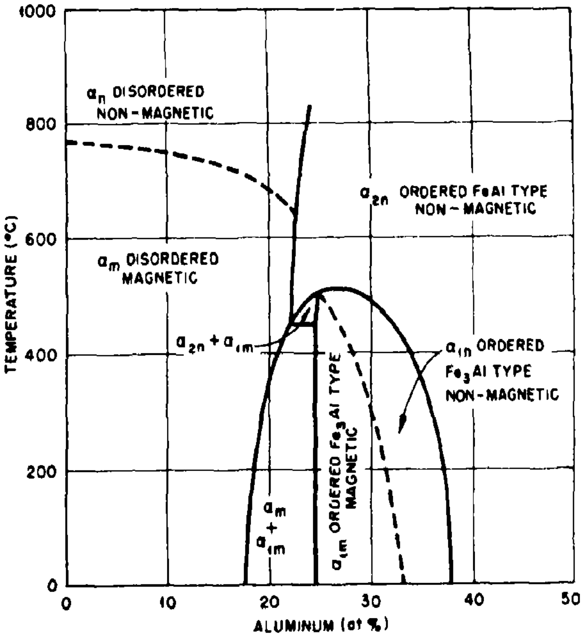

Fig. 2. Phase diagram assuming Fe_3Al disorders by a first order transformation in alloys containing less than about 25 at % Al after Rudman[9].

Alloys containing between about 20 and 23 at.% Al have proved to be especially puzzling[13] in that anomalous X-ray diffraction peak widths[5], erratic variations of Young's modulus[14], double Curie points[1], and high values of coercive force[15] have been reported. Corresponding structural changes in these alloys have not been firmly established.

In spite of the large amount of research performed on this alloy system, no X-ray diffraction study of the phase relations utilizing single crystal samples has been reported. It has been the purpose of the present investigation to take advantage of the enhanced intensity and ease of interpretation of diffraction effects obtained using single crystal samples in order to study relatively weak superlattice reflections which might not be observable by the methods which have been used previously in studying the Fe-rich Fe–Al alloys.

2. MATERIALS, EQUIPMENT AND PROCEDURES

Fe and Al advertised to be 99·999 and 99·9999 per cent pure, respectively, were purchased from United Mineral and Chemical Corporation. It was later ascertained [3] that this measure of quality did not apply to interstitial impurities, and, in particular, that there may have been as much as 0·03 to 0·05 wt% C present in the Fe.

After sectioning, the Fe was pickled in nitric acid and heated to 600°C for about 2 hr in a stream of dry hydrogen. The bulk sections of Al were cleaned with hot caustic solution. Charges of roughly 150 g each were weighed out to the desired compositions and melted in a resistance furnace under a pressure of five psig. of argon in high-purity, recrystallized alumina crucibles (99·7% Al_2O_3). These charges were then directionally solidified by two modifications of the Bridgman technique in order to grow large crystals. In either case the solid–liquid interface moved at about 0·75 in. per hr. The alloys were homogenized by holding at temperatures between 1000° and 1200°C for periods of 2–4 hr in the argon atmosphere, followed by an anneal at 850°C in a stream of dry hydrogen for periods of at least 1 week.

These crystal growing efforts were never completely successful in that no single crystals as such were obtained; however, a reasonable percentage of the attempts resulted in large grained samples from which single crystal discs about 0·125 in. thick and 0·60–0·75 in. in dia. could be cut. The discs were crystallographically oriented in such a way that the normal to the face was rotated about four degrees from the [210] direction toward the [200]. This orientation was used because it provided easy accessibility to the region of reciprocal space which was of principal interest and also maintained the sample at equal angles with the incident and scattered beams. The desired orientation was achieved within 0·2° for each crystal.

Primarily because of the wide difference in melting points of Fe and Al some weight was lost in each of the melting operations. This required that each ingot be analyzed chemically. The composition of each sample was determined by wet analysis of a section cut from the ingot at a location which was immediately adjacent to the single crystal disc. Because of the reported difficulty of chemically analyzing alloys of Fe and Al[13], samples of known composition, made by mixing metallic powders, were submitted simultaneously with the ingot samples. The composition of these control samples was determined satisfactorily and is the basis for reporting the compositions of the five, Fe-alloy single crystal samples used in the investigation as 14·0, 15·8, 18·3, 21·3 and 22·8 (each ± 0·16) at.% Al.

Sample heat treatment was carried out in flowing dry hydrogen; temperature control was maintained within ±3°C of the reported value. Unless otherwise specified, the sample was quenched to room temperature in water. After heat treatment, the samples were prepared for X-ray investigation by alternate mechanical and chemical polishing in a 50–50 solution of HCl and HNO_3 (by vol.). Back reflection Laue patterns of crystals prepared in this manner showed no evidence for deformed surface layers or pronounced mosaic structure. Further, Debye-Scherrer patterns of filings taken from the edges of the single crystals and stress relieved for one-half hour at 800°C had well resolved $K\alpha_1$–$K\alpha_2$ doublets in the back reflection region; this indicated that composition gradients in the alloy samples were eliminated by the homogenization treatment.

The X-ray measurements were made using MoKα radiation monochromated by diffraction from the (200) planes of a doubly bent LiF crystal in the Warren–Chipman[16, 17] type diffuse scattering geometry. The main advantage of this geometry is increased intensity. This enhanced intensity makes it possible to detect and study scattering from samples which do not have well developed superstructure reflections. The half-wave-length component and other submultiples of the Mo$K\alpha$ radiation were avoided by operating the X-ray tube at 31 kV and 20 ma. A scintillation detector [NaI (Tl doped)] equipped with a single channel pulse height analyzer was used to record the scattered intensity. Because the K fluorescence from the Fe in the samples was so energetically different from the Mo$K\alpha$ radiation, it could be removed by use of the pulse height analyzer. Beam confining and receiving slits limited the divergence in the primary and scattered beams to less than 2°.

Additional precautions which are more pertinent to the quantitative measurements of short-range order but which were also used for the present measurements are described in the subsequent paper, part II.

3. RESULTS

For the five alloy single crystals containing between 14·0 and 22·8 at.% Al in Fe, the X-ray scattering has been measured at room temperature after a series of selected heat treatments. A summary of the heat treating schedules is given in Table 1. Within this composition range, two long-range ordered structures, based on the stoichiometric compounds FeAl (B2) and Fe_3Al (DO_3) have been observed. The B2 type structure yields superlattice reflections when hkl are all even and $h+k+l$ is an odd multiple of 2*. The intensity of these reflections is sensitive to the distribution of Fe and Al atoms between the corners and centers of the small b.c.c. unit cells. The DO_3 type structure is characterized by Al atoms occupying centers of alternate small b.c.c. unit cells. This atomic arrangement gives rise to spectra at the same positions as the B2 structure and to an additional set of superlattice reflections when hkl are all odd.

Within the composition range investigated, the order intensity may vary from short-range order diffuse scattering to relatively intense superlattice reflections, depending on the composition of the alloy and its thermal history. This is illustrated in Fig. 3 which shows the distribution of intensity in the h_1h_20 plane of reciprocal space for the 18·3 at.% Al alloy. The diffuse intensity maxima displaced from the superlattice positions shown in Fig. 3(a) are characteristic of the short range ordered structures formed in this and the more dilute alloys. When the alloys are heat treated so as to produce long-range order, relatively intense superlattice reflections are produced as shown in Fig. 3(b).

The absence, in all the cases investigated, of order intensity maxima at or near positions for which hkl are mixed is taken as conclusive evidence that the $Fe_{13}Al_3$ structure which has been proposed[4] is not formed. However, the order reflections present in the h_1h_20 plane do not permit one to distinguish between the DO_3 and B2 types of structure. To distinguish

---

*All Miller indices cited will refer to a unit cell containing 16 atoms which is obtained by doubling the usual b.c.c. unit cell parameter in each of its axial directions. These will be referred to as large and small unit cells, respectively, in the discussion

Table 1. *Summary of the compositions and heat treatments investigated*

Composition (at % Al)	Heat treatment*	Composition (at.% Al)	Heat treatment	Composition (at.% Al)	Heat treatment
14·0	(1) 12 hr at 850°C, *Q*	18·3	(7) 2 hr at 850°C, *Q* 24 hr at 425°C, *Q*	21·3	(3) 1 hr at 850°C, *Q*, 12 hr at 475°C, *Q*.
	(2) 24 hr at 850°C, *Q*, 9 hr at 250°C, *Q*		(8) 6 hr at 850°C, *Q* 4 hr at 480°C, *Q*.		(4) 6 hr at 850°C, *Q*, 14 hr at 500°C, *Q*
15·8	(1) 12 hr at 850°C, *Q*.		(9) 6 hr at 850°C, *Q* 3 hr at 500°C, *Q*		(5) 1 hr at 850°C, *Q*, 12 hr at 525°C, *Q*
	(2) 1 hr at 850°C, *Q*, 70 hr at 140°C, *Q*		(10) 6 hr at 850°C, *Q* 14 hr at 530°C, *Q*	22·8	(1) 2 hr at 850°C, *Q*.
	(3) 1 hr at 850°C, *Q*, 10 hr at 250°C, *Q*		(11) 6 hr at 850°C, *Q*, 3 hr at 700°C, *Q*		(2) 8 hr at 850°C, *Q*, 24 hr at 250°C, *Q*.
18·3	(1) 8 hr at 850°C, *Q*.		(12) 12 hr at 850°C, *Q*.		(3) 2 hr at 850°C, *Q*, 21 hr at 425°C, *Q*.
	(2) 8 hr at 850°C, *Q*, 24 hr at 250°C, *Q*.		(13) same as (12) plus 15 min at 250°C, *Q*		(4) 6 hr at 850°C, *Q*, 16 hr at 470°C, *Q*
	(3) 8 hr at 850°C, *Q*, 24 hr at 325°C, *Q*		(14) same as (13) plus 15 min at 250°C, *Q*.		(5) 6 hr at 850°C, *Q*, 5 hr at 500°C, *Q*
	(4) 6 hr at 850°C, *Q*, 5 hr at 340°C, *Q*.		(15) same as (14) plus 30 min at 250°C, *Q*.		(6) 6 hr at 850°C, *Q*, 28 hr at 512°C, *Q*.
	(5) 2 hr at 850°C, *Q*, 24 hr at 375°C, *Q*.		(16) same as (15) plus 2 hr at 250°C, *Q*.		(7) 2 hr at 850°C, *Q*, 18 hr at 525°C, *Q*
	(6) 6 hr at 850°C, *Q*, 14 hr at 400°C, *Q*.		(17) same as (16) plus 7 hr at 250°C, *Q*.		(8) 6 hr at 850°C, *Q*, 14 hr at 530°C, *Q*.
		21·3	(1) 5 hr at 850°C, *Q*		(9) 6 hr at 850°C, *Q*, 4 hr at 550°C, *Q*.
			(2) 8 hr at 850°C, *Q*, 24 hr at 250°C, *Q*.		(10) 6 hr at 850°C, *Q*, 6 hr at 600°C, *Q*.
					(11) 6 hr at 850°C, *Q*, 1 hr at 750°C, *Q*.
					(12) 8 hr at 850°C, *Q*, 14 hr at 250°C, *Q*, 24 hr at 520°C, *Q*.
					(13) 4 hr at 850°C, *Q*, *directly* to 512°C, 74 hr at 512°C, *Q* to r.t.

*All treatment was done in flowing dry hydrogen. Unless otherwise specified, *Q* indicates the sample was quenched to room temperature in water.

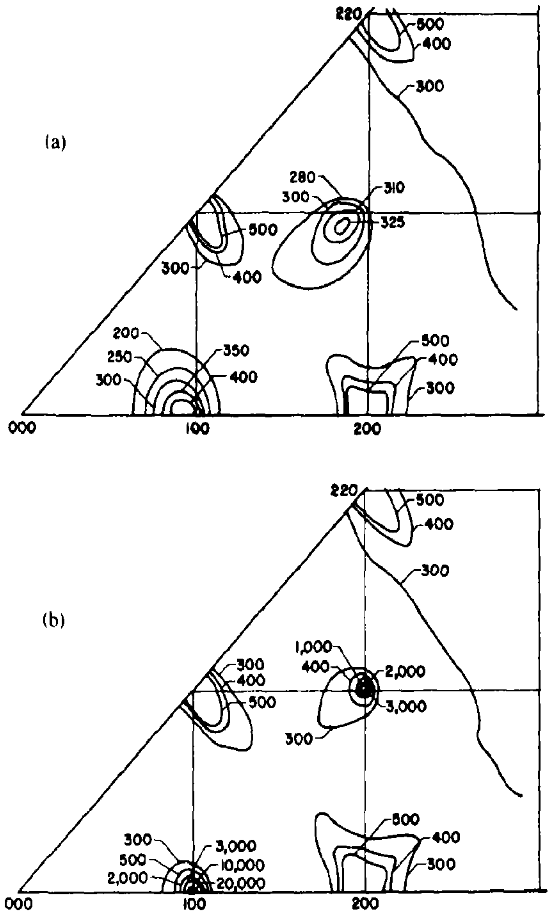

Fig. 3. Distribution of scattered intensity in the $h_1h_2 0$ plane of reciprocal space for the iron–18·3 at. % Al alloy. Uncorrected data in arbitrary units. (a) Sample quenched in water from 850°C; (b) sample annealed 168 hr at 250°C after quenching from 850°C.

between these two types of order, it is convenient to measure the scattered X-ray intensity along the cube diagonal in reciprocal space. This has been done for each of the five alloys after annealing at temperatures between 140° and 850°C. From the results of these X-ray measurements, a revised segment of the Fe–Al phase diagram as shown in Fig. 4 is proposed. The proposed phase diagram based on the present results is fundamentally different from previously reported experimental work in that an elevated temperature region in which long-range ordered phases based on FeAl and Fe_3Al coexist has been established.

The temperature dependence of the order in the 22·8 at. % Al alloy is illustrated by the intensity distributions shown in Fig. 5. Extensive long-range order of the DO_3 type is found at 250°C as shown by the intense superlattice reflections in Fig. 5(a). Similar diffraction patterns are obtained when this alloy is annealed at 425° and 470°C, except that the intensity of the superlattice reflections decreases with increasing annealing temperature.

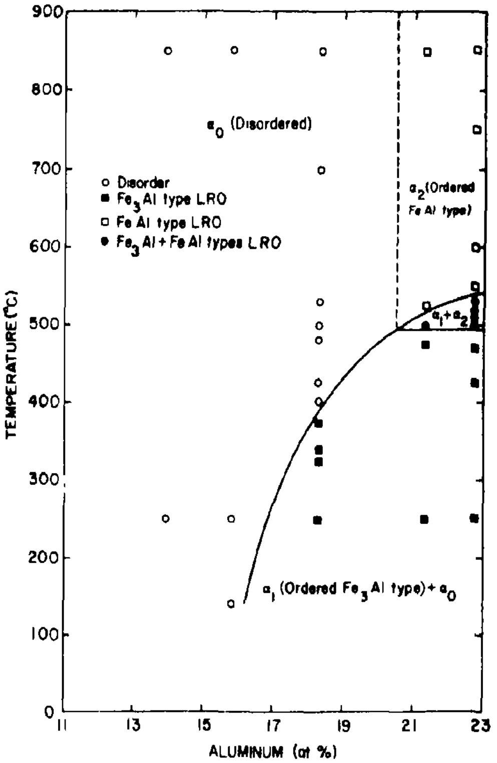

Fig. 4. Revision of the Fe–Al phase diagram according to the present results

Another characteristic type of diffraction pattern is obtained when the 22·8 at. % alloy is annealed between about 495° and 540°C as is shown in Fig. 5(b). The fact that the (222) superlattice reflection is more intense than the (111) results from the fact that the B2 type structure contributes only to this (222) reflection and not to the (111) and (333), the latter two being superlattice reflections for the DO_3 phase.

In order to confirm the existence of this two-phase region, equilibrium has been approached from the DO_3 type, highly ordered, low temperature state and also from the B2 type, weakly ordered, higher temperature state. Within the sensitivity of the experimental method being used, identical results were obtained. Similar results were obtained for an alloy containing 21·3 at. % Al as is reflected in the construction of Fig. 4.

In contrast, when the 22·8 at. % Al alloy is annealed at higher temperatures, between about 540°C and 850°C, a diffraction pattern of the type shown in Fig. 5(c) is obtained. The presence of the broad (222) reflection (at about 24·6°2θ) and the absence of (111) and (333) superstructure reflections denotes the presence of B2 type order. That the domains of the B2 type order are small is indicated by the broad (222) peak. In addition, the presence of diffuse intensity maxima in the vicinity of the (111) and (333) superlattice reflection positions is interpreted to mean that on a scale even smaller than the size of the ordered domains, there is a definite tendency for Al atoms to avoid being second nearest neighbors.

The temperature dependence of order in the 18·3 at. % Al alloy is fundamentally different from that of the higher Al alloys. For annealing temperatures between about 395° and 850°C, there is no evidence for the presence of long-range order; however, there is considerable short-range order in the atomic arrangement. Figure 6 presents two typical diffraction patterns showing modulations in the diffuse scattering observed along the $h_1 = h_2 = h_3$ line in reciprocal space. In addition to the order diffuse maxima in the vicinity of the DO_3 type superlattice positions, there are other features characteristic of these patterns which are due to atomic displacements. The background is always high between the (111) and (222) positions, there is a sharp decrease in the background intensity immediately beyond the (222) position, and the order diffuse maximum associated with the (222) position is displaced toward lower angles. These modulations in the diffuse scattering caused by atomic displacements (or atomic size-effect) will be discussed more extensively in part II.

As will be discussed at length in part II, the short-range order present in these more dilute Al alloys is predominantly of the DO_3 type; however, there is qualitative information that some B2 character is assumed in the 18·3 at. % Al alloy for annealing temperatures

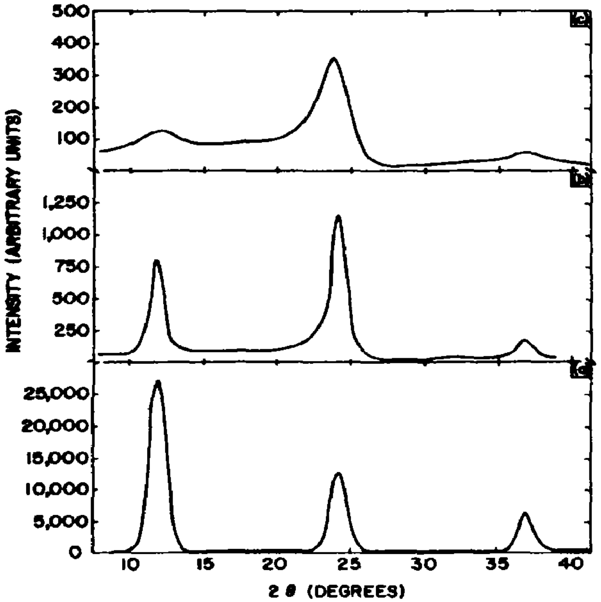

Fig. 5. Uncorrected X-ray intensity scattered along the $h_1 = h_2 = h_3$ line in reciprocal space for the Fe–22·8 at.% Al alloy annealed at (a) 250°C, (b) 512°C, and (c) 850°C. (See Table 1)

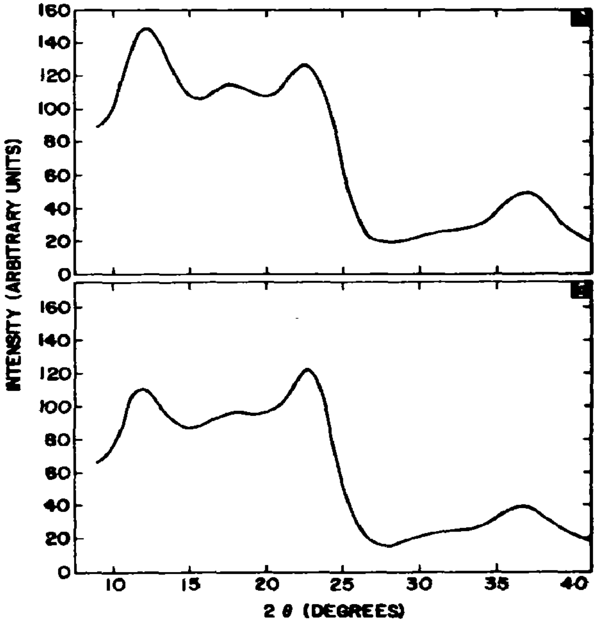

Fig. 6 Uncorrected X-ray intensity scattered along the $h_1 = h_2 = h_3$ line in reciprocal space for an Fe alloy containing 18·3 at.% Al. (a) annealed at 500°C; (b) annealed at 850°C.

between about 480° and 530°C. It may be significant that this corresponds approximately to the temperature range in which long-range order of the DO_3 and B2 types coexist in the higher Al alloys.

No long-range order was observed in alloys containing 15·8 and 14·0 at. % Al; however, there was considerable structure in the diffuse scattering. Typical diffraction patterns for these more dilute alloys are shown in Fig. 7. The 14·0 at. % Al alloy is practically unresponsive to annealing at 250°C following quenching from 850°C.

4. DISCUSSION

In constructing the phase diagram shown in Fig. 4, recourse has been made to published experimental results in labelling the phase field denoted as disordered (α_0) plus ordered Fe_3Al (α_1). This construction, at low temperature, is consistent with the lattice parameters

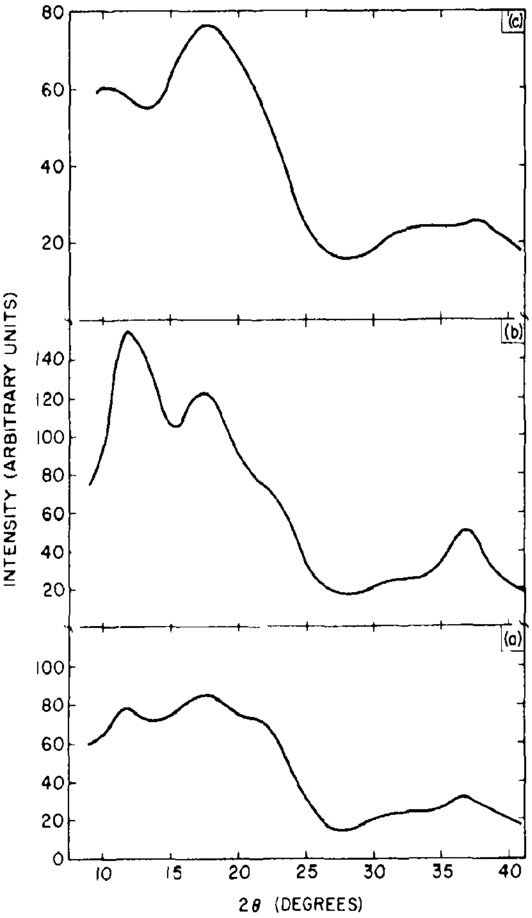

Fig 7. Uncorrected X-ray intensity scattered along the $h_1 = h_2 = h_3$ line in reciprocal space by two alloys which do not exhibit long-range ordering. (a) Fe–15·8 at.% Al quenched from 850°C. (b) Fe–15·8 at.% Al quenched from 850°C and annealed 10 hr at 250°C. (c) Fe–14·0 at.% Al quenched from 850°C.

measured at temperature by Taylor and Jones[4] and with the anomalous peak widths reported by Lihl and Ebel[5]. In addition recent dark field electron microscopy by Lutjering and Warlimont[18, 19] has yielded primary evidence for the coexistence of a disordered phase and the ordered DO_3 type structure below about 500°C.

The present work is the first to demonstrate the existence of the elevated temperature region comprised of ordered phases based on the DO_3 and B2 type structures. The present results are in excellent agreement in this respect with the statistical theoretical results by Rudman[9] as shown in Fig. 2. Consequently, the present experimental results can be taken as evidence for the correctness of Rudman's assumption that, in alloys containing less than about 25 at. % Al, the Fe_3Al type phase disorders by a first order transformation.

The construction of the Fe–Al phase diagram in the composition range from 20 to about 25 at. % Al and at temperatures above the two-phase $(\alpha_1+\alpha_2)$ field remains in question. Earlier work[9, 13] has been interpreted as evidence that the B2 type structure disorders by a second order transformation. However, recent transmission electron microscopy work by Swann and Fisher[20] has been interpreted in terms of the coexistence of a disordered phase with the B2 type ordered phase and, hence, that this transformation is also of the first order. This interpretation is not inconsistent with the diffraction effects observed in the present investigation but would simply imply that the horizontal line in Fig. 4 at about 495°C represents a eutectoid. However, the experimental technique being used in the present research is not well suited for detecting the presence of a disordered phase if an ordered phase having a similar unit cell size is also present. It is for this reason that a dotted vertical line at 20 at. % Al is shown in Fig. 4.

There is an interesting correlation between the phase relations in the Fe-rich Fe–Al alloys according to the present investigation (Fig. 4) and the occurrence of the *K*-state phenomenon as reported by Thomas[11] and Davies[6]. Thomas noted that within certain composition ranges marked increases in electrical resistance could be induced by subjecting the alloy to a low temperature anneal following quenching from high temperature or following cold-working. For example, an 18·8 at. % Al alloy exhibited the *K*-state behaviour while one containing 21·4 at. % Al did not. Except for the very dilute alloys, this *K*-state behavior could be produced by the low temperature anneal following quenching of the alloys from within the disordered field. The lower concentration limit for which the *K*-state phenomenon occurs corresponds approximately to the lower limit for which short-range order has been observed.

In general, for a given alloy the change in electrical resistivity is inversely related to the disorder in the structure. However, when a range of composition is considered, it is found[11, 21] that the specific electrical resistance of alloys equilibrated at 300°C and quenched to room temperature, for example, goes through a maximum somewhere within the two-phase field and subsequently decreases to a value at stoichiometric Fe_3Al which is lower than that for the disordered phase. This composition variation of the resistance is suggestive of significant contributions due to strain energy changes accompanying the ordering process, an effect which has been noted in other systems[22].

Strain energy considerations of this type, however, are inadequate for explaining the changes in electrical resistance on annealing for a given composition. The explanation of this behavior may lie in changes in the electronic structure which occur when Al is alloyed with Fe. The transition element Fe has unfilled 3*d* states and is slightly more electro-negative than the solute Al. There is evidence in the literature which supports the concept that there is some departure from the metallic type bonding in going from the disordered to ordered states in this alloy system. Studies of the fine structure of the absorption edge of Fe in the pure material and in some of its alloys with Al by Murty and Azaroff[23]; Nemnonov and Kolobova[24]; and Nemnonov, Finkel'shtein, and Kolobova[25] have been interpreted in terms of changes in the electronic structure of the absorbing atom, Fe, on alloying. It was concluded that there is a tendency toward formation of covalent type bonds in the ordered FeAl and Fe_3Al structures, Fe_3Al being intermediate between pure Fe and ordered FeAl in this respect. In view of these arguments, it does not appear unreasonable to conclude that the anomalous decrease in electrical resistivity observed when a *K*-state alloy is deformed or disordered by heat treatment results basically from the disruption of the tendency to form covalent bonds and the attendant return toward metallic type bonding.

REFERENCES

1. SYKES C. and EVANS H., *Proc. R. Soc.* **A145**, 529 (1934).
2. BRADLEY A. J. and JAY A. H., *Proc. R. Soc.* **A136**, 210 (1932).
3. EPPERSON J. E., University of Tennessee Dissertation (1968).
4. TAYLOR A. and JONES R. M., *J. Phys. Chem. Solids* **6**, 16 (1958).
5. LIHL F. and EBEL H., *Arch. Eisenhüttenwes.* **32**, 483 (1961).
6. DAVIES R. G., *J. Phys. Chem. Solids* **24**, 985 (1963).
7. SEYBOLT A. U., *Trans. AIME* **218**, 570 (1960).
8. McQUEEN H. J. and KUCZYNSKI G. C., *Trans. AIME* **215**, 619 (1959).
9. RUDMAN P. S., *Acta metall.* **8**, 321 (1960).
10. HOUSKA C. R., *J. Phys. Chem. Solids* **24**, 95 (1963).
11. THOMAS H., *Z. Metallk.* **41**, 185 (1950).
12. EPPERSON J. E. and SPRUIELL J. E., *J. Phys. Chem. Solids* **30**, 1733 (1969).
13. LAWLEY A. and CAHN R. W., *J. Phys. Chem. Solids* **20**, 204 (1961).
14. YAMOMOTO M. and TANIGUCHI S., *Sci. Rep. RITU* **A8**, 193 (1956).
15. BENNETT W. D., *J. Iron Steel Inst.* **171**, 372 (1952).
16. WARREN B. E., *J. appl. Phys.* **25**, 814 (1954).
17. CHIPMAN D. R., *Rev. scient. Instrum.* **27**, 164 (1956).
18. LUTJERING G. and WARLIMONT H., *Acta Metall.* **12**, 1460 (1964).
19. LUTJERING G. and WARLIMONT H., *Z. metall.* **56**, 1 (1965).
20. SWANN P. R. and FISHER R. M., *Appl. Phys. Lett.* **9**, 279 (1966).
21. MARCINKOWSKI M. J. and SMOLUCHOWSKI R., *J. Phys. Chem. Solids* **26**, 185 (1965).
22. STARKE E. A., Jr, GEROLD V. and GUY A. G., *Acta metall.* **13**, 957 (1965).
23. MURTY H. N. and AZAROFF L. V., *Acta metall.* **15**, 1655 (1967).
24. NEMNONOV S. A. and KOLOBOVA K. M., *Fiz. metal. metalloved* **6**, 183 (1958).
25. NEMNONOV S. A., FINKEL'SHTEIN L. D. and KOLOBOVA K. M., *Fiz. metal. metalloved.* **9**, 243 (1960).

J. Phys. Chem. Solids Pergamon Press 1969. Vol. 30, pp. 1733–1744. Printed in Great Britain.

AN X-RAY SINGLE CRYSTAL INVESTIGATION OF IRON-RICH ALLOYS OF IRON AND ALUMINUM–II. DIFFUSE SCATTERING MEASUREMENTS OF SHORT-RANGE ORDER IN ALLOYS CONTAINING 14·0 AND 18·3 AT.% ALUMINUM

J. E. EPPERSON* and J. E. SPRUIELL
Department of Chemical and Metallurgical Engineering, University of Tennessee, Knoxville, Tenn. 37916, U.S.A.

(*Received* 6 *November* 1968)

Abstract—The X-ray diffuse scattering from alloy single crystals of Fe-14·0 and Fe-18·3 at.% Al quenched from 850°C has been measured throughout a volume in reciprocal space sufficient to permit the order and atomic displacements modulations to be separated. From these separated components, three-dimensional order and atomic displacements coefficients were determined. The short-range order in the arrangement of the atoms is tending toward the DO_3 type arrangement, the ordered structure being more fully developed in the more concentrated alloy The modulations associated with the atomic displacements are shown to be responsible for many of the characteristic features of the diffuse intensity distributions.

1. INTRODUCTION

IN THE preceding paper[1], referred to hereafter as part I, an X-ray investigation of Fe-rich single crystals containing between about 14 and 23 at.% Al was discussed from the standpoint of the equilibrium phase relations. It was shown there that the Fe-rich terminal solid solution contains a high degree of short-range order as well as a large atomic size (or displacements) modulation of the diffuse X-ray scattering. The present paper presents quantitative measurements of the short-range order and atomic displacements parameters in two alloys containing, respectively, 14·0 and 18·3 at.% Al.

The fact that the Fe-rich terminal solid solution is short-range ordered has also been shown by several previous investigators. Lawley and Cahn[2] and Davies[3] have surveyed the diffuse scattering of several alloys in the range 16–23 at.% Al using polycrystalline samples. While these investigators showed that short-range order occurs in the terminal solid solution, no quantitative interpretation was attempted.

Vlasova[4] and Vlasova and Iveronova[5] have investigated alloys containing from 6 to 28·2 at.% Al using single crystal samples and film registration to study the diffuse intensity distribution. Based on their measurements it was suggested that observed displacements of the diffuse maxima were produced by a large atomic size-effect and that the solution may consist of small aluminum enriched zones randomly dispersed in a disordered matrix. These zones were thought to have Fe_3Al (DO_3) type structure but to be so small that order probably did not extend beyond the third coordination shell.

The only previous investigation which attempted to obtain quantitative information on the atomic arrangements in the short-range ordered solutions was that of Houska and Averbach[6]. These investigators measured the X-ray diffuse scattering from surface-ground polycrystalline strips containing between 15 and 20 at.% Al. The first three order and size-effect coefficients were derived from the corrected diffuse intensity, and the order coefficients indicated a tendency toward the DO_3 type structure in the dilute Al alloys.

**Present address:* Oak Ridge National Laboratory, Oak Ridge, Tenn. 37830, U.S.A.

Because the single crystal technique is inherently more accurate and more easily interpreted and because no quantitative three-dimensional single crystal measurements had been made, it was thought to be worthwhile to make this analysis using recently devised three-dimensional analytical techniques[7] for separating the size-effect modulations from those due to the short-range order. The Fe–Al system, with its large atomic size-effects, seemed to be a logical system to which to apply this separation technique.

2. X-RAY DIFFRACTION THEORY

According to kinematic diffraction theory, the total coherently scattered X-ray intensity, I_{eu}, at a given position in reciprocal space is given in electron units as

$$I_{eu} = \sum_p \sum_q f_p f_q e^{i\mathbf{k}\cdot\mathbf{R}_{pq}}, \tag{1}$$

where f_p and f_q are the scattering factors of the atoms situated at sites p and q, $\mathbf{k}$ is 2π times the diffraction vector, and $\mathbf{R}_{pq}$ is the interatomic vector. It is conventional to consider the coherently scattered intensity from binary solid solutions as being composed of two parts, one part associated with the sharp fundamental reflections and the other with the diffuse scattering. For a linear approximation of the displacement of the atoms off the average lattice sites, the diffuse intensity associated with the atomic order and atomic displacements, specialized for body- or face-centered cubic binary alloys, can be expressed as

$$\begin{aligned} I(h_1, h_2, h_3) &= NX_AX_B(f_A-f_B)^2 \sum_l \sum_m \sum_n \\ &\times \alpha_{lmn} \cos 2\pi(h_1l+h_2m+h_3n) \\ &- NX_AX_B(f_A-f_B)^2 \sum_l \sum_m \sum_n (h_1\gamma^l_{lmn}+h_2\gamma^m_{lmn} \\ &+ h_3\gamma^n_{lmn}) \sin 2\pi(h_1l+h_2m+h_3n). \end{aligned} \tag{2}$$

Relative to an arbitrarily chosen origin, the average interatomic vector is given by

$$\langle \mathbf{R}_{lmn}\rangle = l\frac{\mathbf{a}_1}{2}+m\frac{\mathbf{a}_2}{2}+n\frac{\mathbf{a}_3}{2}, \tag{3}$$

where l, m and n are integers and $\mathbf{a}_1$, $\mathbf{a}_2$ and $\mathbf{a}_3$ are the translation vectors of the cubic unit cell. The continuous variables in reciprocal space, h_1, h_2 and h_3, are related to the diffraction vector by the relationship

$$\frac{\hat{s}-\hat{s}_0}{\lambda} = h_1\mathbf{b}_1+h_2\mathbf{b}_2+h_3\mathbf{b}_3, \tag{4}$$

where $\mathbf{b}_1$, $\mathbf{b}_2$ and $\mathbf{b}_3$ are vectors reciprocal to $\mathbf{a}_1/2$, $\mathbf{a}_2/2$ and $\mathbf{a}_3/2$. The Warren order parameter α_{lmn} is defined by

$$\alpha_{lmn} = 1 - \frac{P_{lmn}}{X_B} \tag{5}$$

where P_{lmn} is the probability of finding a B atom as an (lmn) neighbor of an A atom. The atomic displacements parameters are defined by relationships of the form

$$\begin{aligned} \gamma^l_{lmn} = \frac{2\pi}{f_A-f_B}\Bigg[&\left(\frac{X_A}{X_B}+\alpha_{lmn}\right) f_A L^{AA}_{lmn} \\ &- \left(\frac{X_B}{X_A}+\alpha_{lmn}\right) f_B L^{BB}_{lmn}\Bigg]. \end{aligned} \tag{6}$$

The L's are components of displacement off the average atomic sites,

$$\delta^{AA}_{lmn} = L^{AA}_{lmn}\frac{\mathbf{a}_1}{2}+M^{AA}_{lmn}\frac{\mathbf{a}_2}{2}+N^{AA}_{lmn}\frac{\mathbf{a}_3}{2}. \tag{7}$$

Equation (2) represents a generalization by Borie and Sparks[8] of the treatment of short-range order due to Cowley[9] which had been modified by Warren, Averbach and Roberts [10] to include the first-order size-effect.

The treatment by Borie[11], later generalized by Sparks and Borie[7], which takes advantage of the fact that the atomic order and atomic displacements modulations exhibit different symmetry in reciprocal space can be employed to separate the diffuse intensity represented by equation (2) into components from which the α's and γ's can be recovered by Fourier inversion.

3. PROCEDURES

The details of single crystal growth and sample preparation were discussed in part I, and many of the details pertaining to equipment and experimental procedures used in making X-ray scattering measurements were also described. Those matters which were not discussed in part I and which are important for the present paper will now be described.

For the quantitative determination of the Warren short-range order parameters, α_{lmn}, and the atomic displacement coefficients, γ_{lmn}^{m}, the diffuse intensity was measured by counting for 100 sec at each of 1014 points located on a cubic grid throughout the volume element in reciprocal space shown heavily outlined in Fig. 1. Data must be available throughout at least this volume in order to make the three-dimensional atomic size-effect separation by the procedure of Sparks and Borie[7].

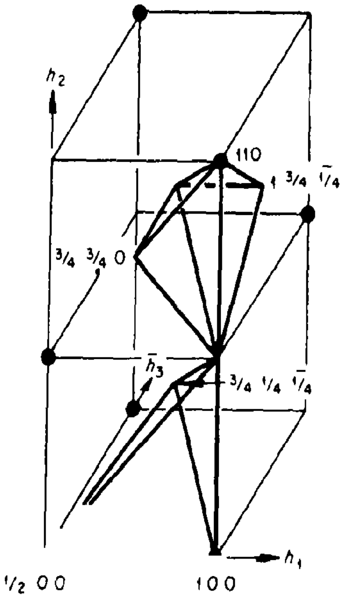

Fig. 1. The volume in reciprocal space in which intensity data are required for b.c.c. structures when using the separation procedure based on the linear displacement approximation.

Since the present determinations were to be quantitative, sources of scattering other than that due to the local atomic arrangements had to be eliminated experimentally or appropriate corrections applied to the data. To this end the sample was mounted in an evacuated chamber of a liquid nitrogen cryostat; the radiation entered and left the chamber through beryllium windows covered with a polyester film. The evacuated sample chamber and appropriately placed baffles and scatter slit eliminated air scattering while an approximate correction for temperature diffuse scattering (TDS) was evaluated by making measurements at both room temperature and 136°K. Assuming that the TDS varies linearly with temperature, this TDS correction was determined by extrapolation of the data to 0°K. A correction for Compton modified scattering was computed using the incoherent scattering functions calculated by Freeman[12, 13]; this correction was applied after the data were converted into absolute units.

The intensity measurements were converted to absolute units (electron units per atom, I_{eu}/N) using the expression

$$\frac{I_{eu}}{N} = \frac{2M_s(\mu/\rho)}{N_a P_0 p}\left(\frac{mc^2}{e^2}\right)^2 R^2 I \qquad (8)$$

where M_s is the molecular weight of the sample; μ/ρ is the mass absorption coefficient; N_a is Avogadro's number; p is the appropriate polarization factor; (e^2/mc^2) is the classical electron radius; R is the distance from the sample to the detector; I is the measured intensity; and P_0 is the power in the incident X-ray beam. All the parameters appearing in this expression are either tabulated or are easily obtained experimentally with the exception of P_0. The value of P_0 was measured using the 'nearly perfect' crystal technique proposed by Batterman, Chipman and De Marco[14]. The atomic scattering factors of Fe and Al used in the analysis of the present results were measured experimentally and are being reported elsewhere[15].

The bulk of the laborious calculations necessary for conversion of the raw intensity data into absolute units, application of the necessary correction factors, and Fourier inversion of the separated components was facilitated by use of a series of digital codes [16] and an IBM 7040 computer.

4. RESULTS AND INTERPRETATION

The diffuse X-ray scattering was measured throughout the volume element shown in Fig. 1 for the Fe-18·3 and Fe-14·0 at. % Al alloys after water quenching from 850°C. These data were converted into absolute units and corrected for TDS and Compton scattering as described above. The Bragg peaks and the Huang scattering in their immediate neighborhood were removed by a smooth extrapolation of the diffuse scattering data. The remaining diffuse intensity was separated into components due to the short-range order and to the first-order size-effect. Warren short-range order parameters, α_{lmn}, were obtained by Fourier inversion of the local order component of the diffuse intensity and are presented in Table 1, columns two and four. Tables 2 and 3 present the atomic displacements parameters for the Fe-18·3 and Fe-14·0 at. % Al alloys, respectively.

For purposes of easy comparison, the order coefficients for perfectly ordered stoichio-

Table 2. Three-dimensional first-order size-effect parameters for the iron-18·3 at. % aluminum alloy quenched from 850°C

lmn	γ_{lmn}^{m}	γ_{mnl}^{n}	γ_{nlm}^{l}
000	0·000	0·000	0·000
111	−0·260	−0·260	−0·260
002	0·000	0·416	0·000
022	0·039	0·040	0·000
113	0·022	−0·022	0·022
222	0·036	0·036	0·036
004	0·000	0·001	0·000
133	−0·013	−0·013	0·014
024	−0·020	0·043	0·000
224	−0·010	0·017	−0·010
333	−0·032	−0·032	−0·032
044	0·005	0·005	0·000
244	0·005	0·005	0·000
444	0·005	0·005	0·005

Table 1. Three-dimensional short-range order parameters α_{lmn} for the iron-14·0 and iron-18·3 at. % aluminum alloys quenched from 850°C

	Fe-18·3 at % Al		Fe-14·0 at. % Al	Perfect FeAl LRO	Perfect Fe_3Al LRO
lmn	Experimental α_{lmn}	α_{lmn} Calculated from model	Experimental α_{lmn}	Calculated α_{lmn}	Calculated α_{lmn}
000	1·331	1·000	1·924	1·000	1·000
111	−0·202	−0·201	−0·113	−1·000	−0·333
200	−0·007	−0·007	−0·037	1·000	−0·333
220	0·024	0·022	−0·017	1·000	1·000
311	0·011	0·021	0·035	−1·000	−0·333
222	−0·013	0·037	−0·003	1·000	−0·333
400	0·035	0·036	0·004	1·000	1·000
331	−0·032		−0·029	−1·000	−0·333
420	−0·015		−0·022	1·000	−0·333
422	0·047		0·024	1·000	1·000
333	−0·006		0·002	−1·000	−0·333
440	0·013		0·000	1·000	1·000
442	−0·009		0·002	1·000	−0·333
444	0·005		−0·003	1·000	1·000

Table 3. *Three-dimensional first-order size-effect parameters for the iron*-14·0 *at.* % *aluminum alloy quenched from* 850°C

lmn	γ_{lmn}^{n}	γ_{mnl}^{n}	γ^{l}_{nlm}
000	0·000	0·000	0·000
111	−0·334	−0·334	−0·334
002	0·000	0·439	0·000
022	0·055	0·054	0·000
113	0·036	0·001	0·036
222	0·015	0·015	0·015
004	0·000	0·025	0·000
133	−0·019	−0·019	0·008
024	−0·046	0·029	0·000
224	−0·012	0·000	−0·012
333	−0·017	−0·017	−0·017
044	0·028	0·027	0·000
244	0·011	0·011	−0·002
444	−0·003	−0·003	−0·003

metric FeAl (B2) and Fe_3Al (DO_3) are also included in Table 1. From the sixth column, it can be seen that if the local atomic arrangements were of the kind which, if extended, yield DO_3 type long-range order, the first two coordination shells would show a preference for atoms unlike the one at the origin, the third shell would show a preference for like atoms, etc. This sequence of preference is altered when the local atomic arrangements are of the B2 type as can be seen from column five. In particular, one finds in the case of B2 type order that the first coordination shell shows a preference for unlike neighbors, but the second and third shells tend to be populated with atoms like the one at the origin, etc.

Short-range order in the Fe-18·3 *at.* % *Al alloy*

Comparison of the experimental α's in column two of Table 1 with the calculated values in columns five and six indicates that the atoms in this sample are tending toward an arrangement similar to that in long-range ordered Fe_3Al. This statement is based on the observation that the signs of the α's are 'correct' through the first eleven coordination shells, except for the fourth (α_{311}); however, this characterization must be explored further because the magnitudes of the order coefficients are quite small beyond the first shell. The value of zero corresponds to random occupancy of the coordination shell in question.

The large negative value of α_{111} is proof that unlike first nearest neighbors are strongly preferred in the 18·3 at. % Al alloy. The maximum negative value α_{111} can take on for this composition is −0·224. The value of −0·202 obtained in the present experiment means that when this alloy is quenched from 850°C, on the average about 98 per cent of the first nearest neighbors of the Al atoms are Fe atoms.

In view of the facts that rather well defined diffuse intensity maxima are found in the vicinity of the Fe_3Al superlattice reflection positions (see Fig. 6(b), part I) and that first nearest neighbor ordering is so nearly complete, it is somewhat surprising that the experimental value of α_{200} is so small. The value of −0·007 for α_{200} means that on the average about 82 per cent of the second nearest neighbors of Al atoms are Fe atoms. The surprising fact is that this is only about one half of one per cent above the random value.

The explanation of this virtual random occupancy of the second coordination shell about the Al atoms is thought to be associated with the fact that α_{200} differs in sign for the DO_3 and B2 type structures. It does not seem unreasonable to describe qualitatively the local-order structure of the Fe-18·3 at. % Al alloy after quenching from 850°C as consisting of a mixture of regions in some of which there is a tendency toward the DO_3 structure and in others a tendency toward the B2 structure, with the predominant tendency being to form the DO_3 type short-range order. A more appropriate characterization might be to describe the structure as having a strong tendency toward superposition of DO_3 type short-range order on the B2 type.

In order to assess the validity of these conclusions, a model incorporating these requirements for the atomic arrangements has been developed. A schematic representation of the model for the short-range structure of the 18·3 at. % Al alloy after quenching from 850°C is presented in Fig. 2. The section of crystal shown in this figure contains 290 atoms, 53 of which are Al, and its composition corresponds to that of the experimental alloy. The planes shown in Fig. 2 are stacked one above another, plane (b) above plane (a), etc.

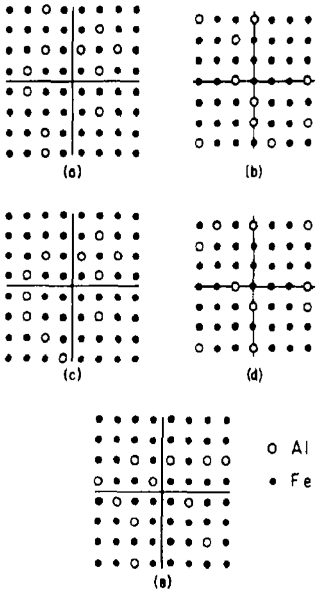

Fig. 2. Model for the short-range structure in the Fe-18·3 at % Al alloy after quenching from 850°C.

The α_{lmn} for the atom arrangements shown here were calculated from their definition by counting the number of Al atoms in the appropriate coordination shell about each of the 53 Al atoms. For this model, the calculations were performed on the assumption that all atoms outside the region shown are 'statistically average' atoms, except that there can be no first nearest neighbor Al–Al pairs formed with the atoms in the surfaces of the region shown in Fig. 2. The partial B2 character of the short-range order was built into the model by requiring that α_{200} from the model agree with the experimental value. Order coefficients for the first six coordination shells calculated from this model are given in Table 1, column three.

Through the first three coordination shells, the atom positions were adjusted manually in such a manner as to optimize the agreement between the calculated and experimental order coefficients. From the resulting atom arrangement, the next three order parameters were calculated. This was done for convenience and also in order to determine to what degree the inner shell coordination parameters are capable of characterizing the ordered system, i.e. to determine whether an arrangement of atoms forced to be consistent with the first three order parameters will predict satisfactorily the atom preferences in the succeeding shells. The tabulated results show that only limited success was attained. The moderate agreement with respect to α_{311} was gratifying in that, as has already been noted, the experimental value is different in sign from the calculated value for both DO_3 and B2 types of order. Also the calculated value is in excellent agreement with respect to the sixth shell (α_{400}); however, the model calculation is in serious disagreement with respect to the fifth shell. Present experience leads one to be confident that better agreement of the values calculated from the model with the experimental α's could be obtained by increasing the number of atoms in the model and by continuing to make minor adjustments in atom arrangements. However, when doing the computation manually, this becomes an extremely laborious task, and the anticipated results do not adequately justify the expenditure of time.

Short-range order in the Fe-14·0 at. % Al alloy

The order coefficients for the 14·0 at. % Al alloy are given in column four of Table 1. The large negative value of α_{111} ($-0{\cdot}113$) indicates that only about five per cent of the closest neighbors of the Al atoms are other Al atoms. For the higher order coordination shells, there is a marked tendency for agreement between the order coefficients for the two alloys, the principal exception being α_{220}.

Thus a tendency to form the same type of short-range order for the two alloys is indicated; however, it is considered prudent to inject a word of caution at this point. As will be shown in the following section, the modulations in the diffuse intensity due to the atomic displacements are quite large in comparison to those due to the short-range order for the alloy containing 14·0 at. % Al. For this reason it is felt that the order parameters for the more dilute alloy are less accurate than are the corresponding parameters for the 18·3 at. % Al alloy.

The atomic displacements (size-effect)

The effects due to the short-range order of the atoms do not, in themselves, adequately describe the observed modulations in the diffuse intensity scattered from Fe-rich Fe–Al solid solutions. This fact is obvious from a casual inspection of the distributions of the diffuse intensity; for example, see Figs. 3(a), 6 and 7, of part I. This fact is further illustrated by Fig. 3 of this paper. Parts (a) and (b) of Fig. 3 show the intensity scattered from the 18·3 at. % Al alloy along the $h_2 = h_3 = 0$ and $h_1 = h_2 = h_3$ lines, respectively, in reciprocal space expressed in absolute Laue monotonic units. In Fig. 4 the large atomic displacements modulations alone are shown along the $h_1 = h_2 = h_3$ line. The smoothed atomic displacements function shown in Fig. 4 was reconstructed from its definition using the appropriate component of the separated data. The atomic displacements modulations along the $h_1 = h_2 = h_3$ line clearly illustrate the origin of the peculiar features of the diffraction patterns shown in Fig. 3(b) of this paper and in Figs. 6 and 7 of part I. The high background between the (111) and (222) positions and the sharp decrease in intensity immediately beyond the (222) position result from the asymmetry of the atomic displacements function about the (222) position. The convolution of the short-range order and atomic displacements modulations also causes the diffuse maximum associated with the (222) position to be displaced toward lower angles and to have a higher peak intensity. There is a lesser effect of atomic displacements on the (111) position. It is also the atomic displacements effect which is responsible for the

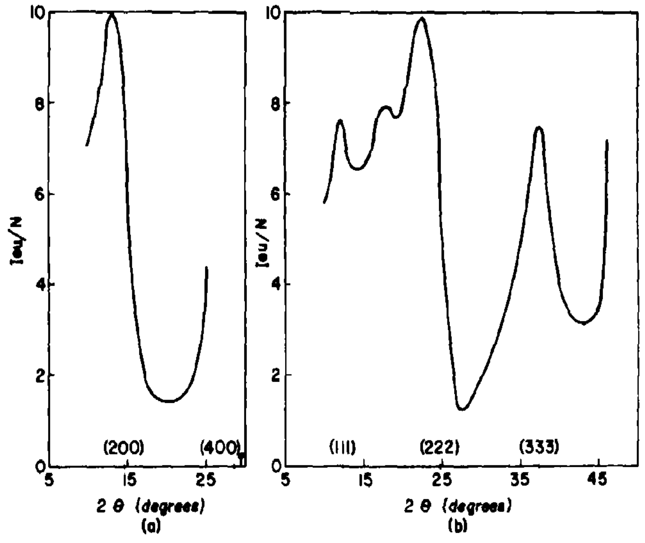

Fig. 3. Scattered X-ray intensity for the Fe-18·3 at. % Al alloy after being quenched from 850°C. Data were corrected from Compton scattering and divided by the Laue monotonic unit.

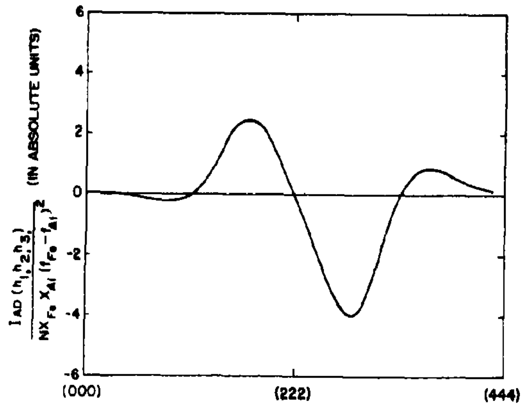

Fig. 4 Atomic-displacements modulations along the $h_1 = h_2 = h_3$ line for the Fe-18·3 at. % Al alloy quenched from 850°C.

subsidiary maximum between the (111) and (222) positions, a feature which is especially prominent in the more dilute alloys.

As was discussed in the previous section, the diffuse scattering modulations due to short-range order decrease with decreasing Al content. However, the coefficients presented in Tables 2 and 3 indicate that the modulations due to the atomic displacements increase somewhat with decreasing Al content in the compositions investigated. The differences between the values of the atomic displacements coefficients for the lower order coordination shells for the 14·0 and 18·3 at. % Al alloys are quite real as is apparent even in the separated data. Hence, for the Fe–Al alloys which have been heat treated so as to produce short-range ordered structures, the atomic displacements modulations are comparable in magnitude to those due to the atomic order, and in the more dilute alloys, the size-effect modulations tend to dominate.

Effects of atomic displacements have also been noted in diffraction patterns from some of the higher Al alloys heat treated so as to yield long-range order of the DO_3 type. In particular the subsidiary maximum due to the atomic displacements between the (111) and (222) positions has been observed to persist even after long-range order is well established. Of course in the long-range ordered structures, it is weak in comparison to the superlattice reflections. Its intensity decreases with increased Al content from 18·3 to 22·8 per cent. The atomic displacements modulations observed in these higher Al alloys appear to be associated with the proposed two-phase nature of these alloys after low temperature heat treatment (see part I). The disordered terminal solid solution in equilibrium with the long-range ordered Fe_3Al type phase should still exhibit short-range order and the atomic displacements effect. Since the amount of terminal solid solution decreases with increasing Al content in the two-phase region, the diffraction effects associated with the atomic displacements in the terminal solid solution should also decrease with increasing Al content in agreement with observations.

Since the atomic displacements coefficient is a measure of the mean local deviation of an atom off the average lattice site, depending on the type of atoms at the termini of the interatomic vector, the occurrence of both positive and negative γ's in Tables 2 and 3 is significant. This means that, although the Al atom is larger than that of the Fe, the distance between Al–Al pairs is less than the interatomic distance computed from the average lattice for some coordination shells. This must be due to the high probability of smaller Fe atoms occupying sites in the neighborhood of the interatomic vector connecting two Al atoms for these coordination shells.

The experimental parameters given in Tables 2 and 3 also show that the Warren–Averbach–Roberts size-effect theory[10] is not quite adequate for representing the atomic displacements in these alloys. As was discussed by Borie and Sparks[8], the WAR theory assumes that all the displacements off the average lattice sites are parallel to the interatomic vector, and it yields a set of size-effect coefficients, β_{lmn}, which are independent of the order of l, m and n. In other words, all β_{lmn} should be the same for a given coordination shell. If this assumption were adequate, the γ's reported here would be related to the WAR β's by $\gamma^l_{lmn} = 2\pi l\beta_{lmn}$, $\gamma^m_{lmn} = 2\pi m\beta_{lmn}$ and $\gamma^n_{lmn} = 2\pi n\beta_{lmn}$. Thus $\gamma^l_{lmn}/l = \gamma^m_{lmn}/m = \gamma^n_{lmn}/n$. These relationships certainly hold for the highly symmetric combinations of lmn such as 111, 222, 200, 220, etc. However, for the less symmetric combinations, the above relationships are found not to hold. For example, from Table 2 for the 18·3 at. % Al alloy $\gamma^1_{113}/1 = 0\cdot022$, but $\gamma^3_{131}/3 = -0\cdot007$. Similarly from Table 3 for the 14·0 at. % Al alloy $\gamma^1_{113}/1 = 0\cdot036$, but $\gamma^3_{131}/3 = 0\cdot000$.

Since there are so few Al–Al nearest neighbor pairs in these alloys, 2 per cent in the 18·3 and 5 per cent in the 14·0 at. % Al alloy, it is possible to obtain a good approximation of the atomic displacements in the first coordination shell. For purposes of this calculation, it is assumed that there are no nearest neighbor Al–Al pairs. For the Fe-18·3 at. % Al alloy, the Fe–Fe nearest neighbor pairs are found to be closer than would be calculated from the average lattice by the amount;

$$\delta^{\mathrm{FeFe}}_{111} = -0\cdot0052\left(\frac{\mathbf{a}_1}{2}+\frac{\mathbf{a}_2}{2}+\frac{\mathbf{a}_3}{2}\right).$$

Since volume must be conserved for a given coordination shell, it is also possible to calculate the displacement of the Fe–Al closest neighbor pairs. These unlike nearest neighbors are found to be more widely separated than one would calculate from the average lattice by

$$\delta^{\mathrm{FeAl}}_{111} = 0\cdot0090\left(\frac{\mathbf{a}_1}{2}+\frac{\mathbf{a}_2}{2}+\frac{\mathbf{a}_3}{2}\right).$$

Similar calculations for the Fe-14·0 at. % Al alloy yield the following;

$$\delta^{\mathrm{FeFe}}_{111} = -0\cdot0047\left(\frac{\mathbf{a}_1}{2}+\frac{\mathbf{a}_2}{2}+\frac{\mathbf{a}_3}{2}\right),$$

and

$$\delta^{\mathrm{FeAl}}_{111} = 0\cdot012\left(\frac{\mathbf{a}_1}{2}+\frac{\mathbf{a}_2}{2}+\frac{\mathbf{a}_3}{2}\right).$$

It is interesting to compare the experimental atomic displacements parameters with some calculations based on a hard sphere model. For purposes of this comparison, it is assumed that both the Fe and Al atoms retain their pure state size, Fe having its normal eightfold coordination and Al having a hypothetical bcc structure[17]. Because there are so few Al–Al pairs in the first coordination shell, the calculated result is relatively insensitive to the choice of the size of the Al atom. On the basis of the hard sphere model, γ^1_{111} is calculated to be $-0\cdot327$ and $-0\cdot297$ for the Fe-18·3 and Fe-14·0 at. % Al alloys, respectively. Expressed alternately, these results give

$$\delta^{\mathrm{FeFe}}_{111} = -0\cdot0064\left(\frac{\mathbf{a}_1}{2}+\frac{\mathbf{a}_2}{2}+\frac{\mathbf{a}_3}{2}\right)$$

and

$$\delta^{\mathrm{FeAl}}_{111} = 0\cdot011\left(\frac{\mathbf{a}_1}{2}+\frac{\mathbf{a}_2}{2}+\frac{\mathbf{a}_3}{2}\right)$$

for the 18·3 at. % Al alloy. For the 14·0 at. % Al alloy, one finds

$$\delta^{\mathrm{FeFe}}_{111} = -0\cdot0040\left(\frac{\mathbf{a}_1}{2}+\frac{\mathbf{a}_2}{2}+\frac{\mathbf{a}_3}{2}\right)$$

and

$$\delta^{\mathrm{FeAl}}_{111} = 0\cdot010\left(\frac{\mathbf{a}_1}{2}+\frac{\mathbf{a}_2}{2}+\frac{\mathbf{a}_3}{2}\right).$$

These calculations of the nearest neighbor atomic displacements based on the hard sphere model are in sufficiently good agreement with the experimental results to indicate that it is reasonable, as a first order approximation, to assume that the Fe and Al atoms in solution maintain their pure state size. Thus, for the Fe–Al alloys very significant atomic displacements modulations in the diffuse scattering could have been predicted on the basis of this crude model.

5. GENERAL DISCUSSION

The results of the present investigation have shown that the Fe-rich Fe–Al terminal solid solutions quenched from 850°C are highly short-range ordered. The local atomic arrangements are such that a tendency toward the formation of a DO_3 type superlattice is distinguishable in the short-range structure, although there are also a greater number of second nearest neighbor Al pairs than might be expected on this basis alone. That there is some FeAl character in the local order is not surprising in view of the fact that B2 type superlattice reflections are possible in alloys containing as low as about 20·5 at. % Al as shown by Fig. 4 of part I. As has been pointed out in Part I, the FeAl character in the order appears to be most significant between about 480° and 530°C in alloys slightly less rich in Al than those for which long-range ordered DO_3 and B2 type superlattices have been shown to exist. It would be of interest if order coefficients were determined in this region.

The experimental order coefficients reported by Houska and Averbach[6] afford some comparison with the present results. They measured only the first three α's using surface ground polycrystalline samples. A direct comparison with the present results is not possible because of differences in composition and measuring temperatures. Nevertheless, both investigations are in general agreement that the atomic arrangement in the locally ordered alloys is tending toward a DO_3 type structure. There are some points, however, which appear to be in substantial disagreement. For example, the present results indicate that there are far fewer Al–Al nearest neighbor pairs in the 18·3 at. % Al alloy than Houska and Averbach reported. Furthermore, the previous work indicated little difference in the short-range order parameters of 14·8 and 18·2 at. % Al alloys; whereas, the present investigation indicates quite large differences in α_{111} for the 14·0 and 18·3 at. % Al alloys.

Houska and Averbach also reported a set of Warren–Averbach–Roberts size-effect coefficients. Again these coefficients cannot be compared directly to the present atomic displacement parameters for the same reasons that the order coefficients could not and also because of the inadequacies in the Warren–Averbach–Roberts treatment which have already been discussed. These difficulties being recognized, the two sets of measurements are in general agreement. Both investigations are in agreement that the size-effect parameter for the first coordination shell is negative and it is positive for the next two shells. In magnitude, too, the coefficients are in satisfactory agreement, except that the present single crystal measurements indicate that the values given by Houska and Averbach for β_{111} in the 14·8 at. % alloy are somewhat low.

If only Laue monotonic scattering modulated by short-range order and the first order atomic displacements effect is present in the distribution of diffuse intensity, the value of α_{000} should be unity. Abnormally large values of α_{000}, such as those observed in the present investigation, have plagued all previous investigators who have made quantitative measurements of short-range order parameters using single crystal samples and an independent method of standardizing the power in the incident beam[7, 18, 19]. There are several factors which could contribute to abnormally large values for α_{000}. These include parasitic scattering, fluorescence, absorption, polarization, incoherent scattering, errors in atomic scattering factors (including the dispersion correction), temperature diffuse scattering, Huang (second order atomic displacement) diffuse scattering, and standardization of the beam power. The methods used in the present investigation to eliminate or to correct for these effects have already been discussed.

A new technique for separating the order diffuse intensity from the components due to static atomic displacements (first and second order effects) and thermal motion has recently become available[20]. This technique, referred to here as the quadratic separation technique, should improve the correction of the data for Huang and thermal diffuse scattering. Although in the present investigation data was not collected in a volume in reciprocal space sufficient to permit this quadratic separation technique to be applied to recover three-dimensional α's, sufficient data was available for the 18·3 at. % Al alloy to permit recovery of two-dimensional order parameters, A_{lm}. The A_{lm}'s are given in terms of the α_{lmn} by

$$A_{lm} = \sum_{n} \alpha_{lmn}.$$

A direct comparison of the value of α_{000} using these two separation procedures is thus not possible. We may, however, compare values of A_{00} obtained from the two separation procedures. The value of A_{00} obtained from the older separation technique, namely 1·659 is significantly greater than the value of 1·145 obtained by the quadratic separation technique. This result appears to confirm that the thermal and Huang scattering corrections are partially responsible for the abnormally large values of α_{000}. If an error is involved which contributes a uniform background intensity throughout the repeat volume, only α_{000} would be affected. On the other hand, if an error is involved which is not constant in the repeat unit, other α's which characterize the shape of the intensity distribution will be altered also. A final decision on this will have to wait until three-dimensional data have been taken which can be analyzed according to both separation procedures. However, the shape of the order component of the diffuse intensity in the h_1h_20 plane obtained from the quadratic separation is not very different from the shape of this component obtained from the older separation technique. Hence, it is unlikely that low order α's, other than α_{000}, will be appreciably affected.

Acknowledgements—The authors wish to thank C. J. Sparks and B. S Borie for many useful discussions during the course of this investigation, and to express their appreciation to Sparks and J. V. Cathcart for reviewing this and the previous paper. The financial support of the National Aeronautics and Space Administration is also gratefully acknowledged.

REFERENCES

1. EPPERSON J. E and SPRUIELL J. E., *J Phys. Chem. Solids* **30**, 1721 (1969).
2. LAWLEY A. and CAHN R. W., *J. Phys. Chem Solids* **20**, 204 (1961).
3. DAVIES R. G., *J Phys Chem. Solids* **24**, 985 (1963).
4 VLASOVA Y. N, *Fiz metal. metalloved.* **16**, 355 (1963)
5 VLASOVA Y. N and IVERONOVA A. A., *Fiz. metal. metalloved.* **15**, 254 (1963).
6. HOUSKA C. R and AVERBACH B. L., *J. Phys Chem. Solids* **23**, 1763 (1962).
7. SPARKS C. J. and BORIE B. S., Local Atomic Arrangements Studied by X-ray Diffraction, *Metallurgical Society Conf. 36* (Edited by J. B Cohen and J. E. Hilliard), pp. 5–46 Gordon and Breach. New York (1966).
8 BORIE B. S. and SPARKS C. J, *Acta crystallogr* **17**, 827 (1964).
9. COWLEY J M., *J. appl. Phys.* **21**, 24 (1950).
10. WARREN B. E., AVERBACH B L. and ROBERTS B. W., *J. appl Phys.* **22**, 1493 (1951).
11. BORIE B, *Acta crystallogr.* **14**, 472 (1961)
12. FREEMAN A. J., *Phys Rev* **113**, 176 (1959).
13 FREEMAN A. J., *Acta crystallogr.* **13**, 618 (1960).
14. BATTERMAN B. W, CHIPMAN D. R. and De MARCO J. J., *Phys. Rev.* **122**, 68 (1961).

15. EPPERSON J. E. and SPRUIELL J. E., To be submitted for publication.
16. EPPERSON J. E., University of Tennessee Dissertation (1968).
17. TAYLOR A and JONES R. M., *J. Phys. Chem. Solids* **6**, 16 (1968).
18. MOSS S. C., *J. appl. Phys.* **35**, 3547 (1964).
19. AMMONS A. M. and SPRUIELL J. E., *J. appl. Phys.* **39**, 3682 (1968).
20. BORIE B. and SPARKS C. J., Jr., To be submitted for publication.

J. Phys. Chem. Solids Pergamon Press 1969. Vol. 30, pp. 1745–1750. Printed in Great Britain.

EXCHANGE CONSTANTS IN ORTHOFERRITES $YFeO_3$ AND $LuFeO_3$*

G. GORODETSKY
Department of Electronics, The Weizmann Institute of Science, Rehovot, Israel

(*Received* 1 *November* 1968)

Abstract—The exchange interaction with nearest neighbors J_1, next nearest neighbors J_2, and the spectroscopic splitting factor g were determined for two orthoferrites $YFeO_3$ and $LuFeO_3$. A high temperature analysis of the paramagnetic susceptibility yielded the following results: For $YFeO_3$, $J_1/k \approx -27{\cdot}2 \pm 1°K$, $J_2/k = -1{\cdot}2 \pm 0{\cdot}2°K$, $g = 2{\cdot}05 \pm 0{\cdot}1$, and for $LuFeO_3$, $J_1/k = -24{\cdot}2 \pm 1°K$, $J_2/k = -1 \pm 0{\cdot}1°K$, $g = 2{\cdot}00 \mp 0{\cdot}05$. Compatible values of J_1 were found from the low temperature susceptibility measurements and Néel point.

1. INTRODUCTION

THE ORTHOFERRITES $YFeO_3$ and $LuFeO_3$ represent a class of weak ferromagnets with a perovskite structure, in which the magnetically ordered ions lie approximately on a simple cubic lattice. Each iron ion is coupled through the O^{2-} ions by a superexchange to six nearest neighbors (n.n.) in an *essentially antiferromagnetic* ordering[1, 2]. Weak ferromagnetism arises from a canting of the predominantly antiferromagnetic spins, due to an antisymmetric exchange term, $-\mathbf{D}_{ij}(\mathbf{S}_i \times \mathbf{S}_j)$. This interaction tends to tilt the two interacting spins $\mathbf{S}_i$, $\mathbf{S}_j$ from a strict antiferromagnetic alignment in a plane perpendicular to the constant sector $\mathbf{D}_{ij}$. In the orthoferrites studied the vector $\mathbf{D} = \sum_{i>j} \mathbf{D}_{ji}$ coincides with the b-axis of the orthorhombic unit cell, the spontaneous magnetic moment lies along the c-axis and the antiferromagnetic direction is parallel to the a-axis.

Evidence indicating the existance of an antiferromagnetic coupling through more than one diamagnetic ion has been given by Blasse[3] for isostructural compounds in which the nearest neighbors to each iron ion on the Fe^{3+} sublattice are replaced by diamagnetic ions; e.g. Sr_2FeSbO_6. Here, the next nearest neighbors (n.n.n.) exchange interaction is found to be ~3 per cent of the n.n. interaction in rare earth orthoferrites. We therefore might expect a similar magnitude of n.n.n. coupling in the orthoferrites studied, $YFeO_3$ and $LuFeO_3$.

In Section 2 of this article the experimental techniques are described.

In Section 3 the derivation of the n.n. and the n.n.n. exchange interaction is carried out from the measurements of the paramagnetic susceptibility, using the high temperature expansion.† We also calculate the n.n. exchange interaction from measurements of the low temperature perpendicular susceptibility.

In Section 4 the results are compared with those obtained from the Néel point.

2. EXPERIMENTAL AND RESULTS

The magnetic susceptibility of some single crystals‡ of $LuFeO_3$ and $YFeO_3$ was measured at 4·2°K, and above the transition temperature T_N, (622° and 643°K, respectively)[2] to 1000°K. The measurements at 4·2°K were carried out using a motor driven vibrating sample magnetometer[5]. The sample was vibrated between pick-up coils mounted in a bore of a superconducting magnet wherein the magnetic field is applied parallel to the axis of vibration and the axis of the pick-up coils. The magnetic susceptibility was measured along the two principle crystallographic axes perpendicular to the antiferromagnetic a-axis. The results obtained at 4·2°K for $YFeO_3$ are: $\chi_b = (2{\cdot}8 \pm 0{\cdot}1)\ 10^{-3}$ (e.m.u./mole), $\chi_c = (2{\cdot}7 \mp 0{\cdot}1)\ 10^{-3}$ (e.m.u./mole) and for $LuFeO_3$, χ_b, $\chi_c = (2{\cdot}8 \pm 0{\cdot}2)\ 10^{-3}$ (e.m.u./mole). Where χ_b and χ_c donote the perpendicular susceptibilities along the orthorhombic axes b and c respectively.

---

*The research reported in this document has been sponsored in part by the Air Force Materials Laboratory Research and Technology Division AFSC through the European Office of Aerospace Research, United States Air Force Contract F61052-67C-0040.

†Preliminary results of the exchange constants in $LuFeO_3$ found by the high temperature analysis, have been used already for the expression of the paramagnetic susceptibility by a Padé approximant [4].

‡The single crystals were kindly provided by J. P. Remeika from The Bell Telephone Laboratories

The magnetic susceptibility was also measured in powder samples above the Néel point up to 1500°K. These measurements were done by a balance magnetometer. The value of the paramagnetic susceptibility was obtained from the measured susceptibility by substracting the calculated diamagnetic contribution[6]. The results obtained are presented in Fig. 1. Susceptibility measurements from above T_N up to ~1000°K were also done by a vibrating sample magnetometer wherein the magnetic field was applied perpendicular to the direction of vibration. The data obtained by the vibrating sample magnetometer agree to within 2 per cent with those obtained using the balance method.

The anisotropy in the susceptibility above the Néel temperature was measured in single crystals using a torquemeter. It was found that for $T/T_N > 1{\cdot}01$, the anisotropy $(\chi_i - \chi_j)/\chi_i < 0{\cdot}01$ $(i,j = a,b,c)$. This amount of anisotropy is negligible for our purposes.

3. ANALYSIS OF THE EXPERIMENTAL DATA

(i) *High temperature susceptibility*

The high temperature series expansion is an exact asymptotic series expansion for the susceptibility when $T > T_N$.

Rushbrooke and Wood[7] have calculated the first six terms for the nearest neighbors Heisenberg ferromagnet and antiferromagnet. Wojtowicz and Joseph[8], Dalton[9] and Pirnie *et al.*[10] have extended these calculations to next nearest neighbors interactions for which, in the presence of an external magnetic field H, the Heisenberg Hamiltonian has the form:

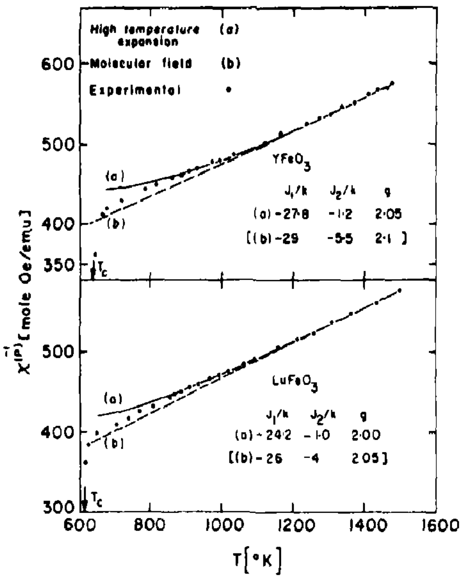

Fig. 1. The inverse paramagnetic susceptibility $\chi^{(p)^{-1}}$ vs. temperature for $LuFeO_3$ and $YFeO_3$. The value of $\chi^{(p)}$ were obtained by subtracting the calculated diamagnetic contribution from the experimental values measured by a balance magnetometer

$$\mathcal{H}_1 = -2J_1 \sum_{<i,j>} \mathbf{S}_i \cdot \mathbf{S}_j - 2J_2 \sum_{<i,j>} \mathbf{S}_i \cdot \mathbf{S}_j - g\mu_B \mathbf{H} \sum \mathbf{S}_i. \quad (1)$$

The first term represents the n.n. interaction with an exchange integral J_1. The summation is carried out over all pairs of n.n. The second term represents the n.n.n. with an exchange integral J_2, where the summation extends over all pairs of n.n.n. Zeeman energy for the entire crystal is represented by the third term. Here, μ_B denotes Bohr magneton and g is a spectroscopic splitting factor. Assuming that the ratio $\alpha = J_2/J_1 \simeq 0{\cdot}03$ deduced previously for a similar perovskite structure, Sr_2FeSbO_6 as noted above, holds also for the orthoferrites we find that the antisymmetric exchange energy and the anisotropy energy are significantly smaller than the n.n.n. exchange interaction[11–13]. We shall therefore confine our discussion to the Hamiltonian (1) and thus the high temperature series for the inverse susceptibility may be written in the form[8]:

$$\chi^{-1} = T/C \sum_{n,m}{}' (1+b_{nm}(J_1/kT)^n (J_2/kT)^m) \tag{2}$$

where T denotes temperature, C is the Curie constant and k is the Boltzman constant. The prime in the summation sign exclude $m = n = 0$. Numerical expressions for the coefficients b_{nm} up to $n+m = 6$ have been tabulated by Pirnie *et al.*[10].

The determination of the exchange integrals J_1, J_2 and the Curie-Weiss constant C was undertaken by fitting equation (2) to the experimental results, using a least squares method to obtain the best fit[8, 14]. The fitting procedure was carried out systematically for points with physical validity in a plane defined by J_1 and C. Values of J_2 were chosen for each set (J_1, C) to give least mean square deviation [14]. The three parameters were then determined from the coordinates J_1, J_2 and C of the point that had the smallest deviation. The error in determining J_1, J_2 and C due to the convergence properties can be estimated by calculating these parameters in different temperatures regions where the convergence of the power series equation (2) is fairly rapid. The results obtained for $YFeO_3$ are presented in Table 1. No well defined minima were found in the region 1000°K < T < 1500°K, the accuracy in determining J_1, J_2 and C for each temperature region is better than the spread of the results given in Table 1 (e.g. in the region $2{\cdot}5 > T/T_c > 1{\cdot}5$, a deviation of 1 per cent in J_1 and C increases the root mean square deviation, by a factor ~2. At this point (J_1, C) a deviation of 10 per cent in J_2 causes the same increase in the root mean squares deviation). The same analysis was undertaken for $LuFeO_3$. The results obtained from the temperature region 850°K < T < 1500°K are $J_1/k = -24{\cdot}2$°K, $J_2/k = -1{\cdot}0$°K, $C = 4{\cdot}35$ (e.m.u. °K/mole).

Table 1. The exchange constants and the Curie constant in $YFeO_3$ *as obtained by fitting the high temperature series expansion to the experimental data in various temperature regions*

Temperature region	$J_{1/k}$ (°K)	$J_{2/k}$ (°K)	C (e.m.u. °K/mole)
$1500 > T > 850$°K	−27·2	−1·2	4·61
$1500 > T > 900$°K	−27·4	−1·2	4·63
$1500 > T > 950$°K	−27·8	−1·2	4·67
$1500 > T > 1000$°K	−27·9	−1·4	4·69

It is of interest to consider the molecular field approximation in the same temperature range. Using a least squares fitting the Curie constant C and the paramagnetic Curie-Weiss temperature θ_p can be determined from the well known relation $\chi^{(p)} = C/(T-\theta_p)$ where $\chi^{(p)}$ is the paramagnetic susceptibility. It was found that $\theta_p = -1400$°K for $YFeO_3$ and $\theta_p = -1200$°K for $LuFeO_3$. The exchange constants were calculated from θ_p and T_N using the following relations for a simple cubic lattice[15]:

$$T_N = \frac{2S(S+1)}{3k}(-6J_1+12J_2).$$

$$\theta_p = \frac{2S(S+1)}{3k}(6J_1+12J_2). \tag{3}$$

Here $S = 5/2$ is the spin value of a S-state ion, Fe^{3+}. The results obtained for J_1, J_2 and the spectroscopic splitting factor $g = \sqrt{3kC/N\mu_B^2S(S+1)}$ are given in Table 2.

(ii) *Low temperature susceptibility*

According to the molecular field theory for a weak ferromagnet, the susceptibility along the orthorhombic axes, b and c (perpendicular to the antiferromagnetic a-axis) is temperature independent and given by[13]:

$$\chi_\perp = Ng^2\mu_B^2/4Z_1|J_1|. \tag{4}$$

Here, χ denotes a molar perpendicular susceptibility. Equation (4) is the same as the

Table 2. *The exchange constants with n.n. and n.n.n.,* J_1/k *and* J_2/k *respectively and the spectroscopic splitting factor* g, *as derived by various theories*

	Theory	YFeO$_3$			LuFeO$_3$		
		J_1/k (°K)	J_2/k (°K)	g	J_1/k (°K)	J_2/k (°K)	g
(1) Paramagnetic susceptibility	Molecular field	−29	−5·5	2·1	−26	−4	2·05 ± 0·1
	High temperature expansion	−27·2 ± 1	−1·2 ± 0·2	2·05 ± 0·1	−24·2 ± 1	−1 ± 0·1	2·0 ± 0·05
(2) Néel temperature	Rushbrooke & Wood	−28			−27		
(3) Perpendicular susceptibility	Molecular field & Green-function R.P.A	−23 ± 1			−22·5 ± 2		
(4) Sublattice magnetization	Spin wave[19]	−25 ± 2			−25 ± 2		

well known expression for the perpendicular susceptibility of a pure antiferromagnet. An identical expression for $\chi_\perp$ in an antiferromagnet is given by the random phase approximation[16]. Other approaches such as Callen decoupling and the Oguchi spin wave theories yield within the first order approximation the same results[16]. The numerical values are summarized in Table 2.

4. DISCUSSION

The analysis of the paramagnetic susceptibility by the high temperature expansion was found to be a useful approach for determining the exchange interactions and the g factor in the orthoferrites $YFeO_3$ and $LuFeO_3$. In both cases the quantities J_1, J_2 and g, given in Table 2, yielded a well defined minima in the fitting procedure. The results obtained for the n.n. interaction are in reasonable agreement with those obtained from the low temperature susceptibility (see Table 2). The ratio $\alpha = J_2/J_1 \simeq 0{\cdot}05$, obtained for the two perovskites is supported by the value found in the isomorphic structure Sr_2FeSbO_6. The g factor calculated from the Curie constant C by the high temperature analysis ($g_{YFeO_3} = 2{\cdot}05 \pm 0{\cdot}1$, $g_{LuFeO_3} = 2{\cdot}00 \pm 0{\cdot}05$) are in the agreement with the expected one for an S-state ion. By comparing these results with the one obtained by the molecular field theory (see Table 2) it is apparent that the latter are rather poor; J_2 in this case is significantly too high.

Additional experimental data from which the exchange interaction can be derived is the Néel temperature. Rushbrooke and Wood[17] have determined the antiferromagnetic ordering temperature for a Heisenberg antiferromagnet having only n.n. interaction, $T_N(\alpha = 0)$ $(\alpha = J_2/J_1)$ from the high temperature staggered susceptibility. The result is:

$$T_N(\alpha = 0) = 5/192(J_1/k)(z_1 - 1) \times [11S(S+1) - 1][1 + 0{\cdot}63/z_1S(S+1)]. \quad (5)$$

The dependence of the transition temperature $T_N(\alpha)$ on the ratio J_2/J_1 was calculated by Tahir-Kheli *et al.*[18] using the random phase approximation. In the region where $\alpha \ll 1$, this dependence to the first approximation is linear in α. For a simple cubic lattice one finds

$$m = 1/T_N(\alpha = 0)\frac{\mathrm{d}T_N(\alpha)}{\mathrm{d}\alpha} \simeq -2. \quad (6)$$

A similar result is obtained from the molecular field theory, where $m = -2{\cdot}0$. The solution of equation (6) yields.

$$T_N(\alpha) \simeq T_N(\alpha = 0)[1 - 2\alpha], \quad \alpha \ll 1. \quad (7)$$

The exchange constant J_1 was calculated from $T_N(\alpha)$ using equations (5) and (7). The results obtained for J_1 are presented in Table 2.

Eibschütz *et al.*[19] have evaluated the n.n. exchange interaction in the orthoferrites using Oguchi spin wave theory. The value of J_1 was extracted by fitting of the experimental low temperature sublattice magnetization to the dependence by spin wave theory. The results obtained for J_1 (see Table 2) are in agreement with those derived from the low temperature susceptibility. It should be noted that the values of the exchange constant J_1 obtained from the low temperature region are on the average lower than those obtained from the high temperature region. The dependence of the exchange integral on the thermal expansion could be roughly estimated from the relation $\partial \ln T_N/\partial \ln v \simeq 2$ that was found for the orthoferrites[2]. Here v denotes the volume of a unit cell. The use of an average thermal expansion coefficient for ceramics ($\sim 5 \cdot 10^{-5}$, cubic) should yield a decrease of ~ 5 per cent over the entire temperature range. This effect would lead to a better agreement between the observed values for J_1.

Acknowledgements—The author thanks Professor R. Pauthenet for his kind hospitality in CNRS, Grenoble, where part of the reported measurements were carried out. He is indebted to Professor S. Shtrikman for guidance and helpful suggestions

REFERENCES

1. TREVES D., EIBSCHUTZ M. and COPPENS P., *Phys. Lett.* **18**, 216 (1965).
2. TREVES D., *J. appl. Phys.* **36**, (part 2) 1033 (1965).
3. BLASSE G., *Philips Res. Rep.* **20**, 327 (1956).
4. GORODETSKY G., *Solid State Commun.* **6**, 159 (1968).
5. FLANDERS P. J. and DOYLE W. D., *Rev. scient. Instrum.* **33**, 691 (1962).
6. SELWOOD P. W., In *Magnetochemistry*, 2nd Edn., p 78, Interscience, New York (1956).
7. RUSHBROOKE G. S. and WOOD P. J., *Molec. Phys.* **1**, 257 (1958).
8. WOJTOWICZ P. J. and JOSEPH R. I., *Phys. Rev.* **135**, A1314 (1964).
9. DALTON N. W., *Proc. phys. Soc.* **88**, 659 (1966)
10. PIRNIE K., WOOD P. J. and EVE J., *Molec. Phys.* **11**, 551 (1966).
11. TREVES D., *Phys. Rev.* **125**, 1843 (1962).
12. HERMANN G. F., *Phys. Rev.* **A133**, 1334 (1964).
13. GORODESTKY G., SHTRIKMAN S., TENNENBAUM J. and TREVES D., To be published.
14. JOSEPH R. I., *Phys. Rev.* **A138**, 1441 (1965).
15. NAGAMIYA T., YOSHIDA K. and KUBO R., *Advan. Phys.* **4**, 1 (1956).
16. ANDERSON B. and CALLEN H. B., *Phys. Rev.* **A136**, 1068 (1964).
17. RUSHBROOKE G. S. and WOOD P. J., *Molec. Phys.* **6**, 409 (1963).
18. TAHIR-KHELI, CALLEN H. B. and JARRET H., *J. Phys. Chem. Solids* **27**, 23 (1966).
19. EIBSCHÜTZ M., SHTRIKMAN S. and TREVES D., *Phys. Rev.* **156**, 562 (1967).

J. Phys. Chem. Solids Pergamon Press 1969. Vol. 30, pp. 1751–1761. Printed in Great Britain.

ELECTRON PARAMAGNETIC RESONANCE SPECTRA FROM GAMMA-IRRADIATED POTASSIUM THIOCYANATE

ROGER KEWLEY

Department of Chemistry, Queen's University, Kingston, Ontario, Canada

(*Received* 20 *August* 1968; *in revised form* 22 *January* 1969)

Abstract—The electron paramagnetic resonance spectra of two distinct radical species have been observed following the gamma-irradiation of potassium thiocyanate single crystals. The spectrum of the first species appears when a crystal is irradiated at 77°K. For this radical there are two magnetic sites, each characterized by principal g values $g_{\parallel} = 2{\cdot}004$ and $g_{\perp} = 2{\cdot}025$ and by principal values of the hyperfine coupling tensor $A_{\parallel} = 8{\cdot}9$ and $A_{\perp} = 1{\cdot}4$ Mc/s. For the two sites the radical axis makes angles of 22° and 158° with the (010) axis and in each case the radical axis lies in the (100) plane of the crystal. The five line hyperfine pattern shows that this radical contains two equivalent N^{14} nuclei and it is identified as the V-center $(NCS)_2^-$. The spectrum of the second radical is observed in the temperature range 103°–181°K. This species is also situated at two magnetic sites and has principal g values 2·034, 2·018 and 2·014. It exhibits a three line hyperfine pattern from one N^{14} nucleus, the principal values of the hyperfine coupling tensor being 5·6, 6·6 and 6·4 Mc/s. The nature of this second radical is discussed.

INTRODUCTION

IT HAS BEEN found that solid carbonyl sulfide, OCS, may be photolyzed by u.v. radiation at 77°K to yield long chain sulfur radicals which give an electron paramagnetic resonance spectrum[1]. It is also known that low temperature X-irradiation of alkali halide crystals produces oriented (halogen)$_2^-$ V_k-centers[2] and that the analoguous radical $(CN)_2^-$ is formed when sodium or potassium cyanide or potassium chloride doped with cyanide is irradiated at 77°K[3]. Gamma-irradiation of potassium azide at 77°K gives *N* atoms and the radicals N_2^- and N_4^-[4] and the latter two species may also be produced by u.v. photolysis of KN_3[5]. Nitrogen atoms have been found to be present in sodium azide following irradiation with X-rays[6].

It was therefore judged to be of considerable interest to investigate the effects of both u.v. and gamma radiation on potassium thiocyanate, KNCS, in which the NCS^- ion is isoelectronic with the OCS molecule and yet, being an ion derived from a pseudohalogen, is also chemically related to the ions (halogen)$^-$, CN^- and N_3^-.

EXPERIMENTAL PROCEDURE

In order to test the behavior of potassium thiocyanate under conditions closely similar to those used in the OCS study, u.v. irradiation of polycrystalline potassium thiocyanate was carried out at 77°K The sample, which was about 4 cm in length, was sealed in a 3 mm quartz EPR tube which was then placed in the V-4546 quartz liquid nitrogen dewar and subjected to radiation from an Osram high pressure mercury lamp for a period of three hours. The lamp was placed 3–5 cm from the sample as in the OCS investigation[1]. During irradiation the KNCS sample remained colorless; and when the dewar containing the sample tube was transfered at once to the cavity of the spectrometer, no EPR signal could be detected near $g = 2$. The temperature of the sample was maintained at 77°K throughout

When a similar sample was exposed to the gamma-radiation from a 12·3 k Co^{60} source for 30 min at 77°K, the crystals turned dark brown and gave a strong EPR absorption near $g = 2$ The gamma ray dosage was 4×10^{17} eV/g/min. Subsequent experiments were carried out using single crystals of KNCS, prepared in the manner described below, which were also gamma-irradiated for 30 min and maintained and studied initially at 77°K. A second dewar was employed when maintaining the single crystal sample at 77°K during gamma-irradiation. The transfer operation from this dewar to the V-4546 dewar was achieved very rapidly to prevent any loss of radicals. In this manner the possibility of observing an EPR signal due to the dewar was eliminated. The absorption due to the pyrex sample holder was much weaker than that due to the sample and for almost all orientations it did not overlap the sample signal. It was found unnecessary to take this weak signal into account when analyzing the KNCS spectra.

Single crystals of potassium thiocyanate were grown by dissolving reagent grade KNCS in acetone and then allowing the solvent to evaporate slowly at room temperature. Potassium thiocyanate is orthorhombic and crystals may also be grown by solvent evaporation from an aqueous solution[7] These crystals have the (100) and (010) faces predominating whereas the ones grown from acetone solution[7] were found to be elongated along the (010) or *b* axis with the (101) prisms developed. Similar crystals were obtained from acetone solution in the present investigation and the observed EPR spectra from them are in agreement with the assignment of the crystal faces, see Fig. 1 It is quite possible that a small amount of impurity (~ 1 per cent) might have been introduced during the crystallization procedure. However, the signals from the polycrystalline and single crystal KNCS samples are sufficiently alike in intensity and *g* value spread that they can be identified as due to the same species. Also the analysis of the single crystal spectrum given below is entirely consistent with the signal being due to KNCS itself rather than to any impurity. In order to counteract the deliquescence of KNCS the crystal was dipped momentarily in hot paraffin wax. In this way one crystal could be preserved so that its spectra for rotation about three perpendicular axes could be obtained The presence of the wax did not have an observable effect on the spectra. After being coated with wax the crystal was attached to a 2 mm pyrex rod by means of silicone grease. The crystal orientation was determined by means of growth faces. The main error in the measurements stems from the difficulty in orienting the wax-covered crystal on the end of the rod. The orientation error was found to be as much as 8° in some cases. The rod was mounted on a scale calibrated in degrees. No evidence was found for twinning. The number of radical sites observed for each radical species in the investigation is consistent with a single crystal having been used in taking each set of observations.

The spectrometer used throughout the investigation was a Varian model 4502 equipped with a 12 in. magnet which was operated at a field close to 3330 G. The magnetic field was modulated at 100 kc/s for the sample cavity and at 400 c/s for the standard cavity of the V-4532 dual cavity accessory. The standard used was a solution containing the *p*-benzosemiquinone ion, which was taken to have a *g* value of 2·0057 ± 0·0004 and a hyperfine separation of 6·54 ± 0·06 Mc/s between the adjacent peaks of the 1:4:6:4:1 pattern[8]. The frequency was near 9·3 Gc/s and was measured to an accuracy of 0·1 per cent with a Hewlett Packard X532B frequency meter. Frequency readings were taken before and after the spectrum was recorded for a particular orientation of the crystal. For work at temperatures above 77°K the V-4557 variable temperature accessory was employed together with a thermocouple, allowing temperatures to be measured to ± 3°K.

RESULTS

(i) *Spectra from a KNCS single crystal gamma-irradiated and maintained at 77°K*

The EPR spectrum characteristic of a single crystal irradiated at 77°K and kept at that temperature is, for a particular orientation, one consisting of two groups of lines, each group being made up of five hyperfine components with an intensity distribution 1:2:3:2:1, see Fig. 2. Both the hyperfine

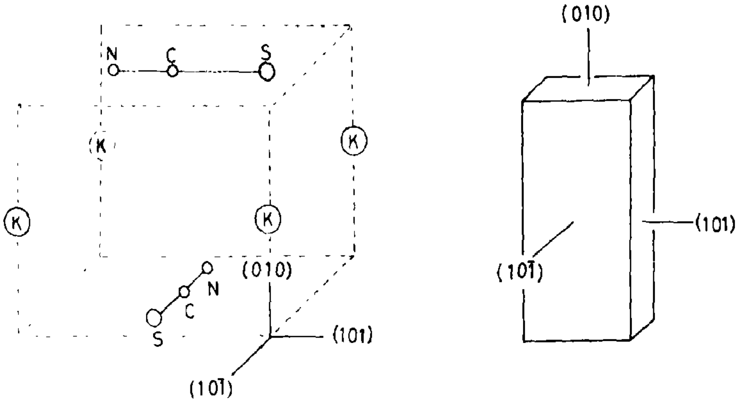

(a) (b)

Fig. 1. (a) Atomic positions in the crystal structure of potassium thiocyanate, after Klug[7] (b) Form of crystal and axes of rotation used in the present investigation.

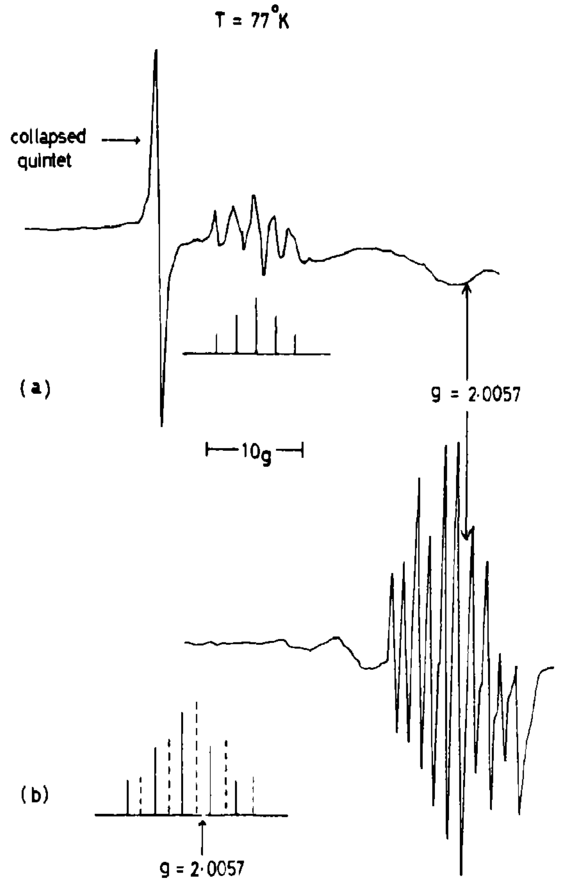

Fig. 2. Traces of first derivative electron paramagnetic resonance absorption spectra from a single crystal of potassium thiocyanate, gamma-irradiated and maintained at 77°K. The frequency is 9325 Mc/s. The axis of rotation is (101). (a) Field direction 75° from (010), showing near maximum *g* and near minimum hyperfine splitting for one site and intermediate values for the other site. (b) Field direction 5° from (010), showing near minimum *g* and near maximum hyperfine splitting for both magnetic sites. In the 'stick' diagram the peaks due to the two sites are differentiated by use of dashed and continuous lines.

separation and the *g* value corresponding to the center line of a group are markedly dependent on the orientation of the crystal with respect to the applied magnetic field, see Fig. 3. For a given orientation the group of lines situated at higher field or having a lower *g* value at its center line is more intense than the group appearing at lower field. For either group the intensity maximum corresponds with the maximum observed hyperfine splitting. When both groups are exhibiting approximately maximum hyperfine splitting their intensities become equal, see Fig. 2(b).

When the crystal is rotated about the (010) axis the hyperfine splitting remains small at all angles while the *g* values for both group centers stay close to the maximum value. For rotation about the (101) and $(10\bar{1})$ axes the variations in the hyperfine splitting and *g* are more pronounced with the minimum *g*

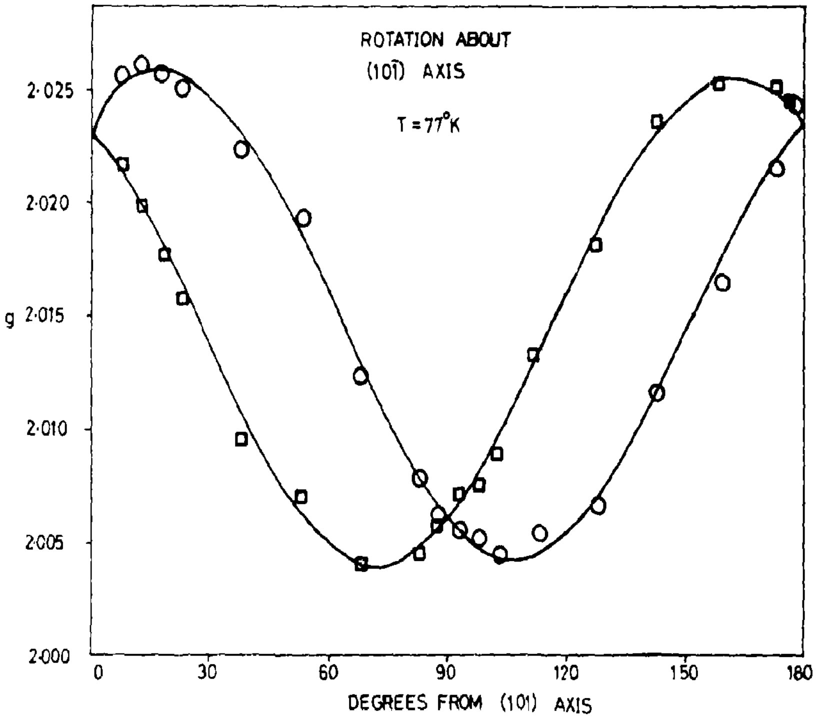

Fig. 3. Variation of g with orientation for the two sites of the radical present in a potassium thiocyanate single crystal following gamma-irradiation at 77°K. The frequency is 9323 Mc/s. The solid lines are the least squares fits to the experimental data for the two magnetic sites. □ site 1; ○ site 2.

occurring at the same angle as the maximum hyperfine splitting and vice versa. The spectra observed for rotation about the (101) and (10$\bar{1}$) axes are equivalent. The whole spectrum can be attributed to a single radical containing two equivalent N^{14} nuclei and situated at two magnetic sites in the crystal lattice. The principal values of the spectroscopic splitting factor g and the hyperfine coupling tensor A are given in Table 1, from which it may also be seen that the principal axes of the two tensors coincide. The errors in the values of g and A stem from the difficulty of resolving the closely spaced hyperfine components when rotation is being carried out about the (010) axis.

(ii) *Spectra observed at temperatures above 77°K*

When the temperature of the irradiated sample in the EPR spectrometer cavity was raised gradually a new spectrum appeared,

Table 1. Principal values and axes of the g *and* A *tensors for the paramagnetic species formed at 77°K*

g	A (Mc/s)	Direction of axis
$g_{\parallel} = 2{\cdot}004 \pm 0{\cdot}004$	$A_{\parallel} = 8{\cdot}9 \pm 0{\cdot}5$	Site 1: 22° to (010) axis in (100) plane
		Site 2: 158° to (010) axis in (100) plane
$g_{\perp} = 2{\cdot}025 \pm 0{\cdot}004$	$A_{\perp} = 1{\cdot}4 \pm 0{\cdot}5$	Perpendicular to $g_{\parallel}$-$A_{\parallel}$ axis

being first observed at 103°K. At that temperature the new signal overlapped with the original five line patterns for some orientations. The new spectrum consists of a pair of three line groups, each with intensity distribution 1 : 1 : 1, showing the production of a radical containing one N^{14} nucleus. This radical occupies two magnetic sites in the crystal. The intensities of the two triplets vary with orientation, the one at higher field having the greater intensity. By a temperature of 110°K the original five line patterns are about to disappear, leaving the three line groups, see Fig. 4. A search 500 G on either side of the three line groups showed that they are the only ones in the region.

Table 2. Principal values and axes of the g *and* A *tensors for the paramagnetic species present between* 103° *and* 181°*K*

g	A(Mc/s)	Direction of axis	
2·014 ± 0·002	6·4 ± 0·3	Site 1: (010)	Site 2 (010)
2·018 ± 0·002	6·6 ± 0·3	(101)	$(10\bar{1})$
2·034 ± 0·002	5·6 ± 0·3	$(10\bar{1})$	(101)

The presence of three hyperfine components in each of the two groups of lines in the spectrum suggests that the species responsible might be the nitrogen atom. However, even with only one magnetic site populated it would be expected that three triplets would occur because of zero field splitting effects in addition to the nuclear spin-electron spin hyperfine interaction. Also if fine structure were present the line positions would be slightly temperature dependent, due to variation of the fine structure parameters D and E. No temperature dependence was detected over the range 103°–178°K, indicating a lack of fine structure. This, together with the fact that only two triplets are observed, shows that

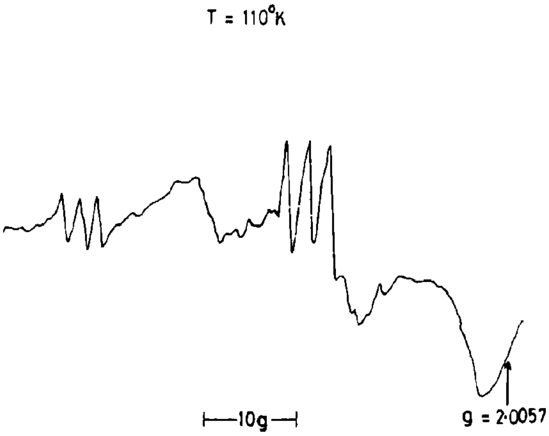

Fig. 4. Trace of first derivative electron paramagnetic resonance spectrum from a potassium thiocyanate single crystal which was irradiated at 77°K and then warmed to 110°K and maintained at that temperature. The frequency is 9256 Mc/s and the magnetic field is parallel to the (101) direction. Between the two three line groups can be seen a broad absorption due to the species originally present at 77°K.

Rotation of the crystal around the (010) axis at 120°K shows that the two radicals become magnetically equivalent when the field is directed along the (100) axis or along the (001) axis, see Fig. 5. These results combined with those for rotation about the (101) and $(10\bar{1})$ axes show that the radical occupies sites which have the maximum g along the (101) axis in one case and along the $(10\bar{1})$ axis in the other as shown in Table 2.

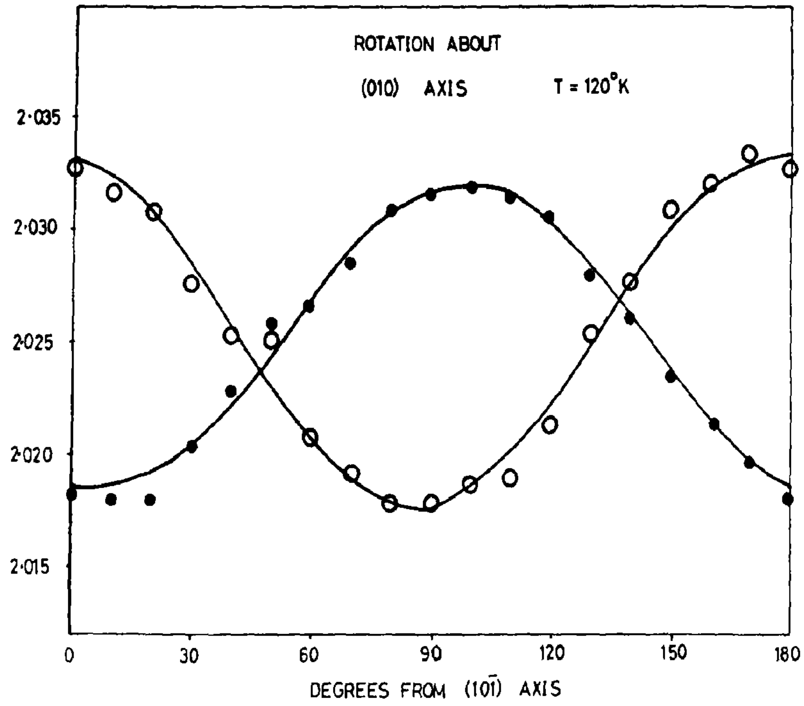

Fig. 5. Variation of g with orientation for the two sites of the radical produced by gamma-irradiation of a potassium thiocyanate single crystal at 77°K followed by warming above 103°K. The frequency is 9254 Mc/s. The solid lines are the least squares fits to the experimental data for the two magnetic sites, which become magnetically equivalent at 45° and 135°. ○ site 1; ● site 2.

the radical has only one unpaired electron and therefore cannot be the nitrogen atom. Studies carried out at different power levels, from 0·0003 to 0·3 mW at 77°K and from 0·003 to 3 mW at 110°K, failed to reveal the presence of any further paramagnetic species. The power variations were carried out in 10 dB steps at both temperatures.

When the spectrum was recorded initially at 110°K and then the temperature was returned to 77°K the three line spectrum increased in intensity as did also the five line pattern to a smaller extent, showing that the transition from one species to the other is apparently not a reversible process. A study was undertaken of the disappearance of the three line spectrum at higher temperatures. Starting from a temperature of 132°K it was found that a rapid decay of the signal began above 143°K and that the spectrum finally disappeared at 181°±5°K.

DISCUSSION

(i) *Species observed at 77°K*

The EPR spectrum of the radical present following gamma-irradiation at 77°K can be accounted for by the Hamiltonian:

$$\mathcal{H} = \beta H \cdot g \cdot S + I_{(1)} \cdot A \cdot S + I_{(2)} \cdot A \cdot S$$

in which the interaction between the nuclear magnetic moment of each nitrogen and the applied field and also the interaction between the two nitrogen nuclear magnetic moments are neglected. The nuclear spin operators for C^{13} and S^{33} are not included as hyperfine splittings from these atoms were not observed at 77°K or at higher temperatures. The hyperfine interaction between the electron spin magnetic moment and the nuclear magnetic moment of nitrogen is considered to be sufficiently small that a first order perturbation treatment is satisfactory. The frequency expression is then

$$h\nu = \beta H_0 (g_\parallel^2 \cos^2\theta + g_\perp^2 \sin^2\theta)^{1/2} + KM_I$$

where

$$K^2 g^2 = A_\parallel^2 g_\parallel^2 \cos^2\theta + A_\perp^2 g_\perp^2 \sin^2\theta$$

and

$$g = (g_\parallel^2 \cos^2\theta + g_\perp^2 \sin^2\theta)^{1/2}$$

θ being the angle between the applied field and the radical axis. M_I takes the values 2, 1, 0, −1, −2. The numerical values for g and A are given in Table 1.

The value of $g_\perp = 2{\cdot}025$ suggests that the radical may contain sulfur because of the tendency towards larger spin-orbit interaction for atoms other than those in the first row of the periodic table. It is, however, unwise to rely heavily on the g value for the identification of a radical in a crystal since a number of radicals are known which contain only first row elements and yet which show large deviations from the free spin g value of 2·0023 and moreover exhibit large changes in g from one lattice to another; for example the O_2^- ion in NaO_2 has its principal g values in the range 2·002 − 2·175[9] but has a range 1·9512–2·4359 in a KCl lattice[10]. A more reliable way of identifying a radical appears to be by means of its hyperfine coupling constants, which are less sensitive to environmental changes than are the deviations of its principal g values from the free spin value. A possibility is that the radical under consideration here might be N_2^-, which is quoted by one group of authors as having principal A values of 11, 33 and 11 Mc/s[5] and by another group as having the values 11, 18 and 11 Mc/s[4], in both cases in a KN_3 lattice. These figures are quite different from those for the radical present at 77°K in the present study, see Table 1, and it can therefore be concluded that the radical N_2^- is not the one responsible for the spectrum.

A more likely possibility is that the entity $(NCS)_2^-$ is formed by ejection of an electron from an NCS^- ion to give NCS·, followed by the sharing of the resulting electron deficiency with a second NCS^-. The position of the principal $g_\parallel$ axis argues strongly for this model. If the points representing the S atom positions in two adjacent layers of the KNCS crystal structure are joined, see Fig. 1, a line is obtained the inclination of which to the (010) direction is 29°. This angle is to be compared with the observed inclination of 22° of the radical axis with the (010) direction. The fact that the results can be accounted for by an axially symmetric spin Hamiltonian shows that the dominating symmetry is that of the $(NCS)_2^-$ radical itself, which would be axially symmetrical with the proposed model, rather than the local crystal symmetry. Evidentally the unpaired electron is to some extent localized either between two N atoms or between two S atoms in the $(NCS)_2^-$ radical. To decide this question the hyperfine coupling constants must be considered in more detail.

Since the signs of $A_\parallel$ and $A_\perp$ are not determined there are four possibilities for the values of $A_{\text{iso}} = (2A_\perp + A_\parallel)/3$ and $2B = A_\parallel - A_{\text{iso}}$, where A_{iso} is the isotropic hyperfine coupling constant and $2B$ is the largest component of the anisotropic hyperfine coupling tensor, the other two components being $-B$. The possibilities are

(i) $A_\parallel = \pm 8{\cdot}9$; $A_\perp = \pm 1{\cdot}4$ Mc/s
$2B = \pm 5{\cdot}0$; $A_{\text{iso}} = \pm 3{\cdot}9$ Mc/s
$c_p^2 = 0{\cdot}0052$; $c_s^2 = 0{\cdot}003$

(ii) $A_\parallel = \pm 8{\cdot}9$; $A_\perp = \mp 1{\cdot}4$ Mc/s
$2B = \pm 6{\cdot}9$; $A_{\text{iso}} = \pm 2{\cdot}0$ Mc/s
$c_p^2 = 0{\cdot}072$; $c_s^2 = 0{\cdot}001$

where c_p^2 and c_s^2 are obtained by comparison of $2B$ and A_{iso} with the one electron atomic N values of 96 and 1540 Mc/s respectively [11]. Even with possibility (ii) only about 15 per cent of the unpaired electron density is concentrated on the two nitrogen atoms. This low spin density on nitrogen indicates that the unpaired electron is concentrated mainly between the two sulfur atoms, most probably in a molecular orbital of essentially $p\sigma$ character. For this model consideration of the values of the quantity $(3\cos^2\phi - 1)$ at various points leads to the conclusion that the anisotropic coupling constant for the $A_\parallel$ direction should be negative and that for the $A_\perp$ direction positive. ϕ is the angle between the $A_\parallel$ axis and the radius vector of the unpaired electron with a nitrogen nucleus taken as origin. Also the coupling constant for the $A_\parallel$ direction should be the largest in magnitude. These predictions agree with the observed values provided that the experimental $A_\parallel$ is taken to have a negative sign. The experimental $A_\perp$ can be assumed to have either a positive or a negative sign and still give a negative value for the quantity $2B$.

The species $(NCS)_2^-$ is an unusual case of a V_k type center, the only other similar radical known at present being the $(CN)_2^-$ radical in which the two carbon atoms are joined and the planar radical lies in the (100) plane of the KCl host crystal [3]. The $(NCS)_2^-$ radical differs from this insomuch as the join takes place between atoms in adjacent layers of the host lattice. The $(NCS)_2^-$ is thus not planar and the unpaired electron occupies a different type of molecular orbital from the one occupied in $(CN)_2^-$, since the possibility of the formation of a π system extending over all the atoms is ruled out. KNCS is observed to turn dark brown on gamma-irradiation. This suggests that data could be obtained which would complement the EPR results by carrying out a study of the optical absorption by the V_k center in a KNCS single crystal. Also the effect on the optical absorption of illumination with polarized light could be studied as in the work on Pb-doped KCl by Delbecq *et al.*[17].

(ii) *Species observed above* 103°*K*

The spectrum of the higher temperature species can be fitted to the Hamiltonian:

$$\mathscr{H} = \beta H \cdot g \cdot S + I \cdot A \cdot S$$

with spectroscopic constants as shown in Table 2. As noted above the lack of fine structure effects makes it most unlikely that the spectrum is due to the nitrogen atom. Also comparison of the observed hyperfine coupling constants with the isotropic coupling constant for the N atom of 15·3 Mc/s in KN_3 [4], 15·9 Mc/s in NaN_3[6] and 12·1 Mc/s in solid nitrogen [12], supports the same conclusion. The observed g values in the present case show considerable anisotropy, whereas the N atom has an isotropic g in either KN_3 or NaN_3 matrices.

For the species yielding the three line hyperfine pattern the principal axes located in the (010) plane are along the same directions as the axes of the NCS^- ions in the unirradiated KNCS crystal, which strongly suggests that the radical also contains the three atoms N, C and S but differs by one electron from the NCS^- ion. The two possibilities are therefore either $NCS\cdot$ or $NCS^=$. It would appear to be more favorable energetically for the $(NCS)_2^-$ radical to break down into $NCS\cdot$ and NCS^- so that in both of the products the highest energy electrons would be accommodated in weakly bonding π orbitals, assuming for the present that both $NCS\cdot$ and NCS^- would be linear. If, on the other hand, breakdown resulted in the formation of $NCS^=$, then an equivalent amount of NCS^+ should be formed. If bent, the latter would be diamagnetic but if linear, as expected, could be a biradical with two unpaired electrons occupying a degenerate π molecular orbital, see Fig. 6. No spectrum from the species NCS^+ was observed although it would probably be difficult to observe and would lie outside the $g = 2$ region. The annealing data is thus consistent with the occurrence of the process $(NCS)_2^- \rightarrow$

$NCS^- + NCS\cdot$ in the temperature range 77°–103°K, followed by the disappearance of the $NCS\cdot$ radical in the range 103°–181°K as diffusion becomes increasingly more possible.

In the free state the radical $NCS\cdot$ would be linear according to the Walsh correlation diagram for BAC molecules[13] since the unpaired electron in a fifteen valence electron molecule would occupy the highest bonding orbital, which correlates with an orbital of π symmetry if the molecule BAC is linear, see Fig. 6. For a bent molecule this becomes divided into two orbitals of symmetry A' and A'' for the C_s symmetry group, with the unpaired electron occupying the A' level. The A' level is of higher energy than the A'' level but is also of higher energy than the linear molecule π level so that the molecule tends to remain linear*. A free linear $NCS\cdot$ radical would therefore have the unpaired electron in an energy level degenerate as regards the x and y directions, where z is defined as the molecular axis for a molecule of symmetry $C_{\infty v}$. In that case two of the three g values should be exactly equal, which is not in accord with the observed values of Table 2. It seems quite impossible, however, that the $NCS\cdot$ radical could be slightly bent due to the crystal field. On account of the close equivalence of the (101) and $(10\bar{1})$ directions in KNCS such a distortion would probably take place along the (010) direction. Even allowing for the possible nonlinearity of the $NCS\cdot$ radical it is difficult to account for the observed g values, all of which are greater than the free spin value. To see this the symmetry of the ground state molecular orbital in which the unpaired electron is situated must be compared with that for each nearby energy level. The group theory relation which allows the estimation of $\Delta g_i = g_i - 2{\cdot}0023$ for a molecule of C_s symmetry is that g_i will deviate from the free spin value due to interaction between the ground state and a nearby state if the product of the representations of the two orbitals in the C_s group gives a representation which is that of rotation about the i axis[14]. The sign of Δg_i for a particular interaction is determined by whether the interacting energy level lies above or below the level which contains the unpaired electron in the ground state. For a bent $NCS\cdot$ radical the energy level immediately below the one containing the unpaired electron in the ground state is of symmetry A''. Since $A' \times A'' = A''$, which is the representation of R_x and R_y in the C_s group, and since the A'' level is of lower energy, then this interaction should result in increases of both g_x and g_y above 2·0023, where x and y are now defined as in the molecular plane for a molecule of C_s symmetry. Taking this to be the main interaction the observed values 2·014 and 2·018 could be assigned to the x and y directions. However if this is done, to account for the observed g_z of 2·034 it is necessary that a level of symmetry A' lie just below the ground state level of the unpaired electron and be even closer than the A'' level just discussed because the representation of R_z is A'. It may be seen from Fig. 6 that this requirement cannot be satisfied.

If the species present is instead taken to be $NCS^=$, there is less difficulty in giving a qualitative explanation of the observed g values. For this bent molecule the unpaired electron would be the seventeenth valence electron and would occupy the level of symmetry A' which correlates with the next highest and weakly antibonding orbital of the linear molecule. The $NCS^=$ could be bent to such an extent that the interaction between this level and the A' level just below could give the main contribution to Δg_z, which would be positive, with important contributions to Δg_x and Δg_y coming from interaction with the next lowest level of symmetry A''. In this way Δg_z could be larger than Δg_x and Δg_y.

It remains to attempt to differentiate be-

---

*In the flash photolysis of CH_3SCN and C_2H_5SCN the NCS radical is known to give an electronic absorption spectrum characteristic of a linear molecule. HOLLAND R., STYLE D. W. G., DIXON R. N. and RAMSAY D. A., *Nature* **182**, 336 (1958).

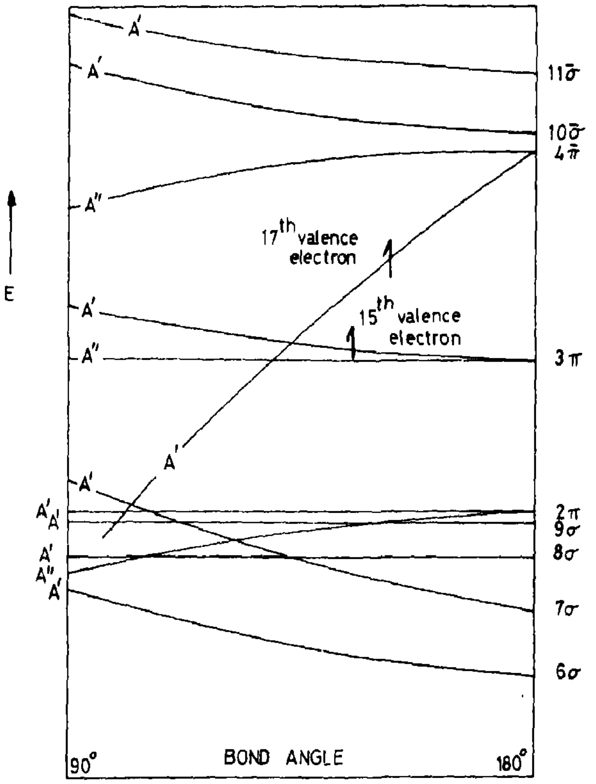

Fig. 6. Correlation diagram for a BAC triatomic molecule after Walsh[13] The order of the energy levels on the right hand vertical axis corresponds to that calculated by McLean and Yoshimine for the NCS^- ion[16]. The 15th and 17th valence electrons would be unpaired in the ground states of NCS· and $NCS^{=}$ respectively. The symmetries of the orbitals in the C_s group are shown as A' or A''.

tween the two possibilities NCS · and $NCS^{=}$ by consideration of the hyperfine coupling. Like the CO_2^- radical[15], the radical $NCS^{=}$ would have seventeen valence electrons and approximately the same bond angle of 128°. The unpaired electron in CO_2^- occupies the $4A_1$ orbital, which is made up largely of C(2s) and C($2p_z$) atomic orbitals, where the z axis bisects the OCO angle for the molecule of C_{2v} symmetry. Similarly in $NCS^{=}$ the unpaired electron would occupy a molecular orbital consisting mainly of carbon 2s and 2p orbitals and of symmetry A'. Again a consideration of the sign of $(3\cos^2\phi - 1)$ in various regions allows an estimation of the signs and relative magnitudes of the components of the anisotropic hyperfine coupling tensor. It is deduced that with the unpaired electron concentrated on the carbon the largest value of the N^{14} tensor corresponding to a principal axis would occur when the field is perpendicular to the molecular plane and that the sign in this case would be negative. The other two components of the anisotropic hyperfine tensor should be smaller with positive signs. As the observed coupling constant 5·6 Mc/s corresponds to the direction for which $g = 2{\cdot}034$, thought to be perpendicular to the molecular plane of $NCS^{=}$, then this coupling constant is taken to be negative and the other two values, 6·4 and 6·6 Mc/s, to be positive. This gives $A_{\text{iso}} = 2{\cdot}5$ Mc/s and the tensor (3·9, 4·1, −8·1) for the anisotropic part of the hyperfine coupling. This is in satisfactory agreement with the deductions from the $(3\cos^2\phi - 1)$ expression. The figure 8·1 Mc/s gives a value $c_p^2 = 0{\cdot}085$. That about 8 per cent of the unpaired electron be in a nitrogen p orbital is in satisfactory agreement with the assumed electronic configuration. This may be compared with the value of c_p^2 at each oxygen in CO_2^- which is 0·157. The observed hyperfine coupling is not incompatible with the NCS · radical, in which the unpaired electron would occupy the highest energy A' bonding orbital, assuming a bent molecule. This orbital would be largely made up of $N(2p_z)$, $C(2p_z)$ and $S(3p_z)$ atomic orbitals, still using z in the sense indicated for the C_s group. In this model the largest value of the anisotropic tensor would be of positive sign and would correspond to the field being approximately along the NS direction. The other two values would be smaller and of negative sign. Since the absolute signs of the experimental coupling constants are not known, it is not at present possible to distinguish between NCS · and $NCS^=$ solely on the basis of hyperfine interaction.

Acknowledgements—The author wishes to thank O. P. Strausz and Professor H. E. Gunning for helpful discussions. He is also indebted to F. W. Birss for help in setting up the computer programs and to G. Bigam for assistance in the initial stages of the experimental work.

REFERENCES

1. STILES D. A., KEWLEY R., STRAUSZ O. P. and GUNNING H. E., *Can. J. Chem.* **43**, 2442 (1965).
2. CASTNER T. G. and KÄNZIG W., *J. Phys. Chem. Solids* **3**, 178 (1957).
3. ROOT K. D. J. and SYMONS M. C. R., *J. chem. Soc.* **A1968**, 21.
4. WYLIE D. W., SHUSKUS A. J., YOUNG C. G. and GILLIAM O. R., *Phys. Rev.* **125**, 451 (1962).
5. HORST R. B., ANDERSON J. H. and MILLIGAN D. E., *J. Phys. Chem. Solids* **23**, 157 (1962)
6. CARLSON F. F., *J. chem. Phys.* **39**, 1206 (1963).
7. KLUG H. P., *Z. Kristallogr.* **85**, 214 (1933).
8. VENKATARAMAN B. and FRAENKEL G. F., *J. Am. chem. Soc.* **77**, 2707 (1955).
9. BENNETT J. E., INGRAM D. J. E., SYMONS M. C. R., GEORGE P. and GRIFFITHS J. S., *Phil. Mag.* **46**, 443 (1955).
10. KÄNZIG W. and COHEN M. H., *Phys. Rev. Lett.* **3**, 509 (1959).
11. MORTON J. R., *Chem. Rev.* **64**, 456 (1964).
12. FONER S. N., JEN C. K., COCHRAN E. L. and BOWER V. A., *J. chem. Phys.* **28**, 352 (1958).
13. WALSH A. D., *J. chem. Soc.* 1953, 2269.
14. see, for example, ATKINS P. W. and SYMONS M. C. R., In *The Structure of Inorganic Radicals*. App. 3 Elsevier, New York 1967
15. OVENALL D. W. and WHIFFEN D. H., *Molec. Phys.* **4**, 135 (1961).
16. MCLEAN A. D. and YOSHIMINE M., In *Tables of Linear Molecule Wave Functions*. IBM Corporation, New York (1967).
17. DELBECQ C. J., SMALLER B. and YUSTER P. H., *Phys. Rev.* **111**, 1235 (1958).

J. Phys. Chem. Solids Pergamon Press 1969. Vol. 30, pp. 1763–1767. Printed in Great Britain.

ISOMER SHIFTS OF ^{151}Eu IN DIVALENT EUROPIUM COMPOUNDS*

O. BERKOOZ†
Department of Electronics, The Weizmann Institute of Science, Rehovot, Israel

(*Received* 5 *December* 1968; *in revised form* 16 *January* 1969)

Abstract—The isomer shifts of the 21·6 keV. Mössbauer absorption of the ^{151}Eu nuclei, were studied in various divalent europium compounds. It is shown that the interpretation of the results, on the basis of covalency effects due to low electronegativity of the anions alone, is unsatisfactory. On the other hand it is shown that the isomer shift is very sensitive to the actual distances between the europium ions and their nearest neighbour anions.

INTRODUCTION

THE ISOMER shifts of the recoilless resonant absorption of the 21·6 keV. γ radiation in ^{151}Eu nuclei, were discussed in many articles[1–6]. The experimental values of the isomer shifts were found to be in the range between −15 mm/sec to +4 mm/sec, and to depend on the ionization states of the europium ions in the investigated compounds. The absorption lines, of divalent europium compounds, are shifted, with respect to Eu_2O_3 by −15 mm/sec to −10 mm/sec. The observed isomer shifts were interpreted[1, 3–5] as due to covalency effects which increase the s electron density at the Eu^{151} nuclei. It was believed that such effects increase as the electronegativity of the anions in the compound decreases[4]. However, no monotonic variation of the isomer shift with the electronegativity of the anions is found (Fig. 1). Thus, we suggested [7] that one should get more insight into the crystallographic structure of the investigated compounds, in order to get better understanding of the isomer shifts in divalent europium compounds.

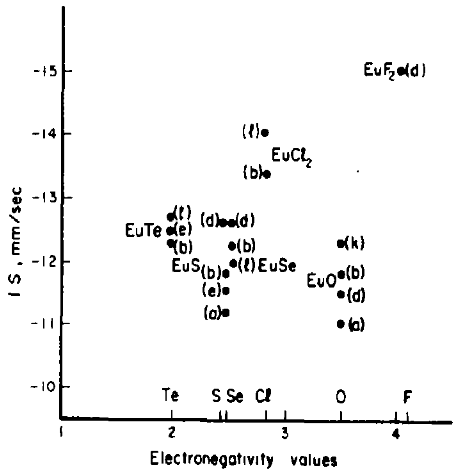

Fig. 1 Isomer shifts of some divalent europium compounds as a function of the electronegativity of the anions. No monotonic relation is found between these two quantities. (a) [18], (b) [19]; (d) [3]; (e) [1], (k) [20], (l) [21].

In order to clarify this problem, we measured the isomer shifts of the resonance lines of ^{151}Eu nuclei, in the three series of divalent europium compounds: sulfides, selenides and oxides. The results are given below, and are correlated with the crystallography of the compounds studied.

EXPERIMENTAL

The isomer shift measurements were carried out using a commercial constant acceleration

---

*The research reported in this document has been sponsored in part by the Air Force Materials Laboratory Research and Technology Division AFSC through the European Office of Aerospace Research, United States Air Force Contract F61052-67C-0040, and was done in partial fulfillment of the Ph.D requirements of the author.

†Department of Chemistry, Polytechnic Institute of Brooklyn, 333 Jay St., N.Y. 11201.

Mössbauer effect spectrometer[8]. The source was ^{151}Sm as a sesquioxide[9]. Apart from the measurement of the Eu_3S_4 (for reasons given in [10]), all the spectra were taken at room temperature. The velocity range of the spectrometer was set between −25 mm/sec to +20 mm/sec, and the reference velocity (zero velocity) was taken as the resonance absorption of the Eu^{151} nuclei in Eu_2O_3. The velocity scale of the spectrometer was calibrated with the resonance absorption of the ^{57}Fe nuclei in α-Fe_2O_3, and was checked with Eu_2O_3 and EuF_2 absorbers.

The results, as well as some crystallographic parameters, for the three series, are given in Tables 1-3. For 3 of the compounds we were able to find data in the literature, and these compared favourably with our results.

DISCUSSION

In view of the results, listed in the tables, it can be clearly seen that the isomer shifts, in each one of the series studied, are not limited to one value, as should be expected from electronegativity considerations. It is seen that the isomer shifts of the sulfides are found in the range (−11·9)mm/sec-(−13·8) mm/sec, those of the selenides are found between (−12·2) mm/sec and (−13·8) mm/sec and those of the oxides between (−12·6) mm/sec and (−14·1) mm/sec. Thus, the interpretation based on the electronegativity of the anions, is not completely satisfactory and it is suggested that the actual arrange-

Table 1. Isomer shifts of divalent europium sulfides. $\bar{d}$ is the mean Eu^{2+}–S^{2-} distance as was estimated from crystallographic considerations

Compound	Crystal structure	d Å (estimated)	Isomer shift ±0·2 (mm/sec)
$EuGd_2S_4$	Th_3P_4	2·94	−11·9
$EuEu_2S_4$	Th_3P_4	2·95	−12·6 (200°K)
$EuSm_2S_4$	Th_3P_4	2·96	−12·6
EuS*	NaCl	2·984	−12·7
$EuLa_2S_4$	Th_3P_4	3·02	−12·9
$EuSc_2S_4$	$CaFe_2O_4$	3·07	−13·0
$EuYb_2S_4$	$CaFe_2O_4$	3·13	−13·8
EuY_2S_4	$CaFe_2O_4$	3·16	−13·6

*References [1, 6, 18, 19].

Table 2. Isomer shifts of divalent europium selenides. $\bar{d}$ is the mean Eu^{2+}–Se^{2-} distance as was estimated from crystallographic considerations

Compound	Crystal structure	d Å (estimated)	Isomer shift ±0·2 (mm/sec)
$Eu_{0\cdot6}Gd_{0\cdot4}Se$	NaCl	2·985	−12·2
$EuNd_2Se_4$	Th_3P_4	3·09	−12·9
EuSe*	NaCl	3·095	−12·6
$EuLa_2Se_4$	Th_3P_4	3·14	−13·1
$EuSc_2Se_4$	$CaFe_2O_4$	3·17	−13·4
$EuLu_2Se_4$	$CaFe_2O_4$	3·25	−13·6
$EuHo_2Se_4$	$CaFe_2O_4$	3·28	−13·8
EuY_2Se_4	$CaFe_2O_4$	3·29	−13·8

*References [1, 6, 20].

Table 3. Isomer shifts of divalent europium oxides. $\bar{d}$ is the mean Eu^{2+}–O^{2-} *distances as is known from crystallographic data*

Compound	Crystal structure	$\bar{d}$ Å (estimated)	Isomer shift (mm/sec)
EuO*	NaCl	2·984	[1, 6, 18, 20]
Eu_3O_4†	$CaFe_2O_4$	2·711	−12·6 ± 0·1
$EuTiO_3$	Perovskite	2·75	−13·5 ± 0·1
$EuZrO_3$	Perovskite	2·96	−14·1 ± 0·2

*Not measured in this work.

†See also reference [11].

ments of the europium neighbours influence the isomer shifts in these compounds.

This suggestion is based on the experimental and calculated results of the isomer shifts of the ^{57}Fe resonance absorption lines in CoO and FeF_2[12–15]. It was shown by Simanek *et al.*[14,15] that applying pressure to the Mössbauer samples, results in a net increase of the *s* electrons density at the ^{57}Fe nuclei, as much as the interionic distances decrease. This is an effect of 'overlap distortion' of the electronic wave functions[16].

Assuming that this effect also holds for the europium ions in compounds, we plotted the isomer shifts, obtained from the spectra, as a function of the mean ionic distances $\bar{d}$, between the divalent europium ions and their nearest neighbours divalent anions (Figs. 2–4). (In Fig. 4 we also included the results obtained from EuO from the literature). Since not all the $\bar{d}$ values had been known, we estimated them from crystallographic considerations[7](Appendix).

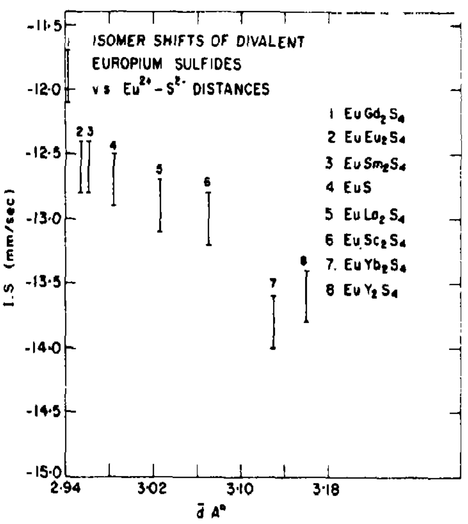

Fig. 2. Isomer shifts of divalent europium sulfides vs. Eu^{2+}–S^{2-} mean distances $\bar{d}$. The $\bar{d}$ values were estimated by crystallographic considerations [7] (Appendix).

The plotted results, of the isomer shift vs. $\bar{d}$, show a monotonic increase of the isomer shift (towards the positive velocity) as the mean ionic distances $\bar{d}$ decrease, thus indicating the increase of the *s* electron density at the ^{151}Eu nuclei. Such an increase of the *s* electron densities at the nuclei was found also in the pressure induced isomer shifts in ^{57}Fe nuclei[12–15]. We thus suggest that the same effect occurs here with the exception that instead of applying pressure to one sample we use the differences of the ionic distances in the various compounds.

The influence of the electronegativity of the anions on the isomer shifts is mostly seen in the longer $\bar{d}$ limits of the 3 series of compounds. Since the electronegativity of *S* and Se is nearly the same (2·44 and 2·48)[17], it seems that the isomer shifts of the sulfides and the selenides in this limit are the same, while the isomer shift found in the oxides, for long $\bar{d}$, is more negative, because of the higher electronegativity of the oxygen.

Finally it should be noted that, by invoking

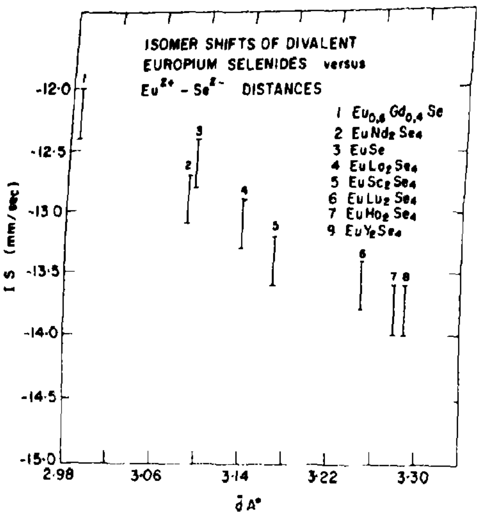

Fig. 3. Isomer shifts of divalent europium selenides vs. $Eu^{2+}-Se^{2-}$ mean distances $\bar{d}$. The $\bar{d}$ values were estimated by crystallographic considerations [7] (Appendix).

overlap distortion effects, we are able to understand the isomer shift in EuO, which has not been understood on the basis of the electronegativity considerations[4].

Acknowledgements—The author wishes to thank Professor S. Shtrikman for his interest; Dr. F. Hulliger for supplying us with the samples of $EuGd_2S_4$, $EuLa_2S_4$, $EuSc_2S_4$, $EuYb_2S_4$, EuY_2S_4, $EuNd_2Se_4$, $EuLa_2Se_4$, $EuLu_2Se_4$, $EuHo_2Se_4$ and EuY_2Se_4, Dr. R. C. Rau for his Eu_3O_4 sample, Dr. S. Methfessel for his EuSe and $Eu_{0.6}Gd_{0.4}Se$; Dr. T. R. McGuire for the $EuZrO_3$ compounds. He is especially indebted to Mr. Y. Tenenbaum for his kind help in the preparation of this manuscript.

REFERENCES

1. BRIX P., HUFNER S., KIENLE P. and QUITMAN D., *Phys. Lett.* **13**, 140 (1964).
2. STEICHELE E., *Z. Phys.* **201**, 331 (1967).
3. DANON J. and DeGRAFF A.M., *J. Phys. Chem. Solids* **27**, 1953 (1966).
4. DEENEY F.A., DELANEY J. A. and RUDDY V. P., *Phys. Lett.* **25A**, 370 (1967)
5. WICKMAN H. H., WERNICK J. H., SHERWOOD R. C. and WAGNER C. F., *J. Phys. Chem. Solids* **29**, 181 (1968).
6. WICKMAN H. H., NOWIK I., WERNICK J. H., SHIRLEY D. A. and FRANKEL R. B., *J. appl. Phys.* **37**, 1246 (1966).
7. BERKOOZ O., Ph. D. thesis, unpublished.
8. Produced by 'Elron', Electronic Industries of Israel, Haifa, Israel.
9. Purchased from 'New England Nuclear Corp', U.S.A.
10. BERKOOZ O., MALAMUD M. and SHTRIKMAN S., *Solid State Commun.* **6**, 185 (1968).

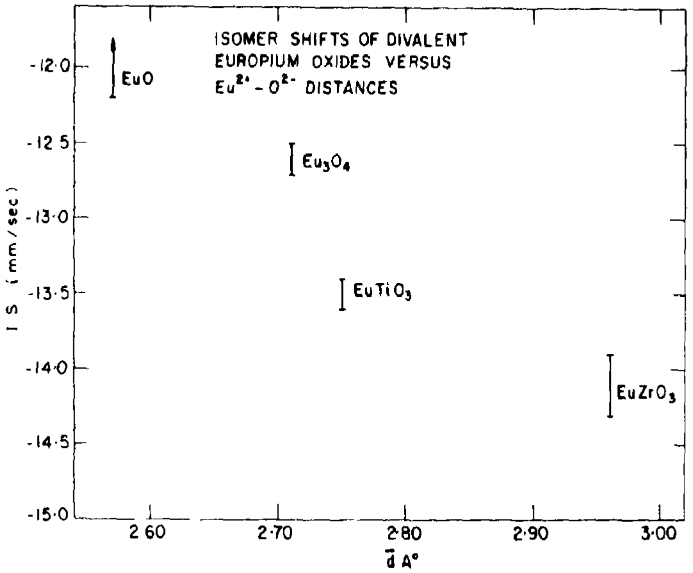

Fig. 4. Isomer shifts of divalent europium oxides vs. $Eu^{2+}-O^{2-}$ distances $\bar{d}$. The $\bar{d}$ values are known from crystallographic data.

11. WICKMAN H. H. and CATALANO E., *J. appl. Phys.* **39**, 1248 (1968).
12. COSTON C. J., INGALS R. and DRICKAMER H. G., *J. appl. Phys.* **37**, 1400 (1968).
13. INGALS R. COSTON C. J., DePASQUALI G., DRICKAMER H. G. and PINAJIAN J. J., *J. chem. Phys.* **45**, 1057 (1966).
14. SIMANEK E. and ZROUBEK Z., *Phys. Rev.* **163**, 275 (1967).
15. SIMANEK E. and WONG A. Y. C., *Phys. Rev.* **166**, 348 (1968).
16. MARHSALL W. In *Sec. Int. Conf. on Mossbauer Effect* (Edited by D. M. J Compton and A. G. Schoen, p. 263 (1961).
17. ROYER D. J., In *Bonding Theory*. McGraw Hill, New York (1968).
18. BARRET P. H. and SHIRLEY D. A., *Phys. Rev.* **131**, 123 (1963).
19. HUFNER S., KIENLE P., QUITMAN D. and BRIX P., *Z. Phys.* **187**, 67 (1965).
20. STEICHELE E., HUFNER S. and KIENLE P., *Phys. Lett.* **21**, 220 (1966).
21. NOWIK I. and OFER S., *Phys. Rev.* **153**, 409 (1967)
22. SHAFER M. W., *J. appl. Phys.* **36**, 1145 (1965).
23. DONNAY J D. H. and DONNAY G., (Editors), In *Crystal Data*. Am. Cryst. Ass. (1963).
24. HOLTZBERG F., McGUIRE T. R., METHFESSEL S. and SUITZ J. C., *Phys. Rev. Lett.* **13**, 18 (1964).
25. McGUIRE T R., SHAFER M. W., JOENEK R. J., ALPERIN H. A. and PICKART S. J., *J. appl. Phys.* **37**, 981 (1966).
26. HOLTZBERG F. and METHFESSEL S, *J. appl. Phys.* **37**, 1433 (1966).
27. RAU R. C., *Acta crystallogr.* **20**, 716 (1966).
28. WYCKOFF R. W., In *Crystal Structures*. Interscience, New York (1965).
29. TJEN V., FLAHAUT J. and DOMANGE L., *C. r. hebd. Séanc. Acad. Sci., Paris* **267**, 278 (1966).
30. FLAHAUT J., In *Prog. Sci. Tech. of the Rare Earths* (Edited by L. Eyring), Vol. 3, Chaps. 5, 6. Pergamon Press, Oxford (1968).
31. HULLIGER F. and VOGT O., *Phys. Lett.* **21**, 138 (1966).

APPENDIX

The isomer shifts of the ^{151}Eu recoilless absorption were studied in four typical structures found in divalent europium compounds. Thus, the mean ionic distances, between the divalent europium ions and their nearest neighbours divalent anions, should be estimated in an appropriate way for each structure. In these estimations we used only the lattice constants and the geometrical structures of the studied compounds, so that the changes of the ionic radii due to coordination numbers were not involved here.

For the NaCl type of compounds, i.e. EuO, EuS, EuSe and $Eu_{0.6}Gd_{0.4}Se$, the distances between the cations and the anions were taken as half of the lattice constants, where the latter are given in the literature[22–24] The calculations of the $\bar{d}$ values for the perovskite compounds, i.e. $EuTiO_3$ and $EuZrO_3$, were based on the lattice constants and the crystallographic discussions given in [22] and [25]. The estimated values of both the NaCl type and the perovskite compounds are not mean values and are accurate to the same degree as the lattice constants accuracy.

The estimations of the $\bar{d}$ values of the Th_3P_4 type compounds and the $CaFe_2O_4$ type compounds, were somewhat more complicated since the crystallographic descriptions of these compounds involve also u or x, y, z parameters, respectively. In the Th_3P_4 type compounds there are two sets of 4 anions as nearest neighbours to the metal ion, while the appropriate distances for each set was given by[26]:

$$d_4 = a_0 \,.\, \sqrt{3}(u^2 + u/12 + 5/192)^{1/2}[\text{Å}]$$

$$d_5 = a_0 \,.\, \sqrt{3}(u^2 - 5u/12 + 13/192)^{1/2}[\text{Å}].$$

Both distances are equal for $u = 1/12$ where then

$$d_4 = d_5 = a_0 \,.\, 0{\cdot}346[\text{Å}]$$

Since the u parameters of the studied compounds have not been yet known, we used the value of $u = 1/12$ which was found for some other compounds of this structure [28]. The values of the lattice constants were taken from [29] and [30].

The estimations of the $\bar{d}$ values of the $CaFe_2O_4$ type compounds were based upon the investigations of Eu_3O_4 [27] and the value of the mean distance between the divalent europium ions and their nearest neighbours divalent oxygen ions, (2·711 Å) which was found there. We estimated the $\bar{d}$ values, for the other compounds of this structure, using the relations between the lattice constants of these compounds[31] and the lattice constants of Eu_3O_4[27] Both the $\bar{d}$ values estimated for the Th_3P_4 compounds and the $CaFe_2O_4$ compounds have less accuracy than those obtained for the NaCl compounds and the perovskite compounds because of lack of detailed crystallographic information.

J. Phys. Chem. Solids Pergamon Press 1969. Vol. 30, pp. 1769–1777. Printed in Great Britain.

THE JAHN–TELLER INSTABILITY WITH ACCIDENTAL DEGENERACY

A. M. STONEHAM* and M. LANNOO†‡

Theoretical Physics Division, AERE Harwell, Berkshire, United Kingdom

(*Received* 17 *October* 1968; *in revised form* 6 *January* 1969)

Abstract–The Jahn–Teller theorem predicts that orbitally degenerate complexes in solids can lower their energy by a distortion which lowers their symmetry. Exact degeneracy is not necessary for this instability; usually it suffices if the actual separation of the energy levels involved is less than the energy reduction which would result if they were exactly degenerate. We discuss various cases of accidental degeneracy in cubic and tetrahedral systems. With accidental degeneracy it is possible to get mixed distortions which involve both trigonal and tetragonal distortions. These have probably been observed for the negative vacancy in silicon, and possibly for the neutral vacancy in diamond. The theory is applied to both these cases, and it is compared with the earlier qualitative arguments of Watkins.

1. INTRODUCTION

THE JAHN–TELLER theorem asserts that orbitally degenerate molecules or complexes in solids can lower their energy by a distortion which lowers their symmetry[1]. The instability occurs because the Hamiltonian has matrix elements linear in the distortion, whereas the elastic restoring forces are quadratic in this distortion. The theorem is usually applied to cases where the degeneracy of the energy levels is exact and arises from some symmetry of the system. However, exact degeneracy is not necessary for an instability [2]. Usually it is sufficient if the reduction of energy by distortion for exact degeneracy exceeds the actual separation of the levels involved. Near degeneracies can occur even when there is no underlying symmetry reason, and are known as 'accidental' degeneracies.

Accidental degeneracy is particularly interesting because the matrix elements linear in the distortion, responsible for the instability, may connect states which transform according to different representations of the appropriate symmetry group. Usually, with exact degeneracy, matrix elements within one representation alone are considered. For this reason more varied phenomena occur with accidental degeneracy, and inter-level terms are important in the examples considered here.

Opik and Pryce discussed the near degeneracy of the $2s$ and $2p$ levels of the F centre. These states are coupled by odd modes parity of T_{1u} symmetry. For suitable values or parameters the system was unstable with respect to these distortions. The interesting feature here is that a system with full cubic symmetry can lose its inversion symmetry by a Jahn–Teller instability. As the selection rules for optical transitions depend on the parities of the states involved this particular instability may profoundly affect the observed properties of the centre.

This article is mainly concerned with nearly degenerate E and T levels in tetrahedral or cubic symmetry. The calculations show that configurations may be achieved which are of lower symmetry than those obtained ignoring the near degeneracy. Also the inter-level terms may alter the relative importance of trigonal and tetragonal distortions for relatively isolated levels. The results are particularly relevant to defects in the valence crystals diamond, Si and Ge. Two cases are discussed

---

*[*] *Present address:* Coordinated Science Laboratory, University of Illinois, Urbana, Ill. 61801, U.S.A.

[†] *Permanent address:* Institut Supérieur d'Électronique du Nord, Lille, France.

[‡] This article is based on part of a thesis submitted by M.L. for the degree of Doctorat d'Etat en Sciences Physiques (Centre National pour les Recherches Scientifiques No. A.O. 2646).

in detail. The first is the negative vacancy in Si, where Watkins[3] observed mixed trigonal and tetragonal distortions. His description in terms of a one-electron model is related to a new description, appropriate to a many-electron model of the type introduced by Coulson and Kearsley[4], for diamond. The second case discussed is the neutral vacancy in diamond. The stress-splitting of the zero phonon line of the GR 1 band shows anomalies, and these may be related to the low-symmetry distortions discussed here[5].

2. COMBINED TRIGONAL AND TETRAGONAL DISTORTIONS

The Jahn–Teller instability arises from matrix elements of the Hamiltonian which are linear in the distortions of the environment. As an example of a system in which the matrix elements of importance connect non-degenerate levels, we discuss in detail the case where a T_2 level (comprising the states $|\xi\rangle$, $|\eta\rangle$, $|\zeta\rangle$) lies close to an E level (comprising states $|\epsilon\rangle$ and $|\theta\rangle$). For zero distortion the T level lies Δ above the E level. Within these levels the use of symmetry simplifies the matrix elements linear in the distortion to the form:

$$\begin{array}{c|ccc|cc|}
\langle\xi| & G_{ET}(\sqrt{3}\,\epsilon-\theta) & G_{TT}\zeta & G_{TT}\eta & -G_{TX}\xi & +\sqrt{3}G_{TX}\xi \\
\langle\eta| & G_{TT}\zeta & -G_{ET}(\sqrt{3}\,\epsilon+\theta) & G_{TT}\xi & -G_{TX}\eta & -\sqrt{3}G_{TX}\eta \\
\langle\zeta| & G_{TT}\eta & G_{TT}\xi & 2G_{ET}\theta & 2G_{TX}\zeta & \\
\hline
\langle\theta| & -G_{TX}\xi & -G_{TX}\eta & 2G_{TX}\zeta & -G_{EE}\theta & +G_{EE}\epsilon \\
\langle\epsilon| & \sqrt{3}G_{TX}\xi & -\sqrt{3}G_{TX}\eta & & G_{EE}\epsilon & G_{EE}\theta
\end{array} \qquad (2.1)$$

The G_{IJ} are coupling coefficients, where $I = E, T$ labels the symmetry of the mode involved, and $J = E, X, T$ indicates the states involved. The matrix elements within the T state have $J = T$ and those connecting the T and E states have $J = X$. The notation $\epsilon, \theta, \xi, \eta, \zeta$ for the normal modes of even parity is standard.*

In addition to these linear terms there are elastic energy terms quadratic in the distortions. The matrix elements of these have the form:

$$[K_E(\epsilon^2+\theta^2)+K_T(\xi^2+\eta^2+\zeta^2)]\,\hat{1} \qquad (2.2)$$

where $\hat{1}$ is the unit matrix.

The static distortions of this system will now be discussed, giving the configurations $Q \equiv (\epsilon, \theta, \xi, \eta, \zeta)$ which minimise the total energy. As general solutions of the secular equation are so complicated as to hide the important features the results will be given for various degrees of intra-level coupling and inter-level coupling. Dynamic effects and spin-orbit coupling are ignored.

2.1 *Intra-level coupling only*

We first consider the case when there is no coupling between the E and T_2 levels, i.e. G_{TX} is zero. This is the standard case, where there is only coupling within each state. Opik and Pryce concluded that the E states would distort tetragonally, with energy reduction G_{EE}^2/K_E. The T state distorts trigonally if the reduction of energy by trigonal distortion, $G_{TT}^2/3K_T$, exceeds G_{ET}^2/K_E; otherwise a tetragonal distortion results. Mixed tetragonal and trigonal distortions do not provide stable distortions; this result has recently been verified with more general assumptions by Wysling and Müller[6].

2.2 *Inter-level coupling only*

In this section G_{TX} is assumed to dominate, and we treat the case $G_{EE} = G_{ET} = G_{TT} = 0$. The eigenvalues can be obtained, as functions of G_{TX}. From these configurations of minimum energy are found; there are minima for each of the five energy surfaces $E(Q)$. Subsequently Section 2.3 discusses the effects of intra level coupling.

---

*In tetrahedral symmetry there are, in general, two sets of T_2 normal modes. We will only discuss vacancy centres with this symmetry; for vacancy centres there is just one set of T_2 modes, and no ambiguity arises.

When G_{EE}, G_{ET} and G_{TT} are all zero the eigenvalues for an arbitrary configuration Q are:

$$E_a = K_T q^2 + \frac{2}{5}\Delta,$$

$$E_{b,c} = K_T q^2 - \frac{1}{10}\Delta + \sqrt{\left[\left(\frac{\Delta}{2}\right)^2 + 2G_{TX}^2 q^2 (1 \pm \surd 1 - \phi)\right]} \tag{2.3}$$

$$E_{d,e} = K_T q^2 - \frac{1}{10}\Delta - \sqrt{\left[\left(\frac{\Delta}{2}\right)^2 + 2G_{TX}^2 q^2 (1 \pm \surd 1 - \phi)\right]}$$

in which $q^2 = \xi^2 + \eta^2 + \zeta^2$ and $\phi = 3(\xi^2\eta^2 + \eta^2\zeta^2 + \zeta^2\xi^2)/q^4$. The origin of energy is taken to be the centre of gravity of the electronic energy levels for zero distortion. The energy surfaces are labelled a, b, c, d and e*.

The results can be conveniently expressed in terms of F, a dimensionless parameter defined by:

$$F = (\Delta/4)/(G_{TX}^2/K_T). \tag{2.4}$$

F is a measure of the inter level coupling, and tends to zero as the coupling becomes large.

It is easily shown that the lowest energy is always found with $|d\rangle$, and is achieved with $\phi = 0$. This corresponds to one of six distortions with (ξ, η, ζ) equal to $(\pm q, 0, 0)$, $(0, \pm q, 0)$ or $(0, 0, \pm q)$. Minimising the lowest eigenvalue, E_d, with respect to q gives:

$$|q_0| = \frac{|G_{TX}|}{K_T}\surd(1 - F^2) \tag{2.5}$$

so there will be an instability in state $|d\rangle$ if $|F| < 1$. The energy levels for the equilibrium configuration of the ground state ($Q = Q_{d0}$) are given in Fig. 1 as a function of F; the energies are in units of G_{TX}^2/K_T. In this configuration the ground state for the $(0, 0, q_0)$ distortion is:

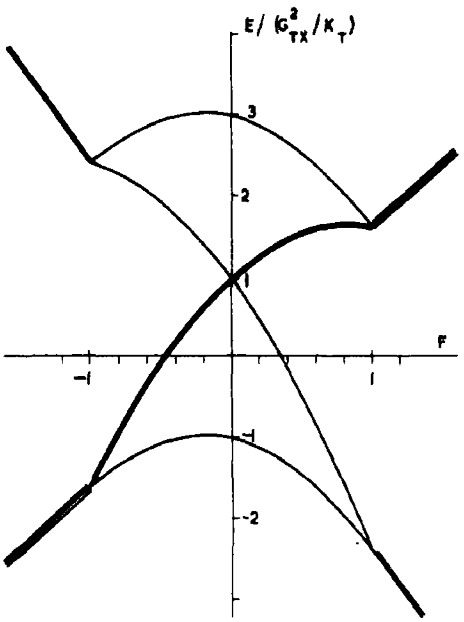

Fig. 1. The energy levels in the $E + T_2$ case are shown in units of G_{TX}^2/K_T as a function of $F = \Delta/(4G_{TX}^2/K_T)$. In all cases the levels are calculated for the configuration which minimises the energy in the ground state.

$$|d\rangle = \surd(\tfrac{1}{2}(1+F))|\theta\rangle - \surd(\tfrac{1}{2}(1-F))|\zeta\rangle \tag{2.6}$$

with energy

$$E = -(G_{TX}^2/K_T)(1 + \tfrac{2}{5}F + F^2). \tag{2.7}$$

The state $|d\rangle$ also shows an extremum with $\phi = \frac{3}{4}$ if $|F| < \frac{3}{4}$. This is a saddle point, not a minimum, and corresponds to a $(0, q_0', q_0')$ distortion with energy

$$-(G_{TX}^2/K_T)(\tfrac{3}{4} + \tfrac{2}{5}F + \tfrac{1}{3}F^2).$$

Similarly, there is a saddle point in $|e\rangle$ with energy

---

*E_d and E_e do not represent separate energy surfaces, but give different sections of two intersecting energy surfaces. E_e comprises the upper two branches at the line of intersection and E_d the lower two branches. Failure to recognise this can lead one to identify spurious minima, such as the one on the line of intersection $\phi = 1$.

$$-(G_{TX}^2/K_T)(\tfrac{1}{4}+\tfrac{2}{5}F+4F^2)$$

if $|F| < (1/4)$ and $\phi = 3/4$.

The other states, $|a\rangle$, $|b\rangle$ and $|c\rangle$, show no instability from interlevel coupling. They are, of course, still affected by the coupling within the E and T levels.

2.3 *Arbitrary intra level and inter level coupling*

We follow the method of Öpik and Pryce [2], and express the wave function Ψ as a linear combination of the basis functions, ψ_i, of the nearly degenerate states:

$$\Psi = \sum_j a_j\psi_j$$

$$\sum a_j^2 = 1. \qquad (2.8)$$

where Q is one of the normal coordinates θ, ϵ, ξ, η or ζ. With these equations we can express the Q in terms of the a_i. Inserting these values for the Q in equation (2.9) we obtain a set of equations in the unknowns E and a_i. These equations can be solved exactly.

It is easily shown that the extrema obtained with zero inter level coupling always exist. Their energies were given in Section 2.1.

The first mixed solution obtained gives the six possible distortions with $(\theta, \epsilon, \xi, \eta, \zeta)$ equal to $(\rho, 0, 0, 0, \pm q)$, $\left(-\tfrac{1}{2}\rho, -\frac{\sqrt{3}}{2}\rho, 0, \pm q, 0\right)$ or $\left(-\tfrac{1}{2}\rho, +\frac{\sqrt{3}}{2}\rho, \pm q, 0, 0\right)$.

The energy at these minima is:

$$E = -\frac{G_{TX}^2}{K_T}\left[\frac{2F}{5} + \frac{1-\dfrac{K_T}{2K_E}\left\{\dfrac{G_{ET}.G_{EE}}{G_{TX}^2}+\dfrac{G_{ET}^2-\frac{1}{4}G_{EE}^2}{G_{TX}^2}.F\right\}+F^2}{1-\dfrac{K_T}{4K_E}\left(\dfrac{G_{ET}+\frac{1}{2}G_{EE}}{G_{TX}}\right)^2}\right] \qquad (2.11)$$

and ρ and q are given by:

$$\rho = \frac{1}{2}\left[(G_{FT}-\tfrac{1}{2}G_{EE})-F(G_{FT}+\tfrac{1}{2}G_{EE})\right]\Big/\left[\frac{K_T}{4}\left(\frac{G_{ET}+\frac{1}{2}G_{EE}}{G_{TX}}\right)^2-K_E\right];$$

$$q = \frac{|G_{TX}|}{K_T}\,\frac{\sqrt{\left(\left[1-F-\dfrac{G_{EE}(G_{ET}+\frac{1}{2}G_{EE}).K_T}{G_{TX}^2\qquad .4K_E}\right]\left[1+F-\dfrac{G_{EE}(G_{ET}+\frac{1}{2}G_{EE}).K_T}{G_{TX}^2\qquad .2K_E}\right]\right)}}{1-\left(\dfrac{G_{ET}+\frac{1}{2}G_{EE}}{G_{TX}}\right)^2\dfrac{K_T}{4K_E}}. \qquad (2.12)$$

The coefficients a_j are solutions of the equations:

$$Ea_i = \sum_j \mathscr{H}_{ij}a_j \qquad (2.9)$$

where $\mathscr{H}_{ij}$ is the sum of a Jahn–Teller matrix element and an elastic energy term. The extrema of the energy are given by:

$$0 = \sum_{ij} a_i\frac{\partial\mathscr{H}_{ij}}{\partial Q}a_j \qquad (2.10)$$

These formulae are only valid if F lies between

$$1-\frac{K_T}{4K_E}\frac{G_{EE}(G_{ET}+\frac{1}{2}G_{EE})}{G_{TX}^2}$$

and

$$\frac{K_T}{2K_E}\frac{G_{ET}(G_{ET}+\frac{1}{2}G_{EE})}{G_{TX}^2}-1;$$

these limits exclude any divergences in the denominator of E. In the limit of zero intra level coupling this state gives the minimum of $|d\rangle$ with $\phi = 0$ discussed in Section 2.2. For sufficiently strong interlevel coupling the solution with mixed distortions is the absolute minimum of energy. This result is important. In all cases treated previously the distortions which minimise the energy have been pure trigonal or pure tetragonal; mixed distortions do not provide absolute minima in isolated E or T levels.

Other mixed solutions correspond to $|d\rangle$ and $|e\rangle$ with $\phi = 3/4$; both are saddle points, and neither of these are minima. The solution for $|d\rangle$ has displacements $(\theta, \epsilon, \xi, \eta, \zeta)$ equal to $(-p', 0, \pm q', \pm q', \pm p')$ and cyclic permutations in the five-coordinate space. The $|e\rangle$ solution has distortions $(p'', 0, \pm q'', \pm q'', \pm p'')$ together with cyclic permutations.

3. OTHER CASES OF NEAR DEGENERACY

Certain other cases of near degeneracy lead to mixed distortions, and these will be discussed in the present section. Although we shall not discuss all cases of near degeneracy, the ones we omit $(A+A, A+E, E+E)$ are straightforward, and need no special comment. In the $E+E$ case the secular equation can be factorised and, as for an isolated E level, the energies are functions of $(\epsilon^2+\theta^2)$ and not of ϵ or θ separately. For $A+E$, as has been observed by Elkin and Watkins[7], in an analogous case, the energy does depend on ϵ and θ separately; the interaction with the A state effectively produces a cubic anharmonic term which stabilises certain combinations of ϵ and θ distortions.

In all our analysis below we refer the final energies to the centroids of the two levels for zero distortion. Our convention is arbitrary, but it simplifies discussion when the order of the levels is inverted.

(*a*) A_1+T_2 *or* A_2+T_1

For zero distortion the T level has energy $-\Delta/4$ and the A level $3\Delta/4$. The matrix giving the Jahn–Teller terms is:

$$\begin{bmatrix} G_{ET}(\sqrt{3}\epsilon-\theta) & G_{TT}\zeta & G_{TT}\eta & G_{TX}\xi \\ G_{TT}\zeta & -G_{ET}(\sqrt{3}\epsilon+\theta) & G_{TT}\xi & G_{TX}\eta \\ G_{TT}\eta & G_{TT}\xi & 2G_{ET}\theta & G_{TX}\zeta \\ G_{TX}\xi & G_{TX}\eta & G_{TX}\zeta & \end{bmatrix} \tag{3.1}$$

There are three types of extremum. The first is the pure tetragonal distortion found for an isolated T level, with energy $-\Delta/4-G_{ET}^2/K_E$. There are three equivalent minima of this type. Secondly, there are the four equivalent trigonal distortions with $|\xi| = |\eta| = |\zeta|$. These correspond to the trigonal minima of an isolated T level. Although the distortions which give energy minima for an isolated T level still give extrema, they are only minima when G_{TX} is zero. At the minima in the present case the energy has a complicated form which we give only in the limit $\Delta = 0$:

$$E = -\{|G_{TT}|+\sqrt{(G_{TT}^2+3G_{TX}^2)}\}^2/12K_T. \tag{3.2}$$

The distortion has, for example:

$$\xi = \eta = \zeta = \{|G_{TT}|+\sqrt{(G_{TT}^2+3G_{TX}^2)}\}/6K_T. \tag{3.3}$$

Finally, there is a mixed distortion, with six equivalent minima. One such minimum has $\epsilon = \xi = \eta = 0$ and finite values of θ and ζ:

$$\begin{aligned} \theta &= \frac{G_{ET}}{2K_E}\frac{(\Delta+G_{TX}^2/K_T)}{(G_{ET}^2/K_E)-(G_{TX}^2/K_T)} \\ \zeta &= \pm\frac{G_{TX}}{2K_T}\frac{\{[\Delta+G_{TX}^2/K_T][G_{TX}^2/K_T-\Delta-2G_{ET}^2/K_E]\}^{1/2}}{(G_{ET}^2/K_E)-(G_{TX}^2/K_T)} \end{aligned} \tag{3.4}$$

The energy of this mixed state is:

$$E=\frac{\Delta}{4}-\frac{G_{TX}^2}{2K_T}+\frac{1}{4}\frac{[\Delta+G_{TX}^2/K_T][2G_{ET}^2/K_E-G_{TX}^2/K_T+\Delta]}{G_{ET}^2/K_E-G_{TX}^2/K_T}. \tag{3.5}$$

This expression is only valid if Δ lies between $-G_{TX}^2/K_T$ and $G_{TX}^2/K_T-2G_{ET}^2/K_E$. The last term in E is always finite if this condition is satisfied.

The energies (3.2) and (3.5) are equal for purely interlevel coupling, when G_{TT} and G_{ET} are zero. When there is weak intra level coupling and $\Delta=0$ the trigonal solution has lower energy; in general cases the relative energies depend on the actual magnitudes of the coupling coefficients.

(*b*) T_1+T_1 *or* T_2+T_2

For simplicity we consider the case of interlevel coupling alone. The energy levels are $\pm\Delta/2$ in the absence of distortion. The relevant part of the Jahn–Teller matrix is:

$$\begin{bmatrix} G_{EX}(\sqrt{3}\epsilon-\theta) & G_{TX}\zeta & G_{TX}\eta \\ G_{TX}\zeta & -G_{EX}(\sqrt{3}\epsilon+\theta) & G_{TX}\xi \\ G_{TX}\eta & G_{TX}\xi & 2G_{EX}\theta \end{bmatrix}. \tag{3.6}$$

The solutions are analogous to those for an isolated T level, in that there are both tetragonal and trigonal extrema, and the mixed distortions have energies intermediate between these values. Further, the trigonal distortion is again favoured if $G_{TX}^2/3K_T$ exceeds G_{EX}^2/K_E. However, there are now six equivalent tetragonal minima, with energy

$$E=-\frac{G_{EX}^2}{K_E}\left\{1+\left(\frac{\Delta/4}{G_{EX}^2/K_E}\right)^2\right\} \tag{3.7}$$

provided $|\Delta|<4G_{EX}^2/K_E$. The distortions here are, for instance:

$$\theta=\pm\frac{G_{EX}}{K_E}\sqrt{\left(1-\left(\frac{\Delta/4}{G_{EX}^2/K_E}\right)^2\right)}. \tag{3.8}$$

When $|\Delta|<4G_{TX}^2/3K_T$ there are eight equivalent trigonal minima, with energy

$$E=-\frac{G_{TX}^2}{3K_T}\left\{1+\left(\frac{\Delta/4}{G_{TX}^2/3K_T}\right)^2\right\} \tag{3.9}$$

and with distortions such as:

$$\xi=\eta=\zeta=\pm\frac{G_{TX}}{3K_T}\sqrt{\left(1-\left(\frac{\Delta/4}{G_{TX}^2/3K_T}\right)^2\right)}. \tag{3.10}$$

The degeneracies which are associated with the different possible signs of θ and of ξ,η and ζ may be lifted by anharmonic terms or by the intralevel coupling. Inclusion of these extra terms greatly increases the difficulty of the problem, and we have not examined these features in detail. When there is both interlevel and intralevel coupling, mixed distortions can occur. This can be easily seen by considering the effect of weak coupling to E modes from intralevel coupling when interlevel coupling gives a trigonal distortion. However, the general case is extremely complicated, and we have not treated the most general form.

(*c*) T_1+T_2

Again we consider zero intralevel coupling. When the distortions are zero the T_2 level lies Δ above the T_1 level. The interlevel part of the matrix linear in the distortions is:

$$\begin{bmatrix} -G_{EX}(\sqrt{3}\theta+\epsilon) & -G_{TX}\zeta & G_{TX}\eta \\ G_{TX}\zeta & +G_{EX}(\sqrt{3}\theta-\epsilon) & -G_{TX}\xi \\ -G_{TX}\eta & G_{TX}\xi & 2G_{EX}\epsilon \end{bmatrix} \tag{3.11}$$

The results are completely different from the (T_1+T_1) and (T_2+T_2) cases. There are three classes of distortion which give minima in $E(\mathbf{Q})$. As the solutions are complicated, we introduce the abbreviations:

$$\left.\begin{aligned}\gamma_E &= G_{EX}^2/K_E\\ \gamma_T &= G_{TX}^2/K_T\\ \gamma_2 &= (3\gamma_E+\gamma_T)/4\\ \gamma_3 &= \gamma_T(\gamma_T+2\gamma_E)/(4\gamma_T-\gamma_E)\ .\end{aligned}\right. \tag{3.12}$$

The first solution gives six equivalent minima. These are orthorhombic, one of them having ϵ finite and $\theta=\xi=\eta=\zeta=0$. Its energy is

$$E_1=-\gamma_E\left\{1+\left(\frac{\Delta}{4\gamma_E}\right)^2\right\} \tag{3.13}$$

and the distortion is:

$$\epsilon=\pm\frac{G_{EX}}{K_E}\sqrt{\left(1-\left(\frac{\Delta}{4\gamma_E}\right)^2\right)}. \tag{3.14}$$

These are valid when $4\gamma_E > |\Delta|$. The second solution gives a mixed distortion, with θ and ζ finite, and $\epsilon=\xi=\eta=0$. It has C_2 symmetry, and energy:

$$E_2=-\gamma_2\left\{1+\left(\frac{\Delta}{4\gamma_2}\right)^2\right\} \tag{3.15}$$

valid when $4\gamma_2 > |\Delta|$. There are 12 such distortions, for example:

$$\left.\begin{aligned}\theta &= \pm\frac{\sqrt{3}}{2}\frac{G_{EX}}{K_E}\sqrt{\left(1-\left(\frac{\Delta}{4\gamma_2}\right)^2\right)}\\ \zeta &= \pm\frac{1}{2}\frac{G_{TX}}{K_T}\sqrt{\left(1-\left(\frac{\Delta}{4\gamma_2}\right)^2\right)}\end{aligned}\right\}. \tag{3.16}$$

The third solution also gives a mixed distortion, but with $\theta=\zeta=0$, and $|\xi|=|\eta|$. The energy at this minimum is:

$$E_3=-\gamma_3\left\{1+\left(\frac{\Delta}{4\gamma_3}\right)^2\right\} \tag{3.17}$$

valid when $4\gamma_3 > |\Delta|$ and $4\gamma_T > \gamma_E$. In this case the symmetry is C_1, and there are 24 equivalent sets of distortions, corresponding to the various permutations of signs and interchange of cube axes with:

$$\left.\begin{aligned}|\epsilon| &= 3\frac{G_{EX}}{K_E}\sqrt{\left(1-\left(\frac{\Delta}{4\gamma_3}\right)^2\right)}\frac{\gamma_T}{4\gamma_T-\gamma_E}\\ |\xi| &= |\eta|\\ &= \frac{G_{TX}}{K_T}\left[1-\frac{\Delta}{4\gamma_3}\right]\frac{\sqrt{((2\gamma_T+\gamma_E)(\gamma_T-\gamma_E))}}{4\gamma_T-\gamma_E}\end{aligned}\right\}. \tag{3.18}$$

To summarise, we have:

(i) $\gamma_E < \gamma_T$: $E_2 < E_3 < E_1$
(ii) $\frac{1}{4}\gamma_E < \gamma_T < \gamma_E$: $E_3 < E_1 < E_2$
(iii) $\gamma_T < \frac{1}{4}\gamma_E$: $E_1 < E_2$.

(d) $E+T_1$

This is very similar to the example given in detail in Section 2, $(E+T_2)$. The Jahn-Teller matrix elements differ from the earlier example in that the elements involving $|\epsilon\rangle$ and $|\theta\rangle$ should be interchanged, and those in $|\theta\rangle$ changed in sign. The energy reductions and distortions are not affected, but the wave functions are altered. The results for T_1+E can be obtained from the earlier results by the substitution of $-|\theta\rangle$ for $|\epsilon\rangle$ and of $|\epsilon\rangle$ for $|\theta\rangle$.

4. COMPARISON WITH EXPERIMENT

In this section we discuss briefly a number of systems which illustrate the Jahn-Teller effect for near, rather than exact, degeneracy. The systems described all show mixed trigonal and tetragonal distortions. Examples are the negative vacancy in silicon[3] and the transition ions Pd⁻ and Pt⁻ in silicon and Ni⁻ in germanium[8]. The neutral vacancy in diamond may exhibit mixed distortions also, but the evidence is less direct. We will only discuss the vacancy centres in valence crystals, and will outline the reasons for expecting them to show the effects of near degeneracy. Watkins has emphasised[9, for example] that the Jahn-Teller terms are particularly large in silicon.

It is easy to show that, for these vacancy centres, there are likely to be energy levels nearly degenerate with the ground state of the centre. The electronic properties of vacancies in valence crystals are largely determined by the so-called 'defect electrons'. In the neutral vacancy, for instance, four bonds were broken in forming the centre; the four electrons on the neighbours which previously participated in the bonds are the defect electrons. New molecular orbitals can be formed by taking linear combinations of the broken bond orbitals. In particular the molecular orbital of lowest energy, $|v\rangle$, has A_1 symmetry; above it are three degenerate T_2 orbitals, $|t_x\rangle$, $|t_y\rangle$ and $|t_z\rangle$. These one-electron orbitals are filled successively by the defect electrons, giving electronic configurations $v^n t^m$. However, from any one configuration a number of many-electron states may be constructed, and these states will, in general be close in energy[4]. For the negative vacancy in silicon three states of the same spin (^2E, $^2T_1$ and $^2T_2$) and one other ($^4A_2$) derive from the configuration v^2t^3. For the neutral vacancy in diamond there are again three states of the same multiplicity (^1E, $^1T_2$ and $^1A_1$) and one of different multiplicity ($^3T_1$) which all derive from v^2t^2.

In the simplest models of the vacancy centres all states which derive from the same configuration $v^n t^m$ are exactly degenerate. The degeneracy will be removed by the electron–electron interaction, which admixes states of the same symmetry derived from $v^{n-1}t^{m+1}$, $v^{n-2}t^{m+2}$,…. Such configuration interaction is very important in diamond and, as we shall show, may cause large enough splittings to inhibit Jahn–Teller instabilities. On the other hand, in silicon, Watkins has found that the configuration interaction is much smaller, and may often be ignored. For this reason he has been able to interpret his data in terms of a one-electron model, rather than in terms of Jahn–Teller coupling between many-electron states which are close in energy. The two pictures have much in common, for example, both recognise that the matrix elements which cause the instability are linear in the distortions, and indeed the one-electron model can be considered as a special case of the many-electron picture. We shall not compare the two viewpoints in detail here, but merely observe that Watkins' model is particularly useful for understanding the nature of the ground states of these centres *a posteriori*, when the configuration interaction is known to be weak. The approach via the many-electron states of low energy is more appropriate when one wants to predict the ground state *a priori*, since this approach involves a more general formulation of the Jahn–Teller problem and also detailed consideration of the energy separations of the various many electron states.

We conclude this section by discussing the neutral vacancy in diamond, since the centre has been studied extensively theoretically, and it is possible to give some idea of the relative importance of the configuration interaction and Jahn–Teller terms. Although the Jahn–Teller terms dominate in silicon, the situation is less clear in diamond. The evidence for mixed trigonal and tetragonal distortions of the neutral vacancy in diamond comes from the stress splitting of the zero-phonon line of the GR1 band, often attributed to the neutral vacancy[4, 5]. Theoretical treatments suggest that the ground state is ^1E, separated by some 0·05 eV from the $^3T_1$ state; the next state, $^1T_2$, is about 2 eV higher in energy. The GR1 band is attributed to transitions between the ^1E and $^1T_2$ states. The interlevel coupling which gives rise to the mixed distortions can occur in two obvious ways: coupling between ^1E and $^3T_1$, or coupling between ^1E and $^1T_2$. Although ^1E and $^3T_1$ are very close in energy, their coupling depends on the spin-orbit coupling. In diamond the spin-orbit coupling is very weak, and the difference in multiplicity effectively reduces G_{TX} by about 10^{-3}. The interaction is then too weak; mixed distortions would only occur if the two levels were only separated by about 10^{-7} eV. The ^1E and $^1T_2$ levels have a larger separation, and should exhibit an instability if G_{TX} exceeds about 4 eV/Å. Calculations based on the point-ion model [10, 11] give 2·6 eV/Å, and those based on the

LCAO method[12] give 0·26 eV/Å. These results are not conclusive; what the calculation does emphasise is that, if the interpretation of the experiments is correct, the Jahn–Teller coupling between the ^1E and $^1T_2$ states is only just large enough to cause the instability.

To summarise, we see that near degeneracies occur quite naturally for vacancy centres in valence crystals. The degeneracy of states derived from any one configuration is removed by the interaction between the defect electrons. In silicon the Jahn–Teller terms are much larger than the splittings due to the electron–electron interaction, but the two terms are comparable for diamond. The near degeneracies which are important in both these cases involve states with the same spin. It is clear, however, that in systems where there is appreciable spin-orbit coupling the near degeneracy of states with different multiplicity may be important.

CONCLUSION

Nearly degenerate levels are coupled by terms linear in the distortions of the environment. When the coupling is sufficiently strong, and the levels are sufficiently close, a Jahn–Teller instability occurs. In combination with this the Jahn–Teller coupling within the levels can lead to mixed trigonal and tetragonal distortions; these cannot occur if there is no coupling between the levels.

These mixed distortions are of importance for defects in valence crystals, and offer an explanation of the spin resonance data for the negative vacancy in Si. It is possible that the low symmetry distortions also explain the unusual stress-splitting of the zero phonon line of the GR1 line in diamond.

Acknowledgements—We are indebted to Dr. G. D Watkins for a stimulating correspondence, and to Dr K. A. Müller for a copy of his work prior to publication.

REFERENCES

1. JAHN H. and TELLER E., *Proc. R. Soc.* **A161**, 220 (1937).
2. OPIK U. and PRYCE M. H. L., *Proc. R Soc.* **A238**, 425 (1957).
3. WATKINS G. D, *Radiation Damage in Semiconductors*, pp. 97–113. Dunod, Paris (1964).
4. COULSON C. A. and KEARSLEY M. J, *Proc. R. Soc.* **A241**, 433 (1957).
5. LANNOO M. and STONEHAM A M., *J Phys Chem. Solids* **29**, 1987 (1968).
6. WYSLING P. and MÜLLER K. A., *Phys. Rev.* **173**, 327 (1968).
7. ELKIN E. L. and WATKINS G. D., *Phys. Rev.* **174**, 881 (1968).
8. LUDWIG G. W. and WOODBURY H., *Solid St. Phys* **13**, 223 (1962).
9. LIDIARD, A. B., Report of Panel Discussion in *Radiation Damage in Semiconductors*, p. 335. Dunod, Paris (1964).
10. STONEHAM A. M., *Proc. Phys Soc.* **88**, 135 (1966).
11. LIDIARD A. B. and STONEHAM A. M., *Science Techn. Industrial Diamonds* **1**, 1 (1966).
12. FRIEDEL J., LANNOO M. and LEMAN G, *Phys. Rev.* **164**, 1056 (1967).

J. Phys. Chem. Solids Pergamon Press 1969. Vol. 30, pp. 1779–1791. Printed in Great Britain.

CALCULATION OF III-V TERNARY PHASE DIAGRAMS: In–Ga–As and In–As–Sb

G. B. STRINGFELLOW and P. E. GREENE
Hewlett-Packard Laboratories, Palo Alto, Calif 94304, U.S.A.

(*Received* 25 *September* 1968; *in revised form* 24 *December* 1968)

Abstract—It has been demonstrated that certain thermodynamic properties of III–V systems can be described using the quasi-chemical equilibrium treatment of a lattice model for the liquid and solid solutions where each atom interacts with only its nearest neighbor atoms. The calculated activity of In in In–Sb solutions, activity of As in Ga–As solutions, and liquidus curves in the In–Sb, Ga–As and In–As systems all agree well with available experimental data. The quasi-chemical equilibrium approach has been used as the basis for a calculation of the phase diagram for a general ternary system A, B, C containing the binary compounds AC and BC which are stoichiometric and completely miscible. The parameters needed for the calculation are the melting temperature and entropy of fusion for both AC and BC and the interaction parameters, Ω_{A-C}, Ω_{B-C}, Ω_{A-B}, Ω_{AC-BC}, which are constants representing the interaction energies in each of the binary systems. The calculation was carried out numerically for two ternary systems In–Ga–As and In–As–Sb. The excellent agreement between calculated and experimental results indicates that the quasi-chemical equilibrium model is valid for the description of the liquid and solid solutions involving elements from groups III and V of the periodic table.

1. INTRODUCTION

A METHOD of calculating the ternary phase diagrams for III–V systems from the available thermodynamic data is extremely desirable because such diagrams are useful in the growth of III–V mixed crystals from equilibrium liquid phases. The experimental determination of the phase diagrams including liquidus curves and tie lines is a prohibitive task because of the time required and the large degree of uncertainty in the results. It is the purpose of this paper to present a method of calculating III–V ternary phase diagrams using the quasi-chemical equilibrium approach of Guggenheim[1]. The results of the calculation for the In–Ga–As and In–As–Sb systems will be presented.

Previous attempts to calculate III–V phase diagrams have been restricted to applying the regular solution approach to the interpretation of III–V binary phase diagrams[2–6], and the extrapolation and interpolation of experimental points in ternary systems[7–10]. However, the III–V binary systems studied do not behave as regular solutions[5, 6, 13]. The quasi-chemical equilibrium approach has been used successfully to describe the Cd–Bi–Pb, Cd–Sn–Pb, and Al–Bi–Pb systems[11], but not until now applied to III–V systems.

2. THE MODEL

The lattice model is commonly chosen to represent the III–V solution. In a solution of N_A atoms of A and N_B atoms of B, each atom is surrounded by Z nearest neighbors. The energy of the solution is regarded as a linear function of the number of the various types of bonds between nearest neighbor atoms. The energy of solution or interaction parameter, Ω_{AB}, may be expressed

$$\Omega_{AB} = Z\left(E_{AB} - \tfrac{1}{2}(E_{AA} + E_{BB})\right). \tag{1}$$

The E_{ij} term represents the interaction energy of an i–j nearest neighbor pair.

In principle, an exact statistical theory can be used to derive the thermodynamic properties of this model solution. The configurational partition function can be written,

$$(P.F.) = \sum_{N_{AB}} g(N_A, N_B, N_{AB}) \exp(-\Omega_{AB}N_{AB}/RT) \quad (2)$$

but the function $g(N_A, N_B, N_{AB})$, the number of arrangements of $N_A - A$ atoms and $N_B - B$ atoms so that there are $N_{AB} - AB$ pairs, cannot be formulated explicitly; so, it is necessary to use an approximate theory.

The simplest and most often used approximation is to assume a random distribution of A and B atoms. This leads to a regular solution defined[12] as one in which the excess enthalpy of mixing is non-zero, while the excess entropy of mixing is zero. This approach is internally inconsistent since it assumes a random distribution of atoms even though certain configurations are energetically more favorable than others.

An internally consistent and more reasonable approximation is the quasi-chemical equilibrium approach of Guggenheim[1]. The distribution of pairs is weighted exponentially in energy, analogous to the law of mass action, hence the name quasi-chemical equilibrium. The following equations completely determine the thermodynamic properties of the solution:

$$N_{AA}N_{BB}/(N_{AB})^2 = \tfrac{1}{4}\exp(2\Omega_{AB}/ZRT) \quad (3a)$$

$$2N_{AA} + N_{AB} = ZN_A \quad (3b)$$

$$2N_{BB} + N_{AB} = ZN_B. \quad (3c)$$

This approach can be used to derive the activity coefficients of A and B in the solution:

$$\gamma_A = \left\{\frac{\beta - 1 + 2X}{X(\beta+1)}\right\}^{Z/2} \quad (4a)$$

$$\gamma_B = \left\{\frac{\beta + 1 - 2X}{(1-X)(\beta+1)}\right\}^{Z/2} \quad (4b)$$

where $\beta = [1 + 4X(1-X)(\eta^2 - 1)]^{1/2}$,

$X = N_A/(N_A + N_B)$, and $\eta = \exp(\Omega_{AB}/ZRT)$.

To determine the applicability of this model to III–V systems, it is necessary to see how well calculated thermodynamic properties fit the experimental data in several binary systems. The activity of In in the In–Sb system has been determined by Hoshino *et al.*[13] using high temperature e.m.f. measurements. Their results at 900°K (Fig. 1) are in excellent agreement over the entire composition range with the results calculated from equations (4a, b), using $\Omega_{\text{In-Sb}} = -3980$ cal/mole, which are shown as a solid line in Fig. 1. A value of $Z = 6$ was used and will be used in all calculations involving the liquid state. This is supported by the X-ray measurements of Buschert, Geib and Lark Horowitz [14] on InSb liquid where they found the number of nearest neighbors, Z, to be 5·7.

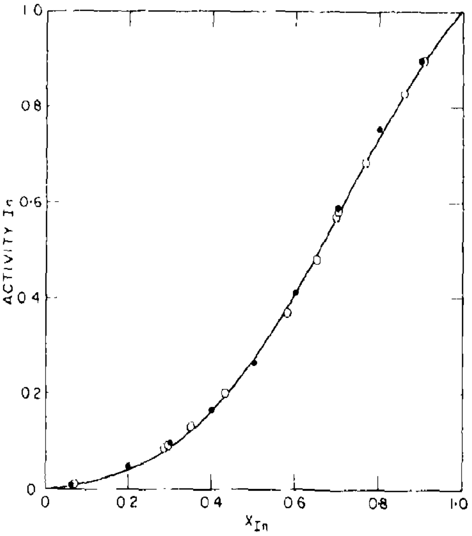

Fig. 1. Activity of In vs. atom fraction In in In–Sb solution at 900°K. —— present calculation; ○ Hoshino *et al.*[14]; ● Terpilowski[35].

A quantitative measure of how well the curves fit the experimental data is the root mean squared[15] deviation:

$$\sigma(X) = \left\{\sum_{i=1}^{N}(X_i, \text{obs.} - X_i, \text{calc.})^2/N\right\}^{1/2}. \quad (5)$$

The r.m.s. deviation in activity for the data presented in Fig. 1 is 0·008.

Arthur[6] has determined the activity coefficients along the liquidus line in the GaAs system from As vapor pressure measurements. Using a regular solution approach he found the interaction parameter to be linear in temperature,

$$\Omega_{Ga-As} = -3{\cdot}7T.$$

Thurmond[5] determined the interaction parameter along the liquidus from the T–X phase diagram of Hall[16] using the formula of Wagner[2] and Vieland[4], based on a regular solution theory. He found

$$\Omega_{Ga-As} = 9960 - 11{\cdot}15\,T.$$

Both Arthur and Thurmond concluded that the Ga–As system does not behave as a regular solution. Arthur's[6] activity coefficient data plotted in Fig. 2 is in good agreement with the solid line in the figure which was calculated using the quasi-chemical equilibrium approximation from equations (4a, 4b) with a temperature independent interaction parameter,

$$\Omega_{Ga-As} = -4380\ \text{cal/mole}.$$

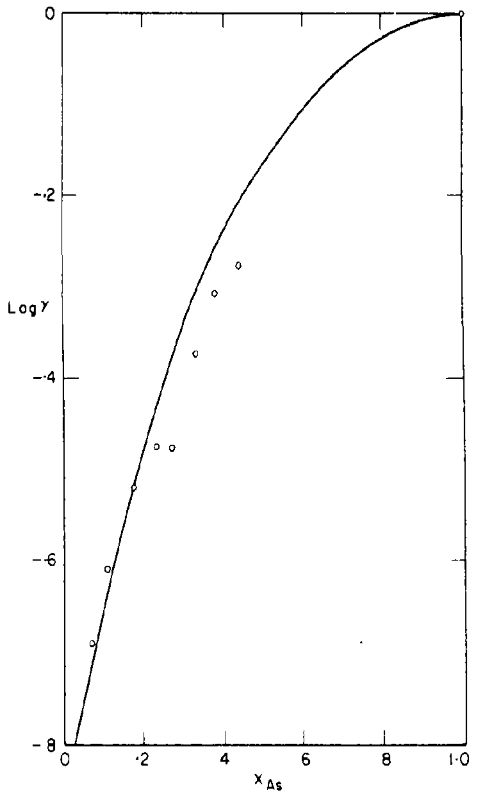

Fig 2. As activity coefficient vs. atom fraction As along the Ga–As liquidus. ——— present calculation; ○ Arthur[6]

The r.m.s. deviation in activity is calculated from equation (5) to be 0.018. The maximum disagreement of 15 per cent occurs in the region $X_{As} = 0{\cdot}3 - 0{\cdot}5$, where the maximum error in the experimental determination of P_{As_4} and thus ϕ_{As} occurs.

The Ga–As liquidus line on the $T - X$ phase diagram was calculated using Vieland's expression[4],

$$\ln\left[\frac{1}{4X(1-X)}\right] + \ln\left(\frac{\gamma_A^{s.l.}\gamma_B^{s.l.}}{\gamma_A\gamma_B}\right) = \frac{\Delta S^F}{R}\left(\frac{T^F}{T} - 1\right) \quad (6)$$

for the GaAs-liquid equilibrium, with the activity coefficients expressed in equations (4a, 4b). (The superscript s.l. indicates stoichiometric liquid, i.e. $X = 0{\cdot}5$) The resultant equation can be solved numerically for $X = f(T)$, which is shown as a solid line in Fig. 3. The liquidus line for the As-liquid equilibrium was determined in a similar manner. Since the solid has only one component, equation (6) simplifies to

$$\ln\left(\frac{1}{\gamma_B X_B}\right) = \frac{\Delta S_B^f}{R}\left(\frac{T_B^f}{T} - 1\right). \quad (7)$$

The calculated liquidus lines agree well with the experimental data. The r.m.s. deviation which results mainly from scatter in the data is 16°C. Figure 3 also contains the results of the calculation compared with the

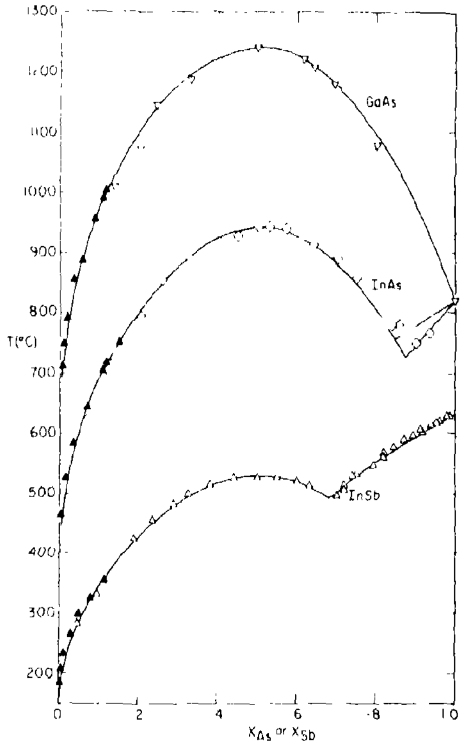

Fig. 3. Liquidus curves for the Ga–As, In–As and In–Sb systems. The calculated liquidus, represented by the solid line, is compared with the data of Hall[16] ▲ Koster and Thoma[36] ▽, Liu and Peretti[37, 38] ◇, △.

experimental liquidus data for In–As and In–Sb. The r.m.s. deviation in the liquidus for the InAs-liquid equilibrium is 11°C. For the As-liquid equilibrium, the liquidus data is very poor. In addition, the ΔS^F_{As} is only estimated[34]. Therefore, two liquidus lines were calculated for $\Delta S^F_{As} = 6{\cdot}07$ e.u. (the upper line) and 3·21 e.u. The standard deviation of the In–Sb liquidus lines is 7°C. The parameters used were:

$$\Omega_{Ga-As} = -4380, \Omega_{In-As} = -6070, \text{and} \quad \Omega_{In-Sb} = -3980.$$

The values of ΔS^l and T^l are listed in Table 1.

The comparisons of experimentally determined thermodynamic properties with the calculated properties strongly support the use of the quasi-chemical equilibrium treatment for III–V systems, even though in each case cited the regular solution approach has been shown to be invalid[5, 6, 18].

3. CALCULATION OF THE TERNARY PHASE DIAGRAM *A, B, C*

Vieland's[4] regular solution method of treating the equilibrium between a liquid and a binary compound of virtually invariant composition can be generalized to ternary systems of sub-regular solutions by using the quasi-chemical equilibrium approximation. The liquidus becomes a surface and the solid phase field, a line in the binary system, becomes a plane. A schematic phase diagram for the system *A, B, C* is shown in Fig. 4. The equilibrium treated is between the liquid and III–V mixed crystal solid solution, *AC–BC*. The chemical potentials in the liquid phase may be expressed as:

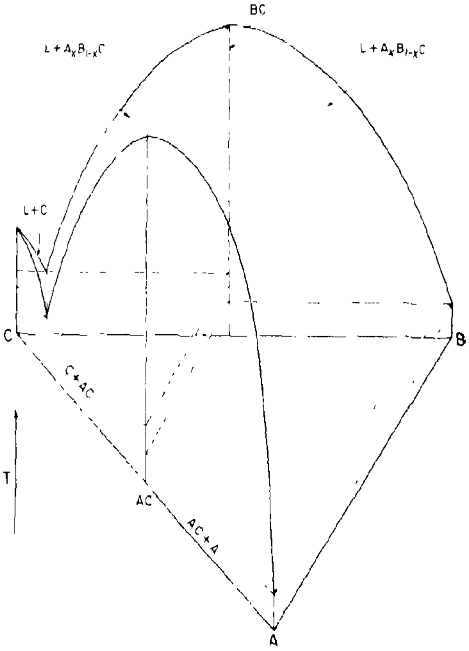

Fig. 4. Schematic *A-B-C* ternary phase diagram. The compounds, *AC* and *BC* are completely miscible. The solubility of *A*, *B* and *C* in $A_xB_{1-x}C$ is zero.

$$\mu_i^l(T) = \mu_i^{l0}(T) + RT \ln \gamma_i N_i, \quad i = A, B, C \tag{8}$$

Table 1. Parameters used in the calculation of the In–Ga–As *and* In–As–Sb *ternary phase diagrams*

Parameter P	Value used	Literature value
T^F_{GaAs}	1511°K	
T^F_{InAs}	1215°K	
T^F_{InSb}	803°K	
T^F_{As}	1090°K	
T^F_{Sb}	903°K	
$\Delta S^F_{\mathrm{GaAs}}$	14·7 eu	13·9[30], 15·3[31], 16·64[6]
$\Delta S^F_{\mathrm{InAs}}$	14·7 eu	21·4[30], 10·4[31], 11·5[33]
$\Delta S^F_{\mathrm{InSb}}$	13·3 eu	11·3[30], 11 9[31], 14·4[33] 14·1[32], 12·2[3]
ΔS^F_{As}	3·67 eu	3·67[34]
ΔS^F_{Sb}	5·27 eu	5·27[34]
Ω_{GaAs}	−4380 cal/mole	
$\Omega_{\mathrm{In\text{-}As}}$	−6070 cal/mole	
$\Omega_{\mathrm{In\text{-}Sb}}$	−3980 cal/mole	
$\Omega_{\mathrm{In\text{-}Ga}}$	+1066 cal/mole	
$\Omega_{\mathrm{As\text{-}Sb}}$	610 cal/mole	
$\Omega_{\mathrm{GaAs\text{-}InAs}}$	2800 cal/mole	
$\Omega_{\mathrm{InAs\text{-}InSb}}$	2900 cal/mole	

where $\mu_i^{l0}(T)$ is the chemical potential in the standard state of $N_i = 1$ and γ_i is the activity coefficient of component i. The chemical potentials in the solid phase are

$$\mu^c_{AC}(T) = \mu^{c0}_{AC}(T) + RT \ln \gamma_{AC} X \qquad (9a)$$

$$\mu^c_{BC}(T) = \mu^{c0}_{BC}(T) + RT \ln \gamma_{BC}(1 - X) \qquad (9b)$$

where X is the mole fraction of AC in the solid solution. At equilibrium,

$$\mu^c_{AC}(T) = \mu_A{}^l(T) + \mu_C{}^l(T) \qquad (10a)$$

$$\mu^c_{BC}(T) = \mu_B{}^l(T) + \mu_C{}^l(T). \qquad (10b)$$

The chemical potential of pure AC may be determined in terms of the chemical potentials of the stoichiometric liquid, $\mu_A{}^{s\,l}(T)$ and $\mu_B{}^{s\,l}(T)$, the entropy of fusion, ΔS^F_{AC}, the melting temperature, T^F_{AC}, and ΔC_p, the difference in specific heat between the compound and its supercooled liquid, by considering the total change in chemical potential as the compound AC at $T < T^F_{AC}$ is heated to the melting temperature, melted, and the resulting stoichiometric liquid supercooled to T. The resulting expression is[4]

$$\begin{aligned}\mu^{c0}_{AC}(T) = {} & \mu_A{}^{s\,l}(T) + \mu_C{}^{s\,l}(T) \\ & - \Delta S^F_{AC}(T^F_{AC} - T) \\ & + \Delta C_p[T^F_{AC} - T - T \ln(T^F_{AC}/T)].\end{aligned} \qquad (11)$$

μ^{c0}_{BC} may be expressed similarly. Neglecting the small terms in ΔC_p, the equilibrium conditions equations (10a, 10b) may be combined with equations (8–11). The result is

$$\begin{aligned}\ln(\gamma_{AC} X) = {} & \ln\left(\frac{4\gamma_A \gamma_C N_A N_C}{\gamma_A{}^{s\,l} \gamma_C{}^{s\,l}}\right) \\ & + \Delta S^F_{AC}(T^F_{AC} - T)/RT\end{aligned} \qquad (12a)$$

$$\begin{aligned}\ln\left(\gamma_{BC}(1 - X)\right) = {} & \ln\left(\frac{4\gamma_B \gamma_C N_B N_C}{\gamma_B{}^{s\,l} \gamma_C{}^{s\,l}}\right) \\ & + \Delta S^F_{BC}(T^F_{BC} - T)/RT\end{aligned} \qquad (12b)$$

$$N_A + N_B + N_C = 1. \qquad (12c)$$

The activity coefficients may now be calculated in terms of temperature and composition using the quasi-chemical equilibrium theory. The following six equations specify the thermodynamic properties of the solution:

$$N_{AA}N_{BB}/(N_{AB})^2 = \tfrac{1}{4}\exp(2\Omega_{AB}/ZRT) \quad (13a)$$

$$N_{BB}N_{CC}/(N_{BC})^2 = \tfrac{1}{4}\exp(2\Omega_{BC}/ZRT) \quad (13b)$$

$$N_{AA}N_{CC}/(N_{AC})^2 = \tfrac{1}{4}\exp(2\Omega_{AC}/ZRT) \quad (13c)$$

$$2N_{AA} + N_{AB} + N_{AC} = ZN_A \quad (14a)$$

$$2N_{BB} + N_{AB} + N_{BC} = ZN_B \quad (14b)$$

$$2N_{CC} + N_{AC} + N_{BC} = ZN_C. \quad (14c)$$

The following notation is introduced to simplify the expressions:

$$X_{ij} = N_{ij}/Z; \quad i,j = A,B,C$$

$$\eta_{ij} = \exp(\Omega_{ij}/ZkT); \quad i,j = A,B,C$$

Combining equations (13–14), results in a set of three simultaneous equations from which X_{ij} and hence N_{ij} may be determined.

$$(N_A - X_{AB} - X_{AC})(N_B - X_{AB} - X_{BC}) - \eta_{AB}^2 X_{AB}^2 = 0 \quad (15a)$$

$$(N_B - X_{AB} - X_{BC})(N_C - X_{AC} - X_{BC}) - \eta_{BC}^2 X_{BC}^2 = 0 \quad (15b)$$

$$(N_A - X_{AB} - X_{AC})(N_C - X_{AC} - X_{BC}) - \eta_{AC}^2 X_{AC}^2 = 0. \quad (15c)$$

These equations cannot be solved analytically, but can be solved numerically on a digitial computer for a given temperature and composition, giving

$$\Delta H_M = X_{AB}\Omega_{AB} + X_{AC}\Omega_{AC} + X_{BC}\Omega_{BC}. \quad (16)$$

The activity coefficient γ_A is related to ΔH_M through the excess free energy of mixing.

$$\Delta F^{xs} = \Delta F_M - \Delta F_M{}^{\text{ideal}}. \quad (17)$$

ΔF^{xs} may be obtained from ΔH_M by integrating the Gibbs–Helmholtz equation; i.e.

$$\int_{\Delta F_M{}^{\text{ideal}}/T}^{\Delta F_M/T} d(\Delta F_M/T) = \int_0^{1/T} \Delta H_M d(1/T) \quad (18)$$

since as $T \rightarrow \infty, \Delta F_M \rightarrow \Delta F_M{}^{\text{ideal}}$. Thus,

$$\ln\gamma_A = \left(\frac{\partial(\Delta F^{xs}/RT)}{\partial N_A}\right)_{N_B,N_C}$$

$$= 1/R\left[\frac{\partial}{\partial N_A}\left(\int_0^{1/T}(X_{AB}\Omega_{AB} + X_{AC}\Omega_{AC} + X_{BC}\Omega_{BC})\,d(1/T)\right)\right]_{N_B,N_C}. \quad (19)$$

The calculation is carried out numerically to yield the three activity coefficients in the liquid phase. The activity coefficients in the solid phase, which has only two components, are given by equations (4a, 4b), Z is taken as 4 for the solid since it has the zinc-blende structure.

The activity coefficients γ_A, γ_B, γ_C, γ_{AB}, γ_{AC} can all be determined; thus equations (12a–c) can be solved numerically with N_A and N_B given to yield N_C, the liquidus temperature, and the solidus composition in terms of the following parameters: T^F_{AC}, T^F_{BC}, ΔS^F_{AC}, ΔS^F_{BC}, Ω_{A-B}, Ω_{A-C}, Ω_{B-C}, and Ω_{AC-BC}, which can be obtained from the published thermodynamic data for the binary III–V systems.

4. CALCULATION OF THE In–Ga–As TERNARY PHASE DIAGRAM

The melting temperature and entropy of fusion for InAs and GaAs can be extracted directly from the literature. See Table 1. $\Omega_{\text{Ga-As}}$ was determined in Section 2 from activity data and the binary liquidus. $\Omega_{\text{In-As}}$ may be determined from the activity coefficients calculated from the As vapor pressure data along the liquidus, which is plotted in Fig. 5. Only the As_2 pressures determined by Goldfinger and Jeunehomme[17] are presented because Arthur[6] found their As_4 pressure measurements over GaAs to be in error. Because the extrapolation of Goldfinger and Jeunehomme's data does not agree with the results of Folberth[18] and Boomgard and Schol[19], Renner[20] calculated P_{As_2} at 1000°K from thermodynamic data. His estimated As_2 curve, which

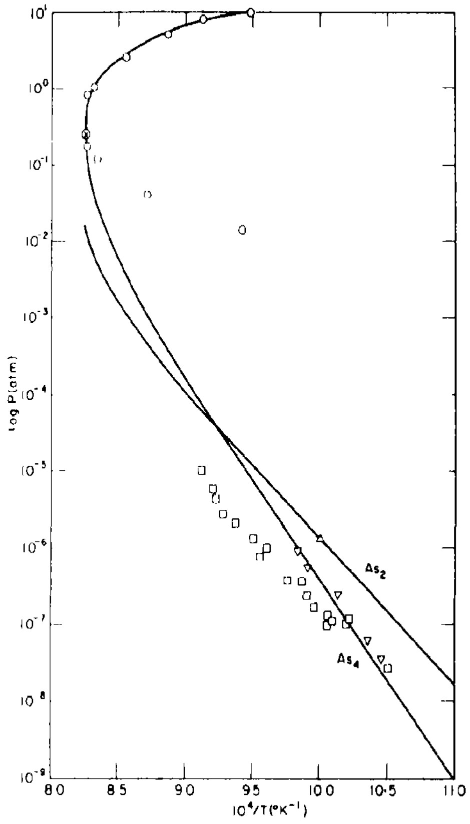

Fig. 5. Arsenic pressure as a function of $1/T$ for InAs. ○ Van den Boomgard and Schol[19]; ⊗ Folberth[18]; ☐ Goldfinger and Jeunehomme[17]; ∇ Sirota[21]; Δ Renner[20].

agrees approximately with Sirota's[21] estimates, is plotted in Fig. 5. The P_{As_4} curve shown was calculated from the As_2 curve using the As_2–As_4 equilibrium constant determined by Arthur[6]. These values of P_{As_4} were used in the following expression to calculate the activity coefficients:

$$\gamma_{As} = \frac{1}{X_{As}}\left(\frac{P_{As_4}}{P^0_{As_4}}\right)^{1/4}.$$

$P^0_{As_4}$ was obtained from Thurmond[5] and X_{As} from Hall[16]. η_2 vs. $1/T$ was calculated from the data using equations (4a, 4b). The slope of η^2 vs. $1/T$, shown in Fig. 6, is equal to $2\Omega_{In-As}/ZRT$ giving $\Omega_{In-As} = -6070$ cal/mole. Included in Fig. 6 for comparison is η^2 for GaAs, which yields $\Omega_{Ga-As} = -4380$ cal/mole.

Macur, Edwards, and Wahlbeck[22] investigated the activity coefficients in In–Ga solutions. Using the regular solution treatment, they found $\Omega_{In-Ga}/RT = 0{\cdot}42$ at 1269°K. At high temperatures ($\Omega \gg kT$), the regular solution approximation becomes equivalent to the quasi-chemical equilibrium approach so Ω_{In-Ga} was taken as 1066 cal/mole.

The InAs–GaAs interaction parameter was determined from the pseudobinary phase diagram[23–25] by adjusting $\Omega_{InAs-GaAs}$ to give agreement between the calculated and experimental solidus point at 1300°K. The value of $\Omega_{InAs-GaAs}$ used in the calculation was 2800 cal/mole.

The calculated In–Ga–As ternary phase diagram is presented in Fig. 7. Two families of curves are drawn on the diagram. Isothermal liquidus curves at 50°K temperature intervals are presented as solid lines. Each member of the set of dashed curves represents the liquidus compositions in equilibrium with a fixed solid composition. The curves are drawn for solid compositions of 10, 30, 50, 70, 80, 90 and 95 per cent GaAs. The two sets of lines together allow one to determine the temperature-coordinate liquid composition pairs with tie lines leading to a given solid composition.

The applicability of the quasi-chemical equilibrium approach to the In–Ga–As ternary system can be further tested by comparing the available experimental phase diagram data with the calculated results. In Fig. 8, the calculated InAs–GaAs pseudobinary phase diagram is plotted along with the experimentally determined data[23–25]. Even though the InAs–GaAs interaction parameter was determined by fitting one calculated solidus point to the experimental value, the excellent agreement between calculation and experiment for the liquidus and solidus across the entire diagram is valid evidence in support of the model. The r.m.s. deviation is 2·7°, comparing the Van Hook and Lenker[25]

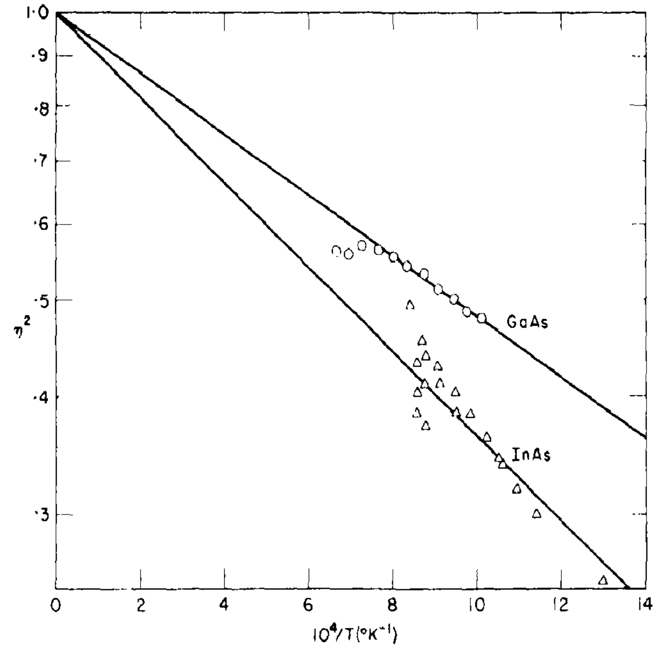

Fig. 6. The parameter η^2 (defined by equation (4)) as a function of $1/T$ for GaAs and InAs

liquidus and Woolley and Smith[23] solidus data with the calculated curves.

The calculation is further verified by several experimental points on the In–Ga–As ternary phase diagram obtained by Ewing[26]. InAs–GaAs crystals were grown epitaxially on InAs substrates by slowly cooling (5°C/hr.) an In–Ga–As solution, in contact with an InAs substrate, from near the liquidus temperature. The composition of the resultant crystal was determined with an accuracy of ±2 per cent, using X-ray diffraction. The results are plotted in Fig. 9.

It should be understood that these were not strictly equilibrium measurements. During growth of crystals which have a different composition than the liquid, concentration gradients are built up near the growing interface. The magnitude of the gradient depends on the cooling rate. For the growth of InAs–GaAs crystals reported, one would expect a region depleted in As to be built up especially when the total As concentration in the liquid is low. From the ternary phase diagram, one can see that such a depletion layer would cause the growing crystal to have a higher GaAs content. Thus, the crystal grown from a liquid containing 2 per cent As and 38 per cent Ga produced a crystal of 99 ± 2 per cent GaAs even though the phase diagram indicates the solidus to be 95 per cent GaAs. The phase diagram indicates that at low Ga concentrations the solidus concentration is not sensitive to the As concentration, but is sensitive to Ga concentration; however, the crystals grown from solutions low in Ga have low Ga contents. Thus, the Ga depletion should be small.

5. CALCULATION OF In–As–Sb TERNARY PHASE DIAGRAM

The parameters for the calculation of the In–As–Sb phase diagram, except Ω_{As-Sb}, have been discussed above or can be obtained directly from the literature. They are sum-

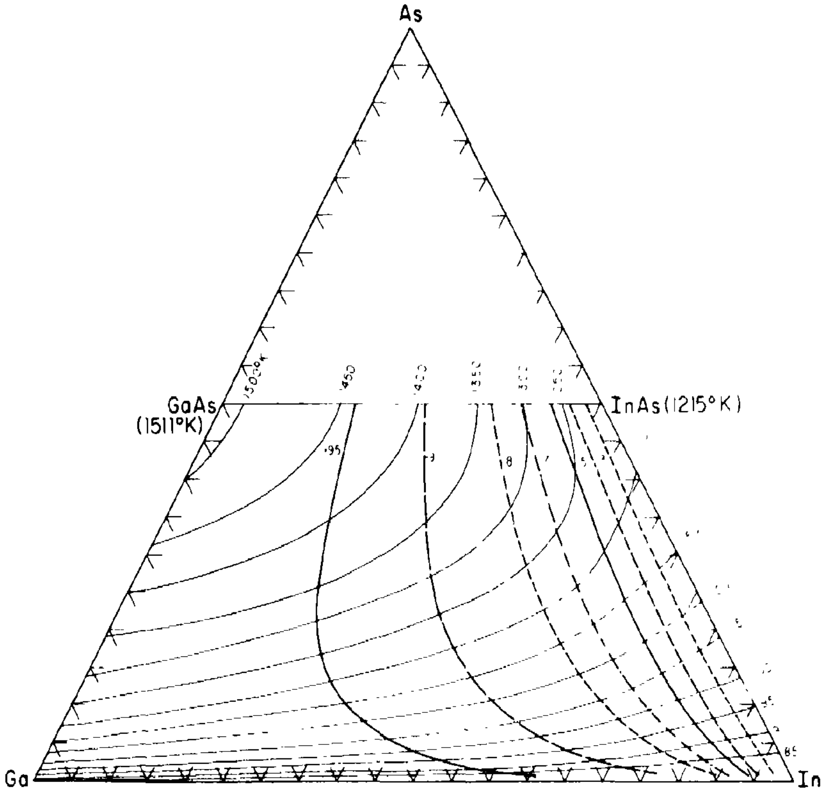

Fig. 7. In-Ga-As ternary phase diagram. The set of solid lines are liquidus isotherms taken at 50° intervals between 850° and 1500°K. The set of dashed lines are iso-solidus-concentration lines. Each line represents the liquid concentrations in equilibrium with a fixed solid concentration. The curves are drawn for solid compositions of 10, 30, 50, 70, 80, 90 and 95 per cent GaAs.

marized in Table 1. No information is available from which $\Omega_{\text{As-Sb}}$ could be calculated. An estimate can be made from the As-Sb phase diagram[27, 28]. The minimum in the liquidus curve and the tentative existence of a solid immiscibility indicate $\Omega_{\text{As-Sb}}$ to be positive. The As-Sb interaction parameter was determined to be 610 cal/mole by fitting the calculated As-Sb liquidus curve to the experimentally determined phase diagram[28]. The r.m.s. deviation between calculated and experimental values is 2·7°.

The calculated In-As-Sb phase diagram is presented in Fig. 10. Liquidus curves only for the $\text{InAs}_{1-x}\text{Sb}_x$-liquid equilibrium were calculated. The boundary between this liquidus and the liquidus in equilibrium with As-Sb alloys was estimated from three experimental points: the In-As and In-Sb binary eutectics and the 'eutectic' in the InAs-Sb pseudobinary[29].

The InAs-InSb pseudobinary phase diagram calculated is shown in Fig. 11. Again the experiment-calculation agreement supports the model for the In-As-Sb system. The r.m.s. deviation is 19°C.

6. SUMMARY

It has been demonstrated that certain thermodynamic properties of III-V systems can be described using the quasi-chemical

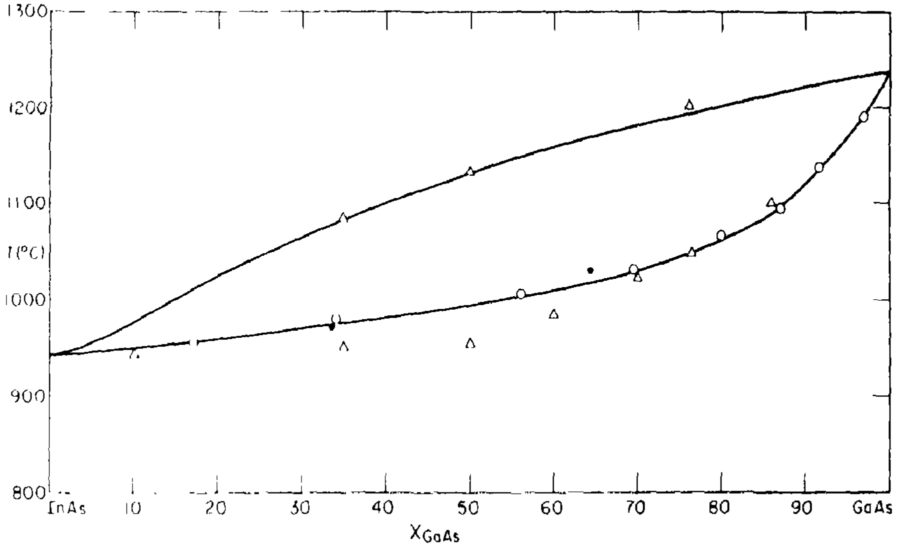

Fig. 8. The InAs–GaAs pseudobinary phase diagram ——— calculated; Δ Van Hook and Lenker [25]; ○ Woolley and Smith [23]; ● Hockings *et al.*[24].

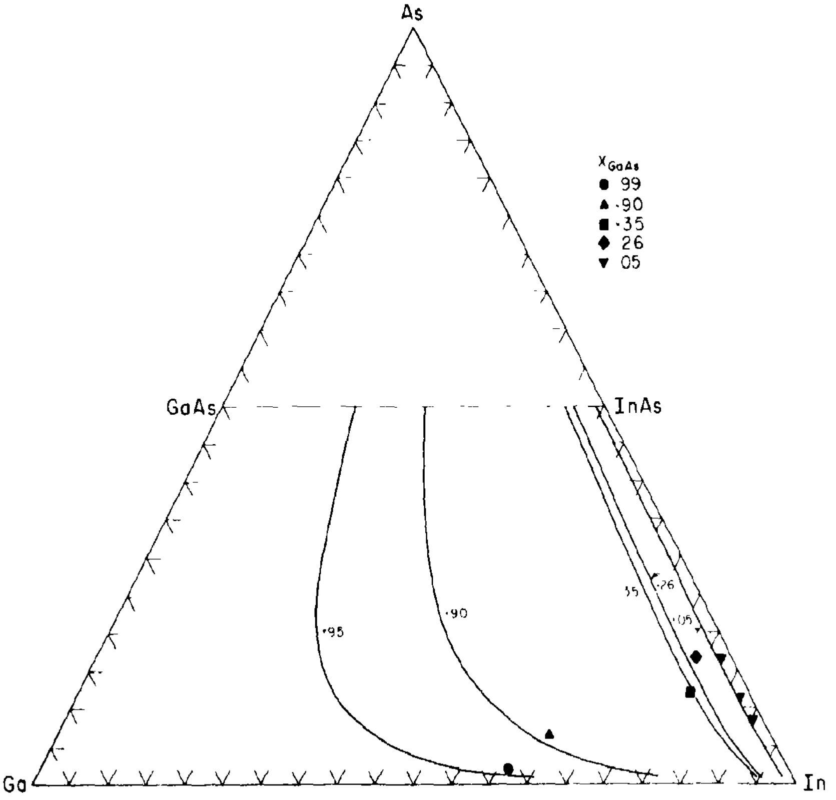

Fig. 9. Comparison of calculated and experimental data on the In–Ga–As ternary phase diagram.

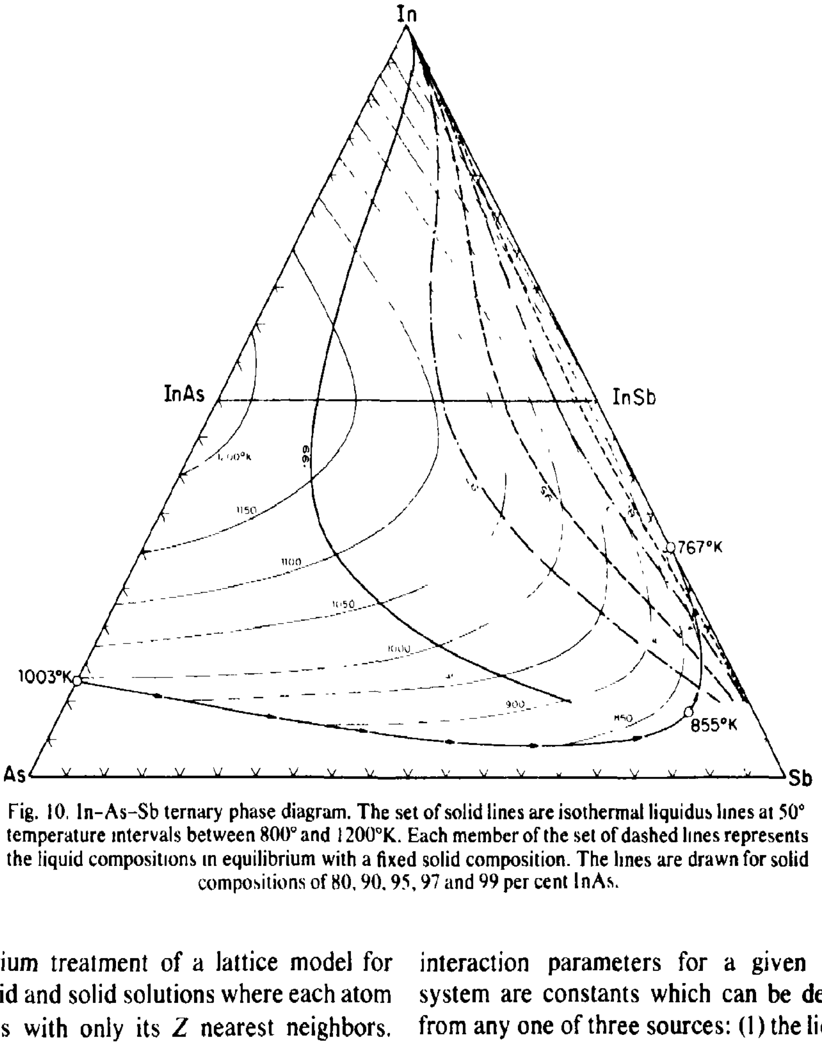

Fig. 10. In–As–Sb ternary phase diagram. The set of solid lines are isothermal liquidus lines at 50° temperature intervals between 800° and 1200°K. Each member of the set of dashed lines represents the liquid compositions in equilibrium with a fixed solid composition. The lines are drawn for solid compositions of 80, 90, 95, 97 and 99 per cent InAs.

equilibrium treatment of a lattice model for the liquid and solid solutions where each atom interacts with only its Z nearest neighbors. The calculated activity of In in In–Sb solutions, activity of As in Ga–As solutions, and liquidus curves in the In–Sb, Ga–As, and In–As systems all agree well with available experimental data.

The quasi-chemical equilibrium approach has been used as the basis for a calculation of the phase diagram for a general ternary system A, B, C containing the binary, stoichiometric, completely miscible compounds AC and BC. The parameters needed for the calculation are the melting temperature and entropy of fusion for both AC and BC, and the interaction parameters, $\Omega_{A\text{-}C}$, $\Omega_{B\text{-}C}$, $\Omega_{A\text{-}B}$, $\Omega_{AC\text{-}BC}$. The interaction parameters for a given binary system are constants which can be deduced from any one of three sources: (1) the liquidus or solidus curves for the binary systems; (2) the vapor pressure of one component over the binary solution as a function of $1/T$; or (3) the activity vs. concentration data at one temperature.

The calculation was carried out numerically for two ternary systems, In–Ga–As and In–As–Sb. The agreement between the calculated and experimentally determined phase diagrams was excellent, indicating the validity of the quasi-chemical equilibrium model for the description of liquid and solid solutions involving elements from groups III and V of the periodic table.

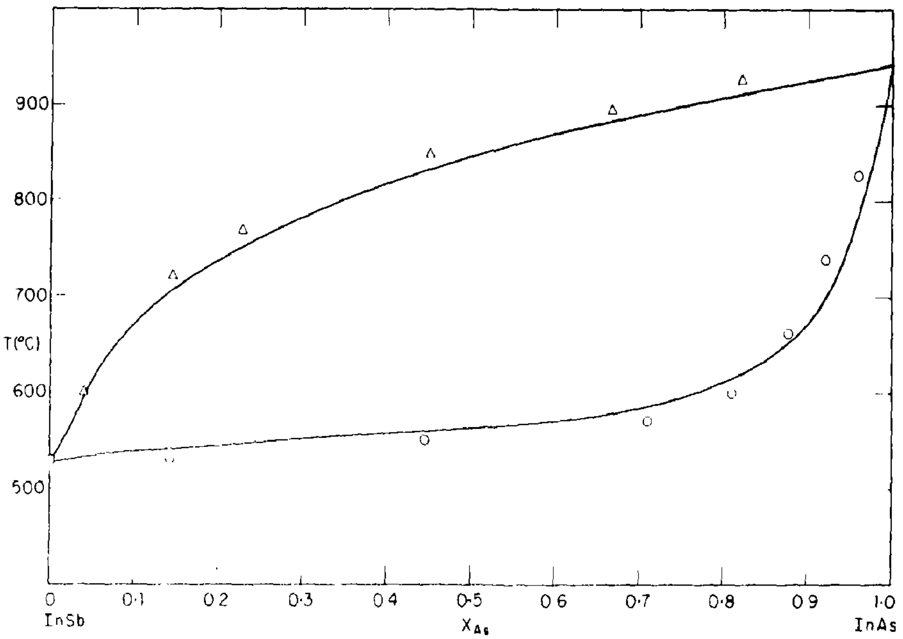

Fig. 11. InAs–InSb pseudobinary phase diagram. ——— —calculated; Δ Shih and Peretti[29]; ○ Woolley and Smith[23]

REFERENCES

1. GUGGENHEIM E. A., In *Mixtures* Oxford University Press, Oxford (1952)
2. WAGNER C., *Acta. Metall* **6**, 309 (1958).
3. SCHOTTKY W. F. and BEVER M. B., *Acta. Metall.* **6**, 320 (1958)
4. VIELAND L. J., *Acta Metall.* **11**, 137 (1963).
5. THURMOND C. D., *J. Phys Chem. Solids* **27**, 785 (1965).
6. ARTHUR J. R., *J. Phys. Chem. Solids* **28**, 2257 (1967).
7. FURUKAWA Y. and THURMOND C. D., *J. Phys. Solids* **26**, 1535 (1965).
8. PANISH M. B., *J. Phys Chem. Solids* **27**, 291 (1966).
9. PANISH M. B., *J. electrochem. Soc.* **113**, 224 (1966).
10. PANISH M. B., *J. electrochem. Soc.* **114**, 516 (1967).
11. HAGEMARK K., *J. phys Chem.* **72**, 2316 (1968).
12. HILDEBRAND J. H., *J. Am. chem Soc.* **51**, 66 (1929).
13. HOSHINO H., NAKAMURA Y., SHIMOJI M and NIWA K., *Ber Bunsen phys Chem.* **69**, 114 (1965)
14. BUSCHERT R., GEIB I. G. and LARK-HOROWITZ K., *Bull. Am. phys. Soc. Ser. II*, 1, 111 (1956).
15. BENNETT C. A. and FRANKLIN N. L., In *Statistical Analysis in Chemistry and the Chemical Industry*, p. 28 Wiley, New York (1954).
16. HALL R. N., *J. electrochem. Soc.* **110**, 385 (1963).
17. GOLDFINGER P. and JEUNEHOMME M., In *Advances in Mass Spectrometry* (Edited by J. D. Waldron), p. 534. Pergamon Press, Oxford (1959).
18. FOLBERTH O. G., *J. Phys. Chem. Solids* **7**, 295 (1958)
19. VAN DEN BOOMGAARD J. and SCHOL K., *Phillips Res. Rep.* **12**, 127 (1957).
20. RENNER T., *Solid St. Electron.* **1**, 39 (1960)
21. SIROTA N. N., In *Semiconductors and Semimetals*, Vol. 4, Chap. 2. Academic Press, New York (1968).
22. MACUR G. J., EDWARDS R. K. and WAHLBECK P. G., *J. phys. Chem.* **72**, 1047 (1968).
23. WOOLLEY J. C. and SMITH B. A., *Proc. phys. Soc.* **72**, 214 (1958).
24. HOCKINGS E. F., KUDMAN I., SEIDEL T. E., SCHMELZ C. M. and STEIGMEIER E. F., *J. appl. Phys* **37**, 2879 (1966).
25. VAN HOOK H. J. and LENKER E. S., *Trans. metall. Soc. AIME* **227**, 220 (1963).
26. EWING R. E., Private communication.
27. HANSEN M., In *Constitution of Binary Alloys.* McGraw-Hill, New York (1958).
28. SHIH C. H. and PERETTI E. A., *Trans. Am. Soc. Metals* **48**, 709 (1956).
29. SHIH C. and PERETTI E. A., *Trans. Am Soc. Metals* **46**, 389 (1954).
30. RICHMAN D. and HOCKINGS E. F., *J. electrochem. Soc.* **112**, 461 (1965).
31. GLAZOV V. M., KRESTOVNIKOV A. N. and MALYNTINA G. L., *Dokl. Akad. Nank. SSSR* **175**, 631 (1967).

32. NACHTRIEB N. H. and CLEMENTI N., *J. phys. Chem.* **62**, 876 (1958).
33. LUDIN C. E., POOL M. J. and SULLIVAN R. V., Final Report, Contract No. AF19(604)-7222. University of Denver (1963).
34. KELLEY K. K., *U.S. Bur. Mines, Bull.* 584 (1958).
35. TERPILOWSKI J., *Arch. Hutnictwa* **3**, 227 (1958).
36. KOSTER W. and THOMA B., *Z. Metallk.* **46**, 291 (1955).
37. LIU T. S. and PERETTI E. A., *Trans. Am. Soc. Metals* **45**, 677 (1953).
38. LIU T. S. and PERETTI E. A., *Trans. Am. Soc. Metals* **44**, 534 (1952).

J. Phys. Chem. Solids Pergamon Press 1969. Vol. 30, pp. 1793–1799. Printed in Great Britain.

SOME STUDIES OF DEFECTS IN CALCIUM OXIDE–I. IMPURITY EFFECTS

A. C. TOMLINSON and B. HENDERSON
Physics Department, Keele University, Keele, Staffordshire, England

(*Received* 16 *September* 1968; *in revised form* 16 *December* 1968)

Abstract– In some CaO crystals grown by the arc fusion technique, paramagnetic resonance lines due to impurity ions are considerably narrower than have usually been reported. Thus it has been possible to resolve the hyperfine structure from the nuclei ^{155}Gd and ^{157}Gd associated with the Gd^{3+} electron spin resonance spectrum. An isotropic g-shift of order 0·00008 between the ^{47}Ti and ^{49}Ti hyperfine lines in a spectrum due to octahedrally co-ordinated Ti^+ ions is also apparent. In annealed and quenched crystals these linewidths are noticeably increased as a result of the lattice disorder present after quenching.

Pairs of sharp lines in the electron spin resonance spectrum of Mn_{2+} are assigned to the double-quantum transitions between pairs of non-adjacent levels. In the absence of strain, the levels involved are unequally spaced and double quantum transitions are not observed. A range of internal distortions in the crystals yields equality of spacing between the levels for some ions, so that $\Delta M_s = 2$ transitions may occur with simultaneous absorption of two microwave photons of identical frequency.

1. INTRODUCTION

COMMERCIALLY available single crystals of calcium oxide contain significant concentrations of transition metal impurities substituted on cation sites. Electron spin resonance studies show that the symmetry around these ions is accurately cubic despite considerable dislocation structure consequent upon the growth process. The valencies of these ions may be varied by annealing the crystals in vacuum or in oxidising atmospheres. The ease with which the valency changes may be effected depends upon the degree of misfit between the impurity ion and the matrix, and upon the need to maintain electrostatic neutrality in the lattice through the incorporation of charge compensating vacancies. Valency changes are also produced by ionising radiation, in which case charge compensation is achieved through electron or hole trapping elsewhere in the lattice.

Since numerous impurity ions occur in the trivalent state, cation vacancies are favoured. Holes formed during irradiation are trapped preferentially on the oxygen ions near these vacancies and may be observed by electron spin resonance. Trapped electron centres are less easily produced in calcium oxide since there are very few anion vacancies in thermodynamic equilibrium, and also because the binding energy of the divalent host lattice precludes the possibility of ionic displacement by ionizing radiation. Anion vacancies are, however, present in crystals which have been subjected to either heavy particle irradiation or to annealing treatment at high temperatures in several atmospheres of calcium vapour. The present crystals were selected from regions of the melt closest to the electrodes since they had been electrolytically coloured during the growth process. The crystals were coloured dark brown, suggesting the presence of colloidal metal particles in addition to the single anion vacancies. In Part I we discuss some interesting features of the impurity spectra of these electrolytically coloured samples.

2. EXPERIMENTAL PROCEDURE

The calcium oxide crystals were grown by Muscle Shoals Inc., Tuscumbia, Alabama, U.S.A. and had been accidentally electrolytically coloured during the growth process. The crystals were not chemically analysed but concentrations of 10^{14}–10^{16} cm^{-3} of paramagnetic ions were detected. Most crystals were examined in the as-received condition, but a few were annealed in oxidising atmospheres by suspending them from platinum wires in air inside an electric furnace.

Preliminary electron spin resonance measurements were made with a simple spectrometer which used a helix in place of the more familiar resonant cavity. For more quantitative measurements a Varian V4502 superheterodyne spectrometer with facilities for 100 kHz and audio frequency field modulation was used. The magnetic field was produced by a 9″ magnet on a rotatable base and controlled with the Varian Fieldial device. The microwave frequency was measured with a Hewlett Packard 524C frequency counter by zero beating against a 540B transfer oscillator. The field could then be accurately calibrated over a wide range, since the Hamiltonian parameters of such impurities as Mn^{2+} are well established. Irradiation was accomplished with a high pressure mercury lamp through precisely machined slots in the end wall of a rectangular H_{012} cavity. Paramagnetic resonance measurements were made at 290°, 77° and 4°K, using cold finger dewars when required. At 4°K and using the lowest possible power on the superheterodyne spectrometer commensurate with good sensitivity, no transitions were observed. Presumably this indicates that for all ions the relaxation times are very long: rapid cross-relaxation via other impurities seems to be unimportant compared with the same ions in MgO.

3. RESULTS AND DISCUSSION

Although nominally 'undoped', all crystals showed resonance absorption from Gd^{3+}, Mn^{2+}, Fe^{3+}, Cr^{3+}, V^{2+}; the linewidths (Table 1) for these ions were much smaller than has previously been reported. This emphasises the accurate cubic symmetry around the ions and the absence of line broadening by lattice defects or by magnetic hyperfine interaction with nuclei of the host lattice. The increased linewidths in quenched crystals are a consequence of the increased disorder present in such crystals. Quenching tends to retain the high temperature concentration of vacancies and also produces significant plastic deformation as a result of the thermal stresses: both these effects will broaden the lines inhomogeneously as a result of the distortions of the cubic crystal field[1].

Table 1. Paramagnetic resonance linewidths in calcium oxide single crystals. Derivative peak-to-peak width in gauss

	As grown		*Annealed and quenched*	
	300°K	77°K	300°K	77°K
Gd^{3+}	0·8	0·1	0·8	0·8
Mn^{2+}	0·6	0·1	1·0	0·7
Fe^{3+}	*	8		12
Cr^{3+}	1·0	P 15	1·0	0·7
V^{2+}	1·0	0·15	*	*
Li^{+}	1·0	0·15	*	*
F^{+} centres	0·02	0·02	*	*
V centres	*	1·0	*	1·0

*Defect not detected or spectrum too broad to measure

3.1 *The Gd hyperfine structure*

The fine structure spectrum of the $^8S_{7/2}$ ground state of Gd^{3+} in calcium oxide has been reported previously both by Shuskus[2] and Low and Rubins[3]. The fine structure parameters measured in the present experiments are in good agreement with those already reported. No evidence was obtained for $\Delta M_S > 1$ forbidden transitions of Gd^{3+}, nor of axially symmetric spectra consequent upon the localization of a charge compensating vacancy near the Gd^{3+} ion. However, the electron spin resonance linewidths reported earlier are almost two orders of magnitude greater than those reported here. The lines in the previous work were probably inhomogeneously broadened by interaction with lattice defects, although we have noted that they are also quite sensitive to the microwave power level. Consequently Shuskus[2] and Low and Rubins[3] failed to detect the hyperfine structure of the Gd^{3+} ion in calcium oxide. Figure 1 shows the hyperfine structure associated with the $\Delta M_s = +\frac{1}{2} \leftrightarrow -\frac{1}{2}$ transition at 77°K. The nuclei involved in this structure have nuclear spin $I = \frac{3}{2}$ and are associated with ^{157}Gd and ^{155}Gd, which have 15·64 and 14·68 per cent isotopic abundance respectively. Hyperfine structure parameters for these two nuclei in calcium oxide and some other solids are compared in Table 2.

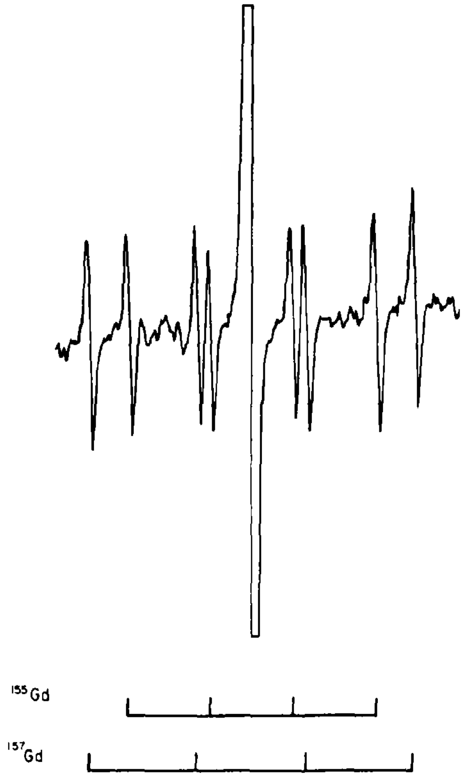

Fig. 1. The ^{155}Gd and ^{157}Gd hyperfine structure attendant upon the $M_s = \frac{1}{2} \leftrightarrow -\frac{1}{2}$ transition for Gd^{3+} ions at 77°K

The classical contribution to magnetic hyperfine interaction arises from electronic orbital motion, electron spin magnetization outside the nucleus and spin magnetization at the nucleus. Relativistic effects may contribute to all three interactions but unlike core polarization do not contribute to a hyperfine anomaly. This is because a hyperfine anomaly may arise from a non-uniform distribution of unpaired electron spin density over the volume occupied by the nuclear magnetization. The hyperfine anomaly can then be determined from

$$^{155}\left(\frac{A}{g_n}\right)\,^{157}\left(\frac{g_n}{A}\right) = 1+\Delta$$

where the nuclear g-values and hyperfine constants are to be determined for Gd^{3+} in the oxide. Usually, and for the systems noted in Table 2, this has not been the adopted procedure. In the absence of ENDOR measurements, the nuclear g-values used have been those determined optically for Gd^4 atoms or from NMR measurements on GdN[5]. Using this method we determine Δ for Gd^{3+} in CaO to be about 1·2 per cent, which is within the range of values reported for other solids. However, it is realised that this is not conclusive evidence for the presence of a hyperfine anomaly, since the nuclear g-values should be measured directly using ENDOR.

Table 2. Hyperfine parameters in gauss for Gd^{3+} *and* Gd

Crystal	^{155}A	^{157}A	$^{155}A/^{157}A$	Reference
Free Atom			0·80 ± 0·02	[4]
$Bi_2Mg_3(NO_3)_{12} \cdot 24H_2O$	4·0 ± 0 3	5·34 ± 0·17	0·75 ± 0 07	[6]
SrS	3·68 ± 0·06	5·0 ± 0·05	0·73 ± 0·03	[7]
ThO_2	4·25 ± 0·15	5·73 ± 0·12	0·744 ± 0·0007	[8]
$CaWO_4$	4·45 ± 0 02	5·84 ± 0 02	0·763 ± 0·0006	[9]
CaO	3·97 ± 0·10	5 19 ± 0·10	0·767 ± 0·010	This paper

3.2 Ti^+-*spectrum*

Prolonged irradiation at 77°K of the electrolytically coloured crystals revealed a new spectrum, the central component of which is essentially isotropic, indicating that the defect responsible is present in sites of cubic symmetry. The spectrum was somewhat broadened at 300°K. After production at 77°K it decayed to half the intensity at room temperature in a few hours. Irradiation at room temperature produced the spectrum transiently; decay to undetectably low intensities occurring within tens of seconds after the cessation of irradiation. Figure 2 shows the isotropic hyperfine structure associated with this spectrum to consist of eight lines, the inner six of which almost overlap a second set of six lines. Consequently isotopes with nuclear spins $I = \frac{5}{2}$ and $I = \frac{7}{2}$ are involved, with the latter the less abundant. This indicates that the spectrum is due to titanium, for which the abundance of ^{47}Ti is 7·75 per cent and ^{49}Ti is 5·51 per cent. The spectrum is centred at $g = 1{\cdot}9866$ $(\pm 0{\cdot}005)$ and we observe $^{47}A = {}^{49}A = 10{\cdot}8 \times 10^{-4}\,cm^{-1}$. A shift of 130 mG is observed for the ^{49}Ti components relative to ^{47}Ti, corresponding to a difference in g-value of 0·00008 for these isotopes. No such isotopic g-shift has been previously reported, although an isotopic change in D-value of Cr^{3+} in axially symmetric sites in magnesium oxide was reported[10].

We assign this spectrum to Ti^+ ions in substitutional cation sites. Wertz *et al.*[11] have suggested that Ti^{4+} is stable in magnesium oxide and that Ti^{3+} in axially symmetric sites may be detected after X-irradiation. The ionic radii of the various titanium ions are Ti^{4+}, 0·68 Å; Ti^{3+}, 0·76 Å; Ti^{2+}, 0·90 Å and Ti^+, 0·96 Å while the radius for Ca^{2+} is 0·99 Å Ti^{4+} and Ti^{3+} are very small relative to Ca^{2+} and are unlikely candidates for a substitutional site in calcium oxide. The presence of F^+-centres in the crystals may bias them against the formation of such ions. Intuitively, therefore, one expects Ti^{2+} to exist in calcium oxide, since no charge compensation is required and little elastic distortion results from the small ionic size. Ti^{2+} is a $3d^2$ ion, and although other $3d^2$ ions (V^{3+}) exist in calcium oxide they may have not been detected using electron spin resonance. There is not *a priori* reason why Ti^{2+} should be detected. In addition electron spin resonance spectra from Ti^{2+} ($3d^2$) and Ti^{3+}($3d^1$) in octahedral coordination are unlikely to have the properties reported for this spectrum[12]. Ti^{2+} has been observed substituting for Ca^{2+} in calcium fluoride[13], where the eightfold cubic coordination reverses the order of the levels relative to that of the octahedral coordination. The magnetic resonance spectrum is readily observable in that case.

The Ti^+ ion is isoelectronic with V^{2+}, Cr^{3+} and Mn^{4+}, which in octahedral crystal fields have the orbital singlet state $^4A_{2g}$ lowest. Thus in a magnetic field the transitions between the $\pm\frac{3}{2}$ and $\pm\frac{1}{2}$ levels are isotropic and coincide precisely. The isotropic g-value of 1·9866 is consistent with this, and an appropriately simple spin Hamiltonian including only the effects of isotropic Zeeman and hyperfine interactions may be used to describe the present results. The g-value in the Zeeman term is given as:

$$g = 2{\cdot}0023 - \frac{8\lambda'}{\Delta}$$

where λ' is the spin-orbit coupling constant and Δ the splitting between the $^4A_{2g}$ ground term and the $^4T_{2g}$ excited state. Thus the isotropic g-shift is derived from the quotient λ'/Δ. The two isotopes will have different vibrational frequencies associated with their different masses: this causes the admixture of other excited state wavefunctions into the $^4T_{2g}$ level to differ for the two isotopes. Thus the orbital angular momentum generated in the ground state by mixing of the $^4A_{2g}$ and $^4T_{2g}$ levels due to the spin-orbit coupling operator $\lambda L.S$ will also differ for the two isotopes. The effect is usually negligibly small, and in the present case $\Delta g = 0{\cdot}00008$.

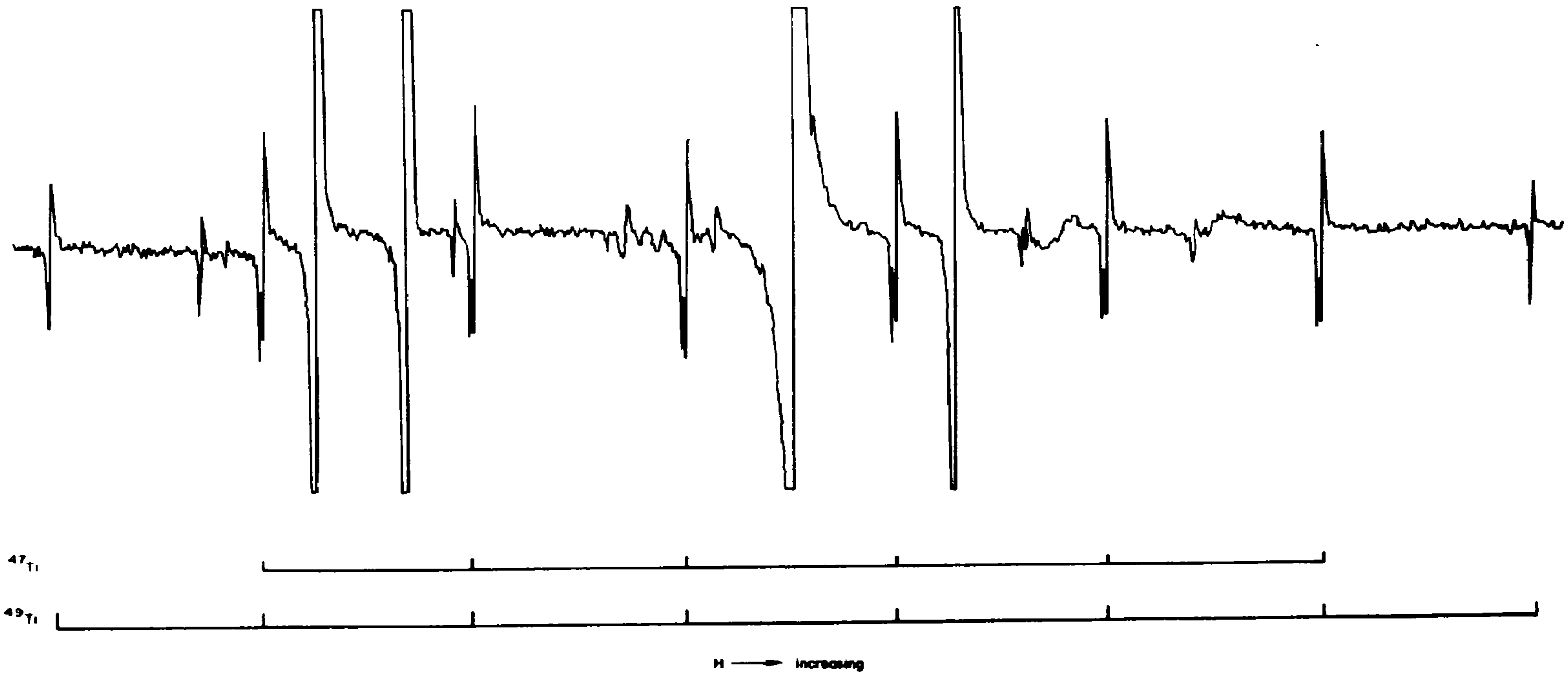

Fig. 2. The paramagnetic resonance spectrum of Ti^+ in calcium oxide. This spectrum is observed after irradiation with light in the F-band (3·1 eV) at 77°K. The shift of only 130 mg between the hyperfine components of ^{47}Ti and ^{49}Ti is clearly discernible.

The appearance of the Ti^{+} spectrum during irradiation is apparently due to electron trapping by Ti^{2+} ions. The stability of the spectrum evidently depends on the irradiation temperature, and this is most probably due to different defect centres acting as electron donors in the different temperature ranges. At room temperature the F^{+} spectrum increases transiently with irradiation up to sevenfold, due to liberation of electrons from F-centres[13]. At 77°K this process is less efficient, but Fe^{3+} and Cr^{3+} ions are formed from the divalent ions, and their stability is similar to that of the Ti^{+} centre formed at this temperature.

3.3 *Double quantum transitions in the* Mn^{2+} *spectrum*

In as-received crystals the spectrum from Mn^{2+} ions is always present. Transitions other than those corresponding to $\Delta M_s = +\frac{1}{2} \leftrightarrow -\frac{1}{2}$ are considerably broadened especially after quenching, when a new twelve line spectrum is observed. This spectrum, which is enhanced following ultra violet irradiation at 77°K, consists of 6 pairs of sharp lines each centred on one of the principal manganese $\Delta M_s = +\frac{1}{2} \leftrightarrow -\frac{1}{2}$ lines.

The similarities of this spectrum with those reported earlier by Auzins and Wertz[14] for the double-quantum transitions of the Fe^{3+} and Mn^{2+} in magnesium oxide have prompted further comparison. The non-adjacent transitions $+\frac{3}{2} \rightarrow -\frac{1}{2}$ and $+\frac{3}{2} \rightarrow +\frac{5}{2}$ as well as $-\frac{5}{2} \rightarrow -\frac{3}{2}$ and $+\frac{1}{2} \rightarrow +\frac{3}{2}$ occur with simultaneous absorption of two quanta. Equality of spacing between the two sets of levels for each pair is produced by a small tetragonal distortion of the cubic symmetry, which introduces a D-term into the spin Hamiltonian. To first order in perturbation theory, the $+\frac{3}{2}$ levels are shifted by 2D and

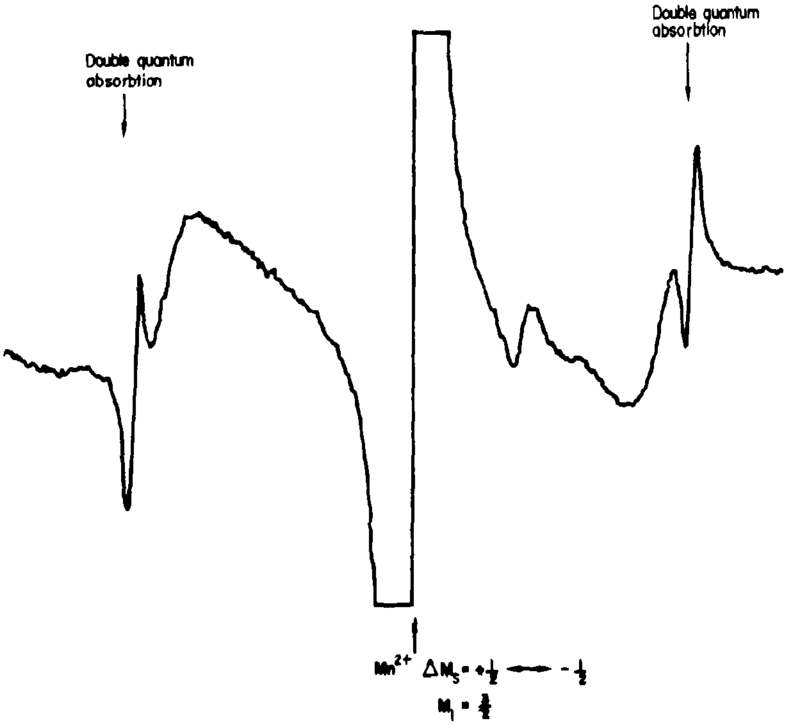

Fig. 3. Double quantum transitions in the e.p.r. spectrum of Mn^{2+} in CaO: the spectrum shown is for the $m_I = \frac{1}{2}$ pentad with H along the principal axis.

the $\pm\frac{5}{2}$ levels by 6D compared with the $\pm\frac{1}{2}$ levels. The value of D necessary in the case of Mn^{2+} in CaO is only 0·55 G. The resonance condition for double quantum transitions to be observed from suitably distorted Mn^{2+} ions occurs when the separation between the $-\frac{5}{2}\rightarrow-\frac{3}{2}$ and the $+\frac{3}{2}\rightarrow+\frac{5}{2}$ lines is subdivided by 2D and 4D[14]. In the case of manganese the energy level scheme is complicated by a large hyperfine interaction, and the fine structure splittings consequently vary for each of the six hyperfine pentads. In Fig. 3 the double quantum transitions are shown for the $m_1 = \frac{3}{2}$ pentad along a principal axis, where the usual fine structure positions are reversed, i.e. in this case the $\pm\frac{3}{2}\rightarrow\pm\frac{5}{2}$ transitions lie outside the $\pm\frac{1}{2}\rightarrow\pm\frac{3}{2}$ transitions. The measured line positions are within one gauss of the predicted positions for double quantum transitions, taking into account second-order effects from fine and hyperfine splittings. A further check was made by measuring the increase in line intensity as a function of the microwave magnetic field vector $\mathbf{H}_1$ at the sample, keeping crystal bias current constant. At low power levels the twelve line spectrum increased more than linearly with H_1, consistent with double quantum transitions.

The effect of quenching the crystals clearly introduces the distortions necessary for the resonance condition for double quantum transitions to be satisfied. The spectrum was considerably stronger at 77°K than at room temperature, in contrast to the case for Mn^{2+} in MgO, for which the intensity of the lines increased with increasing m_I value[14]. The mechanism coupling the intermediate states of the double quantum transitions is not understood. If the coupling between the states is phonon assisted, it is not surprising that the temperature dependence of the intensity of the double quantum lines for Mn^{2+} should be different in calcium oxide than in magnesium oxide.

Acknowledgements—The authors are indebted to the United Kingdom Atomic Energy Authority, Harwell, and the Science Research Council for support of the experimental programme. Informative discussions with Professor D.J.E. Ingram and Dr. M. J. Baker were much appreciated.

REFERENCES

1. STONEHAM M. A., U.K.A.E.A. Res. Rep R5530 (1967).
2. SHUSKUS A. J., *Phys. Rev.* **127**, 2022 (1962)
3. LOW W. and RUBINS R. S., *Proc. 1st Int. Conf. Paramagnetic Res.* 1, 79 (1962)
4. SPECK D. R., *Phys. Rev.* **101**, 1725 (1956)
5. BOYD C. A. and GAMBINO R. J., *Phys. Rev. Lett.* **12**, 20 (1964)
6. LOW W., *Phys. Rev.* **103**, 1309 (1956)
7. MANENKOV A. A. and PROKHOROV A. M., *Soviet Phys. JETP* **6**, 860 (1958).
8. LOW W. and SHALTIEL D., *J. Phys. Chem. Solids* **6**, 315 (1958).
9. HEMPSTEAD C. F. and BOWERS K. D., *Phys. Rev.* **118**, 131 (1960).
10. MARSHALL S. A., HODGES J. A. and SERWAY R. A., *Phys. Rev.* **136**, A1024 (1964)
11. WERTZ J. E., SAVILLE G. S., HALL L. and Auzins P., *Proc. Br. ceram. Soc.* 1, 59 (1963).
12. ZARIPOV M. M., KROPOTOV V. S., LIVANOVA L. D. and STEPANOV V. G., *Soviet Phys. solid St.* 9, 992 (1967)
13. KEMP J. C., ZINIKER W. and HENSLEY E. B., *Phys. Lett.* **25A**, 43 (1967)
14. AUZINS P. V. and WERTZ J. E., *J. phys. Chem.* **71**, 211 (1967).

J. Phys. Chem. Solids Pergamon Press 1969. Vol. 30, pp. 1801–1809. Printed in Great Britain.

SOME STUDIES OF DEFECTS IN CALCIUM OXIDE–II. INTRINSIC LATTICE DEFECTS

B. HENDERSON and A. C. TOMLINSON
Physics Department, Keele University, Keele, Staffordshire, England

(*Received* 16 *September* 1968, *in revised form* 16 *December* 1968)

Abstract–The optical absorption spectrum of electrolytically coloured calcium oxide shows the presence of both F^+- and F-centres Low temperature measurements of absorption and emission from the F^+-centre suggest that the electron-phonon coupling at the defect is strong enough to suppress the zero-phonon transition probability to undetectably small values.

In electrolytically coloured crystals, although not in neutron irradiated crystals, the paramagnetic resonance linewidth of the F^+-centre is < 15 mG and the hyperfine interaction from ^{43}Ca without isotopic enrichment has been identified for the first time. Analysis of this hyperfine structure proves the de Boer model of the F^+-centre in calcium oxide There are further hyperfine interactions of the F^+-centre electron which have not been unambiguously identified. However, a group of lines has been assigned to an interaction with a nucleus having a spin $I = 5/2$; tentatively it is suggested that this associated with ^{17}O nuclides in the next-nearest-neighbour position.

Surprisingly, V_1-centres are observed in these crystals after heat treatment alone. Enhancement of the V_1-centre concentration by u v irradiation is more efficient than in the isostructural magnesium oxide. Several spectra with identical symmetry but with different g-tensors from the V_1-centre are apparently associated with holes trapped at cation vacancies near other defects. The magnetic resonance spectrum of the antimorph of the F-centre, corresponding to two trapped holes localised on opposite sides of the cation vacancy, has been identified

1. INTRODUCTION

IN THE alkaline earth oxides anion vacancies may trap one or two electrons to form F^+- and F-centres*. The F^+-centre is paramagnetic and should show characteristic magnetic resonance absorption. However, the only magnetic isotope of calcium is the 0·13 per cent abundant ^{43}Ca nucleus, which has nuclear spin $I = \frac{7}{2}$. Consequently magnetic hyperfine interaction from this nucleus is expected to be exceedingly difficult to observe without isotopic enrichment, a process precluded for single crystal growth of calcium oxide. Thus the F^+-centre has been characterised only by the g-value and its difference from the g-values of the other alkaline earth oxide. Such evidence does not conclusively demonstrate the anion vacancy (de Boer) model of the defect. In a remarkable application of magnetic resonance techniques to powder samples, Tench and Nelson[1] showed that in powders enriched with 2 per cent ^{43}Ca, hyperfine structure was associated with the narrow line at $g = 2·0001$, originally identified as being due to the F^+-centres[2]. Even this is not conclusive evidence, since the orientation dependence of the nuclear hyperfine structure is a necessary prerequisite to determining the symmetry of the defect. Such evidence, including possible interaction with next nearest neighbour ^{17}O ions, is presented in this paper. We discuss also some optical properties of intrinsic lattice defects in calcium oxide.

In annealed crystals V_1-centres i.e. holes trapped on oxygen ions adjacent to cation vacancies, are observed. Pairs of trapped holes, coupled by dipolar interaction, have been observed for the first time in calcium oxide, and the magnetic resonance spectrum of this defect is also discussed.

---

*These definitions differ from those currently used in the literature: they indicate the charge state of the defect, in addition to its anion vacancy nature, and emphasise the differences between the defects in oxides and the alkali halides.

2. EXPERIMENTAL PROCEDURE

The experimental procedures are largely those discussed in Part I. However some crystals were examined after fast neutron irradiation in the Harwell Pluto reactor to doses of 10^{17}–10^{19} nvt at an ambient temperature of 45°C. For photo excitation in the resonance cavity of the magnetic resonance spectrometer, filtered u.v. light from a high pressure mercury lamp was used. Kodak-Wratten filters were used to ensure that photo excitation occurred mainly in the $^1S \rightarrow {}^1P$ band of the F-centre. Optical absorption spectra were made at 4°K, using a Cary 14 spectrophotometer. Emission spectra measured using a medium quartz spectrograph, photographic recording and microdensitometer.

3. RESULTS AND DISCUSSION

3.1 *The* ^{43}Ca *hyperfine structure*

Fortunately, in some crystals coloured by electrolytic processes during growth, the linewidth of the F^+-centre E.S.R. spectrum was extremely narrow, typically < 15 mG. This is one of the narrowest paramagnetic resonance lines yet observed in solids. As a result of the small linewidth, sidebands are observed separated from the centre of the line by approximately ±36 n mG when using 100 kHz detection (Fig. 1). The sidebands are a consequence of the frequency modulation of the magnetic field, and measurement of the number and position of the sidebands permits accurate calibration of the modulation amplitude. When the 100 kHz modulation amplitude is small compared with the linewidth, the maximum observed linewidth is not greater than that observed using 400 Hz detection. Figure 1 shows the appearance of the sideband spectrum for various modulation amplitudes. In the neutron irradiated crystals the linewidths are larger and varied slightly according to neutron dose. This increase is attributed to inhomogeneous strain broadening consequent upon the increased lattice disorder present after neutron irradiation.

The exceptional narrowness of the lines in the electrolytically coloured samples also permitted measurement of the ^{43}Ca nuclear hyperfine structure without isotopic enrichment. This structure is shown in Fig. 2(a) as sixteen lines, eight of which are superposed doublets resulting from the simple orientation used. For this spectrum the static Zeeman field was directed along one of the cube axes. In a general orientation twenty four lines are observed, the line positions varying with magnetic field orientation according to:

$$\Delta H = M_I\{A_S + B(3\cos^2\theta - 1)\}$$

where A_S and B are the isotropic and anisotropic components of the hyperfine tensor. The total intensity of the hyperfine lines relative to the central component is given by the probability of one of the six nearest neighbour cations being $^{43}Ca^{2+}$: this probability is just 0·0013, and the intensity of each hyperfine line is thus only 0·00005 the intensity of the central component. Thus for a concentration of about 10^{15} F^+-centres cm^{-3} we see that with a 15 mG linewidth, the signal-to-noise ratio for the hyperfine lines is favourable. The observed intensities are substantially in agreement with these ideas. The measured hyperfine parameters are $A_S = -9{\cdot}17 \pm 0{\cdot}1$* and $B = -0{\cdot}97 \pm 0{\cdot}1$ G, indicating the exceptional accuracy obtained in Tench and Nelson's[1] powder studies. The hyperfine line positions are shifted relative to the line for which $I = 0$, giving different g-values for the hyperfine spectrum and for the central component. For F-centres the correction to the hyperfine structure g-value has been calculated for interaction with a single nucleus by Holton and Blum[3], and is given by

$$g_{\mathrm{corr}} = g_{\mathrm{meas}}\left\{1 - \tfrac{1}{2}\left(\frac{a}{H_0}\right)^2 (I(I+1) - M_I^2)\right\}.$$

---

*The sign of A_S for both ^{43}Ca and ^{17}O is determined by the known sign of the nuclear moment.

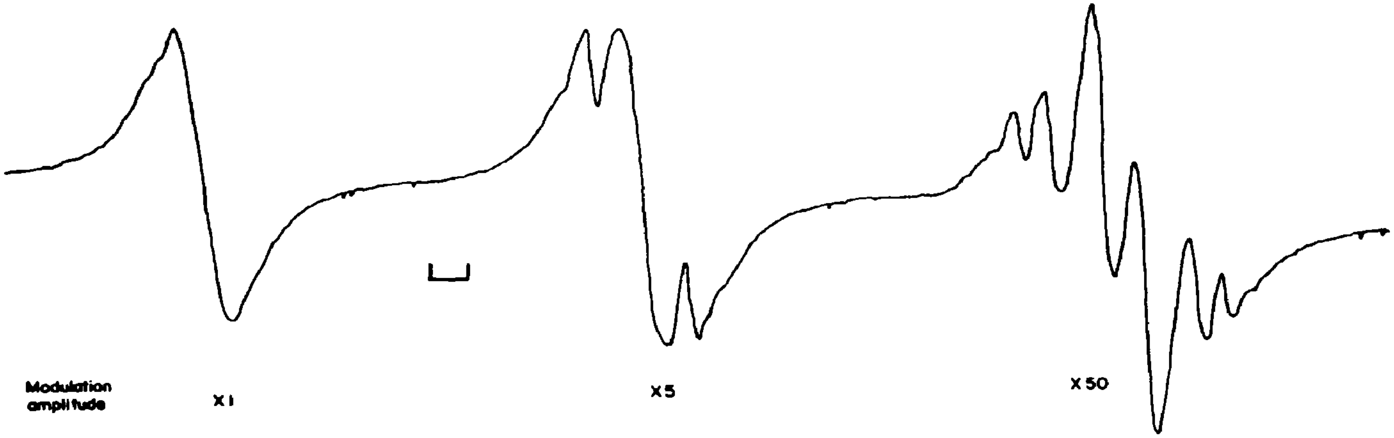

Fig. 1. The development of modulation sidebands on the F^+-centre electron spin resonance line in CaO as the 100 kHz modulation amplitude is increased from a very low value, starting at the left.

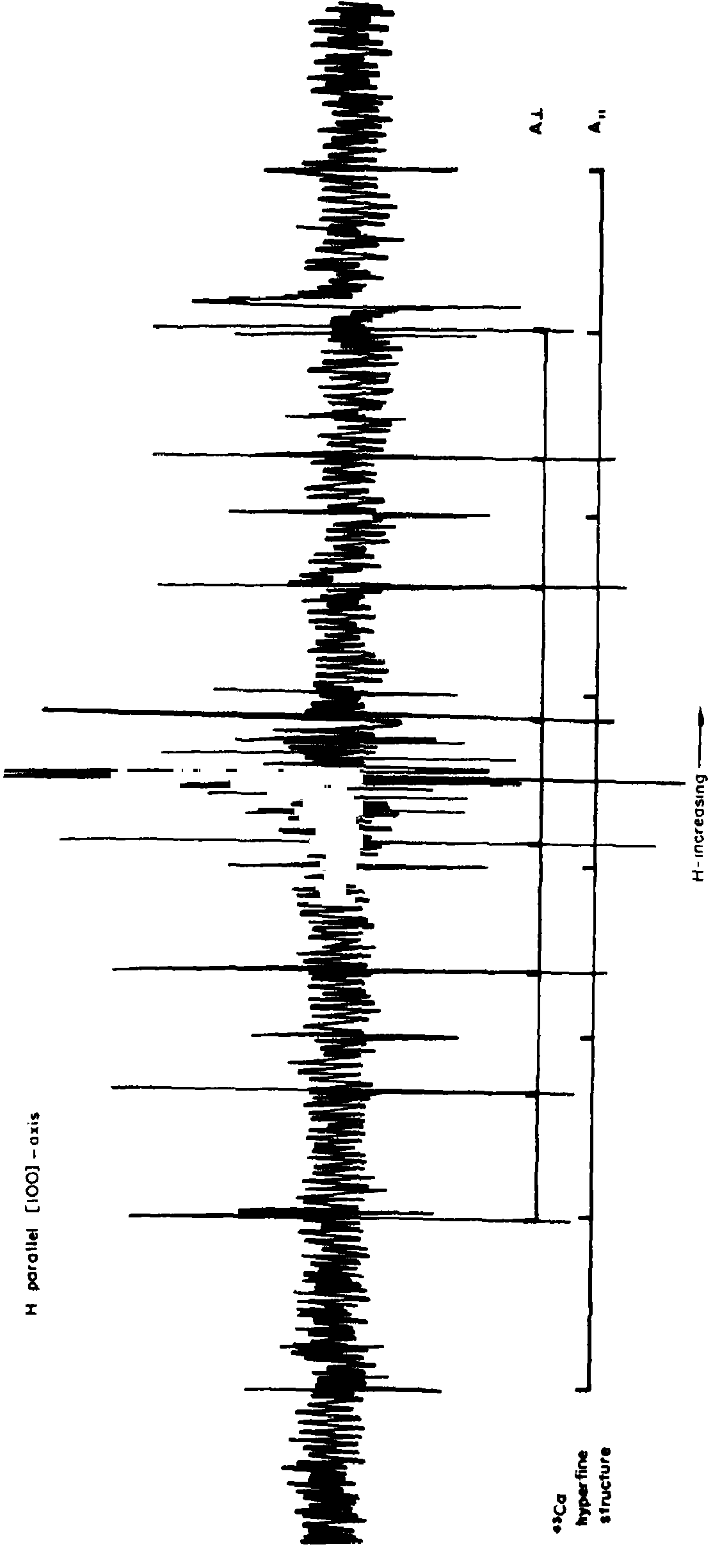
H parallel [100]-axis
A⊥
A∥
43Ca hyperfine structure
H-increasing

Fig. 2(a).

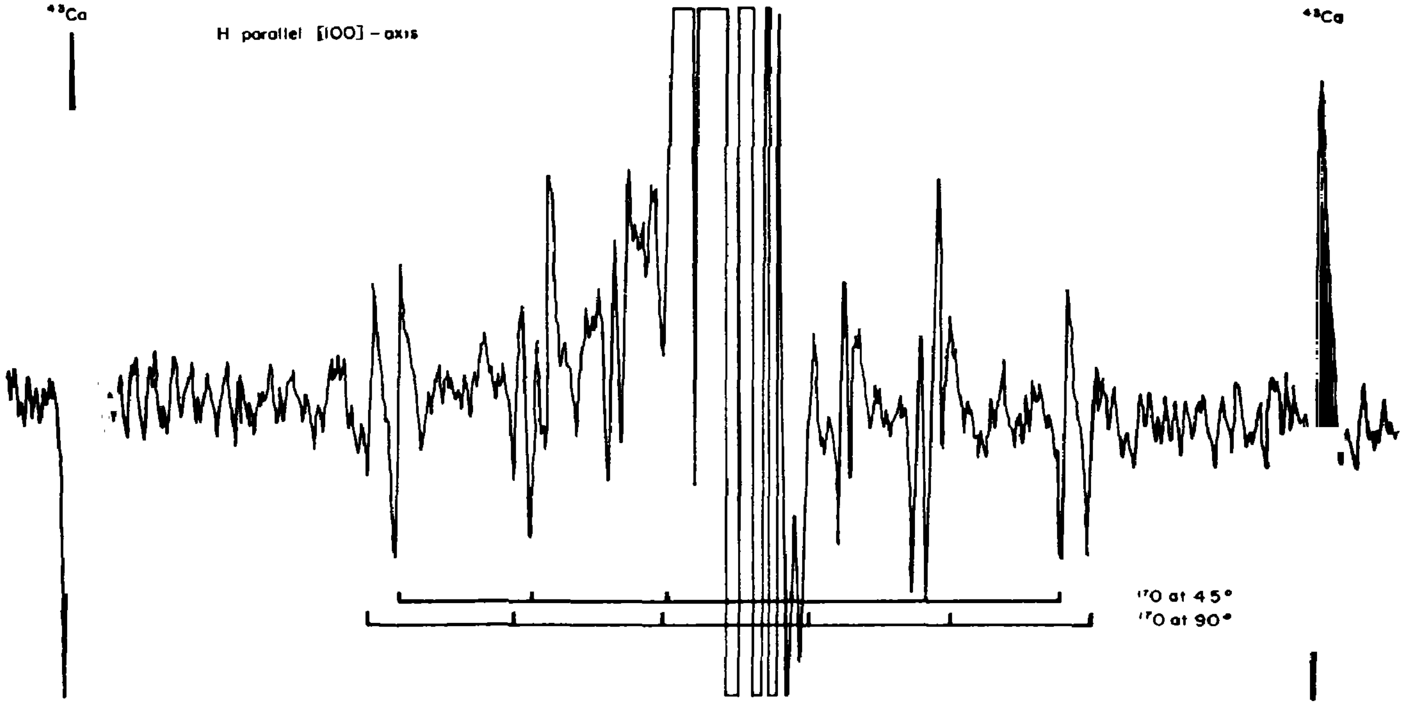

Fig 2(b)

Fig. 2 The hyperfine structure associated with the F^+-centre in CaO. (a) due to 0·13 per cent abundant ^{43}Ca-nuclei (b) due to 0·037 per cent abundant ^{17}O-nuclei Both spectra are recorded with magnetic field along a cube axis

For the inner pair of ^{43}Ca hyperfine lines, neglecting the insignificant anisotropic component, a g-shift of $-0{\cdot}00015\pm0{\cdot}00005$ is found, in good agreement with the calculated value of $-0{\cdot}00015$.

3.2 *The ^{17}O hyperfine structure*

Close examination of the region within the innermost pair of ^{43}Ca hyperfine lines shows that there are further groups of lines. This part of the spectrum is expanded in Fig. 2(b) and reveals two groups of six lines. Other lines are also present, but these will not be discussed in this paper. The magnetic field is again along a cube axis. The splittings are about an order of magnitude smaller than the ^{43}Ca hyperfine splittings; thus it seems probable that these lines may arise from interactions of the F^+-centre electron with ^{17}O nuclei which occur with a natural abundance of 0·037 per cent, in next-nearest-neighbour positions. This nucleus has a spin $I=\frac{5}{2}$, and thus one expects groups of six lines. Along the principal axis, the F^+-centre has four equivalent n.n.n. sites perpendicular to the magnetic field and eight equivalent n.n.n. sites at 45° to the field. Thus from the intensity of the two groups of six lines, the one with the larger splitting is apparently due to the ^{17}O ions perpendicular to the magnetic field. This implies that A and B for this hyperfine interaction are opposite in sign. The perpendicular group should be about one half the intensity of the innermost pair of ^{43}Ca hyperfine lines, also shown on Fig. 2(b), as is observed. A full angular variation study was not of much assistance in this case, owing to the large number of inequivalent sites away from the axis, interference from other weak spectra, and magnetic field uncertainties. Although this sixfold splitting may arise from an interaction of the F^+-centre electron with a non-magnetic ion with spin $I=\frac{5}{2}$, the intensity of the spectrum relative to the nearest neighbour ^{43}Ca spectrum is such as to give reasonable confidence in the assignment to the ^{17}O-nuclide, in which case the parameters are; $A_S=-0{\cdot}87\pm0{\cdot}1$ and $B=+0{\cdot}05\pm0{\cdot}02$ G.

The hyperfine interaction for both ^{43}Ca and ^{17}O may be written as the sum

$$A_S+(A_d+A_\sigma)(3\cos^2\theta_\sigma-1)+A_\pi(3\cos^2\theta_\pi-1).$$

A_S is Fermi contact term, A_d gives the strength of the dipolar interaction, and A_σ and A_π represent the overlap of the F^+-centre electron onto the bonding and antibonding orbitals of the neighbouring ions. As expected, A_s is the largest term for both ^{43}Ca and ^{17}O. Usually for F-centres the anisotropic component is dominated by the dipolar contribution A_d. This situation obtains for the ^{43}Ca anisotropic interaction since the measured value of B is $-0{\cdot}97$ G compared with the computed value $A_d=-0{\cdot}92$ G. The ^{17}O interaction is apparently somewhat different since the sign of both A_s and A_d should be the same, being determined only by the sign of the nuclear moment. The computed value of A_d for ^{17}O is $-0{\cdot}36$ G which is to be compared with $B=+0{\cdot}05$ G. Since $B=A_d+A_\sigma+A_\pi$, then $A_\sigma+A_\pi=-0{\cdot}41$ G. This is an unusual result for F-centres, since it implies that the contribution from the antibonding orbitals is relatively important.

It is of some interest to compare the relative magnitudes of the isotropic hyperfine components for ^{43}Ca and ^{17}O. The procedure adopted assumes that the isotropic interaction with a nucleus α is related to the electron spin density $|\psi(R_1)|^2$ at the nucleus by:

$$A_s=\frac{16\pi}{3}\frac{\mu_\alpha}{I_\alpha}\beta G_\alpha|\Psi(R_1)|^2$$

where μ, I and β have their usual significance, and G_α is an amplification factor which is proportional to $Z^{3/2}$, at least in the alkali halides[2]. Thus we find that $|\psi(R_1)|^2$ is $0{\cdot}176\times10^{24}$ cm^{-3} and $0{\cdot}054\times10^{24}$ cm for ^{43}Ca and ^{17}O respectively. These quantities emphasize the extent to which the electronic charge is localized within the vacancy in the alkaline earth oxides.

3.3 *Some optical studies*

Typical optical absorption spectra of additively coloured and neutron irradiated single crystals of calcium oxide are shown in Fig. 3.

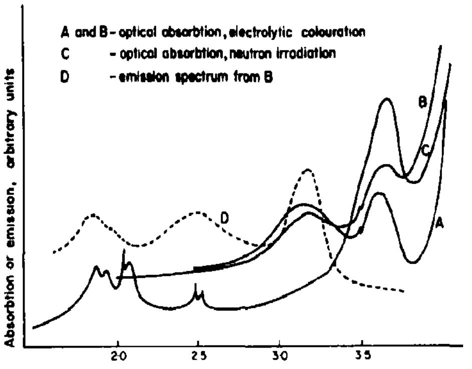

Fig. 3. Optical absorption and emission spectra from additively coloured and neutron irradiated calcium oxide.

The former have a high background absorption, on which is superimposed two broad bands at 3·6 and 3·1 eV due to F$^+$- and F-centres respectively[4, 5]. The F$^+$-band has a full width at half height of 0·25 eV: the F-band is a little broader. No F-centres are present in neutron irradiated samples although large numbers of F$^+$-centres are detected. The zero phonon line at 3557 Å has been the subject of several recent investigations; the defect species associated with its presence is still a matter of conjecture[10]. The fluorescence spectrum in Fig. 3 was measured at 77°K using light filtered to allow only F- and F$^+$-band radiation. Strong emission is expected from both these centres since allowed electric dipole transitions are involved. Consequently we identify the two peaks at 3·18 and 2·50 eV with the F$^+$- and F-centres respectively. Independent excitation of the bands using monochromatic light in the F$^+$-band or F-band incident upon the sample confirm this assignment. The emission bands appear to be slightly broader than the corresponding absorption bands, although it is possible that other underlying bands produce this effect. Due to non linearity in the response of photographic plates, the band peaks and widths are regarded as approximate. However, we note the energy or Stokes shift between the absorption and emission bands of the F$^+$-centre is about 0·4 eV.

The breadth of the absorption and emission bands is a consequence of the electron-phonon coupling at the defect. The low temperature half width of the absorption band H(O), and the Stokes shift, Δ, are related to the frequency ν of the dominant modes broadening the transition by,

$$S = \left[\frac{H(O)}{2{\cdot}36\, h\nu}\right]^2 = \frac{\Delta}{2h\nu}$$

S being the effective number of phonons interacting with the defect states. Bessent's [6] unpublished results show that this mode has an energy of 210 cm^{-1}, giving S values between 8 and 16. A value of $\nu = 260\,\text{cm}^{-1}$ is obtained using the relationship $2\pi\nu\beta = 10$, where β is the compressibility. The relationship works well for F-centres in the alkali halides[7] and in magnesium oxide[8]. This frequency implies $S \simeq 9$ if used with the bandwidth. In practice since the zero phonon line probability relative to the whole band is e^{-S}, the zero phonon line is only observed when $S \leq 6$. Thus the criterion for observing the zero phonon transition implies that the zero phonon line at 3557 Å is unlikely to be associated with the F$^+$-centre. However, underlying structure may appear to broaden the F$^+$-band. Kemp *et al.*[9], argue from optical Faraday rotation measurements that this line is the F$^+$-centre zero phonon line, a view apparently difficult to reconcile with the piezospectroscopic studies of Hughes and Runciman[10].

Further emission bands are observed below 2 eV, and at least one of these has a long lifetime, as shown by the red glow of the additively coloured crystals for many seconds following ultra irradiation, both at room temperature and 77°K. Selective irradiation, using a monochromator indicated that this long lived fluorescence was excited by radiation in the 3·1 eV region of the spectrum. It is tempting therefore to associate it with the F-centre. Of the excited state levels of this defect the ^3P lies lowest and it may be populated by radiationless transitions. The optical transition to the ground state is spin forbidden, and hence this state would have a long lifetime. Unpublished calculations, by Bartram indicate that the E.S.R. of this state would not be readily observable owing to the Jahn–Teller effect[11]. Another possibility is that the fluorescence arises from the formation of other charge states of impurity ions, of which we have already shown Ti^+ to be an important ingredient (Part I).

3.4 *Hole centres*

Contrary to earlier experiences[12] we observed V_1 centres in calcium oxide after annealing at 1300°C in oxidizing atmospheres, the highest concentration being present in crystals quenched from this temperature after annealing for 24 hr. Although none of the crystals shattered during this process, considerable strain was introduced as was shown by considerable linewidth increases in E.S.R. spectra. Thermally generated V_1 centres were stable at room temperature for periods up to two months. In addition to the simple V_1 centre, several centres are observed with identical symmetry properties, but differing from the V_1-centres only in the g-values. Possible models for these defects would include the calcium oxide analogue of the V_{OH}-centres in magnesium oxide[13] and V_1 centres associated with diamagnetic charged defects such as substitutional Al^{3+} ions.

Larger numbers of centres are observed in quenched crystals after irradiation with u.v. light 77°K. However, a few hours at room temperature was sufficient to reduce this concentration to that originally present in the quenched crystal. After such irradiation, the calcium oxide analogue of the V_2-centre produced in MgO by X-irradiation at 77°K was observed. The model for this defect consists of two holes trapped on diametrically opposite anions across the cation vacancy [14]. The coupled state of the defect has $S = 1$, and in axially distorted symmetry sites the $M_S = 0, \pm 1$ levels are split in the absence of a magnetic field. Thus the spectrum consists of six lines corresponding to the two transitions of the defects for the three inequivalent [100]-axes. The spin Hamiltonian appropriate to this defect is

$$\mathscr{H} = \beta S \,.\, \mathrm{g} \,.\, H + D\{S_z{}^2 - \tfrac{1}{3}S(S+1)\}$$

where $S = 1$, $g = 2{\cdot}0683$, $g = 2{\cdot}0023$ and $D = 114$ G. We note the measured g-values are not different, from those relevant to the V_1-centre. Small concentrations of these defects were present in some samples after quenching. It is of interest to note that if the coupling between the O^- ions is assumed to be principally dipolar, the zero field splitting term D is related to the dipolar separation by $D = 111\, g^2\beta^2/(10r_3)$. Thus one obtains a value of $r = 5{\cdot}89$ Å for the separation of the dipole pair, compared with 4·80 Å for the normal lattice spacing. In magnesium oxide the value of r for the analogous defect is 5·0 and 4·20 Å for the normal lattice spacing. In the present case, the increased deviation from a for calcium oxide possibly reflects an increased delocalization of the trapped holes compared with the analagous case in magnesium oxide. This difference is not surprising since the assumption of dipole–dipole coupling is an abvious over-simplification. A similar exaggeration in the apparent separation of pairs of coupled F^+-centres in CaO was reported earlier[15].

Acknowledgements—The authors are indebted to the Atomic Energy Research Establishment, Harwell, and the Science Research Council for support of the experimental programme. We have also enjoyed numerous discussions with Drs. R. G. Bessent and A. M. Stoneham (Harwell) and Professor D. J. E. Ingram (Keele University).

REFERENCES

1. TENCH A. J. and NELSON R. L., *Proc. phys. Soc.* **92**, 1055 (1967).
2. WERTZ J. E., ORTON J. W. and AUZINS P. V., *Discuss. Faraday Soc.* **30**, 40 (1961).
3. HOLTON W. C. and BLUM H., *Phys. Rev.* **125**, 89 (1962).
4. KEMP J. C., ZINIKER W. M. and GLAZE J. A., *Proc. Br. ceram. Soc.* **9**, 109 (1967).
5. WARD W. C. and HENSLEY E., *Bull. Am. phys. Soc.* **10**, 307 (1965).
6. BESSENT R., Private Communication (1968).
7. PODINI P. and SPINOLO G., *Solid State Commun.* **4**, 205 (1966).
8. HENDERSON B., KING R. D. and STONEHAM A. M., *J. Phys. C (Proc. Phys. Soc.)* **1**, 586 (1968)
9. KEMP J. C., ZINIKER W. M., GLAZE J. A. and CHENG J. C., *Phys. Rev.* **171**, 1024 (1968).
10. HUGHES A. E. and RUNCIMAN W. A., *J. Phys. C (Proc. Phys. Soc.)* **2**, 37 (1968).
11. BARTRAM R. H., Private Communication (1968).
12. SHUSKUS A. J., *J. chem. Phys* **39**, 849 (1963).
13. KIRKLIN P. W., AUZINS P. and WERTZ J. E., *J. Phys. Chem. Solids* **26**, 1067 (1965)
14. WERTZ J. E., AUZINS P., GRIFFITHS J. H. E. and ORTON J. W., *Discuss. Faraday Soc.* **28**, 136 (1959).
15. TANIMOTO D. H., ZINIKER W. M. and KEMP J. C., *Phys. Rev. Lett.* **14**, 645 (1965).

J. Phys. Chem. Solids Pergamon Press 1969. Vol. 30, pp 1811-1821. Printed in Great Britain.

DOPING OF EPITAXIAL SILICON-BEHAVIOR OF SOLID SOLUTIONS*

P. RAI-CHOUDHURY†
Metallurgical and Materials Engineering Department, University of Pittsburgh, Pittsburgh, Penn. 19104, U.S.A.

(*Received* 16 *December* 1968)

Abstract—This paper presents a theoretical model for the behavior of solid solutions of group III and V impurities in silicon. The impurities are considered as weak electrolytes dissolved in an ionizing medium. The Fermi level, the activity coefficient and the dissociation equilibrium constants for the dopants are calculated, using Fermi-Dirac statistics, as functions of temperature and doping level. The solid solutions obey Henry's law at very low concentrations and exhibit positive deviations as the concentration is increased. Ionization of impurities or dopants as a function of their concentrations are discussed.

INTRODUCTION

Semiconductor technology consists essentially in the preparation of solid solutions of impurities with controlled concentration. Preparation of these solid solutions by the epitaxial growth technique is extremely versatile in that any desired concentrations and gradients of impurities can be obtained. The process consists of injection of appropriate amounts of hydrides (or other suitable volatile compounds) of group III and V elements into a silicon tetrachloride-hydrogen gas stream from which epitaxial layers of silicon are grown. Silane is also used instead of silicon tetrachloride when low temperature growth is desired. Due to the complexity of the process most of the preparations of solid solutions are carried out on an empirical basis. Since the epitaxial process is being used successfully in a limited scale by the industry little effort has been spent in investigating the fundamentals of the process. It should be emphasized that the potential of the epitaxial growth technique is enormous and largely untapped from the point of view of the applications to device fabrication. To mention a few of the potential applications, the technique can be used to produce devices that require localized control of properties such as lifetime of carriers, high power rectifiers and thyristors, rectifying heterojunctions, etc.

Wagner[1] has treated defects in solids as chemical reactants and provided a basis for viewing defect interactions in terms of the principles of mass action and thermodynamics. Reiss[2] used the concept of dilute electrolytes such as aqueous solutions of acetic acid and developed a parallel argument for solid solutions of impurities in semiconductors. This analogy seems valid at very dilute solutions where complete ionization of impurities or dopants prevails. However, at relatively high concentrations it may not be possible to draw such an analogy with aqueous solutions due to the presence, in the latter case, of incomplete ionization via clustering and hydrogen bonding. Concepts will be developed here which will show that the ionization of impurities is enhanced, rather than retarded, with increasing concentration, although incomplete ionization of dopants is possible in Si through formation of impurity clusters.

At the epitaxial growth temperatures (1200°–1600°K) the dopant bearing compounds such as PH_3 or $(CH_3)_3$Ga are unstable and decompose to the respective pure components, the form of which depends on the thermochemistry of the process and the mechanism involved. These dopants then enter the silicon lattice to form solid solutions. The conductivity of these doped epitaxial layers depend on the concentration, degree of ionization and association of the incorporated dopants. The purpose of this communication is to attempt to treat the process of doping and dissolution from essentially two points of view – band structure and thermodynamics. In what follows, some useful equations are derived to examine the type of solid solution. Ionization of the dopants in solid solution and the effect of increasing concentration are briefly treated. Due to the very nature of the epitaxial process compensation is essentially absent and thus avoiding the complex problem of treating donors and acceptors simultaneously. The equilibrium gas phase composition and the mechanisms of transfer from the gas to the solid is the subject of the next paper of this series.

---

*Extracted from research in partial fulfilment of Ph.D. thesis.

†*Present address*: Westinghouse Research Laboratories, Pittsburgh, Penn. 15235, U.S.A.

SOLID SOLUTIONS

Consider a dilute solid solution of donor in Si, such that ϵ_v represents the energy of the highest state of the valence band, ϵ_c the energy of the lowest state in the conduction band, ϵ_D the energy of the donor level, and μ the Fermi level. The middle of the forbidden energy gap is used as a zero, to which all the energetic quantities are referred.

The concentration n_D of electrons in the donor level can be expressed, using Fermi–Dirac statistics, as

$$n_D = \frac{N_D}{1+\frac{1}{2}\exp[(\epsilon_D-\mu)/kT]} \tag{1}$$

where N_D is the total concentration of donor atoms (dissociated and undissociated), k is the Boltzmann constant and T is the absolute temperature. Application of Henry's law to the undissociated donor concentration n_D gives for p_D the donor pressure,

$$\begin{aligned} p_D &= K'_D n_D \\ &= K'_D\left[\frac{N_D}{1+\frac{1}{2}\exp[(\epsilon_D-\mu)/kT]}\right] \end{aligned} \tag{2}$$

where K'_D is a constant, dependent upon temperature. If K'_D is written as

$$K_D = K'_D\left[\frac{1}{1+\frac{1}{2}\exp(\epsilon_D/kT)}\right] \tag{3}$$

where K_d is another constant, then (2) becomes

$$\begin{aligned} p_D &= K_D\left[\frac{1+\frac{1}{2}\exp(\epsilon_D/kT)}{1+\frac{1}{2}\exp[(\epsilon_D-\mu)/kT]}\right]N_D \\ &= K_D\gamma_D N_D \end{aligned} \tag{4}$$

where

$$\gamma_D = \left[\frac{1+\frac{1}{2}\exp(\epsilon_D/kT)}{1+\frac{1}{2}\exp[(\epsilon_D-\mu)/kT]}\right] \tag{5}$$

is an activity coefficient which approaches unity at infinite dilution when μ goes to zero as the semiconductor becomes intrinsic. The above treatment is derived from the work of Reiss[1]. Reiss has developed expressions to calculate μ using Boltzmann approximation and made sample calculations for donor impurities in Ge. In the present study μ is calculated for Si using only Fermi–Dirac statistics so that the calculations can be extended to degenerate materials.

The total number of donors are given by

$$N_D = n_c + n_D \tag{6}$$

n_D is given by (1). A general expression for n_c, the electron concentration in the conduction band, is given by

$$n_c = 4\pi\left(\frac{2m_e}{h^2}\right)^{3/2}\int_{\epsilon_c}^{\infty}\frac{(\epsilon-\epsilon_c)^{1/2}\,d\epsilon}{1+\exp[(\epsilon-\mu)/kT]} \tag{7}$$

where m_e is the effective mass of the electron. When $(\epsilon-\mu)/kT \gg 1$, then (7) reduced to

$$n_c = 4\pi\left(\frac{2m_e}{h^2}\right)^{3/2}\int_{\epsilon_c}^{\infty}(\epsilon-\epsilon_c)^{1/2}$$

$$\exp[-(\epsilon-\mu)/kT]\,d\epsilon$$

$$= 2\left(\frac{2\pi kTm_e}{h^2}\right)^{3/2}\exp[-(\epsilon_c-\mu)/kT]. \quad (8)$$

The use of (7) or (8) is governed by the doping level or the position of the Fermi level. Let us assume the solution to be dilute, i.e. the approximation leading to (8) is justified. Then substituting (1) and (8) in (6) we obtain

$$N_D = 2\left(\frac{2\pi kTm_e}{h^2}\right)^{3/2}\exp[-(\epsilon_c-\mu)/kT]$$

$$+\frac{N_D}{1+\frac{1}{2}\exp[(\epsilon_D-\mu)/kT]}. \quad (9)$$

For a rigorous determination of μ as a function of N_D, (7) instead of (8) must be used giving the equation to be solved as

$$N_D = 4\left(\frac{2m\epsilon}{h^2}\right)^{3/2}\int_{\epsilon_c}^{\infty}\frac{(\epsilon-\epsilon_c)^{1/2}\,d\epsilon}{1+\exp[(\epsilon-\mu)/kT]}$$

$$+\frac{N_D}{1+\frac{1}{2}\exp[(\epsilon_D-\mu)/kT]}. \quad (10)$$

The above integral can be solved accurately with the aid of a computer, and (10) may then be solved for μ as a function of temperature at different values of N_D. Consequently, γ_D can be calculated from (5). Since μ increases with increasing N_D, and therefore γ_D increases, the solution should exhibit positive deviation from Henry's law.

The partial dissociation of the N_D donors (into ions D_s^+) and electrons (e^-) within the semiconductor enables the dissolution process to be described by the following chemical equation:

$$D_g \rightleftharpoons D_s \rightleftharpoons D_s^+ + e \quad (11)$$

where D_g represents the donor in the gas phase, D_s the undissociated donor in the solid phase, D_s^+ the ionized donor, and e^- the electrons in the solid. At the same time the electrons and holes of the semiconductor itself are continuously undergoing dissociation and association, corresponding to transitions from the valence to the conduction band and vice versa. This process also can be described as a chemical reaction:

$$e^+e^- \rightleftharpoons e^+ + e^- \quad (12)$$

where the symbol e^+ represents a hole. Corresponding to the equilibrium process in (11) and (12), the following mass action expression can be written:

$$p_D = K'_D[D_s] \quad (13)$$

$$K_+ = \frac{[D_s^+][e^-]}{[D_s]} \quad (14)$$

$$K_0 = [e^+][e^-] \quad (15)$$

where the symbols in square brackets denote concentrations. The main reason for using concentrations rather than activities in the above expressions is that the resultant equations cannot be solved because of the unavailability of the activity data of various species. Also, as will be seen later, the errors involved in such an approximation do not render the interpretation of the equilibrium constants meaningless. $[D_s]$ is given by the concentration of undissociated donors n_D, $[D_s^+]$ by (N_D-n_D), $[e^+]$ by n_c and $[e^+]$ by h_v. Therefore, (14) and (15) become

$$K_+ = \frac{(N_D-n_D)n_c}{n_D} \quad (16)$$

$$K_0 = h_v n_c \quad (17)$$

N_D can be eliminated from (16) using (1), which results in

$$K_+ = \tfrac{1}{2}\exp[(\epsilon_D-\mu)/kT]n_c \quad (18)$$

as before n_c is obtained from (7) or (8), depending on the degree of dilution or the *position of the Fermi level. If (8) is applicable, then (18) reduces to*

$$K_+ = (2\pi m_e kT)^{3/2}/h^3] \exp[(\epsilon_D - \epsilon_c)/kT]. \quad (19)$$

Using a weak electrolyte analogy, *i.e. the approximation* $\epsilon_D = \epsilon_c$, *(18) further simplifies to*

$$K_+ = (2\pi m_e kT)^{3/2}/h^3. \quad (20)$$

As is seen, when the electrolyte or the dopant is present in very low concentrations and has a low ionization energy, K_+ becomes independent of μ.

In order to calculate k_0, it is necessary to obtain an expression for h_v in terms of known parameters. A general expression for the hole concentration in the valence band is given by

$$h_v = 4\pi\left(\frac{2m_h}{h^2}\right)^{3/2} \int_{-\infty}^{\epsilon_v} \frac{(\epsilon_v - \epsilon)^{1/2}\, d\epsilon}{1 + \exp[(\mu - \epsilon)/kT]} \quad (21)$$

where m_h is the effective mass of the hole. When $(\mu - \epsilon)/kT \gg 1$, then (21) reduces to

$$h_v = 4\pi\left(\frac{2m_h}{h^2}\right)^{3/2} \int_{-\infty}^{\epsilon_v} (\epsilon_v - \epsilon)^{1/2}$$

$$\exp[-(\mu - \epsilon)/kT]\, d\epsilon$$

$$= 2\left(\frac{2\pi kT m_h}{h^2}\right)^{3/2} \exp[-(\mu - \epsilon_v)/kT] \quad (22)$$

therefore, K_0 is given by the product of (7) and (21), or using Boltzmann approximation by the product of (8) and (22) as follows:

$$K_0 = 16\pi^2\left(\frac{4m_e m_h}{h^2}\right)^{3/2}\left[\int_{\epsilon_c}^{\infty} \frac{(\epsilon - \epsilon_c)^{1/2}\, d\epsilon}{1 + \exp[(\epsilon - \mu)/kT]}\right.$$

$$\left. + \int_{-\infty}^{\epsilon_v} \frac{(\epsilon_v - \epsilon)^{1/2}\, d\epsilon}{1 + \exp[(\mu - \epsilon)/kT]}\right] \quad (23)$$

or the approximate form is

$$K_0 = 4\left(\frac{2\pi kT}{h^2}\right)^3 (m_e m_h)^{3/2} \exp\left[-\frac{\epsilon_c + \epsilon_v}{kT}\right]$$

$$= 4\left(\frac{2\pi kT}{h^2}\right)^3 (m_e m_h)^{3/2} \exp\left[-\frac{\epsilon_G}{kT}\right] \quad (24)$$

ϵ_G, *the width of the forbidden energy gap, is given by*

$$\epsilon_G = 1{\cdot}21 - 2{\cdot}79 \times 10^{-4}\, T. \quad (25)$$

The above expression[3] is not accurate below 300°K. Thus for dilute solutions, K_0 is a function of temperature alone, provided the effective masses remain constant. However, at increasing solute concentration when Boltzmann approximation fails, K_0 is a function of temperature as well as the position of the Fermi level.

Similar considerations may be applied to acceptors which dissociate to form negative ions and positive holes. The concentration h_A of holes in the acceptor level can be expressed as

$$h_A = \frac{N_A}{1 + \frac{1}{2}\exp[-(\epsilon_A - \mu)/kT]} \quad (26)$$

where N_A is the total concentration of acceptor atoms and ϵ_A is the energy of the acceptor level. Equations analogous to (4) and (5) may now be readily derived for acceptors. These are:

$$p_A = K_A \gamma_A N_A \quad (27)$$

where

$$\gamma_A = \left[\frac{1 + \frac{1}{2}\exp(-\epsilon_A/kT)}{1 + \frac{1}{2}\exp[-(\epsilon_A - \mu)/kT]}\right]. \quad (28)$$

It is now necessary to calculate μ as a function of N_A and T, so that γ_A can be calculated. The total number of acceptors are given by

$$N_A = h_A + h_v. \quad (29)$$

Substituting for h_A and h_v from (26) and (21) into (29), we obtain an expression which gives μ as a function of N_A:

$$N_A = \frac{N_A}{1+\frac{1}{2}\exp\left[-(\epsilon_A-\mu)/kT\right]} + 4\pi\left(\frac{2m_h}{h^2}\right)^{3/2} \int_{-\infty}^{\epsilon_v} \frac{(\epsilon_v-\epsilon)^{1/2}\,d\epsilon}{1+\exp\left[(\mu-\epsilon)/kT\right]}. \quad (30)$$

Using dilute solution approximation, (30) simplifies to

$$N_A = \frac{N_A}{1+\frac{1}{2}\exp\left[-(\epsilon_A-\mu)/kT\right]} + 2\left(\frac{2\pi kTm_h}{h^2}\right)^{3/2} \exp\left[-\frac{(\mu-\epsilon_v)}{kT}\right]. \quad (31)$$

Since μ becomes increasingly negative with increasing N_A, (28) predicts that γ_A should increase with increasing doping level.

The dissociation of N_A acceptors into ions (A_s^-) and holes (e^+) within the semiconductor enables the dissolution process to be described by the following chemical equation:

$$A_g \rightleftharpoons A_s \rightleftharpoons A_s^- + e^+ \quad (32)$$

where A_g represents the acceptors in the gas phase, A_s the undissociated acceptor in the solid phase and A_s^- the ionized acceptor in the solid. The equilibrium constant for the acceptor dissociation reaction can be written as:

$$K_- = \frac{[A_s^-][e^+]}{[A_s]} = \frac{(N_A-h_A)h_v}{h_A} \quad (33)$$

N_A can be eliminated from (33) by substitution of h_A from (26) which results in

$$K_- = \tfrac{1}{2}\exp\left[-(\epsilon_A-\mu)/kT\right]h_v \quad (34)$$

h_v is obtained from (21) or (22), depending on the degree of dilution. Using a weak electrolyte analogy, i.e. approximation $\epsilon_A \simeq -\epsilon_v$ and very dilute solution, equation (34) simplifies to

$$K_- = (2\pi m_h kT)^{3/2}/h^3. \quad (35)$$

Thus K_- and K_+ differ from each other by the ratio $(m_e/m_h)^{3/2}$ and are functions of temperatures only.

To summarize these, using the above treatment it is possible to calculate γ_D and γ_A as a function of N_D and N_A respectively at our temperatures of interest. This will provide information regarding the extent of validity of the dilute solution approach. Also, variation of K_+, K_- and K_0 with temperature yields free energies of these dissociation reactions.

IMPURITY IONIZATION AND CONDUCTION

It is instructive to view the doping process as the gradual broadening of the impurity band with increasing dopant concentration. Let us examine the case of n-type Si, although, p-type Si behaves in a similar manner. The lightly doped material is characterized by the absence of any intra-band conduction, i.e. conduction within the impurity band observable at liquid He temperature. The donors have a well defined ionization energy, ϵ_d. As the donor concentration is increased the impurity band gradually broadens, and above a critical concentration, electrons begin to delocalize from the donor atoms and are able to move from one donor atom to another. Above a second critical concentration in heavily doped Si the Fermi level moves into the conduction band and the impurity band becomes sufficiently broad to enter the conduction band. These transitions have recently been observed by Alexander and Holcomb[4] in Si doped with P at liquid He temperatures. The delocalization of electrons are observed at a donor concentration of 3×10^{18} atom/cm^3 and the movement of the Fermi level into the conduction band at a donor concentration of 2×10^{19} atom/cm^3.

In heavily doped material, i.e. when the Fermi level is in the conduction band and the impurity band overlaps the conduction band, Si should behave as a metal rather than a semiconductor. The activation energy for the ionization of donors is essentially zero. With the exception of those donors that are associated, each donor atom gives one electron into the conduction band and therefore a linear increase in conductivity with increasing doping may be expected. However, with each electron an extra ionized donor atom is introduced which increases electron-impurity scattering, i.e. decreases conductivity. The net effect is that the conductivity is independent of the doping level above the impurity concentration where the Fermi level enters conduction band.

The foregoing discussion is valid as long as a stable solid solution is maintained without the formation of any precipitates, compounds or excessive lattice straining. Arsenic should conform well to the above treatment because of the small differences in atomic radii (0·01 Å) and electronegativity (0·2) with Si. Experimental results in support of this model are already available in part and will be reported in a future communication.

RESULTS

Values of μ for n-type Si are computed from (10) for different values of N_D at different temperatures. The integral does not have any closed form solution and consequently various approximations were made in the past such as those by McDougall and Stoner[5]. In the present study the integration is carried out using the Romberg integration procedure [6, 7] stored in the computer program library. Since the integral converges rapidly its value between the limits ϵ_c and (ϵ_c+1) eV at room temperature is many orders of magnitude greater than the value between the limits ϵ_c+1 and ϵ_c+2. Hence the upper limit is conveniently set at ϵ_c+2. However, the error involved in setting this upper limit increases with temperature and is less than 0·2 per cent at the highest temperature used here. γ_D is then calculated from (5) using the values of μ at different doping levels. K_+ is also obtained from (18). Similarly, values of μ, γ_A and K_- for the p-type are obtained from (30), (28) and (34) respectively.

For the above computations it is assumed that the effective masses of the holes and electrons are independent of temperature, having the following values: $m_e = 1{\cdot}08$ m, $m_h = 0{\cdot}59$ m, where m is the electron rest mass. Arsenic is used for the computations in n-type Si with ϵ_D taken as $(\epsilon_c - 0{\cdot}49)$ eV and boron is used for p-type Si with ϵ_A taken as $(\epsilon_V - 0{\cdot}045)$ eV. Ionization energies of these dopants are assumed to be independent of the doping level which is precise only at low doping levels.

Values of Fermi level, activity coefficient and dissociation equilibrium constant as functions of doping level and temperature are presented in Tables 1 and 2. Fermi level enters the conduction band for n-type Si or the valence band for p-type Si at doping levels of 10^{20}–10^{21} atom/cm^3. Activity coefficient data indicate that at room temperature very large positive deviations from ideality are observed and the values approach unity as N_D or N_A approaches the intrinsic carrier concentration ($1{\cdot}45\times10^{10}$ carriers/cm^3). Some of the values of activity coefficients and dissociation equilibrium constants are plotted in Figs. 1–4. At low concentrations and high temperatures the behavior of the solid solution approaches ideality fairly well from the point of view of activity coefficients. The levelling off of activity coefficients at high doping density is due to the fact that with increasing μ the denominator of (5) or (28) approaches a constant value, the numerator being assumed constant. Plots of equilibrium constants vs. $1/T$ indicate that in both Figs. 3 and 4 the upper curve represents an ideal solution at and above 600°K, whereas the lower curve represents a non-ideal behavior throughout. Several points of interest may be noted from these curves. The negative slope indicates that

Table 1. Values of Fermi level (μ), donar activity coefficient (γ_D) and equilibrium constant (K_+) at different doping level and temperature

N_D	μ	γ_D	K_+
$T = 300$°K			
$1\cdot000 \times 10^{11}$	$7\cdot376 \times 10^{-2}$	$1\cdot732 \times 10^{1}$	$2\cdot112 \times 10^{18}$
$1\cdot000 \times 10^{12}$	$1\cdot373 \times 10^{-1}$	$2\cdot021 \times 10^{2}$	$2\cdot112 \times 10^{18}$
$1\cdot000 \times 10^{13}$	$2\cdot010 \times 10^{-1}$	$2\cdot372 \times 10^{3}$	$2\cdot112 \times 10^{18}$
$1\cdot000 \times 10^{14}$	$2\cdot556 \times 10^{-1}$	$1\cdot957 \times 10^{4}$	$2\cdot112 \times 10^{18}$
$1\cdot000 \times 10^{15}$	$3\cdot120 \times 10^{-1}$	$1\cdot736 \times 10^{5}$	$2\cdot112 \times 10^{18}$
$1\cdot000 \times 10^{16}$	$3\cdot708 \times 10^{-1}$	$1\cdot684 \times 10^{6}$	$2\cdot112 \times 10^{18}$
$1\cdot000 \times 10^{17}$	$4\cdot311 \times 10^{-1}$	$1\cdot683 \times 10^{7}$	$2\cdot110 \times 10^{18}$
$1\cdot000 \times 10^{18}$	$4\cdot836 \times 10^{-1}$	$1\cdot061 \times 10^{8}$	$2\cdot098 \times 10^{18}$
$1\cdot000 \times 10^{19}$	$5\cdot173 \times 10^{-1}$	$2\cdot545 \times 10^{8}$	$2\cdot063 \times 10^{18}$
$1\cdot000 \times 10^{20}$	$5\cdot553 \times 10^{-1}$	$4\cdot258 \times 10^{8}$	$1\cdot921 \times 10^{18}$
$1\cdot000 \times 10^{21}$	$6\cdot009 \times 10^{-1}$	$5\cdot110 \times 10^{8}$	$1\cdot413 \times 10^{18}$
$1\cdot000 \times 10^{22}$	$6\cdot322 \times 10^{-1}$	$5\cdot263 \times 10^{8}$	$9\cdot045 \times 10^{17}$
$T = 600$°K			
$1\cdot000 \times 10^{11}$	$0\cdot000 \times 10^{0}$	$1\cdot000 \times 10^{0}$	$1\cdot545 \times 10^{19}$
$1\cdot000 \times 10^{12}$	$0\cdot000 \times 10^{0}$	$1\cdot000 \times 10^{0}$	$1\cdot545 \times 10^{19}$
$1\cdot000 \times 10^{13}$	$0\cdot000 \times 10^{0}$	$1\cdot000 \times 10^{0}$	$1\cdot545 \times 10^{19}$
$1\cdot000 \times 10^{14}$	$0\cdot000 \times 10^{0}$	$1\cdot000 \times 10^{0}$	$1\cdot545 \times 10^{19}$
$1\cdot000 \times 10^{15}$	$0\cdot000 \times 10^{0}$	$1\cdot000 \times 10^{0}$	$1\cdot545 \times 10^{19}$
$1\cdot000 \times 10^{16}$	$1\cdot025 \times 10^{-1}$	$7\cdot251 \times 10^{0}$	$1\cdot545 \times 10^{19}$
$1\cdot000 \times 10^{17}$	$2\cdot184 \times 10^{-1}$	$6\cdot776 \times 10^{1}$	$1\cdot545 \times 10^{19}$
$1\cdot000 \times 10^{18}$	$3\cdot358 \times 10^{-1}$	$6\cdot236 \times 10^{2}$	$1\cdot539 \times 10^{19}$
$1\cdot000 \times 10^{19}$	$4\cdot396 \times 10^{-1}$	$3\cdot434 \times 10^{3}$	$1\cdot502 \times 10^{19}$
$1\cdot000 \times 10^{20}$	$5\cdot176 \times 10^{-1}$	$7\cdot547 \times 10^{3}$	$1\cdot374 \times 10^{19}$
$1\cdot000 \times 10^{21}$	$5\cdot989 \times 10^{-1}$	$1\cdot033 \times 10^{4}$	$1\cdot020 \times 10^{19}$
$1\cdot000 \times 10^{22}$	$6\cdot695 \times 10^{-1}$	$1\cdot113 \times 10^{4}$	$6\cdot032 \times 10^{18}$
$T = 900$°K			
$1\cdot000 \times 10^{11}$	$0\cdot000 \times 10^{0}$	$1\cdot000 \times 10^{0}$	$3\cdot895 \times 10^{19}$
$1\cdot000 \times 10^{12}$	$0\cdot000 \times 10^{0}$	$1\cdot000 \times 10^{0}$	$3\cdot895 \times 10^{19}$
$1\cdot000 \times 10^{13}$	$0\cdot000 \times 10^{0}$	$1\cdot000 \times 10^{0}$	$3\cdot895 \times 10^{19}$
$1\cdot000 \times 10^{14}$	$0\cdot000 \times 10^{0}$	$1\cdot000 \times 10^{0}$	$3\cdot895 \times 10^{19}$
$1\cdot000 \times 10^{15}$	$0\cdot000 \times 10^{0}$	$1\cdot000 \times 10^{0}$	$3\cdot895 \times 10^{19}$
$1\cdot000 \times 10^{16}$	$0\cdot000 \times 10^{0}$	$1\cdot000 \times 10^{0}$	$3\cdot895 \times 10^{19}$
$1\cdot000 \times 10^{17}$	$0\cdot000 \times 10^{0}$	$1\cdot000 \times 10^{0}$	$3\cdot895 \times 10^{19}$
$1\cdot000 \times 10^{18}$	$1\cdot595 \times 10^{-1}$	$7\cdot653 \times 10^{0}$	$3\cdot887 \times 10^{19}$
$1\cdot000 \times 10^{19}$	$3\cdot250 \times 10^{-1}$	$5\cdot477 \times 10^{1}$	$3\cdot822 \times 10^{19}$
$1\cdot000 \times 10^{20}$	$4\cdot615 \times 10^{-1}$	$1\cdot742 \times 10^{2}$	$3\cdot519 \times 10^{19}$
$1\cdot000 \times 10^{21}$	$5\cdot764 \times 10^{-1}$	$2\cdot682 \times 10^{2}$	$2\cdot753 \times 10^{19}$
$1\cdot000 \times 10^{22}$	$6\cdot947 \times 10^{-1}$	$3\cdot062 \times 10^{2}$	$1\cdot586 \times 10^{19}$
$T = 1200$°K			
$1\cdot000 \times 10^{11}$	$0\cdot000 \times 10^{-1}$	$1\cdot000 \times 10^{0}$	$7\cdot012 \times 10^{19}$
$1\cdot000 \times 10^{12}$	$0\cdot000 \times 10^{-1}$	$1\cdot000 \times 10^{0}$	$7\cdot012 \times 10^{19}$
$1\cdot000 \times 10^{13}$	$0\cdot000 \times 10^{-1}$	$1\cdot000 \times 10^{0}$	$7\cdot012 \times 10^{19}$
$1\cdot000 \times 10^{14}$	$0\cdot000 \times 10^{-1}$	$1\cdot000 \times 10^{0}$	$7\cdot012 \times 10^{19}$
$1\cdot000 \times 10^{15}$	$0\cdot000 \times 10^{-1}$	$1\cdot000 \times 10^{0}$	$7\cdot012 \times 10^{19}$
$1\cdot000 \times 10^{16}$	$0\cdot000 \times 10^{-1}$	$1\cdot000 \times 10^{0}$	$7\cdot012 \times 10^{19}$
$1\cdot000 \times 10^{17}$	$0\cdot000 \times 10^{-1}$	$1\cdot000 \times 10^{0}$	$7\cdot012 \times 10^{19}$
$1\cdot000 \times 10^{18}$	$0\cdot000 \times 10^{-1}$	$1\cdot000 \times 10^{0}$	$7\cdot012 \times 10^{19}$
$1\cdot000 \times 10^{19}$	$1\cdot977 \times 10^{-1}$	$6\cdot111 \times 10^{0}$	$6\cdot930 \times 10^{19}$
$1\cdot000 \times 10^{20}$	$3\cdot917 \times 10^{-1}$	$2\cdot452 \times 10^{1}$	$6\cdot461 \times 10^{19}$
$1\cdot000 \times 10^{21}$	$5\cdot520 \times 10^{-1}$	$4\cdot300 \times 10^{1}$	$5\cdot144 \times 10^{19}$
$1\cdot000 \times 10^{22}$	$7\cdot055 \times 10^{-1}$	$5\cdot102 \times 10^{1}$	$3\cdot108 \times 10^{19}$

Table 1 (*cont.*)

N_A	μ	γ_A	K
$T = 1500°\text{K}$			
$1\cdot000 \times 10^{11}$	$0\cdot000 \times 10^{0}$	$1\cdot000 \times 10^{0}$	$1\cdot073 \times 10^{20}$
$1\cdot000 \times 10^{12}$	$0\cdot000 \times 10^{0}$	$1\cdot000 \times 10^{0}$	$1\cdot073 \times 10^{20}$
$1\cdot000 \times 10^{13}$	$0\cdot000 \times 10^{0}$	$1\cdot000 \times 10^{0}$	$1\cdot073 \times 10^{20}$
$1\cdot000 \times 10^{14}$	$0\cdot000 \times 10^{0}$	$1\cdot000 \times 10^{0}$	$1\cdot073 \times 10^{20}$
$1\cdot000 \times 10^{15}$	$0\cdot000 \times 10^{0}$	$1\cdot000 \times 10^{0}$	$1\cdot073 \times 10^{20}$
$1\cdot000 \times 10^{16}$	$0\cdot060 \times 10^{0}$	$1\cdot000 \times 10^{0}$	$1\cdot073 \times 10^{20}$
$1\cdot000 \times 10^{17}$	$0\cdot000 \times 10^{0}$	$1\cdot000 \times 10^{0}$	$1\cdot073 \times 10^{20}$
$1\cdot000 \times 10^{18}$	$0\cdot000 \times 10^{0}$	$1\cdot000 \times 10^{0}$	$1\cdot073 \times 10^{20}$
$1\cdot000 \times 10^{19}$	$5\cdot675 \times 10^{-2}$	$1\cdot507 \times 10^{0}$	$1\cdot069 \times 10^{20}$
$1\cdot000 \times 10^{20}$	$3\cdot102 \times 10^{-1}$	$7\cdot222 \times 10^{0}$	$1\cdot008 \times 10^{20}$
$1\cdot000 \times 10^{21}$	$5\cdot158 \times 10^{-1}$	$1\cdot429 \times 10^{1}$	$8\cdot223 \times 10^{19}$
$1\cdot000 \times 10^{22}$	$7\cdot098 \times 10^{-1}$	$1\cdot775 \times 10^{1}$	$5\cdot120 \times 10^{19}$

Table 2. *Values of Fermi level* (μ), *acceptor activity coefficient* (γ_A) *and equilibrium constant* (K_-) *at different doping level and temperature*

N_A	μ	γ_A	K
$T = 300°\text{K}$			
$1\cdot000 \times 10^{11}$	$-5\cdot443 \times 10^{-2}$	$8\cdot204 \times 10^{0}$	$3\cdot232 \times 10^{19}$
$1\cdot000 \times 10^{12}$	$-1\cdot104 \times 10^{-1}$	$7\cdot156 \times 10^{1}$	$3\cdot232 \times 10^{19}$
$1\cdot000 \times 10^{13}$	$-1\cdot689 \times 10^{-1}$	$6\cdot861 \times 10^{2}$	$3\cdot232 \times 10^{19}$
$1\cdot000 \times 10^{14}$	$-2\cdot306 \times 10^{-1}$	$7\cdot468 \times 10^{3}$	$3\cdot232 \times 10^{19}$
$1\cdot000 \times 10^{15}$	$-2\cdot966 \times 10^{-1}$	$9\cdot562 \times 10^{4}$	$3\cdot232 \times 10^{19}$
$1\cdot000 \times 10^{16}$	$-3\cdot533 \times 10^{-1}$	$8\cdot564 \times 10^{5}$	$3\cdot231 \times 10^{19}$
$1\cdot000 \times 10^{17}$	$-4\cdot088 \times 10^{-1}$	$7\cdot319 \times 10^{6}$	$3\cdot224 \times 10^{19}$
$1\cdot000 \times 10^{18}$	$-4\cdot665 \times 10^{-1}$	$6\cdot693 \times 10^{7}$	$3\cdot167 \times 10^{19}$
$1\cdot000 \times 10^{19}$	$-5\cdot254 \times 10^{-1}$	$5\cdot534 \times 10^{8}$	$2\cdot729 \times 10^{19}$
$1\cdot000 \times 10^{20}$	$-5\cdot770 \times 10^{-1}$	$1\cdot971 \times 10^{9}$	$1\cdot589 \times 10^{19}$
$1\cdot000 \times 10^{21}$	$-6\cdot223 \times 10^{-1}$	$2\cdot953 \times 10^{9}$	$6\cdot452 \times 10^{18}$
$1\cdot000 \times 10^{22}$	$-6\cdot692 \times 10^{-1}$	$3\cdot236 \times 10^{9}$	$1\cdot923 \times 10^{18}$
$T = 600°\text{K}$			
$1\cdot000 \times 10^{11}$	$0\cdot000 \times 10^{0}$	$1\cdot000 \times 10^{0}$	$3\cdot841 \times 10^{19}$
$1\cdot000 \times 10^{12}$	$0\cdot000 \times 10^{0}$	$1\cdot000 \times 10^{0}$	$3\cdot841 \times 10^{19}$
$1\cdot000 \times 10^{13}$	$0\cdot000 \times 10^{0}$	$1\cdot000 \times 10^{0}$	$3\cdot841 \times 10^{19}$
$1\cdot000 \times 10^{14}$	$0\cdot000 \times 10^{0}$	$1\cdot000 \times 10^{0}$	$3\cdot841 \times 10^{19}$
$1\cdot000 \times 10^{15}$	$0\cdot000 \times 10^{0}$	$1\cdot000 \times 10^{0}$	$3\cdot841 \times 10^{19}$
$1\cdot000 \times 10^{16}$	$-5\cdot498 \times 10^{-4}$	$2\cdot890 \times 10^{0}$	$3\cdot840 \times 10^{19}$
$1\cdot000 \times 10^{17}$	$-1\cdot718 \times 10^{-1}$	$2\cdot763 \times 10^{1}$	$3\cdot837 \times 10^{19}$
$1\cdot000 \times 10^{18}$	$-2\cdot925 \times 10^{-1}$	$2\cdot788 \times 10^{2}$	$3\cdot801 \times 10^{19}$
$1\cdot000 \times 10^{19}$	$-4\cdot052 \times 10^{-1}$	$2\cdot069 \times 10^{3}$	$3\cdot529 \times 10^{19}$
$1\cdot000 \times 10^{20}$	$-5\cdot038 \times 10^{-1}$	$6\cdot854 \times 10^{3}$	$2\cdot556 \times 10^{19}$
$1\cdot000 \times 10^{21}$	$-5\cdot909 \times 10^{-1}$	$1\cdot021 \times 10^{4}$	$1\cdot296 \times 10^{19}$
$1\cdot000 \times 10^{22}$	$-6\cdot768 \times 10^{-1}$	$1\cdot123 \times 10^{4}$	$4\cdot863 \times 10^{18}$
$T = 900°\text{K}$			
$1\cdot000 \times 10^{11}$	$0\cdot000 \times 10^{0}$	$1\cdot000 \times 10^{0}$	$5\cdot274 \times 10^{19}$
$1\cdot000 \times 10^{12}$	$0\cdot000 \times 10^{0}$	$1\cdot000 \times 10^{0}$	$5\cdot274 \times 10^{19}$
$1\cdot000 \times 10^{13}$	$0\cdot000 \times 10^{0}$	$1\cdot000 \times 10^{0}$	$5\cdot274 \times 10^{19}$
$1\cdot000 \times 10^{14}$	$0\cdot000 \times 10^{0}$	$1\cdot000 \times 10^{0}$	$5\cdot274 \times 10^{19}$
$1\cdot000 \times 10^{15}$	$0\cdot000 \times 10^{0}$	$1\cdot000 \times 10^{0}$	$5\cdot274 \times 10^{19}$

Table 2 (*cont.*)

N_A	μ	γ_4	K
$1\cdot000 \times 10^{18}$	$-9\cdot054 \times 10^{-2}$	$3\cdot172 \times 10^{0}$	$5\cdot253 \times 10^{19}$
$1\cdot000 \times 10^{16}$	$0\cdot000 \times 10^{0}$	$1\cdot000 \times 10^{0}$	$5\cdot274 \times 10^{19}$
$1\cdot000 \times 10^{17}$	$0\cdot000 \times 10^{0}$	$1\cdot000 \times 10^{0}$	$5\cdot274 \times 10^{19}$
$1\cdot000 \times 10^{19}$	$-2\cdot609 \times 10^{-1}$	$2\cdot490 \times 10^{1}$	$5\cdot028 \times 10^{19}$
$1\cdot000 \times 10^{20}$	$-4\cdot090 \times 10^{-1}$	$9\cdot248 \times 10^{1}$	$4\cdot046 \times 10^{19}$
$1\cdot000 \times 10^{21}$	$-5\cdot381 \times 10^{-1}$	$1\cdot498 \times 10^{2}$	$2\cdot361 \times 10^{19}$
$1\cdot000 \times 10^{22}$	$-6\cdot658 \times 10^{-1}$	$1\cdot697 \times 10^{2}$	$9\cdot821 \times 10^{18}$
$T = 1200°K$			
$1\cdot000 \times 10^{11}$	$0\cdot000 \times 10^{0}$	$1\cdot000 \times 10^{0}$	$6\cdot951 \times 10^{19}$
$1\cdot000 \times 10^{12}$	$0\cdot000 \times 10^{0}$	$1\cdot000 \times 10^{0}$	$6\cdot951 \times 10^{19}$
$1\cdot000 \times 10^{13}$	$0\cdot000 \times 10^{0}$	$1\cdot000 \times 10^{0}$	$6\cdot951 \times 10^{19}$
$1\cdot000 \times 10^{14}$	$0\cdot000 \times 10^{0}$	$1\cdot000 \times 10^{0}$	$6\cdot951 \times 10^{19}$
$1\cdot000 \times 10^{15}$	$0\cdot000 \times 10^{0}$	$1\cdot000 \times 10^{0}$	$6\cdot951 \times 10^{19}$
$1\cdot000 \times 10^{16}$	$0\cdot000 \times 10^{0}$	$1\cdot000 \times 10^{0}$	$6\cdot951 \times 10^{19}$
$1\cdot000 \times 10^{17}$	$0\cdot000 \times 10^{0}$	$1\cdot000 \times 10^{0}$	$6\cdot951 \times 10^{19}$
$1\cdot000 \times 10^{18}$	$0\cdot000 \times 10^{0}$	$1\cdot000 \times 10^{0}$	$6\cdot951 \times 10^{19}$
$1\cdot000 \times 10^{19}$	$-1\cdot054 \times 10^{-1}$	$2\cdot569 \times 10^{0}$	$6\cdot803 \times 10^{19}$
$1\cdot000 \times 10^{20}$	$-3\cdot062 \times 10^{-1}$	$1\cdot063 \times 10^{1}$	$5\cdot766 \times 10^{19}$
$1\cdot000 \times 10^{21}$	$-4\cdot763 \times 10^{-3}$	$1\cdot848 \times 10^{1}$	$3\cdot682 \times 10^{19}$
$1\cdot000 \times 10^{22}$	$-6\cdot463 \times 10^{-1}$	$2\cdot156 \times 10^{1}$	$1\cdot645 \times 10^{19}$
$T = 1500°K$			
$1\cdot000 \times 10^{11}$	$0\cdot000 \times 10^{0}$	$1\cdot000 \times 10^{0}$	$8\cdot671 \times 10^{19}$
$1\cdot000 \times 10^{12}$	$0\cdot000 \times 10^{0}$	$1\cdot000 \times 10^{0}$	$8\cdot671 \times 10^{19}$
$1\cdot000 \times 10^{13}$	$0\cdot000 \times 10^{0}$	$1\cdot000 \times 10^{0}$	$8\cdot671 \times 10^{19}$
$1\cdot000 \times 10^{14}$	$0\cdot000 \times 10^{0}$	$1\cdot000 \times 10^{0}$	$8\cdot671 \times 10^{19}$
$1\cdot000 \times 10^{15}$	$0\cdot000 \times 10^{0}$	$1\cdot000 \times 10^{0}$	$8\cdot671 \times 10^{19}$
$1\cdot000 \times 10^{16}$	$0\cdot000 \times 10^{0}$	$1\cdot000 \times 10^{0}$	$8\cdot671 \times 10^{19}$
$1\cdot000 \times 10^{17}$	$0\cdot000 \times 10^{0}$	$1\cdot000 \times 10^{0}$	$8\cdot671 \times 10^{19}$
$1\cdot000 \times 10^{18}$	$0\cdot000 \times 10^{0}$	$1\cdot000 \times 10^{0}$	$8\cdot671 \times 10^{19}$
$1\cdot000 \times 10^{19}$	$0\cdot000 \times 10^{0}$	$1\cdot000 \times 10^{0}$	$8\cdot671 \times 10^{19}$
$1\cdot000 \times 10^{20}$	$-1\cdot954 \times 10^{-1}$	$3\cdot027 \times 10^{0}$	$7\cdot704 \times 10^{19}$
$1\cdot000 \times 10^{21}$	$-4\cdot094 \times 10^{-1}$	$5\cdot650 \times 10^{0}$	$5\cdot208 \times 10^{19}$
$1\cdot000 \times 10^{22}$	$-6\cdot169 \times 10^{-1}$	$6\cdot756 \times 10^{0}$	$2\cdot507 \times 10^{19}$

the free energies of these dissociation reactions are negative ($\Delta F = -RT \ln K$) and becomes increasingly negative with increasing temperature. With decreasing temperature ionization becomes difficult and the free energy should become less negative or more positive. This point is well demonstrated in Fig. 4. The fact that complete ionization of dopants may be expected at room temperature is not due to a negative free energy but due to the availability of many empty states in the respective bands. In fact energetically no ionization should occur (i.e. having very low probability of ionization) at room temperature ($kT = 0{\cdot}025$ eV). The curves in Fig. 4 also indicate that near room temperature the slope or the free energy becomes more negative with increasing impurity concentration, i.e. ionization is enhanced.

Some of the inferences of the above computations are outlined here under the epitaxial growth conditions, namely at 1400°–1500°K, the solute obeys Henry's law up to a concentration of 1×10^{18} atom/cm^3 beyond which rapid deviations may be expected. At doping levels of 10^{20}–10^{21} atom/cm^3 metallic behavior may be expected and conductivity should increase linearly with doping level. However, this increase in conductivity may be completely masked by the scattering center

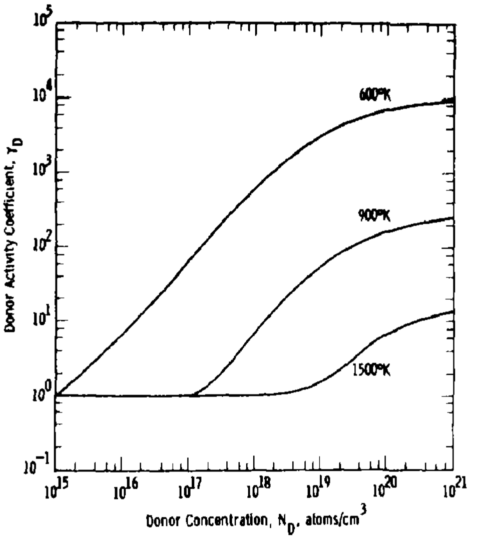

Fig. 1. Dependence of γ_D on N_D at different temperatures for arsenic in silicon.

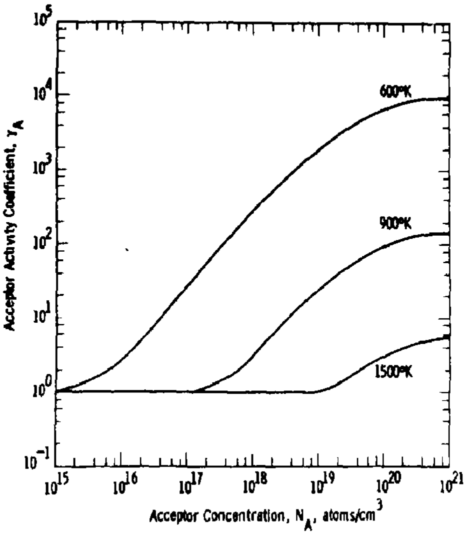

Fig. 2. Dependence of γ_A on N_A at different temperatures for boron in silicon.

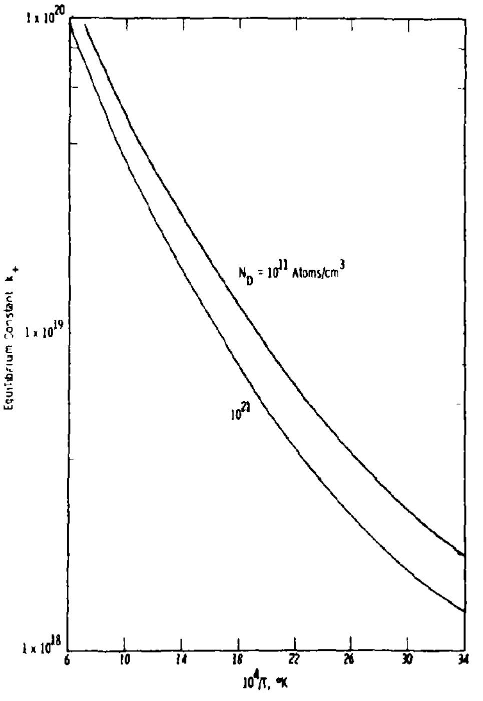

Fig. 3. Variation of k_+ with temperature at different donor doping levels.

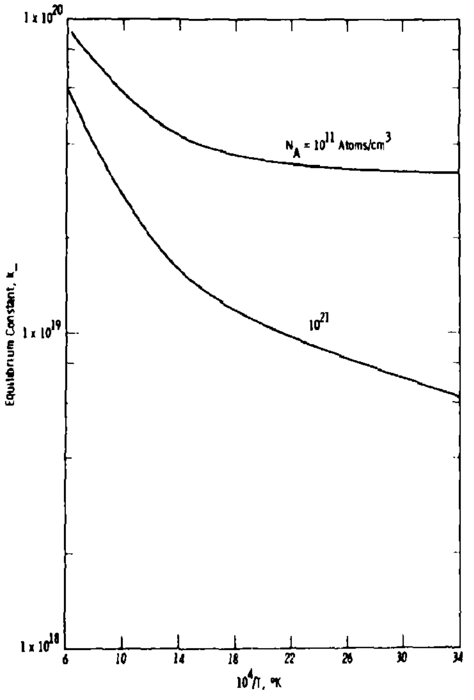

Fig. 4. Variation of k_- with temperature at different acceptor doping levels.

(i.e. the donor or the acceptor ion) that results from each electron liberated in the conduction band.

As another application of these computations the mobility of the impurity atoms in the Si matrix can be calculated from diffusivity data using Nernst–Einstein relation. From the computations for the n-type Si, we can safely say that at 1200°C and $N_D = 1 \times 10^{18}$ atom/cm^3 the activity coefficient γ_D has a value of unity. Further, the difference between the activity coefficients for P doping and As doping is small. We can therefore use the Nernst–Einstein equation and obtain a value of mobility, B, for the dopant atom:

$$B = \frac{D}{kT}$$

Here D is the diffusivity of the dopant atom. Maekawa[8] has measured diffusivity of P in Si at different temperatures and surface concentrations. Using his data at 1200°C a value of D equal to $1{\cdot}5 \times 10^{-12}$ cm^2/sec is obtained at a surface concentration of $2{\cdot}2 \times 10^{18}$ atom/cm^3. Thus, the mobility at 1200°C is calculated to be $1{\cdot}2 \times 10^{-11}$ cm^2/sec V using consistent units. This is a reasonable value of the atom mobility and may be compared with the corresponding mobility of vacancies from the self diffusivity in Si which is about 4×10^{-13} cm^2/sec V[9]. Divacancies are thought to be responsible for the self-diffusion in Si and should therefore yield a mobility value considerably lower than that of a single vacancy. In view of the existing uncertainties in the detailed mechanism of diffusion the mobility of the P atom calculated here must await further confirmation. Since, at high doping levels the activity coefficient is greater than one and increases with concentration, the correction due to non-ideal solution[10]. $\partial \ln \gamma_D / \partial \ln N_D$, is positive. Thus, we cannot only predict that the diffusivity increases with concentration, but can calculate diffusivities at high concentrations using the mobility and activity coefficient data.

SUMMARY

Solid solutions of group III and V impurities in Si are examined and their deviations from ideal behavior are determined by the activity coefficients. It is shown that under the epitaxial growth conditions Henry's law can be applied to the system up to a carrier concentration of about 1×10^{18} atom/cm^3 above which considerable deviations may be expected. These activity data can be utilized to calculate atom mobility and the correction required in the Nernst–Einstein relation to calculate diffusivities at high concentratons. Dissociation equilibrium constants are evaluated and their dependence on the non-ideality of the solid solution is small. The slopes or the free energies of these dissociation reactions become more positive with decreasing temperature. In the case of B doping near room temperature it is clearly seen that the free energy becomes more negative with increasing impurity concentration, i.e. ionization is enhanced. Ionization of impurities as a function of their concentration is described with the ions acting as strong scattering centers when the impurity band penetrates the conduction band.

Again, the two basic assumptions or limitations in these computations and (i) the effective masses are assumed to be constants, and (ii) ionization energies of the dopant are assumed to be independent of the doping level.

Acknowledgement—The author is indebted to Westinghose Electric Corporation for making this work possible

REFERENCES

1. WAGNER C., *Z. phys. Chem.* **B21**, 25 (1936)
2. REISS H., *J. chem. Phys.* **21**, 1209 (1953)
3. McFARLANE G. G., McLEAN T. P., QUARRINGTON J. F. and ROBERTS V., *Phys. Rev.* **111**, 1245 (1958).
4. ALEXANDER M. N. and HOLCOMB D. F., *Solid State Commun.* **6**, 355 (1968).
5. McDOUGALL J. and STONER E. C., *Phil. Trans. R. Soc.* **337A**, 67 (1938)
6. WILF H. S., In *Advances in Numerical Quadrature* (Edited by A. Ralston and H. S. Wilf), Vol. 2, Chap. 6. Wiley, New York (1967).
7. BANER F. L., *Comm ACM* **4**, No. 6 (1961)
8. MAEKAWA S., *J. phys. Soc. Japan* **17**, 1592 (1962).
9. GHOSHTAGORE R. N., *Phys. Rev. Lett.* **16**, 890 (1966)
10. BARDEEN J. and HERRING C., In *Atom Movements*, p. 87 ASM, Cleveland (1951).

J. Phys. Chem. Solids Pergamon Press 1969. Vol. 30, pp. 1823–1825. Printed in Great Britain.

PREPARATION AND PROPERTIES OF POLYCRYSTALLINE CERIUM ORTHOFERRITE ($CeFeO_3$)

M. ROBBINS, G. K. WERTHEIM, A. MENTH and R. C. SHERWOOD
Bell Telephone Laboratories, Incorporated, Murray Hill, N.J 07971, U.S.A.

(*Received* 16 *December* 1968)

Abstract—Cerium orthoferrite ($CeFeO_3$) was prepared by the reaction $3CeO_2 + Fe_2O_3 + Fe \rightarrow 3CeFeO_3$. $CeFeO_3$ forms with an orthorhombic unit cell where a = 5·541 Å, b = 5·577 Å, and c = 7·809 Å. Magnetic measurements and Mossbauer spectra both show that the cation valencies in $CeFeO_3$ are Ce^{3+} and Fe^{3+}. $CeFeO_3$ undergoes spin reorientation at 230°K and has a Curie temperature of 719°K.

INTRODUCTION

THE CRYSTALLOGRAPHIC and magnetic properties of most of the rare earth orthoferrites ($ReFeO_3$) have been very extensively studied. Of these, only cerium orthoferrite ($CeFeO_3$) which has been reported[1] to be an orthorhombic orthoferrite has not been studied magnetically or by Mössbauer effect. In this paper we report the preparation and magnetic properties of single phase polycrystalline $CeFeO_3$. Also investigated was the question of valence states of the Ce and Fe ions, in order to distinguish between the two possible valence distributions, (Ce^{4+}, Fe^{2+}) or (Ce^{3+}, Fe^{3+}). The magnetic properties and the valence distribution were both determined from magnetic and Mössbauer measurements.

EXPERIMENTAL

$CeFeO_3$ was prepared by the reaction $3CeO_2 + Fe_2O_3 + Fe \rightarrow 3CeFeO_3$. This reaction was carried out by firing pressed pellets of the appropriate mixture in a sealed evacuated quartz tube at 800°–850°C for 48 hr. The resulting material was single phase within the limitations of X-ray diffraction. Unit cell parameters (using CrKα radiation) and unit cell volume are shown in Table 1 along with those which have been reported for $LaFeO_3$ and $PrFeO_3$[2]. The a- and b-unit cell parameters are consistent with the trends which were observed for the other rare earth orthoferrites[2]. The c-parameter was found to be only slightly smaller in $CeFeO_3$ than in $PrFeO_3$. The unit cell volume falls between that of $LaFeO_3$ and $PrFeO_3$ (as shown in Table 1), and is in better agreement with cell volume systematics than that of [1].

MAGNETIC MEASUREMENTS

Magnetic measurements as a function of temperature (using applied fields of 15·3, 9·9

Table 1. *Crystallographic properties of* $CeFeO_3$

	Unit cell parameters (Å)			Unit cell
	a	b	c	volume (Å)^3
$LaFeO_3$[2]	5·556	5·565	7·862	243·1
$CeFeO_3$	5·541	5·577	7·809	241·3
$CeFeO_3$[1]	5·519	5·536	7·819	238·9
$PrFeO_3$[2]	5·495	5·578	7·810	239·4

and 4·9 kOe) in the 1·5°–300°K region are shown in Fig. 1. $CeFeO_3$ exhibits, at room temperature, a small magnetic moment similar to that observed in the other orthoferrites[3], which is due to the occurrence of canted antiferromagnetism. As shown in Fig. 1 there is a broad maximum in the magnetic moment at 230°K followed by an increase in moment at ~60°K. This magnetic behavior is very similar to that of $TmFeO_3$[4], in which a maximum in the magnetic moment occurs at 90°K. This maximum was shown to be due to a change in the easy direction of magnetization, which results in a temporary lowering of the anisotropy. Thus, 230°K appears to be the spin reorientation temperature of $CeFeO_3$. The Mössbauer measurements discussed below support this contention. The low temperature (60°K) increase in moment is undoubtedly caused by the presence of a paramagnetic rare earth ion. This indicates that the valence state of the cerium ion is Ce^{3+}, since Ce^{4+} is a nonmagnetic ion. The presence of trivalent cerium means that the iron must also be trivalent.

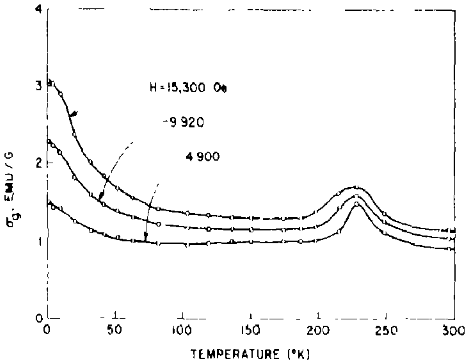

Fig. 1. Magnetization vs. temperature between 1·5° and 300°K

Magnetic measurements as a function of temperature in the region 300°–1200°K yield an effective paramagnetic moment, obtained from the high temperature susceptibility data of 5·20 μ_B. The Curie temperature was measured by differential thermal analysis techniques and found to be 719°K.

MÖSSBAUER STUDY

The ^{57}Fe Mössbauer effect absorption spectrum[*] of $CeFeO_3$ shows only trivalent iron, Fig. 2. The trivalent nature of the iron in $CeFeO_3$ is established by the isomer shift and hfs effective field which are very similar to those of Fe_2O_3 and the other orthoferrites [5] (see Table 2).

The Mössbauer effect quadrupolar line shift shows clearly that there is a spin reorientation near 230°K. For small quadrupolar admixture the magnetic hfs lines are shifted by an amount $e^2qQ(e\cos^2\theta - 1)/8$ provided the electric field gradient, EFG, tensor has

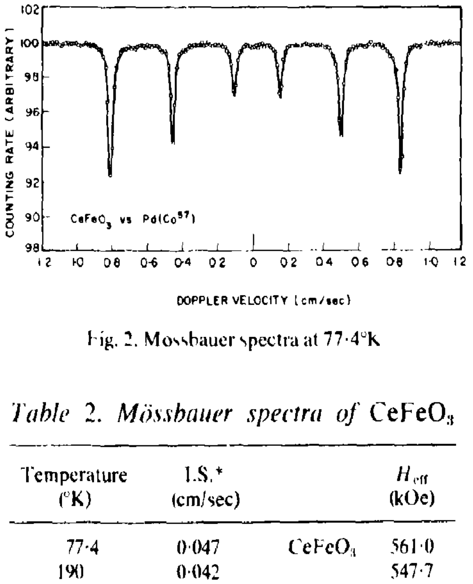

Fig. 2. Mossbauer spectra at 77·4°K

Table 2. Mössbauer spectra of $CeFeO_3$

Temperature (°K)	I.S.* (cm/sec)		H_{eff} (kOe)
77·4	0·047	$CeFeO_3$	561·0
190	0·042		547·7
225	0·041		538·6
260	0·038		528·3
298	0·036		516·9
R.T.	0·0362	Fe_2O_3	515·7
		$LaFeO_3$	
R.T.			521†
85			562†

*Isomer shift relative to metallic iron
†From [5].

---

[*] A conventional constant-acceleration Doppler spectrometer using a ^{57}Co in Pd source was employed

axial asymmetry, and θ is the angle between the symmetry axis of the EFG tensor and spin direction. Even though this case is not strictly applicable in the orthoferrites the data, Fig. 3, show a change in the sign of the line shift at 230°K. This is interpreted as an indication that the spin direction which is approximately perpendicular to the c-axis above 230°K becomes parallel below that temperature. In the same region of temperature the hfs effective magnetic field and isomer shift are continuous and show no discontinuity in slope indicating that there is no phase transition. The hyperfine effective field as a function of temperature for $CeFeO_3$ falls between those of $LaFeO_3$ and $NdFeO_3$[5] as shown in Fig. 4.

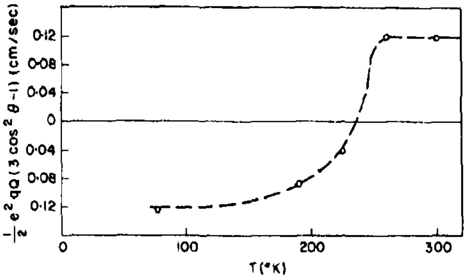

Fig. 3. Temperature dependence of the quadrupolar line shift.

DISCUSSION AND CONCLUSIONS

The measured paramagnetic effective moment (5.20 μ_B) is in agreement with values (5·20 – 6·00μ_B) which have been previously obtained for Fe^{3+}[6]. The spin reorientation temperature of 230°K, for $CeFeO_3$ is the second highest of the rare earth orthoferrites, $SmFeO_3$ having the highest reorientation temperature (483°K)[7]. The Curie temperature (T_c) of $CeFeO_3$ (719°K) falls midway between those of $LaFeO_3$ and $PrFeO_3$[5, 8]. All of the properties of $CeFeO_3$ which have been determined are in agreement with the systematics of the rare earth orthoferrites.

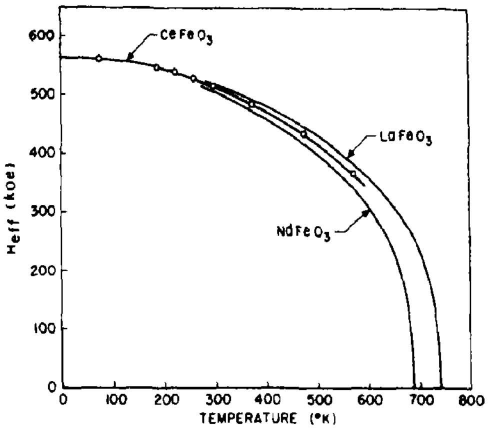

Fig. 4. Hyperfine effective field vs. temperature for CeFeO, $LaFeO_3$ and $NdFeO_3$[4].

Acknowledgements—We are indebted to M. R. Monforte for the determination of the Curie Point by differential thermal analysis.

REFERENCES

1. BERTAUT F. and FORRAT F., *J. Phys.* **17**, 129 (1956).
2. GELLER S. and WOOD E. A., *Acta crystallogr.* **9**, 563 (1956)
3. BOZORTH R. M., KRAMER V. and REMEIKA J. P., *Phys. Rev. Lett.* 1, 3 (1958); GORODETSKY G. and TREVES D., *Proc. Intl Conf. on Magnetism, Nottingham, 1964* The Institute of Physics and the Physical Society, London
4. WOLFE R., PIERCE R. D., HASZKO J. E. and REMEIKA J. P., *Appl. Phys. Lett.* **11**, 245 (1967).
5. FIBSCHUTZ M., SHTRIKMAN S. and TREVES D., *Phys. Rev.* **156**, 562 (1967)
6. SELWOOD P. W., In *Magnetochemistry*, p. 159 Interscience, New York (1956).
7. SHERWOOD R. C., REMEIKA J. P. and WILLIAMS H. J., *J. appl. Phys.* **30**, 217 (1959)
8. EIBSCHUTZ M., GORODETSKY G., SHTRIKMAN S., and TREVES D., *J. appl. Phys.* **35**, 1071 (1964)

J. Phys. Chem. Solids Pergamon Press 1969. Vol. 30, pp. 1827–1833. Printed in Great Britain.

LOW TEMPERATURE ELECTRICAL RESISTIVITIES OF SOME DILUTE *Pd* Fe ALLOYS*

GWYN WILLIAMS and J. W. LORAM
School of Mathematical and Physical Sciences,
University of Sussex, Brighton, U.K.

(*Received* 13 *December* 1968)

Abstract – The electrical resistivity of several dilute *Pd* Fe alloys has been measured in the temperature range 0·5°–77°K. Immediately below the Curie temperature (T_c) a linear decrease of the incremental resistivity ($\Delta\rho$) with temperature is observed, while at lower temperatures ($T \ll T_c$), $\Delta\rho$ is proportional to $T^{3/2}$. The experimental results are compared with the theoretical predictions of a model based on *s* electron–magnon scattering. Estimates of the effective exchange integral *J* are made.

INTRODUCTION

PALLADIUM and its alloys, especially with the trio Fe, Co and Ni, has attracted much experimental and theoretical interest. Paramagnetic susceptibility and ferromagnetic saturation magnetisation measurements[1, 2] on dilute *Pd* Fe and *Pd* Co indicate giant magnetic moments associated with the impurity atoms, while the fact that as little as 0·1 per cent of Fe (or Co) in Pd leads to ferromagnetism indicates a long range ferromagnetic spin coupling associated with a long range spin polarization in the host metal.

Recent investigations, both experimental and theoretical[3], into the low temperature electrical resistivities of Pd and several dilute *Pd* Ni alloys have indicated the importance of *s*-electron scattering from spin density fluctuations (paramagnons) in the nearly-ferromagnetic itinerant *d* band. Similar considerations should also be important in dilute *Pd* Fe (or Co), however, in the ferromagnetic state *s*-electron scattering from *real* spin waves in the coupled impurity moment – *d* band system should dominate the low temperature electrical resistivity. Indeed, a recent theoretical paper[4] directed along these lines has prompted the measurement of the low temperature resistivity of a series of dilute *Pd* Fe alloys.

METHODS AND MATERIALS

The phase constitution of binary (Pd–Fe) alloys is well established[5]. At high temperatures they form a complete range of solid solutions with a f.c.c. structure. In alloys containing less than 60 At.% Fe, quenching from high temperatures suppresses super-lattice formation (these are centred about the compositions Pd Fe and Pd_3Fe) and produces a disordered f.c.c. solid solution.

The alloys were prepared by melting 5*N* pure Pd with 5*N* pure Fe (both provided in sponge form by Johnson Matthey and Co.) in a water cooled 'Cu boat induction furnace' [6], surrounded by an argon atmosphere. Initially a 'master alloy' of approximate composition Pd – 5 At.% Fe (Pd – 4·6 At.% Fe as estimated from the initial weights of each material) was prepared by melting together the appropriate proportions of the two elements: this alloy was inverted and remelted five times to ensure that it was homogeneous. This 'master alloy' was etched in a solution of nitric acid and hydrogen peroxide, cold-rolled to a thickness of about 0·01 in., annealed in vacuo for 24 hr at 1150°C and finally quenched.

---

*This work has been sponsored in part by the Air Force Materials Laboratory (AFSC) through the European Office of Aerospace Research (OAR), United States Air Force, under Contract F61052-68-C-0011.

Alloys containing roughly 0·2, 0·3, 0·5, 0·7 and 1·0 At.% Fe were prepared by diluting the 'master alloy' with the appropriate amounts of Pd (obtained by melting the 5*N* pure Pd sponge); each alloy was subjected to the homogenising treatment described above. They were then etched, cold-rolled to thicknesses varying from 0·003 in. (0·2 At.% Fe) to 0·008 in. (1 At.% Fe), cut into strips 8 cm long and 0·2–0·3 cm wide. The samples were etched after cutting and then subjected to the same annealing treatment as the 'master alloy'.

The specimen resistances were measured in a conventional He^4 cryostat operating in the temperature range 0·5°–300°K, using a normal four-probe d.c. potentiometric circuit, incorporating a Tinsley Disselhorst potentiometer and galvanometer amplifier capable of reproducible measurements to 2×10^{-8} V. A sample holder accommodating six specimens (one 'pure' metal and five alloys) was employed, and a sample current of 30 mA was used. Temperatures below 4·2°K were stabilised and measured to within ± 1 mdeg, and above 4·2°K to better than ± 1 per cent.

RESULTS AND DISCUSSION

Figures 1(a) and 1(b) reproduce some of the experimental data in the form $\Delta\rho(\rho_{\text{Alloy}}(T) - \rho_{\text{Pd}}(T))$ vs T; the fact that the Pd and the

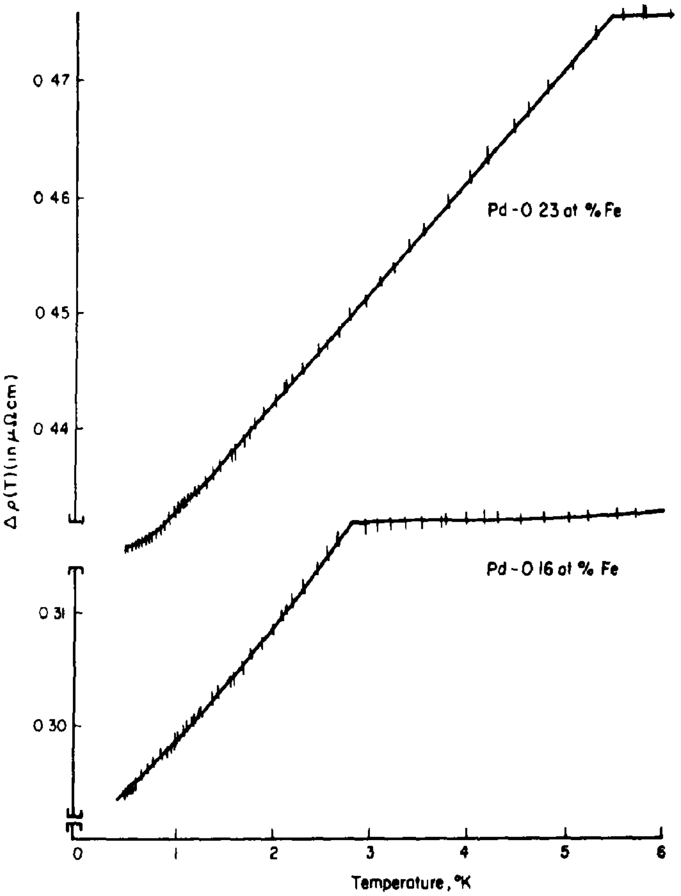

Fig 1(a) Experimental data on Pd-0·16 At.% Fe and Pd-0·23 At.% Fe. Vertical bars correspond to a voltage uncertainty of ±2 . 10^{-8} V.

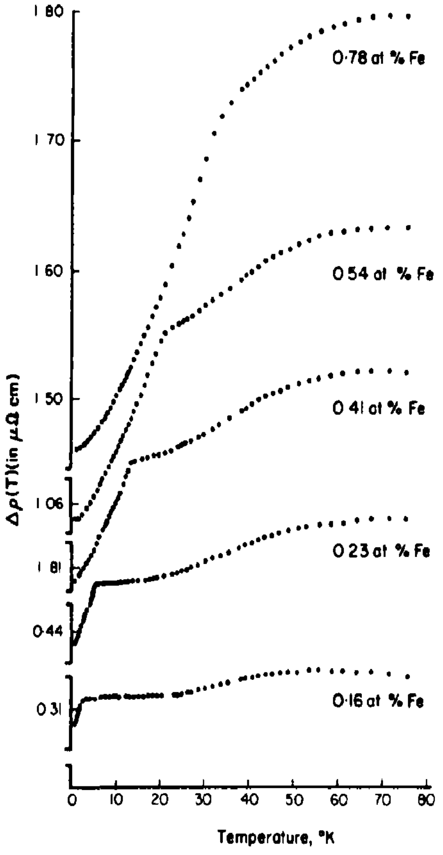

Fig. 1(b). $\Delta\rho$ (T) (in $\mu\Omega$ cm) vs. T (in °K) for all five alloys examined. Note the changes of zero for the incremental resistivities.

Pd Fe alloys were subjected to the same heat treatment means that in examining the difference $\Delta\rho(T)$, the temperature independent contribution to the resistivity arising from scattering due to lattice imperfections should be eliminated. The temperature dependence of the Pd resistivity is in very good agreement with the data of Rice and Schindler[3], while the general features of the ($\Delta\rho(T)-T$) plots for the alloys seem to agree with previous measurements on the *Pd* Fe system[7] although a detailed comparison with the published data is difficult. Careful examination of the present results enable the following comments to be made about the overall character of the incremental resistivity $\Delta\rho(T)$ of the alloys.

(i) Above the Curie temperature, T_c, this quantity is not independent of temperature. Apart from the 'usual' deviations from Matthiessen's Rule, this result could originate from *s*-electron scattering from enhanced spin *density* fluctuations in this paramagnetic region.

(ii) In the temperature region immediately below T_c, the experimental data indicates that $\Delta\rho(T)$ decreased linearly with T (as predicted in [4]). The 'coefficient' of this linear decrease is approximately $10^{-2}\,\mu\Omega$ cm/°K in *all* the alloys examined.

(iii) At lower temperatures deviations from the linear behaviour discussed in (ii) are observed.

According to the theoretical approach contained in reference 4, the form of the incremental resistivity, $\Delta\rho(T)=\rho(T)-\rho_{Pd}(T)$, in dilute systems at temperatures $T \ll T_c$ (the Curie temperature) is:

$$\Delta\rho(T) \approx Ac+\frac{B}{c^{1/2}}\times T^{3/2} \qquad (1)$$

A and B are constants and c is the concentration. The first term on the right hand side of equation (1) comes from elastic (potential) scattering; there are, however, three contributions to the second term. *S*-electron spin flip scattering from the coupled impurity moment-*d* band system results in the creation of a spin deviation in this system, which propagates as a spin wave. The coupled system does not possess translational symmetry, consequently such processes do not result in the limiting T^2 form of the low temperature resistivity from electron-magnon scattering, familiar in 'pure' ferromagnets, but gives rise to the $T^{3/2}$ limiting relationship. The second contribution comes from the non spin-flip (elastic) part of the exchange scattering[8]; it is proportional to $\langle M^2\rangle$, the mean of the squared magnetization (consequently increases with decreasing temperature). The third contribution comes from 'interference' effects between the potential scattering and the non spin-flip part of the exchange scattering[8]; such effects, in the limit of strong potential scattering, contribute a term to the incremental resistivity $\Delta\rho(T)$ which decreases as $\langle M\rangle^2$, the mean magnetisation, squared. For the case of a ferromagnetic system, in the low temperature limit, $\langle M^2\rangle$ and $\langle M\rangle^2$ have the same dependence on temperature, which leads in the present case to both terms being proportional to $T^{3/2}$.

Figure 2 reproduces some of the experimental data in the form $\Delta\rho(T)$ vs. $T^{3/2}$. It is clear from this figure that for $T \ll T_c$, the difference $\Delta\rho(T)$ follows the predicted $T^{3/2}$ power law for all five alloys examined. From this limiting behaviour $\Delta\rho(T=0)$ can be estimated; this quantity is plotted against the (analysed) concentration in Fig. 3(a). Again, as predicted, $\Delta\rho(0) = Ac$ where experimentally $A \approx 1{\cdot}9\,\mu\Omega$ cm/At.%Fe. Figure 3(b) indicates the concentration dependence of the coefficient of the $T^{3/2}$ term; it shows that this is not proportional to $c^{-1/2}$ as suggested in [4], but is best represented by Bc^{-1}, with B estimated at $\approx 1{\cdot}08\times10^{-3}\,\mu\Omega$ cm at.% Fe/(°K)$^{3/2}$. This disagreement is not really surprising since the theoretical model employs a molecular field approach in which the d-band splitting (and hence T_c) depends linearly on the impurity concentration, whereas previous measurements[7] and the present results (Table 1) show that T_c varies in a more complicated manner with concentration. Thus although the general predictions of the theoretical model of [4] are expected (and indeed have been shown) to be correct the more subtle concentration dependent effects can hardly be expected to agree.

Aside from the considerations already discussed, one of the more interesting results of the present investigation concerns the change in resistivity ($\Delta\rho_{\max}$) between 0°K and the Curie temperature T_c ($\Delta\rho_{\max.} = \Delta\rho(T_c) - \Delta\rho(0)$). This difference has a complicated dependence on impurity concentration, as an examination of Fig. 3(c) reveals. The theories of Yosida[8] and Kasuya[9] however, predict that $\Delta\rho_{\max.}$ should be proportional to c, but the present system is undoubtedly more complicated than that discussed by these authors, owing to the presence of 'persistent fluctuations' in the itinerant d-band, and their

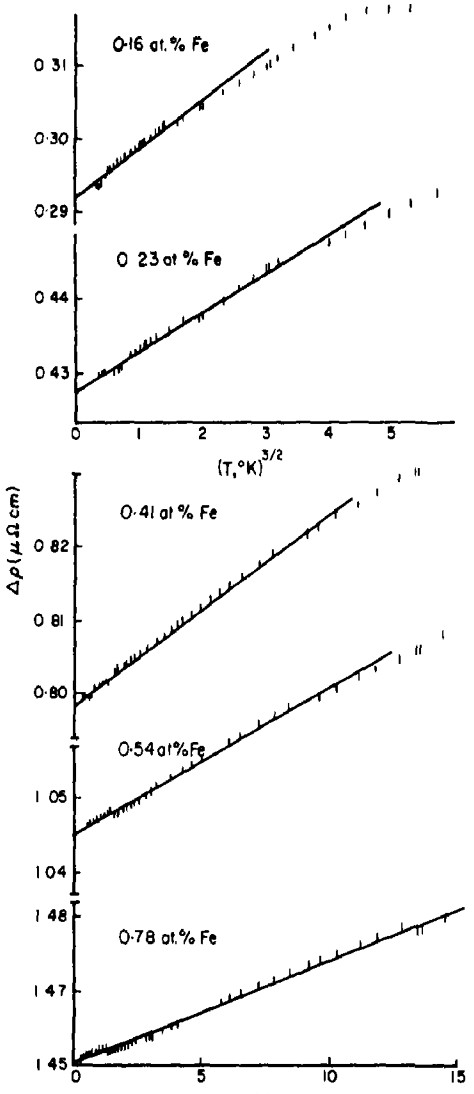

Fig. 2. $\Delta\rho(T)$ (in $\mu\Omega$ cm) vs. $T^{3/2}$. Note the changes of zero for the incremental resistivities.

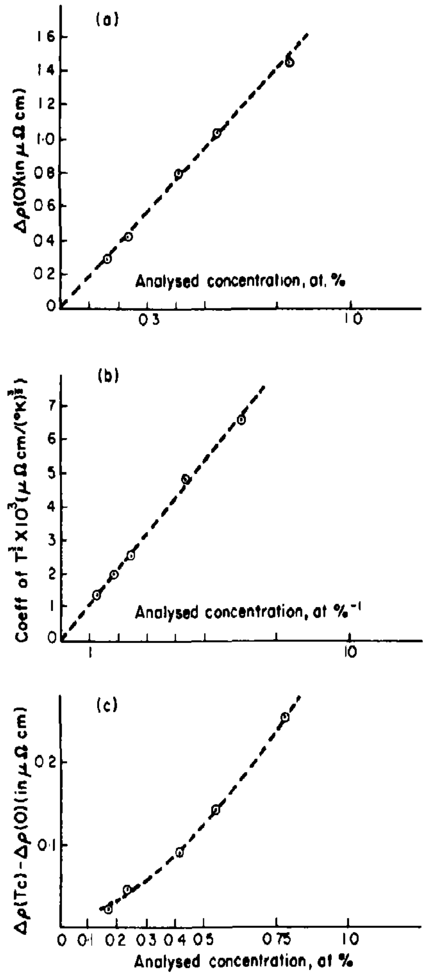

Fig. 3. (a) $\Delta\rho$ (0) (in $\mu\Omega$ cm) vs. analysed concentration (in at. %). (b) Coefficient of $T^{1/2}$ (in $\mu\Omega$ cm/(°K)$^{1/2}$) vs (analysed concentration[in at.%])$^{-1}$. (c) $\Delta\rho$ (T_c) - $\Delta\rho$ (0) (in $\mu\Omega$ cm) vs. analysed concentration (in at %).

attendent effect on the resistivity. Nevertheless their expressions can be used to estimate the magnitude of an 'effective' exchange integral J from the present results. For a system ordering ferromagnetically one obtains (from [8]) in the limit of *strong potential scattering:*

$$\Delta\rho_{\text{max.}} = \frac{8{\cdot}67\,J^2(\text{eV})}{E_f(\text{eV})}\,S(1+4S)\,\mu\Omega\ \text{cm/at.\%} \qquad (2)$$

where S is the impurity spin, and E_f the Fermi energy (having made use of the effective mass of s-electrons in Pd reported by Vuillemin[10, 11]), while in *the same limit:*

$$\Delta\rho(0) = \frac{8{\cdot}67}{E_f}\,V^2\,\mu\Omega\ \text{cm/at.\%}. \qquad (3)$$

(V representing the deviation of the spin-independent potential from perfect periodicity owing to the presence of the impurity). Figure 3(a) indicates that $\Delta\rho(0) \approx 1{\cdot}9\,\mu\Omega$ cm/at.% Fe, which using equation (3), gives $V \approx 0{\cdot}57$ eV. However, as Fig. 3(b) indicates, $\Delta\rho_{\text{max.}}$ varies from $0{\cdot}16\,\mu\Omega$ cm/at.%Fe (in the Pd – 0·16 at.% Fe alloy) to $0{\cdot}32\,\mu\Omega$ cm/at.% Fe (in the Pd – 0·78 at% Fe alloy), from which the magnitude of J varies (Table 1, using $E_f \sim 1{\cdot}5$ eV* and $S = \frac{3}{2}$) from 0·051 eV in the most dilute, to 0·073 eV in the most concentrated alloy examined. These values for V and J conclusively demonstrate that the limit taken in equation (2) and (3) is the correct one.

It is apparent from Fig. 1(b) that $\Delta\rho(T)$ is not independent of temperature above the Curie temperature, T_c. The form of its temperature dependence strongly suggests that it has the same origin as similar effects observed in dilute non-magnetic alloys. In the latter case this is the result of the breakdown of Matthiessen's Rule, which is to be expected whenever several comparable scattering mechanisms with different k dependences are present[12]. Thus, making direct use of the measured values of $\Delta\rho_{\text{max.}}$ in estimating the magnitude of J means that these deviations from Matthiessen's Rule (*above* T_c) have been completely ignored. In the present context this would be a legitimate procedure only if these deviations originated *entirely* from enhanced paramagnon scattering above T_c (this is the approach used in estimating the magnitudes of J quoted in Table 1). The alter-

---

*This is approximately the value of E_f obtained using an effective mass approach with $m^*/m_0 = 2{\cdot}2$, and with 0·36 s-electrons per atom, as quoted in [10] and [11]

Table 1

Estimated from initial weights	Analysed*	T_c (°K)	$\Delta\rho$ (0) (in $\mu\Omega$ cm)	Coeff of T $^{3/2}$ ($\mu\Omega$ cm/°K$^{3/2}$)	$\Delta\rho_{max}$. ($\mu\Omega$ cm)	Coeff. of linear decrease below T_c	J (eV)
Pd	~ 15 ppm Fe	0	0*	0	0	0$\mu\Omega$ cms/°K	$\mu\Omega$ cm/°K$^{3/2}$
Pd-0·18 at % Fe	0·16 at.%Fe	2·8	0·2919	6·62(5) × 10^{-3}	0·0256	0·0113	0·051
Pd-0·27	0·23	5·4	0·4275	4·86	0·0480	0·0098	0·059
Pd-0·45	0·41	13·0	0·7985	2·56	0·0914	0·0084	0·060
Pd-0·60	0·54	20·1	1·0449	1·97	0·1420	0·0095	0·065
Pd-0·90	0·78	32·6	1·4603	1·36	0·2528	0·0112	0·073

*Analysis carried out by Daniel Griffiths & Co., London.

†Quenching from 1100°C results in a high dislocation density and consequently a low resistance ratio. A subsequent strain relieving from 500°C produced a resistance ratio $R300/R4{\cdot}2 \simeq 1200$.

native extreme is to regard the deviations as due *entirely* to the cause first listed, in which case, in estimating the magnitude of J, the measured value of $\Delta\rho_{max}$ must be corrected for the deviation.

An examination of Fig. 1(b) suggests that these deviations begin to manifest themselves (within the present experimental error) around 10°K; the same figure, when examined in the 35°–50°K temperature interval, also suggests that these deviations scale approximately linearly with concentration (see Table 2). Consequently, since there appears to be virtually no such deviation at the Curie temperature in either the Pd – 0·16 or 0·23 at.% Fe alloy, the deviation at T_c in any *other* alloy can be estimated by observing the deviation at the appropriate temperature in the most dilute alloy, and scaling for the concentration. Table 2 summarises data obtained in this manner, and, for example indicates that the estimated value of $\Delta\rho_{max}$ is reduced by this correction from the measured value of 0·32 to 0·25 $\mu\Omega$ cm/at% Fe in the most concentrated alloy examined, with an associated reduction in the estimated magnitude of J from 0·073 to 0·064 eV.

The present investigation is being extended to examine the low temperature form of the electrical resistivity in *Pd* Co alloys, as well

Table 2

Alloy (at % Fe)	$\Delta\rho$(50°K)-$\Delta\rho$(35°K) ($\mu\Omega$ cm)	$\Delta\rho_1(T_c)$-$\Delta\rho_1$(2·8°K)† ($\mu\Omega$ cm)	Estimated correstion at T_c ($\mu\Omega$ cm)	"New" step height ($\mu\Omega$ cm)	J (eV)
1 Pd-0·16	0·0103	0	0	0·0256	0·051
2 Pd-0·23	0·0171	0	0	0·0480	0·059
3 Pd-0·41	0·0270	0·0010	0·0026	0·0888	0·060
4 Pd-0·54	0·0351	0·0027	0·0091	0·1329	0·064
5 Pd-0·78	0·0468	0·0116	0·0566	0·1952	0·064

†Suffix 1 refers to alloy number 1

as the possible enhanced paramagnon scattering above T_c in both the *Pd* Fe and *Pd* Co alloy systems.

Acknowledgements—We would like to thank Dr. R. E. Turner and Mr. P. D. Long for communication and discussion of their results prior to publication, and Mr. R. J. White for his assistance in part of the experimental work.

REFERENCES

1. CRANGLE J., *Phil. Mag.* **5**, 335 (1960).
2. BOZORTH R. M. WOLFF P. A., DAVIS D. D., COMPTON V. B and WERNICK J., *Phys. Rev.* **122**, 1157 (1961).
3. SCHINDLER A. I. and RICE M. J., *Phys. Rev.* **164**, 759 (1967).
4. TURNER R. E. and LONG P. D., To be published.
5. HANSEN M., In *Constitution of Binary Alloys*, p 696. McGraw-Hill, New York (1958).
6. STERLING H. F. and WARREN R. W., *Metallurgia* **67**, 24 (1963).
7. COLES B. R., WASZINK J. H. and LORAM J. W., *Proc. Intl. Conf. Magnetism, Nottingham 1964.* I.P.P.S., London (1965).
8. YOSIDA K., *Phys. Rev.* **107**, 396 (1957); the relationship between the elastic part of the exchange scattering and the 'interference' term can be obtained from the low temperature limit of equation (19) of the above paper, for a *ferromagnetic* system. The residual resistivity can also be obtained from the same equation.
9. KASUYA T., *Prog. theor. Phys.* **22**, 227 (1959).
10. VUILLEMIN J. J. and PRIESTLEY M. G., *Phys. Rev. Lett.* **14**, 307 (1965)
11. VUILLEMIN J. J., *Phys. Rev.* **144**, 396 (1966)
12. DUGDALE J. S. and BASINSKI Z. S., *Phys. Rev.* **157**, 552 (1967).

J. Phys. Chem. Solids Pergamon Press 1969. Vol. 30, pp. 1835–1847. Printed in Great Britain.

CHARGE TRANSFER IN TRANSITION METAL CARBIDES AND RELATED COMPOUNDS STUDIED BY ESCA

LARS RAMQVIST
The Axel Johnson Institute for Industrial Research, Nynashamn, Sweden

and

KJELL HAMRIN, GUNILLA JOHANSSON, ANDERS FAHLMAN and CARL NORDLING
Institute of Physics, Uppsala University, Uppsala, Sweden

(*Received* 3 *December* 1968)

Abstract—Electron spectroscopic measurements of binding energy shifts of C1*s* electrons in Group 4*b*, 5*b* and 6*b* carbides and of core electrons in Ti and V compounds are presented The results are discussed and compared with X-ray spectroscopic investigations and energy band calculations It is shown that electrons are transferred from the metal to the carbon atoms when a carbide of this type is formed.

1. INTRODUCTION

THE ELECTRONIC structure and the origin of the cohesive energy of transition metal carbides have frequently been discussed in the literature[1]. The interesting and outstanding physical and chemical properties of the carbides and their simple crystallographic structures have made these compounds particularly attractive for theoretical considerations. The question of electron transfer between the metal and the carbon atoms, i.e. whether the metal atom is an electron donor or acceptor with respect to the carbon atom, was raised early in the discussions and still remains the most frequently discussed

Due to the difficulties in making accurate measurements of electron transfer between the atoms, there has been a lack of definitive experimental data. Unfortunately, there is also serious disagreement between the different theories that have been proposed[1]. Even quantum mechanical methods have given contradictory results due to the lack of accurate experimental data to support the basic theoretical assumptions.

The experimental method that has been used in this study is based on high resolution electron spectroscopy and was originally developed for high precision determination of electron binding energies. Since it has been found to have great potential in chemical structure and chemical bonding research it is referred to as ESCA (Electron Spectroscopy for Chemical Analysis)[2]. This method gives an experimental check on the proposed theories and quantum mechanical calculations

Our purpose has been to perform an accurate experimental study of the electron transfer between the metal and the carbon atoms in transition metal carbides. We have concentrated the experiments on measurements of the energy shifts of the core electrons in TiC_x and VC and in the related materials TiB_2, TiN, TiO, TiO_2, pure Ti and pure V. C1*s* shifts showing the electron transfer for other Group 4*b* and 5*b* carbides together with 6*b* carbides are also presented. This investigation can be regarded as an introduction to further accurate experimental studies on the electronic structures of interstitial compounds. Measurements can also be performed of the outer electronic levels which define *more directly the chemical and physical* properties of the material[3].

The ESCA results presented here are supported in a parallel investigation by Ramqvist *et al.*[4] on the metal K emission and absorption X-ray spectra of TiC and related compounds.

2. TEST MATERIALS

In the present investigation the use of well defined test samples is stressed. The starting materials have been of the highest purity practically and economically possible. Electronic Space Products, Inc., Calif., USA, and K & K Laboratories Inc., N.Y., USA, have supplied the metal and the metal hydride powders. The metal dioxide powder was supplied by J. T. Baker Chemical Co., New Jersey, USA, and the graphite powder together with the pure reference vanadium metal by Johnson, Matthey & Co., Ltd., London, England. The reference titanium rod was produced by Koch-Light Laboratories Ltd., Colnbrook, Bucks, England. The test samples were analysed chemically with special attention to carbon and gas contents. The lattice parameter was used for phase identification, homogeneity and purity tests. The preparation and test methods are described in the following sections and relevant data of the materials are summarized in Table 1.

It should be noticed that some of the test materials used in the present investigation have also been used

Table 1. Properties of the test materials and the reference metals

Hot pressed samples Compound	C/Me +0·003	Lattice parameter (Å)	O (wt.%)	N,H (wt.%)	Me impurities (wt.%)
TiC	0·967	4·3278 ± 0·0002	0·08	0·10	<0·2
	0·876	4·3272 ± 0·0002	0·09	0·10	<0·2
	0·775	4·3253 ± 0·0001	0·12	0·11	<0·2
	0·675	4·3188 ± 0·0004	0·16	0·15	<0·2
ZrC	0·913	4·6974 ± 0·0002	0·08	0·10	<0·1
HfC	0·915	4·6391 ± 0·0002	0·08	0·11	<0·3
VC	0·876*	4·1670 ± 0·0001	0·02	0·07	<0·1
NbC	0·976	4·4702 ± 0·0001	0·08	0·04	<0·5
TaC	0·990	4·4550 ± 0·0002	0·05	0·03	<0·1
Cr_3C_2	0·654	a = 5·5274 ± 0·0003 b = 2·8289 ± 0·0001 c = 11·4838 ± 0·0007	0·03	0·05	<0·1
Mo_2C	0·495	a = 4·7306 ± 0·0006 b = 6·0297 ± 0·0006 c = 5·2010 ± 0·0006	0·02	0·02	<0·1
WC	0·998	a = 2·9060 ± 0·0001 c = 2·8371 ± 0·0002	0·02	0·05	<0·1
	B/Me				
TiB_2	2·0†	a = 3·0298 ± 0·0002 c = 3·2306 ± 0·0003	0·24	0·10	<0·1
	N/Me				
TiN	1·0	a = 4·2416 ± 0·0001	0·52		<0·2
Arc melted samples					
	C/Me				
TiC	0·590 ± 0·005	a = 4·3134 ± 0·0005	0·07	0·01	<0·2 W = <0·05
	O/Me				
TiO	1·0	a = 4·1763 ± 0·0002		0·12	<0·2 W = <0·05
TiO_2	2·0	a = 4·5998 ± 0·0005 c = 2·9578 ± 0·0006		0·15	<0·2 W = <0·05
Reference metals					
Ti rod					<0·4
V filament					<0·1

*Total carbon C/V 0·993

†*B* content estimated.

in the X-ray emission investigation[4] mentioned in the introduction.

2.1 *Preparation methods*

Since ESCA is a surface method[2] it is very important to have test samples with pure and chemically well defined surfaces. It was shown experimentally that weak carbide but relatively strong oxygen signals were obtained from carbide powders of 1–10 μm grain size. The optimum signals from the carbide were obtained from highly polished dense surfaces. In this investigation high density test samples with a 0·5 cm² source area were prepared by hot pressing and arc melting methods. As pointed out previously[5, 6] these two preparation methods suffer from contamination problems. Although other methods, such as the gascarburization method, produce purer samples[5], it is difficult by these methods to fabricate large, dense and chemically well defined surfaces on the specimens. Attempts to make ESCA measurements on gascarburized wires of 0·3 mm dia. failed due to difficulties in surface polishing and handling of the brittle wires.

2.1.1 *Hot pressing*. The carbides were prepared starting from high purity metal or hydride and spectroscopically pure carbon powders. After mixing and pressing, the produced bars were placed upon supports made of the same material to avoid contamination and put into a furnace under a vacuum of $< 10^{-5}$ Torr, and heated for 1 hr at the appropriate reaction temperature, around 2000°C for most 4*b* and 5*b* carbides, 1700°C for the TiC_x series formed from TiH_2 and C, and around 1700°C for the 6*b* carbides. After grinding and reheating three times homogeneous carbide powders with sharp X-ray diffraction patterns were obtained in all cases. The carbide powders were then hot pressed according to methods described in previous papers[5–8]. Carborundum boron nitride grade HP was used in contact with the non-stoichiometric carbides and the other titanium compounds to avoid carbon pick-up and gradients from the graphite die. The hot pressing was carried out under a pure argon atmosphere in order to prevent carbon loss and gradients, an especially important consideration for the non-stoichiometrical carbides. After hot pressing the BN and the underlying layer of the specimen were ground to ensure a pure carbide surface which was polished down to 1 μm. For the TiC_x-series a vacuum annealing under a pressure of $\approx 10^{-6}$ Torr. at 1700°C for 8 hr was added in order to lower the content of entrapped gases. A higher annealing temperature would probably lower the gas content further but, at the same time, would initiate loss of Ti and C resulting in serious gradients and inhomogeneities[9]. Discs of dense and gas free non-stoichiometric TiC can thus be prepared only with great care.

After the ESCA measurements the discs were subject to X-ray and chemical analyses. The carbon analyses were carried out using the 'Avecarbon 100' recently developed at Avesta Jernverks AB, The Axel Johnson Group, Sweden[10]. This equipment works according to the low pressure method, an absolute method capable of high accuracy[11]. The oxygen and nitrogen analyses were performed according to the vacuum liquid extraction method with a Leybold GAO 1 equipment.

The lattice parameters were measured with a 80 mm diameter Guinier-Hagg camera using $CuK\alpha_1$ radiation with $\lambda = 1{\cdot}54051$ Å. Silicon with a lattice parameter of $(5{\cdot}43054 \pm 0{\cdot}00017)$ Å was used as an internal standard in all measurements. The parameters were refined with a least squares program[12]. All samples used in this project proved to be of the homogeneous single phase type with sharp diffraction patterns. Since the lattice parameters are relatively sensitive to the gas content in the carbide, the X-ray data can be put to advantage as an indirect gas analysing method. Using the literature survey by Storms[9] as a guide the present lattice parameters showed low gas contents.

A hot pressed TiB_2 disc and TiN powder were obtained from Soderfors bruk, Sweden and Institute of Inorganic Chemistry, University of Stockholm, Sweden respectively. These samples were prepared and analysed in accordance to the method described above.

2.1.2 *Arc melting*. The arc melting method often gives lower gas content than the hot pressing method, especially in non-stoichiometric carbides[6,9]. However, if the homogeneity problems, which can occur even after remeltings, are solved by long time annealings the samples are generally contaminated with gases. In the present investigation we have chosen to improve the homogeneity of the samples by remeltings only. As a complement to the hot pressed samples one non-stoichiometric carbide, $TiC_{0{\cdot}580}$, and two oxides, TiO_2 and TiO, were arc melted in pure argon using Ti–Zr melts as oxygen getters. TiO was produced starting from pure Ti and TiO_2 powders. The arc melted samples were then prepared for the ESCA measurements in accordance with the method described for the hot pressed samples. Since this procedure utilizes a tungsten electrode in the melting procedure, a tungsten analysis was added. This analysis was made with a Perkin Elmer Atomic Absorption Spectrophotometer 303.

3. EXPERIMENTAL TECHNIQUES

The ESCA technique has been described in detail elsewhere[2], but a short summary will be given of the procedure used in this experiment. Electrons emitted from a sample upon irradiation with X-rays are analysed in an iron-free double-focussing spectrometer[13] and detected with a windowless channel electron multiplier. The number of electrons is recorded as a function of the spectrometer current which is proportional to the electron momentum.

In the photoelectric process the electron binding energy, E_b, is obtained from the expression

$$E_b = E_{\text{X-ray}} - E_{\text{kin}}$$

where $E_{\text{X-ray}}$ is the characteristic X-radiation energy, known from X-ray spectroscopy, and E_{kin} the kinetic energy of the ejected electrons, obtained from the momentum analysis. The Fermi level is chosen as a reference level for the electron binding energies and a correction for the work function ϕ_{sp} of the spectrometer material then has to be applied[14].

In the de-excitation process following the photoelectric emission Auger electrons are emitted from the specimen. The Auger process is the radiationless alternative to X-ray emission for the de-excitation of atoms with inner shell vacancies. The energy of such electrons is independent of the primary X-radiation. For example, the kinetic energy of a $KL_{\text{II}}L_{\text{III}}$ ($^1D_2$) Auger electron is given by the following expression[15]:

$$\begin{aligned} E_{\text{kin}}[KL_{\text{II}}L_{\text{III}}(^1D_2)] &= E_b(K)-2E_b(L_{\text{II}}) \\ &\quad -F^0(21,21)+2/25F^2(21,21)+\tfrac{9}{4}\xi_{21} \\ &\quad -[(3/25F^2(21,21)+\tfrac{1}{4}\xi_{21})^2+\tfrac{1}{2}\xi_{21}^2]^{1/2}-\phi_{sp} \end{aligned}$$

where $E_b(K)$ and $E_b(L_{\text{II}})$ are the electron binding energies of the K and L_{II} shells, $\xi_{21}=\frac{2}{3}[E_b(L_{\text{II}})-E_b(L_{\text{III}})]$ is a measure of the spin-orbit coupling, and $F^0(21,21)$ and $F^2(21,21)$ are matrix elements of the electrostatic interaction between two electrons. The notation $KL_{\text{II}}L_{\text{III}}$ means that the atom has initially one vacancy in the K shell and vacancies in the L_{II} and L_{III} subshells after the de-excitation.

The core electron energy levels are shifted when a chemical bond is formed. The observed chemical shifts can be explained in a simple model as follows. The valence electron orbitals define a spherical 'valence shell' of electric charge. If charge is added to or removed from this valence shell, the electric potential inside the shell is changed. This potential is also modified due to the interaction with the neighbouring atoms. The core electron binding energies are thus changed by almost the same amount ΔE_b. The kinetic energies of the photo and Auger electron lines are shifted as follows

$$\Delta E_{\text{kin}}(K) = -\Delta E_b(K)$$

and

$$\begin{aligned} &\Delta E_{\text{kin}}(KL_{\text{II}}L_{\text{III}}) \\ &\quad = \Delta E_b(K)-\Delta E_b(L_{\text{II}})-\Delta E_b(L_{\text{III}}) \end{aligned}$$

with neglect of changes in the electrostatic interaction integrals in the expression for the Auger transition energy. Since ΔE_b is almost the same for inner shells

$$\Delta E_{\text{kin}}(KL_{\text{II}}L_{\text{III}}) \sim -\Delta E_b$$

which means that both photoelectron lines and Auger lines are shifted in the same direction and by about the same amount. Furthermore since

$$\begin{aligned} K\alpha_1 &= E_b(K)-E_b(L_{\text{III}}) \\ K\alpha_2 &= E_b(K)-E_b(L_{\text{II}}) \end{aligned}$$

the following relations hold

$$\begin{aligned} &\Delta K\alpha_1 = \Delta E_b(K)-\Delta E_b(L_{\text{III}}) \\ &\Delta K\alpha_2 = \Delta E_b(K)-\Delta E_b(L_{II}) \\ &\Delta E_{\text{kin}}(KL_{\text{II}}L_{\text{III}}) = \Delta K\alpha_1-\Delta E_b(L_{\text{II}}) \\ &\qquad\qquad = \Delta K\alpha_2-\Delta E_b(L_{\text{III}}) \\ &\Delta E_{\text{kin}}(K)-\Delta E_{\text{kin}}(KL_{\text{II}}L_{III}) \\ &\qquad = -2\Delta E_b(K)+\Delta E_b(L_{\text{II}})+\Delta E_b(L_{\text{III}}) \\ &\qquad = -(\Delta K\alpha_1+\Delta K\alpha_2) = -2\Delta K\alpha. \end{aligned}$$

Different characteristic X-radiations have been used in this work depending on the' energy of the atomic level studied. The radiations were Cu$K\alpha_1$, Al$K\alpha_{1,2}$ and Mg$K\alpha_{1,2}$, having quantum energies equal to 8047·8, 1486·6 and 1253·6 eV, respectively[16]. The inherent widths of the Al$K\alpha_{1,2}$ and Mg$K\alpha_{1,2}$ emission lines are less than one eV[14]. Since the contributions from the spectrometer and from the levels studies are of the same magnitude, the resultant electron lines are narrow. When soft X-rays are used, the detected electrons come mainly from the first hundred Å of the sample. This means that ESCA is a surface method, sensitive to surface contamination and oxidation.

The electron spectra were calibrated against carbon in the hydrocarbon layer which forms on the sample when this is introduced into the spectrometer. This contamination comes from the rotary pump oil and the O-ring grease. In most cases it is convenient to use this carbon 1*s* electron line for calibration purposes. The momentum of the line has been determined from an absolute calibration of copper $2p_{3/2}$ lines excited with two different X-rays of well known energies[17]. It has been found that carbon in graphite has the same 1*s* binding energy as carbon in hydrocarbons, within the resolution limits of these experiments.

The electron spectra excited with Cu$K\alpha_1$ radiation could not be calibrated in the same way. Instead, a comparison was made between the momenta of corresponding electron lines from two sources.

4. RESULTS

4.1 *Carbon in transition metal carbides*

The carbon 1*s* electron spectra from the transition metal carbides, TiC, ZrC, HfC, VC, NbC, TaC, $\mathrm{Cr_3C_2}$, $\mathrm{Mo_2C}$, and WC, consist of two lines, the hydrocarbon line, the intensity of which increases with time, and a second line originating from carbon in the carbide. The latter line was in all cases found at a higher kinetic energy than the hydrocarbon line indicating that carbon in carbides has a lower 1*s* binding energy than in saturated hydrocarbons.

Figure 1 shows the C1*s* electron spectra for HfC, TaC, and WC compared with the hydrocarbon line. The energy separation between the two lines varies with the metal component from about 2 up to 4 eV, Table 2. The energy shifts are largest for 4*b* carbides. This is in agreement with Pauling's electro-negativity scale[18]. Each carbide was studied with Al$K\alpha_{1,2}$ as well as with Mg$K\alpha_{1,2}$ radiation. Electron spectra excited by these two different radiations gave the same energy differences between the carbide line and the hydrocarbon reference.

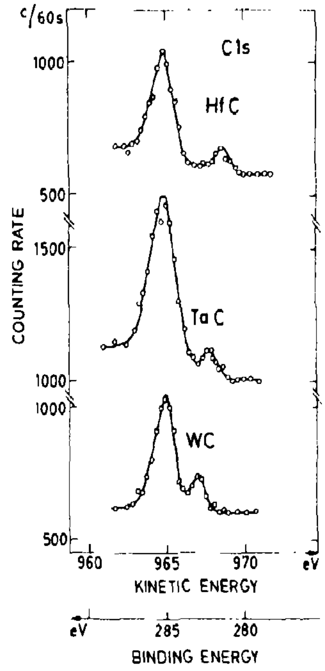

Fig. 1. C1*s* electron spectra from HfC, TaC and WC excited with Mg$K\alpha$ radiation. In each spectrum two lines are seen, one from the hydrocarbon layer and one from the carbide. The latter line corresponds to a lowered binding energy of the C1*s* level, which shows that electronic charge is transferred from the metal to the carbon atom.

Table 2. Shift in binding energy (eV) of the 1s level of carbon in transition metal carbides referred to carbon in the hydrocarbon layer

	Group		
Period	4*b*	5*b*	6*b*
4	TiC −3·3	VC −2·6	$\mathrm{Cr_3C_2}$ −2·0
5	ZrC −3·7	NbC −2·9	$\mathrm{Mo_2C}$ −2·1
6	HfC −4·0	TaC −2·9	WC −2·1

ESCA studies of chemical shifts in electron spectra have been performed for a number of elements and the measurements have given strong evidence that the core electron binding energies in an atom increase when charge is removed from the atom[2]. Correlations between energy shifts and a charge parameter have been established for sulfur, nitrogen and carbon[19–21]. These studies, therefore, suggest that carbon in metal carbides is more negative than in saturated hydrocarbons and provide evidence that charge is transferred from the metal atom to the carbon atom when metal carbide is formed.

The bond energies in an interstitial compound may in principle be related to its heat of formation. The heat of formation is generally given in energy per mole of MeC_x, $-\Delta H_{298K}$, but for a more exact correlation to the bond strength, this energy per atom, $-\Delta H/1+x$, is more appropriate. In Fig. 2 it is shown that the C1*s* energy shifts for those carbides which are cubic can be correlated with the heats of formation per mole for stoichiometric carbides. The values per atom would not be more accurate since the variations of $-\Delta H$ with carbon content are not fully elucidated. The values of the heats of formation are taken from the review by Storms[9]. The value of $-\Delta H$ for VC is in some doubt.

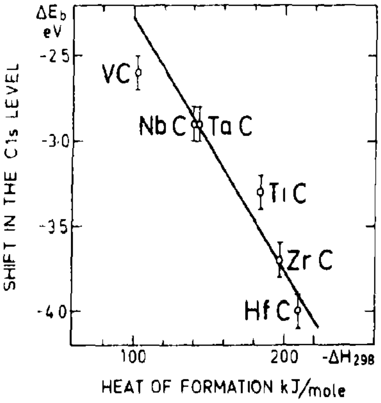

Fig. 2. Relationship between the shift of the C1s level and the heat of formation of cubic Group 4*b* and 5*b* carbides. Standard deviations are indicated

Figure 2 demonstrates that the ESCA shifts measured for these carbides are proportional to their heats of formation. As heats of formation and bond strengths are similarly related, the ESCA measurements might be used directly to estimate bond strengths. However, ESCA is a measure of charge transfer; the linear correlation of Fig. 2 is strongly suggestive that bond strength differences in these carbides are due to differences in the ionic rather than the covalent contribution to the binding energy.

4.2 *Titanium in titanium carbide and related titanium compounds*

Further evidence of the charge transfer can be obtained from the binding energies of the core electrons of the metal constituent. These should then be compared with the energies for the same metal in other metal-interstitial compounds. For this reason a series of titanium compounds was also studied.

Electron spectra of stoichiometric and non-stoichiometric TiC and the related materials (TiO_2, TiO, TiN, TiB_2, and Ti) were recorded using Al$K\alpha_{1,2}$ excitation. The Ti$2p_{1/2}$ and $2p_{3/2}$ electron lines from some of these compounds are shown in Fig. 3 together with the 1*s* electron lines from the non-metals. The shifts in binding energies referred to the $2p_{3/2}$ binding energy in metallic Ti are given in Table 3.

The TiO_2 spectrum, Fig. 3(a), shows two narrow electron lines corresponding to the spin doublet Ti$2p_{1/2}$, $2p_{3/2}$ and a broad O1*s* line. Figure 3(b) shows the electron spectrum recorded for TiO. Two lines with the same binding energies as observed for TiO_2 are found together with a line of lower binding energy and lower intensity. This suggests that the sample surface is oxidized to such an extent that the dioxide is predominant. This explanation is further supported by a study of the relative intensities of the 1*s* line of oxygen and the $2p_{3/2}$ line of titanium as follows. Empirically it has been

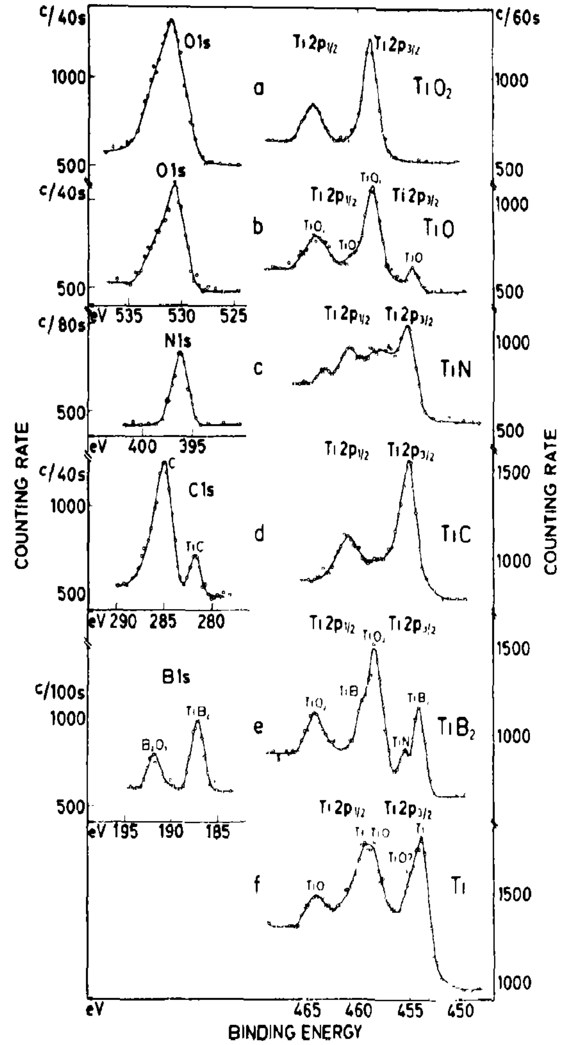

Fig. 3. Electron spectra of titanium compounds excited with Al$K\alpha_{1,2}$ radiation. (a) O1s, Ti2$p_{1/2}$ and Ti2$p_{3/2}$ electron lines from TiO_2. (b) Electron lines from TiO. Ti2$p_{1/2}$ and Ti2$p_{3/2}$ lines from TiO_2 and TiO are found together with an O1s line with about the same relative intensity as in (a) (c) N1s, Ti2$p_{1/2}$ and Ti2$p_{3/2}$ electron lines from TiN. (d) C1s, Ti2$p_{1/2}$ and Ti2$p_{3/2}$ electron lines from TiC. The C1s calibration line from the hydrocarbon layer marked C is also shown. (e) Electron lines from TiB_2. Since the surface is oxidized, electron lines corresponding to TiO_2 and B_2O_3 are also present (f) Ti2$p_{1/2}$ and Ti2$p_{3/2}$ electron lines from polished Ti metal. The surface is oxidized into TiO_2 probably with TiO as an intermediate state

found that the photoelectric cross section is proportional to Z^k, where Z is the atomic number of an element[22]. The relative intensities of the lines Y1s (Y = B,C,N,O) and Ti2$p_{3/2}$ from the titanium compounds are given in Table 3. Setting $k = 3$ and choosing the intensity ratio of one boron atom and one titanium atom as unity gives a reasonably

Table 3. Binding energy shifts and relative intensities for titanium compounds from Fig. 3

Compound	Ti2$p_{1/2}$ binding energy shift relative to metallic titanium (eV)	Electro-negativity difference [18]	Relative intensity $Y1s$/Ti2$p_{1/2}$ (Y = B,C,N,O) from Fig. 3	Relative photoelectric cross section of normalized to B/Ti Exp.	$\left(\frac{z}{5}\right)^3$
TiB_2	0·3 ± 0·2	0·5	0·48	1	1
TiC	1·3 ± 0·1	1·0	0·44	1·8	1·7
TiN	1·5 ± 0·2	1·5	0·6	2·5	2·7
TiO	1·0 ± 0·2		7	29	
	4·8 ± 0·2	2·0	1·6	3·3	4·1
TiO_2	4·9 ± 0·2	2·0	1·7	3·5	4·1

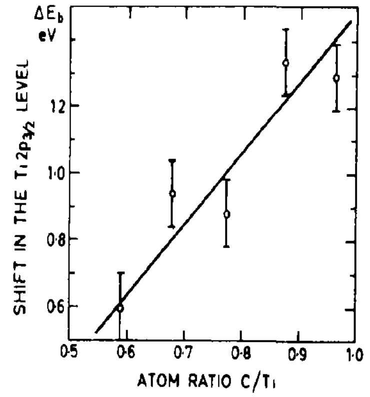

Fig. 4. Relationship between the shift of the Ti2$p_{3/2}$ level and the atom ratio, C/Ti, for TiC_x ($x = 0{\cdot}590$–$0{\cdot}967$). Standard deviations are indicated.

good fit for the carbon and nitrogen lines and supports the assumption that the composition of the surface layer of the monoxide sample is Ti_2O_3 or TiO_2 rather than TiO.

The Ti2p spectrum from TiN, Fig. 3(c), shows four lines, of which the two weaker originate from an oxidized surface but with smaller binding energies than in Fig. 3(a). The N1s binding energy shift suggests electron transfer from titanium to nitrogen[20].

The titanium carbide spectra were free from titanium oxide lines due to the method of making the samples. Different non-stoichiometric compounds of TiC_x ($x = 0{\cdot}590$–$0{\cdot}967$) were studied and the Ti2$p_{3/2}$ binding energy was found to increase as the carbon content was increased, Fig. 4. The binding energies are referred to the Ti2$p_{3/2}$ binding energy of Ti metal. The C1s shifts were the same for all carbides within error limits. The results are in good agreement with the Ti$K\alpha_1$ shifts for non-stoichiometric titanium carbides[4].

The heat of formation per mole, $-\Delta H_{298K}$, increases with increasing carbon content of Group 4b carbides. Morozova *et al* [23] have reported the heat of formation to increase linearly from ≈ 110 kJ/mole for $TiC_{0{\cdot}5}$ to ≈ 230 kJ/mole for $TiC_{1{\cdot}0}$. Even if their $-\Delta H_{298}$ values may be somewhat too high[1, 9] their result points to the principal relationship between carbon concentration and heat of formation. It is important to notice that the value of the heat of formation per atom, i.e. a value which is more exactly related to the bond strength than the value of the heat of formation per mole, also increases when carbon atoms are added. Figure 5 implies that the ESCA Ti2$p_{3/2}$ energy shifts are proportional to the heats of formation for TiC with varying carbon content. Figure 5, like Fig. 2 as discussed above, is strongly suggestive that bond strength differences in TiC_x ($x = 0{\cdot}590$–$0{\cdot}967$) are ionic (*vis-á-vis* covalent). An increase in carbon content within the range studied increases the ionicity of the bond and the stability of the carbide.

The spectrum from titanium boride, Fig. 3(e), shows several lines; the Ti2$p_{1/2}$, 2$p_{3/2}$ from TiB_2, along with the same lines from

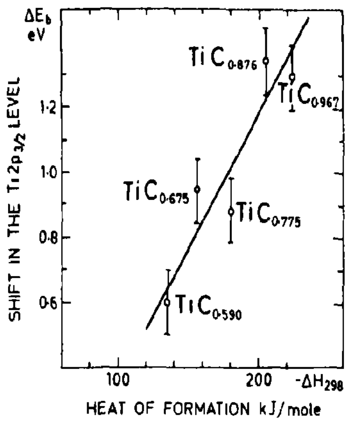

Fig. 5. Relationship between the shift of the Ti$2p_{3/2}$ level and the heat of formation, $-\Delta H_{298}$, for TiC with increasing carbon content.

TiO_2 and from TiN. The corresponding 1*s* lines from boron, nitrogen and oxygen were also recorded. Boric acid was probably formed on the sample surface since two lines appeared in the B1*s* spectrum. The sample was prepared in BN which explains the appearance of nitrogen lines.

Titanium metal was polished to reduce the oxide layer. The resulting spectrum, Fig. 3(f), shows three lines which can be resolved into two spins doublets, one corresponding to TiO_2 and one to Ti metal. The Ti$2p_{3/2}$ line from the metal is also broader than normal which indicates the presence of Ti-oxide in lower oxidation states. The sample surface is thus oxidized to TiO_2 presumably with TiO as an intermediate state. The Ti$2p_{3/2}$ energy in titanium metal, 453·8 eV, is used as a reference for the shifts given in Table 3, since the Ti$2p_{3/2}$ line from Ti is well resolved from the Ti$2p_{3/2}$ line from TiO_2.

X-ray spectroscopy has established decreasing energies for the Ti$K\alpha_1$ emission lines for the series Ti, TiO, TiN, and TiC. It is therefore of interest to investigate the energy shifts of the Ti1*s* lines and the Ti$KL_{II}L_{III}$ Auger lines. The shift in the Auger transition may be considered as shifts in the $K\alpha$ transition and the $2p$ level as previously explained. These kinetic energy shifts are summarized in Table 4 together with X-ray emission data from[4]. The differences $\Delta E_{\text{kin}}(2p_{3/2}) - \Delta E_{\text{kin}}(1s)$ and $\Delta E_{\text{kin}}(KL_{II}L_{III}) - \Delta E_{\text{kin}}(2p_{3/2})$ agree fairly well with the shift in the Ti$K\alpha_1$ transition energy.

For certain titanium compounds the $2p_{3/2}$ level is thus shifted more than the 1*s* level. The Auger transition is changed still more since it takes account of the energy shifts of the two $2p$ levels and the 1*s* level. This particular behavior of the core electron levels has been found dependent on $3d$ electron transfer[4,24]. When $3p$ electrons constitute the bonding electrons, however, the 1*s* level is shifted more than the $2p$ levels[2,24].

In Table 4 data from electron spectra recorded from VC and vanadium metal are included. The results are quite similar to those for Ti compounds. The kinetic energies of the V1*s*, V$2p_{3/2}$ and V$KL_{II}L_{III}$ lines are lower in the carbide than in the metal. This result confirms the conclusion drawn from the C1*s* spectrum that electrons are transferred from the metal atoms to the carbon atoms.

Table 4. Shift in kinetic energy (eV) for the 1s, $2p_{3/2}$ and $KL_{II}L_{III}(^1D_2)$ lines, and for the $D\alpha_1$ transition energy, relative to the pure metal

Compound	1*s*	$2p_{3/2}$	$KL_{II}L_{III}(^1D_2)$	$K\alpha_1$[4]
TiC	−1·0 ± 0·4	−1·3 ± 0·1	−1·5 ± 0·4	−0·33 ± 0·02
TiN	−1·2 ± 0·4	−1·5 ± 0·2	−1·9 ± 0·4	−0·19 ± 0·04
TiO	−1·0 ± 0·4	−1·0 ± 0·2	−1·6 ± 0·5	−0·09 ± 0·03
TiO_2	−4·3 ± 0·4	−4·9 ± 0·2	−5·8 ± 0·4	
VC	−1·5 ± 0·4	−1·8 ± 0·3	−2·4 ± 0·4	

5. COMPARISON WITH THE LITERATURE

Since the literature on the electronic structures of metallic carbides is very extensive we will deal only with experiments and theories of current interest. For a more detailed discussion of the theoretical works see the parallel X-ray investigation[4] on the Ti*K* absorption and emission bands of TiC_x and related compounds.

Holliday has studied the carbon *K* and metal L_{II} and L_{III} X-ray emission bands of stoichiometric and non-stoichiometric metal carbides[25], and suggested from the wavelength shifts of the emission bands that the vanadium and titanium atoms are more negative in the carbide than in the metal, contradicting the interpretation of our ESCA results, and those of [4]. However, a direct comparison of the ESCA spectra and Holliday's emission bands is quite suggestive and requires further comment.

The electron transfer cannot be determined from the shift of the peak of the emission band. The profile of the emission band is defined by the band structure which, in the metal spectra in question, cannot be obtained since the relative intensity of the L_{II} and L_{III} bands is unknown. The shift of the inner level should be measured relative to the Fermi level; i.e. to the edge at the high energy side of the emission band. But since the L_{II} and L_{III} bands lie so close to each other there are difficulties in resolving the bands and obtaining the edges. The present ESCA study has aided this problem. As can be seen in Fig. 6 the ESCA peak, $Ti2p_{3/2}$, fits Holliday's emission band of pure Ti at the high energy side and shows the Fermi level. The experimental consensus between Holliday and this investigation is thus obvious. Since the ESCA peak and the high energy edge of the L_{III} emission band of TiC do not coincide as they did for the pure metal, we can conclude that the density of states is low at the Fermi level for TiC. This is also the conclusion from the comparison of Holliday's C*K* emission bands and the ESCA C1s peaks for various carbides of which TiC and VC are shown in Fig. 7. It is important to note that the shifts of the ESCA peaks are opposite to those of

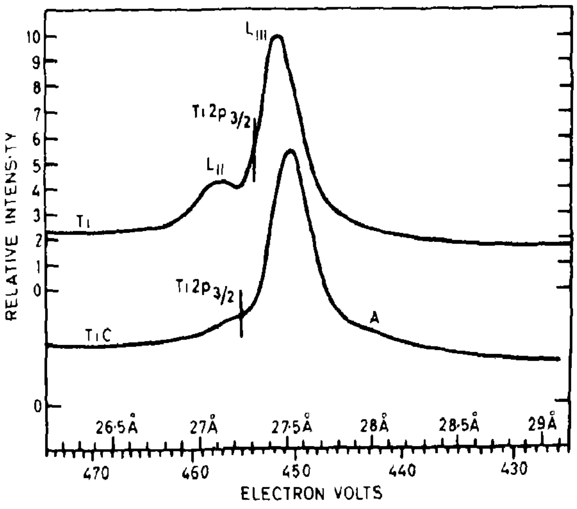

Fig. 6. Ti$L_{II,III}$ emission bands of Ti and TiC as recorded by Holliday [25]. Corresponding ESCA binding energies, $Ti2p_{1/2}$, are also indicated. The ESCA peak fits the high energy edge for Ti but not for TiC indicating that the density of states is low at the Fermi level for carbides.

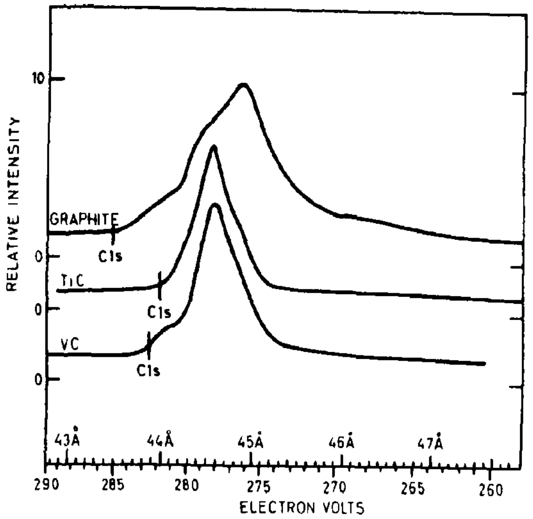

Fig. 7. C*K* emission bands of graphite, TiC and VC as recorded by Holliday[25] with the corresponding ESCA binding energies indicated, C1*s*. The peaks of the emission bands of TiC and VC are shifted in the opposite direction to the ESCA binding energies

the maximum of the peaks for the carbide emission bands given. For the Ti–O system, however, Holliday[26] obtains the same results as we do; in this system the shifts of the peaks and the edges are in the same direction.

The X-ray absorption and emission investigation on TiC_x and related compounds show that, indeed, the density of states at the Fermi level is low. The binding energies measured by X-ray absorption and ESCA also appear in close agreement for the samples examined.

Quantum mechanical calculations by Costa and Conte[27] and by Lye and Logothetis[28] suggest charge transfer from carbon to metal atom, in contradiction to our conclusions. In their LCAO calculation for TiC and TiN Costa and Conte neglect all but the *d*-functions' interactions, but, nevertheless, emphasize a stronger metal–metal interaction in the compound than in the metal due to carbon overlap in the $3d_\varepsilon$ orbital.

Lye and Logothetis[28] report a semi-empirical, tight-binding calculation of the band structure of TiC, parametrized to fit optical properties from dispersion analyses of the measured reflectivity. Considering C2*s* and 2*p* and Ti3*d*, 4*s* and 4*p* orbitals, Lye and Logothetis find a surprisingly high, largely unoccupied 2*p* level responsible for the transfer of 1½ electrons from carbon to titanium. They get C2*p* states of much higher energy relative to the Ti3*d* bands than most other quantum mechanical calculations on TiC. Lye, Hollox and Venables have recently used the same method to examine the electronic structure of VC and predict an analogous type of bonding for this carbide[29].

The relative energy of these calculated 2*p* levels is quite different from that calculated earlier by Bilz[30] for cubic interstitial compounds. His tight-binding approximation, considering only carbon 2*p* and titanium 3*d* and 4*s* orbitals, suggested electron transfer in qualitative agreement with our ESCA results.

APW calculations by Ern and Switendick [31] and more recently by Conklin and Silversmith[32], also predict 2*p* states lower than

Lye and Logothetis. For TiC the self-consistent APW calculation by Conklin and Silversmith[32] give a loss of less than one Ti3*d* electron. This is in excellent agreement with the interpretation of the measured energy shifts of the Ti$2p_{3/2}$ and Ti1*s* levels as discussed above[4, 24]. The less accurate, non self-consistent APW calculation by Ern and Switendick[31], on the other hand, has a greater occupancy of the Ti3*d* states for TiC than for the neutral atom. Ern and Switendick[31] also predict, in contradiction to the present results, increasing ionicity in the order TiC–TiN–TiO. Their results indicate, in agreement with the electronegativity concepts, a more localized non-metal 2*p* band and as a consequence fewer Ti3*d* electrons in that order. Although Denker[33] in his localized orbital model for the same compounds suggests a similar increase of the ionicity as in [31], it is evident from his discussion that at the same time as the non-metal bonding levels will be more localized from carbide to oxide the additional valence electrons in TiN and TiO partially enter the next levels which are antibonding and predominantly localized around the Ti atoms; i.e. the Ti3*d* levels. A balance between the increasing electronegativity and the filling of antibonding orbitals thus occurs; a balance, which, as discussed in [4], is likely to be rather sensitive to the choice of the effective potential A self-consistent APW calculation for TiO recently made by Switendick[34] indicates a somewhat higher occupancy of the Ti3*d* states compared to TiC and thus confirms our results.

It is noteworthy that the two different APW calculations[31, 32], in spite of the discrepancies regarding the transfer of the Ti3*d* electrons, both give a low density of states at the Fermi level, in agreement with the present ESCA results.

6. CONCLUSIONS

The present measurements on the core level shifts in various transition metal carbides and in the related compounds TiN, TiO, TiO_2, and TiB_2 show that electronic charge is transferred from the metal to the non-metal constituent. This agrees with the conclusions of the parallel X-ray study of TiC and related compounds by Ramqvist, Ekstig, Källne, Noreland and Manne[4]. The soft X-ray measurements on transition metal carbides by Holliday[25] can also be interpreted in agreement with our results if the energy shifts of his emission bands are re-evaluated as indicated in the text. The approximately self-consistent APW calculation for TiC by Conklin and Silversmith[32] gives a charge transfer from the Ti to the C states and thereby confirms the earlier APW calculations by Ern and Switendick[31].

The shift towards higher binding energy of the Ti1*s* level was shown to be smaller than the corresponding shift of the Ti$2p_{3/2}$ level in TiC, TiN, TiO and TiO_2 implying a loss of Ti3*d* electrons. In their APW calculation Conklin and Silversmith[32] also give a lower occupancy in the Ti3*d* states for TiC than for the pure metal. The same relationship between the 1*s* and $2p_{3/2}$ shifts was found for the VC phase. It thus appears likely that the metal atom always has fewer *d*-electrons in atom interstitial compounds than in pure metals. The present investigation further indicates that the charge transfer decreases in the order (TiC–TiN)–TiO. This trend is in agreement with that experimentally found in [4] but in disagreement with that theoretically predicted by Ern and Switendick[31] in their APW calculations. However, a self-consistent APW calculation for TiO quite recently made by Switendick[34] indicates a higher occupancy of the Ti3*d* states compared to TiC.

The experimentally found low density of states for carbides at the Fermi level is also predicted by the APW calculations[31, 32]. It might be concluded that the approximately self-consistent APW calculation for TiC by Conklin and Silversmith[32] obtains strong support by the present ESCA results.

Acknowledgements—We thank Professor Kai Siegbahn for his interest in this investigation. Thanks are also due to Drs. Rolf Manne and Michael C. Zerner, Quantum Chemistry Group, Uppsala University, for stimulating discussions and valuable comments on the manuscript. The work has been supported in part by the U.S. Air Force through the European Office of Aerospace research contract AF 61(052)-795.

REFERENCES

1. For a survey see RAMQVIST L., *Jernkont. Annlr.* **153**, In press (1969).
2. SIEGBAHN K., NORDLING C., FAHLMAN A., NORDBERG R., HAMRIN K., HEDMAN J., JOHANSSON G., BERGMARK T., KARLSSON S. E., LINDGREN I. and LINDBERG B., *Nova Acta Regiae Societatis Scientiarum Upsaliensis*, Ser. IV, Vol. 20 (1967).
3. HAMRIN K., JOHANSSON G., GELIUS U., FAHLMAN A., NORDLING C. and SIEGBAHN K., *Chem. Phys. Lett.* 1, 613 (1968); and [2], Chap. IV.
4. RAMQVIST L., EKSTIG B., KÄLLNE E., NORELAND E. and MANNE R., *J. Phys. Chem. Solids* **30**, 1849 (1969).
5. RAMQVIST L., *Jernkont. Annlr.* **152**, 465 (1968).
6. RAMQVIST L., *Jernkont. Annlr.* **152**, 517 (1968).
7. RAMQVIST L., *Powder Metall.* **17**, 2 (1966).
8. RAMQVIST L., *Powder Metall.* **17**, 26 (1966).
9. STORMS E. K., In *The Refractory Carbides*. Academic Press, New York (1967).
10. *Scandinavian Steel and Metal News*, No. 4, p. 7, (1968).
11. RAMQVIST L. and LUNNER S E., To be published.
12. TEGENFELDT J., *Program Celsius, for CDC3600*. Available from the Institute of Chemistry, Uppsala University.
13. FAHLMAN A., HAGSTRÖM S., HAMRIN K., NORDBERG R., NORDLING C and SIEGBAHN K., *Ark. Fys.* **31**, 479 (1966).
14. SIEGBAHN K., NORDLING C., FAHLMAN A., NORDBERG R., HAMRIN K, HEDMAN J., JOHANSSON G., BERGMARK T., KARLSSON S. E., LINDGREN I. and LINDBERG B., *Nova Acta Regiae Societatis Scientiarum Upsaliensis*, Ser. IV, Vol 20, Chap. II (1967)
15. ASAAD W. N. and BURHOP E. H. S., *Proc. phys. Soc.* **71**, 369 (1958).
16. BEARDEN J. A., *Rev. mod. Phys.* **39**, 78 (1967).
17. LINDBERG B J, HAMRIN K., JOHANSSON G., GELIUS U, FAHLMAN A., NORDLING C. and SIEGBAHN K., Rep. No. UUIP-638 (1969).
18. PAULING L., In *The Nature of the Chemical Bond*, 3rd Edn. Wiley, New York (1960)
19. HAMRIN K., JOHANSSON G, FAHLMAN A., NORDLING C, SIEGBAHN K. and LINDBERG B., *Chem. Phys. Lett.* 1, 557 (1968).
20. NORDBERG R., ALBRIDGE R G., BERGMARK T, ERICSON U., HEDMAN J., NORDLING C, SIEGBAHN K and LINDBERG B. J., *Ark. Kemi* **28**, 257 (1968)
21. NORDBERG R, GELIUS U., HEDÉN P. F., HEDMAN J., NORDLING C., SIEGBAHN K and LINDBERG B. J, Rep. No. UUIP-581 (1968).
22. SIEGBAHN K, NORDLING C., FAHLMAN A., NORDBERG R, HAMRIN K., HEDMAN J., JOHANSSON G., BERGMARK T., KARLSSON S. E., LINDGREN I. and LINDBERG B., *Nova Acta Regiae Societatis Scientarum Upsaliensis*, Ser. IV, Vol 20, Chap. V: 7, VII (1967)
23. MOROZOVA M. P., KHRIPUN M. K. and ARIYA S. M., *Zh. Obs. Khim.* **32**, 2072 (1962) (English translation).
24. LINDGREN I, In *Röntgenspektren und chemische Bindung* (Edited by A. Meisel), p. 182. Phys. Chem. Inst. der Karl-Marx-Univ., Leipzig (1966).
25. HOLLIDAY J. E., *J. appl. Phys.* **38**, 4720 (1967).
26. HOLLIDAY J. E., In *Soft X-ray Band Spectra and the Electronic Structure of Metals and Materials* (Edited by D. J. Fabian), p. 101. Academic Press, New York (1968).
27. COSTA P. and CONTE R. R. In *Nuclear Metallurgy Symposium*, Vol. X, p. 3. Met. Soc. AIME, New York (1964).
28. LYE R. G. and LOGOTHETIS E. M, *Phys. Rev* **147**, 622 (1966).
29. LYE R. G., HOLLOX G. E. and VENABLES J. B. Rep. No. AD 655456. Research Institute for Advanced Studies, Baltimore, Maryland, USA (1967).
30. BILZ H., *Z. Phys.* **153**, 338 (1958)
31. ERN V. and SWITENDICK A C, *Phys. Rev* **A137**, 1927 (1965).
32. CONKLIN Jr, J B and SILVERSMITH D. J., *Bull. Am. Phys. Soc.* **12** 416 (1967). *Int. J. Quantum Chem.* **25**, 243 (1968).
33. DENKER S. P., *J. Less common Metals* **14**, 1 (1968).
34. SWITENDICK A. C, Private communication.

J. Phys. Chem. Solids Pergamon Press 1969. Vol. 30, pp. 1849–1860. Printed in Great Britain.

X-RAY STUDY OF INNER LEVEL SHIFTS AND BAND STRUCTURE OF TiC AND RELATED COMPOUNDS

LARS RAMQVIST
The Axel Johnson Institute for Industrial Research, Nynäshamn, Sweden

and

BÖRJE EKSTIG, ELISABETH KÄLLNE and ERIK NORELAND
Institute of Physics, Uppsala University, Uppsala, Sweden

and

ROLF MANNE
Quantum Chemistry Group, Uppsala University, Uppsala, Sweden

(*Received* 30 *September* 1968; *in revised form* 3 *December* 1968)

Abstract—New measurements are presented of Ti *K* absorption and emission spectra from TiC, TiN, TiO, TiB_2, and Ti. It is shown that in all investigated compounds the number of Ti 3*d* electrons is lower than in the pure metal. For the three cubic compounds the order of increasing ionicity is TiO, TiN, TiC. The results are discussed in conjunction with other X-ray and electron spectroscopical investigations and are shown to be in agreement with recent energy band calculations using the self-consistent Augmented Plane Wave method.

INTRODUCTION

THE ELECTRONIC structure of transition metal carbides has been the object of many theoretical and experimental investigations. Two schools have evolved, one advocating that the metal acts as electron donor, the other that it acts as electron acceptor[1]. In the present investigation experimental evidence is presented in favor of the former school. We examined the metal *K* absorption and emission spectra for the following materials: Ti, TiB_2, TiC, TiN, and TiO and also for the non-stoichiometric carbide $TiC_{0.7}$. Comparisons to theoretical work are made in two respects: (i) the band structure as displayed in the absorption and emission band spectra is compared to band structure calculations, (ii) the direction and the relative magnitudes of inner level shifts in compounds are compared to those theoretically predicted.

Parallel to the present work an investigation was made of the inner level shifts in the same materials by electron spectroscopy (ESCA)[2]. These results and earlier soft X-ray measurements[3] are shown to be consistent with the present results.

Experimental determinations of titanium *K* spectra in chemical compounds have previously been performed mostly by investigators in the Soviet Union, e.g. Vainshtein, Chirkov and Blokhin[4, 5], Blokhin and Shuvaev[6], and by Nemnonov and Kolobova [7, 8]. It has, however, been shown for other physical properties of transition metal carbides that the mode of preparation greatly influences the results[9]. Many investigations in the literature are therefore not reproducible because of ill-defined test materials. To avoid that problem extensive tests were made of the purity and homogeneity of the materials in this investigation.

EXPERIMENTAL

Test materials

Except for the TiO specimen, the same test materials were used in the electron spectroscopy investigation[2]. Full information regarding the sources of supply, the preparation and test methods are given in that paper, and therefore only summarized here.

For the emission measurements test samples with a surface of approximately 0·5 cm^2 were required. These samples were obtained by a hot pressing technique. For the absorption measurements the compacts were ground to powders. The TiO phase was hot pressed at 1500°C for 30 min.

Special attention was paid to carbon and gas contents and to the homogeneity of the samples. The lattice parameter was used for identification, homogeneity and purity tests. It was measured with a 80 mm dia. Guinier–Hägg camera using Cu$K\alpha_1$ irradiation with $\lambda = 1{\cdot}54051$ Å and an internal standard of Si having the lattice parameter of $5{\cdot}43054 \pm 0{\cdot}00017$ Å. The parameters were refined using a computerized least squares program. The carbon analyses were carried out with the equipment Avecarbon 100, recently developed at Avesta Jernverks AB of the Axel Johnson Group[10]. Oxygen and nitrogen analyses were made with the vacuum liquid extraction method with a Leybold GAO 1 equipment. The results are summarized in Table 1. Other physical measurements on TiC and $TiC_{0{\cdot}7}$ are published elsewhere[9].

Apparatus

The $K\alpha_1$ and $K\beta_{1,3}$ emission lines, the K emission band, and the K absorption edge were recorded with a 2 meter bent crystal vacuum spectrometer of Johann type. The emission spectra were recorded in primary radiation. The analyzer crystal was quartz with reflections from the $10\bar{1}0$ planes. A proportional counter was used as detector and the spectra were recorded automatically in the 2nd order of reflection, the dispersion in this order being 2·11 XU/mm. The pressure in the tank was less than 5×10^{-5} Torr. The spectrometer has been described in greater detail elsewhere[11, 12].

Emission measurements

The samples were prepared as solid X-ray anodes from the source material described above. Due to the low evaporation temperatures of pure titanium and some of its compounds at the pressure used in the vacuum tank, the power over the water-cooled X-ray tube was kept at a minimum. The emission current ranged between 2–8 mA and the applied voltage between 8–10 kV. A typical value of the $K\alpha_1$ peak counting rate was 4500 cps. To test any influence of successive contamination of the samples every recording of a compound was immediately followed by

Table 1. *Properties of the test materials and the reference metal*

Compound	a_0 (Å)	O (wt.%)	H, N (wt.%)	Me impurities (wt.%)
Hot pressed samples				
$TiC_{1{\cdot}0}(TiC_{0{\cdot}987+0{\cdot}002})$	$4{\cdot}3278 \pm 0{\cdot}0002$	0·08	0·10	< 0·2
$TiC_{0{\cdot}7}(TiC_{0{\cdot}675+0{\cdot}002})$	$4{\cdot}3188 \pm 0{\cdot}0004$	0·16	0·15	< 0·2
$TiN_{1{\cdot}0}$	$4{\cdot}2416 \pm 0{\cdot}0001$	0·52		< 0·2
$TiB_{2{\cdot}0}$	$a = 3{\cdot}0298 \pm 0{\cdot}0002$ $c = 3{\cdot}2306 \pm 0{\cdot}0003$	0·24	0·10	< 0·1
$TiO_{1{\cdot}0}$	$4{\cdot}1714 \pm 0{\cdot}0007$		0·57	< 0·2
Reference metal				
Ti powder	$a = 2{\cdot}9515 \pm 0{\cdot}0002$ $c = 4{\cdot}6908 \pm 0{\cdot}0007$			< 0·3
Ti rod				< 0·01*

*According to supplier. Johnson, Matthey & Co. Ltd., London, England a recording of the pure metal and this procedure was repeated at least twice. The shifts of the line peaks were calculated from such pairs of curves. Typical values for the total scanning time for one run over the spectrum was for the $K\alpha_1$ line 20 min, for the $K\beta_{1,3}$ line 60 min, and for the K emission band 8 hr.

Absorption measurements

The absorbers were made of powder with grain sizes of 1–10 μm suspended in a zapon solution and spread onto mylar film. In this way the compounds were kept intact. For metallic titanium two absorbers were made, one powder absorber and one absorber prepared by vacuum deposition of spectrographically pure metal onto mylar backing. The intensity of the continuous radiation from an X-ray tube with tungsten anode operated at 13 kV and 22 mA was first recorded without absorber and was found to be constant over the energy region of interest. Then the transmitted intensity spectra were recorded. The pulse counting rate in the 2nd order of reflection without absorber in the X-ray beam was 120 cps. Each absorption spectrum was registered in a region of 40 XU around the absorption edge. The spectra were recorded once or twice depending on the thickness of the absorber. The measuring time for one total scan of the spectrum was about 8 hr.

RESULTS

The recorded emission and absorption spectra are reproduced by the solid lines in Figs. 1–3 and 5–7. The emission spectra are given in a linear intensity scale. Due to the grain sizes of the powder, uniform absorbers of optimal thickness could not be made. Thus no precise determination of the absorption coefficients was possible. Consequently the absorption spectra are presented as transmitted intensity in a negative logarithmic scale.

The absorption spectra from the two titanium metal absorbers are reproduced in Fig. 1. It is observed that the first absorption structure at the low energy side of the edge as displayed in the evaporated absorber curve dominates the whole absorption jump in the curve for the powder absorber. This is obviously due to the nature of the powder absorber where the transmitted radiation has passed through absorbing material of varying thickness. The other powder absorption spectra display similar shapes. Thus little information about the band structure above the Fermi level is gained. It should be emphasized, however, that the increase of the absorption starts at the Fermi edge, the determination of which was the main reason for recording the absorption spectra. The determination of the Fermi level is more uncertain for the compounds due to the low density of states at that position. Therefore both absorption and emission spectra were considered for the determination of the Fermi level.

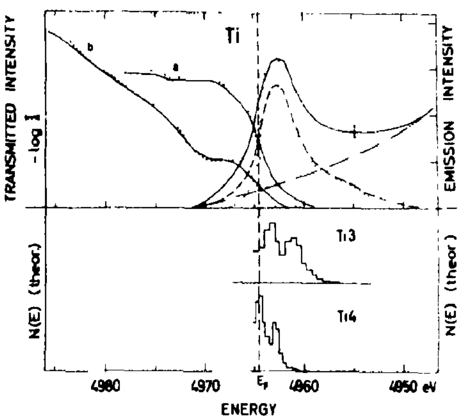

Fig. 1. K absorption spectrum and emission band for metallic titanium compared to theoretical density of states histograms by Altmann and Bradley[23]. Solid lines = experimental spectrum. Dashed-dotted line = tail of $K\beta_{1,3}$ line. Dashed line = resolved emission band. Dotted lines = corrected and resolved spectra. The absorption and emission intensities are in arbitrary units. E_f denotes the Fermi energy. The two absorption curves (a) and (b) show the spectrum from a powder and an evaporated absorber, respectively

The K emission band was resolved from the tail of the $K\beta_{1,3}$ line and is indicated by the dashed line in Figs. 1–3 and 5–7. The resolved emission spectra and the absorption spectra were then corrected for spectrometer smearing and partly for inner level smearing. This was done by a numerical iteration procedure described in [13]. The smearing function was of Lorentzian shape with the width 1·2 eV. This does not give a complete correction but was found to be optimal since a broader smearing function gave rise to difficulties due to uncertainties in the recorded spectra, especially in the tails. Through this correction a more accurate determination of the Fermi level was made possible. The dotted lines in the figures show the corrected spectra.

The wavelength and energy scales for the band spectra were calibrated with the Ti $K\beta_{1,3}$ as reference. The wave-length of this line and the conversion factor from X-units to eV were taken from Bearden and Burr[14]. The errors in the ordinate scale of the graphs denote the errors from the statistics of photon counting.

The results of the measurements of K level shifts are given in Table 2. Note that we follow the experimentalist convention to give levels in terms of binding energies which have the opposite sign from the orbital energies of atomic and molecular physics. Also included in the table are the same shifts recorded by photoelectron spectroscopy.

Table 2. Shifts of K absorption edge (binding energy) relative to metallic titanium (eV) *(TiK*: 4965·3 eV[14])

	This paper	ESCA[2]
TiB_2	−0·5 ± 0·4	
$TiC_{0·7}$	−0·1 ± 0·4	
$TiC_{1·0}$	0·7 ± 0·4	1·0 ± 0·4
TiN	1·8 ± 0·3	1·2 ± 0·4
TiO	0·5 ± 0·3	1·0 ± 0·4

Table 3 gives the shifts of the $K\alpha_1$ lines. A comparison of the L_{III} shifts calculated from the present data with the corresponding photoelectron spectra is also made in the same table. The shifts of the $K\beta_{1,3}$ lines and the shifts in the $M_{II,III}$ level calculated from the present data are given in Table 4. The errors in the energy values are estimated standard errors. Agreement between K and L_{III} binding energy shifts of the present investigation and as determined by electron spectroscopy[2] is in all cases satisfactory, see Tables 2 and 3.

Nemnonov and Kolobova[7] who report absorption and emission band spectra of TiC, TiN and TiO appear to have a K-level shift of +0·5 eV relative to Ti for all compounds. Chirkov, Blokhin and Vainshtein[5] who also measured the K emission band do not report the K-level shifts, though they appear to have had the necessary data available.

For the $K\alpha_1$ shifts Chirkov *et al.*[5] give an accuracy of 0·1 eV while Blokhin and

Table 3. Shifts of the $K\alpha_1$ line and the L_{III} binding energy relative to metallic titanium (eV) (Ti$K\alpha_1$: 4510·84 eV[15], TiL_{III}:454·5 eV[14])

	$K\alpha_1$			L_{III}	
	This paper	Blokhin[6]	Chirkov *et al.*[5]	This paper*	ESCA[2]
TiB_2	−0·18 ± 0·04	−0·25 ± 0·02		−0·4 ± 0·4	0·3 ± 0·2
$TiC_{0·7}$	−0·09 ± 0·04	−0·62 ± 0·02		0·0 ± 0·4	0·9 ± 0·1
$TiC_{1·0}$	−0·33 ± 0·02	−0·16 ± 0·02	$-0·5_6 \pm 0·1$	1·0 ± 0·3	1·3 ± 0·1
TiN	−0·19 ± 0·04	−0·11 ± 0·02	$-0·2_0 \pm 0·1$	2·0 ± 0·3	1·5 ± 0·2
TiO	−0·09 ± 0·03	−0·38 ± 0·10[16]	$-0·0_5 \pm 0·1$	0·6 ± 0·3	1·0 ± 0·2

*Calculated from the K absorption edge and the $K\alpha_1$ line.

Table 4. Shifts of the $K\beta_{1,3}$ line and the $M_{\mathrm{II,III}}$ binding energy relative to metallic titanium (eV) (Ti$K\beta_{1,3}$: 4931·8 eV[15], Ti $M_{\mathrm{II,III}}$: 33·5 eV[14])

	$K\beta_{1,3}$		M_{III}	
	This paper	Blokhin[6]	Chirkov *et al* [5]	This paper*
TiB_2	−0·41±0·12	−0·75±0·05		−0·1±0·4
$TiC_{0\cdot7}$	−0·50±0·09			0·4±0·4
$TiC_{1\cdot0}$	−0·44±0·09	−0·80±0·05	$-0{\cdot}6_0\pm0{\cdot}1$	1·1±0·4
TiN	−0·25±0·09	−0·80±0·05	$-0{\cdot}9_0\pm0{\cdot}1$	2·0±0·3
TiO	−0·39±0·09	−0·70±0·05	$-0{\cdot}5_4\pm0{\cdot}1$	0·9±0·3

*Calculated from the *K* absorption edge and the $K\beta_{1,3}$ line.

Shuvaev[6] claim 0·02 eV. With these limits of accuracy agreement with the present results is satisfactory except for TiC where our shift is markedly smaller in magnitude. The Ti $K\alpha_1$ shift for TiO measured by Meisel[16] is larger than those obtained by other investigators.

For the $K\beta_{1,3}$ shifts variations between different investigations are more dominant. On the whole, our measurements give shifts smaller in magnitude than those recorded by Chirkov *et al.*[5] and by Blokhin and Shuvaev [6]. Comparison with the reported band spectra are made later in this paper. In Soviet literature there is a tendency to try to decompose the emission band in a main peak $K\beta_5$ and one or several 'satellites', $K\beta'$, $K\beta_5'$, etc. In our view this nomenclature is confusing and hides the origin of the features which is found in the band structure and is in no way connected with ordinary X-ray satellites. We will therefore avoid this terminology as far as possible here.

DISCUSSION

Theory

The literature on the electronic structure of transition metal carbides is extensive, and we will here only discuss a few theories of current interest. For a discussion of chemical bonding only the outer orbitals of the constituent atoms are of interest. For titanium we consider the 3*d* and the 4*s* orbitals, for the non-metals the 2*s* and 2*p* orbitals. The description of the chemical bonding depends largely on the energetical ordering of these orbitals, especially the relation of the non-metal 2*p* orbitals to the metal 3*d* orbitals. Free atom Hartree–Fock calculations by Clementi[17] give the carbon 2*s* as the lowest one, and the metal 4*s* as the highest one, while the carbon 2*p* and titanium 3*d* are very similar in energy. One can therefore assume that the 4*s* orbitals, which are fully occupied in the ground state, loose some of their electrons to the carbon 2*p* orbitals, which in the free atom contain two out of six possible electrons. With this kind of redistribution of valence electrons electrostatic fields emerge, and the atomic orbital energies are no longer a good measure of the ordering of the energy levels. To get further insight we will have to consider theoretical calculations on the materials themselves.

The tight-binding approximation was used by Bilz[18], who excluded the 2*s* orbitals, which were considered as fully occupied, and who obtained an electron distribution with titanium as electron donor. The same approach was used by Lye and Logothetis who parametrized it to make the results fit their measurements of optical properties[19]. The most marked difference from Bilz is the high energy of the carbon 2*p* orbitals which are largely unoccupied. Their picture of the electronic structure is thus opposite to the one obtained by Bilz[18]. Calculations by the Augmented Plane Wave (APW) method have been performed by Ern and Switendick[20] and more recently by Conklin and Silversmith [21]. These calculations do not attempt to interpret optical properties or other 'finer details' in the electronic structure. On the other hand they are more firmly based on the Schrödinger equation than is the calculation by Lye and Logothetis. Conklin and Silversmith present the first approximately self-consistent band calculation for TiC and Switendick has recently made a similar calculation for TiO[22]. These calculations are thus independent of the initial assumptions regarding the potential. It is noteworthy that all APW calculations show electron transfer from metal to non-metal and that the choice of potential influences the results only to a minor extent.

Metallic titanium band calculations of a non-empirical nature by the cellular method have been performed by Altmann and Bradley[23]. Three different potentials were used but so far no attempt at self-consistency has been made. The calculations are discussed further below in conjunction with the experiments.

In the literature on the transition metal carbides numerous papers appear by Samsonov and coworkers who recently have discussed the ionic-covalent character with arguments based on Hund's rules for atoms[24]. It should be pointed out that the 'exchange forces' which determine the electronic configurations of free atoms and molecules are an order of magnitude smaller than the electrostatic forces occurring in a (partially) ionic crystal. The theoretical work by Samsonov is thus of doubtful validity.

The inner-electron levels of pure elements preserve their identities in chemical compounds. The observed energy shifts, which may be large chemically speaking, are small compared to the spacing between different levels in the same compound. Perturbation theory is thus applicable and the measured shifts are to first order attributed to changes in the effective potential due to redistribution of valence electrons[25]. The transfer of a valence electron from one atom to another due to a partially ionic bond decreases the electrostatic potential experienced by core electrons on the first atom. This is the basis for the assignment of polarities from binding energy measurements. The same model is used for X-ray emission spectra from transitions between two core levels on the same atom. In that case contributions from other atoms to the effective potential cancel out for the two states, and the shift is attributed to the valence electron distribution only on the emitting atom. Calculations of free atoms in various stages of ionization may therefore help in the interpretation of chemical effects in X-ray emission spectra not involving outer electrons. Lindgren[26] calculated the shift in the $K\alpha$ ($2p \rightarrow 1s$) transition energy due to one electron hole in various outer shells. He studied a series of atoms with $13 \leq Z \leq 36$ and used a Hartree–Fock–Slater method with an improved exchange approximation. The two states involved were calculated separately and the transition energy taken as the total energy difference between the two states. Interpolation in his results gives for the Ti $K\alpha$ line a shift of $+0{\cdot}08$ eV for the loss of a $4s$ electron and $-0{\cdot}82$ eV for the loss of a $3d$ electron. Thus, unless the observed shift is very small, $3d$ electrons dominate the chemical shift of the Ti $K\alpha$ emission line.

Further information on shifts of inner-electron levels can be obtained from Clementi's tables of Hartree–Fock calculations[17]. These calculations do not include holes in inner shells and one has therefore to use Koopmans' approximation to obtain the relevant information. The transitions are taken as differences between the appropriate orbital energies, and the various transitions obtained this way are given in Table 5. The general trends found by Lindgren for the $K\alpha$ line are supported and the shifts agree fairly well. For the $K\beta$($3p \rightarrow 1s$) line the shift is found to be positive both on the removal of $4s$ and of $3d$ electrons.

Experimental evidence in support of the

Table 5. ***Shifts in the emission lines for various ionized states of titanium calculated from Clementi's tables***[17] ***by Koopmans' approximation*** (eV)

	$K\alpha_{1,2}(2p \rightarrow 1s)$	$K\beta_{1,3}(3p \rightarrow 1s)$
$Ti^- 4s^2 3d^3\ ^4F$	0·53	−0·12
$Ti\ 4s^2 3d^2\ ^3F$		
$Ti^+ 4s^2 3d^1\ ^2D$	−0·79	0·92
$Ti^+ 4s^0 3d^3\ ^4F$	0·96	−0·13
$Ti^{2+} 4s^0 3d^2\ ^3F$	0·18	0·29

views presented here as to the cause of *Kα* chemical shifts in transition metal compounds are given by Meisel[16].

With binding energy shifts giving the direction of the charge transfer in heteropolar compounds the *Kα* shifts thus give an indication of which orbitals are involved in the process. We want to point out, however, that this perturbation approach is better the closer to the nucleus the core one-electron holes are located. The approach is thus inapplicable to transitions from the valence bands where the electron distribution is very different from that in free atoms.

Core level shifts

The *K* absorption edge energies in Table 2 show that the metal 1*s* orbitals for the compounds are shifted toward higher binding energies. This indicates a loss of valence electrons to the non-metal, the 1*s* orbitals of which are shifted toward smaller binding energies as found from the photoelectron spectra[2]. A quantitative estimate of the charge transfer from the binding energy shifts is, however, likely to be somewhat uncertain since the Fermi level cannot be considered fixed relative to vacuum in the various materials. The rigid band model of Bilz is in support of this. Transitions between core levels are, however, free from complications concerning the Fermi level. Table 3 shows that the metal $K\alpha_1(2p \rightarrow 1s)$ emission lines of the compounds are shifted towards lower energies relative to the pure metal. In the interpretation of the previous section these shifts are attributed to a loss of 3*d* electrons from the metal. For the cubic compounds TiC, TiN, and TiO the results indicate that Ti is most positive for TiC, less so for TiN and TiO.

The magnitude of the $K\alpha_1$ shift for TiC, − 0·33 eV, represents in the light of Lindgren's and Clementi's calculations a loss of 0·3–0·5 Ti 3*d* electrons. This result is in agreement with the self-consistent band calculation by Conklin and Silversmith which gives a loss of less than one 3*d* electron[21]. Also, the two Ti 4*s* electrons are transferred to carbon 2*p* orbitals. Since these orbitals largely occupy the same region of space, the effect of this transfer on the $K\alpha_1$ line is likely to be still smaller than theoretically predicted.

For TiO the self-consistent APW calculation by Switendick gives a 3*d* population approximately 0·15 electrons larger than that obtained by the same method for TiC [22]. The free-ion calculations attribute a difference in the $K\alpha_1$ energy of about 0·12 eV from this result; the experimental difference is 0·24 eV. The shift of the TiO $K\alpha_1$ line relative to metallic titanium is − 0·09 eV, which according to the free ion model represents a charge transfer of 0·1–0·2 3*d* electrons. Accurate comparisons of the charge distributions are hard to make due to the nature of the available data; the theoretical charges are estimated from the electron population within the titanium sphere with the free atom as reference while the experimental shifts are measured relative to titanium metal. Further theoretical work is apparently necessary, including self-consistent band calculations involving core levels and on the metal itself. Still, we want to stress that available self-consistent APW calculations give considerable support to our interpretation of the origin of the $K\alpha_1$ shifts.

The earlier APW calculations on TiC, TiN and TiO by Ern and Switendick[20] were not self-consistent and show deviations from the more recent accurate calculations and are also in disagreement with the free ion model for core level shifts. The Ti $3d$ population for TiC was slightly larger than for the neutral titanium atom and decreased in the order TiC, TiN and TiO, leaving the latter as the most ionic compound of the three. Our work gives the reverse order.

All APW calculations and also the localized molecular orbital model of Denker[27] have an uppermost filled band of TiC consisting mainly of non-metal $2p$ orbitals with some admixture of metal $3d$. In TiN and TiO this band is more localized on the non-metal atoms in agreement with electronegativity rules. The additional electrons occupy antibonding states which are mainly Ti $3d$, and the resultant charge distribution is determined by the balance between these two competing effects which apparently is very sensitive to the choice of effective potential. The density of states is on the other hand largely independent of this choice as is clear from the comparison in the following section.

The results for TiB_2 are somewhat inconclusive. The Ti K shift is negative indicating a loss of $3d$ electrons. The Ti K and L_{III} binding energies are, however, also shifted towards lower energies, although the accuracy of this result is rather low. The two most accurate measurements, the $K\alpha_1$ line and the L_{III} binding energy measured by electron spectroscopy, give results completely in line with those for other compounds. It therefore appears safe to conclude that Ti lacks electrons also in TiB_2 and that some of these electrons are lost from Ti $3d$ orbitals. The same reasoning applies to $TiC_{0.7}$ where we conclude from the $K\alpha_1$ line and L_{III} binding energy measured by electron spectroscopy that Ti is positive though less so than in $TiC_{1.0}$.

It is observed from Table 4 that the direction of the $K\beta_{1,3}$ shift in all cases follows that of the $K\alpha_1$ shift. This is in contradiction to the results of the free ion model. The $M_{II,III}$ ($3p$) binding energy for titanium is 33·5 eV [14] and the separation of this state from the non-metal $2s$ band in TiC, TiN and TiO is in this investigation 23·9, 17·4 and 13·7 eV, respectively. These energy differences are apparently too small to safely neglect the mixing of Ti $3p$ with the non-metal valence bands compared to the effective electrostatic interaction caused by the redistribution of valence electrons. Such a neglect is necessary in order to apply the free ion model. That the Ti $3p$ band is not completely localized in TiC is also indicated by the band width of 0·4 eV obtained for this band by Conklin and Silversmith[21].

Band structure

Ti. Figure 1 shows the results of absorption and emission measurements on metallic titanium. The emission band of Nemnonov and Kolobova[8] is in agreement with ours while their absorption spectrum has an absorption maximum near the edge not seen in the present investigation. Furthermore, they report a low density of states at the Fermi level in contrast to the present result.

The band calculations by Altmann and Bradley[23] are not self-consistent; instead, results of three different potential fields are given. The density of states from two of these (in Altmann and Bradley's notation Ti3 and Ti4) are reproduced in Fig. 1. The third choice, Ti2, gives a maximum in the density of states more than 4 eV below the Fermi level. This does not agree very well with the present results. As discussed by Altmann and Bradley, Ti3 is in agreement with experimental heat capacity data and with the band width as determined from soft X-ray measurements.

The experimental K emission band shows a considerable broadening on the low energy side, reaching some 10 eV from the main peak. It is generally assumed that this broadening, which is present in all X-ray band spectra, is produced by an Auger process within the band[28]. Due to this broadening, as well as to the transition probability function and the inner level smearing, an accurate determination of the band width is difficult to obtain from X-ray band spectra. As the totality of the mentioned effects in general increase the width of the emission band, the present results may be in better agreement with a narrower band width than that obtained from Ti3, one very likely intermediate between Ti3 and Ti4.

TiC. The corrected emission and absorption spectra of TiC and TiC$_{0.7}$ in Figs. 2 and 3 show that the density of states at the Fermi level is low. The same conclusion is drawn from a comparison of the carbon *K* emission band and the photoelectron spectra in various transition metal carbides[2]. As shown by Fig. 2 the shape of the emission bands is in good agreement with the density of states from self-consistent as well as non-self-consistent APW calculations[20–22]. With the C *K* binding energy determined by photoelectron spectroscopy, the peak of the C *K* emission band in TiC measured by Holliday agrees well with the main peak of the present band[3]. This is in support of the C2*p* character of the valence band. The low energy peak (often referred to as *K*β'') is identified as the cross transition from the non-metal 2*s* level to Ti 1*s*. This transition is not found in the C*K* emission band in TiC, in full agreement with the selection rules, see Fig. 4. The Ti $L_{\rm II,III}$ band also studied by Holliday has a structure approximately at the position of the C 2*s* band but cannot be used to further verify the present results. The main reason is that the relative intensity of the $L_{\rm II}$ and $L_{\rm III}$ bands is unknown, and a resolution of the bands, therefore impossible.

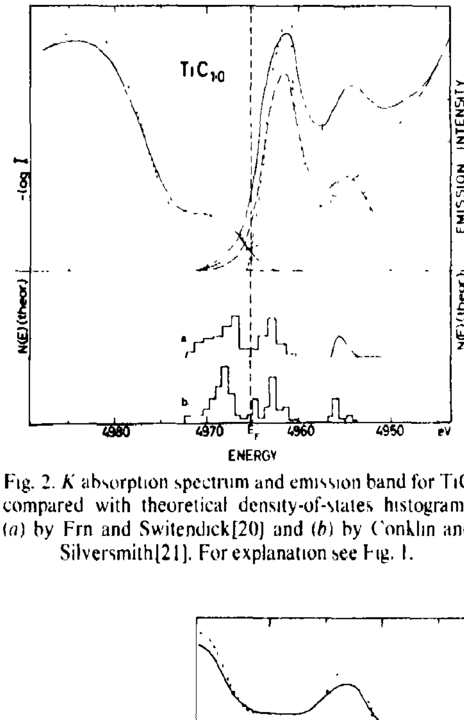

Fig. 2. *K* absorption spectrum and emission band for TiC compared with theoretical density-of-states histograms (*a*) by Ern and Switendick[20] and (*b*) by Conklin and Silversmith[21]. For explanation see Fig. 1.

The band calculation of Lye and Logothetis [19] also has a peak in the density of states on the low energy side of the valence bands attributed to C2*s*. On the other hand, their calculated density of states shows many more irregularities closer to the Fermi level and is somewhat higher at this level, which does not agree so well with the experiments. Most important is, however, that the polarity of

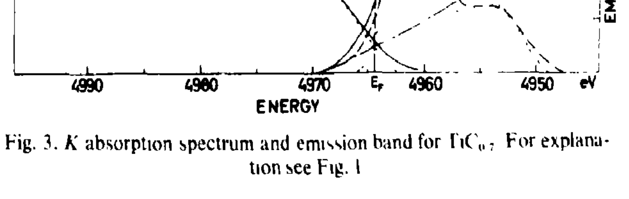

Fig. 3. *K* absorption spectrum and emission band for TiC$_{0.7}$. For explanation see Fig. 1

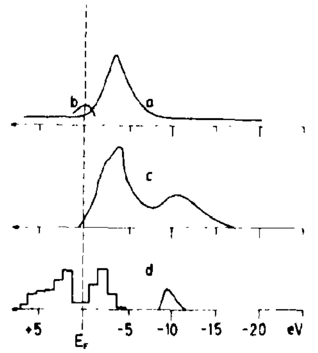

Fig. 4. Comparison of experimental and theoretical investigations of the band structure of TiC. (*a*) the carbon *K* emission band after Holliday[3], (*b*) carbon 1*s* photoelectron spectrum[2], (*c*) the Ti *K* emission band (present investigation) and (*d*) the theoretical density of states histogram after Ern and Switendick[20].

their charge distribution is opposite to the result of the present experiments, and to the electron spectroscopy studies. Though Lye and Logothetis claim better agreement with optical properties than obtained from APW calculations we contend that the evidence from the core levels cannot be overruled. The calculation by Bilz[18], is, as pointed out previously, in agreement with the experimentally determined polarity, but the neglect of C 2*s* levels makes the results of less interest here.

A comparison of the areas of the resolved *K* emission band and the $K\beta_{1,3}$ emission line was made for $TiC_{1.0}$ and $TiC_{0.7}$. The result is

$$\frac{\text{Area of } K \text{ band}}{\text{Area of } K\beta_{1,3} \text{ line}} = \begin{cases} 0{\cdot}033 \pm 0{\cdot}003 \text{ for } TiC_{0.7} \\ 0{\cdot}050 \pm 0{\cdot}003 \text{ for } TiC_{1.0}. \end{cases}$$

The area of the emission band has increased with the increase of carbon content. Figures 2 and 3 show that the main change is due to an increase of the low energy peak thus further supporting the carbon character of the corresponding band.

TiN, TiO and TiB_2. TiN and TiO have the same crystal structure as TiC and also a similar band spectrum. The density of states histograms of Ern and Switendick agree well with the recorded spectra, Figs. 5 and 6.

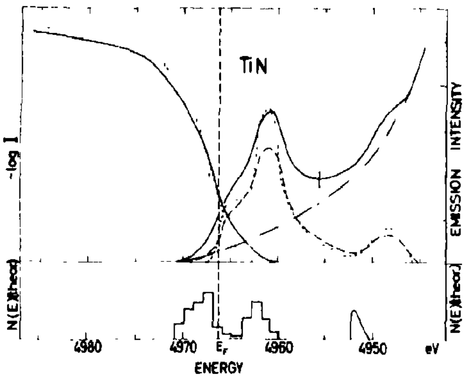

Fig. 5. *K* absorption spectrum and emission band for TiN compared to theoretical density of states histogram by Ern and Switendick[20]. For explanation see Fig. 1.

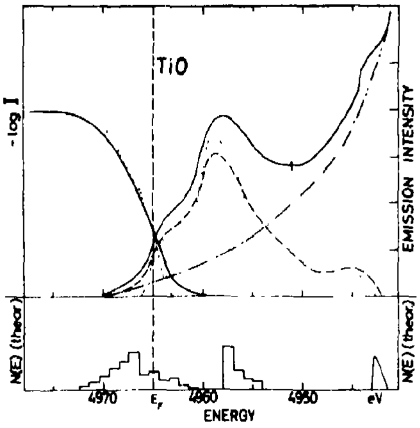

Fig. 6. *K* absorption spectrum and emission band for TiO compared to theoretical density of states histogram by Ern and Switendick[20]. For explanation see Fig. 1.

For TiB_2 no theoretical band calculation has been found. The band spectra for these compounds by Nemnonov and Kolobova[7] and by Chirkov, Blokhin and Vainshtein[5] are in qualitative agreement with the present results. In addition to the low energy (2*s*) peak a structure on the high energy side of the main peak appears for TiN and TiO accompanied by an increased density of states at the Fermi level compared to TiC. In the light of the APW calculations and the $K\alpha_1$ shift measurements this is attributed to the increasing occupancy of the Ti 3*d* states in these compounds.

The TiB_2 band spectrum in Fig. 7 is very close to that for TiC although with a less pronounced low energy peak.

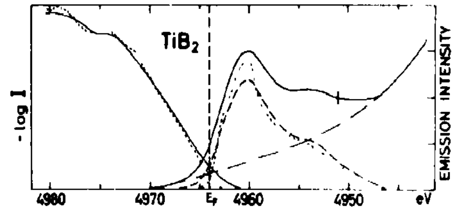

Fig. 7 *K* absorption spectrum and emission band for TiB_2. For explanation see Fig. 1.

CONCLUSIONS

Shifts of the titanium *K* absorption edge and of the $K\alpha_1$ line in TiC, TiN and TiO relative to the pure metal show that the electron transfer in these compounds is from metal to non-metal, and that the occupancy of $3d$ states is less in the compounds than in the metal. The charge transfer is largest for TiC, less for TiN and TiO. The magnitude of the charge transfer, 0·3–0·5 $3d$ electrons for TiC, 0·1–0·2 $3d$ electrons for TiO, is in agreement with self-consistent APW calculations for these materials. Agreement with APW calculations for TiC, TiN and TiO is good with regard to the shape of the density of states.

The electron spectra recorded for the same compounds by Ramqvist, Hamrin *et al.*[2] are consistent with the present results as are the carbon *K* emission band spectra of Holliday[3].

For titanium metal, the agreement with the calculated density of states for the valence bands is satisfactory.

Non-empirical electron energy band calculations by the APW and cellular methods thus appear to give sufficient information to explain the X-ray and electron spectra of the investigated compounds.

Acknowledgements – Thanks are due to Dr. J. B. Conklin, Jr. and Dr. A. C Switendick for information about their calculations prior to publication. This work was partially supported by the Swedish Natural Science Research Council and the Air Force Office of Scientific Research (OSR) through the Eurpoean Office of Aerospace Research (OAR), United States Air Force under Grant AF EOAR 67-50 to the Quantum Chemistry Group, Uppsala University.

REFERENCES

1. RAMQVIST L., *Jernkont. Annlr.* **153**, In press (1969).
2. RAMQVIST L., HAMRIN K., JOHANSSON G., FAHLMAN A. and NORDLING C., *J. Phys. Chem. Solids* **30**, 1835 (1969).
3. HOLLIDAY J. E., *J. appl. Phys.* **38**, 4720 (1967).
4. VAINSHTEIN E. E. and CHIRKOV V. I., *Dokl. Akad. Nauk SSSR* **145**, 1031 (1962), transl. *Soviet Phys. Dokl* 7, 724 (1963).
5. CHIRKOV V. I., BLOKHIN S. M. and VAINSHTEIN E. E., *Fiz. Tverd. Tela* **9**, 1116 (1967); transl. *Soviet Phys. solid St.* **9**, 873 (1967).
6. BLOKHIN M. A. and SHUVAEV A T., *Izv. Akad. Nauk SSSR, ser. fiz.* **26**. 429 (1962); transl. *Bull. Acad. Sci. USSR, Phys. Ser.* **26**. 429 (1963)
7. NEMNONOV S. A. and KOLOBOVA K. M., *Fiz. metal. metalloved.* **22**, 680 (1966); transl. *Physics Metals Metallogr.* **22**, 36 (1966).
8. NEMNONOV S. A. and KOLOBOVA K. M., *Fiz. metal. metalloved.* **21**, 476 (1966), transl. *Physics Metals Metallogr.* **21**, 168 (1966)
9. RAMQVIST L., *Jernkont. Annlr.* **152**, 517 (1968).
10 *Scand. Steel Metal News* **4**, 7 (1968).
11. NORDFORS B., *Ark. Fys.* **19**, 259 (1961).
12 NORELAND E. and EKSTIG B., *Ark. Fys.* **26**, 161 (1963).
13. EKSTIG B., To be published.
14. BEARDEN J. A. and BURR A F., *Atomic Energy Levels*. U.S. Atomic Energy Commission, NYO-2543-1, Oak Ridge, Tenn. (1965).
15. BEARDEN J A., *X-Ray Wave Lengths*. U.S. Atomic Energy Commission, NYO-10586, Oak Ridge, Tenn. (1964).
16. MEISEL A., In *Rontgenspektren und Chemische Bindung* (Edited by A. Meisel). p 212 VEB Reprocolor, Leipzig (1966).
17. CLEMENTI E., *IBM Jl. Res. Dev.* **9**, 2 (1965), *suppl.*
18. BILZ H., *Z. Phys.* **153**, 338 (1958)
19. LYE R G. and LOGOTHETIS E M., *Phys. Rev* **147**, 622 (1966).
20. ERN V and SWITENDICK A. C., *Phys. Rev.* **137**, A1927 (1965).
21. CONKLIN J. B., Jr. and SILVERSMITH D. J., *Bull. Am. phys. Soc.* **12**, 416 (1967); *Int. J. Quantum Chem.* **25**, 243 (1968).
22. SWITENDICK A. C., Private communication.
23. ALTMANN S. L. and BRADLEY C J., *Proc. phys. Soc.* **92**, 764 (1967).
24 SAMSONOV G. V., *Poroshkovaya metall Ukr SSR* **12** (48), 49 (1966), PRYADKO Y F., *ibid.* **12** (48), 61 (1966); KUCHMA A Ya. and SAMSONOV G. V., *Neorg. mat.* **2**, 1970 (1966); Earlier work by this group of qualitative nature is

collected in SAMSONOV G. V., *Refractory Transition Metal Compounds*. Academic Press, New York (1964).

25. See e.g. MANNE R., *J. chem. Phys.* **46**, 4645 (1967)
26. LINDGREN I., In *Rontgenspektren und Chemische Bindung* (Edited by A. Meisel), p.182. VEB Reprocolor, Leipzig (1966).
27. DENKER S. P., *J. Less-common Metals* **14**, 1 (1968).
28. PIRENNE J. and LONGE P., *Physica* **30**, 277 (1964).

J. Phys. Chem. Solids Pergamon Press 1969. Vol. 30, pp 1861–1871 Printed in Great Britain

SPACE CHARGE LIMITED CURRENTS IN *P-N* JUNCTIONS

A. TARONI
University of Modena, Italy

and

G. ZANARINI
University of Bologna, Italy

(*Received* 18 *November* 1968)

Abstract—The system of partial differential equations which describes the motion of charge carriers inside the space charge region of an inversely biased *p–n* junction is numerically solved, taking into account the influence of the density of electron-hole pairs on the electric field.

It is shown that there are remarkable variations in the theoretically predicted current signals when the density is raised Particularly interesting is the appearance of a peak closely resembling the one predicted by the theory of SCL currents in insulators. The time position of the above mentioned peak is not influenced by diffusion (at least when a realistic order of magnitude is considered for the diffusion term).

These theoretical previsions could be very useful in the study of charge transport in semiconductors at low fields

INTRODUCTION

MANY PAPERS have been written on the collection of charge carriers generated inside the depletion region of a *p–n* junction by ionizing radiations[1–3]. The density of the generated electron-hole pairs, however, was always supposed to be so low as to give rise, at most, to a small perturbation of the electric field inside the junction.

In this paper a more general approach to the collection problem is presented. It leads to the numerical solution of the system of partial differential equations (continuity equations and Poisson's equation) which describes the motion of charge carriers inside the depletion region. The assumption is made throughout this paper that these processes can be adequately described by means of one space variable only*.

This approach takes into account in an exact way the non linear effects due to the density of the created pairs. It permits then to study the dependence of the current signal on this parameter (besides, obviously, the dependence on the electric field and on the range of the ionizing radiation).

It will be shown that the shape and the time characteristics of the current pulses are strongly dependent on the initial density of the created pairs. Particularly interesting is the appearance, at moderately high densities, of a peak closely resembling the one predicted in the theory of SCL currents in insulators [4–6].

This result was never obtained before for *p–n* junctions, and it could be very useful in the study of charge transport in semiconductors at low fields.

Finally, the influence of diffusion on the results will be discussed.

STATEMENT OF THE PROBLEM

Let us consider a *p–n* junction where the *p*-type material is much more heavily doped than the n-type material. When a reverse bias voltage is applied to the junction, the space charge region then extends essentially in the n-type material (this is also the case of a Schottky junction made on n-type material) [7].

---

*This assumption is certainly valid when the ionizing radiation impinges on a sufficiently large surface, so that transverse diffusion (i.e. diffusion normal to the electric field direction) can be disregarded. This can be the case with a burst of electrons, with a short low-penetration light flash, or also with a burst of ions.

A short range ionizing radiation sent through the junction[†] into the space charge region gives rise to a distribution of e–h pairs. These pairs are then collected by the electrodes owing to the electric field inside the space charge region. The electric field, however, depends (through Poisson's equation) not only on the external bias voltage and the ionized donors density inside the space charge region, but also on the density of the carriers to be collected. The motion of the carriers inside the space charge region then obeys a system of non linear partial differential equations (the continuity equations and Poisson's equation).

Let us suppose to neglect direct recombination and trapping phenomena and consider, as previously stated, the uni-dimensional case; let us also suppose mobilities to be independent on the electric field. The influence of diffusion is for now disregarded and will be discussed in a following section.

Under these assumptions, the system of differential equations is written[7]:

$$\frac{\partial n}{\partial t} = \mu_p\left[E\frac{\partial n}{\partial x} + n\frac{\partial E}{\partial x}\right]$$

$$\frac{\partial p}{\partial t} = -\mu_n\left[E\frac{\partial p}{\partial x} + p\frac{\partial E}{\partial x}\right] \tag{1}$$

$$\frac{\partial E}{\partial x} = \frac{q}{\epsilon}(p - n + N_d)$$

where x is the space variable (normal to the electrodes) with origin on the junction.

The initial conditions are

$$\begin{aligned} n(x,0) &= f(x) \\ p(x,0) &= f(x) \\ E(x,0) &= -\frac{qN_d}{\epsilon}(w-x) - \frac{V_a - V_d}{w}. \end{aligned} \tag{2}$$

The function $f(x)$ is determined by the specific energy loss of the incident radiation[*]. The initial condition on the electric field contains the term $(V_a - V_d)/w$ only when the applied voltage is higher than the depletion voltage.

The boundary conditions on $n(x,t)$ and $p(x,t)$ are

$$\begin{aligned} n(x,t) &= 0 \quad \text{for } x < 0 \text{ and } x > w \\ p(x,t) &= 0 \quad \text{for } x < 0 \text{ and } x > w. \end{aligned} \tag{3}$$

The boundary condition on the electric field will be found under a 'short circuit' assumption, i.e. assuming the voltage across the junction to be independent of the time and equal to the bias voltage. This is a very good approximation when the junction is connected to a circuit with a low input impedance, which is the case when observing the current signal [9].

Performing a first integration of Poisson's equation, we have

$$\begin{aligned} E(x) &= \frac{q}{\epsilon}\int_0^x (N_d + p - n)\,\mathrm{d}\xi + E(0) \\ &= \frac{q}{\epsilon}N_d x + \frac{q}{\epsilon}\int_0^x (p-n)\,\mathrm{d}\xi + E(0). \end{aligned}$$

Integrating again between 0 and w:

$$\int_0^w E(x)\,\mathrm{d}x = \frac{qN_d w^2}{2\epsilon} + \frac{q}{\epsilon}\int_0^w \int_0^x (p-n)\,\mathrm{d}\xi\,\mathrm{d}x + E(0)w$$

[†] If the ionizing radiation is sent through the opposite side or the space charge region extends in the p-type material, there are only minor changes to introduce in the statement of the problem.

[*] For the purpose of numerical computation the expression $f(x) = Ax^4(R-x)^2$ was assumed[8], where A is a constant and R is the range of the ionizing radiation. The shape of the initial distribution, however, has only a weak influence on the results

whence

$$E(0)=\frac{1}{w}\int_0^w E(x)\,\mathrm{d}x-\frac{qN_dw}{2\epsilon}$$
$$-\frac{q}{w\epsilon}\int_0^w\int_0^x (p-n)\,\mathrm{d}\xi\,\mathrm{d}x.$$

On the other hand, the 'short circuit' condition implies that

$$\int_0^w E(x)\,\mathrm{d}x=-V_a$$

and therefore

$$E(0)=-\frac{V_a}{w}-\frac{qN_dw}{2\epsilon}-\frac{1}{w\epsilon}\int_0^w\int_0^x(p-n)\mathrm{d}\xi\,\mathrm{d}x.$$

Remembering that* $V_d=(qN_dw^2/2\epsilon)$ we can at last write

$$E(0,t)=-\frac{qw}{\epsilon}\left[N_d+\frac{1}{w^2}\times\int_0^w\int_0^x(p-n)\,\mathrm{d}\xi\,\mathrm{d}x\right]-\frac{V_a-V_d}{w}. \quad (4)$$

Let us now introduce normalized variables, as follows:

$$x'=x/w;\quad t'=t/T_0;\quad E'=\frac{E}{qN_dw/\epsilon};$$
$$n'=\frac{n}{N_d}\cdot\quad p'=\frac{p}{N_d}$$

with:

$$T_0=\frac{1}{(q\mu_eN_d/\epsilon)};\quad R_3=\frac{V_a}{(qN_dw^2/2\epsilon)};$$
$$R_1=\frac{\mu_h}{\mu_e}.$$

The system (1) becomes

$$\frac{\partial n'}{\partial t'}=E'\frac{\partial n'}{\partial x'}+n'\frac{\partial E'}{\partial x'}$$
$$\frac{\partial p'}{\partial t'}=-R_4\left(E'\frac{\partial p'}{\partial x'}+p'\frac{\partial E'}{\partial x'}\right)\quad(5)$$
$$\frac{\partial E'}{\partial x'}=1+(p'-n')$$

with the initial conditions

$$n'(x',0)=f(x')$$
$$p'(x',0)=f(x')$$
$$E'(x',0)=x'-\frac{R_3}{2}-\frac{3}{2}=x'-1-\frac{R_3+1}{2}\quad(6)$$

and the boundary conditions

$$n'(x',t')=0\quad\text{for}\quad x'<0\ \text{and}\ x'>1$$
$$p'(x',t')=0\quad\text{for}\quad x'<0\ \text{and}\ x'>1$$
$$E'(0,t')=-\frac{R_3+1}{2}-\int_0^1\int_0^{x'}(p'-n')\,\mathrm{d}\xi\,\mathrm{d}x'.\quad(7)$$

The difficult mathematical problem of solving the above system was transformed into the much simpler problem of solving a system of finite difference equations. These difference equations were obtained from the previous ones by substituting the time and space derivatives with their linear difference analogs. The width of the space charge region was divided into a large number of intervals (from 100 to 400, according to the range of the ionizing radiation) and the time step was chosen according to the rapidity of variation of the various quantities. We reduced them to a system of only two difference equations by solving Poisson's equation and substituting the so obtained expression of the electric field into the continuity equations. It was then possible in this way to obtain the charge densities and the electric field as functions of x' and t'.

---

*We introduce here the assumption that the 'built in' voltage be negligible with respect to the total depletion voltage.

The current density due to the motion of carriers inside the space charge region has the expression

$$J = J_c + J_d \tag{8}$$

where J_c is the conduction current density and J_d is the displacement current density. Substituting the familiar expressions for J_c and J_d into (8), we have

$$J = q(\mu_e n + \mu_p p)E + \epsilon \frac{\partial E}{\partial t}.$$

Integrating this expression on the space variable x between 0 and w and remembering that, by definition, J does not depend on x, we have

$$J(t) = \frac{q}{w}\left[\int_0^w (\mu_e n + \mu_p p)E\,\mathrm{d}x + \epsilon \frac{\partial}{\partial t}\int_0^w E\,\mathrm{d}x\right]$$

By virtue of the 'short circuit' assumption:

$$J(t) = \frac{q}{w}\int_0^w (\mu_e n + \mu_p p)E\,\mathrm{d}x$$

Introducing normalized variables:

$$J(t) = \frac{q^2\mu_e N_d^2 w}{\epsilon}\int_0^1 (n' + R_4 p')E'\,\mathrm{d}x'$$

whence, if $J_0 = (q^2\mu_e N_d^2 w/\epsilon)$, we have:

$$J'(t) = J(t)/J_0 = \int_0^1 (n' + R_4 p')E'\,\mathrm{d}x'. \tag{9}$$

Having written the system of equations in normalized form, we are in a position to obtain results of general validity as functions of the following dimensionless parameters: R_1 = ratio between range of ionizing radiation and space charge region width; R_2 = ratio between average density of carriers generated at the initial instant by the ionizing radiation and ionized donors density inside the depletion region; R_3 = ratio between external bias voltage and depletion voltage; R_4 = ratio between hole and electron mobilities.

In this work we shall limit ourselves to $R_4 = 0{\cdot}33$, which corresponds to ambient temperature[7].

DISCUSSION OF RESULTS

Figures 1 and 2 show the increasing importance of the modification of the electric field by the ionized pairs when their initial density is raised. The only difference between the two situations is the value of R_2, while R_1 and R_3 are held fixed ($R_1 = 0{\cdot}2$, $R_3 = 5$).

It is easily seen that the separation of electrons from holes takes place more slowly when the initial density is higher, owing to the increasing influence on the electric field of the charges which, when separation begins, are no more neutralized by charges of opposite sign. In particular, when the initial density is sufficiently high, charge collection takes place through a slow erosion of the ionized region.

The shape and the time characteristics of the current signals are strongly dependent on the initial density of electron-hole pairs. Figures 3 and 4 show the normalized current signals corresponding to two different ionizing radiation ranges, two different applied voltages and various initial densities.

The most important feature in these current signals is the peak which appears at moderately high densities and becomes more and more evident when the initial density is raised. Its time position t_0, however, as it can be seen in Figs. 3 and 4, does not depend on density, but only on electric field and ionizing radiation range. This dependence is shown in Fig. 5.

This peak very closely resembles the one predicted by the theory of SCL currents in insulators[4, 6]. It is to be noted, in particular, that when the ionizing radiation range goes to zero the time t_0 raises to the value predicted by the above mentioned theory, i.e. $t_0 \simeq 0{\cdot}8\,t_t$, where t_t is the electron transit time through the space charge region. We have, in fact:

$$t_t = \frac{w^2}{\mu_e V_a} = \frac{2\rho\epsilon}{R_3}.$$

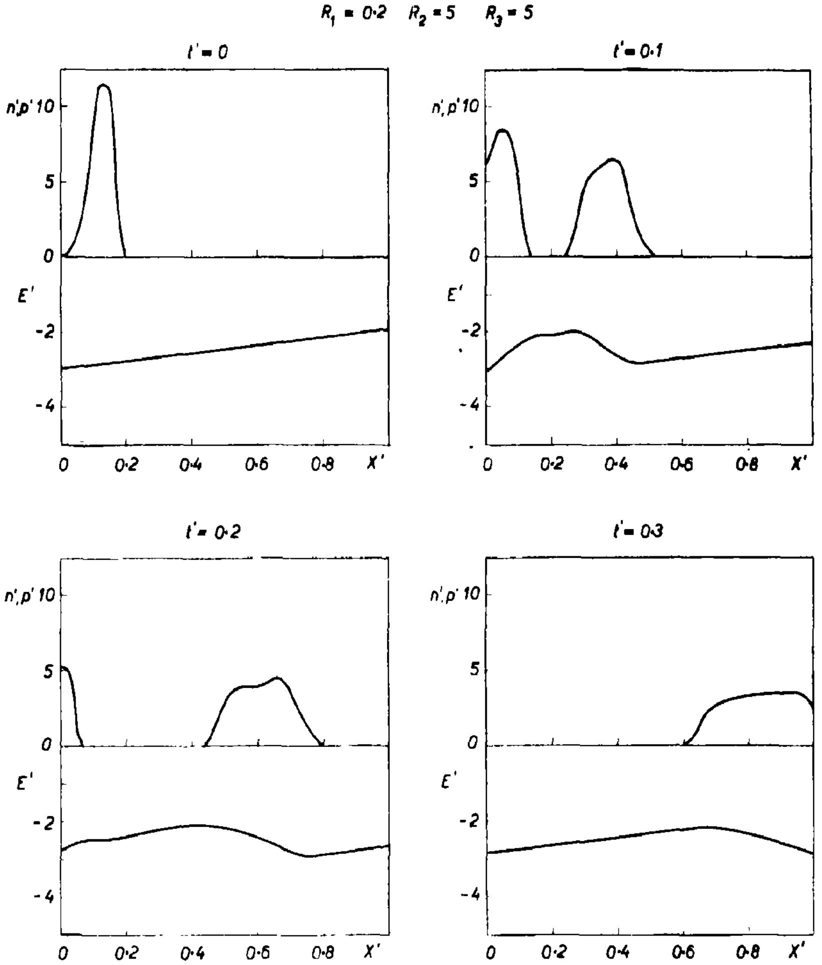

Fig. 1. Normalized density of holes and electrons and normalized electric field inside the space charge region of a p–n junction as functions of the space coordinate normal to the junction, at four different time instants. $R_1 = 0{\cdot}2$, $R_2 = 5$, $R_3 = 5$.

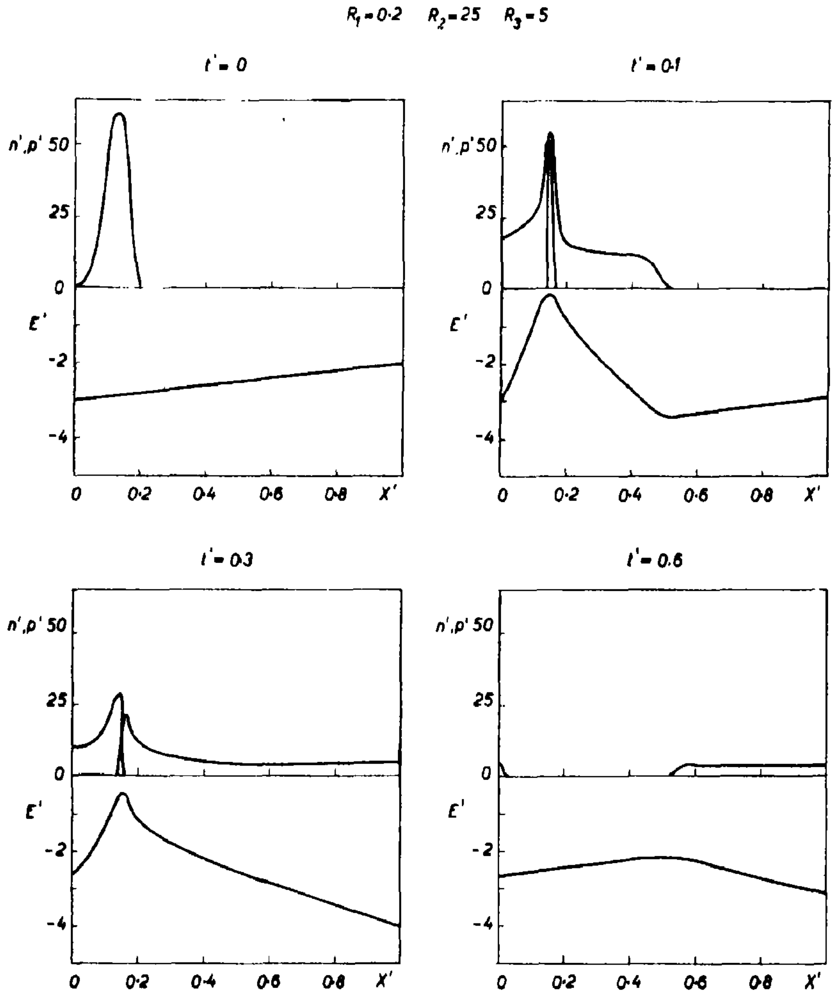

Fig. 2. Normalized density of holes and electrons and normalized electric field inside the space charge region of a p-n junction as functions of the space coordinate normal to the junction, at four different time instants. $R_1 = 0{\cdot}2$, $R_2 = 25$, $R_3 = 5$.

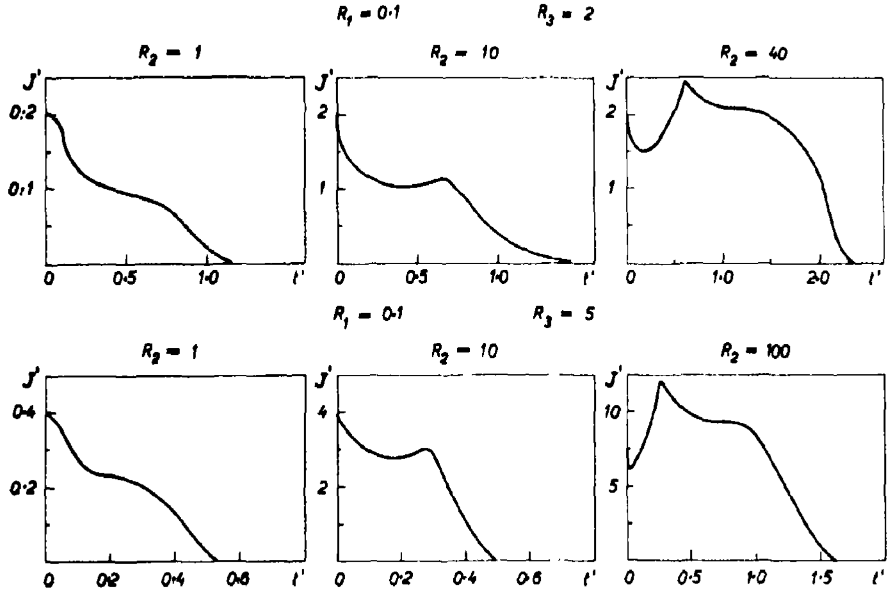

Fig. 3. Normalized current density as a function of time in a p–n junction for two different applied voltages, various initial densities and $R_1 = 0{\cdot}1$.

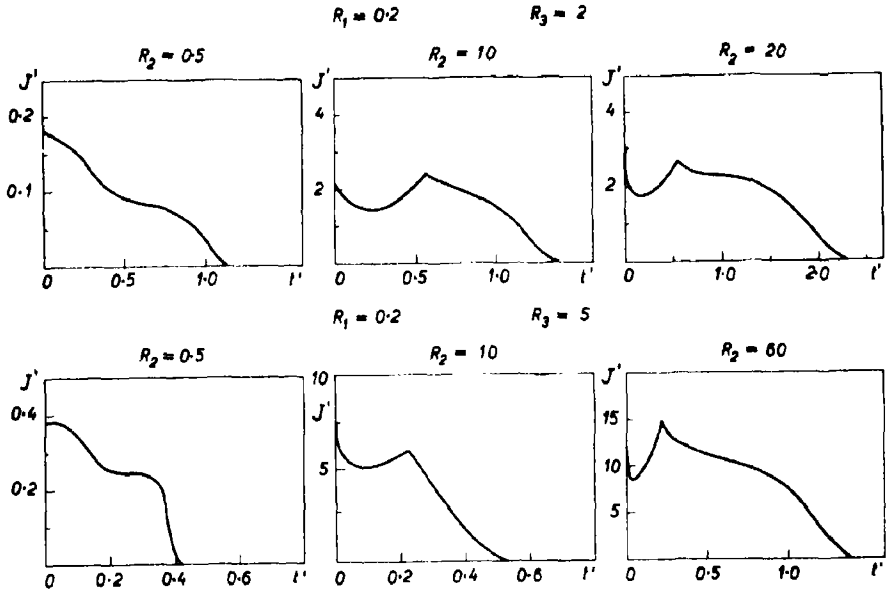

Fig. 4. Normalized current density as a function of time in a p–n junction for two different applied voltages, various initial densities and $R_1 = 0{\cdot}2$.

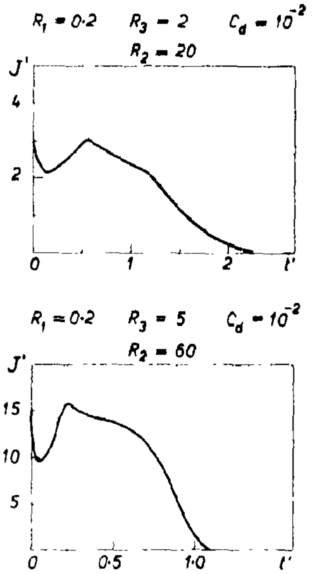

Fig. 7. Normalized current density as a function of time in a p–n junction for two different values of initial densities with $R_1 = 0{\cdot}1$, $R_3 = 2$ and 5, $C_d = 10^{-2}$.

interest of our theoretical previsions, which also suggest the possibility of obtaining similar results by sending suitable ionizing radiations on a reverse biased p–n junction.

These theoretical previsions could then be remarkably useful for the design and interpretation of experiments on SCL currents. By means of experiments of this kind it would be possible to evaluate charge transport coefficients in semiconductors also at low electric fields, where difficulties arise with usual methods[11, 12], using the same philosophy of the classical experiments on insulators[13–15].

NOTATION

C_d	normalized diffusion coefficient
D_e	electron diffusion constant, m^2 sec^{-1}
E	electric field, V m^{-1}
K	Boltzmann's constant, J °K^{-1}
J	current density, A m^{-2}
J_c	conduction current density, A m^{-2}
J_d	displacement current density, A m^{-2}
n	density of electrons generated by ionizing radiation, m^{-3}
N_d	ionized donor density, m^{-3}
p	density of holes generated by ionizing radiation, m^{-3}
q	electronic charge, C
R	range of ionizing radiation, m
R_1	ratio between range of ionizing radiation and space charge region width
R_2	ratio between average density of carriers generated by ionizing radiation and ionized donors density inside the depletion region
R_3	ratio between external bias voltage and depletion voltage
R_4	ratio between hole and electron mobilities
t_0	time position of the peak in current signals, sec
t_t	electron transit time through the space charge region, sec
T	absolute temperature, °K
V_a	bias voltage, V
V_d	depletion voltage, V
ϵ	dielectric constant, F m^{-1}
μ_e	electron mobility, m^2 V^{-1} sec^{-1}
μ_h	hole mobility, m^2 V^{-1} sec^{-1}
ρ	resistivity, Ω m

Acknowledgements—Thanks are due to Professor A. Alberigi Quaranta for his constant interest in our work, to Professor J. W. Mayer (California Institute of Technology) for some stimulating discussions and to Dr. P. Cinti for his valuable help in performing the calculations.

REFERENCES

1. TOVE P. A. and FALK K., *Nucl. Instr. Meth.* **29**, 66 (1964).
2. ALBERIGI QUARANTA A., CASADEI G., MARTINI M., OTTAVIANI G. and ZANARINI G., *Nucl. Instr. Meth.* **35**, 93 (1965).
3. PAPADAKIS A. C. and KEATING P. N., *Br. J. appl. Phys.* **16**, 613 (1965)
4. MANY A. and RAKAVY G., *Phys Rev.* **126**, 1980 (1962)
5. SCHWARTZ L. M. and HORNIG J. F., *J. Phys. Chem. Solids* **26**, 1821 (1965)
6. TREDGOLD R. H., In *Space Charge Conduction in Solids*, Elsevier, Amsterdam (1966).
7. MOLL J. L., In *Physics of Semiconductors*. McGraw Hill, New York (1964).
8. TARONI A. and ZANARINI G., *Nucl. Inst Meth.* **67**, 277 (1969).

9. ALBERIGI QUARANTA A., MARTINI M., OTTAVIANI G and ZANARINI G., *Nucl. Instr. Meth.* **57**, 131 (1967).
10. LEMKE H and MULLER G. O., *Phys. Status Solidi* **24**, 127 (1967).
11. ALBERIGI QUARANTA A., MARTINI M., OTTAVIANI G., REDAELLI G. and ZANARINI G., *Solid-St. Electron.* **11**, 685 (1968)
12. ALBERIGI QUARANTA A., TARONI A. and ZANARINI G., *IEEE Trans. Nucl. Sci.* **NS-15**, 373 (1968)
13. MARK P. and HELFRIK W., *J appl. Phys.* **33**, 205 (1961)
14. SILVER M., MARK P., OLNESS D., HELFRIK W. and JARNAGIN R. C., *J. appl. Phys* **33**, 2988 (1962).
15. MANY A., SIMHONY M., WEISZ S. Z. and TEUCHER Y., *J. Phys. Chem Solids* **25**, 721 (1964).

J. Phys. Chem. Solids Pergamon Press 1969. Vol. 30, pp. 1873–1883. Printed in Great Britain.

BLOCH ELECTRONS IN A MAGNETIC FIELD PERTURBATION APPROACH†

S. P. MORRIS

Physics Department, Sir George Williams University, Montreal, Quebec, Canada

(*Received* 16 *September* 1968; *in revised form* 15 *November* 1968)

Abstract—The wave functions and energy levels of an electron in a periodic potential and a uniform magnetic field are found by means of a modified perturbation theory.

The expansion functions for these generalized Bloch wave functions are products of the field-free Bloch wave function and the Landau wave function for a free electron in a magnetic field.

The formalism should facilitate calculations for which the effective mass formalism is not suitable, such as those involving interband matrix elements.

1. INTRODUCTION

THE PROBLEM of determining the wave function for an electron in a magnetic field moving in a periodic potential—the crystal potential—has been treated by several authors from various points of view. The importance of this question is immediately obvious when we consider the role played by the Fermi surface in present theory, and that the shape of the Fermi surface is often determined experimentally by methods which depend upon the use of a strong magnetic field. Two main avenues have been followed in the investigation of the Bloch electrons in a magnetic field. Some authors have considered the translational properties in the presence of the magnetic field[1], while others have pursued the effective Hamiltonian approach[2–6].

A review of the earlier literature may be found in the paper by Kohn[2] who discusses the different approximations made in these earlier theories. Kohn has derived an effective single-band Hamiltonian with corresponding basis functions, but has not diagonalized the Hamiltonian nor discussed the resulting energy levels or wave functions. It should be acknowledged that the paragraph commencing Section 1.3 of this paper, which concerns the effect of even very weak magnetic fields, indirectly stimulated the approach to be followed here. In brief, the objection to using perturbation theory is simply that the terms considered as a perturbation involve the coordinates. One cannot, therefore, use basis functions which are indefinitely extended in space, as are plane waves and the Bloch wave functions. We have circumvented this difficulty by using functions which involve the harmonic oscillator functions. These are relatively short-ranged in addition to aiding naturally to describe the response of the system to the magnetic field.

Blount[3] has developed a formalism which simplifies Kohn's derivation of the effective Hamiltonian. Spin-orbit effects are included, but the expansion is again to various orders in the magnetic field. The effective Hamiltonian is also derived by Roth[4] and by Wannier and Fredkin[5] who simplify the theory while approaching the same problem from different points of view. As has been pointed out by Chambers[6], it is often useful to have an explicit expression for the wave function of the electron, and this is not available from the previous treatments. In fact, no reported method produces a simple useful expression for the wave function, analogous to the expression for the Bloch wave function itself as the product of the

---

†The research reported in this paper has been sponsored by the National Research Council of Canada.

free electron wave function exp ($i\,\mathbf{k}\cdot\mathbf{r}$) times a periodic modulating function $U_{n\mathbf{k}}(\mathbf{r})$.

It is true that many authors[7] have used the result of the effective mass, or effective Hamiltonian theory, as extended by Luttinger and Kohn[8], and used the wave function $F(\mathbf{r})U_{n0}(\mathbf{r})$ with $F(\mathbf{r})$ satisfying the effective Schrodinger equation

$$\{E_n[-i\nabla+(e/\hbar c)\mathbf{A}(\mathbf{r})]\}F(\mathbf{r})=EF(\mathbf{r}).$$

The energy in the region of the band minimum is given by

$$E=E_0+(N+\tfrac{1}{2})(e\hbar/m^*c)H+\hbar^2k^2/2m^* \qquad (1)$$

with m^* the effective mass, and the eigenfunction is equivalent to the basis function to be introduced in Section 2. However, these results are severely limited. In particular, the derived wave functions should not be used if interband matrix elements[9] are to be taken, nor are they easily extended to non-parabolic bands.

Moreover, as indicated by McLean[10], the variation of the wave function for high Landau states becomes very rapid and the effective mass approximation cannot then be used.

The purpose of this paper is to develop an improvement to the effective mass wave function currently in use. The wave function for a Bloch electron in a magnetic field is obtained as a series expansion

$$\sum_{n,N} a_N{}^n(m,M,k_z)\psi^N_{n\mathbf{k}_\perp}(\mathbf{r})$$

where the functions $\psi^N_{n\mathbf{k}}(\mathbf{r})$ are discussed in Section 2. In Section 3 a perturbation approach is taken to the evaluation of the coefficients in the expansion.

Although the splitting of the Hamiltonian is here dependent upon which basis function is the operand, the standard results of perturbation theory are seen to be valid. The results are only taken to second order, but could be extended to any order, if necessary.

In Section 4 the resulting wave functions are shown to form an orthonomal set (to second order). This of course is merely a confirmation of the results obtained by means of the perturbation method.

The formalism is applicable to semiconductors and may be extended to metals when magnetic breakdown does not occur, when there is no significant coupling between orbits.

2. THE BASIS FUNCTIONS

We seek a solution of the steady state Schrödinger equation for a single electron moving in a periodic potential in the presence of a uniform magnetic field of magnitude H in the direction which we wish to consider as the Z-axis. The Hamiltonian $\mathscr{H}$ for an electron of mass m and charge $-e$ is then given by

$$\mathscr{H}=\frac{1}{2m}\left(\mathbf{P}+\frac{e\mathbf{A}}{c}\right)^2+V(\mathbf{r}) \qquad (2)$$

where $V(\mathbf{r})$ is the periodic potential, and $\mathbf{A}$ is the vector potential associated with the uniform magnetic field $\mathbf{H}$, given by

$$\mathbf{A}=\tfrac{1}{2}\mathbf{H}\times\mathbf{r}. \qquad (3)$$

The physical periodicity of the crystal is unaltered by the presence of the magnetic field. We assume the usual boundary conditions, namely periodicity of a large box of volume V, with linear dimensions L_x, L_y, L_z.

The Schrödinger equation corresponding to (2) is

$$\frac{1}{2m}\left(\mathbf{P}+\frac{e\mathbf{A}}{c}\right)^2\Psi+V(\mathbf{r})\Psi=E\Psi. \qquad (4)$$

The wave function Ψ is to be expanded in terms of the set of basis functions $\psi^N_{n\mathbf{k}_\perp}(\mathbf{r})$ which are defined as follows:

$$\psi^N_{n\mathbf{k}_\perp}(\mathbf{r})=\left(\frac{L_x}{V}\right)^{1/2}e^{i(eH/2c)(xy/\hbar)}\,e^{i\mathbf{k}_\perp\cdot\mathbf{r}}\,U_n(\mathbf{r})\Lambda^N_{k_y}(x), \qquad (5)$$

where $\mathbf{k}_\perp = (o, k_y, k_z)$, restricted to the first Brillouin Zone, and $U_n(\mathbf{r}) \equiv u_{no}(\mathbf{r})$ is the periodic part of the Bloch wave function, defined by

$$\phi_{n\mathbf{k}}(\mathbf{r}) = (V)^{-1/2} u_{n\mathbf{k}}(\mathbf{r}) \exp(i\mathbf{k}\cdot\mathbf{r}) \tag{6}$$

for $\mathbf{k} = 0$, and

$$\Lambda^N_{k_y}(x) \equiv \Lambda^N\left(\frac{x+\lambda^2 k_y}{\lambda}\right) \tag{7}$$

are the harmonic oscillator functions centered at $-\lambda^2 k_y$ for the energy levels specified by the integer N. The quantity $\lambda = (c\hbar/eH)^{1/2}$ has dimensions of length and is the radius of the first cyclotron orbit.

These functions satisfy the following equations:

$$-\hbar^2/2m\nabla^2 U_n(\mathbf{r}) + V(\mathbf{r}) U_n(\mathbf{r}) = \epsilon_{no} U_n(\mathbf{r}) \tag{8}$$

where ϵ_{no} is the energy of the n th Bloch band at $\mathbf{k} = 0$, and

$$-\frac{\hbar^2}{2m}\frac{\mathrm{d}^2}{\mathrm{d}x^2}\Lambda^N_{k_y}(x) + \frac{1}{2m}(\hbar k_y + m\omega_c x)^2 \Lambda^N_{k_y}(x) = E^N \Lambda^N_{k_y}(x), \tag{9}$$

where the cyclotron frequency ω_c is defined by

$$\omega_c = eH/mc = \hbar/m\lambda^2 \tag{10}$$

and the energy of the Nth Landau[11] level is

$$E^N = (N+\tfrac{1}{2})\hbar\omega_c. \tag{11}$$

These functions satisfy the following orthogonality relations:

$$V^{-1}\int \mathrm{d}^3\mathbf{r}\, U_{n'}(\mathbf{r}) U_n(\mathbf{r}) = \delta_{nn'} \tag{12}$$

and

$$\int \mathrm{d}x \Lambda^N_{k_y}(x) \Lambda^{N'}_{k_y}(x) = \delta^{NN'}. \tag{13}$$

The basis functions so defined form a complete orthonormal set, subject to the approximation discussed below. We consider the orthogonality integral

$$\begin{aligned} I &= \int \mathrm{d}^3\mathbf{r}\, \psi^{*N'}_{n'\mathbf{k}'_\perp}(\mathbf{r}) \psi^N_{nk_\perp}(\mathbf{r}) \\ &= (L_x/V)\int \mathrm{d}^3\mathbf{r} \exp[i(\mathbf{k}_\perp - \mathbf{k}'_\perp)\cdot\mathbf{r}] U_{n'}(\mathbf{r}) U_n(\mathbf{r}) \\ &\quad \times \Lambda^{N'}_{k'_y}(x)\Lambda^N_{k_y}(x). \end{aligned} \tag{14}$$

Define $\mathbf{q}_\perp$ by the relation $\mathbf{k}'_\perp = \mathbf{k}_\perp + \mathbf{q}_\perp$ and Fourier-analyze the product function

$$\begin{aligned} \Lambda^{N'}_{k'_y}(x)\Lambda^N_{k_y}(x) &\equiv P^{N'N}_{q_y k_y}(x) \\ &= \sum_{q_x} P^{N'N}_{q_y k_y}(q_x) \exp[-iq_x x] \end{aligned} \tag{15}$$

so that upon substitution into equation (14) we obtain

$$\begin{aligned} I = (L_x/V) \sum_{q_x} P^{N'N}_{q_y k_y}(q_x) \int \mathrm{d}^3\mathbf{r} \exp[-i\mathbf{q}\cdot\mathbf{r}] \\ \times U_{n'}(\mathbf{r}) U_n(\mathbf{r}). \end{aligned} \tag{16}$$

We now make use of the periodicity of the functions $U_n(\mathbf{r})$ and write within the integral $\mathbf{r} = \mathbf{r}' + \mathbf{R}_n$ where $\mathbf{R}_n$ is a translation vector of the lattice joining the point $\mathbf{r}$ to the corresponding point $\mathbf{r}'$ within an arbitrarily chosen fundamental unit cell of the crystal. The integral over the crystal can now be written as the sum of integrals over the unit cell, and we obtain

$$\begin{aligned} I &= (L_x/V) \sum_{q_x} P^{N'N}_{q_y k_y}(q_x) \sum_{\mathbf{R}_n} \exp[-i\mathbf{q}\cdot\mathbf{R}_n] \\ &\quad \times \int_0 \mathrm{d}^3\mathbf{r}' \exp[-i\mathbf{q}\cdot\mathbf{r}'] U_{n'}(\mathbf{r}') U_n(\mathbf{r}') \\ &= (L_x/V) \sum_{q_x} P^{N'N}_{q_y k_y}(q_x) N \delta_{q0} \int_0 \mathrm{d}^3\mathbf{r}'\, U_{n'}(\mathbf{r}') U_n(\mathbf{r}') \\ &= (L_x/V) P^{N'N}_{0k_y}(O) \delta_{\mathbf{q}_\perp 0} \int \mathrm{d}^3\mathbf{r}\, U_{n'}(\mathbf{r}) U_n(\mathbf{r}) \\ &= \delta_{n'n} \delta_{\mathbf{q}_\perp 0} \int \mathrm{d}x P^{N'N}_{q_y k_y}(x) \end{aligned}$$

or

$$\int \mathrm{d}^3\mathbf{r}\, \psi^{*N'}_{n'\mathbf{k}'_\perp}(\mathbf{r}) \psi^N_{n\mathbf{k}_\perp}(\mathbf{r}) = \delta^{N'N} \delta_{n'n} \delta_{\mathbf{k}'_\perp \mathbf{k}_\perp} \tag{17}$$

where we have made use of the inverse transformation to equation (15), as well as the orthogonality and normalization of both the Bloch wave functions and the oscillator functions.

To obtain the above result, we have kept only the dominant term in the expression. The other terms will now be considered. The sum

$$\sum_{\mathbf{R}_n} \exp(i\mathbf{q}\cdot\mathbf{R}_n) = N\Delta_{\mathbf{q}0} \tag{18}$$

where $\Delta_{\mathbf{q}0}$ is a crystalline δ-function which vanishes unless $\mathbf{q} = \mathbf{K}_n$, where $\mathbf{K}_n$ is a vector of the reciprocal lattice, in which case it is unity[4]. In order to obtain equation (17) we have considered only the term with $\mathbf{q} = 0$. The other terms, corresponding to values $\mathbf{q} = \mathbf{K}_n$, $q_x = Q_x$, give values which depend upon the value of

$$P^{N'N}_{0\mathbf{k}_y}(Q_x) = (L_x)^{-1} \int \mathrm{d}x \exp[iQ_x x]\Lambda^{N'}_{k_y}(x)\Lambda^{N}_{k_y}(x).$$

We restrict q_y to the value zero since it, by definition, must be within the first Brillouin zone. There is no such restriction on $\mathbf{q}_x$ since it arises from the Fourier expansion.

Integrals of this type have been considered in Appendix *A*, with the result that

$$P^{N'N}_{0k_y}(Q_x) = (L_x)^{-1} \exp[-i\lambda^2 Q_x k_y] Q_{N'N}(Q_x)$$

where the $Q_{N'N}(Q_x)$ can be related to the associated Laguerre polynomials, as is seen in the equations (A.7). Thus the function $P^{N'N}_{0k_y}(Q_x)$ is related to the radial dependence of the hydrogen atom wave function. Using the notation of Slater[12] where these are denoted by $P_{nl}(\mathrm{r})$ with the normalization

$$\int_0^\infty [P_{nl}(r)]^2 \,\mathrm{d}r = 1$$

we have, apart from constant and oscillating factors,

$$P^{N'N}_{0k_y}(Q_x) = \xi^{-(l+1/2)} P_{nl}(\xi)$$

where $\xi = \lambda^2 Q_x{}^2/2$, and we have made the correspondence $N = n + l$, and $N' - N = 2l + 1$.

Moreover, the maximum value of N is restricted by the maximum energy attainable by the particles, as governed by an equation similar to equation (1).

The value of ξ for representative crystals is seen to be a significant factor greater than the maximum value of N. For energy difference of 10 eV and lattice spacing 2 Å, for lowest value of Q_x and $m/m^* = 10$, we find that the ratio is about 50 : 1. Thus, for the lowest value of ξ concerned we are still far beyond the significant region of the wave function. Moreover, we also have the factor $\xi^{-(l+1/2)}$ which decreases the value even further. We conclude that the equation (17) holds and that the basis functions do form an orthonormal set. Their orthogonality is assumed when they are taken as the eigenfunctions of the effective Hamiltonian[7].

It is shown in Appendix C that these functions form a complete set, with the sum over N going up to $N = \infty$.

The previous argument may not be valid for much larger values of N, but the departure from orthogonality would occur only when the difference $N - N'$ is small. We will proceed as if all the basis functions are orthogonal, with the following justification.

One of the results of Section 3 is that the coefficients corresponding to these larger values of N are of no interest, being negligible. Formally, a Schmidt orthogonalization could be carried out, mixing the higher values of N. This would then alter the higher coefficients, but these will never enter into a calculation.

3. PERTURBATION APPROACH

We will now investigate the result of operating with the Hamiltonian on the basis function $\psi^N_{n\mathbf{k}}(\mathbf{r})$ defined by equation (5). This function involves some magnetic field dependence in addition to a modulating factor with the periodicity of the crystal lattice. It is the combination of these two properties which will enable us to fruitfully expand the eigenfunctions of the Hamiltonian in terms of this set of basis functions.

Since the magnetic field is assumed to act in the Z-direction the Hamiltonian becomes, upon combining equations (2) and (3):

$$\mathscr{H}=-\frac{\hbar^2}{2m}\nabla^2-\frac{ie\hbar}{2mc}H\left(x\frac{\partial}{\partial y}-y\frac{\partial}{\partial x}\right)+\frac{H^2e^2}{8mc^2}(x^2+y^2)+V(\mathbf{r}). \qquad (19)$$

The exponentials can be passed through the operator and we obtain

$$\mathscr{H}\psi^N_{n\mathbf{k}_\perp}(\mathbf{r})=(L_x/V)^{1/2}\exp\left\{\frac{ieH}{2c}\frac{xy}{\hbar}+i\mathbf{k}_\perp\cdot\mathbf{r}\right\}\times\mathscr{H}^{(1)}U_{n0}(\mathbf{r})\Lambda^N_{k_y}(x) \qquad (20)$$

where

$$\mathscr{H}^{(1)}\equiv-\hbar^2/2m\nabla^2+(\hbar k_y+m\omega_c x)^2/2m+V(\mathbf{r})-i\hbar^2/m(k_y\partial/\partial y+k_z\partial/\partial z)-i\hbar\omega_c x\partial/\partial y+\hbar^2k_z{}^2/2m. \qquad (21)$$

We now make use of the defining relations (8) and (9) to obtain:

$$\begin{aligned}\mathscr{H}^{(1)}U_n(\mathbf{r})\Lambda^N_{k_y}(x)=&\left\{\epsilon_{n0}+\frac{\hbar^2k_z{}^2}{2m}+(N+\tfrac{1}{2})\hbar\omega_c\right\}U_n(\mathbf{r})\Lambda^N_{k_y}(x)\\&-\frac{\hbar^2}{m}\frac{\partial U_n(\mathbf{r})}{\partial x}\frac{\mathrm{d}\Lambda^N_{k_y}(x)}{\mathrm{d}x}-i\hbar\omega_c x\Lambda^N_{k_y}(x)\frac{\partial U_n(\mathbf{r})}{\partial y}.\\&-\frac{i\hbar^2}{m}\left(k_y\frac{\partial U_n(\mathbf{r})}{\partial y}+k_z\frac{\partial U_n(\mathbf{r})}{\partial z}\right)\Lambda^N_{k_y}(x),\end{aligned} \qquad (22)$$

Thus we could write

$$\mathscr{H}\psi^N_{n\mathbf{k}_\perp}(\mathbf{r})=(H_0+H'^N_n)\psi^N_{n\mathbf{k}_\perp}(\mathbf{r}), \qquad (23)$$

where we define

$$\begin{aligned}H_0\psi^N_{n\mathbf{k}_\perp}(\mathbf{r})&=\{\epsilon_{n0}+\hbar^2k_z{}^2/2m+(N+\tfrac{1}{2})\hbar\omega_c\}\psi^N_{n\mathbf{k}_\perp}(\mathbf{r})\\&\equiv E^N_{nk_z}\psi^N_{n\mathbf{k}_\perp}(\mathbf{r}),\end{aligned} \qquad (24)$$

and

$$\begin{aligned}H'^N_n\psi^N_{n\mathbf{k}_\perp}(\mathbf{r})=&\left(\frac{L_x}{V}\right)^{1/2}\mathrm{e}^{i(eH/2c)(xy/\hbar)}\,\mathrm{e}^{i\mathbf{k}_\perp\cdot\mathbf{r}}\\&\times\left\{-\frac{\hbar^2}{m}\frac{\partial U_n(\mathbf{r})}{\partial x}\frac{\mathrm{d}\Lambda^N_{k_y}(x)}{\mathrm{d}x}\right.\\&-\frac{i\hbar^2}{m}\Lambda^N_{k_y}(x)\mathbf{k}_\perp\cdot\nabla U_n(\mathbf{r})\\&\left.-i\hbar\omega_c x\Lambda^N_{k_y}(x)\frac{\partial U_n(\mathbf{r})}{\partial y}\right\},\end{aligned} \qquad (25)$$

Although the Hamiltonian $\mathscr{H}$ does not actually separate into these two parts until it operates on the function $\psi^N_{n\mathbf{k}_\perp}(\mathbf{r})$, equations (23–25) can still be used in a modified form of perturbation theory. This is shown below, where it is seen that the dependence of the operator division on the operand does not interfere with the formal derivation of the standard results of perturbation theory.

We consider the 'perturbed' part of the Hamiltonian to be linear in a variation parameter γ which will eventually be put equal to unity. This procedure enables us to evaluate the expansion coefficients.

We write,

$$\mathscr{H}\psi^N_{n\mathbf{k}_\perp}(\mathbf{r})=H_0\psi^N_{n\mathbf{k}_\perp}(\mathbf{r})+\gamma H'^N_n\psi^N_{n\mathbf{k}_\perp}(\mathbf{r}) \qquad (26)$$

with H_0 and H'^N_n defined by equations (24) and (25). We now put

$$\psi=\psi_0+\gamma\psi_1+\gamma^2\psi_2+\dots. \qquad (27a)$$

$$E=W_0+\gamma W_1+\gamma^2W_2+\dots. \qquad (27b)$$

The functions ψ_l are then expanded in terms of the basis functions in the form,

$$\psi_l=\sum_{n,N}a^{ln}_N\psi^N_{n\mathbf{k}_\perp}(\mathbf{r}) \qquad (28)$$

where we have temporarily suppressed the **k** dependence of the coefficients. We now substitute into equation (4) to obtain:

$$\mathscr{H}\sum_{n,N,l}\gamma^{(l)}a^{ln}_N\psi^N_{n\mathbf{k}_\perp}=\left(\sum_j W_j\gamma^{(j)}\right)\sum_{n,N,l}\gamma^{(l)}a^{ln}_N\psi^N_{n\mathbf{k}}$$

where $\gamma^{(i)}$ is γ raised to the power i. Using equation (26) this becomes

$$\sum_{n,N,i} \gamma^{(i)} a_N^{in}(H_0\psi^N_{nk_\perp} + \gamma H'^N_n \psi^N_{nk_\perp}) = \sum_{i,j,n,N} \gamma^{(i+j)} W_j a_N^{in} \psi^N_{nk_\perp}. \qquad (29)$$

Equating equal powers of γ in equation (29) and using the orthogonality of the basis functions, we have the standard results, which we express in terms of the bracket notation

$$\langle Kk\mathbf{k}'_\perp | H'^M_m | Mm\mathbf{k}_\perp\rangle \equiv \int \psi^{*K}_{k\mathbf{k}'_\perp} H'^M_m \psi^M_{m\mathbf{k}_\perp} \,\mathrm{d}^3\mathbf{r}. \qquad (30)$$

Investigation of these in Appendix B leads to the conclusion that the only non-zero matrix elements of H′ are the following:

$$\langle Nm\mathbf{k}_\perp | H'^N_n | Nn\mathbf{k}_\perp\rangle = -\frac{i\hbar^2}{m} k_z \left(U_m \middle| \frac{\partial U_n}{\partial z}\right)$$

$$\langle N+1, m, \mathbf{k}_\perp | H'^N_n | Nn\mathbf{k}_\perp\rangle = \frac{\hbar^2}{m\lambda}\left(\frac{N+1}{2}\right)^{1/2}\left(U_m \middle| \frac{\partial U_n}{\partial x} - i\frac{\partial U_n}{\partial y}\right)$$

and

$$\langle N-1, m, \mathbf{k}_\perp | H'^N_n | Nn\mathbf{k}_\perp\rangle = -\frac{\hbar^2}{m\lambda}\left(\frac{N}{2}\right)^{1/2}\left(U_m \middle| \frac{\partial U_n}{\partial x} + i\frac{\partial U_n}{\partial y}\right)$$

where

$$\left(U_m \middle| \frac{\partial U_n}{\partial \mathbf{r}_i}\right) = V^{-1}\int U_m(\mathbf{r}) \frac{\partial U_n(\mathbf{r})}{\partial \mathbf{r}_i}\,\mathrm{d}^3\mathbf{r}. \qquad (31)$$

We also find that it is not necessary to carry the indices on H′, since it is always true that

$$\langle Nn\mathbf{k}_\perp | H'^M_m | Mm\mathbf{k}_\perp\rangle = \langle Mm\mathbf{k}_\perp | H'^N_n | Nn\mathbf{k}_\perp\rangle^*$$

The results to second order are summarized below. We denote the state specified by m, M as $\Psi^M_{m\mathbf{k}}(\mathbf{r})$. We have

$$\Psi^M_{m\mathbf{k}_\perp} = \sum_{n,N,i} a_N^{in}(m, M, k_z)\, \psi^N_{n\mathbf{k}_\perp} \qquad (32)$$

with energy to second order given by

$$W = W_0 + W_2$$

where

$$W_0 = E^M_{mk_z} = \epsilon_{m0} + \frac{\hbar^2 k_z{}^2}{2m} + (M + \tfrac{1}{2})\hbar\omega_c \qquad (33a)$$

$$W_2 = \sum_{n,N}{}' \frac{\langle Mm\mathbf{k}_\perp | H' | Nn\mathbf{k}_\perp\rangle \langle Nn\mathbf{k}_\perp | H' | Mm\mathbf{k}_\perp\rangle}{E^M_{mk_z} - E^N_{nk_z}} \qquad (33b)$$

and the coefficients are given by

$$a_N^{on}(m, M) = \delta_{mn}\delta^{MN}$$

$$a_K^{1k}(m, M, k_z) = \frac{\langle Kk\mathbf{k}_\perp | H' | Mm\mathbf{k}_\perp\rangle}{E^M_{mk_z} - E^K_{kk_z}}$$

$$a_K^{2k}(m, M, k_z) = \sum_{n,N}{}' \frac{\langle Kk\mathbf{k}_\perp | H' | Nn\mathbf{k}_\perp\rangle \langle Nn\mathbf{k}_\perp | H' | Mm\mathbf{k}_\perp\rangle}{(E^M_{mk_z} - E^N_{nk_z})(E^M_{mk_z} - E^K_{kk_z})}$$

and

$$a_M^{2m}(m, M, k_z) = -\frac{1}{2}\sum_{n,N}{}' \frac{|\langle Nn\mathbf{k}_\perp | H' | Mm\mathbf{k}_\perp\rangle|^2}{(E^M_{mk_z} - E^N_{nk_z})^2} \qquad (34)$$

These coefficients, together with the non-zero matrix elements of H', are seen to allow the difference K-M to have the maximum value i. For the perturbation approach to be successful, i will take on only small values. Thus K will remain in the neighbourhood of M, and is correctly restricted by the energy considerations of Section 2.

It is seen in the following section that the wave functions obtained with these coefficients do form an orthonormal set.

4. ORTHONORMALITY OF THE WAVE FUNCTIONS

We wish to examine here the orthogonality of the wave functions $\Psi^M_{m\mathbf{k}_\perp}(\mathbf{r})$, defined by equation (32) with coefficients to second order given by equations (34). We consider the integral

$$\int \mathrm{d}^3\mathbf{r}\Psi^{*M'}_{m\mathbf{k}_\perp}\Psi^{M}_{m\mathbf{k}_\perp}$$

$$= \sum_{l,l',n,n',N,N'} a^{*l'n'}_{N'}(m', M', k_z')\, a^{ln}_{N}(m, M, k_z)$$

$$\times \int \mathrm{d}^3\mathbf{r}\psi^{*N'}_{n'\mathbf{k}'_\perp}\psi^{N}_{n\mathbf{k}_\perp}$$

$$= \sum_{l,l',n,N} a^{*l'n}_{N}(m', M', k_z)\, a^{ln}_{N}(m, M, k_z)\delta_{\mathbf{k}_\perp\mathbf{k}'_\perp} \quad (35)$$

We will expand this expression to second order only. We are merely confirming the results of Section 3, as summarized by equations (34). If the investigation there had been carried to higher order, we could do so here as well. Consider the sum

$$\sum_{l,l',n,N} a^{*l'n}_{N}(m', M', k_z)a^{ln}_{N}(m, M, k_z) = \delta_{mm'}\delta^{MM'}$$

$$+ [a^{1m'}_{M'}(m, M, k_z) + a^{*1m}_{M}(m', M', k_z)]$$

$$+ [a^{2m'}_{M'}(m, M, k_z) + a^{*2m}_{M}(m', M', k_z)$$

$$+ \sum_{n,N} a^{*1n}_{N}(m'\, M'\, k_z)\, a^{1n}_{N}(m, M, k_z)]$$

$$= \delta_{mm'}\delta^{MM'} \quad (36)$$

where we have used equations (34) and have anticipated the results given below. We have from equation (34) using equation (B. 12)

$$a^{1m'}_{M'}(m, M, k_z) + a^{*1m}_{M}(m', M', k_z) =$$

$$\frac{\langle M'm'\mathbf{k}_\perp|H'|Mm\mathbf{k}_\perp\rangle}{E^{M}_{mk_z} - E^{M'}_{m'k_z}} + \frac{\langle Mm\mathbf{k}_\perp|H'|M'm'\mathbf{k}_\perp\rangle^*}{E^{M'}_{m'k_z} - E^{M}_{mk_z}}$$

$$= 0.$$

The remaining term leading to (36) becomes:

$$a^{2m'}_{M'}(m, M, k_z) + a^{*2m}_{M}(m', M', k_z)$$

$$+ \sum_{n,N} a^{*1n}_{N}(m', M', k_z)\, a^{1n}_{N}(m, M, k_z)$$

$$= \sum_{n,N}{}' \frac{\langle M'm'\mathbf{k}_\perp|H'|Nn\mathbf{k}_\perp\rangle\langle Nn\mathbf{k}_\perp|H'|Mm\mathbf{k}_\perp\rangle}{(E^{M}_{mk_z} - E^{N}_{nk_z})(E^{M}_{mk_z} - E^{M'}_{m'k_z})}$$

$$+ \frac{\langle Mm\mathbf{k}_\perp|H'|Nn\mathbf{k}_\perp\rangle \cdot \langle Nn\mathbf{k}_\perp|H'|M'm'\mathbf{k}_\perp\rangle^*}{(E^{M'}_{m'k_z} - E^{N}_{nk_z})(E^{M'}_{m'k_z} - E^{M}_{mk_z})}$$

$$+ \frac{\langle Nn\mathbf{k}_\perp|H'|M'm'\mathbf{k}_\perp\rangle^*\langle Nn\mathbf{k}_\perp|H'|Mm\mathbf{k}_\perp\rangle}{(E^{M'}_{m'k_z} - E^{N}_{nk_z})(E^{M}_{mk_z} - E^{N}_{nk_z})}$$

$$= \sum_{n,N}{}' \frac{F}{(E^{M}_{mk_z} - E^{N}_{nk_z})(E^{M'}_{m'k_z} - E^{N}_{nk})(E^{M}_{mk_z} - E^{M'}_{m'k_z})}$$

where we have defined

$$F = (E^{M'}_{m'k_z} - E^{M}_{mk_z})\langle M'm'\mathbf{k}_\perp|H'|Nn\mathbf{k}_\perp\rangle$$

$$\times \langle Nn\mathbf{k}_\perp|H'|Mm\mathbf{k}_\perp\rangle - (E^{M}_{mk_z} - E^{N}_{nk_z})$$

$$\times \langle Mm\mathbf{k}_\perp|H'|Nn\mathbf{k}_\perp\rangle$$

$$\times \langle Nn\mathbf{k}_\perp|H'|M'm'\mathbf{k}_\perp\rangle$$

$$+ (E^{M}_{mk_z} - E^{M'}_{m'k_z})\langle Nn\mathbf{k}_\perp|H'|M'm'\mathbf{k}_\perp\rangle$$

$$\times \langle Nn\mathbf{k}_\perp|H'|Mm\mathbf{k}_\perp\rangle$$

$$= E^{M'}_{m'k_z}\langle Nn\mathbf{k}_\perp|H'|Mm\mathbf{k}_\perp\rangle$$

$$\times [\langle M'm'\mathbf{k}_\perp|H'|Nn\mathbf{k}_\perp\rangle$$

$$- \langle Nn\mathbf{k}_\perp|H'|M'm'\mathbf{k}_\perp\rangle\ ]$$

$$+ E^{M}_{mk_z}\langle Nn\mathbf{k}_\perp|H'|M'm'\mathbf{k}_\perp\rangle$$

$$\times [\langle Nn\mathbf{k}_\perp|H'|Mm\mathbf{k}_\perp\rangle$$

$$- \langle Mm\mathbf{k}_\perp|H'|Nn\mathbf{k}_\perp\rangle^*]$$

$$+ E^{N}_{nk_z}[\langle Mm\mathbf{k}_\perp|H'|Nn\mathbf{k}_\perp\rangle$$

$$\times \langle Nn\mathbf{k}_\perp|H'|M'm'\mathbf{k}_\perp\rangle$$

$$- \langle M'm'\mathbf{k}_\perp|H'|Nn\mathbf{k}_\perp\rangle$$

$$\times \langle Nn\mathbf{k}_\perp|H'|Mm\mathbf{k}_\perp\rangle]$$

$$= 0.$$

We have used equation (B.12) to obtain the final result.

Thus we have confirmed equation (36) which gives upon substitution into equation (35) the desired result:

$$\int \mathrm{d}^3\mathbf{r}\Psi^{*M'}_{m'\mathbf{k}_\perp}(\mathbf{r})\Psi^{M}_{m\mathbf{k}_\perp}(\mathbf{r}) = \delta_{m'm}\delta^{M'M}_{m\mathbf{k}_\perp}\delta_{\mathbf{k}'\ \mathbf{k}_\perp}.$$

5. SUMMARY

We have obtained an expression for the Bloch wave function in a magnetic field which should facilitate various calculations. The derivation is valid regardless of the shape of the energy bands, as long as the band extrema are at the origin of k-space. This restriction should present no difficulties, and in a succeeding paper the formalism will be generalized for any position of the extrema. When applied to parabolic bands, the results are comparable to the accepted ones. In a following paper it will be demonstrated that the energy levels are just those in use, a generalization of equation (1), but the wavefunctions are more complicated, valid for calculations involving inter-band matrix elements. The application to crossed electric and magnetic fields can also be handled by this method, and the derivation of the longitudinal dielectric constant follows easily.

In a recent paper Miller and Kwok [13] have calculated the effect of the periodic potential on helicon attenuation using the effective-mass approximation. The large quantum oscillations arising from $\Delta N = 0$ transitions can easily be obtained with the wave functions developed in this paper, and calculations are in progress.

REFERENCES

1 BROWN E., *Phys Rev.* **133**, A1038 (1964); HARPER P. G , *J. Phys. Chem. Solids* **28**, 495 (1967), PRADDAUDE H. C., *Phys. Rev.* **140**, A1292 (1965); WANNIER G. H., *Rev. Mod Phys.* **34**, 645 (1962). ZAK J , *Phys. Rev. Lett.* **19**, 1385 (1967), *Phys Rev.* **139**, A1159 (1965).
2. KOHN W , *Phys Rev.* **115**, 1460 (1959).
3. BLOUNT E. I , *Phys. Rev.* **126**, 1636 (1962).
4. ROTH L., *J Phys. Chem. Solids* **23**, 433 (1962).
5 WANNIER G. H. and FREDKIN D. R., *Phys. Rev* **125**, 1910 (1962)
6. CHAMBERS R. G., *Proc. phys. Soc.* **89**, 695 (1966).
7. DRESSELHAUS M S. and DRESSELHAUS G., *Phys Rev* **125**, 499 (1962).
8 LUTTINGER J M. and KOHN W., *Phys Rev.* **97**, 869 (1955).
9 SMITH A. C , JANAK J. F. and ADLER R. B , In *Electronic Conduction in Solids*. McGraw-Hill, New York (1966).
10 McLEAN T P., In *Proceedings of the International School of Physics 'Enrico Fermi' Course XXII. Semiconductors* (Edited by R. A. Smith), p. 479. Academic Press, New York (1963).
11. LANDAU L., *Z. Phys.* **64**, 629 (1930).
12 SLATER J. C , In *Quantum Theory of Atomic Structure*, Vol. I. McGraw-Hill, New York (1960).
13. MILLER P. B. and KWOK P. C., *Phys. Rev.* **161**, 629 (1967).
14. SCHIFF L. E., In *Quantum Mechanics*. McGraw-Hill, New York (1955).

APPENDIX A

We wish to evaluate

$$P^{N'N}_{0k_y}(Q_x) \equiv (L_x)^{-1} \int \mathrm{d}x \exp(iQ_x x)\Lambda^{N'}_{k_y}(x)\Lambda^{N}_{k_y}(x)$$

We must therefore use the explicit form of the oscillator functions which are known [14] to be

$$\Lambda^N\left(\frac{x+\lambda^2 k_y}{\lambda}\right) = N_N H_N\left(\frac{x+\lambda^2 k_y}{\lambda}\right)\exp\left\{-\frac{1}{2}\left(\frac{x+\lambda^2 k_y}{\lambda}\right)^2\right\}, \tag{A.1}$$

where $H_N(\zeta)$ is the Hermite polynomial of order N, and N_N is the normalization constant given by

$$N_N = (\pi^{1/2} 2^N N! \lambda)^{-1/2}.$$

We can, without error, take the limits of the integral to be from $-\infty$ to $+\infty$ and we have

$$P^{N'N}_{0k_y}(Q_x) = \frac{N_N N_{N'}}{L_x} \int_{-\infty}^{\infty} \mathrm{d}x\, e^{iQ_x x} e^{-((x+\lambda^2 k_y)/\lambda)^2} \times H_{N'}\left(\frac{x+\lambda^2 k_y}{\lambda}\right) H_N\left(\frac{x+\lambda^2 k_y}{\lambda}\right) \tag{A.2}$$

We now make use of the generating function for the Hermite polynomials, $H_n(Z)$, namely the relation

$$\exp(-t^2 + 2tZ) = \sum_{N=0} H_N(Z) t^N/N! \tag{A.3}$$

and we obtain, from equation (A.2)

$$L_x \sum_{N,N'=0}^{\infty} \frac{P^{N'N}_{0k_y}(Q_x)}{N_N N_{N'}} \frac{t^{N'}}{N'!} \frac{S^N}{N!} = \sum_{N,N'=0}^{\infty} \int_{-\infty}^{\infty} \mathrm{d}x \left\{ e^{iQ_x x} e^{-((x+\lambda^2 k_y)/\lambda)^2} \times \frac{t^{N'}}{N'!} H_{N'}\left(\frac{x+\lambda^2 k_y}{\lambda}\right) \frac{S^N}{N!} H_N\left(\frac{x+\lambda^2 k_y}{\lambda}\right)\right\}.$$

Let $Z = (x+\lambda^2 k_y)/\lambda$, $\bar{Q}_x = \lambda Q_x$, $\bar{k}_y = \lambda k_y$ so that we now have with the help of equation (A.3)

$$\begin{aligned} L_x \sum_{N,N'=0}^{\infty} \frac{P^{N'N}_{0k_y}(Q_x)}{N_{N'} N_N} \frac{t^{N'}}{N'!} \frac{S^N}{N!} &= \int_{-\infty}^{\infty} \mathrm{d}x\, e^{i\bar{Q}_x x} e^{-Z^2} e^{-t^2+2tZ} e^{-S^2+2SZ} \\ &= \lambda \int_{-\infty}^{\infty} \mathrm{d}Z\, e^{i\bar{Q}_x(Z-\bar{k}_y)} e^{-Z^2} e^{-S^2-t^2+2Z(S+t)} \\ &= \lambda e^{-i\bar{Q}_x \bar{k}_y} e^{-1/4\bar{Q}_x^2} e^{i\bar{Q}_x(S+t)} e^{2tS} \\ &\quad \times \int_{-\infty}^{\infty} \mathrm{d}Z\, e^{-\{Z-(t+S+i\bar{Q}_x/2)\}^2}. \end{aligned} \tag{A.4}$$

However we know that $\int_{-\infty}^{\infty} \exp(-Z^2)\,\mathrm{d}Z = \pi^{1/2}$ and we can show by a simple contour integration that:

$$\int_{-\infty}^{\infty} \exp(-Z^2)\,\mathrm{d}Z = \int_{-\infty}^{\infty} \exp\{-(Z-a+ib)^2\}\,\mathrm{d}Z$$

so that the equation (A.4) becomes

$$\sum_{N,N'=0}^{\infty} \frac{L_x P^{N'N}_{0k_y}(Q_x)}{N_{N'} N_N} \frac{t^{N'}}{N'!} \frac{S^N}{N!} = \pi^{1/2} \lambda e^{-i\bar{Q}_x \bar{k}_y} e^{-1/4\bar{Q}_x^2} e^{i\bar{Q}_x(S+t)} e^{2tS}. \tag{A.5}$$

We now expand the last three exponentials into a sum of the form $\sum_{N,N'} B_{N'N} t^{N'} S^N$, whereupon we can equate the coefficients of corresponding powers of S and t on both sides of the equation.

There results

$$P^{N'N}_{0k_y}(Q_x) = (L_x)^{-1}\exp(-i\lambda^2 Q_x k_y)Q_{N'N}(Q_x) \quad \text{(A.6)}$$

where we define

$$Q_{N'N}(Q_x) = e^{-1/4\lambda^2 Q_x^2}\left[\frac{N'!N!}{2^{N'}2^N}\right]^{1/2} \times \sum_{l=0}^{[N,N']} \frac{2^l(-1)^{N-l}(-1)^{N'-l}(i\bar{Q}_x)^{N+N'-2l}}{(N-l)!(N'-l)!l!}.$$

The sum over l goes up to $[N,N']$, the smaller of N,N'. The sum can be related to the associated Laguerre polynomials $L_n{}^a$ as follows: For $N' > N$, we have

$$Q_{N'N}(Q_x) = \left(\frac{N!}{N'!}\right)^{1/2} e^{-1/4\lambda^2 Q_x^2}\left(\frac{i\lambda Q_x}{2^{1/2}}\right)^{N'-N} L_N^{N'-N}\left(\frac{\lambda^2 Q_x{}^2}{2}\right), \quad \text{(A.7a)}$$

whereas, for $N > N'$ we have

$$Q_{N'N}(Q_x) = \left(\frac{N'!}{N!}\right)^{1/2} e^{-1/4\lambda^2 Q_x^2}\left(\frac{i\lambda Q_x}{2^{1/2}}\right)^{N-N'} L_{N'}^{N-N'}\left(\frac{\lambda^2 Q_x{}^2}{2}\right), \quad \text{(A.7b)}$$

and for $N = N'$

$$Q_{NN}(Q_x) = e^{-1/4\lambda^2 Q_x^2} L_N\left(\frac{\lambda^2 Q_x{}^2}{2}\right), \quad \text{(A.7c)}$$

APPENDIX B: THE MATRIX ELEMENTS

We wish to evaluate the matrix element $\langle Mm\mathbf{k}'_\perp|H'n^N|Nn\mathbf{k}_\perp\rangle$ and to determine some of its properties. According to equation (25)

$$H'^N_n\psi^N_{n\mathbf{k}_\perp} = \left(\frac{Lx}{V}\right)^{1/2} e^{i(eH/2c)(xy/\hbar)}e^{i\mathbf{k}_\perp\cdot\mathbf{r}} \times\left\{-\frac{\hbar^2}{m}\frac{\partial U_n(\mathbf{r})}{\partial x}\frac{d\lambda^N_{k_y}(x)}{dx} - i\hbar\omega_c x\lambda^N_{k_y}(x)\frac{\partial U_n(\mathbf{r})}{\partial y} - \frac{i\hbar^2}{m}\Lambda^N_{k_y}(x)\mathbf{k}_\perp\cdot\nabla U_n(\mathbf{r})\right\}.$$

We consider separately the three integrals defined by

$$\langle Mm\mathbf{k}'_\perp|H^N_{1n}|Nn\mathbf{k}_\perp\rangle \equiv -\hbar^2/mI_1 \quad \text{(B.1a)}$$

$$\langle Mm\mathbf{k}'_\perp|H^N_{2n}|Nn\mathbf{k}_\perp\rangle \equiv -i\hbar\omega_c I_2 \quad \text{(B.1b)}$$

$$\langle Mm\mathbf{k}'_\perp|H^N_{3n}|Nn\mathbf{k}_\perp\rangle \equiv -i\hbar^2/m\mathbf{k}_\perp\cdot\mathbf{I}_3 \quad \text{(B.1c)}$$

where we have written

$$H'^N_n\psi^N_{n\mathbf{k}_\perp} = (H^N_{1n}+H^N_{2n}+H^N_{3n})\psi^N_{n\mathbf{k}_\perp} \quad \text{(B.2)}$$

and we see that if we define $\mathbf{q}_\perp$ by

$$\mathbf{k}'_\perp = \mathbf{k}_\perp + \mathbf{q}_\perp$$

then it follows that

$$I_1 = (Lx/V)\int d^3\mathbf{r}\exp(-i\mathbf{q}_\perp\cdot\mathbf{r})U_m(\mathbf{r})\frac{\partial U_n(\mathbf{r})}{\partial x} \times \Lambda^M_{k'_y}(x)\frac{d\Lambda^N_{k_y}(x)}{dx}, \quad \text{(B.3a)}$$

$$I_2 = (Lx/V)\int d^3\mathbf{r}\exp(-i\mathbf{q}_\perp\cdot\mathbf{r})U_m(\mathbf{r})\frac{\partial U_n(\mathbf{r})}{\partial y} \times \Lambda^M_{k'_y}(x)\Lambda^N_{k_y}(x), \quad \text{(B.3b)}$$

$$\mathbf{I}_3 = (L_x/V)\int d^3\mathbf{r}\exp(-i\mathbf{q}_\perp\cdot\mathbf{r})U_m(\mathbf{r}) \times\nabla U_n(\mathbf{r})\Lambda^M_{k'_y}(x)\Lambda^N_{k_y}(x) \quad \text{(B.3c)}$$

since both $U_m(\mathbf{r})$ and $\Lambda^N_{k_y}(x)$ are real functions.

Consider a general integral of the type (B.3)

$$I = (L_x/V)\int d^3\mathbf{r}\exp(-i\mathbf{q}_\perp\cdot\mathbf{r})U_m(\mathbf{r})\frac{\partial U_n(\mathbf{r})}{\partial \mathbf{r}_i} \times P^{NM}_{q_yk_y}(x) \quad \text{(B.4)}$$

where $P^{NM}_{q_yk_y}$ is any one of the product functions occuring in the equations (B.3). We follow the same procedure as in Section 2 and Fourier-analyze the function $P^{NM}_{q_yk_y}(x)$:

$$P^{NM}_{q_yk_y}(x) = \sum_{q_x} P^{NM}_{q_yk_y}(q_x)\exp(-iq_xx) \quad \text{(B.5a)}$$

with

$$P^{NM}_{q_yk_y}(q_x) = L_x{}^{-1}\int dx P^{NM}_{q_yk_y}(x)\exp(iq_xx). \quad \text{(B.5b)}$$

We obtain after substitution into equation (B.4)

$$I = (L_x/V)\sum_{q_x} P^{NM}_{q_yk_y}(q_x)\int d^3\mathbf{r}\exp(-i\mathbf{q}\cdot\mathbf{r})U_m(\mathbf{r})\frac{\partial U_n(\mathbf{r})}{\partial \mathbf{r}_i} \quad \text{(B.6)}$$

The function $\partial U_n(\mathbf{r})/\partial \mathbf{r}_i$ is periodic with the same period as $U_n(\mathbf{r})$, so that the transformation to a unit cell is again effective, and we obtain

$$I = \delta_{\mathbf{q}_\perp 0}\left(U_m\left|\frac{\partial U_n}{\partial \mathbf{r}_i}\right.\right)\int P^{NM}_{0k_y}(x)dx \quad \text{(B.7)}$$

where we define

$$\left(U_m\left|\frac{\partial U_n}{\partial \mathbf{r}_i}\right.\right) = V^{-1}\int d^3\mathbf{r}U_m(\mathbf{r})\frac{\partial U_n(\mathbf{r})}{\partial \mathbf{r}_i} \quad \text{(B.8)}$$

The argument required to obtain the result (B.8) is the same as that in Section 2, only the $Q_x = 0$ term will contribute. The function $P^{NM}(q_x)$ is either the same one met in Section 2 or it can be related directly to that one. We see from the equation (B.3) and the result (B.8) that we must now investigate the following three integrals:

$$I^{MN} = \int dx\Lambda^M_{k_y}(x)\Lambda^N_{k_y}(x) \quad \text{(B.9a)}$$

$$I^{MN}_d = \int dx\Lambda^M_{k_y}(x)\frac{d\Lambda^N_{k_y}(x)}{dx}, \quad \text{(B.9b)}$$

$$I^{MN}_x = \int dx\Lambda^M_{k_y}(x)x\Lambda^N_{k_y}(x). \quad \text{(B.9c)}$$

Using the properties of the oscillator functions as discussed in Schiff[13], these become

$$I^{MN} = \delta^{MN}, \quad \text{(B.10a)}$$

$$I^{MN}_d = \lambda^{-1}\left\{\left(\frac{N}{2}\right)^{1/2}\delta^{M,N-1} - \left(\frac{N+1}{2}\right)^{1/2}\delta^{M,N+1}\right\} \quad \text{(B.10b)}$$

$$I^{MN}_x = \lambda\left\{\left(\frac{N}{2}\right)^{1/2}\delta^{M,N-1} + \left(\frac{N+1}{2}\right)^{1/2}\delta^{M,N+1}\right\}. \quad \text{(B.10c)}$$

We are now in a position to write down the value of the matrix elements considered in equations (B.1). These are related to the above results through equations (B.3) (B 7) and (B.9). We first write the equations in the form:

$$\langle Mm\mathbf{k}'_\perp|H^N_{1n}|Nn\mathbf{k}_\perp\rangle = -\frac{\hbar^2}{m}\left(U_m\left|\frac{\partial U_n}{\partial x}\right.\right)I^{MN}_a\delta_{\mathbf{k}'_\perp\mathbf{k}_\perp}$$

$$\langle Mm\mathbf{k}'_\perp|H^N_{2n}|Nn\mathbf{k}_\perp\rangle = -i\hbar\omega_c\left(U_m\left|\frac{\partial U_n}{\partial y}\right.\right)I^{MN}_x\delta_{\mathbf{k}'_\perp\mathbf{k}_\perp}$$

$$\langle Mm\mathbf{k}'_\perp|H^N_{3n}|Nn\mathbf{k}_\perp\rangle = -\frac{i\hbar^2}{m}\mathbf{k}_\perp\cdot(U_m|\nabla U_n)\delta^{MN}\delta_{\mathbf{k}'_\perp\mathbf{k}_\perp}$$

which become, with the help of the equations (B.9)

$$\langle Mm\mathbf{k}'_\perp|H^N_{1n}|Nn\mathbf{k}_\perp\rangle = -\frac{\hbar^2}{m\lambda}\left(U_m\left|\frac{\partial U_n}{\partial x}\right.\right)\times\left\{\left(\frac{N}{2}\right)^{1/2}\delta^{M,N-1}-\left(\frac{N+1}{2}\right)^{1/2}\delta^{M,N+1}\right\}\delta_{\mathbf{k}'_\perp\mathbf{k}_\perp}$$

$$\langle Mm\mathbf{k}'_\perp|H^N_{2n}|Nn\mathbf{k}_\perp\rangle = -i\hbar\omega_c\lambda\left(U_m\left|\frac{\partial U_n}{\partial y}\right.\right)\times\left\{\left(\frac{N+1}{2}\right)^{1/2}\delta^{M,N+1}+\left(\frac{N}{2}\right)^{1/2}\delta^{M,N-1}-k_y\lambda\delta^{MN}\right\}\delta_{\mathbf{k}'_\perp\mathbf{k}_\perp}$$

$$\langle Mm\mathbf{k}'_\perp|H^N_{3n}|Nn\mathbf{k}_\perp\rangle = -\frac{i\hbar^2}{m}\mathbf{k}_\perp\cdot(U_m|\nabla U_n)\delta^{MN}\delta_{\mathbf{k}'_\perp\mathbf{k}_\perp}$$

We recall that $\lambda = (\hbar c/eH)^{1/2}$ and that $\omega_c = eH/mc$ so that $\hbar^2/m\lambda = \hbar\omega_c\lambda = \hbar(e\hbar H/c)^{1/2}/m$. We can now use the defining relation (B 2) along with the above results to isolate the non-zero terms of $\langle Mm\mathbf{k}'_\perp|H'^N_n|Nn\mathbf{k}_\perp\rangle$. The only non-zero matrix elements are found to be.

$$\langle Nm\mathbf{k}_\perp|H'^N_n|Nn\mathbf{k}_\perp\rangle = -\frac{i\hbar^2}{m}\mathbf{k}_z\left(U_m\left|\frac{\partial U_n}{\partial z}\right.\right)$$

$$\langle N+1,m\mathbf{k}_\perp|H'^N_n|Nn\mathbf{k}_\perp\rangle = \frac{\hbar^2}{m\lambda}\left(\frac{N+1}{2}\right)^{1/2}\left(U_m\left|\frac{\partial U_n}{\partial x}-\frac{i\partial U_n}{\partial y}\right.\right)$$

$$\langle N-1,m\mathbf{k}_\perp|H'^N_n|Nn\mathbf{k}_\perp\rangle = -\frac{\hbar^2}{m\lambda}\left(\frac{N}{2}\right)^{1/2}\times\left(U_m\left|\frac{\partial U_n}{\partial x}+\frac{i\partial U_n}{\partial y}\right.\right). \quad \text{(B.11)}$$

We note that as a result of periodocity

$$\left(U_m\left|\frac{\partial U_n}{\partial \mathbf{r}_i}\right.\right) = -\left(U_n\left|\frac{\partial U_m}{\partial \mathbf{r}_i}\right.\right) = 0 \quad \text{if} \quad m = n.$$

It then follows directly that

$$\langle Nn\mathbf{k}_\perp|H'^M_m|Mm\mathbf{k}_\perp\rangle = \langle Mm\mathbf{k}_\perp|H'^N_n|Nn\mathbf{k}_\perp\rangle^*, \quad \text{(B.12)}$$

and therefore we need not maintain the labelling of H' when matrix elements are taken. This result follows when we consider separately each of the possibilities $M = N$, $M = N+1$ and $M = N-1$, as shown below.

(i) $M = N$

$$\begin{aligned}\langle Nn\mathbf{k}_\perp|H'^M_m|Mm\mathbf{k}_\perp\rangle &= -\frac{i\hbar^2}{m}k_z\left(U_n\left|\frac{\partial U_m}{\partial z}\right.\right)\\ &= \frac{i\hbar^2}{m}k_z\left(U_m\left|\frac{\partial U_n}{\partial z}\right.\right)\\ &= \langle Mm\mathbf{k}_\perp|H'^N_n|Nn\mathbf{k}_\perp\rangle^*.\end{aligned}$$

(ii) $M = N+1$

$$\begin{aligned}\langle Nn\mathbf{k}_\perp|H'^M_m|Mm\mathbf{k}_\perp\rangle &= -\frac{\hbar^2}{m\lambda}\left(\frac{N+1}{2}\right)^{1/2}\left(U_n\left|\frac{\partial U_m}{\partial x}+\frac{i\partial U_m}{\partial y}\right.\right)\\ &= \frac{\hbar^2}{m\lambda}\left(\frac{N+1}{2}\right)^{1/2}\left(U_m\left|\frac{\partial U_n}{\partial x}+\frac{i\partial U_n}{\partial y}\right.\right)\\ &= \langle N+1,m\mathbf{k}_\perp|H'^N_n|Nn\mathbf{k}_\perp\rangle^*\\ &= \langle Mm\mathbf{k}_\perp|H'^N_n|Nn\mathbf{k}_\perp\rangle\end{aligned}$$

(iii) $M = N-1$

$$\begin{aligned}\langle Nn\mathbf{k}_\perp|H'^M_m|Mm\mathbf{k}_\perp\rangle &= \frac{\hbar^2}{m\lambda}\left(\frac{N}{2}\right)^{1/2}\left(U_n\left|\frac{\partial U_m}{\partial x}-\frac{i\partial U_m}{\partial y}\right.\right)\\ &= \frac{-\hbar^2}{m\lambda}\left(\frac{N}{2}\right)^{1/2}\left(U_m\left|\frac{\partial U_n}{\partial x}-\frac{i\partial U_n}{\partial y}\right.\right)\\ &= \langle N-1,m\mathbf{k}_\perp|H'^N_n|Nn\mathbf{k}_\perp\rangle^*\\ &= \langle Mm\mathbf{k}_\perp|H'^N_n|Nn\mathbf{k}_\perp\rangle^*.\end{aligned}$$

APPENDIX C: COMPLETENESS OF THE BASIS FUNCTIONS

We wish to demonstrate that the set of basis functions $\psi^N_{n\mathbf{k}_\perp}(\mathbf{r})$ defined by equation (5) are complete i.e. we wish to show that an arbitrary function $f(\mathbf{r})$ can be expanded uniquely in terms of this set in the form

$$f(\mathbf{r}) = \sum_{n,N,\mathbf{k}_\perp} a_N{}^n(\mathbf{k}_\perp)\,\psi^N_{n\mathbf{k}_\perp}(\mathbf{r}). \quad \text{(C.1)}$$

The proof follows. Define the function

$$g(\mathbf{r}) = f(\mathbf{r})\exp(-ieHxy/2c\hbar). \quad \text{(C.2)}$$

Any function $g(\mathbf{r})$ can be expanded as a Fourier series,

$$g(\mathbf{r}) = \sum_{\mathbf{k}'} C(\mathbf{k}')\exp(i\mathbf{k}'\cdot\mathbf{r}). \quad \text{(C.3)}$$

where the sum goes over all of $\mathbf{k}'$ − space.

Write $\mathbf{k}' = \mathbf{k}+\mathbf{K}_m$, where $\mathbf{K}_m$ is a vector of the reciprocal lattice, and $\mathbf{k}$ is a vector in the first Brillouin Zone. The sum then becomes

$$g(\mathbf{r}) = \sum_{\mathbf{k}\in Bz}\exp(i\mathbf{k}\cdot\mathbf{r})\sum_{K_m}C(\mathbf{k}+\mathbf{K}_m)\exp(i\mathbf{K}_m\cdot\mathbf{r}). \quad \text{(C.4)}$$

We treat these sums separately.

$$\sum_{\mathbf{K}_m}C(\mathbf{k}+\mathbf{K}_m)\exp(i\mathbf{K}_m\cdot\mathbf{r})$$

is a function which is periodic with the period of the lattice, and which can consequently be expanded in terms of the set of functions $U(\mathbf{r}) \equiv u_{n0}(\mathbf{r})$, which are known[8] to be complete for the expansion of such functions. We write

$$\sum_{\mathbf{K}_m} C(\mathbf{k}+\mathbf{K}_m)\exp(i\mathbf{K}_m\cdot\mathbf{r}) = \sum d_n(\mathbf{k})U_n(\mathbf{r}). \qquad (\text{C}.5)$$

This is substituted into (C.4) and the remaining sum is broken up as follows:

$$\sum_{\mathbf{k}} d_n(\mathbf{k})\exp(i\mathbf{k}\cdot\mathbf{r}) = \sum_{\mathbf{k}_\perp}\exp(i\mathbf{k}_\perp\cdot\mathbf{r}) \times \sum_{\mathbf{k}_x} d_n(\mathbf{k})\exp(ik_xx). \qquad (\text{C}.6)$$

The x-dependent function $\sum_{\mathbf{k}_x} d_n(\mathbf{k})\exp(ik_xx)$ can be expanded in terms of the set of oscillator functions $\Lambda^N_{k_y}(x)$ which are complete, so that we write

$$\sum_{\mathbf{k}_x} d_n(\mathbf{k})\exp(ik_xx) = \sum_N b_N{}^n(\mathbf{k}_\perp)\Lambda^N_{k_y}(x). \qquad (\text{C}.7)$$

Substituting the expansions (C.5–C.7) back into (C.4) we have

$$g(\mathbf{r}) = \sum_{n,N,k_\perp} b_N{}^n(\mathbf{k}_\perp)\exp(i\mathbf{k}_\perp\cdot\mathbf{r})U_n(\mathbf{r})\Lambda^N_{k_y}(x). \qquad (\text{C }7)$$

Using the relationship (C.2) between $f(\mathbf{r})$ and $g(\mathbf{r})$ we see that the original arbitrary function $f(\mathbf{r})$ has been expanded uniquely in the form

$$\begin{aligned} f(\mathbf{r}) &= \sum_{n,N,\mathbf{k}_\perp} b_N{}^n(\mathbf{k}_\perp)\, e^{i(eH/2c)xy/\hbar}\, e^{i\mathbf{k}_\perp\cdot\mathbf{r}}\, U_n(\mathbf{r})\Lambda^N_{k_y}(x) \\ &= \sum_{n,N,\mathbf{k}_\perp} a_N{}^n(\mathbf{k}_\perp)\psi^N_{n\mathbf{k}_\perp}(\mathbf{r}) \qquad (\text{C }8) \end{aligned}$$

where we define

$$a_n{}^N(\mathbf{k}_\perp) = b_n{}^N(\mathbf{k}_\perp)(V/Lx)^{1/2}.$$

The basis functions are seen to form a complete set of functions, and an arbitrary function $f(\mathbf{r})$ can be expanded in terms of them.

The expansion in Section 3 does not involve a sum over $\mathbf{k}_\perp$ since the Hamiltonian is seen to be diagonal with respect to the $\mathbf{k}_\perp$-dependence.

J. Phys. Chem. Solids Pergamon Press 1969. Vol. 30, pp. 1885–1895. Printed in Great Britain.

ANODIC GROWTH, DIELECTRIC BREAKDOWN AND CARRIER TRANSPORT IN AMORPHOUS SiO_2 FILMS

C. R. FRITZSCHE
Institut für Elektrowerkstoffe, Freiburg, Germany

(*Received* 12 *September* 1968)

Abstract—Dielectric breakdown has been studied in anodically grown SiO_2 and compared with the growth conditions It is found that avalanche multiplication of electrons and ionic conductivity are closely related. This supports the impact ionization theory of anodization recently published[1]. An improved theory is given which supplies equations for efficiency of anodization, growth at constant current, and current decay at constant voltage in excellent agreement with experimental results. The effective mass ratio of electrons to ions, the mean free time of the electrons, the mean time between ionizing collisions and the electron drift velocity are estimated from experimental data.

1. INTRODUCTION

THERE are several facts of breakdown and anodization challenging the theory of anodic growth. Anodic growth of SiO_2 occurs at the very high field strength of $1{\cdot}9 \times 10^7$ V/cm but, as will be shown later, in a substantial part of the total oxide area dielectric breakdown happens below this value if well conducting electrodes are applied. *Revesz*[2] has found that during anodization the electronic current is at least 100 times the ionic current at current densities in the order of 10^{-3} to 10^{-2} A/cm^2 but, as we found, the total current density at a field just before breakdown is definitely smaller than 4×10^{-4} A/cm^2. Since the ratio of ionic to electronic current decreases with decreasing current these values show that there is practically no ionic current before breakdown and not only the ionic current but also the electronic current increases rapidly when the field strength of anodic growth is reached.

In a previous paper[1] it has been assumed that impact ionization takes place during anodic growth and that the ionic conductivity is caused by breaking chemical bonds. With the very rough assumption that the current is inversely proportional to the mean time between the ionizing collisions it was possible to derive the law of current decay at constant voltage. The according experimental results are presented now. Since we did not find a substantial voltage dependence of the decay constant a more careful calculation of the relationship between current and ionization time has been made. Voltage dependence could be concluded from the previous theory but has not been described explicitly in[1]. The improved theory does not only give a more reasonable decay constant but also renders possible the extention of the theory to the time dependence of voltage at constant current.

2. EXPERIMENTAL

1 Ohm . cm single crystalline silicon polished on one side and nickel plated on the backside has been anodized in a solution of $0{\cdot}4$ g KNO_3 in 100 cm^3 ethylene glycol at 25°C. Platinum was used as cathode and its distance from the silicon was $1{\cdot}2$ cm. The water content of the glycol was checked by Karl Fischer titrations and in most cases kept between $0{\cdot}06$ and $0{\cdot}08$ per cent. Aluminum electrodes $0{\cdot}5$ mm in diameter were evaporated for breakdown measurement. Breakdown voltage was measured with dc as well as pulse methodes as described elsewhere[3], however, an improved pulse amplifier was used and the current limiting resistor was only 220 Ω at pulse measurement.

3. ANODIZATION

Several investigations of anodic growth have been published[2, 4–6, 8], most of them being in agreement with our own results which are presented here for quantitative evaluation of the theory. Some of our results are new and give additional evidence of the proposed growth mechanism.

Figure 1 shows the increase of voltage with time at constant current. There is, particularly at low current and for *n*-type material, a minimum of slope between 70 and 150 V depending upon current. This can be seen in more detail from Figs. 2 and 3, where the scale is enlarged and the curves show an average over several runs.

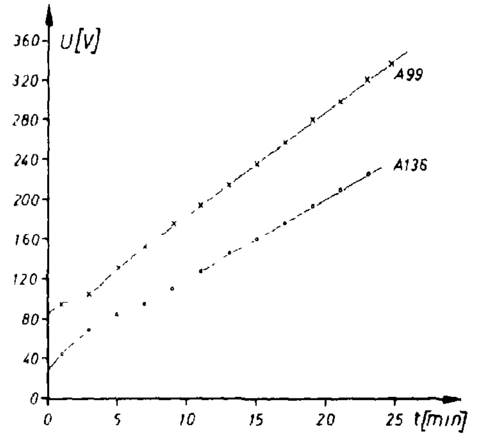

Fig. 1. Forming voltage *U* vs. time *t*. A 99 *n*-type silicon 25 ma. A 136 *p*-type silicon 25 ma.

Figure 4 shows oxide thickness vs. forming voltage. From the two curves for *p*-type silicon it can be seen that the thickness increases during current decay at constant voltage. The currents indicated correspond to an area of 3 . 14 cm^2 Since the positive bias of the semiconductor causes a barrier in *n*-type material the behaviour of the *p*-type material is more characteristic for the growth process.

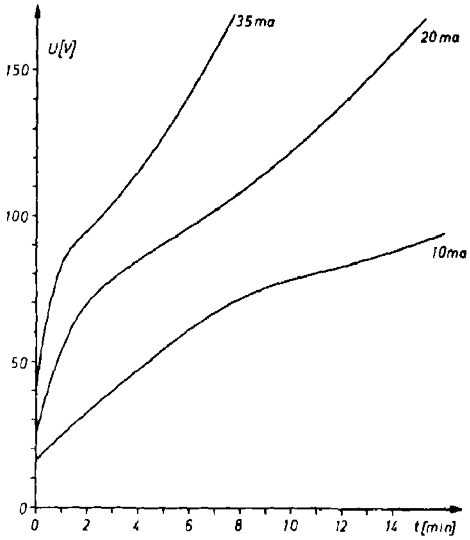

Fig. 2. Forming voltage *U* vs. time *t*, *p*-type silicon.

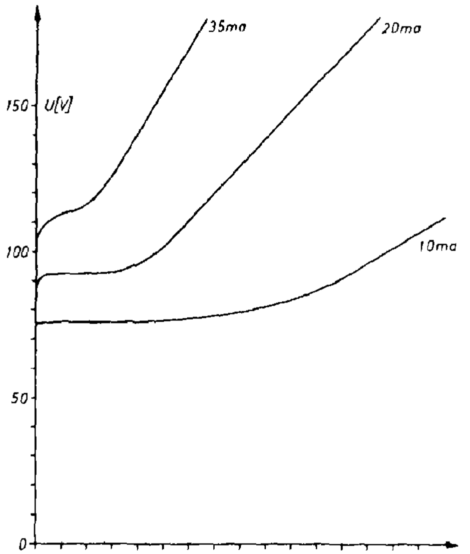

Fig. 3. Forming voltage *U* vs. time *t*, *n*-type silicon.

At high voltages the time dependence of voltage becomes linear. For *p*-type silicon and 25 ma the linear part is at least reached at 100 V (Fig. 1). This voltage corresponds to a thickness of about 550 to 600 Å (Fig. 4). (The data from samples with 15 sec current decay at constant voltage must be used here because during a decay of several minutes the thickness increases.) We will need this value later on in the theory.

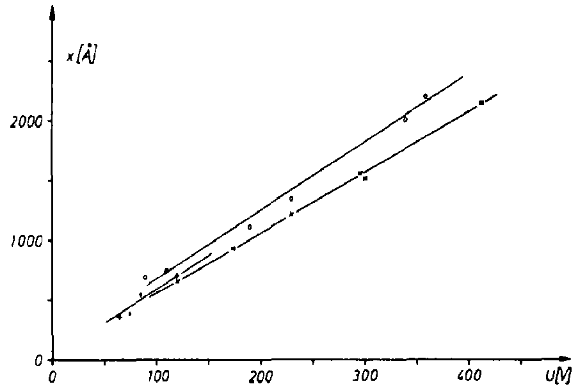

Fig 4 Oxide thickness vs. forming voltage ○ p-type Si, 25 ma, 10 min current decay at forming voltage, + p-type Si, 25 ma, 15 sec current decay at forming voltage, × n-type Si, 20 ma, 2 min current decay at forming voltage

If the forming voltage is kept constant after a certain thickness has been reached the current decreases with reciprocal of time. It has been suggested[2] that this is due to rearrangement of the oxide structure. If this is true one would expect that after the current has been diminished by an order of magnitude an accordingly high increase of voltage would be necessary to bring the current to its original value or that the oxide would break down rather than grow again. Figure 5 shows the voltage vs. time for two experiments, where after anodizing at 40 ma the voltage was kept constant at 170 and 210 V respectively until the current had decreased to 5 ma. The voltage step necessary to increase the current again by a factor of 8 to 40 ma is only 40 V in both cases and can, therefore, be attributed to a small increase in thickness during the constant voltage phase. When the original current is readjusted the voltage increases with the same slope as before. To explain the current decay at constant voltage we have, therefore, to look for a mechanism which changes the current rapidly with electric field. A suitable process is carrier multiplication by impact ionization as will be shown later.

Figure 6 shows the efficiency measured by the weight gain per unit charge (relative efficiency) and the thickness vs. current density. The layers have been grown to 340 V and subsequently kept at this voltage for 4 min. Circles correspond to experiments where the glycol has been dried by molecular sieve. This increases efficiency and thickness slightly.

A remark is necessary on the voltages. The total voltage applied to the cell we call forming voltage. At 20 ma there is a voltage drop of about 7 V across the electrolyte. The barriers between the electrodes and the electrolyte as well as between the semiconductor and the oxide are not known and may depend upon oxide thickness. The threshold voltage U_{th} to get the wanted current can be taken from Figs. 2 and 3 and is 25 V for p-type silicon at 20 ma. Thus, for p-type silicon and 20 ma any voltage between 7 and 25 V has to be subtracted from the forming voltage to get the real voltage across the oxide.

4. DIELECTRIC BREAKDOWN

For reasons already discussed elsewhere [3] we generally watch the first selfhealing breakdown as well as the breakdown which destroys the sample definitively. We will call these two types of events first breakdown and

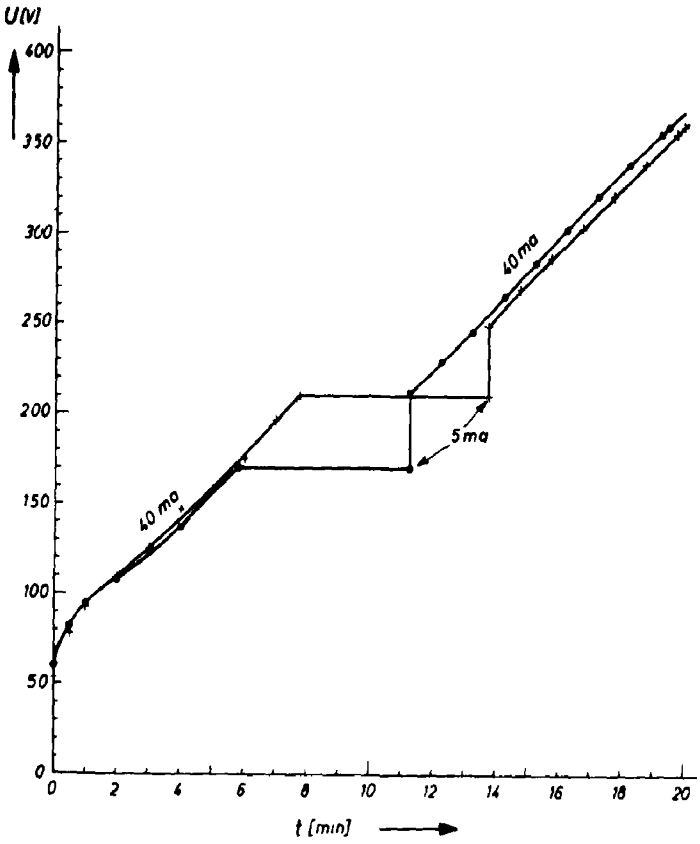

Fig. 5. Forming voltage vs. time. Anodization interrupted by current decay.

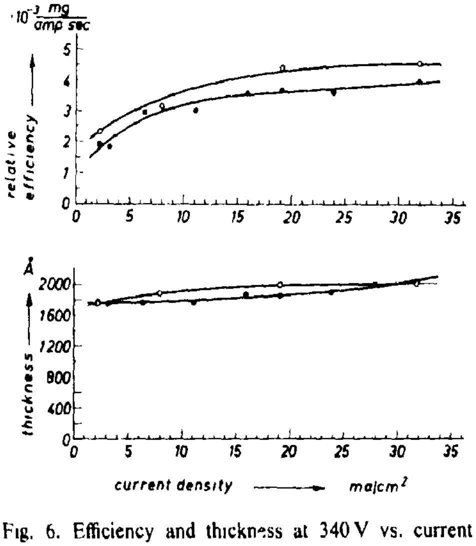

Fig. 6. Efficiency and thickness at 340 V vs. current density. ○ glycol dried; ○ glycol undried.

definitive breakdown. The probability of breakdown at specific point defects depends upon electrode diameter. Therefore in the first experiments we usually evaporate electrodes of various diameters. Tables 1 and 2 show how many electrodes of a given diameter have their breakdown in a certain range of voltage. As can be seen from the tables there is, in contrast to thermally grown oxide [3], no point defect breakdown prefering a certain voltage range. The first breakdown which occurs at the weak spots, is simply the less probable the lower the voltage. The most important fact is that, with only very few exceptions, the breakdown voltage is smaller than the forming voltage and even smaller than the difference between forming voltage and threshold voltage. This demonstrates that

Table 1. *Breakdown distribution of* SiO_2 *grown on* n-*type* Si *to* 300 *V at* 20 *ma.* d.c. *measurement. Aluminum positive.* $U - U_{th} = 275$ V, *thickness* 1510 Å

Breakdown voltage (V)	Electrode diameter (mm) First breakdown 0·5	0·7	1·0	1·4	2·0	Definitive breakdown 0·5	0·7	1·0	1·4	2·0
0–19					1					1
20–39			1					1		
40–59										
60–79										
80–99				1					1	
100–119					1					
120–139				1	1					1
140–159	1					1				
160–179		1	1	4			1	1		
180–199		1	3				1	2	1	
200–219	3	2	1			3	1		1	1
220–239	1					1			3	
240–259		2					2			
260–279							1	2		
Total	5	6	6	6	3	5	6	6	6	3

Table 2. *Breakdown distribution of* SiO_2 *grown on* p-*type* Si *to* 360 *V at* 50 *ma,* d.c. *measurement. Aluminum negative.* $U - U_{th} = 302$ V, *thickness* 2075 Å

Breakdown voltage (V)	Electrode diameter (mm) First breakdown 0·5	0·7	1·0	1·4	2·0	Definitive breakdown 0·5	0·7	1·0	1·4	2·0
0–27					1					1
28–55				1	1				1	1
56–83	1					1				
84–111										
112–139				1						
140–167				1	1					1
168–195			1	5	3					
196–223	1	3	7	4						
224–251	5	5	3			2	1	2	1	2
252–279	2	4	1				1		2	1
280–307	2					4	8	9	2	
308–335						2	1	1	2	
336–363	1					3	1		1	
364–391									1	
392–419									2	
Total	12	12	12	12	6	12	12	12	12	6

a theory of anodization must not neglect the electronic processes which cause dielectric breakdown.

In agreement with *Fröhlich's* theory of electronic breakdown in amorphous materials [7] the dielectric strength decreases with increasing temperature (Fig. 7). Figure 7 also shows that the water content of the electrolyte decreases the dielectric strength. Statistics are shown in Fig. 8. Sample A 79 was prepared with 1 per cent water added to the glycol. For A 80 no water was added but the electrolyte was purposely handled without care. A 81 is a normal run. For A 82 the glycol was dried with molecular sieve.

There are several hints on influence of ion

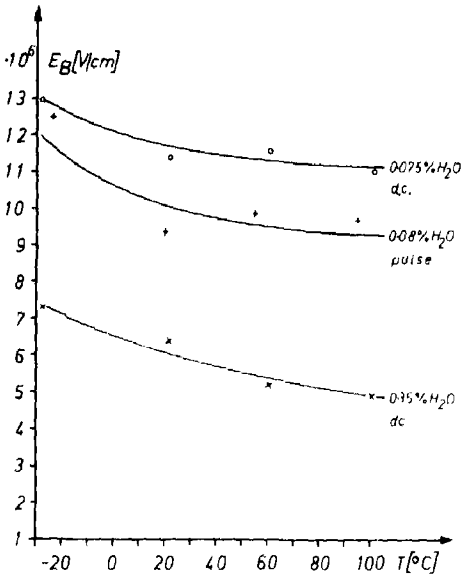

Fig. 7. Temperature dependence of dielectric strength

Table 4. Dependence of breakdown field E$_B$ *upon repetition time at* 15 *μsec pulse width*

Rep. time (msec)	0·06	0·3	3·0
E_B (10^6 V/cm)	10·6	11·3	12·1

migration on breakdown phenomena. At low oxide thickness the breakdown depends upon polarity and pulse repetition rate the latter dependence leading to a large difference between d.c. and pulse measurements which becomes smaller at higher thickness and disappears above 1300 Å. This is shown in Tables 3 and 4. Table 5 shows that the breakdown does not depend upon pulse width if the repetition rate is sufficiently low.

The dependence on layer thickness was also investigated. For layers which were grown in an electrolyte with low water content and measured with positive polarity of the silicon we have not been able to find any increase in dielectric strength with decreasing thickness down to 400 Å. This indicates that the mean free path of the electrons is substantially lower than 400 Å.

5. THE IMPACT IONIZATION THEORY OF ANODIZATION

Because of the high field strength necessary for anodization, the accordingly short path an electron needs to gain the ionization energy, and the breakdown behaviour of the oxide there is hardly any doubt that impact ionization takes place during anodic growth of SiO_2[1]. The main assumption of the theory is that every ionizing collision produces one additional free electron and one mobile ion. *Schmidt* and *Owen*[8] have found that silicon anodization occurs by cation migration. Although in their work the anodization has been carried out in solutions of 15 per cent pyrophosphoric acid in tetrahydrofurfuryl alcohol and statements about the mechanism of oxide growth should be restricted to the actual system investigated we may assume that silicon ions are the migrating species also in our case. This is probable since the growth and breakdown behaviour of oxides grown in the electrolyte used here is very similar to that of oxides grown in the electrolyte used by *Schmidt* and *Owen* as preliminary investigations have shown.

According to our assumption on the production of mobile ions the concentration of mobile

Table 3. Dependence of d.c. and pulse breakdown field E$_B$ *upon layer thickness* x

x (Å) E$_B$ (10^6 V/cm)	390	680	740	970	1110	1335	1670	2000	2200
Pulse	13·6	12·6	14·3	14·3	15·5	13·6	14·4	14·4	12·9
d.c.	1·6	3·6	9·1	11·7	14·4	15·0	15·5	14·8	14·2

Table 5. Dependence of breakdown field E$_B$ *upon pulse width. rep. time* 6 *msec*

Pulse width (μsec)	60	20	6·0	1·8
E_B (10^6 V/cm)	11·6	12·4	11·3	11·8

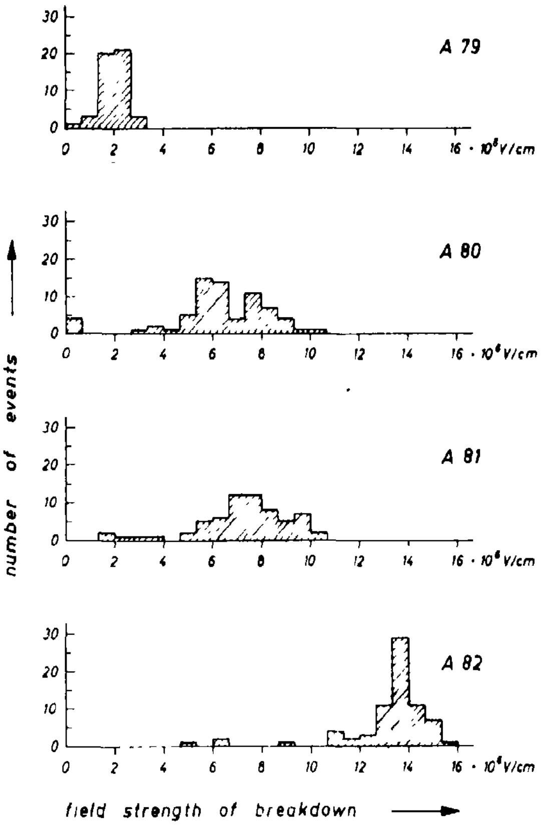

Fig. 8. Influence of water content in the electrolyte on dielectric strength (first breakdown). Water content decreases from 1 per cent at sample A79 to about 0·05 per cent at A 82

ions equals the concentration n_{coll} of electrons produced by collision, and the ratio of ionic current to total current may be written

$$\eta = \frac{\mu_{\text{ion}} n_{\text{coll}}}{\mu_{\text{el}}(n_0 + n_{inj} + n_{\text{coll}}) + \mu_{\text{ion}} n_{\text{coll}}} \tag{1}$$

where n_0 is the concentration of electrons excited thermally n_{inj} the concentration of electrons injected from the electrolyte[2], and μ_{ion} and μ_{el} are the mobilities of ions and electrons respectively.*

---

*For simplicity the factor a in [1] is set to unity. This of course influences the evaluation of η in Fig. 9. However, Fig. 9 is based on a very rough estimation and has to be considered as a qualitative statement only. To get η from the relative efficiency shown in Fig. 6 it is commonly assumed that 4 electronic charges have to be transported to form one neutral SiO$_2$[5]. This however is not certain

Introducing the mobility ratio

$$q = \mu_{\mathrm{el}}/\mu_{\mathrm{ion}}$$

the total current j, and the leakage current j_l caused by n_0 and n_{inj} we get

$$\eta = \frac{j-j_l}{j(1+q)} \qquad (1a)$$

Hence

$$j_{\mathrm{ion}} = j \,.\, \eta = \frac{j-j_l}{1+q}. \qquad (1b)$$

Using (1b) we can estimate q and j_l from Fig. 6. This was done by calculating η from the relative efficiency (see footnote) and solving (1b) for $(1+q)$ with two different pairs of η and j values found experimentally. It was assumed that q and j_l vary only slightly with j. The difference of the two j values must be small and the error will be large. The result is shown in Fig. 9. It is interesting that q shows high values only at very low current density and is rather small under normal growth conditions. If an Si^+ ion is migrating q has to be multiplied by a factor of 4.

The thickness x is assumed to increase proportional to the number of transported ions. Let x_0 be the thickness reached at the time t_0 at which the voltage is kept constant. Then we have according to (1b)

$$x = x_0 + C \int_{t_0}^{t} \frac{j-j_l}{1+q} \, \mathrm{d}t \qquad (2)$$

where C is a constant.

The current decay at constant voltage is due to the fact that increasing thickness decreases the field and increases the time t_i per ionizing collision. Thus we need a relationship between j and t_i or x. Let t_t be the transit time an electron needs to cross the oxide film, and let one electron produce N_{coll_1} electrons on its way. Then

$$1 + N_{\mathrm{coll}_1} = 2^{t_t/t_i - 1} \cong 2^{t_t/t_i}.$$

The primary electron may be neglected if the film is sufficiently thick. Taking into account all primary electrons we can set (see appendix)

$$n_{\mathrm{coll}} = p\,(n_0 + n_{\mathrm{inj}}) \,.\, 2^{t_t/t_i}$$

Writing j_{ion} in terms of n_{coll}, using (1b), and introducing the leakage current again we get

$$j - j_l = p \cdot \frac{1+q}{q} j_l \,.\, 2^{t_t/t_i}$$

and since $q \gg 1$

$$\ln \frac{j-j_l}{j_l \cdot p} = \frac{t_t}{t_i} \ln 2 \qquad (3)$$

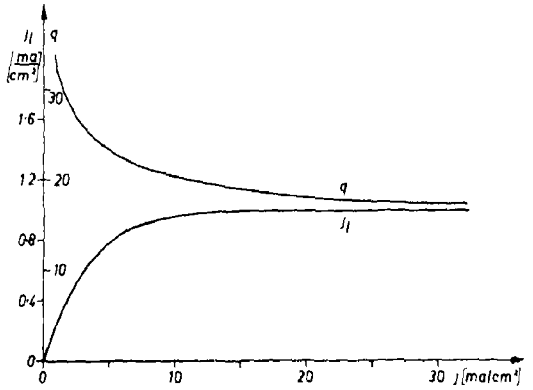

Fig. 9. Mobility ratio and leakage current density vs. total current density.

where p is a constant. Now we consider the time needed to gain the ionization energy I in the case of free acceleration. If m is the effective mass of the electron, e the electronic charge, U the voltage, and τ the mean time between collisions of all types we have [9]

$$t_i = \frac{\sqrt{2mI}}{eU/x}\exp\frac{\sqrt{2mI}}{\tau eU/x}. \tag{4}$$

Now we substitute (4) and (2) into (3). The increase in thickness during the constant voltage phase is small compared to x_0. Therefore we use the integral only in the exponential term and replace U/x by E_0 in the other one. This leads to

$$\ln\frac{j-j_1}{j_1 p} = t_i \ln 2\,\frac{eE_0}{\sqrt{2mI}}$$
$$\exp\left\{-\frac{\sqrt{2mI}}{eU\tau}\left(x_0 + C\int_{t_0}^{t}\frac{j-j_1}{1+q}\,\mathrm{d}t\right)\right\}. \tag{5}$$

Expanding the exponential function into series at x_0 and differentiating (5) we get

$$\frac{j_1}{j-j_1}\cdot\frac{\mathrm{d}}{\mathrm{d}t}\frac{j-j_1}{j_1} = -Bj_1\frac{j-j_1}{j_1} \tag{6}$$

where

$$B = t_i\ln 2\cdot\frac{C}{1+q}\cdot\frac{E_0}{U\,.\,\tau}\exp\left(-\frac{\sqrt{2mI}}{eE_0\tau}\right). \tag{7}$$

Instead of t_i we can introduce the drift velocity v and (7) may be written

$$B = \frac{1}{v}\ln 2\cdot\frac{C}{1+q}\cdot\frac{1}{\tau}\exp-\frac{t_l}{\tau} \tag{7a}$$

where t_l is the time needed to gain the ionization energy in the case of free acceleration, and because of (see [9])

$$\frac{t_i}{t_l} = \exp+\frac{t_l}{\tau}. \tag{8}$$

we get

$$B = \frac{1}{v}\ln 2\,\frac{C}{1+q}\cdot\frac{t_l}{\tau t_i}. \tag{7b}$$

Integration of (6) is possible, if we consider not too large a current range so that q and j_1 may be regarded as constant. We get

$$\frac{1}{j-j_1} - \frac{1}{j_0-j_{1_0}} = B(t-t_0). \tag{9}$$

This is the current decay at constant voltage. B can be determined experimentally. In agreement with (7a) it was found to depend not upon voltage. With $B = 0{\cdot}82\ \mathrm{A}^{-1}\mathrm{sec}^{-1}$ and j_1 from Fig. 9 we calculated curves for $j_0 = 20$ ma as well as 35 ma. These are shown in Fig. 10 together with experimental values. The agreement between theory and experiment is quite satisfactory.

The theory can also be applied to the growth

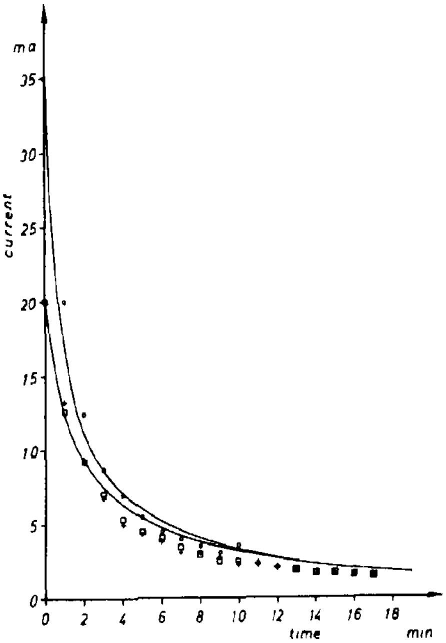

Fig. 10. Current decay at constant voltage ○ 35 ma, 270 V, n-type; □ 20 ma, 300 V, p-type; + 20 ma, 360 V, p-type, – theoretical curves.

under constant current. With $x_0 = 0$ equations (2) and (3) yield

$$x(t) = \frac{Cj}{1+q}\int\left(1-\frac{1}{1+p\,.\,2^{x/vt_i}}\right)\mathrm{d}t. \quad \text{(2a)}$$

Hence

$$\frac{\mathrm{d}x}{\mathrm{d}t} = \frac{C.j}{1+q}\left(1-\frac{1}{1+p\,.\,2^{x/vt_i}}\right).$$

Here p cannot be regarded as constant. Substituting for p with the expression derived in the appendix we get

$$\frac{\mathrm{d}x}{\mathrm{d}t} = \frac{C.j}{1+q}\left(1-\frac{1}{1+\dfrac{v\,.\,t_i}{x\,.\ln 2}(2^{x/vt_i}-1)}\right).$$

If $x \geqq 4vt_i$ practically no deviation from linear growth can be observed. As has been shown above this happens at $x = 575$ Å. Thus we have

$$vt_i \approx 1{\cdot}4\times 10^{-6}\,\mathrm{cm}. \quad (10)$$

Since I is known[3] t_l can be calculated from classical mechanics. The quantity $C/1+q$ can be taken from Figs. 1 and 4 using (2). With (10), (7b), and (8) we have all we need to determine τ, t_i, and v.

We have found:

from experiment for $j = 25$ ma

$$B = 0{\cdot}82\,\mathrm{A}^{-1}\,\mathrm{sec}^{-1}; \quad \frac{C}{1+q} = 3{\cdot}5\times 10^{-7}\,\mathrm{cm\,A^{-1}\,sec^{-1}}$$

$$E_0 = 1{\cdot}9\times 10^{7}\,\mathrm{V\,cm}^{-1}, \quad I = 11\,\mathrm{eV}\ \text{(see [3])}$$

from theory

$$t_l = 5{\cdot}9\times 10^{-15}\sqrt{\frac{m}{m_0}}\,\mathrm{sec}; \quad \frac{t_l}{\tau} = 4{\cdot}8$$

$$t_i = 120\times t_l; \quad v = 2\times 10^{6}\sqrt{\frac{m_0}{m}}\,\mathrm{cm\,sec}^{-1}.$$

It may be that the evaluation of anodization is not a very accurate method to determine these values. However, the fact that they all are obtained in a reasonable order of magnitude supports the theory much more convincingly than the agreement between theory and experiment in current decay (Fig. 10).

Acknowledgements—The author is indebted to Professor R. Mecke for his support and to Dr. A. Bresch, Dr. A. Goetzberger and W. Rothemund for critical reading of the manuscript. Thanks are also expressed to G. Gerdes, O. Kramer, J. Schaub and H. Vogt who collaborated in the experimental work.

REFERENCES

1. FRITZSCHE C. R., *Solid State Commun.* **6**, 341 (1968).
2. REVESZ A. G., *Phys. Status Solidi* **24**, 115 (1967).
3. FRITZSCHE C. R., *Z. angew. Phys.* **24**, 48 (1967).
4. SCHMIDT P. F. and MICHEL W., *J. electrochem Soc.* **104**, 230 (1957).
5. DUFFEK E. F., MYLROIE C. and BENJAMINI E. A., *J. electrochem. Soc.* **111**, 1042 (1964).
6. DUFFEK E. F., BENJAMINI E. A. and MYLROIE C., *Electrochem. Technol.* **3**, 75 (1965).
7. FROEHLICH H., *Proc. R. Soc.* **A188**, 521 (1947).
8. SCHMIDT P. F. and OWEN A. E., *J. electrochem. Soc.* **111**, 682 (1964).
9. FRANZ W., Dielektrischer Durchschlag in *Handb. Phys* **17**, 155 (1956).

APPENDIX

Calculation of the factor p

Consider a unit area and let N_{coll} be the total number of electrons produced by collisions. Then we can define an average density n_{coll} by

$$x\,.\,n_{\mathrm{coll}} = N_{\mathrm{coll}}.$$

This number can be calculated by integrating the contributions of (n_0+n_{ini}). dξ electrons starting in a surface layer of the width dξ and travelling over a distance ξ. Since these electrons need the time ξ/v we have

$$x\,.\,n_{\mathrm{coll}} = \int_0^x (n_0+n_{ini})\,.\,2^{\xi/vt_i}\mathrm{d}\xi.$$

Hence

$$n_{\mathrm{coll}} = \frac{1}{x}\frac{v\,t_i}{\ln 2}\cdot(n_0+n_{ini})(2^{x/vt_i}-1).$$

Comparing this with our assumption

$$n_{\mathrm{coll}} = p\,.\,(n_0+n_{ini})\,.\,2^{t/t_i}$$

we see that

$$p = \frac{v \,.\, t_l}{x \,.\, \ln 2} \cdot (1 - 2^{-(x/v\, t_l)}).$$

During the current decay at constant voltage x remains almost constant. Thus p can be regarded as a constant in equation (5).

J. Phys. Chem. Solids Pergamon Press 1969. Vol. 30, pp. 1897–1900. Printed in Great Britain.

TECHNICAL NOTES

Multiphonon processes in amorphous selenium

(*Received* 9 *September* 1968; *in revised form* 24 *January* 1969)

THE FUNDAMENTAL vibration modes of amorphous selenium have recently been identified assuming a structural model involving the presence of Se_8 molecules as well as polymeric Se chains[1]. In the present work the temperature dependence of the i.r. spectrum of amorphous selenium has been measured and used to assign the non-fundamental absorption bands. The temperature dependence of the absorption edge has been discussed previously[2]. In the wavelength range between the absorption edge and the highest frequency fundamental vibration (i.e. between 1 and 39 μm) several absorption bands have been reported in the literature [3–5] but disproved by later publications [6, 7]. However, none of the absorption bands discussed in this paper are due to impurities or different preparation techniques of the specimens.

The measurements were carried out with a Perkin–Elmer 13U spectrometer in the wavelength range 1–25 μm and with a Perkin–Elmer Model 301 spectrophotometer for the rest of the spectrum. The liquid selenium was kept in heated Vycor tubes with KBr windows and teflon seals. Temperature gradients in the longer cells (up to 10 cm length was used) were compensated by keeping the windows slightly hotter than the main body of the tube. The transmission of the empty cell at each temperature was measured separately since the transmission of the KBr and CsI windows is strongly temperature dependent near the cutoff frequency.

Figure 1 shows a plot of absorption coefficient α against wavenumber for three different temperatures. In the shorter wavelength range the absorption at 77° and 300°K exceeds that of liquid selenium (623°K) indicating a nearly wavelength independent background scattering. In fact, when amorphous specimens were cooled several times to liquid nitrogen temperature and reheated, irreversible changes of the background absorption were observed. The background absorption of liquid selenium is much smaller and was assumed to be caused by the wing of the 257 cm^{-1} fundamental band:

$$\alpha_{\text{f.r.}} = \frac{\alpha_{\max}\gamma^2\omega^2}{(\omega_0{}^2-\omega^2)^2+\gamma^2\omega^2}$$

and

$$\gamma = \frac{\omega_0{}^2-\omega_H{}^2}{\omega_H{}^2}$$

where $\alpha_{\max}$ is the absorption, ω_0 the resonance frequency and ω_H the halfwidth of the fundamental band. The temperature dependence of ω_H was adjusted to make the value of $\alpha_{\text{f.r.}}$ equal to the smallest measured absorption at 900 cm^{-1}(Fig. 1).

The three absorption bands at 983, 743 and 490 cm^{-1} are considered as combination bands due to Se_8 molecules in the amorphous phase. The phonon frequencies of the Se_8 molecules are taken from the observed frequencies of monoclinic selenium[1]. Table 1 shows our assignment together with the fundamental vibrations of amorphous selenium as assigned by Lucovsky[1]. The band positions are given at room temperature.

Our assignment agrees well with the observed temperature dependence of the combination bands. This is shown in Fig. 2,

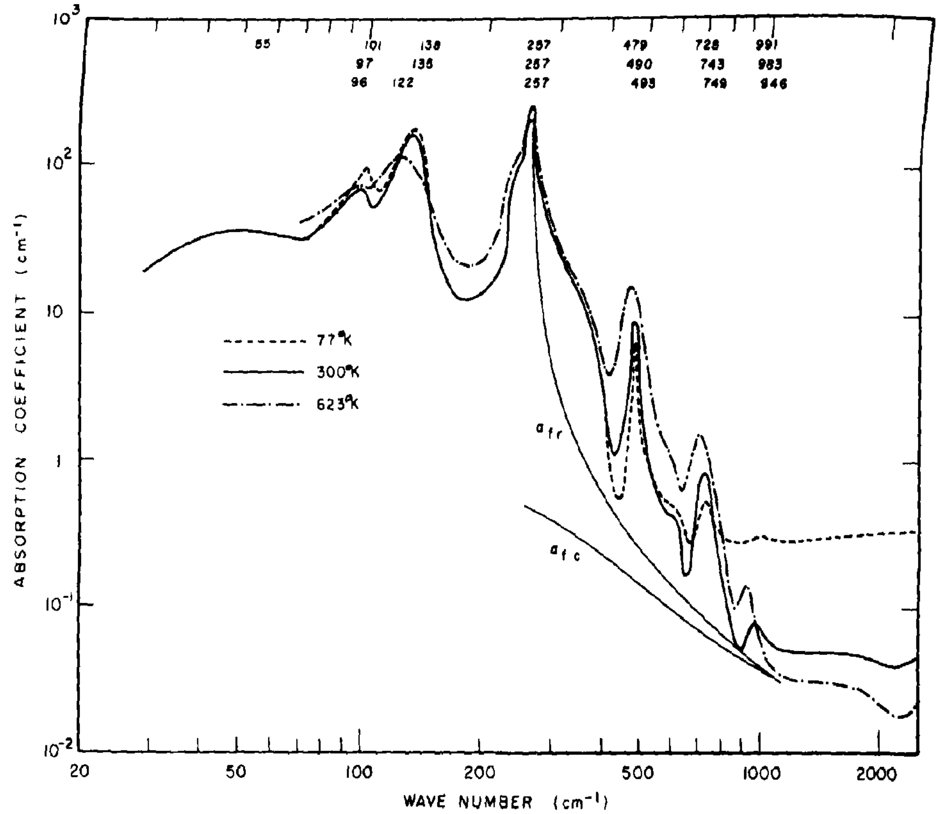

Fig. 1. Absorption coefficient as a function of wavenumber for three different temperatures. The numbers on top denote the band positions in wavenumbers. α_{fr} background absorption due to the wing of the fundamental resonance at 257 cm^{-1}, α_{fc} background absorption due to free carriers with $\mu = 100$ cm^2/Vsec and $N = 10^{15}$

Table 1. Fundamental and overtone bands in amorphous selenium

Frequency by Lucovsky (cm^{-1})	Assignment by Lucovsky	I.R. frequency observed in our work (cm^{-1})
50 Raman	Se$_8$, E_2	55 (very broad)
80 Raman	Se$_8$, E_2	
95 I.R.	Se$_8$, E_1	97
112 Raman	Se$_8$, A_1	
120 I.R.	Se$_8$, B_2	
135 I.R.	Polymeric chain, E	138
138 Raman	Polymeric chain, E	
235 Raman	Polymeric chain, A_1, E	
250 Raman	Se$_8$, A_1, E_2	
254 I.R	Se$_8$, E_1	257

I.R. frequency observed in our work (cm^{-1})	Assigned by us	
490	$254 + 239 = 493$	(Se$_8$, E_2) + (Se$_8$, E_3)
743	$254 + 249 + 233 = 742$	(Se$_8$, E_2) + (Se$_8$, A_1) + (Se$_8$, E_3)
983	$(2 \times 254) + (2 \times 239) = 986$	2(Se$_8$, E_2) + 2(Se$_8$, E_3)

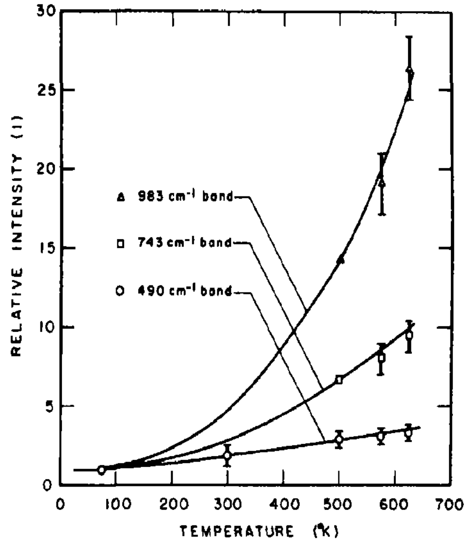

Fig. 2. Plot of the integrated intensity ($\int \alpha d\lambda$) in relative units against the temperature. The thin lines denote the theoretical curves for a 4-phonon, 3-phonon and 2-phonon process. The dots are the measured values using the background absorption ($\alpha_{f,r}$). The error lines are determined by assuming either no background absorption at all or straight lines between the minima of the bands.

where the theoretical temperature dependence is plotted together with the integrated band intensities. The integration was carried out numerically after subtracting the background absorption. The theory of multiphonon absorption[8, 9] requires in the case of a 3-phonon process, a temperature dependence of the band intensity according to

$$I_3 \propto [1+I(h\nu_1)] \times [1+I(h\nu_2)] \times [1+I(h\nu_3)] - I(h\nu_1) \times I(h\nu_2) \times I(h\nu_3)$$

where $I(h\nu) = (\exp h\nu/kT - 1)^{-1}$.

Naturally the population of higher states is insufficient to cause significant absorption at temperatures as low as 77°K, therefore the theoretical curves for all three bands start close to unity. The true intensities however differ considerably between the bands expressing clearly the smaller probability for the higher phonon processes. The normalisation was done for the 490 cm^{-1} band at 77°K, and for the other two bands at 500°K (dots without error indication in Fig. 2).

Considering the entire i.r. spectrum of amorphous selenium as shown in Fig. 1, the absorption band at 983 cm^{-1} has been observed by Vasko[4] but never discussed any further since it appeared too weak. The band at 743 cm^{-1} has been assigned by Vasko [5] as a 4-phonon combination which is inconsistent with the measured temperature dependence. The band at 490 cm^{-1} has been assigned[5] as a 3-phonon combination, again inconsistent with the temperature dependence. Our assignment (Table 1) is based on the measured temperature dependence and on the closest frequency matching. It is definite in the number of phonons involved but does not exclude other possible phonon combinations which would come equivalently close in their frequency sum.

The band at 257 cm^{-1} has been assigned by Lucovsky[1] as a type E_1 fundamental vibration of the Se_8 molecule (254 cm^{-1}). This assignment agrees well with the observed temperature independence of its position and intensity. The band at 138 cm^{-1} was assigned by Lucovsky[1] as due to the type E rotational vibration of the polymeric Se chains. In the trigonal selenium single crystals, this band is located at 144 cm^{-1} and in the liquid selenium we observed it at 122 cm^{-1}. Hass and Rosenstock[10] calculated the frequency and intensity changes which would occur when an infinite chain is shortened so that the end conditions become effective. Apart from some additional absorption bands which would be too far in the i.r., they propose the absorption of the fundamental mode to be directly proportional to the chain length. Thus we obtain an excellent support for the assignment by Lucovsky and confirm the conception that increasing temperature in amorphous Se leads to a drastic shortening of the polymeric Se chains. From viscosity measurements by Keezer and Bailey[11], the decreasing chain length with increasing temperature has been indirectly derived. The absorption band at 97 cm^{-1} was assigned by Lucovsky[1] as due to the type E_1 vibration of the Se_8 molecule (95 cm^{-1}). This seems to be consistent with our results in the liquid phase. However, it could be caused equally well by the type A_2 vibration of the polymeric chains which occurs in the trigonal crystals at 102 cm^{-1}. The slight shift observed between liquid nitrogen and room temperature supports the latter assignment and this would then be similar to the shift of 138 cm^{-1} band. The last absorption band at about 55 cm^{-1} was too weak and broad to be further analysed.

Acknowledgements – The experiments were supported jointly by Canadian Copper Refiners Limited and the Directorate of Industrial Research of the Defence Research Board of Canada. The authors are grateful to F. Rosenblum for technical assistance, and to K. M. Baird and C. H. Champness for valuable discussions.

Noranda Research Centre,
Pointe Claire, Quebec,
Canada
K. J. SIEMSEN*

and

National Research Council,
Division of Applied Physics,
Ottawa, Ontario,
Canada
H. D. RICCIUS

REFERENCES

1. LUCOVSKY G., MOORADIAN A., TAYLOR W., WRIGHT G. B. and KEEZER R. C., *Solid State Commun.* **5**, 113 (1967).
2. SIEMSEN K. J. and FENTON E. W., *Phys. Rev.* **161**, 632 (1967).
3. GOBRECHT H. and TAUSEND A., *Z. Phys.* **161**, 205 (1961).
4. VASKO A., *Czech. J. Phys.* **B11**, 664 (1961).
5. VASKO A., *Czech. J. Phys.* **B13**, 827 (1963).
6. VASKO A., *Czech. J. Phys.* **B15**, 170 (1965).
7. ABDULLAEV G. B., MEKHTIEVA S. I., ALIEV B. M., ABDINOV D. SH. and KERIMOVA T. G., *Phys. Status Solidi* **16**, K31 (1966).
8. KLEINMAN D. A., *Phys. Rev.* **118**, 188 (1960).
9. LAX M. and BURSTEIN E., *Phys. Rev.* **97**, 39 (1955).
10. HASS M. and ROSENSTOCK H. B., *Appl. Optics* **6**, 2079 (1967).
11. KEEZER R. C. and BAILEY M. W., *Materials Res. Bull.* **2**, 185 (1967).

---

*Present address: National Research Council, Division of Applied Physics, Ottawa, Ontario, Canada

---

J. Phys. Chem. Solids Vol. 30, pp. 1900–1902.

Exploding wire phenomena in the coinage metals

(*Received 6 March 1967; in revised form 4 October 1968*)

MUCH OF the interest in Exploding Wire Phenomena (EWP) has been concerned with the physics of the processes occurring, while little work has been done in studying the chemical and physico-chemical aspects of EWP. In exploding wire experiments one obtains, among other things, an oscilloscopic trace of current *versus* time, and in many instances the trace will show two current maxima, the time interval between these maxima being known as the 'dwell' time. One explanation of this behavior[1] is that the second maxima (restrike) is due to ionization which was prevented during the dwell period by high gas density.

Chace, Morgan and Saari[2] measured the current as a function of voltage during the dwell period and found that the data could not be fitted in all cases to Childs' Law[3]. However, when Childs' Law is modified to take into consideration the Schottky effect[4] the results are in agreement with the modified law which indicates that the charge carriers are produced by thermionic emission. In this case, the current should be related to the thermionic work function by the Richardson-Dushman equation[5], and the dwell time might be expected to be dependent upon the work function as has been suggested by Woffinden[6]. We wish to report the results of a study of the effect of the nature and dimensions of the coinage metal wires, Cu, Ag and Au, on EWP.

EXPERIMENTAL RESULTS AND DISCUSSION

In order to ascertain the relationship of dwell time to work function, metals in the same family were chosen and the wire dimensions used were the same so as to eliminate the dependence of the dwell time on wire size. If it is assumed that restrike occurs because of ionization due to electronic or ionic impact, then the magnitude of the current and hence the dwell time would be expected to be a function of the ionization potential of the gaseous atoms as well as the work function of the metals. We have found that the dwell time for the coinage metals increases as the ionization potential of the gaseous ion and the work function of the metal for Cu, Ag and Au increase. The experiments have been carried out in air at two different pressures and the results are given in Table 1. We feel, in particular, that the relationship of the ionization potential to dwell time supports one of the proposed models of EWP[1].

Table 1. *Dwell times, ionization potentials and work-functions for* Cu, Ag and Au*

	Dwell time (μsec)		Ionization energy† (eV)	Work function‡ (eV)
	P = 760 mm	P = 1500 mm		
Ag	38	27	7·54	4·28
Cu	48	38	7·68	4·47
Au	68	58	9·18	4·58

*Wires 12·70 cm in length and 0·0508 cm dia. were used. The initial charge on the capacitor bank was 7 KV.

†In *Handbook of Chemistry and Physics*, 45th Edn, p. E41

‡MICHAELSON H. B., *J. appl. Phys.* 21, 536 (1950).

The observed decrease in dwell times with increasing ambient pressure appears to be contrary to most published work. However, most investigations along these lines have utilized very thin wires, hence the arc terminating the dwell occurs through the core of the vapor cloud. Thick wires produce more uniform, dense vapor clouds, and Korneff *et al.*[7] have shown that restrike occurs through the surface of these clouds due to a rapid decrease in pressure behind the shock front. It is possible, therefore, that under the conditions of our explosions, the duration of the dwell is determined by this pressure drop following shock propagation.

The explosions were performed with an apparatus consisting of five 31·25 μF oil-filled capacitors connected in parallel using a copper/polyethylene/Mylar/polyethylene/copper sandwich constructed as follows: Two sheets of copper (0·32 cm thick) separated by two sheets of thin (0·076 cm) polyethylene which in turn were separated by one sheet of Mylar (0·013 cm) were connected to the capacitor terminals. The three insulation sheets extended about 5 cm beyond the copper plates to prevent arcing at the edges from plate to plate. The polyethylene, being smooth, prevents surface corona and the Mylar prevents breakdown through the insulation. To prevent arcing at the capacitor terminals, a 10 cm dia. hole was drilled in the copper sheet at each terminal not connected to that particular sheet. Through the use of the sandwich, the leads were held very close together thus reducing the inductance to a reasonable level (0·39 μH) by decreasing the magnetic field induced by the large current changes during discharge. The capacitor bank may be charged to 10 KV, and the stored energy discharged through the wire by firing a Lovotron switch[8] with a modified Theophanis hydrogen thyratron trigger[9]. Current-time traces were obtained with a commercially available current-viewing resistor and a Tektronix 517A oscilloscope. Dwell times were reproducible to within ± 1 μsec.

The oscilloscopic traces (current vs. time) obtained for the Group IB metal wire explosions are essentially identical; however, the actual numerical values of the current maxima and dwell times do differ. We have found that it is essential to hold at least four variables constant when comparing results for different members of a chemical series: wire length, wire diameter, initial charge on the capacitor bank and the pressure of the surrounding atmosphere. An increase in either wire dimensions *always* causes an increase in the dwell time. Both Keilhacker[10] and Oktay[11] have observed increases in dwell time for increasing wire diameter, but neither have observed a consistent dependence on wire length. Similarly, an increase in either voltage or surrounding gas pressure causes a decrease in dwell time. Therefore, in comparing dwell phenomena for any series of metal wires, the above four variables should be held constant.

Department of Chemistry,
Michael Faraday Laboratories,
Northern Illinois University,
Dekalb, Ill. 60115,
U.S.A.

J. D. GRAHAM
C. W. SPANGLER
S. K. LOTT
M. J. JONCICH

REFERENCES

1. CHACE W. G., In *Exploding Wires* (Edited by W. G. Chace and H. K. Moore), Vol. 1, p. 7. Plenum Press, New York (1959).
2. CHACE W. G., MORGAN R. L. and SAARI K. R., In *Exploding Wires* (Edited by W. G. Chase and H. K. Moore), Vol. 1, p. 59. Plenum Press, New York (1959).
3. HARNWELL G. P., In *Principles of Electricity and Electromagnetism*, p. 224. McGraw-Hill, New York (1949).
4. HARNWELL G. P., In *Principles of Electricity and Electromagnetism*, p 211. McGraw-Hill, New York (1949).
5. HARNWELL G. P., In *Principles of Electricity and Electromagnetism*, p. 209. McGraw-Hill, New York (1949).
6. WOFFINDEN G. J., In *Exploding Wires* (Edited by W. G. Chace and H. K. Moore), Vol. III, p. 193. Plenum Press, New York (1964).
7. KORNEFF T., BOHN J., and NADIG F., In *Exploding Wires* (Edited by W. G. Chace and H. K. Moore), Vol. 1, p 104. Plenum Press, New York (1959).
8. CULLINGTON E. H., CHACE W. G. and MORGAN R. L., Instrumentation for Geophysical Research. Rep. No. 5, AFCRC-TR-55-227 (1955).
9. THEOPHANIS G. A., *Rev. scient. Instrum* **31**, 427 (1960)
10. KEILHACKER M., *J. appl. Phys.* **12**, 49 (1960).
11. OKTAY E., *Rev. scient Instrum.* **36**, 1327 (1965).

J. Phys. Chem. Solids Pergamon Press 1969. Vol. 30, pp. 1903-1904. Printed in Great Britain.

ERRATA

I

R. W. DREYFUS: Tunneling states of CN^- in RbCl crystals. *J. Phys. Chem. Solids* **29**, 1941 (1968).

THE AUTHOR notes that in the *Acknowledgements*, the following should be included:

B. Gilbert kindly synthesized the pure RbCN.

II

J. C. HO and R. VISWANATHAN: Low temperature specific heat of h.c.p. Mo–Ru and Mo–Rh alloys. *J. Phys. Chem. Solids* **30**, 169 (1969).

THE AUTHORS regret that on page 170, line 9 should read:

however, had no significant effect on the

III

G. LEHMANN: Interstitial incorporation of di- and trivalent cobalt in quartz. J. Phys. Chem. Solids **30**, 395 (1969).

THE AUTHOR regrets that on page 396 the first sentence after paragraph (d) should read:

> The sites (a), I_4 and I_8 are expected to lead to the same type of spectrum and to similar band positions.

IV

W. J. BITER, INDRADEV and FERD WILLIAMS: Experimental and theoretical studies of low-voltage electroluminescence of ZnS single crystals. *J. Phys. Chem. Solids* **30**, 503 (1969).

IN THE above article the name of Ferd Williams was misspelled as Fred Williams owing to an error made by the printers after the title had appeared in page proof. The printers greatly regret this unfortunate error.

J. Phys. Chem. Solids Pergamon Press 1969. Vol. 30, pp. 1905–1908. Printed in Great Britain.

ELASTIC CONSTANTS OF LiBr FROM 300° to 4·2°K*

B. J. MARSHALL and C. R. CLEAVELIN
Department of Physics, Texas Technological College, Lubbock, Texas 79406, U.S.A.

(*Received* 6 *November* 1968; *in revised form* 17 *March* 1969)

Abstract – The adiabatic elastic constants have been measured in single crystals of lithium bromide in the temperature range of 300°–4·2°K. The values of the elastic constants at 0°K, extrapolated from 4·2°K, are $c_{11} = 4{\cdot}721$, $c_{44} = 2{\cdot}052$, and $c_{12} = 1{\cdot}590$ in units of 10^{11} dyn/cm². The variation from the Cauchy Relation is $\Delta = c_{12} - c_{44} = -0{\cdot}462 \times 10^{11}$ dyn/cm² at 0°K. The Debye characteristic temperature calculated from the elastic constants θ_D^{el} at 0° is 276·6°K according to Betts *et al.* The lattice energy at 0°K is calculated to be 185 kcal/mole.

INTRODUCTION

WITHIN THE last ten years much progress has been made in understanding the nature of the bonding forces between ions in alkali halide crystals. Phenomena such as the failure of the Cauchy relation ($c_{12} \neq c_{44}$), the crystal stability and the fact that many of them exhibit polymophism under pressure at low temperatures have been theoretically investigated by Lowdin[1], Lothe[2], Herpin[3], Dick[4] and recently by Lombardi *et al.*[5].

Accurate low temperature measurements of the elastic constants provide the theoreticians with a means of checking their fundamental theories. Therefore, in a continuing effort to supply basic information on the elastic and thermal properties of crystalline solids, we have measured the adiabatic elastic constants of LiBr from 300° to 4·2°K.

EXPERIMENTAL

The single crystal specimens used in these measurements were approximately cylindrical with a diameter of 0·63 in. and a length of 1·0 in. The crystals were obtained from Semi-Elements, Inc. with the end faces of one crystal oriented perpendicular to the [100] axis of the crystal, and the end faces of the other were oriented perpendicular to the [110] axis of the crystal. The end faces were polished parallel to within ±0·001 inch. LiBr is extremely hygroscopic, thus requiring that the specimens be handled in a dry atmosphere at all times. This was accomplished by making all preparations in a 'dry box' containing a helium atmosphere.

Due to the symmetry of a cubic crystal, there are only three independent elastic constants c_{11}, c_{44} and c_{12}[6]. To obtain c_{11} and c_{44}, one simply measures the velocities (V) of 10 MHz longitudinal and transverse sound waves propagated in the [100] direction. Then if the density ρ is known, the following relations may be used: $c_{11} = \rho V_L^2$ and $c_{44} = \rho V_T^2$. To obtain c_{12}, one measures the velocity of longitudinal sound waves along the [110] direction (V_l') from which we obtain $c_{12} = 2\rho V_l'^2 - (c_{11} + 2c_{44})$. The elastic constants c_{12} and c_{44} may also be obtained by using polarized transverse sound waves propagated in the [110] direction. Thus to obtain c_{12}, one measures the velocity (V_T) of a transverse wave propagated along the [110] direction with its particle motion polarized perpendicular to the [001] direction giving $c_{12} = c_{11} - 2\rho V_T^2$. Then in order to determine c_{44}, a transverse sound wave is again propagated along the [110] direction, but this time the particle motion is polarized parallel to the [001] direction. The velocity (V_T') associated with this wave gives $c_{44} = \rho V_T'^2$.

---

*This work was supported by the Robert A. Welch Foundation of Texas.

For measurements on LiBr, c_{11} was measured as first mentioned; c_{44} was measured by both methods giving excellent agreement, and c_{12} was measured by the polarized transverse wave technique.

The method employed to measure the sound velocities in the crystals was the well-known pulse-echo technique. The equipment has been described in an earlier publication[7].

The pulse-echo technique requires that a rigid bond exist between the quartz wafer transducer and the crystal. In the temperature range over 300°–160°K Nonaq stopcock grease was used as a binder. For measurements between 160°–80°K, an organic mixture of 5 parts ethyl ether, 6 parts pentane, and 2 parts ethyl alcohol was used as a binder. The mixture was applied as a liquid at approximately 160°K. Finally for measurements below 80°K, dried natural gas was the binder. It was applied as a liquid at approximately 80°K.

The temperature measurements were made with a Copper-Constantan thermocouple which was placed in contact with the crystal. The crystals were cooled at a constant rate of 10°K per hour.

RESULTS AND DISCUSSION

In order to compute the velocity of sound through the LiBr crystal, it is necessary to know the length of the crystal as a function of temperature. The room temperature length measurements were corrected down to 4·2°K by utilizing the thermal expansion coefficient of LiBr: ($\alpha = 50{\cdot}0 \times 10^{6}(°\mathrm{K})^{-1}$ at 22°C)[8]. Since there were no data available on either the temperature dependence of the expansion coefficient or the specific heat of LiBr, the temperature dependence of the expansion coefficient was approximated by assuming the dependence proportional to the specific heat data modeled after LiCl; see Grüneisen[9]. The value of the density at 22°C is given by S. Haussühl[10] to be $\rho = 3{\cdot}4703$ g/cm³. Then with the above calculated expansion coefficient, the density may be calculated as a function of temperature.

In Table 1 the value of the adiabatic elastic constants and $\rho V_T^2 = \frac{1}{2}(c_{11} - c_{12})$ are given over the temperature range 300°–4·2°K. The values of the elastic constants shown are from smoothed curves of the data. Also given in this table are the calculated values of density

Table 1. Elastic constants and $\rho V_T^2 = \frac{1}{2}(c_{11} - c_{12})$ *of* LiBr *in units of* 10^{11} *dyn/cm², densities in units of g/cm³, and compressibilities in units of* 10^{-12} *cm²/dyn*

T(°K)	c_{11}	c_{12}	c_{44}	ρV_T^2	ρ	β
300	3·920	1·890	1·885	1·015	3·4678	3·896
280	3·972	1·877	1·898	1·048	3·4781	3·883
260	4·034	1·862	1·913	1·086	3·4885	3·867
240	4·095	1·843	1·929	1·126	3·4987	3·856
220	4·160	1·823	1·945	1·168	3·5089	3·843
200	4·224	1·800	1·960	1·215	3·5189	3·834
180	4·289	1·776	1·975	1·256	3·5286	3·826
160	4·355	1·750	1·990	1·302	3·5379	3·819
140	4·425	1·723	2·005	1·351	3·5468	3·811
120	4·496	1·697	2·019	1·400	3·5550	3·802
100	4·565	1·680	2·033	1·451	3·5624	3·785
80	4·626	1·648	2·043	1·517	3·5686	3·787
60	4·682	1·630	2·049	1·530	3·5732	3·777
40	4·710	1·618	2·052	1·546	3·5759	3·775
20	4·721	1·603	2·052	1·559	3·5768	3·785
0	4·721	1·590	2·052	1·565	3·5768	3·797

and the compressibilities as calculated from

$$\beta = 3/(c_{11}+2c_{12}).$$

The estimated possible error for c_{11}, c_{44}, c_{12}, and ρV_T^2 at 4·2°K are ±0·8%, ±0·8%, ±3·9%, and ±0·8%, respectively. The error in c_{12} is greater due to the cumulative error of c_{11} and ρV_T^2 since c_{12} is a difference equation and is directly dependent upon the values of c_{11} and ρV_T^2.

The elastic constants of LiBr have been measured at room temperature (22°C) by K. Spangenberg and S. Haussühl[10]. The values they give, in units of 10^{11} dyn/cm², are $c_{11} = 3·94$, $c_{12} = 1·88$, $c_{44} = 1·91$.

Figure 1 shows the temperature dependence of the elastic constants of LiBr. c_{11} and c_{44} show a decrease with increasing temperature, while c_{12} shows an increase with increasing temperature. The percentage changes over the range 300°–0°K are c_{11} (17%), c_{44} (8·2%), and c_{12} (15·9%) which are in line with the other alkali halides of NaCl structure.

Another quantity, which expresses the elastic behavior of LiBr, is the anisotropy factor. $A = 2c_{44}/[c_{11}-c_{12}]$. At 300° and 0°K this quantity is equal to 1·857 and 1·204, respectively. For an isotropic material, the anisotropy factor is equal to one. Thus, it is observed that LiBr tends to become more isotropic for decreasing temperature. The temperature dependence of the anisotropy of the alkali halides has been discussed by

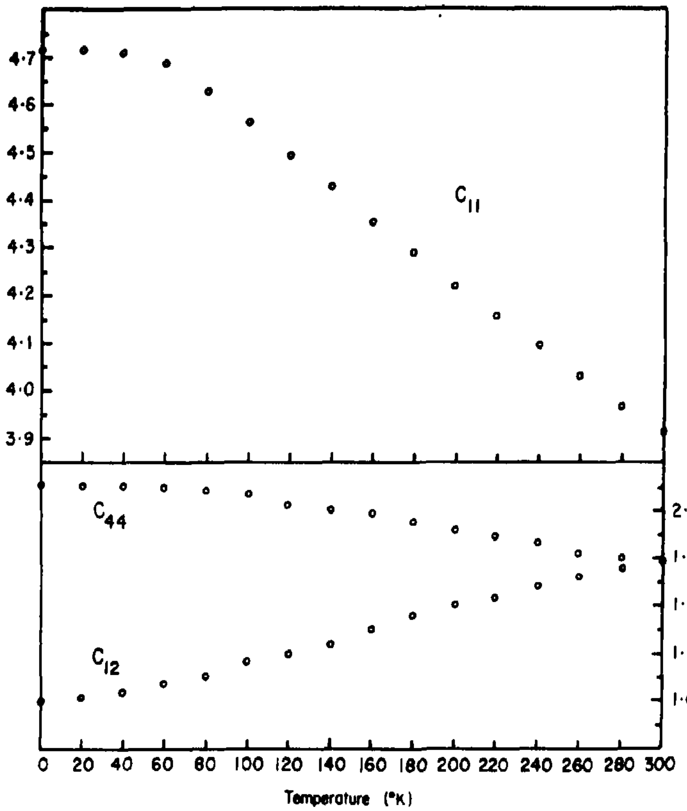

Fig. 1. The elastic constants of LiBr as a function of temperature in units of 10^{11} dyn/cm².

Lewis *et al.*[11] and Nikanorov *et al.*[12]. In addition, Huntington[6] has discussed the fact that $(\frac{1}{2}c_{11}-c_{12}) < c_{44}$ for Li halides.

DEBYE TEMPERATURE AND LATTICE ENERGY

The Debye temperature, Θ_D, at 0°K, was calculated from the extrapolated values of the elastic constants. Using the approximation of Betts, Bhatia, and Wyman[13] we obtained a value of $\theta_D^{el} = 276{\cdot}6$°K. According to Betts *et al.* if $0{\cdot}5 \leq 2c_{44}/(c_{11}-c_{12}) \leq 1{\cdot}5$ for cubic crystals, then θ_D^{el} is in error at most by a fraction of a per cent. For LiBr we get the anisotropy factor to be $A = 1{\cdot}204$. Therefore, θ_D^{el} for LiBr should lie within the above error.

The DeLaunay's approximation[14] could not be used in these calculations since $(c_{11}-c_{12})/2c_{44}$ is not greater than or equal to one.

Utilizing the Madelung's constant $\alpha = 1{\cdot}747558$ and the compressibility β at 0°K, we have calculated the lattice energy of LiBr[15] to be $U_0 = 184{\cdot}8$ kcal/mole.

FAILURE OF CAUCHY RELATION

Quantities which provide information on the forces between ions in a solid are the Cauchy Relations which for a cubic system reduce to $c_{12} = c_{44}$[6]. It was found for LiBr as has been found with the other alkali halides that $\Delta = c_{12} - c_{44}$ is not equal to zero.* The value for Δ obtained in these measurements was $-0{\cdot}462$° at 4·2°K and $-0{\cdot}010$ at 295°K (both in units of 10^{11} dyn/cm^2). Our value at 300°K is very near to the room temperature value obtained by Spangenberg and Haussühl [10] of $-0{\cdot}03$ (in units of 10^{11} dyn/cm^2). As can be seen from the experimental results of LiF[16] and LiCl[7] the deviation of the Cauchy Relation becomes more marked for decreasing temperature, i.e. the differences in the deviations between 300° and 4·2°K being $-0{\cdot}17$ and $-0{\cdot}234$, respectively (both in units of 10^{11} dyn/cm^2). Therefore, our value of $-0{\cdot}462$ (in units of 10^{11} dyn/cm^2) seems very reasonable at 4·2°K.

Acknowledgements—The authors would like to express their appreciation to Dr. W. O. Milligan and the late Dr. W. V. Houston for their discussions during the course of this work.

---

*For a theoretical discussion of the deviations of the Cauchy Relations, see, for example, the work of P. O. LOWDIN and more recently the work of E. LOMBARDI *et al.*

REFERENCES

1. LOWDIN P. O., *A Theoretical Investigation into Some Properties of Ionic Crystals*, Almquist and Wiksell, Uppsala (1948); *Advan. Phys. (Phil. Mag. Suppl.)* **5**, 1 (1959).
2. LOTHE J., *Arch. Math. Naturwidenskab.* **55**, 1 (1959).
3. HERPIN A., *J. Phys. Radium* **14**, 611 (1953).
4. DICK B. G., *Phys. Rev.* **129**, 1583 (1963).
5. LOMBARDI E. and JANSEN L., *Phys. Rev.* **136**, A1011 (1964); *ibid.* **140**, A275 (1965); *ibid.* **151**, 694 (1966).
6. HUNTINGTON H. B., In *Solid State Physics*, Vol 7, pp. 214–349. Academic Press, New York (1958).
7. MARSHALL B. J., PEDERSON D. O. and DORRIS G. G. *J. Phys. Chem. Solids* **28**, 1061 (1967).
8. WEYL W. A., Office of Naval Research Tech. Reps. Nos 64–66, Pennsylvania State University (1965)
9. KITTEL C., In *Introduction to Solid State Physics*, p. 154. Wiley, New York (1963).
10. SPANGENBERG K. and HAUSSUHL S., *Z. Kristallogr.* **109**, 4 (1957).
11. LEWIS J. T., LEHOCZKY A. and BRISCOE C. V., *Phys. Rev.* **161**, 877 (1967).
12. NIKANOROV S. P. and STEPANOV A. V., *Fiz. Tverd. Tela* **6**, 1987 (1964); *Soviet Phys. solid St.* **6**, 1569 (1965); NIKANOROV S. P., NRANYOU A. A. and STEPANOV A. V., *Fiz. Tverd. Tela* **6**, 1996 (1964), *Soviet Phys. solid St.* **6**, 1576 (1965).
13. BETTS D. D., BHATIA A. B. and WYMAN M., *Phys. Rev.* **104**, 37 (1956).
14. DE LAUNAY J., *J. chem. Phys.* **30**, 91 (1959).
15. KITTEL C., In *Introduction to Solid State Physics*, pp. 77–79 Wiley, New York (1963)
16. SQUIRE C. F. and BRISCOE C. V., *Phys. Rev.* **106**, 1175 (1958)

J. Phys. Chem. Solids Pergamon Press 1969. Vol. 30, pp 1909–1916 Printed in Great Britain.

SOME TRANSITION PROPERTIES OF THE ISING MODEL SUPER-EXCHANGE ANTIFERROMAGNET

D. W. WOOD
Mathematics Department, University of Nottingham, Nottingham, England

and

N. W. DALTON
Theoretical Physics Division, Atomic Energy Research Establishment, Harwell, England

(*Received* 24 *December* 1968; *in revised form* 25 *February* 1969)

Abstract—The partition function and related thermodynamic functions of a two-dimensional antiferromagnet where exchange interactions are present between (i) magnetic and non-magnetic spins with an exchange integral J_1 and (ii) non-magnetic spins with an exchange integral J_2 are obtained exactly in an arbitrary magnetic field H and for an arbitrary magnetic spin quantum number S. The model is a simple quadratic lattice with non-magnetic spins at each vertex and decorated with a magnetic spin on each bond. The effect of interactions present between non-magnetic spins on the critical temperature $T_c(\alpha)(\alpha = J_2/J_1)$ and critical field $H_c(\alpha)$; and on the transition temperature $T_t(\alpha)$ and transition field $H_t(\alpha)$ is examined in detail It is found that $T_c(\alpha)$ approaches zero linearly as $\alpha \rightarrow \alpha^* = -2S$, and that when $\alpha > 0$ there exists a temperature T_x below which the transition magnetic field is infinite The dependence of the zero field internal energy $E(\alpha, T)$, and the zero field susceptibility $\chi_0(\alpha, T)$ upon α is evaluated, and exact expressions are derived for the critical point values of $E(\alpha, S, T_c)$ and $\chi_0(\alpha, S, T_c)$.

1. INTRODUCTION

CONSIDER an Ising model[1] ferromagnetic lattice assembly of N spins, where the Hamiltonian is given by

$$\mathcal{H} = -\sum_{r=1}^{n} J_r \sum_{(r)} S_i^z S_{i+r}^z - \mu H \sum_{i=1}^{N} S_i^z$$

and where J_r is the exchange constant between rth neighbouring spins S_i^z and S_{i+r}^z, $\sum_{(r)}$ denotes the sum over all rth neighbour spins, μ is the magnetic moment per spin, and H is the external magnetic field. It is well known that exact solutions can be obtained for the partition function and related thermodynamic functions of any two-dimensional planar lattice when, (a) the interactions are limited to those between nearest neighbour spins, (b) the spin quantum number S of each lattice site is $\frac{1}{2}$, and (c) the external magnetic field is zero.

Of all the present day methods which are capable of re-deriving the Onsager solution not one of them is able to incorporate a relaxation of any one of the constraints (a), (b) or (c). An interesting exception to this deadlock is the two-dimensional super-exchange model of an antiferromagnet which was proposed by Fisher[2] and is based on the Ising model. The model is a member of a class of exactly solvable problems known as the decorated bond transformations, which have been discussed by Fisher[3]. The basic idea of the model is to represent at low temperatures an antiferromagnetic ordering in terms of magnetic atoms interacting via a non-magnetic intermediary atom; a phenomena labelled super-exchange by Anderson [4, 5]. Fisher has given a very thorough treatment of a super-exchange simple quadratic lattice deriving exact results for the thermodynamic functions in the presence of a field (condition (c) relaxed), and discusses in detail their magnetic field dependence. The super-exchange Ising model is even more versatile, and exact results can be obtained when all three of the constraints (a–c) are relaxed simultaneously.

It is the main purpose in this paper to examine the effects of a second neighbour interaction on the transition properties of a two-dimensional super-exchange model of an antiferromagnet (condition (a) relaxed). The paper contains three further sections. In Section 2 the model is briefly described and the partition function obtained; a semi-classical Ising-Heisenberg model is introduced as the limiting case of the super-exchange model ($S \to \infty$).

In Section 3 the transition points are discussed as functions of the strength of the second neighbour interactions, and in Section 4 we discuss the behaviour of some of the critical thermodynamic properties in zero magnetic field.

2. FISHER'S SUPER-EXCHANGE MODEL

A section of Fisher's[2] super-exchange simple quadratic lattice is shown in Fig. 1. The open circles at the vertices of the net represent non-magnetic spins S_i^0 which do not interact with the external magnetic field, and have quantum numbers of $\frac{1}{2}$. The crosses on the bonds of the square net represent magnetic spins S_j^+ (vertical bonds) and S_k^- (horizontal bonds). The magnetic spins may have an arbitrary quantum number S. To ensure that the low temperature ordering is antiferromagnetic Fisher introduces ferromagnetic coupling between neighbouring S_j^+ and $S_i^0(-J_1 S_{iz}^0 S_{jz}^+)$, and antiferromagnetic coupling between neighbouring S_k^- and $S_i^0(J_1 S_{iz}^0 S_{kz}^-)$.

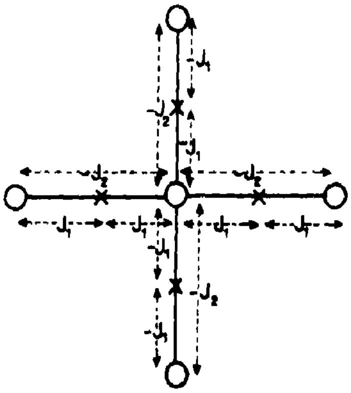

Fig. 1. A section of Fisher's super-exchange lattice where the open circles at each vertex represent non-magnetic spins, and the crosses on each bond represent magnetic spins. The exchange interactions included in the assembly are also shown, a negative J_r denotes a ferromagnetic exchange.

Consider now an exchange coupling $-J_2 S_{iz}^0 S_{jz}^0$ present between the neighbouring non-magnetic vertex spins; this effectively introduces a next-nearest-neighbour interaction in the form of a direct ferromagnetic exchange interaction. The exchange interactions present are shown in Fig. 1; we can write the Hamiltonian of the assembly in the form

$$\mathscr{H} = 4J_1\left\{-\sum S_{iz}^0 S_{jz}^+ + \sum S_{iz}^0 S_{kz}^- - \alpha \sum S_{iz}^0 S_{jz}^0\right\} - 2\mu H \sum S_{jz}^+ - 2\mu H \sum S_{kz}^- \qquad (2)$$

where $\alpha = J_2/J_1$ and is a measure of the relative strength of the next-nearest neighbour interactions.

The Hamiltonian (2) is a particular case of a decorated lattice where the decoration is the addition of a magnetic spin to each bond of the undecorated s.q. lattice. Following Fisher[3] the partition function Z_D of the decorated super-exchange lattice in the presence of a field can be expressed in terms of the partition function Z of the undecorated lattice in zero magnetic field. The decorated bond transformation yields the relation

$$Z_D(K_1, K_2, S, L) = \{f(K_1, S, L)\}^{N_D} Z(K', K_2) \qquad (3)$$

where N_D is the number of decorated bonds,

$$K_r = J_r/kT, \quad L = \mu H/kT \qquad (4)$$

and

$$K' = K'(K_1, S, L). \qquad (5)$$

In (3) the new interaction parameter K' is defined by the transformation equation (5) which following Fisher[3] can be expressed in terms of a single function $\psi(S^0_{1z}, S^0_{2z}; H)$. For our particular model

$$\psi(S^0_{1z}, S^0_{2z}; H)$$

$$= \sum_{S_j^+=-S}^{S} \exp\{4K_1 S_j^+ (S^0_{1z}+S^0_{2z}) + 2LS_j^+\} \quad (6)$$

$$= \sinh X\{2K_1(S^0_{1z}+S^0_{2z})+L\}/$$

$$\sinh[2K_1(S^0_{1z}+S^0_{2z})+L] \quad (7)$$

where $X = 2S+1$. The functions f and K' are now defined by

$$e^{4K'} = \psi(++)\psi(--)/\psi(+-)\psi(-+) \quad (8)$$

and

$$f = \psi(++)\psi(--)\psi(+-)\psi(-+) \quad (9)$$

where $\psi(++) = \psi(\frac{1}{2}, \frac{1}{2}; H)$ and so on. The complete transformation reduces Z_D to the form

$$Z_D = (2S+1)^{2N} f^{2N} Q(K'+\alpha K_1) \quad (10)$$

where Q is the partition function of the Ising model square net in zero magnetic field.

In the limit $S_j^+, S_j^- \to \infty$ the above model tends to a semiclassical Ising-Heisenberg model of a super-exchange antiferromagnet where the non-magnetic spins remain with quantum number $\frac{1}{2}$. We introduce a unit vector **k** in the direction of the magnetic field and define the non-magnetic Ising spins $\mathbf{S}_i^0$ by

$$\mathbf{S}_i^0 = S_i^0 \mathbf{k} \quad (11)$$

where $S_i^0 = \pm 1$. The magnetic spins become classical unit vectors $\mathbf{S}_j^+$ and $\mathbf{S}_k^-$ which can orientate in any direction. The Hamiltonian corresponding to (2) becomes

$$\mathscr{H}'_{\text{classical}} = -J_1' \sum \mathbf{S}_i^0.\mathbf{S}_j^+ + J_1' \sum \mathbf{S}_i^0.S_k^-$$

$$-J_2' \sum \mathbf{S}_i^0.\mathbf{S}_j^0 - \mu' \sum \mathbf{H}.\mathbf{S}_k^- - \mu' \sum H.\mathbf{S}_j^+ \quad (12)$$

where $SJ_1 \to J_1'$, $S^2J_2 \to J_2'$ and $S\mu \to \mu'$ in the limit of infinite spin.

Again the decorated bond transformation is completely defined by $\psi(S_1^0, S_2^0; H)$, which is given by

$$\psi(S_1^0, S_2^0; H)$$

$$= \frac{1}{4\pi} \int \exp\{[K_1(S_1^0+S_2^0)+L]\,\mathbf{k}.\mathbf{S}_j^+\}\,d\Omega_j^+ \quad (13)$$

$$= \sinh(K_1(S_1^0+S_2^0)+L]/[K_1(S_1^0+S_2^0)+L] \quad (14)$$

where the range of integration extends over the solid angle Ω_j^+ subtended by the classical spin on the bond. The classical partition function is given by

$$Z_{\text{classical}} = f^{2N} Q(K'+\alpha K_1) \quad (15)$$

where f and K' are again defined by (8) and (9).

3. TRANSITION FIELDS AND TEMPERATURES

In order to discuss the effects of the magnetic field on the various transition properties it is convenient to introduce the reduced magnetic field $H^* = \mu H/J_1$. The variation of (i) the critical temperature $kT_c(\alpha, S)/J_1 = K_c^{-1}(H{=}O)$, (ii) the critical magnetic field $H_c^*(\alpha, S)$ $(T{=}O)$, (iii) the transition temperature $kT_t(\alpha, S)/J_1 = K_t^{-1}(H \neq 0)$, and (iv) the transition magnetic field $H_t^*(\alpha, S)$ $(T > 0)$ with changes in J_2/J_1, and the magnetic spin quantum number are all contained in the single equation

$$\exp\{2K'(K_t, H_t^*) + 2\alpha K_t\} = 1+\sqrt{2} \quad (16)$$

which follows from the solution of the Ising model square net.

The variation of $T_c(\alpha)/T_c(0)$ with α for values of α between -1 and 1 obtained from the solution to (16) is shown in curves (c) and (a) of Fig. 2 for the cases $S = \frac{1}{2}$, and classical spins respectively. For positive $\alpha(J_1 > 0, J_2 > 0)\, T_c$ increases rapidly with

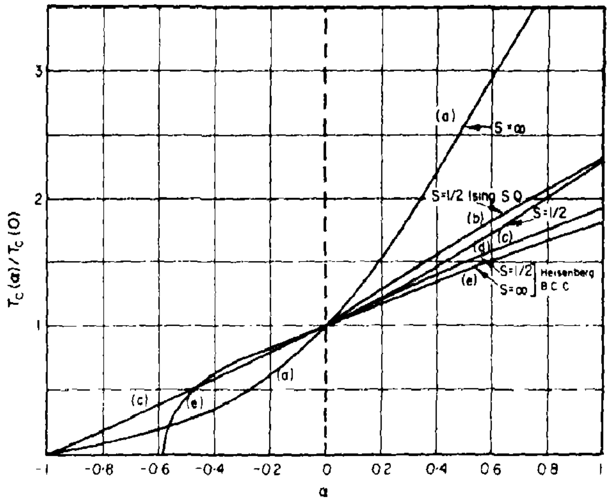

Fig. 2. Comparisons of behaviour of $T_c(\alpha)/T_c(0)$; (a) the Classical super-exchange model s.q lattice (b) the Ising model s.q. lattice, $S = \frac{1}{2}$ (c) the super-exchange model s.q lattice, $S = \frac{1}{2}$ (d) the Heisenberg model b.c.c. lattice, $S = \frac{1}{2}$ and (e) the Classical Heisenberg model b.c.c. lattice.

α, and for $S = \frac{1}{2}$ the change in T_c between $\alpha = 0$ and $\alpha = 1$ is given by

$$T_c(1)/T_c(0) = 2\cosh^{-1}(1+\sqrt{2})/\ln(1+2\sqrt{2}) = 2{\cdot}277 \quad (17)$$

which is slightly less than the corresponding figure of 2·323 for the Ising model square net, which has been obtained from the high temperature ($T > T_c$) series expansions of the zero field susceptibility[6, 7]. In the region $\alpha \to 0$ the curves of $T_c(\alpha)/T_c(0)$ vs. α for various spin values ($S = \frac{1}{2}, 1, \frac{3}{2}, \ldots$) begin to show a marked curvature, and from (16) we can obtain the expansion

$$\frac{T_c(\alpha)}{T_c(0)} = 1 + \frac{1}{F(2K_c(0))}\alpha + \frac{K_c(0)D(2K_c(0))}{\{F(2K_c(0))\}^3}\alpha^2 + 0(\alpha^3) \quad (18)$$

where

$$F(y) = X\coth Xy - \coth y$$

and

$$D(y) = \operatorname{cosech}^2 y - X^2 \operatorname{cosech}^2 Xy. \quad (19)$$

In the case of $S = \frac{1}{2}$ (18) reduces to

$$\frac{T_c(\alpha)}{T_c(0)} = 1 + 1{\cdot}099\alpha + 0{\cdot}1739\alpha^2 + 0(\alpha^3). \quad (20)$$

For the Ising model square net the linear term in (20) has been evaluated from series expansion data[7] and is 1·35.

In the negative α region ($J_1 > 0$, $J_2 < 0$) where the exchange interactions between the non-magnetic spins are antiferromagnetic, the critical temperature decreases with negative α and becomes identically zero at $\alpha = \alpha^* = -2S$; for classical spins $\alpha^* = -1$. In the neighbourhood of α^* the critical point approaches zero according to the linear relation

$$kT_c/J_1 \simeq 2(\alpha-\alpha^*)/\log\{X(1+\sqrt{2})\} \quad \alpha \gtrsim \alpha^* \quad (21)$$

and for the classical magnetic spins the slope at α^* becomes zero, and (21) is replaced by the logarithmic approach to zero

$$\tfrac{1}{2}(kT_c/J_1)\log(kT_c/2J_1) \simeq \alpha^* - \alpha \qquad \alpha \gtrsim \alpha^*. \quad (22)$$

This behaviour in the region of α^* is unexpected in relation to what little is known about it for other models. There is no reliable information on this region for Ising model lattices, however there is some theoretical evidence available for the three-dimensional Heisenberg model lattices. In this case the evidence from both a first order Greens function approach[8] and a high temperature expansion approach[9] indicates that $T_c(\alpha)$ approaches zero very rapidly in the region $\alpha > \alpha^*$ and that the curves intersect the α axis perpendicularly at α^*. We have illustrated this in Fig. 2 where we have compared the plots of $T_c(\alpha)/T_c(0)$ vs. α for the super-exchange model ($S = \frac{1}{2}, S = \infty$) with the Ising model square net ($S = \frac{1}{2}$, and $\alpha > 0$), the Heisenberg model b.c.c. lattice ($S = \frac{1}{2}$ and $\alpha > 0$), and the classical Heisenberg model b.c.c. lattice. The Ising and Heisenberg model curves in Fig. 2 are all based on data obtained from series expansion methods[7, 9].

Interesting effects can occur in the presence of a magnetic field, here (16) can be thought of as the equation for the transition magnetic field $H_t^*(T,\alpha,S)$. At a given temperature below T_c the long range order of an antiferromagnet can be reduced by increasing the magnetic field, and becomes zero at the transition field H_t^*. At zero temperatures the transition field is known as the critical field H_c^*. In the region $\alpha \leq 0$ (16) yields the equation

$$H_c^* = \alpha/S + 2, \quad \alpha < 0 \qquad (23)$$

hence the critical field becomes zero at α^*.

The curves of H_t^* vs. kT/J_1 are plotted in Fig. 3 for the case $S = \frac{1}{2}$, here α is a parameter and takes values between $-0{\cdot}6$ and $0{\cdot}5$. These transition field curves illustrate clearly the essential differences in behaviour which exist between the positive and negative α regions. In both regions H_t^* decreases with increasing temperature and finally becomes zero at T_c. In the neighbourhood of $T_c (T < T_c) H_t^*$ tends to zero according to the relation

$$H_t^* \simeq \frac{2[F(2K_c)+\alpha]^{1/2}}{\cdot\,[\frac{1}{3}(X^2-1)-D(2K_c)]^{1/2}} \{K_c^{-1}-K_1^{-1}\}^{1/2}\Big|_{T\to T_c^-}. \qquad (24)$$

For $\alpha < 0$ H_t^* increases as the temperature falls below T_c and approaches the critical field linearly in the limit of zero temperature. The most striking behaviour is shown for $\alpha > 0$ where the transition field becomes infinite at a temperature T_∞ which is given by

$$T_\infty = (J_2/k)/\tfrac{1}{2}\ln(1+\sqrt{2}). \qquad (25)$$

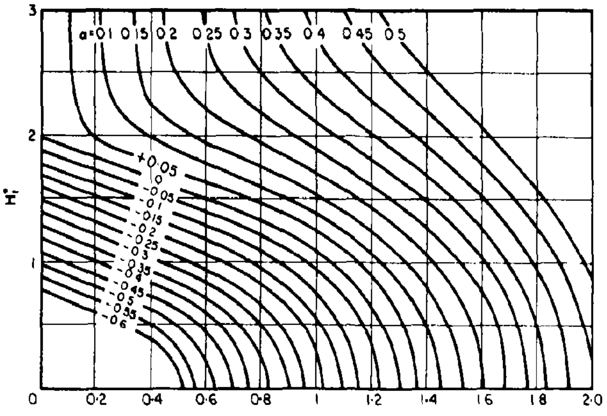

Fig. 3. The variation of the transition magnetic field H_t^* with temperature for $S = \frac{1}{2}$ with α as a parameter.

For a given positive value of J_2, the long range order cannot be removed from the assembly simply by increasing the magnetic field when the temperature is below T_λ, but for $T > T_\tau$ this will always be possible.

4. THE INTERNAL ENERGY, MAGNETIC SPECIFIC HEAT, AND SUSCEPTIBILITY IN ZERO MAGNETIC FIELD

The behaviour of the thermodynamic properties of the super-exchange antiferromagnet in the presence of a field have been thoroughly discussed by Fisher[2], particularly in the neighbourhood of H_c^*. Here we restrict the discussion of the thermodynamic properties to the zero field case and consider the effects of the direct exchange interactions on the critical properties of the model.

The internal energy per non-magnetic spin $U(K_1, \alpha, H)$ is given by

$$U(K_1, \alpha, H) = N^{-1}\frac{\partial}{\partial K}\ln Z(K_1, \alpha, H)$$
$$= -E(K_1, \alpha, H)/NJ_1. \quad (26)$$

The behaviour of the internal energy is shown in Fig. 4, where $U(K_1, \alpha, 0)$ is plotted against K_1^{-1} for values of α in the range -1 $(=\alpha^*)$ to 0·8 for the case $S = \frac{1}{2}$ in (26). At zero temperature the energy is given by

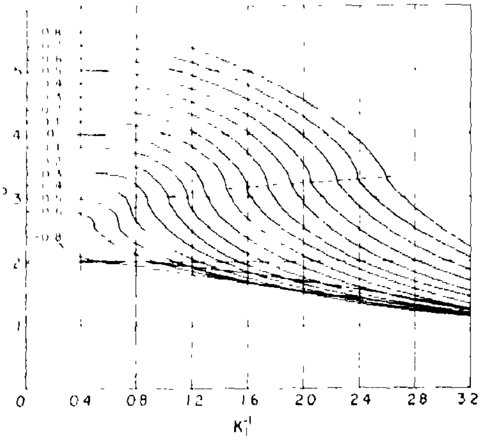

Fig. 4. The internal energy per non-magnetic spin U obtained from (26) with $S = \frac{1}{2}$ plotted against temperature with α as a parameter. The dashed curve is the locus of the critical point.

$$\lim_{T\to 0} U = 8S + 2\alpha \quad (27)$$

and decreases steadily from this point until a sharp kink is encountered in the region of the critical point. The dashed curve in Fig. 4 is the locus of the critical points. At the critical point all the curves have a vertical slope (except for the case $\alpha = \alpha^*$, where $T_c = 0$); beyond T_c the energy decreases to zero in the high temperature limit. The internal energy is continuous through T_c and for a given α behaves as

$$U \simeq U_c - AK_c\left(\frac{T_c}{T} - 1\right)\ln\left|\left(\frac{T_c}{T} - 1\right)\right|_{T \approx T_c}$$

where U_c is the value of the internal energy at T_c, and A depends on α and is given by

$$A = \frac{8}{\pi}(F(2K_c) + \alpha)^2. \quad (29)$$

At the critical point we can obtain $U_c(\alpha)$ from (26), which simplifies to give

$$U_c(\alpha) = F(2K_c)(2+\sqrt{2}) + \sqrt{2}\alpha \quad (30)$$

where for example

$$U_c(\alpha) = (2+\sqrt{2})\tanh 2K_c + \sqrt{2}\alpha,$$
$$S = \tfrac{1}{2} \quad (31)$$

and

$$U_c(\alpha) = (2+\sqrt{2})(\coth 2K_c - 1/2K_c) + \sqrt{2}\alpha,$$
$$S = \infty. \quad (32)$$

If we denote the specific heat per non-magnetic spin vertex by C_v', then the area under the curves of C_v' vs. T between temperatures T_1 and T_2 is given by

$$\int_{T_1}^{T_2} C_v' \mathrm{d}T = (J_1/k)[U(T_1) - U(T_2)] \quad (33)$$

and so $(J_1/k)U_c(\alpha)$ is the area above T_c under the specific heat curve. If we plot the specific heat C_v' on a reduced scale of temperature $t(=T/T_c)$ the area under the curve above T_c is given by $K_cU_c(\alpha)$ which is a quantity often compared with experimental work[10–12]. Plots of $K_cU_c(\alpha)$ against α are shown in Fig. 5 for the cases $S=\frac{1}{2}$, $S=1$, $S=\frac{3}{2}$ and $S=\infty$. These curves are also compared with the corresponding curve for the Ising model square net with $S=\frac{1}{2}$ and $\alpha>0$, which has been determined from high temperature series expansions[7].

To discuss the susceptibility χ we define the reduced susceptibility ξ given by

$$\begin{aligned}\xi(K_1,\alpha,H) &= kT\chi(K_1,\alpha,H)/N\mu^2\\ &= N^{-1}\partial^2\ln Z(K_1,\alpha,H)/\partial L^2 \qquad (34)\end{aligned}$$

which in zero magnetic field yields the equation

$$\begin{aligned}\xi(K_1,\alpha,0) &= \xi_0\\ &= \frac{\{D(2K_1)+\frac{1}{3}(1-X^2)\}\{\frac{1}{2}U(K_1,\alpha,0)+\alpha\}}{\{F(2K_1)+\alpha\}}\\ &\quad -\tfrac{2}{3}(1-X^2). \qquad (35)\end{aligned}$$

From (35) we see that ξ_0 in the critical region is closely connected to the behaviour of the internal energy, and for temperatures close to T_c is of the form

$$\xi_0 \simeq \xi_c + B(\alpha)\left(\frac{T_c}{T}-1\right)\ln\left|\frac{T_c}{T}-1\right|_{T=T_c}$$

where $B(\alpha)$ is readily obtained from (35) and (29). In (36) ξ_c is the value of the reduced susceptibility at the critical temperature. The detailed behaviour of the susceptibility is shown in Fig. 6 where we plot the susceptibility for various values of α and for the case $S=\frac{1}{2}$ in (35). These curves show that the near vertical sections about the kinks rapidly decrease in size as α increases, and for $\alpha>1$ the transition kink would be practically unobservable in these plots. At high temperatures ξ_0 approaches asymptotically the value of $8S(S+1)/3$.

At the critical point (35) simplifies, and the critical reduced susceptibility is given by

$$\begin{aligned}\xi_c &= \{D(2K_c)\}(1/\sqrt{2}+1)\\ &\quad +\tfrac{1}{3}(X^2-1)(1-1\sqrt{2}). \qquad (37)\end{aligned}$$

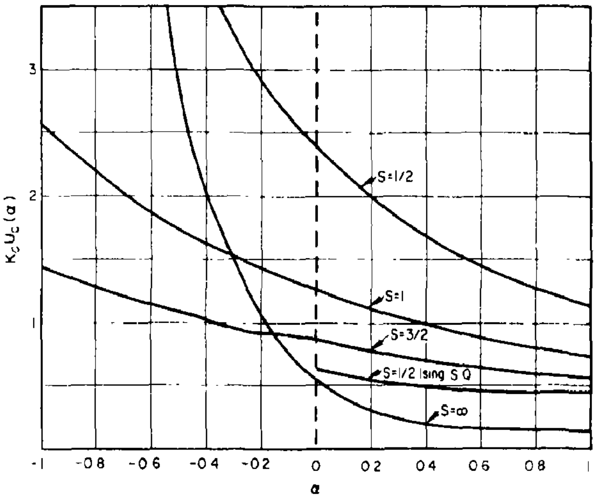

Fig. 5 The variation of K_cU_c with α for the cases $S=\frac{1}{2}$, 1, $\frac{3}{2}$ and ∞; and for the Ising model s.q. lattice with $S=\frac{1}{2}$.

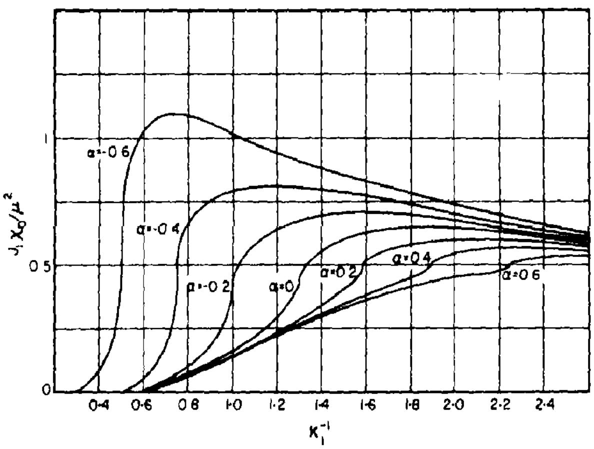

Fig. 6. The zero field susceptibility χ_0 plotted against temperature with α as a parameter and for $S = \frac{1}{2}$.

In the limit of zero critical temperature ξ_c approaches a finite limit given by

$$\xi_c(\alpha^c) = \tfrac{1}{4}(X^2 - 1)(1 - 1/\sqrt{2}). \qquad (38)$$

Although the artificial nature of the present two-dimensional model rules out any comparisons with experimental work, the properties discussed in these last two sections are likely to retain a qualitatively accurate picture of the effects of mixed exchange interactions on the transition and thermodynamic properties of an antiferromagnet. At the cost of losing an exactly solvable model three-dimensional models could be similarly set up, and the standard techniques of series expansions and extrapolations[11] could be employed to reconstruct the properties discussed above for a three-dimensional lattice.

REFERENCES

1. The literature on the Ising model is extensively covered in the following reviews: DOMB C., *Advan. Phys* **9**, 34, 35 (1960); Fisher M. E., *Rep Prog. Phys* **30**, 615 (1967).
2. FISHER M. E., *Proc R. Soc* **A254**, 66 (1960); *ibid.* **A256**, 502 (1960).
3. FISHER M. E., *Phys. Rev.* **113**, 969 (1959).
4. ANDERSON P. W., *Phys Rev.* **79**, 350 (1950)
5. ANDERSON P. W., *Solid St. Phys.* **14**, 99 (1963).
6. DOMB C and DALTON N W, *Proc phys Soc.* **89**, 859 (1966).
7. DALTON N. W. and WOOD D. W., *J. Math. Phys.* To be published (1969).
8. TAHIR-KHELI R., CALLEN H. B and JARRETT H. S., *J. Phys Chem. Solids* **27**, 23 (1966)
9. WOOD D. W. and DALTON N. W., *Phys. Rev.* **159**, 384 (1967)
10. DOMB C. and MIEDEMA A R., *Proc Low Temp. Phys* **4**, 296 (1964).
11. MIEDEMA A. R., VAN KEMPEN H. and HUISKAMP W. J., *Physica* **29**, 1266 (1963).
12. WOOD D. W. and DALTON N. W, *Proc. phys. Soc* **87**, 755 (1966).

J. Phys. Chem. Solids Pergamon Press 1969. Vol. 30, pp. 1917–1920. Printed in Great Britain.

THE ENERGY OF ORDERING IN THE ALLOY CuPt

CARL M. WU* and **BARTON ROESSLER**
Division of Engineering, Brown University, Providence, R. Is. 02912, U.S.A.

(*Received* 27 *November* 1968; *in revised form* 5 *February* 1969)

Abstract – The energy of ordering in the alloy CuPt was measured by means of tin solution calorimetry. The energy difference between a specimen quenched from above the critical temperature and a specimen completely long-range ordered is 1400 ± 60 cal/g-atom.

1. INTRODUCTION

THE ORDER–DISORDER transformation in the CuPt system which occurs in the alloy of 50 at. % is somewhat unusual, since in the ordered condition the number of unlike first nearest neighbors is the same as it is, on the average, in the random disordered condition [1]. Changes in the number of unlike second and more distant neighbors must be considered if the ordering tendency is to be attributed to a reduction in pairwise interaction energy. These facts have led several authors [2–6] to suggest that the ordering may be caused, instead, by a lowering of the electron energies. Thermodynamic data, which would be helpful in understanding the transformation are not extensive. In particular, the energy of ordering is not known. The present investigation describes the experimental determination of this quantity by means of tin solution calorimetry.

2. EXPERIMENTAL PROCEDURE AND RESULTS

Preparation of alloys

Copper of 99·999 per cent purity (Asarco A-58) and platinum sponge of 99·999 per cent (Johnson Mathey 1010) in the appropriate amounts were induction melted in a high purity graphite crucible under a protective atmosphere of helium. The resulting ingot was homogenized in the crucible by holding between 1250° and 1350°C for 5 hr. Chemical analysis showed no significant composition difference between the top and bottom of the ingot; the mean concentration of copper was 24·51 wt. %, the stoichiometric composition being 24·57 per cent. The resulting ingot was then rolled to produce strip of thickness 0·01 in.

To produce long-range ordered material, the strip was sealed under vacuum in a Vycor tube and held for approximately 24 hr at a series of temperatures starting at 850°C (T_c = 815°) and decreasing approximately 50°C every 24 hr down to 490°C. It was then held for 4 days at 490°C, cooled to 200°C in steps over the next two weeks and, finally, furnace cooled to room temperature. Recrystallization occurred during this heat treatment to give an equiaxed structure having a mean intercept grain size of 0·11 mm. Specimens suitable for the calorimetric measurements (approximately ¼ × ¼ × 0·01 in.) and for resistivity measurements (approximately 1·5 × 0·030 × 0·01 in.) were cut from the ordered strip by a spark discharge machine. A number of these specimens were then resealed in an evacuated Vycor tube, placed in a furnace at 877°C for 2·5 hr, and then quenched by dropping the tube into an ice water mixture and smashing it as soon as it landed in the quenching tray. These specimens will be referred to as disordered, although, in fact they contain short-range order [7].

The state of order in the specimens was checked by X-ray diffraction and electrical resistivity measurements. Back reflection X-ray photographs from the ordered specimens showed superlattice reflections which were completely absent in the disordered specimens. The photographs were substantially the same as those shown by Roessler and Rayne [8].

The results of electrical resistivity measurements at 24°, −81°, and −196°C are presented in Table 1. The estimated limits of error for the resistivity values are due to the limitations in the measurements of the specimen dimensions. The resistivity values at room temperature for the slowly cooled alloys are

---

*Based on a thesis by Carl M. Wu submitted in partial fulfillment of the requirements for the Sc.M. degree at Brown University.

Table 1. Resistivity of ordered and disordered CuPt

Specimen No	Temperature, T_1 (°C)	Resistivity* ($\mu\Omega$-cm)	Temperature, T_2 (°C)	Resistivity* ($\mu\Omega$-cm)	Temperature, T_3 (°C)	Resistivity* ($\mu\Omega$-cm)	Temperature, coefficient of resistivity† ($\mu\Omega$-cm °C)
			Ordered CuPt				
1	24·4	10·15	−81	8·15	−196	6·01	0·0188
2	24·9	9·92	−81	8·01	−196	5·92	0·0181
3	24·4	9·81	−81	7·89	−196	5·85	0·0180
4	24·5	9·76	−81	7·87	−196	5·77	0·0181
5	25·0	9·95	−81	7·95	−196	5·91	0·0183
			Disordered CuPt				
2	25·5	91·07	−81	90·23	−196	89·37	0·0077
3	24·1	91·89	−81	91·26	−196	90·39	0·0068
4	24·0	90·02	−81	89·34	−196	88·46	0·0079

*Limits of error ± 1·4 per cent

†Temperature coefficient calculated from $\alpha = \dfrac{\rho(T_1)-\rho(T_3)}{T_1-T_3}$.

substantially the same as the lowest previously reported value[9] ($\rho = 10{\cdot}15\,\mu\Omega$-cm) and confirm that the specimens were completely long-range ordered. The temperature coefficient of resistivity for ordered specimens is more than twice that for disordered specimens, a finding which is similar to that for Cu_3Au[10]. The resistivity at 24°C for the ordered alloy is approximately equal to that of pure platinum, whereas at −196°C, where the value is more nearly just the residual resistivity, it has fallen to about $6\,\mu\Omega$-cm, an extremely low value for a transition metal alloy. These extremely low resistivity values indicate that the lattice periodicity in the ordered structure was very perfect indeed.

Calorimetric measurements

The heats of solution in liquid tin at 466°C were measured in a tin solution calorimeter which is substantially identical to that described by Howlett *et al.*[11].

The calorimeter was calibrated by adding a known weight of tin from 0°C using 4605 cal/g-atom for the enthalpy increment from 0°C to 700°K and a value of 6·85 cal/g-atom-deg[12] for the heat capacity above 700°K. The temperature was measured with a double iron constantan thermocouple in a Pyrex protective tube, it having been found that the Kovar protective cup usually used[11] deteriorated at these temperatures. The difference between the thermocouple signal and a bucking potential supplied by a K-2 potentiometer was amplified by a Keithley 150A microvoltmeter and was then recorded on a strip chart recorder[13].

The temperature first decreased as the cold specimen entered the tin bath, and then increased above that prevailing before the specimen was added to the calorimeter to give a resulting exothermic heat effect. The adiabatic temperature change[11] for each addition was computed using a technique especially developed for this purpose[13]. Constancy of the calculated adiabatic temperature change indicated that, at 466°C, the specimens were in solution in 3 to 6 min.

Specimens of disordered and ordered CuPt were added alternately to the calorimeter from a temperature of 0°C, and the resultant heat effects were plotted as a function of composition in the bath. The difference, at constant bath composition, of the heat effects for disordered and ordered specimens yielded the energy of ordering. The results of the calorimetric run having least scatter, shown in Fig. 1, are E_{ord} = 1409 cal/g-atom. Two other runs gave values of 1340 and 1460 cal/g-atom as the energy of ordering. On the basis of these measurements the energy difference between disordered and ordered CuPt is 1400 ± 60 cal/g-atom.

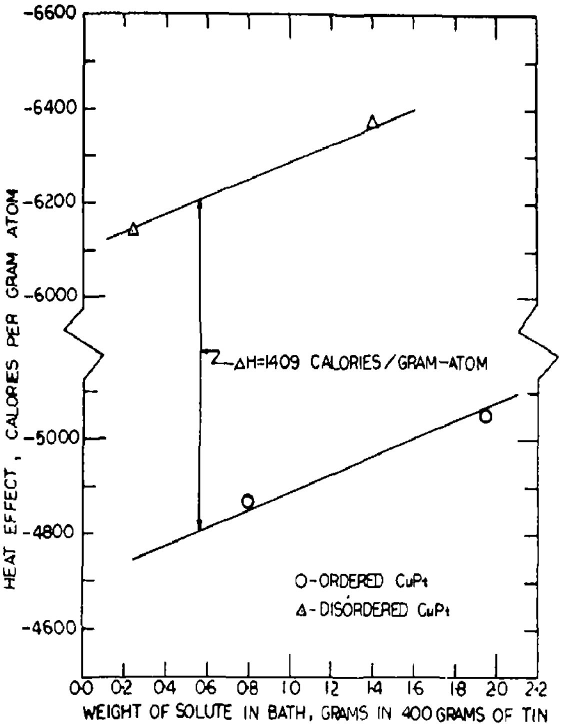

Fig. 1. Heat effect of ordered and disordered CuPt in tin at 466°C as a function of weight of solute in bath.

DISCUSSION

The only previous thermodynamic measurements with which the results reported here can be compared are those of Oriani and Murphy[14] and of Weibke and Matthes[15]. Oriani's extrapolation of his data on the enthalpy of formation of disordered specimens suggests a value of about 800 cal/g-atom for the energy difference between disordered and ordered specimens at 640°C. From measurements of the temperature dependence of the e.m.f., Weibke and Matthes suggest a value of 910 cal/g-atom for the difference between a disordered specimen at 800°C and an ordered specimen at 550°C and about 800 cal/g-atom when the ordered specimen is at 650°C. Since the ordered specimens in these previous investigations had a degree of order corresponding to temperatures of 640°, 550°, and 650°C, respectively, and hence were not fully ordered[7], it is to be expected that the energy differences of 800–910 cal/g-atom are considerably smaller than that determined here.

Since the alloy used here was very slowly cooled it is reasonable to assume that the cooling rate was sufficiently slow to allow the establishment of equilibrium at temperatures several hundred degrees below the critical temperature for long-range order. There will then be some minimum temperature for which atomic diffusion is sufficiently rapid so that equilibrium occurs in the time the cooling rate allows. The degree of order in the slowly cooled alloys used here, then, may be thought of as equal or greater than and, in fact, considerably greater than that characteristic of this 'lowest equilibrium temperature.' Although the resistivity, of course, depends in a complicated way[16] on details of the electronic structure such as the number and kind of carriers, and not just on the periodicity (or the scattering probability), the resistivity measurements suggest that the lattice was very perfectly ordered in the slowly cooled specimens used here. The state of order in the quenched specimens was undoubtedly greater than that which would prevail in equilibrium at the quench temperature of 877°C. It is evident, however, from the resistivity and X-ray measurements (see also [7] and [8]) that no long-range order was present in the quenched specimens. The energy difference of 1409 cal/g-atom, then, corresponds to the difference between an alloy containing only short-range order and one which is perfectly long-range ordered.

Acknowledgements—The support of this work by the Advanced Research Projects Agency under Contract SD 86 is gratefully acknowledged. The authors wish also, to thank the Westinghouse Electric Corporation for the preparation of alloys and for its generous gift to Brown University of the calorimeter used in this investigation. The numerical computations were carried out at the Brown University Computing Center with financial support from the National Science Foundation.

REFERENCES

1. WARREN B. E., *Frontiers Chem.* **5**, 101 (1948).
2. DEHLINGER U., *Z. Phys.* **105**, 588 (1937).
3. MUTO T., *Sci. Rep. Inst. Phys. Chem. Res. Tokyo* **34**, 377 (1938).
4. LIPSON H., *Prog. Metal Phys.* **2**, 1 (1950).
5. SLATER J. C., *Phys. Rev.* **84**, 179 (1951).
6. NICHOLAS J. F., *Proc. phys. Soc.* **A66**, 201 (1953)
7. WALKER C. B., *J. appl. Phys.* **23**, 118 (1952).
8. ROESSLER B. and RAYNE J. A., *Phys. Rev.* **136**, A1380 (1964).
9. LINDE J. O., *Annln. Phys.* **5**, 30, 151 (1937).
10. COHEN J. B. and BEVER M. B., *Trans. metall. Soc. A.I.M.E.* **218**, 155 (1960).
11. HOWLETT B. W., LEACH J. S. Ll., TICKNOR L. B. and BEVER M. B., *Rev. scient. Instrum.* **33**, 619 (1962)
12. HULTGREN R., ORR R. L., ANDERSON P. D. and KELLEY K. K., *Selected Values of Thermodynamic Properties of Metals and Alloys*. Wiley, New York (1963).
13. WU CARL M., M. S. Thesis, Brown University (1967).
14. ORIANI R. A. and MURPHY W. K., *Acta metall.* **10**, 879 (1962).
15. WEIBKE F. and MATTHES H., *Z. Elektrochem* **47**, 421 (1941).
16. SIVERTSEN J. M. and NICHOLSON M. E., *Prog. Mater. Sci.* **9**, 303 (1961).

J. Phys. Chem. Solids Pergamon Press 1969. Vol. 30, pp. 1921–1928. Printed in Great Britain.

HEAT OF EXCHANGE BETWEEN GASEOUS IONS AND IONS IN ANHYDROUS ZEOLITES

R. M. BARRER and **J. A. DAVIES**
Physical Chemistry Laboratories, Imperial College, London, S.W 7

(*Received* 28 *October* 1968; *in revised form* 3 *February* 1969)

Abstract – From heats of ion exchange of hydrated zeolites with aqueous solutions of ions, heats of immersion of dehydrated zeolites, and heats of hydration of gaseous ions, it has been possible to obtain heats of ion exchange between a gaseous ion and a second ion in an anhydrous zeolite for zeolites *X*, *Y*, *A* and chabazite. These heats are considerable, and their significance has been discussed in relation to several aspects of zeolite chemistry, including solvation energies of gaseous ions in some anhydrous and hydrated zeolites.

1. INTRODUCTION

THERMODYNAMIC and thermochemical data have been obtained for cation exchange between certain inorganic exchangers and aqueous solutions[1–4]. However, to interpret these data in terms of the binding energies between the cations and the anionic frameworks, one must consider not only interaction between the exchanging cations and the anionic frameworks, but also between the cations and solvent molecules, both in the hydrated exchanger and in the external solution. Although hydration energy differences for cations in solutions are well established, it is only recently that data have become available for the differences in the heats of solvation of two cations in a given hydrated zeolite[2–4]. However, in view of the notable catalytic activity of anhydrous molecular sieve zeolites, and of the part which the cations may play in catalysis[5], much interest centres upon the energetics of binding of different cations within the anhydrous structures.

2. HEATS OF ION EXCHANGE IN ANHYDROUS ZEOLITES

One approach to the energy of cation binding requires evaluation of heats of ion exchange between a gaseous cation of element A and a cation of element B within the anhydrous zeolite lattice. This exchange is represented by the equation:

$$B(Z)+\frac{1}{z}.A^{z+}(\text{gas})\xrightarrow{\Delta H}\frac{1}{z}.A(Z)_z+B^{+}(\text{gas}) \qquad (1)$$

In equation (1), A^{z+}, B^+ are the exchangeable cations and (Z) is one equivalent of solid anhydrous anionic framework. The ion of A has charge z^+ and the univalent ion initially present in the exchanger, i.e. B^+, is Na$^+$. The heat, ΔH, of the reaction in equation (1) is an indication of the differences in the binding energies of the cations in the anhydrous zeolite. This heat cannot be measured directly but can be determined from experimental quantities by the following thermochemical cycle:

$$\begin{tikzcd}
B(Z) \arrow[d, "\Delta H^{W}_{B(Z)}"'] & + & \frac{1}{z}.A^{z+}(\text{gas}) \arrow[r, "\Delta H"] \arrow[d, "\frac{1}{z}.\Delta H^{h}_{A^{z+}}"] & \frac{1}{z}.A(Z)_z \arrow[d, "\frac{1}{z}.\Delta H^{W}_{A(Z)_z}"] & + & B^{+}(\text{gas}) \arrow[d, "\Delta H^{h}_{B^+}"] \\
B(Z).n_s^{B}\text{H}_2\text{O} & + & \frac{1}{z}A^{z+}(\text{aq}) \arrow[r, "\Delta H^{w}"] & \frac{1}{z}[A(Z)_z.z\,n_s^{A}\text{H}_2\text{O}] & + & B^{+}(\text{aq})
\end{tikzcd}$$

where $\Delta H^{W}_{B(Z)}$ and $\Delta H^{W}_{A(Z)_z}$ are the heats of immersion in water of the dehydrated exchangers; $\Delta H^{h}_{A^{z+}}$, $\Delta H^{h}_{B^+}$ are the heats of hydration of the gaseous ions; and ΔH° is the standard heat[1] of the complete exchange for the reaction involving the hydrated zeolites and aqueous solutions. n_s^A, n_s^B are the numbers of water molecules per equivalent of exchanger after equilibration with water under standard conditions[1]. They refer to intracrystalline water only and do not include water molecules attached to the external surface of the crystals. The measured heats of immersion are the heats for the complete saturation of the dehydrated crystals, and therefore include any heat evolved during surface hydration. It has been shown previously[1-4] that these surface heats are small and contribute less than 1 per cent of the total heat of immersion for the zeolite crystals employed. Thus they need not be considered here.

From the heat cycle, one may determine ΔH of equation (1) as

$$\Delta H = \left[\Delta H^{W}_{B(Z)} - \frac{1}{z}\,.\,\Delta H^{W}_{A(Z)_z}\right] + \left[\frac{1}{z}\,.\,\Delta H^{h}_{A^{z+}} - \Delta H^{h}_{B^+}\right] + \Delta H^\circ. \quad (2)$$

The standard heat of complete exchange, ΔH° has been obtained for several cation pairs in synthetic zeolites A[1], X[2], Y[3] and in natural chabazite[4]. Heats of immersion of various cationic forms of the same zeolites in anhydrous form have recently been measured[6], while the hydration heats of gaseous ions are readily available[7]. The values of ΔH are then summarised in Table 1.

3. DISCUSSION OF TABLE 1

Several points emerge from Table 1.

(a) The heats of exchange, ΔH, of gaseous ions with anhydrous zeolites are approximately ten times larger than these heats when exchange occurs between aqueous solution and hydrated zeolites.

(b) The sign of ΔH is always opposite to that of the corresponding standard heat ΔH° of complete exchange between aqueous solutions and hydrated crystals.

(c) The numerical magnitudes of ΔH (whether positive or negative) are normally in the sequence:

chabazite < zeolite A, zeolite X, zeolite Y.

The large numerical magnitudes of ΔH reflect the very energetic nature of the 'solvation' of cations by the anhydrous zeolite frameworks. The anionic oxygens in aluminosilicates are rather similar to the anionic oxygen in water in solvating properties such as polarity and polarisability. Solvation of an ion by anhydrous zeolite is therefore very energetic, but because of the lattice rigidity is somewhat less so than solvation in water since the oxygens of the mobile water molecules can group closely around the ion. The energy of solvation of an ion by hydrated zeolite should lie between the other two, since the ion is solvated in part by framework oxygens and in part by water. This is shown by the small values of ΔH°[1-4]. For each zeolite the curve of ΔH against the Pauling ionic radii (Fig. 1) is comparatively smooth, with the possible exception of that for Sieve A. Also the curves for uni-univalent pairs are well above those for uni-divalent pairs. For those zeolites that have mixed cation compositions, (Table 1), the ionic radius has been taken as that of the most abundant ion. ΔH for the uni-univalent ion pair Na^+ and Li^+ exchanging between gas phase and water is more negative when Na^+ leaves the water and Li^+ enters than is ΔH for the same process in the anhydrous zeolites. Likewise for the same reaction involving Na^+ and either K^+, Rb^+ or Cs^+, ΔH is more positive. This indicates that solvation energies of gaseous ions in water are greater than these energies for corresponding ions in anhydrous zeolites.

As mentioned above, the curve for Sieve A is less smooth. Before measuring the heats of immersion[6] the zeolites were heated at

Table 1. *Heats of ion exchange between anhydrous zeolites and the gas phase*

In chabazite		In zeolite *X*		In zeolite *Y*		In zeolite *A*	
Exchange	ΔH*	Exchange	ΔH	Exchange	ΔH	Exchange	ΔH
Na$^+$ → Li$^+$	−23·0	Na$^+$ → Li$^+$	−24·2	Na$^+$ → Li$^+$	−24·9	Na$^+$ → Li$^+$	−25·2
Na$^+$ → K$^+$	12·9	Na$^+$ → K$^+$	17·0	Na$^+$ → K$^+$	16·6	Na$^+$ → K$^+$	18·3
Na$^+$ → Rb$^+$	16·9	Na$^+$ → 0·65 Rb$^+$, 0·35 Na$^+$	21·6	Na$^+$ → 0·70 Rb$^+$, 0·30 Na$^+$	22·6	Na$^+$ → 0·93 Rb$^+$, 0·07 Na$^+$	15·5
Na$^+$ → 0·84 Cs$^+$, 0·16 Na$^+$	22·1	Na$^+$ → 0·65 Cs$^+$, 0·35 Na$^+$	29·2$_5$	Na$^+$ → 0·70 Cs$^+$, 0·30 Na$^+$	29·1	Na$^+$ → 0·93 Cs$^+$, 0·07 Na$^+$	27·1
Na$^+$ → Tl$^+$	7·2	—	—	Na$^+$ → 0·69 Tl$^+$, 0·31 Na$^+$	10·9	—	—
—	—	Na$^+$ → ½ Ca^{2+}	−88·3	Na$^+$ → ½(0·72 Ca^{2+} 0·56 Na$^+$)	−89·4	—	—
—	—	Na$^+$ → ½ Sr^{2+}	−69·5	Na$^+$ → ½(0·69 Sr^{2+}, 0·62 Na$^+$)	−70·8	—	—
—	—	Na$^+$ → ½(0·74 Ba^{2+}, 0·52 Na$^+$)	−57·1	Na$^+$ → ½(0·70 Ba^{2+}, 0·60 Na$^+$)	−54·5	—	—

*Values of ΔH are in kcals/g eq of exchanger. For the reactions when incomplete exchange was observed, the figures for the Na$^+$ contents given in the table have been obtained by difference, and may therefore include some H$^+$.

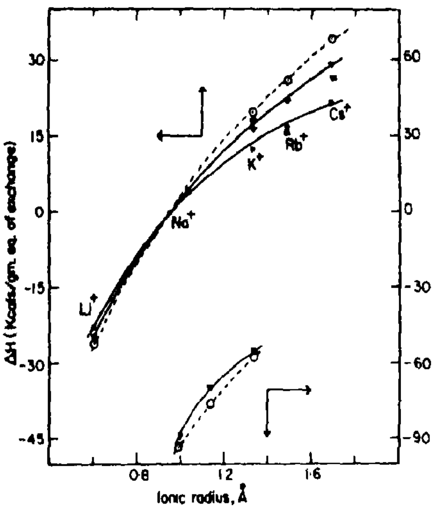

Fig. 1. Variation of ΔH with ionic radius for exchange in several anhydrous zeolites. ● In chabazite. ■ in Linde Sieve *A*. ▼ in Linde Sieves *X* and *Y*. ○ differences in the heats of solvation of two ions in water, i.e. $\Delta H^h_{Na^+} - \frac{1}{z}\Delta H^h_{M^{z+}}$.

360°C *in vacuo* for 24 hr. During this outgassing some decomposition of certain cation forms is possible. Our heats of immersion[6] and also those from elsewhere[8], both suggest that the partly exchanged Na, Rb–*A* form may have decomposed although this was not verified by X-ray diffraction. Sherry and Walton[9] found that Ba-*A*, outgassed at 350°C in dry air, failed to sorb *n*-hexane or to resorb water, and that X-ray powder diffraction patterns indicated loss of crystallinity. Also relevant to ΔH values in Sieve *A* is the degree of exchange of the mixed Na, Rb–*A* and Na, Cs–*A* zeolites. The exchange compositions given in Table 1 for these forms are based on an experimental exchange capacity corresponding with $\frac{12}{13}$ths of the total Na^+ content[1]. In the evaluation of ΔH from equation (2) the values of $\Delta H°$ correspond with these exchange limits[1] for the Na → Rb and Na → Cs exchanges. However, in view of the sigmoid shape of the isotherms for ion exchanges between hydrated zeolites and aqueous solutions it is likely that the Na, Rb–A and Na, Cs–A samples used to measure the heats of immersion[6] contained more residual Na^+ than given by the compositions of Table 1. For these reasons we regard the subsequent results for Sieve *A* as less accurate than for the other zeolites.

The similarity in ΔH for a given ion-pair in anhydrous zeolites *X* and *Y* is interesting in view of the difference in framework charge and cation density within otherwise virtually iso-structural crystals. Exothermal electrostatic energy components (ions with anionic oxygens) and endothermal components (ions with ions) evidently add to about the same in each zeolite independently of possible differences in cation distribution. One may also compare the sequence in ΔH given in (c) above with that for standard heats, $\Delta H°$, of complete exchange between aqueous solution and hydrated zeolite. For the uni-univalent exchanges at least, this sequence[1–4] is

$$\text{chabazite} > \text{zeolite } A > \text{zeolite } X, \text{zeolite } Y$$

and so is the reverse of the sequence for ΔH.

Because ΔH for univalent ions in chabazite has its lowest numerical values (Table 1) the binding energy of these cations is on average likely to be less than in the other zeolites. This in turn indicates that a larger proportion of cations in chabazite is less well solvated by anionic oxygens (see also Table 5). The more exposed the cations the greater the electric fields in their vicinity. This should mean more energetic sorption and enhanced catalytic activity. Exceptionally strong affinity is indeed shown by chabazite for polar sorbates such as CO_2[10] and H_2O[11]. Also Miale *et al.*[12] have established that an ammonium-hydrogen chabazite is a superactive catalyst for cracking *n*-hexane into propane and propene, despite the more difficult accessibility of its intracrystalline channels as compared with those in zeolites *X* and *Y*. Univalent cations in chabazite have not been located but some ions are believed to be in the large cavities either in or near the 8-ring windows[13]. In zeolites *X* and *Y*[14, 15] some univalent ions are thought to be inside hexagonal prisms or sodalite cages where they are less exposed than ions in the largest 26-hedral cavities. In anhydrous X and Y binding energies of ions in the former sites might be expected to exceed those of ions in the 26-hedra.

ESTIMATION OF LOCAL DIELECTRIC CONSTANTS

The electrostatic self-energy, U_i, of an ion i of radius r_i and valence Z_i in a continuum of dielectric constant ϵ is

$$U_i = \frac{(Z_i e)^2}{2r_i\epsilon} = \frac{165{\cdot}98 Z_i^2}{r_i\epsilon} \qquad (3)$$

where r_i is in Å units and U_i is in kcals/g. ion. Values of r_i according to three methods of estimation are given in Table 2, together with the corresponding values of U_i *in vacuo* ($\epsilon = 1$).

An approximation to the energy or heat of the exchange reaction in equation (1) is obtained by treating the zeolites as structureless dielectrics. Assuming that the ions A^+ and B^+ have radii r_A and r_B which are the same in both zeolite and gaseous phases then*

$$\Delta H \sim \Delta U = \frac{e^2}{2}\left\{\frac{1}{r_B}\left(1-\frac{1}{\epsilon_B}\right) - \frac{1}{r_A}\left(1-\frac{1}{\epsilon_A}\right)\right\} \qquad (4)$$

where ϵ_A, ϵ_B are the dielectric constants of the pure ion exchangers $A(Z)_z$ and $B(Z)$. This model is simple in principle although possibly only semi-quantitative in application. It is however the most useful because no information is required about the geometrical arrangment of cations. Indeed cation siting and the relative populations of sites in the zeolites are not well understood, nor is the distribution of charge among Si, Al and O atoms of the anionic framework. As a further approximation we have taken $\epsilon_A = \epsilon_B = \epsilon$. This is justified at least in chabazite if we consider the relationship $\epsilon = n^2$ where n is the high frequency refractive index. In hydrated cationic forms of chabazite n varies only to a limited extent with the exchange ion (Table 3).

Table 2. Cationic radii and self potentials of ions in vacuo

Cation	Ion radius (Å)†			Electrostatic self potential‡ (kcals/g ion)		
	(i)	(ii)	(iii)	(i)	(ii)	(iii)
Li^+	0·60	0·78	0·93	276·6	212·7	178·5
Na^+	0·95	0·98	1·17	174·7	169·4	141·9
K^+	1·33	1·33	1·49	124·8	124·8	111·4
Rb^+	1·48	1·49	1·64	112·1	111·4	101·2
Cs^+	1·69	1·65	1·83	98·2	100·6	90·7

† (i) Pauling radii, (ii) Goldschmidt radii, (iii) radii from electron density maps[16].

Table 3. Refractive indices of pure cationic forms of chabazite [17]

Cationic form	n	Cationic form	n	Cationic form	n
Li	1·472	Ca	1·486	Cu	1·497
Na	1·467	Sr	1·490	Ag	1·516
K	1·472	Ba	1·499	Tl	1·559
Rb	1·476				

---

*More strictly ΔH is a free energy. However equation (4) is found experimentally to be more successful in the evaluation of heats or energies than free energies[2, 3].

The values of n in Table 3 are upper bounds only, since when the zeolitic water is removed n should decrease.

The dielectric constants, ϵ, calculated from equation (4) with $\epsilon_i = \epsilon_{ii} = \epsilon$, are given in Table 4. At first sight they appear low compared with the macroscopic dielectric constants[18]. However, they are near to values found from $\epsilon = n^2$ and to the dielectric constant of water calculated from Born charging theory:

$$\Delta H_i = \frac{-NZ_i^2 e^2}{2r_i}\left(\frac{1}{\epsilon_{n}} - 1\right). \qquad (5)$$

Table 4. Calculated dielectric constants of the zeolite phases[1]

Cation pair	Chabazite (i)	Chabazite (ii)	Chabazite (iii)	Linde Sieve X (i)	Linde Sieve X (ii)	Linde Sieve X (iii)
Na^+/Li^+	1·3	2·2	2·8	1·3	2·3	3·0
Na^+/K^+	1·4	1·5	1·8	1·5	1·6	2·3
Na^+/Rb^+	1·4	1·4	1·7	1·5	1·6	2·1
Na^+/Cs^+	1·4	1·5	1·8	1·6	1·8	2·3

Cation pair	Linde Sieve Y (i)	Linde Sieve Y (ii)	Linde Sieve Y (iii)	Linde Sieve A (i)	Linde Sieve A (ii)	Linde Sieve A (iii)
Na^+/Li^+	1·3	2·4	3·1	1·3	2·5	3·2
Na^+/K^+	1·5	1·6	2·2	1·6	1·7	2·5
Na^+/Rb^+	1·6	1·6	2·3	1·4	1·4	1·7
Na^+/Cs^+	1·6	1·7	2·3	1·6	1·7	2·1

[1] The columns labelled (i), (ii), (iii) correspond to those similarly headed in Table 2

ϵ_{n} from equation (5) is thus well below the macroscopic value of 78·5 at 25°C. In the immediate vicinity of ions, i.e. at distances less than ~ 3 Å, there is a remarkably high electric field ($\sim 10^7$ V cm^{-1}) resulting in local dielectric saturation. Other estimates of this local dielectric constant of water also give values comparable with those of Table 4 for the zeolites[19]. The nearest neighbours to the cations in zeolites are anionic oxygens (as for cations in water), and therefore it is not surprising that values of ϵ are similar to those of ϵ_{n} calculated from equation (5) or reported elsewhere[17].

ΔH in Table 1 measures the difference between the heats of solvation of pairs of gaseous ions in anhydrous zeolites. To obtain individual heats of solvation a further relation is required. Therefore we have assumed that

$$\frac{\Delta H^s_{Na^+}}{\Delta H^h_{Na^+}} = \frac{\Delta H^s_{A^+}}{\Delta H^h_{A^+}} \qquad (6)$$

and hence that

$$\frac{\Delta H^s_{Na^+}}{\Delta H^h_{Na^+}} = \frac{\Delta H^s_{Na^+} - \Delta H^s_{A^+}}{\Delta H^h_{Na^+} - \Delta H^h_{A^+}} = \frac{-\Delta H}{\Delta H^h_{Na^+} - \Delta H^h_{A^+}}. \qquad (7)$$

The superscripts s and h denote solvation in the zeolite and hydration in water respectively. Since ΔH, $\Delta H^h_{Na^+}$ and $\Delta H^h_{A^+}$ for the ion A^+ are known, $\Delta H^s_{Na^+}$ is obtained from equation (7). Four values of $\Delta H^s_{Na^+}$ can be obtained for each zeolite, for $A^+ = Li^+, K^+, Rb^+$ and Cs^+, and the test of equation (6) is that $\Delta H^s_{Na^+}$ does not change significantly over the four values. For zeolites X and Y the maximum deviation of $\Delta H^s_{Na^+}$ from the mean value is <10 per cent. In zeolite A, because of suspected breakdown of the Rb-enriched form (*loc. cit.*) only three values were taken, and the maximum individual variation of any of these from the mean was again <10 per cent. In chabazite $\Delta H^s_{Na^+}$, derived from the Na^+/Li^+ pair was also out of line and was therefore not considered. The maximum deviation from the mean for the remaining three values was ~ 1 per cent. Using the mean value of $\Delta H^{s}_{Na^+}$ and equation (6) the individual heats of solvation of the gaseous ions A^+ (Table 5) were then calculated. As predicted in discussing Table 1, the heat of solvation by chabazite is less exothermic than for the other zeolites, the sequence of exothermicity being

Water > Sieve A > Sieve Y > Sieve X > Chabazite.

From the heats of ion exchange between hydrated zeolites and aqueous solutions, together with the heats of hydration of gaseous ions, individual heats of solvation of gaseous ions by hydrated zeolites can also be estimated. To do this we again assume

$$\frac{\Delta' H^{s}_{Na^+}}{\Delta H^{h}_{Na^+}} = \frac{\Delta' H^{s}_{A^+}}{\Delta H^{h}_{A^+}} \tag{8}$$

where the prime now indicates that the solvation is by the hydrated zeolites. From equation (8)

$$\frac{\Delta' H^{s}_{Na^+}}{\Delta H^{h}_{Na^+}} = 1 - \frac{\Delta H^{\circ}}{(\Delta H^{h}_{Na^+} - \Delta H^{h}_{Li^+})}. \tag{9}$$

As before four values of $\Delta' H^{s}_{Na^+}$ were obtained for $A^+ = Li^+$, Na^+, Rb^+ and Cs^+. For none of the zeolites was the maximum deviation from the mean more than 2·5 per cent, so that equation (8) appears well justified. Using the mean $\Delta' H^{s}_{Na^+}$ heats of solvation for the other ions were then calculated from equation (8). All the values are collected in Table 5.

As predicted in discussing Table 1, the individual heats of solvation of a given ion in the hydrated zeolite lie between those for solvation by anhydrous zeolites and water. The sequence of exothermicity is now

Water > Sieve Y > Sieve X > Sieve A > Chabazite.

The increase in exothermicity of ion solvation is now greatest for chabazite, supporting the view already given that the cations being solvated are on average more exposed in this zeolite than in the others.

The information in Table 5 is of considerable interest because it provides the first relatively direct estimate of ion-bonding in anhydrous and hydrated zeolites.

Table 5. Heats of solvation of gaseous ions by water and by zeolite frameworks

Cation	Heat of solvation of gaseous ion (kcal/g ion)								
	In Chabazite		In Sieve X		In Sieve Y		In Sieve A		
	Hydrated	Anhyd†	Hydrated	Anhyd	Hydrated	Anhyd	Hydrated	Anhyd‡	In Water*
Li^+	−117·9	—	−122·7	−111·6	−123·4	−117·0	−118·4	−117·4	132·0
Na^+	94·6	68·4	−98·4	−89·5	−99·0	−93·8	−95·0	−94·2	−105·9
K^+	−76·6	−55·4	79·6	−72·4	−80·1	75·9	76·9	−76·2	−85·7
Rb^+	−71·3	51·5	74·1	−67·4	74·6	−70·7	−71·6		−79·8
Cs^+	−64·2	−46·4	−66·6	−60·8	−67·2	63·7	−64·5	−64·0	−71·9

*The figures for ion hydration have been determined from the relative heats of ion hydration[7] by subtracting the absolute heat of proton hydration, i.e. 269·7 kcal/g ion[19].

†Values have been determined by ignoring the Na/Li system

‡Values have been determined by ignoring the Na/Rb system

REFERENCES

1. BARRER R. M., REES L. V. C. and WARD D. J., *Proc. R. Soc.* **A273**, 180 (1963)
2. BARRER R. M., REES L. V. C. and SHAMSUZZOHA M., *J. inorg. nucl. Chem.* **28**, 629 (1966)

3. BARRER R. M., DAVIES J. A. and REES L. V. C., *J. inorg. nucl. Chem.* **30**, 3333 (1968).
4. BARRER R. M., DAVIES J. A. and REES L. V. C., J. inorg. nucl. Chem. **31**, 219 (1969).
5. MAYS R. L. and PICKERT P. E., *Molecular Sieves*, p. 112. Soc. Chem. Ind., London (1968).
6. BARRER R. M. and CRAM P. J., In preparation.
7. BENJAMIN L. and GOLD V., *Trans. Faraday Soc.* **50**, 797 (1954).
8. RASTRENEKO A. I, ANTONOVSKAYA S. N and NEIMARK I. E, *Kolloid Zh.* **27**, 269 (1965).
9. SHERRY H. S. and WALTON H F, *J phys Chem.* **71**, 1457 (1967).
10. BARRER R M. and COUGHLAN B., *Molecular Sieves*, pp 233, 241 Soc Chem. Ind, London (1968).
11. BARRER R. M. and FENDER B. E. F., *J. Phys Chem. Solids* **21**, 1 (1961).
12. MIALE J. N. and WEISZ P. B., *J. Catal.* **4**, 527 (1965).
13. SMITH J. V., *J. chem. Soc.* 3759, (1964).
14. BRECK D. W. and FLANIGEN E. M., *Molecular Sieves*, p. 47. Soc. Chem. Ind., London (1968).
15. EULENBERGER G. R., SHOEMAKER D. P. and KEIL J. G., *J. phys. Chem.* **71**, 1812 (1967).
16. MORRIS D. F. C., *Structure and Bonding* **4**, 63 (1968).
17. BARRER R. M. and SAMMON D. C., *J. chem. Soc.* 2838, (1955).
18. BARRER R. M. and SAXON-NAPIER E. A., *Trans. Faraday Soc.* **58**, 156, (1962).
19. ROSSEINSKY D. R., *Chem. Rev.* **65**, 467 (1965).

J. Phys. Chem. Solids Pergamon Press 1969. Vol. 30, pp. 1929–1934. Printed in Great Britain.

ELECTRIC AND MAGNETIC PROPERTIES OF B2 STRUCTURE COMPOUNDS: NiAl, CoAl

S. R. BUTLER,* J. E. HANLON and R. J. WASILEWSKI†

Central Research Department‡, E. I. du Pont de Nemours and Company, Experimental Station, Wilmington, Delaware 19898, U.S.A.

(*Received* 6 *January* 1969; *in revised form* 3 *February* 1969)

Abstract – Electrical resistivity, thermoelectric power, and magnetic susceptibility or magnetization have been measured at room temperature and below on compositions surrounding NiAl (49–51 at % Al) and CoAl (42–54% Al). The resistivity-composition plots show a minimum near 50 per cent. The slopes of the ρ vs. composition plots are markedly different on opposite sides of the minimum. The thermoelectric power is *n*-type with a distinct shoulder at 50 per cent. NiAl is Pauli paramagnetic for all compositions as is CoAl for Al-rich compositions. Co-rich CoAl is ferromagnetic with the magnetization approaching zero at about 50 per cent. These results are used to suggest a qualitative energy band model. The main features of this model are similar to those of Goodenough, i.e. a broad hybrid *s*-*p* band and several narrow *d*-bands formed from transition metal atomic orbitals.

INTRODUCTION

THE ORDERED b.c.c. (B2) structure compounds NiAl and CoAl have been the subject of several studies of physical[1–6] and mechanical properties[7, 8]. One of the most interesting features of these materials is the large composition range over which the ordered structure is stable[9]. This range is not symmetric with respect to the equiatomic, being much larger in the Ni- or Co-rich side. In addition, the 'defects' responsible for non-stoichiometry are different[10–12]. Similar defects have recently been reported[13] on the related compound NiGa.

The measurements reported include electrical resistivity, thermoelectric power, and magnetic susceptibility or magnetization for compositions within the respective stability fields. The results suggest that substantial changes in the electronic structure occur over the stability range.

PREPARATION OF SAMPLES

The samples were prepared from high purity elements [Ni 99·9+%,§ Co 99·9+% (zone-melted), Al 99·999%]. The only impurities present in amounts >50 ppm were Fe and Co in NiAl at 200 ppm each and Fe and Ni at the same level in CoAl. The elements were combined by repeated non-consumable arc melting under gettered argon. Balance of materials was used to check maintenance of composition. In all samples the resulting uncertainty in composition was < ±0·05 per cent. The composition range was 49–51% Al for NiAl and 42–54% Al for CoAl. X-ray and metallographic examination showed all samples to be single phase with the ordered B2 structure. High-temperature X-ray studies showed NiAl and CoAl to be ordered to 1200°C. Annealing at 1000°C for over 100 hr and rapid cooling did not affect the microstructure or physical properties significantly.

EXPERIMENTAL METHODS AND RESULTS

The techniques used to measure electrical resistivity and thermoelectric power have been previously described[14]. The accuracy of the measurements is 2 per cent for resistivity and 10 per cent for thermoelectric power (the precision of these measurements is 0·2 and 5 per cent, respectively). The uncertainty bars shown in Fig. 2 for CoAl are much larger because of difficulties in preparing samples with good geometry. The results are presented in Figs. 1-4. The magnetic susceptibility measurements for NiAl were made with a Faraday balance at fields up to 8 KOe. and are accurate to 2 per cent

---

*Now at National Science Foundation, Washington, D.C.

†Now at Battelle Memorial Institute, Columbus, Ohio.

‡CRD Contribution No 1491.

§All compositions in atomic per cent (at. %).

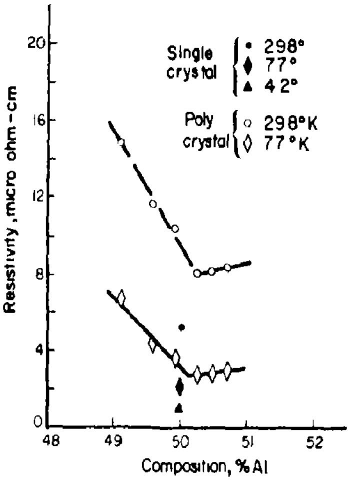

Fig. 1. Electrical resistivity of nickel aluminum samples annealed at 1000°C.

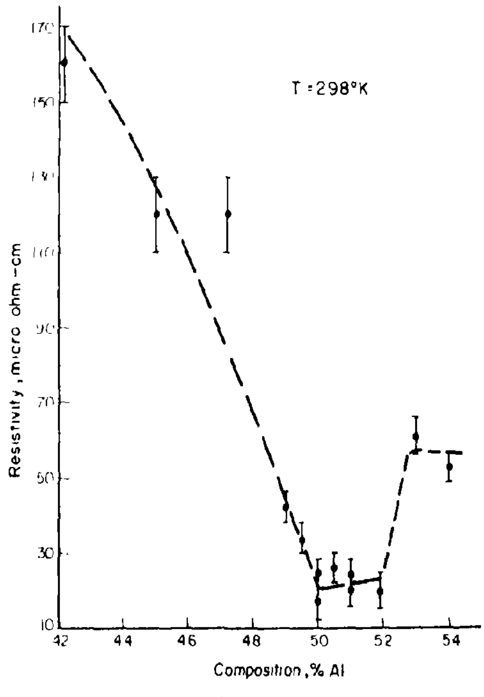

Fig 2. Electrical resistivity of cobalt aluminum samples annealed at 1000°C

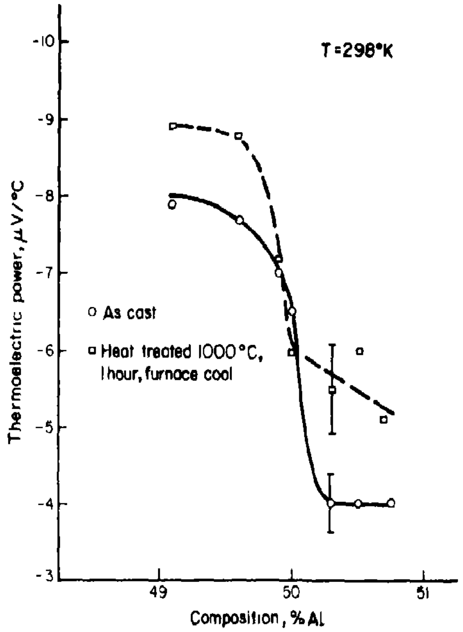

Fig. 3. Thermoelectric power of nickel aluminum samples in as cast and annealed conditions

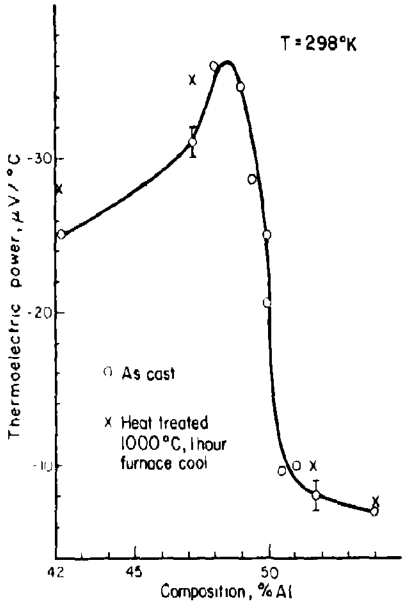

Fig 4. Thermoelectric power of cobalt aluminum samples in as cast and annealed conditions. In the range 48-51 per cent the two sets of points are within experimental error.

(Fig. 5). The magnetic field dependence corresponded to <5 ppm ferromagnetic nickel. The magnetic measurements on CoAl samples (Fig. 6) were made with a vibrating sample magnetometer[22]. The accuracy is related to the magnitude of the effect observed and is indicated by uncertainty bars in the figure. The isothermal field dependence of the magnetization and the temperature dependence of the magnetic moment indicate that the samples with ≤49% Al were ferromagnetic.

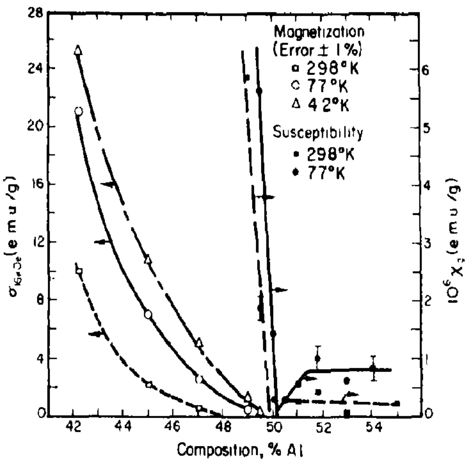

Fig. 6. Magnetic susceptibility and saturation magnetization of cobalt aluminum samples in the as cast condition The horizontal arrows on the curves indicate that the magnetic moment results (on the left) are read on the scale on the left and susceptibility results (on the right) are read on the scale on the right.

DISCUSSION

NiAl

The resistivity shows the expected minimum, but at a composition of 50·4% Al. This deviation from the ideal stoichiometry may be interpreted in terms of the suggestion[11] that the slightly Al-rich composition, which has the maximum lattice parameter, also has the minimum lattice defect concentration. The occurrence of a minimum defect concentration off ideal composition may result from interactions between order-disorder defects and those due to deviation from the stoichiometric[12]. These results are consistent with low temperature resistivity measurements on a float-zone grown [15] single crystal (50·0% Al) of at least comparable purity[7]. Even carefully annealed crystals have never had resistivity values at 4·2°K below 1 μΩ cm. The general trend of the results at 298°K is not completely consistent with the results of Yamaguchi *et al.* [4, 16]. First, their maximum resistivity ratio is at a slightly Ni-rich composition, which does not agree with our results. Second, because of their widely spaced compositions, they have not seen the dramatic differences in the slope of the ρ vs. composition plot on either side of the minimum. For both NiAl and CoAl the increase in resistivity for Al-rich samples is very much less than for the transition metal rich side. It appears that the transition metal vacancies present (in Al-rich samples) have a much smaller scattering power than the transition metal antistructure

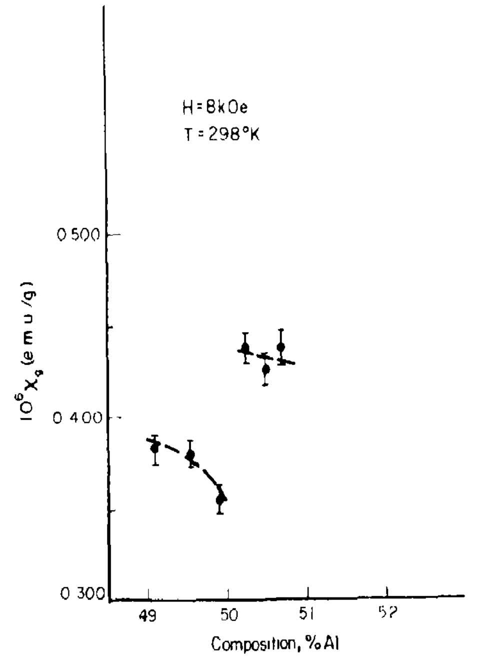

Fig. 5 Magnetic susceptibility nickel aluminum samples annealed at 1000°C.

atoms present in Al-deficient compositions. We shall return to this point after considering the magnetic properties of CoAl.

The magnetic susceptibility reported here for Al-rich compositions is consistent with the value given by Höhl[5] for a single composition (50·1% Al). The rapid decrease in the thermoelectric power (T.E.P.) at 50% can be interpreted[17] as either a rapid change in the density of states vs. energy or a change in the area of the Fermi surface due to contact with a Brillouin zone boundary. One Hall effect measurement on a 50·0 per cent sample at 298°K gave $R = 3{\cdot}2 \pm 0{\cdot}1 \times 10^{-5}$ cm^3/C. If this value of R is converted to a carrier density for a single band (i.e. $R = 1/ne$) one finds $n = 4{\cdot}7$ carriers per NiAl. The large apparent carrier density and the compositional dependence of thermoelectric power imply that a single band and/or a simple Fermi surface does not exist in this compound. This conclusion is further strengthened by the electronic specific heat measurement[3], which gives a calculated density of states of 1/2 electron/eV/NiAl.

CoAl

The above discussion of lattice defects and band structure should apply generally to CoAl as well. The resistivity data of Yamaguchi *et al.*[4] are rather incomplete but show the same general trend, i.e. minimum near 50 per cent. However, as noted above, they have not reported the flat region for small excess Al compositions. Their resistivity values are all about an order of magnitude larger than for NiAl, in disagreement with our values: The difference found here is only a factor of 2. If this increase from NiAl to CoAl is due to defect scattering as suggested by Yamaguchi *et al.*[4] the defect content must either be much larger or the scattering power per defect must be greater. No information is available on the relative defect concentrations at present. However, the dramatic difference in magnetic properties implies significant differences in electronic effects, which favors the differences in scattering power as the origin of the resistivity differences. The drop in T.E.P. (Fig. 4) for CoAl is much more pronounced than in NiAl and, as noted above, may indicate the appearance of hole-like behavior or a shoulder in the density of states.

The magnetic properties observed in CoAl are also much more striking (Fig. 6) than for NiAl. The ferromagnetism observed for Co-rich compositions has not been observed previously. Höhl[5] showed data for a 50·1% Co sample with a paramagnetic Curie temperature of 30°K. This is not consistent with our results. Extrapolating our 4·2°K data for σ vs. $1/H$ to zero gives saturation moments between 1·5 and 2·5 μ_B per excess cobalt atom for the data between 42 and 49·0% Al (the 49·5 sample was far from saturation at 16 KOe). The magnetization varies nearly as x^2 for positive x defined in terms of the composition by $Co_{1+x}Al_{1-x}$. The minimum resistivity for CoAl also does not occur at 50 per cent but at an Al-rich composition (51–52 per cent) which is close to the maximum lattice parameter composition[11]. We may thus speculate that the defects (antistructure atoms) which give rise to the ferromagnetic behavior are also the scattering centers responsible for the high electrical resistivity.

Finally we consider several aspects of a simplified electron energy band scheme for these materials along the lines presented by Goodenough[19]. We do not consider the 'classical 3:2' electron to atom description (Hume-Rothery[18]) realistic since it neglects two important features of these materials, namely the effect of the atomic order on Brillouin zone boundaries and the importance of the *d*-bands in determining the stability of the structure.

First, following Goodenough, we consider the broad conduction band to be a hybrid band of *s* and *p* states. This means the first b.c.c. zone (110) will contain 8 electrons/atom instead of 2 as in the *s* band of the 'classical 3:2' model. Since the first zone of the ordered B2 structure is bounded by (100) and contains half the volume of the (110) zone it should contain four electrons/atom. The volume ratio of the inscribed sphere to cubic zone is $\pi/6$ and thus would contain $4\pi/6 = 2{\cdot}1$ electrons/atom. If we assume the number of electrons contributed to this band to be 3 per aluminum and 2 per transition metal, there would be 2·5 electrons/atom in this zone. An 8 per cent increase in the radius of the inscribed sphere would have sufficient volume inside the (100) zone to contain 2·5. We would therefore postulate a Fermi surface which contacts the (100) zone boundaries in ⟨100⟩ directions. This Fermi surface will therefore have electron-like and hole-like portions with the former in the majority (to be consistent with the T.E.P. data).

Secondly, turning to the *d*-electrons we use the same choice of coordinates as Goodenough[19] so that *t* orbitals point toward nearest neighbors while *e* orbitals point toward next-nearest neighbors. Since the nearest neighbors to a transition metal atom are aluminum atoms (the stoichiometric composition is considered first) with no *d* electrons the *t* orbtals will be undisturbed and full, t^6. The *e* orbitals pointing toward next-nearest neighbors, i.e. a transition metal, will have some overlap and form a narrow band with a bimodal character for the density of states (bonding and antibonding).

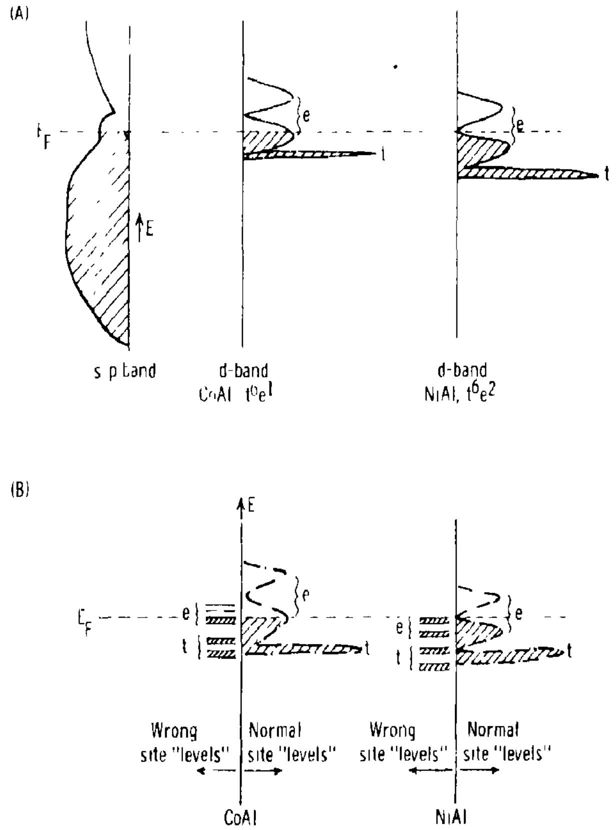

Fig. 7 Schematic density of states plots for nickel aluminum and cobalt aluminum. (A) Applies to the stoichiometric compounds. (B) Indicates the positions of the *d*-levels of the transition metal atoms which occupy aluminum atom sites in non-stoichiometric compositions

Since the transition metal has given 2 electrons to the s–p band the filling of the d-bands will be t^6e^1 for Co and t^6e^2 for the Ni. The filling of the e band to 1/4 and 1/2 for Co and Ni is considered to be the important contribution to the stability of these ordered B2 structures. For Fe the e band is empty, so FeAl is not very stable, as the phase diagram demonstrates[9]. A simplified (one-dimensional) density of state vs. energy plot for this model is given in Fig. 7(a).

The last important consideration is the position of the 'd-levels' of the excess transition metal atoms which go onto aluminum sites in the non-stoichiometric compositions. First we can feel fairly sure that the t orbitals will be strongly affected since they will overlap the full (t^6) orbitals of the nearest neighbor transition metal. Thus there will be splitting of these levels and localized t-bonding will take place. For CoAl, since the lower half of the e-band is only half full, electron transfer to this band is relatively easy. For NiAl, the lower half of the e band is full, so the local electronic rearrangement requires more energy. We show in Fig. 7(b) a possible arrangement for these wrong atom d levels. The e levels of the wrong atom will point toward next-nearest neighbors which are aluminum atoms and will thus be completely localized if occupied. We have positioned the e-levels in a way that is consistent with the observed magnetic measurements: the observed magnetic moment of excess Co in CoAl is ~ 2 Bohr magnetons/excess atom (e^2) while no ferromagnetism is observed in NiAl (e^1).

The high density of empty d-states at the Fermi level in CoAl should enhance the s–d scattering, consistent with the higher resistivity of stoichiometric CoAl compared with NiAl. Finally we suggest that the strong composition dependence of the T.E.P. which appears in both NiAl and CoAl is most likely associated with changes in the electron concentration in the s–p band. At present we cannot distinguish between the contributions of the density of states and the area of Fermi surface to this change in T.E.P.

Acknowledgements—The authors wish to express their appreciation to C. G. Frederick for magnetic measurements, J. T. Bailey and D. Worden for property measurements and sample preparation. We also appreciate the helpful discussions of R. J. Bouchard and J. B. Goodenough.

REFERENCES

1. RECHTIEN J. J., *et al.*, *J. appl. Phys.* **38**, 3045 (1962).
2. MIZANANI K., *et al.*, *J. phys. Soc. Japan* **18**, 1345 (1963).
3. SEITCHIK J. A. and WALMSLEY R. H., *Phys. Rev.* **131**, 1473 (1963)
4. YAMAGUCHI Y., *et al.*, *J. appl. Phys.* **39**, 231 (1968)
5. HOHL M., *Z. metallk.* **51**, 85 (1960).
6. WEST G. W., *Phil. Mag.* **9**, 979 (1964).
7. WASILEWSKI R. J., *et al.*, *Trans. AIME* **239**, 1357 (1967).
8. BALL A. and SMALLMAN R. E., *Acta Metall.* **14**, 1349 (1967).
9. HANSEN M., In *Constitution of Binary Alloys*, pp. 79–118 McGraw-Hill, New York (1961).
10. BRADLEY A. J. and TAYLOR A., *Proc. R. Soc.* **159A**, 56 (1937).
11. COOPER M. J., *Phil. Mag.* **8**, 805 (1963).
12. WASILEWSKI R. J., *J. Phys. Chem. Solids* **29**, 39 (1968)
13. WASILEWSKI R. J., *et al.*, *J. appl. Phys.* In press.
14. HANLON J. E., *et al.*, *Trans. AIME* **239**, 1323 (1967)
15. Single crystals were grown by WORDEN D. of this laboratory
16. A resistivity vs. composition plot more similar to that of YAMAGUCHI *et al.* was found in a preliminary series of samples more widely spaced in composition, 44–54% Al. However, samples were more than 52% Al showed a second phase.
17. SHRODER K. and YESSIK M., *J. Phys. Chem. Solids* **28**, 1713 (1967)
18. HUME-ROTHERY W., In *Phase Stability in Metals and Alloys* (Edited by P. Rudman, J. Stringer and R. Jaffee). McGraw-Hill, New York (1967).
19. GOODENOUGH J. B., In *Magnetism and the Chemical Bond*, Chap. III. Interscience, New York (1967)
20. Unpublished results from this laboratory show NiGa does not exhibit a sharp shoulder at 50 per cent.
21. The notation used here is that of GOODENOUGH, reference[19].
22. A Foner type instrument manufactured by Princeton Applied Research, Inc., Princeton, New Jersey, U.S.A., Model FM-1, was employed for these measurements.

J. Phys. Chem. Solids Pergamon Press 1969. Vol. 30, pp 1935–1940. Printed in Great Britain.

PREPARATION AND PROPERTIES OF SINGLE CRYSTAL $CuAlS_2$ AND $CuAlSe_2$

W. N. HONEYMAN
Department of Applied Physics,
Brighton College of Technology, Brighton, Sussex, England

(*Received* 12 *September* 1968; *in revised form* 24 *January* 1969)

Abstract – Single crystals of the I–III–VI_2 ternary semiconductors $CuAlS_2$ and $CuAlSe_2$ have been prepared by vapour transport with iodine. Optical transmission measurements give energy gaps of about 3·35 eV (sulphide) and 2·5 eV (selenide). Double refraction is observed, and the refractive indices extrapolated to infinite wavelength are 2·300, 2·325 (sulphide) and 2·437 (selenide). The selenide shows large photoconductive effects, while both semiconductors have electrical resistivities from 10^4 to 10^7 Ω cm and mobilities less than 60 $cm^2 V^{-1} sec^{-1}$

1. INTRODUCTION

THE I–III–VI_2 ternary semiconductors have been studied by many workers[1–9]. These compounds are formed by combinations of the elements Cu, Ag with Al, Ga, In, Tl, and S, Se, Te. Their crystal structures have been analysed by Hahn *et al*[1] and the polycrystalline compounds containing aluminium briefly mentioned by Goodman and Douglas[2]. The properties of single crystals of the group containing aluminium have not been examined previously and this paper gives the results measured for two members of the group.

2. PREPARATION

Both compounds were prepared by reaction of the elements to form the polycrystalline material followed by vapour transport [12] using iodine to grow the single crystals.

The elements in powder form (99·999 per cent pure) were obtained from Koch Light Laboratories. Stoichiometric quantities were weighed out and sealed under a high vacuum either in an alumina crucible held in a quartz tube or directly in the tube. The total quantity of material was about two grammes. The elements were mixed by shaking and then reacted by gradually increasing the temperature to 1000°C over a period of several days followed by slow cooling. The sulphide ampoules often exploded if the temperature was raised too quickly, presumably due to sulphur pressure. The selenide did not show this characteristic. The resulting material was crushed with an agate mortar and pestle to give a black sulphide or a brown-red selenide powder.

The powder was then placed in a 15 mm dia., 15 cm long cleaned quartz tube, which was evacuated to remove moisture. Iodine was added to give a concentration of 5 mg/cm^3 of tube volume and the tube re-evacuated and sealed. The tube was placed in a horizontal, double wound, furnace with a temperature gradient along it so that the ends of the tube were maintained at different temperatures, usually 800°C (powder end) and 700°C. This was maintained for a period of several days, during which crystals were formed along the cool half of the tube.

It was found that aluminium powder tends to react with the quartz resulting in a whitening of the tube. This does not happen in the vapour transport after the compound has been formed. Hence if silicon impurities are important it is essential to use an alumina crucible in the polycrystalline preparation.

3. GENERAL MEASUREMENTS

The sulphide crystals were dark green or black depending on their thickness. Either needle-like crystals one to two cm long and several mm wide, or plates several mm wide and about 100μ thick were obtained, both having highly reflecting mirror-like faces. The needles were very regular, having interfacial angles of 78°, 102° and 38° 41′, the latter angle being measured more precisely for use in refractive index measurements. Some of the larger needles were hollow.

The selenide crystals were yellow-orange and more transparent than the sulphide. Needles and plates of similar dimensions to the sulphide were obtained, the needles having identical interfacial angles although the faces were less perfect.

X-ray powder photographs of the crushed crystals gave a chalcopyrite structure with $a = 5{\cdot}312$ Å, $c = 10{\cdot}42$ Å for the sulphide and $a = 5{\cdot}60$ Å, $c = 10{\cdot}90$ Å for the selenide, in good agreement with the results of Hahn *et al.*[1]. In addition, Laue back reflection photographs indicated the material was single crystal, although the crystal axis was not determined.

Chemical analysis of the sulphide showed that copper, aluminium and sulphur were present in the relative atomic proportions of 1 : 1 : 1·9. The apparent deficiency of sulphur is probably due to an analytical error resulting from slight sulphur loss on oxidation with nitric acid.

4. COPPER ALUMINIUM SULPHIDE

4.1 *Optical absorption*

These measurements were taken on a Unicam SP700 spectrophotometer using only the plate samples which were 25–100 μ thick. Although they were not perfectly parallel, attempts to grind more uniform samples proved unsuccessful. The beam was stopped to about 0·06 in dia. by the crystal mount. A typical transmission plot is shown in Fig. 1 showing two maxima in the transmission at wavelengths of 5200 and 8300 Å before the intrinsic energy gap decrease. The maximum at 5200 Å accounts for the crystals' green colouration. A plot of the absorption coefficient α near the intrinsic absorption edge is given in Fig. 2, the reflectivity being calculated from the measured refractive index values. A plot of α to the power of either 2, $\frac{1}{2}$ or $\frac{1}{3}$ against wavenumber does not yield a good straight line, although all approximate to a straight line at the high absorption end. Therefore, the energy gap can only be found approximately and is $3{\cdot}35 \pm 0{\cdot}1$ eV.

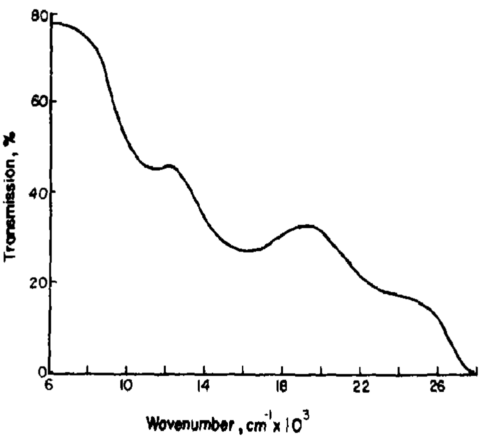

Fig. 1. Transmission through a CuAlS$_2$ crystal $2{\cdot}7 \times 10^{-4}$ cm thick as a function of wavenumber.

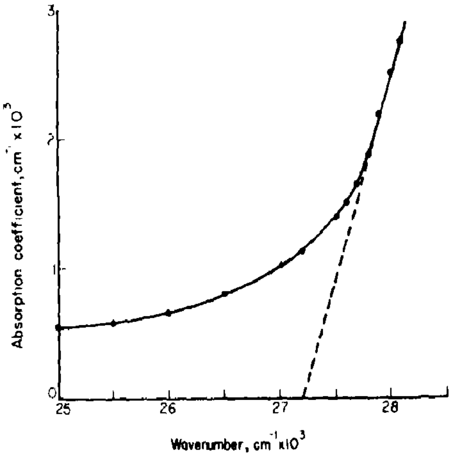

Fig 2 Absorption coefficient of a CuAlS$_2$ crystal $2{\cdot}7 \times 10^{-4}$ cm thick as a function of wavenumber.

4.2 *Refractive index*

A needle-shaped sample was used to measure the refractive index. The crystal with a well defined 38° 41′ interfacial angle was mounted with its axis vertical, on the table of a spectrometer. Monochromatic light from a Hilger and Watts monochromator was focused on the collimator slit and the refracted image from the 38° 41′ interfacial angle observed. The refracted image was double, the two lines being polarised parallel and perpendicular to the needle axis with an angular separation of about 1°. The refractive indices, n, of the sulphide with light polarised parallel and perpendicular to the needle axis were obtained by measurement of the angles of minimum deviation of the two images. Typical results are shown in Fig. 3. A plot of $(n^2-1)^{-1}$ against (wavelength, $\lambda)^{-2}$ gives a nearly straight line, although slight residual curvature is still present. It yields values of refractive indices, extrapolated to infinite wavelength, of $n_\infty = 2{\cdot}300$ when the electric field of the light is parallel to the crystal axis and $n_\infty = 2{\cdot}325$ with light polarised perpendicular to the axis. The results were confirmed by measurement of the Brewster angle of a clean crystal face, although the latter measurement was not accurate enough to show either polarisation or wavelength changes.

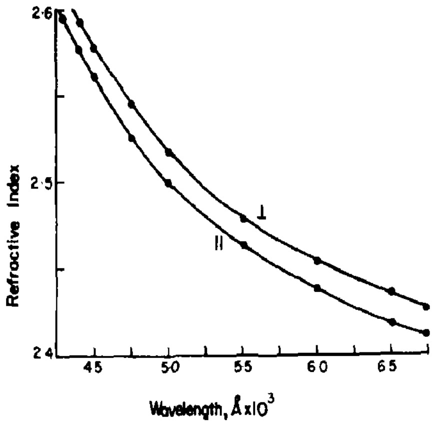

Fig. 3. Refractive index of $CuAlS_2$ as a function of wavelength for light polarised parallel (‖) and perpendicular (⊥) to the needle axis.

4.3 *Electrical measurements*

A variety of contacts were made including evaporated indium, evaporated gold, indium solder, silver loaded araldite and silver aquadag. The indium evaporated contacts were ohmic and were used in the Hall measurements. The silver loaded araldite contacts were used in the resistivity measurements up to 400°C, although they were noisier than the indium contacts.

Typical room temperature resistivities for the sulphide varied from 10^5 to $10^7\,\Omega$ cm. A needle-shaped sample with two silver loaded araldite contacts was mounted in an evacuated tube placed in a furnace and its resistence-temperature curve is shown in Fig. 4. The curve shows a strong impurity level with an activation energy of 0·7 eV. The intrinsic line is not reached by 400°C ($10^3/T = 1{\cdot}49$).

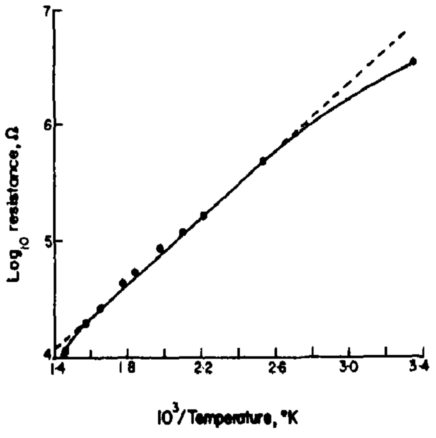

Fig. 4. Resistance-temperature curve for a $CuAlS_2$ crystal.

Irreversible changes in the crystals' resistance prevented the measurements from being extended to higher temperatures.

Several plate samples were prepared with four indium evaporated contacts at the edges and a room temperature Hall measurement carried out using the Van der Pauw method [10] with a d.c. magnetic field of 0·9 Wb m^{-2} and d.c. current. The Hall voltage was less than 0·5 mV, giving a Hall coefficient of less than $0{\cdot}2\ \mathrm{m^3\,C^{-1}}$. The carrier mobility was less than $5\ \mathrm{cm^2\,V^{-1}\,sec^{-1}}$.

Measurements using a hot probe method to measure the sign of the Seebeck coefficient indicates that all samples were *n*-type semiconductors.

No photocurrent was observed when one of the samples was illuminated with a focused 50 W white light source.

5. COPPER ALUMINIUM SELENIDE

5.1 *Optical absorption*

Measurements were made using the apparatus described for the sulphide. Unlike the sulphide, the transmission for the selenide did not show peaks but increased rapidly from zero transmission followed by a gradual increase. A graph of absorption coefficient, α, as a function of wavenumber is shown in Fig. 5. Again plots of various powers of absorption coefficient against wavenumber do not give straight lines except at the high absorption end. The energy gap is $2{\cdot}5 \pm 0{\cdot}1$ eV.

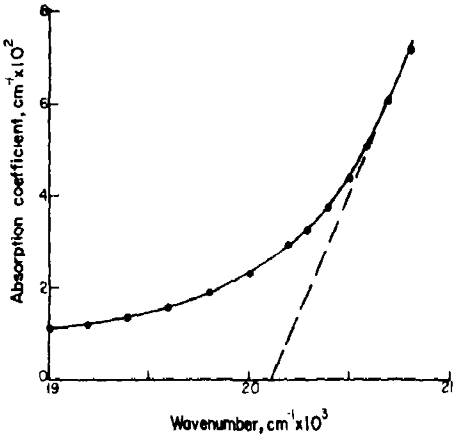

Fig. 5. Absorption coefficient of a $CuAlSe_2$ crystal 9×10^{-3} cm thick as a function of wavenumber.

5.2 *Refractive index*

The minimum deviation method was used. Due to crystal imperfections, the two polarised images were almost blurred together although they could just be distinguished. Consequently only the centre of the image was measured, giving the mean refractive index shown in Fig. 6. The mean refractive index extrapolated to infinite wavelength is $n_\infty = 2{\cdot}437$.

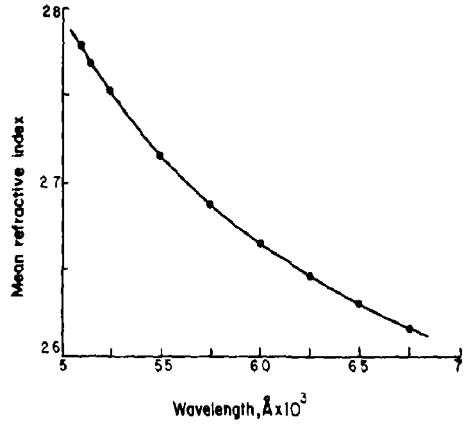

Fig. 6. Mean refractive index of $CuAlSe_2$ as a function of wavelength.

5.3 *Electrical measurements*

The same contact materials were used and again the indium evaporated contacts proved to be ohmic and gave minimum noise. The electrical resistivity was only measured at room temperature and it varied between 10^4 and $10^5\ \Omega$ cm with different specimens. Hall measurements were tried, but the Hall voltage with a field of $0{\cdot}9\ \mathrm{Wb\,m^{-2}}$ was less than 1 mV giving a mobility of less than $60\ \mathrm{cm^2\,V^{-1}\,sec^{-1}}$.

Measurement of the sign of the Seebeck coefficient indicates that all samples were *p*-type.

5.4 *Photoconduction*

The crystals show large photoconduction effects, the dark current being increased by a factor of about 20 when a 100 W white light source was focused on the crystal.

Indium evaporated contacts were used on the needle-shaped crystals and the photoconductivity wavelength response measured by focussing monochromatic light from a Hilger and Watts monochromator on to the crystal. The beam was 'chopped' at 10 Hz and the photocurrent was detected by measurement of the 10 Hz voltage across a small series resistor. This method eliminates the effect of any dark current drift. The equipment was calibrated using a thermopile and the results shown in Fig. 7. The relative height of the two peaks varied from batch to batch, but the intrinsic or short wavelength peak remained in the same position. The intrinsic photoconduction peak can be extrapolated to give a long wavelength limit of 4950 Å corresponding to an energy gap of 2·5 eV. This agrees with the value measured by optical absorption.

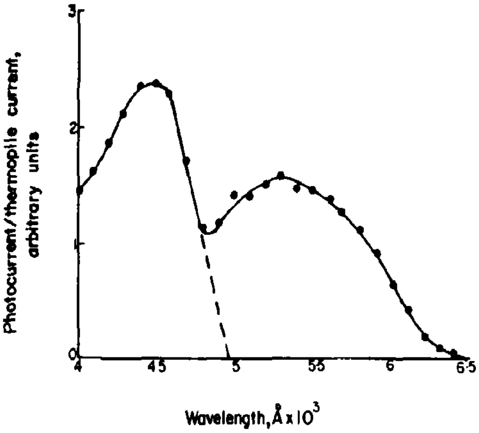

Fig. 7. Photocurrent from a $CuAlSe_2$ crystal, normalised with respect to a thermopile current, as a function of wavelength

6. SUMMARY AND DISCUSSION

Single crystals of $CuAlS_2$ and $CuAlSe_2$ have been prepared by iodine vapour transport. Their energy gaps have been measured by optical absorption and are about 3·35 and 2·5 eV respectively, although the absorption coefficient data could not be analysed in detail. The crystals show slight double refraction effects. The refractive indices for $CuAlS_2$ extrapolated to infinite wavelength are 2·300 and 2·325. The average extrapolated value for the selenide is 2·437. The selenide showed marked photoconductive effects with a double peak in the photoconductivity-wavelength curve. Mobilities in both compounds are low, the sulphide being less than 5 $cm^2 V^{-1} sec^{-1}$ and the selenide less than 60 $cm^2 V^{-1} sec^{-1}$ at room temperature. Resistivities of both compounds lie between 10^4 and 10^7 Ω cm at room temperature.

The I-III-VI_2 compounds are analogous to the II-VI compounds and so ZnS[14] can be compared with $CuAlS_2$ and ZnSe[13] with $CuAlSe_2$ as shown in Table 1. Here the refractive indices parallel and perpendicular to the needle axis have been averaged. The refractive indices obey the approximate law stating that $n_\infty{}^4E_G$ is constant; this quantity is shown in the last column of Table 1. The high photoconductivity of $CuAlSe_2$ compares directly to ZnSe[11], both semiconductors showing an intrinsic and impurity maxima.

The forbidden energy gaps of the two compounds measured are compared with the reported values for the copper containing members of the I-III-VI_2 semiconductors in Table 2.

Further work is being carried out on $CuAlTe_2$, but unfortunately the telluride does not appear to form by vapour transport, possibly due to the low vapour pressure of tellurium.

Table 1

	Energy gap E_G	Average refractive index n_∞	$n_\infty{}^4E_G$
$CuAlS_2$	3·35	2·312	95·7
ZnS	3·7	2 27	98 3
$CuAlSe_2$	2·5	2 437	88 2
ZnSe	2·68	2 43	93·5

Table 2. Energy gaps (eV) *of the semiconductors* $CuXY_2$ *with reference in brackets*

Y/X	Al	Ga	In
S	3·35	–	1·2[3]
Se	2 50	1·60[6] – 1·63[6, 4]	0·92[3] – 1·07[4]
Te	–	1·0[4] – 1·17[8]	0·95[3, 4] – 1·04[7]

Acknowledgements—The author is indebted to the members of staff and research assistants of the Physics Department of Brighton College of Technology for their invaluable assistance; to Mr. R, White for the chemical analysis and to the Pharmacy Department for use of the spectrophotometer.

REFERENCES

1. HAHN H., FRANK G., KLINGLER W., MEYER A., and STORGER G., *Z. anorg allg. Chem.* **271**, 153 (1953).
2. GOODMAN C. H. L. and DOUGLAS R. W., *Physica* **20**, 1107 (1954).
3. AUSTIN I. G., GOODMAN C. H. L. and PENGELLY A. E., *J. electrochem. Soc.* **103**, 609 (1956).
4. ZHUZE V. P., SERGEEVA V. M. and SHTRUM E. L., *Soviet Phys. tech. Phys.* **3**, 1925 (1958).
5. ZALAR S. M., and CADOFF I. B., *Trans. AIME* **224**, 436 (1962).
6. LERNER L. S., *J. Phys. Chem. Solids* **27**, 1 (1966).
7. ZALAR S. M., *J. electrochem. Soc.* **113**, 230 (1966).
8. WOOLLEY J. C. and WILLIAMS E. W., *J. electrochem. Soc.* **113**, 899 (1966).
9. PALATNIK L. S., *et al.*, *Soviet Phys. Crystallogr.* **10**, 395 (1966).
10. VAN DER PAUW L. J. *Phillips Res. Rep.* **13**, 1 (1958).
11. BUBE R. H. and LIND E. L., *Phys. Rev.* **110**, 1040 (1958).
12. SCHAFER H. *Chemical Transport Reactions.* Academic Press, New York (1964).
13. MARPLE D. T. F., *J. appl. Phys.* **35**, 539 (1964).
14. BIENIEWSKI T. M. and CZYZAK S. J. C., *J. Opt. Soc. Am.* **53**, 496 (1963).

J. Phys. Chem. Solids Pergamon Press 1969. Vol. 30, pp. 1941–1948. Printed in Great Britain.

POLARISED NEUTRON DIFFRACTION STUDY OF NICKEL FERRITE

S. I. YOUSSEF*, M. G. NATERA†, R. J. BEGUM,
B. S. SRINIVASAN and N. S. SATYA MURTHY
Nuclear Physics Division, Bhabha Atomic Research Centre, Trombay, Bombay-85, India

(*Received* 22 *January* 1969)

Abstract—Polarised neutrons have been used to solve the existing ambiguities in the chemical and magnetic structures of $NiFe_2O_4$. The results show conclusively that it has a completely inverted spinel structure with an oxygen parameter of 0·2573±0·0003. The observed magnetic moments at room temperature show that nickel ferrite exhibits the Neel ferrimagnetism with $m(A)\mathrm{Fe} = 4{\cdot}86\mu_B$, $m(B)\mathrm{Fe} = 4{\cdot}73\mu_B$ and $m(B)\mathrm{Ni} = 2{\cdot}22\mu_B$ leading to a net moment of $2{\cdot}09\mu_B$ The Debye–Waller temperature correction was determined with the constant $B = 0{\cdot}8 \times 10^{-16}$ cm².

INTRODUCTION

THE CRYSTAL structure of nickel ferrite has been the subject of several investigations in recent years. Due to the fact that nickel and iron are near neighbours in the periodic table and the neutron scattering amplitudes of the two elements are very close to each other, it is difficult to ascertain the cation distribution of nickel ferrite using either X-ray methods or from nuclear intensities alone in the case of neutron work.

Hastings and Corliss[1], using unpolarised neutron diffraction data, have concluded that the computed intensities are not sensitive to incomplete inversion, that the cation distribution is at least 80 per cent inverted and that the magnetic structure is of the collinear, Neel type. However, the nuclear intensities are not appreciably different for degrees of inversion between 80 and 100 per cent. In a recent Mössbauer work, Kedem and Rothem [2] reported that $NiFe_2O_4$ possesses the Yafet–Kittel type of triangular spin arrangement, while Chappert and Frankel[3] using the same technique have contradicted this and have concluded that $NiFe_2O_4$ has the collinear model.

In an earlier publication[4], we reported the unpolarised neutron work on $NiFe_2O_4$ and some of its solutions with $ZnFe_2O_4$. By studying the systematics of these solid solutions, it was established in that paper that $NiFe_2O_4$ is a collinear ferrimagnet at all temperatures below its Neel point. In this paper we present our results on $NiFe_2O_4$ obtained by means of polarised neutron diffraction and show the usefulness and the enhanced sensitivity of the method over the usual unpolarised neutron work in determining the cation distribution as well as the individual magnetic moments of each cation present on the tetrahedral and the octahedral sites. This method is specially applicable in the case of magnetic substances in which the spin arrangements are known to be collinear and there is no large magnetic anisotropy so that it is possible to saturate the specimen with the applied field in any direction.

Takei, Shirane and Frazer[5] in the study of Mn_4N, and Satya Murthy *et al.*[6] in the study of Mn_2Co_2C have adopted the polarised neutron technique in resolving the ambiguities in the magnetic structure and were able to choose between different models which unpolarised neutrons could not differentiate. In the present case, however, the basic magnetic structure being known, the coherence between the nuclear and magnetic scattering processes in the case of polarised neutrons has been used to amplify the variations of the nuclear structure factor with respect to inversion.

---

*Guest Scientist from the U.A.R. Atomic Energy Establishment, Cairo, U.A.R.

†I.A.E.A. Fellow from the Philippine Atomic Research Center, Diliman, Quezon City, Philippines.

PRINCIPLE

In the case of unpolarised neutrons the scattering intensity is given by

$$I(0) = \text{Const.} \times jL(N^2 + \tfrac{2}{3}M^2)\mathrm{e}^{-2W}. \qquad (1)$$

For polarised neutrons with their spins parallel to the magnetisation the intensity is given by

$$I(+) = \text{Const.} \times jL(N^2 + M^2 + 2PDNM)\mathrm{e}^{-2W} \qquad (2)$$

and for the opposite state i.e. with r.f. flipper coil on, the intensity is given by

$$I(-) = \text{Const.} \times jl(N^2 + M^2 - 2PD\,\overline{2F-1}\,NM)\mathrm{e}^{-2W}. \qquad (3)$$

In the above equations, j is the multiplicity of the reflecting planes. L is the Lorentz factor, N and M are the nuclear and magnetic structure factors, P is the incident beam polarisation, D is the polarisation transmission by the sample and F is the flipping efficiency of the r.f. coil.

It is evident from equations (2) and (3) that the polarised neutron intensities are significantly different and are very sensitive to the nuclear and magnetic parameters, which depend on the degree of inversion (ν). This enables an accurate determination of ν.

The polarisation ratio is defined as

$$R = \frac{I(+)}{I(-)} = \frac{N^2 + M^2 + 2PDNM}{N^2 + M^2 - 2PD(2F-1)NM} = \frac{\gamma^2 + 2\mathrm{PD}\gamma + 1}{\gamma^2 - 2PD(2F-1)\gamma + 1} \qquad (4)$$

where $\gamma = M/N$. For a certain value of PD and F, the polarisation ratio is sensitive to relative signs and magnitudes of M and N. In the case of $R > 1$, N and M have same sign, while in the case of $R < 1$, N and M have opposite signs.

The sum and difference of the total structure factors for the two states of polarisation can be given in a relation such as

$$(\Sigma/\Delta)\,(\text{Actual}) = \frac{I(+) + I(-)}{I(+) - I(-)} = \frac{1}{2PDF}\left(\gamma + \frac{1}{\gamma}\right) + \frac{(1-F)}{F}. \qquad (5)$$

In the case of ideal PD and F, i.e. $PDF = 1$, equation (5) reduces to

$$(\Sigma/\Delta)\,(\text{Ideal}) = \tfrac{1}{2}\left(\gamma + \frac{1}{\gamma}\right) \qquad (6)$$

and

$$(\Sigma/\Delta)\,(\text{Ideal})/(\Sigma/\Delta)\,(\text{Actual}) = PDF \qquad (7)$$

assuming that F is very close to 1·0.

A detailed description of the principles and applications of the polarised neutrons in magnetic structure determination is given elsewhere[7].

EXPERIMENTAL RESULTS AND DISCUSSION

(a) Sample preparation

The nickel ferrite sample was prepared by the usual ceramic sintering process. NiO and Fe_2O_3 were mixed intimately in the appropriate molar proportions and heated in air at a temperature of 900°C for several hours. The resulting mass was powdered and pressed into pellets having 15 mm dia. and 3 mm thickness. The pellets were then sintered in air at 1250°C for 8 hr and slowly cooled in a controlled furnace. Chemical analysis for metals showed the correct composition, and X-ray diffraction failed to reveal the presence of any other phase. The lattice constant was determined to be $a_0 = 8{\cdot}325 \pm 0{\cdot}008$ Å.

(*b*) *Determination of the oxygen parameter*, u, *and* PD

We have selected three reflections, which, in the case of unpolarised neutrons, have negligible magnetic contributions and are insensitive to the degree of inversion because of the nature of their structure factors. These reflections are (311), (511,333) and (440). The calculated magnetic contributions with respect to the corresponding total intensities for 100 and 80 per cent inversion were estimated to be 0·093 and 0·506 per cent respectively for the (311), 0·183 and 0·255 per cent for the (511,333) and 0·252 and 0·271 per cent for the (440). The graphical method of plotting the ratios of observed and calculated nuclear structure factors as a function of u was employed to determine the oxygen parameter as shown in Fig. 1 and it is found to be 0·2573 ± 0·0003.

The polarised neutron data was taken on the spectrometer described previously[8] with the sample in a vertical magnetic field of 8 KOe which was found to be well above the field required to eliminate all magnetic contributions to the unpolarised neutron pattern. Table 1 gives the absolute values of the total structure factors for the polarised neutron case relative to the (440) reflection based on the assumptions that it is purely

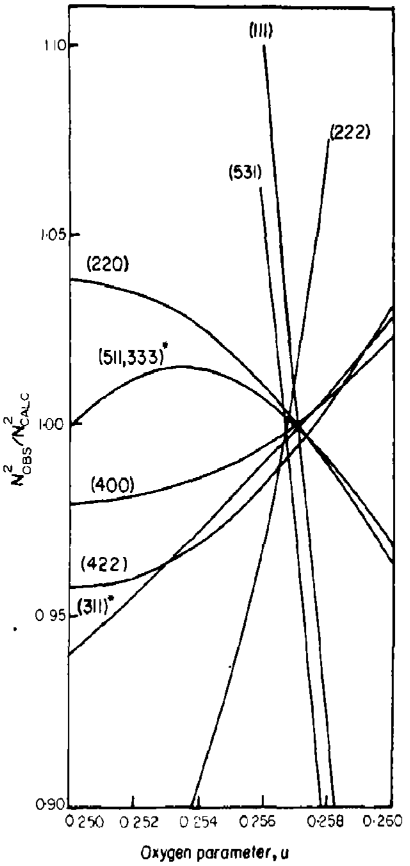

Fig. 1. Dependence of the ratio N^2_{Obs}/N^2_{Calc} upon the oxygen parameter for various Bragg reflections. Curves with asterisks are from unpolarised neutron data, others from polarised neutron data.

Table 1. *Comparison of observed and calculated polarised neutron total structure factors for* $NiFe_2O_4$

hkl	$F^2_{hkl}(10^{-24}\,cm^2)$					
	I(0)Obs.	*I*(0)Calc	*I*(+)Obs.	*I*(+)Calc.	*I*(−)Obs.	*I*(−)Calc.
111			263·89	263·71	108·33	108 26
220			17·39	17·56	204·69	202·95
311	168·25	168·40	179·25	179·18	159·93	159·04
222			65·28	65·37	144·01	143·35
400			1570·19	1563·40	337·37	337·04
331			63·49	63·33	50·68	50·69
422			21·17	21·61	118 43	117·90
511 333	358 00	358·53	389·08	389·81	331·86	331·55
440	1730·00	1734·20	1922·00	1916·93	1570·00	1577·06
531			57 06	56·32	8·64	7·71

$m(A)Fe = 4{\cdot}86\mu_B$, $m(B)Fe = 4{\cdot}73\mu_B$, $m(B)Ni = 2{\cdot}22\mu_B$, $b_{Fe} = 0{\cdot}956 \times 10^{-12}$ cm, $b_{Ni} = 1{\cdot}04 \times 10^{-12}$ cm; $u = 0{\cdot}2573 \pm 0{\cdot}0003$, $B_{R,T} = 0{\cdot}80 \times 10^{-16}$ cm², $a_0 = 8{\cdot}325 \pm 0{\cdot}008$ Å.

nuclear and independent of the cation distribution in the case of unpolarised neutrons.

The value of PD has been determined by solving equations (1–3) and using the measured value for $F = 0{\cdot}945$ corresponding to each of the reflections (311), (511,333) and (440) and it is not found to be significantly different being 0·85, 0·842 and 0·856 for the three reflections respectively. An average value of 0·85 has been used in the following analysis. (This corresponds to a polarisation transmission in the sample of $D = 0{\cdot}89$, if a value of $P = 0{\cdot}955$, as measured independently, is used.)

(*c*) *Determination of nuclear and magnetic structure factors*

The solution of the structure factors determined from the observed $I(+)$ and $I(-)$ enables one to extract the nuclear and magnetic structure factors separately and their relative signs. This is also represented graphically in Fig. 2 which very clearly brings out the role of the signs of N and M. From the comparison of the 'r.f. off' and 'r.f. on' patterns which are shown in Fig. 3 and the nature of the structure factor formulae the proper signs and magnitudes of M and N can be determined.

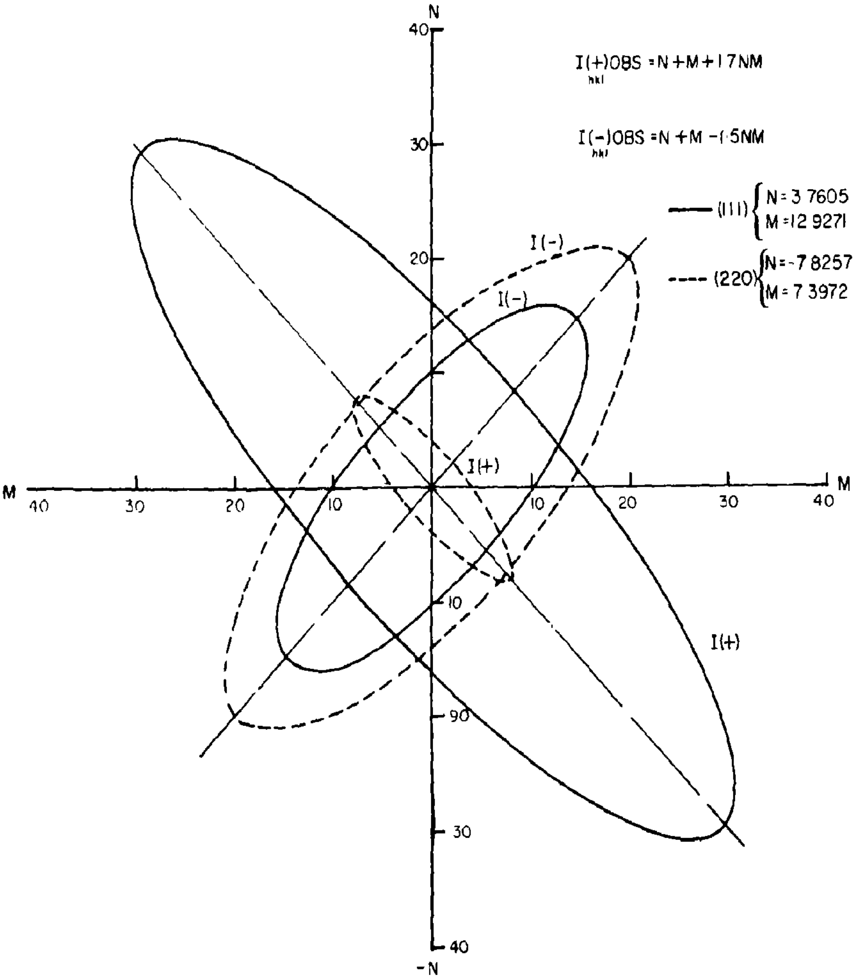

Fig. 2. Plot of all possible combinations of N and M as deduced from observed $I(+)$ and $I(-)$. The intersection points of the two curves represent those values of N and M and their relative signs which satisfy both the reflections.

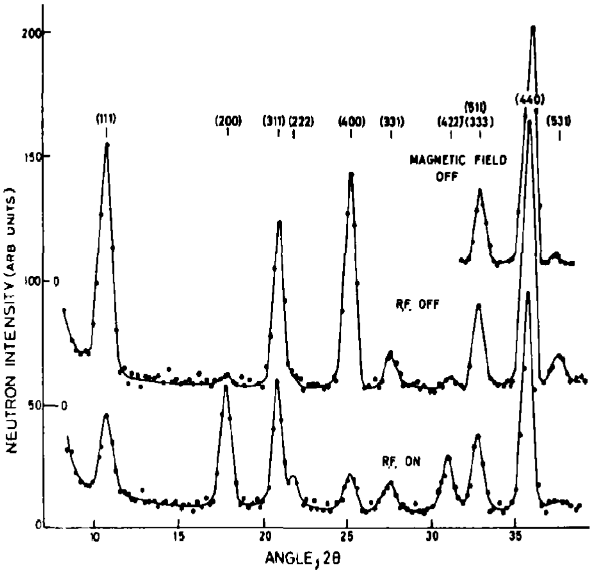

Fig. 3. Neutron diffraction patterns of polycrystalline $NiFe_2O_4$ for polarised and unpolarised neutrons at room temperature. The 'r.f. off' and 'r.f. on' patterns show the polarised neutron intensities with spin parallel and antiparallel to the magnetisation respectively, while the 'magnetic field off' pattern shows two of the unpolarised neutron intensities for comparison.

(*d*) *Determination of the degree of inversion*, ν

In Fig. 1 a family of curves has been obtained by plotting the ratios of $N^2_{\text{Obs.}}/N^2_{\text{Calc}}$ for various reflections as a function of u, for both polarised and unpolarised data. The values of $F^2_{\text{Obs.}}/F^2_{\text{Calc.}}$ as a function of ν for the polarised neutron data has been plotted in Fig. 4. This method yields precisely the values of u and ν simultaneously. Figure 4 definitely establishes that $NiFe_2O_4$ cannot be less than 100 per cent inverted. Figure 5 shows a comparison between the polarised and unpolarised neutron intensities and their relative sensitivity to the degree of inversion.

The Debye–Waller temperature factor was estimated to give $B = 0{\cdot}8 \times 10^{-16}\,\text{cm}^2$.

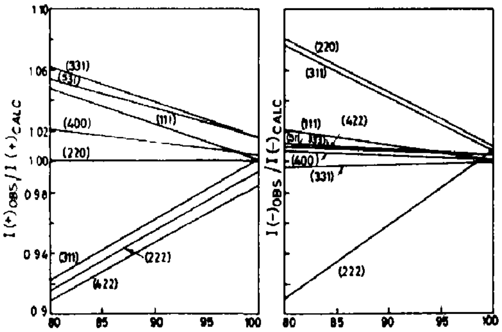

Fig. 4. Dependence of the ratio $I_{\text{Obs}}/I_{\text{Calc}}$ upon the degree of inversion for the two states of neutron polarisation.

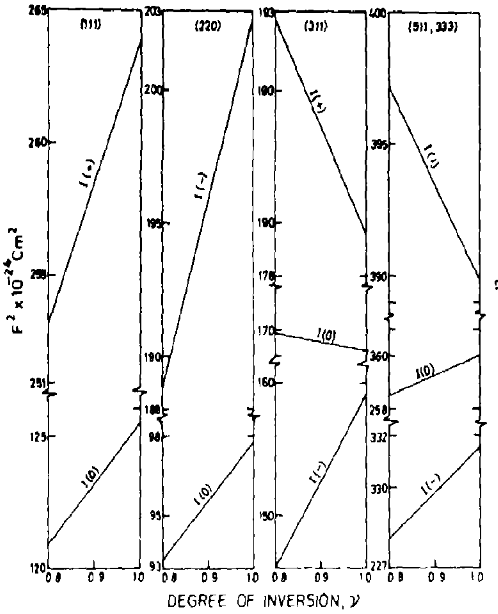

Fig. 5. Comparison between relative structure factor magnitudes for polarised and unpolarised cases and their relative sensitivities to the degree of inversion.

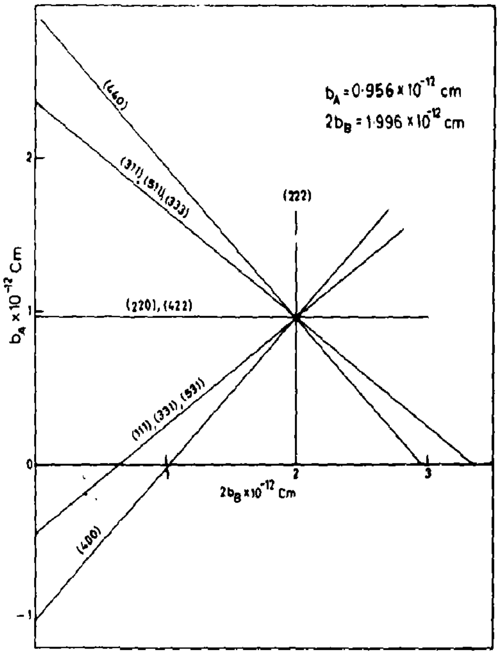

Fig. 6. The *A*- and *B*-sublattice nuclear scattering amplitudes for various nuclear structure factors.

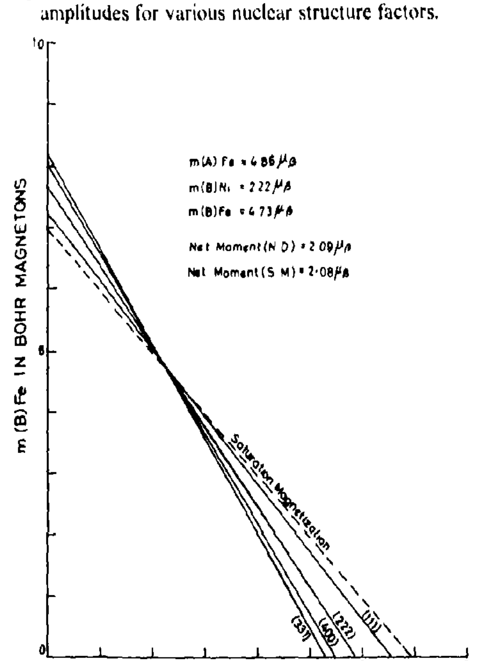

Fig. 7. The *B*-sublattice magnetisation for various magnetic structure factors after determining the *A*-sublattice magnetisation from the (220) and (422) reflections. The broken line is from the saturation magnetisation (S.M.) data.

(e) *Determination of the individual nuclear scattering amplitudes and magnetic moments*

After correcting every nuclear structure factor for its oxygen contribution, a graphical examination of all reflections are shown in Fig. 6 which leads to values of $b_A = 0{\cdot}956 \times 10^{-12}$ cm and $2b_B = 1{\cdot}996 \times 10^{-12}$ cm with $b_{Fe} = 0{\cdot}956 \times 10^{-12}$ cm and $b_{Ni} = 1{\cdot}04 \times 10^{-12}$ cm, these values of b_A and b_B clearly show that there is no Ni on the tetrahedral sites. A similar examination has been employed for the magnetic structure factors, using the calculated form factor of $3d^5$ by Freeman and Watson[9] for Fe^{3+} and Alperin's[10] experimental form factor for Ni^{2+}, $m(A)Fe = 4{\cdot}86\mu_B$, $m(B)Fe = 4{\cdot}73\mu_B$ and $m(B)Ni = 2{\cdot}22\mu_B$ were obtained. These are in excellent agreement with the saturation magnetisation measurement of $2{\cdot}08\mu_B$ at room temperature. The difference in the Fe^{3+} moments on the *A* and *B* sites is presumably due to the different Brillouin functions that they follow. Figure 7 shows the graphical determination of the moments for Fe and Ni ions in the *B*-sites

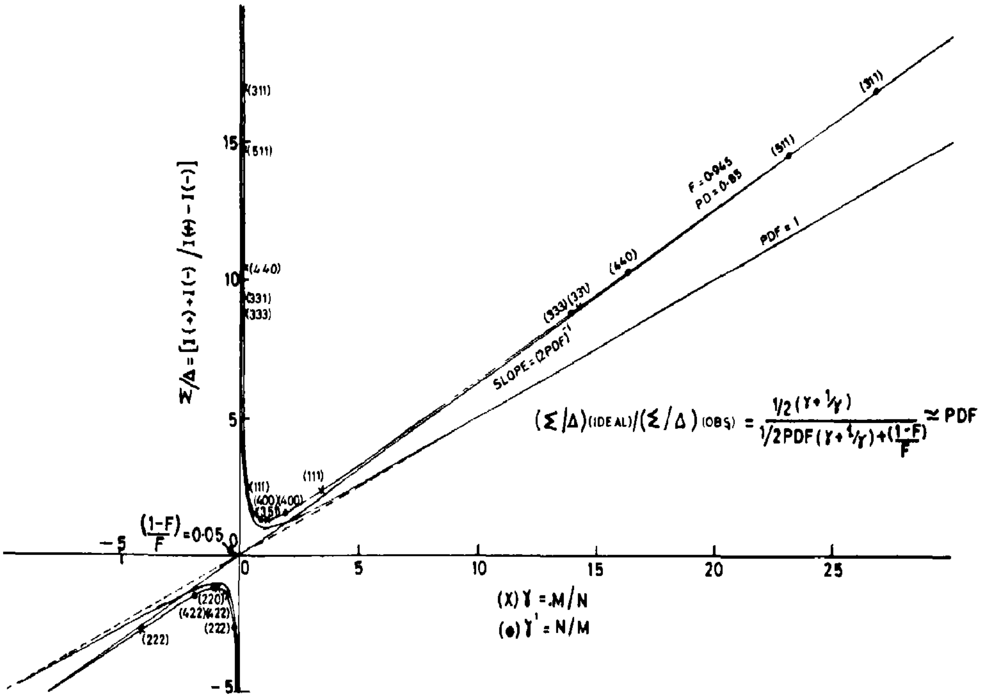

Fig. 8. Plot of observed (Σ/Δ) for several reflections as a function of the ratio of nuclear and magnetic structure factors. The ratio of (Σ/Δ) (Ideal)/(Σ/Δ) (Obs) gives the value of *PDF* ≈ 0·803.

for several reflections after determining the moment of the Fe ions in the *A*-site from the (220) and (422) reflections.

The calculated intensities based on the extracted nuclear and magnetic parameters are given in Table 1 which indicates excellent agreement with the observed intensities. Moreover, Fig. 8 shows the plot of equations (5) and (6) which indicate that the observed (Σ/Δ) values fit very well with the calculated curve based on the extracted parameters.

CONCLUSION

Our polarised neutron results show conclusively that $NiFe_2O_4$ has completely inverted spinel structure and is a collinear, Neel ferrimagnet. This agrees with the recent work of Robertson and Pointon[11]. They determined experimentally the preference energy of Ni^{2+} ions for the *B*-sites to be 0–80 eV, which implies that Ni^{2+} at the *A*-sites should be less than 1 per cent even for samples quenched from near the melting point of the ferrite. The present result is an improvement over the earlier neutron diffraction results of Hastings and Corliss[1] and is in agreement with the Mossbauer results of Chappert and Frankel[3] as well as with the most recent neutron diffraction results of Satya Murthy *et al.*[4].

Acknowledgements—We are indebted to Dr. P. K. Iyengar for his encouragement and keen interest in the work. We wish to thank Dr. C. M Srivastava of I.I T., Bombay for supplying the sample. Our thanks are also due to Mr. M. R. L. N. Murthy for help in the experimental work.

REFERENCES

1. HASTINGS J. M. and CORLISS L. M., *Rev. mod. Phys.* **25**, 114 (1953).
2. KEDEM D. and ROTHEM T., *Phys. Rev. Lett.* **18**, 165 (1967).
3. CHAPPERT J. and FRANKEL R B, *Phys. Rev. Lett.* **19**, 571 (1967).

4. SATYA MURTHY N. S., NATERA M. G., YOUSSEF S. I., BEGUM R. J. and SRIVASTAVA C. M., *Phys. Rev.* To be published (1969).
5. TAKEI W. J., SHIRANE G. and FRAZER B. C., *Phys. Rev.* **119**, 122 (1960).
6. SATYA MURTHY N. S., BEGUM R. J., SOMANATHAN C. S., SRINIVASAN B. S. and MURTHY M. R. L. N., *J. Phys. Chem. Solids* **30**, 939 (1969).
7. NATERA M. G., YOUSSEF S. I., BEGUM R. J. and SATYA MURTHY N. S., To be published.
8. SATYA MURTHY N. S., SOMANATHAN C. S., BEGUM R. J., SRINIVASAN B. S., and MURTHY M. R. L. N., *Indian J. Pure Appl. Phys.* To be published (1969).
9. FREEMAN A. J. and WATSON R. D., *Phys. Rev.* **118**, 1168 (1960).
10. ALPERIN H. A., *Phys. Rev. Lett.* **6**, 55 (1961).
11. ROBERTSON J. P. and POINTON A. J., *Solid State Commun.* **4**, 257 (1966); POINTON A. J. and ROBERTSON J. P., *Phil. Mag.* **17**, 703 (1968).

J. Phys. Chem. Solids Pergamon Press 1969. Vol. 30, pp. 1949–1956. Printed in Great Britain.

SUPERCONDUCTING, THERMAL AND MAGNETIC SUSCEPTIBILITY BEHAVIOR OF SOME INTERMETALLIC COMPOUNDS WITH THE FLUORITE STRUCTURE

J. H. WERNICK, A MENTH, T. H. GEBALLE*, G. HULL and J. P. MAITA
Bell Telephone Laboratories, Incorporated, Murray Hill, N.J. 07971, U.S.A

(*Received* 8 *January* 1969)

Abstract – $AuGa_2$ becomes superconducting at 1·12°K. The superconducting critical temperature rises rapidly with small additions of Pd. For the composition corresponding to $Au_{0\cdot95}Pd_{0\cdot05}Ga_2$, $T_c = 1\cdot79$°K, and then remains essentially constant with further increase in Pd content. The electronic contribution to the heat capacity, γ, increases in a similar manner. At $Au_{0\cdot95}Pd_{0\cdot05}Ga_2$ the change in γ amounts to 18·4 per cent per atomic per cent Pd. All of the $Au_{1-x}Pd_xGa_2$ materials are diamagnetic and the diamagnetism decreases with increasing Pd content The behavior of the susceptibility per gram atom, χ_1, at 0°K as a function of Pd content parallels the behavior of.T_c, γ, and the ^{71}Ga Knight shift in these allows[2]. $AuAl_2$ and $AuIn_2$ becomes superconducting below 0·1°K and both show temperature independent diamagnetism, in contrast to the behavior of $AuGa_2$.

INTRODUCTION

THE FLUORITE structure (cubic CI type – four formula units per cell) is common to a number of phases of stoichiometry AB_2 and comprise metals, semiconductors, and insulators. In this structure, each B atom has $4A$ atom neighbors at a distance a $\sqrt{3}/4$ while each A atom has $8B$ neighbors at the same distance. The A atoms are arranged in a FCC sublattice while the B atoms form a simple cubic subcell within the unit cell. It is important to note that for the metallic phases, three of which will be considered here ($AuGa_2$, $AuAl_2$ and $AuIn_2$), the A–B distance is about 0·2 Å less than the sum of the coordination 12 radii of the constituent atoms, suggesting considerable covalent character of the bonds. This is also true for $PtGa_2$. The colors of these materials are also very interesting and reflect differences in optical transitions and band structure. $AuGa_2$ is silvery-gray, $AuAl_2$ purple, $AuIn_2$ silvery, and $PtGa_2$ yellow and d-electron states may be important regarding the optical properties of these materials.

An NMR study of these materials by Jaccarino *et al.* showed that the ^{71}Ga Knight shift in $AuGa_2$ exhibited an unusual temperature dependence[1]. The shift is negative at low temperatures, changes sign at about 68°K and approaches a constant value at higher temperatures[1, 2]. On the other hand, the Al and In shifts are positive and essentially temperature independent. However, the substitution of Pd for Au in $AuGa_2$ results in a monotonic change in the Ga Knight shift with increasing Pd until at $Pd_{0\cdot05}Au_{0\cdot95}Ga_2$ the Knight shift is positive at all temperatures.† In this context the 'phase' $PdGa_2$ does not exist. On the other hand, Pt is very slightly soluble in $AuGa_2$ and in addition, does not behave as Pd regarding the NMR properties.† We shall show below that the superconducting properties of $AuGa_2$ are affected drastically by small amounts of Pd and the dependence on Pd content correlates with the Ga Knight shift behavior and the heat capacity data to be given below.

---

*Also at Stanford University where the work was supported in part by the Air Force Office of Scientific Research, Office of Aerospace Research, United States Air Force under AFOSR grant 68-1510.

†JACCARINO V., WERNICK J H. and MENTH A., Unpublished results.

Because these intermetallic compounds exhibit comparatively low residual resistivities in the zone melted single crystal state*, they have been studied in recent years by means of galvano-magnetic measurements and experimental methods which give information regarding the Fermi surfaces[3–7]. All three compounds show maxima in the thermoelectric power between $\frac{1}{4}\theta_D-\frac{1}{5}\theta_D$ and this is attributed to phonon drag effects. However, away from these maxima at both high and low temperatures, the thermoelectric power of $AuGa_2$ is negative while the other two remain positive. The resistivity of $AuGa_2$ does not show any anomaly at 68°K. It is significantly larger than either $AuIn_2$ or $AuAl_2$ at all temperatures. Regarding the interpretation of de Haas–van Alphen effect measurements made on all of these materials, there appears to be approximate agreement between the experimental results and a Fermi surface based on a free electron model. However, differences between them do exist but apparently not sufficient enough to explain the thermoelectric and NMR behavior of $AuGa_2$[3]. Low temperature heat capacity data for $AuGa_2$, $AuIn_2$, and $AuAl_2$ show the electronic contributions to be similar in these materials[8].

For the isostructural intrinsic semiconductors Mg_2Si, Mg_2Ge and Mg_2Sn (8 valence electrons/3 atoms), the volume of the Brillouin zone is such that there are just 8/3 states per atom within the zone[16]. Thus, the number of available valence electrons is equal to the number of states within the zone. An interesting observation regarding $AuGa_2$, $AuAl_2$ and $AuIn_2$ (7 valence electrons/3 atoms), worth mentioning here in the context of covalent character of these materials, is that they contract on melting, a characteristic feature of semiconductors and semimetals, such as Bi and γ-brass. With the present electron-to-atom ratio, the free electron sphere intersects the zone boundaries, a situation characteristic of semimetals. In addition, this may be the reason why each of these phases do not form extensive solid solutions with the other isostructural phases and elements when the usual conditions of crystal structure and atomic size are satisfied. Finally, crystals in which the Fermi surface is near or at zone boundaries may have high diamagnetic susceptibilities from conduction electrons and holes and changes which can alter by small amounts the proximity of the Fermi surface to the zone boundaries may result in rather significant changes in electronic properties.

EXPERIMENTAL RESULTS AND DISCUSSION

All of the materials were prepared from elements of 99·999+ per cent purity. Stoichiometric amounts of the constituent elements were first melted in recrystallized Al_2O_3 crucibles by induction heating in an argon atmosphere. Zone melting was subsequently carried out in quartz ampoules. The Pd bearing samples, prepared in the same manner, were subjected to zone melting (2 passes) and we refer to this operation on these samples as a quasi-zone leveling, as far as the Pd is concerned. Our analytical data indicates that for the compositions of interest to us, the distribution coefficient of Pd in $AuGa_2$ is near unity. Table 1 shows the results of atomic absorption analysis on the $Au_{1-x}Pd_xGa_2$ samples used for all measurements. Because of the good agreement with the nominal com-

Table 1. Atomic absorption analytical results

	Wt. % Pd (Nominal)	Wt. % Pd (Analysis)
$Au_{0.98}Pd_{0.02}Ga_2$	0·64	0·64 ± 0·013%
$Au_{0.95}Pd_{0.05}Ga_2$	1·60	1·60 ± 0·032%
$Au_{0.9}Pd_{0.1}Ga_2$	3·25	3·40 ± 0·068%

---

*This suggests that these intermetallic compounds are truly stoichiometric 'line' phases and perhaps is a result of the covalent character of these materials.

positions, we shall refer to our materials in terms of the nominal compositions. All materials were examined by powder X-ray diffraction. The variation of the lattice constant with Pd content in $AuGa_2$ is shown in Fig. 1. The maximum solid solubility of Pd in $AuGa_2$ appears to be close to $x = 0{\cdot}15$. The decrease in average unit cell size results in an increase in average volume of the Brillouin zone and a corresponding decrease in proximity of the Fermi surface to the zone boundaries.

Heat capacities were determined by the heat pulse method[9], and the data are shown in Fig. 2. Examination for superconductivity was made in an apparatus described previously [10] down to 0·36°K using the resonant-frequency shift circuit of Shawlow and Devlin [11] and a frequency of 16 kc/sec. Good agreement was obtained with the critical temperatures which could be observed by heat capacity measurements (Table 2). The transition breadth is indicated. As shown in Fig. 3, T_c rises rapidly with increasing Pd and is close to the maximum value at $Au_{0{\cdot}95}Pd_{0{\cdot}05}Ga_2$. Previous workers have reported $AuGa_2$ to be not superconducting down to 0·34°K[14].

A Faraday method, utilizing a Cahn balance, was used for the magnetic susceptibility measurements in the temperature range 4·2°–300°K. The susceptibility per gram atom values, χ_A, are accurate to within 3 per cent. The χ_A vs. temperature data and χ_A at 0°K as a function of Pd content in $AuGa_2$ are shown on Figs. 4 and 5 respectively.* All of the $Au_{1-x}Pd_xGa_2$ materials are diamagnetic and exhibit a temperature dependence to the susceptibility. The diamagnetism decreases with increasing Pd content. The degree of temperature dependence decreases with increasing Pd content. The behavior of χ_A at 0°K (Fig. 5) as a function of Pd content parallels the behavior of T_c, γ (below) and Ga^{71} Knight shift[2]. In contrast to the behavior of $AuGa_2$, $AuAl_2$ and $AuIn_2$ show temperature independent diamagnetism.

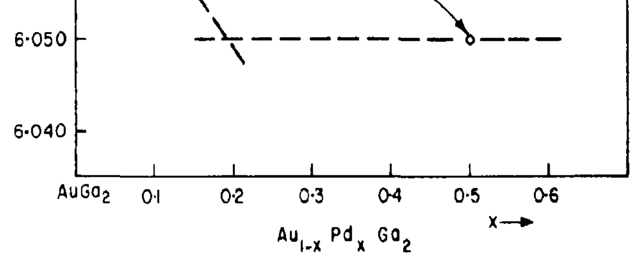

Fig. 1. The variation of lattice constant with Pd content in the system $Au_{1-x}Pd_xGa_2$. The presence of some second phase for $x = 0{\cdot}15$ indicates the maximum solid solubility is perhaps somewhat below this value.

---

*The measurements were performed on the heat capacity samples and in some cases also repeated on different samples obtained from different regions of the ingot.

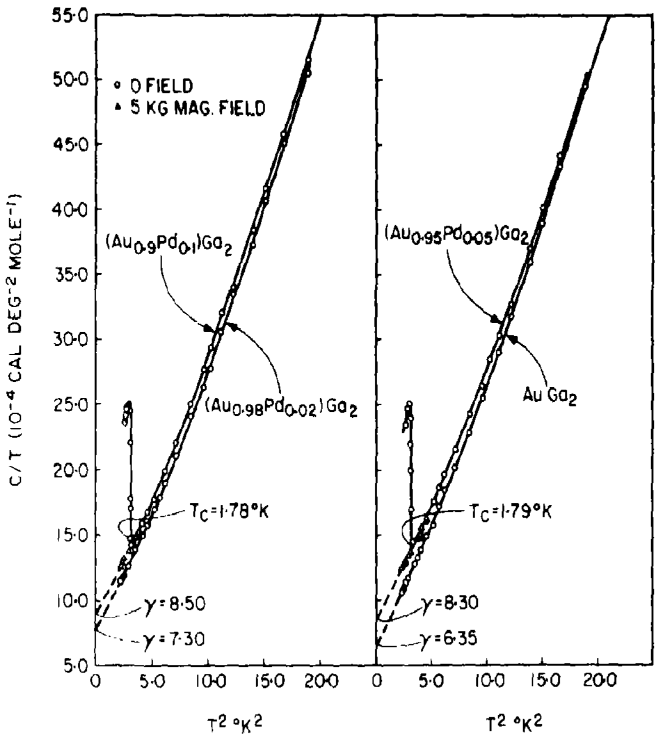

Fig. 2. Heat capacity data for $Au_{1-x}Pd_xGa_2$ compositions studied for this research.

A summary of some of the experimental results is shown on Table 2. Note the large increase in the electronic contribution to the heat capacity, γ, of $AuGa_2$ due to the substitution of Pd for Au. For $Au_{0.9}Pd_{0.1}Ga_2$, there is a 33·8 per cent increase (~10·5 per cent per atomic per cent Pd), with the bulk of the increase (30·7 or 18·4 per cent per atomic per cent Pd) obtained in $Au_{0.9}Pd_{0.05}Ga_2$. The variation in T_c follows the change in γ (Fig. 3). Furthermore, the composition near which T_c and γ saturate ($Au_{0.95}Pd_{0.05}Ga_2$) corresponds to the composition at which the Ga Knight shift becomes positive at all temperatures.

The contribution of the ion cores to the susceptibility can be estimated by using the value for Ga^{3+}($-0{\cdot}8\times10^{-5}$) given by Klemm [15]. Klemm proposes a value for Au^{1+} smaller than $-4{\cdot}0\times10^{-5}$. If one chooses $-4{\cdot}3\times10^{-5}$ for Au^{1+} the remaining susceptibility is zero at the same temperature at which the Knight shift is zero. The difference between the ion part and the total susceptibility can be attributed to the susceptibility of the free carriers, χ_c. A direct correlation of χ_c and Knight shift data results in a unreasonable large and negative hyperfine field. An attempt to correlate the magnetic susceptibility, Knight shift, and nuclear relaxation data in a consistent manner leads to a larger temperature independent diamagnetic contribution given above[2]. Blount[17] pointed out that in materials with large spin orbit coupling (heavy ions) and small band gaps, additional terms to the Pauli–Landau susceptibility occur resulting in larger diamagnetism. These additional terms do not contribute to the Knight shift.

Also shown in Table 2 are the size of the

Table 2. Summary of superconductivitynand heat capacity results

Material	T_c(°K)	γ (10^{-4} cal/mol-deg²)	θ_D (°K)	$C_{es}/\gamma T_c$	g	λ	$N_{bs}(0)$, (states/eV-atom)	Remarks
$AuGa_2$	1·12–1·05	6·35(a)	196, 198 ± 8(g)		0·199	0·43	0·13	Zone melted single crystal, $R_{273}/R_{4\cdot2} = 255$. Powder, bulk behavior. Superconductivity (SC) destroyed at $H = 66$ G.
$Au_{0\cdot98}Pd_{0\cdot02}Ga_2$	1·35–1·25	7·30(c)	196		0·204	0·455	0·15	Powder, bulk behavior.
$Au_{0\cdot95}Pd_{0\cdot05}Ga_2$	1·75–1·69, 1·79(e)	8·30(c)	198	1·33	0·218	0·49	0·16	Powder, bulk behavior. SC quenched at 150 G.
$Au_{0\cdot9}Pd_{0\cdot1}Ga_2$	1·73–1·72 1·78(e)	8·50(c)	197	1·30	0·218	0·49	0·17	Powder, bulk behavior. SC quenched at 350 G.
$Au_{0\cdot85}Pd_{0\cdot15}Ga_2$	1·75–1·73							Powder, bulk behavior, although X-ray pattern indicated some second phase. SC quenched at 300 G.
$AuIn_2$	0·096–0·093(f)	7·54(b)	187(b)		0·135	0·30	0·17	As-cast ingot. SC destroyed at $H = 25$ G.
$Au_{0\cdot9}Pd_{0\cdot1}In_2$	(d,f)							Zone leveled.
$AuAl_2$	0·095–0·074	7·25(b)	297(b)		0·127	0·29	0·17	Zone melted. SC destroyed at $H = 50$ G.

(a)This research and in good agreement with Rayne (reference [8]) – 6·45 × 10^{-4}.
(b)From reference [8].
(c)This research.
(d)Normal to 0·36°K.
(e)From heat capacity measurements.
(f)Lattice constant for $AuIn_2$ = 6·517 Å; for $Au_{0\cdot9}Pd_{0\cdot1}In_2$, 6·484 Å.
(g)From sound velocity measurements by L. R. TESTARDI.

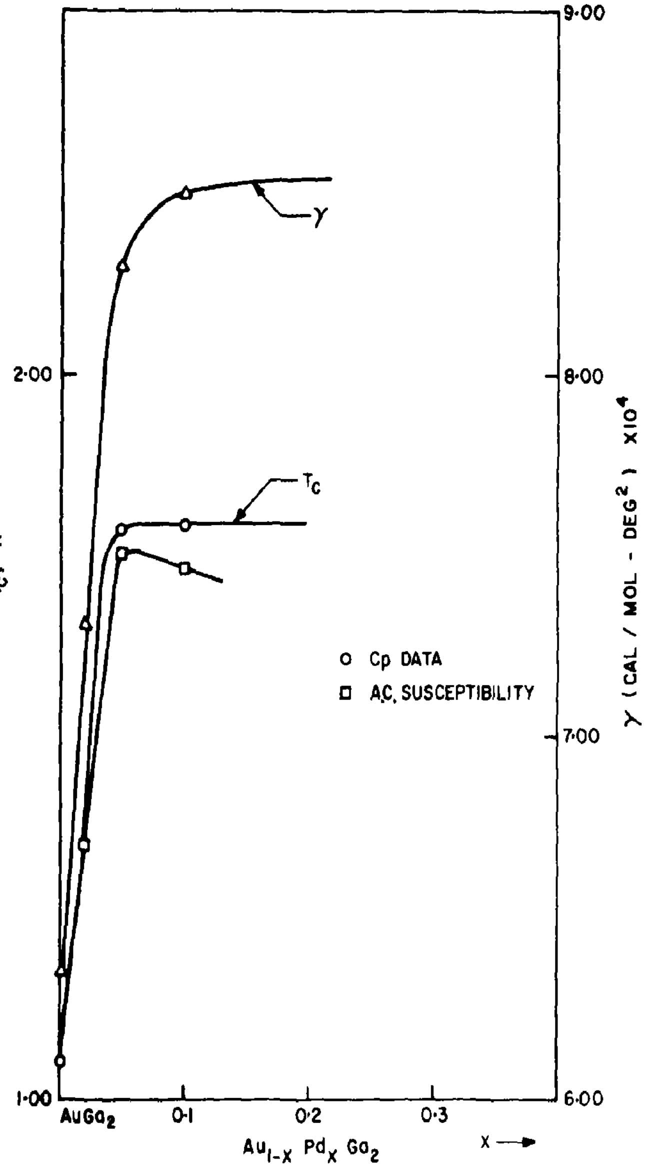

Fig. 3. Variation of T_c and γ with Pd content in $Au_{1-x}Pd_xGa_2$ alloys.

heat capacity anomaly $(C_{es}/\gamma T)_{T_c}$, where C_{es} is the electronic contribution to the superconducting state specific heat, and the *g*-factor obtained from the relation

$$T_c = 0{\cdot}85\theta_D e^{1/g}.$$

In the BCS relation, $g = N(E_F)A$, where $N(E_F)$ and A are the normal density of electronic states and electron–electron pairing potential arising from the electron–phonon interaction respectively. The increase in γ of 30 per cent is more than enough to account for a '*g*' increase of 10 per cent.

The superconducting critical temperatures,

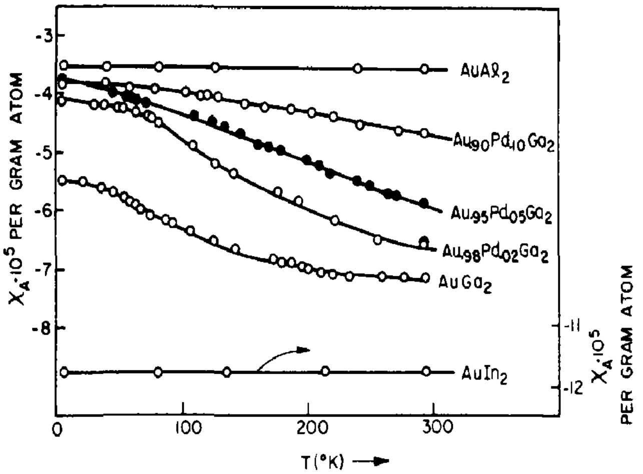

Fig. 4. The susceptibility per gram atom as a function of temperature for $AuAl_2$, $Au_{1-x}Pd_xGa_2$ alloys, and $AuIn_2$

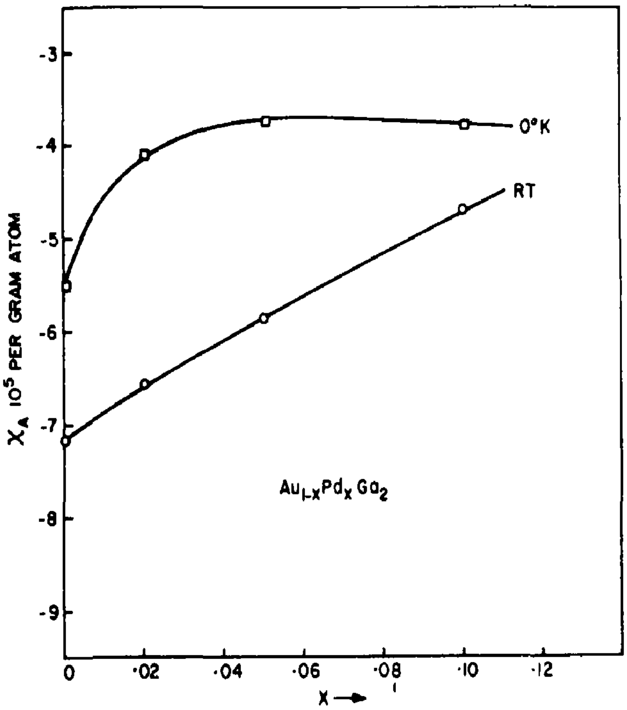

Fig. 5. The susceptibility per gram atom at 0°K and room temperature for the $Au_{1-x}Pd_xGa_2$ alloys. The 0°K data was obtained by extrapolation of the data shown on Fig. 4.

the Debye temperatures θ_D, and the γ-values $[\gamma = \frac{2}{3}\pi^2 k^2 N(E_F)]$ can be used to discuss the superconducting behavior of these materials within the framework of strong-coupling theory[13]. The formula for T_c is

$$T_c = \frac{\theta_D}{1{\cdot}45}\exp\left[-\frac{1{\cdot}04(1+\lambda)}{\lambda-\mu^*(1+0{\cdot}62\lambda)}\right]$$

λ is an electron–phonon coupling constant and μ^* is the Coulomb pseudopotential. The density of states $N(E_F)$ obtained from the specific heat data is the 'band-structure' or 'bare' density of states $[N_{bs}(0)]$ enhanced by the factor $(1+\lambda)$, i.e. $n(E_F) = [N_{bs}(0)](1+\lambda)$. $N_{bs}(0)$ contains the enhancement due to Coulomb interaction between electrons. Table 2 contains the λ and $N_{bs}(0)$-values computed from the above equation assuming $\mu^* = 0{\cdot}1$, which, according to McMillan, is reasonable for nearly free electron metals. For the $Au_{1-x}Pd_xGa_2$ materials, there is nearly a 50 per cent enhancement of the band-structure density of states. It should be noted that the sharp rise in the density of states from 0·13 to 0·15 states per eV per atom as 2% of the Au is replaced by Pd corresponds to a rate of increase of one state per eV per Pd atom. This large increase is undoubtedly a feature of the fact that the Fermi level lies near a zone edge.

According to the arguments of McMillan, the superconducting transition temperature is less related to changes in γ than to changes in the phonon spectrum. In contrast, however, the measurements show that the low temperature Debye data show no significant dependence upon Pd concentration. Also there is no evidence of dispersion in the low frequency portion of the spectrum since θ_D for $AuGa_2$ measured by Testardi from velocity of sound measurements is in agreement with the C_p value. However, it is still possible that considerable structure does exist in the higher frequency range and that a study of those phonons by tunnelling or optical means would show that their frequencies would be lowered by the addition of Pd as would be predicted by McMillan.

The pronounced changes in the electronic properties of $AuGa_2$ resulting from alloying with Pd cannot be attributed simply to the reduction of conduction electrons in a rigid band model or an expansion of the Brillouin zone, but must be considered to be a consequence of changes in band structure, as for example, change in the relative position of bands.

Acknowledgements—It is a pleasure to acknowledge A. M. Clogston, V. Jaccarino and A. C. Gossard for discussions, the experimental assistance of D. Dorsi, K. Andres for the critical temperature measurements of $AuIn_2$ $AuAl_2$, L. Testardi for the sound velocity data, and T. Kometani for the atomic absorption analyses.

REFERENCES

1. JACCARINO V., BLUMBERG W. E. and WERNICK J. H., *Bull. Am. phys. Soc.* **6**, 104 (1961).
2. JACCARINO V., WEGER M., WERNICK J. H. and MENTH A., *Phys. Rev. Lett.* **21**, 1811 (1968).
3. JAN J.-P., PEARSON W. B., SAITO Y., SPRINGFORD M. and TEMPLETON I. M., *Phil. Mag* **12**, 1271 (1965).
4. HALLORAN M. H and WERNICK J. H., *Bull Am. phys. Soc.* **10**, 450 (1965).
5. JAN J.-P and PEARSON W. B, *Phil. Mag* **8**, 279 (1963)
6. LONGO J T, SCHROEDER P. A. and SELLNYER D. J., *Phys. Lett* **25A**, 747 (1967).
7. BECK A, JAN J.-P, PEARSON W. B. and TEMPLETON I. M, *Phil Mag.* **8**, 351 (1963).
8. RAYNE J. A., *Phys. Lett.* **7**, 114 (1963).
9. MORIN F. J and MAITA J. P, *Phys. Rev.* **129**, 1115 (1963).
10. GEBALLE T. H, MATTHIAS B T., HULL G. W., Jr and CORENZWIT, *Phys. Rev. Lett* **6**, 275 (1961).
11. SHAWLOW A. L. and DEVLIN G. E, *Phys Rev.* **113**, 120 (1959).
12. STORM A. R, WERNICK J. H. and JAYARAMAN A., *J. Phys. Chem. Solids* **27**, 1227 (1966).
13. McMILLAN W. L., *Phys. Rev.* **167**, 331 (1968).
14. HAMILTON D. C., *et al.*, *J. Phys. Chem. Solids* **26**, 665 (1965).
15. In *Landolt-Bornstein: Tabellenwerk*, 6th Edn. Vol. II, part 6, p. 931. Springer, Berlin (1959).
16. MOTT N. F. and JONES H., *The Theory of the Properties of Metals and Alloys.* Dover, New York (1958).
17. BLOUNT E. I., *Phys. Rev.* **126**, 1636 (1962).

J. Phys. Chem. Solids Pergamon Press 1969. Vol. 30, pp. 1957-1962. Printed in Great Britain.

EFFECTIVE SPIN-ORBIT COUPLING OF IMPURITY STATES IN METALS

Y. YAFET
Bell Telephone Laboratories, Incorporated, Murray Hill, N.J. 07971, U.S.A.

(*Received* 2 *January* 1969)

Abstract—The correction to the spin-orbit constant of an impurity *d* orbital due to the admixture of nearest-neighbor host *d* orbitals is calculated for a transition element impurity in a noble metal. The expressions of the *g* shift and of the spin-flip scattering cross section are accordingly modified. Experimental data is not sufficiently accurate or complete at present to allow comparison with this refinement in the theory.

THIS PAPER is concerned with the modification of the spin-orbit coupling of a transition element impurity (which may or may not be magnetic) by the admixture into the localized wave function of nearest neighbor host orbitals. This effect is the analog in a metal of the charge transfer corrections to the properties of transition ions in salts, and we shall refer to it as covalency corrections.

The simplest case to consider is that of a 3*d* impurity in a noble metal. Here the energy of the virtual level is well separated from the *d* band of the host but the separation is not so large as to make the interaction negligible, and the *d*–*d* admixture can be treated as a perturbation[1]. The effect is of some interest because when the spin-orbit coupling of the host is appreciably larger than that of the impurity, even a small admixture can give a sizable correction. Unfortunately, for the cases of 3*d* impurities in copper studied so far, the corrections we find, although not small, add no new light on the interpretation of the data mainly because none of the parameters of the virtual level is known with any accuracy.

We assume that the *d* band of the host can be described in tight binding and that the energy separation between the higher lying impurity *d* state and the *d* band is large enought to split-off a localized state. The energy transfer integrals ($dd\sigma$), ($dd\pi$), ($dd\delta$), (which will be abbreviated as σ, π, δ) between the impurity and the nearest neighbors are responsible for mixing host *d* functions into the localized state. It was found[1] that in a f.c.c. lattice, the ϵ(or Γ_5') orbitals on the nearest neighbors give rise to three Γ_5 and one Γ_3 representation (the center of the rotations being at the impurity site) and the γ orbitals give two Γ_3 and one Γ_5 representation. Let $|\epsilon^{(0)}\rangle$ denote the Γ_5 orbitals of the impurity $|\epsilon^{(i)}\rangle$, $i = 1$–4 denote the Γ_5 states on the nearest neighbors, and similarly let $|\gamma^{(0)}\rangle$ and $|\gamma^{(i)}\rangle$, $i = 1$–3, refer to the corresponding Γ_3 states. The wave functions of the localized states are:

$$|\epsilon\rangle = (1-\Sigma_{(i)}|c_i|^2)^{1/2}|\epsilon^{(0)}\rangle + \Sigma_{(i)}c_i|\epsilon^{(i)}\rangle \quad (1)$$

$$|\gamma\rangle = (1-\Sigma_{(i)}|d_i|^2)^{1/2}|\gamma^{(0)}\rangle + \Sigma_{(i)}d_i|\gamma^{(i)}\rangle. \quad (1')$$

The explicit expressions of $\epsilon^{(i)}$ and $\gamma^{(i)}$ as well as the matrix elements that determine c_i and d_i are given in the appendix.

In tight binding, the spin-orbit Hamiltonian of the *d* states is:

$$\lambda_{\epsilon\epsilon} = \lambda_i \mathbf{l}_0 \cdot \mathbf{s} + \sum_{m\neq 0} \lambda_h \mathbf{l}_m \cdot \mathbf{s} \quad (2)$$

where λ_i and λ_h are the spin-orbit constants of the impurity (located at lattice site 0) and host atom respectively, and $\mathbf{l}_m$ is the angular momentum operator around site m. To calculate the matrix elements of (2) over the states (1) and (1′), we use the extension of the Wigner-Eckart theorem given by Koster [2]: *the operator* Λ transforms as Γ_5; *the number of times* Γ_5 *is contained in the products* $\Gamma_5\times\Gamma_5$, $\Gamma_5\times\Gamma_3$, and $\Gamma_3\times\Gamma_3$ is respectively one, one, and zero. Hence Λ can be represented by two constants,

$$\Lambda = \lambda_{\epsilon\epsilon}\mathbf{l}+\lambda_{\epsilon\gamma}\mathbf{l} \qquad (3)$$

where the constant $\lambda_{\epsilon\epsilon}$ is to be used between two $|\epsilon>$ states in (1), and $\lambda_{\epsilon\gamma}$ is to be used between a $|\epsilon>$ and a $|\gamma>$ state. The representation of $\mathbf{l}$ here is that appropriate to the $|\epsilon^{(0)}>$, $|\gamma^{(0)}>$, basis of a single ion.

The constants $\lambda_{\epsilon\epsilon}$ *and* $\lambda_{\epsilon\gamma}$ *are calculated* using the wave functions (1) and (1′) and the matrix elements of Λ which are given in the Appendix. The result is:

$$\lambda_{\epsilon\epsilon} = \lambda_l\left[1-\frac{1}{V^2}(3\sigma^2+4\pi^2+5\delta^2)\right] + \lambda_h\left(\frac{6\sigma\delta+8\pi\delta-2\delta^2}{V^2}\right) \qquad (4)$$

$$\lambda_{\epsilon\gamma} = \lambda_l+\lambda_h\frac{3\sigma\pi+\pi^2+(3/2)\sigma\delta+5\pi\delta+(3/2)\delta^2}{V^2} \qquad (4')$$

where V is the energy separation between the impurity d level (or center of the virtual state) and the weighted mean d band energy of the host.

The corrections to λ_l are second order in the ratio of the transfer integrals to V and hence depend fairly sensitively on this ratio. For magnetic states the values of V for the two spin directions will differ by the electrostatic splitting energy and so the spin-orbit coupling of the majority and minority spins will be different.

The magnitudes of σ, π, δ are in the order $|\sigma| > |\pi| > |\delta|$, and σ and π tend to have opposite signs while δ tends to be small. For pure copper, their values have been estimated[3] and we may use these values as a guide, since no actual calculations for *impurities are available. We then see that* $\lambda_{\epsilon\epsilon}$ *will usually be very close to* λ_l *(since* δ *occurs as a factor in the second term)* but $\lambda_{\epsilon\gamma}$ may differ significantly from λ_l. In particular $\lambda_{\epsilon\gamma} < \lambda_l$, i.e. *the opposite signs of* σ *and* π *tend to reduce the spin-orbit coupling.*

We now discuss the application of (3) to the g shift of a magnetic impurity and to the spin-flip cross section of a nomagnetic impurity.

(1) *The g shift*

This has already been considered in the Hartree-Fock approximation to the Anderson model by Yosida *et al.*[4]. These authors neglected the covalent contribution to λ, thus taking $\lambda=\lambda_l$, but included the effect of unequal population of impurity d orbitals due to the crystalline splitting. Their result (equation (28)) corrected for some misprints is:

$$\delta g = \frac{4\lambda_l}{N\uparrow - N\downarrow}\left[\sum_{(m\sigma,n\sigma)}{}' (s_z)_\sigma| < m\sigma|l_z|n\sigma > |^2 \times\frac{(N_{m\sigma}-N_{n\sigma})}{E_{m\sigma}-E_{n\sigma}} -\frac{1}{2}\sum_{m\sigma}(s_z)_\sigma| < m\sigma|l_z|m\sigma > |^2 \times\frac{\rho_{m\sigma}(E_F)}{1-(U-J)\rho_{m\sigma}(E_F)}\right] \qquad (5)$$

where the double summation is over pairs of impurity spinorbitals $m\sigma \neq n\sigma$, the $E_{m\sigma}$ are the energies of these states uncorrected for the Hartree-Fock energy, $N_{m\sigma}$ is the occupation number, $\rho_{m\sigma}(E_F)$ the density of states at the Fermi level E_F, $N\uparrow$ and $N\downarrow$ the total number of ↑ and ↓ spin localized electrons, and z the direction of the magnetic field. For a cubic crystal (5) reduces to

$$\delta g = +\frac{2\lambda_l}{N_\uparrow - N_\downarrow}\left[4\left(\frac{N_{\epsilon\uparrow} - N_{\gamma\uparrow}}{E_{\epsilon\uparrow} - E_{\gamma\uparrow}} - \frac{N_{\epsilon\downarrow} - N_{\gamma\downarrow}}{E_{\epsilon\downarrow} - E_{\gamma\downarrow}}\right)\right.$$

$$\left.-\left(\frac{\rho_{\epsilon\uparrow}(E_F)}{1-(U-J)\rho_{\epsilon\uparrow}(E_F)} - \frac{\rho_{\epsilon\downarrow}(E_F)}{1-(U-J)\rho_{\epsilon\downarrow}(E_F)}\right)\right] \tag{6}$$

It is to be noted that the contributions of ↑ spin electrons are opposite in sign to those of ↓ spin electrons, so that if the ↑ and ↓ virtual levels are nearly symmetrical there will be a tendency for the g shift to vanish. This is apparently the case for chromium[5] which has $S \simeq \frac{5}{2}$ and a value of $N_\uparrow + N_\downarrow$ near 5. The g shift is very small and positive.

It was seen in[1] that the crystalline splitting $\delta E_\sigma = E_{\gamma\sigma} - E_{\epsilon\sigma}$ is small, the ratio of δE_σ to the level width Δ ranging from perhaps 0·1 for *Cu*-Ni to 0·25 for *Cu*-Ti. It is then of interest to see how δg depends on the splitting when the total number of localized electrons $N_\uparrow + N_\downarrow$ is kept constant. We find, upon expanding equation (5) in powers of the splittings, that the first order term is:

$$\delta g_1 = -\frac{2\lambda_l}{N_\uparrow - N_\downarrow}\sum_{m\sigma}\left(\frac{\partial\rho}{\partial\epsilon_{m\sigma}}\right)_0$$

$$\times \frac{1}{1-(U-J)\rho^0_{m\sigma}}(s_z)_\sigma$$

$$\times\left[|\langle m|l_z|m\rangle|^2\delta\epsilon_{m\sigma} + \frac{1}{2}\sum_{n\neq m}{}' |\langle m|l_z|n\rangle|^2\right.$$

$$\left.\times(\delta\epsilon_{m\sigma} + \delta\epsilon_{n\sigma})\right] \tag{7}$$

where the $\delta\epsilon_{m\sigma}$ are the crystalline splittings and obey the relation $\Sigma_{(m)}\delta\epsilon_{m\sigma} = 0$. Note that usually the sign of $(\partial\rho/\partial\epsilon_{m\sigma})$ changes with σ when there is a local moment, hence the contributions of ↑ and ↓ spins to the first order shift are of the same sign.

For cubic crystals, using the matrix elements of l_z (Appendix) it is easy to see that equation (7) vanishes.* The effect of the splitting on δg will therefore be second order in $\delta E\sigma/\Delta$, which is expected to be quite small. It is important then to include the covalency corrections to the spin-orbit coupling constant. As will be seen in the case of *Cu*-Cr below, the magnitude of these corrections is in fact of the order of the observed g shift.

The covalency effect is incorporated in the derivation of (5) merely by using $\lambda_{\epsilon\epsilon}$ or $\lambda_{\epsilon\gamma}$ in the appropriate spin-orbit matrix elements, and the result for a cubic crystal is:

$$\delta g = \frac{2}{N_\uparrow - N_\downarrow}\left[4\left(\lambda_{\epsilon\gamma\uparrow}\frac{N_{\epsilon\uparrow} - N_{\gamma\uparrow}}{E_{\epsilon\uparrow} - E_{\gamma\uparrow}} - \lambda_{\epsilon\gamma\downarrow}\right.\right.$$

$$\left.\times\frac{N_{\epsilon\downarrow} - N_{\gamma\downarrow}}{E_{\epsilon\downarrow} - E_{\gamma\downarrow}}\right)$$

$$-\left(\lambda_{\epsilon\epsilon\uparrow}\frac{\rho_{\epsilon\uparrow}(E_F)}{1-(U-J)\rho_{\epsilon\uparrow}(E_F)} - \lambda_{\epsilon\epsilon\downarrow}\right.$$

$$\left.\left.\times\frac{\rho_{\epsilon\downarrow}(E_F)}{1-(U-J)\rho_{\epsilon\downarrow}(E_F)}\right)\right]. \tag{8}$$

If the crystal field splitting is neglected, this reduces to

$$\delta g_{sph} = -\frac{2}{N_\uparrow - N_\downarrow}\left[(\lambda_{\epsilon\epsilon\uparrow} + 4\lambda_{\epsilon\gamma\uparrow})\right.$$

$$\frac{\rho_\uparrow(E_F)}{1-(U-J)\rho_\uparrow(E_F)}$$

$$\left.-(\lambda_{\epsilon\epsilon\downarrow} + 4\lambda_{\epsilon\gamma\downarrow})\frac{\rho_\downarrow(E_F)}{1-(U-J)\rho_\downarrow(E_F)}\right]. \tag{9}$$

There are two spin-orbit constants for each spin direction in (8), which reflects the Hartree-Fock splitting of the spin state. It is to be noticed that the constant most affected by covalency, namely $\lambda_{\epsilon\gamma}$, occurs with the largest coefficient in the g shift. Let us now compare the g shift one would expect from equations (5–9) with the experimental values for *Cu*-Mn and *Cu*-Cr.

---

*In hexagonal structures equation (7) does not vanish in general. The crystal field terms that can split the d levels have symmetry $Y_2{}^0(\theta,\varphi)$ and $Y_4{}^0(\theta,\varphi)$. Direct computation shows that the $Y_4{}^0$ term does not contribute to δg_1 for any direction of the magnetic field while $Y_2{}^0$ contributes an anisotropic first order shift, but not an average first order shift.

(*a*) *Cu*-Mn. The experimental value is [6] $\delta g = +0{\cdot}011$. The spin-orbit constant of Mn$^+$ is estimated[7] to be $\lambda \approx 290\,\mathrm{cm}^{-1}$. The spin of the localized moment is nearly 2, and if we assume $N_\uparrow + N_\downarrow = 6$, the ↑ spin shell becomes filled and only the ↓ spin shell contributes to δg, with a positive sign. Taking typical values of $\Delta = 0{\cdot}8\,\mathrm{eV}$ for the ↓ spin level and $(U-J) = 2{\cdot}5\,\mathrm{eV}$, one finds from Yosida's expression (6) the value $\delta g = 0{\cdot}015$. The covalency correction is small and has been neglected because the ↓ spin level is far from the Cu d levels. If a value smaller than 6 is assumed for $N_\uparrow + N_\downarrow$ the predicted δg becomes smaller. Considering the uncertainties in the values of the parameters, a more accurate comparison with theory is not possible.

(*b*) *Cu*-Cr. The measured value is [5] $\delta g = +0{\cdot}0037 \pm 0{\cdot}002$. This g shift is quite small, which is consistent with having nearly $N_\uparrow = 4$ and $N_\downarrow = 1$. To estimate the covalency correction to $\lambda_{\epsilon\gamma\uparrow}$ we assume the $d_\uparrow$ level of Cr to lie $1{\cdot}5\,\mathrm{eV}$ above the host d level, and lacking calculated values of σ, π and δ, use for these the values[3] for pure Cu based on Burdick's band calculation. We then find that the coefficient of λ_h in equation (4′) is equal to $-0{\cdot}073$. Using the values[7] $\lambda_i = 280\,\mathrm{cm}^{-1}$ for Cr$^+$ and $\lambda_h = 750\,\mathrm{cm}^{-1}$ for Cu, we find $\lambda_{\epsilon\gamma\uparrow} \approx 0{\cdot}77\,\lambda_i$, a sizable correction. The correction to $\lambda_{\epsilon\gamma\downarrow}$ will be about ten times smaller. If we take $N_\uparrow = 4$ and $N_\downarrow = 1$, the g shift is given entirely by the difference $\lambda_{\epsilon\gamma\uparrow} - \lambda_{\epsilon\gamma\downarrow}$. For values $\Delta = 1\,\mathrm{eV}$ and $U - J = 2{\cdot}0\,\mathrm{eV}$, one finds $\delta g = +0{\cdot}002$ which is comparable to the experimental value. Again there are too many uncertainties for a meaningful comparison of calculation and experiments.

It might be possible to demonstrate experimentally the importance of the covalency correction by measuring the g shift of Cr in Au which has a very large spin-orbit constant, $\lambda^{\mathrm{Au}} \approx 4800\,\mathrm{cm}^{-1}$. The effect of the nearest neighbors would be sufficiently large that it could reverse the sign of $\lambda_{\epsilon\gamma}$ and on that basis the g shift would be expected to be positive and larger than that of *Cu*-Cr by a factor of perhaps 4–10. However it must be remembered that the total magnetic moment has a small contribution from the conduction band as the 'cancellation theorem' of Anderson and Clogston is only approximate[8]. If V_{sd} denotes the matrix element for s–d mixing, the relative s to d contribution to the moment will be of order $(V_{sd}/E_F)^2$ which may range from 0·01 to 0·1. The contribution to the g shift of the localized state is not negligible when the g shift of the host conduction band, as is probably the case for gold, is considerably larger than that of the impurity. A more complete analysis is probably necessary for *Au*-Cr, and perhaps even for *Cu*-Cr.

(2) *The spin-flip relaxation rate*

A nonmagnetic impurity presents a large spin-flip cross section to the conduction electrons when the virtual d level is near the Fermi level[9]. The covalency correction to λ can be taken into account as follows: let f be the fraction of Γ_5 orbitals at the Fermi level (i.e. each Γ_5 state has weight $f/3$). Then, since $\lambda_{\epsilon\epsilon}$ connects the ϵ orbitals and $\lambda_{\epsilon\gamma}$ connects ϵ and γ orbitals, and since the orbital angular momentum matrix element in the latter transitions is a factor 2 larger, the unperturbed value λ_i^2 in equation (2) of[9] must be replaced by

$$\lambda_i^2 \rightarrow \frac{1}{5}\left[\frac{f^2}{f_0^2}\lambda_{\epsilon\epsilon}^2 + 4\frac{f(1-f)}{f_0(1-f_0)}\lambda_{\epsilon\gamma}^2\right] \qquad (9)$$

where $f_0 = \frac{3}{5}$ is the value corresponding to spherical symmetry. Substituting in equation (2) of[9] and neglecting the crystal-field corrections to ρ_d, we obtain:

$$\sigma_{sf} = (4\pi^3/3k_F^2)(50/3)[1-(U-J)\rho_d(E_F)]^{-2}$$
$$\times f[f\lambda_{\epsilon\epsilon}^2 + 6(1-f)\lambda_{\epsilon\gamma}^2]\rho_d^2(E_F). \qquad (10)$$

In the spherical case the last bracket reduces to $(\frac{3}{5})[\lambda_{\epsilon\epsilon}^2+4\lambda_{\epsilon\gamma}^2]$. For Ti in Cu, $\lambda_{\epsilon\gamma}$ is expected to be about 15 per cent smaller than λ_i so that a reduction in σ_{sf} of about 25 per cent may be expected. As is the case for the g shift, quantitative comparison with experiment [10] is not presently feasible.

If Ag or Au is used as the solvent, there will be a larger effect on $\lambda_{\epsilon\gamma}$, and one might expect the cross section for spin-flip scattering to decrease significantly. However the spin-orbit coupling of the $5p$ or $6p$ states in the pure metal is now comparable to or larger than λ_i. As a consequence, in addition to d wave scattering, p wave scattering will also flip the spin and this contribution is likely to be important.

In conclusion, the effect of the nearest neighbors on the spin-orbit constant of a transition impurity in noble metals can be a significant correction, especially when the host has a much larger spin-orbit constant then the impurity. However a detailed comparison with experiment is not possible at present, both because there are too many uncertain parameters (N_i+N_i, Δ, $U+4J$) and also because the experimental accuracy of δg is (in the case of Cr) limited.

Acknowledgments—The author is grateful to P. Monod and S. Schultz for a copy of their paper before publication.

REFERENCES

1. YAFET Y., *Phys. Lett.* **26A**, 481 (1968).
2. KOSTER G. F., *Phys. Rev.* **109**, 227 (1958).
3. MUELLER F. M., *Phys. Rev.* **153**, 659 (1967).
4. YOSIDA K., OKIJI A. and CHIKAZUMI S., *Prog. theor. Phys.* **33**, 559 (1965).
5. MONOD P. and SCHULTZ S., *Phys. Rev.* **173**, 645 (1968).
6. SCHULTZ S., SHANABARGER M R and PLATZMAN P. M., *Phys. Rev. Lett.* **19**, 749 (1967).
7. BLUME M. and WATSON R. E., *Proc. R. Soc.* **A271**, 565 (1963).
8. ANDERSON P. W., *Phys. Rev.* **124**, 41 (1961).
9. YAFET Y., *J. appl Phys.* **39**, 853 (1968).
10. GOSSARD A. C., HEEGER A. J., and WERNICK J. H., *J. appl. Phys.* **38**, 1251 (1967).

APPENDIX

We give here the details of the calculation leading to equations (4) and (4′). We take as bases for Γ_5 and Γ_3 the d orbitals having angular dependence $\epsilon_1=xy$, $\epsilon_2=yz$, $\epsilon_3=zx$ and $\gamma_1=3z^2-r^2$, $\gamma_2=\sqrt{3}\;(x^2-y^2)$. The only non-vanishing matrix elements of l_z are:

$$(\epsilon_1, l_z\gamma_2)=-2i;\ (\epsilon_2, l_z\epsilon_3)=i \tag{1a}$$

where the orbitals are normalized to unity. Let $\epsilon_i^{(0)}$, $\gamma_i^{(0)}$ refer to the impurity orbitals at the site (0,0,0) and $\epsilon_i(a,b,c)$, $\gamma_i(a,b,c)$ refer to the orbitals located at lattice sites (a,b,c), where for the nearest neighbors the (a,b,c) run over the set of $(\pm1,\pm1,0)$ and their cyclic permutations. Using the standard method of projection operators, we find the four linear combinations of nearest-neighbor orbitals that transform like the first row, ϵ_1, of Γ_5:

$$\begin{aligned}
\epsilon_1^{(1)}&=(1/2)\Sigma_{(a,b)}\epsilon_1(a,b,0)\\
\epsilon_1^{(2)}&=(1/2\sqrt{2})\Sigma_{(a,b)}[\epsilon_1(a,0,b)+\epsilon_1(0,a,b)]\\
\epsilon_1^{(3)}&=(1/2\sqrt{2})\Sigma_{(a,b)}ab[\epsilon_2(a,0,b)+\epsilon_3(0,a,b)]\\
\epsilon_1^{(4)}&=(1/2)\Sigma_{(a,b)}ab\gamma_1(a,b,0)
\end{aligned} \tag{2a}$$

Here, the indices a and b run over the values +1 and −1. Similarly the three states transforming like the second row, γ_2, of Γ_3, are:

$$\begin{aligned}
\gamma_2^{(1)}&=(1/4\sqrt{2})\Sigma_{(a,b)}\{\sqrt{3}[\gamma_2(a,b,0+\gamma_2(a,0,b)]\\
&\quad+[\gamma_1(a,b,0)-\gamma_1(a,0,b)]\}\\
\gamma_2^{(2)}&=(1/4\sqrt{6})\Sigma_{(a,b)}\{4\gamma_2(0,a,b)+\gamma_2(a,0,b)+\gamma_2(a,b,0)\\
&\quad+\sqrt{3}[\gamma_1(a,0,b)-\gamma_1(a,b,0)]\}\\
\gamma_2^{(3)}&=(1/2\sqrt{2})\Sigma_{(a,b)}ab[\epsilon_2(0,a,b)-\epsilon_1(a,0,b)].
\end{aligned} \tag{3a}$$

The matrix elements of the energy (transfer integrals) between these states and $\epsilon_1^{(0)}$, $\gamma_2^{(0)}$ are:

$$\begin{aligned}
&(\epsilon^{(0)}, \mathscr{H}\epsilon^{(1)})=(3/2)\sigma+(1/2)\delta;\quad (\epsilon^{(0)}, \mathscr{H}\epsilon^{(2)})=\sqrt{2}(\pi+\delta)\\
&(\epsilon^{(0)}, \mathscr{H}\epsilon^{(3)})=\sqrt{2}(\pi-\delta);\quad (\epsilon^{(0)}, \mathscr{H}\epsilon^{(4)}=-(\sqrt{3}/2)(\sigma-\delta)\\
&(\gamma^{(0)}, \mathscr{H}\gamma^{(1)})=(\sqrt{3}/4)(\sigma+4\pi+3\delta)\\
&(\gamma^{(0)}, \mathscr{H}\gamma^{(2)})=(\sqrt{3}/4)(\sigma-4\pi+3\delta)\\
&(\gamma^{(0)}, \mathscr{H}\gamma^{(3)})=-(3/2\sqrt{2})(\sigma-\delta)
\end{aligned} \tag{4a}$$

Assuming the energy separation V of the impurity d level from the mean host d band energy to be large compared to these matrix elements, the coefficients c_i and d_i of equations (1), (1′) can be taken to first order. To obtain the matrix elements of Λ among the resulting wave functions $|\epsilon\rangle$, $|\gamma\rangle$ we need the matrix elements of l_z between the $\epsilon^{(i)}$ and $\gamma^{(i)}$. Direct evaluation of these, using expressions (1a) and (3a) gives.

$$(\epsilon_2^{(1)}, l_z\epsilon_3^{(2)} = i/\sqrt{2} = (\epsilon_2^{(2)}, l_z\epsilon_3^{(1)})$$

$$(\epsilon_2^{(2)}, l_z\epsilon_3^{(2)}) = i/2 = -(\epsilon_2^{(3)}, l_z\epsilon_3^{(3)})$$

$$(\epsilon_2^{(3)}, l_z\epsilon_3^{(4)}) = \sqrt{(3/2)}\,i = (\epsilon_2^{(4)}, l_z\epsilon_3^{(3)})$$

$$(\epsilon_1^{(1)}, l_z\gamma_2^{(1)}) = -(2/\sqrt{3})i = -(\epsilon_1^{(1)}, l_z\gamma_2^{(2)})$$

$$(\epsilon_1^{(2)}, l_z\gamma_2^{(1)}) = -(2\sqrt{2}/\sqrt{3})i = +2(\epsilon_1^{(2)}, l_z\gamma_2^{(2)})$$

$$(\epsilon_1^{(3)}, l_z\gamma_2^{(3)}) = -i. \tag{5a}$$

Use of these values in the matrix elements $\langle\epsilon|\Lambda_z|\epsilon\rangle$ and $\langle\epsilon|\Lambda_z|\gamma\rangle$ gives equations (4) and (4′) in the text.

J. Phys. Chem. Solids Pergamon Press 1969, Vol. 30, pp. 1963–1972. Printed in Great Britain.

ELECTRONIC STRUCTURE OF THE NEUTRAL ISOLATED DIVACANCY IN DIAMOND

C. A. COULSON and F. P. LARKINS
Mathematical Institute, Oxford, England

(*Received* 20 *December* 1968)

Abstract—A defect-molecule model has been used to calculate the electronic structure of a neutral isolated divacancy in an otherwise perfect diamond crystal, using the molecular-orbital theory. The result suggests that there is a spin- and orbitally-allowed transition of symmetry ${}^1A_{2u} \rightarrow {}^1A_{1u}$ which contributes to the broad u.v. band observed in irradiated diamonds. It is also predicted that this centre should be paramagnetic and show optical dichroism.

INTRODUCTION

THE MOST successful theoretical studies so far to explain quantitatively the absorption spectra of irradiated diamonds have used a defect molecule approximation for isolated defects in the crystal. The most complete studies in this field are those of Coulson and Kearsley[1] for the single isolated vacancy in its various charge states and Yamaguchi's studies[2, 3] for the single vacancy and the interstitial carbon atom in the diamond lattice. Such studies have proved that they can provide a valuable basis on which to interpret experimental results.

Further theoretical work on the static Jahn–Teller effect for a single vacancy in diamond [4] and on the Huang–Rhys factor for the neutral vacancy in diamond[5] have been based upon a defect-molecule approach. This work has provided support for the model and for the findings of Coulson and Kearsley that the *GR1* band observed in the absorption spectrum of irradiated diamonds is associated with an electronic transition between the ${}^1E$ and ${}^1T_2$ localized energy levels of the neutral isolated vacancy.

In view of the uncertainty which still exists in the interpretation of many of the features of the absorption spectrum of irradiated diamonds a study of the neutral isolated divacancy in diamond has been undertaken using a similar defect-molecule approximation to that used for the single vacancy. A preliminary study of this problem was undertaken by Kearsley[6].

MODEL FOR THE ISOLATED DIVACANCY

A detailed discussion of the localized model and its limitations may be found in the original paper by Coulson and Kearsley. It will suffice for the purposes of the present calculation to give a brief outline of the essential features as applied to the divacancy. As for the limitations of the model, these will be at least as serious in the case of the divacancy as they are for the single vacancy. At present, however, there seems no better alternative way of dealing with the problem.

The carbon atoms of the perfect diamond crystal are considered to be in a tetrahedral sp^3 state, with each atom at the centre of a regular tetrahedron formed by its four nearest neighbours, to which it is covalently bonded. In order to create the divacancy it is necessary to remove two adjacent carbon atoms as shown in Fig. 1. Although there will be some deformation of the lattice around the divacancy, at the time of this study there was no quantitative evidence to suggest its extent. Therefore, in the first approximation we have neglected this effect and used the undistorted lattice parameters to specify the model, since this case provides the basis for further electronic calculations. A recent study by

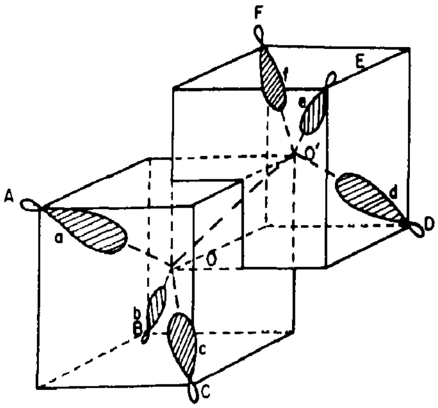

Fig. 1. Isolated divacancy in diamond-defect molecule of D_{3d} symmetry.

Hasiguti[7] using a simplified model and a restricted relaxation procedure suggests that the maximum displacement of any of the nearest neighbour atoms to the divacancy in diamond is less than 0·05 Å. In our model each of the six nearest carbon atoms to the defect will have three of its valence electrons still involved in the formation of localized carbon–carbon bonds to second nearest neighbour atoms to the divacancy. There remains a fourth valence electron which in the undisturbed lattice would be bonded with valence electrons on one of the two missing atoms.

Following Coulson and Kearsley it is assumed that the electronic properties of the system in the immediate neighbourhood of the defect are dependent on just these six electrons–termed vacancy electrons. The distribution of these vacancy electrons in the electric field of the neighbouring atoms and the much weaker field of the rest of the lattice is therefore to be determined. The contribution to the potential field of the vacancy electron due to atoms which are not nearest neighbours to the defect will be small, because all these carbon atoms are fully covalently bonded and appear electrically neutral to a vacancy electron.

This model involves two assumptions.

Firstly, it is assumed that the vacancy electrons occupy orbitals which are localized in the region of the defect.

Secondly, it is assumed that the energy levels of the vacancy electrons may be considered without detailed allowance being made for such effects as exchange or polarisation by other electron clouds. Coulson and Kearsley have shown that the transition energies are reasonably insensitive to the exchange effects, even though the absolute energies are dependent upon them.

Because of the molecular character of the problem we are able to use the well-established techniques of molecular-orbital theory to simplify the calculations. Even if the rest of the lattice is not perfect, the present simple model will be applicable provided that the other defects are sufficiently separated from one another such that the interaction between their potential fields is negligible.

MOLECULAR-ORBITAL WAVE FUNCTIONS FOR THE DEFECT MOLECULE

The model of the defect molecule for the isolated neutral divacancy in the diamond lattice is shown in Fig. 1. We shall be primarily interested in the six vacancy electrons which, before the defect was created, were in the tetrahedral hybrid orbitals, a–f, associated with the atoms A–F. These vacancy electrons originally formed covalent bonds with the valence electrons of a carbon atom at either O or O'.

Three different internuclear distances are involved in the present calculation. $AB = 4{\cdot}766$ a.u., $AE = 5{\cdot}586$ a.u. and $AD = 7{\cdot}343$ a.u.

The symmetry group of the defect molecule is D_{3d}. A solution of our problem may be achieved using either resonance among valence-bond structures, of which there are five canonical structures, or the method of molecular orbitals. We have chosen to use the latter method incorporating the linear combination of atomic orbitals approximation (l.c.a.o. method) and to apply configuration interaction to states of the same symmetry to obtain improved energy values. This method is more convenient than the valence-bond method because of the non-orthogonality of the hybrid orbitals and the complexity of using the valence-bond method for such a large number of electrons. However, both methods become identical when ionic structures are included in the valence-bond method.

It can be shown that in a field of D_{3d} symmetry and single-electron molecular orbitals belong to the following irreducible representations

$$a_{1g}, a_{2u}, e_u \text{ and } e_g.$$

A suitable set of real non-localized single-electron wave functions, which are mutually orthogonal and correspond to these symmetry irreducible representations are as follows:

$$v = N_1(a+b+c+d+e+f) \qquad a_{1g}$$

$$u = N_2(a+b+c-d-e-f) \qquad a_{2u}$$

$$\left.\begin{aligned} x &= \sqrt{3}N_3(a+b-2c+d+e-2f) \\ y &= N_3(3a-3b+3d-3e) \end{aligned}\right\} e_g$$

$$\left.\begin{aligned} z &= \sqrt{3}N_1(a+b-2c-d-e+2f) \\ t &= N_4(3a-3b-3d+3e) \end{aligned}\right\} e_u$$

where normalization constants are given by

$$N_1^{-2} = 6(1+2S_{ab}+2S_{ae}+S_{ad})$$

$$N_2^{-2} = 6(1+2S_{ab}-2S_{ae}-S_{ad})$$

$$N_3^{-2} = 36(1-S_{ab}-S_{ae}+S_{ad})$$

$$N_4^{-2} = 36(1-S_{ab}+S_{ae}-S_{ad}).$$

S_{ab}, S_{ae}, and S_{ad} are the overlap integrals.

It is possible to obtain a more symmetrical complex set of orbitals, but these were less convenient to use in the present calculation.

Each non-degenerate orbital may be occupied by at most two electrons, while each of the doubly-degenerate orbitals by at most four electrons. Since there are 12 possible spin orbitals and six vacancy electrons there are 924 possible six-electron wave functions for the system. For this system of vacancy electrons we have in all 37 possible configurations of the form $a_{1g}{}^m a_{2u}{}^n e_g{}^r e_u{}^s$. Because of the restriction imposed by the Pauli Principle that the occupation number of any orbital cannot be greater than two the following restrictions are placed on m, n, r and s.

$$0 \leq m, n \leq 2, 0 \leq r, s \leq 4.$$

The symmetry states of the six-electron wave functions corresponding to the particular configurations may be determined using the method of Mulliken[8] of reducing through states of lower symmetry. Since holes transform like particles it follows that $e_u{}^3$ will transform like e_u and $e_u{}^4$ like a_{1g}, since the 'e_u shell' is filled at four electrons, and similarly for e_g. The symmetry and spin multiplicities of the resultant states for eleven of these 37 configurations are shown in Table 1.

THE HAMILTONIAN FOR THE SYSTEM

The spin-independent Hamiltonian for the defect-molecule system (excluding exchange with non-vacancy electrons) may be written, in atomic units, in the following form

$$H = H_0 + H_1$$

$$\text{where } H_0 = \sum_i (T_i + V_i) \text{ and } H_1 = \sum_{i\,j} \frac{1}{r_{ij}}$$

$i, j = 1, 2 \ldots\ldots n$ where n is the number of vacancy electrons. For the isolated neutral divacancy n will be 6.

$T_i = -\frac{1}{2}\nabla_i{}^2$ = kinetic energy operator for the ith electron. V_i represents the potential energy of interaction of the vacancy electron i with the nuclei, the K-shell electrons

Table 1. Some allowed states for the neutral divacancy

Configuration Number	Description	Symmetry of resultant states
1	$a_{1g}^2a_{2u}^2e_g^2$	${}^1A_{1g}+{}^3A_{2g}+{}^1E_g$
2	$a_{1g}^2a_{2u}^2e_ge_u$	${}^3A_{1u}+{}^1A_{1u}+{}^3A_{2u}+{}^1A_{2u}+{}^3E_u+{}^1E_u$
3	$a_{1g}^2a_{2u}^2e_u^2$	${}^1A_{1g}+{}^3A_{2g}+{}^1E_g$
4	$a_{1g}^1a_{2u}^2e_g^3$	${}^3E_g+{}^1E_g$
5	$a_{1g}a_{2u}^2e_g^2e_u$	${}^5E_u+4{}^3E_u+3{}^1E_u+{}^3A_{2u}+{}^1A_{2u}+{}^3A_{1u}+{}^1A_{1u}$
6	$a_{1g}a_{2u}^2e_ge_u^2$	${}^5E_g+4{}^3E_g+3{}^1E_g+{}^3A_{2g}+{}^1A_{2g}+{}^3A_{1g}+{}^1A_{1g}$
7	$a_{1g}a_{2u}^2e_g^3$	${}^3E_u+{}^1E_u$
8	$a_{1g}^2a_{2u}e_g^3$	${}^3E_u+{}^1E_u$
9	$a_{1g}^2a_{2u}e_g^2e_u$	${}^5E_g+4{}^3E_g+3{}^1E_g+{}^3A_{2g}+{}^1A_{2g}+{}^3A_{1g}+{}^1A_{1g}$
10	$a_{1g}^2a_{2u}e_ge_u^2$	${}^5E_u+4{}^3E_u+3{}^1E_u+{}^3A_{2u}+{}^1A_{2u}+{}^3A_{1u}+{}^1A_{1u}$
11	$a_{1g}^2a_{2u}e_u^3$	${}^3E_g+{}^1E_g$

surrounding the nuclei of the divacancy atoms and with the bonded valence electrons of these atoms. The latter electrons may be considered to be in localized tetrahedral hybrids directed along the sets of unbroken bonds at $A.....F$.

Therefore,

$$V_i = \sum_K V_{Ki} \text{ where } K = A, B, C, D, E, F$$

and, for example,

$$V_{1i} = \frac{-6}{r_{1i}} + \text{repulsion from the two } K\text{-shell electrons around atom } A + \text{repulsion from the tetrahedral hybrids around } A$$

As in the previous study, only Coulomb repulsions are considered to contribute to V_{1i} and use is made of the Geoppert–Mayer and Sklar approximation[9] to evaluate V_{1i} as has been outlined in the previous investigation by Coulson and Kearsley. The neglect of exchange terms is most serious in the case of intra-atomic integrals such as $\langle a|V_{1i}|a\rangle$, referred to as 'self penetration integrals'. However, the previous workers have shown that the energy separations of the lowest states are fairly insensitive to the value of $\langle a|V_{1i}|a\rangle$ so that the above approximation is considered to be adequate for the present calculation.

For the calculations reported here simple analytic forms proposed by Slater[10] for the $2s$ and $2p$ wave functions were chosen. As in the earlier work, the screening constant, c, for these functions is chosen to have the value of 3·19, the usual free atom value.

A variational calculation for c was not attempted, because of the difficulty which exists in evaluating accurately three- and four-centre integrals and also it was desired to obtain a comparison with the previous work for the neutral vacancy.

In principle it is possible to evaluate all the energy levels for each separate configuration. The interaction problem between the 924 six-electron wave functions arising from the 37 possible configurations, simplifies on account of the overall symmetry properties of the Slater determinants. Thus there are 198 six-electron wave functions with symmetry ${}^3E_u$, 180 with symmetry ${}^3E_g$, 60 with symmetry ${}^1E_g$ and 54 with symmetry ${}^1E_u$. Even if we make maximum use of the double degeneracy of the E-type levels, we shall still have secular determinants of order 30×30. In order to reduce this problem to manageable proportions some further simplification is needed.

The aim of the present calculation is to determine the ground-state level and the excited levels near this state which result from the presence of a neutral isolated divacancy in the crystal. Therefore, we have argued as follows, on the basis of a one-electron model.

If we assume that there is no interaction between the vacancy electrons then it is possible to calculate the relative energies of the single-electron molecular-orbital states. Such a calculation using an empirical value for the one-centre Coulomb integral $Q(Q = 12{\cdot}856\,\text{eV})$ and the calculated 'self penetration integral' $P(P = -7{\cdot}75\,\text{eV})$, see page 1968 for details, results in the following values for the energies

$$A = \frac{\langle v|H^0|v\rangle}{\langle v|v\rangle} = -45{\cdot}650\,\text{eV}$$

$$B = \frac{\langle u|H^0|u\rangle}{\langle u|u\rangle} = -43{\cdot}080\,\text{eV}$$

$$C = \frac{\langle x|H^0|x\rangle}{\langle x|x\rangle} = -34{\cdot}789\,\text{eV}$$

$$D = \frac{\langle z|H^0|z\rangle}{\langle z|z\rangle} = -36{\cdot}741\,\text{eV}$$

where H^0 is the single-particle operator of the Hamiltonian H.

In the six-electron system, therefore, if there were no interaction between the vacancy electrons, one would expect that the three configurations $a_{1g}{}^2a_{2u}{}^2e_u{}^2$, $a_{1g}{}^2a_{2u}{}^2e_ue_g$ and $a_{1g}{}^2a_{2u}{}^2e_g{}^2$ would be lowest in energy. Configurations in which one electron was excited from an orbital of a_{1g} or a_{2u} symmetry, namely orbital v or u, to an orbital of e_g or e_u symmetry would be expected to constitute the next group of configurations lowest in energy. There are eight such configurations. A further group of 15 configurations results from the promotion of two electrons from the non-degenerate molecular orbitals into the doubly-degenerate ones. Interaction between the electrons will cause the levels from any one configuration to split. It would appear to be a reasonable approximation to assume that a calculation considering the interaction between the first eleven configurations mentioned above would enable the relative ordering of the levels near the ground state to be determined accurately. The present work has been concerned exclusively with the first eleven configurations with the exception that the highest spin symmetry state, ${}^7A_{2u}$, arising from the configuration $a_{1g}a_{2u}e_g{}^2e_u{}^2$ has also been considered.

With these approximations the problem, while still being formidable, becomes at least manageable.

WAVE FUNCTIONS FOR THE SIX VACANCY ELECTRONS

In order to represent the symmetry states of each particular configuration, shown in Table 1, suitable six-electron wave functions are formed. These are linear combinations of Slater determinants and have the appropriate space transformation properties. These functions must also be chosen to be simultaneous eigenfunctions of the square of the total spin, S^2, and its z component, S_z. In this way all the necessary wave functions for the various symmetry states may be written down.

The energy levels of the various configurations, before configuration interaction, are now given by

$$E(R) = \frac{\int \psi^*(R)H\psi(R)\mathrm{d}\tau}{\int \psi^*(R)\psi(R)\mathrm{d}\tau}$$

where $\psi(R)$ is the six-electron wave function corresponding to a given irreducible representation R of the group D_{3d}, for a particular configuration and given S and S_z.

On substitution of the appropriate wave-functions the integration may be reduced to a series of one- and two-electron integrals involving the molecular orbitals v, u, x, y, z and t. These integrals may in turn be expressed in terms of one- and two-electron integrals involving the localized atomic hybrid orbitals a, b, c, d, e, and f. Finally, all these integrals may be broken down into one- and two-centre integrals, of Coulomb, hybrid, exchange and ionic type together with some three- and four-centre integrals.

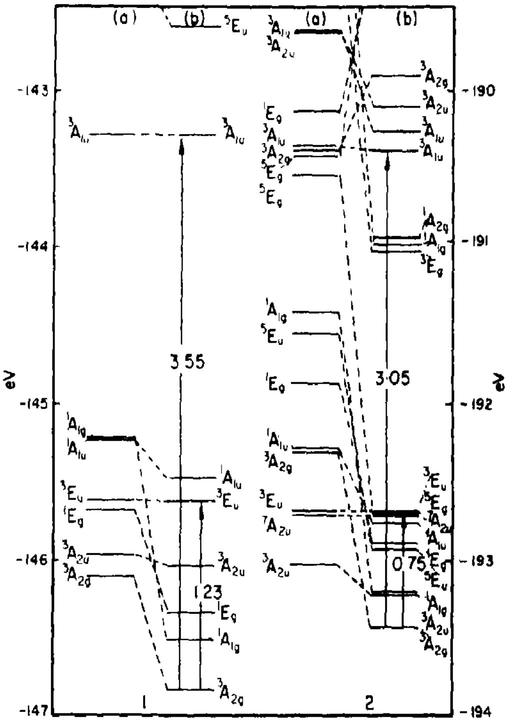

Fig. 2. Energy levels of a neutral isolated divacancy on the modified a.s.m.o. theory, (1) calculated using $Q = 12·856$, $P = -7·75$ eV, (2) calculated using $Q = 12·856$, $P = -16·42$ eV. (a) Before configuration interaction; (b) After configuration interaction.

tions. The general effect of this dependence is that all the energy levels become more compressed and hence configuration-interaction effects even more significant as P decreases. This effect was also observed in the neutral vacancy calculation.

For the divacancy system of D_{3d} symmetry the components of the electric dipole operator, which are proportional to x, y, z, transform as follows

$$z \subset A_{2u};\quad x, y \subset E_u$$

Therefore, the allowed electric dipole transitions shown in Table 4 may occur provided the spin selection rule is satisfied.

The energies of the allowed transitions from the $^3A_{2g}$ ground state and from the $^1A_{1g}$ level, which is within 0·3 eV of the ground state, are given below. If the $^1A_{1g}$ level is 0·3 eV above the lowest level the transition from $^1A_{1g} \rightarrow {}^1E_u$ would be very weak, if observable at all at room temperature. However, it is possible that the $^1A_{1g}$ level is closer to the ground state than this in the actual crystal.

	Case 1 $P = -7·75$ eV	Case 2 $P = -16·42$ eV
$^3A_{2g} \rightarrow {}^3E_u$	1·23 eV	0·75 eV
$^3A_{2g} \rightarrow {}^3A_{1u}$	3·55 eV	3·05 eV
$^3A_{2g} \rightarrow {}^3A_{1u}$	(6·73 eV)	3·17 eV
$^1A_{1g} \rightarrow {}^1E_u$	4 12 eV	3·59 eV

There are other possible transitions from the $^3A_{2u}$ level, but these are even less likely, especially since the true value of P is probably closer to $-7·75$ eV than to $-16·42$ eV, such that case 1 more closely resembles the true situation using the present approximations. It is noteworthy that for the neutral isolated divacancy the transition energy decreases with decreasing values of P, whereas, for the neutral isolated vacancy the reverse trend is observed.

The explanation for this is that for the neutral isolated vacancy before configuration interaction the ^1E and $^1T_2$ levels involved in the transition arise from the v^2t^2 configuration and therefore contain equal admixtures of the one-electron molecular integrals. Even after configuration interaction the lowest levels arise predominantly from this configuration. However, for the neutral divacancy transitions must occur between levels of gerade and ungerade symmetry and these will, of course, arise from different con-

Table 4. *Allowed transitions with* D_{3d} *symmetry*

Initial state		A_{2g}	A_{2u}	A_{1g}	A_{1u}	E_g	E_u
Final state	z	A_{1u}	A_{1g}	A_{2u}	A_{2g}	E_u	E_g
	x, y	E_u	E_g	E_u	E_g	A_{1u}, A_{2u}, E_u	A_{1g}, A_{2g}, E_g

figurations and so contain different admixtures of the one-electron molecular integrals A, B, C and D. The varying dependence of these integrals on P, is the basic cause of the decrease of transition energies as P decreases.

It is also interesting to note that if only the lowest group of states is considered it is easy to understand why the states of gerade symmetry are lowered much more in energy by configuration interaction than the ungerade symmetry states. The former arise from the configuration $a_{1g}{}^2a_{2u}{}^2e_u{}^2$ and interact strongly with the gerade states arising from the configuration $a_{1g}{}^2a_{2u}{}^2e_g{}^2$ which also belongs to the 'ground state group of configurations' and lie just above the lowest group of levels. However, to find suitable symmetry states to interact with the lowest ungerade states we must consider levels from higher configurations. These are, in general, of much higher energies and interact less with the lowest-lying states.

The second-lowest ${}^3A_{1u}$ level arises from the configuration $a_{1g}{}^2a_{2u}e_ge_u{}^2$ and shows a strong dependence on P for reasons discussed previously.

The present calculation predicts that since the lowest level is non-degenerate there would be no Jahn–Teller effect causing distortion of the nuclear framework in the ground state. However, there is always the possibility that Jahn–Teller effects could split the ${}^1E_g$ level and shift one of its components to a lower level, below the ${}^3A_{2g}$ level. But since the lowering would need to exceed ½ eV we are inclined to think that this is rather unlikely.

Since the lowest level is a triplet we expect the defect to be paramagnetic and hence to exhibit resonance in an E.P.R. study, whereas the neutral vacancy is predicted to be diamagnetic in the ground state. Many lines with spin $S = 1$ have been observed in E.P.R. studies and it is therefore possible that the origin of some of these lines lies in the electronic behaviour of the defect electrons of the divacancy in the neutral state.

Also it is interesting to note that a transition between the ${}^3A_{2u}$ and ${}^3A_{1u}$ levels is allowed only in the z direction. Therefore polarisation effects should be observed which would manifest themselves in optical dichroism studies. Also the low energy transition between ${}^3A_{2u}$ and ${}^3E_u$ is allowed only in the x and y directions.

RELATION WITH EXPERIMENT

We are now ready to compare our purely theoretical values with the results of absorption experiments. In view of the various approximations inherent in our model we must not expect exact agreement, and in any case the interpretation of the experimental absorption curve of irradiated diamonds is itself uncertain. We may therefore expect that our theoretical predictions might be of help in assigning the different parts of the measured absorption spectrum.

The spectrum for irradiated type II diamonds obtained by Clark *et al.*[15] showed a broad absorption band between 1·65 and 2·4 eV with an intense line at 1·673 eV known as the GRI band and also a band in the u.v. region of the spectrum. This intense band commenced at about 2·8 eV and the absorption increased to a maximum near 4 eV after which it decreased only to be masked by the beginning of the region of continuous absorption. There are also sharp lines at 3·315 and 4·133 eV which have been used to measure the strength of the band[16, 17]. There have been several studies, for example[18], which suggest that GRI and u.v. bands arise from transitions within the same centre or from associated defect centres.

It is also clear from many studies that the u.v. band is very complex. However, on the basis of the present quantitative calculation, it is suggested that at least part of this absorption band may arise from electronic transitions involving the electrons immediately surrounding the isolated neutral divacancy as the result of the spin- and orbitally-allowed ${}^3A_{2u} \rightarrow {}^3A_{1u}$ transition. There also exists the possibility of a transition between the ${}^1A_{1u}$ and ${}^1E_u$ levels.

This calculation does not substantiate the possible association of the isolated neutral divacancy with the GR1 band (1·65–2·4 eV) or with the TH5 band (2·3–2·8 eV)[19], produced as a result of annealing the sample. It seems more likely that this latter band arises from some complex impurity defect being formed.

The association of at least part of the u.v. band with a neutral isolated divacancy and the GR1 band with the neutral isolated vacancy provides a consistent explanation as both these bands are produced by room temperature irradiation. The formation of divacancies should be possible at the energies of irradiation used in most investigations so far. Their formation involves the rupture of only seven bonds, whereas two single vacancies involve the breaking of eight bonds, and therefore they are quite likely to exist on energetic grounds.

The predicted low energy transition between the ${}^3A_{2u}$ and ${}^3E_u$ level is also of interest. However, there seems to be no published work available of any investigations in this region.

CONCLUSION

The present calculation using a modified molecular-orbital treatment predicts electronic transitions among the electrons surrounding an isolated neutral divacancy which would correspond to absorptions in the u.v. region of the spectrum. The spin- and orbitally-allowed ${}^3A_{2u} \rightarrow {}^3A_{1u}$ transition is predicted as well as a low energy transition between the ${}^3A_{2u}$ and ${}^3E_u$ level.

A broad band would be expected, because of lattice vibrations within the crystal and the influence of other atoms not considered in this calculation. This centre should be paramagnetic and show optical dichroism.

Acknowledgement—One of us (F.P.L.) would like to thank the Rhodes Trust for the award of the Victorian Rhodes Scholarship

REFERENCES

1. COULSON C. A. and KEARSLEY M. J., *Proc. R. Soc.* **241A**, 433 (1957).
2. YAMAGUCHI T., *J. phys. Soc. Japan* **17**, 1359 (1962).
3. YAMAGUCHI T., *J. phys. Soc. Japan* **18**, 368 (1963).
4. FRIEDEL J., LANNOO M. and LEMAN G., *Phys. Rev.* **164**, 1056 (1967).
5. LANNOO M. and STONEHAM A. M., *J. Phys. Chem. Solids* **29**, 1987 (1968).
6. KEARSLEY M., D.Phil. Thesis, Oxford (1956)
7. HASIGUTI R. R., *Lattice Defects in Semiconductors* (Edited by Hasiguti), p. 131. Tokyo Press, Tokyo (1968).
8. MULLIKEN R. S., *Phys. Rev.* **43**, 279 (1933).
9. GOEPPERT-MAYER M. and SKLAR A. L., *J. chem. Phys.* **6**, 645 (1938)
10. SLATER J. C., *Phys. Rev.* **36**, 57 (1930).
11. CORBATO F. J. and SWITENDICK A. C., *Methods of Computational Physics* (Edited by Adler, Fernbach and Rotemberg), Vol. 2. Academic Press, New York (1963).
12. MULLIKEN R. S., *J. chim. Phys.* **46**, 500 (1949).
13. MOFFITT W., *Proc. R. Soc.* **210A**, 224, 245 (1951).
14. PARR R. G. and PARISER R., *J. chem. Phys.* **21**, 466, 767 (1953).
15. CLARK C. D., DITCHBURN R. W. and DYER H. B., *Proc. R. Soc.* **234A**, 363 (1956).
16. DUNCAN I., Thesis, Reading University (1963).
17. CLARK C. D., KEMMEY P. and MITCHELL E. W. J., *Discuss. Faraday Soc.* **31**, 96 (1961).
18. DYER H. B. and Du PREEZ L., *J. chem. Phys.* **42**, 1898 (1965).
19. CLARK C. D., DITCHBURN R. W. and DYER H. B., *Proc. R. Soc.* **237A**, 75 (1956).

J. Phys. Chem. Solids Pergamon Press 1969. Vol. 30, pp. 1973–1976. Printed in Great Britain.

IONIC CONDUCTION IN PURE AND DOPED SINGLE-CRYSTALLINE LITHIUM IODIDE

B. J. H. JACKSON and D. A. YOUNG
Department of Chemical Engineering and Chemical Technology, Imperial College,
London S.W. 7, England

(*Received* 8 *November* 1968)

Abstract – The free energy of defect formation and the activation energy for motion of the most mobile defect have been determined from the ionic conductivity of as-grown and Mg-doped single crystals of lithium iodide. Values obtained are $s_f = 4{\cdot}5\,k$, $h_f = 1{\cdot}06$ eV with k_m(cation vacancy) $= 0{\cdot}43$ eV, giving a defect concentration at the melting point $x_0(T_m) = 0{\cdot}18$ at. %, concordant with the other alkali halides.

INTRODUCTION

HAVEN's examination[1] of ionic conduction in the lithium halides suggested that lithium iodide was untypical in that the defect concentration at the melting point was an order of magnitude greater than values now accepted as representative for the alkali halides. In particular, conductivity enhancement in the extrinsic region by Mg-additions was less than proportional to the dopant concentration. Evidently the Mg-ion did not exert its full electrical effect either because it had been extracted from substitutional solid solution by aggregation, or was paired with an unidentified polyvalent anion.

Attempts to grow lithium iodide single crystals by open-crucible techniques demonstrated that this substance is a good deal more reactive than hitherto recognised. Thus the molten salt oxidises freely in dry air releasing iodine, whilst the solid salt is both extremely hygroscopic and readily hydrolysed. Specifically, the trihydrate can not be dehydrated without decomposition above its melting point (63°C). For these reasons it is likely that Haven's experimental procedures led to crystals contaminated by oxide which could combine with the added magnesium.

Accordingly we have re-examined the ionic conductivity of lithium iodide single crystals grown in closed ampoules by the Bridgman technique. It has not proved possible to analyse for oxide ion.

EXPERIMENTAL

Preparation

Lithium iodide trihydrate containing less than 100 ppm of altervalent cations was finely powdered in a glove box flushed with dried oxygen-free nitrogen and introduced into bulb *A* of the purification apparatus illustrated in Fig. 1, where it was dehydrated at about 50°C under a pressure of 10^{-5} Torr. for 20 hr. The temperature was then first gradually raised over some 10 hr to 230°C in order to complete dehydration without incipient melting, and finally to 50°C above the melting point of the anhydrous salt (446°C), when a dried mixture of hydrogen and hydrogen iodide was bubbled through the melt for 2–3 hr to displace oxide and hydroxide. The so-purified melt was then run successively into the pre-heated globe *B* and through the glass fibre filter into globe *C*, where it solidified and remained while the ampoule was evacuated and sealed at point *D*.

Crystals grown in ampoule *E* in a Bridgman furnace with a temperature differential at the baffle of 500:430°C at a lowering rate of 6 mm/hr were transparent, colourless single-crystalline boules which did not adhere to or etch the Pyrex ampoule and could be cleaved on (100) into 5 mm cubes.

Doped crystals were prepared by adding the appropriate amount of dehydrated magnesium iodide to anhydrous lithium iodide from previous preparations and re-

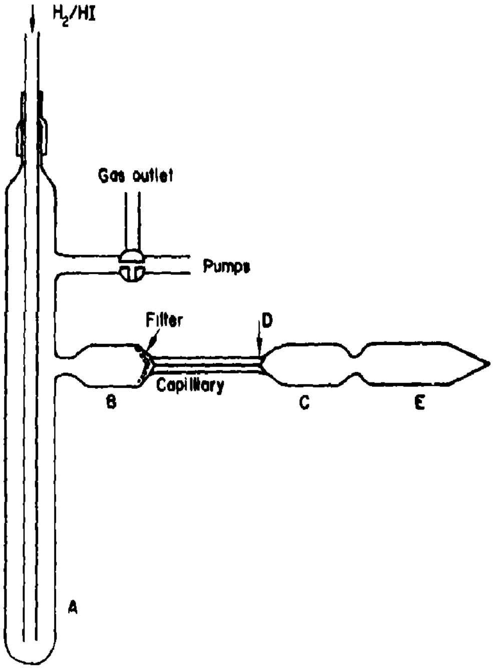

Fig. 1. Arrangement for filling the growth ampoule with anhydrous lithium iodide.

peating the procedure starting with the H_2/HI treatment.

Electrodes were applied with a soft graphite rod. All handling took place in an atmosphere of dried nitrogen.

Analysis

All crystals proved to contain approximately 40 ppm of ferrous ion, determined by emission spectroscopy and standard colorimetric techniques. Magnesium added in concentrations ranging from 1000 to 10,000 ppm produced concentrations in the single crystals of only 30–120 ppm as determined by sodium EDTA as titrant with Eriochrome Black *T* as indicator. Evidently the solubility of magnesium ion in lithium iodide is low. Analyses for four crystals are summarised in Table 1.

Conductivity measurement

The general techniques are reported elsewhere[2]. In this work, the conductivity was measured at 10 kHz.

Table 1.

Crystal No.	Impurity content ($Mg^{2+} + Fe^{2+}$) ppm
1 (as-grown)	70
2 (doped)	70
3 (doped)	100
4 (doped)	160

RESULTS

Plots of $\log_{10} \sigma T$ vs. $1000/T$ °K over the whole temperature range are illustrated in Fig. 2 for two specimens cut from Crystal No. 1. Note that the intrinsic region I is straight within experimental error, and that a so-called 'knee-temperature' ($1000/T$) can be defined as the intersection of region I with the extrinsic region II. This extrinsic region is plotted on a larger scale in Fig. 3 for four crystals. The intrinsic regions of these crystals are superimposable, and extrinsic conductivities are reproducible within 5 per cent. In spite of appearances, there is no

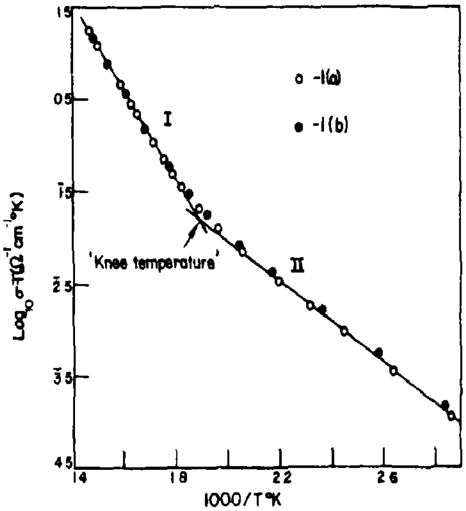

Fig 2. The intrinsic (I) and extrinsic (II) regions of the ionic conductivity plot for two specimens of as-grown material.

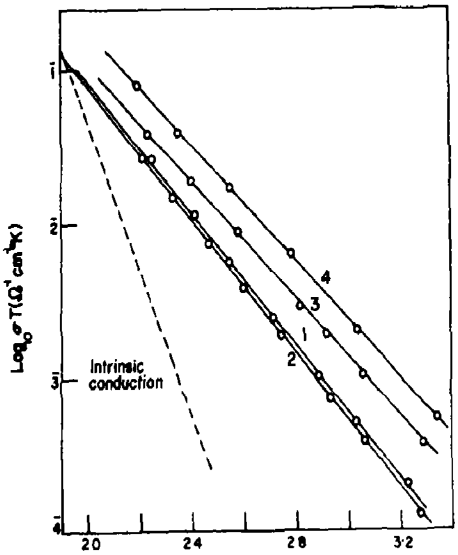

Fig. 3. The extrinsic regions for four representative crystals listed in Table 1.

systematic dependence of the slope of region II on dopant concentration.

ANALYSIS OF THE DATA

The linearity of region I supports the view that one charge-carrier is dominant. Since the conductivity at low temperatures is enhanced by magnesium additions and the intrinsic region at no stage falls below the extrinsic region, we conclude that such Frenkel disorder for which the interstitial is more mobile than the vacancy can be excluded, and that the single charge-carrier is the cation vacancy, probably arising from Schottky disorder. Accordingly the Stasiw-Teltow no-association theory[3] as formulated by Dreyfus and Nowick[4] is applicable.

Within this framework, the site fraction of cation vacancies in equilibrium at the 'knee-temperature' is characteristic of pure material, and is equal to the concentration of added divalent cations[5]; the slope of region I is given by $(\frac{1}{2}h_f + h_m)/k$ and the slope of region II by h_m/k. Adopting the most reproducible value of $h_m = 0{\cdot}43$ eV one obtains from the slope of region I (0·96 eV) a value for $h_f = 1{\cdot}06$ eV. Using 'knee-temperatures' (1000/T) for crystals 1, 2, 3 and 4 of 1·90; 1·91; 1·87 and 1·80, respectively, with the above value of h_f the entropy s_f is calculated to be 4·5k. This corresponds to a defect concentration at the melting point of $x_0(T_m) = 0{\cdot}18$ at.%.

The present results contrast sharply with values given earlier by Haven of $h_f = 1{\cdot}34$ eV; $h_m = 0{\cdot}42$ eV with $x_0(T_m) = 1{\cdot}17$ at.%, but are concordant with entropies of formation of 6·2k for NaCl[6] and 5·4k for KCl[7]. No reliable values of $x_0(T_m)$ greater than 0·2 at.% have been reported for Schottky disorder in other alkali halides[8], so we surmise that Haven's material contained a high concentration of electrically ineffective magnesium combined with oxide. Neglect of residual oxide impurity means that the present value of $x_0(T_m)$ is an upper bound.

Acknowledgement – We thank the Science Research Council for the award of a Studentship to B. J.

REFERENCES

1. HAVEN Y., *Rec. Trav. chim. Pays-Bas Belg* **69**, 1471 (1950).
2. JACKSON B. J. H. and YOUNG D. A., *Trans. Faraday Soc.* **63**, 2246 (1967).

3. STASIW O. and TELTOW J., *Annln. Phys.* **1**, 261 (1947).
TELTOW J. *Annln. Phys.* **5**, 63, 71 (1949).
4. DREYFUS R. W. and NOWICK A. S., *J. appl. Phys.* **33**, 473 (1962).
5. ETZEL H. W. and MAURER R. J., *J. chem. Phys.* **18**, 1003 (1950).
6. KIRK D. L. and PRATT P. L., *Proc. Br. ceram. Soc.* **9**, 215 (1967).
7. BEAUMONT J. H. and JACOBS P. W. M., *J. chem. Phys.* **45**, 1496 (1966).
8. SÜPTITZ P. and TELTOW J., *Phys. Status Solidi* **23**, 9 (1967).

J. Phys. Chem. Solids Pergamon Press 1969. Vol. 30, pp. 1977–1980. Printed in Great Britain.

THE EFFECT OF PREFERRED CRYSTAL GROWTH ON THE ANGULAR DEPENDENCE OF THE MAGNETIC-TRANSITION FIELD IN QUENCHED THIN In FILMS*

C. K. SCHILLER and H. BULOW
Department of Physics, Wayne State University, Detroit, Mich. 48207 U.S.A

(*Received* 9 *September* 1968)

Abstract–The critical field behavior of superconducting thin In films, quenched on substrates held at liquid He temperatures, is investigated right after the evaporation and during the annealing. The experimentally determined angular dependence of the critical field, H_c, is compared with the prediction of the Tinkham[1] theory. For all quenched In-films a departure of the angular dependence of H_c from the theory of Tinkham is found for the 300°K anneals for angles in the range from approximately 0°–30° This departure is explained by the preferred growth of In crystallites on annealing. The purpose of our investigation was to examine the angular dependence of the critical field, and its relation to changes in defect concentration and crystallization processes.

EXPERIMENTAL CONCEPT AND PROCEDURE

THERE ARE two commonly used approaches for studying the effects of defects in solids which can accomplish this. It is possible to begin with a very pure material into which defects may be introduced by doping, alloying, radiation, plastic deformation, or other similar methods. A second procedure, the one which was employed in the experiments described herein, is to begin with as high a concentration of defects as possible, and subsequently anneal them. A similar approach is taken, for instance, in radiation damage experiments where depletion zones are produced and then annealed.

The films were formed as in previous papers [2–4] by quenching the metal vapor on a perpendicular cut quartz single crystal substrate held at liquid He temperature. After the evaporation process measurements were begun of the dependence of H_c on θ, where θ is the angle between the field and the plane of the film. The transition was measured resistively, using currents of 0·80 mA, orthogonal to the field and the normal to the film. The films were warmed up to successive higher temperatures up to room temperature. After each annealing stage measurements would be made with the film recooled to liquid He temperature. The magnetic field was produced by a Varian V-3400 rotable magnet with 9 in.-pole faces and 2·5 in. gaps. The field strength was calibrated periodically with a rotating coil gaussmeter checked against an NMR probe, and had a maximum value of 11·2 kG. For the total arrangement of experiment see [14].

The relative orientation between magnetic field and film plane was such, that an angle $\theta = 0$ meant, that magnetic field direction and film plane were parallel to each other.

For the analysis of the experimental results the theory of Tinkham [1] was used. Tinkham made in his paper the prediction that the perpendicular critical field is given by

$$H_{c\perp}^{(T)} = \frac{4\pi\Lambda_c^2(T)H_{cb}^2(T)}{\phi_0}$$
$$= 6\cdot06\times10^7\Lambda_c^2(T)H_{cb}^2(T) \qquad (1)$$

which depends only on known quantities, $\Lambda_c(T)$ and $H_{cb}(T)$, and thus leads to a

---

*Partly supported by the Atomic Energy Commission under AEC Contract No. AT(11-1)-1054.

parameter free determination of $H_{c\perp}$. This result is equivalent to that of Abrikosov[6] for the critical field H_{c2} of bulk Type II superconductors, in which the flux is shown to penetrate in a vortex structure similar to that described by Tinkham.

For angular dependence of the critical field Tinkham predicts a critical field vs. angle relation of the form:

$$\frac{H_c \sin\theta}{H_{c\perp}} + \left[\frac{H_c \cos\theta}{H_{c\parallel}}\right]^2 = 1 \qquad (2)$$

where $H_{c\perp}$ is given by equation (1) and $H_{c\parallel}$ by equation (2) in Tinkham's paper[1]. θ is the magnitude of the angle between the field and the plane of the film. For a thin film $H_{c\perp} \ll H_{c\parallel}$, and the first term will dominate over a considerable angular range. The fact that the variation is with $\sin\theta$ rather than $\sin^2\theta$ is important for explaining the extreme sensitivity of critical field measurements to small perpendicular field components.

In the analysis of our experimental results we used Tinkham's theory in the following way. The angular dependence results are compared directly with equation (2). Knowing the extreme values $H_{c\perp}$ and $H_{c\parallel}$, that equation predicts a curve for intermediate values of H_c which can be compared directly with our measured values.

The temperature dependences for $\Lambda_e(t)$ and $H_{cb}(t)$ are approximated by the usual Gorter–Casimir relations:

$$\Lambda_e^2(t) = \Lambda_e^2(0)(1-t^4)^{-1}$$
$$H_{cb}(t) = H_{cb}(0)(1-t^2)$$

where $t = T/T_c$.

In another paper we have shown that Tinkham's theory works very well in the cases of quenched Pb- and Sn-Films[4] with randomly oriented crystallites. Of special interest in this investigation was whether or not a preferred orientation of the crystallites within the film would lead to a disagreement between experiments and theory. Earlier experiments done by the author[7] showed that indium would be a good element to choose for this study, since it showed a preferred orientation for the majority of crystallites on annealing between 90° and 180°K, and continued t grow with this preferred orientation unti room temperature was reached. The growth i such that either the 202 or 220 planes ar perpendicular to the surface of the substrate 60 per cent of the oriented crystallites hav the 202 plane perpendicular to the substrat with the remaining 40 per cent in the 22 orientation. An advantage of choosing indiu would be the fact that for the first two anneal at low temperatures, the film would be ran domly oriented, and should agree with th theoretical predictions, whereas if there wer going to be any deviation, it would be expecte only for the higher temperature anneals (fo example the 180° and 300°K anneals).

PRESENTATION AND ANALYSIS OF THE EXPERIMENTAL RESULTS

The experimental results and the theoretic curves for indium are shown in Fig. 1 (a, b). should be noted that for some of the anneal the critical field was beyond the measurin capability of the equipment for angles ne 0°, in which case the measured critical fiel for the angles nearest zero which could b obtained were used to extrapolate a value f $H_{c\parallel}$, using equation (2) and this value of H would then be used to generate the enti curve. The end point determined in this wa may be in error by a large amount, but th effect of such an error in the generation of th curve is relatively minor due to the fact th *the first term predominates over such a lar angular range. For example, if $H_{c\parallel}$ for th 6·0°K anneal curve for Film 109 is taken to b 20 kG rather than 17 kG, an increase of 1 per cent, the resultant increase in the predicte value of H_c for $\theta = 10°$ is only 3·6 per cent.*

This extrapolation did not have to be per formed for the 300°K annealing temperature since H_c was within our capability. This is a important point since it is the angular depen

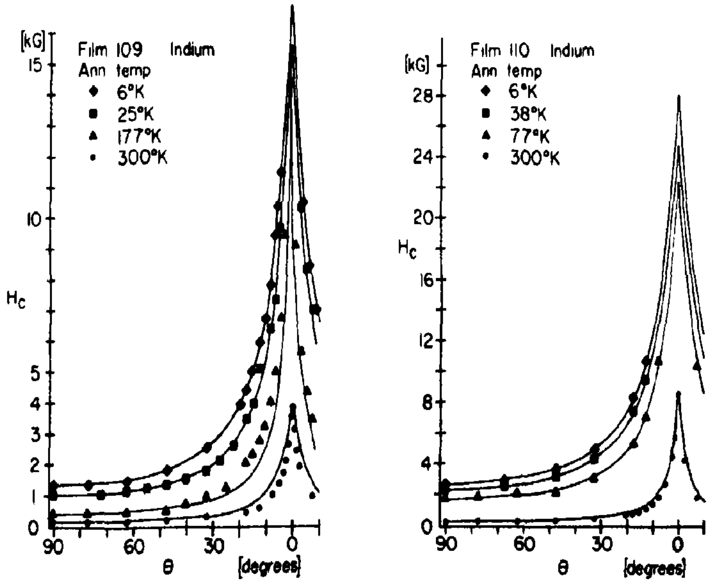

(a) (b)

Figs. 1 (a, b). Angular dependence of the critical field (measuring temperature for In-Film 109 = 3·7°K, for In-Film 110 = 3·8°K; thickness of In-Film 109 = 1750 Å, of In-Film 110 = 1072 Å).

dence for this annealing temperature which shows the greatest deviation from the theoretical predictions.

Returning to Figs. 1 (a, b), we note that as expected the experimental points and theoretical curve are in close agreement for the first two anneals. For room temperature anneals the deviation from the predicted angular dependence is evident. The maximum deviations are 32 per cent for Film 109 and 12·3 per cent for Film 110. These maximum deviations occur within 15° of 0°, and the deviation is very small for angles greater than 45°.

These results are interpreted in the light of the known preferred orientation of the crystallites on annealing as follows. For 0° the magnetic field 'sees' a cross-sectional area of the film equal to the thickness of the film times the length. The orientation of the crystallites can not have a large effect, since so small an area is shown to the field (about 10^{-5} cm^2). As soon as θ is increased from 0°, however, the cross-sectional area presented to the magnetic field is enhanced by the oriented crystallites, and the larger area presented to the field causes a lower critical field value to be observed.*

Thus as θ is increased the experimental points will lie below the theoretical curve, until the projected area of the film surface normal to the field has masked out the effect of the orientation. This is what is expected and found.

For Film 109 the third anneal took place at 177°K and shows the effect produced by retarded crystallization. This anneal also shows a large deviation of the experimental points from the theoretical curve, which is in the opposite direction from the observed deviation for the 300°K anneals. The reason for this behavior is some mechanism which has retarded the recrystallization until about 177°K, and this contention is supported by the behavior of the resistivity changes of this film, (not shown here).

---

*The basis for this statement is the same argument as presented in Tinkham's paper concerning the difference in magnitude in H_c for parallel and perpendicular fields.

The cause of retarded growth would be an impurity or impurities of some kind, and the most suspect is the presence of some water in the film.

This is supported by the fact that some of the electron diffraction patterns show additional rings at about 180°K which had the correct radii to correspond with ice. These rings disappeared upon further annealing. It is our belief that this impurity would be the most likely to cause the behavior which we observe.

CONCLUSION

A good agreement of the angular dependence data with the theoretical predictions for In for films with randomly oriented crystallites is found; the defect concentration does not greatly affect the angular dependence of the measured critical fields, since the theoretical and experimental points are in accord for several annealing temperatures for films with very different concentrations. The behavior of quenched indium films annealed to room temperature demonstrates that the orientation of the crystallites is important, however.

The large increase in H_c right after the quenching follows from the high density of defects with consequent increase in the penetration depth and a correspondingly small mean free path. The decrease in H_c during the annealing of defects is coupled with a decrease in θ and an increase in l.

In summary, these experiments show that the theory of the behavior of the critical field of thin metal films as presented by M. Tinkham based on the concept of flux quantization and vortices, provides a good description for such films, as long as no preferred orientation of crystallites within the films exists!

REFERENCES

1. TINKHAM M., *Phys. Rev.* **129**, 2413 (1963).
2. BULOW H. and SCHILLER C. K., *Phys. Lett.* **22**, 136 (1966).
3. BULOW H. and SCHILLER C. K., *Phys. Lett.* **24A**, 673 (1967).
4. BULOW H. and SCHILLER C. K., To be published.
5. MONCH WINIFRIED and SANDER W., *Z. Phys.* **157**, 149 (1959).
6. ABRIKOSOV A. A., *Zh. eksp. teor. Fiz.* **32**, 144 (1957); translation, *Soviet Phys. JETP* **5**, 1174 (1957).
7. BULOW H. and BUCKEL W., *Z. Phys.* **145**, 14 (1956).

J. Phys. Chem. Solids Pergamon Press 1969. Vol. 30, pp. 1981–1988. Printed in Great Britain.

INTERMOLECULAR INTERACTION AND INFRA-RED SPECTRA OF THE THREE CRYSTALLINE PHASES OF POTASSIUM NITRATE–II. INTERNAL-LATTICE COMBINATION BAND REGION

A. A. SHULTIN and S. V. KARPOV
Institute of Physics, Leningrad State University, Leningrad, U.S.S R.

(*Received* 15 *August* 1968)

Abstract—Polarized i.r. absorption spectra (in the region 700–1300 cm^{-1}) of binary combinations between internal and lattice vibrations for the three crystalline phases of potassium nitrate are investigated. They are treated mainly according to the selection rules in the factor group representation. However, the branch dispersion and the state density are important for the interpretation of low-temperature and ferroelectric phase spectra. The broad combination absorption maxima in the high-temperature spectrum are associated with the orientational lattice disorder in the (001) plane

INTRODUCTION

IN THE previous article[1] we gave the principal results on fundamental nitrate-ion internal vibrations in the three crystalline modifications. Numerous absorption bands due to combinations of lattice modes were observed in the course of that work.

The general features of the optical behavior of the crystal both in absorption and in the second order Raman scattering, were discussed by a number of writers[2–5], who established the basic principles of obtaining selection rules and noted a possible significance of the phonon branch dispersion.

Combined with the properties of the frequency distribution function in the vicinity of the Brillouin zone critical points, this may lead to the observation of a most complex spectrum. These data must form the basis of a detailed interpretation of the second order spectra but they are now available only for a few simple crystals.

In a recent paper Nusimovici[6] discussed in detail the symmetry properties of the KNO_3 lattice in different phases and obtained, in particular, selection rules for the second order i.r. and Raman spectra. We shall consider his results further.

KNO_3-II

The KNO_3 low-temperature phase has a simple orthorhombic Bravais lattice ($D_{2h}^{16} = Pnma$, $z = 4$). The number and types of the lattice modes can be obtained by taking into account the unit cell transformation properties by Bhagavantam's method[7]. These data are given in Table 1. Separation into external and internal cell vibrations is possible due to the large differencies between corresponding frequencies. Separation into translational and librational lattice modes appears to be a more difficult approximation, since there are only qualitative considerations as to the true form of normal vibrations for lattices built of molecular ions[8–11]. For this reason and owing to the relative lattice complexity (see[1], Fig. 1), we do not present drawings of the unit cell external vibrations.

Raman spectra have been studied in [12, 13]. The most complete data available [14] give the following lattice frequencies at room temperature: 50 (B_{2g}, B_{3g}), 65 (B_{1g}), 83 (B_{2g}, B_{3g}), 103 (B_{3g}), 122 (B_{3g}), 133 (B_{1g}), 138 (A_g) cm^{-1}.

The far i.r. study[15] of a powdered sample reveals frequencies of 130 and 152 cm^{-1}.

The spectra of KNO_3-II obtained in this

Table 1. The number and types of the KNO_3–II *unit cell vibration symmetry*

Symmetry type	Total number of vibrations	Number of translations	Number of librations	Number of internal vibrations
A_g	9	4	1	4
B_{1g}	6	2	2	2
B_{2g}	6	2	2	2
B_{3g}	9	4	1	4
A_u	6	2	2	2
B_{1u} (z)	9	3 + 1	1	4
B_{2u} (y)	9	3 + 1	1	4
B_{3u} (x)	6	1 + 1	2	2

work at 80° and 300°K are plotted in Figs. 1 and 2. Apart from the nitrate ion internal vibration bands, many internal-lattice combination bands were observed.

The combination absorption bands in the spectra taken with orientations E ∥ *a* and E ∥ *b* show a marked similarity. This is due to the local field around nitrate ions which is only slightly different than the trigonal one. The arrangement of cations K^+ with respect to anions is of C_{3r} symmetry, whereas the anion's site-symmetry is C_S. This symmetry lowering is due to a vertical shift (by ¼ of the cell parameter) and a 60° rotation in the ion plane suffered by one half of the total numbe of nitrate-ions. The angle between the optic axes of KNO_3–II is about 7°, the refractio indices in the (001) plane differing by onl 10^{-3}.

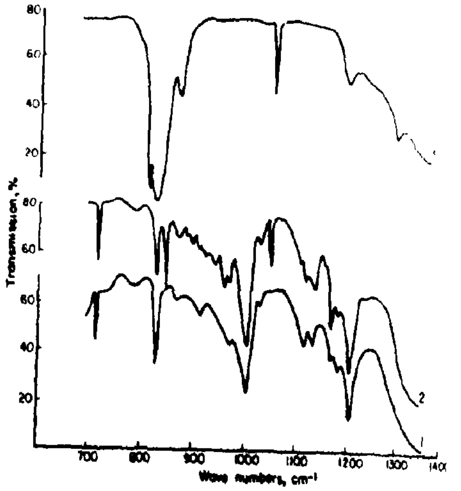

Fig. 2. Polarized i.r. spectra of KNO_3–II single crystal a 80°K 1–E∥*a*; 2–E∥*b*, (001) plate 350μ thick 3-E∥ (010) plate 150μ thick.

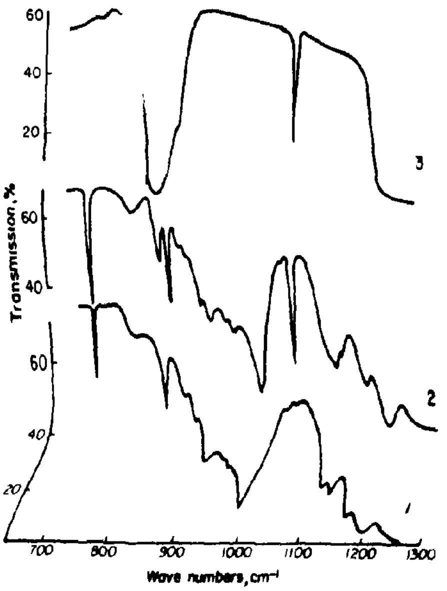

Fig. 1. Polarized i.r. spectra of KNO_3*–II single crystal at 300°K. 1–E ∥ a; 2–E ∥ b, (001) plate 300μ thick 3–E ∥ c, (100) plate 150μ thick.*

Since there is little information on the val of the intermolecular interaction constant we must consider the factor-group selecti rules (i.e. Brillouin zone Γ-point), assumi that the transitions allowed in this approxim *tion are more probable [2].*

Selection rules for binary combinations wi internal vibrations ν_1 *and* ν_2*, allowed in ab sorption in the Brillouin zone centre are give in Table 2.*

The pattern of combination bands with a totally symmetric internal vibration, ν_1*, is*

Table 2. Selection rules for binary combination transitions in the lattice with ν_1 and ν_2 internal vibrations in the zone centre

ν_1 and ν_2 intramolecular vibration symmetry types	Symmetry types of lattice vibrations active in combination transitions		
	along *a*	along *b*	along *c*
B_{1u}	B_{2g}	B_{3g}	A_g
B_{2u}	B_{1g}	A_g	B_{3g}
A_g	B_{3u}	B_{2u}	B_{1u}
B_{3g}	A_u	B_{1u}	B_{2u}

the simplest, since the insignificant value of the vibration resonance splitting[1] causes no extra complications. The strongest lines with maxima near 1202 cm^{-1} (Fig. 1, spectra 1 and 2) can be assigned to combinations of the internal mode A_g with external vibrations B_{2u} and B_{3u}. These, in turn, result from the coupling between K^+ and NO_3^- sub-lattice translational vibrations in the opposite phase towards the *a* and *b* axes and nitrate-ion librations.

Similar combinations with internal vibration ν_4 can give rise to the bands at 863 cm^{-1} (E ∥ *a*, E ∥ *b*) and a shoulder at 860 cm^{-1} (E ∥ *c*). These bands are more distinct in the spectra obtained at a liquid nitrogen temperature (Fig. 2).

Despite the identity of selection rules for binary combinations occurring with internal modes ν_1 and ν_2, the region of sum transitions with the latter differs from that of the ν_1 mode. This is due primarily to the ν_2 vibration component splitting by approximately 15–17 cm^{-1}. By taking into account the symmetry considerations and comparing the values of the lattice sums in the point dipole approximation, it is possible to locate the inactive vibration components*. The scheme of the ν_2 mode resonance splitting in an NO_3^- ion in the lattice of KNO_3-II is presented in Fig. 3. However, comparison of the absorption curves in the regions under consideration (1202 → 988 cm^{-1}, 1165 → 946 cm^{-1}, 1125 → 908 cm^{-1} and 1113 → 892 cm^{-1}, Fig. 1, curve 1) does not completely fit in with such a diagram, because in this case the component ν_2 (A_g) must have a frequency of about 845 cm^{-1} in the zone centre. Since the internal mode branch dispersion has a value of approximately the distance between the extreme multiplet components[16], one can assume that the phonon interaction occurs mainly when the exciton states of the ν_2 mode are located near the Brillouin zone boundary.

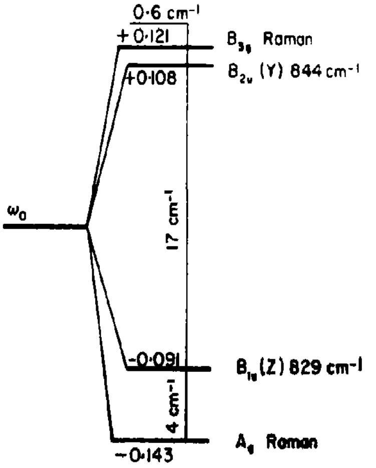

Fig. 3. Correlation splitting of the nitrate-ion ν_2 mode in KNO_3–II at 300°K. The value of the dipole lattice sum *is given for each term.*

The factor-group selection rules are different for combination translations in polarizations E ∥ *a* and E ∥ *b*. In the first case, the translational modes may occur along the *a* axis, whereas in the second case, similar vibrations may occur along axes *b* and *c*.

---

*The writers wish to express their appreciation to M. V. Belousov who performed a number of calculations of dipole lattice sums for the aragonite structure.

On the contrary, librational movements of molecular ions can make the greatest contribution to the combination absorption in polarization E ∥ *a* (Table 2). Therefore, the simplicity of the spectrum in this polarization (curve 1, Figs. 1 and 2) suggests, in contrast to the conclusions of [17], that the combination absorption bands are essentially of a translational origin.

At 80°K a number of combination bands reveal a more complex structure. The lack of quantitative data on KNO_3-II lattice dynamics, however, prevents a detailed interpretation of a number of absorption bands.

In Figs. 1 and 2 the combination absorption bands are seen to be sharply polarized in the (001) plane. This fact is of particular interest due to the identical factor-group selection rules for binary combinations in E ∥ *b* and E ∥ *c* polarizations, whereas the consideration of a possible contribution by the rest of the Brillouin zone points leads to absorption band depolarization[2]. Such a result can be explained by the difference in intermolecular interactions in the (001) plane and in the perpendicular direction, this difference manifesting itself, in particular, in a considerable anysotropy of the crystal thermal expansion.

According to [18] $\alpha_1 = 23{\cdot}5 \times 10^{-6}$, $\alpha_2 = 22 \times 10^{-6}$ and $\alpha_3 = 182{\cdot}6 \times 10^{-6}$ in the 30°–100° C range. In this case the thermal expansion ellipsoid axes are parallel to the *a*, *b* and *c* axes.

Therefore, the intermolecular interaction should be weakest along the *c* axis.

INFRA-RED SPECTRA OF THE FERROELECTRIC PHASE FOR CRYSTALS KNO_3, $K_{0·7}Rb_{0·3}NO_3$ AND $K_{0·6}(NH_4)_{0·4}NO_3$

The KNO_3-III structure is the simplest one: the lattice is the primitive, space group $C^5_{3v} - R\bar{3}m$, $Z = 1$.

The number and symmetry types of the unit cell vibrations are given in Table 4, the lattice vibration form being given in Fig. 4. The crystals in which part of the K^+ cations are replaced by Rb^+ or $NH_4{}^+$ possess a similar structure. The ferroelectric phase of a $K_{1-x}(NH_4)_xNO_3$ crystal becomes stable (for $x > 0{\cdot}2$), whereas the phase $K_{1-x}Rb_xNO_3$, being metastable at atmospheric pressure, occurs in a broader temperature range. Therefore, it was of interest to study the mixed crystal spectra as well.

Experimental data on i.r. and Raman spectra of KNO_3-III are scarce[14, 19]. Balkanski, Teng and Nusimovici reported a broad band near 120 (*E*) cm^{-1} in the Raman spectrum as well as 3 lines corresponding to the nitrate ion internal vibrations: 716 (*E*), 1057 (A_1) and 1352 (*E*) cm^{-1}.

Infra-red spectra of KNO_3, $K_{0·7}Rb_{0·3}NO_3$ and $K_{0·6}(NH_4)_{0·4}NO_3$ crystals obtained simultaneously with the observation of the dielectric hysteresis loop are given in Figs. 5–7. The frequencies of absorption maxima are presented in Table 5.

The spectra of the same polarizations are quite similar for all of the samples. The most

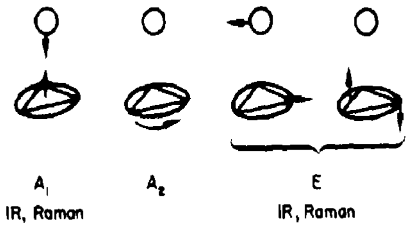

Fig. 4. Form of KNO_3-III unit cell normal vibrations.

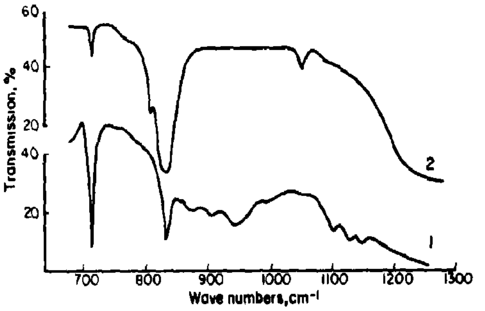

Fig. 5. Polarized i.r. spectra of KNO_3-III single crystal at 387°K. 1–E ⊥ *c*, (001) plate; 2–E ∥ *c*, (010) plate 150 μ thick each.

Table 3. KNO_3–II *i.r. band frequencies*

80°K	300°K	Polarization	Assignment*	80°K	300°K	Polarization	Assignment
714·5	715·2	*a*	$\nu_4(B_{3u})$	1002	989	*b*	$\nu_2+152\,(B_{2u})$
715·2	716·0	*b*	$\nu_4(B_{2u})$	1004	988	*a*	$\nu_2+154\,(B_{3u})$
770		*a, b, c*	ν_4+53	1030	1030	*a, b*	$\nu_1\,(N^{14}O^{18}O_2^{16})$
797	790	*a, b, c*	ν_4+81	1049 9	1050·0	*b*	$\nu_1\,(B_{2u})$
814	812	*c*	$\nu_2\,(N^{15}O_3^-)$	1051·0	1051·0	*c*	$\nu_1\,(B_{1u})$
829	829	*c*	$\nu_2\,(B_{1u})$	1105		*b*	ν_1+54
846	844	*b*	$\nu_2\,(B_{2u})$	1115	1112	*a, b*	ν_1+65
870	863	*a, b, c*	ν_4+155 (B_{2u}, B_{3u})	1130	1125	*a*	ν_1+82
890	874	*b*		1133	1125	*b*	
899	891	*b*	ν_2+54	1154		*b*	ν_1+103
913	906	*a, b*	ν_2+65	1167	1164	*a, b*	ν_1+116
917		*b*	ν_2+82	1181		*a, b*	ν_1+130
923		*b*		1192	1207	*c*	$\nu_1+141\,(B_{1u})$
942		*b*	ν_2+103	1203	1202	*b*	$\nu_1+152\,(B_{2u})$
958	933	*b*	ν_2+116	1206	1202	*a*	$\nu_1+154\,(B_{3u})$
970	946	*a, b*	ν_2+130	1294	1207	*c*	$\nu_1-56\,(?)$

*Frequency values in this column refer to the spectrum at 80°K.

Table 4. *The number and types of the* KNO_3–III *unit cell vibration symmetry*

Symmetry type	Total number of vibrations	Number of translations	Number of librations	Number of internal vibrations
$A_1\,(Z)$	4	1+1	0	2
A_2	1	0	1	0
$E(x, y)$	5	1+1	1	2

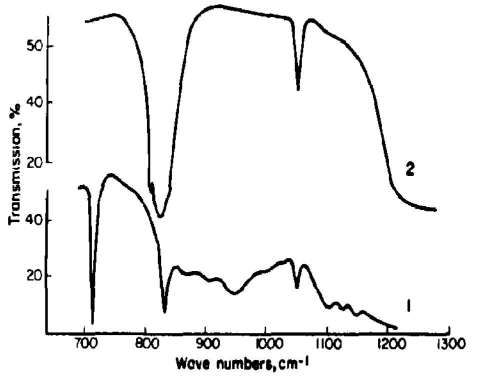

Fig. 6. Polarized i.r. spectra of $K_{0·7}Rb_{0·3}NO_3$–III single crystal. 1–E ⊥ *c*, 380°K (001) plate 350 μ thick; 2–E ∥ *c*, 387°K (100) plate 150 μ thick.

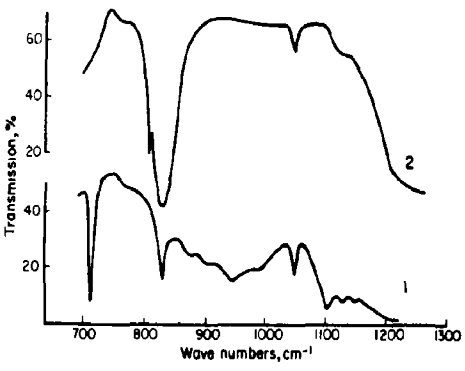

Fig. 7. Polarized i.r. spectra of $K_{0·6}(NH_4)_{0·4}NO_3$–III single crystal. 1–E ⊥ *c*, 387°K (001) plate 350 μ thick, 2–E ∥ *c*, 390°K (010) plate 150 μ thick.

essential difference is in the appearance of the ν_1 band in $K_{0·6}(NH_4)_{0·4}NO_3$ and $K_{0·7}Rb_{0·3}NO_3$ spectra with E ⊥ *c*. This is probably due to the lowering of the nitrate-ion site-symmetry in mixed crystals to C_1 (ionic radius $R_{K^+} = 1·33$ Å, $R_{Rb^+} = 1·48$ Å). Weak bands in the 870–990 cm⁻¹ and 1100–1150 cm⁻¹ regions belong to transitions that result from the coupling with lattice vibrations (Figs. 5–7, E ⊥ *c*).

Table 5. KNO_3 *crystal i.r. band frequencies for the ferroelectric phase*

KNO_3-III			$K_{0\cdot7}Rb_{0\cdot3}NO_3$-III			$K_{0\cdot6}(NH_4)_{0\cdot4}NO_3$-III		
116°C	Polarization	Assignment	107·5°C, 114°C*	Polarization	Assignment	114°C, 117°C†	Polarization	Assignment
717	$\perp c$	ν_4	716·5	$\parallel c, \perp c$	ν_4	716·5	$\parallel c, \perp c$	ν_4
811	$\parallel c$	$\nu_2(N^{15}O_3^-)$	810	$\parallel c$	$\nu_2(N^{15}O_3^-)$	811	$\parallel c$	$\nu_2(N^{15}O_3)$
836	$\parallel c$	ν_2	834	$\parallel c$	ν_2	833	$\parallel c$	ν_2
876	$\perp c$	See text	872	$\perp c$	See text	880	$\perp c$	See text
905	$\perp c$		905	$\perp c$		906	$\perp c$	
942	$\perp c$		947	$\perp c$		949	$\perp c$	
997	$\perp c$	$\nu_1 - 56\ (E)$	996	$\perp c$	$\nu_1 - 55\ (E)$	996	$\perp c$	$\nu_1 - 54\ (E)$
1029	$\parallel c$	$\nu_1(N^{14}O^{18}O_2^{16})$	1030	$\parallel c$	$\nu_1(N^{14}O^{18}O_2^{16})$			
1053	$\parallel c$	ν_1	1051	$\parallel c, \perp c$	ν_1	1050·5	$\parallel c, \perp c$	ν_1
1103	$\perp c$	$\nu_1 + 50\ (E)$	1102	$\perp c$	$\nu_1 + 51\ (E)$	1103	$\perp c$	$\nu_1 + 52\ (E)$
1128	$\perp c$	See text	1126	$\perp c$	See text	1127	$\perp c$	See text
1149	$\perp c$	$\nu_1 + 96\ (E)$	1149	$\perp c$	$\nu_1 + 98\ (E)$	1150	$\perp c$	$\nu_1 + 100\ (E)$

*Temperature 107·5°C refers to the spectrum with **E** $\perp c$. 114°C refers to the spectrum with **E** $\parallel c$.

†Temperature 114°C refers to the spectrum with E $\perp c$; 117°C refers to the spectrum with **E** $\parallel c$.

Selection rules for binary combination transitions[6] allow the appearance of $A_1 \otimes E$, $E \otimes E$ combinations in this polarization in the centre zone, as well as a number of combinations of the type $Z_1 \otimes Z_1, Z_3 \otimes Z_3$ and $A_i \otimes A_j$, $D_i \otimes D_j$ $(i, j = 1, 2)$, where Z_i, A_i and D_i are irreducible representations in the respective points on the Brillouin zone boundary.

It should be noted that separations of combination bands from the ν_1 band in the 1100–1150 cm^{-1} region do not coincide with those for similar bands in the vicinity of ν_2 absorption (870–950 cm^{-1}). Since ν_1 and ν_2 internal modes belong to the same representations, their binary combinations are formed with the same lattice vibrations.

Therefore, the difference in the observed combination band separations are due to a difference in the branch width of ν_1 and ν_2 vibrations.

The data on the combination $\nu_2 + \nu_L$ bands may suggest that the ν_2 branch width is about 10 cm^{-1}, the frequency of this vibration having a lower value on the zone boundary. Certain difficulties are faced in the attempts to attribute the combination absorption maxima to a definite lattice vibration. Two degenerate lattice vibrations (Fig. 4) form coupled vibrations. The broad band near 120 (E) cm^{-1} as well as the weak peak observed near 50 cm^{-1} in the Raman spectrum[14] may be due to this coupling. Combination bands $\nu_1 + (97 \sim 100)$ cm^{-1}, $\nu_1 + (50 \sim 52)$ cm^{-1} and $\nu_2 + (40 \sim 45)$ cm^{-1} are probably due to the participation of these vibrations.

The occurrence of $\nu_2 + 70$ cm^{-1} and $\nu_1 + (74 \sim 77)$ cm^{-1} bands can be attributed to the singularities of the frequency density distribution function in the vicinity of Z, A and D normal critical points.

The participation of acoustic vibrations in combination bands is allowed by selection rules, but additional investigations are required to explain their role in combination absorption bands. The absence of an absorption maxima in the $\nu_2 - \nu_L$ region is noteworthy since the spectra were taken at $T = 380°$–$390°$K. Under these conditions, the Boltzman distribution must lead to the bands of difference combinations (for $\nu_L \simeq 50$–100 cm^{-1}) comparable in intensity to the sum bands.

Unfortunately, we failed to observe combination bands with the type A_1 lattice optical mode connected with ferroelectric KNO$_3$-III properties.

The combinations of this mode with ν_1 and ν_2 internal vibrations are forbidden for $\mathbf{E} \perp c$; all the spectra with $\mathbf{E} \parallel c$ polarization, as in the case of KNO$_3$-II, contain almost no combination bands.

KNO$_3$-I

The structure properties for the KNO$_3$ high-temperature phase were discussed briefly in our earlier paper[1].

Some data, in particular the analysis of the band width temperature dependence for certain internal vibrations[20], does not confirm the hypothesis of a free nitrate-ion rotation previously suggested.

A two-dimensional orientational nitrate-ion disorder ('orientational melting') in layers perpendicular to the axis must lead to a broadening of the bands corresponding to the ordered lattice vibrations.

The data for the low frequency Raman spectra of KNO$_3$-I are somewhat contradictory. Nedungadi[12] reported the disappearance of 100, 126 and 143 cm^{-1} bands at $T = 120°$C; according to his data, the 82 cm^{-1} band becomes very broad at $T = 170°$C.

Chisler[21] observed in KNO$_3$-I the disappearance of the 50 and 81 cm^{-1} bands and the occurrence of a broad band near 120 cm^{-1}.

Balkanski *et al*[14] did not observe any bands in the low-frequency region of the Raman spectrum for this phase.

Chisler excited the Raman spectrum by means of a mercury arc, while the authors of the latter paper[14] used the Ne–He laser.

If the assumption of the KNO$_3$-I lattice consisting of 'micro-domains' is true, then under certain conditions the interference of coherent light scattered on the 'micro-domain' low-frequency vibrations may considerably diminish its intensity. Apart from considerations given in [14] this hypothesis seems to us to be worth verifying.

In the interferometric study of the KNO_3 reflection spectrum at 24° and 146°C in the 12–100 cm^{-1} range, Chen and Chernow[22] obtained an almost flat curve at a level of $(15 \pm 3)\%$.

The KNO-I spectra observed in this paper are given in Fig. 8, the absorption band frequencies being given in Table 6. There are two combination absorption regions near 1137 and 965 cm^{-1} in the $E \perp c$ polarization. The former is due to the sum combination of the $\nu_1 + \nu_L$ type and the latter to the difference, $\nu_1 - \nu_L$, type, with the lattice vibrations being translational (in the (001) plane) and librational (around C_2 axes) nitrate-ion movements in changing local force fields.

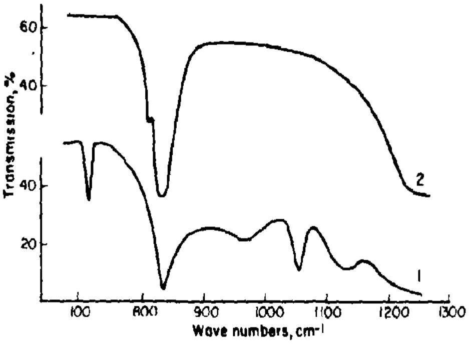

Fig. 8 Polarized i.r. spectra of KNO_3-I crystal at 413°K 1–$E \perp c$, (001) plate 150 μ thick; 2–$E \parallel c$. (010) plate 100 μ thick.

Table 6. KNO_3-I *i.r. band frequencies*

140°C	Polarization	Assignment
716	$\perp c$	ν_4
812	$\parallel c$	$\nu_2(N^{15}O_3^-)$
835	$\parallel c$	ν_2
965	$\perp c$	$\nu_1 - 82, \nu_2 + 82$
1055	$\perp c$	ν_1
1137	$\perp c$	$\nu_1 + 82$

No combination absorption bands were observed in $E \parallel c$ polarizations.

Acknowledgements—The authors thank Professor E. F. Gross for his interest, Professor S. S. Mitra for drawing the writers' attention to certain peculiarities in the second order i.r. spectra, and Dr. M. A. Nusimovici for sending a reprint of his article on KNO_3 lattice dynamics.

REFERENCES

1. KARPOV S. V. and SHULTIN A. A., *J. Phys. Chem. Solids* **29**, 475 (1968).
2. WINSTON H. and HALFORD R. S., *J. chem. Phys.* **17**, 607 (1949).
3. BIRMAN J. L., *Phys Rev.* **127**, 1093 (1962); *ibid.* **131**, 1489 (1963).
4. MITRA S. S., *J. chem. Phys.* **39**, 3031 (1963).
5. MITRA S. S., In *Progress in Infrared Spectroscopy*, Vol. 2. Plenum Press, New-York (1964).
6. NUSIMOVICI M. A., In *Ferroelectricity* (Edited by E. F. Weller, p. 123. Elsevier, Amsterdam (1967).
7. BHAGAVANTAM S. and VENKATARAYUDU T., *Theory of Groups and its Application to Physical Problems*. Andhra University, Waltair (1951).
8. KASTLER A., *Proc. Indian Acad. Sci.* **28A**, 348 (1948).
9. KASTLER A., *C.r. hebd. Séanc. Acad. Sci., Paris* **227**, 1024 (1948).
10. GIULOTTO L. and OLIVELLI G., *J. chem. Phys.* **16**, 555 (1948).
11. WICKERSHEIM K. A., *J. chem. Phys.* **31**, 863 (1959).
12. NEDUNGADI T. M. K., *Proc. Indian. Acad. Sci.* **14A**, 242 (1941).
13. COUTURE L., *Annls Phys.* **12**, 5 (1947).
14. BALKANSKI M., TENG M. K. and NUSIMOVICI M. A., *Raman Scattering in KNO_3 Phase I, II and III*. Rep. Laboratoire de physique des solides, Faculté des Sciences de Paris, (1967).
15. FERRARO J. R. and WALKER A., *J. chem. Phys.* **42**, 1273 (1965).
16. DAVYDOV A. S. and MYASNIKOV E. N., *Phys. Status Solidi* **20**, 153 (1967).
17. SCHROEDER H. A., WEIR C. E. and LIPPINCOTT E. R., *J. Res. natn. Bur. Stand. A. Phys. Chem.* **66A**, 407 (1962).
18. LONAPPAN M. A., *Proc. Indian Acad. Sci.* **41A**, 239 (1955).
19. KARPOV S. V. and SHULTIN A. A., *Soviet Phys. solid St.* **11**, 2761 (1966).
20. YANAGI T., *J. phys. Soc. Japan* **20**, 1351 (1965).
21. CHISLER E. V., *Fiz. Tverd. Tela* **8**, 1938 (1966).
22. CHEN A. and CHERNOW F., *Phys. Rev.* **154**, 49 (1967).
23. SHINNAKA Y., *J. phys. Soc. Japan* **17**, 820 (1962).

J. Phys. Chem. Solids Pergamon Press 1969. Vol. 30, pp. 1989–1997. Printed in Great Britain.

PREPARATION AND PROPERTIES OF FERRIMAGNETS IN THE $RbMgF_3$-$RbCoF_3$ SYSTEM

M. W. SHAFER and T. R. McGUIRE
IBM Watson Research Center, Yorktown Heights, N.Y. 10598, U.S.A.

(*Received* 27 *January* 1969; *in revised form* 25 *February* 1969)

Abstract—Previously reported ABF_3-type ferrimagnets with the hexagonal $BaTiO_3$ structure all contain Ni^{2+} as the predominant magnetic ion. This paper reports the discovery of new ferrimagnetic compositions in the $RbMgF_3$–$RbCoF_3$ system where Co^{2+} is the only magnetic ion. Phase studies on this system show that at high temperatures the hexagonal phase is stable to about 70% $RbCoF_3$. Single crystals were grown over this compositional range and their magnetic and optical properties studied. Compositions containing in excess of about 35% $RbCoF_3$ are ferrimagnetic and their magnetic moments (as high as 24 e.m.u./g) and Curie temperatures (up to 36°K) vary with Co^{2+} concentration. The magnetization data are consistent with a model of a $\frac{1}{3}$–$\frac{2}{3}$ ferrimagnetic spin arrangement. The B–B interaction, which is the resultant of the 90° Co^{2+}–F–Co^{2+} and the direct Co^{2+}–Co^{2+} interactions appears to be positive. Anisotropy measurements at 4·2°K yielded values from $2{\cdot}2 \times 10^{-6}$ to $8{\cdot}9 \times 10^{-6}$ ergs/cm³ for K. Optical absorption data were used to determine the magnitude of the crystal field parameter *Dq* (870–880 cm^{-1}) and the spin orbit interaction constant λ (190 cm^{-1}). From the *Dq* values it is concluded that the strength of the crystalline field acting on the Co^{2+} ion in the hexagonal structure, where $\frac{2}{3}$ of the CoF_6 octahedra share faces, is not too different from that in cubic $KCoF_3$ and $RbCoF_3$, where they share corners.

INTRODUCTION

THE ABF_3-type ferrimagnetic fluorides with the hexagonal $BaTiO_3$ structure have recently received considerable attention as a result of their interesting magnetic and optical properties[1–6]. Previously reported ferrimagnets with this structure all contained Ni^{2+} as the predominant B ion and either Rb^+, Tl^+, or $NH_4{}^+$ as the A ion[7]. For example, the $RbNiF_3$, $TlNiF_3$, and NH_4NiF_3 compounds are hexagonal ferrimagnets, but when other divalent transition metals as Co, Fe, and Mn replace Ni^{2+}, cubic or pseudo-cubic perovskites are formed which order antiferromagnetically at low temperatures* [8]. This paper reports further on the discovery of new hexagonal ABF_3 ferrimagnetic compositions containing cobalt as the only magnetic ion[9]. These are found in the $RbMg_{1-x}Co_xF_3$ system where $0{\cdot}35 < x < 0{\cdot}68$.

The origins of the ferrimagnetism in the nickel-containing hexagonal compounds have been studied and can be understood with reference to its crystal structure and by comparison with the cubic or pseudo-cubic antiferromagnetic perovskites [5, 6]. In the ideal form of the cubic ABF_3 perovskites, the large A ions have 12 fluoride neighbors and the B ions have 6. Thus, the B ion and its 6 fluoride neighbors can be considered a BF_6 octahedron, which is linked to neighboring BF_6 octahedra by the sharing of corners throughout the structure. As a consequence of this configuration, each B ion has 6 nearest neighbor B ions separated by a fluoride ion and any resulting magnetic exchange interactions will be predominantly the 180° superexchange type, which are usually negative. In the hexagonal structure, two-thirds of the BF_6 octahedra occur in pairs which share a face to form B_2F_9 polyhedra (site 4*f*). The remaining one-third of the octahedra are linked to the B_2F_9 groups by sharing corners (site 2*a*). Magnetically, the distinguishing feature between the cubic and hexagonal structures is that in the cubic case the predominant exchange is the 180° B–F–B interaction, whereas in the hexagonal structure there is also a 90° B–F–B interaction plus the direct interaction, which may also be significant because of the relatively short B–B distance. It is believed that one or both of these latter interactions i.e. 90° or direct, are ferromagnetic [10] and, coupled with a negative AB interaction the resulting magnetic order is such that the spins of all ions occupying equivalent sites are parallel and those on inequivalent sites are antiparallel. This would yield an arrangement where one-third of the spins are antiparallel to the other two-thirds, which for pure $RbNiF_3$ is consistent with the measured magnetic moment.

---

*The exception to this is $RbFeF_3$ which although cubic at room temperature, undergoes several phase transitions as the temperature is lowered. The magnetic order also changes from antiferromagnetic to some complex spin arrangement.

Pure $RbCoF_3$ is a pseudo-cubic perovskite; hence, it is an antiferromagnet and has a Néel temperature of 32°K [11]. The system $RbNiF_3$–$RbCoF_3$ has been investigated [6] and the hexagonal solid solution extends to about 55% $RbCoF_3$. These compositions remain ferrimagnetic, but with a rather linear decrease in the Curie temperature from 138° to 90°K. An objective of this work was to study the effect of the face sharing of CoF_6 octahedra on the magnetic interactions of the Co^{2+} ion by preparing a series of compositions with the hexagonal structure containing Co^{2+} as the only magnetic ion. The system chosen for study was the $RbMgF_3$–$RbCoF_3$ because of the strong similarity in the crystal chemistry of the Mg^{2+} and the Ni^{2+} ions, and the fact that we had previously shown that $RbMgF_3$ could be prepared with the hexagonal structure [7].

EXPERIMENTAL

Both polycrystalline and single crystal compositions were used in this investigation. The starting materials were HF treated CoF_2 and MgF_2, and well crystallized RbF. The initial solid solutions of $RbMg_{1-x}Co_xF_3$ were prepared by solid state reactions in sealed platinum tubes and single crystals were grown in platinum crucibles by the Stockbarger method. Phase equilibria studies were carried by sealing the desired compositions in small platinum tubes, heating for a given amount of time (up to 380 hr in some cases), and then rapidly quenching. The phases formed were examined by X-rays and the petrographic microscope. Differential thermal analysis was also used, particularly in the determination of the liquidus temperatures. Magnetic moment measurements were made over the temperature range 4·2°–300°K and in fields up to 25,000 Oe. Curie temperatures were also obtained by an ac susceptibility method. The optical absorption data were taken on a Carey Model 14 at 300°, 77° and 10°K. The final compositions of the single crystals were determined by chemical analysis: the rubidium by precipitation with sodium tetraphenylboron, and the Mg and Co by atomic absorption spectroscopy.

RESULTS AND DISCUSSION

$RbMgF_3$

Previous X-ray work on $RbMgF_3$ indicated it to have a modification of the perovskite-type structure, but with monoclinic symmetry [12]. Our results on $RbNiF_3$–$RbMgF_3$ solid solutions [6] prepared at high temperatures showed the hexagonal $BaTiO_3$ structure to be stable over all composition ranges. For this to be true, it is necessary that $RbMgF_3$ have the hexagonal structure at some temperature. This was checked by preparing pure $RbMgF_3$ by several different methods and investigating its structure after heating at various temperatures. These results showed that, when prepared by the solid state reaction of pure RbF and MgF_2 below 500°C, a two-phase mixture consisting of a pseudo-cubic perovskite and a hexagonal phase is initially formed, and as the temperature or the reaction time is increased the cubic phase is slowly converted to hexagonal. Under no conditions could a pure cubic phase be formed by solid state reaction of the component fluorides. However, when $RbMgF_3$ was precipitated at room temperature from methanol solutions of the RbF and $MgBr_2$ [13], digested at 65°C, and then dried at 180°C, a rather poorly crystallized cubic phase ($a_0 = 4{\cdot}006$ Å), completely free of hexagonal, was formed. This did not convert to hexagonal at 400°C after 4 hr heating, but was completely converted at 400°C after 100 hr. Thus, it appears the hexagonal $BaTiO_3$ phase is the stable one for $RbMgF_3$ at high temperatures. Because of the sluggishness of the transition from cubic to hexagonal, no definite transition temperature was observed by differential thermal analysis. Since both the cubic and hexagonal phases are observed to coexist over a wide temperature range, it is concluded that cubic $RbMgF_3$ is metastable in the intermediate temperature range, i.e. 200°–600°C. However, further work on the kinetics of this transformation, plus a phase study of the RbF–MgF_2 system, are necessary to understand detailed relationships between the two phases.

$RbMgF_3$–$RbCoF_3$ *System*

A phase diagram for the $RbMgF_3$–$RbCoF_3$ system is shown in Fig. 1. Although some uncertainties still exist, as indicated by the dashed portion, this represents an effort to draw an equilibrium diagram which best fits both the quenching and the DTA data. The nonreproducibility of certain data is an obvious result of failure to achieve equilibrium, especially at temperatures below 500°C, and at higher temperatures in the compositional range 10–30 mol. % $RbCoF_3$.

Several rather unusual features of this diagram are evident. First, the flat and extremely narrow two-phase region separating the solid and liquid regions. $RbMgF_3$ and $RbCoF_3$ with melting points of 868° ± 5 and 882° ± 5 respectively, have their eutectic at 866° ± 5°C at about 70% $RbCoF_3$. The slight maximum (876°C) on the liquidus (solidus) curve at about 45% $RbCoF_3$ is associated with the melting of the hexagonal solid solution. There is experimental evidence, mainly from the DTA results, to indicate that the liquidus and solidus curves were not separated by any more than about 2°–3°C, which is the experimental error in determining the melting temperatures from the DTA curves. This so-called 'nonexistent' two-phase region has previously been observed in other halide systems [14, 15].

The hexagonal phase region is shown to

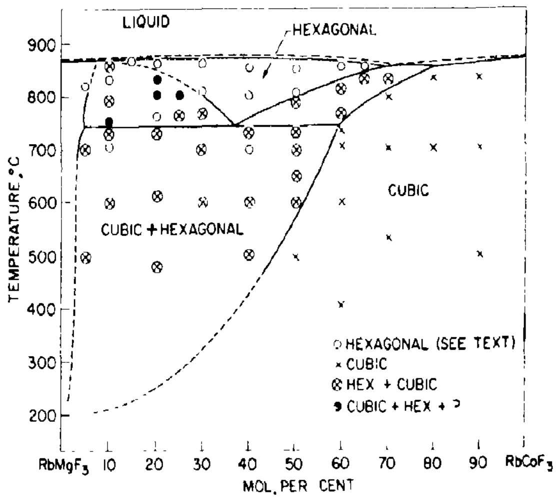

Fig. 1. Phase diagram for the $RbMgF_3$–$RbCoF_3$ system

extend to about 68% $RbCoF_3$ and is stable only at high temperatures, i.e. greater than about 750°C. An exact characterization of the phase in the area enclosed by the dashed 'dome' between about 5 and 25% $RbCoF_3$ was not undertaken because of nonreproducibility. Also, the question whether this 'multiphase' region intersects the solidus curve at about 10–15% Co^{2+} has not been firmly answered. If there is no intersection, then just one continuous solid section region, extending from pure $RbMgF_3$ to about 68% $RbCoF_3$, will exist. On the other hand, two distinct hexagonal phases would be present if the 'dome' does intersect the solidus. The fact that hexagonal single crystals of the composition in question, i.e. 10–20% $RbCoF_3$, have been grown from the melt is evidence for a continuous solid solution region. However, we were unable to prepare single phase polycrystalline hexagonal materials of the same compositions by solid state reactions at temperatures just a few degrees below the solidus. This may suggest that the presence of a liquid phase is essential for the equilibrium formation of the hexagonal phase in this region. The lattice parameters of the hexagonal phase as a function of cobalt concentration are shown in Fig. 2 and a rather linear increase with no major discontinuities is observed.

The phase transition in pure $RbMgF_3$, shown in Fig. 1 at about 300°, indicates its polymorphism and, because of its sluggishness, should not be associated with a true equilibrium transition temperature. As expected, there is extensive solid solution of the cubic phase, particularly for the high $RbCoF_3$ concentrations.

Magnetic properties

The magnetic data for the hexagonal phase with high Co^{2+} concentrations are shown in Figs. 3 and 4. Compositions containing in excess of about 35% $RbCoF_3$ are ferrimagnets as evidenced by the typical M–H curves taken on single crystals. A curve for an $x = 0{\cdot}65$ composition is shown in Fig. 4. It is seen that the easy axis of magnetization is parallel to the *c* axis of the crystal. This is consistent with previous work [4] where Co^{2+} substitutions in this hexagonal structure yielded positive anisotropy constants K_1. The saturation moments for various compositions are shown in the lower portion of Fig. 3 and the expected linear increase with Co^{2+} is evident. Saturation moments as high as 22 e.m.u./g have been measured on a $RbMg_{0{\cdot}32}Co_{0{\cdot}68}F_3$

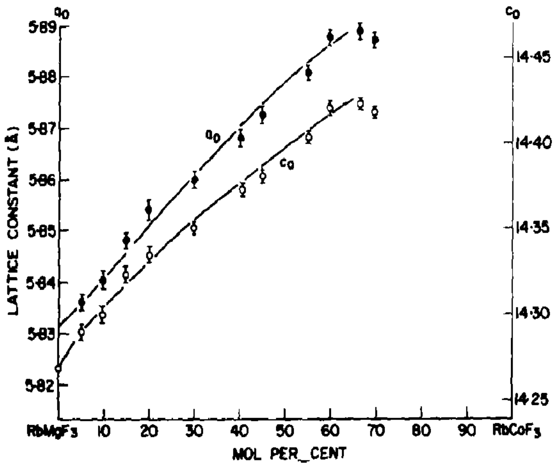

Fig. 2. Lattice parameter vs. composition for the hexagonal solid solutions in the $RbMgF_3$–$RbCoF_3$ system.

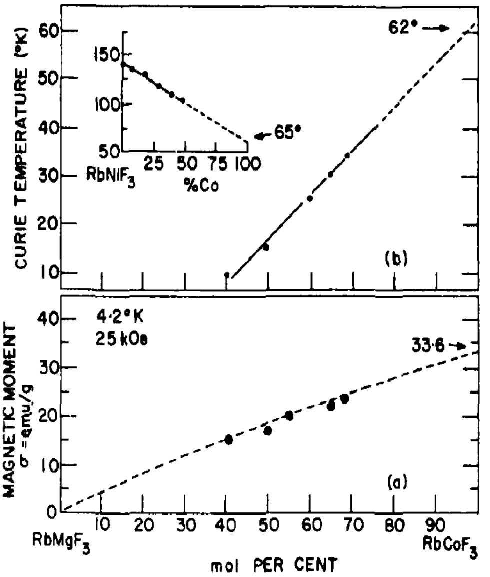

Fig. 3. (a) Magnetic moment vs. composition and (b) Curie temperature vs. composition for hexagonal solid solutions

composition, the limit of the hexagonal solid solution range.

The dashed curve in Fig. 3a represents the calculated moments based on the following three assumptions: (1) there is a random distribution of the Mg^{2+} and Co^{2+} ions on both the 2*a* and 4*f* sites, it being understood that there are twice as many 4*f* as 2*a* sites available, (2) one-third of the Co^{2+} moments (on the 2*a* sites) are aligned antiparallel to the other two-thirds (on the 4*f* sites), and (3) the moment of the Co^{2+} in the ordered state is $3{\cdot}6\,\mu_B$/atom. Obviously a magnetic structure determination by neutrons would be necessary to completely verify these assumptions, but a good case can be made to justify them from existing data. First, with respect to assumption [1], from ionic size and other crystal chemical considerations, Co^{2+} and Mg^{2+} are quite similar and would be expected to have no great differences in site preferences. Also, previous substitution studies in $RbNiF_3$ [6] showed that for higher concentration ($> \sim 25$ per cent) both Mg^{2+} and Co^{2+} replace Ni^{2+} rather randomly, further indicating an equal preference for both sites. Finally, there is a regular increase in the lattice parameter with increased Co^{2+} concentration and no evidence of a discontinuity which might be observable should atomic

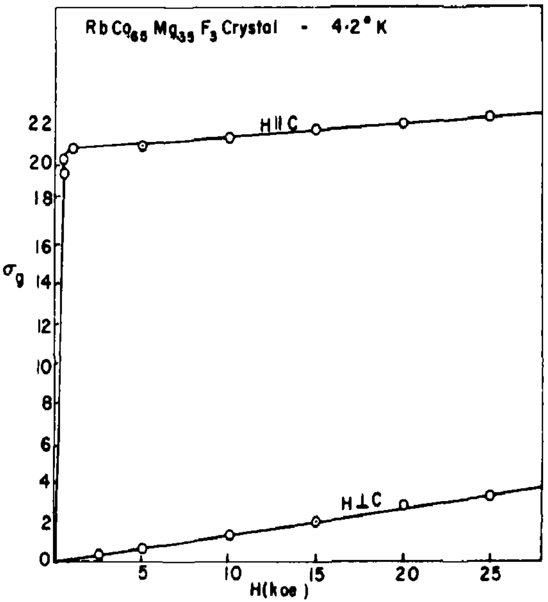

Fig. 4. Magnetization vs. applied field for a $RbCo_{0.65}Mg_{0.35}F_3$ single crystal.

ordering occur. Assumption (2), i.e. that the Co^{2+} spins are aligned in a $\frac{1}{3}$–$\frac{2}{3}$ antiparallel arrangement, is based only on the fact that pure $RbNiF_3$ has this arrangement and, as the Ni^{2+} is replaced by Co^{2+} in single crystals, a moment increase consistent with the higher moment of the Co^{2+} ion is observed. Of course this implies that the ordered moment of Co^{2+} is known and indeed higher than that of Ni^{2+} (assumption (3)). One has difficulty in determining the exact moment of Co^{2+} from the high temperature paramagnetic susceptibility because of uncertainties in the population of the energy levels comparable to kT. EPR measurements on dilute cobalt in $RbMgF_3$ at low temperatures were used to determine an average g value of 4·4. From magnetic susceptibility, also on dilute samples, in the temperature range 1·3°–4·2°K where Curie–Weiss behavior was observed, μ_{eff} was determined to be $4\mu_B$. Providing $J = \frac{1}{2}$, this value is consistent with a $g = 4{\cdot}6$ (comparable to the EPR result). For higher concentrations, i.e. $x = 0{\cdot}13$ Co^{2+}, $\mu_{eff.}$ decreases to 3·6. This is apparently caused by exchange field induced mixing between $J = \frac{1}{2}$ and $J = \frac{3}{2}$. At still higher concentrations, $x > 0{\cdot}4$ Co^{2+} we use the value $3{\cdot}6\,\mu_B/Co^{2+}$ ($J = \frac{3}{2}$, $g = 2{\cdot}4$), which is in good agreement with the moments observed for Co^{2+} in similar matrices, i.e. $KCoF_3$ [16], and $CoFe_2O_4$ [17].

A final argument in favor of the validity of the three assumptions is that they are, in total, the most plausible essential conditions that explain the experimental results. In other words, they are necessary to select the simplest model to explain the observed magnetic properties in the $RbMg_{1-x}Co_xF_3$ system. Obviously, other models implying more complex spin arrangements, site preferences, quenched moments, etc., can be proposed that also fit the experimental data, but we feel that such models, in addition to being more complex than necessary, would also be no more plausible.

The above model would yield a value of about 34 e.m.u./g for the magnetization of pure $RbCoF_3$ if it were possible to prepare it with the hexagonal structure. The upper part of Fig. 3 shows the Curie temperature behavior of these materials. A linear increase is observed with the highest value being at 36°K for a $RbCo_{0{\cdot}68}Mg_{0{\cdot}32}F_3$ composition. The extrapolated Curie temperature for 'hexagonal $RbCoF_3$' is about 62°K, which is in good agreement with the extrapolated value obtained (65°K) from the $RbNi_{1-x}Co_xF_3$ system (shown in inset). Thus, from the moment and Curie temperature data we speculate that 'hexagonal $RbCoF_3$', would be a colinear $\frac{1}{3}$–$\frac{2}{3}$ ferrimagnet with an expected moment of about 33–35 e.m.u./g and a Curie temperature of 62°–64°K. These data further indicate that the magnitudes of the exchange interactions of the Co^{2+} in this structure are about half of those for Ni^{2+}, but of the same sign.

In a previous paper on $RbNiF_3$ [6] we analyzed the high temperature susceptibility using the Néel theory to obtain the magnitude of the exchange interactions. A similar analysis was less successful in this system ($RbMg_{1-x}Co_xF_3$) because the splitting of the unquenched orbital contribution comparable to kT, which at high temperatures results in wide departures from Curie's Law. A more detailed study of the temperature dependence (of the orbital contributions) is required before we can give meaningful values for the three principal exchange interactions (AA, AB and BB). Indications are that the AA and AB are negative while the BB is positive. Thus the 90° Co^{2+}–F–Co^{2+} interaction is ferromagnetic while the 180° Co^{2+}–F–Co^{2+} is antiferromagnetic. The direct Co^{2+}–Co^{2+} interaction, through the common face of the shared octahedra, is apparently weak and ferromagnetic.

Anisotropy

The crystalline anisotropies of four compositions in the $RbMg_{1-x}Co_xF_3$ system were obtained from magnetization measurements on single crystals. For $x = 0{\cdot}41, 0{\cdot}55, 0{\cdot}60,$

and 0·65, the c-axis is the easy direction of magnetization and is also the spin direction of the Co^{2+} ion.

In the hard direction, perpendicular to the c-axis, the anisotropy can be determined from the relation

$$\frac{H}{M} = \frac{4K_2}{M_s^4}M^2 + \frac{2K_1}{M_s^2}$$

where M_s is the saturation magnetization at the temperature of measurement. We find, however, the dependence of M on H is linear in fields up to 25 kOe, the maximum used, and consequently the coefficient of M^2 which gives K_2 cannot be determined. K_1 is simply given as $\frac{1}{2}\frac{H}{M}M_s^2$.

An example of the measurement from which K_1 is obtained is shown in the $H \perp$ to C curve in Fig. 4 and values of K_1 are listed in the following table.

$RbMg_{1-x}Co_xF_3$

x	y	K_1(ergs/cm³)
0·41		$2{\cdot}2 \times 10^6$
0·55		4·0
0·60		4·9
0·65		8·9
1·00		≥13·5
	*1·00	≥12 6

*From [6] based on $RbNi_{1-y}Co_yF_3$.

The values for 'hexagonal' $RbCoF_3$, ($x = 1$ and $y = 1$) are linear extrapolations from the highest cobalt concentrations that were available. Such a procedure is essentially based on the one-ion model, where, given the contributions to the anisotropy of each individual ion, the anisotropy constants for the crystal are found simply as the sum over the ions contained in the crystal. In using the $RbNi_{1-Y}Co_YF_3$ data it was necessary to subtract out the contribution to K_1 and K_2 from the Ni^{2+} as obtained from pure $RbNiF_3$. It is seen that there is good agreement in the extrapolated values for $x = 1$ and $y = 1$ for the two systems. However, the values of K_1 do not plot linearly with either x or y and it is possible that the values for $x = 1$ or $y = 1$ can be considerably higher than as given in the table. Details of the anisotropy in these hexagonal systems will be discussed in a subsequent paper.

Optical properties

The optical absorption in the 4000–20,000 cm^{-1} region for samples with various Co^{2+} concentrations has been measured at 298°, 77° and 10°K. A typical spectrum at $T = 298°$ and 10°K is shown in Fig. 5. Only the three strongest transitions, i.e. $^4T_1 \rightarrow {}^4T_2, {}^4A_2, {}^4T_1$, are observed at room temperature and these are very similar in oscillator strength

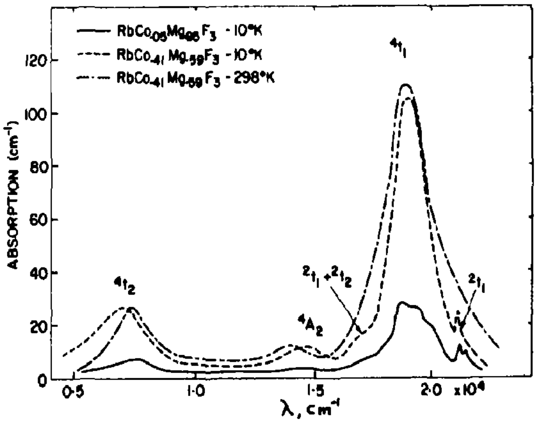

Fig. 5. Optical absorption curves for two compositions in the system $RbMg_{1-x}Co_xF_3$.

and position to those previously reported for cubic $RbCoF_3$ [19]. The spectrum taken at 10°K is somewhat sharper and the $^4T_1 \rightarrow {}^2T_1+{}^2T_2$ and the $^4T_1 \rightarrow {}^2T_1$ transitions are resolved. These have also been observed in pure $RbCoF_3$ at 77° by Pisarev and Prokhorova [20] who showed by studying Na, K, and Rb cobalt trifluorides that a slight shift of the Co^{2+} levels to high energy takes place with decreasing Co–F bond distance. Our results are consistent with this since at low temperatures the crystal field splitting is expected to increase as a result of the smaller cell. Further, in Table 1 it is seen that a small systematic decrease of the transition maxima in the absorption spectra occurs as the Co^{2+} concentration is increased in the hexagonal structure. This can also be explained on the basis of larger Co–F distances since the cell size increases as the cobalt concentration increases (Fig. 2). Also shown in Table 1 are Pizarev's and Prokhorova's [20] data for cubic $RbCoF_3$ and $KCoF_3$ where the Co–F distances are 2·06 and 2·03 Å, respectively. The fact that for all concentrations, the transitions of the Co^{2+} ion in the hexagonal structure fall between those of $RbCoF_3$ and $KCoF_3$ indicates that the average Co–F distances in the hexagonal structures should be close to 2·04–2·05 Å. This is slightly inconsistent with the distances calculated from the cell dimensions. These were slightly larger and varied from 2·05–2·08 Å. However, because of distortions within the octahedra, particularly in the case of the hexagonal material, a complete structure analysis is necessary to obtain the exact distances. In the case of $CsMnF_3$, which also has the hexagonal $BaTiO_3$ structure, a structure determination by Zalkin *et al.* [21] showed that there is surprisingly little variation in the Mn–F distances even through the Mn^{2+} occupies two nonequivalent sites, i.e. $2a$ and $4f$. In view of this, it is probable that the Co–F distances of the CoF_6 octahedra are relatively constant regardless of whether the octahedra share faces as they do in the hexagonal structure, or just corners as is the case in the cubic perovskites $RbCoF_3$ and $KCoF_3$. Since the strength of the crystalline field acting on the Co^{2+} ion by the 6 fluorides is not appreciably different in the cubic and hexagonal structures (other than the effect caused by the Co–F distance variations) it may be assumed that the local symmetry of the Co^{2+} ion is not too different in the two structures, i.e. probably close to O_h.

The magnitude of the crystal field parameter (Dq) is shown in Table 1 and also reflects the uniform shift to higher crystalline fields with decreasing Co–F bond lengths. The Dq values were obtained from the near infrared $^4T_1 \rightarrow {}^4T_2$ transition, which was previously shown [19, 22] to have an energy separation of roughly 8 Dq in other materials where Co^{2+} is in a similar environment, i.e. octahedrally coordinated by 6 fluorides.

Table 1. *Positions of maxima for transitions and* Dq *values for a series of hexagonal compositions*

Compound	$^4T_1 \rightarrow {}^4T_2$ cm^{-1}	$^4T_1 \rightarrow {}^4A_2$ cm^{-1}	$^4T_1 \rightarrow {}^4T_1(P)$ cm^{-1}	Dq cm^{-1}
$RbCoF_3{}^*{}_{(cubic)}$	6750	13,460	18,780	844
$RbCo_{0\cdot65}Mg_{0\cdot35}F_3$	6950	13,950	18,800	870
$RbCo_{0\cdot41}Mg_{0\cdot59}F_3$	6960	14,100	18,850	872
$RbCo_{0\cdot30}Mg_{0\cdot70}F_3$	7010	14,250	18,870	878
$RbCo_{0\cdot05}Mg_{0\cdot95}F_3$	7040	14,250	18,900	880
$KCoF_3{}^\dagger{}_{(cubic)}$	7230	14,500	18,970	904

*Data from [18].

†Data from [23].

The well-known absorption band around

18,850 cm^{-1} corresponding to the $^4T_1(F) \rightarrow {^4T_1}$ (P) transition was used to determine the extent of the spin-orbit interaction. For rather dilute samples, such as $RbCo_{0\cdot 02}Mg_{0\cdot 98}F_3$ and $RbCo_{0\cdot 05}Mg_{0\cdot 95}F_3$, a definite splitting of the $^4T_1$ band is observed at 77° and 10°K (Fig. 5). But at room temperatures, or in samples with high cobalt concentrations, we could not detect any splitting. A total splitting, 6λ, (λ = spin-orbit interaction constant) of -1150 cm^{-1} was obtained and is consistent with previously reported values for compounds containing CoF_6 octahedra [23, 24]. It is unlikely this will change significantly as the Co^{2+} concentration is increased because at 10°K, the half-width of the $^4T_1$ band for a concentrated sample ($RbCo_{0\cdot 65}Mg_{0\cdot 35}F_3$) was only about 200–300 cm^{-1} greater than for the diluted ones. Should this increased broadening be entirely the result of spin-orbit effects, a 6λ value of -1300–1350 cm^{-1} is obtained. However, since this concentrated sample is magnetically ordered at this temperature, it is possible the increased width is at least partly due to the increase in the noncubicity of the crystal field.

The sharp $^2T_1$ band at about 21,000 cm^{-1} splits to a well resolved doublet at low temperatures, presumably due to spin-orbit effects. The possibility that this is not splitting and only single $^2T_1$ absorption bands from each of the two sites (2*a* and 4*f*) also exists. Because of the usual difficulties of resolving the spin-orbit splitting of solid complexes by optical absorption, and the fact that it is relatively weak (compared with the $^4T_1$), it is not surprising that no splitting of the $^4T_2$ band was observed.

Acknowledgements—The authors acknowledge the most helpful assistance of R. A. Figat, J. W Mitchell, H. Lilienthal and R. Bush for their help with the sample preparation and the magnetic and optical measurements. We are also grateful to Dr's. J. Swalen and R. Title for the EPR measurements and to Dr. J. Slonczewski for many helpful discussions.

REFERENCES

1. RUDORFF W., KANDLER J. and BABEL D., *Z. anorg. allg. Chem.* **317**, 261 (1962).
2. SMOLENSKII G. A., YUDIN V. M., SYRNIKOV P. P. and SHERMAN A. B., *Zh. eksp. teor. Fiz.* **3**, 416 (1966); *Soviet Phys. solid St.* **8**, 2368 (1967).
3. SHAFER M. W., McGUIRE T. R., ARGYLE B. E. and FAN G., *Appl. Phys. Lett.* **10**, 202 (1967).
4. SUITS J. C., McGUIRE T. R. and SHAFER M. W., *Appl. Phys. Lett.* **12**, 406 (1968).
5. BOKY L. P., SYRNIKOV P. P., YUDIN V. M. and SMOLENSKII G. A., *Solid State Commun.* **4**, 927 (1967).
6. McGUIRE T. R. and SHAFER M. W., *J appl. Phys.* **39**, 1130 (1968).
7. SHAFER M. W. and McGUIRE T. R., *133rd Meeting Electrochemical Society*, Extended abstracts. Boston (1968).
8. TESTARDI L. R, LEVINSTEIN H. J. and GUGGENHEIM H. J., *Phys. Rev. Lett.* **19**, 503 (1967).
9. SHAFER M. W. and McGUIRE T. R., *Phys. Rev. Lett.* **27A**, 676 (1968).
10. GINSBERG A. P., MARTIN R L. and SHERWOOD R. C., *Chem. Comm* **18**, 856 (1967)
11. WANG F. F. and KESTIGIAN M., *Bull Am phys. Soc.* **10**, 352 (1965).
12. LUDEKERS W. L. W. and WELCH A. J. E., *Acta crystallogr* **5**, 841 (1952).
13. CROKET D. S. and HAENDLER H. M., *J. Am. chem. Soc.* **82**, 4158 (1960).
14. TOMA R., WEAVER C., FRIEDMAN H., INSLEY H. and GRIMES R, ORNL Rep. No. 2458, p. 97 (1959).
15. SACKMAN H., SCHAAF H. and ARNOLD H., *Z. anorg. allg. Chem.* **294**, 127 (1958).
16. SCATTURIN V., CORLISS L., ELLIOTT N. and HASTINGS J. M., *Acta crystallogr* **14**, 19 (1961)
17. WICKHAM D., WHIPPLE E. and LARSON E *J. inorg. nucl. Chem.* **14**, 217 (1960)
18. NESTEROVA N. N., SINII I. G., PISAREV R. V. and SYRNIKOV P. P., *Fiz Tverd. Tela* **9**, 21 (1967); *Soviet Phys. solid St.* **9**, 15 (1967)
19. PIZAREV R. V. and PROKHOROVA S. D., *Fiz Tverd Tela* **9**, 1879 (1967): *Soviet Phys solid St.* **9**, 1482 (1968)
20. ZALKIN A., LEE K. and TEMPLETON D., *J. chem. Phys.* **37**, 697 (1962).
21. BALLHAUSEN C. J., *Introduction to Ligand Field Theory*. McGraw Hill, New York (1962).
22. LOW W., *Phys. Rev* **101**, 1827 (1956).
23. FERGUSON J. F., WOOD D. L. and KNOX K., *J. chem. Phys.* **39**, 881 (1963).

J. Phys. Chem. Solids Pergamon Press 1969. Vol. 30, pp. 1999-2005. Printed in Great Britain.

CORRELATION BETWEEN BOND ENERGIES AND FORBIDDEN GAPS OF INORGANIC BINARY COMPOUNDS

ASHOK K. VIJH
Sprague Electric Company North Adams, Mass. 01247, U S.A.

(*Received* 16 *January* 1969; *in revised form* 25 *February* 1969)

Abstract – It has been shown that Manca's empirical relation between bond energies and band gaps is approximately valid for a wide variety of binary semiconductors and insulators. This relationship has also been theoretically derived for the case of ionic compounds, e.g. alkali halides. The procedure of derivation involves application of the Madelung approach and the Born–Haber cycle. The possible theoretical significance of our previous empirical correlation between band gaps and heats of formation per equivalent has also been indicated.

INTRODUCTION

In the chemical approaches to the approximate prediction of band gaps of semiconductors, correlations have been proposed between band gaps and various other quantities, e.g. single bond energies[1], heats of formation per mole[2], heats of formation per equivalent[3], atomic numbers[4], electronegativities[5] etc. Some of these approaches, especially those seeking relationships between binding and band gaps have also been presented in the form of reviews, either detailed[6] or synoptic[1].

In the present paper, only one aspect of these approaches will, however, be examined. Following the original suggestion of Manca [1] that single bond energies of certain *restricted* classes of compounds are related to their band gaps, an attempt has been made here to explore a similar relationship for a large variety of semiconductors and insulators. An analysis has also been attempted of the possible theoretical origin of the empirical relationship of Manca[1], according to which:

$$E_g = a(E_S - b) \qquad (1)$$

where E_g is the band gap; E_S is the single bond energy; a and b are constants with the value of a approximately equal to 2 for the compounds investigated by Manca.

DEFINITIONS AND RELATED CONSIDERATIONS

(*A*) *Bond energies*

For the calculation of bond energies, two procedures are available and are as follows:

(1) *Pauling's Method.* Here, bond energy of an isolated diatomic molecule formed between uni-univalent atoms, e.g. NaCl, is estimated by the empirical equation:

$$D(\text{Na–Cl}) = \tfrac{1}{2}\{D(\text{Na–Na}) + D(\text{Cl–Cl})\} + 23(X_{\text{Na}} - X_{\text{Cl}})^2 \qquad (2)$$

where D(Na–Cl) is the required bond energy between Na and Cl in NaCl; D(Na–Na) is the bond energy between two Na atoms; D(Cl–Cl) is the bond energy between two chlorine atoms; X_{Na} and X_{Cl} are the electronegativities of Na and Cl respectively on the Pauling Scale. The procedure of Pauling gives fairly accurate estimates of bond energy between two uni-univalent atoms held together by a single bond, e.g. NaCl. However, when more than one bond is involved, e.g. in NH_3, Pauling's procedure would not give a good estimate of the average N–H bond energy, but, instead would only yield a value for the last dissociation energy, i.e. a N–H bond when one H is present on N. When applied to cases involving either divalent or multivalent atoms, e.g. AlN, ZnS, Al_2O_3 etc., Pauling's procedure yields the estimate of energy of the last bond in the molecule after all other bonds have been removed. Such a quantity, however, would not be very representative of the general magnitude of binding in a complex molecule, which must be represented by an average bond energy. The average bond energy thus obtained, it is believed, is more relevant to the discussion of relation between binding and band gaps in inorganic compounds. This bond energy is calculated from the appropriate thermochemical data.

(2) *Thermochemical prodecure.* Here the bond energy of, e.g. NaCl would be obtained from the equation:

$$D(\text{Na–Cl}) = \Delta H_S + \tfrac{1}{2}\Delta H_{\text{diss}} + \Delta H_f^0 \quad (3)$$

where D(Na–Cl) is the required bond energy; ΔH_S is the heat of sublimation of Na metal per *mole*; ΔH_{diss} is the heat of dissociation of Cl_2 molecule into Cl atoms, again, per mole; ΔH_f^0 is the heat of formation of NaCl in its standard state, again per mole. The quantity given by equation (3) (i.e. bond energy) is nothing but heat of atomization of NaCl.

For the case of NaCl, only one shared electron pair is involved in the bonding. For the case of complex compounds, e.g. Ta_2O_5, more than one bond (i.e. shared electron pair) is involved and hence a suitable normalizing factor must be used to obtain from equation (3), the bond energy per *bond* and not the total energy for all the bonds in Ta_2O_5. This may be carried out by calculating first from equation (3) the heat of atomization per mole and then normalizing it with respect to the participating valences to obtain heat of atomization per equivalent, which is, of course, the bond energy. For example, heat of atomization per equivalent (i.e. the bond energy) for Ta_2O_5 is 1/10 of the heat of atomization per mole as calculated from equation (3). Further details on these and related matters are available elsewhere[7,8].

The bond energies (i.e. heat of atomization per equivalent) thus obtained, after some second order corrections (e.g. spin correlation stabilization energies, coordinate valence) as discussed by Howald[8] are the actual values of the average bond energies as obtained from the experimental thermochemical data. The bond energies used by us (Fig. 1) have been calculated by this procedure. The accuracy of these bond energies is limited only by the accuracy of the thermodynamic data used in computing them. These data have been obtained from reliable compilations [8,9]. Second order corrections to the bond energies have been included only for spin correlation stabilization energies[8]. The possible presence of coordinate valence has been neglected, however, since unambiguous estimates of the extent of participation of coordinate valence in compounds are not always easily obtained as discussed by Howald[8]. Since the main arguments to be presented in this paper are claimed to be strictly valid for alkali halides only, this neglect of coordinate valence in the calculation of bond energies is not serious, because alkali halides do not involve any coordinate bonds.

(*B*) *Band gaps*

Some problems associated with the selection of appropriate band gap values in Fig. 1 merit discussion. As mentioned earlier, since the arguments to be presented in the theoretical part of this paper are claimed to be valid for alkali halides only, the problems involved in the selection of band gaps will be illustrated mainly with reference to the alkali halides. All the band gaps for alkali halides except for NaF have been obtained from [10]. The band gap value for NaF has been taken from [11]. These are optical band gaps. Further, these band gaps refer to k space at $k = 0$. The values of band gaps of other compounds have been obtained from

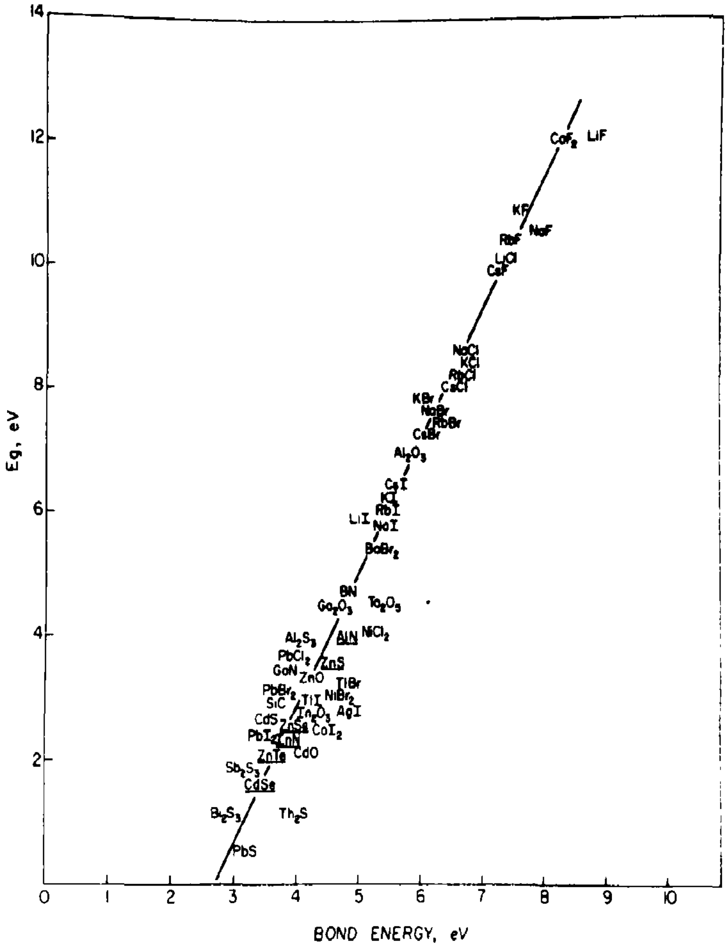

Fig. 1. E_g vs. bond energy for 52 binary semiconductors and insulators; bond energies for CdSe, ZnTe, InN, ZnSe, ZnS and AlN approximate and were estimated by Pauling's equation (*cf.* Manca in [11]) since reliable thermodynamic data are not available for the calculation of bond energies. For the origin and assessment of the data used in this figure, see text.

references[2, 10, 11] and are probably of varying degrees of accuracy. Since the relation represented in Fig. 1 is, as intrinsically all such *general* relations are, rather approximate, a slight uncertainty in the band gaps, E_g, quoted in Fig. 1 would not change the general relationship presented in Fig. 1. Precise definition and determination of band gaps involves some real difficulties. For example, in large band gap semiconductors like alkali halides, experimental values quoted are strongly influenced by Coulomb effects, even though there is no great difference between the direct and indirect gap since the bands are very narrow. This arises because the optical absorption is determined rather by the exciton structure in front of the energy gap than by the energy gap itself [12]. Small band gap semiconductors involve a different problem in that there are significant differences between direct and indirect gaps since the bands are rather wide[12]. The significance of values of band gaps quoted in Fig. 1 must be accepted only in relation to difficulties mentioned in the foregoing discussion. It is believed, however, that the aforementioned difficulties in the precise definition and determination of band gaps, would not render values of band gaps in Fig. 1 so uncertain as to make the relationship presented invalid.

RELATIONSHIP BETWEEN BANDGAPS AND BOND ENERGIES

In Fig. 1, bond energies calculated by the thermochemical procedure (see, however, caption to Fig. 1) have been plotted against the band gaps for a large number of inorganic binary semiconductors and insulators.

It may be seen from Fig. 1 that Manca's relation (i.e. equation (1)) is approximately obeyed by a wide variety of semiconductors and insulators. It may be noted that the relationship shown in Fig. 1 is rather a general one and includes compounds which cover the following spectrum of behavior:

(i) A wide range of band gap values, i.e. 0·5–12 eV.
(ii) Semiconductors and insulators covering a wide range of ionicity, i.e. from 9 per cent ionicity (Sb_2S_3) to 93 per cent ionicity (CsF) on the basis of Pauling's electronegativity criteria. Strictly, Pauling's criteria are not applicable to solids; however, they constitute a convenient scale on which to express, albeit crudely, the range of ionicity covered here.
(iii) A significant number of polyatomic (i.e. greater than even three atoms) binary compounds formed between *polyvalent* ions, it seems, also obey the relationship shown in Fig. 1; e.g. Al_2O_3, Ta_2O_5, Ga_2O_3, In_2O_3, Sb_2S_3, Bi_2S_3, Al_2S_3.
(iv) Compounds belonging to most of the important crystal structures have been included in Fig. 1; these structures include NaCl, CsCl, wurzite, zinc blende, corundum, cuprite, and fluorite.

Hence it may be concluded (Fig. 1) that the empirical relation first proposed by Manca for certain restricted classes of semiconductors may actually be applied in a rather general way. The general application of equation (1) would not be expected to be anything but approximate since several classes of semiconductors, otherwise unrelated, have been included in Fig. 1. Hence, it is noted that the scatter in Fig. 1 is not entirely unexpected.

Previously[1], no theoretical justification has been presented for equation (1) (or Fig. 1). Here, it will be shown that for the case of compounds which are predominantly ionic, e.g. alkali halides, the relationship may actually be derived theoretically.

Theoretical derivation of the relationship between band gaps and the bond energies for ionic compounds, e.g. alkali halides

According to Mark[13], the band gap energy, E_g, of e.g. NaCl is given by (13):

$$E_g = 2M - (I_m - A_x) \qquad (4)$$

where M is the Madelung energy, I_m is the ionization potential of Na; A_x is the electron affinity of Cl. From equation (4),

$$E_g = 2M - I_m + A_x \qquad (5)$$

or

$$E_g = 2(U - R) - I_m + A_x \qquad (6)$$

where U is the experimental (thermochemical) lattice energy and R is an energy term which includes repulsive and London components of theoretical lattice energy (14) so that,

$$M = (U - R) \qquad (7)$$

is quite valid.

From the first law of thermodynamics, it may be readily shown by means of a Born–Haber cycle that[14]:

$$\Delta H_f^0 = \Delta H_s + I_m + \tfrac{1}{2}\Delta H_D + A_x + U \qquad (8)$$

where, ΔH_f^0 is the heat of formation, e.g. of NaCl; ΔH_s is the heat of sublimation of Na; I_m is the ionization potential of Na; ΔH_D is the energy of dissociation of Cl_2 (g) into atoms; A_x is the electron affinity of Cl; U is the lattice energy of NaCl.

All the quantities defined above are per *mole* of the corresponding substance.

On obvious rearrangement, equation (8) gives:

$$-U = \Delta H_s + I_m + \tfrac{1}{2}\Delta H_D + A_x - \Delta H_f^0. \quad (9)$$

Here we note that, U, A_x and ΔH_f^0 are exothermic quantities (hence with − sign) and ΔH_s, I_m and ΔH_D are endothermic quantities (hence with + sign) for the case of alkali halides. Making these substitutions for exothermicity and endothermicity in equation (9), we obtain:

$$U = \Delta H_s + I_m + \tfrac{1}{2}\Delta H_D + \Delta H_f^0 - A_x. \quad (10)$$

Substituting equation (10) in equation (6)

$$E_g = 2\Delta H_s + 2I_m + \Delta H_D + 2\Delta H_f^0 - 2A_x - I_m + A_x - 2R \quad (11)$$

or

$$E_g = 2\Delta H_s + I_m + \Delta H_D + 2\Delta H_f^0 - A_x - 2R \quad (12)$$

Here, we make an approximation that I_m is roughly equivalent to A_x in magnitude, and then obtain:

$$E_g = 2\Delta H_s + 2\Delta H_f^0 + \Delta H_D - 2R \quad (13)$$

or

$$E_g = 2(\Delta H_a - R) \quad (14)$$

where ΔH_a is the heat of atomization per *mole*, and, for a diatomic molecule formed between uni-univalent ions (e.g. NaCl) is equal to the heat of atomization per equivalent, which is the same thing as bond energy[7, 8, 15, 16].

For a polyatomic compound formed between either univalent or polyvalent ions, equation (14) has to be appropriately modified. This is because equations (4) and (6) refer to the transfer of *one* valence electron, e.g. from Na to Cl; in order to maintain the validity of equation (11), U in equation (10) must also be taken as per valence electron, i.e. as per equivalent. As a consequence, the ΔH_a term in equation (14) must be changed from ΔH_a/mole to ΔH_a/eq. for the case of polyatomic compound. As mentioned earlier, ΔH_a/eq., is, of course, the bond energy E_s. Hence,

$$E_g = 2(E_s - R) \quad (15)$$

For a given class of related compounds, e.g. alkali halides, R may approximately be treated as a constant. Hence, equation (13) may be written in the form:

$$E_g = 2(E_s - b) \quad (16)$$

where 'b' is a constant. This equation (16) is identical with Manca's equation, i.e. equation (1) in this paper.

The approximation involved in the derivation of equation (13) will now be examined. If I_m is not roughly equivalent to A_x, then R in equation (13) may be transformed into R' where,

$$R' = R + \tfrac{1}{2}I_m - \tfrac{1}{2}A_x. \quad (17)$$

For a given class of structurally related compounds, R' may again be assumed as, *roughly*, a constant. For example, for several alkali halides, R' would assume values close to 2·5 ± 0·5 eV. It is obvious, of course, that equation (17) may be suitably modified for classes of compounds involving positive electron affinities.

Theoretical origin of our previous relationship between E_g and heat of formation per equivalent

It has been previously shown[3] empirically, that for a large variety of inorganic semiconducting compounds,

$$E_g \pm 20\% = 2\Delta H_f^0/\text{eq}. \qquad (18)$$

It is now possible to extend the theoretical analysis to this relation on the basis of arguments developed in the foregoing discussion. Rewriting equation (13) by substituting equation (17) in it, we get,

$$E_g = (2\Delta H_s + \Delta H_D - 2R') + 2\Delta H_f^0. \qquad (19)$$

In a large number of cases it is possible to show that, fortuitously, the quantities in the parentheses roughly cancel each other out. For example, for NaCl, the net value of the quantities in the parenthesis in equation (19) would be *ca.* 0·5 eV. If the values of the quantities in parentheses make only a small contribution to E_g, it follows that:

$$E_g \simeq 2\Delta H_f^0. \qquad (20)$$

Like all quantities in such comparisons, ΔH_f^0 must be 'normalized', i.e. taken as per equivalent[3, 15, 16] which for a diatomic compound formed between uni-univalent ions is, of course, the same thing as per mole.

Hence,

$$E_g \simeq 2\Delta H_f^0/\text{eq}. \qquad (21)$$

It must be emphasized that ΔH_f^0 refers to the formation of a compound from its standard, and not atomic state.

Limitations of the present analysis

Even though the empirical relationship of Manca is found to be approximately valid for a large variety of binary compounds (Fig. 1), the possible theoretical origin of this correlation can be understood for the case of alkali halides only. At the present, theoretical foundations of equation (1), as applied to other classes of compounds, are not at all clear.

For the case of some covalent compounds, e.g. those included in Fig. 1, it is possible that increase in cohesive energy due to homopolar binding approximately cancels out the decrease in lattice energy that may result from partial ionicity[13] of the compound. In such cases, experimental lattice energy values, U, would be very nearly equivalent to the $(M+R)$ values that would have been obtained, had the compound been completely ionic. In fortuitous cases of this type, equations (7) and (16) and the entire analysis presented here would still be valid, despite significant covalent bonding.

In other cases of covalent compounds, the analysis presented here would be invalid in its present form. In principle, however, the present analysis may be extended even to those compounds by modifying equation (16) to give:

$$E_g = 2(E_s - b) \pm \Delta U \qquad (22)$$

where ΔU is the difference between the thermochemical and theoretical lattice energies (14) again taken as per equivalent.

Finally, the present analysis would not be applicable at all to either the elemental semiconductors (e.g. Ge, Si) or the molecular semiconductors, e.g. anthracene.

It must be emphasized once again that it is just fortuitous that several covalent compounds obey the relationship shown in Fig. 1, despite the fact that no correction for covalence has been applied to them.

Acknowledgements—The author would like to thank Drs. R. S. Alwitt and K. Lehovec of these laboratories for some comments. Thanks are also due to Dr. A. Rose of R. C. A., Professor R. Howald of Mantana State University, Professor W. J. Moore of Indiana University and Dr. M. Tosi of Argonne National Laboratory, for personal communications that clarified the author's understanding of various matters discussed in this paper.

REFERENCES

1. MANCA P., *J. Phys. Chem. Solids* **20**, 268 (1961).
2. RUPPEL W., ROSE A. and GERRITSEN H. J., *Helv. Phys. Acta* **30**, 238 (1957); See also, ROSE A., *Concepts in Photoconductivity and Allied Problems*, Final Chapter. Interscience, New York (1963).
3. VIJH A. K., *J. Phys. Chem. Solids* **29**, 2233 (1968).
4. BUBE R. H., *Photoconductivity of Solids*. Wiley, New York (1960).

5. HANNAY N. B., *Solid State Chemistry*. Prentice-Hall, New York (1967).
6. GATOS H. and ROSENBERG A., *The Physics and Chemistry of Ceramics* (Edited by C. Klingsberg). Gordon and Breach, New York (1963).
7. PAULING L., *The Nature of the Chemical Bond*. Cornell Press, New York (1960).
8. HOWALD R., *J. chem. Educ.* **45**, 163 (1968).
9. ROSSINI R. *et al.*, *Selected Thermodynamic Properties*, N.B.S. 500. U.S. Gov't. Printing Office, Washington, D.C. (1952).
10. *American Institute of Physics Handbook*. McGraw-Hill, New York (1963).
11. LANDERS J. J., In *Semiconductors* (Edited by N. B. Hannay). Reinhold, New York (1959).
12. Anonymous referee of one of our previous papers.
13. MARK P., *J. Phys. Chem. Solids* **29**, 689 (1968).
14. MOORE W. J., *Seven Solid States*. Benjamin, New York (1967).
15. SANDERSON R. T., *Chemical Periodicity*. Reinhold, New York (1960).
16. VIJH A. K., *J. electrochem. Soc.* **115**, 1096 (1968).

J. Phys. Chem. Solids Pergamon Press 1969. Vol. 30, pp. 2007-2009. Printed in Great Britain.

SURFACE BARRIERS ON LAYER SEMICONDUCTORS: GaS, GaSe, GaTe*

STEPHEN KURTIN and C. A. MEAD
California Institute of Technology, Pasadena, Calif. 91109, U S.A.

(*Received* 11 *February* 1969)

Abstract—Surface barriers formed on the gallium-chalcogenide layer semiconductors GaS, GaSe and GaTe are studied by the photoresponse technique. The observed behavior is qualitatively similar to that of non-layer compounds.

INTRODUCTION

RECENT study[1] of metallic surface barriers on the layer compound GaSe revealed that at the crystal surface the Fermi level is partially stabilized by surface states. A linear relationship with a slope, S, of approx. 0·6 was found for the dependence of barrier energy on electronegativity of the metal employed. It is of fundamental importance to an understanding of the relationship between chemical bonding and metal-semiconductor interface properties to determine whether this result is intrinsic to layer compounds, and hence a consequence of their unique spatial atomic configuration. We report here the results of barrier energy measurements on the isostructural layer compounds GaS[2] and GaTe[3]. These measurements indicate that there is *no* Fermi level stabilization in GaS ($S \sim 1{\cdot}0$) and significant Fermi level stabilization in GaTe ($S \sim 0{\cdot}3$). Therefore, the unique spatial atomic configuration of layer compounds plays little or no role in Fermi level stabilization at the semiconductor surface.

SAMPLE PREPARATION

GaTe for this investigation was grown from a stoichiometric mixture of 99·9999 per cent pure Ga and 99·9999 per cent pure Te by the modified Bridgman, gradient-freeze technique. The resulting boule was polycrystalline with several large single crystal regions. Samples were constructed by peeling flakes from one of these single crystal regions. Large area In–Ag solder contacts were affixed to one side of each flake. The flakes were then cleaved, in air, to expose a fresh (0001) surface. Surface barriers were formed by vacuum deposition, through a wire screen mesh, of semitransparent metallic dots. Measurements of capacitance as a function of voltage of such surface barriers fabricated on GaTe indicate that our material is p-type with $p \sim 3\times10^{14}/\text{cm}^3$. Samples of p-type GaS were prepared by similar techniques from bulk material kindly furnished by Strauss of Lincoln Laboratories.

Metals used for surface barrier fabrication were, in all cases, evaporated from directly heated tungsten filaments. Care was taken to allow the evaporation source to thoroughly outgas before allowing metal to deposit on the semiconductor surface.

PHOTORESPONSE MEASUREMENTS

Barrier energies of GaS and GaTe surface barrier structures were measured primarily by the photoresponse technique. Samples were illuminated with a 50 Hz chopped light system and photocurrent detected with a lock-in amplifier. The light source employed was an iodine-quartz lamp in conjunction with a quartz prism monochromator. Intensity calibration was performed with a Santa Barbara Research Center evaporated thermopile.

---

*This work was supported in part by the Office of Naval Research and the Jet Propulsion Laboratory.

The dependence of photocurrent on photon energy was generally found to follow a square law as expected from the simple theory of photoemission from metals.

Typical curves of the square root of photoresponse per incident photon vs. photon energy, for several metals on both GaS and GaTe, appear in Fig. 1. Intercepts on the *hν* axis correspond to the semiconductor-metal barrier energy measured from the semiconductor valence band to the Fermi level of the metal.

From photoresponse data as in Fig. 1 it is possible to plot, for each semiconductor material, barrier energy vs. electronegativity of the different metals. Such plots, including data on GaSe from[1], appear as Fig. 2.

Although the data of Fig. 1 were obtained on air cleaved surfaces, essentially identical

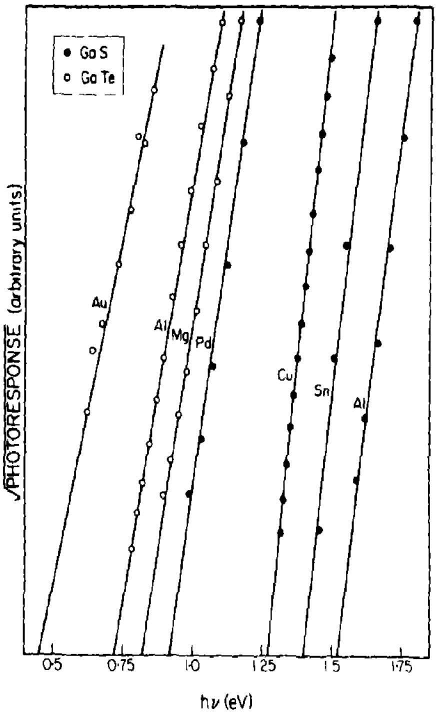

Fig. 1. Typical plots of photoresponse per incident photon vs. photon energy for several metals on both GaS and GaTe.

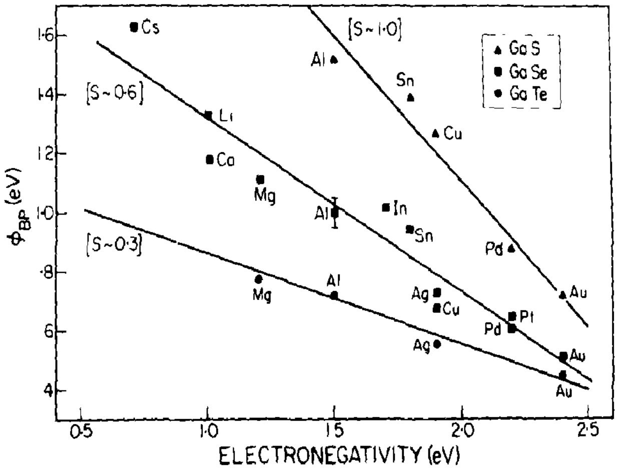

Fig. 2. Barrier energy vs. electronegativity of metal for GaS, GaSe, and GaTe. Values are best averages of several samples. Slope of the reference lines are $S \simeq 1{\cdot}0$ for GaS, $S \simeq 0{\cdot}6$ for GaSe, and $S \simeq 0{\cdot}3$ for GaTe.

results were obtained on vacuum cleaved surfaces for the case of gold barriers on GaSe. The vacuum cleaved data are shown in Fig. 2 of[4]. On many other compound semiconductors, barriers formed from active metals have been found to be less affected by the presence of an adsorbed layer than barriers formed from more noble metals such as gold. Thus we believe the data shown here represent, within the scatter, the properties of the gallium–chalcogenide metal interface.

CONCLUSION

We note that the compounds of the gallium-chalcogenide system display Fermi level stabilization ranging from nonexistant in the case of GaS, to virtually complete in the case of GaTe. As a result, the behavior of GaSe may be regarded as the consequence of a smooth transition from the properties of GaS to those of GaTe, similar to that observed on the CdS-Se system[5]. Since the Fermi level stabilization behavior of GaS and GaTe is similar to that observed for non-layer compounds[6], we believe that Fermi level stabilization, and hence surface state density, is more closely allied to the chemical properties of the constituents of a given compound than to the spatial atomic configuration of the compound.

Acknowledgements—The authors are indebted to A. J. Strauss of Lincoln Laboratories for providing bulk specimens of GaS, and to N. Stevens of the Santa Barbara Research Center for providing an evaporated thermopile.

REFERENCES

1. KURTIN S. and MEAD C. A., *J. Phys. Chem. Solids* **29**, 1865 (1968).
2. AKHUNDOV G A, GOSANOVA N. A. and NIZAMETDINOVA M. A, *Phys. Status Solidi* **15**, K109 (1966).
3. FIELDING P., FISHER G. and MOOSER E., *J. Phys. Chem. Solids* **8**, 434 (1959).
4. LEUNG P C., ANDERMANN G., SPITZER W. and MEAD C. A., *J. Phys. Chem. Solids* **27**, 849 (1966).
5. MEAD C. A., *Appl. Phys. Lett.* **6**, 103 (1968).
6. MEAD C. A., *Solid-St. Electron.* **9**, 1023 (1966).

J. Phys. Chem. Solids Pergamon Press 1969. Vol. 30, pp. 2011-2021. Printed in Great Britain.

ORDRE A COURTE DISTANCE, DEPLACEMENTS LOCAUX DES IONS ET ENERGIE ELECTROSTATIQUE DANS $FeLiO_2$*

M. BRUNEL et F. de BERGEVIN

Laboratoire d'Électrostatique et de Physique du Métal, C N R S , B P. Cedex No. 166,
38 Grenoble-Gare, France

(*Received 2 August 1968; in revised form 10 February 1969*)

Résumé—Nous étudions, par diffusion et diffraction des rayons-X, des échantillons désordonnés de $FeLiO_2$. L'ensemble des paramètres d'ordre à courte distance obtenus indique une similitude entre les structures désordonnée et antiphase Q_{II}, ces deux phases étant différentes de la phase ordonnée Q_I. Ceci nous permet d'expliquer le mécanisme des transformations.

Nous montrons aussi, par étude des réflexions de Bragg et par le fond continu, l'existence de déplacements locaux de tous les ions, et, en particulier, des anions qui se rapprochent des ions Fe^{3+} très chargés.

Même en introduisant l'ordre à courte distance et les déplacements, la différence d'énergie électrostatique entre les phases désordonnée et ordonnée Q_I, calculée en négligeant les déformations des ions, reste de l'ordre de 40 KT_c (T_c = température de transition ≃ 1000°K). Pour expliquer l'existence d'une transition ordre-désordre, il semble que l'on soit obligé d'introduire la polarisation des ions oxygène; nous montrons que cet effet favorise plus la phase désordonnée que la phase ordonnée.

Abstract—We have studied, by diffusion and diffraction of X-rays, disordered samples of $FeLiO_2$. The short range order parameters obtained show similarity between the disordered and antiphase Q_{II} structures, these two phases being different from the ordered phase Q_I. We can explain thus the mechanism of the transformations. We show also, by studying the Bragg reflexions and the background, the existence of local displacements of all the ions, and in particular the anions which come close to the strongly positive Fe^{3+} ions.

Even with the introduction of the short-range order and the displacements, the difference in electrostatic energy between the disordered and the ordered Q_I phases, calculated disregarding the deformation of the ions, is of the order of 40 KT_c (T_c being the transition temperature ≃ 1000°K) To explain the existence of an order-disorder transition, it seems that one must introduce a polarization of the oxygen-ions. We show that this effect favours the disordered phase more than the ordered phase.

INTRODUCTION

LE FERRITE de lithium $FeLiO_2$ existe sous trois formes différentes. Une phase ordonnée Q_I (ou γ)[1] (Fig. 1). Une phase ordonnée Q_{II} (ou β) dont nous avons précédemment déterminé la structure[2]. Un plan (0 0 1) de Q_{II} (Fig. 2) s'obtient à partir d'un plan (0 0 1) de Q_I en intervertissant les atomes Fe^{3+} et Li^+ dans des domaines plans antiphases limités par des droites parallèles à (1 1 0) et de largeur $a\sqrt{2}$, c'est-à-dire les domaines (R S) (T U). L'ordre selon c est toujours Fe–Li–Fe. A cause de la dissymétrie introduite dans ce plan, les plans (0 0 1) immédiatement adjacents peuvent être placés de deux façons différentes (domaines parallèles ou perpendiculaires) entraînant deux structures possibles: quadratique ou monoclinique. Une phase désordonnée α de type NaCl: les ions Fe^{3+} et Li^+ se répartissent au hasard sur les sites d'un réseau cubique faces centrées.

Nous avions déterminé les paramètres d'ordre à courte distance dans le spinelle Fe_5LiO_8[3] et montré que le paramètre d'ordre des premiers voisins conserve dans l'état désordonné la valeur − 1/3 qu'il a dans l'état ordonné. La disposition géométrique des sites octaèdriques des spinelles, occupés par les ions Fe^{3+} et Li^+, permet de désordonner le cristal, c'est-à-dire d'obtenir une entropie non nulle, en conservant l'ordre des premiers voisins [4]; ceci entraîne une variation d'énergie faible à la transition et permet d'expliquer une température de transition expérimentale T_c beaucoup plus faible (de l'ordre de 50 fois) que celle obtenue à partir des variations d'énergie entre état ordonné et état totalement désordonné. Or, dans $FeLiO_2$, l'arrangement cubique faces centrées des ions Fe^{3+} et Li^+ ne permet plus ce type de désordre et pourtant les températures de transition ordre-désordre des deux ferrites de lithium sont peu différentes. C'est pourquoi nous nous sommes intéressés à l'ordre à courte distance dans $FeLiO_2$.

---

*Ce travail fait partie d'une thèse de Doctorat ès Sciences Physiques, qui sera soutenue prochainement par M. Brunel, et enregistrée au Centre de Documentation du C.N.R.S., sous le no. A.O. 2719.

DEPLACEMENTS LOCAUX DES IONS

Dans la structure Q_I quadratique (groupe d'espace D_{4h}^{19}) (Fig. 1), les ions oxygène sont placés en $00z$ avec $z = 1/4$. En réalité, z est différent de 0,25 et Cox *et al.* [5] déterminent un paramètre $z = 0{,}23$, soit un rapprochement de 0,17 Å des distances Fer-oxygène selon c. L'ion Fe^{3+} est ainsi entouré d'un octaèdre régulier d'oxygènes (alors que l'environnement d'un lithium est très déformé), avec des distances fer-oxygène égales à 2,02 Å.

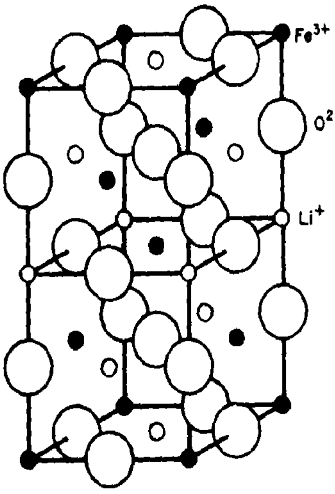

Fig. 1. Structure de la phase Q_I (ou γ).

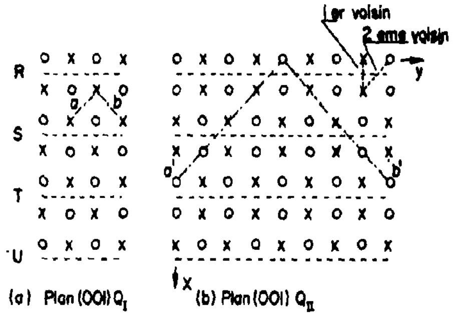

Fig. 2. Construction d'un plan (001) de Q_{II} à partir d'un plan (001) de Q_I. Seuls les cations Fe^{3+} et Li^+ sont représentés.

On peut supposer de même que, dans la structure désordonnée α, les ions oxygène se déplacent de leur position idéale pour se rapprocher des Fe^{3+} très chargés, car la distance moyenne cation-oxygène dans α est de 2,075 Å. Les ions Fe^{3+} étant répartis au hasard sur un site, ce déplacement des anions sera donc non périodique et local.

L'intensité totale de diffraction et diffusion d'un cristal est donnée par:

$$I = \sum_{ij} f_i f_j \exp i\mathbf{k}(\mathbf{r}_i - \mathbf{r}_j)$$

f_i et f_j étant les facteurs de diffusion atomique des atomes i et j placés en $\mathbf{r}_i$ et $\mathbf{r}_j$.

Si $\mathbf{r}_i = \mathbf{R}_i + \delta\mathbf{r}_i$ et $\mathbf{r}_j = \mathbf{R}_j + \delta\mathbf{r}_j$, $\mathbf{R}_i$ et $\mathbf{R}_j$ étant les positions idéales et $\delta\mathbf{r}_i$ et $\delta\mathbf{r}_j$ les déplacements, on a, en supposant $\delta\mathbf{r}_i$ et $\delta\mathbf{r}_j$ petits devant $\mathbf{R}_i$ et $\mathbf{R}_j$:

$$I = \sum_{ij} f_i f_j \exp i\mathbf{k}(\mathbf{R}_i - \mathbf{R}_j)(1 + i\mathbf{k}(\delta\mathbf{r}_i - \delta\mathbf{r}_j) - \tfrac{1}{2}((\mathbf{k}\,.\,\delta\mathbf{r}_i)^2 + (\mathbf{k}\,.\,\delta\mathbf{r}_j)^2 - 2(\mathbf{k}\,.\,\delta\mathbf{r}_i)(\mathbf{k}\,.\,\delta\mathbf{r}_j))).$$

Dans notre cas, une partie des atomes est répartie au hasard sur un site dans un désordre binaire.

Le premier terme introduit les raies de diffraction de Bragg et une diffusion reliée à l'ordre à courte distance, et, pour les suivants:

(a) le terme d'ordre 1 entraîne une diffusion (effet de taille dans les alliages)[7], (b) les termes $(\mathbf{k}.\delta\mathbf{r})^2$ se traduisent, dans les raies de diffraction, par une réduction en exp $-(B_i \sin^2\theta/\lambda^2)$ du facteur de diffusion atomique de l'atome analogue à un effet thermique; soit B_{iS} ce facteur statique. (c) Ces mêmes termes entraînent une diffusion en:

$$\sum_i f_i^2(1-\exp -2(B_i \sin^2\theta/\lambda^2))$$

qui s'ajoute à la diffusion thermique. (d) Le terme $(\mathbf{k}.\delta\mathbf{r}_i)(\mathbf{k}.\delta\mathbf{r}_j)$ entraîne une modulation du fond continu (c) dépendant des corrélations entre les déplacements des atomes. Ce terme est difficile à évaluer et Borie[6] montre qu'il n'introduit des perturbations qu'au voisinage des raies de structure. Nous avons supposé que les déplacements des atomes étaient indépendants, même pour des distances assez rapprochées, et négligé cette diffusion.

Dans $FeLiO_2$, tous les ions se déplacent et nous évaluerons successivement les variations moyennes $\delta r_{ij} = (\delta r_i - \delta r_j)$ des distances r_{ij} et pour chaque ion le terme B_{iS} statique.

Dans le terme (a) on retrouve: (1) Lorsque i et j décrivent les sites occupés par les ions Fe^{3+} et Li^+, c'est-à-dire les liaisons Fe–Fe, Fe–Li et Li–Li, l'effet de taille habituel aux alliages est remplacé ici par un effet de charge. (cf. paragraphe Discussion). (2) Lorsque $\mathbf{R}_{ij}$ décrit les liaisons oxygène-oxygène, le terme (a) est nul car $\Sigma\ \delta r_{\text{oxy oxy}} = 0$ quel que soit $\mathbf{R}_{ij}$. (3) Lorsque $\mathbf{R}_{ij}$ décrit les liaisons fer-oxygène, le terme (a) est donné par:

$$I_{\text{Feroxy}}(\text{diffusion}) = \sum_{ij} f_{\text{oxy}} f_{\text{Fe}} \cdot i \times (\mathbf{k}.\delta\mathbf{r}_{ij} \exp(i\mathbf{k}.\mathbf{R}_{ij})$$

et, par raison de symétrie, seule la projection de $\delta\mathbf{r}_{ij}$ sur $\mathbf{R}_{ij}$ intervient. (4) Les variations des distances oxy-lithium entraînent un terme analogue à (3) mais en $(f_{\text{oxy}} f_{\text{lithium}})$.

En ajoutant les termes (1), (3), (4), et la diffusion d'ordre à courte distance, et après avoir éliminé le terme (c) et son équivalent thermique, nous obtenons la diffusion totale $I(s)$. Celle-ci, pour un volume contenant N/2 cations Li et N/2 cations Fe, est reliée à l'ordre à courte distance et aux déplacements, dans le cas d'un diagramme de poudre, par la relation:

$$\begin{aligned} K(s) &= \frac{4I(s)}{N(f_{\text{Fe}}-f_{\text{Li}})^2} - 1 \\ &= \sum_{i=1}^{\infty} C_i \alpha_i \frac{\sin(sr_i)}{sr_i} - \sum_{i=1}^{\infty} C_i \beta_i \left(\frac{\sin(sr_i)}{sr_i} - \cos(sr_i)\right) - \sum_{j=1}^{\infty} \frac{f_{\text{oxy}}}{(f_{\text{Fe}}-f_{\text{Li}})} 4C_j \epsilon_{j\text{Fer-oxy}} \\ &\left(\frac{\sin(sr_j)}{sr_j} - \cos(sr_j)\right) \end{aligned} \tag{1}$$

dans laquelle

$$s = 4\pi\frac{\sin\theta}{\lambda} = |\mathbf{k}|.$$

Les indices i correspondent, aux liaisons cation–cation et les indices j aux liaisons anion–cation. α_i est le paramètre d'ordre à courte distance; $\alpha_i = 1-(P_{AB,i})/m_B$ où $P_{AB,i}$ est la probabilité de trouver un atome B à la distance r_i d'un atome A (m_A et m_B sont les concentrations); C_i = nombre d'atomes dans la ième couche; β_i = le coefficient d'effet de charge;

$$\beta_i = \frac{1}{\eta-1}\left(-\left(\frac{m_{\text{Fe}}}{m_{\text{Li}}}+\alpha_i\right)\epsilon_{\text{FeFe},i} + \left(\frac{m_{\text{Fe}}}{m_{\text{Li}}}+\alpha_i\right)\eta\,\epsilon_{\text{LiLi},i}\right)$$

$$\epsilon_{AA,i} = \frac{r_{AA,i} - r_{\text{moyen},i}}{r_{\text{moyen},i}}$$

et comme:

$$\eta = \frac{f_{\text{Li}}}{f_{\text{Fe}}} \simeq 0$$

$$\beta_i \simeq \left(\frac{m_{\text{Fe}}}{m_{\text{Li}}}+\alpha_i\right)\epsilon_{\text{FeFe},i} = (1+\alpha_i)\frac{r_{\text{FeFe},i} - r_{i,\text{moyen}}}{r_{i,\text{moyen}}}$$

(les termes 3 et 4 se simplifient en utilisant la relation $\epsilon_{\text{Fer-oxy}} = -\epsilon_{\text{Li-oxy}}$).

PARTIE EXPERIMENTALE

Détermination des coefficients B_{iS}

Nous avons vu que les termes du 2° ordre agissaient sur les diffractions de Bragg, comme un effet thermique. Dans le cas d'un échantillon désordonné de $FeLiO_2$, le facteur de structure d'une raie h, k, l, est donc:

$$F(h,k,l) = \sum_i f_i \exp -\left((B_{iT}+B_{iS})\frac{\sin^2\theta}{\lambda^2}\right) \times \exp 2i\pi(hx_i+ky_i+lz_i)$$

avec B_{iT} = facteur thermique, B_{iS} = facteur statique de l'ion i. Pour un échantillon ordonné:

$$F(h,k,l) = \sum_i f_i \exp -\left(B_{iT}\frac{\sin^2\theta}{\lambda^2}\right) \times \exp 2i\pi(hx_i+ky_i+lz_i).$$

Nous avons donc affiné à la même température les structures ordonnée Q_1 et désordonnée; ceci nous permet, *en supposant que le facteur* B_{iT} *ne varie pas pour le même atome* i *entre les 2 types de structures*, de déterminer les facteurs B_{iS} pour les ions fer et oxygène.

Pour l'échantillon désordonné, les mesures ont été effectuées à la radiation $K\alpha$ du molybdène et avec un compteur à scintillation. Par contre, les raies de la structure quadratique Q_1 étant très nombreuses et rapprochées, nous n'avons pu utiliser que la radiation $CoK\alpha$, ce qui entraîne une précision bien plus faible sur les paramètres B_i.

Toutes les mesures de raies ont été faites par diffractomètrie sur poudre, et à des vitesses de défilement très lentes (30 min/deg θ). A − 185°C, nous avons obtenu:

Structure désordonnée α:

$$B \text{ total}(Fe^{3+}) = 0{,}33 \pm 0{,}03$$
$$B \text{ total (oxygène)} = 0{,}57 \pm 0{,}075$$

Le résidu, $\Sigma\ (I-I_{\text{cal}})^2/\Sigma\ (I_{\text{cal}})^2 = 0{,}0014$ (facteur de véracité cristallographique 3,8%) et les précisions données sont égales à ± 1,5σ (σ = écart quadratique moyen).

Structure ordonnée Q_1:

Les facteurs B_{iT} selon a et b et B_{iT} selon c sont différents. Cependant, le programme de calcul sur ordinateur ne permet pas de les distinguer, aussi n'avons-nous utilisé qu'une approximation isotrope.

Le paramètre de position de l'oxygène déterminé est:

$$z = 0{,}233 \pm 0{,}001$$

et les coefficients de température:

$$B_{\text{FeT}} = 0{,}23 \pm 0{,}12$$
$$B_{\text{oxyT}} = 0{,}06 \pm 0{,}20$$

avec un résidu de 0,0014 (facteur de véracité 3,9%), soit donc, pour l'octaèdre d'oxygène autour d'un Fe^{3+}, 6 distances fer–oxygène égales à 2,03 Å (les paramètres de mailles à −185°C sont: $a = b = 4{,}047$ Å $c = 8{,}716$ Å). Les termes B_{iS} sont donc de l'ordre de: 0,10 Å^2 pour Fe^{3+}, et 0,50 Å^2 pour O^{2-}.

Détermination des coefficients d'ordre à courte distance et des termes du 1er ordre liés aux déplacements locaux

(1) *Conditions expérimentales:* Elles sont identiques à celles décrites pour Fe_5LiO_8 [3] c'est-à-dire: étude sur échantillon en poudre, recuit à des températures supérieures à 700°C et trempé à l'eau. La diffusion des rayons-X (radiation du cobalt) est mesurée par diffractométrie. Nous avons éliminé: La diffusion par l'air en plaçant l'échantillon sous vide; la diffusion Compton aux angles supérieurs à 20°θ en plaçant un monochromateur réglé sur $CoK\alpha$ entre échantillon et compteur, et réduit les diffusions thermiques en refroidissant l'échantillon à l'azote liquide.

Les diffusions thermiques ou pseudothermiques et Compton qui subsistent sont éliminées en utilisant la diffusion d'un échantillon ordonné, corrigées en fonction des variations de B mesurées précédemment.*

Le montage utilisé ne nous permet pas de normaliser par la méthode habituelle de mesure de la diffusion d'un corps amorphe. Aussi avons-nous déterminé les intensités en valeur absolue par la mesure de l'intensité des diffractions de Bragg d'un échantillon de fer en poudre (f et B bien connus [8]).

Dans le cas d'une mesure en diffractométrie, on a les relations:

$$P_{\text{raie intégrée}} = R \,.\, C_\lambda \,.\, \frac{p|F|^2}{\mu V} \times \frac{1+\cos^2 2\theta \cos^2 2\alpha}{(1+\cos^2 2\alpha)\sin 2\theta \sin\theta} \,.\, \delta$$

$$P_{\text{fond continu}} = R \,.\, \frac{I}{\mu'} \,.\, \frac{1+\cos^2 2\theta \cos^2 2\alpha}{1+\cos^2 2\alpha}$$

$$R = c^{te} \,.\, I_0;\ C_\lambda = 1{,}14\,\lambda^3$$

dans lesquels: I_0 est l'intensité du faisceau incident; P_{raie}: intensité intégrée d'une raie sur un enregistrement si δ est la longueur de papier pour 1°θ. $P_{\text{fond continu}}$: hauteur du fond continu. I est l'intensité absolue de diffusion pour un volume d'absorption μ'. F est le facteur de structure d'une raie, de multiplicité p, calculée dans une maille de volume V et d'absorption μ et en introduisant le facteur thermique. α: angle de Bragg du monochromateur.

(2) *Calculs et résultats*. Par la méthode des moindres carrés, nous avons recherché la concordance entre:

$$F_1(r) = \int_{S\text{min.}}^{S\text{max.}} sp(s)\, K_1(s) \sin sr\, ds \quad \text{(Fig. 3)}$$

et

$$F_2(r) = \int_{s\text{min}}^{S\text{max.}} sp(s)\, K_2(s) \sin sr\, ds$$

($K_1(s)$ et $K_2(s)$ sont respectivement les formes expérimentale et théorique de $K(s)$) dans un domaine compris entre $r = 1$ Å et $r = 6,8$ Å, incluant les distances $r_1 = 2{,}94$ Å, $r_2 = 4{,}15$ Å, $r_3 = 5{,}1$ Å, $r_4 = 5{,}89$ Å et $r_5 = 6{,}58$ Å,

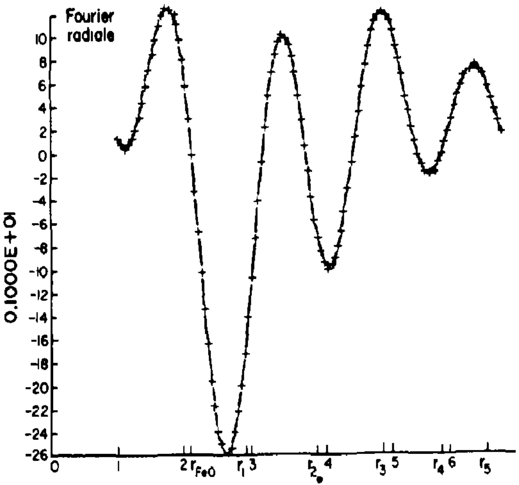

Fig. 3. Transformée de Fourier radiale

$$F_1(r) = \int_{s\text{min}}^{s\text{max}} s e^{a^2 s^2} K_1(s) \sin sr\, ds$$

(échantillon trempé depuis 742°C, a = 0.15) ainsi que $r_{\text{Fer-oxy}} = 2{,}075$ Å. Le domaine d'intégration est pris entre $S\text{min.} = 0{,}6$ Å^{-1} et $S\text{max.} = 5$ Å^{-1}. La fonction de pondération $p(s)$ est choisie en $e^{-a^2s^2}$ ($a = 0{,}15$) pour diminuer l'importance des données aux grands angles, très imprécises.

---

*Les diffusions dues au terme du second ordre ne sont aux grands angles que de l'ordre du 1/4 de la diffusion totale. Par ailleurs, les erreurs dans l'évaluation de la diffusion thermique se retrouvent près de l'origine lors de la transformée de Fourier radiale [7].

Pour ne pas introduire trop de variables et par là des corrélations, nous avons supposé que les paramètres β_3, β_4 et β_5 ainsi que les variations des distances fer–oxygène autres que premiers voisins, étaient nuls ou très faibles.

Les paramètres obtenus sont reportés Tableau 1. Dans l'affinement (a) de l'échantillon trempé depuis 742°C, nous avons supposé que le paramètre $\epsilon_{\text{Fer-oxy}}$ était nul, c'est-à-dire que les anions restaient en position idéale: les variables introduites sont alors α_1, α_2, α_3, α_4 et α_5 ainsi que β_1 et β_2. Dans l'affinement (b) pour les mêmes intensités expérimentales, ainsi que pour l'échantillon trempé depuis 857°C, nous avons introduit comme variable supplémentaire le paramètre $\epsilon_{\text{Fer-oxy}}$.

Tableau 1. Valeurs des paramètres obtenues; *dans le cas* (*a*) *le paramètre* $\epsilon_{1,\text{FeO}}$ *est bloqué à la valeur* O

Nature	α_1	α_2	α_3	α_4	α_5	β_1	β_2	$\epsilon_{\text{Fer oxy}}$	Résidu
Trempé 742°C (a)	−0,21	−0,33	0,01	−0,05	0,035	0,035	0,021	0	0,032
(b)	−0,16	−0,23	0,05	−0,01	0,06	0,030	0,013	−0,016	0,0087
Trempé 857°C	−0,15	−0,19	0,07	−0,01	0,08	0,025	0,012	−0,022	0,010
Ordonné Q_{I}	−0,33	0,33	0,33	−0,33	−0,33	0,010	−0,034	−0,02	
Ordonné Q_{II}	−0,17	−0,33	0,17	0	0,17				

La précision sur les différents paramètres est difficile à évaluer car l'affinement est fait sur la transformée de Fourier radiale, c'est-à-dire sur des informations non indépendantes[9]. Cependant, en supposant qu'il n'y a pas d'erreur systématique, et en prenant comme nombre d'informations indépendantes le nombre de points mesurés, on obtient des erreurs de l'ordre de ±0,02 sur α_i, ±0,022 sur β_i et ±0,002 sur ϵ.

Les ions Fe^{3+} et Li^+ sont dans la structure Q_{I} sur des positions sans paramètre, et les variations de distance entraînées par les effets de charge sont soumises aux contraintes de la symétrie, il est donc normal qu'il n'y ait pas concordance entre les valeurs de β_1 et β_2 dans la structure désordonnée et dans Q_{II}. L'oxygène est par contre, beaucoup plus libre (Tableau 1).

Les paramètres de position atomique dans la structure Q_{II} ne sont connus que dans le cas idéal, aussi n'avons nous pu calculer β_1, β_2 et $\epsilon_{\text{Fer-oxy}}$.

DISCUSSION

(1) *Existence des déplacements d'oxygène*

La diminution par un facteur 4 du résidu

$$R = \frac{\Sigma\, |F_1(r) - F_2(r)|^2}{\Sigma\, F_1{}^2(r)}$$

entre les affinements (a) et (b) confirme l'existence de ces déplacements. Nous avons reporté Fig. 4 les courbes $F_1(r) - F_2(r)$, (F_2 calculé d'après les paramètres du Tableau 1), et Fig. 5 les fonctions $K(s)$ expérimentale et $K(s)$ théorique dans les cas (a) et (b)*.

La distance moyenne d'un oxygène à ses premiers voisins Fer est égale à $2{,}075 + (\epsilon_{1,\text{Fer-oxy}} \times r_{1,\text{Fer-oxy}})$, soit 2,035 Å. Il faut souligner que cette valeur est peu différente de celle trouvée pour la phase ordonnée.

---

*Il est possible de calculer grossièrement le paramètre $\epsilon_{2\,\text{Fer,oxy}}$ correspondant à la 2° distance fer–oxygène. Celui-ci est trouvé de l'ordre de $\epsilon_{(1,\text{Fer-oxy})/3}$ et l'introduction de cette valeur dans l'affinement ne change notablement, ni le résidu, ni les paramètres.

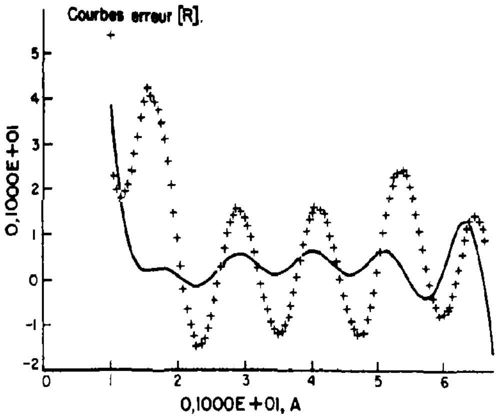

Fig. 4. Courbe d'erreurs $F_1(r) - F_2(r)$ $F_2(r)$ est calculée d'après les paramètres du Tableau 1:+++ affinement fait en introduisant $\epsilon_{1,Fer-oxy} = 0$(cas a); —— affinement fait en introduisant $\epsilon_{1,Fer-oxy}$ comme variable (cas b). Dans le cas (a), le déplacement des ions oxygène est mis en évidence par la forme de la courbe au voisinage de $r = 2$ Å: c'est la dérivée d'une fonction delta (élargie par les effets de coupure et perturbée par les autres variables).

Le problème des relations entre les paramètres α_i, β_i et B_{statique} ne pourrait être résolu que par l'introduction d'une hypothèse sur la propagation des déplacements. Dans le cas de certains alliages, Borie [6], en supposant que chaque noeud du réseau est occupé par un centre de distorsion à symétrie sphérique, et que $r_{1,AB} = \frac{1}{2}(r_{1,AA} + r_{1,BB})$, relie les paramètres α_1 et B_{st}.

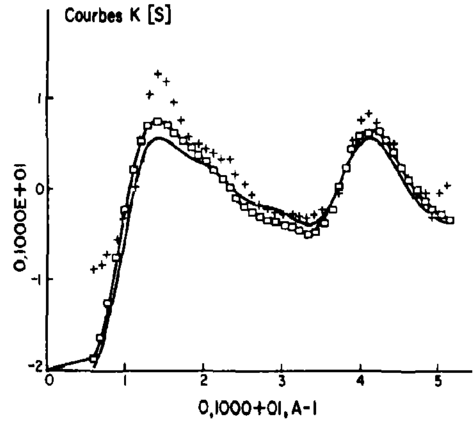

Fig. 5. Courbes $K(s)$ dans l'espace réciproque: ++++ courbe expérimentale; —— calculée pour le cas (a); O—O calculée pour le cas (b).

Si, dans les corps ioniques, les variations de distance sont dues aux différences de charges, on peut penser que les cations de même charge s'éloignent au maximum, les liaisons premiers voisins les plus courtes étant les liaisons entre cations de charges différentes*. Ainsi, dans FeLiO$_2$, l'ensemble des cations fer et lithium peut être remplacé par un cation unique de charge +2 occupant les positions idéales. Les ions Fe^{3+} ont alors, par rapport à cette charge moyenne, une charge +1, les ions Li$^+$ une charge −1, et les distances Fer-Fer correspondant à l'interaction de deux charges +1 sont égales aux distances Li-Li correspondant à l'interaction de deux charges −1. On a donc une relation différente de celle de Borie entre les distances AA, AB et BB, et le calcul n'est pas possible avec les mêmes hypothèses.

---

*C'est pourquoi nous avons appele ces déplacements 'effet de charge'.

(2) *Etude des paramètres d'ordre à courte distance*

Dans le Tableau 1, nous avons indiqué, pour comparaison, les valeurs des paramètres d'ordre à courte distance dans les structures Q_I et Q_{II}. *Les paramètres d'ordre à courte distance* α_i *des échantillons désordonnés sont peu différents de ceux de la structure* Q_{II}. La structure désordonnée se rapproche donc localement de la structure Q_{II}. Même pour des voisins éloignés, les α_i de la phase désordonnée conservent des signes et des rapports concordant avec leurs valeurs dans Q_{II}. Les variations assez faibles des α autres que 1er voisins permettent cependant de passer d'un état ordonné à un état désordonné correspondant à une infinité de configurations.

Par contre, *les structures désordonnée et* Q_{II} *sont très différentes de* Q_I.

Cette analogie des phases α et Q_{II} se retrouve dans les mesures magnétiques[10] et permet de comprendre le mécanisme des transformations. En effet, la transformation de la phase désordonnée en Q_I ne se fait que par l'intermédiaire de Q_{II}[11]. Or, le changement de la structure $\alpha \rightarrow Q_{II}$ se fait avec peu de sauts de cations. Il est donc plausible que, dans la matrice désordonnée, les germes de Q_{II} se forment plus facilement que ceux de Q_I. La transformation $Q_{II} \rightarrow Q_I$ se réalise ensuite par échange de position entre les cations, plus facile ici car les deux structures sont comparables par leurs déformations quadratiques.

ENERGIE ELECTROSTATIQUE DES DIFFERENTES PHASES

La différence d'énergie entre une phase ordonnée et une phase désordonnée est de l'ordre de RT_c par mole, pour une température de transition T_c; dans le cas de $FeLiO_2$ ($T_c \sim 1000°K$) on trouve ainsi 2 kcal/mole. Nous allons tenter de retrouver cette différence d'énergie entre la phase Q_I et la phase α, en introduisant tous les paramètres déterminés ci-dessus.

Energie coulombienne

Dans l'hypothèse d'interactions électrostatiques coulombiennes, nous avons déterminé la différence d'énergie entre Q_I et α en tenant compte dans le calcul de l'ordre à courte distance et des déplacements des ions. Les distances interatomiques changeant peu, nous avons négligé les variations de l'énergie de répulsion. Nous avons pu introduire facilement ces termes par un calcul dans l'espace réciproque en utilisant la méthode de Bertaut[12] et le diagramme de rayons-X[13], les facteurs de diffusion atomique étant remplacés par des charges.

Si l'on ne tient compte que des interactions entre charges, sans effet de polarisation, la variation d'énergie électrostatique entre Q_I et α est[13].

$$W_d - W_0 = \frac{1}{2\pi V_d} \sum_i \frac{|F_d(\mathbf{h}_i)|^2}{h_i^2} |\phi(h_i)|^2 + 2\int_0^{h_0} j(h)|\phi(h)|^2 dh - \frac{1}{2\pi V_0} \sum_i \frac{|F_0(\mathbf{h}_i)|^2}{h_i^2} |\phi(h_i)|^2$$

avec $|h| = 2 \sin\theta/\lambda = s/2\pi$

$F_0(\mathbf{h}_i)$ et $F_d(\mathbf{h}_i)$ sont les facteurs de structure des réflexions de Bragg des phases Q_I et α respectivement, les facteurs de diffusion atomique f_i étant remplacés par les charges q_i, et $J(h)$ une fonction de l'espace réciproque précisée plus loin. $\phi(h_i)$ est la transformée de Fourier d'une sphère pleine, de rayon choisi égal à 0,95 Å pour éviter les recouvrements entre atomes voisins (la self-énergie, étant la même dans les deux phases, n'intervient pas). La limite d'intégration h_0 utilisée pour les raies et le fond continu donne une précision de l'ordre de 0,5 %.

Pour le terme relatif à la phase ordonnée, nous avons introduit le paramètre de position de l'oxygène déterminé précédemment.

$J(h)$ provenant de la répartition non périodique des charges est relié à l'ordre à courte distance et aux déplacements, par une relation analogue à celle donnant $I(s)$ (relation

1). Cette fonction se divise donc, comme $I(s)$, en trois parties que nous avons intégrées séparement dans l'espace réciproque. Ce sont: (1) le terme d'ordre à courte distance: il a été obtenu en retranchant du fond continu expérimental, les diffusions dues aux distorsions; f_{Fe} et f_{Li} y sont ensuite remplacées par les charges $+3$ *et* $+1$[13]; nous avons pu ainsi tenir compte de toutes les interactions, même celles entre voisins éloignés, alors qu'un calcul dans l'espace direct ne nous aurait permis d'introduire que les 5 premiers voisins. Cependant, les ions ne sont pas en position idéale et il s'ajoute; (2) le terme du aux variations des distances cation–cation: nous le calculons, pour les premiers et deuxièmes voisins en supposant que les distances lithium-lithium inconnues sont égales aux distances fer–fer (voir plus haut discussion 1). Il suffit de remplacer dans l'expression de β le terme:

$$\eta = f_{Li}/f_{Fe} \text{ par } q_{Li}/q_{Fe}.$$

(3) Le terme du aux déplacements des anions: nous n'avons considéré que les liaisons anion-cation premiers voisins. L'énergie totale d'interaction coulombienne de la phase ordonnée Q_1 est de 2474 kcal/mole (somme sur les raies de Bragg moins self-énergie) si l'oxygène est placé dans sa position réelle, 2435 kcal/mole s'il est en position idéale, soit une différence de 40 kcal/mole. L'énergie de la phase α supposée totalement désordonnée, c'est-à-dire avec $J(h)$ = fond continu de Laue, est de 2235 kcal/mole, soit une différence d'énergie de 240 kcal/mole entre l'état ordonné réel et l'état totalement désordonné.*

L'évaluation ainsi faite est correcte pour Q_1; pour α, elle doit être corrigée des termes (1–3) ci-dessus. Les corrélations ne sont pas nulles et le terme (1) augmente l'énergie de la phase α de 82 kcal/mole, le terme (2) (allongement des distances Fer–Fer et Li–Li par rapport aux distances Fer–Li) de 32 kcal/mole et le terme (3) (différence entre les distances Fe–O et Li–O) de 56 kcal/mole.

Il subsiste donc une variation d'énergie de $W_d - W_0 = -70$ kcal/mole entre l'état ordonné et l'état désordonné. Bien que plus faible que les 240 kcal entre phase ordonnée et phase totalement désordonnée, cette différence d'énergie est cependant beaucoup trop importante pour la température de transition observée.

Il semblerait que cet écart provienne des effets de polarisation des ions oxygène. En effet, les environnements des anions en cations sont très dissymétriques.

Evaluation de l'énergie de polarisation

Dans la structure ordonnée Q_1, nous avons déterminé l'énergie due à la polarisation des ions oxygène par la méthode utilisée par Kingsbury[14]. La diminution d'énergie entraînée par la polarisation est donnée par

$$\tfrac{1}{2} \sum_i q_i V_i$$

dans laquelle V_i est le potentiel créé par les dipôles oxygène P(ox) sur l'ion i de charge q_i (ou par la relation équivalente $\frac{1}{2}$P(ox) E_c(ox) dans laquelle E_c(ox) est le champ des charges sur l'oxygène).

Tous les calculs ont été faits sur un ordinateur. Les potentiels sont calculés par la méthode d'Evjen par intégration sur des couches: si a, b, c sont les paramètres de la maille, la couche n est formée par le volume compris entre les parallélépipèdes rectangle de côté $2na$, $2nb$, $2nc$ et $2(n-1)a$ $2(n-1)b$, $2(n-1)c$. La maille $a = b = 4{,}05$ Å et $c = 8{,}722$ Å, étant grande, il suffit de 3 couches plus la maille centrale (soit environ 3000 atomes) pour obtenir une précision de l'ordre de 0,1 %.

En placant en chaque position d'un ion oxygène, un dipôle unité $P(u)$ ($P(u) = 1$ électron Å) orienté selon **c** (orientation de l'axe de symétrie passant par un oxygène), nous avons déterminé le potentiel du à ces dipôles en deux positions situées à $\pm 0{,}05$ Å (selon **c**) de part et d'autre du centre O d'un oxygène: on obtient ainsi le champ $\mathbf{E}_d$ au point O; Simultanément nous avons calculé les potentiels des charges en ces points, et ensuite le champ $\mathbf{E}_c$ des charges en O.

---

*Avec le signe adopté, une phase est d'autant plus stable que son énergie est plus grande.

Si $A\mathbf{P}(u)$ est la valeur du dipôle **P** réel on a:

$$\mathbf{P} = A\mathbf{P}(u) = \alpha(\mathbf{E} + A\mathbf{E}_d)$$

avec $\alpha =$ polarisabilité de l'ion oxygène $= 2{,}4.10^{-24}$ cm^3[15].

On trouve $E_c = 3{,}25 . 10^{10}$ V/m, et $E_d = 1{,}42 . 10^{10}$ V/m, d'où $A = 0{,}71$ soit une énergie $\frac{1}{2}PE_c$ de 53 kcal/mole $FeLiO_2$.

Nous avons aussi déterminé les potentiels dus aux charges et aux dipôles.

Sur les sites des ions Fe^{3+}, Li^+ et O^{2-} respectivement, les potentiels dipolaires sont de $-2{,}36$, $2{,}16$ et $-0{,}07$ V et les potentiels des charges de $-33{,}44$, $-15{,}23$ et $24{,}77$ V, soit une énergie d'interaction charge-charge de 2473 kcal/mole en accord avec la valeur obtenue précédemment.

Dans Q_1, parmi les 3 segments de droite cation-oxygène-cation concourants sur un oxygène (Fig. 1) un seul est dissymétrique, pour 2 dans Q_{II} (en réalité 1 ou 3 selon la position de l'oxygène) et 1,8 dans α d'après la valeur du paramètre d'ordre à courte distance α_2. Les énergies de polarisation sont donc beaucoup plus importantes dans Q_{II} et α que dans Q_1. A défaut de pouvoir le faire dans la phase, α, nous avons déterminé l'énergie de polarisation dans la phase Q_{II} mais en ne considérant que les interactions charges-dipôles et en plaçant tous les atomes en position idéale, ce qui simplifie les calculs.

Dans l'une ou l'autre des deux structures possibles de la phase Q_{II}[2] les oxygènes appartiennent à deux positions.

Nous avons trouvé un champ de $8{,}2.10^{10}$ V/m sur l'une des positions et $4{,}03.10^{10}$ V/m sur l'autre, ces deux champs étant presque orthogonaux.

Soit une énergie de 158 kcal/mole (les interactions dipôles–dipôles doivent entraîner une énergie de l'ordre de 10% de cette dernière).

On peut admettre que pour α, l'énergie de polarisation est du même ordre que celle de Q_{II}, d'autant plus que les premiers voisins doivent y jouer un rôle important car les voisins plus éloignés sont sans doute assez désordonnés*. La différence d'énergie liée à la polarisation entre Q_{II} et Q_I est de 105 kcal/mole; on peut expliquer par ces phénomènes les 70 Kcal/mole qui subsistent lors du calcul d'énergie d'interaction charge-charge, entre Q_1 et α†.

Nous avons montré par ailleurs[16] que dans l'hypothèse d'interactions de paires jusqu'au 2° voisins avec un rapport d'énergie $V_1 = 2V_2$ (avec $V_i = V_{\mathrm{FeFe},i} + V_{\mathrm{LiLi},i} - 2V_{\mathrm{FeLi},i}$ dans laquelle $V_{AB,i}$ est l'énergie d'interactions entre un atome A et un atome B distant de r_i) la relation $4\alpha_1 + \alpha_2 = -1$ correspondait à un minimum d'énergie et qu'elle permettait une structure désordonnée; or l'observation des paramètres d'ordre à courte distance montre que cette relation se conserve assez bien (-1 pour Q_I et Q_{II}, $-0{,}87$ pour α). Il semblerait donc que toutes les interactions intervenant dans la variation d'énergie entre les trois phases de $FeLiO_2$ puissent être traduites par la relation d'énergie $V_1 = 2V_2$ entre cations premiers et deuxièmes voisins. Malheureusement, nous n'avons pas pu établir de rapport entre ce type d'explication et les calculs développés ci-dessus.

---

*Dans Q_I, l'effet des premiers voisins d'un oxygène est atténué par les suivants ce qui explique la valeur de 200 kcal/mole trouvé par Fayard pour l'énergie de polarisation dans Q_I en ne considérant que les premiers voisins.

†Nous avions effectué pour le spinelle Fe_5LiO_8 un calcul analogue[13] qui nous a conduit à un résultat plausible sans la prise en compte de l'énergie de polarisation. Sans-doute, les effets de polarisation n'interviennent que très faiblement dans ce corps, car l'environnement en cations d'une oxygène varie très peu entre les états ordonné et désordonné.

REFERENCES

1. BARBLAN F. BRANDERBERGER E et NIGGLI P., *Helv. Chim. Acta* **27**, 88 (1944).
2. BRUNEL M. et de BERGEVIN F., *J. Phys. Chem. Solids* **29**, 163 (1968).
3. BRUNEL M. et de BERGEVIN F., *Solid State Commun.* **4**, 165 (1966).
4. ANDERSON P. W., *Phys. Rev.* **102**, 1008 (1956).
5. COX D. E., SHIRANE G., FLINN P. A., RUBY S. L. et TAKEI W. J., *Phys. Rev.* **132**, 1547 (1963).
6. BORIE B., *Acta crystallogr.* **10**, 89 (1957).
7. FLINN P. A., AVERBACH B. L. et RUDMAN P. S., *Acta crystallogr.* **7**, 153 (1954).
8. BATTERMAN B. W., CHIPMAN D. R. et de MARCO J. J., *Phys. Rev.* **122**, 68 (1961).
9. MORINO Y., JUCHITSU K. et MURATA Y *Acta crystallogr.* **18**, 549 (1965); MURATA Y. et MORINO Y., *Acta crystallogr.* **20**, 605 (1966)
10. ANDERSON J. C., DEY S. K. et HALPERN W., *J. Phys. Chem. Solids* **26**, 1555 (1965).
11. FAYARD M., *Annls. Chim.* **6**, 1279 (1961).
12. BERTAUT E. F, *J. Phys. Radium, Paris* **13**, 499 (1952).
13. BRUNEL M. et de BERGEVIN F., *C. r. hebd. Séanc. Acad. Sci., Paris* **260**, 3598 (1965).
14. KINGBURY P., *Acta crystallogr.* **A24**, 578 (1968).
15. TESSMAN J., KAHN A. et SHOKLEY W., *Phys. Rev.* **92**, 890 (1953)
16. de BERGEVIN F. et BRUNEL M., *Bull Soc. fr. Minér. Cristallogr.* **91**, 621 (1968).

J. Phys. Chem. Solids Pergamon Press 1969. Vol. 30, pp. 2023-2035. Printed in Great Britain

THE OPTICAL CONVERSION OF F CENTERS TO M CENTERS IN KCl WITH REPETITIVE LIGHT PULSES†‡

FREDERICK J. DUDEK§ and L. I. GROSSWEINER
Physics Department, Illinois Institute of Technology, Chicago, Ill. 60616, U.S.A.

(*Received* 27 *December* 1968; *in revised form* 6 *February* 1969)

Abstract—The optical conversion of F centers to M centers in KCl by 1 μsec light pulses has been studied as a function of repetition rate, temperature, pulse intensity, and F center density. The initial rate of growth after a delay period increases with decreasing repetition rate while the maximum M band yield increases with increasing repetition rate, for both KCl-K and Co-60 irradiated samples. The results obtained with irradiated crystals follow a kinetics model based on the combination of an anion vacancy with a nearby F' center, in competition with thermal and optical ionization of the F' center. It is proposed that the electronic motion during the delay period and the first stage of M center formation takes place via tunneling, while the later stages of aggregation in which bulk processes control involves the combination of anion vacancies with F centers or M centers. The relationship of this work to steady illumination measurements is discussed.

INTRODUCTION

THE OPTICAL conversion of F centers to M centers is one of the most fundamental of the color center transformations involving both ionic and electronic motions. Although this process has been known since at least 1940 from the work of Molnar[1], the mechanism remains a subject of current investigation. Most of the available information derives from kinetic studies, in which the dependence of the M band growth rate on pertinent variables such as F-center density, temperature and light intensity, have been measured. Unfortunately, there is considerable lack of agreement among the experimental results. For example, for the case of additively-colored KCl, activation energies for the $F \rightarrow M$ optical conversion have been reported as follows: Bron and Nowick[2] 0·35±0·05 eV (based on the data of Petroff [3]), van Doorn[4] 0·58 eV, Delbecq[5] 0·46 eV, Itoh and Suita[6] 0·95±0·20 eV (pulsed F light) Asai and Okuda[7] 0·41 eV. The dependence of the initial rate of M center formation in KCl on absorbed F light intensity $(I_F)^n$ and the initial F center density $[F]^p$ have been reported as follows: van Doorn[4] $n = 0$ at high I_F to $n = 1$ at low I_F. Delbecq[5] $n = 0{\cdot}27$; $p = 1{\cdot}3$, Asai and Okuda[7] $n = 0{\cdot}65$; $p = 1{\cdot}34$.

The wide variation of these results can be attributed to several factors. The work of Delbecq[5] has shown that the growth of the M band is preceded by a 'delay period' in which the quantum efficiencies of both F center fluorescence and the formation of F' centers are reduced by ~3 times, which are explained by a condensation of F centers prior to actual aggregation. The supression of F' center formation during the delay period was confirmed in KCl at 85°K by McCall and Grossweiner[8] using pulse bleaching and in KI at 113°K by Schneider and Patterson[9] using a Q-switched ruby laser. As discussed in more detail below, the formation of aggregate centers probably occurs in several stages and the measured activation energy may vary with the particular conditions of the

---

†Supported by the U.S. Atomic Energy Commission. This is AEC publication COO-1052-10.

‡A preliminary report of this work was given at the American Physical Society meeting in Chicago, 27-30 March, 1967.

§This work is based on the MS Thesis of FJD submitted to the Physics Department of IIT.

experiments. The complicated dependence of the *M* center growth rate on light intensity suggests that a short-lived intermediate is influenced by the light, a possibility that does not appear to have been considered in detail in the previous work.

In this work the initial conversion of *F* centers to *M* centers in KCl induced by repetitive light pulses of short duration has been studied as a function of repetition rate, pulse intensity, initial *F*-center density, and temperature. This approach has the advantage of providing information about the dark processes that accompany the photochemical effects and makes it possible to work at low average light intensities, where non-linear effects are most significant. The early work of Itoh and Suita[6] showed that the growth of the *M* and *R* bands in KCl is remarkably sensitive to the pulsing period, but their limited results could not be analyzed in terms of a specific model for *M* center formation. The new measurements have been made with both additively colored KCl (KCl-K) and cobalt-60 irradiated (KCl-γ) with similar results. It has been found that the first stage of *M* center growth, following the delay period, cannot be explained by a conventional mechanism in which uniform volume kinetics is assumed. However, the results are in excellent agreement with a modified Lüty mechanism[10], in which both condensation and the first stage of aggregation take place via tunnelling of the electron from the excited *F* center to a nearby *F* center, followed by thermal and light-induced return of the electron to the anion vacancy, in competition with migration of the vacancy to the F' center. This process has been referred to as the F'-α mechanism (in contrast to the F-α mechanism in which ionized *M* centers are formed by the combination of the anion vacancy with an *F* center) and is consistent with the kinetics results obtained in this investigation and also the suppression of *F* center luminescence and ability to form F' centers during the delay period.

The analysis in this paper is confined to the results with KCl-γ samples obtained under refined experimental techniques subsequent to our earlier work with KCl-K samples. The latter work is reported in the thesis of Wier [11], which is referred to for comparison purposes in the Results.

EXPERIMENTAL PROCEDURES

The KCl samples were taken from 1 in. cubes supplied by Harshaw Chemical Co. Additive coloring was done by the van Doorn method[12], followed by annealing at 450°C for 45 sec and rapid cooling to room temperature. The irradiations were done in a Co-60 chamber at room temperature, after which the crystals were cleaned by the chemical method of Zwicker[13]. The sample dimensions were 1 cm × 1 cm × 1–2 mm thick.

Pulse bleaching and measurement of *M* band growth was done in a modified Beckman DU spectrophotometer, in which an E.G. & G. type FX-6A flashtube was located in a housing attached to the sample chamber, with the output focussed on the crystal perpendicular to the measuring beam. The crystal was located in an evacuated double-wall metal sample holder with the face oriented at 45° to both the measuring and irradiation beams. (This necessitated a Snell's law correction of 1·14 to the optical path length which was made for all reported data). The crystal was in good thermal contact with a copper plate attached to the inner can of the sample holder and the copper-constantan measuring thermocouple was attached firmly to the copper plate adjacent to the crystal. The temperature was controlled to ±0·2°C by circulating fluid through the well of the inner can from a Haake type *F* thermostat bath unit using water above room temperature and an isopropanol-water mixture below room temperature.

The flashtube was operated repetively by charging a 0·1 mfd capacitor to 600 V. The light pulse of 0·8 μsec risetime and 0·9 μsec halfwidth provided $3{\cdot}6\times10^{-7}\,\mathrm{J/cm^2}$ through a Corning CS No. 4-64 glass filter (475–590 nm pass) as measured with an E.G. & G. Lite-Mike. The spectral intensity distribution was measured with a set of narrow-band interference filters from 420 to 800 nm using the Lite-Mike, to enable the calculation of the absorbed energy. For a typical KCl-γ sample with $1{\cdot}5 \times 10^{17}$ *F* centers/cm^3 (based on Smakula's relation with $f = 0{\cdot}81$) the energy absorbed in the *F* band per pulse was $(1{\cdot}0 \pm 0{\cdot}2) \times 10^{13}$ photons per cm^3 in the irradiated crystal. The light pulses were monitored with a 929 phototube and displayed on a Tektronix 531A oscilloscope to ensure constant intensity at different repetition rates. In addition, the phototube output was counted with timer-decade scaler unit of a GE XRD-3 X-ray diffraction unit to determine the repetition rate. The rate was controlled by triggering the flashtube with a 2D21 thyratron, which was triggered in turn with a Hewlett-Packard model 212 A pulse generator from 50 to 200 sec^{-1} and with the gate of the Tektronix oscilloscope at lower repetition rates. The growth of the *M* band was measured by coupling the spectrophotometer output to a Leeds and Northrup type G Speedomax chart recorder using a Beckman ERA unit. The *M* center density was calculated with Smakula's relation using $f = 0{\cdot}23$ for the M_1 band. The results are reported as *M* centers formed per pulse, where the actual run time varied from minutes to many hours depending on the repetition rate. The analog computer used for function generation was an EAI type TR-20 with non-linear expansion and Moseley type 2S *x*–*y* recorder readout.

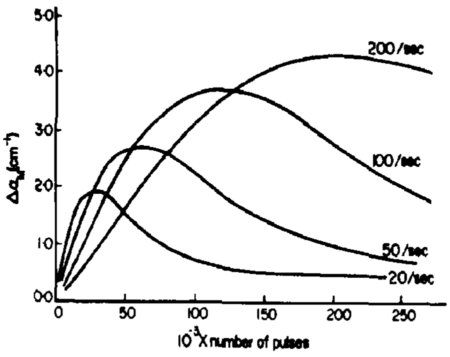

Fig. 1. *M* band growth induced by *F* light pulse illumination of KCl-γ at 25°C. *F* center density $8{\cdot}0 \times 10^{16}$/cc.

RESULTS

Typical data for the growth of the *M* band in KCl-γ induced by repetitive pulsed illumination at 25°C are shown in Fig. 1. It is apparent that the initial yield (per pulse) is higher at low repetition rates **R**, while the maximum yield of *M* centers increases with increasing **R**. Analogous effects were observed with KCl-K as shown by typical data in Fig. 2. A summary of initial growth rates (per pulse) with a uniform set of KCl-γ samples is given in Table 1. The dependence of the growth curve on **R** becomes less significant at higher temperatures. Figure 3 shows data for KCl-K obtained at 50°C with three different values of **R**. The same general effect is shown by the initial rates in Table 1. The delay period reported by Delbecq[5] was observed also in this work, particularly at low temperatures and high **R**. Results for both types of crystals are shown in Fig. 4. The effect of light pulse intensity on the initial growth rate in KCl-γ is shown as a logarithmic plot in Fig. 5. At low intensities the exponent *n* is $0{\cdot}75 \pm 0{\cdot}05$. A saturation effect occurs at higher intensities, and is attained more rapidly at the higher value

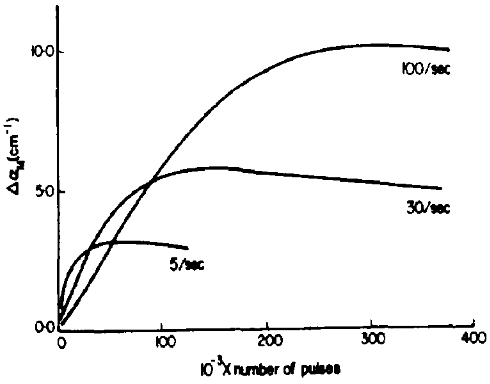

Fig. 2. *M* band growth induced by *F* light pulse illumination of KCl-K at 0°C: *F* center density $1{\cdot}6 \times 10^{17}$/cc[*11*]

Table 1. *Dependence of initial* M *band growth rate on temperature and repetition rate for* Co-60 *irradiated* KCl

Temperature (°C)	Repetition rate† (c/s)	Initial growth rate‡ (M centers/cm³-pulse)
0·0	200	$0{\cdot}19 \times 10^{11}$
0·0	100	$0{\cdot}43 \times 10^{11}$
0·0	50	$0{\cdot}80 \times 10^{11}$
0·0	20	$1{\cdot}59 \times 10^{11}$
0·0	10	$2{\cdot}67 \times 10^{11}$
8·0	200	$0{\cdot}40 \times 10^{11}$
8·0	100	$0{\cdot}76 \times 10^{11}$
8·0	50	$1{\cdot}27 \times 10^{11}$
8·0	20	$2{\cdot}65 \times 10^{11}$
8·0	10	$3{\cdot}74 \times 10^{11}$
15·0	200	$0{\cdot}71 \times 10^{11}$
15·0	100	$1{\cdot}42 \times 10^{11}$
15·0	50	$2{\cdot}43 \times 10^{11}$
15·0	20	$3{\cdot}30 \times 10^{11}$
15·0	10	$5{\cdot}00 \times 10^{11}$
25·0	200	$1{\cdot}38 \times 10^{11}$
25·0	100	$1{\cdot}98 \times 10^{11}$
25·0	50	$3{\cdot}06 \times 10^{11}$
25·0	20	$4{\cdot}48 \times 10^{11}$
25·0	10	$5{\cdot}36 \times 10^{11}$

†$(1{\cdot}0 \pm 0{\cdot}2) \times 10^{13}$ photons per cm³ per pulse absorbed.
‡Initial F center density $(1{\cdot}50 \pm 0{\cdot}08) \times 10^{17}$ per cm³.

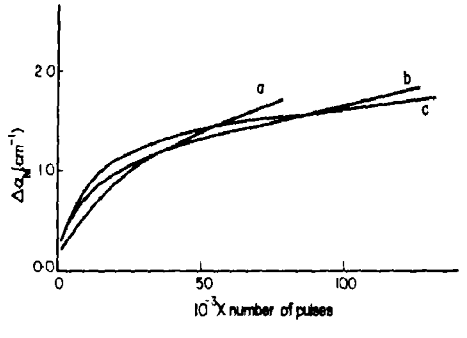

Fig. 3. M band growth induced by F light pulse illumination of KCl-K at 50°C: F center density $1{\cdot}6 \times 10^{17}$/cc, repetition rate (a) 5/sec, (b) 30/sec, (c) 100/sec[11].

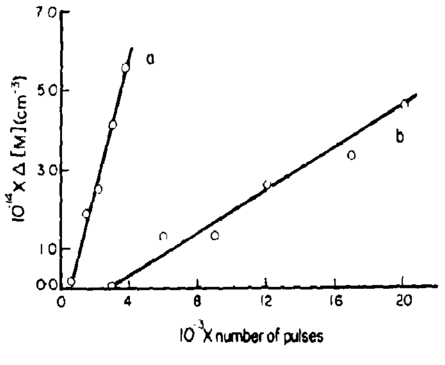

Fig. 4. Initial M center growth induced by F light pulse illumination: (a) KCl-K, $2{\cdot}2 \times 10^{17}$ F centers/cc, 3°C, 50 pulses/sec, pulse dose 1×10^{13} photons/cc; (b) KCl-γ, $1{\cdot}5 \times 10^{17}$ F centers/cc, 0°C, 20 pulses/sec, pulse dose $0{\cdot}025 \times 10^{13}$ photons/cc.

of **R**. The measured dependence of the initial growth rate on initial F center density is shown as the points in Fig. 6. The dashed line was obtained by making an approximate correction for the change in absorption from sample to sample based on the factor $(1 - \exp - \alpha_{F_0} d)$ where α_{F_0} is the absorption coefficient at the F band peak and d is the thickness.

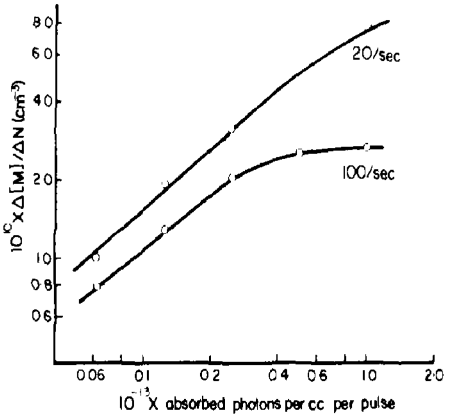

Fig. 5. Dependence of initial *M* center growth rate on *F* light pulse intensity: KCl-γ, $1{\cdot}5 \times 10^{17}$/cc, 0°C.

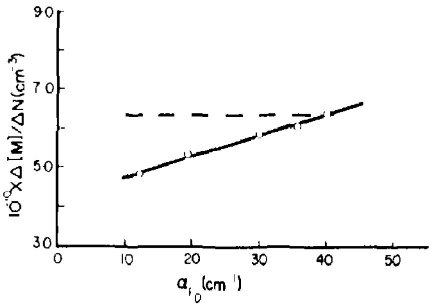

Fig. 6. Dependence of initial *M* center growth rate on *F* center density: KCl-γ, 0°C, 50 pulses/sec. The dashed line is obtained after correcting for the light absorption rate.

(1) *Rationale of the proposed model*

It is convenient to introduce the proposed model in terms of the kinetics of *M* center growth induced by steady *F* light illumination. In the absence of aggregation effects it is generally accepted (e.g. [14]) that the *F* center is excited to a higher state (F^*) in which luminescence and the other deactivation processes compete with thermally-assisted ionization. The conduction electrons may be trapped by *F* centers to form F' centers or by α centers to give F^*. The F' centers decay thermally and also via photoionization to reform an *F* center and a conduction electron. For the case of KCl near room temperature the steady state concentrations of F' and α centers are related as follows:

$$[\alpha][F'] \sim CI_F\tau_{F'}[F]/(1+\gamma I_F\tau_{F'}) \quad (1)$$

where I_F is the rate of light absorption by *F* centers, $\tau_{F'}$ is the thermal lifetime of an F' center, γ is a constant factor that depends on the photoionization efficiency of the F' and the overlap of the *F* and F' absorptions integrated over the spectrum of the incident light, and *C* is a constant that includes other transition probabilities and cross sections (Appendix A). The predictions of this mechanism for *M* center growth depend on the model considered:

(I) F′-α model

$$\mathrm{d}[M]/\mathrm{d}t \sim \begin{array}{ll} (I_F)^1[F]^1 & \text{if} \quad \gamma I_F \ll 1/\tau_{F'} \\ (I_F)^0[F]^1 & \text{if} \quad \gamma I_F \gg 1/\tau_{F'} \end{array}$$

(II) *F*-α model

$$\mathrm{d}[M]/\mathrm{d}t \sim \begin{array}{ll} (I_F)^{1/2}[F]^{3/2} & \text{if} \quad \gamma I_F \ll 1/\tau_{F'} \\ (I_F)^0[F]^{3/2} & \text{if} \quad \gamma I_F \gg 1/\tau_{F'}. \end{array}$$

In both cases the initial rate of *M* center growth saturates with increasing light intensity as was observed by van Doorn[4]. However, both models predict a strong dependence on *F* center density that was not observed in this work. It is concluded that bulk kinetics are not applicable in the initial *M* center growth stage. The clustering of *F* centers prior to *M* center formation suggests an alternative mechanism, in which the rate controlling processes take place between the geminate F' and α centers in proximity. It is assumed that the electron ejected from the excited *F* center tunnels to a nearby *F* center, so that the resulting vacancy has a higher chance of recombining with the nearby F' center than with other *F* centers or F' centers distributed through the crystal. The neighboring vacancy-F' center entity is referred to as "F_α'" to emphasize that its transitions are pseudo-first order with respect to the component defects. The rate controlling step is taken to be the competition between the thermal and optical conversion of F_α' to the original *F* centers with coagulation to form an M center, so that the proposed mechanism is a modification of the Lüty [10] F'-α model. It should be noted that this model does not rule out an F-α mechanism in the later stages of bleaching or in purely thermal aggregation processes.

(2) *The* F'_α *mechanism*

According to the proposed model the kinetics of M center formation can be represented by the following steps:

$$F + h\nu_F \xrightarrow[F]{} F'_\alpha \qquad \text{(a)}$$

$$F'_\alpha \longrightarrow M \qquad \text{(b)}$$

$$F'_\alpha \longrightarrow 2F \qquad \text{(c)}$$

$$F'_\alpha + h\nu_F \begin{array}{l} \nearrow \ \alpha + F' \\ \searrow \ 2F \end{array} \qquad \text{(d)}$$

which lead to the following rate equations:

$$\mathrm{d}[F'_\alpha]/\mathrm{d}t = \eta I_F - \eta' I'_F - (k_1 + k_2)[F'_\alpha] \qquad (2)$$

$$\mathrm{d}[M]/\mathrm{d}t = k_1[F'_\alpha] \qquad (3)$$

where η is the quantum efficiency for the formation of the F'_α entity and η' is the quantum efficiency for its destruction by F light, I_F and I'_F are the light absorption rates in F and F'_α centers, and k_1 and k_2 are the pseudo-first order rate constants for steps (b) and (c), respectively. It is assumed that the short light flashes can be approximated by square pulses of duration τ and period t_0, which should not introduce a significant error for $t_0 \gg \tau$. For optically 'thick' samples in the F center absorption it is assumed that:

$$I_F(t) = \begin{cases} I_0 & nt_0 < t < nt_0 + \tau; \\ 0 & \text{otherwise} \end{cases}$$

$$(n = 0, 1, 2, 3, \ldots)$$

where I_0 is the integrated rate of light absorption. On the other hand, the F'_α optical density must always be low giving $I'_F(t) = BI_F(t)[F'_\alpha]$, where B is a constant determined by the overlap of the F and F' absorption bands and the spectrum of the incident light.

A straight forward integration gives the contribution to M center growth of each light pulse and during the dark period between the pulses (Appendix B). A considerable simplification follows if it is assumed that a sufficient number of pulses have been absorbed to make $N(k_1 + k_2)t_0 \gg 1$ (i.e. the time average F'_α concentration has attained steady state) and that negligible M band growth occurs during the short light pulse compared to the much longer dark time leading to:

$$\Delta[M]/\Delta N = \frac{k_1 \eta I_0 (1 - \mathrm{e}^{-k\tau - \eta' B I_0 \tau})(1 - \mathrm{e}^{-kt_0})}{k(k + \eta' B I_0)(1 - \mathrm{e}^{-kt_0 - \eta' B I_0 \tau})} \qquad (4)$$

where $k \equiv k_1 + k_2$. Equation (4) predicts the dependence of the initial M center growth rate on pulsing period t_0 and light intensity I_0. The measured dependence of the initial M band growth rate on t_0 (from Table 1) is shown by the points in Fig. 7. In order to examine the

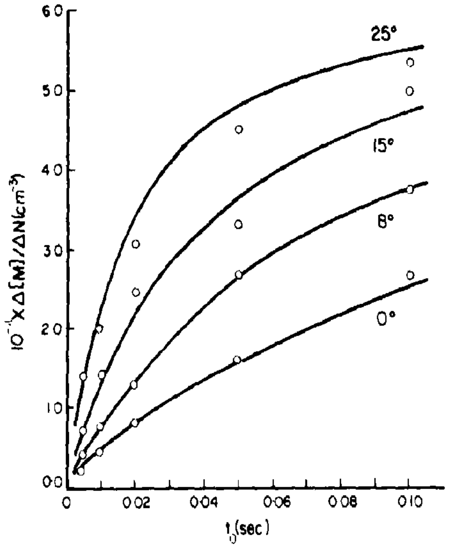

Fig. 7. Dependence of initial M center growth rate on pulsing period and temperature: KCl-γ, F center density $1{\cdot}5 \times 10^{17}$/cc. The points are taken from Table 1. The lines are the analog computer fit to equation (5′) based on $\eta' B I_0 \tau = 0{\cdot}60$, $k(25°\mathrm{C}) = 25\ \mathrm{sec}^{-1}$, and an activation energy for k of 0·59 eV.

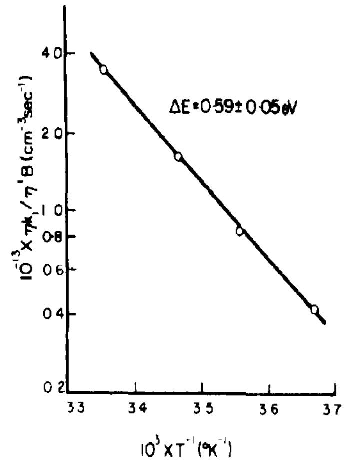

Fig. 9. Arrhenius plot of the reciprocal slope of the lines in Fig. 8.

agreement with the model it is assumed that $e^{-kt_0} \cong 1 - kt_0$ and that $\eta' B I_0 \gg k$, in which case equation (4) reduces to:

$$(\Delta[M]/\Delta N)^{-1} = (\eta' B/\eta k_1) t_0^{-1} + [(\eta' B/\eta)(k/k_1)\, e^{-\eta' B I_0 \tau}]/(1 - e^{-\eta' B I_0 \tau}) \quad (5)$$

which is the limit of high light intensities with high repetition rates. The fit of the data in Table 1 to equation (5) holds over the range of temperatures and **R** investigated; Fig. 8. An Arrhenius plot of the slope in Fig. 9 gives $0{\cdot}59 \pm 0{\cdot}05$ eV as the activation energy of ηk_1, which is the effective temperature-dependent quantity controlling *M* center formation. This result is in excellent agreement with 0·58 eV reported by van Doorn[4], particularly in that he obtained the same type of non-linear intensity dependence observed in this work, suggesting that the initial aggregation stage is being measured in both cases. The convergence of the lines to a common intercept implies that k and k_1 have the same temperature dependence. The probable explanation is that step (c) does not contribute to F_α' decay at high light intensities so that the k_2 term is insignificant in the integrated relationship. At infinitely high light intensity equation (5) predicts that the saturation rate of *M* center formation (per unit time) is the reciprocal of the slope in Fig. 8. At 0°C the latter quantity is $4{\cdot}0 \times 10^{12}\,\mathrm{cm}^{-3}\,\mathrm{sec}^{-1}$. The conversion of the Fig. 5 data to rates per unit time gives for the extrapolated growth rate $2{\cdot}9 \times 10^{12}\,\mathrm{cm}^{-3}\,\mathrm{sec}^{-1}$ at 100 c/s and $\sim 3 \times 10^{12}\,\mathrm{cm}^{-3}\,\mathrm{sec}^{-1}$ at 20 c/s. The agreement is considered quite good, since data for constant light intensity and variable **R** (Fig. 8) are compared with data for constant **R** and variable light intensity (Fig. 5) obtained with a different crystal sample.

The comparison between the model and the data was extended by fitting the predicted dependence of initial growth rate on pulsing period to the points in Fig. 7. Rearranging equation (5) leads to:

$$\Delta[M]/\Delta N = A(1 - e^{-kt_0})/(1 - e^{-\eta' B I_0 \tau}\, e^{-kt_0}) \quad (5')$$

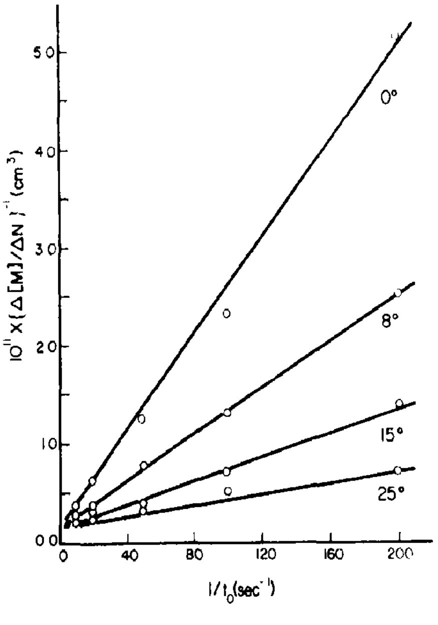

Fig. 8. Plot of the data of Table 1 according to equation (5) in which the slope of the lines leads to relative values of k_1 and the common intercept shows that the thermal step (c) is unimportant.

where A is independent to t_0. The functional dependence on t_0 was generated with the analog computer and matched to the data, using one value of $\eta' BI_0\tau$ for all temperatures and all values of **R**. The constant k was selected to give the best fit to the t_0 dependence at 0°C and was adjusted according to the activation energy of 0·59 eV for the higher temperatures. The lines in Fig. 7 are the direct readout of the analog computer on the x–y plotter, based on $\eta' BI_0\tau = 0{\cdot}60$ and $k(25°\text{C}) = 25\ \text{sec}^{-1}$. The corresponding values of k at other temperatures are 11·5 at 15°C, 6·2 at 8°C, and 2·9 at 0°C, all sec^{-1}. Thus, a 'high' repetition rate at 0°C occurs for $\mathbf{R} > 3$ c/s, while $\mathbf{R} > 25$ c/s is required at 25°C. The magnitude of these time constants for M center formation supports the approximations leading to equation (5) and the calculation of the activation energy. The energy of 0·59 eV applies to the rate constant k_1 of step (b), since step (c) has been shown to be unimportant under these conditions. However, it is shown that a steady-state analysis based on the time average light intensity leads to 0·61 eV for the high **R** growth rates, so that this result should be applicable also to the initial stage of M center formation under steady illumination of moderate intensity. (For example, the average intensity at 10 c/s in this work corresponds to $\sim 1 \times 10^{13}$ photons/cm^2-sec absorbed in the F band).

In the earlier work of Wier[11] with KCl-K, the numerical parameters were obtained by trial and error fitting of the growth data to a function equivalent to equation (5′). His results led to $k = 6\ \text{sec}^{-1}$ at $2{\cdot}2 \times 10^{17}$ F centers/cm^3 which did not change with temperature from 3° to 25°C. However, the quantity $\eta' BI_0\tau$ varied by a factor of two over this temperature range which indicates that the fitting procedure used was not successful. We have attempted to analyze Wier's data with the method of equation (5) and were not able to obtain a reliable value of the activation energy because of scatter. The most likely cause of such scatter is the non-reproducibility of the initial condition after the rapid quenching of the crystal, which does not arise with Co-60 irradiations. On the other hand, the qualitative aspects of Wier's results parallel the present work and the essential features of the mechanism probably apply to both KCl-K and KCl-γ.

(3) *Implications of the* F'_α *mechanism*

It is reasonable to assume that the delay period and the initial stage of M center formation are a continuous process, in which randomly distributed F centers in the unbleached crystal first condense and then coagulate. Significantly, a considerable extent of F center luminescence quenching takes place prior to optical bleaching at moderate F center densities. For example, the data of Delbecq[5] shows that the F center fluorescence efficiency at 0°C for a mean separation between F centers of 17 lattice spacings ($\sim 1{\cdot}9 \times 10^{17}$/cm^3) is approximately four times smaller than at a density corresponding to 50 lattice spacings. Since F centers located in adjacent anion sites are already M centers, it follows that the concentration quenching is a moderately long-range interaction. This conclusion argues against resonant transfer from the relaxed excited state of the F center to the ground state which should follow a R^{-6} dependence on distance. Furthermore, the poor overlap of the emission and absorption bands and the relatively long lifetime of the F center excited state are unfavourable for this type of process[15]. Delbecq's data show also that an additional reduction in the fluorescence efficiency by a factor ~ 3 has taken place at the end of the delay period, which corresponds to a mean separation of F centers (in an unbleached crystal) of 15 lattice spacings. Since the ability to form F' centers has decreased by about the same factor, it cannot be assumed that fluorescence quenching involves only a process which competes with fluorescence. However, the fast transfer of the electron from the excited F center to a nearby F

center followed by non-radiative recapture of the electron in the anion vacancy is equivalent to 'physical' quenching and also explains the decreased yield of F' centers. Furthermore, the migration of the vacancy towards the F' center under the influence of the coulombic attraction would explain both the condensation during the delay period and our results pertaining to the initial stage of M center formation. In the case of additively colored KI, Schneider and Patterson[9] have proposed that the decrease in the ability to form F' centers at 113°K induced by F light bleaching at 238°K is due to a tunneling transformation of the type proposed in this work. The important distinction between this mechanism and the conduction band process of F center photoionization is that the return step ($F'+\alpha \rightarrow 2F$) must be non-radiative to account for the decrease in fluorescence efficiency, and that kinetics are pseudo-first-order in the F' or α center concentrations, as indicated by the F'_α notation.

In terms of the tunneling model, η is the quantum efficiency for tunneling of the electron from the excited F center, k_1 is the probability per second that the vacancy migrates to a lattice position adjacent to the F' center during the actual F' lifetime, and k_2 is the probability per second that the F' electron tunnels back to the original vacancy. The kinetics do not distinguish between the two possible paths of step (d), i.e. return of the electron to the original vacancy or formation of separated F' and α centers via photoionization of the F'_α entity, so that the interpretation of η' cannot be expanded. As noted above, step (d) is responsible for the dependence of the initial M center formation rate on repetition rate and predominates over the dark process step (c) in our measurements. The transition to the next stage of bleaching is readily explained if the path leading to separated α and F' centers is the correct one, because the subsequent M centers would be formed also by bulk processes. The conversion of F centers to M centers in this work is <1 per cent at 0°C and <3 per cent at 25°C. The non-dependence of the initial growth rate on F center density supports the hypothesis that condensed F centers are involved in this stage. A possible reason for the F center density dependence reported by Delbecq[5] and Asai and Okuda [7] is that the F-α mechanism takes over as soon as a random distribution of F' and α centers is established (see *Discussion*). In fact the occurrence of volume processes in the later stages would explain the higher M center maximum yields at higher **R** observed in this work (Figs. 1 and 2), because the higher time average light intensity establishes higher steady-state densities of F' and α centers. An additional factor is the use of radiation coloration in this work compared to additive coloration in [5] and [7]. The low M band formed after irradiation of KCl suggests that some condensation occurs in the un-bleached crystal, which would enhance the significance of the F'-α stage.

DISCUSSION

It is interesting to compare the pulse bleaching analysis with the equivalent solution for steady irradiation. The steady-state solution of equation (3) for constant intensity light I_r leads to:

$$d[M]/dt = k_1\eta I_r/(\eta' B I_r + k) \qquad (6)$$

so that a plot of $(\Delta[M]/\Delta t)^{-1}$ against I_r^{-1} should give a series of straight lines at high R, where $I_r \equiv I_0(\tau/t_0)$. The data in Table 1 graphed in Fig. 10 are in agreement with equation (6). An Arrhenius plot of the intercepts at the different temperatures gives 0·61 eV for the activation energy of ηk_1, which is in good agreement with the result obtained by the pulse analysis. Furthermore, the parallel lines (at high **R**) for the different temperatures indicates that $k \equiv k_1+k_2$ has the same temperature dependence as k_1, deduced also in the pulse analysis. It is concluded that the activation energy of M center formation

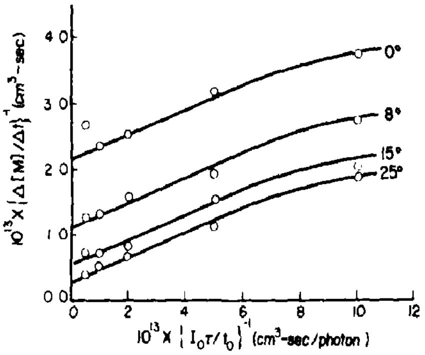

Fig. 10 Fit of the Table I data to the constant light intensity approximation based on equation (6) with $I_e = I_0(\tau/t_0)$. The approximation is valid at high average light intensity (high repetition rate) where the parallel straight lines show that the thermal step (c) is unimportant.

obtained in this work is equivalent to the activation energy that would be observed in steady illumination measurements made in the early stages of aggregation. The unimportance of the k_2 term emphasizes that photobleaching of the F' centers is the dominant back process for the temperatures and F-center densities involved.

Equation (6) predicts a linear dependence of growth rate on light intensity at low light intensities and saturation at high light intensities, as were actually observed by van Doorn[4]. The variation of the exponent n reported by other workers is probably due to the non-applicability of the $(I_F)^n$ dependence. As shown in Appendix A, the assumption of bulk processes leads to strong dependence of the initial growth rate on $[F]$, while the F'_α tunneling model predicts a rate independent of $[F]$. The experimental results of the earlier investigations indicate that bulk processes are controlling above 0°C in KCl, probably because the short F' lifetime establishes a random distribution of F' and α centers in a time short compared to the measurements. On the other hand, our light pulses are $\sim 10^5$ times more intense than typical steady sources, with a corresponding increase in the initial concentration of near-by F' and α centers and the possibility of their combining prior to thermal ionization of F' or by the next light pulse.

The activation energy of 0·59 eV can be interpreted as the jump activation energy of the anion vacancy to the F' center, since η is not expected to require thermal activation in the tunneling process. Reported values for the activation energy of the anion self-diffusion constant in KCl range from 0·8 to 2·5 eV[16], which is at least consistent with the view that the coulombic attraction contributes to the initial aggregation process. It is interesting to note that Hirai and Scott[17] have estimated that the monopole-induced dipole interaction between an F center and a vacancy could contribute only $-0{\cdot}04$ eV to the activation energy for the F-α mechanism.

The tunneling of an electron from the excited F center to a nearby F center in the ground state was proposed by Markham *et al.* [18] to explain the reversible optical bleaching of the F band in KBr at 300°C, and more recently by Schneider and Patterson[9] as noted above. The critical tunneling distance can be estimated with a theory proposed by Nelson[19] in connection with electron transfer from an adsorbed dye molecule in the excited state to a semiconductor conduction band. According to this model, the temperature-independent part of the tunneling probability is the order of: $f_c t/(\tau^{-1}+f_c t)$, where f_c is the classical frequency of the electron in the potential well, τ is the lifetime of the excited state, and t is the barrier transparency. Taking $t \simeq \exp[-2a(2m\Delta E)^{1/2}/h]$ gives for the critical distance a^* (i.e. the distance at which $p = 1/2$): $a^*(\text{Å}) \simeq 2{\cdot}25 \log_{10} f_c\tau/(\Delta E)^{1/2}$. For the excited F center in KCl: $\Delta E = 0{\cdot}16$ eV and $\tau = 6 \times 10^{-7}$ sec[20], and taking $f_c \sim 10^{15}\ \text{sec}^{-1}$ gives $a^* \simeq 50$ Å. Although this calculation is highly oversimplified, the conclusion that the excited electron can tunnel over a number of lattice spacings is probably correct, in view of the low barrier and the long excited state lifetime. On the other hand, the long lifetime is unfavorable for resonant dipole transfer with a probability ~ $(1/\tau)R^{-6}$[15].

It should be emphasized that the mechanism proposed in this work to explain optical *M* center formation in KCl may not be operative in related thermal processes, such as aggregation by the rapid warming of additively-colored crystals bleached at low temperature observed by van Doorn[4] and studied in detail by Hirai and Scott[17]. The latter workers proposed that *F'* electrons are trapped at a center associated with the *A* band above −50°C, while *M* centers are formed above −40°C by the *F*-α process followed by capture of the trapped electrons. However, their estimate of the α center jump probability based on high temperature anion diffusion constants is incompatible with the *M* center yield and they suggest that 'amomalous' low temperature diffusion constants may be more appropriate. Aggregate centers are formed also by irradiating at low temperature followed by warming. This effect was observed by Rabin[21] in KCl, and studied in detail for LiF by Farge *et al.* [22] and Nahum[23] in which the *F*-α mechanism was proposed. These findings and the proposed explanations do not conflict with the present work, which postulates the *F'*-α mechanism only for the first stage of aggregation (after the delay period) in the photochemical process. The complications resulting from higher aggregates and the growth of new absorptions under the *F* band make the extension of our method to the later stages more difficult. We have made some preliminary measurements on the growth of the *R* band in KCl-γ induced by repetitive pulse irradiation and observed a marked dependence of the initial growth rate per pulse on the repetition rate that parallels the *M* band case, i.e. faster growth at smaller values of **R**. However, there are two differences from the *M* band results: (a) the influence of **R** on the growth rate does not become smaller as the temperature is raised from 0° to 25°C; (b) a very rapid formation of *R* centers takes place during the first few hundred pulses prior to the establishment of linear growth. The rapid rise can be explained by the *M'*-α process utilizing the small concentration of *M* centers already in the irradiated crystal. The next stage, which competes with *M* band growth, probably involves the *M*-α process because the temperature dependence indicates that the stability of the intermediate is higher than that of F'_α which rules out the M'_α center.

The relationship between these results and the formation of the *M* center triplet state is of interest. The work of McCall and Grossweiner[8] and Schneider[24] has shown that low-temperature illumination of KCl containing *F* and *M* centers with *F* light induces the formation of the *M* center triplet state. The proposed mechanism is short-range energy transfer from the excited *F* center to nearby *M* centers, which is consistent with a number of experimental results such as the linear dependence of the yield on *M* center density[8], the action spectrum peaking at the *K* band[8], and the non-dependence of the yield on the polarization of the incident light for oriented *M* centers [24]. This conclusion raises the question as to why resonant transfer from F^* to the *M* center is possible while tunneling appears to be favoured for the F^*-F interaction. Based on the temperature dependence of the ^3M lifetime, it was suggested in [8] that the lowest triplet-state wave function of $^3\Sigma_u^+$ character is stabilized by the nearest neighbor cations, so that the potential energy surface has a minimum before it contacts the ground state. This situation might lead to a substantial enhancement of the exchange integral with F^* (particularly for *K* band excitation) and permit spin-conserving resonant transfer. On the other hand, electron transfer would be less favorable in this case because of the low stability of *M'* compared to *F'* centers. These considerations are admittedly speculative and a detailed theoretical treatment of the tunneling and resonant transfer transitions between F^* and F or M centers is necessary.

SUMMARY

The irradiation of KCl-K or KCl-γ with repetitive pulses of F light near room temperature induces the formation of M centers after a delay period in which the initial linear growth rate decreases with increasing repetition rate **R**, while the maximum height of the M band increases with increasing **R**. The results of this work with KCl-γ show that the initial growth rate is essentially independent of the F center density and increases with light pulse intensity up to a saturation value. The dependence of the initial growth rate on **R** is strongest at 0°C and tends to disappear above 25°C.

These results are explained by a kinetic model in which the shortlived intermediate formed by optical excitation of the F center generates M centers in a pseudo-first-order process, in competition with thermal and optical destruction of the intermediate. The data are in quantitative agreement with this model and lead to an activation energy of $0{\cdot}59 \pm 0{\cdot}05$ eV for the conversion of the intermediate to M centers.

It is proposed that the condensation of F centers during the delay period and the initial growth of M centers follow the same mechanism, in which tunneling of an electron from the excited F center to another F center leads to and F' center and α center in proximity. This entity is referred to as "F_α'". The quenching of F center fluorescence and the diminished ability to form F' centers during the delay period are explained by tunneling of the F' electron back to the α center in a non-radiative process. The initial stage of M center formation is attributed to the diffusion of the α center to the coupled F' center in a pseudo-first order process. The competing photo-ionization of F_α' by F light leads to separated F' and α centers, so that the later stages of M center growth probably takes place by the F-α process. The higher maximum yield of M centers at higher average light intensities (i.e. higher **R**) can be explained by the occurrence of such bulk processes in the later stage. Although the resonant transfer of energy from F^* to F centers appears unlikely in KCl, short-range resonant transfer from F^* centers to M centers is favorable at low temperatures and accounts for the formation of the M center triplet state.

REFERENCES

1 MOLNAR J. P., Thesis. Mass. Inst. of Technol. (1940).
2. BRON W. E. and NOWICK A. S., *Phys. Rev.* **119**, 114 (1960).
3. PETROFF St., *Z. Phys.* **127**, 443 (1950).
4. VAN DOORN C. Z., *Philips Res. Rep. Suppl.* **4**, 1 (1962).
5. DELBECQ C., *Z. Phys.* **171**, 560 (1963).
6. ITOH N. and SUITA T., *J. phys. Soc. Japan* **17**, 348 (1962).
7. ASAI K. and OKUDA A., *J. phys. Soc. Japan* **21**, 2197 (1966).
8. McCALL R. T. and GROSSWEINER L. I., *J. appl. Phys.* **38**, 284 (1967).
9. SCHNEIDER I. and PATTERSON D. A., *Phys. Rev.* **164**, 1136 (1967).
10. LÜTY F., *Z. Phys.* **165**, 17 (1961).
11. WIER K. E., M. S. Thesis, Ill. Inst. of Technol. (1967).
12. VAN DOORN C. Z., *Rev. scient. Instrum.* **32**, 755 (1961).
13. ZWICKER E., *J. appl. Phys.* **38**, 1983 (1967).
14 MARKHAM J. J., In *Solid State Physics* (Edited by F. Seitz and D. Turnbull), Suppl 8. Academic Press, New York (1966).
15. DEXTER D. L., *J. chem. Phys.* **21**, 836 (1953).
16. ALLNATT A. R. and JACOBS P. W. M., *Trans. Faraday Soc.* **58**, 116 (1962).
17. HIRAI M. and SCOTT A. B., *J. chem. Phys* **46**, 2896 (1967).
18. MARKHAM J. J., PLATT R. T., Jr. and MADOR I. L., *Phys. Rev.* **92**, 597 (1953).
19. NELSON R. C., *J. phys. Chem.* **71**, 2517 (1967).
20. SWANK R. K. and BROWN F. C., *Phys. Rev.* **130**, 34 (1963).
21. RABIN H., *Phys. Rev.* **129**, 129 (1963).
22. FARGE Y., LAMBERT M. and SMOLUCHOWSKI R., *Solid State Commun.* **4**, 333 (1966).
23. NAHUM J., *Phys. Rev.* **158**, 814 (1967).
24. SCHNEIDER I., *Phys. Rev. Lett.* **17**, 1009 (1966).
25. FEDDERS H., HUNGER M. and LÜTY F., *J. Phys. Chem. Solids* **22**, 299 (1961)
26 IKEZAWA M., HIRAI M. and UETA M., *J. phys. Soc. Japan* **17**, 1474 (1962).

APPENDIX A

Optical conversion of F *centers to* M *centers by bulk processes*

For conditions where aggregation does not occur, the photoequilibrium between F and F' centers induced by F light illumination can be explained by competition between photoionization of F and F' centers and electron capture by F centers and anion vacancies (α centers) according to the following scheme [14]:

$$\begin{array}{rll}
F + h\nu_F \rightarrow F^* & & I_F \\
F^* \rightarrow F & & k_1[F^*] \\
F^* \rightarrow \alpha + e^- & & k_2[F^*] \\
F + e^- \rightarrow F' & & k_F[e^-]\,[F] \\
\alpha + e^- \rightarrow F^* & & k_\alpha[e^-]\,[\alpha] \\
F' \rightarrow F + e^- & & k_3[F'] \\
F' + h\nu_{F'} \rightarrow F + e & & I_{F'} = \gamma I_F[F']
\end{array}$$

where it has been postulated that the capture of electrons by α centers leads to the excited F center[25]. It is assumed that the short-lived species e^-, F^*, and α are at steady-state leading to

$$[\alpha]\,[F'] = (k_F/k_\alpha)(k_2/k_1)\frac{[F]I_F\tau_{F'}}{1+\gamma I_F\tau_{F'}}, \qquad \text{(A1)}$$

where $\tau_{F'} = 1/k_3$.

We distinguish between two possible mechanisms of M center formation:

$$\begin{array}{ll}
\text{(I) } F'\text{-}\alpha \text{ model} & F' + \alpha \rightarrow M \\
\text{(II) } F\text{-}\alpha \text{ model} & F + \alpha \rightarrow M^+ \\
 & M^+ + e^- \rightarrow M
\end{array}$$

where the first step of (II) is taken to be rate controlling. If it is assumed that the formation of M centers does not alter (A1) significantly, then the initial rate of M center growth for the cases of high and low light intensity are given in paragraph one of the *Results*.

It is interesting to obtain the F' band lifetime predicted by the above model. Taking $I_F = 0$ and assuming that e^- and F^* remain at steady state during F' decay leads to a complex rate equation. A considerable simplification results when $k_F[F] \gg k_\alpha[F']$, which should be valid in KCl where a high conversion of F centers to F' centers is not usually obtained, leading to:

$$-\mathrm{d}[F']/\mathrm{d}t = \frac{k_1 k_\alpha[F']^2}{(k_1+k_2)\{k_F[F]I_{F'}+1\}}. \qquad \text{(A2)}$$

Thus, the decay of the F' band should be second order in the F' center concentration (in contrast to the first-order lifetime of the individual F' center) with a rate constant that decreases at higher F center density. The bimolecular decay of the F' band in KCl with a rate constant proportional to $1/[F]$ was reported by Ikezawa *et al.*[26] and their analysis leads to an equation similar to (A2) except for the unity in the denominator.

APPENDIX B

Calculation of M *center growth induced by repetitive illumination according to the* F'_α *model*

The general solution of equation (2) is:

$$F'_\alpha(t) = \eta I_0 K^{-1}[1 - \mathrm{e}^{-K(t-t_i)}] + F'_\alpha(t_i)\,\mathrm{e}^{-K(t-t_i)} \qquad \text{(B1)}$$

where t_i is any initial time, $k \equiv k_1 + k_2$, and $K \equiv k + \eta' B I_0$. (It is convenient in this section to represent the concentrations of F'_α and M centers by the symbols themselves). The net yield of F'_α during the n'th pulse is:

$$F'_\alpha(nt_0+\tau) = \eta I_0 K^{-1}[1 - \mathrm{e}^{-K\tau}] + F'_\alpha(nt_0)\,\mathrm{e}^{-K\tau} \qquad \text{(B2)}$$

while the F'_α concentration immediately before the $(n+1)$'th pulse is:

$$F'_\alpha[(n+1)t_0] = F'(nt_0+\tau)\,\mathrm{e}^{-k(t_0-\tau)} \qquad \text{(B3)}$$

The geometric series obtained by letting n range from 0 to n is summed to give:

$$F'_\alpha(nt_0) = F'_\alpha(\tau)\frac{[1-\mathrm{e}^{-n[k(t_0-\tau)+K\tau]}]}{1-\mathrm{e}^{-k(t_0-\tau)-K\tau}}\,\mathrm{e}^{-k(t_0-\tau)}$$

$$\text{(light on)} \qquad \text{(B4)}$$

$$F'_\alpha(nt_0+\tau) = F'_\alpha(\tau)\,\frac{[1-\mathrm{e}^{-(n+1)[k(t_0-\tau)+K\tau]}]}{1-\mathrm{e}^{-k(t_0-\tau)-K\tau}}$$

$$\text{(light off)} \qquad \text{(B5)}$$

where

$$F'_\alpha(\tau) \equiv \eta I_0 K^{-1}(1-\mathrm{e}^{-K\tau}). \qquad \text{(B6)}$$

For the experimental case where $t_0 \gg \tau$ we can ignore the growth of M centers during the pulse, and obtain the growth of M centers during the dark period after the n'th pulse but before the $(n+1)$'th pulse by substituting (B1) in equation (2) and integrating:

$$\begin{aligned}
\Delta M &\equiv M[(n+1)t_0] - M(nt_0+\tau) \\
&= k_1 k^{-1} F'_\alpha(nt_0+\tau)[1-\mathrm{e}^{-k(t_0-\tau)}] \qquad \text{(B7)}
\end{aligned}$$

Finally, for sufficient irradiation times that $Nkt_0 \gg 1$, i.e. when the time *average* F'_α concentration is at steady state, (B7) reduces to equation (4) of the text.

J. Phys. Chem. Solids Pergamon Press 1969. Vol. 30, pp. 2037–2043. Printed in Great Britain.

THERMAL IONIZATION ENERGY OF LITHIUM AND LITHIUM-OXYGEN COMPLEXES IN SINGLE-CRYSTAL SILICON

ROGER KEITH CROUCH
NASA Langley Research Center
and
T. E. GILMER, Jr.
Virginia Polytechnic Institute, Blacksburg, Va. 24061, U.S.A.

(*Received* 8 *July* 1968; *in revised form* 30 *January* 1969)

Abstract – Recent optical studies[1, 2] have found that for float-zone crystals, having a relatively low oxygen content (less than 10^{16} cm^{-3}), the ionization energy of the lithium impurity was about 32 meV, whereas for pulled-crucible crystals, having a higher oxygen concentration (approximately 10^{18} cm^{-3}), the ionization energy was 39 meV. Previous measurements by means of Hall effect studies had indicated that the ionization energy in a pulled crucible sample was about 33 meV which seemed to agree with the optical float-zone value. In an attempt to clarify the situation, Hall effect measurements were made on pulled-crucible and float-zone silicon samples containing lithium as an impurity, and ionization energies were calculated. It was found that this new Hall effect data seemed to be in agreement with the optical data, the ionization energy being 37 meV for the pulled crucible sample and 29·5 meV for the float-zone.

1. INTRODUCTION

THE PROPERTIES of lithium as an impurity in the elemental semiconductor silicon are of great interest due to an increasing number of electronic devices which use lithium doped silicon as a basic material. Optical studies[1, 2] have recently shown that the interstitial lithium impurity exhibits an excitation spectrum which is similar to that exhibited by a Group V impurity; however, the energy levels of this spectrum are different for float-zone and pulled-crucible silicon. The primary difference in these two types of silicon is the concentration of oxygen with which the lithium is known to interact[3]. Measurements of the thermal ionization energy of the lithium impurity in silicon have been made by a group from Bell Laboratories[4] on a sample which almost certainly contained a large amount of oxygen, but the values they obtained agree closely with values determined optically for material which had a low oxygen content. This study deals with a determination of the thermal ionization energy of the lithium impurity in a float-zone crystal (low oxygen content) and a pulled-crucible crystal (high oxygen content), and a comparison of these values with those determined by the optical studies. The thermal data is analyzed taking the splitting of the degenerate ground state into account. It is found that failure to consider this splitting can lead to significant errors in values for ionization energy as well as donor and acceptor concentrations.

2. DESCRIPTION OF THE EXPERIMENT

Silicon crystals

Pulled-crucible crystal. Silicon crystals grown by the Czochralski or pulled-crucible method typically have on the order of 10^{18} atoms/cm^3 of oxygen as an impurity. Kaiser and Keck[5] have given values of the absorption coefficient at the nine micron band as a function of oxygen concentration. Using their values, the oxygen content of the pulled-crucible sample used in these tests was 5×10^{17} atoms/cm^3. The major active impurity prior to doping was boron. The sample resistivity measured on a four-point probe was approximately 5000 Ω-cm, indicating an acceptor concentration of approximately $10^{12}\,\mathrm{cm}^{-3}$. The major inert impurity is believed to be carbon having a concentration of a few parts per million.

Float-zone crystal. Float-zone refined silicon crystals have much lower oxygen concentration than the pulled-crucible crystal. The oxygen content of the float-zone sample used in these tests was not detectable by i.r. techniques and thus has an upper limit of $10^{16}/\mathrm{cm}^3$[5]. Also, there were probably a few parts per million of carbon present.

Doping procedure. The samples were doped using essentially the same technique used by Aggarwal *et al.*[2]. Silicon wafers were coated with a commercially available suspension of lithium in mineral oil. The wafers were then heated for 2 hr in a helium environment at 200°C to drive off the oil. The temperature was raised to 400°C and held for 30 min to drive the lithium into the silicon crystal. The wafers were then removed from the furnace and the excess lithium cleaned off before being heated in a helium environment at 600°C for 2 hr to assure a homogeneous distribution of the lithium and anneal any 'thermal conversion' of the type described by Fuller and Logan[6].

Hall measurements

Sample preparation[7]. Standard 'bridge-shaped' samples were cut from the doped silicon wafers with an ultrasonic impact grinder. Surface contaminants were removed by etching the samples in CP-4 (a mixture of hydrofluoric, nitric, and acetic acid). The tabs were then sandblasted and plated with nickel by an electrodeless process. A tesla coil was used on each tab to aid in removing any rectifying contacts which may have been present. Indium solder was used to connect the sample to the measuring circuitry of the cryostat.

Measuring system. The cryostat was similar in design to that described in reference [8], using liquid helium as a coolant and gaseous helium in the sample chamber as an exchange gas to insure uniform temperatures. Temperatures below 100°K were measured by a germanium resistance thermometer, while temperatures greater than 100°K were measured by a copper-constantan thermocouple. All voltages were measured on a precision digital voltmeter except those instances where the circuit resistance became comparable to the resistance of the voltmeter. In these cases an electrometer was used. The magnet provided a uniform field of 4000 G over the entire sample for all Hall measurements.

At each temperature a series of four measurements was taken, reversing the electric and magnetic field in all possible combinations to minimize errors due to misalignment of the Hall probes and other galvanomagnetic and thermomagnetic effects [9].

Calculations

Hall coefficient. In order to calculate the Hall coefficient, R_H, from the measured quantities: i.e. V_H, H, I; the Hall voltage, magnitude of the magnetic field and current through the sample, respectively, as well as t, the thickness of the sample, the equation

$$R_H = (V_H t/HI) \times 10^8 \qquad (1)$$

was used[10]. Values for the electron concentration in the conduction band, n, were determined from the equation

$$n = (1/R_H e). \qquad (2)$$

For temperatures less than about 100°K, Long and Myers have shown that ionized impurity scattering is important and that the proportionality term between R_H and n is a complex function of temperature and concentration[11]. Since the proportionality term is never too different from unity, it is assumed to be 1·0 for all calculations in this paper.

Ionization energy. Kohn and Luttinger have calculated the type of energy level scheme which a substitutional donor impurity would be expected to have, taking into account the known structure of the bottom edge of the conduction band[12, 13]. Since the wave function for the effective mass ground state was constructed from the Bloch functions of the six equivalent minima of the conduction band, it would be six-fold degenerate. Since the theoretical values for the effective mass ground state energy level did not agree with the experimental value for the ionization energy of various donor impurities, but the predicted levels for the various excited states agreed closely with the experimental i.r. data, Kohn and Luttinger pointed out that the effective mass theory was not applicable in the region rather close to the donor ion due to the failure of some of the assumptions, mainly, the form of the potential. However, calculations of the so-called valley-orbit splitting[13] show that the six-fold degenerate ground state is split into three levels with degeneracies of 1, 2 and 3. The singlet state has the lowest energy for a group V impurity and calculations considering the valley-orbit splitting give ionization energies that agree very well with the experimental values[14]. The doublet and triplet states are relatively close in energy and can normally be considered to be equivalent to a five-fold degenerate level, close to the predicted value for the effective mass ground state energy.

Using an energy level structure similar to that of Kohn and Luttinger, the distribution of electrons among all the states of the conduction band and any compensating impurities in n type silicon is given by the statistical equation[11]:

$$\frac{n(n+N_a)}{N_d-N_a-n}=\frac{2\cdot 75\times 10^{15}\,T^{3/2}\exp(-E_d/kT)}{1+5\exp(\Delta/kT)+\sum_{i=2}^{N} g_i\exp(\Delta_i/kT)}. \tag{3}$$

The factor $2\cdot 75\times 10^{15}$ is the effective density of states in the conduction band, E_d, is the energy separation between the singlet ground state and the conduction band and g_i is the degeneracy of the ith excited electronic state. $\Delta = E_m - E_d$ and $\Delta_i = E_i - E_d$ where E_m and E_i is the energy separating the conduction band from the five-fold degenerate ground state and the ith excited state respectively.

Δ_i will always be less than zero and if Δ is also less than zero, as it generally will be, then an expression for E_d can be obtained from equation (3) such that

$$E_d=\frac{k}{1/T_2-1/T_1}\ln\frac{n_1/T_1^{3/2}}{n_2/T_2^{3/2}}+\ln\frac{1+5\exp(\Delta/kT_1)}{1+5\exp(\Delta/kT_2)} \tag{4}$$

where the subscripts 1 and 2 correspond to experimental values at temperatures where $n \ll N_a$. Using values of N_a determined from the low temperature equation

$$N_a=\frac{N_d-N_a}{n}\,\frac{2\cdot 75\times 10^{15}\,T^{3/2}\exp(-E_d/kT)}{1+5\exp(\Delta/kT)}, \tag{5}$$

Long and Myers[15] determined the optimum value of Δ to give a best fit of equation (3) to experimental Hall data which they had obtained. They found Δ to be between minus 9–12 meV for phosphorous. Aggrawal and Ramdas[16] later made optical measurements of the splitting which agree very well with the thermal data, being − 11·85 meV. (Aggarwal found that the doublet and triplet state in phosphorous were split by 1·35 meV, the triplet state having the lowest energy.)

The data presented in this paper were analyzed by means of a computer program which fitted equation (3) to the experimental data by the method of least squares with respect to the three parameters N_d, N_a and E_d. Comparison of values calculated using equations (4) and (5) and values calculated by the computer program for phosphorous data showed very good agreement (differences around 0·5 per cent for E_d and 5 per cent for N_a). These calculations also showed that consideration of the excited states other than the upper 1S states made essentially no difference in the results. Appropriate values of Δ are a required input of the program and were obtained from the literature.

3. RESULTS AND DISCUSSION

Pulled-crucible sample

Figure 1 presents a plot of the carrier concentration as a function of temperature for the pulled-crucible sample. (This impurity has been previously identified as LiO[1, 2].) The curve in the figure corresponds to the values predicted by the computer program using $\Delta = -7{\cdot}7$ meV[2]. The values for E_d, N_a and N_d from the computer program were 37·3 meV, $2{\cdot}17 \times 10^{12}\,\text{cm}^{-3}$ and $3{\cdot}74 \times 10^{15}\,\text{cm}^{-3}$, respectively. The values for N_d agree with values of n in the region where nearly all uncompensated donors are ionized, *viz.* $3{\cdot}67 \times 10^{15}\,\text{cm}^{-3}$, and N_a is in agreement with the acceptor concentration prior to doping ($2{\cdot}6 \times 10^{12}\,\text{cm}^{-3}$). The value for the ionization energy is slightly lower than the optical value of 39 meV[1], but seems to agree with the optical value much better than the thermal value of 33 meV reported by Morin *et al.*[4]. Using the values obtained from the computer program for N_d, N_a and E_d, Fig. 2 shows the effect which consideration of the upper ground state has on the fit of the curve to the experimental data. The curve labeled $\Delta = -\infty$ is simply equation (3), neglecting all terms except unity in the denominator on the right hand side, whereas the curve labeled $\Delta = -7{\cdot}7$ meV is equation (3), neglecting the summation terms. It is apparent that the upper

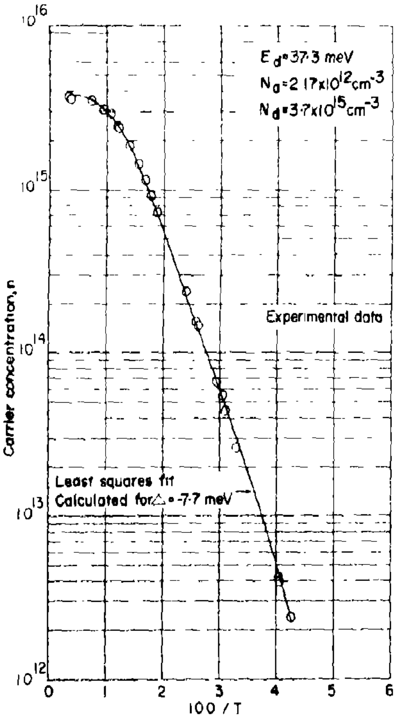

Fig. 1. Carrier concentration as a function of temperature for LiO impurity

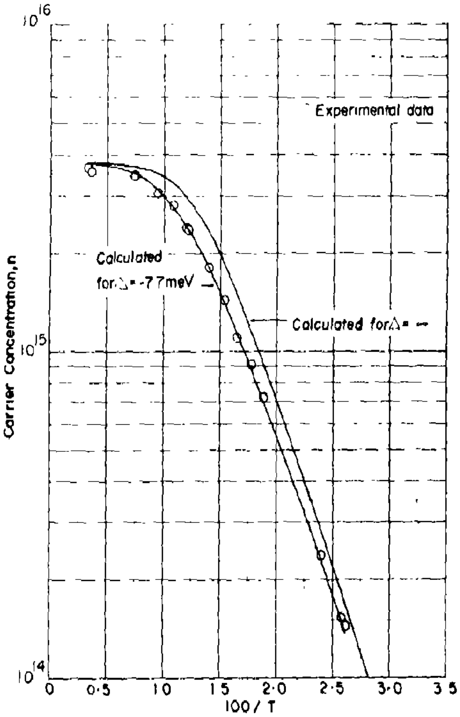

Fig. 2. Effect of consideration of upper level ground state for LiO data.

level of the ground state affects the shape of the curve over an intermediate temperature range.

The difference between the present thermal value for the ionization energy and the optical value, as well as the difference in the present and previous thermal value can, at least partially, be explained by a consideration of the excited impurity states. Kohn commented about the difference in thermal and optical values for ionization energy but offered no explanation[13]. Various papers have noted a difference in thermal ionization energy as a function of concentration[10, 17]. This dependency of E_d upon concentration appears to be fairly well explained by the model proposed by Erginsoy[18] and elaborated somewhat by Baltensperger[19] in which the excited impurity states form bands which overlap with the conduction band, effectively lowering the conduction band edge. An increase in concentration would result in more overlap for a lower excited state; thus, the conduction band would be lowered even further. It is believed that this model could also aid in explaining the differences between optical and thermal values. The optical value for E_d is determined by adding the value calculated by effective mass theory for the depth of an excited state to the optically determined value for a transition from the ground state to the excited state[13]. The excited state used is generally the $3p_\pm$[1, 2]. The effect of the overlap of the higher order states would not be seen except in the disappearance of such states as the $6p_\pm$, $5p_\pm$, $4p_\pm$, and so forth, from the optical spectra as the concentration is increased. Eventually, the $3p_\pm$ peak would itself disappear; however, before this point is reached, the number of free carriers still in the conduction band even at these lower temperatures is usually such that for a reasonably thick sample, most of the i.r. radiation is absorbed by the sample, and resolution of the absorption peaks becomes very difficult. Therefore, other than for some concentration broadening of the peaks, the optical ionization energy would generally be unchanged for different impurity concentrations. Thus, it seems that this model would partly explain the discrepancy between the thermal value obtained here and optical values. Another possibility for the difference in thermal and optical values of lithium in silicon could be occupation by electrons of energy levels close to that identified as a LiO state but having a slightly higher energy. Gilmer, Franks and Bell identified six donor-like series of spectra in a sample similar to the one in this paper[1]. If these were possible electron states, their energies could not be separated by Hall measurements, and the ionization energy deduced from the Hall data would be a weighted average of the energy of each of these states. Since they would have a lower ionization energy than the primary state at 39 meV, the resultant thermal ionization energy would be smaller.

Float-zone sample

The carrier concentration as a function of temperature for the float-zone sample is presented in Fig. 3. (This impurity has been identified as an isolated lithium atom[1, 2].) The solid line corresponds to the fitted curve from the computer program using $\Delta = 1{\cdot}6$ meV[2]. Calculated values of N_d and N_a were $1{\cdot}08 \times 10^{17}\,\text{cm}^{-3}$ and $7{\cdot}4 \times 10^{14}\,\text{cm}^{-3}$, respectively, which compare quite well with the experimentally determined values of $9{\cdot}9 \times 10^{16}\,\text{cm}^{-3}$ and $10^{15}\,\text{cm}^{-3}$ for N_d and N_a. The value for E_d, the energy separation between the singlet ground state and the conduction band, was 27·9 meV. The curve in Fig. 3 was calculated using the structure of the ground state which Aggarwal *et al.* used to explain their optical data. In this model the energy separation between the five-fold degenerate ground state and the conduction band is greater than the energy separation between the singlet ground state and the conduction band; therefore, the ionization energy in this case would be E_m or 29·5 meV, from the relationship $E_m = E_d + \Delta$. (This 'anomalous' ground

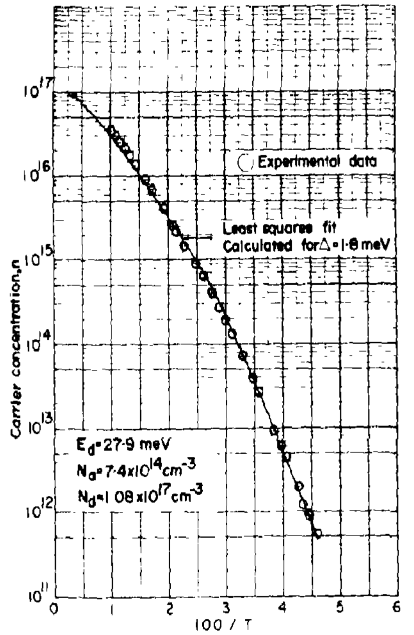

Fig. 3. Carrier concentration as a function of temperature for Li impurity.

state structure could be due to the interstitial location of lithium.) This value of 29·5 meV seems to be comparable to the optical value of 32 meV[1, 2], particularly in view of the relatively high impurity concentration of this sample. The agreement between the calculated values and the experimental data using the model proposed by Aggarwal *et al.* seems to imply that their description of the ground state structure is adequate for this type of study.

Consideration of the degenerate ground state is essential in the analysis of the lithium data. Failure to consider this degeneracy results in errors for the values obtained by the computer program for E_d, N_d and N_a, and a resultant poor fit of predicted to measured values of n. Figure 4 presents a plot of the carrier concentration as a function of temperature where the solid line represents the least square fit considering only a singlet ground state. Values for E_d, N_d and N_a were 25·9 meV, $5{\cdot}7 \times 10^{16}$ cm^{-3}, and $1{\cdot}7 \times 10^{16}$ cm^{-3}, respectively. Thus neglecting the degeneracy gives a value of N_d that is in error by about a factor of 2, and N_a that is an order of magnitude higher than it should be compared to predope resistivity measurements, and an ionization energy that is too small by about 12 per cent.

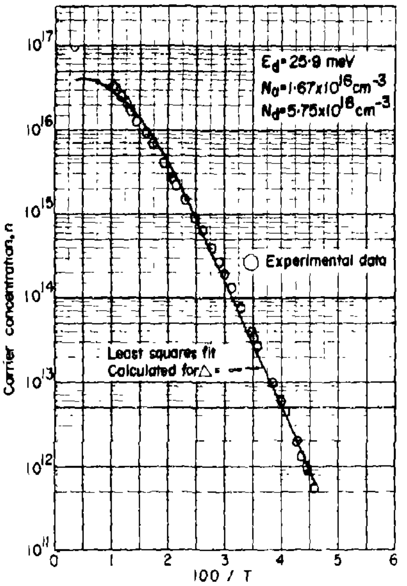

Fig. 4. Carrier concentration as a function of temperature for Li impurity neglecting ground state degeneracy

4. CONCLUDING REMARKS

Measurements of the thermal ionization energy of lithium impurities in single-crystal silicon by means of the Hall effect have shown that the ionization energy is a function of the oxygen concentration in the silicon. Values determined were 29·5 meV for a float-zone crystal (believed to have about 10^{15} oxygen atoms per cm^3) and 37·3 meV for a pulled-crucible crystal (having about 5×10^{17} oxygen atoms per cm^3 by i.r. measurements) which tend to agree with values previously determined optically. These measurements also showed the importance of considering the degeneracy of the ground state in calculating the ionization energy, particularly in the float-zone crystals where the splitting of the ground state is relatively small. The ground state structure proposed by Aggarwal *et al.*, wherein the five-fold degenerate state has a lower energy than the singlet state, seems to adequately describe the data.

Acknowledgements—The help of M. F. McNear in sample preparation and equipment construction was very beneficial and the authors wish to thank him.

REFERENCES

1. GILMER T. E., Jr., FRANKS R. K. and BELL R. J., *J. Phys. Chem. Solids* **26**, 1195 (1965).
2. AGGARWAL R. L., FISHER P., MOURZINE V. and RAMDAS A. K., *Phys. Rev.* **138**, A882 (1965).
3. PELL E. M., In *Solid State Physics in Electronics and Telecommunications*, Vol. 1, p. 261. Academic Press, New York (1960).
4. MORIN F. J., MAITA J. P., SHULMAN R. G. and HANNAY N. B., *Phys. Rev.* **96**, 833 (1953)
5. KAISER W. and KECK P. H., *J. appl. Phys.* **28**, 882 (1957).
6. FULLER C. S. and LOGAN R. A., *J. appl. Phys.* **28**, 1427 (1957).
7. BRECKENRIDGE R. A. and DEBNAM W. A., Jr., Private communication.
8. FRITZSCHE H., In *Methods in Experimental Physics* (Edited by K. Lark-Horovitz and Vivian A. Johnson), Vol. 6, Part B, p. 157. Academic Press, New York (1959).
9. LINDBERG OLOF, *Proc. Instn Radio Engrs* **40**, 1414 (1952)
10. SHOCKLEY W., In *Electrons and Holes in Semiconductors*, p. 213. Van Nostrand, New York (1950).
11. LONG D. and MYERS J., *Phys. Rev.* **115**, 1107 (1959)
12. KOHN W. and LUTTINGER J. M., *Phys. Rev.* **98**, 915 (1955).
13. KOHN W., In *Solid State Physics* (Edited by F. Seitz and D. Turnbull), Vol. 5, pp. 257–320. Academic Press, New York (1957).
14. NARITA K. and SHIMIZU T., *J. phys. Soc. Japan* **16**, 2588 (1961).
15. LONG D. and MYERS J., *Phys. Rev.* **115**, 1119 (1959)
16. AGGARWAL R. L. and RAMDAS A. K., *Phys. Rev* **140**, A1246 (1965).
17. DEBYE P. and CONWELL E., *Phys. Rev.* **93**, 693 (1954).
18. ERGINSOY C., *Phys. Rev.* **80**, 1104 (1950), *ibid.* **88**, 893 (1952)
19. BALTENSPERGER W., *Phil. Mag.* (*Series 7*) **44**, 1355 (1953).

J. Phys. Chem. Solids Pergamon Press 1969. Vol. 30, pp. 2045–2051. Printed in Great Britain.

THE PRESSURE DEPENDENCE OF THE TRANSITION TEMPERATURE IN KDP AND ADP[*]

J. SKALYO, Jr., B. C. FRAZER and G. SHIRANE
Brookhaven National Laboratory, Upton, N.Y. 11973, U.S.A.

and

W. B. DANIELS
Princeton University, Princeton, N.J. 08540, U.S.A.

(*Received* 24 *January* 1969)

Abstract—The pressure dependence of the ferroelectric transition temperature for KD_2PO_4 and for $K(D_{0.55}H_{0.45})_2PO_4$ has been measured to 10 kbar. The dependence in both cases was linear, with slopes of $-2{\cdot}40 \pm 0{\cdot}01$°K/kbar and $-2{\cdot}93 \pm 0{\cdot}01$°K/kbar respectively. Measurements on $ND_4D_2PO_4$ and $NH_4H_2PO_4$ over a smaller pressure range gave linear fits with slopes of $-1{\cdot}43 \pm 0{\cdot}04$°K/kbar and $-3{\cdot}39 \pm 0{\cdot}06$°K/kbar respectively. The results were obtained by neutron diffraction wherein the transition was detected by the sharp decrease of extinction effects on transforming to the low temperature phase. The present results on KDP are consistent with previous neutron diffraction measurements utilizing samples with 0 per cent and approx. 90 per cent deuteration. The values for dT_c/dP are found to be approximately 1°K/kbar less negative than those determined from dielectric constant measurements.

1. INTRODUCTION

KH_2PO_4 (abbreviated as KDP) is a well-known ferroelectric prototype. The importance of the role of the hydrogen bonds in explaining the ferroelectric mechanism in KDP-type crystals is evident from the large shift in transition temperature which occurs upon substitution of deuterium for hydrogen [1]. More recently, the effect of pressure on the transition temperature has also indicated differences due to deuteration[2–4]. The pressure dependence is observed to be linear but with a slope dependent upon the deuteration level.

The structure of KDP has been determined by both X-rays[5] and neutron diffraction[6] in both the paraelectric and ferroelectric phases. The important structural feature of both phases is the network of hydrogen bonds which links each phosphate group to neighboring phosphate groups in a tetrahedral array. Similar hydrogen bonding of phosphate groups has been verified for the case of $NH_4H_2PO_4$ (abbreviated to ADP)[7], in which the transformation at low temperature is to an antiferroelectric phase.

The length of the O–H . . . O bond is rather critical in determining the positioning of the H atom[8]. If the bond is longer than about 2·55 Å, a double-well potential exists along the bond with a central barrier of sufficient height to effectively lock the hydrogen into one well. For a very short bond, a symmetric single well results. In the region of intermediate bond length, as is the case for KDP-type crystals, the nature of the bond can be either an anharmonic single well or a double well with low barrier. The neutron diffraction results on paraelectric KDP indicate that the hydrogen atom is either statistically disordered, and located in the minima of a double potential, or that the hydrogen is making large vibrations about the bond center[6]. Nuclear magnetic resonance measurements have been able to prove the latter and that either a "hopping' in an anharmonic single well or a true tunneling through a low barrier is occurring[9].

---

[*] Work performed under the auspices of the U.S. Atomic Energy Commission and the National Science Foundation.

Apart from the initial success of Pirenne[10] with a model utilizing a square-well potential along the bond (an extreme case of an anharmonic single well), it appears that most subsequent theories have centered on the tunneling model[11]. In that context, recent theoretical estimates of the change in transition temperature with pressure based on a tunneling mode agree within 30 per cent of the observed dependence[12, 13]. More important, the effect on the slope caused by the deuteration level is also predicted.

The measurements of $T_c(P)$ by neutron diffraction[2] in KDP and in a 90 per cent deuterated isomorph display different slopes than dielectric constant measurements of $T_0(P)$ [3, 4]. The difference appears to be systematic with dT_c/dP about 1°K/kbar less negative than dT_0/dP. The present results confirm the previous neutron diffraction measurements on KDP and also indicate a similar dependence of the antiferroelectric transition temperature (T_N) in ADP and its deuterated isomorph.

2. SAMPLE AND APPARATUS

The samples were 10 mm long and 1 mm in dia. with an *a*-axis parallel to the rod axis. The sample was mounted in an unconstrained manner in a maraged-steel high-pressure cell as indicated in Fig. 1. The cell was fastened to the temperature-controlled base of a helium cryostat, and the temperature was measured to ±0·05°K with a platinum resistance thermometer implanted in the copper control block. Pressure was applied to the cell through 1/16 in. O.D. high-pressure tubing which was thermally grounded to the radiation shield. Helium gas was used as the pressure-transmitting medium in a system using a diaphragm-type compressor up to 2 kbar and a pressure intensifier from 2 to 10 kbar. In order to check for possible effects due to diffusion of He into the sample, the transition temperature of $K(D_{0\cdot55}H_{0\cdot45})_2PO_4$ was measured also at 3·5 kbar with argon as the transmitting medium. No difference with the He result was observed.

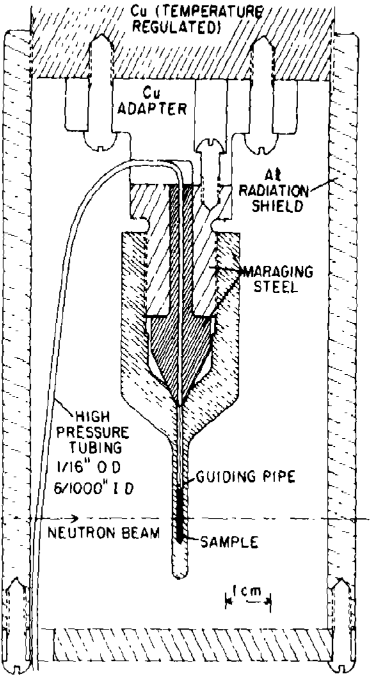

Fig. 1. High pressure cell for neutron diffraction measurements up to 10 kbar. An additional shield at 77°K and a vacuum jacket are not depicted.

The pressure of the system was measured with a maganin gauge calibrated to 7 kbar with a bourdon gauge. The calibration was linear to within 200 psi over this range and it was estimated that an extrapolation to 10 kbar would be precise to at least 0·5%. The gauge calibration also agreed to 0·2 per cent with a similarly constructed gauge fashioned from the same spool of wire which was calibrated against the freezing point of mercury at 0°C. The accuracy would appear to be better than ±1 per cent.

The deuteration percentages of the samples are indicated in Table 1. The values are those specified by the supplier[14] and have been determined by NMR for the ADP and by destructive distillation for the KDP. The accuracy of these values after the samples have been stored and handled must be in-

Table 1

% Deuteration	$T_{c,P=0}$	$\frac{dT_c}{dP}$ (°K/kbar)	Method
	KDP		
0	122	−4·52 ± 0·06	Neutrons [2]
	120·8	−5·7	
0	120·0	−5·5	Dielectric constants [3]
	120·4	−5·7	
55·1 ± 0·5	183·0	−2·93 ± 0·01	Neutrons, this work
≈90	213	−2·63 ± 0·05	Neutrons [2]
≈90	208	−3·9 ± 0·2	Dielectric constant [4]
99·0 ± 0·5	220·6	−2·40 ± 0·01	Neutrons, this work
	ADP		
0	151·2	−3·39 ± 0·06	Neutrons, this work
99·0 ± 0·2	235·1	−1·43 ± 0·04	Neutrons, this work

ferred by the measured transition temperature at zero pressure. A possible decrease in deuteration could occur due to the small size of the samples. In the case of the 99 per cent deuterated samples, a comparison of the transition temperature at 1 bar can be made with values obtained by other investigators. The value for 99 per cent deuterated KDP observed here was 220·6 ± 0·2°K which compares excellently with the value of 222 ± 1°K obtained by Sliker and Burlage[15]. The value for 99 per cent deuterated ADP is 235·1 ± 0·2°K which is 7°K lower than the value of Mason and Matthias[16] obtained by measuring the discontinuous change of the dielectric constant. Another recently reported value of 240°K for a 96 per cent deuterated sample[17] is in agreement with the value of Mason and Matthias. While it appears that our sample would have lost some 7 per cent of its deuteration, a check of two other large crystals (~1 cm^3) deuterated to 99 per cent (also obtained from Isomet Corporation) gave transition temperatures of 234·0 ± 0·5°K and 234·0 ± 0·3°K. The source of discrepancy would appear, therefore, not to be due to improper handling. Table 1 also correctly identifies a KDP sample inferred to be ~ 100 per cent deuterated by Umebayashi *et al.* as nominally 90 per cent deuterated[18].

The transition in ADP has the nature of shattering a single crystal into a multitude of crystallites[7]. In order to keep the crystallites from falling apart, the sample was coated with flexible collodion before mounting in the sample cell. This precaution permitted the measurement of the $T_c(P)$ with one sample. Collodion was not applied to the two large crystals whose transition temperature was measured; the clamping of the collodion was therefore minimal.

3. METHOD AND RESULTS

The measurements were made on a double-axis spectrometer at the Brookhaven High Flux Beam Reactor. The method consisted of monitoring the peak intensity of a Bragg reflection as the temperature was changed at constant pressure. Passage through the transition was accompanied by a sharp change in intensity. The increase in intensity in the low temperature phase is attributed to a reduction of extinction as a consequence of structural change; the crystals are now composed of oppositely polarized domains. A typical measurement is shown in Fig. 2.

The temperature was changed continuously at a constant rate. The massive pressure cell and temperature shield effected a temperature difference between the thermometer and the sample. Corrections to zero-rate were made to all data; i.e. the temperature indicated in Fig. 2 should be decreased by 0·20°K. In addition, all points on the KDP samples were

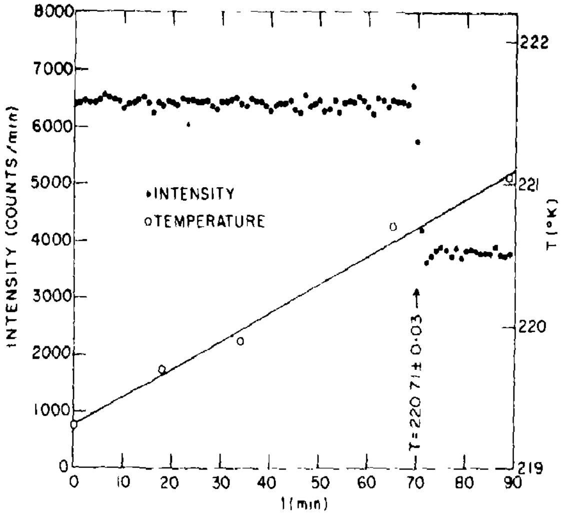

Fig. 2. Heating determination of T_c for KD_2PO_4 at 1 bar. The intensity of the (004) Bragg peak is shown.

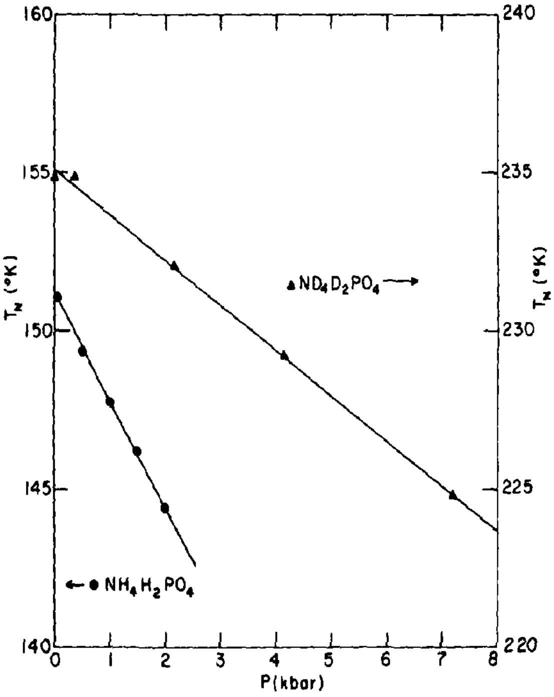

Fig. 3. Transition temperature vs. pressure for $NH_4H_2PO_4$ and $ND_4D_2PO_4$.

measured by heating and cooling curves; the corrected transition temperatures agreed to within 0·1°K. This latter check was not possible on the ADP samples due to a hysteresis of 1°–4°K. However, the ADP points were obtained at approximately the same cooling rate to minimize the error in dT_N/dP.

The results of the measurements on the two samples of ADP are depicted in Fig. 3 and summarized in Table 1. We have included only the points obtained upon cooling. As the phase change is of first order in ADP, and since the crystal is grown in an unstrained state in the paraelectric phase, the cooling curve is felt to be a more reliable measure of the effects of pressure on T_N. The measurements on the KDP samples are shown in Fig. 4 and summarized in Table 1.

4. DISCUSSION

An interpretation of the negative slope for dT_c/dP by Umebayashi *et al.*[2] was based qualitatively on a tunneling mode. Novakovic [12] utilized a molecular field model incorporating the tunneling mode to calculate dT_c/dP, obtaining $-3{\cdot}13$°K/kbar for KH_2PO_4 and $-1{\cdot}89$°K/kbar for KD_2PO_4. A similar calculation by Blinc and Zeks[13] evaluated for a four-particle cluster approximation gave values of $-4{\cdot}70$°K/kbar for KH_2PO_4 and $-3{\cdot}36$°K/kbar for KD_2PO_4. The theoretical results assume two harmonic oscillator potential wells for the potential. The agreement with experiment is within 30 per cent, and the predicted less negative slope for the deuterated sample is observed. It would appear that the slope of dT_c/dP vs. deuteration could be fitted by an adjustment of the bond potential barrier.

The variation of the transition temperature with pressure is found to be linear up to 10 kbar for KD_2PO_4 and $K(D_{0{\cdot}55}H_{0{\cdot}45})_2PO_4$. The linear behavior has been previously noted for KH_2PO_4 and $K(D_{0{\cdot}9}H_{0{\cdot}1})_2PO_4$[2-4]. All results are listed in Table 1 and shown in Fig. 5, where the lines are drawn as an aid to the eye in connecting the points. From

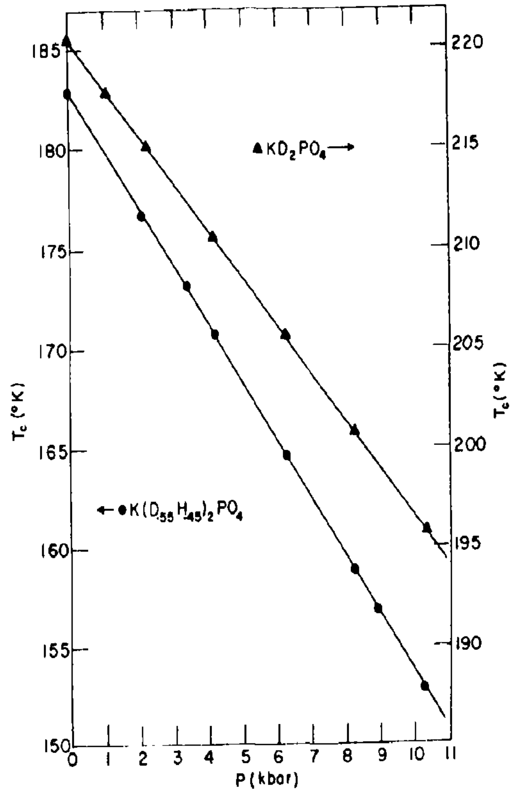

Fig 4. Transition temperature vs. pressure for KD_2PO_4 and $K(D_{0{\cdot}55}H_{0{\cdot}45})_2PO_4$.

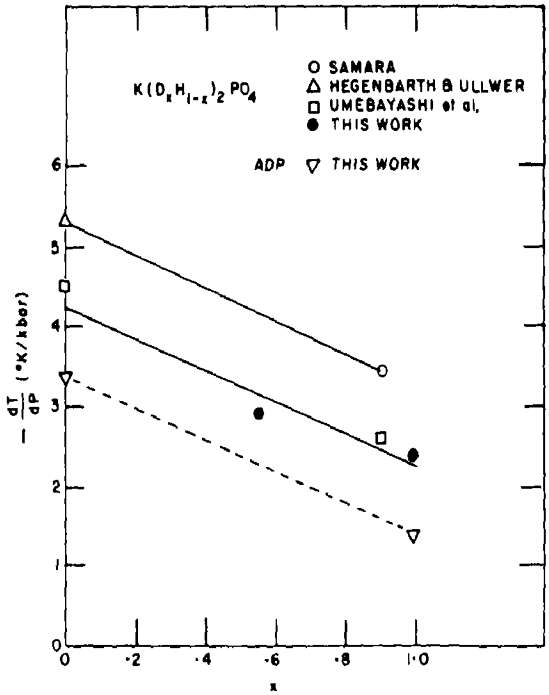

Fig. 5. dT/dP for KDP and ADP vs. relative deuteration. Lines have been drawn through the points as an aid to the eye.

Fig. 5, it is apparent that the results of the neutron diffraction experiments are in disagreement with the results utilizing dielectric constant measurements. The dielectric constant measurements give dT_0/dP where

$$\epsilon \cong \frac{C}{T-T_0};\ T > T_0$$

An extrapolation of $1/\epsilon$ to zero gives the value T_0. If, instead, T_c is taken as the point where the dielectric constant is a maximum, Samara finds no significant difference between dT_c/dP and dT_0/dP[19].

The source of the discrepancy is not apparent. As the crystals are grown from solution near room temperature, sample purity would not appear to be paramount. The effect may be due to some slight constraining of the sample in the dielectric constant measuring apparatus or due to measurements being made with the application of a field.

$NH_4H_2PO_4$ and $ND_4D_2PO_4$ are also found to have negative values of dT_N/dP, with the deuterated sample again giving a less negative slope. The results are listed in Table 1 and plotted in Fig. 5. The values of dT_N/dP are of the same magnitude as for the KDP samples and the change of dT_N/dP with deuteration level is similar. This is probably indicative of the similarity of the bond potential along O–H . . . O. Though the O–H . . . O bond may be similar in KDP and ADP, an explanation of the resultant antiferroelectric state will probably necessitate consideration of the N–H . . . O bond.

Acknowledgements—We would like to acknowledge the help of H. Umebayashi in the early stages of this work and the technical help of W. Lenz in constructing the high pressure apparatus.

REFERENCES

1. JONA F. and SHIRANE G., *Ferroelectric Crystals*, p. 87. Pergamon Press, Oxford (1962).
2. UMEBAYASHI H., FRAZER B. C., SHIRANE G. and DANIELS W. B., *Solid State Commun.* **5**, 591 (1967).
3. HEGENBARTH F. and ULLWER S., *Cryogenics* **7**, 306 (1967).
4. SAMARA G. A., *Phys. Lett.* **25A**, 664 (1967).
5. FRAZER B. C. and PEPINSKY R., *Acta crystallogr.* **6**, 273 (1953).
6. BACON G. E. and PEASE R. S., *Proc. R. Soc.* **A230**, 359 (1955).
7. TENZER L., FRAZER B. C. and PEPINSKY R., *Acta crystallogr.* **11**, 505 (1958).
8. HAMILTON W. C. and IBERS J. A., *Hydrogen Bonding in Solids*, p. 52. Benjamin, New York (1968).
9. BJORKSTAM J. L., *Phys. Rev.* **153**, 599 (1967).
10. PIRENNE J., *Physica* **15**, 1019 (1949)
11. BLINC R. and HADZI D., *Mol. Phys* **1**, 391 (1958)
12. L. NOVAKOVIC L., *J. Phys. Chem. Solids* **29**, 963 (1968)
13. BLINC R and ŽEKŠ B., *Phys. Lett.* **26A**, 468 (1968).
14. KDP from Clevite Corporation, Cleveland, Ohio and ADP from Isomet Corporation, Palisades Park, New Jersey.
15. SLIKER T. R. and BURLAGE S. R., *J appl. Phys.* **34**, 1837 (1963).
16. MASON W. P. and MATTHIAS B. T., *Phys. Rev.* **88**, 477 (1952).
17. VASILEVSKAYA A. S, VOLKOVA E. N., KOPTSIK V. A., RASHKOVICH L. N, REGUL'SAYA T. A., REZ I. S, SONIN A. S. and SUVOROV V. S, *Soviet Phys crystallogr* **12**, 446 (1967).
18. This clarification was brought to our attention by CARLSON A., Clevite Corporation, Cleveland, Ohio.
19. SAMARA G. A., Private communication

J. Phys. Chem. Solids Pergamon Press 1969. Vol. 30, pp. 2053–2059. Printed in Great Britain.

LOW TEMPERATURE SUPPRESSION BY CHLORINE OF DIFFUSION OF GOLD IN SILVER CHLORIDE*

A. P. BATRA, A. L. LASKAR† and L. SLIFKIN
Department of Physics, University of North Carolina at Chapel Hill, Chapel Hill,
N C. 27514, U.S.A.

(*Received* 24 *December* 1968)

Abstract—The tracer-sectioning technique was used to study the diffusion of aurous ion in silver chloride. Above 260°C, the diffusion proceeds interstitially with an activation energy of 0·47 eV. When the diffusion anneal was carried out in an external chlorine atmosphere, the diffusion coefficient was depressed This behavior is explained in terms of the effect of chlorine on the cation vacancy concentration, and agrees quantitatively with results obtained from optical absorption studies by Ulrici, Koswig and Stasiw. Analysis of the data yields 0·62 eV for the heat of the reaction $\frac{1}{2}Cl_2 = Cl^- +$ cation vacancy + hole.

INTRODUCTION

COMPARISON of ionic conductivity with self-diffusion measurements of silver and halide ions in the silver halides[1, 2] has yielded information on the mechanism of mass transport. One finds that of the two ions, the silver is much more mobile and that its diffusion proceeds predominantly by the interstitialcy mechanism.

Only two monovalent cationic impurities, copper[3] and sodium[4], have so far been examined. Copper diffuses interstitially in both silver chloride and silver bromide. In contrast, sodium diffuses in silver chloride by a vacancy mechanism; also the Arrhenius plot shows a slight upturn at about 300°C which is attributed to the "extra" increase in the intrinsic Frenkel disorder at higher temperatures.

For the diffusion of divalent cations in the silver halides the Arrhenius plots are either linear over the entire temperature range (strontium[5] and calcium[6]) or curved, with a break at about 320°C (manganese[7] and cadmium[8]). It has been suggested[7] that the outer electronic configuration of the diffusing ion determines the nature of the Arrhenius plot. Ions with outer *d*-shell electrons may diffuse by a combination of vacancy and interstitial mechanisms, whereas those with no outer *d*-electrons are likely to diffuse only by a vacancy mechanism.

Previous diffusion measurements in the silver halides have all been carried out in a vacuum or in an inert atmosphere, with the exception of one measurement by Tannhauser [2]. He found that at 351°C the diffusion of bromide in silver bromide is unaffected by a bromine atmosphere of approximately 60 Torr. Other workers, however, have found that the presence of halogen at higher pressures does measurably affect some of the physical properties of the silver and alkali halides For example, near the intrinsic-extrinsic break-point temperature, Müller[9] notices a slight increase in the ionic conductivity of pure silver chloride under a chlorine atmosphere and a rather large increase for silver bromide under a bromine atmosphere. The ionic conductivity of potassium iodide was found by Forbes and Lynch[10] to be enhanced when additively colored with iodine. These results are consistent with the idea that

---

*Work supported by the U.S. Atomic Energy Commission (Contract AT-(40-1)-2036) and the Advanced Research Projects Agency (Contract SD-100)

†Now at the Department of Physics, Clemson University, Clemson, S. C. 29631, U.S.A.

each adsorbed halogen molecule introduces two cation vacancies and two holes in the crystal. In support of this, Ulrici, Koswig and Stasiw[11] have observed that when silver chloride is placed in chlorine at temperatures above 200°C, there appears a new optical absorption, which they attributed to free holes. In addition, it has been shown that silver bromide exposed to bromine vapor exhibits hole conduction[12]. In view of these facts, it seems probable that an external halogen atmosphere of sufficiently high pressure should affect diffusion measurements in the silver halides. The results of a study of gold diffusion in silver chloride, both in primarily inert and in chlorine atmospheres, are reported here.

EXPERIMENTAL AND RESULTS

The experimental procedures have been described in detail elsewhere[13]. Right parallelepiped single crystal specimens of Harshaw silver chloride were used in this work. High-specific activity $Au^{198}Cl_3$ was obtained from Nuclear Science and Engineering Corporation and a thin layer, no more than 20 Å in thickness, was deposited on each specimen, thus satisfying the boundary condition for the thin-film solution to the diffusion equation.

Specific to this particular experiment was the problem of loss of mobile tracer, either by evaporation of $AuCl_3$ or as a result of its decomposition to form immobile gold metal. Evaporation was minimized by surrounding the specimen by a gas, usually a mixture of helium and chlorine, and in some cases by also wrapping the crystal in silver foil. The function of the chlorine in the ambient atmosphere was to inhibit decomposition, although, as will be seen, at pressures of the order of one atmosphere chlorine was found to have more profound effects.

Each of the plated specimens was annealed for one hour, this unusually short period being imposed by the very large diffusion coefficient. The annealing temperature was measured frequently by a chromel-alumel thermocouple placed within the furnace cavity, just outside the encapsulated specimen. Warm-up corrections, which are appreciable for such short diffusion times, were applied. The determination of the diffusivity followed the standard microtome sectioning technique and tracer assay.

In very short runs such as these, the principal error is in the measurement of the instantaneous diffusion temperature, since when the sample is warming up the specimen and thermocouple are not at exactly the same temperature. In a calibrating experiment, this time-dependent temperature difference between the monitoring thermocouple and the specimen was determined. The effective annealing temperatures are believed to be correct to within 2°C, and the diffusion coefficients in error by no more than 10 per cent.

Figure 1 shows three plots for the temperature dependence of the diffusion coefficient of

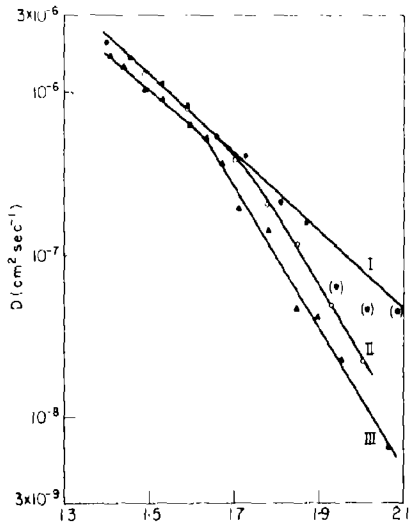

Fig. 1. Arrhenius plots for the diffusion of Au^+ in AgCl. Plot I shows results obtained with an ambient atmosphere of 1 Torr. of chlorine and 400 Torr. of helium. The three low temperature points enclosed in parentheses are only roughly approximate, because of extensive surface hold-up of activity. Plots II and III were obtained using specimens wrapped in silver foil, and annealed in 0·7 and 2 atm of chlorine, respectively.

gold in silver chloride under different annealing atmospheres. The conditions of anneal and the corresponding results are given as follows.

(i) *Diffusion in a mixture of* 1 *Torr. chlorine and* 400 *Torr. helium*

For these runs, the active face of the encapsulated specimen rested on a quartz disc. The diffusion penetration profiles obtained above 260°C were very good Gaussians, as expected from the boundary conditions, and the resulting values of the diffusion coefficient D are given in Table 1 and are shown as curve I of Fig. 1. Below 260°C, however, though still well within the intrinsic conductivity range, the original activity was largely blocked at the specimen surface and only an insignificant amount seemed to have penetrated. It appears unlikely that the solubility of $AuCl_3$ in silver chloride is only infinitesimally small at these temperatures. The blocking, however, may have been due to decomposition of $AuCl_3$, which could become increasingly important at lower temperatures if the activation energy for the decomposition reaction were much less than that for solution. The fact that the activity could be readily washed off almost completely from the surface by aqua regia, but not by water or methyl alcohol, lends support to this view. The values of D at these low temperatures, calculated from the few points in the tails of the penetration profiles are also included, with parentheses, in curve I. These low-temperature diffusion coefficients are not at all reliable but it seems that they lie below the Arrhenius plot extrapolated from the higher temperatures, presumably an effect of the blocking.

Table 1. *Diffusion of* Au^+ *in stoichiometric* AgCl

Temperature (°C)	Diffusion coefficient (cm²/sec)
442·2	$2{\cdot}02 \times 10^{-6}$
414·2	$1{\cdot}63 \times 10^{-6}$
380·0	$1{\cdot}14 \times 10^{-6}$
355·5	$8{\cdot}35 \times 10^{-7}$
329·4	$5{\cdot}36 \times 10^{-7}$
306·2	$4{\cdot}09 \times 10^{-7}$
279·3	$2{\cdot}11 \times 10^{-7}$
261·9	$1{\cdot}60 \times 10^{-7}$

The data in curve I above 260°C presumably represent the intrinsic diffusion of aurous ion Au^+, in AgCl. They are described by the following Arrhenius relation (D in cm²/sec):

$$D = 5{\cdot}0 \times 10^{-3} \exp(-0{\cdot}47\,\mathrm{eV}/kT). \quad (1)$$

(ii) *Diffusion under moderate pressure of chlorine*

In the diffusion measurements represented by plot II of Fig. 1, the specimens, each with its active face against a quartz disc, were wrapped in silver foil. They were then encapsulated in approximately 0·7 atm of chlorine; it seems reasonable, however, to assume that much of the chlorine reacted with the silver foil, particularly at the higher temperatures, so that the effective chlorine pressure is less and also uncertain. Generally, the high temperature penetration profiles were good Gaussians. The low temperature plots exhibited a slight upturn in a small region near the specimen surface, possibly caused by slight decomposition or the evaporation of some of the tracer and its subsequent return into the crystal at later times. The major portion of each of these plots, however, defined the diffusion coefficient quite sharply.

The Arrhenius plot II consists of two approximately linear segments with a break at about 300°C. Above 300°C the data may be represented by equation (1). Below 300°C, one finds, approximately (D in cm²/sec):

$$D = 14 \exp(-0{\cdot}87\,\mathrm{eV}/kT) \quad (2)$$

(iii) *Diffusion under high chlorine pressure*

The annealing conditions for the Arrhenius plot III were the same as in (ii) except that the specimens were sealed in about 2 atm of chlorine. (During the encapsulation, the chlorine was frozen by immersion of the specimen tube in liquid nitrogen). The penetration profiles for these runs were similar to those obtained in (ii). The Arrhenius plot here also is comprised of two segments, both lying below those of plot II, with the breakpoint occurring at a somewhat higher temperature, 340°C. Above the breakpoint, the activation energy is, within experimental error, approximately equal to that of curve I, although the diffusivities themselves appear to be slightly lower. Below the breakpoint, the curve parallels the low-temperature segment of curve II.

DISCUSSION

(1) *Diffusion in primarily inert atmosphere*

The data shown in Fig. 1 as curve I would appear to represent the intrinsic diffusion of Au^+ in AgCl, the very low chlorine pressure of 1 Torr, presumably having no measurable effect on the diffusivity. Equation (1) gives the activation energy E to be 0·47 eV and the frequency factor $D_0 = 5{\cdot}0 \times 10^{-3}$ cm²/sec. These low values of E and D_0 are typical of interstitial diffusion. For example, the only other monovalent impurity known to diffuse interstitially in AgCl is copper[3], for which E and D_0 have been found to be 0·40 eV and $9{\cdot}8 \times 10^{-3}$ cm²/sec, respectively.

One can evaluate the components of E and D_0 by application of the mass action law to the reaction: substitutional gold ion $\xrightarrow{G_i}$ interstitial gold ion + cation vacancy[3], where G_i is the Gibbs free energy of the reaction. Thus, if the fraction, x_i, of the gold ions in interstitial sites is much less than unity, so that the concentration of substitutional gold ions is essentially independent of x_i, we have

$$x_i x_v = \exp\left[-G_i/kT\right] \tag{4}$$

where x_v is the fractional concentration of cation vacancies. If, in addition, the temperature is sufficiently high and the gold concentration sufficiently low that the intrinsic concentration of cation vacancies is much larger than the concentration of interstitial gold ions, then x_v is independent of x_i, and equals $\exp(-G_f/2kT)$, where G_f is the Gibbs free energy of formation of a cation Frenkel pair. We now have

$$x_i = \exp\left[-(G_i - G_f/2)/kT\right]. \tag{5}$$

The diffusion coefficient of the interstitial fraction of gold ions in the silver chloride is given by[14]

$$D_i = a^2 \nu_i \exp(-G_m/kT) \tag{6}$$

where a is the cation–anion separation; ν_i is the vibration frequency; G_m is the free energy of activation for interstitial migration; and the correlation factor is here unity. The gold diffusion coefficient, D, will be given by the product $D_i x_i$. If both G_m and G_f are resolved into their component energies and entropies, one obtains from equations (5) and (6)

$$D = a^2\nu_i \exp\left[(S_i + S_m - S_f/2)/k\right] \exp\left[-(E_i + E_m - E_f/2)/kT\right]. \tag{7}$$

With $E_f = 1{\cdot}44$ eV and $S_f = 9{\cdot}4k$[15], and inserting values for a (2·78 Å) and ν_i (which we take to be 2×10^{12} sec^{-1}),

$$D = 1{\cdot}4 \times 10^{-5} \exp\left[(S_i + S_m)/k\right] \exp\left[-(E_i + E_m - 0{\cdot}72)/kT\right]. \tag{8}$$

Thus, for gold diffusion in silver chloride,

$$E_i + E_m = (0{\cdot}47 + 0{\cdot}72) = 1{\cdot}19\ \text{eV}. \tag{9}$$

E_m is perhaps not very much different from that of interstitial silver ion in silver chloride which, although there is some disagreement amongst the several published values[9, 15, 16], appears to be approximately 0·1 eV. Therefore, E_i is approximately 1·1 eV. This result is consistent with the proposed interstitial mechanism: E_i is low enough to guarantee that a non-negligible fraction, exp $-(G_i/$

$2kT$), of the gold ions is present as highly mobile interstitials. On the other hand, the overall concentration of gold is so small that the formation of gold interstitial ions cannot measurably perturb the cation vacancy concentration, and hence will make no contribution to substitutional diffusion.

Considering the fact that the ionic radius of the aurous ion is slightly larger than that of silver, one might intuitively expect the formation energy of the gold interstitial to be greater than the 1·44 eV required for the intrinsic silver Frenkel defect. On the other hand, there may be large contributions to these energies from polarization effects. In any event, E_i is of the expected order of magnitude. By way of comparison, the value of E_i for Cu^+ in AgCl has been deduced, from the ionic conductivity of copper-doped AgCl, to be 1·03 eV[17].

The observed frequency factor, $D_0 = 5{\cdot}0 \times 10^{-3}$ cm^2/sec, seems reasonable for diffusion by an interstitial mechanism. From equation (8) one concludes that $S_i + S_m \approx 6k$. Since S_m is probably very small (the low E_m implies that there is little local distortion of the lattice during the jump), therefore a value of $5k$ for S_i would explain the observed D_0; this does not seem unreasonable.

It therefore appears that the diffusion of gold in silver chloride proceeds predominantly by an interstitial mechanism. This conclusion is consistent with the idea[7] that ions with outer d-shell electrons are likely to dissolve in part interstitially in silver halides.

(2) *Effect of chlorine atmosphere*

The results obtained when the diffusion anneals were performed under nominal chlorine pressures of 0·7 and 2 atm have been shown in Fig. 1 as curves II and III, respectively. Above their respective breakpoints, both curves appear to have the same slope as does curve I. The small difference at these high temperatures between the actual diffusivities of curve III and those of I and II is probably an artifact, produced by a combination of very short anneal time and the sensitivity of the specimen warm-up rate to variations in ambient gas and the silver foil wrapping. It thus appears that the high-temperature segments of each curve represent intrinsic behavior, and defects introduced by the chlorine atmosphere being far outweighed by the native Frenkel pair concentrations.

The most striking feature, however, of curves II and III is the depression of the diffusivity in the low-temperature region, the breakpoint appearing at higher temperature for greater chlorine pressure. Although the scatter is greater for the data below the breakpoint – probably due to variations in the actual chlorine pressure from run to run, and perhaps also reflecting a varying dislocation density introduced by the liquid nitrogen treatment during encapsulation – both low-temperature segments appear to have the same activation energy, 0·86 eV. This value is almost twice that for the intrinsic, high-temperature region.

A similar break was observed for the diffusion of Cu^+ in silver chloride by Süptitz, occurring at roughly the same value of D but at a much lower temperature (150°C). The effect of impurity-induced vacancies of interstitial diffusion could possibly explain the Süptitz data below 150°, but the breakpoint in the present experiments is much too high above the temperature of the onset of intrinsic ionic conductivity to be attributed to residual impurities.

It is proposed that the chlorine-induced depression of the low-temperature diffusivity is due to a deviation from stoichiometry. The absorption of excess chlorine by the crystal produces extra silver vacancies, V_{Ag}, and electronic holes, e^+, by the reaction:

$$\tfrac{1}{2}Cl_2\,(\text{gas}) = Cl\ (\text{lattice}) + V_{Ag} + e^+. \quad (10)$$

At high temperatures, above the breakpoint, the concentration of these extra vacancies is negligible compared to that of the intrinsic Frenkel defects. At lower temperatures, however, if the chlorine pressure is sufficiently great, these extra vacancies and holes could well outnumber the intrinsic defects. In such a case, the fractional vacancy concentration, x_v, in equation (4) will vary as $\exp(-H/2kT)$ instead of as $\exp(-E_f/2kT)$, where H is the heat of the reaction (10). The activation energy for diffusion will now equal $(E_i+E_m-H/2)$, instead of the $(E_i+E_m-E_f/2)$ of equation (7). The difference in the activation energies for the low- and high-temperature regions, 0·39 eV, must then be equal to $E_f/2-H/2$, from which we deduce that $H = 0{\cdot}66$ eV.

This result may be compared with an analysis of the data of Ulrici, Koswig and Stasiw[11] on the optical absorption of AgCl in equilibrium with a chlorine atmosphere. These workers found a very broad absorption, centered near 7000 Å, which they attributed to the free holes introduced by reaction (10), the intensity of which could be fitted to an Arrhenius relation. Assuming an oscillator strength of unity, they concluded that the concentration of holes was much less than the intrinsic Frenkel defect concentration, and they were able to obtain a value for H, the heat of the reaction (10).

We have modified their treatment of the absorption data in two ways. First, since the optical absorption involves the transition (of the fraction of holes that are free) from a delocalized silver d-like state down to a localized chlorine p-like state, it would seem that the effective oscillator strength would be very small. If it were, in fact, as low as 10^{-3}, then the concentrations of holes and cation vacancies deduced from their data would be much greater than the intrinsic concentrations over most of the temperature range. We have, therefore, analyzed their data on this basis. Second, under these conditions one would expect the temperature dependence of the optical absorption to show a breakpoint similar to that observed in the diffusion data. Indeed, the Arrhenius plot given by Ulrici *et al.* is better fitted in this way, giving an activation energy some 7 per cent greater than they obtained by drawing the best straight line through all of the points. With these two modifications, the optical absorption results yield a value for H of 0·58 eV. Within the experimental uncertainties of both experiments, this seems to be in quite good agreement with the value 0·66 eV from the diffusion experiment, and lends support to the proposed mechanism. Taking the average of the two numbers, one has 0·62 eV as the heat of solution of $\frac{1}{2}Cl_2$ in AgCl, forming one cation vacancy and one hole.

CONCLUSIONS

It can be concluded from the present investigation that the gold ion diffuses interstitially in silver chloride with an activation energy of

depressed if the anneal takes place in a chlorine atmosphere. This is probably due to a decrease in the number of gold interstitials as a result of induced silver ion vacancies. The heat of solution of $\frac{1}{2}Cl_2$ in silver chloride is found to be 0·62 eV.

Acknowledgements—Numerous helpful discussions with M. Greene, Dr. G. Brébec and Dr. W. Alexander, and suggestions of Dr R. Condit, Dr R. Borg and Dr. C. E Birchenall are gratefully acknowledged

REFERENCES

1. COMPTON W. D., and MAURER R., *J. Phys. Chem. Solids* **1**, 191 (1956), MILLER A. and MAURER R., *J. Phys. Chem. Solids* **4**, 196 (1958), FRIAUF R., *J. appl. Phys.* **33**, 494 (1962)
2. TANNHAUSER D., *J. Phys. Chem. Solids* **5**, 224 (1958)
3. SUPTITZ P., *Phys. Status Solidi* **7**, 653 (1964)
4. SÜPTITZ P., *Phys. Status Solidi* **12**, 555 (1965).
5. LASKAR A. L., BATRA A. P. and SLIFKIN L., *J. Phys. Chem. Solids* **30**, 2061 (1969).
6. BRÉBEC G. and SLIFKIN L., To be published.
7. LASKAR A. L. and SLIFKIN L., *Bull. Am. Phys. Soc.* **11**, 838 (1966) and to be published; SÜPTITZ P. and WEIDMANN R., *Phys. Status Solidi* **27**, 631 (1968).
8. HANLON J., *J. chem. Phys.* **32**, 1492 (1960); READE R. and MARTIN D., *J. appl. Phys.* **31**, 1965 (1960).
9. MÜLLER P., *Phys. Status Solidi* **12**, 775 (1965).
10. FORBES III H. L and LYNCH D. W., *J. Phys. Chem. Solids* **25**, 621 (1964).
11. ULRICI W., KOSWIG H. D. and STASIW O., *Phys. Status Solidi* **12**, 545 (1965)

12. LUCKEY G. W. and WEST W., *J. chem. Phys.* **24**, 879 (1956); RALEIGH D. O., *J. Phys. Chem. Solids* **26**, 329 (1965).
13. BATRA A. P. and SLIFKIN L., *J. Phys. Chem. Solids* **30**, 1315 (1969).
14. GIRIFALCO L. A., *Atomic Migration in Crystals*, p. 92. Blaisdell, New York (1964).
15. ABBINK H. C. and MARTIN D. S., *J. Phys. Chem. Solids* **27**, 205 (1966).
16. EBERT I. and TELTOW J., *Annls Phys.* **15**, 268 (1955).
17. ABBINK H. C., Ph.D Thesis, Iowa State University of Science and Technology, Ames, Iowa (1964)

J. Phys. Chem. Solids Pergamon Press 1969. Vol. 30, pp. 2061–2064. Printed in Great Britain.

DIFFUSION OF STRONTIUM ION IN SILVER CHLORIDE*

A. L. LASKAR,† A. P. BATRA and L. SLIFKIN
Department of Physics, University of North Carolina at Chapel Hill, Chapel Hill, N.C. 27514, U.S.A

(*Received* 24 *December* 1968)

Abstract – The activation energy for diffusion of Sr^{2+} in AgCl has been found to be 0·98 eV, by means of a standard sectioning technique. The results are consistent with a vacancy mechanism and corroborate the hypothesis that ions with no outer *d*-shell electrons diffuse almost entirely substitutionally in silver halides.

INTRODUCTION

In order to explain non-linear Arrhenius plots in the diffusion of divalent cations in silver halides, it has recently been suggested [1] that the electronic configuration of the diffusing ion determines the characteristics of its diffusion: ions with outer *d*-electrons dissolve in part interstitially, thus giving rise to diffusion both by interstitial and vacancy mechanisms. On the other hand, ions with no outer *d*-shell electrons are expected to dissolve entirely substitutionally and therefore to diffuse only by a vacancy mechanism. Work already done on diffusion of sodium[2], which has no outer *d*-electrons, and on silver[3], copper[4], gold[5], cadmium[6] and manganese[1, 7], all having outer *d*-shells, can be understood in terms of such a model.

One additional test of the proposal that the presence or absence of outer *d*-electrons is a determining factor would be provided by measurement of the diffusion of alkaline earth ions. Unlike Cd^{2+} and Mn^{2+}, these divalent ions have no outer *d*-electrons and are expected to show typical substitutional migration. A measurement of the diffusion of Ca^{2+} will be reported later[8]; the present paper describes the results of a study of the diffusion of Sr^{2+} in silver chloride. Radioactive strontium is readily available as carrier-free Sr^{85}, thereby allowing such an experiment to be carried out with extremely small quantities of impurity tracer. The advantages of this opportunity will be made clear later in the paper.

EXPERIMENTAL AND RESULTS

Microtome-sectioning and radiotracer assay methods, with Harshaw single crystals of silver chloride, were used to determine the diffusion coefficients, employing experimental procedures described earlier[9]. One microcurie, or less, of carrier-free $Sr^{85}Cl_2$, obtained from Nuclear Science and Engineering Corporation, was deposited on one face of each specimen. The specimens were diffusion-annealed in ultra-pure helium, at a temperature constant to within ±0·5°C The smallest diffusion anneal time was 9 hr; thus, the warm-up time corrections, although applied, were not significant. Except for a slight upturn near the surface, the penetration profiles were good Gaussians. The resulting diffusion coefficients are given in Table 1.

A number of additional runs were also made using tracer of lower specific activity,

---

*Work supported by the U.S. Atomic Energy Commission (Contract AT-(40-1)-2036) and the Advanced Research Projects Agency (Contract SD-100).

†Now at the Department of Physics, Clemson University, Clemson, S.C. 29631, U.S.A.

Table 1. *Diffusion of carrier-free* Sr^{2+} *in* AgCl

Temperature (°C)	Diffusion coefficient (cm^2/sec)
397·5	$1{\cdot}49 \times 10^{-8}$
363·0	$6{\cdot}75 \times 10^{-9}$
320·8	$1{\cdot}61 \times 10^{-9}$
287·0	$6{\cdot}23 \times 10^{-10}$
255·1	$1{\cdot}56 \times 10^{-10}$

11 curies per g of strontium. For these runs, the ambient atmosphere was approximately 1 Torr. of chlorine, and the diffusion times were considerably shorter, being only one hour at the highest temperatures.

The temperature dependence of the diffusion coefficient obtained using the carrier-free isotope is plotted as solid triangles in Fig. 1. The overall error in the individual diffusion coefficient is estimated to be no more than 5 per cent. The data are well represented by

$$D = D_0 \exp(-E/kT) \qquad (1)$$

with $E = 0{\cdot}98$ eV and $D_0 = 0{\cdot}33$ cm^2/sec. The statistical probable error in the activation energy is ±0·02 eV, and for D_0 is ±0·12 cm^2/sec.

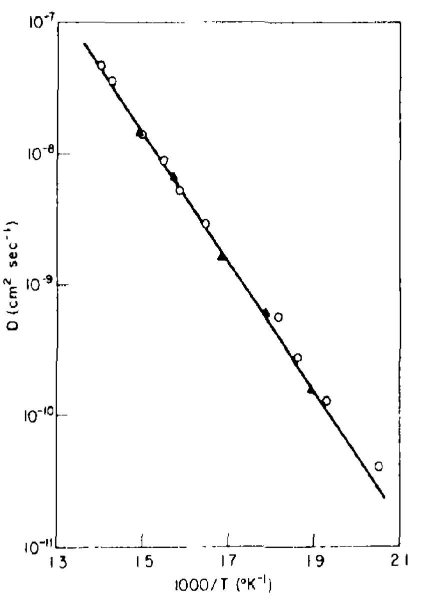

Fig. 1. Diffusion coefficient plotted logarithmically as a function of reciprocal temperature. The solid triangles show results obtained with carrier-free tracer and presumably represent true 'tracer' diffusion. The open circles are data obtained with the lower specific activity tracer.

The results obtained with the lower specific activity tracer are also shown, as open circles, in Fig. 1. The diffusion coefficients at the higher temperatures agree with those obtained with carrier-free isotope. This agreement indicates that the warm-up corrections for the 1-hr runs are reliable, even though the thermocouple was outside the glass capsule containing the specimen. At low temperatures, however, the diffusion coefficients from this set of runs are about 30 per cent high. This can be understood in terms of the effect of the impurity tracer on the concentration of cation vacancies. Thus, at low temperatures, the diffusion penetration depths were small enough that, during the anneal, the average strontium concentration in the diffusion zone was of the order of the thermal vacancy concentration. In such a situation, one would expect a small downward curvature in the penetration profile, due to the effect of the impurity concentration gradient on the diffusion coefficient. The profiles, however, appear to be good Gaussians, although there is somewhat more scatter in the data. The measured values of D are thus average values over the entire diffusion zone and are somewhat higher, as expected. If one drew, as is possible, a straight line through the data points for the tracer of lower specific activity, an activation energy slightly lower than the correct value would be obtained. These apparently 'well-behaved' results emphasize the danger that can arise in the study of diffusion of polyvalent ions in monovalent ionic crystals. The tracer specific activity must be so high that chemical concentrations may be low enough so as not to disturb the equilibrium thermal disorder.

DISCUSSION

The activation energy E of 0·98 eV and a frequency factor D_0 of 0·33 cm²/sec obtained for the diffusion of Sr^{2+} in AgCl are typical of a vacancy mechanism. The diffusion coefficient of an impurity ion under conditions of negligible impurity concentration gradient is given by [10]

$$D = 4a^2 f\nu \exp\left[-(E_f/2+E_m-E_a)/kT\right] \times \exp\left[(S_f/2+S_m-S_a)/k\right] \qquad (2)$$

where a is the cation–anion separation distance (2·78 Å); f is the correlation factor which allows for the fact that successive tracer jumps are not random; ν is the vibration frequency of the diffusing ion, usually taken as the Debye frequency ($3{\cdot}7\times10^{12}\,\mathrm{sec}^{-1}$); E and S represent enthalpy (or energy) and entropy, respectively; the subscripts f, m, and a refer to the formation of a Frenkel pair, activation for migration, and impurity-vacancy association, respectively.

If one assumes the Sr^{2+}-vacancy association energy to be of the order of 0·2 eV, then one would expect that the diffusion coefficient of Sr^{2+} would be much larger than that of substitutional Ag^+ in AgCl unless the jump frequency of the Sr^{2+}-vacancy exchange, ω_2, is much less than that of Ag^+-vacancy exchange, ω_1. The observed value of D_{Sr} at the highest temperatures is only about 1/3 that of the substitutional component of D_{Ag}. From these data, one estimates that $\omega_2 \sim 0{\cdot}006\,\omega_1$. This small value of ω_2 implies that the correlation factor, f, must be nearly unity[11], the argument being valid over the entire temperature range. Taking $E_f = 1{\cdot}44$ eV and $S_f = 9{\cdot}4k$[12] and inserting the experimental values, $E = 0{\cdot}98$ eV and $D_0 = 0{\cdot}33$ cm²/sec, into equation (2), one obtains

$$E_m - E_a = 0{\cdot}26\,\mathrm{eV}, \qquad (3)$$

$$S_a - S_m \sim 1{\cdot}4k. \qquad (4)$$

If E_m were known, then equation (3) would determine the association energy, E_a. Conflicting values of E_m for vacancy migration in pure AgCl have been reported [12, 13], but it appears to be about 0·3 eV. The migration activation energy for Sr^{2+} diffusion, however, will be higher than this since, because of electrostatic relaxation, the doubly charged strontium ion will see a tighter 'gate' than does the monovalent silver ion. Thus, all that we can say about the association energy is that it is greater than 0·04 eV. The difference between the entropies S_m and S_a, equation (4), appears not to be in conflict with the accepted notions for a vacancy mechanism.

The analysis thus indicates that the diffusion of Sr^{2+} in AgCl proceeds by a vacancy mechanism. Further support is lent to this assumption by the fact that an increase of about 25 per cent in D at 255°C was observed in one additional experiment in which the diffusion anneal was carried out in an atmosphere of 260 Torr. of chlorine. This chlorine-induced increase is almost certainly due to the extra silver ion vacancies produced in the crystal as a result of absorption of excess chlorine[5].

This study of Sr^{2+} diffusion in AgCl thus provides further support to the contention that, in contrast to transition metal and group B ions, these ions with no outer d-shell electrons diffuse by a vacancy mechanism over the entire temperature range.

Acknowledgement—The authors are appreciative of the assistance of Marvin Greene

REFERENCES

1. LASKAR A. L. and SLIFKIN L., *Bull. Am. Phys. Soc.* **11**, 838 (1966); *J. Phys. Chem. Solids* To be published (1969)
2. SÜPTITZ P., *Phys. Status Solidi* **12**, 555 (1965).
3. COMPTON W. D. and MAURER R. J., *J. Phys. Chem. Solids* **1**, 191 (1956)
4. SÜPTITZ P., *Phys. Status Solidi* **7**, 653 (1964)
5. BATRA A. P., LASKAR A. L. and SLIFKIN L., *J. Phys. Chem. Solids* **30**, 2053 (1969).
6. HANLON J., *J. Chem. Phys.* **32**, 1492 (1960).

READE R. and MARTIN D., *J. appl. Phys.* **31**, 1965 (1960).
7. SÜPTITZ P. and WEIDMANN R., *Phys. Status Solidi* **27**, 631 (1968).
8. BRÉBEC G. and SLIFKIN L., To be published.
9. BATRA A. P. and SLIFKIN L., *J. Phys. Chem. Solids* **30**, 1315 (1969).
10. GIRIFALCO L. A., *Atomic Migration in Crystals*, p. 92. Blaisdell, New York (1964).
11. LIDIARD A. B., In *Handbuch der Physik*, Vol. XX, p. 337. Springer, Berlin (1957).
12. ABBINK H. C. and MARTIN, Jr. D. S., *J. Phys. Chem. Solids* **27**, 205 (1966).
13. MÜLLER P., *Phys. Status Solidi* **12**, 775 (1965).

J. Phys. Chem. Solids Pergamon Press 1969. Vol. 30, pp. 2065–2075. Printed in Great Britain.

STRESS RELAXATIONS IN INTERNALLY OXIDIZED Ag(Cu)

J. C. SWARTZ

Edgar C. Bain Laboratory for Fundamental Research, United States Steel Corporation, Research Center, Monroeville, Penna. 15146, U.S.A.

(*Received* 10 *October* 1968; *in revised form* 24 *December* 1968)

Abstract—Internal friction spectra of oxidized Ag, Ag 0·2% Al, Ag 0·4% Al, Ag 0·26% Au and Ag 0·26% Cu are presented. Only the Ag(Cu) alloy oxidized at 250° or 300°C exhibited stress relaxations which could be attributed to point defects. In this case two relaxations were observed with activation energies approximately 0·10 and 0·20 eV. The magnitude and anisotropy of the 0·20 eV relaxation indicate a relatively strong ⟨100⟩ tetragonal dipole. Experiments on the effects of oxidation pressure and temperature suggest that relatively few Cu–O pairs formed at 250° or 300°C are sufficiently isolated to relax; the majority of the pairs are in larger, non-relaxing clusters. A defect model based on the structure of bulk CuO is suggested to account for the low energies of these relaxations.

INTRODUCTION

INTERNAL oxidation of copper in silver produced stoichiometric CuO above 700°C and submicroscopic clusters of $CuO_{1\cdot3-1\cdot7}$ at 300°C[1]. The clusters are relatively stable to vacuum deoxidation at 300°C: in one experiment[1] with $AgCu_{0\cdot0024}$ the O/Cu ratio decreased only 3 per cent (from 1·37 to 1·32) when the external oxygen pressure decreased from 450 to 0·65 Torr. at 300°C. Isotope exchange experiments[2] at 300°C have shown that most of the O^{16} in the clusters can be replaced readily by O^{18}. Apparently the clusters are so small that most of the Cu atoms have at least one filled and one empty oxygen site exposed to the silver matrix.

The present experiments were undertaken to learn if the CuO_x clusters are capable of stress relaxation. The possible ionic character of the Cu–O bond suggests that a Cu–O pair might have an appreciable elastic dipole strength.* Assuming a dipole strength ~ 10^{-1} a stress relaxation could be detected if ≳ 10^{-4} atomic fraction of such dipoles reoriented with a unique activation energy. In the alloy of the present study there are 26×10^{-4} atomic fraction Cu–O pairs. Hence there is ample sensitivity to test whether these pairs are asymmetric and sufficiently isolated to reorient. Similar tests were made on internally oxidized silver-aluminum alloys.

A previous study[4] of Ag(Mg) alloys internally oxidized at 600°C failed to reveal any relaxation peak between 77° and 290°K at 1 Hz. On the other hand this study did show that pure silver charged with ~ 300 ppm oxygen exhibited small relaxation peaks at 130°, 180° and 270°K. The magnitude of the 130° and 180°K peaks increased with the square of the oxygen concentration. The activation energy obtained for 180°K peak (0·5 eV) equals that for diffusion of oxygen in silver. The orientation dependence implies that the 130° peak is due to a ⟨110⟩ orthorhombic defect and the 180° peak to a ⟨100⟩ tetragonal defect[5]. Papazian suggested that these two peaks were caused respectively by a pair of oxygen atoms in a silver atom vacancy and by a pair of interstitial oxygen atoms.

At the frequencies of the present study (20–80 Hz) the peaks observed by Papazian would fall near 140°, 200° and 300°K. A few efforts to observe these peaks were made in the present work.

---

*The dipole strength of a pair of impurity atoms is a measure of the difference in the misfit strains parallel and perpendicular to the pair axis[3, 5].

EXPERIMENTAL TECHNIQUES

Specimens were prepared from 99·999% Ag(Cominco Electronics Co.) and vacuum melts of Ag with Al, Au and Cu. The alloys were homogenized typically 18 hr at 900°C in pressure nominally $\langle 10^{-5}$ Torr. These materials were swaged, drawn and chemically polished to form 0·7 mm dia. wire. Specimens 5–10 cm long were recrystallized at 870°C in a vacuum furnace at a pressure $\langle 10^{-5}$ Torr.

A few single crystal wires of the AgCu alloy were prepared in a Bridgeman furnace from 1·3 mm dia. wires in vertical 1·5 mm dia. holes in graphite. After growth the crystals were electropolished to 1·2 mm dia. Combustion analysis of one of the crystals indicated $\langle 5$ ppm carbon by weight. Crystal orientations were determined by the Laue method. The axis of one crystal was within 1° of a $\langle 100 \rangle$ direction; the other crystals were approximately 15° from a $\langle 100 \rangle$ direction.

Oxidation of the specimens was accomplished in sealed glass containers containing sufficient oxygen to bring the oxygen pressure to one atmosphere at the oxidation temperature. In several experiments the soluble oxygen was later removed by heating the specimens in evacuated and sealed glass containers. From the amount of oxygen evolved[1] and the container volume we estimate the final pressure for these 'deoxidation' treatments was ~1 Torr. Occasionally oxidized Ag(Cu) specimens were reverted to homogeneous Ag(Cu) solutions by heating above 800°C in vacuum or flowing argon. In some cases the changes in oxygen content of a specimen was followed gravimetricly using a Sartorius microbalance.

The stress relaxations were revealed as peaks in the internal friction measured as a function of temperature. These data were obtained with an inverted torsional pendulum operating in free decay at frequencies between 20 and 70 Hz[6].

RESULTS

Typical internal friction spectra of most of the alloys did not exhibit any pronounced stress relaxation (Fig. 1). Occasionally, however, broad maxima were observed as shown in Fig. 2. The excessive width and the annealing behavior of these maxima are suggestive of dislocation relaxations. For an oscillation frequency of 50 Hz the Bordoni peak[7] and deformation peaks α, β and γ of Hasiguti *et al.*[8] are expected around 53°, 143°, 175° and 215°K, respectively. The temperatures of the major peaks in Fig. 2 (50°, 130° and 210°K) roughly correlate with those of the Bordoni, α and γ peaks. No further study was made of these relaxations.

Spectrum 1*c* fails to show any significant peak near 200°K which would correlate with the 'oxygen-pair' peak observed by Papazian. In another attempt to observe an oxygen-pair relaxation, an Ag 0·26 *a*/o Cu specimen which had been oxidized at 300°C was pulsed briefly to 543°C. During the pulse much of the oxygen in excess of that in stoichiometric CuO (~10^3 ppm) is expected to dissociate from the clusters. According to the silver–oxygen phase diagram, the limit of the α field at this temperature corresponds to ~600 ppm dissolved oxygen. Figure 3 shows the internal friction of a specimen held one minute at 543°C, then dropped into liquid nitrogen. During transfer of the specimen from the nitrogen bath to the torsional pendulum the specimen temperature did not exceed 200°K. A narrow peak at 207°K (33 Hz) is evident in the spectrum of the first warm-up. Two similar experiments failed to reproduce this peak (e.g. spectrum *c* of Fig. 6). Therefore, there is too little evidence to decide whether the peak in Fig. 3 is a transient dislocation damping or a stress relaxation of oxygen pairs. In any event the sensitivity of the peak to subzero annealing contrasts considerably

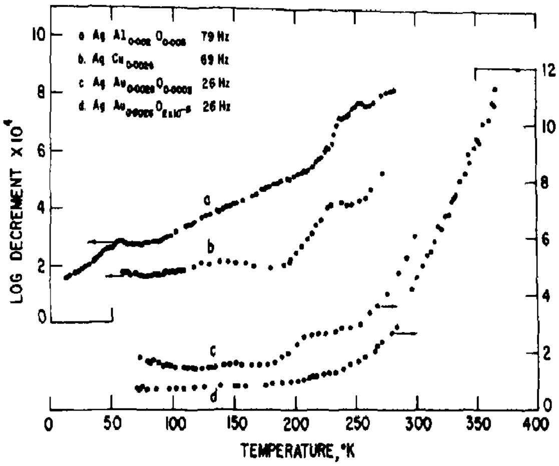

Fig. 1. Several cases in which the internal friction spectrum fails to exhibit any pronounced relaxation. (*a*) Ag 0·2% Al oxidized 312 hr @ 300°C in 1 atm O_2 then held 216 hr @ 300°C in an evacuated capsule; (*b*) Ag 0·26% Cu after vacuum anneal at 800°C; (*c*) Ag 0·26% Au oxidized 1·3 hr @ 810°C in 1 atm O_2. (d) Ag 0·26% Au oxidized 400 hr @ 300°C in 1 atm O_2.

with the stability of the peak observed by Papazian at 180°K (2 Hz).

The remainder of this report concerns internal friction spectra of the silver copper alloy oxidzed at low temperature. A typical spectrum after oxidation at 300°C is shown in Fig. 4(a). A small peak designated *B* is apparent at 80°K (20·6 Hz). Spectrum 4*b* was obtained after this specimen had been deformed 3 per cent in torsion at 97°K and warmed to room temperature. The height of *B* was unaffected by the deformation and a new peak at 160°K appeared which corresponds in temperature to deformation peak *β* of Hasiguti *et al.* [8].

After the measurements of Fig. 4 specimen 1 was cut into three segments (1*a*, 1*b* and 1*c*) of about equal length. Figure 5 shows the results of a sequence of further treatments on one of these segments. Spectrum 5*a* reveals a new peak (designated *A*) near 40°K. Upon aging the specimen in a static vacuum at 300°C, *A* decreased slightly and *B* increased an order of magnitude. Spectra 5*c* and 5*d* show that brief pulse at 543°C causes *A* and *B* to disappear irreversibly. Finally 5*e* shows that *B* can be reintroduced after reversion at 800°C.

Figure 6 shows further examples of *A* and *B* in spectra of another specimen. Clearly these peaks are strongly sensitive to the temperature and oxygen pressure of the final equilibration.

Table 1 lists the heights of *A* and *B* after sequential treatments of each polycrystalline specimen. Occasional spectra contain Bordoni damping (e.g. 5*b*) which prevents an unambiguous estimate of the *A* height. In these cases only an upper limit of *A* is listed. No such difficulty exists for *B*.

Several of the observations contained in Table 1 warrant explicit statement. After oxidation at 300°C *B* is small and decreases slowly with room temperature aging, but after the vacuum treatment *B* is high and relatively stable to room temperature storage or to brief warmings to 300°C. Furthermore after evacuation *B* is independent of cooling rate from 300°C, whether one air cools in a glass container, quenches directly into water, or 'quenches' directly into liquid nitrogen and measures before warming above 150°K. Final

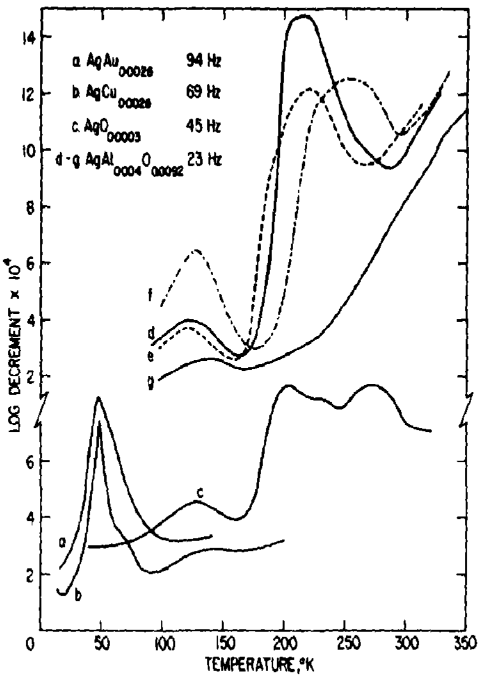

Fig 2 Spectra which exhibit broad maxima characteristic of dislocation relaxations (*a*) Ag 0·26% Au oxidized 400 hr @ 300°C in 1 atm O_2 and subsequently heated 216 hr @ 300°C in static vacuum; (*b*) Ag 0·26% Cu after vacuum anneals first @ 800°C then 339 hr at 300°C; (*c*) 99·999% silver oxidized 41 hr @ 830°C in 1 atm O_2, water quenched. (*d*) Ag 0·4% Al oxidized 137 hr @ 447°C in 1 atm O_2 and further held 166 hr @ 447°C in argon, air cooled (O/Al = 2·3–) (Kindly prepared by D F. Wriedt of the author's laboratory); (*e*) Ag 0·4% Al oxidized 137 hr @ 447°C in 1 atm O_2, air cooled. (O/Al = 2·3+) (Kindly prepared by D. F. Wriedt of the author's laboratory); (*f*) same as (*e*) after 10 min anneal at 195°C; (*g*) same as (*f*) after 10 min anneal at 371°C.

equilibration at 250° or 300°C seems to affect *A* and *B* oppositely. *A* is higher after 250° equilibration and *B* is higher after 300° equilibration.

Figure 7 displays the height of *B* as a function of inverse absolute equilibration temperature. An increase in oxygen pressure at a constant temperature of 300°C reduced *B*. At low oxygen pressure *B* varies reversibly between 250° and 300°C and decreases irreversibly with time at 350°C. The energy governing the reversible temperature dependences is roughly 0·4 eV.

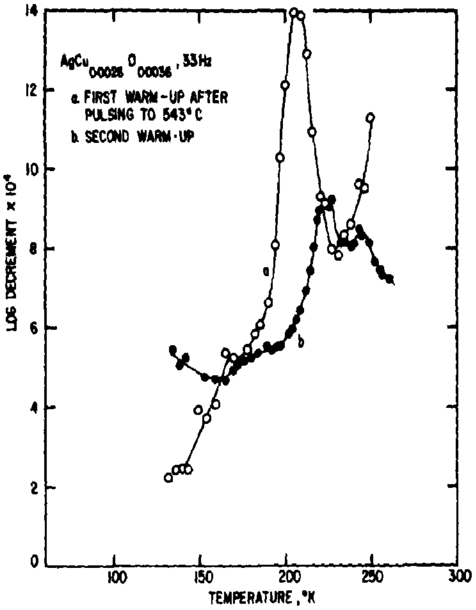

Fig. 3. A transient peak at 207°K. Ag 0·26% Cu oxidized 797 hr @ 300°C, heated 1 min @ 543°C and 'quenched' into liquid nitrogen.

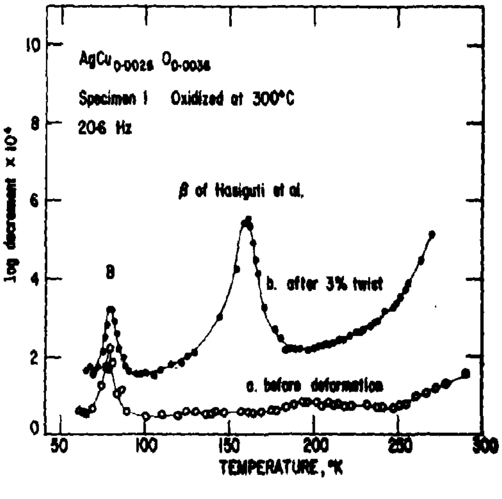

Fig. 4. Initial observation of *B* relaxation and effect of deformation. Specimen 1 oxidized 797 hr @ 300°C in ~1 atm O_2.

The activation energies of relaxations *A* and *B* from the Wert-Marx relation[9] are 0·10 and 0·20 eV. The peak temperatures vary in rough accord with these activation energies for frequencies in the range 20–80 Hz. The average width of *A* from the

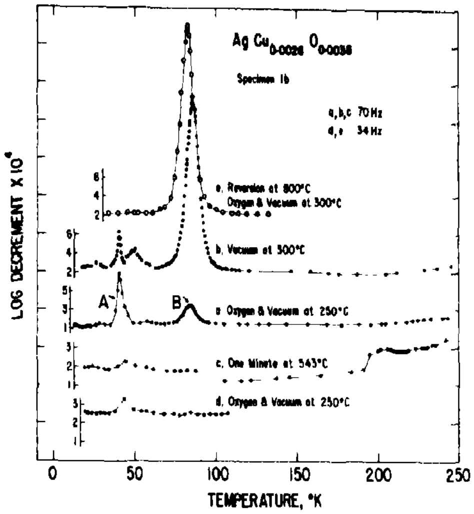

Fig. 5 Effect of sequential treatments on relaxations *A* and *B*. Specimen of Fig. 4 further oxidized 284 hr @ 250°C then: (*a*) heated 65 hr @ 300°C in static vacuum; (*b*) further heated 66 hr @ 350°C in static vacuum; (*c*) first warm up after heating 1 min @ 543°C and 'quenching' in liquid nitrogen; (*d*) reoxidized 432 hr @ 250°C and held 504 hr @ 250°C in static vacuum; (*e*) deoxidized 16 hr @ 820°C in argon, reoxidized 695 hr @ 300°C and treated 455 hr @ 300°C in static vacuum.

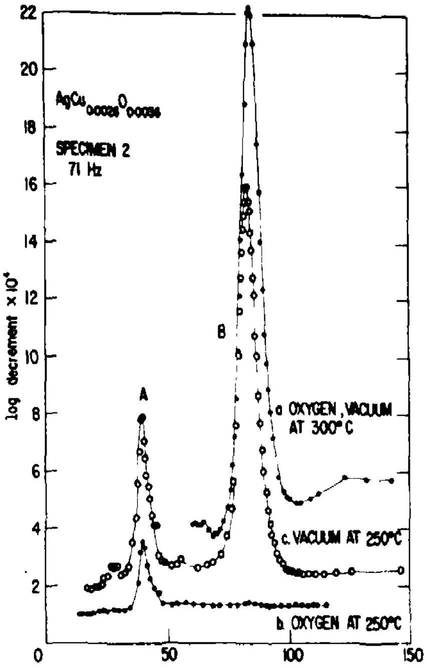

Fig. 6. Effect of sequential treatments on internal friction of Specimen 2. (*a*) Oxidized 797 hr @ 300°C in 1 atm oxygen then sealed in vacuum and held 312 hr at 300°C. (*b*) further treated at 304 hr @ 250°C in 1 atm oxygen. (*c*) 160 hr @ 250°C sealed in vacuum.

spectra with negligible Bordoni damping is 10 per cent greater than the theoretical width of an 0·10 eV relaxation. Similarly the average width of *B* is 5 per cent greater than the theoretical width. Apparently the Wert–Marx method gives reasonably correct estimates of the activation energies of these relaxations. Also the distributions in activation energy and attempt frequency are relatively narrow.

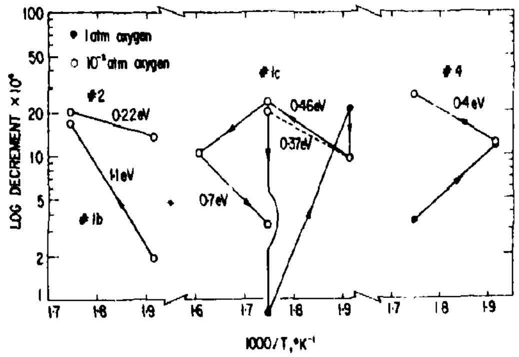

Fig. 7. Dependence of *B* relaxation strength on oxidation temperature and pressure.

Table 1. *Effects of sequential treatments on relaxations of* Ag(Cu, O)

Specimen	Hr at T(°C) and P(atm) of oxygen					Other treatments	Peak height log dec. × 10^4	
	T 250		300		350			
	P 1	10^{-3}	1	10^{-3}	10^{-3}		A	B
1			797				—	1·7
						3% twist	—	1·7
2			797	312			—	20·5
						½ yr @ 25°C		20·5
						3 yr @ 25°C		18·0
	304						2·3	0·1
		160					5·3	13·4
3			797			3 yr @ 25°C	—	0·1
				506			<0·3	12·9
					188		<0·4	3·9
			305				<0·4	0·5
				0·1			<0·4	0·5
1*a*	284						2·4	<0·1
		28					6·9	9·8
		232					7·5	14·5
1*b*	284	43					5·4	1·95
				70			3·3	17·9
						1 min @ 543°C	<0·3	<0·2
	432	504					<0·7	<0·2
						800°C reversion	—	—
			695	455			<0·2	20·0
1*c*	284			65			6·9	14·3
					66		<0·2	11·9
						½ min @ 543°C	4·7	2·8
	432	504					0·5	6·8
						800°C reversion	—	—
			695	455			<0·1	20·0
			427				<0·1	0·8
	189						0·6	21·0
		426					5·2	9·6
				196			≤4·8	23·8
					121		<1·0	10·5
			98	138			<1·0	3·3
4			501				≤5·3	3·5
	260						6·5	11·6
		220					2·4	12·0
				240			<0·3	26·5
					215		<0·2	<0·2
			189	115			<0·2	<0·3

The results on the few single crystals are summarized in Table 2. The crystals are identified by values of the orientation parameter $\Gamma = \alpha_1^2\alpha_2^2 + \alpha_2^2\alpha_3^2 + \alpha_3^2\alpha_1^2$, where α_1, α_2 and α_3 are the direction cosines of the wire axis with the [100], [010] and [001] crystal axes. The O/Cu ratios in Table 2 are calculated from the average weight change. These data suggest incomplete oxidation for the treatments at 250° and 300°C. This is possible since the diameter of these crystals was about 1·7 times that of the polycrystalline specimens. The peaks for these early treatments are also abnormally low.

According to the general theory[3] of torsional anelasticity the relaxation strength Δ_G(= $2\pi^{-1}$ × peak log dec.) is related to the crystal orientation by the equation:

$$\Delta_G G^{-1} = \delta G^{-1} = \delta s + 2(\delta s' - \delta s)\Gamma \quad (1)$$

Table 2. *Heights* (log dec. × 10⁴) *of peaks* A *and* B *in oxidized* Ag(Cu) *crystals*

Treatment	O/Cu	$\Gamma = 0{\cdot}0004$		0·056		0·059		0·073	
		A	*B*	*A*	*B*	*A*	*B*	*A*	*B*
737 hr Ox @ 300	*a*		<0·1		2·3		0·7		0·7
Above plus 280 hr Ox @ 250 + 410 hr Deox @ 250	(*a*) + 0·33	0·5[b]	0·4	2·0	2·2	2·7[b]	2·3	1·2	2·4
Deox @ 820 426 hr Ox @ 250 392 hr Deox @ 250				0·2	0·5			0·8	0·6
Deox @ 800 670 hr Ox @ 300 500 hr Deox @ 300	0·82	<0·2	<0·3	<0·3	2·5	<0·3	2·0	<0·5	3·8
Above plus 578 hr Ox @ 350	1·33								
354 hr Deox @ 350	1·20	<0·2	0·5	<0·2	5·6	<0·2	4·7	<0·2	7·2

[a] Not measured.

[b] Upper limit (spectrum includes extraneous damping between 40° and 50°K).

where G is the unrelaxed rigidity modulus for the orientation Γ. δG^{-1} is the difference in relaxed and unrelaxed reciprocal modulus, δs is a similar difference for the compliance coefficient s_{11} and $\delta s'$ is that for the coefficient $2(s_{11} - s_{12})$. Figure 8 shows δG^{-1} as a function of Γ for the B peak after the 350° treatment (Table 2) using rigidity moduli calculated from the compliance coefficients of pure silver[10]. The estimated uncertainties in Γ and Δ_G are indicated. The remaining scatter from the linear relation (1) must be ascribed to small variances in the oxidation treatments.

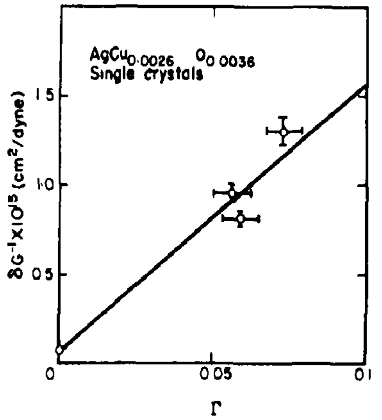

Fig. 8 Orientation dependence of B relaxation after 350°C treatment described in Table 1.

From Fig. 8 we obtain $\delta s = 0{\cdot}06 \pm 0{\cdot}01$ and $\delta s' = 7{\cdot}6 \pm 1$ in units of 10^{-15} cm²/dyne for the B relaxation after equilibration at 350°C. Extrapolation of the linear relation to $\Gamma = 0{\cdot}2$ (the average Γ for a random polycrystalline aggregate) predicts a peak height (log decrement) of 12×10^{-4}, which compares favorably with data in Table 1. The strong anisotropy ($\delta s'/\delta s \approx 130$) indicates that the dipoles responsible for the B relaxation have strong $\langle 100 \rangle$ tetragonal symmetry.

DISCUSSION

The absence of any pronounced peak near 200°K in spectrum 1c contrasts with the experience of Papazian. He found that a similar oxidation treatment of pure silver introduced a peak of magnitude about 2×10^{-4} (log decrement units): any such peak in spectrum 1c must be smaller than $0{\cdot}5 \times 10^{-4}$. Perhaps silver oxide precipitates more readily in our particular silver than in the silver used by Papazian. Spectra 2c, e and f show that a dislocation relaxation sometimes occurs at a temperature close to that anticipated for the oxygen pair relaxation. Hence it will be difficult to identify the pair relaxation unambiguously until the nearby dislocation relaxation is eliminated or otherwise controlled.

Spectrum Ic also determines an upper limit for the possible relaxation strength of oxygen-gold impurity pairs. In a completely random solution of this composition there would be about 5 ppm oxygen in interstices near neighbor to isolated gold atoms. Assuming this concentration and the upper limit on the height of any peak in spectrum Ic we calculate from equation (2) (subsequently presented) an upper limit of ~ 0·3 for the magnitude of the dipole strength ($\Delta\lambda$) of an oxgyen-gold pair in silver.

Let us consider peaks A and B exhibited by the oxidized Ag(Cu) alloy. Figure 4 demonstrates that B is not sensitive to deformation. Moreover the widths of A and B are too small to ascribe them to dislocation relaxations. Therefore the peaks seem to be caused by certain strain dipoles (hereafter designated $\mathscr{A}$ and $\mathscr{B}$) among the CuO_x clusters. Treatments at and above 350°C, which presumably increase the average cluster size, irreversibly decrease the peaks. Evidently the relaxing dipoles are among the smallest clusters. Even if the larger clusters also have dipolar strain fields, their reorientation probably would require too many independent or coupled activations and hence would be unlikely.

The two-fold difference in activation energies of these relaxations suggests that relaxation B requires two activation processes of the type responsible for relaxation A. For example, if A is associated with an isolated Cu–O pair which has a mean time of stay $\tau_{\mathscr{A}} = t_0 \exp(Q_{\mathscr{A}}/kT)$, B could be associated with two such pairs so interacting that relaxation of the complex is not effected unless both pairs are activated within a time $\sim \tau_{\mathscr{A}}$. The probability of two independent $\mathscr{A}$ activations in a unit time would be proportional to $\tau_{\mathscr{A}}^{-2}$ so that the activation energy for reorienting the $\mathscr{B}$ complex would be $2Q_{\mathscr{A}}$.

Relaxation B is particularly sensitive to the oxygen pressure during the final equilibration at 250° and 300°C. Apparently the small concentration of loosely bound oxygen ($\sim 1{\cdot}3 \times 10^{-4}$ atomic fraction at 300°C)[1] can immobilize the $\mathscr{B}$ dipoles. Perhaps this is accomplished by filling the occasional oxygen ion sites which link the $\mathscr{B}$ dipoles to other clusters. At any rate each loosely bound oxygen can be assumed to suppress on the average no more than one of the $\mathscr{B}$ dipoles. Therefore the concentration of $\mathscr{B}$ dipoles formed at 300°C is $\leqslant 1{\cdot}3 \times 10^{-4}$. The thermodynamic theory of anelasticity for a dilute solution of ⟨100⟩ dipoles yields[5]

$$\Delta_G G^{-1} \approx C V_0 \Gamma (\Delta\lambda)^2/RT \qquad (2)$$

where C is the dipole concentration, V_0 is the molar volume of the solution, and $\Delta\lambda$ is the dipole strength. Substituting in equation (2): $\Delta_G = 2(20 \times 10^{-4})/\pi$, $C < 1{\cdot}3 \times 10^{-4}$, $G = 2{\cdot}7 \times 10^{11}$ d/cm^2, $\Gamma = 0{\cdot}2$, $V_0 = 10{\cdot}3$ cm^3 and $T = 80$°K, we find $|\Delta\lambda| \gtrsim 0{\cdot}34$, which is a rather large dipole strength. Assuming similar strengths for the $\mathscr{A}$ and $\mathscr{B}$ dipoles and respectively one and two Cu atoms per dipole we can account for no more than 15 per cent of the total Cu concentration. The great majority of the copper would seem to be in larger (hence non-relaxing) clusters.

In the foregoing paragraph we suggest that a reaction of the type

$$0 + \mathscr{B} = \mathscr{C} \qquad (3)$$

can account for the strong dependence of the $\mathscr{B}$ concentration on the equilibrium pressure of oxygen. In equation (3) $\mathscr{C}$ signifies a non-relaxing cluster. Now let us try to interpret the reversible temperature dependence in Fig. 7 using the same reaction.

From the thermodynamics of defect association[11], the binding free energy ΔG of reaction (7) is related to the concentrations of the reactants by

$$[\mathscr{C}]/[\mathscr{B}] = Z[O] \exp(\Delta G/kT) \qquad (4)$$

here Z is the number of distinguishable O sites about $\mathscr{B}$ and the square brackets signify mole fractions. The concentration of oxygen is expected to vary with oxidation temperature and pressure as in the case of pure silver:

$$[\mathrm{O}] = 1{\cdot}39\times 10^{-3}\,p^{1/2}\exp(-0{\cdot}45\,\mathrm{eV/kT}) \quad (5)$$

where P is the oxygen pressure in Torr[1]. Assuming $[\mathscr{C}]$ is not a strong function of temperature around 300°C, equations (4) and (5) determine the following temperature dependence of $[\mathscr{B}]$:

$$\frac{\partial(\ln[\mathscr{B}])}{\partial(1/T)} \approx (0{\cdot}45\,\mathrm{eV} - \Delta H)/k \qquad (6)$$

where ΔH is the binding enthalpy. In conjunction with the data in Fig. 7, equation (6) leads to the possibility that ΔH is about 0·9 eV. In comparison the enthalpy difference at 300°C between bulk CuO and dissolved Cu and O is approximately 2·4 eV.* Hence the oxygen which might immobilize $\mathscr{B}$ according to reaction (3) would be bound considerably weaker than oxygen is bound in bulk CuO. While this result is qualitatively reasonable, the possibility that equation (3) is indeed the major reaction controlling the concentration of $\mathscr{B}$ is certainly not proven.

If oxygen can be weakly bound to sites with perhaps only two copper atoms within the second neighbor shell, gradual replacement of the remaining silver neighbors by copper provides a spectrum of increasing oxygen binding energies. This suggests an explanation for the excess stoichiometry of the clusters: silver ions frequently included in the Cu–O structure provide excess oxygen sites with sufficient binding energy to remain filled during even low pressure equilibration.

Let us now discuss some conceivable models of the dipole clusters. Since clustering is an intermediate state between a homogeneous solid solution and a two phase mixture, we can speculate on the clustered state from either limiting perspective. From the perspective of a solid solution we imagine a weak interaction between the dilute substitutional and interstitial components and obtain the usual model of an interstitial-substitutional impurity atom pair. The pair axis in the present case would lie in a ⟨100⟩ direction and its reorientation would be accomplished by a jump of the oxygen atom between the octahedral interstices adjacent to a copper atom. With this model one expects the activation barrier for reorientation to be similar to that for the diffusion of the interstitial in the pure solvent. Many relaxations have been reported which seem to conform to this model[14]. In contrast, relaxations A and B are activated far easier (0·1 and 0·2 eV) than the diffusion of oxygen in silver (0·5 eV). Obviously the copper atom drastically alters the atomic or electronic structure around the oxygen atom. Realizing the possibility of some ionic character to the Cu–O bond, we can conceive of the copper ion becoming smaller than the oxygen ion. Then it becomes a moot question: which is the interstitial ion whose motion energy presumably governs the relaxation?

One also can envision a relaxation mechanism involving thermally activated electron exchange which fluctuates the Cu–O bond between two states of different ionicity and in this case different ⟨100⟩ distortions. Fine *et al.*[15, 16] have used such a model for certain stress relaxations of ferrites at low temperature. In any such reaction between two species of dipoles there is likelihood of a hydrostatic component of the relaxation[5]. The present experiments utilizing torsional stresses only, do not test for a possible hydrostatic relaxation component.

Let us next consider the clusters from the perspective of a two phase mixture. In the monoclinic structure of bulk CuO the copper ions occupy a face-centered lattice which is shorter in the [001] and longer in the [110] direction than the cubic lattice of silver[17].

---

*Derived from data[1, 12, 13] on the following reactions:

$$\mathrm{Cu}(s)+\tfrac{1}{2}\mathrm{O}_2(g)=\mathrm{CuO}(s)$$
$$\tfrac{1}{2}\mathrm{O}_2(g)=\mathrm{O}\ (\text{in Ag})$$
$$\mathrm{Cu}(s)=\mathrm{Cu}\ (\text{in Ag}).$$

The oxygen ions are situated within copper tetrahedra but instead of occupying the tetrahedral centers they are offset toward the [110] edges.

The number of copper atoms required for a nucleus of CuO in silver is not known. The fact that AgO is nearly isomorphous with CuO probably stabilizes small nucleii. One might even say that in the presence of a few copper impurity atoms the solubility of silver oxide (strictly $Ag_xCu_{1-x}O$) is exceeded perhaps at one atmosphere of oxygen at 300°C.

Figure 9 shows a possible configuration for a nucleus of CuO containing three copper atoms constrained to the fcc silver lattice and a pair of oxygen atoms. For this configuration of Cu atoms there are two equivalent positions of the pair of oxygen atoms: both oxygens can be close to the [110] edge of their respective tetrahedra or alternatively to the $[01\bar{1}]$ edge. Figure 9 illustrates the former configuration. To reorient the cluster axis from [100] to $[01\bar{1}]$, both oxygen atoms must move a small distance within their respective tetrahedra. (Recall that a double activation process was suggested for the B relaxation.) The small displacement of each oxygen atom in reorienting such Cu–O clusters is qualitatively consistent with the low activation energies of the observed relaxations. If the atom positions in bulk CuO are applicable to such a small nucleus, this ⟨110⟩ dipole would be expected to have dipolar strains in both [110] and [001] directions. Only a ⟨100⟩ distortion is indicated by the observed anisotropy of the B relaxation.

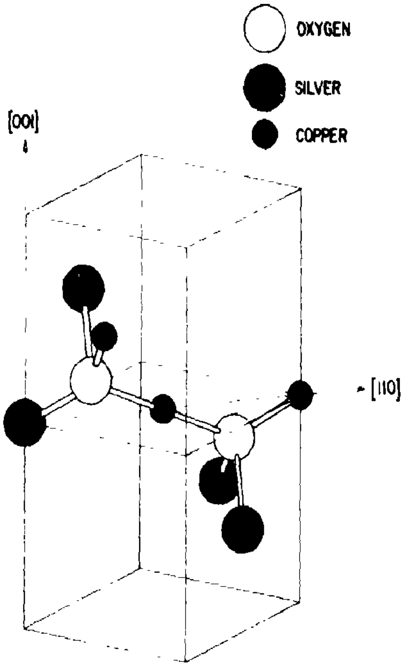

Fig 9. A model for the $\mathscr{B}$ dipole in Ag(Cu, O).

Coincidentally the primary example of a ⟨110⟩ dipole[5], the silicon A center, involves an oxygen atom in a bond arrangement similar to that in Fig. 9 and moreover has its major dipolar distortion along ⟨100⟩. Furthermore the A center in silicon is activated to reorient by 0·38 eV which is far below the 2·55 eV for interstitial diffusion of oxygen in silicon [18, 19]. There is also another stress relaxation attributed to the A center with an activation energy about half that ascribed to the motion of the oxygen ion[18]. Here the parallelism with the present defects may break down since there is no indication that the strengths of the two relaxations in silicon can vary independently.

SUMMARY

Two unique stress relaxations have been observed in an Ag 0·26% Cu alloy internally oxidized at 250°–300°C. The relaxations, designated A and B, are activated respectively by 0·10 and 0·02 eV. The orientation dependence of the B relaxation indicates a ⟨100⟩ tetragonal dipole; the strength of this dipole has been estimated $\gtrsim 0·34$. The magnitudes of both relaxations are strong functions of the oxidation temperature and pressure. It is concluded that the relaxing dipoles are among the smallest CuO_x clusters; most of the copper in specimens oxidized at 300°C is in larger, non-relaxing clusters. A dipole model based on the structure of bulk CuO

provides a possible explanation for the low activation energies of these relaxations.

Efforts to observe reproducible relaxations due to pairs of oxygen atoms in silver were unsuccessful.

Acknowledgements—The author wishes to thank A. J. Schwoeble for his assistance with the measurements and H. H. Podgurski and J. C. M. Li of this laboratory for helpful discussion.

REFERENCES

1. PODGURSKI H. H. and DAVIS F. N., *Trans AIME* **230**, 731 (1964).
2. PODGURSKI H. H., Unpublished research. U.S. Steel Research Center, Monroeville, Pa. (1964).
3. NOWICK A. S. and SERAPHIM D. P., *Acta Metall.* **9**, 40 (1961).
4. PAPAZIAN J. M., U.S. AEC Rep No UCRL-11017 (1963).
5. NOWICK A. S. and HELLER W. R., *Adv. Phys* **12**, 251 (1963)
6. WAGENBLAST H. and SWARTZ J. C., *Acta Metall.* **13**, 42 (1965).
7. OKUDA S., *Appl. Phys. Lett.* **2**, 163 (1963).
8. HASIGUTI R. R., IGATA N. and KAMOSHITA, G., *Acta Metall.* **10**, 176 (1962).
9. WERT C. and MARX J., *Acta Metall.* **1**, 113 (1953).
10. HUNTINGTON H. B., In *Solid State Physics* (Edited by F. Seitz and D. Turnbull), Vol. 7, p. 214. Academic Press, New York
11. For example: DAMASK A. C. and DIENES, G. J., In *Point Defects in Metals*. Gordon and Breach. New York (1963)
12. KUBASCHEWSKI O., EVANS E. L. and ALCOCK C. B., In *Metallurgical Thermochemistry*, p. 423. Pergamon Press, Oxford (1967)
13. WRIEDT H. A., *Trans. AIME* **221**, 377 (1961).
14. NACKEN M. N. and KUHLMANN V., *Arch. Eisenhuttenw.* **37**, 235 (1966); RITCHIE I. G. and RAWLINGS R., *Acta Metall* **15**, 491 (1967), BUNN P. M., CUMMINGS D. G. and LEAVENWORTH H. W., *J. appl. Phys.* **33**, 3009 (1962); VIDAL G. and BIBRING H., *C. r. hebd. Séanc. Acad. Sci., Paris* **260**, 857 (1965), MILLER D. R., *Trans. AIME* **224**, 275 (1962), BISOGNI E., MAH G. and WERT C., *J. Less-common Metals* **7**, 197 (1964), YANG C. Y. and KAMBER K. T., *J. appl. Phys* **34**, 3405 (1963), ELIAS M. J. and RAWLINGS R., *J. Less-common Metals* **9**, 305 (1965); KE T. S. and TSIEN C. T., *Scientific Sinica* **5**, 625 (1956), MAH G. and WERT C., *Trans. AIME* **230**, 16 (1964), VERNER V. D., *Soviet Phys. solid St.* **7**, 1874 (1966).
15. FINE M. E. and KENNEY N. T., *Phys. Rev.* **84**, 1573 (1954).
16. GIBBONS D. F., *J. appl. Phys.* **28**, 810 (1957)
17. WYCOFF R. W. G., In *Crystal Structures*, Vol. 1, p. 140. Interscience, New York (1948).
18. WATKINS G. D. and CORBETT J. W., *Phys. Rev.* **121**, 1015 (1961)
19. HASS C., *J. Phys. Chem. Solids* **15**, 108 (1960).

J. Phys. Chem. Solids Pergamon Press 1969. Vol. 30, pp. 2077–2089. Printed in Great Britain.

CUBIC FIELDS WITH TETRAGONAL AND TRIGONAL DISTORTIONS IN CRYSTAL FIELD THEORY OF TRANSITION METAL IONS

UDO SCHERZ
III. Physikalisches Institut der Technischen Universitat, Berlin, Germany

(*Received* 13 *December* 1968)

Abstract—The most general effective Hamiltonians including spin-orbit coupling, crystal fields of lower symmetry and spin-spin coupling in various orders of perturbation theory are given for three symmetry groups. Spin tensor operators which transform as basis functions of these groups are also presented. From the effective Hamiltonians, energy matrices are derived for d^1–d^9 configurations in trigonally and tetragonally distorted tetrahedral and octahedral crystal fields, the eigenvalues of which give the fine structure energy levels observable in the optical spectra of transition metal ions in II–VI-compounds. The corresponding eigenfunctions, necessary to calculate the g-factors of these levels, are also included.

1. INTRODUCTION

IN THE analysis of optical spectra of transition metal ions in II–VI compounds trigonally and tetragonally distorted tetrahedral fields are of special interest. The fine structure of the infrared spectrum of Cu^{2+} centers in ZnO, for example, is strongly influenced by a trigonal crystal field arising from the crystal structure (wurtzite lattice)[1]. More complex spectra have been observed from Cu^{2+} centers in ZnS crystals consisting of various polytypes[2–4]. A Jahn–Teller effect may also lower the symmetry of the crystal field[4]. On the other hand arbitrary distortions may be produced by applied stress[5].

If a tetrahedron, with symmetry group T_d, is distorted in the direction of a twofold symmetry axis, the symmetry is reduced to that of the subgroup D_{2d}; if an octahedron, with symmetry group O_h is distorted in the same way the subgroup D_{4h} results. The distortion along a threefold symmetry axis leads to groups C_{3v} and D_{3d} for T_d and O_h respectively. If I is the group which consists of the identity and inversion only, we may write $O_h = O \times I$, $D_{3d} = D_3 \times I$, $D_{4h} = D_4 \times I$, and we have the following isomorphisms: $T_d \triangleq O$, $C_{3v} \triangleq D_3$, $D_{2d} \triangleq D_4$[6]. For the irreducible representations of the groups and double groups Prather's notation[7] is used as well as Bethe's Γ_i symbols:

$$T_d, O: A_1, A_2, E, T_1, T_2; \Gamma_6, \Gamma_7, \Gamma_8.$$
$$D_{2d}, D_4: A_1, A_2, B_1, B_2, E: \Gamma_6, \Gamma_7.$$
$$C_{3v}, D_3: A_1, A_2, E: \Gamma_4, \Gamma_5, \Gamma_6.$$

The irreducible representations of the groups O_h, D_{4h} and D_{3d} are given by simply adding an index g or u. The qualitative splitting of crystal field energy levels characterized after representations of T_d or O_h by the distortions is given in Table 1. The level Γ_4, Γ_5 is still degenerate (unless a magnetic field is present) for time inversion reasons and is called a Kramers-doublet.

In the frame of crystal field theory the optical spectra of ions in crystals are determined by various forces. For transition metal ions in II–VI compounds they are, in decreasing order of magnitude in energy: Coulomb interaction between electrons in non-closed shells, a crystal field arising predominantly from the nearest neighbors, spin-orbit interaction, another crystal field of lower symmetry, spin-spin interaction, an external magnetic field, interaction of electrons with the

Table 1. Splitting of octahedral and tetrahedral crystal field energy levels by trigonal and tetragonal distortions

Tetragonal		Trigonal
D_4	O	D_3
D_{2d}	T_d	C_{3v}
A_1	A_1	A_1
B_1	A_2	A_2
A_1+B_1	E	E
A_2+E	T_1	A_2+E
B_2+E	T_2	A_1+E
Γ_6	Γ_6	Γ_4
Γ_7	Γ_7	Γ_4
$\Gamma_6+\Gamma_7$	Γ_8	$\Gamma_4, \Gamma_5+\Gamma_6$

nucleus and so on. As a first step Tanabe and Sugano[8] considered the Coulomb interaction and a crystal field with symmetry T_d or O_h. They calculated energy matrices in terms of Racah parameters B, C and the crystal field parameter D_q, from which the energy levels may be derived.

The fine structure of these levels has been treated by many authors. Tanabe and Kamimura[9] developed a general theory and Liehr and Ballhausen[10] calculated energy matrices for d^2-d^8 in a cubic crystal field with spin-orbit coupling included. Euwema [11] gave spin-orbit coupling matrix elements for d^n and Druzhinin *et al.*[12] calculated energy matrices for d^n. A trigonal crystal field has been considered by Liehr[13] and Gladney and Swalen[14] for d^1 and by Sugano and Tanabe[15] and Perumareddi[16] for d^3.

The general method of effective Hamiltonians developed by Tanabe and Kamimura [9], however, makes it possible to use the most general Hamiltonian, consistent with symmetry requirements, giving non-vanishing matrix elements. This effective Hamiltonian then includes spin-orbit interaction, crystal fields of lower symmetry and spin-spin interaction in first and higher order perturbation theory. It includes the maximum number of possible parameters which may be used in the frame of crystal field theory. Moreover, since the effective Hamiltonian is set up for every multiplet $^{2S+1}\Gamma$ separately, orbital reduction may be taken into account. With these covalency extensions, the treatment can be used to explain the Zeeman effect of the optical spectra in nearly all cases[1, 17].

2. EFFECTIVE HAMILTONIANS

The method of effective Hamiltonians may not only be used to determine the splitting of a given multiplet $^{2S+1}\Gamma_0$ but also to calculate matrix elements between different multiplets $^{2S+1}\Gamma$ and $^{2S+1}\Gamma'$. The spin-orbit interaction, however, may also give nonvanishing matrix elements between multiplets $^{2S+1}\Gamma$ and $^{2S'+1}\Gamma'$. As a first approximation we therefore restrict ourselves to the lowest multiplet ^{2S+1}L which is determined by Hund's rule. The influence of the higher multiplets $^{2S'+1}L'$ on the fine structure of the ground multiplet is neglected. This is a good approximation for Co^{2+} $(3d^7)$ ions and for Fe^{2+} $(3d^6)$ ions in II–VI compounds. For d^1–d^9 ions there are no higher multiplets at all.

From this we conclude that the method of an effective Hamiltonian constructed from tensor operators is adequate for d^1–d^9 and should give satisfactory results for all others. The fine structure of the higher levels $^{2S+1}\Gamma$ may also be calculated by the method of effective Hamiltonians.

A magnetic field could be included in the effective Hamiltonian (linear and quadratic). However, since the magnetic field removes any degeneracy, the resulting energy matrices are usually of such a high dimension, that the evaluation of the eigenvalues in terms of the unknown parameters is tedious. It is much easier to calculate eigenvalues and eigenfunctions of the effective Hamiltonian without a magnetic field and then find the g-factors from the eigenfunctions by the operator L_z+2S_z (magnetic field in z-direction)[18].

The most general effective Hamiltonian, invariant under the symmetry group considered may be set up by taking products of irreducible orbital tensor operators $X_\gamma(\Gamma)$ [9, 19], with $\Gamma = A_2, E, T_1, T_2$ and $X(A_1) = 1$, and irreducible spin tensor operators $C_{K\mu}$, $S_{K\mu}$ which are defined by:

$$C_{K\mu} = \left(\frac{1}{2}\right)^{-1/2} [T_{K\cdot\mu} + (-1)^\mu T_{K\mu}],$$

$$S_{K\mu} = \frac{i}{\sqrt{2}} [T_{K-\mu} - (-1)^\mu T_{K\mu}]$$

$$0 < \mu \leqslant K, C_{K0} = T_{K0}, K > 0.$$

The $T_{K\mu}$ are defined by (Racah[20]):

$$[S_z, T_{K\mu}] = \mu T_{K\mu},$$

$$[S_\pm, T_{K\mu}] = \sqrt{((K \mp \mu)(K \pm \mu + 1))}\, T_{K\mu\cdot 1}$$

$$T_{KK} = \left(\frac{-1}{\sqrt{2}}\right)^K S_+{}^K$$

with $S_\pm = S_x \pm iS_y$.

Spin tensor operators in terms of S_z and S_+ may be found in the book of Watanabe[21]. Matrix elements of these operators may easily be found by using the Wigner–Eckart theorem:

$$\langle SM|T_{K\mu}|SM'\rangle = \langle S\|T_K\|S\rangle\langle SM|SM'K\mu\rangle.$$

The double barred matrix elements needed for transition metal ions are (up to $S = 2$):

$$\langle \tfrac{1}{2}\|T_1\|\tfrac{1}{2}\rangle = \tfrac{1}{2}\sqrt{3}; \qquad \langle \tfrac{3}{2}\|T_3\|\tfrac{3}{2}\rangle = \tfrac{3}{2}\sqrt{\tfrac{7}{2}}$$

$$\langle 1\|T_1\|1\rangle = \sqrt{2}; \qquad \langle 2\|T_1\|2\rangle = \sqrt{6}$$

$$\langle 1\|T_2\|1\rangle = \sqrt{\tfrac{5}{3}}; \qquad \langle 2\|T_2\|2\rangle = \sqrt{21}$$

$$\langle \tfrac{3}{2}\|T_1\|\tfrac{3}{2}\rangle = \tfrac{1}{2}\sqrt{15}; \qquad \langle 2\|T_3\|2\rangle = 6\sqrt{\tfrac{7}{5}}$$

$$\langle \tfrac{3}{2}\|T_2\|\tfrac{3}{2}\rangle = \sqrt{\tfrac{15}{2}}; \qquad \langle 2\|T_4\|2\rangle = \tfrac{18}{\sqrt{3}}.$$

Matrices of spin tensor operators $C_{K\mu}$ and $S_{K\mu}$ may simply be constructed from those of $T_{K\mu}$.

Next we have to look for spin tensor operators which transform as the basis functions of the irreducible representations of the three symmetry groups. These basis functions are defined after Watanabe[21] and Griffith[22]. The reduction for cubic symmetry has been given by Ray[23] Table 2 shows spin tensor operators up to $K = 5$ which transform as basis functions of the irreducible representations of the symmetry groups considered. It must be remembered, that the z-axis is a twofold symmetry axis for T_d, O, D_{2d} and D_4 while it is a threefold symmetry axis for C_{3i} and D_3 (trigonal axis). For groups O_h, D_{4h} and D_{3d} one has to add an index g to the basis functions. This is due to the fact that spin tensor operators $T_{K\mu}$ transform under rotations as $|K\mu\rangle$ but commute with the inversion operator.

The irreducible orbital tensor operators may be divided in imaginary operators $T_\gamma(\Gamma)$ which may only occur in connection with a spin tensor operator or a magnetic field, and real operators $V_\gamma(\Gamma)$. Their matrix elements may also be found by using the Wigner-Eckart theorem[9, 24]

$$\langle \Gamma\gamma|V_{\bar\gamma}(\bar\Gamma)|\Gamma'\gamma'\rangle = (d_\Gamma)^{-1/2}\langle\Gamma\|V(\bar\Gamma)\|\Gamma'\rangle\langle\Gamma\gamma|\Gamma'\gamma'\bar\Gamma\bar\gamma\rangle$$

where d_Γ denotes the dimension of the irreducible representation Γ, and the Clebsch-Gordan coefficients may be found for instance in reference[8]. The definition of the double barred matrix elements depends on the definition of the parameters occuring in the effective Hamiltonian. They should be chosen so as to produce simple eigenvalues of the effective Hamiltonian. For d electrons the definition of parameters in terms of one particle integrals may then be derived using the method and tables of Tanabe and Kamimura [9]. Double barred matrix elements of the form $\langle\Gamma\|X(\bar\Gamma)\|\Gamma\rangle$ are therefore given by:

$$\langle E\|V(E)\|E\rangle = 2; \qquad \langle E\|T(A_2)\|E\rangle = -i\sqrt{2}$$

$$\langle T_1\|V(E)\|T_1\rangle = \sqrt{6}; \quad \langle T_1\|T(T_1)\|T_1\rangle = i\sqrt{6}$$

$$\langle T_1\|V(T_2)\|T_1\rangle = 3\sqrt{2}.$$

$$\langle T_2\|V(E)\|T_2\rangle = 2\sqrt{3}; \quad \langle T_2\|T(T_1)\|T_2\rangle = i\sqrt{6}$$

$$\langle T_2\|V(T_2)\|T_2\rangle = 3\sqrt{2}.$$

Table 2. Spin tensor operators which transform as basis functions of irreducible representations of various groups

	C_{3v}, D_3	T_d, O	D_{2d}, D_4
$K = 1$	$a_2 = C_{10}$ $u = -S_{11}$ $v = C_{11}$	$\alpha = C_{11}$ $\beta = S_{11}$ $\gamma = C_{10}$	$a_2 = C_{10}$ $u = C_{11}$ $v = S_{11}$
$K = 2$	$a_1 = C_{20}$ $u^{(1)} = C_{21}$ $v^{(1)} = S_{21}$ $u^{(2)} = C_{22}$ $v^{(2)} = -S_{22}$	$u = C_{20}$ $v = C_{22}$ $\xi = S_{21}$ $\eta = C_{21}$ $\zeta = S_{22}$	$a_1 = C_{20}$ $b_1 = C_{22}$ $b_2 = S_{22}$ $u = S_{21}$ $v = -C_{21}$
$K = 3$	$a_1 = S_{33}$ $a_2^{(1)} = C_{30}$ $a_2^{(2)} = C_{33}$ $u^{(1)} = -S_{31}$ $v^{(1)} = C_{31}$ $u^{(2)} = S_{32}$ $v^{(2)} = C_{32}$	$a_2 = S_{32}$ $\alpha = \sqrt{\frac{5}{8}}C_{33} - \sqrt{\frac{3}{8}}C_{31}$ $\beta = -\sqrt{\frac{5}{8}}S_{33} - \sqrt{\frac{3}{8}}S_{31}$ $\gamma = C_{30}$ $\xi = -\sqrt{\frac{3}{8}}C_{33} - \sqrt{\frac{5}{8}}C_{31}$ $\eta = -\sqrt{\frac{3}{8}}S_{33} + \sqrt{\frac{5}{8}}S_{31}$ $\zeta = C_{32}$	$a_2 = C_{30}$ $b_1 = S_{32}$ $b_2 = C_{32}$ $u^{(1)} = C_{31}$ $v^{(1)} = S_{31}$ $u^{(2)} = C_{33}$ $v^{(2)} = -S_{33}$
$K = 4$	$a_1^{(1)} = C_{40}$ $a_1^{(2)} = C_{43}$ $a_2 = S_{43}$ $u^{(1)} = C_{41}$ $v^{(1)} = S_{41}$ $u^{(2)} = C_{42}$ $v^{(2)} = -S_{42}$ $u^{(3)} = C_{44}$ $v^{(3)} = S_{44}$	$a_1 = \sqrt{\frac{7}{12}}C_{40} + \sqrt{\frac{5}{12}}C_{44}$ $u = -\sqrt{\frac{5}{12}}C_{40} + \sqrt{\frac{7}{12}}C_{44}$ $v = C_{42}$ $\alpha = -\sqrt{\frac{1}{8}}S_{43} - \sqrt{\frac{7}{8}}S_{41}$ $\beta = -\sqrt{\frac{1}{8}}C_{43} + \sqrt{\frac{7}{8}}C_{41}$ $\gamma = S_{44}$ $\xi = \sqrt{\frac{7}{8}}S_{43} - \sqrt{\frac{1}{8}}S_{41}$ $\eta = -\sqrt{\frac{7}{8}}C_{43} - \sqrt{\frac{1}{8}}C_{41}$ $\zeta = S_{42}$	$a_1^{(1)} = C_{40}$ $a_1^{(2)} = C_{44}$ $a_2 = S_{44}$ $b_1 = C_{42}$ $b_2 = S_{42}$ $u^{(1)} = S_{41}$ $v^{(1)} = -C_{41}$ $u^{(2)} = S_{43}$ $v^{(2)} = C_{43}$
$K = 5$	$a_1 = S_{53}$ $a_2^{(1)} = C_{50}$ $a_2^{(2)} = C_{53}$ $u^{(1)} = -S_{51}$ $v^{(1)} = C_{51}$ $u^{(2)} = S_{52}$ $v^{(2)} = C_{52}$ $u^{(3)} = -S_{54}$ $v^{(3)} = C_{54}$ $u^{(4)} = S_{55}$ $v^{(4)} = C_{55}$	$u = S_{54}$ $v = -S_{52}$ $\alpha^{(1)} = \sqrt{\frac{63}{128}}C_{55} - \sqrt{\frac{35}{128}}C_{53} + \sqrt{\frac{30}{128}}C_{51}$ $\beta^{(1)} = \sqrt{\frac{63}{128}}S_{55} + \sqrt{\frac{35}{128}}S_{53} + \sqrt{\frac{30}{128}}S_{51}$ $\gamma^{(1)} = C_{50}$ $\alpha^{(2)} = \frac{1}{16}(\sqrt{10}C_{55} + \sqrt{162}C_{53} + \sqrt{84}C_{51})$ $\beta^{(2)} = \frac{1}{16}(\sqrt{10}S_{55} - \sqrt{162}S_{53} + \sqrt{84}S_{51})$ $\gamma^{(2)} = C_{54}$ $\xi = -\sqrt{\frac{15}{32}}C_{55} - \sqrt{\frac{3}{32}}C_{53} + \sqrt{\frac{14}{32}}C_{51}$ $\eta = \sqrt{\frac{15}{32}}S_{55} - \sqrt{\frac{3}{32}}S_{53} - \sqrt{\frac{14}{32}}S_{51}$ $\zeta = C_{52}$	$a_1 = S_{54}$ $a_2^{(1)} = C_{50}$ $a_2^{(2)} = C_{54}$ $b_1 = S_{52}$ $b_2 = C_{52}$ $u^{(1)} = C_{51}$ $v^{(1)} = S_{51}$ $u^{(2)} = C_{53}$ $v^{(2)} = -S_{53}$ $u^{(3)} = C_{55}$ $v^{(3)} = S_{55}$

All others are zero. Double barred matrix elements of the form $\langle \Gamma\nu \| X(\bar{\Gamma}) \| \Gamma\mu \rangle$ with $\nu > \mu$ which are needed here are

$$\langle T_2 \| V(T_2) \| E \rangle = 2\sqrt{3},\ \langle T_2 \| T(T_1) \| E \rangle = -i2\sqrt{3},\ \langle T_2 \| T(T_2) \| E \rangle = i2\sqrt{3}.$$

Double barred matrix elements with $\nu < \mu$ are then not necessary, since one can use the fact that matrices of the effective Hamiltonian are Hermitian.

The most general form of the effective Hamiltonian may be found by the following rules given by Tanabe and Kamimura[9]:

1. orbital tensor operators alone must be real,
2. spin tensor operators alone must have K even,
3. products of orbital tensor operators with spin tensor operators must be either a real orbital operator multiplied by a

spin operator with K even, or an imaginary orbital operator multiplied by a spin operator with K odd,

4. $K \leqslant 2S$ for multiplets with spin S.

Tables 3–5 give the most general effective Hamiltonians invariant under the transformations of various symmetry groups. The terms are listed in order of increasing K up to $K = 4$. For groups O_h, D_{4h} and D_{3d} one has to add an index g to the subscripts denoting the basis function.

It must be remembered that the theory applies not only to d-electrons but more generally to t_2 and e electrons. That means that only the symmetry properties of the wave functions are required here. Thus allowance is made for wave functions constructed by the LCAO–MO-method and this is an extension of crystal field theory taking covalency into account. As a consequence more parameters appear, which can only be determined by fitting to experimental results. One may therefore speak of a 'semiempirical' theory[1].

3. ENERGY MATRICES FOR d^1, d^9 IN TETRAHEDRAL OR OCTAHEDRAL CRYSTAL FIELDS

Energy matrices for these cases have been given by Liehr[13] without orbital reduction. We include here the most general case. A d^1 ion has only one multiplet, ^2D, which is split by a tetrahedral crystal field into two levels with energies: $E(^2T_2) = 4Dq$, $E(^2E) = -6Dq$. The effective Hamiltonian from Table 3 consists of spin-orbit coupling only and vanishes for ^2E. For $^2T_2$ and for configuration mixing of the two levels it reads

$$H(^2T_2) = \zeta(T_\alpha(T_1)S_x + T_\beta(T_1)S_y + T_\gamma(T_1)S_z)$$

$$H(^2T_2, {}^2E) = \zeta'(T_\alpha(T_1)S_x + T_\beta(T_1)S_y + T_\gamma(T_1)S_z)$$

Table 3. Effective Hamiltonian invariant under symmetry groups $\mathrm{T_d}$ *and* O

Terms for $S = \frac{1}{2}$:

$$\frac{1}{\sqrt{3}}(T_\alpha(T_1)C_{11} + T_\beta(T_1)S_{11} + T_\gamma(T_1)C_{10}).$$

Additional terms for $S = 1$:

$$\frac{1}{\sqrt{2}}(V_u(E)C_{20} + V_v(E)C_{22}), \frac{1}{\sqrt{3}}(V_\xi(T_2)S_{21} + V_\eta(T_2)C_{21} + V_\zeta(T_2)S_{22}).$$

Additional terms for $S = \frac{3}{2}$:

$T(A_2)S_{32}$

$$\frac{1}{\sqrt{3}}\{T_\alpha(T_1)[\sqrt{\tfrac{5}{8}}C_{33} - \sqrt{\tfrac{3}{8}}C_{31}] + T_\beta(T_1)[-\sqrt{\tfrac{5}{8}}S_{33} - \sqrt{\tfrac{3}{8}}S_{31}] + T_\gamma(T_1)C_{30}\}.$$

$$\frac{1}{\sqrt{3}}\{T_\xi(T_2)[-\sqrt{\tfrac{3}{8}}C_{33} - \sqrt{\tfrac{5}{8}}C_{31}] + T_\eta(T_2)[-\sqrt{\tfrac{3}{8}}S_{33} + \sqrt{\tfrac{5}{8}}S_{31}] + T_\zeta(T_2)C_{32}\}$$

Additional terms for $S = 2$.

$$\sqrt{\tfrac{7}{12}}C_{40} + \sqrt{\tfrac{5}{12}}C_{44}, \frac{1}{\sqrt{2}}\{V_u(E)[-\sqrt{\tfrac{5}{12}}C_{40} + \sqrt{\tfrac{7}{12}}C_{44}] + V_v(E)C_{42}\},$$

$$\frac{1}{\sqrt{3}}\{V_\xi(T_2)[\sqrt{\tfrac{1}{8}}S_{43} - \sqrt{\tfrac{7}{8}}S_{41}] + V_\eta(T_2)[-\sqrt{\tfrac{1}{8}}C_{43} - \sqrt{\tfrac{7}{8}}C_{41}] + V_\zeta(T_2)S_{42}\},$$

$$\frac{1}{\sqrt{3}}\{V_\alpha(T_1)[-\sqrt{\tfrac{7}{8}}S_{43} - \sqrt{\tfrac{1}{8}}S_{41}] + V_\beta(T_1)[-\sqrt{\tfrac{7}{8}}C_{43} + \sqrt{\tfrac{1}{8}}C_{41}] + V_\gamma(T_1)S_{44}\}$$

Table 4. Effective Hamiltonian invariant under symmetry groups C_{3v} *and* D_3

Terms for $S = 0$.

$V_0(T_2)$,

Additional terms for $S = \frac{1}{2}$:

$T(A_2)C_{10}, T_0(T_1)C_{10}$

$\frac{1}{\sqrt{2}}(-T_u(E)S_{11}+T_v(E)C_{11}), \frac{1}{\sqrt{2}}(-T_u(T_1)S_{11}+T_v(T_1)C_{11}),$

$\frac{1}{\sqrt{2}}(-T_u(T_2)S_{11}+T_v(T_2)C_{11}),$

Additional terms for $S = 1$

$C_{20}, V_0(T_2)C_{20},$

$\frac{1}{\sqrt{2}}(V_u(E)C_{21}+V_v(E)S_{21}), \frac{1}{\sqrt{2}}(V_u(E)C_{22}-V_v(E)S_{22}),$

$\frac{1}{\sqrt{2}}(V_u(T_1)C_{21}+V_v(T_1)S_{21}), \frac{1}{\sqrt{2}}(V_u(T_1)C_{22}-V_v(T_1)S_{22}),$

$\frac{1}{\sqrt{2}}(V_u(T_2)C_{21}+V_v(T_2)S_{21}), \frac{1}{\sqrt{2}}(V_u(T_2)C_{22}-V_v(T_2)S_{22}),$

Additional terms for $S = \frac{3}{2}$.

$S_{33}, T(A_2)C_{30}, T(A_2)C_{33}, T_0(T_1)C_{30}, T_0(T_1)C_{33}, T_0(T_2)S_{33},$

$\frac{1}{\sqrt{2}}(-T_u(E)S_{31}+T_v(E)C_{31}), \frac{1}{\sqrt{2}}(T_u(E)S_{32}+T_v(E)C_{32}),$

$\frac{1}{\sqrt{2}}(-T_u(T_1)S_{31}+T_v(T_1)C_{31}), \frac{1}{\sqrt{2}}(T_u(T_1)S_{32}+T_v(T_1)C_{32}),$

$\frac{1}{\sqrt{2}}(-T_u(T_2)S_{31}+T_v(T_2)C_{31}), \frac{1}{\sqrt{2}}(T_u(T_2)S_{32}+T_v(T_2)C_{32}),$

Additional terms for $S = 2$:

$C_{40}, C_{43}, V(A_2)S_{43}, V_0(T_1)S_{43}, V_0(T_2)C_{40}, V_0(T_2)C_{43},$

$\frac{1}{\sqrt{2}}(V_u(E)C_{41}+V_v(E)S_{41}), \frac{1}{\sqrt{2}}(V_u(E)C_{42}-V_v(E)S_{42}),$

$\frac{1}{\sqrt{2}}(V_u(E)C_{44}+V_v(E)S_{44}), \frac{1}{\sqrt{2}}(V_u(T_1)C_{41}+V_v(T_1)S_{41}),$

$\frac{1}{\sqrt{2}}(V_u(T_1)C_{42}-V_v(T_1)S_{42}), \frac{1}{\sqrt{2}}(V_u(T_1)C_{44}+V_v(T_1)S_{44}),$

$\frac{1}{\sqrt{2}}(V_u(T_2)C_{41}+V_v(T_2)S_{41}), \frac{1}{\sqrt{2}}(V_u(T_2)C_{42}-V_v(T_2)S_{42}),$

$\frac{1}{\sqrt{2}}(V_u(T_2)C_{44}+V_v(T_2)S_{44})$

With the abbreviations: (X stands for V or T)

$X_0(T_1) = \frac{1}{\sqrt{3}}(X_\alpha(T_1)+X_\beta(T_1)+X_\gamma(T_1)),$

$X_0(T_2) = \frac{1}{\sqrt{3}}(X_\xi(T_2)+X_\eta(T_2)+X_\zeta(T_2)),$

$X_u(T_1) = \frac{1}{\sqrt{2}}(X_\alpha(T_1)-X_\beta(T_1)),$

$X_v(T_1) = \frac{1}{\sqrt{6}}(X_\alpha(T_1)+X_\beta(T_1)-2X_\gamma(T_1)),$

$X_u(T_2) = \frac{1}{\sqrt{6}}(X_\xi(T_2)+X_\eta(T_2)-2X_\zeta(T_2)),$

$X_v(T_2) = \frac{1}{\sqrt{2}}(X_\eta(T_2)-X_\xi(T_2))$

---

where the factor $1/\sqrt{3}$ has been included in the parameters for convenience, and where $C_{11} = S_x$, $S_{11} = S_y$, $C_{10} = S_z$ have been used. The matrices of the spin operators are simply $\frac{1}{2}$ times Pauli's spin matrices, and the matrices of the T operators are:

$$\text{for } T_2: \langle T_\alpha\rangle = \begin{pmatrix} 0 & 0 & 0 \\ 0 & 0 & i \\ 0 & -i & 0 \end{pmatrix},$$

$$\langle T_\beta\rangle = \begin{pmatrix} 0 & 0 & -i \\ 0 & 0 & 0 \\ i & 0 & 0 \end{pmatrix}, \langle T_\gamma\rangle = \begin{pmatrix} 0 & i & 0 \\ -i & 0 & 0 \\ 0 & 0 & 0 \end{pmatrix}$$

$$\text{for } T_2, E: \langle T_\alpha\rangle = \begin{pmatrix} -i\sqrt{3} & -i \\ 0 & 0 \\ 0 & 0 \end{pmatrix},$$

$$\langle T_\beta\rangle = \begin{pmatrix} 0 & 0 \\ i\sqrt{3} & -i \\ 0 & 0 \end{pmatrix}, \langle T_\gamma\rangle = \begin{pmatrix} 0 & 0 \\ 0 & 0 \\ 0 & 2i \end{pmatrix}.$$

The definitions of the spin-orbit coupling parameters ζ, ζ' are then as follows:

$$\zeta = -2i\langle t_2\xi\tfrac{1}{2}|\zeta(r)s_z l_z|t_2\eta\tfrac{1}{2}\rangle$$
$$\zeta' = -i\langle t_2\zeta\tfrac{1}{2}|\zeta(r)s_z l_z|ev\tfrac{1}{2}\rangle$$

and for pure d electrons one has $\zeta = \zeta'$.

Table 5. *Effective Hamiltonian invariant under symmetry groups* D_{2d} *and* D_4

Terms for $S = 0$:

$V_u(E)$,

Additional terms for $S = \frac{1}{2}$

$T_\gamma(T_1)C_{10}, \frac{1}{\sqrt{2}}(T_\alpha(T_1)C_{11} + T_\beta(T_1)S_{11}), \frac{1}{\sqrt{2}}(T_\xi(T_2)C_{11} - T_\eta(T_2)S_{11})$.

Additional terms for $S = 1$·

$C_{20}, V_u(E)C_{20}, V(A_2)C_{22}, V_v(E)C_{22}, T_\zeta(T_2)S_{22}$,

$\frac{1}{\sqrt{2}}(V_\alpha(T_1)S_{21} - V_\beta(T_1)C_{21}), \frac{1}{\sqrt{2}}(V_\xi(T_2)S_{21} + V_\eta(T_2)C_{21})$.

Additional terms for $S = \frac{3}{2}$.

$T_\gamma(T_1)C_{30}, T(A_2)S_{32}, T_v(E)S_{32}, T_\zeta(T_2)C_{32}$,

$\frac{1}{\sqrt{2}}(T_\alpha(T_1)C_{31} + T_\beta(T_1)S_{31}), \frac{1}{\sqrt{2}}(T_\alpha(T_1)C_{33} - T_\beta(T_1)S_{33})$,

$\frac{1}{\sqrt{2}}(T_\xi(T_2)C_{31} - T_\eta(T_2)S_{31}), \frac{1}{\sqrt{2}}(T_\xi(T_2)C_{33} + T_\eta(T_2)S_{33})$.

Additional terms for $S = 2$.

$C_{40}, C_{44}, V_u(E)C_{40}, V_u(E)C_{44}, V_\gamma(T_1)S_{44}, V(A_2)C_{42}, V_v(E)C_{42}, V_\zeta(T_2)S_{42}$,

$\frac{1}{\sqrt{2}}(V_\alpha(T_1)S_{41} - V_\beta(T_1)C_{41}), \frac{1}{\sqrt{2}}(V_\alpha(T_1)S_{43} + V_\beta(T_1)C_{43})$,

$\frac{1}{\sqrt{2}}(V_\xi(T_2)S_{41} + V_\eta(T_2)C_{41}), \frac{1}{\sqrt{2}}(V_\xi(T_2)S_{43} - V_\eta(T_2)C_{43})$.

The three fine structure energy levels $\Gamma_7(^2T_2)$, $\Gamma_8(^2T_2)$, $\Gamma_8(^2E)$ are now given by the eigenvalues of the matrix

$$\langle H\rangle = \begin{pmatrix} \langle H(^2T_2)\rangle & \langle H(^2T_2, {}^2E)\rangle \\ \langle H(^2T_2, {}^2E)\rangle^+ & \langle H(^2E)\rangle \end{pmatrix}.$$

After an unitary transformation one finds the following energy matrices: (energies of $^2T_2$ and ^2E added)

Γ_7: $4Dq + \zeta$ with eigenfunctions c, c'

$$\Gamma_8: \begin{pmatrix} 4Dq - \frac{1}{2}\zeta & -\sqrt{\frac{3}{2}}\zeta' \\ -\sqrt{\frac{3}{2}}\zeta' & -6Dq \end{pmatrix}$$

with eigenfunctions $\begin{pmatrix} a \\ u- \end{pmatrix}, \begin{pmatrix} b \\ v- \end{pmatrix}, \begin{pmatrix} a' \\ u+ \end{pmatrix}, \begin{pmatrix} b' \\ v+ \end{pmatrix}$ with

$$(abc) = (\xi + \eta + \zeta -)\begin{pmatrix} \frac{i}{\sqrt{2}} & \frac{i}{\sqrt{6}} & \frac{1}{\sqrt{3}} \\ \frac{-1}{\sqrt{2}} & \frac{1}{\sqrt{6}} & \frac{-i}{\sqrt{3}} \\ 0 & \frac{2i}{\sqrt{6}} & \frac{-1}{\sqrt{3}} \end{pmatrix},$$

$$(a'b'c') = (\xi - \eta - \zeta +)\begin{pmatrix} \frac{i}{\sqrt{2}} & \frac{i}{\sqrt{6}} & \frac{1}{\sqrt{3}} \\ \frac{1}{\sqrt{2}} & \frac{-1}{\sqrt{6}} & \frac{i}{\sqrt{3}} \\ 0 & \frac{-2i}{\sqrt{6}} & \frac{1}{\sqrt{3}} \end{pmatrix}$$

and ± denotes z-component of spin $\pm\frac{1}{2}$.

To find the energy matrices for d^9 one has to replace Dq, ζ and ζ' by their negative values[9]. Energy matrices of an octahedral potential are given by replacing Dq by its negative value.

4. ENERGY MATRICES FOR d^1, d^9 IN A TRIGONALLY DISTORTED TETRAHEDRAL OR OCTAHEDRAL CRYSTAL FIELD

These cases have been studied extensively by Dietz *et al.*[1] and by Liehr[13]. The difference in this treatment is that complete energy matrices are given here for the most general effective Hamiltonians. A new term has been included which arises by an interplay of spin-orbit coupling and a trigonal crystal field in configuration mixing matrix elements. The new parameter ζ_0' gives an additional term to spin-orbit coupling and represents the modification of spin-orbit coupling by the crystal field. Schmidke[25], however, has estimated this effect and found that it should be small for transition metal ions in complexes.

The parameter ζ_0', which leads to a different spin-orbit coupling for Γ_6 and $\Gamma_4\Gamma_5$ levels, is therefore presumed to be small compared with $\zeta_\perp'$ defined below.

d^1 in a tetrahedral crystal field is considered first, the other cases may be found merely by changing some signs. The trigonal crystal field has symmetry C_{3v}. From Table 4 the following effective Hamiltonians are found:

$$H(^2E) = DT(A_2)S_z$$

$$\begin{aligned} H(^2T_2) = {} & KV_0(T_2) + \zeta_\perp(T_v(T_1)S_x \\ & - T_u(T_1)S_y) + \zeta_\parallel T_0(T_1)S_z \end{aligned}$$

$$\begin{aligned} H(^2T_2, {}^2E) = {} & K'V_0(T_2) + \zeta_\perp'(T_v(T_1)S_x \\ & - T_u(T_1)S_y) \\ & + \zeta_\parallel' T_0(T_1)S_z \\ & + \zeta_0'(T_v(T_2)S_x - T_u(T_2)S_y) \end{aligned}$$

where factors $1/\sqrt{2}$ have been included in the parameters, and where $C_{11} = S_x$, $S_{11} = S_y$, $C_{10} = S_z$ have been used. The matrices of spin operators are simply Pauli's spin matrices times $\frac{1}{2}$. New basis functions are introduced for convenience [9]:

$$\begin{pmatrix} a_+ \\ a_- \\ a_0 \end{pmatrix} = \Omega \begin{pmatrix} \alpha \\ \beta \\ \gamma \end{pmatrix}, \begin{pmatrix} x_+ \\ x_- \\ x_0 \end{pmatrix} = \Omega \begin{pmatrix} \xi \\ \eta \\ \xi \end{pmatrix},$$

$$\Omega = \frac{1}{\sqrt{3}} \begin{pmatrix} -\omega & -\bar{\omega} & -1 \\ \bar{\omega} & \omega & 1 \\ 1 & 1 & 1 \end{pmatrix}, \omega = e^{i(2\pi/3)}$$

$$\begin{pmatrix} u_+ \\ u_- \end{pmatrix} = \frac{1}{\sqrt{2}} \begin{pmatrix} -1 & -i \\ 1 & -i \end{pmatrix} \begin{pmatrix} u \\ v \end{pmatrix}$$

and the matrices of the orbital operators are therefore:

$$\text{for} \quad E: \langle T(A_2) \rangle = \begin{pmatrix} 1 & 0 \\ 0 & -1 \end{pmatrix}$$

$$\text{for } T_2: \langle V_0(T_2) \rangle = \begin{pmatrix} -1 & 0 & 0 \\ 0 & -1 & 0 \\ 0 & 0 & 2 \end{pmatrix},$$

$$\langle T_v(T_1) \rangle = \frac{1}{\sqrt{2}} \begin{pmatrix} 0 & 0 & 1 \\ 0 & 0 & 1 \\ 1 & 1 & 0 \end{pmatrix}$$

$$\langle T_u(T_1) \rangle = \frac{i}{\sqrt{2}} \begin{pmatrix} 0 & 0 & 1 \\ 0 & 0 & -1 \\ -1 & 1 & 0 \end{pmatrix},$$

$$\langle T_0(T_1) \rangle = \begin{pmatrix} -1 & 0 & 0 \\ 0 & 1 & 0 \\ 0 & 0 & 0 \end{pmatrix}$$

$$\text{for } T_2, E: \langle V_0(T_2) \rangle = \sqrt{2} \begin{pmatrix} 1 & 0 \\ 0 & 1 \\ 0 & 0 \end{pmatrix},$$

$$\langle T_v(T_1) \rangle = \begin{pmatrix} 0 & 1 \\ -1 & 0 \\ -1 & -1 \end{pmatrix}$$

$$\langle T_u(T_1) \rangle = i \begin{pmatrix} 0 & -1 \\ -1 & 0 \\ 1 & -1 \end{pmatrix},$$

$$\langle T_0(T_1) \rangle = \sqrt{2} \begin{pmatrix} -1 & 0 \\ 0 & 1 \\ 0 & 0 \end{pmatrix}$$

$$\langle T_v(T_2)\rangle = \begin{pmatrix} 0 & -1 \\ 1 & 0 \\ -1 & -1 \end{pmatrix}, \langle T_u(T_2)\rangle = i\begin{pmatrix} 0 & 1 \\ 1 & 0 \\ 1 & -1 \end{pmatrix}$$

The definition of the parameters is:

$$D = \langle eu_+ | t(A_2) | eu_+ \rangle$$

(this parameter must not be confused with D in Dq)

$$K = -\langle t_2x_+ | v_0(T_2) | t_2x_+ \rangle$$

$$\begin{aligned} \zeta_\perp &= \sqrt{2}\langle t_2x_0\tfrac{1}{2} | s_xt_v - s_yt_u | t_2x_+ -\tfrac{1}{2}\rangle \\ &= \sqrt{2}\langle t_2x_0\tfrac{1}{2} | \zeta(r)(s_x1_x + s_y1_y) | t_2x_+ -\tfrac{1}{2}\rangle \end{aligned}$$

$$\begin{aligned} \zeta_\parallel &= -2\langle t_2x_+\tfrac{1}{2} | s_zt_0 | t_2x_+\tfrac{1}{2}\rangle \\ &= -2\langle t_2x_+\tfrac{1}{2} | \zeta(r)s_z1_z | t_2x_+\tfrac{1}{2}\rangle \end{aligned}$$

$$K' = \frac{1}{\sqrt{2}}\langle t_2x_+ | v_0(T_2) | eu_+ \rangle$$

$$\begin{aligned} \zeta'_\perp &= -\langle t_2x_0\tfrac{1}{2} | s_xt_v - s_yt_u | eu_+ -\tfrac{1}{2}\rangle \\ &= -\langle t_2x_0\tfrac{1}{2} | \zeta(r)(s_x1_x + s_y1_y) | eu_+ -\tfrac{1}{2}\rangle \end{aligned}$$

$$\begin{aligned} \zeta'_\parallel &= -\sqrt{2}\langle t_2x_+\tfrac{1}{2} | s_zt_0 | eu_+\tfrac{1}{2}\rangle \\ &= -\sqrt{2}\langle t_2x_+\tfrac{1}{2} | \zeta(r)s_z1_z | eu_+\tfrac{1}{2}\rangle \end{aligned}$$

$$\zeta'_0 = -\langle t_2x_+\tfrac{1}{2} | s_xt_v(T_2) - s_yt_u(T_2) | eu_- -\tfrac{1}{2}\rangle$$

The 5 doubly degenerate fine structure energy levels

$$\Gamma_4\Gamma_5(^2T_2), \Gamma_4\Gamma_5(^2E), \Gamma_6(^2T_2), \Gamma_6(^2T_2), \Gamma_6(^2E)$$

are then given by the eigenvalues of the following energy matrices

The corresponding eigenfunctions are:

$$\text{for } \Gamma_6: \begin{pmatrix} |x_+ & -\tfrac{1}{2}\rangle \\ |x_0 & \tfrac{1}{2}\rangle \\ |u_+ & -\tfrac{1}{2}\rangle \end{pmatrix} \text{and} \begin{pmatrix} |x & \tfrac{1}{2}\rangle \\ |x_0 & -\tfrac{1}{2}\rangle \\ |u_- & \tfrac{1}{2}\rangle \end{pmatrix}$$

$$\text{for } \Gamma_4\Gamma_5: \begin{pmatrix} \alpha|x_+\tfrac{1}{2}\rangle - \beta|x_- -\tfrac{1}{2}\rangle \\ |u_+\tfrac{1}{2}\rangle \end{pmatrix}$$

$$\text{and} \begin{pmatrix} \beta|x_+\tfrac{1}{2}\rangle + \alpha|x_- -\tfrac{1}{2}\rangle \\ |u_- -\tfrac{1}{2}\rangle \end{pmatrix}$$

with

$$\alpha = \frac{K' - \tfrac{1}{2}\zeta'_\parallel}{\sqrt{((K' - \tfrac{1}{2}\zeta'_\parallel)^2 + \tfrac{1}{2}(\zeta'_\perp - \zeta'_0)^2)}}$$

$$\beta = \frac{\frac{1}{\sqrt{2}}(\zeta'_\perp - \zeta'_0)}{\sqrt{((K' - \tfrac{1}{2}\zeta'_\parallel)^2 + \tfrac{1}{2}(\zeta'_\perp - \zeta'_0)^2)}}.$$

To find the energy matrices for d^9 all parameters have to be replaced by their negative values. Energy matrices for a trigonal distorted octahedral potential are readily found by replacing Dq by its negative value.

5. ENERGY MATRICES FOR d^1, d^9 IN A TETRAGONALLY DISTORTED TETRAHEDRAL OR OCTAHEDRAL CRYSTAL FIELD

d^1 in a tetragonally distorted tetrahedral field is considered first. The most general effective Hamiltonian invariant under the symmetry group D_{2d} is then after Table 5 with

$$\Gamma_6: \begin{pmatrix} 4Dq - K + \tfrac{1}{2}\zeta_\parallel & \frac{1}{\sqrt{2}}\zeta_\perp & \sqrt{2}K' + \frac{1}{\sqrt{2}}\zeta'_\parallel \\ \frac{1}{\sqrt{2}}\zeta_\perp & 4Dq + 2K & -\zeta'_\perp - \zeta'_0 \\ \sqrt{2}K' + \frac{1}{\sqrt{2}}\zeta'_\parallel & -\zeta'_\perp - \zeta'_0 & -6Dq - \frac{D}{2} \end{pmatrix}$$

$$\Gamma_4\ \Gamma_5: \begin{pmatrix} 4Dq - K - \tfrac{1}{2}\zeta_\parallel & \sqrt{\left(\left(\sqrt{2}K' - \frac{1}{\sqrt{2}}\zeta'_\parallel\right)^2 + (\zeta'_\perp - \zeta'_0)^2\right)} \\ \sqrt{\left(\left(\sqrt{2}K' - \frac{1}{\sqrt{2}}\zeta'_\parallel\right)^2 + (\zeta'_\perp - \zeta'_0)^2\right)} & -6Dq + \frac{D}{2} \end{pmatrix}$$

respect to double barred matrix elements:

$$H\,(^2E) = D\,V_u(E)$$

$$\begin{aligned}H(^2T_2) = {} & FV_u(E) + \zeta_\perp(T_\alpha(T_1)S_x \\ & + T_\beta(T_1)S_y) + \zeta_\parallel T_\gamma(T_1)S_z\end{aligned}$$

$$\begin{aligned}H(^2T_2, {}^2E) = {} & \zeta'_\perp(T_\alpha(T_1)S_x + T_\beta(T_1)S_y) \\ & + \zeta'_\parallel T_\gamma(T_1)S_z \\ & + \zeta'_0(T_\xi(T_2)S_x - T_\eta(T_2)S_y).\end{aligned}$$

Again the parameter ζ'_0 arises from the modification of spin-orbit coupling by the crystal field and is expected to be small compared with $\zeta'_\perp$. In the effective Hamiltonians, factors $1/\sqrt{2}$ have been included in the parameters, and $C_{11} = S_x$, $S_{11} = S_y$, $C_{10} = S_z$ have been used. The matrices of spin operators are simply Pauli's spin matrices times $\frac{1}{2}$ and the matrices of the other operators are:

$$\text{for } E \quad : \langle V_u(E)\rangle = \begin{pmatrix} -1 & 0 \\ 0 & 1 \end{pmatrix}$$

$$\text{for } T_2 \quad : \langle V_u(E)\rangle = \begin{pmatrix} -1 & 0 & 0 \\ 0 & -1 & 0 \\ 0 & 0 & 2 \end{pmatrix}$$

$$\langle T_\alpha(T_1)\rangle = \begin{pmatrix} 0 & 0 & 0 \\ 0 & 0 & i \\ 0 & -i & 0 \end{pmatrix}, \langle T_\beta(T_1)\rangle = \begin{pmatrix} 0 & 0 & i \\ 0 & 0 & 0 \\ i & 0 & 0 \end{pmatrix}$$

$$\langle T_\gamma(T_1)\rangle = \begin{pmatrix} 0 & i & 0 \\ -i & 0 & 0 \\ 0 & 0 & 0 \end{pmatrix}$$

$$\text{for } T_2, E : \langle T_\alpha(T_1)\rangle = \begin{pmatrix} -i\sqrt{3} & -i \\ 0 & 0 \\ 0 & 0 \end{pmatrix}.$$

$$\langle T_\beta(T_1)\rangle = \begin{pmatrix} 0 & 0 \\ i\sqrt{3} & -i \\ 0 & 0 \end{pmatrix}$$

$$\langle T_\gamma(T_1)\rangle = \begin{pmatrix} 0 & 0 \\ 0 & 0 \\ 0 & 2i \end{pmatrix}$$

$$\langle T_\xi(T_2)\rangle = \begin{pmatrix} -i & i\sqrt{3} \\ 0 & 0 \\ 0 & 0 \end{pmatrix},$$

$$\langle T_\eta(T_2)\rangle = \begin{pmatrix} 0 & 0 \\ -i & -i\sqrt{3} \\ 0 & 0 \end{pmatrix}.$$

The definition of the seven parameters is

$$D = -\langle eu|v_u(E)|eu\rangle$$

$$F = \tfrac{1}{2}\langle t_2\zeta|v_u(E)|t_2\zeta\rangle$$

$$\begin{aligned}\zeta_\perp = {} & 2\langle t_2\zeta\tfrac{1}{2}|t_\alpha s_x + t_\beta s_y|t_2\xi - \tfrac{1}{2}\rangle = 2\langle t_2\zeta\tfrac{1}{2}|\zeta(r) \\ & \times(1_x s_x + 1_y s_y)|t_2\xi - \tfrac{1}{2}\rangle\end{aligned}$$

$$\begin{aligned}\zeta_\parallel & = -2i\langle t_2\xi\tfrac{1}{2}|t_\gamma(T_1)s_z|t_2\eta\tfrac{1}{2}\rangle \\ & = -2i\langle t_2\xi\tfrac{1}{2}|\zeta(r)1_z s_z|t_2\eta\tfrac{1}{2}\rangle\end{aligned}$$

$$\zeta'_\perp = -2\langle t_2\eta\tfrac{1}{2}|t_\alpha(T_1)s_x + t_\beta(T_1)s_y|ev - \tfrac{1}{2}\rangle$$

$$\zeta'_\perp = -2\langle t_2\eta\tfrac{1}{2}|\zeta(r)(1_x s_x + 1_y s_y)|ev - \tfrac{1}{2}\rangle$$

$$\begin{aligned}\zeta'_\parallel & = -i\langle t_2\zeta\tfrac{1}{2}|t_\gamma(T_1)s_z|ev\tfrac{1}{2}\rangle \\ & = -i\langle t_2\zeta\tfrac{1}{2}|\zeta(r)1_z s_z|ev\tfrac{1}{2}\rangle\end{aligned}$$

$$\zeta'_0 = 2\langle t_2\eta\tfrac{1}{2}|t_\xi(T_2)s_x - t_\eta(T_2)s_y|eu - \tfrac{1}{2}\rangle.$$

The five doubly degenerate fine structure energy levels $\Gamma_6(^2E)$, $\gamma_6(^2T_2)$, $\Gamma_7(^2E)$, $\Gamma_7(^2T_2)$, $\Gamma_7(^2T_2)$ are then given by the eigenvalues of the matrices:

$$\Gamma_6: \begin{pmatrix} 4Dq - F - \frac{1}{2}\zeta_\parallel & -\sqrt{\frac{3}{2}}\zeta'_\perp - \frac{1}{\sqrt{2}}\zeta'_0 \\ -\sqrt{\frac{3}{2}}\zeta'_\perp - \frac{1}{\sqrt{2}}\zeta'_0 & -6Dq - D \end{pmatrix}$$

$$\Gamma_7: \begin{pmatrix} 4Dq - F + \frac{1}{2}\zeta_\parallel & +\frac{i}{\sqrt{2}}\zeta_\perp & -\frac{1}{\sqrt{2}}\zeta'_\perp + \sqrt{\frac{3}{2}}\zeta'_0 \\ -\frac{i}{\sqrt{2}}\zeta_\perp & 4Dq + 2F & -i\zeta'_\parallel \\ -\frac{1}{\sqrt{2}}\zeta'_\perp + \sqrt{\frac{3}{2}}\zeta'_0 & i\zeta'_\parallel & -6Dq + D \end{pmatrix}$$

The corresponding basis functions are:

$$\Gamma_6: \begin{pmatrix} \frac{i}{\sqrt{2}}|\xi\tfrac{1}{2}\rangle - \frac{1}{\sqrt{2}}|\eta\tfrac{1}{2}\rangle \\ |u - \tfrac{1}{2}\rangle \end{pmatrix}$$

$$\text{and} \begin{pmatrix} \frac{i}{\sqrt{2}}|\xi - \tfrac{1}{2}\rangle + \frac{1}{\sqrt{2}}|\eta - \tfrac{1}{2}\rangle \\ |u\tfrac{1}{2}\rangle \end{pmatrix}$$

$$\Gamma_7: \begin{pmatrix} \frac{i}{\sqrt{2}}|\xi\tfrac{1}{2}\rangle + \frac{1}{\sqrt{2}}|\eta\tfrac{1}{2}\rangle \\ |\zeta-\tfrac{1}{2}\rangle \\ |v-\tfrac{1}{2}\rangle \end{pmatrix}$$

$$\text{and} \begin{pmatrix} \frac{i}{\sqrt{2}}|\xi-\tfrac{1}{2}\rangle - \frac{1}{\sqrt{2}}|\eta-\tfrac{1}{2}\rangle \\ -|\zeta\tfrac{1}{2}\rangle \\ |v\tfrac{1}{2}\rangle \end{pmatrix}.$$

To find the matrices for d^9 all parameters have to be replaced by their negative values. Energy matrices for a tetragonally distorted octahedral potential are readily found by replacing Dq by its negative value.

6. ENERGY LEVEL DIAGRAMS FOR Cu^{2+} CENTERS

The energy levels of Cu^{2+} ions ($3d^9$) in a tetrahedral coordination are:

$$E(\Gamma_8(^2E)) = Dq+\tfrac{1}{4}\zeta+\tfrac{1}{2}\sqrt{((10\,Dq-\tfrac{1}{2}\zeta)^2+6\zeta'^2)}$$
$$\simeq 6\,Dq+\frac{3\zeta'^2}{20\,Dq}$$

$$E(\Gamma_8(^2T_2)) = Dq+\tfrac{1}{4}\xi$$
$$-\tfrac{1}{2}\sqrt{((10\,Dq-\tfrac{1}{2}\xi)^2+6\zeta'^2)}$$
$$\simeq -4\,Dq+\tfrac{1}{2}\zeta-\frac{3\zeta'^2}{20\,Dq}$$

$$E(\Gamma_7(^2T_2)) = -4\,Dq-\zeta$$

where $\zeta \ll 10\,Dq, \zeta' \ll 10\,Dq$ have been used to simplify the square roots. An energy level diagram is given in Fig. 1.

The energy levels of Cu^{2+} ions ($3d^9$) in a trigonally distorted tetrahedral coordination are approximately:

$$E(\Gamma_6(^2E)) = 6\,Dq+\tfrac{1}{2}D$$
$$+\frac{1}{10\,Dq}(\tfrac{3}{2}\zeta'^2+2\,K'\zeta')$$

$$E(\Gamma_4\Gamma_5(^2E)) = 6\,Dq-\tfrac{1}{2}D$$
$$+\frac{1}{10\,Dq}(\tfrac{3}{2}\zeta'^2-2\,K'\zeta')$$

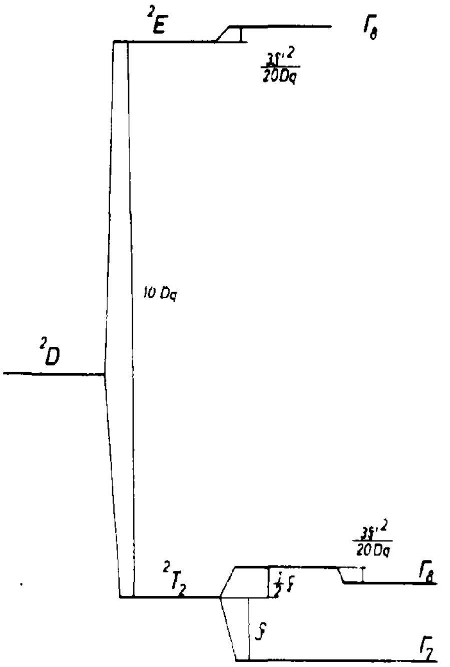

Fig. 1. Energy level diagram of Cu^{2+} in a tetrahedral coordination

$$E(\Gamma_4\Gamma_5(^2T_2)) = -4\,Dq+\tfrac{1}{2}\zeta$$
$$+K-\frac{1}{10\,Dq}(\tfrac{3}{2}\zeta'^2-2\,K'\zeta')$$

$$E(\Gamma_6(^2T_2)) = -4\,Dq+\tfrac{1}{2}\zeta$$
$$-K-\frac{1}{10\,Dq}(\tfrac{3}{2}\zeta'^2+2\,K'\zeta')$$

$$E(\Gamma_6(^2T_2)) = -4\,Dq-\zeta$$

where

$$\zeta_\perp = \zeta_\parallel = \zeta \ll 10\,Dq, \zeta'_\perp = \zeta'_\parallel = \zeta' \ll 10\,Dq,$$
$$K \ll \zeta, K' \ll \zeta', \zeta'_\parallel \ll \zeta'_\perp$$

have been used. The energy level diagram for this case is given in Fig. 2.

The energy levels of Cu^{2+} ions ($3d^9$) in a tetragonally distorted tetrahedral coordination are approximately:

$$E(\Gamma_6(^2E)) = 6\,Dq+D+\frac{3\zeta'^2}{20\,Dq}$$

$$E(\Gamma_7(^2E)) = 6\,Dq-D+\frac{3\zeta'^2}{20\,Dq}$$

J. Phys. Chem. Solids **Pergamon Press 1969. Vol. 30, pp. 2091–2103. Printed in Great Britain.**

ON THE COMPRESSIBILITY OF THE ALKALI METALS*

R. GROVER, R. N. KEELER and F. J. ROGERS
Lawrence Radiation Laboratory, University of California, Livermore, Calif 94550, U.S.A
and
G. C. KENNEDY
Institute of Geophysics and Planetary Physics, University of California, Los Angeles, Calif. 90024, U.S.A

(*Received* 26 *August* 1968)

Abstract – A detailed comparison of shock wave and static compression data for alkali metals reveals serious inconsistencies above 40 kbar. The reduction of shock wave results is reviewed, and the Bridgman high-pressure data on the alkali metals are described. It is shown that the most likely cause of this disagreement is inaccuracy in the static high-pressure data.

INTRODUCTION

It is generally believed that the pressure-volume compression relationships for solids has been reliably determined by experiment below 100 kbar because of the reasonable agreement between high pressure compression data from both static and dynamic compression techniques. The conclusion was reached, for instance, on the basis of the consistency of X-ray compression data[1] when normalized to the shock compression of several different metals. Such comparisons, however, have been restricted mainly to solids of moderate to-small compressibilities. Because of the great importance of the highly compressible alkali metals in solid-state physics, attention should be called to the fact that static and shock compression data on these metals below 100 kbar are in obvious and serious disagreement.

This situation is illustrated in Figs. 1–4 wherein Bridgman's isothermal compression data of 1948[2] for Li, Na, K and Rb are compared with the locus of shock compression points (the 'Hugoniot' curve) obtained by Rice[3] and Bakanova *et al.*[4]. A similar data comparison for Cs is not included because of the complication of two first-order solid-solid phase transitions at low pressure[2]. The two sets of shock compression data are in agreement except in the case of Li. The higher compressibility of Li as shown by the Russian data is not understood, but for the present purposes it may be overlooked since it only increases the disagreement we are pointing out. In all cases the shock compression data and Bridgman's isothermal data are nearly coincident, with Bridgman reporting slightly lower compressibilities in all cases. Recently, additional static compression measurements have been made at several temperatures on sodium[5] and potassium[6] up to 20 kbar, as well as ultrasonic velocity measurements up to 10 kbar[7, 8]. However, it appears that the extrapolation of these data to the range of 50–100 kbar cannot be done with sufficient accuracy to be useful in our data comparison. Below 50 kbar the various sets of data are consistent within experimental error.

In the case of highly compressible solids

---

*Work performed under the auspices of the U.S. Atomic Energy Commission Publication # 695, Institute of Geophysics and Planetary Physics, University of California, Los Angeles, Calif 90024, U S.A

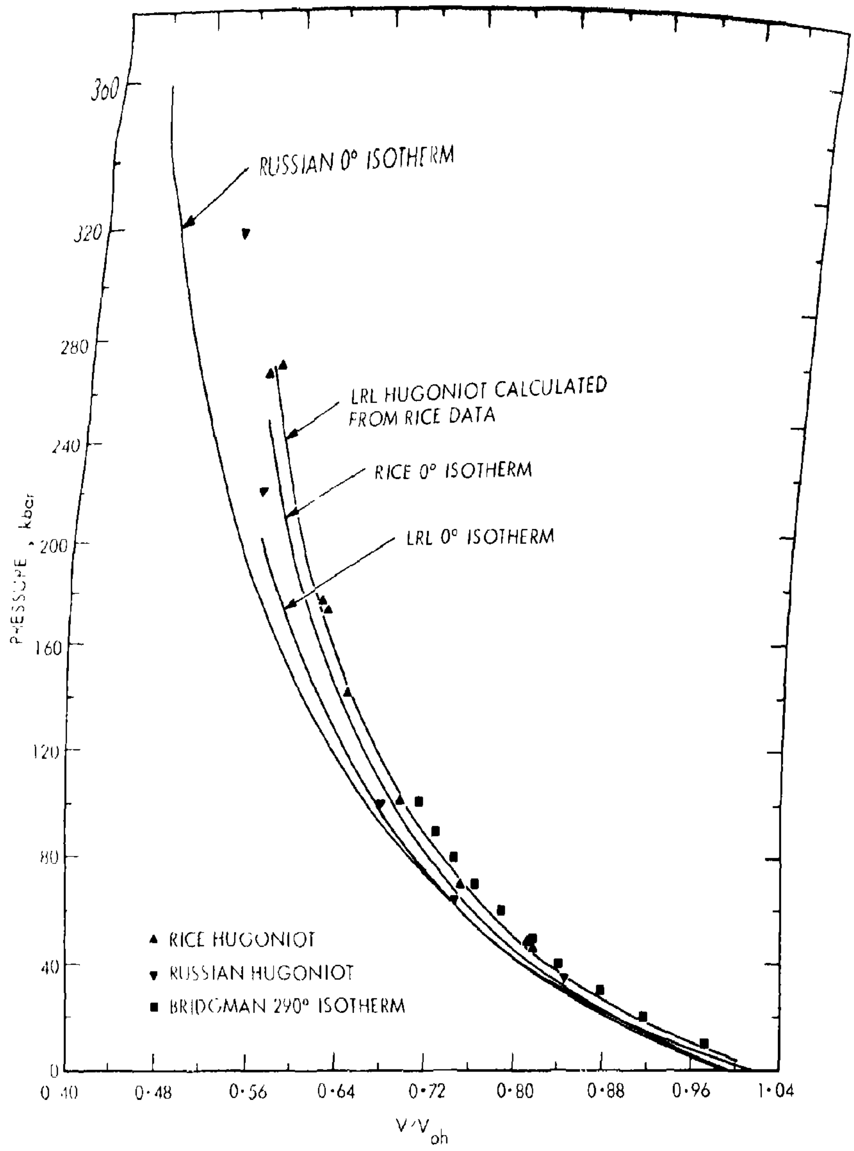

Fig. 1. Comparison of Bridgman isothermal compression data with shock data and calculated isotherms for lithium

like the alkali metals, a large thermal correction must be made to the shock Hugoniot to obtain a 25°C isotherm for comparison with the Bridgman's data. The irreversible heating that occurs upon shock compression causes the temperature along the Hugoniot to increase with compression. Assuming that the compressed state of the metal behind the shock front is a state of thermodynamic equilibrium, the calculated shock temperatures are not a sensitive function of the assumed thermal equation of state of the metal. The increase in shock temperature with compression, as calculated from Rice's data, is seen in Tables 1-4 to be very rapid for these compressible metals.

The reduction of a Hugoniot to yield a 25°C isotherm, however, depends sensitively

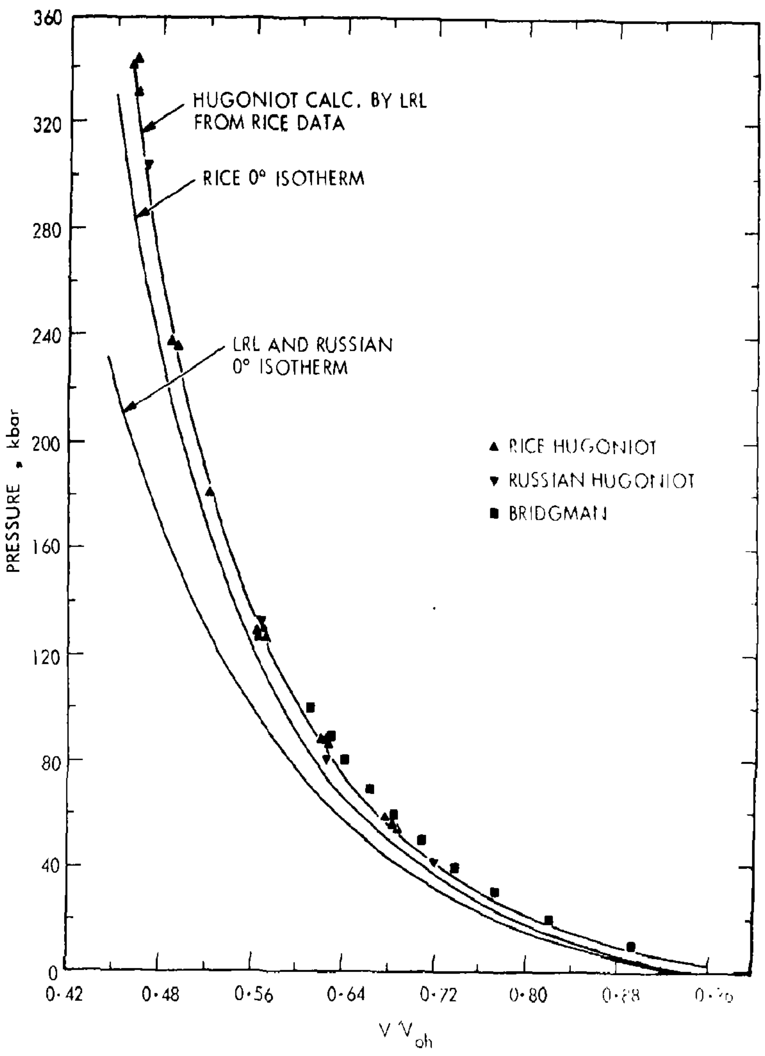

Fig. 2 Comparison of Bridgman isothermal compression data with shock data and calculated isotherms for sodium.

on the assumed equation of state, as is illustrated in Figs. 1–4, by the large differences between the zero degree isotherm calculated with different theories by the Russian experimenters and by Rice from very similar data. As we shall later argue in some detail, Rice's estimates of the 0° or 298°K isotherms for the alkali metals, although in considerably better agreement with Bridgman data, do not appear to have any reasonable basis in theory and are likely to be incorrect. Using Rice's data, we also calculate by a somewhat different theory an isotherm which is indistinguishable from the Russian curves (except for Li). The disagreement between the Russian and Bridgman isotherms is extremely large, averaging to ~30 kbar at a pressure of 100 kbar. Specifically, the pressure differences systematically increase with compression for each element and increase

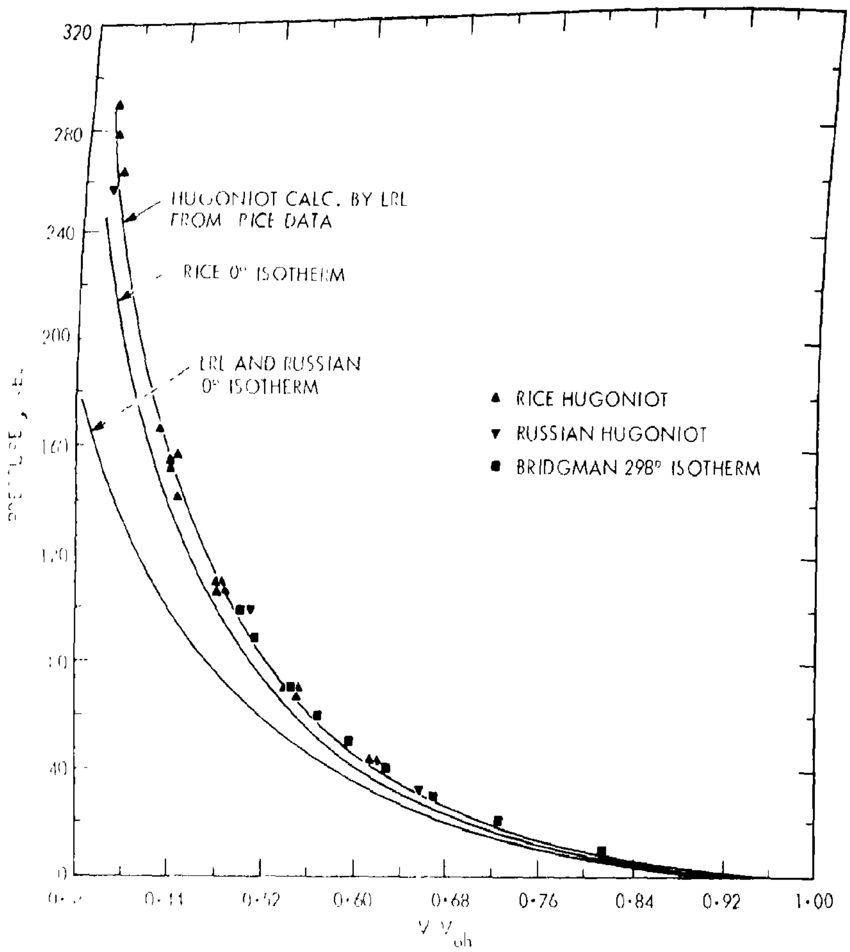

Fig. 3. Comparison of Bridgman isothermal compression data with shock data and calculated isotherms for potassium

with the initial compressibility of the metal. Such discrepancies are outside the range of quoted experimental error and unusually large in view of the general agreement found for the less compressible elements[11].

BRIDGMAN DATA ON ALKALI METALS

It is important at this point to briefly review the consistency of Bridgman's measurements of the compressibility of the alkali metals. Bridgman[9(a)] first reported data on the compressibility of the alkali metals in 1922. The maximum reported pressure in these experiments was 12 kbar. In 1935, Bridgman [9(b)] extended his maximum pressure to 20 kbar in Li, Na, and K. In these experiments, he measured the difference between the compressibility of alkali metals and the compressibility of iron. Shortening of a test specimen was observed by motion of a lever along a slide wire potentiometer inside his press. The pressure was determined by reading from a manganin cell pressure gauge. Lever arms were used to magnify the apparent motion of the sample as it shortened in length.

The measurements reported in 1935 differed sharply from the earlier 1922 measurements

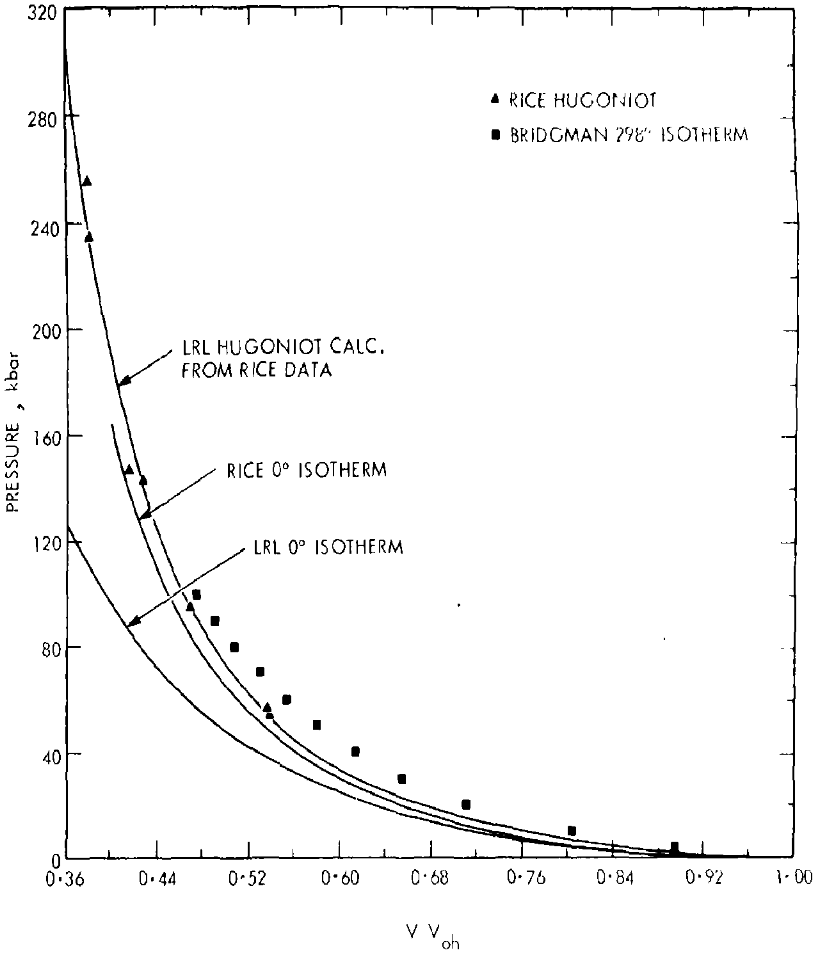

Fig. 4 Comparison of Bridgman isothermal compression data with shock data and calculated isotherms for rubidium

where the data overlap. Much of this change was found to be due to an error in reduction of the earlier data. Considerable difficulties, however, were encountered in measuring the compressibility of the alkali metals even to 20 kbar. Unfortunately, the pressure-transmitting medium becomes quite viscous, and permanent deformation of his samples took place resulting in nonlinear readings.

Bridgman[9(c)] again reported on compressibility of the alkali metals having extended his range to 45 kbar. Bridgman's 45-kbar measurements were made by observing motion of a piston which compressed a sample approximately ½ in. dia. × 1½ in. long, sheathed in lead. Dilation of the cylinder was obtained by assuming a compressibility of iron. Results from this apparatus gave compressibilities slightly smaller than previously determined. Potassium is reported to have a compression of 0·2764 at 20 kbar in 1934, and is reported in 1937 as 0·268. The change is only a little more than 3 per cent. Unfortunately, it is difficult to evaluate the precision of these measurements, as Bridgman does not give his low-pressure results. He

Table 1. Calculated properties according to DM theory for lithium

V/V_0	Temperature (0°K)	Gamma	$P(0)$ ($mb = 10^3$ kbar)	$P(298)$ (mb)	P(HUG) (mb)
0·95823	3·1495 × 10^2	1·2453	0·00048	0·00500	0·00515
0·92165	3·3145	1·1935	0·00563	0·01000	0·01054
0·89102	3·4786	1·1537	0·01074	0·01500	0·01591
0·86421	3·6496	1·1225	0·01583	0·02000	0·02131
0·84052	3·8319	1·0976	0·02090	0·02500	0·02673
0·81928	4·0284	1·0773	0·02595	0·03000	0·03220
0·80006	4·2407	1·0605	0·03099	0·03500	0·03771
0·78251	4·4701	1·0465	0·03603	0·04000	0·04327
0·76636	4·7171	1·0340	0·04106	0·04500	0·04888
0·75145	4·9823	1·0231	0·04608	0·05000	0·05455
0·72457	5·5675	1·0041	0·05613	0·06000	0·06606
0·70097	6·2266	0·9876	0·06617	0·07000	0·07781
0·67996	6·9593	0·9725	0·07621	0·08000	0·08980
0·66106	7·7651	0·9584	0·08625	0·09000	0·10204
0·64391	8·6430	0·9452	0·09628	0·10000	0·11452
0·61385	1·0615 × 10^3	0·9209	0·11635	0·12000	0·14024
0·58812	1·2870	0·8991	0·13641	0·14000	0·16696
0·56576	1·5408	0·8795	0·15646	0·16000	0·19472
0·54602	1·8226	0·8617	0·17651	0·18000	0·22351
0·52840	2·1326	0·8455	0·19655	0·20000	0·25337

Table 2. Calculated properties according to DM theory for sodium

V/V_0	Temperature (0°K)	Gamma	$P(0)$ ($mb = 10^3$ kbar)	$P(298)$ (mb)	P(HUG) (mb)
0·93072	3·3138 × 10^2	1·3679	0·00118	0·00500	0·00527
0·87816	3·6374	1·2910	0·00624	0·01000	0·01076
0·63704	3·9838	1·2423	0·01126	0·01500	0·01629
0·80327	4·3731	1·2099	0·01626	0·02000	0·02191
0·77464	4·8149	1·1870	0·02124	0·02500	0·02764
0·74982	5·3142	1·1698	0·02621	0·03000	0·03349
0·72794	5·8740	1·1558	0·03118	0·03500	0·03947
0·70841	6·4958	1·1436	0·03616	0·04000	0·04558
0·69079	7·1806	1·1325	0·04113	0·04500	0·05183
0·67476	7·9286	1·1221	0·04611	0·05000	0·05822
0·64655	9·6163	1·1025	0·05607	0·06000	0·07142
0·62235	1·1560 × 10^3	1·0841	0·06605	0·07000	0·08519
0·60124	1·3761	1·0668	0·07603	0·08000	0·09954
0·58255	1·6219	1·0505	0·08602	0·09000	0·11449
0·56584	1·8938	1·0353	0·09601	0·10000	0·13005
0·53700	2·5167	1·0078	0·11600	0·12000	0·16305
0·51280	3·2475	0·9837	0·13599	0·14000	0·19868
0·49204	4·0903	0·9622	0·15599	0·16000	0·23709
0·47393	5·0501	0·9430	0·17599	0·18000	0·27845
0·45792	6·1319	0·9255	0·19599	0·20000	0·52294

Table 3. Calculated properties according to DM theory for potassium

V/V_0	Temperature (V°K)	Gamma	$P(0)$ ($mb = 10^3$ kbar)	$P(298)$ (mb)	$P(\mathrm{HUG})$ (mb)
0·87789	3·5856 × 10^2	1·1928	0·00291	0·00500	0·00535
0·80160	4·2622	1·1093	0·00790	0·01000	0·01088
0·74681	5·1265	1·0661	0·01287	0·01500	0·01659
0·70421	6·2120	1·0385	0·01782	0·02000	0·02252
0·66950	7·5286	1·0169	0·02278	0·02500	0·02870
0·64034	9·0794	0·9978	0·02774	0·03000	0·03512
0·61529	1·0864 × 10^3	0·9801	0·03271	0·03500	0·04179
0·59342	1·2882	0·9635	0·03768	0·04000	0·04873
0·57404	1·5133	0·9478	0·04266	0·04500	0·05591
0·55671	1·7617	0·9331	0·04764	0·05000	0·06336
0·52679	2·3285	0·9062	0·05761	0·06000	0·07907
0·50169	2·9896	0·8824	0·06758	0·07000	0·09588
0·48017	3·7469	0·8612	0·07756	0·08000	0·11384
0·46139	4·6027	0·8422	0·08754	0·09000	0·13301
0·44480	5·5600	0·8249	0·09752	0·10000	0·15344
0·41661	7·7943	0·7946	0·11749	0·12000	0·19835
0·39334	1·0485 × 10^4	0·7685	0·13746	0·14000	0·24911

Table 4. Calculated properties according to DM theory for rubidium

V/V_0	Temperature (0°K)	Gamma	$P(0)$ ($bm = 10^3$ kbar)	$P(298)$ (mb)	$P(\mathrm{HUG})$ (mb)
0·83762	3·9226 × 10^2	1·2190	0·00340	0·00500	0·00544
0·75022	5·0554	1·1421	0·00835	0·01000	0·01118
0·69098	6·5794	1·1060	0·01328	0·01500	0·01728
0·64649	8·5349	1·0791	0·01822	0·02000	0·02380
0·61114	1·0935 × 10^3	1·0548	0·02318	0·02500	0·03074
0·58199	1·3778	1·0321	0·02814	0·03000	0·03811
0·55733	1·7075	1·0110	0·03311	0·03500	0·04594
0·53603	2·0831	0·9916	0·03808	0·04000	0·05423
0·51735	2·5055	0·9736	0·04306	0·04500	0·06299
0·50077	2·9760	0·9571	0·04804	0·05000	0·07226
0·47241	4·0658	0·9276	0·05800	0·06000	0·09238
0·44884	5·3660	0·9019	0·06797	0·07000	0·11476
0·42878	6·8915	0·8792	0·07794	0·08000	0·13960
0·41139	8·6634	0·8589	0·08792	0·09000	0·16716
0·39610	1·0702 × 10^4	0·8404	0·09790	0·10000	0·19769
0·37024	1·5682	0·8077	0·11786	0·12000	0·26890
0·34902	2·2084	0·7793	0·13784	0·14000	0·35616

merely states low-pressure results were 'adjusted'[9(c)] to agree with earlier values obtained at 10,000 kg/cm.

Results to 100,000 kg/cm^2 were published by Bridgman[9(d)] in 1941. In these particular experiments, measurements were made in a carbide cell immersed in isopentane which could be compressed to 25–30,000 bar. The diameter of his sample was $\frac{3}{16}$ in., the total length of the sample was under $\frac{1}{2}$ in. In this apparatus, internal pressure was measured electrically by changes in resistance of a hardened steel grid, and piston displacement was obtained through remote readings with an Ames dial gage. Dilation calibrations in this apparatus was measured by assuming a compression of gold extrapolated to 100,000 atm from measurements made only to 12,000 atm. Double values of friction of as high as 20 per cent were reported in these measurements. Bridgman reported a final accuracy for these numbers between 1 and 2 per cent. It is clear that Bridgman's pressure measurements were not good in this apparatus as he reported a transition in barium at 60 kbar which is now known to lie at 55 kbar, and reported a transition in bismuth at 90 kbar which is now known to lie at 77·5 kbar. Thus, his error in measuring pressure was 10–15 kbar at values of approximately 100 kbar. Further, all of Bridgman's measurements on the alkali metals were made with the alkalis in copper capsules which occupied two-thirds of the total volume of the system. Rigidity of copper is large and there is no evidence that a satisfactory fraction of the pressure generated inside this apparatus was actually transmitted to the alkali metal. The compressibility of copper which enters as a first-order correction to his results was extrapolated to 100 kbar from results of 12 kbar. The new data on the alkali metals obtained in this apparatus were normalized to the earlier 45 kbar data. However, the slopes of the compressibility curves are quite different and the two sets of curves meet at a rather sharp angle. Further, there is a suggestion that there is an uncertainty of at least 10 per cent in the amount of the alkali metal present. Bridgman says that "the volume of the alkali metal found (by measuring the dimensions of the charge) in this way agreed within 10 per cent with less accurate volumes given by weighing." In this apparatus Bridgman's raw measurement of the compression of potassium at 50 kbar were $\Delta V/V_0$ of 0·462 in contrast to his earlier measurements of 0·416. The raw data from the 100 kbar set of measurements, however, were 'normalized' against his earlier 50 kbar (45 kbar) measurements.

Bridgman[9(e)] published new measurements of the alkali metals to 100 kbar. These new measurements involved a certain amount of modification of the method for measuring displacement of the piston. However, the technique and apparatus were essentially similar to his previous 100 kbar measurements. In these new measurements on the alkali metals, aluminum sheaths were used rather than the copper sheaths of the previous determinations. Bridgman's new volume for the alkali metals at 100,000 kg/cm² contrast very markedly from his previously published values. The earliest 100,000 kg/cm² value for potassium was $\Delta V/V_0 = 0{\cdot}573$; whereas his newer, and presumably, better value is 0·500. Rubidium was changed from an initial value of $\Delta V/V_0$ of 0·638 at 100 kbar to a value of 0·527, with correspondingly large changes for the other alkali metals. In general, the newer sets of measurements show a revision downward in the compressibilities of 10–20 per cent from the prior measurements. Unfortunately, from the point of view of the shock wave results, these revisions are in the wrong direction, as the first and presumably the least accurate set of compressibility measurements show closest agreement to shock wave densities computed from the model outlined in this paper.

Thus, in view of the fact that Bridgman revised earlier numbers by 20 per cent in $\Delta V/V_0$ on a number of occasions where newer data overlapped older data at the upper end of a pressure range, disagreement between Bridgman's results and shock wave results of this magnitude should, perhaps, not be so surprising.

REDUCTION OF HUGONIOT DATA

The source of the differences in the reduction of the Hugoniot to the isotherm between Rice and the Russian group can be easily understood without resort to numerical calculations in terms of thermal equation of state of the metal. Where the thermal pressure of the metal is much less than its low-temperature bulk modulus at the same volume, it may be taken to be proportional to the thermal energy according to the accepted Mie–Grüneisen equation of state for solids.

Experimentally, the Grüneisen coefficient $\gamma_G \equiv V(\delta P/\delta E)_V$ is found at not too high temperatures to depend only on the volume according to a function which is characteristic of the material. A good first-order estimate of the thermal energy along the Hugoniot can be obtained directly from the shape of the Hugoniot in the P-V plane. The usual steady-state conservation conditions across a shock front imply that the change in total internal energy in shock compression is equal to the area of the triangle formed by the initial state, the shock state, and the $P = 0$ line in the P-V plane. On the other hand, the gain in lattice potential energy is approximately the internal energy gain along the isentrope through the initial point which, in turn, is simply the area under the isentrope, or approximately the area under the Hugoniot. Thus the thermal shock energy is approximately the area between the Hugoniot and a straight line connecting the initial and final states, independent of the precise form of the equation of state. In the range where the solid has a constant molar specific heat of $3R$, an approximate shock temperature is thereby determined. However, to evaluate the thermal pressure arising from this thermal energy at any particular density along the Hugoniot, additional information is required in the form of an estimate of Grüneisen's γ_G for the material at that volume.

Rice's estimate of $\gamma_G(V)$ along the Hugoniot was apparently based on the then most extensive high-pressure thermodynamic data on alkali metals, which was the work on Na by Beecroft and Swenson[5]. In their analysis of the behavior of the compressibility along different isotherms, the latter authors concluded that their low-pressure data could be represented most economically by an isothermal compressibility which was independent of temperature. This assumption, applied to the adiabatic compressibility and combined with the Mie–Grüneisen equation of state, predicts a simple, explicit volume dependence for γ_G which is independent of the shape of the zero-degree isotherm,

$$\gamma_G(V) = \frac{V/V_0}{(\gamma_0+1)/\gamma_0 - V/V_0} \tag{1}$$

where $\gamma_0 \equiv \gamma_G(V_0)$. This volume dependence for Na is shown in Fig. 5 where γ_G is seen to decrease to very small values at high compression. By thus legislating γ_G to be small, Rice's calculated zero-degree isotherm is forced to be close to the Hugoniot at high compression, as shown in Figs. 1–4. However, as we shall argue below, such small values of γ are not to be expected for these alkali metals on the basis of conventional theories for the thermal properties. Moreover, Monfort and Swenson[6] have more recently concluded that the analysis of the static Na data was faulty on the basis of a comparison with newer ultrasonic data.

Since a complete theory of the thermal equation of state of metallic solids is not available, it has been necessary in interpreting shock data to resort to rather crude approximate phenomenological theories for calculating the volume dependence of the Grüneisen coefficient, γ_G. A brief review of these theories is therefore useful in order to clarify our reasons for using them in the analysis of the alkali metal data.

The thermal properties of the monatomic metallic solids are thought to consist of two independent additive components arising from thermal excitations of lattice vibrational modes and electrons. The electronic component is generally negligible at pressures below 100 kbar and will be ignored (see below). In theories for the lattice component, γ_G is related to the shape of the zero-degree isotherm $P_0(V)$. By making simplifying approximations in standard models of the thermal behavior of solids, a single formula for γ_G can be obtained.

$$\gamma_G = \frac{t-2}{3} - \frac{1}{2}\frac{d\ln\left[d(P_0V^{2t/3})/dV\right]}{d\ln V} \tag{2}$$

from the Debye, lattice dynamic, and Einstein (or 'free volume') models for $t = 0$, 1 and 2.

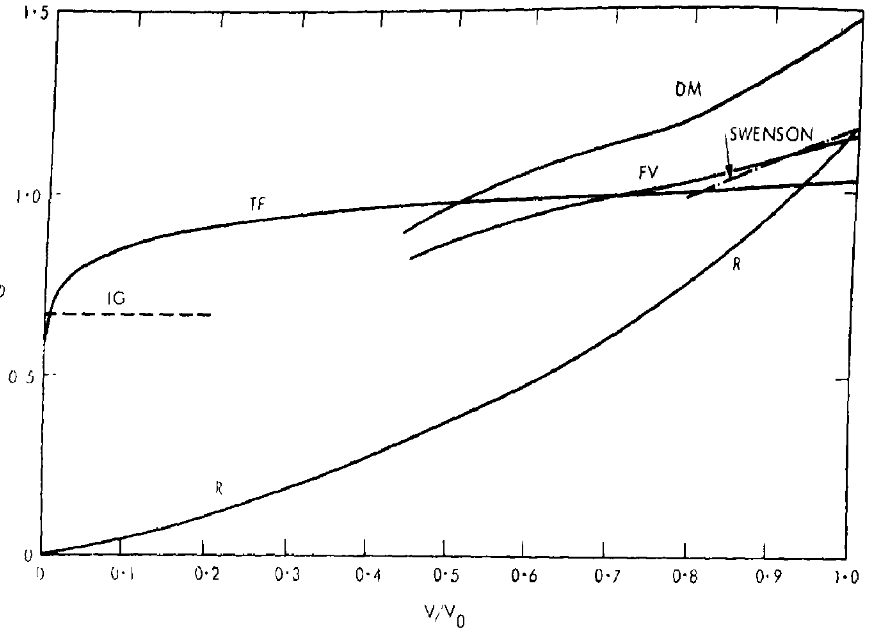

Fig. 5. Various estimates of the volume dependence of γ_G. DM, Dugdale–MacDonald formula, $t = 1$; FV, free-volume, $t = 2$, R, Rice's form, TF, Thomas–Fermi model, Swenson, thermal data of [5]; IG, ideal gas value of $\frac{2}{3}$

respectively. These cases are identified with Slater (SL) and Dugdale and MacDonald (DM) who first derived the cases $t = 0$ and 1 respectively, and the case $t = 2$ is denoted here as the free-volume (FV) approximation[10]. When combined with the Mie–Grüneisen equation for the energy $E_H(V)$ and pressure $P_H(V)$ along the Hugoniot, i.e.

$$\gamma_G = V\frac{P_H(V) - P_0(V)}{E_H(V) - E_0(V)}. \tag{3}$$

Equation (2) can be numerically solved to obtain $P_0(V)$ and $\gamma_G(V)$.

In spite of the approximations involved, this approach has proved very useful in obtaining $\gamma_G(V)$ and $P_0(V)$ from shock data on the monatomic solids. The calculated behavior of $P_0(V)$ is nearly identical in typical solids for the SL, DM and FV approximations and, as noted previously, in agreement with static X-ray compression data on the less compressible solids. The similarity in the calculated functions $P_0(V)$ is, in turn, a result of the fact that calculated values of $\gamma_G(V)$ for the different forms of equation (2) differ usually by decreasing amounts with increasing compression. This is illustrated in Fig. 5 where the DM and FV values of γ_G for Na are compared as functions of volume. The largest differences occur near $P_0(V_0) = 0$ where it can be shown directly from equation (2) that for the DM and FV formulas $\gamma_G(V_0)$ is respectively $\frac{1}{3}$ and $\frac{2}{3}$ less than its value according to the Slater formula. However, at low pressures and small compressions where these differences in γ are largest, the Hugoniot and the isentrope through the initial state can only differ by very small amounts (of third order in the compression). At higher compressions, the differences between the calculated γ are small enough to result in nearly the same thermal pressure corrections. Tables 1–4 present the results of the DM calculation for Li, Na, K and Rb, using the experimental data of Rice. The calculated

0°K isotherms are also plotted in Figs. 1-4 and are seen to be in close agreement with the Russian calculations. A constant specific heat of $3R$ has been assumed, and the 298°K isotherm $P_{DM}(298°)$ has been calculated for comparison with Bridgman data. The differences between this isotherm and that for the SL and FV approximations are indicated in Table 5 in the range 50–100 kbar. The discrepancy between Bridgman's isotherm and $P_{DM}(298°)$ is also tabulated and is seen to be an order of magnitude larger. Therefore, the three approximations for the lattice γ_G expressed by equation (2) show the same large inconsistency with Bridgman's compression data.

Table 5. Comparison of values of γ_G and $P(298°)$ isotherm calculated in SL, DM and FV approximation from shock data. Differences from the DM 298°K isotherm are shown for SL qnd FV as well as Bridgman data in the range of densities corresponding to shock pressures from 50 to 100 kbar

Mat.	γ_G^*	γ_{SL}	γ_{DM}	γ_{FV}	P_{FV}-P_{DM}	P_{DM}-P_{SL} (kbar at 298°)	P_{BR}-P_{DM}
Li	0·81	1·541	1·208	0·975	1–3	1–2	8-16
Na	1·17	1·817	1·484	1·151	1–3	1–3	10–24
K	1·23†	1·719	1·386	1·053	2-4	1–3	11–30
Rb	1·06	1·797	1·464	1·131	2–5	1–3	19–39

*Thermodynamic data in [3].

†Varies from 1·05–1·23, depending on thermal expansion coefficient.

In their reduction of Hugoniot data, the Russian group has also made use of the DM equation in a somewhat different way. The DM form of equation (2) is integrated, assuming γ_G has the form

$$\gamma_G(V) = \tfrac{2}{3} + \left[\gamma_G(V_0) - \tfrac{2}{3}\right]\left(\frac{V}{V_0}\right)^M$$

and the value of M is chosen which predicts a Hugoniot in best agreement with the data.

Use of equation (2) is further justified by the significant correlation of calculated γ_G at zero pressure with thermodynamic values of $V(\partial P/\partial E)_V$ over the whole range of atomic numbers of the solid metallic elements[11]. The best average fit is obtained for the DM approximation where it was found that over a range of thermodynamic values from 1 to 3, γ_G was fit on the average to ±10 per cent using shock wave data[10]. The fit is somewhat better when ultrasonically measured values of the pressure variation of compressibility are used. For certain groups of elements it is, however, possible to get better fits for the other values of t, and a reasonable recipe for analyzing the shock data for these cases is to use the value of t in equation (2) which produces the zero pressure agreement with thermodynamic data. The FV formula gives best agreement for the alkali metals as can be seen in Table 5. In addition, shock wave data on metals, together with the above theory, show γ_G initially decreasing with compression at a rate which is consistent with rates derived from the variation of melting temperature with pressure or the temperature dependence of the elastic constants[12] where such data exist.

The mathematical reason for the similarity of the solutions of the various equations (2) for γ_G is as follows: When $P_0(V)$ varies as V^{-n}, then equation (2) shows that $\gamma_G = \frac{1}{2}(n-\frac{1}{3})$ independent of t. On the other hand, there is an increasing tendency for the pressure along the experimental 0°K isotherm to have a power law dependence of volume, as is seen when the *P-V* experimental isotherms are displayed in a ln − ln plot. This volume dependence is also observed in a Thomas–Fermi equation of state for the zero-degree isotherm of the elements[13] at high compression. In the latter theory, the pressure of the atomic electron gas slowly approaches a volume dependence of $V^{-5/3}$ in the limit of high compression for which equation (2) implies γ_G, the ideal gas value → $\frac{2}{3}$. In a more correct calculation of the lattice modes in a Thomas–Fermi picture[14], γ_0 decreases very slowly with volume from values ~ 1 at normal densities to a high compression limit of $\frac{1}{2}$. The results of this calculation for γ_G are also shown in Fig. 5 for comparison with the other estimates of γ_G. Thus all theories predict γ_G to be considerably above the value Rice has used in the vicinity of two-fold compression.

The closeness of the Thomas–Fermi estimate to the thermodynamic γ_G reflects the similarity of the Thomas–Fermi model of the Na atom in a solid to the Bardeen–Fuchs force model which is used to explain many normal properties of the alkali metals[7, 8]. The Russian group also find the 0°K isotherm calculated from the Bardeen model in close agreement with the isotherm obtained from shock data on Na and K. When the compression becomes sufficient to cause additional energy bands of the alkali atoms to overlap, a more complicated behavior than shown by either the Bardeen model or the TF curve in Fig. 5 can be expected. Such effects are presumably already present at normal density in other metals exhibiting larger values of γ, such as the noble metals. In these other metals, the interatomic forces, both attractive and repulsive, depend on higher powers of the interatomic spacing. However, all compression data on the alkali metals are smoothly varying and show no evidence of new force laws. Also, the systematics of changes of electronic configuration with pressure which are shown by nearby elements in the periodic table[15] do not indicate such a change in these alkali metals in the range of compressions discussed here.

There is an additional thermal component of the equation of state arising from electronic excitation in the solid which, however, plays a minor role in the data below 100 kbar. This component was introduced by the Russian authors[4] mainly because of its importance at much higher pressures. A free electron model for electronic pressure P_e suggests a value of $\frac{2}{3}$ for $V(\mathrm{d}P_e/\mathrm{d}E_e)$. However, this value is so close to the lattice values of the alkali metals that the net change in the thermodynamic γ is entirely negligible below 100 kbar.

In our analysis, there remains a possible source of error which is currently under investigation. It arises from the fact that all measured Hugoniot points in Figs. 1–4 for the alkali metals are actually above the melting line. A more complicated equation of state is therefore necessary to account for the heat of fusion and the additional temperature dependence of thermodynamic quantities in the liquid state. In the past, such corrections have not proved significant, but their importance for the compressible materials should be checked.

On the basis of these arguments, the 298° isotherm obtained from shock wave data for the alkali metals should be reliable to ~ 5 per cent. In view of the much larger disagreement with static data and the scatter in Bridgman data, it appears desirable to recheck the static compression data for the alkali metals, particularly above 40 kbar, by improved or different techniques to see if unexpected thermal behavior does exist below 100 kbar, or if unexpected systematic errors are present in the shock wave data.

REFERENCES

1. DRICKAMER H. G., LYNCH R. W., CLENDENEN R. L. and PEREZ-ALBUERNE E. A., *Solid St. Phys* **19**, 135 (1966); DRICKAMER H. G., *Comments Solid St. Phys.* **1**, 11 (1968).

2. BRIDGMAN P. W., as given in *A.P.S. Handbook*, 2nd Edn., Section 2, p. 81. McGraw-Hill, New York (1963).
3. RICE M. H., *J. Phys. Chem. Solids* **26**, 483 (1965).
4. BAKANOVA A. A., DUDOLADOV I. P. and TRUNIN R. F., *Soviet Phys. solid St.* **7**, 1307 (1965).
5. BEECROFT R. I. and SWENSON C. A., *J. Phys. Chem. Solids* **18**, 329 (1961).
6. MONFORT III C. E. and SWENSON C. A., *J. Phys. Chem. Solids* **26**, 291 (1965).
7. DANIELS W. B., *Phys. Rev.* **119**, 1246 (1960).
8. SMITH P. A. and SMITH C. S., *J. Phys. Chem. Solids* **26**, 279 (1965).
9. BRIDGMAN P. W., (a) *Proc. Natl Acad. Sci.* **8**, 361 (1922); (b) *Proc. Natl Acad. Sci.* **21**, 109 (1935). (c) *Proc. Am. Acad. Arts Sci.* **72**, 207 (1937); (d) *Phys. Rev.* **60**, 351 (1941), (e) *Proc. Am. Acad. Arts Sci.* **76**, 55 (1947).
10. RICE M. H., McQUEEN R. G. and WALSH J. M., *Solid St. Phys.* **6**, 1 (1958); VASHCHENKO V. Ya. and ZUBAREV V. N., *Soviet Phys. solid St.* **5**, 653 (1963).
11. GSCHNEIDNER K. A., *Solid St. Phys.* **16**, 275 (1964).
12. GROVER R., Unpublished
13. LATTER R., *J. chem. Phys.* **24**, 280 (1956).
14. KOPYSHEV V. P., *Soviet Phys. Dokl.* **10**, 338 (1965).
15. ROYCE E. B., *Phys. Rev.* **164**, 929 (1967).

J. Phys. Chem. Solids Pergamon Press 1969. Vol. 30, pp. 2105–2108. Printed in Great Britain.

TECHNICAL NOTES

Equilibrium concentration of impurity-vacancy complexes

(*Received* 13 *December* 1968)

IN RECENT years the transport properties of alkali halide crystals have been discussed in terms of five defects, i.e. isolated anion vacancies, isolated cation vacancies, isolated impurity ions, nearest neighbor vacancies of opposite electric charge (divacancies) and nearest neighbor impurity-vacancy complexes [1]. Originally these defects were treated as noninteracting particles located at appropriate lattice sites (the presence of divacancies and complexes was not assumed) and the defect concentrations were obtained from statistical mechanics. Subsequently the defects were allowed to interact with oppositely charged defects located at nearest neighbor lattice sites and the concentrations of divacancies and complexes were included in the analysis of experimental data. In 1954, Lidiard improved the theory of ionic conductivity by including the long-range Coulomb interactions between isolated defects[2]. Lidiard obtained closed-form equations for ionic conductivity by using the Debye-Hückel approximation for the Coulomb interactions. Recently these equations have become more widely used in the analysis of ionic conductivity data[3–5]. Now nonrandom deviations between the Lidiard-Debye-Hückel equations (LDH) and experimental ionic transport data have been reported[4–6]. This has on the one hand led to speculation about other defects being important in ionic transport phenomena. Cation Frenkel defects[4–6] and cation trivacancies[5–7] have both been discussed in recent conductivity and diffusion papers. On the other hand, the deviations between experiments and the LDH equations may arise from the assumptions and approximations implicit in those equations[8, 9]. In particular, the LDH derivation[2] assumes that the Helmholtz free energy of an alkali halide crystal can be written as the sum of two parts: (a) a configurational term directly dependent on the presence of impurities and (b) a vibrational term which is independent of the arrangement of the impurities and vacancies in the lattice. This paper presents an alternative to the assumption that the vibrational term of the free energy is independent of the arrangement of the impurities and vacancies.

We begin by dealing with the cation sublattice of an alkali halide crystal containing n_i impurity ions and n_c vacant lattice sites. The impurities and vacancies are assumed to interact with energy $-B$ and hence form a number n_k of bound impurity-vacancy complexes. We further assume that there is a definite change in vibrational motion when an impurity moves from an isolated site to a bound site near a vacancy. We treat this change in vibrational motion in the Einstein approximation, i.e. each impurity ion is an independent oscillator with the same frequency, but a different frequency is assigned to the bound impurity ions (complexes) than to the isolated impurity ions. The isolated impurity ions vibrate in shallow potential wells with energy level spacings of $\hbar\omega_I$ and the tightly bound impurity ions vibrate in deep potential wells with energy level spacings of $\hbar\omega_k$[10].

In general, when c_j states of energy ϵ_j are available for N particles subject to Boltzmann statistics the number found in the jth state is given by [11]

$$n_j = c_j \exp(-\alpha - \beta\epsilon_j). \qquad (1)$$

In the present situation this becomes

$$(n_k)_j = (c_k)_j \exp(-\alpha - j\beta(-B + \hbar\omega_k)) \quad (2)$$

and

$$(n_i - n_k)_j = (c_L)_j \exp(-\alpha - j\beta\hbar\omega_L) \quad (3)$$

with $c_k = Zn_v$ where Z is the number of possible bound sites near a vacancy and n_v is the number of cation vacancies and $c_L = N - Zn_v$ where N is the total number of sites available. When equations (2) and (3) are summed over j the following results are obtained.

$$n_k = Zn_v e^{-\alpha} e^{\beta B}(1 - e^{-\hbar\omega_k\beta})^{-1} \quad (4)$$

$$n_i - n_k = (N - Zn_v)e^{-\alpha}(1 - e^{-\hbar\omega_L\beta})^{-1} \quad (5)$$

where β is identified as $(kT)^{-1}$. Then equations (4) and (5) can be cast into a form similar to the usual law of mass action equation for complex concentration,

$$\frac{(N - Zn_v)n_k}{(n_i - n_k)n_v} = Z\exp(B/kT) \times \left[\frac{1 - \exp(-\hbar\omega_L/kT)}{1 - \exp(-\hbar\omega_k/kT)}\right]. \quad (6)$$

The term in square brackets results from allowing the crystal energy to be dependent upon the arrangements of the impurities in the lattice. The LDH result is readily incorporated into our result by replacing the $\exp(B/kT)$ term in equation (6) by the more complete expression from the LDH equation (See for example equation (12)[2]).

An illustration of the usefulness of equation (6) can be found in the analysis of the temperature dependence of the ionic conductivity of an alkali halide crystal containing a divalent-cation impurity. For example, an analysis of the conductivity data for a KCl:SrCl$_2$ crystal containing 375 ppm mole fraction of strontium has already been reported[5]. The data was fitted to the LDH equations by the method of least squares with eleven adjustable parameters. In that analysis values were obtained for a jump attempt frequency $\bar{\omega}$, for an impurity-vacancy binding energy B, expressed as an enthalpy minus the temperature-entropy product, and for the cation migration enthalpy and entropy.

To compare least square analyses of experimental data using two different sets of theoretical equations, i.e. the LDH equations and the LDH equations modified by equation (6), it is desirable to use the same number of adjustable parameters in each analysis. So values for the quantities in equation (6) that do not appear in the LDH equations were estimated in terms of LDH parameters. These estimates were obtained from Einstein oscillator models of the isolated and bound impurity ions. The jump attempt $\bar{\omega}$ as determined from the LDH analysis of the conductivity was taken as the average of the potassium and chlorine ion vibration frequencies and was related to the masses of the potassium (M_K) and chlorine (M_{Cl}) ions by the following equations:

$$\bar{\omega} = \tfrac{1}{2}(\omega_K + \omega_{Cl}) \propto \tfrac{1}{2}(M_K^{-1/2} + M_{Cl}^{-1/2}), \quad (7)$$

and the Einstein frequency ω_L for an isolated Sr ion was estimated to be

$$\omega_L = \frac{2M_K^{1/2}M_{Cl}^{1/2}\bar{\omega}}{M_{Sr}^{1/2}(M_K^{1/2} + M_{Cl}^{1/2})} = 0{\cdot}65\bar{\omega}. \quad (8)$$

The binding energy B as determined from the least squares analysis was related to ω_k and ω_L in a simple harmonic approximation. It seems reasonable that the particles in deeper traps would vibrate with higher frequency. To simply estimate the frequency difference let us assume that both bound and isolated impurity ions oscillated with a maximum displacement of $a/2$. The two oscillators were taken to have force constants of $M_{Sr}\omega_k^2/2$ and $M_{Sr}\omega_L^2/2$ respectively. Furthermore, the lowest energy levels of the two

Table 1. *Results of analyses of conductivity of* KCl : SrCl$_2$ *crystal containing* 375 *ppm* Sr

Quantity	Our result LDH theory modified by equation (6)	LDH theory[5]
Cation vacancy migration enthalpy (eV)	0·74	0·74
Cation vacancy migration entropy	2·4k	2·4k
Divalent-cation-impurity-cation-vacancy binding enthalpy (eV)	0·66	0·60
Divalent-cation-impurity-cation-vacancy binding entropy	2·3k	2·3k
Jump attempt frequency $\bar{\omega}$(sec^{-1})	37·1 × 10^{12}	37·7 × 10^{12}
Average rms fractional deviation	0·33%	0·67%

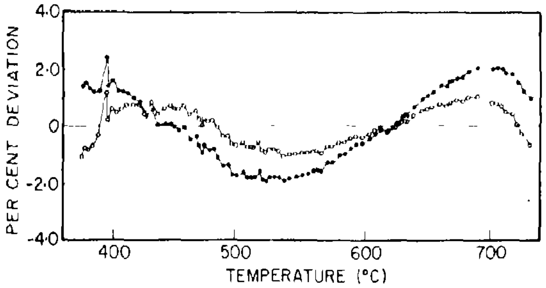

Fig. 1. Per cent deviation as a function of temperature for the KCl crystal containing 375 ppm Sr. ●, per cent deviation between theoretical and experimental values of conductivity with Lidiard–Debye–Hückel theory. ○, per cent deviation between theoretical and experimental values of conductivity with the Lidiard–Debye–Huckel theory modified by the square bracketed term in equation (6).

oscillators differ by an energy of B[10]. On the basis of such a model the following relationship can be derived for ω_k and ω_L:

$$\omega_k^2 = \omega_L^2 + \gamma B \qquad (9)$$

where

$$\gamma = 8/M_{Sr}a^2. \qquad (10)$$

A value of 207 × 10^{26} sec^{-2} eV^{-1} for γ gave the best fit to the experimental data. This leads to $a/2 = 0{\cdot}10$ Å, a reasonable value for the maximum displacement amplitude, and to $\omega_k = 26{\cdot}6 \times 10^{12}$ sec^{-1} at room temperature as compared to 24·1 × 10^{12} sec^{-1} for ω_L.

The results of analyses before and after inclusion of equation (6) are shown in terms of parameter values in Table 1 and in terms of the per cent deviation between theoretical and experimental values of conductivity as a function of temperature in Fig. 1. (The complete discussion of the computer analysis procedure is contained in [5].) The theoretical values of ionic conductivity calculated with the LDH equations modified by equation (6) do provide the better fit to the experimental conductivity data, and reduce the rms percent deviation from 0·67 to 0·33 per cent.

In summary an equation for the equilibrium concentration of impurity-vacancy complexes has been derived. This derivation has included the dependence of the vibrational term of the crystal free energy upon the arrangement of the impurity ions. The vibrational changes in a simple Einstein approximation have been incorporated into the equation for complex concentration. It is encouraging to note that even in this simple approximation the resulting equations for ionic transport are more in accord with experimental data than transport equations which neglect the vibrational effects of the arrangement of the impurity ions.

Acknowledgements – The authors gratefully acknowledge helpful discussions with Drs Manuel Gomez and Michael H Reilly.

Solid State Division,
Naval Research Laboratory,
Washington, D.C 20390
U S A

R. G FULLER
H. B. ROSENSTOCK

REFERENCES

1 SUPTITZ P and TELTOW, J., *Phys. Status Solidi* **23**, 9 (1967).
2 LIDIARD A B., *Phys. Rev.* **94**, 29 (1954).
3 KANZAKI H, KIDO K. and TAMURA S., *J. phys Soc Japan* **20**, 2305 (1965).
4. ALLNATT A. R. and PANTELIS P., *Solid State Comm.* **6**, 309 (1968)
5 FULLER R G., MARQUARDT C L., REILLY M. H. and WELLS J. C., *Phys. Rev.* **176**, 1036 (1968)
6 NELSON V. C. and FRIAUF R. J., U.S. Atomic Energy Commission, Tech Rep C00-1197-32, The University of Kansas (1968)
7 FULLER R G and REILLY M. H., *J. Phys. Chem. Solids* **30**, 457 (1969).
8 ALLNATT A. R and COHEN M. H., *J chem. Phys* **40**, 1860 (1964).
9. ALLNATT A. R and COHEN M. H., *J. chem. Phys.* **40**, 1871 (1968).
10 Here B represents the energy between the lowest vibrational levels and is less than the binding energy defined in other papers (See FULLER R. G., MARQUARDT C L., REILLY M. H. and WELLS J. C., *Phys. Rev.* **176**, 1036 (1968).) by $\hbar/2(\omega_k - \omega_l)$, the zero point energy terms.
11. MAYER J. E and MAYER M. G., In *Statistical Mechanics*, p 114 Wiley, New York (1940).

J. Phys. Chem. Solids Vol. 30, pp. 2108–2111.

Mössbauer resonant absorption in the Garnet-type compound ferric molybdate

(*Received* 6 *December* 1968)

RECENT discussion of the crystal structure of ferric molybdate, $Fe_2(MoO_4)_3$, has emphasized the presence of the garnet pattern and the relationship of this compound to other iso-structural natural and synthetic garnets [1,2]. Since we recently measured Mössbauer spectra for a series of natural garnets, and spectra have been published for a variety of synthetic ferrimagnetic garnets, we felt that it would be of interest to study the Mössbauer absorption spectrum for this compound.

The experimental procedure was conventional. An Austin Science Associates Mössbauer spectrometer with flyback adaptation was used in conjunction with a 400 channel Victoreen pulse height analyzer. A 50-mCi source of Co^{57} in copper foil was used. Measurements were made using a standard transmission geometry and both source and absorber were at room temperature. Samples of ferric molybdate were made available to us by the Climax Molybdenum Company Research Laboratory, Ann Arbor, Michigan. The andradite garnet measured for comparison purposes originated at Stanley Butte, Graham County, Arizona, and was obtained from Southwest Scientific Company, Hamilton, Montana. The absorbers were prepared by forming hot molded lucite discs with the powdered sample material distributed uniformly throughout the lucite. Each absorber had a sample areal density of 38 mg/cm^2.

In garnets such as the yttrium iron garnet, $Y_3^{3+}Fe_2^{3+}(Fe^{3+}O_4)_3$, or the andradite, $Ca_3^{2+}Fe_2^{3+}(Si^{4+}O_4)_3$, the first cation in the

Table 1. *Mössbauer parameters for octahedral ferric iron in Garnet-type compounds*

	Isomer shift* (mm/sec)	Electric quadrupole splitting (mm/sec)
Ferric molybdate	+0·39 ± 0·03	0·25 ± 0·06
Andradite garnet	+0·38 ± 0·03	0·57 ± 0·03
YbIG, octahedral site†	0·44	0·50
YIG, octahedral site†	0·40	0·52

*Isomer shifts are reported with respect to the center of the iron spectrum.
†Adapted from reference [4].

formulas (Y or Ca) has eight-fold coordination, the second (Fe^{+3}), octahedral coordination, and the third (Fe^{3+} or Si), tetrahedral coordination. In ferric molybdate, the eight-fold coordinated cations are missing. The ferric ions are in octahedral coordination to oxygen, and the Mo^{6+} ions are tetrahedrally coordinated to oxygen[1,2]. This results in a structure with the Fe octahedra and the Mo tetrahedra linked at their vertices. This arrangement of the octahedra is similar to the case of grossularite, $Ca_3Al_2(SiO_4)_3$, or andradite. In the ferric molybdate structure, four Fe octahedra have been distinguished[1,2].

A spectrum of ferric molybdate is shown in Fig. 1. For comparison purposes a spectrum of an andradite garnet, which was measured under similar conditions, is shown in Fig. 2. From these spectra it is clear that the environments of the ferric ions are quite different in these two compounds. The spectrum of ferric molybdate consists of a superposition of unresolved absorption peaks. The separations in energy resulting from electric quadrupole interactions of the ferric ions at the octahedral sites, and from possibly different isomer shifts at different sites, are not sufficiently large compared to the line width to resolve the individual lines from each other.

On the basis of the Mössbauer spectra observed for ferric molybdate, it can be concluded that all iron sites in this compound have isomer shifts of approximately +0·39 mm/sec. (All velocities are quoted with respect to the center of the iron spectrum.) This is in the range typical for high spin ferric iron[3], and, within experimental error, is equal to the measured isomer shift for andradite garnet[3]. The ferric ions at the octahedral sites in synthetic ferrimagnetic rare earth iron garnets also exhibit a comparable isomer shift[4]. Therefore, it appears that the electronic charge density at the nucleus of the octahedrally coordinated ferric ions in these garnet-type compounds does not differ appreciably between the ferrimagnetic and paramagnetic compounds, and, in fact, is not affected appreciably by the complete absence of the eight-coordinated cations in structures of this type.

We have not attempted computer fitting of the spectrum to distinguish four sites as this does not appear to be justified by the data. The most straightforward interpretation of this absorption spectrum is that all of the iron atoms in this crystal structure exhibit very nearly the same isomer shift and have electric quadrupole splittings near the value listed in Table 1. This latter parameter (which would be the full peak separation in the case of a simple doublet, or twice the level shift) is approximately 0·25 mm/sec, an unusually small value. The andradite garnet exhibits an electric quadrupole splitting that is more than twice as large, being equal to approximately 0·57 mm/sec, a value that is comparable to the electric quadrupole splittings present for the octahedrally coordinated

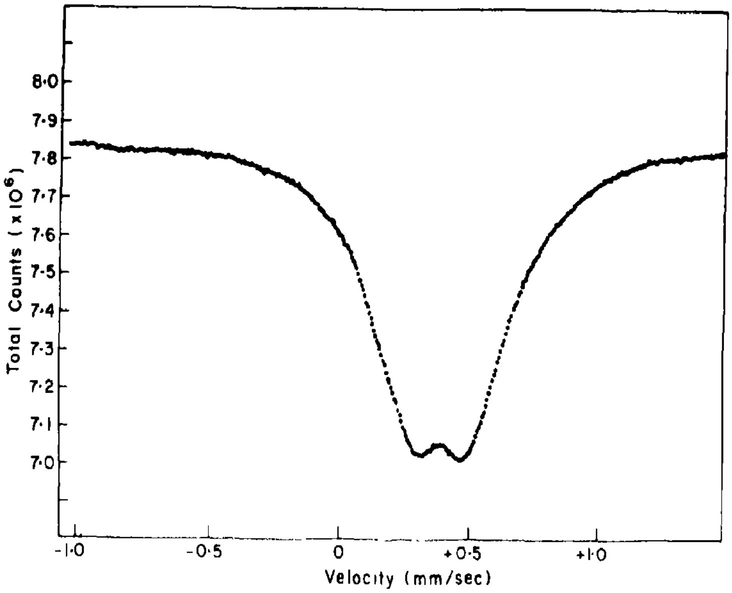

Fig. 1. Mossbauer hyperfine absorption spectrum of ferric molybdate.

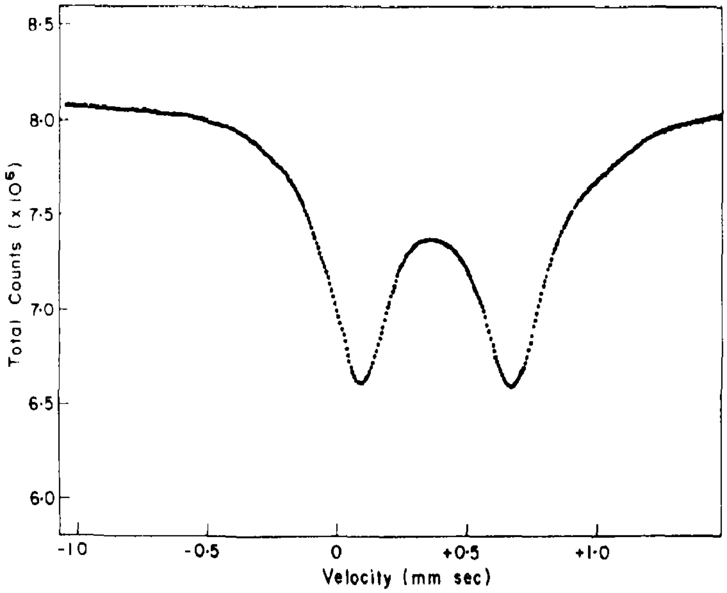

Fig 2. Mossbauer hyperfine absorption spectrum of andradite garnet.